Acta METALLURGICA

VOL. 2 JAN. 1954

Author Index to Volume II

(References with (L) are to Letters to the Editor)

Contents of Volume 2, 1954

(References with (L) are to Letters to the Editor)

ACTIVITY OF IRON IN IRON-PLATINUM SOLID SOLUTIONS*

HUGO R. LARSON† and JOHN CHIPMAN‡

Slags of known iron activity were brought into equilibrium with platinum at 1550°C, the platinum absorbing a quantity of iron which depended upon the iron activity of the slag.

The activity coefficient of iron was thus determined in platinum alloys containing from zero to eleven per cent iron. The iron-platinum alloys show strong negative deviation from ideality.

L'ACTIVITÉ DU FER DANS LES SOLUTIONS SOLIDES FER-PLATINE

Des laitiers, dont l'activité du fer était connue, ont été amenés à l'équilibre avec du platine à 1550°C; la quantité de fer absorbé par le platine dépendait de l'activité du fer du laitier.

Le coefficient d'activité du fer fut ainsi déterminé dans des alliages de platine contenant de zéro à onze pour cent de fer.

Les alliages fer-platine manifestent un écart négatif, important, par rapport à l'idéalité.

DIE AKTIVITÄT DES EISENS IN FESTEN EISEN-PLATIN LÖSUNGEN

Schlacken mit bekannter Eisenaktivität wurden bei 1550°C mit Platin ins Geichgewicht gebracht, wobei das Platin eine von der Aktivität der Schlacke abhängige Eisenmenge absorbiert.

Auf diese Weise wurde der Aktivitätskoeffizient des Eisens in Platinlegierungen, die zwischen null und elf Prozent Eisen enthielten, bestimmt. Die Eisen-Platin Legierungen zeigten starke negative Abweichungen vom Idealzustand.

The usefulness of platinum as a structural material in metallurgical research is limited by its propensity for alloying with other metals. Crucibles and thermocouples are readily contaminated by metals reduced from fused salts or slags but the exact conditions governing this phenomenon have not been described. This paper contains data on the contamination of platinum by iron from melts consisting of CaO, FeO and Fe_2O_3 under controlled conditions of known activity of iron and oxygen. The data permit calculation of the activity coefficient of iron in the Pt-Fe solid solution in the range 0–11 per cent Fe.

Iron activity in lime-iron oxide slags

The procedure used in these experiments was similar to that used by Darken and Gurry [1] and has been described in detail elsewhere [2]. Carbon-dioxide-carbon monoxide mixtures were passed over the melt contained in a small platinum crucible until equilibrium was reached. The melt was quenched and analyzed for CaO, FeO and Fe_2O_3. Four atmospheres were employed at a temperature of 1550°C: air, CO_2, $CO_2/CO = 11.4$ and $CO_2/CO = 2.50$. The data of Fetters and Chipman [3] and of Darken and Gurry [1] permitted extending the results to lime-iron oxide slags in equilibrium with iron. The corresponding oxygen pressures covered a range from about 10^{-1} to 10^{-9} atmospheres. The experimentally determined oxygen pressures, interpolated to even values of p_{O_2}, are shown in Figure 1.

Wagner [4] has developed, from the Gibbs-Duhem relation, a formula by which it is possible

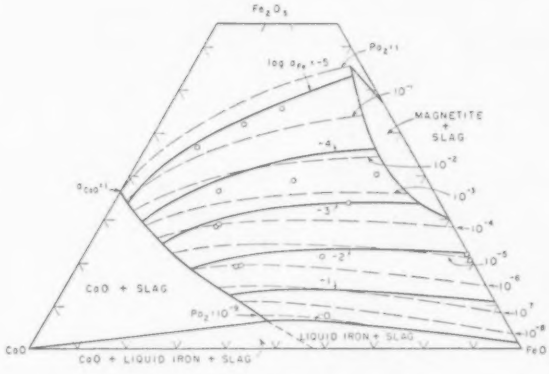

FIGURE 1. Oxygen pressures and iron activities in the system CaO-FeO-Fe_2O_3 at 1550°C.

to calculate the activities of two components in a ternary system over a range in which the activity of the third component is known:

$$\left(\frac{\partial \ln a_1}{\partial N_2}\right)_y = \frac{-y}{(1-N_2)^2}\left(\frac{\partial \ln a_2}{\partial y}\right)_{N_2} - \frac{N_2}{1-N_2}\left(\frac{\partial \ln a_2}{\partial N_2}\right)_y$$

where the N's are mole fractions and y is $\frac{N_3}{N_3 + N_1}$.

In the lime-iron oxide system the components can be chosen as Fe, O and CaO. The activity of oxygen is taken as $P^{\frac{1}{2}}_{O_2}$ and y is then $\frac{N_{CaO}}{N_{CaO} + N_{Fe}}$.

Integrating the equation yields:

*Received June 27, 1953.

†Metallurgist, American Brake Shoe Company, Mahwah, New Jersey.

‡Department of Metallurgy, Massachusetts Institute of Technology, Cambridge, Massachusetts.

$$\log a_{Fe}(N_O, y) = -y\int_{N'_O}^{N_O} \frac{\partial \dfrac{\log a_O}{(1-N_O)^2}}{y} \, dN_O$$

$$-\int_{N'_O} \frac{N_O}{1-N_O} d \log a_O$$

The integration is carried out for various constant y values from zero to that represented by lime saturation. If the standard state for iron is chosen as pure liquid iron, the lower integration limit, N'_O, is the mole fraction of oxygen for the slag in equilibrium with iron.

The results of graphical integration over the experimental composition range are shown by lines of constant iron activity in Figure 1.

Iron activity in iron-platinum alloys

At equilibrium the iron activity in the iron-platinum solid solution equals that in the slag. Rather than destroy the crucible for analysis, a thin piece of platinum foil weighing about 0.2 gram was coiled and placed in the bottom of the crucible. Slag compositions and atmospheres were chosen to give a range of iron activities indicated by the points in Figure 1. After equilibrium had been reached, the crucible was quenched in mercury, the slag was analyzed to permit calculating the iron activity and the platinum foil was analyzed for iron.

A summary of the experimental results is given in Table I. The first series of three samples was used to determine the time necessary to attain equilibrium. Evidently four hours was sufficient, although longer times were used in most subsequent experiments.

In the second series of five samples an attempt was made to melt slags with different lime contents but equal iron activity. Although the iron activities did not come out equal, the iron content of the platinum increased in a regular fashion as the calculated iron activity increased. Samples 228 and 229 should be compared to samples 236 and 238. The calculated iron activity and the percent iron in the platinum were almost identical although there was a considerable difference in the lime contents and atmospheres under which the two slags were melted. In the third group two slags with different lime contents but the same iron activity were melted. The iron content of the platinum foil was almost identical for each sample. These constitute good checks of the ternary activity calculations.

The iron activities in Table I and Figure 2 have been based on pure liquid iron as the standard state. The standard state can be changed to pure solid iron by using the known heat of fusion of iron. However, the experimental temperature, 1550°C, is so close to the melting point, 1535°C, that the difference, 0.003 log units, is insignificant.

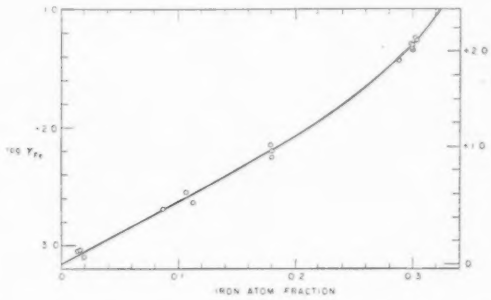

FIGURE 2. Activity coefficient of iron in iron-platinum alloys at 1550°C.

For these dilute solutions it is possibly more informative to use as the standard state the infinitely dilute solution of iron in platinum. The activity coefficients based on this standard state are shown on the right-hand scale of Figure 2.

TABLE I

SUMMARY OF EXPERIMENTAL RESULTS

Sample	Time hrs.	CO_2/CO	Slag* FeO Weight %	Slag* Fe_2O_3 Weight %	Fe in Pt Per cent	Fe in Pt Mol. Fr.	$-\log a_{Fe}$	$-\log \gamma_{Fe}$
228	6	11.4	63.10	37.10	10.90	0.299	1.87	1.34
229	4	11.4	63.20	37.00	10.92	0.300	1.87	1.35
230	2	11.4			9.28	0.257		
338	9	13.5	61.68	38.57	10.46	0.288	1.98	1.44
236	7.5	7.76	40.20	40.40	10.84	0.298	1.83	1.30
238	4.5	7.76	40.18	40.50	10.90	0.299	1.83	1.31
245	7.75	4.64	29.0	38.45	10.95	0.301	1.76	1.24
247	5.5	4.64	28.19	38.62	11.06	0.303	1.79	1.27
347	8	67.6	34.60	55.00	5.84	0.179	3.00	2.25
340	6	35.5	19.09	50.96	5.82	0.178	2.90	2.15
342	3.5	35.5	19.05	51.56	5.84	0.179	2.95	2.20
352	6	CO_2	33.72	61.18	3.47	0.112	3.59	2.64
354	6	CO_2	23.78	61.40	3.27	0.106	3.54	2.56
356	6	CO_2	14.60	60.52	2.63	0.086	3.75	2.69
361	8	Air	14.36	75.65	0.54	0.019	4.83	3.10
362	8	Air	10.90	74.05	0.45	0.016	4.85	3.04
363	8	Air	6.99	70.55	0.35	0.013	4.97	3.05

*Balance CaO.

References

1. DARKEN and GURRY. J. Am. Chem. Soc. **67** 1938 (1945); **68** (1946) 798.
2. LARSEN and CHIPMAN. J. Metals **5** (1953) 1089.
3. FETTERS and CHIPMAN. Trans A.I.M.E. **140** (1940) 170.
4. WAGNER. Thermodynamics of Alloys (Cambridge, Mass., Addison-Wesley, 1952) p. 19.

WORK-HARDENING IN STRETCHED AND TWISTED ALUMINIUM CRYSTALS*

H. W. PAXTON† and A. H. COTTRELL‡

The effects of plastic twisting on the tensile deformation of aluminium crystals are examined. After such a twist the tensile stress needed to continue tensile straining is sharply increased and, in some cases, this is followed by a period of increased work hardening. These effects are most pronounced when the twisting is applied during the period of "easy glide" in crystals oriented for single slip in tension, but they also appear in crystals which undergo multiple slip and work harden more severely during tensile straining. An explanation of the results is proposed in terms of the difficulty which those dislocations producing the tensile strain have in cutting through intersecting dislocations introduced during the twisting. The observed magnitude of the stress increment following a plastic twist can be predicted reasonably well by means of a formula deduced from theory, and the results provide evidence in favour of the view that multiple slip is a cause of work hardening.

L'ÉCROUISSAGE DES CRISTAUX D'ALUMINIUM ALLONGÉS ET TORDUS

Un examen est fait des effets de torsion plastique sur la déformation de cristaux d'aluminium par traction. Après une telle torsion, la tension de traction, nécessaire à la continuation de la déformation par traction, augmente brusquement et, dans certains cas, est suivie d'une période d'écrouissage accru.

Ces effets sont le plus prononcés quand la torsion est appliquée pendant la période de "glissement facile" dans un cristal orienté de façon à donner du glissement simple en traction, mais ils apparaissent également dans des cristaux qui se déforment par glissement multiple et subissent un écrouissage plus sévère pendant la déformation par traction. On propose une explication de ces résultats en termes de la difficulté qu'auraient les dislocations qui produisent le glissement, à passer les dislocations entrecoupantes, introduites lors de la torsion. La valeur observée de l'accroissement de tension, à la suite d'une torsion plastique, peut être assez exactement prédite au moyen d'une formule déduite de la théorie; ces résultats appuient l'opinion que le glissement multiple constitue la cause de l'écrouissage.

VERFESTIGUNG VON GESTRECKTEN UND GEDRILLTEN ALUMINIUMKRISTALLEN

Die Wirkung der plastischen Verdrillung auf die Zugverformung von Aluminiumkristallen wurde untersucht. Nach einer solchen Verdrillung steigt die zur Fortsetzung der Zugverformung notwendige Spannung stark an; in einigen Fällen folgt darauf eine Periode verstärkter Verfestigung. Diese Effekte treten am stärksten hervor, wenn die Verdrillung in einer Periode der "leichten Gleitung" in Kristallen, die für einfache Gleitung unter Zug orientiert sind, erfolgt. Aber sie treten auch an Kristallen auf, die mehrfache Gleitung erfahren, und die sich während der Zugverformung stärker verfestigen. Es wird eine Erklärung dieser Ergebnisse vorgeschlagen, die davon ausgeht, dass die Versetzungen, die die inneren Spannungen hervorrufen, Schwierigkeiten haben, sich durch die ihren Weg kreuzenden Versetzungen, die während der Verdrillung eingeführt wurden, zu bewegen. Die beobachtete Grössenordnung der Spannungszunahme nach plastischer Verdrillung kann mit zufriedenstellender Genauigkeit aus einer Formel, die aus dieser Theorie entwickelt wurde, vorausgesagt werden. Die Ergebnisse unterstützen die Ansicht, dass mehrfache Gleitung eine Ursache der Verfestigung ist.

Introduction

During tensile straining work hardening appears almost fortuitously in a single crystal since there is nothing in the macroscopic deformation, apart perhaps from bending at the grips, to cause dislocations to accumulate in the material. The observations of easy glide in crystals oriented for single slip bear this out [1; 2; 3]. In such cases dislocations accumulate only because obstacles, e.g., deformation bands, are created where the slip happens to deviate from the simple laminar flow that satisfies the macroscopic requirements of the deformation. Rather than rely on these somewhat arbitrary groupings of dislocations it seemed preferable, in the experiments described below, to explore the possibility of introducing a macroscopically controlled distribution of dislocations by giving the crystal a suitable non-uniform plastic strain at some stage during the tensile experiment. For simplicity, a uniform distribution of dislocations was desired and this uniformity could be obtained, over distances large compared with the spacing of slip bands, by giving a plastic strain that varied linearly across the section of the specimen. Either twisting or bending was suitable for this, and of these twisting was chosen since it maintained the straightness of the specimen.

The procedure in making the experiments was therefore as follows. A cylindrical aluminium crystal was strained in tension and its stress-strain curve taken. While the extension was still small,

*Received July 8, 1953.

†Formerly Research Fellow in Theoretical Metallurgy at the University of Birmingham; now Member of Staff, Metals Research Laboratory, Carnegie Institute of Technology, Pittsburgh.

‡Professor of Physical Metallurgy, University of Birmingham.

however, the tensile straining was temporarily halted in order to give the crystal a small plastic twist about the tensile axis. The tensile straining was then resumed and a note taken of the effect of the twist on the subsequent stress-strain curve.

Experimental Method

Ingots of 99.996 per cent aluminium, kindly given by the Aluminum Company of America, were swaged to round bars 2–3 cm diameter, machined and reduced to 1 cm diameter in grooved rolls, and etched and drawn to 0.32 cm diameter, without annealing. Spectrographic analyses of the finished wire detected only manganese and zinc, in amounts less than 0.001 per cent. Pieces of the wire were then recrystallized in a salt bath at 650°C for 15 seconds, strained 2 per cent in tension at room temperature, and finally moved axially at 2 cm per hour through a cylindrical furnace at 650°C. This produced single crystals in lengths up to 15 cm. Their orientations, given in Figure 1, were measured by the back-reflection Laue method.

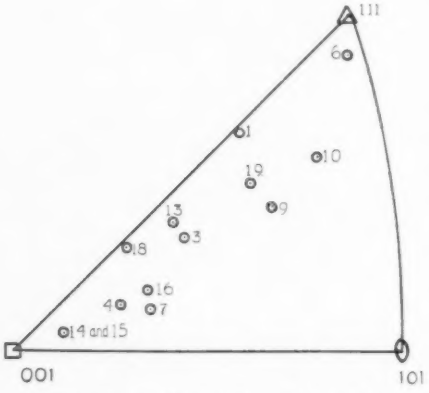

FIGURE 1. Orientations of crystals.

To mount crystals for straining, their ends were fitted into axial holes, 1 cm long, in duralumin end-pieces and secured there by a bonding resin ('Araldite'). The working portions of the specimens between the end-pieces were usually 5–7 cm long. The end-pieces were suspended vertically between the grips of a small hard-beam tensile machine and tensile strain applied at the rate of 1.5×10^{-5} per second. To twist a crystal plastically, its upper end-piece was temporarily clamped while the lower one was rotated in a light bearing. The angle of rotation was measured optically with mirrors attached to the end-pieces.

The movements of these mirrors revealed some slight and adventitious twisting and bending of the specimens during the tensile straining, particularly at the beginning of the experiment. The twisting was shown by horizontal deflections of the light beam, and amounted in extreme cases to a relative rotation of the end-pieces, about the tensile axis, of 20 minutes of arc. The bending was shown by vertical deflections and usually amouted to a relative rotation of the end-pieces, about a horizontal axis, of 30 minutes of arc, although in two specimens known to be poorly aligned it rose to 1 degree. It seems likely that this twisting and bending is caused by the specimens and their end-pieces settling down into axial alignment. Nishimura and Takamura [4] have recently observed plastic twisting, of about the same amounts as in the present work, when straining aluminium strip crystals in tension.

To ascertain whether the intentionally applied twist was distributed uniformly along the gauge length, several small mirrors were mounted with spots of adhesive along one specimen. After giving rotations of up to 3 degrees, the ensuing plastic twists were found to be distributed very uniformly over the central portion of the gauge length, but did not extend to the ends. This end-effect, due to the constraints of the end-pieces, was unexpectedly large. Twisting could not be detected within 1 cm from the end-pieces, and the uniform region only began at about 1.5 cm from them.

Results

The high purity of the aluminium was reflected in the low values obtained for the critical resolved shear stress (Table I); furthermore, this stress did not vary appreciably with temperature over the range from −185°C to +20°C, a result similar to

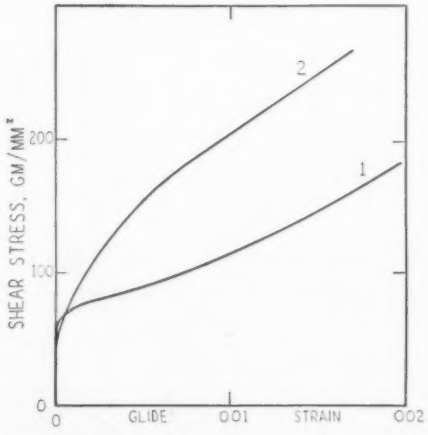

FIGURE 2. Stress-strain curves of aluminium crystals; curve 1—crystal no. 9; curve 2—crystal no. 15.

TABLE I
CRITICAL RESOLVED SHEAR STRESSES OF ALUMINIUM CRYSTALS*

Reference number of specimen	Temperature of experiment °C	Shear stress, gm/sq mm
1	+20	51
3	20	55
4	20	66
6	20	75
7	−74	72
9	+20	68
10	−185	62
13	+20	57
14	20	55
15	20	49
16a	20	45
16b	20	52
18	20	74†
19	−185	78

*Where the stress-strain showed easy glide (linear hardening) preceded by a small rounded portion the critical stress was found by extrapolating the linear part to zero strain. In other cases the critical stress was taken as the stress at which plastic flow was first detected.

†This result is doubtful because of the irregular form of the stress-strain curve at the start of plastic flow (see Figure 6).

that obtained by Neurath and Koehler [5] on pure copper crystals. Two typical stress-strain curves are shown in Figure 2. The greater rate of work-hardening in crystal no. 15, the orientation of which was nearly suitable for multiple slip, as compared with that of no. 9, oriented for single slip, agrees with the observations of Lücke and Lange [2]. In crystals oriented for single slip the length of the easy glide was smaller, and the rate of work-hardening larger than expected in view of the purity of the material, although Nishimura and Takamura [4] obtained very similar results.

Some typical effects of applying a twist during the tensile experiment are shown in Figures 3 to 6.

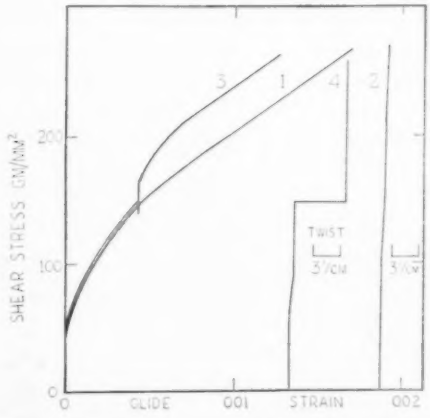

FIGURE 3. Stress-strain and stress-twist curves of two crystals of the same orientation; curves 1 and 2—crystal no. 15; curves 3 and 4—crystal no. 14.

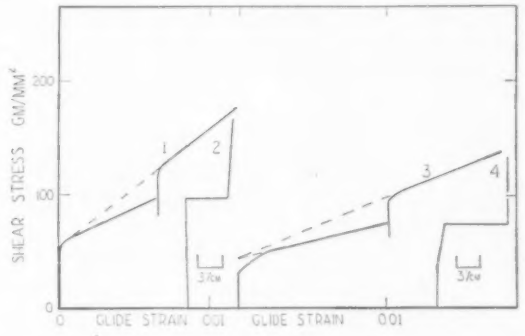

FIGURE 4. Stress-strain and stress-twist curves; curves 1 and 2—crystal no. 13; curves 3 and 4—crystal no. 16a.

In all cases the total rotation, Θ, given to the lower end-piece was of the order 10^{-2} radian. The over-all shear strain, $\Theta r/l$, at the surface, where r is the radius and l the length, was thus of order 3×10^{-4}. From the slopes of the stress-strain curves of these crystals, the work-hardening due to an equivalent increment of tensile strain would be of order 3 gm/sq mm.

Figure 3 compares two curves from specimens out of the same crystal. One was strained continuously in tension, while the tensile straining of the other was interrupted, at a glide strain of 4.3×10^{-3}, to give a twist of 6 minutes of arc/cm, corresponding to a shear strain at the surface of about 3×10^{-4}. This twist caused a sharp increase of 16 gm/sq mm in the stress needed to continue tensile deformation, followed by a period of enhanced work-hardening. The curve eventually settled down at the same slope as that of the uninterrupted specimen, but at a

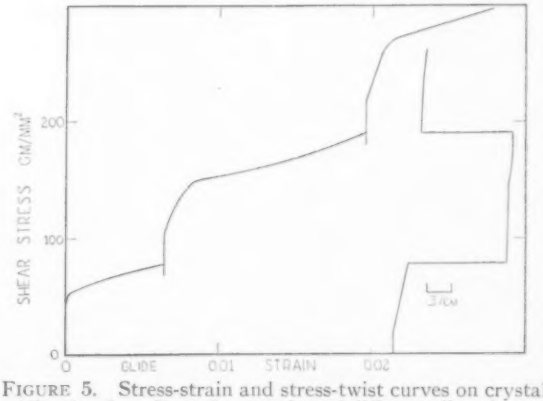

FIGURE 5. Stress-strain and stress-twist curves on crystal no. 16b, showing effect of two twists of different directions.

stress 35 gm/sq mm greater than it. From the slope of the curves in this range of strain, the glide strain in tension needed to produce an increment of 35 gm/sq mm would be 3.6×10^{-3}. The twist of both specimens, as a function of stress, is shown in the figure. The adventitious twist should be noticed.

The effect of twisting was particularly striking in specimens whose orientations favoured single slip and easy glide, such as those of Figure 4. Here the twist produced a sharp step in the stress-strain curve, followed by an increase in the rate of work-hardening. It should be noticed that this part of the curve extrapolates back approximately to the critical shear stress at zero strain; this appeared to occur generally after small twists (Figure 6 shows a less convincing example) but not after large ones (see Figure 5).

The specimen of Figure 5 was given two rather large twists, one in each direction. In each case a substantial increase in flow stress occurred. When the steps on the stress-strain curve were large, as in this case, they began vertically but became inclined further up, rather like part of a hysteresis loop. Figure 6 also shows the effects of two twists,

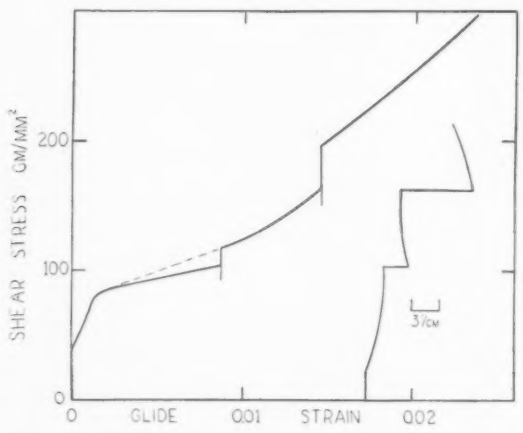

FIGURE 6. Stress-strain and stress-twist curves on crystal no. 18, showing effect of two twists of different magnitudes.

taken in the same direction but with different magnitudes. The second twist was three times larger than the first, and produced a stress increment 2.4 times larger than that produced by the first. An unusual feature in this experiment was the partial untwisting which occurred when the tensile straining was resumed after twisting.

Discussion

Ever since Taylor's theory [6] it has been believed that the most common and severe form of work-hardening in a single crystal is that caused by the mutual interactions of dislocations which accumulate during plastic straining. Recent studies have emphasized that the important interactions are those between dislocations in different glide systems [7; 8]. In some cases these dislocations may combine to form sessile ones [9; 10]. In others, intersecting dislocation lines have to cut through each other in order to continue their glide motions, and energy has to be supplied to make the jogs which are then formed at the points of intersection [11]. A simple calculation [8; 12] shows that the applied stress $\Delta\sigma$ needed to drive a dislocation line through a field of intersecting lines, whose density across its slip plane is ρ per sq. cm, is given in order of magnitude by

$$\Delta\sigma = \alpha\mu b\rho^{\frac{1}{2}}, \tag{1}$$

where $\alpha \simeq 1$, μ is the shear modulus, and b is the length of the Burgers vector; here the energy of a jog is taken as $\alpha\mu b^3$. This formula does not take account of thermal fluctuations, which enable the dislocations to cut through one another at somewhat lower stresses.

The results of the present work can be explained in terms of intersecting dislocations. The plastic twisting produces dislocation lines in slip systems which intersect those used during the tensile straining, and the tensile stress has to be raised to provide the energy for the jogs which form when the dislocations cut through one another. The detailed distribution of the dislocations introduced by twisting depends on the orientations of the slip systems, and a detailed treatment would involve a separate analysis for each crystal. However, it is easy to see that in general the systems used in stretching and twisting intersect one another.

In plastic twisting there are two ideal orientations, corresponding to the fact that, at any point in an elastically twisted circular cylinder, the shear stress is a maximum in two directions, respectively perpendicular and parallel to the axis of twist. In the first of these ideal orientations the slip plane is perpendicular to the axis of twist and 'rotational slip' occurs [11; 13; 14], ideally producing a crossed grid of screw dislocations in each active slip plane [15].

The mode of deformation in the second ideal

orientation is more difficult to visualize, but is analogous to that which occurs when a bundle of parallel wires is twisted, allowing free sliding between contacting wires. In this case the active slip planes are parallel to the axis of twist, and can be regarded as dividing the crystal up into a bundle of long, thin parallel columns, across the interfaces of which little or no shear stress can be sustained. An example of the operation of such slip systems has been noted by Gough, Wright and Hanson [16].

In practice, the slip systems actually used during twisting will be those that lie close to these ideal orientations. Since these ideal orientations lie at 45 degrees to the ideal orientation for slip during tensile straining i.e., the plane of maximum resolved shear stress, the slip systems used in stretching and twisting will generally intersect one another.

It should be possible to predict the increment of work-hardening due to the plastic twisting by first calculating the density of intersecting dislocations and then using equation (1) to find the stress needed to drive a dislocation through them. At this stage of the work, however, an accurate calculation would be unprofitable; because of the approximate nature of equation (1) and the complication of the non-uniformity of the twist along the gauge length, only an order of magnitude estimate can be significant.

Such an estimate is easily made. Let the angle of twist be θ radians/cm. Then a slip surface that intersects the slip systems used in twisting no longer remains plane but is twisted by an angle of the same order. Consider a small square, $ABCD$, with sides of length d, marked out in the slip plane before twisting (Figure 7). After twisting, the

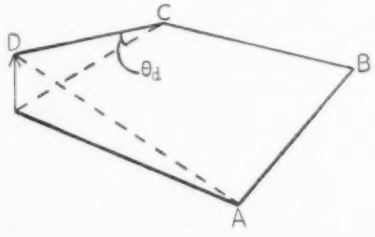

FIGURE 7. Displacement of a corner, D, of a small square, $ABCD$, by plastic twisting.

three points A, B, and C, still define a plane, but D no longer lies in it. Proceeding along BC, the lattice rotation about this line is of order θ/cm. Thus CD is rotated an angle θd, relative to AB, about the axis BC. The distance that D is moved out of the plane, on the end of the rotated arm CD, is θd^2, if the angle of rotation is small. Let the number of dislocations, each of strength b, passing through the square be ρd^2. The displacement they produce in a Burgers circuit taken round the square is $\rho d^2 b$. Equating this to θd^2 gives

$$\rho = \theta / b \tag{2}$$

as the order of magnitude of the density of dislocations introduced by twisting. Substituting this result in equation (1) and taking $\alpha = 1$, gives the increment in shear stress $\Delta\sigma$ caused by a plastic twist θ per cm to be of the order

$$\Delta\sigma = \mu(\theta b)^{\frac{1}{2}}. \tag{3}$$

Table 2 compares the stress increments given by this formula with experimental values, taking $\mu = 2.5 \times 10^6$ gm. per sq. mm. and $b = 2.9 \times 10^{-8}$ cm. The agreement is better than expected in view of

TABLE II

COMPARISON OF THEORETICAL AND EXPERIMENTAL STRESS INCREMENTS CAUSED BY TWISTING

Specimen	θ, radians/cm	$\Delta\sigma$, gm/sq mm, calculated	$\Delta\sigma$, observed
13	1.75×10^{-3} "	18	23.5
14	1.45 "	16	* 16.0 / 35.0
16a	2.25 "	20	23.5
16b (i)	3.5 "	25	* 24.5 / 70
16b (ii)	3.3 "	24	* 24.5 / 75
18 (i)	0.73 "	11.5	14.0
18 (ii)	2.2 "	20	33.3

*Where two values are given the smaller refers to the height of the vertical part of the step and the larger to the total stress increment at which the curve regains its normal slope (see Figures 3 and 5).

the approximate nature of the calculation, suggesting that some of the neglected factors largely cancel one another. No account of end-effects has been taken when setting down the values of θ; by shortening the effective gauge length, these effects should increase the density of intersecting dislocations but this will be partly compensated by the fact that the active slip planes for tensile straining should intersect a lower density of dislocations than is given by equation (2) because they intersect the ideal slip systems for twisting at about 45 degrees.

These results thus provide evidence in favour of the view that multiple slip is a cause of work-

hardening. It is interesting to note that the intersecting slip not only has an immediate effect on the stress to continue the original mode of slip; it also increases the subsequent rate of work-hardening. On the basis of Mott's theory [7], this can be interpreted in terms of an increase, due to the presence of the intersecting dislocations, in the number of places where a piled-up group of dislocations is likely to form during the subsequent tensile deformation.

Acknowledgments

These experiments were made in the Department of Theoretical and Physical Metallurgy under the general direction of the late Professor D. Hanson who, until his untimely death, gave us unfailing support and encouragement. We had the benefit of several useful discussions with Dr. R. W. Cahn, and Dr. P. L. Pratt constructively criticised the manuscript. Financial assistance was provided by the Atomic Energy Research Establishment (Metallurgy Division), Harwell.

References

1. Masing, G. and Raffelsieper, J. Z. Metallk. **41** (1950) 65.
2. Lücke, K. and Lange, H. Z. Metallk. **43** (1952) 55.
3. Andrade, E. N. da C. and Henderson, C. Phil. Trans. Roy. Soc. **A.244** (1951) 177.
4. Nishimura, H and Takamura, J. Tech. Rep. Eng. Res. Inst., Kyoto University **2** (1952) 139.
5. Neurath, P. W. and Koehler, J. S. J. App. Phys. **22** (1951) 621.
6. Taylor, G. I. Proc. Roy. Soc. **A145** (1934) 362.
7. Mott, N. F. Phil. Mag. **43** (1952) 1151.
8. Cottrell, A. H. Dislocations and Plastic Flow in Crystals (Oxford University Press, 1953).
9. Lomer, W. M. Phil. Mag. **42** (1951) 1327.
10. Cottrell, A. H. Phil. Mag. **43** (1952) 645.
11. Heidenreich, R. D. and Shockley, W. Report on Strength of Solids, Physical Society of London (1948) 57.
12. Cottrell, A. H. J. Mech. Phys. Solids **1** (1952) 53.
13. Evans, D. M., Layton, D. N., and Wilman, H. Proc. Roy. Soc. **A205** (1951) 17.
14. Jillson, D. C. Trans. Amer. Inst. Min. Met. Eng. **188** (1950) 1009.
15. Frank, F. C. Report on Strength of Solids, Physical Society of London (1948) 46.
16. Gough, H. J., Wright, S. J., and Hanson, D. J. Inst. Metals **36** (1926) 173.

ON THE STRENGTH OF SOLID SOLUTION ALLOYS*

J. C. FISHER†

Short-range order is shown to give an important contribution to the strength of highly alloyed solid solutions. Because motion of a dislocation through a crystal with short-range order partially destroys the order and produces an interface of positive mean energy γ per unit area, an additional stress $\tau = \gamma/b$ is required to force the dislocation along the slip plane.

SUR LA RÉSISTANCE DES ALLIAGES DU TYPE SOLUTION SOLIDE

On montre que l'ordre à petite distance fait une importante contribution à la résistance des solutions solides fortement alliées. Du fait que le mouvement d'une dislocation à travers un cristal avec ordre à petite distance détruit partiellement le dit ordre, et produit une interface possédant une énergie moyenne, positive γ par unité de surface, il est nécessaire d'appliquer une tension supplémentaire $\tau = \gamma/b$ pour forcer la dislocation à se déplacer le long du plan de glissement.

ZUR FESTIGKEIT VON LEGIERUNGEN, DIE FESTE LÖSUNGEN SIND

Es wird gezeigt, dass die Naheordnung einen erheblichen Beitrag zur Festigkeit von hochlegierten festen Lösungen leistet. Da die Bewegung einer Versetzung durch einen Kristall mit Naheordnung diese Ordnung zum Teil zerstört und eine Grenzfläche mit einer positiven mittleren Energie γ per Oberflächeneinheit schafft, ist eine zusätzliche Spannung $\tau = \gamma/b$ erforderlich, um eine Versetzung in der Gleitebene zu bewegen.

Introduction

Single crystals and polycrystals of solid solution alloys are considerably stronger than crystals of pure metals. Two strengthening mechanisms are of particular interest, one previously proposed by Cottrell and modified by Suzuki for close-packed crystals, and another now to be proposed. The two mechanisms complement each other.

Strength Produced by Segregation of Solute Atoms at Dislocations

Cottrell [1] has suggested a strengthening mechanism that is of particular importance at low solute concentrations. According to him, solute atoms cluster preferentially in the neighborhood of dislocations, effectively decreasing the dislocation energy. If deformation is to proceed at a temperature where diffusion of solute atoms is inhibited, dislocations must break away from their associated solute atoms, increasing their energy in the process. For body-centered cubic crystals, where dislocations are not dissociated into partials, the act of breaking away is thermally activated, leading to a sharp increase of strength with decreasing temperature. It is likely that this mechanism also is responsible for the rapid increase of strength produced in body-centered cubic alloys by relatively minor solute additions. Subsequent additions of solute have decreasing effect, for once a dislocation is pinned, which requires only a small solute concentration, additional solute causes relatively little additional pinning.

For face-centered cubic crystals, on the other hand, dislocations are dissociated into partials. Suzuki [2] has pointed out that segregation of solute elements can occur throughout the faulted regions of dissociated dislocations, giving a much broader and weaker potential energy valley. Because of the width of the valley, thermal activation is not important in the yield process and the yield stress is relatively insensitive to temperature. Since the partition of solute element between the stacking fault and the normal crystal should be constant at low alloy concentrations, the yield strength of dilute solutions in close-packed crystals should be proportional to the concentration.

Strength Produced by Short-Range Order

There is a second strengthening mechanism, of particular importance at higher solute concentrations. Consider first a dislocation in a stress-free single crystal of a pure metal. The dislocation is in neutral equilibrium; for if it glides, perfect crystal is re-created. Consider next a dislocation in a crystal of completely random substitutional solid solution. Here again it is in neutral equilibrium under zero stress, for its motion re-creates random matching of atoms across the glide plane. In most solid solutions, however, the atoms will not be located at random. In an alloy composed of large and small atoms, for example, the neighbours of a small atom will be large ones more often than in a random alloy, and the neighbours of a large atom will tend to be small ones.

*Received July 10, 1953.
†General Electric Research Laboratory, The Knolls, Schenectady, New York.

Consider now a crystal of an alloy with short-range order, i.e., with any type of short-range departure from randomness. A dislocation in such a crystal is in stable equilibrium under zero stress, for its motion would destroy the equilibrium short-range order across the glide plane, producing a more nearly random configuration of higher energy. As Griffith [3] pointed out before the invention of crystal dislocations, a positive energy interface would be produced by the glide process, so that glide would be opposed in either direction. Only under the application of a definite stress, therefore, can a dislocation move in an alloy with short-range order. The stress increment that is required to just maintain the displacement of such a dislocation (in the absence of diffusion) is a measure of the strengthening effect. This increment is not determined by a thermal activation process, and (when measured in units of the rigidity modulus) should be independent of temperature at low temperatures where self-diffusion is inhibited and a fixed degree of order is frozen in.

Long-range order need not lead to a strengthening effect of the type described for short-range order, because long-range order significantly alters the distribution of dislocations in an annealed crystal. In the simplest ordered alloys, for example, dislocations regroup themselves into pairs, each pair having a Burgers vector equal to twice that for the disordered lattice. Since the motion of a dislocation pair re-creates the ordered structure, the pair is in neutral equilibrium under zero stress. The long-range order itself provides the driving force for grouping dislocations into pairs, for each single dislocation must form the edge of a surface of misfit between ordered regions that are out of step. This surface will tend to contract, pulling the dislocation along until it leaves the crystal or meets another of like or of opposite Burgers vector, producing a pair or an annihilation. The pairs that are formed can exist as line discontinuities in ordered material.

Returning now to a consideration of the strengthening effect of short-range order, let γ be the energy of the disordered interface produced by the passage of a dislocation through (short-range) ordered material, let τ be the resolved shear stress and b the magnitude of the Burgers vector. Then the energy change associated with the motion of a unit length of dislocation line through unit distance is

$$\Delta E = \gamma - b\tau. \tag{1}$$

At equilibrium with respect to dislocation glide, $\Delta E = 0$ and the stress increment due to short-range order hardening is

$$\tau = \gamma/b. \tag{2}$$

An estimate of the order of magnitude of τ requires a knowledge of the misfit energy γ. As an example, a rough calculation based upon a nearest-neighbour bond energy model gives $\gamma \approx 10$ ergs/cm^2 for 70–30 alpha brass, and a stress increment of about $5 \cdot 10^8$ dynes/cm^2 or 8000 psi. This value is several times the yield strength of brass single crystals, suggesting that a significant fraction of the strength of brass is caused by short-range order.

Conclusion

A portion of the strength of solid solution alloys with short-range order results from the fact that dislocation motion destroys the order, creating an interface of positive energy γ. A stress $\tau = \gamma/b$ or greater is required if a dislocation is to move, for the decrease in strain energy accompanying slip must at least equal the energy of the interface that is produced. In contrast to the type of hardening proposed by Cottrell, which is associated with segregation of solute atoms near a dislocation, and which leads in body-centered cubic alloys to a yield stress that decreases rapidly as the temperature is raised, it is predicted that order hardening should be nearly independent of temperature at low temperatures. The temperature-independence of order strength is very similar to that suggested by Suzuki for the yield strength of close-packed crystals with solute segregation.

The connection between the thermodynamic properties of an alloy and its mechanical properties, which is provided by the order-hardening mechanism, should be of considerable utility in investigating the strength of solid solutions.

References

1. Cottrell, A. H. *Report on the Strength of Solids*, Physical Society, London (1948) p. 30. See also Cottrell, A. H. and Bilby, B. A. Proc. Phys. Soc. **62A** (1949) 49.
2. Suzuki, H. Sci. Rep. RITU **A4** (1952) 455.
3. Griffith, A. A. Phil. Trans. Roy. Soc. **221A** (1920–1) 163.

SOLUBILITY OF CARBON IN FERRITE*

MATS HILLERT†

The solubility of cementite in ferrite is known from several determinations. Now the solubility of graphite in ferrite has been determined by a computation.

The two solubility curves have been compared from a theoretical point of view. It is shown that the entropy of formation of the substance, with which the solution is in equilibrium, plays an important rôle in the absolute value of the solubility.

LA SOLUBILITÉ DU CARBONE DANS LA FERRITE

La solubilité de la cementite dans la ferrite est connue; elle a été déterminée à plusieurs reprises. Cette fois la solubilité du graphite dans la cementite fut déterminée mathématiquement. Les deux courbes de solubilité furent comparées du point de vue théorique.

Il est montré que l'entropie de formation de la substance avec laquelle la solution est en équilibre, oue un rôle important dans la valeur absolue de la solubilité.

DIE LÖSLICHKEIT DES KOHLENSTOFFS IN FERRIT

Aus verschiedenen Bestimmungen ist die Löslichkeit von Zementit in Ferrit bekannt. Die Löslichkeit von Graphit in Ferrit wurde im Folgenden rechnerisch bestimmt.

Die beiden Löslichkeitskurven wurden nach theoretischen Gesichtspunkten verglichen. Es wird gezeigt, dass die Bildungsentropie eines Stoffes, mit dem die Lösung im Gleichgewicht steht, eine wichtige Rolle im Absolutwert der Löslichkeit spielt.

1. Computation of the Graphite Solubility in Ferrite

The solubility of carbon in α-iron, ferrite, represents two key-functions to the understanding of important behaviour and properties of steel for temperatures up to some 720°C. There are two such functions because ferrite can be saturated with carbon either to equilibrium with graphite or to equilibrium with cementite. In Figure 1 these functions have been plotted as the natural logarithm of the mole fractions of the carbon content ($\ln x$) versus absolute temperature. This information has been compiled in the following way.

Curve I, for "the solubility of cementite," is the one compiled by Wert [1], from measurements by the damping method by Dijkstra [2] and Wert [1] and by a diffusion method by Stanley [3]. A different method of arriving at the solubility function is the calorimetric one used by Borelius *et al.* [4]. This yields much lower values; and the calorimetric results have not been included in curve I. Wert has found it possible to represent the data by the function

$$x = 0.119\, e^{-\frac{9700}{RT}} = e^{-\frac{9700}{RT} - 2.13} \qquad (1)$$

This straight-line approximation is good over the entire temperature region where measurements have been performed; that is, down to 150°C.

Curve II, for "the solubility of graphite," has been computed from curve I with the aid of data for the carbon activity of ferrite in equilibrium with cementite according to curve I. This activity is shown as a function of temperature in curve III of Figure 1. The curve was drawn by using the computed increase in free energy $4\Delta g$ when that amount of cementite, Fe_3C, is formed from graphite

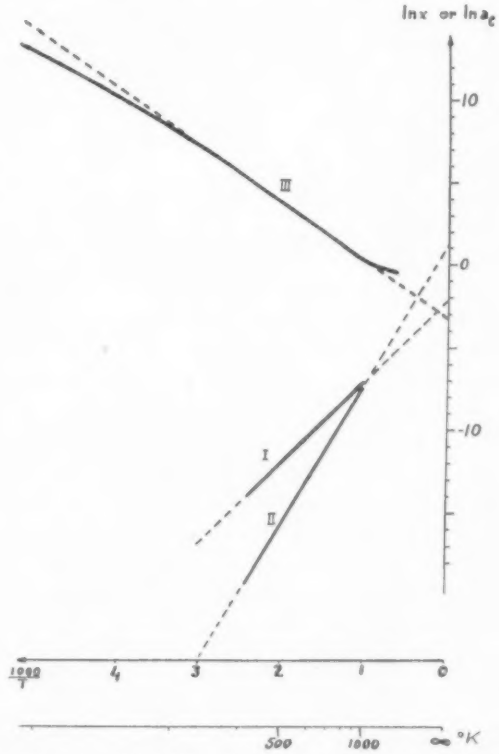

FIGURE 1. Solubility of carbon in ferrite. Curve I— Solubility of cementite. Curve II— Solubility of graphite. Curve III— Carbon activity of ferrite in equilibrium with cementite.

*Received July 16, 1953.

†Swedish Institute for Metal Research, Stockholm, Sweden.

and ferrite, which contains one mole carbon. This increase can easily be evaluated from thermodynamic data for cementite, ferrite and graphite, published by Darken and Gurry [5], Darken and Smith [6], and Rossini *et al* [7]. The data concerning formation of cementite are given in Table I. Curve III for the carbon activity of ferrite in equilibrium with cementite in Figure 1 was then simply taken as

$$\ln a_C^{\text{cem}} = \frac{4\Delta g}{RT} \tag{2}$$

This involves, first, the customary normalization convention of adjusting the activity scale for each temperature so that the activity for equilibrium with graphite becomes 1, and, second, the assumption of an iron activity unity both in ferrite that is in equilibrium with graphite and in ferrite in equilibrium with cementite. The latter assumption is justified by the exceedingly small solubilities actually involved. Curve III, for the "cementite activity," can be approximated by a straight-line expression of the same form as (1):

$$a_C^{\text{cem}} = 0.0353\, e^{\frac{6900}{RT}} = e^{\frac{6900}{RT} - 3,34} \tag{3}$$

This approximation is shown dotted adjoining the solid curve III in Figure 1. It becomes a very bad approximation near and above 768°C and near and below 190°C, which are the Curie temperatures of ferrite and cementite. This is more clear from a diagram with $4\Delta g$ against T.

Knowing the carbon content (curve I) and the corresponding carbon activity (curve III) for ferrite in equilibrium with cementite at any chosen temperature, one can compute the carbon content of the ferrite, which at the same temperature would correspond to a carbon activity of unity, on the further assumption of full proportionality between activity and concentration of solute at these very low concentrations—that is, assuming the validity of Henry's law. The concentration at activity 1 is by definition the solubility at that temperature of carbon in ferrite in equilibrium with graphite. In this way, then, the solubility curve for graphite (II) in Figure 1 is obtained. The straight-line approximation for this curve, shown dotted, obviously must be

$$x = 3.36\, e^{-\frac{16600}{RT}} = e^{-\frac{16600}{RT} + 1.21} \tag{4}$$

It seems quite reasonable to assume that Henry's law is valid for the very dilute solutions of carbon in ferrite. Thus, it is evident that straight-line approximation of both curves I and II at the same time is permissible only when curve III can be approximated to a straight line. According to Figure 1, this is not the case at low temperatures. Thus, at least one of the straight-line approximations of the curves I and II must become very poor.

For several years it has been generally accepted that cementite is a metastable, and graphite a stable, phase at all temperatures. It is possible to describe the metastable character of a phase in a more precise manner than is usually used. Thus, we can say that cementite in equilibrium with ferrite at, for example, 700°C, is metastable with respect to graphite. This is a way of stating the fact that cementite and ferrite in equilibrium at 700°C have a carbon activity higher than 1. From Figure 1 we get the value 1.25. It is an interesting feature in Figure 1 that the carbon activity in the ferrite-cementite equilibrium approaches and then goes below the value 1 with increasing temperature. This means that above a certain temperature cementite in equilibrium with ferrite is not metastable but stable with respect to graphite. For unalloyed steel this does not occur until the temperature is so high that the equilibrium state between cementite and ferrite is metastable with respect to austenite.

It is interesting that a different line of computing the carbon activity of the ferrite-cementite equilibrium for these higher temperatures leads to the same conclusion that cemetite is not metastable but stable with respect to graphite under these conditions. This line is as follows. R. P. Smith [8] has measured the carbon activity in ternary alloys Fe-C-Si of a number of different compositions at a temperature 1000°C. It appears possible to perform an extrapolation to compositions of vanishing Si-content. In this way one finds that unalloyed ferrite with 0.7 atomic per cent carbon has the carbon activity 1 at 1000°C. By extrapolation of curve I in Figure 1 one finds that ferrite should contain only 0.25 atomic per cent carbon in equilibrium with cementite at this temperature. Thus, the ferrite-cementite equilibrium at 1000°C must have a carbon activity considerably lower than 1.

2. Theoretical Discussion

Suppose that a phase, 1, mainly consists of one component, A, and that it can contain small amounts of another component, B. This phase 1 is in equilibrium with a B-rich phase, 2, with the composition A_lB_m, which eventually is pure $B(l = 0,\ m = 1)$. The thermodynamic condition for equilibrium, i.e., of saturation, is

$$\frac{\partial G^1}{\partial n_2} = \frac{\partial G^2}{\partial n_2}, \tag{6}$$

where G^1 and G^2 are the Gibbs free energy of the two phases; ∂n_2 is the infinitely small amount of phase 2, measured as mole, that is thought to be transferred to phase 1. (In this paper one mole is defined as N atoms. N is the Avogadro number.) By introducing heat content, H, and entropy, S, instead of G in (6) and by multiplying with the factor $\frac{l+m}{m}$, the following is obtained:

$$\frac{l+m}{m}\left(\frac{\partial H^1}{\partial n_2} - \frac{\partial H_2}{\partial n_2}\right) = T \cdot \frac{l+m}{m}\left(\frac{\partial S^1}{\partial n_2} - \frac{\partial S^2}{\partial n_2}\right) \tag{7}$$

The left-hand side is the heat absorbed by the system, when that amount of phase 2 is dissolved in phase 1, which contains one mole of component B. This can be called the heat of solution of B and designed L_B. The right-hand side of (7) is the temperature multiplied by the entropy increase of the system, when the same amount of phase 2 is dissolved. This entropy increase can be split into two terms. The first of these depends on the change in the randomness of the atom positions and for low B-content it can be computed to $-R[\ln x - \ln q]$. x is the mole fraction that indicates the B-content in phase 1. For substitutional solutions q is 1 and thus $\ln q$ is zero and can be omitted. For interstitial solutions, q is the number of holes per atom in the mother lattice; q is 1 for carbon in austenite and 4 for carbon in ferrite. The other entropy term represents the increase from other causes—for instance, changes of the thermal vibrations and of the distribution of electron spin directions. This term is here designed s^*. Now (7) gives

$$x = e^{\frac{s^*}{R} + \ln q} \cdot e^{-\frac{L_B}{RT}} \tag{8}$$

On the assumption that the temperature dependence of s^* and L_B is negligible, the heat of solution of carbon from cementite and from graphite into ferrite can be evaluated by comparison of (1) and (4) with (8). The result is $L_C^{gr} = 16600$ cal and $L_C^{cem} = 9700$ cal. From the cementite solubility values, determined by Borelius *et al* [4] by the calorimetric method, one gets $L_C^{gr} = 19400$ cal and $L_C^{cem} = 12500$ cal. R. P. Smith [9] has determined L_C^{gr} from carbon activity measurements at temperatures above A_1 and he found $L_B^{gr} = 20000$ cal.

Under the same assumption of temperature independence, s^*/R can be evaluated from the solubility expressions. Zener [10] has determined s^*/R from data on the solubility of several elements in aluminum and for all elements he found positive and rather small values. He has explained this from a theoretical point of view, too, by calling attention to the fact that the decrease of the elastic modulus that foreign atoms always give rise to in a lattice must involve an increase of the vibrational entropy in the region surrounding each solute atom. This effect seems to be capable of explaining all the experimental data that Zener has analysed. Thus, he can assume that there was no other important contribution to s^*/R, which means that the solute atoms have nearly the same entropy in the solution as in the substance with which the solution is in equilibrium.

This condition may eventually be realized very well, if the two kinds of atoms have the same lattice structure in their pure states and if the solution is in equilibrium with the solute kind of atom in its pure state, e.g., the solution of copper in aluminum in equilibrium with pure copper. Zener has evaluated s^*/R for the solution of copper in aluminum when in equilibrium with ϑ-phase. Thus Zener's interpretation of s^*/R is exactly right only if ϑ-phase is formed from pure copper and pure aluminum without any entropy change. It would be interesting to compare the values of s^*/R obtained from the solubilities of ϑ-phase and of pure copper in aluminum, but unfortunately the latter solubility is probability very difficult to determine.

For solutions of carbon in ferrite a similar comparison can be made. By means of (8) we can determine s^*/R from the cementite solubility (1) compiled by Wert and we find $s^*/R + \ln 4 = -2.1$ and $s^*/R = -3.5$. This negative value cannot be explained by the effect discussed by Zener. From the solubility of graphite (4) we find $s^*/R + \ln 4 = 1.2$ and $s^*/R = -0.2$.

According to our interpretation the difference between the two values of $s^*/R (3.5 - 0.2 = 3.3)$ should depend on the entropy of formation of cementite, when formed from graphite and ferrite. This should then be $3.3R$. Available data, $4\Delta s$ in Table I, show that the entropy of formation has this value at about 560°C. This temperature lies in the temperature region where the solubilities have been investigated.

Borelius *et al.* [4] propose that an appreciable negative value of s^*/R for the solution of cementite in ferrite can be due to ferromagnetism. At the temperatures of interest the cementite is not ferromagnetic and therefore the three iron atoms, which are dissolved in the ferrite with each carbon atom,

are transformed into a ferromagnetic state. This involves a redistribution of the electron spin directions and consequently a large entropy change. As the temperature is increased towards the Curie point of ferrite, the experimentally determined entropy of formation of cementite strongly decreases but it does not tend to reach the zero value, as is shown in Table I. Thus, the ferromagnetism can only explain about half the observed value of s^*/R. The entropy of formation decreases even when the temperature is decreased below a certain value. This happens because the cementite then becomes ferromagnetic too.

By means of (8), s^*/R can be evaluated from the graphite solubility in austenite ($q = 1$). The result is very close to zero and consequently close to the value found for graphite in ferrite.

TABLE I

T	$4\Delta h$	$4\Delta g$	$T.4\Delta s$	$4\Delta s$
300	5986	4755	1231	4.10
400	6498	4262	2236	5.59
500	7081	3637	3444	6.88
600	7320	2916	4404	7.35
700	7238	2185	5053	7.22
800	6961	1478	5483	6.85
900	6323	827	5496	6.10
1000	5080	·273	4807	4.81
1100	3566	−120	3686	3.35
1200	3081	−434	3515	2.93
1300	2798	−715	3513	2.70
1400	2578	−979	3557	2.54
1500	2400	−1230	3630	2.42

References

1. WERT, C. A. J. Metals **2** (1950) 1242.
2. DIJKSTRA, L. J. J. Metals, **1** (1949) 252.
3. STANLEY, J. K. J. Metals. **1** (1949) 752.
4. BORELIUS, G. and BERGLUND, S. Ark. Fys. **4** (1952) 173.
5. DARKEN, L. S. and GURRY, R. W. J. Metals **3** (1951) 1015.
6. DARKEN, L. S. and SMITH, R. P. Industr. Engng. Chem. **43** (1951) 1815.
7. ROSSINI, F. D. *et al.* Nat. Bur. Standards Circular **461** (1947).
8. SMITH, R. P. J. Amer. Chem. Soc. **70** (1948) 2724.
9. ———. J. Amer. Chem. Soc. **68** (1946) 1163.
10. ZENER, C. Thermodynamics in Physical Metallurgy. Amer. Soc. Metals (Cleveland, Ohio, 1950) p. 16.

THE FORMATION OF MECHANICAL TWINS*

B. A. BILBY† and A. R. ENTWISLE‡

It is suggested that the nucleation of mechanical twins is controlled by large local stresses which are set up in a crystal round inhomogeneities of various kinds. An examination is made of the stress fields round two types of inhomogeneity arising during plastic deformation, the bounded slip band, and the kink band. It is shown that in hexagonal metals, twin nuclei on planes containing the slip direction of the dislocations in the inhomogeneity are unlikely to be formed. The theory is compared with available data on these metals, and critical experiments are suggested to distinguish between this hypothesis and that which proposes a macroscopic critical resolved twinning stress.

LA FORMATION DE MACLES MÉCANIQUES

Il est suggéré que la germination de macles mécaniques est contrôlée par de grandes tensions locales, créées autour de diverses hétérogénéités dans un cristal. On a examiné les champs des tensions de deux types d'hétérogénéités engendrées par la déformation plastique, à savoir, la bande de glissement limitée et la bande de pliage. Il est montré que dans les métaux hexagonaux, la formation de germes de macles, sur des plans contenant la direction de glissement des dislocations dans l'hétérogénéité, est peu probable. La théorie est comparée aux données expérimentales, disponibles, concernant ces métaux. On suggère des expériences qui faciliteraient la distinction entre cette hypothèse et celle qui propose une tension critique, macroscopique de maclage.

DIE MECHANISCHE ZWILLINGSBILDUNG

Es wird angenommen, dass der Beginn der mechanischen Zwillingsbildung durch die grossen örtlichen Spannungen bestimmt wird, die in einem Kristall um die verschiedensten Gitterstörungen bestehen. Die Spannungsfelder um zwei Arten von Störungen, die im Verlauf der plastischen Verformung auftreten—das begrenzte Gleitband und das "kink" Band—werden untersucht. Es wird gezeigt, dass es unwahrscheinlich ist, dass in hexagonalen Metallen Zwillingskeime auf Ebenen entstehen, die die Gleichrichtung der Versetzung in der Störung enthalten. Die Theorie wird mit den für diese Metalle vorhandenen Daten verglichen. Neue Versuche werden vorgeschlagen, die es ermöglichen, zwischen dieser Theorie und einer Hypothese, die eine makroskopische kritische spezifische Spannung der Zwillingsbildung postuliert, zu entscheiden.

1. Introduction

There is some evidence in support of the hypothesis that in metal crystals mechanical twinning begins when the applied shear stress on the twinning plane resolved in the twinning direction reaches a critical value (Thompson and Millard [1], King [2]). The measured critical twinning stress, however, usually varies within wide limits, and the criterion for the onset of twinning is not so well established as the corresponding one for slip. Experiments on twinning and untwinning under reversed stresses, for example those of Jillson [3], show on the other hand, that under certain conditions the growth of twins of macroscopic size is controlled by the externally applied stress. It is the purpose of this paper to make a preliminary examination of the hypothesis that the nucleation of mechanical twins is controlled by large local stresses which are set up in the crystal round inhomogeneities of various kinds. We shall not be concerned here with the subsequent growth of the twin nuclei. It will be assumed that the nucleation is determined by the resultant local shear stress on the twinning plane resolved in the twinning direction, although, as will appear, an important conclusion of the theory is valid under a less restrictive assumption.

Recently, suggestions have been made by various workers about the role of specific inhomogeneities of stress in initiating mechanical twinning (Burke and Hibbard [4], Frank and Stroh [5], Low and Feustel [6]). We consider here two types of inhomogeneity produced by previous plastic deformation, namely, the bounded slip band and the bend plane. The discussion is confined to crystals with a hexagonal close-packed structure, since it is for these that most data are available. The idea that twin formation in hexagonal metal crystals is influenced by previous plastic deformation has received considerable attention in the past. Empirical rules have been formulated relating the operative slip direction to the operative twin planes (Gough and Cox [7; 8], Bakerian and Mathewson [9]). There is also some indication that the rules have a wider application (Andrade and Hutchings [10]). We shall examine these rules in the light of the above hypothesis.

2. The Stresses round Bounded Slip Bands

Let X, Y, U and Z denote the conventional axes of reference for a crystal with the hexagonal close

*Received July 17, 1953.

†Royal Society Sorby Research Fellow, Department of Metallurgy, The University, Sheffield.

‡Research Fellow, Department of Metallurgy, The University, Sheffield.

packed structure, and consider a region of the crystal where the Y slip direction is operative. It is anticipated (Mott [10]) that if dislocation groups at the ends of bounded slip bands exist in hexagonal metal crystals deforming by basal slip, they will be composed of screw rather than of edge dislocations. We therefore examine the stresses on the twinning planes produced by a group of long, straight screw dislocations parallel to the $[\bar{1}2\bar{1}0]$ direction. The elastic field of such a group is one of anti-plane strain, and if we take axes x_1, x_2, x_3 parallel to $[10\bar{1}0]$, $[\bar{1}2\bar{1}0]$ and [0001] respectively, the only non-zero components of the stress tensor are p_{12} and p_{23}. Let new axes x_j' whose direction cosines with respect to the axes x_i' are l_{ij}, be chosen for each twinning plane so that x_3' is the normal to the twinning plane and x_1' is the twinning direction. The shear stress on the twinning plane resolved in the twinning direction, p'_{13}, and the normal stress on this plane, p'_{33} are then readily calculated from the relation:

$$p'_{mn} = p_{ij} l_{im} l_{jn}$$

Both p'_{13} and p'_{33} are of the form $tp_{12} + up_{23}$, and the values of t and u for p'_{13} are shown in Table I.

TABLE I

VALUES OF THE STRESS p'_{13}

Twinning plane	State of anti-plane strain, axis $[\bar{1}2\bar{1}0]$		State of plane strain, axis $[10\bar{1}0]$		
	t	u	f	g	h
$TX(01\bar{1}2)$	$+a$	$-b$	$+A$	$-B$	$-C$
$TU(1\bar{1}02)$	$-a$	$+b$	$+A$	$-B$	$+C$
$TX'(0\bar{1}12)$	$+a$	$+b$	$+A$	$-B$	$+C$
$TU'(\bar{1}102)$	$-a$	$-b$	$+A$	$-B$	$-C$
$TY(\bar{1}012)$	o	o	$+G$	$-H$	o
$TY'(10\bar{1}2)$	o	o	$+G$	$-H$	o

The expressions for p'_{33} are obtained by replacing the constants a, b and o by the constants c, $2a$ and o respectively. For a hexagonal structure of axial ratio s, the values of the constants in units of m^2, where m^2 stands for $1/\{4(3 + s^2)\}$ are : $a = 6s$, $b = 2\sqrt{3}(s^2 - 3)$, $c = 2s^2\sqrt{3}$.

In preparing this table, x_1' has been chosen so that when p'_{13} is positive it assists the twinning in zinc and cadmium where $s^2 > 3$. For the other hexagonal metals, where $s^2 < 3$, p'_{13} must be negative if it is to assist twinning. The notation TX, TX' etc., indicates the pair of complementary twinning planes containing the X slip direction, and is used by Gough and Cox.

The table shows that both p'_{13} and p'_{33} are zero for the twinning planes containing the operative slip direction. Thus if either of these stresses (or any combination of them) controls the local nucleation of twins, we should not expect twinning to occur on these planes. This result depends only on the assumption of anti-plane strain and is independent of the form of the expressions p_{12} and p_{23} for the stresses due to the dislocation group.

We shall later require the results of a corresponding analysis for a state of plane strain with stress components $p_{11} = \nu(p_{22} + p_{33})$, p_{22}, p_{33} and p_{23}, where ν is Poisson's ratio. The field of a group of edge dislocations lying along $[10\bar{1}0]$ with Burgers vectors along $[\bar{1}2\bar{1}0]$ is of this kind. The stresses p'_{13} and p'_{33} are now of the form $fp_{22} + gp_{33} + hp_{23}$, where the values of f, g and h for p'_{13} are shown in Table I. Expressions for p'_{33} are obtained by substituting the constants D, $-E$, $-F$, K, $-L$, o for A, B, C, G, H, o respectively, and in units of m^2, the constants have the values:

$$A = s\sqrt{3}\,(3 + \nu), B = 2\sqrt{3}\,(4 - \nu),$$
$$C = 2\sqrt{3}\,(s^2 - 3),\ D = s^2\,(3 + \nu),$$
$$E = (12 + \nu s^2),\ F = 12s,\ G = 4\nu s\sqrt{3},$$
$$H = G(1 - \nu)/\nu,\ K = 4\nu s^2,\ L = 4(3 + \nu s^2).$$

The stresses p'_{13} and p'_{33} on TY and TY' are thus not zero for a state of plane strain, and to proceed further it is necessary to specify the distribution of dislocations in the group. A detailed analysis for groups of both edge and screw dislocations is in progress and the results will be published shortly. However, both at large distances and also in the region very near to the leading dislocation, the field of the group is of the same form as that of a single edge dislocation, and it is easily shown that for such a field the stress p'_{13} favouring twinning is less on the planes TY and TY' than on the other twinning planes.

Table I shows that both for states of plane and anti-plane strain, the stresses on TY and TY' differ in form from those on the other twinning planes. We cannot, however, distinguish between the complementary pairs TX, TX' and TU, TU'. For an edge group the stresses on TX and TU' (and on TX' and TU) are the same, while for a screw group the stress components p_{12} and p_{23} are anti-symmetric and symmetric in the x_3 coordinate respectively, and this implies that if TX operates so also does TU'. For any complementary pair the

stresses p'_{13} are not very different because the planes are nearly perpendicular to one another.

Distinctions can, however, be made when we consider the effect of the applied stress in addition to that of the dislocation groups. The general conclusion then follows that twinning on planes containing the operative slip direction will not occur, and of the other twinning planes, that complementary pair will operate on which the macroscopic resolved shear stress is the greatest. This is true if the twins are nucleated by screw groups, and probably true if they are nucleated by edge groups. There may, however, be a considerable variation in the macroscopic resolved shear stress at which the first twinning is observed, since the nucleation is not controlled by the macroscopic stress only.

The empirical rule formulated by Bakerian and Mathewson [9] as a result of some experiments on the compression of magnesium crystals at various temperatures was: "The operative pair of planes is the pair for which the intersection with the slip plane makes an angle of as near 90 degrees as is geometrically possible with the projection of the compression axis on the same plane." Thompson and Millard [1] have pointed out that this rule is approximately equivalent to the statement that the favoured planes are those for which the macroscopic resolved twinning stress p'_{13} is the greatest. Computations show that when the compression axis lies in any 30 degrees sector bounded by directions $\langle 2\bar{1}\bar{1}0\rangle$ and $\langle 10\bar{1}0\rangle$ in the conventional hexagonal stereogram, there is a region near [0001] where the p'_{13} stress opposes twinning on all the twinning planes, while in the remainder of the sector there is one twinning plane for which the p'_{13} stress is the greatest, and this is in fact the plane selected by the above empirical rule. The hypothesis of the present paper would predict that the same twinning planes operate, since in this set of experiments the exclusion of the twinning planes containing the operative slip direction automatically follows from either hypothesis. This is so because, with the stress system employed, there are always other twinning planes for which the macroscopic stress p'_{13} is greater. Stress systems can, however, be applied where this is not the case, for example, if the magnesium crystals are deformed in tension and the angles χ_0 and λ_0 are small and nearly equal.

Gough and Cox [7; 8] subjected cylindrical zinc crystals to alternating torsional stresses and found that in any region of the crystal, twinning occurred on one or other of the complementary pairs of twinning planes not containing the operative slip direction. They were unable to formulate a rule selecting which of these two pairs operated, although they divided their crystals into two types according as the operative slip–operative twinning sequence was XYU or XUY.* In their second paper, they show the shear stress on the twinning plane resolved in the twinning direction as a function of λ, the angular distance about the torsion axis measured from a reference mark on the crystal surface. Their stresses are, however, not correct. We have recalculated them and have also performed a similar calculation for the crystal examined in their first paper. The stresses for the crystals examined in their second paper, which were all of similar orientation, are shown in Figure 1. The graphs are divided by vertical lines separat-

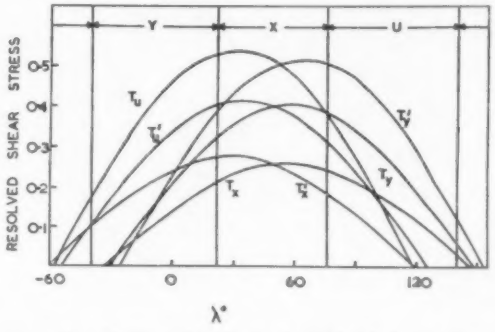

FIGURE 1. Corrected values of resolved shear stress p_{13}' on the twinning planes for the crystal *Z5B* of Gough and Cox [8]. The resolved shear stress is expressed as a fraction of the tangential surface shear stress on the plane perpendicular to the torsion axis. Only the region where the stresses are positive is shown.

ing regions in which the X, Y and U slip directions are operative (as determined by the maximum resolved shear stress criterion). It is clear that here also, the stress system applied fails to distinguish the two hypotheses since in any region of the crystal the twinning planes with the highest resolved twinning stress are not those containing the operative slip direction. We should predict in either theory that in these crystals the slip-twinning sequence would be as follows: in region Y, twinning on TU, TU'; in region U, twinning on TY, TY'; and in region X twinning on both TY, TY' and TU, TU'. This prediction does not in fact agree with either of the sequences XYU, XUY observed. Figure 2 shows the stresses for the crystal of the first paper [7], in which only twinning on

*The sequence XYU means that when the slip direction is X, the operative twins are TY, TY', and when it is Y, they are TU, TU', and so on.

TY, TY' was observed. The fact that the resolved twinning stresses on these planes are small compared with those on the other twinning planes is evidence against the simple hypothesis of a critical resolved stress for twinning, although when $\lambda \backsim 180°$, where maximum twinning was observed, the largest twinning stress is that on TY. However, there is no explanation on either theory of the absence of TU, TU' twins in the X-region and of TX, TX' twins in

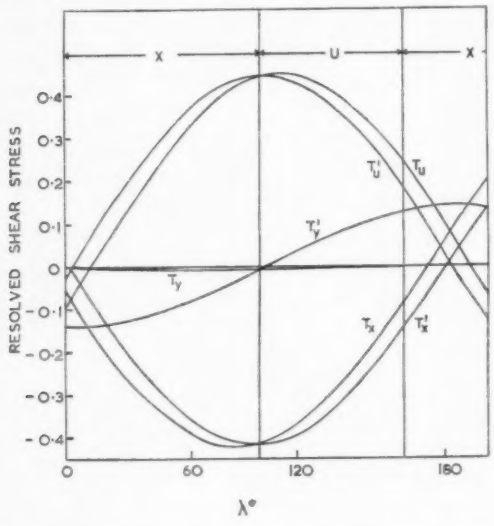

FIGURE 2. Resolved shear stress on the twinning planes for crystal *Z3A* [7]. The resolved shear stress is expressed in the same units as that for Figure 1.

the U-region. The results of Gough and Cox thus find no complete explanation, and it is possible that in their experiments the twinning was initiated by other inhomogeneities. However, the interpretation is made more difficult because their crystals were subjected to many hundreds of thousands of alternating stress cycles. Experiments on crystals subjected to static torsion are desirable.

3. The Initiation of Twinning by Bend Planes

Frank and Stroh [5] have suggested that kink bands formed of parallel walls of edge dislocations of opposite sign may originate at stress concentrations. Once it exceeds a certain length a kink band under a shear stress can lengthen in a direction normal to the slip plane by continuous creation of dislocation pairs at its tip. After the band has propagated in this way the two dislocation walls can separate to form isolated bend planes. We shall now make a rough calculation of the stresses p'_{13} on the twinning planes of a hexagonal crystal in the neighbourhood of the tip of a kink band. If b is the Burgers vector of the dislocations, D their spacing in the walls, and w the distance between the walls, then at distances $R > w$ the stress field near the tip of a long kink band approximates to that of an edge dislocation with Burgers vector $B = wb/D$ [5]. The vector B lies normal to those of the dislocations of the walls, that is, along the length of the kink band itself. The elastic field is one of plane strain and we use the results of section 2, taking the dislocation line along x_1 and the Burgers vector B along x_3, the normal to the basal plane. In Figure 3

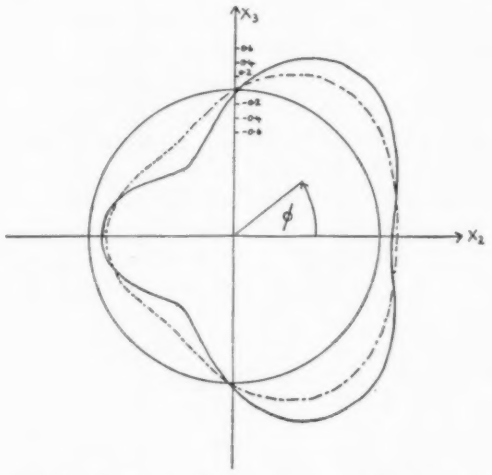

FIGURE 3. The stresses on twinning planes near the end of a kink band in magnesium. The X_1-axis lies perpendicular to the plane of the paper. The dislocations in the band lie parallel to the X_1-axis with their Burgers vectors parallel to the X_2-axis. The stress field near the tip approximates to that of a single dislocation parallel to X_3. The stresses on the twinning planes TY, TY' (– – – – –) and TX, TU' (————) are shown as functions of ϕ in units of $GB/2\pi(1-\nu)R$ where G is the shear modulus and R the radial distance from the dislocation line. The stress is zero on the circle and its magnitude is proportional to the radial distance from this circle, positive stresses being plotted outwards.

the stress $-p'_{13}$ is plotted as a function of the angle ϕ for $\nu = \frac{1}{4}$. This is the resolved twinning stress for a crystal such as magnesium for which $s^2 < 3$. Only the stresses on TY, TY' and TX, TU' are shown, since the stresses on TX', TU are nearly equal to those on TX, TU'. For all the twinning planes, $-p'_{13}$ is positive on one side of the kink band and negative on the other, and it is always greater numerically on the planes TX, TU', than on the planes TY, TY', except in one region, where the stresses are small. We assume that the motion of the kink band as it extends along its length does not greatly alter the form of the stresses at its tip. Consequently, if twins are nucleated at the tip of the band as it propagates, we expect to find them on one side only, and predominantly of the kind

which do not contain the slip direction of the dislocations in the walls. Similarly, if the other wall of the kink band moves away, we expect to find a bend plane, with twins on one side only.

We suggest that this is the explanation of the Figure 14 in the paper of Burke and Hibbard [4] on the deformation of magnesium crystals, where twins are shown on one side of a bend plane. Our interpretation is that, since the single-bend plane has only a very localised stress field, the twins were nucleated on the right side of the tip of a kink band as it moved downwards in the Figure 14, and that the left side wall subsequently moved away during the bending and no longer appears in the figure. There are two sets of twin bands in the figure, and analysis shows that as we should expect neither set contains the slip direction of the dislocations in the bend plane. This interpretation could be tested by direct observation of the formation of the twins by a high-speed camera.

4. Discussion

In twinning and martensite transformations, deformations occur which are macroscopically homogeneous. A dislocation mechanism for producing deformations of this kind has been proposed [1; 11] and it has been shown that the necessary arrangement of dislocations can always be found at the junction of the two structures which are undergoing mutual transformation [12;13]. No difficulty arises therefore in understanding the growth of a twin nucleus once formed. In iron it is geometrically possible for twins to develop from monolayer nuclei [11], but there are difficulties in extending this idea to other materials [14]. It is therefore important to examine possible explanations of the origin of twin nuclei. The suggestion has been made [15] that such nuclei originate during the growth of the crystal. The present hypothesis is a possible alternative to this proposal.

We have shown in this note that stresses favouring the nucleation of mechanical twins in hexagonal metals exist round two specific inhomogeneities caused by plastic deformation. It is clearly implied that some previous plastic deformation is a necessary condition for twin formation, although its amount may be very small. In addition to the experiments already mentioned, interesting evidence in support of this has been obtained recently by Cahn [16]. Of course, we do not wish to imply that this requirement is a universal one, since there may be other inhomogeneities not caused by previous plastic deformation which are equally effective in producing twins. This seems particularly likely in brittle materials like calcite.

In designing experiments to test this hypothesis, it is clear that it is very important to choose a stress system suitably oriented with respect to the slip and twinning elements of the crystals. Otherwise, as has been shown, the results may be ambiguous. In particular the more usual experiments on the deformation of zinc in tension (or magnesium in compression) are not sufficiently discriminating.

A number of interesting consequences follow from this theory. For example, if the stresses round dislocation groups initiate both twinning and fracture, we may expect certain parallels between these processes. It is to be noted, for instance, that low temperatures and impact testing, generally favour deformation by twinning or fracture rather than deformation by slip. More detailed consideration of these problems is, however, required, and we shall not discuss them further here.

Acknowledgments

We are indebted to Professor A. G. Quarrell for providing facilities to enable this work to be carried out, and to Mr. E. Smith for checking some of the computations.

References

1. THOMPSON, N. and MILLARD, D. J. Phil. Mag. **43** (1952) 421.
2. KING, R. Nature **169** (1952) 544.
3. JILLSON, D. C. Trans. A.I.M.M.E. **188** (1950) 1009.
4. BURKE, E. C. and HIBBARD, W. R. J. Metals, **4** (1952) 295.
5. FRANK, F. C. and STROH, A. N. Proc. Phys. Soc. **B65** (1952) 295.
6. LOW, J. R. and FEUSTEL, R. G. Acta Met. **1** (1953) 185.
7. GOUGH, H. J. and COX, H. L. Proc. Roy. Soc. **A123** (1929) 143.
8. GOUGH, H. J. and COX, H. L. Proc. Roy. Soc. **A127** (1930) 453.
9. BAKERIAN, P. W. and MATHEWSON, C. H. Trans. A.I.M.M.E. **152** (1943) 226.
10. MOTT, N. F. Phil. Mag. **43** (1952) 1151.
11. COTTRELL, A. H. and BILBY, B. A. Phil. Mag. **42** (1951) 573.
12. BILBY, B. A. Phil. Mag. **44** (1953) 782.
13. BASINSKI, Z. and CHRISTIAN, J. W. Phil. Mag. **44** (1953) 791.
14. BILBY, B. A. Year Book of the Royal Society (1953) p. 218.
15. OLIVER, D. S. Research **5** (1952) 45.
16. CAHN, R. W. Private communication.

TRANSITION METAL DIBORIDES*

BENJAMIN POST,† FRANK W. GLASER‡ and DAVID MOSKOWITZ‡

Structural characteristics of eight transition metal diborides have been investigated. It was found that in these hexagonal compounds the length of the "a" axis is determined primarily by boron-boron contacts in the case of diborides of the smaller metal atoms, whereas in the diborides of the larger metal atoms, the metal atoms are the determining factor. Enlarged metal atoms were postulated to explain variations in lattice dimensions and "c/a" ratios. An examination of the melting points of the diborides relative to those of their respective metals indicated that they reflect primarily the strength of the Me-B bonds in these structures. The extent of mutual solid solubility appeared to depend mainly upon size factor considerations. In cases of solid solution between two diborides where one of these was of a more highly ordered structure than the other, the more disordered phase was favored.

LES BIBORURES DES MÉTAUX DE TRANSITION

Les biborures de huit métaux de transition furent examinés afin d'étendre la connaissance de leurs caractéristiques structurales.

On a constaté que la longueur de l'axe "a" de ces composés hexagonaux est déterminée, soit par les contacts bore-bore, soit par les contacts entre les atomes métalliques; le premier cas s'applique aux biborures des métaux à petits atomes, et le deuxième cas aux biborures des métaux à grands atomes. Un accroissement des dimensions des atomes métalliques a été proposé pour expliquer les variations dans les dimensions des réseaux et dans les rapports "c/a". Un examen des points de fusion des biborures, en comparaison avec les points de fusion de leurs métaux respectifs, a permis de constater que ceux-là reflètent principalement l'intensité des liaisons Me-B dans ces structures. L'étendue de solubilité solide, mutuelle, dépend surtout du facteur de dimensions.

Dans les cas de solution solide entre deux biborures, dont un a une structure plus ordonnée que l'autre, la phase la plus désordonnée prédomine.

DIBORIDE DER ÜBERGANGSMETALLE

Strukturelle Eigenschaften der Diboride von acht Übergangsmetallen wurden untersucht. Es zeigte sich, dass in diesen hexagonalen Verbindungen die Länge der a-Achse in Diboriden mit kleineren Metallatomen in erster Linie von den Bor-Bor Kontakten bestimmt ist, während bei Diboriden mit grösseren Metallatomen die Metallatome die grösse—bestimmenden Faktoren sind. Es wurde eine Vergrösserung der Metallatome postuliert, die die Veränderungen in den Gitterkonstanten und im "c/a" Verhältnis erklären kann. Ein Vergleich der Schmelzpunkte der Diboride und der der entsprechenden Metalle deutet darauf hin, dass der Schmelzpunkt der Diboride in erster Linie die Stabilität der Me-B Bindung reflektiert. Das Ausmass der gegenseitigen festen Löslichkeit scheint hauptsächlich vom jeweiligen Raumbedarf abzuhängen. In festen Lösungen von zwei Diboriden, von denen eine Verbindung einen höheren Ordnungsgrad als die andere aufwies, wurde die Phase geringeren Ordnungsgrades bevorzugt.

Introduction

Isomorphous diborides of eight transition metals (Ti [1], Zr [2], Hf [3], V [4], Nb [5], Ta [6], Cr [7] and Mo [8a,b]), have been described in the extensive literature of metallic borides. Most of these, as well as the closely related Mo_2B_5 and W_2B_5 compounds, have been described by Kiessling in a comprehensive review article [9].

In this paper some structural and physical properties of these borides and their solid solutions will be discussed.

The crystal structures of the diborides are simple. They are of the C-32 type. The primitive hexagonal unit cell contains one formula weight of MeB_2. The space group is D'_{6h}–C 6/mmm, with the metal atom at 0,0,0, and boron atoms at $\frac{2}{3}$, $\frac{1}{3}$, $\frac{1}{2}$ and $\frac{1}{3}$, $\frac{2}{3}$, $\frac{1}{2}$. As shown in Figure 1, the metal and boron atoms lie in alternate planar layers. Each metal atom has six equidistant closest metal neighbors in its plane, and twelve equidistant boron neighbors, six in the layer above and six in the layer below the metal atom. Correspondingly, each boron atom has three closest boron neighbors in its plane, and also forms six boron-to-metal bonds.

Kiessling [10] has determined the crystal structures of the closely related Mo_2B_5 and W_2B_5. These resemble ordered modifications of the MeB_2 structure and are discussed below.

A diboride of uranium, apparently isomorphous with those listed above, has recently been prepared [11]; it is not included in this discussion, which is limited to diborides of transition metals of the first, second and third long periods.

I. Structural Considerations

1. *Lattice Dimensions*

Lattice constants of the isomorphous diborides are listed in Table I in order of increasing length of the "a" axis. Boron-to-boron distances are also listed.

*Received August 21, 1953.
†Polytechnic Institute of Brooklyn, Brooklyn, New York.
‡American Electro Metal Corporation, Yonkers, New York.

Studies of a number of compounds in which boron-boron bonds exist indicate that the "normal" boron radius is 0.87 Å, i.e., the "normal" boron-boron separation is 1.74 Å [9]. In the MeB_2 structure, the length of the "a" axis is $\sqrt{3}$ times the boron-boron separation. In the borides of the smaller metal atoms (e.g., Cr and V)the length of the "a" axis is determined primarily by boron-boron contacts. The length of the "a" axis increases with increasing size of the metal atoms. Thus, in ZrB_2, the boron-boron separation, which must equal $a/\sqrt{3}$, is 1.83 Å, or 0.09 Å in excess of the "normal" value. Evidently, in such borides, the metal atoms are in "contact" and determine the length of the "a" axis.

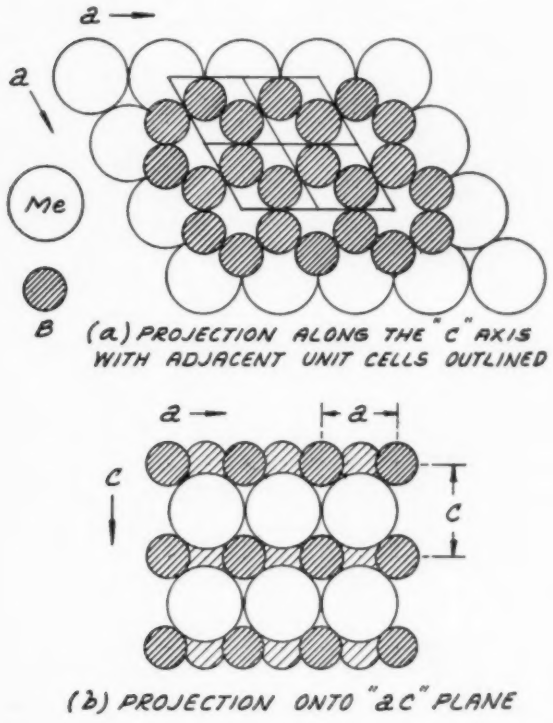

FIGURE 1. Arrangement of metal (Me) atoms and Boron (B) atoms in MeB_2.

These elementary considerations of atomic size indicate that, regardless of other factors, it is doubtful whether metal atoms much smaller than Cr, or much larger than Zr, can form diborides of the type discussed. The excessive separation of metal atoms in one case, and of boron atoms in the other, would undoubtedly lead to structural instability.

2. "c/a" *Ratios and Me-B Bond Lengths*

Values of the "c/a" ratios are listed in Table I. Norton *et al* [4] and Kiessling [9] have noted the fairly regular increase in this ratio which accompanies increasing size of the metal atom. It is of some interest to investigate this effect more closely.

Values of interatomic distances in the pure metals and in their diborides are listed in Table II. It will be noted that in all cases the "observed" Me-B bond length exceeds the corresponding calculated value by 0.07 ± .01 Å. This Me-B separation is related to the axial lengths in the following way:

$$(1) \qquad d_{(Me-B)} = \left(\frac{a^2}{3} + \frac{c^2}{4}\right)^{\frac{1}{2}}$$

TABLE I

UNIT CELL DIMENSIONS OF METAL DIBORIDES (IN Å)

	"a"	"c"	c/a	(B–B)
CrB_2 [7]	2.97	3.07	1.03	1.72
VB_2 [4]	3.00	3.06	1.02	1.73
TiB_2 [1]	3.03	3.23	1.07	1.75
MoB_2 [8a]*	3.05	3.08	1.01	1.75
TaB_2 [6]	3.08	3.27	1.06	1.78
NbB_2 [5]	3.09	3.30	1.07	1.78
HfB_2 [3]	3.14	3.47	1.10	1.81
ZrB_2 [2]	3.17	3.53	1.11	1.83

*Bertaut and Blum [8b] have reported a = 3.05 Å and c = 3.11 Å for MoB_2.

TABLE II

INTERATOMIC DISTANCES IN METALS AND METAL DIBORIDES (IN Å)

	(1)	(2)	(3)	(4)	(5)
Metal	r(Me) in Metal C.N. in brackets	r(Me) for C.N.12*	r(Me) (C.N.12) plus r(B) r(B) = 0.87 Å	r(Me–B) obs. in MeB_2	(4) minus (3)
Ti	1.45 (12)	1.45	2.32	2.38	0.06
Zr	1.59 (12)	1.59	2.46	2.54	0.08
Hf	1.57 (12)	1.57	2.44	2.51	0.07
V	1.32 (8)	1.37	2.24	2.31	0.07
Nb	1.43 (8)	1.48	2.35	2.43	0.08
Ta	1.43 (8)	1.48	2.35	2.41	0.06
βCr**	1.36 (12)	1.36	2.23	2.30	0.07
Mo	1.36 (8)	1.41	2.28	2.34	0.06
W	1.37 (8)	1.42	—	—	—

*Where values for C.N. 8 were the only ones available, the values for C.N. 12 were computed using Pauling's equation $R(12) - R(8) = .300 \log n$ [12].

**Values for β Cr have been used somewhat arbitrarily in this Table in place of the more common α Cr. The latter is so small (r = 1.25 Å) that it appears probable that in CrB_2 the Cr atom has a configuration similar to that in β Cr.

The calculated values are simply the sums of the "normal" boron radius and the radii of the metal atoms for twelve-fold coordination.

Evidently, the effective radii of either the metal or boron atoms, or both, are substantially greater than the radii used for these "calculated" values.

Considerable light is shed on this point by a consideration of the variation of the lattice constants of NbB_2 and TaB_2 with boron content [6; 13]. These compounds show relatively wide homogeneity ranges. Comparable data are not available for other diborides.

Kiessling [6] has reported that at the lower boron limit for TaB_2 (*ca.* 64 atomic per cent) "*a*" = 3.099Å and "*c*" = 3.224 Å. At the upper boron limit (*ca.* 72 atomic per cent) "*a*" = 3.057 Å and "*c*" = 3.291 Å. Similar results have been reported by Brewer *et al* [13] and have also been obtained in the course of this investigation.

In the case of NbB_2, Brewer *et al.* [13] found that, at the lower boron limit (the exact homogeneity range was not reported) $a = 3.110$ Å and $c = 3.285$ Å; at the upper boron limit $a = 3.085$ Å and $c = 3.311$ Å.

In both compounds, however, the Me-B distances remain substantially constant throughout the homogeneity ranges: these are 2.41 Å in TaB_2 and 2.43 Å in NbB_2. It is clear from equation (1) that, if $d_{(Me-B)}$ remains constant, an increase in "*a*" must be compensated for by a decrease in "*c*", and vice versa, as is observed.

In both cases, too, "*a*" decreases as the boron content of the phase increases, and increases as the boron content goes down. In the MeB_2 structure a boron content in excess of the stoichiometric amount indicates that the boron layers are filled while the metal layers are only partially full; the converse is true in cases of boron deficiencies.

In these borides the length of the "*a*" axis appears to be determined by the balance between two opposing forces: expansive forces due to "enlarged" metal atoms, which are opposed by strong cohesive forces within the boron network which resist any increases in the boron-boron separations. In these circumstances the "*a*" dimension decreases when the cohesive forces of a full boron layer are opposed by the weakened expansive forces of a partially filled metal layer. (It must be borne in mind that when the boron content rises to 72 atomic per cent, as in the case of TaB_2, the metal content is only 28 atomic per cent, and there are, therefore, 8 vacancies out of every 36 available metal positions.) Similar considerations explain the increase in "*a*" when the boron content is decreased. The observed variations in "*c*" simply compensate for the changes in "*a*" while $d_{(Me-B)}$ is maintained constant.

"Enlarged" metal atoms have been postulated to explain the variations in lattice dimensions. The magnitude of this "enlargement" appears to correspond closely to the values listed in column 5 of Table II (i.e. the radii for twelve-fold coordination appear to increase by these amounts in MeB_2). The length of the "*a*" axis will be close to twice this "enlarged" metal radius in cases where this increase does not involve a large increase in the boron-boron separation over the "normal" (1.74 Å) value. However, in cases like ZrB_2 and HfB_2, the effective radius of the metal atom in the "*a*"-direction is no greater than the metal radius for twelve-fold coordination. In both ZrB_2 and HfB_2 the strong cohesive forces in the "stretched" boron lattice (B-B = 1.83 Å in ZrB_2) prevent any expansion of the metal atoms in the "*a*"-direction. No such restraints are present in the "*c*" or the "Me-B" directions, and in these directions these metal radii increase by approximately 0.07 Å.

The variation in the *c/a* ratio can be explained on this basis. Where, as in CrB_2 and VB_2, even the expanded metal atoms are not in contact, the *c/a* ratio is small. It can readily be shown that, when the metal atoms are in "contact" and the boron-boron separation is "normal" or close to "normal," the *c/a* ratio will be about 1.08. In the case of the largest metal atoms the "normal" increase in "*a*" is prevented by factors mentioned above and the *c/a* ratio rises to 1.10 and 1.11.

3. *Melting Points of the Diborides*

A comparison of the melting points of the metals and their diborides (Table III) is of interest. The melting points of diborides that had not previously been reported were determined in the course of this investigation. The ratios of the melting points of the diborides to the melting points of their respective metals are also listed in Table III. These ratios (which reflect the thermal stabilities of the diborides relative to the pure metals) decrease regularly in going from Group IV to Group VI, and decrease also within each group in going from lower to higher atomic numbers. The melting points of the pure metals behave in the opposite fashion; they increase in going from Group IV to Group VI, as well as in going from lower to higher atomic numbers within a group.

It is evident that the bonds which determine the thermal stability of the diborides are not simply

Me-Me bonds. Nor do they appear to be B-B bonds. The melting points of diborides of large metal atoms have the highest melting points, although in these compounds the B-B separations are greatest, and the B-B bonds presumably weakest. It therefore appears probable that the melting points of the diborides reflect primarily the strength of the Me-B bonds.

The data in Table III indicate, too, that the diborides of Group VII would, if they existed,

TABLE III

MELTING POINTS OF METALS AND THEIR DIBORIDES

	MP°C. Metal	MP°C. MeB_2	Ratio MP (MeB_2) in °K / MP (Me)
Ti	1700	2920	1.62
Zr	1850	3050	1.57
Hf	2250	3240	1.40
V	1735	2400	1.33
Nb	2500	3050	1.20
Ta	2990	3200	1.06
Cr	1850	1900	1.02
Mo	2620	2100	.83
W	3410	2200*	.67

*Refers to melting point of W_2B_5; it is probable that W_2B_5, like Mo_2B_5, transforms to the MeB_2 form near the melting point.

probably exhibit low thermal stability relative to the pure metals. So far as is known diborides of these metals have never been prepared.

These results may be compared with recent findings of Hagg and Kiessling [14]. Their studies of ternary metal-boron systems indicate that, in transition metals of the first series, the strength of the Me-B bonds (in MeB and Me_2B) decreases with increasing atomic numbers.

II. Solid Solutions

It is evident that metal-to-metal replacement to form solid solutions should occur readily in the diborides. In this section we shall discuss the results obtained in the course of an investigation of these solid solutions.

1. *Preparation of Raw Material and Samples*

All the metal diborides were prepared by direct synthesis from the elements. The purity of the products was controlled by chemical and X-ray diffraction analyses.

To obtain solid solutions, two borides were mixed in the desired proportions and hot pressed into bars approximately $\frac{1}{4} \times \frac{1}{2} \times 1''$. Very high currents were then passed through these boride test samples. Samples were heated in this way very rapidly to their melting points in a helium atmosphere. Surfaces which had been in contact with carbon dies during hot pressing were carefully ground to remove all surface carbon. All samples were chemically analyzed; these latter values, rather than the proportions mixed, were used in determining composition.

Solid solutions of diborides of Zr, Ti and Cr with all the other diborides were studied. It was felt that results obtained with these three diboride systems would be fairly typical of all the diborides. Zr is the largest metal atom of the group studied; Cr is the smallest; and Ti is intermediate in size.

The extent of mutual solubility was estimated from X-ray diffraction measurements; a Norelco Geiger Counter spectrometer was used for all diffraction experiments.

A preliminary series of experiments conducted at 1500°C indicated complete solid solution in only two of a large number of trials. Even in these two cases (Cr-V and Nb-Ti) the similarities in lattice constants could easily have disguised incomplete solid solution. Much higher reaction temperatures were clearly needed. Sample bars were then heated until they melted. All temperatures were measured optically.

2. *Results*

The results of these experiments are outlined in Table IV. Table IV also shows the reaction temperatures reached during all these experiments. The ratios of the effective radii of the metal in the diborides, as computed in Part I above, are shown in column 2. In addition, mutual solubilities, as estimated from X-ray diffraction measurements, are shown in column 4.

3. *Discussion of Results*

It can be seen, from the data in Table IV, that in general the so-called "15 per cent rule" is obeyed for the systems studied. In addition, measurements of the lattice constants of the solid solutions indicated a practically linear variation of parameters with composition. These measurements are summarized in Table V. In a few cases, where X-ray diffraction measurements of 50–50 compositions of two diborides with favorable radius ratios showed clear evidence of only one solid solution phase, further measurements were considered unnecessary for the purposes of this investigation.

The deviations from Vegard's Law which occurred in a few cases were generally positive in the case of measurements of the "c" axis. This type of devia-

TABLE IV

MUTUAL SOLUBILITIES OF METAL DIBORIDES

(1) ZrB_2 in MeB_2	(2) Approx. Reaction Temp. (°C.)	(3) Radius Ratio % Diff.	(4) Solubility Mole %	(1) MeB_2 in ZrB_2	(3) Radius Ratio % Diff.	(4) Solubility Mole %
ZrB_2 in TiB_2	3000±100	11	100	TiB_2 in ZrB_2	10	100
" " HfB_2	3100±100	2	100	HfB_2 " "	2	100
" " VB_2	2500±200	16	0–5	VB_2 " "	14	10–15
" " NbB_2	3000±100	8	100	NbB_2 " "	7	100
" " TaB_2	3000±100	8	100	TaB_2 " "	8	100
" " CrB_2	2100±100	17	0–5	CrB_2 " "	14	10–15
" " MoB_2	2600±100	14	100	MoB_2 " "	12	100
" " W_2B_5	2700±100	13	*	WB_2 " "	12	*
TiB_2 in MeB_2				MeB_2 in TiB_2		
TiB_2 in ZrB_2	3000±100	10	100	ZrB_2 in TiB_2	11	100
" " HfB_2	3000±100	8	100	HfB_2 " "	9	100
" " VB_2	2700±100	5	100	VB_2 " "	5	100
" " NbB_2	3000±100	3	100	NbB_2 " "	3	100
" " TaB_2	3000±100	2	100	TaB_2 " "	2	100
" " CrB_2	2100±100	6	100	CrB_2 " "	5	100
" " MoB_2	2500±100	3	100	MoB_2 " "	3	100
" " W_2B_5	2700±100	2	*	WB_2 " "	2	*
CrB_2 in MeB_2				MeB_2 in CrB_2		
CrB_2 in TiB_2	2100±100	5	100	TiB_2 in CrB_2	6	100
" " ZrB_2	2100±100	14	10–15	ZrB_2 " "	17	0–5
" " HfB_2	2500±100	13	5	HfB_2 " "	15	0–5
" " VB_2	2000±100	—	100	VB_2 " "	—	100
" " NbB_2	2500±100	8	100	NbB_2 " "	8	100
" " TaB_2	2500±100	7	100	TaB_2 " "	8	100
" " MoB_2	2000±100	3	100	MoB_2 " "	3	100
" " W_2B_5	2100±100	3	*	WB_2 " "	3	*

*Exact limits not as yet determined.

TABLE V

CALCULATED AND OBSERVED LATTICE CONSTANTS OF METAL DIBORIDE SOLID SOLUTIONS

(50–50 Mole Per cent)

	"a"		"c"	
	Calc. $\left(\frac{a_1+a_2}{2}\right)$	Observed	Calc. $\left(\frac{c_1+c_2}{2}\right)$	Observed
Cr/Ti	3.00	2.99	3.147	3.14
V	2.984	2.99	3.061	3.045
Nb	3.029	3.03	3.185	3.20
Ta	3.023	3.025	3.165	3.21
Mo	3.005	3.01	3.065	3.12
Ti/Zr	3.098	3.10	3.379	3.392
Hf	3.085	3.085	3.35	3.368
V	3.013	3.01	3.142	3.15
Nb	3.054	3.06	3.266	3.264
Ta	3.053	3.05	3.246	3.246
Mo	3.035	3.035	3.147	3.206
Zr/Hf	3.155	3.155	3.50	3.497
Nb	3.129	3.128	3.426	3.42
Ta	3.124	3.12	3.397	3.40
Mo	3.105	3.085	3.30	3.40
Ti	3.098	3.098	3.38	3.39

tion is consistent with the considerations discussed above in Part I. In Table IV a number of reactions where only limited solubility could be observed are listed. The extent of solubility was estimated from X-ray diffraction measurements of lattice constants. It was assumed that, in the regions of interest, lattice constants varied linearly with composition. It was estimated that solubility limits could be approximated in this way to within 5 per cent by interpolation.

It will be noted that the behavior of the MoB_2 solid solutions showed anomalous variation of lattice constants with composition. Large and positive deviations of the "c" axis were observed in the solid solutions with ZrB_2, TiB_2 and CrB_2. The cause of these deviations is difficult to determine; it is, however, probably related to the variations which have been observed in the reported values of the lattice constants of pure MoB_2 (Table I).

Efforts were also made to prepare solid solutions of Mo_2B_5 and W_2B_5. As was mentioned above, the structures of these two compounds are very similar;

they differ only in the lengths of the "c" axes, i.e., in the extent of ordering in the "c" direction. In W_2B_5 the sequence of metal sheets in the "c" direction is $AABBAA$; in Mo_2B_5 it is $AABBCCAA$. Planar and puckered layers of boron atoms alternate between layers of metal atoms. In both W_2B_5 and Mo_2B_5 separations between layers of metal atoms are of two types; they are 3.07 Å and 3.85 Å in W_2B_5, and 3.13 Å and 3.82 Å in Mo_2B_5.

It was found that larger amounts of Mo_2B_5 can be accommodated in the W_2B_5 structure than vice versa. The W_2B_5 phase is the more disordered of the two and its structure is favored in solid solution formation.

Similar results were observed in the TiB_2–W_2B_5 system. In solid solutions containing 50 mole per cent of each compound, the phase present had the MeB_2 structure.

The result in this latter case is of particular interest since repeated efforts to prepare pure WB_2 were unsuccessful. It is possible that this compound, like MoB_2 [8*a*], forms at high temperatures; however, this phase (WB_2) was not observed at room temperature even after very rapid quenching of the high temperature reaction product.

Acknowledgment

The authors would like to thank the Office of Naval Research, Washington, D.C., under whose sponsorship this work was carried out, for permission to publish this paper.

Thanks are also due to Messrs. W. Ivanick and W. Arbiter for their cooperation in carrying out some of the experimental work.

References

1. EHRLICH, P. Angeu. Chemie, **59** (1947) 163.
2. MCKENNA, P. Ind. Eng. Chem. **28** (1936) 767.
3. GLASER, F. W., MOSKOWITZ, D., POST, B. Submitted to J. Metals.
4. NORTON, J. T., BLUMENTHAL, H., SINDEBAND, S. J. Trans. A.I.M.E. **185** (1949) 749.
5. KIESSLING, R. Acta. Chem. Scand. **4** (1950) 160.
6. ——— Acta. Chem. Scand. **3** (1949) 603.
7. ——— Acta. Chem. Scand. **3** (1949) 595.
8a. STEINITZ, R., BINDER, I., MOSKOWITZ, D. J. Metals **4** (1952) 983.
8b. BERTAUT, F., BLUM, P. Acta Cryst. **4** (1951) **72.**
9. KIESSLING, R. Acta Chem. Scand. **4** (1950) **209.**
10. ——— Acta Chem. Scand. **1** (1947) 893.
11. DAANE, A., BAENZEGER, N. C. U.S.A.E.C. Report I.S.C. **53** (July 1949).
12. PAULING, L. J. Am. Chem. Soc. **69** (1947) 542.
13. BREWER, L., SAWYER, D. L., TEMPLETON, D. H., DAUBEN, C. H. J. Am. Ceram. Soc. **34** (1951) 173.
14. HAGG, G., KIESSLING, R. J. Inst. Metals **81** (1952) 57.

OBSERVATIONS ON THE STRUCTURAL CHANGES ACCOMPANYING RECOVERY IN SUPER-PURITY ALUMINIUM*

E. C. W. PERRYMAN†

The structure of super-purity aluminium has been examined by metallographic and X-ray examination directly after cold rolling at room and liquid air temperatures and after annealing at temperatures in the range, room temperature to 375°C. Hardness and micro-hardness tests have also been carried out. A small amount of work has been done on a super purity aluminium-1% magnesium alloy.

It is shown that there exists directly after cold working at room temperature a subgrain structure, the subgrains of which become increasingly perfect on annealing. This increase in perfection of the subgrains is accompanied by a decrease in hardness and it is found that the percentage softening brought about by this recovery process is about 50–60% irrespective of the amount of cold work. Furthermore it is shown that recovery can proceed both before and at the same time as recrystallization. The subgrain size decreases with increasing cold reduction, decreasing annealing temperature and with additions of magnesium.

It is concluded that during recovery dislocations within the subgrains diffuse, those of opposite sign cancelling each other out and others diffusing into the subgrain boundary regions. It is shown that this residual strain energy in the subgrain boundaries is probably the driving force for the growth of recrystallization nuclei.

OBSERVATIONS SUR LES MODIFICATIONS STRUCTURALES QUI ACCOMPAGNENT LA RESTAURATION DANS L'ALUMINIUM DE TRÈS HAUTE PURETÉ

La structure de l'aluminium de très haute pureté a été examinée au moyen de méthodes métallographiques et aux rayons X, immédiatement après le laminage à froid à la température ambiante et à la température de l'air liquide, et ensuite après des recuits aux températures allant de l'ambiante à 375°C. Des essais macroscopiques et microscopiques de dureté ont aussi été faits. Quelques expériences furent faites avec un alliage d'aluminium de haute pureté avec 1% de magnésium. Il est montré qu'immédiatement après l'écrouissage à la température ambiante il existe une sous-structure, dont les sous-grains deviennent de plus en plus parfaits lors du recuit. L'accroissement de la perfection des grains est accompagné d'une diminution de dureté. Le pourcentage de diminution de dureté, produit par cette restauration, est d'environ 50–60% quel que soit le degré d'écrouissage. Il est montré, de plus, que la restauration peut s'opérer avant la recristallisation ou en même temps que cette dernière. La grosseur de sous-grains diminue quand le pourcentage de réduction par laminage augmente, quand la température de recuit est abaissée et quand on ajoute du magnésium à l'aluminium. On conclut, que pendant la restauration, les dislocations contenues dans les sous-grains diffusent, les dislocations de signe contraire s'annulent et les autres diffusent vers les régions des joints des sous-grains. Il est montré que cette énergie résiduelle de déformation constitue probablement la force motrice pour la croissance des germes de recristallisation.

BEOBACHTUNGEN VON STRUKTURVERÄNDERUNGEN DIE BEI DER ERHOLUNG VON REINSTALUMINIUM AUFTRETEN

Die Struktur von Reinstaluminium wurde metallographisch und röntgenographisch direkt nach Kaltwalzen bei Zimmertemperatur und bei der Temperatur der flüssigen Luft wie auch nach Glühen im Temperaturbereich zwischen Zimmertemperatur und 375°C untersucht. Weiterhin wurden Härte- und Microhärtemessungen und einige Versuche an einer Reinstaluminium-1% Magnesium Legierung durchgeführt.

Es wird gezeigt, dass das Aluminium unmittelbar nach der Kaltbearbeitung bei Zimmertemperatur eine Feinkornstruktur zeigt, und dass die Feinkörner durch Glühen fehlerfreier werden. Diese wachsende Vergütung der Feinkörner geht Hand in Hand mit einer Verminderung der Härten und es zeigt sich, dass der Erweichungsgrad der durch diesen Erholungsvorgang hervorgerufen wird, etwa 50%–60% beträgt und zwar unabhängig von dem Ausmass der Kaltbearbeitung. Es wird weiterhin gezeigt, dass die Erholung sowohl vor als auch während der Rekristallisation erfolgen kann. Die Grösse der Feinkörner nimmt mit zunehmender Kaltbearbeitung, mit abnehmender Glühtemperatur und beim Zusatz von Magnesium ab.

Aus diesen Beobachtungen wird geschlossen, dass während der Erholung Versetzungen innerhalb der Subkörner diffundieren, dass sich dabei Versetzungen ungleichen Vorzeichens gegenseitig auslöschen, und die verbleibenden Versetzungen in die Feinkorngrenzen diffundieren. Es wird gezeigt, dass die Verzerrungsenergien dieser Korngrenzen wahrscheinlich die treibende Kraft im Wachstum der Rekristallisationskeime ist.

Introduction

In recent years the structural changes which accompany the recovery‡ of lightly strained aluminium single crystals and coarse grained polycrystalline aluminium have received wide attention. Little work has been done, however, on the recovery of heavily cold rolled aluminium and furthermore little notice seems to have been taken of the possibility that recovery can proceed at the same time as recrystallization.

Heidenreich [1], using an electron transmission microscope method, has shown that the grains of high purity aluminium, heavily cold worked by

*Received August 31, 1953.

†Physical Metallurgist, Division of Physics and Physical Metallurgy, Aluminium Laboratories Limited, Kingston, Canada

‡Throughout this paper recovery will be taken to mean any modification of properties or structure, which is brought about by annealing plastically deformed material but without the formation of new recrystallized grains.

hammering at room temperature, consist of slightly disoriented, imperfect subgrains of an average diameter of about 2 microns. Smaller subgrains were observed if the hammering was done at −196°C. Because of the lack of sharp "extinction contours" Heidenreich concluded that these subgrains, immediately after being formed, have considerable strain. However, on standing at room temperature all subgrains showed extinction contours such as were observed with grains of fully recrystallized aluminium from which he concluded that during recovery the subgrains became more perfect. Heidenreich also found that during recovery at room temperature and even at elevated temperatures below those required for recrystallization the subgrain size remained essentially constant. Hirsch and Kellar [2] using an X-ray micro-beam technique confirmed the findings of Heidenreich and moreover found that the subgrains in high purity aluminium (99.99%) exhibited a limiting size of approximately 2 microns after about 10% cold reduction; with smaller amounts of cold work they found the subgrain size to increase, it being about 5 microns at 3% cold reduction. Impurities were found to decrease the subgrain size. Later work by Gay and Kelly [3] has shown that similar structures exist after cold working copper, nickel, iron, zinc, lead and cadmium.

Similar observations to those described above have been made by Beck and Hu [4] on severely rolled (95% cold reduction) high-purity aluminium. Using electrolytic etching and a polarising microscope they found that the subgrain size was about 2 microns and that this size was independent of annealing temperature up to 220°C. It is interesting to note the authors' statement that in some deformed grains recrystallization did not commence with annealing temperatures up to 330°C and that when this occurred the subgrain size had increased to about 20 microns, and furthermore, the orientation difference between adjacent subgrains had increased. Tate and McLean [5] have also observed subgrains in cold rolled aluminium but the size of the subgrains was much coarser (20 microns) than those observed by other workers. They also found that as the temperature of rolling was decreased the subgrain structure became less distinct, it not being evident after rolling at −73°C. The large size of the subgrains observed by Tate and McLean may be due to lack of sensitivity of their metallographic technique. They may in fact have been observing groups of much smaller subgrains, not being able to detect the very small orientation difference between the individual units of such groups.

The present work was carried out to investigate further the recovery process and to see what relationship, if any, exists between recovery and recrystallization.

Experimental Procedure

(a) *Material Used*

While the major part of this investigation has been carried out on super-purity aluminium, a little work has been done on super-purity base aluminium-magnesium alloys. The chemical analyses are given in Table I.

TABLE I

Identification	Mg	Fe	Si	Cr	Mn	Cu
CPB	<0.001	0.003	0.002	<0.002	<0.001	0.002
CRP	0.99	0.002	0.001	<0.002	<0.001	0.002

(b) *Fabrication*

Two permanent mould castings 6 in. × 4 in. × 2 in. were cast in a cast iron mould which had been thoroughly washed with alumina. After scalping, the ingots were soaked at 450°C for 16 hours and pressed to a thickness of 1 inch. The pressed ingots were then soaked at 450°C for 16 hours prior to hot rolling to 0.25 inch. After hot rolling the slabs were alternately annealed ½ hour and cold rolled 30% between anneals. After the last anneal of 3 hours at 450°C the sheet was rolled to 0.036 inch, giving final reductions of 20 to 80%. The grain size prior to the last cold rolling operation was about 450 microns. For one experiment some material was rolled 80% at liquid air temperature. This was accomplished by immersing the specimen in liquid air, giving it a light pass through the rolls and immersing again in liquid air immediately after rolling. This procedure was repeated until 80% reduction was obtained.

(c) *Heat Treatment*

Annealing was carried out in a salt bath except for that at 100°C when short time anneals were done in boiling water and long time anneals in an ageing oven. The temperature of the salt bath was controlled to ±2°C.

(d) *Metallographic Examination*

Specimens were ground down on emery papers, and the scratches removed by metal polish. They

were then electrolytically polished in a solution containing five parts methyl alcohol and one part perchloric acid [6] and finally electrolytically etched in a solution containing 49 parts water, 49 parts methyl alcohol and 2 parts hydrofluoric acid [6]. Specimens were then examined under polarised light.

Another technique used was to etch in a solution containing 25% nitric acid, 2% hydrofluoric acid and 73% water. The etchant was maintained at 50°C and specimens were etched for short times with intermediate washings. The total etching time was generally about 1 minute. Specimens were then examined under phase contrast illumination. For the examination of very fine substructures this method was better than the polarised light technique, because the grain contrast using the latter method decreases with increasing numerical aperture of the objective. With phase contrast there is no such limitation on the magnification which can be used.

(e) *Micro-hardness Testing*

An Eberbach micro-hardness tester was used for surveying the hardness of different regions after annealing. This tester utilizes a normal Vickers diamond and the load is applied by means of a spring.

(f) *X-ray Examination*

The normal back reflection Laue technique and an oscillating beam method were used. The latter method is similar to that used by Barrett [7] for studying the spread of orientation of a worked grain. The specimen is irradiated with a beam of unfiltered X-radiation from a Copper target at a glancing angle of about 20°, while the specimen and film are oscillated together through ±5°. So that the diffraction photographs could be examined at a magnification of about ten times, a fine grain film was used.

Results

(a) METALLOGRAPHIC EXAMINATION

(1) *Examination of Cold-Worked Material*

Careful examination of super-purity aluminium directly after heavy cold rolling (80%) at room temperature revealed the presence of fine bands and small subgrains about 1–2 microns in size; see Figure 1. Similar structures were observed after smaller cold reductions down to 20 per cent. It should be noted that the structures, such as that shown in Figure 1, were never sharp and after rolling at liquid air temperature the structures were even more diffuse; in fact no subgrains could be seen.

(2) *Annealing at Room Temperature*, 100°C *to* 240°C *and* 325°C

After the material had stood at room temperature for one year the substructures were much sharper and the bands appeared to have split up into subgrains; compare Figure 1 with Figures 2 and 3. With decreasing amounts of cold work the structures observed were slightly coarser than those observed after 80 per cent cold reduction. Furthermore with the smaller cold reductions the equiaxed subgrains were more difficult to see, probably because of smaller orientation differences between adjacent ones. Although there had been an appreciable change in structure on standing at room temperature, the Vickers Hardness Number of material cold rolled 80 per cent had only decreased from 42.1 to 39.8.

Similar observations were made on specimens annealed at 100°C directly after cold rolling 80 per cent. After five minutes annealing, fine equiaxed subgrains 1–2 microns were observed and were much sharper than those observed directly after cold working. With longer annealing times the subgrains did become slightly coarser in some areas; see Figure 4. In other areas, however, the equiaxed subgrains were still about 1–2 microns. As before, the bands became split up into subgrains. Sometimes one grain would consist completely of the banded structure and in other cases there would be both equiaxed subgrains and bands in the same grain. Again the hardness decrease was small: it falling from 42.1 to 40.2 after 16 hours at 100°C and to 38.2 after 6 days at 100°C.

After annealing at 200°C and 325°C new recrystallized grains were formed but the same structural changes as those described above were observed in the unrecrystallized areas, except that the equiaxed subgrains were slightly larger; see Figure 5. New recrystallized grains (marked by arrows) are also apparent in Figure 5. Although the recovered structures observed after annealing at 240°C were similar to those found after standing at room temperature and after annealing at 100°C, micro-hardness tests showed that recovery was much more advanced with the 240°C annealing treatment. For example, after 16 hours at 100°C little change in hardness had occurred whereas after 16 hours at 240°C the hardness of unrecrystallized areas had fallen to about 30.5, i.e., about 50 per cent softening had taken place.

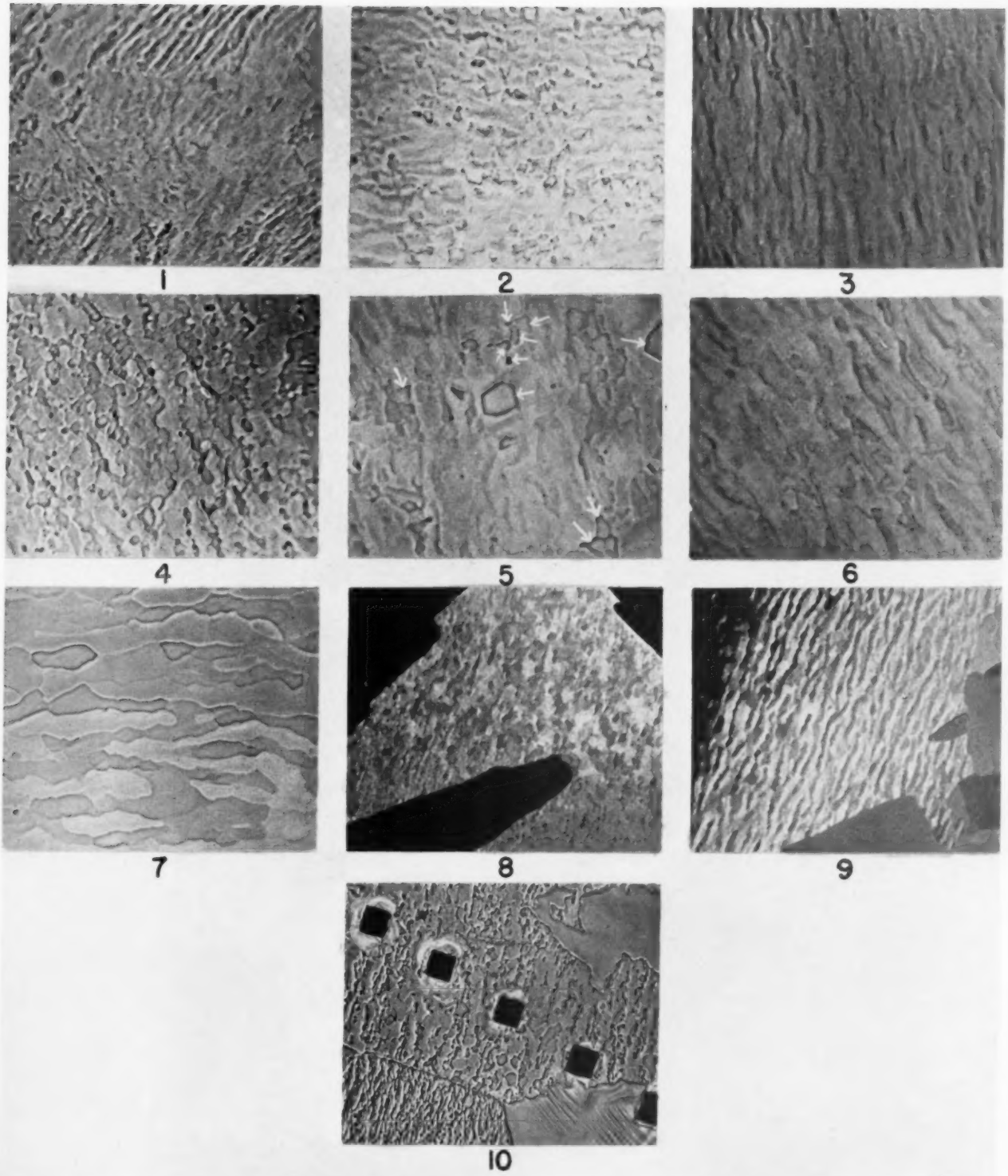

PLATE I (all figures reduced by ¾). Figure 1—Super-purity aluminium directly after cold working 80% at room temperature. Etched in $25HNO_3$, 2HF, $73H_2O$-phase contrast (×1000). Figure 2—Super-purity aluminium cold worked 80% and annealed 1 year at room temperature. Etched in $25HNO_3$, 2HF, $73H_2O$-phase contrast (×1000). Figure 3—Same as Figure 2 another field (×1000). Figure 4—Super-purity aluminium cold worked 80% and annealed 16 hours at 100°C. Etched in $25HNO_3$, 2HF, $73H_2O$-phase contrast (×1000). Figure 5—Super-purity aluminium cold worked 80% and annealed 3 hours 240°C. Etched in $25HNO_3$, 2HF, $73H_2O$-phase contrast (×1000). Figure 6—Super-purity aluminium cold worked 80% and annealed 20 seconds 350°C. Etched in $25HNO_3$, 2HF, $73H_2O$-phase contrast (×1000). Figure 7—Super-purity aluminium cold worked 20% and annealed 20 seconds 350°C. Etched in $25HNO_3$, 2HF, $73H_2O$-phase contrast (×1000). Figure 8—Super-purity aluminium cold worked 20% and annealed 4 minutes 375°C. Electrolytically etched-polarised light (×200). Figure 9—Same as Fig. 8 another field (×200). Figure 10—Super-purity aluminium cold worked 40% and annealed 10 seconds 375°C. Etched in $25HNO_3$, 2HF, $73H_2O$-phase contrast (×200).

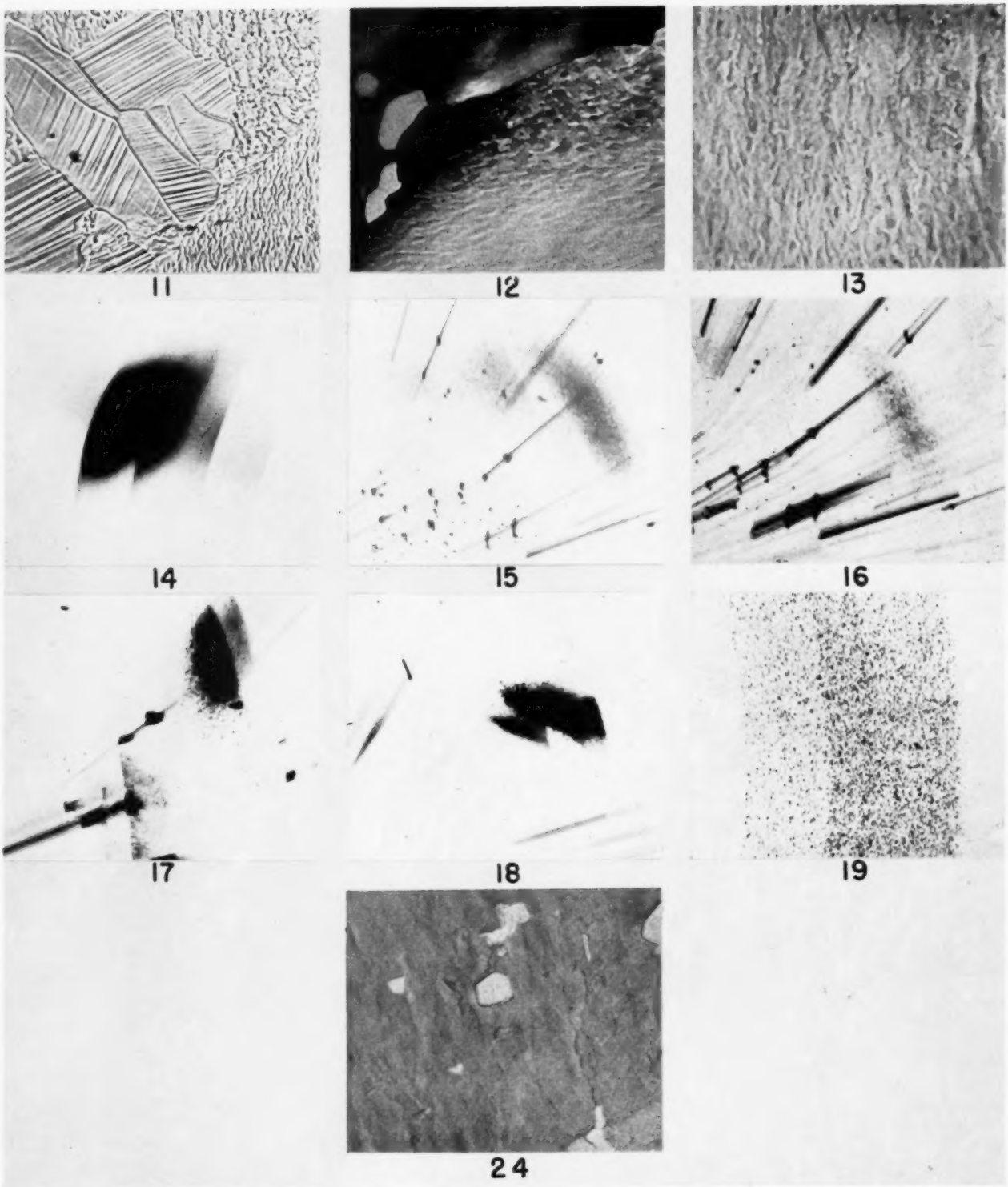

PLATE II (all figures reduced by $\frac{3}{4}$). Figure 11—Super-purity aluminium cold worked 50% and annealed 10 seconds 375°C. Etched in $25HNO_3$, 2HF, $73H_2O$. Bent slightly after etching. Phase contrast (×200). Figure 12—Super-purity aluminium cold worked 20% and annealed 1 minute 375°C. Electrolytically etched-polarised light (×200). Figure 13—Super-purity base aluminium 1% magnesium alloy cold worked 80% and annealed 20 seconds 350°C. Etched in $25HNO_3$, 2HF, $73H_2O$-phase contrast (×1000). Figure 14—Oscillating beam, X-ray pattern from super-purity aluminium cold worked 50% (×4). FIGURE 15—Oscillating beam X-ray pattern from coarse subgrain area. Super-purity aluminium cold worked 50% given two separate anneals of 10 seconds 375°C (×4). Figure 16—Oscillating beam X-ray pattern from same coarse subgrain area as Fig. 15 but after two more anneals of 10 seconds 375°C (×4). Figure 17—Oscillating beam X-ray pattern from area shown in Fig. 8 (×4). Figure 18—Oscillating beam X-ray pattern from area shown in Fig. 9 (×4). Figure 19—Oscillating beam X-ray pattern from fully recrystallized commercial purity aluminium–5.5% magnesium alloy. Grain size 10μ (×4). Figure 24—Same field as shown in Fig. 5 after electrolytic etching-polarised light (×1000).

(3) *Annealing at* 350°C, 375°C, *and* 400°C

Annealing at these higher temperatures gave similar substructures to those described in the previous section. Figure 6 shows the equiaxed subgrain structure in material cold-rolled 80 per cent. As with the lower annealing temperatures the subgrains increased in size with decreasing cold work (see Figure 7).

In addition to the fine substructures already described, annealing at these higher temperatures produced areas showing much coarser subgrains (10–30 microns). Furthermore it was possible to observe these coarse subgrains by electrolytic etching and polarised light examination. Only indications of the fine substructures could be obtained using this electrolytic etching technique which suggests that the orientation difference between adjacent subgrains is larger with the coarse than with the fine subgrain areas. Although in general these coarse subgrains were equiaxed (Figure 8), they were sometimes elongated (Figure 9). These coarse subgrain areas could also be observed by chemical etching and phase contrast examination. Figure 10 is a photograph of an area showing fine subgrains, coarse subgrains and new recrystallized grains. It will be noticed in Figure 10 that while slip lines are apparent around the microhardness impressions in the new recrystallized grains, they are virtually absent around the impressions in the subgrain areas. This indicates that the subgrain areas are much more resistant to plastic deformation than are the new recrystallized grains. This was confirmed by bending a specimen after electrolytic polishing and chemical etching. Figure 11 shows the resultant structure and clearly demonstrates the difficulty of plastically deforming a subgrain area; in fact, the coarse subgrain areas behave in a similar way to the areas in which fine subgrains are present.

It is interesting to note that recrystallization nuclei were never seen in areas showing coarse subgrains. Figure 12 illustrates this point and shows recrystallization nuclei at the grain boundary and also within a grain in which no substructure appears to be present. However, on chemical etching and phase contrast examination this grain was found to have fine subgrains present (2–4 microns). Figure 5 shows the presence of recrystallization nuclei within a fine subgrain area. Once the recrystallization nuclei had formed they appeared to be able to grow within both fine and coarse subgrain regions. The rate of growth of these nuclei was measured by using the technique described by Sperry [8] for studying grain boundary migration. This consists of stripping the oxide film off after electrolytic etching and re-etching after successive annealing treatments. For super-purity aluminium, cold-rolled 20 per cent and annealed at 375°C, the rate of growth was found to be the same in both fine and coarse subgrain areas, namely 5×10^{-4} cm/sec.

(4) *Effect of Magnesium*

Magnesium in solid solution was found to decrease the size of both the fine and the coarse subgrains. For example, while subgrains 1–2 microns in size were observed in super-purity aluminium cold rolled 80 per cent and maintained at room temperature for one year, none were observed in an aluminium–1% magnesium alloy, probably because their size was below the resolving power of the microscope. On annealing at higher temperatures similar but finer substructures to those found in super-purity aluminium were observed. Figure 13 shows the fine subgrain structure in an aluminium-1% magnesium alloy at 350°C. The subgrains compare in size with those observed in super-purity aluminium after standing at room temperature. Fine subgrain structures were not observed in alloys containing 4 and 5 per cent magnesium. The examination of these alloys was made difficult by the tendency of the etchant to pit so that it may well be that fine subgrains were present although they could not be seen. Coarse subgrains were occasionally seen; they were, however, very much less prevalent than in super-purity aluminium or alloys of low magnesium content.

(b) X-RAY EXAMINATION

(1) *Back-reflection*

Back reflection Laue photographs were taken directly after rolling at room temperature and at liquid air temperature. In both cases diffuse Debye-Scherrer rings were obtained, these being slightly more diffuse after rolling at liquid air temperature than at room temperature. After annealing at low temperatures the rings became sharper but did not sharpen completely until times much longer than were needed for the fine substructures to become sharp and clear after etching. For example with a specimen rolled 80 per cent and maintained at room temperature for one year the diffraction pattern from an area such as that shown in Figure 2 consisted of sharp rings while the diffraction pattern from an area in a specimen annealed 16 hours at 100°C, such as that shown in Figure 4, gave moderately diffuse rings; in fact it needed 3

days at 100°C to give rings comparable to those obtained after one year at room temperature even though the metallographic structure after one year at room temperature was similar to that after 16 hours at 100°C. Coarse subgrain areas such as those shown in Figure 8 always gave sharp Debye-Scherrer rings.

The diffraction photographs referred to above were examined in a recording densitometer and the half-peak breadth determined. The results, together with the Vickers hardness values are given in Table II. No great accuracy is claimed for these results but they do show that there is a marked reduction in line breadth during recovery.

TABLE II

HALF-PEAK BREADTHS FROM SUPER-PURITY ALUMINIUM AFTER RECOVERY

Condition	Half-peak breadth (cms)	Vickers Hardness Number
(a) Rolled 80% at liquid air temperature	5.24	44.7
(b) Rolled 80% at room temperature	4.85	42.1
(c) (b)+16 hours at 100°C	3.76	40.2
(d) (b)+3 days at 100°C	2.63	39.8
(e) (b)+6 days at 100°C	3.02	38.2
(f) (b)+1 year at room temperature	2.74	39.8

(2) *Oscillating Beam Method*

Figure 14 shows a diffraction pattern taken from coarse grained super-purity aluminium cold worked 50 per cent. It will be seen that the reflection is drawn out into a smeary shape which covers an area on the film corresponding to a spread of about 10 degrees in the orientation of the reflecting grain. Diffraction photographs taken from areas showing the fine subgrain structures did not show any sign of break up of the reflections which would correspond to separate reflections from the fine subgrains; in fact patterns similar to that shown in Figure 14 were obtained. Coarse subgrain areas (10–30 microns) gave reflections which were broken up into small sharp streaks, these being the reflections from the subgrains. Figure 15 shows the pattern obtained from a coarse subgrain area (10–20 microns) in super-purity aluminium cold worked 50% and given two successive anneals of 10 seconds at 375°C. The reflection from the unrecrystallized area is broken up into streaks, each streak being a doublet owing to the presence of α_1 and α_2 components of the characteristic radiation. The same area was followed after successive anneals of 10 seconds at 375°C and it was found that with increasing annealing time the streaks became more distinct and the general diffuse background less. Figure 16 shows the pattern obtained from the same area as that shown in Figure 15 but after two further anneals of 10 secs. at 375°C, that is, after a total annealing time of 40 seconds. Comparing Figures 15 and 16 it will be noticed that there is a smaller number of streaks after 40 seconds annealing than after 20 seconds. This is probably due to growth of the new recrystallized grains within the subgrain areas. Measurements taken from these diffraction patterns show that the total range of misorientation within the unrecrystallized grain is about 5 degrees and the orientation difference between adjacent reflections from the subgrains is about 1–4 minutes. It must be emphasized that this figure does not necessarily represent the orientation difference between adjacent subgrains. Figures 17 and 18 show the diffraction patterns from the equiaxed and elongated coarse subgrain areas shown in Figures 8 and 9 respectively. It will be noticed that the break-up of the X-ray reflection from the elongated subgrains is not so complete as from the equiaxed subgrains. This is due to insufficient resolving power of the X-ray technique, for examination of a similar but slightly finer elongated subgrain structure than that shown in Figure 9 showed practically no signs of break-up of the X-ray reflection.

It is interesting to note than when the same specimen was given a number of separate short anneals the streaks in the oscillating beam picture became clearer with less background intensity than with specimens annealed at the same temperature but for longer times. Similar observations to this have been made by Eborall [9]. This diffuse background could result either from residual strain or from particle size. The latter seems unlikely, but to check this a fully recrystallized aluminium–5% magnesium alloy with a grain size of 10μ was examined. This gave sharp streaks with no diffuse background (see Figure 19), thus confirming that residual strain is probably the cause of the diffuse background in the oscillating beam photographs.

(c) MICRO-HARDNESS TESTS

Micro-hardness tests were carried out on specimens of super-purity aluminium cold-rolled 20, 40, and 60 per cent at room temperature and annealed at 375°C for various times. Hardness impressions were made in three different kinds of area, (1) areas

showing coarse equiaxed subgrains,—e.g., see Figure 8; (2) areas showing fine substructures—e.g., see Figures 6 and 7; and (3) areas consisting of new recrystallized grains. Wherever possible hardness tests were also made in areas showing the elongated type of subgrain structure (see Figure 9). In order to identify the respective areas, specimens were etched prior to hardness-testing and tests were carried out after both electrolytic and chemical etching.

The results obtained from chemically and electrolytically etched surfaces were the same and so only those from electrolytically etched surfaces are given in Tables III, IV and V and are shown plotted in Figures 20, 21 and 22. Each result is the

TABLE III

MICRO-HARDNESS TESTS ON S.P. ALUMINIUM COLD-WORKED 20% AND ANNEALED AT 375°C.—LOAD 25.17 GRAMS

Annealing time (secs)	% Recrystallization	MICRO-HARDNESS NUMBER		
		Equiaxed coarse subrgains	Fine subgrains	New recrystallized grains
As cold-rolled	0		29.2±2.5	
30	2.2	23.5±0.6	27.1±0.9	
60	6.0	28.4±1.3	26.7±0.8	
120	25.8	24.5±0.8	23.4±1.0	18.5±0.8
240	50.0	23.9±0.8	24.2±0.6	
240	50.0	24.7±0.8*		
480	75.0	24.0±0.7	24.0±1.2	
960	94.0		24.8±1.1	
1800	95.3	22.3±1.1	21.4±0.6	

*These impressions made in areas showing elongated subgrains.

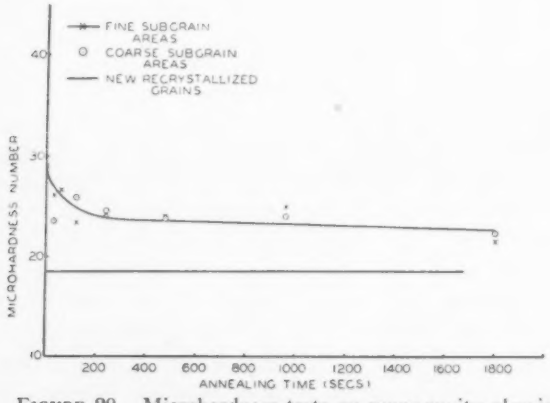

FIGURE 20. Microhardness tests on super-purity aluminium cold-rolled 20% and annealed at 375°C—specimens electrolytically etched—load 25.95 grams.

TABLE IV

MICRO-HARDNESS TESTS ON S.P. ALUMINIUM COLD-WORKED 40% AND ANNEALED AT 375°C.—LOAD 36.78 GRAMS

Annealing time (secs)	% Recrystallization	MICRO-HARDNESS NUMBER		
		Equiaxed coarse subgrains	Fine subgrains	New recrystallized grains
As cold-rolled			29.8±1.2	
10	20.0	25.3±1.8	28.2±1.2	19.3±1.2
20	35.0	23.0±1.0	27.5±1.3	18.8±0.4
60	60.0	23.7±0.9	26.0±1.4	18.4±0.5
120	80.0	24.1	25.3±1.0	19.4±1.4

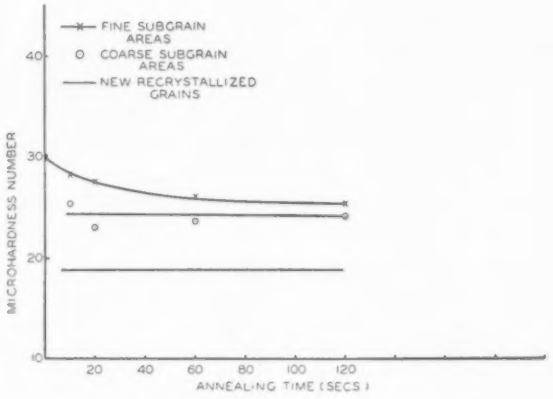

FIGURE 21. Microhardness tests on super-purity aluminium cold-rolled 40% and annealed at 375°C—specimens electrolytically etched—load 36.78 grams.

TABLE V

MICRO-HARDNESS TESTS ON S.P. ALUMINIUM COLD-WORKED 60% AND ANNEALED AT 375°C.—LOAD 36.78 GRAMS

Annealing time (secs)	% Recrystallization	MICRO-HARDNESS NUMBER		
		Equiaxed coarse subgrains	Fine subgrains	New recrystallized grains
As cold-rolled			33.4±1.1	
10	30.0	25.8±1.5	27.7±1.0	18.6±1.2
20	48.0	24.5±1.8	27.2±1.1	

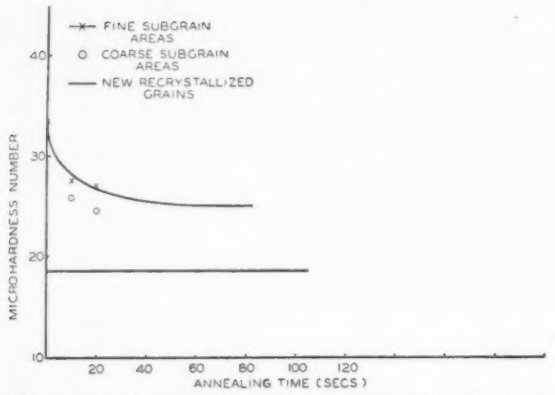

FIGURE 22. Microhardness tests on super-purity aluminium cold-rolled 60% and annealed at 375°C—specimens electrolytically etched—load 36.78 grams.

mean of about 15 impressions. The percentage recrystallizations was determined by taking five photographs of each condition and measuring the recrystallized areas with a planimeter.

From these results it is clear that (1) both coarse and fine subgrain areas are considerably harder than the new recrystallized grains; (2) the hardness of the areas showing fine subgrain structures decreases with annealing time, ultimately reaching a value approximately equal to that of the coarse subgrain areas; (3) the hardness of the areas showing elongated substructures is slightly higher than that of equiaxed subgrain areas; (4) the major part of the decrease in hardness due to recovery takes place after short annealing times; and (5) recovery can proceed at the same time as recrystallization. Table VI gives the percentage softening due to recovery as determined from the micro-hardness tests where

$$\% \text{ Softening} = \frac{H_{cw} - H_t}{H_{cw} - H_{cr}}$$

H_{cw} = Hardness of cold-worked material
H_{cr} = Hardness of completely recrystallized material
H_t = Hardness after annealing for t seconds.

From Table VI it appears that within the limit of experimental error the percentage softening due to recovery is independent of the percentage cold reduction. Further support for the above result is given in Figure 23 which shows the percentage recrystallization as a function of the macroscopic Vickers Hardness Number (2.5 kilogram load). The rate of softening is much more rapid in the early stages of the recrystallization process than in the later stages where there is a linear relationship.

TABLE VI

PERCENTAGE SOFTENING DUE TO RECOVERY AT 375°C.

Surface preparation	% Cold reduction	% Softening
Electrolytically etched	20	57
Electrolytically etched	40	53
Electrolytically etched	60	57
Chemically etched	20	63
Chemically etched	40	67

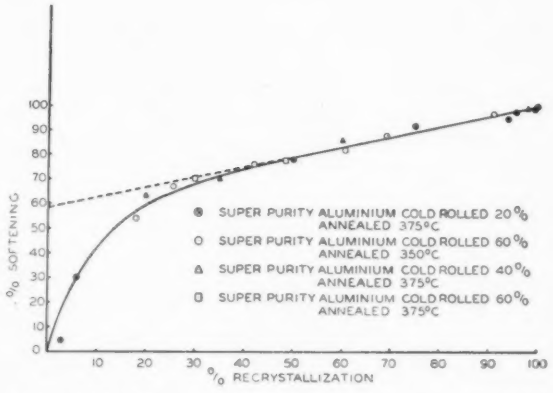

FIGURE 23. Percentage recrystallization as a function of percentage softening.

It is clear from the micro-hardness tests that the rapid softening in the beginning of the process is due to the fact that recrystallization and recovery are going on together. If the straight line is extrapolated to zero percentage recrystallization we arrive at a figure of 58 per cent softening which represents the amount of softening due to recovery. This agrees very well with the values obtained by the micro-hardness tests.

Discussion of Results

It has been shown that subgrains 1–2 microns in diameter are present in super-purity aluminium heavily cold worked at room temperature. No subgrains however, could be seen in the same material rolled at liquid air temperature. This result is in contradiction to Heidenreich's [1] findings but may simply be due to the lower sensitivity of the technique used here. After annealing, the subgrains appear much sharper after etching and moreover the banded structure is found to be broken up into subgrains. These structural changes produce a sharpening of the Debye Scherrer rings in back reflection Laue photographs and also cause a slight

decrease in hardness. The subgrain size decreases with increasing amounts of cold work, decreasing temperature, and with additions of magnesium. These results are similar to the effect of the respective variables on the as recrystallized grain size except that the subgrain size increases with annealing temperature and does not alter very much with annealing time. The fact that the subgrain size increases with annealing temperature strongly suggests that the mechanism of formation of these substructures is different from that of recrystallization because it is known that the as recrystallized grain is either independent or decreases with increasing annealing temperature. It is generally supposed that the driving force for grain growth in a completely recrystallized structure is the grain boundary surface energy, this being a function of the orientation difference between neighbouring grains. Thus when this orientation difference is very small, such as it is between neighbouring subgrains, there will be little tendency for subgrain growth with increasing annealing time.

With annealing temperatures of 350°C, 375°C and 400°C coarse subgrains 10 to 30 microns in diameter were observed in addition to the fine subgrains approximately 4 microns in size. Furthermore, the hardness of the former was practically independent of annealing time while the hardness of the latter decreased with annealing time, ultimately reaching the same value as that of the coarse subgrains. Another difference between these coarse and fine subgrains areas was that recrystallization nuclei were never observed in the former but were observed in the latter type of area.

The hardness tests have shown that recovery proceeds both before and during the recrystallization process and within the experimental error the percentage softening brought about by recovery is about 50–60 per cent and is independent of the amount of cold work. Similar results were obtained by Kornfeld [10] who found that with aluminium single crystals the percentage softening brought about by recovery was about 40 per cent and was independent of the amount of cold work. X-ray and metallographic examination has shown that this softening is accompanied by an increasing perfection of the subgrains formed during cold working. This, together with the fact that little subgrain growth has been observed with increasing annealing time, is in direct contradiction to the recent conclusions of Beck [11] who claims that "Present evidence indicates that only a minor component of the work hardening is released in recovery, while subgrain growth is capable of releasing the remaining larger portion which is connected with the subboundaries."

Back reflection Laue photographs from fully recovered areas which showed either the coarse or fine subgrain structures gave sharp Debye Scherrer rings, thus indicating that long-range strains have disappeared during recovery. Oscillating beam X-ray patterns obtained from recovered areas showing coarse subgrains always consisted of a diffuse background upon which discrete spots were superimposed. It has been shown that this diffuse background is probably due to residual strain which is supported by the fact that the subgrain areas are considerably harder and more resistant to plastic deformation than the fully recrystallized material. The question remains as to the distribution of this strain within the separate subgrains. In this connection it is interesting to note that Hirsch and Kellar [2], using a micro-beam X-ray technique, found that the reflections from the small subgrains were superimposed on a diffuse background and from an analysis of these patterns Hirsch [12] concluded that the diffuse background was due to a highly strained boundary region. Such a distribution of strain could explain the diffuse background observed in this work. In this connection, it is interesting to note that during this work a relatively wide dark fringe around the subgrain boundaries has always been observed during examination under the phase contrast microscope. This means that the boundary region has been attacked by the etchant to a greater degree than have the centres of the subgrains. Such a result would be expected if the subgrain boundary region was heavily strained relative to that of the centre of the subgrain.

This work does not help to clarify the position as to whether the subgrains in the as cold worked metal are formed by the polygonisation mechanism as postulated by Cahn [13] or are formed by the cold working operation itself as suggested by Beck [14]. It is clear, however, from the work reported here and also from that of Heidenreich [1] and Hirsch and Kellar [2] that the subgrains are relatively imperfect directly after cold working.

Heidenreich [1] and Hirsch and Kellar [2] have found that for super-purity aluminium the subgrain size directly after cold working at room temperature is independent of cold work above 20 per cent cold reduction. The work reported here confirms this observation. However, after annealing, the subgrain size has been found to increase with

increasing annealing temperature and decreasing amounts of cold work. This suggests that subgrain growth takes place in the very early stages of annealing, the subgrains quickly reaching an equilibrium value. Furthermore, on annealing, the subgrains become more perfect probably because the dislocations within the subgrains diffuse, dislocations of opposite sign cancelling each other out and others diffusing into the subgrain boundary region. The dislocation density of the subgrain boundary regions thus increases, thereby producing an increase in the orientation difference between adjacent subgrains. This is probably the reason why it was much easier to observe the subgrains after annealing than directly after cold working.

The effect of magnesium in decreasing the size of the subgrains is in agreement with the findings of Heidenreich [1] and Hirsch and Kellar [2]. Heidenreich found that 4 per cent copper in high-purity aluminium reduced the subgrain size and Hirsch and Kellar found that the subgrain size was smaller in 99.2% aluminium than in 99.99% aluminium. This effect may be due to the formation of an atmosphere of impurity atoms around dislocations thus hindering their movement (Cottrell [15]).

Recrystallization nuclei have only been observed in the fine subgrain areas while growth of recrystallization nuclei with a completely different orientation has been observed to take place within both fine and coarse subgrain areas. Measurements of the growth rate of recrystallization nuclei showed that for super-purity aluminium cold-worked 20 per cent and annealed at 375°C the rate of growth was about 5×10^{-4} cm/sec irrespective of the type of subgrain area into which the nucleus was growing. This result, together with the fact that the coarse subgrain areas were found to be much harder than the fully recrystallized material, casts some doubt on Beck and Hu's [4] conclusions that "recrystallization *in situ* leads to an apparently complete return to the fully annealed condition." Furthermore, it has been suggested by Beck [16] that the driving energy for grain growth within the subgrain areas is the grain boundary surface energy. Beck *et al* [17] investigated primary grain growth in super-purity aluminium and found that with a grain size of about 200 microns the rate of growth at 400°C was about 8×10^{-7} cm/sec. The subgrain size on which the measurements reported here were performed varied between 5 to 20 microns so that the grain boundary surface energy would be about 10 to 40 times that of material with a grain size of 200 microns. Assuming that the driving force for primary grain growth is the grain boundary surface energy, then the rate of growth within the subgrain areas should be about 3×10^{-5} to 8×10^{-6} cm/sec. The actual rate of growth would probably be much less than this because the grain boundary surface energy is a function of orientation difference between adjacent grains and thus would be smaller for the subgrain areas where the orientation difference is a few minutes of arc than for the fully recrystallized material used by Beck *et al* where the orientation difference would probably be several degrees. From the above and also the fact that the rate of growth of the recrystallization nuclei were the same irrespective of the subgrain size into which they were growing strongly suggests that the increased grain boundary surface energy brought about by the small subgrains is not sufficient to explain the rapid growth of new grains in such areas. It is far more likely that the driving force is the strain energy which is concentrated in the subgrain boundary zones.

It has been suggested by Cahn [18] that the subgrains formed during recovery may act as the nuclei for recrystallization. Figure 5 suggests that this may be so but as will be seen from Figure 24 the recrystallization nuclei shown in Figure 5 have a completely different orientation from that of the fine subgrain matrix. Some effort has been made to measure the orientation of such recrystallization nuclei by the etch pit technique but due to the high chemical activity of the subgrain areas the etch pits are confined to the unrecrystallized areas and the boundary between the recrystallization nucleus and the unrecrystallized matrix. It is interesting to note that the etch pits within the subgrain areas were formed preferentially at the subgrain boundaries. The fact that recrystallization nuclei are only observed in areas which show the fine subgrain structure does, however, indicate that these fine subgrains may be acting as the nuclei for recrystallization.

Acknowledgment

The author wishes to express his thanks to Mr. W. Marsh for help in the experimental work.

References

1. Heidenreich, R. D. Bell Syst. Tech. J. (Oct. 1951).
2. Hirsch, P. B. and Keller, J. H. Acta Cryst. **5** (1952) 162.
3. Gay, P. and Kelly, A. Acta Cryst. **6** (1953) 165 and 172.
4. Beck, P. A. and Hu, Hsun. Trans. A.I.M.E. **194** (1952) 83.

5. TATE, A. E. L. and MCLEAN, D. J. Inst. Metals **80** (1951-52) 390.
6. PERRYMAN, E. C. W. Metal Industry **79** (1951) 71.
7. BARRETT, C. S. Metals and Alloys **8** (1937) 13.
8. SPERRY, P. R. Trans. A.I.M.E. **188** (1950) 103.
9. EBORALL, R. E. Private communication.
10. KORNFELD, M. O. Phys. Z. Sowjetunion **6** (1934) 329.
11. BECK, P. A. Acta Met. **1** (1953) 422.
12. HIRSCH, P. B. Acta Cryst. **5** (1952) 168.
13. CAHN, R. W. J. Inst. Metals **76** (1949) 121.
14. BECK, P. A. A.S.M. Symposium on Metal Interfaces (1952) 208.
15. COTTRELL, A. H. Progress in Metal Physics **1** (1949) 77.
16. BECK, P. A. J. Metals **4** (1952) 979.
17. BECK, P. A., KREMER, J. C., DEMER, L. J. and HOLZWORTH, M. L. Metals Technology Tech. Pubn. No. 2280 (Sept. 1947).
18. CAHN, R. W. Proc. Phys. Soc. **63** (1950) 323.

INTERSTITIAL AND VACANCY MIGRATION IN Cu_3Au AND COPPER*

J. A. BRINKMAN, C. E. DIXON, and C. J. MEECHAN†

Vacant lattice sites and interstitial atoms in excess of the equilibrium concentrations have been introduced into the alloy Cu_3Au by quenching rapidly from high temperatures and by irradiating with cyclotron particles. Experiments of other investigators, involving the introduction of interstitials and vacancies into copper by cold work and irradiation, have been discussed. Two annealing states have been observed between −100°C and +200°C in both Cu_3Au and copper. For each material, the low-temperature state is found in the vicinity of −30°C and the high-temperature state in the vicinity of +150°C. Vacancy migration has been assigned to upper-state and interstitial migration to the lower in Cu_3Au, on the basis of arguments which show that only the former should order the alloy. From other arguments, the same assignments have been made for copper, and the similarity of the two materials has been discussed. The following assignment of migration activation energies has been made for copper: vacancies −1.19 ev, interstitials −0.7 ev.

LA MIGRATION DES ATOMES INTERSTITIELS ET DES LACUNES RÉTICULAIRES DANS Cu_3Au ET DANS LE CUIVRE

Des lacunes réticulaires et des atomes interstitiels ont été introduits dans l'alliage Cu_3Au, en excès de la concentration d'équilibre, au moyen d'une trempe rapide à partir de températures élevées et par irradiation avec des particules du cyclotron. Les expériences d'autres chercheurs, se rapportant à l'introduction d'atomes interstitiels et de lacunes dans le cuivre, par écrouissage et par irradiation, ont été discutées. Deux états de recuit ont été observés entre −100°C et +200°C dans Cu_3Au et dans le cuivre. Dans les deux cas l'état caractéristique des basses températures se trouve dans le voisinage de −30°C, et celui caractéristique des températures plus élévées, dans le voisinage de +150°C. En se basant sur certains arguments, on montre que seule la migration de lacunes permettrait la mise en ordre de l'alliage. Par conséquent, ce mécanisme fut attribué à l'état supérieur, alors que la migration des atomes interstitiels fut réservée à l'état inférieur. D'autres arguments ont conduit à l'attribution des mêmes mécanismes au cuivre; la similitude des deux matériaux fut discutée. Les valeurs suivantes ont été attribuées à l'énergie d'activation de migration pour le cuivre: lacunes −1.9 ev, atomes interstitiels −0.7 ev.

DIE BEWEGUNG VON LEERSTELLEN UND ZWISCHENGITTERPLÄTZEN IN Cu_3Au UND Cu

Es wurden Leerstellen und Atome in Zwischengitterplätzen über die Gleichgewichtskonzentrationen hinaus durch schnelles Abschrecken von hohen Temperaturen und durch Bestrahlen mit Cyklotron Teilchen in die Legierung Cu_3Au eingebaut.

Es wurden die Versuche anderer Autoren, die die Einführung von Leerstellen und Zwischengitteratomen in Kupfer durch Kaltbearbeitung und Bestrahlung untersuchten, diskutiert. Sowohl in Cu als auch in Cu_3Au wurden zwei Glühstadien zwischen −100°C und +200°C beobachtet. In beiden Stoffen zeigte sich das Tieftemperaturstadium in der Umgebung von −30°C und das Hochtemperaturstadium in der Umgebung von +150°C. Wanderung der Leerstellen kann dem Hochtemperaturstadium zuschrieben werden und Wanderung der Zwischengitteratome dem Tieftemperaturstadium, und zwar auf Grund von Überlegungen die zeigen, dass nur der erste Mechanismus die Legierung ordnen sollte. Auf Grund weiterer Überlegungen werden die gleichen Beziehungen für Kupfer postuliert, und die Ähnlichkeit der beiden Materialien wird erörtert. Kupfer wurden die folgenden Aktivierungsenergiewerte zugeschrieben: Für Wanderung der Leerstellen −1.19 ev, für Wanderung der Zwischengitteratome − 0.7 ev.

Introduction

It is well known that lattice imperfections, particularly interstitial atoms, vacant lattice sites, and dislocations, are important in determining the physical properties of metals. It has been difficult, however, to isolate the effects of specific defects, because many properties are affected in a similar manner by more than one of them. Annealing studies offer a possible means of separating these effects. However, as long as more than one type of defect is present in a metal, the annealing will probably be complicated by interactions among the various defects.

The methods of defect production which are used have an important bearing on the problem of separating the effects of the various defects. Certainly a method in which only one type of defect is produced can be used to great advantage. Also, methods which produce equal numbers of defects, and others which produce one type in excess, will be helpful. Such methods as these, which have been employed in the present work and by others, are heating to high temperatures and quenching, irradiating with high-energy particles, and cold-working. The first of these methods involves the production of only a single type of defect, namely, vacancies, although the concentrations which can be retained are quite small.

The order-disorder alloy Cu_3Au can be used to detect the presence of vacancy concentrations too small to be detected in pure metals, since the

*Received May 26, 1953; in revised form, September 4, 1953.

†North American Aviation, Inc., Atomic Energy Research Department, Downey, California.

migration of vacancies increases the degree of order of the alloy. Each vacancy makes a large number of jumps during its lifetime, thus producing considerable atomic rearrangement. The resistance decrease associated with the increased degree of order resulting from the migration of a single vacancy is generally much larger than the resistance decrease associated with the disappearance of the vacancy. Therefore, considerable use of Cu_3Au has been made in the present experiments for the purpose of observing extremely small vacancy concentrations.

Investigations of irradiation effects in Cu_3Au have been made by Siegel [1], Blewitt and Coltman [2] and Adam, Green, and Dugdale [3], as well as others. The latter two papers demonstrate that defects produced by irradiation can accelerate the ordering rate under suitable conditions. Overhauser [4] and Eggleston [5] have studied irradiation effects in copper. They both found a well defined annealing state in the vicinity of −30°C. Bowen, Eggleston, and Kropschot [6] have studied the annealing kinetics of copper, cold-worked at room temperature, and measured an activation energy of 1.2 ev, associated with an annealing state in the temperature range 100°C to 200°C. These experiments all involve the introduction of interstitial atoms and vacant lattice sites into these materials.

This paper describes experiments on the alloy Cu_3Au which indicate the existence of two annealing states, and makes specific assignments of interstitial migration and vacancy migration to these annealing states, as well as to the corresponding states in copper. In the *Discussion of Experiments*, these assignments are made for each material independently. In the *Conclusions*, the assignments made for Cu_3Au are compared with those for copper.

Discussion of Experiments

A. *Effect of Quench Temperature on the Ordering Rate of Cu_3Au*

The following experiments demonstrate that the isothermal ordering rate of Cu_3Au at 150°C is considerably enhanced by quenching the alloy rapidly from a temperature in the vicinity of 600°C. The ordering rate, as determined by the rate of change of electrical resistivity, increases with increasing quench temperature. This effect is interpreted as evidence of having frozen in the vacancy concentration which exists in thermal equilibrium at the quench temperature. The interpretation is based on the assumption that vacancy diffusion is responsible for the ordering process.

Cu_3Au specimens of dimensions 0.020 × 0.020 × 0.5 inch were water-quenched from various temperatures in a modified Rosenhain apparatus similar to that described by Taylor [7]. Resistance measurements were made at −196°C after annealing for various times in a wax bath. During preliminary measurements the initial resistivity was found to be 10.0 micro-ohm-cm at −196°C, independent of quench temperature within the errors of the dimensional measurements; hence all initial resistances in the different specimens were assumed to correspond to a resistivity of 10.0 micro-ohm-cm.

The data in Figure 1 show the effect of quench temperature on the ordering rate at 150°C. The

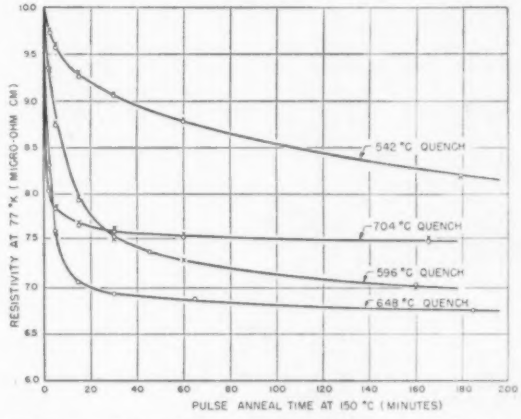

FIGURE 1. Dependence of the ordering rate of Cu_3Au on the quench temperature.

initial slope of each resistivity-time curve is used as a measure of the ordering rate. The ordering rate is seen to increase with quench temperature between 542°C and 648°C. The 704°C curve is not appreciably different from the 648°C curve, which may indicate that the quenching rate was too slow to freeze in the equilibrium concentration of vacancies at the higher temperature. It is probable that the initial states of short-range order which exist at the different quench temperatures will influence the initial slopes and shapes of these curves to some extent, and quantitative values of the relative numbers of vacancies will not be reliable. One cannot, however, attribute the major effect of the quench temperature dependence to short-range order, since any reasonable assumption concerning its effect on the ordering rate suggests the opposite temperature dependence to that which was observed.

The data of Figure 2 were obtained by the following procedure. A specimen was quenched from

542°C and annealed at 182°C for 210 minutes, at which time the ordering rate was essentially zero. The annealing temperature was changed to successively higher temperatures of 232°C, 245°C and 300°C for 5 minutes, 3 minutes and 2 minutes, respectively, and then was lowered to 182°C again. The purpose of this procedure was to determine the extent of the atomic diffusion and to show that the ordering rate decreased with time as would be expected if non-equilibrium vacancies were retained by the quench. The increases in resistivity which occurred at the higher annealing temperatures indicate that the first flattening of the curve was a result of the attainment of the equilibrium degree of order at 182°C within antiphase domains

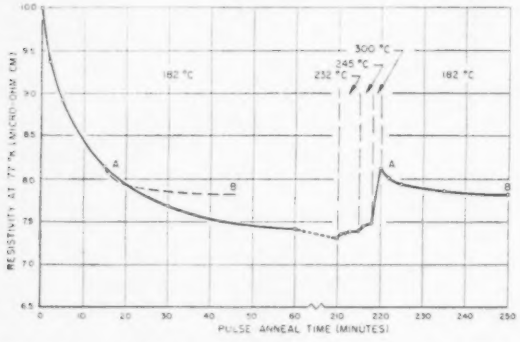

FIGURE 2. Ordering and disordering behavior of Cu_3Au after quenching from 542°C.

[8], rather than a result of the disappearance of the non-equilibrium vacancies. The resistivity increases are undoubtedly due to partial disordering within antiphase domains. If one assumes that the disordering relaxation time [9] is characterized approximately by the time required for the resistivity to attain two-thirds its maximum value at each temperature (e.g., 5 minutes at 232°C, 3 minutes at 245°C) and compares these relaxation times with a 60-minute value which was observed at 250°C in a well-ordered alloy containing no non-equilibrium vacancies, it can be concluded that a few non-equilibrium vacancies still exist after 3 hours at 182°C. Evidence that the number of excess vacancies had decreased was obtained by a comparison of the ordering rates at 15 minutes and 220 minutes where the alloy had identical resistivities. The superposition of the two rates shows that the ordering rate depends primarily on the vacancy concentration rather than on the resistivity.

Further data for Cu_3Au quenched from 542°C and annealed at successively higher temperatures between 110°C and 204°C are shown in Figure 3. These data were taken for the purpose of determining the activation energy for vacancy migration in Cu_3Au by observing changes in the slopes of the resistivity-time curves with changes in temperature. The curves are unusual in that each exhibits an initial negative curvature followed by an inflection point, indicating that the annealing is not a single-stage process. Hence an interpretation in terms of a single activation energy will probably have no significance.

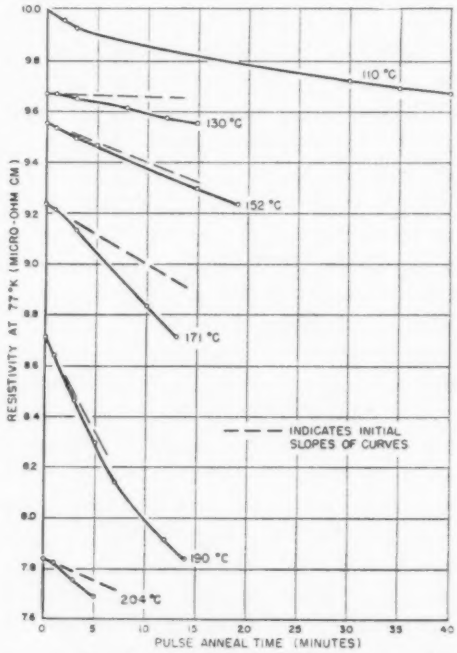

FIGURE 3. Continuous annealing of Cu_3Au quenched from 542°C at successively higher temperatures showing a complex ordering process.

B. *Electron Irradiation of Cu_3Au*

In Part A of this section, it is shown that a non-equilibrium concentration of vacancies can be quenched into Cu_3Au, and that these vacancies have appreciable mobility at 150°C. Let us now examine irradiated Cu_3Au and look for evidence of vacancy migration. Probably the simplest kind of damage, consisting only of interstitial-vacancy pairs, is produced by 1 Mev electron irradiation. This irradiation is not capable of producing high-temperature thermal spikes and the associated types of damage, perhaps dislocations, because the maximum energy which can be transferred from a 1 Mev electron to an atom is only of the order of 50 ev.

The first such irradiation was made at room temperature by Adam, Green and Dugdale [3]. They

observed that a type of defect was stored up in ordered Cu_3Au which produced no measurable electrical resistivity increase, but which annealed at 100°C and 130°C, producing additional ordering of the alloy. The same result has been observed in this laboratory [10] and, in addition, an irradiation of an ordered alloy was performed at −190°C which, by the absence of a disordering effect, confirmed the belief that thermal spike effects are unimportant from such irradiation. To identify the defect responsible for the ordering observed by Adam, Green and Dugdale, let us consider whether or not interstitial migration can order Cu_3Au, since it has already been established in Part A of this section that vacancy migration produces ordering.

Since there is no known method of introducing exclusively interstitials into a metal, analogous to quenching in a non-equilibrium vacancy concentration, one must resort to theoretical considerations to determine whether interstitial migration will produce ordering. One might expect a gold interstitial atom in Cu_3Au to have a higher energy of formation than a copper interstitial in the same material, because of its larger size. The "interstitialcy" migration mechanism of Huntington and Seitz [11] requires the replacement of the interstitial by a different atom during each elementary jump. For ordering to occur, both copper and gold atoms must participate in this process. However, because of the difference in formation energies of copper and gold interstitials, interstitial migration will probably occur only among the copper atoms of the alloy. Hence one would not expect interstitial migration to produce ordering. A more detailed treatment of this problem is given in the Appendix. On the basis of the arguments above, it may be concluded that the 100°C to 150°C annealing state in electron-irradiated Cu_3Au is a result of vacancy migration. This is consistent with the observation that quenched-in vacancies migrate in Cu_3Au in the same temperature range.

C. *Cyclotron Irradiation of Cu_3Au*

In the preceding part of this section, it is shown that electron irradiation produces vacancies in Cu_3Au which migrate at 100°C and 130°C. A moderate cyclotron irradiation should produce larger interstitial-vacancy concentrations than were obtained from the electron irradiation. Because of these larger concentrations, one may be able to observe another annealing state in Cu_3Au which can be associated with interstitial migration. The need of a larger interstitial concentration arises from the inability of the interstitials to order the alloy; hence the concentration of interstitials must be sufficiently large to produce a measurable resistivity increase resulting from the associated lattice distortion. The results of a cyclotron irradiation of Cu_3Au are described below.

Two .003 inch foils of Cu_3Au were irradiated simultaneously with 9 Mev protons to an integrated beam intensity of 5×10^{17} protons/cm^2. The specimen temperatures were maintained below −100°C during the irradiation. One of the specimens, O, was well ordered, and its initial resistivity was 1.7 micro-ohm-cm. The other specimen, D, was disordered by air quenching from 420°C, and its initial resistivity was 10.1 micro-ohm-cm. All resistance measurements in this experment were made at −180°C, and resistivity values are given for this temperature. After the irradiation, the specimens were simultaneously heated for intervals of about 15 minutes at successively higher temperatures, the temperature intervals being approximately 20°C.

The irradiation caused an increase in the resistivity of specimen O of 4.25 micro-ohm-cm, while the increase in D was only 0.65 micro-ohm-cm. Upon pulse annealing these specimens, a decrease of about 0.60 micro-ohm-cm was observed in each in the range −60°C to 0°C. Further pulse annealing to 130°C caused a resistivity decrease in specimen O of another 0.45 micro-ohm-cm, while that in D was less than 0.05 micro-ohm-cm.

The major part of the large resistivity increase in O is a result of radiation disordering, an irradiation effect first reported by Siegel [1]. The resistivity increase in D cannot be attributed to disordering since this specimen was completely disordered before the irradiation; hence it is attributed to the lattice distortion associated with interstitials and vacancies. If one assumes that equal interstitial-vacancy concentrations are produced in O and D, and that these concentrations produce an equal resistivity increase in each, the 4.25 micro-ohm-cm increase in O can be separated into two parts: 3.60 micro-ohm-cm due to disordering and 0.65 micro-ohm-cm due to lattice distortion.

Since the total resistivity decrease in D did not exceed the increase, which is associated with lattice distortion, the decrease is associated with the recovery of lattice distortion rather than with ordering. This viewpoint is supported by the fact that all of the decrease occurred in the range −60°C to 0°C, while if it was due to ordering, one should

expect a further change in the range 0°C to 130°C. Furthermore, the fact that the resistivity decrease in D was nearly equal to the radiation-induced increase indicates that both the interstitials and the vacancies were annihilated during the low-temperature annealing. Assuming, therefore, that the dominant process involves the annihilation of interstitials and vacancies resulting from the migration of one, a simple argument can be used to show that a small concentration of the less mobile defects will remain after the annihilation. For the sake of simplicity, and in anticipation of later conclusions, it will be assumed that the defects migrating at the lower temperature are interstitials.

An interstitial migrating randomly through the lattice will have a given probability, P_v, of encountering and annihilating a vacancy on each jump, and another probability, P_d, of being annihilated at an edge dislocation or grain boundary, either of which presumably can act as an infinite sink for vacancies and interstitials. P_v should be proportional to the vacancy concentration, while P_d should remain constant. Hence not all of the vacancies will be annihilated by the interstitials, as P_v will eventually become smaller than P_d and the remainder of the interstitials will go mainly to dislocations and grain boundaries. The vacancy concentration remaining after the interstitials have annealed should be nearly independent of the original interstitial-vacancy pair concentration, as long as it was large enough so that $P_v > P_d$ before annealing.

A comparison of the resistivity changes in O and D in the two temperature ranges enables one to conclude that ordering occurred in O. Since the resistivity decreases in O and D in the range −60°C to 0°C were the same, it is concluded that the decrease in O resulted from the recovery of lattice distortion, just as in D. In the range 0°C to +130°C, O exhibited a further decrease of 0.45 micro-ohm-cm which was not observed in D. This decrease is attributed to an increase in the degree of order of O. The fact that no ordering was observed in D can be explained by the lack of previously established domains of long-range order. Sykes and Evans [8] point out that ordering within domains is a much easier process than the growth of new domains of long-range order. The domains were already established in specimen O, and thus an increase in the degree of order within domains was observed.

The above data indicate the presence of two annealing states in cyclotron irradiated Cu_3Au, one above and the other below room temperature. Ordering is associated only with the high-temperature state. Since cyclotron damage consists predominantly of interstitials and vacancies, and ordering is associated with only the high-temperature state, interstitial migration has been assigned to the low-temperature state and the ordering observed at high temperatures is interpreted as the result of the migration of a small vacancy concentration which escaped annihilation by the interstitials.

D. *Cyclotron Irradiation of Copper*

The annealing of damage produced in copper by cyclotron irradiation has been studied by Overhauser [2] and Eggleston [3]. By means of electrical resistivity measurements, they found a well-defined annealing state in the vicinity of −30°C, characterized by an activation energy of 0.7 ev. A large part of the total radiation-induced resistivity change is associated with this annealing state. Both investigators failed to find another well-defined activation energy in the temperature range −100°C to +200°C. Interstitial migration and vacancy migration both should exhibit well-defined activation energies; thus it is believed that the 0.7 ev activation energy characterizes the migration of one of these defects.

The annealing kinetics of this state also were studied by Overhauser. He was able to show that a second-order reaction was consistent with the data, and concluded that the process involved the annihilation of interstitial-vacancy pairs. This conclusion is consistent with the absence of a second well-defined activation energy, since both defects are produced in equal numbers by irradiation.

The above consideration indicates that both the migration of interstitials and that of vacancies cannot be studied by electrical resistivity measurements in cyclotron-irradiated copper. Therefore one must resort to other means of interstitial-vacancy production in which one of the defects is produced in greater numbers than the other. Part E will consider such experiments, involving the annealing of cold-worked copper.

E. *Cold Work of Copper*

It has been suggested by Seitz [12] that vacancies and interstitials are produced in metals by cold work, and that the vacancy concentration will probably exceed that of the interstitials. He indicates that vacancies should be produced in preference to interstitials when the production is a result

of dynamic instability of the in-phase motion of atoms during the passage of a dislocation.

If the above result is accepted, a means is provided for determining whether interstitials or vacancies migrate more easily in copper. If the vacancies move first, and disappear primarily by interstitial-vacancy annihilation, only a single annealing state should exist. On the other hand, if interstitials move at a lower temperature than vacancies, a second annealing state should exist at a higher temperature, resulting from the migration of the unannihilated vacancies.

Eggleston [5] has observed an annealing state for cold-worked copper in the vicinity of −30°C which is characterized by an activation energy of about 0.7 ev. Both he and Overhauser suggest that the same mechanism is involved in this state and the 0.7 ev state in irradiated copper. A high-temperature annealing state in cold-worked copper has been studied by Bowen, Eggleston and Kropschot [6]. The annealing between 100°C and 200°C of the resistivity change produced in copper by cold work appeared to be characterized by a well-defined activation energy of 1.25 ev.

Two annealing states exist in cold-worked copper in the temperature range −100°C to +200°C, as shown above, each possessing a well-defined activation energy; in irradiated copper, however, only one was found in this temperature range. Let us assume that the upper state results from the migration of either interstitials or vacancies, rather than that of a third defect. Then the mere existence of the high-temperature state implies that it involves the migration of the defects produced in greater numbers, namely, vacancies.

F. *Annealing Kinetics*

Let us examine in more detail the assumption that the activation energy characterizing the upper annealing state in cold-worked copper is that for vacancy migration. The actual process could involve the annealing of other defects in addition to vacancies. Annealing of dislocations, for example, might result in the following manner from the migration of vacancies. Stresses present in cold-worked metals tend to move dislocations which are restrained from moving by high vacancy concentrations [12]. These dislocations will be free to move and annihilate upon the removal of the vacancies. It is thus possible that a part of the physical property change associated with this annealing state results from the annealing of such complex defects as dislocations, while the thermally activated process is simply the migration of vacancies.

If the annealing observed from 100°C to 250°C is actually such a process as we have suggested above, one should be able to make certain predictions concerning the shape of the resistivity annealing curves. First, one should expect the initial part of the resistivity decrease to be the result of the disappearance of vacancies, and the final part to result from the disappearance of both vacancies and dislocations, predominantly the latter. If it is true that the first part of the annealing is due to the loss of vacancies, and if these vacancies anneal by true volume diffusion to dislocations and grain boundaries, then a fairly accurate calculation of the fraction of the vacancies remaining at any time during an isothermal anneal can be made by solving the problem of diffusion of an initially uniform concentration of defects out of a region whose boundary is maintained at zero concentration. This calculation will be described below.

The physical analogs of the boundaries of the region are grain boundaries and edge dislocations, which presumably can act as sinks for vacancies. The solution is rather insensitive to the actual shape of the region, and a sphere will be assumed as the simple shape which most nearly approximates the physical situation. If one were dealing with a highly anisotropic material in which diffusion were predominantly one- or two-dimensional instead of three-, the appropriate shapes would be a slab and a cylinder, respectively.

Diffusion out of a sphere has been treated by Serin and Ellickson [13]. The expression for the fraction of vacancies remaining, n/n_0, after a time, t, is

$$n/n_0 = \frac{6}{\pi^2}\sum_{\nu=1}^{\infty}\frac{1}{\nu^2}e^{-\nu^2 t/\tau}, \tag{1}$$

where

$$\tau = \frac{r_0^2}{\pi^2 D},$$

r_0 being the radius of the sphere and D the diffusion coefficient of the vacancies. One can treat r_0 as representing some distance of the order of the average separation between dislocations. The diffusion coefficient, D, should have the following temperature dependence:

$$D = D_0 e^{-E_m/kT}, \tag{2}$$

where E_m represents the activation energy for migration of vacancies. By measuring the temperature dependence of τ and plotting ln τ *vs* $/1T$,

one should be able to determine E_m from the slope of the resulting straight line.

Assuming that the resistivity arising from the vacancies is at all times proportional to the average density of vacancies present, the measured resistivity change should be proportional to $(1-n/n_0)$ until most of the vacancies have annealed. The experimental curve should then begin to fall below the calculated curve as dislocations begin to anneal. With this assumption, one can transform the resistivity data as follows:

$$n/n_0 = \frac{\rho - \rho_0}{\rho_{\max} - \rho_0}, \tag{3}$$

where $\rho_{\max}$ is the residual resistance of a given specimen before the anneal was begun, and ρ_0 represents the residual resistance which the same specimen should have after all of the vacancies have annealed and before the dislocations have begun to anneal. This, of course, is an idealized case and cannot be achieved; nevertheless, ρ_0 can be determined from the asymptote of the calculated curve if the experimental points follow the theoretical vacancy decay curve sufficiently far to determine it accurately. Thus one is free to adjust two constants in order to fit the experimental data to the calculated curve: ρ_0, determining the fraction of the total resistivity change which is associated with the vacancies, and the relaxation time, τ, involving the density of dislocations and the diffusion coefficient of vacancies.

The numerical data of Bowen, Eggleston and Kropschot were kindly furnished to us by R. R. Eggleston, and it has been possible to obtain a good fit by use of the above expressions, as shown in Figure 4. The calculated curve is shown as the

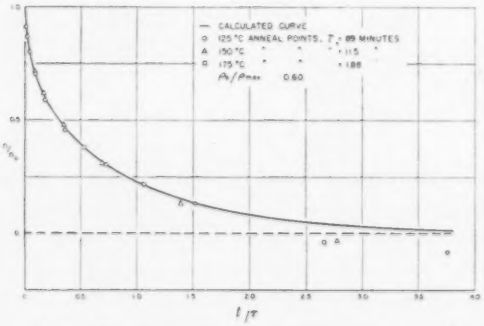

FIGURE 4. Fraction of vacancies remaining in cold-worked copper, n/n_0, after annealing for time, t.

solid line, and it can be seen that the experimental points accurately follow the curve until over 90 per cent of the vacancies are gone. Subsequently the points fall below, indicating that the dislocations do not begin to disappear until most of the vacancies have been removed. It was found that $\rho_0/\rho_{\max} = 0.60 \pm 0.02$ for all three curves, while τ varied with temperature as shown in Table I.

TABLE I

T (°K)	τ (min)
398	89
423	11.5
448	1.88

From the ln τ *vs* $1/T$ plot in Figure 5, one finds a well-defined activation energy: $E_m = 1.19 \pm 0.01$ ev.

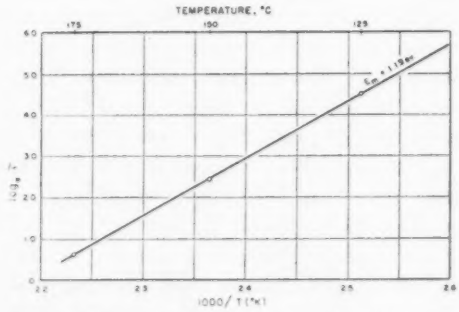

FIGURE 5. Determination of the activation energy for migration of vacancies in cold-worked copper.

The copper used in this work was oxygen-free with less than 0.05 per cent silver, but otherwise its purity was not definitely established. The cold work was performed by successively drawing through dies at room temperature to a total reduction in cross-sectional area of 96.9 per cent. Recent work still in progress, using 99.999 per cent pure copper, indicates that cold work produces more dislocations and fewer vacancies in the purer material, because $\rho_0/\rho_{\max}$ for similar amounts of cold work is found to be higher and τ to be lower at a given temperature. The activation energy for vacancy migration, however, remains essentially unchanged.

Bowen, Eggleston and Kropschot measured an activation energy of 1.25 ev. According to the present interpretation, they observed a complex process involving the annealing of both vacancies and dislocations. While the predominant thermally activated process responsible for all of the annealing is probably vacancy migration, it is believed that there may exist other obstacles, as well as vacancies, tending to impede the motion of the disloca-

tions. This would give a value somewhat too high for the observed activation energy if determined from the entire annealing range. It is believed, therefore, that the value of 1.19 ev, obtained above from the part of the measurements involving the vacancies only, represents the better value for the activation energy for migration of vacancies in copper.

It should be pointed out that the annealing curve calculated above possesses certain characteristics which serve to distinguish it from one describing a process which obeys a chemical rate equation of the form:

$$\frac{dn}{dt} = -\nu n^a e^{-E/kT}. \tag{4}$$

A curve governed by such a rate equation always has a finite initial slope; hence, for sufficiently short times, one should be able to approximate the elapsed portion of the curve by a straight line. By making sufficiently close measurements, one should find that during the very early part of the annealing the amount of damage removed is proportional to the time. In the diffusion-to-boundary-type process, on the other hand, the rate should be proportional to the concentration gradient at the boundaries, rather than to the average defect concentration, as is demanded by the chemical rate equation. Equation (1) can be shown to approach

$$1 - n/n_0 \rightarrow \frac{6}{\pi^{3/2}}\sqrt{t/\tau} \tag{5}$$

for t sufficiently small. The initial slope in this case is infinite, and by making measurements at sufficiently small times one should find that the amount of damage annealed is proportional to $\sqrt{t}$. This is actually observed for the first few points of the 125°C anneal shown in Figure 4, indicating that the annealing mechanism involves the diffusion of defects to an infinite sink. However, in the case of the low-temperature annealing observed by Overhauser and Eggleston, the interstitials presumably migrate to vacancies, each of which can act only once as a sink. Therefore no tendency should exist for the defect concentration to be depleted in a non-uniform manner, as it is in the neighbourhood of dislocations and grain boundaries in the event that the defects are required to migrate to them to be destroyed. One should therefore expect the low temperature state to obey the chemical rate equation.

One can present additional arguments demonstrating that the first part of the 100°C to 200°C annealing is the disappearance of vacancies rather than interstitials or dislocations. Because of the sharply defined activation energy obtained from Figure 5, it seems unlikely that this part of the process is the disappearance of dislocations. It is difficult to imagine a large number of dislocations so uniform in shape and size as to require exactly the same energy to move each. Even if this is assumed to be the case, diffusion from a slab or cylinder should be a more accurate model, since each dislocation is limited to one or two degrees of freedom. The experimental points, however, fit the curve for three-dimensional diffusion much better than for one or two dimensions, indicating that the annealing is that of simple defects, such as interstitials or vacancies, capable of diffusing in three dimensions.

Conclusions

The experiments discussed in the preceding section involve various methods of producing lattice defects in the alloy Cu_3Au and the pure metal copper. The first four columns of Table II summarize the experimental data pertinent to the present discussion. The specific assignments of the defects to the various annealing states are shown in Column 5. They are based on a series of arguments given in the previous section which are summarized below.

TABLE II

OBSERVED ANNEALING STATES

Material	Treatment	Approx. Temps.	Activation Energy	Migrating Imperfections
Cu_3Au	Rapid quench	150°C	—	Vacancies
Cu_3Au	Electron irradiation	130°C	—	Vacancies
Cu_3Au	Cyclotron irradiation	−30°C	—	Interstitials
		130°C	—	Vacancies
Cu	Cyclotron irradiation	−30°C	0.7 ev	Interstitials
Cu	Cold work	−30°C	0.7 ev	Interstitials
		150°C	1.19 ev	Vacancies

Two annealing states have been observed in Cu_3Au: (1) a high temperature state in the vicinity

of 150°C, and (2) a low-temperature state in the vicinity of −30°C. It has been concluded independently from the quenching experiments and from the irradiation experiments that the high-temperature state is a result of vacancy migration. In the quenching experiments, only vacancies are expected to be present. In the irradiation experiments the annealing state is observed by an ordering effect. Since interstitial migration has been shown to be incapable of ordering this alloy, the high-temperature state is again attributed to vacancy migration. The most probable mechanism for the low-temperature state seems to be interstitial migration because cyclotron damage is believed to consist primarily of interstitial-vacancy pairs.

Two annealing states are found in both copper and Cu_3Au at approximately the same temperatures. Overhauser's analysis of cyclotron-irradiated copper has established the low-temperature state as interstitial-vacancy annihilation. This annihilation must be a consequence of the migration of one of these defects. The presence of only a single well-defined annealing state in irradiated copper, where interstitials and vacancies are produced in equal numbers, supports the conclusion that the low-temperature state involves interstitial-vacancy annihilation. On the other hand, in cold-worked copper, where vacancy production is believed to predominate, the high-temperature state as well as the low-temperature state is observed. Since the low-temperature state involves interstitial-vacancy annihilation, causing the interstitials to be entirely removed in the lower state, the high-temperature state cannot result from interstitial migration. The annealing kinetics of this state favor the assignment of it to the annealing of vacancies rather than to a third defect.

The discussion thus far has been limited to an independent analysis of each experiment and comparisons among the Cu_3Au experiments as well as comparisons among those involving copper. However, if one assumes that there is a close similarity in the respective temperatures at which vacancies and interstitials migrate in Cu_3Au and in copper, then the same assignments can be made on the basis of this assumption alone. Since two annealing states have been observed in each material in the same temperature ranges, this assumption seems tenable. The assignment of vacancy migration to the high temperature state in Cu_3Au, from the quenching experiments, then enables one to assign the same mechanism to the high temperature state in copper. As the low temperature state in copper involves interstitial-vacancy annihilation, interstitial migration must be assigned to this state in both materials. Thus the same conclusions are obtained by making the above assumption as those obtained from the previous approach.

Having determined the activation energy for vacancy migration in copper, one can now obtain the formation energy for vacancies. The activation energy for self-diffusion in copper, 2.07 ev [14], should be the sum of the activation energy for motion of vacancies and their formation energy. Subtracting 1.19 ev from this value, one obtains the formation energy of 0.88 ev for vacancies in copper.

If one compares the activation energies in Table II with the predicted activation energies for vacancy migration in various metals given by Mott [15], it is evident that the annealing state which we have associated with interstitial migration is the one which has been assumed by Mott to be due to vacancy migration. Overhauser [4] also assigned vacancy migration to the low temperature annealing state, basing this assignment on an experiment of Kauffman and Koehler [16], in which partial annealing of a resistivity change quenched into gold wire was observed below room temperature. They interpreted this resistivity change as arising from quenched-in vacancies. Our conclusions disagree with the above assignments.

On the other hand, support for the present assignment of 1.19 ev and 0.88 ev as the activation energy for vacancy migration, E_{mv}, and the formation energy of vacancies, E_{fv}, respectively, is obtained from recent measurements of Nowick and Sladek [17]. They determined E_{fv} and E_{mv} for quenched-in vacancies in 70–30 silver-zinc from anelastic measurements, and found that in this alloy E_{fv} was somewhat smaller than E_{mv}. Furthermore, since the activation energy for diffusion in copper is 2.07 ev, in comparison with 1.36 ev in 70–30 silver-zinc, one would expect similar processes to occur at correspondingly higher temperatures in copper than in the silver-zinc alloy. The temperatures at which Nowick and Sladek observed vacancy migration were in the neighbourhood of 50°C; hence, from this experiment, one would expect vacancies in copper to migrate at higher temperatures. Theoretical calculations of the activation energies for migration of interstitials and vacancies in copper have been made by Huntington and Seitz [11; 18]. Their calculations indicate that E_{mv} should exceed E_{mi}, the activation energy for inter-

stitial migration, by about 1/2 ev; i.e., interstitials should anneal at lower temperatures than vacancies.

Appendix

We wish to estimate the difference in the energy of formation of gold and copper interstitial atoms in a Cu_3Au lattice. The formation energy of interstitial atoms in copper has been calculated by Huntington and Seitz [11]. It was found that about half of this energy arises from the closed shell repulsive interaction, the remainder coming from the change in the electronic energy. We shall neglect the electronic energy in the present calculation, as it should be approximately the same for either a copper or gold interstitial. Thus it should be possible to estimate the difference in formation energies of gold and copper interstitials by simply calculating the difference in the repulsive energy contributions.

We shall use a Born-Mayer type [19] exponential repulsion interaction, $Ae^{-r/\rho}$, in calculating the repulsive energy contributions to the interstitial formation energies, allowing relaxation of nearest neighbour atoms only, as was done by Huntington and Seitz. The values of A and ρ for copper interstitials in copper will be taken as $A_{Cu} = 7.67 \times 10^5$ ev/ion pair and $\rho_{Cu} = 0.150$ Å, following Huntington and Seitz.

The radius of the gold atom's closed shell electron core is about 13 per cent larger than that of the copper atom; thus one should expect the corresponding value of ρ in a similar exponential repulsion representing the interaction of two gold atoms to be about 13 per cent larger than the above value for copper. More precisely, we shall take

$$\rho_{Au} = \rho_{Cu} \frac{a_{Au}}{a_{Cu}},$$

where a represents the lattice parameter of the metal designated by the subscript. It should be noted that this is equivalent to holding α constant and substituting the appropriate values of both a and r_0 for gold into Zener's form of the Born-Mayer potential [20],

$$U(r) = A' e^{-\alpha(r-r_0)/a},$$

where a represents the lattice constant of the metal in question and r_0 is the distance between nearest neighbours in the equilibrium configuration of the lattice.

The value of A should also be larger for the gold atom than for the copper, due to the larger number of electrons in closed shells of the gold atom. We shall not attempt to estimate any other value for A, but shall simply take

$$A_{Au} = A_{Cu}$$

and remember that this is the direction which will give a conservative estimate of the difference in formation energies.

The repulsive potential to be used for gold, $Ae^{-r/\rho_{Au}}$, then gives a stronger repulsive interaction between two gold atoms than between two copper atoms at any given separation, a result which one intuitively feels must be true.

If one were to consider the interaction between a gold and copper atom, as would be encountered, for example, in the case of a copper interstitial in gold, one should expect the value of ρ in such an interaction to be approximately the average of ρ_{Cu} and ρ_{Au}. That use of such an approximation is justified is indicated by the fact that the lattice parameter for Cu_3Au is very close to $\frac{3}{4}a_{Cu} + \frac{1}{4}a_{Au}$. As we are interested in gold and copper interstitials in Cu_3Au, we shall define an effective ρ for Cu_3Au as follows:

$$\rho_{Cu_3Au} = \rho_{Cu} \frac{a_{Cu_3Au}}{a_{Cu}}.$$

Then the value of ρ to be used for interactions of a copper interstitial with its surrounding atoms in Cu_3Au will be taken as $\frac{1}{2}\rho_{Cu} + \frac{1}{2}\rho_{Cu_3Au}$, while for a gold interstitial, we shall use $\frac{1}{2}\rho_{Au} + \frac{1}{2}\rho_{Cu_3Au}$.

Using the above expressions and the measured lattice parameters,

$$a_{Cu} = 3.61 \text{ Å}$$
$$a_{Au} = 4.07 \text{ Å}$$
$$a_{Cu_3Au} = 3.74 \text{ Å},$$

one obtains a value of 8.8 ev for the repulsive energy contribution to the formation energy of a gold interstitial in Cu_3Au, and 3.9 ev for that of a copper interstitial.

As pointed out by Huntington and Seitz [21], such values may be slightly high due to inaccuracies in the exponential form for the closed shell repulsion. It is also probable that allowing next nearest neighbours to relax would lower these values slightly. It is believed that neglecting to estimate a higher value for A_{Au} than for A_{Cu} will cancel such errors and that 5 ev represents a fair estimate of the difference in the formation energies of copper and gold interstitial atoms in

Cu_3Au. However, even if it is only as much as 1 ev, the following arguments should still be valid.

Consider now the annealing of interstitial atoms in Cu_3Au. A copper interstitial will probably require an activation energy for migration of the order of 0.5 ev, the value calculated for copper interstitials in copper by Huntington and Seitz [11]. The migration involves the pushing of a normal lattice atom into a new interstitial position, its site subsequently being occupied by the old interstitial. If both new and old interstitials are copper, then the initial and final energies should be very nearly the same, the only energy barrier overcome being the 0.5 ev activation energy. If, however, the new interstitial is a gold atom, an additional energy of the order of 5 ev must have been furnished to form this gold interstitial. On the other hand, if the original interstitial was gold and the final is copper, 5 ev will have been given up as heat to the lattice.

It immediately becomes apparent that any gold interstitials formed in the lattice will, upon the first jump, replace copper atoms on normal lattice sites, and that the annealing of the interstitials will subsequently proceed only among the copper atoms of the lattice. For ordering to occur, both the copper and gold atoms must participate in migration and exchange of lattice sites. Therefore, while the activation energy for annealing of interstitial atoms in Cu_3Au is probably of the order of 0.5 ev, the activation energy for ordering by interstitial migration is probably of the order of 5 ev. Thus, for all practical purposes, interstitial ordering is prohibited.

Acknowledgment

The proton irradiation of Cu_3Au was performed on the 60-inch cyclotron at the Crocker Laboratory, Berkeley, by W. S. Gilbert. The authors wish to express their appreciation to R. R. Eggleston and A. W. Overhauser for making available manuscripts of papers in advance of publication.

The work is based upon studies conducted for the Atomic Energy Commission under Contract At-11-1-Gen. 8.

References

1. Siegel, S. Phys. Rev. **75** (1949) 1823.
2. Blewitt, T. H. and Coltman, R. R. Phys. Rev. **85** (1952) 384.
3. Adam, J., Green, A., and Dugdale, R. A. Phil. Mag. **43** (1952) 1216.
4. Overhauser, A. W. Phys. Rev. **90** (1953) 393.
5. Eggleston, R. R. Acta Met. **1**(1953) 679.
6. Bowen, D. B., Eggleston, R. R., and Kropschot, R. H. J. Appl. Phys. **23** (1952) 630.
7. Taylor, A. X-Ray Metallography (New York, Wiley, 1949) p. 142.
8. Sykes, C. and Evans, H. J. Inst. Met. **58** (1936) 255.
9. Bragg, W. L. and Williams, E. J. Proc. Roy. Soc. **A145** (1934) 699.
10. Dixon, C. E., Meechan, C. J., and Brinkman, J. A. Phil. Mag. **44** (1953) 449.
11. Huntington, H. B. and Seitz, F. Phys. Rev. **61** (1942) 315.
12. Seitz, F. Advances in Physics **1** (1952) 43.
13. Serin, B. and Ellickson, R. T. J. Chem. Phys. **9** (1941) 742.
14. Maier, M. S. and Nelson, H. R. Trans. A.I.M.E. **147** (1942) 39.
15. Mott, N. F. Phil. Mag. **43** (1952) 1151.
16. Kauffman, J. W. and Koehler, J. S. Phys. Rev. **88** (1952) 149.
17. Nowick, A. S. and Sladek, R. J. Acta Met. **1** (1953) 131.
18. Huntington, H. B. Phys. Rev. **61** (1942) 325.
19. Born, M. and Mayer, J. E. Z. Physik **75** (1932) 1.
20. Zener, C. Acta Cryst. **3** (1950) 346.
21. Huntington, H. B. and Seitz, F. Phys. Rev. **76** (1949) 1728.

SLIP PLANES AND THE ENERGY OF DISLOCATIONS IN A BODY-CENTERED CUBIC STRUCTURE*

N. K. CHEN and R. MADDIN†

Based upon a consideration of the energy of dislocations and the possible slip planes in body-centered cubic metals, modified values of the Chalmers and Martius parameter β—the ratio of the Burgers vector to the interplanar spacing— for {112} and {123} planes are derived assuming an alternate {110} slip process. It is shown that the modified β-values are in good agreement with the general theory of Chalmers and Martius in that the additional slip systems correspond to the next lowest value of β. Thus, it is concluded that the alternate {110} slip process is energetically favored.

LES PLANS DE GLISSEMENT ET L'ÉNERGIE DES DISLOCATIONS DANS LA STRUCTURE CUBIQUE CENTRÉE

On a déterminé des valeurs modifiées du paramètre β de Chalmers et Martius, c'est-à-dire le rapport entre le vecteur de Burgers et la distance interplanaire, pour les plans {112} et {123}, en se basant sur l'énergie des dislocations, les plans de glissement possibles dans les métaux cubiques centrés et en admettant un processus de glissement alternant sur {110}. Il est montré que les valeurs modifiées de β sont en bon accord avec la théorie de Chalmers et Martius, en ce que les systèmes additionnels de glissement correspondent aux valeurs de β se rapprochant le plus de la valeur de β pour le système principal de glissement.

On conclut que le processus de glissement alternant sur {110} est avantageux du point de vue énergétique.

GLEITEBENEN UND DIE ENERGIE DER VERSETZUNGEN IM RAUMZENTRIERT—KUBISCHEN GITTER

Auf Grund von Betrachtungen der Energie der Verzerrungen und den möglichen Gleitebenen in raumzentriert-kubischen Metallen wurden modifizierte Werte des Chalmers and Martius Parameters β—das Verhältnis des Burgers Vektors zum Netzebenenabstand—für die {112} und {123} Ebenen abgeleitet. Dabei wird angenommen, dass ein umschichtiger {110} Gleitprozess vorliegt. Es wird gezeigt, dass eine gute Übereinstimmung zwischen den modifizierten β-Werten und der Theorie von Chalmers und Martius besteht, da die zusätzlichen Gleitsysteme den nächst-niedrigen β-Werten entsprechen. Daraus wird geschlossen, dass ein umschichtiger {110} Gleitprozess energetisch günstig ist.

Chalmers and Martius [1; 2] have shown that the energy of a dislocation in a crystal depends on the orientation of its plane as well as on its Burgers vector. This may be seen in the following way: The shear strain in the crystal caused by the displacement by a Burgers vector "s" is proportional to the angle of shear $\beta = s/d$ where d is the interplanar spacing of the crystallographic planes parallel to the plane of the dislocation. If the displacement occurs in a closely packed plane having a large interplanar distance from its neighbor, the shear strain of the lattice will be smaller than when the same displacement is brought about in planes with closer spacing. Since the energy of a dislocation is a function of the state of strain of the crystal, it follows that the energy must depend on the orientation of the plane of the dislocation as well as on the Burgers vector [1; 2]. Hence the dislocations of lowest energy are those of lowest β, and the lowest value of β is expected to correspond to the dislocations that are active in actual glide. Chalmers and Martius [1; 2] have calculated a series of values of β for each crystal structure and have confirmed that in every case the lowest β-value corresponds to the most frequently observed slip plane and slip direction.

They have also demonstrated that when more than one slip system is reported, the additional slip system corresponds to that indicated by the next lowest value of β. In this respect, however, a significant "discrepancy" arises in the case of the body-centered cubic metals. This "discrepancy" can be seen in Table I which shows the values of β for the body-centered cubic structure and also the observed slip systems.

TABLE I [2]

β-VALUES AND OBSERVED SLIP SYSTEMS FOR BODY-CENTERED CUBIC METALS

	s	d	$\beta = s/d$	Slip systems "observed"
1.	$\frac{1}{2}\,a\,[111] = \frac{1}{2}\,a\sqrt{3}$	$d_{(110)} = a/\sqrt{2}$	1.2225	Yes
2.	$a\,[100] = a$	$d_{(110)} = a/\sqrt{2}$	1.42	No
3.	$a\,[100] = a$	$d_{(100)} = \frac{1}{2}\,a$	2	No
4.	$a\,[110] = a\sqrt{2}$	$d_{(110)} = a/\sqrt{2}$	2	No
5.	$\frac{1}{2}\,a\,[111] = \frac{1}{2}\,a\sqrt{3}$	$d_{(112)} = a/\sqrt{6}$	2.12	Yes
6.	$a\,[110] = a\sqrt{2}$	$d_{(100)} = \frac{1}{2}a$	2.84	No
7.	$\frac{1}{2}\,a\,[111] = \frac{1}{2}\,a\sqrt{3}$	$d_{(123)} = a/\sqrt{14}$	3.22	Yes

*Received September 7, 1953.

†School of Engineering, The Johns Hopkins University, Baltimore, Maryland.

It has been suggested [3; 4] that the experimentally observed slip on {112} and {123} planes is actually slip on alternating segments of two nonparallel {110} planes. This possibility has been further explored recently [5] with experiments on molybdenum single crystals. It is the purpose of this note to indicate from theoretical considerations of the energy of dislocations that the process of alternate {110} slip is energetically favored. It will be seen that, based on this assumption, a modified value of β can be derived for {112} and {123} which is 1.414 and 1.38 respectively. This is in agreement with the general theory of Chalmers and Martius [1; 2] that the additional slip system corresponds to the next lowest value of β.

Consider a plane perpendicular to the Burgers vector (Figure 1). In this figure, the trace of {110},

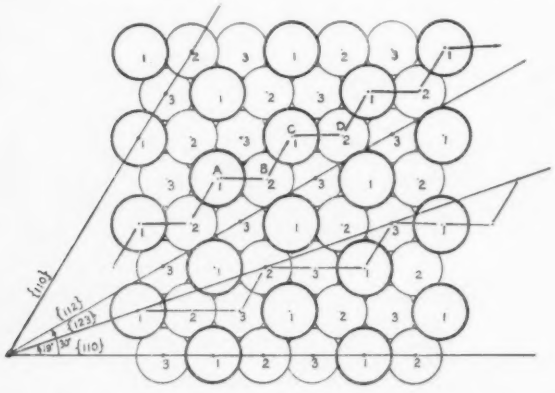

FIGURE 1. Atomic configuration of a (111) plane, perpendicular to the Burgers vector in a body-centered cubic structure.

{112}, and {123} planes has been indicated. These three planes are all perpendicular to the paper and contain the same Burgers vector ⟨111⟩.

In order to estimate the relative energy of dislocations in terms of the parameter, β, for {112} planes, assuming that they are composed of alternate {110} slip planes, the following steps have been taken: A segment of a {110} plane, formed by atoms A and B, is assumed to slip first by the movement of a dislocation. This movement, termed as a "unit {110}" slip, is followed by another "unit {110}" slip on a nonparallel {110} plane, formed by atoms B and C. This implies that the Burgers vector and the line of dislocations are always contained in two alternating {110} planes, or that the screw component of the dislocation travels through the crystal on a {110} plane via another nonparallel {110} plane, integrating into an apparent {112} slip plane.

Thus, the energy of the dislocation of both the segments, AB and BC of a "composite {112}" plane (ABC), can be separately regarded as being a function of the same parameter, $\beta_{\{110\}}$, as derived earlier by Chalmers and Martius, [1; 2] above. Nevertheless, in estimating the relative energy of dislocations on a "composite {112}" plane over a certain width, an additional factor, l, the width of the dislocation along the slip plane, has to be considered. It can be shown that within a width l there are $l/(\sqrt{2}/\sqrt{3})a$ "unit {110}" slip movements along a {110} plane, but $(l/\sqrt{2}\,a) \times 2$ "unit {110}" slip movements along a "composite {112}" slip plane. Therefore a modified parameter, $\beta'_{\{112\}}$, for a "composite {112}" plane, would be

$$\beta'_{\{112\}} = \beta_{\{110\}} \times \frac{l/(\sqrt{2}a) \times 2}{l/(\sqrt{2}/\sqrt{3})a} = \beta_{\{110\}} \cdot \frac{2}{\sqrt{3}}$$
$$= \frac{\sqrt{3} \cdot \sqrt{2}}{2} \times \frac{2}{\sqrt{3}} = \sqrt{2} = 1.414.$$

In the same manner the energy of dislocations for a "composite {123}" plane, consisting of alternate {110} dislocation movements, can be represented by a modified parameter,

$$\beta'_{\{123\}} = \beta_{\{110\}} \times \frac{l/(\frac{1}{3}a\sqrt{42}) \times 3}{l/(\sqrt{2}/\sqrt{3})a}$$
$$= \beta_{\{110\}} \times \frac{3}{\sqrt{7}} = 1.384.$$

Thus it becomes evident that since the parameters $\beta'_{\{123\}}$ and $\beta'_{\{112\}}$ are only slightly larger than $\beta_{\{110\}}$, the {123} and {112} planes should be the next additional slip systems in the body-centered cubic metals.

Several problems concerning the slip process in the body-centered cubic metals can be now considered. First, it seems justifiable to take the ratio of the energy of dislocations on different planes to be roughly the same as the ratio of the corresponding critical resolved shear stresses. Thus, $S_{\{112\}}/S_{\{110\}}$ is taken to be approximately equal to $\beta'_{\{112\}}/\beta_{\{110\}} = 1.154$, and $S_{\{123\}}/S_{\{110\}} = \beta'_{\{123\}}/\beta_{\{110\}} = 1.134$. These two ratios for the critical resolved shear stresses turn out to be exactly the same as the values estimated by Smoluchowski [6]. According to Smoluchowski [6] a rough estimate of the relative values of the critical shear stresses can be made on {110}, {112}, and {123} planes if it is assumed that the shear is proportional to the ratio of the length of a dislocation to the length of its projection on the slip plane. Since "the length of a dislocation" in his assumption is actually the path of dislocation movements on alternate {110} planes, it is not surprising to see that his estimate and the present one give the same

ratios of the critical shear stresses for {110}, {112} and {123} planes. It should be noted that, if slip on the {112} and {123} planes were actually dislocation movements on these planes, the high ratios, ($S_{\{112\}}/S_{\{110\}} = \beta_{\{112\}}/\beta_{\{110\}} = 1.73$ and $S_{\{123\}}/S_{\{110\}} = \beta_{\{123\}}/\beta_{\{110\}} = 2.64$), would appear to prohibit slip on {112} and {123} planes.

The ratios $S_{\{112\}}/S_{\{110\}}$ and $S_{\{123\}}/S_{\{110\}}$, as estimated above, would be expected to be influenced by temperature, composition, and perfection of the crystals concerned. In general, the ratios will be decreased as the temperature or imperfection of the crystals increases [6]. On the other hand, the ratios will increase with the addition of solute elements [7]. For a single crystal under axial tension, the variation of resolved shear stress on different planes can be calculated in the usual manner, *viz.*, $S = P/A \sin X \cos \lambda$, where P is the applied load, A is the cross-sectional area, X is the angle between the stress axis and the slip plane and λ is the angle between the stress axis and the slip direction. It can be seen that the orientation of the crystal can dictate the activity of a slip plane, if the limiting ratios, ($S_{\{112\}}/S_{\{110\}} = 1.154$ and $S_{\{123\}}/S_{\{110\}} = 1.134$), theoretically estimated on the premise of dislocation movement on alternating {110} planes, are not exceeded.

The crystallography of slip planes in the deformation of ferrite single crystals has been extensively investigated recently by Brick and co-workers [8; 9]. They found that plastic deformation occurs by glide in the ⟨111⟩ direction on planes which are not necessarily crystallographically significant. The identity of the noncrystallographic slip plane is determined by the orientation of the crystal with respect to the stress axis and by the variation of the resistance to shear of these planes. The latter function according to Steijn and Brick [9] is continuous between $\psi = 0$ and $\psi = 30$, where ψ is the angle between the observed glide plane and the plane {110} in the zone ⟨111⟩. In order to explain slip on high-index planes and the continuous variation of the resistance to shear of these planes, they proposed a model based on the movements of individual rows of atoms along the ⟨111⟩ direction. Thus {110} slip is considered to be composed of A movements, and {112} slip is made up of an equal number of type B and of type C movements. All the other slip planes can then be described as being made up of A and B plus C movements. Referring to Figure 1, the A-type movements are characterized by the movements of atoms A and B on the *track 231*, the {110} plane. The B type movements are characterized by the movements of A and C on the *track 333*, the {112} plane and the C type, by the movements of B and D on *track 333*, also the {112} plane. There is a great difference between this model and the model of alternate {110} slip in the respective assumptions involved in the slipping process. The model of Steijn and Brick [9] implicitly assumes that atoms A and C, B and D are linked together in their movement along a {112} track, so that they can be differentiated as type-B and type-C movements. Without this assumption, the movement of any single row of atoms is indistinguishable. The model of alternate {110} slip, however, assumes that Segments A,B move together and are then accompanied by the movements of Segment B,C. This assumption is essential since the energy of dislocations depends on the plane containing the Burgers vector as well as on the Burgers vector itself.

The hypothetical curves, $S_\psi/S_{\{110\}}$ versus ψ, which show the variation of the resistance to shear along the ⟨111⟩ zone can be derived on the assumption of alternate slip on {110} segments to give the same results as those obtained by Steijn and Brick [9] using their model. However there are two advantages in proposing the mechanism of alternate {110} slip: (1) It gives a limiting ratio $S_{\{112\}}/S_{\{110\}} = (1.154)$ above which {112} slip by alternate {110} slip is improbable, and (2) it furnishes a basis for explaining the continuous function of S_ψ/S_{110} versus ψ, and thus the possible occurrence of slip on "high-indices" planes.

Acknowledgment

This work was sponsored by the Office of Naval Research under Contract Nonr 248(05).

References

1. CHALMERS, B. and MARTIUS, U. M. Nature, London **167** (1951) 681.
2. CHALMERS, B. and MARTIUS, U. M. Proc. Roy. Soc. **213A** (1952) 175.
3. ELAM, C. F. Proc. Roy. Soc. **153A** (1936) 273.
4. GRENINGER, A. B., in discussion of a paper by BARRETT, ANSEL and MEHL, Trans. A.I.M.E. **25** (1937) 702.
5. CHEN, N. K. and MADDIN, R. Trans. A.I.M.E. **191** (1951) 937.
6. SMOLUCHOWSKI, R. Phy. Rev. **86** (1952) 787 (ii).
7. BARRETT, C. S., ANSEL, G. and MEHL, R. F. Trans. A.I.M.E. **25** (1937) 702.
8. VOGEL, F. L. and BRICK, R. M. J. Metals **5** (1953) 700.
9. STEIJN, R. P. and BRICK, R. M. Tech. Rep. No. **2**, January, 1952 to Flight Research Laboratory (WCRRL) Wright-Patterson Air Force Base from University of Pennsylvania, Philadelphia, Pennsylvania. To be published in Trans. A.S.M., 1954.

EFFECT OF NEUTRON IRRADIATION ON A SUPERSATURATED SOLID SOLUTION OF BERYLLIUM IN COPPER*

G. T. MURRAY† and W. E. TAYLOR‡

The effects of neutron irradiation on the electrical resistivity, hardness, X-ray line shape and position, and density of a solution annealed copper-beryllium alloy were investigated. Temperature during irradiation was 0°C to 40°C. With the exception of X-ray line effects, the observed changes were found to be similar to those caused by aging the alloy at low temperatures. Retrogression phenomena of irradiated samples were also found to be similar to retrogression following low-temperature aging. The property changes during irradiation are attributed to the formation of small precipitate nuclei. These nuclei are presumed to result from the acceleration of the diffusion rate on a microscale by the presence of excess vacancies and interstitials. The investigation revealed anomalous changes in density during irradiation which were found to be duplicated by low-temperature aging of single crystals. Lower rates of property changes in cold-worked samples than in solution-annealed samples were also found to occur at low aging temperatures after being first observed in irradiated samples. Lattice parameter decreases observed during irradiation were apparently related to density increase. These observations indicate the value of irradiation studies as a means of investigating metallurgical phenomena.

L'EFFET DE L'IRRADIATION AUX NEUTRONS SUR UNE SOLUTION SOLIDE DE GLUCINIUM DANS LE CUIVRE

On a investigué les effets de l'irradiation aux neutrons sur la résistivité électrique, la densité, la forme et la position de raies de diffraction de rayons X et de la densité d'un alliage cuivre-glucinium non précipité. Pendant l'irradiation, la température variait de 0°C à 40°C. A l'exception des effets sur les raies des rayons X, les changements observés ressemblaient aux modifications causées par un vieillissement de l'alliage aux basses températures.

On a aussi constaté que les phénomènes de rétrogradation des échantillons irradiés ressemblaient à la rétrogradation qui suit le vieillissement aux basses températures. Les changements des propriétés pendant l'irradiation sont attribués à la formation de petits germes de précipitation. Il est supposé, que ces germes résultent d'un accroissement de la vitesse de diffusion sur une échelle microscopique, par la présence d'un excès de lacunes et d'atomes interstitiels. Cette investigation a révélé des modifications anormales de la densité pendant l'irradiation, qui peuvent être reproduites par vieillissement de monocristaux aux basses températures. Dans des échantillons écrouis, on a constaté que les vitesses de changement des propriétés, aux basses températures de vieillissement, étaient inférieures à celles des échantillons non précipités; le même effet fut auparavant constaté dans des échantillons irradiés. Les diminutions du paramètre de réseau, observées pendant l'irradiation, étaient apparemment liées à l'accroissement de la densité. Ces observations soulignent l'importance des études des irradiations dans la recherche relative aux phénomènes métallurgiques.

DIE WIRKUNG VON NEUTRONENBESTRAHLUNG AUF ÜBERSÄTTIGTE FESTE LÖSUNGEN VON BERYLLIUM IN KUPFER

Es wurde die Wirkung von Neutronenbestrahlung auf den elektrischen Widerstand, die Härte, die Form und Lage der Röntgenstrahlreflexionen und die Dichte von einer nach Glühen und Abschrecken als feste Lösung vorliegenden Kupfer-Beryllium Legierung untersucht. Die Temperatur während der Bestrahlung betrug 0°C und 40°C. Es zeigte sich dass mit Ausnahme der Röntgenstrahleffekte die beobachteten Veränderungen den durch Altern der Legierung bei tiefen Temperaturen hervorgerufenen Veränderungen entsprechen. Die Erholungserscheinungen in bestrahlten Proben entsprachen ebenfalls der Erholung nach Alterung bei tiefer Temperatur. Die Eigenschaftsänderungen während der Bestrahlung werden auf die Bildung kleiner Ausscheidungskeime zurückgeführt. Es wird angenommen, dass diese Keime die Folge der durch zusätzliche Leerstellen und Zwischengitteratome hervorgerufenen örtlichen Vergrösserung der Diffusionsgeschwindigkeit sind. Die Untersuchungen zeigten anomale Dichteveränderungen während der Bestrahlung, die bei der Tieftemperaturalterung von Einkristallen reproduziert werden konnten. In kaltbearbeiteten Proben wurden geringere Geschwindigkeiten der Eigenschaftsänderungen bei zur festen Lösung ausgeglühten Proben gefunden; dies wurde ebenfalls für tiefe Alterungs-temperaturen gefunden, nachdem es zuerst an bestrahlten Proben beobachtet worden war. Die während der Bestrahlung beobachteten Abnahmen der Gitterkonstanten hingen anscheinend mit der Dichtezunahme zusammen. Diese Versuche zeigen den Wert der Bestrahlungsstudien als Hilfsmittel zur Untersuchung metallurgischer Erscheinungen.

Introduction

Experience in the application of nuclear energy has shown that the properties of solids may be markedly altered by the radiation (i.e., energetic particles) which is present in reactors. In this paper experiments will be described in which specimens of copper containing 13.5 atomic per cent beryllium were exposed in the ORNL uranium-graphite reactor. The energetic particles with which we are concerned are the fast neutrons resulting from nuclear fission of the fuel atoms [1]. The charged particles (protons, beta-particles, alpha-

*Received May 18, 1953; in revised form September 23, 1953.

†Presently at Bendix Aviation Corporation Research Laboratories, Detroit, Michigan.

‡Presently at Motorola, Inc. Research Laboratory, Phoenix, Arizona.

particles, and fission fragments) have a very short range in solids as a result of the strong coulomb interaction with the lattice ions. On the other hand, fast neutrons penetrate through large distances of the lattice, producing an effect throughout the volume of the material. The slow (or thermal) neutrons may also affect the material as a consequence of transmutations which introduce impurity atoms.

Theory

The theory developed by Bohr [2] for the interaction of fast nucleons with gaseous atoms has been extended to solids by Seitz [1], James [3], and others [4; 5]. The results of their calculations show that incident fast neutrons will knock atoms from lattice positions, and that during their recoil movement these atoms will dissipate recoil energy by:

1. Excitation of the valance electrons in the solid.
2. Elastic collisions with other atoms in the lattice causing additional (secondary and tertiary) displaced atoms.
3. Elastic collisions in which the atom which has been struck does not receive sufficient energy to be displaced, but is excited to a higher vibrational energy condition.

The term "knock-on" has been used to describe the recoiling atoms which receive enough energy to be displaced from a normal lattice site. After coming to rest the knock-on will result in the presence of a vacant lattice site and an occupied interstitial site which will be referred to as displacements. The track of the primary knock-on has been referred to as a "thermal spike" because of the high kinetic energy imparted to the atoms in this region.

The number of interaction events, Q, between the bombarding particles and atoms in the lattice per cubic centimeter in a time, t, is given by:

$$Q = N_0 \sigma_q \phi t \tag{1}$$

where N_0 is the number of atoms per cubic centimeter, σ_q is the cross section of the atomic species for the event Q, and ϕ is the total neutron path length per cubic centimeter per second = $cm^{-2}sec^{-1}$.

For a copper alloy containing 13.5 atomic per cent beryllium, the concentration of transmutations (after complete radioactive decay) and of primary displacements for an integrated neutron flux (ϕt) of 10^{18} cm^{-2}, will be approximately 3.16×10^{-6} and 2.9×10^{-6} respectively. (Since the thermal neutron flux is not usually the same as the fast neutron flux, the exposure times for the two processes will not usually be the same.) This concentration of impurities and defects is so small that no changes of appreciable magnitude should be observed in the physical properties. The average distance which a fast neutron travels between collisions is 3.9 cm for the alloy. It is evident that the distribution of primary displacements will be homogeneous in samples of the size of one centimeter.

The average energy imparted to a primary knock-on by a fast neutron is given by [1]:

$$\bar{E} = \frac{2E_0 m M}{(m + M)^2} \tag{2}$$

where E_0 is the energy of the neutron, m is the mass of the neutron, and M is the mass of the atom.

For 2 mev fission neutrons this equation gives 360 kev for the energy of the primary beryllium knock-ons and 61 kev for the primary copper knock-ons. These energy values are well above the energy required to displace the atom [2; 6] (approximately 30 ev)—the excess energy must be dissipated as the atom moves through the lattice. Calculations based on the method developed by Seitz show that most of the energy of the primary beryllium knock-ons will be dissipated by excitation of the valence electrons, since only about 2 or 3 kev are dissipated by elastic collisions. On the other hand, almost all of the energy of the primary copper knock-ons will be lost in elastic collisions. The contribution of the beryllium primaries to the total concentration of higher-order knock-ons therefore will be neglected.

The average energy, $\bar{E}'$, of the secondary knock-ons is given by

$$\bar{E} = 30 \ln \frac{E'_0}{30} \tag{3}$$

where E'_0 is the energy of the primary knock-on at which the elastic collisions predominate over electronic excitation. The average energy of the secondary knock-ons obtained in this way for the copper primaries is 230 ev. The secondaries will, in turn, produce tertiary displacements for which equation (3) can be applied. The average energy of the tertiary knock-ons will be about 60 ev, which is too small to lead to a continuation of the chain.

The total number of secondary knock-ons can be obtained by dividing the available energy of the primary by the average energy of the secondaries. Following Seitz [1] we will assume that half of the energy lost in elastic collisions excites lattice vibrations rather than knock-ons. The available energy for creation of secondary knock-ons is

therefore about 30 kev, which will produce on the average about 130 secondaries. Similarly, one can calculate the number of tertiaries produced per secondary. The resulting estimate of two tertiary knock-ons per secondary is probably too high. A value of one tertiary per secondary will be assumed. Thus there is a total of about 260 knock-ons per primary displacement.

The atomic fraction of all displacements will be 0.65×10^{-3}, or 0.065 atomic per cent of vacancies with an equal quantity of interstitials, for an integrated flux of 10^{18} cm^{-2}. These vacancies and interstitials will be introduced in the vicinity of the primary knock-on; within these clusters the concentration will be higher than is given by the above estimate. Since the tertiary knock-ons receive energies of only about 60 ev, it seems unlikely that they could move more than one or two lattice distances. The resulting vacancy-interstitial pair should be highly unstable, and there may be a rapid annihilation of these defects by recombination.

The average distance between the damaged regions associated with primary knock-ons will be

$$\bar{L} = \sqrt[3]{\frac{1}{\text{atomic fraction primaries} \times \text{atoms per cc}}}$$

For copper-beryllium $N_0 = 8.8 \times 10^{22}$, so that $\bar{L}$ is 1.2×10^{-6} cm for an integrated flux of 10^{18} cm^{-2}.

The results of these considerations, summarized in Table I, indicate that the response of the lattice ions to the incident neutrons will lead to:

1. A small number of transmutation impurities.
2. A small number of primary vacancy-interstitial pairs.
3. A large number of secondary and tertiary vacancy-interstitial pairs (distributed in random clusters throughout the alloy).
4. Local thermal excitation of the lattice resulting from the dissipation of about 30 kev of energy along the track of the primary knock-on.

The energy loss by the primary beryllium knock-ons is mainly due to electronic excitation. The energy imparted to the electrons will be rapidly spread through the lattice by electronic motion and will not result in permanent alteration of the metal.

Previous Studies

The earliest studies of neutron irradiation of metals described in the general literature were those of Billington and Siegal [7] who observed hardness and resistivity changes in several metals and alloys as the result of neutron irradiation.

TABLE I

INTERACTION CHARACTERISTICS OF 2 MEV NEUTRONS WITH LATTICE IONS IN 13.5 ATOMIC PER CENT BERYLLIUM IN COPPER (INTEGRATED FLUX = 10^{18} CM^{-2})

Atomic fraction transmutation impurities		3.16×10^{-6}
Atomic fraction primary displacements	Cu	6.0×10^{-6}
	Be	0.93×10^{-6}
Neutron mean free path between primary displacements		1.63 cm
Average energy of primary displacements	Cu	61 kev
	Be	360 kev
Average energy of secondary knock-ons		230 ev
Average energy of tertiary knock-ons		60 ev
Average number of secondaries per primary*		130
Total number of displacements per primary*		260
Atomic per cent of vacancies and interstitials*		0.15
Average distance between damage regions		1.2×10^{-6} cm

*From copper primary knock-ons only.

They found that the increase of hardness and electrical resistivity of a solution annealed copper-beryllium alloy during neutron irradiation were much greater than in the case of pure metals or stable alloys. The effects were attributed to the presence of vacancies and interstitials introduced by the irradiation.

As will be seen from the phase diagram (Figure 1), the 13.5 atomic per cent beryllium alloy which they used exceeds the solubility of beryllium in copper at low temperatures. By quenching from 820°C,

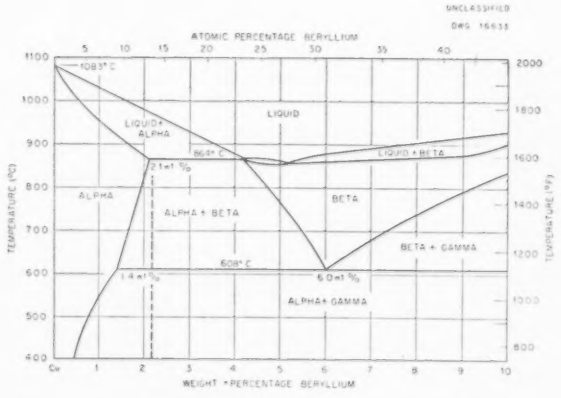

FIGURE 1. Equilibrium diagram for copper-beryllium system (after Filnow and Mack, Journal of Metals, October, 1950, p. 1230).

most of the excess beryllium is retained in a supersaturated solid solution. With time, this solution decomposes to form a precipitate of the gamma-phase in the copper-rich matrix. At temperatures below 40°C, the rate of precipitation is so slow that no changes are observed over a long period of time. The formation of precipitate nuclei during aging at higher temperatures is known to be accompanied by [8]:

1. Increase in hardness.
2. Increase in electrical resistivity for short aging periods at low temperatures.
3. Decrease in electrical resistivity at high temperatures or long periods at low temperatures.

The differences which were observed by Billington and Siegal between the solution-annealed copper-beryllium alloy and other metals are of the correct sign and magnitude to be accounted for by the formation of small nuclei in the copper-beryllium alloy during the irradiation. This hypothesis is in contradiction to the tentative conclusions of Billington and Siegel, who did not consider the effect of aging conditions on the resistivity changes.

Experimental Methods

Two lines of attack were followed in the present investigation in order to investigate the possibility of irradiation-induced nucleation. First, the property changes accompanying the neutron irradiation of a supersaturated solid solution of copper-beryllium were compared with the changes occurring during normal aging of this alloy. A good correspondence was found between irradiation and low-temperature aging. Secondly, the stability of the irradiation-induced changes in copper-beryllium at elevated temperatures was compared with the stability of changes resulting from normal low-temperature nucleation. The results of these experiments also showed a correspondence between irradiation and low-temperature aging.

The alloys used and their composition are given in Table II. The copper-beryllium alloy was part of the special binary alloy obtained from the Beryllium Corporation by Billington and Siegel. The beryllium content of this alloy exceeded the solubility of beryllium in copper at the solution annealing temperature; consequently, a small amount of the beta-phase was retained in the solution-annealed specimens. Material for the preparation of single crystals was obtained by remelting the original alloy in vacuum with sufficient copper added to produce a single phase alloy (11.4 atomic per cent beryllium). Single crystals were grown by the Bridgman method. The unsaturated solid solution alloys Cu-Zn, Cu-Ge, Cu-Ga, and Cu-As were melted under argon atmosphere. Borax flux was used to prevent vaporization of the alloying element. The Cu-Sn, Cu-Mn, and Cu-Si alloys were generously provided by O. T. Marzke of the Naval Research Laboratory.

Electrical resistivity measurements were made on a Kelvin double bridge or by a potentiometric method, using round rods 0.32 cm in diameter and 6.3 cm long for specimens. In the potentiometric method, the voltage drop across the sample was compared with the voltage drop across a standard resistance in series with the specimen. Voltages were measured with a Leeds and Northrup type K2 potentiometer. The reproducibility of measurements was ± 0.10 per cent for the bridge method and ± 0.05 per cent for the potentiometric method.

TABLE II

COMPOSITION OF ALLOYS USED

Alloy	Per cent alloying element by weight
Cu-Be (polycrystalline)	2.2% Be
Cu-Be (single crystal)	1.8% Be
Cu-Zn	4.1% Zn
Cu-Ga	4.4% Ga
Cu-Ge	4.6% Ge
Cu-As	4.7% As
Cu-Si	1.6% Si
Cu-Sn	5.1% Sn
Cu-Sn	10.0% Sn
Cu-Mn	20.0% Mn

Hardness specimens were prepared by rolling flat shapes 0.32 cm thick from round stock. A Tukon hardness-tester with a pyramid indenter was used for all hardness measurements. Each hardness number was obtained by averaging results obtained from five indentations; the maximum deviation was $\pm$ 5DPH numbers.

Specimens for the study of the X-ray line shape consisted of filings which had been passed through a 100 mesh screen. A Norrelco high-angle spectrometer with a GM counting tube was employed to measure the diffracted beam for a counting period of 64 seconds. The ratio of the number of counts to the number of counts obtained in the background was used for the intensity of the diffracted beam. The intensity was measured at half-degree inter-

vals through the intense region of the diffracted beam. The line position, defined as the mid-point at half-height, was reproducible to within $-0.01°$.

Copper-beryllium samples were annealed in vacuum at 820°C for one hour and quenched in water to retain the supersaturated solution as a metastable state. For purposes of comparison, samples were prepared from the same stock and solution treated together in order to eliminate any possible differences between samples which might result from variations in temperature or quenching rate.

All aging experiments conducted at temperatures higher than 200°C were carried out in a constant temperature nitrate (50% KNO_3, 50% $NaNO_2$) salt bath. For aging experiments conducted below 200°C a constant temperature oil bath was employed. Temperatures of aging baths were held to ± 1°C.

Specimens were irradiated by inserting them in the Oak Ridge Uranium-graphite reactor. The fast neutron flux was estimated to be 1×10^{12} cm^{-2}sec^{-1}. The thermal neutron flux was estimated to be 0.4×10^{12} cm^{-2} sec^{-1}. The samples were contained in aluminum carriers which were cooled by the cooling system of the reactor. Thermocouple measurements indicated that the sample temperature varied between 0°C and 40°C, depending on the ambient atmospheric temperature.

Comparison of Irradiation and Low-temperature Aging

The effect of irradiation on the resistance and hardness of a number of alloys and the effect of aging at low temperature on the copper-beryllium alloy are given in Table III.

The increase in electrical resistivity of the copper-beryllium alloy as a function of integrated flux is shown in Figure 2. The increase appears to approach

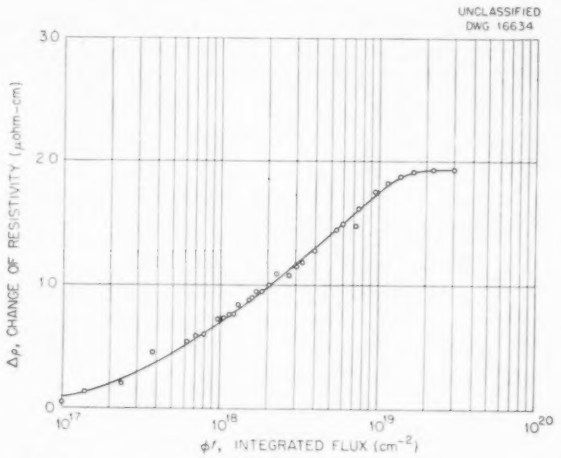

FIGURE 2. Change of resistivity of solution annealed copper-beryllium during neutron irradiation.

an upper limit at an integrated flux of 3×10^{19} cm^{-2}. This may be a saturation value or a true maximum in the curve. The behavior described by this curve was found to apply to both single-crystal and polycrystal samples, indicating that the irradiation effect is not associated with grain boundary phenomena.

Resistivity changes during aging of polycrystals at various temperatures are shown in Figure 3. The comparison of the curves for irradiation and

TABLE III

	Alloy hardness before	Alloy hardness after	(ΔH)	Resistance before	Resistance after	(ΔR)	Fast flux
Cu-Zn				131.	130.7	−0.23	1.5×10^{18}
	48.9	73.4	24.3				2.5×10^{18}
Cu-Ga				313.6	313.2	−0.13	1.5×10^{18}
	57.2	78.6	21.8				2.5×10^{18}
Cu-Ge				737.5	737.9	+0.10	1.5×10^{18}
	64.6	80.2	15.6				2.5×10^{18}
Cu-As				135.4	135.6	+0.15	1.5×10^{18}
	77.4	95.5	18.1				2.5×10^{18}
Cu-Sn (5.1%)	68.3	86.2	17.9	364.4	364.0	−0.08	1.4×10^{18}
Cu-Sn (10%)	86.4	96.4	10.	681.5	681.8	+0.04	1.4×10^{18}
Cu-Mn (10%)	69.2	81.4	12.2	135.5	135.0	−0.37	1.4×10^{18}
Cu-Mn (20%)	91.2	103.2	12.0	311.8	311.5	−0.10	1.4×10^{18}
Cu	40.8	56.2	15.7	116.3	116.5	+0.17	1.5×10^{18}
Cu-Be	98	145	47.	468.4	520.3	+11.1	2.3×10^{18}
Cu-Be (Single crystal)				278.	306.6	+10.3	2.5×10^{18}
Cu-Be	111	139	28.	467.6	513.1	9.5	

aging of polycrystals and single crystals is shown in Figure 4.

Billington and Siegel [7] reported that the magnitude of the resistance change due to irradiation was reduced by cold-working the solution-annealed specimens prior to the irradiation. This observation was verified. For an exposure of 2.5×10^{18} cm^{-2},

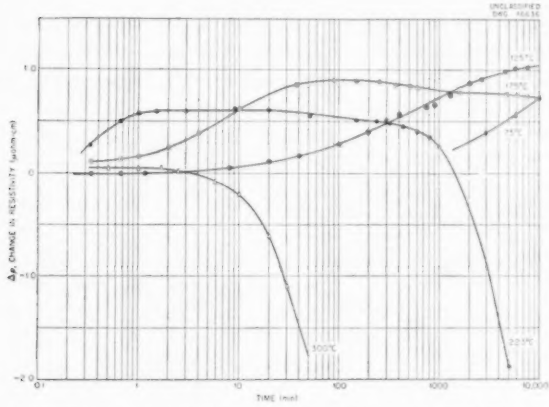

FIGURE 3. Resistivity changes during aging of copper-beryllium at temperatures below 300°C.

the resistivity of specimens which had been solution-annealed and cold-swaged to a 50 per cent reduction of area increased 0.20 micro-ohm centimeters or 1.7 per cent whereas the resistivity of specimens which had been only solution-annealed increased by 1.31 micro-ohm centimeters, or 13 per cent. A similar retardation was observed in the

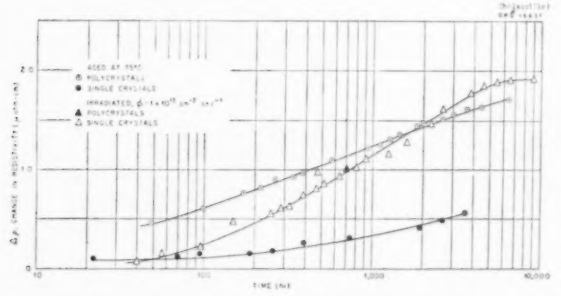

FIGURE 4. Resistivity changes in copper-beryllium during irradiation and during aging at 75°C.

case of cold-worked samples which were aged at 75°C. Polycrystal samples which had been cold-worked (50% R.A.) by swaging after solution annealing appeared to age more slowly than specimens which had been solution-annealed. The resistivity changes during aging for these two conditions are compared in Figure 5.

It was found that the shape of the (331) X-ray line was altered considerably, with a shift of the line to larger Bragg angles as a result of irradiation.

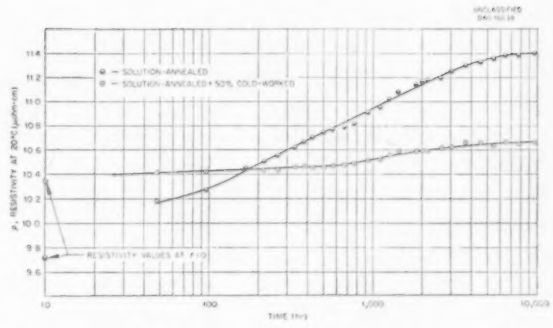

FIGURE 5. Resistivity changes of solution annealed and cold-worked copper-beryllium during aging at 75°C.

The line shape and position before and after irradiation are compared in Figure 6. The amount of shift as a function of the integrated flux is

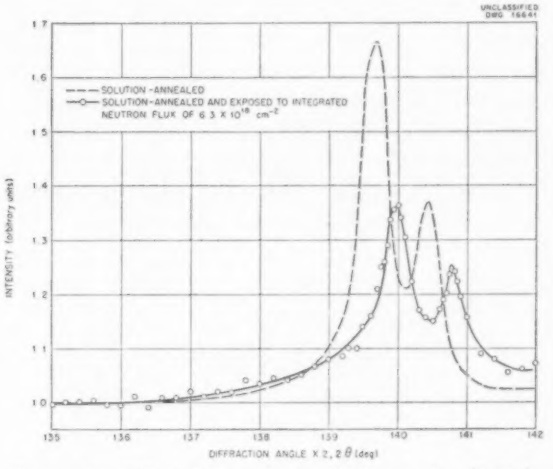

FIGURE 6. Effect of neutron irradiation on the (331) line of copper-beryllium.

shown in Figure 7. A corresponding shift was found for other lines. Specimen filings were aged at 125°C for 122 hours, a treatment which produced on solid polycrystalline specimens an increase

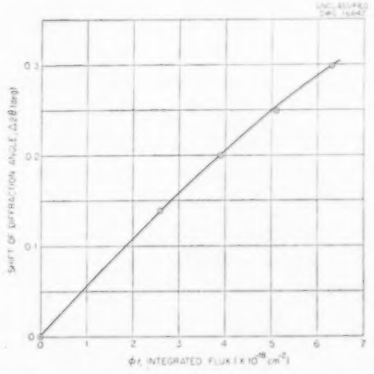

FIGURE 7. Shift of diffraction angle of (331) line resulting from neutron irradiation of copper-beryllium.

in resistivity of the order of 15% and a hardness increase of approximately 100 DPH numbers. This treatment produced no effect on the (331) line shape or position. During aging at higher temperatures, the diffraction lines broaden and decrease in intensity as new lines appear at a smaller diffraction angle for the alpha-phase, and at a larger diffraction angle for the gamma-(precipitate) phase [9].

Density measurements were made by the immersion method on two copper-beryllium rods approximately 0.64 cm in diameter and 5.1 cm long. One specimen was exposed to an integrated neutron flux of 3.8×10^{18} cm^{-2}, and the other specimen retained as a standard. Using the standard to correct for temperature changes, an increase in density of 0.18% was measured for the irradiated specimen. An increase of 0.19% in density is to be expected on the basis of the lattice parameter change for an exposure of 3.9×10^{18} cm^{-2}. The density change to be expected during precipitation in copper-beryllium is in the direction of a decrease. Such decreases have been observed at high aging temperatures [10]. Aging of solution-annealed polycrystal samples for 25 hours at 125°C produced no alteration in the density. However, aging a single crystal at 200°C for 6 hours caused an anomalous increase in density of 0.26%.

Retrogression Experiments

Several experiments were conducted to determine the effect of irradiation on the subsequent aging of the copper-beryllium alloy. It was observed that a recovery process appeared as the aging temperature increased; part of the irradiation effects were rapidly removed, part remained and affected the course of the precipitation reaction. At sufficiently high temperatures, complete recovery of the irradiation effects occurred and the precipitation followed a course which showed no effect of the irradiation. A similar recovery process occurred in specimens which had been aged at low temperatures. These observations can be most readily explained as the result of retrogression, or redissolving of precipitate particles which are too small to be stable at the higher temperatures. The observations and explanation correspond to the retrogression phenomena observed by Masing [11] in aluminum-copper specimens which had been aged at low temperatures.

The subsequent aging behavior at 300°C and at 325°C of irradiated samples as measured by electrical resistivity is compared with unirradiated standard specimens in Figures 8 and 9. The major differences between the behavior of the irradiated specimens and non-irradiated standards are (1) rapid partial recovery of the irradiation effect, and (2) accelerated aging of the irradiated specimens. Partial recovery of the irradiation effect was obtained at temperatures as low as 175°C.

The effect of low-temperature aging (125°C) on subsequent aging at a higher temperature (325°C) is shown in Figure 10. Here there was also observed a rapid recovery of the resistivity increase caused

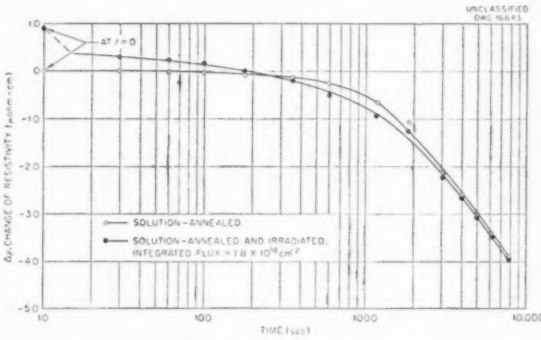

FIGURE 8. Resistivity measurement of retrogression at 300°C in copper-beryllium nucleated by neutron irradiation.

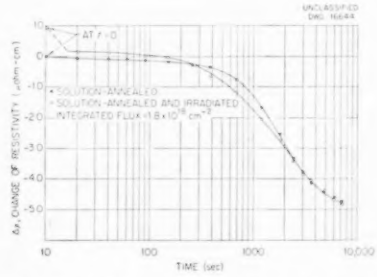

FIGURE 9. Resistivity measurement of retrogression at 325°C in copper-beryllium nucleated by neutron irradiation.

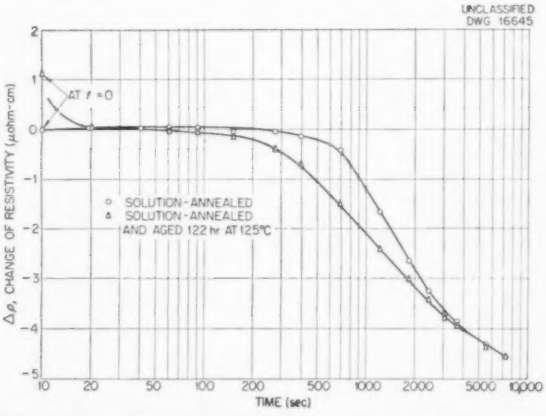

FIGURE 10. Resisitivity measurement of retrogression at 325°C in copper-beryllium nucleated by aging at 125°C.

by the prior aging, together with accelerated aging at a later stage. The subsequent aging behavior at 375°C of an irradiated specimen and a specimen aged at a low temperature (125°C) are shown in Figure 11. In both cases the rapid recovery occurred, but the accelerated aging which was observed at 325°C is absent.

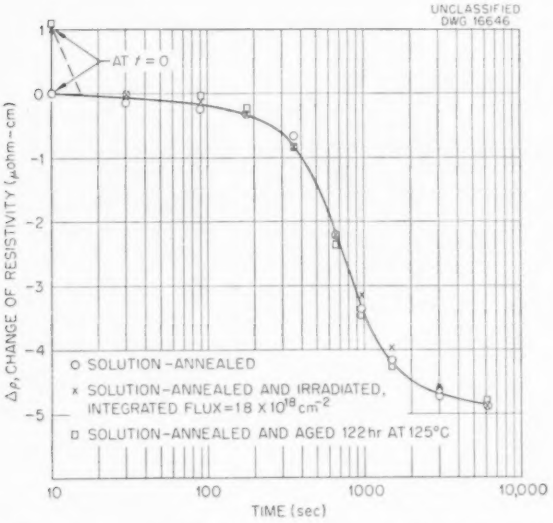

FIGURE 11. Resistivity measurement of retrogression (complete) at 375°C in copper-beryllium nucleated by neutron irradiation and by aging at 125°C.

Hardness specimens were irradiated in the solution-annealed condition and subsequently aged with a corresponding standard at 300°C and at 325°C (Figures 12 and 13). At the higher temperature the irradiated specimen exhibited almost complete recovery, whereas no apparent recovery occurred at 300°C. The irradiated specimens apparently aged at a more rapid rate than the corresponding standards at both temperatures.

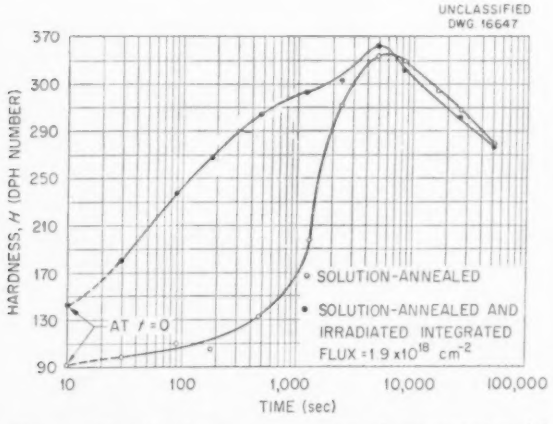

FIGURE 12. Hardness measurement of retrogression (absent) at 300°C in copper-beryllium nucleated by neutron irradiation.

The subsequent aging at 325°C of a specimen which had been previously aged at 125°C is shown in Figure 14. Practically no recovery occurred at 325°C. An accelerated aging rate resulted as in the case of the irradiated specimens. The subsequent aging at 375°C of an irradiated specimen and a

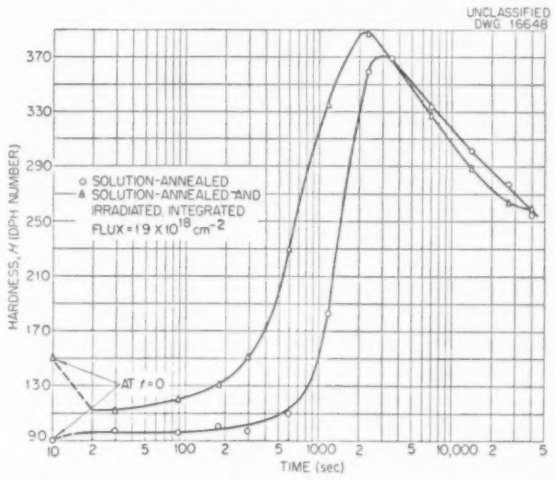

FIGURE 13. Hardness measurement of retrogression at 325°C in copper-beryllium nucleated by neutron irradiation.

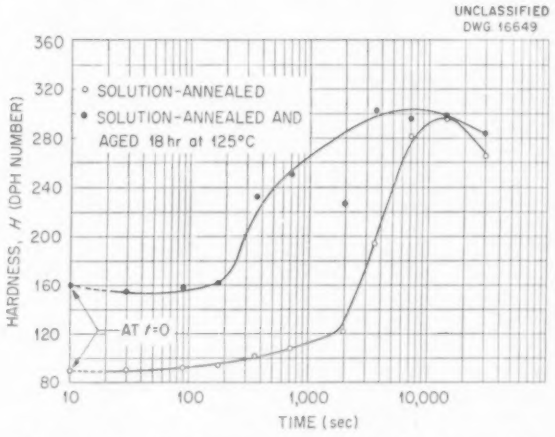

FIGURE 14. Hardness measurement of retrogression at 325°C in copper-beryllium nucleated by aging at 125°C.

specimen aged at low temperature is compared with a standard in Figure 15. At this temperature complete recovery occurred for both nucleated samples, and the aging was not accelerated.

Solution-annealed filings were irradiated and subjected to short periods of aging at 300°C simultaneously with non-irradiated solution-annealed filings. After 30 seconds at 300°C no change

in the line shape or position was observed in either the irradiated or the standard specimens. Another set of specimens, standard and irradiated, was held at 350°C for 30 seconds. The line shape and positions of the standard remained unchanged, but

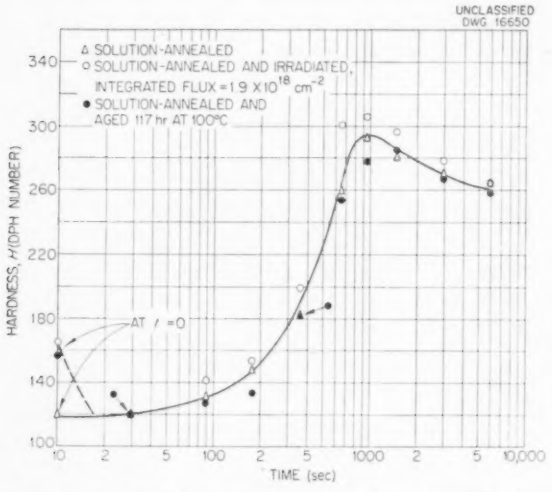

FIGURE 15. Hardness measurement of retrogression (complete) at 375°C in copper-beryllium nucleated by neutron irradiation and by aging at 100°C.

approximatly 75 per cent recovery was observed for the line shape and position of the irradiated filings (Figure 16).

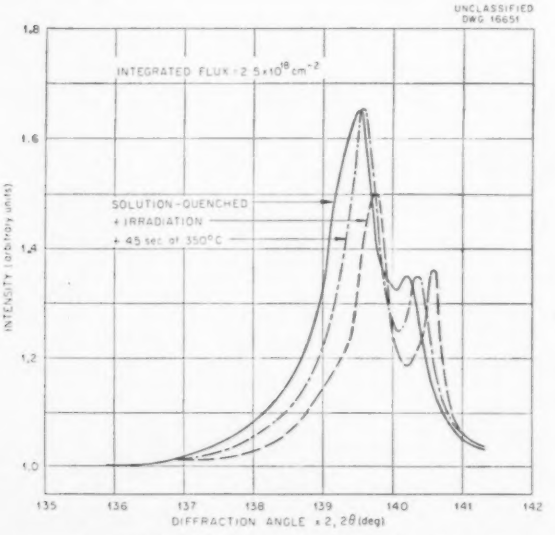

FIGURE 16. Effect of retrogression at 350° on the shape and position of the (331) line of irradiated copper-beryllium (integrated flux of $2.5 \times 10^{18}/cm^2$).

Discussion

The effects of irradiation in nuclear reactors on the properties of supersaturated solutions of beryllium in copper were found to be in agreement with the results of Billington and Siegel [7]. Because of a more extensive investigation of the effects of low-temperature aging, it is possible to explain the effects of irradiation in a different way. Billington and Siegel [7] rejected the hypothesis that the precipitation process was partially responsible for the observed effects because of (1) the increase of resistance during irradiation, and (2) the smallness of the irradiation effects in cold-worked samples. Both of these observations are in opposition to the effects of aging at the usual commercial heat-treatment temperatures. The data obtained for low-temperature aging remove these objections, since it was found that both of these abnormalities occur during the initial stages of precipitation occurring at temperatures in the range of 100°C or lower. The possibility of precipitation effects associated with irradiation must therefore be reconsidered.

Although the changes in hardness and resistivity due to irradiation can be explained by precipitate nucleation, a new difficulty is introduced by the shift of the X-ray diffraction line. This is difficult to explain on the basis of induced precipitation for two reasons:

1. The shift is anomalous; i.e., depletion of the parent solution should expand the lattice. This would be accompanied by a broadening of the X-ray diffraction line, and possibly a shift in the opposite direction from that observed.
2. Such an effect on the X-ray line as that obtained during irradiation could not be obtained by aging at low temperatures, as was the case for hardness and resistivity.

The same difficulties are encountered when attempting to explain the increase in density due to irradiation on the basis of induced nucleation of the precipitate. The agreement between the density increase calculated from the line shift and the measured density increase resulting from irradiation suggests that these two phenomena are related.

It may be assumed that such properties as X-ray diffraction and density, which depend on the bulk of the material, will not be affected appreciably by nuclei concentrated at the grain boundaries. The density change and shift of diffraction angle during irradiation occurred under conditions where there was a homogeneous distribution of nuclei. The nuclei distribution in the single crystal aged at 200°C was probably relatively homogeneous. On the other hand, in the filings and polycrystalline

density sample, the nuclei obtained during aging at 125°C were almost certainly clustered at the grain boundaries. Since the retrogression of irradiation-induced line shift corresponds temperaturewise to the hardness retrogression, it is probable that the line shift and density increase resulted from the coherent strains of relatively homogeneously dispersed precipitate nuclei.

The effects of irradiation on copper-beryllium which were not observed in stable alloys and pure copper support the hypothesis that during irradiation precipitate particles are formed. The correspondence obtained between irradiation and low-temperature aging indicate that the nuclei formed during irradiation resemble those which form at about 100°C.

On the basis that the nature of the precipitate nuclei induced by irradiation resemble those which form at low-aging temperatures there should be a similarity in the stability of the nuclei formed under these two conditions. This should appear as a similarity of retrogression phenomena in samples nucleated by the two methods. Such an agreement was found. The occurrence of retrogression corresponded in such details as the resolution between particle sizes which cause resistivity increase and hardness increase. This resolution of particle sizes results from the almost complete recovery of resistivity at 300°C as contrasted to the complete absence of recovery of hardness at this same temperature.

A more complete description of the retrogression is given by the ratio of the amount of recovery, $\Delta P'$, of the physical property, P, to the original change of the property, ΔP, during irradiation or low temperature aging. The retrogression ratio is plotted as a function of temperature in Figure 17. Although there is considerable scatter of the data, the points for resistivity and hardness fall into well-defined scatter bands which are resolved for the two

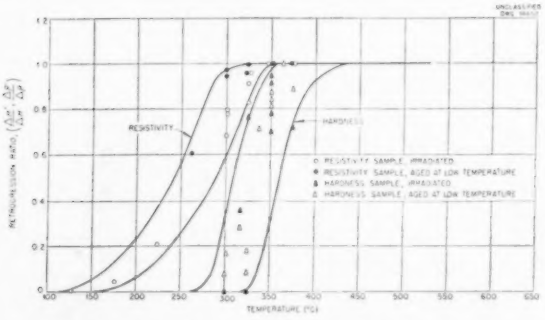

FIGURE 17. Retrogression of copper-beryllium as measured by hardness and resistivity.

properties. It may therefore be concluded that the particles responsible for the resistivity increase differ from those responsible for hardening.

The aging curves at 375°C (Figures 11 and 15) do not show the accelerated aging which occurs for the nucleated samples at 300°C and at 325°C. The acceleration at the lower temperatures should occur if all of the nuclei are not dissolved. The absence of acceleration at 375°C indicates that all of the nuclei have been removed at this temperature.

The mechanism of formation of precipitate nuclei during irradiation is not clearly established. Presumably the rate of diffusion is accelerated on a microscale by the presence of excess vacancies and interstitials resulting from the displacements created during the irradiation. The possibility of nuclei formation as a result of lattice excitation (thermal spikes) cannot be discounted.*

The experiments described indicate that nuclei which form as a result of irradiation or aging at low temperatures affect the properties of the material in different ways than do the nuclei which form at higher temperatures. The difference is presumably related to the smaller size of nuclei which are stable at lower temperatures, although there may also be a difference in orientation, shape, or structure [13]. Very large resistance increases have been observed to be associated with low-temperature nuclei in the copper-beryllium alloy. Retrogression experiments indicate that this effect is not related to the coherent lattice strains which cause hardening. The mechanism of the resistance increase here may be the coherent scattering of electrons suggested by Mott [14] a number of years ago.

Summary

Comparison of the effects of irradiation and aging suggest the possibility of precipitate nucleation induced by fast neutron irradiation. The retrogression phenomenon provides convincing evidence for the presence of precipitate nuclei in the irradiated specimens. The results of both types of experiments indicate a similarity between irradiation

*More recent experiments [12] suggested by the hypothesis of accelerated diffusion on a microscale show that during low-temperature irradiation the abnormally large changes do not occur. The capacity for change is introduced as a latent characteristic so that when the irradiated sample is raised to room temperature the properties assume values which would result from irradiation at the higher temperatures. This result precludes the possibility of nucleation during the thermal spike cycle, since there is no way in which the mechanism could be latently stored. On the other hand one would expect a decrease in diffusion of the vacancies at the low temperature; upon raising the temperature, nucleation could rapidly proceed at all damage centers introduced by the irradiation.

induced nuclei and those which naturally form at low aging temperatures.

In addition to indicating the existence of precipitate nuclei resulting from neutron irradiation, these experiments have shown:

1. In copper-beryllium very large increases in electrical resistivity can be obtained by irradiation or by aging at sufficiently low temperatures.
2. The nuclei that produce an increase in resistivity in copper-beryllium are not the same as those that cause hardness increases.
3. Cold worked copper-beryllium samples aged at low temperatures show a slower rate of resistivity change than annealed samples.
4. Copper-beryllium exhibits anomalous lattice parameter and density changes when nuclei which form at low temperatures are homogeneously distributed through the lattice.

Acknowledgment

The authors wish to express their appreciation to the many members of the Oak Ridge National Laboratory who assisted directly or indirectly in this work. Especially to be noted are Dr. D. S. Billington for much encouragement and many suggestions, F. H. Blacksher who assisted with the measurements, and W. E. Busby who prepared many drawings. Many helpful discussions were had with Drs. T. H. Blewitt, J. H. Crawford, and D. K. Holmes.

References

1. Seitz, F. "On the Disordering of Solids by Action of Fast Massive Particles," Discussions of the Faraday Society 5–6 (1948) 271.
2. Bohr, N. The Penetration of the Atomic Particles through Matter (Denmark, Bianco Lunos Bogtrykkeri, 1948).
3. James, H. Oak Ridge National Laboratory, ORNL-307.
4. Ozcroff, J. "Atomic Displacements by Fission Fragments and Fission Neutrons in Matter," Knolls Atomic Power Laboratory, KAPL-205.
5. Brooks, H. Knolls Atomic Power Laboratory, KAPL-360.
6. Klontz and Lark-Horovitz. "Electron Bombardment of Germanium," USAEC TID 5010.
7. Billington, D. and Siegel, S. Metal Progress **58** (1950) 847.
8. Guy, A., Barrett, C., and Mehl, R. Cu-Be, Trans. A.I.M.M.E. **175** (1948) 216.
9. Dahl, O., Holm, E., and Masing, G. X-ray Investigation of the Age Hardening Process in Beryllium Copper Alloys; *Beryllium*, translated by Rimbach, R. and Michel, A. (New York, Chemical Catalog Company, 1932) p. 188.
10. Masing, G., and Dahl, O. "Changes in Electrical Conductivity and Volume during Age Hardening of Beryllium Copper Alloys"; *Beryllium*, translated by Rimbach, R. and Michel, A. (New York, Chemical Catalog Company, 1932) p. 151.
11. Masing, G. Trans. A.I.M.M.E. **104** (1933) 27.
12. Cleland, J. W., Billington, D. S., and Crawford, J. H. Phys. Rev. **91** (1953) 238.
13. Geisler, A., Malbery, J., and Steigert, F. J. Metals **4** (1952) 307.
14. Mott, N. J. Inst. Metals **60** (1937) 267.

ORDER-DISORDER IN Cu-Au ALLOYS
II. THE NATURE OF THE ORDER-DISORDER TRANSFORMATION AND LONG-RANGE ORDER*

FRANK E. JAUMOT, JR. AND CHARLES H. SUTCLIFFE†

The order-disorder transformation has been studied in Cu-Au alloys containing from 15.5 to 34.2 atomic per cent gold. This has been accomplished by observing high-angle fundamental X-ray reflections from single crystals, at temperatures ranging from room temperature to 450°C. The data indicate that the transformation is a classical phase transformation for alloys containing more than 25 atomic per cent gold. For samples containing less than 25 atomic per cent gold, it cannot be stated that the transformation is a heterogeneous one. Rather, the evidence appears to favor a homogeneous transformation for copper-rich samples.

The degree of long-range order present in samples of the above compositions has been determined by measurement of the integrated X-ray intensity of the (3,0,0) superstructure reflection. All measurements were made at the temperature of interest, using monochromatic Cu-K_α radiation and single crystal samples. Values of the long-range order parameter, S, as a function of temperature, are given for each composition.

LA TRANSFORMATION ORDRE-DÉSORDRE DANS LES ALLIAGES Cu-Au
II. LA NATURE DE LA TRANSFORMATION ORDRE-DÉSORDRE ET L'ORDRE À GRANDE DISTANCE

La transformation ordre-désordre a été étudiée dans des alliages Cu-Au contenant de 15,5 à 34,2 pour cent d'or en atomes. Cette étude fut effectuée par l'observation des réflexions fondamentales à grand angle, de rayons X, provenant de monocristaux, à des températures allant de l'ambiante à 450°C. Les données expérimentales indiquent que dans le cas des alliages contenant plus de 25 pour cent d'or en atomes, c'est une transformation classique de phases. Il ne peut pas être affirmé que pour des échantillons contenant moins de 25 pour cent d'or, la transformation soit hétérogène. Il paraît plutôt, que dans les échantillons riches en cuivre, la transformation est aussi homogène. Le degré d'ordre à grande distance, dans les échantillons dont les compositions sont mentionnées ci-dessus, fut déterminé par des mesures d'intensité intégrée de réflexion des rayons X de la surstructure (3,0,0). Toutes les mesures ont été faites sur des monocristaux, en employant la radiation monochromatique K_α du Cu.

Des valeurs du paramètre S d'ordre à grande distance sont données pour chaque composition, en fonction de la température.

DER ORDNUNGSGRAD IN Cu-Au LEGIERUNGEN
II. DAS WESEN DES ÜBERGANGS VON GEORDNETER ZU UNGEORDNETER ATOMVERTEILUNG UND DIE FERNORDNUNG

Der Übergang von geordneter zu ungeordneter Atomverteilung wurde in Cu-Au Legierungen, die zwischen 15, 5 and 34, 2 Atomprozent Gold enthielten, untersucht. Dies wurde durch Beobachtung der prinzipiellen Röntgenstrahlreflexionen von Einkristallen unter grossen Winkeln bei Temperaturen zwischen Zimmertemperatur und 450°C erreicht. Die Resultate deuten darauf hin, dass für Legierungen mit mehr als 25 Atomprozent Gold der Übergang eine klassische Phasenumwandlung ist. Für Legierungen mit weniger als 25% Gold kann die Umwandlung nicht als heterogen bezeichnet werden. Das vorhandene Material deutet für kupferreiche Legierungen vielmehr auf eine homogene Umwandlung hin.

Der Fernordnungsgrad in den Proben der oben angegebenen Zusammensetzung wurde durch Messung der integrierten Röntgenstrahlintensität der (3, 0, 0) Überstrukturlinie bestimmt. Alle Messungen wurden bei der Temperatur von Interesse mit monochromatischer Cu-K_α Strahlung und Einkristallproben durchgeführt. Die Werte des Fernkoeffizienten S werden für jede Zusammensetzung als Funktion der Temperatur angegeben.

Introduction

The majority of the experimental work on order-disorder in Cu-Au alloys has been made on the stoichiometric alloys Cu_3Au and CuAu, and has indicated that the transformation in the neighbourhood of Cu_3Au is a homogeneous one. Thus, one would expect a reversible transformation with a precipitous drop at the critical temperature, T_c, in the degree of order present. Evidence has been given in support of these phenomena in the alloy Cu_3Au [1] and much of the theoretical work has been based on the premise of a homogeneous phase transformation.

More recently, arguments have been advanced supporting the suggestion first made by Nix and Shockley [1] that the transformation could reasonably be a classical or heterogeneous phase change with ordered and disordered phases present in equilibrium at a given temperature. Evidence has been given in support of this type of phase change for the alloy Co-Pt [2], and somewhat less convincing evidence [3;4] has been given for the Cu-Au system.

*Received July 21, 1953.

†Randal Morgan Laboratory of Physics, University of Pennsylvania. Present address: The Philco Corporation, Philadelphia, Pennsylvania.

It is interesting to consider why the nature of the order-disorder transformation has never been definitely demonstrated. If the ordering reaction were a heterogeneous one, occurring by nucleation and growth, the volume of the ordered phase would gradually increase at the expense of the disordered phase, and the equilibrium diagram would show the ordered phase separated from the disordered phase by a two-phase region. There are two possible reasons why this situation may have gone undetected although recognized as possible. In the Cu-Au system, the low critical temperatures result in a low diffusion rate at low ordering temperatures, and thus a low rate of growth combined with a high nucleation rate. Without highly refined techniques, conventional X-ray patterns may not detect the resulting finely dispersed areas of order and disorder. Secondly, most of the work has been attempted close to the stoichiometric composition of the ordered region, since only then are the various theories of ordering applicable. In this region one would expect a two-phase region, if present, to be quite narrow and hence likely to escape detection.

It has been shown [5; 6] that alloys of Cu-Au near the composition Cu_3Au exhibit an anomalous increase in the thermal expansion near the critical temperature. This may be explained either as an increase in cell size with a decrease in order, or if two phases be present, it may be explained on the basis of a larger cell in the disordered phase. Sykes and Evans [7] have shown that disordered samples of Cu_3Au have a substantially larger cell size than ordered samples. Consequently, a fundamental X-ray reflection from a sample containing both the ordered and disordered phases would appear as a split line, and the relative intensities of the two reflections would give a measure of the amount of each phase present. Thus it would appear that very careful measurements on a high angle fundamental X-ray reflection, made at temperature, should give concrete evidence as to the nature of the order-disorder transformation.

However, the situation is not entirely favorable. Assuming for the moment that one has an ideal classical phase change, it is interesting to ask what one should expect to find regarding the positions of the portions of the split fundamental reflection due to the two phases, at different compositions. The maximum separation of the lines due to ordered and disordered phases will occur at 25 atomic per cent gold, which would make resolution of the two lines easier than for any other composition. However, the temperature range over which one could detect the two phases in equilibrium is theoretically zero (along BB' in Figure 1) at the stoichiometric composition. Thus, a study of the nature of the transformation using samples containing 25 atomic per cent gold is almost certain to produce a discontinuity in line position and lead one to believe the transformation to be homogeneous.

At compositions above or below stoichiometric, one would expect a considerably wider temperature range (along AA' or CC' in Figure 1) in which the

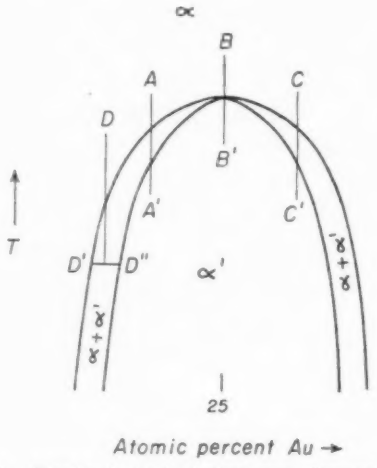

FIGURE 1. Idealized classical phase transformation.

phases coexist. At the same time, in these regions one has an insufficiency of one of the constituents so that one would expect the line positions of the ordered and disordered phases to be less widely separated and consequently resolution of the lines should be more difficult.

The Experiment

Single crystals of alloys containing 15.5, 20.25, 23.45, 28.25, 30.4, and 34.2 atomic per cent gold (hereafter referred to as 15, 20, 23, 28, 30, and 34 per cent samples) were grown in a furnace designed by Nix [8]. Samples $\frac{1}{4}$ inch in diameter and $\frac{1}{8}$ inch thick were cut from these crystals and oriented with crystal faces parallel to the (1,0,0) planes. These samples were polished and electrolytically etched in a 5 per cent solution of potassium cyanide. They were then annealed and ordered using the following procedures: 48 hours at 875°C, 24 hours at 600°C, 24 hours at 400°C, 200 hours at 360°C, 300 hours at 300°C, slowly cooled to 200°C and held there for 72 hours, followed by slow cooling to room temperature. After annealing and ordering the samples were again etched and checked for orientation.

The first set of measurements were made with

the samples mounted in the furnace described in Part B of this paper, using CuK_α radiation monochromated by a bent quartz crystal monochromator and collimated by a series of "home-made" slits. These slits did not employ the principle of Soller slits. Consequently, we found that the narrowest line width obtainable was approximately 10 minutes in 2θ.

Inasmuch as the first set of experiments indicated that the fundamental reflections were split, but were not resolved, it was decided that higher resolution would have to be achieved. To this end, Soller slits* of the following specifications were used: beam slit, high resolution Soller, 0.4° divergence; detector slits; high resolution Soller, 0.02° divergence. The combination of the extreme collimation and the absorption by the nickel foil reduced the intensity of the monochromatic beam to a point below the maximum efficiency of the Geiger counter used for detection. Thus we were forced in the second set of measurements to use continuous radiation. However, it was found that the resolution of the α-doublet was even better, due to the improved slit arrangement, than that found using the monochromatic radiation. Since the measurements were being repeated anyway, and since the preliminary work indicated results of great interest, it was decided to no longer rely on the rotational alignment being kept exact by a fitted pin. Consequently, in spite of the advantage of studying six samples essentially simultaneously, it was decided to use the furnace-sample holder and mount shown in Figure 2, and study the samples one at a time.

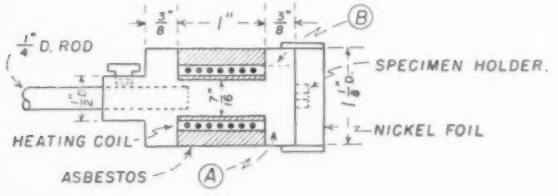

FIGURE 2. Furnace-sample holder used in determination of diffraction line position as a function of temperature.

The temperature of the furnace was controlled by a Chromel-Alumel thermocouple placed near the furnace windings. The thermocouple potential was balanced against a reference potential using a Brown Converter. The amplified difference voltage provided the bias voltage for the electronic control circuit used. This control circuit supplied a differential current to the furnace using an impedance reflection principle. The temperature in the furnace was controlled to an amazing degree. The fluctuations in the temperature in most cases did not exceed $\neq 0.05$°C over periods as long as 12 hours. It is not intended to imply that the temperature of the sample surface was known to 0.05°C, since the temperature was measured at the rear of the sample and the gradient was undetermined.

*Kindly loaned to us by The Franklin Institute, Laboratories for Research and Development, Philadelphia, Pa.

Results

The angular position of the (4,0,0) fundamental reflection was used throughout as a means of studying the nature of the order-disorder transformation. The measurements of the peak position were taken by recording the intensities using a Leeds and Northrup Speedomax Recorder while turning the crystal through the Bragg angle at the rate of 0.1° in θ per minute. The Geiger counter turned synochronously at a rate of 0.2° in 2θ per minute. The line positions were read from the recorder chart with an accuracy of $\pm 0.02°$ in 2θ.

The heating program followed was essentially to heat the initially well-ordered sample to a given temperature and allow it to remain at that temperature until it reached equilibrium. The criterion used for equilibrium was that the line position should not change, or the half-width of the line diminish, within a period of at least 12 hours. Even so, it is probable that absolute thermal equilibrium was not attained, particularly as regards agglomeration of fine, widely-dispersed nuclei of a second phase. Table I gives a typical set of equilibrium times.

TABLE I

TYPICAL VALUES FOR THE TIME ALLOWED FOR SAMPLES TO COME TO EQUILIBRIUM AT VARIOUS TEMPERATURES

Temperature °C	Time hours	Temperature °C	Time hours
26	—	335	50
150	150	340	75
197	125	363	75
220	50	380	25
238	75	386	25
262	50	393	24
271	75	402	24
280	75	420	24
285	25	460	24
297	100	482	24
328	125	505	24

Figures 3*a* through 3*f* show the curves of line position of the (4,0,0) fundamental reflection as a function of temperature for the composition indicated. Also listed in the figures are the half-widths of the lines below, approximately at, and above the so-called critical temperature.

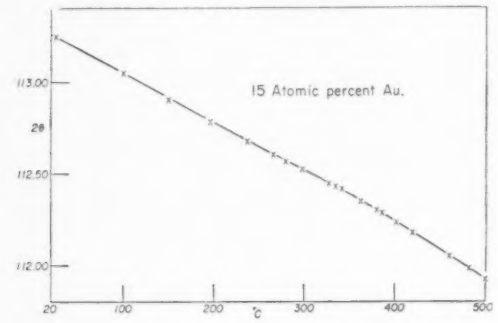

(*a*)

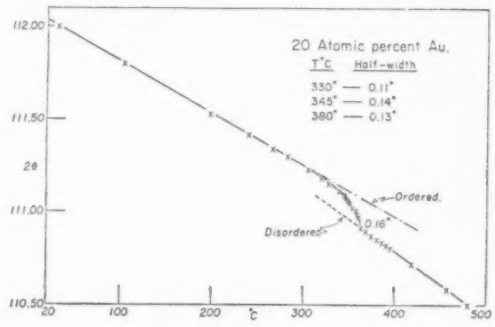

(*b*)

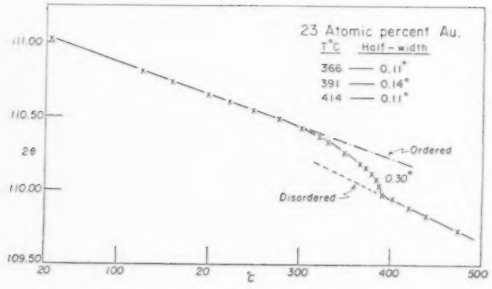

(*c*)

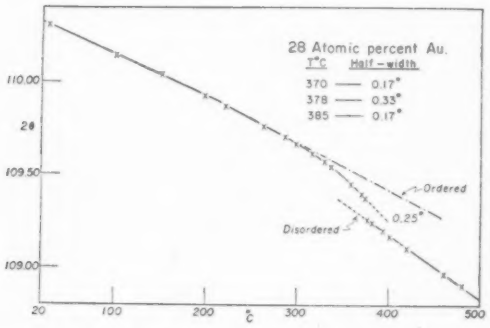

(*d*)

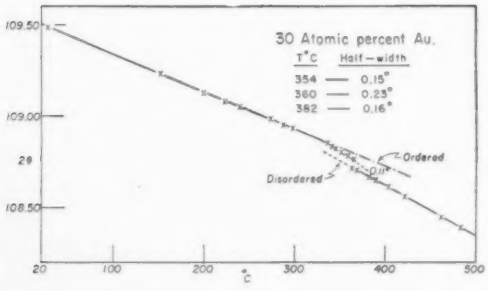

(*e*)

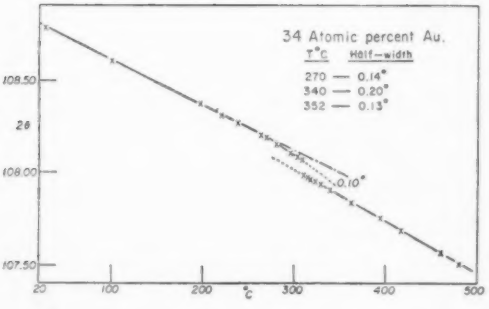

(*f*)

FIGURE 3. (4,0,0) Line position as a function of temperature.

Figures 4*a* through 4*d* show line shapes for these lines for temperatures below, in, and above the critical region. These lines are direct tracings of the recorder chart.

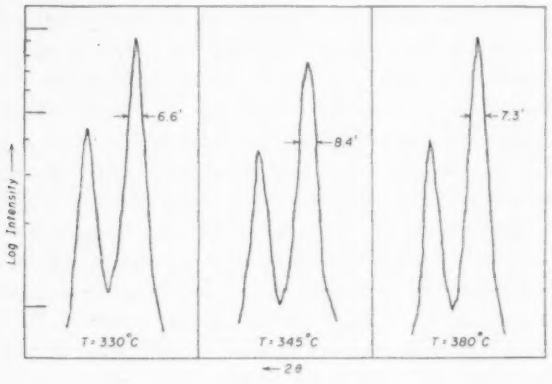

(*a*)

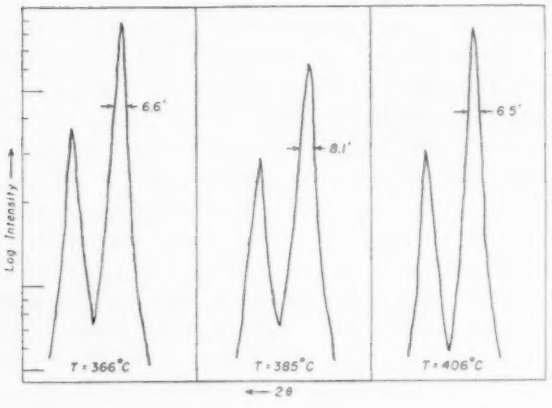

(*b*)

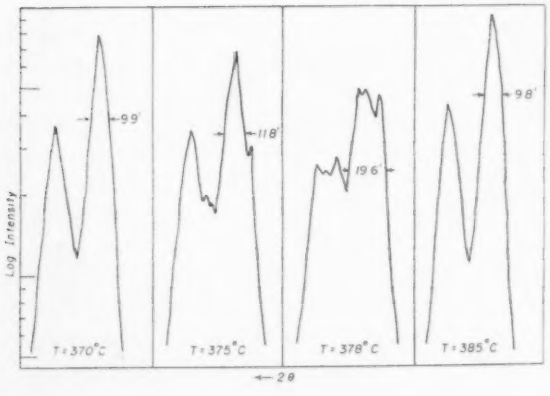

(*c*)

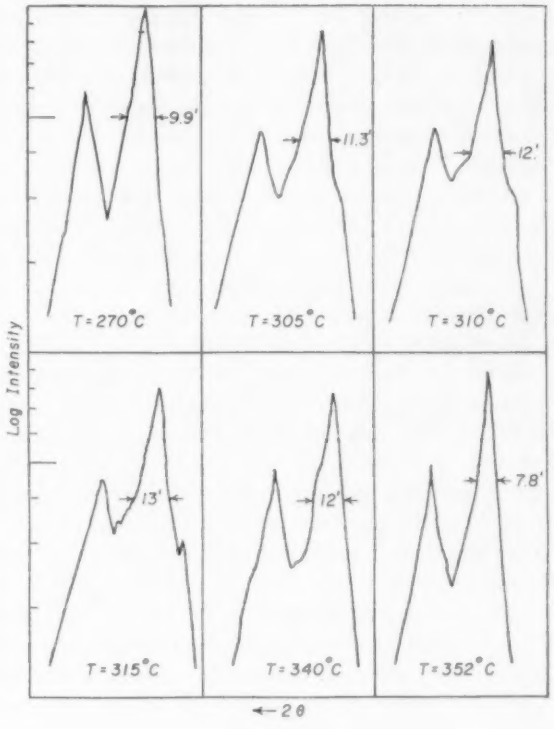

(*d*)

FIGURE 4. (4,0,0,) Line shapes of (*a*) 20% sample, (*b*) 23% sample, (*c*) 28% sample, (*d*) 34% sample. Half-intensity widths are given in minutes in 2θ.

Discussion of Results

The 15 per cent sample gave relatively uninteresting results. The points can be fitted to one straight line at the lower temperatures and to another straight line with a slightly different slope at the higher temperatures. These two straight lines can be joined smoothly by a line having a slight curvature. The curved region of the plot of the line position *versus* temperature extends from approximately 290°C to 360°C. Thus, no marked effect on line position due to ordering was detected for the 15 per cent sample although a very weak superstructure maximum was detected (see Part B of this paper).

Generalizing, the remainder of the data can be divided into two regions, the gold-rich and the copper-rich. On the gold-rich side of Cu_3Au the transformation is apparently a heterogeneous one rather than a homogeneous one. This conclusion is based on fairly definite evidence of two separate diffraction peaks (Figures 4*c*, *d*). The use of the phrase "fairly definite" is not intended to convey the impression that we have obtained two clearly resolved peaks for all compositions. On the con-

trary, in Figures 3*d* through 3*f*, the curves are shown as dotted lines to a considerable extent in the critical regions, since they depend on positions taken from the recorder chart for peaks that were not clearly resolved (see Figures 4*c*, *d*). The upper dashed line in all plots of angle *versus* temperature is an extrapolation of the straight line portion of the curve in the ordered region, and the distance between this line and the disordered line is the maximum angular separation in 2θ, one could expect between the peaks (this value is given in hundredths of a degree on the plots).

Figures 4*c* and 4*d* clearly indicate the manner in which the second phase becomes evident. First, an asymmetry appears on the low-angle side of the line and increases with increasing temperature in such a way that it can be regarded only as another peak. At still higher temperatures the line becomes quite broad and relatively flat at the peak (see Figure 4*c*), and finally the asymmetry appears on the high angle side of the line. We believe that this behaviour can be interpreted only in terms of a two phase transformation. It must be admitted that we obtained apparently resolved peaks of approximately equal magnitudes only for the 28 per cent sample, but this is presumably due to the small separation of the peaks, and the practical limit on the size of the temperature increments. For example, at the temperature at which one would hope to get the two peaks with equal intensity for the 34 per cent sample, the peak separation is less than 6 minutes in 2θ and the half-width of the K_α line at temperatures in this region is greater than 12 minutes. Thus, complete resolution is not physically possible and the combined peaks appear simply as a considerably broadened line.

The half-widths of the lines themselves provide strengthening for the contention of two phases. The half-width of the line for the 34 per cent sample (Figure 4*d*) for example, was 7.2′ in 2θ at room temperature, and only 7.8′ at 352°C. However, in the critical region the line broadened considerably with a maximum half-width of more than 12 minutes. This broadening began as much as 10 degrees below the first real indications of asymmetry. It is important to note that the intensity scale in Figures 4*a* through 4*d* is logarithmic, in order to get a proper perspective of the half-intensity measurements.

The valley between the K_{α_1}, and K_{α_2} peaks gives still a third indication of the presence of two phases. (Incidentally, no implication is intended that the three indications mentioned are unrelated.) At temperatures above and below the critical region, this valley is deep and symmetric. In the critical region the valley becomes relatively shallow and takes on an asymmetry compatible with that described for the K_{α_1} peak. This is clearly shown in the 3rd, 4th, and 5th illustrations in Figure 4*d*.

There is one unusual feature of the line positions. Assuming two phases, the evidence is that from the initial inception (as nearly as we can guess the positions of the peaks from the asymmetries) the change in line position with temperature is linear for the disordered phase, but the curve of line position *versus* temperature for the ordered region shows a marked concave curvature, beginning in fact, at temperatures below those at which the asymmetry is first apparent. This is demonstrated in the curves of line position *versus* temperature.

The samples containing less than 25 per cent gold (copper-rich) present an altogether different picture than the gold-rich samples. As illustrated in Figures 4*a* and 4*b*, none of the three points mentioned above as evidence for a two-phase system is clearly observed for the copper-rich samples. There does seem to be a slight broadening of the diffraction peaks in the critical region. In fact, the curves show that the half-maximum widths of these lines have their greatest values in the critical region. However, the broadening is so slight that it can hardly be regarded as anomalous. No definite asymmetry was observed in the peak of any copper-rich sample, and the peak positions were relatively definite throughout (as contrasted to the wide, irregular peaks described above). The curve of peak position *versus* temperature can be drawn as a smooth curve joining the more or less linear portions of the ordered and disordered phases. Thus, based on the evidence at hand it would be very difficult to state that the transformation is heterogeneous for samples containing less than 25 per cent gold.

There is a possibility that the transformation on the copper-rich side of Cu_3Au is a heterogeneous one, with the failure to detect the two phases being due primarily to the difference in size of the two atoms. The combination of circumstances which make the detection of two phases difficult in this region can be seen more clearly by referring to Figure 1.

Consider the disordered composition D, which when cooled to a certain temperature separates into the two phases with compositions D' and D''. D', the disordered phase, is relatively poorer in gold and thus has a smaller cell size than composition D. D'', although ordered and consequently reduced in cell size from a disordered alloy of composition D'',

is rich in gold compared to D and thus is relatively larger. It is possible that these conditions combine to cause a near superposition of the peaks so that two phases, if present, are not detected by the present method.

A sort of "inverse" reasoning applies in the gold-rich side of Cu_3Au so that there the condition is more favorable for detection of two phases than might be expected if both atoms were of the same size.

Summarizing, the most we can say of the transformation on the copper-rich side is that if it be two phase, the two-phase region must span a narrow composition range.

It is impossible to state that one has demonstrated an equilibrium process in an experiment such as the present one if the desired temperatures are approached only from one direction. All the work discussed to this point was done by heating well-ordered samples. This method was used because equilibrium is reached much more quickly on heating than on cooling.

In order to determine whether or not we were dealing with an equilibrium phenomena, the 28 per cent sample was repeated, using a cooling technique. The results are shown in Figure 5. The sample was heated to 422°C and held at that temperature for 48 hours. It was then cooled to approximately 380°C and held at that temperature for 21 days. No effect on the line, other than a slight broadening, was noted until the sample had been at temperature for over ten days. After 15 days it was clearly evident that the initial results were reproducible. This long "incubation" period supports the evidence found by other workers [4] studying electrical resistivity.

It is both interesting and surprising that on cooling to lower temperatures (in 2 or 3°C intervals) the equilibrium was much faster. In fact, the sample was held at no temperature (other than 380°C) for more than 200 hrs. In spite of this, the stages in the transformation are clearly indicated as illustrated in Figure 5. We have included in the figure a tracing of the line obtained from the sample when it was quenched from 422°C. This allows a comparison with the line taken at temperature. The higher temperature apparently produces approximately a 15 per cent increase in half-width.

We would like to emphasize that although we have used the word "equilibrium" in our discussion, we do not believe that we attained an absolute thermal equilibrium in all cases. However, we do believe that we have approached equilibrium to the degree that the conclusions are valid. In all cases the evidence was that the situation could not be materially improved in any reasonable time (for example, 21 days at 380°C for the 28 per cent sample).

Figure 6 gives a qualitative picture of the transformation as determined from our data. There is no claim made for accuracy, since the individual points have a possible error of at least ±5°C. The

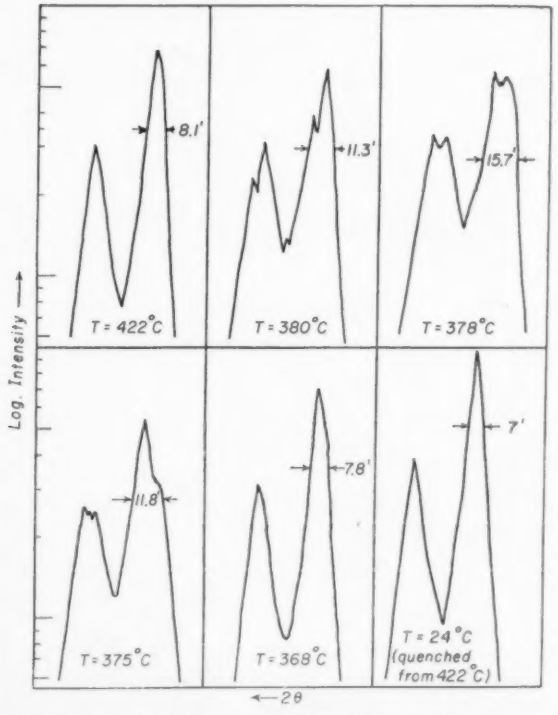

FIGURE 5. (4,0,0) Line shapes of 28% sample for decreasing temperatures.

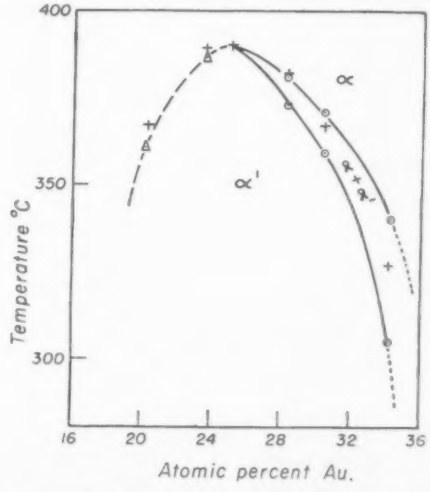

FIGURE 6. Phase boundaries of ordered region as determined from X-ray diffraction study.

points on the copper-rich side were taken as the lowest temperatures at which definite asymmetry was first visible on the low-angle side of the line, and the highest temperature at which it was seen on the high-angle side of the line. The points on the copper-rich side were taken as the temperature at which the slope of line position *versus* temperature was steepest. The dashed line thus represents what would be the critical temperature for a homogeneous transformation.

It is probable that somwhat more positive evidence could be obtained from an experiment of this kind by incorporating a few changes in the experimental set-up. First of all, it is obvious that one should measure the line position at the highest possible angle, in order to obtain maximum resolution. In order to do this, one could use CoK_α radiation. Unfortunately no cobalt target X-ray tube was available to us. Secondly, it would be advisable to set more stringent criteria on the equilibrium conditions. These would include allowing the samples to remain at a given temperature for very long periods of time, perhaps more than 30 days. This, of course, would require several years to complete the range of compositions studied here, and consequently is impractical except under the most unusual conditions. However, it remains that really incredibly long times are going to be required to make certain that the samples are in their most perfect equilibrium condition, and particularly that nuclei of the second phase have had a chance to grow to their maximum size.

B. LONG-RANGE ORDER IN CU-AU ALLOYS

Introduction

Alloys of copper and gold, near the composition Cu_3Au, at temperatures above the critical temperature for ordering, exhibit a disordered face-centered cubic structure, but below the critical temperature, in the ideal case, the structure is ordered with the copper atoms occupying the face-centered position. In the non-ideal, or normal situation, varying degrees of long-range order may be ascribed to the crystal, the most common designation being the Bragg-Williams long-range order parameter, S.

The degree of long-range order present in a particular alloy as designated by the parameter S can be interpreted in two ways. The first interpretation arises when it is established that there is only one phase present in the alloy, i.e. the ordered phase, below the critical temperature. In this case, S is to be interpreted in the manner of Bragg-Williams, as a parameter indicating to what degree the correct sites are occupied by the correct atoms. On the other hand, if the classical phase change is assumed, so that ordered and disordered phases are present in equilibrium near the critical temperature, then the square of the long-range order parameter gives a measure of the material in the ordered state. Thus, regardless of the nature of the transformation, values of the parameter S are of interest.

To date, too little work has been done on the determination of the long-range order parameter by X-ray means [9; 10; 11], and these have been determined for the stoichiometric composition. Hence it was decided to measure this parameter for alloys not having the stoichiometric Cu_3Au composition, since the samples were available under the proper conditions in the course of the preliminary work on the nature of the transformation. It must be admitted that the use of single crystals does not represent the most desirable sample condition for measuring long-range order. However, the nature of the transformation work required single crystals and was regarded as relatively more important in our choice of samples.

A value of S can be obtained experimentally at the desired temperature by comparing the X-ray integrated intensity of superstructure reflections to the integrated intensity of principle reflections. It has been shown [11] that if the long-range order parameter is S_0 at room temperature, at some elevated temperature it can be obtained from

$$S = S_0\left[\left(\frac{P_T}{P_0}\right)_{\text{sup.}} \times \left(\frac{P_0}{P_T}\right)^{\gamma}_{\text{fund}}\right]^{\frac{1}{2}}$$

where

$$\gamma = (h^2 + k^2 + l^2)_{\text{sup}}/(h^2 + k^2 + l^2)_{\text{fund}}$$

$\left(\frac{P_T}{P_0}\right)_{\text{sup}}$ = ratio of elevated and room temperature intensities of a superstructure reflection

$\left(\frac{P_0}{P_T}\right)_{\text{fund}}$ = ratio of room and elevated intensities of a fundamental reflection.

The value of S_0 can be obtained from detailed comparison with a fundamental line, if secondary extinction can be ignored. This has not been done in the present work since single crystals were used, and no reliable way has been devised to correct for extinction in single crystals [12]. Instead, perfect order for the given composition has been assumed at room temperature, and the calculated

value of S_0 used. S_0 has been calculated assuming maximum possible order from the expression:

$$S = r_\alpha + r_\beta - 1$$

where r_α and r_β are the fractions of α and β sites properly occupied. The expression for S has been chosen from a consideration of the X-ray structure factors. It is important to recognize that if any different value of S_0 were the correct one, the only result would be to multiply the given values by a constant factor.

The Experiment

The same crystals were used for this work as were used for the work described in Part A of this paper. They were also given the same "ordering" treatment as described there.

The samples were mounted in a specially constructed furnace which is shown schematically in Figure 7. The samples were mounted on one inch

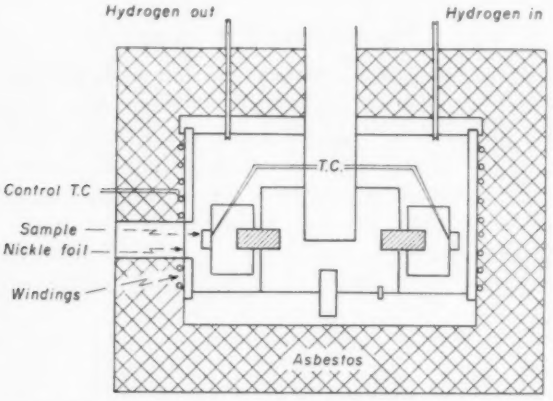

FIGURE 7. Furnace used for studying six samples concurrently, at temperature.

diameter cylindrical copper blocks 5/8 inch thick, which were threaded onto studs fitted into the main furnace post. This permitted the samples to be moved in a horizontal plane to the center of the spectrometer table for alignment in the beam. The main furnace post was a carefully milled hexagonal copper block which rotated on a copper pin fitted into the copper base. The rotational position was defined by a pin fixed in the base positioned so that the hexagonal faces of the main furnace post allowed the crystal faces (which were parallel to the hexagonal faces) to satisfy the Bragg condition at all times. The hexagonal post was raised and rotated by means of a refractory tube which also served as a means of entry for thermocouples which were placed in contact with the rear of the samples (see Figure 7). The resistance heating element was wound on a cylindrical copper can which screwed onto the base. A 120 degree entrance and exit slit was milled into this winding support and covered with a 0.0002-inch nickel foil. Refractory tubes through the top of the furnace and through the asbestos insulation which surrounded the entire assembly provided an inlet and outlet for the hydrogen gas which was used to prevent oxidation. The temperature was controlled by Chromel-Alumel thermocouples placed near the furnace winding. This thermocouple was used in conjunction with the electronic control circuit mentioned in Part A of this paper.

Monochromatic CuK_α radiation and the "homemade" slit arrangement previously mentioned were used throughout the experiment.

The samples were heated to a given temperature and allowed to remain at that temperature until the integrated intensity of the superstructure reflection approached an equilibrium value. The superstructure line used in the present work was the (3,0,0) reflection, the fundamental line used was the (4,0,0) reflection. It was found that just below, as well as above, the critical temperature, the superstructure intensity approached equilibrium with extreme rapidity, but a minimum of two hours was allowed in this region (when points were taken every few degrees) to avoid a possible non-equilibrium situation. The times allowed for the samples to reach equilibrium at the different temperatures were not greatly different from those given in Table I, except at the high temperatures where the time was approximately 4 hours.

The actual technique used to obtain the integrated intensities of the lines was as follows: The beam slits limited the monochromatic beam to a divergence of less than one-half a degree, illuminating an area of 0.044 in. by 0.20 in. of the approximately 1/4 in. diameter samples. The reflected radiation passed through a counter slit with enough (2.2° in 2θ) to allow all the radiation from a diffraction peak to enter the counter chamber. The diffuse background was taken on both sides of the peaks with the same slit arrangement, and one-half the sum subtracted from the peak intensity.

Results

Values of S, at various temperatures, for the various samples are given in Tables II and III. The value of S for the 15 per cent sample does not appear in the tables since we were unable to obtain a quantitative value of the long-range order para-

TABLE II

VALUE OF THE LONG-RANGE ORDER PARAMETER FOR VARIOUS TEMPERATURES

20 Atomic Per cent Au				23 Atomic Per cent Au			
Temp. °C	S/S_0	S^*	S^2	Temp. °C	S/S_0	S^*	S^2
26	1	.810	.657	26	1	.938	.880
100	.981	.795	.631	258	.965	.905	.819
150	.994	.805	.649	300	.943	.885	.782
220	.989	.801	.641	325	.932	.874	.762
238	.982	.795	.631	333	.908	.851	.723
262	.983	.796	.632	348	.872	.818	.669
327	.887	.719	.517	363	.757	.710	.503
335	.859	.695	.483	366	.732	.687	.472
340	.817	.662	.439	372	.684	.641	.411
346	.812	.658	.433	373	.680	.638	.405
349	.756	.613	.375	379	.363	.341	.116
315	.723	.583	.340	382	.283	.266	.071
354	.705	.571	.327	384	.217	.202	.041
357	.557	.451	.204	386	.171	.160	.026
360	.388	.314	.098				
362	.330	.268	.072				
363	.282	.228	.052				
368	.190	.154	.024				

*S_0 calculated from $S = r_\alpha + r_\beta - 1$, assuming maximum possible order.

meter for this sample. However, for temperatures below 350°C, some order was present as evidenced by an extremely broad maximum in the region of the expected superstructure peak. This maximum is illustrated for one temperature in Figure 8, and spans an angular breadth of at least 30 degrees in 2θ. This maximum is presumably due to the equivalent of a high degree of short-range order; long-range order being absent simply because of an insufficiency of gold atoms.

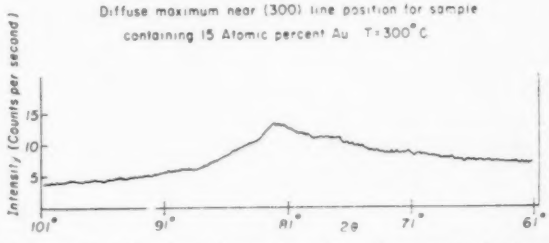

FIGURE 8. Tracing of recorder chart (reduced) obtained for 15 per cent gold sample.

In Figures 9*a* through 9*e*, values of S and S^2 are plotted against temperature for the 20, 23, 28, 30, and 34 per cent samples. The lowest data points shown represent the highest temperature at which quantitative measurements could be made. These curves are extrapolated to $S = 0$ at those temperatures for which a peak such as is shown in Figure 8 was no longer observable.

Discussion of Results

Both S and S^2 are plotted in Figures 9*a* through 9*e* because of some uncertainty in the nature of the transformation. It appears as though the transformation in samples containing less than 25 per cent gold atoms could well be a homogeneous one. At the same time, for samples containing more than 25 per cent gold atoms, there is little doubt that the data in Part A indicates a two-phase transformation.

TABLE III

VALUES OF THE LONG-RANGE ORDER PARAMETER FOR VARIOUS TEMPERATURES

28 Atomic Per cent Au				30 Atomic Per cent Au				34 Atomic Per cent Au			
Temp. °C	S/S_0	S^*	S^2	Temp. °C	S/S_0	S^*	S^2	Temp. °C	S/S_0	S^*	S^2
26	1	.957	.915	26	1	.927	.861	26	1	.877	.769
197	.925	.885	.782	150	.984	.912	.831	197	1.003	.880	.773
220	.939	.898	.807	197	.950	.881	.777	220	.980	.860	.739
327	.833	.796	.632	238	.897	.832	.692	238	.956	.839	.703
335	.819	.784	.612	262	.850	.779	.621	262	.901	.790	.624
340	.813	.778	.603	280	.820	.761	.580	280	.816	.716	.512
363	.749	.716	.512	297	.816	.758	.573	297	.581	.510	.260
366	.738	.706	.499	327	.750	.696	.485	304	.447	.392	.154
369	.724	.692	.479	335	.728	.675	.455	308	.360	.316	.100
373	.662	.634	.401	340	.722	.670	.449	310	.329	.288	.083
376	.573	.548	.300	354	.627	.582	.339	313	.286	.251	.063
378	.412	.394	.156	363	.296	.275	.076	318	.237	.208	.043
379	.297	.284	.081	366	.197	.183	.033	320	.183	.161	.026
380	.176	.168	.028	370	.120	.113	.013	323	.155	.136	.018
382	.115	.110	.012								

*S_0 calculated from $S = r_\alpha + r_\beta - 1$, assuming maximum possible order.

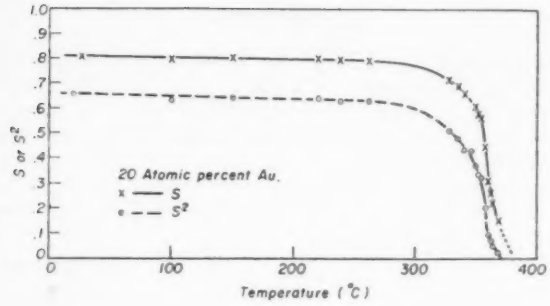

(a)

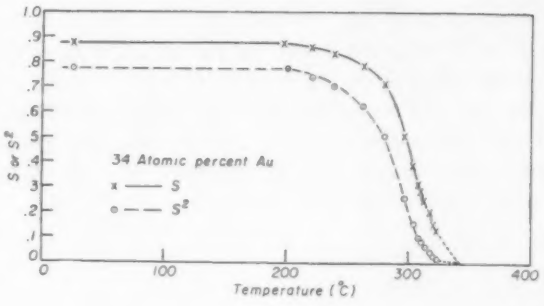

(e)

FIGURE 9. Variation of long-range order with temperature.

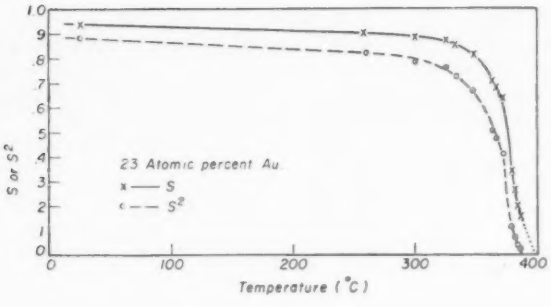

(b)

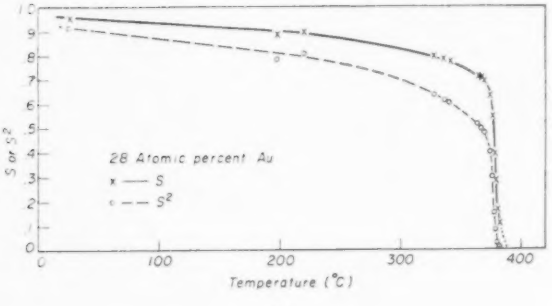

(c)

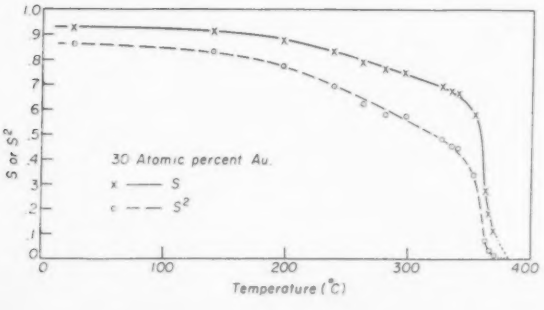

(d)

Since the transformation throughout the region investigated is possibly a two-phase one as mentioned previously, the "tail" on the plot of *S versus* temperature no longer seems to be as much a result of experimental limitations as originally thought. One would not expect the volume of an ordered phase to diminish slowly initially followed by a precipitous disappearance. Rather one would expect the dimunition of the ordered phase to occur slowly initially, then becoming more rapid until nearly all the material is in the disordered state, followed by a "tailing-off." That the completion of the disordering process occurs slowly is borne out by the detection of short-range order at temperatures considerably above the so-called critical temperature [10; 13]. It should be pointed out that the detection of short-range order at temperatures considerably above the so-called critical temperature, and for relatively large distances from a given origin atom, in no way invalidates the conclusion of a two-phase transformation. The short-range order observations, previously reported [10; 13], do not indicate the presence of a distribution which for each shell would be somewhere between randomness and perfect order. The identical result would be achieved for a system containing very small regions of ordered material widely dispersed, due to the averaging process inherent in the method of analysis.

The meaning of a critical temperature is at best uncertain in view of the results of the present experiment. However, since the term has had such venerable usage, and since a critical temperature can be defined from the results of long-range order studies, we have included in Figure 6 (the + points) the "critical" temperatures taken from the plot of *S versus* temperature. We have defined the "critical" temperature in the present work by an extrapolation of the relatively precipitous portion of the

curves of *S versus* temperature. On the gold-rich side of Cu_3Au the points so defined fall generally within the two-phase region. On the copper-rich side the points are all above the points determined from line position as a function of temperature. No particular significance is attached to this, other than experimental uncertainty.

Acknowledgments

The authors would like to express their appreciation to Professor Foster C. Nix for his interest and advice throughout the course of this work. Also a note of thanks goes to Mr. Fred Witt, Jr. for his aid in solving many of our experimental problems. The work was supported by the Flight Research Laboratory, U.S.A.F.

References

1. See for example, the review article by Nix, Foster C. and Shockley, William. Rev. Mod. Phys. **10** (1938) 1.
2. Newkirk, J. B., Geisler, A. B., Martin, D. L., and Sholuchowski, R. Trans. Amer. Inst. Min. Met. Engr. **188** (1950) 1249.
3. Borelius, G. J. Inst. Metals **74** (1947) 17.
4. Rhines, F. N. and Newkirk, J. B. Trans. Amer. Soc. Met. **45** (1953) 1209.
5. Nix, F. C. and MacNair, D. Phys. Rev. **60** (1941) 320.
6. Sanville, W. W., Nix, F. C., and Jaumot, Frank E. Jr. Bull. Am. Phys. Soc. (for North Carolina Meeting, March 1953, Paper 4–5).
7. Sykes, C. and Evans, H. Jr. Inst. Metals **58** (1936) 255.
8. Nix, F. C. Rev. Sci. Instr. **9** (1938) 426.
9. Wilchinsky, Z. W. J. App. Phys. **15** (1944) 806.
10. Cowley, J. M. J. App. Phys. **21** 24 (1950).
11. Keating, D. T. and Warren, B. E. J. App. Phys. **22** 286 (1951).
12. James, R. W. The Optical Principles of the Diffraction of X-rays (London, G. Bell and Sons, Ltd., 1950).
13. Sutcliffe, C. H. and Jaumot, F. E. Jr. Acta Met. **1** (1953) 725.

COHERENT GROWTH OF MARTENSITE DURING TEMPERING*

T. KO†

It is shown that martensite plates in a 1.5% C 5.0% Ni steel can, during tempering, thicken or grow into bainite. It is suggested that this supports the author's view on bainite formation that the reduction in volumetric strain by the removal of carbon in the form of carbide during the formation of bainite provides part of the additional driving force needed for the coherent growth to proceed. The results also suggest that the austenite-martensite interface remains coherent after the development of a martensite plate has ceased.

LA CROISSANCE COHÉRENTE DE LA MARTENSITE PENDANT LE REVENU

Il est montré que pendant le revenu d'un acier à 1,5% de C et 5,0% de Ni, des lamelles de martensite peuvent grossir, ou se transformer en bainite. Il est suggéré que ce fait appuie l'opinion de l'auteur, que la réduction de la déformation volumétrique par l'enlèvement de carbone sous forme de carbure, pendant la formation de la bainite, fournit une partie de la force supplémentaire, nécessaire à la croissance cohérente. Les résultats suggèrent aussi, que l'interface austenite-martensite reste cohérente après la fin du développement d'une lamelle de martensite.

STETIGES WACHSEN VON MARTENSIT BEIM TEMPERN

Es wird gezeigt, dass Martensit-Plättchen in einem Stahl mit 1,5% C und 5% Ni während des Temperns durch Dicken- oder Längenwachstum in Bainit übergehen können. Es wird angenommen, dass das die Ansicht des Verfassers über die Bainit-Bildung unterstützen konnte, wonach die Verminderung der räumlichen Verzerrung durch die Entfernung des Kohlenstoffs als Karbid während der Bainit-Bildung einen Teil der zusätzlichen treibenden Kraft darstellt, die für die Fortsetzung des stetigen Wachstums notwendig ist. Die Resultate deuten weiterhin darauf hin, dass die Austenit-Martensit Grenzfläche kontinuierlich bleibt, nachdem die Bildung des Martensitplättchens beendet ist.

Introduction

Bainite in steel forms by a mechanism very similar to that of martensite except that the coherent growth of bainite is very slow. It has been suggested [1; 2; 3] that the growth of a bainite plate is controlled by the removal of carbon, which occurs by diffusion into the austenite, by precipitation of carbide within the bainite, or by a combination of both. These processes (i) reduce the strain due to the specific volume change, and (ii) increase the chemical free energy of the transformation; they thus increase the driving force for coherent growth.

According to these views it might be expected that, during tempering, growth of a martensite plate would take place due to a reduction in strain provided that the austenite-martensite interface remains coherent after the initial formation of the plate. Such growth would take place as a result of the reduction in strain, independent of the chemical free energy, because the free energy change due to the removal of carbon from the martensite on tempering is available only for the precipitation of carbide.

A study of the possible growth of martensite plates is also useful for providing a direct indication of whether the cessation of their initial growth is due to the destruction of interfacial coherency, as was suggested by Kurdjumov (4).

Experimental

The coherent growth of martensite during tempering should lead to the formation of either martensite or bainite, depending on the relative rate of tempering and of bainite formation from existing nuclei. It may be expected therefore that a high carbon steel, which can be tempered readily but is slow in bainite formation, is most suitable for observing the growth of martensite.

A high-frequency-induction melted steel containing 1.5% C, 5.0% Ni, 0.45% Si and 0.3% Mn was used. The forged bars, 1.4 cm diameter, were homogenized in vacuo for two weeks at 1050°C and sliced into half-round discs 2.5 mm thick. These were austenitized in argon at 1220°C for one hour and water-quenched to 5°C. The specimens were then polished electrolytically in a solution containing 7 volumes of ethyl alcohol, 2 volumes of perchloric acid and 1 volume of glycerine, sealed in vacuo, and tempered at 100°C and 300°C or 350°C for various periods. A few specimens made by carburizing a 5% Ni steel [5] were also used.

The surface of a specimen after tempering is shown in Figure 1. Surface distortion adjacent to the martensite plates (white) could be clearly seen. When it appeared on both sides of the martensite plate, one side usually consisted of a ridge, the other a valley; but the change more often took

*Received July 13, 1953.

†Formerly Lecturer, The University of Birmingham, England.

place on one side only. By anodically colouring the austenite before tempering, the distortion could be shown to take place always in the austenitic regions.

These distortions corresponded, after polishing, to a rim round the martensite plate. After one hour of tempering at 100°C a few martensite plates could be seen to have grown, with a rim lighter-etching than the tempered martensite (Figure 2). The number of plates possessing this rim increased with increasing time of tempering, but there was no evidence that the rim grew in thickness. Specimens tempered for long periods up to 10 days showed only dark-etching martensite, occasionally with traces of the rim. This indicates that the formation of the rim took place in the early stages of tempering.

Tempering at 300°C for 30 seconds was sufficient to produce a light-etching rim, and after one minute, a dark-etching rim began to appear, the thickness of which increased with increasing time. Similar results were obtained at 350°C except for the shorter time required to produce these effects. The dark rim could form directly on the original martensite (Figure 3) or on the light-etching rim (Figure 4). Dark-etching whiskers, closely resembling the bainite directly formed from the austenite in this type of steel, appeared on the dark-etching rim after about 15 minutes of tempering at 300°C and 10 minutes at 350°C and the transformation was completed by bainite formation. Both the kinetics and the structure indicate that the dark-etching rim was formed by the bainite mechanism, and the light-etching rim by the martensite mechanism.

Discussion

(i) *The Growth of Martensite*

In the steels used, both martensite and bainite can form from the martensite by further coherent growth. In the photographs of martensite shown by Lucas [6], light-etching rims were also present around the slightly dark-etching martensite formed from an austenite containing about 1.5% carbon [6, Figures 8 and 17]. These rims were probably formed by the tempering effect of mechanical polishing [7]. In the case of steels with lower carbon contents, such as 1.0% C, 1.5% Cr, 1.2% C 2.5% Ni and 1.0% C 5% Ni steels [8], only bainite has been observed to form directly from the initial martensite plates. Jellinghaus (9) has also observed the formation of bainite as a dark rim on martensite in a 1.2% C 3.2% Mn steel.

The martensitic rims cannot be new martensite plates formed adjacent to the original plate, as the martensite plates in these steels always form at an angle, presumably to reduce the residual stresses [10]. It is also clear that the martensite had grown at tempering temperatures and not during the subsequent cooling, since the bainite structure could form around the light-etching martensitic rim.

The present study also indicates that the growth of martensite plates does not take place uniformly along all the austenite-martensite interface. Furthermore, martensite plates having the same habit planes and orientation relationship in a single austenite grain do not all grow at the same time, although the rate of tempering may be expected to be very similar. This suggests that there are imperfections at the interface which interfere with the growth.

The formation of a bainitic rim which is more readily attacked by etchants than the martensitic rim formed earlier at the same temperature indicates that the dark-etching nature of the lower bainite cannot be attributed entirely to precipitation of carbide during or after its formation. It appears that some changes in the austenite occur during incubation, which facilitate the precipitation of carbide during bainitic growth. Clustering of carbon has been suggested as a possible occurrence [1].

(ii) *The Coherency of the Austenite-Martensite Interface*

Kurdjumov [4] has suggested that, when a martensite plate grows to a certain thickness, the strain may become so large that plastic deformation takes place at the vicinity of the moving interface. The coherency would thus be destroyed, and the growth of martensite stopped. Similar arguments have been advanced by others [11; 12]. The present observation that martensite can grow coherently on tempering indicates that this suggestion is not correct, at least in the high carbon steels. In such steels the habit planes of martensite and the slip planes of austenite are not the same, and any plastic deformation in austenite accompanying the transformation must take place by slipping in planes different from the moving interface. Although the coherency of the interface may be interrupted at some places, it should be maintained at others.

In low carbon steels where the habit planes of martensite are the same as the slip systems of austenite, Kurdjumov's mechanism may be operating. There is evidence, however, that in such steels

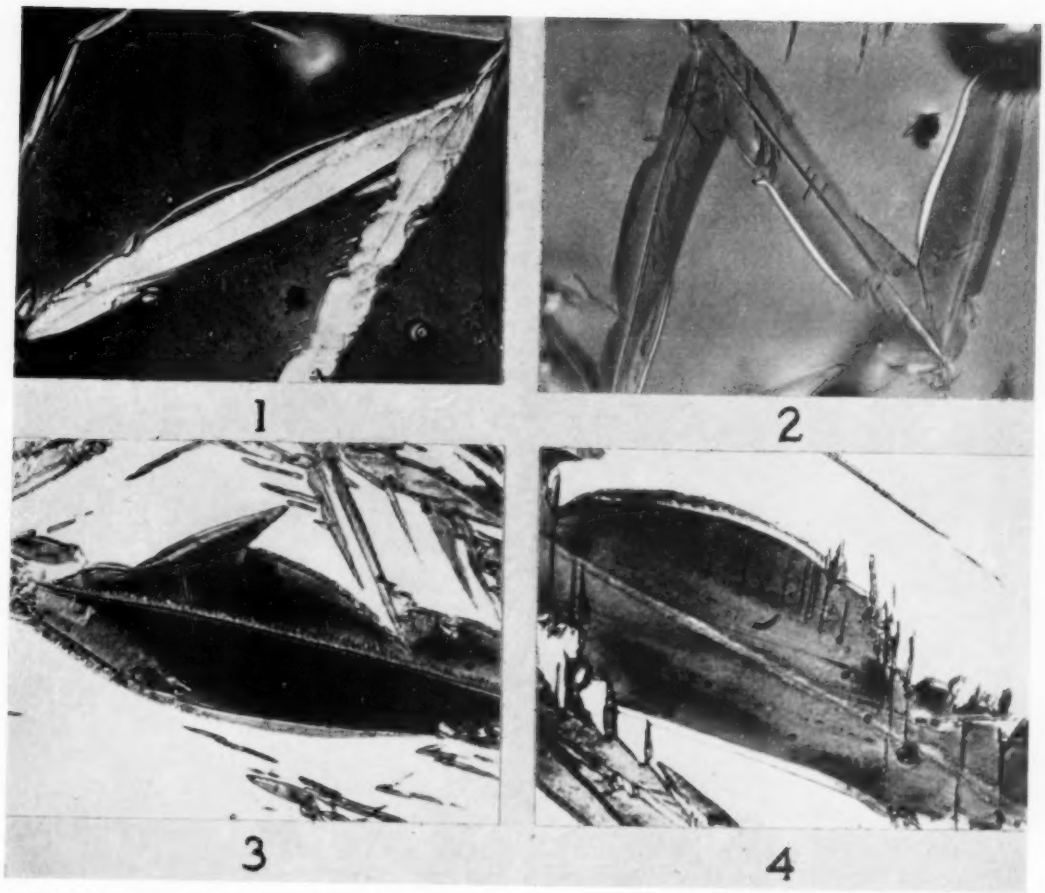

PLATE I. FIGURE 1—The surface relief associated with rim formation (600×). FIGURE 2—Martensitic rims associated with tempered martensite plates. Tempered 1 hour at 100°C (500×). FIGURE 3—The formation of martensitic and bainitic rims directly on martensite. Tempered 4 minutes at 350°C (1200×). FIGURE 4—The formation of bainitic rim on a martensitic rim. Tempered 4 minutes at 350°C (2000×).

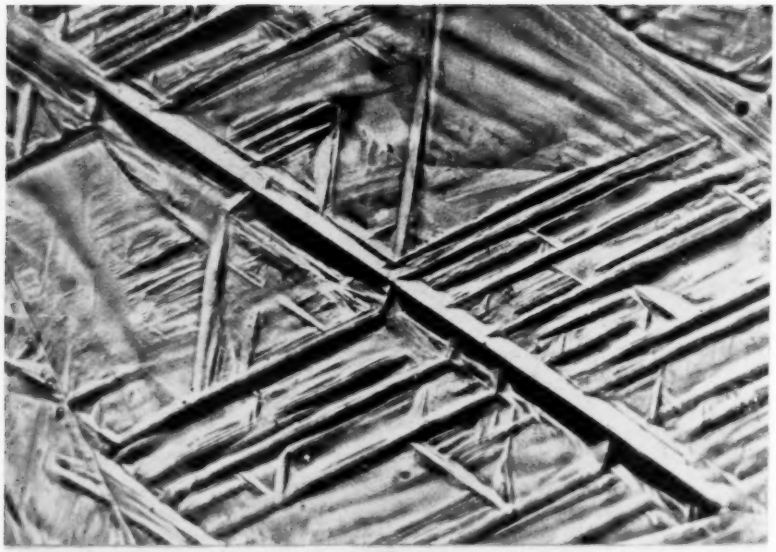

5

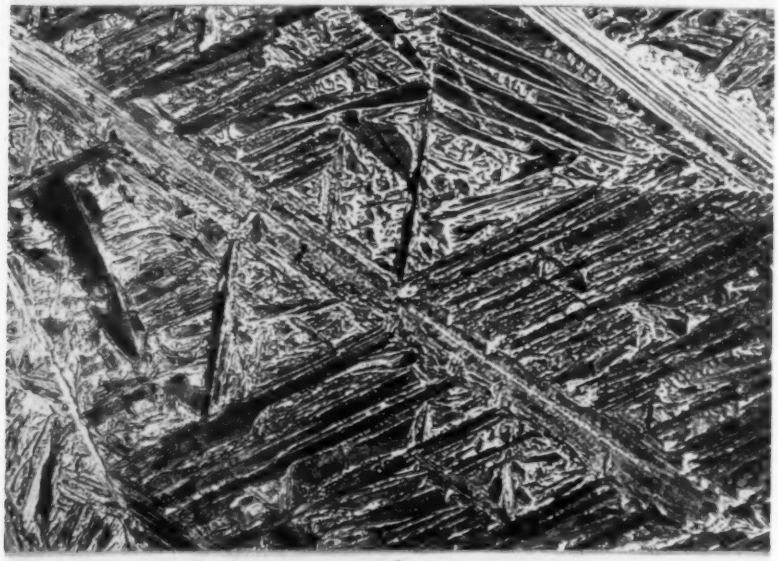

6

PLATE II. FIGURE 5—Surface relief associated with the formation of martensite in a 0.3% C 3.5% Ni steel (600×). FIGURE 6—Same as Fig. 5. Surface relief removed (600×).

plastic deformation may also take place without destroying the interfacial coherency. Figures 5 and 6, taken from a low carbon steel containing 3% Ni and 0.33% C, before and after surface relief due to martensite formation had been removed, show a number of small parallel martensite plates joining the main plate in the centre of the grain at the middle of its sloping surfaces. This indicates that the formation of these plates must have begun along their ridges. The parallel martensite plates in Figure 5 correspond to the smooth halves of the parallel ridges (in shadow in Figure 6), while the other halves are occupied by a number of smaller plates. These smaller plates formed, probably later from the accommodating austenite, in this manner presumably because the movement of the accommodating austenite was limited by the presence of adjacent martensite plates, and it was much easier to form a series of martensite plates each with limited movement of material. Alternatively, as martensite can only form from austenite by shear in one direction, further growth of martensite into the accommodating austenite without deformation must result in an increase in the height of the surface relief without any change in the slope. In other words, martensite formed without deformation should correspond to only one uninterrupted inclined surface. In the case of the central plate, however, both sides of the hill belong to the same martensite plate; the large scale movement of the iron atoms involved, during the crystallographic shear in the same direction when the accommodating austenite changed to martensite by further growth, must have been compensated by plastic deformation during transformation. This deformation had not prevented the development of the full plate or caused the destruction of the interfacial coherency.

It has been observed [13] that plastic deformation of austenite during the formation of martensite also occurs in regions far away from the martensite. This uniform distribution of slip lines in austenite could not occur if Kurdjumov's suggestion was correct, as the martensite growth should have stopped before the deformation became so extensive.

Kurdjumov [4] made a valuable suggestion that there must be martensite transformations in which the whole deformation is elastic, and there should be no hysteresis between the transformation on cooling and the reversed transformation on heating. This led to the discovery of totally thermo-elastic martensite in a Cu-Al-Ni alloy [14]. In the light of present results, it appears that while their interpretation of the mechanism of thermo-elastic martensite formation remains correct, their suggestion that the hysteresis between cooling and heating martensitic transformations is due to the destruction of interfacial coherency must be modified. It is more reasonable to suggest that it is the plastic deformation accompanying the nonelastic martensitic transformation that makes the reversal more difficult, by increasing the resistance to the formation of the new phase. That this view is substantially correct has been shown [13] by the depression of the martensitic transformation temperature in an Fe-Ni alloy during cooling, from about -80°C in virgin austenite to below -180°C after repeated cycles of transformations. In this alloy both the transformation during cooling and the reversed transformation during heating had been accompanied by extensive plastic deformation in the austenite, which rendered subsequent transformation more arduous. Consequently, the Ms was depressed and the temperature hysteresis between heating and cooling transformations increased after the alloy had been subjected to repeated transformations.

Acknowledgments

This research was carried out under the general direction of the late Professor D. Hanson, Director of the Departments of Metallurgy and Industrial Metallurgy, to whom the author's gratitude is due for his interest and encouragement. He owes much to Dr. H. M. Otte, who carried out some of the experimental work in the earlier stages. Thanks are also due to many of his other colleagues, especially to S. G. Glover, B. Edmondson and R. B. G. Yeo, for their assistance. The Mond Nickel Company Research Laboratory in Birmingham supplied one of the steels used in the investigation.

References

1. Ko, T. and Cottrell, S. A. J. Iron Steel Inst. **172** (1952) 307.
2. Cottrell, S. A. and Ko, T. J. Iron Steel Inst. **173** (1953) 224.
3. Ko, T. J. Iron Steel Inst. In the press.
4. Kurdjumov, G. V. Z. Tek. Fiz. **18** (1948) 999.
5. Otte, H. M. and Ko, T. J. Iron Steel Inst. **173** (1953) 31.
6. Lucas, F. F. Trans. Amer. Soc. Steel Treat. **6** (1924) 669.
7. Lucas, F. F. Trans. Amer. Soc. Steel Treat. **15** (1929) 339.
8. Private communications from S. G. Glover and B. Edmondson.
9. Jellinghaus, W. Arch. Eisenhüttenw. **23** (1952) 459.
10. Orowan, E. Symposium on Internal Stresses in Metals and Alloys. (London, Institute of Metals, 1948) p. 47.
11. Lyubov, B. Ya. Dok. Akad. Nauk SSSR **78** (1951) 895.
12. Frank, F. C. Acta Met. **1** (1953) 15.
13. Edmondson, B. and Ko, T. To be published.
14. Kurdjumov, G. V. and Khandros, L. G. Dok. Akad Nauk SSSR **66** (1949) 211.

MECHANICAL DEFORMATION OF ALUMINIUM BICRYSTALS*

R. CLARK† and B. CHALMERS‡

Aluminium specimens composed of two symmetrically oriented crystals having a common ⟨111⟩ axis were subjected to a tensile test. It was observed that the yield stress and the rate of work hardening increased with the orientation difference between the crystals. In the initial stages of plastic deformation a linear stress-strain region was observed; the length of this region became shorter as the rate of work hardening (i.e., the orientation difference) increased.

LA DÉFORMATION MÉCANIQUE DE BICRISTAUX D'ALUMINIUM

Des échantillons d'aluminium consistant en deux cristaux orientés symétriquement, ayant un axe ⟨111⟩ commun, furent soumis à un essai de traction. Il a été constaté que la limite élastique et la vitesse d'écrouissage augmentaient en même temps que la différence d'orientation entre les deux cristaux. Une région linéaire de la relation tension-déformation fut observée durant les premiers stades de la déformation plastique; la longueur de cette région diminuait quand la vitesse d'écrouissage (c.-à-d., la différence d'orientation) augmentait.

DIE MECHANISCHE VERFORMUNG VON ALUMINIUM BI-KRISTALLEN

Es wurden Zugversuche an Aluminiumproben, die aus zwei symmetrisch orientierten Einkristallen mit gemeinsamer ⟨111⟩ Achse bestanden, unternommen. Es wurde beobachtet, dass die Fliessspannung und die Verfestigungsgeschwindigkeit mit zunehmendem Unterschied in der kristallographischen Orientierung der Kristalle zunahm. In den Anfangsstadien der plastischen Verformung wurde ein Gebiet mit linearer Spannungs-Verzerrungs Beziehung gefunden. Die Ausdehnung dieses Gebiets nahm mit zunehmender Verfestigungsgeschwindigkeit (d.h. zunehmendem Unterschied in der kristallographischen Orientierung) ab.

Introduction

It has long been observed during the plastic deformation of polycrystals that there exists a mutual interaction between neighbouring crystals that influences the mode and the extent of the deformation in each crystal concerned [1–7]. Chalmers' [5] experiments with tin bicrystals, for example, showed that neighbouring crystals have a marked effect in inhibiting slip in each other. The specimens consisted of two crystals identical with respect to the specimen axis (the axis of applied stress) but rotated about this axis with respect to each other. It was observed that the stress necessary to cause an arbitrary amount of plastic deformation increased with the orientation difference.

Boas and Hargreaves [3] have shown that in coarse grained polycrystalline samples, the strain near a boundary may either be greater or less than in the interior of the same crystal depending on the deformation of the neighbouring grain. It is evident that for the metal to remain continuous, the stress system must cause slip on systems that would not be observed in single crystals stressed in a similar manner. Chalmers [8] was of the opinion that this concept should be extended to include families of slip planes and directions never observed in the deformation of single crystals. More recently, an example of a new slip system becoming active has been observed by Craig and Chalmers [9]. They showed that, while the deformation of a zinc single crystal could be accounted for entirely in terms of slip on the basal plane in a $\langle 11\bar{2}0 \rangle$ direction, the deformation of a 'tricrystal' could not be so described. It was shown that, with boundaries present, slip occurred on an entirely new family of planes, as well as on the basal plane, in the boundary region. The boundary inhibited slip on the normal system sufficiently to allow the application of resolved shear stresses on other slip systems higher than those possible in a single crystal.

Cottrell [10] suggests that there may be three forces acting on a dislocation as it approaches a boundary, one long range, and two short range forces. The long-range force exists where the elastic constants are different beyond the boundary; as the dislocation approaches the boundary more of its strain field is imposed on the material beyond the boundary, and the energy to deform this is different from that to deform the material on the near side of the boundary. For a free surface, Koehler [11] showed that this force is inversely proportional to the distance of the dislocation from the surface. It should be remembered, however, that most metal surfaces are coated with oxide (or other metal compound) layers. Even internal boundaries in 'pure' metals may differ in composition from the crystals [12]. There is much experimental evidence to show that oxide films make slip more difficult in soft metal crystals [13–18]. This implies that such

*Received July 27, 1953.

†University of Toronto, Canada. Now at Norton Company, Chippawa, Ontario.

‡University of Toronto, Canada. Now at Harvard University, Cambridge, Massachusetts.

surfaces generally repel dislocations approaching from inside the crystal. Barrett [19] has demonstrated that a pressure of piled-up dislocations existed in plastically twisted, oxide-coated, zinc crystals. When the oxide layer was removed from a freshly twisted crystal, the crystal would spontaneously twist a little further as the piled-up dislocations were allowed to run out.

A study of the effects of intercrystalline junctions (i.e., the mutual interaction of neighbouring grains) would be quite difficult in ordinary polycrystalline metals. However, the problem can be greatly simplified by the use of specimens containing only a few large crystals and by preparing samples consisting of two or three crystals of controlled orientation. Such specimens can be produced by using 'seed' crystals of the desired orientation. This technique provides a powerful tool of the investigation of the properties and effects of grain boundaries as functions of the orientation difference existing across a boundary.

In the work to be described, rectangular bars composed of two crystals separated by a longitudinal boundary were subjected to a tensile test. The orientations were arranged such that there was a slip plane common to both crystals and inclined at 45 degrees to the specimen axis. A rotation through an angle ϕ about the normal to the common slip plane would bring one crystal into coincidence with the other.

Experimental

The experimental work consisted of (*a*) preparing rectangular bars of pure aluminium as single and bicrystals of controlled orientations, and (*b*) recording the stress-strain characteristics of the specimens when subjected to a gradually increasing stress.

The specimens were grown from the melt in an argon atmosphere using a technique described previously [20]. The aluminium was obtained from the Aluminum Company of Canada, and was reported to be 99.99 per cent aluminium. Spectrographic analysis showed the presence of small amounts of iron, magnesium, silicon, copper and titanium. Comparison of the original ingot metal with that in specimen form revealed no change in impurity concentration with the exceptions that silver and zinc appeared as new trace impurities in the specimens. Chemical analysis showed the major impurity, iron, to be 0.005 per cent and revealed an acid (HCl) insoluble residue amounting to 0.012 per cent (oxidized). Spectrographic analysis showed the major component of the residue to be titanium, with smaller amounts of magnesium, silicon, aluminium, copper and iron.

To produce uniform specimens, a machined graphite boat equipped with a cover was used. The boat is illustrated in Figure 1. The specimens (Figure 2) were approximately 1.3 cm wide, 0.5 cm

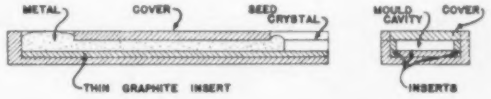

FIGURE 1. Graphite boat used to prepare specimens.

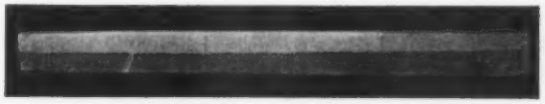

FIGURE 2. Typical specimen showing the direction of boundary and the gauge length markers.

thick, and 14–15 cm long. The metal was melted in a graphite crucible and poured into the boat. The specimens were parted from the excess metal at one end and the seed crystals at the other by means of a fine toothed saw.

Each specimen was etched in a solution of 9 parts HCl, 3 parts HNO_3, 2 parts HF, and 5 parts water; this revealed the presence of any stray crystals and showed the direction of the boundary in the bicrystals. The crystal orientations were determined by Greninger's back-reflection Laue method [21]. The striations [22] occurring caused an orientation distribution of 4 degrees to exist within the crystals.

A 5-cm (approx.) gauge length was marked on each specimen and accurately measured with a travelling microscope. The width and thickness of each specimen were measured with a micrometer, and the average cross-sectional area of their gauge lengths calculated. The specimens were annealed in air for five days at 630°C $\pm 5°$ and etched immediately prior to straining.

The tensile testing machine [23] was, in essence, the type described by Andrade and Chalmers [24]. Water was used as the load; the extension was measured with a single-mirror optical extensometer. The 'stresses' were calculated on the original specimen area and measured to the nearest gram/mm^2. Strain was measured to the nearest 2×10^{-5} cm/cm.

A slip plane, {111}, was fixed at 45 degrees to the specimen axis, the position of maximum resolved shear stress. Further, a ⟨110⟩ slip direction in the

slip plane was also fixed at 45 degrees to the specimen axis. This orientation is illustrated in Figure 3. A seed crystal, having the orientation shown in Figure 3, was rotated about the normal to the {111} plane (both clockwise and counter-clockwise) to prepare seeds for the single and bicrystal specimens. These rotations were labelled positive and negative respectively and caused the ⟨110⟩ slip directions to rotate in the {111} plane;

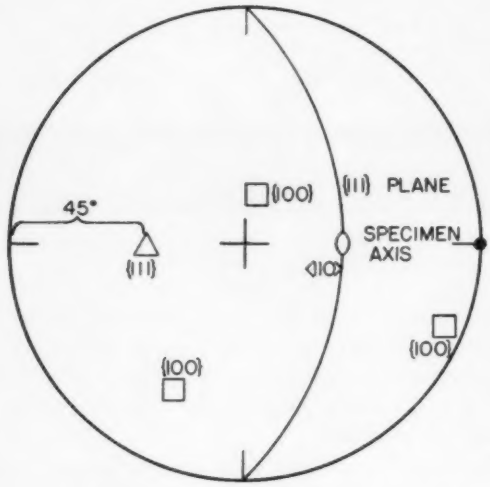

FIGURE 3. Stereographic projection showing initial orientation $\phi = 0°$.

the angle of rotation from the initial position was called θ. The seeds prepared by rotating the initial seed about the ⟨111⟩ axis, were 'paired' so that the average values of θ were equal ($\pm 1°$), but of opposite sign. Each pair of crystals was used to prepare a bicrystal seed; the difference in orientation between the crystals in these seeds was designated by $\phi = 2\theta$ degrees.

Observations and Results

Some difficulty was experienced in preparing aluminium crystals sufficiently free of 'striations' (22). Figure 4 illustrates an exceptionally large orientation distribution due to striations. The largest pin hole available (1–2 mm diam. spot.) was used to give good coverage to determine the widest orientation difference existing in any one crystal. In general, the spread was found to be 2–4 degrees. The 'best' crystals were prepared in a boat with graphite inserts as illustrated in Figure 1. The use of these thin inserts effectively reduces the lateral heat loss, and the ratio of the heat flow across the liquid-solid interface to that through the graphite boat is increased. These conditions favour the growth of single crystals free from striations and stray crystals. This effect has also been observed by other investigators [25].

Examination of the stress-strain curves obtained from the bicrystal specimens showed that the general form of the curve is as illustrated in

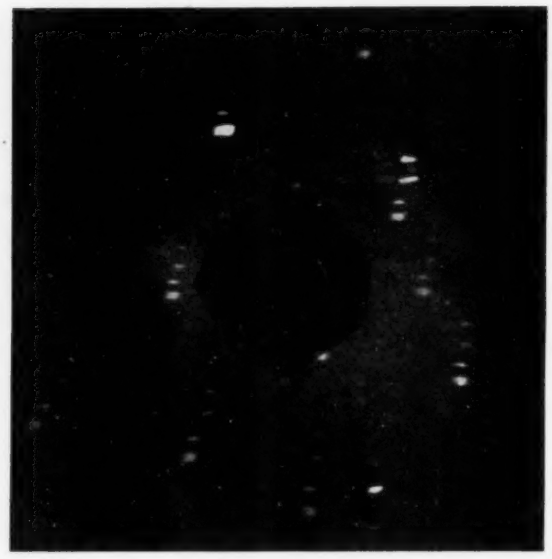

FIGURE 4. Unusually large orientation distribution caused by 'striations.'

Figure 5. There is an elastic range OA (approximately) where the stress is proportional to the strain, followed by the plastic region B–C where the stress-strain relation is linear but the slope of the curve is much less. Beyond point C, the proportionality between the stress and strain disappears and the curve rises more steeply. When no definite

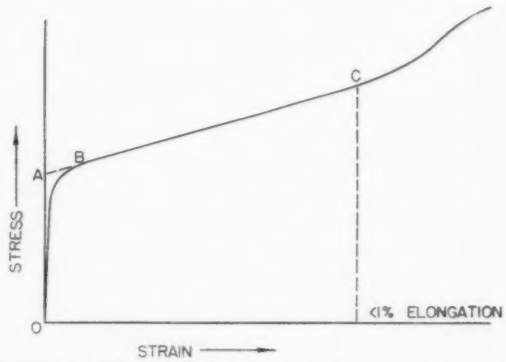

FIGURE 5. General form of observed stress-strain curve.

yield point is observed (as with these crystals) the normal procedure is to define the yield stress as the stress that causes a stated elongation of the speci-

men, e.g., 0.1 per cent. However, in this case, because of the linearity of the plastic region *B–C*, the yield stress was defined as that value of stress obtained by extrapolating the line *C–B* to zero strain. In Figure 5 the yield stress is represented by *OA*.

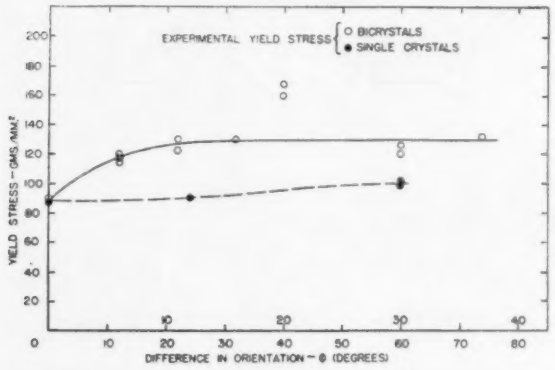

FIGURE 6. Plot of yield stress versus difference in orientation ϕ.

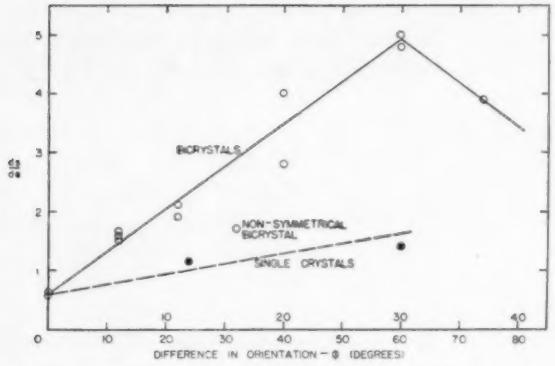

FIGURE 7. Plot of rate of work-hardening (ds/de) versus difference in orientation ϕ.

TABLE I

Specimen	ϕ Degrees	Strain at point *C* cm/cm × 10^4	Average strain cm/cm × 10^4
Single crystals		<80	
4*A*	12	>80	
4*B*	12	80	
4*C*	12	80	80
5*A*	22	80	
5*B*	22	70	75
6*A*	40	>35	
6*B*	40	40	40
7*A*	60	25	
7*B*	60	25	25
8*A*	74=46	40	40

The experimental results are shown as graphs in Figures 6 and 7. Figure 6 relates the observed yield stresses to the difference in crystal orientation, while Figure 7 relates the slope of the plastic region *B–C* to the difference in crystal orientations. The approximate strains at which the linear stress-strain regions ended (Point *C* in Figure 5) are shown in Table I. The presence of the boundary shortened the linear region as the orientation difference between the crystals was increased.

Discussion

As noted before, the specimens were prepared with a {111} plane common to both crystals. Before discussing the results described above, it may be useful to consider the relations between the crystals' axes as they are rotated with respect to each other about the common axis.

The ⟨111⟩ axis of rotation has three-fold rotational symmetry with respect to the unit cell of the crystals. Thus, when a crystal is rotated about this axis it reaches an identical position every 120 degrees. The position of maximum difference with respect to the original orientation occurs at a rotation of 60 degrees. Considering the ⟨110⟩ slip directions in the plane of rotation, it can be seen (Figure 8) that they have six-fold symmetry and thus repeat themselves every 60 degrees. Therefore, the maximum possible angular difference from the original and corresponding identical positions is 30 degrees.

The specimens used were composed of a 'pair' of crystals rotated about the common ⟨111⟩ axis through the same angle θ, one clockwise (positive) and the other counterclockwise (negative). When both rotations are 30 degrees, the angular difference (ϕ) between the crystals is 60 degrees. We see from the foregoing discussion that the slip directions in the common plane are again codirectional. That is, in terms of the ⟨110⟩ slip directions in the common plane the specimen would appear to be a single crystal. However, considering the general crystal orientations as defined by the ⟨100⟩ axes, the orientation difference between the crystals is the maximum. Figure 8 is a stereographic projection showing the relative positions of the major axes of the two crystals for $\phi = 60°$. It can be seen from the projection that the crystals are twins, i.e., mirror images in the common {111} plane. The projection shows the slip directions of the two crystals as being codirectional in the common plane. Utilizing the fact that the crystals are twins, it is possible to build a model illustrating the rela-

tive positions of the successive layers of atoms in the two crystals. The ideal face centered cubic structure can be described as an *ABCABC*..... stacking sequence of close-packed {111} planes, where the *B*- and *C*-layers are situated above alternate sets of hollows between the atoms of the

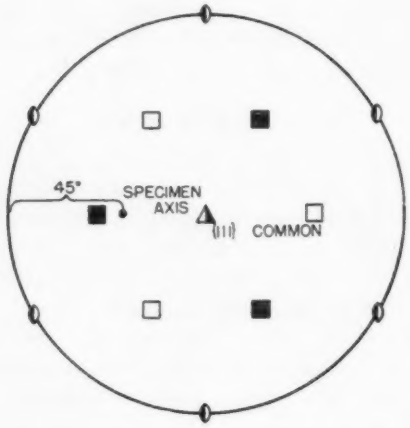

FIGURE 8. Stereographic projection showing the relative orientation of the crystals when $\phi = 60°$.

A-layer. In face-centered cubic structures the twinning plane is {111} and so the relation between twinned crystals may be illustrated by

A B C A B C A C B A C B A
Crystal I | Crystal II
Twinning plane.

The crystals in the specimen $\phi = 60°$ are twins and the relation between them is illustrated as follows:

Crystal I *A B C A B C A B C A B C* crystal
——————————— boundary
Crystal II *A C B A C B A C B A C B*

The crystals are looking, as it were, into the same side of the mirror plane. The boundary between the crystals is a noncoherent twin boundary. It can be seen that two out of four {111} planes (the *A*-layers) are identical; in the intermediate layers, the close-packed directions are codirectional but not collinear. The displacement is illustrated in Figure 9.

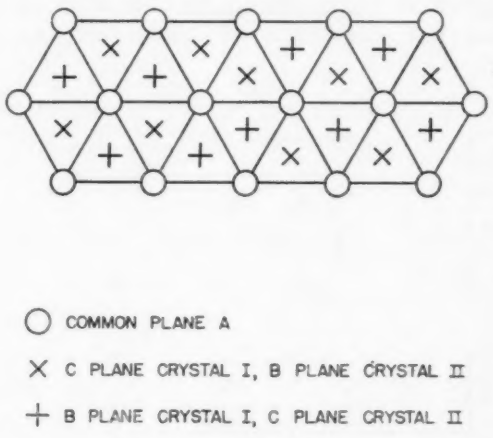

FIGURE 9. Diagram illustrating the stacking sequence of parallel common {111} planes for a bicrystal in which $\phi = 60°$.

Consideration of Figure 6 shows that the yield stress reached a maximum value of 130 gms/mm² at approximately $\phi = 30°$ (the maximum slip direction orientation difference) and remained constant up to $\phi = 60°$. There is a notable exception to this at $\phi = 40°$ Here the yield stress values reach as high as 170 gms/mm². These values were first considered to be in error since the operation of the slip system considered to be active (Figure 1) would result in a yield stress curve symmetrical about $\phi = 60°$. It was pointed out, however, that a new slip system becomes more favourably oriented for slip (in one crystal only) at approximately $\phi = 40°$.* The original slip system again becomes operative beyond $\phi = 60°$. It is possible that the operation of a different slip system could cause the large yield stress observed at $\phi = 40°$.

It is possible that the bicrystal specimens do actually begin yielding at the same stresses as the corresponding single crystals. Dislocations within the crystals far removed from the boundary would be expected to move at the same stress as in the single crystal. It is suggested that the boundary causes the moving dislocations to 'pile up' and effect a rapid increase in the stress necessary to (1)

*The authors are indebted to Dr. R. Maddin for this suggestion. At $\phi = 40°$ the slip system in both crystals was expected to correspond to $\chi = 45°$, $\lambda = 48°$($\sin\chi\cos\lambda = 0.472$). However, in the crystal rotated 20° in the counterclockwise direction, a system having $\chi = 42°$ and $\lambda = 44°$ ($\sin\chi\cos\lambda = 0.474$) is more likely to operate. At least, it could interfere with the initiation of slip.

move other dislocations and (2) produce the large number of new dislocations required to cause observable deformation. In this way, it would be possible to reach the stress required to overcome the slip inhibiting effect of the boundary before any observable plastic deformation had occurred. It might well be expected that the inhibiting effect would become less as the position $\phi = 60°$ is approached. Here, the crystals have one out of every three planes common in every sense to both crystals. Examination of Figure 6 shows that while the yield stress of the bicrystals is essentially constant from $\phi = 30°$ to $\phi = 60°$, the yield stress of the single crystals is increasing and reaches a maximum at $\theta = 30°$ (equivalent to $\phi = 60°$). The differences between the yield stresses of single crystals and the corresponding bicrystals are a measure of the inhibiting effect of the boundary; they are listed in Table II. It can be seen that at $\phi = 60°$ the boundary causes a smaller increase in the yield stress than at $\phi = 30°$.

TABLE II

Yield Stress gms/mm²		Difference gms/mm²	ϕ Degrees
S. Crystals	*Bicrystals*		
90	90	0	0
90	118	28	12
92	126	34	22
95	130	35	40
100	130	30	60

Examination of Figure 7 shows that, as well as inhibiting the initiation of the deformation process, the presence of the boundary increased the rate of strain hardening. In the initial stages of the plastic deformation, the relation between the stress and strain was linear. The slope of this region was greatest at $\phi = 60°$ the position of maximum orientation difference. The difference between the slope $\left(\frac{ds}{de}\right)$ for the bicrystals and the single crystals is a measure of increase in the rate of strain hardening caused by the boundary. These differences are listed in Table III.

Comparison of the increase in yield stress (Table II) with the increase in the rate of work-hardening (Table III) shows that the boundary has a more marked effect in inhibiting the progress of the deformation process than in its initiation. Since no definite yield point was observed (as for example with mild steel) the values used are relative to one another and may or may not be of physical significance with regard to the initiation of the deformation process. The slope $\left(\frac{ds}{de}\right)$, however, is an experimental observation not dependent on a definition; it is a direct measure of the mutual interaction effect of the two crystals.

TABLE III

$\left(\frac{ds}{de}\right)$ gms/mm²		Difference gms/mm²	ϕ Degrees
S. Crystals	*Bicrystals*		
0.6	0.6	0	0
0.8	1.4	0.6	12
0.9	2.2	1.1	22
1.2	3.4	2.2	40
1.5	4.9	3.4	60
1.4	3.8	2.4	74 = 46

The general stress-strain curve for single crystals of face-centered cubic metals is parabolic in form and shows intense work-hardening. However, such single crystals of high purity oriented for single slip have shown regions of 'easy' glide similar to the laminar flow of hexagonal metals [26–30]. Masing and Raffelsieper [29] found that the region of 'easy' glide in aluminium crystals became smaller as the initial orientation approached one of multiple slip. The initial orientation $\phi = 0°$ is one of single slip. At $\phi = 60°$ the crystals are oriented for double slip; specimens 7_A and 7_B ($\phi = 60°$) showed the shortest 'easy' glide regions. The termination of the 'easy' glide has been related to the start of double glide in α-brass [28]. The general conclusion is that when the "laminar flow" breaks up into a more complex process, the work-hardening becomes more intense. Comparison of the single and bicrystal stress-strain curves (Table I) shows that the presence of the boundary made the 'easy' glide region shorter as the orientation difference between the crystals increased. This might well be interpreted as evidence of a more complex deformation process in the boundary vicinity, since the termination of laminar flow is associated with multiple slip or inhomogeneous lattice rotations. Since slip is increasingly inhibited as the orientation difference of the crystals is increased, greater resolved shear stresses can be applied to latent slip systems causing the most favourable of them to become active. The more active slip systems there are, the more complex is the deformation process and, as a result, the greater is the rate of work-hardening.

From the experimental yield-stress values obtained at $\phi = 0°$, the critical resolved shear stress (δ) necessary to cause plastic deformation was calculated to be 45 gms/mm^2. Using this value and the relation $\delta = \rho \sin \chi \cos \lambda$ the curve relating the yield stress ρ to the crystal orientations was plotted. It can be seen from Figure 6 that the observed and expected yield-stress values agree extremely well.

Acknowledgment

The financial assistance of the Defense Research Board of Canada, and a summer grant from the School of Engineering Research, University of Toronto, are gratefully acknowledged.

The authors wish to thank their colleagues in the Department of Metallurgical Engineering, University of Toronto, for their helpful discussion.

References

1. Aston, R. L. Cambridge Phil. Soc. **23** (1926) 549.
2. Barrett, C. S. and Levenson, C. H. Trans. A.I.M.E. **137** (1940) 112.
3. Boas, W. and Hargreaves, M. E. Proc. Roy. Soc. A **193** (1948) 89.
4. Carpenter, H. C. H. and Elam, C. F. Proc. Roy. Soc. A **100** (1921) 329.
5. Chalmers, B. Proc. Roy. Soc. A **162** (1937) 120.
6. ——— Proc. Phys. Soc. **52** (1940) 127.
7. Hibbard, W. R. Trans. A.I.M.E. **162** (1937) 120.
8. Chalmers, B. Metal Interfaces, A. S. M. Seminar, National Metals Congress, October, 1951.
9. Craig, G. B. and Chalmers, B. In course of publication.
10. Cottrell, A. H. Progress in Metal Physics, Vol. IV.
11. Koehler, J. S. Phys. Rev. **60** (1941) 397.
12. Stewart, M. T., Thomas, R., Wauchope, K., Winbgard, W. C. and Chalmers, B. Phys. Rev. **83** (1951) 83.
13. Andrade, E. N. da C. and Randall, R. F. Y. Nature (London) **163** (1948) 890; 164: 1127, 1949.
14. Harper, S. and Cottrell, A. H. Proc. Phys. Soc. B **63** (1950) 331.
15. Kemsley, O. S. Nature (London) **163** (1949) 404.
16. Phillips, D. J. and Thompson, N. Proc. Phys. Soc. B **63** (1950) 839.
17. Roscoe, R. Phil. Mag. **21** (1936) 399.
18. Menter, J. W. and Hall, E. O. Nature (London) **165** (1950) 611.
19. Barrett, C. S. Acta Met. **1** (1953) 2.
20. Chalmers, B. Proc. Roy. Soc. A **196** (1949) 64.
21. Greninger, A. B. A.I.M.E., Inst. Metals Div. Tech. Pub. No. 583, 1934.
22. Teghtsoonian, E. and Chalmers, B. Can. J. Phys. **29** (1951) 370.
23. Clark, R. and Chalmers, B. In course of publication.
24. Andrade, E. N. da C., and Chalmers, B. Proc. Roy. Soc. A **138** (1932) 348.
25. Craig, G. B. (Zn) and Karna, K. (Ag). Dept. of Metallurgical Engineering University of Toronto, Private Communication.
26. Andrade, E. N. da C., and Henderson, R. Phil. Trans. Roy. Soc. A, **244** (1951) 177.
27. Lücke, K and Lange, H. Z. Z. Metallk. **43** (1952) 55.
28. Maddin, R., Mathewson, C. H. and Hibbard, W. R. Trans. A.I.M.E. **175** (1948) 86; **185** (1950) 527.
29. Masing, G. and Raffelsieper, J. Z. Metallk. **41** (1950) 65.
30. Röhm, F. and Kochendorfer, A. Z. Metallk. **41** (1950) 265.

THE CHANGE IN RESISTIVITY, ON PLASTIC DEFORMATION, OF SILVER-COPPER AND SILVER-GOLD ALLOYS*

W. H. AARTS and R. K. JARVIS†

Wires of silver, gold, and copper and some silver-copper and silver-gold alloys were stretched at room temperature, −80°C and at the liquid air point. The change of resistivity was determined as well as the recovery of resistivity on warming from the low temperatures to room temperature. The silver-copper alloys behaved as the pure metals did, but some of the silver-gold alloys showed an increase in resistivity after being warmed up to room temperature and being returned to the air point. This is explained by assuming that the elastic strain at the low temperature increases the order and the warming to room temperature then produces more disorder which remains on cooling to liquid air temperature.

LE CHANGEMENT DE RÉSISTIVITÉ LORS DE LA DÉFORMATION PLASTIQUE DES ALLIAGES ARGENT-CUIVRE ET ARGENT-OR

Des fils d'argent, d'or, de cuivre et de certains alliages argent-cuivre et argent-or ont été étirés à la température ambiante, à −80°C et à la température de l'air liquide. On a déterminé le changement de la résistivité et sa restauration lors du retour des basses températures à la température ambiante. Les alliages argent-cuivre se comportaient de la même façon que les métaux purs, mais certains alliages argent-or ont manifesté un accroissement de résistivité après avoir été rechauffés à la température ambiante et ensuite refroidis à la température de l'air liquide. Ce phénomène est expliqué en faisant l'hypothèse que la déformation élastique aux basses températures accroît l'ordre alors que le chauffage subséquent à la température ambiante produit un plus grand désordre, qui subsiste lors du refroidissement jusqu'à la température de l'air liquide.

DIE WIDERSTANDSÄNDERUNG VON SILBER-KUPFER UND SILBER-GOLD LEGIERUNGEN BEI PLASTISCHER VERFORMUNG

Silber, Gold, Kupfer und einige Silber-Kupfer und Silber-Gold Legierungen wurden in Drahtform bei Zimmertemperatur, −80°C und bei der Temperatur der flüssigen Luft verformt. Es wurde sowohl die Änderung des Widerstandes als auch die Widerstandserholung beim Wiedererwärmen von tieferer Temperatur auf Zimmertemperatur gemessen. Die Silber-Kupfer Legierungen verhielten sich wie die reinen Metalle, einige der Silber-Gold Legierungen zeigten jedoch eine Zunahme des Widerstandes, nachdem sie auf Zimmertemperatur erwärmt und dann auf die Temperatur der flüssigen Luft zurückgebracht worden waren. Das ist erklärlich, wenn man annimmt, dass die elastischen Spannungen bei tiefen Temperaturen den Ordnungsgrad vergrössern und das Erwärmen auf Zimmertemperatur weitere Unordnung hervorruft, die dann beim Abkühlen zur Temperatur der flüssigen Luft erhalten bleibt.

I. Introduction

A considerable amount of work has been done on the change of resistivity of pure metals [1–5]. Considerably less has been done on alloys [4; 5; 6].

As the processes occurring in alloys are more complex it was decided to investigate two alloy systems of different types—viz., silver-copper, in which each metal is only slightly soluble in the other at low temperatures, and silver-gold, in which the metals are completely soluble in each other. Seitz [7] is of the opinion that "the alloy character may have a strong influence on the events which occur during plastic flow, for the degree of short-range order may decrease, as the relatively large change in resistivity with cold-work implies is the case. In addition it is possible that vacant lattice sites are entrained in the lattice by imhomogeneities associated with fluctuations in composition."

In the experiments here described the wires were stretched at room temperature (20°–29°C), at −80°C to −84°C, and at −185°C to −195°C.

The resistance of the specimens in all cases was measured with no tension acting on the wire. The specimens drawn at the liquid air point were allowed to warm up to room temperature after a certain extension (approximately 10 to 20 per cent) and then cooled down to the air point again, the resistance redetermined, and they were then extended further. The silver-gold alloys were merely extended at −80°C, while the silver-copper alloys extended at −80°C were allowed to warm up after a certain extension, cooled down to −80°C again and stretched further. At room temperature the specimens were merely stretched without any annealiug at a higher temperature.

II. Silver, Copper, and Silver-Copper Alloys

The silver and copper wires were annealed at 550°C and furnace-cooled. The silver-copper alloys were annealed at 550°C and then quenched. As can be seen from the graphs, in which the relative change in resistivity is plotted against the strain, (Figures 1–7) the silver-copper alloys behaved similarly to the pure metals. This can be expected,

*Received August 11, 1953.
†Department of Physics, University of the Witwatersrand, Johannesburg, South Africa.

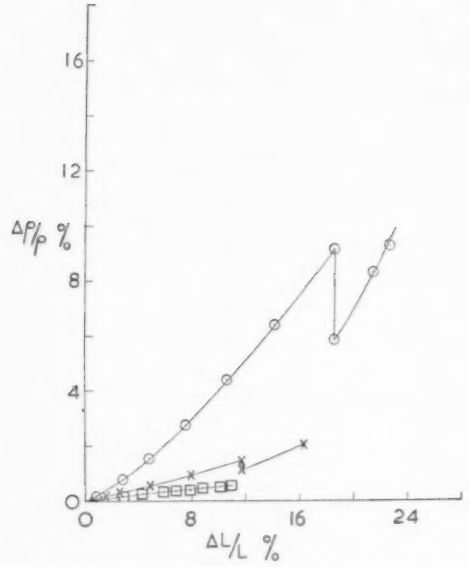

FIGURE 1. Pure Silver. Supplied by Johnson Matthey, spectrographically standardised. The relative change of resistivity is plotted against the strain. Observations at the air point are denoted by ⊙, at the CO_2 point by X and at room temperature by ⊡. The wire at the air point was extended for approximately 18 per cent, warmed to the room temperature and cooled to the air point, the resistance again determined and then extended further. The wire at the CO_2 point was extended 12 per cent before warming to room temperature and cooling again.

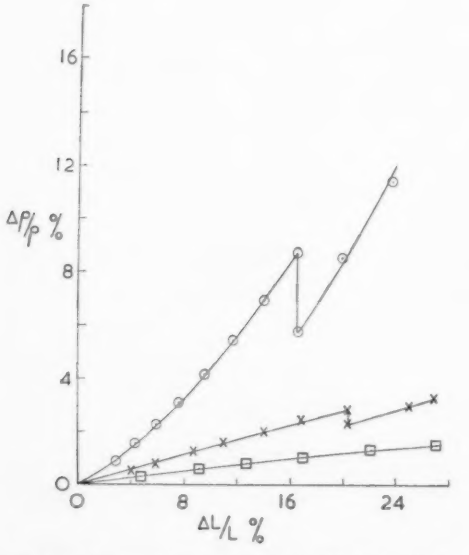

FIGURE 2. 0.5 atomic per cent copper 99.5 atomic per cent silver, as Fig. 1.

as, owing to the slight solubility of the metals in each other, the alloys consist of two phases differing only slightly from the pure metals. The compositions of the alloys are given in atomic percentages, and the air point observations are denoted by ⊙, the CO_2 point by × and room temperature by ⊡. The change of resistivity of the alloys is higher than for the pure metals as can be seen in Table I, where the standard deviation of $\Delta\rho$ is also given. The values given in the tables are average values, whereas the graphs are drawn from the observations on a particular specimen. The increase of $\Delta\rho$ of the alloys could be due to the disruption of partial order besides the effects occurring in pure metals,

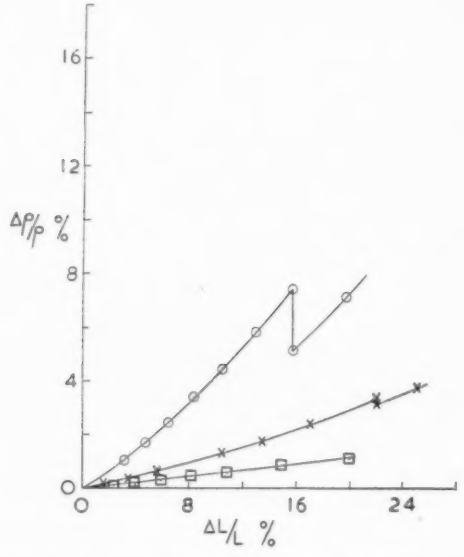

FIGURE 3. 2 atomic per cent copper; 98 atomic per cent silver.

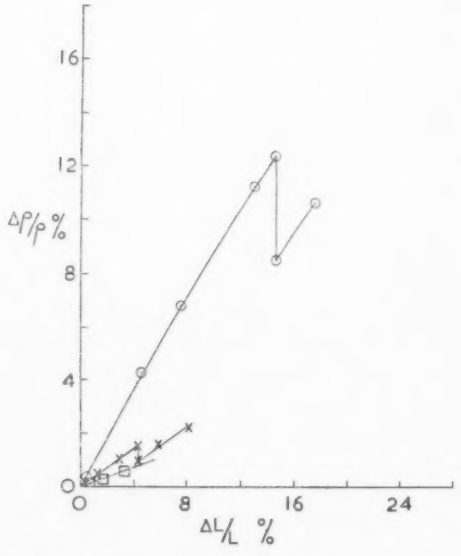

FIGURE 4. The eutectic alloy: 39 atomic per cent copper; 61 atomic per cent silver. (Owing to the wire hardening quickly and then breaking, only small extensions could be produced.)

and also due to precipitation of the solute, unless this was nearly complete, in which case it would tend to reduce the resistivity.

TABLE I

Atomic per cent		$\Delta\rho$ in ohm-cm $\times 10^{-8}$ at 10% extension		
Ag	Cu	Air point	CO_2 point	Room temperature
100	0	1.33±.06	1.16±.06	.75±.04
99.5	0.5	1.52±.03	1.28±.06	.93±.05
98	2	1.61±.04	1.34±.05	.96±.04
61	39	4.62±.07	1.98±.04*	1.31±.04†
2	98	1.67±.06	1.69±.06	1.33±.05
0.5	99.5	1.34±.04	1.46±.08	1.07±.06
0	100	1.23±.04	1.25±.12	.91±.09

*At approximately 4.5% strain.
†At approximately 3.5% strain.

III. Silver, Gold, and Silver-Gold Alloys

The silver, gold, and silver-gold alloys were all annealed before extension at 550°C and furnace-cooled. Figure 8 gives the curves for 2 per cent gold in silver. It is similar to the diagram for pure silver. Figure 9 gives the results for 25 per cent gold in silver: There is hardly any recovery for specimens extended at the air point and annealed at room temperature and then returned to the air point. In Figure 10 (50 atomic per cent gold) an *increase* of resistivity is produced when the specimen is extended 10 per cent at the air point, warmed up to room temperature, and again cooled to the air point. The extension immediately after this reduces the resistivity slightly before it again increases it. In Figure 11 we see the effect in a 75 atomic per cent gold alloy. In Figure 12 the graphs for pure gold are given. In Figure 13 the relative change of resistivity for an extension of 10 per cent and the recovery on warming up to room temperature are both plotted against the composition of the alloy.

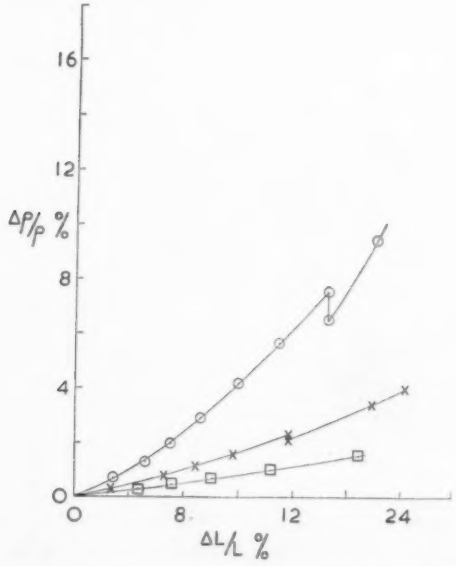

FIGURE 5. 98 atomic per cent copper; 2 atomic per cent silver.

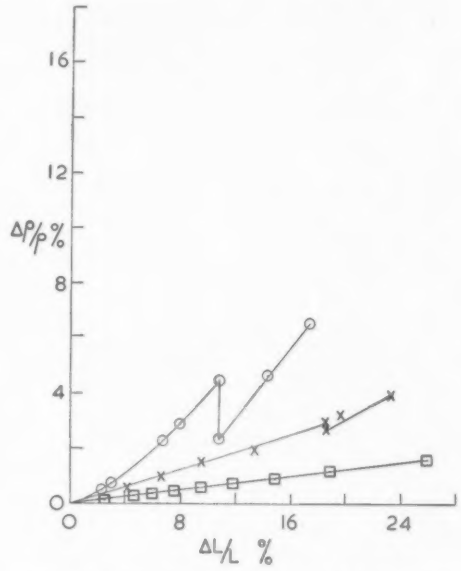

FIGURE 6. 99.5 atomic per cent copper; 0.5 atomic per cent silver.

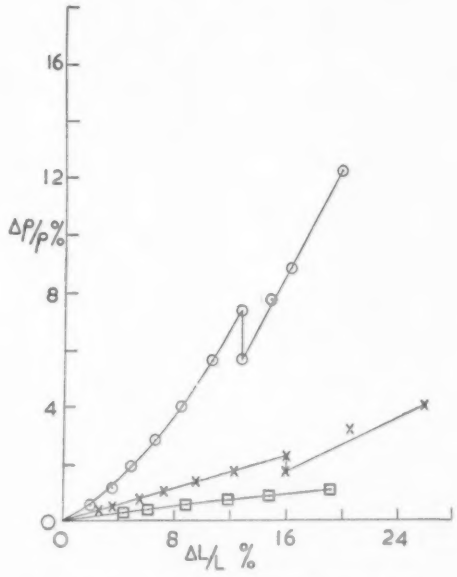

FIGURE 7. Pure copper (99.999 per cent).

In Table II the change of resistivity for a 10 per cent extension is shown, as well as the recovery of $\Delta\rho$.

TABLE II

Atomic per cent		$\Delta\rho$ in ohm-cm $\times 10^{-8}$ at 10% extension			
Ag	Au	Air point	Recovery	CO_2 point	Room temperature
100	0	1.5 ±.1	− .59±.08	1.16±.06	.75± .08
98	2	1.3 ±.2	− .49±.08	1.34±.17	.94± .15
75	25	7.67±.14	− .08±.08	—	5.7 ±1.4
50	50	11.8 ±.6	+1.66±.53	10.1±1.3	8.25±1.8
25	75	7.3 ±.6	+1.42±.26	—	4.3 ± .4
0	100	2.68±.15	− .61±.03	1.8± .4	1.8 ± .2

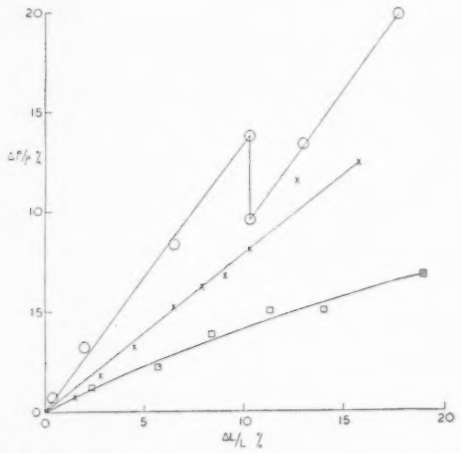

FIGURE 8. 98 atomic per cent silver; 2 atomic per cent gold.

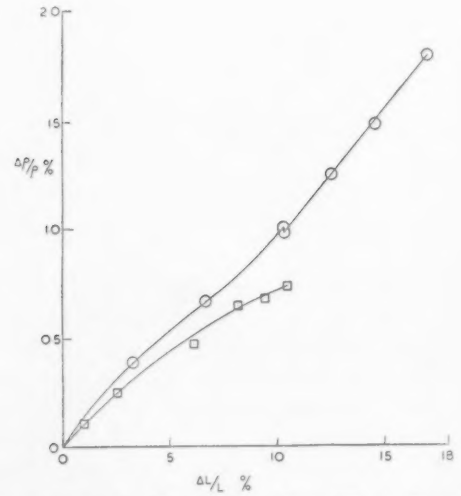

FIGURE 9. 75 atomic per cent silver; 25 atomic per cent gold.

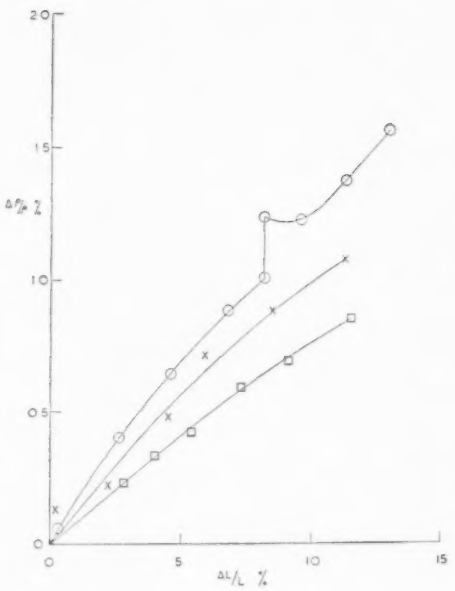

FIGURE 10. 50 atomic per cent silver; 50 atomic per cent gold.

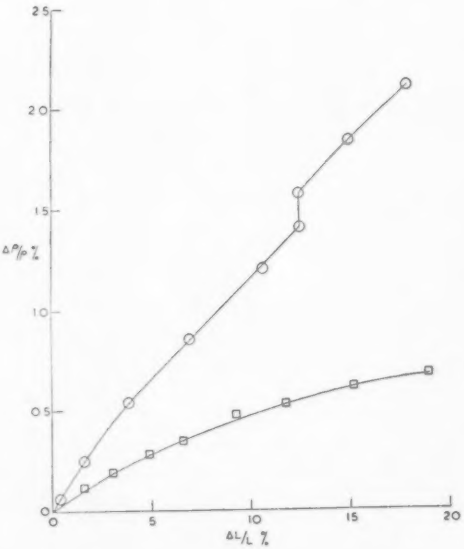

FIGURE 11. 25 atomic per cent silver; 75 atomic per cent gold.

The discrepancy between the values of $\Delta\rho$ for pure silver at the air point in Tables I and II is due to the fact that the determination of ρ does not

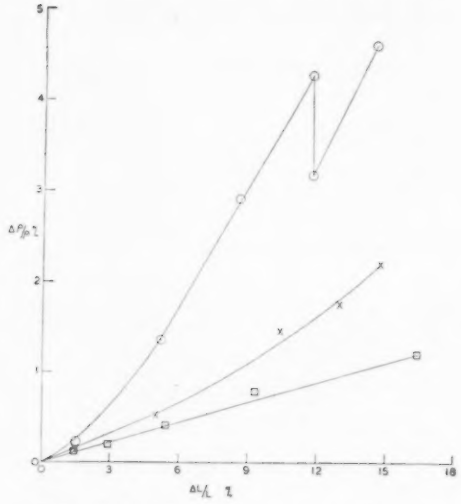

FIGURE 12. Pure gold. Johnson Matthey spectrographically standardised.

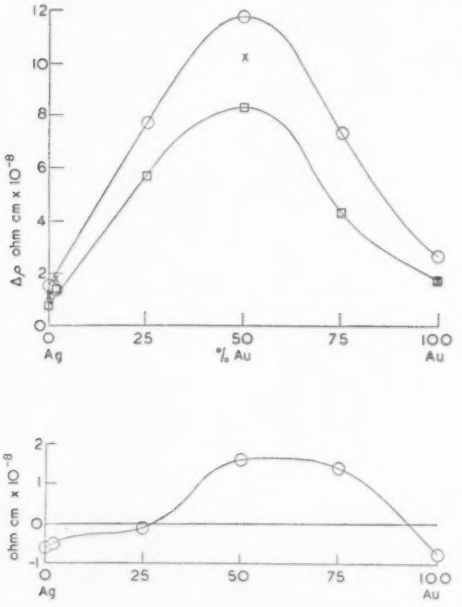

FIGURE 13. In the upper diagram the change of resistivity for an extension of 10 per cent of the silver-gold alloys is plotted against the alloy composition. In the lower diagram the recovery due to annealing at room temperature after an extension of 10 per cent at the air point is plotted against the alloy composition.

occur at exactly the same temperature as the determination of $\Delta\rho/\rho$. The liquid air bath varied in temperature from $-185°C$ to $-195°C$, depending on the oxygen content.

IV. Conclusion

It is clear that for small extensions the increase of resistivity is considerably larger for all the alloys than for the pure metals. That the degree of partial order produced by the passage of dislocations is important is shown by graphs of the silver-gold alloys of compositions likely to produce a high degree of order. Here the increase of resistivity of the specimens drawn at the air point and annealed at room temperature shows an effect which can be explained by assuming that the elastic strain at the low temperature increases the order and that the warming to room temperature produces more disorder, which remains on cooling to the air point. Especially is this indicated for the 50 per cent Ag-Au alloy, where further extension, and hence increase of the internal elastic strain, initially reduces the resistivity again and only further strain increases the resistivity again.

Acknowledgment

The authors wish to thank Professor M. J. Druyvesteyn for the initial introduction to this line of research.

References

1. TAMMAN *et al.* 1953. Ann. Phys. **161** (1933) 111; 657; 680.
2. MOLENAAR, J. and AARTS, W. H. Nature **166** (1950) 690.
3. DRUYVESTEYN, M. J. and MANINTVELT, J. A. Nature **168** (1951) 868.
4. BROOM, T. Proc. Phys. Soc. **B65** (1952) 871.
5. MASIMA, M. and SACKS, G. Z. Phys. **51** (1928) 321; **54** (1929) 666.
6. AARTS, W. H. S. Afr. J. Sci. **49** (1952) 183.
7. SEITZ, F. Adv. Phys. **1** (1952) 43.

SOLID SOLUTION FORMATION IN THE GOLD-NICKEL SYSTEM*

B. L. AVERBACH,† P. A. FLINN,‡ and MORRIS COHEN†

The local atomic configurations measured from diffuse X-ray scattering in the gold-nickel system cannot be reconciled with the observed heats and entropies of mixing on the basis of a statistical treatment of chemical bonding energies. The heats of mixing are positive (heat absorbed), and yet there is a preference for *unlike* neighbours in solutions above the solubility gap. It is shown that these positive heats of mixing may be explained in terms of the elastic strain energy required to form solutions from atoms of different size. The sizes of the ions in gold-nickel solutions, also measured from the diffuse X-ray measurements, are used to calculate the strain energies and reasonable agreement with the observed heats of mixing is obtained.

The strain energy contribution to the heat of mixing in Cu_3Au is also evaluated approximately from an X-ray determination of the atomic size effect; in this system it appears that a significant negative contribution to the heat of mixing may arise from a change in the electronic configuration on alloy formation.

LA FORMATION DE SOLUTION SOLIDE DANS LE SYSTÈME OR-NICKEL

Les configurations atomiques locales, dans le système or-nickel, mesurées par la dispersion diffuse des rayons X, ne peuvent pas être mises en accord avec les chaleurs et entropies de mélange sur la base d'un traitement statistique des énergies de liaison chimique. Malgré que les chaleurs de mélange soient positives (chaleur absorbée), il y a préférence pour des voisins dissemblables dans les solutions au-dessus de la lacune de solubilité. Il est montré que les chaleurs de mélange positives peuvent être expliquées en termes de l'énergie élastique de déformation, nécessaire pour la formation de solutions à partir d'atomes de dimensions différentes. Les dimensions des ions dans les solutions or-nickel, également mesurées par la dispersion diffuse des rayons X, sont utilisées pour calculer les énergies de déformation, et un accord raisonnable est obtenu avec les chaleurs de mélange observées. La contribution de l'énergie de déformation à la chaleur de mélange dans Cu_3Au est aussi évaluée approximativement, en se basant sur la détermination, au moyen des rayons X, de l'effet des dimensions atomiques; dans ce système, il paraît qu'une contribution négative, appréciable, à la chaleur de mélange puisse provenir du changement de la configuration électronique lors de la formation de l'alliage.

DIE BILDUNG VON FESTEN LÖSUNGEN IM SYSTEM GOLD-NICKEL

Die Einzelheiten der Anordnung der Atome im System Gold-Nickel, die mit Hilfe der diffusen Streuung von Röntgenstrahlen gemessen wurde, stimmen nicht mit den entsprechenden Daten aus den beobachteten Mischungswärmen und Mischungsentropien überein. Die Mischungswärmen sind positiv (Wärme wird absorbiert) und trotzdem findet man bevorzugt *ungleiche* Nachbarn oberhalb der Mischungslücke. Es wird gezeigt, dass diese positiven Mischungswärmen als die elastische Verzögerungsenergie verstanden werden kann, die verbraucht wird, wenn sich Lösungen von Atomen verschiedener Grösse bilden. Die Grösse der Ionen in Gold-Nickel Lösungen wurde mit Hilfe der Röntgenstrahlstreuung gemessen. Mit den so erhaltenen Werten der Ionenabmessungen wurden die Verzerrungsenergien berechnet. Die Übereinstimmung mit den beobachteten Mischungswärmen ist zufriedenstellend.

Der Beitrag der Verzerrungsenergie zur Mischungswärme von Cu_3Au wurde ebenfalls näherungsweise aus dem röntgenographisch bestimmten Atomformfaktor berechnet. Ein beträchtlicher, negativer Beitrag zur Mischungswärme in diesem System scheint von der Umwandlung der Elektronenanordnung bei der Legierungsbildung herzurühren.

1. Introduction

There have been frequent attempts [1; 2; 3] to deduce the local atomic configuration in a binary alloy from the macroscopic thermodynamic properties of the system. In most cases the heat of mixing of the alloy is described in terms of chemical bonding energies between nearest neighbors, and the calculated entropy of mixing is based on the nearest-neighbor configuration. The Kopp-Neumann rule is also assumed i.e., the heat capacity of the system is taken to be a linear function of the composition. Although there have been refinements which extend these theories to neighbors beyond the first shell [2], the essential features of the results have remained the same.

A typical nearest-neighbor theory is that of Takagi [3]. The average number of unlike nearest neighbors is given by:

$$(1)\quad \frac{p_{AB}}{(ZN_0)/2} = \frac{-1 + \{1 + 4m_Am_B[\exp(2\nu/kT) - 1]\}^{\frac{1}{2}}}{\exp(2\nu/kT) - 1}$$

where

p_{AB} = number of A–B pairs per mol of solution,

m_A, m_B = atom fraction of A and B atoms,

k = Boltzmann constant,

*Received July 18, 1953; in revised form September 19, 1953.

†Department of Metallurgy, Massachusetts Institute of Technology, Cambridge 39, Massachusetts.

‡Present address, Department of Physics, Wayne University, Detroit, Michigan.

Z = number of nearest neighbors (coordination number),
N_0 = Avogadro's number,
$ZN_0/2$ = number of nearest-neighbor pairs per mol of solution,
T = absolute temperature,
ν = net chemical interaction energy
$= \epsilon_{AB} - 1/2(\epsilon_{AA} + \epsilon_{BB})$,
ϵ_{AB} = chemical bonding energy of an A–B pair, etc.

The quantity $2p_{AB}/(ZN_0)$, which is the fractional number of unlike pairs, is thus expressed as a function of the chemical interaction energy. On expanding the radical and the exponential, the approximate relationship given by Wagner [4] is obtained:

$$\frac{p_{AB}}{(ZN_0)/2} = 2m_A m_B\left(1 - 2m_A m_B \frac{\nu}{kT}\right). \quad (2)$$

If $\nu = 0$, the configuration is random, and the fractional number of unlike pairs becomes $2m_A m_B$. The molar heat of mixing is given by:

$$\Delta H = p_{AB}\nu. \quad (3)$$

The general type of configuration predicted by this quasi-chemical theory may be seen from equations (2) and (3). If the heat of mixing is positive (heat absorbed), ν is positive, and the fractional number of A–B bonds is less than random. In the lattice, this requires the presence of A-rich or B-rich clusters or both. If the heat of mixing is negative, the fractional number of A–B bonds exceeds the random number and the lattice exhibits short range order. For the systems Au-Ag and Cu-Au, the thermodynamic properties and X-ray measurements of the average atomic configurations are available, and a comparison of these data is summarized in Table I. The quantity $(N_0\nu)$ was calculated either from the heat of mixing or from the thermodynamic activities, assuming a regular solution. The quantity p_{AB}/N_0 (i.e., number of unlike bonds per atom) calculated from equation (1) in the third column agrees fairly well with the X-ray measurement of the same quantity in the fourth column. It should be noted, however, that both of these systems have negative heats of mixing; equivalent data for alloys with positive heats of mixing have not been available until recently [12].

Solid solutions with positive heats of mixing may exhibit a miscibility gap at lower temperatures, and hence an understanding of the statistical atomic arrangements in such alloys is important in connection with the mechanism and kinetics of the precipitation process. The thermodynamic and the X-ray data for the gold-nickel system are compared in this paper. These alloys have positive heats of mixing and form a continuous series of face-centered cubic solid solutions above 840°C. On cooling, the solutions decompose into nickel-rich and gold-rich solutions, also face-centered cubic. Thus the number of nearest neighbors about an atom, Z, remains unchanged.

TABLE I

COMPARISON OF X-RAY AND THERMODYNAMIC MEASUREMENTS OF SHORT RANGE ORDER

Alloy	$N_0\nu$ (Cal/mol)	p_{AB}/N_0 (thermodynamic)	p_{AB}/N_0 (X-ray)	p_{AB}/N_0 (random)	$\Delta H = p_{AB}\nu$ (Cal/mol)
Cu_3Au	−550*	2.49	2.58 [6]	2.25	−1370
Cu Au	−550*	3.40	3.40 [7]	3.00	−1870
Ag_3Au	−250†	2.45‡	2.36 [9]	2.25	−610
Ag Au	−250†	3.30‡	3.24 [9]	3.00	−825

*Calculated from data of Weibke and Quadt [5] at 500°C assuming that the solution is regular and that $\frac{Z\nu}{kT}(1 - m_{Cu})^2 = \ln \gamma_{Cu}$ where γ_{Cu} = activity coefficient of copper.

[6] Single crystal data of Cowley [6] interpolated at 500°C.
[7] Single crystal data of Roberts [7; 8] interpolated at 500°C.
[9] Single crystal data of Norman and Warren [9] on slowly cooled alloys at room temperature.
†Calculated from data of Kubaschewski and Huchler [10], and Schmahl [11], at 500 and 550°C respectively.
‡Calculated on basis that short range order on slow cooling is that characteristic of 300°C.

On the basis of equations (2) and (3), a preference for *like* nearest neighbors would be predicted, and the corresponding A-rich and B-rich clusters might be expected to provide embryos for the precipitation reaction. The X-ray evidence shows, however, that there is an excess of *unlike* neighbors in solutions above the miscibility gap.

It is now apparent that the quasi-chemical approach by itself is inadequate since it predicts the wrong atomic configuration in this system. It is necessary to consider the elastic strain energy arising in the formation of a solid solution from atoms of different sizes in order to account for the measured thermodynamic properties. The sizes of the gold and nickel ions in solid solution, obtained from the diffuse X-ray measurements, are used to calculate the elastic strain contribution to the heat of mixing. The results suggest that the strain energy plays a much more significant role than the chemical bonding energy in the thermodynamic behavior of solid gold-nickel alloys.

In fact, the excellent agreement between the X-ray measurements of short-range order and the thermodynamic calculations based on the quasi-chemical theory (as shown in Table I) may be fortuitous, at least in the case of Cu_3Au. The atomic sizes in this alloy can be estimated from available diffuse scattering data, and it is found that the corresponding strain energy is relatively large. However, it appears that the positive contribution to the heat of mixing arising from the strain energy may be more or less offset by a postulated negative contribution arising from a change in the electronic configuration (which does not occur in the gold-nickel alloys) and the net heat of mixing is negative.

2. The Gold-Nickel System

The gold-nickel system lends itself to a critical evaluation of the quasi-chemical theory since thermodynamic and X-ray determinations quite similar to those available for copper-gold can be made. The free energies and entropies of mixing for gold-nickel alloys were measured recently by the emf method [12], and the local atomic arrangements were determined from the diffuse X-ray scattering [13].

The gold-nickel phase diagram and the thermodynamic data obtained at 900°C are shown in Figures 1 and 2 [12]. The heats of mixing are positive and quite large. The entropies of mixing are also unexpectedly large, being approximately twice the ideal configurational entropy, $-kN_0(m_A \ln m_A + m_B \ln m_B)$. Aside from the anomalous entropy values, the thermodynamic properties are just those expected from the phase diagram.

The results of the diffuse X-ray scattering measurements on gold-nickel solutions are summarized in Figure 3 [13]. Two kinds of information were

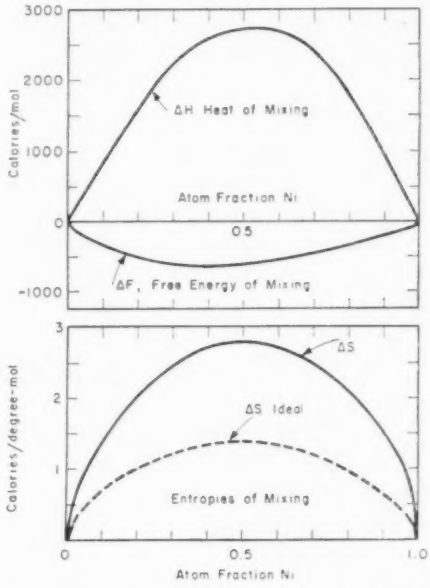

FIGURE 2. Thermodynamic properties of gold-nickel alloys at 900°C.

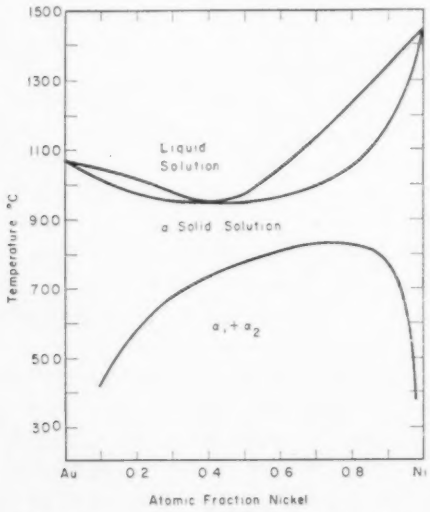

FIGURE 1. Gold-nickel phase diagram.

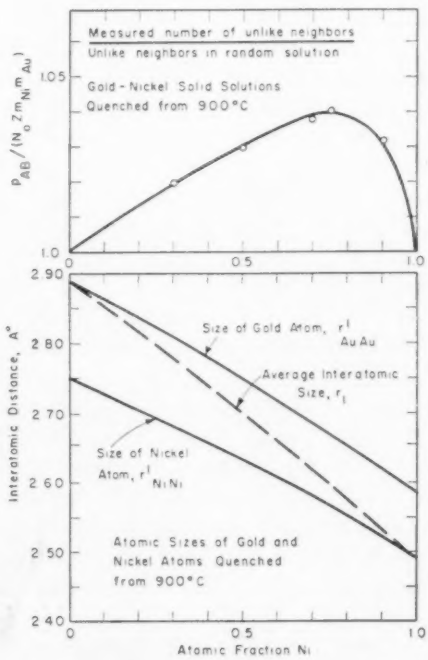

FIGURE 3. Degree of short-range order and atomic sizes in gold-nickel solid solutions.

obtained from these observations: the average nearest neighbor identity and the mean atomic sizes as functions of composition.

It is immediately evident that the quasi-chemical approach is unable to reconcile the thermodynamic and X-ray measurements. A large positive heat of mixing predicts a strong preference for *like* nearest neighbors according to equations (1–3) whereas the X-ray data clearly show that gold-nickel solid solutions exhibit a preference for *unlike* nearest neighbors. In fact, the short-range ordering in this system is very similar in kind to that observed in the gold-copper system which forms a series of superlattices on cooling.

An alternate explanation for the positive heat of mixing in gold-nickel alloys seems possible. Elastic strain energy may be required to form a close-packed lattice from two atoms of different sizes, and a positive heat of mixing arising from this factor would have little relationship to the nearest neighbor identity as given by equations (1–3). It is likely that some alternation of large and small atoms would tend to reduce the strain energy, while the formation of clusters of like atoms would appear to increase the strain energy. This effect has been suggested as the driving force for the formation of superlattices [14], but it is still possible that the observed short-range order may arise from a small quasi-chemical preference for unlike bonds over like bonds, with a negative contribution to the heat of mixing. However the liquid solutions in the gold-nickel system are ideal [12], i.e., the heat of mixing is zero. Since the chemical bonding tendencies should persist in the liquid while lattice strain disappears on melting, the hypothesis that the non-ideal behavior of these solid solutions arises from elastic strain rather than quasi-chemical effects receives support.

3. Strain Energy in Alloy Formation

The X-ray measurements of atomic size must be interpreted carefully. The average interatomic distance, averaged over a large number of atoms, may be calculated from the lattice parameter, and this is shown in Figure 3 as r_1. The actual first neighbor distance is, however, a function of the identity of the neighboring atom, and the true interatomic distances r^1_{AuAu} and r^1_{NiNi} are obtained from the diffuse X-ray scattering [13]. Figure 3 shows that the interatomic distance between two like atoms varies with composition and lies between the average interatomic distance and the distance between the atoms in the pure metals. We may consider that these interatomic distances denote the "sizes" of the atoms. It is also convenient to think of these interatomic distances as representing the diameters of spherical ions in the lattice. The X-ray results are, however, independent of any assumption of the shapes of the ions. These data indicate that the ions are not precisely on the average lattice points, as determined from parameter measurements.

Several points of view have been taken in order to calculate the strain energy required to form a lattice from ions of different size. Lawson [15] has assumed that the ions behave as incompressible spheres, but this assumption is not justified on the basis of the new X-ray data which clearly show that the ions do change in size on mixing. Heumann [12; 12A] has assumed that the ions lie on the average lattice and that the bonds are stretched or shrunk relative to their original sizes in the pure metals. The heat of mixing for gold-nickel alloys has been calculated by these two methods [12] and the predicted values are 1.5–2 times as large as the observed values.

It appears that at least three contributions to the strain energy should be considered in the packing of large and small ions in a lattice: the increase in energy due to the imperfect close-packing of the ions, the energy associated with the distortion of the ions from a spherical shape, and the hydrostatic energy arising from the hydrostatic pressure required to change the ion size from that in the pure metal to that found in the lattice. In the gold-nickel system the first two factors are probably negligible compared to the third. The molar volume is linear with composition (see Figure 4), and therefore any energy associated with a failure of close-packing is likely to be small. It is not known whether the ions in solution are greatly distorted from a spherical shape, but the neglect of this possible contribution would tend to be compensated by a corresponding overestimation of the volume change required to account for the observed interatomic distances.

The hydrostatic work required to change the atomic diameter is given by:

$$E = \frac{9}{2} B_a \left(\frac{\Delta d}{d}\right)^2 \tag{4}$$

where B_a is the effective bulk modulus of the atom, d is the atomic diameter, and Δd is the difference between atomic diameter in solution and that in pure metal. The effective bulk modulus for a single atom differs from the modulus measured for the

lattice containing the atom. Part of the resistance to hydrostatic deformation for the crystalline material arises from a change in Fermi energy with volume, and the rest from ion core interactions. Only the second effect is thus associated with the individual atom. Using the method outlined by Fuchs [16] it is possible to calculate the Fermi

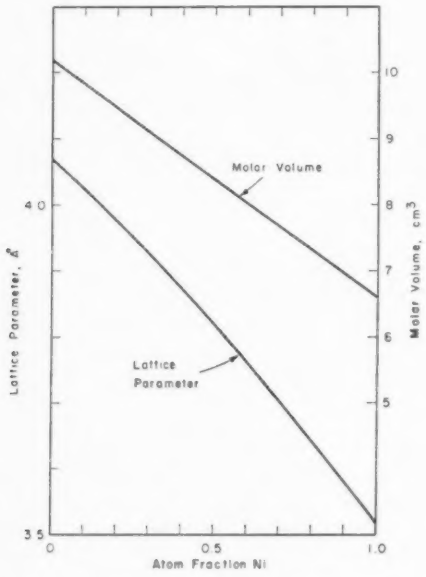

FIGURE 4. Molar volumes and lattice parameters of gold-nickel alloys.

energy contribution and subtract it from the observed bulk moduli. Fuchs employed the free-electron approximation where:

$$\frac{1}{B_f} = K_f = \frac{8\pi^2 m}{h^2}\,(2.843)\,r_0{}^5 n, \tag{5}$$

where K_f is the compressibility arising from Fermi energy and r_0 is the atomic radius; n is the number of free electrons per unit volume. With this approximation and Bridgman's [17] values for compressibilities, the effective moduli were evaluated for gold, nickel and copper, and are listed in Table II. In each case the ion core contribution to the bulk modulus is about 87 per cent of the total.

TABLE II

LATTICE AND ATOMIC BULK MODULI
in units of 10^{12} dynes/cm²

	B (experimental)	Fermi Contribution	B (atomic)
Gold	1.79	0.26	1.53
Nickel	1.87	0.21	1.66
Copper	1.49	0.19	1.30

With the atomic bulk moduli and the values of the ionic sizes shown in Figure 3, the distortion energy required to change an ion from its size in the pure metal to the size found in each solution was calculated. These values were weighted by the corresponding atomic fractions and the results are shown in Figure 5 along with the experimentally measured heats of mixing. The agreement is reasonably good. Both curves have the same shape with the peak slightly on the nickel side of the equi-atomic composition; the calculated curve is within 20 per cent of the measured data. No attempt was made to estimate the possible contribution to the heat of mixing arising from the filling of the d-band in the nickel atoms, but the direction of this effect should help the agreement.

It thus appears that the principal portion of the

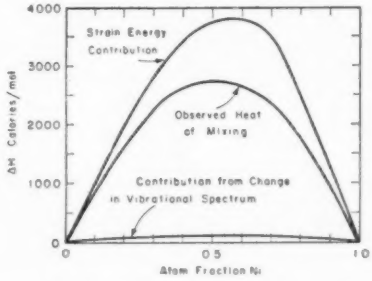

FIGURE 5. Heats of mixing gold-nickel alloys.

observed heat of mixing in the gold-nickel system can be accounted for in terms of the energy required to change the ion size without considering any chemical bonding effects at all. This system is not necessarily typical, however, of all solid solutions with a positive heat of mixing. The aluminum-zinc system also has a solubility gap and the heat of mixing has been shown to be positive [18]. However, the X-ray results for these alloys [19] indicate that the atoms have almost exactly the same size and the strain energy is therefore negligible. Clustering of like atoms has been found in these solutions, suggesting that chemical bonding effects may be controlling in this case. Furthermore, liquid solutions of aluminum-zinc alloys exhibit a positive heat of mixing [18A] indicating that a true chemical bonding effect may be a strong nearest neighbor phenomenon which persists even after the lattice is melted.

In the gold-nickel system, the heat of mixing and the separation into two phases on cooling seem to be determined primarily by strain energy considerations, and the relative strengths of the like and

unlike atomic bonds have little to do with these phenomena or even with the local atomic configurations. In fact, the existence of short range order in the gold-nickel solutions above the miscibility gap is contrary to the postulation that the solutions contain embryonic clusters of the gold-rich and nickel-rich phases which eventually precipitate. This situation is also reflected in the subsequent precipitation rates. Precipitation in the gold-nickel system is very sluggish and appears to start only at grain boundaries. In the aluminum-zinc system, however, embryos of the zinc-rich clusters exist in equilibrium above the critical, and the precipitation on cooling is so rapid that it cannot be easily suppressed by quenching.

4. The Excess Entropy

Although the large positive heats of mixing of the gold-nickel solid solutions can be accounted for by strain energy considerations, the excess entropy (i.e., the measured entropy of mixing minus the ideal entropy of mixing) cannot be explained in terms of the strain energy. Since the ions do not lie on the average lattice points in the solution, let us assume that the excess entropy arises from a change in the vibrational spectrum and hence in the heat capacity. In the derivation of equation (1), the heat capacity is taken to be a linear function of the composition, i.e., the Kopp-Neumann rule is assumed. If this rule does not hold, there will be two contributions to the entropy of mixing on alloy formation: the configurational entropy, and the entropy increment $(\int_0^T (\Delta C_p/T)\, dT)$ due to the change in heat capacity associated with the change in the vibrational spectrum.

The degree of short range order in the gold-nickel solid solutions at 900°C (see Figure 3) is sufficiently close to random so that the configurational contribution to the entropy is given approximately by $S_{\text{ideal}} = -R(m_{\text{Ni}} \ln m_{\text{Ni}} + m_{\text{Au}} \ln m_{\text{Au}})$. The ideal entropy of mixing is plotted in Figure 2, and the difference between this and the measured entropy in Figure 2 is the excess entropy.

Using the Debye theory [21; 22] the vibrational entropies of pure gold and nickel were calculated with Debye temperatures of 170°K for gold and 375°K for nickel [20]. Inasmuch as the Debye temperatures of the solid solutions are not available, the vibrational entropy (S_v) for each intermediate composition was taken as the mean entropy $(S_{\text{mean}} = m_{\text{Ni}}S_{\text{Ni}} + m_{\text{Au}}S_{\text{Au}})$ plus the previously determined excess entropy. The results are plotted in Figure 6. The Debye temperatures of the alloys were then calculated from the S_v values, and are presented in Figure 7 along with the Debye temperatures corresponding to the mean vibrational entropies.

It is also possible to estimate the contribution to the heat of mixing arising from the change in the vibrational spectrum. With the aid of the Debye theory, it is possible to calculate the heat capacity,

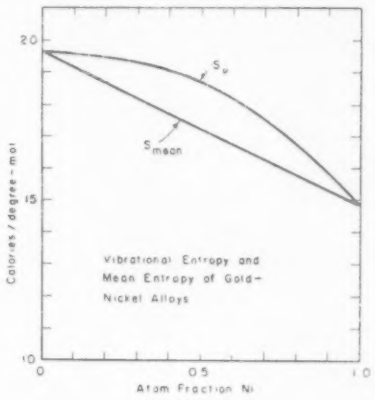

FIGURE 6

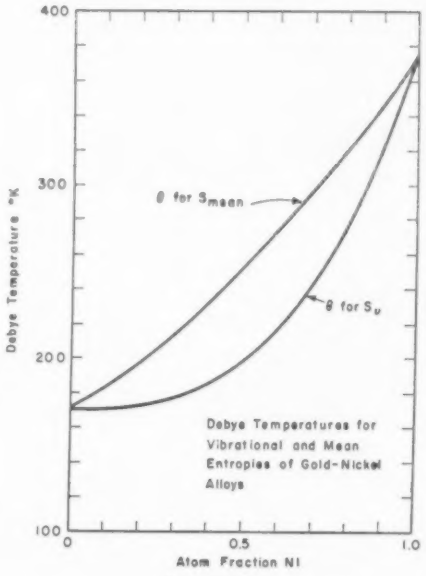

FIGURE 7

C_v, as a function of temperature for the pure metals and for each alloy, using the Debye temperatures shown in Figure 7. The change in heat capacity on mixing is $\Delta C_v = C_{v_{\text{soln.}}} - m_{\text{Ni}}C_{v_{\text{Ni}}} - m_{\text{Au}}C_{v_{\text{Au}}}$, and is sufficiently close to ΔC_p for present purposes. Thus, the contribution to the heat of mixing $\left(\int_0^T (\Delta C_p)\, dT\right)$ due to the change in the vibra-

tional spectrum can be evaluated as a function of composition. The results are given in Figure 5. This contribution is positive, but is quite small compared to the strain energy, the maximum effect being only about 110 cal/mol for the 50 atomic per cent solution at 900°C.

The heat capacity of the 50 atomic per cent solution is now being measured over a wide range of temperatures by Dr. W. de Sorbo at the General Electric Company Laboratory; from this, it will be possible to determine whether the excess entropy actually arises from a change in the vibrational spectrum on mixing, as postulated here.

5. Strain Energy Contribution to the Heat of Mixing of Cu_3Au

Since the strain energy in gold-nickel solid solutions contributes a large positive increment to the heat of mixing, a similar calculation for gold-copper alloys should also prove significant because the copper and nickel atoms have similar sizes. The size effect in the alloy Cu_3Au has recently been measured [23]. Unfortunately, the sizes were not determined as a function of composition, but the available data permit the following estimate for the sizes of the copper and gold atoms in Cu_3Au*:

$$r^1_{CuCu} = 2.60\text{Å}$$
$$r^1_{AuAu} = 2.68\text{Å}.$$

Using the compressibilities listed in Table II, the strain energy was calculated in the same manner adopted for the gold-nickel solutions. The resulting strain energy is 1870 calories per mol of Cu_3Au, which can be compared to the corresponding value of 3000 calories per mol for Ni_3Au.

The observed heat of mixing for disordered Cu_3Au is -1370 calories per mol. This must be reconciled with the necessity of providing 1870 calories per mol for strain energy while still yielding a net negative heat of mixing. If it is assumed that the bonding energy has a correspondingly larger negative value (i.e., $-1370-1870 = -3240$ calories per mol), the alloy would have to be almost completely ordered at 500°C according to equation (1). Experimentally, the short-range order is only about ⅓ of the way towards complete ordering. This suggests that a negative contribution, not considered thus far, comes into play to counterbalance the positive strain energy.

Independent evidence is on hand to suggest that there is a significant electronic contribution to the heat of formation in the disordered alloy Cu_3Au. On ordering, superlattice reflections appear in reciprocal space and the new inner Brillouin zone is bounded by the planes {001} and {110}. The volume of the zone is $2/a^3$ corresponding to one electron per atom, and the inscribed sphere can contain only 0.52 electrons per atom. Since each atom contributes one conduction electron it appears that the new zone boundaries intersect and closely approach the Fermi surface. Following the arguments of Slater [26] and Nicholas [27] the Fermi energy of electrons in k space just below the energy gap introduced at the zone boundaries is lowered, and the net decrease in energy tends to stabilize the superlattice. Such effects have been postulated for the layered superlattices CuAu, CuPt, and Ag_3Mg [26; 27]; the restriction to layered structures is unnecessary, however, and it appears that this electronic contribution may be equally important in superlattices of the Cu_3Au type. An experimental indication of the intersection of the zone boundaries is provided by Hall measurements [24]. On ordering, the Hall coefficient reverses sign from negative to positive in the alloy Cu_3Au and becomes considerably less negative in the alloy CuAu. Thus, in the ordered alloy Cu_3Au the first zone appears to be almost full but with unfilled corners.

It is customary to consider only the sharp lattice reflections in the construction of the Brillouin zone. The structure factor is assumed to be zero in all regions of reciprocal space other than at the Bragg reflections. If the thermal scattering is neglected, this is true for crystals containing only one kind of atom. In alloys, however, there is an additional diffuse scattering arising from the uncertainty in the identity of the atom at a given lattice site. In the alloys Cu_3Au [2] (as well as in CuAu [3]) the solution is not completely random above the critical temperature, and there are regions of strong diffuse scattering in regions of reciprocal space where superlattice reflections appear in the ordered structure. The structure factor is, therefore, not strictly zero at such reciprocal lattice points as (100) and (110) etc., and there is thus a vestige of the small inner Brillouin zone which appears on ordering. Even in the disordered alloy, therefore, there are weak zone boundaries in the vicinity of the Fermi surface. The energy of the conduction electrons near these energy gaps is lowered, although not as much as for the ordered alloys. This lowering of the Fermi energy as a result of alloying could thus constitute a significant negative contri-

*The gold atom has a diameter of 2.88 Å and the copper atom of 2.55 Å in the pure metals. The average nearest neighbor distance in Cu_3Au calculated from the lattice parameter is 2.62 Å.

bution to the heat of mixing. Recent Hall measurements on disordered gold-copper alloys [25] tend to confirm this viewpoint and indicate that the Fermi energy changes on alloy formation.

Similar Hall measurements in gold-nickel alloys show that there is a much smaller concentration of conduction electrons, presumably because of the filling of the nickel 3*d* band. The Fermi surface is thus well within the corresponding fine structure arising from the short range order above the miscibility gap. As a result, there is little electron contribution to the heat of mixing, and it is significant to note that superlattices are not formed in this system.

It now seems possible that there may be little, if any, chemical bonding effect in gold-copper alloys. The short range order above the critical temperature may be due principally to the strain relief arising from arranging atoms of different sizes within the face-centered cubic lattice. It is still possible, however, that there may be a small nearest neighbor bonding effect, since the liquid solutions are reported to have a small negative heat of mixing [5], but this effect may be inconsequential in comparison to the other components of the heat of mixing.

6. Summary

Experimental data on the heats and entropies of mixing in the gold-nickel system cannot be correlated with the local atomic configurations by a statistical treatment involving only the chemical bonding energies. In gold-nickel alloys, the heat of mixing is positive, yet diffuse X-ray scattering measurements disclose that the solid solutions exhibit a preference for *unlike* nearest neighbors. It appears that this positive heat of mixing is due almost entirely to the lattice strain energy required to form an alloy from atoms of different sizes. Data for the size of the atoms in solid solution, also obtained from the diffuse X-ray observations, were used to calculate the strain energies.

It is reasonable to assume that the excess entropy observed in this system arises from a change in the vibrational spectrum on alloy formation. The Debye temperatures of the alloys have been calculated, taking this excess entropy into account, and the additional heat of mixing attributable to the change in the vibrational spectrum has also been evaluated. This contribution is quite small, having a maximum value of only 110 calories per mol, and can be neglected in comparison with the maximum strain energy of 3800 calories per mol.

It is evident that a positive heat of mixing and a miscibility gap in the phase diagram do not necessarily lead to the presence of *A*-rich and *B*-rich clusters in the parent solution. Although this does seem to be the case in some instances (e.g., aluminum-zinc), it is not true in the gold-nickel system. Here, the miscibility gap and the short range order above the gap seem to arise primarily from a tendency to lower the strain energy introduced by the difference in size of atoms.

The quasi-chemical approach to the calculation of short range order in Cu_3Au also appears to require reexamination. Since the atomic sizes here are significantly different, a strain energy term requiring a positive contribution to the heat of mixing of 1870 calories per mol must be taken into consideration. Therefore, the consistency between the observed heat of mixing of -1370 calories per mol and the measured short range order (Table I) may be largely fortuitous. A possible explanation is given in terms of changes in the Fermi energy arising from changes in energy levels on alloy formation.

Unfortunately there seems to be no way at present of ascertaining the nature of the local atomic arrangements from the phase diagram or the macroscopic thermodynamic properties. If the atoms have different sizes, the strain energy component may be very large. Thus, the apparent agreement with the quasi-chemical predictions in some systems may be quite accidental. It is necessary to consider both the strain energy and the electronic changes on alloy formation in order to account for the observed heats of mixing.

7. Acknowledgments

The authors would like to acknowledge the assistance of the Atomic Energy Commission in the sponsorship of this research. They also appreciate the cooperation of L. L. Seigle and E. E. Underwood in connection with the calculations summarized in Table I, and are indebted to Professor John C. Slater for a stimulating discussion.

This work was sponsored by the U.S. Atomic Energy Commission under Contract No. AT(30–1)–1002. Scope II.

References

1. FOWLER, R. and GUGGENHEIM, E. H. Statistical Thermodynamics (Cambridge University Press 1939).
2. COWLEY, J. M. Phys. Rev. **77** (1950) 669.
3. TAKAGI, Y. Proc. Phys. Math. Soc. (Japan) **23** (1941) 44.
4. WAGNER, C. Thermodynamics of Alloys (Cambridge, Mass. Addison Wesley, 1952).

5. WEIBKE, F. and QUADT, U. F. Z. Elektrochem. **45** (1939) 715.
6. COWLEY, J. M. J. App. Phys. **21** (1950) 24.
7. ROBERTS, B. W. JR. "Short and Long Range Order in CuAu," Ph.D. Thesis, Massachusetts Institute of Technology. 1951.
8. WARREN, B. E. and AVERBACH, B. L. Modern Research Techniques in Physical Metallurgy (American Society for Metals, 1953).
9. NORMAN, N. and WARREN, B. E. J. App. Phys. **22** (1951) 483.
10. KUBASCHEWSKI, O. and HUCHLER, O. Z. Elektrochem. **52** (1948) 170.
11. SCHMAHL, N. G. Z. Anorg und Allg. Chemie, **266** (1951) 1.
12. SEIGLE, L. L., COHEN, M., and AVERBACH, B. L. A.I.M.E. J. Metals **4** (1952) 1320.
12A. HEUMANN, T. Zeit. Metallk. **42** (1951) 182.
13. FLINN, P. A., AVERBACH, B. L., COHEN, M. Submitted to Acta Met.
14. HUME-ROTHERY, W. and POWELL, H. M. Z. Krist. **91** (1935) 23.
15. LAWSON, A. W. J. Chem. Phys. **15** (1947) 831.
16. FUCHS, K. Proc. Roy. Soc. **A151** (1935) 585.
17. BRIDGMAN, P. W. Proc. Amer. Acad. Arts and Sci. **77** (1949) 187; also NEIGHBORS, J. R., BRATTEN, F. W., and SMITH, C. S. J. App. Phys. **23** (1952) 389.
18. HILLIARD, J. Private communication.
18A. SCHNEIDER, A. and STOLL, E. K. Z. Elektrochem. **47** (1941) 527.
19. RUDMAN, P. S., FLINN, P. A., and AVERBACH, B. L. J. App. Phys. **24** (1953) 365.
20. SEITZ, F. Modern Theory of Solids (New York, McGraw-Hill, 1940).
21. LUMSDEN, J. Thermodynamics of Alloys (London, Institute of Metals, 1952).
22. SLATER, J. C. Introduction to Chemical Physics (New York, McGraw-Hill, 1939).
23. WARREN, B. E., AVERBACH, B. L., and ROBERTS, B. W. J. App. Phys. **22** (1951) 1493.
24. SIEGEL, S. Phase Transformations in Solids, (New York, Wiley, 1951) p. 366.
25. FLANAGAN, W. E. Research now in progress.
26. SLATER, J. C. Phys. Rev. **84** (1951) 179.
27. NICHOLAS, J. F. Proc. Phys. Soc. **A66** (1953) 201.

CRYSTALLOGRAPHY OF DEFORMATION BY TWIN BOUNDARY MOVEMENTS IN INDIUM-THALLIUM ALLOYS*

Z. S. BASINSKI and J. W. CHRISTIAN†

The geometrical effects of steps ("twinning dislocations") in the (101) twin boundaries of face-centered tetragonal crystals are outlined. By introduction of edge-type twinning dislocations, a set of parallel twins may be tapered uniformly to give a single crystal lattice, rotated slightly with respect to one of the twin orientations. The tapering is equivalent to a macroscopic shear, approximately on the $(10\bar{1})$-plane of the untwinned lattice. The deformation of specimens consisting of sets of fine parallel twins is considered in detail. A distribution of edge twinning dislocations gives uniform plane bending to a maximum curvature determined by the orientation of the specimen. The geometrical results are closely related to those derived by Nye for glide deformation, but the condition for maximum bending is different. The variation of strain energy with twin thickness is calculated; minimum total energy corresponds to a twin thickness of $\sim 10^{-3}$ cm. Three-dimensional bending is possible if screw-type twinning dislocations are introduced, though Nye's tensor relations cannot be satisfied exactly. For pure screw bending, the specimen has the approximate shape of a solid torus. The predictions were confirmed by experimental work on indium-thallium alloys. At room temperature, the behaviour is perfectly plastic, but the material exhibits rubber-like elastic properties when deformed at lower temperatures. The transition between plastic and pseudo-elastic behaviour is governed by a temperature controlled relaxation process. There is also a high temperature rubber-like behaviour, which may be explained by postulating stress induced transformation from the cubic to the tetragonal form above the normal M_s temperature.

LA CRISTALLOGRAPHIE DE DÉFORMATION PAR DES MOUVEMENTS DES JOINTS DE MACLES DANS DES ALLIAGES INDIUM-THALLIUM

On expose les effets géométriques de gradins (dislocations de maclage) dans les joints (101) de macles de cristaux tétragonaux à faces centrées. En introduisant des dislocations-coin de maclage, des macles parallèles, en rangée, peuvent être amincies uniformément de façon à donner finalement un réseau de monocristal, tourné légèrement par rapport à l'orientation d'une des macles. L'amincissement est équivalent à un cisaillement macroscopique approximativement sur le plan $(10\bar{1})$ du réseau non maclé. La déformation d'échantillons consistant en des rangées de fines macles parallèles est examinée en détail. Une distribution de dislocations-coin de maclage donne une flexion plane, uniforme, jusqu'à une courbure maximum, déterminée par l'orientation de l'échantillon. Les résultats géométriques se rapprochent des résultats obtenus par Nye pour le cas de déformation par glissement, mais la condition de flexion maximum est différente. On a calculé la variation de l'énergie de déformation en fonction de l'épaisseur de la macle; le minimum de l'énergie totale correspond à une épaisseur de macle d'environ 10^{-3} cm. Une flexion à trois dimensions est possible, si on introduit des dislocations-vis de maclage, quoique les tenseurs de Nye ne puissent pas être complètement satisfaits dans ces cas. Dans le cas de flexion hélicoïdale, pure, l'échantillon a approximativement la forme d'un tore. Les prédictions furent confirmées par les expériences effectuées sur des alliages indium-thallium. A la température ambiante, le comportement est parfaitement plastique, mais lors de la déformation aux basses températures, le matériau manifeste des propriétés élastiques semblables à celles du caoutchouc. La transition entre le comportement plastique et pseudo-élastique est un processus de relaxation contrôlé par la température. Aux températures élevées, on trouve aussi un comportement semblable à celui du caoutchouc, qui peut être expliqué, si on admet l'existence de transformation de la forme cubique à la forme tétragonale, induite par des tensions, au-dessus de la température M_s normale.

DIE KRISTALLOGRAPHIE DER VERFORMUNG VON INDIUM-THALLIUM LEGIERUNGEN DURCH WANDERUNG VON KORNGRENZEN VON ZWILLINGSKRISTALLEN

Die geometrischen Effekte von Stufen ("Zwillings-Versetzungen") in den (101) Zwillings Kristallgrenzen flächenzentriert tetragonaler Kristalle werden beschrieben. Durch Einführung von Zwillings-Versetzungen des Stufen-types können parallele Zwillingskristalle gleichförmig abgeschrägt werden, und es ergibt sich ein Einkristallgitter, das in Bezug auf die eine der Zwillingsorientierungen ein wenig rotiert ist. Diese Abschrägung isteiner makroskopischen Scherung ungefähr auf der (101) Ebene des ursprünglichen Gitters gleichbedeutend. Die Verformung von Proben, die aus einem System schmaler, paralleler Zwillings-kristalle bestehen, wird in Einzelheiten diskutiert. Eine Verteilung von Stufen-Zwillings-Versetzungen ergibt gleichmässige, ebene Biegung bis zu einem maximalen Biegungsradius, der von der Orientierung der Probe abhängt. Die geometrischen Resultate sind den von Nye für Verformung durch Gleitung abgeleiteten Angaben verwandt, die Bedingung für maximale Biegung ist jedoch verschieden. Es wird die Änderung der Verzerrungsenergie mit der Zwillingsdicke berechnet. Das Minimum der Gesamtenergie entspricht einer Zwillingsdicke von 10^{-3} cm. Es ist möglich, dreidimensionale Biegung zu behandeln, wenn Schrauben-Zwillings-Versetzungen eingeführt werden; Nye's Tensorbeziehungen können jedoch nicht exakt erfüllt werden. Im Falle einer reinen "Schraubenbiegung" hat die Probe etwa die Form eines vollen Torus. Diese Voraussagen wurden durch Experimente mit Indium-Thallium Legierungen bestätigt. Das Verhalten dieser Legierungen ist bei Zimmertemperatur völlig plastisch, jedoch zeigt das Material bei Verformung bei tiefen Temperaturen ein gummiartiges elastisches Verhalten. Der Übergang zwischen plastischem und pseudo-elastischem Verhalten wird durch einen temperaturabhängigen Relaxionsvorgang bestimmt. Man findet auch ein gummiartiges Verhalten bei hohen Temperaturen, das sich erklären lässt, wenn man eine spannungsausgelöste Transformation von der kubischen zur tetragonalen Form oberhalb der normalen M_s Temperatur postuliert.

*Received August 10, 1953.
†The Inorganic Chemistry Laboratory, Oxford University, England.

1. Introduction

F.c.c. single crystals of In-Tl alloys may be transformed martensitically to give a single set of fine parallel f.c.t. twins. The twin boundaries are very mobile and lead to unusual mechanical properties, including rubber-like behaviour at low temperatures. In this paper we first consider the crystallography of tetragonal twinning, and in particular the lattice curvatures produced by steps in twin boundaries. The geometrical relations are applicable to any form of deformation twinning, and are closely related to the results recently obtained by Nye [1] for the curvatures produced by inhomogeneous slip. Simple experiments on the deformation of In-Tl alloys have confirmed some of the predictions. The modes of deformation are also closely related to processes occurring during the martensitic transformation; these are described in a separate paper.

A tetragonal crystal is brought into a twin orientation by a simple shear on (101)-planes in a $[10\bar{1}]$-direction. In the conventional description of deformation twinning (see e.g., Cahn [2]), the twinning elements are:

K_1	K_2	η_1	η_2
(101)	$(10\bar{1})$	$[10\bar{1}]$	$[\bar{1}01]$

2ϕ	s	3ϵ
$2\tan^{-1}\frac{a}{c}$	$\frac{c^2-a^2}{ac}$	$2\tan^{-1}\frac{c}{a}-\frac{\pi}{2}$

The symbols have the meanings used by Cahn: 3ϵ, introduced in addition, is the acute angle between the [001]-direction of the parent lattice and the [100]-direction of the twin. We shall be concerned only with structures in which $|(c/a-1)| \ll 1$, so that the angle of shear becomes

$$s = 2\left(\frac{c}{a}-1\right) = 6\epsilon$$

The indium-thallium alloys used for the experimental work have $c/a \simeq 1.04$ and $s \simeq 0.08$.

2. Lattice Rotations Produced by Steps in Tetragonal Twin Boundaries

Two tetragonal lattices in twin orientation will fit together on a (101) composition plane with only a very small energy due to the change in interatomic distance across the boundary. Regions of strain are produced whenever the boundary moves from one composition plane to a neighbouring plane; the step in the boundary is the twinning dislocation described by Frank [3], and Thompson and Millard [4]. Twinning dislocations may lie in any direction of the composition plane and have Burgers vector $\mathbf{b} = h.\mathbf{s}$, where h is the step height. In a f.c.t. structure, the minimum step height is $h = ac/2(a^2+c^2)^{\frac{1}{2}}$, and is equal to half the repeat distance in the direction perpendicular to (101). The minimum step in a simple tetragonal structure is twice as high. In both structures, the atoms can all be placed on the points of a Bravais lattice, and a homogeneous shear of the unit cell produces the twin orientation without the need for atomic "shuffles."

When the step is parallel to [010], the twinning dislocation is of edge type, when parallel to $[10\bar{1}]$ it is of screw type. Figure 1 shows two edge-type

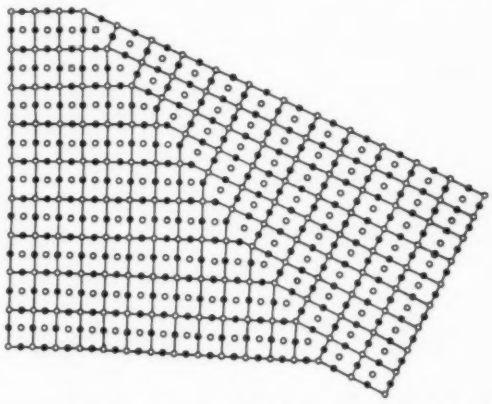

FIGURE 1. Two edge-type twinning dislocations in a (101) twin boundary of a face-centered tetragonal lattice. The plane of the figure is perpendicular to [010]. Open circles are atomic positions in the plane of the figure: filled circles the projection of the next atomic layer on this plane. The lattice curvatures are visible if the diagram is viewed at glancing incidence.

twinning dislocations in an f.c.t. lattice. If the total thickness of parent and twin crystal in the direction normal to the twinning plane is t, the effect of each step is to produce a bend in the specimen, the lattices being rotated by b/t about the [010]-axis. Figure 2 similarly shows a screw-type twinning dislocation, drawn for simplicity in a simple tetragonal lattice. The lattices on either side of the step (viewed from any direction) are oppositely sheared in the $[10\bar{1}]$ direction through an angle b/t.

Deformation twins are usually lenticular in shape and the progressive thinning may conveniently be described in terms of closed loops of twinning dislocations. We now discuss an apparently less probable situation, in which the twin thickness decreases in one direction only, remaining uniform in a perpendicular direction. This obviously corre-

sponds to a parallel array of straight twinning dislocations on successive atomic planes.

We consider a set of (101) twins which have lattice orientations 1 and 2 and mean thicknesses p and q perpendicular to (101). The twins are assumed to taper uniformly in the [10$\bar{1}$]-direction, so that the twins of orientation 2 are wedge-shaped and end in a series of [010] lines. If the angle of

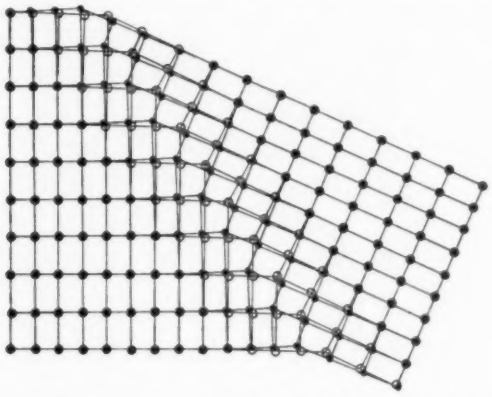

FIGURE 2. A screw-type twinning dislocation in a simple tetragonal lattice. Lattice orientation and atomic symbols are as in Fig. 1.

taper is very small, the twin boundaries consist of coherent sections with widely spaced steps of the type shown in Figure 1. Each step will produce a small bend in a finite specimen, and the twin planes become curved in the tapered region. We assume that the tapering occurs in such a way that strain energy is minimised. Since the atomic movements (slip vectors) all lie along the (101)-twinning planes, it follows that the distance between any two (101)-planes must remain constant if long-range stresses are to be avoided.

Consider two neighbouring sections, perpendicular to the twin planes, at which the mean thicknesses of twins of orientation 1 are p_1 and p_2 respectively. If there are n twins of each kind there are $2n$ twin boundaries and the total number of twinning steps between the two sections is $(p_2 - p_1)n/h$. Each step produces a rotation $b/n(p + q)$ and the total rotation between the two sections is thus:

$$(1) \qquad \theta_2 - \theta_1 = \frac{b(p_2 - p_1)}{h(p + q)} = \frac{s(p_2 - p_1)}{p + q}$$

If the tapering takes place in such a way that the mean twin thickness decreases uniformly along the twinning planes, each of these will have constant curvature. The twinning planes will thus lie on the surfaces of a series of concentric circular cylinders with axes in the [010]-direction. The curvature of the twinning planes decreases slowly, and the distance between steps, measured along the (101)-planes, increases slowly as we move out from the centre of curvature. The maximum curvature of the innermost plane must be small because of the restriction to small angles of taper.

Figure 3 shows the way in which the twinned lattices 1 and 2 change into the untwinned single-crystal region of orientation 1′. From (1) we see that lattice 1′ is rotated about the [010]-axis with respect to lattice 1 by an angle

$$(2) \qquad \theta = \frac{qs}{p + q}.$$

This change in the orientation of the lattice planes should not be confused with the change in direction of a line marked on the crystal before untwinning began. Such a line, i.e., a 'labelled' set of atoms, will in general change its crystallographic orientation relative to the lattice. In particular, we consider a labelled row of atoms passing through point × (Figure 3) and perpendicular to the original twin boundaries. After untwinning, an atom of this row distant $n'(p + q)$ from × will have slipped a distance $n'sq$ along the (101)-planes

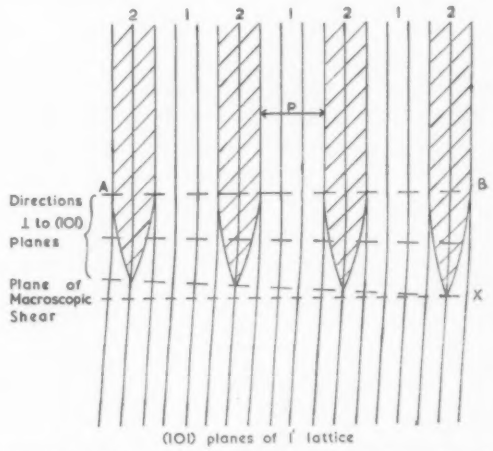

FIGURE 3. Tapering of twin orientation 2 to give single lattice slightly rotated from orientation 1. [101] perpendicular to plane of figure.

with respect to ×. The original line will thus have turned through an angle $n'sq/n'(p + q) = \theta$ with respect to its original lattice direction, and will therefore still be a straight line parallel to AB. We deduce from this that macroscopic planes perpendicular to the original [10$\bar{1}$]-directions remain undistorted. The macroscopic effect of the tapering is thus equivalent to a simple shear of amount θ on

the planes of the 1′ lattice at an angle $(\pi/2 - \theta)$ from the (101)-planes of this lattice. We may describe this as a virtual or distributed shear, since there is no composition plane and the transition is continuous over the regions in which tapering occurs.

When $p = q$, the undistorted K_1 plane of the macroscopic shear is the plane at an angle $(\pi/2 - s/2)$ to the (101)-plane of the 1′ lattice. This is the $(10\bar{1})$-plane. Since s is small, we also see that for any ratio of p/q, the K_1 plane of the macroscopic shear is approximately $(10\bar{1})$ of the 1′ lattice.

The macroscopic effect of this virtual shear may also be obtained by a macroscopically homogeneous real shear on $(10\bar{1})$. If we have a series of fine parallel twins, orientations 1′ and 3 and mean thicknesses p and q, adjacent to an untwinned region of 1′ lattice, the two portions of the specimen are related by a macroscopic shear of $qs/(p + q)$ on the $(10\bar{1})$-plane of the 1′ lattice. Such a macroscopic shear may thus be obtained by a series of fine parallel $(10\bar{1})$ twins or by a set of fine tapered (101) twins, having the same thickness ratio. In the first case, the surface of the specimen would show a sharp bend about its intersection with the $(10\bar{1})$-plane joining twinned and untwinned regions, whereas for (101) twins there would be a gradual bend over the region of taper. Both kinds of shear are important in the martensitic transformation.

The above results may be shown to be self-consistent by a hypothetical example in which two lattices having orientations corresponding to $(10\bar{1})$ twinning are joined by tapered (101) twins. In Figure 4 a set of (101) twins are made to taper in opposite ways producing orientations 1′ and 2′. If orientation 1′ is related to 1 by a rotation of θ about [010], orientation 2′ is similarly obtained from 2 by a rotation of $s - \theta$. The relative orientations of 1′ and 2′ are thus obtained from those of 1 and 2 by a relative rotation of s. Such a rotation interchanges the K_1 and K_2 planes, so the orientations 1′ and 2′ correspond to those obtained from twinning on $(10\bar{1})$-planes. This is readily seen from the virtual shears, the total distributed shear between 1′ and 2′ being s. The situation in Figure 4 might be described as a distributed twin boundary: obviously it would have a much higher energy than a normal $(10\bar{1})$ twin boundary.

The above discussion refers to tapering by edge-type twinning dislocations. We may also imagine a situation in which a set of wedge-shaped twins end in a series of $[10\bar{1}]$ lines. An array of screw dislocations produces a long-range shear of the lattice, and by introducing only screw-type twinning steps it is not possible to avoid accumulating stresses. The twins cannot be tapered so as to produce an unstrained single-crystal region, and the change in lattice orientations is not describable as a single rotation. We discuss this in more detail in Section 4.

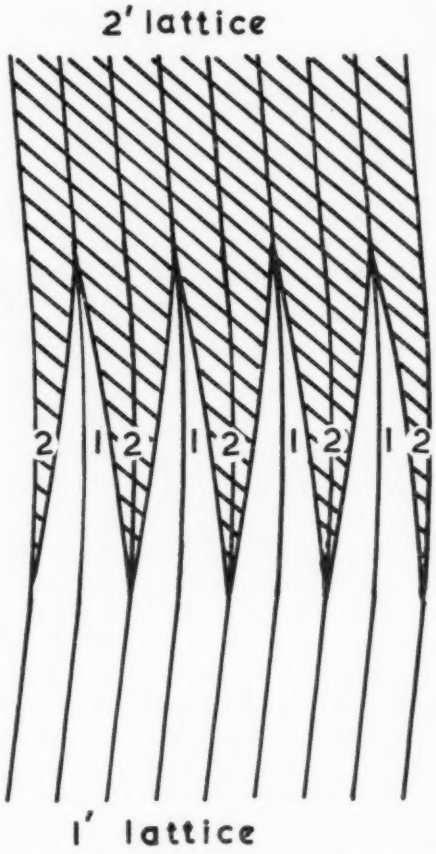

FIGURE 4. A distributed twin boundary. Curved vertical lines are traces of (101) planes.

3. Deformation by Movement of Twin Boundaries

A specimen consisting of a series of fine parallel twin crystals may be deformed by movements of the twin boundaries. The simplest deformation results from the application of a uniaxial tensile or compressive stress. Although the basic formulae are well known [5], we shall briefly treat this problem first, as it is convenient to introduce some approximations. If the twin boundaries are sufficiently mobile, they will move perpendicular to themselves, increasing or decreasing the proportion of the orientation appropriate to the sign of the stress. Thus with a compressive stress, the twins

having a smaller repeat distance along the stress axis will grow at the expense of the others. This process can continue until the specimen becomes a single crystal, and the maximum strain obtainable will depend both on the orientation of the stress axis and the relative amounts of the two twins initially present. The maximum difference in length along the stress axis in compression and tension will depend only on the orientation of the axis.

For a volume of material sheared through a uniform angle s', we have the well-known result for the change in length of any vector **l** [5]

$$\frac{l'}{l} = (1 + 2s' \sin \chi \cos \lambda + s'^2 \sin^2 \chi)^{\frac{1}{2}}$$

where χ is the angle between **l** and the K_1 plane, and λ is the angle between **l** and η_1. This equation gives the ratio of the maximum and minimum lengths along the stress axis if we replace s' by the twinning shear s. Since s is small, we may neglect s^2 and the change in length is then more conveniently specified by other angles. In Figure 5, which shows

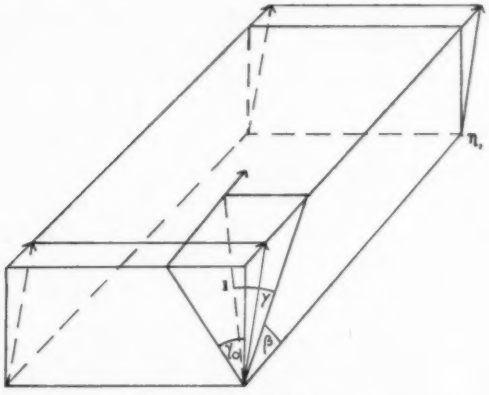

FIGURE 5. Angles used in defining homogeneous shear.

a rectangular parallelepiped sheared to a new position, γ is the angle between an arbitrary direction **l** and the plane of shear, and β the angle between η_1 and the projection of **l** on the plane of shear. The change in length of **l** for a shear s may be written:

$$\frac{\Delta l}{l} = \frac{s}{2} \sin 2\beta \cos^2 \gamma. \tag{3}$$

Alternatively, we may introduce the angle γ_0 between the plane containing **l** and η_1 and the plane of shear. We then have:

$$\frac{\Delta l}{l} = \frac{s}{2} \sin 2\lambda \cos \gamma_0. \tag{4}$$

As a result of the shear, the direction **l** rotates relative to K_1 and η_1. The change in orientation for a shear s' is given by

$$\frac{\sin \chi'}{\sin \chi} = \frac{\sin \lambda'}{\sin \lambda} = \frac{l}{l'}. \tag{5}$$

The effect of neglecting s^2 in equations (3) and (4) is to leave directions in the plane perpendicular to K_1 unchanged in length, whereas this is only strictly true for directions in K_1 and K_2.

4. Uniform Plane Bending

Suppose, for simplicity, we have a bar of rectangular cross-section, and one face a (010) plane. The traces of (101) twinning planes in this face will then appear as in Figure 6(a). The specimen

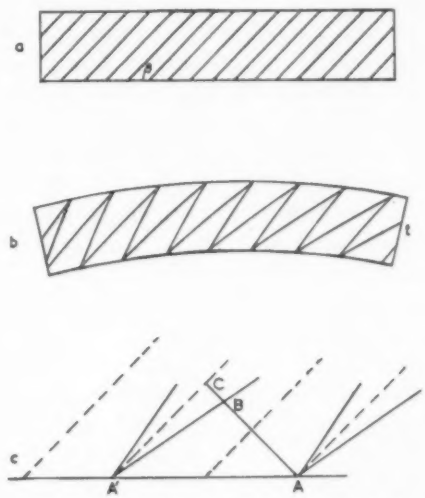

FIGURE 6. Bending of specimen by edge twinning dislocations. (a) Traces of (101) planes in unbent specimen. (b) Traces of (101) planes in bent specimen. (c) Two neighbouring twins meeting compressed surface.

can bend under applied stress if the twin boundaries are able to rotate through small angles from their original positions, tapering in opposite directions so that the top surface of the specimen is entirely composed of lattices from one of the original twins, and the bottom surface from the other. (Figure 6(b)). If we take the axis of the specimen as **l** in Figure 5, $\gamma = 0$ and β is the angle between the axis and the trace of a twinning plane. If there is no macroscopic strain, the radius of curvature, ρ_c, of the bent specimen is given by:

$$\frac{1}{\rho_c} = \frac{\Delta l}{tl} = \frac{s \sin 2\beta}{2t} \tag{6}$$

where t is the thickness after deformation. Planes

parallel to the top surface are curved into cylindrical shape, the generators lying along [010].

Instead of using this macroscopic argument, we may obtain the same result by considering the rotation produced by the steps in the twin boundaries, which are obviously twinning dislocations of edge type. Figure 6(c) shows the positions of two adjacent boundaries where they meet the lower face of the bent specimen: the directions of the original boundaries are shown by dotted lines. The results of Section 2 show that the orientation of each of the lattices will be constant along a line such as ABC, perpendicular to the (101) planes. There will, therefore, be a change of orientation between A and A′, which from equation (1) is equal to $s2BC/AC \simeq s \cdot AC \cos \beta/t$. If the original twin thicknesses were p and q, we have the mean misorientation between neighbouring points A and $A' = s(p + q) \cos \beta/t$. The average distance between A and A' is $(p + q)/\sin \beta$ and hence the total misorientation between the ends of the bottom surface of the specimen is $ls \sin 2\beta/2t$. This corresponds to the radius of curvature given by equation (6).

In neither of the above arguments have we considered the position of the neutral plane or the curvature of the lattice planes. It is clear that the ordinary definition of the neutral plane is without significance. The final bent state is independent of the proportions of the twins initially present, but the filament unchanged in length does depend on these proportions. The specimen may be extended or compressed (so long as only twin boundary movements occur) prior to bending, without changing the final shape. We may therefore suppose that we start with a specimen containing equal proportions of the two twins, and it is useful to define the neutral plane as the plane containing equal proportions of the twins after bending.

For a consideration of lattice curvatures, the following model is useful. The specimen is cut into thin strips, each parallel to the top plane and of thickness dx. The strips are then extended or compressed by twin movements, so that in a given strip the length changes to l' and the thickness to dx'. For some strip Δl will be zero and we take the origin of x' in this plane. If each strip is now bent elastically into cylindrical shape, the strips can be fitted together again without long-range stress, provided only that Δl is proportional to x'. The surfaces of the strips, originally flat, are now corrugated, and strain energy is required to fit two strips together. As $dx \to 0$, the strain energy in each bent strip also tends to zero. However, we are not able to make dx indefinitely small because of the finite spacing between dislocations. If each twinning step is of minimum height h, there must be one twinning dislocation of Burger's vector $\mathbf{b} = \mathbf{s}h$ on every atomic (101) plane. The total number of twinning dislocations N is thus fixed, and as $dx \to 0$ the twin thickness p increases, and the number of dislocations in the interface between any two strips decreases. The elastic energy required to fit the strips together shows a corresponding increase. To a first approximation, the two energy effects cancel, so that for fixed $\mathbf{b}$ the strain energy of the bent specimen is independent of twin width. If it were possible to increase the number of dislocations by decreasing $\mathbf{b}$ indefinitely, a different result would be obtained. If $\mathbf{b} \to 0$, keeping $N\mathbf{b}$ constant, we can allow both dx and p to tend to zero simultaneously, and the strain energy then becomes zero. This corresponds to a model of slip deformation described by Nye [1]. With fixed $\mathbf{b}$, the strain energy remains finite, but the model clearly gives the arrangement of dislocations which has minimum strain energy. In Section 6, we shall show that to a higher approximation the strain energy may be further reduced by decreasing p.

The condition Δl proportional to x' implies that the neutral plane, defined as above, is the central plane of the deformed specimen. Consider a strip for which the macroscopic shear is s' and the fractional change in length is therefore $s' \sin 2\beta/2$. The corresponding change in thickness is given by:

$$\frac{dx' - dx}{dx} = -\frac{s'}{2} \sin 2\beta.$$

The total change in length between the neutral filament and the most extended filament is $sl \sin 2\beta/4$ and this is accompanied by a contraction of $x' - x = -xs \sin 2\beta/4$ in the strips above the neutral filament. Since $x' = t/2$, we have the original thickness of the strips above the neutral plane as

$$x_a = \frac{t}{2}\left(1 + \frac{s}{4} \sin 2\beta\right).$$

Similarly the original thickness of the strips below the neutral plane is

$$x_b = \frac{t}{2}\left(1 - \frac{s}{4} \sin 2\beta\right).$$

The total thickness of the specimen thus remains unchanged, but the neutral plane is originally

situated at a distance $ts \sin 2\beta/8$ below the central line. If the specimen originally has $p \neq q$ there will be a change of thickness during the bending.

When each strip is compressed the lattice rotates relative to its length, as shown by equation (5). In our specimen $\chi = \beta$, so that the angle between the twinning plane and any filament is given by:

$$\frac{\sin \beta'}{\sin \beta} = \frac{l}{l'} = \frac{\rho_e}{\rho_e + x}$$

where ρ_e is the radius of curvature of the neutral filament. As shown by Nye [1], this relation implies that the twinning planes are the involutes of a circle.

We may now consider what happens if we attempt to bend a rectangular bar specimen in which the top surface contains [010], but this is no longer perpendicular to its length. If the twin boundaries again taper by edge type twinning dislocations, the top surface will again be bent about the [010] axis with identical radius of curvature. The top surface of a long rod specimen now appears to twist as well as bend. The specimen lies between the surfaces of two coaxial cylinders of radii $\rho_e \pm t/2$, and with the specimen axis inclined to the cylinder axis. Directions in the extended (top) surface are converted into circular helices, so that if straight lines are ruled on this surface before bending, both the curvature and torsion of the surface remain constant along such lines.

In practice, it is easier to measure the total curvature in the plane of the applied bending moment than the true curvature along a direction inclined to the specimen axis. If a rod or bar specimen is allowed to rest freely on its side, its shape may be projected orthogonally on to a flat plane. This shape will clearly be a section of the cylinder by a plane containing the direction of the original length; i.e., an ellipse with major axis along the specimen length. Taking x and y axes in the section parallel and perpendicular to the specimen axis, the equation is:

$$\frac{x^2}{\rho_e^2 \sec^2 \gamma} + \frac{y^2}{\rho_e^2} = 1.$$

The radius of curvature in the projected section is thus

$$\rho = \rho_e \sec^2 \gamma \left[1 - \frac{x^2 \sin^2 2\gamma}{4\rho_e^2} \right]^{3/2}$$

and at the centre of the specimen ($x = 0$)

$$\rho = \rho_e \sec^2 \gamma.$$

If the specimen is sufficiently short [$l \sin 2\gamma \ll \rho_e$ i.e., $l/t \ll 1/(s \sin 2\gamma \sin 2\beta)$], the section will approximate to a circle with this curvature. Substituting for ρ_e from (6), we see that to a first approximation directions along the specimen axis are bent into circular arcs of radii $\rho = tl/\Delta l$.

We have assumed that application of the bending moment in the plane through **l** and η_1 produces the same result as application of the stresses in the plane perpendicular to [010]. Only the component of the bending moment in this plane is utilised in the deformation: a little consideration shows there is no other way of bending a specimen by movement of twin boundaries. Uniform plane bending is therefore possible in all specimens if the bending moment is applied perpendicular to the plane containing the specimen axis and the [010] direction, but the bending becomes progressively more difficult as γ increases. Bending is impossible for $\gamma = \pi/2$, when the twin planes are parallel to the specimen axis.

The maximum curvature in any specimen occurs when $\beta = \pi/4$ as is physically obvious, and is given by $1/\rho = s/2t$. When $\gamma = 0$, this curvature is along the specimen length.

5. Relation to Nye's Treatment

The mean curvatures produced in a single crystal by unevenly distributed glide have recently been analysed mathematically by Nye [1]. The results of the previous section correspond closely to his conclusions for plane bending. This is expected since the fundamental assumption in both problems is identical; namely, that the lattice attains a minimum energy state in which there are no cumulative long-range stresses.

To relate our results to those of Nye, we may regard the deformation as the result of slipping movements on the twinning planes. The finite number of dislocations, however, imposes an additional restriction on the twin movements. Assuming all steps are of minimum height, the total number of steps in a specimen containing n twins of each kind is:

$$N = n(p + q)/h.$$

The traces of the twinning or glide planes in a (010) plane are the involutes of a circle, and the excess density of dislocations of one sign decreases as we move radially across the specimen from the compressed to the extended surface. When deformation occurs by slip, there is no limit to the way in which the dislocations may be distributed over the glide planes, and maximum bending is possible when

$\chi = \beta = 0$. For deformation by twin boundary movements, however, the restricted number of dislocations give maximum variation of radial dislocation density when $\beta = \pi/2$, and this variation is zero for $\beta = 0$. We shall now show that this leads to maximum bending for $\beta = \pi/4$.

From Nye's results, we have the number of dislocations per unit area along a filament distant x from the neutral plane is

$$\nu = \frac{l}{b[(\rho_e + x)^2 - \rho_e^2 \sin^2 \beta]^{\frac{1}{2}}}$$

where ρ_e is the radius of curvature of the neutral plane, and β the angle the twinning planes make with this plane. The length of this filament is

$$l = \frac{n(p+q)(\rho_e + x)}{\rho_e \sin \beta}$$

and hence the total number of twinning dislocations in the specimen is given by

$$N = \int_{-t/2}^{t/2} \nu l \, dx = \frac{2n\,(p+q)}{b \sin 2\beta} \frac{t}{\rho_e} \text{ since } t \ll \rho_e \cos \beta.$$

Equating the expressions for N, we obtain finally:

$$\rho_e = \frac{2t}{s \sin 2\beta}$$

in agreement with (6). The maximum curvature is very much smaller than the maximum curvature in glide, which corresponds to an infinite density of dislocations on the innermost filament.

6. Energy Considerations

We may now consider again the variation of strain energy with twin thickness. Nye showed that his model leads to an expression for the strain energy density of the form:

$$\kappa G b \ln \frac{b}{\kappa r_0^2}$$

where κ is the local curvature of the glide planes, G an elastic constant, and r_0 a length of atomic dimensions. This expression is applicable to an element of volume containing several active glide planes or twin boundaries, and shows the strain energy to depend only on the number of dislocations in this volume and the strain energy of each. To a higher approximation, there is a dependence of energy upon the detailed distribution of dislocations which arises in the following way. Within the volume characterised by κ, each dislocation may be regarded as lying along the axis of a prismatic sub-volume which is fixed in magnitude per unit length of dislocation line. Local redistributions of dislocations which do not disturb the mean density change the shape of the sub-volumes, and hence the elastic energy of the dislocation contained in each. For example, a dislocation in a flat rectangular prism with its Burger's vector along the longer side of the section will have a lower energy than a dislocation in a square prism of the same volume. Thus there is a lowering of energy if the dislocations are arranged so that there is a minimum separation in the direction normal to the Burger's vector at the expense of an increased separation parallel to the Burger's vector; this is polygonisation. In our present problem, a larger separation of twinning dislocations parallel to **b** implies a larger number of fine twins. We calculate the strain energy on the assumption that the mean twin thickness, p, may be varied in any way we choose. Consider a small unit cube with sides parallel and perpendicular to the (101) planes. If this cube contains m dislocations, the mean curvature of the twinning planes is specified by $\kappa = mb$, and the mean separation of dislocations along these planes by $y = 1/mp$. By analogy with ordinary polygonisation, we expect the strain energy to be reduced by an increase in y and corresponding decrease in p. We can write approximate expressions for the strain energy under the limiting conditions $y \gg p$ or $y \ll p$. In the former case we have $1/y$ linear arrays of twinning dislocations perpendicular to the boundaries of the very fine (submicroscopic) twins. Each of these pseudo-polygon boundaries produces an angular tilt of κy in both lattices, so their total energy may be written [6]:

$$(7) \qquad \begin{aligned} E &= \frac{1}{y} \frac{\mu b}{4\pi(1-\nu)} mby(A - \ln mby) \\ &= \frac{\mu b^2 m}{4\pi(1-\nu)} (A - \ln b + \ln p) \end{aligned}$$

where μ is the shear modulus, ν is Poisson's ratio and $A \simeq 0.5$. This expression gives the elastic energy per unit volume in the region where the density of dislocations is m. For given m, it has a minimum value when p is as small as possible; i.e., when the angle of taper is minimised.

If $y \ll p$, we treat each twin as a continuously bent beam, instead of a series of sharply tilted regions. The filament strain then has maximum values of $\pm b/2y$, and the strain energy density may be written:

$$(8) \qquad E = \frac{Yb^2}{6y^2} + C = \frac{\mu(1+\nu)\, b^2 m^2 p^2}{3} + C$$

where Y is Young's modulus, and C allows for the core energy of the dislocations. The elastic energy thus increases with p^2.

For the specimens used in the experimental part of this paper, a typical value of py is 2.10^{-8} cm^2, giving $m = 5.10^7$ lines per cm^2, and $b = .10^{-9}$ cm. Assuming $\nu = 1/3$, we obtain for the elastic energy density:

$$\frac{E}{\mu} = 5.10^{-12}(21 + \ln p) \qquad p \ll y$$

or

$$\frac{E}{\mu} = .10^{-3}p^2 + C' \qquad p \gg y$$

Neither of these equations is strictly valid when $p \doteq y \doteq 10^{-4}$ cm, but it is interesting to note they both then give values of E/μ of order 10^{-11} if C' is taken to be $\backsim 5.10^{-11}$. As expected the strain energy density is very small, even when compared with the energy stored in material deformed by glide.

Equations (7) and (8) show that the strain energy decreases continually with p, but this does not necessarily minimise the total energy. Unlike glide planes, the coherent sections of the twin boundaries have a finite energy, which increases as p decreases. If this energy is W per unit area, the energy density due to this term is W/p. We thus expect a minimum total energy at some definite twin thickness p_c given by

$$p_c = \frac{4\pi(1-\nu)}{b^2 m}\,\frac{W}{\mu}$$

or

$$p_c^3 = \frac{3}{2(1+\nu)\,b^2m^2}\,\frac{W}{\mu}$$

depending on whether the value of W/μ makes p_c less than or greater than y. For copper the ratio of the twin boundary energy to the shear modulus is $\backsim 4.10^{-11}$ cm. If we assume a ratio of the same order of magnitude and substitute numerical values, we see that the first equation is inappropriate, and the equilibrium twin thickness is about 10^{-3} cm.

The above discussion is without significance unless there is some physical mechanism by which p may be changed. In an actual experiment, we start with a number of twins of small but finite thickness, so that a certain coherent energy per unit volume is effectively frozen into the specimen. Only small stresses are used to move the twin boundaries, and there is thus no plausible physical mechanism by which p may be reduced, since this requires creation (or activation) of new twin nuclei. However, neighbouring twins coalesce on the top and bottom surfaces when the specimen is bent to its maximum curvature, so it is physically possible by bending and unbending a specimen to eliminate some of the twins and so increase p. Thus if we start with a value of p appreciably lower than the equilibrium value for a fully bent specimen, we may be able to approach p_e by periodic bending and unbending. This means formally that we use the elastic energy of bending to help overcome the activation barrier for twin movements, and thus approach closer to thermodynamic equilibrium in the straight specimen. True equilibrium in the straight specimen requires that $p = \infty$ and this is attainable only by the use of uniaxial compression or extension.

The rather large value for p_e deduced above raises the question of why specimens with very narrow twins are found after the martensitic transformation. The reason for this lies in the large localised strain energy near the transformation interface. As we describe elsewhere (7), p is submicroscopic immediately behind this interface, and reaches its observed value by twin coalescence.

7. Three Dimensional Bending

The plane bending discussed above is ascribable simply to the change in length between top and bottom surfaces of the specimen when these are oppositely twinned. If a bending moment is applied to any specimen with arbitrary lattice orientation, we may envisage a similar deformation. The top and bottom surfaces will again be oppositely twinned, giving a progressive change in length in the plane of the applied bending moment. The change in relative amounts of the two twins will require the introduction of twinning dislocations having directions parallel to the intersection of the top surface and the twinning planes. Since all such twinning steps may be resolved into edge and screw components, we need only consider the other extreme case. Twinning dislocations of pure screw character are formed if the top surface of the specimen contains the η_1 direction. In terms of Figure 5, this top surface is thus the plane through **l** and η_1, where **l** lies in the plane of the bending moment.

Using equation (4) for the changes in length of directions in the top surface, we find $\Delta l/l$ has maximum and minimum values of $\pm s \cos\gamma_0$ when $\lambda = \pm\pi/4$. To a first approximation, we may assume that the change of length in any direction gives the corresponding radius of curvature. Planes perpendicular to the applied bending moment are

thus converted into anticlastic surfaces, the principal curvatures of which are equal and opposite and of magnitude

$$\frac{1}{\rho_s} = \frac{s}{2t}\cos\gamma_0. \tag{9}$$

The directions of the principal curvatures correspond to the length and breadth of the specimen if η_1 was originally at $\pi/4$ to **l**. A rod specimen will then bend without twisting. When $\gamma_0 = 0$, $1/\rho_s$ has a maximum value which is equal to the maximum value of $1/\rho_e$ for bending by edge dislocations. We conclude that an 'ideal' rod specimen ($\beta = \pi/4$, $\gamma = 0$) will bend about its length in any direction without twisting. If the specimen has circular cross-section, the maximum curvature will be constant and given by $1/\rho = s/2t$ where t is the diameter.

The above reasoning is only approximate, and we must now consider the lattice changes associated with the deformation. From Section 7 of Nye's paper, it follows that a distribution of screw dislocations of one Burger's vector (or of parallel dislocations of one general type) cannot be arranged so as to give a non-accumulating stress. To illustrate this, we again use a model of the deformation. For simplicity we deal with the ideal specimen, in which the top surface is the plane of shear, (010). We imagine the straight specimen cut into thin strips parallel to (010), each having thickness dx in the [010] direction. The strips are then compressed or extended along their lengths by twin boundary movements, so that in a given strip the changes in length and breadth are related by the equation $\Delta w/w = -\Delta l/l$: there is no change in dx. If we make Δl proportional to x, choosing the origin of x where $\Delta l = 0$, the strips will fit together again without accumulating stress in the x-direction, provided each can be bent into a suitable anticlastic surface. Since such a surface is not developable from a plane, the bending cannot be accomplished without extension or compression of the middle parts of each strip. The displacements in each strip are large compared with dx, and hence the stress required for the elastic bending of the strip increases with at least one dimension in the plane of the strip. The strain energy thus increases with the size of the strip, even if $b \to 0$.

For specimens which are long in comparison with their cross section, we may reasonably assume that directions in the plane of the applied bending moment are bent into circular arcs. The stress at any point will then not accumulate with increase in length of the specimen, which could be cut into two transversely without release of strain energy. If only screw-type twinning dislocations are involved, the transverse bending must be produced by the elastic stretching of longitudinal filaments near the sides of the specimen with respect to those in the centre. Considering the strip for which $\Delta l = \Delta w = 0$, we find the fibre strain of the outermost filament is given approximately by

$$\frac{\Delta' l}{l} = \frac{s^2 w^2}{32 t^2}$$

where w is the total width of the specimen. This strain thus increases rapidly with w.

A more probable physical description is obtained if we allow the introduction of some edge-type twinning dislocations. For a given strip, we now make Δl proportional to w^2, so that the relative amounts of the two orientations are a function of w as well as of x. On the top surface untwinning is complete only at the edges, on the bottom surface only along the centre line. The maximum curvature is decreased slightly, but only by quantities of order s^2. In each strip there is a density of edge dislocations which increases linearly with w.

The shape of the specimen specified by the above distribution of twins is approximately a solid torus, obtained by rotating two circles of radii $\rho_s \pm t/2$, about a line distant $2\rho_s$ from their centre. This distribution may be shown not to satisfy Nye's tensor relations exactly, but it does so approximately if we neglect the differences in curvature of the (010) planes. For w, $t \ll l$, the stress is everywhere small, so the deformation seems physically plausible. In the present problem we are considering a rather widely spaced distribution of dislocations of small Burger's vector, and the physical significance of an array which rigidly satisfies Nye's conditions is much smaller than in the more general problem of slip deformation.

Equation (5) now shows that the lattice twists about the [010] (x)-direction, the total rotation between top and bottom planes of the ideal specimen again being $s/2$. Returning to the more general case of screw dislocation bending when $\gamma_0 \neq 0$ there will clearly be a macroscopic twist of the specimen as well as a bend about its length. We now assume that lengths in the direction of principal curvature nearest to the applied bending moment are bent into circular arcs, and the previous argument can be repeated. It becomes increasingly difficult to bend a specimen as the stress axis moves away from a direction of curvature. The condition for no twist in edge bending ($\gamma = 0$)

is different from that in screw bending ($\lambda = \pi/4$), so that a twist in one case does not imply a twist in the other. In theory, it should be possible to twist a specimen about its length without bending if $\lambda = 0$.

If we again use the projection of the specimen shape as a measure of the curvature along the length, we find by considering a section through a torus or similar figure that the radius of curvature is once again given by $\rho = tl/\Delta l$. For a circular rod specimen, the apparent maximum curvature along the length is thus identical for all planes of applied bending moment.

8. Experimental Work

Large single crystals of indium-thallium alloys containing ~18.5% thallium were grown from the melt, and as described in another paper these could be obtained in the form of fine parallel tetragonal twins. Cylindrical crystals with lengths of up to 10 cm. and diameters up to 10 mm. were prepared, but for most of the work rather smaller specimens were used. Plane surfaces were obtained when desired by careful cutting with a razor blade or an ordinary wood plane, after which the strained layer was dissolved away electrolytically. The specimens were examined under the microscope, using etching or relief effects, and by taking back reflection Laue photographs.

Twinned specimens were all extremely soft at room temperature, and could be deformed in the fingers. The behaviour was perfectly plastic, the permanent deformation remaining after removal of stress. The alloys became softer as the temperature was raised, and a little way below the transformation temperature (~100°C) specimens bent under their own weight. If bent specimens were heated through this temperature, they straightened abruptly during transformation to a cubic single crystal.

Simple experiments were made to test the predictions of the previous sections. A specimen could be compressed or extended along its axis up to a certain minimum or maximum length; after this it became very much harder. Microscopical examination showed that during this process the thicknesses of the twins of one orientation steadily increased at the expense of those of the other, and X-ray photographs proved the specimen of minimum or maximum length was a single crystal.

After compressing or extending to a single crystal, reversal of the stress produced the other twin crystal. This change did not proceed by the appearance of a set of fine twins which gradually thickened, but by the production of a single twin interface which moved across the whole of the macroscopic crystal. This mode of deformation was very similar to single interface movements observed during the martensitic transformation (7). The stress required to compress or extend a single crystal was larger than that required for a specimen consisting of fine parallel twins. Once formed it was difficult to arrest the interface within the crystal, so the higher stress is evidently needed to form the interface rather than move it. This is in agreement with Cottrell and Bilby's suggestion of a yield stress for the onset of twinning [8]. The difference in lengths in compression and tension was measured accurately for two specimens of arbitrary orientation: the results agreed with equations (3) and (4) to within the experimental accuracy in determining c/a. The production of a single twinning interface suggests that remaining nuclei of the original twins were not readily activated by a uniaxial stress applied to the single crystal. On the other hand, bending of such a crystal resulted in the reappearance of the fine twins, so it appears certain that the twins were not completely eliminated by extension or compression.

Specimens were bent about their length to a maximum curvature by the application of a very small bending stress, after which the stress for further bending became much larger. The tapering of the twin boundaries was verified by microscopical examination of the twin traces in a plane parallel to the applied bending moment. The specimen could easily be straightened again and then rebent or bent in the opposite direction. With repeated bending and unbending there was no work hardening; indeed there was an apparent work softening effect and bending became easier after a few cycles. During the first few cycles, the mean twin thickness increased to a roughly constant value.

Figure 7 shows the twin boundaries in a straight specimen, after bending and unbending a few times to increase the twin thickness. The photograph is taken near the top surface of the specimen, and Figures 8 and 9 show the same region after bending in opposite directions to the maximum curvature. The tapering of twin boundaries in opposite senses in the two photographs can be seen clearly by using inclusions as fiducial marks. Since the region is very close to the top surface Figures 8 and 9 consist almost entirely of twins of one orientation. The actual tapering is very gradual and corresponds to about one twinning step in 500 atomic distances

along the twinning planes. The width of the twins is $\sim 1/50$ mm, and this agrees so well with the equilibrium value of ρ_c calculated in the last section that we are inclined to regard it as accidental.

With cylindrical specimens, the apparent curvature along the length was independent of the direction of the applied stress as required by the above discussion. Measurement of this curvature gave results for $\Delta l/l$ agreeing with equation (3) or (4). In some specimens, flat planes were cut to contain the [010] or [10$\bar{1}$] directions. Bending by edge dislocations was seen visually to result in the distortion of the plane containing [010] into a cylindrical surface. Similarly the double curvature in a plane containing the [10$\bar{1}$] direction could clearly be seen when the specimen was bent by twinning dislocations of screw type.

Laue photographs were used to determine the orientations of the lattice in a specimen, bent as far as could be determined by screw dislocations alone. These confirmed that on the bottom (compressed) face the principal curvature directions were at angles of $\pm\pi/4$ from the shear direction η_1. By taking two photographs, one of the top face and one of the bottom face at exactly 180 degrees, on the same film, the existence of the lattice twist between these two faces was confirmed. All photographs showed small asterisms, because of the finite range of orientations covered by the X-ray beam.

9. Rubber-like Elasticity

Chang and Read observed a pseudo rubber like behaviour in gold-cadmium alloys transformed by multiple interfaces. In the present work we have found similar behaviour in indium-thallium alloys (*a*) just above the transformation temperature and (*b*) at temperatures below about 0°C. At intermediate temperatures the alloys were perfectly plastic as already described.

Twinned specimens could be deformed at liquid air temperature exactly as at room temperature, except that slightly higher stresses were required. On removal of the stress, however, the specimen sprang back into its original position. The results were identical for both homogeneous uniaxial stresses and for bending stresses. Specimens bent plastically at room temperature could be straightened at liquid air temperature, but rebent when the stress was removed.

The rubber-like properties persisted at temperatures up to $\sim$0°C. The change to completely plastic properties took place gradually over a temperature interval: in the intermediate range there was a dependence on time. Thus the specimen returned rapidly to its original position when the stress was removed rapidly, but remained in the deformed position if the stress was applied for some time. At higher temperatures, the deformation became permanent in smaller and smaller times until practically instantaneous plastic behaviour was obtained. These characteristics are clearly those of a relaxation process with time constant of the order of seconds in the intermediate range, but we have not investigated this quantitatively in the present work.

The high temperature elastic properties were similar, except that no relaxation was possible and higher stresses were required. The high temperature elasticity is a result of the martensitic transformation, and its mechanism seems likely to be different from that of the low temperature rubber-like behaviour.

10. Discussion

Recent results on the variation of grain boundary energy with relative grain orientation (6) suggest that sharp cusp-like minima are associated with coherent twin boundaries. The energy is very sensitive to the orientation of the boundary as well as to those of the grains, and the theories usually predict that the torque resisting rotation of a coherent twin boundary is almost infinite. While this may be true for {111} twins in f.c.c. materials, the present results show that tetragonal twin boundaries may be rotated as well as moved perpendicular to their length. In terms of quantities previously defined, the angle which the twin boundary makes with its coherent position (the angle of taper) is given by $\psi = h/y = bmp/s$. From equation (8) we see therefore that the energy density is proportional to ψ^2, and hence the torque resisting rotation is linear in ψ, so long as the rotation is small enough for the present treatment to apply.

Rotation of the boundaries may be regarded as the movement of small sections through unequal distances perpendicular to their plane. The atomic problem in both homogeneous and inhomogeneous deformation may therefore be reduced to finding a mechanism for this movement. There are currently two possible accounts of the way in which the boundary between two related crystal regions may be propagated without thermal activation. If the habit plane is irrational, stress induced movement of the whole dislocation array in a manner analagous to that found for small angle kink boundaries

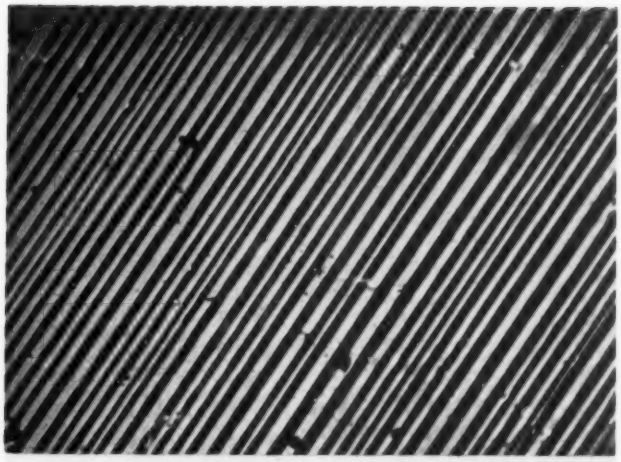

7

8

9

PLATE I (all figures reduced by 1/4 in reproduction). FIGURE 7—Twins in straight specimen of indium-thallium alloy. Unetched. Oblique illumination. ×75. FIGURE 8—Twins in bent specimen of indium-thallium alloy. Same area as Fig. 7. FIGURE 9—Twins in bent specimen of indium-thallium alloy. Same area as Fig. 8 but specimen bent in opposite direction.

[10] may be allowed. For rational habit planes, the movement of a single dislocation through the agency of a generating node may be a more acceptable description. A general account of the theory of generating nodes has recently been given by Bilby [11]. If this is the mechanism for twin boundary movements in indium-thallium alloys, rotation or tapering of the boundaries could result from the action of a number of nodes suitably spaced along the boundaries.

Two sets of conditions must be satisfied for the operation of a generating node to be feasible. If two lattices have a common plane of zero distortion, Bilby has shown that the geometrical conditions can always be fulfilled. In addition it is essential that one or both pole dislocations be firmly anchored in its lattice. The structure may be defined by the inter-atomic vectors **a**, **b** and **h** + **p**, where **a**, **b** and **p** lie in the twinning plane and **h** is the normal to the atomic twinning planes. The pole dislocation must thread the twinning plane and have a component vector **h** normal to them. Nabarro [12] has shown that imperfect dislocations of vector **h** exist only in special lattices and then are ineffective, since they must lie in the twinning planes. Dislocations 2**h** can always exist but are only useful if there is a second set of twinning planes at 60 degrees to the first, as in b.c.c. twinning. In all other cases, it seems that the pole dislocations must be formed from the perfect dislocations **h** + **p**, **h** − **p**, of the parent and twin lattices. In general, perfect dislocations are mobile, but this is not always true; h.c.p. twinning [4] and the martensitic transformation in cobalt [11; 12] may be possible because of the resistance to glide of hexagonal dislocations with Burger's vector c [00.1].

In tetragonal twinning, the dislocation 2**h** represents the boundary of a twin stacking fault, say on the $(01\bar{1})$ plane. By analogy with b.c.c. twinning, this might be expected to form a suitable pole for twinning on (101) planes. However, the angle between these planes is given by

$$\cos^{-1}\left\{\frac{1}{1 + c^2/a^2}\right\}$$

and so the component of the Burger's vector normal to (101) is not exactly **h**. The perfect dislocations **h** + **p**, **h** − **p** are c[001] vectors in parent and twin crystals. It seems improbable that they could glide readily, so they might form suitable poles. The dissociation

$$\begin{aligned} c[001] &= \tfrac{1}{2}[a0c] + \tfrac{1}{2}[\bar{a}0c] \\ &= \tfrac{1}{2}[0ac] + \tfrac{1}{2}[0\bar{a}c] \end{aligned}$$

is possible and leads to a slight reduction of elastic energy. However, the pairs of dislocations formed in this way can only glide in different {111} planes.

For b.c.c. twinning, the shear direction is common to two intersecting sets of twinning planes. Cottrell and Bilby (8) showed how this enables twin crystals to grow from monolayer stacking faults. In general, this does not seem to be possible, since twinning dislocations would become stuck when attempting to pass one another on neighbouring planes. The problem has been considered in detail by Bilby [14] who estimates a nucleus 50 atomic spacings thick is required if b is a tenth of an atomic spacing. The observation that fine twins reappeared when a bending moment was applied to a compressed specimen seems to be clear evidence for the retention of twin nuclei. Once twin orientations are present, the retention of nuclei is expected, since the argument above can be reversed to show that interaction between twinning dislocations prevents the twin from shrinking to a monolayer fault.

The rubber-like behaviour at high temperatures is believed to be due to stress induced transformation from cubic to tetragonal phases above the M_s temperature. If this is possible, the regions of tetragonal phase will have higher free energies when the stress is removed, and this will produce a force on the transformation interface driving it backwards again. We have found that a transformation interface formed during spontaneous transformation can be reversed by application of a suitable external stress.

The change in mechanical properties at low temperatures is obviously caused by a temperature controlled relaxation process. At high temperatures the twin boundaries come rapidly to equilibrium in any position, the strain energy being minimised. At lower temperatures this is not possible, and the boundaries return spontaneously to their original positions when the stress is removed. The present experimental results do not distinguish between the two possibilities that the twin interfaces move back continuously from their new positions to their original positions, or that nuclei of the original orientation are left behind during the straining and grow into macroscopic regions which amalgamate to give the original twin pattern. The first possibility is analagous to the high temperature elasticity, but there is now no difference in the volume free energy of the material on the two sides of the interface, and it is difficult to envisage a plausible atomic mechanism for providing long range forces.

The force cannot be attributed directly to the presence of twinning steps since it is present in homogeneously compressed specimens. It seems conceivable that the torque on the slightly incoherent boundaries produced by bending might be sufficient to rotate them back into coherent positions, but a normal force on coherent boundaries is unexpected.

The second possibility was suggested to us by Dr. Lomer. If the twin boundary encounters regions of crystal which are difficult to twin, these may be left behind as islands of the original orientation. On removal of stress, the strain field round each might be sufficient to cause growth. Unfortunately this theory seems ro raise as many difficulties as the alternative account, for either the number of these regions must be so large as to make the process implausible, or we are faced with the same problem of forces acting on twin boundaries over large distances.

In the neighbourhood of a twin boundary, there will probably be a concentration gradient of solute atoms, thus reducing the strain energy by formation of suitable Cottrell atmospheres. When a twin boundary is displaced there will be a redistribution of solute atoms, leading to a typical relaxation process with an activation energy equal to that for atomic diffusion. Atmospheres of this kind, however, would produce forces only over atomic distances, so this type of relaxation cannot be responsible for the elastic-plastic transition. A possible, though unconvincing, model for the long-range force may be obtained if we accept the dislocation node theory and suppose that a given boundary moves forward by the independent action of a number of double twinning nodes. The closed loops of twinning dislocation will amalgamate on each atomic plane, but occasionally internal obstacles may prevent this happening. Each twin will then contain thin layers of untwinned material, separated by spiral loops of twinning dislocation from neighbouring nodes. These loops have line energy and would tend to contract, pulling back the boundary to its original position. The relaxation process would enable the spiral loops of twinning dislocation to be eliminated by supplying thermal energy to overcome the barriers.

The above theories are speculative and obviously unsatisfactory. An investigation of the activation energy, e.g., by internal friction measurements, would be of value in determining the atomic nature of the relaxation process.

Acknowledgments

We should like to acknowledge helpful discussion with Dr. W. M. Lomer who kindly read the first draft of this paper. We also wish to thank Dr. W. Hume-Rothery, F.R.S., for laboratory accommodation and for his interest in this work.

References

1. Nye, J. F. Acta Met. **1** (1953) 153.
2. Cahn, R. W. Acta Met. **1** (1953) 49.
3. Frank, F. C. Phil. Mag. **42** (1951) 809.
4. Thompson, N. and Millard, D. J. Phil. Mag. **43** (1952) 422.
5. Schmid, E. and Boas, W. Plasticity of Crystals (London, F. A. Hughes, 1950).
6. Read, W. T. and Shockley, W. Phys. Rev. **78** (1950) 275.
7. Basinski, Z. S. and Christian, J. W. To be published.
8. Cottrell, A. H. and Bilby, B. A. Phil. Mag. **42** (1951) 573.
9. Chang, L. C. and Read, T. A. Trans. A.I.M.E. **191** (1951) 47.
10. Li, Choh Hsien, Edwards, E. H., Washburn, J. and Parker, E. R. Acta Met. **1** (1953) 223.
11. Bilby, B. A. Phil. Mag. **44** (1953) 782.
12. Nabarro, F. R. N. Adv. Phys. **1** (1952) 269.
13. Basinski, Z. S. and Christian, J. W. Phil. Mag. **44** (1953) 791.
14. Bilby, B. A. Private communication.

THE CRYSTALLOGRAPHY OF THE β–α TRANSFORMATION IN TITANIUM*

A. J. WILLIAMS,† R. W. CAHN,† and C. S. BARRETT‡

The orientation relationships, habit plane and surface contour associated with the martensitic transformation in iodide titanium were investigated. The transformation markings studied were those on the natural facets of the specimens, which had originally been single crystals of β-phase. The orientation relationship was close to but not quite identical with the Burgers relationship: $(0001)_\alpha \| \{110\}_\beta$; $\{11\bar{2}0\}_\alpha \| \{111\}_\beta$; the deviations were $\frac{1}{2}$–1°. The habit plane was close to $\{8, 9, 12\}$, to an accuracy of 1°. The orientations associated with individual habit plane variants were analysed and fitted into a consistent scheme which was close to that expected if the transformation mechanism proposed by Burgers operated. Each habit plane was 10° from the variant of $\{112\}$ predicted as shear plane by Burgers. Data on the surface contour showed that the direction of atom motion was close to the variant of $\langle 111 \rangle$ required by Burgers, though the magnitude of the surface tilt was smaller than predicted. The precise contour of individual plates, as revealed by multiple beam interferometry, showed that accommodation slip had occurred which would reduce the surface tilt. The results could not be satisfactorily interpreted on the basis of Frank's theory of the martensitic transformation, but they provide some support for Geisler's views.

LA CRISTALLOGRAPHIE DE LA TRANSFORMATION β–α DANS LE TITANE

Une investigation a été faite des relations d'orientation, du plan limite et du contour de surface associés à la transformation martensitique dans l'iodure de titane. On a étudié les marques de transformation sur les facettes naturelles des échantillons, qui étaient initialement des monocristaux de la phase β. La relation d'orientation était proche de la relation de Burgers $(0001)_\alpha \| \{110\}_\beta$; $\{11\bar{2}0\}_\alpha \| \{111\}_\beta$; l'écart était de $\frac{1}{2}$–1°. Le plan limite était proche de $\{8, 9, 12\}$, à 1° près. Les orientations associées avec des variantes individuelles du plan limite furent analysées et incorporées dans un système auquel on s'attendrait si la transformation s'opérait suivant le mécanisme proposé par Burgers. Chaque plan limite se trouvait à 10° de la variante de $\{112\}$ prédite comme plan de cisaillement par Burgers. Les données concernant le contour de surface ont montré que la direction du mouvement atomique était proche d'une variante $\langle 111 \rangle$ requise par Burgers, quoique la rotation de la surface fût inférieure à celle qu'on a prédite. Le contour précis de lamelles individuelles a été révélé au moyen d'interférométrie à rayons multiples. Il a aussi été montré qu'un glissement d'adaptation a lieu, ce qui réduit la rotation de la surface. Les résultats n'ont pas pu être interprétés d'une manière satisfaisante en se basant sur la théorie de la transformation martensitique de Frank, ils appuient, toutefois, les vues de Geisler.

DIE KRISTALLOGRAPHIE DER β–α UMWANDLUNG IN TITAN

Die Beziehungen der kristallographischen Orientierung, die Habitusebene und die Oberflächenkontur, die bei der martensitartigen Umwandlung von Titanjodid auftreten, wurden untersucht. Die Umwandlungsmarkierungen wurden auf den natürlichen Fazetten von Proben, die ursprünglich Einkristalle der β-Phase gewesen waren, untersucht. Die Beziehung der kristallographischen Orientierung war nahezu, aber nicht völlig, identisch mit Burgers' Beziehung: $(0001)_\alpha \| \{110\}_\beta$; $\{11\bar{2}0\}_\alpha \| \{111\}_\beta$; die Abweichungen betrugen $\frac{1}{2}$–1°. Die Habitusebene war nahezu $\{8, 9, 12\}$ mit einer Genauigkeit von 1°. Die Orientierungen, die im Zusammenhang mit den einzelnen Habitusebenen auftraten, wurden analysiert. Sie fügten sich in ein eindeutiges Bild, das nahezu der Erwartung entsprach, wenn man den von Burgers vorgeschlagenen Mechanismus annimmt. Jede Habitusebene war 10° von einer Ebene der $\{112\}$ Familie entfernt. $\{112\}$ war von Burgers als Scherungsebene vorausgesagt worden. Die Daten der Oberflächenkontur zeigten, dass die Richtung der Atombewegung nahezu eine Richtung des $\langle 111 \rangle$ Typs war, wie es nach Burgers erforderlich ist, obwohl das Ausmass der Oberflächenneigung kleiner als vorausgesagt war. Die genaue Kontur der einzelnen Plättchen, wie sie mit "multiple beam interferometry" gemessen wurde, zeigte, dass "Anpassungsgleitung" ("accommodation slip") aufgetreten war. Dies würde die Oberflächenneigung verringern. Die Ergebnisse liessen sich nicht zufriedenstellend mit Franks Theorie der martensitartigen Transformationen erklären, unterstützten jedoch die Ansichten Geislers einigermassen.

1. Introduction

Crystallographic studies have been published of the martensitic transformation of a body-centred cubic structure to a close-packed hexagonal one, in zirconium [1; 2], lithium [3] and a copper-aluminium alloy [4]. At about the time when the present work reached its conclusion, nothing had been published about the crystallography of the transformation in titanium or its alloys, but since its completion, Newkirk and Geisler [5] and McHargue [6] have published results on the subject, while Liu and Margolin [7] have published data on a titanium-manganese alloy. The results of the present work, given below, agree with some of the recently published results, disagree with others, and provide some new information about the mechanism of transformation.

*Received August 19, 1953; in revised form, September 16, 1953.

†Department of Metallurgy, University of Birmingham, England.

‡Institute for the Study of Metals, Chicago, Illinois.

Since the cubic (β) phase cannot be retained at room temperature in pure zirconium and titanium, special methods have to be used to determine the orientation relationship between the β- and α-phases, and the indices of the habit plane (referred to the β-phase lattice). Burgers [1] and van Ginneken and Burgers [2] did this by studying rod specimens of iodide zirconium in their original form, using the arrangement of the facets as an indication of the orientation of the single crystal of β-phase which had originally occupied the whole volume of each specimen. The orientations of the plates of α-phase produced by the transformation were approximately determined by means of X-ray oscillation and Laue photographs, and refined by applying the hypothesis (which all investigators have implicitly made) that all orientations so found are *variants* of a single type. The recent data on titanium [5; 6] were obtained from an examination of prepared sections of metal which had originally contained coarse β-grains. Because in transformed titanium quite large volumes are sometimes occupied by parallel plates of α-phase of uniform orientation, Laue photographs could be taken of different such regions which were within the confines of an original β grain. If the orientation relationship in titanium is the same as in zirconium (as is to be expected in view of the crystallographic similarity between the metals) then (0001) poles in such neighbouring regions should be inclined at 60 or 90 degrees to each other, these being the angles between different variants of the form $\{110\}$; moreover certain $\{11\bar{2}0\}$ planes should be mutually inclined at $70\frac{1}{2}$ degrees, which is the angle between $\{111\}$ planes. This was indeed found to be the case.

In the present work these two techniques have been combined. Iodide titanium rods were used with the original facets intact, and Laue photographs were taken of identifiable regions of uniform orientation. This has enabled the orientation in a particular region to be correlated with the habit plane variant in that same region.

The indices of the habit plane have been found for zirconium [2] and for titanium [5; 6] by the earlier workers. For zirconium the plane is either $\{569\}$ or $\{145\}$, the ambiguity being due to an ambiguity in deriving the original orientation of an iodide zirconium rod from its external symmetry. $\{569\}$ was believed to be correct. There is however reason to believe that both alternatives are in error by several degrees. Van Ginneken and Burgers [2] used the same six-sided specimen as Burgers [1] had used in his original work, but while Burgers had shown that in this specimen the rod axis made an angle of 6 degrees with a former [111] direction, in the later paper this angle was assumed to be zero. For titanium, Newkirk and Geisler determined the habit plane to be approximately $\{8, 8, 11\}$, which is not far from $\{569\}$. McHargue determined $\{331\}$, which is quite different. In all these cases, habit plane indices were derived from surface traces revealed by polishing and etching.* There is no certainty that the surface lines produced by etching are parallel to the habit planes, or it may be that this is true only for some etchants. Whether or not the disparity between Newkirk and Geisler's, and McHargue's habit planes is due to some such source of error, there is room for further data. Liu and Margolin found $\{334\}$ as one habit plane in titanium-manganese specimens, which is very close to $\{8, 8, 11\}$. Orientation relationships for this alloy are not known.

In copper-aluminium alloy containing 12.9–13.6 per cent aluminium [4; 8] the habit plane is near $\{221\}$, while the orientation relationship is closely similar to that in zirconium, with the addition of extra orientations attributable to mechanical twinning. When the aluminium content is increased, the habit plane moves to near $\{331\}$. In lithium [3], the habit plane is $\{441\}$, while the orientation relationship is again similar to the Burgers relationship, though not identical.

Burgers [1] put forward a mechanism for the transformation in zirconium, based on a shear on (112) planes in the $[11\bar{1}]$ direction, followed by homogeneous dilatation in two directions and contraction in a third. The magnitude of the postulated shear is 0.22; the shear direction is that $\langle 111 \rangle$ direction which is parallel to a $\langle 11\bar{2}0 \rangle$ direction of the transformed phase. Apart from X-ray tests which provided some indirect evidence for the aptness of the mechanism for copper-aluminium alloys [8], no attempts have been made to test its validity experimentally. This can be done by checking whether in each transformed region the habit plane is parallel to the particular $\{112\}$ variant appropriate for that region, and by comparing the observed tilts on a free surface with those calculated from Burgers' model. Such checks were made in the course of the present experiments.

*McHargue [6] refers to relief markings in the surface which were "intensified" by etching; but since the surface was prepared when the metal was in the α-range, the significance of relief markings seen after the double transformation is difficult to assess.

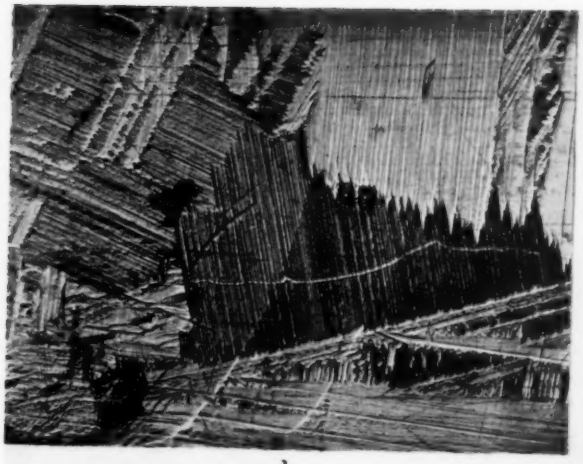

1

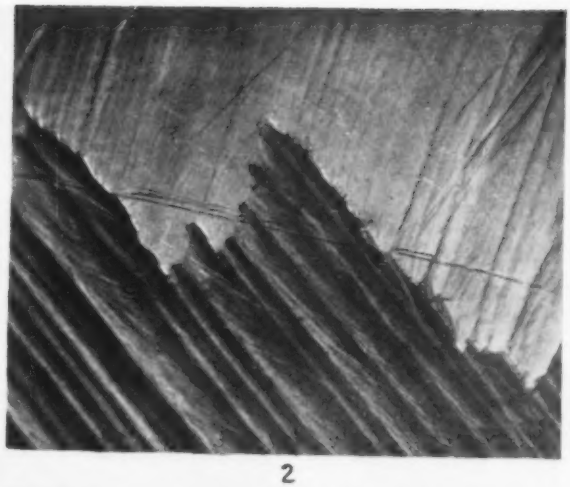

2

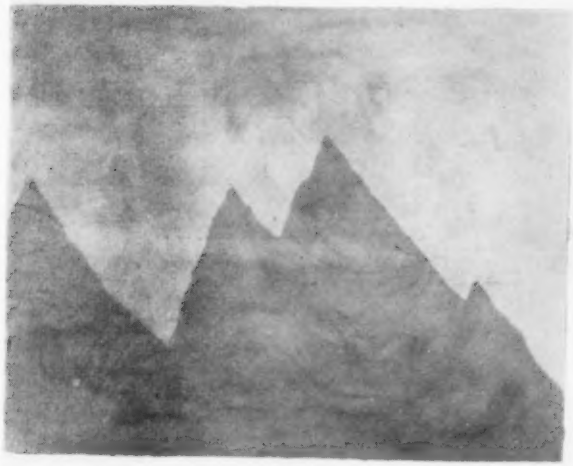

3

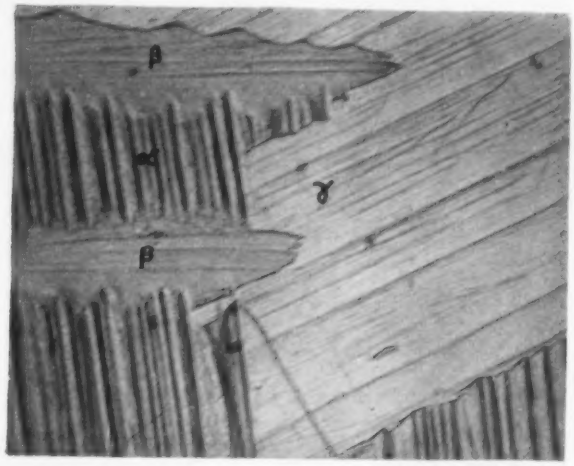

6

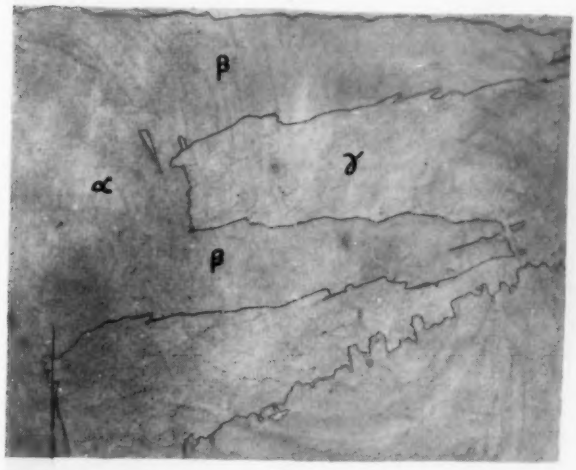

7

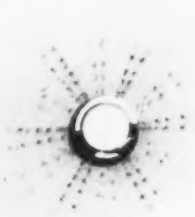

8

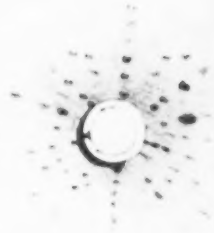

9

PLATE I (all figures reduced by 1/8). FIGURE 1—Portion of facet A of specimen 1 (×10). FIGURE 2—Two areas on specimen 1, as received. Polarised light (×300). FIGURE 3—Same region as in previous figure, after deep polishing. Polarised light (×300). FIGURE 6—Three areas on specimen 1, as received. Polarised light (×100). FIGURE 7—Same region as in previous figure after deep polishing. Polarised light (×100). FIGURE 8—Superimposed Laue photographs of two areas with nearly parallel basal planes. FIGURE 9—Laue photograph of two areas differing only slightly in orientation.

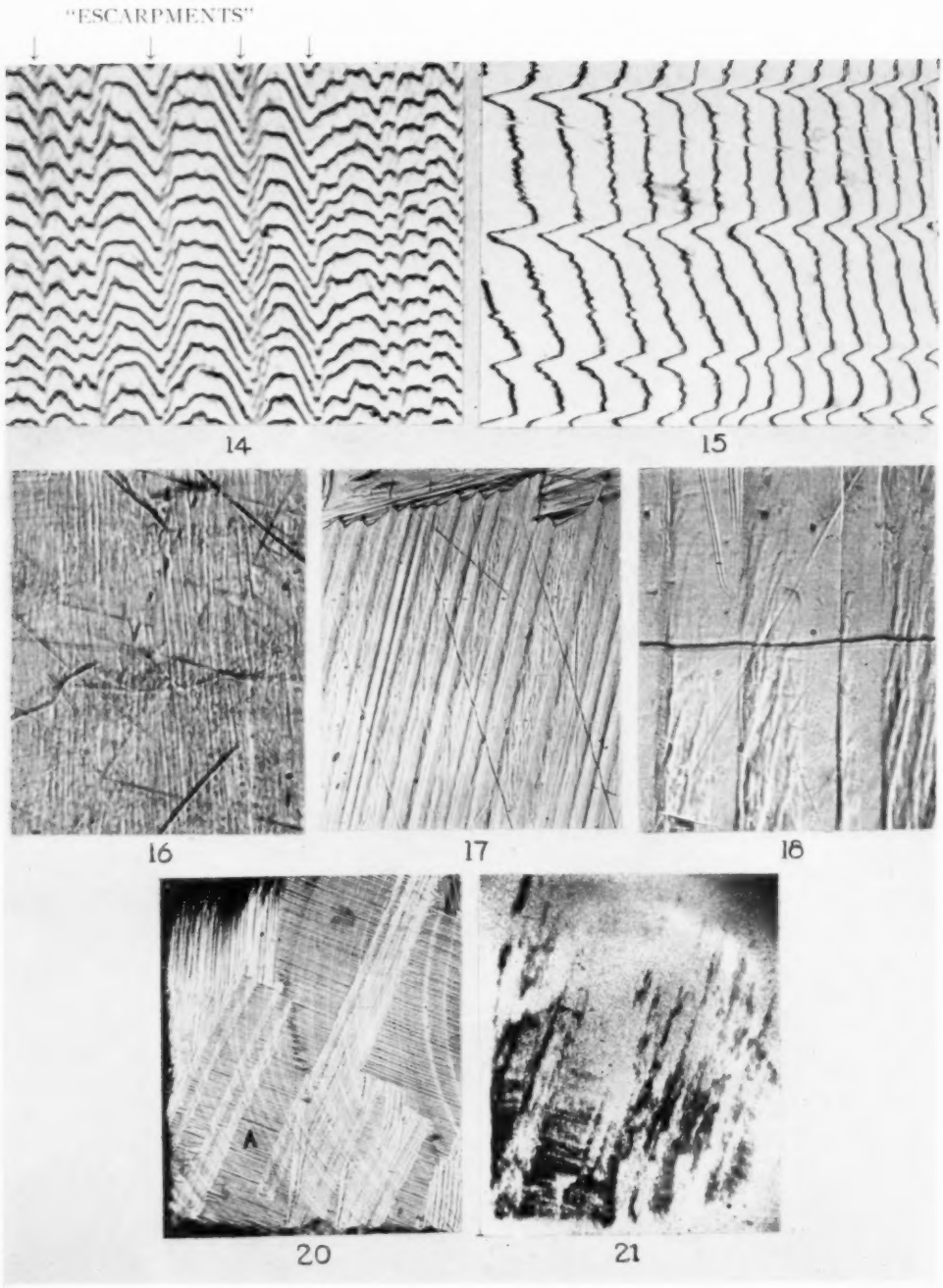

PLATE II (all figures reduced by 1/4). Figure 14—Multiple-beam interferogram of strong area, specimen 1 (negative × 240, enlarged 3 times). Figure 15—Multiple-beam interferogram of weak area, specimen 1 (negative × 100, enlarged 3 times). Figure 16—Weak area on specimen 3. The *almost* vertical markings are slip lines. The faint habit traces are vertical (×250). Figure 17—Strong area on specimen 1. The narrow black lines are deformation twins, which must have been formed after transformation, and consequently serve to reveal contour. (×300). Figure 18—Light-profile micrograph of strong area on specimen 1. The slip-free regions are the "escarpments" (×1200). The wavy black line is the "light-profile" and reveals contour with a vertical magnification of 1200×. Figure 20—Surface of a region on specimen 1, as received (×10). Figure 21—Berg-Barrett photograph of the same region as in previous figure, after deep polishing.

2. Experimental Methods

(a) *Materials*

Specimens of iodide titanium rod with particularly well-formed facets were presented by the New Jersey Zinc Company (specimen 1), the Research Laboratory of Associated Electrical Industries (specimen 2) and Philips Gloeilampenfabrieken (specimen 3). The first two had roughly regular hexagonal cross sections, while the last had an accurately regular octagonal section. Following Burgers' argument, these types had originally had $\langle 111 \rangle_\beta$ and $\langle 100 \rangle_\beta$, respectively, parallel to the prism axis. The first two were bounded by $\{110\}_\beta$ facets only, the last by four $\{110\}_\beta$ and four $\{100\}_\beta$ facets. On most of the facets there were some areas several tenths of a mm across in which all martensite needles were parallel. Specimen 2 did not have such large areas as the other samples and was not used for precision work. Qualitatively, results obtained with this specimen were consistent with those obtained with the other two.

(b) *X-ray Techniques*

Back-reflection Laue photographs were taken of individual areas of parallel plates (referred to hereafter simply as *areas*). The X-ray beam was correctly located, at first by painting around the area with fluorescent paint, later by using a modified version of the microbeam camera described by Cahn [9]. This apparatus provided a beam 0.2 mm in diameter which could be located with an accuracy of about 0.02 mm on an area previously selected under a microscope. To determine the relative orientations of several different areas on the same facet as accurately as possible, Laue photographs from two areas at a time were superimposed on the same film. One of these was always the same reference area. The problem of the accurate setting-up of the camera is thus by-passed.

Some areas were also examined by the Berg-Barrett technique of "X-ray microscopy" [10]. The specimen was set so that the selected area gave a Bragg reflection with copper radiation. Individual areas were so small that the diffracted beam could not be detected by means of a fluorescent screen, but the use of a Geiger counter, provided with a filter to cut out fluorescent radiation from the specimen, met this difficulty.

(c) *Optical Techniques*

A complete photomicrographic map was made of specimen 1, which was the largest and also had the largest areas. This map was later used for the determination of habit planes. Figure 1 shows a portion of one facet. The arc-shaped markings are a growth feature and are not connected with the phase transformation. Specimen 3, which had accurately flat facets (unlike specimen 1) was used for an independent derivation of the habit plane.

Some areas were also examined by polarized light after the appropriate facet had been electrolytically polished [11]. This permitted a check on the orientations of certain areas the hexad axes of which were believed to be parallel, or else equally inclined to the specimen surface and with parallel projections in the specimen surface. Because titanium is optically uniaxial, such areas should be optically indistinguishable in polarized light, as was indeed found. Some specimens were etched in an HF/H_2O_2 reagent, to attack grain boundaries.

The surface of each facet had been smooth while in the β-condition, but ridges were thrown up during transformation by the associated shear. The surface contours so produced were examined by the light-profile method [12] and more sensitively by multiple-beam interferometry. Since the facets were not perfectly flat, it was necessary to use an optical reference flat in the form of a small truncated cone [13]. The smaller section of the cone could be brought up very close to the surface of the specimen, which is essential for the attainment of narrow fringes and therefore of good resolution [14]. The cones were coated with evaporated multiple layers of zinc sulphide and cryolite, which gives better optical contrast than half-silvering [15]. Monochromatic green light was used. Several photographs, (e.g., Figures 2, 16, 17, 18) include scratches due to handling. These can be distinguished in many cases by the fact that they are discontinuous where they cross the valleys of the surface structure.

3. Experimental Results

(a) *Uniformity of Orientation of Areas*

Laue photographs of areas containing a single set of striations were always found to correspond to single orientations, and there were no Laue spots unaccounted for. This uniformity was further confirmed by observations in polarized light. Figures 2 and 3 show the same pair of areas, respectively in the original condition and by polarized light after polishing and etching. The uniform colourations bespeak uniform orientations.

(b) *Relative Orientations of β- and α-Phases*

The orientations of 21 areas on samples 1 and 3

were determined. The positions of the poles of (0001) and $\{11\bar{2}0\}$ planes were plotted on two stereograms, one for each specimen, having the direction of the specimen axis at the centre. Figure 4 is the stereogram for specimen 1. (Only a few $\{11\bar{2}0\}$ poles are included to avoid overcrowding.)

If the facets were assumed to have been exactly parallel to the former $\{110\}_\beta$ planes, then the Burgers relationship is not exactly obeyed. However, a rotation of the stereogram through 6 degrees about a point on the primitive circle rotates all those groups of (0001) poles which are near the primitive circle in Figure 4, in such a way that they all now lie almost exactly on this circle. It was therefore assumed that the $[111]_\beta$ direction had been at 6 degrees to the prism axis. On the rotated stereogram (0001) poles other than those falling on the primitive also coincide with $\{110\}_\beta$ poles (Figure 4). The hypothesis that $(0001)_\alpha \parallel \{110\}_\beta$ *always*, removes the ambiguity which troubled van Ginneken and Burgers. The external symmetry alone does not permit one to distinguish between the alternative orientations of the parent β-crystal shown in Figures 5a and 5b, but the alternative of Figure 5a is excluded because the groups of basal plane poles at X, Y and Z (Figure 4) would not then coincide with $\{110\}$ poles.

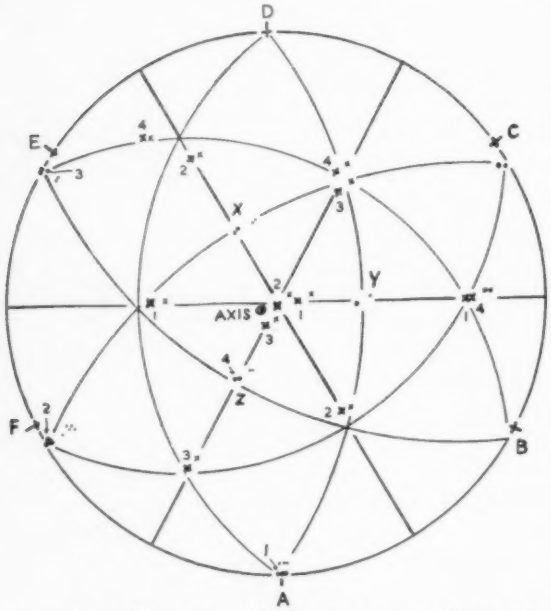

FIGURE 4. Orientations of areas on specimen 1. Small dots and crosses are (0001) and $\{11\bar{2}0\}$ poles before adjustment of specimen axis; large dots and crosses, the same after adjustment.

A similar analysis was made for sample 3, and here again (0001) and $\{110\}$ poles were parallel if the original [100] axis was assumed to have been tilted through 5 degrees with respect to the rod axis.

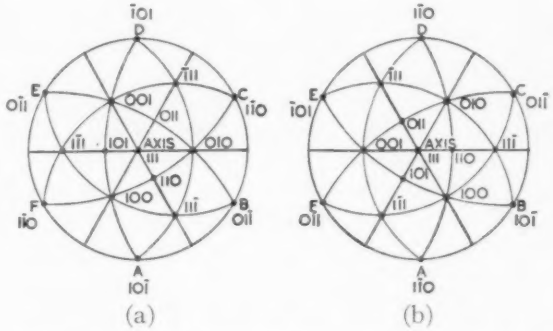

FIGURE 5. Two alternative orientations for a hexagonal pseudo-crystal.

The accuracy of determination of the orientation relationships was not better than about 2 degrees, because of the difficulty of setting the facets correctly with respect to the X-ray beam. By the method of superimposed Laue photographs, however, (0001) planes in different areas on the same facet were found to be nearly parallel, or at 60 or 90 degrees to each other, but there was generally a deviation of 1–1½° degrees. The estimated maximum experimental error here was ½ degree.

The Burgers relationship requires that of the three normals to $\{11\bar{2}0\}$ planes in any one area, one should be accurately parallel to $\langle 111\rangle$, one of the others being 10°32′ from another $\langle 111\rangle$ direction. It follows from this that two differently oriented areas which happen to have parallel basal planes should differ in azimuth about the hexad axis by 10°32′. Superimposed Laue photographs such as Figure 8 have shown that the azimuths of such pairs of areas systematically differed by less than this angle. For the six pairs examined, the azimuth difference was always $9\pm\frac{1}{2}°$.

One Laue, reproduced as Figure 9, had most of its spots subdivided. The arrangement of the subspots was consistent with the presence of two contiguous areas with slightly different orientations, related by a tilt of 1 degree, approximately about a $[10\bar{1}0]$ axis. As a consequence, the basal planes in these contiguous areas were mutually inclined at 1 degree. It follows from the hypothesis that all areas represent variants of a single orientation relationship, that (0001) cannot be exactly parallel to $\{110\}$, but is removed from parallellism by about ½ degree. The basal planes in the con-

tiguous areas are each inclined by ½ degree to the same (110) plane, but in opposing senses.

Areas which according to Laue photographs have parallel basal planes and differ only in azimuth about the hexad axis, were indistinguishable by polarized light, as was expected. Areas α and β in Figures 6 and 7 are a case in point. Boundaries between areas such as α and β appear to be of low energy, for they are not attacked by the etchant (Figure 7). In area γ, however, the basal plane is inclined at 60 degrees to the basal plane in α and β, and correspondingly the γ–α and γ–β boundaries have been attacked by the etchant.

(c) *Habit Plane*

The striations in the areas of uniform orientation were assumed to be traces of the habit planes in those areas. Their direction was usually constant to 1 degree in any one area. In the case of specimen 3, widely separated areas of similar orientation had accurately parallel markings, which verifies that the original β-crystal had been of strictly uniform orientation. Specimen 1 was not so good in this respect.

To derive the habit plane, a stereogram of each specimen was drawn in the corrected orientation. (The corrected orientation was obtained by trial and error so as to get all basal planes to obey the ideal Burgers relationship as nearly as possible. The maximum error of ½ degree caused by the fact that this relationship is not exactly obeyed is less than the experimental errors.) The loci of possible poles of the habit plane consistent with each family of striations were first entered on this stereogram and then all collected in one elementary stereographic triangle, as originally described by Bowles [3]. This was done for 30 areas on specimen 1 and 24 on specimen 3. All loci for specimen 3 passed through a small circle of 1 degree radius and there was no other common intersection. Four sample loci are shown in Figure 10. The pole {8, 9, 12}, which is the point of intersection of all four loci, is marked by an open circle. The loci for specimen 1 all passed within 2½ degrees of {8, 9, 12} and this was the nearest approach to a common intersection. For several reasons, referred to above, the results for this specimen cannot be as accurate as for specimen 3, and were regarded only as confirmation of the validity of the method used.

In Figure 11 are assembled the data referred to in the Introduction. The circles indicate published estimates of experimental error; the 5-degree errors for van Ginneken and Burgers' data are our estimate. The present results agree most closely with those of Newkirk and Geisler, though they used a two-surface method and stated that the single surface method did not yield consistent results.

Occasionally an area at the edge of one facet could be followed across to the next facet, so that the correctness of the habit plane indices could be

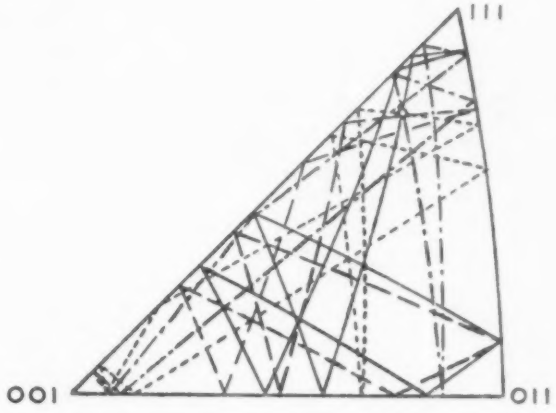

FIGURE 10. Mode of determination of the habit plane.

checked by measuring the directions of the traces on the two surfaces. In each of the three instances investigated, the habit plane so obtained was close to {8, 9, 12}.

McHargue's habit plane, {331}, was obtained by the one-surface method, 15 sets of striations being included in the determination. The disagreement between {331} and our indices cannot be due to

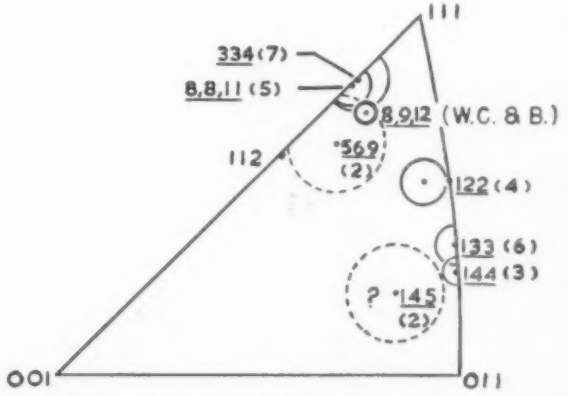

FIGURE 11. Published habit plane for b.c.c.–h.c.p. transformations. Numbers in brackets are reference numbers.

McHargue's having unwittingly mistaken the β-orientations after the fashion of van Ginneken and Burgers, because this can only happen if all the basal planes of areas within a former β-grain are

cozonal, as they were not in his work. The source of the disagreement is not clear.

(d) *Correlation of Habit Plane with Orientation*

Frank [16] remarked that for the theorist it was desirable to know which particular variant of the orientation relationship applied to martensite plates which are parallel to a particular variant of the habit plane. This information was accordingly obtained. Since the habit plane was known to be {8, 9, 12}, the habit plane variant for each area of known orientation could be deduced from the direction of the surface striations on that area. For all such areas, without exception, the following rules were found to hold:

(i) Each of the six lattice planes of the form {110} has associated with it four habit plane variants each at an angle of about 87 degrees to it. Transformed areas of α-phase possessing any of these four habit plane variants all have basal planes approximately parallel to the (110) plane in question. No other areas have basal planes parallel to it.

(ii) Of the four variants mentioned, one pair differs by about 9 degrees in azimuth about the hexad axis from the other pair. The difference of orientation between the members of either pair is a tilt of about 1 degree, roughly about that $[10\bar{1}0]_\alpha$ $[112]_\beta$ axis which is normal to the common $[11\bar{2}0]_\alpha$, $[111]_\beta$ direction. This last conclusion is based on a single Laue photograph.

In Figure 12 one such group of four variants is set forth.

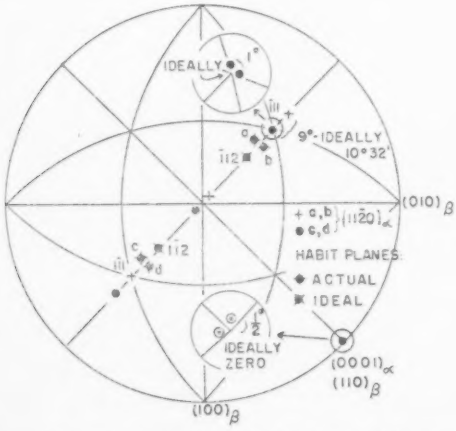

FIGURE 12. Orientations and habit planes of four variants with approximately parallel basal planes. "Ideal" refers to the Burgers orientation relationship.

The universality of rule (i) is perhaps the best evidence for the correctness of the habit plane obtained by the single-surface method. If this plane had been obtained merely by a chance intersection of the pole loci in the unit triangle, then there could have been no sort of regular correlation between the variants of such a spurious habit plane and the orientations of the corresponding areas. The rule is, by the same token, a confirmation of the observed orientation relationships and of the hypothesis that all areas are variants of the same relationship.

The above rules can be compared with predictions made on the hypothesis that the Burgers mechanism operates. The above four variants are actually reduced to two in this idealized case. The two observed variants with habit planes *a* and *b* become one idealized variant with habit plane $(\bar{1}12)$, while those with *c* and *d* become a variant with habit plane $(1\bar{1}2)$. Each actual habit plane variant is thus 10 degrees from the predicted plane. The basal planes of the two idealized variants are exactly parallel to {110} and the azimuths differ by 10°32′. Thus far the Burgers mechanism seems to be a fair approximation to the facts.

The shear direction required by the Burgers mechanism is $[1\bar{1}1]$ for the idealized variant with habit plane $(\bar{1}12)$ and $[\bar{1}11]$ for the variant with habit plane $(1\bar{1}2)$. The actual mechanism cannot at first sight be a true shear in a close-packed direction, since the observed habit planes are not exactly parallel to any ⟨111⟩ direction, but a comparison of surface contour of different areas has shown that in this respect, too, the Burgers mechanism is a close approximation to the truth. This is explained in the next section.

(e) *Surface Contour and its Correlation with Habit Plane and Orientation*

Examination of Figure 1 will show that the striations are strong in some areas, weak in others. The contrast between strong and weak areas was even more marked on the facets of specimen 3 than on those of specimen 1. Inspection of the feeble markings on "weak" areas of specimen 3 suggested that they were due to slip since they were short and ragged. Careful examination of a high-power micrograph of such an area revealed faint habit markings somewhat inclined to the slip lines (Figure 16), but as these could not be properly measured they were not included in the habit plane analysis.

The strength of the striations was analysed on the hypothesis that the striations were weak or absent when the shear direction (rigorously, the direction of motion of the transforming atoms) was parallel to the plane of the facet on which they were observed. If the shear direction was inclined to the

plane of the facet, the striations were strong. By means of this hypothesis the shear direction could be approximately identified.

What follows refers to specimen 1. It was found that (1) all areas in which the basal planes were approximately parallel to the facet under examination, were weak. In addition (2) *some* of those areas with basal planes at 60 degrees to the facet under examination were also weak. All other areas were strong.

Consider now only areas with basal planes parallel to $(1\bar{1}0)$, i.e., A in Figure 13. Any such

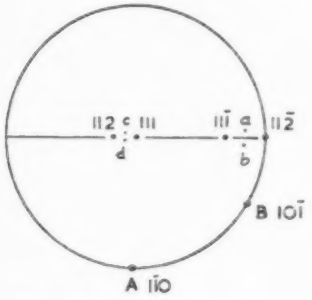

FIGURE 13. Stereogram for determination of direction of atom motion.

areas visible on the facet parallel to A fall in class (1) above, and are weak. It follows that the shear direction $\underline{D}$ is parallel to $(1\bar{1}0)$. Any such areas visible on the facet parallel to B $(10\bar{1})$ are found experimentally to be weak if they have habit planes at a or b, or $(11\bar{2})$ in the idealized case; but they are not weak if the habit plane is c or d, or (112) in the idealized case. The shear direction D for the weak areas on facet B must be parallel to $B(10\bar{1})$. Thus for areas with habit planes a or b, D is parallel both to A and to B, and therefore to their intersection, which is [111]. This direction is almost parallel to the habit planes a and b.

We have therefore shown that to a first approximation the direction of atom motion is parallel to the common $(110)_\beta$, $(0001)_\alpha$ planes, and to the habit plane. This is just what Burgers' mechanism requires (compare Figure 5 of Burgers' paper).*

The weak areas on the eight-sided sample were restricted to the four facets which had originally been $\{110\}_\beta$ facets. The other four facets, originally $\{100\}_\beta$, had only strong areas. Reasoning similar to the above led to the same conclusions.

More detailed information about the surface contour was obtained from the interferograms:

*Examination of areas with (0001) planes parallel to x, y or z (Fig. 4) confirmed this conclusion.

(i) *Weak areas.* Figure 15 is a typical interferogram of a weak area on specimen 1. There is virtually no surface tilt, but there are deep grooves which presumably mark the boundaries between neighbouring plates. The absence of tilt is consistent with the hypothesis that the shear direction is nearly parallel to the surface. Within individual plates, the fine serrations on the fringes show that there has been some slip, the slip traces being roughly parallel to the habit plane traces. Grooves, as well as faint slip lines slightly inclined to them, can be seen on the weak areas in Figures 1, 2 and 6. The weak areas on sample 3 did not have any grooves.

It was thought at first that the grooves had been formed by thermal etching at sub-boundaries of some kind, during the time the specimen was cooling below the transformation temperature. However, an attempt to develop grooves in the weak areas of specimen 3, which were originally without them, by annealing in high vacuum at 830°C, was unsuccessful. The grooves are perhaps due to accommodation slip, but in that case their shape is hard to understand.

(ii) *Strong areas.* Figure 14 is a representative interferogram of a strong area on specimen 1. The cross section of each plate is roughly in the form of a flat-topped hill with a uniform escarpment on one side and a slope, which may be steep or gentle, on the other. The escarpments were taken to be due to the surface tilt accompanying the transformation shear, while the shape of the remainder of the cross section was believed to be controlled by accommodation slip. Fine serrations on the fringes show that such slip had indeed occurred. This evidence of slip was concentrated on the slopes (as distinct from the escarpments). This is also well brought out in Figure 2 and in Figures 17 and 18. These micrographs show neighbouring slipped and almost slip-free regions.

Numerous measurements on interferograms showed that the surface tilt at the escarpments was always in the range $3\frac{1}{4}$–$4\frac{3}{4}$ degrees. It was computed that, according to the Burgers mechanism, the angular tilt of the strong areas concerned should be 9 degrees.

Figure 19 shows in a diagrammatic form how these observations can perhaps be accounted for. In (i), a first martensite plate has been formed. Point b and all the surface beyond it are now raised. The neighbouring material must exert a constraint tending to lower this part of the surface to its original height, and this is achieved by accommoda-

tion slip, as shown in (ii). Slip is largely inhibited between b and b' because of the proximity of the plate (just as slip in a polycrystal is inhibited near grain boundaries) but further along slip takes place more freely. If the specimen could be retained in this condition the ridge through b would look like a "midrib". In (iii) the metal transforms on the same habit plane up to point c, but the apparent surface tilt is smaller than before because previous

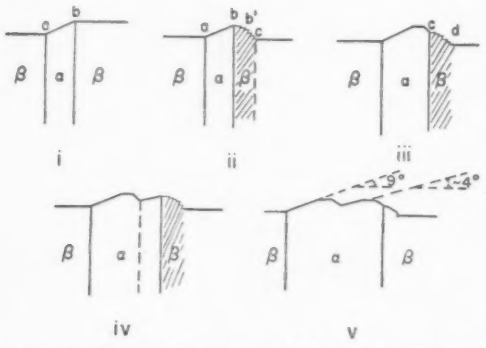

FIGURE 19. Schematic sections of a β-grain showing stages in the progress of an α-plate.

slip had caused the surface to slope the other way. The region bb', which had been least affected by slip, forms a plateau. There is now renewed accommodation slip, between c and d. When (iv) this region in turn transforms, it will again be tilted less steeply than is calculated. (v) is the stage when two "plates" have appeared. This scheme is not entirely satisfactory; in particular, it does not explain why the tilt of the escarpments is always so much smaller than 9 degrees, in spite of the fact that they are largely devoid of slip. No attempt has been made to consider the possible role of accommodation slip in the α-phase.*

The demands on accommodation slip are much more severe when the whole area consists of a single family of plates, than in the more usual case (as in steels) where interpenetrating plates on different habit plane variants help to accommodate each other.

It is probable that the accommodation slip is combined with a very slight rotation of the β-lattice adjoining the plate. The inhibition of slip near the α/β boundary implies the presence of a deformation gradient along each slip line, and hence a slight lattice curvature due to the retained dislocations. There should also be a pronounced lattice curvature along the dotted line through c, which is a locus of slip discontinuity. There will therefore be a small difference in orientation, after transformation, along the dotted line in sketch (iv). The proposed lattice rotation and the associated sub-boundaries are consistent with (i) the fact that faint etch-markings parallel to the original striations can often be seen on a polished and etched section (Figure 7, γ), and that appropriate etching renders such markings quite bold [5; 6]; and (ii) the observed slight departure from the Burgers orientation relationship. If it were not for the problem of accommodation and its consequences, each area should consist of a single α-grain of strictly uniform orientation, featureless when etched. On this view, also the Burgers orientation relationship is accurately obeyed at the instant of transformation, but impaired by *subsequent* lattice rotation.

In Figures 20 and 21 are reproduced an optical and a Berg-Barrett micrograph, respectively, of a part of a facet. The Berg-Barrett micrograph was taken after the surface had been smoothed by electrolytic polishing. (This led to some alteration in distribution of the areas.) The striations in Figure 21 in the area corresponding to A in Figure 20 are parallel to the surface striations visible there. This is further evidence of the existence of lattice misorientations consistent with the above scheme.

4. Discussion

All the experimental results point to the conclusion that Burgers' idealized mechanism is a close approximation to what actually happens in the titanium transformation. The major discrepancies which have not yet been accounted for are the divergence of about 10 degrees between the observed and predicted habit planes, and the unexpectedly small surface tilt. Geisler [17] has recently published an analysis of the habit plane problem for steels, in which he proposes that the nucleus of a martensite plate is related to the austenite lattice precisely according to the Kurdjumov-Sachs relationship [18], with {111} as the true habit plane. The observed deviations from this habit plane and simple orientation relationship are ascribed to accommodation slip in either the martensite or the austenite. The theory is not an inescapable inference from experimental observations, nor has it the power of predicting precise habit planes and surface tilts directly from crystallographic data at present available, yet it is consistent with a large number of observations. It appears to be capable of contribut-

*No satisfactory way has been found of accounting for the sharp division between slipped and unslipped regions (cf. Figure 18). Perhaps slip in the α-phase must be invoked.

ing to an understanding of the titanium transformation, if the Burgers orientation relationship and {112} habit is assumed for transformation nuclei.

The 10-degree deviation of the habit plane in titanium from an ideal {112} can be viewed as resulting from accommodation slip of the type postulated by Geisler. Indeed, this deviation is smaller than the angular deviation between {111} and most of the habit planes reported for steels. On Geisler's picture, the smaller deviation for titanium may well be a consequence of the smaller shear required according to the Burgers mechanism and the correspondingly smaller lattice distortion which has to be taken up by accommodation slip. Burgers' shear is 0.22, while the magnitude of the first shear of the Sachs mechanism is 0.71. Moreover, while steels undergo a volume change of over 2 per cent during transformation, in titanium this change is less than 0.1 per cent. No attempt has been made at a detailed interpretation of the 10 degrees deviation after the manner of Geisler, since nothing is known about the operative slip planes in β-titanium.

Continuing with Geisler's theory, the small deviation from the Burgers orientation relationship may also be put down to accommodation slip; the smallness of this deviation is to be attributed to the same cause as the smallness of the habit plane deviation. For steels, as for titanium, the absolute angle of deviation from the ideal is smaller for the orientation relationship than for the habit plane.

The readiness with which large volumes of β-titanium transform into a single family of parallel plates, which is in such contrast with the finely interlaced pattern of plates found in steels, can presumably also be attributed to the smaller distortion accompanying the transformation in titanium.

Before Geisler's paper was to hand, attempts had been made to analyse the habit plane on the basis of the observed orientation relationship. The method of analysis proposed by Frank [16] was adopted, using lattice parameters appropriate to the transformation temperature (880°C) obtained from recent publications [19–21]. Frank's treatment was chosen because it is presented in a form that facilitates its extension to a non-ferrous case. The procedure was to assume the correctness of the observed habit plane, and then to find which lattice rows in the α- and β-lattices, if any, were parallel to each other *and* to this habit plane. Then the analysis of section 7 of Frank's paper was applied to find which of the infinity of planes containing the lattice rows in question was to be expected as habit plane. Self-consistency required that this should be the habit plane originally assumed, i.e., the observed one. This was found to be so, within 3–4 degrees. The remaining difficulties were twofold. Firstly, no set of dislocations could be found that would satisfactorily accommodate the difference in spacing along the common lattice rows (which were $[120]_\beta$, $[11\bar{2}1]_\alpha$). Frank was able to provide for this in the case of steel (section 5 of his paper) because the lattice rows common to the austenite and martensite were identical in direction with the Burgers vectors of the dislocations commonly available for slip in these lattices, but this was not the case for titanium. The second difficulty was that the observed habit plane was not consistent with the observed shear direction. Frank's treatment allows the shear direction to be related to the orientation relationship (cf. p. 18 of his paper); actually several alternative directions came out of the calculation, but none were even roughly in agreement with the deductions made from surface contour.

Next the observed habit plane was ignored, and the method of Frank's section 7 applied straightforwardly, this time taking $[111]_\beta$, $[11\bar{2}0]_\alpha$ as the significant common lattice rows (which follows directly from the Burgers orientation relationship). As these are slip directions, the first difficulty is met. The habit plane calculated on this assumption was between {145} and {011}, which does not agree with experiment.

Thus Frank's analysis, though it works nicely for steel, is inconsistent with observation in the case of titanium, and for this reason it has not been thought worth while to publish details of the calculations. The failure in this instance of Frank's theory, which is one of the most incisive of recent attempts to interpret the austenite-martensite transformation without regard to accommodation slip, provides more presumptive evidence in favour of Geisler's approach. This is not to say that Burgers' mechanism necessarily represents the exact truth for titanium. The large anisotropic dilatations and contraction, though not leading to much net change of volume, make it probable that slight modifications of the mechanism should be invoked so as to reduce the magnitude of these readjustments.

In spite of what has been said above about Frank's treatment, it may be that Bowles' [22] approach to the austenite-martensite transformation may be capable of generalization to cover the

titanium transformation in a way that would account quantitatively for the tilt of the escarpments and for the {8; 9; 12} habit plane. As detailed attention is being directed to possible generalization of the theory by Bowles and Mackenzie [23] it will not be discussed here except to point out that it should be directly applicable at most to those portions of the titanium plates within which slip is least prominent, the escarpments. In the adjoining portions (the slopes) slip is believed to have tilted the surface with respect to the escarpments. The difference in tilt between escarpments and slope cannot be assigned to any distortion mechanism that would result in pronounced reorientation of the lattice away from the orientation in the escarpments because such reorientation is observed to be very small.

Experiments are currently being undertaken with titanium-manganese alloys, in which the β-phase is metastable at room temperature after quenching, in order to obtain more information about the early stages of the transformation, and, indirectly, about the transformation mechanism.

Acknowledgments

We are deeply indebted to the late Professor D. Hanson for his support throughout the period of this work. One of us (A. J. W.) was in receipt of an Athlone Fellowship. We are obliged to Drs. D. C. Jillson, J. Fast and A. E. Geach for providing titanium samples. Professor Tolansky and members of his staff gave invaluable instruction in the art of interferometry.

References

1. Burgers, W. G. Physica, **1** (1934) 561.
2. Van Ginneken, A. J. J. and Burgers, W. G. Acta Cryst. **5** (1952) 548.
3. Bowles, J. S. Trans. Amer. Inst. Min. Met. Eng. **191** (1951) 44.
4. Greninger, A. B. Trans. Amer. Inst. Min. Met. Eng. **133** (1939) 204.
5. Newkirk, J. B. and Geisler, A. H. Acta Met. **1** (1953) 370.
6. McHargue, C. J. Acta Cryst. **6** (1953) 529.
7. Liu, Y. C. and Margolin, H. J. Metals **5** (1953) 667.
8. Kurdjumov, G. Trans. Amer. Inst. Min. Met. Eng. **133** (1939) 222.
9. Cahn, R. W. J. Sci. Instr. **30** (1953) 201.
10. Barrett, C. S. Trans. Amer. Inst. Min. Met. Eng. **161** (1945) 15.
11. Sutcliffe, D. A., Forsyth, J. I. M. and Reynolds, J. A. Metallurgia, **41** (1950) 283.
12. Tolansky, S. Z. Elektrochem. **56** (1952) 263.
13. Tolansky, S. and Omar, M. J. Sci. Instr. **30** (1953) 337.
14. Tolansky, S. "Multiple-Beam Interferometry" (Oxford, Clarendon Press, 1948) p. 18.
15. Turnbull, D. T. and Belk, J. A. Laboratory Practice **1** (1952) 403.
16. Frank, F. C. Acta Met. **1** (1953) 15.
17. Geisler, A. H. Acta Met. **1** (1953) 260.
18. Kurdjumov, G and Sachs, G. Z. Physik, **64** (1930) 325. Sachs, G. Z. Metallk. **24** (1932) 241.
19. Eppelsheimer, D. S. and Penman, R. R. Nature, **166** (1950) 960.
20. Levinger, B. W. J. Metals **5** (1953) 195.
21. Berry, R. L. P. and Raynor, G. V. Research (Supplement) **6** (1953) 21S.
22. Bowles, J. S. Acta Cryst. **4** (1951) 162.
23. Bowles, J. S. and Mackenzie, J. K. Trans. Amer. Inst. Min. Met. Eng. **194** (1952) 1201, and further work, to be published.

THE CRYSTALLOGRAPHY OF MARTENSITE TRANSFORMATIONS I*

J. S. BOWLES and J. K. MACKENZIE†

The atomic displacements involved in a martensite transformation cannot be described consistently by means of a homogeneous strain because the homogeneous strain that describes the change in shape accompanying the formation of a martensite plate usually does not convert the initial lattice into the final lattice. To obtain a consistent description of the atomic displacements it is supposed that the strain describing the change in shape is followed by another strain which generates the final lattice in its observed orientation without causing any further change in shape. Such a strain can only be homogeneous on a submicroscopic scale.

From an analysis of the available experimental data the first strain is shown to be composed of a dilatation, and an invariant plane strain which leaves the habit plane invariant. On the assumption that the second strain is also an invariant plane strain, it is shown to be a simple shear either on a twinning plane or in a twinning direction of the final lattice. This strain need not cause any observable change in shape if it is accompanied by slip on closely spaced planes parallel to the shear plane.

The resultant of these two strains is determined by the correspondence between the points of the initial and final lattices, their dimensions and their relative orientations. It is shown that the resolution of this strain into component strains of the above types is uniquely determined. Finally, it is proposed that the second strain is a part of a twinning shear in the final structure.

LA CRISTALLOGRAPHIE DES TRANSFORMATIONS MARTENSITIQUES I

Les déplacements atomiques impliqués dans une transformation martensitique ne sont pas compatibles avec une déformation homogène, car la déformation homogène décrivant le changement de forme dont est accompagnée la formation d'une lamelle de martensite, ne transforme habituellement pas le réseau initial en réseau final. En vue d'obtenir une description des déplacements atomiques, conforme à la réalité, il est supposé que la déformation relative au changement de forme est suivie d'une autre déformation; cette dernière engendrerait le réseau final dans son orientation observée, sans causer de changement de forme extérieure. Une telle déformation ne peut être homogène qu'à l'échelle submicroscopique. Une analyse des données expérimentales, disponibles montre que la première déformation est composée d'une dilatation et d'une déformation plane, invariante, qui laisse le plan limite invariant.

En supposant que la deuxième déformation soit aussi plane et invariante, on montre qu'elle est un cisaillement simple, soit sur un plan de maclage, soit dans une direction de maclage du réseau final. Cette déformation ne causerait pas de changement de forme observable, si elle était accompagnée d'un glissement sur des plans peu espacés et parallèles au plan de cisaillement. La résultante de ces deux déformations est déterminée par le rapport entre les points du réseau initial et du réseau final, ainsi que par les dimensions et orientations relatives de ces derniers. Il est montré que la résolution de cette déformation en deux composantes, décrites plus haut, est déterminée d'une façon unique. On propose aussi que la deuxième déformation est une partie d'un cisaillement de maclage dans la structure finale.

DIE KRISTALLOGRAPHIE DER MARTENSIT TRANSFORMATIONEN I

Die Atombewegungen, die mit einer Martensit-Transformation verbunden sind, lassen sich nicht völlig durch homogene Verzerrungen beschreiben. Die homogene Verzerrung, die die Formänderung, die mit der Bildung eines Martensitplättchens verbunden ist, beschreibt, wandelt im allgemeinen das ursprüngliche Gitter nicht in das Endgitter um. Um eine eindeutige Beschreibung der Atombewegungen zu erhalten, wird angenommen, dass auf die Verzerrung, die die Formänderung beschreibt, eine andere Verzerrung folgt, die das Endgitter mit seiner bekannten kristallographischen Orientierung ohne eine weitere Formänderung bildet. Eine solche Verzerrung kann nur submikroskopisch homogen sein.

Aus der Analyse der vorhandenen experimentellen Angaben kann gezeigt werden, dass sich die erste Verzerrung aus einer Dehnung und einer invarianten ebenen Verzerrung, die die Habitus Ebene invariant erhält, zusammensetzt. Wenn man annimmt, dass die zweite Verzerrung ebenfalls eine invariante ebene Verzerrung ist, kann gezeigt werden, dass es sich hier um eine einfache Scherung, entweder in einer Zwillingsebene oder in einer Zwillingsrichtung des Endgitters handelt. Eine derartige Verzerrung braucht keine sichtbare Formänderung hervorzurufen, wenn sie von einer Gleitung auf nahe benachbarten, der Scherungsebene parallelen Ebenen begleitet ist.

Die Resultierende dieser beiden Verzerrungen ist bestimmt durch die Beziehung zwischen den Punkten des ursprünglichen und des Endgitters, den Gitterdimensionen und den relativen kristallographischen Orientierungen. Es wird gezeigt, dass die Zerlegung dieser Verzerrung in Verzerrungskomponenten wie oben beschrieben eine eindeutige Zerlegung ist. Es wird ausserdem vorgeschlagen, die zweite Verzerrung als einen Teil der Zwillingsscherung in der Endstruktur anzusehen.

1. Introduction

In recent years various attempts [1–5] have been made to deduce from the geometrical properties of martensite transformations the over-all atomic displacements involved, and the mechanism by which these displacements occur. While these attempts have been fairly successful no general theory of the atomic displacements has yet emerged, nor have the interrelations between the various geometrical properties of the transformations been completely

*Received February 9, 1953.

†Division of Tribophysics, University of Melbourne, Victoria, Australia.

clarified. The object of the present series of papers is to provide such a theory and to compare its predictions with experimental data for a variety of individual transformations. In the formulation of this general theory it has been necessary to re-examine previous arguments and to make certain corrections and extensions; but in the interests of brevity and continuity of argument the historical background has been omitted (see, however, Greninger and Troiano [1; 2], Jaswon and Wheeler [6], Bowles [3], Bowles and Barrett [7], Machlin and Cohen [5]).

Part I of the present work is concerned with clarifying the interrelation between the main geometrical features of martensite transformations and with developing a general hypothesis consistent with these features. Briefly, this hypothesis is that the atomic displacements can be described by a homogeneous strain of the parent structure followed by a strain which is part of a twinning shear in the final structure, but occurs inhomogeneously. The homogeneous strain has the important property that all lines in one plane (the habit plane) are unrotated.

In Part II this hypothesis is developed into a quantitative theory and in later papers it will be shown that it yields predictions of habit planes, orientation relationships and other geometrical features which agree satisfactorily with the experimental values. Furthermore, it has been suggested [7] that during the stage of coherent growth many nucleation and growth transformations may be geometrically similar to martensite transformations. The theory also provides satisfactory predictions at least in some such cases.

The theory is phenomenological and is concerned only with the initial and final states. It follows that nothing can be deduced about the actual paths taken by the atoms during transformation: only a description of the correspondence in position between atoms in the two structures can be obtained. However, the theory is not altogether unrelated to the problem of discovering a mechanism. For, once a proposed mechanism is shown to fulfil the above hypothesis it is automatically assured that the model is consistent with all the different geometrical features. The task of ensuring this consistency is thereby greatly reduced.

2. The Nature of the Problem

The problem is to find a set of atomic displacements which is consistent with the geometrical and crystallographic features of the transformation. These atomic displacements must generate the final crystal lattice from the initial, and, in cases where the structures contain superlattices, must generate the final superlattice from the initial superlattice. They must also produce the observed orientation relationship between the two lattices, and finally, they must produce the observed change in shape of the transformed regions. The historical development of the whole problem has recently been reviewed by Bowles and Barrett [7].

Jaswon and Wheeler [6] have suggested that the total atomic displacements can be described by a homogeneous strain which distorts the initial lattice into the final lattice and produces the correct orientation relationship. Such a strain can always be found but is not unique. Any particular strain satisfying these requirements uniquely associates lattice points in the initial lattice with the points they become in the final lattice. Conversely, when this "correspondence" and the relative orientation of the two lattices are specified the strain is uniquely determined. Jaswon and Wheeler proposed that, of all possible correspondences, the correct one is that which involves the smallest displacements in the associated strain. This criterion for selecting the correspondence has been shown to yield correct predictions of the positions of interstitial atoms, and of superlattices, for those martensite structures to which it has been applied [6; 3; 8].

The homogeneous strain derived in this way provides a description of the atomic displacements that is consistent with some, but not all, of the requirements. In this paper this strain is assumed to be known and will be referred to as the total strain, $\mathbf{S}_t$. Since the above choice of the correspondence ensures that all atoms undergo the least possible relative displacements, the total strain must describe the displacements of atoms correctly, at least in the neighbourhood of the origin. However, if the total strain is to describe the displacements of *all* atoms in a martensite plate it must also describe the macroscopic change in shape that accompanies the formation of the plate. Although the change in shape can be described by a homogeneous strain, this strain is generally ***not*** the same as the total strain [3]. For this reason most transformations cannot be described consistently by a strain which is homogeneous throughout the volume of a plate: the strain describing the atomic displacements is inhomogeneous.

To derive a description that is consistent with all requirements it is convenient to resolve the

atomic displacements into 'homogeneous' and 'inhomogeneous' components. The 'homogeneous' displacements are defined by the observed change in shape of the plate, and the strain they define will be called the homogeneous strain. The 'inhomogeneous' displacements are those additional displacements which are required to generate the final lattice in its observed orientation, without causing any observable change in shape. Although the combination of these two sets of atomic displacements cannot be described throughout large volumes by a homogeneous strain, the strain they define must be locally homogeneous (on a submicroscopic scale) since it distorts one lattice into another and involves only small displacement of atoms relative to their neighbours. Thus, within such homogeneously-strained regions this strain can be identified with the total strain, $\mathbf{S}_t$.

It is clear that the required 'inhomogeneous' displacements will be different depending on whether they are considered to occur before or after the 'homogeneous' displacements. As far as a description of the total atomic displacements is concerned this order is immaterial, and in the present analysis the usual convention [1; 2], that the homogeneous component of the strain occurs first, will be adopted.

This paper is concerned primarily with finding the geometrical conditions which determine this resolution of the atomic displacements into 'homogeneous' and 'inhomogeneous' components. These conditions are deduced from a detailed consideration of the nature of the component strains, and from the implications of the observed coexistence of twins in martensite plates. Since the problem is concerned with finite, though small, homogeneous strains a matrix representation is appropriate.* In the following section the notation is described and some well-known basic formulae are collected for convenient reference. For general information concerning matrix and vector algebra the reader is referred to Jeffreys and Jeffreys [11].

3. Notation and Basic Formulae

(*a*) *Notation*

The use of matrices to represent vectors and homogeneous strains requires the specification of a definite set of non-coplanar base vectors. The non-coplanar base vectors $\mathbf{a}_1$, $\mathbf{a}_2$, $\mathbf{a}_3$ used in the following treatment are quite general; they are not assumed to be either orthogonal or equal in length. This set will be described as the basis A.

Small letters in **bold face type** will be used to represent vectors. The components of a vector $\mathbf{x}$ relative to the basis A will be denoted by the corresponding *italics* x_1, x_2, x_3, while the column matrix with these components will be written in **sans serif type** as x. Thus,

$$(3.1) \qquad \mathbf{x} = x_1\mathbf{a}_1 + x_2\mathbf{a}_2 + x_3\mathbf{a}_3, \qquad \mathsf{x} = \begin{bmatrix} x_1 \\ x_2 \\ x_3 \end{bmatrix}.$$

In order to conserve space the matrix x will be written $\mathsf{x} = [x_1, x_2, x_3]_A$, where the square brackets indicate that x is a column matrix, and the subscript $_A$ is added only when it is necessary to specify the basis explicitly. The two kinds of type will be used in a similar fashion to distinguish between a particular strain $\mathbf{S}$ and its matrix representation S relative to a specified basis.

The set of reciprocal base vectors $\mathbf{a}_1^*$, $\mathbf{a}_2^*$, $\mathbf{a}_3^*$ will be described as the basis A* and when necessary the components of a vector relative to this reciprocal basis will be denoted by the corresponding starred italic symbols. Thus,

$$(3.2) \qquad \mathbf{x} = x_1^*\mathbf{a}_1^* + x_2^*\mathbf{a}_2^* + x_3^*\mathbf{a}_3^*,$$

$$\mathsf{x}^* = [x_1^*, x_2^*, x_3^*]_{A^*}.$$

The reciprocal base vectors have the important property that the scalar product

$$(3.3) \qquad \mathbf{a}_r \,.\, \mathbf{a}_s^* = \begin{cases} 1 \text{ for } r = s, \\ 0 \text{ for } r \neq s. \end{cases}$$

The components of a vector $\mathbf{x}$ relative to the basis A* are related to the components of the same vector relative to the basis A by the matrix equation

$$(3.4) \qquad \mathsf{x}^* = \mathsf{G}\mathsf{x},$$

where the metric G is a symmetrical square matrix with components g_{rs} given by

$$(3.5) \qquad g_{rs} = g_{sr} = \mathbf{a}_r \,.\, \mathbf{a}_s.$$

In the special case where the basis A is an orthonormal basis, i.e., consists of orthogonal unit vectors, the bases A and A* are identical and the metric G is the identity matrix I.

The transpose of a matrix, which is obtained by interchanging rows and columns, will be denoted by adding a dash to the corresponding symbol. Thus, the transpose of x is the row matrix

$$(3.6) \qquad \mathsf{x}' = (x_1, x_2, x_3),$$

*Matrices are used in preference to tensors because they are immediately suited to numerical representation and calculation.

where the parentheses (and the prime) indicate that $\mathbf{x}'$ is a row matrix. Since directions will usually be referred to the basis A and appear in equations as column vectors, while normals to planes when referred to the reciprocal basis A* will usually appear as row vectors, the use of these types of bracket conforms with established crystallographic conventions.

(b) Scalar Products and Normals to Planes

The scalar product of two vectors $\mathbf{x}$ and $\mathbf{y}$ is most easily calculated when one of the vectors is referred to the basis A*, while the other is referred to the basis A. Using equation (3.3),

$$\begin{aligned}\mathbf{x}\,.\,\mathbf{y} &= x_1^* y_1 + x_2^* y_2 + x_3^* y_3 = \mathbf{x}^{*\prime}\mathbf{y}, \\ &= x_1 y_1^* + x_2 y_2^* + x_3 y_3^* = \mathbf{x}'\mathbf{y}^*.\end{aligned} \tag{3.7}$$

The scalar product can therefore be calculated in the simple way that holds for an orthonormal basis. When both $\mathbf{x}$ and $\mathbf{y}$ are referred to the basis A, the transformation (3.4) gives†

$$\mathbf{x}.\mathbf{y} = \mathbf{x}'\mathsf{G}\mathbf{y} = \mathbf{y}'\mathsf{G}\mathbf{x}. \tag{3.8}$$

The vector equation to a plane normal to the vector $\mathbf{h}$ is

$$\mathbf{h}.\mathbf{x} = c \tag{3.9}$$

where $\mathbf{x}$ is the position vector of any point on the plane and c a scalar constant. The usual convention is that $\mathbf{x}$ is referred to the basis A, while $\mathbf{h}$ is referred to the reciprocal basis A* so that equation (3.9) becomes

$$\mathbf{h}^{*\prime}\mathbf{x} = h_1^* x_1 + h_2^* x_2 + h_3^* x_3. \tag{3.10}$$

In all that follows, unless the contrary is stated, normals to planes will be referred to the reciprocal basis A*, and the stars will be omitted from the notation for components.

(c) Representation of Homogeneous Strains

In a homogeneous strain $\mathbf{S}$ a point with position vector $\mathbf{x}$ is transformed into a point with position vector $\mathbf{y}$ determined by the homogeneous linear transformation

$$\mathbf{y} = \mathsf{S}\mathbf{x}, \tag{3.11}$$

where S is a nonsingular square matrix and both $\mathbf{x}$ and $\mathbf{y}$ refer to the basis A. On substituting [100], [010] and [001] in turn for $\mathbf{x}$, it is clear that the successive columns of S are the components (relative to A) of the vectors, S A, into which the set of base vectors A are transformed by the strain $\mathbf{S}$.

The strain $\mathbf{S}$ transforms points lying in a plane with normal $\mathbf{n}$ into points lying in a plane with normal $\mathbf{m}$ given by

$$\mathbf{m}' = \mathbf{n}'\mathsf{S}^{-1}, \tag{3.12}$$

where the components of the row vectors $\mathbf{m}'$ and $\mathbf{n}'$ are those of $\mathbf{m}$ and $\mathbf{n}$ relative to A*.

The determinant of S is equal to the ratio of the final volume V_f of any particular closed region to its initial volume V_i

$$V_f/V_i = |\,\mathsf{S}\,| = 1 + \Delta, \tag{3.13}$$

where Δ is the dilatation which must be greater than minus one for a physically realizable strain.

(d) Unrotated Lines and Planes

The non-zero solutions of the equations

$$\mathsf{S}\mathbf{x} = \lambda\mathbf{x}, \quad \mathbf{n}'\mathsf{S} = \lambda\mathbf{n}', \tag{3.14}$$

where λ is some constant, define lines and planes respectively that are not rotated by the strain $\mathbf{S}$. These equations have non-zero solutions only if λ satisfies the determinantal equation

$$|\,\mathsf{S} - \lambda\mathsf{I}\,| = 0. \tag{3.15}$$

Equation (3.15) has either one or three real (characteristic) roots so there is always at least one unrotated line and a corresponding unrotated plane. A characteristic root λ_r determines the ratio $1/\lambda_r$ of the length of the corresponding vector $\mathbf{x}_r$ to the length of the vector into which it is transformed by the strain. Similarly λ_r is the ratio of the final to the initial spacing of a set of equidistant parallel planes with normal $\mathbf{n}_r$. Thus, if a $\lambda_r = 1$ the corresponding line is an invariant line and the corresponding plane has an invariant normal. Note that a plane in which all lines are invariant, i.e. an invariant plane, does not necessarily have an invariant normal.

4. The Nature of the Homogeneous Strain

In this section an analysis is made of the relief effects which martensite transformations produce on polished surfaces and the nature of the strain producing them is determined.

The relief effects produced by all martensite transformations are essentially similar. In the region where a martensite plate meets a free plane surface, the surface remains plane and is simply tilted about its intersection with the habit plane (the plane of the plate). Similarly, where a martensite plate

†Unlike the scalar product $\mathbf{x}.\mathbf{y}$, the matrix product $\mathbf{x}^{*\prime}\mathbf{y}$ is not commutative; for, by the rule for matrix multiplication, $\mathbf{y}\mathbf{x}^{*\prime}$ is a 3×3 matrix.

intercepts a straight line, scribed on a plane surface prior to transformation, the line is changed in direction but remains straight. Furthermore, the matrix is displaced in such a way that the line remains continuous across the interface. Since planes (straight lines) are distorted into planes (straight lines) the observed change in shape can be described by a homogeneous strain.

If the habit plane were rotated by this strain, plastic deformation of the matrix would be required in order to preserve the continuity between a plate and the surrounding matrix. Since the ratio of the length to the thickness of a martensite plate is large, the amount of plastic deformation would be extensive even for small rotations of the habit plane. Moreover, if the boundaries of the parent crystal are constrained, as in a polycrystalline aggregate, rotation of the habit plane would involve transport of material from one side of a plate to the other. The amount of plastic deformation in the matrix, as revealed by the lateral displacement of scratches on a polished surface, is not compatible with any appreciable rotation of the habit plane. It can, therefore, be concluded that the habit plane is not rotated by the homogeneous strain.

Since any free surface is simply rotated about its intersection with the habit plane, no line in this plane can be rotated by the homogeneous strain. A direct test of the accuracy of this conclusion is furnished by the observation that a martensite plate and the neighbouring matrix can be kept in focus under a microscope while traversing the whole length of the plate. Since plates can be a centimetre or more in length no line can be rotated within the habit plane by more than a few minutes.

Hence, the change in shape on transformation can be described as a homogeneous strain $\mathbf{S}$ in which the habit plane and all lines in it are unrotated. Thus, if $\mathbf{x}_1$ and $\mathbf{x}_2$ are non-parallel vectors lying in the habit plane, then

$$\mathbf{S}\mathbf{x}_1 = \lambda_1\mathbf{x}_1, \quad \mathbf{S}\mathbf{x}_2 = \lambda_2\mathbf{x}_2, \tag{4.1}$$

where λ_1,λ_2 are constants. Since any other vector $a\mathbf{x}_1 + b\mathbf{x}_2$ lying in the habit plane is also unrotated

$$\mathbf{S}(a\mathbf{x}_1 + b\mathbf{x}_2) = \lambda(a\mathbf{x}_1 + b\mathbf{x}_2),$$

or

$$a\lambda_1\mathbf{x}_1 + b\lambda_2\mathbf{x}_2 = a\lambda\mathbf{x}_1 + b\lambda\mathbf{x}_2. \tag{4.2}$$

This last equation is true for all a,b so that $\lambda_1 = \lambda_2 = \lambda$. Hence, the strain $\mathbf{S}/\lambda$ is such that the plane defined by $\mathbf{x}_1,\mathbf{x}_2$ is invariant: an invariant plane strain. This strain differs from $\mathbf{S}$ by a pure dilatation $\lambda\mathbf{I}$. Since scratches crossing the interface remain continuous after transformation the value of λ can only differ from unity by at most a few per cent.

Apart from this small dilatation, the homogeneous strain which describes the change of shape is an invariant plane strain in which the habit plane is invariant. The next section is devoted to a consideration of the properties of such strains.

5. Properties of Invariant Plane Strains

It can be shown that the strain

$$\mathbf{S} = \mathbf{I} + \mathbf{d}\mathbf{p}' \equiv \mathbf{P}, \tag{5.1}$$

where $\mathbf{d}$ is any vector, is the most general strain for which the plane with normal $\mathbf{p}$ is invariant; the symbol $\mathbf{P}$ will be used hereafter to denote such invariant plane strains. The expanded representation of $\mathbf{P}$ is

$$\mathbf{P} = \begin{pmatrix} 1 + d_1p_1 & d_1p_2 & d_1p_3 \\ d_2p_1 & 1 + d_2p_2 & d_2p_3 \\ d_3p_1 & d_3p_2 & 1 + d_3p_3 \end{pmatrix}. \tag{5.2}$$

The displacement of any point $\mathbf{x}$ by the strain $\mathbf{P}$ is given by†

$$\mathbf{P}\mathbf{x} - \mathbf{x} = (\mathbf{p}'\mathbf{x})\,\mathbf{d}, \tag{5.3}$$

which is always in the direction of $\mathbf{d}$ and proportional** to the perpendicular distance of the point $\mathbf{x}$ from the plane $\mathbf{p}'\mathbf{x} = 0$. Since the displacement of all points in the plane $\mathbf{p}'\mathbf{x} = 0$ is zero, this plane is clearly invariant. Such a strain occurring in a crystal lattice is particularly easy to visualize. The set of lattice planes parallel to the invariant plane $\mathbf{p}'\mathbf{x} = 0$ are neither distorted nor rotated so that the strain can only consist of a displacement of these planes relative to each other in a fixed direction. Two limiting cases of invariant plane strains can readily be identified. When $\mathbf{d}$ and $\mathbf{p}$ are perpendicular the strain is a simple shear and when they are parallel it is a simple extension.

The determinant of $\mathbf{P}$ is

$$|\mathbf{P}| = 1 + d_1p_1 + d_2p_2 + d_3p_3 = 1 + \mathbf{p}'\mathbf{d}, \tag{5.4}$$

and the inverse of $\mathbf{P}$ is

$$\mathbf{P}^{-1} = \mathbf{I} - \mathbf{d}\mathbf{p}'/(1 + \mathbf{p}'\mathbf{d}) \tag{5.5}$$

which is an invariant plane strain on the same plane and in the opposite direction.

†Note that $\mathbf{p}'$ is a row matrix with elements equal to the components of $\mathbf{p}$ referred to the reciprocal basis. The product $\mathbf{p}'\mathbf{x} = \mathbf{p}.\mathbf{x}$ is a scalar and must be distinguished from the products like $\mathbf{d}\mathbf{p}'$ which is a three-by-three square matrix.

**A suitable measure of the magnitude of $\mathbf{P}$ is the magnitude of the displacement of a point in an invariant plane at unit distance from the origin; this is equal to the product of the magnitudes of $\mathbf{p}$ and $\mathbf{d}$.

The displacement of any normal $\mathbf{n}$ by the invariant plane strain $\mathbf{P}$ is given by

$$(5.6) \qquad \mathbf{n}'\mathbf{P}^{-1} - \mathbf{n}' = -(\mathbf{n}'\mathbf{d})\mathbf{p}'/(1 + \mathbf{p}'\mathbf{d})$$

which is always in the direction of $\mathbf{p}$ and proportional to the distance of the point $\mathbf{d}$ from the plane $\mathbf{n}$. Thus, the initial and final positions of the normal to a plane are coplanar with the normal to the invariant plane.

The characteristic roots of the matrix $\mathbf{P}$ are $1 + \mathbf{p}'\mathbf{d}$,1,1. The unrotated line and normal corresponding to the first root are in the direction of $\mathbf{d}$ and $\mathbf{p}$ respectively. Since the other roots are equal and unity there is a whole plane of invariant lines and a zone of planes with invariant normals. This plane and zone axis are the plane $\mathbf{p}$ and the direction $\mathbf{d}$ of the strain $\mathbf{P}$.

The condition that the resultant of two consecutive invariant plane strains be another invariant plane strain will be required in the following section. If the product $\mathbf{P}_2\mathbf{P}_1$ represents an invariant plane strain, then $\mathbf{p}'$ and $\mathbf{d}$ exist such that

$$(5.7) \qquad (\mathbf{I} + \mathbf{d}_2\mathbf{p}_2')(\mathbf{I} + \mathbf{d}_1\mathbf{p}_1') = \mathbf{I} + \mathbf{d}\mathbf{p}'.$$

Hence, for all $\mathbf{x}$ and $\mathbf{n}'$

$$(5.8) \quad \left.\begin{aligned} \mathbf{d}(\mathbf{p}'\mathbf{x}) &= \mathbf{d}_1(\mathbf{p}_1'\mathbf{x}) + \mathbf{d}_2[(\mathbf{p}_2'\mathbf{x}) + (\mathbf{p}_2'\mathbf{d}_1)(\mathbf{p}_1'\mathbf{x})], \\ (\mathbf{n}'\mathbf{d})\,\mathbf{p}' &= [(\mathbf{n}'\mathbf{d}_1) + (\mathbf{p}_2'\mathbf{d}_1)(\mathbf{n}'\mathbf{d}_2)]\,\mathbf{p}_1' + (\mathbf{n}'\mathbf{d}_2)\,\mathbf{p}_2', \end{aligned}\right\}$$

so that $\mathbf{d}$ and $\mathbf{p}'$ are linear combinations of $\mathbf{d}_1,\mathbf{d}_2$ and $\mathbf{p}_1',\mathbf{p}_2'$ respectively. Suppose that $\mathbf{d}_1$ and $\mathbf{d}_2$ are not parallel; then for any $\mathbf{x}$ such that $\mathbf{p}'\mathbf{x} = 0$ the coefficients of $\mathbf{d}_1$ and $\mathbf{d}_2$ in equation (5.8) must be zero. Hence,

$$\mathbf{p}_1'\mathbf{x} = 0, \quad \mathbf{p}_2'\mathbf{x} + (\mathbf{p}_2'\mathbf{d}_1)(\mathbf{p}_1'\mathbf{x}) = \mathbf{p}_2'\mathbf{x} = 0,$$

so that the planes with normals $\mathbf{p}_1$, $\mathbf{p}_2$ and $\mathbf{p}$ all coincide. Similarly, if $\mathbf{p}_1$ and $\mathbf{p}_2$ are not parallel, it follows that $\mathbf{d}_1$, $\mathbf{d}_2$ and $\mathbf{d}$ are all parallel.

Thus, *if the resultant of two invariant plane strains is to be another invariant plane strain it is necessary that the two component strains be either on the same plane or in the same direction.* It is easily verified that either of these conditions is also sufficient. The corresponding result for simple shears follows as a special case and will be needed in the following section.

6. The Nature of the Inhomogeneous Strain

Since the change of shape can be described, apart from a small dilatation, by a homogeneous strain in which one plane, the habit plane, is invariant, it is clear that this strain alone cannot possibly describe the total atomic displacements unless the atomic configuration in the habit plane is the same in both the initial and the final structures. In all other cases, additional atomic displacements are required. These additional displacements constitute a strain in which the lattice generated by the homogeneous strain is distorted into the final lattice. Thus, like the total strain $\mathbf{S}_t$, this strain must be homogeneous within volumes having at least the dimensions of a unit cell. In spite of its local homogeneity this strain must be inhomogeneous on a larger scale since it produces no observable change of shape. Thus, the additional 'inhomogeneous' displacements can be described by means of a homogeneous strain together with some kind of localised inhomogeneity. For convenience, this homogeneous strain will be called hereinafter the complementary strain.

The complementary strain cannot be accompanied by any dilatation, for, regardless of the kind of inhomogeneity, such a dilatation would inevitably be cumulative and would, therefore, already be included in the observed homogeneous strain. This is the only general restriction on the nature of the complementary strain.

In order that the 'inhomogeneous' displacements shall cause no observable change in shape it is clear that the inhomogeneity must arise from localised displacements which counteract the change in shape that would otherwise accompany the complementary strain. Since these localised displacements must leave the final lattice continuous and undistorted, they can only be slip displacements in the lattice.† When the complementary strain is a simple shear, an observable change of shape need not occur if slip takes place on closely spaced planes parallel to the shear plane. When the complementary strain is more complex, slip on several systems is required to avoid change of shape.

It is assumed in the present work that the complementary strain is an invariant plane strain, which means, since there is no dilatation, that it is a simple shear. This condition, together with the observation that martensite plates are frequently twinned, leads to additional restrictions on the nature of the complementary strain.

When a transformation produces twinned martensite plates, the observed change in shape caused by the transformation is the same for both twins. This means that the atomic displacements involved

†The combination of a complementary strain and the required lattice slip is achieved automatically if each atom simply moves to the nearest available position in the final lattice.

in producing the twin orientations differ only in their 'inhomogeneous' components. The complementary strains are, therefore, two simple shears $\mathbf{P}_2$,$\mathbf{P}_3$ which generate twin orientations of the final structure from the hypothetical intermediate lattice generated by the common homogeneous strain. It is clear that the twinning shear $\mathbf{P}^T$, which is the strain that distorts one orientation into its twin, can be regarded as the resultant of the reversed shear $\mathbf{P}_2^{-1}$, which would distort this orientation back to the intermediate lattice, and the shear $\mathbf{P}_3$ which distorts this lattice into the twin orientation. Thus, $\mathbf{P}^T = \mathbf{P}_3\mathbf{P}_2^{-1}$. Since it was proved in section 5 that the resultant of two simple shears can be another simple shear only if the shear plane or the shear direction is the same for all three shears, it follows that the complementary strains, which are simple shears, occur either on a twinning plane‡ or in a twinning direction of the final structure.

7. The Composition of the Total Strain

The concept has now been reached that the total strain is composed of a dilatation and two consecutive invariant plane strains, the second of which is a simple shear on a known plane (twinning plane) or in a known direction (twinning direction). In succeeding sections it will be shown that this information not only suffices to determine a unique resolution of the total strain into its component strains, but also provides certain information concerning the nature of the total strain.

The dilatation is identified by considering the nature of the remaining part of the total strain. The resultant of any two invariant plane strains is an invariant line strain because the line of intersection of their invariant planes is obviously invariant throughout. Thus, the dilatation is that which must be removed from the total strain to convert it into an invariant line strain. The requirement that this be possible does not provide any information about the total strain, because in a homogeneous strain there is always at least one unrotated line and, by removing an appropriate dilatation, this line can always be made invariant in the remaining strain. Thus, apart from a possible multiplicity of unrotated lines the dilatation is uniquely determined.

The remaining problem is to resolve the invariant line strain into an invariant plane strain, and a simple shear on a specified plane or in a specified direction. Now any resolution of an invariant line strain into two invariant plane strains must be such that the two invariant planes intersect along the invariant line. Similarly, the two directions of displacement must lie in the plane with the invariant normal, because a normal to a plane can only be invariant if all displacements take place within that plane. Thus, the total strain must be such that either the twinning plane contains the invariant line, or the twinning direction lies in the plane with the invariant normal. These conditions restrict the nature of the total strain.

8. Resolution of an Invariant Line Strain

It will first be shown that an invariant line strain that is not itself an invariant plane strain, can always be resolved into two invariant plane strains on arbitrarily chosen planes containing the invariant line. The directions and magnitudes of these strains are uniquely determined when their planes are specified.

An invariant line strain $\mathbf{S}$ is characterized by the existence of an invariant line in the direction of $\mathbf{x}_i$ and an invariant normal $\mathbf{n}'_i$ such that

$$\mathbf{S}\mathbf{x}_i = \mathbf{x}_i, \quad \mathbf{n}'_i\mathbf{S} = \mathbf{n}'_i. \tag{8.1}$$

When $\mathbf{S}$ is not itself an invariant plane strain the directions of $\mathbf{x}_i$ and $\mathbf{n}'_i$ are uniquely defined. The first step towards establishing an explicit factorization of $\mathbf{S}$ is to show that the displacements of all vectors lying in a given plane $\mathbf{p}'_2$ containing $\mathbf{x}_i$ can be achieved by an invariant plane strain on any other plane $\mathbf{p}'_1$ containing $\mathbf{x}_i$.

Let $\mathbf{y}_2$ be some definite vector, other than $\mathbf{x}_i$, lying in the plane $\mathbf{p}'_2$. Then $\mathbf{p}'_2\mathbf{y}_2 = \mathbf{p}'_2\mathbf{x}_i = 0$, and any vector lying in the plane $\mathbf{p}'_2$ can be written $\mathbf{x} = a\mathbf{y}_2 + b\mathbf{x}_i$ where a and b are numbers. The displacement of $\mathbf{x}$ by the invariant line strain is

$$\begin{aligned} \mathbf{S}\mathbf{x} - \mathbf{x} &= a[\mathbf{S}\mathbf{y}_2 - \mathbf{y}_2] + b[\mathbf{S}\mathbf{x}_i - \mathbf{x}_i], \\ &= a[\mathbf{S}\mathbf{y}_2 - \mathbf{y}_2], \end{aligned} \tag{8.2}$$

and is, therefore, in the same direction for all $\mathbf{x}$ in the plane $\mathbf{p}'_2$. Since $\mathbf{n}'_i[\mathbf{S}\mathbf{x} - \mathbf{x}] = \mathbf{n}'_i\mathbf{x} - \mathbf{n}'_i\mathbf{x} = 0$, for all $\mathbf{x}$, this direction necessarily lies in the plane with the invariant normal.

An invariant plane strain on a plane $\mathbf{p}'_1$ and in the common direction of displacement of all vectors in the plane $\mathbf{p}'_2$ is given by

$$\mathbf{P}_1 = \mathbf{I} + k[\mathbf{S}\mathbf{y}_2 - \mathbf{y}_2]\,\mathbf{p}'_1. \tag{8.3}$$

‡The terms 'twinning plane' and 'twinning direction' are used throughout to denote the plane and direction, respectively, of the twinning shear. It should be noted that if the twinning is of Type II, in the terminology of Schmid and Boas [9], the twinning plane is not the reflection plane relating the two twins.

The displacement of the vectors $\mathbf{x}$ above by $\mathbf{S}$ and $\mathbf{P}_1$ are the same provided

$$(8.4) \qquad a = k\mathbf{p}_1'[a\mathbf{y}_2 + b\mathbf{x}_i] = ak\mathbf{p}_1'\mathbf{y}_2,$$

since $\mathbf{p}_1'\mathbf{x}_i = 0$. Thus, because the planes $\mathbf{p}_1'$ and $\mathbf{p}_2'$ are distinct $\mathbf{p}_1'\mathbf{y}_2 \neq 0$ and k is uniquely determined for all possible $\mathbf{x}$. Hence,

$$(8.5) \qquad \mathbf{P}_1 = \mathbf{I} + [\mathbf{S}\mathbf{y}_2 - \mathbf{y}_2]\,\mathbf{p}_1'/(\mathbf{p}_1'\mathbf{y}_2),$$

is the unique invariant plane strain which displaces all vectors in the plane $\mathbf{p}_2'$ to their final positions and leaves the plane $\mathbf{p}_1'$ invariant.

The remaining part of $\mathbf{S}$ is a strain which must leave invariant the plane generated from $\mathbf{p}_2'$ i.e. the plane $\mathbf{p}_2'\mathbf{S}^{-1}$ and it is, therefore, an invariant plane strain on this plane. It must also displace all vectors in the plane $\mathbf{p}_1'$ to their final positions.

The preceding theory can now be applied again provided the planes $\mathbf{p}_1'$ and $\mathbf{p}_2'\mathbf{S}^{-1}$ are distinct. Thus, if $\mathbf{y}_1$ is any vector lying in the plane $\mathbf{p}_1'$ and distinct from $\mathbf{x}_i$ the required additional strain is unique and given by

$$(8.6) \qquad \mathbf{P}_2 = \mathbf{I} + [\mathbf{S}\mathbf{y}_1 - \mathbf{y}_1]\,\mathbf{p}_2'\mathbf{S}^{-1}/(\mathbf{p}_2'\mathbf{S}^{-1}\mathbf{y}_1).$$

The final factorization of $\mathbf{S}$ is therefore

$$(8.7) \qquad \mathbf{S} = \{\mathbf{I} + [\mathbf{S}\mathbf{y}_1 - \mathbf{y}_1]\,\mathbf{p}_2'\mathbf{S}^{-1}/(\mathbf{p}_2'\mathbf{S}^{-1}\mathbf{y}_1)\}\{\mathbf{I} + [\mathbf{S}\mathbf{y}_2 - \mathbf{y}_2]\,\mathbf{p}_1'/(\mathbf{p}_1'\mathbf{y}_2)\}.$$

It is easily verified that the product on the right transforms the three non-coplanar vectors $\mathbf{x}_i,\mathbf{y}_1,\mathbf{y}_2$ into $\mathbf{x}_i,\mathbf{S}\mathbf{y}_1,\mathbf{S}\mathbf{y}_2$ respectively, and so the equality is established independently. This factorization shows that when the planes of the two component strains are known† the direction (and magnitude) of each strain is uniquely determined by the displacement of vectors lying in the invariant plane of the other strain. This has also been demonstrated stereographically by Bowles [3].

It can also be shown that an invariant line strain can always be resolved into two invariant plane strains occurring in arbitrarily chosen directions lying in the plane with the invariant normal. In this case, when the two directions are specified, the plane (and magnitude) of each strain is uniquely determined by the displacement of normals that are invariant to the other strain, i.e., normals to planes containing the direction of the other strain. Thus, if $\mathbf{d}_1,\mathbf{d}_2$ are arbitrarily chosen directions lying in the plane $\mathbf{n}_i'$ with the invariant normal, and $\mathbf{m}_1',\mathbf{m}_2'$ are normals to any planes (except the plane $\mathbf{n}_i'$) containing $\mathbf{d}_1,\mathbf{d}_2$ respectively, then $\mathbf{n}_i'\mathbf{d}_1 = \mathbf{n}_i'\mathbf{d}_2 = 0$ and $\mathbf{m}_1'\mathbf{d}_1 = \mathbf{m}_2'\mathbf{d}_2 = 0$ and the alternative factorization is

$$(8.8) \qquad \mathbf{S} = \{\mathbf{I} - \mathbf{S}\mathbf{d}_2(\mathbf{m}_1'\mathbf{S}^{-1} - \mathbf{m}_1')/(\mathbf{m}_1'\mathbf{d}_2)\}\{\mathbf{I} - \mathbf{d}_1(\mathbf{m}_2'\mathbf{S}^{-1} - \mathbf{m}_2')/(\mathbf{m}_2'\mathbf{S}^{-1}\mathbf{d}_1)\}.$$

Note that $\mathbf{d}_2$ must be distinct from $\mathbf{d}_1$ and $\mathbf{S}^{-1}\mathbf{d}_1$ and that $\mathbf{d}_2$ (like $\mathbf{p}_2'$) is the direction which is transformed by $\mathbf{S}$ into the direction $\mathbf{S}\mathbf{d}_2$ of the second strain.

The equivalence of these two factorizations is ensured by the condition that $\mathbf{S}$ is not itself an invariant plane strain. Provided the plane $\mathbf{p}_1'$ is distinct from the planes $\mathbf{p}_2'$ and $\mathbf{p}_2'\mathbf{S}^{-1}$, the unique directions of displacement determined from the first factorization satisfy the conditions that $\mathbf{d}_1$ is distinct from $\mathbf{d}_2$ and $\mathbf{S}\mathbf{d}_2$; otherwise $\mathbf{S}$ would be an invariant plane strain.‡ The second factorization can, therefore, be applied and, since its result is unique, the planes of the two component strains must be $\mathbf{p}_1'$ and $\mathbf{p}_2'\mathbf{S}^{-1}$. When $\mathbf{S}$ is itself an invariant plane strain, the two factorizations, although valid, lead to mutually exclusive sets of possibilities.

Equations (8.7) and (8.8) enable any invariant line strain to be factorized into two invariant plane strains in a double infinity of ways. It remains to show how the requirement that the second component strain be a simple shear in a known direction (or on a known plane) determines a unique factorization except in certain special cases. In the present problem the known direction (plane) is of course a twinning direction (plane) of the final structure.

If the direction $\mathbf{S}\mathbf{d}_2$ (and hence $\mathbf{d}_2$) of the second strain is known, the plane $\mathbf{p}_1'$ of the first strain is uniquely determined by equation (8.8). Further, the plane $\mathbf{p}_2'\mathbf{S}^{-1}$ (and hence $\mathbf{p}_2'$) of the second strain is uniquely determined by the condition that it contain the shear direction $\mathbf{S}\mathbf{d}_2$ and the invariant line $\mathbf{x}_i$, provided these are not in the same direction, and provided $\mathbf{S}$ is not itself an invariant plane strain. Using these two uniquely determined planes, equation (8.7) gives the required unique factorization. Alternatively, if the plane $\mathbf{p}_2'\mathbf{S}^{-1}$ is known, $\mathbf{d}_1$ is determined and $\mathbf{S}\mathbf{d}_2$ must be the intersection of the plane $\mathbf{p}_2'\mathbf{S}^{-1}$ and the plane with the invariant normal $\mathbf{n}_i'$ (unless, of course, these normals coincide), and equation (8.8) gives the

†Although the planes $\mathbf{p}'_1$, $\mathbf{p}'_2$ can be chosen in a double infinity of ways, there is a minor physical restriction on this choice. The volume must not pass through zero during either of the component strains and so $\mathbf{p}'_2\mathbf{S}\mathbf{y}_2/\mathbf{p}'_1\mathbf{y}_2 > 0$ and $\mathbf{p}'_2\mathbf{y}_1/\mathbf{p}'_2\mathbf{S}^{-1}\mathbf{y}_1 > 0$. These conditions are always satisfied when one component is a simple shear.

‡It is easily shown that

$$\mathbf{S} = \{\mathbf{I} + \mathbf{S}\mathbf{d}_2\mathbf{p}_2'\mathbf{S}^{-1}\}\{\mathbf{I} + \mathbf{d}_1\mathbf{p}_1'\},$$
$$= \{\mathbf{I} + \mathbf{d}_1\mathbf{p}_1'\}\{\mathbf{I} + \mathbf{d}_2\mathbf{p}_2'\},$$

are alternative factorizations of $\mathbf{S}$.

required result. Similar arguments can be used if the first strain is to be a simple shear (see footnote on p. 136).

A convenient way of determining the plane and direction of $\mathbf{P}_1$, when $\mathbf{P}_2$ is a simple shear, is as follows. Since $\mathbf{Sd}_2$ and $\mathbf{p}_2'\mathbf{S}^{-1}$ are invariant to $\mathbf{P}_2$, $\mathbf{P}_1$ must have displaced $\mathbf{d}_2$ and $\mathbf{p}_2'$ to their final positions. Thus, $\mathbf{P}_1\mathbf{d}_2 = \mathbf{Sd}_2$, $\mathbf{p}_2'\mathbf{P}_1^{-1} = \mathbf{p}_2'\mathbf{S}^{-1}$ and so

$$\left.\begin{array}{l}\mathbf{d}_1 \text{ parallel to } \mathbf{Sd}_2 - \mathbf{d}_2,\\ \mathbf{p}_1' \text{ parallel to } \mathbf{p}_2'\mathbf{S}^{-1} - \mathbf{p}_2'.\end{array}\right\} \tag{8.9}$$

9. Conclusion

It has been shown that the change in shape that accompanies the formation of a martensite plate can be described by an invariant plane strain together possibly with a small dilatation. Further, for transformations which produce twinned martensite plates, the assumption that the complementary strain is an invariant plane strain has been shown to imply that it is a simple shear on the twinning plane or in the twinning direction of the final structure. Finally, it has been shown how either of these conditions determines a unique resolution of the total strain into suitable homogeneous and complementary strains.

The question that now arises is which of these conditions applies in any specific transformation? Since the interface between the twins has been found in all cases so far analysed to be the twinning plane [2; 10; 4; 12], shearing on this plane is more likely to be the relevant condition. However, in all cases where the transformation has been consistently resolved into component strains [3; 4; 12] it has been found that the complementary strain is part of the twinning shear. We therefore propose as a working hypothesis that both conditions are simultaneously satisfied for all martensite transformations.* The fact that twins have not been observed in all transformations does not detract from this hypothesis; for the physical processes involved in producing the twin orientations are not, in general, equivalent (they have different orientation relationships) and one of the twin orientations may not be formed for energetic reasons.

This hypothesis imposes certain restrictions on the nature of the total strain $\mathbf{S}_t$. The complementary strain can be a part of a twinning shear, only if the invariant line strain derived from $\mathbf{S}_t$ (by removing the appropriate dilatation) is such that the invariant line lies in the twinning plane, and the plane with the invariant normal contains the twinning direction. In principle, when the correspondence is known, it should be possible to check the validity of these requirements by measuring the orientation relationship. Unfortunately, however, variations in orientation within the usual experimental error of about $\frac{1}{2}$ degree can sometimes cause large movements of unrotated lines and planes, so that this test alone is likely to be inconclusive.

For this reason a different procedure will be adopted in subsequent papers. It will be shown in Part II that the above requirements of the hypothesis, together with the correspondence and the dimensions of the initial and final lattices, determine $\mathbf{S}_t$ (and hence the orientation relationship) apart from a single parameter. If a value of this parameter can be chosen to give agreement with, say, the observed habit plane, $\mathbf{S}_t$ can then be calculated and the factorization carried out.

The first test of the hypothesis is, of course, to see whether the observed habit plane is compatible with any value of the unknown parameter. If this is so, the hypothesis can be tested further by comparing the predicted direction of the first invariant plane strain and the predicted orientation relationship with those measured experimentally.

*In discussing the results of Machlin and Cohen [5] the authors have suggested that shearing in the twinning direction is the relevant condition, and Machlin and Cohen's results appear to lend support to this view. However, in Part III of this series, Machlin and Cohen's experimental data will be shown to be compatible with the present hypothesis.

Acknowledgment

The authors are indebted to Professor T. M. Cherry for helpful discussions during the preparation of the manuscript.

References

1. GRENINGER, A. B. and TROIANO, A. R. Trans. Amer. Inst. Min. Met. Eng. **145** (1941) 289.
2. GRENINGER, A. B. and TROIANO, A. R. Trans. Amer. Inst. Min. Met. Eng. **185** (1949) 590.
3. BOWLES, J. S. Acta Cryst. **4** (1951) 162.
4. BOWLES, J. S., BARRETT, C. S. and GUTTMAN, L. Trans. Amer. Inst. Min. Met. Eng. **188** (1950) 1478.
5. MACHLIN, E. S. and COHEN, M. J. Metals **3** (1951) 1019. See Discussion by Bowles and Mackenzie. J. Metals **4** (1952) 1201.
6. JASWON, M. A. and WHEELER, J. A. Acta Cryst. **1** (1948) 216.
7. BOWLES, J. S. and BARRETT, C. S. Progress in Metal Physics. III (London, Pergamon Press, 1952).
8. CHANG, L. C. Acta Cryst. **4** (1951) 320.
9. SCHMID, E. and BOAS, W. Plasticity of Crystals, §33 (English translation, London, Hughes, 1950).
10. GRENINGER, A. B. Trans. Amer. Inst. Min. Met. Eng. **133** (1939) 204.
11. JEFFREYS, H. and JEFFREYS, B. Methods of Mathematical Physics (Cambridge, University Press, 1946). Chaps. 2 and 4.
12. BASINSKI, Z. S. and CHRISTIAN, J. W. J. Inst. Metals **80** (1952) 659.

THE CRYSTALLOGRAPHY OF MARTENSITE TRANSFORMATIONS II*

J. K. MACKENZIE and J. S. BOWLES†

The hypothesis advanced in Part I requires that the total strain in a martensite transformation be such that a twinning direction in the final structure lie in an unrotated plane and the twinning plane contain an unrotated line of the strain. From these conditions, together with the correspondence, and the dimensions of the initial and final structures, an explicit expression for the total strain is obtained. Hence, the orientation relationship and the component strains are determined.

LA CRISTALLOGRAPHIE DES TRANSFORMATIONS MARTENSITIQUES II

L'hypothèse proposée dans la première partie exige, que lors d'une transformation martensitique, la déformation totale soit compatible avec un arrangement par lequel une direction de maclage, dans la structure finale, soit comprise dans un plan qui n'a pas tourné, et que le plan de maclage renferme une ligne de déformation qui n'a pas tourné. Ces conditions, en même temps que le rapport entre le réseau initial et le réseau final, ainsi que leurs dimensions, conduisent à une expression explicite de la déformation totale. De là on peut déterminer la relation d'orientation et les composantes de déformation.

DIE KRISTALLOGRAPHIE DER MARTENSIT-TRANSFORMATIONEN II

Die in Teil I dargestellte Hypothese verlangt, dass die Gesamtverzerrung in einer Martensit Transformation so gestaltet ist, dass die Zwillingsrichtung der Endstruktur in einer Ebene liegt, die in der Transformation nicht rotierte, und die Zwillingsebene eine nicht rotierte Grade des Verzerrungstensors enthält. Aus diesen Bedingungen zusammen mit ihrer notwendigen Gleichzeitigkeit und den Dimensionen der ursprünglichen und der Endstruktur wurde ein expliziter Ausdruck für die Gesamtverzerrung erhalten. Folglich sind damit die Beziehungen der kristallographischen Orientierungen und die Verzerrungskomponenten bestimmt.

1. Introduction

In Part I it has been shown that the displacements of atoms in martensite transformations can be described consistently by means of a homogeneous strain, which is defined by the change in external shape produced by the transformation, together with inhomogeneous displacements which produce no observable change in shape. The homogeneous strain is composed of an invariant plane strain and, possibly, a small dilatation. Within sufficiently small volumes the inhomogeneous displacements can be described by a homogeneous strain, and the hypothesis has been advanced that this homogeneous strain, which is called the complementary strain, is part of a twinning shear in the final structure. The hypothesis requires the twinning direction to lie in a plane which is not rotated by the total strain and the twinning plane to contain the corresponding unrotated line. It has also been shown that, provided the total strain satisfies these conditions, its resolution into components of the required type is always possible and is uniquely determined.

In this paper it will be shown that the above conditions, together with the correspondence between the initial and final structures and their dimensions, determine the total strain, apart from a correction due to the small dilatation mentioned above. The total strain will be calculated explicitly and all the geometrical features of the transformation, including the orientation relationship, can then be determined, apart from this small correction. In particular, the normal to the habit plane should lie in a certain surface and this can be checked experimentally; if so, its precise direction can be used to fix the unknown small dilatation.

When twins are formed it is unlikely that the two correspondences are not crystallographically equivalent. If they are equivalent, it will be shown that the twinning direction is determined when the twinning plane is known and that this plane must be generated from a plane of symmetry in the initial structure. The initial structure would then have at least the symmetry of a monoclinic crystal.

2. Notation

The notation used in the present paper conforms with that used in Part I. However, some extension is necessary to deal adequately with the problems that arise when the same vector or strain has to be referred to different bases. The extension consists in adjoining basis symbols A, B, etc., as indicated below.

(a) *Vectors*

The set of non-coplanar base vectors $\mathbf{a}_1$, $\mathbf{a}_2$, $\mathbf{a}_3$, will be described as the basis A. The column matrix, whose elements are the components of a

*Received February 9, 1953.
†Division of Tribophysics, University of Melbourne, Victoria, Australia.

vector $\mathbf{x}$ relative to this basis will be written in extended notation as

$$\mathbf{x} = [x_1,x_2,x_3]_A = [\mathrm{A};\mathbf{x}], \tag{2.1}$$

while the transpose of $\mathbf{x}$ will be written

$$\mathbf{x}' = (x_1,x_2,x_3)_A = (\mathbf{x};\mathrm{A}). \tag{2.2}$$

Note that transposition is denoted both by a change in the type of bracket and by the reversal of the order of the symbols. This reversal of order ensures that, in products, like basis symbols occur in adjacent positions.

(*b*) *Metric and Scalar Product*

The metric associated with the basis A will be written $(\mathrm{A}^*\mathbf{G}\mathrm{A})$. The relation $\mathbf{x}^* = \mathbf{G}\mathbf{x}$ between the components of $\mathbf{x}$ referred to the reciprocal basis A^* and its components referred to the basis A becomes

$$[\mathrm{A}^*;\mathbf{x}] = (\mathrm{A}^*\mathbf{G}\mathrm{A})[\mathrm{A};\mathbf{x}]. \tag{2.3}$$

Since the metric is symmetrical

$$(\mathrm{A}^*\mathbf{G}\mathrm{A})' = (\mathrm{A}^*\mathbf{G}\mathrm{A}), \tag{2.4}$$

and the scalar product

$$\mathbf{x}.\mathbf{y} = (\mathbf{x};\mathrm{A}^*)[\mathrm{A};\mathbf{y}] = (\mathbf{x};\mathrm{A})(\mathrm{A}^*\mathbf{G}\mathrm{A})[\mathrm{A};\mathbf{y}]. \tag{2.5}$$

(*c*) *Strains*

A homogeneous strain $\mathbf{S}$ transforms a point with position vector $\mathbf{x}$ into a point with position vector $\mathbf{y}$. When these vectors are referred to the basis A this transformation will be written

$$[\mathrm{A};\mathbf{y}] = (\mathrm{A}\mathbf{S}\mathrm{A})[\mathrm{A};\mathbf{x}], \quad \mathbf{y} = \mathsf{S}\mathbf{x}, \tag{2.6}$$

where $(\mathrm{A}\mathbf{S}\mathrm{A}) = \mathbf{S}$ is the matrix representation of $\mathbf{S}$ referred to the basis A. Note that letters in **bold face type** stand for physical entities, and that the extended notation is simply a way of denoting their matrix representations relative to explicitly specified bases. When there is no doubt which bases are involved these matrices are denoted by the corresponding symbol in **sans serif type**, as in Part I.

A plane with normal $\mathbf{n}$ is transformed by the strain $\mathbf{S}$ into a plane with normal $\mathbf{m}$ given by

$$(\mathbf{m};\mathrm{A}^*) = (\mathbf{n};\mathrm{A}^*)(\mathrm{A}\mathbf{S}\mathrm{A})^{-1}. \tag{2.7}$$

The basis symbols A and A^* are adjacent in this relation because $(\mathrm{A}\mathbf{S}\mathrm{A})^{-1}$ has been substituted for $(\mathrm{A}^*\mathbf{S}^*\mathrm{A}^*)'$, where $\mathbf{S}^*$ is the corresponding strain in the reciprocal lattice.

(*d*) *Change of Basis*

The components of any vector $\mathbf{x}$ referred to a new basis B, comprised of the vectors $\mathbf{b}_1$, $\mathbf{b}_2$, $\mathbf{b}_3$, are related to the components of the same vector referred to the old basis A by the transformation

$$[\mathrm{B};\mathbf{x}] = (\mathrm{B}\mathbf{T}\mathrm{A})[\mathrm{A};\mathbf{x}], \tag{2.8}$$

where $(B\mathbf{T}A)$ is a non-singular matrix. The successive columns of this matrix are the components of the old base vectors $\mathbf{a}_1 = [100]_A$, $\mathbf{a}_2 = [010]_A$, $\mathbf{a}_3 = [001]_A$ referred to the new basis B.

The **bold face** symbol $\mathbf{T}$ can be interpreted either as representing the process of transforming from one basis to another (A to B, say), or as a function symbol operating on the basis symbols A and B to give the matrix representation $(\mathrm{B}\mathbf{T}\mathrm{A})$ of the transformation process. Thus, $(\mathrm{A}\mathbf{T}\mathrm{B})$ is the matrix representation of the transformation from the basis B to the basis A. If

$$(\mathrm{B}\mathbf{T}\mathrm{A}) = \mathsf{T}, \tag{2.9}$$

then it follows that

$$(\mathrm{A}\mathbf{T}\mathrm{B}) = (\mathrm{B}\mathbf{T}\mathrm{A})^{-1} = \mathsf{T}^{-1}. \tag{2.10}$$

Similarly, to preserve the juxtaposition of like basis symbols it is convenient to introduce another function symbol $\mathbf{T}'$ (different from $\mathbf{T}$) defined by

$$(\mathrm{B}\mathbf{T}\mathrm{A})' = (\mathrm{A}\mathbf{T}'\mathrm{B}) = \mathsf{T}'. \tag{2.11}$$

The transformation of components of normals (referred to the reciprocal basis) is clearly

$$[\mathrm{B}^*;\mathbf{n}] = (\mathrm{B}^*\mathbf{T}\mathrm{A}^*)[\mathrm{A}^*;\mathbf{n}],$$

which becomes on transposition

$$(\mathbf{n};\mathrm{B}^*) = (\mathbf{n};\mathrm{A}^*)(\mathrm{A}^*\mathbf{T}'\mathrm{B}^*).$$

However, it can be shown that $(\mathrm{A}^*\mathbf{T}'\mathrm{B}^*) = (\mathrm{A}\mathbf{T}\mathrm{B})$ and so the convenient relation

$$(\mathbf{n};\mathrm{B}^*) = (\mathbf{n};\mathrm{A}^*)(\mathrm{A}\mathbf{T}\mathrm{B}), \tag{2.12}$$

is obtained.

The convenience of the extended notation is clearly illustrated by the following transformation formulae. The metric $(\mathrm{B}^*\mathbf{G}\mathrm{B})$ corresponding to the new basis B is given by

$$\begin{aligned}(\mathrm{B}^*\mathbf{G}\mathrm{B}) &= (\mathrm{B}^*\mathbf{T}\mathrm{A}^*)(\mathrm{A}^*\mathbf{G}\mathrm{A})(\mathrm{A}\mathbf{T}\mathrm{B}),\\ &= (\mathrm{B}\mathbf{T}'\mathrm{A})(\mathrm{A}^*\mathbf{G}\mathrm{A})(\mathrm{A}\mathbf{T}\mathrm{B}).\end{aligned} \tag{2.13}$$

Similarly, the strain $\mathbf{S}$ referred to the new basis becomes

$$(\mathrm{B}\mathbf{S}\mathrm{B}) = (\mathrm{B}\mathbf{T}\mathrm{A})(\mathrm{A}\mathbf{S}\mathrm{A})(\mathrm{A}\mathbf{T}\mathrm{B}). \tag{2.14}$$

The following relations between strains and axis transformations are often useful. Since the suc-

cessive columns of a strain matrix $({}_A\mathbf{S}_A)$ are the components relative to the basis A of the vectors ${}_S A$ into which the base vectors A are transformed by the strain, it follows that

$$({}_A\mathbf{S}_A) = ({}_A\mathbf{T}_{S\,A}). \tag{2.15}$$

Hence, the strain $\mathbf{S}$ which transforms the set of vectors B into the set C is given by

$$\begin{aligned}({}_A\mathbf{S}_A) &= ({}_A\mathbf{T}_B)({}_B\mathbf{S}_B)({}_B\mathbf{T}_A),\\ &= ({}_A\mathbf{T}_B)({}_B\mathbf{T}_C)({}_B\mathbf{T}_A),\\ &= ({}_A\mathbf{T}_C)({}_B\mathbf{T}_A).\end{aligned} \tag{2.16}$$

Note that the substitution for $({}_B\mathbf{S}_B)$ immediately means that like basis symbols are no longer adjacent.

3. Correspondences

In Part I it was shown that a martensite transformation can be described, at least locally, by a homogeneous strain $\mathbf{S}_t$. This total strain clearly defines a one to one correspondence between lattice vectors in the initial and final lattices. Although $\mathbf{S}_t$ is not known, the associated correspondence can be determined from physical considerations [1; 2]. It will be shown that this correspondence provides an essential piece of information in the calculation of the total strain.

The initial and final lattices $\mathscr{A}$ and $\mathscr{B}$ can be described by means of bases A and B and their associated metrics $({}_A{}^*\mathbf{G}_A)$ and $({}_B{}^*\mathbf{G}_B)$. The correspondence associates every lattice vector $[{}_A\,;\mathbf{x}]$ in $\mathscr{A}$ with a unique lattice vector $[{}_B\,;\mathbf{y}]$ in $\mathscr{B}$, and can be described by the relation*

$$[{}_B\,;\mathbf{y}] = ({}_B\mathbf{C}_A)[{}_A\,;\mathbf{x}], \tag{3.1}$$

where $({}_B\mathbf{C}_A)$ is a non-singular matrix which has integral elements and determinant ± 1 provided the bases A and B both define primitive unit cells. The successive columns of $({}_B\mathbf{C}_A)$ are the components referred to the basis B of the lattice vectors, ${}_C A$, in $\mathscr{B}$ which correspond to the base vectors A in $\mathscr{A}$. By a suitable choice of bases the correspondence matrix can always be made the identity matrix; for example, $({}_{C\,A}\mathbf{C}_A) = \mathbf{I}$.

The above correspondence between vectors implies that points in a plane with normal $\mathbf{m}$ in $\mathscr{B}$ given by

$$(\mathbf{m}\,;{}_B{}^*) = (\mathbf{n}\,;{}_A{}^*)({}_A\mathbf{C}_B), \tag{3.2}$$

correspond to points in the plane with normal $\mathbf{n}$ in $\mathscr{A}$. The correspondence can be referred to new bases in the lattices $\mathscr{A}$ and $\mathscr{B}$ as follows

$$({}_{B'}\mathbf{C}_{A'}) = ({}_{B'}\mathbf{T}_B)({}_B\mathbf{C}_A)({}_A\mathbf{T}_{A'}). \tag{3.3}$$

4. Principal Axes of the Total Strain

When a body undergoes a homogeneous strain there is always at least one set of mutually orthogonal directions, called the principal axes, which are transformed into a set of orthogonal directions by the strain. It is clear that the correspondence between two known lattices $\mathscr{A}$ and $\mathscr{B}$ determines the initial and final angle between pairs of corresponding lattice vectors, and hence the principal axes. It can be shown that the principal axes are determined by the non-zero solutions for $[{}_A\,;\mathbf{x}]$ of the equations

$$\{({}_A\mathbf{C}'_B)({}_B{}^*\mathbf{G}_B)({}_B\mathbf{C}_A) - \mu^2({}_A{}^*\mathbf{G}_A)\}[{}_A\,;\mathbf{x}] = 0, \tag{4.1}$$

where μ^2 must satisfy the determinantal equation

$$|\mathsf{C}'\mathsf{G}_B\mathsf{C} - \mu^2\mathsf{G}_A| = 0, \tag{4.2}$$

using an obvious notation. Since G_A and G_B are symmetric positive definite matrices this equation gives three positive values of μ^2 and the three associated vectors $[{}_A\,;\mathbf{x}_r]$ where $r = 1, 2, 3$, can always be chosen to be mutually orthogonal unit vectors [3].

The identification of the vectors so determined with the principal axes is made as follows. Let $\mathbf{y}_1, \mathbf{y}_2, \mathbf{y}_3$ be the vectors in $\mathscr{B}$ which correspond to the above $\mathbf{x}_1, \mathbf{x}_2, \mathbf{x}_3$. Then,

$$\begin{aligned}\mathbf{y}_1.\mathbf{y}_2 &= (\mathbf{y}_1\,;{}_B)({}_B{}^*\mathbf{G}_B)[{}_B\,;\mathbf{y}_2],\\ &= (\mathbf{x}_1\,;{}_A)({}_A\mathbf{C}'_B)({}_B{}^*\mathbf{G}_B)({}_B\mathbf{C}_A)[{}_A\,;\mathbf{x}_2].\end{aligned}$$

On multuplying equation (4.1) on the left by $(\mathbf{x}_1\,;{}_A)$ and putting $\mathbf{x} = \mathbf{x}_2$ and $\mu^2 = \mu_2^2$, it follows that

$$\mathbf{y}_1.\mathbf{y}_2 = \mu_2^2\mathbf{x}_1.\mathbf{x}_2, \tag{4.3}$$

and, since $\mathbf{x}_1$ and $\mathbf{x}_2$ are perpendicular, $\mathbf{y}_1$ and $\mathbf{y}_2$ are also perpendicular. Further, a similar calculation gives $\mathbf{y}_1.\mathbf{y}_1 = \mu_1^2\mathbf{x}_1.\mathbf{x}_1$ so that μ_1^2 is the square of the ratio of the final to the initial length of $\mathbf{x}_1$. Other pairs of these vectors behave similarly. Thus, the mutually perpendicular vectors $\mathbf{x}_1, \mathbf{x}_2, \mathbf{x}_3$ correspond to mutually perpendicular vectors $\mathbf{y}_1, \mathbf{y}_2, \mathbf{y}_3$ and μ_1, μ_2, μ_3 determine the corresponding principal strains.

If the orthonormal set of vectors $\mathbf{x}_1, \mathbf{x}_2, \mathbf{x}_3$ is taken as a new basis P in $\mathscr{A}$ and the corresponding orthogonal set $\mathbf{y}_1, \mathbf{y}_2, \mathbf{y}_3$ as a new basis P_f in $\mathscr{B}$, then in terms of these bases the correspondence matrix

*It should be remembered that in the present problem $({}_B\mathbf{C}_A)$ only describes the correspondence within the small homogeneously strained regions.

$({}_P\mathbf{C}_{P_f})$ and the metric $({}_{P^*}\mathbf{G}_P)$ are both identity matrices. The successive columns of the transformation matrix $({}_A\mathbf{T}_P)$ are the components of $\mathbf{x}_1, \mathbf{x}_2, \mathbf{x}_3$ referred to A which have just been determined; the corresponding transformation in $\mathscr{B}$ is given by

(4.4)
$$({}_B\mathbf{T}_{P_f}) = ({}_B\mathbf{C}_A)({}_A\mathbf{T}_P)({}_P\mathbf{C}_{P_f}) = ({}_B\mathbf{C}_A)({}_A\mathbf{T}_P)$$

Further, on introducing the diagonal matrix $\mathbf{M}^2$, with diagonal elements $\mu_1^2, \mu_2^2, \mu_3^2$, the three equations obtained from (4.1) by putting $\mathbf{x} = \mathbf{x}_1$, $\mu^2 = \mu_1^2$ *etc.* can be compactly written

$$\mathbf{C}'\mathbf{G}_B\mathbf{C}({}_A\mathbf{T}_P) = \mathbf{G}_A({}_A\mathbf{T}_P)\mathbf{M}^2. \tag{4.5}$$

On multiplying this equation on the left by $({}_P\mathbf{T}'_A)$ and using (2.13) for transforming metrics, together with (4.4) it follows that

$$({}_{P_f^*}\mathbf{G}_{P_f}) = \mathbf{M}^2, \tag{4.6}$$

is the new metric in $\mathscr{B}$. The matrix $\mathbf{M}$ represents the strain referred to P which merely extends the base vectors P to their final lengths without rotation.

When the relation between the bases A and B is known the strain associated with the correspondence $({}_B\mathbf{C}_A)$ is clearly

$$\mathbf{S} = ({}_A\mathbf{S}_A) = ({}_A\mathbf{T}_B)({}_B\mathbf{C}_A). \tag{4.7}$$

Using equation (2.13), it follows that

$$\mathbf{S}'\mathbf{G}_A\mathbf{S} = \mathbf{C}'\mathbf{G}_B\mathbf{C}, \tag{4.8}$$

so that the principal axes and their associated principal strains can equally be determined when $\mathbf{S}$ is given.

5. Determination of the Total Strain

The total strain $\mathbf{S}_t$ is required to transform a lattice $\mathscr{A}$ into a lattice $\mathscr{B}$ in accordance with a specified correspondence. The invariant line strain $\mathbf{S}$, derived from $\mathbf{S}_t$ by the removal of a suitable dilatation $\mathbf{I}/\delta$, is to satisfy the conditions that a twinning plane in lattice $\mathscr{B}$ contains the invariant line of $\mathbf{S}$ and that the associated twinning direction in lattice $\mathscr{B}$ lies in the plane with the invariant normal (§7, Part I).

The results of the last two sections show that the correspondence, together with the two metrics, determines a set of principal axes P in $\mathscr{A}$ and a diagonal matrix $\mathbf{M}$ that represents the strain (referred to P) which extends all vectors to their final lengths but does not rotate the principal axes. It follows that the total strain is given by

$$\mathbf{S}_t = ({}_P\mathbf{S}_{t\,P}) = \mathbf{RM}, \tag{5.1}$$

and

$$\mathbf{S} = ({}_P\mathbf{S}_P) = \delta\mathbf{RM}, \tag{5.2}$$

where $\mathbf{R}$ is the matrix which describes the rotation of the principal axes to their final directions.* It remains to show that the other conditions effectively determine $\mathbf{R}$ and hence the orientation relationship.

In the remainder of this section all strains and vectors will be referred to the basis P in $\mathscr{A}$. Since these other conditions are given relative to the lattice $\mathscr{B}$, it is necessary first to find equivalent conditions referred to the lattice $\mathscr{A}$. It was shown in Part I that the displacement of any point by the invariant line strain $\mathbf{S}$ lies in the plane with the invariant normal. Since the final position of the twinning direction in $\mathscr{B}$ is to lie in this plane, so must the direction in $\mathscr{A}$ from which it is generated. This initial direction is determined from the twinning direction by means of the correspondence. A similar argument shows that the plane from which the twinning plane is generated contains the invariant line.

Unit vectors $\mathbf{u}$ and $\mathbf{h}$ in the known initial positions of the twinning direction and the normal to the twinning plane will be denoted in *all* succeeding sections by

$$[\mathrm{P}\,;\mathbf{u}] = \mathbf{u},\ (\mathbf{h};\,\mathrm{P}^*)' = [\mathrm{P}\,;\mathbf{h}] = \mathbf{h}, \tag{5.3}$$

respectively.† Thus, a unit vector $\mathbf{x}_i$ parallel to the invariant line of $\mathbf{S}$ lies in the plane with normal $\mathbf{h}$, while a unit vector $\mathbf{n}_i$ parallel to the invariant normal lies in the plane with normal $\mathbf{u}$. It will now be shown that the possible positions of $\mathbf{x}_i$ and $\mathbf{n}_i$ in their respective planes are determined by the condition that $\mathbf{S}$ leaves their lengths unchanged. The further condition that they are not rotated by $\mathbf{S}$ then determines the rotation $\mathbf{R}$.

Since the rotational part, $\mathbf{R}$, of $\mathbf{S}$ does not change the length of any vector, all changes in length must be due entirely to $\delta\mathbf{M}$. Thus, if a unit vector $\mathbf{x}$ lies in the plane with normal $\mathbf{h}$ and is not changed in length by $\mathbf{S}$

$$\left.\begin{aligned} \mathbf{h}'\mathbf{x} &= 0, \\ \mathbf{x}'\mathbf{x} &= 1, \\ \text{and}\qquad \delta^2\mathbf{x}'\mathbf{M}^2\mathbf{x} &= \mathbf{x}'\mathbf{x} = 1, \end{aligned}\right\} \tag{5.4}$$

because the strain $\delta\mathbf{M}$ changes $\mathbf{x}$ into $\delta\mathbf{M}\mathbf{x}$. The $\mathbf{x}$ satisfying these three equations lie respectively on a plane, a sphere and an ellipsoid. The intersections

*Since P is an orthonormal basis $\mathbf{RR}' = \mathbf{I}$, and $\mathbf{S}_t'\mathbf{S}_t = \mathbf{M}^2$.
†The bases P, P* are identical since both are orthonormal.

of the circle and the ellipse, defined by the intersection of the plane with the sphere and the ellipsoid respectively, give the $\mathbf{x}$ satisfying all three equations. Provided the elements of $\delta\mathbf{M}$ lie between certain limits two possible $\mathbf{x}$ are thereby determined and these give the possible positions of the invariant line $\mathbf{x}_i$.

The corresponding equations for determining a unit normal $\mathbf{n}$ which lies in the plane with normal $\mathbf{u}$ and is not changed in length are

$$\left.\begin{aligned} \mathbf{n}'\mathbf{u} &= 0, \\ \mathbf{n}'\mathbf{n} &= 1, \\ \mathbf{n}'\mathbf{M}^{-2}\mathbf{n} &= \delta^2. \end{aligned}\right\} \tag{5.5}$$

These likewise determine two possible positions of the invariant normal $\mathbf{n}_i$. Further, the angle between an $\mathbf{x}$ and an $\mathbf{n}$, determined by equations (5.4) and (5.5), is left unchanged by the strain $\delta\mathbf{M}$. This follows, since $\mathbf{n}$ is transformed into $\delta^{-1}\mathbf{M}^{-1}\mathbf{n}$, and $\mathbf{x}$ into $\delta\mathbf{M}\mathbf{x}$, so that $(\delta^{-1}\mathbf{M}^{-1}\mathbf{n})'\,\delta\mathbf{M}\mathbf{x} = \mathbf{n}'\mathbf{x}$, identically.

There are now four possible ways of identifying the pair of vectors $\mathbf{x}_i$ and $\mathbf{n}_i$ with the possible $\mathbf{x}$ and $\mathbf{n}$. This multiplicity of possible solutions will be considered in detail later (§§8, 9), but having made a choice, the rotation matrix $\mathbf{R}$ is uniquely determined as follows. The strain $\mathbf{S}$ is composed of $\delta\mathbf{M}$ followed by the rotation $\mathbf{R}$. Since the direction $\mathbf{x}_i$ and the normal $\mathbf{n}_i$ are not rotated by $\mathbf{S}$, it follows that $\mathbf{R}$ is the unique rotation which reverses the rotations of $\mathbf{x}_i$ and $\mathbf{n}_i$ due to $\delta\mathbf{M}$. Both the lengths of $\mathbf{x}_i$ and $\mathbf{n}_i$ and the angle between them are not changed by $\delta\mathbf{M}$, so this restoration can always be accomplished by a rotation.

It is now clear that the conditions imposed determine four distinct possible total strains. Thus, the whole problem is, in principle, solved. However, the direct calculation of $\mathbf{R}$, as above, is complicated and this is avoided in the calculation of $\mathbf{S}$ in the next section.

6. Calculation of the Invariant Line Strain

The explicit calculation of the invariant line strain $\mathbf{S}$ will be carried out in two stages. The first step is to calculate the strain $\mathbf{S}_1$ which, (*a*) has an invariant line lying in the plane with normal $\mathbf{h}$, (*b*) has the specified principal axes P, with their correct extensions, and (*c*) leaves the plane with normal $\mathbf{h}$ unrotated. This strain satisfies all requirements except that its invariant normal does not necessarily lie in the plane with normal $\mathbf{u}$. The required invariant line strain can only differ from $\mathbf{S}_1$ by a rotation about the invariant line, since this is the only additional strain which affects neither the invariant line nor the principal axes and their extensions. The second step, therefore, is to determine a rotation $\mathbf{R}_1$ about the invariant line, such that in the combination of $\mathbf{S}_1$ with $\mathbf{R}_1$ the invariant normal lies in the plane with normal $\mathbf{u}$.

The simplest way to define the positions of the invariant line, and the invariant normal, relative to known directions, is to introduce the orthonormal basis I for which

$$(6.1)\quad \mathbf{i}_2 = [\mathrm{P}\,;\mathbf{i}_2] = \mathbf{u},\ \mathbf{i}_3 = [\mathrm{P}\,;\mathbf{i}_3] = \mathbf{h},\ \mathbf{i}_1 = \mathbf{i}_2 \times \mathbf{i}_3.$$

The positions of the invariant line $\mathbf{x}_i$ and the invariant normal $\mathbf{n}_i$ in the planes with normals $\mathbf{h}$ and $\mathbf{u}$ are then fixed relative to the vector $\mathbf{i}_1$ by the angles α and β shown in Fig. 1. Thus,

$$(6.2)\quad [\mathrm{I}\,;\mathbf{x}_i] = \mathbf{x}_i = [\cos\alpha,\ \sin\alpha,\ 0]_I,$$

$$(6.3)\quad (\mathbf{n}_i\,;\mathrm{I}) = \mathbf{n}_i' = (\cos\beta,\ 0,\ \sin\beta)_I,$$

are unit vectors in the required planes.

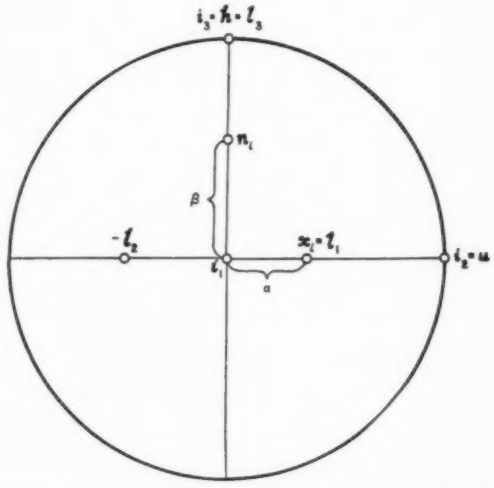

FIGURE 1. Stereographic projection showing the orientations of the bases I and L relative to the twinning plane normal $\mathbf{h}$ and the twinning direction $\mathbf{u}$.

The equations determining α and β are derived, as before, by equating to unity the final lengths of these vectors after the strain $\mathbf{S}$. Since the metric associated with the basis I is identity, the square of the final length of any vector $\mathbf{x}$ after the strain $\mathbf{S}$ is

$$(6.4)\quad (\mathbf{x}\,;\mathrm{I})(\mathrm{I}\mathbf{S}\mathrm{I})'(\mathrm{I}\mathbf{S}\mathrm{I})[\mathrm{I}\,;\mathbf{x}],$$

and because $(\mathrm{I}\mathbf{S}_1\mathrm{I})$ only differs from $(\mathrm{I}\mathbf{S}\mathrm{I})$ by a rotation, $\mathbf{S}_1$ may be substituted for $\mathbf{S}$. Now,

$$\begin{aligned} (\mathrm{I}\mathbf{S}\mathrm{I})'(\mathrm{I}\mathbf{S}\mathrm{I}) &= (\mathrm{I}\mathbf{T}'\mathrm{P})(\mathrm{P}\mathbf{S}\mathrm{P})'(\mathrm{P}\mathbf{S}\mathrm{P})(\mathrm{P}\mathbf{T}\mathrm{I}), \\ &= (\mathrm{I}\mathbf{T}'\mathrm{P})\,\delta^2\mathbf{M}^2(\mathrm{P}\mathbf{T}\mathrm{I}) \\ &= (\mathrm{S}\mathrm{I}^*\mathbf{G}\mathrm{S}\mathrm{I}) = \mathbf{G} \end{aligned} \tag{6.5}$$

where S1 is the basis generated from 1 by the strain.

To evaluate $\mathbf{G}$, and so determine the square of the final length of $\mathbf{x}$, the transformation matrix ($_P\mathbf{T}_1$) must be found. The successive columns of ($_P\mathbf{T}_1$) are the components of the vectors $\mathbf{i}_1$, $\mathbf{i}_2$, $\mathbf{i}_3$ referred to the basis P, and this is conveniently indicated by the notation

$$(6.6) \qquad (_P\mathbf{T}_1) = (\mathbf{i}_1, \mathbf{i}_2, \mathbf{i}_3) = (\mathbf{i}_1, \mathbf{u}, \mathbf{h}).$$

It follows that†

$$(6.7) \quad (_1\mathbf{S}_1)'(_1\mathbf{S}_1) = \mathbf{G} = \begin{pmatrix} \mathbf{i}_1' \\ \mathbf{i}_2' \\ \mathbf{i}_3' \end{pmatrix} \delta^2\mathbf{M}^2(\mathbf{i}_1, \mathbf{i}_2, \mathbf{i}_3),$$

and the elements of this important matrix $\mathbf{G}$ will be denoted in *all* succeeding sections by g_{rs} while the elements of $\mathbf{G}^{-1}$ will be denoted by g^*_{rs}. These elements are determined by the equations†

$$(6.8) \qquad \left.\begin{aligned} g_{rs} &= \mathbf{i}_r'\,\delta^2\mathbf{M}^2\mathbf{i}_s, \\ g^*_{rs} &= \mathbf{i}_r'\,\delta^{-2}\mathbf{M}^{-2}\mathbf{i}_s, \end{aligned}\right\}$$

and, given δ, are easily calculated in terms of known quantities. The determinant $|\mathbf{G}|$ will be denoted by g^2 so that

$$(6.9) \qquad |\mathbf{G}|^{\frac{1}{2}} = g = \delta^3\mu_1\mu_2\mu_3.$$

The squares of the final lengths of $\mathbf{x}_i$ and $\mathbf{n}_i$ are $\mathbf{x}_i'\mathbf{G}\mathbf{x}_i$ and $\mathbf{n}_i'\mathbf{G}^{-1}\mathbf{n}_i$ respectively and hence, using equations (6.2), (6.3) and (6.8) the angles α and β are determined by

$$(6.10) \quad g_{11}\cos^2\alpha + 2g_{12}\cos\alpha\sin\alpha + g_{22}\sin^2\alpha = 1,$$

$$(6.11) \quad g^*_{11}\cos^2\beta + 2g^*_{13}\cos\beta\sin\beta + g^*_{33}\sin^2\beta = 1.$$

There are two solutions (if any) to each of these equations in agreement with the results of the last section.

The invariant line strain $\mathbf{S}_1$ which does not rotate the plane with normal $\mathbf{h}$ is conveniently calculated by introducing yet another orthonormal basis L for which

$$(6.12) \quad [1\,;\mathbf{l}_1] = \mathbf{x}_i,\ [1\,;\mathbf{l}_3] = \mathbf{i}_3,\ \mathbf{l}_2 = \mathbf{l}_3 \times \mathbf{l}_1,$$

so that

$$(6.13) \qquad (_1\mathbf{T}_L) = \begin{pmatrix} \cos\alpha & -\sin\alpha & 0 \\ \sin\alpha & \cos\alpha & 0 \\ 0 & 0 & 1 \end{pmatrix}.$$

It is clear that the strain $\mathbf{S}_1$ for which $\mathbf{l}_1 = [100]_L$ is invariant, and the plane with normal $\mathbf{h} = \mathbf{l}_3 = (001)_L$ is unrotated, can be written in the form

$$(6.14) \qquad (_L\mathbf{S}_1{}_L) = \begin{pmatrix} 1 & a_{12} & a_{13} \\ 0 & a_{22} & a_{23} \\ 0 & 0 & a_{33} \end{pmatrix},$$

so that $|\mathbf{S}_1| = a_{22}a_{33}$ (which must be equal to $g = \delta^3\mu_1\mu_2\mu_3$). Hence,

$$(6.15) \qquad (_L\mathbf{S}_1{}_L)^{-1} = \begin{pmatrix} 1, & -a_{12}/a_{22}, & (a_{12}a_{23} - a_{13}a_{22})/a_{22}a_{33} \\ 0, & 1/a_{22}, & -a_{23}/a_{22}a_{33} \\ 0, & 0, & 1/a_{33} \end{pmatrix}$$

Now the principal axes and their extensions are determined by the matrix product

$$(6.16) \qquad (_L\mathbf{S}_1{}_L)'(_L\mathbf{S}_1{}_L) = (_L\mathbf{T}_1)\mathbf{G}(_1\mathbf{T}_L).$$

On substituting equation (6.14) for ($_L\mathbf{S}_1{}_L$) on the left and equation (6.13) for ($_1\mathbf{T}_L$) on the right and equating like components of the resulting matrices, equations which determine the unknown a_{rs}, are obtained. The most compact solutions of these equations are obtained if one considers simultaneously the corresponding set of equations obtained from the inverse relation

$$(6.17) \quad (_L\mathbf{S}_1{}_L)^{-1}(_L\mathbf{S}_1{}_L)'^{-1} = (_L\mathbf{T}_1)\mathbf{G}^{-1}(_1\mathbf{T}_L).$$

The values of a_{rs} thus obtained are

$$(6.18) \qquad \left.\begin{aligned} a_{12} &= (g_{22} - g_{11})\cos\alpha\sin\alpha + g_{12}(\cos^2\alpha - \sin^2\alpha) \\ &= (g_{22} - 1)\tan\alpha + g_{12}, \\ a_{13} &= g_{13}\cos\alpha + g_{23}\sin\alpha, \\ a_{22} &= g\,g^{*\frac{1}{2}}_{33}, \\ a_{23} &= g\,g^{*-\frac{1}{2}}_{33}(g^*_{13}\sin\alpha - g^*_{23}\cos\alpha), \\ a_{33} &= g^{*-\frac{1}{2}}_{33}, \end{aligned}\right\}$$

where α is determined by equation (6.10). Other useful results are

$$(6.19) \qquad \left.\begin{aligned} (a_{12}a_{23} - a_{13}a_{22})/a_{22}a_{33}^2 &= g^*_{13}\cos\alpha + g^*_{23}\sin\alpha, \\ a_{23}/a_{22}a_{33}^2 &= g^*_{13}\sin\alpha - g^*_{23}\cos\alpha. \end{aligned}\right\}$$

The final step is to determine the rotation $\mathbf{R}_1$ about the invariant line $\mathbf{l}_1 = \mathbf{x}_i$, such that the invariant normal of the strain ($_L\mathbf{R}_1{}_L$)($_L\mathbf{S}_1{}_L$) = ($_L\mathbf{S}_L$) lies in the plane with normal $\mathbf{u} = \mathbf{i}_2$. Let

†Note that ($_P\mathbf{T}_1$) = ($_P\mathbf{T}'_1$) since both are transformation matrices between orthonormal bases and are, therefore, rotation matrices.

$$(\text{L}\mathbf{S}\text{L}) = \begin{pmatrix} 1 & 0 & 0 \\ 0 & \cos\omega & -\sin\omega \\ 0 & \sin\omega & \cos\omega \end{pmatrix} \begin{pmatrix} 1 & a_{12} & a_{13} \\ 0 & a_{22} & a_{23} \\ 0 & 0 & a_{33} \end{pmatrix},$$

(6.20)

$$= \begin{pmatrix} 1, & a_{12}, & a_{13} \\ 0, & a_{22}\cos\omega, & a_{23}\cos\omega - a_{33}\sin\omega \\ 0, & a_{22}\sin\omega, & a_{23}\sin\omega + a_{33}\cos\omega \end{pmatrix},$$

where ω is the angle through which the plane with normal $\mathbf{h}$ is rotated by the strain $\mathbf{S}$. The condition determining ω is equivalent to the requirement that $[\text{L}\,;\mathbf{u}]$ and $(\text{L}\mathbf{S}\text{L})[\text{L}\,;\mathbf{u}]$, (which is in the twinning direction), define the plane with the invariant normal. Now $[\text{L}\,;\mathbf{u}] = [\sin\alpha, \cos\alpha, 0]_L$, and using (6.20) to calculate $(\text{L}\mathbf{S}\text{L})[\text{L}\,;\mathbf{u}]$ it follows that the plane defined by these directions has the normal

$$(a_{22}\sin\omega\cos\alpha,\ -a_{22}\sin\omega\sin\alpha,\ (a_{22}\cos\omega - 1)\sin\alpha - a_{12}\cos\alpha)_L.$$

The condition that this be an invariant normal leads to the equation

(6.21)

$$[(a_{12}a_{23} - a_{13}a_{22})\cos\alpha + a_{23}\sin\alpha]\sin\omega + [(a_{22} + a_{33})\sin\alpha + a_{33}a_{12}\cos\alpha]\cos\omega = (a_{33}a_{22} + 1)\sin\alpha + a_{12}\cos\alpha,$$

and on substituting for the a_{rs} this may be reduced to

(6.22)

$$g\overset{*}{g}_{13}\sin\omega + [(g\overset{*}{g}_{33} + g_{22})\sin\alpha + g_{12}\cos\alpha]\cos\omega = \overset{*}{g}_{33}^{\frac{1}{2}}[(g + g_{22})\sin\alpha + g_{12}\cos\alpha].$$

In general, this equation is satisfied by two distinct values of ω, and remembering the two possible values for α, this gives four solutions in all. In effect, ω replaces the previous variable β.

A corresponding development can be carried out by working in an orthonormal basis K for which

(6.23) $\quad [\text{I}\,;\mathbf{k}_1] = \mathbf{n}_i,\ [\text{I}\,;\mathbf{k}_2] = \mathbf{i}_2,\ \mathbf{k}_3 = \mathbf{k}_1 \times \mathbf{k}_2,$

and calculating the strain

$$(6.24) \qquad (\text{K}\mathbf{S}_2\text{K}) = \begin{pmatrix} 1 & 0 & 0 \\ b_{21} & b_{22} & b_{23} \\ b_{31} & 0 & b_{33} \end{pmatrix},$$

in which the normal $\mathbf{k}_1 = \mathbf{n}_i$ is invariant and the direction $\mathbf{k}_2 = \mathbf{u}$ is unrotated. The condition that this strain have the specified principal axes leads to

(6.25)

$$b_{22} = g_{22}^{\frac{1}{2}},$$

$$b_{33} = g\,g_{22}^{-\frac{1}{2}},$$

$$b_{31} = -\,g\,g_{22}^{-\frac{1}{2}}[(\overset{*}{g}_{33} - \overset{*}{g}_{11})\sin\beta\cos\beta + \overset{*}{g}_{13}(\cos^2\beta - \sin^2\beta)],$$

$$b_{21} = g_{22}^{-\frac{1}{2}}(g_{12}\cos\beta + g_{23}\sin\beta),$$

$$b_{23} = g_{22}^{-\frac{1}{2}}(-\,g_{12}\sin\beta + g_{23}\cos\beta),$$

where β is given by equation (6.11). An additional rotation $\mathbf{R}_2$ through an angle ϕ about the invariant normal is required to make the invariant line lie in the plane with normal $\mathbf{h}$. The rotation $(\text{K}\mathbf{R}_2\text{K})$ is obtained from $(\text{L}\mathbf{R}_1\text{L})$ on replacing ω by ϕ and then ϕ is given by

(6.26)

$$-g_{12}\sin\phi + [(g\overset{*}{g}_{33} + g_{22})\sin\beta + g\overset{*}{g}_{13}\cos\beta]\cos\phi = g_{22}^{\frac{1}{2}}[(g\overset{*}{g}_{33} + 1)\sin\beta + g\overset{*}{g}_{13}\cos\beta].$$

7. Calculation of the Twinning Shear†

So far it has been assumed that both the twinning direction and the twinning plane in the final lattice are known. However, only the twinning plane can be determined by direct observation and so the appropriate twinning direction remains to be determined. It will now be shown that, provided the correspondences for both twins are crystallographically equivalent, the twinning plane must be generated from a plane of symmetry in the initial structure, and that the associated twinning direction is completely determined. In this case, the initial structure has at least the symmetry of a monoclinic crystal.

Bases A and A′ in lattice $\mathscr{A}$ are crystallographically equivalent if one basis can be brought into coincidence with the other by a symmetry operation of the lattice. Consider now the bases B_1 and B_2 in two lattices $\mathscr{B}_1$, $\mathscr{B}_2$ which are generated from A and A′ respectively; the correspondences $(\text{B}_1\mathbf{C}_1\text{A})$ and $(\text{B}_2\mathbf{C}_2\text{A}')$ are then, of course, both identity. The correspondences for these two transformations are equivalent if the basis B_2 can be brought into coincidence with the basis B_1 by means of a rotation and/or a reflection operation. When B_1 and B_2 describe twin orientations, this operation is reflection in the common twinning plane of lattices $\mathscr{B}_1$, $\mathscr{B}_2$.

In the transformation from A to B_1 a vector $[\text{A}\,;\mathbf{x}]$ in $\mathscr{A}$ is transformed into the vector

†This calculation and the conditions arising from it apply only to Type I twinning [4] where the twin orientations are related by reflection across the common twinning plane. An analogous development can easily be carried out for the case of Type II twinning, but so far no example of Type II twinning in a martensite structure has been reported.

$(B_1\mathbf{C}_1A)[A;\mathbf{x}]$ in the orientation $\mathscr{B}_1$, while in the transformation A′ to B_2, the same vector in $\mathscr{A}$ is transformed into $(B_2\mathbf{C}_2A')(A'\mathbf{T}A)[A;\mathbf{x}]$ in the twin orientation $\mathscr{B}_2$. The two vectors so obtained must correspond in the shear which transforms $\mathscr{B}_1$ into its twin $\mathscr{B}_2$. Thus, the twinning correspondence

$$(7.1)\quad (B_2\mathbf{C}^TB_1) = (B_2\mathbf{C}_2A')(A'\mathbf{T}A)(A\mathbf{C}_1B_1) = (A'\mathbf{T}A),$$

since the correspondences on the right are both identity. It follows that the twinning shear referred to the basis B_1 is

$$(7.2)\quad (B_1\mathbf{S}^TB_1) = (B_1\mathbf{T}B_2)(B_2\mathbf{C}^TB_1) = (B_1\mathbf{T}B_2)(A'\mathbf{T}A).$$

The matrix $(B_1\mathbf{T}B_2)$ describes the transformation between bases related by reflection in the twinning plane. Denoting the normal to this plane by $\mathbf{k}$, the reflection $\mathbf{x}^r$ of any vector $\mathbf{x}$ is given by

$$(7.3)\qquad \mathbf{x}^r = \mathbf{x} - 2\mathbf{k}(\mathbf{k}.\mathbf{x})/\mathbf{k}.\mathbf{k}.$$

Thus, if $\mathbf{k} = [B_1^*;\mathbf{k}]$

$$(7.4)\quad (B_2\mathbf{T}B_1) = \mathbf{I} - 2\mathbf{G}_B^{-1}\mathbf{k}\mathbf{k}'/\mathbf{k}'\mathbf{G}_B^{-1}\mathbf{k} = (B_1\mathbf{T}B_2),$$

and, since the twinning plane must be a lattice plane, $\mathbf{k}$ may be supposed to have integral elements. The important point is that $(B_2\mathbf{T}B_1)$ can be regarded as an invariant plane strain on the plane with normal $\mathbf{k}$. Because its determinant is -1, it is not a physically possible strain but this is immaterial in the argument which follows.

Since the twinning shear $(B_1\mathbf{S}^TB_1)$ is an invariant plane strain, and the transformation $(B_2\mathbf{T}B_1)$ can be regarded as a strain in $\mathscr{B}_1$ with the same invariant plane, their resultant, which by equation (7.2) must have the matrix representation $(A'\mathbf{T}A)$, must also be an invariant plane strain on the plane with normal $\mathbf{k}'$. (See Section 5 in Part I). Thus,

$$(7.5)\qquad (A'\mathbf{T}A) = \mathbf{I} + \mathbf{m}\mathbf{k}',$$

for some vector $\mathbf{m}$. This result must now be interpreted relative to the lattice $\mathscr{A}$. Because the correspondence $(B_1\mathbf{C}_1A)$ is identity, the twinning plane in $\mathscr{B}_1$ is generated from the plane in $\mathscr{A}$ whose normal has components $\mathbf{k}'$ relative to A* *i.e.* $(\mathbf{h};A^*) = \text{const}\ \mathbf{k}'$. Thus, $(A'\mathbf{T}A)$ can also be regarded as an invariant plane strain in $\mathscr{A}$ on the plane with normal $\mathbf{h}$. However, $(A'\mathbf{T}A)$ also represents a symmetry operation in $\mathscr{A}$ and must, therefore, be the resultant of a real rotation and/or a reflection. Such a combination can only be an invariant plane strain if $(A'\mathbf{T}A)$ is a reflection in the plane from which the twinning plane is generated. Thus,

$$(7.6)\qquad (A'\mathbf{T}A) = \mathbf{I} - 2\mathbf{G}_A^{-1}\mathbf{k}\mathbf{k}'/\mathbf{k}'\mathbf{G}_A^{-1}\mathbf{k},$$

Substituting equations (7.4) and (7.6) into equation (7.2) gives†

$$(7.7)\quad (B_1\mathbf{S}^TB_1) = \mathbf{I} - 2\mathbf{G}_A^{-1}\mathbf{k}\mathbf{k}'/\mathbf{k}'\mathbf{G}_A^{-1}\mathbf{k} + 2\mathbf{G}_B^{-1}\mathbf{k}\mathbf{k}'/\mathbf{k}'\mathbf{G}_B^{-1}\mathbf{k}.$$

Since $(A'\mathbf{T}A)$ is a symmetry operation,

$$\mathbf{m} = -2\mathbf{G}_A^{-1}\mathbf{k}/\mathbf{k}'\mathbf{G}_A^{-1}\mathbf{k}$$

has integral elements and is such that $\mathbf{k}'\mathbf{m} = -2$. It is now easy to verify that the strain $(B_1\mathbf{S}^TB_1)$ is in fact a twinning shear on the plane with normal $\mathbf{k}$. On substituting the bases P, P_f for A, B_1 respectively in equation (7.7) and, therefore, also $\mathbf{h}$ for $\mathbf{k}$, the twinning shear may be written

$$(7.8)\qquad (P_f\mathbf{S}^TP_f) = \mathbf{I} + c\mathbf{u}\mathbf{h}',$$

where

$$(7.9)\quad c\mathbf{u} = 2[\mathbf{M}^{-2}\mathbf{h}/\mathbf{h}'\mathbf{M}^{-2}\mathbf{h} - \mathbf{h}].$$

The magnitude of the twinning shear is $c(g_{22}^*g_{33}^*)^{\frac{1}{2}}$ since the magnitudes of the vectors which are represented by the matrices $\mathbf{h}$ and $\mathbf{u}$ when referred to P_f are no longer unity.

8. The Relationship between the Solutions

The relation between $\mathbf{u}$ and $\mathbf{h}$ obtained in the last section can be used to simplify the strain matrix $(L\mathbf{S}L)$. The vector with components $\delta^{-2}\mathbf{M}^{-2}\mathbf{h}$ relative to the basis P, can be expressed in terms of the basis I as

$$(8.1)\qquad \delta^{-2}\mathbf{M}^{-2}\mathbf{h} = g_{13}^*\mathbf{i}_1 + g_{23}^*\mathbf{u} + g_{33}^*\mathbf{h}.$$

Substituting in equation (7.9) then gives

$$g_{33}^*c\mathbf{u} = 2(g_{13}^*\mathbf{i}_1 + g_{23}^*\mathbf{u}),$$

so that

$$(8.2)\qquad g_{13}^* = 0,$$

$$(8.3)\qquad c = 2g_{23}^*/g_{33}^*.$$

The fact that $g_{13}^* = 0$, implies the useful relations

$$(8.4)\qquad -g_{23}^*/g_{33}^* = g_{23}/g_{22} = g_{13}/g_{12}.$$

The most important simplification occurs in equation (6.22) for ω which now reads

†Because the correspondence is chosen, in this section, to be identity, the matrix $\mathbf{G}_B$ in equations (7.4) and (7.7) is not necessarily the same as the matrix $\mathbf{G}_B$ introduced in §4.

$$(8.5)\quad [(g g^*_{33} + g_{22}) \sin\alpha + g_{12} \cos\alpha] \cos\omega = g^{*\frac{1}{2}}_{33} [(g + g_{22}) \sin\alpha + g_{12} \cos\alpha],$$

giving two opposite values of ω immediately. After some reduction this gives,

$$(8.6)\quad \sin\omega = \pm g g^{*\frac{1}{2}}_{33} [(g^*_{33} - 1)(1 - g^*_{11})]^{\frac{1}{2}} / [(g g^*_{33} + g_{22}) \sin\alpha + g_{12} \cos\alpha],$$

from which ω is most conveniently calculated. The simplified expression for the invariant line strain is

$$(8.7)\quad ({}_L\mathbf{S}_L) = \begin{pmatrix} 1, & (g_{22} - 1)\tan\alpha + g_{12}, & g_{13}\cos\alpha + g_{23}\sin\alpha \\ 0, & g g^{*\frac{1}{2}}_{33}\cos\omega, & -(g g^*_{23}\cos\alpha\cos\omega + \sin\omega)/g^{*\frac{1}{2}}_{33} \\ 0, & g g^{*\frac{1}{2}}_{33}\sin\omega, & (-g g^*_{23}\cos\alpha\sin\omega + \cos\omega)/g^{*\frac{1}{2}}_{33} \end{pmatrix}.$$

With the two values of ω determined above and the two values of α obtained from equation (6.10) there are, in all, four solutions with the same principal axes.

When twins are generated with equivalent correspondences a 'parent' orientation of the final structure and one of the variants of its twin must have the same principal axes. Thus, the above four solutions can be classified into two pairs, each pair being related in this way. There are, therefore, two independent solutions of the whole problem, and these correspond to the two values of α. For a given α, the two values of ω give a pair of solutions related as above. In a monoclinic crystal there are only two equivalent sets of principal axes and these are related by the symmetry operation of rotation about the normal to the plane of symmetry. Since twin orientations are generated by strains with different but crystallographically equivalent principal axes, it follows that a pair of solutions describes a parent **1** and the twin of parent **2**, where parents **1** and **2** are related by the above symmetry operation.

The relation between a pair of solutions $({}_L\mathbf{S}_L)_{\pm\omega}$ with the same principal axes and with the same α is verified as follows. The strain matrices describing parents **1** and **2** are the same when referred to their respective L-bases, L_1 and L_2, which are related by the symmetry operation; thus, $({}_{L_1}\mathbf{T}_{L_2})$ is equal to the diagonal matrix with elements $-1, -1, 1$. The strain required to generate the twin of parent **2** is, when referred to L_1,

$$({}_{L_1}\mathbf{T}_{L_2})({}_{L_2}\mathbf{S}^T{}_{L_2})({}_{L_2}\mathbf{S}_{L_2})_{+\omega}({}_{L_2}\mathbf{T}_{L_1}).$$

On substituting

$$({}_{L_2}\mathbf{S}^T{}_{L_2}) = ({}_{L_2}\mathbf{T}_{L_{2f}})({}_{L_{2f}}\mathbf{S}^T{}_{L_{2f}})({}_{L_{2f}}\mathbf{T}_{L_2}),$$

and using equation (2.15) to give $({}_{L_2}\mathbf{T}_{L_{2f}}) = ({}_{L_2}\mathbf{S}_{L_2})_{+\omega}$ this becomes,

$$({}_{L_1}\mathbf{T}_{L_2})({}_{L_2}\mathbf{S}_{L_2})_{+\omega}({}_{L_{2f}}\mathbf{S}^T{}_{L_{2f}})({}_{L_2}\mathbf{T}_{L_1}).$$

Finally, substituting

$$(8.8)\quad ({}_{L_{2f}}\mathbf{S}^T{}_{L_{2f}}) = \begin{pmatrix} 1 & 0 & c\sin\alpha \\ 0 & 1 & c\cos\alpha \\ 0 & 0 & 1 \end{pmatrix},$$

it is easily verified from equation (8.7) that the result is $({}_L\mathbf{S}_L)_{-\omega}$.

9. Factorization of the Strain

It remains to resolve the invariant line strain **S** into an invariant plane strain $\mathbf{P}_1$ followed by a part $\mathbf{P}_2$, of the twinning shear in the final structure.

The plane **p** and direction **d** of $\mathbf{P}_1$ are parallel to the plane $(\mathbf{h}; L)({}_L\mathbf{S}_L)^{-1} - (\mathbf{h}; L)$ and the direction $({}_L\mathbf{S}_L)[L; \mathbf{u}] - [L; \mathbf{u}]$, respectively. (Equation (8.9) of Part I). Since $(\mathbf{h}; L) = (001)_L$ and $[L; \mathbf{u}] = [\sin\alpha, \cos\alpha, 0]_L$, it follows from equation (6.20) that

$$(9.1)\quad (\mathbf{p}; L) = (0, \sin\omega, a_{33} - \cos\omega)_L,$$

$$(9.2)\quad [L; \mathbf{d}] = [a_{12}, a_{22}\cos\omega - 1, a_{22}\sin\omega]_L,$$

and substituting for the a_{rs} from equations (6.18) Gives

$$(9.3)\quad (\mathbf{p}; L) = (0, \sin\omega, g^{*-\frac{1}{2}}_{33} - \cos\omega)_L,$$

$$(9.4)\quad [L; \mathbf{d}] = [(g_{22} - 1)\tan\alpha + g_{12}, g g^{*\frac{1}{2}}_{33}\cos\omega - 1, g g^{*\frac{1}{2}}_{33}\sin\omega]_L,$$

where α and ω are given by equations (6.10), (8.6). Thus,

$$(9.5)\quad ({}_L\mathbf{P}_1{}_L) = \mathbf{I} + \operatorname{cosec}\omega\,[L; \mathbf{d}](\mathbf{p}; L),$$

where the constant cosec ω is obtained by equating $({}_L\mathbf{S}_L)[L; \mathbf{u}]$ to $({}_L\mathbf{P}_1{}_L)[L; \mathbf{u}]$.

The invariant plane strain $\mathbf{P}_1$, together with the dilatation $\mathbf{I}/\delta$, determine the homogeneous component of the total strain. A convenient way of determining the magnitude of the inhomogeneous shear $\mathbf{P}_2$ is to consider the alternative factorization in which the homogeneous strain $\mathbf{P}_1$ occurs second. The basis used in this paragraph is irrelevant, but in order that the symbols may have their previously defined meanings it is assumed to be the basis P. The strain $\mathbf{P}_2$ is clearly

$$\mathbf{P}_2 = \mathbf{I} + ck\mathbf{S}\mathbf{u}\mathbf{h}'\mathbf{S}^{-1},$$

where k is the fraction of the total twinning shear involved. Thus,

$$\mathbf{S} = \mathbf{P}_2\mathbf{P}_1 = \mathbf{S}(\mathbf{I} + ck\mathbf{u}\mathbf{h}')\mathbf{S}^{-1}\mathbf{P}_1,$$

which on solving for $\mathbf{S}$ gives

$$\mathbf{S} = \mathbf{P}_1(\mathbf{I} + ck\mathbf{u}\mathbf{h}'). \tag{9.6}$$

Thus, $\mathbf{P}_3 = \mathbf{I} + ck\mathbf{u}\mathbf{h}'$ is the simple shear which must precede $\mathbf{P}_1$ to give $\mathbf{S}$. As stated in Part I the inhomogeneous strain required to complete the transformation is different according to whether it is considered to occur before or after the homogeneous strain. The above result gives the relation between these alternative inhomogeneous strains.

Since $\mathbf{P}_1 = \mathbf{S}\mathbf{P}^{-1}{}_3$ and $(\mathrm{L}\mathbf{P}_3\mathrm{L})$ is the matrix on the right of equation (8.8) with c replaced by ck, it follows after some simplification that

$$(\mathrm{L}\mathbf{P}_1\mathrm{L}) = \begin{pmatrix} 1, & (g_{22}-1)\tan\alpha + g_{12}, \\ & \qquad (1+2k)(g_{13}\cos\alpha + g_{23}\sin\alpha) \\ 0, & g g_{33}^{*\frac{1}{2}}\cos\omega, \\ & \qquad -[(1+2k)\, g g_{23}^{*}\cos\alpha\cos\omega + \sin\omega]/g_{33}^{*\frac{1}{2}} \\ 0, & g g_{33}^{*\frac{1}{2}}\sin\omega, \\ & \qquad [-(1+2k)\, g g_{23}^{*}\cos\alpha\sin\omega + \cos\omega]/g_{33}^{*\frac{1}{2}} \end{pmatrix}. \tag{9.7}$$

This matrix can only represent an invariant plane strain if

$$\begin{aligned} 1 + 2k &= [(1 + g g_{33}^{*})\cos\omega - g_{33}^{*\frac{1}{2}}(1+g)]/ \\ &\qquad g g_{33}^{*}\cos\alpha\sin\omega, \\ &= \operatorname{sgn}\omega[(g_{22}-1)\tan\alpha + g_{12}](g_{33}^{*}-1)^{\frac{1}{2}}/ \\ &\qquad (1 - g_{11}^{*})^{\frac{1}{2}} g g_{23}^{*}, \end{aligned} \tag{9.8}$$

on substituting for $\sin\omega$ and $\cos\omega$. Equation (6.10), defining α, gives

$$(g_{22}-1)\tan\alpha + g_{12} = \pm\,[g_{12}^2 - (g_{11}-1)(g_{22}-1)]^{\frac{1}{2}} \tag{9.9}$$

so that $1 + 2k$ changes only in sign for the four possible solutions.

For the same α

$$k_{+\omega} + k_{-\omega} = -1, \tag{9.10}$$

and the values of $k_{+\omega}$ and $k_{-\omega}$ are interchanged on changing from one value of α to the other. Consideration of equation (9.10) shows that the magnitude of the shears involved in producing a parent and a twin are complementary with respect to the twinning shear. This result was to be expected because twin orientations are derived from the common intermediate lattice generated by the homogeneous strain. Since changing the value of α leads to the same values of k, the same intermediate lattice is generated (in different orientations) in all solutions.

10. Conclusion

The theory has now been developed to a stage where it can be applied to the analysis of specific transformations and its predictions compared with experimental results. The relevant correspondence between the initial and final lattices is first determined from the experimental information and this is used to determine the positions of the principal axes and the elements μ_1, μ_2, μ_3 of the matrix $\mathbf{M}$ (equations (4.1) and (4.2)). Now the invariant line strain $\mathbf{S}$ given in equation (8.7) and its resolution into appropriate components (§9) are expressed, ultimately, in terms of the g_{rs} defined in equation (6.8). However, the g_{rs} are determined by $\delta\mathbf{M}$ rather than $\mathbf{M}$ and, since δ is initially unknown, it must be detrmined indirectly as follows.

Consider a class of transformations which differ from one another only in the sizes of the initial and final unit cells. For all transformations belonging to such a class the ratio $\mu_1 : \mu_2 : \mu_3$ is the same, because the μ_r are simply the ratios of the final to the initial lengths of the principal axes. Thus, within a class the elements of $\mathbf{M}$, and hence $\delta\mathbf{M}$, are in the same ratio. If $\mathbf{M}_0$ is any diagonal matrix with elements in the required ratio, it follows that $\delta\mathbf{M} = \theta\mathbf{M}_0$, where θ is a scalar parameter.

Having chosen $\mathbf{M}_0$ the values of the g_{rs} depend only on the parameter θ. Thus, the normal to the habit plane, (equation (9.3)) also depends only on θ and, therefore, always lies in a certain surface. If the observed normal to the habit plane does lie in this surface a value of θ can be determined and so the dilatation $\mathbf{I}/\delta$ accompanying the homogeneous strain is determined. Further, this value of θ defines the relevant invariant line strain, and so the orientation relationship and the other elements of the component strains can be obtained explicitly.

References

1. JASWON, M. A. and WHEELER, J. A. Acta Cryst. **1** (1948) 216.
2. CHANG, L. C. Acta Cryst. **4** (1951) 320.
3. JEFFREYS, H. and JEFFREYS, B. Methods of Mathematical Physics (Cambridge, University Press, 1946), chap. 4.
4. SCHMID, E. and BOAS, W. Plasticity of Crystals, §33 (English translation, London, Hughes, 1950).

EXPERIMENTS ON THE MARTENSITIC TRANSFORMATION IN SINGLE CRYSTALS OF INDIUM-THALLIUM ALLOYS*

Z. S. BASINSKI† and J. W. CHRISTIAN†

The transformation from the face-centred cubic phase to the face-centred tetragonal phase has been studied in alloys containing ~18.5% thallium, using ciné-photography and X-ray methods. After suitable annealing, single crystals transformed by the migration of either a single or a double interface from one end of the specimen to the other. In single-interface transformations, a twinned tetragonal structure is produced in accordance with the previously postulated double shear mechanism. The twins are visible under the microscope, except in an accommodation region immediately behind the interface. There are no long-range stresses, provided the twins have mean thickness ratio 2:1. Two types of double interface ("X" and "λ" interfaces) have been observed to lead to a tetragonal single crystal. Each region of the crystal is first transformed to twinned tetragonal, and then untwinned again; accumulating strains are again avoided. There is also a type of double interface which leads to twinned tetragonal crystals. The kinetics of the transformation are similar to those of gold-cadmium alloys. Thermal stabilisation by a diffusion-controlled relaxation process occurs readily, and interfaces were often halted permanently in this way. Applied stresses were able to reverse the direction of interface motion during transformation. The results may be related to the more complex structures found in polycrystalline alloys. A group of main bands grows progressively from one end, but new bands are formed ahead of the set, and grow backwards to meet the advancing group. The atomic processes occurring during transformation are discussed in terms of current theories.

UNE EXPÉRIENCE SUR LA TRANSFORMATION MARTENSITIQUE DANS DES MONOCRISTAUX D'ALLIAGES INDIUM-THALLIUM

La transformation de la phase cubique à faces centrées en la phase tétragonale à faces centrées a été étudiée dans des alliages contenant ~18,5% de thallium, au moyen de méthodes cinématographiques et aux rayons X.

Après un recuit convenable, des monocristaux se transformaient par la migration d'une interface simple ou double, d'une extrémité de l'échantillon à l'autre. Dans les transformations à interface simple, il y a formation d'une structure tétragonale, maclée, en accord avec le mécanisme de double cisaillement proposé antérieurement. Les macles sont visibles au microscope, sauf dans une région d'adaptation immédiatement derrière l'interface. Il n'y a pas de tensions à grande distance, pour autant que le rapport d'épaisseur moyenne des macles soit 2:1. On a observé deux types d'interfaces doubles (interfaces "X" et "Y") donnant lieu à un monocristal à réseau tétragonal. Chaque région du cristal est d'abord transformée en tétragonale, maclée, ensuite démaclée; l'accumulation des déformations est ainsi évitée. Il existe aussi un type d'interface double qui donne lieu à des cristaux à structure tétragonale, maclée.

La cinétique de la transformation est semblable à celle des alliages or- cadmium. Une stabilisation thermique due à un processus de relaxation contrôlé par la diffusion, est presque instantané; certaines interfaces furent, de ce fait, arrêtées d'une façon permanente. Il y a moyen de renverser le sens du mouvement de l'interface par l'application d'une tension extérieure. Ces résultats peuvent être appliqués aux structures plus complexes qu'on trouve dans les alliages polycristallins.

Un groupe de bandes principales croît progressivement à partir d'une extrémité, mais en même temps d'autres bandes se forment en avant du groupe principal et croissent en sens inverse, pour finalement rencontrer les bandes principales. Les processus atomiques qui ont lieu pendant la transformation sont discutés en termes des théories courantes.

EXPERIMENTE ZUR MARTENSITARTIGEN UMWANDLUNG VON EINKRISTALLEN VON INDIUM-THALLIUM LEGIERUNGEN

Die Umwandlung der kubisch-flächenzentrierten in die tetragonal-flächenzentrierte Form wurde an Thallium-Indium Legierungen mit etwa 18, 5% Thallium röntgenographisch und mit Hilfe von Kinephotographie untersucht. Nach hinreichender Glühung wandeln sich die Einkristalle durch Wanderung einer einzigen oder einer doppelten Grenzfläche von einem Ende der Probe zum anderen um. Bei Umwandlungen mit einer einzigen Grenzfläche entsteht eine tetragonale Zwillingsstruktur, wie es auf Grund des früher vorgeschlagenen doppelten Scherungsmechanismus zu erwarten ist. Die Zwillingskristalle sind unter dem Mikroskop sichtbar, mit Ausnahme einer Übergangszone unmittelbar hinter der Grenzfläche. Wenn die Zwillingskristalle ein mittleres Dickenverhältnis von 2:1 haben, liegen keine weitreichenden inneren Spannungen vor. Es wurde beobachtet, dass zwei verschiedene Arten von doppelten Grenzflächen ("X" und "λ" Grenzflächen) zur Bildung eines tetragonalen Einkristalles führen. Jede Kristallhälfte wandelt sich im ersten Stadium in eine verzwillingte tetragonale Struktur um, im darauffolgenden zweiten Stadium wird die Zwillingsbildung rückgängig gemacht. Grosse innere Spannungen werden wiederum vermieden. Es wurde ausserdem eine Art der doppelten Grenzfläche gefunden, die zu verzwillingten tetragonalen Kristallen führt. Die Umwandlungskinetik entspricht der der Gold-Kadmium Legierungen. Thermische Stabilisierung mit Hilfe eines diffusionsbestimmten Relaxionsvorgangs tritt leicht auf, und Grenzflächen werden oft auf diese Weise permanent festgehalten. Äussere Spannungen konnten während der Umwandlung die Richtung der Grenzflächenwanderung unkehren. Die hier angegebenen Resultate können auf die komplizierteren Strukturen polykristalliner Legierungen angewandt werden. Dort wächst eine Gruppe von Bändern von einem Ende aus, während sich neue Bänder vor der Gruppe formen und ihr rückwärts entgegen wachsen. Die atomaren Vorgänge während der Umwandlung werden im Licht der gegenwärtigen Theorien diskutiert.

*Received September 9, 1953.

†The Inorganic Chemistry Laboratory, Oxford.

1. Introduction

Martensitic transformations from high temperature f.c.c. phases to low temperature f.c. tetragonal phases are found in indium-thallium alloys, and in many alloys of manganese. The atomic movements are equivalent to two shears on {110}-planes at 60 degrees to each other [1; 2]. In polycrystalline alloys, the original cubic grains are divided into sets of parallel bands by the transformation, each set representing a region in which the first shear is on the same {110}-plane but in opposite ⟨110⟩ directions in neighbouring bands.The second shear subdivides the main bands, but the finer bands cannot always be seen under the microscope. A set of fine bands is really a series of f.c.t. twins, and there are two such sets possible in each main band. The complexity of the transformed structure impedes detailed investigation of the mechanism of transformation.

Chang and Read [3] have described how single crystals of gold-cadmium alloys may be transformed by the migration of a single interface across the specimen. This method, when applicable, seems to be the ideal way of investigating martensitic transformations. In this paper we describe experiments on the transformation of indium-thallium alloys by single and double interfaces.

2. Crystallography of Transformation

Before describing the experimental work we briefly summarise the orientation relations which follow from the two shear transformation mechanism. This mechanism now seems to be well established, although an alternative description of the atomic movements has recently been proposed by Geisler [4]. Geisler's theory has been discussed in detail elsewhere [5], and has been shown to be inconsistent with the experimental results. In the present paper, we assume the validity of the two shear mechanism; the results of this section are all implicit in the original treatment given by Bowles and co-workers [1].

The tetragonal structure may be produced by oppositely directed shears on two of the four {110}-planes at 60 degrees to the undistorted, unrotated plane of the "first"shear.* Shears on the other two {110}-planes produce a tetragonal structure with the wrong sign for $(c/a - 1)$, but give the correct structure if the direction of the first shear is reversed. For each cubic {110}-plane, there are, therefore, 8 possible tetragonal orientations, 4 for each direction of the first shear. These orientations are all different from those produced by a first shear on the {110}-plane at 90 degrees, but there is one common orientation in the sets produced by first shears on planes at 60 degrees to each other. Each cubic crystal may thus give tetragonal crystals of 36 different orientations.

The orientations produced by a first shear (101), $[10\bar{1}]$, 2ϵ are shown in Figure 1. Here y is the original [010]-axis, while x' is derived from the original [100]-direction by a rotation of ϵ about [010]. The twin pairs (a) and (b) can be converted into (c) and (d) by a rigid rotation of $3\epsilon = s/2$, and a relative rotation of $6\epsilon = s$ about the z'-axis. The twins are thus reciprocal twins; ϵ and s have the meanings used in the previous paper [6].

A first shear $(10\bar{1})$, [101], 2ϵ will give 4 tetragonal orientations identical with those shown in Figure 1,

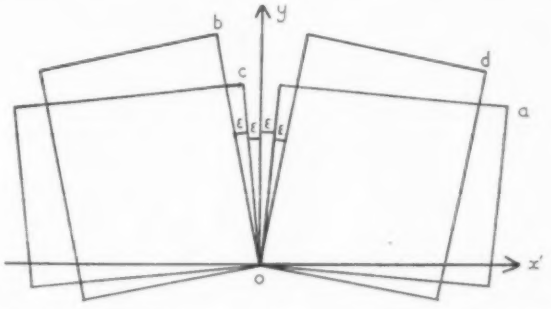

FIGURE 1. Lattice orientations produced by a first shear $(101)[10\bar{1}]$ 2ϵ. The second shears are: (*a*) $(\bar{1}10)$ $[1\bar{1}0]$ 2ϵ; (*b*) (110) $[\bar{1}10]$ 4ϵ; (*c*) $(1\bar{1}0)[110]$ 2ϵ; (*d*) $(1\bar{1}0)$ $[\bar{1}\bar{1}0]$ 4ϵ.

except that x' is now rotated about [010] in the opposite sense. The tetragonal orientations produced by corresponding first shears on perpendicular {110}-planes thus differ only by a rigid rotation of 2ϵ about the cube axis common to the two planes.

The orientation relations between the parent phase and the transformed regions may be represented as a single homogeneous deformation for each tetragonal orientation. We define the cubic unit cell of the f.c.c. structure by the three equal vectors $\mathbf{e}_1$, $\mathbf{e}_2$, $\mathbf{e}_3$. The atoms then lie at points:

$$\mathbf{r} = \tfrac{1}{2} m_i \mathbf{e}_i \qquad (i = 1, 2, 3)$$

where the summation convention is used, and m_i are integers such that $\sum_i m_i$ is even. After transformation, the atoms lie at points:

$$\mathbf{r}' = \tfrac{1}{2} m_i \mathbf{e}'_i$$

*We do not necessarily imply any physical resolution of the atomic movements into two components: the terms first and second are used for convenience, but may have only mathematical significance.

where the vectors $\mathbf{e}'_i$ define the tetragonal unit cell. The quantities m_i are identical in the two equations, since both directions and planes in the cubic lattice are related to directions and planes in the tetragonal lattice by the unit matrix **I**. This means that a row of atoms lying along the $[uvw]_c$-direction before transformation forms the $[uvw]_t$-direction after transformation, and atoms in the $(hkl)_c$ plane before transformation all lie in the $(hkl)_t$ plane after transformation. The vectors $\mathbf{e}'_i$ are related to $\mathbf{e}_i$ by the equation:

$$\mathbf{e}'_i = \mathbf{M}\,\mathbf{e}_i.$$

The components of the strain matrix **M** form a nonsymmetrical tensor. For a transformation specified by the shears (101) $[10\bar{1}]$ 2ϵ; (110) $[1\bar{1}0]$ 2ϵ (orientation (a) of Figure 1) we have [1]

$$\mathbf{M}_a = \begin{pmatrix} 1 + 2\epsilon + 2\epsilon^2 & -\epsilon - \epsilon^2 & -\epsilon - \epsilon^2 \\ \epsilon + 2\epsilon^2 & 1 - \epsilon - \epsilon^2 & -\epsilon^2 \\ \epsilon & 0 & 1 - \epsilon \end{pmatrix}.$$

Two atoms in the cubic structure having position vectors $\mathbf{r}_1$, $\mathbf{r}_2$ are related by the translation $\mathbf{v} = \mathbf{r}_1 - \mathbf{r}_2$. After transformation, the interatomic vector is given by $\mathbf{v}' = \mathbf{M}\,\mathbf{v}$. The relative displacement of the two atoms is thus

$$d\mathbf{v} = \mathbf{v}' - \mathbf{v} = (\mathbf{M} - \mathbf{I})\,\mathbf{v} = \mathbf{S}\,\mathbf{v}$$

where the strain matrix **S** has components $S_{ij} = M_{ij}$ $(i \neq j)$, $S_{ii} = M_{ii} - 1$. From the matrix $\mathbf{M}_a$ it follows that $d\mathbf{v} = 0$ if **v** is parallel to $[1\bar{1}\bar{1}]$. Rows of atoms in this direction are therefore unrotated and undistorted by the transformation, as is physically obvious, since $[1\bar{1}\bar{1}]$ is the direction common to the unrotated, undistorted (K_1) planes of the two shears. We also see that directions $[01\bar{1}]$, $[2\bar{1}\bar{1}]$ are unrotated during the transformation, provided we may neglect ϵ in comparison with ϵ^2. This is justified since $\epsilon \approx 0.01$. These unrotated directions define three unrotated planes, which are (111), (011) and (211). The results agree with the orientation relation postulated by Geisler [4] which is $:(111)_c \,/\!/\, (111)_t$, $[01\bar{1}]_c \,/\!/\, [01\bar{1}]_t$. For a transformation specified by the shears (101) $[10\bar{1}]$ 2ϵ, (110)$[\bar{1}10]$ 4ϵ we have the transformation matrix:

$$\mathbf{M}_b = \begin{pmatrix} 1 - \epsilon - 2\epsilon^2 & 2\epsilon & -\epsilon - 2\epsilon^2 \\ -2\epsilon - 2\epsilon^2 & 1 + 2\epsilon & 2\epsilon^2 \\ \epsilon & 0 & 1 - \epsilon \end{pmatrix}$$

and interatomic vectors in the $[1\bar{1}\bar{1}]$-direction are again common to both structures.

Consider an atom with position vector given by

$$\mathbf{r} = \sum_n (a_n\,\mathbf{i} + b_n\,\mathbf{i})$$

where **i** is a unit vector and $a_1, a_2 \ldots b_1, b_2 \ldots$ are scalar quantities such that $\sum_n (a_n + b_n) = |\mathbf{r}|$.

Now suppose the transformation occurs heterogeneously, so that the lattice is changed to tetragonal orientation (a) in a region traversed by the vector $a_1\,\mathbf{i}$, while an adjacent region (traversed by $b_1\,\mathbf{i}$) is changed to orientation (b), and so on. The position vector of our atom is now:

$$\mathbf{r}' = \sum_n \mathbf{M}_a\,a_n\,\mathbf{i} + \sum_n \mathbf{M}_b\,b_n\,\mathbf{i}.$$

The effect of the two separate distortions may be combined to give a macroscopic transformation:

$$\mathbf{r}' = \mathbf{M}_m\,\mathbf{r}$$

where

$$\mathbf{M}_m = \frac{\sum_n (a_n\,\mathbf{M}_a + b_n\,\mathbf{M}_b)}{\sum_n (a_n + b_n)}.$$

Of particular interest is the situation when $\Sigma a_n / \Sigma(a_n + b_n) = 2/3$. The macroscopic strain tensor is then:

$$\mathbf{S}_m = \mathbf{M}_m - \mathbf{I} = \begin{pmatrix} \epsilon & 0 & -\epsilon \\ 0 & 0 & 0 \\ \epsilon & 0 & -\epsilon \end{pmatrix}.$$

Directions in the (101) planes are represented by vectors

$$\mathbf{v} = \alpha(\mathbf{e}_1 - \mathbf{e}_3) + \beta\,\mathbf{e}_2$$

and for these directions the macroscopic distortion

$$d\mathbf{v} = \mathbf{S}_m\,\mathbf{v} = 0.$$

The (101) plane is thus a plane of zero macroscopic strain if the tetragonal twins have mean thickness ratio of 2:1. This is physically obvious, since the mean effect of the second shears then cancels out, and the only macroscopic strain corresponds to a shear of 2ϵ on the (101) planes in the $[10\bar{1}]$-direction. It is also clear that the cubic and tetragonal phases cannot co-exist without long-range strains, unless the tetragonal crystals are twinned on a fine scale to give a $\{101\}$-plane of zero macroscopic distortion.

The actual magnitude of the strains will depend on the width of the twin bands. If the tetragonal crystal has orientation (a), $d\mathbf{v} = 0$ for the $[1\bar{1}\bar{1}]$-direction, and in the perpendicular direction of the (101)-plane, $[1\bar{2}\bar{1}]$, the strain has a maximum value of

$$dv = 3\epsilon\,\frac{x}{6}\,(\mathbf{e}_1 - \mathbf{e}_2),$$

where x is the number of atomic $[1\bar{1}\bar{1}]$ rows traversed

by **v**. If we postulate that no atom is displaced by more than one atom radius, we find $x \simeq 40$. Similarly $x \simeq 20$ for orientation (b). The shear must then be reversed every 40 and 20 atomic planes as concluded by Bowles *et al.* [1]. The sub-bands observed in the microstructures of indium-thallium alloys are very much thicker than this, and hence require much larger strains. If these strains are concentrated at the interface, they must be plastic; i.e., the shears must be heterogeneous and the interface must contain slip dislocations. Alternatively, we may suppose the strains are spread out in an "accommodation region" extending back from the interface for a distance at least equal to the mean thickness of a twin. If the accommodation occurs without slip, however, the mean width of the twins of orientation (a) must always be twice that of those of orientation (b).

3. Experimental Methods

Single crystals of alloys with ~18.5% thallium were obtained by slow solidification in evacuated glass capsules, divided into two by a flat strip of glass. Semicylindrical crystals up to 4 cm in length and 0.6 cm in diameter, each having a smooth flat surface were thus obtained. The crystals were annealed about 5°C below the solidus for 2–7 days in order to induce single or double interface transformation. After cooling, the flat surface was electropolished. If more than one crystal was present, this was revealed by etching occurring during polishing.

The transformation was studied optically and by back-reflection Laue photographs. The specimen was placed in a close-fitting copper boat, heated from one end to give a small temperature gradient. Temperatures were measured approximately by chromel-alumel thermocouples placed in contact with the specimen. Visual observations under the microscope were made with slightly oblique illumination, or else an opaque stop was used to facilitate observations of small differences of surface orientation [7]. Moving film photographs were taken at speeds of 4–16 frames per second. Polarised light was sometimes useful for the room temperature examination of a transformed specimen, but it was not suitable for kinetic studies.

X-ray photographs were taken both at room temperature and at elevated temperatures up to ~110°C. The specimen was so mounted in the Laue camera that rotation through 180 degrees enabled the portion of the surface being photographed to be observed through a microscope. In this way X-ray methods were used to study the orientation changes occurring during a transformation.

We shall find it convenient to distinguish between two experimental arrangements used throughout the work. The slight longitudinal segregation, inevitably present in crystals grown from the melt, was utilised either to aid or oppose the temperature gradient. In the "normal" position, the end of the crystal which solidified first was placed at the unheated end of the copper boat. Since both freezing temperatures and transformation temperatures decrease with increasing thallium content, this implies any concentration gradient formed during freezing cooperates with the temperature gradient. Both gradients tend to make the transformation begin from the hotter end of the specimen on heating, and the other end on cooling. In the "reverse" position, the specimen was placed so that the two gradients opposed one another, and tended to promote transformation from opposite ends. The temperature gradient was increased considerably in some experiments by using specimens larger than the copper boat in which they were heated, so that one end of the specimen projected freely into the air.

4. Characteristics of Single-Interface Transformation

After suitable annealing, all specimens have been observed to transform by the migration of a single interface, lying along a {110}-plane, from one end of the specimen to the other. The trace of this interface is visible in a microsection either as a narrow white or black line, or as the boundary between two regions of different brightness. The surface of the specimen is tilted about the trace, so that the interface represents the limit of a region of homogeneous shear. Measurements of the surface tilt confirmed that the shear angle is given by $2\epsilon = 2/3(c/a - 1)$, as required by the accepted transformation mechanism [1]. The motion of the trace in the microsection is always perpendicular to itself, and it remains a straight line, so that any steps or irregularities in the boundary of the sheared region are of atomic dimensions only.

The interface leaves behind it a set of fine parallel bands as the crystal cools. These bands are visible as opposite tilts of the originally flat surface, and correspond to oppositely directed shears on a second {110}-plane. The lattice ahead of the interface is thus a single cubic crystal, while behind it are formed a series of parallel f.c.t. twins. After cooling right through the transformation range,

specimens consisting entirely of parallel tetragonal twins were obtained in this way; as described previously [6], these could be changed into single crystals by compression or extension. The appearance of a typical microsection during cooling is shown in Figures 2–4.

With the specimen in a normal position, the velocity of the interface was roughly proportional to the rate of cooling, and was of the order 0.05 cm per second for a cooling rate of 20°C per minute. These figures are very approximate, since the mean velocity of the interface varied considerably in different specimens. The movement was never completely smooth, but occurred as a series of discontinuous jerks with intermediate pauses.

In the simplest transformations, the changes occurring on heating were the reverse of those on cooling, the interface "wiping out" the secondary bands to leave a cubic single crystal of the original orientation. There was a temperature hysteresis of ~2°C between the heating and cooling transformations. During either heating or cooling, the interface could be halted in an intermediate position by regulation of the power input. When held completely stationary, the trace in the microsection became diffuse, and sometimes invisible, although the surface tilts were unaltered, except presumably in the immediate neighbourhood of the interface. If the interface were allowed to oscillate slightly in position, its definition was unchanged. After holding an interface stationary for some time, thermal stabilisation was found to have taken place. The interface then did not begin to move again until the specimen was heated or cooled some little way above or below the temperature at which the movement was arrested.

Figure 5 is a photomicrograph of a stationary single interface taken immediately after halting. The fine twins do not extend right up to the interface, and the surface appears to level out in a distance of about 10 twin thicknesses. Gaps of this kind were observed in all single- and double-interface transformations (see also Figures 2–4), and may be identified with the accommodation region referred to in section 2. With slow-moving interfaces the region in which no twins were visible was comparable with that shown in Figure 5, but during transformation on cooling, the gap increased with the speed of interface motion, and reached dimensions of the order of 1 mm in extreme cases. When such a rapid interface was halted or slowed down, the visible twins grew forward again almost to the interface in about a second. Examination of the twin boundaries behind a moving interface showed that they gradually became further apart over macroscopic distances. The twin thickness was usually close to the resolving power of the microscope, so it was difficult to observe how this thickening occurred. Occasionally, however, a twin band was seen splitting into narrower bands as the interface was approached.

The gap between the interface and the visible twins was always narrow during heating transformations, and seemed to be independent of the interface velocity. In fact the interface motion was always slower during heating. Figures 6–8 show the same single interface as Figures 2–4, but are taken during transformation from tetragonal to cubic.

A strange phenomenon occasionally observed with stationary interfaces was the increase in length of fine bands, which extended across the interface a little way into the cubic region. This change took place slowly, the contrast in the extended bands gradually increasing. When transformation was subsequently resumed, either by heating or by cooling, the portion of the bands which had crossed the interface remained visible as surface tilts. Figure 9 is a photograph of a group of such "bands," taken above the transformation temperature, when the specimen was entirely cubic.

Simple transformation on heating by the motion of an identical interface was most readily obtained by beginning heating again as soon as the interface had left the specimen on cooling. In the same way, if cooling was started as soon as the heating transformation appeared to be complete, the new cooling interface lay along the same {110}-plane. There was a tendency to obtain reproducible behaviour even after heating above the transformation range for some time, but this treatment sometimes resulted in the appearance of a new single interface, or in a two-interface transformation, described in the next section. On cooling, the interface seemed to pass out of the specimen perfectly regularly, but on heating there was a sudden acceleration when the interface was near the end of the specimen. This acceleration was observed under differing conditions in a large number of specimens.

The above description refers to the simplest mode of single interface transformation. More complex behaviour resulted when the heating transformation was accomplished by an interface moving on a different {110}-plane. In all cases observed, this was the plane perpendicular to the

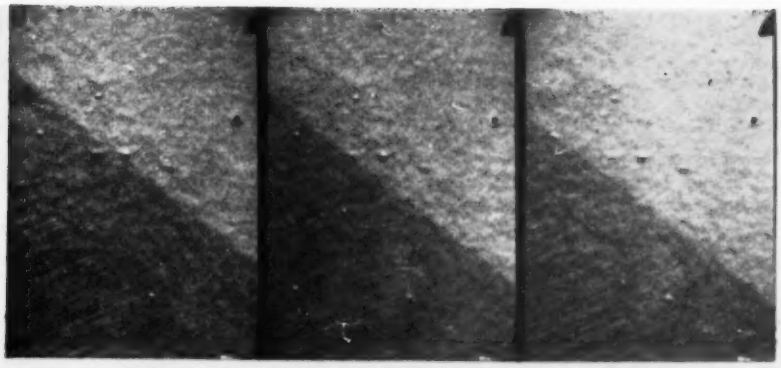

2 3 4

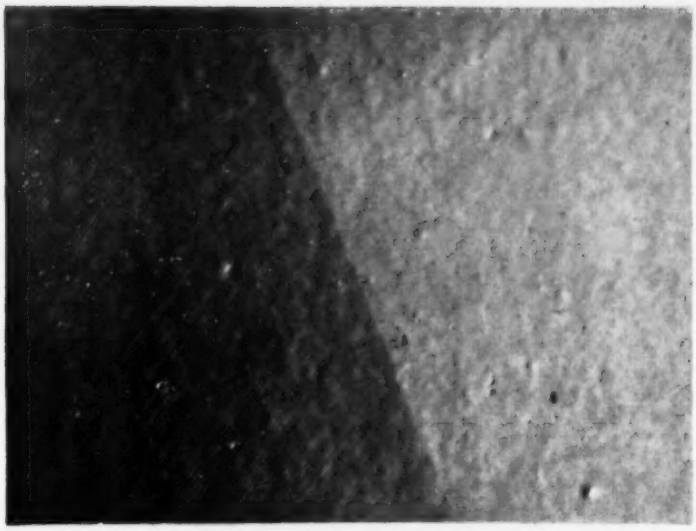

5

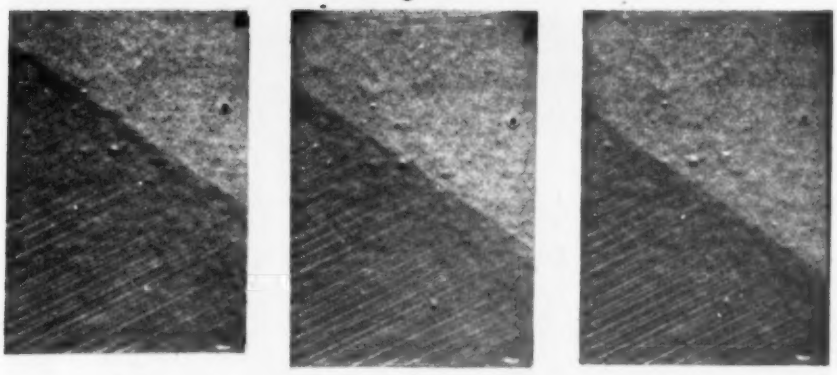

6 7 8

PLATE I. Figures 2–4—Motion of a single interface on cooling. Oblique illumination. 70×. The dark region is tetragonal, and the twin traces are just visible. Interval between frames 1/16 sec. Figure 5—Stationary single interface showing accommodation region for fine twins. Oblique illumination. 150×. Figures 6–8—Motion of single interface on heating. Oblique illumination. 70×. Interval between frames 5/16 sec.

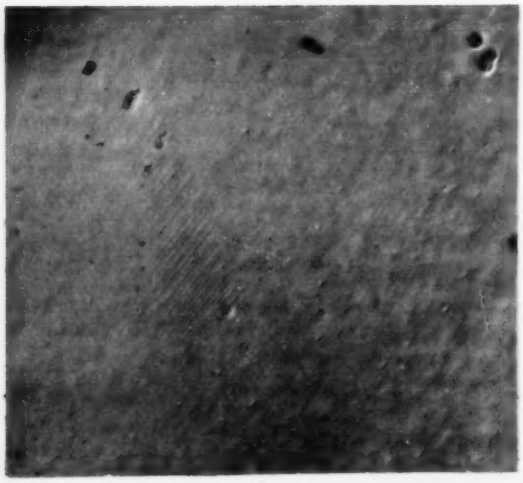

9

11

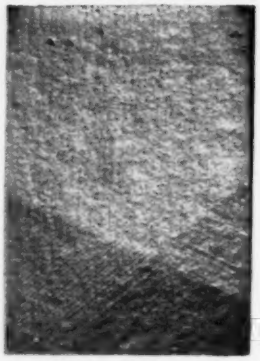

12

13

15

17

PLATE II. Figure 9—Surface tilts produced by fine bands which have extended across a stationary single interface. Photographed in cubic region at 120°C. Normal illumination. 150×. Figures 11–13—Motion of an *X*-interface on heating. The cubic region (AOB in Fig. 10) is at the top of the photographs: the single tetragonal region at the bottom. Oblique illumination. 70×. Interval between frames ¼ sec. Figure 15—Thermally stabilised λ-interface photographed at room temperature. Oblique illumination. 65×. The cubic region is on the left of the photograph, and the tetragonal single crystal on the right. The bottom of the photograph corresponds to AOX of Fig. 14, the top to BOY. The twins in the top cannot be seen since their shear direction is almost in the surface plane; their presence was confirmed by X-rays. For the same reason, the bend round OY is not readily visible. Figure 17—A double interface transformation of the type shown in Fig. 16. The cubic region is at the bottom of the photograph. The twins in the region on the left are not visible because their shear direction is almost in the surface plane. Oblique illumination. 70×.

original interface, and produced a cubic single crystal of the original orientation. This type of reverse transformation is possible, since the two sets of twins formed by first shears on perpendicular planes, and identical second shears, are connected by a rigid rotation. In a completely transformed specimen such a rigid rotation has no physical meaning, and reverse transformation by an interface on either plane is crystallographically possible. In one specimen, this behaviour was very reproducible, the same cooling interface and its perpendicular heating interface appearing in a large number of cycles.

As pointed out in section 2, one cooling interface should be able to produce two sets of tetragonal crystals, of the relative orientations shown in Figure 1. This was observed only once in a normal transformation: the two sets of twins met along a straight line but there was no orientation difference of the macroscopic surface of the two twinned regions. In this specimen, the heating interface removed both sets of twins to form a single crystal. The heating interface was perpendicular to the cooling interface, as is possible since all four orientations of Figure 1 are changed by a rigid rotation into those produced by the first shear on the perpendicular plane.

With specimens in reversed positions, the observations were qualitatively similar to those above, but some important differences were noted. Using the normal (small) temperature gradient, the transformation began from the colder end on heating, so that the composition gradient apparently controlled the process. An attempt to detect this gradient by analysis of the ends of one specimen gave inconclusive results, so this assumption may not be justified. Nevertheless, it seems almost certain that the method of growth would result in a macroscopic composition gradient, and reference to Guttman's paper [8] shows that a very small composition difference produces an appreciable difference in transformation temperature. The interface motion was similar to that described above, but was much faster for a given rate of heating or cooling. Experiments with an increased temperature gradient were successful in inducing double-interface transformation from the indium rich (hotter) end; these are described in the next section. The results indicate that transformation against the temperature gradient is a consequence of the composition gradient, and not of preferred nucleation round some crystal imperfection frozen in at one end of the specimen.

5. Characteristics of Double-Interface Transformations

Single interface transformations result in a series of fine tetragonal twins. A single tetragonal crystal may be produced by the simultaneous motion of two primary interfaces across the crystal. These interfaces lie along {110}-planes at 60 degrees to each other in the cubic crystal, and the single tetragonal crystal has the orientation common to first shears in these two planes. The *directions* of the first shears are thus not independent; each first shear must be a possible second shear of the other interface.

Two types of double interface have been observed to lead to the production of tetragonal single crystals; we shall call them "X" and "λ" interfaces, for convenience. The X-transformation is the simplest type. Each interface leaves behind it a set of tetragonal twins, with twinning plane parallel to the other interface. Figure 10 represents an arbitrary surface of the crystal when two such interfaces have crossed. We have already noted that if the twins have the width ratio 2:1, the only macroscopic strain produced by a single interface is that due to the first shear. There will thus be a macroscopic

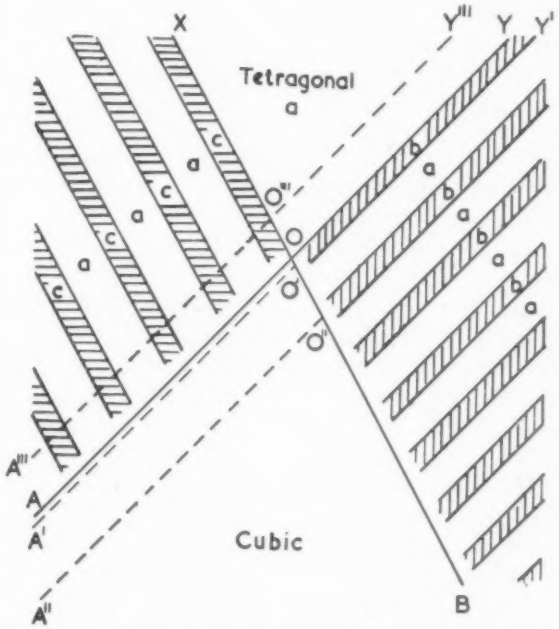

FIGURE 10. To illustrate production of a single tetragonal crystal by an "X" interface (diagrammatic only). AOY, BOX are the traces of {110}-planes at 60 degrees to each other.

surface tilt about OB if the twins (a) are twice as wide as (b). Similarly there will be a macroscopic tilt corresponding to a shear of 2ϵ along the {110}-plane having trace OX, if the twins (a) and (c) have width ratio 2:1 (see section 2 of reference [6]). There will therefore be a macroscopic shear of 2ϵ along the {110} plane through BOX, and similarly on the plane through AOY. The surfaces AOB, XOY, AOX and BOY will all be macroscopically flat, but will be tilted sharply with respect to each other about AOY and BOX. The point O is the apex of a flat pyramidal elevation or depression of the macroscopic surface.

Now suppose the interface OA moves to a new position $O'A'$ during cooling, while OB remains stationary. The twins (a) and (c) are extended, and the macroscopic tilt is now about $O'A'$. This produces a strain in the region OO', and a force on OY tending to move it towards $O'Y'$ and thus untwin the first twin region (b). If OY remains stationary, the force increases rapidly as $O'A'$ moves away from OA, and eventually will be large enough to move OY. Actually the twin boundaries are so mobile that OY always appears to remain in line with $O'A'$, so far as can be seen under the microscope.

Clearly when the region (b) is completely untwinned, the accommodation forces will tend to make $O'A'$ move further forward to $O''A''$. As the interface OA advances, the accommodation strains may be supposed to supply a small force, alternately aiding and opposing its motion. This effect is necessarily very small, and it is doubtful whether we may justifiably make use of forces due to macroscopic accommodation of the lattices over distances of the order of the twin widths.

Exactly equivalent arguments apply to the motion of OB. In an actual transformation, both interfaces advance together, leaving a single tetragonal crystal of orientation (a). The term "X-interface" is a little misleading, since only the portions OA, OB represent the traces of first shear planes. The motion of OX and OY is discontinuous, but under the microscope there is an optical illusion of the two traces moving across each other.

After a double-interface transformation, the whole of the specimen will be a single crystal only if both interfaces pass right out of the crystal together. If one interface does this first, there will be a region of tetragonal twins bounded by the other interface, and this region should persist since there are no longer any accommodation forces tending to untwin it. Many transformed specimens were found to contain small twinned regions of this type.

The changes on heating may occur by the exact reversal of the motion on cooling. It is necessary for the single tetragonal crystal to twin before it can be transformed into cubic. Referring to Figure 10 again, an advance of the interface OA to a position $O'''A'''$ on heating will transform the region $OO'''A'''A$ and the accommodation stresses then require the twinned region BOY to extend to $BO'''Y'''$. Obviously the initiation of the heating transformation is facilitated if a set of twins are left in a finite volume of the specimen by the cooling transformation. This seems to have usually occurred, and the same two interfaces were observed on heating. The appearance of an X-interface on heating is shown in Figures 11–13.

The double-interface transformation does not necessarily appear as an "X" in the microstructure. The line of intersection of the interfaces need not cut the microsection; if it does not, the transformation appears to take place by the passage of one trace, leaving fine bands, followed by a second trace which removes them again.

In a normal position, the kinetics of the double-interface transformation were similar to those of single-interface transformation. The movement of one interface was often much more rapid than that of the other, and the interfaces could be halted by regulation of the temperature. The thermal stabilization produced by prolonged holding in one position was often so great that one or both interfaces became permanently locked in this position. Subsequent transformation on cooling then required the formation of a new interface.

The appearance of an arbitrary crystal surface during a λ transformation is shown in Figure 14. Each single interface again leaves a set of tetragonal twins, but those left by the interface OB now have a twinning plane perpendicular to OA. The macroscopic tilts along XOB and OA are exactly as in Figure 10, and the accommodation stresses therefore require a macroscopic tilt along OY, as the result of a macroscopic shear along the {110}-plane through OY. This shear is produced by tapering of the twin boundaries as shown in Figure 9. If this tapering takes place by the formation of edge-type twinning dislocations in such a way that the twin boundaries end in ⟨100⟩ lines which are randomly distributed in a planar region parallel to the {100}-plane through OA, the tapering is equivalent to a macroscopic shear along OY. We have called this a distributed or virtual shear [6]. The lattice orientation (d) changes into the orientation (a)

during this tapering, providing the thickness ratio of (d) to (e) is 2:1. The accommodation requirements are again satisfied, and there are no long range strains present. The interface thus acts in a manner essentially similar to the X-interface, except that the macroscopic shear along OY is gradual not sharp. This is readily visible in the microsection where the change in surface orientation from XOY to YOB occurs gradually over the distance in which the twins taper. As OA advances, the

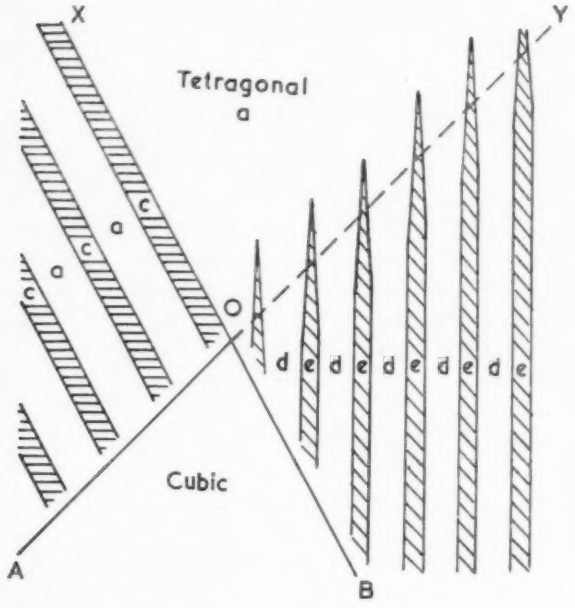

FIGURE 14. To illustrate the production of a tetragonal single crystal by a λ-interface. AOY, BOX are traces of {110}-planes at 60 degrees to each other. The twinning plane of orientations d and e, represented as a vertical trace, is a {110}-plane at 90 degrees to the plane having trace AOX.

accommodation stresses again tend to untwin the region YOB, and a single crystal of orientation (a) is again obtained. During transformations of this kind, the interface YOA was usually much less mobile than XOB.

λ interfaces could be stabilised thermally, and Figure 15 shows such an interface after cooling to room temperature, the transformation having resumed on a different plane. Specimens in which the interface XOB moved right out on cooling, leaving a diffuse bend about OY were found to slowly straighten at room temperature. This implies slow untwinning, i.e., the slow migration of OY out of the crystal.

From the above description, it is clear that a double interface transformation of "V" type should also be possible, each interface leaving twins perpendicular to the other, and the tilts about OX and OY both being gradual. In the present work, this has not been observed.

Double-interface transformations in reversed specimens with small temperature gradients were similar to normal transformations. Increasing the temperature gradient by using a specimen longer than the copper boat, resulted in a transformation controlled in direction by the temperature gradient. The interface motion was then so rapid that visual observation with the eye rather than under the microscope had to be used. The initial velocity of the interface on heating was even then too great to be observed, and it was not possible to decide whether the transformation began at the hot end of the specimen, or somewhere in the middle. A loud click was heard when transformation began; fainter clicks were heard in some normal transformations. The interface motion became much slower when it reached the cooler end of the specimen and it could then be halted or reversed in the usual way.

6. Double Interface Transformations leading to Twinned Tetragonal Crystals

In section 5 we emphasised that the shear directions of the two interfaces are not independent, if a single tetragonal crystal is to be obtained. We have also observed a double interface transformation in which the first shears are on {110} cubic planes at 60 degrees to each other, but in which there is no common orientation in the resultant tetragonal crystals. The operation of such an interface is shown in Figure 16. The interfaces OA, OB may be supposed to lie along the same {110}-planes as in Figure 10, but the direction of shear on OA is now reversed. OA is thus the trace of a possible second shear plane for the first shear along OB, but the reverse statement is no longer true. As in the X-interface the macroscopic tilts along OA and OB require similar shears along the planes through OY and OX. The macroscopic shear along OY is obtained by a change in the thickness ratio of twins (a) and (b), which have OY as their twinning plane. In the region BOY, this ratio is 2:1; a shear of 2ϵ along OY converts the ratio into 1:2 (see section 2 of [6]). The region AOX is twinned on a completely different plane from OXY, and the macroscopic shear along OX must correspond to a meeting plane of the two sets of twins. In contrast to the X-interface, the shape of the macroscopic surface is now obtained by folding a sheet of paper upwards along AOY, and downwards along BOX, or vice versa.

The action of this double interface should now be clear from the previous description. If OA advances along OB, the line OY will be pulled along with it, exactly as in Figure 10. Similarly, the line OX will be subject to a force if OB advances along OA. The situation along OX is rather more complex, since the material traversed by this interface must retwin on a different plane. In view of the great ease of twin boundary movements, this presents no great difficulty. A double interface of this type is shown in Figure 17. It is clear that if the second

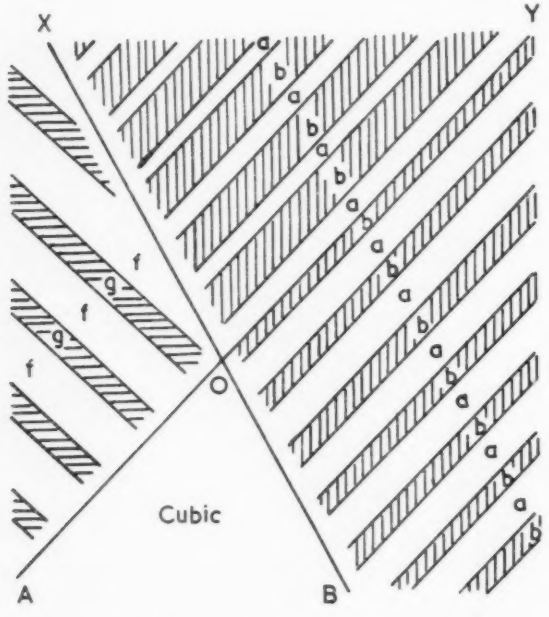

FIGURE 16. To illustrate the production of twinned tetragonal crystals by a double-interface transformation. The {110}-planes having traces AOX, BOX are at 60 degrees to each other. The twinning plane of orientations f and g is at 60 degrees to both AOY and BOX.

shear in the region BOY were along the {110}-plane perpendicular to OA, we should have the analogue of the λ interface of the last section. This has not been observed.

7. Effect of Stress on the Transformation

Qualitative experiments on the effect of stress illustrated the remarkable similarity in transformation and deformation properties, both of which depend on the mobility of twin boundaries or shear interfaces under small stresses. Specimens transformed under small compressive or extensive loads were rather more likely to give single tetragonal crystals than specimens under no external constraints. As described in the previous paper [6], specimens transformed by one interface could be changed into single crystals by the application of such a load.

Specimens supported on knife edges, and thus subjected to small bending moments from their own weight, remained straight in the cubic region, but bent as soon as transformation occurred. When such a specimen was reheated, it straightened again on the reverse transformation. This straightening was very rapid; the specimen emitted a loud click, and seemed almost to jump in the air. In the same way, specimens transformed by a single interface, and then deliberately bent by twin boundary movements, straightened during the reverse transformation.

Some experiments were made on the opposing effects of stress and volume free energy of the phases in moving an interface. A small compressive stress, suitably applied, was able to halt and reverse the motion of a cooling interface in both single- and double-interface transformations. In an X-transformation, the effect was greatest on the interface having the largest component of the stress acting on it.

Application of a rather large stress to a cubic single crystal just above the transformation temperature produced a macroscopic bend. On removal of the stress, however, the specimen returned instantaneously to its original position. These results seem to be exactly comparable with those reported by Reynolds and Bever [9] for copper-zinc alloys. The rubber like elasticity may be taken as evidence of stress induced transformation above the equilibrium temperature.

8. Multiple Interface Transformation and Transformation in Polycrystalline Specimens

Single-crystal specimens which had not been well annealed, or had been mishandled, transformed by multiple interfaces. One or two specimens consisting of a few large crystals were also available. In both cases the transformation pattern was reminiscent of that produced in polycrystalline specimens, but was simpler and on a larger scale. Most of the characteristic features of polycrystalline transformation can be explained in terms of the single and double interface movements described above.

The production of a series of parallel main bands corresponds to the motion of a number of single interfaces on parallel planes but having opposite shear directions. On a macroscopic scale, the formation of these main bands always occurred progressively from one end of the series to the other, and

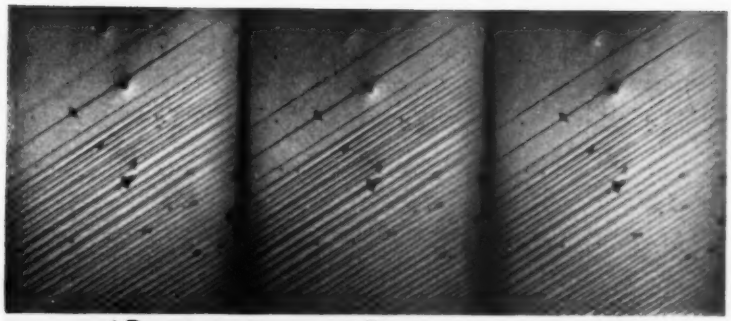

18 19 20

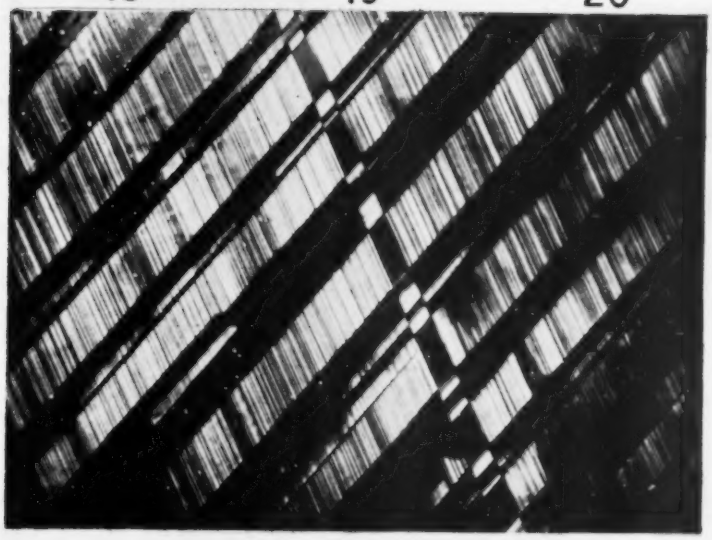

21

22

PLATE III. Figures 18–20—The growth of a main band at the head of an extending set of main bands. Oblique illumination. 70×. Interval between frames 1/16 sec. Figure 21—Interpenetrating main bands showing twin pattern characteristic of *X*-interfaces. Etched specimen. Two-hour exposure with polarised light. 100×. Figure 22—Part of the area of Figure 21 showing twinning pattern. Etched specimen. Normal illumination. 500×.

the bands grew mainly by motion of interfaces perpendicular to their length. On a microscopic scale, however, it was observed that bands continually formed ahead of the main group and the interface advanced "backwards" to meet the existing bands. These results are in agreement with those previously reported for polycrystalline copper manganese alloys [2].

Growth of main bands by lengthwise extension was also observed. Under the microscope this lengthening appeared to be very rapid compared with the sideways motion of an interface. Motion picture studies show that in such an extension the surface tilt is not discontinuous but builds up gradually. Figures 18–20 are three successive frames of a region near the edge of an advancing set of main bands. It can be seen that two or three bands have formed ahead of the main interface. The centre of the most advanced band (at the bottom of the photographs) is visible as a diffuse region in the first frame, and this becomes sharp in the two successive frames.

Bowles, Barrett and Guttman [1] observed that main bands on planes at 60 degrees to each other interpenetrated, others did not. This interpenetration is clearly analogous to the double-interface transformation; in fact, each crossing main band may be regarded as a small X-interface. The relation between X-interfaces and the transformation pattern in polycrystalline specimens is shown clearly in Figures 21 and 22. The rather broad interpenetrating main bands show the twinning pattern characteristic of X-interfaces.

9. Discussion

(1) *Mechanism of the Two Shear Transformation*

A full description of a martensitic transformation involves not only a knowledge of the atomic paths during the reaction, but also a reasonable atomic model for these movements. As with other types of transformation, we require mechanisms both for nucleation of the new phase, and for the subsequent growth of the nuclei. The nucleation problem presents considerable difficulties, and we deal first with the growth mechanism.

In the temperature region where the tetragonal phase is thermodynamically stable, there will be an effective force on the boundary between the phases provided by the higher free energy of the cubic structure. The boundary may advance into the cubic region (*a*) if atoms are able to jump separately across the interfaces under the influence of thermal agitation, or (*b*) if the stress is able to move the boundary as a whole. The first assumption is the basis of the theories developed by Kurdjumov [10] and by Fisher, Hollomon and Turnbull [11]; under the second we may group the various dislocation theories of martensitic reactions. As we have indicated elsewhere [5], the distinction between the two assumptions is not always very clear, but may sometimes be made on the basis of activation energy. The characteristic of the second assumption is that thermal activation energy is not necessarily required for growth, and the process is very closely related to plastic deformation by mechanical twinning, and to the recently observed stress-induced movements of small angle grain boundaries [12]. The analogy between the effects of temperature and those of mechanical stress in moving a boundary is so very close (see section 7 and reference [6]) that we are inclined to accept the second kind of description as almost established. This theory is also able to account for rapid transformation at very low temperatures [13]. In the more exceptional examples where martensitic reaction is largely isothermal [14], there is growing recognition that the rate limiting step is nucleation of the new phase [15]. These transformations thus do not provide evidence that thermal activation energy is needed for growth.

In the indium-thallium transformation, we must first decide whether or not our separation of the atomic movements into two shears has physical, as distinct from purely mathematical, significance. We have considered the possibility that the strain of the second shear is taken purely elastically. This would imply that the accommodation region of Figure 5, for example, would be described as a strained lattice continuously varying from the single orthorhombic structure produced by the first shear to the final twinned tetragonal structure. It seems most improbable, however, that such an arrangement could be mechanically stable, and the experiments in which the visible twinned regions were left well behind the first shear interface definitely rule out this possibility.

Since there is no experimental evidence to support a physical separation of the two shears, we assume that the atom movements occur together at the visible interface, and that tetragonal structures are produced immediately behind the interface. Frank [16] has recently treated a similar problem in the formation of iron-carbon martensite, and he showed that the macroscopically inhomogeneous second shear could be obtained by an array of screw dislocations moving in the transformation interface

between every sixth pair of (011) planes. These dislocations move blocks of six planes through one interatomic distance relative to each other; each block is homogeneously sheared so that neighbouring atom rows are displaced through 1/6 of an interatomic distance. The atoms between the screw dislocations are obviously mechanically unstable in their original relative positions and move immediately to their new positions. In this sense it is correct to regard the screw dislocations as automatically accomplishing the heterogeneous shear. Nevertheless, it seems to us that it is useful, purely formally, to suppose the small units of homogeneous shear to be obtained by the motion of imperfect dislocations in the interface. These imperfect dislocations will lie between every atomic plane, and have Burger's vectors $-1/6$ of those of the slip dislocations. This formalism has the advantage that the total Burger's vector of the "second" shear is then zero if more than six atomic planes are considered, thus corresponding to zero macroscopic distortion. Since the dislocations are present in the interface, rather than in either of the lattices, it is clear that the mode of description we adopt is largely a matter of convenience.

There are some important differences between the description given by Frank and the corresponding theory for indium-thallium. In the present transformation, the direction of the second shear does not lie in the interface between the phases. The dislocations which generate the second shear are therefore, not pure screw in character; their line is a $\langle 111 \rangle$-direction, but their Burger's vector is in a $\langle 101 \rangle$-direction. These imperfect dislocations may be supposed to move in the $\{110\}$-plane of the second shear, which is their slip plane. The second difference is that the macroscopic effect of the second shear is eliminated by the periodic reversal of its direction, rather than by periodic slip. The second shear of the indium-thallium transformation may be formally obtained by a series of x imperfect parallel dislocations, having Burger's vectors $b = 2\epsilon\, a/2\sqrt{2} = a\epsilon/\sqrt{2}$ between every two atomic $\{110\}$ planes, followed by $x/2$ parallel dislocations with Burger's vectors $-a\epsilon\sqrt{2}$. The number of planes is not known, but x must be less than about 40 unless there are also slip dislocations in the interface.

According to this theory, the tetragonal structure behind a single interface consists of very fine twins. The fine scale twinning is necessary to prevent large strain energy at the interface, but is obviously unfavourable energetically in the more remote regions of the tetragonal phase. The total coherency energy of the tetragonal boundaries is appreciable, and may be reduced by progressive elimination of some of the twins, as sketched in Figure 23. This process leaves the ratio of the thicknesses of the two orientations unchanged, and is responsible for the accommodation region over which the twins thicken to microscopic dimensions. The thickening is accomplished by the motion of arrays of twinning dislocations behind the interface, and the experimental results can best be explained on the assumption that these dislocations are less mobile than the interface itself. When the interface moves very rapidly, the region of sub-microscopic twins is enlarged, and gradually returns to its equilibrium dimensions when the interface is slowed again.

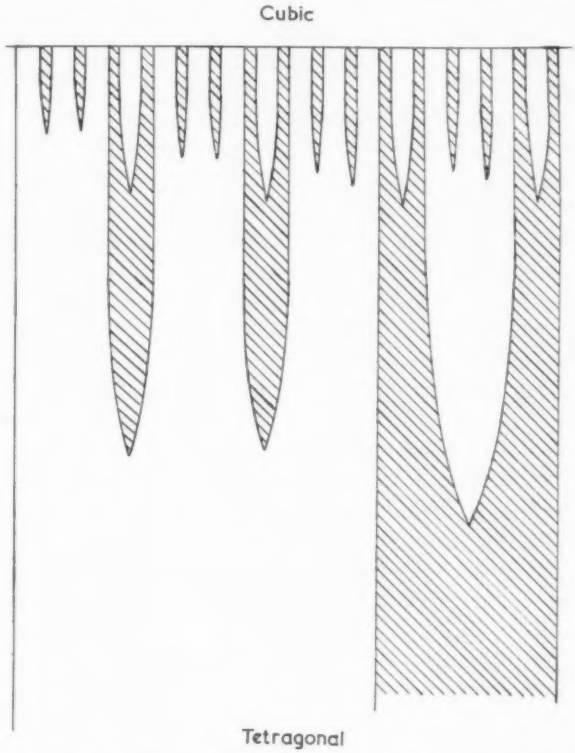

FIGURE 23. Suggested mechanism for thickening of sub-microscopic twins in accommodation region behind interface (diagrammatic only).

Frank [16] and Bowles [1] have both pointed out that an iron-carbon martensite twin may be formed by reversing the direction of the second shear. In this transformation, also, it is thus geometrically possible to avoid a macroscopic strain by periodic reversal of the shear direction, rather than by heterogenous shear. According to Bowles and Mackenzie [17], martensite plates are usually twinned, and we are unaware of any definite evi-

dence that individual plates are not twinned on a fine scale. However, it seems safer to assume that this is not so. The reason why iron-carbon alloys prefer a heterogeneous shear, whereas the indium-thallium alloys prefer to twin, is not known, but is probably connected with the small magnitude of the shear in the latter case. Suppose the second shear is homogeneous for x planes, after which it either reverses in direction or slip takes place. If slip occurs there is a minimum value of x, $x_{\min}$, since the total displacements of the imperfect dislocations (i.e., of the homogeneous shear) must equal at least one lattice vector; otherwise, a stacking fault is left in the lattice. For twin crystals produced by reversing the second shear, this does not apply since the twin boundaries have low energy. The strain energy is proportional to x^2, the energy of the coherent twin boundaries to $1/x$. If the shear is reversed to give twin crystals in a distance $x_{\min}$, the strain energy is equal to that produced by slip, but the total energy will be greater because of the finite twin boundary energy. The energy of the set of twins may be treated as a continuous function of x, and at some value x_0 the total energy will be minimised. In general if $x_0 < x_{\min}$, it is possible for the twin assembly to give the lower total energy, and hence to be preferred to the heterogeneous shear. The conditions for this are obviously favourable when, as in indium-thallium, the shear is very small, so that $x_{\min}$ is large: they are unfavourable when $x_{\min}$ is only 6 atomic planes.

The above discussion refers explicitly to the generation of the second shear. The results show that growth of the tetragonal phase occurs mainly by movement of the interface perpendicular to its plane, i.e., in the same way as the usual growth of mechanical twins. If this interface is irrational, as in iron-carbon alloys, it may be expected to be very mobile. With rational interfaces, however, difficulties are encountered, as in the theory of crystal growth on close-packed planes. A step in the interface corresponds to a transformation or twinning dislocation, and when a stress is applied (either externally or from the free-energy difference between the phases), the dislocation will spread in its plane, increasing the thickness of the martensite plate or twin crystal by one atomic layer. In a perfect lattice, this process results in a plane interface, and the next layer then cannot grow until a nucleus of suitable size is formed by thermal activation. When a few atoms are transferred to form a small island of the product phase on the next atomic plane, the transformation dislocation which surrounds them tends to shrink on itself. It will only expand after reaching a critical size, and the kinetics of the process are therefore governed by an activation energy for two-dimensional nulceation. As discussed elsewhere [5], however, this type of growth would not lead to the large homogeneously strained regions which are observed in martensitic reactions.

The difficulty is avoided in the theory of "generating nodes" developed by Cottrell and Bilby [18] and by Bilby [19], which is essentially a combination of Frank's theory of crystal growth and Frank and Read's mechanism for slip-band formation. In view of the detailed discussions of this theory which have been given elsewhere, we shall not consider it here in greater detail.

The observations of lengthwise growth of the main bands in a multi-interface transformation cannot be fitted easily into the above theory. Such growth may occur by spontaneous generation of new loops of transformation dislocation, as suggested by Frank and Stroh [20] for kink bands. The observations in Figures 18–20 can be explained more simply on the hypothesis that the transformation interface is held up below the surface over part of its length, the resultant strains producing a gradual bend of the surface. As the thickness of the band increases, the strains due to the stuck dislocations increase also, and the surface becomes sharply kinked when the dislocations break through.

(2) *Kinetics of the Transformation*

The velocity of the interface was found to be roughly proportional to the rate of cooling, in agreement with the results for gold-cadmium alloys [21]. Chang interpreted these results in terms of two relaxation processes occurring during transformation, one at the interface itself, and the other a volume relaxation, so that an energy term proportional to the volume transformed opposes further transformation. In the present work, ample confirmation of the relaxation processes at the interface has been obtained. The thermal stabilisation produced by holding the interface stationary increased with time, and in some cases the stresses round the interface were so relaxed that transformation resumed from a different nucleus. As concluded by Chang, it seems probable that the activation energy for the process is that for atomic diffusion, the mechanism presumably being the formation of dilute Cottrell atmospheres of solute atoms with Maxwellian distribution round the interface. Such a relaxation seems especially likely in view of the rapid decrease of the cubic-tetragonal transformation tem-

perature with increasing thallium content. Consider a stationary interface. The stresses which tend to move it into the cubic region depend only on the difference of the volume free energies of the two phases on either side of the interface. These stresses can be relaxed to zero if there is a redistribution of solute atoms, so that the concentration of thallium slightly increases in the cubic region in the immediate vicinity of the interface, and slightly decreases in the tetragonal region. When cooling is resumed, the interface will only begin to move again when a sufficient free energy difference is attained. We emphasise, however, that although such a diffusion mechanism seems reasonable, there is no direct evidence on this point. The results support the view of Morgan and Ko [21] on the nature of stabilisation.

In indium-thallium alloys, the transformation range is much nearer the melting point than in gold-cadmium, so that diffusion is rapid and stabilisation considerable. When the interface is held stationary, the sharp kink in the surface at the junction of cubic and tetragonal regions changed into a gradual bend, and the interface trace became diffuse. This seems to require the material transport of surface atoms, either by diffusion or a kind of creep, as a result of surface energy driving forces. So far as the transformation is concerned, this observation is therefore unimportant, but it shows how rapid diffusion may be. The extension of the small surface tilts in the tetragonal region across the interface into the cubic region (Figure 5) is presumably a similar phenomenon. The persistence of the tilts, even after transformation to a cubic single crystal, shows that their formation does involve the transport of matter.

In addition to relaxation at the interface, Chang also postulated a relaxation term proportional to the volume, in order to explain why continuous cooling is required to effect the transformation. Such a term is obviously present in polycrystalline specimens because of the stresses in the parent phase round a developing crystal of the product phase, but there seems no reason to expect it in single crystals. The present work suggests that part of the reason for transformation proceeding only on cooling may be trivial, and due only to a small macroscopic composition gradient along the specimen: it is difficult to see how else to interpret the results obtained with reversed specimens and very small temperature gradients. However, we think it unlikely that this can be the whole explanation, especially in view of Chang's results.

A purely formal theory of the transformation may perhaps be developed on the following lines, assuming for convenience there is no temperature or composition gradient. We postulate some suitable nucleus, either formed in the cubic region, or during cooling. If cooling is continuous from the cubic region, the stresses round this nucleus will not be fully relaxed, and the interface will begin moving when the stress on it reaches a value τ_0, corresponding to temperature differential (transformation temperature − actual temperature) ΔT_0. As the interface moves, solute atoms continuously reorientate themselves to relax stresses, so that for a given ΔT_0 the interface velocity will be roughly constant: in effect a partially formed Cottrell atmosphere is dragged along. Eventually the interface encounters some obstacle which halts it or slows it down sufficiently for relaxation to occur. The stress necessary for further advance is then $\tau_1 > \tau_0$, and the temperature has to be lowered to ΔT_1. Repetition of the process leads to the observed jerky movement. After passing the obstacle, the interface will have a larger force acting on it, and we might expect that a second obstacle would have to exert a back stress of at least $\tau_1 - \tau_0$ to stop it. If this were true, the ability of obstacles to arrest the interface would rapidly diminish, and we should obtain isothermal transformation at some value ΔT_r. The volume relaxation is equivalent to assuming that after passing the first obstacle, the stress necessary to just move the interface is τ_1 rather than τ_0, and so on. On this interpretation, each obstacle continues to exert an influence after the interface has passed it. To take a specific example: this might happen if passage of the interface through the obstacle involved the intersection of screw dislocations, so that the jog in the interface leaves a trail of lattice imperfection.

It is interesting to note that the account above implies that although the single-interface transformation only proceeds on cooling or heating, the movements may be regarded as a series of short isothermal advances. In more normal transformations, there will be a similar effect, except that the volume energy opposing further transformation is now large, being mainly due to the stresses round a martensitic plate, so that each plate grows rapidly (and isothermally) to its final size. Further transformation then requires the activation of new nuclei on subsequent cooling. The phenomenon of isothermal martensitic transformation may similarly be interpreted as involving rapid isothermal growth to a limiting size followed by a time interval for the thermal creation of a new nucleus.

Finally, we should consider the magnitude of the interface velocity. At slow rates of cooling or heating, this is presumably limited by the relaxation processes discussed above. With very large temperature gradients, interfaces moved with speeds of the order 10 cm/sec or greater. The mechanism discussed by Cottrell and Bilby however, shows that velocities of the order 500 cm/sec may be obtained with quite small stresses, so that no difficulties arise in explaining the higher speeds.

(3) *Nucleation of the Transformation*

We have previously pointed out that the often observed reversibility of the transformation implies the existence of nuclei of the martensite phase which are not entirely eliminated by heating into the stability region of the parent phase. In the present work, the same single or double interface was found on repeated cycles, although a change was occasionally produced by heating for some time in the cubic region. Since the interface always appeared and disappeared from the same part of the crystal surface, it seems probable that a nucleus of the appropriate tetragonal orientation was retained at the surface. It may be possible to draw a parallel with Turnbull's theory of the effect of thermal history on the supercooling of liquids [23], but this was not investigated in the present work.

The nature of the nucleus itself is unknown, but some observations on multi-interface transformations, made both in the present work and in the previous work on copper-manganese alloys [2], are of interest. According to the dislocation node theory, we should expect small nuclei of the cubic phase to be retained between every two main bands, since the transformation dislocations cannot pass each other below a certain minimum separation. Providing insufficient time is allowed for the dissipation of these nuclei by thermal means, the main bands should transform more or less randomly back to cubic. This is in fact observed. On cooling, however, a set of main bands form progressively from one end to the other, the mechanism being either the activation or the creation of nuclei by the matrix stresses ahead of the advancing set of bands.

It is fairly certain that nucleation is heterogeneous, and probably occurs at or near the surface in single-interface transformations. In Cottrell and Bilby's theory of twinning in α-iron, the nucleus can be a monolayer stacking fault, but in general this does not seem to be possible, and much larger nuclei are required before growth can occur by shear processes. There seems at present no alternative to the assumption that nuclei are formed thermally at the transformation temperature, or athermally by cooling from above this temperature.

According to Geisler [4], nuclei are formed coherently on {111} planes. Although we have criticised his theory of growth, this seems a feasible method of nucleation. If we refer the strain tensor $\mathbf{S}_a$ of section 2 to axes $[01\bar{1}]$, $[\bar{2}11]$ $[111]$, we find

$$\mathbf{S}_a = \begin{pmatrix} -\epsilon & 0 & 0 \\ 0 & \epsilon & 0 \\ 0 & -2\sqrt{2\epsilon} & 0 \end{pmatrix}.$$

The strain in the {111}-planes thus corresponds to a homogeneous shear, and there is no stress normal to these planes, since their spacing is unchanged. A small coherent nucleus on such a plane would thus have relatively low strain energy.

The existence of double shear interfaces requires explanation. If a single interface is formed, and for some reason one of the tetragonal twins is rather thicker than usual, the strain energy might be reduced by the propagation of the shear across the interface, thus producing a new single interface in the cubic region. All types of double interface could conceivably be accounted for in this way.

Acknowledgements

We should like to thank Dr. W. Hume-Rothery, F.R.S. for laboratory accommodation and other facilities, and for his interest in this work. One of us (J. W. C.) also wishes to acknowledge the award of a Pressed Steel Co. Ltd. Fellowship by the University of Oxford.

References

1. BOWLES, J. S., BARRETT, C. S. and GUTTMAN, L. Trans. A.I.M.E. **188** (1950) 1478.
2. BASINSKI, Z. S. and CHRISTIAN, J. W. J. Inst. Metals **80** (1951–2) 659.
3. CHANG, L. C. and READ, T. A. Trans. A.I.M.E. **191** (1951) 47.
4. GEISLER, A. H. Acta Met. **1** (1953) 260.
5. BASINSKI, Z. S. and CHRISTIAN, J. W. Note submitted to Acta Met.
6. BASINSKI, Z. S. and CHRISTIAN, J. W. Acta Met. **2** (1954).
7. LOMER, W. M. and PRATT, P. L. J. Inst. Metals **80** (1951–2) 409.
8. GUTTMAN, L. Trans. A.I.M.E. **188** (1950) 1472.
9. REYNOLDS, J. E. and BEVER, M. B. Trans. A.I.M.E. **194** (1952) 1065.
10. KURDJUMOV, G. V. and MAKSIMOVA, O. P. Doklady Akademii Nauk SSRR **61** (1948) 83.

11. Fisher, J. C., Hollomon, J. H. and Turnbull, D. Trans. A.I.M.E. **185** (1949) 691.
12. Li, C. H., Edwards, E. H., Washburn, J. and Parker, E. R. Acta Met. **1** (1953) 223.
13. Kulin, S. A. and Cohen, M. Trans. A.I.M.E. **188** (1950) 1139.
14. Cech, R. E. and Hollomon, J. H. Trans. A.I.M.E. **197** (1953) 685.
15. Fisher, J. C. Acta Met. **1** (1953) 32.
16. Frank, F. C. Acta Met. **1** (1953) 15.
17. Bowles, J. S. and Mackenzie, J. K. Trans. A.I.M.E. **194** (1952) 1201.
18. Cottrell, A. H. and Bilby, B. A. Phil. Mag. **42** (1951) 573.
19. Bilby, B. A. Phil. Mag. **44** (1953) 782.
20. Frank, F. C. and Stroh, A. N. Proc. Phys. Soc. **65(B)** (1952) 811.
21. Chang, L. C. J. Appl. Phys. **23** (1952) 725.
22. Morgan, E. R. and Ko, T. Acta Met. **1** (1953) 46.
23. Turnbull, D. J. Chem. Phys. **18** (1950) 198.

A Yield Point in Steel Due to Hydrogen*

It has been thought for some time that there may well be a yield point in steel due to hydrogen. This letter is to describe experiments that demonstrate the presence of such a yield point.

The base material used was commercial hot-rolled SAE 1020. The specimens were plunge-ground from 1/2 in. rod to an 0.20-in. specimen diameter. They were subsequently polished, using 1, 0, 3/0 emery paper, degreased, annealed in dry hydrogen for 1 hour at 600°C and cooled in the same atmosphere in a water-cooled extension of the furnace. In an attempt to remove any dissolved hydrogen, this treatment was followed by vacuum annealing at 600°C for 7 hours, and cooling under vacuum.

In order both to eliminate the carbon and nitrogen yield points and to allow for the subsequent absorption of large quantities of hydrogen, the specimens were prestrained 15% at −78°C in a bath of dry ice and alcohol, unloaded, and placed immediately in liquid nitrogen to eliminate possible aging.

Group I of the specimens was tested at −150°C in a bath of liquid Freon 12 immediately after up-quenching from −196°C.

Group II was charged with hydrogen electrolytically for 4 hours in a solution of 4% H_2SO_4 with addition of As_2O_3 as a catalytic poison. Current density was in the neighborhood of 0.2 amp/in², and the bath temperature never rose above 30°C. The specimens were washed and placed in liquid nitrogen immediately, then tested at −150°C as for Group I.

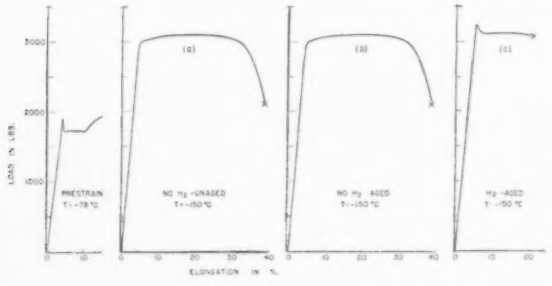

FIGURE 1

Group III of the specimens were warmed to room temperature from the −196°C storage following prestraining, and aged 4 hours at 25°C to allow possible aging, then quenched in liquid nitrogen and tested as for Group I.

Load-elongation curves for all three treatments are shown in Figure 1. A yield-point is present in the hydrogen-charged specimen, and in neither of the others. Preliminary experiments also indicate that this yield point is not observed above about −120°C.

I am indebted to Drs. G. Ardley, J. C. Fisher, J. H. Hollomon, and J. R. Low, Jr., for their stimulating and helpful discussions.

H. C. ROGERS

General Electric Research Laboratory
Schenectady, New York

*Received November 18, 1953.

X-Ray Diffraction by a Deformed Crystal Lattice*

Under the appropriate experimental conditions, a rather large amount of information can be obtained about the distortion of a crystal from the appearance of its transmission Laue spots. Thus, Guinier and Tennevin [1] developed a transmission Laue method which can detect and measure very slight amounts of bending about an axis lying in the plane of a plate-shaped crystal specimen. Julien and Cullity [2] extended this technique and developed a method of measuring torsion about a similar axis. The purpose of this note is to describe a method of detecting bending about an axis *perpendicular* to the plane of the specimen. Distortion of this kind is ordinarily very difficult to detect by means of X-ray diffraction.

The experimental conditions duplicate those of Julien and Cullity [2]. A Soller slit, with its plates horizontal, was placed in the incident beam issuing from a vertical line source of X-rays. We are here concerned with Laue reflections on the equator line of the film, i.e., so-called 90°-reflections [2] made by diffracted beams lying in a horizontal plane. It has been shown [3] that such reflections contain *inclined* striations if the crystal has been twisted. However, some broadened 90° reflections from deformed aluminum crystals were observed to contain *horizontal* striations. Now the mere fact that the reflection is broadened indicates that the reflecting planes are bent about a vertical axis lying in the plane of the specimen [1], while the presence of horizontal striations is indicative of another kind of distortion.

*Received December 2, 1953.

The combination of a Soller slit and a line source of X-rays is equivalent to a set of virtual point sources spaced along a vertical line [3]. Figure 1 shows one source in this set, located at *S*. ABEF is a reflecting lattice plane normal, or approximately normal, to the surface of the crystal and A′B′E′F′ is its extension. If this lattice plane is flat, incident rays such as SO and SO′ would continue to diverge vertically after diffraction, the amount of divergence being given by the angle β. However, if A′B′E′F′ is bent about the horizontal axis SI, parallel to A′B′E′F′, then the reflected rays OI and O′I will converge to a focus at I, as shown in Figure 1. There will be one such focus for every

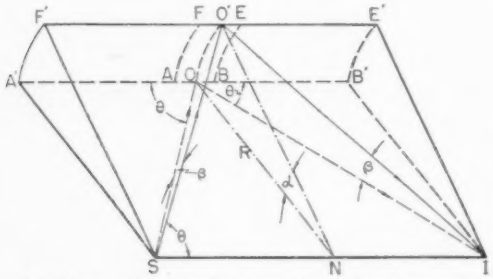

FIGURE 1. X-ray reflections from a bent crystal.

source S in the set of virtual sources. If, now, the crystal is bent about a vertical axis through O and O′, each focus I will be broadened horizontally to form a line and the whole reflection will consist of a set of horizontal lines or striations. The presence of a horizontally striated 90° reflection is therefore evidence of (a) bending about a vertical axis in the plane of the crystal and (b) bending about a horizontal axis normal, or approximately normal, to the surface of the crystal. The extent of the former is related to the amount of horizontal broadening of the reflection, while the extent of the latter is discussed below.

ON and O′N are normals to the bent reflecting plane at O and O′ and *N* is the center of curvature for the segment OO′. The angle α measures the angular disorientation of the bent plane between O and O′.

$$R = (SO) \sin \theta$$

$$\alpha = \frac{(SO)\,\beta}{R} = \frac{\beta}{\sin \theta} \tag{1}$$

where R = ON = radius of curvature of the bent plane. This relation is valid when the source-to-crystal distance SO equals the crystal-to-film distance OI.

θ is normally about 10 degrees and SO and OI are each normally quite large, 30–50 cm, for sensitivity in detecting bending about a vertical axis. If focused striations are detected when SO = OI = 50 cm, then $R = 50 \sin 10° = 8.7$ cm. This represents rather severe bending. As the radius of curvature increases, OI also increases and it may be shown that R approaches 2 (SO) $\sin \theta$ as OI/SO approaches infinity. Therefore, the minimum curvature detectable under the above conditions would correspond to R = 17.4 cm. Further decrease in curvature causes the reflected rays to diverge vertically rather than converge to a focus.

It is practically impossible to bend a thin plate-shaped specimen about an axis normal to its surface, but such deformation has been found in compressed aluminum crystals when the compression axis is normal to the surface of the crystal plate. Horizontally striated Laue reflections were obtained from every compressed specimen examined, indicating curvatures with radii of the order of 5–10 cm, but only occasionally from specimens bent or twisted about an axis parallel to the plate surface. In the compression specimens, lattice bending about an axis normal to the plate was accompanied by bending about an axis parallel to the plate.

The writer is grateful to the Office of Naval Research for financial support of this work and to Professor B. D. Cullity for help and suggestions.

S. S. HSU

Department of Metallurgy
University of Notre Dame
Notre Dame, Indiana

References

1. GUINIER, A. and TENNEVIN, J. Acta Cryst. **2** (1949) 133.
2. JULIEN, C. A. and CULLITY, B. D. Acta Met. **1** (1953) 588.
3. CULLITY, B. D. and JULIEN, C. A. J. Appl. Phys. **24** (1953) 541.

The Micro-Mechanism of Fracture in Ferrite*

The writer has shared with only a few others the belief that mechanical twinning in alpha-iron is related to the incidence of cleavage fracture and that twinning may on occasion be directly responsible for the onset of cleavage. There are many more who consider mechanical twinning as merely incidental to brittle fracture; hence it may be of interest to present some information as to twin behavior derived from a continuing investigation of brittle fracture. The prior data are available under my authorship in Welding Jour., N.Y., vol. 29, p. 467s, 1950, and vol. 30, p. 459s, 1951. The methods of investigating the micro-mechanism of

*Received November 12, 1953.

fracture with tension impact specimens subjected to varied load are presented in the references cited.

Armco iron was employed for impact specimens which were variously loaded to cause complete or partial fracture. Metallographic examination of the mechanical twins in these specimens established the following as barriers to the propagation of twins; other twins, cells of the alpha-veining substructure, nonmetallic inclusions and the alpha-grain boundaries. Sometimes the twins were stopped at such barriers and at other times were deflected, pinched or otherwise changed in propagating through the barriers. Micro-hardness tests (loads ca. 1 gm) of twinned volume were made but found too difficult to apply as a general method of search. Recrystallization techniques were found to be quite effective in showing strained regions of the micro-structure in which slip resulted from the energy diverted from a propagating twin at some barrier.

Figure 1 shows a new, recrystallized grain at the intersection of two twin traces and to the left a pinched section of the twin where a tiny new grain has formed at the twin interface. Figure 2 shows that one of several twins has a new grain along its path. Figure 3 shows two twin traces, one of which has been cut by a cleavage trace. The twin-twin intersection has a new grain and the twin-cleavage intersection just at the start of cleavage, has a number of new grains, as does a portion of the twin volume itself near the cleavage. The twin cut by the cleavage can be observed clearly while the other twin not intersected by the cleavage is quite indistinct. This indistinctness is a characteristic of twins which are associated with large clusters of recrystallized grains. That these "disturbed" twins have met a particularly effective barrier is shown by the recrystallization behavior of the regions in or near the twins affected. From the study of twins, cleavages and the associated micro-areas of recrystallization it is postulated that when the propagating twin meets an effective barrier, its energy may be diverted into producing slip and thereby initiating cleavage fracture. Figure 3 is one of several recorded instances which are considered to be *prima facie* evidence of the twin-slip-cleavage sequence.

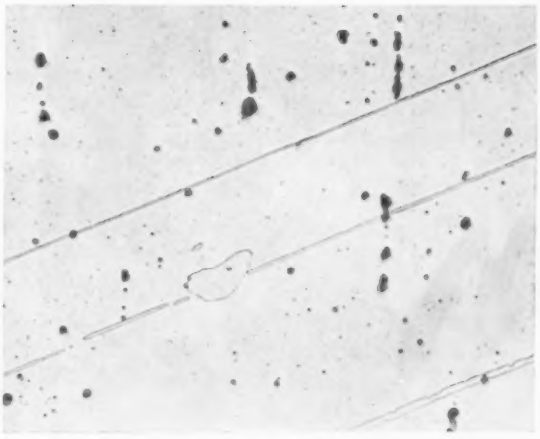

FIGURE 2. Recrystallized grain along path of twin. 5 per cent nital etch, magnification 500×.

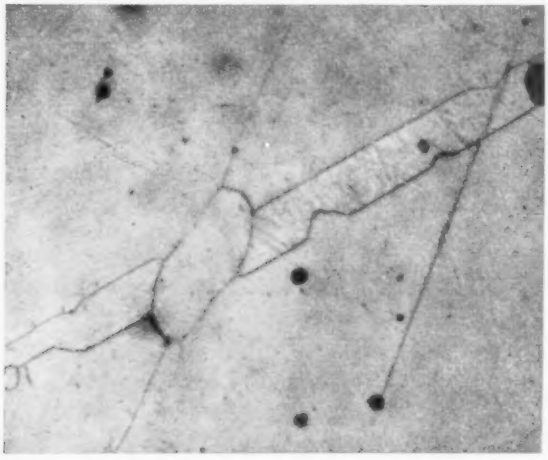

FIGURE 1. Recrystallized grain at intersection of two twins. 5 per cent etch, magnification 1500×.

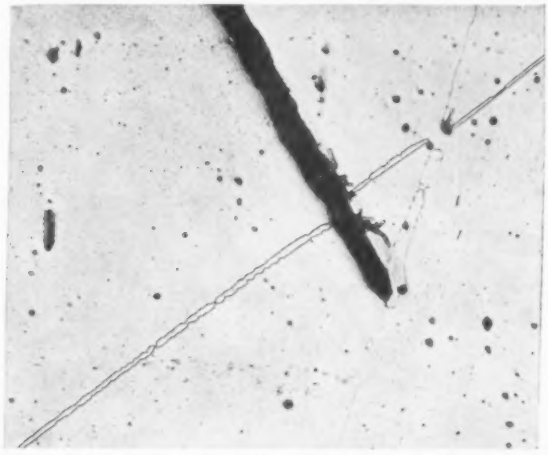

FIGURE 3. Intersecting twins and cleavage with recrystallized grains at twin-twin and twin (No. 2)-cleavage intersection. 5 per cent nital etch, magnification 500×.

W. H. BRUCKNER

Department of Mining
and Metallurgical Engineering
University of Illinois
Urbana, Illinois

BOOK REVIEW

Dislocations and Plastic Flow in Crystals. By A. H. Cottrell. Oxford: Clarendon Press, 1953.
Dislocations in Crystals. By W. T. Read, Jr. New York: McGraw-Hill Book Company. 1953.

The science of metals made its biggest step forward when the experimental techniques of X-ray crystallography made it possible to identify the "grain" of the metallographer with the "crystal" of the crystallographer. Many of the properties of metals, now known as the "non structure sensitive" properties, could be explained in terms of the geometrical arrangement of atoms in crystals. It was found, however, that some of the properties could not be accounted for in terms of perfect crystals; the most prominent example was plastic deformation, which takes place, in single crystals, far more easily than would be expected for a perfect crystal.

In 1934, Taylor, Orowan and Polanyi realized, independently and simultaneously, that a particular kind of departure from crystal perfection would in principle account for the salient features of plastic deformation. Such imperfections are known as "dislocations." Since that time, the development of the theory of dislocations has been very rapid and has taken many different directions. Many interesting consequences of the existence of dislocations have been predicted, and there have been a surprising number of instances in which experimental verification has been achieved.

There have, in general, been two main lines of research which have contributed to the development of dislocation theory; one is to examine the geometry and energetics of dislocations, to calculate the forces between them and their response to externally applied stresses and to predict the geometrical consequences of their motion. The other approach has been to consider the experimental observations that are not accounted for in terms of perfect crystals, and to determine whether they could be explained by the presence of dislocations; such explanations led in several cases to the prediction of as yet unobserved effects, which were susceptible to experimental study.

The publication of the two books under review represents a very timely stocktaking in both these methods of approach. Dr. Read's book is a step by step development of the "geometrical" theory of dislocations, both qualitative and quantitative, followed by a detailed discussion of two topics in which dislocation theory has provided the basis for predictions that have since been verified experimentally; namely crystal growth from vapour and solutions, and the structure, energy and motion of grain boundaries. The book is written as a text-book, with numerous questions and examples to help the student to test his comprehension of the material he has read. The book is extremely clearly written and well arranged and can be wholeheartedly recommended to the serious student who is prepared to devote a considerable amount of time to learning about the firmly established aspects of dislocation theory. Dr. Read points out in his preface that he offers "only fragments of a theory of mechanical properties, strength, plastic deformation and work hardening . . ." because, he writes "there is no systematic general theory that is convincing or widely accepted."

Professor Cottrell's book, on the other hand, is a very lucid and readable account of the theory of dislocations largely in relation to plastic deformation; while Dr. Read regards plastic deformation as an area in which dislocation theory has not yet reached the text-book stage, Dr. Cottrell's book demonstrates that it was ripe for reviewing and discussing in detail in monograph form.

The emphasis in Dr. Read's book is a rigorous mathematical treatment, while Dr. Cottrell's, being mainly concerned with qualitative physical ideas, is not intended as a permanent record of firmly established results, although undoubtedly most of it will fall into this category. Dr. Cottrell has included some discussion of the more speculative aspects of his subject. This book is recommended as strongly as Dr. Read's; it is, however, intended for a slightly different (but largely overlapping) group of readers. It is intended primarily for the reader whose real interest is in understanding the mechanical properties of crystalline solids, whether these can be understood in terms of dislocations or not, while Dr. Read's book is intended for the student of dislocations, whether they are applied to plastic deformation, crystal growth, etc., or whether they are regarded as a consequence of purely geometrical concepts.

The reviewer is compelled to make the recommendation, more popular with the authors than with the reader, that a serious interest in the present position and future possibilities of dislocations calls for the possession of both books.

B. CHALMERS

CURRENT PAPERS IN OTHER JOURNALS

Acta Crystallographica, Vol. 6

Part 11–12, November, 1953 (Partial Contents)

A new method of calculating the scale factor in structure analysis. GOPINATH KARTHA.

Unusual X-ray diffraction effects from a crystal of wollastonite. J. W. JEFFERY.

The multiple-film technique: the effect of angle of incidence on the factor. G. J. BULLEN.

Change of structure of ferrous oxide at low temperature. B. T. M. WILLIS and H. P. ROOKSBY.

The structure of dimethyl oxalate. MARYON W. DOUGILL and G. A. JEFFREY.

The structure of 1: 1: 6: 6 Tetraphenylhexapentaene. M. M. WOOLFSON.

Etude de la concentration de la solution autour d'un cristal en voie de croissance. STANISLAUS GOLDSZTAUB et RAYMOND KERN.

Structure analysis of single crystals by electron diffraction. III. Modifications of alumina. J. M. COWLEY.

The structure of α(AlCrSi)–$Cr_4Si_4Al_{13}$. KEITH ROBINSON.

Polarization dichroism, form birefringence, and molecular orientation in crystalline haemoglobins. M. F. PERUTZ.

The form birefringence of macromolecules. W. L. BRAGG and A. B. PIPPARD.

Archiv für das Eisenhüttenwesen

Heft 9–10 (September-Oktober, 1953)

Modellversuche zur Klärung von Strömungsvorgängen in Tieföfen. MICHAEL HANSEN, HANS SCHOLZ und OSKAR J. STEBEL.

Photometrische Bestimmung des Titans mit Chromotropsäure in Roheisen und Stählen, einschliesslich der Chrom-Nickel-Stähle, ohne Abtrennung des Eisens und der Legierungsmetalle. WALTER KOCH und HEINRICH PLOUM.

Flammenspektralanalytische Untersuchung von Schwermetallen, besonders zur Bestimmung der Ferritzusammensetzung in Stählen. FRANZ WEVER, WALTER KOCH und GERT WIETHOFF.

Einige Beobachtungen über das Kriechverhalten zirkonlegierter Stähle bei 500°. WILHELM ANTON FISCHER.

Eine mathematische Gleichung der Spannungs-Dehnungs-Kurve des Zugversuches. ALFRED KRISCH.

Die Biegefliessgrenze, eine zusätzliche Kennzeichnung für dünne Bleche. WALTER FACKERT.

Prüfung verwickelt geformter Teile mit Überschall. ERICH MARTIN und KARL WERNER.

Einfluss der Verformung bei tiefer Temperatur auf die Eigenschaften nichtrostender austenitischer Stähle. KARL BUNGARDT, RUDOLF OPPENHEIM und ROBERT SCHERER.

Zur Abkühlungskurve des Gusseisens mit Kugelgraphit. ADALBERT WITTMOSER.

Das Zustandsschaubild Eisen—Eisensilizid—Kupfersilizid—Kupfer. RUDOLF VOGEL und DIETRICH HORSTMANN.

Alterungsuntersuchungen an stabförmigen Dauermagneton bei verschiedenen Temperaturen. KLAUS KRONENBERG.

Journal of the Chemistry Society

November, 1953 (Partial Contents)

The Anodic Oxidation of Metals at Very Low Current Density. Part II. Nickel. S. E. S. EL WAKKAD, (MISS) S. H. EMARA.

The Anodic Oxidation of Metals at Very Low Current Density. Part. III Copper. S. E. S. EL WAKKAD, (MISS) S. H. EMARA.

December, 1953 (Partial Contents)

The Photochemistry of Selenium. Part IV. Photogalvanic Effects with Grey Selenium. R. W. PITTMAN.

The Production of Active Solids by Thermal Decomposition. Part I. Introduction. S. J. GREGG.

The Production of Active Solids by Thermal Decomposition. Part II. Ferric Oxide. S. J. GREGG and K. J. HILL.

Anodic Processes. Part I. Anodisation at Low Current Densities of Mercury in Hydrochloric Acid. R. H. COUSENS, D. J. G. IVES, and R. W. PITTMAN.

Anodic Processes. Part II. Oscillographic Studies of Processes at the Mercury Anode in Hydrochloric Acid. R. H. COUSENS, D. J. G. IVES, and R. W. PITTMAN.

Anodic Processes. Part III. The Passivation of Mercury in Hydrochloric Acid. R. H. COUSENS, D. J. G. IVES, and R. W. PITTMAN.

Journal of the Institute of Metals, Vol. 81

December, 1953

Symposium on making the best of metals (in **Bulletin,** not in **Journal**).

The low-stress torsional creep properties of pure aluminium. W. BETTERIDGE.

The copper-silicon eutectoid transformation. A. D. HOPKINS.

The melting point of titanium. T. H. SCHOFIELD and A. E. BACON.

Lamellae in chromium. W. E. CARRINGTON.

The system uranium-lead. B. R. T. FROST and J. T. MASKREY.

The effects of some constitutional factors on the creep and fatigue properties of lead and lead alloys. L. M. T. HOPKIN and C. J. THWAITES.

Journal of Metals, Vol. 5

No. 11, November, 1953

Metallurgical aspects of the development of small gas turbines. W. L. SLOSSON.

CF & I opens streamlined tube mill at Pueblo, Colorado.

Ultra-pure metals produced by zone melting technique. EARLE E. SCHUMACHER.

Composition control of steel castings improved by new furnace sampling methods. VINCENT E. BELUSKO.

Programs underway to increase U.S. production of strategic beryllium. B. H. CLEMMONS and J. S. BROWNING.

Hurley furnace and boiler description and design. E. A. SLOVER.

Preparation of metallic iron of high purity. G. A. MOORE.

Manganese as an indicator of blast furnace slag oxidation and desulphurizing power. N. J. GRANT, J. W. DOWDING, JR., and R. J. MURPHY.

Diffusion of calcium ion in liquid slag. H. TOWERS, M. PARIS, and J. CHIPMAN.

Neptunium-Aluminum intermetallic compounds. O. J. C. RUNNALLS.

Diffusion and solubility of boron in iron and steel. P. E. BUSBY, M. E. WARGA, and C. WELLS.

Effects of temperature on the flow and fracture characteristics of molybdenum. J. H. BECHTOLD.
Bending of molybdenum single crystals. K. T. AUST, R. MADDIN, and N. K. CHEN.
Change in ingot shape during zone melting. W. G. PFANN.
The habit plane of beta in alpha titanium. P. A. ALBERT.
The silver-cadmium beta and zeta phases. L. MULDAWER, M. AMSTERDAM, and F. ROTHWARF.
Formation of sigma phase in the Mn-Mo system. B. F. DECKER, R. M. WATERSTRAT, and J. S. KASPER.

No. 12, December, 1953.
Can the electric furnace compete with the open hearth? C. F. RAMSEYER.
McQuaid-Ehn grain size determined by spectrochemical analysis. G. E. RESSLER.
Reconstruction of CF and I mill increases capacity and flexibility. W. BRILL and R. H. WRIGHT.
Electric steel foundries control dust emissions in Los Angeles area. O. E. ERICKSON.
Review of Russian practice reveals rail steel production methods. C. A. ZAPFFE.
Gas combustion practice described for copper smelters of the southwest. HAROLD FOARD.
Sintering zinc concentrates on the Blackwell 12 by 168 ft. machine. A. E. LEE, JR.
Some observations of slag-metal relations in the acid open hearth steel furnace. G. R. FITTERER.
Solid phase identification in partially reduced iron ore. G. BITSIANES and T. L. JOSEPH.
Exchange of iron between liquid metal and iron silicate slag. G. DERGE and C. E. BIRCHENALL.
After-effects in polycrystalline cadmium. C. S. BARRETT.
Torsional after-effect measurement and applications to aluminum. C. S. BARRETT, P. M. AZIZ, and I. MARKSON.
A crystallographic analysis of the ductile-brittle transition in body-centered cubic single crystals. A. J. OPINSKY.
Surface structure on single crystals produced from melt. F. D. ROSI.

La Metallurgia Italiana, Vol. XLV

No. 9, Septembre, 1953
Attuali orientamenti nei criteri di scelta e nella tecnologia dei materiali refrattari. F. DE CARLI.
La corrosione per aerazione differenziale. Ricerche sullo zinco. G. BIANCHI.
Prove di fatica su acciai deformati a freddo ed aventi subito una diminuzione de durezza. L. MATTEOLI e B. ANDREINI.

No. 10, Octobre, 1953
Impostazioni tecnologiche suggerite dagli attuali orientamenti nell'impiego dei refrattari. F. DE CARLI.
Le fasi di Hume-Rothery nelle leghe a più di due componenti. La composizione delle fasi di Hume-Rothery in leghe con più di due componenti. F. MAZZOLENI.
Attualita nelle applicazioni del rame. P. LOMBARDI.

Revue de Métallurgie, 50 Année

Numéro 11, Novembre, 1953
La transformation isotherme de l'austenite et le partage des éléments speciaux dans les aciers faiblement alliés. AXEL HULTGREN et ses COLLABORATEURS.
Essai de pièces moyennes à la flexion rotative. P. CORON.
Etude par la méthode des radio-éléments, de la ségrégation des impuretés dans les joints fondus des aluminiums de haute pureté. F. MONTARIOL, Ph. ALBERT et G. CHAUDRON.
Sur l'emploi d'un microanalyseur de l'oxygène dans le fer pur. L. MOREAU, J. TALBOT et J. BOURRAT.
Etude de quelques aciers à faible teneur en éléments d'alliage traités par trempe classique et par trempe étagée. G. DELBART et F. MARATRAY.

Zeitschrift für Metallkunde, Band 44

Heft 9, September, 1953
Untersuchungen des Bruchfeingefüges im System Wismut-Antimon. CARL A. ZAPFFE.
Über den Zerfall des hexagonalen Aluminiumborids AlB_2. FRANZ LIHL und PETER JENITSCHEK.
Wesen und Eigenschaften der Korngrenzen polykristalliner Metallkörper (Fortsetzung und Schluss). KURT LUCKE.
Lösungskalorimeter zur genauen Bestimmung von Lösungs- und Bildungswärmen. FRANZ EBERHARD WITTIG.
Zur frage der Bildungswärmen im System Aluminium-Magnerium. FRANZ EBERHARD WITTIG und GEORG PILLER.

Heft 10, Oktober, 1953
Beitrag zum System Chrom-Silizium und über einige Silizid-Mischsysteme. RICHARD KIEFFER, FRIEDRICH BENESOVSKY und HERMANN SCHROTH.
Über die Gesetzmässigkeiten der plastischen Verformung von Metallen unter einem mehrachsigen Spannungszustand I. Theoretische Grundlagen. WERNER SAUTTER, ALBERT KOCHENDORFER und ULRICH DEHLINGER.
Der Wärmeübergang durch freie Konvektion in Metallschmelzen. HANS KLEIN.
Zur Kristallchemie der B.-Metalle. II. Diskussion und Untersuchung trigonal verzerrter NaCl-Strukturen. KONRAD SCHUBERT und HORST FRICKE.
Die Platzwechselreaktionen im System Eisen-Silizium. ERICH FITZER.
Der Einfluss mechanischer Spannungen bei der magnetinduktiven Fehlerprüfung von Stahlrohren. KURT MATTHAES.

Heft 11, November, 1953
Zur Metallographie der Leichtmetalle VII. Beobachtungen über die dendritische Kristallisation von Reinaluminium. HANS KOSTRON und MARGARETE SCHIPPERS.
Zur Metallographie der Leichtmetalle IX. Beobachtungen am Gefüge von Wassergussbarren aus Aluminium 99,5. HANS KOSTRON und MARGARETE SCHIPPERS.
Über die Aushärtung von Aluminium-Silber-Legierungen VIII. Messung der Hallkonstante und der magnetischen Suszeptibilität. WERNER KOSTER und ADOLF FREI.
Beitrag zur Kristallisation der Aluminium-Silizium-Legierungen. GUSTAV GURTLER.
Über die Eigenschaften metallischer Schmelzen VII. Innere Reibung von flüssigem Aluminium und Aluminiumlegierungen. ERICH GEBHARDT, MANFRED BECKER und STEFAN DORNER.
Störung der Gleitung bei Aluminium-Einkristallen II. Mikroskopische Untersuchung des Gleitlinien-Bildes und Diskussion des Verformungsmechanismus. HANSHEINZ LANGE und KURT LUCKE.
Schubverformung von langen Aluminium-Einkristallen. HERBERT SCHOLL.
Diskontinuierliche Erstarrungsvorgange beim Stranggiessen von Raffinal und Reinaluminium. DIETRICH ALTENPOHL.

COLD-ROLLED AND PRIMARY RECRYSTALLIZATION TEXTURES IN COLD-ROLLED SINGLE CRYSTALS OF SILICON IRON*

C. G. DUNN†

Quantitative pole figures are given for the cold-rolled textures and the primary recrystallization textures obtained from single crystals of silicon iron. The orientation changes produced by cold rolling, by primary recrystallization, and by secondary recrystallization are discussed. Each primary recrystallization texture is shown to consist of several preferred orientations with one component predominant. Minor components are shown to have the orientations found for components of the secondary recrystallization texture when secondary recrystallization occurs on further annealing. The conclusion is reached that large primaries from a minor component of the primary recrystallization structure grow and become secondaries of the same preferred orientation, provided they are large enough to grow in competition with other primaries and do not come from a component which by itself or together with a twin component represents too large a fraction of the texture. The results obtained for both primary and secondary recrystallization agree better with the oriented-nucleation growth-selectivity theory than with other current theories.

LES TEXTURES DE LAMINAGE À FROID ET DE RECRISTALLISATION PRIMAIRE DANS DES MONOCRISTAUX DE FER AU SILICIUM LAMINÉS À FROID

On donne des figures polaires, quantitatives, des textures de laminage à froid et des textures de la recristallisation primaire, obtenues de monocristaux de fer au silicium. Les changements d'orientation produits par le laminage à froid et par les recristallisation primaire et secondaire, sont discutés. Il est montré que chaque texture de recristallisation primaire consiste en plusieurs orientations privilégiées, avec la prédominance d'une composante. Il est montré que des composantes secondaires ont les mêmes orientations qu'on trouve dans les textures de la recristallisation secondaire, quand on obtient de la recristallisation secondaire en prolongeant le recuit. On en conclut que de grands cristaux primaires d'une composante secondaire de la structure de recristallisation primaire croissent et deviennent des cristaux secondaires de la même orientation privilégiée, pourvu qu'ils soient suffisamment grands pour pouvoir croître malgré la compétition d'autres cristaux primaires, et ne proviennent pas d'une composante qui par elle-même, ou avec une composante en macle, représente une trop grande fraction de la texture.

Les résultats obtenus dans les deux cas de recristallisations primaire et secondaire sont en meilleur accord avec la théorie de la germination orientée et croissance sélective qu'avec les autres théories courantes.

WALZTEXTUREN UND PRIMÄRE REKRISTALLISATIONSTEXTUREN IN KALT GEWALZTEN SILICON-EISEN EINKRISTALLEN

Es werden quantitative Polfiguren für die Kaltwalztexturen und für die primären Rekristallisationstexturen von Silicon-Eisen Einkristallen mitgeteilt. Die Orientierungsänderungen, die durch Kaltwalzen, durch primäre und durch sekundäre Rekristallisation hervorgerufen werden, werden diskutiert. Es wird gezeigt, dass jede primäre Rekristallisationstextur aus mehreren bevorzugten Orientierungen besteht, von denen eine überwiegt; (Hauptanteil). Die andern bevorzugten Orientierungen (Nebenanteile) sind identisch mit denen der Komponenten der sekundären Rekristallisationstexturen, die sich nach weiterem Glühen bilden. Es wird aus diesen Beobachtungen geschlossen, dass grosse Primärkeime der Nebenanteile der primären Rekristallisationsstruktur wachsen und Sekundärkeime der gleichen bevorzugten Orientierung werden, vorausgesetzt dass sie sowohl gross genug sind um gleichzeitig mit anderen Primärkeimen zu wachsen, als auch von keinem Anteil herrühren, der–allein oder zusammen mit einer Zwillingskomponente–einen zu grossen Bruchteil der Gesamttextur darstellt. Sowohl die für die primäre als auch für die sekundäre Rekristallisation gewonnenen Resultate stimmen besser mit der Theorie der orientierten Keimbildung mit selektivem Wachstum als mit anderen bekannten Theorien überein.

Introduction

The present paper is the second in a series dealing with recrystallization phenomena in cold-rolled single crystals of silicon iron and to a considerable degree is a supplement to the first paper [1]. In the first paper microstructure data showed the presence of large primaries in deviating orientations. Also orientation data on four early forming primaries and the lack of secondaries in equivalent orientation positions eliminated to a large degree the possibility that the observed secondary recrystallization textures were produced by selective growth of large randomly oriented primaries. Instead, the data indicated that the large deviating primaries (nuclei) more probably occurred in preferred orientations. The following conception was advanced for the origin of secondary recrystallization textures: "When primary recrystallization produces a high percentage of primaries in one preferred orientation and the remaining primaries in other preferred orientations in such a way that a number of the latter have diameters two or three times the average, then these large primaries in deviating orientation grow into secondaries."*

*Received August 20, 1953.
†General Electric Company, Pittsfield, Massachusetts.

*Somewhat similar ideas were presented earlier [2] but these were based entirely on theoretical conceptions.

Quantitative information on the primary recrystallization textures, particularly if sufficiently sensitive to detect extremely weak preferred orientations representing minor components of the texture or even the presence of randomly oriented primaries, would add valuable information on the problem of the origin of secondaries and would permit an evaluation of orientation relationships between primaries and secondaries. Quantitative information on the cold-rolled textures, in turn, would add information on both the origin of the primary recrystallization textures and the cold-rolled textures. These are the considerations which comprise the present paper.

Experimental Procedure

In the course of the previous investigation [1], cold-rolled specimens and annealed specimens of suitable size were set aside for pole figure determinations. Briefly, single crystals of silicon iron (3.25 per cent Si) in three different orientations designated as specimens 1, 2, and 3 were cold-rolled from a thickness of 0.050 inch to 0.014 inch. (Initial orientations, referred to the plane and direction of rolling, are given below in the section on results.) Mechanical twinning early in the deformation produced a number of Neumann bands, which were particularly noticeable in specimen 1. Annealing consisted of a one-minute treatment at 980°C in an atmosphere of hydrogen, except for one sample of specimen 1 which received a 64-hour anneal at 550°C prior to the one-minute anneal at 980°C.

X-ray specimens 0.002 inch thick were prepared from the central regions of the 0.014-inch pieces by surface grinding followed by iodine etching.

X-ray data were obtained by a Geiger-counter integrating camera transmission method [3] using a 1-degree slit, Mo K_α–radiation, and diffraction from (110) planes. Intensities were obtained on a Speedomax recorder after the radiation was filtered at the Geiger tube with zirconium to remove white radiation diffraction from other planes. Chart records were calibrated in terms of counts per second and then converted directly into pole density units* by means of a comparison method [3] employing a randomly oriented sample of the same effective thickness (powdered iron and a binder sprayed on to paper). In the comparison method no significant background correction was found.

The choice of (110) planes instead of (200) planes was made upon realization that with the Geiger counter set for (200) diffraction, sufficient white radiation remained even after filtering to give Laue-

*Pole density, which is measured in terms of fraction of sample per unit solid angle falling in an element of solid angle, has been defined in absolute units [4]. For (110) poles the integral of pole density over a hemisphere equals 6, which is the number of (110) poles for a single crystal and therefore the number of times the crystal is counted in the integration. In such units the (110) pole density of a random orientation texture is 6.

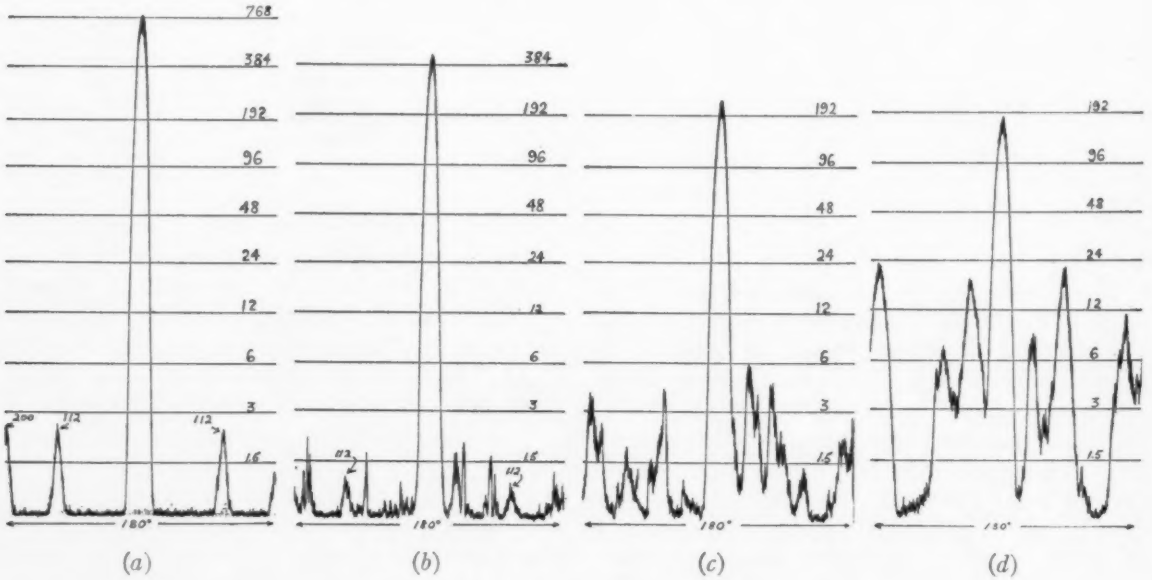

FIGURE 1. Recorder chart traces for Mo K_α-diffraction from (110) planes and calibrated pole density levels. (*a*) lightly deformed single crystal; (*b*) specimen 1 after 1 minute at 980°C; (*c*) specimen 2 after 1 minute at 980°C; (*d*) specimen 3 after 1 minute at 980°C.

type diffraction from very strong concentrations of (110) planes and thus produce (200) ghost peaks, which would be troublesome to handle. Even with the Geiger counter set for (110) diffraction, weak (110) ghost peaks, caused by diffraction from (200) and (112) concentrations, were found. For example, Figure 1*a* shows a chart record from a (110) single crystal cold-rolled about 5 per cent in a $[1\bar{1}0]$ direction, and Figure 1*b* that of a fine-grained sample (specimen 1 recrystallized) with nearly single orientation texture like that of the lightly deformed single crystal, and both examples show weak peaks due to (200) and (112) reflections, as can be seen in the figures. The magnitude of such peaks was found to be about 0.3 per cent of the strong (110) peak, a negligible figure except for identification of real (110) peaks of comparable strength (note minor peaks in Figure 1*b*). Minor peaks above the 0.3 per cent value, which appear in Figure 1*c* and 1*d*, for specimens 2 and 3 presented no problem in the analysis.

Each specimen was scanned over a rotation angle of 360 degrees for each of twelve tilt positions. Tilt positions varied in 5-degree steps to cover the region from the basic circle to within 30 degrees of the center of each stereogram. The 5-degree steps proved to be too large to determine successfully all small but sharp isolated (110) concentrations with peak heights of 1.5 to 3 pole density units. To avoid ambiguities and cluttering in the stereograms, many of these weak (110) concentrations (those shown in Figure 1*b* for specimen 1 are examples) were omitted in plotting the data.

The pole figure plots consist of constant pole density contour lines. For an isolated pole concentration these lines start with a lowest value of 1.5 and increase in steps toward the peak point according to the following sequence: 1.5, 3, 6, 12, 24, etc. as drawn in the charts of Figure 1.

Results

Cold-Rolled Textures

The cold-rolled textures of specimens 1, 2, and 3 are given in Figures 2, 3, and 4, respectively. Black dots give initial orientations, which are near (110) [001], (331) $[\bar{1}\bar{1}6]$, and (332) $[\bar{1}\bar{1}3]$ for specimens 1, 2, and 3, respectively.

The texture of specimen 1 consists of a strong (111) $[\bar{1}\bar{1}2]$ component, a weak (111) $[11\bar{2}]$ component, and a weak (100) [011] component. The orientation of the Neumann bands that formed early in specimen 1 would be near $(\bar{1}\bar{1}4)$ [221], which is an orientation that rotates into the stable

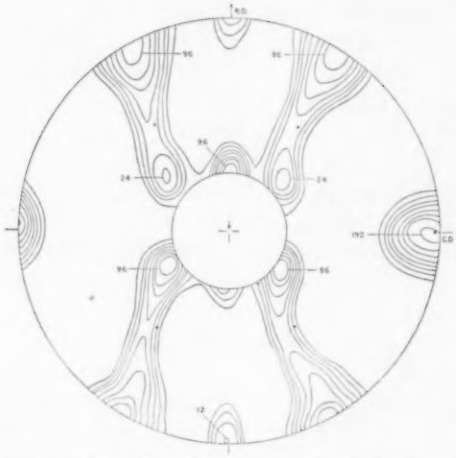

FIGURE 2. Pole density stereogram of (110) poles of specimen 1 cold-rolled 70 per cent. Black dots give original orientation.

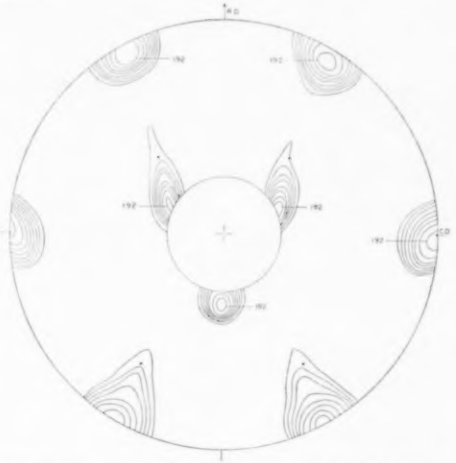

FIGURE 3. Pole density stereogram of (110) poles of specimen 2 cold-rolled 70 per cent. Black dots give original orientation.

FIGURE 4. Pole density stereogram of (110) poles of specimen 3 cold-rolled 70 per cent. Black dots give original orientation.

(100) [011] end orientation; thus the (100) [011] component of the texture can be accounted for in this way. The weak (111) [11$\bar{2}$] component will be discussed later.

The textures of specimens 2 and 3 are mainly those of the (111) [$\bar{1}\bar{1}$2] component.

The end orientations reached by the specimens—namely, (111) [$\bar{1}\bar{1}$2] or (111) [$\bar{1}\bar{1}$2] plus (111) [11$\bar{2}$]—are in excellent agreement with the results obtained by Barrett and Levenson [5] for single crystals of iron cold-rolled between 80 and 95 per cent. One of their crystals (No. 11-1), initially within 5 degrees of the orientation (110) [001], ended in a texture with two (111) ⟨112⟩ components. Decker and Harker [6] found, however, that if individual grains in a coarse-grained sheet of 3.5 per cent silicon iron were within 5 degrees of (110) [001], no significant rotation occurred, whereas if they were beyond 7 degrees (but still in a (110) [001] classification) rotation away from (110) [001] occurred during cold-rolling reductions of 40 per cent. On the other hand, Dunn [7], using a single crystal of silicon iron within 2 degrees of (110) [001], obtained two orientations separated by 12 degrees in a cold-rolling reduction of only 10 per cent and ascribed this result to the formation of deformation bands. The latter type deformation would readily account for the second (111) ⟨112⟩ component observed in specimen 1. The different behavior noted by Decker and Harker may be due to some difference in the manner of rolling specimens.

Primary Recrystallization Textures

The primary recrystallization textures of specimens 1, 2, and 3 after a one-minute anneal at 980°C are given in Figures 5, 6, and 7 respectively.

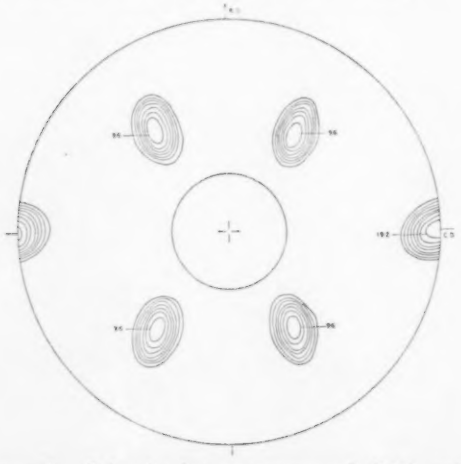

FIGURE 5. Pole density stereogram of (110) poles of sample of specimen 1 recrystallized 1 minute at 980°C.

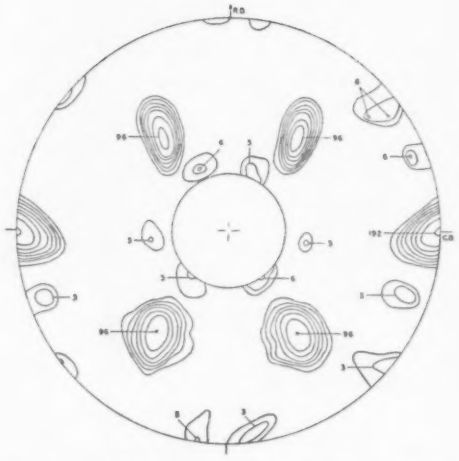

FIGURE 6. Pole density stereogram of (110) poles of specimen 2 recrystallized 1 minute at 980°C.

FIGURE 7. Pole density stereogram of (110) poles of specimen 3 recrystallized 1 minute at 980°C.

The primary recrystallization texture of specimen 1 after a double anneal consisting of 64 hours at 550°C, followed by one minute at 980°C is given in Figure 8.

The stereogram of Figure 5 shows that the recrystallization texture of specimen 1 produced in a one-minute anneal at 980°C is a sharp (110) [001] preferred orientation.* This result is in agreement with the almost single crystal appearance of Lauegrams and of magnetic torque values reported by Dunn [1] for specimen 1.

The textures of specimens 2 and 3 recrystallized at 980°C are shown in Figures 6 and 7 and consist

*As stated earlier, minor components of the texture with peak pole concentrations in the range 1.5 to 3 units have been omitted in the stereograms, this statement applying to Figures 5, 6, 7, and 8.

mainly of three components: namely, (110) [001] and two weak orientations near (111) [1$\bar{1}$0] and (111) [$\bar{1}$10], which are twin orientations. We shall refer to the latter two components as C-orientations. Each is rotated about 8 or 9 degrees either clockwise or counterclockwise from its nearest (111) ⟨110⟩ counterpart. These C-orientation compon-

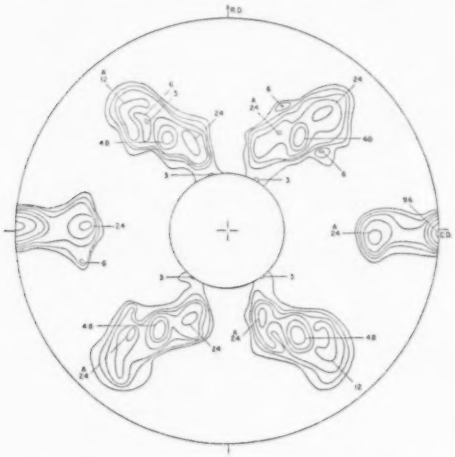

FIGURE 8. Pole density stereogram of (110) poles of sample of specimen 1 annealed 64 hours at 550° and then annealed one minute at 980°C to complete recrystallization (see reference 1).

ents of the texture can be designated as (111) [$\bar{6}$51] and (111) [5$\bar{6}$1]. They produce the minor peaks shown in Figures 1*c* and 1*d*. Quantitatively, the texture of specimen 3 consists of a higher percentage of (111) ⟨651⟩ components than does that of specimen 2.

The texture of specimen 1 recrystallized in a double anneal consisting of 64 hours at 550°C and one minute at 980°C is shown in Figure 8 and consists mainly of three components: namely, (110) [001], (120) [001] marked with the letter A in the figure, and (210) [001]. The highest pole density contour lines drawn in the figure for these components are 48, 24, and 24, respectively. Other concentrations with levels marked 6 or 3, excepting one where the 3-level is within the 6-level for a depression in the plot, are associated with other minor components that either have not been plotted or have not been located in the 5-degree steps. The levels marked 3 on the circle 30 degrees from the center are associated with C-orientation components, which were identified and which could have been completely plotted. Incidentally, the minor peaks adjacent to the strong peak in Figure 1*b* for specimen 1 recrystallized directly at 980°C can be associated with C-orientation components.

From magnetic torque data Dunn [1] predicted a lateral tilt of the average texture of specimen 1 annealed first at low temperatures. The results of Figure 8 confirm this prediction. The pole figure also shows, of course, that the main component—namely, (110) [001]—is unrotated and that the lateral tilt is due to the tremendous increase in the (120) ⟨001⟩ components over that obtained on rapid recrystallization at 980°C.

Some additional and summarizing remarks need to be made about the weak unplotted (110) concentrations of specimens 1, 2, and 3 recrystallized directly at 980°C. First there was substantial evidence of the presence of (12$\bar{0}$) ⟨001⟩ components in all three specimens. Furthermore, if these components are accepted in addition to the identified (111) ⟨651⟩ components, one still has a residue of unexplained (110) peaks.

Calculations

In cold-rolled specimens and in annealed specimens the crystal fragments or crystal grains, as the case may be, are distributed among a number of preferred orientations. An estimate of the fraction in each preferred orientation has been made using methods derived from the normal type distribution [4]. Results appear in Table I in percent. More exact values would require numerical integration of the quantitative pole figures.

TABLE I

ESTIMATE OF FRACTION OF TEXTURE IN EACH PREFERRED ORIENTATION

Specimen	(111) [1$\bar{1}$2]	(111) [11$\bar{2}$]	(100) [011]	(110) [001]	(120) ⟨001⟩	(111) ⟨651⟩
1. cold rolled	75	18	7	—	—	—
2. " "	97	—	—	—	—	—
3. " "	95	—	—	—	—	—
1. after 980°C	—	—	—	95	<2	2
2. " "	—	—	—	88	<2	8
3. " "	—	—	—	72	<2	25

Orientation Relationships

Cold-Rolled and Primary Recrystallization Orientations

Figure 9 gives a stereogram of the cube poles of the principal preferred orientations before and after primary recrystallization. The cold-rolled orientation is shown by open triangles—also closed triangles for the second (111) ⟨112⟩ component of specimen 1. The recrystallized orientations are designated by M, A, and C and are further identified in Table II.

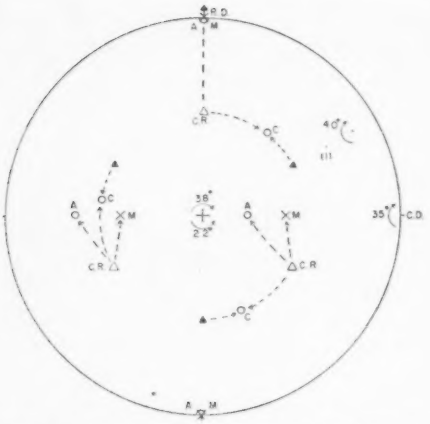

FIGURE 9. Stereogram of cube poles showing orientation relationship between cold-rolled orientation and the three principal preferred orientations obtained by primary recrystallization (see Table II).

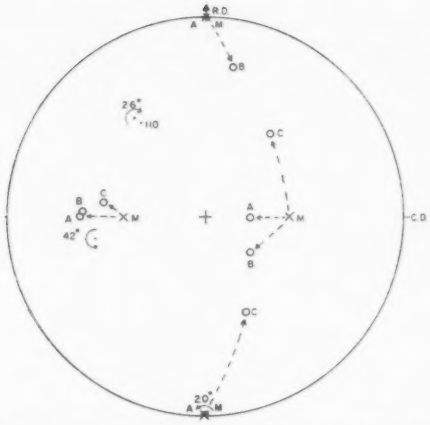

FIGURE 10. Stereogram of cube poles showing orientation relationship between the strongest component of the primary texture and the three strongest components of the secondary recrystallization texture (see Table III).

TABLE II

AXES AND ANGLES OF ROTATION FOR PRIMARY RECRYSTALLIZATION

Orientation of primaries	Axis of rotation	Angle of rotation
M: (110) [001]	CD, also a common ⟨110⟩ direction	35°
A: (120) [001]	11° from ⟨111⟩ of C. R.	40°
C: (111) [$\bar{6}$51]	Normal to sheet and a common ⟨111⟩ direction	38° or 22° from closed triangles

TABLE III

AXES AND ANGLES OF ROTATION FOR SECONDARY RECRYSTALLIZATION

Orientation of secondaries	Axis of rotation	Angle of rotation
A: (120) ⟨001⟩	R. D. or [001] of M or A	20°
B: (362) ⟨013⟩ to (121) ⟨012⟩	near a common ⟨110⟩ direction	26°
C: near (111) ⟨110⟩	a common ⟨821⟩ direction	42°

Table II also gives the axes and angles of rotation to transform the cold-rolled orientation into the specified preferred orientation obtained by recrystallization.

The first of these orientation relationships is in good agreement with the 30-degree rotation about a ⟨110⟩ axis found by Dunn [8] for recrystallization in silicon ferrite following small deformations. The second and third are new relationships, although in the earlier work other unclassified orientations were noted.

Primary and Secondary Recrystallization Orientations

Figure 10 gives a stereogram of the cube poles of the main component (M) of the primary texture and the preferred orientations A, B, and C of the secondary texture reported by Dunn [1]. Table III gives the axes and angles of rotation to transform M into the specified preferred orientations obtained by secondary recrystallization, which occurred after increased annealing time at 980°C.

It can be noted that none of these transformations, except perhaps the second, agrees with the relationships found for primary recrystallization.

Discussion of Results

Secondary Recrystallization

Considering the secondary recrystallization process first, we note from the tables and the stereograms that the primary recrystallization texture has minor components in the orientations found in the secondary recrystallization texture. This is obvious for the (120) ⟨001⟩ preferred orientations which occurred in both the primary and secondary recrystallization textures. To show the relationship for (111) ⟨110⟩ secondaries of specimen 1 reported by Dunn [1], we replot his data in Figure 11 with the two (111) ⟨110⟩ components combined. Since specimen 1 had two (111) ⟨112⟩ components in the

cold-rolled texture, two C-orientations are required to represent the orientations of this type of component in the primary recrystallization texture. These are marked C and C′ in the figure. Open-line circles in the figure show a range of 10 degrees from these orientations. The orientations of secondaries,

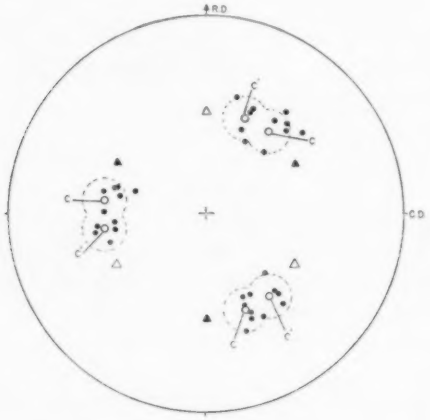

FIGURE 11. Stereogram of cube poles showing orientation relationship between the C-orientation primary recrystallization component and that of 11 secondaries.

indicated by the solid black dots, clearly lie in or near these indicated areas. Thus the agreement between the orientations of C-oriented primaries and C-oriented secondaries is excellent.

Regarding other important relationships, no primary component of the B-orientations of secondaries was established. A plot of (110) poles of B shows that a B-orientation would be difficult to resolve in the presence of stronger M, A, and C components; so we cannot conclude without an exceedingly careful determination of the pole figure (perhaps use of purer K_α-radiation and steps smaller than 5 degrees) that no such preferred orientation exists. Also, it will be remembered that a few secondaries were noted with orientations different from A, B, and C.

Consideration of the present data and known theory of growth phenomena leads us to modify the previously stated conception [1] for the origin of secondaries in silicon iron produced from original single crystals. This modification involves putting limits on the strength of a minor component if primaries from it are to become secondaries.

Thus we set down the following three necessary conditions for primaries to grow into secondaries, the modification entering as the third condition:

1. Whether observable or not in a texture analysis primaries must exist in the correct orientation—that is, be in the orientations of secondaries.
2. If grain-boundary energy provides the driving force, such primaries must be above a critical size.
3. Primaries above the critical size when present in a minor component of the texture cannot become secondaries if the minor component (or its twin) represents too large a fraction of the texture. (In the present materials this fraction may be set at, say, not over 5 per cent.)

Applying these conditions to specimen 3 which had no C-orientation secondaries, we note that C-orientation primaries exist (25 per cent) and from such a large group some ought to be above a critical size. Therefore, the reason for no C-orientation secondaries in specimen 3 is due to the presence of too much material of the same orientation. In exactly the same way the principle of growth selectivity has been applied by many investigators to account for the failure of a sharp single orientation texture to transform into a single crystal of the same orientation. In agreement with this principle we note that as component C increases from less than 2 per cent to about 25 per cent in the three specimens, the incidence of secondaries of the same orientation decreases.

Increase in the A-component of primaries in specimen 1 upon recrystallizing at low temperatures likewise could be cited as a factor favoring normal grain growth, which was observed for this sample [1] upon prolonged annealing at 980°C. In this case, another important factor is the kind of grain structure developed during primary recrystallization.

Although the existence of minor components of the primary recrystallization texture in the (120) ⟨001⟩ orientation was not definitely established for specimens 2 and 3, partial evidence like that for specimen 1 recrystallized at 980°C could be mentioned. If such primaries were present, then the necessary conditions 1 and 3 for them to become secondaries would be satisfied. Since no such secondaries were noted in the rather limited data presented, one would conclude that such primaries lacked the necessary size (condition 2) or, since growth is a competitive process, remained too long in the slow-growth stage and were engulfed by growth of B-orientation grains, which produced the major component of the secondary recrystallization texture of these specimens.

Pole figure data were not obtained for specimens 2 and 3 recrystallized first at 550°C, but recent

results obtained in this Laboratory from magnetic torque data on samples so treated indicate a marked change in the textures. The (110) [001] component is greatly reduced. Further annealing at 980°C produced only normal grain growth, which was accompanied by a further reduction in the torque peak.

Pole figure data showing the texture changes produced by normal grain growth in specimens 1, 2, and 3, which occurs if these specimens are annealed first at 550°C, no doubt would be interesting.

Primary Recrystallization

From the cold-rolled textures we note that there are no preferred orientations in the orientations observed for primaries. Only (110) [001] orientations can be said to be present in the scatter of the cold-rolled texture, i.e., in the low-density region, which reached levels below the 1.5 pole density value for specimen 2, and which is relatively stronger in the bridging region of the two (111) ⟨112⟩ components of specimen 1. From this point of view specimen 2 has the least amount of (110) [001] material prior to annealing. After annealing, however, specimen 2 surpasses specimen 3 for amount of (110) [001] developed. In other words, there is no clear relationship between amount of (110) [001] present before recrystallization and amount obtained in the recrystallization process. The difficulty is obviously not resolved by invoking condition 3 listed previously. Actually, the amount of (110) [001] material in the cold-rolled textures is probably small enough to avoid selective growth interference.

Nevertheless, we can say that there are two possible sources of nuclei: namely, (1) potential nuclei with material already in essentially the correct orientation and (2) stressed regions, which undergo a change in orientation during a nucleation process.

Relation of Results to Current Theories

Current Theories

The following summaries, covering the main points of three current theories on how sharp annealing textures occur, are given as a basis for discussion of the present results.

1. *The Oriented-Nucleation Growth-Selectivity Theory*: growth selectivity requires nuclei to be different from same or twin orientation of the matrix texture and in a narrow orientation range since growth selectivity alone cannot sharpen the texture sufficiently. Induction periods and numbers of nuclei are very important [9; 10].
2. *The Modified Oriented-Growth Theory*: oriented nucleation occurs but in too broad a range; growth selectivity narrows the orientation range for necessary sharpness of the texture [11; 12*a*].
3. *The Oriented-Growth Theory*: sufficient nuclei are available in all orientations; the matrix texture alone determines the final texture through growth selectivity [13].

There seems to be general agreement on the qualitative aspects of growth selectivity and therefore agreement on the matrix texture influencing rates of growth of nuclei. However, even if the quantitative nature of the relationships were known, knowledge of the texture would permit one to make accurate predictions of growth behavior only over macroscopic regions. Rate of growth is determined by other factors besides orientation relationships, and one of these is a free energy per unit volume in (*a*) the worked state; (*b*) the partially recovered state; (*c*) the polygonized state; and (*d*) the completely recrystallized state. On the microscopic scale the free energy per unit volume, available as a driving force for growth to occur, is quite variable; so it is doubtful that this factor could average out the same for nuclei of all possible orientations. Because so many important factors enter the picture, Burgers and Tiedema's detailed consideration of what may happen on annealing [10] is a well-taken point of view.

Origin of Secondary Recrystallization Textures

It is of interest to ask if the oriented-growth theory can predict from a broad point of view what the secondary recrystallization textures will be for specimens 1, 2, and 3 of the present work from a knowledge of their primary recrystallization textures. One should look first for that orientation which is most favorably related to all components, strong or weak, because such an orientation is the most favored to grow, a point well made by Beck [14]. Since all the primary components come from a (111) [$\bar{1}\bar{1}2$] cold-rolled texture by primary recrystallization, each component must have been favorably oriented for growth according to the oriented-growth theory and therefore (111) [$\bar{1}\bar{1}2$] must be an orientation favorably related to all the primary components. But do any (111) [$\bar{1}\bar{1}2$] secondaries occur? To date none has been found. Recent work in our Laboratory along the lines recommended by

Burgers [9], who referred to unpublished work of Tiedema on growing crystals through bent portions of specimens, show that a secondary grain, when reoriented to a (111) [$\bar{1}\bar{1}2$] orientation, grows with apparently unchanged rate. Similarly, an orientation such as (110) [$\bar{1}12$] (i.e., one rotated 35 degrees about [110] of M), which was not observed, was obtained by the reorientation method and found to grow with ease. Therefore the idea that there are sufficient nuclei in all orientations must be abandoned. Furthermore, application of the main factor in the oriented-growth theory—namely, growth selectivity—predicts that (111) [$\bar{1}\bar{1}2$] primaries cannot be expected to grow well in a (111) [$\bar{1}\bar{1}2$] single-orientation matrix, in agreement with present data and in disagreement with (111) [$\bar{1}\bar{1}2$] nuclei being available for secondary recrystallization.* It is therefore concluded that application of oriented-growth theory leads to contradictions.

On the other hand, if we know the primary recrystallization texture, including amount and distribution of each component, and know also that there are large primaries in one or more components, which are sufficiently weak, we probably can predict the secondary recrystallization texture. In other words, the oriented-nucleation growth-selectivity theory appears adequate for this case.

To decide whether or not the modified oriented-growth theory is also adequate to account for present data would require more detailed knowledge on the distribution of orientations for the very large primaries. It can be argued, however, from growth selectivity operating during primary recrystallization that the largest primaries should be near the peak pole density positions, which is in reasonable agreement with the position of secondary grains. Also, qualitative and relative values of rates of growth were determined in the present specimens for a variety of orientations obtained by the reorientation of a seed crystal and were not found to vary enough to account for the secondary recrystallization data. Similar work on relative growth rates versus orientation in commerical fine-grained polycrystalline silicon iron [2] when compared with secondary recrystallization textures indicates that oriented-nucleation is needed in addition to selective growth to account for the sharpness of the (110) [001] texture developed by secondary recrystallization. Oriented-nucleation for this case would be described in terms of a standard deviation of large primaries in an exceedingly weak (110) [001] component of the texture. The writer therefore favors the oriented-nucleation growth-selectivity theory for secondary recrystallization in silicon iron.

That the correct orientation relationships for secondary recrystallization in face-centered cubic metals can be supplied by oriented primaries has been proposed recently by Liu and Hibbard [15] and Dunn [16].

Origin of Primary Recrystallization Textures

At the outset we need to note the marked effect of recrystallizing specimen 1 at different temperatures, which is not unlike results obtained by other investigators (see, for example, [17; 18]). In specimen 1 the effect is the marked dependence on recrystallization temperature of the relative amounts of (110) [001] primaries (M-primaries) and (120) ⟨001⟩ primaries (A-primaries) which arise from M-nuclei and A-nuclei. It seems doubtful that growth selectivity alone could explain this effect.

On the other hand, the old idea that low temperatures can give certain nuclei with short induction periods a special advantage is very applicable. According to this point of view, low temperatures favor A-oriented nuclei because of their considerably shorter induction periods, whereas at high temperatures the induction periods of M-nuclei are relatively short enough for them to become competitive with A-nuclei. According to the microstructure data reported by Dunn [1], one can conclude that the number of M-nuclei far outweighs the number of A-nuclei. Therefore, by giving the A-nuclei a special advantage, which happens to occur at low temperature, one can enhance the A-component at the expense of the M-component.

The oriented-nucleation growth-selectivity theory therefore seems generally adequate to deal with present primary recrystallization phenomena. However, it is not at all clear what a nucleus is and how it is formed. The so-called "preformed" nucleus looks attractive. Generally, it has been difficult to visualize a preformed nucleus in one specific orientation (oriented nucleation) arising in the most severely worked regions of a crystal, i.e., along slip planes, etc., where nucleation occurs. This difficulty may be met, however, using arguments along the lines suggested by Burgers [9], who considered that certain adjustments for the nucleus orientation could lead to an energy cusp boundary between nucleus and mother crystal, which would

*A cold-rolled polycrystalline sample, of course, offers better opportunity for producing large primaries in nearly all orientations, but here again the number of such large primaries, which is an aspect of oriented-nucleation, probably varies with orientation.

be relatively lower in value than those for adjacent orientations. Call this an "energy cusp" nucleation theory. In this theory the mother crystal would be the frame of reference for determining the orientation of the nucleus just as it is in the oriented growth theory. Rate of nucleation would depend on rate of adjustment leading to the low-energy nucleus and rate of growth in the initial stages. Early rates of growth would depend on variable local driving forces, which reasonably could be distributed in a normal way not unlike the distribution of curvatures in the Cahn theory [19] of nucleus formation by polygonization and growth processes.

If during deformation material is put into the nucleus orientation by large rotations on the slip planes about axes either perpendicular to the slip direction or perpendicular to the slip plane, the relatively lower energy of the nucleus orientation would favor accumulation of material in this orientation over adjacent orientations. This is a second factor favoring such oriented nuclei.

What is the evidence for energy cusp nuclei? First, there is the third-order twin relationship for primary recrystallization in silicon ferrite [8]. Another example is the present rotation of 35 degrees about a ⟨110⟩ axis. This position is between the third-order twin and the second-order twin position, which correspond to rotations of 31°36′ and 38°56′ respectively about a ⟨110⟩ axis. Low-energy boundaries for these could be common {552} planes and common {114} planes, respectively. Still another illustration, the one mentioned by Burgers [9], is the Kronberg-Wilson relationship of 38-degree rotation about a ⟨111⟩ axis [20], which also was observed for the prominent minor components of recrystallization in the present work. The energy cusp boundary could be composed of those common {541} planes that correspond to a relative rotation of 38°13′.

Since there are several equivalent positions—twelve second-order twins positions and eight of the Kronberg-Wilson type—a variety of orientations may appear possible from primary recrystallization. Figure 12 illustrates the positions of four orientations obtained from (111) [$\bar{1}\bar{1}2$] by a 35-degree rotation about two ⟨110⟩ axes; the other eight can be visualized from symmetry considerations.

The important question is: How does the cold rolling provide nuclei in only a few of the equivalent positions? Knowledge of the deformation process beyond that presently available could provide the answer. Nevertheless, there seems to be evidence

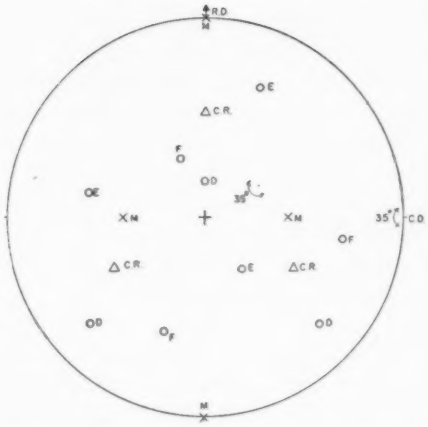

FIGURE 12. Stereogram showing four orientations M, D, E and F obtained by 35° rotations about two specific ⟨110⟩ axes of the cold-rolled orientation.

favoring slip on {110} planes over slip on {112} and {123} planes in body-centered cubic lattices [21]. To account for the observed rotation of the original crystals into the (111) [$\bar{1}\bar{1}2$] orientation one can visualize a proper combination of {110} planes and ⟨111⟩ slip directions. After the crystal reaches a stable end orientation, slip systems must operate in such a way to retain this orientation. Successive or simultaneous operation of several slip systems can produce a rocking motion of the crystal about certain axes.

To illustrate important possibilities, let us refer to a standard (110) projection [22]. Figure 13 gives the poles of the {111} and {110} planes. We rule out the following slip systems because of their unfavorable position in a (111) [$\bar{1}\bar{1}2$] orientation: ($10\bar{1}$) plane and [111] slip direction, ($1\bar{1}0$) and [111], ($0\bar{1}1$) and [111], ($10\bar{1}$) and [$1\bar{1}1$], ($1\bar{1}0$) and [$11\bar{1}$], and ($0\bar{1}1$) and [$\bar{1}11$]. The six slip systems that remain

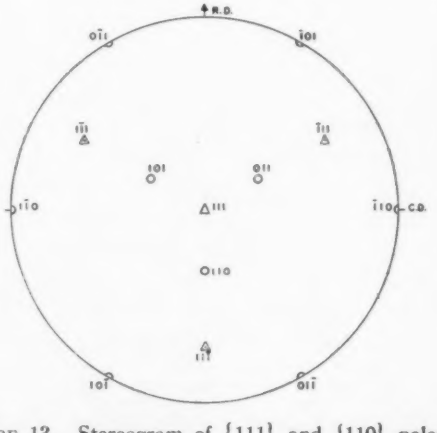

FIGURE 13. Stereogram of {111} and {110} poles of a crystal in the (111) [$\bar{1}\bar{1}2$] orientation.

have been grouped into combinations in Table IV.

From Table IV it can be seen that combinations 1 and 2, operating in succession, rocks the crystal about [$\bar{1}$10] or C.D. as an axis and that combinations 3 and 4, operating in succession, rocks the crystal about [111], or the normal direction.

It will be noted also from Table IV that combination 2 is equivalent to slip on a (112) plane and is the one responsible for rotating the crystals into

TABLE IV

COMBINATIONS OF SLIP SYSTEMS

Slip systems	Axis of rotation	Type of rotation
1. (110) and [1$\bar{1}$1], (110) and [$\bar{1}$11]	[$\bar{1}$10]	[111] moving toward R.D.
2. (101) and [11$\bar{1}$], (011) and [11$\bar{1}$]	[$\bar{1}$10]	[111] moving away from R.D.
3. (110) and [1$\bar{1}$1], then (011) and [11$\bar{1}$], then (101) and [$\bar{1}$11] in succession	[111]	clockwise
4. (110) and [$\bar{1}$11], then (011) and [1$\bar{1}$1], then (101) and [11$\bar{1}$] in succession	[111]	counterclockwise

the (111) [$\bar{1}\bar{1}$2] orientation. During cold-rolling this combination would have to operate more in specimen 1 than in specimens 2 and 3. Further rotation of this type in small regions could produce nuclei in the D-orientation (see Figure 12). No primaries were observed in this orientation. The first combination in Table IV, however, could provide M-orientation nuclei, but it is not clear how this combination would favor specimen 1 over specimens 2 and 3. If there were an analogue to the opposite rotation of a detached portion on a slip plane or the local curvature produced by a piling up of dislocations (12*b*), then a more active combination 2 should produce more M-nuclei in small regions separating slip planes.

On the other hand, operation of combination 3 or combination 4, which could produce C-oriented nuclei, reasonably could lead to more C-oriented nuclei, the greater the reduction, while the crystal is in the (111) [$\bar{1}\bar{1}$2] orientation. This may explain the observed maximum for amount of (110) [001] primaries with amount of cold-rolling [1], which occurred near 70 per cent reduction, because an appreciable amount of cold-rolling is first required to rotate a (110) [001] crystal away from the original (110) [001] orientation as well as to set up the required conditions for producing a strong (110) [001] primary recrystallization texture; whereas reductions exceeding 70 per cent could generate more and more C-oriented nuclei and thus produce an enhancement of this component of the primary recrystallization texture and a loss in the (110) [001] component.

If these ideas are correct, cold-rolling a (111) [$\bar{1}\bar{1}$2] single crystal should lead to even more C-oriented primaries than those observed in the in the present specimens. Further work is being done in this Laboratory to clarify the role orientation plays in the development of recrystallization textures.

Acknowledgments

Dr. H. O. Spauschus and Mr. J. U. Druck provided X-ray diffraction chart recordings and Mr. H. T. Sagendorph aided in the preparation of specimens and the plotting of pole figures. Drs. W. R. Hibbard and D. Turnbull read and criticized the manuscript.

References

1. DUNN, C. G. Acta Met. **1** (1953) 163.
2. DUNN, C. G. In "Cold Working of Metals" (Cleveland, Am. Soc. Metals, 1949) p. 113.
3. GEISLER, A. H. In "Modern Research Techniques in Physical Metallurgy" (Cleveland, Am. Soc. Metals, 1953) p. 131.
4. DUNN, C. G. J. Appl. Phys. In press.
5. BARRETT, C. S. and LEVENSON, L. H. Trans. A.I.M.E. **145** (1941) 281.
6. DECKER, B. F. and HARKER, D. J. Appl. Phys. **22** (1951) 900.
7. DUNN, C. G. Trans. A.I.M.E. **167** (1946) 373.
8. DUNN, C. G. Trans. A.I.M.E. **167** (1946) 357.
9. BURGERS, W. G. In "L'état solide" (Brussels, Institut Internationale de Physique, 1951) p. 73.
10. BURGERS, W. G. and TIEDEMA, T. J. Acta Met. **1** (1953) 234.
11. GOW, K. V. and CAHN, R. W. Acta Met. **1** (1953) 238.
12. BARRETT, C. S. Structure of Metals (2nd ed., New York, 1952): (*a*) p. 503, (*b*) p. 419.
13. BECK, P. A. Acta Met. **1** (1953) 230.
14. BECK, P. A. Trans. A.I.M.E. **191** (1951) 474.
15. LIU, Y. C. and HIBBARD, W. R. To be published.
16. DUNN, C. G. To be published in *Acta Met.*
17. COHEUR, P. and LEJEUNE, L. M. Rev. Métall. **46** (1949) 439.
18. LIU, Y. C. and HIBBARD, W. R. J. Metals **5** (1953) 672.
19. CAHN, R. W. Proc. Phys. Soc. (London) **A63** (1950) 323.
20. KRONBERG, M. L. and WILSON, F. H. Trans. A.I.M.E. **185** (1949) 501.
21. CHEN, N. K. and MADDIN, R. Trans. A.I.M.E. **191** (1951) 937.
22. SCHIEBOLD, E. and SACHS, G. Ztsch. Krist. **63** (1926) 34.

GRAIN BOUNDARY SELF-DIFFUSION IN ZINC*

EDWARD S. WAJDA†

The grain boundary self-diffusion in zinc has been measured in the temperature range from 75°C to 200°C with the use of Zn^{65} as a tracer and the usual lathe sectioning technique. Two different high-purity grades of zinc gave an activation energy of 14.5 kcal/mol to within experimental error. It is concluded that the grain boundary self-diffusion activation energy is 37 per cent less than the lattice self-diffusion energy of activation.

L'AUTODIFFUSION DANS LES JOINTS INTERCRISTALLINS DU ZINC

L'autodiffusion dans les joints intrecristallins du zinc a été mesurée dans l'intervalle de températures allant de 75°C à 200°C, en se servant de Zn^{65} comme indicateur, et en employant la méthode usuelle des sections au tour. Deux qualités différentes de zinc de haute pureté ont donné une énergie d'activation de 14,5 kcal/mol, à l'erreur expérimentale près. On en conclut que l'énergie d'activation pour l'autodiffusion dans les joints intercristallins est de 37 pour cent inférieur à l'énergie d'activation pour l'autodiffusion dans le réseau.

KORNGRENZEN—SELBSTDIFFUSION IN ZINK

Die Korngrenzen-Selbstdiffusion in Zink wurde mittels Zn^{65} als Indikator und der üblichen mechanischen Schnittmethode im Temperaturgebiet zwischen 75°C und 200°C gemessen. Zwei verschiedene Grade Reinstzink ergaben innerhalb der experimentellen Fehlergrenze die gleiche Aktivierungsenergie von 14,5 kcal/mol. Es wird daraus geschlossen, dass die Aktivierungsenergie der Korngrenzen-Selbstdiffusion 37% geringer ist als die Aktivierungsenergie der Kristallgitter-Selbstdiffusion.

Introduction

In a previous paper [1] the rate of self-diffusion in single crystals of zinc was discussed. The rate was found to depend markedly on the direction in which it was measured. In conjunction with those measurements, the grain-boundary self-diffusion has also been investigated. Information on grain-boundary diffusion rates promises to be extremely valuable because it appears that the rates of many important physical and metallurgical processes, such as grain growth, recrystallization, plastic deformation and crystal strength, are more directly related to grain boundary than to lattice diffusion coefficients. Also, a quantitative relation for D_b and D_v which are the grain-boundary and lattice diffusion coefficients, respectively, should be valuable in the development and testing of the different proposed models for grain boundaries.

Recent work by Hoffman and Turnbull [2] and Slifkin, Lazarus, and Tomizuka [3] has shown quantitatively that the grain-boundary self-diffusion in silver was much larger than the lattice diffusivity in the same metal at lower temperatures. Numerous other workers have also given qualitative verification that $D_b \gg D_v$.

It is the purpose of this work to measure the rate of grain-boundary diffusion in an anisotropic crystal such as zinc, and compare it with the rate of self-diffusion through the bulk crystal lattice of the same metal. This work also shows the application of Fisher's theory [4] for diffusion along uniform grain boundaries, to a material where the diffusion is anisotropic.

Experimental Procedure

Two grades of zinc as obtained from the New Jersey Zinc Company were used. One grade was the chemically pure (C–P) zinc (99.999%) and the other was a commercially prepared zinc known as Horsehead (H–H) which was 99.99% pure.

The (C–P) specimens were cut directly from the cast rods as received from the supplier. The crystallites in these rods displayed a marked radial orientation. The size of the crystallites used was about 0.1 mm × 3 mm. Back reflection X-ray photographs showed that the crystallites had a preferred orientation with respect to the cylinder specimen axis, and were positioned with their hexagonal axes in the radial direction.

The (H–H) specimens were made by melting stock (H–H) zinc and casting it into a slug 1 inch in diameter × 4 inches long. This slug was then alternately cold-rolled and annealed until a small grain size was obtained (2×10^{-2} cm mean linear dimension). Small cylindrical specimens were then cut from the cold-worked slug in a manner such that the cylindrical specimen axis was perpendicular to the direction of rolling of the slug.

The specimens were then polished and annealed at the highest temperature used in the investigation to minimize grain-boundary migration and crystal growth during the diffusion anneal. The

*Received September 8, 1953.
†Rensselaer Polytechnic Institute, Troy, New York; now at Union College, Schenectady, New York.

average grain sizes of the two series of specimens were measured on the part of the specimen that remained after sectioning, and in no case was there an appreciable change in grain size during the diffusion process.

After radioactive Zn^{65} was electrodeposited on the specimen surfaces, the samples were diffused at different temperatures and then sectioned in a lathe, and the activities measured in the manner described in reference [1].

Results and Discussion

As yet no general solution of the diffusion equation for diffusion along uniform grain boundaries has been obtained. However, Fisher [4] has derived an approximate solution appropriate to the region beyond the influence of pure bulk diffusion, which is easily applicable to the interpretation of the experimental data. Roe [5] and Whipple [6] have also considered the same problem in more detail using more rigorous mathematical analysis, but their results are rather complicated and extremely difficult to correlate with experimental data.

With the same assumptions outlined in Fisher's paper [4], one obtains a simple analytical expression for the ratio of the lattice diffusivity to the grain boundary diffusivity as follows:

$$D_v/D_b = \frac{\delta(\pi D_v t)^{\frac{1}{2}}}{2}\left[\frac{d \ln a}{d\bar{y}}\right]^2,$$

where a is the isotope activity per unit volume at a distance $\bar{y}$ measured in a direction normal to the free surface on which the original isotope was deposited and δ is the thickness of the uniform grain boundary. Using the experimentally measured value of the slope of the activity-penetration curve, together with the known value of the bulk diffusion coefficient obtained from the work of Shirn, Wajda, and Huntington [1] at the same temperature, and assuming a value of 5×10^{-8} cm for δ, one can find the absolute value of the grain boundary diffusivity (D_b).

Typical activity penetration curves are shown in Figures 1, 2, and 3. The vertical lines through some of the points give an indication of the counting errors involved. In Figure 1 is shown penetration data on a polycrystalline sample which was diffused at a high temperature where lattice diffusion is more pronounced than grain-boundary diffusion. When the data are plotted against $(\bar{y})^2$, the average diffusion distance squared, a straight line results as is required by the theory of homogenous diffusion, whereas a plot against $\bar{y}$ gives a

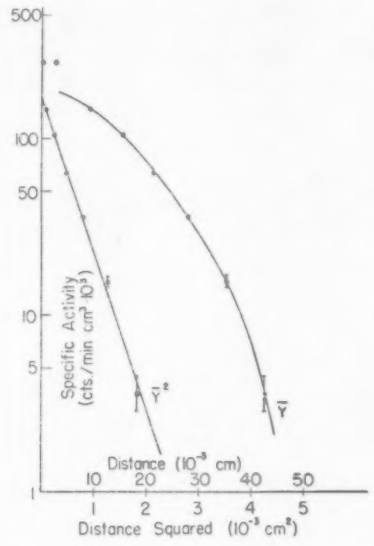

FIGURE 1. High-temperature diffusion: $T = 268.1$°C; $t = 169$ hours.

pronounced curvature. This indicates that the major portion of the diffusion took place through the lattice. Figure 2 shows similar data on a polycrystalline sample which was diffused at a very low temperature, where one would expect the grain-boundary diffusion to be more effective than the lattice diffusion. This expectation is verified very nicely because a linear relationship appears when log activity is plotted against $\bar{y}$ as predicted by Fisher's theory, whereas a marked curvature is observed for the log activity versus $(\bar{y})^2$. Further-

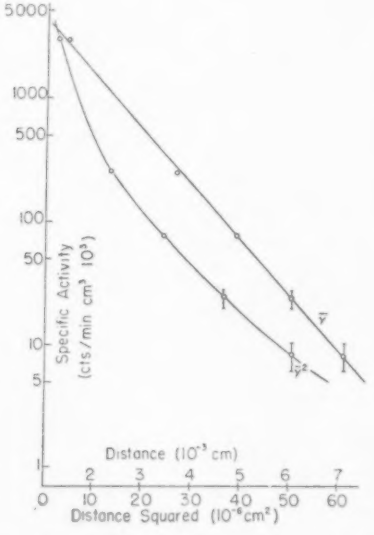

FIGURE 2. Low-temperature diffusion: $T = 90$°C; $t = 501.5$ hours.

more, one would expect, in a temperature range where both types of diffusion are important, that the experimental data would not agree with either the lattice or grain-boundary diffusion theories. This is seen in Figure 3. Here a plot of log activity against $(\bar{y})^2$ and $\bar{y}$ gives a straight line over a limited portion only. This temperature region is termed the "apparent lattice diffusion region." It is extremely difficult to separate the contributions to diffusion from the lattice and grain-boundary effects in this region.

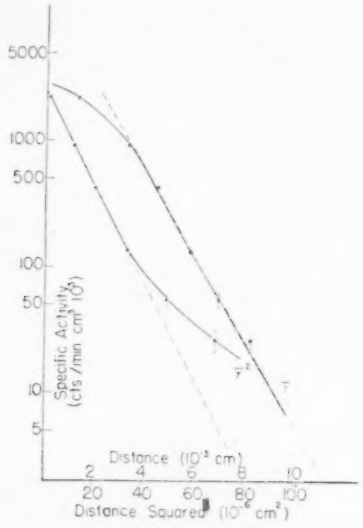

FIGURE 3. Apparent diffusion: $T = 157°C$; $t = 312.5$ hours.

The rate of polycrystalline self-diffusion was measured in the temperature range from 75°C to 200°C and the results are summarized in Table I. The diffusion coefficients calculated in the apparent lattice diffusion region were termed D_A when calculated on the basis of the lattice diffusion theory and D_b when calculated from Fisher's grain-boundary theory.

The average root-mean-square probable error for the diffusion coefficient was 11 per cent. This error arose from many sources, such as weighing of the sections, time of diffusion, sample activity counting, and extrapolated values for lattice diffusion coefficients at low temperatures.

Assuming that the temperature dependence of the diffusivity is described by

$$D = D_0 \exp(-Q/RT),$$

the log of the diffusivity can be plotted against $1/T$

TABLE I

$1/T$ (°K) $\times 10^{-3}$	Crystal	t (hrs)	D_b (cm²/sec) $\times 10^{-10}$ (C–P)	D_b (cm²/sec) $\times 10^{-10}$ (H–H)	D_A (cm²/sec) $\times 10^{-10}$	D_v (cm²/sec) $\times 10^{-14}$
1.6420	1	16			19.18	
1.8484	2	169			2.00	
2.075	3	261			0.146	570
2.174	20	92	803		0.0916	170
2.217	7	314	1180		0.059	100
2.217	10	287.5	1286		0.0614	100
2.268	21	92	401		0.0548	56
2.299	11	96	183.6		0.0247	37
2.326	23	312.5	182.8		0.0176	27
2.335	6	361.5		297		43.3
2.387	33	69.5	70.0			
2.392	9	576	171.6		0.016	12
2.439	32	166		64.1		12.6
2.445	25	189	56.1			6.4
2.481	24	312.5	32.6			4.2
2.493	18	170.5	33.2			3.6
2.532	29	337.5		28.3		4.4
2.597	17	241	22.9			1.0
2.653	27	355.5	10.1			0.50
2.667	16	93.5	9.02			0.43
2.674	28	528		12.21		0.83
2.703	13	167	7.23			0.29
2.710	30	404		6.69		0.55
2.755	26	501.5	5.75			0.13
2.824	31	959		3.50		0.15
2.857	15	118	2.53			0.043

and the slope and intercept will give, respectively, the activation energy (Q) and the temperature-independent part of the diffusivity (D_0). The plot of the data is shown in Figure 4. A least-square fit was applied to the points and the data can be described by:

	D_0 (cm²/sec)	Q (kcal/mol)
(C–P) (99.999%)	0.22	14.3 ± 0.2
(H–H) (99.99%)	0.38	14.6 ± 0.2

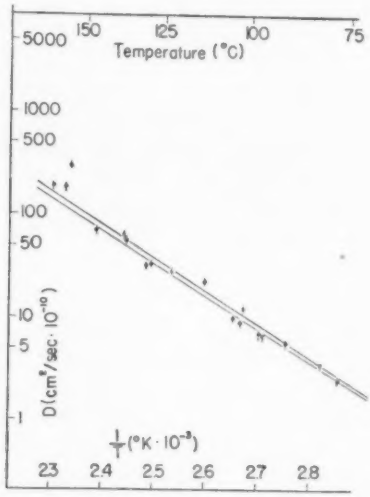

FIGURE 4. Log D vs $1/T$. ● = (C–P), + = (H–H).

The difference between the (C–P) and (H–H) is very small and it is questionable whether any special significance can be attached to this difference beyond experimental error. However, a part of this difference might be attributed to the anisotropy for motion in the grain boundaries, as was found by Couling and Smoluchowski [7].

Figure 5 shows the over-all picture of self-diffusion in zinc as determined from the experiments in this Laboratory. On the left are the single-crystal data which were reported on in reference [1]. On the right are the grain-boundary data described here. In the reciprocal temperature range ($1/T = 2.07$ to 2.36) is the apparent lattice diffusion region where both types of diffusion phenomena are prominent, and a marked deviation from both straight-line plots is observed. The diffusivity in this region can be described by:

$$D_A = (2 \times 10^{-3}) \exp(-17{,}500/RT) \quad (\text{cm}^2/\text{sec}).$$

This apparent diffusion coefficient for the lattice is not a unique constant like D_v or D_b but is a mixed coefficient made up from some average of intragranular and intergranular diffusion.

In summary, it can be concluded that the grain-boundary activation energy is about 37 per cent less than the lattice activation energy, giving a larger self-diffusivity for the grain boundary than for pure bulk self-diffusion in zinc.

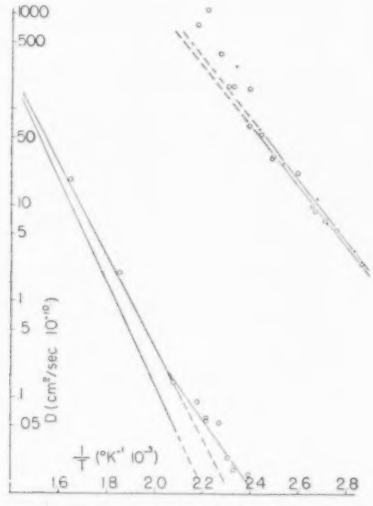

FIGURE 5. Self-diffusion in zinc.

Acknowledgement

The author wishes to express his appreciation to Professor Hillard B. Huntington for his enthusiastic direction and encouragement in this project. The preparation of the radioactive plating solution was made with the help of Professor Herbert Clark. A special note of thanks is also extended to Mr. George A. Shirn for his help in making some of the experimental measurements and to Professor Francis T. Worrell for the kind use of the X-ray equipment. The work was performed under the sponsorship of the Atomic Energy Commission, Contract AT-(30-1)-1044.

References

1. SHIRN, G. A., WAJDA, E. S., HUNTINGTON, H. B. Acta Met. **1** (1953) 513.
2. HOFFMAN, R. E., and TURNBULL, D. J. Appl. Phys. **22** (1951) 634.
3. SLIFKIN, L., LAZARUS, D., and TOMIZUKA, T. J. Appl. Phys. **23** (1952) 1032.
4. FISHER, J. C. J. Appl. Phys. **22** (1951) 74.
5. ROE, G. M. Knolls Atomic Laboratory, Schenectady, New York.
6. WHIPPLE, R. T. A.E.R.E. Report T/R 1026 (1952). Ministry of Supply, Harwell, England.
7. COULING, L., and SMOLUCHOWSKI, R. Phys. Rev. **91** (1953) 245.

ORIGIN OF SPIRAL EUTECTIC STRUCTURES*

R. L. FULLMAN and D. L. WOOD†

Eutectic structures in which the two phases appear as intertwined spirals in cross section have been observed in zinc-magnesium and aluminum-thorium alloys. The spatial form of the eutectic structure in zinc-magnesium alloys is a spiral cone. A theory of the solidification conditions necessary for formation of this type structure is advanced based on a particular type of anisotropy in the difference in growth rates of the two phases.

L'ORIGINE DES STRUCTURES EUTECTIQUES, SPIRALIFORMES

On a observé dans des alliages zinc-magnésium et aluminium-thorium, des structures eutectiques dans lesquelles les deux phases apparaissent, dans une coupe transversale, en forme de spirales entrelacées. Dans l'espace la structure eutectique dans les alliages zinc-magnésium est en forme d'une hélicoïde conique. On propose une théorie des conditions nécessaires lors de la solidification pour former ce type de structure. Cette théorie est basée sur l'anisotropie de la différence entre les vitesses de croissance des deux phases.

DER URSPRUNG DER EUTEKTISCHEN SPIRALSTRUKTUREN

In Zink-Magnesium und Aluminium-Thorium Legierungen wurden eutektische Strukturen beobachtet, in denen die beiden Phasen als verschlungene Spiralen im Schnitt erschienen. Die räumliche Form der eutektischen Strukturen der Zink-Magnesium Legierungen ist ein Spiralkegel. Es wird eine Theorie der Erstarrungsbedingungen, die für die Bildung einer derartigen Struktur erforderlich sind, dargelegt. Diese Theorie gründet sich auf eine bestimmte Form der Anisotropie in der Differenz der Wachstumsgeschwindigkeiten der beiden Phasen.

Scheil [1] and Bückle [2] have published illustrations of eutectic structures in which the polished and etched cross section reveals the two phases wrapped around each other in the form of spirals. The structures were found in the zinc-magnesium [1] and aluminum-thorium [2] systems. This paper reports the results of an investigation of the spatial arrangement of the phases in eutectic spirals of an alloy of zinc plus 3 per cent magnesium. A theory of the prerequisites for the formation of spiral eutectic structures is advanced.

Experimental Procedure

Small heats of the alloy were melted in air, and cast into simple ingots suitable for metallographic preparation. A wide range of cooling rates was obtained by varying the casting conditions (i.e., from extremely rapid cooling obtained by casting onto a large cold brass block, to extremely slow cooling obtained by allowing the heat to cool in a small furnace). Cross sections were prepared for metallographic examination by mechanical polishing and were etched with 1 per cent Nital.

Specimens showing well-developed spiral structures were used to investigate the spatial arrangement of the phases. A "Knoop" micro-hardness indentation was made on the surface of each specimen to be investigated. Since the long axis of the "Knoop" diamond indenter has a base angle of 172 degrees, the depth polished away is equal to 0.0306 times the change observed in the indentation length. The indentation was photographed at a magnification of 250×, and one or more spirals were photographed at a magnification of 2000×. The specimen was then repolished and etched, and the same spirals were photographed, along with the indentation as shown in Figure 1. Alternate polishing and photographing were continued until a considerable depth of the specimen had been examined. When an indentation had shrunk to near zero size, a new indentation was placed on the specimen, and both indentations were photographed so as to provide continuity in the record of the depth removed by polishing.

Experimental Observations

It was found that well-developed spiral structures were produced over a wide range of cooling rates. At the fastest cooling rates used, the microstructure revealed small spiral segments, but the numerous eutectic colonies impinged before any attained sufficient size for a spiral of several turns. At the slowest cooling rates used, the phases were distributed in a typical spheroidized structure. A 5-minute anneal at about 15°C below the eutectic temperature caused similar spheroidization of the structure of a sample that had a well-developed spiral structure before annealing. Hence the formation of the spiral morphology does not appear to require any special range of cooling rates, except for limitations imposed by high nucleation rate: growth-rate ratios at high cooling rates, or spheroid-

*Received October 13, 1953.
†General Electric Research Laboratory, Schenectady, N.Y.

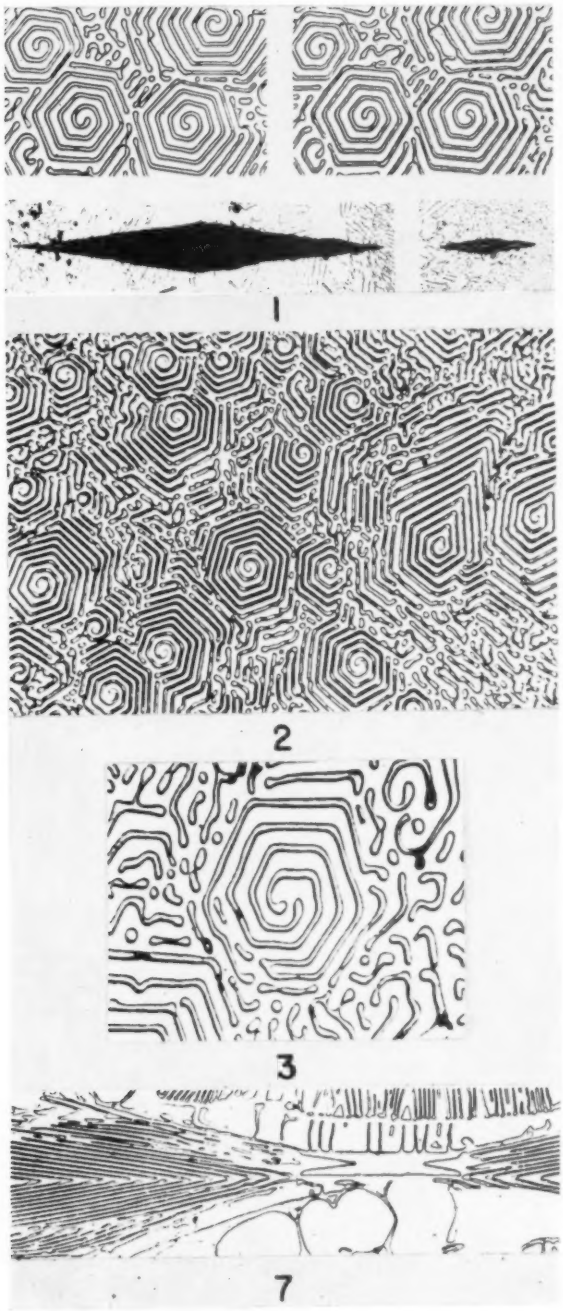

PLATE I. Figure 1—Top, two cross sections of same area of zinc plus 3% magnesium alloy, 1000×. Bottom, "Knoop" microhardness indentation corresponding to the cross sections above. 200×. Figure 2—Typical microstructure of zinc plus 3% magnesium alloy. As cast. 750×. Figure 3—Double spiral structure. Zinc plus 3% magnesium. 1500×. Figure 7—Nearly axial cross section of zinc plus 3% magnesium eutectic colony. 250×.

ization at low cooling rates. Most of the spirals were single, as shown in Figure 2, but occasional closed loops or double spirals, as shown in Figure 3, were found. The spirals had approximately regular hexagonal form, and neighboring spirals were usually of nearly identical orientation.

On repolishing samples to investigate the spatial arrangement of the phases, it was found that the spiral centers wound farther around or unwound as material was removed. One spiral was found that unwound at first, and then wound up as more material was removed. The general shape to be inferred from this observation is that of a spiral cone, as shown in Figure 4. As the cone widens out,

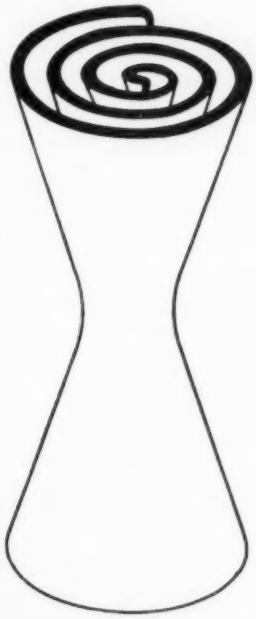

FIGURE 4. Schematic diagram of spiral cone morphology.

the spiral winds farther around, filling in the center of the figure. Hence, unwinding of the spiral center is observed if the direction of polishing is toward the center of the cone, and winding of the spiral center is observed if the direction of polishing is away from the cone center. The spiral center first unwinds and then winds if the initial direction of polishing is toward the cone center and polishing is continued beyond the cone center.*

The product of number of revolutions that the spiral center turns times the spacing of the spiral turns measures the distance that the cone opens or closes in a given distance along the axis. Hence, if the shape is actually a regular cone, a graph of spiral revolutions times spiral spacing versus the distance polished should consist of two straight lines of equal slope but opposite sign. The slope of the lines is equal to the half-angle of the cone. Data

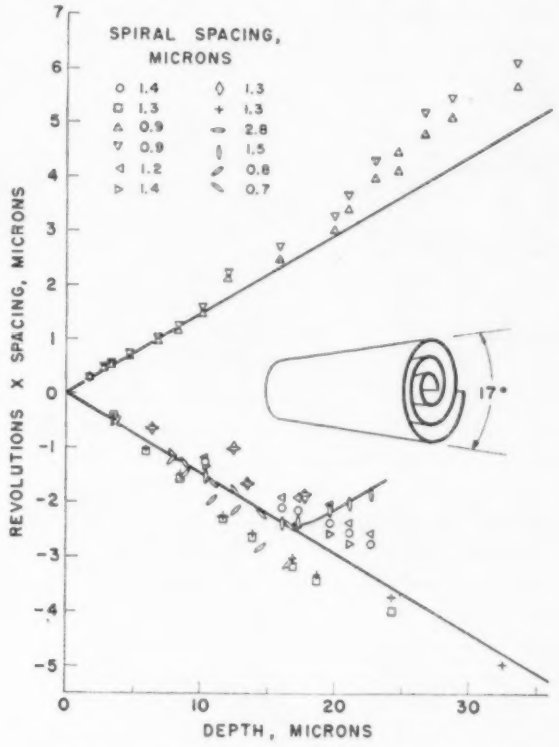

FIGURE 5. Analysis of spatial form of spiral eutectic colonies in zinc plus 3% magnesium.

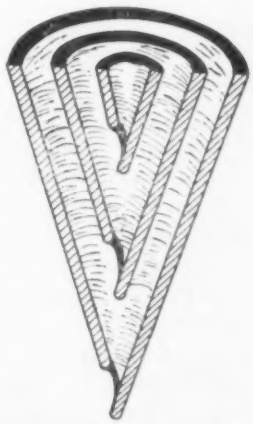

FIGURE 6. Schematic diagram of axial cross section through a spiral cone.

*The alloys studied contained primary dendrites, and most of the spiral cones appeared to start from dendrites. Hence only one half of the ideal double cone was observed in most of the spirals investigated. Nucleation from a common dendrite is no doubt responsible for the similar orientations of neighboring spirals, apparent in Figures 1, 2 and 3.

from 12 spiral eutectic colonies are plotted in this manner in Figure 5. The cone angle is about 17 degrees, and is independent of the spacing of the spiral turns, within experimental scatter.

A longitudinal section through a spiral cone would appear as shown in Figure 6, if the section were exactly along the cone axis. The discontinuities of alternate branches would disappear if the section were off the cone axis. The appearance of these discontinuous branches over a considerable distance in the photomicrograph of Figure 7 indicates that the section is nearly parallel to the cone axis. Hence the observed angle between branches of the cone is approximately equal to the true cone angle. The angle found is again 17°.

Theory of Formation of Spiral Eutectic Structures

In order to understand the attributes of a eutectic system necessary for the formation of spiral eutectic structures, it is convenient to consider first the behavior of a hypothetical eutectic system of two-dimensional crystals. Typical eutectic solidification would consist of the growth of adjacent rods of the two phases, as shown in the upper part of Figure 8. The composition of liquid

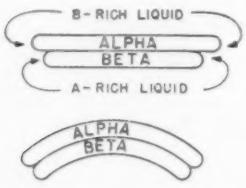

FIGURE 8. Schematic growth of rods during solidification of a hypothetical two-dimensional eutectic alloy.

ahead of the rapid-growth directions of each rod is shifted toward the composition of the other phase. As a result, the liquid at the ends of the slower-growing beta-rod is more supercooled with respect to growth of phase alpha than is the liquid at the ends of the alpha-rod. Hence the faster-growing phase tends to grow around the slower-growing phase, as shown in the lower part of Figure 8. Continued growth of the pair of two-dimensional rods would then lead to formation of a spiral unless there were no error of closure of the loop formed. If a complete loop were formed, repeated alternate nucleation of alpha- and beta-crystals at the liquid-solid interface could lead to the formation of a series of rings. If the closure error were larger than that required for the development of a single spiral, subsequent nucleation of another crystal on the lateral liquid-solid interface could lead to the formation of a double spiral.

In most real (three-dimensional) eutectic systems, the faster-growing phase grows around the slower growing phase in all directions, so that the slower growing phase is surrounded and isolated from the liquid, without formation of a spiral. If the difference in growth rates is approximately isotropic, the slower-growing phase will be roughly spherical. If the difference in growth rates is small in a single direction, the isolated phase will be in the form of rods, while if the difference is large in a single direction plates will be formed.

A conical spiral eutectic morphology can be produced if the anisotropy in growth rates is so large that the growth-rate difference changes in sign as well as magnitude as a function of direction. Consider the hypothetical growth rate plot shown in Figure 9. In this idealized model it is assumed

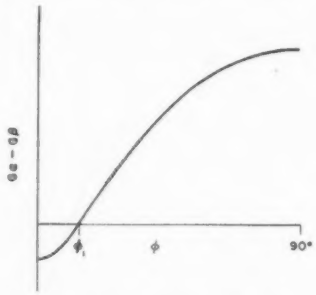

FIGURE 9. Hypothetical growth rate anisotropy required for formation of spiral cone eutectic structure.

that the growth-rate difference is a function only of the angle ϕ from some crystallographic direction. For the situation considered, beta-crystals grow faster than alpha-crystals for all values of ϕ from 0 to ϕ_1, and alpha grows faster at larger values of ϕ. If contiguous crystals were growing from the melt, the growth-rate anisotropy shown in Figure 9 would cause phase alpha to grow around phase beta in all directions in the plane $\phi = 90°$, while phase beta would grow around phase alpha in the direction $\phi = 0°$, leading to the configuration shown in Figure 10. But as phase beta grows around phase alpha the direction of the growing edge changes from $\phi = 0$ to larger values of ϕ. When the direction of the edge reaches ϕ_1, the growth rates become equal and the two phases grow out as a cone with half-angle ϕ_1. The cone axis is the direction $\phi = 0°$. Since with this configuration there is no opportunity for the faster-growing phase to surround the slower-growing phase, the arguments

predicting spiral morphology in a hypothetical two-dimensional eutectic system are not invalidated. Only growth directions between ϕ_1 and 90 degrees are operative, so that G_α–G_β ranges from zero to a maximum positive value in the plane $\phi = 90°$. The result is a spiral cone morphology, as shown in Figure 4.

The growth rates of real crystals do not depend on only a single orientation parameter ϕ, as has been assumed above. The growth rates of the two crystal types can be described as functions of ϕ and an angle θ measured in the plane perpendicular to the spiral axis. Then for each value of θ a plot

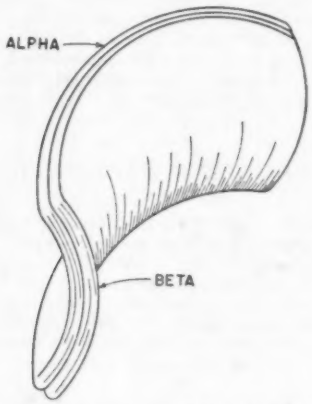

FIGURE 10. Elementary growth form leading to formation of spiral cone eutectic morphology.

of the growth-rate difference as a function of ϕ may be drawn, similar to Figure 9. For each value of θ there will be a value $\phi_1(\theta)$ at which the growth-rate difference is zero, but the angle ϕ_1 and the growth rate at which this occurs will depend on the value of θ chosen. Since the longitudinal growth of the spiral colony involves only directions for which the two growth rates are equal, it behaves like a single phase, and only the slowest growth rate operates. Hence the group of crystallographically equivalent directions $\phi_1(\theta)$ which have the smallest growth rate are the only active growth directions, and the spiral is faceted.

Conclusions

The spatial form of eutectic colonies that appear as spirals in cross sections of zinc + 3 per cent magnesium alloy has been analyzed. The colonies have the form of spiral cones with hexagonal faceting and a cone angle of 17 degrees. The formation of eutectic colonies with this morphology can be rationalized on the basis of a particular type of anisotropy in growth rates of the two phases.

Acknowledgement

The authors wish to express their appreciation to Miss D. Kontoleon for assistance in the preparation of the several hundred photomicrographs required in this investigation.

References

1. SCHEIL, E. Z. für Metallkunde, **37** (1946) 1.
2. BÜCKLE, H. Z. für Metallkunde, **37** (1946) 43.

THE SUPERSATURATION AND PRECIPITATION OF VACANCIES DURING DIFFUSION*

R. W. BALLUFFI†

Some metallographic evidence is presented which supports the viewpoint that the porosity formed during diffusion is produced by the heterogeneous nucleation of supersaturated vacancies which are pumped into one side of the diffusion zone by the unequal diffusion currents of the Kirkendall effect. From observations of the distribution of porosity in various sandwich type diffusion couples it is estimated that the required relative excess concentration necessary for precipitation is probably $\leqslant 0.01$. Additional diffusion data are cited which indicate that large deviations from the equilibrium vacancy concentration do not occur in the diffusion zone during any significant portion of the diffusion cycle.

LA SURSATURATION ET LA PRÉCIPITATION DE LACUNES RÉTICULAIRES PENDANT LA DIFFUSION

On présente certains faits métallographiques supportant le point de vue que la porosité qui apparaît pendant la diffusion est produite par la germination hétérogène de lacunes réticulaires, sursaturées, transférées d'un côté de la zone de diffusion par les courants inégaux de diffusion dus à l'effet de Kirkendall. Des observations de la distribution des porosités, faites sur divers couples de diffusion en forme de sandwichs, ont permis d'estimer que l'excès relatif de concentration, nécessaire à la précipitation, est probablement $\leqslant 0{,}01$. D'autres données relatives à la diffusion sont aussi rapportées; elles indiquent que de fortes déviations de la concentration d'équilibre des lacunes n'ont jamais lieu pendant des parties appréciables du cycle de diffusion.

DIE ÜBERSÄTTIGUNG UND AUSSCHEIDUNG VON LEERSTELLEN WÄHREND DER DIFFUSION

Metallographische Versuchsergebnisse werden beschrieben, die die Ansicht unterstützen, dass die während der Diffusion auftretende Porosität durch die heterogene Formation von übersättigten Leerstellen, die durch die ungleichen Diffusionsströme des Kirkendall-Effekts in eine Seite der Diffusionszone hineingepumpt werden, hervorgerufen wird. Aus Beobachtungen der Porositätsverteilung in verschiedenen schichtförmigen Diffusionspaaren kann die zur Ausscheidung notwendige relative Überschusskonzentration zu etwa $\leqslant 0{,}01$ abgeschätzt werden. Es werden weitere Diffusionsdaten mitgeteilt, die zeigen, dass in keinem wesentlichen Teil des Diffusionskreislaufs grosse Abweichungen von der Gleichgewichtskonzentration der Leerstellen in der Diffusionszone auftreten.

I. Introduction

Seitz [1] has recently presented the first detailed analysis of the porosity formation which has been observed in diffusion couples exhibiting a Kirkendall effect [2; 3; 4; 5]. In the above work the viewpoint is taken that the holes form by the precipitation of supersaturated vacancies produced by the unequal diffusion currents of the Kirkendall effect. Seitz postulates that the process occurs by heterogeneous nucleation and calculates a value of about 10^{11} for the lifetime number of vacancy jumps by using some porosity observations of Barnes [3] and the rather arbitrary value of 1 for the critical relative excess vacancy concentration necessary to form holes. He is careful to point out, however, that nuclei could be present which would nucleate holes at a relative excess concentration of 0.01 or less.

In the present paper we first give some experimental evidence which supports the basic premise that the holes form from a supersaturated solution by a process of heterogeneous nucleation. The problem of hole formation is then considered somewhat differently and the results indicate that the required relative excess vacancy concentration for hole formation in most specimens studied to date is probably $\leqslant 0.01$. If this conclusion is valid the estimate used by Seitz of 10^{11} for the number of jumps may be too high and a high vacancy supersaturation would not be maintained during any appreciable portion of the diffusion cycle. Diffusion data which are cited later in this paper seem to support the conclusion. Briefly, the diffusion coefficient seems to be a unique function of local concentration. The fact that points of constant concentration have always been found to move parabolically with time is evidence of this point. Diffusion coefficients calculated at a given concentration from widely different couples have been found recently to agree within expected experimental error. In addition, Kirkendall marker movements have been found to vary parabolically even at comparatively short diffusion times. Such results would not be expected if excess relative concentrations of the order of 1 were maintained over appreciable portions of the diffusion cycle.

*Received September 20, 1953.
†Atomic Energy Division, Sylvania Electric Products Inc., Bayside, New York.

II. Evidence for the Heterogeneous Nucleation of Holes

As Seitz [1] has indicated, the exact nature of the nucleating sites responsible for the heterogeneous nucleation of holes is unknown at present. However, it seems almost certain that such sites must be present since the supersaturation required for precipitation in the perfect crystal is prohibitively high. Most probable nucleating sites are small foreign particles or imperfections which are present in a sufficiently wide distribution to be capable of operating over a range of supersaturations. As shown later, we suspect that in most metals nucleating sites are present which can operate at relative excess concentrations of 0.01 or less.

We have found a number of obvious cases of heterogeneous nucleation while observing porosity formation in diffusion zones in alpha-brass sheet where the zinc was diffused out by heating *in vacuo*. In Figure 1a a number of randomly distributed holes have formed in the diffusion zone adjacent to the surface where zinc loss has occurred, but in addition there is a distinct row of holes present. These holes most likely originated on a string of impurity particles which were rolled out parallel to the surface during the original forming of the sheet. In another experiment nucleating sites were introduced in a specimen by welding two brass sheets together without first cleaning the welded faces. The welded sandwich was then annealed in an evacuated capsule until grain growth occurred across the bonded interface and then the specimen was diffused by heating *in vacuo*. As shown in Figure 1b a distinct row of holes was observed along the position of the former welded interface and must be due to the effect of foreign particles and possible imperfections introduced at the former join. While these observations do not prove directly that the randomly distributed holes throughout the volume form by heterogeneous nucleation, it appears most likely that they form at sites quite similar to those just discussed.

Another interesting feature of the precipitation process is shown in Figure 2 where a porous zone near the surface of a vacuum-annealed brass sheet is again shown. The holes become smaller and more closely spaced as the surface is approached. This observation may be explained on the basis of the maximum level of supersaturation reached in various parts of the diffusion specimen. At the beginning of the process the highest supersaturation is reached in the volume adjacent to the surface. The wave of maximum supersaturation then moves into the specimen but also decreases in intensity. The greater density of holes near the surface must be due to the presence of nucleating sites throughout the specimen which could only become effective at the relatively high supersaturations reached near the specimen surface.

III. Precipitation of Holes in the Diffusion Zones of Various Systems

The rate at which vacancies accumulate in a unit volume of the diffusion zone is given by [1]

$$\frac{\partial N_v}{\partial t} = -\operatorname{div} I_v - \frac{N_{vo} R}{T}. \tag{1}$$

We retain the notation used by Seitz where N_v is the actual number of vacancies per unit volume, N_{vo} is the equilibrium number, $R = (N_v/N_{vo} - 1)$ is the relative excess concentration, I_v is the vacancy current and T is the vacancy lifetime. By making reasonable approximations in (1) it is possible to obtain an order of magnitude value for the ratio R_c/T for the condition that holes are just capable of forming. Since the number of vacancies created and destroyed within the unit volume must be large compared to the change in the number maintained there the term $\partial N_v/\partial t$ must be relatively small. In addition, we assume that the motion of the vacancies is largely determined by the pumping action of the chemical gradient and not by any vacancy gradients which are established during diffusion. This appears to be reasonable since it is known that vacancies actually are continuously pumped against their own gradient into regions of higher vacancy concentration e.g., the brass side of copper/alpha-brass sandwich couples. Div I_v may, therefore, be approximated by

$$\frac{\partial}{\partial x}\left[(D_2 - D_1)\frac{\partial N_2}{\partial x}\right],$$

where D_1 is the intrinsic diffusivity. Using the relationship $D = N_1 D_2 + N_2 D_1$, where D is the chemical diffusity, and assuming that the ratio of intrinsic diffusities $K = D_1/D_2$ is relatively independent of concentration, equation (1) may be rewritten as

$$\frac{N_{vo}}{N}\frac{R}{T} \sim -\left[\frac{(1-K)}{N_1 + KN_2}\right] \tag{2}$$
$$\left[D\frac{\partial^2 N_2}{\partial x^2} + \left\{\frac{\partial D}{\partial N_2} + D\frac{(1-K)}{(N_1 + KN_2)}\right\}\left(\frac{\partial N_2}{\partial x}\right)^2\right].$$

where N is the total number of atoms per unit volume. The above relationship should also apply in the case of interstitial diffusion if every atom which diffuses interstitially out of a volume in the diffusion zone leaves a vacancy behind.

An order of magnitude value of $(N_{v_0}/N)(R_c/T)$ where R_c is the critical relative excess concentration required to just form holes, may be obtained directly from relation (2) by locating the position in the diffusion zone of the region where holes just stop appearing and then evaluating the right-hand side of the equation from the corresponding diffusion curve and diffusivity data. Use of equation (2) in this way assumes, of course, that the porous region is still advancing at the time diffusion is interrupted and that the wave of maximum supersaturation has not fallen below the level necessary for hole formation. We have calculated this quantity for a number of cases in the copper/nickel, copper/alpha-brass and copper/copper-aluminum systems where suitable data are available in the literature and resulting values are given in Table I. The positions in the diffusion zone where the holes just ceased appearing were obtained from a number of micrographs prepared in this Laboratory and elsewhere. In a number of cases the porosity did not disappear at a sharply defined interface, but, instead, a few widely separated holes appeared considerably deeper into the specimen as in Figures 3a and 3b, for example. In this case the location where the majority of the holes ceased forming was used, and the few randomly scattered holes further into the specimen were ignored (see locations marked by arrows in Figures 3 and 4). Since these latter holes must have formed on unusually effective nucleating sites this procedure gives the location where all but these few widely scattered sites became ineffective. The micrographs in Figure 3 indicate that the porous zone was still advancing in the copper/nickel specimen after 91 hours at 1020°C and, therefore, that the supersaturation had not yet fallen below the value required for hole formation. The same condition is true for the copper/alpha-brass specimen diffused for 6.5 hours at 800°C as shown in Figure 4. In the case of the copper/copper-aluminum couples the condition is probably closely satisfied in the lesser diffused couple annealed for 25 hours at 903°C. The corresponding diffusion curves for these specimens were obtained from available diffusion data by using the following approximate relationship given by da Silva and Mehl [7] for transforming a given diffusion curve to correspond to any time and temperature:

$$x_2 = \sqrt{\frac{t_2}{t_1}} \cdot \exp\left[\frac{Q(T_2 - T_1)}{2R\,T_2T_1}\right] \cdot x_1 \qquad (3)$$

The values in Table I suggest that holes will form in all of these systems when vacancies are pumped into any small region of the diffusion zone at the rate of about 10^{16}/sec/cc [div $I_v \sim (-N_{v_0}R_c/T)$]. The lower values obtained for the copper/alpha-brass and copper/copper-aluminum couples of Buckle and Blin which were diffused for the comparatively long period of 600 hours may be due to the condition that holes are no longer forming, since the vacancy supersaturation is too low by this time. A notable exception in Table I is the result based upon the observations of Barnes. Barnes found a localized row of holes to appear in the copper side of copper-nickel couples in contrast to the wider distribution of holes in Figure 3. The most reasonable explanation for this difference seems to be that the specimens of Barnes were unusually free of effective nuclei and that, therefore, higher supersaturations were required for hole formation. Using the width of the porous zone shown by Barnes for the specimen diffused for the short time of 2.25 hours at 1000°C we estimate that vacancies were pumped into this specimen at the rate of $\geqslant \sim 10^{17}$/per/cc, without forming holes. This observation emphasizes the difficulty in comparing results from various laboratories and the great importance of any variations in the type and size of the nucleating sites present. It is interesting to note that Seith and Kottmann

TABLE I

VACANCY DATA FOR VARIOUS SYSTEMS

System	Diffusion treatment	Width of porous zone (cm)	$\left(\frac{N_{v_0}}{N}\right)\left(\frac{R_c}{T}\right)$	Source
Cu/Ni	91 hr. at 1020°C	.016	$\sim 10^{-7}$	Fig. 3*a*, 3*b*
	239 hr. at 1055°C	.026	—	Fig. 3*c*
	2.25 hr. at 1000°C	.003	$\geqslant \sim 10^{-6}$	Barnes [3]
	68 hr. at 1080°C	.005	—	Barnes [3]
Cu/brass	6.5 hr. at 880°C	.040	$\sim 10^{-6}$	Fig. 4
	16 hr. at 880°C	.080	—	Fig. 4
	24 hr. at 785°C	.024	$\sim 10^{-7}$	Sylvania Laboratory
	600 hr. at 800°C	.090	$\geqslant 10^{-8}$	Buckle and Blin [2]
Cu/Cu-Al	26 hr. at 903°C	.025	$\sim 10^{-7}$	Rhines and Mehl [6]
	600 hr. at 800°C	.025	$\geqslant \sim 10^{-8}$	Buckle and Blin [2]

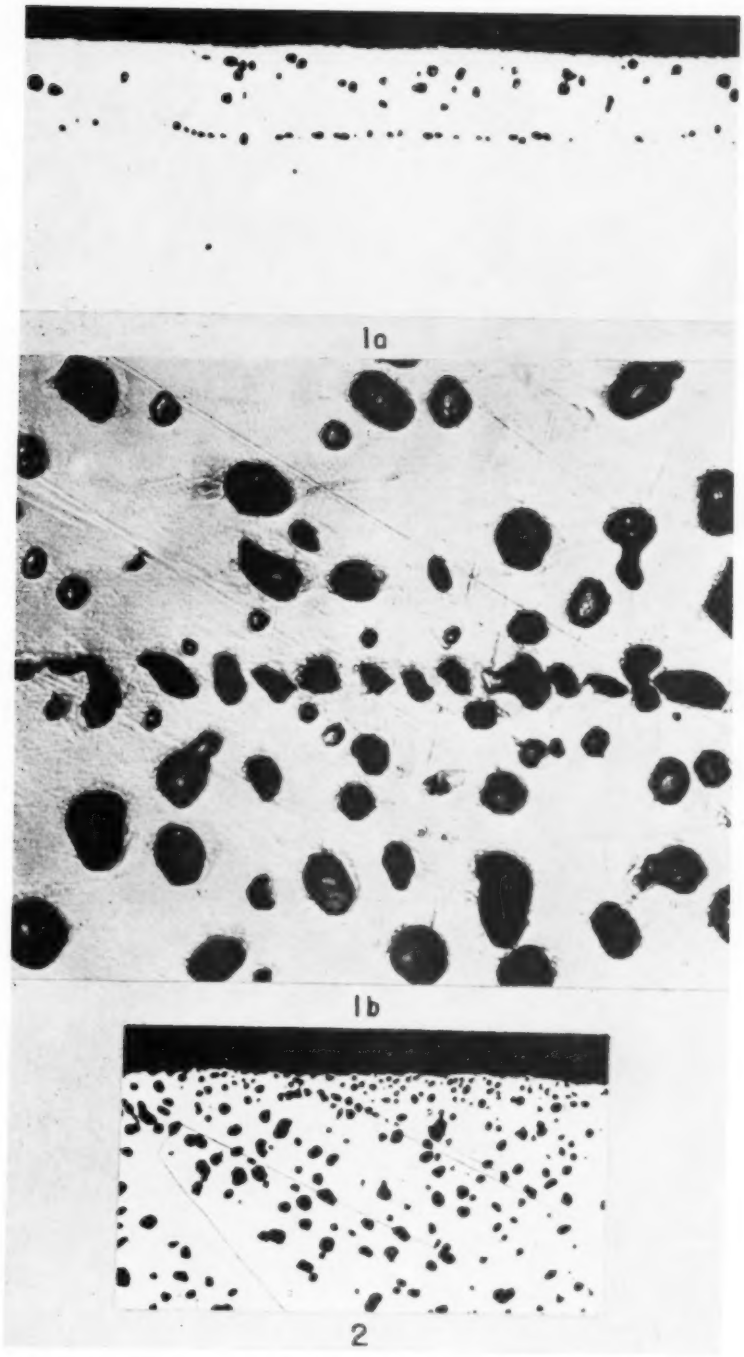

PLATE I (figures reduced to seven-eighths in reproduction). Figure 1—Diffusion zones of single-crystal alpha-brass sheet specimens heated *in vacuo*. (*a*) 2 hours at 700°C. (400×) (*b*) 88 hours at 800°C. (500×) Figure 2—Region near surface of alpha-brass specimen heated 86 hours at 800°C *in vacuo* (100×)

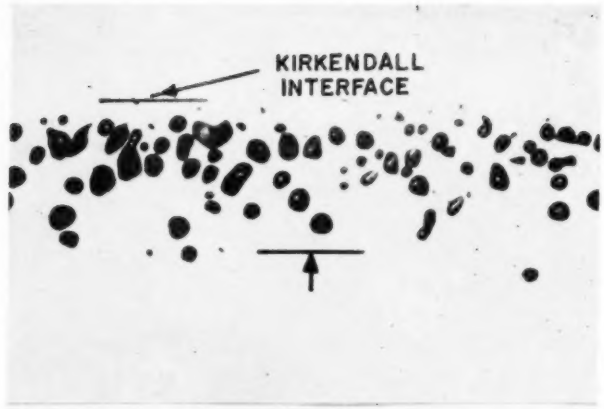

3a

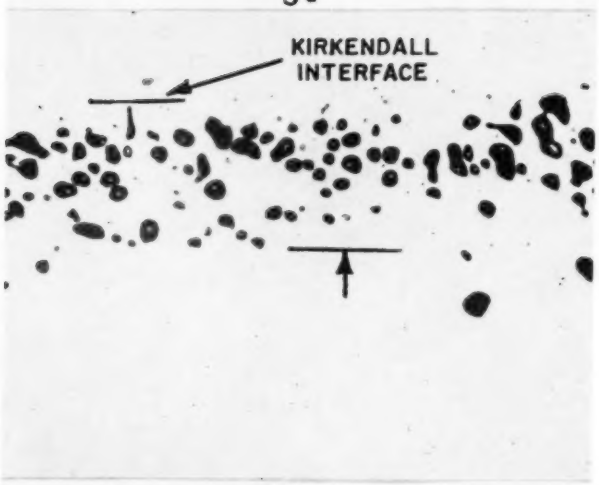

3b

3c

PLATE II (figures reduced to seven-eighths in reproduction). Figure 3—Porosity developed in copper/nickel sandwich couples in hydrogen. Arrow indicates limit of porous region. (*a*) 91 hours at 1020°C. (*b*) 91 hours at 1020°C. (*c*) 239 hours at 1050°C. (150×)

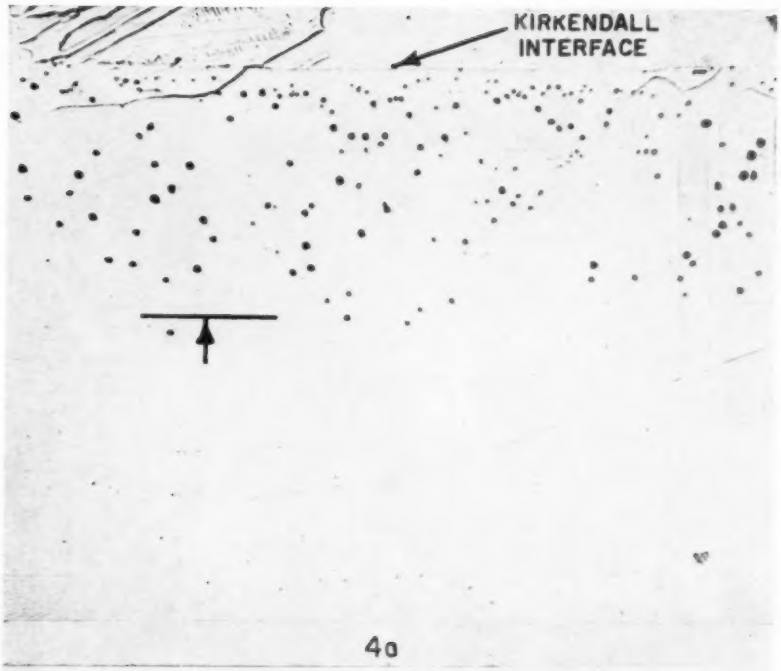

4a

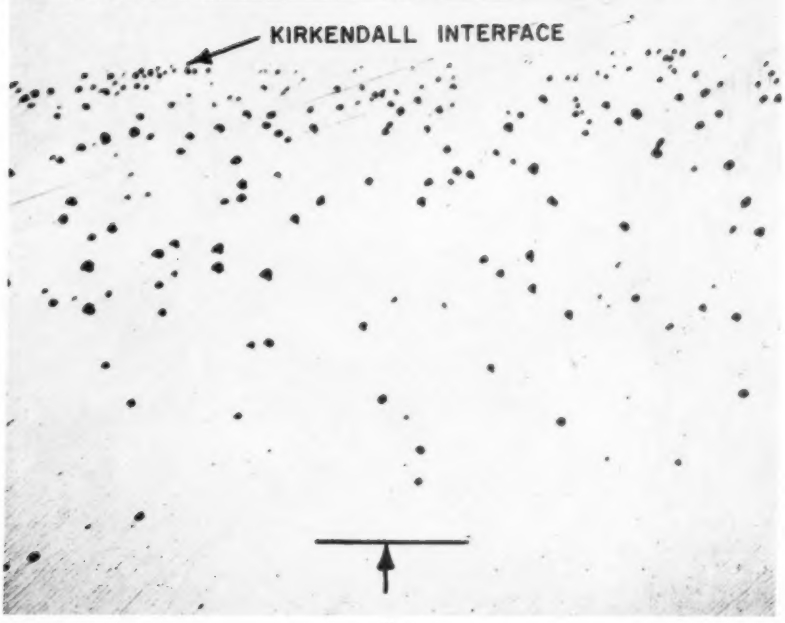

4b

PLATE III (figures reduced to seven-eighths in reproduction). Figure 4—Porosity developed in copper/alpha brass sandwich couples at 880°C in hydrogen. Arrow indicates limit of porous region. (*a*) 6.5 hours (*b*) 16 hours. (100×)

[4] have observed widely distributed porosity in copper/nickel couples which is similar to that shown in Figure 3. The wide distribution of porosity often observed in copper/alpha-brass couples may be easily explained on the basis of these results. Since diffusion is more rapid in this system, vacancies are pumped into regions comparatively distant from the original interface at a rate sufficient to form holes.

IV. The Supersaturation Necessary for Precipitation

Since $(N_{v0}/N)/(R_c/T) \sim 10^{-7}$ seems to be a typical value for porosity to just form in the present couples we may next estimate the relative excess concentration required to form holes. Since a good estimate for the free energy of formation of a vacancy is about one half the observed activation energy for diffusion the mol fraction of vacancies is given by:

$$\frac{N_{v0}}{N} \sim \exp\left(-\frac{20{,}000}{RT}\right). \tag{4}$$

The magnitude of this quantity is about 10^{-4} at diffusion temperatures and therefore R_c/T must be equal to about 10^{-3}. In order to obtain an approximate value for R_c we must next estimate the vacancy lifetime. A reasonable upper limit for the lifetime based upon the concept of dislocations acting as sinks for vacancies may be obtained. If only one site in every thousand along the dislocation line is capable of acting as an effective sink the vacancy must make about 10^{10} jumps before capture since about 1 site in 10^7 lies on a dislocation line according to current estimates. The lifetime under these conditions is about 10 sec. since

$$T \sim n_j \cdot 10^{-13} \exp\left(\frac{20{,}000}{RT}\right) \tag{5}$$

where n_j is the lifetime number of jumps and 20,000 cal/mol is the estimated activation energy for vacancy exchange. If $T_c \sim 10$ sec. the relative excess concentration for hole formation must be about 0.01 in the present specimens. Nowick and Sladek [8] have recently given a lower limit of 10^6 for the number of vacancy jumps in a 70–30 silver zinc alloy which was obtained from anelastic measurements. This value seems too low on the basis of the above results, since it would require an unusually low supersaturation for hole formation. Since 10^{10} represents a probable upper limit for the number of jumps it is probable that the required relative excess concentration is < 0.01. These obviously approximate calculations suggest that holes are able to form at supersaturations considerably below the value of $R_c = 1$ tentatively used by Seitz.

Additional evidence that probably $T < 10$ sec. and that $R_c < 0.01$ is provided by several diffusion data. If the vacancy diffusion mechanism holds, the diffusion process should be markedly affected by large deviations from the equilibrium vacancy concentration throughout the diffusion zone which might occur during an appreciable portion of the diffusion cycle. The effect would arise from the presence of a vacancy gradient term and the fact that the diffusion coefficients themselves are proportional to the vacancy concentration. In this case any calculated diffusion coefficients should depend upon the type of couple used and upon the time of diffusion since the vacancy concentration would in turn be a function of these parameters.

It has long been apparent that points of constant concentration move parabolically with time thereby justifying application of the Matano analysis and indicating that the diffusion coefficient is a function of the local composition only. A comparison of some of the most recent diffusion data indicates that the diffusion coefficients determined from different type couples agree within expected experimental error. Birchenall and Thomas [9] find D-values at 947°C in the copper/nickel system using incremental couples which agree within about 15 per cent with corresponding values obtained by da Silva and Mehl [7] using pure copper/pure nickel couples. Balluffi and Seigle [10] find that the D-values in alpha-brass at 800°C obtained from vapor-solid type couples agree within about 20 per cent with the most recent sandwich type couple data of da Silva and Mehl [7]. In the silver/gold system the data obtained from pure metal sandwich type [4], incremental sandwich type [11; 12], and vapor-solid type [10] couples all agree within about 10 per cent. In addition, no deviation from parabolic motion of Kirkendall markers has as yet been found, even at comparatively short diffusion times when deviations of the vacancy concentration and the vacancy gradient term would have maximum values. Balluffi and Seigle [10] find no deviation from parabolic marker movement in silver/gold and copper/alpha brass couples even during the first few hours of diffusion. All these presently available results indicate again that deviations from the equilibrium vacancy concentration

must be relatively small during all but perhaps the very initial period of the diffusion cycle and that hole formation which actually does occur during an appreciable period of the diffusion cycle must proceed in the presence of a relatively low superconcentration of vacancies.

Acknowledgment

The writer wishes to thank Dr. L. L. Seigle for several helpful discussions and for critically reading the present paper. The work was done under AEC Contract AT-30-1 GEN 367.

Note Added in Proof

At this point it would be highly desirable to carry out experiments designed specifically to detect possible non-equilibrium vacancy effects in diffusion couples at very short diffusion times. L. Slifkin and T. Tomizuka have informed the author (private communication) that such experiments have been started at the University of Illinois.

References

1. Seitz, F. Acta Met. **1** (1953) 355.
2. Buckle, H. and Blin, J. J. Inst. Metals **80** (1952) 385.
3. Barnes, R. S. Proc. Phys. Soc. **65B** (1952) 512.
4. Seith, W. and Kottmann, A. Z. angew. Chemie **64** (1952) 379.
5. Balluffi, R. W. and Alexander, B. H. J. Appl. Phys. **23** (1952) 953; **23** (1952) 1237.
6. Rhines, F. N. and Mehl, R. F. Trans. A.I.M.E. **128** (1938) 185.
7. da Silva, L. C. C. and Mehl, R. F. Trans. A.I.M.E. **191** (1951) 155.
8. Nowick, A. S. and Sladek, R. J. Acta Met. **1** (1953) 131.
9. Thomas, D. E. and Birchenall, C. E. J. Metals (1952) 867.
10. Balluffi, R. W. and Seigle, L. L. To be published.
11. Johnson, W. A. Trans. A.I.M.E. **147** (1942) 331.
12. Ebert, H. and Trommsdorf, G. Z. Electrochem. **54** (1950) 294.

INTERNAL FRICTION IN TITANIUM AND TITANIUM-OXYGEN ALLOYS*

J. N. PRATT†, W. J. BRATINA‡ and B. CHALMERS§

A low-frequency torsional pendulum technique has been used to study internal friction in alpha-titanium and in some titanium-oxygen alpha-solid-solutions containing up to 4.5 atomic per cent oxygen. Characteristic grain-boundary relaxation peaks are exhibited by the pure titanium and by the alloys; the respective heats of activation were found to be 46,000 cal/mol and 75,000 cal/mol. The introduction of oxygen results in the appearance of an additional relaxation peak at approximately 700°K; the mechanism involved is not established but the associated heat of activation is estimated as 48,000 cal/mol.

LE FROTTEMENT INTERNE DANS LE TITANE ET LES ALLIAGES TITANE-OXYGÈNE

La méthode du pendule de torsion à basse fréquence a été utilisée pour l'étude du frottement interne dans le titane alpha et dans quelques solutions solides, du type alpha, d'oxygène dans le titane. Sur les courbes de frottement interne du titane pur et des alliages, apparaissent les maxima caractéristiques de la relaxation aux joints intercristallins; les énergies d'activation furent évaluées respectivement à 46000 cal/mol et 75000 cal/mol. L'introduction d'oxygène conduit à l'apparition d'un autre maximum de relaxation aux environs de 700°K, le mécanisme impliqué dans ce second cas n'est pas établi, mais l'énergie d'activation associée à ce phénomène est évaluée à 48000 cal/mol.

DIE INNERE REIBUNG IN TITAN UND TITAN—SAUERSTOFF LEGIERUNGEN

Die innere Reibung von α-Titan und einigen festen α-Lösungen von Titan und Sauerstoff, die bis zu 4, 5 Atom% Sauerstoff enthielten, wurde mit Hilfe einer Niederfrequenz-Torsionspendelmethode untersucht. Reines Titan und die Legierungen zeigen charakteristische Korngrenzen Relaxationsmaxima; die entsprechenden Aktivierungsenergien betrugen 46,000 cal/mol bezw. 75,000 cal/mol. Der Zusatz von Sauerstoff rief ein weiteres Maximum bei etwa 700°K hervor. Der dazugehörige Elementarvorgang ist noch nicht bekannt, aber die damit verbundene Aktivierungsenergie kann zu ca. 48,000 cal/mol abgeschätzt werden.

Introduction

The profound effect of certain interstitial solute elements on the physical properties of α-titanium is well established. Previous work has shown, for example, that while pure titanium has a high ductility, contamination by very small quantities of nitrogen or oxygen induces marked embrittlement [1; 2; 3]. A rigorous interpretation of the influence of these elements on α-titanium is not possible on the basis of the existing data; the effects are not attributable to the equilibrium precipitation of a second phase since they become significant at compositions far below the equilibrium solubility limits and cannot be explained in terms of the observed lattice parameter changes [2; 4; 5; 6]. It is possible that the fundamental embrittlement mechanism involves an inhomogeneous distribution of solute atoms within the specimen, accompanied by incipient precipitation or lattice faulting. With the aim of obtaining further information concerning the exact role of the interstitial solutes in α-titanium, an investigation is being made of their influence on its internal friction characteristics, particularly their modification of grain boundary relaxation phenomena [7; 8]. The present publication reports the results of experiments on commercially pure titanium and titanium-oxygen alloys.

Experimental Details

The titanium employed in the present investigation was in the form of wire of 0.05-inch diameter. It was supplied by the Titanium Metals Corp. of America who reported its analysis to be: 0.10% Fe; 0.02% N; trace O; 0.04% C; 0.03% W; remainder Ti. Heat treatment of specimens was carried out either *in situ* in the internal friction apparatus or in evacuated quartz capsules in an auxiliary tube furnace; in the latter case the specimens were wrapped in similar titanium wire to prevent contamination by reaction with the containers. Oxygen-bearing samples were prepared by heating lengths of the wire under suitable conditions to give a uniform oxide coat, followed by prolonged annealing *in vacuo* until a uniform distribution of the oxygen throughout the specimen had been achieved. The change of the weight of the specimen was taken as a measure of its oxygen content. Owing to the inherent difficulties, it was not possible to prepare alloys with a high degree of precision by this method. All annealing procedures were such as

*Received October 6, 1953.

†Department of Metallurgical Engineering, University of Toronto; now I.C.I. Research Fellow, Department of Metallurgy, University of Manchester.

‡Department of Metallurgical Engineering, University of Toronto.

§Division of Applied Science, Harvard University, Cambridge, Massachusetts.

to result in uniform α-titanium structures. In the subsequent internal friction experiments the final temperature of the preliminary anneal was generally not exceeded in order to avoid grain growth during their progress. Nor in the present work were observations made above approx. 860°C, since it was desired to exclude any possible complications resulting from the allotropic transformation of titanium.

Measurements of internal friction were made by the standard method [7] of studying the free decay of the oscillations of a simple torsion pendulum, the suspension of which consisted of a wire of the material under investigation. The normal apparatus was elaborated to permit the experiments to be carried out in high vacuum (approx. 5×10^{-5} mm Hg.). This eliminated the possibility of contamination of the specimens during the experiments and also greatly increased the sensitivity of the method. Frequencies of vibration of approximately 1 cycle per second and 0.5 cycle per second were used. The maximum pendulum deflection employed corresponded to a maximum torsional strain of the order of 10^{-5} at the surface of the specimen. The variation of temperature along the length of the specimen was found to be little more than 1°C.

Internal friction is here defined as

(1) $\tan \delta$ = logarithmic decrement/π

where the logarithmic decrement is the natural logarithm of the ratio of the amplitudes of successive swings. The variation of $\tan \delta$ with temperature has been studied and the relaxation spectra plotted. From the frequency dependence of $\tan \delta$ the heat of activation, H, for a relaxation process may be calculated using the expression

$$H = R \cdot \ln \frac{f_1}{f_2} \Big/ \Delta(1/T) \tag{2}$$

where $\Delta(1/T)$ is the shift to superpose the curves of $\tan \delta$ versus $(1/T)$ obtained from experiments on a single specimen using two frequencies of vibration, f_1 and f_2, and where T is expressed in degrees absolute. The temperature dependence of the rigidity modulus may be observed by determining the vibrational frequency, f, at each temperature, since for a torsional pendulum

$$G = \frac{128 \cdot l \cdot \pi}{d^4} \cdot I \cdot f^2 \tag{3}$$

where l, d and G are respectively the length, diameter and shear modulus of the suspension and I the moment of inertia of the oscillating member.

Experimental Results and Discussion

1. Titanium

The variation of internal friction with temperature has been determined for a number of specimens of pure titanium; the results were found to be satisfactorily reproducible. Typical $\tan \delta$ versus $1/T$ plots are shown in Figure 1. Curves (*a*) and (*b*) were obtained from the same small-grained sample (mean grain diameter 0.019 mm) using two different frequencies of vibration, while curve (*c*) is that obtained under similar conditions for a sample having a very large grain size.

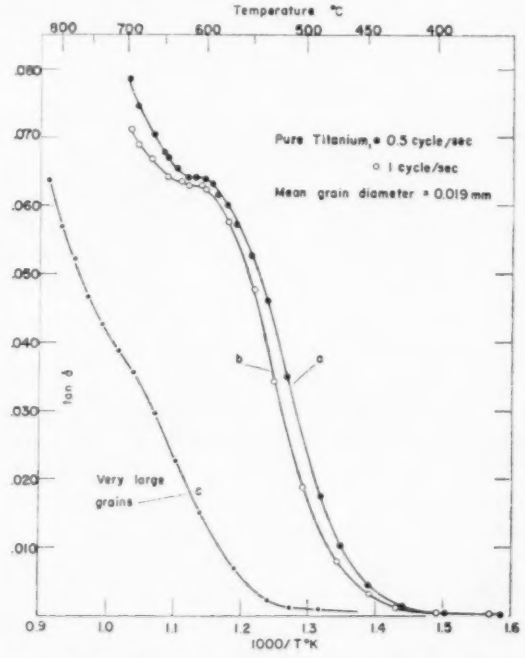

FIGURE 1. Variation of internal friction with 1000/(absolute temperature) in pure titanium (frequency of vibration is equal 0.5 cycles/sec and 1 cycle/sec for grains of mean grain diameter = 0.019 mm, and 0.5 cycles/sec for very large grains).

It is evident that the relaxation spectrum of polycrystalline titanium consists of two component parts, a background steadily increasing with temperature and a peak confined to a limited temperature range. The nature of the peak is revealed by its behavior as the grain size of the specimen is modified. As the grain size increases but remains small compared with the diameter of the specimen the peak is observed to occur at higher temperatures but remains unchanged in magnitude. However, when the point is reached where some grains extend completely across the specimen, the peak begins to be reduced in size. These observa-

tions show that the peak is due to stress relaxation by grain-boundary slip. It is difficult to assess precisely the contribution of the background internal friction in the vicinity of the peak; however, it is certain that at the temperatures where tan δ first begins to rise most rapidly the form of the curve is mainly determined by that of the relaxation peak. The magnitude of the shift, $\Delta(1/T)$, to superpose the curves in this region should, therefore, on substitution in equation (2), give a value for H which corresponds to the heat of activation for the grain-boundary slip process responsible for the peak. The observed value is 46,000 cal/mol.

No detailed study of the background internal friction has been made in the present work, but it is evident that its magnitude decreases rapidly with increasing grain size; this would appear to be in accord with the views of Pearson et al [9], who regard it as due to creep at regions of stress concentration arising from shear stress relaxation along grain boundaries. Few measurements are available which can be considered to be wholly attributable to this source; however, examination of such high-temperature regions of spectra as were obtained suggests that the heat of activation for the background internal friction in polycrystalline titanium is identical with that for grain-boundary relaxation.

The variation of the rigidity modulus with temperature is illustrated in Figure 2, where values of

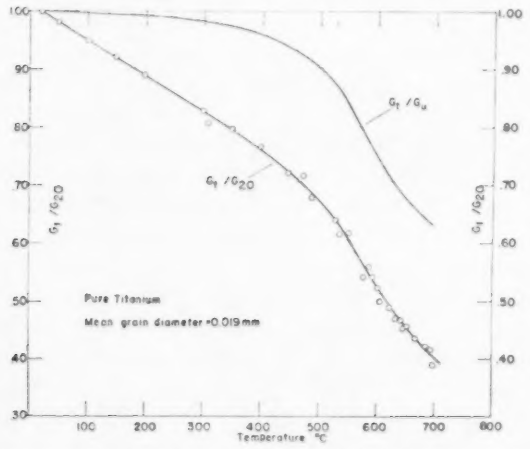

FIGURE 2. Variation of rigidity modulus with temperature in pure titanium (G_t and G_{20} are rigidity moduli at t°C and 20°C; G_u is "unrelaxed modulus").

G_t/G_{20} (i.e., f_t^2/f_{20}^2), G_t being the modulus at t°C, are plotted. The results shown are those associated with internal friction curve (a) in Figure 1. Most rapid reduction of the modulus begins when the temperature reaches that at which the amount of grain-boundary slip starts to become significant. At temperatures well below that of the relaxation peak, the "unrelaxed modulus," G_u, is observed and in this region the curve for polycrystalline specimens should be identical with that for a single crystal of titanium. G_u falls slowly and approximately linearly with increasing temperature. The extent of the modulus variation directly associated with grain-boundary slip is best illustrated by a plot of G_t/G_u versus temperature; this is shown also in Figure 2. A computation of the maximum effect that stress relaxation at the grain boundaries can have on the elastic modulus has been made by Zener [10]. Theoretically, with increasing temperature, the modulus should approach a limiting value known as the "relaxed modulus," G_r, where

$$G_r/G_u = \frac{2\,(7 + 5\sigma)}{5\,(7 - 4\sigma)}, \qquad \sigma = \text{Poisson's ratio.}$$

For titanium $\sigma = 0.36$ [11] so that $G_r/G_u = 0.63$. As indicated by the graph of G_t/G_u (Figure 2), the modulus relaxation exhibited in the temperature range corresponding to the relaxation peak is close to this theoretical value, providing confirmation that both these effects are associated with grain-boundary slip. It appears, however, that the modulus will continue slowly to fall below the theoretical limit, the further reduction of the modulus being associated with the mechanism responsible for the background internal friction.

2. *Titanium-oxygen alloys*

Alloys ranging in composition from approximately 0.8 to 4.5 atomic per cent oxygen have been examined and typical of the relaxation spectra observed are those shown in Figure 3. They may be resolved into three component parts, a background increasing with temperature and two characteristic peaks.

The peak appearing in the temperature range around $1000/T$ = approx. 1.0 has been shown, by its dependence on grain size and the magnitude of the associated modulus decrement, to be due to grain-boundary relaxation. This peak is found at higher temperatures in titanium-oxygen alloys than is the corresponding one in pure titanium; it has been calculated that in the 4.5 atomic per cent oxygen alloy the grain-boundary peak occurs at a temperature 95°C above that in pure titanium of the same grain size, the frequency of vibration being approximately 0.5 cycles per second. However, the grain-boundary peak in the alloys is reduced in size as the oxygen content increases,

and there is some evidence of a simultaneous tendency to move to slightly lower temperatures.

It is considered, therefore, that the grain-boundary peaks in pure titanium and in the oxygen alloys are distinct phenomena, characteristic of the individual materials, and are not simply related by a temperature transition. This type of phenomenon has been observed by Pearson [12] in copper- and silver-base substitutional alloys. In certain specimens he was able to distinguish two grain-boundary relaxation peaks, one typical of the pure metal, the other of the solid solution; the first was rapidly eliminated while the latter increased to its maximum value as the solute content was increased. It was not possible to resolve two grain-boundary peaks in any of the alloys examined in the present work.

This view of the effect of oxygen on the grain-boundary relaxation of titanium seems necessary to account for the superficially contradictory observation that although the characteristic temperature of the peak in alloys is higher than in pure titanium it falls as the oxygen content increases.

The gradual reduction of size and characteristic temperature, with increasing solute content, of the grain-boundary peak in alloys may be attributed respectively to the reduction in the amount of slip and of the mean relaxation distance arising from a locking effect of oxygen segregated at the grain boundaries.

The heat of activation for grain-boundary relaxation in the alloys is considerably larger than that for the corresponding process in pure titanium. From the results plotted in Figure 3, a value for H

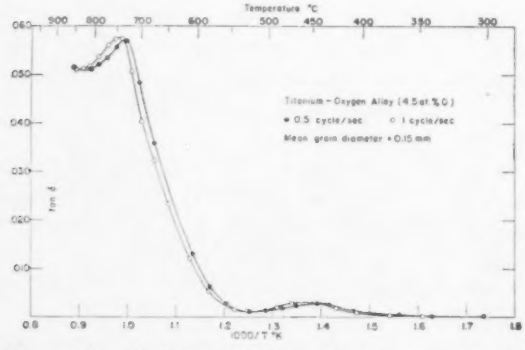

FIGURE 3. Variation of internal friction with 1000/(absolute temperature) in titanium-oxygen alloy.

of 75,000 cal/mol. is found for the 4.5 atomic per cent oxygen alloy; very similar values for H were observed for alloys with other oxygen concentrations.

The value of the background internal friction of titanium at both high and low temperatures is reduced by the addition of oxygen. The near identity of the maxima in the relaxation spectra for the two frequencies suggests that the heat of activation for the background internal friction mechanism is again the same as that for grain-boundary slip.

The introduction of oxygen also results in the appearance of the very small additional relaxation peak at approximately $1000/T = 1.4$. The additional peaks observed in three specimens having increasing oxygen contents are shown on an enlarged scale in Figure 4. It is clear that the size of

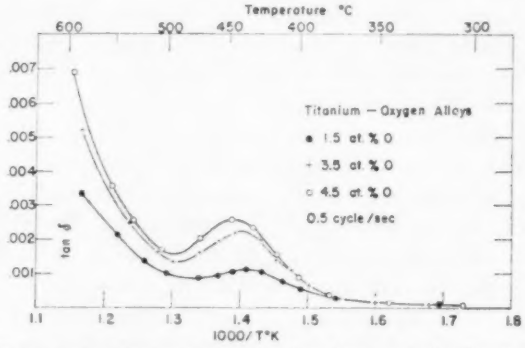

FIGURE 4. Oxygen-induced relaxation peak in titanium-oxygen alloys of different composition.

peak increases with the oxygen content. However, if allowance is made for the internal friction from other sources it appears that the size is not directly proportional to the solute content and possibly approaches a limiting value at comparatively low percentages of oxygen. The position of the peak appears to be independent of grain size but the dependence of its magnitude upon this factor has not been determined owing to the difficulty of separating other contributions in fine-grained specimens. It will be seen that at temperatures well above the peak the internal friction is greater the greater the oxygen content; since oxygen reduces the magnitude of the background and of the grain-boundary slip relaxation effects, this increase must be due to the movement of the grain-boundary peak to lower temperatures.

The frequency dependence of the additional peak in a 3.5 atomic per cent oxygen alloy is illustrated in Figure 5, and from these curves it is found that the associated heat of activation is 48,000 cal/mol. Similar calculations using data from other samples indicate that the heat of activation is independent of composition. Examination of the half-maximum width of the peaks obtained for several specimens

suggests only a very slight spread of relaxation times for the process involved.

Micrographic examination revealed all the titanium-oxygen alloys to consist entirely of a uniform α-solid solution. No signs of precipitation of any second phase were found; neither were there any indications of twinning or any similar modification having occurred in the α-phase. The second peak cannot be attributed, therefore, to either of these sources, so that it would seem that it must be associated more directly with the diffusion of

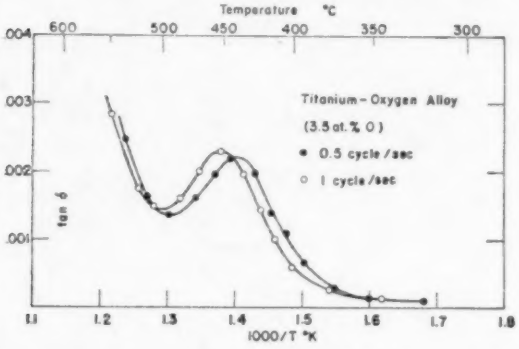

FIGURE 5. Frequency dependence of the oxygen-induced relaxation peak in a 3.5 atomic per cent oxygen alloy.

oxygen in solution in titanium. However the values of 48,000 cal/mol for the heat of activation and of approximately 0.4 for D_0 (estimated by means of the Dushman-Langmuir equation [13] are considerably higher than are normally observed for the diffusion of interstitial solutes, while the diffusion distance indicated by the relaxation time is very small. Furthermore, no suitable diffusion process is readily apparent.

The work of Ehrlich [4] indicates that in titanium-oxygen alloys the solute atoms occupy the octahedral interstices at the $(\frac{3}{4}, \frac{1}{4}, \frac{1}{4})$ and $(\frac{3}{4}, \frac{1}{4}, \frac{3}{4})$ positions in the close-packed hexagonal unit cell. Thus simple stress-induced diffusion, analogous to that of the interstitial solutes in body-centred cubic structures [14; 15] does not provide a mechanism in the present case.

An atom pair process [16] could operate for an interstitial solid solution in a closed-packed lattice; the occupation of neighbouring pairs of interstices will give rise to an anisotropic strain, so that in the presence of an oscillating stress diffusion should take place in a continual striving to maintain coincidence between the interstitial pair axis and the direction of maximum applied strain. However, a significant number of such pairs could only occur at fairly high oxygen contents, which would indicate it to be improbable that such a mechanism is responsible for the peak given by the small amounts of oxygen involved in the present alloys.

A possible stress-induced diffusion process might result from the effect of applied stress on the equilibrium distribution of oxygen between the grains and the grain boundaries. Since the solution of oxygen increases the axial ratio of the titanium lattice, a grain on which the net effect of the applied stress was also to increase the axial ratio might be expected to absorb oxygen from that adsorbed at the grain boundary, while ejection of solute into surrounding interfaces would occur from grains whose axial ratios were reduced by the applied stress. However, this mechanism would seem to be precluded as an interpretation of the present results because of the excessive relaxation time which it would involve.

Thus it is not possible at present to define the mechanism responsible for the additional oxygen-induced relaxation peak. Further experiments are being made in an effort to establish its exact nature and in order to obtain a more precise relationship between the oxygen content and the detailed form of the relaxation spectrum. An analogous series of experiments are proposed on titanium-nitrogen alloys.

Summary

The internal friction characteristics of pure α-titanium have been examined using a low-frequency torsion pendulum method of high sensitivity. The relaxation spectrum was found to consist of a background which rises continuously with temperature and a peak arising from stress relaxation by slip at the grain boundaries. The heat of activation for the latter process was found to be 46,000 cal/mol.

The investigation of titanium-oxygen alloys has shown their relaxation spectra to be characterised by a background curve, a grain-boundary relaxation peak and a small additional relaxation peak. In the alloys, the peak characteristic of grain-boundary slip occurs at higher temperatures than in pure titanium and the heat of activation for the process is increased to approximately 75,000 cal/mol. It has been established that the additional relaxation peak is due to the presence of oxygen. The process involved has not been determined, but the associated heat of activation has been shown to be 48,000 cal/mol. While the grain-boundary relaxation peak in alloys is reduced in size and temperature by additional oxygen, the second peak increases in size with increasing solute content,

but not apparently in any direct proportion. The background internal friction decreases with increasing oxygen content.

The rigidity moduli of titanium and of the alloys decrease in the usual manner with increasing temperature. It was observed that, at room temperature, the addition of approximately 4.5 atomic per cent of oxygen raised the rigidity modulus of titanium to approximately 4500 kg/mm^2; the corresponding value for the original material was 3840 kg/mm^2.

Acknowledgements

The authors wish to thank Professor L. M. Pidgeon for his interest and for the provision of laboratory facilities, and Mr. D. H. Laing for his assistance in constructing the apparatus. The financial support of the Defence Research Board of Canada is also gratefully acknowledged (Grant No. 289).

References

1. Finlay, W. L. and Snyder, J. A. Trans. A.I.M.E. **188** (1950) 277.
2. Jaffee, R. I., Ogden, H. R. and Maykuth, D. J. Trans. A.I.M.E. **188** (1950) 1261.
3. Jenkins, A. E. and Worner, H. W. J. Inst. Metals **80** (1951) 157.
4. Ehrlich, P. Angew. Chem. May/June, 1947, 163; Z. anorg. allgem. Chem. **247** (1941) 53.
5. Clark, H. T. Trans. A.I.M.E. **185** (1949) 588.
6. Rostocker, W. Trans. A.I.M.E. **194** (1952) 981.
7. Kê, T. S. Phys. Rev. **71** (1947) 533; **72** (1947) 41; **73** (1948) 267.
8. Zener, C. Elasticity and Anelasticity of Metals (Chicago, University of Chicago Press, 1948).
9. Pearson, S., Greenough, G. B., and Smith, A. D. N. Nature **167** (1951) 1021.
10. Zener, C. Phys. Rev. **60** (1941) 906.
11. Köster, W. American F.I.A.T. Rev. **31**, 56.
12. Pearson, S. R.A.E. Report No. Met. 67, 1951; R.A.E. Report No. Met. 71, 1953.
13. Dushman, S. and Langmuir, I. Phys. Rev. **20** (1922) 113.
14. Snoek, J. Physica **6** (1939) 591; **8** (1941) 711; **9** (1942) 862.
15. Kê, T. S. Phys. Rev. **74** (1948) 9; **74** (1948) 914.
16. Zener, C. Trans. A.I.M.E. **152** (1943) 122; Phys. Rev. **71** (1947) 34.

RESIDUAL LATTICE STRAINS IN IRON SINGLE CRYSTALS*

J. H. AULD† and G. B. GREENOUGH‡

X-ray diffraction measurements of the change in interplanar spacing of iron single crystals on plastic extension have been made and the "residual lattice strains" have been found to be negligible. This is interpreted as showing that the residual lattice strains observed in polycrystalline iron are due to an intergranular stress system rather than due to stresses associated with trapped dislocations.

LES DÉFORMATIONS RÉSIDUELLES DU RÉSEAU DANS DES MONOCRISTAUX DE FER

On a effectué, au moyen de la diffraction des rayons X, des mesures des changements des distances entre les plans réticulaires lors de l'extension plastique de monocristaux de fer, et il fut constaté que les déformations résiduelles du réseau étaient négligeables. L'interprétation en est que les déformations résiduelles du réseau, observées dans du fer polycristallin, sont dues à un système de tensions intergranulaires, plutôt qu'aux tensions associées aux dislocations immobilisées.

INNERE GITTERVERZERRUNGEN IN EISEN EINKRISTALLEN

Es wurden röntgenographische Messungen der Veränderung des Netzebenenabstands in durch Zug plastisch verformten Eiseneinkristallen durchgeführt, und die "inneren Gitterverzerrungen" wurden vernachlässigbar klein gefunden. Daraus wird geschlossen, dass die in polykristallinem Eisen beobachteten inneren Gitterverzerrungen durch ein interkristallines Spannungssystem und nicht so sehr durch die von festliegenden Verzetzungen herrührenden Spannungen bedingt sind.

1. Introduction

Much work has been reported in which the movement of the peaks of X-ray diffraction lines given by polycrystalline metals has been measured during and after the application of stresses. This movement allows the average change of interplanar spacing of those grains contributing to the diffraction line to be determined and curves can be drawn showing the relation between applied stress and the lattice strain. One of the more important details of the work has been the demonstration that if the metal has been plastically deformed, the lattice strain does not usually disappear completely when the applied stress is removed.

A discussion of the various papers referring to these residual lattice strains, and their possible causes, is available elsewhere [1]. It is generally accepted that the strain is due to a stress in the volume of metal contributing to the diffraction line, and the various explanations put forward have discussed the type and cause of the residual stress system in the metal. Following the discovery that different reflection lines showed residual lattice strains of varying magnitude and sign, it was thought probable that an intergranular stress system (arising because of the variation of yield stress of the grains with orientation) was responsible for the residual lattice strains. This idea was later treated quantitatively and agreement between theory and experiment found for the face-centred cubic metals aluminium, copper and nickel [2], although it became clear later that a macroscopic surface stress was superposed on this Heyn intergranular stress system [3].

However, an alternative explanation is possible for the part of the residual lattice strain which varies with the reflection line examined. This was first proposed during an unpublished discussion in 1943 between Bragg, Orowan, Smith and Wood, and is that the stresses around groups of dislocations left in the crystals after plastic deformation might be responsible for the X-ray line shifts. The lattice near the dislocations is probably insufficiently regular to contribute to the diffraction line, but at greater distances the strain varies less rapidly and can well cause a shift in the X-ray diffraction peak. These stresses vary with crystallographic direction, and hence the residual lattice strain with the reflection line examined. That plastic deformation does leave dislocations trapped in the crystals producing residual stresses is clear from the experimental observation that single crystals show a Bauschinger effect [4; 5]. It is also an essential feature of the recent theory of work-hardening put forward by Mott [6].

While it was not possible to see precisely how the existing residual lattice strain results on polycrystal specimens could be interpreted in terms of dislocations, it was felt that the explanation was qualitatively sufficiently attractive to justify an experimental attempt to distinguish between this explanation and one based on Heyn intergranular stresses. The simplest method of carrying this out

*Received October 6, 1953.
†Defence Research Laboratories, Melbourne, Australia; formerly Department of Metallurgy, University of Sheffield.
‡Department of Metallurgy, University of Sheffield.

is to measure the residual lattice strains in plastically extended single crystals. If the Heyn intergranular stresses are largely responsible for the residual lattice strains observed in polycrystalline material, then single crystals should show negligible residual lattice strains, but if dislocation stresses are largely responsible then single crystals should show residual strains of similar magnitudes to those shown by polycrystalline metals. No observations of the required type on single crystals have yet been reported.

Residual lattice strains in polycrystalline metals are not very large compared with the experimental errors in their determination, usually about $\pm 3 \times 10^{-5}$ (e.g., relatively large observed values are, for the 310 reflection from iron $+25 \times 10^{-5}$, and for the 400 reflection from aluminium $+8 \times 10^{-5}$). Since iron shows the largest residual strains in the polycrystalline state, it was to be expected that single crystals of iron would show the largest value if the dislocation hypothesis were valid. So as to reduce the importance of experimental error we therefore decided to examine iron single crystals, despite the fact that the strains, if present, would be more difficult to interpret theoretically than any found in single crystals of a face-centred cubic metal.

2. Experimental Technique

The accuracy of interplanar spacing determination obtained in ordinary single crystal rotation photographs is normally much less than that required in this work. However, the same principles used in obtaining accurate measurements from polycrystalline material may be adapted for single crystals. High Bragg angle reflections were used and recorded on a flat film, using a calibrating powder on the surface of the crystal to assist in the elimination of errors. The single crystals were in the form of wires, about $\frac{3}{4}$ mm diameter, completely bathed by the X-ray beam and were rotated about an axis accurately perpendicular to the incident beam. Co, Cr and Fe Kα radiations were used to record reflections of the types 310, 211, and 110 at sufficiently high Bragg angles.

In order to obtain a reflection, say, of the 310 type, one of the directions $\langle 310 \rangle$ must be almost perpendicular to the axis of rotation. In general, if the axis of the wire crystal coincides with the axis of rotation this condition is not satisfied, and the wire axis must be tilted in order to bring one of $\langle 310 \rangle$ into a suitable orientation. Figure 1 shows a cubic stereographic projection and the direction corresponding to the wire axis of crystal No. 3. The shaded area shows the region lying $90° \pm 8°$ from this axis. It will be seen that [310], [$2\bar{1}1$] and [$\bar{1}\bar{2}1$] all lie at nearly 90 degrees from the wire axis, and in this case these reflections can be obtained by rotating the crystal about its axis. However, the nearest $\langle 110 \rangle$, viz. [$0\bar{1}1$], lies at 81 degrees from the wire axis, and in order to obtain this reflection the

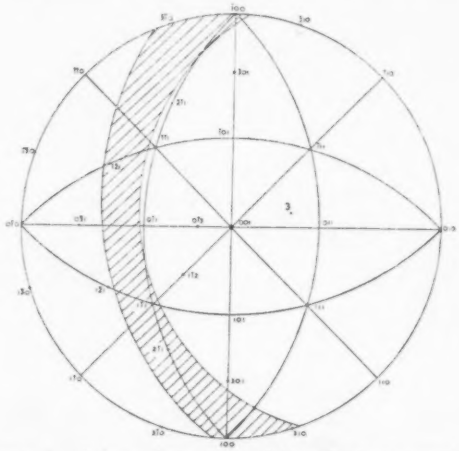

FIGURE 1. Orientations of possible reflecting normals.

wire axis must be tilted relative to the axis of rotation. It should be noted that if a reflection is obtained from planes to which the normal is [*hkl*], a reflection is also obtained from [$\bar{h}\bar{k}\bar{l}$]. Figure 1 shows the [*hkl*] normals to all the planes from which reflections were obtained.

Figure 2 shows some typical photographs from

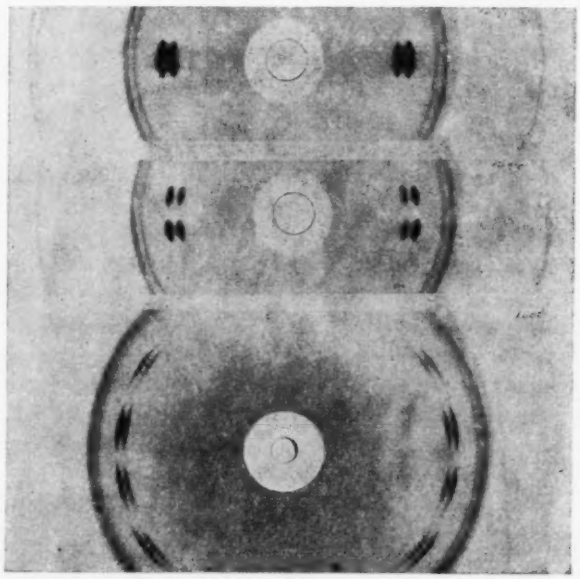

FIGURE 2. Typical X-ray photographs. (*a*) and (*b*) taken with Co K-radiation; (*c*) taken with Cr K radiation.

the annealed crystals. In 2(*a*) [301] was at 90 degrees to the axis of rotation and only 2 arcs are seen; but in 2(*b*) the angle was about 85 degrees and 4 arcs result. Figure 2(*c*) shows the case referred to for crystal No. 3 using Cr radiation, where reflections are obtained from two normals of the type ⟨211⟩. The continuous rings outside the single crystal arcs are given by the calibrating material—silver for Co and Fe radiations and chromium for Cr radiation. A consideration of the geometry of the diffraction process shows that the reflection from $[\bar{h}\bar{k}\bar{l}]$ always occurs at the opposite end of a diameter of a diffraction 'ring' to $[hkl]$. This is an important point in the elimination of errors in the determination of the Bragg angles, since it is essential to measure ring diameters.

Apart from some minor variations, the elimination of errors in the lattice strain measurements follows closely the procedure used for polycrystalline substances. In the tables of results an indication is given of the probable limits of experimental error appropriate to the various cases.

The crystals were grown by the strain-anneal method and initially were 2 mm diameter and length 3.5 cm or more. The analysis of the material was Si, 0.1–0.2%; S, 0.05%; P, 0.05%; Mn 0.3–0.45%; C, estimated 0.003%. The crystals were electrolytically polished and etched, examined visually to check that they were single crystals, and their orientations determined by a back-reflection Laue method. There was a tendency for the orientations to have a ⟨110⟩ parallel to the wire axis, but a selection of seven crystals was made to cover as large an area of the stereographic unit triangle as possible. Later, crystal No. 14 was selected as being as close in orientation to No. 2 as could be attained.

These crystals were then prepared in the form of miniature cylindrical test pieces. The ends were covered in rubber solution, and the central 2 cm etched to a diameter of approximately $\frac{3}{4}$ mm. This gauge length was then electrolytically polished to remove the roughness produced by etching. Finally, the crystals were annealed in a vacuum at 700°C for one hour to remove any hydrogen, or strains, picked up during the preparation. The interplanar spacings of the various planes in the annealed crystals were measured.

The crystals were then extended plastically using grips designed to give as near axial loading as possible. It is interesting to note however that the two diffraction arcs forming the ends of a ring diameter are from opposite sides of the specimen, i.e., any small differences in strain on the two sides of the crystal due to non-axial loading will be eliminated from the measurements. Since in polycrystalline iron the residual lattice strains increase with increasing stress applied to cause plastic deformation, the deformation given to the crystals was as high as could be attained while maintaining the uniformity of strain along the gauge length. This was about 15 per cent elongation. The load required to produce this was measured for all crystals except No. 1 and the orientations of the crystals were redetermined after deformation. At least three rotating back reflection photographs were taken of each strained crystal with each radiation. Both circumferential spreading and radial broadening of the reflection arcs was seen, but the latter was not so great as to make the α-doublets confused and visual measurements of the positions of the peaks of the lines were possible. The interplanar spacings for each strained crystal were obtained from a mean of the three photographs, and hence the residual lattice strains were determined.

3. Experimental Results

Table I lists the values of the elongations of the crystals and of the applied tensile stresses necessary to produce them. The initial and final orientations of all the crystals used in the work are shown in Figure 3. Knowing the orientations of the strained crystals it is possible to determine the reflection planes giving rise to the arcs on which measurements were made, and the angle between the reflecting normal and the axis of crystal. This information, together with the observed residual lattice strains is given in the Table II.

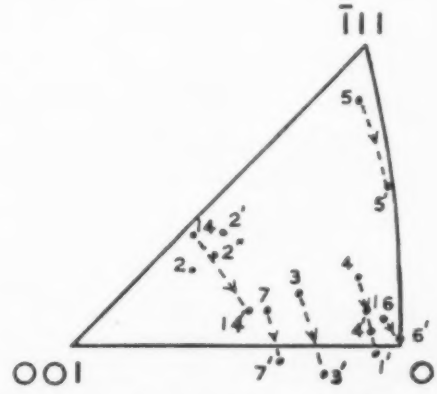

FIGURE 3. Details of initial (x) and final (x') orientations of crystals.

TABLE I

PLASTIC ELONGATION OF THE SPECIMENS

Crystal	1	2	3	4	5	6	7	14
Elongation %	10	15	17	12	12	13	18	14
True Stress ($\times 10^3$ lb/in^2)	—	36	28	27	24	23	23	22

TABLE II

RESIDUAL LATTICE STRAINS

(*a*) Cobalt Kα radiation. Limits of error $\pm 3 \times 10^{-4}$.

Crystal	Reflecting planes	Angle between [*hkl*] and wire axis	Residual lattice strain
1	—	—	—
2	$(0\bar{3}1)$	87 °	$+12 \times 10^{-4}$
	(301)	$87\frac{1}{2}$°	
3	$(3\bar{1}0)$	84°	0
4	(310)	87°	+3
5	(310)	85°	+3
	(301)	85°	
6	(310)	77°	+4
	(301)	$76\frac{1}{2}$°	
7	$(3\bar{1}0)$	83°	−1
14	(310)	88°	−2

(*b*) Chromium Kα radiation. Limits of error $\pm 4 \times 10^{-4}$.

Crystal	Reflecting planes	Angle between [*hkl*] and wire axis	Residual lattice strain
1	$(\bar{2}\bar{1}1)$	$89\frac{1}{2}$°	$+1 \times 10^{-4}$
2	$(1\bar{2}1)$	$89\frac{1}{2}$°	+2
	$(2\bar{1}1)$	$88\frac{1}{2}$°	
3	$(\bar{2}\bar{1}1)$	88°	+2
4	$(2\bar{1}1)$	89°	+3
	$(\bar{2}\bar{1}1)$	87°	
5	$(1\bar{1}2)$	82°	−3
6	$(2\bar{1}1)$	89°	+2
	$(\bar{2}\bar{1}1)$	89°	
7	$(1\bar{2}1)$	88°	+3
14	$(1\bar{2}1)$	90°	−1

(*c*) Iron Kα radiation. Limits of error $\pm 7 \times 10^{-4}$.

Crystal	Reflecting planes	Angle between [*hkl*] and wire axis	Residual lattice strain
1	$(0\bar{1}1)$	87°	$+2 \times 10^{-4}$
2	(110)	86°	+14
3	$(0\bar{1}1)$	81°	+8
4	$(0\bar{1}1)$	87°	−7
5	$(0\bar{1}1)$	90°	−2
6	$(0\bar{1}1)$	90°	−1
7	$(0\bar{1}1)$	75°	+3
14	(110)	76°	0

4. Discussion

It is apparent from the results in Tables I and II that crystal No. 2 differed in behaviour from the remainder. Not only was it the only crystal which gave residual lattice strains of appreciable magnitude, but the stress necessary to extend it was higher. Other qualitative differences were observable. All crystals deformed uniformly except No. 2 where the cross section varied irregularly along the gauge length. Also, the spread of the diffraction arcs from the strained crystal No. 2 was appreciably larger than for the remainder.

There were two possible causes of this difference in behaviour: either the orientation of No. 2 was responsible, or crystal No. 2 was not a single crystal. To check the first possibility, crystal No. 14, which had a similar orientation, was examined; the results show that it behaves as did crystals 1, 3–7. To check the second possibility an intensive micrographic and X-ray examination was made of sections of crystal No. 2. Micrographic work failed to reveal definite evidence of a grain boundary, but from two different sections of the crystal Laue photographs showing two sets of diffraction spots were obtained. The orientations of the two parts are shown in Figure 3 as 2′ and 2″, the orientation difference being about 5 degrees. It appears, then, that after deformation, crystal No. 2 was a bicrystal. Similar examinations of several of the other deformed crystals showed no evidence whatever of any bicrystal structure; they were all apparently good single crystals.

It is strange that crystal No. 2 showed no evidence of the bicrystal nature in the annealed condition. While it is conceivable that during the optical examination of the curved etched surface, a small orientation difference between different parts could have been overlooked, it might be expected that the diffraction arcs on the initial rotation photographs would have shown some evidence. It is possible, then, that the orientation difference between the two parts of crystal No. 2 was enhanced during the deformation.

It was decided that the results from crystal No. 2 should be ignored when drawing general conclusions from the experimental work, on the grounds that it was not a single crystal in the deformed state. In the remainder of the crystals, the residual lattice strains observed are less than the limits of experimental error.

There are two possible reasons why the residual stresses associated with the dislocations trapped in

the deformed crystals should not produce any observable lattice strain. The first is that the directions of measurement are such that the strains due to the stresses are zero. (Such a direction, for instance, would be one parallel to the length of edge dislocations.) It is not feasible to examine this possibility in detail for a general case in iron, but since the normals to the reflecting planes cover a wide range of possible orientations relative to the active slip elements, the chance that in every case a direction of approximately zero strain was selected is very remote.

The second possibility is that the volume of metal contributing to the diffraction line contains many stressed regions, the sign of the stress varying so that the average stress in the volume is zero. If the depth of penetration of the beam, which is about 0.02 mm, exceeds the length of the lines of piled-up dislocations [6], then this will necessarily be true since the stresses on opposite sides of a dislocation are equal in sign but opposite in magnitude. Another way in which the averaging of the stresses may be achieved is by the presence of regions of opposite states of stress along the irradiated length of the crystal surface, which was about 2 mm. In either case this averaging of stresses would lead to an absence of X-ray line displacement but would cause a line-broadening and this was, in fact, observed. It seems most likely that this second possible explanation of the absence of appreciable residual lattice strains is correct.

5. Conclusions

Single crystals of iron do not show residual lattice strains after plastic extension. Thus the residual lattice strains found in polycrystalline metal after a similar deformation must be due to their polycrystalline nature. These experimental results, then, give strong, although indirect, support to the Heyn intergranular stress theory.

It seems likely that the residual stresses associated with trapped dislocations in crystals do not cause a movement of the diffraction line peaks because the metal diffracting includes roughly equal volumes in opposite states of stress.

6. Acknowledgments

We are greatly indebted to Dr. Paxton of Birmingham University for supplying the iron single crystals used in this work. We would also like to thank the Director, Royal Aircraft Establishment, for the loan of a camera-stand in the early stages of the work, and Professor A. G. Quarrell for providing general facilities for the research. One of us (J. H. Auld) wishes to thank the Chief Scientist, Department of Supply (Australia) for making it possible for him to carry out this work at the University of Sheffield and for permission to publish this paper.

References

1. GREENOUGH, G. B. Progress in Metal Physics, vol. 3 (London, Pergamon Press, 1952) p. 187.
2. GREENOUGH, G. B. Proc. Roy. Soc. **A197** (1949) 556.
3. GREENOUGH, G. B. J. Iron. Steel Inst. **169** (1951) 235.
4. SACHS, G. and SHOJI, H. Z. f. Phys. **45** (1927) 776.
5. COOGAN, C. K. Ph.D. thesis, Bristol University (1952).
6. MOTT, N. F. Phil. Mag. **43** (1952) 1151.

DIFFUSION OF HYDROGEN IN MILD STEEL*

AL. DEMAREZ†, ARTHUR G. HOCK‡, and FRANCIS A. MEUNIER§

From experiments on the rate of removal of hydrogen from steel, a number of writers have suggested that this element exists in two forms, with different effects upon the physical properties.

This hypothesis is not confirmed by new experiments which show that there is reasonable agreement with expectation based upon the laws of normal diffusion.

It is thus possible to estimate the course of hydrogen removal from the usual rolled products if the diffusion coefficient is known. The apparatus used in these experiments can be used readily for the rapid determination of the total hydrogen content and of the diffusion coefficient.

LA DIFFUSION DE L'HYDROGÈNE DANS LES ACIERS DOUX

En se basant sur des expériences sur la vitesse d'extraction de l'hydrogène des aciers, plusieurs chercheurs ont suggéré que cet élément existe sous deux formes, dont les effets sur les propriétés physiques sont différents. Cette hypothèse n'est pas confirmée par de nouvelles expériences montrant qu'il y a accord avec les prévisions basées sur les lois de la diffusion normale. Il est ainsi possible d'estimer le cours de l'extraction de l'hydrogène des produits laminés, usuels, quand le coefficient de diffusion est connu. L'appareil employé dans ces expériences peut aussi servir à la détermination rapide de la teneur totale en hydrogène et du coefficient de diffusion.

DIE DIFFUSION VON WASSERSTOFF IN WEICHEM STAHL

Auf Grund von Versuchen über die Geschwindigkeit der Wasserstoffentgasung des Stahls haben eine Anzahl Autoren angenommen, dass dieses Element in zwei Formen, die verschiedene Effekte auf die physikalischen Eigenschaften haben, vorliegt.

Neue Experimente bestätigen diese Hypothese nicht; sie zeigen eine zufriedenstellende Übereinstimmung mit den nach den Gesetzen der normalen Diffusion zu erwartenden Resultaten.

Es ist somit möglich, den Verlauf der Wasserstoffentgasung der üblichen gewalzten Materialien abzuschätzen, wenn der Diffusionskoeffizient bekannt ist. Die in den vorliegenden Untersuchungen benutzte Apparatur lässt sich unmittelbar zur Bestimmung des Gesamtwasserstoffes und des Diffu sionskoeffizienten benutzen.

I. Introduction

Since the assessment of the influence of hydrogen upon the mechanical and physico-chemical properties of steels [1–5] much work has been carried out with the object of obtaining accurate determinations of this gaseous impurity [6–10].

Owing to its relatively unreactive character in solution, hydrogen is not readily determined by chemical means. Of the physical methods which have been proposed the most favoured are those based upon the vacuum extraction from samples heated either above the melting point (with or without addition of tin) or below it.

Two of the authors have discussed in detail [10] the reasons for preferring the use of temperatures a little below the A_1 transformation point for carbon and low-alloy steels.

Other reports [8–11], based essentially upon the same fundamental principles, have suggested the existence of two distinct processes of hydrogen evolution [Figure 1 and reference 8]:

1. A rapid evolution in which the quantity of gas collected appeared to depend upon the previous history of the sample, i.e., melting, working, and heat treatment. The length of this initial period is, however, fairly constant.

2. A second period of much slower evolution following an approximately exponential course

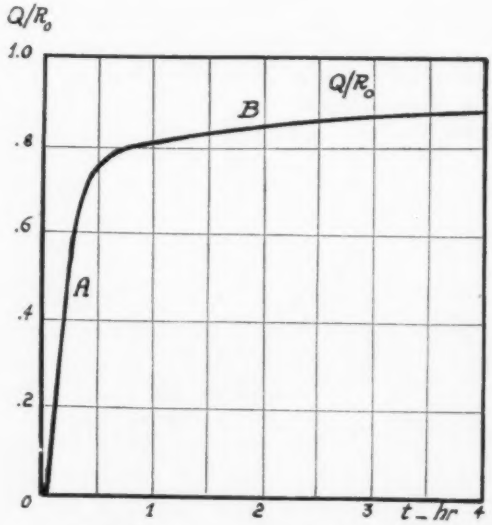

FIGURE 1. Curve of extraction of hydrogen in vacuum at 600°C, showing two apparently different regimes [8]. *A:* period of rapid evolution, *B:* period of slow evolution, Q/R_0 = ratio of hydrogen extracted at any time to the total hydrogen collected after 40 hours. Samples ½ inch diameter and ½ inch long.

*Received July 1, 1953.

†Aciéries et Minières de la Sambre, Belgium.
‡Workington Iron and Steel Ltd., Great Britain.
§Faculté Polytechnique, Mons, Belgium.

which ends practically in a few dozen hours. The quantity of gas evolved in this period would appear to be of the same order for most ordinary steels.

Other experimenters [12; 13] mention the existence of two forms of hydrogen, defined respectively as more readily and less readily diffusible. It is sometimes inferred also that these two forms may possess or induce different properties.

It is of interest to enquire into the reasons which have led to the above hypotheses.

Curves have been given [10] for the quantity, R, of hydrogen remaining in samples $\frac{1}{2}$ inch long and $\frac{1}{2}$ inch in diameter, as a function of the time of extraction in vacuum at 650°C. Such a curve is reproduced in Figure 2 where the broken line

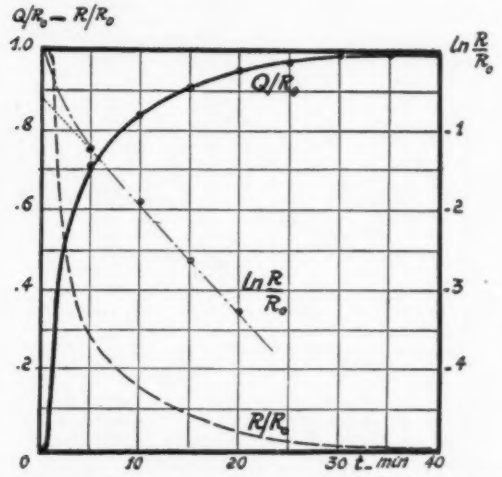

FIGURE 2. Extraction curves in vacuum at 650°C [10]. *Q:* hydrogen extracted at time *t*. *R:* hydrogen remaining in sample at time *t*. R_0: total hydrogen collected at end of experiment (1 hour). Samples ½ inch diameter and ½ inch high.

represents the proportion R/R_0 of hydrogen which has still to be extracted. This curve does not suggest as strongly as Figure 1 that there may be two different kinds of evolution of gas but if the natural logarithm of R/R_0 is plotted in terms of the time, t, there is a clearer suggestion of two different laws of extraction (Figure 2, chain-dotted line). It can be seen that the extraction is accurately exponential for values greater than 5. For values less than 5 the quantity of gas removed is greater than the value expected from this law.

Is this due to the existence of two forms of hydrogen in steel? The problem merits attention because the separation of these two forms and the study of their respective influences might lead eventually to an accurate correlation between the mechanical properties of a steel and its hydrogen content, which is a matter which investigations [3; 4; 5] have not yet solved.

II. Diffusion of Hydrogen from a Finite Cylinder

It is generally accepted that the loss of hydrogen from steel, under ambient conditions and at higher temperatures, is due to the diffusion of this element [14; 15] in the atomic state, probably as protons H^+.

Diffusion is not the only phenomenon which determines the rate of loss because hydrogen must escape at the surface by some rather complicated process which has been studied by Barrer [16].

It is evident that the slower of these two phenomena will determine the over-all speed of the evolution of gas and it is pertinent, therefore, to mention two interesting conclusions. Fast [15] states that, in the system Fe-H, the exit of hydrogen occurs rapidly and does not mask the diffusion process. Chang and Bennett [17] have shown recently, from measurements of the permeability through the walls of a hollow cylinder (i.e., in a system which presents a process of entry as well as one at exit), that the process of diffusion is the slowest in the chain of phenomena when the temperature is greater than about 400°C to 450°C.

We may thus consider that the evolution of hydrogen at 650°C is controlled only by diffusion and it becomes apposite to apply the following theoretical considerations.

Consider a circular cylinder of radius ρ and of length l. From the proportionality of the rate of flow to the instantaneous concentration gradient, it follows that Fick's equation holds, at constant temperature, in the form: $D \cdot \nabla^2 c = \partial c/\partial t$, and if we take cylindrical co-ordinates r, θ, z, we have:

$$(1) \qquad D\left\{\frac{\partial^2 c}{\partial r^2} + \frac{1}{r}\cdot\frac{\partial c}{\partial r} + \frac{\partial^2 c}{\partial z^2}\right\} = \frac{\partial c}{\partial t}$$

for flow independent of the co-ordinate θ, where D is the diffusion coefficient under experimental conditions and C is the concentration at the point r, θ, z at time t.

The solution of this equation was given by Fourier, over a century ago, for arbitrary initial conditions, in the form of a double series in terms of functions which are now better known as Bessel coefficients of zero order. The double series is difficult to handle, at first sight, but it is possible to proceed quickly, as follows, for the case of constant initial concentration.

Let v be the solution of

$$(2) \qquad D\left\{\frac{\partial^2 v}{\partial r^2} + \frac{1}{r}\cdot\frac{\partial v}{\partial r}\right\} = \frac{\partial v}{\partial t}$$

with

$v = c_0$ when $t = 0$ in $0 < r < \rho$, for all z

$v = 0$ for $t > 0$ at $r = \rho$, for all z

and let w be the solution of

$$(3) \qquad D\frac{\partial^2 w}{\partial z^2} = \frac{\partial w}{\partial t}$$

with

$w = 1$ for $t = 0$ in $0 < z < 1$, for all r

$w = 0$ for $t > 0$ at $z = 0$ and at $z = 1$, for all r.

It is easily verified that $c = vw$ is the solution of (1) with

$c = c_0$ for $t = 0$ in $0 < r < \rho$ and $0 < z < 1$

$c = 0$ for $t > 0$ at $r = \rho$; $z = 0$; $z = 1$

Since

$$v = 2C_0 \cdot \sum_{n=1}^{\infty} \frac{e^{\frac{-D\beta_n^2 t}{\rho^2}} \cdot J_0\left(\frac{\beta_n r}{\rho}\right)}{\beta_n \cdot J_1(\beta_n)}$$

where β_n is a root of $J_0(\beta) = 0$ which can be found in tables, and

$$w = \frac{4}{\pi}\sum_{n=0}^{\infty}\frac{1}{2n+1}\sin\frac{(2n+1)\pi z}{l}\, e^{-D(2n+1)^2\pi^2 t/l^2}$$

c becomes a product of two series which may be computed separately.

The total quantity, R, of hydrogen remaining in the cylinder at any time t is evidently:

$$R = 2\pi\int_0^{\rho}\int_0^1 crdrdz.$$

Performing the indicated integrations, we obtain after some reductions:

$$R = \frac{32}{\pi}C_0\rho^2 l\left[\sum_{n=0}^{\infty}\frac{e^{-(2n+1)^2\pi^2 Dt/l^2}}{(2n+1)^2}\right]\left[\sum_{n=1}^{\infty}\frac{e^{-D\beta_n^2 t/\rho^2}}{\beta_n^2}\right]$$

The equation represents the theoretical law of reduction of the hydrogen content in a finite cylinder, of *constant initial concentration*, subject to vacuum extraction. If R_0 is the total quantity of hydrogen at the beginning of the experiment and if the cylinder has a length equal to its diameter we may write:

$$(5) \qquad \frac{R}{R_0} = \frac{32}{\pi_2}\left[\sum_{n=0}^{\infty}\frac{e^{-(2n+1)^2\pi^2 Dt/l^2}}{(2n+1)^2}\right]\left[\sum_{n=1}^{\infty}\frac{e^{-4\beta_n^2 Dt/l^2}}{\beta_n^2}\right]$$

It may be noted that the equation may be written in terms of the parameter Dt/l^2, and with the result that the form $R/R_0 = f(Dt)/l^2$, is the general solution of the problem of diffusion in a cylindrical sample of length equal to diameter.

With the first six roots of $J_0(x)$ (2.405; 5.524; 8.654; 11.792; 14.931; 18.071) sufficiently accurate values can be computed readily for most values of Dt/l^2.

For very small values of the parameter, the series must be transformed. The steps required are beyond the compass of this note but it should be recorded that accurate computations are possible for all values of t. These are illustrated in Figure 3.

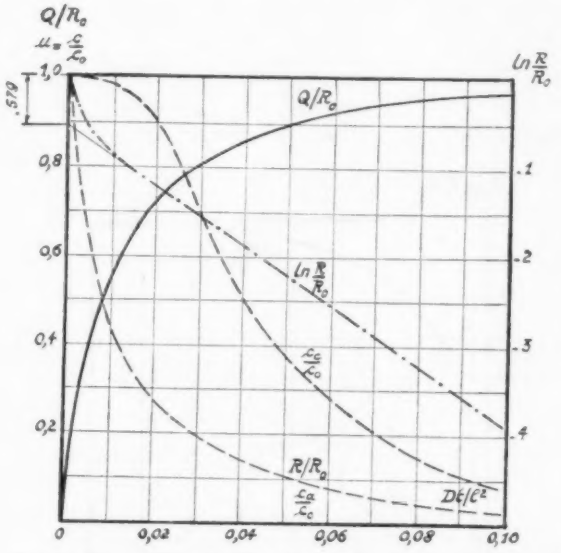

FIGURE 3. Extraction of hydrogen from samples of length equal to diameter. Theoretical curves obtained from the integration of the diffusion equation. Q, R and R_0 as in Fig. 2. C_0 = initial concentration of hydrogen, assumed to be constant in the sample. C_c = concentration at centre of sample at time t. C_a = average concentration at time t. D = diffusion coefficient. l = height or diameter of sample. t = time.

The theoretical and experimental curves can thus be compared if the following quantities are known:

(*a*) the total amount of hydrogen in the sample

(*b*) the dimension of the sample

(*c*) the diffusion coefficient of the sample at the temperature of the experiment (650°C).

The total quantity of hydrogen can be found by complete vacuum extraction.

The diffusion coefficient presents some difficulty because published experimental results are rather discordant. From theoretical considerations and from results of permeability measurements selected from existing publications, some writers [18; 19] give: $D = 13.2 \times 10^{-8}$ cm²/min at 650°C. Chang and Bennett [17] find: $D = 3.6 \times 10^{-8}$ cm²/min, from measurements of permeability through the wall of a hollow cylinder. Examination of equation

(5) yields a solution of this problem which is perhaps more elegant. For values of t greater than some threshold t_0, the series degenerate to their first terms with adequate accuracy and

$$\frac{R}{R_0} = \frac{32}{\pi^2\beta_1^2}\, e^{-[\pi^2+4\beta_1^2]Dt/l^2} \text{ for } t > t_0,$$

which is an exponental law in accordance with the results of experiments [reference 10 and Figure 2].

Since β_1 and l are known, the slope of the straight line $\ln R/R_0 = f(t)$ leads to the determination of D.

III. Comparison of Theoretical and Experimental Rates of Extraction of Hydrogen at 650°C in Vacuum

(A) *Considerations Arising from Previous Results*

The fact that the law of extraction has been found, by experiment, to become exponential after some lapse of time is the first matter of interest.

The chain-dotted lines in Figures 4 and 5, which are obtained from Figures 5 and 6 in reference [10] give the plot of $\ln R/R_0 = f(t)$.

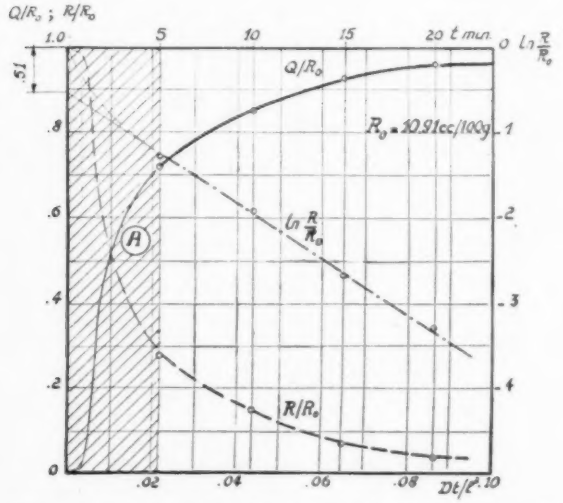

FIGURE 4. Extraction of hydrogen at 650°C from sample of length equal to diameter, rich in hydrogen. Shaded zone: not observed during experiment. Curves drawn from experiments reported in reference 10 (Fig. 5).

A change of scale transforms these curves into $\ln R/R_0 = f(Dt)/l^2$ which yields a direct comparison with the theoretical law plotted in Figure 3. The shapes of the curves are similar. For abscissae: Dt/l^2: greater than 0.02 the points lie on a straight line and for values less than 0.02 the curves bend upwards in the same way.

Since the object in view in reference [10] was the determination of total hydrogen, the process of evolution between 0 and 5 minutes was not specially studied and only the values for 0 and 5 minutes are known. Nevertheless, certain other observations led to the hope that the theory of diffusion might be in agreement with experiment. For instance, equation (6) valid for values of t which are not too small, shows that *for all the extractions*, the straight-line portion of the curve for $\ln R/R_0$ should, if produced, give an ordinate at $t = 0$ of $\ln 32/\pi^2\beta_1^2$ or minus .579.

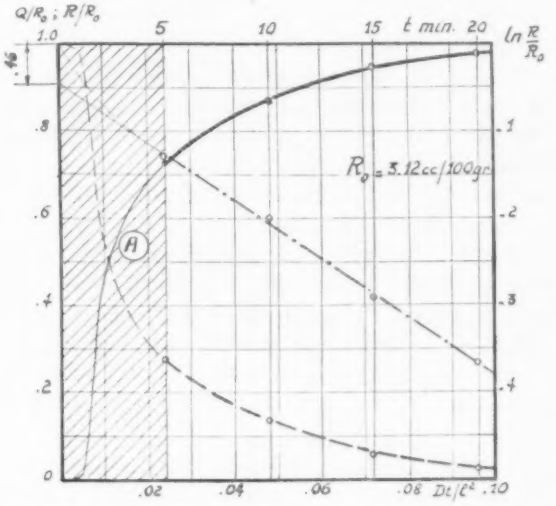

FIGURE 5. Extraction of hydrogen at 650°C from sample containing an average quantity of hydrogen. (Length = diameter.) Shaded zone: not observed. Curves taken from reference 10 (Fig. 6).

The ordinates measured on Figures 5 and 7 of reference [10] are respectively 0.46, 0.51, 0.42, which is fairly satisfactory when we consider that certain conditions assumed in the calculation, and discussed later, cannot be realised accurately in the practical work.

Similarly, a comparison of the theoretically expected and the experimentally established times required for the extraction of 80, 90, 95, 98 per cent of the total hydrogen have been compared in Table I.

The agreement is reasonably good. When the difference is greater than the experimental error (steel M) it is interesting to note that the experiment gives higher results, which may well be due to the fact that some of the experimental conditions differ appreciably from those assumed in the calculation.

(B) *New Experiments*

In order to complete a critical examination of the

TABLE I

Steel	Composition			D Calculated from (6) cm²/min	Time required for extraction of							
					80 per cent		90 per cent		95 per cent		98 per cent	
	C	Si	Mn		Theor.	Exp.	Theor.	Exp.	Theor.	Exp.	Theor.	Exp.
M	.05	.01	Tr	7.97×10^{-3}	5.9	8	10.8	11.5	15.1	16	20.5	22
Q	.10	.12	.60	6.98×10^{-3}	6.8	7	12.4	12.5	17.3	17	23.5	24
R	.04	.01	Tr	6.62×10^{-3}	8.4	8.5	15.3	15	21.4	21	28.9	28.5

results predicted by theoretical considerations, it is necessary to examine the phase in which extraction is not of exponential form, namely, the early stages, with the small values of *t which do not enter into the calculation of D from the results of the experiment.*

It is necessary, therefore, to provide an apparatus capable of bringing the sample quickly to the required temperature and of accurate and rapid measurement of the quantities of hydrogen collected in the first five minutes. (It will be recalled that the solution of the diffusion equation is based on the supposition that the temperature is attained at once.)

The equipment reported in detail in reference [10] and sketched in Figure 6, included a high-frequency induction furnace 2; immediate pumping of evolved gas by high-capacity mercury diffusion pump, 6, and collection of the gas into the calibrated volume, 8, in which the pressure could be determined by thermoelectric gauge 16 or by McLeod gauge 7.

The equipment is suitable for the purpose in view when the thermo-electric gauge has been carefully calibrated in order to provide instantaneous and continuous measurements.

The apparatus is fitted with means of introducing and removing samples without breaking the vacuum [8]. It is thus possible to maintain high vacua permanently with consequent elimination of much of the trouble associated with "degassing" periods.

A nonmagnetic rod, 9, with a 180-degree bend, has two small platforms attached at one end. The sample is immersed in the mercury trough 14, then placed between the platforms, brought up to the cross-tube 17 and moved by external magnet to the mercury lift 5, of the usual type.

The sample is removed by reversing the procedure. The fused silica furnace tube is connected by ground joint 4, to the remainder of the apparatus

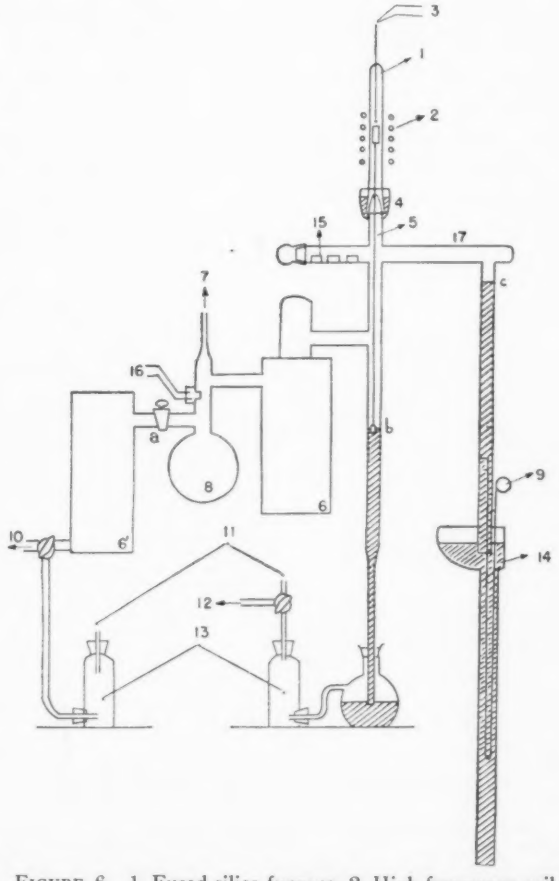

FIGURE 6. 1. Fused silica furnace; 2. High-frequency coil; 3. Thermocouple; 4. Silica to Pyrex joint with mercury seal; 5. Mercury lift; 6 and 6′. Mercury diffusion pumps; 7. Connection to McLeod gauge; 8. Calibrated space for collecting gas; 9. Guide rod for insertion and removal of samples; 10. Connection to primary vacuum; 11. Connection to atmosphere; 12. Connection to rough vacuum; 13. CaC 12 bottles; 14. Mercury reservoir; 15. Degassed samples; 16. Thermoelectric gauge.

constructed in Pyrex glass. Used either dry or very slightly greased, this joint is fitted with a mercury seal which has proved to be very satisfactory and vacuum-tight.

TABLE II

1	2	3	4	5	6	7
Time T minutes	Q Hydrogen extracted ml/100 gm	R Hydrogen left in sample ml/100 gm	$\ln \frac{R}{R_0}$	$\frac{Q}{R_0}$	$\frac{Dt}{l^2}$	$\frac{Dt}{l^2}$
.5	.10					
.75	.21					
1.0	.33	8.05	− .040	.039	5.3×10^{-3}	0×10^{-3}
1.25	.79	7.59	− .099	.094	6.7 "	1.4 "
1.50	1.32	7.06	− .171	.157	8.0 "	2.7 "
1.75	1.91	6.47	− .259	.228	9.3 "	4.0 "
2.25	2.92	5.46	− .428	.348	12.0 "	6.7 "
3.0	3.65	4.73	− .571	.435	16.0 "	10.7 "
5.0	5.89	2.49	−1.214	.703	26.7 "	21.4 "
7.0	6.95	1.43	−1.769	.830	37.3 "	32.0 "
9.0	7.41	.97	−2.156	.884	47.0 "	41.7 "
12.0	7.78	.60	−2.637	.929	64.1 "	58.8 "
15.0	7.96	.42	−2.994	.950	80.1 "	74.8 "
20.0	8.22	.16	−3.956	.980	106.8 "	101.5 "
25.0	8.33	.05		.994	133.3	128.0 "
60.0	8.38			1.000	309.8	304.5 "

1. *First experiment.* This has been performed with deposited weld metal of composition: C = .08 per cent; Si = .40 per cent; Mn = .75 per cent. The results are shown in Table II.

The hydrogen contents are given to two places of decimals. For values of Q greater than 2, only the first place is significant (sensitivity of measurements: .05 ml/100 gm).

R_0 has been taken as the quantity of gas collected after 60 minutes, i.e., $R_0 = 8.38$. Evolution was practically completed after 35 minutes.

For the determination of D by means of equation (6), only the experimental results for times of 5 to 20 minutes have been used. (After 20 minutes the quantity of hydrogen to be collected is less than the sensitivity of the measurements.) The regression line for $\ln R/R_0$ has been calculated in the usual manner, with the result:

$$\ln R/R_0 = -.174t - .486.$$

It follows that $D = 8.61 \times 10^{-3}$ cm²/minute and column 6 can be drawn up.

The results of this experiment give rise to the following considerations:

The heating of the sample has been carried out as follows: At $t = 0$ the high-frequency source was switched on at the normal power required for reaching and maintaining 650°C. The values of Q/R_0 show a gradually increasing evolution during the first minute which has not yet attained the subsequent rate. This is undoubtedly due to the fact that the sample has not reached the required temperature of 650°C and in order to compensate for this effect, values of Dt/l^2 have been corrected rather arbitrarily by subtracting 60 seconds from the actual time in order to obtain coincidence of the beginning of rapid evolution with the zero of time for the theoretical curve.

The speed of the various phenomena and the heterogeneous heating effects caused by induced currents do not allow accurate appreciation of the temperature in the early stages and, in all probability, a temperature as high as 500°C has not been reached in the first minute.

Hence, the correction is still too small. As D varies rapidly with the temperature $D(500°C) \simeq \frac{1}{2}D(650°C)$, [19] it is to be expected that the corrected experimental values of Q/R_0 may be lower than the theoretically predicted values.

These theoretical results are also based upon a homogeneous repartition of hydrogen in the sample (equation (4)). The sample had been exposed to the atmosphere for four to five weeks and may have lost constancy of hydrogen concentration because the outer layers lose gas more quickly than the core. (See the theoretical curve for C/C_0 in Figure 3, which is applicable to cylinders of length equal to diameter.)

Our lack of sufficient knowledge of the value of D and of other surface phenomena which may occur under ambient conditions does not allow accurate

appreciation of the perturbations in the initial conditions of the experiment but it is apparent that the ratio Q/R_0 will increase less quickly than in the case of homogeneous samples [19].

Taking these considerations into account, the agreement found would appear to be reasonably good (Figure 7).

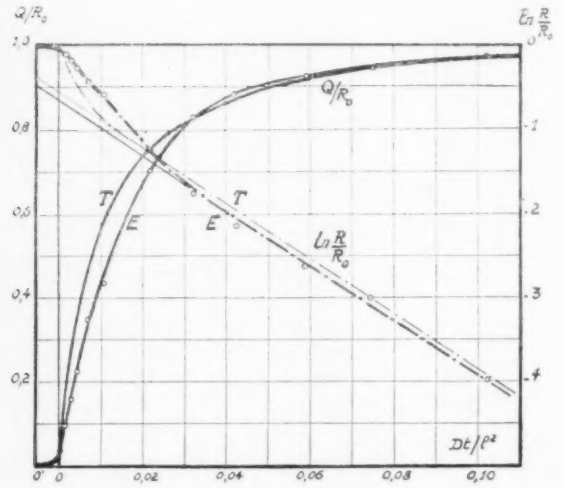

FIGURE 7. Comparison of extraction curves for sample of length equal to diameter. *T:* theoretical curve. *E:* experimental curve. 0′: uncorrected origin of abscissae, 0: corrected origin, Deposited weld metal with *C:* .08%, Si: .40%; Mn, .75%.

2. *Second experiment.* Closer agreement has been sought by minimising the disturbing influences already described.

Heating has been accelerated during the first 30 seconds by trebling the input energy; subsequently the normal power was applied to the coil.

The sample (S.A.E. 1041 steel with .4%C, 1.5%Mn, .18% Si, with S. and P. less than .03%) has been taken from a 45 mm steel ingot forged as rapidly as possible to a diameter of 30 mm in order to obtain physical homogeneity of the steel. The sample was machined to 12 mm as quickly as possible and kept in solid carbon dioxide. The best solution would have been to trepan a 30-mm round from the centre of a large bloom but the necessary equipment was not available.

The hydrogen content of the small ingot was probably 5.4 ml/100 gm, which was the value obtained from a chilled sample taken during the pouring of the cast. After forging and machining the hydrogen was found to be 1 ml/100 gm. In spite of this, the small sample cut from the axis of the forging may be expected to possess a reasonably constant concentration of the gas.

The results of the experiment are embodied in Table III.

TABLE III

1	2	3	4	5	6
Time T Minutes	Q Hydrogen extracted ml/100 gm	R Hydrogen left in sample ml/100 gm	$\ln \frac{R}{R_0}$	$\frac{Q}{R_0}$	$\frac{Dt}{l^2}$
.33	.108	.872	− .117	.110	3.5×10^{-2}
.66	.248	.732	− .292	.253	$7.0 \times$ "
1.0	.346	.634	− .435	.353	10.5 "
1.33	.432	.548	− .582	.441	14.0 "
1.66	.550	.430	− .824	.562	17.5 "
2.0	.626	.354	−1.017	.633	21.1 "
2.5	.724	.256	−1.341	.734	26.4 "
3.0	.778	.202	−1.581	.795	31.6 "
3.5	.820	.160	−1.812	.837	36.9 "
4.0	.843	.137	−1.968	.860	42.2 "
4.5	.865	.114	−2.152	.883	47.5 "
5.0	.886	.094	−2.345	.905	52.7 "
7.5	.939	.041	−3.188	.958	79.0 "
10.0	.969	.011		.989	105.4 "
15.0	.980			1.000	158.1 "
30.0	.980			1.000	316.2 "

The amounts of hydrogen are given to three decimals. With the small quantities of extracted gas, the sensitivity of the thermoelectric gauge is at its highest (.01 to .015 ml/100 gm) and the first two decimals are significant. Three decimals have been used in the calculations. Figure 8 gives a comparison between experimental and expected values of $\ln R/R_0$.

The evolution in the early stages is greater than in the first trial but it is decidedly less than the rate expected theoretically. In spite of the steps

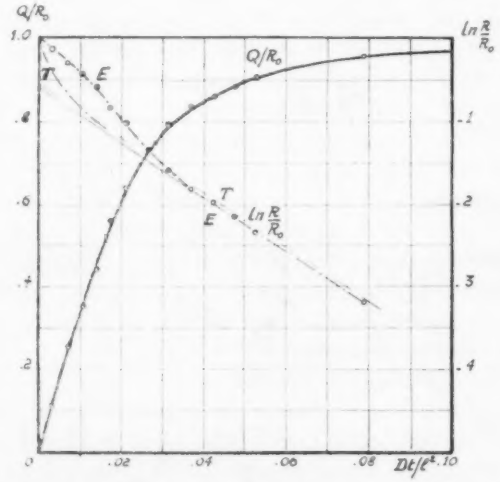

FIGURE 8. Comparison of extraction curves. *T:* theoretical curve; *E:* experimental curve. Samples ½ inch long and ½ inch diameter of S.A.E. 1041 Steel with C, .4%; Si, 18%; Mn, 1.5%.

taken, 30 seconds were necessary to bring the sample to a dull red heat and it seems difficult, if not impossible, to realise better agreement during the first few minutes.

The other elements of comparison remain satisfactory, since, in spite of the reduced precision of measurement brought in by the small quantity of hydrogen present in the sample, the regression line of $\ln R/R_0$ on t for values of $t > 3$ is represented by

$$\ln \frac{R}{R_0} = -0.344t - 0.608$$

The ordinate at the origin of t is .608, compared with the expected value of .579 given by equation (6). A rather lower value would be expected and the probable reason is the relatively large error in the values of R used in the calculations.

IV. Conclusion

Considering the difficulties already described and the nature of their influence upon the experiment, we may conclude that there is reasonable agreement between the results obtained and those expected from the hypothesis of normal diffusion.

The fact that a quantity (the diffusion coefficient) measured experimentally has been used, in order to establish the theoretical curve, implies only the identity of the slopes of the straight portion of the relation $\ln R/R_0 = f(Dt/l^2)$.

This relation represents a curve passing through the origin, and the important part of the verification seems to be the ordinate at $t = 0$ obtained by producing the straight portion of the curve. It is thus interesting to note that the measured values (.48 and .608) are close to the figure of .579 expected from a purely diffusional process.

In addition, the values obtained for the diffusion coefficient (5.6 to 16×10^{-3} cm²/min) are in agreement with the best determinations hitherto published [17; 18; 19].

Lastly, the values of Dt/l^2 at which the evolution becomes exponential in character are only slightly greater than the theoretical values and the difference may be explained by the impossibility of realising in practice the simpler and more rigid conditions considered in the calculations.

V. Consequences

These experiments, which may appear to have only a speculative character, give indications of practical interest.

1. The rapid evolution of hydrogen in the early stages of the extraction is a normal manifestation of the process of diffusion and is not to be attributed to the existence of two different states of this element such as a rapidly extracted and a slowly diffusing kind of hydrogen.

2. The time necessary for the extraction of a given substantial proportion of the hydrogen is independent of the total content of the gas and depends only on the diffusion coefficient and on the dimensions of the sample.

In determinations of the total hydrogen content, the size of the sample is fairly constant and the very long extraction times mentioned by some experimenters are justified only by low values of D, as in the case of some highly alloyed and austenic steels.

The time of extraction depends on the square of linear dimensions, not only for cylinders of similar aspect but also for rounds and squares of great length and for linear flow in slabs and plates. We recall in this connection that relations of the type:

$$\frac{t_2}{t_1} = \left(\frac{l_1}{l_2}\right)^n,$$

when n is not equal to 2, have been proposed.

3. The satisfactory agreement found with the cylinders used shows that solutions of the diffusion equation can be applied to solids of other shapes. It will be apparent that the case we have considered can be decomposed into a combination of the solution for an infinite cylinder and for an infinite slab. It is easy to transform these results in order to apply them to the simpler mill sections such as rounds, billets, slabs and plates.

4. Such solutions are valid for diffusion into a medium containing no hydrogen atoms or molecules, such as a vacuum or an inert atmosphere free from H_2 and H_2O. It is again easy to generalize these solutions for practical cases if we know the concentration of hydrogen at the surface, C_1, which is in equilibrium with the partial pressure of this gas in the surrounding atmosphere.

Sievert's law gives:

$$C_1 = K\sqrt{P_{H_2}}$$

and K is related to the absolute temperature T by means of the thermodynamical relation

$$K = K_1 T \frac{\mu}{2} e^{-\lambda/2kT} \tag{19}$$

As it has been found that $\mu/2$ is approximately equal to unity, we find on writing $T_1 = \lambda/2k$:

$$C_1 = K_1 T\, e^{-T_1/T}\sqrt{P_{H_2}}.$$

From a review of existing experimental results, Kawai [19] proposes the following values for K_1 and T_1.

α and δ Fe: $K_1 = 40.4 \times 10^{-3}$ and $T_1 = 3{,}250$

γ Fe: $K_1 = 14.5 \times 10^{-3}$ and $T_1 = 1{,}500$

With P_{H2} expressed in atmospheres, these values give C_1, in ml/100 gm.

Fick's equation $D \cdot \nabla^2 C = \dfrac{\partial c}{\partial t}$ with initial concentration C_0 and surface concentration C_1, is transformed by the substitution $C = C_1 + (C_0 - C_1)u$ into the simpler form $D\nabla^2 u = du/dt$ with:

$u = 1$ for $t = 0$ in the whole solid

$u = 0$ for $t > 0$ at the surface.

The solution for u is then readily applicable to all values of C_0 and C_1.

Values have been calculated for cases of much practical interest and these are illustrated in Figures 9 and 10.

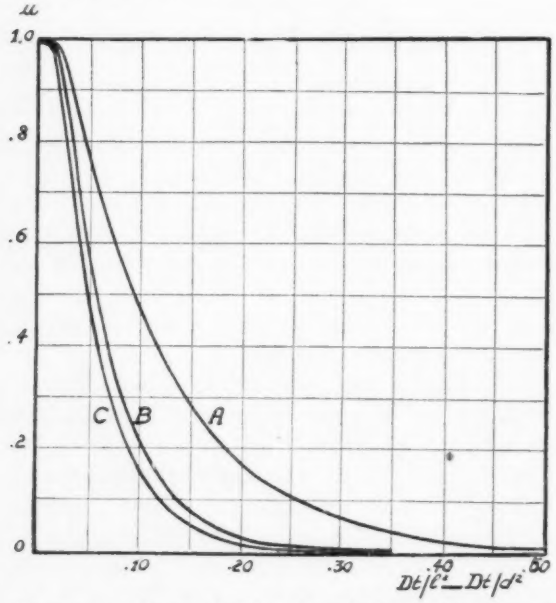

FIGURE 9. Curves showing the relative axial concentration, u, for homogeneous samples. A: slab of thickness l, B: parallelopiped of square section of a side l, C: cylinder of diameter d.

Figure 9 shows the axial concentration, u, for infinite cylinders and billets and slabs in terms of Dt/l^2 and Dt/d^2, where l represents the side of the square or thickness of the slab and d stands for the diameter of the round.

Figure 10 shows the average concentration t, on the scale of u, of the hydrogen remaining in the sample in terms of the same parameters.

These two graphs are easy to use and they require only the values of D. Published values [17; 18] will give a useful result, at least for temperatures above 450°C when phase-boundary reactions do not interfere.

5. It is valuable to notice that the apparatus which has been described can be used for determining the diffusion coefficient, which is a fundamental property of interest.

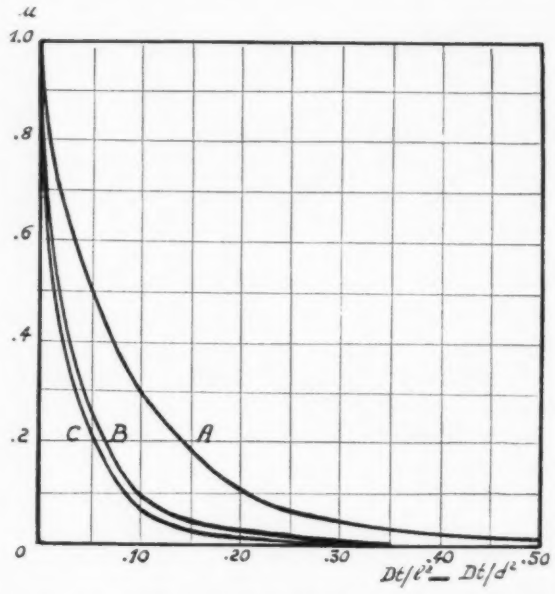

FIGURE 10. Mean value of u for homogeneous samples. *A:* slab of thickness l, *B:* parallelopiped of square section of side l, *C:* cylinder of diameter d.

Should it be confirmed that the exit process at the surface is more rapid than the rate of diffusion below 450°C, it will be possible to measure this diffusion coefficient correctly at lower temperature —a procedure which measurements of permeability through plane or circular walls cannot achieve readily for reasons established by Chang and Bennett.

References

1. ZAPFFE and HASLEN. Trans. A.I.M.E. **134** (1943) 10.
2. BASTIEN. Rev. Metall. **37** (1940) 225 and 272; **42** (1945) 205. C.R. Acad. Sci. **228**, No. 16 (1949) 1337; **228**, No. 21 (1949) 1651; **229**, No. 11 (1949) 549; **231**, No. 2 (1950) 147; **232**, No. 1 (1951) 69.
3. MEUNIER and DEMAREZ. Mémoires du Centre Nat. de Recherches Métallurgiques. Section du Hainaut, Decembre, 1950, 1.
4. SIMS, MOORE and WILLIAMS. Metals Techn. **25** (October, 1948) T. P. 2454.
5. HOBSON and SYKES. J. Iron Steel Inst. **169** (1951) 209.
6. Trans. A.I.M.E. **162** (1945) 355. Symposium on estimation of H_2 in steels.

7. Iron and Steel Institute (1937) Special report No. 16, Section IV, 82; (1939) Special report No. 25, Section IV, (2A) 82. J.I.S.I. **141** (1940), 243P; J.I.S.I. **148** (1943), 278P; J.I.S.I. **155** (1947), 27.
8. BLETON, MISCHONSNIKY, COIN and BASTIEN. Rev. Metall. **48** (1951) 471.
9. CARNEY, CHIPMAN and GRANT. J. Metals **2** (1950) 397.
10. MEUNIER and DEMAREZ. Rev. Metall. **48** (1951) 598.
11. SIMS and MOORE. Trans. A.I.M.E. **176** (1948) 248; Metals Techn. **15** (June, 1948) T. P. 2369.
12. GELLER, TAK-HO-SUN and WILLEMS. Archiv. Eisenh. **17** (1944) 207.
13. BENNEK und KLOTZBACK. Stahl u. Eisen **61** (1941) 597.
14. SMITHELLS. Gases and Metals. Cantor lectures (1938) February, March.
15. FAST. Chemisch Weekblad. (1941). Philips Review No. 1528.
16. BARRER. Phil. Mag. **38** (1939) 148.
17. CHANG and BENNETT. J.I.S.I. **170** (1952) 205.
18. SYKES, BURTON and GEGG. J.I.S.I. **156** (1947) 155.

THE CRYSTALLOGRAPHY OF MARTENSITE TRANSFORMATIONS III. FACE-CENTRED CUBIC TO BODY-CENTRED TETRAGONAL TRANSFORMATIONS*

J. S. BOWLES and J. K. MACKENZIE†

The theory developed in Parts I and II is applied to transformations from face-centred cubic to body-centred tetragonal in the alloys Fe-C, Fe-Ni, Fe-Ni-C. The theoretical predictions of habit planes, orientation relationships and directions of the homogeneous strain are found to be in satisfactory agreement with all the available experimental data. Thus, the hypothesis that the inhomogeneous shear is a part of the twinning shear in the final structure has been substantiated for the transformations considered.

The habit plane interface envisaged by Frank is shown to be a special case of the type of interface expected on the present theory: all planes in the zone of the invariant line, and in particular the twinning plane, meet edge to edge in the interface.

LA CRISTALLOGRAPHIE DES TRANSFORMATIONS MARTENSITIQUES III. LES TRANSFORMATIONS DU SYSTÈME CUBIQUE À FACES CENTRÉES EN TÉTRAGONAL CENTRÉ

La théorie développée dans les Parties I et II est appliquée aux transformations du système cubique à faces centrées en tétragonal centré, dans les alliages Fe-C, Fe-Ni, Fe-Ni-C. Il est constaté que les prédictions théoriques des plans limites, des relations d'orientation et des directions de déformation homogène sont en accord satisfaisant avec toutes les données expérimentales, disponibles. Ainsi, l'hypothèse que la tension non-homogène fait partie de la tension de maclage dans la structure finale, a été confirmée pour le cas des transformations considérées. Il est montré que l'interface constituée par un plan limite, envisagée par Frank, n'est qu'un cas particulier de l'interface proposée par la présente théorie, à savoir: tous les plans dans la zone de la ligne invariante, et en particulier le plan de maclage, se rencontrent suivant une arête commune dans l'interface.

DIE KRISTALLOGRAPHIE DER MARTENSIT TRANSFORMATIONEN. III. TRANSFORMATIONEN VON KUBISCH-FLÄCHENZENTRIERTEN ZU TETRAGONAL-RAUMZENTRIERTEN GITTERN

Die in Teil I und II entwickelte Theorie wird auf die Umwandlungen kubisch-flächenzentriert zu tetragonal-raumzentriert in Fe-C, Fe-Ni und Fe-Ni-C Legierungen angewandt. Die theoretischen Voraussagen über Habitusebenen, Beziehungen der kristallographischen Orientierungen und Richtungen homogener Verzerrungen stimmten zufriedenstellend mit allen vorhandenen experimentellen Angaben überein. Somit ist die Hypothese, dass die inhomogene Scherung einen Teil der Zwillingsscherung in der Endstruktur darstellt, für die hier betrachteten Transformationen bestärkt worden.

Es wird gezeigt, dass die von Franck vorgeschlagene Habitusebenengrenzfläche ein Spezialfall des nach der vorstehenden Theorie zu erwartenden Grenzflächentyps ist. Alle Ebenen in der Zone der invarianten Richtung und im besonderen die Zwillingsebene schneiden sich in der Grenzfläche.

1. Introduction

In this paper the geometrical theory of martensite transformations which was developed in Parts I and II‡ [1] will be applied to transformations from face-centred cubic to body-centred tetragonal lattices, and its predictions of habit planes, orientation relationships and other geometrical features will be compared with the available experimental data for iron-carbon, iron-nickel and iron-nickel-carbon alloys.

In I and II a phenomenological theory of the relations between the various crystallographic features of martensite transformations was developed. This theory aims at describing the total atomic displacements produced by martensite transformations but not necessarily the motions of atoms during transformation. It has been shown that the total atomic displacements can be described consistently by means of a homogeneous strain which is composed of an invariant-plane strain on the habit plane and a small dilatation, followed by an inhomogeneous shear which produces no further observable change in shape. This shear can only be homogeneous within small volumes and it was proposed that within such volumes it is a part of a twinning shear in the final lattice. It has been shown that these conditions, together with a knowledge of the correspondence between the two lattices, their dimensions, and the twinning plane involved, is sufficient to determine the total strain in terms of a single parameter, θ, and, further, that the resolution of this total strain into component strains of the required types is uniquely determined.

In §§2, 3, of the present paper the correspondence between the initial and final lattices, and also the relevant twinning plane, are shown to be

*Received September 5, 1953.

†Division of Tribophysics, University of Melbourne, Victoria, Australia.

‡These papers will be referred to as I and II.

the same for all the transformations considered. In these sections the experimental origins of this information are described and quantities which are required for direct substitution into the equations of the theory are derived. In §4 the parameter θ is introduced and substitution into the main equations of the general theory is carried out. To apply the theory to a particular transformation it is necessary to find the appropriate value of θ by calculating the variation of the habit plane with θ and determining that value for which the predicted and observed habit planes agree. Of course the extent to which there is agreement between the observed and the theoretically possible habit planes is a first test of the hypothesis that the inhomogeneous shear is a part of a twinning shear. The actual comparisons of predicted and observed habit planes are carried out in §5 and the appropriate values of θ are determined for the various transformations. The remaining sections of the paper are concerned with detailed analyses of individual transformations and show that the predictions of the theory are in substantial agreement with experiment.

The notation used in this paper is the same as that used in I and II.

2. The Correspondence and the Principal Axes

Jaswon and Wheeler [2] have determined the correspondence between *f.c.c.* and *b.c.t.* lattices for those transformations in iron-carbon alloys which produce the Kurdjumow-Sachs orientation relationship [3]. For the variant of this relationship shown in Figure 1, their correspondence is

$$(2.1) \qquad ({}_{\mathrm{B}}\mathbf{C}_{\mathrm{F}}) = \begin{pmatrix} 1 & 0 & 1 \\ 1 & 0 & \bar{1} \\ 0 & 1 & 0 \end{pmatrix},$$

where the bases B and F define the *b.c.t.* and *f.c.c.* unit cells respectively; the corresponding metrics* are $({}_{\mathrm{B}}{}^{*}\mathbf{G}_{\mathrm{B}}) = (\mathrm{diag}: a'^{2}, a'^{2}, \gamma^{2}a'^{2})$ and $({}_{\mathrm{F}}{}^{*}\mathbf{G}_{\mathrm{F}}) = (\mathrm{diag}: a^{2}, a^{2}, a^{2})$ where a' and a are the respective lattice parameters and γ is the axial ratio of the tetragonal cell. This correspondence was chosen by Jaswon and Wheeler because it ensures that the atomic displacements involved in the transformation are as small as possible. It has been shown [4; 2] that the arrangement of interstitial carbon atoms in iron-carbon martensite is precisely that expected from this correspondence. It has also been shown [5] that the same correspondence results from a consideration of the analogous variants of all orientation relationships between Nishiyama [6] and Kurdjumow-Sachs, including that of Greninger and Troiano [7].

*The notation (diag: a, b, c) represents a square diagonal matrix with elements a, b, c in the leading diagonal, all other elements being zero.

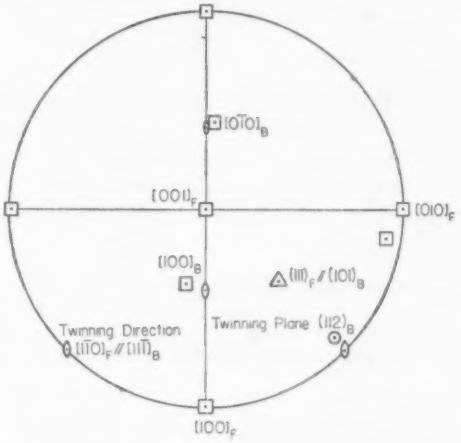

FIGURE 1. Stereographic projection showing the variant of the Kurdjumow-Sachs orientation relationship considered in this paper. The relevant twinning plane and twinning direction are also shown. The subscripts F and B refer to the f.c.c. and b.c.t. lattices respectively.

The correspondence and the metrics of the two bases B and F determine the principal axes, and the associated principal strains of the total strain, as described in II-§ 4. In the present case the results are easily obtained by inspection, for the mutually orthogonal directions $[101]_{\mathrm{F}}$, $[10\bar{1}]_{\mathrm{F}}$, $[010]_{\mathrm{F}}$ correspond to the mutually orthogonal directions $[100]_{\mathrm{B}}$, $[010]_{\mathrm{B}}$, $[001]_{\mathrm{B}}$. The former set of directions can therefore be chosen as principal axes and the basis P, comprised of unit vectors in these directions (Figure 2) defined to be $[\mathrm{F}; \mathbf{p}_1] =$

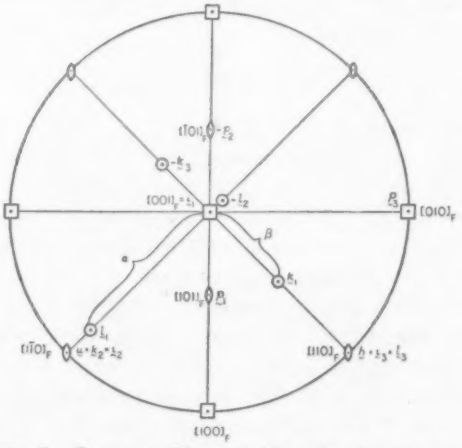

FIGURE 2. Stereographic projection showing the orientation of the bases P, I, L, K relative to the f.c.c. lattice. The invariant line and the invariant normal make angles α and β respectively with $[001]_{\mathrm{F}}$.

$[1/\sqrt{2}, 0, 1/\sqrt{2}]_F$, $[F; \mathbf{p}_2] = [1/\sqrt{2}, 0, -1/\sqrt{2}]_F$, $[F; \mathbf{p}_3] = [0, 1, 0]_F$.
Thus,

$$(2.2) \qquad (P\mathbf{T}F) = \begin{pmatrix} 1/\sqrt{2}, & 0, & 1/\sqrt{2} \\ 1/\sqrt{2}, & 0, & -1/\sqrt{2} \\ 0 & , 1, & 0 \end{pmatrix} = (F\mathbf{T}P)'.$$

The elements of the diagonal matrix $\mathbf{M}$, representing the strain referred to the basis P which extends the base vectors P to their final lengths without rotation, are simply the ratios of the final to the initial identity periods along the principal axes. Thus,

$$(2.3) \qquad \mathbf{M}^2 = (a'/a)^2 \,(\text{diag: } 2, 2, \gamma^2).$$

3. The Twinning Plane and Direction

Greninger and Troiano [7] have observed twinned martensite plates in an iron-22% nickel-0.8% carbon alloy and have determined the indices of the twinning plane. Examination of their pole figure shows that the operative twinning plane is $(112)_B$ for the variant being considered in this paper.

That the twinning plane is the same for transformations which lead to the Kurdjumow-Sachs orientation relationship can be shown as follows. This orientation has the property that its variants are twin-related in pairs. The twinning shear relating such a pair variants can be obtained by stereographic analysis [5] making use of the correspondences for these variants. The relevant twinning plane is again found to be $(112)_B$ and the associated twinning direction is $[11\bar{1}]_B$. This twinning direction is the same as that obtained from the general equation for the twinning shear, II-(7.7), which gives

$$(3.1) \qquad (B\mathbf{S}^T B) = \mathbf{I} - f[1, 1, \bar{1}](1, 1, 2),$$

where $f = (2 - \gamma^2)/2(\gamma^2 + 2)$.

The intermediate basis I used in the general theory can now be determined explicitly. The base vector $\mathbf{i}_2 (= \mathbf{u})$ is a unit vector parallel to the direction in the initial lattice from which the twinning direction is generated. The base vector $\mathbf{i}_3 (= \mathbf{h})$ is a unit vector normal to the plane from which the twinning plane is generated, while $\mathbf{i}_1$ is a unit vector perpendicular to both. Using the correspondence (2.1) it follows that the twinning direction $[11\bar{1}]_B$ is generated from the direction $(B\mathbf{C}F)^{-1}[11\bar{1}]_B = [2\,\bar{2}\,0]_F$, so that $[F; \mathbf{i}_2] = [1/\sqrt{2}, -1/\sqrt{2}, 0]_F$. Similarly, the twinning plane $(112)_B$ is generated from the plane $(112)_B(B\mathbf{C}F) = (220)_F$ so that $[F; \mathbf{i}_3] = [1/\sqrt{2}, 1/\sqrt{2}, 0]_F$ and $[F; \mathbf{i}_1] = [0, 0, 1]_F$. These base vectors are shown in Figure 2. Finally, using (2.2) to transform the components of these base vectors to the basis P it follows that the transformation

$$(3.2) \quad (P\mathbf{T}I) = \begin{pmatrix} 1/\sqrt{2}, & 1/2, & 1/2 \\ -1/\sqrt{2}, & 1/2, & 1/2 \\ 0 & , -1/\sqrt{2}, & 1/\sqrt{2} \end{pmatrix} = (I\mathbf{T}P)'.$$

It should be noted that the twinning plane $(112)_B$ is generated from a plane of symmetry $(110)_F$ as required by the general theory, II-§ 7.

4. The Invariant Line Strain

The invariant line strain $\mathbf{S}$ that is obtained from the total strain $\mathbf{S}_t$ by removing a suitable dilatation $\mathbf{I}/\delta$, is calculated in II-§§6, 9 and is expressed ultimately in terms of the elements g_{rs} of a matrix.

$$(4.1) \qquad \mathbf{G} = (I\mathbf{T}P)\,\delta^2\mathbf{M}^2(P\mathbf{T}I).$$

The dilatation δ is the only unknown quantity in this equation, and is therefore the only adjustable parameter in the theory. However, δ itself is not the most convenient parameter to use. Equation (2.3) shows that $\delta^2\mathbf{M}^2 = \delta^2(a'/a)^2\,\mathbf{M}_0^2$, where $\mathbf{M}_0^2 = (\text{diag: } 2, 2, \gamma^2)$, which for a fixed γ is independent of the sizes of the initial and the final cells. Thus, if a new parameter θ is defined by the relation

$$(4.2) \qquad \theta = \delta(a'/a),$$

all transformations with the same γ can be treated simultaneously for they differ only with respect to the value of θ. In terms of the parameter θ

$$(4.3) \quad \mathbf{G} = (g_{rs}) = \theta^2 \begin{pmatrix} 2, 0 & , & 0 \\ 0, 1 + \gamma^2/2, & & 1 - \gamma^2/2 \\ 0, 1 - \gamma^2/2, & & 1 + \gamma^2/2 \end{pmatrix},$$

$$(4.4) \quad \mathbf{G}^{-1} = (g^*_{rs}) = \frac{1}{\theta^2} \begin{pmatrix} \frac{1}{2}, & 0 & , & 0 \\ 0, & (2 + \gamma^2)/4\gamma^2, & & (\gamma^2 - 2)/4\gamma^2 \\ 0, & (\gamma^2 - 2)/4\gamma^2, & & (2 + \gamma^2)/4\gamma^2 \end{pmatrix},$$

and

$$(4.5) \qquad |\mathbf{G}| = g^2 = 4\gamma^2\theta^6.$$

In II it was shown that the matrix representing the invariant line strain $\mathbf{S}$ has a simple form when referred to a basis L, such that $\mathbf{l}_1$ is parallel to the invariant line. The base vectors $\mathbf{l}_1$, $\mathbf{l}_2$, $\mathbf{l}_3$ are shown in Figure 2. The transformation

$$(4.6) \quad (I\mathbf{T}L) = \begin{pmatrix} \cos\alpha, & -\sin\alpha, & 0 \\ \sin\alpha, & \cos\alpha, & 0 \\ 0 & , 0 & , 1 \end{pmatrix},$$

where $\alpha(|\alpha| \leqslant 90°)$ is the angle between $\mathbf{l}_1$ and $[001]_F = \mathbf{i}_1$, and is determined by equation II-(6.10). On substituting the $g_{r\theta}$ given in (4.3) into this equation it is found that

$$(4.7)\quad \cos\alpha = (1 - \theta^2 - \theta^2\gamma^2/2)^{\frac{1}{2}}/\theta(1 - \gamma^2/2)^{\frac{1}{2}},$$

$$(4.8)\quad \sin\alpha = (2\theta^2 - 1)^{\frac{1}{2}}/\theta(1 - \gamma^2/2)^{\frac{1}{2}},$$

giving two values of α which are merely opposite in sign. It should be noted that these equations only determine real values of α provided $1/\sqrt{2} \leqslant \theta < 1/(1 + \gamma^2/2)^{\frac{1}{2}}$, thus imposing limits on the possible values of θ; the minimum and maximum values of θ correspond to $\alpha = 0°$ and $90°$ respectively.

The matrix representing $\mathbf{S}$ referred to the basis L is given by II-(8.7), (6.18)

$$(4.9)\quad (\mathrm{L}\mathbf{S}\mathrm{L}) = \begin{pmatrix} 1, & (g_{22} - g_{11})\cos\alpha\sin\alpha, & g_{23}\sin\alpha \\ 0, & g g_{33}^{*\frac{1}{2}}\cos\omega, & -(g g_{22}^{*\frac{1}{2}}\cos\alpha\cos\omega + \sin\omega)/g_{33}^{*\frac{1}{2}} \\ 0, & g g_{33}^{*\frac{1}{2}}\sin\omega, & (-g g_{23}^{*\frac{1}{2}}\cos\alpha\sin\omega + \cos\omega)/g_{33}^{*\frac{1}{2}} \end{pmatrix},$$

where ω is the angle between the initial and final positions of the twinning plane and is found from II-(8.5) to be

$$(4.10)\quad \cos\omega = (2\theta\gamma + 1 + \gamma^2/2)/(1 + \theta\gamma)(2+\gamma^2)^{\frac{1}{2}},$$

giving two values of ω, opposite in sign. It should be noted that $\cos\omega$ must be positive since the criterion for selecting the correspondence ensures that the total strain is as small as possible: if $\cos\omega$ were negative the twinning plane would have to be rotated by more than $90°$ by the transformation. Considerations such as this show that all the square roots must be taken positively unless the contrary is stated.

The two values of α taken together with the two for ω determine four possible invariant line strains, all of which have the same principal axes and associated principal strains, and the twinning plane is generated from the same plane $(110)_F$ in all four cases. The solution obtained by taking α and ω both positive, say, will be referred to as the $(\alpha+, \omega+)$-solution and so on. In II-§ 8, it was shown that the $(\alpha+, \omega-)$-solution refers to the twin of that variant of the $(\alpha+, \omega+)$-solution which is obtained by a rotation of $180°$ about the normal to the $(110)_F$ symmetry plane. The $(\alpha-, \omega-)$- and the $(\alpha-, \omega+)$-solutions are related in the same way. In general, the $(\alpha+, \omega+)$- and $(\alpha-, \omega+)$-solutions are distinct, but in the present case they are variants related by a rotation through $180°$ about the normal to the $(001)_F$ symmetry plane. The other pair are, of course, related in the same way. Examination of Figure 2 shows that this symmetry operation leaves the principal axes, principal strains and the plane $(110)_F$ invariant* while it changes $\mathbf{l}_1(\alpha+)$ into $\mathbf{l}_1(\alpha-)$. This result can be demonstrated formally by showing that the $(\alpha-, \omega+)$-solution, when referred to the variant of its L basis, is identical with the $(\alpha+, \omega+)$-solution.

The factorization of $\mathbf{S}$ can now be carried out making use of the relations given in II-§ 9. In the present class of transformations certain simplifications arise and the formulae can be given geometrical interpretations which are sometimes useful. For the $(\alpha+, \omega+)$-solution, unit vectors along the normal to the habit plane and in the direction of the displacement in the invariant plane strain are given by

$$(4.11)\quad \begin{aligned} (\mathbf{p};\ \mathrm{L}) &= (0, -1, \cos\beta)_L/(1 + \cos^2\beta)^{\frac{1}{2}}, \\ (\mathbf{p};\ \mathrm{I}) &= (\sin\alpha, -\cos\alpha, \cos\beta)_I/(1+\cos^2\beta)^{\frac{1}{2}}, \end{aligned}$$

$$(4.12)\quad \begin{aligned} [\mathrm{K};\ \mathbf{d}] &= [0, \cos\alpha, -1]_K/(1 + \cos^2\alpha)^{\frac{1}{2}}, \\ [\mathrm{I};\ \mathbf{d}] &= [\sin\beta, \cos\alpha, -\cos\beta]_I/(1+\cos^2\alpha)^{\frac{1}{2}}, \end{aligned}$$

where K is the basis introduced at the end of II-§6 and β, the angle between $[100]_I$ and the invariant normal of $\mathbf{S}$, is given by II-(6.11)

$$(4.13)\qquad \sin\beta = \sqrt{2}\gamma(2\theta^2 - 1)^{\frac{1}{2}}/(2 - \gamma^2)^{\frac{1}{2}}.$$

It follows from (4.11) that for constant β the habit plane is a fixed plane in the L-basis. Since the L-basis only varies by a rotation about $[110]_F$, the normal to the habit plane varies in the same way for constant β. Similarly for constant α the direction only varies by a rotation about $[1\bar{1}0]_F$. Further, the magnitude m (I-§5) of the invariant plane strain reduces to

$$(4.14)\qquad m = \sqrt{2}\,\theta(1 - \theta\gamma),$$

while the fraction k of the twinning shear involved in the complementary strain is given by

$$(4.15)\qquad 1 + 2k = \cos\alpha\cos\beta.$$

*Since $[001]_F$ is a line of symmetry in the initial position of the twinning plane $(110)_F$, these facts show that the two possible values of α can differ only in sign.

5. The Habit Plane

It was shown in II-(9.3) that the habit plane referred to the basis L is of the form $(0, \sin\omega, g_{33}{}^{*-\frac{1}{2}} - \cos\omega)_L$. On substituting for ω and $g_{33}{}^*$ this becomes

$$(5.1)\quad (0, \operatorname{sgn}\omega\,(1-\gamma^2/2)^{\frac{1}{2}}, -[1-\gamma^2(4\theta^2-1)/2]^{\frac{1}{2}})_L.$$

The habit plane can now be referred to the basis F using the transformation

$$(5.2)\quad \begin{aligned}(\mathrm{F}\mathbf{T}\mathrm{L}) &= (\mathrm{F}\mathbf{T}\mathrm{P})(\mathrm{P}\mathbf{T}\mathrm{I})(\mathrm{I}\mathbf{T}\mathrm{L}),\\ &= \begin{pmatrix} \sin\alpha/\sqrt{2}, & \cos\alpha/\sqrt{2}, & 1/\sqrt{2}\\ -\sin\alpha/\sqrt{2}, & -\cos\alpha/\sqrt{2}, & 1/\sqrt{2}\\ \cos\alpha & -\sin\alpha, & 0\end{pmatrix}.\end{aligned}$$

The variation of the habit plane with θ for $\gamma = 1$, i.e., for body-centred cubic structures, is shown in Figure 3 for all four solutions, and the relationship between the solutions is clearly that described previously. Since the four habit planes are crystallographically equivalent, it is only necessary to consider one eighth of the whole projection in order to compare experimental habit planes with those predicted by the theory. Accordingly, in Figure 4 the variation of the habit plane with θ and γ has been plotted for the $(\alpha+, \omega+)$-solution.

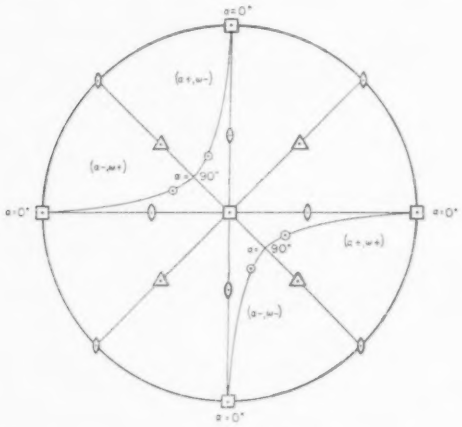

FIGURE 3. Stereographic projection showing the variation of the habit plane with θ for $\gamma = 1$. As θ^2 varies between the limits 1/2 and 2/3, α varies from 0 to 90 degrees. The open circles represent the four solutions obtained for the habit plane for some particular value of θ.

The compositions of those alloys for which habit planes have been determined are given in Table I, which also shows the corresponding values of γ and $(a'/a)^2$. In all the experimental work, with one exception [7] only the general indices of the habit plane have been determined. In

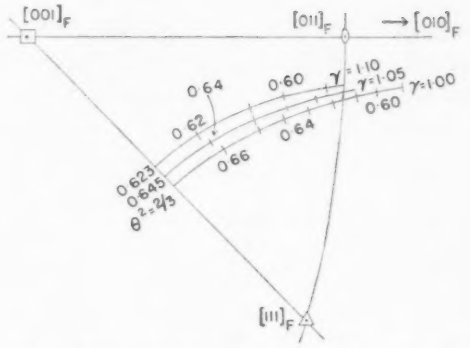

FIGURE 4. Stereographic projection showing the variation of the habit plane with θ and γ.

Figures 5, 6, 7, where the measured habit planes are compared with the theory, the experimental habit planes have been plotted in the stereographic triangle containing the predicted curves. It will be shown in the next section that Greninger and Troiano's habit plane does indeed lie in this triangle.

It is evident from these diagrams that the experimental results are in general agreement with the theory. The observed habit planes lie close to the calculated curves for the relevant γ, and the predicted lateral shift of the habit plane curves as γ increases is in good agreement with observation (Figure 5).

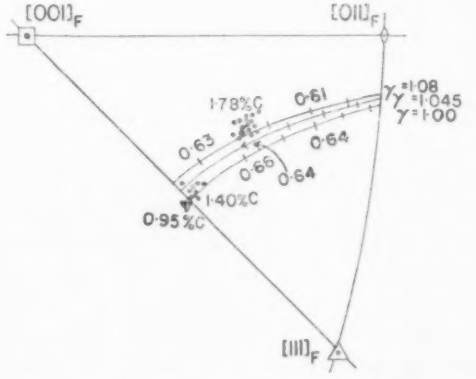

FIGURE 5. Comparison of the predicted habit planes with those measured by Greninger and Troiano [7] for various iron-carbon alloys. Following Greninger and Troiano, the results for 0.95%C. have been plotted in the adjoining triangle. According to the theory each group of points should lie somewhere on the curve for the appropriate γ.

The exact location of a habit plane on a particular curve is determined by the value of the parameter $\theta = \delta a'/a$. Although the exact values of δ are not known, they must be close to unity (I-§4). Thus, by regarding θ as equal to a'/a, a crude comparison of the predicted with the observed

effects of varying θ can be made. The theory then predicts that a'/a decreases either as γ increases or as the habit plane is displaced along a curve towards $(010)_F$. Examination of the data in Table I shows that a'/a always decreases as γ increases. Furthermore, in those transformations for which $\gamma = 1$ (Fig. 7) and also in those for which $\gamma = 1.041$, 1.045 (Fig. 6) the habit plane moves in

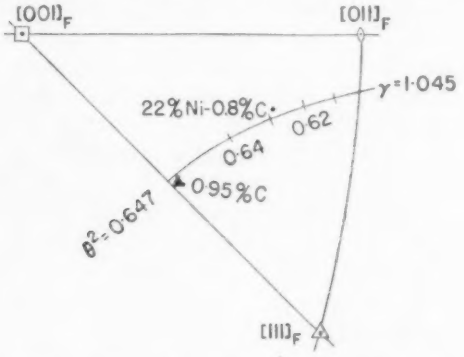

FIGURE 6. Comparison of the predicted and measured habit planes for transformations with $\gamma \simeq 1.045$.

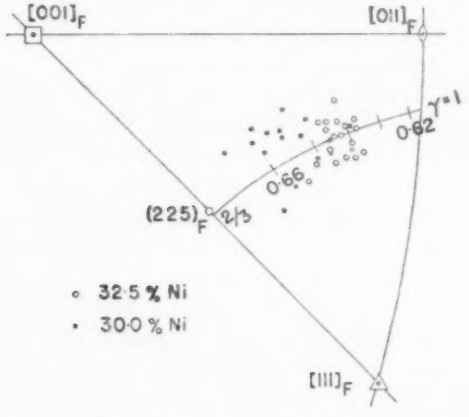

FIGURE 7. Comparison of the predicted and measured habit planes for transformations with $\gamma = 1$. The results for 30.0% and 32.5% Ni are those obtained respectively by Machlin and Cohen [14] and Greninger and Troiano [7].

the predicted direction as a'/a varies. Thus, the theory accounts for the general trends of habit plane variation. Quantitative agreement is achieved by evaluating the adjustable parameter δ.

The values of θ^2 which lead to the best agreement with the experimental habit planes have been estimated for each transformation, and are given in Table I, together with the values of δ derived therefrom. The values of δ are all within 1.5% of unity, in agreement with the observational evidence that any dilatation of the habit plane could not exceed a few per cent. (I-§4).

The feature of the experimental data that seems

TABLE I

Composition	γ	$(a'/a)^2$	θ^2	$\delta = \theta a/a'$	References
Carbon Steels					
0 %C.	1.000	0.650	0.6667†	1.013	
0.35%C.	1.016	0.642	0.6596†	1.014	
0.92%C.	1.041	0.630	0.6481†	1.014	Roberts* [8]
1.40%C.	1.063	0.620	0.6386†	1.015	
1.78%C.	1.080	0.612	0.620	1.006	
Fe–30% Ni	1.000	0.642	0.647‡	1.004‡	Owen, Yates and Sully [9]; Bradley, Jay and Taylor [10]; Jette and Foote [11]; Phragmen; [12]; Nishiyama [6].
Fe–32.5%Ni	1.000	0.640	0.645	1.004	
Fe–0.8%C. –22%Ni	1.045	0.627	0.630	1.002	Greninger and Troiano [7].

*For Fe–C alloys Roberts summarises all the existing data and gives $a = (3.548 + 0.044x)kX$, $a' = (2.861 - 0.013x)kX$, $\gamma = 1.000 + 0.045x$, where x is the wt. % carbon. For pure iron, Barrett [13] gives $a = 3.564$Å $= 3.557kX$ differing from Roberts' extrapolated value and obtained by extrapolation of high-temperature data.

†$\theta^2 = 1/(1 + \gamma^2/2) = \theta^2_{max}$.

‡The wide scatter of the observed habit planes makes it difficult to estimate θ^2. The value given has been obtained by assuming $\delta = 1.004$ (as for Fe–32.5% Ni) and using the value of $(a'/a)^2$ to calculate θ^2. The theoretical habit plane for $\theta^2 = 0.647$ lies within the scatter of the observations.

most difficult to reconcile with the theory is the wide scatter of the observed habit planes, particularly in the iron-nickel alloys (Fig. 7). Since it seems unlikely that the whole of this scatter can be due to experimental error other possibilities must be considered. The scatter parallel to the predicted curves could, of course, be attributed to variations in θ from plate to plate. Such variations could arise from changes in δ and/or a'/a due to inhomogeneneity of composition. The scatter normal to the predicted curves cannot be explained in this way, and, if it is a true effect, it may be necessary to abandon the hypothesis that the complementary shear occurs on the twinning plane and in the twinning direction and examine the consequences of fulfilling only one of these conditions (I-§§6, 9). However, it is clear that all the general features of habit plane variation are accounted for satisfactorily by the present hypothesis, and in the remaining sections it will be shown that by using the values of θ determined above, other crystallographic features of the transformations can also be accounted for quantitatively.

6. Greninger and Troiano's (259)-Transformation

The most complete experimental analysis of a martensite transformation is that made by Grenin-

ger and Troiano [7] of the transformation in Fe–0.8% C–22% Ni. They determined the habit plane and orientation relationship for a particular variant and also the direction of the homogeneous strain, assuming this strain to be a simple shear on the habit plane. The predictions of the theory for this transformation will now be compared with their observations.

It is clear from Figure 6 that the predicted and experimental habit planes are in good agreement for $\gamma = 1.045$, if $\theta^2 = 0.63$. Of the four possible strain matrices which can now be obtained using these values it is only necessary to consider any two which characterise a parent and a variant of its twin; the other two solutions are just real variants of these. A suitable pair is the $(\alpha+, \omega+)$- and the $(\alpha+, \omega-)$-solutions, and of these it is the $(\alpha+, \omega+)$-solution which leads to agreement with Greninger and Troiano's orientation relationship. For this transformation $\alpha = 72° 26.87'$ and $\omega = 4° 57.30'$ and the $(\alpha+, \omega+)$-solution* is

$$(6.1) \qquad (\mathrm{L}\mathbf{S}\mathrm{L}) = \begin{pmatrix} 1, & -0.082238, & 0.272696 \\ 0, & 1.103662, & 0.016254 \\ 0, & 0.095683, & 0.948345 \end{pmatrix},$$

while the transformation $(\mathrm{F}\mathbf{T}\mathrm{L})$ is obtained from equation (5.2) with $\sin\alpha = 0.953443$ and $\cos\alpha = 0.301574$.

The relative orientation of the two lattices can now be found very simply, for the indices, relative to the basis F, of any direction $[u\,v\,w]_B$ are $(\mathrm{F}\mathbf{S}\mathrm{F})(\mathrm{F}\mathbf{C}\mathrm{B})[u\,v\,w]_B$ while a plane $(hkl)_B$ has indices $(hkl)_B(\mathrm{B}\mathbf{C}\mathrm{F})(\mathrm{F}\mathbf{S}\mathrm{F})^{-1}$ relative to F. In Table II the

TABLE II

COMPARISON OF PREDICTED AND MEASURED ORIENTATION RELATIONSHIPS IN FE–22% NI–0.8% C.

Corresponding directions	Measured angle	Predicted angle
$[1\bar{1}0]_F$—$[11\bar{1}]_B$	2.5°	2.7°
$[0\bar{1}1]_F$—$[1\bar{1}\bar{1}]_B$	6.5°	6.6°
$[1\bar{2}1]_F$—$[10\bar{1}]_B$	2.0°	1.9°
$(111)_F$—$(101)_B$	about 1°	0.2°

predicted angles between various corresponding directions and planes are compared with those measured by Greninger and Troiano [7; Figs. 3 and 6]. It is evident that the two sets of angles are in very good agreement. The greatest discrepancy (0.8°) is in the angle between $(111)_F$ and $(101)_B$ but this is of doubtful significance since it is not indicated in Greninger and Troiano's paper whether the angle was measured directly or obtained by graphical construction. Since a gnomonic projection was used the latter possibility seems the more likely, and in this case the discrepancy is not surprising. Notwithstanding its magnitude, the predicted displacement of the $(101)_B$-pole from the $(111)_F$-pole is, as far as can be judged, in the observed direction. The other three angles appear to have been rounded off and the values given are, in fact, inconsistent with a tetragonal structure with $\gamma = 1.045$. (The results imply an angle of not more than 69.0° between $[1\bar{1}\bar{1}]_B$ and $[11\bar{1}]_B$ whereas the correct angle is 69.3°). Thus, the small discrepancies in these three angles may be even further reduced, and since these three angles define the fourth, the estimate of 1° may need some amendment.

For this transformation the theory not only predicts the observed orientation relationship but also the observed orientation of the habit plane relative to both lattices. It is readily demonstrated that a pole figure showing the austenite axes, the predicted martensite axes and habit plane, can be rotated into coincidence with the pole figure determined by Greninger and Troiano [7; Fig. 6]. The theory, therefore, predicts the correct habit plane: not merely a plane of the correct form.

The orientation relationship derived from the $(\alpha+, \omega-)$-solution is simply a variant of the $(112)_B$-twin of the orientation just considered. Greninger and Troiano have observed twins on this plane so that all orientations predicted by the theory actually occur. However, the reported orientation is produced in preference to its twin. A rational explanation of this observation becomes apparent on carrying out the factorization into component strains of both the $(\alpha+, \omega+)$- and the $(\alpha+, \omega-)$-solutions. The homogeneous strains are, of course, variants of the same strain, while the inhomogeneous strains differ with respect to the fraction of the twinning shear involved. It is found [II-(9.8)] that 0.4077 of the twinning shear is involved in the $(\alpha+, \omega+)$-solution, while the other solution involves the fraction 0.5923. It is reasonable to suppose that the twin orientation is less favoured because of the larger fraction of the twinning shear that is involved in its formation.

The only experimental data which remain to be considered concern the magnitude and direction of the homogeneous strain. According to the theory

*The six-figure accuracy is needed to obtain self-consistent numerical results.

(II-§9) this strain is represented when referred to the basis F by the matrix

$$(6.2) \qquad ({}_F\mathbf{p}_1{}_F) = \mathbf{I} + m\,\mathbf{d}\mathbf{p}',$$

where

$$(6.3) \quad -\mathbf{d} = [0.21017, 0.61850, -0.75715]_F,$$

$$(6.4) \quad \mathbf{p}' = (0.18726, 0.55102, 0.81321)_F,$$

represent unit vectors parallel to the direction of the strain and the normal to the habit plane respectively, and

$$(6.5) \qquad m = 0.19144,$$

is the magnitude (I-§5) of this strain.

In their analysis of this strain, Greninger and Troiano assumed it to be a simple shear on the habit plane, and determined the shear direction as the intersection of the habit plane with a plane defined by direction of a specimen edge before and after transformation. If the theory is correct all such planes should intersect along the predicted direction (6.3). The observed scatter of Greninger and Troiano's shear direction is just that expected, provided all specimen edges studied were within about 60° of the normal to the habit plane. The direction of their trial shear "*A*" is about 1° from the projection of the predicted direction on the habit plane. The measured angles of shear range from 8° to 14° with a mean of about 11° which compares favourably with the prediction that the direction normal to the habit plane rotates by 11.0°. Thus, the theory is not inconsistent with these observations.

7. Machlin and Cohen's (259)-Transformation

Machlin and Cohen's [14] analysis of the transformation in Fe–30% Ni is the most recent measurement of the homogeneous strain accompanying the transformation. The predictions of the theory for this case are summarized below using $\gamma = 1$ and $\theta^2 = 0.647$.

The invariant line strain for α and ω positive now becomes

$$(7.1) \quad ({}_L\mathbf{S}_L) = \begin{pmatrix} 1, & -0.093129, & 0.308397 \\ 0, & 1.114712, & 0.016826 \\ 0, & 0.115080, & 0.935472 \end{pmatrix},$$

and $\cos\alpha = 0.301977$. The angle between $[1\bar{1}0]_F$ and $[11\bar{1}]_B$ is now 3.1°, while the angle between $(111)_F$ and $(101)_B$ is 24′. This orientation relationship is about ½° nearer the Nishiyama relationship than the previous one (§6). No precision determination of the orientation relationship has been made but the predicted orientation does lie within the scatter of the results obtained by the pole figure method [6; 15].

The homogeneous strain is given by an expression of the form (6.2) where

$$(7.2) \quad -\mathbf{d} = [0.23008, 0.63891, -0.73407]_F,$$

$$(7.3) \quad \mathbf{p}' = (0.20226, 0.56166, 0.80227)_F,$$

$$(7.4) \quad m = 0.22254,$$

while the inhomogeneous shear is 0.4031 of the twinning shear. Machlin and Cohen estimate that the homogeneous strain has a shear component of 0.20 and a component normal to the habit plane of 0.05; the corresponding values predicted by the theory are 0.219 and 0.041.

In comparing the predicted direction (7.2) with Machlin and Cohen's observations, it must be remembered that they were only able to measure the projection of the direction on the $(111)_F$-plane. In Figure 8, their measured direction is compared

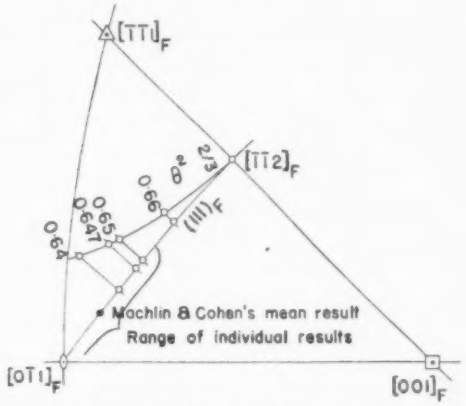

FIGURE 8. Stereographic projection showing the predicted variation (for $\gamma = 1$) of the direction of the homogeneous strain. The projection of this direction on the $(111)_F$-plane is compared with Machlin and Cohen's results.

with the projection of the predicted direction on this plane. The direction given by Machlin and Cohen is a mean of all their results. Since the scatter of their individual measurements is conservatively estimated, from the data in their Table I*, to be ±10° the agreement between theory and experiment is reasonable. The predicted direction is about 5° out of the $(111)_F$-plane which is consistent with the errors stated in Machlin and Cohen's paper [16].

The scatter of the habit planes determined by Machlin and Cohen (Fig. 7) corresponds to the range of θ^2 from 0.64 to 0.66. The use of the value

*The projection of $\mathbf{d}$ on the $(\bar{1}11)_F$-plane is $[t_{xz}/t_{yz}, 1, 0]$ referred to axes in the directions $[\bar{1}\bar{1}2]_F$, $[1\bar{1}0]_F$, $[111]_F$.

$\theta^2 = 0.647$ in the above comparisons is not of particular significance because the corresponding range of predicted directions lies almost entirely within the scatter of the experimental results (Fig. 8). If the scatter of the habit planes is real, it will be necessary to make measurements on individual martensite plates and then, perhaps, it may be possible to distinguish between the present hypothesis and those for which the complementary strain is either on the twinning plane or in the twinning direction.

8. The (225)-Transformations

In iron-carbon alloys containing less than 1.4% carbon the habit planes all contain a close-packed direction $\langle 110 \rangle_F$. Above 0.9%-carbon the habit planes are in the vicinity of $(225)_F$ (see Fig. 5), but as the carbon content is lowered below 0.9% the martensite plates degenerate first into laths and then into needles. Although the habit planes have not been determined in these cases the long axes of the crystals are in $\langle 110 \rangle_F$ directions. Accordingly in applying the theory to these transformations θ^2 is taken to have its maximum value. Thus, $\alpha = 90°$ and the invariant line is parallel to the twinning direction $[110]_F$ or $[11\bar{1}]_B$. Equation (4.10) for (LSL) now simplifies somewhat and it can readily be shown that the $(\alpha+, \omega+)$- and $(\alpha+, \omega-)$-solutions represent the same strain; similarly, for the other pair. Remembering the relations between solutions described in section 4, it follows that the variants are twin related in pairs. Hence, this group of transformations is a degenerate case of the general theory.

Since $[1\bar{1}0]_F$ and $[11\bar{1}]_B$ are now always parallel, the orientation relationships can be described conveniently by the angle ψ between the planes $(111)_F$ and $(101)_B$. The angle ψ increases as the pole $(101)_B$ moves from $(111)_F$ towards $(001)_F$ and is given by

$$\psi = \omega + \xi - \eta, \tag{8.1}$$

where ω is the angle (equation (4.11)) between $(110)_F$ and $(112)_B$, ξ the angle between $(101)_B$ and $(112)_B$, and η the angle between $(111)_F$ and $(110)_F$. Thus,

$$\left.\begin{aligned} \sin\omega &= (2-\gamma^2)^{\frac{1}{2}}[(2+\gamma^2)^{\frac{1}{2}} - \sqrt{2}\gamma]/2(2+\gamma^2)^{\frac{1}{2}}, \\ \sin\xi &= \gamma/\sqrt{2}(1+\gamma^2)^{\frac{1}{2}}, \\ \sin\eta &= 1/\sqrt{3}, \end{aligned}\right\} \tag{8.2}$$

and the calculated variation of ψ with γ is shown in Figure 9. The predicted orientation relationship is exactly that of Kurdjumow-Sachs for $\gamma = 1$ and never differs from it by more than about 15′. This is in agreement with the pole figure determinations of Kurdjumow-Sachs [3] and of Wassermann [17].

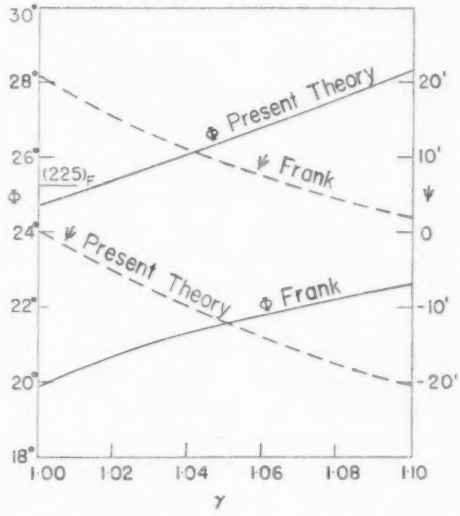

FIGURE 9. Comparison of the predictions of the present theory with that of Frank. Φ is the angle between the habt plane and $(111)_F$, and ψ the angle between the planes $(111)_F$ and $(101)_B$.

The homogeneous strain is given by an expression of the form (6.2) where

$$-\mathbf{d} = [(2-\gamma^2)^{\frac{1}{2}}, (2-\gamma^2)^{\frac{1}{2}}, -2\gamma]_F/\sqrt{2}(2+\gamma^2)^{\frac{1}{2}} \equiv [11\bar{2}]_F, \text{ for } \gamma = 1, \tag{8.3}$$

$$\mathbf{p}' = ((2-\gamma^2)^{\frac{1}{2}}, (2-\gamma^2)^{\frac{1}{2}}, \sqrt{2}(2+\gamma^2)^{\frac{1}{2}})_F/2\sqrt{2}, \equiv (2, 2, 4.90)_F, \text{ for } \gamma = 1, \tag{8.4}$$

$$m = 2[(2+\gamma^2)^{\frac{1}{2}} - \sqrt{2}\gamma]/(2+\gamma^2). \tag{8.5}$$

The inhomogeneous shear is always one-half of the twinning shear. It follows that twin orientations with same habit plane are produced equivalently and are therefore variants as stated above.

The above predictions for this special case are exactly the same as those obtained by Bowles [5] but differ somewhat from those of Frank [18]. Frank suggested that the habit plane is determined by the condition that the close-packed planes $(111)_F$, $(101)_B$ meet edge to edge in the habit plane. This is automatically true in the present theory provided that the $(111)_F$-plane intersects the habit plane (and the twinning plane) along the invariant line $[1\bar{1}0]_F$. This condition is satisfied in the present case ($\alpha = 90°$) but will not always hold, so that Frank's theory cannot be extended to more general cases.

The predictions of the two theories are compared

in Figure 9. The angle ψ (equation (8.1)) between the planes $(111)_F$ and $(101)_B$ is defined in the same way as in Frank's paper, while his angle ϕ between $(111)_F$ and the normal to the habit plane is here denoted by Φ and, on the present theory, is given by

$$\cos \Phi = [\sqrt{2}(2 - \gamma^2)^{\frac{1}{2}} + (2 + \gamma^2)^{\frac{1}{2}}]/2\sqrt{3}. \tag{8.6}$$

The curves labelled "Frank" have been computed from the equations in §-7 of Frank's paper using the uncorrected parameters given therein. The habit planes so predicted are clearly incompatible with observation. To improve the agreement Frank has suggested that before applying the theory the experimental lattice parameters should be adjusted so that the atoms in the $[1\bar{1}0]_F$, $[11\bar{1}]_B$ rows match. One way of doing this is to change all the parameters of one structure by the same factor; this is equivalent to the introduction of the dilatation δ in the present theory. When this is done the two theories give the same result. Frank employed a different method of correction but apparently applied the correction in the wrong sense for his procedure leads to even worse agreement with observation.

In the development of his theory Frank has taken as clues the parallelism of the close-packed directions $[1\bar{1}0]_F$, $[11\bar{1}]_B$, and the close parallelism of the close-packed planes $(111)_F$, $(101)_B$. He envisages a simple type of interface in which these planes meet edge to edge along these directions. In the development of the present theory the authors have argued (Part I) that twinning is of fundamental significance. The twinning plane $(112)_B$ is generated from $(110)_F$ and since, in the present theory, these planes always intersect along the invariant line they necessarily meet edge to edge in the interface in all cases. The agreement between the two theories for $(225)_F$-transformations stems from the coincidence that in these transformations the invariant line is $[1\bar{1}0]_F$ which also lies in the plane $(111)_F$.

9. Discussion

The general conclusion to be drawn from the preceding analysis of specific transformations is that the theory is in substantial agreement with the available experimental data, although this data is inadequate for a conclusive test. To distinguish between the present hypothesis and the alternative ones where the complementary shear is either on the twinning plane or in the twinning direction, measurements of properties such as the habit plane, orientation relationship, direction and magnitude of the homogeneous strain, will have to be made on individual martensite plates.

The present hypothesis provides a description of the overall atomic displacements produced by a transformation, which is certainly very nearly correct. If it is correct, the problem of finding suitable mechanisms for these transformations is reduced to discovering those which are compatible with the hypothesis; any such mechanism would automatically be consistent with all the geometrical properties of the transformations. It seems almost certain that a satisfactory mechanism will involve the motion of dislocations and the theory suggests that these dislocations will be related in some way to twinning in the final structure.

The theory contains one adjustable parameter, δ, which has been estimated from the observed habit plane. It may be asked what physical or geometrical requirement determines its value. If the requirement were purely geometrical, it might be hoped that its nature would emerge from a study of the transformations as a whole. Although this has not proved to be the case, an interesting feature of the iron-carbon group of transformations has been noticed and may be of some significance.

The habit planes observed in iron-carbon alloys containing 0–1.78% carbon are plotted in Figure 10, together with the predicted variation of the habit plane, for $\beta = 54° 44'$ ($\cos \beta = 1/\sqrt{3}$), and $\beta = 56° 20'$.* Along these latitude circles the

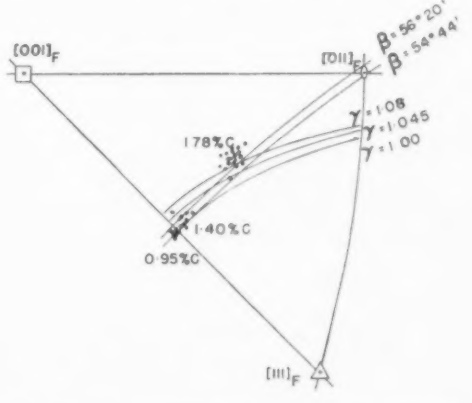

FIGURE 10. The same as figure 5, together with the lines along which β takes the values 54° 44′ and 56° 20′.

*For $\alpha = 90°$, $\tan (54° 44' - \Phi) = \cos \beta$, and then these values of β correspond to habit planes 30° and 29° from $(001)_F$ respectively.

angle ψ between the close-packed planes is zero and approximately 7′ respectively. Although the data is inadequate, it is in agreement with a requirement that as the carbon content increases ψ increases to about 7′ and thereafter remains approximately constant. As γ increases the transformations can be of the $(225)_F$-type until ψ reaches 7′; thereafter, the habit plane would move rapidly out into the centre of the triangle along the line $\beta = 56°\ 20'$, for the lines γ = const. cross the lines β = const. at a small angle. Such a rapid change of habit plane with γ could account for the reported discontinuous variation of the habit plane at 1.4% carbon [19].

Another feature of interest is that the latitude circle corresponding to $\cos\beta = 1/\sqrt{3}$ and $\psi = 0$, passes through $(011)_F$. If this latitude circle has any particular significance one might expect that a transformation with γ about $\sqrt{2}$ would have a habit plane in the neighbourhood of $(011)_F$. This is the case for transformations such as In-Tl [20; 21] or Cu-Mn [22]. These transformations are special cases of the present class.

References

1. Bowles, J. S. and Mackenzie, J. K. Acta Met. **2** No. 1 (1954). p. 129.
2. Jaswon, M. A. and Wheeler, J. A. Acta Cryst. **1** (1948) 216.
3. Kurdjumow, G. and Sachs, G. Z. Phys. **64** (1930) 325.
4. Lyman, T. Discussion to N. J. Petch. J. Iron Steel Inst. **147** (1943) 221.
5. Bowles, J. S. Acta Cryst. **4** (1951) 162.
6. Nishiyama, Z. Sci. Rep. Tohoku Univ. **23** (1934–35) 638.
7. Greninger, A. B. and Troiano, A. R. Trans. Amer. Inst. Min. (Metall.) Engrs. **185** (1949) 590.
8. Roberts, C. S. J. Metals **5** (1953) 203.
9. Owen, E. A., Yates, E. L. and Sully, A. H. Proc. Phys. Soc. **49** (1937) 315.
10. Bradley, A. J., Jay, A. H. and Taylor, A. Phil. Mag. **23** (7) (1937) 547.
11. Jette, E. R. and Foote, F. Trans. Amer. Inst. Min. (Metall.) Engrs. **120** (1936) 259.
12. Phragmén, G. J. Iron Steel Inst. **123** (1931) 465.
13. Barrett, C. S. Structure of Metals (New York, McGraw-Hill, 1943).
14. Machlin, E. S. and Cohen, M. J. Metals **3** (1951) 1019.
15. Mehl, R. F. and Derge, G. Trans. Amer. Inst. Min. (Metall.) Engrs. **105** (1937) 215.
16. Bowles, J. S. and Mackenzie, J. K. J. Metals **4** (1952) 1201.
17. Wassermann, G. Mitt. K. Wilh. Inst. Eisenforsch. **17** (1935) 149.
18. Frank, F. C. Acta Met. **1** (1953) 15.
19. Greninger, A. B. and Troiano, A. R. Trans. Amer. Inst. Min. (Metall.) Engrs. **140** (1940) 307.
20. Guttman, L. Trans. Amer. Inst. Min (Metall.) Engrs. **188** (1950) 1472.
21. Bowles, J. S., Barrett, C. S. and Guttman, L. Trans. Amer. Inst. Min (Metall.) Engrs. **188** (1950) 1478.
22. Christian, J. W. and Basinski, Z. S. J. Inst. Metals **80** (1952) 659.

SPONTANEOUS DEFORMATION OF AUSTENITE DURING MARTENSITIC TRANSFORMATIONS*

B. EDMONDSON† and T. KO†

Metallographic examination has shown that plastic deformation takes place in austenite during the martensitic transformations occurring in a 34 per cent Ni iron alloy during both heating and cooling. There is a permanent distortion remaining after all the martensite has reverted to austenite. This distortion is shown to have an important effect on the subsequent formation of martensite. Slip lines in austenite have also been observed in 18 per cent Ni 1 per cent C and 5 per cent Ni 1.5 per cent C steels. The effects of spontaneous deformation on the kinetics of martensitic transformation are discussed.

LA DÉFORMATION SPONTANÉE DE L'AUSTENITE LORS DES TRANSFORMATIONS MARTENSITIQUES

Un examen métallographique a permis de constater que l'austenite est déformée plastiquement lors des transformations martensitiques dans un alliage Fe-Ni à 34% de Ni, aussi bien au chauffage qu'au refroidissement. Une distortion permanente persiste après la transformation de toute la martensite en austenite. Il est montré que cette distortion joue un rôle important dans la formation ultérieure de martensite. Des lignes de glissement furent aussi observées dans des aciers à 18% de Ni 1% de C et à 5% de Ni 1,5% de C. On discute les effets de la déformation spontanée sur la cinétique des transformations martensitiques.

DIE SPONTANE VERFORMUNG VON AUSTENIT WÄHREND MARTENSITARTIGER UMWANDLUNGEN

Metallographische Untersuchungen einer 34% Ni-Eisenlegierung haben gezeigt, dass während der Martensittransformationen sowohl beim Erwärmen als auch beim Kühlen plastische Verformungen im Austenit auftreten. Selbst nachdem aller Martensit in Austenit zurückverwandelt worden war, verblieb eine permanente Verzerrung. Es wird gezeigt, dass diese Verzerrung einen wesentlichen Einfluss auf die künftige Martensitbildung hat. In 18% Ni, 1% C und 5% Ni, 1,5% C Stählen wurden ebenfalls Gleitlinien im Austenit beobachtet. Die Einflüsse der spontanen Verformung auf die Kinetik der Martensittransformationen werden erörtert.

1. Introduction

Despite the considerable interest shown recently in martensitic transformations, complete understanding of their mechanism and kinetics has not yet been attained. One of the most important problems yet to be solved concerns the factors which determine the amount of martensite forming under given conditions. The phenomena which must be explained are:

(i) The athermal nature of the transformation usually observed.

(ii) The isothermal formation of martensite in certain alloys.

(iii) The stabilization and conditioning of the high temperature phase with respect to further transformation.

(iv) The effect of externally applied deformation.

(v) The temperature hysteresis between the transformations occuring during cooling and heating in most reversible martensitic transformations.

Most theories [1; 2; 3] have attempted to solve the problem from the standpoint of nucleation and suggest that the factor controlling the amount of martensite obtained is the availability of martensite nuclei for transformation. The effects of external variables (temperature, stress, ageing, etc.), it is suggested, are due to changes in the availability of these nuclei as a result of the variation of these external factors.

Recently, the suggestion has been made that one of the important factors determining the amount of martensite at a given temperature is the resistance of the parent phase to the growth of the nuclei of the new phase. According to this view, the rapid movement of the coherent austenite-martensite interfaces is hindered by imperfections such as dislocations, lattice defects, or aggregates of solute atoms, and some driving force must be provided to overcome these obstacles before the growth of the martensite can proceed. The interaction of such imperfections with the interfaces will be quite different from that during a slow transformation, even in the case of a slow shear transformation such as the formation of bainite [4; 5], when there is time for thermal agitation to play a part. This view has been applied by Morgan and Ko [6] to explain the phenomenon of thermal stabilization of austenite.

The 'growth-resistance of austenite' hypothesis of athermal formation of martensite considers that,

*Received October 9, 1953.

†Department of Metallurgy, University of Birmingham, England.

when a martensite plate forms, more imperfections are generated in the surrounding austenite by plastic deformation due to the volumetric and shear strains; the formation of martensite from this deformed austenite is thus rendered more difficult and a greater driving force is required before the austenite can transform further. This extra driving force can be provided by further cooling of the austenite.

Recently, Geisler [7] has postulated that the irrational habit planes of martensite observed may be the result of such plastic deformation, which he suggested should be called spontaneous deformation.

Before the 'growth-resistance' hypothesis can be considered plausible, it is necessary to demonstrate conclusively that a reasonable amount of plastic deformation of austenite accompanies the formation of martensite and that the deformation has an effect on the subsequent transformation. The present work consists of a metallographic examination directed towards this end.

2. Experimental

An iron nickel alloy containing 34 per cent Ni, prepared by vacuum-melting electrolytic iron and carbonyl nickel, was used, since:

(i) The transformation is reversible and the effect of any deformation on subsequent re-transformation could be studied.

(ii) As the cooling transformation takes place below room temperature, and most of the heating transformation above it, the examination of relief effects after transformation could conveniently be made.

(iii) Some indication of plastic deformation during transformation in a similar alloy has been observed [8].

Specimens were austenitized *in vacuo* at 1220°C for one week, and water-quenched to room temperature. They were then electrolytically polished and partly transformed by quenching to various temperatures down to −189°C. Dilatometric measurements indicated that the cooling transformation took place mainly below −60°C and the reverse transformation during heating at about 0°C. There was some inhomogeneity in the alloy which was not removed completely after long annealing, and the temperature difference observed between M_s during cooling and that during heating may not be the true hysteresis in a uniform 34 per cent Ni iron alloy. To accomplish the reverse transformation, the specimens were rapidly heated *in vacuo* to 450°C.

The observations and the conclusions reached are not in any way affected by the presence of heterogeneity in the material, because important and critical observations were normally made on the same locations in a specimen.

2.1 *Spontaneous Deformation of Austenite*

The specimen surface after partial transformation to martensite is illustrated in Figures 1 to 5. Sets of fine lines outlining crystallographic directions were observable on the surface. Stereographic analyses showed that, within the experimental scatter, they lay in {111} planes of the austenite. These lines when resolvable appeared in clusters and formed steps on the surface (Figures 1 and 2).

These fine lines were not observed in the regions of austenite remote from any martensite. It is certain therefore thay they were slip lines formed during the formation of martensite and that their appearance was a direct result of the transformation and not caused by stresses set up on quenching.

When these lines were intersected by a martensite plate, they were always bent at the austenite-martensite interface. Evidently the slip lines were already present, produced by previous transformation, when the intersecting martensite plate formed and were bent by the shear associated with the transformation in the same way that scratches on the surface are distorted (see for example, [9]).

Slip lines were also observed in an 1.0 per cent C 18 per cent Ni steel, though on a much finer scale. They were not observable on the surface of a 1.5 per cent C 5 per cent Ni alloy, but could be revealed within the specimen by tempering, during which precipitation of carbide presumably took place along the slip lines (Figure 6). The deformation in the region shown in this photograph was so severe that the fine martensite needles were heavily distorted. It has also been observed that martensite plates are broken up into several portions in regions where plastic deformation is severe.

When a partly martensitic specimen, untouched after transformation, was heated to 400°C, the reverse transformation was complete and all the martensite was removed. The surface, however, remained distorted. Three phenomena were observed (compare Figure 3 with Figure 7, and Figure 5 with Figure 8): (i) The number of slip lines in the austenite increased; (ii) there was a residual tilting of the areas formerly occupied by the martensite; and (iii) these areas were rippled (Figure 9).

Figure 3 also shows a martensite plate which

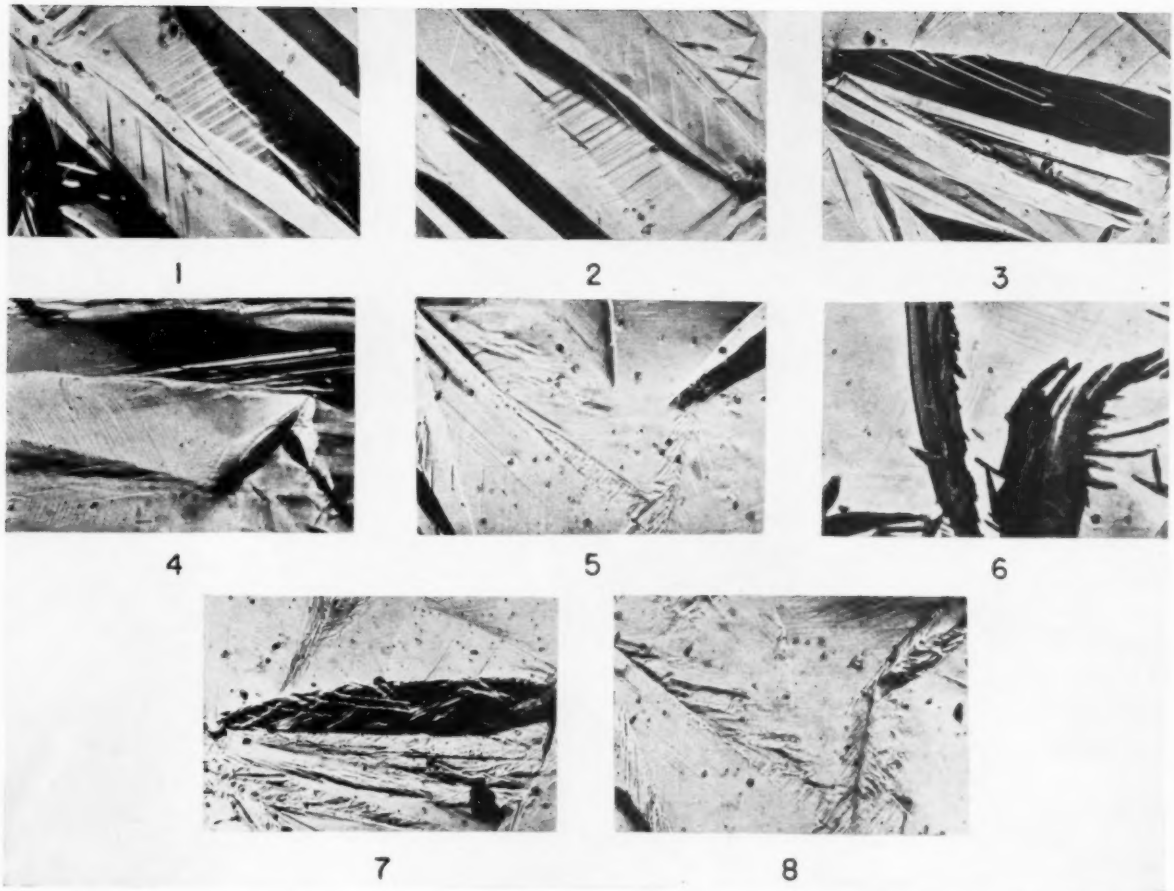

PLATE I (All figures reduced to two-thirds in reproduction). Figure 1—Iron nickle alloy. Oblique illumination. Surface relief and slip lines in austenite due to martensite formation. ×250. Figure 2—As Fig. 1, rotated through 180°. Figure 3—Iron nickel alloy. Oblique illumination. Surface relief and slip lines in austenite due to martensite formation. ×250. Figure 4—Iron nickel alloy. Oblique illumination. Surface relief and slip lines in austenite due to martensite formation. ×250. Figure 5—Iron nickel alloy. Oblique illumination. Surface relief and slip lines in austenite due to martensite formation, and residual distortion after reverse transformation. ×250. Figure 6—5% Ni 1.5% C steel. Quenched from 1200° to −33°C and tempered at 450°C. Slip lines in austenite and distortion of martensite. ×1200. Figure 7—Iron nickel alloy. Oblique illumination. Same as Fig. 3, but after reheating to 450°C. Residual distortion after reverse transformation. ×220. Figure 8—Iron nickel alloy. Oblique illumination. Same as Fig. 4, but after reheating to 450°C. Residual distortion after reverse transformation. ×250.

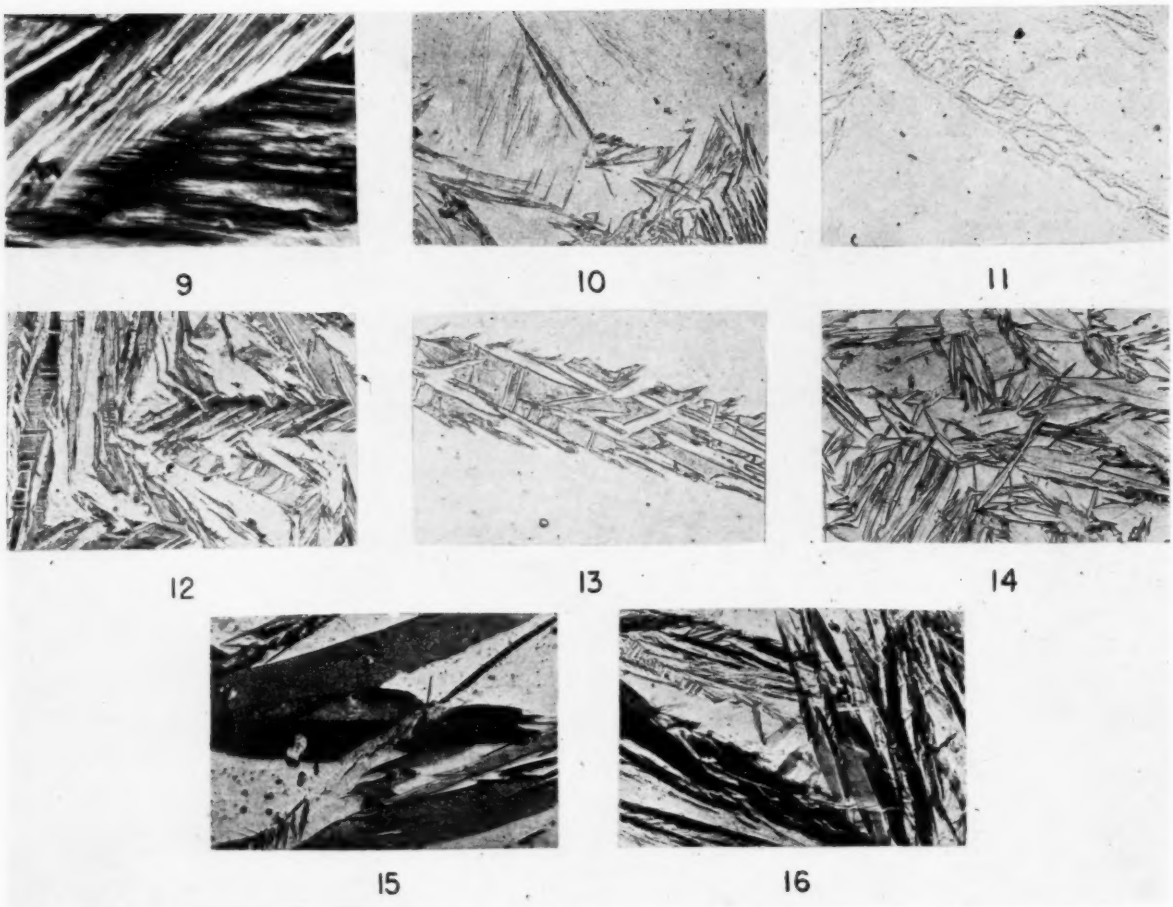

PLATE II (all figures reduced to two-thirds in reproduction). Figure 9—Iron nickel alloy. Oblique illumination. Distortion in the transformed region after reverse transformation. ×2000. Figure 10—Iron nickel alloy. Ghost structure of martensite after reverse transformation and martensite formed after second cooling. Etched with 4% nital. ×200. Figure 11—Iron nickel alloy. Recrystallization at the martensitic sites. Annealed 4 hours at 800°C after reverse transformation. Etched with 4% nital. ×800. Figure 12—Iron nickel alloy. Martensite formed during second cooling. Etched with nital. ×200. Figure 13—Iron nickel alloy. Martensite formed during second cooling. Etched with nital. ×500. Figure 14—Iron nickel alloy. Martensite formed from virgin austenite. Etched with nital. ×200. Figure 15—Iron nickel alloy. Oblique illumination. Martensite formed during second cooling. Etched with nital. ×500. Figure 16—Iron nickel alloy. Oblique illumination. Surface distortion due to cooling and heating transformations and retransformation on second cooling to −189°C. ×350.

contained several twins. The surface tilt due to the twinning of the martensite was clearly seen and was retained after the reverse transformation was carried out (Figure 7).

Deformation by slipping in the austenite during reverse transformation was also demonstrated by reheating a specimen, which had been polished after sub-zero quenching, thus removing the surface distortion and slip lines due to the first cooling transformation. The plastic deformation in the untransformed austenite during reverse transformation was not so extensive as during cooling, as considerable deformation took place in the regions which had been martensitic before the reverse transformation set in. This concentration of plastic deformation in the transforming regions was probably due to the restriction of slipping within them by their permanent tilting, and by the previous hardening of the untransformed surrounding austenite.

Scheil [10] has reported the appearance of deformation markings on the surface of a polished specimen (*loc. cit.* Figure 31, p. 35). He suggested that they were slip lines in the austenite associated with the formation of martensite underneath the surface. This explanation is doubtful, and comparison of his photograph with Figure 8 clearly shows that the markings in Scheil's photograph were very similar to the residual deformation after reverse transformation in the regions which were formerly martensitic. Presumably reverse transformation had begun in his specimen between quenching and examination. This had happened in the specimen shown in Figure 5.

The residual deformation after reverse transformation in the austenite regions formerly occupied by martensite could be revealed by heavily etching a polished specimen after one complete cycle of cooling and heating. Figure 10 shows the ghost structure of the martensitic regions, which appeared very differently from the true martensite plates present. The heavy residual deformation was also demonstrated by recrystallization in these regions when the specimen was annealed at higher temperatures after the reverse transformation had been carried out (Figure 11).

2.2 *Effects of Spontaneous Deformation on the Subsequent Transformation*

If the spontaneous deformation has an effect on the subsequent formation of martensite, it may be expected that:

(i) The appearance of martensite plates formed from the imperfect austenite may be different from that of plates formed from a virgin austenite, and

(ii) The amount of martensite at a given temperature should be less in a specimen which has been subjected to cooling and heating transformation cycles, unless recovery sets in during heating so as to cause 'conditioning.'

Both of these effects have been observed. Figures 12 and 13 show the martensite formed from austenite which had been subjected to one complete cycle of transformation before quenching. Compared with the martensite formed from virgin austenite (Figure 14) the martensite plates from imperfect austenite were fragmented, although the general shape was maintained. The interference of the formation of martensite during second cooling by the ghost of a martensite plate is also illustrated in Figure 15.

Figure 16 shows the surface structure of a specimen after re-transformation without intermediate polishing. It is obvious that the new martensite plates did not form during the second cooling in the same places as the first generation of plates. This is very different from the thermoelastic martensite observed by Kurdjumov and Khandros [11] in a CuAlNi alloy, in which the martensite transformation is probably accompanied by little spontaneous deformation.

The cumulative effect of spontaneous deformation in depressing the martensitic transformation has also been observed. It was found that after 15 cycles of cooling and heating between −189° and 450°C, no transformation took place on subsequently cooling the specimen to −189°C. This could also be accomplished by externally applied plastic deformation.

3. Discussion

The present investigation has shown that, in a 34 per cent Ni iron alloy:

(i) Plastic deformation takes place during the formation of martensite, mainly by slipping in the austenite. Slip lines in austenite have also been observed in 1 per cent C 18 per cent Ni and 1.5 per cent C 5 per cent Ni steels.

(ii) Plastic deformation also occurs during the reverse transformation from martensite to austenite during heating. This occurs mainly by deformation in the regions originally occupied by martensite, although some slipping also occurs in the untransformed austenite. The residual deformation in austenite after a complete cycle of cooling and heating transformations consists, therefore, of (*a*) slipping in austenite, (*b*) severe deformation in the regions transformed to martensite during

cooling, (*c*) any twinning which may have occurred in the martensite during its formation, and (*d*) a permanent surface tilt of the martensitic regions.

(iii) The severe deformation in the martensitic regions after a complete cycle of transformations has an obstructing effect on the formation of martensite during subsequent cooling.

(iv) The martensite plates formed during the second cooling do not occupy the same sites as the plates formed during the first cooling; evidently the spontaneous deformation renders the original nuclei ineffective.

3.1 *Spontaneous Deformation and Athermal Martensitic Transformation*

The effect of spontaneous deformation on the subsequent formation of martensite is evident during second cooling after a complete transformation cycle. It is less easy to demonstrate directly, however, its effect on the transformation during first cooling. It might be argued that the remarkable fragmentation of martensite formed from austenite which had been subjected to a previous transformation cycle was solely associated with the reversion of martensite to austenite; the fragmentation is not direct evidence that the suggested obstructing effect exists in the case of transformation from virgin austenite.

However, if the disturbances cause a complete stoppage of growth of martensite through these regions, it is reasonable to expect that the lighter disturbance of austenite due to spontaneous deformation during first cooling will cause an increase in the resistance to the movement of austenite-martensite interfaces during the growth of martensite. Although martensite eventually formed can pass through slip bands, or even through deformation bands [12], the transformation of regions containing concentrations of imperfections must consume some extra energy. In the extreme case, the growth of martensite may be completely prevented by the presence of slip bands, as was observed by Scheil [13] and others [14].

Furthermore, the deformation in the residual austenite after a considerable amount of martensite has formed must be very heavy and cannot be very different from that occurring during a complete cycle of transformation.

In addition to the above direct effect of increasing obstruction to the movement of a coherent interface due to an increase in the number of imperfections of various kinds, there is also the indirect effect of work-hardening of the austenite. Plastic deformation of the austenite will render more difficult further spontaneous deformation and the formation of more martensite, as this must be accompanied by further deformation. Considering also the well-established observation that external plastic deformation of austenite has a stabilizing effect on its subsequent transformation, it can only be concluded that the formation of martensite becomes progressively more difficult as the transformation proceeds in regions which become progressively more deformed. A continually increasing driving force must be provided therefore if the transformation is to continue. The athermal nature of the heating transformation can be explained in a similar manner, since it is also accompanied by plastic deformation.

The observation of plastic deformation in austenite in three alloys does not demonstrate conclusively that all martensitic transformations are accompanied by plastic deformation, but since these alloys cover a wide range of carbon composition up to 1.5 per cent carbon, there are sufficient grounds to believe that plastic deformation takes place in all steels during the formation of martensite, and probably in all martensitic transformations in which the volumetric and shear strains are large.

It is likely that the factors affecting the 'growth-resistance' of austenite—the slip mechanism, the amounts of work-hardening and recovery obtained, and the effect of the imperfections—all vary considerably with temperature and with the composition of the steel. Probably this can account, in part at least, for the wide temperature range between M_s and M_f (the temperature at which further transformation to martensite becomes negligible) and for the greater amounts of austenite retained at M_f as the carbon and alloying element contents increase.

It may also be expected that, as plastic deformation is easier in a single crystal of austenite than in a polycrystalline specimen, the formation of martensite in a single crystal of austenite should take place within a narrower range of transformation, and, if the difference between M_0 (the temperature at which austenite and martensite are in thermodynamic equilibrium) and M_s is partly due to the resistance of austenite to shear transformation, M_s should also be higher for the monocrystalline austenite. This is in agreement with the observation [15] that austenite grains electrolytically isolated from an 18 per cent Cr 8 per cent Ni 3 per cent Mo 1 per cent Ti steel, which has an M_s

below room temperature in the polycrystalline state, were martensitic at room temperature and remained unchanged on further quenching to −189°C.

The energy required to overcome the resistance of the parent phase to the growth of a new phase is of a nonreversible kind, unlike that required to fulfill surface energy and strain energy requirements. Energy of the latter kind stored in a transformed specimen would assist the reverse transformation, whereas nonreversible energy must be supplied again before the reverse transformation can occur. Thus the concept of resistance to motion of the austenite-martensite interfaces may well explain, in part, the temperature hysteresis between the cooling and heating transformations.

3.2 *Spontaneous Deformation and Interfacial Coherency*

It has been suggested [1] that plastic deformation in austenite which occurs when a martensite plate grows to its full size, will destroy the coherency of the austenite-martensite interface and thus cause the cessation of growth. A similar suggestion has also been made by Frank [16]. The deformation required by these theories cannot be identified with that observed in the present investigation. In fact, Ko [17] has observed, in support of his theory of bainite formation [4; 5], that martensite can thicken or grow coherently into bainite during tempering, and concluded that the austenite-martensite interfaces remain coherent after the initial growth of a martensite plate has ceased.

4. Conclusion

The observation of spontaneous deformation during the transformation of austenite to martensite and of the effect of this deformation on the subsequent transformation, together with the known stabilizing effect of external plastic deformation on the spontaneous transformation to martensite, provide sufficient grounds for the belief that the athermal nature of martensitic transformations is, partly at least, related to the spontaneous deformation associated with the transformation. It appears likely that theories based solely on nucleation and not considering the factors discussed above, even when the energy contribution due to stresses [18] has been taken into consideration, are oversimplified. A more quantitative study of the spontaneous deformation and the effect of the deformation on nucleation and growth of martensite, and a careful investigation of spontaneous deformation, if any, associated with isothermal martensite, will assist in achieving a better understanding of martensitic transformations.

Acknowledgements

The investigations were made in the Department of Metallurgy, the University of Birmingham, England, under the general direction of the late Professor D. Hanson, to whom the authors' gratitude is due for his encouragement. The work was carried out while one of the authors (B. E.) was in receipt of a maintenance allowance from the Department of Scientific and Industrial Research.

References

1. KURDJUMOV, G. V. Z. Tek. Fiz. **18** (1948) 999.
2. FISHER, J. S., HOLLOMAN, J. H., TURNBULL, D. Trans. Amer. Inst. Min. Met. Eng. **185** (1949) 691.
3. COHEN, M., MACHLIN, E. S. and PARANJPE, V. G. Thermodynamics in Physical Metallurgy (Cleveland, Amer. Soc. Metals, 1950) p. 242.
4. KO, T. J. Iron Steel Inst. (1953). In the press.
5. KO, T. and COTTRELL, S. A. J. Iron Steel Inst. **172** (1952) 307.
6. MORGAN, E. R. and KO, T. Acta Met. **1** (1953) 36.
7. GEISLER, A. H. Acta Met. **1** (1953) 260.
8. MACHLIN, E. S. and COHEN, M. Trans. Amer. Inst. Min. Met. Eng. **191** (1951) 746.
9. BOWLES, J. S. and BARRETT, C. S. Progress in Metal Physics, vol. 3 (London, Pergamon Press, 1952) p. 1.
10. SCHEIL, E. Harterei-Technishe Mitteilunge **5** (1952) 9.
11. KURDJUMOV, G. V. and KHANDROS, L. G. Dok. Akad. Nauk. SSSR. **66** (1949) 211.
12. BOWLES, J. S. and CLIFTON, D. Quoted by Bowles and Barrett [9].
13. SCHEIL, E. Z. anorg. Chem. **207** (1932) 21.
14. KO, T. and OTTE, H. M. Unpublished work.
15. HOAR, T. P. and BOWEN, K. W. J. Trans. Amer. Soc. Metals **45** (1953) 443.
16. FRANK, F. C. Acta Met. **1** (1953) 15.
17. KO, T. Acta Met. **2** (1954) 75.
18. FISHER, J. C. and TURNBULL, D. Acta Met. **1** (1953) 310.

THERMODYNAMICS OF THE LIQUIDUS AND THE SOLIDUS OF BINARY ALLOYS*

CARL WAGNER†

(1) For alloys completely miscible in the liquid and the solid state, formulae are derived in order to calculate from the phase diagram the difference in the excess integral molar free energies of the solid and the liquid phase, which is essentially equal to the strain energy due to the difference in size of the constituent atoms.

(2) The width of the gap between the liquidus and the solidus in the system Ag–Au is calculated to be 1.3°at $N_{Au} = 0.5$ in contrast to an experimental value of 10°. The divergence between the calculated and the observed value is due to incomplete attainment of equilibrium during thermal analysis.

(3) Formulae for the liquidus and the solidus in the vicinity of a minimum are derived and applied to the system Au–Cu.

LA THERMODYNAMIQUE DU LIQUIDUS ET DU SOLIDUS DES ALLIAGES BINAIRES

(1) Des formules sont dérivées pour le calcul, à partir du diagramme des phases, de l'excès des énergies libres, molaires, du solide et du liquide, dans le cas de solubilité complète dans l'état liquide et dans l'état solide. Cet excès est essentiellement égal à l'énergie de déformation due à la différence entre les dimensions des atomes constituants.

(2) La valeur calculée de l'espacement entre le liquidus et le solidus, dans le système Ag–Au, est de 1.3° à $N_{Au} = 0.5$, alors que la valeur expérimentale est de 10°. Cette différence entre la valeur calculée et la valeur expérimentale est due au fait que l'équilibre n'est pas atteint pendant l'analyse thermique.

(3) On dérive des formules pour le liquidus et le solidus au voisinage d'un minimum et on les applique au système Au–Cu.

THERMODYNAMIK DER LIQUIDUS- UND SOLIDUSKURVE VON BINÄREN LEGIERUNGEN

(1) Für Legierungen, die sowohl im festen wie auch im flüssigen Zustand völlig mischbar sind, werden Formeln abgeleitet, um aus dem Phasendiagram die Differenz der überschüssigen freien Energien (pro Mol) der festen und flüssigen Phase zu berechnen. Diese Differenz ist praktisch gleich der durch die Grössenunterschiede der Legierungsatome hervorgerufenen Verzerrungsenergie.

(2) Die Breite der Lücke zwischen der Liquidus- und der Soliduskurve im System Ag-Au wurde bei $N_{Au} = 0.5$ zu 1.3° im Gegensatz zu dem experimentellen Wert von 10° berechnet. Die Diskrepanz zwischen dem berechneten und dem experimentell beobachteten Wert kann auf ein nicht vollständig erreichtes Gleichgewicht während der thermischen Analyse zurückgeführt werden.

(3) Formeln für die Liquidus- und die Soliduskurve in der Umgebung eines Minimums werden abgeleitet und auf das System Au-Cu angewandt.

Introduction

If the free energies of the liquid and the solid phase of a binary alloy are given as functions of composition and temperature, the liquidus and the solidus may be derived from the condition that the partial molar free energies of each component must be equal in coexisting phases. In many cases, the solidus and the liquidus are more easily obtainable than the free energy functions. Consequently, one may try to deduce free energy functions from data given by the phase diagram.

Scheil [1] and Chipman [2] have derived relatively simple formulae for the case that the coexisting solid phase contains practically only one component and the liquid phase is a regular solution.

If the concentrations of the two components in the liquid and the solid phase are of the same order of magnitude, one may assume special functions for the concentration dependence of the molar free energies and then determine the parameters of these functions which are compatible with observations of the liquidus and the solidus as has been suggested by Seltz [3; 4] and Scatchard and Hamer [5]. The accuracy of the values obtained in this way, however, is limited because of the lack of accuracy of most phase diagram data and the special assumptions used for the representation of the concentration dependence of the molar free energies.

If an alloy exhibits complete miscibility in both the liquid and the solid state, the liquidus and the solidus lie in general close together. In the following it is shown that under these conditions it is profitable to calculate the difference of the excess free energies in the solid and in the liquid state rather than quantities for the individual phases.

*Received October 13, 1953.

†Department of Metallurgy, Massachusetts Institute of Technology, Cambridge, Mass., U.S.A.

Evaluation of the Terminal Slopes of the Liquidus and the Solidus of an Alloy Completely Miscible in the Liquid and the Solid State

According to Scatchard [6] the partial molar free energy $\bar{F}_i$ of component i in a mixture involving mole fraction N_i may be expressed as the sum of the partial molar free energy of a hypothetical ideal mixture and the "excess partial molar free energy" $F_i^E = RT \ln \gamma_i$ where γ_i is the activity coefficient defined for pure substance i as reference state. Thus

$$\bar{F}_i = F_i^\circ + RT \ln N_i + F_i^E \tag{1}$$

where F_i° is the molar free energy of pure component i in the phase under consideration.

At the melting point T_{mi} of pure component i the molar free energies of component i in the liquid and the solid state, $F_i^{\circ(l)}$ and $F_i^{\circ(s)}$, respectively, are equal. The difference $F_i^{\circ(l)} - F_i^{\circ(s)}$ at a temperature sufficiently close to T_{mi} may then be expressed as

$$F_i^{\circ(l)} - F_i^{\circ(s)} = -(T - T_{mi})\,\Delta S_{fi}^\circ \tag{2}$$

where ΔS_{fi}° is the entropy of fusion of component i.

The partial molar free energies of any constituent i in coexisting liquid and solid phases are equal. Thus

$$\bar{F}_i^{(l)} - \bar{F}_i^{(s)} = 0, \tag{3}$$

or in view of Eqs. (1) and (2),

$$-(T - T_{mi})\,\Delta S_{fi}^\circ + RT \ln N_i^{(l)} - RT \ln N_i^{(s)} + F_i^{E(l)}(T, N_2^{(l)}) - F_i^{E(s)}(T, N_2^{(s)}) = 0, \tag{4}$$

where quantities referring to the liquid and the solid state are marked by superscripts (l) and (s), respectively.

For small concentrations of component 2, the difference between the melting point T_{m1} of pure component 1 and the equilibrium temperature Θ of an alloy may be calculated with the help of the generalized van't Hoff formula for the depression of the freezing point,

$$T_{m1} - \Theta = (N_2^{(l)} - N_2^{(s)})\,RT_{m1}/\Delta S_{f1}^\circ \tag{5}$$

if $N_2^{(l)} \ll 1, \quad N_2^{(s)} \ll 1.$

Substituting $T_{m1} = T$ in equation (4) for $i = 2$, the distribution ratio of component 2 between the solid and the liquid phase is obtained as

$$\frac{N_2^{(s)}}{N_2^{(l)}} = \exp\left[\frac{-(T_{m1} - T_{m2})\,\Delta S_{F2}^{\ 0} - (F_2^{E(s)} - F_2^{E(l)})_{N_2=0}}{RT_{m1}}\right] \tag{6}$$

if $N_2^{(l)} \ll 1, \quad N_2^{(s)} \ll 1, \quad$ and $\quad T_{m1} \sim T_{m2}.$

Upon elimination of $N_2^{(s)}$ from equation (5) with the aid of equation (6), it follows that

$$-\left(\frac{\partial\theta}{\partial N_2^{(l)}}\right)_{N_2^{(l)}=0} = \frac{RT_{m1}}{\Delta S_{f1}^\circ}\left\{1 - \exp\left[\frac{-(T_{m1} - T_{m2})\,\Delta S_{f2}^\circ - (F_2^{E(s)} - F_2^{E(l)})_{N_2=0}}{RT_{m1}}\right]\right\}. \tag{7}$$

If conversely $N_2^{(l)}$ is eliminated from equation (5), it follows that

$$-\left(\frac{\partial\theta}{\partial N_2^{(s)}}\right)_{N_2^{(s)}=0} = \frac{RT_{m1}}{\Delta S_{f1}^\circ}\left\{\exp\left[\frac{(T_{m1} - T_{m2})\,\Delta S_{f2}^\circ + (F_2^{E(s)} - F_2^{E(l)})_{N_2=0}}{RT_{m1}}\right] - 1\right\}. \tag{8}$$

The excess partial molar free energies of components 1 and 2 in any phase of a binary mixture and the integral molar free energy F^E (= molar free energy of the real mixture minus molar free energy of a hypothetical ideal mixture) are interrelated by

$$F_1^E = F^E + (1 - N_1)(\partial F^E/\partial N_1) \tag{9a}$$

$$F_2^E = F^E + (1 - N_2)(\partial F^E/\partial N_2). \tag{9b}$$

Since the integral excess molar free energy vanishes for a pure component, i.e., $F^E = 0$ if $N_2 = 0$ or $N_2 = 1$, it follows from equation (9b) that

$$(F_2^{E(s)} - F_2^{E(l)})_{N_2=0} = [\partial(F^{E(s)} - F^{E(l)})/\partial N_2]_{N_2=0}. \tag{10}$$

Upon solving equation (7) for $F_2^{E(s)} - F_2^{E(l)}$ and using equation (10),

$$[\partial(F^{E(s)} - F^{E(l)})/\partial N_2]_{N_2=0} = -(T_{m1} - T_{m2})\,\Delta S_{f2}^\circ - RT_{m1} \ln\left[1 + \frac{\Delta S_{f1}^\circ}{RT_{m1}}\left(\frac{\partial\theta}{\partial N_2^{(l)}}\right)_{N_2^{(l)}=0}\right]. \tag{11}$$

Likewise, upon solving equation (8) for $F_2^{E(s)} - F_2^{E(l)}$ and using equation (10),

$$[\partial(F^{E(s)} - F^{E(l)})/\partial N_2]_{N_2=0} = -(T_{m1} - T_{m2})\,\Delta S_{f2}^\circ + RT_{m1} \ln\left[1 - \frac{\Delta S_{f1}^\circ}{RT_{m1}}\left(\frac{\partial\theta}{\partial N_2^{(s)}}\right)_{N_2^{(s)}=0}\right]. \tag{12}$$

Analogous equations are obtained for a dilute solution of component 1 in component 2 as solvent.

According to Scatchard and Hamer [7] and Guggenheim [8] the excess molar free energy of a solid or liquid mixture may be represented by the empirical formula

$$(13)\quad F^E = N_1N_2[A_0 + A_1(N_1 - N_2) + \ldots] = (1 - N_2)\,N_2[A_0 + A_1(1 - 2N_2) + \ldots]$$

where A_0 and A_1 are constants and eventually higher terms may be added. Consequently, the difference $F^{E(s)} - F^{E(l)}$ for a given mole fraction $N_2 = N_2^{(l)} = N_2^{(s)}$ may be represented as

$$(14)\quad F^{E(s)} - F^{E(l)} = (1 - N_2)\,N_2[\Delta A_0 + \Delta A_1(1 - 2N_2) + \ldots],$$

where ΔA_0 and ΔA_1 are the differences of the corresponding constants for the solid and the liquid state. If the liquid and the solid phases are virtually regular solutions and the difference between the melting points of the components is not large, the temperature dependence of the coefficients ΔA_0 and ΔA_1 may be disregarded. Differentiating equation (14) with respect to N_2 at $N_2 = 0$ and $N_2 = 1$ and disregarding higher terms, obtain two equations involving ΔA_0 and ΔA_1. Upon solving these equations for ΔA_0 and ΔA_1 as unknowns, it follows that

$$(15a)\quad \Delta A_0 = \tfrac{1}{2}\{[\partial(F^{E(s)} - F^{E(l)})/\partial N_2]_{N_2=0} - [\partial(F^{E(s)} - F^{E(l)})/\partial N_2]_{N_2=1}\}$$

$$(15b)\quad \Delta A_1 = \tfrac{1}{2}\{[\partial(F^{E(s)} - F^{E(l)})/\partial N_2]_{N_2=0} + [\partial(F^{E(s)} - F^{E(l)})/\partial N_2]_{N_2=1}\}.$$

Upon substitution of equation (15*a*) in equation (14), the value of $F^{E(s)} - F^{E(l)}$ at $N_2 = 0.5$ is obtained as

$$(16)\quad [F^{E(s)} - F^{E(l)}]_{N_2=0.5} = \tfrac{1}{4}A_0 = \tfrac{1}{8}\{[\partial(F^{E(s)} - F^{E(l)})/\partial N_2]_{N_2=0} - [\partial(F^{E(s)} - F^{E(l)})/\partial N_2]_{N_2=1}\}.$$

In most alloys exhibiting complete miscibility in both the liquid and the solid state, the melting points of the two components differ by not more than 20 per cent and the molar entropies of fusion are approximately equal. If the solidus and the liquidus are nearly straight lines interconnecting the melting points of the pure components, the values of $\partial(F^{E(s)} - F^{E(l)})/\partial N_2$ for $N_2 = 0$ and $N_2 = 1$ are much less than RT as readily follows by using a series expansion for the logarithm in equation (11). The same is true for the coefficients ΔA_0 and ΔA_1 and the value of $F^{E(s)} - F^{E(l)}$ for the whole concentration range. For instance, this is the case with the systems Ag–Au and Cu–Ni, i.e., deviations from ideality are virtually equal in the solid and in the liquid state. Numerical values are not presented since percentage wise the limits of error are very high.

Significant results, however, are obtained with alloys whose liquidus and solidus are not virtually straight lines, especially if there is a pronounced minimum of the liquidus and the solidus. Substituting experimental values for the terminal slopes of the liquidus of the system Au–Cu [9; 10] in equation (12) and using equations (14), (15*a*), and (15*b*), we obtain

$$(17)\quad F^{E(s)} - F^{E(l)} = (1 - N_{Cu})\,N_{Cu}[1700 + 190(1 - 2N_{Cu})]\ \text{cal.}$$

According to equation (17), $F^{E(s)} - F^{E(l)}$ equals 418 cal at $N_{Cu} = 0.4$ in close agreement with the value of 421 cal derived below from the minimum of the liquidus and listed in Table I.

For a regular solution the excess integral molar free energy equals the molar heat of mixing. Thus, if both the solid and the liquid phase are virtually regular solutions, $F^{E(s)} - F^{E(l)}$ equals the difference in the molar heats of mixing, $H^{M(s)} - H^{M(l)}$, in the solid and the liquid state. The interaction between nearest neighbors and the interaction between metal ions and electrons are presumably about the same in the solid and in the liquid state. Consequently, both $[F^{E(s)} - F^{E(l)}]$ and $[H^{M(s)} - H^{M(l)}]$ are essentially equal to the strain energy of the solid alloy due to the difference in the size of the constituent atoms.

Significant values of $F^{E(s)} - F^{E(l)}$ are found particularly in systems involving atoms of different size as is shown below in conjunction with values calculated from equation (29) and compiled in Table I.

Evaluation of the Width of the Gap between Liquidus and Solidus

Since according to equations (11) and (12) the terminal slopes of the liquidus and the solidus are determined exclusively by the derivative of the difference $F^{E(s)} - F^{E(l)}$, it follows that thermodynamic quantities characteristic of the liquid or the solid phase alone, i.e., $F^{E(s)}$ and $F^{E(l)}$ or their derivatives, can be deduced only from the middle part of the phase diagram, especially the width of the gap between the liquidus and the solidus.

The width of the gap in the system Au–Pt is unusually large. Assuming a symmetrical parabolic concentration dependence of the excess free energy for either phase, F^E = constant $N_2(1 - N_2)$, Scatchard and Hamer [5] have shown that the observed width of the gap in the system Au–Pt is accounted for by the following values of the excess free energy:

$F^{E(l)}(N_2 = 0.5)$
$= 1320$ cal and $F^{E(s)}(N_2 = 0.5) = 1330$ cal.

The latter value agrees satisfactorily with the value of 1200 cal derived by Borelius [11] from a thermodynamic evaluation of the miscibility gap in the solid state at lower temperatures. This evaluation gives an asymmetrical curve for $F^{E(s)}$ as a function of N_2 in contrast to the symmetrical parabolic concentration dependence presupposed by Scatchard and Hamer. In principle, a more refined analysis of the width of the gap between the liquidus and the solidus may also give information regarding the asymmetry of $F^{E(s)}$ and $F^{E(l)}$ as functions of N_2 but minor errors in the determination of the liquidus and the solidus may lead to large errors in the calculated functions $F^{E(s)}$ and $F^{E(l)}$.

Calculations of this type are very susceptible to errors in the experimental values if both the solid and the liquid phase exhibit negative deviations from ideality, since in this case the width of the gap between the liquidus and the solidus is very narrow.

The slope of the liquidus may be calculated without special assumptions as [12; 13]

$$(18)\quad \frac{\partial\theta}{\partial N_2^{(l)}} = -\frac{(N_2^{(l)} - N_2^{(s)})\,\theta}{(1 - N_2^{(s)})\,\Lambda_1 + N_2^{(s)}\Lambda_2}\,\frac{\partial^2 F_m^{(l)}}{(\partial N_2^{(l)})^2}$$

and likewise the slope of the solidus as

$$(19)\quad \frac{\partial\theta}{\partial N_2^{(s)}} = -\frac{(N_2^{(l)} - N_2^{(s)})\,\theta}{(1-N_2^{(l)})\,\Lambda_1+N_2^{(l)}\Lambda_2}\,\frac{\partial^2 F_m^{(s)}}{(\partial N_2^{(s)})^2}$$

where $F_m^{(l)}$ and $F_m^{(s)}$ are the molar free energies of the liquid and the solid phase, respectively, and Λ_1 is the heat to be supplied for a reversible transfer of one mole of component 1 from the solid to the liquid phase, and Λ_2 is the corresponding quantity for component 2.

In view of equation (1) the molar free energy F_m of a phase involving components 1 and 2 may be written as

$$(20)\quad F_m = N_1\bar{F}_1 + N_2\bar{F}_2$$
$$= N_1(F_1^\circ + RT\ln N_1) + N_2(F_2^\circ + RT\ln N_2) + F^E$$

whence

$$(21)\quad \partial^2 F_m/\partial N_2^2 = RT/N_2(1 - N_2) + \partial^2 F^E/\partial N_2^2.$$

In equation (21) the second derivative of the excess integral molar free energy may be calculated from the excess partial molar free energy of component 1 or 2 by means of the relation

$$(22)\quad \frac{\partial^2 F^E}{\partial N_2^2} = \frac{1}{1-N_1}\,\frac{\partial F_1^E}{\partial N_1} = \frac{1}{1-N_2}\,\frac{\partial F_2^E}{\partial N_2}$$

which follows by differentiation of equations (9*a*) and (9*b*) with respect to N_1 and N_2, respectively.

Upon solving equations (18) and (19) for $N_2^{(l)} - N_2^{(s)}$ and substituting equation (21), the difference in the composition of the liquid and the solid phase for a given temperature Θ is obtained as

$$(23)\quad N_2^{(l)} - N_2^{(s)} = -\frac{(1 - N_2^{(s)})\,\Lambda_1 + N_2^{(s)}\Lambda_2}{R\theta^2/N_2^{(l)}(1 - N_2^{(l)}) + \theta F^{E(l)\,II}}\,\frac{\partial\theta}{\partial N_2^{(l)}}$$
$$= -\frac{(1 - N_2^{(l)})\,\Lambda_1 + N_2^{(l)}\Lambda_2}{R\theta^2/N_2^{(s)}(1 - N_2^{(s)}) + \theta F^{E(s)\,II}}\,\frac{\partial\theta}{\partial N_2^{(s)}}$$

where $F^{E(l)\,II}$ and $F^{E(s)\,II}$ are the second derivatives of the excess integral molar free energy with respect to the mole fraction N_2 for the liquid and the solid phase, respectively.

If $N_2^{(l)} \cong N_2^{(s)}$, the width $\Delta\Theta$ of the temperature gap between the liquidus and the solidus for a given mole fraction N_2 equals

$$(24)\quad \Delta\Theta \cong -(N_2^{(l)} - N_2^{(s)})(d\Theta/dN_2^{(l)}).$$

Substitution of equation (23) in equation (24) yields

$$(25)\quad \Delta\theta \cong \frac{(1 - N_2^{(s)})\,\Lambda_1 + N_2^{(s)}\,\Lambda_2}{R\theta^2/N_2^{(l)}(1 - N_2^{(l)}) + \theta F^{E(l)\,II}}\left(\frac{\partial\theta}{\partial N_2^{(l)}}\right)^2 \text{ if } N_2^{(l)} \cong N_2^{(s)}.$$

Equations (23) and (25) may be applied to the system Ag–Au. If the system Ag–Au were ideal in both the liquid and the solid state, one would obtain $N_{Au}^{(l)} - N_{Au}^{(s)} = -0.023$ and $\Delta\Theta = 2.3°C$ for $N_{Au} = 0.5$. Actually, however, both the liquid and the solid phase exhibit distinct negative deviations from ideality according to electrochemical measurements [14–17], vapor pressure measurements [18], equilibrium investigations [19], and calorimetric measurements [20]. Available data lead to the approximate formula

$$(26)\quad F_{Ag}^{E(l)} \cong F_{Ag}^{E(s)} \cong -4000(1 - N_{Ag})^2 \text{ cal.}$$

Since deviations from ideality in the liquid and the solid phase, are nearly equal, the heats Λ_1 and

Λ_2 may be equated to the heats of fusion of the pure components. Thus it follows from equations (22), (23), (25), and (26) that $N_{Au}^{(l)} - N_{Au}^{(s)} = -0.013$ and $\Delta\Theta = 1.3°C$ at $N_{Au} \cong 0.5$. The calculated value of $\Delta\Theta = 1.3°$ differs widely from the value of 10°C for the temperature interval between beginning and end of solidification observed by Jaenicke [21] and Reydt [22]. This discrepancy is due to the low diffusivity in the solid phase, which precludes establishment of equilibrium during progressing solidification.

Practically, only the liquidus but not the width of the gap between the liquidus and the solidus can be determined with the aid of conventional thermal analysis. The solidus curve may be obtained from investigations in which the beginning of melting of properly homogenized alloys during heating is recorded. If the latter investigations have not been made, the width of the gap between the liquidus and the solidus may rather be calculated with the aid of equation (24) as has been shown above, eventually with estimated values of the deviations from ideality.

Equilibrium Conditions at the Minimum of the Liquidus and the Solidus of a Binary Alloy Completely Miscible in the Liquid and the Solid State

At the minimum of the liquidus and the solidus the mole fractions of the coexisting phases are equal. Hence it follows from equations (3) and (4) that

$$(27)\quad F_1^{E(s)}(T^*, N_2^*) - F_1^{E(l)}(T^*, N_2^*) = (T_{m1} - T^*)\,\Delta S_{f1}^\circ$$

$$(28)\quad F_2^{E(s)}(T^*, N_2^*) - F_2^{E(l)}(T^*, N_2^*) = (T_{m2} - T^*)\,\Delta S_{f2}^\circ$$

where N_2^* is the mole fraction and T^* is the temperature at the minimum of the liquidus and the solidus.

Upon multiplying either side of equations (27) and (28) by the mole fractions of components 1 and 2, $(1 - N_2^*)$ and N_2^*, respectively, and adding corresponding sides, the difference of the integral excess molar free energies $F^{E(s)*}$ and $F^{E(l)*}$ in the solid and the liquid state at mole fraction N_2^* and temperature T^* is obtained as

$$(29)\quad \begin{aligned} F^{E(s)*} - F^{E(l)*} &= [(1 - N_2^*)\,F_1^{E(s)} + N_2^*\,F_2^{E(s)}] \\ &\quad -[(1 - N_2^*)\,F_1^{E(l)} + N_2^* F_2^{E(l)}] \\ &= (1 - N_2^*)(T_{m1} - T^*)\,\Delta S_{f1}^\circ \\ &\quad + N_2^*(T_{m2} - T^*)\,\Delta S_{f2}^\circ. \end{aligned}$$

Numerical values of $F^{E(s)*} - F^{E(l)*}$ calculated from equation (29) with observed values according to Hansen [23], Metals Handbook [24], Kelley [25], and Smithells [26] are presented in Table I. Values for Co–Fe, Fe–Ni, and Fe–Pd alloys refer to the face-centered cubic gamma-phase. Accordingly, the entropy difference between liquid and γ-iron and the unstable melting point of γ-iron, which is 3 degrees lower than the normal melting point, were used, for the evaluation of equation (29). Similarly, the value for Cu–Mn alloys was obtained.

TABLE I

VALUES OF $F^{E(s)*} - F^{E(l)*}$ FOR ALLOYS WITH A MINIMUM OF THE LIQUIDUS AND THE SOLIDUS ACCORDING TO EQUATION (29)

System	Structure	N_2^*	T^* °K	$F^{E(s)*} - F^{E(l)*}$ cal/g-atom	r_1 A	r_2 A
Au-Cu	f. c. c.	0.40	1157	421	1.44	1.28
Au-Ni	f. c. c.	0.40	1123	640	1.44	1.25
Co-Fe	f. c. c.	0.65	1748	103	1.26	1.26
Cr-Fe	b. c. c.	0.75	1778	70	1.28	1.28
Cu-Mn	f. c. c.	0.35	1141	656	1.28	1.37
Fe-Ni	f. c. c.	0.65	1709	112	1.26	1.25
Fe-Pd	f. c. c.	0.55	1576	566	1.26	1.37
K-Rb	b. c. c.	0.65	306	25	2.38	2.51
Ni-Pd	f. c. c.	0.45	1510	603	1.25	1.37

Table I also lists the atomic radii r_1 and r_2 for the structures indicated in the second column. Relatively high values of $F^{E(s)*} - F^{E(l)*}$ are found in systems in which the atomic radii differ to some extent, and therefore a relatively high strain energy may be expected. There is, however, no direct correlation between the values of $F^{E(s)*} - F^{E(l)*}$ and the ratio or the difference of the atomic radii. According to Lawson [27] the compressibility of the alloys is another important factor for the magnitude of the strain energy.

The Liquidus and the Solidus in the Vicinity of a Maximum or Minimum

In the vicinity of a maximum or minimum, the liquidus and the solidus of a binary alloy may be approximated by parabolae with a common horizontal tangent at the maximum or minimum. In many cases, a maximum is characteristic of an intermediate solid phase of virtually invariable composition, thus designated as an intermetallic compound. For the latter case, special relations have been derived previously [28; 29]. In the following, no special assumptions are made. Consequently, the following considerations also apply to a minimum as it is found, e.g., in the system Au–Cu.

Letting

(30a) $$T - T^* = \tau$$

(30b) $$N_2^{(l)} - N_2^* = \xi$$

(30c) $$N_2^{(s)} - N_2^* = \eta$$

and introducing $\frac{1}{2}\alpha$ and $\frac{1}{2}\beta$ as parameters of the parabolae, we obtain

(31) $$\xi^2 = \alpha\tau$$

(32) $$\eta^2 = \beta\tau$$

where α and β are negative in the case of a maximum ($\alpha < \beta < 0$) and positive in the case of a minimum ($0 > \alpha > \beta$).

The partial molar free energies of components 1 and 2 at the maximum or minimum are denoted by $\bar{F}_1^*$ and $\bar{F}_2^*$, respectively. Using Taylor series expansions for the partial molar free energies $\bar{F}_1$ and $\bar{F}_2$, of components 1 and 2 in either phase for the vicinity of the maximum or minimum, and equating the partial molar free energies in the two phases as a necessary condition for their coexistence, we obtain

(33)

$$\bar{F}_1^* + \xi(\partial\bar{F}_1^{(l)}/\partial N_2^{(l)}) + \tfrac{1}{2}\xi^2[\partial^2\bar{F}_1^{(l)}/(\partial N_2^{(l)})^2] + \ldots + \tau(\partial\bar{F}_1^{(l)}/\partial T) + \ldots = \bar{F}_1^* + \eta(\partial\bar{F}_1^{(s)}/\partial N_2^{(s)}) + \tfrac{1}{2}\eta^2[\partial^2\bar{F}_1^{(s)}/(\partial N_2^{(s)})^2] + \ldots + \tau(\partial\bar{F}_1^{(s)}/\partial T) + \ldots$$

(34)

$$\bar{F}_2^* + \xi(\partial\bar{F}_2^{(l)}/\partial N_2^{(l)}) + \tfrac{1}{2}\xi^2[\partial^2\bar{F}_2^{(l)}/(\partial N_2^{(l)})^2] + \ldots + \tau(\partial\bar{F}_2^{(l)}/\partial T) + \ldots = \bar{F}_2^* + \eta(\partial\bar{F}_2^{(s)}/\partial N_2^{(s)}) + \tfrac{1}{2}\eta^2[\partial^2\bar{F}_2^{(s)}/(\partial N_2^{(s)})^2] + \ldots + \tau(\partial\bar{F}_2^{(s)}/\partial T) + \ldots,$$

where the differential quotients are to be taken at $N_2 = N_2^*$ and $T = T^*$.

The derivatives of the partial molar free energies of components 1 and 2 are interrelated by the Gibbs-Duhem equation. To obtain the most symmetrical relations, the partial molar free energies $\bar{F}_1$ and $\bar{F}_2$ in either phase may be expressed by the molar free energy F_m of the respective phase,

(35) $$\bar{F}_1 = F_m - N_2(\partial F_m/\partial N_2)$$

(36) $$\bar{F}_2 = F_m + (1 - N_2)(\partial F_m/\partial N_2).$$

From equations (35) and (36) the derivatives of $\bar{F}_1$ and $\bar{F}_2$ with respect to N_2 may readily be calculated.

Upon substitution of equations (30a) to (30c), (35), and (36) for the liquid and the solid phase in equations (33) and (34), it follows that

(37)

$$-\tau^{\frac{1}{2}}N_2^*(\alpha^{\frac{1}{2}}F_m^{(l)\,II} - \beta^{\frac{1}{2}}F_m^{(s)\,II}) + \tau\{-\tfrac{1}{2}\alpha F_m^{(l)\,II} + \tfrac{1}{2}\beta F_m^{(s)\,II} - \tfrac{1}{2}\alpha N_2^* F_m^{(l)\,III} + \tfrac{1}{2}\beta N_2^* F_m^{(s)\,III} + [(\partial\bar{F}_1^{(l)} - \bar{F}_1^{(s)})/\partial T]\} + \ldots = 0$$

(38)

$$\tau^{\frac{1}{2}}(1 - N_2^*)(\alpha^{\frac{1}{2}}F_m^{(l)\,II} - \beta^{\frac{1}{2}}F_m^{(s)\,II}) + \tau\{-\tfrac{1}{2}\alpha F_m^{(l)\,II} + \tfrac{1}{2}\beta F_m^{(s)\,II} + \tfrac{1}{2}\alpha(1 - N_2^*)F_m^{(l)\,III} - \tfrac{1}{2}\beta(1 - N_2^*)F_m^{(s)\,III} + [\partial(\bar{F}_2^{(l)} - \bar{F}_2^{(s)})/\partial T]\} + \ldots = 0$$

where $F_m^{(l)\,II}$ and $F_m^{(s)\,II}$ are the second derivatives and $F_m^{(l)\,III}$ and $F_m^{(s)\,III}$ are the third derivatives of $F_m^{(l)}$ and $F_m^{(s)}$ with respect to the mole fraction of component 2, respectively. Equations (37) and (38) are compatible only if the coefficients of the first terms involving the factor $\tau^{\frac{1}{2}}$ vanish. Thus,

(39) $$\alpha/\beta = (F_m^{(s)\,II}/F_m^{(l)\,II})^2.$$

Upon multiplying equations (37) and (38) through by $(1 - N_2^*)$ and N_2^*, respectively, adding corresponding sides, and dividing through by τ,

(40) $$-\tfrac{1}{2}\alpha F_m^{(l)\,II} + \tfrac{1}{2}\beta F_m^{(s)\,II} + (1 - N_2^*)[\partial(\bar{F}_1^{(l)} - F_1^{(s)})/\partial T] + N_2^*[\partial(\bar{F}_2^{(l)} - \bar{F}_2^{(s)})/\partial T] = 0.$$

The derivatives of the partial molar free energies with respect to temperature equal the negative values of the partial molar entropies. Thus

(41) $$(1 - N_2^*)\partial[(\bar{F}_1^{(l)} - \bar{F}_1^{(s)})/\partial T] + N_2^*[\partial(\bar{F}_2^{(l)} - \bar{F}_2^{(s)})/\partial T] = -[(1 - N_2^*)(\bar{S}_1^{(l)} - \bar{S}_1^{(s)}) + N_2^*(\bar{S}_2^{(l)} - \bar{S}_2^{(s)})] = -\Delta H_f^*/T^*$$

where ΔH_f^* is the heat of fusion of one gram-atom of alloy of mole fraction N_2^*. Substitution of equation (41) in equation (40) yields

(42) $$-\tfrac{1}{2}\alpha F_m^{(l)\,II} + \tfrac{1}{2}\beta F_m^{(s)\,II} = \Delta H_f^*/T^*.$$

If any two of the four quantities α, β, $F_m^{(l)\,II}$, and $F_m^{(s)\,II}$ are known, equations (39) and (42) may be used in order to calculate the other two quantities. In the first place, the values of α and β may be calculated if $F_m^{(l)\,II}$ and $F_m^{(s)\,II}$ are known,

(43) $$\alpha = \frac{2\Delta H_f^* F_m^{(s)\,II}}{T^* F_m^{(l)\,II}(F_m^{(l)\,II} - F_m^{(s)\,II})}$$

(44) $$\beta = \frac{2\Delta H_f^* F^{(l)\,II}}{T^* F_m^{(s)\,II}(F_m^{(l)\,II} - F_m^{(s)\,II})}$$

Conversely, if the values of α and β are known, the values of $F_m^{(l)\,II}$ and $F_m^{(s)\,II}$ may be calculated as

$$F_m^{(l)II} = \left| \frac{2\Delta H_f^*}{T^*[(\alpha\beta)^{\frac{1}{2}} - |\alpha|]} \right| \tag{45}$$

$$F_m^{(s)II} = \left| \frac{2\Delta H_f^*}{T^*[|\beta| - (\alpha\beta)^{\frac{1}{2}}]} \right|. \tag{46}$$

In the case of an intermediate phase of virtually invariable composition (intermetallic compound), the width of the parabola of the solidus is almost zero and thus $|\beta| \ll |\alpha|$. If β in equation (45) is disregarded, $F^{(l)II}$ and α are directly interrelated. This case has already been discussed in previous papers [28; 29].

Finally, if $F^{(l)II}$ and α are known, it follows by combining equations (39) and (42) that

$$F_m^{(s)II} = \frac{F_m^{(l)II}}{1 + 2\Delta H_f^*/(\alpha T^* F_m^{(l)II})} \tag{47}$$

$$\beta = \alpha[1 + 2\Delta H_f^*/(\alpha T^* F_m^{(l)II})]^2. \tag{48}$$

Equations (39) and (42) to (48) may especially be used in order to check the consistency of phase equilibrium data or to obtain supplementary information as is illustrated in the following.

The activity of copper in solid Au–Cu alloys has been determined by Wagner and Engelhardt [19] and by Weibke and von Quadt [30] with the aid of electrochemical measurements. According to these investigations solid Au–Cu alloys may be considered as approximately regular solutions with a temperature-independent excess free energy. From the data reported by Weibke and von Quadt for 500°C it follows that

$$(\partial F_2^{E(s)}/\partial N_2) = 4785 \text{ cal/g-atom at } N_{Cu} = 0.4 \tag{49}$$

whence in view of equation (22)

$$F^{E(s)II} = 7975 \text{ cal/g-atom at } N_{Cu} = 0.4. \tag{50}$$

Differentiating equation (17) twice with respect to N_{Cu} and substituting equation (50),

$$F^{E(l)II} = 11{,}600 \text{ cal/g-atom at } N_{Cu} = 0.4. \tag{51}$$

Introducing equations (50) and (51) into equation (21) for the solid and liquid phase, respectively,

$$F_m^{(s)II} = 17{,}525 \text{ cal/g-atom at } N_{Cu} = 0.4, \quad T = 1157°K, \tag{52}$$

$$F_m^{(l)II} = 21{,}150 \text{ cal/g-atom at } N_{Cu} = 0.4, \quad T = 1157°K. \tag{53}$$

Upon substitution of equations (51) and (52) in equation (39), the ratio of the widths of the solidus and the liquidus parabola is obtained as

$$\left(\frac{N_2^{(s)} - N_2^*}{N_2^{(l)} - N_2^*}\right)_{T \sim T^*} = \left(\frac{\beta}{\alpha}\right)^{\frac{1}{2}} = \frac{F_m^{(l)II}}{F_m^{(s)II}} = 1.20. \tag{54}$$

This relation seems much more accurate than information obtained from thermal analysis because of incomplete establishment of equilibrium during progressing solidification.

If both the liquid and the solid phase are regular solutions, the heats of mixing, $H^{M(l)}$ and $H^{M(s)}$, are equal to the integral excess molar free energies $F^{E(l)}$ and $F^{E(s)}$. Consequently, the heat of fusion at the minimum of the liquidus may be calculated approximately as

$$\begin{aligned} \Delta H_f^* &= (1 - N_2^*)\,\Delta H_{f1}^\circ + N_2^*\,\Delta H_{f2}^\circ \\ &\quad + (H^{M(l)} - H^{M(s)})_{N_2 = N_2^*} \\ &\cong (1 - N_2^*)\Delta H_{f1}^\circ + N_2^*\Delta H_{f2}^\circ \\ &\quad - (F^{E(s)*} - F^{E(l)*}) \\ &= 2600 \text{ cal/g-atom} \end{aligned} \tag{55}$$

where the heats of fusion have been taken from Kelley's tables [25] and the value of $F^{E(s)*} - F^{E(l)*}$ from Table I. Substitution of these data in equation (43) yields $\alpha = 1.0 \times 10^{-3}$ degree^{-1} in satisfactory agreement with the liquidus observed by Kurnakow and Zemczuzny [9] and Broniewski and Wesolowski [10].

Analogous equations hold for first-order transformations in the solid state, e.g., equilibria between ordered and disordered structures in the system Au–Cu. The molar free energies of the high-temperature and the low-temperature phase have to be substituted for $F_m^{(l)}$ and $F_m^{(s)}$, respectively, and ΔH_f has to be replaced by the heat of transformation. In particular, an analogue to equation (48) may be used in order to check the results of phase equilibrium studies, i.e., the boundaries of the field of the ordered phase. At the present, however, sufficiently consistent equilibrium data do not seem available.

Acknowledgement

This work was done as a part of investigations sponsored by the Atomic Energy Commission under Contract No. AT-30-Gen-1002.

References

1. Scheil, E. Z. Elektrochem. **49** (1943) 242.
2. Chipman, J. Discussions Faraday Society **4** (1948) 23.

3. SELTZ, H. J. Am. Chem. Soc. **56** (1934) 307.
4. SELTZ, H. J. Am. Chem. Soc. **57** (1935) 391.
5. SCATCHARD, G. and HAMER, W. J. J. Am. Chem. Soc. **57** (1935) 1809.
6. SCATCHARD, G. Chem. Rev. **44** (1949) 307.
7. SCATCHARD, G. and HAMER, W. J. J. Am. Chem. Soc. **57** (1935) 1805.
8. GUGGENHEIM, E. A. Trans. Faraday Soc. **33** (1937) 151.
9. KURNAKOW, N. S. and ZEMCZUZNY, S. F. Z. anorg. allg. Chem. **54** (1907) 194.
10. BRONIEWSKI, W. and WESOLOWSKI, W. Compt. rend. **198** (1934) 370.
11. BORELIUS, G. Ann. Physik (5) **28** (1937) 507.
12. SCHOTTKY, W., ULICH, H., and WAGNER, C. Thermodynamik (Berlin, Springer, 1929), p. 511.
13. PRIGOGINE, I. and DEFAY, R. Thermodynamique chimique, Vol. 2 (Liège, Belgium, Editions Desoer, 1946), p. 153.
14. OELANDER, A. J. Am. Chem. Soc. **54** (1932) 3819.
15. WACHTER, A. J. Am. Chem. Soc. **54** (1932) 4609.
16. WAGNER, C. and ENGELHARDT, G. Z. physik. Chem. **A159** (1932) 241.
17. KUBASCHEWSKI, O. and HUCHLER, O. Z. Elektrochem. **52** (1948) 170.
18. MCCABE, C. L., SCHADEL, H. M. and BIRCHENALL, C. E. Trans. A.I.M.E. **197** (1953) 709.
19. SCHMAHL, N. G. Z. anorg. allg. Chem. **266** (1951) 1.
20. TICKNOR, L. B. and BEVER, M. B. Trans. A.I.M.E. **194** (1952) 941.
21. JAENICKE, E. Metallurgie **8** (1911) 599.
22. RAYDT, U. Z. anorg. allg. Chem. **75** (1912) 58.
23. HANSEN, M. Der Aufbau der Zweistofflegierungen (Berlin, Springer, 1936).
24. Metals Handbook (Cleveland, Ohio, American Society for Metals, 1948).
25. KELLEY, K. K. Contributions to the Data on Theoretical Metallurgy X. U.S. Department of the Interior, Bureau of Mines, Bulletin 477 (Washington, D.C., Government Printing Office, 1950).
26. SMITHELLS, C. J. Metals Reference Book (New York, Interscience Publishers, Inc., 1949) pp. 166–167.
27. LAWSON, A. W. J. Chem. Phys. **15** (1947) 831.
28. SCHOTTKY, W., ULICH, H., and WAGNER, C. Thermodynamik (Berlin, Springer, 1929), pp. 400–410.
29. HAUFFE, K. and WAGNER, C. Z. Elektrochem. **46** (1940) 160.
30. WEIBKE, F. and VON QUADT, U. Z. Elektrochem. **45** (1939) 715.

INTERGRANULAR CAVITATION IN STRESSED METALS*

J. NEILL GREENWOOD, D. R. MILLER, and J. W. SUITER†

It has been found that when copper, alpha-brass and magnesium are strained at elevated temperatures, cavities appear in the intercrystalline boundaries. These are more prevalent in boundaries transverse to the tensile stress axis.

This intergranular cavitation is accompanied by a loss of ductility. For any temperature the loss is greater the lower the strain rate and for a given strain rate is greater the higher the temperature.

The cavities appear to nucleate at regular intervals and under the tensile stress ultimately link to form intercrystalline cracks.

The observations seem to be consistent with the suggestion that the cavities nucleate by the agglomeration of sufficient numbers of vacant lattice sites to form a stable 'hole.' They then grow partly by the 'absorption' of more vacancies and partly by stress concentration at the periphery.

Magnesium presents an interesting ductility-temperature relationship which is explained by (*a*) the coming into play of new slip systems as the temperature rises causing increased ductility, and (*b*) the incidence of intergranular cavitation at higher temperature causing a reversal of this trend.

LES CAVITÉS INTERGRANULAIRES DANS DES MÉTAUX SOUS TENSION

Il fut constaté que des cavités apparaissent dans les joints intercristallins, quand on déforme du laiton alpha et du magnésium aux températures élevées. L'apparition des cavités intergranulaires est accompagnée d'une diminution de la ductilité. Pour une température donnée cette diminution est d'autant plus importante que la vitesse de déformation est plus faible et pour une vitesse de déformation donnée la ductilité diminue quand la température s'élève. Les cavités paraissent germiner à des intervalles réguliers et finalement, sous la tension d'extension, s'assembler pour former des fissures intercristallines. Ces observations paraissent être en bon accord avec l'hypothèse que les cavités germinent par l'agglomération d'un nombre suffisant de lacunes réticulaires pour finalement former un "trou" stable. Ensuite elles croissent, en partie par l'absorption d'autres lacunes et en partie à cause de la concentration des tensions à leurs périphéries. Le magnésium présente une relation intéressante ductilité-température. Cette relation est expliquée par (*a*) l'introduction de nouveaux systèmes de glissement quand la température s'élève, ce qui cause une augmentation de la ductilité, (*b*) l'apparition des cavités intergranulaires aux températures plus élevées, ce qui agit en sens contraire.

DIE BILDUNG VON HOHLRÄUMEN IN DEN KORNGRENZEN VERFORMTER METALLE

Es zeigte sich, dass Hohlräume in den Korngrenzen von Kupfer, α-Messing und Magnesium auftraten, wenn diese Metalle bei höheren Temperaturen verformt wurden. Die Hohlräume traten stärker in Korngrenzen hervor, die quer zur Achse der Zugspannung lagen.

Diese Bildung von interkristallinen Hohlräumen ist mit einer Duktilitätsverminderung verbunden. Für eine gegebene Temperatur ist diese Verminderung um so grösser, je geringer die Dehnungsgeschwindigkeit ist, und für eine gegebene Dehnungsgeschwindigkeit um so grösser je höher die Temperatur ist.

Die Hohlräume scheinen in gleichmässigen Abständen zu entstehen. Unter Zug vereinigen sie sich schliesslich zu interkristallinen Rissen.

Die Beobachtungen scheinen die Annahme, dass die Hohlräume durch Zusammenballung von einer zur Bildung eines "stabilen" Loches hinreichenden Anzahl von Leerstellen entstehen, zu unterstützen. Die Hohlräume wachsen dann weiter, z. T. durch "Absorption" weiterer Leerstellen, z. T. durch Spannungskonzentration an ihrer Peripherie.

Magnesium zeigt eine interessante Beziehung zwischen Duktilität und Temperatur, die sich (a) durch das Auftreten neuer Gleitsysteme bei höherer Temperatur, die ein Anwachsen der Duktilität bewirken, und (b) durch die bei höheren Temperaturen auftretende interkristalline Hohlraumbildung, die einer Erscheinung entgegen wirkt, erklären lässt.

Introduction

It is well known that many metals fail under prolonged stress at elevated temperatures by the development of intercrystalline cracks.

In recent communications [1;2] one of the present authors (J. N. G.) has drawn attention to the occurrence of minute cavities in the grain boundaries of α brass strained in tension at elevated temperatures and has suggested that these are a cause of intercrystalline cracks.

Previous workers have observed these cavities. Jenkins [3] *et al.*, examining the creep characteristics of a copper alloy containing nickel and silicon, refer to the formation of 'distortion cavities' which may be within the grains or in the boundaries. In the latter case they say they lead to intercrystalline cracking.

Whitaker [4] strained both α- and β-brasses in air at 200°C at 0.5 per cent per minute. Some of the photographs show intercrystalline cracks having serrated boundaries, which suggest that they have formed by the linking together of series of cavities.

Herenguel and Scheidecker [5] made a very complete examination of the formation of fissures

*Received October 22, 1953.

†Baillieu Laboratory, University of Melbourne, Australia.

in cold worked α-brass under conditions of continuous deformation at elevated temperatures. They do not associate the small cavities with the initiation of intercrystalline cracking but rather suggest that the chains of cavities present in the boundaries result from fragmentation of cracks presumably by a sintering process.

It thus appears that the failure of metals under prolonged stress may be due to the formation of cavities in the grain boundaries leading to intercrystalline cracking and ultimate rupture.

The following investigation was carried out to determine the influence of strain rate and temperature on the formation of intergranular cavities in α-brass, copper, and magnesium.

Experimental Procedure

The specimens cut from strip 0.05 in. thick (0.03 in. for copper) and having a gauge length of 1.0 in. were made a link in a straining system operated by a synchronous motor through a chain of gears. The load at any instant could be measured by the deflection of a calibrated cantilever spring.

Three rates of strain were used:

(1) A high rate of 500/1000 per cent per hour obtained by hand operation.

(2) An intermediate rate of 40 per cent per hour.

(3) A low rate of 0.2 per cent per hour.

The specimen was enclosed so that when necessary an inert atmosphere or vacuum could be used. This was advisable at higher temperatures to avoid undue oxidation.

Experiments with α-Brass

The brass used was made from electrolytic copper and zinc and contained 70.1 per cent copper and 29.8 per cent zinc.

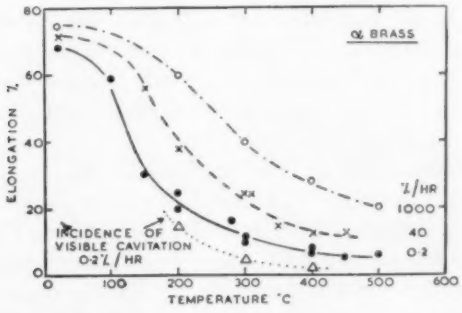

FIGURE 1. Influence of strain rate and temperature on the ductility of α-brass.

Figure 1 shows the relationship between temperature, strain-rate, and the ductility of the specimen expressed as the percentage elongation to cause fracture. It will be seen that the ductility falls off rapidly as the temperature rises, and for any given temperature is lower the lower the rate of strain. The change in ductility is quite remarkable. At ordinary temperature this brass will stretch 70 per cent before fracture, whilst at 400°C at the low rate of strain it will stretch only 5 per cent.

The nature of the fracture also changes. At ordinary temperature it is a silky shear but as the temperature is raised it becomes more and more granular, i.e., it becomes intercrystalline. The facets in the fracture show a micro-roughness (Figure 2) which looks like pitting.

Microsections were prepared by mechanical polish attack, followed by a short (1½ min.) electro-polish.

Examination of the microstructure reveals the cause of the micro-roughness. Figure 4 gives a general impression of the structure near the fracture of a specimen strained 24 per cent at 300°C. There are cavities of various sizes located in the grain boundaries. Figure 5 shows the same kind of thing in more detail after 5 per cent strain at 400°C. These two are typical.

From the examination of large numbers of such specimens fractured over a wide range of strain rate and temperature, there can be no doubt that the micro-roughness apparent on the fractured surface has its origin in the cavities visible in the grain boundaries in the cross section.

It was realised that objection might be raised to the use of even a short-time electro-polish in examining a phenomenon of this kind. Subsequently, by an improvement of mechanical polish attack technique [8] it was possible to eliminate the electro-polish. Similar chains of cavities are again visible as seen in Figure 3.

This micrograph was taken from a specimen strained at 120°C at the low rate until it reached the load corresponding with the ultimate stress. The load was then maintained until the specimen broke after 700 hours. The cavities visible in Figure 3 are the smallest detected and are not greater than 0.5×10^{-4} cm diameter. It has been noticed that the cavities form preferentially in those boundaries transverse to the tensile stress axis.

Some experiments were made to determine the relationship between the strain required to cause visible cavitation (constant strain rate) and temperature. The straining was interrupted at intervals

and the specimen polished. The results are shown in Table I and the dotted line in Figure 1.

TABLE I

STRAIN NEEDED TO CAUSE VISIBLE CAVITATION OF α-BRASS. STRAIN RATE 0.2% PER HOUR. GRAIN SIZE 0.1 MM.

Temperature °C	Elongation %	Comment
200	14.2	No cavitation
	17.9	Cavitation visible
	20.0	Specimen broke
300	2.7	No cavitation
	5.0	Cavitation visible
	11.0	Specimen broke
400	1.5	Cavitation visible
	6.0	Specimen broke

In another series of experiments the straining was carried out in an atmosphere of argon and the surface of the specimen was examined after straining under given conditions. It was found that, as with other metals, the coarse slip which is characteristic of low temperatures became less marked and was almost absent at 300°C (low strain rate). Figures 6 and 7 show the effect of 5 per cent extension at 200°C and 300°C respectively. Although very little slip is evident in Figure 7, examination by phase contrast at higher magnification shows that fine slip is still abundant. On the other hand, an increase in relative displacement of the grains takes place between 200°C and 300°C and is shown by the greater width of the grain boundaries in Figure 7.

Summary of the Characteristics of Intergranular Cavitation in α-Brass

1. For a given temperature of straining, cavitation is more marked, and elongation before fracture is less, the lower the strain rate.

2. For a given strain rate cavitation is more marked the higher the temperature.

3. Visible cavitation was not found below 250°C when the strain rate was 1000 per cent per hour, below 200°C when the strain rate was 40 per cent per hour, nor below 150°C when the strain rate was 0.2 per cent per hour.

4. Visible cavitation was, however, obtained at 120°C when a stress of 36,500 lb/sq in. was maintained for 700 hours.

5. Cavities are most prevalent in those grain boundaries which are transverse to the tensile stress axis.

6. Cavities are not associated with twin boundaries. They do, however, appear to be affected by the orientation difference across a boundary. When twinned areas in a crystal terminate at a boundary, it is frequently noticed that the cavities are associated with one change of orientation but not the other. An instance of this can be seen near the top in Figure 5.

7. The appearance of cavities in the boundaries takes place in a temperature zone where coarse slip diminishes and relative grain movement increases perceptibly.

8. With continuous straining, failure occurs by intercrystalline cracking soon after cavitation has become visible.

9. The cavities are regularly spaced in the early stages of development and the centres of nucleation are further apart the higher the temperature of straining. No precise measurements have been made but the order is 10^{-4} cm at 120°C and 10^{-3} cm at 400°C.

10. The smallest cavities seen are not greater than 0.5×10^{-4} cm diameter.

11. If the straining is continued after cavitation has occurred, the cavities ultimately join up to form continuous cracks. The undulating boundary of the major cracks seen in Fig. 8 indicate the cavity origin.

Experiments on Copper

The material used was O.F.H.C. copper (.03 in. thick) of 99.98 per cent purity. Series of experiments were made at different temperatures using the same straining rates as in the case of α-brass. Since in this case there was no danger of evaporation of any constituent, some of the experiments were carried out in a vacuum of $10^{-2}/10^{-3}$ mm. The tarnish film produced in such cases was so thin that it did not interfere with photography of the surface. The results are shown in Figure 9 and a similarity to Figure 1 is evident. Copper loses its ductility as the temperature is raised or the strain rate is lowered.

Examination of the microstructure again revealed the presence of cavities in the crystal boundaries. Figure 10 is a typical structure. This is taken from a specimen which failed after 7 per cent elongation at the low rate at 300°C. Figure 11, from the same specimen, shows clearly the manner in which the cavities link together to give an intercrystalline crack. It will be noted that, as in the case of brass, the cavities form preferentially in boundaries transverse to the tensile stress.

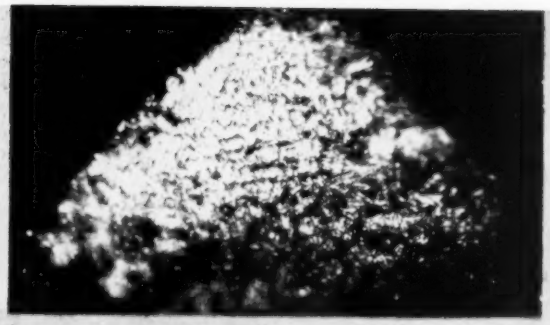

2

3

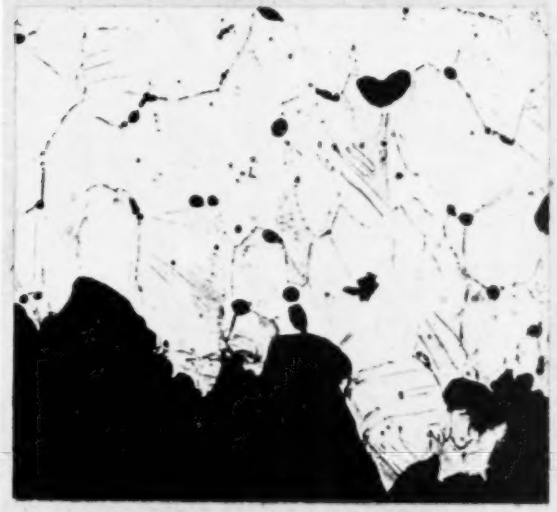

4

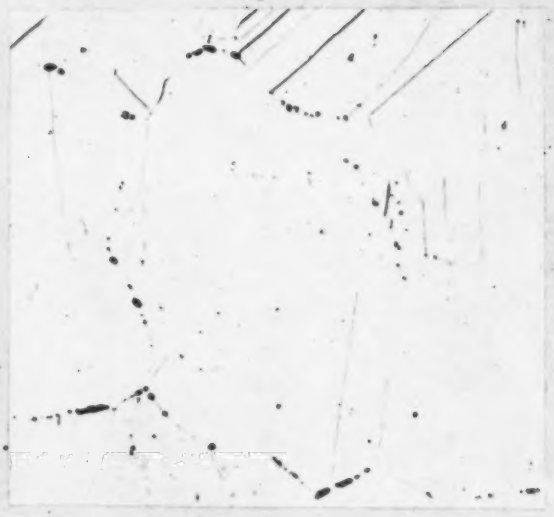

5

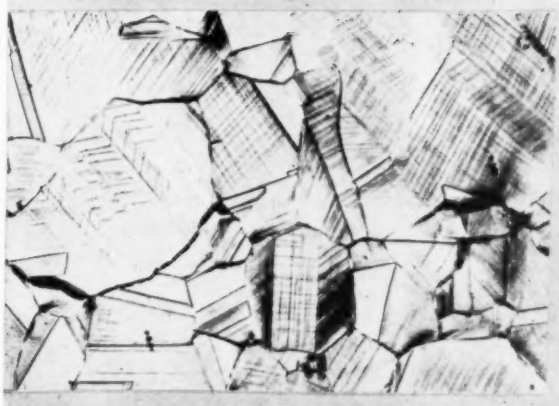

6

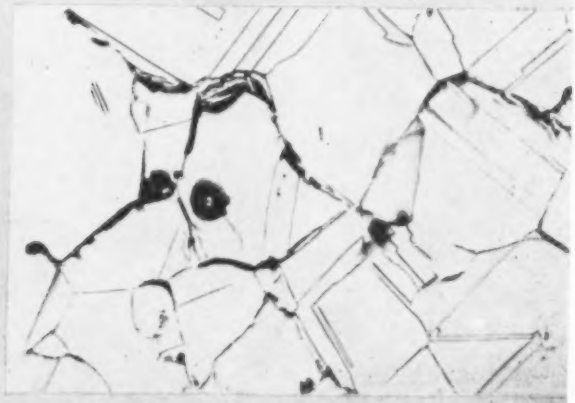

7

PLATE I. Figure 2—Facet in an intercrystalline high-temperature fracture. 500×. Figure 3—After 700 hours under stress at 120°C. Mechanical polish and light etch. 500×. Figure 4—Cavitation near fracture after 24 per cent extension at 300°C. 100×. Intermediate strain rate. Figure 5—Cavitation after 5 per cent extension at 400°C. 200×. Figure 6—surface after 4.5 per cent extension at 200°C. 200×. Figure 7—Surface after 5 per cent extension at 300°C. 200×.

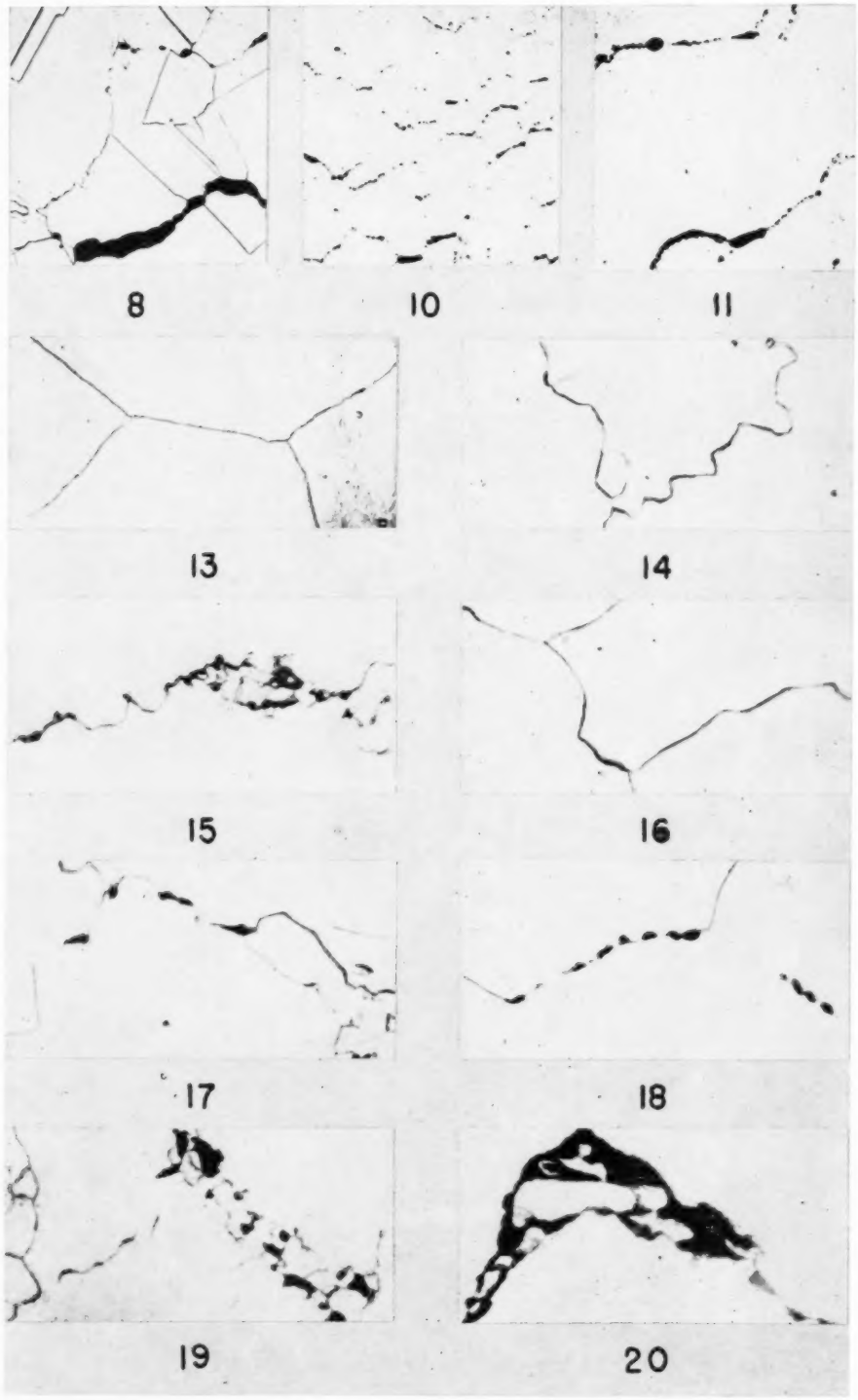

PLATE II (all figures reduced to three quarters in reproduction). Figure 8—α-Brass strained 12 per cent at 300°C. Crack formed from cavities. 200×. Figure 10—Copper slow-strained 7 per cent at 300°C; 100×. Figure 11—Copper slow-strained 7 per cent at 300°C; 500×. Figure 13—Magnesium 14 per cent extension at 100°C. Low strain rate; 400×. Figure 14—Magnesium 40 per cent extension at 200°C; 400×. Figure 15—Magnesium 24 per cent extension at 225°C; 400×. Figure 16—Magnesium 10 per cent extension at 250°C; 400×. Figure 17—Magnesium 14 per cent extension at 250°C; 400×. Figure 18—Magnesium 10 per cent extension at 300°C; 400×. Figure 19—Magnesium 49 per cent extension at 350°C; Int. strain rate. 400× Figure 20—As Fig. 19. Another part.

It was noticed that coarse slip diminished with rise of temperature but was more persistent than in the case of brass, and could be detected even at 500°C. Under the same conditions relative grain movement increases.

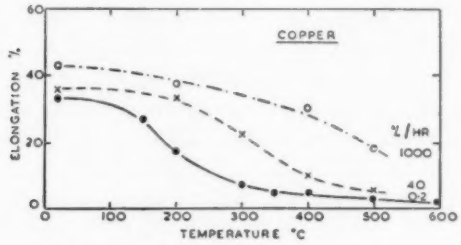

FIGURE 9. Influence of strain rate and temperature on the ductility of copper.

Summary of Results with Copper

Copper behaves similarly to α-brass when strained at elevated temperatures. Intergranular cavitation is visible after straining 28 per cent at 200°C (low rate of strain). The extent of cavitation increases rapidly with temperature. This is coincident with a relative change in the mechanism of deformation, coarse slip diminishing and grain translation increasing.

Experiments on Magnesium

Magnesium crystallises in a different system from copper and brass and also readily forms sub-grains during straining at elevated temperatures [9]. For these reasons it was interesting to examine it for intergranular cavitation.

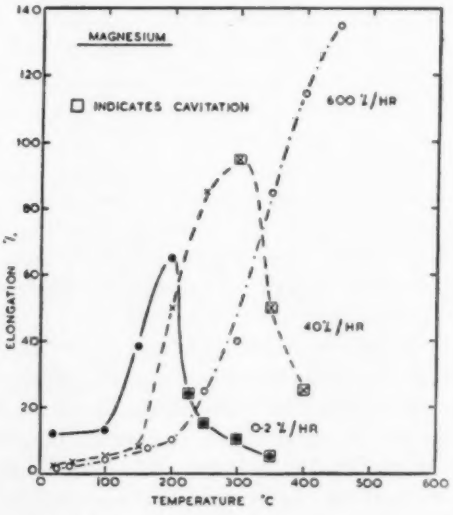

FIGURE 12. Influence of strain rate and temperature on the ductility of magnesium.

The material used contained as major impurities 0.2 per cent lead and 0.02 per cent iron. The lead was in solid solution. Test specimens were prepared similar to those used in the case of brass. The results of the measurement of elongation at fracture are shown in Figure 12 and a distinct difference from Figures 1 and 9 will be noted.

After the specimen had been fractured at a given rate and temperature it was sectioned and polished mechanically using graded alundum powder, and lightly etched with 5 per cent nital.

The elongation, at first low, rises after a temperature 125/250°C (according to the rate of strain) is exceeded, and reaches a maximum value. The maximum is reached at a higher temperature the higher the rate of strain, as shown in Table II.

TABLE II

INFLUENCE OF STRAIN RATE ON DUCTILITY OF MAGNESIUM

Rate of strain %/hour	Temp. °C where increase in ductility begins	Maximum elongation %	Temp. °C of maximum elongation
0.2	125	66	200
40	150	98	300
600	225	132+	450+

After fracture at temperatures below the maxima shown in Figure 12, the structure is similar to either Figure 13 or 14. The boundaries are undulating or 'clean' and smooth, according to whether 'cells' have developed or not. When, however, the maxima have been passed, characteristic dark areas are found in the grain boundaries. These are illustrated in Figures 15–20.

Figure 15 (after 24 per cent extension at 225°C) shows an irregular boundary which appears to have been migrating. The movement has been held up by the presence of cavities. Distinct sub-grains are visible and the sub-boundaries seem also to be the location of cavities. It should, however, be noted that it is only the cells in the neighbourhood of a major grain boundary which are affected in this way. In this specimen areas showing cavities are rare. It follows that this is an early stage of cavitation.

Figure 16, after 10 per cent elongation at 250°C, shows a typical structure without cavitation. After 14 per cent, however, as seen in Figure 17, distinct cavities are present. At this stage fracture occurred. This substantiates the statement in connection with intergranular cavitation of α-brass, that failure occurs soon after cavities appear.

At 300°C the cavities are quite distinct after 10 per cent extension, as shown by Figure 18.

As the temperature is raised the cell size increases, and by 300°C (low rate of strain) has become comparable with the original grain size. It was noted that this was associated with increased regularity of the arrangement of cavities in the boundaries. This is seen by comparing Figures 15, 17, and 18.

Figures 19 and 20 show two stages of cavitation during 49 per cent extension at 40 per cent per hour at 350°C. In Figure 19, the cell structure near the grain boundary is well developed, and the cavities are of the same order of size as the cells. In Figure 20, from the same specimen, the boundaries have parted, several cells have been isolated and the cavity origin of the crack is indicated by the undulations in its outline.

It has been noted with magnesium that the cavities seen in the intergranular boundaries appear to be of two kinds. There are those illustrated in Figures 17 and 18 which are similar to those found in brass and copper, except that they are more shallow, i.e., flat ellipsoids rather than spheres. Then there are those illustrated in Figures 15, 19 and 20, which appear to be associated with the cell structure.

Summary of Results with Magnesium

Magnesium behaves similarly to brass and copper when strained at elevated temperatures in that intergranular cavitation occurs at lower temperatures the lower the strain rate.

In this case there can be no doubt that cavitation leads to the failure of the metal, for until this phenomenon appears, the ductility of magnesium increases with temperature.

The nature of the elongation-temperature relationship is considered later in an appendix.

Discussion

The Origin of Cavities

It has been shown that, in the case of two metals and one alloy, cavities form in the boundaries between crystals when they are subjected to continuous strain at elevated temperatures. The boundaries transverse to the tensile stress axis are the preferred location of these cavities.

Two possible mechanisms have been considered to account for the presence of these cavities:

(*a*) One suggestion is that they formed by the diffusion of interstitial gas atoms. When these small atoms reach the more open structure in the boundary they accumulate in spaces which can accommodate more than individual atoms, and combining to form molecules, are then not able to diffuse back into the lattice. Under such circumstances, pressure would be created which, aided by the tensile stress across the boundary, would create voids which would extend further by stress concentration.

(*b*) The second suggestion is that they are formed by the migration of vacant lattice sites existing in the metal or created during deformation. It is necessary to imagine a sufficient number of these coming together at one instant in order to nucleate a cavity large enough to be stable.

It is, in fact, very difficult to devise experiments which would differentiate between these two suggestions because it is evident that, if cavities form from any cause, interstitial gases will eventually accumulate in them.

The crystal lattice is looked upon as a more or less orderly arrangement of atoms with some vacant sites [10; 11]. Owing to thermal vibrations, and the movement of dislocations under stress, the relative positions of the vacant sites are constantly changing. If now a sufficient number of these arrive simultaneously at a given location a stable hole will be nucleated. It has been shown by Smigelskas and Kirkendall [12], and by Barnes [13] that vacant sites caused by diffusion can form voids readily visible at a magnification of 100 diameters.

The observed fact that under the experimental conditions used, these cavities appear preferentially in boundaries transverse to the tensile stress axis, suggests that the disordered lattice at the boundary acts under these conditions as a trap in which "holes" readily form. Once such a condition has arisen, the vacant sites which have so agglomerated are withdrawn from the lattice and more will be generated to maintain equilibrium. Thus the lattice is a continuous source of vacancies and the cavities continuous sinks.

It is of interest to note that cavitation appears more readily, i.e., with lower strain, under those conditions (rising temperature and falling strain rate) which also cause a change in emphasis from deformation by slip to deformation by grain translation. It is difficult to say whether this latter is a cause or an effect. A sliding movement at the grain boundaries would probably cause localised distortion of the lattice which would aid the formation of cavities. On the other hand, the nucleation of large numbers of cavities would weaken the boundaries and therefore aid movement in those regions.

There appears to be a minimum distance between the centres of cavities. The microstructures

reveal that besides complete parting of the boundaries there are chains of cavities (Figures 3, 5, 10 and 11). Measurements on these show that in the case of α-brass the minimum distance between centres is a function of the experimental conditions. For example, the cavities present in a specimen maintained under stress at 120°C for 700 hours have a spacing of 10^{-4} cm (similar to that of adjoining slip lines) whilst for a specimen strained at 400°C the spacing is of the order of 10^{-3} cm.

If the above picture of nucleation of cavities in the boundaries is correct, as deformation proceeds more vacant sites would be absorbed in existing cavities which would consequently grow. The latter would also spread by tensile stress concentration at their boundaries. This growth, coupled with the tensile stress, would ultimately cause the cavities in any boundary to link up. The grains would part an an intercrystalline crack would have formed.

The effects of temperature and time are of importance. As temperature rises, the density of vacant sites in equilibrium with the lattice increases as does the ease of migration. At the same time the strength of the metal falls rapidly. It would thus be expected that cavitation would be more pronounced the higher the temperature, and between 150°C and 500°C this is the case.

Since the migration of vacancies is time-dependent, it would also be expected that a low rate of strain would facilitate the growth of cavities.

The present experiments are corroborated by the case quoted by Benson *et al.* [6]. Tough pitch copper (with 0.1 per cent silver) broke at 225°C with only 1.5 per cent elongation after the stress had been maintained for 10,000 hours. Micro-examination showed chains of cavities in the intercrystalline boundaries.

It will be seen then that the experimental evidence is consistent with the idea that the phenomenon described has its origin in the migration of vacancies to the crystal boundaries. The absence of cavities from twin boundaries and their appearance preferentially where certain twin boundaries meet another crystal, suggests that a minimum orientation difference is necessary for their nucleation. A tensile stress seems also to be necessary.

A final point refers to the observed fact (Figures 1 and 9) that with brass and copper ductility falls before there is any visible cavitation. There is no reason to assume that cavities are absent because the optical microscope is not able to resolve them. Rather would it appear that the phenomenon is a continuous one, but that in the lower ranges of temperature the accumulation of vacancies in the boundaries produces cavities which are too small to be seen optically.

Appendix

The Temperature-Ductility Relationship for Magnesium

In all three cases mentioned here, the tensile strength of the metals falls continuously as the temperature is raised. In the case of copper and α-brass the ductility-temperature relationship is similar. Intergranular cavitation partly accounts for the loss of strength and appears to be responsible for the loss of ductility.

The case of magnesium is more complicated but helps to clarify the part played by cavitation.

It is evident from Figure 12 that the relationship between ductility (as measured by elongation to fracture) and temperature, can be divided into three zones:

(*a*) In the first zone, from ordinary to slightly elevated temperatures the ductility is low and substantially constant, both with regard to temperature and rate of strain. Under these conditions it is known from the work of Schmid [14] that deformation is by slip on the basal (hexagonal) plane and twinning.

(*b*) In the next zone, the ductility rapidly rises and the rise is greater the greater the rate of strain.

The work of Schmid [14] has shown that under the conditions of tensile stress used, the slip system in single crystals of magnesium changes at 225°C, from the basal plane to the pyramidal set of planes of which more than one may be operative. The work of Bakarian and Mathewson [15] confirmed this change in slip mechanism.

It would seem, therefore, that the increased ductility in this temperature zone is brought about by the operation of additional slip planes.

From the dependence on rate of strain of the temperature at which ductility markedly increases, it is suggested that the temperature at which the extra slip planes become operative is also dependent on strain rate. The new planes apparently come into operation at lower temperature the lower the strain rate.

From the work of Suiter and Wood [9] it is known that the mechanism of deformation is dependent on strain rate. When the rate is of the order of 0.2 per cent extension per hour, coarse slip is abundantly present at 150°C, but is comparatively absent at 200°C. In the present work

it has been found similarly that there is very little coarse slip evident on the surface when the specimen is strained at 300°C at the intermediate rate.

This means that in the temperature zone where ductility is increasing the deformation mechanism is changing in the sense that relative movement of the grains is becoming important. It is of interest to note that the temperature where coarse slip practically disappears coincides with maximum ductility.

(*c*) In the third zone of temperature there is a *loss* of ductility which is as spectacular as the former increase.

Microscopical observation shows that intergranular cavitation appears simultaneously with the loss of ductility. All specimens which have been strained at temperatures higher than those corresponding with maximum ductility for the respective strain rates show cavities in the intercrystalline boundaries.

Since, in this case, ductility was rising rapidly with temperature prior to the incidence of cavitation the sharp reversal is confirmation that this phenomenon does in fact cause loss of ductility as seemed probable in the cases of copper and α-brass.

Acknowledgements

The authors wish to acknowledge the benefit of helpful discussions with their colleagues in the Baillieu Laboratory. They are also indebted to Mr. L. E. Samuels of the Defence Standards Laboratory (Sydney), for micrograph, Figure 7, to Mr. B. Reid for some of the values on copper (Figure 11) and to Miss Y. Tobin for assistance throughout the investigation.

References

1. Greenwood, J. Neill. Bull. Inst. Met. **1** (1952) 104.
2. Greenwood, J. Neill. Bull. Inst. Met. **1** (1952) 120.
3. Jenkins, C. H. M., *et al.* J. Inst. Metals, **70** (1944) 57.
4. Whitaker, M. *et al.* Metallurgia, **39** (1948) 21.
5. Herenguel, J., and Scheidecker, M. Rev. Métall. **48** (1951) 179.
6. Benson, N. D. *et al.* J. Inst. Metals **80** (1951) 131.
7. Richard, K. Proc. 4th Int. Cong. Mech. Eng. Stockholm 1952 (Adv. copy).
8. Samuels, L. E. J. Inst. Metals **81** (1953) 471.
9. Suiter, J. W., and Wood, W. A. J. Inst. Metals **81** (1952) 181.
10. Seitz, F. Advances in Physics **1** (1952) 85.
11. Ellwood, C. D. J. Inst. Metals **80** (1952) 217.
12. Smigelskas, H. D. and Kirkendall, E. O. Trans. A.I.M.M.E. **171** (1947) 130.
13. Barnes, R. S. Proc. Phys. Soc. (B) **65** (1952) 512.
14. Schmid, E. Z. Elektrochem. **37** (1931) 447.
15. Bakarian, P. W. and Mathewson, C. H. Trans. A.I.M.M.E. **152** (1943) 226.

THE MAGNETIC SUSCEPTIBILITY AND ELECTRONIC SPECIFIC HEAT OF TRANSITION METALS IN RELATION TO THEIR ELECTRONIC STRUCTURE*

E. C. STONER†

Information may be obtained about the electronic structure of transition metals by a proper theoretical analysis of the results of experiments of various types, two of which are considered in detail. The collective electron treatment of electronic specific heat and magnetic susceptibility is described, and expressions are obtained for the main relations in a form suitable for application to the experimental results. The density of states at the top of the electron energy band may be derived from the electronic contribution to the specific heat at low temperatures, and from this, combined with results for the magnetic susceptibility, a quantitative measure of the quasi-magnetic interaction may be obtained. The experimental results for the transition metals are collected together and critically discussed. It is shown that the paramagnetic susceptibility is higher than that estimated from the electronic specific heat assuming no additional interactions, and that the positive quasi-ferromagnetic interaction indicated is of the same order of magnitude as in the ferromagnetic metals. Recent experimental work on both the specific heat and susceptibility at low temperatures of alloys of palladium is discussed with particular reference to the determination of the forms of electronic energy bands. Theoretical work on the properties associated with bands of various forms is also described, and an interpretation is given of some of the more unusual types of temperature variation of susceptibility such as that observed for palladium. The coordination of the electronic properties of the transition metals provided by the electron energy band scheme though partial is very promising, but much further experimental work on metals and alloys at low temperatures will be required before a satisfactory overall picture can be obtained.

LA SUSCEPTIBILITÉ MAGNÉTIQUE ET LA CHALEUR SPÉCIFIQUE, ÉLECTRONIQUE, DES MÉTAUX DE TRANSITION EN RELATION AVEC LEURS STRUCTURES ELECTRONIQUES

On indique cinq types d'expériences desquelles il est possible, par une analyse théorique appropriée, d'obtenir des informations sur la structure électronique des métaux de transition. On décrit le traitement collectif des chaleurs spécifiques électroniques et des susceptibilités magnétiques; des expressions sont obtenues pour les relations principales, sous une forme qui convient à l'application aux résultats expérimentaux.

La densité des états au sommet de la bande d'énergie électronique peut être dérivée de la contribution des électrons à la chaleur spécifique aux basses températures, et cela, joint aux résultats sur la susceptibilité magnétique, permet d'obtenir une mesure quantitative de l'interaction quasi-magnétique. Les résultats expérimentaux pour les métaux de transition sont rassemblés et discutés d'une manière critique. Il est montré que la susceptibilité paramagnétique est plus grande que celle qu'on a estimée de la chaleur spécifique, électronique, en supposant qu'il n'y a pas d'interaction supplémentaire et que l'interaction positive, quasi-ferromagnétique, indiquée, est du même ordre de grandeur que dans les métaux ferromagnétiques. On discute des travaux expérimentaux, récents, sur les chaleurs spécifiques et la susceptibilité des alliages de palladium aux basses températures, en soulignant plus particulièrement la détermination des formes des bandes d'énergie électronique. On décrit aussi des travaux théoriques sur les propriétés associées aux bandes de diverses formes, et une interprétation est donnée de certains types peu communs de la variation de susceptibilité en fonction de la température, comme celle qu'on observe dans le palladium. La coordination des propriétés électroniques des métaux de transition donnée par le schéma des bandes d'énergie électronique promet beaucoup, mais est encore incomplète; de nombreuses expériences sur des métaux et alliages aux basses températures seront nécessaires avant qu'il soit possible de donner une image plus complète.

DIE MAGNETISCHE SUSZEPTIBILITÄT UND DIE ELEKTRONENKOMPONENTE DER SPEZIFISCHEN WÄRME DER ÜBERGANGSMETALLE IN BEZIEHUNG ZU DEREN ELEKTRONENSTRUKTUR

Es wird gezeigt, dass man durch geeignete theoretische Analyse von fünf Gruppen von Versuchen Daten über die Elektronenstruktur der Übergangsmetalle erhalten kann. Die Elektronenkomponente der spezifischen Wärme und die magnetische Suszeptibilität werden im Rahmen des kollektiven Elektronenmodells diskutiert, und für die wesentlichen Beziehungen werden Gleichungen in einer zur Anwendung auf experimentelle Resultate geeigneten Form erhalten. Die Dichte der Energieniveaus am oberen Rand des Elektronenbandes kann aus der Elektronenkomponente der spezifischen Wärme der tiefen Temperaturen ermittelt werden. Daraus, zusammen mit den Daten der magnetischen Suszeptibilität, lässt sich ein quantitatives Mass für die quasi-magnetische Wechselwirkung erhalten. Die experimentellen Daten für die Übergangsmetalle werden zusammengestellt und kritisch diskutiert. Es wird gezeigt, dass die paramagnetische Suszeptibilität grösser als der aus dem Elektronenanteil der spezifischen Wärme ohne Annahme weiterer Wechselwirkungen abgeschätzte Wert ist; die auftretende positive quasi-ferromagnetische Wechselwirkung ist in der gleichen Grössenordnung wie die der ferromagnetischen Metalle. Es werden neue Messungen der spezifischen

*Received September 14, 1953; in revised form October 24, 1953.

†Department of Physics, The University of Leeds, England.

Wärme und der Suszeptibilität von Palladiumlegierungen bei tiefer Temperatur diskutiert, vor allem im Hinblick auf die Bestimmung der Form der Elektronenbänder. Theoretische Arbeiten über die Eigenschaften verschieden geformter Bänder werden ebenfalls referiert, und einige ungewöhnliche Arten der Temperaturabhängigkeit der Suszeptibilität, wie z.B. im Palladium, werden interpretiert. Die zusammenfassende Beschreibung der elektronenbedingten Eigenschaften der Übergangsmetalle im Rahmen des Elektronenbändermodells ist teilweise sehr vielversprechend bevor jedoch ein zufriedenstellendes Gesamtbild erhalten werden kann, brauchen wir weitere experimentelle Arbeiten über Metalle und Legierungen bei tiefen Temperaturen.

1. Introduction: Theory, Theories and Experiment

The central problem of transition metals, as indeed of solids generally, is the determination of the energy distribution of states in them, the distribution of electrons among these states, and the spatial distribution of electron charge density. This 'electronic structure' embodies, in principle, an explanation of the observable properties.

In the most thoroughgoing purely theoretical attack on the problem the attempt is made to formulate and to solve the quantum-mechanical equations appropriate to an aggregate of interacting atoms. Even with the approximations and simplifications necessary to make the problem in any way manageable, it is a remarkable achievement that the elaborate calculations required have now been carried through with some completeness for a number of metals. The results, such as the derived electronic energy band forms, assuredly show qualitatively what will happen, and to some extent how it will happen, in an atomic aggregate. Where comparison with experiment can be made of associated properties the quantitative agreement is usually poor. This indeed is to be expected in view of the complexity of the problem, and does not put in question the correctness of the underlying theory any more than does the lack of agreement between the theoretically calculated and the 'observed' energy level values for any but the simplest atoms.

Most of the so-called theories of the transition metals (in which, for example, particular mixtures of ions are postulated, or particular numerical subdivisions of different types of bond) are on an entirely different level, and are little more, in effect, than speculative guesses as to what might be good approximations to the rigorous solution if this were known. These are not theories in any proper sense, but as speculations they may have some value. If they are to be worth considering, they must be compatible with the fundamental theoretical scheme which is known to be applicable to physico-chemical phenomena, and the various parts of the treatment must be consistent with each other. If these conditions are satisfied, the value of the treatment will depend on the extent of the coordination of experimental results which it brings about, without additional purely ad hoc hypotheses and without implications which are in essential contradiction with other experimental results. From this point of view, some of the 'theories' which have been put forward are of no value at all; there have been other suggestions, however, which, though similar in status, have illuminated the whole field.

The progress made in the theoretical calculation of band forms has recently been reviewed by Raynor [1] and will not be considered here. A brief indication will, however, be given (§2, §6) of the results of work on the related problem of determining, by the appropriate statistical treatment, the temperature variation of some of the electronic properties for bands of particular forms.

For atoms the energy level scheme is obtained with great accuracy (and is understood even though not quantitatively explained in detail) from an analysis of experimental results, in particular those on spectra. This suggests that a much better understanding could be gained of the transition metals if more attention were devoted to careful experimental measurements of which the results could be most directly related to the energy band structure. There are various types of experiment from which partial information can be obtained. (1) Measurements of the specific heat at very low temperatures can give the electronic contribution with considerable accuracy, and from this the energy density of states at the top of the occupied range can be determined. Further information is obtainable from a study of suitable alloy series, and, though with less certainty, from the temperature variation of the specific heat. (2) Measurements of the magnetic susceptibility over a wide temperature range, but necessarily including the lowest temperatures, will then give further information about the magnetic moment distribution, and about the character of the interactions. (3) Soft X-ray spectroscopy would seem to be particularly promising as a means of obtaining

almost direct information about energy band forms, but very skilful experimental technique is required, the immediate results are lacking in the precision of optical or ordinary X-ray spectroscopy, and the interpretation of them is usually difficult and uncertain. (4) Intensity measurements in X-ray diffraction provide in principle a means of attacking experimentally the problem of the spatial distribution of electron charge density, but it is doubtful whether clear-cut quantitative conclusions could be reached for the transition metals and their alloys except in very special cases. This is, however, a matter worthy of careful consideration by those engaged in the study of metals and alloys by X-ray methods. (5) Experiments on neutron diffraction give information complementary or additional to that obtainable by X-ray methods, in particular, in favourable cases, on the spatial distribution of magnetic moment density. Remarkably rapid progress has been made in recent years in this field, of which a detailed survey has been given by Bacon and Lonsdale [2].

In this paper attention will be directed mainly to work under (1) and (2). A summarizing survey of experimental results on the electronic heats of the transition elements is given in §3, and of those on magnetic susceptibilities in §4. Some of the recent work at Leeds, in which interrelated measurements have been made on the magnetic susceptibilities and specific heats at low temperature, is then outlined (§5), this being linked with further theoretical studies of the properties associated with bands of various forms (§6). The brief report on this work at Leeds is not intended to present general conclusions, which it would be premature to draw from measurements so far made on a limited number of metals and alloys over limited ranges of temperatures, but rather to give an impression of the general character of the combined attack which is being made on some of the fundamental problems of transition metals and alloys.

2. Theory of Magnetic Susceptibility and Electron Specific Heat

The form of band for which the associated electronic properties have been most fully investigated is that in which the energy density of states is proportional to the square root of the energy measured from an appropriate origin. Denoting the number of states by ν, the distribution is represented by

$$d\nu/d\epsilon = a\epsilon^{\frac{1}{2}}. \tag{1}$$

This 'standard' type of distribution (Figure 1a) applies not only when the energy is purely kinetic (for 'free' electrons, for example) but also, at least as an approximation, much more widely. It will also apply to the upper part of a band when, with the energy measured downwards from the top of the band, the distribution expression (1) holds over an adequate range (Figure 1b). This application is particularly important when there

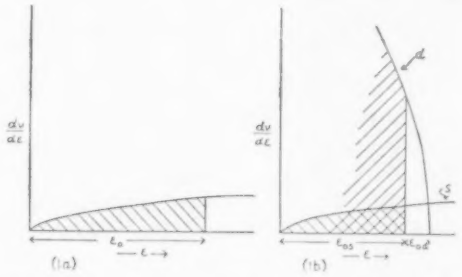

FIGURE 1. Parabolic energy bands. (1a) Form for free electrons and idealized form for *s*-electrons; (1b) Idealized form of overlapping *s*- and *d*-bands in nickel. The occupied ranges in the lowest energy state are shaded.

are overlapping bands, as for nickel and other transition elements. In nickel the *d*-band, believed to be approximately parabolic at its upper end, is overlapped by a much wider *s*-band. It is convenient to consider the distribution of 'holes' in the *d*-band rather than of the electrons. The properties associated with a band containing a given number of holes, the energy being measured from the top, are in general the same as with a 'mirror-image' band containing the same number of electrons, the energy being measured from the bottom. In determining the distribution of electrons among the states, and its variation with temperature and other conditions, Fermi-Dirac statistics must be used, based essentially on the premises that the particles are indistinguishable, and that not more than one may occupy a given quantum state. (For electrons there are two directions of spin, and two electrons may occupy a given translational state only if the spins are antiparallel.)

Normally, at absolute zero, the lowest energy states in a band would be occupied by electrons in pairs, the band being filled up to an energy ϵ_0 (the change in wording for Figure 1b will be obvious). The electronic system corresponding to a single band may therefore be specified by the band form, such as is represented by (1), the number of electrons, N, in it (or the number of electrons per atom, q), and the energy width of

the occupied portion, ϵ_0, in the lowest energy state. It is sometimes convenient to express the energy, ϵ_0, as a temperature, θ_F, where

$$\epsilon_0 = k\theta_F, \tag{2}$$

referring to θ_F as the Fermi temperature (by analogy with the Debye temperature, θ_D). It may be noted that the numerical relation between the energy expressed in ergs, ϵ_0, in electron volts, ϵ_0', and as a temperature, θ_F, is

$$\epsilon_0 = 1.6020 \times 10^{-12}\, \epsilon_0' = 1.3805 \times 10^{-16}\, \theta_F. \tag{2a}$$

With increase in temperature a 'tail' develops, the electrons spreading into the higher energy ranges. Ultimately, at very high temperatures ($T \gg \theta_F$) the distribution approximates to that given by Maxwell-Boltzmann statistics. The effect of a magnetic field is to favour energetically spin directions parallel to the field, so that with N_+ spins parallel and N_- antiparallel to the field, the relative magnetization, ζ, is given by

$$\zeta = \frac{N_+ - N_-}{N_+ + N_-} = \frac{N_+ - N_-}{N}. \tag{3}$$

It may be noted that ferromagnetics are distinguished by the occurrence, below a critical temperature, of magnetization in the absence of an applied field (spontaneous magnetization). This may be formally attributed to a quasi-magnetic molecular field, which arises from the interactions between the electrons, and which, to a first approximation, is proportional to the magnetization.

The determination of the temperature dependence of physical properties associated with electrons in a band is much more troublesome with Fermi-Dirac than with Maxwell-Boltzmann statistics. The quantities required may be expressed in terms of certain Fermi-Dirac integrals. Except for low and high temperatures ($T/\theta_F \to 0$ and $T/\theta_F > 1$ respectively), for which convenient series expressions are obtainable, these integrals must be evaluated numerically. Extensive tables are available of Fermi-Dirac integrals which are immediately applicable to the standard distribution of states [3], and with the aid of these, detailed precise calculations have been made by Stoner of the temperature dependence of various characteristic properties. Extensive tables have been given for electronic energy and specific heat [4], spin paramagnetism [5], collective electron ferromagnetism [6], [7], and the general thermodynamic functions [8]. More recently accounts of the treatment have been included in general surveys having particular reference to ferromagnetism [9], [10]. For the present purpose it will be sufficient to indicate the general character of the results for electronic specific heat and paramagnetism. The variation effectively over the whole temperature range for the standard band form will be shown by curves, and formulae appropriate in the low-temperature limit will be given both for the standard band and for bands of any form.

Specific heat. In Figure 2 is shown, in reduced form, the variation with temperature of the electronic energy and specific heat.

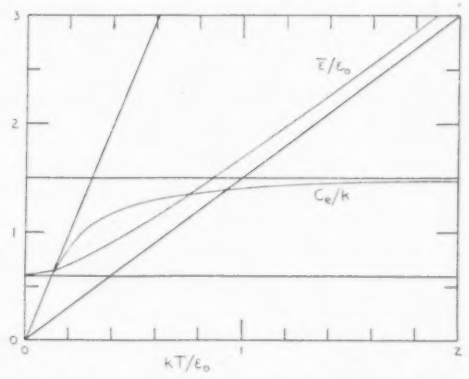

FIGURE 2. Variation with temperature of electronic energy and specific heat for standard band form. ϵ_0, maximum electron energy (band with) at absolute zero. $\bar{\epsilon}$, mean energy per electron. C_e specific heat per electron; k, Boltzmann constant. The straight lines are the tangents at $kT/\epsilon_0 = 0$, and the asymptotes to the curves.

For free electrons θ_F (equal to ϵ_0/k) may be of the order of 10,000°, so that the corresponding specific heat would be small not only at the lowest temperature, but over most of the ordinary temperature range (the 'low-temperature' approximations would here be adequate). For the holes in the d-band of nickel, and other transition elements, θ_F is of the order of 1000°, and ordinary temperatures correspond to the intermediate range. In certain circumstances, θ_F may be considerably lower than this, so that the results for the ordinary temperature range would correspond closely to those given by classical statistics. The limiting value of the specific heat at low temperatures is given by

$$\frac{C_e}{k} \to \frac{\pi^2}{2}\left(\frac{kT}{\epsilon_0}\right) = \frac{\pi^2}{2}\left(\frac{T}{\theta_F}\right) = 4.9348\left(\frac{T}{\theta_F}\right). \tag{4}$$

The electronic contribution to the gram atomic heat, $(C_A)_e$, expressed in cal. deg.$^{-1}$ mole.$^{-1}$, is

$$(5)\quad \frac{(C_A)_e}{T} \to \frac{\pi^2}{2}\left(\frac{qR}{\theta_F}\right) = 9.8028\left(\frac{q}{\theta_F}\right) = 8.4471 \times 10^{-4}\left(\frac{q}{\epsilon_0'}\right),$$

where q is the number of electrons (Figure 1a) or holes (Figure 1b) in the band per atom, and ϵ_0' is in electron volts.

Whatever the band form, the electronic heat at low temperatures is proportional to the temperature and to the energy density of states at the top of the Fermi distribution, being given by

$$(6)\quad \frac{C_e}{k} \to \frac{2\pi^2}{3}\frac{kT}{q}\left(\frac{d\nu'}{d\epsilon}\right)_{\epsilon_0},$$

where $(d\nu'/d\epsilon)$ is the density of states per atom corresponding to one direction of spin. (For the standard band form, (6) and (4) are equivalent.) The electronic contribution to the gram atomic heat may be usefully be expressed as

$$(7)\quad (C_A)_e/T = 1.1263 \times 10^{-3}\,(d\nu'/d\epsilon')_{\epsilon_0},$$

where $(C_A)_e$ is in cal. deg.$^{-1}$ mole^{-1}, ν' is the number of states per atom for one direction of spin, and ϵ' is in electron volts. Using (7), the energy density of states at the top of the Fermi distribution may at once be found from the coefficient, γ, of the term linear in the temperature in the usual form of expression of the results of specific heat measurements at low temperatures (see §3).

Magnetic susceptibility. The variation with temperature of the magnetic susceptibility of electrons in a parabolic band is shown, in reduced form, in Figure 3.

The statements made about the temperature range covered by the specific heat curve of Figure 2, and the trend towards the results given by classical statistics at high temperatures are applicable to the inverse susceptibility curve of Figure 3. The trend of the susceptibility towards constancy at the low-temperature limit and to a linear variation with the inverse of the temperature (Curie law) at the high-temperature limit is to be noted. The limiting value of the susceptibility at low temperatures is given by

$$(8)\quad (\chi_e) \to \frac{3}{2}\left(\frac{\mu^2}{\epsilon_0}\right) = \frac{3}{2}\left(\frac{\mu^2}{k\theta_F}\right),$$

or, for the electronic contribution to the gram atomic susceptibility,

$$(9)\quad (\chi_A)_e \to \frac{3}{2}\left(\frac{M_B^2 q}{R\,\theta_F}\right) = 5.6279 \times 10^{-1}\,(q/\theta_F) = 4.8496 \times 10^{-5}\,(q/\epsilon_0'),$$

where M_B is the magnetic moment per mole for one Bohr magneton per molecule, q is the number of electrons per atom in the band, and ϵ_0' is the Fermi energy in electron volts. If the quasi-magnetic interaction is negligible, the limiting low-temperature susceptibility is directly proportional to the energy density of states at the top of the Fermi distribution, being given by

$$(10)\quad \chi_e \to 2\mu^2\frac{1}{q}\left(\frac{d\nu'}{d\epsilon}\right)_{\epsilon_0}$$

or, for the electronic contribution to the gram atomic susceptibility,

$$(11)\quad (\chi_A)_e = 6.4661 \times 10^{-5}\,(d\nu'/d\epsilon')_{\epsilon_0},$$

where ν' and ϵ' have the same significance as in (7).

Effect of molecular field. The effect of interactions of the exchange, or more generally overlap, type may be to give rise to terms in the energy expression proportional to even powers of the magnetization. In the simplest case, when terms involving powers higher than the second may be neglected, the effect is equivalent to that covered formally by the Weiss assumption of a quasi-magnetic molecular field proportional to the magnetization. The effect of such interaction may be taken into account in a very simple way, as was first shown by Stoner (11). With the standard band form, using Fermi-Dirac statistics, the susceptibility is increased in a way corresponding to a constant (i.e., temperature-independent) decrease in the inverse susceptibility. In reduced form,

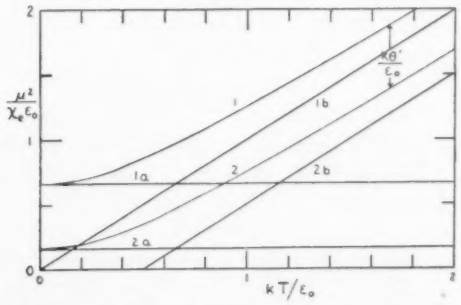

FIGURE 3. Variation with temperature of electronic magnetic susceptibility for standard band form. χ_e, susceptibility per electron; μ, Bohr magneton; ϵ_0, maximum electron energy at absolute zero. (1) Reduced inverse susceptibility against reduced temperature; (1a), (1b) Tangent and asymptote to (1) at low and high temperatures respectively; (2), (2a), (2b) Corresponding curves with positive interaction, for a value 0.5 of the reduced interaction parameter, $(k\theta'/\epsilon_0)$.

$$(12) \qquad \frac{\mu^2}{\chi_e \epsilon_0} = \frac{1}{\zeta}\left(\frac{\mu H}{\epsilon_0}\right) = \frac{T}{\theta_F} f\left(\frac{T}{\theta_F}\right) - \frac{\theta'}{\theta_F},$$

where the first term represents the reduced susceptibility without interaction (and is represented by curve 1 in Figure 3), and θ' is the interaction parameter. This parameter is such that the quasi-magnetic energy per electron in an assembly magnetized to a relative magnetization ζ (see (3)) is equal to $-\frac{1}{2} k\theta'\zeta^2$. It is proportional to the Weiss molecular field coefficient, N_W, the proportionality factor involving constants of the particular material and general physical constants. The variation of susceptibility with temperature when θ'/θ_F is taken as 0.5 is shown in curve 2 of Figure 3.

An important new point becomes evident when the appropriate Fermi-Dirac statistics is applied to this problem. With classical (Maxwell-Boltzmann) statistics a positive molecular field would always give rise to ferromagnetism below a certain temperature. In Figure 3, with $\theta'/\theta_F = 0.5$, spontaneous magnetization would set in at the temperature corresponding to the point at which the straight line 2b crosses the temperature axis. With Fermi-Dirac statistics this crossing will not occur, as is apparent from curve 2, unless θ'/θ_F, that is, effectively, the ratio of the interaction energy to the energy width of the band, exceeds a critical value. From (8) and (12) the condition for ferromagnetism to occur is

$$(13) \qquad \theta'/\theta_F = k\theta'/\epsilon_0 > 2/3.$$

The complications of ferromagnetism will not be considered further here. With an effective interaction coefficient which is positive, and not too large, the paramagnetic susceptibility will be increased by an amount which is calculable over the whole temperature range for the standard band form, and in the low temperature limit for the general band form. Thus, with the standard band form, for the inverse of the susceptibility per electron at low temperatures equation (8) with equation (12) leads to

$$(14) \qquad \frac{1}{\chi_e} \rightarrow \frac{2k}{3\mu^2}\left(\theta_F - \frac{3}{2}\theta'\right),$$

and the corresponding modifications may be made in (9). The quasi-magnetic interaction parameter, θ', may be expressed in terms of the difference of low-temperature limiting values of the inverse susceptibilities with and without interaction. With $(\chi_A)_e$ as the gram atomic susceptibility as observed, and $\{(\chi_A)_e\}_0$ as the value without interaction,

$$(15) \qquad \theta'/q = 3.7519 \times 10^{-1}\,[\{1/(\chi_A)_e\}_0 - 1/(\chi_A)_e].$$

An estimate of $\{(\chi_A)_e\}_0$ may be obtained from the electronic specific heat.

Relation between susceptibility and specific heat. The ratio of the susceptibility (without interaction) to the electronic specific heat for the whole temperature range can be determined for the standard band form. Considering only the low temperature limit (for which the result is the same for any band form), the ratio, from (4) and (8) is given by

$$(16) \qquad \frac{C_e/T}{(\chi_e)_0} = \frac{\pi^2}{3}\left(\frac{k}{\mu}\right)^2.$$

At this low temperature limit the ratio, with the gram atomic heat in cal. deg.$^{-1}$ mole^{-1}, may be expressed in a manner convenient for application to experimental results by

$$(17) \qquad \frac{\{(C_A)_e/T\} \times 10^4}{\{(\chi_A)_e\}_0 \quad \times 10^6} = 1.7418 \times 10^{-1} = \frac{1}{5.7412}.$$

This numerical relation is potentially extremely useful, for if the observed value of χ_A at low temperatures significantly exceeds the value calculated by (17) from C_A/T, there is an immediate indication of a positive molecular field effect, of which a more quantitative estimate is obtainable from (15).

In the next three sections some of the experimental results will be surveyed and briefly considered in the light of the simple form of the collective electron treatment presented in this section.

3. Electronic Heats: Collected Results

It is found that, at sufficiently low temperatures, the gram atomic heat, C_A, of many metals can be represented with good accuracy by an expression of the form,

$$(18) \qquad C_A = \gamma T + bT^3.$$

The term bT^3 may be associated with the lattice vibrations, and on the simple Debye theory is given by

$$(19) \qquad bT^3 = (12\pi^4 R/5)(T/\theta_D)^3 = 4.6440 \times 10^2 (T/\theta_D)^3,$$

where θ_D is the Debye temperature. The term γT is associated with the electronic contribution to the heat capacity, and γ (equal to $(C_A)_e/T$) is given by (5) of §2 for a parabolic band, or generally by (7). Usually measurements must be made in the liquid helium range if reliable values of γ and

b are to be obtained. In some cases (depending on the relative magnitudes of γT and bT^3) apparently satisfactory estimates of γ and b can be made from measurements in the liquid hydrogen range, but even then the values obtained must be treated with reserve, owing, among other things, to the possibility of variations in the effective value of θ_D. In the superconducting state there is considerable evidence that the linear term in the specific heat expression (18) vanishes. In principle, it is possible to derive the value of γ (for the normal state) from measurements of the threshold field over a range of temperatures. Very precise measurements are required and these are difficult to make over the necessary range. With a few exceptions, the values of γ obtained by this method up to the present must be regarded as no more than very rough estimates.

Collected values of γ are given in Table I. For the reasons just indicated little reliance can be placed on the estimates derived from measurements on superconductors, as is brought out strongly by the two values in brackets quoted for niobium.

TABLE I

ELECTRONIC HEATS OF THE TRANSITION ELEMENTS

$\gamma \times 10^4$ ($\gamma = (C_A)_e/T$, cal. mole^{-1} deg.$^{-2}$)

(The values in brackets have been estimated from magnetic measurements on superconducting materials, the remainder from calorimetric measurements.)

Sc	Ti	V	Cr	Mn	Fe	Co	Ni
	8.3	[14.1]	3.7	42.1	12.0	12.0	17.4
Y	Zr	Nb	Mo	Ma	Ru	Rh	Pd
	6.9	21 [60,375]			[3.0]		31.0
La	Hf	Ta	W	Re	Os	Ir	Pt
		14.1 [19.4]	51.1	[4.6]	[2.7]		16.1

Calorimetric measurements

Ti, Cr, Zr FRIEDBERG, S. A., ESTERMANN, I. and GOLDMAN, J. E. Phys. Rev. **85** (1952) 375.

Mn ELSON, R. G., GRAYSON-SMITH, H. and WILHELM, J. O. Can. J. Res. **18** (1940) 82.
ARMSTRONG, L. D. and GRAYSON-SMITH, H. Can. J. Res. **27** (1949) 9.

Fe DUYCKAERTS, G. Physica **6** (1939) 401.
KEESOM, W. H. and KURRELMEYER, B. Physica **6** (1939) 364.

Co DUYCKAERTS, G. Physica **6** (1939) 817.

Ni KEESOM, W. H. and CLARK, C. W. Physica **2** (1935) 513.

Nb BROWN, M., ZERMANSKY, M. W. and BOORSE, H. A. Phys. Rev. **86** (1952) 134.

Pd PICKARD, G. L. Nature **138** (1936) 123.
PICKARD, G. L. and SIMON, F. E. Proc. Phys. Soc. **61** (1948) 1.

Ta KEESOM, W. H. and DESIRANT, M. Physica **8** (1941) 273.

W SILVIDI, A. A. and DAUNT, J. G. Phys. Rev. **77** (1950) 125.

Pt KOK, J. A. and KEESOM, W. H. Physica **3** (1936) 1035.

Measurements on superconductors

V WESLER, A. and CORAK, W. S. Phys. Rev. **79** (1950) 737.

Nb DAUNT, J. A. and MENDELSSOHN, K. Proc. Roy. Soc. **160** (1937) 127.
COOK, D. B., ZERMANSKY, M. W. and BOORSE, H. A. Phys. Rev. **80** (1950) 737.

Ru, Os GOODMAN, B. B. Nature **167** (1951) 111.

Ta DAUNT, J. G. and MENDELSSOHN, K. Proc. Roy. Soc. **160** (1937) 127.

Re DAUNT, J. G. and SMITH, T. S. Phys. Rev. **88** (1952) 309.

The most striking features of the values for γ, as derived from calorimetric measurements, is that all are high, with the exception of that for chromium, as compared with the values for the 'simple' metals. (As examples, the values of $\gamma \times 10^4$ for Cu, Mg and Al are approximately 1.78, 3.25 and 3.48 respectively.) The high values of γ for the transition metals receive an immediate qualitative interpretation in terms of the band picture as arising from the high density of states at the top of the electron distribution (at low temperatures) in the region of the overlap of the relatively wide (and low) s band and the relatively narrow (and high) d band (see Figure 1b). From (7), the energy density of states, expressed as the number of states per atom per electron volt, is given by

$$(20) \qquad (d\nu'/d\epsilon') = 8.8788 \times 10^{-2} (\gamma \times 10^4).$$

This gives values ranging from 2.66 for Pd to 0.61 for Zr (to be compared with 0.16 for Cu). (Although the bands in general are far from parabolic in form, it is interesting to note that if they were the corresponding values of θ_F/q, from (5), would range from about 3160° for Pd to 14200° for Zr, to be compared with 55700° for Cu.)

It is tempting, and it would not be particularly difficult, to devise band forms for the transition elements which are compatible with the γ values given in Table I. Speculative attempts of this kind would, however, serve no useful purpose until many further results are available both for

the metals and for alloys. Where detailed calculations of band forms have been made, the calculated values of γ usually diverge widely from the experimental values. Thus the calculated values of $\gamma \times 10^4$ for iron [12] and tungsten [13] are about 4.6 and 4.8 as compared with the experimental values of 12.0 and 51.1 respectively. Exceptionally, the calculated value for nickel [14] of about 16.9 is very close of the experimental value of 17.4, but, as the author states, this agreement must be regarded as somewhat fortuitous owing to the approximations made in the calculations.

Although there are no obvious defects in the experimental methods or the methods of analysing the experimental results the value obtained for γ for tungsten by Silvidi and Daunt is, as they appreciate, so high as to be out of line with the values for other metals. This will be referred to again in §4. On the other hand there is no reason to doubt the reliability of the low value for chromium, which is compatible with the top of the Fermi distribution falling in a range of the relatively wide composite energy band associated with the *d* and *s* states where the density of states is comparable with that for free electrons.

It will be clear from this short survey that significant information has already been obtained from investigations of specific heat at low temperatures. This information, however, is very fragmentary, and much further extensive and careful work will be necessary before the potentialities of this method of attack on fundamental problems of the electronic structure of the transition metals can be fully realised.

4. Magnetic Susceptibilities: Collected Experimental Results

In the classical investigations of Honda [15] and Owen [16] the magnetic susceptibilities of some sixty elements, including nearly fifty metals, were measured over a range of temperature extending from −170°C to over 1000°C. There has been no such comprehensive investigation since, and the results are by no means entirely superseded. In later work, however, usually on a limited number of elements in each particular investigation, improved methods of measurement may have been adopted and, a most important consideration, materials of higher purity have usually been used. In general, therefore, the results may be presumed to be more reliable. The results obtained for the metals generally have been collected together and discussed from time to time in books, e.g., Stoner [17], Selwood [18], and papers, e.g., Stoner [19], Bommer [20]. During the last few years further work in this field has been carried out in a number of centres. An examination of the results obtained for particular elements by different investigators, giving greater weight to the more recent work, suggests that the room temperature susceptibility of the transition elements cannot usually be regarded as 'established' to better than about 5 per cent (cf. Hoare and Walling [21, p. 340]) and in some cases the uncertainty is much greater than this. This should be borne in mind in connection with the values given for the gram atomic susceptibility, χ_A, in Table II. These are not means of values obtained by different investigators, but are taken from the papers referred to, which are usually the most recent dealing with the particular element. For the present purpose a conspectus of susceptibility values for the transition elements on which reasonable reliance can be placed is all that is required, and an elaborate critical discussion of the various results for each particular element would be out of place. It should be mentioned that the value given by hafnium is from some preliminary results privately communicated.

The results which have been obtained for the temperature variation of the susceptibility are extremely difficult to summarize in a useful way. A considerable number of measurements have been made above room temperature up to about 1000°C, as in the original work of Honda, and very recently a method has been developed for extending the temperature range up to 1850°C by Kriessman [22]. Below room temperature measurements have usually been made only at one or two isolated temperatures, e.g., at 90°K by Bommer [20], at 14.2° and 20.4°K by de Haas and van Alphen [23]. From the theoretical standpoint, extended measurements down to the lowest temperatures would be of very great value. In the absence of adequate information about the low temperature range except for a few of the metals (see §5), an indication of the order of magnitude of the temperature variation has been given in Table II in the form of estimates from available data of $(d\chi_A/dT)$ at room temperature. For most of the transition elements the temperature variation is small at room temperature (palladium is an obvious exception), and where this is so, the aggregate change over the whole temperature range which has been investigated is usually small also, corresponding to a gradual monotonic increase or decrease.

TABLE II

GRAM ATOMIC SUSCEPTIBILITIES OF THE TRANSITION ELEMENTS AT ROOM TEMPERATURE

$\chi_A \times 10^6$.

(The order of magnitude of the temperature variation is shown by the estimated values of 100 $(d\chi_A/dT) \times 10^6$ given in brackets.)

Sc	Ti	V	Cr	Mn	Fe	Co	Ni
315	153	230	160	533			
(−24)	(+4)	(−1)	(0)	(−14)			
Y	Zr	Nb	Mo	Ma	Ru	Rh	Pd
191	122	212	91		44	102	558
(−7)	(+1)	(−2)	(0)		(0)	(+3)	(−140)
La	Hf	Ta	W	Re	Os	Ir	Pt
122	81	154	52	69	10	26	190
(−3)	(+1)	(−1)	(0)	(0)	(+1)	(+2)	(−12)

Sc, Y, La	BOMMER, H. Z. Elektrochem. **45** (1939) 357.
Ti, V, Zr	KLEMM, W. Z. Elektrochem. **45** (1939) 354.
Cr	BATES, L. F. and BAQI, A. Proc. Phys. Soc. **48** (1936) 781.
Mn	SERRES, A. Phys. Rad. **9** (1938) 377.
Nb, Mo, W	DE HAAS, W. J. and VAN ALPHEN, P. M. Proc. Kon. Akad. Amst. **36** (1936) 263.
Ru, Os, Ir	GUTHRIE, A. N. and BOURLAND, L. T. Phys. Rev. **37** (1931) 303.
Rh, Pd, Ta, Pt	HOARE, F. E. and WALLING, J. C. Proc. Phys. Soc. B, **64** (1951) 337.
Hf	KRIESSMAN, C. J. Rev. Mod. Phys. **25** (1953) 122.
Re	PERAKIS, N. and CAPATOS, L. J. Phys. Rad. **6** (1935) 642.

In some cases, however, there is a change of sign in the variation. For manganese, for example, according to recent preliminary measurements of Kriessman, the susceptibility increases with increasing temperature by about 7 per cent from −200°C to −125°C and decreases by 4 per cent from −125°C to +25°C (the curve is gently concave downwards with a rather flat maximum).

The room temperature susceptibilities of the transition elements are plotted effectively against atomic number in Figure 4. This graph brings out more immediately the general character of the regularities and irregularities in the sequence of values along the rows and columns of the periodic table. A somewhat similar graph using the then available results was given by Bommer [20], who appears to have been the first to draw attention explicitly to the peculiar alternation of relatively high and low values for the first five elements in each of the transition series. It is tempting to suggest that this alternation may be connected with the possible occurrence of sub-bands each accommodating two electrons per atom, such as are indicated in the calculations of Manning [12] for iron, but such a suggestion, based on the susceptibilities alone, must be regarded as purely speculative.

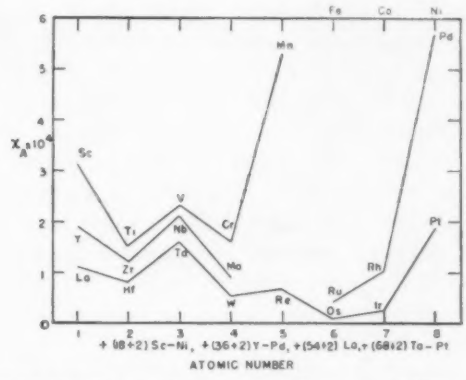

FIGURE 4. Gram atomic magnetic susceptibility of the transition elements at room temperature. (For references, see Table II.)

The susceptibilities of the transition elements are in most cases much higher than those of other metals, for many of which the paramagnetic contribution is of the same order of magnitude as the diamagnetic contribution from the closed electron groups, and the resultant observed susceptibility is as often diamagnetic as paramagnetic. (As examples, the values of $\chi_A \times 10^6$ for the alkali metals Na, K and Rb are in the range +10 to +20, while Cu, Ag and Au are all diamagnetic.) For free electrons, q per atom, from (9) (using the appropriate calculable values of ϵ_0), the calculated values of $\{(\chi_A)_e/q\} \times 10^6$ would lie between about 5 and 25. For very narrow bands, in contrast, the situation would approach that with quasi-classical statistics. With negligible quasi-magnetic interaction, a Curie law would be followed, with a value of $\{(\chi_A)_e/q\} \times 10^6$ at room temperature of about 1280. The collective electron treatment outlined in §2 covers, in a general way, all these possibilities. For the alkali and noble metals the effective Fermi temperature, θ_F, is large, for some of the rare earth metals small, and for the transition metals intermediate.

The temperature variation of the susceptibility of the transition elements raises many points of interest, but in view of the incompleteness of the data for the low-temperature range, only a few comments will be made here. The temperature variation is almost always small compared with

that of a Curie law paramagnetic (for which, at room temperature, the value of 100 $(d\chi_A/dT)$ would be equal to $-0.3413\chi_A$). This type of variation is approached in the room temperature region most nearly by palladium (see §5). In many cases the susceptibility is almost constant. The magnitude of the variation is compatible with the general treatment of §2, though an increase with temperature would not of course occur with an energy band of standard form (see §6). It has been noted by Kriessman [22] that the sign of the variation alternates in successive columns of the periodic table (see Table II), and it is probably significant that there is usually a decrease for elements of higher susceptibility (Table II, Fig. 4). There cannot, however, be a simple general law of this kind, as for some of the elements the sign of the temperature variation changes over the temperature range.

As described in §2, the value of the susceptibility, with zero quasi-magnetic interaction, $\{(\chi_A)_e\}_0$ can be calculated from the low temperature electronic heat (see (17)). Further the sign and magnitude of the quasi-magnetic interaction can be estimated from the difference between this calculated value and the observed value (see (15)). Insufficient experimental results are available to enable a significant extrapolation to absolute zero to be made, but, since the temperature variation is usually small, it is unlikely that results obtained by using the room temperature values will be seriously in error. As the results are of considerable interest, some of the values obtained are collected together in Table III, though it must be stressed that the values must be regarded as very provisional. In view of the special uncertainties in the values of γ derived from measurements on super-conductors, calculations have been made only for those elements for which γ has been determined from calorimetric measurements.

Tungsten is completely out of line with the other elements in Table III, and since there is no reason to expect strongly marked peculiarities in the electronic characteristics, and the values in the literature for the susceptibility are not widely divergent, it seems possible that the value of γ is at fault, as already suggested in §3. Further experiments are obviously desirable.

It cannot be excluded that for the other elements there may be substantial errors in the γ values, most of which rest on a single determination. Further, the observed susceptibility values refer to room temperature, and in most cases can hardly be relied on to better than 5 per cent. For these reasons it would be misguided to discuss the values derived for θ'/q in detail. There can be little doubt however, about the main point brought out by the table. For all the elements listed, except tungsten (that is, for all the transition elements for which there are reasonably reliable experimental results for both the electronic heat and the susceptibility) the observed susceptibility is substantially higher than the value calculated from the electronic heat on the assumption that the quasi-magnetic interaction is negligible. This means that the interaction coefficient which corresponds to the Weiss molecular field coefficient is positive, and that what may for brevity be called 'positive interaction' is by no means restricted, among metals, to the ferromagnetic metals, but is general among the transition elements. This general interpretation of the magnetic properties of the transition elements was put forward a good many years ago by Stoner [11], but the present approach paves the way towards a more quantitative treatment.

With regard to the rough provisional values given in Table III for θ'/q, it may be recalled that q is the effective number of electron spins per atom in the band concerned. (If there are n electrons per atom in a band which can accommodate m electrons, q is equal to n if $n \leqslant m/2$, or to $m - n$ if $n \geqslant m/2$.) For the alkali and noble metals, $q = 1$. For the transition metals it seems

TABLE III

COMPARISON OF OBSERVED VALUES OF SUSCEPTIBILITY AND VALUE CALCULATED FROM THE ELECTRONIC HEAT FOR THE SUSCEPTIBILITY WITH NEGLIGIBLE QUASI-MAGNETIC INTERACTION

$\gamma = (C_A/T)_{T\to 0}$.
$\{(\chi_A)_e\}_0$ estimated values of gram atomic susceptibility with zero quasi-magnetic interaction. (See equation (17) and Table I.)
$(\chi_A)_{obs}$ observed gram atomic susceptibility at room temperature. (From Table II.)
θ' derived interaction parameter (see equation (15)).
q effective number of electrons (or holes) per atom in the band.

	$\gamma\times10^4$	$\{(\chi_A)_e\}_0\times10^6$	$(\chi_A)_{obs}\times10^6$	θ'/q
Ti	8.3	48	153	5 400
Cr	3.7	22	160	15 100
Mn	42.1	242	533	850
Zr	6.9	40	122	6 400
Nb	21	121	212	1 340
Pd	31.0	178	558	1 410
Ta	14.1	81	154	2 200
W	51.1	293	52	− 5 900
Pt	16.1	92	190	2 060

likely that, owing to the occurrence of sub-bands and overlap, the effective value of q will ordinarily be less than unity. The energy per electron is lower when the spins are completely aligned than when the resultant moment is zero by $\frac{1}{2}k\theta'$. Bearing in mind that the value of θ' for nickel is about 2000°, some of the values of θ'/q in Table III may seem large. Superficial consideration might suggest that, in terms of the present symbolism, θ' would be large for ferro-magnetic metals, but small and even negative for other metals. The factor determinative of the occurrence of ferromagnetism is, however, the relative magnitude of θ' and a parameter specifying in some suitable way the energy spread of the band (cf. (13) for a parabolic band). For a widely spread band (which would ordinarily be associated with a small value of γ) θ' may be very large without the so specified quasi-magnetic interaction being large enough to give rise to ferromagnetism. It may be noted that even for free electrons the quasi-magnetic interaction is positive, and for sodium, treating one electron per atom as free, the theoretically calculated exchange effect (cf. Seitz, [24], p. 602) corresponds, with the present symbolism, to a θ' value of the order of 10,000°; but since the effective θ_p is some three times as large, sodium is not merely nonferromagnetic, but it has only a feeble and almost constant paramagnetism. Great difficulties have been encountered in the theoretical treatment of ferromagnetism by methods of the kind initiated by Heisenberg, in which the effective starting point is the Heitler-London treatment of the hydrogen molecule. The exchange interaction integral for hydrogen is negative, and although plausible reasons have been given for the onset of a positive exchange effect for the ferromagnetic metals, and well-known curves showing this have been given, the more detailed calculations by this particular method have persistently given negative exchange effects except in rather special conditions. If the approach is one which takes free or nearly free electrons as the starting point the occurrence of positive exchange effects would be regarded as normal. The present preliminary analysis of the experimental results for the transition elements shows clearly that the relevant interaction effects are positive, and that the occurrence of ferromagnetism is not due simply to positive interaction, but to the relative magnitude of these particular interactions and those determining the energy spread of the states in the electronic energy bands. Some of the recent more fundamental work on the theory of metals (e.g., Slater, [25]; Wohlfarth, [26]) shows much better promise than did most of the earlier work of linking up satisfactorily with the general conclusions reached in the present analysis of the experimental results, and so with the experimental results themselves.

5. Some Recent Investigations on Transition Metals and Alloys at Low Temperatures

A few years ago work was started on the development of a small scale low temperature laboratory in the Physics Department at the University of Leeds. One of the main aims was to make accurate measurements of the magnetic susceptibilities and specific heats of selected metals and alloys such as might lead to more precise information about their electronic structure. It seems appropriate to give some indication of the character of the work which has been carried out and of the general programme envisaged, though it is unnecessary to give details which can be found in recent readily accessible publications. It was thought desirable at first to gain experience in the experimental methods by working with liquid hydrogen, and the measurements so far made have been limited to the range from about 20° to 290°K for susceptibilities, and from about 10° to 20°K for specific heats. It is hoped very shortly to make measurements in the liquid helium range, for which suitable apparatus has been designed and constructed.

It is envisaged that measurements will mainly be made on transition metals and alloys (fairly extensive investigations of diamagnetic metals have been, and are being, carried out in other centres). The aim, however, is not so much to make a broad experimental survey, for this is provided by the results which have been reviewed, but rather to select metals and alloy series for which detailed accurate measurements would be most likely to lead to significant conclusions having a wider bearing. (It should perhaps be mentioned that the choice is partly conditioned by the availability of the metals in a state of high purity, and in a suitable form.) An enormous amount is now known about the ferromagnetic metals iron, cobalt, and nickel, and nickel, in particular, has been the subject of innumerable experimental and theoretical studies of a fundamental kind. For this reason, and bearing in mind the relation indicated by the collective electron treatment between metallic ferromagnetism and paramagnetism, elements in the triads of the other transition series almost pick themselves out as having priority for studies

of the kind in view, and among them, in particular, palladium and platinum, in the same column of the periodic table as nickel. It may be mentioned that a careful analysis in the light of the collective electron treatment, was made a few years ago of the experimental results then available for palladium and platinum by Wohlfarth [27].

The magnetic measurements are made essentially by measuring the force on a small specimen in a nonhomogeneous field, using a Sucksmith balance. This method is very satisfactory for comparative measurements, but it was necessary to make initially absolute measurements, using a Gouy method, on a material to serve as a standard. Tantalum was selected as especially suitable for this purpose, and the first definitive measurements completed in these particular investigations were an absolute determination of the susceptibility of Ta, and a comparative determination of the susceptibilities of Rh, Pd and Pt, all at room temperature [21]. Measurements on the susceptibility at different temperatures were made by a photographic recording method. This enabled the temperature range from liquid hydrogen to room temperature to be traversed in a few hours as the specimen was allowed to warm up, the susceptibility being determinable from the recorded deflections at small temperature intervals over the whole range [28]. In the work referred to the susceptibilities for Rh, Pd and Pt were measured from 20° to 290°K. Measurements have since been made on a number of Pd-Rh alloys [29], and, in conjunction with specific-heat measurements over the range 10° to 20°K, on Pd-Ag alloys [30]. The specific-heat measurements are made by standard methods, with various refinements in detail. It may be mentioned that they are more troublesome than the susceptibility measurements, and that considerably larger quantities of material are required (of the order of 50 gm as compared with 1 gm).

Some of the results obtained by Hoare and his collaborators for the susceptibility of palladium and palladium-silver alloys are shown in Figure 5. The maximum in the susceptibility of palladium had not previously been observed and it raises new and interesting questions which will be referred to again in the next section. From room temperature down to about 100°K the variation of susceptibility with temperature is of a kind corresponding closely to that for a parabolic energy band as shown in Figure 3. The form of the curve shows at once that the band form is more complicated than this. With addition of silver the maximum disappears but the upward turn which occurs with some of the alloys of higher silver content is very intriguing and emphazises the desirability of extending the measurements on all these alloys down to the helium range.

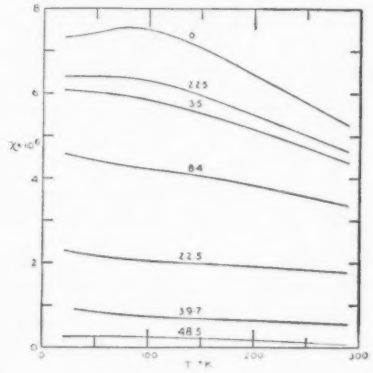

FIGURE 5. Susceptibility against temperature for palladium-silver alloys. Atomic percentage of silver is indicated on the curves.

At room temperatures the susceptibility of the alloys decreases monotonically to about 60% silver after which it remains approximately constant, as had previously been observed [31; 32], and it is reasonable to seek a qualitative explanation of this behaviour in terms of the filling up of holes, approximately 0.6 per atom, in the *d*-band by the *s*-electrons of silver. (This corresponds essentially to the behaviour of nickel on the addition of copper.) Much more direct information is obtainable on this point from specific-heat measurements than from susceptibility measurements. The specific-heat measurements that have been made over the range from 10°–20°K enable the electronic and lattice contributions to be separated with reasonable certainty for the small silver contents, but owing to the falling off in the electronic contribution the separation cannot be convincingly carried out for the higher silver contents until measurements are made in the helium range. Assuming that, for the smaller silver contents at least, alloying does correspond to the filling up of the palladium *d*-band, the form of the band obtained from the measurements is as shown in Figure 6. It must be stressed that this band form is to be regarded as very provisional until measurements at lower temperatures have been made, but it seems unlikely that the initial fairly rapid decrease will be substantially modified.

As for the transition metals generally, a compari-

son of the electronic heats and susceptibilities of the palladium-silver alloy indicates that for the lower silver contents the quasi-magnetic interaction remains positive and comparable in magnitude with that for palladium itself.

The atomic number of rhodium is one less than

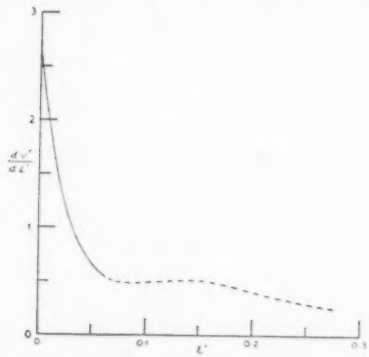

FIGURE 6. Band form for palladium from specific heat measurements. ϵ', energy in electron volts; ν', number of states per atom for one direction of spin.

that of palladium, that of silver one higher. Addition of silver to palladium, as has just been seen, reduces the susceptibility. The susceptibility of rhodium is considerably less than that of palladium (see Table II), but the measurements of Hoare, Kouvelites and Matthews [29] show that in small percentages rhodium increases the susceptibility. In the hydrogen range even 1% of rhodium increases the susceptibility by some 20%; with 5% rhodium the increase is greater but becomes less for 10% after which the susceptibility may provisionally be presumed to decrease monotonically to the rhodium value.

This outline of some of the work so far carried out, though brief, will probably be sufficient to indicate the promise of this type of investigation for elucidating some of the problems of the transition metals and their alloys.

6. Energy Bands of Various Forms

In §2 a quantitative account was given of the physical characteristics associated with energy bands of parabolic form; expressions were also given for the limiting low-temperature characteristics for bands of any form. These latter expressions are essentially the first terms of series of which higher terms may be obtained without undue difficulty (e.g., Stoner, [11]). Unfortunately the range of applicability of these series expressions is usually very limited.

It is in principle possible to determine the necessary integrals numerically for bands of any given form, but the work entailed would be out of all proportion to the value of the results except for bands having well defined general characteristics, or whose form was known to apply accurately and in detail to some actual material of interest.

Useful progress can, however, be made by investigating bands of various well defined types.

(1) The parabolic band is a member of the class of bands whose energy density of states is represented by

$$\frac{d\nu}{d\epsilon} = a\,\epsilon^{\frac{1}{2}(2n+1)}, \tag{21}$$

where $n = 0, 1, 2 \ldots$. The tables prepared by McDougall and Stoner [3] enable bands of this type to be covered without undue difficulty.

(2) The rectangular band, represented by

$$\frac{d\nu}{d\epsilon} = a, \tag{22}$$

is somewhat more artificial than the parabolic band, and the results do not pass over in the same elegant way to those given by quasi-classical statistics. The results do, however, complement most usefully those for the parabolic band, and there are a number of possibilities of application. The great advantage is in simplicity. Almost all the results of physical interest can be obtained, though not without difficulty, in closed analytical form. A very thorough study of this type of band has been made by Wohlfarth [33], covering ferromagnetic as well as paramagnetic and thermal properties.

(3) The rectangular band is a member of the group of bands of the form

$$\frac{d\nu}{d\epsilon} = a\epsilon^n, \tag{23}$$

where $n = 0, 1, 2 \ldots$. Tables prepared by Rhodes [34] effectively enable all bands of this type to be covered satisfactorily. (It should perhaps be noticed that the integrals evaluated in the course of this work have many applications other than those of immediate interest here.)

Although the physical characteristics—that is, in particular, the variation with temperature of quantities such as the magnetic susceptibility and electronic heat—differ in detail for these various forms, the variations are disappointingly similar in general character. It does not seem that any unusual properties (such as an increase in susceptibility over one part of the temperature range

and a decrease over another) is likely to arise with bands of such simple form. More spectacular properties are likely to arise only with overlapping bands of this relatively simple type or with bands requiring a two or more parameter representation. Effects arising from overlapping bands, such as the transfer effect, have been studied by Wohlfarth [35], Lidiard [36] and others. The not unrelated problem of a more complex form of a single band has been studied in recent years by Elcock, Rhodes and Teviotdale [37], and a systematic account of the properties associated with bands of various types is in the course of publication. This will include a preliminary study of certain closed- as well as open-band forms.

It is not intended to discuss this work in any detail here, partly because it is essentially work in progress and partly because there are at present few sufficiently complete sets of experimental results with which comparisons can usefully be made. In view of the attention drawn to the maximum in the susceptibility of palladium, however, it may be of interest to note that this type of behaviour may be associated with a band of the form

$$\frac{d\nu}{d\epsilon} = a + b\epsilon^3, \tag{24}$$

as shown in Figure 7.

Although this form of band may seem somewhat strange, it is not dissimilar to some of the theoretically calculated band forms, and it does appear

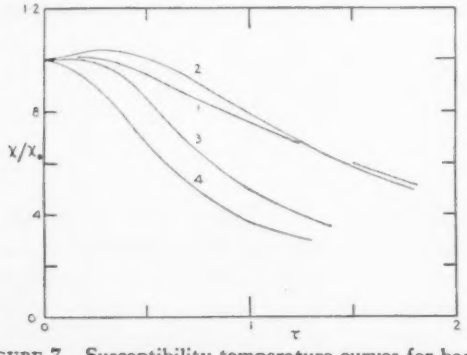

FIGURE 7. Susceptibility temperature curves for bands of the form $d\nu/d\epsilon = a + b\epsilon^3$. τ is a reduced temperature and ϕ a parameter such that $\phi = (b/a)\,\epsilon_0^3$. The curves 1, 2, 3, 4 correspond to ϕ-values of 0.05, 0.146, 2.0 and 5.0, respectively.

to give a quite reasonable fit with both the susceptibility of palladium and the variation of electronic heat on alloying with silver. This illustration is given, however, not as representing a final conclusion but rather as indicating how a combined attack from the theoretical and experimental ends may in due course lead to many interesting results.

Footnote

Since the main text of this paper was written and typed a short abstract has become available giving the results of new measurements in the liquid-helium range of the specific heat of tungsten and molybdenum by M. Horowitz and J. G. Daunt (Phys. Rev. **50** (1953) 379). The value obtained for γ for tungsten is 1.8×10^{-4}, which is 28 times smaller than the earlier value quoted in Table I, and confirms the doubt expressed about that value in the text (§§3, 4). With the new value of γ, the value of θ'/q in Table III would become +29100. This seems very high, but it is more in line with the result for chromium, for which the low value of γ is discussed in the text. The preliminary value of γ for molybdenum is given as 5.1×10^{-4}. This would lead to a value for θ'/q of +8690. The new values for γ, and still more values derived from them, must obviously at present be treated with reserve, but if they are assumed provisionally, it is interesting to note that the highest three values of θ'/q which have so far been obtained are for the three elements Cr, Mo and W, all in the same periodic group.

References

(See also the references to Tables I and II for experimental results on electronic specific heats and magnetic susceptibilities.)

1. RAYNOR, G. V. Rep. Prog. Phys. **15** (1952) 173.
2. BACON, G. E. and LONSDALE, K. Rep. Prog. Phys. **16** (1953) 1.
3. MCDOUGALL, J. and STONER, E. C. Phil. Trans. Roy. Soc. **237** (1938) 67.
4. STONER, E. C. Phil. Mag. **25** (1938) 899.
5. STONER, E. C. Proc. Leeds Phil. Soc. **3** (1938) 403.
6. STONER, E. C. Proc. Roy. Soc. **165** (1938) 372.
7. STONER, E. C. Proc. Roy. Soc. **169** (1939) 339.
8. STONER, E. C. Phil. Mag. **28** (1939) 257.
9. STONER, E. C. Rep. Prog. Phys. **11** (1948) 43.
10. STONER, E. C. J. Phys., Paris **12** (1951) 372.
11. STONER, E. C. Proc. Roy. Soc. **154** (1936) 656.
12. MANNING, M. F. Phys. Rev. **63** (1943) 190.
13. MANNING, M. F. and CHODOROW, M. Phys. Rev. **56** (1939) 787.
14. FLETCHER, G. C. Proc. Phys. Soc. **A65** (1952) 192.
15. HONDA, K. Ann. Physik, Lpz. **32** (1910) 1027.
16. OWEN, M. Ann. Physik, Lpz. **37** (1912) 657.
17. STONER, E. C. Magnetism and Matter (London, Methuen, 1934).
18. SELWOOD, P. W. Magnetochemistry (New York, Interscience, 1943).
19. STONER, E. C. Sci. Rep. Tohoku Univ., Hona Anniversary Vol. (1936) 283.
20. BOMMER, H. Z. Elektrochem **45** (1939) 357.

21. HOARE, F. E. and WALLING, J. C. Proc. Phys. Soc. **B64** (1951) 337.
22. KRIESSMAN, C. J. Rev. Mod. Phys. **25** (1953) 122.
23. DE HAAS, W. J. and VAN ALPHEN, P. M. Proc. Kon. Akad. Amst. **36** (1936) 263.
24. SEITZ, F. The Modern Theory of Solids (New York, McGraw-Hill, 1940).
25. SLATER, J. C. Rev. Mod. Phys. **25** (1953) 199.
26. WOHLFARTH, E. P. Rev. Mod. Phys. **25** (1953) 211.
27. WOHLFARTH, E. P. Proc. Leeds Phil. Soc. **5** (1948) 89.
28. HOARE, F. E. and MATTHEWS, J. C. Proc. Roy. Soc. **212** (1952) 137.
29. HOARE, F. E., KOUVELITES, J. S. and MATTHEWS, J. C. Nature **170** (1952) 537.
30. HOARE, F. E., MATTHEWS, J. C. and WALLING, J. C. Proc. Roy. Soc. **216** (1953) 502.
31. SVENSSON, B. Ann. Physik, Lpz. **14** (1932) 699.
32. WUCHER, J. Ann. Phys., Paris **7** (1952) 317.
33. WOHLFARTH, E. P. Phil. Mag. **32** (1951) 374.
34. RHODES, P. Proc. Roy. Soc. **204** (1950) 396.
35. WOHLFARTH, E. P. Proc. Roy. Soc. **195** (1949) 434.
36. LIDIARD, A. B. Proc. Camb. Phil. Soc. **49** (1953) 115.
37. ELCOCK, E. W., RHODES, P. and TEVIOTDALE, A. Proc. Roy. Soc. **221** (1953) 53.

THE EFFECT OF LATTICE ANISOTROPY ON LOW-TEMPERATURE SPECIFIC HEAT*

W. DeSORBO†

A general analysis has been made in terms of the Debye theory of most of the available low-temperature specific heat data of monatomic solids. The results of the analysis are compared among the various crystal structures including the highly anisotropic lattices. An attempt has also been made to apply for the purpose of general analysis the Tarassov quasi-empirical specific heat integrals to describe lattice anisotropy. The results of such an analysis are summarised for Se, Te, Hg, In, Zn, Cd, Sb, Sn (white) and Li (low-temperature phase). The comparison using this simple model shows that the anisotropy of mercury and indium is "similar" to that of tellurium and selenium, and that the anisotropy of zinc and cadmium is "similar" to that of other "layer" structure elements. The relative number of "soft" and "hard" modes of vibration of these anisotropic lattices have been calculated using simple continuum models. A qualitative method is pointed out for distinguishing between monatomic isotropic lattices, polymeric "chain" lattices and polymeric "layer" lattices from low temperature specific heat data.

L'EFFET DE L'ANISOTROPIE DU RÉSEAU SUR LA CHALEUR SPÉCIFIQUE AUX BASSES TEMPÉRATURES

On a fait une analyse générale en termes de la théorie de Debye des données disponibles, concernant les chaleurs spécifiques des solides mono-atomiques aux basses températures. Les résultats de cette analyse sont comparés suivant les diverses structures cristallographiques, y compris les réseaux fortement anisotropes. Une tentative a aussi été faite d'appliquer, dans une analyse générale, les intégrales quasi-empiriques de chaleur spécifique, de Tarassov, pour la description de l'anisotropie du réseau. Les résultats d'une telle analyse sont exposés sommairement pour Se, Te, Hg, In, Zn, Cd, Sb, Sn (blanc) et Li (la phase stable aux basses températures). La comparaison basée sur ce simple modèle montre que l'anisotropie du mercure et de l'indium "ressemble" à celle du tellure et du sélénium, et que l'anisotropie du zinc et du cadmium "ressemble" à celle des autres éléments ayant une structure en "couches". Le nombre relatif des modes de vibrations "douces" et "dures" de ces réseaux anisotropes a été calculé en se basant sur un modèle simple de milieu continu. On indique une méthode qualitative permettant de distinguer entre les réseaux monoatomiques, isotropes, les réseaux des polymères en "chaînes" et les réseaux des polymères en "couches", en partant des données sur les chaleurs spécifiques aux basses températures.

DIE WIRKUNG DER ANISOTROPIE DES KRISTALLGITTERS AUF DIE SPEZIFISCHE WÄRME BEI TIEFEN TEMPERATUREN

Fast alle vorhandenen Daten über die spezifische Wärme monoatomarer Festkörper bei tiefen Temperaturen wurden im Rahmen der Debye'schen Theorie analysiert. Die Resultate für die verschiedenen Kristallstrukturen, einige stark anisotrop, wurden miteinander verglichen. Es wurde auch versucht, die Tarassov'schen quasi—empirischen spezifischen Wärmeintegrale im Rahmen der allgemeinen Analyse zur Beschreibung der Gitter-anisotropie zu verwenden. Die Resultate einer solchen Analyse werden für Se, Te, Hg, In, Zn, Cd, Sb, Sn (weiss) und Li (Tieftemperaturphase) zusammengestellt. Ein Vergleich, dem dieses einfache Modell zu Grunde liegt, zeigt, dass die Anisotropie des Quecksilbers und des Indiums "ähnlich" der des Tellur und des Selens ist; die des Zinks und Kadmiums ist "ähnlich" der anderer "Schichtstruktur"-Elemente. Unter Zugrundelegung von einfachen Kontinuumsmodellen wurde die relative Anzahl von "harten" und "weichen" Schwingungen in diesen anisotropen Gittern berechnet. Es wird ausserdem eine quantitative Methode angegeben, die gestattet, auf Grund der Daten der spezifischen Wärme bei tiefen Temperaturen zwischen einatomischen, isotropen Gittern, polymeren "Kettengittern" und polymeren "Schichtgittern" zu unterscheiden.

Introduction

During the past several years there has been a revival of interest, both experimental and theoretical, on the effect of lattice anisotropy on low-temperature specific heats. These studies have included the work of Tarassov [1–4], Gurney [5], and Estermann and Kirkland [6]. Prior to this Nernst [7] had recognized the problem in comparing his specific heat data of graphite with the Einstein theory and likewise Magnus [8] had discussed the anisotropy in graphite in terms of the Debye theory. In Tarassov's work [3], two quasi-empirical equations each having two parameters and based on the Debye type of assumptions were proposed and qualitatively accounted for the coupling forces between polymeric "layer" and "chain" structure lattices.

For "chain" lattices Tarassov has proposed the following formula:

$$(1)\quad C_{1(3)} = 3R\left(\frac{T}{\theta_1}\right)\int_0^{\theta_3/T}\frac{x^2e^x}{(e^x-1)^2}\,dx - \left(\frac{\theta_3}{\theta_1}\right)\left[\frac{3RT}{\theta_3}\int_0^{\theta_3/T}\frac{x^2e^x}{(e-1)^2}\,dx - \frac{9RT^3}{\theta_3^3}\int_0^{\theta_3/T}\frac{x^4e^x}{(e^x-1)^2}\,dx\right]$$

*Received October 27, 1953. Presented in part before the A.E.C. Solid-State Conference, University of Illinois, June 11–12, 1953.

†General Electric Research Laboratory, Schenectady, New York.

where θ_1 is the characteristic temperature for the "hard" modes of vibration and θ_3 that for the "soft" modes. Likewise, for "layer" lattices he has presented the following formula:

$$(2) \quad C_{2(3)} = 6R\frac{T^2}{\theta_2^2}\int_0^{\theta_2/T}\frac{x^3e^x}{(e^x-1)^2}\,dx - \left(\frac{\theta_3}{\theta_2}\right)^2 \left[6R\frac{T^2}{\theta_3^2}\int_0^{\theta_3/T}\frac{x^3e^x}{(e^x-1)^2}\,dx - 9R\frac{T^3}{\theta_3^3}\int_0^{\theta_3/T}\frac{x^4e^x}{(e^x-1)^2}\,dx\right]$$

where θ_2 is the characteristic temperature associated with the "hard" modes of vibration and θ_3 that for the "soft" modes. The author has shown that equation (1) can describe the data quite satisfactorily for selenium [9] and tellurium [10]; and equation (2) can describe the data satisfactorily for antimony [11].

Krumhansl and Brooks [12] have extended the Debye theory of specific heat to elastically anisotropic solids and applied it to DeSorbo and Tyler's data on graphite [13]. Their semi-rigorous atomic model substantiates the general form of the assumptions used by Tarassov's simple model for "interacting chain" lattices [14] as well as his simple model for "interacting layer" substances [15]. For a more detailed analysis of the variation of the specific heat of anisotropic monatomic solids, it would be necessary to calculate the vibrational spectrum in each case. These more rigorous dynamical procedures, employing the general methods of Born and Von Karman [16], Blackman [17] and Montroll [18],* are in principle straightforward. To the writer's knowledge, the application of these methods to the study of anisotropic lattices has been independently suggested by Krumhansl [14], Stockmayer and Hecht [19], Montroll [20] and Pry [21]. As a step in this direction, Stockmayer and Hecht [19] have proposed an approximate model for polymeric "chain" lattices following essentially Blackman's [17] method for cubic crystals. Their results are in good agreement with equation (1) above.

It is suggested, then, that the Tarassov simple model, despite its limitations, could become a useful representation of specific heat data for the purpose of general analysis of anisotropic solids as Debye's formula has served, in the past, for isotropic lattices.† For this reason it could be useful on general questions in a simpler manner than the more rigorous and more tedious analysis could accomplish; the detailed methods of analysis often being impossible to carry out when basic information, such as elastic constants, is not readily available. Furthermore, an important application of the Tarassov model could be its use in exploring approximate structural information from observed low temperature specific heat data [19; 76].

The purpose of this paper is to extend the simple Tarassov model for anisotropy and specific heat to other anisotropic monatomic solids whose specific heat data are currently available in the literature and to point out, from this general analysis, certain correlations which have heretofore not been noticeable. The initial step in this simple generalization is brought about in terms of the deviation of the characteristic Debye temperature, θ_D, with temperature [3; 9; 10; 11]. The report also serves to correlate together these Debye characteristic temperatures as a function of temperature for various classes of crystal structures whenever the data have been available.‡ The Debye characteristic temperatures were calculated from specific heat data minus the electronic contribution.§ In a few cases where the electronic specific heat term has not been presented but the data were available in the liquid helium range, it has been approximated by conventional graphical methods. The elements whose specific heat data are still not available between the liquid helium temperature range and liquid nitrogen range have not been included.

(a) *Face-Centered Cubic Lattices*

The characteristic temperatures, θ_D, as a function of temperature for the face-centered cubic lattices are presented in Figure 1 for the low-temperature region. Aluminum [23; 24], platinum [27; 37], silver [31; 38], lead [31; 32] and possibly gold [29; 30] follow the type of deviation predicted by Leighton [40] and Garland and Jura [41]. Nickel [33; 34], aluminum, copper [27; 28] and silver show peaks and/or dips appearing for the most part in the helium range. These variations cannot be accounted for by the theoretical models. They could be due to lattice irregularities, impurities, etc. [42]; incorrect method of accounting

*See also [24].

†Another general method of analysis of interest is that recently introduced by Leibfried and Brenig [22].

‡Bibliographies used: K. K. Kelley, Bulletin No. 477, U.S. Department of the Interior, Bureau of Mines, 1950. C. A. Shiffman, *The Heat Capacities of the Elements below Room Temperature*, General Electric Research Laboratory, 1952.

§In cases where C_v was not determined by the respective authors the Nernst-Lindemann approximate relation, $C_p - C_v = 0.0214\,C_p^2\,(T/T_s)$, has been used to evaluate C_v from the experimental C_p data.

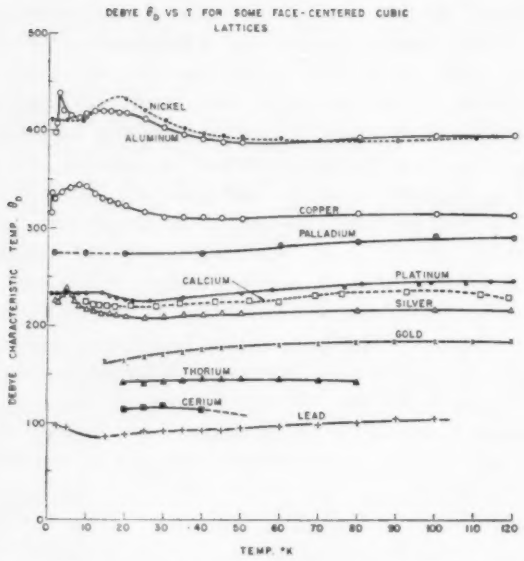

FIGURE 1. The variation with temperature of the Debye characteristic temperature for some face-centered cubic lattices.

for the specific heats of free electrons [43]; experimental factors such as gas adsorption [44; 42]; or a combination of these. No simple generalizations can be made on these variations. Thorium [39], cerium [26], palladium [35; 36], calcium [25], copper, aluminum, and nickel show qualitatively either constant values or increases in θ values with decreasing temperature in the liquid hydrogen temperature region. In Table I are tabulated the electronic terms used in evaluating the lattice contributions to the specific heats.

TABLE I

COEFFICIENT OF LINEAR TERM OF ELECTRONIC SPECIFIC HEAT OF SOME FACE-CENTERED CUBIC METALS

Element	Electronic term (γ) cal-mole^{-1}-deg.$^{-2}$	Reference
Al	3.484×10^{-4}	23
Ca	not available	25
Ce	not available	26
Cu	1.777×10^{-4}*	27
Au	1.74×10^{-4}	30
Pb	7.48×10^{-4}	32
Ni	1.744×10^{-3}	34
Pd	3.1×10^{-3}	35
Pt	1.607×10^{-3}	27
Ag	1.54×10^{-4}†	38, 43
Th	not available	39

*Estermann, Friedberg and Goldman [62] have recently reported a value of $\gamma_{Cu} = 1.80 \times 10^{-4}$.

†Corak and Garfunkel [30] have more recently reported values of $\gamma_{Cu} = 1.60 \times 10^{-4}$ and $\gamma_{Ag} = 1.48 \times 10^{-4}$. The difference in the θ_D values obtained using these more recent values are insignificant in altering the general variation of the θ_D-vs-T curve in the temperature range of interest in this discussion.

(b) *Body-Centered Cubic Lattices*

Figure 2 presents the Debye characteristic temperatures as a function of temperature for some body-centered cubic lattices. Molybdenum [37], potassium [37], and sodium [35; 37] show practically constant θ_D above liquid-hydrogen temperature region.‡ The variation for sodium in the liquid hydrogen region is due to a still unexplained anomaly in the helium region. The θ-value for iron [45; 46; 47] increases with decreasing temperature showing a peak at about 15°K. The electronic specific heat term (γ) for iron is that given by Duyckaerts [45]; i.e., $\gamma = 1.20 \times 10^{-3}$. The electronic terms for the other metals listed are not available from experimental data. Lithium [46] in this temperature region shows a decided drop in θ_D with decreasing temperature.

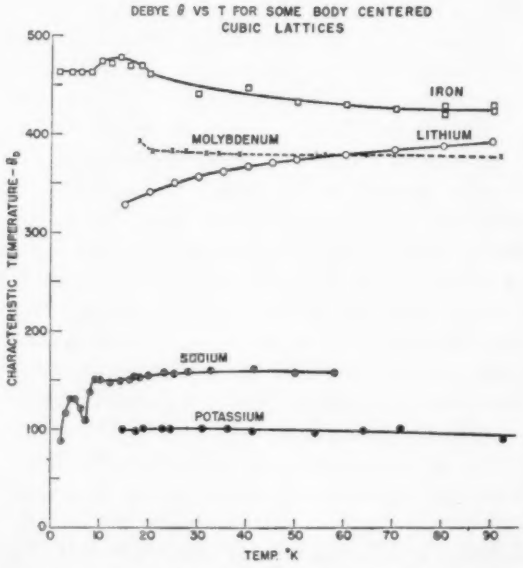

FIGURE 2. The variation with temperature of the Debye characteristic temperature for some body centered cubic lattices.

(c) *Hexagonal Lattices*

The temperature variation for the Debye characteristic temperatures for some hexagonal lattices are presented in Figure 3. Magnesium [52], whose c/a ratio is close to the ideal ratio of 1.633 for hexagonal close-packing, reveals a practically constant θ-value in the upper tempera-

‡For the vibrational spectra of b.c.c. lattice see P.C. Fine, Phys. Rev. **56** (1939) 355.

ture region of the graph followed by a rise in its value with decreasing temperature. Zinc [58; 59; 60] with a c/a ratio of 1.856 and cadmium [49] with a c/a ratio of 1.886 have relatively variable θ's above 20°K. Cobalt [50; 51] with a $c/a = 1.623$ has a variation in θ similar to magnesium except for a slight dip at approximately 55°K (see below). The lattices having a c/a ratio less than ideal,

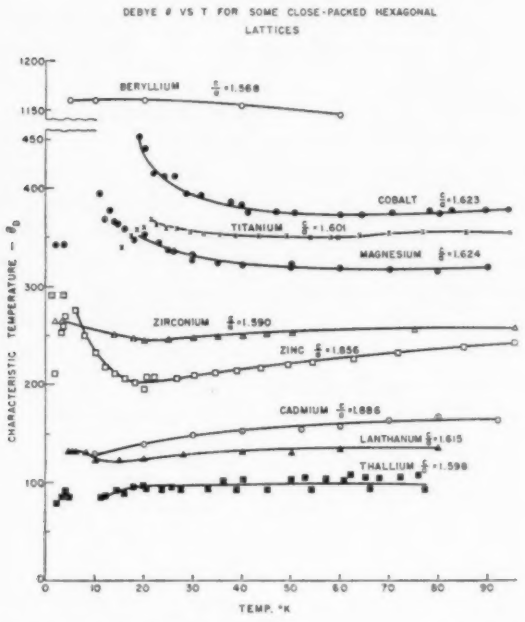

FIGURE 3. The variation with temperature of the Debye characteristic temperature for some close-packed hexagonal lattices.

beryllium [48] ($c/a = 1.568$), zirconium [61; 62] ($c/a = 1.590$), and thallium [25; 56; 57] ($c/a = 1.598$) have a roughly constant θ-vs-T curve. However, these c/a ratios are still very close to the ideal value. The characteristic temperatures for thallium dip down slightly below 18°K. Table II gives a summary of γ, the coefficient of the electronic specific heat term for these substances.

(d) *Other Anisotropic Lattices*

The analysis of the specific heat data for some other anisotropic lattices in terms of the Debye model are shown in Figures 4a and 4b.* These elements (Fig. 4a) are sulfur [63], selenium [10; 64] (hexagonal), crystalline tellurium [64], mercury [35; 66], and indium [67; 68]. The electronic

*The scale used for the ordinate and abscissae are identical in all graphs in order to present a more favorable comparison. The only exception is in presenting the graphite data. The results for some other anisotropic lattices are presented in Fig. 3.

TABLE II

COEFFICIENT OF LINEAR TERM OF ELECTRONIC SPECIFIC HEAT OF SOME CLOSE-PACKED HEXAGONAL METALS

Element	Electronic term (γ) cal-mole^{-1}-deg.$^{-2}$	Reference
Be	5.4×10^{-5}	48
Cd*	not available	49
Co	12.0×10^{-4}	50
La	2.0×10^{-4}	26
Mg	3.25×10^{-4}	53, 62
Ti*	not available	55
Tl	1.8×10^{-3}	56
Zn	1.50×10^{-4}	60
Zr	6.92×10^{-4}	62

*In general, failure to account for the electronic specific heat term does not affect appreciably the characteristic temperature above liquid hydrogen temperatures.

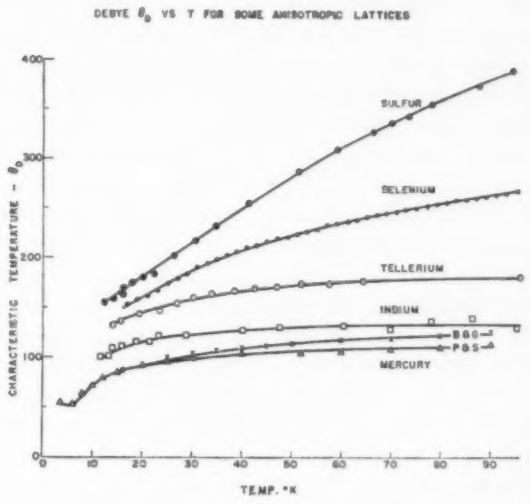

4(*a*)

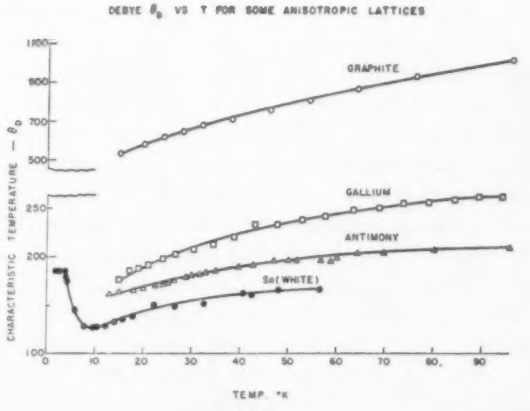

4(*b*)

FIGURES 4(a) and 4(b). The variation with temperature of the Debye characteristic temperatures for some anisotropic lattices.

specific heats were corrected for indium only. ($\gamma = 3.55 \times 10^{-4}$). An anomaly in the helium temperature region for mercury prevents an experimental graphical evaluation of γ. The other three substances have not been studied at low enough temperatures to permit a calculation of γ.* In Figure 4b are presented the Debye characteristic temperatures for graphite [13], gallium [58; 73], tin (white) [70; 71; 72], and antimony [11; 69]. The ordinate scale for graphite is much condensed. An electronic specific heat correction term has been applied to white tin ($\gamma = 4.0 \times 10^{-4}$). Data are not available for determining it for the other three substances.*

Discussion of Results

The general analysis of the data in terms of the Debye model does not reveal any simple generalization about the behavior of θ with temperature for lattices of a given crystal structure. As a crude generalization for the f.c.c. metals, the characteristic temperature θ is more or less constant with some variations in the lower temperature regions; the exceptions to this are gold, lead, platinum and silver. The specific-heat variation in terms of the Debye θ-temperature variation of silver, lead and platinum can be understood in terms of the Leighton model of specific heats of f.c.c. lattices [40]. Gold has a relatively large variation of θ_D with temperature. The data are not available in the liquid-helium region to apply the Leighton model. Other isotropic lattices that deviate considerably from the Debye model are the diamond structure elements germanium, silicon and grey tin. These have been discussed by Hill and Parkinson [77].

With the exception of lithium, the b.c.c. crystals show a constant value or a rise in θ with decreasing temperature. In the c.p.h. lattices the θ variation for Mg and Co, presumably good isotropic lattices, deviate similarly as do the variations of some of the f.c.c. isotropic lattices such as nickel, copper, aluminum, silver and diamond [74]. Cobalt has a slight dip at approximately 55°K which might be due to stacking faults [75] presumably present in the lattice. Lanthanum shows a deviation below 30°K. The data analyzed were those of Parkinson, Simon and Spedding [26] whose sample was reported to have a room temperature structure corresponding to both hexagonal close-packed and cubic close-packed forms. What effect this mixture of structures has on specific heats has not been ascertained. The variation of θ_D for hexagonal lattices having a c/a ratio slightly less than the ideal ratio, reveal almost constant θ-vs-T curves. The variation of θ with temperature for Zn (c/a = 1.886) and cadmium (c/a = 1.886) reveal deviations above 15°K similar to the anisotropic lattices presented in Figures 4a and 4b.

A general comparison of the results shown in Figure 1 through Figure 4b shows that the temperature variation of the normal Debye characteristic temperature for each anisotropic lattice is appreciably more pronounced than that for any of the isotropic lattices presented. In comparing Figures 4a and 4b the results also demonstrate that the three-dimensional Debye theory is incapable of distinguishing between "layer" and "chain" polymeric solids. However, in a very rough and qualitative manner, the simple specific-heat models based on continuum ideas can be utilized to correlate anisotropy with low-temperature specific-heat data. In Figure 5a are shown the variations of the

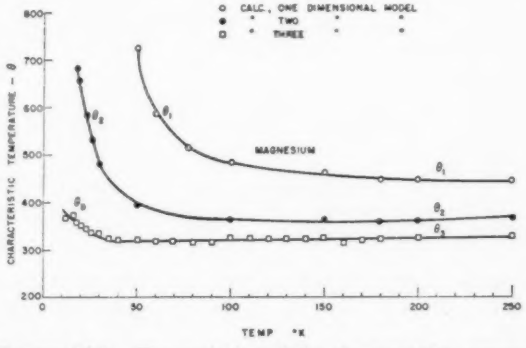

FIGURE 5(a). The variation of the characteristic temperatures θ_3, θ_2 and θ_1 with temperature for magnesium.

characteristic constants θ_3, θ_2 and θ_1 applied to the specific heat data of magnesium, an example of an isotropic lattice. θ_3 is the normal Debye characteristic temperature; θ_2 is the characteristic temperature obtained by using a two-dimensional frequency distribution function, and similarly θ_1 represents the characteristic temperature obtained from a one-dimensional frequency distribution function [3; 9; 10; 11]. These variations in characteristic temperature θ_1, θ_2 and θ_3 (the latter may be increasing with decreasing temperature or constant with decreasing temperature) are representative of a number of isotropic lattices such as aluminum, copper, nickel, iron, molybdenum, potassium, sodium, beryllium, zirconium, and

*In general, failure to account for the electronic specific heat term does not affect appreciably the characteristic temperature above liquid hydrogen temperatures.

titanium (not taking into account any variations in the liquid-helium temperature range.)

Figure 5b shows the deviation of θ_3, θ_2 and θ_1 for cadmium. θ_1 and θ_2 rise with decreasing temperature and θ_3 decreases with decreasing temperature. The elements whose specific heat when analyzed in terms of θ_3, θ_2 and θ_1 behave similarly as in Figure 5b are graphite, antimony, gallium, cadmium, zinc, arsenic, bismuth, lithium (low-

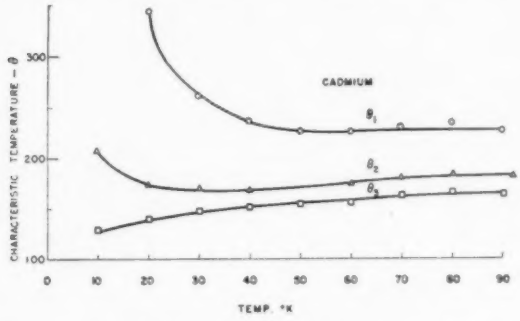

FIGURE 5(b). The variation of the characteristic temperature θ_3, θ_2 and θ_1 with temperature for cadmium.

temperature phase), and tin (white). Similar variations can also be shown for the specific heat data of BN recently reported by Dworkin, Sasmor and Van Artsdalen [78].*

Figure 5c presents the deviation of θ_3, θ_2 and θ_1 for mercury. In this case, θ_3 and θ_2 are decreasing with decreasing temperature while θ_1 is increasing with decreasing temperature (not considering the anomalous variations in the liquid-helium tem-

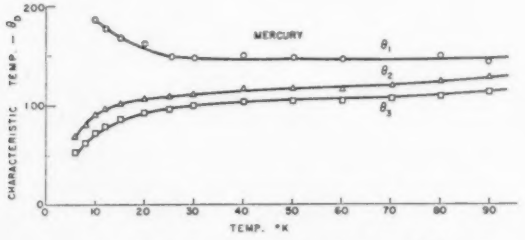

FIGURE 5(c). The variation of the characteristic temperature θ_3, θ_2 and θ_1 with temperature for mercury.

perature range). The elements whose three characteristic temperatures vary in an analogous manner to those of mercury are selenium, tellurium, indium and sulfur.

In general, all the elements falling in the first class (Fig. 5a) have crystal structures that are essentially isotropic. Those mentioned in the second class whose characteristic temperatures in general follow the type of deviation shown in Figure 5b can rather naively be referred to as "layer-like." This term is used loosely to include the rhombohedral structure of Sb, As and Bi. Cadmium and zinc whose c/a ratio is greater than ideal may be considered to be in this class.† In these so-called "layer structures" the main valences occur in the "two-dimensional plane." The bonding perpendicular to the plane is of a weaker character. The main valence forces may be considered to be associated with the higher frequencies in the lattice and on a continuum model represented by a simple two-dimensional distribution function. As the temperature is decreased, however, the higher frequencies, associated with the main valence forces for the layers become less highly excited and leave waves of longer and longer wavelengths as the only ones excited. These longer waves then can better be described, again following the approximations of the continuum model, by a normal Debye three-dimensional distribution function. Therefore, as pointed out previously [3; 11; 12], a possible explanation for the increase in θ_2 and decrease in θ_3 at low temperatures may be that the frequency-distribution function following for the most part a two-dimensional form at the higher frequencies (higher temperatures) is going over into a three-dimensional form with decreasing frequency (lower temperatures). Applying Tarassov's simple two-parameter formula (equation 2) to account for this, we obtain the results shown in Figure 6a where the Debye characteristic temperature (θ_3) vs T has been obtained using in one case the normal three-dimensional Debye function, and in the other case using as data the theoretical specific-heat values obtained from the anisotropic model (equation 2).

Similarly, referring to Figure 5c, one possible explanation for the increase in θ_1 and the decrease in θ_3 with decreasing temperature may be that for this class of elements the frequency-distribution function following initially a one-dimensional form is going over into a three-dimensional form with decreasing temperature [3; 9; 10]. That is to say, as the lower temperatures are attained, the higher frequencies which may be considered to be associated with the main valence forces along the chains (selenium, tellurium) become less highly excited, and leave waves of longer and longer

*The writer is grateful to these authors for their data in advance of publication.

†White Sn whose short bonds (3.02A) do not lie very far out of the a-b plane and whose long bonds (3.17A) are along the c-direction is also included in this class.

wavelengths. At sufficiently low temperatures the remaining waves can be described by the three-dimensional distribution function.

Furthermore, it seems that the anisotropy in mercury and indium based on this model is "similar" to that of selenium and tellurium. The rhombohedral structure of mercury is visualized as a f.c.c. structure deformed along a body diagonal. This geometry brings atoms in neighboring layers closer together at a distance of 3.00 A. Each atom has six nearest atoms at this distance; whereas the Hg-Hg separation within a rhombohedral (111)-plane is 3.47 A.* This anisotropy is of an "opposite" nature compared to that in zinc and cadmium which is brought about in the latter case by the distortions of the hexagonal close-packed layers where the atoms in adjacent planes are farther apart than those in the same layer. In a qualitative way, then, the mercury structure could give rise to stronger net forces along the c-direction compared to the relative weaker forces along the a-direction.

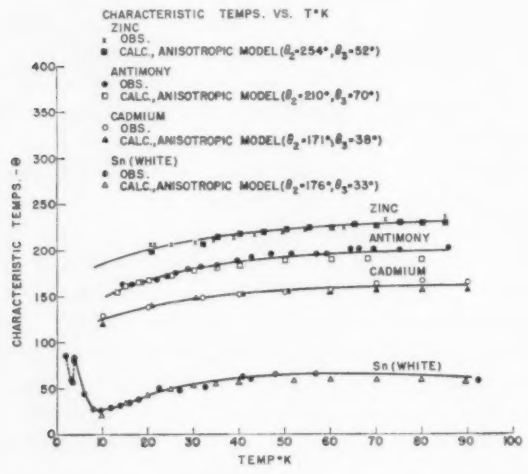

6(a)

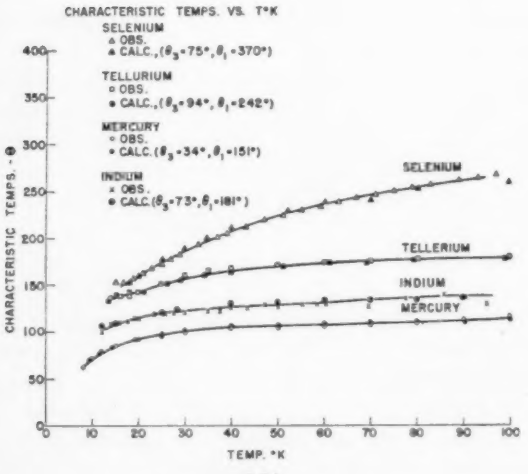

6(b)

FIGURES 6(a) and 6(b). Theoretical curve of Debye θ vs T, using the normal three-dimensional Debye function, and using as data the theoretical specific heat curve for the anisotropic model.

The indium lattice represents a distorted cubic-close-packed grouping where there is an elongation along one of the cube edges. The 12 equidistant neighbors normally present in cubic-close-packed structures go over into one group of four at a distance of 3.24 A and a second group of eight at a slightly larger distance, 3.37 A.* It is difficult, however, to visualize any emphasis of unidirectional forces in this case. Indium could be an anomaly in this scheme.

The results of applying Tarassov's two-parameter formula (equation 1), which accounts for the "soft" and "hard" modes of vibration, are shown in Figure 6b. Here, analogous to Figure 6a, we obtain the theoretical curve of Debye θ vs T obtained in one case with the normal three-dimensional Debye function, and also using as data the theoretical specific-heat values obtained from equation (1). In both Figures 6a and 6b, then, the decrease in the θ_D-vs-T curves can be accounted for in terms of the anisotropy of the lattice using simple continuum models excluding any variations in the helium region.

A rather interesting but qualitative correlation obtained by applying the Tarassov equation to the specific heat of anisotropic lattices is the relative number of "soft" and "hard" modes of vibration [10; 11]. These are summarized in Table III along with some pertinent structural information.† Although there are many detailed effects neglected in this continuum treatment, the summary reveals some interesting correlations, i.e., the larger anisotropy in selenium over that in tellurium which is in agreement with the disparity of bond distances in selenium and tellurium; approximately equal anisotropy in zinc and cadmium whose c/a ratios are about equal; the smaller anisotropy of "layer-structure" antimony compared with graphite [12]. For lithium, equa-

*R. W. G. Wyckoff, *Crystal Structures* (Section I) (New York, Interscience Publishers, Inc., 1948). See also C. S. Barrett, *Structure of Metals* (New York, McGraw-Hill Book Company, Inc., 1952), p. 218.

†The author expresses his gratitude to Dr. J. S. Kasper of our laboratory for his discussions on the structures of these anisotropic lattices.

TABLE III

RELATIVE NUMBER OF "SOFT" AND "HARD" MODES OF VIBRATION IN SOME ANISOTROPIC LATTICES

Element	Crystal Structure	a	c	Simple Description	Closest Approach of Atoms	Second Nearest Distance	θ_1	θ_2	Per cent "Soft" modes	Per cent "Hard" modes
Se	Hexagonal	4.36A	4.95A	Chain	2.32A (2)*	3.46 (4)	370°	75°	20.3	79.7
Te	Hexagonal	4.45	5.91	Chain	2.86 (2)	3.74 (4)	245°	95°	38.8	61.2
Hg	Rhombohedral	3.00		f.c.c. compressed along body diagonal	3.00 (6)	3.47 (6)	163°†	25°	15.3	84.7
In	Face-centered tetragonal	3.24	4.94	f.c.c. compressed along cube edge	3.24 (4)	3.37 (8)	181°	73°	40.3	59.7
							θ_2	θ_3		
Zn	Close-packed hexagonal	2.66	4.94 (c/a = 1.856)	"layer"	2.66 (6)	2.91 (6)	254°	52°	4.2	95.8
Cd	Close-packed hexagonal	2.97	5.61 (c/a = 1.886)	"layer"	2.97 (6)	3.29 (6)	171°	38°	4.9	95.1
Sb	Rhombohedral	4.50		"puckered layer"	2.87 (3)	3.37 (3)	210°	70°	11.1	88.9
Sn (White)	Body-centered tetragonal	5.82	3.17	flattened diamond grouping	3.02 (4)	3.17 (2)	176°	33°	3.5	96.5
Li (Low temp. phase)	close-packed hexagonal	3.09	4.83	Ideal close packing but imperfect stacking of layers	3.00 (6)	3.09 (6)	445°	183°	16.9	83.1

*Number of bonds indicated by number in parenthesis. †Data of Busey and Giauque [66].

tion (2) gives a much better fit [76] to the specific-heat data than did Fuchs' analysis using computed elastic constants and Born's modification of the Debye theory. This agreement is shown in Figure 7.

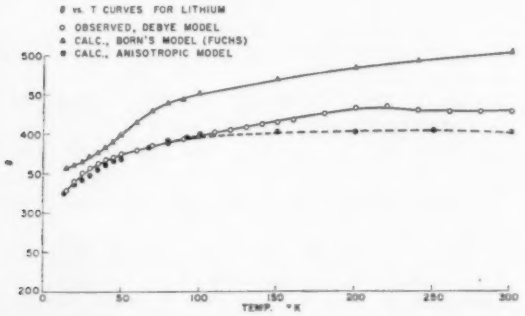

FIGURE 7. The temperature variation of the Debye θ calculated from the Debye model, Born's model (Fuchs) and from the anisotropic model.

In applying the Tarassov model to lithium the assumption has been made that the imperfect stacking sequence present in the low-temperature close-packed hexagonal phase may be responsible for the presence of relative "soft" and "hard" modes of vibration. The frequency spectrum of this phase has been approximated by two distribution functions based on a continuum model. However, the effect of faulting or imperfect stacking sequence on low-temperature specific heat has not yet been studied experimentally. Therefore, this variation of θ with temperature in lithium at present must be looked upon as an anomaly though faulting may be an explanation.

The specific heat of lanthanum whose structure was reported by Parkinson, Simon and Spedding [26] to be a mixture of c.p.h. and b.c.c. can also be described by equation (2) with 22.4 per cent

"soft" modes and 77.6 per cent "hard" modes (i.e., $\theta_2 = 148°$ and $\theta_3 = 68°$). Here again the presence of a "mixture" of two phases may be an explanation for the variation in the Debye characteristic temperature. However, no theory relating heat capacity to the existence of a two-phase mixture has been developed.

Since the main purpose of this report has been to investigate the possibility of the general applicability of the Tarassov model to anisotropic lattices to replace the Debye model for general analysis, it should be pointed out that the specific heat of some anisotropic monatomic substances such as sulfur cannot be described by Tarassov's two-parameter equation.

Summary

The lattice vibration specific heat of monatomic lattices, both isotropic and anisotropic, have been compared in the liquid hydrogen–liquid nitrogen temperature region. This comparison, brought about, in terms of the Debye model, by the usual study of the temperature variation of the Debye characteristic temperature, shows that for the anisotropic lattices the deviations from Debye theory are consistently much higher than for most isotropic lattices; that is, in all cases studied the Debye characteristic temperature decreases significantly with decreasing temperature. These deviations are explainable in a qualitative manner if the data are analyzed in terms of the simple Tarassov continuum model that distinguishes between relatively "soft" and "hard" modes of vibration. The specific heat of Se, Te, Hg and In can be described by Tarassov's integrals applicable to polymeric "chain" lattices; while the specific heat of Sb, Zn, Cd, Sn (white) and Li (low-temperature phase) can be described by Tarassov's integrals derived for polymeric "layer" lattices.

The temperature variation of the Debye characteristic temperature for the f.c.c. lattice in general are in agreement with Leighton's calculation for silver. Exceptions to this are palladium and possibly nickel, calcium and aluminum. The deviation in gold is considerably larger than for any of the other f.c.c. lattices. Peaks and dips present in the liquid-helium temperature region for Ni, Al, Cu and Ag are still not explainable.

In the b.c.c. lattices presented, the variation of θ_D-vs-T curve for Fe, Mo, K and Na (excluding the low temperature anomaly) is typical for isotropic lattices. Lithium shows a decided drop in θ_D with diminishing temperature. Stacking faults present in the c.p.h. phase in the low-temperature region may account for this behavior.

The c.p.h. lattices with a c/a ratio close to the ideal value of 1.63 have a θ_D-vs-T curve similar to the other isotropic lattices. Zinc and cadmium whose c/a ratio is significantly larger than the ideal ratio vary similarly in their θ_D-vs-T curve as the anisotropic lattices.

Acknowledgments

The author wishes to thank Dr. David Turnbull for many helpful conversations and suggestions as well as for his criticism of the manuscript. For the latter as well as for their continued interest in this work the author is also grateful to Professors J. A. Krumhansl and Harvey Brooks and Dr. R. H. Pry. Assistance in calculating the various characteristic constants was rendered by Mrs. M. V. Doyle, Mrs. E. L. Fontanella and Mrs. J. F. Mona to whom the writer also expresses his thanks.

References

1. Tarassov, V. V. C. R. Acad. Sci., U.R.S.S. (1945) XLVI No. 3.
2. Tarassov, V. V. C. R. Acad. Sci., U.R.S.S. (1946) LIV No. 9.
3. Tarassov, V. V. Zhur. Fiz. Khim. XXIV, **1** (1950) 111.
4. Tarassov, V. V. Doklady Akad. Nauk. S.S.S.R. **84** (1952) 321.
5. Gurney, R. W. Phys. Rev. **88** (1952) 465.
6. Estermann, I. and Kirkland, G. I. Unpublished (see ref. 5).
7. Nernst, W. Ann. Phys. **36** (1911) 395.
8. Magnus, A. Ann. Phys. **70** (1923) 303.
9. DeSorbo, W. J. Chem. Phys. **21** (1953) 1144.
10. DeSorbo, W. J. Chem. Phys. **21** (1953) 764.
11. DeSorbo, W. Acta Met. **1** (1953) 503.
12. Krumhansl, J. A. and Brooks, H. J. Chem. Phys. **21** (1953) 1663.
13. DeSorbo, W. and Tyler, W. W. J. Chem. Phys. **21** (1953) 1660.
14. Krumhansl, J. A. Private communication.
15. Brooks, H. Private communication.
16. Born, M. and Von Karman, T. Phys. Z. **13** (1912) 297; **14** (1913) 15.
17. Blackman, M. Proc. Roy. Soc. (London) **A148** (1935) 384; **A159** (1937) 416.
18. Montroll, E. W. J. Chem. Phys. **10** (1942) 218; **11** (1943) 481.
19. Stockmayer, W. H. and Hecht, C. E. J. Chem. Phys. **21** (1953) 1954.
20. Montroll, E. W. Private communication.
21. Pry, R. H. Private communication.
22. Leibfried, G. and Brenig, W. Z. Phys. **134** (1953) 451.
23. Kok, J. A. and Keesom, W. H. Physica **4** (1937) 835; Leiden Comm. **248e** (1937) 1.

24. NEWELL, G. F. J. Chem. Phys. **21** (1953) 1877.
25. CLUSIUS K. and VAUGHEN, J. V. J. Am. Chem. Soc. **52** (1930) 4686.
26. PARKINSON, D. H., SIMON, F. E., and SPEDDING, F. H. Proc. Roy. Soc. (London) **A207** (1951) 137.
27. KOK, J. A. and KEESOM, W. H. Physica **3** (1936) 1035; Leiden Comm. **245a** (1936) 1.
28. GIAUQUE, W. F. and MEADS, P. F. J. Am. Chem. Soc. **63** (1941) 1897.
29. GEBALLE, T. H. and GIAUQUE, W. F. J. Am. Chem. Soc. **74** (1952) 2368.
30. CORAK, W. S. and GARFUNKEL, M. P. Eighth Annual Calorimetry Conference, University of Chicago, September 11–12, 1953.
31. MEADS, P. F., FORSYTHE, W. R. and GIAUQUE, W. F. J. Am. Chem. Soc. **63** (1941) 1902.
32. HOROWITZ, M., SILVIDI, A. A., MALAKER, S. F. and DAUNT, J. G. Phys. Rev. **88** (1952) 1182.
33. BUSEY, R. H. and GIAUQUE, W. F. J. Am. Chem. Soc. **74** (1952) 3157.
34. KEESOM, W. H. and CLARK, W. C. Physica **2** (1935) 513.
35. PICKARD, G. L. and SIMON, F. Proc. Phys. Soc. **61** (1948) 1.
36. CLUSIUS, K. and SCHACHINGER, L. Z. Naturf. **A2** (1947) 9007.
37. SIMON, F. and ZEIDLER, W. Z. phys. Chem. **123** (1926) 383.
38. KEESOM, W. H. and KOK, J. A. Proc. Acad. Sci. Amst. **35** (1932) 301; Leiden Comm. **219d** (1932) 35.
39. GRIFFEL, MAURICE and SKOCHDOPOLE, R. E. J. Am. Chem. Soc. **75** (1953) 5250.
40. LEIGHTON, R. B. Rev. Mod. Phys. **20** (1948) 165.
41. GARLAND, C. W. and JURA, G. Abstract 109 A.C.S. meeting, Los Angeles, March 15–19, 1953.
42. KATZ, E. J. Chem. Phys. **19** (1951) 488.
43. KEESOM, P. H. and PEARLMAN, N. Phys. Rev. **88** (1952) 140.
44. KEESOM, W. H. and CLARK, C. W. Physica **2** (1935) 698.
45. DUYCKAERTS, G. Physica **6** (1939) 401. C.R. Acad. Sci., Paris **208** (1939) 979.
46. SIMON, F. and SWAIN, R. C. Z. phys. Chem. **B28** (1935) 189.
47. KELLEY, K. K. J. Chem. Phys. **11** (1943) 16.
48. HILL, R. W. and SMITH, P. L. Phil. Mag. **44** (1953) 636.
49. LANGE, F. and SIMON, F. Z. phys. Chem. **134** (1928) 372.
50. CLUSIUS, K. and SCHACHINGER, L. Z. Naturf. **A7** (1952) 185.
51. DUYCKAERTS, G. Physica **6** (1939) 817.
52. CRAIG, R. S., WALLACE, W. E., COFFER, L. W., and KRIER, C. A. Progress Report NYO-950, October 10, 1952.
53. ESTERMANN, I. and FRIEDBERG, S. A. Technical Report No. 8, Contract N6ORI-47, Project No. NRO16-403, Carnegie Institute of Technology.
54. FRIEDBERG, S. A., ESTERMANN, I. and GOLDMAN, J. E. Phys. Rev. **85** (1952) 375.
55. KOTHEN, C. W. and JOHNSTON, H. L. J. Am. Chem. Soc. **75** (1953) 3101.
56. KEESOM, W. H. and KOK, J. A. Phyisca **1** (1934) 175; Leiden Comm. **230C** (1934) 1.
57. HICKS, J. F. G. J. Am. Chem. Soc. **60** (1938) 1000.
58. CLUSIUS, K. and HARTECK, P. Z. phys. Chem. **134** (1928) 243.
59. KEESOM, W. H. and VAN DEN ENDE, J. N. Leiden Comm. **219b** (1932) 10. Proc. Acad. Sci. Amst. **35** (1932) 143.
60. SILVIDI, A. A. and DAUNT, J. G. Phys. Rev. **77** (1950) 125.
61. SKINNER, G. B. and JOHNSTON, H. L. J. Am. Chem. Soc. **73** (1951) 4549.
62. ESTERMANN, I., FRIEDBERG, S. A. and GOLDMAN, J. E. Phys. Rev. **87** (1952) 582.
63. EASTMAN, E. D. and MCGAVOCK, W. C. J. Am. Chem. Soc. **59** (1937) 145.
64. ANDERSON, C. T. J. Am. Chem. Soc. **59** (1937) 1036.
65. SLANSKY, C. M. and COULTER, L. T. J. Am. Chem. Soc. **61** (1939) 564.
66. BUSEY, R. H. and GIAUQUE, W. F. J. Am. Chem. Soc. **75** (1953) 806.
67. CLUSIUS, K. and SCHACHINGER, L. Z. Phys. IV (1952) 442.
68. CLEMENT, J. R. and QUINNEL, E. H. Phys. Rev. **79** (1950) 1028.
69. ANDERSON, C. T. J. Am. Chem. Soc. **52** (1930) 2712.
70. LANGE, F. Z. phys. Chem. **110** (1924) 343.
71. KEESOM, W. H. and VAN DEN ENDE, J. N. Leiden Comm. **219b** (1932) 10.
72. KEESOM, W. H. and VAN LAER, P. H. Physica **5** (1938) 193. Leiden Comm. **252b** (1938) 1.
73. ADAMS, G. B., JOHNSTON, H. L. and KERR, E. C. J. Am. Chem. Soc. **74** (1952) 4784.
74. DESORBO, W. J. Chem. Phys. **21** (1953) 876.
75. EDWARDS, O. S. and LIPSON, H. J. Inst. Metals **69** (1943) 177; Proc. Roy. Soc. (London) **A180** (1942) 268.
76. DESORBO, W. Acta Met. **1** (1953) 459.
77. HILL, R. W. and PARKINSON, D. H. Phil. Mag. **43** (1952) 309.
78. DWORKIN, A. S., SASMOR, D. J. and VAN ARTSDALEN, E. R. J. Chem. Phys. **21** (1953) 954.

CREEP OF SILVER BROMIDE AT HIGH TEMPERTURE*†

R. W. CHRISTY‡

The transient and steady-state creep rate of single crystal and polycrystalline specimens of AgBr, stressed in compression from 6 to 150 g/mm², has been investigated between 300° and 410°C, with the emphasis on the steady-state creep of single crystals. The effects on the creep rate of orientation, of hydrostatic confining pressure, and of impurities were studied. Single crystals deformed by slip, though with rather weak conditions on possible slip systems. The steady-state results were reproducible to within about 15 per cent. At higher stresses, for crystals with axis in the [001] direction, the steady-state creep rate was fitted to the empirical formula $\dot{\epsilon} = C \exp\{-Q/RT\} \exp\{B\sigma^{\frac{1}{2}}/RT\}$, with $C = 2.8 \times 10^{17}$ min^{-1}, $Q = 69.1$ kg-cal/mol, $B = 1.21$ (kg-cal/mol)/(g/mm²)$^{\frac{1}{2}}$, σ = compressive stress. For [111] crystals, σ can be replaced by $3/4\ \sigma$; for other orientations the rates were intermediate. At lower stresses the rate decreased more sharply with decreasing stress. The steady-state rate was depressed strongly by high pressure, by the factor $\exp\{-p\Delta V/RT\}$, with $\Delta V = 38 \pm 3$ cm³/mol. The effect of impurities in concentrations of about 10^{-3} was in general to decrease the creep rate, S^{--} being more effective than Cd^{++} or Cl^{-} in this respect. Mott's theory of diffusion-limited creep appears to give a satisfactory interpretation of the temperature, stress, and pressure dependence of the steady-state rate for pure crystals.

LE FLUAGE DU BROMURE D'ARGENT AUX TEMPÉRATURES ÉLEVÉES

Les vitesses de fluage transitoire et de fluage constant d'échantillons monocristallins et polycristallins de AgBr, soumis à des tensions de compression variant de 6 à 150g/mm², ont été investiguées entre 300°et 400°C, avec un accent sur le fluage constant de monocristaux. On a étudié les effets des variables suivantes sur la vitesse de fluage: orientation, pression hydrostatique et impuretés. Les monocristaux se déformaient par glissement, quoiqu'il n'y ait pas eu de conditions bien déterminées concernant les systèmes de glissement possibles. Les résultats du fluage constant étaient reproductibles à 15 pour cent près. Aux tensions plus élevées et dans le cas de cristaux dont l'axe correspondait à la direction [001], le fluage constant a pu être exprimé par la formule empirique $\dot{\epsilon} = C \exp\{-Q/RT\} \exp\{B\sigma^{\frac{1}{2}}/RT\}$, où $C = 2.8 \times 10^{17}$ min^{-1}, $Q = 69.1$ kg-cal/mol, $B = 1.21$ (kg-cal/mol)/(g/mm²)$^{\frac{1}{2}}$, σ = la tension de compression. Dans le cas de cristaux dont l'axe coïncide avec la direction [111], σ peut être remplacé par $3/4\ \sigma$; pour d'autres orientations les vitesses étaient comprises entre ces valeurs. Aux plus basses tensions, la vitesse diminuait plus rapidement avec la diminution de la tension. La vitesse de fluage constant était fortement abaissée par de hautes pressions suivant le facteur $\exp\{-p\Delta V/RT\}$, où $\Delta V = 38 \pm 3$ cm³/mol. L'effet des impuretés aux concentrations d'environ 10^{-3} était en général d'abaisser la vitesse de fluage; S^{--} était plus efficace que Cd^{++} ou Cl^{-}. La théorie de Mott du fluage limité par la diffusion, paraît donner une interprétation satisfaisante de la dépendance du fluage constant de la température, de la tension et de la pression, dans le cas de cristaux purs.

KRIECHVORGÄNGE IM SILBERBROMID BEI HOHEN TEMPERATUREN

Die Anfangs- und die stationäre Kriechgeschwindigkeit von Einkristall- und Polykristallproben von AgBr, die durch Drucke zwischen 6 und 150 g/mm² verformt wurden, wurde im Temperaturgebiet zwischen 300°C und 410°C unter besonderer Betonung der stationären Kriechgeschwindigkeit der Einkristalle gemessen. Der Einfluss der kristallographischen Orientierung, des umgebenden hydrostatischen Druckes und der Verunreinigungen auf die Kriechgeschwindigkeit wurden untersucht. Einkristalle verformten durch Gleitung auf den theoretisch möglichen Gleitsystemen. Die Werte der stationären Kriechgeschwindigkeit waren auf ca. 15 prozent genau reproduzierbar. Bei höheren Spannungen und für Kristalle mit [001] als Achse konnte die stationäre Kriechgeschwindigkeit durch die empirische Formel $\dot{\epsilon} = C \exp\{-Q/RT\} \exp\{B\sigma^{\frac{1}{2}}/RT\}$ mit $C = 2{,}8 \times 10^{17}$ min^{-1}, $Q = 69{,}1$ kg-cal/mol, $B = 1{,}21$ (kg-cal/mol)/(g/mm²)$^{\frac{1}{2}}$, σ = Druckspannung, dargestellt werden. σ kann für [111] Kristalle durch $3/4\ \sigma$ ersetzt werden. Für andere Orientierungen lagen die Geschwindigkeiten zwischen diesen Werten. Im Bereich kleiner Spannungen nimmt die Geschwindigkeit stärker mit abnehmender Spannung ab. Die stationäre Geschwindigkeit wurde stark durch erhöhten Druck herabgesetzt; der Faktor betrug $\exp\{-p\Delta V/RT\}$ mit $\Delta V = 38 \pm 3$ cm³/mol. Verunreinigungs-konzentrationen von etwa 10^{-3} bewirkten im allgemeinen eine Verminderung der Kriechgeschwindigkeit, S^{--} ist darin wirksamer als Cd^{++} oder Cl^{-}. Motts Theorie des diffusionsbestimmten Kriechens scheint die Abhängigkeit der stationären Geschwindigkeit der reinen Kristalle von Temperatur, Spannung und Druck zufriedenstellend zu erklären.

I. Introduction

A correlation between the activation energies for steady-state creep of metal crystals and for self-diffusion has often been suggested. Nabarro [1] has shown how plastic deformation can occur without slip by the diffusion of lattice defects. If a surface where vacancies can form is subjected to a compressive force, at this surface the equilibrium vacancy concentration will be decreased. Under the concentration gradient thus established,

*Received August 27, 1953; in revised form November 3, 1953.

†Based on a dissertation submitted in partial fulfillment of the requirements for the degree of Doctor of Philosophy in the Department of Physics, University of Chicago. The experimental work was carried out in the Institute for the Study of Metals, University of Chicago.

‡Department of Physics, University of Chicago, Chicago 37, Illinois. Now at Department of Physics, Dartmouth College, Hanover, New Hampshire.

vacancies will flow to the surface, resulting in a removal of matter from it. Nabarro's formula for the steady-state strain rate is

$$\dot{\epsilon} = (8\sqrt{2}/d^2)(\sigma a^3/kT)\, D, \tag{1}$$

where σ is the compressive stress, a the lattice spacing, D the coefficient of self-diffusion, and d the dimension of the volume in which there are no sources or sinks of vacancies. This mechanism of course cannot account for the crystallographic features of deformation associated with slip.

Mott [2] has suggested how a dislocation mechanism for creep could be diffusion limited. Dislocations, emitted by a source, pile up on their slip plane behind fixed obstacles. At elevated temperatures the dislocations climb out of the slip plane, allowing further emission by the source. The movement of an edge dislocation one atomic distance normal to the slip plane is accomplished by the addition (or removal) of a line of atoms, i.e., by the diffusion of vacancies from (or to) the dislocation. Mott's formula for the velocity of migration perpendicular to the slip plane for an edge dislocation is

$$(fa^4F/kT)(j/a) \exp\{-W/kT\},$$

where f is the atomic vibrational frequency, F the force per unit length on the dislocation, j/a the number of jogs per unit length in the dislocation, and W the activation energy for self-diffusion.

Since the plastic behavior of ionic crystals at room temperature [3] is similar in many respects to that of metal crystals, measurement of the creep rate of an ionic crystal at elevated temperature should provide an interesting test of these ideas. In ionic crystals, the transport of ion pairs will be limited by the more slowly diffusing ion, and it is with the diffusion coefficient for this ion that a correlation of the creep rate could be expected.

The plasticity of AgBr at room temperature is comparable with that of soft metals, the critical shear stress being about 100 g/mm² [4]. The lattice defects are predominantly cation Frenkel defects [5; 6]. Thus the diffusion of AgBr ion pairs must be limited by the number of Schottky defects and the mobility of the Br^- vacancy, if it is assumed on energetic grounds that the number of interstitial Br^- ions is negligible. The number and mobility of Br^- vacancies is in some doubt. A transport experiment at 406°C shows that any Br^- current is less than 0.3% of the total current [6]. A value of 2.9×10^{-11} cm²/sec at 300°C has been determined [7] for the self-diffusion coefficient of radioactive Br, compared to 1.02×10^{-7} cm²/sec for Ag. The activation energy for Br is therefore probably appreciably greater than that for Ag.

In the present experiments, measurements have been made of the transient and steady-state creep rates of single crystal and polycrystalline specimens of AgBr, stressed in compression from 6 to 150 g/mm² at temperatures from 300° to 410°C. (The melting point of AgBr is 422°C.) The effects of hydrostatic confining pressure and of impurities on the creep rate were observed.

II. Experimental Apparatus

The apparatus for measuring creep in compression at high temperature and atmospheric pressure is illustrated schematically in Figure 1.

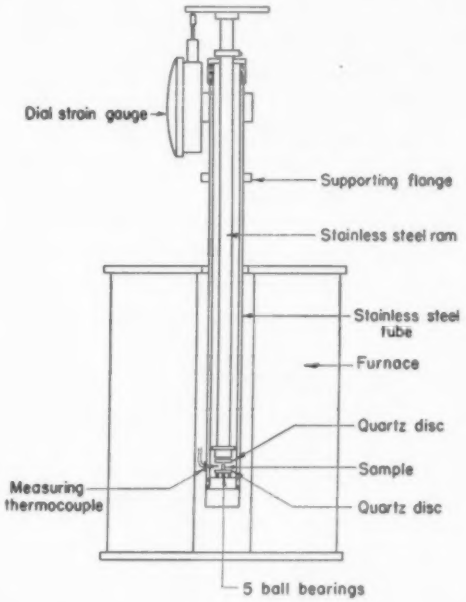

FIGURE 1. Apparatus for measuring creep under compression at high temperature.

The AgBr sample rests between two polished quartz discs, on a stainless steel plug screwed into the bottom of a stainless steel tube. The quartz discs provide a smooth, inert surface bearing on the sample, reduce heat flow from the sample, and eliminate thermoelectric currents. The load is applied to the sample by a stainless steel ram, whose upper end deflects a dial gauge graduated to 0.0001 in. The ram is made of a half-inch tube with 1/32 in. wall, in order to reduce the heat leak up the ram and to permit the application of small

loads. It is rigid enough that the creep of the apparatus, with no specimen, is negligible under the conditions of the experiments. The ram assembly weighs 203 g, and it is loaded at the top with B-B's (weight about 0.3 g) so that the load is nearly continuously variable. The load must be corrected for the spring constant and the friction of the dial gauge. The tube is surrounded by a furnace, whose temperature is held constant to within about 0.5°C by a proportioning controller [8]. The temperature is measured by a chromel-alumel thermocouple about 1/16 in. from the specimen. It is necessary to direct a fan on the upper end of the apparatus in order to overcome spurious gauge deflections caused by the cooling effect of random air currents.

Two types of loading were possible. Since the AgBr specimen sticks firmly to the quartz discs at high temperature, if the latter are constrained against lateral motion the specimen axis must remain vertical. This constraint can be removed by setting the lower quartz platen on five freely rolling ball bearings. (These were "soldered" in place during assembly with naphthalene, which then evaporates when the apparatus is heated.)

The device for measuring creep at high pressure was designed to fit inside the working space of a high-pressure bomb [6]. The sample sat on the bottom of a steel can with a tight fitting lid, shown in Figure 2, with a lead-filled steel weight

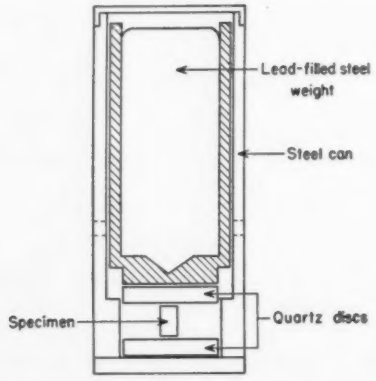

FIGURE 2. Device for loading specimen in a high pressure bomb.

resting on it. Holes in the side of the can admitted the pressure fluid (DC 200 3-centistoke silicone oil), so that a surge while pumping on the oil would not smash down the weight on the specimen. Because the arrangement did not permit strain measurements during the experiment (the working space in the bomb is limited), the specimen was measured with micrometer calipers before and after the deformation. Further, the load was applied to the specimen while the bomb was being heated to the temperature of the experiment, but conditions were arranged so as to minimize the contribution to the strain during this period. The weight weighed 243 g in air; although the stresses were calculated for the bouyancy of the pressure fluid at room temperature and pressure, the failure of thermal expansion to compensate for compressibility is a second order correction.

III. Preparation of Specimens

The AgBr used was precipitated in red light from Mallinckrodt HBr and $AgNO_3$. A qualitative spectrographic analysis indicated about 0.001 per cent of Fe, Mg, and Cu, and less than measurable amounts of Cd, Pb, Sr, Ca, Zn, Ba, Ni, Mn, Sn, Be, and Si present as impurities. Less than 0.0002 per cent sulfur is assumed to have been present, since the addition of about this amount caused a noticeable change in color and in the rate of photolytic darkening of the AgBr. Since the crystals were grown in air, they were presumably saturated with oxygen.

Polycrystalline samples were made by pouring molten salt into a steel die and then pressing under about 30 tons. The single-crystal specimens were sawed from single crystal rods grown by the Czochralski method, a continuous withdrawal from the melt, at 2 in./hr. The specimens were machined into cylinders, from 5 to 8 mm in height and from 2.3 to 5 mm in diameter, with ratios of height to diameter of 0.9 to 2.6, usually about 2. After machining, about 0.001 in. was removed from the surface with sodium thiosulfate solution. After this treatment no recrystallization of the single-crystal specimens ever occurred. The specimens were measured and washed before the experiment. Orientation determinations of the cylinder axis of the specimen were made to within about ½ degree by back reflection X-ray photographs. No attempt was made to handle the crystals in the dark, since photolytic darkening was slight and disappeared at the temperature of the experiments.

IV. Experimental Results

1. *Single Crystal Specimens*

A. *Time dependence of creep*

The strain during the course of a creep experiment at constant stress is commonly divided into three stages: a sudden deformation immediately

on application of the load, a transient phase, in which the strain is in many cases proportional to the cube root of the time according to the Andrade law, and finally a steady state in which the creep rate remains constant. With the present apparatus the sudden compression cannot be measured. After application of the load the strain shows the transient and steady phases. At 300°C the transient state lasts a long time (more than 100 hr), but near 400°C it can be quickly exhausted (about ½ hr). The strain during the transient phase is large at high stress and small at low stress. It is less for crystals with axis near the [111] direction than for those near [001]. The transient phase, however, is not always described by the Andrade law. In fact, the slope, and even the shape, of the strain-time curve during the transient stage is very sensitive to factors beside temperature, stress, and orientation, including previous thermal and mechanical history and purity. The influence of impurities will be described later. In Figure 3 is shown the effect

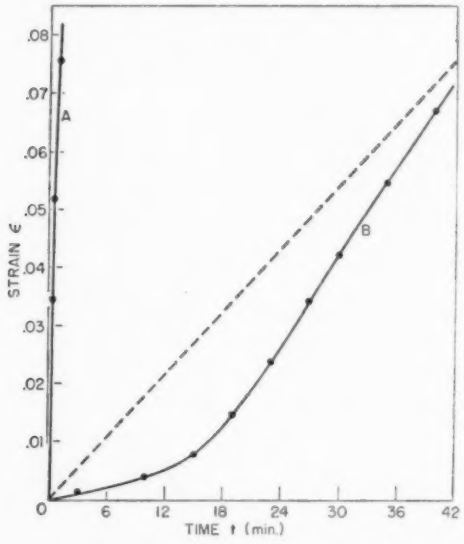

FIGURE 3. Transient creep of an annealed (A) and a cold-worked (B) specimen.

of 2½ per cent compression at room temperature before the run at 370°C (curve B), compared with the behavior of an annealed sample (curve A) and the steady-state rate (dashed line). On the other hand, the steady-state rate is insensitive to these factors, and the emphasis of the experiments has been put on it.

After the steady state is reached, it continues up to a total strain of 10 to 15 per cent, provided the stress is kept approximately constant by an empirical correction to the load to compensate the increase in the diameter of the sample. (This correction never amounts to more than about 5 per cent.) After about this amount of strain the creep rate usually falls off, probably because of the geometrical distortion of the specimen, since if it is then remachined into a cylinder the original creep rate is restored, without the reappearance of a large transient.

During the steady state, if the stress is changed suddenly there is then a new transient phase during which the rate is greater or less than the new steady-state rate according as the stress was increased or decreased. If on the other hand the temperature is changed, no new transient phase is detectable, provided the change is not so fast as to cause thermal stressing nor so slow as to allow, if the load is removed, annealing. The time required for the creep rate to reach equilibrium after changing the temperature is less than the time required for the apparatus to reach temperature equilibrium (about an hour) and is therefore not observable.

The steady-state rate is reproducible to about 15 per cent in a single sample after observing the rate at other temperatures and returning to the original temperature, or among different samples if the height to diameter ratio is between 1.3 and 2.6. For smaller ratios the rate was about 30 per cent low, presumably because of inhibition of slip near the platens. There was no dependence on size, within the limits used.

B. *Temperature and stress dependence*

The reproducibility of the steady-state creep rate among different samples is sufficient to permit measurement of its dependence on temperature and stress over rather large ranges. The stress range which could be investigated was limited at the lower end by the design of the apparatus and at the upper end by the large transient strain produced by high stress. In fact, in samples with the axis near the [001] direction at stresses above 60 g/mm² the transient strain was often so large that it was necessary to remachine the sample before the steady-state could be observed. The procedure was in general first to get the steady-state value at the highest temperature, at which the transient component was most quickly exhausted, then take the lower temperature points in arbitrary order, and finally repeat the highest temperature. This procedure was adopted, in preference to the alternative of varying the stress

at constant temperature, in order to minimize the transient strain during a run. Data will be presented for [001] and [111] samples; for other orientations the creep rates were intermediate.

The logarithm of the creep rate is plotted *versus* inverse temperature in Figures 4 and 5, for these two orientations, at different stresses. In these figures an exponential temperature dependence is apparent. In order to exhibit a stress dependence from the same data, the best straight line was drawn by eye through the points of Figures 4 and 5 for each constant stress, and the ordinates for three fixed temperatures were plotted as a function of stress in Figures 6 and 7. If the data

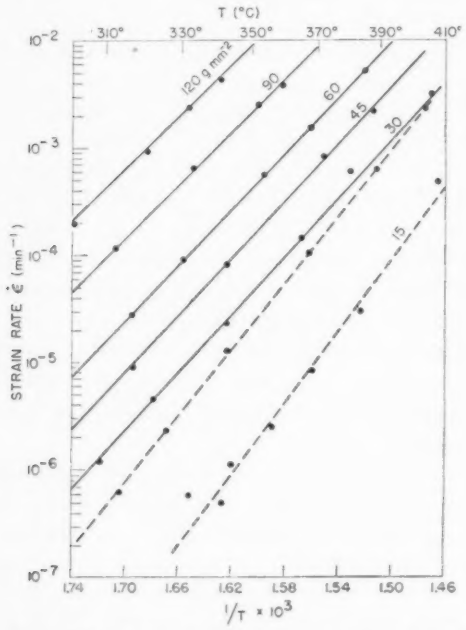

FIGURE 4. Steady-state creep rate of [001] specimens.

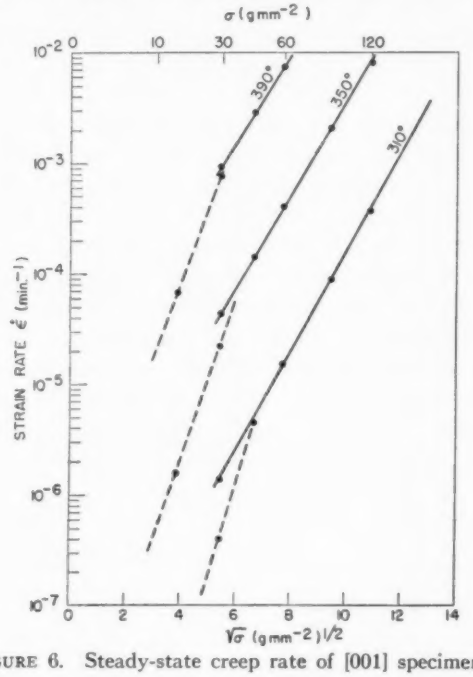

FIGURE 6. Steady-state creep rate of [001] specimens.

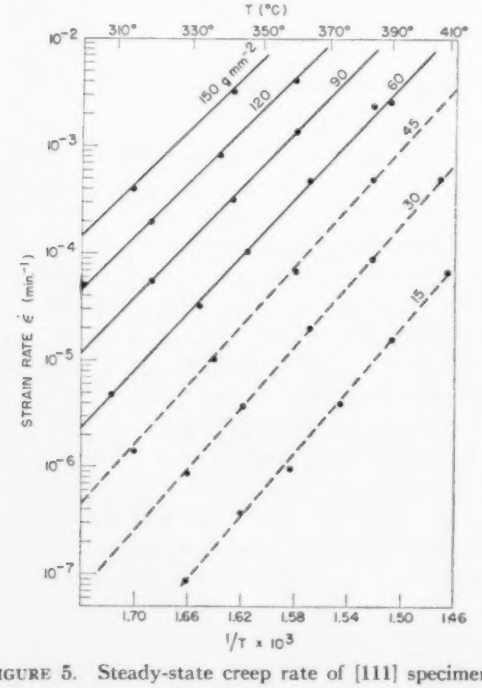

FIGURE 5. Steady-state creep rate of [111] specimens.

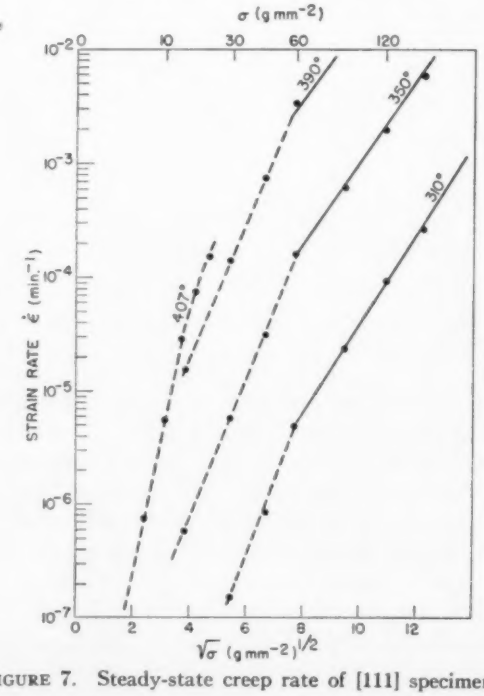

FIGURE 7. Steady-state creep rate of [111] specimens.

of Figure 4 are plotted *versus* the compressive stress, σ, the points show a tendency which indicates that a linear representation could be improved upon. In Figures 6 and 7 the data of Figures 4 and 5 are plotted *versus* the square root of the stress. In these figures the linear representation appears to be adequate in the region of high stress, with no simple function suggested over the whole range. In fact, the function

$$\dot{\epsilon} = C \exp\{-(Q - B\bar{\sigma}^{\frac{1}{2}})/RT\}, \tag{2}$$

with $C = 2.8 \times 10^{17}$ min^{-1}

$Q = 69.1$ kg-cal/mol

$B = 1.21$ (kg-cal/mol)/(g/mm^2)$^{\frac{1}{2}}$

$$\bar{\sigma} = \begin{cases} \sigma & \text{for [001] crystals} \\ 3/4\sigma & \text{for [111] crystals,} \end{cases}$$

represents, within the experimental reproducibility, all the data in the range $\bar{\sigma}$ greater than about 40 g/mm^2. This function is plotted by the full lines in Figures 4–7; the dashed lines are added to connect the data at smaller values of $\bar{\sigma}$. In the case of [001] crystals at 30 g/mm^2, two classes of results were obtained, presumably because of small uncontrolled differences in orientation and loading, and with 15 g/mm^2 the results were not very reproducible.

Because creep by diffusion is expected to vary linearly with stress for small stresses according to (1), a special attempt was made to investigate the stress dependence of the creep rate of a [111] crystal at the lowest stresses achievable with the apparatus. A [111] crystal with height-to-diameter ratio of 0.9 was measured at 407°C. The results appear in Figure 7. Down to the lowest attainable stress (6 g/mm^2), the creep rate is still decreasing faster than linearly.

C. *Effect of hydrostatic pressure*

The procedure for the high-pressure measurements of steady-state creep was as follows. First the specimen was deformed in the atmospheric pressure apparatus at the stress and temperature to be used in the high pressure experiment, in order to exhaust the transient creep and measure the atmospheric pressure steady-state rate. It was then cooled to room temperature, reheated, and remeasured, to verify that the transient component had not returned and that the steady-state rate was unchanged. The sample was then cooled, measured, transferred to the high-pressure apparatus, and brought up to pressure. The temperature was then raised by an external furnace and maintained for a suitable length of time, after which the apparatus was cooled to room temperature and the pressure released. The sample was removed and measured, and the total deformation compared with what it would have been under the same conditions at atmospheric pressure. The procedure for transient creep was the same, except that an unstrained, annealed sample was used.

Five steady-state high pressure runs were made between 3000 and 6000 atmospheres with different applied stresses and using crystals of different

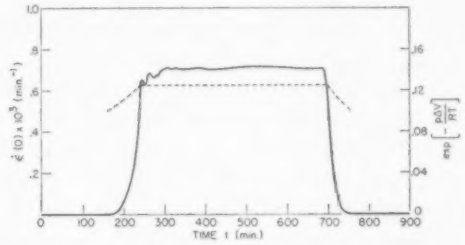

FIGURE 8. Atmospheric pressure creep rate corresponding to high pressure run (full line) and pressure factor (dashed line).

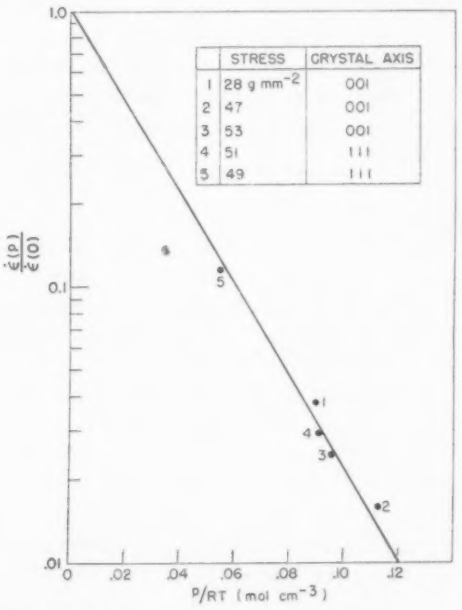

FIGURE 9. Relative steady-state creep rates at high pressure.

orientations. The results are shown in Figure 9, in which the ratio of the strain rate at high pressure $\dot{\epsilon}(p)$ to the strain rate at atmospheric pressure $\dot{\epsilon}(0)$ is plotted *versus* p/RT, where p and T are the pressure and temperature of the run. Because the temperature actually was changing at the beginning and end of the runs, the basis of comparison of the high pressure and atmospheric pressure strains is illustrated for one of the runs by Figure 8,

in which the full curve represents $\dot{\epsilon}(T(t))$ for $p = 0$, $\dot{\epsilon}(T)$ being obtained from the measured atmospheric pressure strain rate and $T(t)$ being the recorded temperature during the high pressure run. The integral of this function is the total strain which would have been observed at atmospheric pressure under the temperature conditions of the high-pressure run. The ratio of the actual strain during the high-pressure run to this integral is assumed to be equal to the ratio of the strain rate at high pressure to the strain rate at atmospheric pressure, $\dot{\epsilon}(p)/\dot{\epsilon}(0)$. If $\log \dot{\epsilon}(p)/\dot{\epsilon}(0)$ is plotted against p/RT, $\dot{\epsilon}(0)$ being referred to the strain rate before the high-pressure run, these data lie approximately on a straight line. The vertical intercept, however, is about 0.5 instead of 1. Furthermore, in all but one case the atmospheric pressure rate was measured also after the high-pressure run, and in each case it was about one-half of the rate before it. Therefore in Figure 9 the data are plotted referred to the rate after the high-pressure run; for the point for which the rate was not measured afterward, the rate obtained beforehand was divided by two. Within the precision of the experiment the points lie on a straight line, regardless of orientation or stress, implying a relation of the form

$$\dot{\epsilon}(p)/\dot{\epsilon}(0) = \exp\{-p\Delta V/RT\}.$$

The slope of the line drawn in the figure is $\Delta V = 38 \pm 3$ cm³/mol. In Figure 8 the dashed line shows $\exp\{-p\Delta V/RT\}$ during the run, showing that this function is slowly varying where the contribution to the strain is significant, and thus that the analysis of the data is consistent.

The retardation of the creep rate after the high-pressure runs was not removed by several hours annealing at high temperature. X-ray diffraction pictures made before and after holding two samples at high pressure and temperature but without loading showed no change in perfection of the crystal structure. Removal of one or two thousandths of an inch from the surface by etching, however, restored the normal creep rate, and the samples, which were slightly discolored after the high pressure runs, regained their normal color. Therefore it is thought that the cause of the retardation was contamination of the surface by an impurity. Spectrographic analysis of the surface of one sample after the high pressure run showed 0.003 per cent Si, 0.007 per cent Fe, and 0.006 per cent Cu.

An annealed [001] sample was loaded with 53 g/mm² for about 260 min at 6000 atmospheres and 378°C. Subtraction of the steady-state strain, computed on the basis of the above results, from the observed strain gave a transient contribution of 1.3 per cent, compared with the usual value of the order of 10 or 20 per cent at atmospheric pressure. Subsequently tested at atmospheric pressure, after removal of the surface, the sample showed a further transient strain of 0.7 per cent and a normal steady-state rate. It thus appears that the transient is also suppressed by pressure, though perhaps less strongly than the steady state.

D. *Effect of impurities*

The effect on the creep rate of additions of a divalent cation, a divalent anion, and a monovalent anion of about the same ionic radius has been observed. Cd^{++}, S^{--}, and Cl^{-} were chosen because the solubility limits were known. For this purpose crystals were grown from melts containing about 0.0006 and 0.25 mol per cent $CdBr_2$, 0.0006 and 0.06 mol per cent Ag_2S, and 0.0017 and 0.17 mol per cent AgCl. The exact impurity content of the resulting single crystals is unknown, although from a crystal grown from a melt containing 0.08 per cent Ag_2S, 0.06 per cent was recovered by chemical analysis.* In the case of sulfur, because of the pronounced color change caused by it, an inhomogeneity associated with the spiral ridges produced on the crystal rods by growth rate, dependent on the temperature gradient in the melt, was seen. Further, in the case of small concentrations of sulfur, richer melts sometimes produced poorer crystals, as evidenced by the rate of photolytic darkening and the effect on the creep rate. Nevertheless, the order of magnitude of the impurity content is believed to be correct, and the following facts emerge.

Sulfur had the greatest effect on the creep rate. The effect on the transient of 0.0006 per cent S^{--}, compared with 'pure' crystals, is shown in Figure 10. Curve A is for an annealed pure crystal which was loaded as soon as temperature equilibrium was attained (about 2 hr after the furnace was turned on); curve C is for a sample containing 0.0006 per cent S^{--} under the same conditions. Curves B and D are, respectively, for a pure crystal annealed 16 hr *in situ* and a sulfur-doped crystal annealed 12 hr *in situ* at 397°C before loading. These specimens were sawed from the same single crystal rods as those of curves A and C, respectively, and all were [001] specimens

*The author is indebted to Dr. Louis Dunicz for performing this difficult analysis.

deformed at 370°C with 60 g/mm². The inhibitory effect, dependent on holding time at high temperature, was similar for other samples tested. The steady-state rate, however, for the sulfur-doped samples was normal, i.e., the same as for the pure samples. But with a stress of 30 g/mm² at 405°C for a sulfur-doped sample, the steady-state rate was 0.7 times normal, and the induction time in the transient stage was an order of magnitude greater.

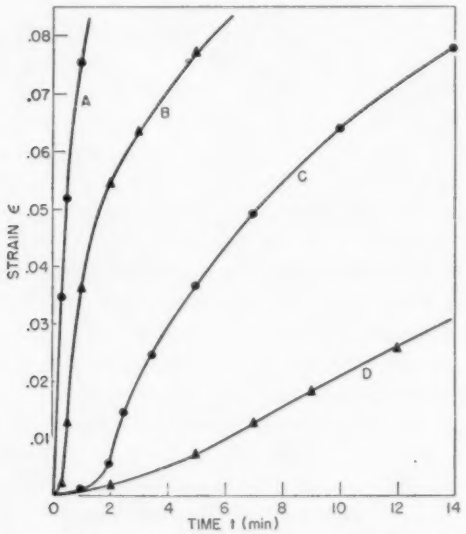

FIGURE 10. Transient creep of pure (A, B) and sulfur-doped (C, D) specimens, loaded immediately (A, C) and after annealing *in situ* (B, D).

Crystals containing 0.06 per cent S^{--} behaved the same at 30 as at 60 g/mm²: there was no measurable transient and the steady-state rate was about 0.2 times normal. (See Table I.)

Additions of Cd^{++} were similar to additions of Cl^- in that the transient behavior was like that of pure crystals, even with the larger concentrations. 0.0017 per cent Cl^- had no effect on the steady-state rate with 60 g/mm². 0.17 per cent Cl^- gave a steady-state rate about 0.6 times normal, and 0.25 per cent Cd^{++} one about 0.8 times normal at 60 g/mm².

TABLE I

EFFECT OF ADDITIONS OF IMPURITIES ON CREEP RATE

Impurity	Atomic per cent	Stress (g/mm_2)	Steady state rate / Normal steady-state rate	Transient
S^{--}	0.0006	60	1.0	induction period
S^{--}	0.0006	30	0.7	induction period
S^{--}	0.06	60	0.2	none
S^{--}	0.06	30	0.2	none
Cl^-	0.0015	60	1.0	normal
Cl^-	0.15	60	0.6	normal
Cd^{++}	0.0006	60	1.0	normal
Cd^{++}	0.25	60	0.8	normal

0.25 per cent Cd precipitated at room temperature in about 8 hr. (In order to observe the effect in solution the sample was maintained at high temperature before loading.) The precipitate had no effect on the transient, and probably none on the steady-state rate, though the latter conclusion is uncertain because of dissolution during the run.

E. *Specimens after deformation*

Slip in AgCl has been studied at room temperature by Nye [9], who concluded that the slip direction is $[0\bar{1}1]$, while the slip plane is not always a crystallographic plane of low indices, but is always near to the plane in an $[0\bar{1}1]$ zone on which the resolved shear stress in the $[0\bar{1}1]$ direction is maximal. Observations of slip lines on the surface of three AgBr samples similar to those used in the high-temperature creep tests, after rapid compression at room temperature, were consistent with Nye's conclusions about AgCl.

After creep at high temperature, slip lines did not always appear on the surface, so that it was difficult to say in all cases what were the active slip systems. This difficulty is the reason for presenting the data in terms of compressive stresses and strains. Nevertheless the occurrence of slip can be inferred from the shape of the specimens after deformation. (See Figure 11.) The very inhomogeneous deformation of the two samples on the left was observed only in specimens with the ends free to move laterally slipping on the (011) plane in the $[0\bar{1}1]$ direction. The avoidance of this type of deformation was the reason for determining the stress and temperature dependence of the creep rate with the ends of the specimen laterally constrained, although the results were about the same in either case. Sometimes planes were traced by not very sharply defined ridges on the surface of the deformed specimen, and occasionally, at high stresses, well-defined slip lines could be seen under low magnification. Measurement of the orientation of these features could only be made within an error of about 10 degrees, however, so that the following statements should be understood to have this uncertainty.

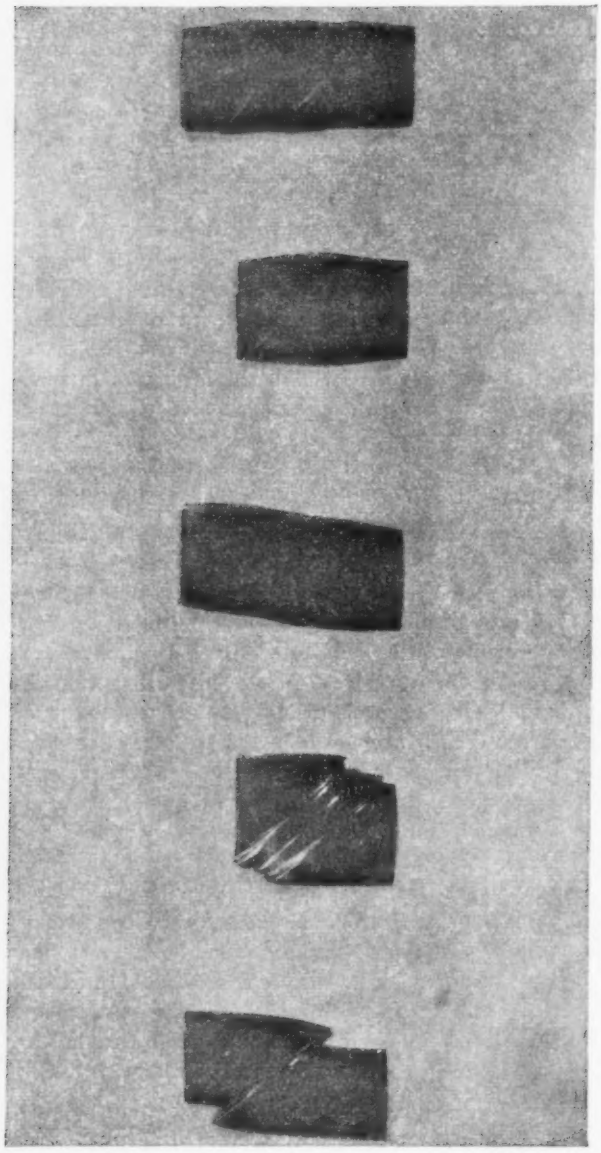

FIGURE 11. Single crystals after deformation of about 10 per cent; in the deformation of the three specimens on the left, the ends were free to move laterally.

These observations indicated first that an (011) plane and an $[0\bar{1}1]$ direction constitute the preferred slip system. For example, a crystal whose axis was [215] was observed to slip in the $[0\bar{1}1]$ direction on the (011) plane, where the resolved shear stress was only 0.79 relative to the maximum resolved shear stress (one half the compressive stress), in preference to the plane, $(1\bar{1}1)$, on which the shear stress resolved in an $[0\bar{1}1]$ direction was greatest, namely 0.95. This conclusion is also supported by the fact that the creep rate was greatest when the specimen axis was [001], when there are four (011)–$[0\bar{1}1]$ systems on which the resolved shear stress is the maximum, and least when the axis was [111], when there are no such systems on which the resolved shear stress is different from zero.

This preference, however, does not appear to be very strong. In every case a slip plane was chosen which was nearly 45 degrees from the specimen axis. In addition, there were cases, particularly when the stress was probably not very homogeneous, when the slip direction apparently cannot have been an $[0\bar{1}1]$ direction. For example, a crystal whose axis was [413] and whose ends were laterally free, after considerable slip in the [110] direction (on the $(1\bar{1}1)$ plane), appeared to have slipped in the $[2\bar{1}0]$ direction (on the (121) plane). In [111] crystals with the ends laterally constrained, traces of (011) planes were seen; since the $[0\bar{1}1]$ direction is 90 degrees from the specimen axis, it cannot have been the slip direction. If [100] and $[2\bar{1}0]$ are also included as possible slip directions, all the observations can be understood. In view of the multiplicity of possible slip systems, the compressive stresses and strains are probably not too bad a measure of the shear stresses and strains.

X-ray orientation determinations made after the deformation only rarely revealed appreciable net rotation of the lattice with respect to the specimen axis [10]. No correlation could be found between the cases in which it occurred and the conditions of the deformation.

After the deformation, except right at the ends of the specimens, in the back-reflection Laue photographs each individual reflection was split up into a number of discrete spots. The number of distinguishable spots varied from about 10 to 35, and they were spread over an angular region of about 2 to 8 degrees. As the area of the incident X-ray beam at the specimen was about 28×10^{-4} cm^2, the crystals appear to have broken up into regions about 10^{-2} cm on a side with a spread in orientation of about 1 to 4°.

2. *Polycrystalline Specimens*

Having the single crystal results, the behavior of polycrystalline specimens could be compared with them. Unfortunately, however, it was not possible to produce very small grained specimens. The results for three of them, with average grain size of about 1 mm, are presented in Figure 12, where the dashed lines represent the results for single crystals of [111] and [001] orientation. The rates do not differ greatly from those for single crystals.

It was found after the runs that grain growth had occurred, the samples now consisting essentially of one or two large grains. Also after the runs relative displacements of the original grains of the order of 0.05 mm normal to the surface could be seen.

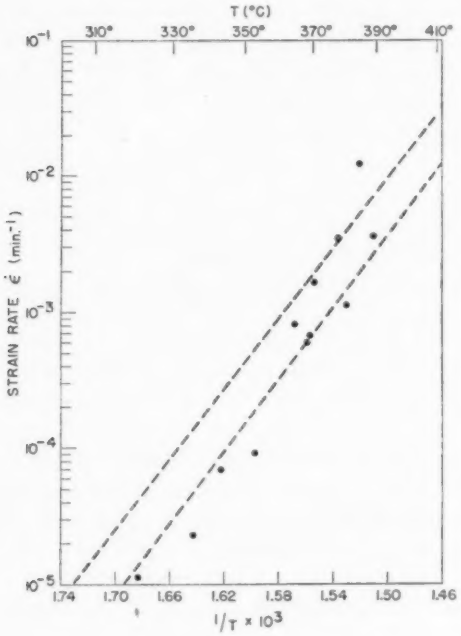

FIGURE 12. Steady-state creep rate of polycrystalline specimens at 60 g/mm².

Two bicrystals with a grain boundary intersecting the plane ends of the specimen were accidentally grown. These were tested, and it was found that slip marks were continuous across the boundary, but with a discontinuous change in direction. The steady-state rate was not greatly lowered by the presence of the boundary, though in both cases there was an initial period of about 90 min, during which the strain was about 3 per cent, in which the strain rate was less than the steady-state rate. This effect was not observed in the polycrystalline samples.

V. Discussion

The most salient features of the experimental results are the large activation energy of the steady-state creep rate, in comparison to soft metals, and the large 'free volume' associated with the high pressure measurements. In this section an attempt will be made to interpret the results in terms of current ideas of plastic flow, the emphasis being put on the Mott mechanism, which appears to give a natural explanation of the large activation energy and strong pressure dependence.

In discussing the results obtained with AgBr, it will be interesting to compare them with the measurements by Cottrell and Aytekin [11] of steady-state creep of single crystals of zinc, a metal which, though not cubic, has about the same melting point and critical shear stress as AgBr. Their results are expressed by

$$\dot{\gamma} = C \exp\{-(Q_0 + B'\tau_0)/RT\} \exp\{B'\tau/RT\},$$

where $\dot{\gamma}$ is the shear strain rate and τ is the shear stress, with

$$C = 10^{10} - 10^{13}\ \text{sec}^{-1},$$
$$Q_0 = 28 - 30\ \text{kg-cal/mol}\ (\tau_0 = 35\ \text{g/mm}^2),$$
$$B' = 0.150 - 0.300\ (\text{kg-cal/mol})/(\text{g/mm}^2).$$

If our high-stress results are expressed in the same form, assuming $\tau = \frac{1}{2}\sigma$, $\dot{\gamma} = 2\dot{\epsilon}$, we have from (2)

$$C = 10^{16}\ \text{sec}^{-1},$$
$$Q_0 = 59\ \text{kg-cal/mol},$$
$$B' = 0.145\ (\text{kg-cal/mol})/(\text{g/mm}^2).$$

Thus the stress dependence is about the same, whereas the activation energy is twice as large and the pre-exponential factor is several orders of magnitude larger.

This comparison can be understood qualitatively if it is assumed that the behavior of dislocations in the two materials is similar, but that the coefficient of self-diffusion appears as a factor in the creep rate. For Zn the smaller of the two diffusion coefficients (perpendicular to the c-axis) is [12] $90 \exp\{-31{,}000/RT\}$, with an activation energy about 2 kg-cal/mol larger than Q_0. For the coefficient of self-diffusion of Br in AgBr, both the activation energy and the pre-exponential factor would be expected to be considerably larger. (For Cl in NaCl [13], $D = 3 \times 10^4 \exp\{-62{,}000/RT\}$.) In addition the linear pressure dependence of $\ln \dot{\epsilon}$, independent of stress and orientation, is easily understood in terms of the effect of pressure on the diffusion coefficient. The value of ΔV for the diffusion of Br should be larger than the molar volume of AgBr, 29 cm³/mol, as is the observed ΔV.

The author [14] has attempted to extend Mott's theory to yield a formula which can be compared with the present experimental results. The resulting expression for the shear strain rate is

$$\dot{\gamma} = N n L l^2 j D \exp\{\Delta W/kT\}, \tag{3}$$

where N is the number of dislocation sources (e.g.,

Frank-Read sources [15]) per unit volume, n is the density of diffusing dislocations per unit area, L is the length of the dislocations, l is the distance on the slip plane in which the dislocations are piled up, j is the proportion of jogs in the dislocations, and D is the coefficient of self-diffusion (for Br, in AgBr). ΔW is the decrease of the energy of formation of a vacancy when the vacancy is formed at a dislocation in a stress field, due to the reduction in strain energy of the dislocation when it climbs. The rate of climb is assumed to be limited by the rate of diffusion of the excess vacancies away from the dislocation. If it is assumed that the driving stress field is primarily that due to the interaction of the accumulated dislocations,* and that the energy of interaction is proportional to the square of the number of dislocations and to a geometrical factor P depending insensitively on their distribution, ΔW is

$$\Delta W = [G\,b\,a^3\,P/4\pi(1-\nu)]\,n\,l, \tag{4}$$

where G is the shear modulus, ν Poisson's ratio, and b the Burgers vector of the dislocation. The main stress dependence arises through $(n\,l)$.

If the theory is to apply both to AgBr and to Zn, the above comparison suggests that the diffusion coefficient for Br is of the order of magnitude $D = 10^6 \exp\{-61{,}000/RT\}$. According to Mott [2], the proportion of jogs in the dislocation is $j = \exp\{-U/RT\}$. Then to give the observed activation energy $Q = 69$ kg-cal/mol, $U = 8$ kg-cal/mol, giving a proportion of jogs between 10^{-3} and 4×10^{-2} between 300° and 400°C. The X-ray diffraction evidence indicated that discontinuities in orientation occur at separations of the order of 10^{-2} cm after deformation,† suggesting that the density of dislocation sources should be $N \approx 10^6$ cm^{-3}. Since the surface layer appears to have an appreciable influence on the creep rate,‡ l should probably be comparable with the dimension of the crystal, and L should probably be of the order of magnitude of l. Substitution of $N = 10^6$ cm^{-3}, $n = 10^7$ cm^{-2}, $L = l = 10^{-1}$ cm, $D = 10^6 \exp\{-61{,}000/RT\}$ into (3) gives the observed value of $C = 10^{16}$ sec^{-1}. In addition, using $G = 10^{11}$ dynes/cm^2, $\nu = 0.25$, $b = a = 6 \times 10^{-8}$ cm, formula (4) gives the correct order of magnitude of ΔW if P is about 5. Thus it appears that the formulas can be made to give the correct order of magnitude for the creep rate of AgBr, and, because of the assumption of D for Br, also of Zn. It should be remarked, however, that the diffusion coefficient assumed for Br· is not in agreement with that measured by Murin and Taush [7] at 300°C.

It might also be noted that dislocations could be blocked by dislocations emitted from a source on a nearby slip plane [18]. The distance h at which two dislocations can block each other under an applied shear stress τ is

$$h = G\,b/8\pi(1-\nu)\,\tau.$$

Such interference might be expected if $h\,l\,L > 1/N$, in which case we would have

$$l \cong (l\,L)^{\frac{1}{2}} = [8\pi(1-\nu)/N\,G\,b]^{\frac{1}{2}}\tau^{-\frac{1}{2}}.$$

Since $h \cong 6 \times 10^{-3}$ cm/σ(g/mm^2), this interference might occur within the range of the experiment, and is a possible explanation of a $\sigma^{\frac{1}{2}}$ stress dependence.

For the magnitude of diffusion creep by the Nabarro mechanism, if we again assume that the diffusion coefficient for Br is $D = 10^6 \exp\{-61{,}000/RT\}$, and if we assume that $d = 6 \times 10^{-4}$ cm, we find from (1) $\dot{\epsilon} = 3 \times 10^{-10}$ sec^{-1} at 407°C and 6 g/mm^2. This value is much less than the experimental rate of 10^{-8} sec^{-1} at this temperature and stress, in agreement with the observation made in Sec. IV. B that the stress dependence was not characteristic of Nabarro creep.

Except in the case of Cd^{++}, the Mott process does not give the observed dependence of creep rate on impurity concentration by its influence on the equilibrium vacancy concentration. Cd^{++} depresses the number of Br^- vacancies, S^{--} increases it, and Cl^- has no effect [19]. On the other hand, S^{--} depressed the creep rate most, next Cl^-, and finally Cd^{++}. Cd^{++} gave about the effect which would be expected from its influence on vacancy concentration. It is thought that the explanation of the effect of S^{--} and Cl^- is to be sought in an interaction of the impurities with the dislocations, leading to an inhibition of their motion on the slip plane. Particularly in the case of S^{--}, the induction time for transient creep, depending on holding time at high temperature, suggests such an explanation [20]. The nature of the interaction, however, is not entirely clear from the experiments. The radii [21] of S^{--} and Cl^- are about 8 per cent smaller than that of Br^-, while Cd^{++} is a little more than 8 per cent smaller than Ag^+, so that an elastic interaction does not

*This assumption appears reasonable in view of the observation [11], that the process of steady-state creep is related to the process of recovery, after the applied stress is removed.

†Hedges and Mitchell [16] have observed optically a polyhedral substructure in AgBr, with dimensions $10^{-3} - 10^{-2}$ cm.

‡Cf., for example [17].

seem to give the observed differences. An electrical interaction between doubly charged impurities and 'incipient vacancies' [22] at jogs in dislocations is conceivable, but also fails to account for the differences. Whatever the nature of the interaction, however, it is believed that accidental impurities account for the sharper decrease of steady-state creep rate at low stress, since the addition of a small amount of S^{--} depressed the rate at 30 but not at 60 g/mm^2.

In alkali halides, slip systems are chosen which do not demand the close approach of ions of like sign when a dislocation moves. In contrast to the alkali halides, the large polarizability of the Ag^+ ion may account for the ductility of the silver halides [4], the monopole repulsion being decreased by dipole interaction [23]. It seems possible to understand qualitatively the comparatively weak conditions on choice of slip system in AgBr on this basis.

Because of the large number of slip systems possible, grain boundaries in polycrystalline AgBr do not appear to inhibit slip in individual grains strongly, in contrast for example to Zn, in which the creep rate of polycrystalline specimens is very much smaller than that of single crystals [11]. On the other hand, grain boundary mobility did not appear to give a large contribution to the strain rate; the contribution would presumably be greater in small grained specimens.

VI. Conclusion

It is concluded that Mott's mechanism for the the limitation of steady-state creep at high temperature by self-diffusion is able to give a satisfactory qualitative explanation of the strong temperature and pressure dependence of the steady-state creep rate of single crystals of pure silver bromide. A reasonable choice of parameters appearing in a model derived from it can give also the correct order of magnitude for Cottrell and Aytekin's results on zinc, and, if an assumption of the diffusion coefficient of Br be made, for the present results on AgBr at higher stress levels. Although the results appear to support Mott's theory, a detailed test of the calculation based on it must await measurement of quantities which are at present unknown. The square-root-of-stress activation energy dependence suggests a mechanism involving the interference of Frank-Read sources on different slip planes. The Nabarro mechanism apparently does not make a significant contribution to the creep in the range of the experiments. At low stresses, the creep rate in AgBr is believed to be controlled by the interaction of impurities with dislocations.

VII. Acknowledgements

The writer is grateful to his sponsor, Professor A. W. Lawson, for suggesting the problem and for guidance in its investigation, and to the Shell Oil Company for the grant of a Fellowship. He is also indebted to Messrs. N. D. Nachtrieb and K. Lindholm for the construction of his apparatus and for advice in its design. The work was supported in part by the Office of Naval Research.

References

1. Nabarro, F. R. N. Rep. of a Conference on the Strength of Solids (London, Phys. Soc., 1948), p. 75.
2. Mott, N. F. Proc. Phys. Soc. London, **B64** (1951) 729.
3. Schmid, E. and Boas, W. "Plasticity of Crystals" (London, F. A. Hughes and Co., 1950), Ch. VII.
4. Stepanow, A. W. Phys. Z. Sowjet. **8** (1935) 25.
5. Teltow, J. Ann. d. Physik **5** (1950) 63.
6. Kurnick, S. W. J. Chem. Phys. **20** (1952) 218.
7. Murin, A. and Taush, Yu. Dokl. Akad. Nauk SSSR, **80** (1951) 579.
8. Lazarus, D. and Lawson, A. W. Rev. Sci. Instr. **18** (1947) 730.
9. Nye, J. F. Nature **162** (1948) 299; Proc. Roy. Soc. **198A** (1949) 190, **200A** (1949) 47.
10. Taylor, G. I. Proc. Roy. Soc. **116** (1927) 16, 39.
11. Cottrell, A. H. and Aytekin, V. J. Inst. Met. **77** (1950) 389.
12. Banks, F. R. and Miller, P. H., Jr. Phys. Rev. **59** (1941) 943.
13. Chemla, M. C. R. Acad. Sci. (Paris) **234** (1952) 260.
14. Christy, R. W. Unpublished.
15. Frank, F. C. and Read, W. T., Jr. Phys. Rev. **79** (1950) 722.
16. Hedges, J. M. and Mitchell, J. W. Phil. Mag. **44** (1953) 223.
17. Andrade, E. N. da C. and Randall, R. F. Y. Proc. Phys. Soc. London, **B65** (1952) 445.
18. Cottrell, A. H. Progress in Metal Physics I (London, Butterworths Sci. Publ., 1949), p. 77.
19. Koch, E. and Wagner, C. Z. f. phys. Chem. **38B** (1937) 295.
20. Seitz, F. Phys. Rev. **88** (1952) 722.
21. Mott, N. F. and Gurney, R. W. "Electronic Processes in Ionic Crystals" (2d ed., Oxford, 1948).
22. Seitz, F. Rev. Mod. Phys. **23** (1951) 328.
23. Weyl, W. A. Glastechn. Ber. **23** (1950) 174.

SUR LE MÉCANISME DE LA DIFFUSION DANS LES SOLUTIONS SOLIDES*

C. CRUSSARD†

La diffusion dans les solutions solides est caractérisée par un temps de relaxation qui n'obéit pas exactement à la loi d'Arrhénius, comme l'ont montré des expériences très précises dûes à Nowick. Diverses hypothèses sont envisagées ici pour expliquer ces écarts : influence d'hétérogénéités de concentration, des lacunes réticulaires, mécanisme de diffusion double (impliquant la diffusion successive d'un atome du solvent et d'un atome du soluté), variation de l'énergie d'activation dans la théorie d'Eyring, mécanisme invoqué par Barrer et différent de celui d'Eyring. On montre qu'aucune de ces hypothèses ne peut rendre compte des écarts observés.

En analysant de plus près le mécanisme de l'agitation thermique, et en utilisant une théorie déjà dévelopée ailleurs par l'auteur, basée sur l'interférence des ondes d'agitation thermique, on arrive à expliquer de façon satisfaisante les écarts à la loi d'Arrhénius.

ON THE MECHANISM OF DIFFUSION IN SOLID SOLUTIONS

The diffusion in solid solutions is characterised by a relaxation time that does not follow exactly Arrhenius' law, as has been shown by very precise experiments carried out by Nowick. Various hypotheses are considered here in order to explain those differences: the influence of heterogeneities of concentration, of vacancies, of the mechanism of double diffusion (involving the successive diffusion of an atom of solvent and an atom of solute), variation of the activation energy in Eyring's theory, the mechanism proposed by Barrer, which differs from the one proposed by Eyring. It is shown that none of those hypotheses can account for the observed discrepancies. By analyzing more closely the mechanism of thermal agitation, and using the theory based on the interference of waves of thermal agitation, developed elsewhere by the author, it is possible to explain in a satisfactory manner the discrepancies in Arrhenius' law.

ÜBER DEN DIFFUSIONSMECHANISMUS IN FESTEN LÖSUNGEN

Diffusion in festen Lösungen ist durch eine Relaxationszeit, die nicht völlig dem Arrhenius'schen Gesetz folgt, charakterisiert. Dieses wurde von Nowick durch sehr präzise Versuche gezeigt. Um diese Differenzen zu erklären werden im Folgenden verschiedene Hypothesen betrachtet: Unstetigkeiten in der Konzentration, Leerstellen, Doppeldiffusion (was eine aufeinander folgende Diffusion eines Atoms des Lösungsmittels und eines Atoms des gelösten Stoffes erfordert) Veränderungen in der Aktivierungsenergie in Eyrings Theorie, ein von Barrer vorgeschlagener Mechanismus, der sich von Eyrings Bild unterscheidet. Es zeigt sich, dass keine dieser Hypothesen die beobachteten Abweichungen erklären kann.

Wenn man jedoch die Elementarvorgänge der thermischen Anregung eingehender analysiert und eine von dem Autor an anderer Stelle veröffentlichte Theorie, die sich auf die Interferenz der Wellen der thermischen Anregung gründet, hinzuzieht, kann man die Abweichungen vom Arrhenius'schen Gesetz zufriedenstellend erklären.

La vitesse de diffusion, mesurée par le coefficient de diffusion par exemple, varie en fonction de la température selon la loi d'Arrhénius:

$$(1) \qquad D = D_0 \exp(-E/RT)$$

La mesure exacte des quantités D_0 et E est très difficile, comme le montrent les écarts considérables entre les résultats trouvés par d'excellents expérimentateurs. Dans le cas des solutions solides métalliques de substitution, il semble que la meilleure mesure de la mobilité des atomes du soluté soit fournie par l'étude du frottement interne. Cette méthode, découverte par Zener [1], a été appliquée récemment par Nowick à des alliages Ag-Zn [2]. Ses résultats contiennent une particularité intéressante qui mérite d'être discutée.

D'après l'équation (1), on doit s'attendre à ce que la représentation en fonction de $1/T$ de log D (ou d'une grandeur qui lui est inversement proportionnelle comme le temps de relaxation déduit des expériences d'amortissement) fournisse une droite. C'est ce qui est communément admis. Mais les expériences de Nowick sont assez précises pour montrer des déviations petites, mais systématiques, par rapport à la loi d'Arrhénius, visibles sur la figure 1 reproduite de son article. Sur cette figure a été ajoutée, en pointillé, une courbe tendue représentant plus exactement les résultats expérimentaux que la droite moyenne; en admettant que cette courbe est une parabole, on peut calculer que la chaleur d'activation apparente (valeur de E déduite de la pente de la courbe à une température donnée) croît de 15% environ (en valeur relative) quand on passe d'un bout à l'autre de la courbe expérimentale. Par exemple, pour un alliage à 15,8% de Zn, où la variation semble la plus forte, la chaleur d'activation moyenne indiquée par l'auteur, soit 36.100 cal/mole, est valable en réalité vers 270°C, milieu de l'inter-

*Received September 9, 1953.

†Institut de Recherche de la Siderurgie, St. Germain-en-Laye.

valle; elle varie entre 32.500 (environ) à 160°C et 39.600 à 400°C.

D'où proviennent ces écarts à la loi d'Arrhénius dans le phénomène de relaxation utilisé ici ? On peut en chercher une explication dans diverses directions.

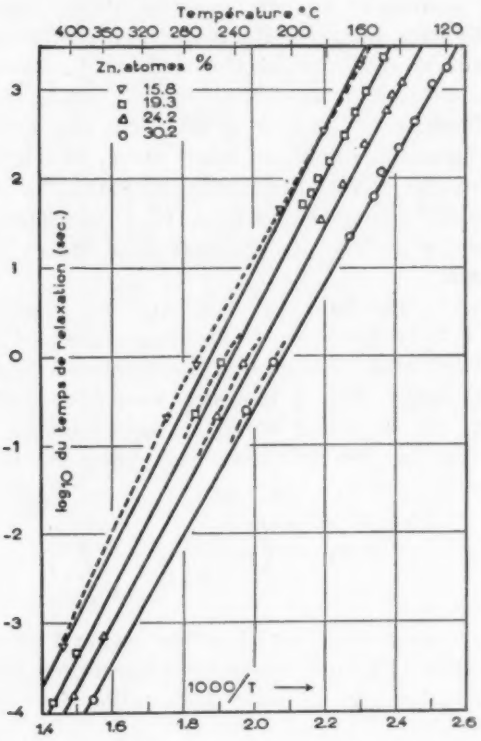

FIGURE 1. Variation du temps de relaxation avec la température, par divers alliages Ag–Zn.

Admettons d'abord que la vitesse de diffusion suive bien la loi d'Arrhénius, mais qu'une particularité du métal ou du processus de relaxation puisse introduire des perturbations.

1. Dans cet ordre d'idées, Nowick a suggéré de ces écarts une première explication : des hétérogénéités de concentration dans la solution solide introduiraient des variations locales dans l'énergie d'activation du processus, donc dans son temps de relaxation τ. Dans cette hypothèse, la valeur du frottement interne, au lieu d'être commandée par un processus à temps de relaxation unique, dépend d'un "spectre" de temps de relaxation, distribué selon une certaine fonction de distribution, F. Comme Nowick a prouvé que les variations du temps de relaxation étaient entièrement attribuables à des variations de l'énergie d'activation E, il faut considérer que cette distribution est faite en fonction de E, ou, ce qui revient au même, du paramètre

$$\lambda = \frac{E}{R} \tag{2}$$

que nous utiliserons dans la suite. Si $F(\lambda)$ est la fonction de distribution ainsi définie, le nombre de "centres de relaxation" dont le temps de relaxation correspondra à une valeur λ, à $d\lambda$ près, sera

$$dN = F(\lambda)\, d\lambda \tag{3}$$

Remarquons en passant qu'il ne faut pas définir la fonction de distribution en fonction de τ,comme l'a fait Zener, car τ varie avec la température, et une distribution ainsi définie n'aurait pas de signification physique intrinsèque au métal et indépendante des conditions d'expérience.

Ceci étant, le frottement interne est égal à

$$\delta = \int_{-\infty}^{+\infty} F(\lambda) \frac{\omega\tau}{1+\omega^2\tau^2}\, d\lambda \tag{4}$$

où ω est la pulsation du pendule de mesure.

Si le processus de relaxation obéit à la loi d'Arrhénius

$$\tau = \tau_0 \exp(\lambda/T) = \exp(A + \lambda x) \tag{5}$$

en posant

$$x = \frac{1}{T} \qquad A = \ln(\tau_0) \tag{6}$$

On peut donc écrire (4) sous la forme suivante:

$$\delta = \int_{-\infty}^{+\infty} F(\lambda) \frac{1}{2\cos\mathrm{h}\, u}\, d\lambda \tag{7}$$

en posant

$$u = A + \lambda x + \ln(\omega) \tag{8}$$

Le pic de la courbe du frottement interne en fonction de la température qui sert à la détermination expérimentale de τ, est donné par l'équation

$$\delta'_x = 0 \tag{9}$$

Le calcul donne

$$\delta'_x = \int_{-\infty}^{+\infty} F(\lambda) \frac{\sin\mathrm{h}\, u}{2\cos\mathrm{h}^2 u}\, \lambda\, d\lambda \tag{10}$$

(9) est donc une équation intégrale qui définit la valeur x_0 de x correspondant au maximum de δ.

En général, on ne peut calculer x_0 qu'en précisant la forme de la fonction F. Mais on peut s'en tirer

par un artifice. Remarquons d'abord que si la distribution des λ se réduisait à une valeur unique, λ_0 (mécanisme à un seul temps de relaxation), à ce mécanisme correspondrait une courbe $\delta(x)$ passant par un maximum (pic de frottement interne) précisément pour la valeur de x annulant u (λ_0, x). Dans le cas général d'une distribution continue, supposons $x = x_0$; on peut développer F en série au voisinage de la valeur λ_0 de λ, inconnue, annulant u (λ, x_0). En se limitant au premier terme, il vient :

$$F(\lambda) = F(\lambda_0) + (\lambda - \lambda_0)\, F'_\lambda(\lambda_0) \tag{11}$$

En portant cette valeur dans le formule (10), on trouve finalement

$$\delta'_x(x_0) = [F(\lambda_0) + \lambda_0 F'(\lambda_0)] \times \int_{-\infty}^{+\infty} \frac{\lambda - \lambda_0}{2} \cdot \frac{\sin h\,[(\lambda - \lambda_0)\, x_0]}{\cos h^2\,[(\lambda - \lambda_0)\, x_0]}\, d\lambda \tag{12}$$

L'intégrale de l'expression (12) a une valeur proportionnelle à $1/x_0^2$; donc, sauf si $x_0 = 0$ ou ∞, le maximum de δ sera atteint pour un couple de valeur λ_0, x_0 satisfaisant aux deux équations

$$F(\lambda_0) + \lambda_0\, F'(\lambda_0) = 0 \tag{13}$$

$$u(x_0, \lambda_0) = 0 \tag{14}$$

La première définit une valeur λ_0 *independante de* x (donc de la température), et légèrement supérieure à la valeur λ_m correspondant au maximum de $F(\lambda)$: λ_0 est donc un peu à droite du maximum de la courbe de distribution, l'écart $\lambda_0 - \lambda_m$ étant faible si la distribution est aigue. Dans ce cas on peut d'ailleurs très sensiblement remplacer l'équation (13) par :

$$F(\lambda_0) + \lambda_m\, F_\lambda'(\lambda_0) = 0 \tag{15}$$

L'équation (14) définit la température correspondante au pic du frottement interne; elle est la même que si la courbe de distribution se réduisait à la valeur unique λ_0, déterminée en portant dans l'équation (5) les valeurs $\tau = 1/\omega$ et λ_0 racine de (15).

Appliquons maintenant ce résultat aux diverses fonctions $F(\lambda)$ que l'on peut imaginer, en remarquant que, d'après les résultats mêmes de Nowick (réf. [2], Fig. 5), λ est fonction linéaire de la concentration, donc que la *courbe de distribution* $F(\lambda)$ *reproduit, à l'échelle près, la courbe de distribution des concentrations*. Nous allons invisager 3 cas.

(*a*) Les fluctuations de concentration se sont produites à haute température (par exemple ségrégations à la coulée), et sont "gelées" à la température de l'expérience. Dans ce cas, l'équation (15) définit un λ_0 différent de λ_m, mais *indépendant de la température* : le pic de frottement interne est légèrement décalé vers la droite (en λ et en T), *mais ce décalage est constant* et ne peut donc introduire aucune variation dans l'énergie d'activation mesurée. Remarquons d'ailleurs que, d'après les résultats donnés par Nowick, l'élargissement du pic de frottement interne correspond à des fluctuations de x de $\pm$ 0,7% environ, donc à des fluctuations de E du même ordre, 10 fois plus petites que les variations de la chaleur d'activation apparente signalées plus haut; elles correspondent à des fluctuations de concentration de $\pm$ 1,2% environ.

(*b*) Les fluctuations de concentration se produisent à la température de l'expérience, sous l'effet de l'agitation thermique (fluctuations thermodynamiques). Soit γ la concentration en chaque point, γm sa valeur moyenne dans l'alliage. On sait que la probabilité de fluctuation est de la forme

$$P = P_0 \exp\left(-\frac{K(\gamma - \gamma_m)^2}{T}\right) \qquad (K \text{ constante}). \tag{16}$$

La courbe $F(\lambda)$ est donc de même forme et l'équation (15) montre que $\lambda_0 - \lambda_m$ est proportionnel à T, donc que l'énergie d'activation E est de la forme

$$E = E_0 + \beta T \qquad (\beta \text{ constante}).$$

En portant cette valeur dans (5), on retrouve la loi d'Arrhénius; les fluctuations envisagées agissent seulement sur l'entropie. Cette hypothèse ne fournit donc pas l'explication des écarts cherchée.

(*c*) Les fluctuations de concentration sont dûes aux tensions internes liées à des défauts de structure. Pour des métaux bien recuits, les seuls défauts que l'on puisse raisonnablement envisager sont des dislocations. Du fait de l'effet Cottrell, d'un côté des dislocations il y a enrichissement, de l'autre côté appauvrissement en atomes dissous. Or des variations locales de concentration sont fonction de la température (les "nuages s'évaporent" quand on chauffe). On connaît la loi de répartition de la concentration dans ces nuages [3]. Elle est de la forme:

$$\frac{a}{r} = -\,b(\gamma - \gamma_m) + kT \ln\left(\frac{\gamma}{\gamma_m}\right) \tag{17}$$

où a et b sont des constantes, et r la distance du point considéré à la dislocation. Quand il y a plusieurs dislocations, il faut remplacer r par une fonction des distances aux dislocations les plus proches. Dans un métal bien recuit, le nombre des dislocations est faible, et il existe de grands espaces éloignés de toute dislocation. Aussi le maximum de la courbe de distribution est très aigu. Dans les espaces en question, γ diffère peu de γ_m, de sorte que (17) peut s'écrire sensiblement

$$(17\text{ bis}) \qquad \frac{a}{r} = \left(-b + \frac{kT}{\gamma_m}\right)(\gamma - \gamma_m)$$

comme b est grand vis-à-vis de kT [3], la distribution dans ces régions est pratiquement indépendante de la température. On retombe donc dans le cas a, avec un maximum plus aigu. Là encore, l'hypothèse envisagée ne peut expliquer les écarts à la loi d'Arrhénius.

2. Il existe un autre genre de défauts de structure dont la répartition, sans agir sur les concentrations, pourrait avoir un effet sur le phénomène étudié: ce sont les *lacunes réticulaires*. Ces lacunes sont attirées par les atomes en solution [3] (ici les atomes de Zn); cette attraction varie avec la température : le nombre de paires Zn-lacune décroît quand la température croît, ce qui rend la diffusion plus difficile. On introduit donc dans le nombre de cas favorables à la diffusion un facteur qui, pour des raisons évidentes, doit être de la forme $\exp(-u/kT)$ (u énergie d'interaction, atome de Zn—lacune; négative); *l'entropie d'activation* de ce fait varie de $-u/kT$. Ce terme, introduit quand l'équation (20), modifie donc seulement l'énergie d'activation apparente d'une quantité constante. Là encore, il n'y a pas d'écart à la loi d'Arrhénius.

3. Nowick a invoqué une autre cause d'écart: le processus de relaxation exige en réalité la diffusion successive d'un atome de zinc et d'un atome d'argent. Le temps de relaxation pour cet ensemble de processus est de la forme

$$(18) \qquad \tau = \tau_1 \exp(\lambda_1/T) + \tau_2 \exp(\lambda_2/T)$$

remplaçant l'équation (5). Ici, d'après ce que l'on sait sur la diffusion, les concentrations des deux espèces d'atomes étant du même ordre, si l'indice 1 est affecté à l'atome diffusant le plus difficilement (ce sera probablement l'argent), $\lambda_1 > \lambda_2$, $\tau_1 < \tau_2$; mais, au total, c'est le premier terme de (18) qui est le plus grand. On peut donc écrire

$$(18\text{ bis}) \qquad \tau = \tau_1 \exp(\lambda_1/T)\left[1 + \frac{\tau_2}{\tau_1}\exp\left(-\frac{\lambda_1 - \lambda_2}{T}\right)\right]$$

d'où très sensiblement

$$(19) \qquad \log \tau = \log \tau_1 + \lambda_1 x + \frac{\tau_2}{\tau_1}\exp(-(\lambda_1 - \lambda_2)x)$$

La courbe correspondante donnant $\log(\tau)$ en fonction de x devrait tourner sa concavité vers le haut. *On trouve donc bien ici un écart à la loi d'Arrhénius, mais du mauvais sens par rapport à* ceux observés. Ceci prouve en passant que le terme $\lambda_1 - \lambda_2$ doit être assez fort pour que le terme correctif soit négligeable.

On ne voit donc pas comment expliquer les écarts observés, si la vitesse de diffusion suit la loi d'Arrhénius. Il fait donc maintenant aller plus à fond dans la théorie et voir si une étude plus approfondie du mécanisme de la diffusion ne montrerait pas qu'elle suit une loi différente de celle exprimée par l'équation (1). Nous continuerons donc la série de nos hypothèses investigatrices comme suit:

4. Si l'on calcule le coefficient de diffusion D d'après la théorie d'Eyring sur la cinétique chimique, on trouve en première approximation la formule

$$(20) \qquad D = A\frac{kT}{h} \cdot \exp(\Delta S/R) \cdot \exp(-E/RT)$$

où A est une constante, k et h respectivement les constantes de Boltzmann et de Planck, ΔS l'entropie de diffusion et E l'énergie d'activation pour la diffusion. L'écart à la loi d'Arrhénius pourrait provenir du terme en T devant l'exponentielle de la formule (20).

Cet écart est bien dans le bon sens; mais en faisant le calcul, on s'aperçoit qu'il n'est pas du bon ordre de grandeur pour expliquer les résultats de Nowick. En effet, d'après la formule (20) la variation de la chaleur d'activation apparente entre 160° et 400° serait seulement de 1,5% (exactement : 480 cal/mole), soit 10 fois plus petite que la variation mesurée.

D'ailleurs, Le Claire a montré [4] qu'une théorie plus exacte faisait disparaître le terme en T devant l'exponentielle. Ce n'est donc pas lui qui peut expliquer les écarts à la loi d'Arrhénius.

On peut alors se demander si des variations de l'énergie d'activation E avec la température ne pourraient être responsable de ces écarts. Mais récemment Dienes a montré [5] que les variations de E étant très approximativement linéaires en T,

au moins dans un large intervalle de température, on peut écrire

$$E = E_0 - \alpha T \tag{21}$$

d'où

$$D = A' \exp(\Delta S + \alpha/R) \cdot \exp(-E_0/RT) \tag{22}$$

ce qui modifie seulement l'entropie d'activation, sans changer la forme de la loi. On ne peut donc expliquer ainsi les écarts observés.

Remarquons enfin que dans le terme A' figure la fréquence des oscillations atomiques. Celle-ci varie avec T, mais beaucoup trop peu pour pouvoir rendre compte des écarts en question.

Ainsi la théorie d'Eyring est incapable d'expliquer correctement les résultats de Nowick.

5. On peut alors, suivant Barrer [6] considérer que le phénomène qui commande la vitesse de diffusion est l'accumulation (aléatoire) d'énergie cinétique dans l'atome *avant* le saut, alors que la théorie d'Eyring suppose que le processus est contrôlé par la vitesse à laquelle les atomes diffusant passent le "col" d'énergie qu'ils ont à franchir. Dans cette hypothèse, on trouve pour le coefficient de diffusion:

$$D = c'^{e} \left(\frac{E}{RT}\right)^{s-1} \exp(-E/RT) \tag{23}$$

où s est le nombre des degrés de liberté sur lesquels l'énergie E est accumulée.

Pour $s = 1$, on retrouve la loi d'Arrhénius. Pour $s > 1$ on trouve des *écarts à cette loi, mais en sens inverse de ceux observés*. Cette théorie ne convient donc pas non plus.

Ainsi, ni les particularités de structure que l'on peut raisonnablement envisager, ni les théories de la diffusion communément admises ne semblent pouvoir rendre compte des expériences de Nowick. Il nous faut donc remonter encore plus loin, et pousser plus à fond l'analyse de l'agitation thermique dans les solides. Nous allons être ainsi conduit à un sixième genre d'explication, qui va nous donner satisfaction.

6. J'ai montré ailleurs (7) que, dans un solide, on ne pouvait appliquer la formule de Boltzmann séparément à l'atome ou au groupe d'atomes où doit se produire l'activation; il faut considérer le couplage très serré avec le reste du solide, notamment les atomes environnants. La méthode la plus naturelle pour traiter le problème est de tenir compte de la décomposition de l'agitation thermique en ondes planes, et de calculer les interférences de ces ondes. Dans le cas du mouvement d'un seul atome (qui doit être le cas de la diffusion), on aboutit [7] pour la probabilité d'activation à la formule

$$W = \exp[-5E/3B^2(T)] \tag{24}$$

où $B^2(T)$ est une fonction définie par une intégrale assez compliquée, et qui, pour $T = 0$, part d'une valeur *finie*, pour se rapprocher ensuite asymptotiquement de T, en sorte qu'aux hautes températures, $B^2(T) \# kT$. Aux basses températures, les variations de $B^2(T)$ resemblent à celles de l'énergie des ondes d'agitation thermique de fréquences voisines de la fréquence limite

$$\epsilon = \frac{k\theta}{2} \operatorname{cotgh} \cdot \left(\frac{\theta}{2T}\right) \tag{25}$$

où θ est la température caractéristique.

Dans ces conditions, la variation des coefficients de diffusion en fonction de la température doit être donnée par une loi de la forme

$$D = D_0 \cdot \exp[-E/B^2(T)] \tag{26}$$

en faisant entrer le facteur 5/3 dans l'énergie d'activation.

Si l'on porte cette valeur dans l'expession du temps de relaxation, on obtient une loi qui s'écarte de celle d'Arrhénius, surtout aux basses températures. Cette fois-ci, *les écarts prévus sont dans le sens de ceux observés par Nowick.*

Voyons si l'ordre de grandeur est correct. Comme

$$\tau = \tau_0 \exp[E/B^2(T)] \tag{27}$$

en assimilant les variations de $B^2(T)$ à celles de ϵ, on trouve

$$\frac{d(\ln \tau)}{dx} \# - E \frac{1}{\epsilon^2} \frac{d\epsilon}{dx} = \frac{E}{k \cosh^2\left(\frac{\theta}{2T}\right)} \tag{28}$$

Dans le cas présent, $\theta = 330°$*; en passant de 430°K à 660°K, $\cosh^2(\theta/2T)$ varie de 1,075 à 1,03, soit de 4,5%.

L'ordre de grandeur de la variation calculée se rapproche de celle observée; elle en représente les

*Les auteurs donnent comme température caractéristique de l'argent 215°. Mais cette température est celle de Debye, calculée d'après une moyenne entre les vitesses des ondes longitudinales et transversales. Ici, il faut tenir compte de ce que les ondes de fréquence maximum sont longitudinales, et que les ondes intéressantes sont celles se propageant dans une direction voisine de 110 (direction dans laquelle se fait le saut au cours de la diffusion). C'est ainsi que l'on trouve la valeur 330°. En toute rigueur, il faudrait faire le calcul de la fonction $B^2(T)$ dans un milieu anisotrope.

3/10. Cette théorie est donc celle qui se rapproche de beaucoup le plus de la réalité.

Il reste néanmoins un écart à combler. A ce sujet, remarquons que, outre les approximations de calcul signalées, nous avons fait une approximation de principe en appliquant à un alliage réel une théorie des ondes thermiques construites pour un cristal parfait. En effet, dans le phénomène qui nous intéresse, c'est-à-dire la diffusion, au moment où un atome va subir un saut, il est accolé à une lacune. Cette lacune constitue un défaut qui diffuse les ondes d'agitation thermique. De ce fait, les atomes voisins subissent une "pression de radiation", qui tend à les rapprocher du centre de la lacune. Cette pression est dûe principalement aux ondes les plus courtes, qui sont les plus diffusées; elle varie donc à peu près proportionnellement à ϵ, c'est-à-dire croît avec la température. Le seuil d'énergie à franchir diminue donc d'une quantité proportionnelle à ϵ^2, de sorte qu'on peut écrire approximativement:

$$\tau = \tau_0 \frac{E - \mu\epsilon^2}{\epsilon} \tag{29}$$

d'où

$$\frac{d(\ln \tau)}{dx} = \frac{E}{k \cosh^2\left(\frac{\theta x}{2}\right)} + \mu \frac{k\theta^2}{4 \sin h^2\left(\frac{\theta x}{2}\right)} \tag{30}$$

Le dernier terme, correctif, croît avec T; la correction est donc du bon sens. Pour en calculer la valeur exacte, il faudrait résoudre le problème mécanique très compliqué que représente l'agitation thermique des atomes autour de la lacune, en tenant compte de la densité électronique dans la lacune et des actions qu'elle exerce de ce fait sur les noyaux atomiques voisins.

Conclusion

L'examen successif de diverses hypothèses, auquel nous venons de procéder, montre que des mesures précises des temps de relaxation de la diffusion à température relativement basse, telles qu'elles ont été faites par Nowick, ne peuvent s'interpréter à l'aide des théories ordinairement admises. On est donc forcé d'abandonner des théories trop simplistes de la diffusion, telle que celle déduite des théories d'Eyring sur la cinétique chimique, pour une théorie complète, à la fois plus mécanique et cristallographique, tenant compte de la vraie nature des ondes d'agitation thermique et, si possible, de leurs interactions avec les lacunes réticulaires responsables de la diffusion.

Bibliographie

1. Zener, C. Trans. A.I.M.E. **152** (1943) 122.
2. Nowick, A. S. Phys. Rev. **88** (1952) 925.
3. Crussard, C. Metaux et Corrosion (1950) p. 203.
4. LeClaire, A. Progress in Metal Physics **4** (1953) 296.
5. Dienes, G. J. Phys. Rev. **89** (1953) 185.
6. LeClaire, A. Progress in Metal Physics **1** (1949) 333.
7. Crussard, C. "L'Etat solide," Rapports Congrès Phys. Solvay (Bruxelles, Stoops, 1951) 345.

ÜBER DIE BERECHNUNG DER VERZERRUNGSENERGIE BEI KEIMBILDUNG IN KRISTALLEN*

E. KRÖNER†

Bei der Bildung von Keimen einer neuen Phase in Kristallen tritt eine Deformation der beteiligten Phasen auf. Es wird eine Methode angegeben, nach der die zugehörige Verzerrungsenergie berechnet werden kann, soweit die Deformation durch den Unterschied im Raumbedarf der beteiligten Phasen bedingt und nur so gross ist, dass die Näherungen der linearen Elastizitätstheorie genügend genau gültig bleiben (§ 1, § 2). Die Rechnung berücksichtigt die Anisotropie der Kristalle in vollem Umfang. Für Keimbildungen innerhalb einer kubischen Phase wird die Verzerrungsenergie als Funktion der elastischen Konstanten und der Molvolumina beider Phasen, sowie der Keimform gegeben (§ 3).

ON THE CALCULATION OF THE STRAIN ENERGY ASSOCIATED WITH THE NUCLEATION OF A NEW PHASE WITHIN A CRYSTAL

When a new phase is nucleated within a crystal a deformation of the phases involved occurs. A method is described which permits the calculation of the strain energy associated with this transformation, provided the deformation is caused by the difference in volume of the phases and is not too large so that the approximations of the linear theory of elasticity are still exactly valid (§1, §2). This calculation takes the anisotropy of the crystals fully into account. For nucleation within a cubic phase the strain energy is given as a function of the elastic constants and the molvolumes of both phases, as well as the shape of the nuclei (§3).

SUR LE CALCUL DE L'ÉNERGIE DE DÉFORMATION ASSOCIÉE AVEC LA GERMINATION D'UNE NOUVELLE PHASE A L'INTÉRIEUR D'UN CRISTAL

La germination d'une nouvelle phase à l'intérieur d'un cristal conduit à une déformation des deux phases en question. On décrit une méthode qui permet de calculer l'énergie de déformation, à condition que la déformation soit causée par la différence entre les volumes des deux phases et ne soit pas trop grande, de sorte que les approximations de la théorie linéaire d'élasticité soient applicables avec une précision suffisante (§1, §2). Ce calcul tient compte de l'anisotropie des cristaux. Dans le cas de germination dans une phase cubique, l'énergie de déformation est donnée en fonction des constantes d'élasticité et des volumes moléculaires des deux phases, ainsi que de la forme des germes (§3).

1. Die Verzerrungsenergie als Funktion der elastischen Moduln und Molvolumina‡

Bezeichnungen:

$\mathfrak{r} = (x, y, z)$	der Ortsvektor mit Schwerpunkt des Bereichs als Bezugspunkt,
$\mathfrak{s} = (u, v, w) = (\mathfrak{s}_x, \mathfrak{s}_y, \mathfrak{s}_z)$	der Vektor des Verschiebungsfeldes,
$\mathfrak{A}$	Flächendichte der äusseren Kräfte auf dem Rand R (bei Zug positiv)
$\mathfrak{M}$	Dichte der äusseren, am Volumenelement angreifenden Kräfte,
$\mathfrak{n} = (\mathfrak{n}_x, \mathfrak{n}_y, \mathfrak{n}_z)$	der äussere Normaleneinheitsvektor von R,
W	die Verzerrungsenergiefunktion,
$E[\mathfrak{s}, \mathfrak{s}] = \iiint_B W d\tau$	die gesamte Verzerrungsenergie des durch $\mathfrak{s}$ verschobenen Bereichs B.

Jede in einem Bereich B überall reguläre Funktion, welche die elastischen Differentialgleichungen für die Verschiebungen bei fehlenden Volumenkräften befriedigt, soll als elastische Funktion in B bezeichnet werden. Unter einem konvexen Bereich soll ein einfach zusammenhängender Bereich mit abteilungsweise stetiger Jordanbegrenzung, welche nirgends konkave Stellen hat, verstanden werden. Als konkaver Bereich wird die sich bis ins Unendliche erstreckende Umgebung eines konvexen Bereichs bezeichnet.

Die Zahl der Atome im Keim soll klein im Verhältnis zur Zahl der Atome in der ursprünglichen Phase, jedoch so gross sein, dass Keim und Wirtsgitter näherungsweise als Kontinua angesehen werden können. Nimmt man den Keim konvex an, so wird das Wirtsgitter mit guter Näherung ein konkaver Bereich. Das soll heissen, man kann so rechnen, als wäre es unendlich ausgedehnt, da die Energie überwiegend in der Nähe des Keimes lokalisiert ist. Die Rechnung selbst wird für einen fiktiven Keim β der Grösse 1 Mol in einer Umgebung α durchgeführt. Dabei soll β dem wirklichen Keim geometrisch ähnlich sein. Man berechnet so die "molare Verzerrungsenergie der Keimbildung" ϵ.

Falls die Deformation allein auf Grund des Unterschieds im Raumbedarf der beteiligten Phasen

*Received August 26, 1953.

†Institut für theoretische und angewandte Physik der Technichen Hochschule und Max Planck-Institut für Metallforschung, Stuttgart.

‡Über die Rolle der Verzerrungsenergie bei der thermodynamischen Behandlung von Phasenumwandlungen in Kristallen vgl. z.B. [1; 2].

auftritt, wirken diese mit Normalkräften konstanten Betrages aufeinander, da dann die zugehörige Energie minimal wird. Diese Behauptung stützt sich auf die Tatsache, dass man solche Kräfte ansetzen muss, wenn man einen konvexen Kristall oder den Hohlraum in einem konkaven Kristallbereich durch Randkräfte mit minimaler Energie maximal dehnen oder zusammendrücken will.*

Grössen, die links oben mit einen Index α bzw. β versehen werden, sollen sich auf die Phasen α bzw. β beziehen. Für die Kräfte zwischen α und β ist nun der Ansatz

$$ {}^{\alpha}\mathfrak{A} = |{}^{\alpha}\mathfrak{A}|{}^{\alpha}\mathfrak{n}, \quad {}^{\beta}\mathfrak{A} = |{}^{\beta}\mathfrak{A}|{}^{\beta}\mathfrak{n} $$

zu machen. Dann hat man als "Übergangsbedingung"

$$ |{}^{\alpha}\mathfrak{A}| = |{}^{\beta}\mathfrak{A}| \equiv |\mathfrak{A}|. $$

${}^{\alpha}v$, ${}^{\beta}v$ seien die Molvolumina von α und β. Da der Keim die Grösse 1 Mol hat, gibt $K = {}^{\alpha}v - {}^{\beta}v$ das Volumen an, das durch die Deformation beider Phasen geschaffen werden muss, damit β gerade in α Platz hat. Bei ${}^{\alpha}v > {}^{\beta}v$ wird der Keim gedehnt, sonst gedrückt. Die Dehnungen von α bzw. β sind

$$ (1)\quad {}^{\alpha}K = \iint_G {}^{\alpha}\mathfrak{s} \cdot {}^{\alpha}\mathfrak{n}\, df, \quad {}^{\beta}K = \iint_G {}^{\beta}\mathfrak{s} \cdot {}^{\beta}\mathfrak{n}\, df, $$

wenn G die Grenzfläche $\alpha - \beta$ ist. Als Bedingung des Problems hat man dann

$$ (2)\qquad {}^{\alpha}K + {}^{\beta}K = K $$

zu erfüllen, wo K als gegebene Konstante angesehen werden kann. Die in β gespeicherte Energie ist

$$ {}^{\beta}E \equiv {}^{\beta}E[{}^{\beta}\mathfrak{s}, {}^{\beta}\mathfrak{s}] = \tfrac{1}{2}\iint_G {}^{\beta}\mathfrak{s} \cdot {}^{\beta}\mathfrak{A}\, df $$

$$ = \tfrac{1}{2}|\mathfrak{A}| \iint_G {}^{\beta}\mathfrak{s} \cdot {}^{\beta}\mathfrak{n}\, df $$

also wegen (1)

$$ {}^{\beta}E = \tfrac{1}{2}|\mathfrak{A}|{}^{\beta}K $$

und genau so

$$ (3)\qquad {}^{\alpha}E = \tfrac{1}{2}|\mathfrak{A}|{}^{\alpha}K $$

Als molare Verzerrungsenergie erhält man

$$ \epsilon = {}^{\alpha}E + {}^{\beta}E = \tfrac{1}{2}|\mathfrak{A}|({}^{\alpha}K + {}^{\beta}K) $$

also

$$ (4)\qquad \epsilon = \tfrac{1}{2}|\mathfrak{A}|K $$

Hierin muss $|\mathfrak{A}|$ bestimmt werden. Zwischen $|\mathfrak{A}|$ und ${}^{\alpha}K$ bzw. ${}^{\beta}K$ hat man wegen der Linearität der Theorie linearen Zusammenhang anzunehmen, also

$$ (5)\qquad |\mathfrak{A}| = ({}^{\alpha}c){}^{\alpha}K|{}^{\beta}v, \quad |\mathfrak{A}| = ({}^{\beta}c){}^{\beta}K|{}^{\beta}v $$

$({}^{\alpha}c)$ und $({}^{\beta}c)$ sind (anisotrope) Kompressionsmoduln der Kristalle α und β. Zwischen ihnen besteht ein fundamentaler Unterschied. Für den konvexen Kristall β ist nach Voigt [3]

$$ ({}^{\beta}c) = 1/[s_{11} + s_{22} + s_{33} + 2(s_{12} + s_{23} + s_{31})] $$

eine für den Kristall spezifische Konstante, die durch Kompressionsversuche im Piezometer leicht gemessen und daher als bekannt angesehen werden kann. Bei kubischen Kristallen β ist auch

$$ (6)\qquad ({}^{\beta}c) = \tfrac{1}{3}(c_{11} + 2c_{12}) $$

Für den konkaven Kristall α hängt der Kompressionsmodul $({}^{\alpha}c)$ ganz wesentlich von der Form der Grenzfläche ab. $({}^{\alpha}c)$ ist eine bestimmte Kombination der elastischen Moduln von α, die erst für jede Grenzfläche rechnerisch bestimmt werden muss. Ist diese Rechnung einmal durchgeführt, so lässt sich der in (4) gesuchte Betrag der Randkräfte leicht ermitteln. Man berechnet aus (2) und (5)

$$ |\mathfrak{A}| = \frac{1}{1/({}^{\alpha}c) + 1/({}^{\beta}c)}\, K/{}^{\beta}v $$

Die gesuchte Energie ist also

$$ (7)\qquad \epsilon = \frac{\tfrac{1}{2}}{1/({}^{\alpha}c) + 1/({}^{\beta}c)} \cdot \frac{({}^{\alpha}v - {}^{\beta}v)^2}{{}^{\beta}v} $$

Als Verhältnis der Energieanteile in α und β ergibt sich

$$ {}^{\alpha}E/{}^{\beta}E = ({}^{\beta}c)/({}^{\alpha}c) $$

Der Kristall mit dem kleineren Kompressionsmodul (mit dem kleineren Widerstand gegen Kompression) nimmt also die grössere Energiemenge auf.

Die Bestimmung von $({}^{\alpha}c)$ ist das eigentliche Problem. Man erhält $({}^{\alpha}c)$ z.B. aus der linken Gleichung (5), wenn man folgendes Randwertproblem löst: Gegeben Normalkräfte konstanten Betrages auf der Grenzfläche G eines konkaven Kristallbereichs α, gesucht die zugehörige Verschiebung in α bzw. die Dehnung des konvexen Hohlraums in α.

*Dieses Theorem wurde von Nabarro (*loc. cit.*) bewiesen. Einen zweiten Beweis enthält die Diplomarbeit des Verfassers (unveröffentlicht).

2. Eine Methode zur Lösung von Randwertproblemen*

Es sei nun $\mathfrak{s}_\nu$ eine endliche oder unendliche Folge von in einem Bereich B mit dem Rand R regulären Verschiebungsvektoren. Dabei soll zunächst offen bleiben, ob die $\mathfrak{s}_\nu$ elastische Funktionen sind oder nicht. Ist letzteres der Fall, so braucht man zur Realisierung einer Verschiebung $\mathfrak{s}_\nu$ ausser Randkräften $\mathfrak{A}_\nu$ auch Volumenkräfte $\mathfrak{M}_\nu$. Der Zusammenhang zwischen diesen äusseren Kräften und den Verschiebungen $\mathfrak{s}_\nu$ ist durch die Gleichungen†

$$(\mathfrak{A}_\nu)_k = c_{iklm}\, n_i \frac{\partial}{\partial m} (\mathfrak{s}_\nu)_l$$

bzw.

$$(\mathfrak{M}_\nu)_k = - c_{iklm} \frac{\partial^2}{\partial i\, \partial m} (\mathfrak{s}_\nu)_l$$

gegeben ($i, k, l, m = x, y, z$).

Es wird nun vorausgesetzt, dass die gesuchte Verschiebung eine Darstellung durch die $\mathfrak{s}_\nu$ in der Form

$$\mathfrak{s}(\mathfrak{r}) = B_\nu \mathfrak{s}_\nu (\mathfrak{r})$$

mit konstanten Koeffizienten B_ν zulässt. Dann kann man Randwertprobleme folgendermassen lösen: Man berechnet die Grössen‡

$$(8)\quad E_{\mu\nu} \equiv E[\mathfrak{s}_\mu, \mathfrak{s}_\nu] = \tfrac{1}{2} c_{iklm} \iiint_B \frac{\partial (\mathfrak{s}_\mu)_m}{\partial l} \cdot \frac{\partial (\mathfrak{s}_\nu)_k}{\partial i}\, d\tau$$

Gleichwertig damit ist

$$E_{\mu\nu} = \tfrac{1}{2} \iint_R \mathfrak{s}_\mu \cdot \mathfrak{A}_\nu\, df + \tfrac{1}{2} \iiint_B \mathfrak{s}_\mu \cdot \mathfrak{M}_\nu\, d\tau$$

Man bildet nun die Determinanten

$$E^\nu \equiv \begin{vmatrix} E_{11} & E_{21} \ldots\ldots E_{\nu 1} \\ E_{12} & E_{22} \ldots\ldots E_{\nu 2} \\ \\ E_{1\nu} & E_{2\nu} \ldots\ldots E_{\nu\nu} \end{vmatrix}$$

Die Unterdeterminanten der letzten Zeile von E^ν sollen E^ν_μ heissen, wo μ von 1 bis ν geht. Dann erfüllen die Verschiebungsvektoren [5]

$$(9)\quad \mathfrak{z}_1 = \mathfrak{s}_1 / \sqrt{E_{11}},\quad \mathfrak{z}_\nu = \frac{1}{\sqrt{E^\nu E^{\nu-1}}} \sum_{\mu=1}^{\nu} E^\nu_\mu \mathfrak{s}_\mu \qquad (\nu = 2, 3, 4 \ldots)$$

die Orthogonalitäts- und Normierungsrelationen

$$(10)\quad E[\mathfrak{z}_\mu, \mathfrak{z}_\nu] = \begin{matrix} 0 \\ 1 \end{matrix} \text{ für } \begin{matrix} \mu \neq \nu \\ \mu = \nu \end{matrix}$$

Durch die Orthogonalisierung wird die Energieform $B_\mu B_\nu E_{\mu\nu}$ auf Hauptachsen gebracht. Mit den $\mathfrak{s}_\nu$ sind auch die $\mathfrak{z}_\nu$ für die Entwicklung der gesuchten Verschiebung vollständig. Die zur Verwirklichung der Verschiebungen $\mathfrak{z}_\nu$ gebrauchten äusseren Kräfte sollen $\mathfrak{A}_\nu'$ und $\mathfrak{M}_\nu'$ heissen. Es sei nun

$$(11)\quad \mathfrak{s}(\mathfrak{r}) = A_\nu \mathfrak{z}_\nu(\mathfrak{r})$$

Zur Bestimmung der konstanten Koeffizienten A_ν bildet man

$$\tfrac{1}{2} \iint_R \mathfrak{s} \cdot \mathfrak{A}_\mu' df + \tfrac{1}{2} \iiint_B \mathfrak{s} \cdot \mathfrak{M}_\mu' d\tau = A_\nu \left(\tfrac{1}{2} \iint_R \mathfrak{z}_\nu \cdot \mathfrak{A}_\mu' df + \tfrac{1}{2} \iiint_B \mathfrak{z}_\nu \cdot \mathfrak{M}_\mu' d\tau \right) = A_\nu E[\mathfrak{z}_\nu, \mathfrak{z}_\mu]$$

oder wegen (10). Diese koeffizientenbestimmung ist bei gegebenen $\mathfrak{s}_\nu$ optimal bezüglich der Energie, da

$$\frac{\partial E[R_n, R_n]}{\partial A_\nu} = 0,$$

wenn

$$R_n = \mathfrak{s} - \sum_{\nu=1}^{n} A_\nu \mathfrak{z}_\nu.$$

$$(12)\quad A_\nu = E[\mathfrak{s}, \mathfrak{z}_\nu] = \tfrac{1}{2} \iint_R \mathfrak{s} \cdot \mathfrak{A}_\nu' df + \tfrac{1}{2} \iiint_B \mathfrak{s} \cdot \mathfrak{M}_\nu' d\tau$$

Mit Bettis Theorem [6] ist auch

$$(13)\quad A_\nu = E[\mathfrak{z}_\nu, \mathfrak{s}] = \tfrac{1}{2} \iint_R \mathfrak{z}_\nu \cdot \mathfrak{A}\, df + \tfrac{1}{2} \iiint_B \mathfrak{z}_\nu \cdot \mathfrak{M}\, d\tau$$

(12) löst das erste Randwertproblem ($\mathfrak{s}$ auf R gegeben), wenn $\mathfrak{M}_\nu = 0$ gesetzt werden kann. Dazu müssen die $\mathfrak{z}_\nu$, also auch die $\mathfrak{s}_\nu$ elastische Funktionen sein.

(13) löst das zweite Randwertproblem ($\mathfrak{A}$ auf R gegeben). Dabei dürfen zusätzlich beliebige stetig verteilte Volumenkräfte vorgeschrieben werden. Die $\mathfrak{z}_\nu$ brauchen keine elastischen Funktionen zu sein. Die Aufstellung eines Funktionensystems $\mathfrak{s}_\nu$, welches die elastischen Differentialgleichungen mit $\mathfrak{M} = 0$ nicht erfüllt, gelingt viel leichter, als die Aufstellung eines Systems elastischer Funktionen. Ein besonderer Vorzug der Verwendung nichtelastischer Funktionen ist aber noch folgender: Für sie ergeben sich wegen (8) die Ausdrücke $E_{\mu\nu}$ als Linearkombinationen der elas-

*Man definiert die Elastizitätsmoduln c_{iklm} etwa durch das Hooke'sche Gesetz $\sigma_{ik} = c_{iklm}\, \epsilon_{ml}$. Es ist $c_{iklm} = c_{kilm}$ $c_{iklm} = c_{lmik}$.

†Vgl. zu diesem § auch St. Bergmann [4].

‡$E_{\mu\mu}$ ist die gesamte Verzerrungsenergie des durch $\mathfrak{s}_\mu$ verschobenen Bereichs B.

tischen Moduln mit Koeffizienten, die von diesen Moduln nicht abhängen. Es gelingt daher, die Randwertaufgaben zu lösen, ohne die Zahlenwerte der elastischen Moduln einsetzen zu müssen. Mit elastischen Funktionen geht das i.allg. nicht, da diese selbst Funktionen der Moduln sind.

Die Funktionen $\mathfrak{s}_\nu$ sollten dem jeweiligen Problem angepasst sein, nur dann ist rasche Konvergenz zu erwarten. Ist S_m irgend eine Kugelflächenfunktion vom Grade m, so bilden die Funktionen

$$(14)\quad (r^n S_m, 0, 0),\ (0, r^n S_m, 0),\ (0, 0, r^n S_m)$$

(n negativ, m positiv)

für das Äussere einer Kugel ein passendes und vollständiges System. Wie der Verfasser in einer zweiten Arbeit gezeigt hat [10], unterliegen dabei n und m der wesentlichen Beschränkung*

$$(15)\qquad n + m + 1 \geqslant 0$$

Für das Äussere eines unendlich langen Kreiszylinders ersetzt man zweckmässig die Funktionen $r^n S_m$ durch die analogen zweidimensionalen Funktionen $\rho^n \sin m\phi$, $\rho^n \cos m\phi$ ($\rho^2 = x^2 + y^2$).

Für das Äussere eines Ellipsoids führt man elliptische Koordinaten λ, μ, ν ein. Es sei $L_m(\mu, \nu)$ irgend ein zweifaches Lamé'sches Produkt vom Grade $m \geqslant 0$. Auf der Oberfläche eines Ellipsoids in elliptischen Koordinaten gegebene Funktionen kann man nach den $L_m(\mu, \nu)$ entwickeln. $K_n(\lambda)$ sei eine Lösung der Lamé'schen Differentialgleichung vom negativen Grade n. Dann treten die Funktionen $K_n(\lambda)\, L_m(\mu, \nu)$ an die Stelle der $r^n S_m$ von (14). Für grosse λ gehen die $K_n L_m$ in die $r^n S_m$ über.

Beschränkt man sich auf Keimbildungen, bei denen die Symmetrieebenen des Ellipsoids mit Symmetrieebenen des Kristalls zusammenfallen,† so kann man für die Verschiebungen die Form

$$u = x\, g_1(x^2, y^2, z^2), v = y\, g_2(x^2, y^2, z^2),$$
$$w = z\, g_3(x^2, y^2, z^2)$$

voraussagen. Dann braucht man von den Lamé'schen Produkten $L_m(\mu, \nu)$ nur diejenigen der zweiten Art und von diesen für die Entwicklung von u, v, w resp. nur die der 1., 2. bzw. 3. Unterart. Die Anzahl der für die Entwicklung einer Verschiebungskomponente benötigten Produkte ist also $(m + 1)/2$ pro Grad m [7].

*Gilt nur für $m = 0$.

†Dies ist nur bei rhomischen, tetragonalen (1. Abt.), hexagonalen und kubischen Kristallen möglich.

3. Berechnung der Verzerrungsenergie bei Keimbildung in tetragonalen Kristallen‡

Es soll nun das am Ende von §1 angegebene Randwertproblem für den Fall, dass α tetragonal ist und das Äussere eines Rotationsellipsoids ausfüllt, gelöst werden. Drehachse des Ellipsoids, z-Achse und [001] sollen zusammenfallen. Man behandelt das Problem zweckmässig für das abgeplattete (flache) und das verlängerte (lange) Ellipsoid gleichzeitig. Dazu bedarf es nur folgender Festsetzungen: Es sei

$$A(\xi) \equiv \begin{matrix}\text{arc ctg } \xi \\ \text{Ar Ctg } \xi\end{matrix} \text{ für das } \begin{matrix}\text{flache} \\ \text{lange}\end{matrix} \text{ Ellipsoid}$$

Ferner sollen in allen Formeln bei doppelter Angabe von Vorzeichen die oberen für das flache, die unteren für das lange Ellipsoid gelten. Man führt zweckmässig durch die Gleichungen [7; 8]

$$(16)\quad x = \pm\sqrt{(\xi^2 \pm 1)(1 - \eta^2)}\cos\phi,$$
$$y = \pm\sqrt{(\xi^2 \pm 1)(1 - \eta^2)}\sin\phi), \qquad z = \xi\eta$$

orthogonale elliptische Koordinaten ξ, η, ϕ ein. Es ist

$$\begin{matrix}0 \\ 1\end{matrix} \leqslant \xi \leqslant \infty,\ -1 \leqslant \eta \leqslant 1,\ 0 \leqslant \phi \leqslant 2\pi$$

für das $\begin{matrix}\text{flache} \\ \text{lange}\end{matrix}$ Ellipsoid

ξ = konst. sind konfokale Ellipsoide mit der Brennlinie $\rho = 1$, $z = 0$ bzw. den Brennpunkten $\rho = 0$, $z = \pm 1$.

Die in den Ausdrücken

$$d\tau = \frac{d\xi\, d\eta\, d\phi}{h_1 h_2 h_3}, \quad df = \frac{d\eta\, d\phi}{h_2 h_3}$$

vorkommenden Grössen h erhält man zu

$$h_1 = \sqrt{\frac{\xi^2 \pm 1}{\xi^2 \pm \eta^2}}, \quad h_2 = \sqrt{\frac{1 - \eta^2}{\xi^2 \pm \eta^2}},$$
$$h_3 = \frac{1}{\sqrt{(\xi^2 \pm 1)(1 - \eta^2)}}$$

Mit ihrer Hilfe berechnet man auch

$$(17)\quad \frac{\partial\xi}{\partial x} = \pm\frac{\xi\sqrt{(\xi^2 \pm 1)(1 - \eta^2)}}{\xi^2 \pm \eta^2}\cos\phi,$$
$$\frac{\partial\xi}{\partial y} = \pm\frac{\xi\sqrt{(\xi^2 \pm 1)(1 - \eta^2)}}{\xi^2 \pm \eta^2}\sin\phi,$$
$$\frac{\partial\xi}{\partial z} = \frac{\xi^2 \pm 1}{\xi^2 \pm \eta^2}\eta$$

‡Bei entsprechender Spezialisierung der Elastizitätsmoduln gelten die folgenden Ergebnisse auch für kubische und hexagonale Kristalle.

Die Gleichung der Ellipsoide ist

$$(18) \qquad F \equiv \frac{x^2+y^2}{\xi^2 \pm 1} + \frac{z^2}{\xi^2} - 1 = 0$$

Ihre Form wird durch das Achsenverhältnis

$$(19) \qquad c/a = \xi/\sqrt{\xi^2 \pm 1}$$

beschrieben. Den äusseren Normaleneinheitsvektor von α gibt ${}^{\alpha}n = \nabla F/|\nabla F|$, für seine Komponenten berechnet man

$$(20) \quad {}^{\alpha}\mathfrak{n}_x = \mp\, l\,\xi\sqrt{\xi^2 \pm 1}\,\underline{\sqrt{1-\eta^2}\cos\phi},$$
$${}^{\alpha}\mathfrak{n}_y = \mp\, l\,\xi\sqrt{\xi^2 \pm 1}\,\underline{\sqrt{1-\eta^2}\sin\phi},$$
$${}^{\alpha}\mathfrak{n}_z = -\,l(\xi^2 \pm 1)\underline{\eta}$$
$$l = 1/\sqrt{(\xi^2 \pm \eta^2)(\xi^2 \pm 1)}$$

Die Ausdrücke (16) befriedigen die Laplace'sche Differentialgleichung, daher sind die unterstrichenen Teile von (20) Lamé'sche Produkte L_1^x, L_1^y, L_1^z vom Grade 1. Durch den oberen Index sollen die drei Unterarten der Lamé'schen Produkte 2. Art unterschieden werden. Zur Entwicklung der gesuchten Verschiebungskomponenten u, v, w braucht man Funktionen $\mathfrak{s}_\nu$ der Form*

$$(21) \quad (K_n L_m^{\,x}, K_n L_m^{\,y}, 0), \quad (0, 0, K_n L_m^{\,z})$$

Ihr Beitrag zur Volumendehnung des Hohlraums in α ist leicht zu übersehen. Es ist, über die Oberfläche des Ellipsoids ξ_0 integriert,

$$(22) \quad 2\iint_G u_\nu\,{}^{\alpha}\mathfrak{n}_x df = \mp\, 2\xi_0(\xi_0^{\,2} \pm 1)\int_{\eta=-1}^{1} \int_{\phi=0}^{2\pi} u_\nu \sqrt{1-\eta^2}\cos\phi\, d\eta\, d\phi$$

bzw.

$$(22a) \quad \iint_G w_\nu\,{}^{\alpha}\mathfrak{n}_z df = -\,(\xi_0^2 \pm 1)\int_{\eta=-1}^{1} \int_{\phi=0}^{2\pi} w_\nu\,\eta\, d\eta\, d\phi$$

Hierbei wurde $ldf = d\eta\, d\phi$ berücksichtigt. Nun sind alle Lamé'schen Produkte in dem Integrationsbereich der beiden letzten Gleichungen orthogonal. Hieraus folgt, dass von den Funktionen (21) nur diejenigen einen Beitrag zur Volumendehnung geben, die L_1^x, L_1^y oder L_1^z enthalten. Für die 1. Näherung nehmen wir die harmonischen Funktionen

$$\mathfrak{s}_1 = (u_1, v_1, 0) = f(\xi)(x, y, 0)$$
$$\mathfrak{s}_2 = (0, 0, w_2) = g(\xi)(0, 0, z)$$
$$f(\xi) \equiv \frac{\xi}{\xi^2 \pm 1} - A(\xi), \quad g(\xi) \equiv 2\left(A(\xi) - \frac{1}{\xi}\right)$$

Ihr Beitrag zur Volumendehnung ist wegen (16), (22), (22a), und mit

$$\iint (1-\eta^2)\cos^2\phi\, d\eta\, d\phi = 4\pi/3,$$
$$\iint \eta^2\, d\eta\, d\phi = 4\pi/3$$
$$\iint \mathfrak{s}_1 \cdot {}^{\alpha}\mathfrak{n}\, df = \frac{8\pi}{3}\,\xi_0(\xi_0^{\,2} \pm 1)\, f(\xi_0)$$
$$\iint \mathfrak{s}_2 \cdot {}^{\alpha}\mathfrak{n}\, df = \frac{4\pi}{3}\,\xi_0(\xi_0^{\,2} \pm 1)\, g(\xi_0)$$

Die aus den Funktionen $\mathfrak{s}_1$ und $\mathfrak{s}_2$ durch Orthogonalisierung zu gewinnenden Verschiebungen $\mathfrak{z}_1$ und $\mathfrak{z}_2$ sind durch (9) gegeben. Man erhält

$$\mathfrak{z}_1 = \mathfrak{s}_1/\sqrt{E_{11}}, \quad \mathfrak{z}_2 = \frac{E_{11}\mathfrak{s}_2 - E_{12}\mathfrak{s}_1}{\sqrt{E_{11}E_{22} - E_{12}^2}}$$

Aus (13) und $\mathfrak{A} = |\mathfrak{A}|\,{}^{\alpha}\mathfrak{n}$ folgt für die Entwicklung (11)

$$A_1 = \frac{4\pi|\mathfrak{A}|}{3\sqrt{E_{11}}}\,\xi_0(\xi_0^{\,2} \pm 1)\, f(\xi_0)$$

$$A_2 = \frac{4\pi|\mathfrak{A}|}{3\sqrt{E_{11}}}\,\xi_0(\xi_0^{\,2} \pm 1)$$
$$\left[-\frac{E_{12}}{\sqrt{E_{11}E_{22}-E_{12}^{\,2}}}\, f(\xi_0) + \frac{E_{11}/2}{\sqrt{E_{11}E_{22}-E_{12}^{\,2}}}\, g(\xi_0)\right]$$

Die zu der Verschiebung $A_1\mathfrak{z}_1 + A_2\mathfrak{z}_2$ gehörige Energie ist wegen (10)

$${}^{\alpha}E = A_1^{\,2} + A_2^{\,2} = \frac{16\pi^2}{9}\,\xi_0^2\,(\xi_0^2 \pm 1)$$
$$\frac{\frac{1}{4}g^2(\xi_0)\,E_{11} + f^2(\xi_0)\,E_{22} - f(\xi_0)\,g(\xi_0)\,E_{12}}{E_{11}E_{22} - E_{12}^{\,2}}$$

Andererseits ist nach (3) und (5) ${}^{\alpha}E = {}^{\beta}v\,|\mathfrak{A}|^2/2({}^{\alpha}c)$, wo man wegen (18) ${}^{\beta}v = 4\pi\xi_0(\xi_0^2 \pm 1)/3$ zu setzen hat. Man erhält so für den gesuchten Kompressionsmodul in 1. Näherung

$$(23) \quad \widetilde{({}^{\alpha}c)} = \frac{3}{2\pi}\,\frac{1}{\xi_0(\xi_0^{\,2} \pm 1)}$$
$$\times \frac{E_{11}E_{22} - E_{12}^{\,2}}{g^2(\xi_0)\,E_{11} + 4f^2(\xi_0)\,E_{22} - 4f(\xi_0)\,g(\xi_0)\,E_{12}}$$

Zur Berechnung der $E_{\mu\nu}$ bedient man sich der folgenden Formeln, in denen der Index 1 bei u, v bzw. 2 bei w einfachheitshalber fortgelassen wurde

*Es gibt $|2\eta+1|$ linear unabhängige Funktionen K_n vom Graden. Von ihnen braucht man für (21) prinzipiell nur eine pro Graden (z.B. die Legendre'sche Funktion 2. Art). Aus rechentechnischen Gründen wurden die K_n im Folgenden etwas anders ausgesucht, was die Vollständigkeit von (21) nicht berührt.

$$E_{11} = \frac{c_{11}}{2}\iiint_\alpha (u_x^2 + v_y^2)\,d\tau + \frac{c_{12}}{2}\iiint_\alpha 2u_x v_y\,d\tau + \frac{c_{44}}{2}\iiint_\alpha (u_z^2 + v_z^2)\,d\tau + \frac{c_{66}}{2}\iiint_\alpha (2u_y v_x + u_y^2 + v_x^2)\,d\tau$$

$$E_{22} = \frac{c_{33}}{2}\iiint_\alpha w_z^2\,d\tau + \frac{c_{44}}{2}\iiint_\alpha (w_x^2 + w_y^2)\,d\tau$$

$$E_{12} = \frac{c_{13}}{2}\iiint_\alpha (u_x w_z + v_y w_z)\,d\tau + \frac{c_{44}}{2}\iiint_\alpha (u_z w_x + v_z w_y)\,d\tau$$

Die notwendigen Differentiationen nach x, y, z bewerkstelligt man mit Hilfe von (17). Sämtliche Integrationen sind geschlossen durchführbar. Sie ergeben ($A_0 \equiv A(\xi_0)$)

$$(24)\quad \begin{cases} E_{11} = \frac{\pi}{3}\Big[-4(\xi_0^2 \pm 1)\,\xi_0 A_0^2 - \xi_0^2 A_0 \pm 3A_0 + 5\xi_0 \mp 2\,\frac{\xi_0}{\xi_0^2 \pm 1}\Big] c_{11} \\ \qquad + \frac{\pi}{3}\Big[-4(\xi_0^2 \pm 1)\,\xi_0 A_0^2 + 5\xi_0^2 A_0 \pm A_0 - \xi_0 \pm 2\,\frac{\xi_0}{\xi_0^2 \pm 1}\Big] c_{12} \\ \qquad + \frac{\pi}{3}\Big[12\xi_0^2 A_0 \pm 4A_0 - 12\xi_0\Big] c_{44} \\ \qquad + \frac{\pi}{3}\Big[-6\xi_0^2 A_0 \pm 2A_0 + 6\xi_0 \mp 4\,\frac{\xi_0}{\xi_0^2 \pm 1}\Big] c_{66} \\ E_{22} = \frac{\pi}{3}\Big[-8(\xi_0^2 \pm 1)\,\xi_0 A_0^2 + 4\xi_0^2 A_0 \pm 4A_0 + 4\xi_0\Big] c_{33} \\ \qquad + \frac{\pi}{3}\Big[12\xi_0^2 A_0 \pm 4A_0 - 12\xi_0\Big] c_{44} \\ E_{12} = \frac{\pi}{3}\Big[8(\xi_0^2 \pm 1)\,\xi_0 A_0^2 - 4\xi_0^2 A_0 \mp 4A_0 - 4\xi_0\Big] c_{13} \\ \qquad + \frac{\pi}{3}\Big[12\xi_0^2 A_0 \pm 4A_0 - 12\xi_0\Big] c_{44} \end{cases}$$

(23) und (24) lösen die gestellte Aufgabe in 1. Näherung. Die Ergebnisse sollen jetzt für kubische Kristalle α näher betrachtet werden. Als elastische Moduln werden

$$\mu' \equiv c_{11} - c_{12} - 2c_{44}, \quad \lambda \equiv c_{12}, \quad \mu \equiv c_{44}$$

verwendet. $\mu' = 0$ bedeutet Isotropie, λ, μ sind die üblichen Laméschen Konstanten.

Besonderes Interesse beanspruchen die Grenzfälle. Für $\xi_0 \to \infty$ erhält man für beide Ellipsoide

$$E_{11} = \frac{16\pi}{135\xi_0^3}(4\mu' + 2\lambda + 17\mu), \quad E_{22} = \frac{16\pi}{135\xi_0^3}(2\mu' + 2\lambda + 7\mu), \quad E_{12} = \frac{16\pi}{135\xi_0^3}(-2\lambda + 3\mu)$$

und

$$(25)\qquad \widetilde{({}^a c)}_{\text{Kugel}} = \frac{4}{15}(\mu' + 5\mu)$$

Man zeigt auch leicht, dass $d({}^a c)/d(c/a)$ für $\xi_0 \to \infty$ verschwindet. $({}^a c)$ hat also für $c = a$ ein Maximum [vgl. (19)].

Für $\xi_0 \to 0$ bzw. $c/a \to 0$ erhält man beim flachen Ellipsoid

$$E_{11} = \frac{\pi^2}{6}(3\mu' + 4\lambda + 12\mu), \quad E_{22} = \frac{\pi^2}{6}(4\mu' + 4\lambda + 12\mu), \quad E_{12} = \frac{\pi^2}{6}(-4\lambda + 4\mu)$$

und

$$(26)\qquad ({}^a c)_{\text{Scheibe}} = \frac{\pi}{4}\left(\mu' + \lambda + 3\mu - \frac{4(-\lambda + \mu)^2}{3\mu' + 4\lambda + 12\mu}\right)\xi_0$$

Für $c/a = 0$ wird also $({}^a c) = 0$. Da für kleine ξ_0 $c/a = \xi_0$, gibt der Faktor von ξ_0 in (26) den Anstieg der Kurve $({}^a c)$ gegen c/a im Ursprung.

Der Grenzübergang $\xi_0 \to 1$ $(c/a \to \infty)$ beim langen Ellipsoid liefert

$$E_{11} = \frac{2\pi}{3}(\mu' + 4\mu)\,\frac{1}{\xi_0^2 - 1}, \quad E_{22} = \frac{4\pi}{3}\mu \ln\frac{\xi_0 + 1}{\xi_0 - 1}, \quad E_{12} = \frac{4\pi}{3}\mu \ln\frac{\xi_0 + 1}{\xi_0 - 1}$$

woraus

$$(27)\qquad ({}^a c)_{\text{Nadel}} = \tfrac{1}{4}(\mu' + 4\mu)$$

folgt. Hierbei ist nur die Verschiebung $\mathfrak{v}_1$ beteiligt, die Deformation ist also zweidimensional. Es ist $d({}^{\alpha}c)/d(c/a) = 0$ für $\xi_0 \to 1$.

4. Diskussion der Ergebnisse

Es fehlt bisher eine Abschätzung für die Güte der erreichten Näherung. Bei Hinzunahme weiterer Funktionen $\mathfrak{v}_\nu$ würde man eine niedrigere Energie ${}^{\alpha}E$ berechnen. Also ist $(\widetilde{{}^{\alpha}c})$ eine obere Grenze von $({}^{\alpha}c)$.

Einen besseren Anhalt für die Güte der Näherung würde die Berechnung der zweiten Näherung $(\widetilde{\widetilde{{}^{\alpha}c}})$ geben. Diese Aufgabe ist für das Ellipsoid umständlich. Man kann jedoch wohl annehmen, dass die Güte der Näherung $(\widetilde{{}^{\alpha}c})$ von c/a annähernd unabhängig ist, da $\mathfrak{v}_1$ und $\mathfrak{v}_2$ der Keimform angepasste Funktionen sind. Die Berechnung von $(\widetilde{\widetilde{{}^{\alpha}c}})$ wurde für das Äussere einer Kugel und das Äussere eines unendlich langen Kreiszylinders durchgeführt.* Die beteiligten Funktionen waren im ersten Fall unter Beachtung von (15) $\mathfrak{v}_\nu = (u_\nu, v_\nu, w_\nu)$ mit

$$w_1 = \frac{z}{r^3}, \quad w_2 = 5\frac{z^3}{r^5} - 3\frac{z}{r^3}, \quad w_3 = 5\frac{z^3}{r^7} - 3\frac{z}{r^5},$$

woraus u_1, v_1 durch zyklische Vertauschung von x, y, z folgten. Im zweiten Fall waren $\mathfrak{v}_\nu = (u_\nu, v_\nu, 0)$ mit

$$u_1 = \cos\phi/\rho, \quad u_2 = \cos 3\phi/\rho, \quad u_3 = \cos 3\phi/\rho^3$$

$$v_1 = \sin\phi/\rho, \quad v_2 = \sin 3\phi/\rho, \quad v_3 = \sin 3\phi/\rho^3$$

Es ergab sich (α kubisch):

$$(\widetilde{\widetilde{{}^{\alpha}c}})_{\text{Kugel}} = (\widetilde{{}^{\alpha}c})_{\text{Kugel}}(1 + \delta_K),$$

$$\delta_K = \frac{-81\,\mu'^2}{7(\mu' + 5\mu)(23\mu' + 20\lambda + 65\mu)}$$

$$(\widetilde{\widetilde{{}^{\alpha}c}})_{\text{Nadel}} = (\widetilde{{}^{\alpha}c})_{\text{Nadel}}(1 + \delta_N),$$

$$\delta_N = \frac{-\mu'^2}{2(\mu' + 4\mu)(\mu' + \lambda + 3\mu)}$$

In der Tat unterscheiden sich δ_K und δ_N nur unwesentlich.

Am ungünstigsten sind grosse negative Werte von μ'. In extremen Fällen reicht die Näherung $(\widetilde{{}^{\alpha}c})$ nicht mehr aus. So bekommt man für β-Messing $\delta_K \approx -0{,}5$. Jedoch bei so stark anisotropen Kristallen wie Kupfer ($\mu' < 0$) ist δ_K nur noch $-0{,}1$. Für $\mu' > 0$ sind die Ergebnisse noch günstiger.† Ein stark anisotroper Kristall ist Kaliumchlorid. Hier wird $\delta_K \approx -0{,}04$. Für Aluminium ist $\delta_K \approx -0{,}004$. In den weitaus meisten Fällen kann man mit der ersten Näherung $(\widetilde{{}^{\alpha}c})$ zufrieden sein. In anderen Fällen bietet die systematische Berechnung höherer Näherungen keine Schwierigkeiten. In diesem Punkte geht die vorliegende Methode über eine Rechnung hinaus, die Nabarro [2] durchgeführt hat. Nabarro berechnete die Energie, die man braucht, um einen Hohlraum der Grösse 1 cm³ in dem konkaven Bereich α um 1% zu dehnen. Nach (3) und (5) ist diese Energie offenbar proportional $({}^{\alpha}c)$. Die Rechnung von Nabarro liefert $({}^{\alpha}c)$ für das Äussere von Kugel, Nadel, und unendlich dünner Scheibe exakt, für die übrigen Formen des rotationsellipsoidförmigen Keimes werden obere und untere Grenzen von $({}^{\alpha}c)$ gegeben. Alle diese Ergebnisse gelten nur bei Isotropie. Die in der folgenden Tabelle enthaltenen Werte der elastischen Moduln zeigen in Verbindung mit den für $({}^{\alpha}c)$ erhaltenen Formeln, dass der Einfluss der Anisotropie sehr merkbar sein kann. Die Formeln (25) und (27) gehen für $\mu' = 0$ in Nabarros exakte Formeln über.

	μ'	λ	μ	(c)	$(\widetilde{\widetilde{{}^{\alpha}c}})$ Kugel	$(\widetilde{\widetilde{{}^{\alpha}c}})$ Nadel	$d({}^{\alpha}c)/d(c/a)$ für $c/a \approx o$
Cu	−10,34	12,3	7,52	13,9	6,62	4,40	18,6
Al	− 1,08	6,22	2,84	7,75	3,5	2,57	9,6
KCl	1,31	0,81	0,79	1,77	1,37	1,07	3,52

Alle Zahlenwerte der Tabelle gelten in cgs-Einheiten, wenn sie mit 10^{11} multipliziert werden. Die elastischen Moduln μ', λ, μ sind dem Buch von Schmid-Boas [9] entnommen. (c) ist der gewöhnliche (anisotrope) Kompressionsmodul, wie er aus (6) folgt. Er ist bei Cu und Al (und wohl bei den meisten Kristallen) wesentlich grösser als der maximale Kompressionsmodul $({}^{\alpha}c)$ für die gleichen Kristalle. Aus dem Vergleich von $(c)_{\text{Cu}} = ({}^{\beta}c)_{\text{Cu}}$ mit $({}^{\alpha}c)_{\text{Al}}$ folgt z.B., dass bei Kupferkeimen in Aluminium der weitaus überwiegende Anteil der Verzerrungsenergie im Aluminium lokalisiert ist. Für flache Einlagerungen gilt das verstärkt. Dasselbe trifft noch in vielen anderen Fällen zu. Daher kommt es i.allg. weniger auf die Genauigkeit von $({}^{\beta}c)$ als gerade auf diejenige von $({}^{\alpha}c)$ an.

Bemerkenswert ist weiter der starke Anstieg der Kurve $({}^{\alpha}c)$ gegen c/a im Ursprung. Man kennt viele Keimbildungen, bei denen sich die Atome der 2. Phase β in einer Gitterebene der Ausgangsphase ansammeln. Enthält ein solcher scheibenförmiger Keim 100 Atome β, so wird man als Verhältnis c/a etwa $0{,}1.4/\pi \approx 0{,}127$ annehmen. Handelt es sich um Cu in Al, so hat man dafür $({}^{\alpha}c)_{\text{Al}} \approx 9{,}6 \cdot 0{,}127$

*Diese Berechnungen sind in der Diplomarbeit des Verfassers enthalten (unveröffentlicht).

†Dieser Fall ist bei Metallen selten.

$\approx 1{,}2 \cdot 10^{11}$ erg/cm³. Die molare Verzerrungsenergie dieser Art von Keimbildung ergibt sich dann mit $(^{\beta}c)_{Cu} \approx 13{,}9 \cdot 10^{11}$ erg/cm³, $^{\alpha}v = 10$ cm³, $^{\beta}v = 7{,}2$ cm³ aus (7) zu $\epsilon \approx 0{,}6 \cdot 10^{11}$ erg/Mol der Phase β.*

Abb. 1 ist mit Hilfe der in der Tabelle enthaltenen Zahlenwerte konstruiert. Sie soll den letzten Betrachtungen noch einen anschaulichen Hintergrund geben.

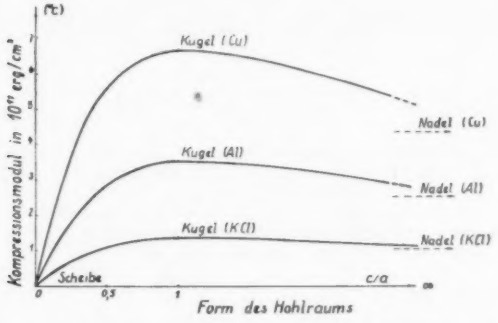

ABB. 1. Anisotroper Kompressionsmodul einiger konkaver Kristalle als Funktion der Kristallform. $\frac{1}{2} \cdot 10^{-4} \cdot (^{\alpha}c)$ ist auch die Energie, die man braucht, um einen Hohlraum der Grösse 1 cm³ in einem konkaven Kristall um 1% zu dehnen.

*Der Unterschied der Molvolumina ist hier allerdings sehr gross, so dass die Zulässigkeit der linearen Elastizitätstheorie fraglich erscheint.

Der Verfasser dankt Herrn Professor U. Dehlinger, Herrn Dr. A. Seeger und Herrn H. Knapp für Anregungen und fruchtbare Diskussionen.

Referenzen

1. FISHER, J. C., HOLLOMON, J. H., and TURNBULL, D. J. Appl. Phys., **19** (1948) 775.
2. NABARRO, F. R. N. Proc. Roy. Soc. (London), **A175** (1940) 519.
3. VOIGT, W. Lehrbuch der Kristallphysik (Teubner, 1910) S. 574.
4. BERGMANN, ST. Mathem. Annalen, **98** (1928) 252 ff.
5. FRANK, P. und v. MISES, R. Die Differential- und Integralgleichungen der Mechanik und Physik, Vieweg, Braunschweig, 2. Aufl. (1930), 1. Bd., VIII, §1, 3.
6. LOVE, A. E. H. A Treatise on the Math. Theory of Elasticity, 4. Aufl. (Cambridge, 1952), S. 173.
7. LENSE, J. Reihenentwicklungen in der mathem. Physik. (Berlin, de Gruyter, 1947) S. 202 ff.
8. WEBSTER, A. G. und SZEGÖ, G. Partielle Differentialgleichungen der mathematischen Physik (Leipzig und Berlin, Teubner, 1930) S. 398 ff.
9. SCHMID, E. und Boas, W. Kristallplastizität. (Berlin, Springer, 1935).
10. KRÖNER, E. Z. Physik, **136** (1953) 402.

THE EFFECTS OF CERTAIN ALLOYING ELEMENTS ON THE ALLOTROPIC TRANSFORMATION IN TITANIUM*

H. W. WORNER†

Alloying elements with atomic sizes close to that of titanium are considered. The change in enthalpy (ΔH) which accompanies the transfer of 1 gram.-atom of any given solute from β-phase to α is used as an indication of the effect of that solute on the $\alpha \rightleftharpoons \beta$ transformation. The estimation of values of ΔH from phase boundaries is outlined. It is shown that the Brillouin zone characteristics of the allotropes of titanium are probably important in determining the influence of the elements discussed on the $\alpha \rightleftharpoons \beta$ transformation.

LES EFFETS DE CERTAINS ÉLÉMENTS ALLIÉS SUR LA TRANSFORMATION ALLOTROPIQUE DU TITANE

On considère des éléments alliés, dont les dimensions atomiques se rapprochent de celles des atomes de titane. Le changement d'enthalpie (ΔH) qui accompagne le passage d'un atome-gramme d'un soluté donné, de la phase β à la phase α, est employé comme indication de l'effet de ce soluté sur la transformation $\alpha \rightleftharpoons \beta$. On indique la méthode utilisée pour l'estimation de (ΔH) à partir des limites des phases. Il est montré que les caractéristiques des zones de Brillouin des deux phases du titane jouent probablement un rôle important dans la détermination de l'influence des éléments discutés sur la transformation $\alpha \rightleftharpoons \beta$.

DER EINFLUSS BESTIMMTER LEGIERUNGSELEMENTE AUF DIE ALLOTROPE UMWANDLUNG VON TITAN

Es wurden Legierungselemente mit titanähnlichen Atomdimensionen betrachtet. Die Enthalpieänderung (ΔH), die mit dem Übergang von 1 Gramm-Atom einer gegebenen Legierungsbeigabe von der β zur α-Form verbunden ist, wird als Mass für den Einfluss der Beigabe auf die $\alpha \rightleftharpoons \beta$ Transformation angesehen. Die Abschätzung von ΔH-Werten aus den Phasengrenzen wird beschrieben. Es wird gezeigt, dass die Eigenschaften der Brillouin-Zonen der allotropen Titanmodifikationen wahrscheinlich bei der Bestimmung des Einflusses der oben erwähnten Legierungselemente auf die $\alpha \rightleftharpoons \beta$ Transformation von Wichtigkeit sind.

Introduction

This note is concerned with the effects of alloying elements which have atomic sizes close to that of titanium and is based on published information, most of which was recently compiled and evaluated by Hansen *et al* [1]. The writer has made use of his own recent results for the systems titanium-tin [2] and titanium-silver [3]. The other alloying elements covered are: aluminium, zirconium, vanadium, niobium, tantalum, chromium, molybdenum, tungsten, manganese, iron, nickel, copper, and silicon. For each of the elements named above, the ratio of atomic radius of alloying element to that of titanium lies in the range 0.85 to 1.15. With the exception of silicon, these elements dissolve in one or both forms of titanium to a maximum extent which exceeds 10 atomic per cent. For silicon, the maximum solid solubility is approximately 6 atomic per cent.

Thermodynamic Expression of Effect of Solute on the Allotropic Transformation

In order to express the effect of a given element on the range of temperature in which the transformation occurs, use has been made of the change in enthalpy (ΔH) which accompanies the transfer of 1 gram-atom of that element from dilute β-solution to dilute α. A large positive value of ΔH corresponds to a marked depression of the transformation range, a small positive value signifies only a slight or moderate depression, and a negative value of ΔH indicates an elevation of the transformation range.

The value of ΔH for any particular system can be estimated from the boundaries of the $(\alpha + \beta)$ field provided (*a*) the calculations are applied only to dilute solutions, and (*b*) it is assumed ΔH varies only slightly with temperature in a range of about 50°C, either below or above the transformation temperature for pure titanium (882°C). If these assumptions are accepted, the following approximate equalities can be used [4]:

$$(1) \qquad \Delta H \simeq \text{R.T.} \, [\ln (C_\beta / C_\alpha) + k]$$

$$(2) \qquad \Delta G_{T_1} \simeq \text{R.T.} \ln (1 - C_\beta)/(1 - C_\alpha)$$

C_β and C_α represent the atom fractions of solute in the β- and α-solutions which are in equilibrium with each other at temperature T(°K). ΔG_{T_1} is the change in free energy which accompanies the transfer of 1 gram.-atom of titanium from β-solu-

*Received September 22, 1953.
†Physical Metallurgy Section, C.S.I.R.O., Baillieu Laboratory, University of Melbourne.

tion to α in the absence of alloying elements. k is a constant, which, for systems involving only substitutional solutes, seems to be small by comparison with $\ln (C_\beta/C_\alpha)$ [4; 5]. Hence,

$$\Delta H \simeq \text{R.T.} \ln (C_\beta/C_\alpha) \quad (3)$$

For a few titanium-base systems, values of ΔH were determined from the $\ln (C_\beta/C_\alpha)$ *versus* $1/T$ relationships. These values of ΔH agreed satisfactorily with those deduced by applying equation (3). This supported the view that the constant k in equation (1) could be ignored in the present consideration of general tendencies.

Comparisons of values of $\text{R.T.} \ln (1 - C_\beta)/(1 - C_\alpha)$ with values of ΔG_{Ti} derived from McQuillan's work on the titanium-hydrogen system [6] provided a means of testing the reasonableness of some of the assumptions stated in relation to equations (1) and (2). In general, values of $\text{R.T.} \ln (1 - C_\beta)/(1 - C_\alpha)$ deduced from the initial portions of $\alpha/(\alpha + \beta)$ and $\beta/(\alpha + \beta)$ boundaries differed from McQuillan's values of ΔG_{Ti} by amounts not exceeding $+20\%$, -5%. The only serious discrepancy was found in the titanium-tungsten system. Estimations of values of $\text{R.T.} \ln (1 - C_\beta)/(1 - C_\alpha)$ were restricted to the ranges of composition and temperature stated below in reference to calculations of ΔH.

Only very approximate values of ΔH could be estimated from the initial portions of published phase boundaries. The calculations were restricted to boundaries extending from 0 to about 5 atomic per cent of solute. This corresponded to a temperature range not exceeding 80°C either below or above the transformation temperature for pure titanium. For any given system, the variation of ΔH with temperature did not exceed $\pm 10\%$ of an average value.

Discussion

Figure 1 shows values of ΔH grouped according to the position of the alloying elements in the Periodic Table. Of the nontransitional elements, copper, silver, silicon and tin cause a slight or moderate depression of the $\alpha \rightleftharpoons \beta$ transformation, whereas aluminium elevates it. All the transitional elements tend to stabilize the β-form of titanium, the effect being more marked, the higher the Group number for metals in any given Period.

If metallic valencies based on the concepts of Pauling [7] are adopted for the alloying elements under consideration (cf. Figure 1), then the following observations emerge.

(a) Elements with a valency of 4 (the assumed valency of titanium) cause only a slight depression of the transformation. Tin, for which the nominal or Group valency is 4, causes a slight depression in the composition region 0 to 5 atomic per cent; additions of tin beyond 5 atomic per cent cause a slight elevation of the transformation range [2]. This is interesting when considered in relation to the fact that tin seems to have a valency of less than 4 in some metallic phases.

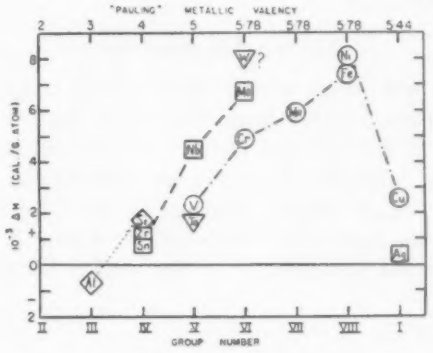

FIGURE 1. Values of ΔH grouped according to the position of the elements in the Periodic Table. "Pauling" valencies are indicated at the top of the chart. ◇..... Elements of 2nd short period. ○—.—. Elements of 1st long period. □ — — — Elements of 2nd long period. ▽ Elements of 3rd long period.

(b) Elements with valencies greater than 4 cause a depression of the transformation range, the effect tending to be more marked, the higher the valency.

(c) Aluminium, with a valency of 3, causes an elevation of the transformation.

In a discussion of the Brillouin zones of titanium and zirconium, Pfeil [8] has pointed out that an increase in the number of electrons per atom above 4 could be tolerated in the β-structure with a smaller increase in the mean Fermi energy than would be the case for the α-structure. Pfeil also indicated that the α-structure would probably be favoured if the electron/atom ratio was reduced below 4. Hence, for the systems considered in this note, there are strong indications that the Brillouin zone characteristics of α- and β-titanium are amongst the important factors which determine the effects of the alloying elements on the relative stabilities of the two forms of the metal. Pfeil (*loc. cit.*) has already made tentative suggestions along these lines, and Rostoker [9] has indicated that Brillouin zone characteristics are probably significant in respect to the stability of the α-phase in the system titanium-aluminium.

One questionable aspect of the above discussion

is the acceptance of the "Pauling" valency of 5.4 for copper and silver. Hume-Rothery *et al.* [10] have shown that the effective metallic valency of metals in Group IB is probably not so high as 5.4. However, any discussion involving metallic valencies, especially those for the transition metals, is fraught with uncertainties. While recognising these and other uncertainties affecting the subject under consideration, the author presents this note in the belief that it may assist the general approach towards a more thorough understanding of titanium-base alloys.

Acknowledgements

This note deals with portion of the programme of the Physical Metallurgy Section of the Commonwealth Scientific and Industrial Research Organization, Australia. The work was carried out in the Baillieu Laboratory, University of Melbourne, under the general direction of Professor J. Neill Greenwood, to whom the author tenders his thanks. The author also desires to thank his colleagues for helpful discussions.

References

1. Hansen, M., McPherson, D. J. and Rostoker, W. Constitution of Titanium Alloy Systems. Wright Air Development Center, Technical Report 53–41, February 1953.
2. Worner, H. W. J. Inst. Metals **81**, (1952–53) 521.
3. Worner, H. W. J. Inst. Metals (in press).
4. Zener, C. Trans. Amer. Inst. Min. Met. Eng. **167** (1946) 513.
5. Oelsen, W. and Wever, F. Archiv für das Eisenhüttenwesen **19** (1948) 97.
6. McQuillan, A. D. Proc. Roy. Soc. **A204** (1950) 309.
7. Pauling, L. J. Amer. Chem. Soc. **69** (1947) 542.
8. Pfeil, P. C. L. A Discussion of the Factors Affecting the Constitution of Zirconium Alloys. Atomic Energy Research Establishment (Harwell) Report M/R 960, June 1952.
9. Rostoker, W. J. Metals **4** (1952) 212.
10. Hume-Rothery, W., Irving, H. M. and Williams, R. P. J. Proc. Roy. Soc. **A208** (1951) 431.

OXIDE GROWTH ON DIFFERENT CRYSTAL FACES OF ALUMINIUM*

MRS. S. J. BASINSKA,† J. J. POLLING† and A. CHARLESBY†

The growth of oxide on different crystal faces of aluminium is studied. According to the theory of the oxidation of a metal proposed by Mott, metallic ions migrate from the metal surface to the oxide-air interface. These ions must first overcome the potential barrier at the metal-oxide interface, and if this is different on different crystal faces, then the oxide thickness will also be different.

The oxide films were formed electrolytically, so that the potential difference across the oxide was known. The orientations of the crystals were found by goniometer measurements and X-ray diffraction methods. The thickness of the oxide was obtained by a study of the interference colours shown by these thin films, the method being capable of showing a change in film thickness of about 40Å. Two known crystal faces were produced by etching techniques, and both etched and electro-polished surfaces were studied. No significant variation in oxide thickness was observed on different crystal faces.

LA CROISSANCE DE L'OXYDE SUR DIFFÉRENTES FACES CRISTALLOGRAPHIQUES DE L'ALUMINIUM

On a étudié la croissance d'oxyde sur différentes faces cristallographiques de l'aluminium. Suivant la théorie de l'oxydation d'un métal, proposée par Mott, les ions métalliques se déplacent de la surface du métal vers l'interface oxyde-air. Ces ions doivent d'abord vaincre la barrière de potentiel à l'interface métal-oxyde, et si cette barrière est différente sur différentes faces du cristal, l'épaisseur de l'oxyde variera d'une face à l'autre. Les couches d'oxyde ont été formées électrolytiquement, et la différence de potentiel à travers l'oxyde était connue. Les orientations des cristaux furent déterminées au moyen de mesures goniométriques et de la diffraction des rayons X.

L'épaisseur de l'oxyde était déterminée par l'étude des couleurs d'interférence obtenues sur ces couches, cette méthode permettant d'évaluer des variations d'épaisseur de l'ordre de 40Å. Deux faces cristallographiques, connues, ont été préparées par attaque, et ensuite les surfaces attaquées et polies électrolytiquement ont été étudiées.

On n'a pas constaté de variations appréciables de l'épaisseur de l'oxyde sur différentes faces.

OXYDBILDUNG AUF VERSCHIEDENEN KRISTALLEBENEN DES ALUMINIUMS

Es wurde die Oxydbildung auf verschiedenen Kristallflächen des Aluminiums untersucht. Nach der von Mott vorgeschlagenen Theorie der Metalloxydation wandern die Metallionen von der Metalloberfläche zur Grenzfläche Oxyd-Luft. Diese Ionen müssen zuerst die Potenzialschwelle an der Grenzfläche Metall-Oxyd überwinden, und falls diese an verschiedenen Kristallebenen verschieden ist. wird auch die Dicke der Oxydschicht verschieden sein.

Die Oxydfilme wurden elektrolytisch geformt, so dass die Potentialdifferenz an den Oxyden bekannt war. Die kristallographische Orientierung wurde röntgenographisch und goniometrisch ermittelt. Die Dicke der Oxydschichten wurde aus den Interferenzfarben, die diese dünnen Filme zeigen, bestimmt. Mit dieser Methode liessen sich Dickenänderungen von ca. 40 Å aufzeigen. Zwei bekannte Kristallebenen wurden mittels Ätzverfahren hergestellt und sowohl geätzte wie auch elektropolierte Flächen untersucht. Die verschiedenen Kristallflächen zeigten keine nennenswerten Unterschiede in der Dicke der entsprechenden Oxydschichten.

Introduction

In the theory of oxidation of certain metals such as aluminium, tantalum and zirconium proposed by Mott [1], oxide growth takes place by the movement of ions from the metal through the oxide to the oxygen rich surface. The factor limiting the rate of growth is the potential barrier at the metal-oxide interface. According to this theory, a potential exists between the two faces of the oxide layer, producing an electrostatic field which assists the metal ions to overcome the potential barrier. Film growth then takes place until the field (equal to the potential divided by the oxide thickness) becomes too small to permit appreciable ion flow.

At any given temperature the limiting oxide thickness depends on the field across the oxide and the dimensions of the potential barrier. Thus on those faces of a single crystal having a lower potential barrier, a lower field should be sufficient to promote oxide growth. When such a crystal is anodised at a constant voltage, one would expect to find increased film growth on faces of lower potential barrier.

In this paper some experiments are described, giving estimates of the oxide thickness on different faces of aluminium crystals. The surface of these crystals was prepared by electropolishing and etching or electropolishing alone. The specimens were then anodised, all crystals of the same specimen being oxidised at the same voltage. The oxide layer thickness can then be estimated from the interference colours produced.

Preparation of Specimens

Formation of large crystals

For this work it was convenient to use large crystals of aluminium. Polycrystalline specimens

*Received September 22, 1953.

†Atomic Energy Research Establishment, Harwell, England.

of high-purity aluminium (99.99%) containing large crystals were made by the following two methods:

(*a*) Standard tensile test pieces cut from aluminium sheet of 0.25-inch thickness were annealed for two hours at 500°C. After annealing, the test pieces were extended by 1.7 per cent over a 2-inch gauge length, then slowly heated from 150°C to 620°C at rate of 50°C per day followed by annealing for two days at the final temperature.

(*b*) Samples of 2-inch square were cut from the same sheet and were annealed for 48–60 hours at 10°C below the melting point.

Method (*a*) tends to give long, narrow crystals, and method (*b*) crystals roughly circular. The crystals produced by these methods were randomly orientated, and their size varied from 0.5 sq cm to about 10 sq cm.

Electropolishing

To remove surface defects, the specimens were electropolished in an electrolyte containing 40 wt% H_2SO_4, 40 wt % H_2PO_4, 20 wt % H_2O at a current density of about 5 amp/sq in and temperature 94°C. A good polish was obtained in about five minutes. The specimens were then washed in warm water and dried in a stream of hot air.

Etching

One function of an etchant is to reveal an equivalent set of faces selectively. Two etchants were used to develop different sets of crystal faces.

(*a*) The first contained 9 parts HCl, 3 parts HNO_3, 2 parts HF and 5 parts water. It was necessary to keep the solution at or below 0°C, and to stir to avoid local heating, otherwise an uneven etch was obtained. Etching time varied from specimen to specimen, but on an average was 90 seconds. For specimens which had developed an oxide film, the proportion of HF in the etchant was increased. This etchant is reported [ref. 2, p. 173] to develop (100) cube faces.

(*b*) The second etchant was dry HCl gas. An aluminium specimen was hung in an atmosphere of dry HCl gas generated by warming concentrated HCl and drying the gas evolved with P_2O_5. After exposure to the dry HCl for about 30 minutes the specimens were washed in acetone and quickly dried. The faces developed by this etchant were investigated, as described below.

Identification of Etch Pit Faces

The faces of the etch pits on any one crystal are all similarly oriented, thus forming a system of small mirrors. Each will reflect an incident beam of collimated light in one direction. The angle between the reflections from each set of faces of the etch pits formed on one crystal will identify those faces. The positions of these reflections relative to the surface of the crystal were measured, for the smaller specimens, with a Unicam two-circle goniometer. The readings were plotted on a Wulff net [ref. 2, p. 25] and the angles between etch pit faces measured along great circles of the projection. From this projection the surface plane of the crystal could be determined. This was usually some irrational crystal plane. The orientations of about 30 crystals which had previously been examined by etch pit technique were also determined by back-reflection Laue X-ray diffraction photographs. The patterns were interpreted using a Greninger chart and were found in every case to be the same as those determined by etching.

For specimens too large for the goniometer, the angles between the facets of the etch pits and the surface of the crystal were determined using a perspex hemisphere. Figure 1 shows the arrangement. A collimated beam of light was directed through a small hole A, in the dome on to a chosen crystal in the specimen B. A beam reflected from a set of etch pit faces of this crystal was apparent at a spot C on the dome surface. The arc lengths *a* and *b* were measured with string previously calibrated to read directly in degrees, i.e., *a* will give angle $C\hat{O}E$ of diagram 1a. Then the angle x between the etch pit face, GO, and the surface of of the specimen is given by,

$$x = 90° - \left[C\hat{O}E + \frac{(90 - C\hat{O}E}{2} \right]^{\circ}.$$

The angle between the normal to the etch pit face and the arbitrary line RS on the specimen is given by the arc length ND (Figure 1). Back-reflection Laue photographs were taken to determine the surface planes of the crystals examined. Knowing this, and the angle x, the indices of the etch pit faces were determined.

By these methods it was confirmed that etching reagent (a) did in fact develop (100) planes and that reagent (b) developed (111) planes.

For some specimens which were badly etched, the light reflected from the etch pit faces was diver-

gent and reflections were therefore recorded over a wide angular range. For this reason to produce sharp reflections it was necessary for the etching technique to be exact. Prolonged etching gave an increased number of etch pits and therefore increased brightness of reflection, but if too prolonged, mutual encroachment occurred and the

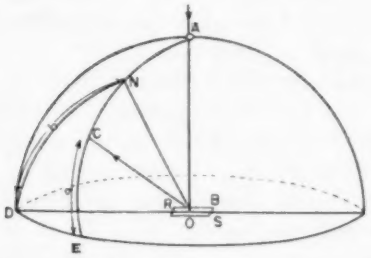

FIGURE 1. Apparatus used and measurements made in determining the angles between etch pit faces and crystal surface. A beam of light enters the dome through a hole at A and strikes the etch pit faces of the chosen crystal. ON is the normal to the reflecting surface giving rise to the spot of light at C.

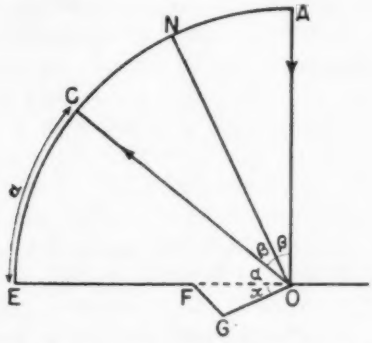

FIGURE 1a. Diagram showing enlarged etch pit. FGO is a cross section of an etch pit, enlarged, GO being the reflecting face considered and ON the normal to that face. The other letters correspond to those of Fig. 1. NO = face normal; OF = specimen surface; FGO = cross section of etch pit, enlarged; C = spot on hemisphere. From geometry, $x = \left\{90 - \left[\alpha + \left(\frac{90 - \alpha}{2}\right)\right]\right\}$.

reflection was less sharp. The best results were obtained with specimens having numerous fairly deep etch pits but whose original surface reflection was still easily visible. Adequate electropolishing prior to etching was essential as surface defects affect the even formation of etch pits and therefore of a sharp reflected beam.

Formation of Oxide Film and Production of Interference Colours

The specimens were anodised in an electrolyte of dilute aqueous ammonium borate. This method has been used in previous experiments [3] and at 20°C gives film thicknesses of approximately 10Å per volt. Unlike oxide films formed on zirconium or tantalum, these films alone do not give rise to interference colours; by evaporating a very thin film of gold over the oxide layer, however, bright interference colours can be produced, the colour being a sensitive indication of the oxide film thickness. These colours, of course, vary with the angle of viewing, but when viewed at normal incidence the colour for a given formation voltage was constant. Several thicknesses of gold were deposited on identically prepared specimens to confirm that no appreciable changes in colour arise from the presence of the gold.

Oxide layers of different thickness were produced on a number of specimens by altering the voltage at which they were formed. It is estimated that in certain regions of the spectrum differences of less than 40Å in oxide thickness would be revealed by the changes in colour.

Examination of Specimens

Electropolished Specimens

Several specimens were etched, electropolished, and anodised at a range of potentials up to 200 volts (corresponding to oxide thicknesses of about 2000Å). When a thin gold layer was deposited on them by evaporation interference colours appeared. For specimens anodised at a particular voltage, the colour for normal incidence was uniform, and there was no indication that different grains were differently coloured. It is concluded that for electropolished crystals oxide growth is equally rapid on all faces.

Etched Specimens

Specimens which were electropolished and then etched prior to anodising showed strong reflections. For any given angle of incidence each crystal in the specimen had three directions in which there were strong reflected beams. After evaporating gold on to the specimen interference colours were observed, which were generally uniform for any one voltage, but which were very bright in the same three directions only. These intense beams are ascribed to reflections from the etch faces. Similar observations were made on some etched, anodised foil.

At first sight, for a specimen anodised at, say, 80 volts and having (100) etch pit faces developed, the crystals appeared to be of different colours,

varying from bright blue to purple. Some crystals appeared very dull, nearly black. On closer examination it was observed that for each position of maximum intensity of reflection from the etch pits of any crystal the same colour was given for the same angle of incidence. This colour was the same as that given by the reflection from the unetched surface of any crystal of the same specimen, again for the same angle of incidence. In general, there were three positions of maximum intensity for the etch pits of each crystal, corresponding to reflections from each of the sets of facets of a particular collection of similarly oriented etch pits. For some adjacent pairs of crystals, there was one position of viewing for which the grain boundary between them disappeared. Back-reflection Laue photographs of such a pair of crystals were taken. The plots of the projections of these photographs in Figure 2 represent the three

FIGURE 2. Projection of 100-plane normals of an adjacent pair of crystals. A and A′ are the almost coincident points. P and Q, R and S are the pairs of non-coincident plane normals. ■ (100)-plane normals of crystal YG; ● (100)-plane normals of crystal YB; W is centre of projection; VW represents reference line on specimen.

TABLE I

CORRESPONDING GONIOMETER READINGS FROM THE TWO CRYSTALS

Crystal	Horizontal circle (degrees)	Vertical circle (degrees)
YB	224–227	60–64
	290–294	192–196
	293–297	293–295
YG	44– 47	225–230
	289–292	295–298
	303–307	183–187

(100) plane normals of each crystal, showing that this pair of crystals has one plane normal in common. The two other plane normals were not coincident. Since one set of (100) plane normals is coincident for the two crystals, then the corresponding sets of etch pit faces are identically oriented with respect to the specimen surface and the arbitrary line. This explains the disappearance of the grain boundary when the maximum reflection from this set of faces is viewed. The two crystals in question can be generated by a simple rotation about a (100) axis.

Goniometer readings showed that the etch pit faces were, in fact, in the positions indicated by the projection from the Laue back-reflection photographs. These readings when plotted on the projection of Figure 1, are almost coincident with the points already marked.

Similar arguments apply to other specimens, except, of course, that the interference colour is different for each formation voltage.

The wavelength of light which undergoes destructive interference after passage through a film is proportional to the cosine of the angle of refraction so that if a specimen is viewed at angles up to 20 degrees from the normal, the colour will hardly alter with angle of viewing, but at greater angles will change rapidly. Thus, when a specimen is held in given position many of the crystals viewed will show only slight differences in colour, but some will appear to be very differently coloured.

Those crystals which appeared dark obviously had none of their etch pit faces in a position to reflect light towards the observer. When the specimen was tilted in such a way that its etch pit facets were in a reflecting position, the colour observed was the same as for other crystals.

Comparison of (100) and (111) etch faces and surface planes

Two specimens, one having (100) planes etched out and the other having (111) planes etched out, were treated identically, i.e., anodised at the same voltage and covered with the same thickness of gold.

The colour of the light which was reflected with maximum intensity from their etch pit faces was identical for equal angles of incidence—within the limits of experimental error which is ca. ± 5%. This colour was also identical with that from the unetched surface, for the same angle of incidence.

From this it is deduced that the oxide film thickness is the same on (100), (111) and on irrational crystal faces.

An apparent discrepancy occurred for films

anodised at a potential of 50 volts when different colours were obtained in the three bright directions. These differences occurred whether (100) or (111) etchants were used, and whether the evaporated metal was silver or aluminium instead of gold. The reason for this exceptional behaviour is not clear; it may be associated with multiple reflection or interference. No such effect was observed at any other formation voltage.

Conclusions

Aluminium specimens anodised up to 200 volts (i.e., 2000 Å oxide film thickness), were examined to determine the oxide thickness on different faces.

The interference colours obtained were constant in each specimen for reflection from all etch pit faces and from the unetched surfaces, for the same angle of incidence. The colours from the (100) and (111) etch pit faces of two specimens which had been anodised at the same voltage and covered with the same thickness of gold were the same for equal angles of incidence. For specimens formed at different voltages the colours were different.

It follows that since the interference colour depends only upon voltage of formation and angle of incidence, and that the structure of the surface plane has no influence, the oxide film is of equal thickness on any crystal face ($\pm 5\%$) for the same voltage of formation. This would indicate that for different crystal faces the potential barrier at the metal-oxide interface which limits the flow of metallic ions into the oxide is not appreciably different.

Acknowledgements

The authors wish to thank Dr. H. M. Finniston and Mr. S. F. Pugh for helpful discussion. This paper is published by kind permission of the Director, Atomic Energy Research Establishment.

References

1. MOTT, N. F. Trans. Far. Soc. **43** (1947) 429.
2. BARRETT, C. S. Structure of Metals (New York, McGraw-Hill).
3. CHARLESBY, A. Proc. Phys. Soc. **B66** (1953) 317.

ON THE USE OF ELECTRICAL RESISTIVITY AS A MEASURE OF PLASTIC DEFORMATION IN COPPER*

R. H. PRY and R. W. HENNIG†

It has been shown that, for fine-grained polycrystalline copper, the stress necessary to continue plastic deformation in tension, below ordinary recovery temperatures, can be determined by measurements of the temperature, strain rate, and residual electrical resistivity measured after a room temperature anneal. Temperature cycling experiments similar to those performed by Dorn and Orowan, some experiments on partially recovered samples, and on pretwisted samples, indicate that the tensile stress for plastic flow is a single valued function of these variables within the accuracy of the experiments.

SUR L'EMPLOI DE LA RÉSISTIVITÉ ÉLECTRIQUE COMME MESURE DE LA DÉFORMATION PLASTIQUE DANS LE CUIVRE

Il a été montré que dans le cas du cuivre polycristallin, à petit grain, la tension nécessaire pour la continuation de la déformation par extension, en dessous des températures normales de restauration, peut être déterminée au moyen de mesures de la température, de la vitesse de déformation et de la résistivité électrique, résiduelle, effectuées après un recuit à la température ambiante. Des expériences sur des cycles de température, ressemblant à celles qui ont été effectuées par Dorn et Orowan, ainsi que certaines expériences sur des échantillons partiellement restaurés et sur des échantillons tordus avant l'expérience, indiquent que la tension d'extension pour l'écoulement plastique est une fonction univalente de ces variables, aux erreurs expérimentales près.

DER ELEKTRISCHE WIDERSTAND ALS MASS FÜR DIE PLASTISCHE VERFORMUNG VON KUPFER

Es wird gezeigt, dass es möglich ist, die zur Fortführung der plastischen Verformung von feinkörnigem, polykristallinem Kupfer unterhalb der üblichen Rekristallisationstemperatur notwendige Zugspannung aus Messungen der Temperatur, der Verzerrungsgeschwindigkeit und des elektrischen Restwiderstandes zu ermitteln. Letzterer wurde nach Glühen bei Zimmertemperatur gemessen. Versuche mit systematisch veränderten Temperaturbedingungen (ähnlich den Dorn und Orowan' schen Experimenten) und einige Versuche mit teilweise erholten und mit vorher verdrillten Proben deuten darauf hin, dass, im Rahmen der experimentellen Fehlergrenzen, die Zugspannung zum plastischen Fliessen eine eindeutige Funktion der oben angegebenen Variablen ist.

Introduction

It has been known for some time that the electrical resistivity increase in copper due to deformation at liquid nitrogen temperatures or below decays in roughly three successive stages of subsequent anneal. These occur in the regions of 160°K, 260°K, and above 360°K [1; 2]. Moreover, it is known that the defects that decay in the lower two temperature anneals do not appreciably affect the strength [3]. That is, if a copper rod is deformed in tension at 78°K, the stress which must be applied to continue plastic deformation is nearly independent of an intervening anneal at room temperature.

The purpose of this paper is to show that the increase in electrical resistivity that remains in deformed copper after a room temperature anneal is closely related to the stress which must be applied to continue the deformation, and that, within certain limitations, the stress during deformation is determined, independent of previous deformation history, by the instantaneous measurement of electrical resistivity, temperature, and strain rate.

Apparatus and Procedure

The material used for these experiments was American Smelting and Refining Company 99.999 per cent pure copper in the form of cold drawn 10-mil diameter wires, cut to 7-in. lengths and annealed one hour at 250°C in a vacuum, thus producing a fairly uniform grain size of .012 mm.

These wires then were carefully mounted in the extension device shown in Figure 1. All electrical measurements were made using a standard potentiometer circuit. Potential leads were attached by soldering No. 36 copper wire to the 10-mil wire at a separation distance of about 5 in. in such a way that the solder was all localized at the potential wires. The test wire was gripped at the ends by means of solder beads as shown in Figure 1, and the current leads were attached to these end grip solder beads. Variations in wire temperature during the measurements were accounted for by measuring the resistance of a copper "dummy" wire with the same dimensions as, and placed close to, the wire being tested. All resistance

*Received October 5, 1953.
†Metallurgy Research Department, General Electric Research Laboratory, Schenectady, New York.

measurements were made with the wire in a bath of liquid nitrogen.

The tensile testing was done with the apparatus shown in Figure 1 mounted in an Instron tensile testing machine which automatically records a load-time curve at constant extension rate. The wire extensions were measured using the extensometer mounted in the machine. Corrections for the wire slipping slightly in the end grips were made by measuring the wire length, between potential leads, with a cathetometer before and after testing. The extension rate was kept constant at .04 in/in. per minute.

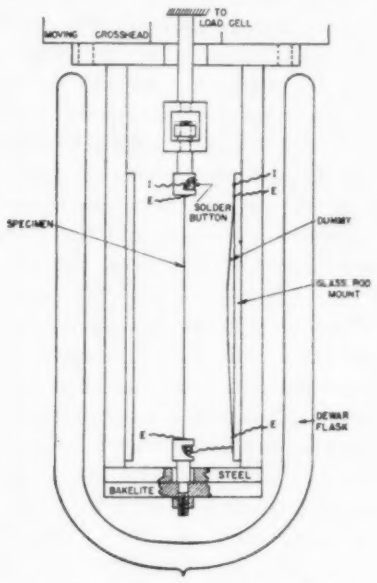

FIGURE 1. Apparatus for making stress, strain, resistivity measurements.

The stress, strain, resistance measurements were made at 78°K and 286°K. Since the resistivity to be measured was not the total resistivity increase after deformation at 78°K, but only that part remaining after a short room temperature anneal, the following procedure was standardized and followed for all measurements.

The wire was placed in the apparatus in an annealed, relaxed, position and its resistance measured at 78°K. The wire was then strained 2 per cent at test temperature (either 78°K or 286°K) and the load, extension data taken continuously. After a 2 per cent strain increment, the wire was relaxed, annealed at 286°K for approximately five minutes, placed in the liquid nitrogen bath and its resistance measured again. This cycle was then repeated for every additional 2 per cent strain. For the wires tested at 78°K the resistance was measured before and after the room temperature anneal to determine the decrease in resistivity after a 2 per cent strain increment at various strain levels. The percentage increase in resistivity above that of the annealed, undeformed wire at 78°K was then calculated from these measurements. Corrections for the dimensional changes in the wires were made on the assumption that the volume of the wire remained constant. It is realized that Matthiessen's rule is not strictly valid for this resistivity increase [4], but since all measurements were made at one temperature, the results should be at least self-consistent.

Results and Conclusions

Some typical stress-strain curves and resistivity-strain curves are shown in Figure 2. The reproducibility of the stress-strain curves was between 1 and 2 per cent in stress. Since these wires showed a small but observable yield point when strained above 10 per cent at 78°K with the above treatment, some stress-strain resistivity measurements were made by continuously straining to 15 per cent. This curve is shown dotted in Figure 2 and is about 7 per cent higher in stress at 15 per cent strain. At 286°K, however, no difference was observed in the two curves.

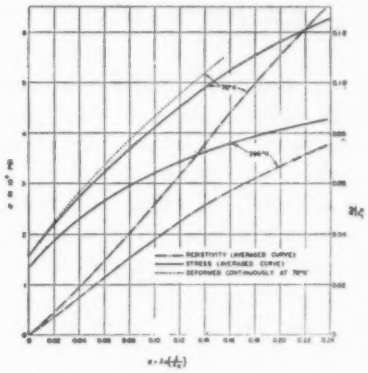

FIGURE 2. Stress-strain, and resistivity-strain curves for copper wires deformed in tension.

In Figure 3 are shown the data of stress versus resistivity increase for the two test temperatures. The points outlined by triangles are the end points of those wires which were pulled continuously to 15 per cent strain. As is seen, although the stress-strain curves at 78°K (from Fig. 2) are appreciably altered by the room temperature anneal, the stress-resistivity curves seem to be fairly independent of this treatment. It must be presumed that

either some dislocation annealing takes place in copper around 286°K, or the defects which decay at low temperatures do affect the strength, at least indirectly. However, since the stress and resistivity seem to behave in the same way, one is encouraged to say that the stress-resistivity curves shown are real.

An interesting feature about Figure 3 is that the stress-resistivity curve at 286°K falls very closely

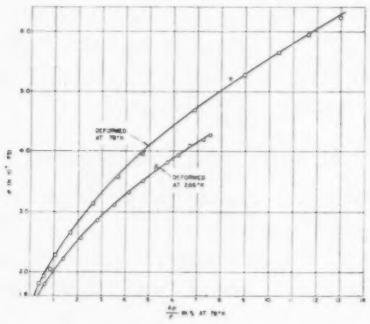

FIGURE 3. Stress-resistivity curves for copper wires deformed in tension.

on the 78°K curve if the higher temperature curve is raised uniformly 14 per cent in stress. In order to examine the significance of these curves, measurements were made on wires that were alternately deformed at 78°K and 286°K. Figures 4a and 4b show the resulting stress-strain curves for these measurements which is a typical behavior

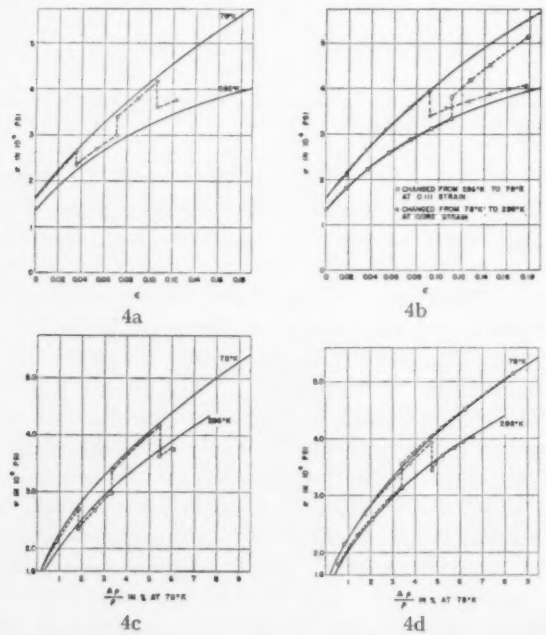

4a 4b 4c 4d

FIGURE 4. Stress-strain and stress-resistivity curves for polycrystalline copper wires deformed in tension alternately at 78°K and 286°K.

for such temperature cycling experiments [5]. That is, the reload stress after some deformation is not a unique function of the instantaneous variables of temperature, strain rate and strain, but depends also on the previous deformation history. Figures 4c and 4d, on the other hand, show that these difficulties are resolved by replacing the strain parameter by resistivity. In this case, at least, it appears that the resistivity increase is a real measure of the work-hardened state. To oversimplify the situation considerably, one might say that the resistivity increase is a measure of the number of dislocations fixed in the metal and so determines the stress at which deformation will proceed, whereas the strain is a measure of their movement and the movement of those dislocations which have already left the material.

The probable criterion for the success of these measurements is that the deformation be sufficiently homogeneous, both for the purpose of talking about an average work-hardened state and for the purpose of making the resistivity increase, as measured along the wire axis, meaningful. This is accomplished by the use of wires with a very small grain size, so that the deformation proceeds, not only on a few planes in a grain, but on many to conform to the deformed state of its neighbors.

In order to explore the regions where the stress-resistivity relation may break down, two wires were strained 10% at 78°K. One was then annealed at 150°C for ½ hour and the other was annealed at 180°C for 1½ hours. Both wires were then strained further at 78°K. These data are shown in Figure 5. Although the stress-resistivity recovery was not very large, the relation between stress and resistivity is still valid.

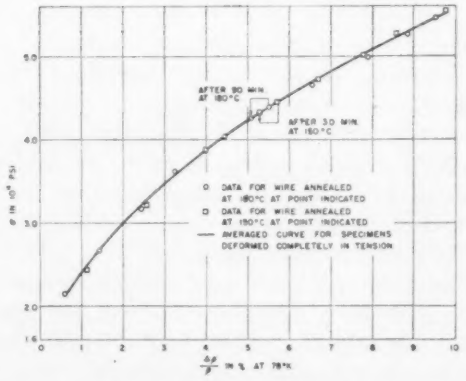

FIGURE 5. Stress-resistivity curves for copper wires deformed in tension in two stages with an intermediate anneal at the temperature indicated.

To test this relation further, two wires were pretwisted, one four and one eight turns per inch at room temperature, and subsequently pulled in tension at 78°K. Even under these conditions, with the exception of the first per cent tensile strain which occurs at a relatively low stress, an example of the Bauschinger effect, the resistivity was a fair measure of the deformed state, as can be seen from Figure 6.

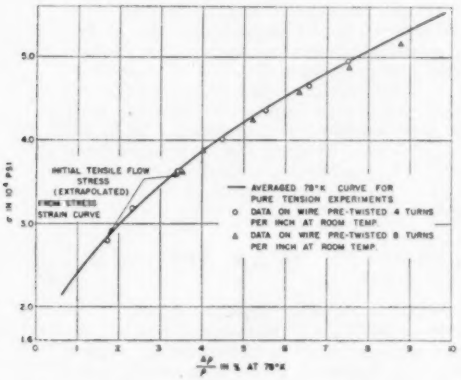

FIGURE 6. Stress-resistivity curves for copper wires pretwisted at room temperature and subsequently deformed in tension at 78°K.

From the stress-resistivity data of the temperature cycling experiments it is clear that part of the flow-stress increase with decreasing temperature, below recovery temperatures, in copper is due to a reversible temperature effect since the temperature cycling data fall on the two isothermal curves. Part of this increase in stress can be attributed to the temperature variation of the elastic constants [5] which probably accounts for a stress change of 7 to 9 per cent between 286° and 78°K. Since the possible energy supplied to dislocation sources by thermal fluctuations would give rise to an effect which is considerably less than the remaining 6 per cent variation, this remainder may be due primarily to a temperature dependent viscous rate effect.

From some experiments by R. P. Carreker [6] on this copper, it is known that the strain rate exponent at 286°K is about .007, so that the increase in stress due to decreasing the temperature to 78°K amounts to an increase in strain rate at 286°K by a factor of about 4000. Unfortunately, not enough is known about the mechanisms involved to really test the plausibility of this connection.

In Figure 7 is plotted the increment of recoverable resistivity per unit strain increment, $\Delta\rho_R/\rho_0\Delta\epsilon$, versus the per cent increase in unrecoverable

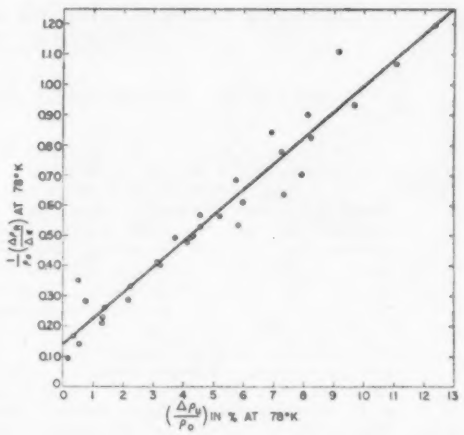

FIGURE 7. Recoverable resistivity increase per unit strain versus total unrecoverable resistivity increase for copper wires deformed in tension at 78°K and recovered at room temperature.

resistivity, $\Delta\rho_u/\rho_0$, referred to the undeformed state, after room temperature anneal, at the midpoint of the strain increment. If one assumes that the resistance after anneal at room temperature is a dislocation resistance, then this indicates that the number of defects produced per unit strain which anneal out below room temperature depends only on the number of dislocations which are bound in the medium. This is in agreement with the idea that the defects produced are lattice vacancies caused by the crossing of screw dislocations [7].

Further work is now in progress to define more clearly the bounds of the validity of the stress resistivity relationship described here by studying this effect on large grain size wires and on wires of different materials.

Acknowledgements

The authors wish to acknowledge the interest and encouragement of J. C. Fisher and E. W. Hart during the progress of this work.

References

1. MANINTVELD, J. A. Nature **169** (1952) 623; EGGLESTON, R. R. J. Appl. Phys. **23** (1952) 1400.
2. BOWEN, EGGLESTON and KROPSCHOT. J. Appl. Phys. **23** (1952) 630.
3. MOLENAAR and AARTS. Nature **166** (1950) 690.
4. RUTTER and REEKIE. Phys. Rev. **78** (1950) 70.
5. DORN, GOLDBERG, and TIETZ. Metals Tech. **15**, No. 6, Tech. Pub. 2445 (1948); OROWAN, E. The Creep of Metals, West of Scotland Iron and Steel Inst., February 14, 1947.
6. CARREKER, R. P. and HIBBARD, W. R. JR. General Electric Research Laboratory Report RL-848, March 1953. Acta Met. **1** (1953) 654.
7. MOTT, N. F. Proc. Phys. Soc. **B64** (1951) 729.

RECENT OBSERVATIONS ON THE MOTION OF SMALL ANGLE DISLOCATION BOUNDARIES*

DOUGLAS W. BAINBRIDGE,† CHOH HSIEN LI,† and EUGENE H. EDWARDS†

The motion of small angle dislocation boundaries in zinc crystals was investigated in the temperature range −196°C to 400°C. Boundaries were made to move by the application of a shear stress acting in the direction of the Burgers vector of the edge dislocations comprising the boundary. The character of this motion was found to vary markedly with temperature. Motion proceeded at a constant rate under a constant stress at elevated temperatures. At +20°C movement was discontinuous, the boundary advancing through an appreciable distance during each jump. At −196°C, motion appeared to be steady. However, at both 20° and −196° a continuously increasing stress was required for continued movement. The boundary angle remained constant during motion at high temperature. At lower temperatures, the magnitude of the angle decreased, and the boundary assumed a more complex shape through interaction with structural defects. Small-angle boundaries of like sign in proximity to one another coalesced during short time annealing treatments at 400°C to form a single boundary. Closely spaced boundaries of like sign could be made to unite at any temperature by the application of a stress, thus establishing a mechanism for the formation of a substructure in the absence of appreciable thermal energy. Boundaries of unlike sign were united through their stress-induced motion and the angle of the resultant boundary equalled the algebraic sum of the angles of the constituent boundaries. The results of boundary motion experiments were compared with the results of simple shear tests on single crystals of zinc. The similarities suggested that motion of dislocations through the structural barriers of the crystal rather than generation of new dislocations may be the factor which determines the yield strength.

OBSERVATIONS RÉCENTES SUR LE MOUVEMENT DE JOINTS À PETIT ANGLE, COMPOSÉS DE DISLOCATIONS

Le mouvement de joints à petit angle, composés de dislocations, dans des cristaux de zinc, a été investigué dans l'intervalle de températures allant de −196° à 400°C. Un mouvement des joints a été obtenu par l'application d'une tension de cisaillement agissant dans la direction du vecteur de Burgers des dislocations-coin qui constituent les joints. Le caractère de ce mouvement varie considérablement avec la température. Aux températures élevées le mouvement a une vitesse constante sous une tension constante. A +20°C le mouvement était discontinu, mais le joint avançait une distance considérable à chaque saut. A −196°C le mouvement paraissait être continu. Cependant, à 20° aussi bien qu'à −196°, il fallait augmenter constamment la tension pour maintenir un mouvement continu. Aux températures élevées l'angle du joint restait constant pendant le mouvement. Aux températures plus basses, l'angle diminuait et le joint prenait une forme plus complexe par l'interaction avec des défauts structuraux. Des joints à petit angle et de même signe s'unissaient pendant un court recuit à 400°C pour former un seul joint. Par l'application d'une tension il était possible d'unir, à n'importe quelle température, des joints de même signe, faiblement espacés; ceci établit un mécanisme pour la formation d'une sous-structure à l'absence d'une agitation thermique, appréciable. Des joints de signe contraire ont été réunis au moyen d'un mouvement induit par une tension; l'angle du joint résultant était égal à la somme algébrique des angles des joints primitifs. Les résultats des expériences sur le mouvement des joints furent comparés aux résultats d'essais de cisaillement simple sur des monocristaux de zinc. Les ressemblances ont suggéré que c'est le mouvement des dislocations à travers les barrières structurales du cristal, plutôt que la génération de nouvelles dislocations, qui détermine la tension d'écoulement.

NEUE BEOBACHTUNGEN ZUR BEWEGUNG VON KLEINWINKEL—VERSETZUNGSKORNGRENZEN

Die Bewegung von Kleinwinkel—Versetzungskorngrenzen in Zinkkristallen wurde im Temperaturgebiet zwischen −196°C and 400°C untersucht. Die Bewegung der Korngrenzen wurde durch Anlegung einer Schubspannung hervorgerufen. Die Schubspannung wirkte in der Richtung des Burgers Vektor der die Korngrenze bildenden Versetzungen. Es zeigte sich, dass die Art der hervorgerufenen Bewegung stark von der Temperatur abhing. Bei höheren Temperaturen zeigte sich eine konstante Bewegungsgeschwindigkeit, wenn eine konstante Spannung angelegt wurde. Bei +20°C war die Bewegung unstetig, und die Korngrenze legte bei jedem Sprung eine beträchtliche Strecke zurück. Bei −196°C erschien die Bewegung gleichförmig. Es war jedoch bei +20°C und bei −196°C notwendig, eine stetig anwachsende Spannung anzulegen, um eine ununterbrochene Bewegung hervorzurufen. Bei hohen Temperaturen blieb der Korngrenzenwinkel während der Bewegung konstant. Bei tieferen Temperaturen verringerte sich der Winkel, und auf Grund des Einflusses von Kristallbaufehlern in ihrem Weg nahm die Korngrenze kompliziertere Formen an. Nahe aneinander liegende Kleinwinkel—Korngrenzen gleichen Vorzeichens vereinigen sich nach kurzem Glühen bei 400°C zu einer einzigen Korngrenze. Nahe benachbarte Korngrenzen gleichen Vorzeichens konnten bei jeder Temperatur durch Anlegung einer Spannung zur Vereinigung gebracht werden. Diese Beobachtung kann auch die Bildung einer Feinstruktur ohne die Zufuhr nennenswerter thermischer Energie erklären. Korngrenzen ungleichen Vorzeichens wurden durch ihre durch die äussere Spannung hervorgerufene Bewegung vereinigt. Der Winkel der resultierenden Korngrenze war gleich der algebraischen Summe der Korngrenzenwinkel der Partner. Die Ergebnisse über die Bewegung der Korngrenzen wurden mit den Ergebnissen von Scherungsversuchen an Zinkeinkristallen verglichen. Die vorhandenen Ähnlichkeiten deuten darauf hin, dass der Faktor, der die Fliessgrenze bestimmt, mehr in der Bewegung von Versetzungen durch strukturelle Unregelmässigkeiten im Kristall als in der Bildung neuer Versetzungen zu suchen ist.

*Received October 13, 1953.

†Research Metallurgist, University of California, Berkeley, California.

Introduction

The possibility that a small-angle crystal boundary might consist of an array of dislocations was pointed out by Burgers [1] and by Shockley and Read [2]. Experimental verification of this concept was obtained in some recent work [3; 4]. It is the purpose of this paper to report further observations on the properties of small angle dislocation boundaries in zinc in the temperature range −196° to 400°C.

After annealing at a temperature close to the melting point, it is presumed that a small-angle boundary consists of an approximately evenly-spaced array of edge dislocations. For a 1-degree boundary in zinc the spacing between dislocations is about 60 interplanar distances. When such an array has been caused to move by an applied shear stress, the volume of crystal through which the array has passed has undergone a shear strain. For a 1-degree boundary a shear strain of about 2 per cent is produced; the magnitude of the strain is determined by the angle of the boundary. The motion of small-angle boundaries can therefore be considered as a particularly uniform type of plastic deformation in which single dislocations traverse every 10th to 100th slip plane rather than 100 to 1,000 dislocations traversing much more widely separated planes. Continued displacement of the boundary involves an enlargement of the strained volume of crystal. As has been pointed out [5], the stress required to set an array of dislocations forming a boundary into motion is approximately the same as the yield stress for the material. Since motion of a boundary only involves movement of dislocations already existing, this implies that the stress necessary to move dislocations may determine the yield strength of zinc rather than the stress necessary to generate new dislocations.

Experimental Techniques

The method of preparing small angle boundary specimens has been described in an earlier paper [4]. Recently an improvement in the shape of specimens was made, in that $0.14'' \times 0.2'' \times 1.0''$ rectangular bars were employed in place of the earlier discs. The rectangular bar specimens were cut to size by means of an acid sawing technique described elsewhere [6]. A specimen of this shape offered the advantage of constant average shear stress on the boundary during its motion. A typical specimen containing a simple edge type boundary is shown in Figure 1. The pronounced change in light intensity existing at the boundary is due to the relative change in orientation of the basal plane across the boundary. The boundary is also visible on the side or $(1\bar{1}00)$ face of the specimen. This effect was attributed to the reflection characteristics of a minute line grating produced by etching during the acid sawing operation. Etched valleys constituting the grating were visible at 500× and appeared randomly spaced but were aligned parallel to the basal plane. The tilting about the $[1\bar{1}00]$ axis was sufficient to cause this optical effect.

The specimens were loaded and observed both at low and high temperature in a manner shown photographically in Figure 2 and schematically in Figure 3. For high-temperature studies, the specimen was supported in a small electrical resistance furnace. At liquid-nitrogen temperatures the specimen was immersed in a Dewar flask. Both the furnace and vacuum flask contained viewing ports of optically flat glass to facilitate the microscopic observation of the boundaries and their motion. Boundary angles were measured optically with a long focal length goniograph capable of an angular resolution of approximately 30 seconds (see Appendix for details).

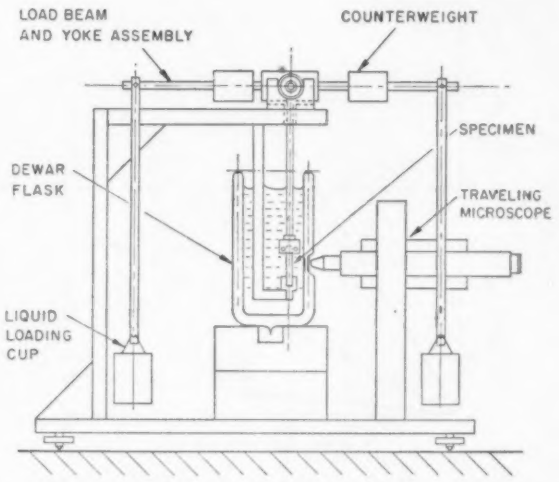

FIGURE 3. Schematic diagram of the loading mechanism used for boundary motion studies.

Observations and Discussion

A. *Effect of Temperature and Stress on Boundary Motion*

Small-angle boundaries used in this study consisted essentially of a planar array of edge dislocations with common Burgers vectors. These boundaries were made to move through the crystal by

the application of a shear stress acting in the direction of the Burgers vector at temperatures varying from that of liquid nitrogen to near the melting point. The characteristics of this motion, however, varied markedly with temperature. In the higher temperature range, i.e., 300° to 400°C, the displacement rate of a boundary was observed to be constant under the action of a constant stress [4]. The rate was dependent upon the temperature, stress level (Fig. 4), and the boundary angle (Fig. 5)

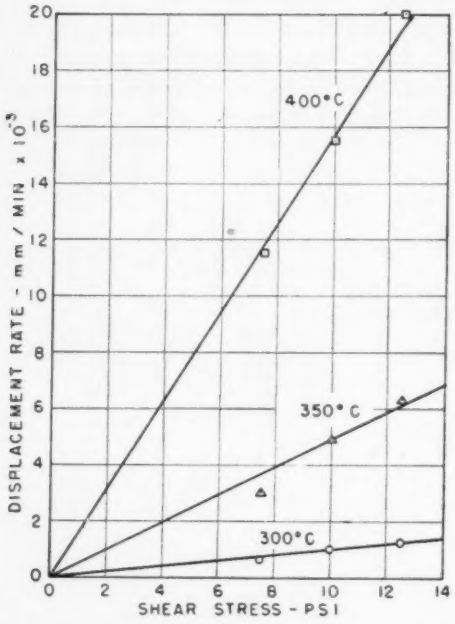

FIGURE 4. Displacement rate of a 2.0° edge dislocation boundary as a function of the shear stress.

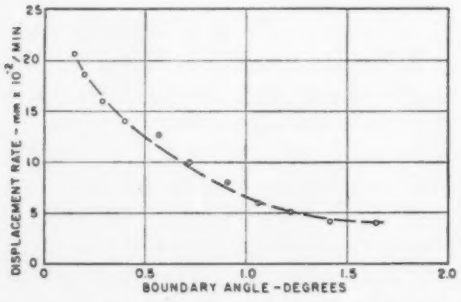

FIGURE 5. Displacement rate of edge dislocation boundaries as a function of the boundary angle under the action of a constant shear stress of 9.19 psi at 350°C.

such that the higher the temperature and stress or the lower the boundary angle, the greater the rate of boundary motion. At high temperatures it was not found possible to establish a lower limit of stress below which no motion would occur. The temperature dependence suggested that a thermal activation process was a major controlling feature. It was thus possible, as reported previously, to determine that an activation energy of approximately 21,500 cal/mole was involved in the motion of a boundary.

From the activation standpoint, only a small amount of thermal assistance is available at room temperature for this shearing process and essentially none exists at the temperature of liquid nitrogen. It was reasonable then to expect that boundaries would behave quite differently at these lower temperatures. In tests at room temperature, boundaries were observed to move in a manner remarkably different from that noted at elevated temperature. As the load was gradually increased, a value would be reached at which the boundary suddenly jumped to a new position at a velocity too rapid to be followed by the eye. The movement was frequently accompanied by a decrease in the angle of the boundary. The length of the jump was observed to be quite erratic. Jump distances as great as 0.5 mm were noted in some instances.

Motion of boundaries at liquid-nitrogen temperature was different from either that at room or

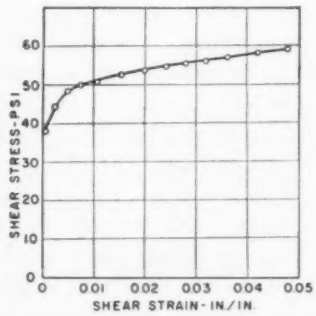

FIGURE 6. Shear stress-strain curve of a Zn single crystal tested in simple shear at −196°C.

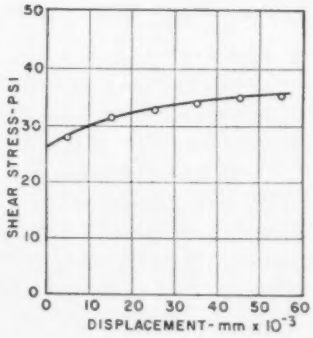

FIGURE 7. Stress-displacement curve of a 1° angle boundary perpendicular to a slip direction at −196°C.

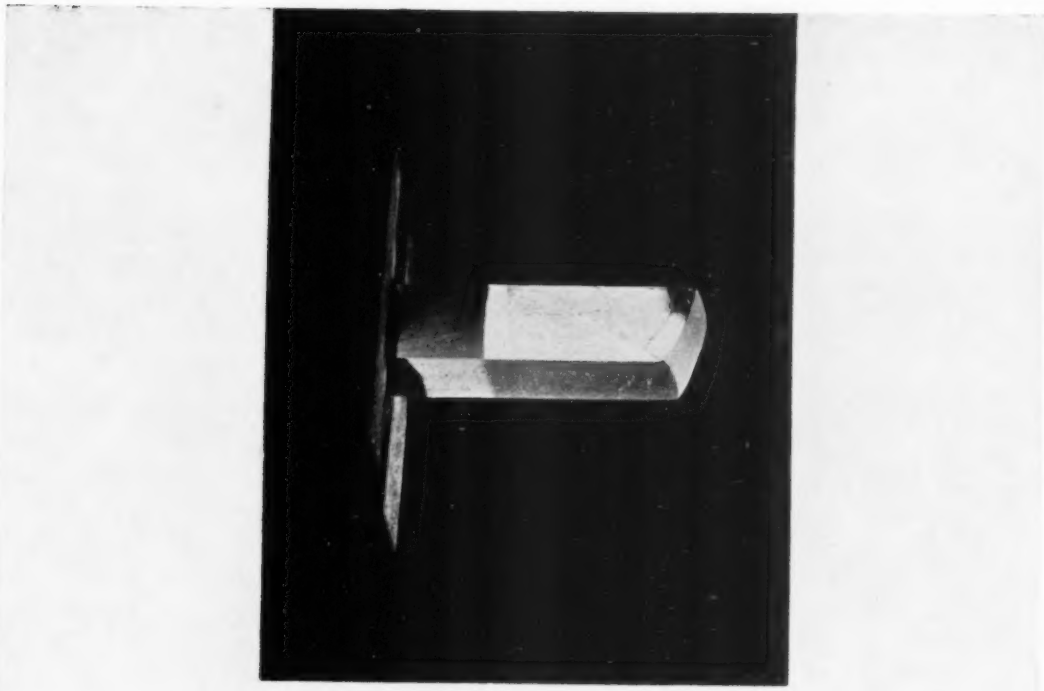

1

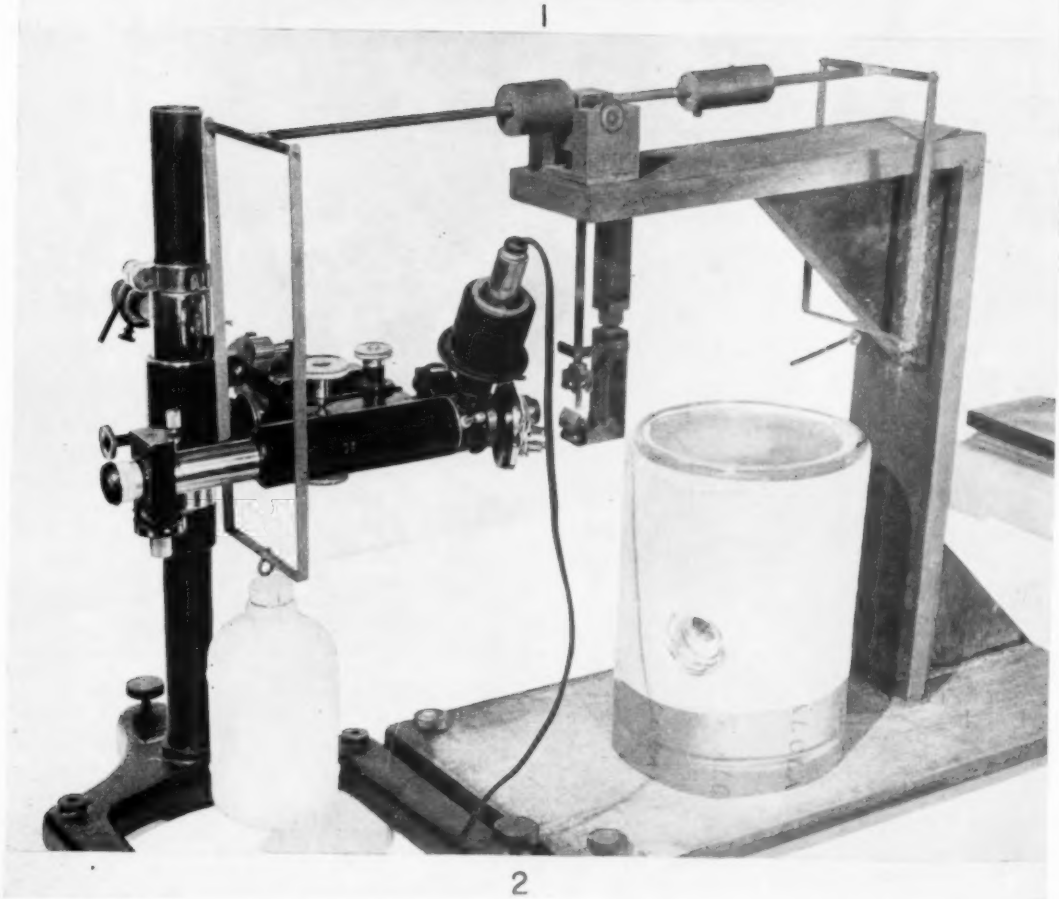

2

PLATE I. Figure 1—Macrophotograph showing a 0.73° edge dislocation boundary in a zinc crystal specimen of the type used for boundary motion studies (4×) Figure 2—Equipment used in studying the motion of small-angle boundaries in zinc crystals.

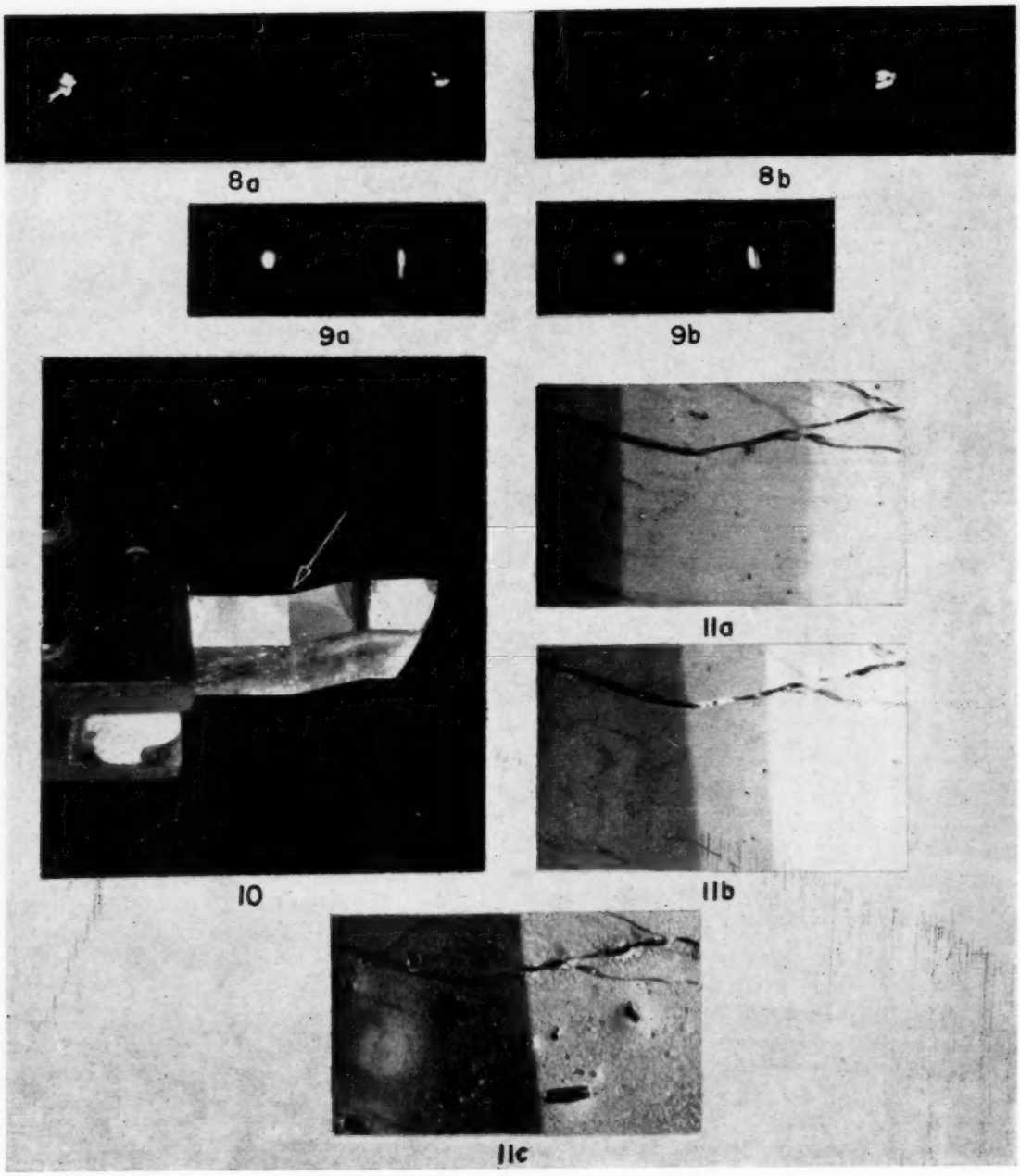

PLATE II (all figures reduced to nine-tenths in reproduction). Figure 8—Photogoniographs from a dislocation boundary showing that the decrease in the boundary angle from 1.26° to 0.63° after a displacement of 0.25 mm at 25°C was accompanied by a dissociation of the boundary into a number of smaller angle boundaries. (1 inch = 30 minutes.) (*a*) Before motion of the boundary. (*b*) After motion of the boundary. Figure 9—Photogoniographs from a 0.89° dislocation boundary showing that the character of the boundary essentially was unchanged after a 0.50 mm displacement at 375°C. (1 inch = 1°.) (*a*) Before motion of the boundary. (*b*) After motion of the boundary. Figure 10—Macrograph showing a 15° boundary developed from a 1° boundary by trapping dislocations generated within the crystal during rapid loading at 375°C. (4×) Figure 11—Micrographs showing union of boundaries of like sign as a result of motion of both boundaries during an anneal at 400°C. (200×) (*a*) Before motion of the boundaries. (*b*) Positions of the boundaries after 5 minutes at 400°C. (*c*) Union of the boundaries after 20 minutes at 400°C.

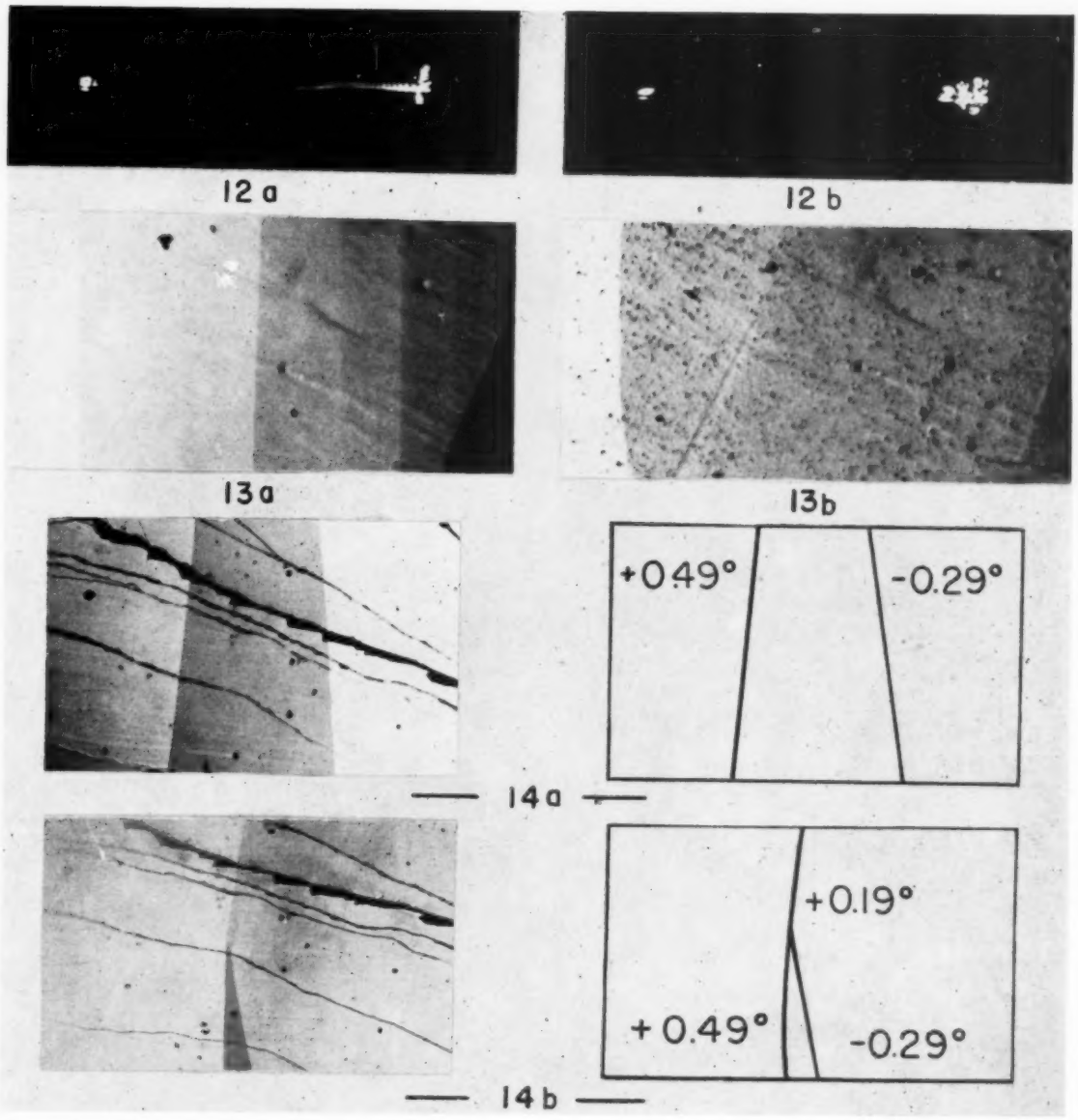

PLATE III. Figure 12—Photogoniographs showing that an apparently curved region of a crystal becomes planar during an anneal at 375°C. (1 inch = 30 minutes.) (*a*) Initial array. (*b*) After 5 minutes at 375°C. Figure 13—Stress-induced union of boundaries of like sign in a zinc crystal at −196°C. (400×) (*a*) Before motion of the boundaries. (*b*) After motion of the boundaries. Figure 14—Stress-induced union of boundaries of unlike sign at 375°C under a constant shear stress of 10 psi. (200×) (*a*) Before motion of boundaries. (*b*) After motion of boundaries.

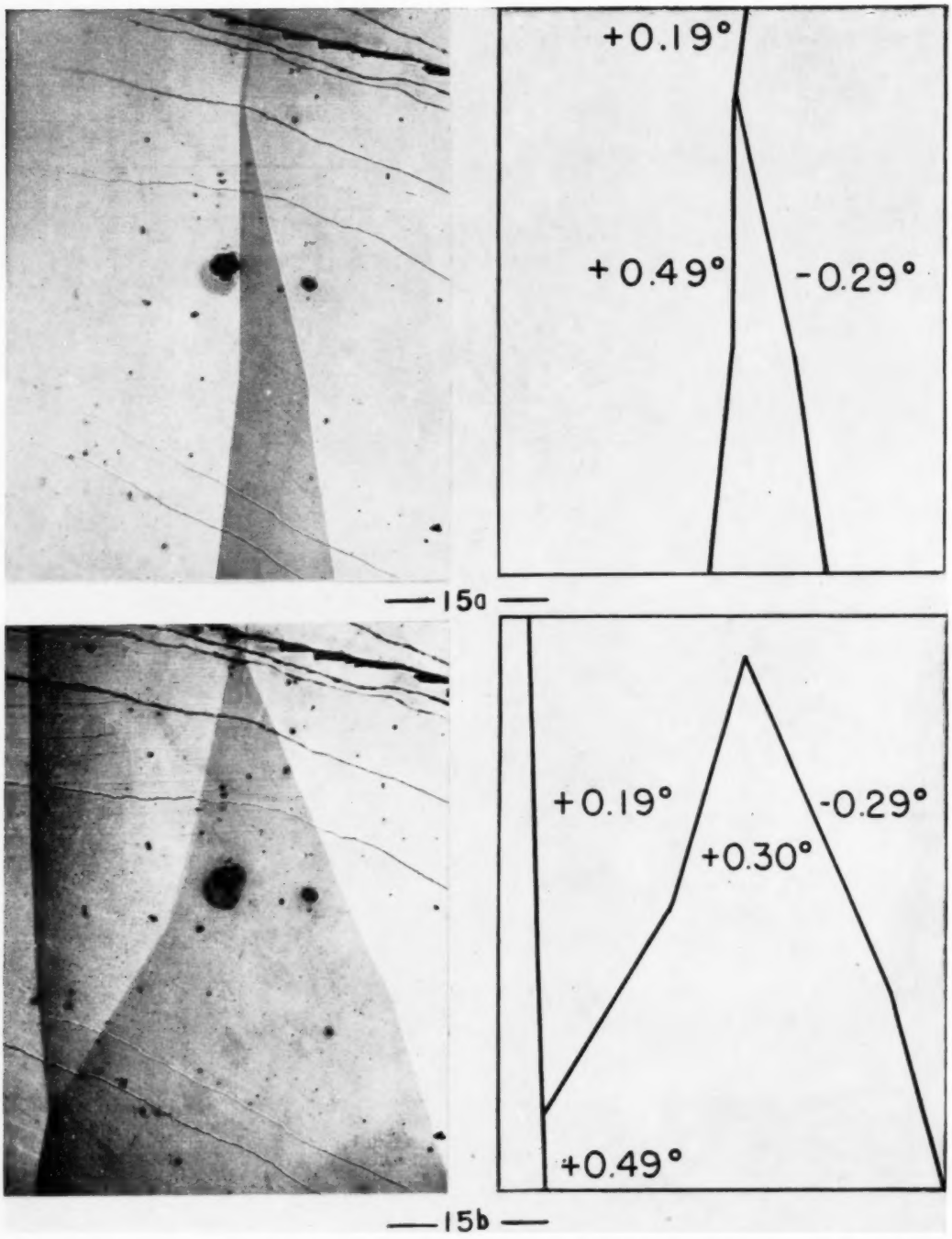

PLATE IV. Figure 15—Effect of reversing the direction of applied stress at 375°C on the motion of the boundaries shown in Figure 14. The +0.19° boundary formed previously by the stress-induced union of the −0.29° and +0.49° boundaries did not separate into these component boundaries. The continued motion of the +0.19° boundary caused the +0.49° boundary to split into +0.19° and +0.30° components. (200×) (*a*) Before reversing the direction of applied stress (see Fig. 14b). (*b*) After reversing the direction of applied stress.

elevated temperatures. Neither creep under constant load as at high temperatures nor sudden jumps over appreciable distances as at room temperature were observed. Motion appeared to be steady when viewed at 50 diameters magnification and a continuously increasing stress was necessary to cause movement to continue. As at room temperature, the boundaries behaved somewhat erratically; changed character during motion, and occasionally refused to move even though the load was continuously increased.

B. *Similarities Between Simple Shear Deformation and Boundary Motion*

A comparison of the deformation of single crystals in simple shear with the motion of edge dislocation boundaries revealed some remarkable similarities. Single crystals of zinc tested at elevated temperatures exhibited steady-state creep characterized by a process having an activation energy of 20,000 cal/mole. This compared favorably with the activation energy for steady state boundary motion noted in the same temperature range.

Creep tests in simple shear on single crystals at room temperature showed that extension frequently occurred in a succession of sudden jumps. This phenomenon is apparently related to the jump-like behavior observed for boundaries at this temperature. Jerky motion of dislocation arrays lends strong experimental support to the concept of interlocking of dislocations with immobile lattice imperfections.

The shear stress for motion of a dislocation array increases with decreasing temperature in a parallel fashion to the increase in critical stress for slip. The stress-strain curve for a single crystal tested in simple shear at liquid nitrogen temperature is given in Figure 6. The stress-displacement curve of a 1-degree boundary obtained at the same temperature is shown in Figure 7. In both cases a continuous increase in stress was necessary to maintain a constant displacement rate.

C. *Changes in a Boundary as a Result of Motion*

A dislocation array in a zinc crystal will be able to assume a low-energy configuration in a relatively short time at 400°C because of rapid diffusion. Edge dislocations of like sign should distribute themselves into a fairly uniform planar array approximately at right angles to the slip vector of the dislocations. The degree of perfection which such a boundary array can attain is difficult to estimate, but it was assumed that after annealing the boundary angle was a reasonably accurate measure of the spacings of dislocations in the array.

When such a boundary is forced to move through the crystal by application of an external stress, the dislocations comprising the boundary presumably encounter obstacles; for example, immobile dislocation segments forming parts of a mosaic network. There is a possibility that during motion of the boundary, some of the dislocations in the array will interact strongly enough with immobile lattice imperfections so as to be left behind the moving array. In this event the boundary angle should decrease during motion. This was actually found to be the case. As shown by the goniographs of Figure 8, when a boundary was moved about 0.25 mm at room temperature, the angle of the boundary decreased from 1.26° to 0.63°. Similar behavior was observed for motion at liquid nitrogen temperature. Despite the decrease in angular magnitude of the boundary, the stress necessary to move the boundary continued to increase. It is not yet possible to choose between numerous possible explanations for this continuous increase in stress. However, a few of the possibilities might be: increase in the number of steps in the dislocation lines due to intersections with screw dislocation segments; back stresses attributable to trapped dislocations in the strained material through which the array has moved; increase in total density of dislocations in the boundary due to trapping of equal numbers of positive and negative dislocations generated in the bulk of the crystal during the test. The last possibility arises from the fact that the stress required for boundary movement is comparable to the yield stress of the crystal.

At high temperatures (300–400°C) the boundary angle did not change during motion. This fact is illustrated by the goniographs of Figure 9. In addition, in this temperature range the boundary continued to move at a constant rate under constant applied shear stress. This indicates that at temperatures where rapid diffusion is possible, any changes in the structure of the boundary and in the strained material through which it has passed can be continuously removed by a diffusion process. Trapped dislocations may be able to escape from immobile obstacles, and positive and negative dislocations captured by the boundary may annihilate each other by the mechanism of climb suggested by Mott [7]. Thus at higher temperatures the boundary can be pictured as maintaining a more or less constant structure during motion.

D. *Boundaries as Barriers to Moving Dislocations*

Frequently at liquid-nitrogen temperatures or upon rapid loading at higher temperatures, a small-

angle boundary was observed to act as a very effective barrier against the motion of other dislocations. Figure 10 shows a specimen which originally contained a 1-degree boundary at the center. Rapid loading at 375°C caused general slip to begin in the region of the specimen between the boundary and the place the load was applied. The bending resulting from this slip, however, was not general along the length of the specimen. As may be seen in the figure, bending occurred at the boundary near the center of the specimen; the angle of the boundary increased to 15 degrees. This behavior clearly indicates the ability of a small-angle boundary to act as a trap for moving dislocations. The specimen also contained another large angle boundary at the place the load was applied. Dislocations collected here because the shear stress fell rapidly from a high value to zero at this location.

E. *Union of Dislocation Boundaries*

When a number of small angle boundaries lie in proximity to one another in a zinc crystal, they may be made to join together by annealing to produce a single boundary having an angle equal to the sum of those of the individual boundaries. Figure 11 shows the union of two boundaries resulting from a 20-minute anneal at 400°C. It has also been observed that a "curved" region of the crystal near a boundary tends to straighten out and become flat during annealing. The goniographs of Figure 12 show that the total angle remained constant. It is apparent that the union of boundaries reduces the strain energy of the crystal.

Dislocation boundaries of like sign can be made to unite by the application of a stress, even at low temperatures. Figure 13 shows nine closely spaced boundaries which were brought together at liquid-nitrogen temperatures by a gradually increasing stress. The total angle of tilt was not changed by the unification. This stress-induced union of boundaries in the absence of thermal activation provides a mechanism for the building up of a substructure during deformation even at low temperatures.

It also was possible to unite boundaries of *unlike* sign both at high and low temperatures. The union of two such boundaries, shown in Figure 14, was brought about by application of a constant stress at 375°C. The +0.49° boundary to the left and the −0.29° boundary to the right in Figure 14a joined to form the +.19° boundary shown in Figure 14b. Although it has been observed that partially united boundaries of like sign may be separated again by a reversal of the applied stress, this has not been found to be true for partially joined boundaries of unlike sign (Fig. 15). These experimental observations imply that the bringing-together of dislocations of opposite sign can result in their annihilation.

Summary

Arrays of edge dislocations which produce low angle boundaries in zinc single crystals can be made to move by the application of an appropriate shear stress at temperatures from −196°C to 400°C. Continued motion at −196°C required the application of a steadily increasing stress. At room temperature the movement was discontinuous; during each advance, the boundary moved very rapidly through an appreciable volume of material. In contrast, at elevated temperature motion was steady and a thermally activated "creep" process seemed to predominate.

The deformation of zinc in simple shear showed characteristics very similar to those of moving boundaries at the same test temperatures. This implies that the propagation of dislocations rather than their generation may be the factor which determines the yield strength of zinc crystals.

During the motion of a boundary at elevated temperature, (300°–400°C), the boundary angle remained constant; at low temperatures the boundary changed in character both with regard to angle and regularity. Diffusion presumably assisted in overcoming barriers at the high temperatures so that the boundary could move as an integral unit. At low temperatures, however, portions of the boundary appeared to become trapped or were forced to assume more complex shapes through interaction with other structural defects.

Small-angle boundaries of like sign in proximity to one another coalesced during short-time annealing treatments at 400°C to form a single boundary. "Curved" boundaries tended to become planar and perpendicular to the slip direction as a result of such treatment. Closely spaced boundaries of like sign were observed to join at −196°C upon the application of a stress, thus establishing a mechanism for the development of substructure in the absence of thermal migration of dislocations. Boundaries of unlike sign were also made to join by means of stress at both high and low temperatures. The angle of a boundary resulting from the union of boundaries of opposite sign at elevated

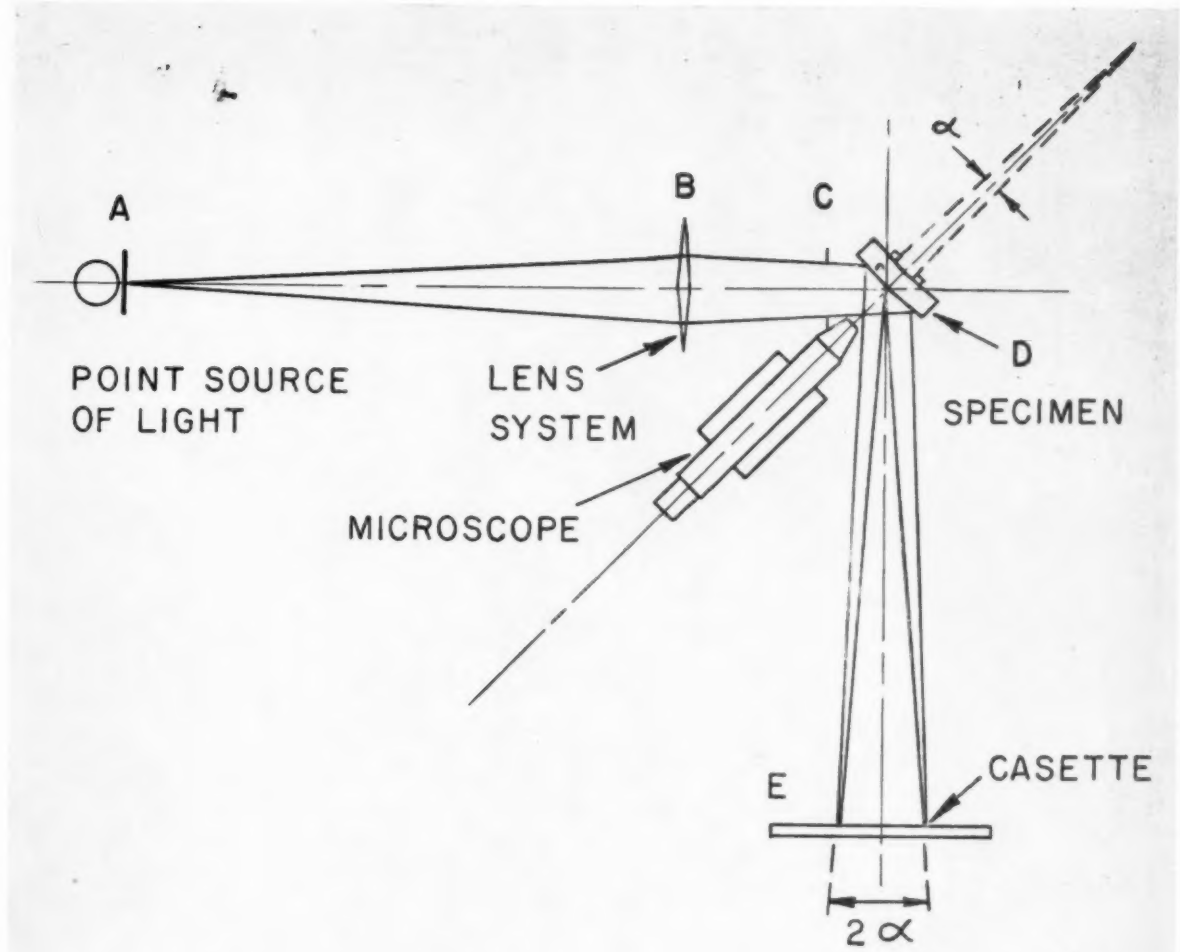

16

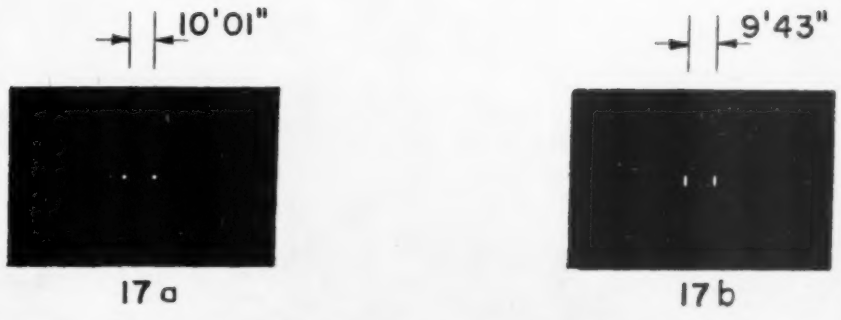

17 a 17 b

PLATE V. Figure 16—Schematic diagram of optical goniograph. Figure 17—Photogoniographs from mirror tilted through a small angle α. (Actual size.) (*a*) Circular aperture 2.54 mm diameter at reflector. (*b*) Slit perpendicular to axis of rotation 0.2 × 1.5 mm at reflector.

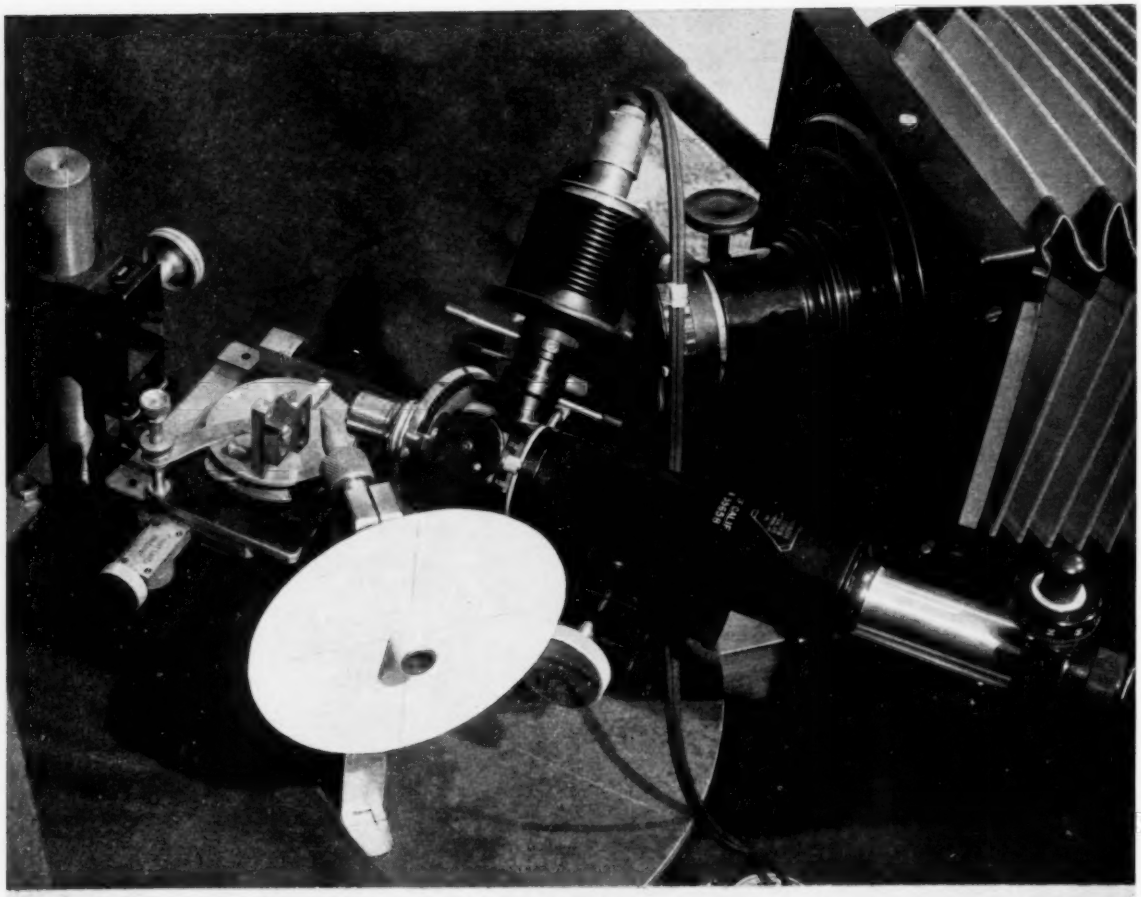

18

PLATE VI. Figure 18—Specimen stage of optical goniograph showing crystal in position for boundary-angle measurements.

temperatures was in accord with theoretical predictions that dislocations of opposite sign can be mutually destructive.

Acknowledgment

This investigation was sponsored by the Office of Naval Research. The authors desire to express their appreciation to the members of the ONR staff and, in particular, Julius Harwood for their continued interest and support. The authors gratefully acknowledge the many constructive suggestions of Jack Washburn and Earl R. Parker and the assistance of L. O. Seaborn and W. R. Arneson in the construction of the apparatus.

APPENDIX

Measurement of Small Angle Boundaries with an Optical Goniograph

For the purpose of determining the magnitude of the boundary angles in zinc, a goniograph employing optical reflection from the cleavage plane was used. The apparatus is shown schematically in Figure 16. An intense light source emanating from a pinhole at "A" was focused by means of a long focal length lens at "B" upon a plane ground glass or photographic film at "E" after approximately 90 degree reflection from a mirror surface, "D". The focused spot at the position of the film thus had the shape of the pinhole source. The position of this focused spot depended only upon the angle of tilt of the mirror and was otherwise independent of the position or extent of the mirror in space, provided that the reflecting plane passed through the point of intersection of the instruments optical axes.

Two reflecting planes differing in orientation by an angle of rotation γ about an axis perpendicular to the incident beam give rise to reflections differing by 2γ. Similar planes differing in orientation by an angle γ' about the incident axis yield reflections separated by the same angle γ'.

In practice, a lens system with an effective focal length of 175 cm was employed in conjunction with a specimen to film distance of 72 cm. The focal spot was sufficiently large under these conditions to permit the film to be examined satisfactorily without magnification. A resolution of 0.008 degrees was obtained with an optically flat mirror reflecting a 0.2-degree cone of light (2.54 mm diameter cross section at mirror). It was considered desirable to be able to limit the reflecting region of the specimen such, for example, that variations in orientation, etc., occurring along a boundary might be evaluated. For this purpose, a mount was supplied at "C," Figure 16, in which slits or other apertures could be positioned. A slit 0.2 mm $\times$ 1.5 mm decreased the resolution considerably in a direction perpendicular to the slit, as shown in Figure 17b, but essentially maintained the resolution in the plane of the slit. By positioning the slit and specimen such that the slit axis and the Burgers vector of edge dislocations comprising the boundary were both in the reflection plane, optimum resolution in the desired direction was maintained. A 0.2 mm length of boundary was thus required for the angle measurements.

Alignment of a specimen in the goniograph was accomplished by means of a microscope whose axis bisected the optical axes of the instrument. This microscope was arranged to focus permanently on the axial intersection of the goniograph. The focus established the correct plane while the eye-piece cross-hairs fixed the axial intersection. A specimen to be studied was brought into position by means of a three-coordinate translation device in conjunction with three leveling screws for rotational adjustment. The portion of the goniograph in the vicinity of the specimen is shown photographically in Figure 18.

Reflections from zinc cleavage surfaces occasionally approached the perfection shown by the mirror but generally were considerably more complicated. In some instances this could be at least partly attributed to cleavage faults. In other cases, double curvatures of the reflecting plane were present in the vicinity of the boundary, indicating the presence of complex arrays of dislocations in the specimen.

References

1. BURGERS, J. M. Proc. Phys. Soc. (Lond.) **52** (1940) 23.
2. SHOCKLEY, W. and READ, W. T. Phys. Rev. **75** (1949) 692.
3. WASHBURN, J. and PARKER, E. R. Trans. A.I.M.E. **194** (1952) 1076.
4. LI, C. H., EDWARDS, E. H., WASHBURN, J. and PARKER, E. R. Acta Met. **1** (1953) 223.
5. EDWARDS, E. H., WASHBURN, J., and PARKER, E. R. Trans. A.I.M.E., T.P. 3645E.
6. PARKER, E. R. and WASHBURN, J. Modern Research Techniques in Physical Metallurgy (ASM 1953) 186.
7. MOTT, N. F. Proc. Phys. Soc. (B) **64** (1951) 729.

ON THE ENERGETICS OF ALKALI HALIDE SOLID SOLUTIONS*

VÄINÖ HOVI†

Heats of formation and of evolution are calculated on the basis of Wasastjerna's statistical theory for such binary alkali halide solid solutions, in which the difference between the interionic equilibrium distances of the components, ΔR, is equal or smaller than that in the case of NaCl-NaBr. The theoretical heat of formation data corresponding to the equilibrium at 50°C in the case of NaCl-NaBr, KCl-KBr, KCl-RbCl, RbCl-RbBr, KBr-RbBr, and KI-RbI are at the same composition closely proportional to the expression $(\Delta R)^2/R_0^3$, where R_0 is the interionic distance of the solid solution. The theoretical heats of formation are in good agreement with the available experimental data. An earlier experimental observation [1] concerning the proportionality above mentioned is supported by the theoretical results of the present paper.

SUR L'ÉNERGÉTIQUE DE SOLUTIONS SOLIDES DES HALOGÈNES ALCALINS

Les chaleurs de formation et d'évolution sont calculées en se basant sur la théorie statistique de Wasastjerna concernant ce genre de solutions solides d'halogènes alcalins, dans lesquels la différence entre les distances d'équilibre entre les ions des composants, ΔR, est égale ou inférieure à la même différence dans le cas NaCl-NaBr. Les données sur la chaleur théorique de formation correspondant à l'équilibre à 50°C pour NaCl-NaBr, KCl-KBr, KCl-RbCl, RbCl-RbBr, KBr-RbBr et KI-RbI sont à la même composition approximativement proportionnelles à l'expression $(\Delta R)^2/R_0^3$, où R_0 est la distance entre les ions de la solution solide.

Les chaleurs théoriques de formation s'accordent bien avec les données expérimentales, disponibles. Une observation expérimentale, antérieure [1], concernant la proportionnalité mentionnée ci-dessus est supportée par les résultats du présent article.

DIE ENERGETIK FESTER ALKALIHALOGENIDLÖSUNGEN

Die Bildungswärmen und Wärmetönungen wurden im Rahmen der statistischen Theorie von Wasastjerna für binäre feste Alkalihalogenidlösungen, in denen die Differenz der Ionen-Gleichgewichtsabstände der Komponenten, ΔR, kleiner oder gleich der im System NaCl-NaBr ist, berechnet. Die theoretischen Werte der Bildungswärmen, bezogen auf Gleichgewicht bei 50°C, sind für NaCl-NaBr; KCl-KBr; KCl-RbCl; RbCl-RbBr; KBr-RbBr und KI-RbI der gleichen Zusammensetzung dem Ausdruck $(\Delta R)^2/R_0^3$ nahezu proportional, wobei R_0 der Ionenabstand in der festen Lösung ist. Die theoretischen Werte der Bildungswärmen stimmen gut mit den vorliegenden experimentellen Daten überein. Eine früher berichtete experimentelle Beobachtung [1] der oben erwähnten Proportionalität wird durch die hier abgeleiteten theoretischen Resultate gestützt.

Introduction

It was shown in a previous paper [1] that the *experimental* heat of formation values of the 50 mole per cent NaCl-NaBr, KCl-KBr, and KCl-RbCl solid solutions are approximately proportional to the expression $(\Delta R)^2/R_0^3$. Here $\Delta R = R_2 - R_1$ $(R_2 > R_1)$ denotes the difference between the interionic equilibrium distances of the components, while R_0 is the interionic equilibrium distance of the solid solution.

The object of the present paper is to re-examine this proportionality. At this time we consider, however, in the first place *theoretical* heat of formation data found by means of Wasastjerna's statistical theory [2–6] for such binary alkali halide solid solutions, in which the quantity ΔR is equal or smaller than in the case of NaCl-NaBr [7, p. 358]. According to the experiments [8; 9] this combination ought to form a complete series of solid solutions at 50°C. When taking into account the available experimental results [10–15], and neglecting the influence of the atmospheric moisture which may be regarded as a secondary factor, we thus may with good reason assume that *all* the solid solutions considered in this investigation can exist at 50°C as a stable state at every composition. In order to obtain thermodynamically with one another comparable data, all the heats of formation were calculated for the equilibrium at that temperature. Theoretical heats of formation were compared with the available experimental data. Furthermore, numerical values were estimated in each case for the energy evolved during the transition of the solid solution from a completely disordered state to that of local order at 50°C.

Heats of Formation and of Evolution

On the basis of his X-ray data [16; 17; 18; 19] Wasastjerna suggested that the actual equilibrium positions of the ions in a KCl-KBr and KCl-RbCl mixed crystal lattice do not coincide with the corresponding positions of an ideal lattice. The lattice of these mixed crystals is characterized by a geometrical long range disturbance, which causes a certain mean displacement of all ions from their theoretical equilibrium positions, and by a superimposed local displacement caused by the asym-

*Received November 3, 1953.
†University of Turku, Turku, Finland.

metry among the immediate neighbouring ions. As shown by Wasastjerna, these displacements give rise in the mixed lattice to a certain degree of local order of ions, which maximizes the thermodynamical probability of the whole system.

It might be reason to mention here that independently of Wasastjerna, Lawson [20] later perceived the analogical phenomenon in his distortion energy calculations for binary *metallic* solid solutions.

For the calculations of the heats of formation and of evolution we assume that the ion displacement phenomenon and the ordering state of the mixed lattice in *all* our cases are similar to those of KCl-KBr and KCl-RbCl solid solutions. Thus, we may calculate the heats of formation from the formula [5]

$$(1) \qquad Q_{IV} = Q_I \left\{ \frac{\vartheta_1}{8}(1 + \sigma(1 - 4q)) + \frac{\vartheta_2}{8}(1 + \sigma(1 - 4p)) + \frac{1 + \sigma}{2} \right\},$$

and the heats of evolution from the formula [21]

$$(2) \qquad \Delta Q = \frac{\sigma Q_I}{8}\theta.$$

In these formulae

$$Q_I = \frac{NCe^2}{R_0} pq \left(\frac{\Delta R}{R_0}\right)^2$$

is the electrostatic part of the heat of formation, while Q_{IV} denotes the heat of formation when the geometrical displacements of the ions are taken into account and the lattice is assumed to be characterized by a certain degree of local order (σ). N stands for Avogadro's number, C for $c\alpha^2$, where c is Madelung's constant and α the ionic charge expressed in elementary units, e for the charge of an electron, p and q for the mole fraction of the components ($p + q = 1$), and ϑ for the characteristic constant defined by Wasastjerna's [22] equation

$$(3) \qquad \frac{-R_\nu \phi_\nu''(R_\nu)}{\phi_\nu'(R_\nu)} = \vartheta_\nu + 2, \qquad (\nu = 1, 2)$$

where $\phi_\nu'(R_\nu)$ and $\phi_\nu''(R_\nu)$ are derivatives of the exchange energies. ΔQ represents the energy evolved from a mixed crystal which transits from a completely disordered state to another, which corresponds to the degree of local order, σ, and θ is the abbreviation $\theta = -(\vartheta_1(1 - 4q) + \vartheta_2(1 - 4p) + 4)$.

Restricting ourselves to the binary cases MX-MY and M_1Z-M_2Z, where M, M_1, and M_2 denote positive, and X, Y, and Z negative ions, respectively, we may use the same method of reasoning as Wasastjerna [2]. Thus, if the lattice is characterized by a certain degree of local order, the probabilities χ, λ, μ, ν of finding a M (or Z) ion surrounded by XX, XY, YX, and YY (or M_1M_1, M_1M_2, M_2M_1, and M_2M_2) respectively in the positive directions of the axes are as follows:

$$(4) \qquad \begin{cases} \chi = p(p - q\sigma), \\ \lambda = pq(1 + \sigma), \\ \mu = qp(1 + \sigma), \\ \nu = q(q - p\sigma). \end{cases}$$

The parameter σ is called here the degree of local order.

When writing the configurational factor Γ of the partition function as follows:

$$(5) \qquad \Gamma(T, \sigma) = g(N, p, z, \sigma) \exp \frac{\Delta Q}{kT},$$

and using for the combinatory number, g, Wasastjerna's expression [2],

$$(6) \qquad g(N, p, z, \sigma) = \left(\frac{p^p q^q}{\chi^\chi \lambda^\lambda \mu^\mu \nu^\nu}\right)^N,$$

we obtain the values of σ, maximizing the configurational partition function, for different crystal compositions from the condition $\partial\Gamma/\partial\sigma = 0$, after the characteristic constants have been calculated from the equation [22]

$$(7) \qquad \vartheta = \frac{3 + 4T\gamma}{K_T \frac{Ce^2}{6R^4} - T\gamma}.$$

Here K_T is the coefficient of compressibility of a cubic-face-centered lattice, while γ stands for the cubic expansion coefficient at constant pressure.

In the numerical calculations for the atomic constants, the following values were used: $N = 6{,}0235.10^{23}$, $e = 4{,}8024.10^{-10}$ esu, and $k = 1{,}38032.10^{-16}$ erg. degree^{-1} [23]. For Madelung's constant, $c = 1{,}7476$, and for the energy equivalent 0,23899 cals/joule were taken. The interionic equilibrium distances of the most salts at 50°C (Table I) were determined by means of the corresponding densities from the interionic distances at 0°C [24] and 25°C [15]. The densities of NaCl we obtained by the graphical method of closest fit from the experimental results in the papers [25; 26; 27]. Similarly, the densities of NaBr we estimated from the data in [25; 27]. For KCl, KBr and RbCl the same quantities were calculated from the density equations determined by the method of the least squares from the experimental values in [28], [29]

and [30] respectively. For RbBr the densities at 25° and 50°C we obtained from [27] and [25]. The interionic distances of KI and RbI were estimated by means of the cubic expansion coefficients from the X-ray results appearing in [15] and [31].

The interionic distances of the solid solutions at 50°C were calculated from the corresponding values of the components according to Vegard's rule.

The initial compressibilities, measured at 30°C by Bridgman [32], were reduced to 50°C in the way presented in [21] using for the temperature coefficient of the compressibility the values appearing in [22].

The values of the cubic expansion coefficient of the components were determined graphically, for 50°C, from the experimental data of the papers [33; 25; 27; 34; 35; 15; 31].

Table I contains the values of some physical quantities used in our calculations. This table also

TABLE I

Salt	Interionic equilibrium distance at 50°C in Å-units	Compressibility coefficient $\times 10^{12}$ in bar^{-1} at 30°C	Compressibility coefficient $\times 10^{12}$ in bar^{-1} at 50°C	Cubic expansion coefficient $\times 10^5$ at 50°C	ϑ
NaCl	$2{,}816_8$	$4{,}26_1$	$4{,}29_5$	$12{,}1_4$	$7{,}53_1$
NaBr	$2{,}983_8$	$5{,}07_8$	$5{,}12_7$	$12{,}4_8$	$8{,}02_9$
KCl	$3{,}142_7$	$5{,}62_7$	$5{,}68_4$	$11{,}3_9$	$8{,}87_6$
KBr	$3{,}295_8$	$6{,}69_7$	$6{,}76_4$	$11{,}3_2$	$9{,}02_8$
KI	$3{,}529_2$	$8{,}53_2$	$8{,}63_5$	$10{,}9_9$	$9{,}28_5$
RbCl	$3{,}287_6$	$6{,}64_6$	$6{,}71_3$	$12{,}0_8$	$9{,}08_8$
RbBr	$3{,}437_1$	$7{,}93_1$	$8{,}01_1$	$10{,}9_2$	$8{,}96_7$
RbI	$3{,}666_2$	$9{,}56_2$	$9{,}67_7$	$12{,}7_0$	$9{,}92_7$

presents the values obtained for the ϑ-quantities of the component salts at 50°C.

In Table II are compiled the values of σ, Q_{I}, Q_{IV} and ΔQ for different alkali halide solid solutions. For the purposes of comparison the available experimental heat of formation values, Q_{exp}, are included in the same table. Figure 1 shows the heat of formation as a function of crystal composition at 50°C for the case of RbCl-RbBr, KBr-RbBr, and KI-RbI. The writer has found no satisfactory experimental or theoretical examination dealing with heat of formation data of these solid solutions.

The heat of formation is represented as a function of $(\Delta R)^2/R_0^3$ in Figure 2. The numbers in connection of each curve indicate the same mole fraction of the lighter component. As seen from this figure, the points corresponding to the values of the heat of formation of the same crystal composition at 50°C lie very nearly in straights. Only in the case of NaCl-NaBr slight deviations from the linearity seem to appear. As an explanation for this it may be pointed out that according to experiments [8, 9] the NaCl-NaBr mixed crystals form a borderline case of the alkali halide solid solutions

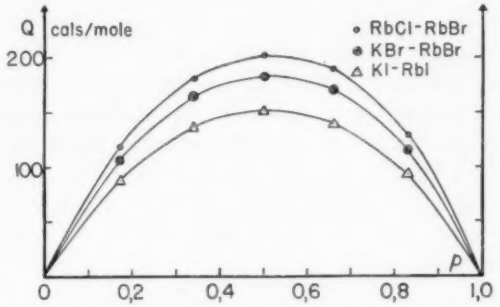

FIGURE 1. The heat of formation as a function of crystal composition at 50°C in the case of RbCl-RbBr, KBr-RbBr, and KI-RbI solid solutions according to Wasastjerna's theory.

stable in the neighbourhood of room temperature. The situation, especially the state of order of this mixed lattice, thus may be more complicated than that of the more stable KCl-KBr and KCl-RbCl solid solutions, and in this way, the premises of Wasastjerna's theory less completely fulfilled.* There may be reason to mention here that the case of NaCl-KCl, for which the expression $10^4(\Delta R)^2/R_0^3 \simeq 40$ Å^{-1}, falls far outside of the alkali halide solid-solution region considered in this paper. The decomposition processes of this particular case have been studied recently by Hyvönen [40], and by Scheil and Stadelmaier [41]. Hyvönen measured directly by means of a calorimetric precision method heats of evolution for some NaCl-KCl solid solutions prepared in different ways, and determined from his experimental data the activation energy. The latter investigators calculated the same quantity on the basis of light absorption measurements.

Table III presents the values obtained for the differences between the electrostatic parts of the heat of formation of the sequent solid solutions. In this table also the differences between the fourth approximations of the heat of formation are included, while the quotients of the differences appear in the edge column. As seen from these values, the quotient $\Delta Q_{\mathrm{IV}}/\Delta Q_{\mathrm{I}}$ is approximately constant $(= 2)$.

Summing up what has been said above, it can be stated that Wasastjerna's theory, when applied

*The experimental verification is in progress at the University of Helsinki.

TABLE II

Solid solution	Mole fraction of the lighter component p	Degree of local order σ	Electrostatic part Q_I (cals/mole)	Heat of formation (cals/mole) Q_{IV}	Heat of formation (cals/mole) Q_{exp}	Heat of evolution ΔQ (cals/mole)
NaCl-	0,17	$0{,}133_4$	88,7	201	181*	16,1
NaBr	0,34	$0{,}277_0$	145,2	298	294	56,5
	0,50	$0{,}357_2$	166,2	321	335	85,7
	0,66	$0{,}301_9$	153,4	306	308	68,7
	0,83	$0{,}152_0$	99,4	220	198	23,0
KCl-	0,17	$0{,}112_9$	54,9	140	136†; 121‡	10,6
KBr	0,34	$0{,}219_2$	89,4	211	213 ; 201	33,8
	0,50	$0{,}269_0$	101,9	231	234 ; 232	47,6
	0,66	$0{,}230_8$	93,6	218	206 ; 216	37,8
	0,83	$0{,}122_8$	60,3	152	127 ; 141	13,1
KCl-	0,17	$0{,}104_7$	49,5	127	119¶	8,9
RbCl	0,34	$0{,}200_1$	80,5	193	197	27,8
	0,50	$0{,}244_0$	91,6	213	217	39,0
	0,66	$0{,}211_5$	84,1	199	199	31,3
	0,83	$0{,}114_8$	54,1	137	138	11,1
RbCl-	0,17	$0{,}101_8$	46,1	119		8,3
RbBr	0,34	$0{,}191_4$	74,9	181		25,3
	0,50	$0{,}229_1$	85,3	201		34,3
	0,66	$0{,}196_9$	78,2	189		26,9
	0,83	$0{,}107_0$	50,3	129		9,3
KBr-	0,17	$0{,}092_6$	41,1	106		6,7
RbBr	0,34	$0{,}171_2$	66,8	164		20,1
	0,50	$0{,}203_8$	75,9	182		27,1
	0,66	$0{,}176_9$	69,5	170		21,5
	0,83	$0{,}097_9$	44,7	115		7,6
KI-	0,17	$0{,}076_4$	31,8	88		4,4
RbI	0,34	$0{,}141_7$	51,6	136		13,5
	0,50	$0{,}171_6$	58,5	151		19,1
	0,66	$0{,}154_0$	53,5	139		16,1
	0,83	$0{,}089_1$	34,3	93		6,1

*Calculated from the interpolation polynom of Fineman and Wallace [36].
†From the interpolation polynom of Hovi [37].
‡From the interpolation polynom recalculated by Wallace and Fineman [38] on the basis of Fontell's experimental data [39].
¶Experimental data by Fontell, Hovi and Hyvönen [1].

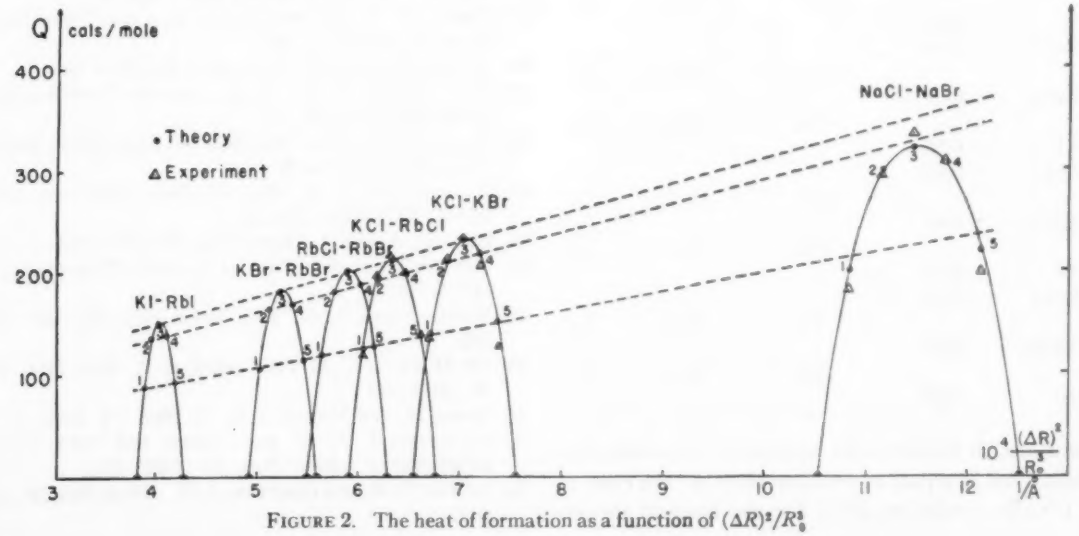

FIGURE 2. The heat of formation as a function of $(\Delta R)^2/R_0^2$

TABLE III

Solid solution	Mole fraction of the lighter component p	Difference between the electrostatic parts ΔQ_I (cals/mole)	Difference between the heats of formation ΔQ_{IV} (cals/mole)	ΔQ_{IV} / ΔQ_I
NaCl-NaBr	0,17			
		33,8	60,9	1,8
KCl-KBr	0,17			
		8,8	21,0	2,4
RbCl-RbBr	0,17			
NaCl-NaBr	0,34			
		55,8	87,3	1,6
KCl-KBr	0,34			
		14,5	29,7	2,0
RbCl-RbBr	0,34			
NaCl-NaBr	0,50			
		64,3	89,1	1,4
KCl-KBr	0,50			
		16,6	30,6	1,8
RbCl-RbBr	0,50			
NaCl-NaBr	0,66			
		59,8	87,7	1,5
KCl-KBr	0,66			
		15,4	29,8	1,9
RbCl-RbBr	0,66			
NaCl-NaBr	0,83			
		39,1	67,7	1,7
KCl-KBr	0,83			
		10,0	22,7	2,3
RbCl-RbBr	0,83			
KCl-RbCl	0,17			
		8,4	20,7	2,4
KBr-RbBr	0,17			
		9,3	18,3	2,0
KI-RbI	0,17			
KCl-RbCl	0,34			
		13,7	29,6	2,2
KBr-RbBr	0,34			
		15,2	27,3	1,8
KI-RbI	0,34			
KCl-RbCl	0,50			
		15,7	30,9	2,0
KBr-RbBr	0,50			
		17,4	30,8	1,8
KI-RbI	0,50			
KCl-RbCl	0,66			
		14,6	29,7	2,0
KBr-RbBr	0,66			
		16,0	30,5	1,9
KI-RbI	0,66			
KCl-RbCl	0,83			
		9,4	22,2	2,4
KBr-RbBr	0,83			
		10,4	21,8	2,1
KI-RbI	0,83			

to such alkali halide solid solutions for which the quantity ΔR is equal or smaller than in the case of NaCl-NaBr, yields at 50°C for the heat of formation values which are in good agreement with available experimental data and, at different crystal composition, closely proportional to the expression $(\Delta R)^2/R_0^3$. Thus, the earlier observation [1] made on the basis of experimental data is supported by the theoretical results of the present paper.

Acknowledgements

The writer wishes to record his indebtedness to the Alfr. Kordelin Foundation and the Finnish Scientific Academy (Suomalainen Tiedeakatemia) for research scholarships.

References

1. Fontell, N., Hovi, V. and Hyvönen, L. Ann. Acad. Sci. Fenn. AI (1949) No. 65.
2. Wasastjerna, J. A. Soc. Sci. Fenn., Comment. Phys.-Math., XIV (1948) No. 3.
3. Wasastjerna, J. A. Soc. Sci. Fenn., Comment. Phys. Math., XIV (1948) No. 7.
4. Wasastjerna, J. A. Soc. Sci. Fenn., Comment. Phys.-Math., XV (1949) No. 3.
5. Hovi, V. Soc. Sci. Fenn., Comment. Phys.-Math., XV (1950) No. 12.
6. Hovi, V. Arkiv för Fysik, **5** (1952) No. 4.
7. Pauling, L. Nature of the Chemical Bond (Ithaca, New York, Cornell University Press, 1948).
8. Simons, E. L., Orlick, C. A. and Vaughan, P. A. J. Amer. Chem. Soc., **74** (1952) 5264.
9. Schobert, E. Dissertation, University of Leipzig (1912).
10. Havighurst, R. J., Mack, Jr., E. and Blake, F. C. J. Amer. Chem. Soc., **47** (1925) 29.
11. Kantola, M. State Inst. for Techn. Res., Finland (1947) No. 2.
12. Simons, E. L. and Blum, S. E. J. Amer. Chem. Soc. **73** (1951) 5717.
13. d'Ans, J. and Busch, F. Z. anorg. Chem. **232** (1937) 361.
14. Hovi, V. Suomen Kemistil. **B23** (1950) 80.
15. Thomas, E. B. and Wood, L. J. J. Amer. Chem. Soc. **56** (1934) 92; **57** (1935) 822.
16. Wasastjerna, J. A. Phys. Rev. **55** (1939) 986.
17. Wasastjerna, J. A. Kungl. Svenska Vetenskapsakad. Handl. **20** (1944) No. 11.
18. Wasastjerna, J. A. Acta Soc. Sci. Fenn., Nova Series A, Tom. III (1944) No. 8.
19. Wasastjerna, J. A. Soc. Sci. Fenn., Comment. Phys.-Math., XIII (1945) No. 5.
20. Lawson, A. W. J. Chem. Phys. **15** (1947) 831.
21. Hovi, V. Soc. Sci. Fenn., Comment. Phys.-Math., XV (1950) No. 15.
22. Wasastjerna, J. A. Phil. Trans. Roy. Soc. **237** (1938) 105.
23. Du Mond, J. W. M. and Cohen, E. R. Rev. Mod. Phys. **21** (1949) 651.
24. Born, M. and Mayer, J. E. Z. Phys. **75** (1932) 1.
25. Henglein, F. A. Z. phys. Chem. **115** (1925) 115; **117** (1925) 285; Z. Elektrochem. **31** (1925) 424.
26. de Foe, O. K. and Compton, A. H. Phys. Rev. **25** (1925) 618.

27. Baxter, G. P. and Wallace, C. C. J. Amer. Chem. Soc. **38** (1916) 265.
28. Gmelin's Handb. d. anorg. Chem., Syst. No. 22 (Kalium) 8. Aufl. (1937) 360-1.
29. *Ibid.* 521–2.
30. Gmelin's Handb. d. anorg. Chem., Syst. No. 24 (Rubidium) 8. Aufl. (1937) 138.
31. Havighurst, R. J. Z. Kryst. **64** (1926) 164.
32. Bridgman, P. W. Proc. Amer. Acad. **67** (1932) 370.
33. Buffington, R. M. and Latimer, W. M. J. Amer. Chem. Soc. **48** (1926) 2312.
34. Biltz, W., Wünnenberg, E., Fischer, W. and Sapper, A. Z. phys. Chem., **A151** (1930) 7.
35. Eucken, A. and Dannöhl, W. Z. Elektrochem. **40** (1934) 819.
36. Fineman, M. A. and Wallace, W. E. J. Amer. Chem. Soc. **70** (1948) 4165.
37. Hovi, V. Ann. Acad. Sci. Fenn. AI (1948) No. 55.
38. Wallace, W. E. and Fineman, M. A. Soc. Sci. Fenn., Comment. Phys.-Math., XIV (1948) No. 6.
39. Fontell, N. Soc. Sci. Fenn., Comment. Phys.-Math., X (1939) No. 6.
40. Hyvönen, L. J. Soc. Sci. Fenn., Comment. Phys.-Math., XVI (1952) No. 15.
41. Scheil, E. and Stadelmaier, H. Z. Metallkunde **43** (1952) 227.

The Effects of Space Charge on the Rate of Formation of Anode Films*

In a recent paper [1] data are presented for the anodic oxidation of tantalum over a range of temperatures and current densities. The data are compared with Mott and Cabrera's theory of very thin films [2]. The author reports three discrepancies: (1) the rate of change of field with logarithm of formation rate (i.e., the Tafel slope) is temperature-independent. The theory predicts a Tafel slope which is directly proportional to the absolute temperature. (2) The "frequency-factor" has the value 10^{-2} instead of 10^{12} which the theory requires. (3) The fields observed are sufficient to completely "obliterate" the barrier for diffusion.

The present note will show that the first of these discrepancies probably results from the inadequacy of the theory when applied to the tantalum oxide system while the last two result from misapplication of the theory.

The theory of Mott and Cabrera is derived on the assumption that the number of ions in transit is small and that therefore space charge makes a negligible contribution to the electric field. The result may be written:

$$(1) \qquad \bar{E} = E_0 = \frac{kT}{bq} \ln \frac{i}{m_s \nu_s} + \frac{\phi}{bq}.$$

The neglect of space charge may be valid for very thin films, but the films in question here are 1000 to 5000 Å thick and, depending upon the values of the lattice and energy parameters, these may be either "thick" or "thin" films. We arrive at this conclusion by considering the growth laws without neglecting space charge. Using a potential-energy profile identical to that of Mott and Cabrera we obtain equation (2) for the average field.†

$$(2) \quad \bar{E} = E_0 + \frac{kT}{aq}\left\{-1 + \left(1 + \frac{1}{\delta}\right) \ln (1 + \delta)\right\}$$

where

$$\delta = \left[\frac{4\pi q^2}{Kk} \frac{(m_s \nu_s)^{a/b}}{\nu}\right] \frac{D}{T} i^{(1-a/b)} \exp\left[U - \phi \frac{a}{b}\right]/kT .$$

The first term in (2) is identical to that of Mott and Cabrera and the second term is due to space charge.

The symbols in these equations have the following meanings:

$\bar{E}$ = average field across the film
$2a$ = distance between interstitial positions in the lattice
b = distance from the metal surface to the first potential barrier
q = charge on the mobile ion
D = film thickness
i = current density (formation rate)
K = dielectric constant of film
k = Boltzman constant
T = absolute temperature
ν = vibration frequency of an ion in an interstitial position $\sim 10^{12}$ sec^{-1}
ν_s = vibration frequency of a surface atom $\approx 10^{12}$ sec^{-1}
U = activation energy for diffusion *through* the film
ϕ = activation energy for diffusion *into* the film
m_s = surface density of atoms in tantalum metal

The dependences stated in equation 2 are simple for $\delta \ll 1$ and $\delta \gg 1$, but are quite complicated in the range when δ is close to 1. However it can be shown that for certain quite reasonable selections of parameters, the Tafel slope can be made temperature independent over a temperature range considerably greater than that represented by the data of Vermilyea. The main requirement is that δ be of the order of 1 at room temperature. One such behavior is shown in Figure 1. Equation (2) predicts that at both very low temperature and very high temperature the Tafel slope should be independent of current density and directly proportional to temperature. Measurements at both higher and lower temperatures are required to check this prediction.

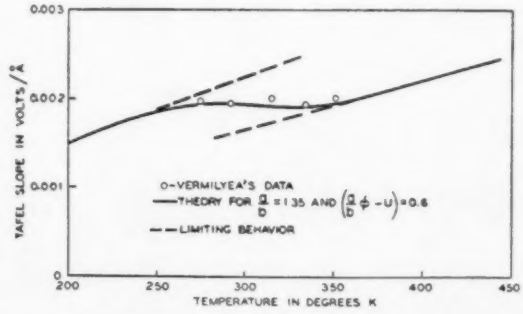

FIGURE 1. The temperature dependence of Tafel slope.

Vermilyea has attempted to calculate the

*Received December 1, 1953.
†The detailed derivation of this equation is in process of publication.

activation energy for the process in question. Plotting the logarithm of the formation rate against the reciprocal of the absolute temperature (electric field remaining constant) he obtains the value .71 e.v. for the "activation energy"; by implication he then equates this to Mott and Cabrera's "activation energy for diffusion." Such a procedure is manifestly incorrect when very high fields are involved. If it must be named, Vermilyea's energy of .71 e.v. is the "activation energy for high-field conduction." To obtain the activation energy for diffusion from these data—and this is the important quantity in the theory—one must correct for the fact that the field depresses the barrier height. In the Mott approximation the barrier is depressed by $\vec{E} \cdot b \cdot q$ which is about .9 volt. Thus the "activation energy for diffusion" is:

$$\phi \approx .9 + .71 \approx 1.6 \text{ e.v.}$$

Although the barrier is depressed to about 1/2 its low-field value when formation occurs there is still quite a barrier left, even at the highest current densities studied.

The frequency-factor discrepancy is automatically accounted for by the recalculation of the activation energy. When we use the value 1.6 e.v. for the activation energy we obtain a frequency factor $\nu_s \sim 10^{11}$ sec^{-1} in reasonable accord with expectation. The jump distance (b) calculated from the data is 2.6 Å.

The recalculation above in terms of the Mott model is only approximate but serves to show the origin of the "discrepancy." In a subsequent paper we present data of our own which largely confirm the experiments of Vermilyea. We postpone until that time the detailed evaluation of parameters.

JACOB F. DEWALD

Bell Telephone Laboratories, Inc.
Murray Hill, N.J.

References

1. VERMILYEA, D. A. Acta Met. **1** (1953) 282.
2. CABRERA, N. and MOTT, N. F. Rep. Progr. Phys. **12** (1948–49) 163.

Work-softening in Aluminium Crystals*

We have recently examined the effects of preliminary plastic deformation at a low temperature upon the plastic properties of aluminium crystals subsequently deformed at a higher temperature. The work-hardening introduced at the low temperature is of course unstable at the higher temperature and slowly disappears when the crystal is held there. The striking feature, however, is the rapidity, almost catastrophic, with which it disappears, giving rise to a sharp yield point, when the crystal is plastically strained at the higher temperature instead of being rested there; the effect can be described as one of *work-softening*.

Tensile specimens of 99.992 per cent aluminium with gauge dimensions $2'' \times 0.3'' \times 0.1''$ were made into single crystals by the strain-anneal method and examined in a hard beam machine at a strain rate of 2.5×10^{-5} sec^{-1} and at temperatures from −185°C to +100°C. During the whole series of deformation and annealing treatments on each specimen, the specimen remained in the machine and the applied load on it was never completely removed, thus maintaining the axial alignment gained from plastic straightening during the first deformation of the series.

Figure 1 is typical of the results obtained and shows many of the features observed. The yield points in curves *d*, *g*, *i*, and *o*, were all produced after preliminary deformations at the standard 'low'

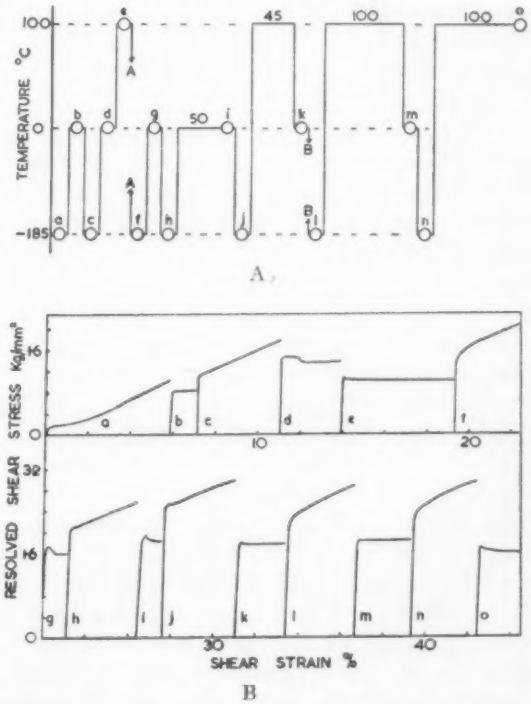

FIGURE 1. (A) Sequence of straining experiments on an aluminium crystal. The numbers on the Figure refer to times of resting in minutes. In the intervals AA and BB the specimen was rested at room temperature for 84 hours and 20 hours respectively. (B) Stress-strain curves obtained in this sequence of experiments.

*Received December 2, 1953.

temperature of −185°C (curves *c*, *f*, *h*, and *n*). Excepting curve *o*, which was taken at 100°C, they were all obtained by using 0°C as the 'high' temperature. That 0°C can also act as a 'low' temperature if followed by a sufficiently higher one is shown by the yield drop in curve *e*, which was obtained at 100°C after curve *d* at 0°C; further examples of this were obtained in other crystals. No yield drop was observed in curve *b*, taken at 0°C after deformation at −185°C, and in fact experiments on several crystals showed that the yield drops were always inappreciable unless the material had first been sufficiently 'charged' with work hardening, enough to raise its shear strength above about 1.5 kgm mm^{-2}.

The yield drops were only produced when the second testing temperature was higher (e.g., by 100 to 200°C) than the first. For example, in Figure 1 none were observed in curves *c*, *f*, *h*, *j*, *l*, and *n*, taken at −185°C. Small irregularities such as those shown in curves *h* and *j* appeared occasionally but these were very indefinite compared with large yield drops that could be produced consistently by the method described above; they are almost certainly due to some other effect, possibly the same as that observed by Blewitt [1] in copper crystals.

Curves *k* and *m*, obtained at 0°C after deformation at −185°C and annealing at 100°C, hardly show yield drops. Thus the softening which could have taken place during straining at 0°C had already occurred during the anneal at 100°C. The slowness with which the material softens on annealing, as compared with its rapidity during straining, is shown by the fact that marked yield drops were observed in curve *i*, obtained at 0°C after 50 minutes at 0°C, and in curve *o*, obtained at 100°C after 100 minutes at 100°C. A comparison of curves *m* and *o* shows further that the annealing treatment at 100°C, even though it removes the work-hardening that is unstable during straining at 0°C, nevertheless leaves in the material some work-hardening that is unstable under strain at 100°C. Thus, at a given softening temperature, plastic straining removes low-temperature work-hardening more completely than does annealing.

In attributing these yield drops to rapid work-softening, it is necessary to be sure that they are not caused in a more familiar manner by impurity atoms, especially as no theory of the mechanism of work softening appears to be known at present. The evidence that they are not examples of the conventional yield phenomenon due to solute atoms is as follows:

1. They are not produced unless the second straining temperature is higher than the first one, and have not been observed so far at −185°C. Yield points due to solute atoms, on the other hand, become stronger at low temperatures.

2. Annealing treatments of the kind that should allow strain ageing to occur, and so increase yield points due to solute atoms, in fact reduce or remove these yield drops (see curves *k* and *m* of Figure 1).

3. The metal is reasonably pure (99.992 per cent), and it is known that appreciable additions are needed to produce impurity yield points in single crystals of aluminium [2].

A fuller account of these experiments will be published later.

R. J. Stokes
A. H. Cottrell

Metallurgy Department,
University of Birmingham, England

References

1. Blewitt, T. Phys. Rev. **91** (1953) 1115.
2. Smallman, R. E., Williamson, G. K., and Ardley, G. W. Acta Met. **1** (1953) 126.

The Rate of Growth of Dendrites in Supercooled Tin*

The results of an investigation relating the rate of growth of dendrites to the degree of supercooling in a melt of tin are presented.

The method employed in this investigation to date is considered to be satisfactory only when the supercooling is greater than about 2.5°C and thus a gap in the experimental data still remains below this value. The method, in brief, involves the supercooling in a shallow graphite boat of a volume of tin 12 × 4.5 × 1 cm in which the temperature distribution was adjusted to ensure growth of the dendrites on the upper surface of the melt. The temperature was measured to within 1/10°C and was substantially uniform throughout the region in which measurements were made. Growth was initiated by touching the surface with a cold steel rod, and the rate of growth of the dendrites along the surface was determined cinematographically.

The main branch of each dendrite was observed to grow 1 to 8 cm in length (depending on the degree of supercooling) before any side branches appeared. The crystallographic direction associated with this main branch was probably the [110] as observed by Weinberg and Chalmers [1]. However,

*Received December 14, 1953.

this direction could be tilted as much as 45 degrees with respect to the surface of the melt; thus dendritic growth rates as recorded on the surface would show a spread of 30 per cent below the maximum or true rate of growth. The average rate would be 8 per cent below the maximum.

The accompanying graph shows the results which were obtained. The solid line represents the

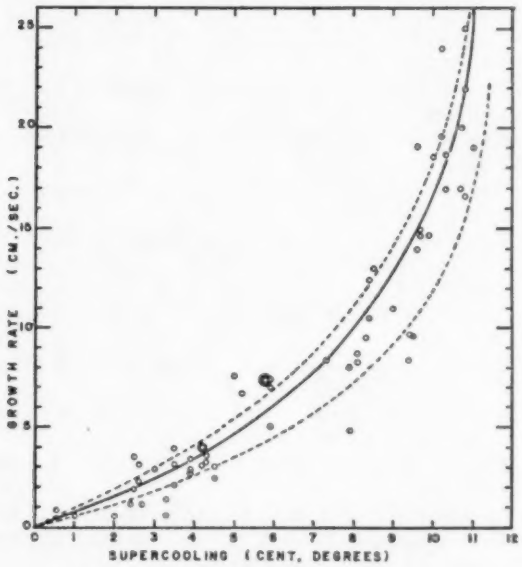

average or least-square curve through the points; the dotted lines represent values 9 per cent above and 23 per cent below this average, delineating the range in which the experimental values should fall. With 3°C supercooling, the growth rate is 3 cm/sec, and this increases to 25 cm/sec with 10.5°C supercooling.

When the results are plotted logarithmically, a straight line is obtained with a slope of 1.8, so that over the range studied it appears that the growth rate varies approximately with the square of the degree of supercooling. This appears to be in agreement with the proposal by Fisher [2] that the growth rate is limited entirely by the diffusion of heat. With steady-state heat flow and no convection he predicts a rate of growth proportional to the square of the degree of supercooling.

A. Rosenberg
W. C. Winegard

Department of Metallurgical Engineering
University of Toronto, Canada

References

1. Weinberg, F. and Chalmers, B. Can. J. Phys. **30** (1952) 488.
2. Fisher, J. C. Private communication, 1953.

The Relation of the Disordering of a Superlattice to the Melting of the Disordered Alloy*

That many binary alloys exhibit superlattices is perhaps not surprising in view of the requirement imposed by the Third Law that at absolute zero a substance in internal equilibrium has zero entropy; hence, an internally equilibrated binary alloy of simple atomic ratio is characterized by perfect order at 0°K, or by separation into the two pure components. However, the temperature at which a superlattice disorders is of interest, and is taken, in the ordinary treatment of the problem [1], to be a measure of the magnitude of the interchange energy occasioned by the exchange of an atom A for an atom B between lattices of pure A and pure B. On the other hand, at a similar level of approximation, the melting temperature of an alloy may be taken as a measure of a mean pairwise binding energy. From this point of view it is not expected that a simple relation should hold between the critical temperature, T_c, of disordering of a superlattice in an alloy and the solidus temperature, T_s, of the disordered alloy of the same composition.

However, an empirical correlation between these two quantities does appear to exist, and the purpose of this note is to point out the approximate constancy of the ratio T_c/T_s for all cases for which, as far as the writer knows, reasonably accurate data are available. The T_c listed in the accompanying table is the maximum critical temperature of disordering, which usually occurs at a simple ratio of the atomic species. The T_s represents the solidus temperature of the alloy at the composition of the superlattice. In some cases, notably AgCd, the separation between the solidus and the liquidus lines is so great that very little significance can be attached to the concept of the melting of the alloy at the composition of the superlattice. In other cases, the disordered solid solution, into which the superlattice transforms, does not melt but goes over into another structure before melting occurs. It is clear that the T_s that is wanted is that of the structure which supports the superlattice, and that this is a smaller number than the T_s of the structure which is actually in equilibrium with the liquid. This may be the explanation for the relatively low value for $CrNi_3$. However, using the numbers as tabulated, the mean Tc/Ts is $0.63 \pm .06$ (standard deviation of an individual value) for

*Received December 16, 1953.

the 1:1 alloys (including two 3:2 alloys) and 0.55± .10 for the 1:3 alloys. The variance of the data for the 1:3 alloys was analyzed statistically yielding a confidence level of 1 per cent for the constancy of Tc/Ts.

TABLE I

RATIO OF DISORDERING TO SOLIDUS TEMPERATURE*

Alloy	Tc°C	Ts°C	(Tc/Ts) °K/°K	References
AgCd	440	700	.75	
AgZn	∽280	700	∽.59	
AuCd	267	627	.61	
AuCu	420	884	.60	
AuMn	680	1230	.63	
CdMg	∽250	410	∽.77	
CoFe	∽800	1480	∽.61	
CoPt	825	1530	.61	
CrFe	815	1510	.61	
Cr_3Pd_3	600	1170	.60	
CuPt	812	∽1500	∽.61	
CuZn	∽460	∽ 880	∽.64	
Fe_3Pd_2	780	1300	.60	2
LiPb	∽200	∽ 480	∽.65	
MnNi	∽670	1100	∽.68	3
NiPt	∽620	∽1480	∽.51	
Ag_3Mg	386	∽ 760	∽.63	4
$AlFe_3$	575	1430	.50	
$AuCu_3$	396	905	.56	
Au_3Cu	∽250	920	∽.44	5
Au_3Mn	690	1000	.74	
Cd_3Mg	85	360	.57	
$CdMg_3$	153	490	.56	6
$CoPt_3$	∽750	∽1650	∽.53	7
$CrNi_3$	540	1380	.49	8
Cu_3Pd	500	∽1100	∽.56	
Cu_3Pt	650	1260	.51	
Cu_3Zn	250	950	.43	9
$FeNi_3$	∽497	∽1440	∽.45	10
$FePd_3$	780	∽1320	∽.66	2
$MnNi_3$	∽510	∽1170	∽.54	11
Ni_3Pt	578	1400	.51	12
Ni_3Sn	875	1180	.79	13

*Except where specified data taken from the compilations of Hansen ("Aufbau der Zweistofflegierungen", Berlin, 1936), Smithells ("Metals Reference Book", New York, 1949), and the A.S.M. Metals Handbook, 1948.

It may be argued that the reason for the approximate constancy of this ratio is that a lower temperature limit to the practical observability of superlattice formation is produced by the immobilization of the atoms that generally sets in at about $0.3T_s$. Nevertheless, the clustering of Tc at values considerably higher than $0.3T_s$ suggests that the disordering and the melting phenomena have something in common that is not contained in the formal treatments accorded to each one separately.

R. A. ORIANI

General Electric Research Laboratory
The Knolls
Schenectady, New York

References

1. GUGGENHEIM, E. A. Mixtures (Oxford, University Press, 1952).
2. HULTGREN, R. and ZAPFFE, C. A. Trans. A.I.M.E. **133** (1939) 58.
3. COLES, B. R. and HUME-ROTHERY, W. J. Inst. Metals **80** (1951) 85.
4. CLAREBROUGH, L. M. and NICHOLAS, J. F. Australian J. Sci. Res. **3A** (1950) 284.
5. HIRABAYASHI, M. J. Jap. Inst. Metals **16** (1952) 67.
6. WELBER, B., WEBELER, R. and TRUMBORE, F. Acta Met. **1** (1953) 374.
7. GEISLER, A. H. and MARTIN, D. L. J. App. Phys. **23** (1952) 374.
8. TAYLOR, A. and HINTON, K. G. J. Inst. Metals **81** (1952) 169.
9. MASUMOTO, H., SAITO, H. and SUGIHARA, M. Sci. Rpts. Tohoku Univ. **A4** (1952) 481.
10. WAKELIN, R. J. and YATES, E. L. Proc. Phys. Soc. **B66** (1953) 221.
11. THOMPSON, N. Proc. Roy. Soc. **52** (1940) 217.
12. ORIANI, R. A. and JONES, T. S. Acta Met. **1** (1953) 243.
13. RAHLFS, P. Metallwirtschafft **16** (1937) 343.

On the Origin of Screw Dislocations in Growing Crystals*

Some of the most convincing evidence for the screw dislocation mechanism of crystal growth has been provided by microscopic observation of the growth of CdI_2 platelets from aqueous solution. [1; 2; 3; 4; 5] Very thin platelets grow at constant thickness to a width of perhaps 1 mm. Suddenly spiral or closed-loop steps many molecular layers high appear on the platelet surface and the crystal starts to thicken by the screw dislocation mechanism.

The mechanism by which the screw dislocations responsible for these large steps form is of great importance to the complete picture of crystal growth. Frank [6] has postulated that the platelets become self-stressed by non-uniform distribution of impurities and as a result ultimately buckle and shear to generate a group of screw dislocations. Forty [3] has suggested that the platelets are sheared

*Received December 19, 1953.

by convection currents. Both of these suggestions are subject to serious objections.

If the non-uniform distribution of impurities were the controlling factor in the origin of screw dislocations, purified material should show significant departures from the behavior of impure material. Screw dislocations should not appear on the faces of a significant fraction of CdI_2 platelets grown from purified material. This is contrary to experimental evidence. Forty [1] reports that unpurified and recrystallized CdI_2 behave alike as regards the appearance of screw dislocations in large faces.

Motion picture records of cadmium iodide platelet growth [4; 5] provide adequate evidence that the platelets move very slowly in solution and therefore cannot be subject to large viscous forces, which would be necessary for the success of the convection current mechanism.

A perfect crystal should not deform plastically until an elastic strain of at least 2.5 per cent is reached. A platelet 5000 Å thick would have to be bent to a radius of curvature of 10 microns to reach this strain. If platelets buckled to the extent required to cause plastic deformation, there would be large irregularities in the effective plate thickness for internal interference, and non-uniformity in the interference color. Experimentally it is observed that the platelets are remarkably uniform in color. Only exceptionally are buckled platelets observed, and even for these platelets growth sources are not formed in the buckled regions [5].

It does not appear that the dislocation responsible for thickness growth in cadmium iodide crystals can arise by plastic deformation of initially perfect crystals. This note suggests that impingement of two crystals is a more likely source of the dislocations. Consider two cadmium iodide platelets growing edgewise toward each other, with their planes nearly parallel. When they touch, the interface is a low-angle grain boundary properly described as a network of dislocations [3], many of which terminate on the flat surfaces of the platelets. Those dislocations that intersect the close-packed surface with a component of the Burgers vector perpendicular to the surface produce perpetual growth steps.

Frequently growth steps are observed to form without observable contact between growing crystals. Here it is supposed that the one observable crystal has come in contact with an unobserved impurity crystal. It is not unreasonable to postulate the presence of impurity crystals, since there is evidence that impurity crystals act as nucleation catalysts for the initial thin cadmium iodide platelets. If an impurity crystal is partially engulfed by a growing cadmium iodide platelet, the grain boundaries on opposite sides of the impurity contain the same number of dislocations, but the screw dislocations that intersect the platelet surface are of opposite hand. Hence, the included crystal provides a source of "closed loop" steps for thickness growth.

If a platelet edge meets an impurity particle that extends beyond the platelet thickness on both sides, the platelet separates around the impurity. When the separated portions recombine on the other side of the impurity, the surface will be offset unless the two parts have remained exactly parallel during their independent growth. The resulting step in the surface provides a "source" for thickness growth of the platelet, leading to a spiral step. If a platelet edge meets a large impurity particle and a low angle interface boundary is formed, a combination "closed loop" and "spiral" growth source may be created. Step patterns consistent with this type source have been observed by Forty [2].

The order of magnitude of the rate of appearance of growth sources on growing crystals can be calculated on the basis of the particle impingement concept. Let n be the number of impurity particles (of sufficient size to be effective growth sources) per unit volume of solution. Since they are very dilute, their osmotic pressure will obey the perfect gas law, and their rate of impingement per unit area will be governed by the effusion equation. Let r be the radius of a platelet at any time, and h be its thickness. Then the rate of impingement $\dot{N}$ of particles on the platelet edges is given by

$$\dot{N} = 2\pi rhn\sqrt{\frac{kT}{2\pi m}} \tag{2}$$

where m is the average mass of the particles, T is the absolute temperature and k is the molecular gas constant. The average time, τ, required for a single particle to impinge on the platelet edge is given by setting the total number of collisions, N, equal to one.

$$1 = N = \int_0^\tau 2\pi\alpha hn\sqrt{\frac{kT}{2\pi m}}\,tdt, \tag{3}$$

where it is assumed that the platelets grow at

constant linear velocity α. Since the final radius, R, of the platelet is given by $R = \alpha\tau$,

$$(4) \qquad 1 = N = \pi R h \tau n \sqrt{\frac{kT}{2\pi m}}.$$

This calculation indicates that 800 particles/cm^3 would be sufficient to cause the observed rate of growth source appearance if $R = 0.5$ mm, $h = 1000$ Å, $m = 10^{-14}$ gm, and $t = 10^3$ sec.

In this calculation, impingement of particles on the large close-packed surfaces of the platelet has not been considered, since it is presumed that particles do not stick to the platelet surface unless they are engulfed as a result of the platelet's growth. Calculation of the average velocity of Brownian motion of particles of the required size indicates that those coming in contact with the advancing platelet edge would be engulfed by it.

A thickness growth source can operate only if the step length associated with the potential source is longer than the critical diameter for two dimensional nucleation of a surface layer. For a "spiral" source, the step length involved is the distance from the source to the crystal edge, while for a "closed loop" source it is the distance between opposite boundaries of the impurity particle. In the neighborhood of an advancing platelet edge the supersaturation is much smaller than elsewhere. Hence, while "spiral" growth sources become effective while the platelet edge is still very near the impinged impurity, "closed loop" growth sources may not start to operate until the edge has advanced some distance beyond the particle.

If the impurity particle on which the platelet formed initially has a structure misfit with the cadmium iodide which requires screw dislocations in the impurity/cadmium iodide interface, this interphase boundary may also act as a "closed-loop" growth source. Sources arising from this type of boundary should appear in the platelet center when the platelet has become large enough so that the required supersaturation is reached at the platelet center. In the motion picture records of cadmium iodide growth [4; 5] it has been observed that "spiral" growth sources always start very near a platelet edge, while "closed-loop" sources may start some distance in from the edge, and occasionally "closed-loop" sources start at the platelet center.

The hypothesis of impurity particle impingement appears to rationalize the observations so far reported of the appearance of dislocation growth sources on crystals. While attention has been directed primarily to the observations on cadmium iodide, the proposed mechanism is general for the genesis of screw dislocations in a crystal face.

J. C. Fisher
R. L. Fullman
G. W. Sears

General Electric Research Laboratory
Schenectady, New York

References

1. Forty, A. J. Phil. Mag. **42** (1951) 670.
2. Forty, A. J. Phil. Mag. **43** (1952) 72.
3. Forty, A. J. Phil. Mag. **43** (1952) 377.
4. Fullman, R. L. and Wood, D. L. Unpublished data.
5. Newkirk, J. B. Unpublished data.
6. Frank, F. C. Phil. Mag. **42** (1951) 1014.

Electron and Photocurrents in Thin Films of ZrO_2*

The mechanism proposed by A. Charlesby [1] to account for the observed variation of the electron current through thin films of anodic ZrO_2 is based upon the assumption that there exists a symmetrical potential barrier of width $2a$ and height U which the electrons must surmount. In the presence of an electric field the barrier is distorted to increase the probability of electron flow in the direction of the field, and the current through the film is given by

$$i = 2A \exp\left(-\frac{U}{kT}\right) \sinh\left(\frac{eaE}{kT}\right)$$

where A is a constant, i the current density, and E the electric field. From the experimental data a value of 7.2Å was deduced for the width of the barrier while the barrier height was found to be 0.375 eV.

There is one objection to the mechanism proposed by Charlesby. As may be seen from the following calculation, the probability of tunneling through a barrier of the dimensions given is greater than the probability that an electron will be thermally excited over the barrier. At 18°C, the temperature at which the data in Figure 1 of reference 1 were taken, the applied electric field strength varied from about 0.7×10^6 to 4.4×10^6 volts/cm. Taking 5×10^6 as the maximum field for which the mechanism should be valid, the energy barrier, given by $U - eaE$, would be 0.195 eV. The probability of thermal excitation over this barrier is 4×10^{-4}.

*Received January 4, 1954.

The probability of tunneling may be calculated from the formula

$$T(E) = f(E) \exp\left[-\frac{2}{\hbar} \int_{X_1}^{X_2} [2m(V-E)]^{\frac{1}{2}}\, dx \right]$$

where $T(E)$ is the transmission coefficient, $X_2 - X_1$ is the distance through the barrier, V is the potential of the barrier, E is the energy of electrons incident on the barrier, and $f(E)$ is a factor depending on the shape of the barrier, but roughly equal to unity. Assuming a square barrier 0.195 eV high, of width 7.2 Å, the probability of tunneling is 5×10^{-2}. This value is considerably too low, since the average height of the barrier is less than 0.195 eV and its average width less than 7.2 Å. If, instead of a square barrier, an initially triangular barrier of peak height 0.375 and width 7.2 Å is assumed, the barrier with a field of 5×10^6 V/cm will be 4.64 Å wide with a peak height of 0.195, and the probability of tunneling becomes 2.5×10^{-1}. The tunneling probability for the actual barrier is probably somewhere between 2.5×10^{-1} and 5×10^{-2}, perhaps 10^{-1}. At any rate, the probability of tunneling through the barrier is certainly much greater than the probability of thermal excitation over it, so that the proposed mechanism is not possible.

An alternative explanation of the observed results may be made as follows. We will assume that there are trapping centers for electrons* in the film, either oxygen vacancies or interstitial zirconium atoms. The potential of an electron in the field of such a center is given by $-e^2/Kr$, where K is the dielectric constant and r the distance from the center. If a strong electric field is applied across the film, the expression for the potential as a function of distance is given by

$$V(x) = -\frac{e^2}{Kx} - eEx \tag{1}$$

where E is the applied field and x is the distance from the trap in the direction of the field. Figure 1 shows a schematic representation of this potential function, which has a maximum at

$$X_0 = \left(\frac{e}{KE}\right)^{\frac{1}{2}} \tag{2}$$

the potential at the maximum being

$$V_0 = -2\left(\frac{e^3E}{K}\right)^{\frac{1}{2}}. \tag{3}$$

In the absence of the field an electron would have to surmount a barrier of height ϵ_0 in order to enter

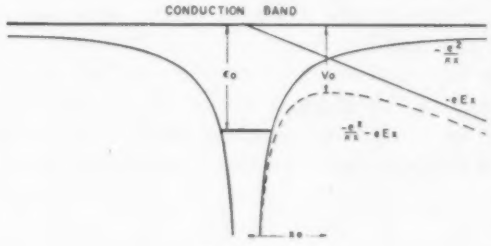

FIGURE 1.

the conduction band. In the presence of the field, therefore, the energy barrier is $\epsilon_0 - |V_0|$, and the conductivity is given by

$$\sigma = A \exp\left(-\frac{\epsilon_0 - |V_0|}{2kT}\right) \tag{4}$$

$$= \sigma_0 \exp\left\{\left(\frac{e^3E}{K}\right)^{\frac{1}{2}} \Big/ kT\right\} \tag{5}$$

where σ_0 is the conductivity in the absence of the field. The conductivity is thus increased by a mechanism similar to the increase in thermionic emission due to the Schottky effect.

According to equation (5), a plot of log i against $E^{1/2}$ should give a straight line. Figure 2 shows a

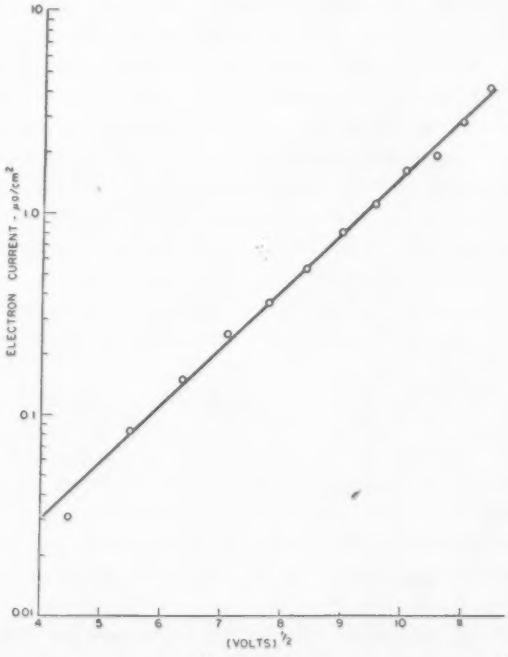

FIGURE 2.

*It is not known whether anodic ZrO_2 films are p-type or n-type. Although the discussion which follows is based on the assumption that electrons are the charge carriers, a similar argument would apply for positive holes.

plot of log i vs $V^{1/2}$ for specimen 12 of Figure 1 of reference 1. It may be seen that except for one point an excellent straight line is obtained. The agreement with theory is better than with the hyperbolic sine curve of Charlesby's paper where the points at low voltages depart seriously from the calculated curve.

It is of interest to determine the height of the barrier in the absence of the electric field. At a field of 2×10^6 V/cm, the current density varied with temperature according to the equation

$$i = i_0 \exp\left(-\frac{W}{kT}\right)$$

where $i_0 = 5$ amp/cm^2 and $W = 0.46$ eV. According to equation (4),

$$W = \frac{\epsilon_0}{2} - \left(\frac{e^3E}{K}\right)^{\frac{1}{2}}.$$

From the slope of the log i vs $V^{\frac{1}{2}}$ plot of Figure 2 we find $K = 18.2$ and thus $\epsilon_0 \sim 1.1$.

According to Mott and Gurney [2], the conductivity of a semiconductor is given by

$$\sigma = Ae^{-\frac{1}{2}(\epsilon/kT)}$$

where $A = 3 \times 10^{-10} v N^{1/2}$, v is the mobility, and N is the concentration of traps. For the ZrO_2 film, $i_0 = 5$ amps/cm^2 at a field of 2×10^6 V/cm, so that $A = 2.5 \times 10^{-6}$. Thus $v \cdot N^{1/2} \sim 10^4$ and if $v = 10$ cm/sec per volt/cm, $N = 10^6$ traps/cm^3. This is an extremely low concentration of traps, the concentrations in many semiconductors being about $10^{14} - 10^{20}$. This low concentration of traps is, however, in accord with the fact that extremely high fields are required to produce appreciable electronic current. Another possible explanation of the low conductivity is that the mobility is less than 10 volts/cm at these high fields with a correspondingly greater concentration of traps. The mobility of electrons and holes in germanium has been found to decrease markedly at high fields [3].

Assuming, therefore, that the anodic ZrO_2 film contains electron traps the depth of which is lowered by the applied field, it is possible to explain the observed variation of electron current with field and temperature. The defect structure deduced from the experimental data is that of a semiconductor with a very small number of fairly deep traps.

The author is pleased to acknowledge helpful criticisms by D. Turnbull, L. Apker, and E. W. Hart of the General Electric Research Laboratory, and by J. K. Bragg of Washington, D.C.

D. A. VERMILYEA

General Electric Research Laboratory
Schenectady, New York

References

1. CHARLESBY, A. Acta Met. **1** (1953) 348.
2. MOTT, N. F. and GURNEY, R. W. Electronic Processes in Ionic Crystals (Oxford, 1940) p. 158.
3. RYDER, E. J. Phys. Rev. **90** (1952) 766.

An Equation for the Solubility Surface of Ternary "Sub-Regular" Solutions*

A subregular binary solution has recently been defined in a communication to this Journal [1] as a regular solution in which the heat of solution is made a linear function of composition. The equation for the free energy is then

$$(1) \qquad \Delta F = A_1x^2y + A_2xy^2 + RT(x \ln x + y \ln y)$$

where x and y are the atomic fractions. The solubility curve obeys the equation.

$$(2) \qquad \begin{aligned}(x_1 + x_2)\, RT \ln x_1/x_2 + (y_1 + y_2)\, RT \ln y_1/y_2 &= A_1(x_1 - x_2)^2(y_1 - y_2) \\ &+ A_2(x_1 - x_2)(y_1 - y_2)^2 \\ &= -(A_1 - A_2)(x_1 - x_2)^3\end{aligned}$$

where (x_1y_1) and (x_2y_2) are the concentrations coexisting in equilibrium. Consequently, only one arbitrary constant is involved, namely $(A_1 - A_2)$, and the solubility data should give a straight line plot when the left-hand side of equation (2) is plotted against $(x_1 - x_2)^3$. The solid solubility curves of Ag-Cu [1], Ag-Pt [1], Al-Zn [1] and Au-Pt [1; 2] and the liquid solubility curve of Pb-Zn [3] alloys give straight lines over appreciable temperature ranges.

The purpose of this note is to set up the equation for the solubility surface of a subregular ternary solution. A linear dependence with composition is obtained by putting the heat of solution as

$$(3) \qquad \Delta H = xy(a + a_1x + a_2y + a_3z) + yz(b + b_1y + b_2z + b_3x) + zx(c + c_1z + c_2x + c_3y).$$

Multiplying axy, byz and czx by $(x + y + z) = 1$, rearrangement and simplification leads to

$$(4) \qquad \Delta F = A_1x^2y + A_2xy^2 + B_1y^2z + B_2yz^2 + C_1z^2x + C_2zx^2 + D\,xyz + RT\,(x \ln x + y \ln y + z \ln z)$$

*Received December 18, 1953; in revised form January 25, 1954.

and the chemical potentials are of the form

$$(5)\quad \mu_x = RT \ln x + y^2 (2A_1 - A_2) + y^3 (2A_2 - 2A_1) + z^2 (2C_2 - C_1) + z^3 (2C_1 - 2C_2) + yz (2A_1 + 2C_2 - D) + y^2 z (-4A_1 + 2A_2 - 2B_1 - 2C_2 + 2D) + yz^2 (-2A_1 - 2B_2 + 2C_1 - 4C_2 + 2D)$$

At equilibrium

$$(6)\quad \mu_x(1) = \mu_x(2);\ \mu_Y(1) = \mu_Y(2);\ \mu_z(1) = \mu_z(2)$$

and these equations are necessary completely to define the solubility curve. Equations (6) are multiplied by $(x_1 + x_2)$, (y_1+y_2) and $(z_1 + z_2)$ respectively, added and rearranged to give

$$(7a)\quad (x_1 + x_2)\, RT \ln x_1/x_2 + (y_1 + y_2)\, RT \ln y_1/y_2 + (z_1 + z_2)\, RT \ln z_1/z_2 = A_1(x_1 - x_2)^2(y_1 - y_2) + A_2(x_1 - x_2)(y_1 - y_2)^2 + B_1(y_1 - y_2)^2(z_1 - z_2) + B_2(y_1 - y_2)(z_1 - z_2)^2 + C_1(z_1 - z_2)^2(x_1 - x_2) + C_2(z_1 - z_2)(x_1 - x_2)^2 + D(x_1 - x_2)(y_1 - y_2)(z_1 - z_2)$$

$$(7b)\quad = (B_2 - B_1)(y_1 - y_2)^3 + (A_2 - B_1 + 2B_2 + C_1 - D)(y_1 - y_2)^2(x_1 - x_2) + (A_1 + B_2 + 2C_1 - C_2 - D)(y_1 - y_2)(x_1 - x_2)^2 + (C_1 - C_2)(x_1 - x_2)^3$$

$$(7c)\quad = \alpha(y_1 - y_2)^3 + \beta(y_1 - y_2)^2 (x_1 - x_2) + \gamma(y_1 - y_2)(x_1 - x_2)^2 + \delta(x_1 - x_2)^3$$

Thus, the solubility surface of a sub-regular ternary solution obeys an equation containing only four arbitrary constants. The surface will be defined completely by two of equations 6 together with equation 7.

Equation 7c does not lend itself to such easy plotting as in the binary alloys. When the tie lines are parallel to the $X - Y$ side, equation (7) reduces to

$$(8)\quad (x_1 + x_2)\, RT \ln x_1/x_2 + (y_1 + y_2)\, RT \ln y_1/y_2 = -(A_1 - A_2)(x_1 - x_2)^3$$
(where $x_1 + y_1 = x_2 + y_2 < 1$)

The terms on the right-hand side of equation (7) vanish when the solution is regular and Meijering's equation (43) is regained [4].

The difficulty in applying equation (7) to ternary metallic solutions is that the tie lines are rarely known with accuracy.

H. K. HARDY

Fulmer Research Institute,
Stoke Poges, Bucks, England

References

1. HARDY, H. K. Acta Met. **1** (1953) 202.
2. HARDY, H. K. J. Inst. Metals, **81** (1952–53) 599 (Discussion).
3. HARDY, H. K. Acta Met. **1** (1953) 610.
4. MEIJERING, J. L. Philips Research Reports **6** (1951) 183.

Faulting in Austenite*

Klier and Troiano [1] in their study of the M_s temperatures of Cr-C steels reported that in certain of the alloys whose M_s was below room temperature, drastic quenching of the austenite (to room temperature) showed under the microscope, markings in the austenite which delineated the {111} planes. A closer examination, presented here, shows that the markings can best be interpreted in terms of stacking faults which are detectable by X-ray diffraction techniques.

The effects of faults in the stacking sequence of CPH and FCC structures on the X-ray diffraction pattern has been analysed mathematically and interpreted in terms of the reciprocal lattice by Wilson [2] and Paterson [3]. The results of Paterson's calculations are seen in Figure 1; the patterns shown repeat themselves throughout space. In the FCC structure, the extreme case of a fault on every (111) layer gives the twin orientation. If the line perpendicular to the (111) planes is labelled the c-axis, then the reciprocal lattices of the FCC and its twin, both given in Figure 1, differ only by a 60 degree rotation about the c*-axis. Superimposing these twin-related lattices thus gives the initial and final positions of the diffraction spots and hence the direction of shift as faulting increases. Those spots that are coincident in the original and twinned orientation do not shift and thus are not affected by faulting. For those spots that shift, the direction of shift is the same whether it results from growth faults or from deformation faults, but the magnitude is different [3]. In the reciprocal lattice this shift is represented during the early stages by short "rods" starting at the reciprocal lattice point and lying in the direction of shift; these "rods" correspond to streaks emerging from spots in the X-ray diffraction pattern.

By assembling (a) and (b) of Figure 1 alternately six times, the complete FCC reciprocal lattice is obtained with the result shown in Figure 2. In this figure the direction of the rods (and hence of the streaks) to be expected when faulting

*Received January 9, 1954.

occurs along the (111) and ($\bar{1}$11) planes is indicated. If faults occur on all four {111} planes it will be seen that all reciprocal lattice points have rods in four directions, except those of {111} planes and multiples of those planes, whose reciprocal lattice points have only three rods.

In Figure 2 reciprocal lattice points of the twinned orientations have not been superimposed.

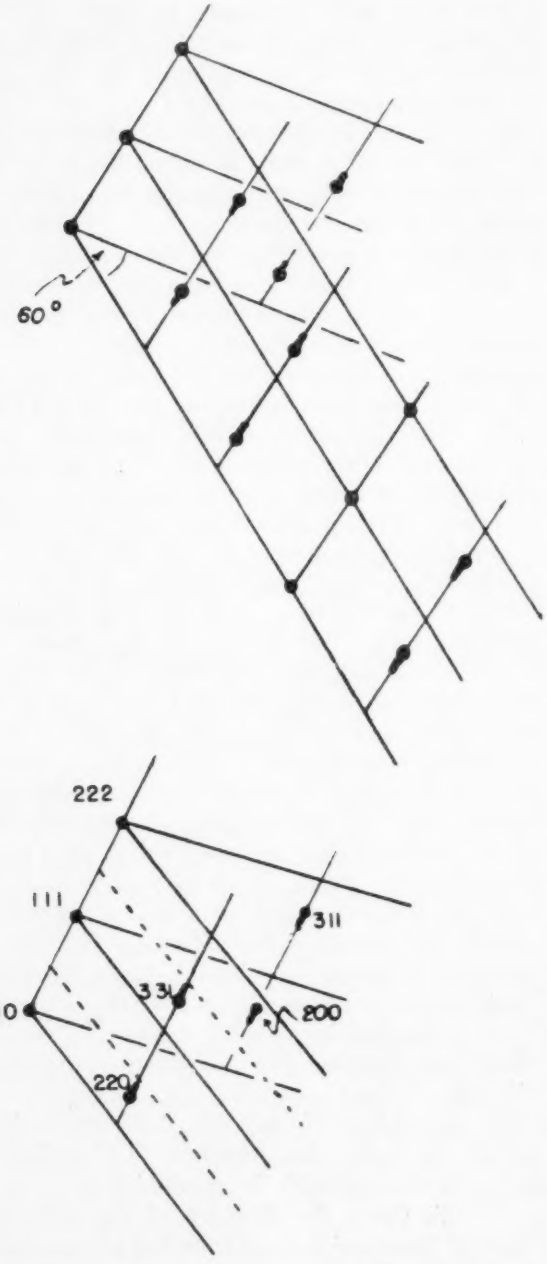

FIGURE 1. Section from the reciprocal lattices of the FCC and its twin orientation.

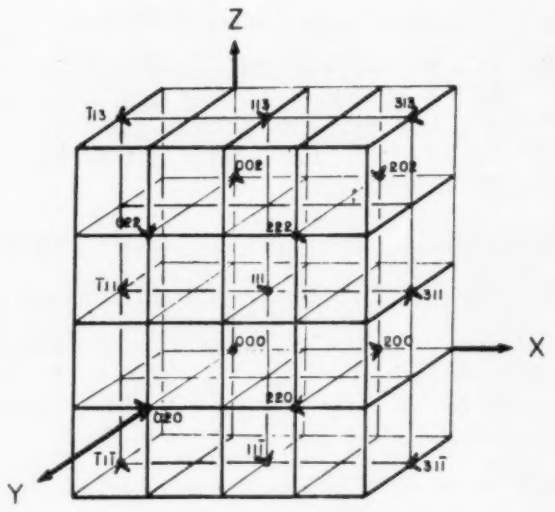

FIGURE 2. The FCC reciprocal lattice showing direction of rods representing X-ray diffraction streaks resulting from faults on two sets of {111} planes.

These may be obtained by rotating the lattice in Figure 2 through an angle of 60 degrees about a line joining the origin to the 111 reciprocal lattice point. This will then give the additional points for a crystal twinned about the (111) plane. If faulting in the twinned orientation also occurs on all four {111} planes, each additional reciprocal lattice point (with the exception of the 111 points) will have four rods emerging from it. The $\bar{1}$11, 1$\bar{1}$1 and 11$\bar{1}$ reciprocal lattice points will have three rods each emerging from them. The (111) twin plane (and multiples of it), however, will have a reciprocal lattice point with six rods emerging from it.

Thus the maximum number of streaks that may emerge from any one X-ray diffraction spot of a faulted (and twinned) FCC lattice is limited to six, and only to the spots from the {111} planes (and multiples of it) on which the crystal is twinned.

The present investigation employed Klier and Troiano's alloy 9Cr100 in the form of specimens one-fourth inch thick, austenitized 23 hours at 1225°C *in vacuo* and quenched into 10 per cent sodium hydroxide solution at 15°C. The M_s temperature was about −15°C and the grain size ASTM number 0 to −2. All specimens examined were electrolytically polished with a solution of 6 per cent perchloric acid and 35 per cent butyl "cellosolve" in methanol.

X-ray diffraction patterns were obtained with filtered cobalt radiation using a cylindrical camera

and a collimator having a 1 mm diameter hole.

The surface of the specimens was set at an angle of 25 degrees to the incident beam and oscillated to 30 degrees.

Figure 3 shows the X-ray pattern obtained from a quenched sample; only austenite spots are

FIGURE 3. (Figure reduced one-half in reproduction.) Oscillation pattern from as-quenched 9Cr100 specimen.

present. Close inspection reveals a 111 spot with a single streak fading out of it and another with six: these are indicated by arrows on the figure. The microstructure of the same specimen is given in Figures 4 and 5; there exists one set of "markings" which are parallel to an austenite twin interface. The relation of these markings to a martensite plate may be seen in Figure 6.

In the oscillation pattern from a sample deformed less than 1 per cent, streaks from 111-spots

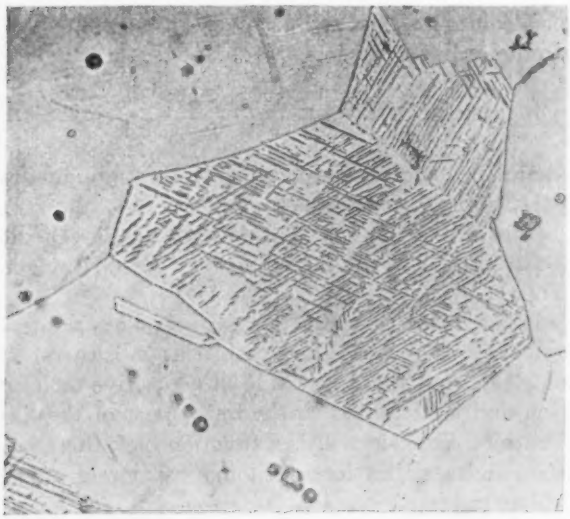

FIGURE 4. Microstructure of as-quenched 9Cr100 specimen. Etched with 45% HCl and 5% HNO_3 in methanol. ×350.

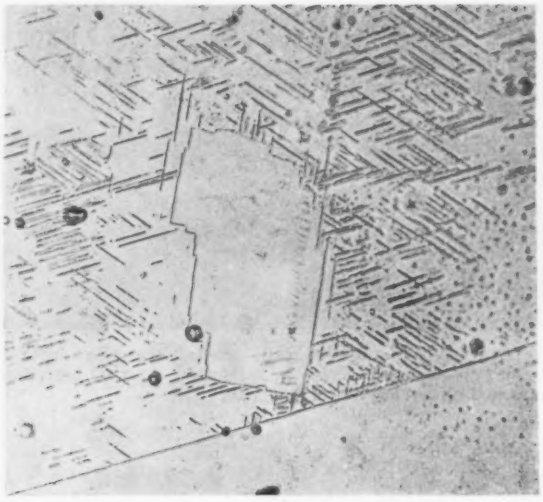

FIGURE 5. Same as for Figure 4.

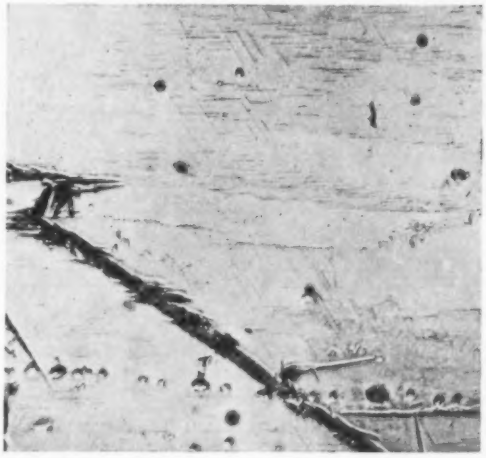

FIGURE 6. 9Cr100 tempered 20 sec at 425°C after sub-zero quenching. Vilella etch. ×350.

could also be found as the arrows in Figure 7 indicate. (111-spots without streaks are probably from grains which have not faulted or from grains unfavorably oriented.) Under the microscope similar markings as in the undeformed sample were observed, but of increased length. Figure 8 is from a specimen deformed about 1.7 per cent at room temperature. Increasing amounts of deformation at room temperature eventually caused some transformation of the austenite to a BCC structure, in agreement with the reports of Klier and Troiano.

The above observations suggest that the "markings" which make their appearance in the quenched austenite of this Cr-C steel and which were first reported by Klier and Troiano, represent some

FIGURE 7. (Figure reduced one-half in reproduction.) Oscillation pattern from a quenched 9Cr100 specimen deformed about 1% at room temperature.

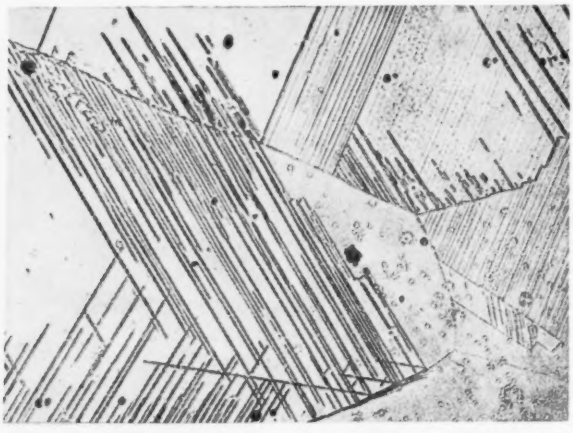

FIGURE 8. (Figure reduced to three-fourths in reproduction.) Microstructure of 9Cr100 specimen quenched and deformed about 1.7% at room temperature. Etched with 45% HCl and 5% HNO_3 in methanol. × 350.

arrangement of faults. A similar effect has been reported in FCC alpha-Cu-Si alloys near 5 per cent Si, by Barrett [4].

An alloy containing 1.5 per cent C, 5 per cent Ni, was also examined but yielded negative results.

I wish to thank Professor A. R. Troiano for his interest and criticism; also Professor T. A. Read for his friendly discussions and Dr. M. S. Paterson for his comments. This work was done under a special grant at Case Institute of Technology.

H. M. OTTE

School of Mines
Columbia University
New York, N.Y.

References

1. KLIER, E. P. and TROIANO, A. R. Trans. A.I.M.E. **162** (1945) 175.
2. WILSON, A. J. C. X-ray Optics (London, Methuen & Co., 1949).
3. PATERSON, M. S. J. Appl. Phys. **23** (1952) 805.
4. BARRETT, C. S. Trans. A.I.M.E. **188** (1950) 123.

The Interaction of Impurity Atoms with Dislocations in Germanium*

It may be expected that the electrical properties of semiconductors are quite structure-sensitive and that the presence of edge-type dislocations and their interaction with solute atoms may be a significant factor in the understanding of certain experimental observations. It is proposed herein that the existence of dislocations in germanium gives rise to certain specific distributions of solute atoms. Although the calculations which have been performed are approximate, the magnitude of the results indicate that these concepts may be of value. The resulting proposed model may be used in predicting and explaining some of the electrical properties of germanium.

Because of its stress field, a dislocation will interact with other sources of internal stress in a crystal. Solute atoms constitute such sources of internal stresses. The energy of a solute atom in a crystal can be considered as the strain energy created by the expansion or contraction of the lattice in order to permit the solute atom to enter the crystal. If the expansion occurs in a region in which a stress field is already present, work must be done against that field. The total strain energy of the system will then change by an amount equal to the interaction energy. Since this energy changes as a function of distance from the center of the dislocation stress field it can be seen that the solute atom will experience a net force drawing it to the region where it can relieve the most stress.

It has been shown that [1] the interaction energy for a solute atom of radius $r(1 + \epsilon)$ in a solvent of atomic radius r can be expressed as:

$$(1) \qquad V = \frac{4}{3} G \epsilon r^3 \lambda \frac{1 + \nu}{1 - \nu} \frac{\sin \alpha}{R}$$

where G is the shear modulus of germanium, ϵ is Poisson's ratio, λ is the Burger's vector, and R is the distance of the solute atom from the dislocation center, and α is the angle between R and the slip plane.

It is evident that V is positive when ϵ is positive and for $0 < \alpha < \pi$. A large solute atom is therefore repelled from the upper side of a positive dislocation and is attracted to the lower part of the dislocation. Also, since V is a function of R there will be a finite radial force tending to attract solute atoms to the dislocation.

Approximate values of V have been calculated

*Received January 21, 1954.

for the interaction of various impurity atoms with dislocations in germanium and the results are given in Table I. The tabulated value of R^* represents

TABLE I

	Atomic Radius	ϵ	R^* in Å	V in ev (for $R = 4$Å)
Cu	1.28	0.0492	10	0.12
As	1.16	−0.0492	10	0.12
Al	1.43	+0.1720	30	0.36
Sb	1.34	+0.0983	17	0.20
In	1.45	+0.1880	40	0.48
P	0.93	+0.2370	45	0.54
Si	1.18	−0.0328	5	0.06

that distance from the center of the dislocation at which the interaction energy is equal to kT at room temperature. This value roughly represents the region over which the stress field effectively acts for each type of solute. One can calculate the approximate depth of the potential well for various values of R using equation (1). Taking $\epsilon \cong 0.05$ (as for Cu or As in germanium), $R = 4$ Å, and $\alpha = -\pi/2$ then $V \cong 0.1$ ev/atom/dislocation. Table I gives values of V for various solute atoms interacting with a dislocation in germanium at a distance of 4 Å from the dislocation center. These calculations indicate that a driving force exists in germanium for the segregation of solute atoms about each dislocation.

It should be pointed out that only the elastic interaction was considered. In a more complete treatment one should include the effects of changing the electronic distribution and the rearrangement of the bonding in the neighborhood of the dislocation.

Mosaics or subgrains can be considered as regions of slightly different orientation in a single crystal. The boundaries between these regions may be accurately described as an array of parallel edge type dislocations [2]. This has the effect of tilting one subgrain with respect to its neighbors. The number of dislocations per unit length of mosaic boundary can be seen to be equal to

$$D = \frac{\theta}{\lambda} \tag{2}$$

where D = number of dislocations per unit length of boundary
λ = lattice spacing
θ = angle disorientation.

Knowing the distribution of mosaic boundaries and the mean angular disorientation between such regions [3], one can compute the average number of dislocations intersecting a unit cross section. Using reasonable values one obtains 10^7 dislocations/cm^2 which is in good agreement with experimentally determined values [4].

We may now represent the equilibrium concentration of solute atoms as a function of distance through the lattice as shown in Figure 1(*a*). The

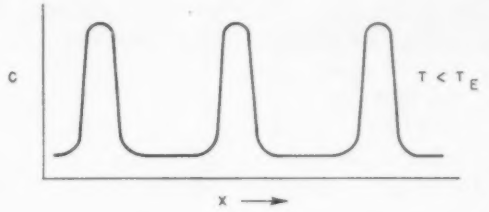

(1*a*)

FIGURE 1(*a*). Schematic depiction of impurity atom concentration versus distance through the lattice.

regions of high solute concentration correspond to boundaries having a high density of dislocations. However, the interior of the mosaics are solute poor regions of correspondingly low dislocation density. On the other hand, if the dislocations have not coalesced to form boundaries, but are randomly distributed throughout the crystal, then the above model is still valid.

It is apparent that as one progressively increases the temperature, certain solute atoms will begin leaving dislocation centers and migrating through the crystal. The escape probability of a solute atom from a dislocation stress field is proportional to $\exp(-V/kT)$, where V is the interaction energy or depth of the potential well; k is Boltzmann's factor, and T is the absolute temperature. When the thermal energy is greater than V one can assume that the solute atoms are dispersed uniformly throughout the crystal as in Figure 1(*b*). It can be shown that this results in an increase in the capture cross section of carriers with a corresponding

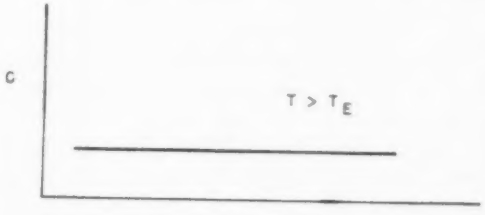

1(*b*)

FIGURE 1(*b*). Schematic depiction of impurity atom concentration versus distance through the lattice. No dislocation atmospheres.

decrease in lifetime.* On fairly rapid cooling from such a high temperature, the random impurity distribution is frozen in because of the low mobility of the solute atoms at low temperatures. However, reheating to some temperature below but in the vicinity of the escape temperature (where $T_E = V/k$) restores the dislocation atmospheres. On subsequent cooling to room temperature an increase in carrier lifetime should be observed.

It is interesting to observe that an edge type dislocation should give rise to additional levels. The lack of atomic continuity produced by this type of defect results in unsaturated bonding. Thus, concurrent with the loss of solute atmospheres is the acquisition of these new levels in the crystal. This phenomenon presumably contributes to thermal conversion. In addition, the defect structure can markedly affect the ability of various solute atoms to ionize; perfect tetrahedral bonding not being present in this region. It is because of this fact that certain impurities may exist in differing degrees of ionization than is found in the bulk of the crystal. It is possible that an impurity such as copper may form an atmosphere of essentially neutral atoms. On heating the copper would be dispersed through the volume of the crystal and ionization would again take place, with a corresponding increase in the number of acceptor levels. Changes in lifetime and electrical conductivity could also result from this phenomenon.

The preceding may be summarized as follows:

1. Since small amounts of impurities have large effects on the electrical behavior of semiconductors, it is expected that the distribution of solute atoms is also important. Atmospheres of solute atoms form under certain conditions in the vicinity of edge dislocations.

2. It is proposed that "atmosphere" formation leads to higher lifetimes. At high temperatures the loss of atmospheres and resulting uniform distribution of impurity atoms produce a corresponding decrease in lifetime.

3. It is also proposed that certain types of thermal conversion such as is produced by copper may result from the mechanism of atmosphere segregation in un-ionized form and the reversion to uniformly distributed ionized impurities on heating. A concurrent change in electrical conductivity would also result.

*The problem of electron capture by impurities is mathematically similar to that of the absorption of thermal neutrons in a pile. This problem has been treated in detail; for example, Elements of Nuclear Reactor Theory by Glasston and Edlund, p. 266.

The research in this document was supported by the Army, Navy, and Air Force under contract with the Massachusetts Institute of Technology.

A. D. KURTZ
S. A. KULIN

Lincoln Laboratory
Massachusetts Institute of Technology
Cambridge, Massachusetts

References

1. COTTRELL, A. H. Report of the Conference on Strength of Solids (London, Phys. Soc., 1948).
2. READ, W. T. and SHOCKLEY, W. Phys. Rev., **78** (1950) 275.
3. KURTZ, A. D., and KULIN, S. A., and AVERBACH, B. L. Unpublished research. Lincoln Laboratory, Massachusetts Institute of Technology.
4. VOGEL, F. L., PFANN, W. G., COREY, H. E., and THOMAS, E. E. Phys. Rev., **90** (1953) 489.

Effect of Dislocations on Minority Carrier Lifetime in Germanium*

Preliminary experimental results indicate that dislocations markedly affect the recombination rate of holes and electrons in germanium. Dislocation densities have been measured by X-ray and metallographic methods and the results have been correlated with measurements of the lifetime of minority carriers. Calculations have been performed to ascertain the magnitude of the change of energy gap resulting from the strains about a dislocation.

An X-ray double crystal spectrometer has been used for precise measurement of diffracted line breadths. The line breadths may be directly related to the density of dislocations, since the double crystal technique eliminates elastic broadening.

If it is assumed that dislocations are randomly distributed in a crystal, one can show that the dislocation density is given by $\beta^2/9\lambda^2$ [1], where β corresponds to the angular width of the diffraction line and λ is the Burgers vector. Values of β were measured with the spectrometer and the dislocation density was then calculated using the above formula.

In addition, under suitable etching conditions it is possible to resolve individual dislocations under the microscope. Thus by counting etch pits one can independently determine the dislocation density. This has been done for a number of samples and the results are in good agreement with the X-ray data.

*Received January 21, 1954.

In order to determine the effect of the density of dislocations on some of the electrical parameters, resistivities, bulk lifetime and mobility were measured on a selected series of germanium specimens. All of the specimens had about the same n-type resistivity (2–8 ohm-cm). In Figure 1 the

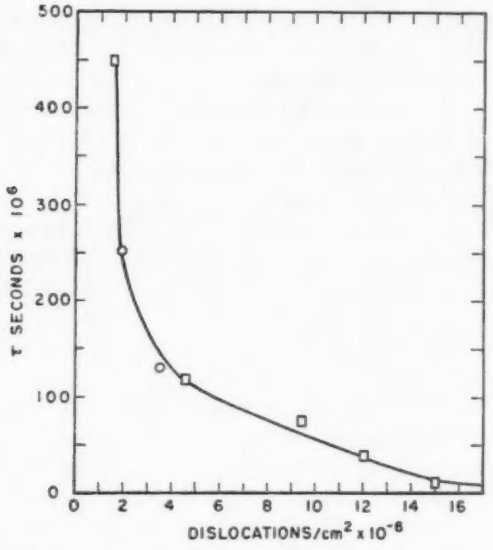

FIGURE 1. Lifetime of minority carriers versus dislocation density.

measured lifetime* is shown as a function of the dislocation density. The results seem to indicate a functional relationship. If one assumes that each dislocation acts as a recombination center, the rate of recombination is given by $\lambda = \Delta p/\tau = \sigma_R N \Delta p$ where Δp is the excess number of minority carriers, N is the number of dislocations and σ_R is a proportionality constant relating to the recombination by a unit length of dislocation. Thus the unit recombination efficiency is given by $1/\tau N$. The value of σ_R is found to be 2×10^{-3}/cm-sec. These experimental results indicate the validity of the proposed hyperbolic relationship.

To explain this correlation one must consider the strains about each dislocation. Using the results of Koehler [2] and Nabarro [3] one can show that the dilation is given by

$$\frac{\Delta V}{V} = \frac{1-2\nu}{2\pi(1-\nu)} \frac{\lambda \sin\theta}{\left[R^2 + \frac{\nu\lambda R\cos\theta}{1-\nu} + \frac{\nu\lambda^2}{2(1-\nu)^2}\right]^{\frac{1}{2}}},$$

where λ is the Burgers vector, ν is Poisson's ratio, and R and θ are the polar coordinates.

These large strains lead to changes in the energy bands in the neighborhood of the dislocation [4]. If the energies of the conduction and valence bands, E_c and E_V respectively, are considered unique functions of the local strain, then following Bardeen and Shockley [5]

$$E_c = E_{c0} + \epsilon_{1c}\Delta V/V \text{ and } E_V = E_{V0} + \epsilon_{1V}\Delta V/V$$

where

$$\epsilon_{1c} = \partial E_c/\partial V$$

and

$$\epsilon_{1V} = \partial E_V/\partial V$$

Thus the change in gap width $\Delta E_G = (\epsilon_{1c} - \epsilon_{1V})\Delta V/V$. Using their values for ϵ_{1c} and ϵ_{1V} the changes in the gap width as a function of position about a dislocation have been determined. Contours of constant gap shift (ΔE_G) are plotted in Figure 2. The

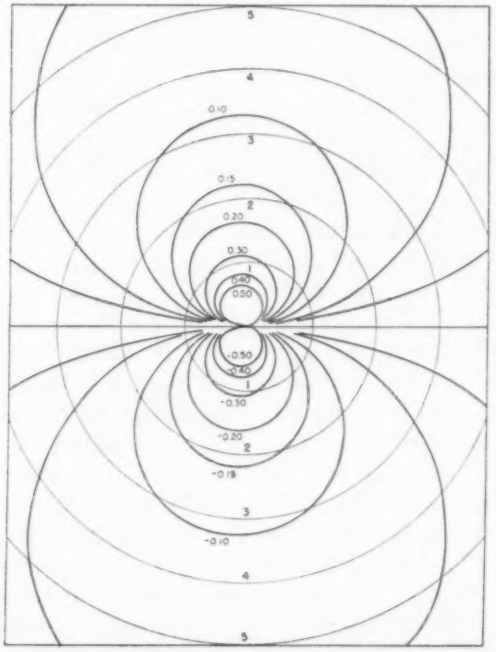

FIGURE 2. Contours of equal change in energy gap about a positive edge-type dislocation in electron volts. R is in units of interatomic spacing.

calculated values are only roughly approximate for $R < 1$. Above the singular line the energy gap widens and below it contracts, corresponding to the change in gap under compression and tension respectively. The same thing is shown schematically in Figure 3. An electron will prefer to be localized in the region BC where its allowed energy

*Bulk lifetimes were measured using a conductivity modulation method on both sandblasted and etched surfaces.

is a minimum. Similarly a hole will tend to reside in the higher energy valence states of this region BC. This energy configuration can thus be used as a model to describe a recombination mechanism.* Furthermore, one might expect the recombination probability to be greater in this volume element than in the undistorted bulk. If so, the reverse process would also occur; i.e. the dislocation must act as a source as well as a sink for hole electron pairs.

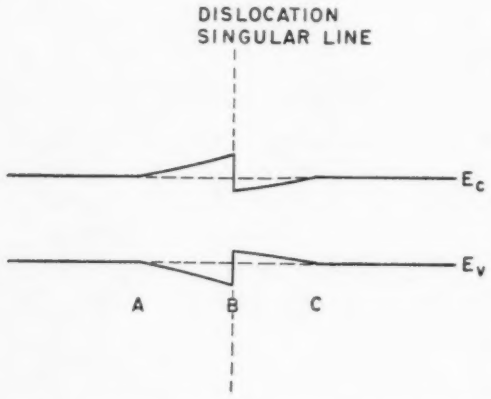

FIGURE 3. Schematic representation of energy levels about a dislocation. Region AB corresponds to the compression side and region BC to the tension side.

This work indicates the important role of dislocations in many aspects of semiconductor theory. Since these imperfections presumably are always present to the extent of about 10^6 per square centimeter (involving roughly 10^{17} atoms per cc in germanium), intrinsic recombination centers will exist even in chemically pure material. Theoretical lifetimes of minority carriers calculated on the basis of a perfect single crystal can therefore probably not be achieved. In addition, certain experimental results might be explained on the basis of the model presented. For example, measurements of light absorption versus frequency to determine the value of the energy gap in germanium do not give a very sharp transition, but result in a band of values. Similarly the breakdown of germanium at liquid helium temperatures as a result of increasing high-frequency electric field does not occur at a single fixed value [6]. These smearing-out effects may possibly result from the additional energy levels associated with the dislocations.

These preliminary results can be summarized in the following manner:

1. The density of randomly distributed dislocations in germanium has been determined by two independent methods. This value varies between 10^6 and 10^8 per square centimeter.

2. A functional relationship exists between the density of dislocations and the lifetime. The recombination efficiency per dislocation is found to be approximately equal to 2×10^{-3}/cm-sec.

3. The change in energy gap has been calculated as a function of position about dislocation. The proposed model may lead to a better understanding of some of the properties of germanium.

The authors wish to express their appreciation to Professor B. L. Averbach of the Department of Metallurgy at Massachusetts Institute of Technology and to Professor J. E. Thomas of Lincoln Laboratory for their continuing advice and assistance in this program. The research in this document was supported by the Army, Navy and Air Force under contract with the Massachusetts Institute of Technology.

S. S. KULIN
A. D. KURTZ

Lincoln Laboratory
Massachusetts Institute of Technology
Cambridge 39, Massachusetts

*Further effects caused by the interactions of Impurities and Dislocations are discussed in a communication appearing in this Journal on page 352.

References

1. GAY, P., HIRSCH, P. B. and KELLY, A. Acta Met. **1** (1953) 315.
2. KOEHLER, J. S. Phys. Rev. **60** (1941) 397.
3. NABARRO, F. R. N. Proc. Phys. Soc. Lond. **59** (1947) 256.
4. BROOKS, H., Private communication.
5. BARDEEN, J. and SHOCKLEY, W. Phys. Rev. **80** (1950) 72.

BOOK REVIEW

Atomic Theory for Students of Metallurgy. By **William Hume-Rothery.** London: Institute of Metals, 1953.

The volume under review here is a revision of a work first published in 1946. With the exception of major changes in two of the thirty chapters the book is essentially the same as the original edition. The principal justification for reviewing this new edition seems to me to be the opportunity to evaluate the success which the book has had, since its first appearance, in teaching the applications of modern atomic theory to metallurgy.

The book was designed for the use of the Honours student in the baccalaureate program of the British university. This level of study corresponds somewhat to the first year of graduate study at American universities, and it is in graduate studies that the main use of the book has been. In this way an entire generation of metallurgists has been introduced to the theories of modern physics which have wide application in their field. Such studies were previously lacking and long overdue in the physical metallurgy curriculum. I doubt, however, whether the book has accomplished nearly so much as should be accomplished in such studies. Almost two thirds of the volume covers material which corresponds to the standard atomic physics course. The treatment of this material is wholly qualitative and not sufficiently fundamental to lead to constructive thinking on the part of the student. A vocabulary is learned without a precise idea of the physical phenomena which underlie it. Much the same criticism can be levelled against the general treatment of the electron theory of metals. Most of the book is written as though all knowledge of the properties of metals came from the development of the quantum mechanics and the important results and viewpoints which were gained from classical physics are omitted entirely. With such omission the student is sure to develop faulty perspective and intuition.

The most satisfactory part of the book is the treatment of the structure of alloys which represents the author's principal competence as well as a field of notable advance in understanding by application of the theory of the electronic structure of metals.

In over-all estimate the book does not seem adequate to its purpose today unless strongly supplemented by some of the better modern texts on atomic theory and theory of solids.

EDWARD W. HART

SOME CURRENT PAPERS IN OTHER JOURNALS

Acta Crystallographica, Vol. 7

Part 1, January, 1954 (Partial contents)

Enregistrement continu par diffraction électronique, de transformations chimiques ou physiques et applications. JEAN-JACQUES TRILLAT et NOBORU TAKAHASHI.

Der Symmetrieeinfluss auf den allgemeinen Lösungsansatz ein-dimensionaler Fehlordnungsprobleme. HEINZ JAGODZINSKI.

Koordination und Symmetric substituierter C6-Strukturen vom Typus $A_nB_{2n-z}C_z$. FRANZ AEBI.

X-ray studies of polycrystalline metals deformed by rolling. III. The physical interpretation of the experimental results. P. GAY, P. B. HIRSCH and A. KELLY.

The crystal structure of Rh_2B. RICHARD W. MOONEY and A. J. E. WELCH.

The crystal structure of TiB. B. F. DECKER and J. S. KASPER.

Contribution à l'étude des Borures à teneur élevée en bore. PIERRE BLUM.

Some lattice indeterminacies. G. D. ARCHARD.

An electron-optical study on the surface of glass. JOHN J. ANTAL and A. H. WEBER.

The crystal structures of ZrBeSi and $ZrBe_2$. J. W. NIELSEN and N. C. BAENZIGER.

Pressure effects on the measurement of lattice parameter. C. R. BERRY, M. H. VAN HORN, and R. L. GRIFFITH.

The atomic scattering factors of Au^+ and Hg^{++}. W. G. HENRY.

Part 2, February, 1954 (Partial contents)

The interpretation of diffuse X-ray scattering from powder patterns of solid solutions. P. A. FLINN, B. L. AVERBACH, and P. S. RUDMAN.

X-ray scattering by aggregates of bonded atoms. IV. Applications to the carbon atom. R. McWEENY.

Ferroelectricity and crystal structure, II. HELEN D. MEGAW.

X-ray study of phase transitions in $PbZrO_3$ containing Ba or Sr. GEN SHIRANE and SADAO HOSHINO.

The reflexion and transmission of X-rays near the Bragg angle in perfect absorbing crystals. GÖSTA BROGREN.

Sur une transformation martensitique de la phase protoxyde de fer. R. COLLONGUES.

Sur les paramètres limites de la phase FeO. J. BÉNARD.

On the basic assumptions and the validity of Zachariasen's sign relations in X-ray crystal analysis. E. F. BERTAUT and R. PEPINSKY.

Subsidiary maxima in electron-diffraction net patterns from molybdenite. RYOZI UYEDA, TAKEO ICHINOKAWA, and YASUSHIGE FUKANO.

Subsidiary maxima of Kikuchi pattern. RYOZI UYEDA, YASUSHIGE FUKANO and TAKEO ICHINOKAWA.

A dynamical theory of the simultaneous reflexion by two lattice planes. I. Simple representation of the dispersion surface. KYOZABURO KAMBE and SHIZUO MIYAKE.

A dynamical theory of the simultaneous reflexion by two lattice planes. II. The effect of the phase factor of the structure amplitude. SHIZUO MIYAKE and KYOZABURO KAMBE.

Atomic resolution in generalized crystal-structure projections. D. C. PHILLIPS.

The intermetallic phase $NpBe_{13}$. O. J. C. RUNNALLS.

Archiv für das Eisenhüttenwesen

Heft 11–12, November-Dezember, 1953

Mikroskopische Untersuchungen an gebranntem Dolomit. GERHARD TRÖMEL.

Beiträge zur Analyse der Gefügebestandteile in Roh-und Gusseisen. WALTER KOCH und JOACHIM BRUCH.

Spektrographischer Nachweis von Randaufkohlungen und -entkohlungen. WERNER LIEDTKE.

Die Abhängigkeit des Steilabfalls der Alterungs-Kerbschlagzähigkeit von der chemischen Zusammensetzung bei unberuhigten Stählen. HEINZ KORNFELD.

Härtbarkeit verschiedener gebräuchlicher Baustähle nach dem Stirnabschreckversuch. HEINZ KIESSLER und KARL SCHWEYHER.

Anisotrope Massänderungen bei der Wärmebehandlung ledeburitischer Chrom-Werkzeugstähle. JOSEF FREHSER.

Anwendung des Zeit-Temperatur-Umwandlungs-Schaubildes für kontinuierliche Abkühlung auf Fragen der Wärmebehandlung. ADOLF ROSE und WERNER STRASSBURG.

Wanddickenmessung an Stahlflaschen in der Fertigung. FRANZ BOLLENRATH und VIKTOR HAUK.

Metallographische Untersuchung nichtmetallischer Einschlüsse in Stahl nach einem neuartigen Dünnschliffverfahren. ERICH FOLKHARD.

Oxydische Dauermagnete aus Bariumoxyd und Eisen (III)-oxyd. HERMANN FAHLENBRACH und WALTER HEISTER.

Der Einfluss von Mangan, Nickel und Vanadin im Zusammenwirken mit Kohlenstoff auf das Verschliess-verhalten von normalgeglühten Stählen. HEINRICH AREND.

Der Oxydationsvorgang bei Titankarbid-Kobalt-Hartmetallen. WILLY KINNA und OTTO RÜDIGER.

Über den Mechanismus der Austenit-Martensit-Umwandlung. HELMUT KNAPP.

Journal of the Chemical Society

December, 1953 (Partial contents)

The photochemistry of selenium. Part IV. Photogalvanic effects with grey selenium. R. W. PITTMAN.

The production of active solids by thermal decomposition. Part I. Introduction. S. J. GREGG.

The production of active solids by thermal decomposition. Part II. Ferric oxide. S. J. GREGG and K. J. HILL.

Anodic processes. Part I. Anodisation at low current densities of mercury in hydrochloric acid. R. H. COUSENS, D. J. G. IVES, and R. W. PITTMAN.

Anodic processes. Part II. Oscillographic studies of processes at the mercury anode in hydrochloric acid. R. H. COUSENS, D. J. G. IVES, and R. W. PITTMAN.

Anodic processes. Part III. The passivation of mercury in hydrochloric acid. R. H. COUSENS, D. J. G. IVES, and R. W. PITTMAN.

January, 1954 (Partial contents)

The mechanism of inhibition of the corrosion of iron by sodium hydroxide solution. Part II. J. E. O. MAYNE and J. W. MENTER.

The mechanism of inhibition of the corrosion of iron by solutions of sodium phosphate, borate, and carbonate. J. E. O. MAYNE and J. W. MENTER.

Further studies of the supercooling of drops of some molecular liquids. H. J. deNordwall and L. A. K. Staveley.
Chemical bonds involving d-orbitals. Part I. D. P. Craig, A. Maccoll, R. S. Nyholm, L. E. Orgel, and L. E. Sutton.
Chemical bonds involving d-orbitals. Part III. D. P. Craig, A. Maccoll, R. S. Nyholm, L. E. Orgel, and L. E. Sutton.

Journal of the Institute of Metals, Vol. 82

Part 5, January, 1954
The constitution of alloys of aluminium, copper, and iron. H. W. L. Phillips.
The oxidation of titanium at high temperatures in an atmosphere of pure oxygen. A. E. Jenkins.
The structure of titanium-silver alloys in the range 0–30 at.-% silver. H. W. Worner.
The metallographic detection of gamma-phase in beta-brass. L. E. Samuels.

Part 6, February, 1954
Mechanism of creep deformation in high-purity aluminium at high temperatures. Hsing C. Chang and Nicholas J. Grant.
Ageing curves at 110°C on binary and ternary aluminium-copper alloys. H. K. Hardy.
Structural ageing characteristics of binary aluminium-copper alloys. (Miss) J. M. Silcock, T. J. Heal, and H. K. Hardy.
Changes of damping capacity in quench-ageing aluminium-rich alloys. K. M. Entwistle.
Some metallographic observations of the creep of aluminium-copper alloys. A. H. Sully and H. K. Hardy.

Part 7, March, 1954
Problems of the control of dimension, shape, and finish in the rolling of sheet and strip and in the drawing of wire. Hugh Ford and J. G. Wistreich.
The control of quality in the hot and cold rolling of aluminium and aluminium alloys. F. King and A. N. Turner.
The control of properties and structure in the hot and cold rolling of copper and copper-base alloys. W. W. Kee.
Some factors affecting the quality of extrusions. Christopher Smith and Norman Swindells.
Statistical control in metal-working operations. M. Whyte.

La Metallurgia Italiana, Vol. XLV

Novembre, 1953
Su alcune anomalie nella emissione spettrale da superfici monocristalline cristallograficamente definite. O. Masi.
Attualita nel campo della produzione del rame. G. Porro.

Revue de Métallurgie, 50e Année

Numéro 12, décembre, 1953
Un exemple de transposition des phénomènes et lois en métallographie: Des alliages légers d'aluminium aux alliages austénitiques résistants à chaud. A. Portevin.
Méthodes de préparation et d'analyse d'échantillons de fer de très haute pureté. J. Talbot, Ph. Albert, M. Caron et G. Chaudron.
Sur l'introduction de carbone 14 dans le fer pur par cémentation gazeuse. Ph. Albert.
Influence de la vitesse de déformation et de la température sur la consolidation du fer Armco. H. Hendus et H. Röhrig.
Influence du vieillissement à 80°C sur les caractéristiques mécaniques du fer Armco et d'un acier à 0,16% C. H. Hendus et H. Röhrig.
Contribution à l'étude des diagrammes fournis par la micro-machine de traction du type Chevenard. H. Hendus, H. Röhrig et G. Kraus.
La transformation isotherme de l'austénite et le partage des éléments spéciaux dans les aciers faiblement alliés. Axel Hultgren et ses Collaborateurs.
La zone de transition de la résilience des aciers doux. J. Ulmo, F. Bastenaire et R. Borione.

Revue de Métallurgie, 51e Année

Numéro 1, janvier, 1954
Particularités et délimitation de la notion de la micro-dureté Vickers. H. Bückle.
Influence du mode de coulée de l'aluminium sur la répartition des impuretés et l'aspect après oxydation anodique. H. Richaud.
La galvanisation continue des bandes en acier selon le procédé Sendzimir. A. Ollivet.
L'atelier de galvanisation de tubes de la Société Lorraine-Escaut. J. Fleischmann.
Influence de la qualité du revêtement sur la résistance à la corrosion des fils d'acier galvanisés. J. Hérenguel.
Une technique opératoire d'élaboration d'acier Thomas à faibles teneurs en azote, en phosphore et en soufre, au moyen d'air enrichi en oxygène. P. Leroy, M. Gombert, et B. Trentini.

Zeitschrift für Metallkunde

Heft 12, Dezember, 1953
Über die Gesetzmässigkeiten der plastischen Verformung von Metallen unter einem mehrachsigen Spannungszustand II. Zug- und Torsionsversuche an Hohlzylindern aus Aluminium. W. Sautter, A. Kochendorfer und U. Dehlinger.
Schnellverfahren zur Bestimmung von Aluminium in Aluminium-Mehrstoffbronzen. H. Wiedmann.
Über ein Geiger-Zählrohr-Goniometer nach dem Seemann-Bohlin Prinzip. G. Wassermann und J. Wiewiorowsky.
Zur Frage der Aktivierung von Metalloberflächen. C. Schaub und W. Liedtke.
Über die Eigenschaften metallischer Schmelzen. VIII. Die Dichte von flüssigem Aluminium und einigen Aluminiumlegierungen. E. Gebhardt, M. Becker und S. Dorner.
Über den Mechanismus von Oxydations—und Korrosionsvorgängen an Metallen und Legierungen. K. Hauffe.

PRECIPITATION OUT OF DUAL SOLID SOLUTIONS OF CARBON AND NITROGEN IN ALPHA-IRON*

C. WERT†

The problem of precipitation in dual solid solutions of C and N_2 in α-iron was examined experimentally. The internal friction of these solutions was found to be a useful property with which to study this change of phase. The effect of either of these elements is to speed up the aging of the one with the slower rate to equal that of the faster. This is interpreted to be an effect of easier nucleation. The structure of the precipitate resulting from aging of this dual solution is unknown. Magnetic coercive force measurements have been made during aging; these are more difficult to interpret than internal friction data. This is thought to be caused by a pronounced particle size effect on the coercive force.

LA PRÉCIPITATION À PARTIR DE SOLUTIONS SOLIDES, DOUBLES DE C ET DE N_2 DANS LE FER-α

On a examiné expérimentalement le problème de précipitation à partir des solutions solides, doubles de C et de N_2 dans le fer-α. Dans l'étude du changement des phases il est avantageux de se servir du frottement interne de ces solutions solides comme propriété indicative. L'effet de chacun de ces éléments est d'accélérer le vieillissement de l'élément dont la vitesse est plus faible, jusqu'à ce qu'il atteigne la vitesse de l'élément le plus rapide. Ceci est interprété comme étant un effet de germination plus facile. La structure du précipité qui apparaît au vieillissement de cette solution double est inconnue. On a mesuré la force coercitive, magnétique pendant le vieillissement; il est, toutefois, plus difficile d'interpréter ces résultats que les données obtenues par la mesure du frottement interne.

On suppose que cette difficulté est causée par l'effet important des dimensions des grains sur la force coercitive.

AUSSCHEIDUNGEN VON ZWEIFACH FESTEN LÖSUNGEN VON C UND N_2 IN α-EISEN

Das Problem der Ausscheidung aus zweifach festen Lösungen von C und N_2 in α-Eisen wurde experimentell untersucht. Es zeigte sich, dass die innere Reibung dieser Lösungen eine zum Studium dieser Phasenumwandlung gut geeignete Eigenschaft ist. Jedes der Lösungselemente hat folgende Wirkung: Es beschleunigt das Altern des Elements mit der geringeren Alterungsgeschwindigkeit um diese der des schneller alternden Elementes anzugleichen. Diese Erscheinung wird als ein Effekt der leichteren Keimbildung erklärt. Die Struktur der beim Altern dieser zweifachen Lösung auftretenden Ausscheidung ist nicht bekannt. Während der Ausscheidung wurden Messungen der magnetischen Koerzitivkraft durchgeführt. Sie sind schwieriger zu interpretieren als die Werte der inneren Reibung. Ein starker Effekt der Teilchengrösse auf die Koerzitivkraft wird als Grund dafür angesehen.

I. Introduction

The precipitation out of solid solutions of C and N_2 in α-iron is accompanied by changes in many physical properties. It is not always easy to follow accurately the kinetics of the precipitation phenomenon, however, since frequently both the precipitate and the solid solution affect the measurement. Furthermore, as more refined methods of experimental technique and interpretation of data are developed, it appears that aging of either solid solution is a more complicated process than was first supposed. A detailed description of the individual steps taking place in precipitation from either solid solution is, for these reasons, not yet known.

The problem of determining what goes on in simultaneous aging of C and N_2 in α-iron is even more troublesome. This is true primarily because most physical properties which might be used to detect aging are affected in much the same way by both C and N_2. It is then difficult to separate the measurements into components caused by either the one or the other. Hence almost no work has been done on the kinetics of precipitation in the dual solid solution. An early attempt at this was the work of Köster [1]. His work was both extensive and well done. It consisted of a large number of measurements of magnetic coercive force and electrical resistance made during aging of various types of solid solutions. He supplemented these measurements by a considerable amount of metallographic inspection of the precipitates. The interpretations he made of interest to this work are chiefly (1) that carbon in solution in iron affects the aging rate of dissolved nitrogen, tending to retard it; (2) that after a certain limiting value of C is reached, aging of nitrogen is even suppressed; (3) that cementite particles can serve as nuclei for precipitation of nitrogen. The first two of these conclusions are not supported by the results of this investigation; no test was made of the third.

Unfortunately the changes in coercive force during aging of these alloys are affected both by the amount of precipitate and by the precipitate particle size (and perhaps shape). Dijkstra and

*Received October 18, 1953.
†University of Illinois, Urbana, Illinois.

Wert have demonstrated a pronounced particle size effect for precipitation of iron carbide [2]. Whether there is such a pronounced effect for nitride particles is not yet completely established; preliminary measurements in our laboratory indicate that some effect of this kind does exist. Köster was aware of these effects but apparently did not consider them serious enough to alter his conclusions. As a result, his intrepretations may not show the true picture.

An important part of the study of aging in these solid solutions is knowledge of the structure of the precipitate produced. Dijkstra has demonstrated that the aging of N_2 in α-iron is a two-stage process; first there forms a metastable precipitate which dissolves and reprecipitates into Fe_4N [3]. Jack has shown Dijkstra's first precipitate to be identical with the α'' nitride, $Fe_{16}N_2$, obtained as a first stage in the decomposition of nitrogen-martensite [4]. The existence of more than one carbide in the decomposition of C in α-iron is a distinct possibility, since several iron carbides have been prepared by other means [5]. The aging of a dual solid solution of C and N_2 may result then in the formation of any of these carbides and nitrides or in the formation of one of a further group of compounds, the carbonitrides, at least two of which have been reported [6].

With such an imposing set of possibilities and considering the experimental difficulties involved, it is unlikely that any single application of any technique will result in a complete understanding of the kinetics of aging in these dual solid solutions. To choose an experimental technique with which to attack the problem, the author was naturally led to a consideration of all physical properties which had been used to study the aging of single solid solutions. The property of the solid solutions finally used as a first technique was their internal friction. Some advances were made with this technique in the understanding of the aging of C and N_2 alone in ferrite [7], and it is not too much to expect that some additional information might be found here. The method does offer one advantage over some other techniques in that the internal friction measurements, when properly made, will give a measure of carbon and nitrogen separately even when both are present. (The details of how this is done will be pointed out later.) Most other property changes—electrical resistance, magnetic coercive force, thermoelectric power, hardness, for example—will not do this.

The present paper is an initial attempt to show that internal friction methods can give new data of use in the study of the dual solid solutions. This was not an exhaustive study since measurements were made at only two aging temperatures and with alloys of only a single carbon-to-nitrogen ratio. The number of conclusions that can be reached from the data presented are not numerous and some of the earlier claims of Köster are not fully tested. These initial measurements do, however, point out some new facts and suggest further measurements that could be made using this method.

II. Experimental Details

The apparatus for making the internal friction measurements was the well-known torsional pendulum [8]. With a specimen .030 in. in diameter and 5 in. long the bob was adjusted to give a frequency of about 1 cps. The specimens were puron wires, swaged and drawn to .030 in. After a decarburizing treatment at 720°C, they were ready for further heat treatment. The grains in the wires were rather uniform in size and were about .001 in. in diameter. This was a somewhat finer grain size than had been used in previous work. As a consequence, part of what is considered in this paper to be precipitation may actually be the trapping of interstitial atoms in the grain boundaries. This should not affect the conclusions presented here since they are based on comparisons of the behavior of the two interstitials in fine grain iron.

Producing the solid solutions of C and N_2 provided the greatest experimental difficulty; once this was solved the measurements were straightforward. To demonstrate the principles involved in producing the desired compositions, parts of the Fe-C and Fe-N_2 phase diagrams are reproduced in Figure 1. These data are taken from the work of Dijkstra [3], Stanley [9], and Paranjpe, Cohen, Bever and Floe [10]. In Figure 1, there are superposed the α-solubility line for C in equilibrium with the carbide, and for N_2 in equilibrium with Fe_4N and the metastable $Fe_{16}N_2$. The composition chosen for these measurements was .015 wt % C and .015 wt % N_2. This is close to the maximum solubility of C in α-iron and is a quantity of C for which aging occurs in reasonable time intervals in the temperature range 100°C to 300°C. For experimental reasons it was desirable to have the N_2 content of the samples about the same as the C content.

Specimens of three types were made: (1) .015% C + iron, (2) .015% N_2 + iron and (3) .015%

C + .015% N_2 + iron. The first was easily made by heating a decarburized specimen at 720°C in a mixture of H_2 and pentane vapor before water quenching. The second type of specimen was made by heating a wire in a mixture of H_2 + 2% NH_3 at 720°C. This is a temperature somewhat higher than that usually used for nitriding (some 590°C). The higher temperature was chosen to eliminate any possible effect on later aging of differences in nucleation which might be caused by differences

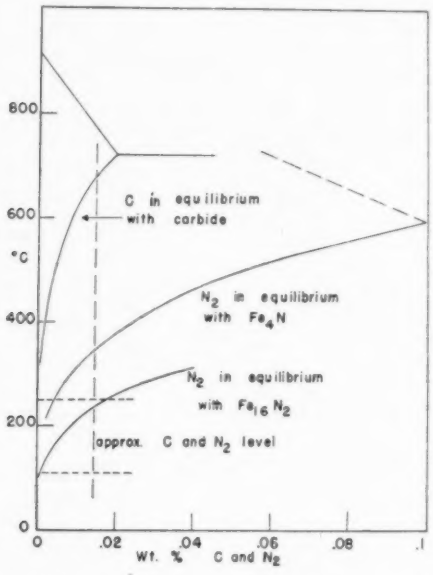

FIGURE 1. A part of the constitution diagrams of the systems Fe-C and Fe-N_2.

in the solution-treating temperature. The third set of specimens was the most difficult to produce since small changes in gas composition would throw one or the other of the components out of the range accepted (.014% to .018% of each). About one third of the samples were suitable and ten specimens of α-iron + C + N_2 in solid solution were prepared. Each of these could be used many times by a short solution-treating exposure at 720°C in dry H_2.

III. Experimental Results

The results of this investigation are conveniently divided into two parts.

1. Precipitation of supersaturated solutions of C, N_2, and C + N_2 was carried out at 110°C and 250°C. Anelastic measurements were made at intervals during aging.

2. Measurements of magnetic coercive force were made during aging at 110°C. These measurements were correlated with anelastic measurements to show in which part of the precipitation process the coercive force experiences its greatest change.

The present section will be devoted to a discussion of the experimental results obtained, together with their interpretation by the author. Final paragraphs will discuss the bearing this work may have on other investigations.

Before it was possible to use internal friction methods to study this problem, it was necessary to learn something of the internal friction behavior of the dual solid solution itself. From the well-known peaks of internal friction vs. temperature, which are found with solutions of C and N_2 alone in α-iron, it is clear that one can expect the two peaks to overlap.*

A measurement of the damping of a solid solution of C + N_2 is given in Figure 2; the experimental points are the circles. The two curves *a* and *b* are the normal nitrogen and carbon peaks whose maxima are adjusted so that the sum curve gives just the measured values at 22°C and 40°C. The entire sum curve is seen to fit the remaining experimental points rather well. This shows that the presence of either interstitial element does not influence the shape or position of the damping peak of the other. It is thus presumed that the internal friction method is a reliable one to use in further precipitation measurements.

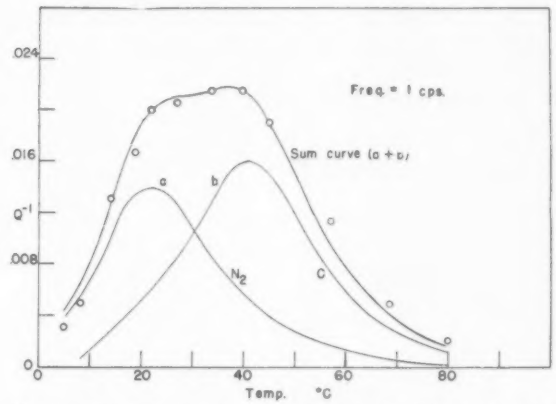

FIGURE 2. The internal friction of a dual solid solution of C and N_2 in α-iron. vs. temperature. Curves *a* and *b* are the normal nitrogen and carbon peaks. The sum curve is *a* + *b*, where the maximum heights of *a* and *b* have been adjusted to give the experimental values at 22°C and 40°C.

During aging, measurements of damping were made at only two temperatures, 22°C and 40°C.

*At 1 cps, the nitrogen peak occurs at 22°C, the carbon peak at 40°C. The contribution of each peak at the temperature of the other is seen from Figure 2 to be some 35 per cent.

The maxima of the two component curves were then calculated. These maxima were taken to be measures of the C and N_2 still in solid solution. It is clear that this technique is most accurate when the two component curves have about the same maxima; when one is several times the other, the error in determining the smaller may be rather great. This is the chief reason for using C and N_2 concentrations of about the same level.

Examination of the constitution diagrams of Figure 1, shows that there are two aging temperatures of interest. The one is a temperature such that the nitride formed (when N_2 is present alone in iron) is the phase $Fe_{16}N_2$. The other temperature is one for which $Fe_{16}N_2$ is soluble and the phase Fe_4N is formed. For the composition of C and N_2 used in this work ($\approx$.015 wt %) the two temperatures which seemed most reasonable were 110°C and 250°C.

Descriptions of measurements made during aging at these two temperatures follow:

1. *Aging at 110°C.*

Typical aging curves for the three types of solid solutions are given in Figure 3.* For C alone, the

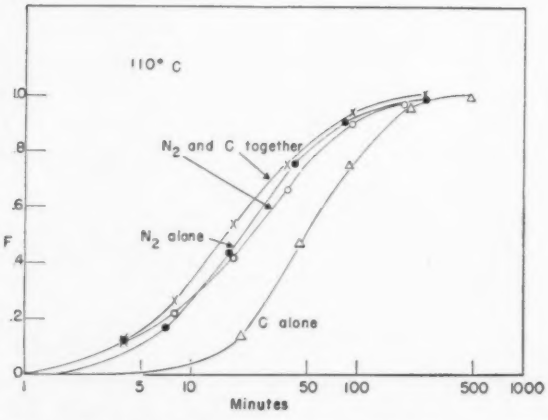

FIGURE 3. Precipitation curves of C and N_2 in iron at 110°C.

precipitation is half-complete in about 50 minutes; for N_2 alone, in about 20 minutes. When C and N_2 are present together, they both precipitate one half in about 20 minutes. This is a rate increase for aging of C of about $2\frac{1}{2}$ times. It is a significant factor since aging curves for a given alloy can be reproduced with a spread in time of about 20 per cent.

2. *Aging at 250°C.*

Similar aging curves for the three solid solutions when they are held at 250°C are given in Figure 4. At this temperature the equilibrium solid solubility

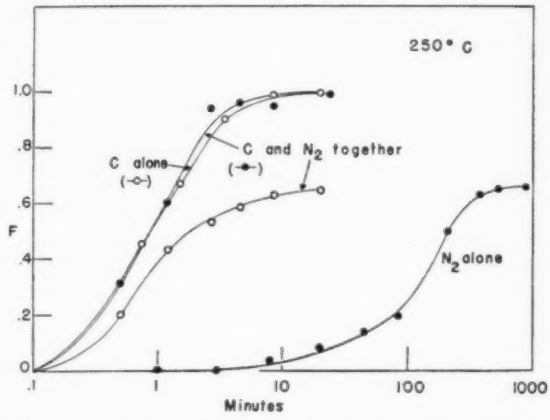

FIGURE 4. Precipitation curves of C and N_2 in iron at 250°C.

of N_2 with $Fe_{16}N_2$ is somewhat greater than the amount of N_2 actually present in the alloy (.015 wt %); hence this phase will not form. For N_2 alone in iron then under these conditions the stable phase Fe_4N forms and ages to half value in about 130 minutes. When C alone is present, aging goes to half-value in slightly less than one minute. When C and N_2 are both present, they both age to half-value in a little less than a minute. This is no change in rate for C, but an increase in rate for N_2 by more than one hundred times.

The reader will note that the fraction of initial nitrogen precipitated in both of these alloys never becomes unity at 250°C. This is so because the solubility of N_2 in equilibrium with Fe_4N at 250°C is itself appreciable. The 35 per cent which does not precipitate corresponds to about .005 wt % N_2; this is about the solubility indicated at 250°C in Figure 1.

These results all by themselves are insufficient to enable one to form a complete and accurate picture of what is going on. Certain facts may be drawn from the data, however, and from them may be made a number of possible explanations. Two of these explanations are given in the paragraphs which follow.

There is no doubt that the rate of aging of one

*The fraction of material precipitated (as plotted in this and the remaining figures is calculated from the damping measurements. Since the internal friction measures the amount of material left in solid solution at time t, the precipitated fraction, F, is given by the expression:

$$F = 1 - (Q^{-1}(t)/Q^{-1}(0)),$$

where $Q^{-1}(t)$ is the damping at time t and $Q^{-1}(0)$ is the initial damping at $t = 0$.

type of interstitial atom is influenced by the presence of the other. The rate of the slower (when it is present alone) is increased to equal the rate of the faster (when it is present alone). This rate increase could be accomplished by either of two means, an increase in number of nuclei available for aging or an increase in diffusion rate; it has previously been demonstrated that both of these factors enter into the aging rate [11]. It is clear from Figure 2, that the diffusion rate of neither C nor N_2 is sensibly altered by the presence of the other in these low concentrations. Hence the important factor must be an increase in the number of nuclei. One would then say that (all other things being considered equal) the number of nuclei present at 110°C in the alloys of N_2 and $N_2 + C$ must be about equal and must be somewhat greater than the number of nuclei present in the alloy of C at this temperature. At 250°C the order must be reversed. Fe_4N must nucleate with great difficulty and the alloys of C and $N_2 + C$ with greater ease. This picture may be somewhat incorrect inasmuch as the physical shape of the precipitate has been demonstrated to play a role in aging rate as well [7].

An important question (and one which cannot be answered by this investigation) is the structure of the precipitates themselves. It has been rather well proved that the precipitates which are formed with N_2 alone (under these experimental conditions) are $Fe_{16}N_2$ and Fe_4N at 110°C and 250°C. The precipitate of carbon formed has been presumed to be cementite; recent investigations show the probability of the precipitate being one of several carbides [12]. At present the structure of the precipitate which forms when both C and N_2 are present is entirely unknown.

In explaining the results of Figures 3 and 4 there are then two main possibilities. The one is that the carbon and nitrogen can nucleate massive precipitates of each other. The carbide and nitride formed in dual aging may then grow from similar nuclei, but may in the end resemble closely the carbide and nitride which would be formed if each were present alone.* This adequately explains the rate increase of the slower aging precipitate. It is also in agreement with the fact (see Figure 4) that at 250°C the N_2 level at the end of aging is the same for both samples—one containing N_2 and the other $N_2 + C$. The second possibility is that the two materials form a mixed carbonitride in both the nuclei and the massive precipitate. The atomic ratio of the two elements, about 1 to 1, is in the range of formation of either the ϵ or ρ carbonitride [6]. This would require that the solubility of N_2 in equilibrium with Fe_4N at 250°C should be the same as that in equilibrium with the carbonitride.

The internal friction is, of course, only one of many physical properties of α-iron which change upon aging of C and N_2. Another property of interest is the magnetic coercive force. Figures 5, 6, and 7 show how the coercive force changes

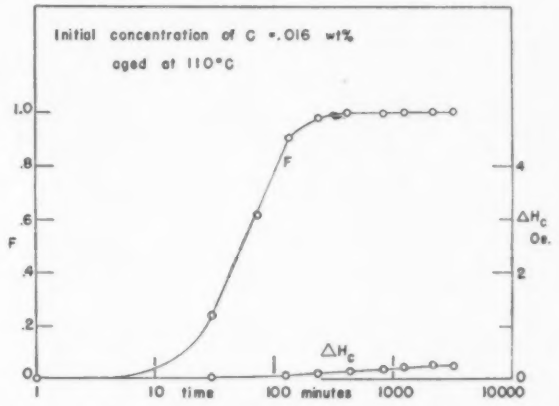

FIGURE 5. Precipitation of C at 110°C and changes in coercive force accompanying it.

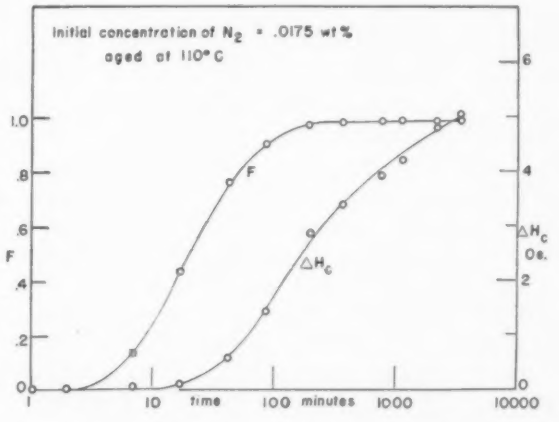

FIGURE 6. Precipitation of N_2 at 110°C and changes in coercive force accompanying it.

during aging at 110°C of C, N_2, and $C + N_2$. These measurements of coercive force were made by the ballistic-galvanometer-method.

The precipitation of C at this temperature is accompanied by almost no change in coercive force. It is only after the precipitation is complete and some coalescence has taken place that H_c will begin to increase. This has been demonstrated to

*Köster claimed that cementite could nucleate the precipitation of dissolved nitrogen.

be due to a particle-size effect [2]. At somewhat higher temperature H_c will indeed follow more closely the actual precipitation curve. The total rise in H_c for precipitation of .015 wt % C under optimum aging conditions is about 1.5 Oe. The curve in Figure 5 would presumably rise to about this level if coalescence were carried far enough.

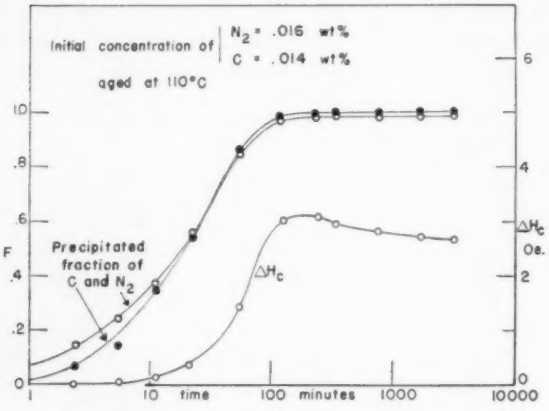

FIGURE 7. Precipitation of C + N_2 at 110°C and changes in coercive force accompanying it.

The precipitation of N_2 at 110°C is more closely followed by an increase in H_c. There seems to be here too, a particle-size effect. The coercive force has barely begun to rise when the precipitation is half-done; it rises steadily while the precipitation is being completed and continues to increase during coalescence of this precipitate. The work of Köster [1] shows that one might expect it to rise to a maximum and then decrease upon even further aging. (Our own unpublished measurements show that this is correct.) For the same amount of material, .015 wt %, the effect on coercive force is clearly considerably greater for N_2 than for carbon. This may indicate an important effect of particle shape as well as particle size.

The precipitation out of solid solution of C + N_2 also causes a change in coercive force. The behavior of H_c in this case is more nitrogen-like than carbon-like, although it does not go as high as for N_2 alone (in spite of a larger amount of precipitate having been formed). Over-aging (magnetically speaking) occurs in a somewhat shorter time also. Comparison of Figures 5, 6, and 7 lends support to the contention that for the alloy C + N_2 a carbonitride is formed, for the behavior of H_c during aging is different from that of either C or N_2. This, too, indicates that, if particle shape is important, the precipitate shape of this supposed carbonitride is somewhat different from that of either the carbide or nitride.

One fact which is clear from these coercive force measurements is that this property is a poor one to use to follow the precipitation. Factors other than the amount of precipitate seem to play an important role. Hence the excellent experimental work of Köster on changes of coercive force during aging apparently does not lend itself well to accurate interpretation.

The work of Tsou, Nutting and Menter, on aging of carbon in iron must be mentioned further. They maintain that the claims of spherical shape of carbide particles made by Wert [11], Zener [13], and Radavich and Wert [14] are erroneous, at least for low aging temperatures. They have evidence to support the contention that the carbides formed during aging of C in α-iron are also plates. Their work is more extensive than any previous work and may indeed show the correct picture. One thing which they failed to do, however, was to remove the N_2 from their material. In the light of the present investigation, this may have been an important factor in their work, for they may have been observing carbonitrides rather than the carbides which they claimed to have.

Summary

The present work shows rather clearly that the precipitation of either C or N_2 out of α-iron is affected strongly by the presence of the other. The minimum amount of one necessary to affect the other is so far not known. The precipitate formed from the dual solid solution is also unidentified; there appears to be a good chance that it is a carbonitride. Since this mutual effect on precipitation of the two does exist, the study of formation of either pure carbides or nitrides in iron may require careful elimination of nitrogen and carbon, respectively.

Acknowledgement

This work was supported in part by the Office of Army Ordnance and by the Westinghouse Research Laboratories.

References

1. KÖSTER, W. Archiv für das Eisenhuttenewesen Fachberichte, **2** (1928–9) 503; **3** (1930) 553; **3** (1930) 637; **4** (1930) 145; **4** (1930) 289.
2. DIJKSTRA, L. and WERT, C. Phys. Rev. **79** (1950) 979.

3. DIJKSTRA, L. Trans. A.I.M.E. **185** (1949) 252.
4. JACK, K. Acta Cryst. **3** (1950) 392.
5. RILEY, H. Quarterly Reviews (London) **3** (1949) 160.
6. JACK, K. Proc. Roy. Soc. ***A*195** (1948) 41.
7. WERT, C. Thermodynamics in Physical Metallurgy (A.S.M., 1950) p. 178.
8. KÊ, T. S. Phys. Rev. **71** (1947) 533.
9. STANLEY, J. Trans. A.I.M.E. **185** (1949) 752.
10. PARANJPE, V., COHEN, M., BEVER, M., and FLOE, C. Trans. A.I.M.E. **188** (1950) 261.
11. WERT, C. J. Appl. Phys. **20** (1949) 943.
12. TSOU, A., NUTTING, J., and MENTER, J. J. Iron and Steel Inst. **172** (1952) 163.
13. ZENER, C. J. Appl. Phys. **20** (1949) 950.
14. RADAVICH, J. and WERT, C. J. Appl. Phys. **22** (1951) 367.

ACCELERATED GROWTH OF TIN WHISKERS*

R. M. FISHER, L. S. DARKEN AND K. G. CARROLL†

It has been shown experimentally that the growth rate of tin whiskers may be accelerated up to 10,000 times the previously observed spontaneous rate by the application of pressure up to 7,500 psi. It is shown that these whiskers may exhibit three stages of growth: (1) an induction period (sometimes unobservably small); (2) a period of constant growth rate, and (3) an abrupt transition to a much slower growth rate. The growth rate during period (2) is directly proportional to the applied pressure. The spontaneous growth rate is shown to correspond to a free-energy dissipation of about 1/10 joule per gram atom of tin and the fastest accelerated rate to about 10^4 times this value. It is verified that tin whiskers grow from the base rather than the tip.

LA CROISSANCE ACCÉLÉRÉE DE "POILS" D'ÉTAIN

Il a été montré expérimentalement que la vitesse de croissance des "poils" d'étain peut être augmentée jusqu'à 10.000 fois la vitesse spontanée, observée antérieurement, par l'application d'une pression allant jusqu'à 7500 livres/pouce carré. Il est montré que ces poils peuvent manifester trois stades de croissance: (1) une période d'induction (parfois trop courte pour être observée); (2) une période de vitesse de croissance constante, et (3) un passage brusque à une vitesse de croissance beaucoup plus faible. La vitesse de croissance de la période (2) est directement proportionnelle à la pression appliquée. On montre que la vitesse de croissance spontanée correspond à une dissipation d'énergie libre d'environ 1/10 de joule par atome-gramme d'étain, et la plus grande vitesse modifiée à environ 10^4 fois cette valeur. Il a été verifié que les "poils" poussent par la base, plutôt que par la pointe.

DAS BESCHLEUNIGTE WACHSTUM VON ZINN"HÄRCHEN"

Es wird experimentell gezeigt, dass die Wachstumsgeschwindigkeit von Zinn"Härchen' bis zum 10,000 fachen der spontanen Wachstumsgeschwindigkeit durch Anwendung von Drucken bis zu 7500 psi gesteigert werden kann. Es wird nachgewiesen, dass diese "Härchen" drei Wachstumsstadien zeigen können: (1) Eine Induktionsperiode (oft unbeachtbar gering); (2) eine Periode konstanter Wachstumsgeschwindigkeit, und (3) einen plötzlichen Umschlag zu einer sehr viel geringeren Wachstumsgeschwindigkeit. Während der Periode (2) ist die Wachstumsgeschwindigkeit dem angewandten Druck nahezu proportional. Es wird gezeigt, dass die spontane Wachstumsgeschwindigkeit einem Fluss der freien Energie von etwa 1/10 Joule pro Grammatom Zinn entspricht, und die höchstbeschleunigte Wachstumsgeschwindigkeit etwa 10^4 mal diesen Wert beträgt. Es wird bestätigt, dass die Zinn"Härchen" vorzugsweise von der Basis aus und nicht von der Spitze wachsen.

The present communication stems from the chance observation that specimens of electrolytic tin plate (as used for tin cans) mounted tightly in an ordinary metallographic clamp and prepared for microscopic examination developed, after a few days standing, a rather pronounced filamentary growth. The nature of these growths is illustrated by Figure 1. Here the growth is along the black lines corresponding to an original tin thickness of about 2.5 microns, the spacings (1/4 mm) correspond to the steel base. These filaments closely resemble the growths or "whiskers" first reported by Compton, Mendizza and Arnold [1], as a spontaneous phenomenon observed after many months on tin- and cadmium-plated capacitors in commercial telephone equipment. These whiskers have since received considerable attention since they pose problems of both theoretical and practical importance. The practical significance lies principally in the fact that these whiskers create short circuits in electrical equipment. Theoretical interest has been spurred by the apparent paradox of macroscopic crystals transforming spontaneously to microscopic crystals (whiskers) of relatively high specific surface.

These whiskers are reported to possess remarkable properties. For example, Herring and Galt [2] reported that their creep rate is much lower than that of bulk tin and that they can be strained as much as 2 per cent without suffering plastic deformation. Each whisker or whisker segment seems to be a single crystal.

The earlier proposed mechanisms called for growth from the tip. For example, Peach [3] proposed that tin atoms were transported along a screw-type dislocation coincident with the whisker axis. Mechanisms of this type are apparently eliminated, for tin at least, by the observation of Koonce and Arnold [4], that tin whiskers grow from the base and not from the tip. This conclusion, i.e., that the whiskers grow from the base, is supported by the present investigation. A careful inspection of some of the whiskers grown in a metallographic clamp, shown in the time sequence of Figure 1, shows that an irregularity at or near the tip of a whisker maintains, with time, a fixed distance from the tip but regularly increases its distance from the base. It will be noted that although many of these

*Received December 8, 1953.
†Research Laboratory, United States Steel Corporation, Kearny, New Jersey.

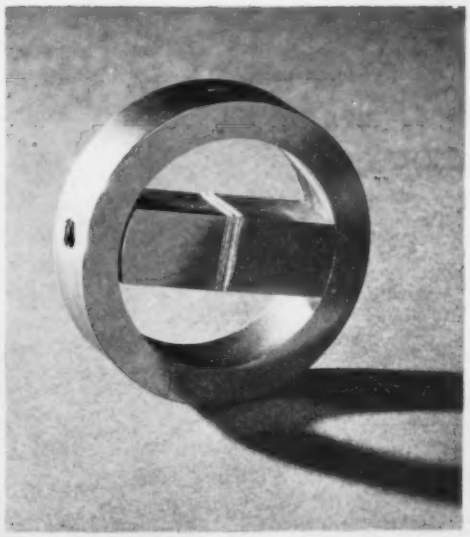

3

PLATE I. FIGURE 1—Time sequence showing whisker growth at low pressure. (*a*) 1 day; (*b*) 2 days; (*c*) 3 days; (*d*) 6 days; (*e*) 7.5 days. FIGURE 3—Ring clamp used for exerting known pressure on specimens.

whiskers are straight, the proportion of kinked or spiral whiskers is considerably greater than that observed by others for spontaneous growth (without pressure application). The spirals usually seem to consist of straight segments; it is not certain that this is always the case. In other respects, except for the markedly increased rate of growth, whiskers here reported are similar to those obtained by spontaneous growth. Examination of some of the longer ones in the electron microscope indicates a diameter of about one micron. X-ray diffraction of a small cluster fixed in a Debye-Scherer powder camera gave about as many spot patterns as whiskers, indicating each to be a single crystal of tin; rotation of the specimen gave a continuous ring powder pattern.

Frank [5] and Eshelby [6] have recently suggested growth mechanisms based on a dislocation at the base of the whisker. Both regard the requisite energy as being supplied by atmospheric oxidation, thus providing a virtual negative surface tension. The crystalline mercury whiskers reported by Sears [7] may grow from the vapor phase, thus involving a different mechanism.

The growth curves of the whiskers marked A, B and C in Figure 1 are plotted in Figure 2. These

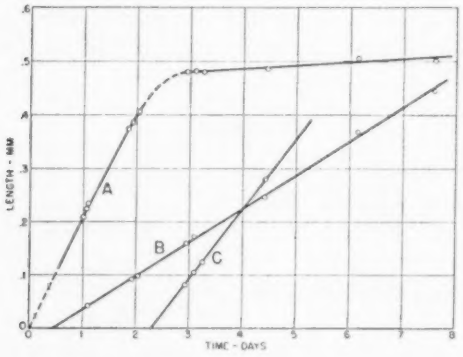

FIGURE 2. Growth behavior of individual whiskers A, B, and C indicated on preceding figure.

three are selected since they grew straight, are nearly parallel to the polished surface (thus remaining in focus), and illustrate various modes of growth. Whisker A apparently started to grow immediately on a retightening of the clamp and continued to grow at a substantially constant rate for about two and one-half days, after which it slowed rather abruptly and continued to grow at a greatly reduced rate. Whisker B started growth only after an induction period of about one-half day; its rate is slower than that of A. The induction period of Whisker C was even greater—two and one-half days—but its growth-rate is comparable to that of A. In general the growth of whiskers here reported, grown under the influence of pressure, is characterized by (1) the presence or apparent absence of an induction period; (2) a period of a substantially constant growth rate; and (3) a rather abrupt transition to a much slower growth rate.

Experiments in Ring Type Clamps

The above-mentioned observation that the rate of whisker growth rises rapidly with the force exerted in tightening the clamp, seemed convincing evidence of the pronounced effect of pressure. However, this is of a qualitative nature only, since the magnitude of force is unknown and it cannot be presumed to act uniformly over the area of the specimens. In order to investigate in a more quantitative manner the relation between pressure and growth rate, special mounting clamps were prepared. These were in the form of hardened steel proof rings 2 inches in outside diameter, $1\frac{1}{2}$ inches in inside diameter and $\frac{1}{2}$ inch thick (see Figure 3). The tin-plated specimens ($\frac{1}{2}$ inch square) were supported inside the ring by end blocks and a single screw through the ring. These rings were calibrated on a tensile machine, and the force exerted by the ring on the specimens was obtained from the calibration chart and the known extension of the ring diameter on loading, as measured by a micrometer. The specimens (about 14) were first mounted, ground, polished and examined under light load (about 100 pounds). Immediately after repolishing the rings were compressed laterally and the screw simultaneously taken up lightly; the specimens were thus still under light load. The lateral compressive force was then released, thus applying the full load on the specimens at a definite starting time. The force exerted by the ring on the specimens did not change noticeably (or only very slightly) during the course of an experiment. Thus, in these experiments, the force—and hence the average pressure—exerted on the specimens was known. Local deviations of pressure are of course unknown; however, pressure equalization brought about by the flow of tin, as well as the results to be discussed, support the opinion that these deviations are not severe in this type of clamp except in the immediate vicinity of the free surfaces.

The whisker growth-rate obtained in these clamps was even more startling than that observed

in the ordinary metallographic clamps. It was planned to maintain the pressure on the clamp and to measure, as a function of time, the number of whiskers which had reached or passed planes at predetermined heights above the polished surface. A pretrial with a substantially static whisker colony indicated this plan to be readily practicable by means of the calibrated focus control on a standard metallographic microscope. However, in the case of specimens under a force of 1200 lbs (4800 psi) the induction and growth periods were so short and the growth-rate so rapid that growth was well advanced in the few minutes required to remove the specimen from the press, measure its diameter, and position it under the microscope. However, this method was satisfactory at lower pressure (2100 psi). At higher pressures (4400 and 7300 psi) the difficulties were obviated by releasing the pressure after a few minutes; this halted or, at least, markedly decreased the growth-rate so that the counts could be made more leisurely. These two methods gave consistent results, as may be seen from the results shown in Figure 4.

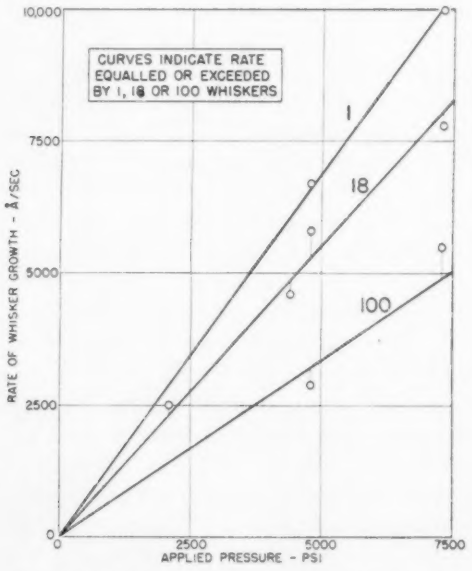

FIGURE 4. Effect of pressure on whisker growth.

It is to be realized that the height measurements (Figure 4) pertain directly only to the vertical component of whisker length. However, the direction normal to the polished surface seems a preferred direction of growth; this, combined with the fact that the earlier whiskers to reach any preassigned plane are those of short induction time which grow straight, tends to minimize the distorting tendency of long induction period and of angular or kinked growth.

The number of shorter whiskers far exceeds that of the longer ones counted—by perhaps a factor of a hundred. An attempt was made to estimate an average height at each of several times by assuming a normal distribution of heights; this statistical treatment was unsuccessful as the presumed average height passed through a maximum as a function of time, and then decreased. This anomalous behavior is undoubtedly associated with the induction time, and with angular and kinked growth as well as with the doubt as to normal distribution of the growth rates.

As can be seen from Figure 4, the fastest growth was 10,000 Å/sec, corresponding to a millimeter (about the maximum length) in 16 minutes; this is about 10^4 times as fast as the reported spontaneous growth rate of a few millimeters per year and is over 100 times as fast as the whiskers grown in ordinary metallographic clamps shown in Figure 1. It should also be noted that the whiskers grown in ring clamps were more prolific the higher the pressure; no quantitative measurements were made of this. Further, the length attained by the end of the period of rapid growth does not vary much; hence the higher the pressure, the greater the growth rate, the shorter is the period of rapid growth.

Discussion

The growth of whiskers under the influence of pressure, as described above, is easier to understand than the previously reported spontaneous growth. In the case of spontaneous whiskers, not only the growth mechanism but even the motive force involved is by no means self-evident; moreover, the source of free energy must be of sufficient magnitude to supply the surface-free energy for the rather large specific surface of the whisker. From the naive view point, at least, the source of energy supply is quite apparent in the case of whiskers grown under the influence of pressure. If it is supposed that a uniform pressure, P, prevails in the major part of the tin and that the pressure drops off in the vicinity of the surface to substantially atmospheric pressure near the base of a whisker, then the free-energy change, ΔF, per gram atom of tin transported from the high-pressure to the low-pressure region is $\Delta F = \int V dP = V(\Delta P)$, V being the gram atomic volume which is essentially constant. Thus the pressure axis of

Figure 4 may equally well be regarded as a free-energy axis; the only restrictions on this transformation are that V remain constant and that a slight change of origin may be required. This slight shift is certainly not enough to affect noticeably the slope of the line in Figure 4; in fact, if a point representing the spontaneous growth-rate were placed on Figure 4, the scale is such that this point would appear to coincide with the origin. Assuming the curves of Figure 4 to be linear to zero growth-rate, it may readily be computed that the spontaneous growth rate (1 Å/sec) corresponds to a ΔF of about 1/10 joule per gram atom of tin above the free energy required for infinitesimal growth-rate. It will be noted that this calculation involves no assumption as to the atomistic nature of the mechanism of whisker growth; this free energy corresponds to that dissipated by the flux of tin from the massive state to the base of the whisker. It is qualitatively compatible with Frank's mechanism. It is tempting to speculate that spontaneous growth is also motivated by pressure—residual stresses in the tin. The magnitude required to account for the observed spontaneous rate is quite low, about 1/10 atmosphere. The present investigation provides no clue as to the verity of this suggestion; the requisite free energy could equally well be provided otherwise.

In the photomicrographic series of Figure 1 we noticed that considerable tin is extruded by the application of pressure. Whiskers seem to grow, not from this extruded tin, but from the vicinity thereof. The speculation might be made that whiskers grow by diffusion of tin from a high-pressure region through a region of steep pressure gradient to the whisker base. Thus, extruded tin, being a region of continuous low pressure, would not form a favorable whisker base. The generalization of Fick's first law to include free-energy gradients not necessarily associated with concentration [8] gives the flux as $(DC/RT)(dF/dr)$, where D is the diffusivity; C, concentration; R, the gas constant; T, the absolute temperature; dF/dr, the free-energy gradient. Setting $dF = VdP$, and assuming that tin is transported by a pseudo-steady-state diffusion process across a hemispherical shell of outer radius large compared to an inner radius (r_0) equal to that of the whisker, the total rate of transport is $2\pi\ r_0\ DP/(RT)$, which corresponds to a linear rate of whisker growth $2\ DPV/(RT\ r_0)$. Setting P equal to the maximum experimental value, the dimensionless quantity $PV/(RT) = 0.4$, this gives a calculated linear growth rate about equal to D/r_0. Taking r_0 as 1 micron, and assuming that the diffusivity is the normal self-diffusivity (10^{-12} cm^2/sec) of tin at room temperature, the calculated linear growth rate is found to be 1 Å/sec—considerably slower than the observed rate of 10^4 Å/sec. The disparity may be occasioned by the enhancement of the diffusivity by a vacancy flux as suggested by Frank, or by an erroneous assumption of a diffusion mechanism, i.e., by the assumption that the sites stay substantially stationary while the atoms move (or, possibly, a surface diffusion mechanism is involved). However, the obvious alternative—the analogy to squeezing tooth paste out of a tube—hardly seems promising when it is recalled that the mechanism invoked must produce a single crystal, a constant growth rate, and should provide some clue as to the induction period and to the termination of the period of rapid constant growth-rate. The diffusion theory combined with the postulate of a dislocation at the base of the whisker does satisfy the first three requisites; on this theory the termination of the rapid growth can be interpreted as a "plugging" of the dislocation by foreign atoms.

References

1. COMPTON, K. G., MENDIZZA, A., and ARNOLD, S. M. Corrosion **7** (1951) 327.
2. HERRING, C., and GALT, J. K. Phys. Rev. **85** (1952) 1060.
3. PEACH, M. O. J. Appl. Phys. **23** (1952) 1401.
4. KOONCE, S. E. and ARNOLD, S. M. J. Appl. Phys. **24** (1953) 365.
5. FRANK, F. C. Phil. Mag. p. 854, August 1953.
6. ESHELBY, J. D. Phys. Rev. **91** (1953) 775.
7. SEARS, G. W. Acta Met. **1** (1953) 457.
8. DARKEN, L. S. Atom Movements (Cleveland, American Society for Metals, 1951).

THE EFFECT OF HYDROGEN ON ULTRASONIC ATTENUATION AND VELOCITY MEASUREMENTS IN TITANIUM*

C. F. YING and R. TRUELL†

Ultrasonic attenuation and velocity were measured in commercially pure titanium over an ultrasonic frequency range from 10 to 50 mc/s before and after heating in hydrogen. The two ultrasonic quantities changed by large amounts when the metal was heated in hydrogen at temperatures near 550°C. The main feature is that the attenuation decreased with the increasing hydrogen content.

The changes induced by heating in hydrogen resulted mainly from the appearance of titanium-hydrogen phases although hydrogen in solution may also have had an effect. Similar treatment of the titanium in vacuum, oxygen, and nitrogen did not produce appreciable changes in attenuation, velocity, or microstructure.

Unfortunately the use of attenuation measurement work at these frequencies is in early stages of development and no unique identification of the mechanisms involved can be given at present. As a consequence this paper is limited to discussion of the experimental observations and effects.

LES EFFETS DE L'HYDROGÈNE SUR LES MESURES DE L'ATTENUATION ET DE LA VITESSE ULTRASONIQUES DANS TITANE

L'attenuation et la vitesse ultrasoniques ont été mesurées dans du titane commercialement pur, dans un intervalle de fréquences allant de 10 à 50 mc/sec, avant et après un chauffage dans de l'hydrogène. Les deux grandeurs ultrasoniques changeaient dans des proportions considérables quand le métal était chauffé dans l'hydrogène aux températures proches de 550°C. La caractéristique principale de ce changement était que l'attenuation diminuait quand la teneur en hydrogène augmentait. Les changements produits par le chauffage dans l'hydrogène étaient dus, avant tout, à l'apparition de phases titane-hydrogène, quoique l'hydrogène en solution eût aussi pu avoir un certain effet. Un traitement similaire du titane dans le vide, l'oxygène et l'azote n'a pas produit de changements appréciables de l'attenuation, de la vitesse ou de la microstructure. L'emploi des mesures de l'attenuation à ces fréquences est encore fort peu développé et il est impossible, en ce moment, d'interpréter les mécanismes impliqués d'une façon unique. Par conséquent, dans cet article, on se borne à discuter les observations et les effets expérimentaux.

DER EINFLUSS VON WASSERSTOFF AUF ULTRASCHALLDÄMPFUNG UND GESCHWINDIGKEITSMESSUNGEN IM TITAN

Ultraschalldämpfung und -geschwindigkeit wurden in technisch reinem Titan vor und nach Glühen in Wasserstoff in einem Ultraschallfrequenzbereich zwischen 10 und 50 mc/sec gemessen. Wird das Metall bei etwa 500°C in Wasserstoff geglüht, so ändern sich die beiden Eigenschaften stark. Die Haupterscheinung ist die mit zunehmendem Wasserstoffgehalt abnehmende Dämpfung.

Die durch Glühen in Wasserstoff hervorgerufenen Eigenschaftsveränderungen beruhen in erster Linie auf dem Auftreten von Titan-Wasserstoff-Phasen, obwohl auch der gelöste Wasserstoff wirksam sein kann. Entsprechende Versuche mit Titan im Vakuum, in Sauerstoff oder Stickstoff rufen keine nennswerten Änderungen in Dämpfung, Schallgeschwindigkeit oder Feinstruktur hervor.

Leider sind die Dämpfungsmessungen in diesen Frequenzbereichen erst im Anfangsstadium ihrer Anwendung, und es kann im Augenblick kein eindeutiger Nachweis der verschieden zugrunde liegenden Elementarvorgänge gegeben werden. Deshalb beschränkt sich die vorliegende Arbeit auf eine Diskussion der experimentellen Beobachtungen.

Introduction

In the course of an investigation of the effect of the occlusion of gases on the ultrasonic attenuation of solids, the effect of hydrogen in titanium was examined. Titanium is known to be capable of absorbing hydrogen in large quantities [1; 2; 3] and hydrides are formed in many cases [4].

Attenuation and velocity measurements of longitudinal ultrasonic waves were made in titanium before and after treating in hydrogen. The frequency range investigated was from 10 to 50 mc/s. The methods of attenuation measurement have been described elsewhere [5]. The equipment used for these measurements has been extensively modified since reference [5] was published. One modification of the previous equipment is the addition of a calibrated exponential decay curve of variable decay rate which can be presented on the scope together with the echo pattern.

In order to introduce the hydrogen into the titanium it was found necessary to heat the samples in hydrogen. Since heating may change the grain size of a metal and since the ultrasonic attenuation properties depend very sensitively on the grain size [6] one must determine whether the hydrogen is really the main feature or whether the changes observed might, for example, arise from heating at the same temperature in vacuum or in the presence of a gas other than hydrogen; such experiments were performed. It is necessary in any given case to examine the microstructure and this

*Received August 23, 1953; in revised form, December 12, 1953.

†Metals Research Laboratory, Brown University, Providence, Rhode Island.

was done in these experiments. On heating titanium in hydrogen it was found that under certain conditions the structure did not change appreciably while under other conditions the structure within the grains changed drastically. The introduction of hydrogen into the titanium by electrolytic methods [7] is not possible with samples large enough for ultrasonic measurements.

Experimental Procedure and Results

All of the samples studied were cut from two commercially pure hot-rolled rods obtained from the Titanium Metals Corporation of America. The rods were labeled grade Ti-75A. The samples used were approximately one-half inch thick and two inches in diameter with opposite faces accurately plane and parallel.

The titanium samples were heated in hydrogen taken from commercial hydrogen tanks and in a furnace designed for growing metal single crystals.

A total of 10 samples was studied in addition to a few samples investigated on preliminary runs. The treatment of the samples together with some of the results on velocity measurements is given in Table I. Samples with consecutive numbers were adjacent to each other in a given rod of titanium. Some of the samples were heated in vacuum in groups before any measurements were made so that these samples were annealed and partially outgassed.

The velocity measurements are shown in Table I and some of the attenuation results are shown in Figures 1–4. In these figures the ultrasonic energy loss is given in decibels per inch of path in the metal as a function of the ultrasonic frequency.

TABLE I

HEAT TREATMENT OF TITANIUM SAMPLES

Sample	Atmosphere	Temp. °C.	Length of time (hours)	Velocity cm/sec	Hydrogen content %	Density change %
507*	Vacuum	750	4	5.85×10^5	—	—
	H_2	440	66	5.88	3.08	−0.2%
506*	Vacuum	750	4	5.83	—	—
	H_2	550	77	5.88	8.2	−1.0%
	H_2	460	50	5.96	11.6	−0.4%
	H_2	500	65	5.96	14.0	−0.4%
508*	Vacuum	750	4	5.87	—	—
	H_2	550	44	6.32	44.4	−7.3%
	H_2	550	61	6.52	55.8	−3.8%
	Vacuum	550	24	6.11	29.1	8.5%
	Vacuum	550	37	5.94	9.4	3.2%
		590	3			
514	Vacuum	750	4	5.89		
513	Vacuum	750	4	not measured		
	H_2	550	114	6.04		
512	Vacuum	750	4	not measured		
	H_2	550	61	6.13		
515*	As received			5.93		
	Vacuum	550	74	5.91		
520	As received			5.86		
	Vacuum	590	77	5.93		
503*	As received			not measured		
	N_2	600	45	5.90		
505*	As received			not measured		
	O_2	600	71	5.95		

*All from one rod; others all from a second rod.

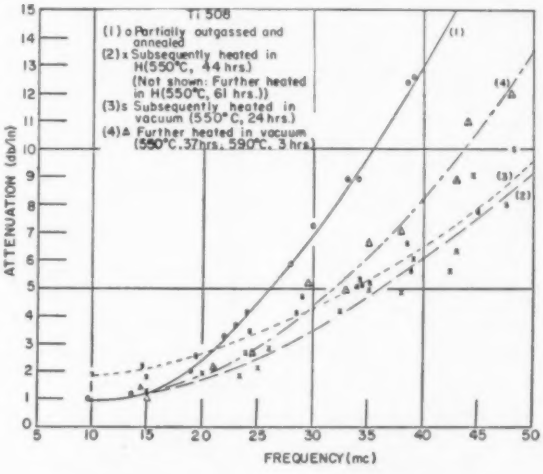

FIGURE 1. Attenuation-frequency plot for Ti 508.

The density changes and the hydrogen content changes produced by heating in hydrogen or in hydrogen and in vacuum were obtained, and these changes are listed in Table I. Volume changes as large as 10 per cent were observed in the titanium after heating sample 508 for 44 hours in hydrogen. Corresponding to this change the density decreased by 7.3 per cent.

The titanium samples did not gain appreciable weight (0.09 gram in 132.30 grams) when heated in commercial oxygen at 600°C. or in commercial nitrogen at 600°C.

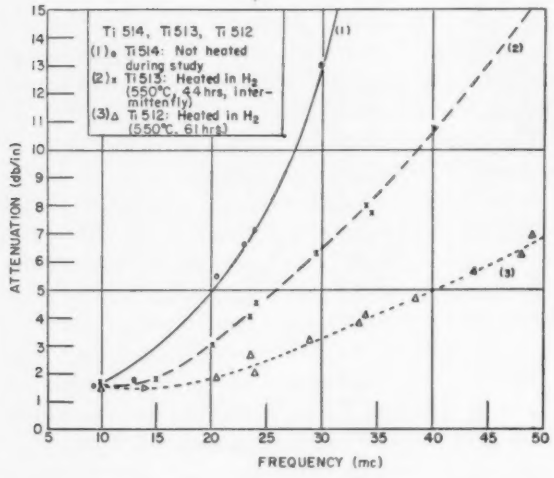

FIGURE 2. Attenuation-frequency plot for Ti 514, Ti 513, and Ti 512.

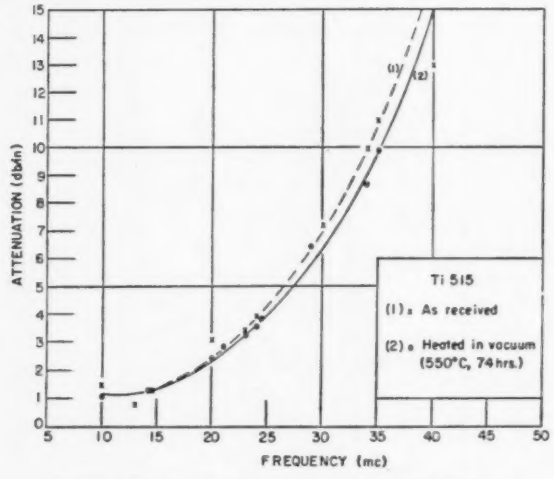

FIGURE 3. Attenuation-frequency plot for Ti 515.

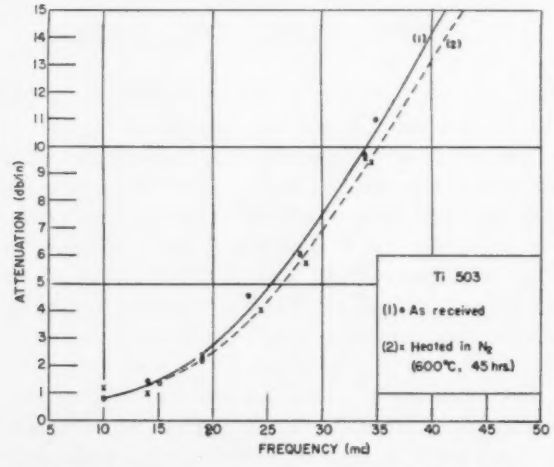

FIGURE 4. Attenuation-frequency plot for Ti 503.

After each stage in the heat treatment the microstructure of most of the samples was examined. Photomicrographs of sample 508 in various stages of heat treatment are shown in Figures *5a, b, c, d, e, f*. The corresponding attenuation-frequency curves for the same sample are shown in Figure 1.

Discussion

It has been established in this experiment that commercially pure titanium on being heated in hydrogen under certain conditions, changes its ultrasonic attenuation and velocity as well as its density.

On comparing the data for sample Ti 508, which was heated only in hydrogen, with the data for Ti 515 and Ti 520 which were heated in vacuum and with the data for Ti 503 and Ti 505 which were heated in nitrogen and oxygen respectively, it can be concluded that heating in the presence of hydrogen and not heating alone is essential for introducing the large changes observed in the ultrasonic properties of titanium. It is not to be inferred that pure heating or that heating in the presence of nitrogen and oxygen will not change these properties under any circumstances. It has only been established that, at the relatively low temperature of 550°C, hydrogen alone produced the effects observed.

The sample marked Ti 508 underwent the most thorough study and it underwent the largest changes on being heated in hydrogen. After the first heating, the attenuation decreased by a factor of 2 to 1 at 40 mc/s, and more at higher frequencies (Figure 1). The largest observed velocity change was about 11 per cent. On being heated for a second time in hydrogen the character of the material changed in a rather remarkable way. The attenuation (not shown) changed by a large amount and echo pattern became markedly nonexponential. When a large energy loss occurs at a given point or interface in the solid an exponential decay factor may no longer be appropriate if the energy lost is no longer proportional to the energy present in the pulse. Such a situation seemed to prevail here and only after the sample was subsequently heated in vacuum, did the echo pattern again become exponential. The remarkable feature is that the attenuation decreased before the pattern became nonexponential. It is interesting to see that with a 10 per cent change in volume the material does not appear to develop faults since the pulse attenuation pattern is very clean.

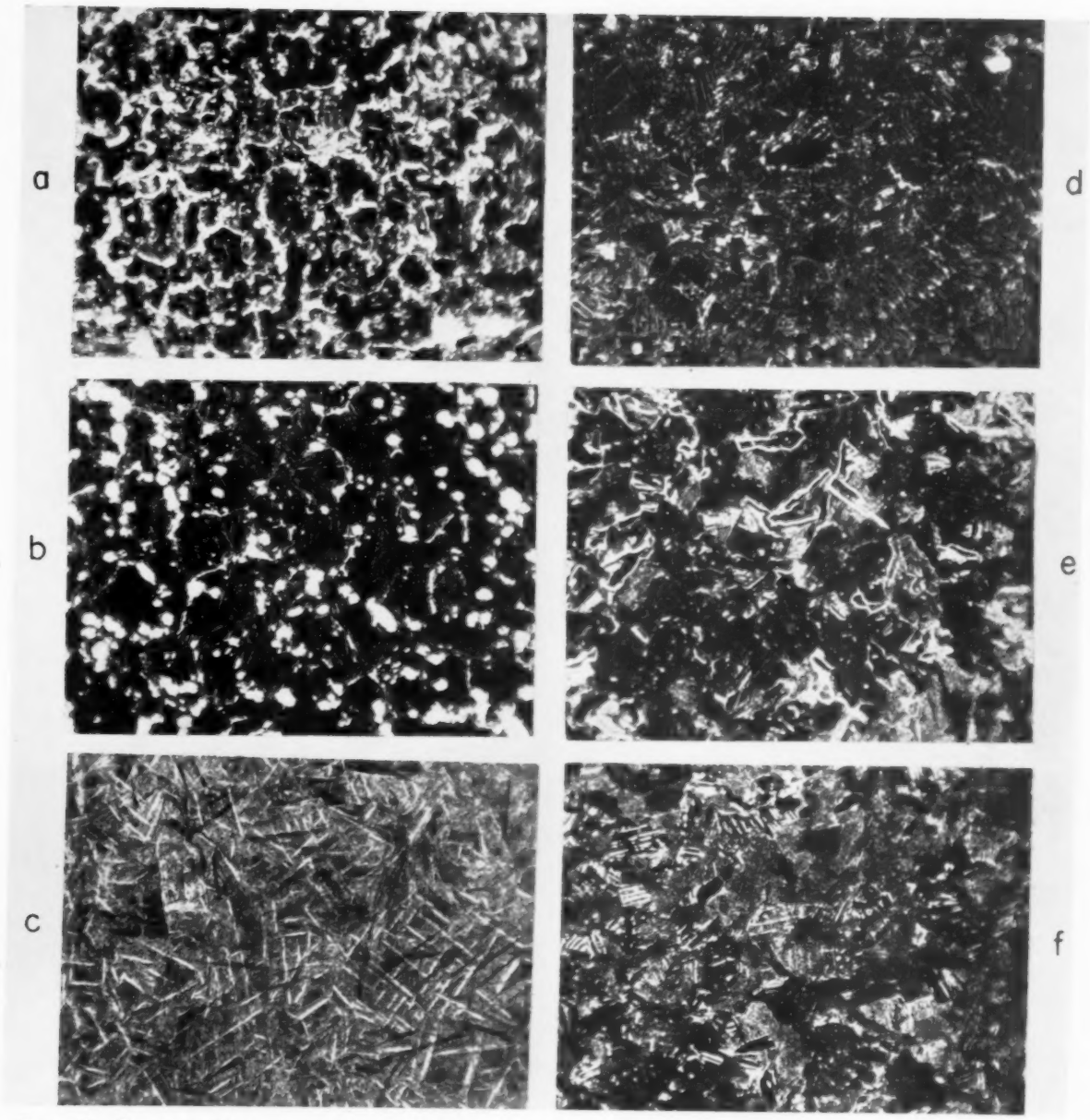

PLATE I. FIGURE 5. Photomicrographs of Ti 508 (300X)—(*a*) Partially outgassed and annealed. (*b*) Heated for the first time in hydrogen (550°C, 44 hrs). (*c*) Heated for the second time in hydrogen (550°C, 61 hrs). (*d*) Heated for the first time in vacuum (after being heated in hydrogen) (550°C, 24 hrs). (*e*) Heated for the second time in vacuum (550°C, 37 hrs; 590°C, 3 hrs). (*f*) Heated for the the third time in vacuum (600°C, 40 hrs). (This heating is not mentioned in the text.)

The effects of heating this sample in hydrogen were not eliminated by heating in vacuum (Figure 1) as far as attenuation is concerned, but they were almost completely removed as far as density and velocity are concerned. The corresponding changes in microstructure are shown in Figures *5a–5f*.

A sample Ti 506 was heated in hydrogen to obtain a hydrogen content of 8 per cent; the microstructure (not shown here) was in our observations unchanged from that before heating. This sample had small but definite changes: about a 1 per cent decrease in density and about 15 per cent decrease in attenuation at 40 mc/s. Two succeeding heatings increased the hydrogen content of this sample to 14 per cent. The ultrasonic properties changed slightly more in the same direction. Other samples behaved in the same way. Between 500°C and 550°C the absorption of hydrogen rises very rapidly.

In order to understand the changes in ultrasonic properties, it is necessary to consider the changes of the sample during heat treatment. Unfortunately, the equilibrium diagram of the system Ti-H is not well known. In older papers titanium was considered to dissolve hydrogen in very high amount (about 33 per cent). However, recently Craighead, Lenning and Jaffee [4] have reported that even at 700°C a second phase appeared when as little as 0.3 per cent of hydrogen was absorbed by titanium. This precipitated second phase was identified as TiH. Our metallographic pictures (Figures *5a–5f*) also show the appearance of a second phase. So it seems to be without doubt that during heat treatment in hydrogen two processes occur; solution and phase change, but it is still not possible to separate the two processes from each other. Therefore it is also not possible to identify the observed change in ultrasonic properties uniquely with only one of the two processes. The decrease in attenuation by addition of hydrogen could perhaps suggest that the effect is caused by dissolved hydrogen,* but then it would not be clear as to why the attenuation continues to decrease after the limit of solution is reached.

The observed changes in velocity of the ultrasound have the same order of magnitude as the changes in density, but the exact application of the formula $v = [(\lambda + 2\mu)/\rho]^{\frac{1}{2}}$ (v = sound velocity, μ = shear modulus, and ρ = density) shows that roughly half of the change in velocity can be attributed to the change in density, and that the other half must be caused by changes in the elastic constants.

Acknowledgement

The authors acknowledge with thanks a number of suggestions of Dr. Kurt Lücke of this Laboratory.

The work described here was supported by the Office of Ordnance Research under Contract DA–19–020–ORD–1512.

References

1. KIRSCHFELD, L. and SIEVERTS, A. Z. phys. Chem. **A145**, (1929) 227.
2. HÄGG, G. Z. phys. Chem. **B11** (1931) 433.
3. EHRLICH, P. Ztsch. anorg. allgem. Chem. **247** (1941) 53.
4. CRAIGHEAD, C. M., LENNING, G. A. and JAFFEE, R. I. Trans. A.I.M.E. **194** (1952) 1317; J. Metals (Dec. 1952).
5. RODERICK, R. L. and TRUELL, R. J. Appl. Phys. **23** (1952) 267.
6. MASON, W. P. and MCSKIMIN, H. J. J. Appl. Phys. **19** (1948) 940.
7. SMITH, D. P. Hydrogen in Metals (Chicago, Illinois, University of Chicago Press, 1947).

*Koehler, Imperfections in Nearly Perfect Crystals (New York, John Wiley, 1952) reports that the introduction of hydrogen into a copper single crystal reduced the damping of sound waves in the crystal. These experiments were, however, performed at frequencies about 1000 times lower.

THE CLIMB OF EDGE DISLOCATIONS IN FACE-CENTRED CUBIC CRYSTALS*

R. S. BARNES†

The climb of edge dislocations in face-centred cubic crystals is described in terms of the atomic movements involved. The conclusion is reached that in a suitable environment such a dislocation will climb even when it is dissociated, although then it will climb less readily. A straight dislocation line will be unable to climb when the departure from the equilibrium number of atomic defects is small, but jogs in the dislocation line will enable the line to climb even under these conditions. Dislocations will climb either to enlarge or reduce the area of the extra {110} planes of atoms which lie perpendicular to the Burgers vector, and with certain special dislocation configurations many parallel adjacent {110} planes of atoms can be either eliminated from, or inserted into, the crystal by a spiral mechanism. By examining the free-surface markings on crystals grown from the vapour it should be possible to distinguish surface steps caused by the climb of dislocations from those due to slip, and also to determine whether it is vacancies or interstitial atoms which are precipitated on cooling such a crystal.

"L'ASCENSION" DES DISLOCATIONS-COIN DANS LES RÉSEAUX CUBIQUES À FACES CENTRÉES

L'ascension de dislocations-coin dans les réseaux cubiques à faces centrées est décrite en termes des mouvements atomiques, impliqués dans ce processus. On en tire la conclusion, que dans un entourage convenable, une telle dislocation "grimpera," même quand elle est dissociée, quoique dans ce cas l'ascension soit plus difficile. Une dislocation en ligne droite ne pourra pas grimper quand le nombre de défauts atomiques se rapproche de la valeur d'équilibre, mais des irrégularités dans la ligne de la dislocation faciliteront l'ascension, même dans ces conditions-là.

Les dislocations, en grimpant, soit augmenteront, soit réduiront l'aire des plans {110} additionnels, qui sont logés perpendiculairement au vecteur de Burgers. Dans le cas de certaines cofigurations des dislocations, de nombreux plans d'atomes {110} parallèles et adjacents, peuvent être éliminés, ou introduits dans le cristal, par un déplacement en spirale. Un examen des surfaces libres de cristaux produits par la condensation des vapeurs, devrait permettre de distinguer entre les gradins sur la surface causés par l'ascension des dislocations, de ceux qui sont dus au glissement, ainsi que de déterminer si ce sont des lacunes réticulaires ou des atomes interstitiels qui précipitent lors du refroidissement d'un tel cristal.

DAS "STEIGEN" VON STUFENVERSETZUNGEN IN KUBISCH-FLÄCHENZENTRIERTEN GITTERN

Das "Steigen" von Stufenversetzungen in kubisch-flächenzentrierten Gittern wird im Rahmen der damit verbundenen Atombewegungen diskutiert. Aus dieser Analyse wird geschlossen, dass eine Versetzung, selbst wenn sie dissoziiert ist in geeigneter Umgebung "steigen" wird, obwohl der Vorgang dann weniger häufig erfolgt. Eine grade Versetzungslinie kann nicht "steigen", wenn die Konzentration der atomaren Fehlstellen nur wenig von der Gleichgewichtskonzentration abweicht. Knoten in der Versetzungslinie können jedoch ein "Steigen" der Versetzungslinie selbst unter diesen Umständen ermöglichen. Versetzungen "steigen", um die Fläche der extra {110} Ebenen die senkrecht zu ihrem Burgers Vektor liegen, entweder zu vergrössern oder zu verkleinern; mit Hilfe spezieller Versetzungskonfigurationen und durch spiralenförmige Bewegungen lassen sich viele parallele, benachbarte {110} Ebenen entweder in das Gitter einführen oder aus dem Verband eliminieren. Es sollte möglich sein, Oberflächenstufen, die durch Gleitprozesse und solche, die durch "Steigen" von Versetzungen erzeugt wurden, voneinander auf Grund von Beobachtungen der auf sublimierten Kristallen vorhandenen Oberflächenmarkierungen zu unterscheiden. Ebenfalls sollte es möglich sein, zu bestimmen, ob Leerstellen oder Zwischengitteratome beim Kühlen eines solchen Kristalls niedergeschlagen werden.

Introduction

Dislocations have two important properties. They can slip along certain well-defined crystallographic planes, and it is this property which is paramount in the plastic deformation of crystals at temperatures well removed from their melting point. However, at temperatures at which atomic diffusion occurs, certain dislocations can move out of their slip plane i.e., climb [1]. This latter property of dislocations has been rather neglected, although at high temperatures it will probably be important. Even at temperatures as low as −180°C the climb of dislocations may play a role in plastic deformation, in view of the results of electrical resistance measurements on cold-worked metals which suggest that atomic defects can, even at these temperatures, diffuse over short distances [2].

Both screw and edge dislocations can be formed by a process of slip in the crystal as is illustrated in Figures 1 and 2. The edge dislocation shown in Figure 2 can also be formed by the insertion of the plane of atoms ABCD into the perfect crystal. The resulting dislocation line AB would be identical with that formed by the slip process. A screw

*Received September 14, 1953; in revised form December 14, 1953.

†Atomic Energy Research Establishment, Harwell, England.

dislocation (Figure 1) can not be formed by such a method, as here no *extra* plane of atoms exists.

In a suitable environment the extra plane of atoms in an *edge* dislocation can steadily either diminish or grow. For instance, if the dislocation line is in a region which is supersaturated with vacancies, then atoms will leave the extra plane at the dislocation line in order to re-establish equilibrium conditions. Under such conditions the

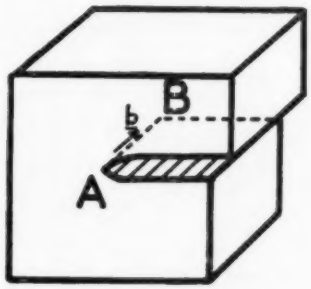

FIGURE 1. Screw dislocation.

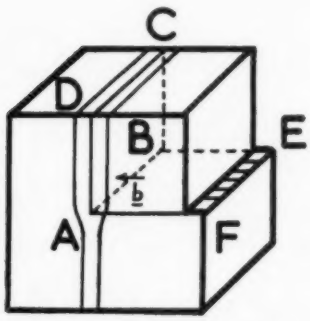

FIGURE 2. Edge dislocation.

dislocation line AB will climb steadily until the whole plane is eliminated and the dislocation ceases to exist. Similarly if vacancies are present in numbers fewer than is necessary for equilibrium, then the extra plane will *increase* its area until the plane is completed, when once again the dislocation line disappears.

Face-Centred Cubic Crystals

We know that in face-centred cubic crystals, slip occurs on a {111} plane along a ⟨110⟩ direction. Thus, if Figure 2 is to represent the state of affairs in a face-centred cubic crystal, then ABEF must represent a {111} plane and AF a ⟨110⟩ direction, so that the plane, ABCD will be a {110} plane. Climb in a face-centred cubic crystal would thus insert or eliminate {110} planes, and an edge dislocation line such as XY (Figure 3) would slip on the (111) plane and climb in a plane perpendicular to this; the $(\bar{1}10)$ plane.

Dissociated Dislocations

Energy considerations suggest that a dislocation line lying in a {111} plane will dissociate into two partial dislocations [3], and the almost universal {111} slip plane in face-centred cubic crystals can be accounted for if dislocations are so dissociated. An edge dislocation XY (Figure 3) lying in the (111) plane LMY with Burgers vector **LM** ($LM = a/\sqrt{2}$, where a^3 is the volume of the unit cell) would dissociate into two partial dislocation lines with Burgers vectors **LO** and **OM** ($LO = OM = a/\sqrt{6}$), which, because the energy is proportional to the square of the Burgers vector [4], will together have lower energy than the original undissociated dislocation line.

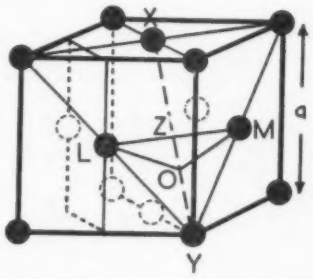

FIGURE 3. Unit cell of a f.c.c. crystal showing an edge dislocation line XY with Burgers vector **LM**.

Consider an edge dislocation formed by the insertion of two adjacent $(\bar{1}10)$ planes into the lattice (two, because the insertion of a single $(\bar{1}10)$ plane would create a stacking fault along this plane), see Figure 4A. This dislocation will dissociate; the two partial dislocations moving apart and causing each atom in the (111) plane lying above the area swept by the dislocation

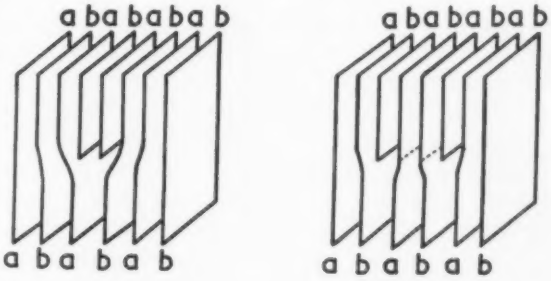

A. Undissociated B. Dissociated

FIGURE 4. The dissociation of an edge dislocation in a f.c.c. lattice in terms of the {110} planes.

lines to move relative to the plane below, a distance equal to the Burgers vector of the partial dislocation line. This will result in a stacking fault lying in that part of the (111) plane, i.e., that plane which is perpendicular to the extra $(\bar{1}10)$ plane, which has been swept by the partial dislocation lines, during their separation. Such a stacking fault, and the partial dislocation which has caused it, is illustrated diagrammatically in Figure 5

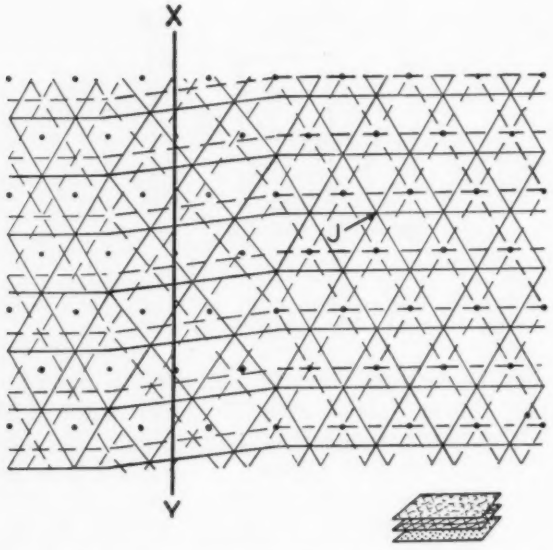

FIGURE 5. Diagram to illustrate the position of the atoms on three adjacent (111) planes near a partial dislocation line XY.

which represents an undistorted (111) plane of atoms as dots, the plane of atoms above this as intersections on a triangular array, and the plane above as intersections on a dashed triangular array. The partial dislocation has swept across the plane from the right-hand side as far as the position XY, leaving in its wake the stacking fault, where the atoms have been moved from positions, such as J (Figure 5) in the direction of the arrow to their present positions. Although the energy of the dislocation is lowered by this dissociation, the final separation of the two partial dislocations will be limited because of the finite energy of the stacking fault which forms between them; this energy is comparable with that of a twin boundary of the same area.

Each {110} plane is composed of atoms arranged in a rectangular array and the atoms of each plane lie directly above the centres of the rectangles formed by the plane of atoms immediately below it (see Figure 3). Successive $(\bar{1}10)$ planes may thus be labelled $a, b, a, b, \ldots$. (Figure 4). On dissociation the two extra $(\bar{1}10)$ planes (which intersect the partial dislocation lines) also separate as a result of the slip process, and "a" planes join "b" planes in the plane of stacking fault (Figure 4B). This discontinuity in the $(\bar{1}10)$ planes is illustrated in Figure 6, where, for simplicity, the displacement of the atoms from their regular lattice positions has been confined to those atoms lying on that

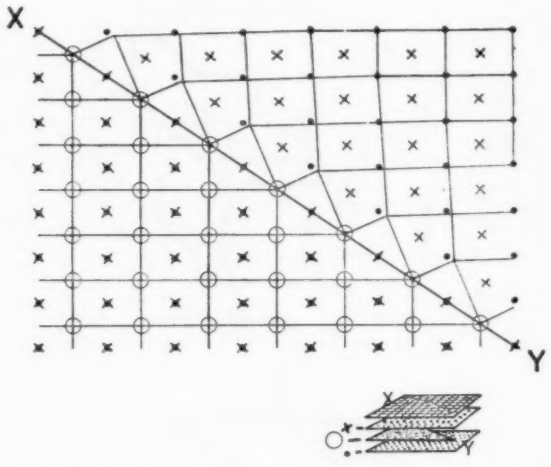

FIGURE 6. Diagram illustrating the position of atoms on a series of adjacent $(\bar{1}10)$ planes near a partial dislocation line XY.

side of the stacking fault (the plane of which lies perpendicular to the paper) removed from the extra atomic plane.

Climb of a Dissociated Dislocation

This situation modifies the simple picture we have formed of the climb process. If the energy of the configuration is not to increase steadily as atoms are added to, or removed from, the extra planes, both partial dislocation lines must climb together, and the ribbon of stacking fault must move with them.

It might be thought that such a stacking fault could not move in a direction perpendicular to itself. However, all that is necessary for the stacking fault to move up one plane is that the plane of atoms above the stacking fault should slip by a distance such as LO (Figure 3). The insertion of a complete *row* of atoms at the edge of the extra $(\bar{1}10)$ plane along the partial dislocation line XY (Figure 5) would cause such a slip to occur. The elastic energy surrounding the partial dislocation, once this row of atoms had been inserted would be sufficient to cause those atoms near to

the dislocation line and lying on the (111) plane above the stacking fault, to slip over the underlying plane of atoms. These atoms near to the dislocation lines were initially displaced from their equilibrium positions and so would slip quite easily. The slip would then spread until the whole of the plane of atoms which lay between the two such inserted rows of atoms had slipped, when the stacking fault would have moved up by an atomic spacing.

The climb velocity of a dissociation dislocation line will be lower than that of the equivalent undissociated dislocation, because the partial dislocation lines, although separated, must climb together. However, there is no fundamental reason why such a dissociated edge dislocation line should not climb, although it is possible that the departure from equilibrium conditions necessary for the climb of a straight dislocation line may have to be large.

Jogs in Dislocations

In reality it is most unlikely that two complete rows of atoms would be inserted (or removed) simultaneously as postulated above. Atoms would be inserted one by one, and probably the departure from equilibrium conditions would have to be large for a sufficient number of atoms to be added to each extra plane to cause the stacking fault to move up an atomic distance across its whole width in any region. The initiation of the insertion or removal of each new row would be difficult. However, there are some dislocation configurations for which this initiation is not difficult.

An edge dislocation line lying on two intersecting {111} planes (Figure 7) can dissociate on these two {111} planes, as shown, although it is then necessary to introduce an extra dislocation line [5] lying along GH to satisfy the dislocation conditions at the nodes.* The simultaneous removal of atoms at G and H would not increase the area of the stacking fault whereas the removal of atoms anywhere else would do so. Thus atoms can be removed more readily from the positions G and H than from other positions along the dislocation line. Also, the removal of an atom at G, for instance, would probably assist the removal of the atom at H because of the high-stacking fault interaction there, whereas the removal of an atom on the straight part of the dislocation line would probably not assist the removal of the extra atom opposite it. An edge dislocation of this form could thus climb when the departure from equilibrium conditions was not very great.

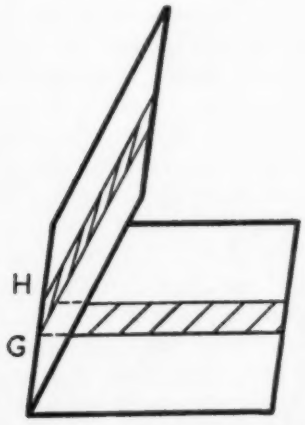

FIGURE 7. Dissociated edge dislocation line which lies partly on one {111} plane and partly on another.

The above argument can be extended to apply to the elimination of atoms at a jog in a dislocation line. A jog can be described as the region of transition of a dislocation line from one plane to a neighbouring parallel plane. The stacking fault joining the parts of the dislocation line lying on two adjacent parallel {111} planes would lie in some other {111} plane (as illustrated in Figure 8), and so the configuration at a jog is related to

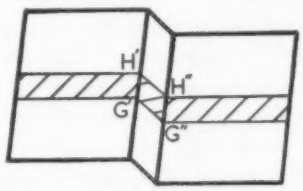

FIGURE 8. A jog in a dissociated dislocation.

that already described; consisting in fact of four positions G', H', G'' and H'' similar to G or H (Figure 7). A jog will, for similar reasons, permit a dislocation to climb in a lower degree of supersaturation than is possible for a perfectly straight dislocation line, where it will anyway be necessary to nucleate two such jogs before a row of atoms can be removed.

Dislocation Nodes

It is possible to consider the climb of dislocations at various types of dislocation node in the same way as has been done for slip by Thompson [5]. However, the processes are somewhat analogous to

*The presence of the dislocation lines along GH, $G'H'$ and $G''H''$ (Figures 7 and 8) modify the shape of the dislocation lines at their junction because of the finite energy of the dislocation lines. However this does not vitiate the argument.

those in the cases he has considered, but it might be worth discussing one dislocation configuration which illustrates a general behaviour.

A dislocation line lying entirely in a {111} plane, bent such that one section of it is a pure edge dislocation, the rest having a screw nature (see Figure 9) would dissociate on this {111}

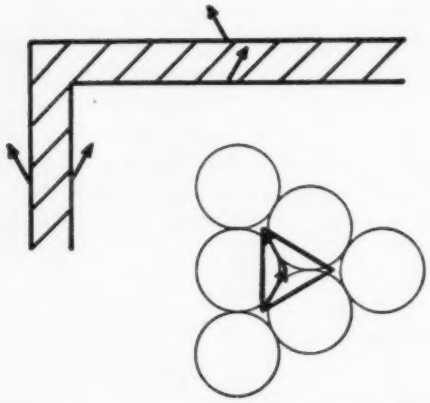

FIGURE 9. A dissociated dislocation line part of which is purely of edge nature and the rest of screw nature.

plane into partial dislocations separated by a ribbon of stacking fault as shown. Now if the region was supersaturated with vacancies, and we postulate the existence of a jog in the edge section, it would climb, whereas the screw section could not. The effective anchoring of the end of the edge section would cause it to spiral around the locked points and eliminate many successive *planes* because of the screw nature of the lock [6].

Surface Markings

The climb of a dislocation to the free surface of the crystal would in general modify the surface, in much the same way as the slip of a dislocation out of the crystal produces a slip line. The elimination (or insertion) of a plane of atoms in the crystal would, unless the plane lay perpendicular to the surface, produce a step in the surface as illustrated in Figure 10. The line of the step in the case of

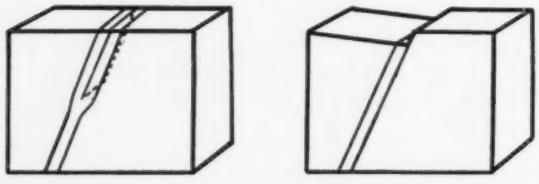

FIGURE 10. The climb of an edge dislocation to the free surface of a crystal.

climb would lie along the intersection of the {110} climb plane and the surface.

The dissocation of the dislocations would not produce double steps which could be thus distinguished from those due to slip, because as the dislocation approaches the surface during its climb, the two partial dislocations will come together. On meeting the surface the stacking fault must disappear entirely and a single step will result.

Observations of Steps on Metal Surfaces

During some recent observations on the free-growth surfaces of single crystals of silver by Forty and Frank [7] some steps of unit atomic height which lie at 45 degrees to slip lines on the free {100} faces of the crystals were seen. The authors suggest that these lines may be due to slip on either {110} or {100} planes. It is interesting to note, however, that the examples of these "anomalous steps" shown in the illustrations to their paper seem to be continuations of normal ({111} plane) slip lines. If the dislocations are in fact dissociated on the {111} planes, it is surprising that they should continue to slip along some different plane.

It seems possible that dislocations which have slipped part of the way through the crystal, have climbed out of the crystal along {110} planes. This does not seem too improbable when it is considered that only those dislocations which move during the very last stages of growth can be detected by examining the growth surfaces. It is during this period that there would be a supersaturation of defects in the crystal, because no doubt the visible growth steps were added only after the temperature had begun to fall. If these anomalous steps are due to climb along {110} planes, their direction on the other natural-growth faces ({111} faces) would be parallel to the lines caused by normal slip.

Examination of these anomalous steps on other surfaces of such metal crystals should distinguish those due to slip from those due to climb, for their interaction with the growth steps on the crystal surface will reveal which is the high side of the step, and the knowledge of the sense of a step all the way round a crystal would give a conclusive verdict as to whether the step was caused by the slip or climb of a dislocation. Also, assuming these anomalous steps do result from the climb of dislocations, then from the sense of the step it can be deduced whether an atomic plane has been

inserted or eliminated by the process, and if, for instance, it is found that an atomic plane has been eliminated during the cooling of the crystal, it can be deduced that more vacancies than interstitial atoms have been precipitated upon that particular dislocation line. Such a study should therefore be able to resolve the effects of vacancies from interstitial atoms; no experiment has up to now succeeded in doing this.

Conclusions

In a face-centred cubic crystal it is expected that in a suitable environment, edge dislocations, which normally lie in {111} planes, and are dissociated, can climb and so insert or eliminate {110} planes, and in special cases a series of adjacent parallel {110} planes. For dislocations to climb there must be a sufficient local departure from the equilibrium number of atomic defects, such as might occur during:

(1) the heating or cooling of a crystal;

(2) deformation, when vacancies and interstitial atoms can be produced by the interaction of dislocations [8];

(3) particle bombardment;

(4) interdiffusion, when large numbers of atomic defects are swept along the concentration gradient as a result of the unequal diffusion rates of the two types of atoms concerned.

A further condition for climb is that the temperature must be sufficiently high, and the non-equilibrium conditions must persist for sufficiently long, for the atomic defects to be able to move distances of the order of the dislocation separation.

The climb of dislocations may therefore be of importance in the following studies:

(1) Creep;

(2) Plastic deformation, particularly at high temperatures;

(3) Polygonisation;

(4) Irradiation;

(5) Interdiffusion;

(6) Crystal growth;

(7) Sintering [9].

Acknowledgements

The author wishes to thank his colleagues, and in particular Dr. W. M. Lomer for valuable discussions, Dr. H. M. Finniston for his encouragement, and the Director of the Atomic Energy Research Establishment for permission to publish this paper.

References

1. Mott, N. F. Proc. Phys. Soc. **64B** (1951) 729.
2. Overhauser, A. W. Phys. Rev. **90** (1953) 393.
3. Heidenreich, R. D. and Shockley, W. Bristol Conference on the Strength of Solids (London, The Physical Society, 1948) 57.
4. Koehler, J. S. Phys. Rev. **60** (1941) 397.
5. Thompson, N. Proc. Phys. Soc. **66B** (1953) 481.
6. Barnes, R. S. Proc. Phys. Soc. **65B** (1952) 512.
7. Forty, A. J. and Frank, F. C. Proc. Roy. Soc. **217** (1953) 262.
8. Seitz, F. Advances in Physics **1** (1952) 43.
9. Barnes, R. S. Phil. Mag. **43** (1952) 1221.

ON THE THEORY OF SECONDARY RECRYSTALLIZATION TEXTURE FORMATION IN FACE-CENTERED CUBIC METALS*

C. G. DUNN†

An oriented-nucleation growth-selectivity theory for secondary recrystallization in face-centered cubic metals is discussed. According to the theory, primary recrystallization produces a texture consisting of strong and weak components, which are related to components of the deformation texture by a ⟨111⟩ relationship (approximately 38 degree rotation). Large primaries from the weak components of the texture are considered to be the nuclei for secondary recrystallization. The theory is applied to explain several results reported in the literature.

SUR LA THÉORIE DE FORMATION DES TEXTURES DE RECRISTALLISATION SECONDAIRE DANS LES MÉTAUX CUBIQUES À FACES CENTRÉES

Une théorie de la recristallisation secondaire dans les métaux cubiques à faces centrées, basée sur le concept de germination orientée et de sélection lors de la croissance, est discutée. Suivant cette théorie, la recristallisation primaire produit une texture qui consiste en composantes "fortes" et "faibles", liées à la texture de déformation par une relation de rotation de ⟨111⟩ (une rotation d'environ 38°). De grands cristaux primaires, appartenant aux composantes faibles de la texture, sont considérés comme germes de la recristallisation secondaire. Plusieurs résultats rapportés dans la littérature sont expliqués en appliquant cette théorie.

ÜBER DIE THEORIE DER BILDUNG EINER SEKUNDÄREN REKRISTALLISATIONSTEXTUR IN KUBISCH-FLÄCHENZENTRIERTEN METALLEN

Eine auf der Hypothese der orientierten Keimung und des bevorzugten Wachstums aufgebaute Theorie der sekundären Rekristallisation der kubisch-flächenzentrierten Metalle wird diskutiert. Nach dieser Theorie erzeugt die primäre Rekristallisation eine aus starken und schwachen Komponenten bestehende Struktur, die mit den Komponenten der Deformationstextur durch eine ⟨111⟩ Beziehung (Drehung von etwa 38°) verknüpft sind. Grosse Primärkristalle der schwachen Komponente der Textur werden als Keime der sekundären Rekristallisation in Betracht gezogen. Die Theorie wird zur Erklärung einiger in der Literatur berichteten Ergebnisse benutzt.

Introduction

In a series of recent papers [1; 2; 3; 4; 5] Beck and coworkers have advanced an oriented-growth theory to account for the origin of both primary and secondary recrystallization textures. In this theory it is assumed that there are randomly oriented nuclei and only those that are related to components of the matrix texture in a proper way —namely, by 30–40 degree rotation about a common ⟨111⟩ axis— grow at the expense of the matrix. To explain the unique relationship, it is necessary to assume that the boundary mobility is high for the ⟨111⟩-type rotation and relatively low for all other orientation relationships. This theory readily accounts for components of the primary recrystallization texture and for some of the main components of the secondary recrystallization texture. The matrix texture (or principal component of the matrix texture) is the frame of reference in each kind of recrystallization.

Arguments against this theory are: (1) the mobility relationship is not sharp enough to determine the observed texture data; (2) the theory does not adequately explain the absence of components of the texture, which, orientation-wise, are equivalent to those obtained; and (3) it does not satisfactorily explain the dependency of primary recrystallization textures on the annealing temperature employed. Arguments against the matrix texture acting entirely as the frame of reference will be considered later.

Some of these arguments are met in a modified oriented-growth theory discussed recently by Gow and Cahn [6]. In this theory nuclei are restricted to certain orientation ranges which are not so sharp as the final components of the recrystallization texture.

Other investigators favor an oriented-nucleation growth-selectivity theory wherein the nuclei are sharply defined and rate of growth or boundary mobility is relatively high for nearly all orientation relationships except the same or the twin orientation. (See, for example, Burgers and Tiedema [7].)

Thus one assumes there are nuclei in certain specific orientations. For secondary recrystallization these may be (*a*) large primaries, (*b*) low-energy primaries adjacent to strained primaries, (*c*) large recovered grains or polygonized grains, or (*d*) low-energy polygonized grains adjacent to strained primaries. For silicon iron, which is a body-centered cubic lattice, Dunn [8; 9] has presented evidence supporting the idea that large

*Received November 12, 1953.
†General Electric Company, Pittsfield, Massachusetts.

primaries are the nuclei for secondary recrystallization, such nuclei occuring in specific preferred orientations. According to this viewpoint what may appear to be a single orientation primary recrystallization texture actually may consist of one strong component and several weak ones. Only weak components can supply nuclei and they may do so depending on the size of primaries and the fraction of the texture represented.

Liu and Hibbard [10] have dealt with the basic question of frame of reference for determining orientation changes in primary and secondary recrystallization. They show that it is possible to derive all components of secondary recrystallization textures as well as all components of primary recrystallization textures by proper ⟨111⟩ rotations from components of the cold-rolled textures. (Such a simplification in analysis is not possible in the oriented-growth theory because in published secondary recrystallization data in cube texture copper there are examples of ⟨100⟩, as well as ⟨111⟩, rotations with the cube orientation taken as the frame of reference.) A similar simplification in analysis holds for silicon iron when the cold-rolled texture is taken as the frame of reference for both primary and secondary recrystallization [9].

In the present paper it is proposed to start with published facts regarding recrystallization phenomena in face-centered cubic metals and to indicate how primary recrystallization may provide appropriate matrix structures and textures for secondary recrystallization. This treatment considers the primary recrystallization texture to be composed of preferred orientations or components. The relative amounts of these components are important. The relative sizes of primaries also are important. When the factors are correct, the conception is that large primaries from one or more minor components grow and produce secondaries having the same preferred orientations as the minor components of the primary recrystallization texture. Examples are given to illustrate these ideas, but no attempt is made to include all published data.

The Description of Textures

The cold-rolled textures of copper and aluminum have been determined quantitatively [11] and have also been described in terms of Miller indices. The latter are somewhat subjective, with several descriptions possible. Thus, there are such descriptions in the literature as near (123) [12̄1], (358) [3$\bar{5}$2], near (146) [21$\bar{1}$], (7 12 22) [84$\bar{5}$], and (135) [$\bar{2}$1$\bar{1}$]. However, some of these orientations are 90 degrees out of position and therefore do not properly represent the data.

To make the necessary corrections and show the similarity of the various descriptions consider first Figure 1, which is a partial reproduction of a

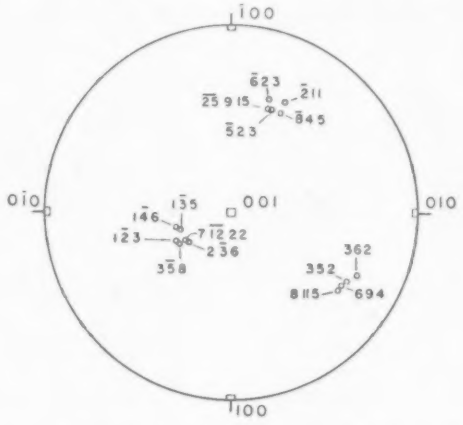

FIGURE 1. Stereogram showing selected directions in a standard [001] projection.

standard [001] projection with higher than usual Miller indices included (see the Appendix for stereographic projection data).

It can be seen that these directions fall into three groups, which are mutually close to 90 degrees apart, with relatively small spread within each group.

The next step is to relate these groups to a new frame of reference—namely, rolling plane and rolling direction—with one group perpendicular to the rolling plane, another group parallel with the rolling direction (R.D.) and the third group parallel with the direction C.D. This change is easily effected in terms of a rotation from an initial orientation (001) [1̄00] to the final orientation (see Figure 2), the direction [1̄1̄1] being a satisfactory axis of rotation. Directions that give a scale of rotations of 30, 34, 38, 42, and 46 degrees have been included in the figure.

The final step, of course, is to select the best indices to represent the data. There are such final orientations as (12$\bar{3}$) [$\bar{5}$23] or approximately (12$\bar{3}$) [$\bar{2}$11], (3$\bar{5}$8) [2$\bar{5}$ 9 15] or approximately (3$\bar{5}$8) [$\bar{5}$23], (13$\bar{5}$) [$\bar{2}$11], approximately (7 1$\bar{2}$ 22) [$\bar{8}$ 4 5], (23$\bar{6}$) [$\bar{6}$ 2 3], etc. These descriptions eliminate the 90-degree error mentioned earlier. Generally speaking, the (23$\bar{6}$) [$\bar{6}$23] orientation appears to be a satisfactory representative of the group; it has

a [$\bar{1}\bar{1}1$] direction common with (001) [$\bar{1}00$] and is 38 degrees from this orientation. The cube and octahedral poles for the (2$\bar{3}$6) [$\bar{6}$23] orientation are plotted in Figure 2.

Besides being representative, the orientation (2$\bar{3}$6) [$\bar{6}$23] has an elegant relationship with (001) [$\bar{1}$00]—it is the Kronberg-Wilson [12] coincidence position expressed in a different way. This relationship involves many common or coinciding planes

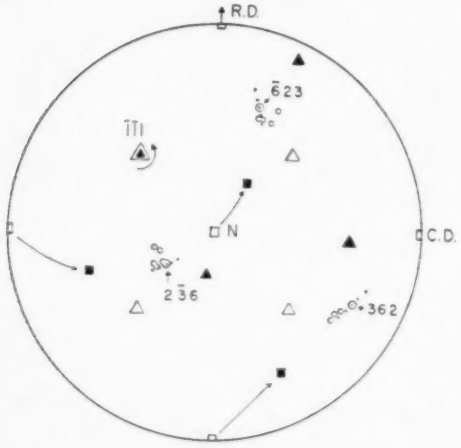

FIGURE 2. Stereogram showing cube and octahedral poles of the (001) [$\bar{1}$00] orientation and of the (2$\bar{3}$6) [$\bar{6}$23] orientation and the other directions in (001) [$\bar{1}$00] that appear in Figure 1. □ and △: cube and octahedral poles of (001) [$\bar{1}$00]. ■ and ▲: cube and octahedral poles of (2$\bar{3}$6) [$\bar{6}$23]. . . ⊙ . . : 30, 34, 38, 42, 46-degree rotation positions.

(see the Appendix). There is, therefore, the possibility of energy-cusp boundaries, which may be important for oriented nucleation [13; 9] or for high boundary mobility [14a]. Furthermore, the orientations of the secondaries reported by Kronberg and Wilson are precisely of the (2$\bar{3}$6) [$\bar{6}$23] type; these will be considered in the next section.

The Formation of the Kronberg-Wilson Secondary Recrystallization Texture in Cube Texture Copper

From orientation data on twin-pairs, Kronberg and Wilson [12] found eight components in the secondary recrystallization texture of copper. These comprised a twofold symmetry group. Four components were related to the cube orientation by specific 38 degree rotations about common ⟨111⟩ axes; the other four were related to the cube orientation by opposite-type rotations of 22 degrees. The latter four were twins of the first four and arose from the twin-pairs. If all possible similar orientations had occurred, there would have been 16 components and fourfold symmetry. On the other hand, the eight similar components observed by Bowles and Boas [15] and by Sharp and Dunn [16] with data on twin-pairs, automatically comprised a fourfold symmetry group because of the observed 30–degree angle of rotation about the four ⟨111⟩ axes.

From a theoretical point of view it is the twofold symmetry result of Kronberg and Wilson that is particularly challenging. No explanation of this result has been given.

As mentioned previously, the (2$\bar{3}$6) [$\bar{6}$23] orientation describes one of the components in the data of Kronberg and Wilson (for simplicity we omit consideration of the twin component).* The four components of the (2$\bar{3}$6) [$\bar{6}$23]-type are plotted in Figure 3. The unobserved ($\bar{3}$26) [$\bar{6}\bar{3}\bar{2}$]-type com-

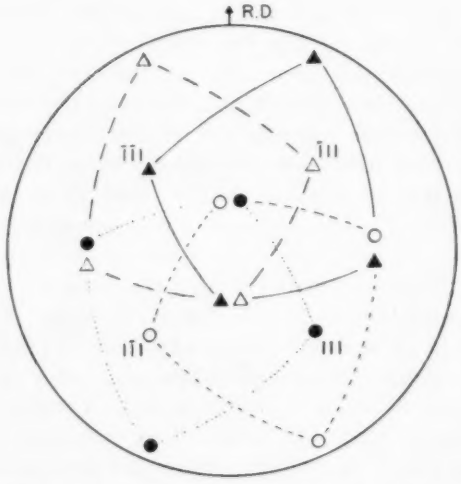

FIGURE 3. Stereogram of octahedral poles giving four orientations of the (2$\bar{3}$6) [$\bar{6}$23] type. ▲: the (2$\bar{3}$6) [$\bar{6}$23] orientation. △: the (236) [$\bar{6}$23] orientation. ●: the ($\bar{2}$36) [$\bar{6}\bar{2}\bar{3}$] orientation. ○: the ($\bar{2}$36) [$\bar{6}\bar{2}\bar{3}$] orientation.

ponents, which result by 38–degree opposite-type rotations, are plotted in Figure 4.

To explain the missing ($\bar{3}$26) [$\bar{6}\bar{3}\bar{2}$]-type components in the Kronberg-Wilson result, consider the following facts and assumptions: First, it is a fact that the cold-rolled texture of suitably prepared copper (and also aluminum) consists only of (2$\bar{3}$6) [$\bar{6}$23]-type components as pointed out in the previous section. Second, it is a fact that primary recrystallization produces a strong (001) [$\bar{1}$00] component—called the cube texture—by a 38–

*The observed twin was described in terms of a 22-degree clockwise rotation from the cube orientation about the [$\bar{1}\bar{1}$1] axis; it is exactly the ($\bar{5}$ 4 20) [$\bar{2}\bar{0}$ $\bar{5}$ $\bar{4}$] orientation.

degree clockwise rotation from (2$\bar{3}$6) [$\bar{6}$23] to the cube orientation, similar relations holding for all components of this type. Third, we assume that primary recrystallization in copper produces minor components with some of them like the major components in aluminum. Specifically, we assume that there are weak (2$\bar{3}$6) [$\bar{6}$23]-type components in cube texture copper (there are strong (2$\bar{3}$6) [$\bar{6}$23]-type components in the recrystallization texture of aluminum).* Fourth, we assume there are primaries in the weak (2$\bar{3}$6) [$\bar{6}$23]-type components,

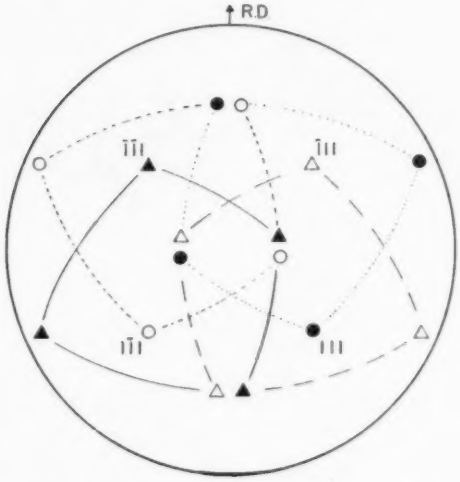

FIGURE 4. Stereogram of octahedral poles giving four orientations of the ($\bar{3}$26) [$\bar{6}\bar{3}\bar{2}$] type. ▲: the ($\bar{3}$26) [$\bar{6}\bar{3}\bar{2}$] orientation. △: the ($\bar{3}$26) [$\bar{6}\bar{3}\bar{2}$] orientation. ●: the (3$\bar{2}$6) [$\bar{6}\bar{3}\bar{2}$] orientation. ○: the (326) [$\bar{6}\bar{3}\bar{2}$] orientation.

which are large enough to grow and become secondaries. Fifth, we assume that these large (2$\bar{3}$6) [$\bar{6}$23]-type primaries grow into secondaries, producing a texture consisting of (2$\bar{3}$6) [$\bar{6}$23]-type components. Therefore, if all the above conditions prevail, we do not expect to find ($\bar{3}$26) [$\bar{6}\bar{3}\bar{2}$]-type components in the secondary recrystallization texture, and thus we have an explanation of the twofold symmetry result obtained by Kronberg and Wilson.

In the oriented growth theory one assumes that primaries are present in all orientations. Among these there are ($\bar{3}$26) [$\bar{6}\bar{3}\bar{2}$]- as well as (2$\bar{3}$6) [$\bar{6}$23]-type primaries. To account for only (2$\bar{3}$6) [$\bar{6}$23]-type secondaries upon further annealing one has to somehow eliminate the ($\bar{3}$26) [$\bar{6}\bar{3}\bar{2}$]-type primaries along with the rest. Beck [3] has suggested that asymmetry in the cube orientation component does this, but further proof seems needed for this argument to be convincing.

Origin of "Near (120) [001]"-Type Secondaries in Copper

It is known that the sharpness of the cube texture developed in copper depends on a number of factors such as impurity content, penultimate grain size, per cent reduction and manner of annealing. Variations in the preparation of materials therefore can account for the observed variations in the primary recrystallization texture. Similarly, we believe these same variations can alter minor components of the texture.

Thus we may produce a texture consisting mainly of the cube component, but having among other minor components, a "near (120) [001]"-type minor component with suitable large primaries capable of growing into "near (120) [001]" secondaries. (Secondaries in the (120) [001] orientation, or near this orientation, have been reported by Dahl and Pawleck [19], Kronberg and Wilson [12] and Sharp and Dunn [16].) In fact, in the particular case at hand we assume such large primaries are highly favored over other primaries in spite of the fact they do not bear a ⟨111⟩ relationship to the cube component. The problem is to explain the origin of (120) [001] primaries in terms of a ⟨111⟩ relationship to some component of the cold-rolled texture.

Because of spread in the pole figure data, the cold-rolled texture is not completely described in terms of (2$\bar{3}$6) [$\bar{6}$23]-type components or equivalent expressions. From the oriented-nucleation point of view, we may be unable to detect all important orientations in the over-all texture. We do know that (110) [1$\bar{1}$2] is a stable cold-rolled orientation; so the (110) [1$\bar{1}$2] orientation reasonably could be present in the cold-rolled texture. Assuming this and referring to Figure 5, we note that cold-rolled regions in a (110) [1$\bar{1}$2] orientation could recrystallize and produce "near (120) [001]" primaries

*Beck [17, 18] has explained in terms of ⟨111⟩ rotations, referred to components of the cold-rolled texture of aluminum, how recrystallization retains the cold-rolled texture. A counterclockwise rotation of 45 degrees about an axis near [$\bar{1}$11] of (2$\bar{3}$6) [$\bar{6}$23], an axis approximately 20 degrees clockwise from R.D. on the basic circle in Figure 2, roughly converts (2$\bar{3}$6) [$\bar{6}$23] into another component of the same type. Actually, this relationship is illustrated better with the modified (3$\bar{5}$8) [$\bar{5}$23] orientation of Liu and Hibbard [10] (see their Figure 5). An alternate method of producing another component of the same type is a clockwise rotation of 40 degrees about an axis near [1$\bar{1}$1] of (2$\bar{3}$6) [$\bar{6}$23], an axis 20 degrees from the center of the stereogram of Figure 2 and 90 degrees from the direction C.D. (see ref. 18).

by a 38 degree rotation about a common [11$\bar{1}$] axis.

The above explanation of the origin of near (120) [001] secondaries by growth of (120) [001] primaries is significant only to the extent that the (110) [1$\bar{1}$2] orientation in the cold-rolled texture is itself significant and worthy of special consideration in a nucleation process.

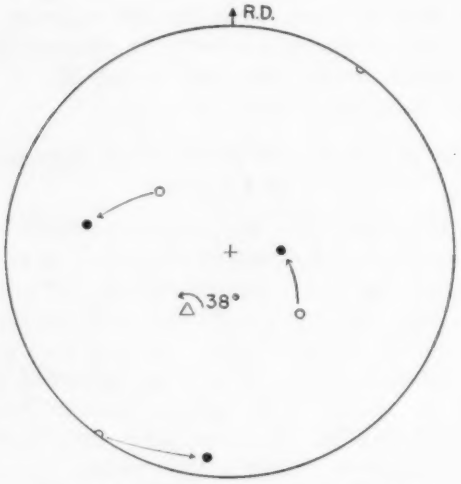

FIGURE 5. Formation of a "near (120) [001]" orientation from a (110) [1$\bar{1}$2] orientation by a 38-degree rotation about an octahedral pole. ○: cube poles of the (110) [1$\bar{1}$2] orientation. ●: cube poles of a "near (120) [001]" orientation. △: octahedral pole and axis of rotation.

Secondary Recrystallization in Aluminum

Secondary recrystallization in fine-grained aluminum occurs when the primary recrystallization texture consists of a strong single orientation texture. These conditions are exemplified best in fine-grained aluminum produced from single crystals [20; 21].

In the work reported by Beck and Hu [1] there is one result of particular interest, because it provides a good illustration for both the oriented-growth theory and the oriented-nucleation growth-selectivity theory. This result (see Figure 5 of reference 1) with some additions has been reproduced in Figure 6.

In making the stereogram, Beck and Hu placed one of the cube poles (actually a pole concentration) of the primary recrystallization texture at the center of the stereogram. The cold-rolled texture in proper relationship was represented by two components corresponding to the orientation of the cold-rolled crystal and its included deformation bands. The secondary recrystallization texture, also in proper relationship, consisted of two components, marked *A* and *B* in the stereogram with cube poles of individual grains plotted.

For purposes which will become clear shortly we have enclosed the cube pole positions of the main component of the cold-rolled texture by solid-line circles of 10-degree radius and have added another orientation. This orientation, indicated by the dotted line circles of 10-degree radius, is related to the cold-rolled orientation by a 38-degree rotation about the octahedral pole marked *P* in the stereogram.

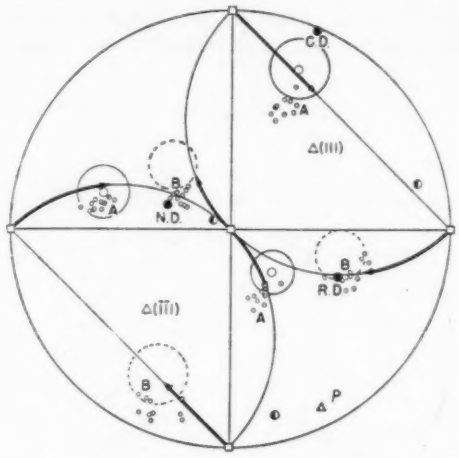

FIGURE 6. (100)-pole figure for textures obtained in Crystal 1. (After Beck). □: recrystallization texture. ○: main component of deformation texture. ◑: deformation bands. ∘: individual secondaries. Large dotted circle gives orientation 38 degrees from main component of the deformation texture.

Consider these data first from the oriented-nucleation point of view. Let Figure 7 represent the cold-rolled single crystal with its deformation bands (deformation bands are marked D.B. in the illustration). Let Figure 8 represent the pri-

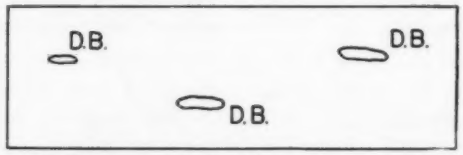

FIGURE 7. Diagram of single deformed crystal with included deformation band regions.

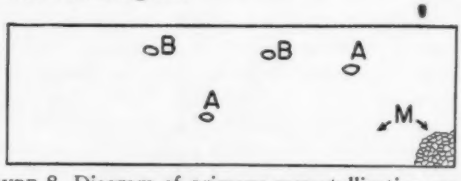

FIGURE 8. Diagram of primary recrystallization structure showing *A*-, *B*-, and *M*-type primaries, the *A* and *B* primaries being embedded in a matrix of *M* primaries.

mary recrystallization structure. The structure consists mostly of M primaries of nearly the same orientation; these are shown in the corner area of the figure but otherwise not indicated. We visualize also that there are two other kinds of primaries marked A and B in the illustration, which are imbedded in a matrix of M primaries. They vary in size, some being appreciably larger than surrounding M primaries.

To specify further these three kinds of primaries let us apply appropriate well-known principles. For instance, a 38-degree rotation about ⟨111⟩ axes of the main component of the cold-rolled texture is responsible for both the M and B primaries. The M primaries involve a $[\bar{1}\bar{1}1]$ axis and many nuclei; the B primaries involve a ⟨111⟩ axis shown at P in Figure 6 and few nuclei. Other equivalent transformations either do not occur or produce only small primaries. The A primaries arise, however, by the phenomenon of strain-induced grain-boundary migration [22] and require D.B. regions of a different orientation for rapid boundary movement. Thus, recovery or polygonization in a small volume adjacent to a D.B. region produces a low-energy nucleus of the cold-rolled orientation, and further growth at the expense of deformed material (a D.B. region) of different orientation produces a primary of sufficient size for it later to grow and become a secondary.

On a competitive basis, growth selectivity would allow little growth of the M primaries. On the other hand, the large primaries of the A and B kind could grow into secondaries at the expense of M primaries. The A secondaries obtained in this way should be within the orientation spread of the cold-rolled crystal. According to Figure 6, many secondaries do lie within and near the arbitrary 10-degree circle; so the agreement seems to be good. B secondaries of the kind predicted should fall within or near the dotted 10-degree circles of Figure 6. Actually, the observed B secondaries occur slightly displaced from this position. The agreement represented by a 35-degree rotation about [111] of the main component of the primary recrystallization texture, however, as suggested by Beck and Hu, is only slightly better.

If one looks for an explanation according to the oriented-growth theory, one has to visualize a primary recrytsallization structure consisting of M primaries and other primaries in all possible orientations. Such a picture is considerably more complicated than the one suggested in Figure 8. Furthermore, one immediately runs into the difficulty of trying to account for the missing equivalent orientations of secondaries when primaries are present in all possible orientations.

Secondary Recrystallization in Fiber Texture Material

From a theoretical point of view it seems possible that significant information on the relative merits of oriented-growth theory and oriented-nucleation theory can be obtained from suitable fiber texture data.

Suppose one has a recrystallized fine-grained wire with a [111] fiber texture that is sufficiently sharp to include most orientations in a range of 20-degree spread. Such a situation is illustrated schematically in Figure 9 in terms of the position of cube poles.

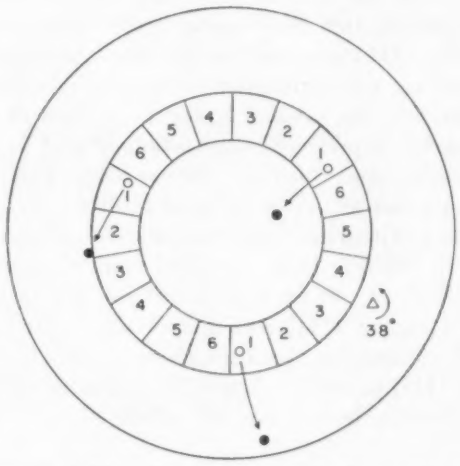

FIGURE 9. {100}-pole figure of [111] fiber texture, which is resolved into six preferred orientations. ○: a [111] primary in preferred orientation 1. ●: a [120] primary related to above [111] primary by a 38-degree rotation about a ⟨111⟩ axis.

Suppose also that the wire undergoes secondary recrystallization in such a way that during growth a secondary consumes primaries in every kind of orientation present in the fiber texture. (This requirement eliminates consideration of secondary recrystallization in local regions where primaries may have a single preferred orientation. For example, all primaries from a deformed grain may occur in a single orientation with the [111] direction parallel with the wire axis.)

For purposes of analysis and discussion let us resolve the [111] fiber texture into six preferred crystal orientations, marked 1, 2, 3, etc. in Figure 9. A single preferred orientation is represented by three {100}-pole concentrations symmetrically located 55 degrees from the center.

If primary recrystallization arises in a cold-drawn wire with a sharp [111] fiber texture and by 40-degree rotations about the [111] axis of individual deformed grains, primaries in orientation 1 of Figure 9 could originate in deformed grains of orientations 3 and 5. Conversely, recrystallization from regions of orientation 1 could produce orientations 3 and 5, with [111] the axis of rotation, or it could produce a deviating primary in a near [120] orientation, as shown in Figure 9, by a 40-degree rotation about any one of the other three ⟨111⟩ directions.*

Let us compare the growth possibilities of a large primary in orientation 1, a [111] primary, and the [120] primary using two kinds of growth selectivity rules.

In the oriented-growth theory the growth selectivity rule is that boundary mobility is high if the orientation relationship is 40-degree rotation about a ⟨111⟩ axis and low for other relationships. Therefore, our particular [111] primary (later a secondary) has available for good growth only primaries in preferred orientations 3 and 5; these represent one third of the matrix. The [120] primary has available for good growth only orientation 1 primaries; these represent one sixth of the matrix. Neither [111] nor [120] primaries (or secondaries) should grow well but, of the two, one would expect [111] secondaries more often than [120] secondaries, because there should be more large [111] primaries than [120] primaries and they also bear a better over-all relationship for good growth.

In the oriented-nucleation growth-selectivity theory the growth-selectivity rule is that growth is poor for the same and for the twin positions and good for other orientations. Therefore, the [111] primary has available for good growth orientations 3, 5, 2, and 6, (two thirds of the matrix), with orientations 1 and 4 (being the same and the twin orientation, respectively), acting to stop growth. On the other hand, the [120] primary is properly related to all six preferred orientations for good growth; this primary (or secondary) therefore should have little difficulty in consuming all the [111] primaries. Consequently, one would expect from the growth point of view [120] secondaries rather than [111] secondaries. The [120] secondaries satisfy the criterion of being in deviating orientation and of coming from a component which itself is very weak.

Before attempting any comparison with published data it should be remarked that the cold-drawn fiber texture usually includes a [100] component [14b]. In the Kronberg-Wilson 38-degree rotation relationship discussed earlier, results showed that every cube pole is replaced by a ⟨236⟩ direction. Therefore recrystallization of a [100] component by a 38-degree ⟨111⟩ rotation can produce nothing but a [236] fiber orientation. Since [236] is within 7 degrees of [112], [112] may be used to describe such a component. According to the argument put forth for growth of [120] secondaries, the [112] primaries should represent a small fraction of the texture; otherwise, those which later become [112] secondaries have difficulty in growing. In the absence of suitable [120] oriented nuclei and with too strong a [112] component, secondary recrystallization should not occur. Under such conditions, however, normal grain growth should occur with retention of components of the primary recrystallization texture.

The theory that secondaries arise from large primaries in a weak component of the primary recrystallization texture, provided this component is sufficiently weak, could be tested with the aid of quantitative pole figures and microstructures. Such data are not available. To some degree of certainty, however, published secondary recrystallization data [23; 24; 14b; 6; 25] point to a preponderance of [120] and [112] secondaries or secondaries very near these orientations. These data, therefore, are in agreement with the above predictions of the oriented-nucleation growth-selectivity theory and are not in agreement with the above predictions of the oriented-growth theory.

Acknowledgment

The author is indebted to Dr. W. R. Hibbard for a critical review of the manuscript and to Drs. D. Turnbull and M. L. Kronberg for helpful discussions.

Appendix

Any crystallographic direction [*uvw*] can be plotted in a stereogram with the aid of a Wulff net if the Wulff-net coordinates of the direction are known. With θ expressing latitude position and ϕ longitude position on the Wulff net, the relation-

*If we use the 38-degree rotation illustrated in Table II of the Appendix, three ⟨111⟩ directions are replaced by three ⟨1 11 5⟩ directions; this holds for either clockwise or counter-clockwise rotations. It follows with this kind of change that a [5 11 1] fiber orientation replaces the [111] fiber orientation. This new orientation, however, is only about 5 degrees from a [120] orientation, so [120] is a suitable description of it.

ships with the Miller indices for a [001] standard projection are

$$\theta = \cos^{-1} u/(u^2 + v^2 + w^2)^{\frac{1}{2}} \quad (1)$$

and

$$\phi = \tan^{-1} w/v \quad (2)$$

Illustrative and useful results for plotting Figures 1 and 2 of the text are given in Tables I and II respectively. (The stereograms in Figures 1 and 2 are also pole figures because a direction [*uvw*] is parallel to the pole of the (*uvw*) plane in the cubic lattice.)

TABLE I

WULFF-NET COORDINATES θ AND ϕ OF DIRECTIONS IN A [001] STANDARD PROJECTION

Group	u	v	w	θ	ϕ
	0	0	1	90	90
	$\bar{1}$	0	0	180	—
	0	1	0	90	0
1	1	$\bar{2}$	3	74.5	123.7
1	3	$\bar{5}$	8	72.4	122.0
1	1	$\bar{3}$	5	80.3	121.0
1	7	$\bar{12}$	22	74.4	118.6
1	1	$\bar{4}$	6	82.1	123.7
1	2	$\bar{3}$	6	73.4	116.5
2	$\bar{2}$	1	1	144.8	45.0
2	$\bar{5}$	2	3	144.2	56.3
2	$\bar{25}$	9	15	145.1	59.0
2	$\bar{8}$	4	5	141.4	51.3
2	$\bar{6}$	2	3	149.0	56.3
3	6	9	4	58.6	24.0
3	3	5	2	60.9	21.8
3	8	11	5	56.5	24.4
3	3	6	2	64.7	18.4

TABLE II

WULFF-NET COORDINATES OF THE CUBE AND OCTAHEDRAL POLES OF $(2\bar{3}6)$ $[\bar{6}23]$ AND PARALLEL DIRECTIONS IN (001) $[\bar{1}00]$

u_2	v_2	w_2	u_1	v_1	w_1	θ	ϕ
0	0	1	$\bar{3}$	2	6	115.4	71.6
1	0	0	6	3	2	31.0	33.7
0	$\bar{1}$	0	2	$\bar{6}$	3	73.4	153.4
$\bar{1}$	$\bar{1}$	1	$\bar{1}$	$\bar{1}$	1	125.3	135.0
$\bar{1}$	1	1	$\bar{11}$	5	1*	155.2	11.3
1	1	1	1	11	5*	85.3	24.4
1	$\bar{1}$	1	5	$\bar{1}$	11*	65.6	95.2

*These directions are within 5.2 degrees of $[\bar{2}10]$, [021], and [102], respectively.

In obtaining the results of Table II one assumes that (001) $[\bar{1}00]$ is a first orientation and $(2\bar{3}6)$ $[\bar{6}23]$ is a second one obtained by rotation from the first. The rotation is effected in terms of identifying parallel directions and calculating the Wulff-net coordinates ([001] of the second orientation is parallel with $[\bar{3}26]$ of the first, etc.).

This procedure is equivalent to the well-known one of rotation of coördinates and leads to general relationships through use of the transformation matrix. Thus a general relationship for parallel directions in (001) $[\bar{1}00]$ and $(2\bar{3}6)$ $[\bar{6}23]$ is

$$u_1 : v_1 : w_1 = (6u_2 - 2v_2 - 3w_2) : (3u_2 + 6v_2 + 2w_2) : (2u_2 - 3v_2 + 6w_2) \quad (3)$$

This simple relationship means, of course, that any direction whatever in the second orientation designated by rational indices will be parallel to a direction in the first orientation having rational indices. For example, the direction [123] in the second orientation is parallel to $[\bar{1}32]$ in the first; $[0\bar{1}3]$ is parallel to $[\bar{1}03]$; etc.

References

1. BECK, P. A. and HU, H. Trans. A.I.M.E. **185** (1949) 627.
2. BECK, P. A. and SPERRY, P. R. and HU, H. J. Appl. Phys. **21** (1950) 420.
3. BECK, P. A. Trans. A.I.M.E. **191** (1951) 475.
4. BECK, P. A. Acta Met. **1** (1953) 230.
5. MERLINI, A and BECK, P. A. Acta Met. **1** (1953) 598.
6. GOW, K. V. and Cahn, R. W. Acta Met. **1** (1953) 238.
7. BURGERS, W. G. and TIEDEMA, T. J. Acta Met. **1** (1953) 234.
8. DUNN, C. G. Acta Met. **1** (1953) 163.
9. DUNN, C. G. Acta Met. **2** (1954) 173.
10. LIU, Y. C. and HIBBARD, W. R. To be published.
11. HU, H., SPERRY, P. R., and BECK, P. A. Trans. A.I.M.E. **194** (1952) 76.
12. KRONBERG, M. L. and WILSON, F. H. Trans. A.I.M.E. **185** (1949) 501.
13. BURGERS, W. G. In L'Etat Solide (Brussels, Institut Internationale de Physique, 1951) p. 73.
14. BARRETT, C. S. Structure of Metals (New York, McGraw-Hill 1952), (*a*) p. 505; (*b*) p. 486.
15. BOWLES, J. S. and BOAS, W. J. J. Inst. Metals **74** (1948) 501.
16. SHARP, M. and DUNN, C. G. Trans. A.I.M.E. **194** (1952) 42.
17. BECK, P. A. Trans. A.I.M.E. **191** (1951) 474.
18. BECK, P. A. and HU, H. Trans. A.I.M.E. **194** (1952) 83.
19. DAHL, O. and PAWLEK, F. Z. Metallkde **28** (1936) 266.
20. VAN ARKEL, A. E. and VAN BRUGGEN, M. G. Z. Physik **51** (1928) 520.
21. BURGERS, W. G. and BASART, J. C. M. Z. Physik **54** (1929) 74.
22. BECK, P. A. and SPERRY, P. R. J. Appl. Phys. **21** (1950) 150.
23. BURGERS, W. G. and SANDEE, J. Physica **9** (1942) 996.
24. BASSI, G. Trans. A.I.M.E. **191** (1951) 533.
25. GOW, K. V. To be published (private communication).

SECONDARY RECRYSTALLIZATION IN ALUMINIUM EXTRUSIONS*

K. V. GOW†

A detailed study was made of the crystallographic orientations of recrystallised grains in a series of extruded and heat-treated rods of commercial and super-pure aluminium. The recrystallization texture was invariably a double ⟨113⟩–⟨013⟩ and ⟨111⟩ fibre texture. The secondary grains, which were found in an annular intermediate zone adjacent to the peripheral zone of the rods, were of the ⟨113⟩–⟨013⟩ component much scattered. A disproportionately high number of ⟨111⟩ component grains were in the intermediate zone and they occurred in long "strings" of grains of closely similar orientations. It was shown that grains which turn into secondaries may initially become slightly larger than other grains by strain-induced grain boundary migration or by the surface tension interaction of grain boundaries. It was concluded that secondary recrystallization is due to these relatively large ⟨113⟩–⟨013⟩ grains encroaching on the strings of ⟨111⟩ grains and that the driving force for secondary recrystallization comes from grain boundary energy.

LA RECRISTALLISATION SECONDAIRE DANS L'ALUMINIUM FILÉ

Une étude détaillée a été faite des orientations cristallographiques des grains recristallisés, dans une série de barres d'aluminium commercial et de très haute pureté, filées et soumises à un traitement thermique. La texture de recristallisation était invariablement une double texture fibreuse ⟨113⟩-⟨013⟩ et ⟨111⟩. Les grains secondaires, trouvés dans une zone annulaire, intermédiaire, adjacente à la zone périphérique des barres, appartenaient à la composante ⟨113⟩-⟨013⟩ fort dispersée. Un nombre hors de proportion de grains appartenant à la composante ⟨111⟩ se trouvait dans la zone intermédiaire; ces grains y étaient disposés en longues "ficelles" de grains d'orientation similaire. Il fut montré que les grains primaires qui deviennent des grains secondaires, peuvent au début devenir légèrement plus grands que les autres, soit par l'action de la migration des joints intergranulaires induite par la déformation, soit par l'interaction des tensions de surface des joints. On en a conclu que la recristallisation secondaire est due au fait que les grands grains appartenant à la composante ⟨113⟩-⟨013⟩ envahissent les ficelles des grains ⟨111⟩, et que la force motrice de la recristallisation secondaire provient de l'énergie des joints intergranulaires.

SEKUNDÄRE REKRISTALLISATION VON ALUMINIUM-STRANGPRESSPROBEN

An einer Reihe von ausgepressten und geglühten Stäben von technisch-reinem und höchst-reinem Aluminium wurde eine detaillierte Untersuchung der kristallographischen Orientierung des rekristallisierten Kornes vorgenommen. Die Rekristallisationstextur war in allen Fällen eine ⟨113⟩-⟨013⟩ und ⟨111⟩ Doppelfasertextur. Die in einer der peripheren Zone der Stäbe benachbarten Ringzone vorkommenden Sekundarkristallite gehörten—mit starken Streuungen—zu der ⟨113⟩-⟨013⟩ Komponenten. In dieser Zwischenzone befand sich eine unverhältnismässig grosse Anzahl von Kristalliten der ⟨111⟩ Komponenten. Diese traten in langen "Ketten" von Kristalliten sehr ähnlicher Orientierungen auf. Es wurde gezeigt, dass Kristallite, die sich in Sekundarkristallite umwandeln, anfangs etwas grösser als die andern Kristallite werden können. Diese Erscheinung geht entweder auf eine spannungsbedingte Korngrenzenwanderung oder auf die auf Grund ihrer verschiedenen Oberflächenspannungen mögliche Einwirkung der Korngrenzen aufeinander zurück. Daraus wurde geschlossen, dass die sekundäre Rekristallisation diesen relativ grossen ⟨113⟩-⟨013⟩ Kristalliten, die auf die Ketten der ⟨111⟩ Kristallite übergreifen, zuzuschreiben ist, und dass die Korngrenzenenergie die treibende Kraft im sekundären Rekristallisationsprozess ist.

I. Introduction

An informative account by Smith [1] of the extrusion of aluminium alloys shows that recrystallization and grain growth are among the most important problems encountered in the production of extruded sections. Depending on the alloy and the extrusion conditions obtaining, it is possible for extruded products to be unrecrystallized, wholly recrystallized, or recrystallized only in part. Heat-treated extruded sections may also be produced in the above three conditions.

Since one of the most valuable physical properties of extruded aluminium alloys is their high tensile strength, the recrystallized grain size, and in particular the growth of extremely large grains during heat treatment are of great industrial interest. Large grains result in a considerably lower proof stress and ultimate stress and a higher elongation than is obtained with fine-grained or unrecrystallized extruded sections [1].

Crystallographic fibring parallel to the extrusion direction, and strain hardening are responsible for the development of the unusually high tensile strength in extruded alloys. The fibring effect is explained by Boas and Schmid [2] on the basis of the three most highly stressed slip systems being active and the resulting deformation texture being composed of orientations which are stable under the action of slip of this kind. That is, the rotations due to slip on these systems cancel one another when the stable position is reached and the rod presents a maximum resistance to further

*Received November 25, 1953.
†Department of Metallurgy, University of Toronto, Canada.

elongation. Boas and Schmid were able in this way to account for the ⟨100⟩ and ⟨111⟩ components of the tension texture in face-centered cubic metals.

Kostron [3] and Unckel [4] have found the deformation texture of extruded aluminium alloys of the duralumin type to be a double fibre texture with ⟨100⟩ and ⟨111⟩ parallel to the extrusion direction. Gow and Cahn [5] report a similar deformation texture in extruded rods of commercial and super pure aluminium, as do Kostron and Schippers in 99.5 per cent aluminium [6].

Changes which occur in the deformed metal upon annealing result in a lower tensile strength. This may be brought about by recovery from strain-hardening and by recrystallization. A recrystallization texture similar to the deformation texture would be in an orientation stable to the action of slip on the principal slip systems. A change in texture upon recrystallization would be expected to lower the tensile strength to a greater extent. Unckel [7] found by X-ray examination that in extruded duralumin alloys the ⟨111⟩–⟨100⟩ texture remained after heat treatment. It was reported recently [5] that the recrystallization texture in super-pure and commercial aluminium extrusions is different from the deformation texture, being a duplex fibre texture with ⟨111⟩ as a minor component and a major component ranging between ⟨113⟩ and ⟨013⟩. It was found that the minor component originated in ⟨111⟩ deformed grains, while both ⟨111⟩ and ⟨100⟩ deformed grains contributed to the major component.

Upon annealing super-pure aluminium extrusions at a high temperature it was observed [5] that extremely large grains of the ⟨113⟩-⟨013⟩ component, much scattered, appeared in the outer layers of the rods. This excessive growth of a limited number of grains has been referred to as "secondary recrystallization," "coarsening" and "abnormal," "discontinuous," or "exaggerated" grain growth. Smith [1] too has observed secondary recrystallization after annealing high-purity aluminium extrusions. He also reports that those alloys which contain large proportions of insoluble compounds are least likely to grow large grains on reheating; but alloys of the duralumin type exhibit a sudden flashing of grain growth during heat treatment as a high proportion of the alloying elements are soluble at the solution treatment temperature. In all instances these large grains occur predominantly in the outer layers of the extrusions and grow most rapidly parallel to the fibre axis.

In the present paper the recrystallization textures of rods of commercial and super-pure aluminium extruded and annealed at various temperatures are reported. The macrostructure of the specimens after recrystallization is discussed. A theory for the origin of secondary grains in aluminium extrusions is advanced. It supports the idea that growth of secondaries depends principally on the surface tension interactions of grain boundaries rather than upon some distribution of strains among primaries. However, a mechanism is proposed by which strain among primaries could account for some grains becoming appreciably larger than others, but the driving force for subsequent growth of these grains into large secondaries is probably grain boundary energy. A theory for the origin of primary grains in recrystallized aluminium extrusions was evolved during the course of the present investigation and it has been described elsewhere [5; 20].

II. Experimental Procedure

(*a*) *Material*

Rods of super-pure and of commercial aluminium were extruded. The impurities in the rods were determined by spectrographic analysis* of sections of the rods adjacent to sections in which the recrystallization textures were studied and are shown in Table I.

TABLE I

Extrusion no.	Fe%	Mn%	Mg%	Si%	Cu%
1S (Super-pure Al)	0.02	nil	<0.01	0.03	0.007
2S (Super-pure Al)	0.02	nil	<0.01	0.02	<0.005
1C (Commercial Al)	0.49	<0.005	<0.01	0.23	<0.005
2C (Commercial Al)	0.49	<0.005	<0.01	0.23	<0.005

No difference was found in impurity concentration along the radius of the rods.

(*b*) *Extrusion*

The extrusion billets were chill-cast in 3 in. diameter cast iron moulds. They were cut to 8 in. lengths and machined to $2\frac{3}{4}$ in. diameter. The billets were preheated for 2 hours and extruded through a 1 in. diameter die. The rods were quenched during extrusion by water sprays at the die orifice to prevent recrystallization. Extrusions were made in a Fielding and Platt 400 tons horizontal extrusion press in these laboratories.† The extrusion conditions are listed in Table II.

*Courtesy of Imperial Chemical Industries Ltd., Metals Division, Kynoch Works, Birmingham 6, England.

†Department of Metallurgy, University of Birmingham, England.

TABLE II

Extrusion no.	Temp °C	Speed (in./sec)*	Pressure (lbs/sq in.)**
1S	485	0.35–0.40	1000
2S	350	0.35–0.40	1300
1C	485	0.35–0.40	1150
2C	350	0.35–0.40	2050

*Speed of ram.
**Maximum pressure developed.

(*c*) *Preparation of Specimens*

Specimens about 1½ in. long were cut radially from the rods with a saw. The ends of these 1-in. diameter cylinders were machined and then etched deeply to remove strained layers. Those specimens to be given similar heat treatments were cut from identical sections near the middle of the 48-in. long rods. After annealing, one half of the cylinder was carefully machined off to expose a longitudinal plane at the centre of the rod. A layer about 0.015 in. thick was then removed by etching in the Hume-Rothery reagent (Table III). This method of surface preparation after annealing eliminates the possibility of machining strains and free surfaces affecting the recrystallization process.

(*d*) *Orientation Determination*

The crystallographic orientations of the grains in the specimens were determined by the reflection of light from etch pits. A two-circle optical goniometer was used [8]. The Hume-Rothery etchant described in Table III was used to develop the (100) etch pits.

TABLE III

150 grams.....$CuCl_2 \cdot 2H_2O$
1000 ml.....H_2O (distilled)

The surface of the specimen was swabbed with this solution and the deposited copper wiped off at 30-sec intervals. The amount of etching did not affect noticeably the sharpness of the reflection from the cubic etch pits. The surface was finally brightened by washing it in a 1:1 HNO_3-water solution.

(*e*) *Annealing*

The specimens were placed in a Birlec air-circulation furnace at the annealing temperature. After the annealing period the specimens were quenched in water. The annealing conditions for the various specimens are given in Table IV.

TABLE IV

Extrusion no.	Specimen no.	Extrusion Temp °C	Annealing Temp °C	Time, min.
1S	1S1	485	485	150
1S	1S2	485	600	150
2S	2S1	350	350	150
2S	2S2	350	600	150
1C	1C1	485	485	150
1C	1C2	485	600	150
2C	2C1	350	350	150
2C	2C2	350	600	150

III. Results

(1) Super-pure Aluminium

(*a*) *General.* An examination of a transverse section of a super-pure aluminium billet prior to extrusion showed the grains to be columnar, about ¼ in. to 1 in. in length and 1/20 in. to ¼ in. in diameter. These columnar grains had grown inwards radially, in the billet with ⟨100⟩ parallel to the columns.

Except for secondary grains the relative recrystallized grain sizes obtained at different extrusion temperatures and pressures, and annealing temperatures, appeared to be consistent with the "laws of recrystallization" [9].

Spectrographic analysis showed the impurity concentration along the radius of the extruded rods to be uniform.

(*b*) *Recrystallization Texture.* A visual inspection of a longitudinal section of the annealed and etched super-pure aluminium extrusions showed that, adjacent to the peripheral layers of the rod, there was a zone in which a relatively high proportion of the recrystallized grains gave a uniform reflection of incident light (see Figures 1a, 1b, 1c). Most of these grains occurred in long "strings" which were approximately parallel to the extrusion direction. Examination of partially recrystallized specimens, such as 2S1 in Figure 1c, showed that each string was restricted to a region formerly occupied by one parent deformed grain. The coning inwards in the direction of extrusion which can be observed in Figure 1c, is due to the mechanism of deformation and flow of the columnar grains in the billet during extrusion. The grains in strings were generally slightly elongated normal to the string direction. Other recrystallized grains were more nearly equiaxed and showed much contrast in their reflection of incident light.

Thus, for the purpose of texture determination, the rod was divided into three longitudinal annular

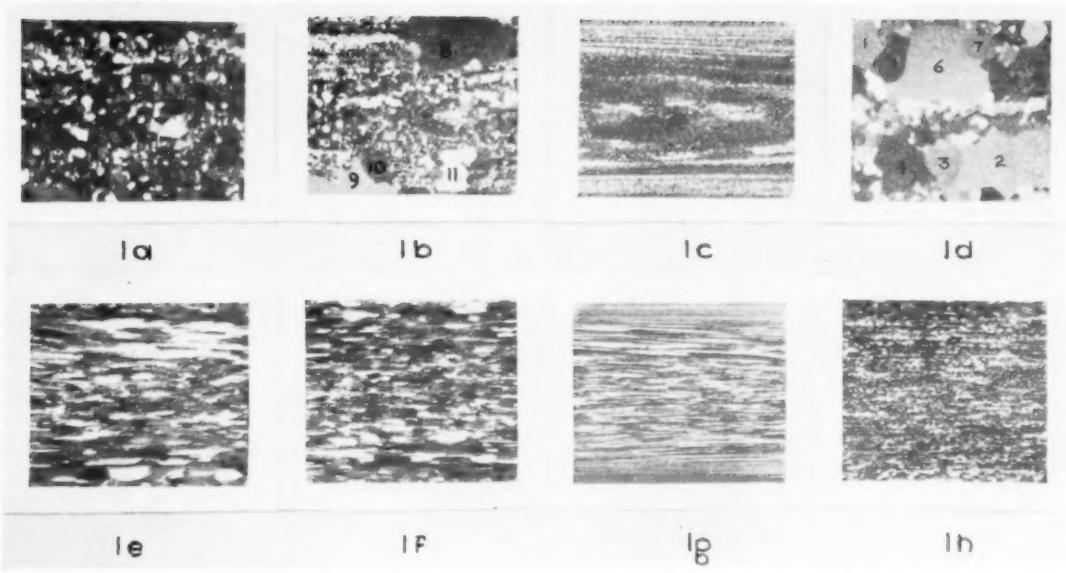

PLATE I. FIGURE 1—Macrostructures in longitudinal planes of extruded and heat-treated rods (×1). See Tables I–IV. (*a*) Specimen 1S1, (*b*) Specimen 1S2, (*c*) Specimen 2S1, (*d*) Specimen 2S2, (*e*) Specimen 1C1, (*f*) Specimen 1C2, (*g*) Specimen 2C1, (*h*) Specimen 2C2.

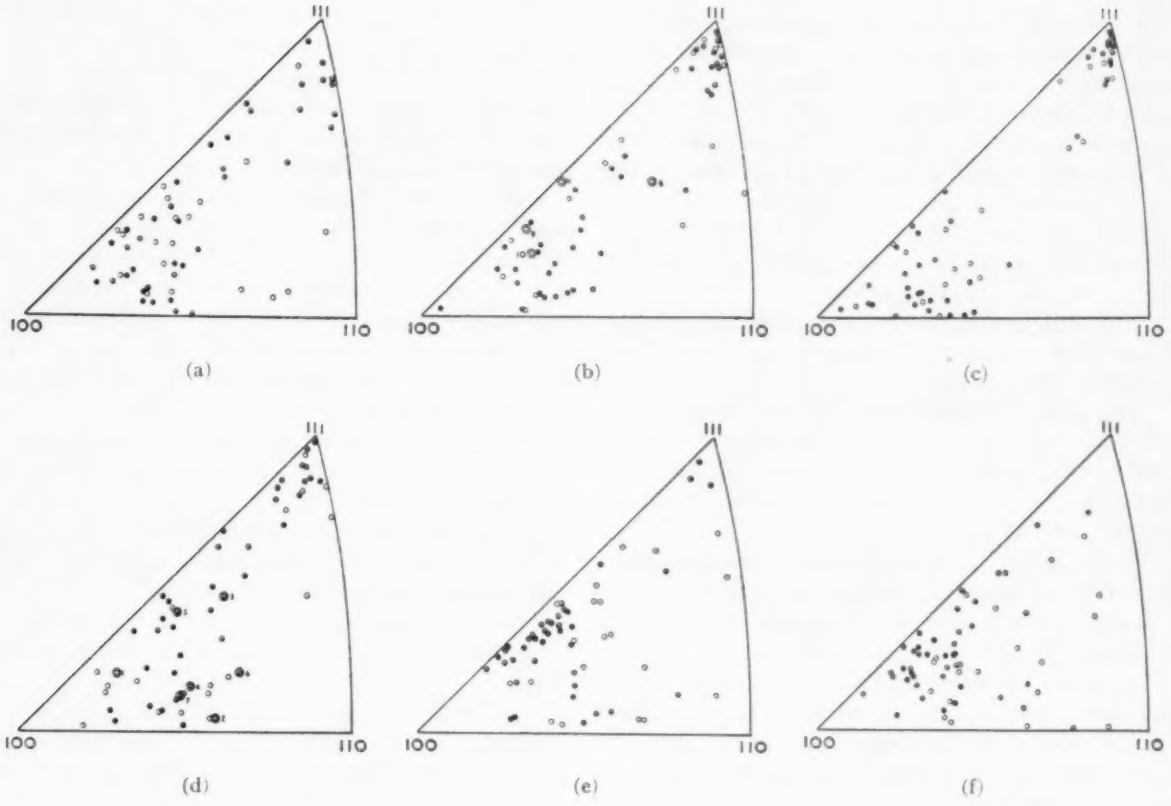

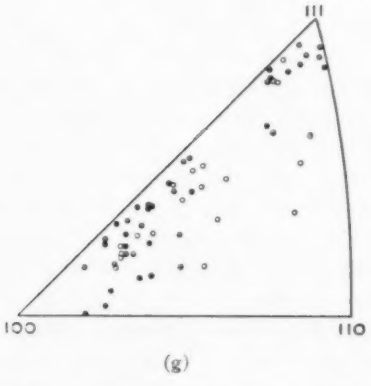

FIGURE 2. Fibre recrystallization textures in the specimens of Fig. 1. The poles represent the extrusion direction. Solid, half-solid, and open circles refer to recrystallized grains in the core, intermediate and peripheral zones respectively. Poles of secondary grains (concentric circles) are numbered to correspond to numbers on the secondary grains in Figs. 1b and 1d. (a) Specimen 1S1; (b) Specimen 1S2; (c) Specimen 2S1; (d) Specimen 2S2; (e) Specimen 1C1; (f) Specimen 1C2; (g) Specimen 2C2.

zones; a peripheral zone 5/32 in. wide, an intermediate zone 5/32 in. wide containing a high proportion of the "strings," and the central core of 3/16 in. radius. Some strings extended into the central core and peripheral zones. For each specimen the crystallographic orientation of 60 grains selected at random, 20 from each zone, are plotted in basic stereographic triangles; see Figures 2a to 2d.

It was found that the elongated grains which form the strings were of the ⟨111⟩ component. The grains in each string had nearly a common crystallographic orientation, the difference in orientation being not more than 3 or 4 degrees for

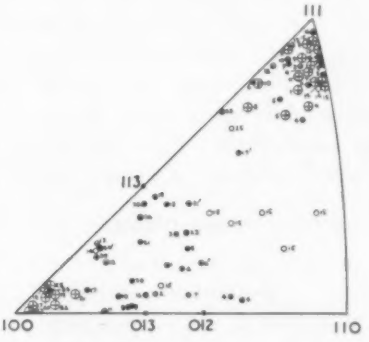

FIGURE 3. Super-pure aluminium extrusion No. 2S. The poles represent the extrusion direction. Crosses refer to the deformed grains; solid, half-solid and open circles as in Fig. 2 caption. Poles of recrystallized grains bear numbers corresponding to their parent deformed grains.

the grains of any one string. Other recrystallized grains belong to the ⟨113⟩–⟨013⟩ component, which is much less sharply defined than the ⟨111⟩ component. Grains in the peripheral zone showed the greatest scatter in orientation. An analysis of the distribution showed that about 54 per cent of the intermediate-zone grains were of the ⟨111⟩ component while only 23 per cent and 13 per cent of the peripheral- and core-zone grains, respectively, belong to the ⟨111⟩ component.

The ⟨111⟩ grains in strings were slightly smaller than neighbouring ⟨113⟩–⟨013⟩ grains, often by a factor as great as two.

The recrystallization textures of extrusion number 1S, made at 485°C and annealed at 485°C and 600°C, were similar to those of extrusion number 2S, made at 350°C and annealed at 350°C and 600°C.

(*c*) *Secondary Recrystallization.* Upon annealing for 150 minutes at 600°C, exaggerated grain growth was observed in specimens 1S2 and 2S2 (Figures 1b and 1d). The orientations of these large grains are shown in Figures 2b and 2d. It can be seen that nearly all these large secondary grains are in the intermediate zones, although most have grown into the two neighbouring zones to some extent. The orientations of the secondary grains are widely scattered throughout the ⟨013⟩–⟨113⟩ component.

Grains number 2 and 6 in specimen 2S2 and grain 8 in specimen 1S2 are much larger than the other secondary grains and their orientations are somewhat further removed from the ⟨113⟩–⟨013⟩ component than other secondary grains. It can be seen that the shape of the grain boundaries of the secondary grains is concave with respect to all the small grains with which they are in contact. Grains 2, 6 and 8 have boundaries concave with respect to adjacent, but smaller, secondary grains. Grain 8 has grown most rapidly along a string of ⟨111⟩ grains. The secondary grains appear to grow most rapidly in a direction parallel to the fibre axis, and their grain boundaries migrate toward their centres of curvature.

(2) Commercial Aluminium

(*a*) *General.* Examination of a transverse section of a commercial aluminium billet prior to extrusion showed the grains to be equiaxed and about 1/20 to 1/100 in. in diameter.

Except for a uniform coarsening in the intermediate zones, the relative recrystallized grain sizes in specimens 1C1, 1C2 and 2C2, Figures 1e, 1f, and 1h respectively, are in accord with the general "laws of recrystallization" [9].

The shape of the recrystallized grains is jagged elongated as compared to the equiaxed grains with smoother boundaries in the recrystallized super-pure aluminium specimens.

Specimen 2C1, Figure 1g, did not recrystallize and it serves to illustrate the "as deformed" structure of the rod. The deformation gradient from the relatively lightly worked central core to the heavily deformed peripheral zone is apparent, as is the coning inwards of the deformed grains in the direction of extrusion and the great elongation of the equiaxed grains of the billet.

Spectrographic analysis showed the impurity concentration along the radius of the extruded rods to be uniform.

The speed of extrusion was maintained the same as for the super-pure aluminium specimens. The extrusion pressures, listed in Table II, show that the lower temperature extrusion, 2C, was much more resistant to flow than the other three extrusions.

(*b*) *Recrystallization Textures.* The strings of similarly oriented grains observed in the super-pure aluminium specimens were much less prominent in the commercial aluminium specimens. However, a careful visual examination showed that a relatively high proportion of grains in and near the intermediate zone of specimen 2C2 occurred as strings of grains which gave a uniform reflection of incident light. These grains were not elongated normal to the string direction and the strings were shorter than those in the super-pure aluminium specimens. The grains in the strings were of the ⟨111⟩ component, and the grains of each individual string had nearly a common crystallographic orientation.

The same longitudinal zoning system was used as for the super-pure aluminium specimens. The recrystallization textures found are shown in the pole figures in Figures 2e, 2f and 2g. The texture of specimen 2C2 is the same double ⟨111⟩ and ⟨113⟩–⟨013⟩ fibre texture found for the super-pure aluminium specimens, but the disproportionately high concentration of ⟨111⟩ grains in the intermediate zone is lacking. The almost complete disappearance of the ⟨111⟩ component in specimens 1C1 and 1C2 is striking. The macrostructures of these two specimens, Figures 1e and 1f, show unusually large grains in and near the intermediate zone. The orientations of many of these grains were determined and they are of the ⟨113⟩–⟨013⟩

component. Relatively large grains have also grown in the intermediate zone of specimen 2C2. The ratio of grain size in the intermediate and peripheral zones to that in the central core is about the same in specimens 2C2, 1C1, and 1C2.

(*c*) *Secondary Recrystallization*. Exaggerated grain growth, on the same scale as in the super-pure aluminium, did not occur in the commercial aluminium specimens. The relatively large ⟨113⟩–⟨013⟩ grains in the intermediate zones of these specimens are the result of a uniform coarsening.

IV. Discussion of Results

The recrystallization textures of extruded rods of super-pure and commercial aluminium are shown to be similar. No attempt was made to obtain annealing conditions which would result in the true primary recrystallization structure. Thus, grains other than the large secondaries are not referred to as primaries, since they must have undergone normal growth after primary recrystallization. Different extrusion and annealing temperatures and the different impurity contents caused no fundamental changes in the recrystallization texture; but the size of the grains other than the secondaries, was affected in a manner which is consistent with the well known "laws of recrystallization" [9]. The uniform distribution of impurities in the rods shows that heterogeneity of composition is not a factor in the phenomena observed.

The disproportionately high concentration of ⟨111⟩ recrystallized grains in the intermediate zone of the super-pure aluminium rods is probably related to the initial orientation of the parent grains in the billet and to the type and amount of deformation which the grains in this zone undergo during extrusion. The occurrence of ⟨111⟩ grains in "strings" has been attributed to the presence of deformation bands in the ⟨111⟩ deformed grains [5].

In the commercial aluminium specimen, 2C2, the ⟨111⟩ component in the intermediate zone appears weaker than in the super-pure aluminium specimens. However, many small strings of ⟨111⟩ grains were observed in and near the intermediate zone and their presence can probably be explained in the same way as for the super-pure aluminium. The finer grain size of the commercial aluminium billets and the fine recrystallized grain size, which resulted in a much smaller proportion of grain orientations being determined, could account for the difference.

In specimens 1C1 and 1C2 the disappearance of the ⟨111⟩ component can probably be attributed to the uniform coarsening of the ⟨113⟩–⟨013⟩ grains in the intermediate zone. In the super-pure aluminium specimens 1S2 and 2S2 it can be seen that further growth of the ⟨113⟩–⟨013⟩ secondaries would result in their consuming all ⟨111⟩ grains in the intermediate zone. This is discussed more fully below.

A number of theories on the origin of secondary grains have been advanced [9]. In general the main point of conjecture is whether secondaries depend principally on (*a*) the surface tension interaction of grain boundaries, or (*b*) some distribution of strains among primaries. Burke and Turnbull [9] state that there is now fairly convincing evidence that the driving energy for secondary recrystallization is surface energy rather than strain energy. In a recent investigation of secondary recrystallization in cold-rolled single crystals of silicon iron [10], Dunn concluded that secondaries originate when relatively large primary grains in orientations deviating markedly from the primary recrystallization texture turn into secondary grains having specific preferred orientations and that the driving force for secondary recrystallization comes from grain boundary energy. Dunn summarizes the conditions to be met by primaries if they are to become secondaries as follows:

1. They must have deviating orientations referred to the average orientation of the primary structure.

2. They must be appreciably larger than average primaries unless neighbouring grains have higher energy due to some form of strain.

3. Regardless of strain differences they must have among them the orientations observed for secondaries.

In the following section it is shown that in extruded aluminium secondaries may originate in two different ways: by (*a*) a mechanism fundamentally similar to that proposed by Dunn to account for the origin of secondaries in cold-rolled silicon iron single crystals, and (*b*) growth in a non-uniformly strained matrix of primaries:

(*a*) In the pole figures, 2a, 2b, 2c and 2d, for super-pure aluminium, the ⟨113⟩–⟨013⟩ component grains have considerable scatter in orientation, while the ⟨111⟩ grains have a relatively sharp texture. A strong preferred orientation inhibits the growth of grains that result from primary recrystallization because, as Beck and Hu [11] point out, grain boundaries between grains of nearly the

same crystallographic orientation migrate only with difficulty. Thus the larger orientation differences between neighbouring ⟨113⟩–⟨013⟩ grains result in their having a higher grain boundary migration rate than the ⟨111⟩ grains which are adjacent to each other in strings. This could account for the ⟨113⟩–⟨013⟩ grains being slightly larger than the ⟨111⟩ grains, since by the process of normal grain growth the former can encroach more readily on their ⟨113⟩–⟨013⟩ component neighbours.

Some ⟨113⟩–⟨013⟩ grains are in contact with smaller ⟨111⟩ grains and because of the large difference in orientation the grain boundary joining them has a high energy and thus is very mobile. Since the ⟨113⟩–⟨013⟩ grains are often as much as two or three times the diameter of an adjacent ⟨111⟩ grain, this size difference provides the larger grains with the ability to encroach on their smaller ⟨111⟩ neighbours [10]. This is due to the fact that curved grain boundaries between undistorted grains migrate toward their centres of curvature [12]. Harker and Parker [13] have shown how a large grain can have its boundaries concave outwards if it is bordered by small grains. The curved grain boundaries of the secondary grains in specimens 1S2 and 2S2 provide an example of this.

A ⟨113⟩–⟨013⟩ grain, in such a position that it can encroach rapidly on a string of ⟨111⟩ grains, will soon reach a size that will permit it to grow with respect to adjacent ⟨113⟩–⟨013⟩ grains which were not so favourably situated for growth. Such a grain can grow rapidly by consuming all its smaller neighbours irrespective of their orientation, and if annealing is continued at a sufficiently high temperature, secondary recrystallization takes place.

Several secondary grains may form in a certain region, as illustrated in specimen 2S2, and some may be much larger than others. Grains 2 and 6 have boundaries concave with respect to their neighbouring secondary grains 3, 5, and 7. Thus it would be expected that had annealing been continued 2 and 6 would eventually have swallowed up the smaller secondary grains. That grains 2 and 6 have been particularly favoured as potential secondary grains after their nucleation as primaries is shown by their orientations, Figure 2d, which lie far removed from the ⟨111⟩ strings and from the centre of their own ⟨113⟩–⟨013⟩ component. There is, therefore, a larger orientation difference between these two grains and their neighbours than there is between most other grains. They also lie in the intermediate zone, close to ⟨111⟩ strings. The orientational relationship between grains 2 and 6 and the ⟨111⟩ grains corresponds to a rotation of about 46 degrees around a ⟨111⟩ axis. Such a relationship is believed to give the highest grain boundary mobility in face-centered cubic metals [5; 8; 14].

(*b*) A second means by which a ⟨113⟩–⟨013⟩ grain may become considerably larger than its neighbours is strain-induced grain boundary migration.

Gow and Cahn [5] have shown that the major ⟨113⟩–⟨013⟩ recrystallization component in super-pure aluminium extrusions is derived from both ⟨111⟩ and ⟨100⟩ deformed grains by mean rotations of 46 degrees and 22 degrees respectively about ⟨111⟩ axes of the deformed grains, while the minor ⟨111⟩ recrystallization component is derived by a mean rotation of 46 degrees about the ⟨111⟩ axis which lies parallel to the fibre axis in ⟨111⟩ deformed grains.

It can be shown on a standard cubic stereographic projection that if a ⟨100⟩ deformed grain with perfect cubic alignment recrystallizes and the new grains are related to the deformed grain by 22-degree rotations about ⟨111⟩ axes, then the crystallographic direction in the new grain which is parallel to the extrusion direction lies on the ⟨110⟩ zone about 1 degree from the ⟨114⟩. Similarly, recrystallized grains related by a 46-degree rotation about ⟨111⟩ axes of a perfectly aligned ⟨111⟩ deformed grain can be shown to form the ⟨013⟩ component if they rotate about any one of the three ⟨111⟩ axes not parallel to the fibre axis, and to form a ⟨111⟩ component if they rotate about the ⟨111⟩ axis that is parallel to the fibre axis. Thus the ideal texture for recrystallized grains related to perfectly aligned parent ⟨100⟩ and ⟨111⟩ deformed grains by rotations of 22 degrees and 46 degrees respectively about ⟨111⟩ axes, may be described as a triple ⟨111⟩–⟨013⟩–⟨114⟩ fibre recrystallization texture.

An investigation [5] of the orientations of recrystallized grains derived from ⟨100⟩ and ⟨111⟩ deformed grains in super-pure aluminium extrusions was carried out (see Figure 3). It was shown that most recrystallized grains with ⟨100⟩ parent deformed grains had orientations near the ⟨113⟩ with some scatter along the ⟨110⟩ zone and toward the ⟨013⟩. Recrystallized grains with ⟨111⟩ parent deformed grains had orientations either near the ⟨013⟩ with scatter toward ⟨113⟩ and ⟨012⟩, or near the ⟨111⟩.

Gow and Cahn also observed [5] that the ⟨111⟩ deformed grains had recrystallized completely before the ⟨100⟩ deformed grains had begun to do so. They postulate that the ⟨111⟩ deformed grains are more highly distorted than the ⟨100⟩ deformed grains. Rathenau and Custers [15] and Tiedema [16] have envisaged a straining of early-forming primaries through release of unbalanced stresses, with only the last-forming primaries free of strain. Strain-free primaries can grow at the expense of strained ones [14]. Thus the last-forming ⟨113⟩ primaries derived from ⟨100⟩ deformed grains are likely to have a lower strain energy than early forming ⟨013⟩ and ⟨111⟩ primaries. These strain-free ⟨113⟩ grains could grow at the expense of neighbouring ⟨013⟩ grains, in spite of the small orientation difference between them, and also at the expense of ⟨111⟩ grains. In this way it is possible for a ⟨113⟩ grain to become considerably larger than its neighbours and eventually to attain the status of a secondary grain.

Specimens 1S2 and 2S2 contain several smaller secondaries, Nos. 1, 3, 5, 10 and 11, which have orientations near ⟨113⟩. For the present discussion it is assumed that they are derived from ⟨100⟩ deformed grains; but it is possible that they may be derived from ⟨111⟩ grains, since, as shown in Figure 3, some grains of such an origin are scattered toward the ⟨113⟩. It is significant that these smaller secondaries occur only in the intermediate and peripheral zones where the ⟨111⟩ strings are concentrated. This could indicate that ⟨113⟩ grains, which eventually become secondaries, may grow slightly larger than their neighbours by strain-induced grain boundary migration, but that surface tension interaction leads to their continued growth into very large grains when they come into contact with ⟨111⟩ strings.

If surface tension is the main driving force for growth, then the shape of the boundaries of the ⟨013⟩ secondaries, 2 and 6, in Figure 1d, is such that they can encroach on the smaller ⟨113⟩ secondaries 3 and 5. If 3 and 5 are less strained than 2 and 6, and strain energy is the main driving force for growth, then the former may be encroaching on the two larger secondaries since the boundary of a strain-free grain encroaching on a strained one migrates away from its centre of curvature. However, when this type of growth occurs, the boundary usually moves in an irregular jagged front, and the boundaries between grains 5 and 6, and between 2 and 3 are smooth [14]. Therefore it is likely that if annealing were continued, grains 2 and 6 would swallow up the smaller grains 3 and 5 and that surface tension is a greater driving force for grain growth than strain difference.

That the ⟨113⟩ secondaries are smaller than secondaries with ⟨111⟩ parent deformed grains would be expected since the orientational relationship between ⟨113⟩ grains and the ⟨111⟩ strings is less favourable for rapid growth, being far removed from the ideal relationship of about 46 degrees around a ⟨111⟩ axis.

The ⟨113⟩ grains can become large enough to develop into secondaries by surface-tension interaction of grain boundaries as well as by strain-induced grain boundary migration. Since the ⟨100⟩ deformed grains, from which the ⟨113⟩ grains are derived, are less highly strained than ⟨111⟩ deformed grains [5], they recrystallize more slowly than the latter. Thus, the ⟨100⟩ deformed grains are likely to have fewer nuclei for primary recrystallization than the more highly strained ⟨111⟩ grains and consequently will recrystallize to a larger grain size. At boundaries between the parent grains there will be relatively large ⟨113⟩ primaries bordering small ⟨111⟩ primaries, which is the condition required for them to be able to grow into secondaries by surface-tension interaction of grain boundaries.

It has been shown above how strain-induced grain boundary migration might lead to secondary recrystallization but that it is likely to be of very minor importance compared to surface-tension forces. As Burke and Turnbull [9] point out, it seems unlikely that strains of the order of magnitude required for conventional nucleation could be retained in the specimen after primary recrystallization.

The above explanations for the origin of secondaries in super-pure aluminium extrusions can also account for the large grains in the intermediate zones of the commercial aluminium extrusions. The more uniform coarsening, as compared to the development of a few very large grains in the super-pure aluminium, is probably due to the much larger impurity content of the commercial aluminium. These impurities inhibit grain boundary migration, and their effect can be seen in the jagged and elongated shape of the grains.

Burgers and Sandee [17] have shown that cold-drawn commercial aluminium wire has a strong ⟨111⟩ fibre deformation texture, with a trace of ⟨100⟩. After primary recrystallization, and upon annealing at a high temperature, a pronounced uniform coarsening took place and these secondary

crystals, about 2 mm long, had a ⟨012⟩ texture. The primary recrystallization texture of aluminium wire is usually reported to be a ⟨111⟩ fibre texture [8]. The results of the present investigation would appear to indicate that some primaries in aluminium wire attain a texture close to the ⟨013⟩ by rotations about ⟨111⟩ axes of the deformed grains which are not parallel to the fibre axis. Primary ⟨013⟩ grains with orientations scattered toward the ⟨012⟩ then grow into secondary grains, upon high-temperature annealing, by encroaching on the abundant ⟨111⟩ primary grains.

An extruded and heat-treated rod of duralumin (3.9% Cu, 0.41% Mn, 0.96% Mg, 0.51% Fe, 0.35% Si), produced under conditions closely similar to the present specimens, had large secondary grains occupying its whole cross section [18]. The largest of these grains were in the intermediate and peripheral zones. The crystallographic orientations of thirty secondaries were determined on the optical goniometer and they were found to be scattered about the ⟨012⟩ direction. As noted previously [3; 4], duralumin-type alloy extrusions have been found to have a double ⟨111⟩–⟨100⟩ fibre deformation texture. Thus it is probable that the same mechanism for the formation of primary textures and the growth of secondaries exists in duralumin as in super-pure aluminium. The sudden flashing of secondary grain growth in duralumin alloys during heat treatment can be associated with partial solution of the alloying elements at grain boundaries at the solution treatment temperature [19]. The alloying element inclusions hold up motion of most boundaries but a few grains are either sufficiently large to grow or the density of inclusions on their boundaries is insufficient to retard their growth. The appearance of secondaries in the outer layers of the extrusions and their rapid growth parallel to the extrusion direction is consistent with the theory that these secondaries grow most rapidly by encroaching on ⟨111⟩ strings due to surface-tension interaction of grain boundaries.

Smith [1] has shown that in extrusion billets there is an annular zone in which the metal is subjected to very high shear stresses during extrusion. In the extruded section the centre of this zone of heavy shear occupies a region which corresponds to the intermediate zone of the present specimens. Smith states that it is the conditions giving rise to this zone which present most of the problems associated with the production of aluminium alloy extrusions, and shows that it is the zone in which secondary recrystallization occurs most readily. He explains the presence of secondary grains in this zone by assuming that it contains a region of critical strain in which the degree of strain is particularly favourable for exaggerated grain growth. The results of the present investigation show that secondary recrystallization is probably due to the disproportionately high concentration of strings of ⟨111⟩ component grains in this zone, and that the growth of secondaries takes place by the surface-tension interaction of grain boundaries rather than by some distribution of strains among primaries.

Smith [1] describes methods which have been used in industry to prevent secondary recrystallization. They are often designed to modify the nature of the flow of metal during extrusion with the idea of relieving or preventing some critical strain in the extruded sections. The present results seem to indicate that such methods will be successful only in so far as they are effective in changing the distribution of, or eliminating, the ⟨111⟩ component deformed grains which produce a disproportionately high percentage of ⟨111⟩ component recrystallized grains in strings in the outer layers of the extruded sections.

V. Summary and Conclusions

The recrystallization textures of a series of super-pure and commercial aluminium rods, extruded and annealed at various temperatures, were determined. Similar double ⟨113⟩–⟨013⟩ and ⟨111⟩ fibre textures were found in all instances. Thus, neither the additional impurities in the commercial aluminium nor the different temperatures of extrusion and annealing brought about fundamental changes in the recrystallization process.

The normal recrystallized grain sizes were consistent with the "laws of recrystallization."

The ⟨111⟩ recrystallized grains occurred most abundantly in the intermediate zones of the specimens and were generally in the form of long "strings" of grains with closely similar crystallographic orientations. Secondary recrystallization took place most profusely in the intermediate zones and the secondary grains were found to belong to the ⟨113⟩–⟨013⟩ component. This accounts for the relative weakness of the ⟨111⟩ component in specimens annealed at higher temperatures, for it is shown that secondary recrystallization takes place when relatively large ⟨113⟩–⟨013⟩ grains

encroach on strings of ⟨111⟩ grains in the intermediate zone.

The growth of a few favourably situated primary grains to a size slightly larger than their neighbours, which is necessarily the origin of secondaries, is attributed to two possible mechanisms: the surface tension interaction of grain boundaries and strain-induced grain boundary migration. It is concluded, however, that subsequent growth of both types of large grains into secondaries is due to surface-tension interaction of grain boundaries and not to strain energy.

Acknowledgements

Thanks are due to the Department of Industrial Metallurgy, University of Birmingham, for provision of facilities and financial support. I am indebted to Professors C. S. Barrett and B. Chalmers, to Doctors C. G. Dunn, A. R. E. Singer, R. W. Cahn, and K. T. Aust, and to Mr. D. H. Locke for much helpful discussion and assistance in this work. The investigation was carried out during tenure of a National Research Council of Canada Post-doctorate Overseas Fellowship.

References

1. Smith, C. J. Inst. Metals **76** (1950) 429.
2. Boas, W. and Schmid, E. Z. Tech. Physik **12** (1931) 71.
3. Kostron, H. Metall. **13/14** (1951) 229.
4. Unckel, H. Metallwirtschaft **21** (1942) 185.
5. Gow, K. V. and Cahn, R. W. Acta Met. **1** (1953) 238.
6. Kostron, H. and Schippers, M. Metall. **1/2** (1953) 25.
7. Unckel, H. Metallwirtschaft **19** (1940) 70.
8. Barrett, C. S. Structure of Metals (New York, McGraw-Hill, 1952).
9. Burke, J. E. and Turnbull, D. Progress in Metal Physics (London, Pergamon Press, 1952) Vol. 3.
10. Dunn, C. G. Acta Met. **1** (1953) 163.
11. Beck, P. A. and Hu, H. J. Metals **1** (1949) 627.
12. Burke, J. E. In "Atom Movements" (Cleveland, American Society for Metals, 1951).
13. Harker, D. and Parker, E. A. Trans. A.S.M. **34** (1945) 156.
14. Beck, P. A. In "Metal Interfaces," (Cleveland, American Society for Metals, 1952).
15. Rathenau, G. W. and Custers, J. F. H. Philips Res. Report **4** (1949) 241.
16. Tiedema, T. J. Doctoral Thesis, Tech. Hogeschool, Delft (1951).
17. Burgers, W. G. and Sandee, J. Physica **9** (1942) 996.
18. Gow, K. V. Unpublished work.
19. Beck, P. A., Holzworth, M. L. and Sperry, P. Trans. A.I.M.M.E. **180** (1949) 163.
20. Gow, K. V. Acta Met. **1** (1953) 610.

EFFECT OF COLD WORK ON THE MAGNETIC SUSCEPTIBILITY OF COPPER AND ALUMINUM*

J. D. McCLELLAND†

The susceptibilities of copper and aluminum have been measured as a function of cold work. Spectroscopically-pure samples were cold-worked both by rolling and compression. A Faraday method was used to determine the specific susceptibility and the mass concentration of the ferromagnetic contaminant simultaneously. No changes were noted in either metal. It is pointed out that trace amounts of ferromagnetic impurity accidentally picked up during the cold working process would result in large apparent changes in the observed susceptibility. This might account for the changes reported previously by other workers.

L'EFFET DE L'ÉCROUISSAGE SUR LA SUSCEPTIBILITÉ MAGNÉTIQUE DU CUIVRE ET DE L'ALUMINIUM

On a mesuré les susceptibilités magnétiques du cuivre et de l'aluminium en fonction du degré d'écrouissage. Des échantillons spectrographiquement purs ont été écrouis par laminage et par compression. Une méthode de Faraday fut employée pour la détermination simultanée de la susceptibilité spécifique et de la concentration de l'impureté ferromagnétique. Aucun changement n'a été constaté dans ces deux métaux. On souligne le fait que des traces d'impuretés ferromagnétiques, introduites accidentellement quand on procède à l'écrouissage, peuvent provoquer de grands changements apparents dans la susceptibilité observée. Ceci peut expliquer les changements que d'autres chercheurs ont rapportés antérieurement.

DIE WIRKUNG DER KALTBEARBEITUNG AUF DIE MAGNETISCHE SUSZEPTIBILITÄT VON KUPFER UND ALUMINIUM

Die Suszeptibilitäten von Kupfer und Aluminium wurden als Funktion der Kaltbearbeitung gemessen. Spektroskopisch reine Proben wurden durch Walzen und durch Kompression kaltbearbeitet. Mit Hilfe einer Faraday-Methode wurde die spezifische Suszeptibilität und die Konzentration der ferromagnetischen Verunreinigung gleichzeitig gemessen. In keiner Probe zeigten sich Änderungen. Es wird gezeigt, dass Spuren von während der Kaltbearbeitung ungewollt aufgenommenen ferromagnetischen Verunreinigungen grosse scheinbare Änderungen in der gemessenen Suszeptibilität hervorrufen würden. Diese Erscheinung mag die von anderen Authoren berichteten Veränderungen erklären.

Introduction

The effect of cold work upon the magnetic susceptibility of pure metals has been the subject of several investigations. Bitter [1] reported that small amounts of cold work drastically changed the susceptibility of copper and silver in the direction of increasing paramagnetism, and Lowance and Constant [2] observed the same effect in bismuth and platinum as well as in copper and silver. Banta [3], however, was unable to observe this effect in copper. Furthermore, by studying the field dependence of the susceptibility, Kussmand and Seeman [4] were able to show that apparent changes noted in the case of copper, silver, and bismuth could be attributed to the presence of traces of ferromagnetic impurity, presumably iron. At the same time they found no apparent change in the case of aluminum, gold, zinc, wolfram, and molybdenum. More recently, Reekie and Hutchison [5] reported that while copper became more paramagnetic upon cold work, aluminum became less paramagnetic. In particular, a 20 per cent reduction in area of a copper wire was found to increase the susceptibility by 14 per cent while a similar reduction in aluminum produced a decrease of 10 per cent.

With the exception of the work of Kussmand and Seeman, all of the work previously mentioned has been done using the Gouy method with no attempt being made to determine the exact amount of ferromagnetic impurities present. The use of spectroscopically-pure samples does not preclude the possibility of the accidental pickup of ferromagnetic contaminant during the cold work process. This is especially true if the samples are drawn through steel dies as is commonly done. It has been our experience in this laboratory that cursory handling of the samples during preparation is sufficient to impart an impurity mass concentration as high as one part per million to the samples. In the case of copper the presence of such a trace amount of impurity may change the susceptibility by 50 per cent when using a Gouy-type apparatus at 10,000 oersteds. The limitations of the Gouy method in detecting such small amounts of iron is well known [6; 7]. It seems imperative, therefore, that the measurements on copper and aluminum be made using a method in which both the sus-

*Received November 27, 1953.

†Atomic Energy Research Department, North American Aviation, Inc., Downey, California.

ceptibility and the ferromagnetic impurity concentration can be measured simultaneously.

Such measurements can be made using a Faraday-type apparatus which differs from the Gouy method in that the whole sample is placed in the magnetic field. This enables one to eliminate unambiguously the unwanted contribution of ferromagnetic contaminant by its dependence on the magnetic field. Following the classic method of Honda and Owen [7], the relation between the apparent susceptibility and the true susceptibility is given by:

$$\chi(\text{apparent}) = \chi(\text{true}) + \frac{c\sigma}{H}$$

where c is the mass concentration of the impurity in parts per million, σ is its saturation magnetization, and H is the magnetic field strength. By measuring the susceptibility at several field strengths and plotting these values against $1/H$, the resulting straight line can be extrapolated to yield χ(true) while the mass concentration of the ferromagnetic contaminant can be determined from the slope.

Observations on copper and aluminum making use of such a method indicated that no changes in the susceptibility occurred during cold work.

Experimental

The apparatus used is that reported by Donoghue [6] in which contoured pole pieces are used to generate a constant force on the sample placed between them. The force on the sample is measured by means of an electrodynamic balance. The susceptibility is measured at four widely separated field strengths, and the true susceptibility as well as the mass concentration of the ferromagnetic impurity is determined from the resulting Honda-Owen plot. In order to insure that σ has a constant value, fields are employed which range from 8,500 to 16,000 oersteds. Donoghue [6] has shown that if the apparatus is calibrated correctly the true susceptibility should be independent of the amount of ferromagnetic contaminant present. To test this, the susceptibility of a piece of copper which inadvertently has picked up some ferromagnetic contamination during the cold-working process was determined. A true susceptibility of .0857 was found with an impurity present in the concentration of 1.1 parts per million assessed as iron with a specific saturation magnetization of 220 ergs/gauss. The sample was then etched in HCl which removed the surface iron but did not react with the copper. The susceptibility was determined once again and a value of .0862 with an impurity concentration less than .1 part per million was found. Figure 1 shows the two sets of data. The difference between the two values of χ(true) is well within the experimental error.

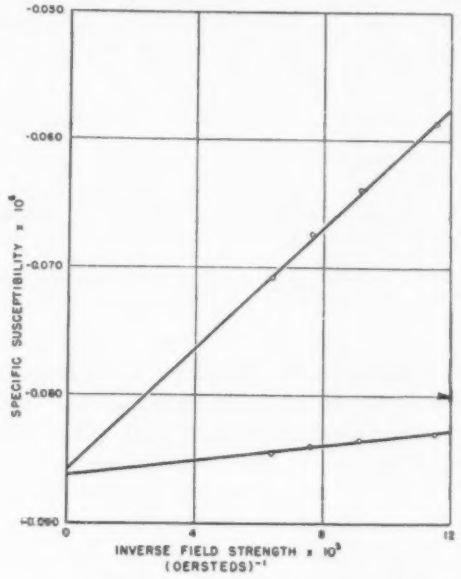

FIGURE 1. Variation of susceptibility with inverse field strength.

The metals studied were obtained from Johnson Matthey Company and were stated to be spectroscopically pure. The samples were first annealed at 550°C for three hours to remove internal strains, and then etched in nitric acid. The specific susceptibility of each sample was determined at room temperature. The samples were then cold-worked. One set of samples was subjected to compression using a power press while a second set of samples was cold-worked by rolling. In all cases the samples were placed between either copper or molybdenum sheets to prevent picking up iron contaminant during the cold-work process. The samples were re-formed to a suitable size and the susceptibility was measured within a 15-minute period. They were then heated in a vacuum furnace to 550°C for three hours, after which the susceptibility was redetermined. The results are shown in Table I where the degree of cold work is represented by the percentage decrease in area of the sample. The apparent ferromagnetic concentration, taken as iron, is shown in the parenthesis. As noted, the iron content did not change appreciably during the cold work, with the exception of

TABLE I

CHANGE IN SUSCEPTIBILITY DURING COLD WORK

Rolling

Metal	% Area Reduction	Susceptibility × 10^6* Annealed	Cold-worked	Re-annealed
Copper	22	−.0858 (.1)	−.0858 (.1)	−.0862 (.1)
Copper	98	−.0856 (.1)	−.0862 (1.1)	−.0863 (.1)
Aluminum	97	+.608 (.1)	+.609 (.1)	+.607 (.1)

Compression

Metal	% Area reduction	Susceptibility × 10^6 Annealed	Cold-worked	Re-annealed
Copper	96	−.0856 (.1)	−.0860 (.1)	−.0856 (.1)
Aluminum	97	+.607 (.1)	+.603 (.2)	+.608 (.1)

*Relative mass concentration of the ferromagnetic impurity present expressed in parts per million is given in the parenthesis.

the compressed copper. This increase can be attributed to the inadvertent use of iron tools to re-form the sample after cold work. This iron was removed by etching in hydrochloric acid which reduced the iron concentration to its previous value but left the value of the susceptibility unaltered, as was previously shown in Figure 1. The values of susceptibility reported have a precision of 1 per cent while the iron concentrations can be determined to within .1 ppm.

Conclusions

In order to determine precisely changes in the susceptibility produced by cold work, one must eliminate any effects due to the presence of trace amounts of ferromagnetic impurities. The use of spectroscopically-pure material is in itself not sufficient. In the case of those observers who reported changes toward increasing paramagnetism, no attempt was made to determine accurately the presence of iron. It is noteworthy that in the cases, including the present study, where care was taken to eliminate the effect of such impurities, no change in susceptibility was noted. The exception to this was the work of Shimizu [8]. However, in this case the copper which was studied was paramagnetic at high fields, indicating the presence of extremely large amounts of iron. This would yield very steep slopes with a corresponding loss of accuracy.

The presence of an undetected ferromagnetic contaminant might explain the observations of Reekie and Hutchison that progressive etching of cold-worked copper restored the original value of susceptibility [5]. In this case the etching would remove the surface iron contamination, producing an apparent change. The changes involved would require the presence of less than one-half part per million of iron, which would be difficult to observe unless a Honda-Owen plot was made. The apparent decrease in paramagnetism in aluminum as observed by Reekie and Hutchsion cannot be explained by the presence of such contaminants. It may be pointed out, however, that no such decrease in aluminum was noted by Kussmand.

Acknowledgement

The author wishes to acknowledge many helpful discussions with Mr. J. J. Donoghue regarding both the interpretation of the data and the experimental techniques used.

This article is based on studies conducted for the Atomic Energy Commission.

References

1. BITTER, F. Phys. Rev. **36** (1930) 978.
2. LOWANCE, F. E. and CONSTANT, F. W. Phys. Rev. **38** (1931) 1547.
3. BANTA, J. E. Phys. Rev. **36** (1931) 498.
4. KUSSMAND, A. and SEEMAN, H. J. Z. Physik **77** (1932) 567–580.
5. REEKIE, J. and HUTCHISON, T. S. Phys. Rev. **74** (1948) 610.
6. DONOGHUE, J. J. NAA–SR–117.
7. BATES, L. F. Modern Magnetism (Cambridge University Press, 1948) p. 115.
8. SHIMIZU, Y. Sci. Rep. Tohoku Univ. **22** (1933) 915.

EVOLUTION DES ALLIAGES ALUMINIUM-CUIVRE PAR CHAUFFAGE DANS LE VIDE*

N. TAKAHASHI ET J.-J. TRILLAT†

1. En utilisant des films composites formés de couches superposées de Cu et Al, il est possible d'obtenir, par chauffage dans le vide, des cristaux uniques de $CuAl_2$, CuAl et Cu_9Al_4 observables par diffraction électronique.
2. Les différentes structures du film résultant de l'interdiffusion des atomes Cu et Al peuvent être aisément étudiées.
3. Il existe des relations d'épitaxie entre $CuAl_2$ et CuAl, ainsi qu'entre CuAl et Cu_9Al_4.

MODIFICATIONS IN ALUMINIUM-COPPER ALLOYS ON HEATING IN VACUUM

1. Using composite films formed by superimposed layers of Cu and Al, it is possible to obtain, by heating in vacuum, single crystals of $CuAl_2$, CuAl and Cu_9Al_4, that can be observed by electron diffraction.
2. The different structures of the film, resulting from interdiffusion of Cu and Al atoms, can be easily studied.
3. There appear to be relations of epitaxis between $CuAl_2$ and CuAl, as well as between CuAl and Cu_9Al_4.

VERÄNDERUNGEN IN ALUMINIUM-KUPFER LEGIERUNGEN BEIM ERHITZEN IM VAKUUM

1. $CuAl_2$-, CuAl- und Cu_9Al_4 Einkristalle lassen sich durch Vakuumerhitzen eines Films von übereinander abgeschiedenen Schichten von Cu und Al herstellen und durch Elektronenbeugung nachweisen.
2. Die verschiedenen, durch die Interdiffusion der Cu- und Al-Atome entstehenden Filmstrukturen lassen sich leicht untersuchen.
3. Sowohl zwischen $CuAl_2$ und CuAl als auch zwischen CuAl und Cu_9Al_4 scheinen Epitaxialbeziehungen zu bestehen.

Introduction

Nous avons étudié antérieurement, par diffraction électronique, la structure des alliages Aluminium-Cuivre et nous avons constaté que cette méthode permet de suivre l'apparition et la transformation des différentes phases obtenues par chauffage dans le vide [1]. Nous avons pu ainsi montrer que le film composite obtenu par évaporation *simultanée* dans le vide des deux métaux et condensation à température ambiante sur une surface fraîchement clivée de sel gemme était en général hors d'équilibre et que, par chauffage ultérieur dans le vide ou par vieillissement à la température ambiante, il donnait naissance à des phases bien cristallisées [2–6].

Le film initial instable correspond à une structure à grains très fins et mal cristallisés caractérisée par des anneaux flous; la maille est intermédiaire à celle des métaux constituants.

Les expériences décrites dans ce travail ont consisté essentiellement à chauffer dans le vide un film Al + Cu obtenu cette fois par évaporation *successive* des deux métaux et condensation à température ambiante sur un support amorphe tel que du parlodion [6]. Dans ces conditions, le film initialement obtenu est un mélange de cristaux d'aluminium et de cuivre et fournit, par diffraction électronique, les anneaux caractéristiques des deux métaux; ce film évolue dans le vide en fonction de la température et du temps, en donnant, par suite de la diffusion des atomes, divers types d'alliages. Les cristaux des composés intermétalliques qui apparaissent dans ce cas ont en général des dimensions suffisantes pour donner lieu à des diagrammes de diffraction électronique du type cristal unique (dimensions comprises entre un et 10 microns). Cette méthode de préparation se rapproche de celle qui est utilisée dans la métallurgie des poudres (frittage); les vitesses de réaction sont cependant beaucoup plus grandes du fait de l'épaisseur très faible du film composite (quelques centaines d'Angströms). Il devient donc ainsi possible de suivre et d'enregistrer les détails des transformations, et ceci dans un temps très court.

Méthode Expérimentale

La méthode utilisée pour la préparation du film composite est basée sur celle qui a été décrite dans nos précédents travaux [2; 3; 4]. Chaque métal est évaporé *successivement* par chauffage sous vide dans deux petits fours constitués par une spirale de tungstène (fig. 1). Afin d'obtenir un film où les deux métaux soient initialement bien différenciés, il est préférable d'employer un support

*Received December 16, 1953.
†Laboratoire de Rayons X du Centre National de la Recherche Scientifique à Bellevue, Seine-et-Oise.

amorphe de parlodion plutôt qu'un cristal de NaCl; dans ce dernier cas en effet, il est nécessaire de dissoudre le sel dans l'eau pour libérer le dépôt métallique, et cette opération est susceptible, comme nous l'avons montré, de donner lieu à des phénomènes parasites d'oxydation ou d'hydratation (notamment du cuivre).

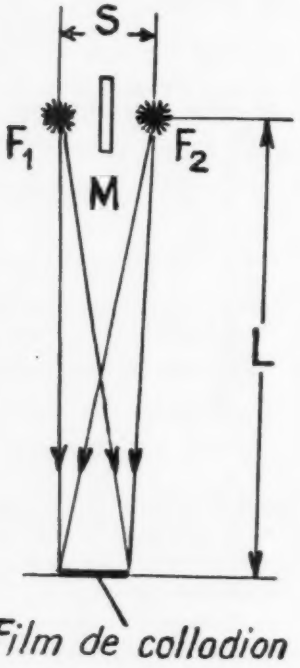

FIGURE 1. Schéma du dispositif d'évaporation. F_1 F_2, fours. M, masque.

Les expériences ont démontré qu'il était nécessaire de vaporiser des proportions de métaux assez différentes de celles qui correspondent à la composition chimique de l'alliage choisi; cela s'explique si l'on tient compte des différences des pressions de vapeur et surtout des vitesses de diffusion du Cuivre et de l'Aluminium. Ainsi, pour obtenir par cette méthode le composé $CuAl_2$ (46% Al + 54% Cu), il faut pour une distance four-support de 6 cm, évaporer environ deux fois plus de cuivre que ne l'exige la formule théorique.

La distance S entre les deux fours (fig. 1) doit être très petite pour assurer un dépôt d'épaisseur uniforme des deux métaux; elle a été choisie égale à 1 cm. La paroi M est nécessaire pour éviter l'évaporation d'un seul métal sur l'autre. La distance L (four-support) est de 6 cm. Dans ces conditions, on obtient un film composite constitué par la superposition d'une couche d'Aluminium et d'une couche de Cuivre, chacun de ces dépôts ayant une épaisseur constante en tous points du support (fig. 2).

L'échauffement d'un tel film permet de suivre la diffusion des atomes d'une couche dans l'autre; cet échauffement est effectué dans un vide de 10^{-4} mm Hg dans *le diffractographe électronique* lui-même, ce qui permet d'observer à chaque instant les modifications de structure dûes à la diffusion, en fonction du temps et de la température. Les variations observées peuvent même être enregistrées d'une façon continue, en utilisant une technique précédemment décrite [1]. Le film support de parlodion disparaît naturellement au cours du chauffage, mais le film métallique subsiste et reste entre les mailles de la grille, comme le prouve l'observation avec la loupe électronique.

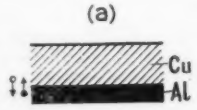

FIGURE 2. Schéma du film composite initial obtenu à froid.

On pourrait penser qu'à cette pression de 10^{-4}mm Hg, la quantité d'air résiduel peut suffire à provoquer des phénomènes d'oxydation; nous avons en effet signalé cette oxydation à propos de la formation d'alumine à partir d'aluminium. Toutefois, jusqu'à la température de 500°C, et pour des durées de chauffage relativement courtes (inférieures à 15 minutes), un tel phénomène ne se produit pas et l'on peut donc exclure complètement cette cause d'erreurs dans les présentes expériences.

Résultats Obtenus

1. *Formation de cristaux uniques de* $CuAl_2$

Si l'on prépare dans les conditions précédentes un film composite d'aluminium et de cuivre, l'examen par diffraction électronique donne d'abord un diagramme de Debye-Scherrer constitué par les anneaux de diffraction des deux métaux (fig. 3a); on peut remarquer que les anneaux du cuivre sont plus élargis et plus intenses que ceux de l'aluminium, ce qui prouve que les microcristaux de Cu sont d'une taille notablement inférieure à ceux de Al. Rappelons qu'à cet état, la préparation est formée de deux couches superposées des métaux (fig. 2).

L'échauffement progressif de ce mélange initial se traduit d'abord par l'affinement des anneaux, notamment de ceux du cuivre (fig. 3b, 3c); ce phénomène est dû à l'accroissement de la taille

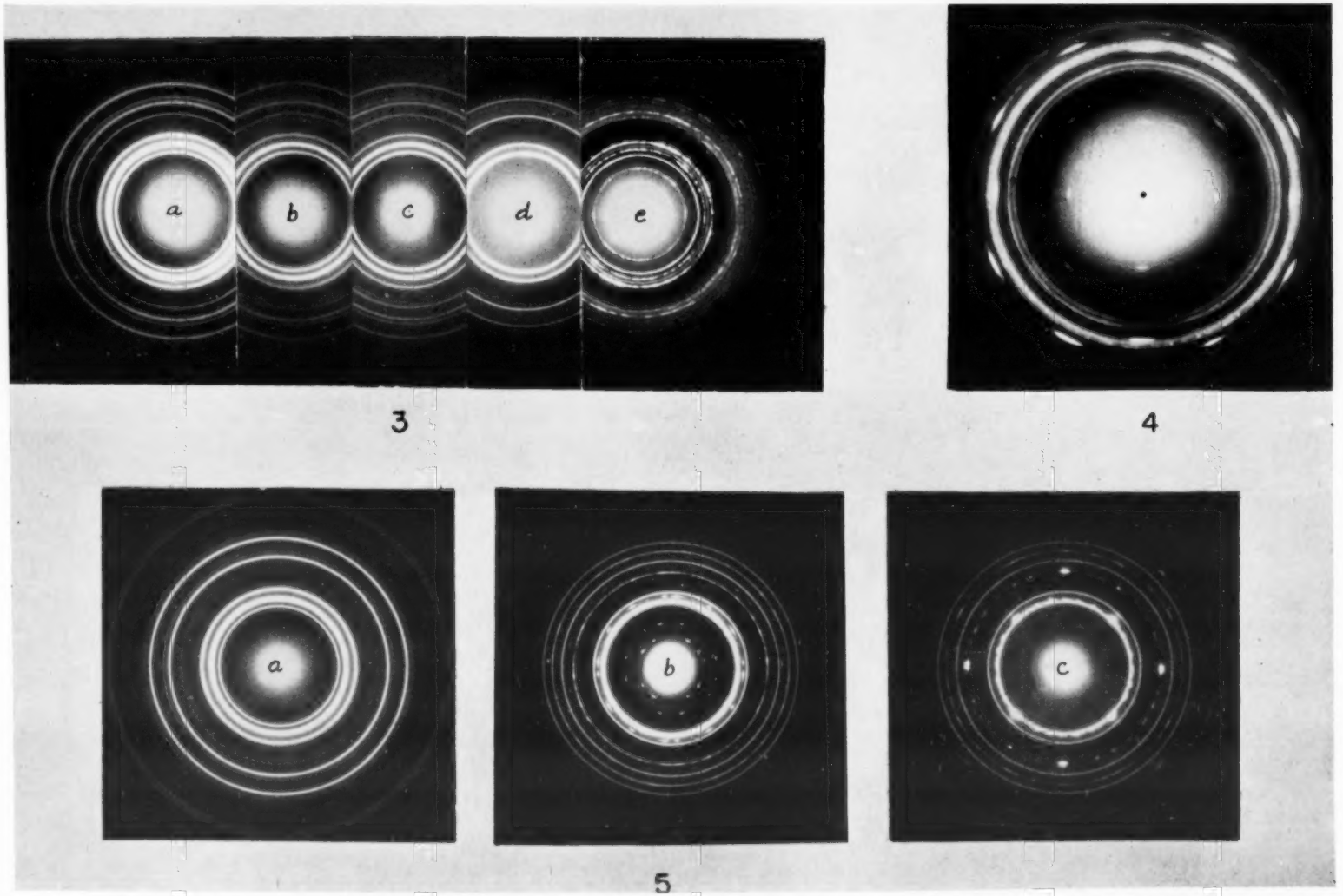

PLATE I. FIGURE 3—Structure d'un film Al + Cu en fonction de la température (composition initiale Al2 : Cu 5). (*a*) 20°C; (*b*) 200°C; (*c*) 400°C; (*d*) 500°C; (*e*) 500°C, durée de chauffage supérieure à 10 minutes. FIGURE 4—Formation d'un cristal unique de $CuAl_2$ (taches isolées). Le diagramme montre également la présence de Cu et Al (anneaux fins) et d'une phase caractérisée par des anneaux ponctués (θ). FIGURE 5—Structure d'un film Al + Cu en fonction de la température (composition initiale Al: 1–Cu 6). (*a*) 20°C—Cu + Al; (*b*) 450°C—$CuAl_2$ (taches isolées correspondant à + CuAl (anneaux) + Cu (anneaux); (*c*) 500°C—CuAl (taches isolées) + Cu.

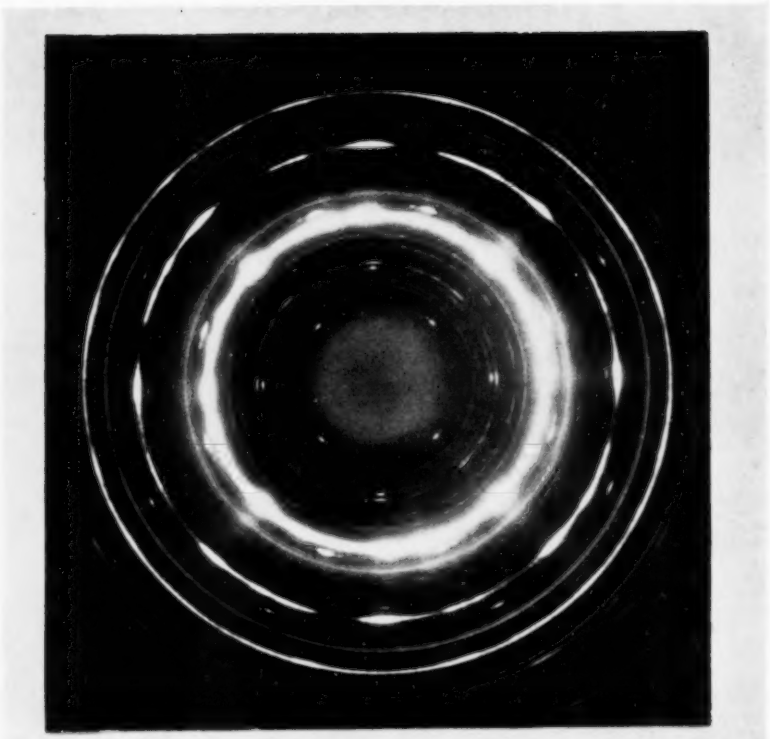

7

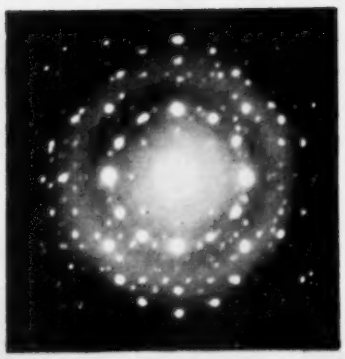

11

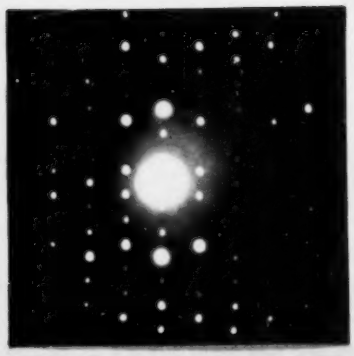

12

PLATE II. FIGURE 7—Formation des cristaux uniques de CuAl et de Cu_9Al_4, après 2 mois de vieillissement à la température ambiante à partir de l'échantillon de la figure 7. Orientation relative (100) CuAl // (100) Cu_9Al_4 et [001] CuAl // [001] Cu_9Al_4. FIGURE 11.—Formation des cristaux uniques de CuAl et de Cu_9Al_4 après 2 mois de vieillissement à la température ambiante à partir de l'échantillon de la figure 7. Orientation relative (100) CuAl // (100) Cu_9Al_4 et [001] CuAl // 001 Cu_9Al_4. FIGURE 12— Même préparation que celle de la figure 11. Orientation relative (110) CuAl // (114) Cu_9Al_4 et [110] CuAl // [110] Cu_9Al_4.

moyenne des microcristaux des métaux purs. En même temps, l'intensité relative des raies Al et Cu se modifie pour, finalement, s'inverser vers 500°C; le cuivre disparaît même presque totalement du diagramme (fig. 3d), et tout se passe comme s'il était dissimulé, ainsi que nous l'avions déjà observé antérieurement [4].

A partir de cette température, la diffusion des atomes Cu et Al donne rapidement naissance au composé tétragonal $CuAl_2$ (fig. 3e); bien entendu, les conditions de formation dépendent de la vitesse de montée en température (dans le cas présent, de l'ordre de 30°C/min. jusqu'à 400°C) et de l'épaisseur du film initial, et il y a intérêt à opérer cette montée lentement.

Le composé $CuAl_2$ qui apparaît dans ces conditions est, en général, constitué de cristaux assez gros (anneaux ponctués fig. 3e); leur dimension est souvent suffisante pour donner lieu à un diagramme de cristal unique (fig. 4) ayant une largeur de quelques microns. Dans ce cas, on peut constater que le plan de base (001) du réseau tétragonal de $CuAl_2$ est disposé parallèlement au plan du support de condensation.

Le tableau I indique les distances réticulaires correspondant aux taches et aux anneaux du diagramme de la figure 4; le film examiné est constitué en majorité par $CuAl_2$, mais contient encore du Cuivre et de l'Aluminium non encore combinés et restés à l'état microcristallin désordonné.

Il est intéressant de remarquer, sur le cliché 4, la présence d'anneaux dédoublés (d = 2,032 Å et d = 2,015 Å) et présentant une ponctuation très nette. De tels anneaux avaient déjà été observés dans le cas où le film était obtenu par vaporisation *simultanée* des deux métaux ou par vaporisation de l'alliage préformé $CuAl_2$ [4]; ils correspondent assez exactement aux anneaux (202) et (220) de la phase intermédiaire θ', mais il est évident que ce résultat demande à être confirmé par un plus grand nombre de raies. Le cliché 4 présente l'intérêt de dissocier nettement la phase supposée θ' (anneaux ponctués) d'avec la phase θ (cristal unique).

Il convient de remarquer que, si l'on augmente la proportion initiale de cuivre vaporisé, cette phase θ' n'apparaît plus.

TABLEAU I

	d(Å)	hkl $CuAl_2$	hkl θ'	hkl Al	hkl Cu
Tache	4.25	110			
	3.78	101			
	3.32		111		
Tache	2.96	200			
	2.43	002			
	2.34	121		111	
Tache	2.112	220–112			
	2.095				111
Ponctuée	2.032		202	200	
Ponctuée	2.015		220		
Tache	1.895	130–202			
	1.804				200
	1.600	222			
	1.493	132			
Tache	1.420	330	400		
	1.396	123			

2. *Formation de cristaux uniques de* CuAl

Nous avons montré antérieurement [4] que lorsque la proportion pondérale de cuivre dans l'alliage dépasse 54%, il apparaît, d'après le diagramme d'équilibre, un composé CuAl; les diagrammes électroniques indiquent que ce composé possède une maille cubique centrée du type CsCl.

Nous avons réussi à obtenir également ce composé sous forme de cristal unique. La figure 5 montre la suite des diagrammes obtenus en fonction de la température. Au départ (fig. 5a), on observe seulement les anneaux de Cu et Al; vers 450°C (fig. 5b), apparaissent $CuAl_2$ (taches caractérisant deux cristaux uniques faisant un angle de 25° entre leurs axes [100]) et CuAl (anneaux). A 500°C, le composé CuAl apparaît sous forme de cristal unique (fig. 5c), accompagné de cuivre en excès. La figure 6 schématise le mécanisme de ces transformations.

Dans quelques cas, nous avons obtenu des diagrammes plus compliqués (fig. 7) où l'on note la présence de $CuAl_2$ (cristal unique), de CuAl fortement orienté (secteurs allongés), et même de

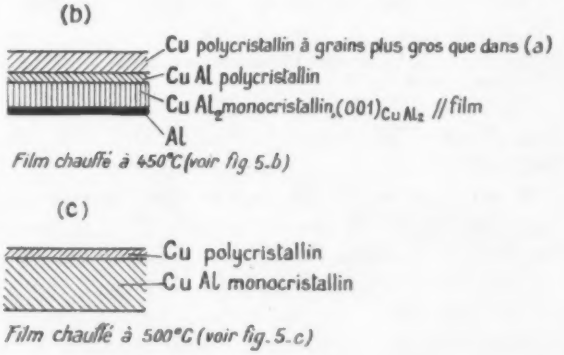

FIGURE 6. Mécanisme de la formation de $CuAl_2$ et CuAl (correspondant à la figure 5).

Cu_9 Al_4 (polycristallin) qui apparaissent donc simultanément*). Entre $CuAl_2$ et CuAl existent la relation d'orientation:

(001) $CuAl_2$ // (001) CuAl et [100] $CuAl_2$ // [100] CuAl.

La figure 8 donne le schéma de la structure du film dans ce cas. La figure 9 donne les indices de Miller pour les taches de diffraction de $CuAl_2$ et CuAl; pour $CuAl_2$, les taches de surstructure (Σh impair et h, l, impairs, k nul) n'apparaissent pas sous cette orientation, mais elles sont visibles

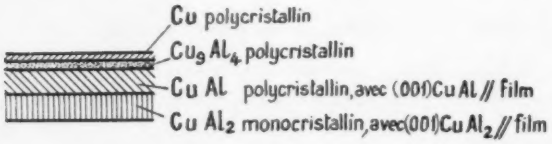

FIGURE 8. Structure du film donnant lieu au diagramme de la figure 7.

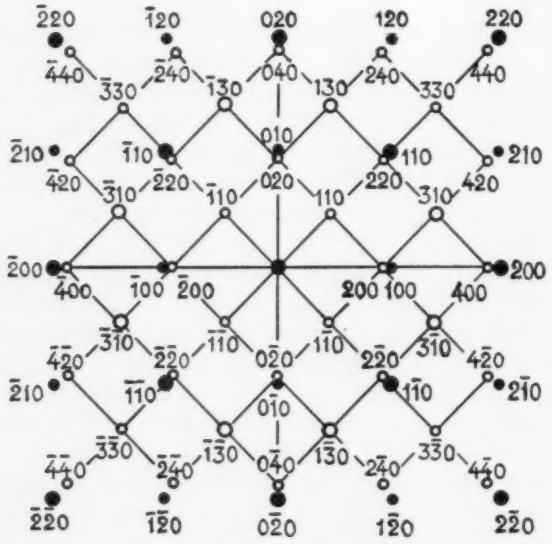

FIGURE 9. Indices des taches de diffraction d'après le diagramme figure 7. Les cercles blancs correspondent à $CuAl_2$, et les cercles noirs à CuAl.

pour CuAl (Σh impair) (taches 010–0$\bar{1}$0–100–$\bar{1}$00, etc).

Il est raisonnable de penser que le composé $CuAl_2$ se produit le premier et que CuAl apparaît ensuite par diffusion des atomes de cuivre; d'après les idées récentes, la disposition des atomes Cu et Al au sein de la maille quadratique $CuAl_2$ est statistiquement variable et, sous l'influence de l'agitation thermique, il peut se former accidentellement des mailles plus riches en Cuivre que ne l'indique la formule moyenne $CuAl_2$. Le CuAl se formerait alors à partir de ces mailles enrichies par introduction de 4 atomes de Cuivre et par déplacement, dans le domaine de transition, de certains atomes de Cu et d'Al. La maille tétragonale correspondant statistiquement au composé $CuAl_2$ pourrait théoriquement donner naissance à 8 mailles cubiques type CsCl, suivant un processus qui sera décrit dans un autre mémoire.

Le domaine du diagramme d'équilibre CuAl correspondant à ces expériences est, comme l'on sait, particulièrement compliqué. Il est donc à prévoir que les résultats dépendront de très faibles fluctuations locales et, en effet, les diagrammes observés varient fréquemment d'un point à un autre, ce qui rend les interprétations plus difficiles.

De plus, si initialement le film composite présente une structure homogène, il n'en est plus de même après chauffage lorsque apparaissent des phases nouvelles : suivant le point examiné, le diagramme obtenu peut varier et cette hétérogénéité est contrôlable au Microscope électronique. La figure 10 par exemple, qui correspond au

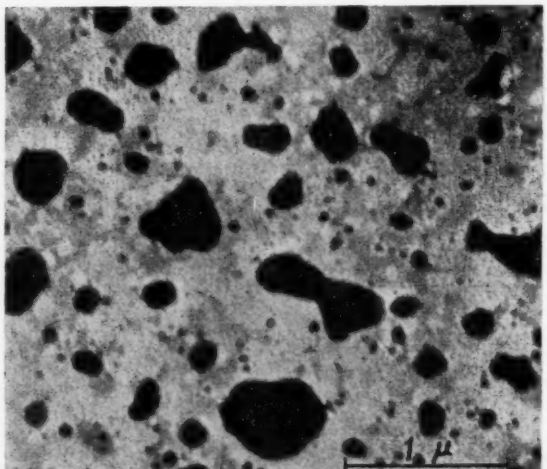

FIGURE 10. Micrographie électronique d'un film Al + Cu après chauffage dans le vide.

diagramme de la figure 7, montre que le film, au lieu d'être homogène comme initialement, présente des agglomérats absorbants irrégulièrement disposés; ce fait peut être attribué aux vitesses de diffusion des atomes Cu et Al, qui varient d'un point à un autre tout en restant statistiquement constantes. En toute rigueur, il serait donc néces-

*Par microdiffraction ces structures apparaissent à l'état parfaitement monocristallin.

saire d'étudier rigoureusement le même point par diffraction électronique et simultanément par Microscopie électronique; ces expériences seront tentées ultérieurement.

3. *Formation de cristaux uniques de* Cu_9Al_4

Enfin, nous avons réussi à obtenir également par la même méthode des cristaux uniques du composé cubique Cu_9Al_4. La figure 11 montre la présence de ce constituant mélangé au composé CuA_4. L'orientation relative entre les deux corps est la suivante :

(100) Cu Al // (100) Cu_9Al_4 et [001] CuAl // [001] Cu_9Al_4.

On observe également parfois une autre orientation (fig. 12) :

(110) CuAl // (114) Cu_9Al_4 et [$\bar{1}$10] CuAl // [$\bar{1}$10] Cu_9Al_4.

L'étude de ces phénomènes est particulièrement nette lorsqu'on utilise une méthode de microdiffraction [7]. La position des atomes dans la maille Cu_9Al_4 est très complexe, mais il semble dès maintenant possible de suivre la transformation CuAl→ Cu_9Al_4.

Ainsi se trouve matérialisée grâce à cette technique expérimentale, l'évolution de la structure de mélanges Al + Cu en fonction de la température, avec l'identification des principaux constituants par des diagrammes de cristaux uniques. Il apparaît donc à nouveau que la méthode de diffraction électronique est susceptible d'apporter des renseignements intéressants quand on l'utilise pour l'étude de la cinétique de réactions; nous en avions déjà donné un exemple à propos de la formation de la cémentite Fe_3C à partir du fer [8].

Bibliographie

1. Trillat, J. J. et Takahashi, N. C.R. Acad. Sci. **236** (1953) 790; Acta Cryst. **7** (1954) 15.
2. Trillat, J. J. et Takahashi, N. C.R. Acad. Sci. **235** (1952) 1306.
3. Trillat, J. J. et Takahashi, N. Rev. Métall. **6** (1953) 427.
4. Takahashi, N., Trillat, J. J., et Saulnier, A. Métaux **28** (1953) 185.
5. Trillat, J. J. et Takahashi, N. C.R. Acad. Sci. **236** (1953) 2245.
6. Takahashi, N. et Trillat, J. J. C.R. Acad. Sci. **237** (1953) 1246.
7. Takahashi, N. et Fert, Ch. C.R. Acad. Sci. **237** (1953) 1664.
8. Trillat, J. J. et Oketani, S. Acta Cryst. **5** (1952) 469.

THE SLIP PROCESS DURING YIELD-POINT DEFORMATION*

EDWARD W. HART†

When Frank-Read dislocation sources are pinned by solute atoms, the mode of dynamic operation of the source is altered. In particular the source may be activated even though the yield-point stress is as much as 15 per cent lower than the critical operating stress of the source, and, further, the number of dislocation loops per burst is strongly dependent on the relative magnitudes of yield stress and critical stress. A qualitative application of these results to the yield-point phenomenon is made.

LE PROCESSUS DE GLISSEMENT PENDANT LA DÉFORMATION À LA LIMITE D'ÉCOULEMENT

Quand les sources de Frank-Read sont arrêtées par des atomes de soluté, le mode d'action dynamique de la source est modifié. La source peut alors être activée, même si la tension de la limite d'écoulement est de 15 pour cent inférieure à la tension critique, nécessaire pour mettre la source en action, en plus de cela, le nombre de noeuds de dislocations par unité de mouvement dépend beaucoup des valeurs relatives de la tension d'écoulement et de la tension critique. Ces résultats sont appliqués au phénomène de la limite d'écoulement.

DER GLEITPROZESS WÄHREND DER VERFORMUNG AM FLIESSPUNKT

Wenn Frank-Read'sche Versetzungsquellen durch Lösungsatome festgelegt sind, ändert sich der dynamische Mechanismus der Quelle. Insbesonders kann die Quelle aktiviert werden, selbst wenn die Fliesspannung bis zu 15% geringer ist als die kritische Auslösungsspannung der Quelle; weiterhin hängt die Anzahl der Versetzungsringe pro Ausbruch der Quelle stark von den relativen Grössen der Zugspannung und der kritischen Spannung ab. Diese Resultate wurden zu einer qualitativen Analyse von Fliesspunkterscheinungen benutzt.

I. Introduction

The production of slip in metals by the operation of Frank-Read [1] sources is strongly modified in case the dislocations are pinned by solute atoms according to either of the two mechanisms proposed by Cottrell [2] and Suzuki [3]. The most notable modification, of course, is the increase of the yield stress and the introduction of the typical yield-point phenomena. A further modification, which is the subject of this paper, is the effect which the changed yield stress has on the production of a slip burst.

As described by Fisher, Hart, and Pry [4], a Frank-Read source, when activated at its critical stress, operates dynamically to produce a burst of a few hundred dislocations. The number of dislocations per burst is independent of the critical operating stress of the source. The following calculations will show that the details of dynamic operation are altered when the critical operating stress is determined by solute pinning rather than by the length of the source.

II. Calculations

The analysis can be briefly sketched as follows, with reference to Figure 1. The energy of the dislocation source is plotted there schematically for a few values of applied stress, τ, as a function of A, the area swept out by the dislocation at any stage of growth of the loop. When no pinning is present, the system continually follows the minimum energy point as the stress is raised until the critical stress, τ_c, is reached when the source is activated for multiplicative operation. In that case

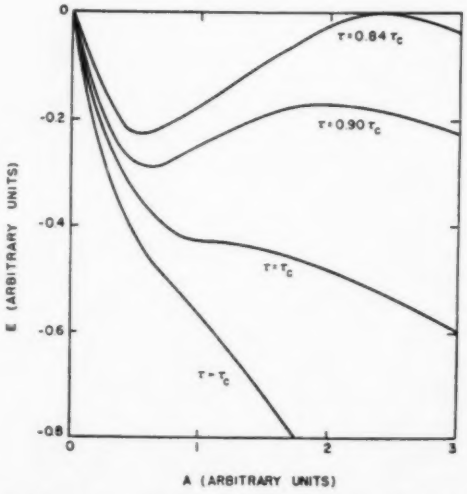

FIGURE 1. Schematic plots of E as a function of A for a variety of values of τ.

it is not possible to achieve the configuration where τ is greater than τ_c. When the source is pinned, however, the system remains at the origin until the yield stress is reached. The system then starts its dynamical motion from the zero energy configuration and with neglect of dissipation can

*Received October 25, 1953.

†General Electric Research Laboratory, Schenectady, New York.

surmount the energy peak, E_c, if E_c is less than zero.

Let us proceed now to a more precise consideration of these ideas.

In the absence of solute pinning the critical shear stress, τ_c, for the operation of a Frank-Read source of length, L, is given by:

$$\tau_c = 2\epsilon/bL \tag{1}$$

where ϵ is the energy per unit length of the dislocation segment and b is the Burgers vector. When solute pinning is present the source is immobilized in its equilibrium straight-line configuration until a yield stress, τ_y, is reached. The source is then freed from the very narrow region in which it is pinned and can subsequently behave dynamically in response to the applied stress. It is clear that for those sources for which τ_y is greater than τ_c, multiplicative loop production will ensue. For the case that τ_y is less than τ_c, we must consider the potential energy for subsequent loop growth referred to the pinned dislocation as the zero of energy. We may ignore the energy of pinning since it is very small compared to the energy involved in subsequent mechanical growth of the loop.

The energy, E, of the source when the dislocation has been blown up to length, l, from its initial length, L, and has swept out area, A, in the slip plane is given by

$$E = (l - L)\,\epsilon - b\tau A. \tag{2}$$

This energy achieves a maximum, E_c, of amount

$$E_c = (\epsilon^2/\tau b)\{\pi - \arcsin(\tau/\tau_c) - (\tau/\tau_c)[2 + \sqrt{1 - (\tau/\tau_c)^2}]\}. \tag{3}$$

Assuming as in reference [4] that there is no dissipation of energy in the motion of the dislocation, the source will operate multiplicatively when τ equals τ_y if E_c is less than zero.

The first consequence of this mode of operation is that the source will be activated by the applied stress even though τ_y may be smaller than τ_c. Figure 2 is a plot of E_c in arbitrary units vs. τ/τ_c. It is evident from the plot that those sources will be activated for which τ_y/τ_c is greater than 0.84.

The number, n, of loops per burst which are thrown off by the source when activated by a stress different from τ_c can be computed on the basis of the model of reference [4]*. On this model

$$n = \exp[2\pi^2(\tau_y/\tau_c) - \sqrt{2}\pi^2]. \tag{4}$$

III. Discussion

Although there is certainly more than only the pinning mechanism involved in the detailed phenomena associated with the yield point in metals, we might nevertheless attempt a qualitative description of the yield-point strain on the basis of the considerations of this paper. The first consideration is that the surface of single crystals just after yield-point deformation exhibits both very deep slip lines and regions of apparently homogeneous deformation. If the depth of the slip lines is to be associated with the number of loops given off by the source after activation, it would appear from equation (4) that there will be a very wide range of slip step-sizes depending on the distribution of Frank-Read sources per unit stress interval. The step size, as determined by n, may vary from about ten atom spaces to possibly a hundred thousand. This contrasts with the well-defined slip-line sizes in the normal deformation

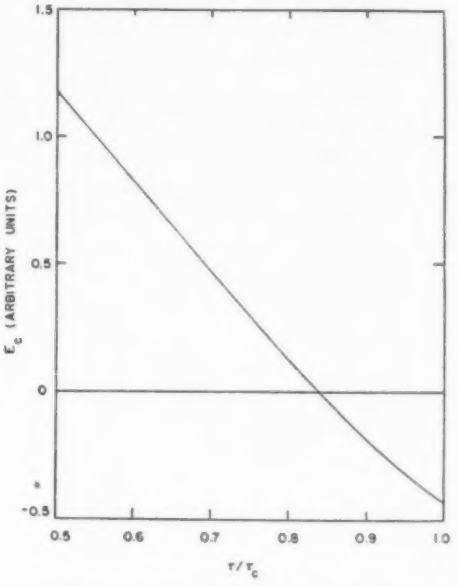

FIGURE 2. E_c in arbitrary units is plotted against τ/τ_c.

*It has been pointed out that the back stress as crudely estimated in equation (2) of reference [4] is in error. However, the loop spacing as estimated by equation (4) of the same paper is also in error, according to a subsequent, more precise unpublished estimate by J. C. Fisher. The two corrections taken together leave the subsequent development of the paper practically unchanged.

range which may there be a result from the fact that n is independent of τ_c when τ equals τ_c. Clearly equation (4) must be in some way limited by strain-hardening effects so that the almost indefinitely large n-values predicted for small τ_c will not be achieved. But in the absence of a theory of strain-hardening it is not possible to state this restriction in any precise manner.

In subsequent plastic deformation beyond the yield-point extension, normal slip-line patterns become evident, and the previous surface appearance becomes somewhat obliterated. This is easily explained as the resumption of the normal critical stress criterion and subsequent uniform slip-step-sizes since all the sources may now be considered as unpinned in the absence of strain aging effects. Usually there is also an appreciable increase in the strain-hardening rate for a small region of strain just after the yield-point strain. This may be attributed to the fact that some of the sources which are activated in this subsequent strain are already somewhat hardened due to having been activated once during the yield-point flow, those having a critical stress closer to τ_y having operated the more intensely in accordance with equation (4).

Acknowledgements

The author wishes to thank Drs. J. C. Fisher, G. W. Ardley, and J. J. Gilman of the General Electric Research Laboratory for valuable discussions and for criticism in preparation of the manuscript.

References

1. Frank, F. C. and Read, W. T. Phys. Rev. **79** (1950) 722.
2. Cottrell, A. H. Rep. Conf. on Strength of Solids (London, Phys. Soc., 1948).
3. Suzuki, H. Science Reports of the Research Institutes, Tohoku University, **A4** (1952) 455.
4. Fisher, J. C., Hart, E. W. and Pry, R. H. Phys. Rev. **87** (1952) 958.

THE EFFECT OF RELATIVE CRYSTAL AND BOUNDARY ORIENTATIONS ON GRAIN BOUNDARY DIFFUSION RATES*

D. TURNBULL and R. E. HOFFMAN†

The rate of self-diffusion of silver in the grain boundaries of bicrystals, misoriented by rotations of θ around a [100] axis, has been measured for $9° \leqslant \theta \leqslant 28°$. Within the experimental uncertainty, the results can be described, using the dislocation model of grain boundaries, with the assumption that the coefficient of self-diffusion, D_p, in grain boundary dislocation pipes is independent of θ (for $\theta \lesssim 28°$) and that D_p is several orders of magnitude larger than the lattice self-diffusion coefficient, D_L (at 500°C, $D_p \sim 4 \times 10^6 D_L$). The dependence of D_p on T is given by:

$$D_p = 0.14 \exp [-19{,}700/RT] \text{ cm}^2 \text{ sec}^{-1}.$$

The activation energy (19.7 ± 2 kcal/gm atom) for D_p is in good agreement with that (20 ± 2 kcal/gm atom) reported earlier for self-diffusion in grain boundaries separating randomly oriented crystals. A marked effect of grain boundary orientation on the diffusion penetration was observed for $\theta = 9°$.

LES EFFETS DES ORIENTATIONS RELATIVES DES CRISTAUX ET DES JOINTS INTERCRISTALLINS SUR LES VITESSES DE DIFFUSION DANS CES JOINTS

La vitesse de l'autodiffusion de l'argent dans les joints intercristallins de bicristaux, dont les réseaux sont tournés, l'un par rapport à l'autre, autour d'un axe commun [100] d'un angle θ, fut mesurée pour $9° \leqslant \theta \leqslant 28°$. Les résultats peuvent être décrits, à l'erreur expérimentale près, en se servant du modèle des joints intercristallins composés de dislocations, en admettant que le coefficient d'autodiffusion, D_p, dans les "canaux" des dislocations des joints ne dépend pas de θ (pour $\theta \lesssim 28°$) et que D_p est de quelques ordres de grandeur supérieur au coefficient d'autodiffusion dans le réseau, D_L, (à 500°C, $D_p \sim 4 \times 10^6 D_L$).

La dépendance de D_p sur T est donnée par:

$$D_p = 0{,}14 \exp [-19{,}700/RT] \text{ cm}^2 \text{ sec}^{-1}.$$

L'énergie d'activation ($19{,}7 \pm 2$ kcal/atome-g) pour D_p est en bon accord avec la valeur rapportée antérieurement ($20 \pm$ kcal/atome-g) pour l'autodiffusion dans les joints intercristallins séparant des cristaux orientés au hasard. Un effet important de l'orientation du joint intercristallin sur la pénétration par autodiffusion a été noté pour $\theta = 9°$.

DIE WIRKUNG DER RELATIVEN KRISTALL- UND KORNGRENZENORIENTIERUNGEN AUF DIE GESCHWINDIGKEIT DER KORNGRENZENDIFFUSION

Die Geschwindigkeit der Selbstdiffusion von Silber entlang der Korngrenzen eines Bikristalles, der durch Rotationen um $\theta°$ um eine der [100] Achsen misorientiert worden war, wurde für $9° \leqslant \theta \leqslant 28°$ gemessen. Die Resultate können im Rahmen der experimentellen Unsicherheit erklärt werden, wenn man annimmt, dass der Selbstdiffusionskoeffizient D_p in den "Versetzungsröhren" der Korngrenzen unabhängig von θ ist (für $\theta \lesssim 28°$) und dass D_p mehrere Grössenordnungen grösser als der Gitterselbstdiffusionskoeffizient D_L ist (bei 100°C, $D_p \sim 4 \times 10^6 D_L$). Die Abhängigkeit von D_p von T wird durch folgenden Ausdruck gegeben:

$$D_p = 0.14 \exp [-19{,}700/RT] \text{ cm}^2 \text{ sec}^{-1}.$$

Die Aktivierungsenergie ($19{,}7 \pm 2$ kcal/Grammatom) für D_p stimmt gut mit dem früher für Selbstdiffusion in Korngrenzen im Kristallhaufenwerk angegebenen Wert überein. (20 ± 2 kcal/Grammatom). Für $\theta = 9°$ wurde ein deutlicher Effekt der Orientierung auf die Eindringtiefe bei der Diffusion beobachtet.

Recent experimental [1; 2] and theoretical developments [3] have strongly supported the dislocation model [4] of grain boundaries. The Read-Shockley theory, derived from this model, successfully predicts the dependence of the energy, σ, of simple types of grain boundaries on crystal misorientation, θ, for $0 \leqslant \theta \leqslant \theta'$, where θ' is nearly the maximum value of θ that is possible in a grain boundary.

It is known [5] that grain boundaries characterized by a large crystal misorientation are very effective "short circuits" (relative to the crystal lattice) in diffusion processes. The use of the dislocation model to derive a theory for the dependence of grain boundary diffusion coefficients, D,‡ on θ has been discussed in some earlier publications [6; 7; 8]. Smoluchowski [7] has derived a semi-quantitative theory relating D to θ. He assumed that any short-circuiting effect of isolated dislocation pipes, such as are supposed to exist in grain boundaries for $\theta \to 0$, is negligible and that dislocation pipes are effective as short circuits only when they are close enough together to interact (e.g., within 2 or 3 atom spacings). In this paper we report the results of some experiments indicating that isolated dislocation pipes are much more effective short circuits for diffusion than Smoluchowski supposed

*Received November 24, 1953.

†General Electric Research Laboratory, Schenectady, New York.

‡In this paper, the symbol D, without subscript, will refer to a generalized grain boundary diffusion coefficient. The lattice diffusion coefficient will be denoted by D_L.

and we develop a theory for the dependence of D on θ based on the assumption that the rate of diffusion in isolated dislocation pipes is many times greater than the diffusion rate in an element of a single crystal lattice.

Theory

Consider a simple "tilt" boundary (Figure 1) formed by fitting together two simple cubic crystals misoriented by a rotation of an angle θ around a common [100] axis. We select a boundary that is a plane of symmetry (zx-plane) between the two crystals that includes the common [100] axis of rotation (parallel to z-direction) and may be described by an array of line dislocations as shown

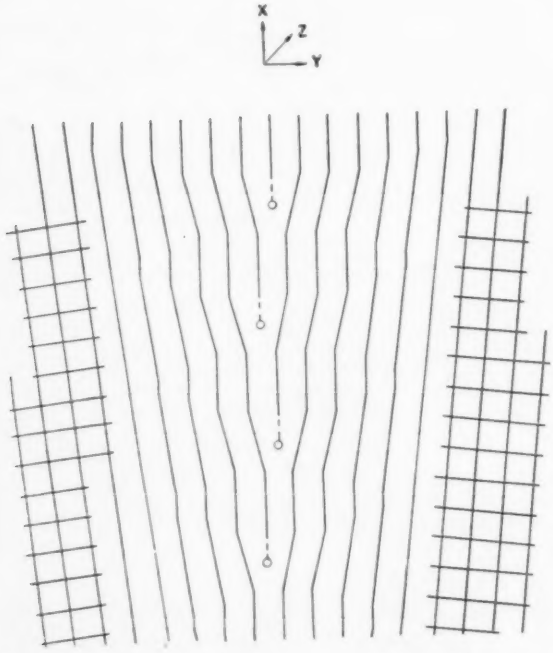

FIGURE 1. Dislocation model of grain boundary (after J. M. Burgers [4]).

in the figure. The dislocation lines extend in the z-direction perpendicular to the plane (xy) of the figure and intersecting this plane at the circled points. Let the spacing between dislocation lines in the boundary be d and the lattice spacing λ; then:[3]

$$d = \lambda/2 \sin(\theta/2). \tag{1}$$

It is presumed that the dislocation line or pipe is highly disordered and that the lattice immediately surrounding the pipe is strained. This strain falls off as the reciprocal of the distance in the xy-plane from the center of the pipe. Now consider the diffusion coefficient, D, in the z-direction of a low-angle boundary as a function of x. We assume that D is uniform, and equal to D_p, in regions of diameter l around the centers of the dislocation pipes located at $x = nd$ $(n = 0, 1, \ldots)$. As already noted, Smoluchowski [7] assumed that, for the purpose of describing grain boundary penetration, D_p may be considered equal to the lattice diffusion coefficient, D_L. However, in view of the marked atomic disorder in the dislocation pipe, we shall investigate the consequences of assuming that $D_p \gg D_L$. In the region between dislocation pipes, D probably decreases sharply to some minimum value, which may still exceed D_L. The supposed dependence of D on x is shown in Figure 2.

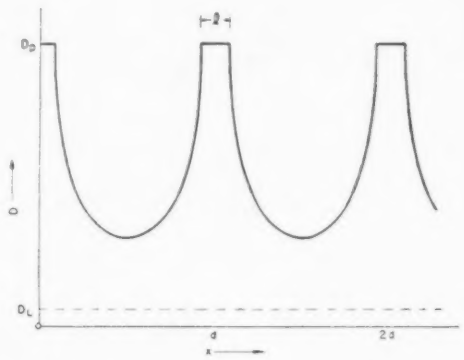

FIGURE 2. The assumed variation of the grain boundary diffusion coefficient in the z-direction as a function of x.

We must now relate the diffusion coefficient of atoms of a diffusing substance, B, in a grain boundary to the observed penetration of B in the z-direction. Let the mean concentration of B in a thin section of the xy-plane be a. Starting with the assumption that the grain boundary is equivalent to a slab of thickness, δ, having a uniform grain boundary diffusion coefficient, D, much larger than the diffusion coefficient, D_L, of the surrounding lattice, Fisher [9] derived an approximate analytical expression for $a = f(z)$ as follows:

$$a \propto t^{1/2} \exp\left[-2^{1/2}(D_L/D\delta)^{1/2}/(\pi D_L t)^{1/4}\right]z + \text{const.} \tag{2}$$

For a constant time, t, of diffusion anneal, equation (2) predicts a straight-line relation between $\log a$ and z.

Using the same model, but without making any restrictive assumptions, Whipple [10] has derived the following equation for the concentration of diffusing substance at any given point:

$$(3)\quad c = \operatorname{erfc}(\eta/2) + \frac{\eta}{2\pi^{\frac{1}{2}}}\int_1^{\Delta} \exp\left(-\frac{\eta^2}{4\sigma}\right)\operatorname{erfc}\left\{\tfrac{1}{2}\left(\frac{\Delta-1}{\Delta-\sigma}\right)^{\frac{1}{2}}\left(\frac{\sigma-1}{\beta}+\xi\right)\right\}\frac{d\sigma}{\sigma^{3/2}}$$

where

$\eta = z/(D_L t)^{\frac{1}{2}}$, $\xi = x/(D_L t)^{\frac{1}{2}}$, $\Delta = D/D_L$, and $\beta = \dfrac{\delta}{2(D_L t)^{\frac{1}{2}}}(\Delta - 1)$.

If $1 \ll \eta \ll \Delta^3/\beta$ and if ξ is "rather small," Whipple shows that equation (3) simplifies to:

$$(4)\quad c = 1.159\beta^{1/3}\eta^{-2/3}\exp\{-0.476\beta^{-2/3}\eta^{4/3} + 0.398\beta^{-4/3}\eta^{2/3}(1-\beta\xi) + \ldots\}.$$

Since we are interested only in the total amount of material, a, in a thin section of the xy-plane and the main contribution to a is from the small values of ξ, it will be assumed that equation (4) is sufficiently accurate to apply to all values of ξ. Then:

$$(5)\quad a = \int_{-\infty}^{\infty} c\,d\xi = 5.824\beta^{2/3}\eta^{-4/3}\exp[-0.476\beta^{-2/3}\eta^{4/3} + 0.398\beta^{-4/3}\eta^{2/3} + \ldots].$$

Although this equation is of a different form than that of Fisher, it may be shown that under certain conditions the two are essentially equivalent. For example, in our previous work [5] it was found that for times and temperatures such that $D_L t \cong 10^{-4}$ cm, $\log a$ varied approximately linearly with z for $z \gtrsim 0.008$ cm, (as predicted by equation 2), with slopes, $d \log a/dz$, in the range -100 cm^{-1} to -200 cm^{-1}. Figure 3 shows $\log a$ vs. z calculated from equation (5) for $\beta = 4000$ and $\beta = 1000$, with $D_L t = 10^{-4}$ cm in both cases. It is seen that these are also essentially linear for $z \gtrsim 0.008$ cm with slopes equal to -95.1 cm^{-1} and -190 cm^{-1}, respectively. For these conditions, then, Fisher's and Whipple's equations are in qualitative agreement with each other and with experimental data, and from the measured slopes the parameter,

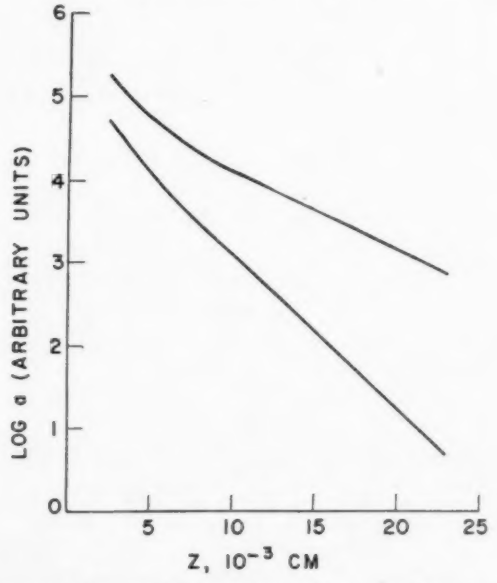

FIGURE 3. Theoretical dependence of $\log a$ on z for $\beta = 4000$ (upper curve) and $\beta = 1000$ (lower curve) according to Whipple [10].

$$(6)\quad \mathcal{P} = D\delta,$$

may be evaluated if values of D_L are known. Actually, for a given slope, the value of $\mathcal{P}$ calculated from equation (5) is larger by a factor of 3.4 than that calculated from equation (2). This discrepancy is not serious, however, since there is, in any case, a large uncertainty in the magnitude of δ.

The model used by Fisher and Whipple should be applicable at least to "incoherent" grain boundaries such that $d \gtrsim 2l(\theta \cong 45°)$, and under these conditions, D and δ should have their maximum values (with respect to changes in θ). If we denote these maximum values by D_M and δ_M, equation (6) becomes:

$$(7)\quad \mathcal{P} = D_M\,\delta_M.$$

For $d \gtrsim 2l(\theta \gtrsim 30°)$, we replace the uniform slab by an array of dislocation pipes, as in Figure 1. But since, under the usual experimental conditions, the perceptible penetration of the diffusing substance normal to the boundary (in the y-direction) is much greater than the pipe spacing, d, we may treat the array of individual pipes as a slab with an effective width, $\delta(\theta)$, of the order of l^2/d, and in which the appropriate diffusion coefficient is D_p. The Fisher-Whipple treatment may then also be applied to this case, and the parameter, $\mathcal{P}$, is given by the equation:

$$(8)\quad \mathcal{P} = D_p l^2/d = 2D_p l^2 \sin\left(\frac{\theta}{2}\right)/\lambda$$

It is difficult to write down a quantitative expression for $\mathcal{P}$ in the intermediate case $d \cong 2l(30° \gtrsim \theta \gtrsim 45°)$, since the effect of the interaction of closely spaced dislocations on D and δ is not known. Presumably, however, $\mathcal{P}$ should be intermediate between the values given by equation (7) and equation (8), tending to the latter as $\theta \to 45°$.

Experimental

The rate of diffusion of radioactive Ag^{110} into silver bicrystals, in the direction z, parallel to the grain boundary and the specimen axis, has been measured as a function of temperature and mis-

orientation. The bicrystals were grown vertically into the melt in an atmosphere of argon, using stock silver of 99.98 per cent purity. Crystal orientations were controlled by the seeding technique of Chalmers [11] so that the two crystals had a common [100] direction parallel to the direction of growth. Bicrystals of various misorientations, θ, were produced by rotation about this [100] axis of the seed crystals in such a way that the grain boundary would approximately bisect the angle between the nearest (100) planes of the two crystals (as in Figure 1). The misorientation was measured using the Laue back-reflection technique.

Diffusion specimens, approximately 1/2 in. in diameter and 1/4 in. thick, were machined from the bicrystal and the two faces perpendicular to the [100] growth axis were alternately polished and etched four times to eliminate cutting strains.

To assure complete recovery from machining strains and equilibration of the grain boundaries the specimens were heated slowly over a 24-hour period to 500°C in a dynamic vacuum system and then annealed in a static vacuum for two to three days at 875°C.

Radiosilver (Ag^{110}), having a very high specific activity (about 10 mc/gm), was electrodeposited to a uniform thickness of about $5(10)^{-5}$ cm on one face of the specimens. After the electrodeposition of radioisotope, each sample was sealed in an evacuated Pyrex tube and given a diffusion anneal for a specified time at a specified constant (± 2°C) temperature. After diffusion the samples were sectioned and the radioactivity of the sections measured as described in an earlier paper [5]. Before sectioning, the specimens were reduced 50 mils in diameter by machining from the outside surface in order to eliminate effects of surface diffusion. Measurements were made at temperatures from 400°C to 525°C, with misorientations in the range 9–28°.*

Results

For the conditions used, a linear relation is expected between the logarithm of the mean concentration, $\log a$, and the depth of penetration, z. Within experimental error, all of our results were described satisfactorily by such a relation, as may be seen by some typical data shown in Figure 4. From the measured slopes, $d \log a/dz$, and the known [12] values of D_L, p has been evaluated from Fisher's equation. Although the absolute magnitudes of p may thus be in error by a factor of about 3.5, the relative uncertainty in p is estimated from the reproducibility to be about ± 25 per cent.

As shown in Figure 5, the dependence of p on absolute temperature, T, may be represented by the equation:

$$p = p_0 \exp(-Q/RT). \tag{9}$$

The values of p_0 and Q for the various values of θ are shown in Table I. The uncertainty in Q is estimated to be ± 5 kcal/gm atom.

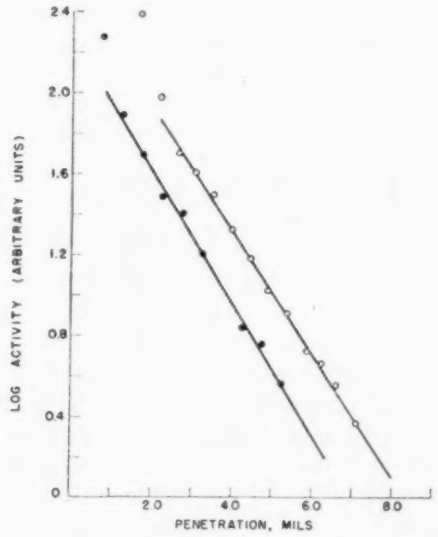

FIGURE 4. Some typical experimental penetration curves.

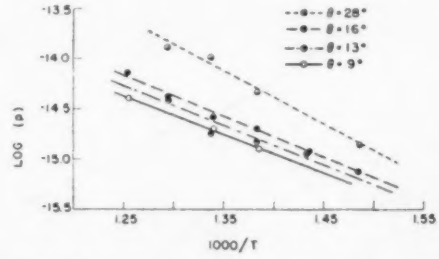

FIGURE 5. Dependence of log p on reciprocal absolute temperature for various values of θ.

TABLE I

SUMMARY OF p_0 AND Q FOR VARIOUS VALUES OF θ

θ, deg.	Q, kcal/gm atom	p_0, cm^2 sec^{-1}
9	17.1	$2.0(10)^{-10}$
13	16.4	$1.4(10)^{-10}$
16	19.2	$1.2(10)^{-9}$
28	24.2	$9.6(10)^{-9}$

*A bicrystal in which $\theta = 2°$ was also investigated, but the activities were too low to permit an accurate measurement of $d \log a/dz$.

The boundary in the bicrystal for which $\theta = 9°$ did not bisect the angle between the (100) planes of the two crystals, but was almost parallel to a (100) plane of one crystal. It was noticed that during the high-temperature anneal, the boundaries in samples from this bicrystal had become wavy, so that the length of the boundary had increased. Since this result suggested that the energy of the 9-degree boundary depends on boundary orientation, the diffusion penetration in this boundary was investigated using the autoradiographic technique. For this purpose, a sample was diffused for 12 days at 500°C and then sectioned at an angle of about 40′ to the plated surface. The exposed surface was put in contact with Eastman Kodak X-Ray No-Screen film for two hours, and the resulting autoradiograph is shown in Figure 6,

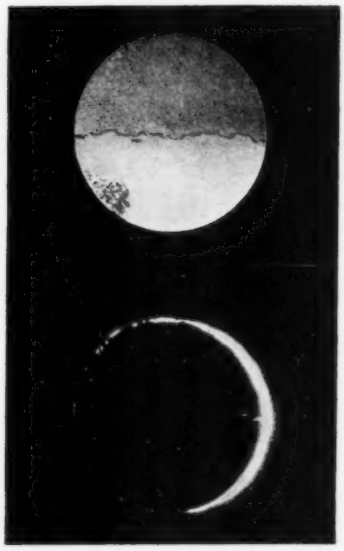

FIGURE 6. (*a*) *Upper* photograph of grain boundary in sample for which $\theta = 9°$. (*b*) *Lower* autoradiograph showing penetration in boundary of (*a*).

together with a photograph of the sample. It is evident that the penetration is non-uniform, and points of high concentration, which appear white in the print of the autoradiograph, correspond to points where the boundary is parallel to a (100) plane of one crystal.

Comparison of Theory and Experience

In order to simplify our discussion, we immediately introduce the assumption $l \cong \lambda \cong 5(10)^{-8}$ cm. Equation (8) may then be rewritten as:

$$D_p = (10)^7 p/\sin(\theta/2) \tag{10}$$

Equation (10) was used to calculate D_p from each of the p-values and in Figure 7 $\log D_p$ is plotted against $1/T$ for all values of θ. This figure indicates no obvious trend of D_p with θ at constant temperature, with the possible exception that at the higher

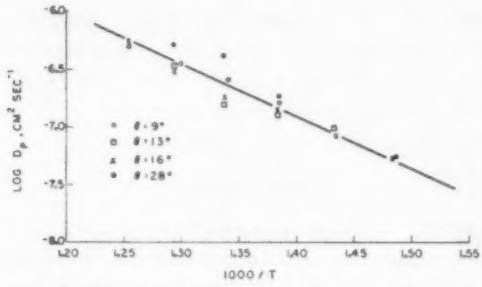

FIGURE 7. The dependence of $\log D_p$ on $1/T$ for various θ values.

temperatures D_p for $\theta = 28°$ may be significantly larger than the average D_p. The dependence of $\log D_p$ on $1/T$ is satisfactorily described by a straight-line relation independent of θ from which we obtain

$$D_p = 0.14 \exp[-19{,}700/RT] \text{ cm}^2 \text{ sec}^{-1}.$$

This activation energy, $Q = 19.7 \pm 2$ kcal/gm atom, is in good agreement with the average, 19.3 kcal/gm atom, of the Q's listed in Table I (these show no significant trend with θ). Thus, the activation energy for silver self-diffusion along a dislocation pipe appears to be independent of θ and agrees, within experimental error, with the activation energy, 20.2 kcal/gm atom, reported earlier [5] for silver self-diffusion in grain boundaries of randomly oriented polycrystals.

In order to show better the quantitative significance of our results, we have listed in Table II the

TABLE II

CALCULATED VALUES OF D_p AND THE RATIO D_p/D_L AT 500°C FOR VARIOUS VALUES OF θ

θ, deg.	p, cm^3 sec^{-1}	D_p, cm^2 sec^{-1}	D_p/D_L
9	$2.9(10)^{-15}$	$3.7(10)^{-7}$	$3.7(10)^6$
13	$3.3(10)^{-15}$	$2.9(10)^{-7}$	$2.9(10)^6$
16	$4.5(10)^{-15}$	$3.2(10)^{-7}$	$3.2(10)^6$
28	$1.4(10)^{-14}$	$5.7(10)^{-7}$	$5.7(10)^6$

values of p at 500 degrees, read from the smoothed curves of Figure 5, and the D_p's for the different θ's calculated therefrom. Confirming our earlier conclusion, D_p is apparently independent of θ for $\theta \ll 16°$. D_p for $\theta = 28°$ is a factor of 1.7 larger

than the average of the other values. However, this larger value of D_p for $\theta = 28°$ at 500 degrees may be without significance since the D_p's for lower temperatures are independent of θ for $\theta \ll 28°$ to well within the experimental uncertainty.

In summary, our results are consistent with the concept that *the coefficient of self-diffusion, D_p, for grain boundary dislocation pipes is independent of the angle of misorientation, θ, for $\theta \gtrsim 30°$, and that D_p is several orders of magnitude greater than the lattice self-diffusion coefficient, D_L.*

Discussion

Results of Smoluchowski and Coworkers

Smoluchowski and coworkers have investigated the grain boundary diffusion of silver [13] and of zinc [14] into columnar copper as a function of misorientation. Their technique consisted of removing successive layers from the diffusion specimen and etching the new surface with reagents that defined a specific concentration of the diffusing substance. They were unable to detect any preferential grain boundary diffusion of silver into copper for $\theta < 18°$ and of zinc into copper for $\theta < 10°$, and these results are the basis for their conclusion that preferential diffusion in isolated dislocation pipes is not distinguishable from lattice diffusion.

It is not to be expected, *a priori*, that quantitatively similar results should be obtained for solute- and self-diffusion in grain boundaries. According to the naive geometrical picture of solid solutions, there is a region of local distortion surrounding a solute atom in a lattice provided that the "sizes" of the solute and solvent atoms are different. It is conceivable, then, that the disorder around a solute atom in a grain boundary is not much greater than in the lattice and the ratio D/D_L is much smaller for solute diffusion than for self-diffusion. However, using Whipple's equation [10] and Smoluchowski's data for $\theta = 45°$, it is estimated that D/D_L is of the order of 10^5 for the diffusion of both silver and zinc in copper at 600–700°C. Therefore, no large disparity is apparent between the magnitudes of D/D_L for solute- and self-diffusion.

One of the very important considerations in evaluating the ratio D/D_L is the resolving power of the technique. Thus, failure to detect any preferential grain boundary penetration by Smoluchowski's technique does not necessarily imply that $D/D_L \cong 1$. Figure 8 shows the general shape of an isoconcentration contour, $c = \bar{c}$, in the vicinity of a grain boundary (at $x = 0$), for diffusion in the z-direction. W is the distance from the diffusion source at which $c = \bar{c}$ as a result of pure lattice diffusion, and ΔW is the additional distance from the source at which $c = \bar{c}$ in the boundary. Figure 9 shows the dependence of ΔW on $(D\delta)$, calculated from Whipple's theory for $D_L = 2(10)^{-10}$ cm^2 sec^{-1}, $t = 5(10)^5$ sec, and $\bar{c} = 0.1\, c_0$, where c_0 is the source

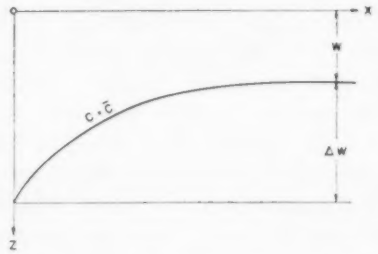

FIGURE 8. The shape of an isoconcentration line in the vicinity of a grain boundary at $x = 0$. Schematic.

concentration,* which conditions closely approximate those used by Achter and Smoluchowski [13] in their study of the diffusion of silver in copper. In those experiments, $\Delta W \ll 0.015$ mm for $\theta \ll 18°$, and $\Delta W \cong 0.30$ mm for $\theta = 45°$. From Figure 9, therefore,

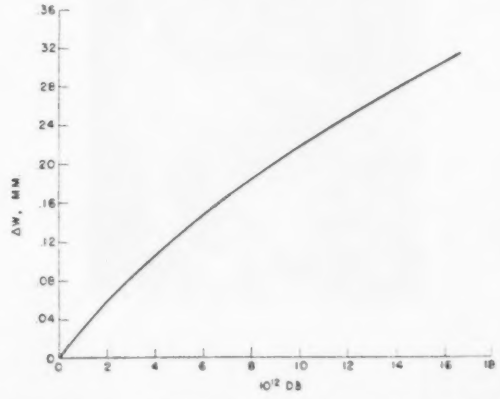

FIGURE 9. Dependence of the excess boundary penetration, ΔW, on $D\delta$, calculated from Whipple's equations for $D_L = 2(10)^{-10}$ cm^2 sec^{-1}, $t = 5(10)^5$ sec, and $\bar{c} = 0.1C_0$.

$$\frac{(D\delta)_{\theta=45°}}{(D\delta)_{\theta=18°}} \cong 35,$$

and since $\delta_{18°} < \delta_{45°}$,

$$\frac{D_{45°}}{D_{18°}} < 35.$$

Since $D_{45°}/D_L$ for the diffusion of silver into copper at 725°C is estimated to be of the order of 10^5, it

*The results are not very sensitive to the particular value chosen for $\bar{c}$.

follows that the grain boundary diffusion coefficient for $\theta = 18°$ is still orders of magnitude larger than D_L.

Comparison with Earlier Results on Silver

Measurements of self-diffusion in silver polycrystalline samples of essentially random orientation were reported earlier [5]. The values of p obtained in that investigation are approximately equal to those found in the present work for $\theta = 9°$. For a specimen consisting of randomly oriented grains, it is inferred from grain boundary energy measurements [15] that most of the misorientations are larger than 9 degrees. However, the common rotational axes for randomly oriented grains are not generally a [100] type; therefore, quantitative agreement between the two sets of results is not necessarily expected.

The Effect of Boundary Orientation

We have no explanation for the fact, demonstrated in Figure 6, that the penetration is a function of boundary orientation for a given crystal misorientation. Further experimentation is necessary to evaluate the effect quantitatively. E. W. Hart and W. T. Read have independently pointed out to us in private conversation that they expect the dislocation configuration and grain boundary energy of the boundary approximately parallel to a [100] of one crystal to be quite different from the boundary 45 degrees to the same [100] direction. Hence, a difference in the rate of diffusion in the two types of boundaries would not be surprising.

Further Consequences of Theory

The most important consequence of our theory is that preferential diffusion in certain directions (parallel to dislocation pipes) of low-angle boundaries, such as lineage and polygonization boundaries, cannot always be ignored. For example, consider self-diffusion in a crystal of silver that consists of mosaic blocks with a mean linear dimension of 10μ and misoriented from each other by an angle of 10′. Of the total amount of isotope, a, in a thin section located at a distance, z, from the source, let a_B and a_L be the amounts which arrived there by diffusion through the mosaic boundaries and through the lattice, respectively. By means of a calculation similar to that described previously, [6] it is found that $a_B/a_L \cong 15$ for $T = 500°C$, $t = 10^6$ sec, and $z = 5(10)^{-4}$ cm. In view of this result, it may be that the anomalously high values obtained [5] for the diffusion coefficient in "single crystals" at 500°C were due to the presence of mosaic boundaries. On the other hand, at temperatures above 700°C, $a_B/a_L \ll 1$ for the usual conditions of a diffusion experiment.

It is expected that the diffusion coefficient in a low-angle boundary will be highly anisotropic reaching a maximum value in a direction (z) parallel to the dislocation pipes and falling to a minimum $D_N \approx D_L$ for diffusion in the direction (x) normal to the pipes.

We presume that the dislocations produced by cold-working a material are not distinguishable from the dislocations in certain low-angle grain boundaries. Therefore, the rate of diffusion along the dislocation pipes produced by cold-working a crystal may be identifiable with D_p, the diffusion coefficient in the dislocation pipes at low-angle boundaries. E. W. Hart of this Laboratory has suggested (private communication) that the major enhancement of diffusion rate by cold-working is due to preferential diffusion along the dislocation pipes produced by cold-working. If so, it is possible in principle to calculate the increase in diffusion rate effected by cold-working from D_p, measured for the proper low-angle boundaries, and the dislocation configuration in the cold-worked state.

For certain conditions, the rate of climb of dislocation is calculable from D_p. Ordinarily it is supposed that dislocations climb by the capture or ejection of lattice vacancies from or to the lattice. However, if the dislocation pipe is attached to a more active source or sink of lattice vacancies, such as a high-angle grain boundary, the dislocation may climb by the migration of lattice vacancies along the pipe to or from the sink. The diffusion coefficient appropriate for this process is D_p.

It now appears that diffusion in silver grain boundaries can be described by a single activation energy, Q_B, equal to 20 ± 2 kcal/gm atom. Thus, $Q_B/Q_L \cong 0.44$, where Q_L is the energy of activation for lattice self-diffusion in silver. Assuming the lattice vacancy mechanism for diffusion, we might naively assume that in grain boundaries all the lattice vacancies necessary for boundary diffusion already exist in the dislocation pipes. Hence, Q_B may be of the order of magnitude of the activation energy Q_0 for moving an atom into a lattice vacancy. The magnitude of Q_B/Q_L is of the same order as the estimates by Huntington and Seitz [16] of the ratio of Q_0/Q_L. However, theory and experience have not progressed to the point where it may be decided whether or not there is a one-to-one correspondence between Q_0 and Q_B.

Acknowledgment

This work was supported by the United States Atomic Energy Commission under Contract No. W-31-109-Eng-52.

We are indebted to E. W. Hart and J. C. Fisher of this Laboratory for helpful criticism of the manuscript.

References

1. Dunn, C. G. and Lionetti, F. J. Metals **1** (1949) 125.
2. Aust, K. T. and Chalmers, B. Proc. Roy. Soc. **201A** (1950) 210.
3. Read, W. T. and Shockley, W. Phys. Rev. **78** (1950) 275.
4. Burgers, J. M. Proc. Phys. Soc. **52** (1940) 23.
5. Hoffman, R. E. and Turnbull, D. J. App. Phys. **22** (1951) 634.
6. Turnbull, D. Atom Movements (Cleveland, ASM, 1951).
7. Smoluchowski, R. Phys. Rev. **87** (1952) 482.
8. LeClaire, A. D. Progress in Metal Physics, Vol. IV. (New York, Interscience Publishers, 1953).
9. Fisher, J. C. J. App. Phys. **22** (1951) 74.
10. Whipple, R. T. P. Atomic Energy Research Establishment Report No. A.E.R.E. T/R 1026 (1952).
11. Chalmers, B. Canadian J. Phys. **31** (1953) 132.
12. Slifkin, L., Lazarus, D. and Tomizuka, T. J. App. Phys. **23** (1952) 1032.
13. Achter, M. R. and Smoluchowski, R. J. App. Phys. **22** (1951) 1260.
14. Flanagan, R. and Smoluchowski, R. J. App. Phys. **23** (1952) 785.
15. Greenough, A. P. and King, R. J. Inst. Metals **79** (1951) 415.
16. Huntington, H. B. and Seitz, F. Phys. Rev. **61** (1942) 315.

THE TUNGSTEN CARBIDE AND NICKEL ARSENIDE STRUCTURES*

NILS SCHÖNBERG†

Four ternary nitrides—$Ti_{0.7}Co_{0.3}N$, $Ti_{0.7}Ni_{0.3}N$, $Mo_{0.8}Co_{0.8}N_{0.9}$, $Mo_{0.8}Ni_{0.8}N_{0.9}$—of the WC structure, and two new sulfides—TiS, NbS—of the NiAs structure have been prepared. The NbS phase of NiAs type is stable with an excess of sulfur, but transforms to the WC type at low sulfur content.

The WC structure has been proposed to be a partially disordered NiAs structure.

The great variation of the axial ratio for compounds of the NiAs structure has been discussed in relation to the degree of ionisation. An expression, in which c/a is a function of the radius ratio of the two components has been found to be valid in all cases, with the exception of those where the degree of ionisation and favourable geometrical conditions for the formation of metallic 8-coordination cause an increase of the c/a value.

LES STRUCTURES DU CARBURE DE TUNGSTÈNE ET DE L'ARSÉNIURE DE NICKEL

On a préparé quatre nitrures ternaires: $Ti_{0.7}Co_{0.3}N$, $Ti_{0.7}Ni_{0.3}N$, $Mo_{0.8}Co_{0.8}N_{0.9}$, $Mo_{0.8}Ni_{0.8}N_{0.9}$, ayant la structure de WC, et deux nouveaux sulfures: TiS, NbS, ayant la structure de NiAs. La phase NbS du type NiAs, est stable avec un excès de soufre, mais elle se transforme en une phase du type WC aux faibles teneurs en soufre. Il fut proposé que la structure de WC est la même que celle de NiAs, mais partiellement désordonnée. La grande variation dans le rapport axial des composés ayant la structure du NiAs a été discutée en relation avec le degré d'ionisation. Il a été constaté qu'une expression donnant c/a en fonction du rapport des rayons des deux constituants est en général valable, à l'exception des cas, où le degré d'ionisation et des conditions géométriques favorables à la formation d'une coordination métallique du type 8, causent une augmentation du rapport c/a.

DIE WOLFRAMKARBID- UND NICKELARSENIDSTRUKTUREN

Es wurden vier ternäre Nitride—$Ti_{0.7}Co_{0.3}N$, $Ti_{0.7}Ni_{0.3}N$, $Mo_{0.8}$, $Co_{0.8}N_{0.9}$, $Mo_{0.8}Ni_{0.8}N_{0.9}$—der WC-Struktur und zwei neue Sulfide—Tis, NbS—der NiAs Struktur hergestellt. Die NbS-Phase des NiAs Typs ist mit überschüssigem Schwefelgehalt stabil, wandelt sich jedoch bei geringerem Schwefelgehalt in den WC Typ um.

Die WC Struktur wird als eine teilweise ungeordnete NiAs Struktur gedeutet.

Die grossen Änderungen im Achsenverhältnis der NiAs Strukturen werden im Bezug auf den Ionisationsgrad diskutiert. Ein Ausdruck, in dem c/a eine Funktion des Radienverhältnisses der beiden Komponenten ist, war in allen Fällen gültig, mit Ausnahme derjenigen Bedingungen, in denen der Ionisationsgrad und die für die Bildung einer metallischen 8-Coordinationsverbindung günstigen geometrischen Verhältnisse eine Vergrösserung des c/a Wertes hervorriefen.

Introduction

The tungsten carbide and nickel arsenide structures are closely related to each other. The ideal formula for both types can be written MeX, although many deviations from the composition 1 : 1 have been found. The metal Me occurs among the transition elements and X is any of the non-metals, metalloids or metals in groups IVb–VIb of the periodical table.

The metal atoms in WC [1] form a "simple" hexagonal unit cell with c/a slightly smaller than unity. It is not possible to determine the position of the carbon atom from X-ray data. The largest space in the cell is available at any of the two centres of trigonal prisms of metal atoms. Such a position is most likely, and the observed Me–X distances for this arrangement in all compounds of the WC structure agree well with the radius sum $r_{Me} + r_X$ calculated for metallic bonds. The positions of the atoms have been described as: 1 Me in 0,0,0 and 1 X in 1/3,2/3,1/2.

In the case of NiAs [2; 3] (B8 type) the metal atoms have the same positions as in WC, but the X-atoms occupy the lattice "holes" giving the largest X–X distances. The atomic arrangement is: 2 Me in 0,0,0; 0,0,1/2 and 2 X in 1/3,2/3,1/4; 2/3,1/3,3/4. As already pointed out by Hägg [4] more than twenty years ago, the analogous grouping of X-atoms may occur in the WC lattice, although it has not been possible to decide it by X-ray methods. The c/a values vary considerably for compounds of the NiAs structure, being usually between 1.2 and 1.7.

Some new nitrides—ternary phases—and sulfides belonging to the two structure types have been prepared in the present investigation. In order to throw light on the relationship between the two groups of structures and on the great variation of the c/a ratio for compounds of the B8 type, all available data in the literature have been collected and discussed.

Experimental

As starting materials for the preparation of nitrides and sulfides, metals of fairly high purities (about 99.5 per cent) were used. The nitrides—

*Received December 18, 1954.

†Institute of Chemistry, University of Uppsala, Uppsala, Sweden.

ternary phases—were prepared by passing oxygen-free dry ammonia over finely powdered binary alloys at various temperatures between 600°C and 800°C. These alloys were made from the powdered metals, by moulding mixtures into brickettes, which were heated in a high frequency vacuum induction furnace [5]. The sulfides were synthethized from the elements in evacuated and sealed silica tubes at a temperature of 700°C and for a time of about four days.

The phase analysis was performed by means of powder photographs taken with Cu–$K\alpha$ radiation in focussing cameras of the Guinier type. The nitrogen content of the nitride samples was determined by means of the Kjeldahl method.

The new compounds investigated in the present study are described under the headings "Nitrides" and "Sulfides." The unit cell dimensions are given in Table I.

Survey of the Compounds of WC and NiAs Type

Carbides

MoC [6] is the only carbide found to be isomorphous with WC.

Nitrides

The existence of the phases $NbN_{0.80-0.90}$, $TaN_{0.80-0.90}$ and WN of the WC structure has recently been reported by the present author [7]. MoN has a slightly deformed WC structure [8; 7].

In the present investigation four ternary nitrides of the WC structure have been prepared with the following approximate formula: $Ti_{0.7}Co_{0.3}N$, $Ti_{0.7}Ni_{0.3}N$, $Mo_{0.8}Co_{0.2}N_{0.9}$, and $Mo_{0.8}Ni_{0.2}N_{0.9}$. As it was only possible to prepare the nitrides in the presence of small amounts of other phases (e.g., TiN, MoN and intermetallic compounds) as impurities, the homogeneity ranges could not be determined with any accuracy. The Me′/Me″/N ratio varies probably to a comparatively large extent. While the diffraction pattern of MoN contains superlattice reflections, easily visible in the powder photograph, no such extra lines could be traced for the $Mo_{0.8}Co_{0.2}N_{0.9}$ and $Mo_{0.8}Ni_{0.2}N_{0.9}$ phases. The reaction between TiN and Co, Ni in a vacuum furnace at temperatures of about 1600°C did not cause the formation of ternary nitrides but so-called "cemented hard metals", i.e., TiN crystals embedded in the Co, Ni phase.

Phosphides

The VP and MoP phases with the NiAs and WC arrangement of atoms respectively have recently been described by the present author [7]. It is of interest to note that no extra reflections caused by ordered P atoms could be traced in the diffraction pattern of MoP. Calculated values of $p|F|^2$ show that at least the 101-reflection should be visible in the photograph for an ordered arrangement of the P atoms analogous to that of the As atoms in NiAs.

Sulfides

The existence of the phases VS [9], CrS [10], FeS [3; 10; 11; 12], CoS [11] and NiS [11] of the B8 type is well established.

The sulfides TiS and NbS were prepared in the present investigation. Both phases are homogeneous close to the composition 1 : 1 and seem to have comparatively small homogeneity ranges. TiS was found to have the NiAs structure, although the reflections exclusively caused by the S atoms—*hkl* reflections with $l = 2n + 1$—were rather diffuse. This may be due to a small degree of disorder of the nonmetal atoms. For the NbS phase in equilibrium with NbS_2 (as will be reported elsewhere, NbS_2 has the C19 type) the NiAs atomic arrangement was observed, while no separate reflections from the S atoms could be traced in photographs of samples with NbS in equilibrium with Nb. It was not possible to determine the homogeneity limits of the NbS phase. But from the observations the conclusion can be drawn that a WC → NiAs type transformation takes place with an increase of the S content, probably when passing the composition 1 : 1. This is most likely a disorder → order transformation of the positions of the nonmetal atoms. If this is true the WC structure ought to be considered as a disordered NiAs structure.

Unit cell dimensions and mean Me-Me distances (designated by d) for all MeX phases, where X = C,N,P,S are listed in Table I. Each Me atom is surrounded by eight Me atoms at the distances of $c/2$ (two atoms) and a (six atoms) Å. The Me-Me distances, calculated for 8-coordination, are those given by Pauling [13]. The Me-X distances—6-coordination—are $\sqrt{a^2/3 + c^2/16}$ Å. In order to facilitate a comparison between the c/a values for the compounds of the WC and NiAs structures the corresponding lengths of the c-axes—$c_{\text{NiAs}} = 2c_{\text{WC}}$—have been chosen in the c/a column.

If the MeX structure—WC or NiAs—is regarded as being of the common "interstitial" type, a contact between the different kinds of atoms is attained, when the r_X/r_{Me} ratio reaches a value of $1/3\ (\sqrt{21} - 1) = 0.53$, when $c/a = 2$. This is in

TABLE I

MeX Compounds of the WC and NiAs Structures, Where X = C, N, P, S.

Me	X	a, Å	c, Å	c/a**	$d_{obs.}$ Å	$d_{calc.}$ Å	r_X/r_M
Mo	C	2.90	2.81	1.94	2.88	2.72	0.57
W		2.90	2.83	1.95	2.88	2.74	0.56
Nb	N	2.94	2.79	1.90	2.91	2.86	0.50
Ta		2.93	2.88	1.97	2.92	2.88	0.49
Mo*		5.73	5.61	1.96	2.85	2.72	0.52
W		2.89	2.83	1.95	2.88	2.74	0.52
$Ti_{0.7}CO_{0.3}$		2.94	2.90	1.97	2.93	2.74	0.52
$Ti_{0.7}Ni_{0.3}$		2.94	2.89	1.96	2.93	2.74	0.52
$Mo_{0.8}Co_{0.2}$		2.84	2.79	1.97	2.82	2.66	0.53
$Mo_{0.8}Ni_{0.2}$		2.84	2.78	1.96	2.83	2.66	0.53
V	P	3.18	6.22	1.96	3.16	2.62	0.81
Mo		3.23	3.20	1.98	3.22	2.72	0.78
Nb	S	3.32	6.46	1.95	3.30	2.86	0.71
Ti		3.30	6.44	1.96	3.28	2.84	0.72
V		3.36	5.81	1.73	3.25	2.62	0.75
Cr		3.45	5.75	1.66	3.31	2.52	0.81
Fe		3.45	5.67	1.64	3.30	2.46	0.83
Co		3.37	5.16	1.53	3.17	2.44	0.84
Ni		3.42	5.30	1.55	3.23	2.44	0.84

*MoN has a slightly deformed WC structure.
**As stated in the text this value refers to the axial system of the NiAs structure.

good agreement with the observed data for the carbides and nitrides, where $r_X = 0.77$ Å and 0.71 Å respectively. For the nonmetals P and S the radius values are 1.06 Å and 1.02 Å respectively. Hence r_X/r_{Me} considerably exceeds the value of 0.53, causing an expansion of the metal lattice. In Figure 1 the d_{obs}/d_{calc} ratio has been plotted against the r_X/r_{Me} ratio for all compounds with X = C,N,P,S.

It is seen from Figure 1 that three different groups of compounds can be specified. The first group includes the carbides and nitrides, where $0.49 \leqslant r_X/r_{Me} \leqslant 0.57$ and $1.9 < c/a < 2.0$. The intermetallic distances are up to 7 per cent greater than those in the pure metals. For VP, MoP, TiS and NbS in the second group $0.71 \leqslant r_X/r_{Me} \leqslant 0.81$. In spite of that the c/a value is slightly smaller than 2. The lattices are expanded, so that the linear increase of the Me-Me distances is between 15 and 21 per cent as compared with the pure metals. The metallic properties have most likely been weakened to a corresponding extent. The VS phase, with $c/a = 1.73$, forms an intermediate stage between the second and third groups, the last one including CrS, FeS, CoS and NiS. The increase of the r_X/r_{Me} ratio has in the third group caused a contraction along the c-axis and consequently an expansion along the a-axis of the unit cell. The limits $1.5 < c/a < 1.7$ are found. The great enlargement of the Me-Me distances indicates a nonmetallic or a very weak metallic character.

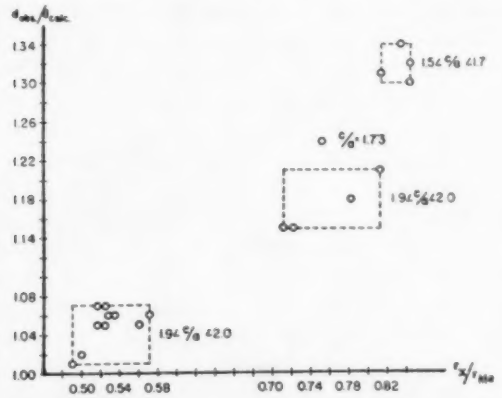

Figure 1. The d_{obs}/d_{calc} ratio *vs.* the r_X/r_{Me} ratio for MeX phases of WC and NiAs types, where X = C, N,P, S.

TABLE II

MeX Compounds of the NiAs Structure, Where X = Sn, Pb, As, Sb, Bi, Se, Te.

Me	X	c/a	r_X/r_{Me}
Ni	Sn	1.27	1.08
Ir		1.40	1.00
Pt		1.32	0.98
Cu		1.21	1.06
Au		1.28	0.92
Pt	Pb	1.28	1.22
Mn	As	1.53	0.79
Ni		1.39	0.97
Cr	Sb	1.33	1.08
Mn		1.40	0.91
Fe		1.26	1.11
Co		1.34	1.11
Ni		1.30	1.11
Pd		1.37	1.02
Pt		1.32	1.01
Mn	Bi	1.42	0.97
Ni		1.32	1.20
Ti	Se	1.75	0.77
V		1.67	0.83
Cr		1.63	0.87
Fe		1.64	0.89
Co		1.59	0.89
Ni		1.46	0.89
Ti	Te	1.67	0.94
Cr		1.56	1.06
Mn		1.62	0.89
Fe		1.49	1.09
Co		1.38	1.10
Ni		1.35	1.10
Pd		1.37	1.00

MeX *phases of the* NiAs *structure, where* X = Sn, Pb, As, Sb, Bi, Se, Te

The existence of 30 compounds belonging to this group has been established, as far as the present author has found in literature. Most phases are reported in Wyckoff: *Crystal Structures I* [14] and the rest in *FIAT Review of German Science, Allgemeine Metallkunde* [15]. They are listed in Table II, where the c/a values, which vary between 1.75 and 1.21, and the r_X/r_{Me} values are also given. The X atoms are surrounded by six Me atoms in the lattice. The radius values of the X elements are corrected for this coordination number, taking the Born exponent $n \sim 6$ [12]. This gives the values $r_{Sn} = 1.32$, $r_{Pb} = 1.65$, $r_{As} = 1.18$, $r_{Sb} = 1.36$, $r_{Bi} = 1.46$, $r_{Se} = 1.09$, and $r_{Te} = 1.34$ Å. Mn has an abnormally great atomic radius in many compounds, for instance in those given in Table II and in MnO and MnS. A calculation gives the approximate value of $r_{Mn} = 1.5$ Å, which has been used in Table II.

General Discussion

Massing and Wallbaum [16], Laves and Wallbaum [17], Nowotny, Schubert and Dettinger [18] point out that the stability of the compounds of the NiAs structure is strongly dependent both on the character of the components and upon the compositions. A continuous transition from nonmetallic to metallic character of the bonds occurs according to Laves and Wallbaum [16]. These two authors note that c/a tends to decrease to a value of $\sqrt{3}/\sqrt{2}$, when the character of the phase approaches the "ideal" NiAs type. However, no definite explanation has been given for the great variation of c/a and why the value of $\sqrt{3}/\sqrt{2}$ should be reached as a lower limit for c/a.

In the following discussion the WC and NiAs structures are treated as belonging to a common type. The phases with WC structure are, therefore, formally described with the c-axis doubled. The disorder only occurs when X is a typical nonmetal (= C,N,P,S), when the degree of ionization of the X atoms is small and when there is space available for a disordered grouping of the X atom layers in the Me lattice, so that the X atoms are partially or entirely isolated from each other.

It is found that $2.0 > c/a > 1.2$ for the phases of WC and NiAs structure. The displacement of electrons from Me to X decreases most likely in the sequence S → N → P → C for a given metal Me. If a fraction of the electrons in the outer s,p,d shells of the transition metal is displaced towards the X atom, there are still a number of electrons left for the formation of intermetallic bonds. Under all circumstances Me-X bonds of ionic nature evidently exist, causing an elongation of the X-X distances. At the same time according to the observations a contraction takes place along the c-axis. Further the degree of Me → X ionisation decreases going from nonmetal via metalloid to metal in a sub-group, i.e., in the sequences C → (Ge) → Sn → Pb, N → P → As → Sb → Bi, (O) → S → Se → Te. No data about germanides of the NiAs structure seem to be available, and the O atom with its very strong tendency as an electron acceptor forms compounds with other structures, commonly of the B1 type.

The unit cell dimensions can be approximately calculated, assuming Me-X as well as Me-Me contacts. The following expressions are valid:

$$\begin{cases} r_{Me} = c/4 \\ (r_{Me} + r_x)^2 = a^2/3 + c^2/16 \end{cases}$$

(1) giving $\begin{cases} c = 4r_{Me} \\ a = \sqrt{3r_x(r_x + 2r_{Me})} \end{cases}$

$$\frac{c}{a} = \frac{4}{\sqrt{3[(rx/r_{Me})^2 + 2(r_x/r_{Me})]}}.$$

It ought to be mentioned that Hägg [4] in 1931 noted that the length of the c-axis was independent of the X atom for a given metal Me in typical NiAs-like compounds. He stated that an increase of r_X thus causes an increase of a and a resulting decrease of the c/a value and used the above-mentioned formula for the calculation of the volume per Me atom. The discussion below is, therefore, to be regarded as a development of Hägg's ideas.

According to formula (1) c/a is a function of the radius ratio of the two elements X and Me. If the degree of ionisation is so large that the diameter of the X atom in the ionized state exceeds the value of a given above, $c > 4r_{Me}$. This occurs for X = S, Se, Te and P (with a few exceptions). As the expression (1) was deduced assuming such Me-X bonds as to cause a decrease of the c-axis, it only has validity for $c/a < 2$. The theoretical lower limit is obtained, when X–X contacts take place between different 001-planes. Hence $(2r_x)^2 = a^2/3 + c^2/4 = 4r_{Me}^2 + 2r_{Me}r_X + r_x^2$, giving $r_X/r_{Me} = 1.54$ and $c/a = 0.99 \sim 1$. This case never occurs. The highest r_X/r_{Me} ratio is obtained for PtPb = 1.22, and the lowest c/a value is observed for CuSn = 1.21.

In Figure 2, c/a has been plotted against r_X/r_{Me} for all MeX phases of the WC and NiAs structures

with the exception of those having X = S, Se, Te in combination with Me = Ti – Fe, Nb, Mo. A curve calculated from equation (1) has also been drawn. It is remarkable that the sulfides, selenides and tellurides of cobalt and nickel and the PdTe phase deviate from the other MeX compounds with the same X component to such a large extent

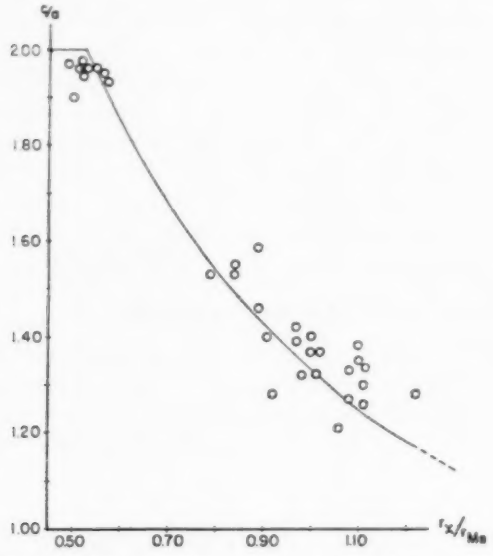

FIGURE 2. The c/a ratio *vs.* the r_X/r_{Me} ratio for all MeX phases of WC and NiAs types with the exception of those having X = P, S, Se, Te in combination with Me = Ti – Fe, Nb, Mo. The drawn curve is calculated.

that they fulfil the requirements for equation (1). This is probably due to a small tendency for these group VIII metals to act as electron donors in combination with the elements S, Se and Te in group VIb.

Figure 3 shows the lattice constants of all monosulfides hitherto known of the WC and NiAs structures. Two horizontal lines have been drawn which represent the values of the lattice constants for an ideal hexagonal close-packing of S^{2-} ions. It is seen that the a-axes of the different compounds vary only slightly, while the c-axes follow the variation of r_{Me} when going from Nb to Fe. The remarkable behaviour of CoS and NiS have been discussed above. The degree of ionisation of S seems to be large and reaches a maximum value for Me = Cr and Fe. In spite of that, NbS and TiS still have metallic properties, as indicated by the comparatively small intermetallic distances (8-coordination).

The P atoms are ionized to a considerably smaller extent than the S atoms in analogous compounds,

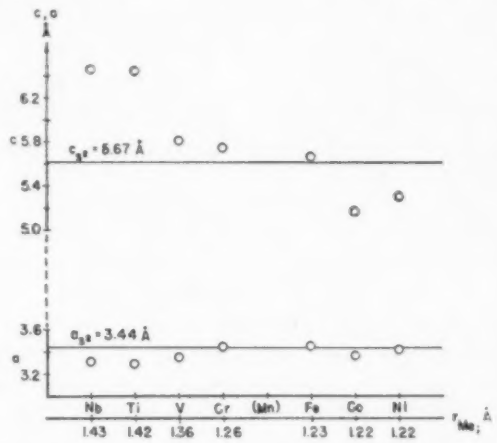

FIGURE 3. The lattice constants for the monosulfides of WC and NiAs types.

as indicated by the lengths of the a-axes in the VP and MoP phases. This is to be expected from the position of P before S in the periodic system.

All compounds which had to be excluded in Figure 2 because of the unfavourable increase in r_x through ionisation, are represented in Figure 4. The axial ratio c/a has been plotted against r_{Me}. The c/a values for the sulfides and selenides follow approximately the variation of r_{Me} and tend to go towards the value 1.63 for Me = Fe, characteristic for a hexagonal close-packing. The lattice constant of FeS corresponds closely with that calculated for an ideal hexagonal S^{2-} lattice. But in FeSe the

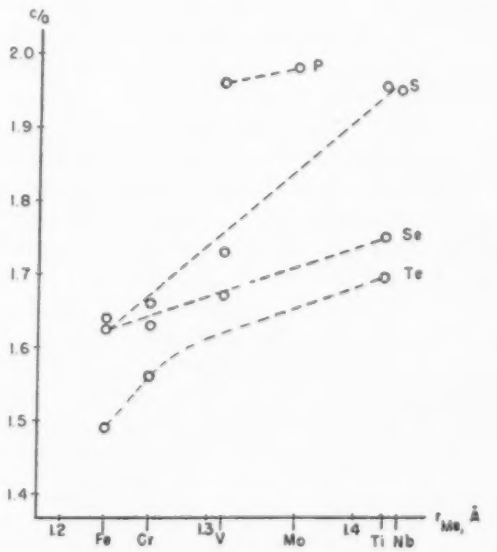

FIGURE 4. The c/a ratio *vs.* r_{Me} for MeX phases of WC and NiAs types, where X = P, S, Se, Te and Me = Ti, V, Cr, Fe, Nb, Mo.

observed value of $a = 3.64$ Å, while $2r_{Se^{2-}} = 3.82$Å, indicating a somewhat smaller degree of ionisation than in FeS. In considering the values for FeTe, CrTe and TiTe one must bear in mind the position of Te between Se and As as regards its electronegativity.

The metallic properties of a compound MeX are dependent on: (*a*) the character of Me, (*b*) the character of X and (*c*) the geometrical conditions for the formation of a stable compound—in this case of WC and NiAs type.

When X is a sub-group metal the MeX compound —of the NiAs structure—can be regarded as an intermetallic phase. The Me atoms are then surrounded by two Me and six X atoms at contact distances, thus having metallic 8-coordination. The X–X bonds are very weak. The X atom is situated at the centre of a trigonal prism of Me atoms. The favourable geometrical conditions for a stable lattice are fulfilled, when c/a is correlated to r_X/r_{Me} as is given in equation (1).

When X is a nonmetal the geometrical conditions have a very great influence on the formation of metallic MeX compounds of WC and NiAs structures, at least for transition metals in groups IV–VI. The ideal r_X/r_{Me} ratio for the interstitial WC structure is 0.53. The carbides and nitrides of this type have $0.49 \leqslant r_X/r_{Me} \leqslant 0.57$. The Me-Me coordination number is 8, and the metallic properties are dependent on the intermetallic distances (Figure 1). For MoP ($r_X/r_{Me} = 0.78$) of the WC structure the Mo-Mo distances are 18 per cent greater than in the pure metal, indicating a corresponding decrease of the metallic character. The partial ionisation of the X atoms in, for instance, the carbides and nitrides gives an explanation of the fact that the nonmetal content does not exceed 50 atomic per cent. If X–X bonds of non-ionic type exist in the carbides and nitrides, it should be possible to place another nonmetal atom in the "simple" hexagonal cell by analogy with the diborides of the AlB_2 structure (C32 type). In most cases the phases are homogeneous at a somewhat smaller X content than 50 atomic per cent. The C and N atoms evidently have ordered positions within an X layer parallel with (001). The separate X layers can be irregularly situated in relation to each other at favourable geometrical conditions, i.e., a small degree of ionisation and a small r_X/r_{Me} ratio. The WC structure may therefore be regarded as a NiAs structure with disordered nonmetal layers. NbS forms a striking example of the influence of the degree of ionisation. The modification with Nb in excess is of the WC structure, and the modification rich in S is of the NiAs structure.

Going from TiS to FeS the bond character changes from metallic to nonmetallic. The S atoms seem to be ionized almost to the S^{2-} state in FeS. In such a case a fraction of the Me atoms can be removed without any breakdown of the lattice. Compounds of the same nature as FeS have been found to have a homogeneity range with the lower limit close to the composition 1 : 1.

A subtraction of one Me atom in a MeX lattice of NiAs type leads to the MeX_2 lattice of $Cd(OH)_2$ type (C 6). A continuous B8–C6 type transformation seems to exist in the following cases: NiTe–$NiTe_2$[19], TiSe–$TiSe_2$[20], TiTe–$TiTe_2$[20]. No similar transition was found to exist in the Ti–S and Nb–S systems.

Acknowledgment

The author wishes to express his gratitude to Professor G. Hägg for his encouraging interest in the present investigation. A grant from Statens Tekniska Forskningsråd is gratefully acknowledged.

References

1. Westgren, A. and Phragmén, G. Z. anorg. Chem. **156** (1926) 27.
2. Aminoff, G. Z. Krist. **58** (1923) 203.
3. De Jong, W. F. Physica **5** (1925) 194.
4. Hägg, G. Z. phys. Chem. **B12** (1931) 33.
5. Kiessling, R. Jernkontorets Ann. **132** (1948) 237.
6. Tutiya, H. Sci. Pap. Inst. Phys. Chem. Res. Tokyo **19** (1932) 384.
7. Schönberg, N. Acta Chem. Scand. **8** (1954) 199.
8. Hägg, G. Z. phys. Chem. **B7** (1930) 339.
9. Biltz, W. and Köcher, A. Z. anorg. Chem. **241** (1939) 324.
10. De Jong, W. F. and Willems, H. W. V. Physica **7** (1925) 74.
11. Alsén, N. Geol. Fören. i Stockholm Förh. **47** (1925) 19.
12. Hägg, G. and Sucksdorff, J. Z. phys. Chem. **B22** (1933) 444.
13. Pauling, L. Nature of the Chemical Bond (London 1948) Chaps. X and XI.
14. Wyckoff, R. W. G. Crystal Structures I (New York, 1951) Table III, 1 and 15.
15. FIAT Review of German Science, Allgemeine Metallkunde **31** (1939–46) p. 31.
16. Massing, G. and Wallbaum, H. J. Nachr. Akad. Wiss. Göttingen **32** (1941).
17. Laves, F. and Wallbaum, H. J. Z. angew. Mineral. **4** (1941–42) 17.
18. Nowotny, G., Schubert, K. and Dettinger, U. Metallforsch. **1** (1946) 137.
19. Klemm, W. and Fralini, N. Z. anorg. Chem. **251** (1943) 222.
20. Ehrlich, P. Habil. Schrift, T. H. Hannover (1945).

INTERSTITIAL CONTENT OF RADIATION-DAMAGED METALS FROM PRECISION X-RAY LATTICE PARAMETER MEASUREMENTS I. PRINCIPLES OF THE MEASUREMENTS*

CHARLES W. TUCKER, JR. AND JOHN B. SAMPSON†

An X-ray method for determining the interstitial content of irradiated metals is suggested and analyzed. This approach offers the following advantages: (*a*) the X-rays "see" mainly the interstitial atoms since their effect outweighs that of vacancies by a 5 : 1 ratio, (*b*) the interpretation is straightforward and may be made quantitative, and (*c*) the method is sensitive since 0.01 atomic per cent, and perhaps less, of interstitials may be detected.

These conclusions are based on a combination of theory and experiment. The theory is based upon an elasticity interpretation which predicts Vegard's law and several other experimentally confirmed X-ray effects.

The possibilities of the method are borne out by preliminary observations in this Laboratory of X-ray-detected lattice expansions of several neutron irradiated metals.

LA TENEUR EN ATOMES INTERSTITIELS DE MÉTAUX ENDOMMAGÉS PAR IRRADIATION, DÉTERMINÉE PAR DES MESURES PRÉCISES DU PARAMÈTRE DU RÉSEAU AU MOYEN DES RAYONS X. I. PRINCIPES DES MESURES

On propose et examine une méthode pour la détermination de la teneur en atomes interstitiels de métaux irradiés, basée sur l'emploi des rayons X. Cette façon d'agir donne les avantages suivants: (*a*) les rayons X "voient", avant tout, les atomes interstitiels, car l'effet de ces derniers est 5 fois plus grand que l'effet des lacunes réticulaires, (*b*) l'interprétation des résultats est simple et peut être quantitative, (*c*) la méthode est sensible, car il y a moyen de détecter 0,01 pour cent, ou peut-être même moins, d'atomes interstitiels. Ces conclusions sont basées sur une combinaison de théorie et d'expérience. La théorie s'appuie sur une interprétation basée sur la notion d'élasticité, qui prédit la loi de Vegard, ainsi que plusieurs autres effets en rayons X, confirmés par l'expérience. Les possibilités de cette méthode sont démontrées par des observations, faites dans ce Laboratoire, sur les expansions des réseaux de quelques métaux irradiés aux neutrons, décelées au moyen des rayons X.

DER ZWISCHENGITTERSTELLENGEHALT STRAHLUNGSGESCHÄDIGTER METALLE AUS RÖNTGENOGRAPHISCHEN PRÄZISIONSMESSUNGEN DER GITTERKONSTANTEN. I. GRUNDLAGEN DER MESSUNGEN

Es wird eine Röntgenmethode zur Bestimmung des Anteils von Zwischengitteratomen in bestrahlten Metallen vorgeschlagen und analysiert. Die Methode hat folgende Vorzüge: (*a*) Die Röntgenstrahlen "sehen" vorzugsweise die Zwischengitteratome, da ihr Effekt den der Leerstellen im Verhältnis 5: 1 überwiegt; die Auswertung ist unkompliziert und kann quantitativ durchgeführt werden; (*c*) die Methode ist empfindlich, denn 0,01 Atom % Zwischengitteratome und wahrscheinlich weniger lässt sich nachweisen.

Diese Schlüsse gründen sich auf eine Kombination von Theorie und Experiment. Der Theorie liegt eine Elastizitätsbetrachtung zugrunde, die Vegards Regel und mehrere andere experimentell beobachteten Röntgeneffekte voraussagt.

In diesem Laboratorium wurden in ersten Versuchen an mehreren mit Neutronen bestrahlten Metallen Gittervergrösserungen röntgenographisch nachgewiesen, und damit die Anwendungsmöglichkeiten der hier beschriebenen Methode gezeigt.

Introduction

It is generally believed that the primary damage in metals caused by heavy particle bombardment is due to the formation of interstitial lattice atoms and vacant lattice sites. However, under continued irradiation and subsequent thermal treatment these interstitial and vacancy defects may enter into various reactions such as mutual annihilation, agglomeration, and interaction with dislocations and other defects. Each of these possible reactions will affect the physical properties of the metal in a characteristic manner. The central problem in the study of radiation damage and its annealing is that of deducing from the changes in physical properties what reactions are occurring among the possible defects.

Specific physical properties which have been studied in the case of irradiated metals [1] include electrical resistivity, critical shear stress, other mechanical properties, and elastic constants. Each of these properties (except possibly the elastic constants) is sensitive to more than one principal defect that may be present. Moreover, the interpretation of these properties in terms of possible defects is complex and subject to various uncertainties. It is therefore desirable to search for a physical property which reveals in a straightforward manner the concentration of a particular defect of importance.

The purpose of this paper is to present a type of measurement, namely, precision X-ray lattice parameter measurements, which gives promise in

*Received January 7, 1954.

†Knolls Atomic Power Laboratory, General Electric Company, Schenectady, New York.

metals of measuring essentially only the interstitial content. For fairly symmetric crystals, a uniform distribution of interstitials causes a uniform lattice dilatation which can be used to measure the concentration of interstitials provided the atomic displacements due to a single interstitial are known. It is true, similarly, that the relaxation around a vacancy produces a contraction of the lattice, but this appears to be nearly an order of magnitude less than the expansion produced by an interstitial. Thus the X-ray method gives a measurement which is dependent essentially only on the interstitial content.

The analysis of crystal dilatation to be discussed here assumes separate interstitials; the possibility of agglomeration of interstitials or their accumulation near dislocations, grain boundaries, or other defects is ignored. This assumption is of course true in some range of temperature and exposure. The interpretation is qualitatively correct even in other ranges since, for example, agglomeration into small clusters should reduce the dilatation but only by a factor of two or three.

By contrast one cannot expect to determine interstitial content from electrical resistivity measurements to any known degree of accuracy. Both vacancies and interstitials scatter the conduction electrons by about an equal amount [2] so that in addition to other information one would also require a knowledge of the ratio of interstitials to vacancies. This ratio is known only if the only possible subsequent reaction is that of direct annihilation of interstitials and vacancies so that the ratio remains fixed. This is a very restrictive assumption. Moreover, it does not appear to be in accord with observations [3; 4] according to which some changes in physical properties in irradiated copper are not annealed at temperatures adequate for the migration of both vacancies and interstitials.

Experimental Possibilities of the X-ray Method

If one assumes the validity of the X-ray method, questions naturally arise whether the method is sufficiently sensitive and whether lattice expansions have ever been observed in metals.

According to Jette and Foote [5], who studied fourteen [14] metallic elements, lattice parameters can be measured using a symmetrical back-reflection focusing camera to a precision of about ± 0.005 per cent. From the relation to be established between interstitial content and lattice parameter change, it can be concluded that the least detectable interstitial content by the X-ray method is about 0.005 per cent.

The interstitial content to be expected for irradiations which are readily achieved in nuclear reactors and which have also been reported for accelerators appear to be well above the least detectable amount. For example, if one assumes equal interstitial and vacancy content for copper which was exposed to 10^{17} deuterons/cm^2 at the University of Illinois [3; 6] by a 12 Mev deuteron beam, the measured resistivity change indicates an interstitial content [3] of 0.02 to 0.2 per cent.*

Actually lattice expansions have been observed in this Laboratory using an X-ray back reflection focusing camera for a number of neutron irradiated metals. These results, which are still preliminary, and others will be presented in a second paper. It is sufficient to say at this point that the changes observed exceed the least detectable amount by about an order of magnitude.

Review of Elastic Description of Interstitials and Vacancies

The changes in the X-ray diffraction pattern as well as the change in volume of a crystalline lattice resulting from an accumulation of either interstitials or of vacancies can in principle be used to measure the concentration of these defects. This measurement is readily amenable to analysis based on an elasticity problem [7] which has been applied by various authors to such phenomena as precipitation from solid solution [8], F-centers [9], dislocations [10], X-ray effects from solid solutions [11], distortion of crystals [12], and to radiation damage [13]. This approach was first considered in this Laboratory by Coffin and Snyder [13], to whom we are indebted for suggesting its applicability to radiation damage effects. The elastic model considers each interstitial or vacancy to be a center of pressure (positive or negative) imbedded in an isotropic elastic medium. This description should be adequate for the common metallic lattices of high symmetry, namely, face-centered cubic, hexagonal close-packed, and body-centered

*Recent measurements of stored energy by Overhauser (to be published) have led him to suggest that the interstitial and vacancy content produced by this irradiation may have been less by an order of magnitude, in which case the theory of the electrical resistivity effects of interstitials and vacancies is seriously incorrect. An X-ray measurement would be of great aid in clarifying this discrepancy.

cubic. The applicability of the model breaks down at higher concentrations due to non-elastic interactions but it should apply up to concentrations of about one atomic per cent.

Recently, a report by Eshelby [12] has appeared which gives in one place a complete and general analysis of the elasticity problem. Before we had learned of this important work we were pursuing similar studies in this Laboratory in order to extend the analysis of Huang [11] who had considered the X-ray effects from dilute solid solutions but who had neglected the effect of a finite medium. The results of the elastic model due principally to Eshelby [12] and Huang [11] which are pertinent to X-ray and volume changes are as follows:

1. A uniform distribution of centers of pressure in a lattice of any finite size and shape produces a uniform volume expansion corresponding to an isotropic linear strain

$$e(n) = \frac{4\pi}{3} nc\gamma \tag{1}$$

where $e(n)$ is the strain produced by a concentration n per unit volume of centers of pressure. The constant c is proportional to the strength of each center of pressure and γ is related to Poisson's ratio, σ, of the medium by

$$\gamma = 3\frac{1-\sigma}{1+\sigma}. \tag{2}$$

2. The positions of the X-ray diffraction maxima shift due to the addition of a uniform distribution of centers of pressure giving a lattice parameter expanded in agreement with equation (1). Huang's analysis predicts the isotropic X-ray expansion incorrectly by the factor $1/\gamma$ because he considered the medium to be infinite. (The same error occurs in considering volume changes if one neglects terms arising from the finite nature of the medium.)

3. Huang predicted additional X-ray effects due to the centers of pressure, namely, no line-broadening, some changes in the intensities of the Bragg reflections, and an effect analogous to thermal diffuse scattering.

4. The elastic displacement around a single center of pressure located at the origin is given by

$$u = c\left[\frac{1}{r^2} + \psi\,(r, \theta, \phi)\right] \tag{3}$$

where ψ is a function which depends upon the shape and location of the outer surface of the body. Quite near the center of pressure the $1/r^2$ term dominates, but the additional effects due to the finite medium result from the ψ-term.*

For the lattice of atomic volume v and atomic concentration p of centers of pressure, the strain and concentration are related by the equation

$$e(p) = \frac{4\pi}{3}\frac{\gamma c p}{v}. \tag{4}$$

This equation is basic to our suggested method of measurement. It will be shown to be consistent with Vegard's law for solid solutions. Evaluation of the constant c in terms of detailed calculations of atomic displacements due to interstitials and vacancies will be discussed in a later section.

Tests of Elasticity Theory Predictions

Several of the predictions of the elasticity theory as applied to X-ray diffraction effects mentioned in the previous section can be tested experimentally. For example, in the case of solid solutions equation (4) can be shown to give

$$e(p) = \frac{r_2 - r_1}{r_1} p, \tag{5}$$

if one assumes that the "elastic constants" of the solute and solvent atoms are identical. In equation (5), r_2 is the atomic radius of a solute atom and r_1 that for a solvent atom. In the simple metallic crystal structures, the atomic radii are proportional to the lattice parameters and it follows that equation (5) is simply a mathematical statement of Vegard's law [14; 15]. This empirical rule states that when two materials of the same crystal structure form a continuous series of solid solutions, the plot of lattice parameter versus composition is a straight line joining the parameters of the pure materials. While Hume-Rothery and his associates [16; 17] have shown that Vegard's law is to be regarded only as an idealization (since they find many factors which influence atomic size in metallic systems), their data indicate that most metallic systems obey Vegard's law to a reasonable

*In an infinite medium ψ is zero; in a sphere of radius R with the center of pressure at the center, ψ is $[2(1-2\sigma)/1+\sigma]\cdot r/R$. For more complex geometries it becomes impractical to calculate ψ. Probably for this reason (and its small value in the vicinity of the center of pressure) ψ has often been ignored, as it was by Huang, with resulting errors in X-ray and volume effects which have been described. Eshelby's work [12] both corrects former errors of others and gives correct results in general, but also avoids the labor of computing ψ explicitly.

first approximation.* Therefore, the elasticity model makes a correct prediction of the lattice expansion.

Another prediction comes from the work of Huang [11], namely, that there should be no broadening of the diffraction lines of solid solutions as compared to pure materials in spite of the rather large local distortions around the solute atoms. This result is in keeping with experiment for a wide variety of solid solutions. Huang also predicted some intensity changes of the diffraction maxima and the production of a type of X-ray scattering analogous to thermal diffuse scattering. While these two effects have not been observed in solid solutions, they have been observed by one of us (C.W.T.) in a nonmetallic radiation damaged material.

Thus it is seen that most of the predictions of the elasticity model have been tested experimentally either in a quantitative or qualitative manner. The success of these tests forms the background for confident application of this approach to the problem of measuring interstitial content.

Interstitial Lattice Atoms and Vacancies

If the interstitial atoms are located in reasonably symmetrical positions, it appears promising to apply equation (4) to the case of interstitial lattice atoms. Owing to the rather small volume available in most interstitial positions of the common metallic crystal structures, it would not be expected that the elastic model, based as it is on Hooke's law, would apply to the region at the periphery of the interstitial atom. Study shows that the region of elastic response lies at and beyond the second or third shell of nearest neighbors of an interstitial. Therefore, the constant c of equation (4) must be evaluated from the equation

$$u = \frac{c}{r^2} \tag{6}$$

using the theoretical calculations of the displacements of those neighboring atoms which are far enough away for the elastic approximation to be applicable.

The required atomic displacement calculations for metals are not yet very numerous. Huntington and Seitz [20] and Huntington [21] have considered copper and Dienes [22] has considered copper and sodium. Since none of these authors had the present application in mind their results were not extended as far or as accurately as desired. Unfortunately, Dienes applied an assumption that the next nearest neighbors are displaced farther than the nearest neighbors, so that only rough conclusions can be based on his work. Huntington [21] considered displacements of the nearest several neighbors of an interstitial and the nearest neighbors of a vacancy. The furthermost neighbors of the interstitial which he considered in detail are displaced 5 per cent or less, and therefore are on the threshold of the elastic range. The atoms immediately beyond these were permitted some relaxation by an approximate treatment. A more accurate treatment would probably give somewhat greater displacements and consequently somewhat greater values for c, but this would increase c only by 40 per cent, at most (H. B. Huntington, private communication). Using the soft potential and configuration B (interstitial atom in the body-centered position of the face-centered cubic lattice) of reference [21] and considering only the outermost atoms regarded by Huntington as movable, one obtains for interstitials the value of 0.15 v for c. Here v is the atomic volume and the second decimal place is not significant. When substituted in equation (4), the following results are obtained:

$$e(p) = 1.1\,p \quad \text{for } \sigma = \tfrac{1}{4}, \qquad e(p) = 0.9\,p \quad \text{for } \sigma = \tfrac{1}{3}. \tag{7}$$

Values for Poisson's ratio for metals vary between about 0.28 and 0.33. Therefore, as a working equation the average of equations (7) has been taken, namely,

$$e\,(p) = 1.0\,p. \tag{8}$$

Thus the interstitial concentration in atomic per cent is equal to the linear lattice expansion expressed as a percent.

The effect of the relaxation around a vacancy on the lattice parameter must also be considered. It is apparent intuitively and it is also substantiated by existing calculations that the relaxation around a vacancy is inward and is less than the outward relaxation around an interstitial. The case of a vacancy in copper has been considered by Huntington and Seitz [20] and by Dienes [22], and both of

*Unfortunately, Eshelby (private communcation) has shown that the above elastic model cannot distinguish between the additivity of atomic radii (Vegard's law) and atomic volumes. As pointed out by Barrett [18], Mehl [19] has questioned the validity of Vegard's law suggesting that a plot of lattice parameter cubed versus concentration should be linear rather than the lattice parameter versus concentration plot (Vegard's law). For such a distinction the elasticity model would require second order elastic theory rather than the much simpler linear elasticity theory used here.

these papers predict an inward displacement of the nearest neighbors of a vacancy of about 2 per cent. This gives a value for the constant c of equation (4) for the case of a vacancy of -0.03 v. Consequently the lattice contraction due to a concentration p_v of vacancies is

$$e_v(p_v) = -0.2\,p_v \tag{9}$$

averaged for values of σ between $\frac{1}{4}$ and $\frac{1}{3}$. Comparison of equations (8) and (9) shows that the effect of vacancies upon the lattice parameter is only 1/5 that of interstitials. The effect of a vacancy is less than the present uncertainty in the knowledge of the constant c for an interstitial, and the effect of vacancies can therefore be ignored at this stage except for cases in which it is clear that the vacancy concentration greatly exceeds the interstitial concentration.

As pointed out in the introduction, it is of course possible that upon annealing the individual interstitials and vacancies agglomerate, accumulate at or near dislocations, grain boundaries, or other defects.* These effects may modify the interpretation of the X-ray method so that interstitial contents are increased by a factor of two or three. However, since it will usually be possible to start with the interstitials and vacancies dispersed, it is felt that much useful information can be obtained by the X-ray method. Further, it is only when our knowledge of the annealing reactions becomes much more precise than at present that any desirable modifications in the interpretation of the X-ray method will become clear.

It is therefore useful to relate X-ray diffraction measurements of the lattice parameter changes to the interstitials content by means of equation (8). For copper the interstitial concentration can be determined to within a factor of less than two, corresponding to the determination of the constant c of equation (4) to within the same factor. Until this constant is determined for other metals it is tempting to apply equation (8) to these other metals, since for the common metal crystal structures (face-centered cubic, hexagonal close-packed, and body-centered cubic) the constant c should not vary greatly from metal to metal. This assumes copper to be typical as far as distortions around an interstitial are concerned. Dienes' work [22] on copper and sodium shows roughly that even in the case of the soft metal sodium the constant c for interstitials is only twice as large as in the case of copper. This indicates that the value for copper should be typical for metals to within a factor of two or three. Clearly, further calculations are desirable to make the assumption of the generality of the copper result unnecessary.

The lattice expansions of irradiated metals observed in this Laboratory indicate that the effect of interstitials outweighs that of vacancies as the above analysis predicts.

Conclusions

The conventional elasticity model which describes substitutional foreign atoms, interstitial atoms, or vacancies as centers of pressure within a crystal lattice provides an adequate description of the effect of a concentration of these defect types upon the crystal lattice. In the case of solid solutions Vegard's law is predicted, which is supported as a first approximation by a large body of experimental data. Other X-ray effects predicted by the theory have been qualitatively observed. This agreement gives one considerable confidence in the correctness of equation (4) which relates defect concentration to lattice expansion.

Equation (4) is applied to the determination of interstitial and of vacancy content with the help of calculations of others which describe in detail for copper and sodium the atomic displacements near the defect. The following results are obtained:

1. Interstitial concentrations of as little as 0.01 per cent are detectable by X-rays.

2. An interstitial is five times as effective in expanding the lattice as a vacancy is in contracting the lattice.

The sensitivity is adequate so the X-rays should determine interstitial content for many conditions of irradiation of metals. X-ray lattice expansions have been observed at this Laboratory for a number of neutron-irradiated metals, and these plus additional results will be presented in a second paper.

The greater sensitivity of X-ray lattice parameter to interstitials, as compared to vacancies, means that such X-ray measurements offer a tool for observing essentially only the interstitial content of radiation-damaged metals, and of following the changes in this concentration with irradiation and with subsequent thermal treatment. Such an unambiguous knowledge of the changes in concentration of this important defect should aid signifi-

*Various possibilities have been widely considered. For example, the case of agglomeration is mentioned in reference [6], among other places, and a special type of agglomerate has been considered in some detail by A. N. Holden of this Laboratory.

cantly in deducing which of the various possible reactions among the defects are occurring.

Acknowledgements

We are indebted to Drs. L. F. Coffin and T. M. Snyder for suggesting the elasticity approach to the radiation damage problem. We are also grateful to Dr. J. D. Eshelby for several helpful discussions of certain aspects of the elasticity model and for sending us a copy of a technical report on his work. It is also a pleasure to acknowledge the stimulating interest of Professor H. B. Huntington in this work.

Note Added in Proof

In a letter submitted to this Journal, H. B. Huntington reports further calculations concerning the elastic strains around an interstitial atom in copper. His conclusion, resulting from two separate approaches, is that the elastic displacement is described by

$$u = \frac{0.04d^3}{r^2}$$

where d is the lattice constant, and the coefficient is estimated to be accurate to within 20 per cent. Since $d^3 = 4v$, this is identical with

$$u = \frac{0.16v}{r^2}$$

which result agrees well with the value $\frac{0.15v}{r^2}$ used in this paper.

References

1. Dienes, G. J. Radiation Effects in Solids. Vol. 2, Annual Review of Nuclear Science, p. 187.
2. Dexter, D. L. Phys. Rev. **87** (1952) 768.
3. Overhauser, A. L. Phys. Rev. **90** (1953) 393.
4. Redman, J. K., Coltman, R. R., and Blewitt, T. H. Phys. Rev. **91** (1953) 448.
5. Jette, E. R., and Foote, F. J. Chem. Phys. **3** (1935) 605.
6. Marx, J. W., Cooper, H. G., and Henderson, J. W. Phys. Rev. **88** (1952) 106.
7. Love, A. E. H. Mathematical Theory of Elasticity (Cambridge, University Press, 1927) p. 142. See also p. 176, example (iv), for an important result concerning volume changes.
8. Mott, N. F. and Nabarro, F. R. N. Proc. Phys. Soc. (London) **52** (1940) 86.
9. Seitz, F. Rev. Mod. Phys. **18** (1946) 384.
10. Seitz, F. and Read, T. A. J. Appl. Phys. **12** (1941) 182.
11. Huang, K. Proc. Roy. Soc. (London) **A190** (1947) 102.
12. Eshelby, J. D. The Distortion of a Crystal by Point Imperfections. Technical Report No. 9, Contract Nonr 177-(00) NR 017-417, Office of Naval Research, Washington, D.C.
13. Coffin, L. F. and Snyder, T. M. Knolls Atomic Power Laboratory Memorandum LFC-5 and work to be published.
14. Vegard, L. ZS. f. Phys. **5** (1921) 17.
15. Vegard, L. and Dale, H. ZS. f. Krist. **67** (1928) 148.
16. Hume-Rothery, W. The Structure of Metals and Alloys (London, Institute of Metals, 1936).
17. Axon, H. J. and Hume-Rothery, W. Proc. Roy. Soc. (London) **A193** (1948) 1.
18. Barrett, C. S. Structure of Metals (2nd ed., New York, McGraw-Hill, 1952) p. 221.
19. Mehl, R. F. Trans. A.I.M.E. **111** (1934) 90.
20. Huntington, H. B. and Seitz, F. Phys. Rev. **61** (1942) 315.
21. Huntington, H. B. Phys. Rev. **91** (1953) 1092.
22. Dienes, G. J. Phys. Rev. **86** (1952) 228.

ACTIVITY OF SILICON IN LIQUID Fe-Si AND Fe-C-Si ALLOYS*

J. CHIPMAN†, J. C. FULTON‡, N. GOKCEN¶ and G. R. CASKEY, Jr.§

Experimental data are presented which establish the solubility of graphite at temperatures of 1290–1690°C in Fe-Si-C solutions up to 20–24 weight per cent Si. The occurrence of βSiC as a stable equilibrium phase is established and its solubility in graphite-saturated iron is determined at temperatures of 1200–1690°C.

The distribution of silicon between the immiscible liquids iron and silver has been studied in the composition range $N_{Si}^{(Fe)} = 0.15$–0.55 and in similar solutions containing substantial additions of carbon.

The experimental data, together with a large amount of collateral information in the literature, are used to establish the following thermodynamic properties of the solution: the heat of mixing and partial molal enthalpies of the components in Fe-Si solutions; the activities of Si and Fe in the binary solutions at temperatures of 1420–1700°C; the molal heat, free energy and entropy of mixing at 1420°; the activities of Si and Fe in graphite-saturated solutions at silicon concentrations from zero to SiC saturation at temperatures of 1420–1700°C.

The results are cross-checked by calculations based on free-energy and equilibrium data for SiC and SiO_2 and are compared wherever possible with published information. Close agreement in these cases and with related data on Fe-C solutions promotes confidence in the tabulated results.

L'ACTIVITÉ DU SILICIUM DANS LES ALLIAGES Fe-Si ET Fe-C-Si LIQUIDES

On présente des résultats expérimentaux montrant que le graphite est soluble, aux températures allant de 1290 à 1690°C, dans des solutions de Fe-Si-C contenant jusqu'à 20 à 24 pour cent de Si en poids. L'apparition de SiC β comme phase d'équilibre stable est démontrée; la solubilité de cette dernière dans du fer saturé en graphite est établie aux températures allant de 1200 à 1690°C. Le partage du silicium entre les liquides non-solubles de fer et d'argent fut étudié dans le domaine de composition $N_{Si}^{(Fe)} = 0{,}15$ à $0{,}55$, ainsi que dans des solutions similaires, contenant des additions appréciables de carbone. Ces données expérimentales, et d'autres informations dans la littérature se rapportant au sujet en question, sont utilisées pour établir les propriétés thermodynamiques de la solution, qui suivent: la chaleur de dissolution et les enthalpies molaires, partielles, des composants dans les solutions Fe-Si; les activités de Si et Fe dans les solutions binaires, aux températures de 1420 à 1700°C; la chaleur, l'énergie libre et l'entropie molaires de dissolution à 1420°C; les activités de Si et Fe dans des solutions saturées en graphite, pour des concentrations en silicium allant de zéro jusqu'à la saturation en SiC, aux températures de 1420 à 1700°C. Ces résultats sont vérifiés par des calculs basés sur les données concernant les énergies libres et les équilibres de SiC et SiO_2, et ensuite, quand c'est possible, comparés aux informations publiées antérieurement. Le bon accord constaté dans ces cas, ainsi que dans le cas de données sur des solutions de Fe-C, inspire confiance dans les résultats rapportés.

DIE AKTIVITÄT DES SILIZIUMS IN FLÜSSIGEN Fe-Si UND Fe-C-Si LEGIERUNGEN

Es wurden experimentelle Resultate berichtet, welche die Löslichkeit von Graphit in Fe-Si-C Lösungen mit einem Si-Gehalt von bis zu 20–24 Gew.%Si in einem Temperaturbereich zwischen 1290–1690°C beweisen. Es wird das Auftreten von β SiC als stabile Geichgewichtsphase sichergestellt, und seine Löslichkeit in graphitgesättigtem Eisen wurde zwischen 1200°C und 1690°C bestimmt.

Die Verteilung von Silizium zwischen flüssigem Eisen und flüssigem Silber (die nicht mischbar sind) wurde im Gebiet der folgenden Zusammensetzungen untersucht: $N_{Si}^{(Fe)} = 0{,}15$–$0{,}55$ und an entsprechenden Lösungen, die beträchtliche Kohlenstoffzusätze enthielten.

Die folgenden thermodynamischen Eigenschaften der Lösung wurden auf Grund der vorliegenden experimentellen Resultate und der reichen vorliegenden Literaturangaben sichergestellt: Die Mischungswärme und die partialen molaren Enthalpien der Komponenten der Fe-Si Lösungen; Die Aktivitäten von Si und Fe in binären Lösungen zwischen 1420°C und 1700°C; die Molwärme, die freie Energie und die Mischungsentropie bei 1420°C; die Aktivitäten von Si und Fe in graphitgesättigten Lösungen mit Siliziumgehalten zwischen Null und SiC Sättigung, zwischen 1420°C und 1700°C.

Die Resultate wurden weiterhin mit rechnerisch auf Grund der freien Energie- und der Gleichgewichtsdaten von SiC und SiO_2 ermittelten Werten und wo immer möglich mit Angaben aus der Literatur verglichen. Die gute Übereinstimmung dieser Daten untereinander und mit den entsprechenden Werten der Fe-C Lösungen lassen die hier zusammengestellten Resultate zuverlässig erscheinen.

The system iron-carbon-silicon is one of the more important ternary systems of ferrous metallurgy and as such it has attracted a substantial amount of experimental attention, particularly with respect to its solid phases. Thermodynamic properties of the liquid solution are known only in rough approximation [1]. The binary solutions Fe–C and Fe–Si exhibit strong negative deviations from ideality, indicating strong attractive forces between unlike atoms. In the ternary solution, because of electrostatic effects or of competition for favored positions

*Received December 22, 1953; in revised form February 4, 1954.

†Department of Metallurgy, Massachusetts Institute of Technology.

‡Allegheny-Ludlum Steel Co.; formerly, Department of Metallurgy, Massachusetts Institute of Technology.

¶Department of Metallurgical Engineering, Michigan College of Mining and Technology.

§E. I. du Pont de Nemours & Co., Inc.; formerly, Department of Metallurgy, Massachusetts Institute of Technology.

as nearest neighbors of Fe atoms [2], the activity of each solute is increased by the presence of the other.

It is the purpose of this paper to present the results of recent studies of the solubility of graphite and silicon carbide in the ternary solutions and of the distribution of silicon between these solutions and molten silver. By means of these two sets of data, and of a variety of subsidiary data already in the literature, the activity of silicon in binary and ternary solutions is determined at temperatures of 1420° to 1700°C.

Solubility of Graphite and of Silicon Carbide

The solubility of graphite in molten iron and in Fe–C–Si alloys containing up to about 23 per cent silicon has been reported [3]. In the binary system the results in the temperature range 1153° (eutectic) to about 1950° are adequately represented by the very simple expression:

$$\% \text{ C} = 1.34 + 2.54 \times 10^{-3} t \text{ (°C)}.$$

In the ternary solutions the graphite solubility could not be determined above 23 per cent silicon because of the precipitation of a second solid phase. This phase has subsequently been isolated and identified by its diffraction pattern as βSiC. This is the cubic form which is stable below 2200°. It differs in structure from the familiar α forms but the thermodynamic properties of the two forms are essentially the same.

New data on ternary solutions in equilibrium with graphite and with graphite and silicon carbide simultaneously are shown in Table I. The melts were held for long periods in graphite crucibles in an atmosphere of argon. Temperatures were determined in submerged graphite tubes both by optical pyrometer and by thermocouple. The presence of silicon carbide in certain heats was assured by charging more than 23 per cent silicon and permitting the precipitate to float out of the bath. Attempts to bring "globar" rods into equilibrium with the bath were less successful. This material dissolves rather slowly, possibly because of an oxide film. The melt was sampled for analysis by sucking a few grams into a thin Vycor tube using an aspirator bulb.

The solubility of graphite at several temperatures is shown in Figure 1. Both old and new data are included. The lines terminate at points representing three-phase equilibrium which were obtained from Figure 2. This includes all data on melts in which both solid phases were present. Unexpected difficulties were encountered in analysis in that the reproducibility was not all that could have been

TABLE I

ADDITIONAL DATA ON SOLUBILITY OF GRAPHITE IN MOLTEN Fe-C-Si ALLOYS

No.	Temp. °C	Silicon Per cent	Carbon Per cent	Note
14–4	1600	22.94	0.33	*
14–5	1600	23.03	0.42	*
15–5	1600	23.39	0.48	*
18–1	1490	21.92	0.34	*
18–2	1690	23.64	0.47	*
18–3	1290	20.53	0.27	*
20–1	1490	19.37	0.64	
20–2	1290	19.56	0.31	
20–3	1690	20.42	0.69	
21–1	1600	22.59	0.36	
22–1	1650	22.59	0.46	
29–2	1490	21.60	0.18	
29–4	1400	21.60	0.19	*
30–1	1290	22.18	0.15	*
30–2	1290	21.52	0.12	*
30–3	1690	23.78	0.41	*
30–4	1690	23.34	0.48	*
48–6	1600	23.23	0.41	*
94–1	1490	16.59	0.85	
94–2	1690	16.71	1.16	
94–3	1290	16.67	0.56	
105–1	1250	20.60	0.19	*
105–2	1200	20.34	0.14	*
235–1	1420	19.64	0.53	**
235–2	1420	19.79	0.44	**
235–3	1420	19.78	0.41	**
235–4	1200	19.98	0.24	**
235–5	1200	19.71	0.24	**
235–6	1600	21.54	0.46	**
235–7	1600	22.06	0.49	**

*Saturated with both graphite and SiC.
**In contact with globar but apparently not saturated with SiC.

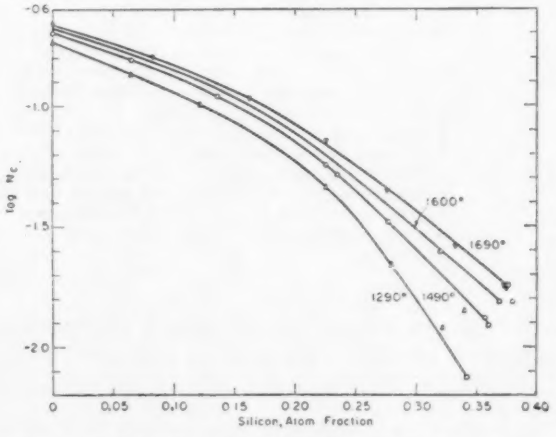

FIGURE 1. Solubility of graphite in Fe-Si-C alloys. Squares indicate two-fold saturation with graphite and β-SiC.

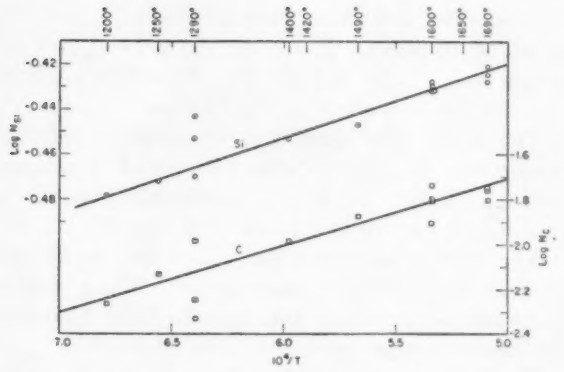

FIGURE 2. Solubility of SiC in graphite-saturated solution.

desired. Errors in sampling and analysis probably exceed those of equilibration and the average results shown by straight lines in Figure 2 are not considered better than ±0.25 per cent Si or ±0.05 per cent C, respectively. Table II shows compositions in equilibrium with graphite and βSiC at several temperatures.

TABLE II

COMPOSITIONS IN EQUILIBRIUM WITH GRAPHITE AND βSiC

Temp. °C	Mol Fraction C	Mol Fraction Si	Weight Per cent C	Weight Per cent Si
1690	0.0184	0.377	0.49	23.7
1600	0.0155	0.370	0.41	23.1
1490	0.0123	0.361	0.33	22.4
1420	0.0105	0.355	0.28	21.9
1290	0.0075	0.342	0.20	20.9
1200	0.0058	0.332	0.15	20.2

A cooling curve was obtained on heat 105 after it had been held for two hours at 1250° and another two hours at 1200° in argon. A prolonged arrest was observed at 1187°. A sample was dipped from the "mushy" mass at this temperature and at 1183° the mass was entirely solid. On reheating, the 1187° arrest was again observed but the metal remained mushy up to about 1200°. A second cooling curve reproduced the 1187° point.

The sample obtained from the "mushy" mass at 1187° was examined microscopically and found to contain graphite, βSiC, αFe and the ε-phase of the binary Fe–Si system. It appears, therefore, that 1187 degrees is a ternary eutectic at which the liquid is in equilibrium with αFe (containing 10–11 per cent Si), εFeSi and either graphite or βSiC. This interpretation requires the existence of a peritectic at some slightly higher temperature at which the liquid is in equilibrium with graphite, βSiC and either αFe or εFeSi. This portion of the ternary system requires a much more detailed study before the phase relations can be established with certainty.

Heat of Solution of Silicon in Iron

In determining the heat of mixing of the liquid elements, Körber and Oelsen [4] carried out two series of measurements. In the first series one of the metals was added as a liquid at 1600° to the crucible of a calorimeter containing the other metal as a solid at 20 degrees. The heat effect, corrected for the heat content of the molten addition, fixed the heat of formation of the alloy at room temperature. In the second series the heat contents of the entire series of alloys and the two elements were determined at 1600 degrees relative to the calorimeter temperature. Combination of the two sets of data yields the heat of mixing at 1600 degrees. The points shown in Figure 3 represent individual

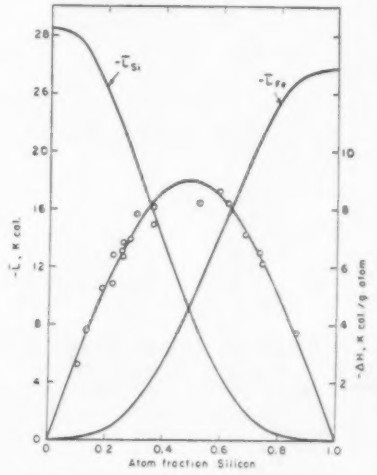

FIGURE 3. Heat of mixing of iron and silicon at 1600°C. Data of Körber and Oelsen.

experiments of the first series adjusted to 1600 degrees by the smoothed curve of the second series.

The data are well represented by the following equation which is of a form suggested by Wagner [5]:

$$\Delta H = N_{Fe} \cdot N_{Si} [-36.0 - 2.5 (N_{Fe} - N_{Si}) + 10.0 (N_{Fe} - N_{Si})^2].$$

Here ΔH is the heat absorbed in kilocalories in forming one gram atom of molten alloy from its molten elements and the N's are atom fractions. The relative partial molal enthalpies of the components, each referred to its pure liquid state and

defined as $\bar{L}_{Fe} = \bar{H}_{Fe} - H^{\circ}_{Fe}$ and $\bar{L}_{Si} = \bar{H}_{Si} - H^{\circ}_{Si}$ are shown graphically. At low concentrations $\bar{L}_{Si} = -28.5$ kcal, in agreement with Körber and Oelsen's computation. This is in good agreement with the value of -29.0 kcal obtained by Chipman and Grant [6] using an entirely different method.

Distribution of Silicon between Liquid Iron and Silver

As a means of studying the activity of silicon in liquid Fe-Si solutions, Chou [7] determined the distribution coefficient of silicon between iron and silver at 1550 and 1650 degrees. The following is an account of a repetition of this work, its extension to a wider range of compositions and its application to Fe-Si-C solutions.

Experiments were carried out in the simple high-frequency induction furnace illustrated in Figure 4.

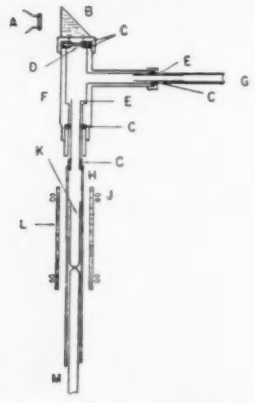

FIGURE 4. Diagram of furnace. *A*, Optical pyrometer. *B*, Prism. *C*, Rubber gasket. *D*, Sight glass. *E*, Glass tube. *F*, Brass furnace head. *G*, Gas inlet. *H*, Furnace tube-vycor. *J*, Induction coil. *K*, Crucible-silica. *L*, Silica sleeve. *M*, Crucible support-vycor.

The charge, consisting of 10 to 11 grams of silver and 9 to 10 grams of alloy prepared from electrolytic iron and refined silicon, was placed in the silica crucible K, approximately 10 mm inside diameter. Argon flowed downward over the crucible and charge. Temperatures were read with an optical pyrometer which had been calibrated previously against a platinum-platinrhodium thermocouple immersed in molten iron-silicon alloys. The correction of the optical reading was essentially the same in 17 per cent and in 43 per cent silicon and the same correction was applied to all melts.

Melts were held at 1420° ± 5° for 40 minutes. Temperature was controlled by frequent observations and hand adjustment of power input. The time allowed was more than adequate for attainment of equilibrium, due to the stirring which accompanies induction heating. This was verified by a few heats made at shorter times.

The heats were quenched by shutting off the power and passing a large volume of hydrogen through the furnace. In general the iron phase was frozen in 5 seconds and black in about 15.

The two phases were separated and each was ground to produce a clean surface. When visible inclusions of one phase were found within the other the heat was rejected.

The results of chemical analysis, reported as mol fraction of silicon in each phase, are shown in Table III and in Figure 5. In general the iron content of the silver phase was less than 0.2 weight per cent. In the iron phase the silver content varied irregularly from about 0.2 per cent in low-silicon iron to 3.5 per cent in iron containing 38 per cent silicon. This was the principal reason for not carrying the experiments to higher silicon concentrations.

TABLE III

DISTRIBUTION OF SILICON BETWEEN IRON AND SILVER AT 1420 DEGREES

No.	Silicon, mol fraction in Fe	Silicon, mol fraction in Ag	$-\log \frac{N_{Si}^{(Ag)}}{N_{Si}^{(Fe)}}$
Series A			
1	0.478	0.102	0.67
2	0.410	0.0399	1.01
3	0.320	0.0076	1.62
5	0.310	0.0069	1.65
6	0.430	0.0595	0.86
13	0.245	0.00138	2.25
14	0.558	0.182	0.49
15	0.499	0.118	0.63
16	0.525	0.165	0.50
Series B			
35	0.169	0.00050	2.53
36	0.146	0.00031	2.68
37	0.144	0.00023	2.80
38	0.248	0.00194	2.11
39	0.346	0.0137	1.40
54	0.312	0.00642	1.69
55	0.194	0.00088	2.34
60	0.182	0.00057	2.50

A similar series of experiments was made with iron-silicon-carbon alloys. The results are shown in Table IV. Since carbon is insoluble in silver, the differences between the two series are due to the effect of carbon on the activity of silicon in the iron phase.

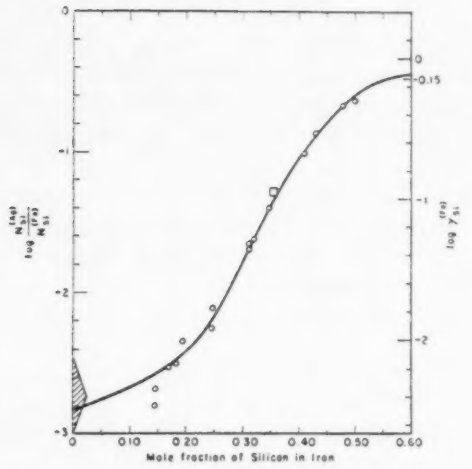

FIGURE 5. Distribution of silicon between molten iron and silver at 1420°C.

TABLE IV

DISTRIBUTION OF SILICON BETWEEN IRON-CARBON ALLOYS AND SILVER AT 1420 DEGREES

No.	Carbon, mol fr. in Fe	Silicon, mol fraction		$-\log \frac{N_{Si}^{(Ag)}}{N_{Si}^{(Fe)}}$
		in Fe	in Ag	
7	0.025	0.210	0.00127	2.22
8	0.046	0.206	0.00169	2.09
9	0.069	0.171	0.00109	2.19
14	0.003	0.349	0.0138	1.40
16	0.087	0.163	0.00100	2.21
23	0.072	0.166	0.00134	2.09
24	0.019	0.251	0.00170	2.17
25	0.008	0.344	0.0152	1.35
26	0.038	0.250	0.00265	1.97
30	0.041	0.248	0.00341	1.86
33	0.007	0.373	0.0189	1.29
41	0.008	0.175	0.00058	2.48
42	0.020	0.174	0.00064	2.44
43	0.032	0.172	0.00067	2.41
44	0.050	0.168	0.00090	2.27
45	0.061	0.168	0.00106	2.20
48	0.012	0.264	0.00364	1.86
49	0.027	0.261	0.00332	1.90
50	0.045	0.247	0.00387	1.81
51	0.076	0.172	0.00125	2.14
52	0.006	0.380	0.0236	1.21
53	0.010	0.350	0.0176	1.30
61	0.004	0.254	0.00228	2.05

Activity of Silicon in Fe-Si Alloys

The distribution experiments are not sufficient to establish the activity of silicon in iron relative to that of the pure liquid element. To accomplish this end there are two avenues of approach, involving, respectively, the phase diagrams of the systems Fe-Si and Ag-Si, both of which have been fairly well established [8].

The Fe-Si Phase Diagram

The melting point of silicon is 1414 degrees and its heat of fusion [4] is 11,100 cal/g atom. A liquid solution of mol fraction 0.73 is in equilibrium with essentially pure solid silicon at 1207 degrees. These data lead to an activity coefficient, $\gamma_{Si} = 0.84$, in the liquid alloy at 1207 degrees. The effect of temperature at constant composition is given by by the formula:

$$\partial \ln \gamma_2/\partial T = -\bar{L}_2/RT^2.$$

From Figure 3, $\bar{L}_{Si}$ in this solution is -1.2 kcal. This leads to a slight increase in γ_{Si} with rising temperature which results in $\gamma_{Si} = 0.89$ at 1420 degrees and $\gamma_{Si} = 0.91$ at 1600 degrees.

For the interval between this composition and highest concentration of the distribution study an extrapolation may be made on the simple assumption that $\log \gamma_{Si}/(1 - N_{Si})^2$ is constant. At $N_{Si} = 0.55$ this gives $\log \gamma_{Si} = -0.15$.

Activity of Silicon in Silver

Liquid Ag-Si solutions are in equilibrium with essentially pure solid silicon over a wide range of compositions. No compounds occur. The diagram permits calculation of γ_{Si} in the liquid phase in the range $N_{Si} = 1.00$ to $N_{Si} = 0.20$. Darken and Gurry [9] have shown that the function $\log \gamma_{Si}/(1 - N_{Si})^2$ varies linearly with concentration within this range. Extrapolation to very dilute solutions gives, approximately, $\log \gamma_{Si} = 0.3$ or $\gamma_{Si} = 2.0$. The uncertainty amounts to at least ± 0.1 in $\log \gamma_{Si}$.

In a system which is so nearly ideal there is little uncertainty in assuming that Henry's law is valid at concentrations such as those used in the distribution experiments. This is supported by experiments [10] which indicate that Henry's law is followed in the dilute solutions. It follows that in our experiments the activity coefficient of silicon in the silver layer, $\gamma_{Si}^{(Ag)}$ is constant and that $\log \gamma^{\circ}_{Si}{}^{(Ag)} = 0.3 \pm 0.1$.

Since the activity of silicon is the same in the iron and silver layers, it follows that:

$$\log \frac{N_{Si}^{(Ag)}}{N_{Si}^{(Fe)}} = \log \frac{\gamma_{Si}^{(Fe)}}{\gamma_{Si}^{(Ag)}} = \log \gamma_{Si}^{(Fe)} - 0.3 \pm 0.1.$$

For the composition $N_{Si} = 0.55$, interpolation on Figure 5 gives

$$\log \gamma_{Si}^{(Fe)} = -0.48 + 0.3 \pm 0.1 = -0.18 \pm 0.1$$

This seems less dependable than the value −0.15 derived from the Fe-Si phase diagram.

Activity Coefficient of Silicon at 1420 Degrees

The entire curve for log γ_{Si} at 1420 can now be obtained simply by adding the scale along the right-hand margin of Figure 5 on the basis that log $\gamma_{Si}^{(Fe)} = -0.15$ at $N_{Si}^{(Fe)} = 0.55$. The extension of the line below the limits of the distribution data will be discussed later.

Effect of Carbon on Activity of Silicon

Let γ_{Si} represent the activity coefficient of silicon in any (ternary) solution and γ'_{Si} that in a binary Fe-Si solution of the same silicon concentration. The effect of a given concentration of carbon may now be expressed in the coefficient $\gamma_{Si}^{(C)}$ defined by the equation:

$$\gamma_{Si}/\gamma'_{Si} = \gamma_{Si}^{(C)}.$$

In principle, it is possible to determine values of $\gamma_{Si}^{(C)}$ at various concentrations of carbon and silicon from the data of Table IV and Figure 5. For this purpose, values of the quantity,

$$\log \gamma_{Si}^{(C)} = \log \frac{N_{Si}^{(Ag)}}{N_{Si}^{(Fe)}} \text{ (Fe-C-Si)} - \log \frac{N_{Si}^{(Ag)}}{N_{Si}^{(Fe)}} \text{ (C Free)}$$

are plotted in Figure 6. The second term on the right is taken from Table IV while the first is read for the same mol fraction of silicon from Figure 5. It is evident that the data are not sufficiently

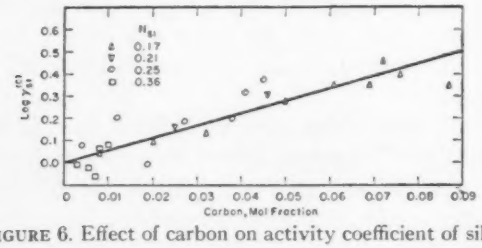

FIGURE 6. Effect of carbon on activity coefficient of silicon.

extensive to show variations in log $\gamma_{Si}^{(C)}$ with changes in silicon concentration. In the range $N_{Si} = 0.17$ to 0.36 the results are represented, within their limits of accuracy, by the equation:

$$\log \gamma_{Si}^{(C)} = 5.5\, N_C.$$

To avoid confusion with other "coefficients" the quantity represented by 5.5 will be termed an "interaction parameter."

The only experimental data which may be compared directly with the foregoing are those of Körber [11] on the equilibrium:

$$Si + 2MnO \text{ (in slag)} = 2Mn + SiO_2 \text{ (solid)}.$$

In these experiments liquid iron containing silicon and manganese was brought into equilibrium with a saturated manganous silicate slag of approximately fixed composition. The effects of carbon and other elements on the equilibrium constant were determined. From the data it has been shown [1] that, assuming no effect of carbon on the activity of manganese, its effect on silicon can be represented by a line whose equation is

$$\log \gamma_{Si}^{(C)} = 0.16\ [\%\ C].$$

At the average composition of Körber's solutions, $N_C = 0.040$ [% C]; therefore, if the concentration of carbon be expressed as mol fraction the above expression corresponds to an interaction parameter of 4.0.

The discrepancy between 4.0 and our figure, 5.5, is due in part to neglect of the effect of carbon on the activity coefficient of manganese. It is known that the solubility of graphite in liquid iron is increased by additions of manganese. The data [3] indicate that γ_C is decreased about 0.5 per cent for each 0.01 increment in N_{Mn}. It follows as a good approximation that γ_{Mn} is decreased a like amount for each 0.01 increment in N_C. Then at 2.5 per cent carbon ($N_C = 0.10$) corresponding to an average of Körber's experiments, $\gamma_{Mn}^{(C)} = 0.95$ or, approximately, $\log \gamma_{Mn}^{(C)} = -0.2N_C$. Since the reaction involves two atoms of manganese for each atom of silicon, the application of this parameter would increase log $\gamma_{Si}^{(C)}$ by 0.4 N_C. In other words, the interaction parameter calculated in this way becomes 4.4 as against the experimental value 5.5. The remaining discrepancy may be ascribed to differences in experimental temperature, since Körber's work was done at 1600–1650 degrees and the parameter would be expected to decrease with increasing temperature.

Activity from Equilibrium Data

Published data [12] on the concentrations of silicon and oxygen in liquid iron in equilibrium with SiO_2 and our data on solubility of SiC furnish important checks on the activity of silicon. Fortunately the thermodynamic data on these two compounds are complete and apparently of high accuracy.

Free Energy of SiO_2 and SiC

The heat of formation of cristobalite, the form of SiO_2 which is stable at high temperatures, has been redetermined recently by Humphrey and King [13].

They report $\Delta H_{298} = -209{,}330 \pm 250$ cal/mol. Entropies and heat contents are contained in Kelley's tables [14] while the heat of fusion of silicon is taken from Körber and Oelsen [4]. The data lead to the following equation which seems unlikely to be in error by as much as 1000 cal in the range 1683–2000°K:

$$\text{Si (l)} + \text{O}_2\ (g) = \text{SiO}_2 \text{ (crist.)}$$
$$\Delta F^\circ = -217{,}700 + 47.0T \text{ cal.}$$

The heat of formation of β-silicon carbide (cubic) from crystalline silicon and graphite was reported by Humphrey, Todd, Coughlin and King [15] to be $-13{,}400 \pm 920$ cal/mol. They also determined its heat capacity at high temperatures and from these and other published data [14] they obtained the free energy of formation. In the range 1683–2000°K the following equation represents their data. The uncertainty is greater than in the corresponding equation for silica.*

$$\text{Si (l)} + \text{C (graphite)} = \text{SiC } (\beta)$$
$$\Delta F^\circ = -24{,}400 + 8.3T \text{ cal.}$$

Activity of Silicon from SiC Data

At 1420 degrees, silicon carbide and graphite coexist in equilibrium with a liquid in which $N_C = 0.0105$ and $N_{Si} = 0.355$. In this liquid the activity of silicon, relative to pure liquid silicon is obtained from the free energy change in the above equation which is $RT \ln a = \Delta F^\circ = -10{,}350$ cal. From this $a_{Si} = 0.046$. In the saturated solution, therefore, $\gamma_{Si} = 0.130$. This is corrected to the carbon-free state on the basis that $\log \gamma_{Si}^{(C)} = 5.5\, N_C$. The resultant is $\gamma_{Si} = 0.113$ in a carbon-free solution in which $N_{Si} = 0.355$. This point is shown in Figure 5. The agreement with the curve is astonishingly good. In fact, the divergence from the curve corresponds to only 500 cal in the heat of formation of SiC, which is less than the estimated error in its determination.

Activity from SiO_2 Equilibria

The concentrations of silicon and oxygen in liquid iron in equilibrium with SiO_2 have been determined by Gokcen and Chipman [16] in the range 1545–1650°C. Their results are expressed in terms of weight per cent thus:

$$K = [\%\ \text{Si}]\ [\%\ \text{O}]^2 \cdot \log K = -29{,}150/T + 11.01.$$

In the range of silicon concentrations from 0.02 to 1.6 per cent at 1600 degrees the standard deviation in 14 experiments was 0.064 in the value of $\log K$ which corresponds to 550 cal in the free energy.

For comparison with other data it is convenient to express the concentration of silicon as mol fraction but to retain units of weight per cent for oxygen. At the low concentrations of these experiments $N_{Si} = 0.0199$ [% Si]. Hence the desired equilibrium constant is obtained by adding $\log 0.0199 = -1.70$ which gives

$$K = [N_{Si}]\ [\%\ \text{O}]^2;\ \log K = -29{,}150/T + 9.31.$$

Expressed in terms of standard free energy, the reference states being the infinitely dilute solutions, this is written:

$$\text{SiO}_2 \text{ (crist.)} = \text{Si (in Fe)} + 2\,\text{O (in Fe, 1\%)}$$
$$\Delta F^\circ = +133{,}300 - 42.60T \text{ cal.}$$

There are two independent series of data from which the standard free energy of oxygen in liquid iron may be obtained. Dastur and Chipman [17] determined the equilibrium in the reaction of oxygen in iron with hydrogen to form water vapor. From the known free energy of formation of the latter [18] they obtained the equation

$$\text{O}_2\ (g) = 2\,\text{O (in Fe, 1\%)}$$
$$\Delta F^\circ = -55{,}860 - 1.14T \text{ cal.}$$

Darken and Gurry [19] determined the ratio CO_2/CO in equilibrium with liquid iron and its oxide at temperatures of 1524–1600°C. Since the solubility of the oxide in the metal is also known [20], the equilibrium constant and standard free energy of the following reaction are also established with the following result:

$$\text{CO}\ (g) + \text{O (in Fe, \%)} = \text{CO}_2\ (g)$$
$$\Delta F^\circ = -38{,}630 + 20.72T.$$

From this and the known free energy change in the oxidation of carbon monoxide [18] we find

$$\text{O}_2\ (g) = 2\,\text{O (in Fe, 1\%)}$$
$$\Delta F^\circ = -57{,}020 - 1.14T \text{ cal.}$$

We shall employ as an average:

$$\Delta F^\circ = -56{,}440 - 1.14T \pm 580 \text{ cal.}$$

We are now in position to calculate the activity coefficient of silicon in dilute solutions. The above equation is combined with that for formation of cristobalite given in the foregoing section and with that for its equilibrium with liquid iron. The result is:

$$\text{Si (l)} = \text{Si (in Fe)}$$
$$\Delta F^\circ = -28{,}000 + 5.54T.$$

*See footnote, p. 449.

This is equivalent, in the infinitely dilute solution, to

$$\log \gamma^{\circ}_{Si} = -6{,}100/T + 1.21.$$

Hence at 1420°C, $\log \gamma^{\circ}_{Si} = -2.40$.

The estimated uncertainties in free energy total about 2100 cal which are equivalent to 0.27 in the value of $\log \gamma^{\circ}_{Si}$. A shaded area corresponding to $\log \gamma_{Si} = -2.40 \pm 0.27$ in the range of the experiments is shown in Figure 5. Direct extrapolation of the distribution data would lead to a lower value of $\log \gamma^{\circ}_{Si}$. The line adopted represents a compromise in which $\log \gamma^{\circ}_{Si} = -2.50$.

Activity Coefficient in Dilute Solution

If there were a sound theoretical basis for determining the value of $d \log \gamma_{Si}/d N_{Si}$ at infinite dilution the task of adjusting the extremity of the curve in Figure 5 would be greatly simplified. A number of related systems have been studied which invite comparison with the slope of 1.6 in the final curve. Richardson and Dennis [21] determined equilibrium constants in the reaction CO_2 (*g*) + *C* (in Fe) = 2CO (*g*). A plot of their data indicates a slope of $d \log \gamma_C/d N_C = 4.7$ at 1560 degrees and 4.2 at 1760 degrees. At 1420 degrees the extrapolated value is 5.1. For the same system the potentiometric data of Sanbongi and Ohtani [22] yield a slope of about 1.9 at 1550 degrees. The formula employed by Smith and Darken [23] for austenite calls for a slope of 2.8.

Temkin and Shvartsman [24] have proposed for carbon in austenite: $\gamma_C = 1/(1 - 5 N_C)$. Samarin and Shvartsman [2] have applied this formula to certain three-component solutions in liquid steel using the sum of the mol fractions in place of N_C. They have shown, for example, that approximate agreement is obtained for C in Fe-Si-C and for S in Fe-C-S. If a similar equation is applied to the problem in hand, it may be rewritten, for very dilute solutions of silicon in iron, $\ln \gamma_{Si} = 5 N_{Si}$. This would make the terminal slope of the line in Figure 5 equal to 2.17.

These considerations point to the possibility that the slope at low concentrations in Figure 5 is a little too small.

In a ternary solution, Wagner [5] defines the following parameters for the limiting case of zero concentration of components 2 and 3:

$$\epsilon_2^{(2)} = \partial \ln \gamma_2/\partial N_2$$
$$\epsilon_2^{(3)} = \partial \ln \gamma_2/\partial N_3, \text{ etc.}$$

He has shown that:

$$\epsilon_2^{(3)} = \epsilon_3^{(2)}.$$

Experimental studies of a number of metallic binary and ternary systems [25] have shown remarkably constant values of ϵ at finite concentrations with deviations occurring only in rather concentrated solutions. On experimental grounds we must expect constancy of $\epsilon_{Si}^{(Si)}$ up to several atom per cent silicon.

Wagner [26] has shown further that the activity of solute metal 2 will be increased by a third component if metals 2 and 3 change the electron/atom ratio in the same direction. Assuming that the interaction energy between similarly charged metal ions is small compared with the interaction energy of metal ions and electrons, he finds the approximate relation:

$$\epsilon_3^{(2)} = \epsilon_2^{(3)} = \pm[\epsilon_2^{(2)} \epsilon_3^{(3)}]^{\frac{1}{2}}$$

The equation provides a rough check on the slopes of the carbon and silicon curves through their relation to the data of Figure 6. Using only the experimental slopes mentioned above,

$$\partial \log \gamma_{Si}/\partial N_C = \epsilon_{Si}^{(C)}/2.3 = [1.6 \times 5.1]^{\frac{1}{2}} = 2.9.$$

This is substantially smaller than the observed slope of Figure 6 which was 5.5. The difference is in the expected direction. The curves of Figure 1 pertain to solutions of constant carbon activity, under which conditions $\partial \ln \gamma_C = -\partial \ln N_C$. The slopes therefore represent experimental values of $\partial \log \gamma_C/\partial N_{Si}$. The curve for 1490 degrees has a slope of 5.0 at high silicon, in agreement with 5.5 for the reciprocal case. At low silicon and high carbon the slope is 1.7. Close agreement with the calculated parameter 2.9 is not expected since the latter applies to dilute solutions. But the figures which have been cited for comparison are sufficient to indicate that the slope of 1.6 in Figure 5 at low concentrations is not inconsistent with the other data.

Activity of Silicon at Higher Temperatures

Since the partial molal enthalpy of silicon is known from the work of Körber and Oelsen (Figure 3), the effect of temperature is readily obtained through the relation $\partial \ln \gamma_{Si}/\partial(1/T) = \bar{L}_{Si}/R$. Since the temperature dependence of the heat of mixing is unknown, $\bar{L}_{Si}$ is treated as a function of composition only. In Table V are shown values of $\bar{L}_{Si}$ and $\log \gamma_{Si}$ at 1420 degrees and the computed values of $\log \gamma_{Si}$ at three higher temperatures.

TABLE V

ENTHALPY AND ACTIVITY COEFFICIENT OF SILICON IN FE-SI ALLOYS

Si mol fr.	$-\bar{L}_{Si}$ K cal	$-\log \gamma_{Si}$ 1420°	1500°	1600°	1700°
1.0	0.0	0.00	0.00	0.00	0.00
0.9	0.1	0.01	0.01	0.01	0.01
0.8	0.4	0.03	0.03	0.03	0.02
0.7	1.7	0.07	0.06	0.05	0.04
0.6	4.4	0.12	0.09	0.07	0.05
0.5	8.4	0.26	0.21	0.16	0.11
0.4	13.4	0.72	0.64	0.55	0.48
0.3	19.3	1.45	1.34	1.21	1.10
0.2	24.1	2.09	1.95	1.79	1.65
0.1	27.8	2.34	2.18	1.99	1.83
0.0	28.5	2.50	2.34	2.14	1.98

Comparison with Other Data

The present results are compared with an earlier attempt [1] to estimate the activity coefficient of silicon in Figure 7. Coefficients obtained from Chou's [7] distribution data are also shown; they are taken from his average distribution ratios for 1550 and 1650 degrees using the value $\gamma^{\circ}_{Si}{}^{(Ag)} = 2.0$. In a very recent study Sanbongi and Ohtani [27] have measured the emf of concentration cells in which the electrodes were respectively pure liquid silicon and iron-silicon alloys and the electrolyte a slag of CaO-SiO_2-Al_2O_3. Their results at a mean temperature of 1500 degrees are also shown. It is noted that our results in general lie between those of the other two experimental studies.

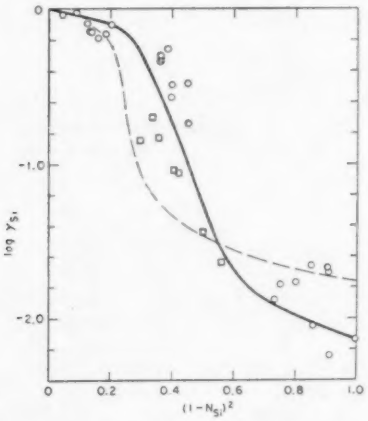

FIGURE 7. Comparison of data: Circles, Sanbongi and Ohtani [27], 1500°; squares, Chou 1550–1650° average; solid line, this investigation, 1600° average; broken line, Chipman [1] calc., 1600°.

Other Properties of the Solution

The Activity Coefficient of Iron

Values $\log \gamma_{Fe}$ at 1420 degrees were obtained by graphical integration of the Gibbs-Duhem equation using the method described by Darken and Gurry [9]. The data of Figure 3 were used to obtain $\log \gamma_{Fe}$ at higher temperatures; the results are contained in Table VI.

TABLE VI

ENTHALPY AND ACTIVITY COEFFICIENT OF IRON IN FE-SI ALLOYS

Si mol fr.	$-\bar{L}_{Fe}$ K cal	$-\log \gamma_{Fe}$ 1420°	1500°	1600°	1700°
1.0	25.7	1.68	1.53	1.36	1.21
0.9	25.3	1.54	1.40	1.22	1.08
0.8	23.5	1.41	1.27	1.11	0.98
0.7	19.4	1.30	1.19	1.05	0.95
0.6	14.6	1.20	1.12	1.02	0.93
0.5	9.7	1.04	0.98	0.92	0.86
0.4	5.5	0.66	0.63	0.59	0.56
0.3	2.5	0.28	0.27	0.25	0.23
0.2	0.7	0.06	0.06	0.05	0.04
0.1	0.2	0.01	0.01	0.01	0.00
0.0	0.0	0.00	0.00	0.00	0.00

Free Energy and Entropy

The free energy and entropy changes accompanying the formation of one gram atom of solution from the liquid elements at 1420 degrees are shown in Figure 8. The methods of calculation are indicated by the equations:

$$\Delta F = RT\,[N_{Si}\,(\ln \gamma_{Si} + \ln N_{Si}) + N_{Fe}\,(\ln \gamma_{Fe} + \ln N_{Fe})]$$

and

$$T\Delta S = \Delta H - \Delta F.$$

For comparison the curve for ΔH is repeated and a curve showing $T\Delta S$ for an ideal solution at the same temperature is added. It will be observed that the entropy of the solution differs greatly from that of the ideal. This may be taken as an indication of strong ordering tendencies in the solution.

The Ternary System Fe-C-Si

Experimental data on the effect of carbon on the activity coefficient of silicon have been shown in Table IV and Figure 6. To obtain an approximation which may be valid over a wider range of compositions, it is postulated that γ_{Si} is a function of $(N_{Si} + N_C)$. Values of $\log \gamma_{Si}$ in ternary solu-

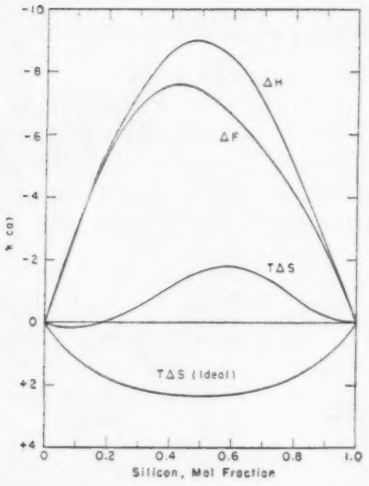

FIGURE 8. Properties of Fe-Si solutions at 1420°.

tions are plotted as such a function in Figure 9, where the experimental line for the binary solution is shown for comparison. It is evident that the ternary data fit the curve almost as well as the binary. Without more extended data it is impossible to estimate how wide a composition range can be described by this simple relation. In the following paragraph it is applied to the range $N_{Si} + N_C = 0.19$ to 0.40.

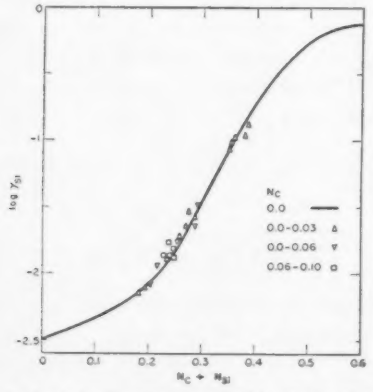

FIGURE 9. Activity coefficient of Si in Fe-Si-C solutions.

Activity of Si in Graphite-Saturated Solutions

Activity coefficients of silicon in graphite-saturated solutions at several temperatures have been computed on the basis of the above postulate. Table VII contains the solubility data, interpolated on a large-scale plot of Figure 1. Corresponding values of log γ_{Si} were read from plots of the data in Table V and these are shown in Table VIII. It is anticipated that these data will be particularly useful in studies of reactions between carbon-saturated alloys and silicate slags.

TABLE VII

SOLUBILITY OF GRAPHITE IN Fe-Si-C ALLOYS

	Carbon, mol fraction			
N_{Si}	1420°	1500°	1600°	1700°
0	0.195	0.200	0.210	0.220
0.05	0.158	0.166	0.174	0.180
0.10	0.127	0.134	0.141	0.149
0.15	0.095	0.102	0.109	0.116
0.20	0.067	0.072	0.078	0.085
0.25	0.041	0.045	0.050	0.057
0.30	0.0216	0.0263	0.0308	0.038
0.35	0.0112	0.0145	0.0188	0.0235
0.355*	0.0105			
0.362*		0.0126		
0.369*			0.0155	
0.376*				0.0186

*Saturated with β SiC.

A check of the reliability of the data can be made by means of the free energy and solubility of silicon carbide discussed in earlier sections. From the free-energy equation quoted, the activity of silicon in the graphite-saturated, SiC-saturated solution is

$$\log a_{Si}\,(\text{sat.}) = -5330/T + 1.81.$$

When this is solved for the four temperatures of Table VII and the results combined with the values of N_{Si} for saturation, the following values of log γ_{Si} are obtained: −0.89 at 1420; −0.76 at

TABLE VIII

ACTIVITY COEFFICIENT OF SILICON IN GRAPHITE-SATURATED IRON

	$-\log \gamma_{Si}$			
N_{Si}	1420°	1500°	1600°	1700°
0	2.10	1.94	1.75	1.59
0.05	2.05	1.88	1.69	1.54
0.10	1.97	1.80	1.61	1.45
0.15	1.86	1.70	1.50	1.35
0.20	1.71	1.57	1.37	1.20
0.25	1.52	1.38	1.21	1.04
0.30	1.28	1.13	0.98	0.82
0.35	0.97	0.86	0.72	0.61
0.355*	0.93			
0.362*		0.79		
0.369*			0.63	
0.376*				0.49

*Saturated with β SiC.

1500; −0.61 at 1600; −0.47 at 1700. The agreement with Table VIII is nearly perfect.*

Activity of Iron in Graphite-Saturated Solutions

Since the activity of carbon is fixed, that of iron is readily obtained through the Gibbs-Duhem equation. It is convenient to write this in the following form:

$$\log \gamma_{Fe}(b) - \log \gamma_{Fe}(a) = \frac{1}{2.3}\int_a^b \frac{N_C}{N_{Fe}} - \int_a^b \frac{N_{Si}}{N_{Fe}} d \log \gamma_{Si}$$

The integration was done graphically on two plots of $1/N_{Fe}$ vs N_C and N_{Si}/N_{Fe} vs $\log \gamma_{Si}$. Limits of integration were, a, the composition corresponding to saturation with SiC and, b, the composition at zero silicon. The activity of iron at limit a is assumed to be the same as that in a binary Fe-Si alloy of equal mol fraction of iron (Table VI). The integration yields activity coefficients at other concentrations down to zero silicon at which point a comparison may be made with data on the iron-carbon system.

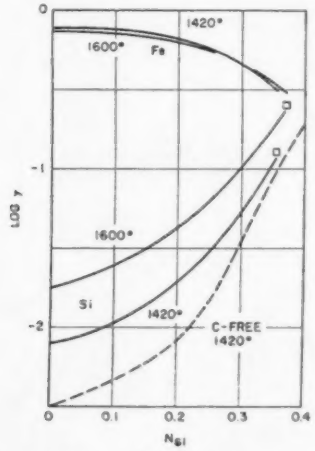

FIGURE 10. Activity coefficients of silicon and iron in graphite-saturated Fe-Si-C alloys. Broken line is for Si in C-free solutions. Squares show calculated $\log \lambda_B$ in equilibrium with SiC.

Darken and Gurry [28] in a careful study of all data on the iron-carbon system proposed for the activity coefficient of iron, $\log \gamma_{Fe} = -4660/T(N_C)^2$. This equation gives $\log \gamma_{Fe} = -0.10$ and -0.11 at 1420 and 1600 degrees respectively. The integration gave -0.11 and -0.13. This is a remarkable agreement.

The results of the calculations on graphite-saturated solutions are plotted in Figure 10. Here the squares show values of $\log \gamma_{Si}$ obtained through the data on βSiC.

In principle, it is possible to learn a great deal about the activity coefficient of carbon from the data here presented. However, since active experimental work on this subject is in progress in this laboratory and elsewhere [21], no calculations on carbon activity are included.

*The remarkable nature of this completely independent check is best appreciated from the reverse calculation. Using the data of Table VIII, the calculated heat of formation of β SiC differs by only 0.3 kcal from the value reported by Humphrey and coworkers in which they recognized an uncertainty of 0.9 kcal. The small discrepancy in $\log \gamma_{Si}$ is removed by adjusting the free energy of formation of β SiC to: $\Delta F^\circ = -24{,}700 + 8.3T$ cal.

Acknowledgments

Experimental work on the solubility of graphite and silicon carbide (J.C.F.) and on the distribution of Si between Ag and Fe-Si and Fe-C-Si solutions (G.R.C.) was supported by a research contract with the American Iron and Steel Institute. Earlier distribution experiments of Table III, Series A (N.A.G.) were sponsored by the Atomic Energy Commission. The authors acknowledge with gratitude the careful analytical work of Donald L. Guernsey.

References

1. CHIPMAN, J. Disc. Faraday Soc., No. 4 (1948) 23.
2. SAMARIN, A. and SHVARTSMAN, L. Izvestiya Akademii Nauk SSSR. No. 3 (1951) 407; *ibid.* No. 11 (1950) 1696.
3. CHIPMAN, J., ALFRED, R. M., GOTT, L. W., SMALL, R. B., WILSON, D. M., THOMSON, C. N., GUERNSEY, D. L. and FULTON, J. C. Trans. Amer. Soc. Metals **44** (1952) 1215.
4. KÖRBER and OELSEN. Mitt. Kaiser Wilhelm Inst. Eisenforch. **18** (1936) 109.
5. WAGNER, C. Thermodynamics of Alloys (Cambridge, Addison Wesley Press, 1952) pp. 48 ff.
6. CHIPMAN, J. and GRANT, N. J. Trans. Amer. Soc. Metals **31** (1943) 365.
7. CHOU, Y. H. Doctorate thesis, Dept. of Metallurgy, Carnegie Institute of Technology (1947).
8. HANSEN, M. Der Aufbau der Zweistofflegierungen (Berlin, Springer-Verlag, 1936).
9. DARKEN, L. S. and GURRY, R. W. Physical Chemistry of Metals (New York, McGraw-Hill, 1953).
10. SCHADEL, A. M., DERGE, G. and BIRCHENALL, C. E. Trans. A.I.M.E. **188** (1950) 1282.
11. KÖRBER, F. Stahl u. Eisen **57** (1937) 1349.
12. GOKCEN, N. A. and CHIPMAN, J. Trans. A.I.M.E. **194** (1952) 171; J. Metals (1953) 1017.
13. HUMPHREY, G. L. and KING, E. G. J. Am. Chem. Soc. **74** (1952) 2041.

14. KELLEY, K. K. U.S. Bur. Mines Bull. 476 (1949); 477 (1950).
15. HUMPHREY, G. L., TODD, S. S., COUGHLIN, J. P. and KING, E. G. U.S. Bur. Mines, Rept. Inv. 4888 (1952).
16. GOKCEN, N. A. and CHIPMAN, J. Reference 12.
17. DASTUR, M. N. and CHIPMAN, J. Trans. A.I.M.E. **185** (1949) 441.
18. National Bureau of Standards. Selected Values of Chemical Thermodynamic Properties (1948).
19. DARKEN, L. S. and GURRY, R. W. J. Am. Chem. Soc. **68** (1947) 798.
20. TAYLOR, C. R. and CHIPMAN, J. Trans. A.I.M.E. **154** (1943) 228.
21. RICHARDSON, F. D. and DENNIS, W. E. Trans. Faraday Soc. **49** (1953) 171.
22. SANBONGI, K. and OHTANI, M. Sci. Repts. Res. Inst., Tohoku Univ., **A5**, No. 3 (1953).
23. SMITH, R. P. J. Am. Chem. Soc. **68** (1946) 1163.
24. TEMKIN and SHVARTSMAN. Zhuranl Fizicheskoi Khimii **23** (1949) 755.
25. CHIPMAN, J. and ELLIOTT, J. F. Thermodynamics in Physical Metallurgy (Am. Soc. Metals, 1950; Trans. Amer. Soc. Metals **42A** (1950) 102).
26. WAGNER, C. J. Chem. Phys. **19** (1951) 626.
27. SANBONGI, K. and OHTANI, M. Sci. Repts. Research Inst., Tohoku Univ. **A5** (1953) 350.
28. DARKEN, L. S. and GURRY, R. W. Reference 9, p. 409.

RESIDUAL LATTICE STRAINS IN PLASTICALLY DEFORMED ALUMINIUM*

CATHERINE M. BATEMAN†

The residual lattice strains in three types of aluminium have been measured using X-ray diffraction methods and have been compared quantitatively with the theory of an intergranular stress system postulated by G. B. Greenough [1]. A discrepancy between theory and experiment has been observed with specimens in the form of tensile test pieces. It is concluded that these results raise doubts as to the validity of the theory in its present form.

LES DÉFORMATIONS RÉSIDUELLES DU RÉSEAU DANS L'ALUMINIUM DÉFORMÉ PLASTIQUEMENT

Les déformations résiduelles du réseau ont été mesurées dans trois types d'aluminium, au moyen de la diffraction de rayons X. Ces déformations furent comparées quantitativement à la théorie d'un système de contraintes intergranulaires, proposée par G. B. Greenough [1]. Une différence entre la théorie et l'expérience a été notée dans le cas d'échantillons en forme d'éprouvettes de traction. On en conclut que ces résultats introduisent des doutes sur la validité de cette théorie dans sa forme actuelle.

INNERE GITTERSPANNUNGEN IN PLASTISCH VERFORMTEM ALUMINIUM

Innere Gitterspannungen wurden röntgenographisch in drei verschiedenen Aluminiumsorten gemessen, und die Resultate wurden quantitativ mit der von G. B. Greenough [1] vorgeschlagenen Theorie eines interkristallinen Spannungssystems verglichen. Wenn das Metall in Form von Zugversuchsproben vorlag, wurde eine Diskrepanz zwischen Experiment und Theorie beobachtet. Daraus wird geschlossen, dass die Gültigkeit der Theorie in ihrer gegenwärtigen Form zweifelhaft erscheint.

Introduction

The existence of a mean lattice strain in the grains of a polycrystalline metal aggregate after plastic deformation, as measured by X-ray diffraction methods, has been observed by many workers. Various explanations of this phenomenon have been advanced but in particular Greenough [1] has put forward an explanation in terms of a micro-stress system existing between the grains of the aggregate due to variation in yield stress with orientation.

He postulated that the residual lattice strains measured by X-ray diffraction methods are due to stresses in those grains suitably oriented to diffract the X-ray beam, these stresses being balanced by stresses of opposite sign in neighbouring grains which do not contribute to the diffraction line. For plastic extension in a metal aggregate takes place by glide and the ease with which a grain deforms depends upon the orientations of its glide planes and glide directions relative to the applied stress. The elastic strain of a grain which glides easily is less than that of its neighbour which is less favourably oriented. When the applied stress is removed the grains tend to return to their strain-free condition but, since each grain contains a different amount of elastic strain, in the final state some are left in tension and others in compression. In this way a micro stress system is established in the aggregate.

The magnitude of the expected residual lattice strains may be estimated by making certain assumptions. To simplify the mathematics it is assumed that the grains are elastically isotropic, in the case of aluminium this probably leads to a very small error. For aluminium is one of the most nearly isotropic of metals, the maximum variation of Young's modulus with crystallographic direction being only 18.8 per cent of the mean value. The second assumption, due to Taylor [2], is that the strain in the individual grains is the same as in the aggregate as a whole.

The strain in any grain may be obtained by compounding five shears. If only slip plane directions operate five of the possible twelve slip plane directions in a face-centred cubic metal must be summed to produce the required strain. Taylor postulated that the operative combination of shears is the one requiring least work.

It may be shown that the residual lattice strain in a grain R

$$= \frac{\nu}{E}(T_{\text{mean}} - T_R) \tag{1}$$

where ν = Poisson's ratio
E = Young's modulus
T_{mean} = the applied stress
T_R = the tensile stress in grain R when the load was applied.

*Received October 12, 1953.
†Royal Aircraft Establishment, Farnborough, Hants., England.

T_R can be expressed in terms of the critical shear stress, τ_c, and orientation; τ_c may in turn be expressed in terms of T_{mean}. The further assumption, that at any stage of the deformation τ_c is the same for all grains, is made.

Taylor has shown that for the aggregate

$$\tau_c \Sigma s = T_x \tag{2}$$

where T is the tensile stress acting on the aggregate, x is the extension of the aggregate, and Σs is the arithmetic sum of the five shears necessary to produce the deformation. The additional assumption is made that this relationship also holds for the individual grains.

To determine the residual lattice strain by X-ray methods the change in interplanar spacing 'd' is measured. The X-ray beam does not select just one orientation but a set of orientations whose 'reflecting normals' are in the correct position for diffraction.

$$\text{i.e., } T_{hkl} = \frac{T_1 + T_2 + \ldots T_n}{n} \tag{3}$$

where n = total number of possible orientations to contribute to the reflection hkl. Then

$$T_{hkl} = \frac{\tau_c}{x} (\Sigma s)_{hkl} \tag{4}$$

and

$$T_{\text{mean}} = \frac{\tau_c}{x} (\Sigma s)_{\text{mean}}$$

The residual lattice strain for the reflection plane hkl is

$$\left(\frac{\delta d}{d}\right)_{hkl}$$

where d is the interplanar spacing for the particular family of planes.

Hence from equations (1) and (4)

$$\left(\frac{\partial d}{d}\right)_{hkl} = \frac{\nu}{E} T_{\text{mean}} \left(1 - \frac{(\Sigma s)_{hkl}}{(\Sigma s)_{\text{mean}}}\right).$$

Therefore a graph of residual lattice strains against $1 - (\Sigma s)_{hkl}/(\Sigma s)_{\text{mean}}$ for the various reflecting planes should be a straight line through the origin with gradient $(\nu/E)T_{\text{mean}}$.

Taylor calculated the values of Σs for face-centred cubic metals for a uniform distribution of orientations over the elementary spherical triangle of cubic symmetry. In these experiments the axis of elongation of the specimens was horizontal and perpendicular to the X-ray beam. Hence the angle between the 'reflecting normal' and the direction of the applied stress is the Bragg angle, θ, and the locus of orientations contributing to a particular reflection is a circle about the hkl-pole with angular radius θ. By means of a stereogram this locus was plotted for the various reflections and $(\Sigma s)_{hkl}$ obtained by taking the mean of the Σs values at 5 degrees around the locus.

Recently a full mathematical treatment of plastic distortion in a polycrystalline aggregate has been published by Bishop and Hill [3]. They first consider a single crystal and then derive a general relationship between stress and plastic strain in the aggregate when the individual grains deform by slip; full account being taken of the mutual constraints between grains. They show that the principle of maximum plastic work, which they adopt, leads to the same result as the principle of minimum shear postulated by Taylor.

In a further paper [4], Bishop and Hill have considered the plastic properties of a polycrystalline face-centred cubic metal. They first determine the stresses needed to produce multislip assuming the aggregate to be elastically isotropic. Then, by conjecturing that the work done in deforming the aggregate is approximately equal to that which would be done if the grains were free to deform equally, and using the principle of maximum plastic work they calculate the yield function of the aggregate. They have found fairly good agreement between the theoretical and experimental values of the yield criteria for aluminium and copper.

With the aid of additional information from Hill [5], the values of Σs have been derived from this work in the same way as described previously.

Greenough also considered the work of Cox and Sopwith [6] who assumed that during the deformation of a polycrystalline aggregate the grains deform as if isolated from their neighbours. This cannot be strictly true for on this basis holes would develop in the aggregate during deformation. Using this work Greenough derived the following expression for the residual lattice strain:

$$\left(\frac{\delta d}{d}\right)_{hk} = \frac{\nu}{E} \frac{T_{\text{mean}}}{\left(\frac{1}{\sin\psi\cos\lambda}\right)_{\text{mean}}} \left\{\left(\frac{1}{\sin\psi\cos\lambda}\right)_{\text{mean}} - \left(\frac{1}{\sin\psi\cos\lambda}\right)_{hkl}\right\} \tag{5}$$

where ψ is the angle between the direction of the applied stress and the glide plane, and λ is the angle between the direction of the applied stress and the glide direction.

Using Taylor's assumptions Greenough found

fairly good quantitative agreement between theory and experiment for several commercially pure metals in the form of wires, but assuming deformation to take place as postulated by Cox and Sopwith, gave poor results. In another experiment with duralumin test pieces Greenough [7] did not find the same measure of agreement between theory and experiment. It was felt that neither the fact that the test pieces were larger than the wires nor that the material was an alloy satisfactorily explained the discrepancy. The present work was designed as a further test of Greenough's hypothesis using specimens dimensionally similar to the duralumin test pieces.

Experimental Work

High purity aluminium (99.93% by weight Al), commercially pure aluminium (99.32% Al) and aluminium alloy to specification D.T.D. 423B (95.23% Al) were the three materials used for these experiments.

The high purity aluminium and commercially pure aluminium specimens were machined from $\frac{1}{8}$ in. thick rolled sheet and then annealed at 450°C for 30 minutes. The respective mean grain diameters were 0.11 mm and 0.04 mm. Some care had to be taken with the alloy, for preliminary measurements indicated that internal stresses were introduced into the material during the normal cold water quench after heat treatment. The $\frac{1}{8}$ in. thick rolled sheet was therefore soaked at 520°C for 45 minutes, air-cooled, aged at 170°C for 8 hours and again air-cooled. Specimens were machined from this heat-treated sheet and used without further heat treatment. The grains in this material were not homogeneous, the grain diameters lying in the range 0.01 to 0.08 mm.

Flat tensile specimens of 1-in. gauge length and nominal cross section 0.125 in. × 0.25 in. were used throughout this work.

Lattice spacings were determined from X-ray diffraction back-reflection photographs. Cobalt, copper and chromium $K\alpha$ radiations were used and reflections obtained from the 331 and 420, the 333–511 and 222 planes respectively. A thin layer of calibrating silver on the specimen surfaces provided an accurate measure of the film-specimen distance. The specimens were oscillated ±2.5° about the X-ray beam during exposures to produce smooth diffraction lines. (It was found necessary to scan the larger grain size high purity aluminium specimens.)

A series of specimens, for each material, was first photographed in the annealed or heat-treated condition. These same specimens were then plastically deformed by suitable loading in a conventional tensile testing machine and a further series of photographs obtained after the removal of the load. The films were measured and the interplanar spacings calculated before and after deformation.

Results

The sign convention that an increase in interplanar spacing is denoted by a positive residual lattice strain has been adopted. The values of the interplanar spacings, from which the residual lattice strains were calculated, were obtained by taking a mean value of the results from all specimens. The probable error for the residual lattice strains is 1×10^{-5} for the high purity and commercially pure aluminium and 2×10^{-5} for the aluminium alloy. The residual lattice strains for the planes investigated in the three materials are given in Table I.

TABLE I

RESIDUAL LATTICE STRAINS IN PLASTICALLY EXTENDED ALUMINIUM

	Residual Lattice Strains × 10^{-5}			
Reflecting plane	High purity aluminium	Commercially pure aluminium		Aluminium alloy
	Extension 10%	Extension 10%	Extension 20%	Extension 4%
hkl	Stress 3 tons/sq in.	Stress 5.5 tons/sq in.	Stress 6.5 tons/sq in.	Stress 21 tons/sq in.
222	−10.9	−5.19	−2.72	−10.4
331	− 1.98	0	−1.23	−15.1
420	− 1.73	+2.22	+3.95	+ 4.2
333 / 511	+1.48	+5.19	+9.14	+17.3

Discussion

In Figures 1–4 the experimental values of the residual lattice strains for the three materials have been plotted against $1-[(\Sigma s)_{hkl}/(\Sigma s)_{mean}]$ using the Σs values derived from Taylor's work.

Similar graphs have been plotted, but are not included, using the Σs values derived from the work of Bishop and Hill and the function obtained from the work of Cox and Sopwith. In Table II the gradients of all these graphs are compared with the gradient to be expected by considering the theoretical expression $(\nu T_{mean})/E$. In addition the relevant results from Greenough's paper are

TABLE II

COMPARISON OF GRADIENTS

Material	Experimental $\times 10^{-4}$			Theoretical $(\nu/E)T_{mean}$ $\times 10^{-4}$
	Taylor	Bishop and Hill	Cox and Sopwith	
High purity aluminium 10%	12.6	13.2	97.0	2.56
Commercially pure aluminium 10%	11.9	12.2	80.0	4.68
20%	14.4	14.4	68.0	5.54
Aluminium alloy 4%	50.0	44.7	300	13.3
Aluminium wire 15% (Greenough)	9.6	7.4	14.1	8.3
Duralumin test pieces 6.3% (Greenough)	66.5	54.3	350	13.9

included and to complete the comparison his experimental results have also been plotted against the Σs values derived from the work of Bishop and Hill.

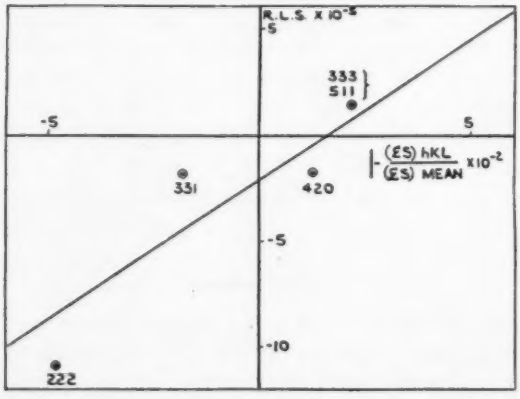

FIGURE 1. High purity aluminium 10 per cent extension.

It should be noted that for the aluminium wire the axis of extension was vertical and therefore the locus of orientations contributing to the reflection is a circle about the *hkl* pole with angular radius 90 degrees.

Greenough pointed out that, since the calculations were of an approximate nature, it would be reasonable if a straight line could be drawn amongst the experimental points with approximately the calculated gradient and which passed near the origin. It can be seen from Figures 1–4 that reasonably straight lines are obtained using the function derived from Taylor. Very similar graphs

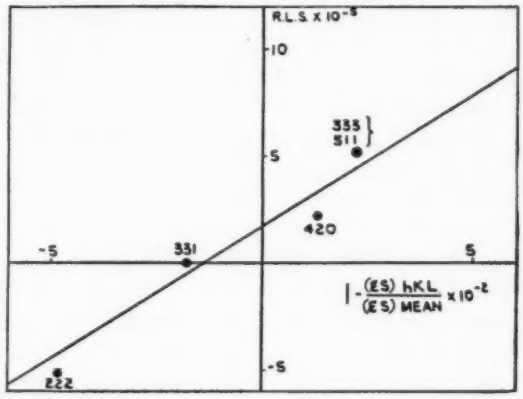

FIGURE 2. Commercially pure aluminium 10 per cent extension.

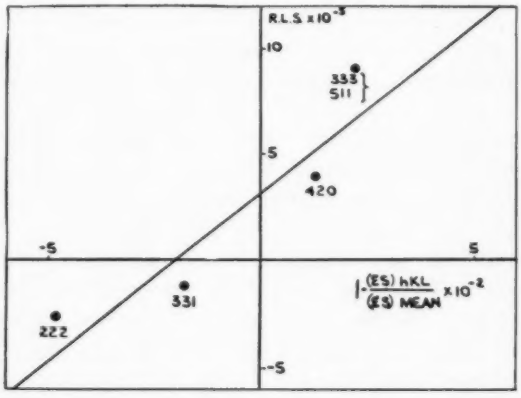

FIGURE 3. Commercially pure aluminium 20 per cent extension.

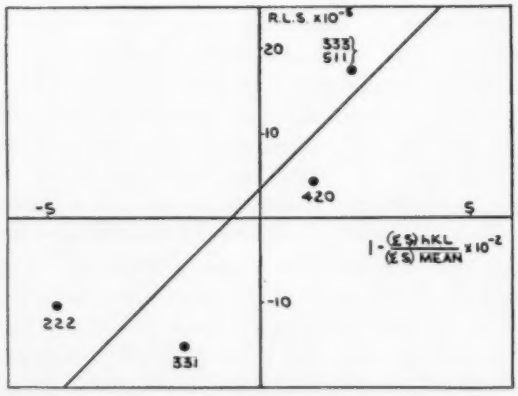

FIGURE 4. Aluminium alloy 4 per cent extension.

are obtained using the Σs values of Bishop and Hill; there is little to choose between them.

The most striking aspect of these results is the discrepancy between the experimental and calculated gradients when the specimens are in the form of test pieces. For the aluminium wire the agreement is as good as can be expected. The fact that all three types of aluminium used here show the discrepancy seems to rule out the possibility that it is caused by impurities dissolved in the metal as seemed likely when only duralumin was being considered. Since Greenough also found remarkably good agreement with theory for other metals in the form of wires, it does seem that it is the shape or size of specimen which is causing the effect.

The gradients obtained from the plots using the function of Cox and Sopwith show very poor agreement with theory; even the gradient for the aluminium wire is too large by a factor of two.

It will be noticed that all the plots give a small intercept on the residual lattice strain axis. With the exception of the high purity aluminium these intercepts are positive. Similar intercepts were noted by Greenough and he suggested that they were caused by the crystals in the surface (i.e., those irradiated by the X-rays) being softer than those which are completely surrounded. They are more likely to go into compression and thus there is an extra positive residual lattice strain at the surface. Greenough [8] has investigated a macroscopic surface stress in mild steel specimens; he showed that this stress was superimposed on the Heyn intergranular stress system and was about two crystals deep. The intercepts in the present instance are so small as to make an accurate investigation of surface stresses impracticable.

It was thought possible that orientation effects introduced into the material by rolling might be a contributory cause of the discrepancy. Examination of the specimens by the usual X-ray methods failed to detect any preferred orientation.

Conclusions

The experiments described here do not confirm the hypothesis put forward by Greenough. While it does not seem possible that the agreement obtained by him in his experiments with wires can be entirely fortuitous, these results from 'test piece' specimens do throw some doubt on the theory. None of the simplifying assumptions made suggests an obvious explanation for the discrepancy nor is it thought probable that preferred orientation effects are introducing errors.

Acknowledgements

The author wishes to thank Dr. G. B. Greenough of Metallurgy Department, Sheffield University (formerly Metallurgy Department, R.A.E.), for much helpful advice. This paper is published by permission of the Chief Scientist, British Ministry of Supply, and the Controller of H.M. Stationery Office, England. British Crown copyright reserved.

References

1. Greenough, G. B. Proc. Roy. Soc. A. **197** (1949) 556.
2. Taylor, G. I. J. Inst. Metals **60** (1938) 307.
3. Bishop, J. F. W. and Hill, R. Phil. Mag. **42** (1951) 414.
4. Bishop, J. F. W. and Hill, R. Phil. Mag. **42** (1951) 1298.
5. Hill, R. Private communication to G. B. Greenough.
6. Cox, H. L. and Sopwith, D. G. Proc. Phys. Soc. **49** (1937) 134.
7. Greenough, G. B. Ph.D. thesis. Cambridge University, 1947.
8. Greenough, G. B. J. Iron Steel Inst. **169** (1951) 235.

THE ORDERING OF ATOMS IN THE CHI-PHASE OF THE IRON-CHROMIUM-MOLYBDENUM SYSTEM*†

J. S. KASPER‡

The crystal structure of the "chi"-phase of composition $Fe_{36}Cr_{12}Mo_{10}$ has been investigated by means of X-ray and neutron diffraction from powdered specimens. It is found that the structure is of an ordered α-Mn type. Mo atoms occupy those sites for which the volume per atom is largest, and Cr atoms tend to segregate in the larger of the remaining positions.

LA MISE EN ORDRE DES ATOMES DANS LA PHASE CHI DU SYSTÈME Fe-Cr-Mo

On a investigué la structure cristalline de la phase "chi," dont la composition est $Fe_{36}Cr_{12}Mo_{10}$ au moyen de la diffraction des rayons X et des neutrons par des échantillons en poudre. Il est constaté que cette structure est du type Mn-α ordonnée. Les atomes de Mo occupent les noeuds qui offrent le maximum de volume par atome et les atomes de Cr occupent les plus grands des emplacements restants.

DIE ATOMARE ORDNUNG IN DER CHI-PHASE DER Fe-Cr-Mo STRUKTUR

Die Kristallstruktur der "Chi" Phase der Zusammensetzung $Fe_{36}Cr_{12}Mo_{10}$ wurde röntgenographisch und mit Hilfe von Neutronenbeugung an gepulverten Proben untersucht. Die Struktur ist ein geordneter α-Mn Typ. Die Mo Atome nehmen diejenigen Gitterplätze ein, für die das Volumen pro Atom am grössten ist, und die Cr-Atome haben die Tendenz, sich in die grösseren der verbleibenden Positionen abzuscheiden.

Introduction

The recent discovery of a new phase with an α-Mn-type structure in steels containing nickel, chromium and molybdenum has been reported by Andrews and Brookes [1], and they have designated this as the "chi"-phase. They were not able to obtain an alloy consisting primarily of this phase, however, or to determine if it was an equilibrium structure. Recent work by McMullin, Reiter and Ebeling [2] on isothermal sections of the iron-chromium-molybdenum ternary diagram at 1500°F and 1650°F has established the existence of the chi-phase as an equilibrium phase in this system. Moreover, from the latter work the range of existence of this phase has been found to be very limited and to be centered about a composition corresponding to integral numbers of each atom in the unit cell, these numbers in turn being suggestive of a possible ordering of the respective atoms (especially molybdenum) among the different positions in the cell. Thus, from the composition, ten of the total of 58 atoms in the unit cell would be molybdenum, suggesting that the two- and eight-fold positions of the α-Mn structure may be occupied by them. Definite evidence for ordering is obtained from the X-ray diffraction patterns of the alloys prepared by McMullin, *et al.* While they conform to the α-Mn structure, they do show definite inversions of intensity relationships when compared to the α-Mn pattern.§ Using alloys of pure chi-phase, kindly prepared by Dr. McMullin, we have been able to determine the nature and degree of ordering of the respective atoms from a consideration of X-ray and neutron diffraction intensities of powdered specimens.

Experimental

The preparation of the alloys studied is described in the report of McMullin, Reiter and Ebeling [2]. They all were of the nominal composition 56 per cent iron, 17 per cent chromium, 27 per cent molybdenum (weight per cent). The chemical analysis and corresponding number of atoms in the unit cell for one of the alloys were:

	Weight %	*Number of atoms per unit cell*
Fe	56·2	36·1
Cr	16·8	11·8
Mo	26·9	10·1

The X-ray diffraction patterns were obtained for Co and Cr radiations in a cylindrical camera of 5 cm radius. The intensities were measured by visual comparison with a standard film intensity scale. Precise values of integrated intensity were not obtained thereby, principally due to the difficulties of allowing for absorption effects.

The neutron diffraction patterns were obtained from a large quantity (285 g) of powdered specimen in a flat holder of dimensions $4 \times 2\frac{1}{4} \times \frac{1}{4}$ in. The

*Received November 21, 1953.

†The neutron diffraction data were obtained at the Brookhaven National Laboratory Pile.

‡General Electric Research Laboratory, Schenectady, New York.

§Similar inversions are apparent in the X-ray pattern given by Andrews and Brookes [1].

TABLE I

X-RAY INTENSITIES FOR χ PHASE

			CrKα			CoKα		
$h^2+k^2+l^2$	hkl	αMn d_{hkl}	αMn I_{obs}	χ I_{obs}	χ d_{hkl}	χ I_{obs}	Disordered I_{calc}	Ordered I_{calc}
2	110	—	—	—	—	*	0.1	12.4
4	200	—	—	2	—	*	0.3	4.0
6	211	3.646	2	3	3.711	7.4	1.8	7.1
8	220	3.174	3	—	—	—	2.4	1.2
10	310	—	—	—	—	—	0.4	0
12	222	2.585	4	2	2.575	3.1	2.3	1.8
14	321	2.389	4	14	2.405	14.8	2.0	13.8
16	400	2.233	18	7	2.239	8.8	13.0	7.8
18	(330)	2.105	>300	>300	2.112	370	306.0	320.0
	(411)							
20	420	1.996	2	—	—	—	1.3	3.4
22	332	1.904	88	83	1.907	64	70.0	51.2
24	422	1.822	36	42	1.825	29.5	25.1	28.1
26	(431)	1.751	59	20	1.749	13.0	33.3	10.9
	(510)							
30	521	1.630	5	—	—	—	2.7	1.9
32	440	1.579	2	—	—	—	0.4	0
34	(433)	1.532	5	—	—	—	2.2	3.1
	(530)							
36	(442)	1.488	7	18	1.490	10.2	3.2	7.7
	(600)							
38	(532)	1.448	9	30	1.448	17.3	4.3	10.5
	(611)							
40	620	1.411	2	—	—	—	0.6	0.1
42	541	1.377	2	4	1.376	1.9	0.7	2.3
44	622	1.345	15	30	1.344	13.7	5.7	8.5
46	631	1.316	6	4	1.315	1.6	1.4	1.7
48	444	1.287	59	87	1.288	20.7	16.5	16.4
	(543)							
50	(550)	1.262	120	120	1.260	29.4	20.1	22.5
	(710)							
52	640	—	—	—	—	—	0	0.1
	(552)							
54	(633)	1.214	335	>300	1.214	66	76.9	74.1
	(721)							
56	642	1.192	67	29	1.192	4.7	13.9	4.7
58	730	1.172	44	21	1.171	3.6	9.2	4.0
62	(732)				1.133	13.0	15.5	15.8
	(651)							
64	800				—	—	0	0.4
	(811)							
66	(741)				1.098	11.1	3.7	8.6
	(554)							
68	(820)							
	(644)				1.080	15.2	8.0	13.1
70	653				1.066	2.2	6.6	5.3
72	(822)				1.051	17.3	38.4	30.7
	(660)							
	(831)							
74	(750)				1.037	11.1	12.5	16.6
	(743)							
76	662				1.023	2.7	3.9	4.0
78	752				1.010	7.4	5.4	5.4
80	840				—	—	0.7	1.3
82	(910)				0.985	9.6	18.5	13.8
	(833)							
84	842				0.973	1.0	6.0	4.4
	(921)							
86	(761)				0.962	1.4	19.7	7.4
	(655)							
88	664				0.951	6.8	15.9	14.1
	(930)							
90	(851)				0.941	19.8	59.0	54.6
	(754)							
94	(932)				0.920	3.6	16.6	16.0
	(763)							
96	844				—	—	9.8	8.4
	(941)							
98	(853)				0.900	52	139.0	192.0
	(770)							

*Not measurable because of high background.

diffracted neutrons were detected by means of a BF_3 counter and integrated intensities of a high degree of precision could be obtained in this case, with due allowance for absorption effects. A beam of neutrons monochromatized by reflection from a single crystal of lead and collimated by Soller slits was used. Its wavelength was 1.05 Å. Integrated intensities were obtained by measuring the areas of peaks with a planimeter.

X-ray Results

The X-ray intensity data are summarized in Table I. For comparison, the pattern of α-Mn is included; Cr radiation was used for this purpose since with other radiations the α-Mn photographs are inferior for intensity measurement. On the other hand, for χ-phase the structural considerations were based mainly on CoKα intensities since these provided more extensive information. Calculated intensities are for the expression

$$I \backsim p|F|^2 \frac{1 + \cos^2 2\theta}{\sin^2 \theta \cos \theta}$$

Accordingly, no allowance is made for absorption, which can be expected to be large, nor for a temperature factor, which should have only a small effect.

It is interesting that the unit cell dimensions of the two structures are so close to one another; $a_0 = 8.895$ Å for α-Mn, and $a_0 = 8.920$ Å for χ. All the reflections for χ were indexed on the basis of a body-centered cubic cell of the given dimensions and there is no doubt that the structure is of the same type as α-Mn.

Inspection of the data in Table I reveals striking discrepancies between the intensities for a disordered model and those observed, the most significant of which are some inversions among adjacent lines, e.g., I_{14} vs I_{16} and I_{24} vs I_{26}. On the other hand, satisfactory agreement is obtained for the ordered model wherein the Mo atoms are placed in the two- and eight-fold positions of the α-Mn structure and the Fe and Cr atoms are distributed at random among the remaining positions.

The intensity comparison has to be made with due allowance for absorption effects. Consequently, only reflections not far from one another in $\sin\theta$ should be compared. In order to facilitate this, Table II gives ratios of intensities of adjacent reflections for some of the more critical cases. It is seen that on this basis the ordered model appears good and the disordered one quite poor. Attempts were made to allow for absorption but this could not be done properly because of the varying breadth of the lines. It did not seem worth while to attempt more quantitative measurement of the intensities with X-rays since this was accomplished more readily with neutrons.

TABLE II

RATIOS OF INTENSITIES (Co Kα) FOR χ-PHASE

	Obs.	Ordered calc	Disordered calc
I_{14}/I_{16}	1.7	1.8	0.2
I_{22}/I_{24}	2.2	1.8	2.8
I_{22}/I_{26}	4.9	4.7	3.0
I_{24}/I_{26}	2.3	2.6	7.6
I_{48}/I_{50}	0.8	0.7	0.8
I_{54}/I_{56}	13.9	15.7	5.5
I_{62}/I_{58}	3.6	4.0	1.7
I_{68}/I_{66}	1.4	1.5	2.2
I_{72}/I_{74}	1.6	1.9	3.1

Despite the apparent complexity of the structure and the several variables in the problem, the location of Mo atoms can be made with considerable certainty from the data at hand. This follows from the high scattering factor of Mo relative to those of Fe and Cr (almost a two-fold difference). The scattering factors of Fe and Cr are so slightly different that, of course, it is not possible to distinguish between them, but this is fortunate for the problem of locating Mo only. The f-values given in Internationale Tabellen, II, p. 571, were used. Corrections for anomalous dispersion would make only slight changes in the calculations.

It may be supposed that the atomic parameters for χ are not precisely those given for α-Mn. Small parameter variations were made and the resulting effect on intensities was minor relative to the scheme of ordering. Not all possible ordering schemes were tried, but because of the sensitivity of the intensities to the placement of Mo, it was found that no significant deviation from the suggested model could be tolerated. Thus, at most only one Mo of those in eight-fold positions could be interchanged with Cr or Fe without significantly changing the intensity agreement for the worse. No such interchange with Mo atoms in the two-fold positions could be allowed. It seems quite certain then, that the Mo atoms are in the two- and eight-fold positions.

Neutron Results

A high degree of precision is readily obtainable

for neutron diffraction intensities. Absorption for the elements concerned is small and can be computed exactly. These data allow, therefore, more quantitative comparisons to be made, and especially afford an opportunity to consider the distribution of Fe and Cr atoms, since their neutron scattering factors are significantly different. The respective neutron f-values are: $f_{Fe} = .96$, $f_{Cr} = .352$, $f_{Mo} = .661$ (all times 10^{-12} cm).

In Table III are given the observed neutron intensities and those calculated for various models by the expression

$$I \sim \frac{p\, e^{-\mu h \sec\theta}}{\sin^2 2\theta} |F|^2,$$

TABLE III

COMPARISON OF OBSERVED AND CALCULATED NEUTRON DIFFRACTION INTENSITIES FOR χ-PHASE

$h^2+k^2+l^2$	I_{obs}	I_{calc} A	B	C	D	D^1
2	0	0	0	9	5	1
4	0	0	0	0	0	0
6	11±2	2	5	3	27	15
8	6±2	2	5	4	7	6
10	0	0	1	0	2	2
12	2±1	3	3	7	5	4
14	4±2	3	1	2	7	3
16	23±2	19	22	23	19	20
18	422±10	422	422	422	422	411
20	0	2	1	0	7	3
22	151±5	127	139	100	186	154
24	50±3	48	48	43	53	46
26	88±3	69	87	74	104	87
30	5±2	6	7	6	14	9
32	3±2	1	2	1	2	2
34	6±2	6	6	7	8	5
36	3±1	9	6	15	6	4
38	6±2	13	13	15	9	7
40	0	2	3	3	3	2
42	0	2	2	4	2	2
44	10±3	18	16	9	26	16
46, 48, 50, 52, 54, 56, 58	375±50	390	473	449	530	358

where p is the multiplicity, μ is the absorption coefficient and h is the thickness of sample. The various models are indicated as follows:

Model	2a	8a	(24g) D_1	(24g) D_2	Temp. factor
A	Random	Random	Random	Random	None
B	Mo	Mo	18, Fe, 6 Cr	18 Fe, 6 Cr	None
C	Mo	Mo	24 Fe	12 Fe,12 Cr	None
D	Mo	Mo	12 Fe,12 Cr	24 Fe	None
D^1	Mo	Mo	15 Fe, 9 Cr	21 Fe, 3 Cr	$B=1.0\times10^{-16}$ cm²

The (24g)-D_2 positions are those for atoms of smaller size in the α-Mn structure, corresponding to the parameters $u = 0.089$, $v = 0.278$. The parameters for (24g)-D_1 are $u = 0.356$, $v = 0.042$.

The intensities of the four models A through D were first calculated without a temperature factor and it seemed that A and C could be eliminated. Model B appears good for the few strong reflections, but shows real discrepancies when the weaker reflections are considered and cannot be improved by a temperature factor. Model D is somewhat better in this respect but still shows definite disagreements. Accordingly, the effect of small variations from these two models were tried and the best fit of data was obtained for the distribution labeled D^1. It includes a reasonable value of the temperature factor, $B = 1.0 \times 10^{-16}$ cm², which also makes the last intensity agree with the observed. The reliability index,

$$R = \frac{\Sigma \mid I_{obs} - I_{calc.} \mid}{\Sigma I_{obs}},$$

has the low value of 0.06.

Again, the effect of a variation of atomic parameters was investigated. It was found that no reasonable changes in parameters could alter the intensities sufficiently to improve an otherwise unsatisfactory model. Though such an investigation could not be done thoroughly, it seemed that for the best model D^1, the parameters cannot be greatly different (±.005) from those in α-Mn.

Discussion of the Structure

The proper description of the structure follows:

$Fe_{36}Cr_{12}Mo_{10}$

Space group I $\bar{4}3m - T_d^3$

2 Mo at 2 (*a*)

8 Mo at 8 (*c*) $u = 0.317$

D_1 15 Fe at 24 (*g*) $u = 0.356$, $v = 0.042$

9 Cr

D_2 21 Fe at 24 (*g*) $u = 0.089$, $v = 0.278$

3 Cr

Nearest neighbor distances are given in Table IV.

TABLE IV

INTERATOMIC DISTANCES AND PAULING VALENCE FOR χ-PHASE

	Neighbors	D (n)	"Valence"	Valence for corresponding positions in $\alpha-Mn$
Mo_I (2a)	4 Mo_{II}	2.82		
	12 D_2	2.71	6.2	3.5
Mo_{II} (8c)	1 Mo_I	2.82		
	3 D_1	2.49		
	3 D_1	2.96		
	3 D_2	2.89		
	6 D_2	2.69	6.6	4.7
D_1 (24g)	1 Mo_{II}	2.49		
	1 Mo_{II}	2.29		
	6 D_1	2.67		
	1 D_2	2.45		
	2 D_2	2.51		
	2 D_2	2.66	4.7	4.6
D_2 (24g)	1 Mo_I	2.71		
	1 Mo_{II}	2.89		
	2 Mo_{II}	2.69		
	1 D_1	2.45		
	2 D_1	2.51		
	2 D_1	2.66		
	1 D_2	2.24		
	2 D_2	2.38	6.4	6.3

It appears, then, that not only are the Mo atoms ordered but that there is a tendency for Cr to occupy preferentially the sites of larger size, leaving the sites of smaller size to be occupied predominantly by Fe. The partially ordered distribution of Fe and Cr atoms may be the result of insufficient annealing time. The completely ordered situation would correspond to the segregation of all Cr atoms in (24g) D_1 positions. The structure would be more understandable on this basis. The subsequent discussion, for purposes of simplicity, will be made for the completely ordered structure, as defined.

It is difficult to see the full significance of the structure, but there are certain features of interest which can be recognized. The atomic arrangements appear reasonable on the basis of size considerations. Thus, the two- and eight-fold positions of coordination number 16 have the largest volume per atom and are found to be occupied by the largest atom, Mo. Also, the positions with smallest volume per atom are occupied by Fe, which is usually smaller than Cr.

The structural features may be best appreciated from a consideration of the polyhedral configurations of nearest neighbors surrounding the different kinds of atoms. In this respect, both Mo atoms appear to be similar. Mo_I has only two kinds of neighbors: twelve D_2 atoms (Fe) and four Mo_{II} atoms. The twelve D_2 atoms form a regular polyhedron depicted in Figure 1, which can be described

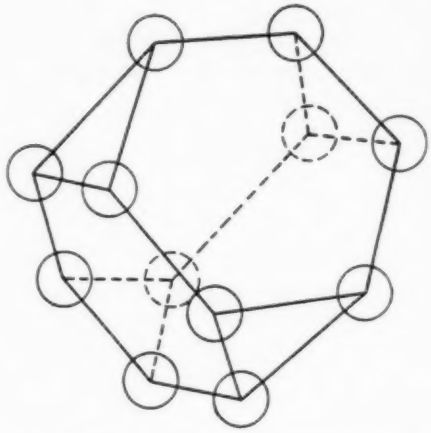

FIGURE 1. The polyhedron of D_2 atoms surrounding Mo_I. Four Mo_{II} atoms, not shown, are along perpendicular directions through the centers of the hexagons.

as formed by positive and negative tetrahedra truncating each other. The four Mo_{II} neighbors on the outside of this figure form a regular tetrahedron. A similar, somewhat distorted, geometrical arrangement of neighbors occurs around Mo_{II}. Here, the twelve-vertex polyhedron is composed of nine D_2 and three D_1 atoms, while the exterior tetrahedron is made up of one Mo_I and three D_1 atoms. For the completely ordered situation, there would then be twelve Fe, three Cr and one Mo neighbors for Mo_{II}. If one attributes to Cr the role of substituting for the chemically similar element, Mo, the similarity of Mo_{II} to Mo_I with respect to its ligands becomes apparent. Both atoms can be described as having two kinds of bonds; twelve with Fe, and four to either Mo only, or to Mo and Cr. It is interesting that only the ratio of 36 Fe to 12 Cr would allow such a simplification of description.

A distorted icosahedral configuration of neighbors occurs about the atoms D_2. Icosahedra which are more regular are found to surround certain atoms in the σ-phase structure. It is also indicated that elements such as Cr or Mo do not occupy the centers of icosahedra in the σ-phase structure [3]. It is of interest then that Cr atoms tend not to occupy the D_2 positions in χ-phase. A relationship of the structures of these two phases may be seen

in that both contain icosahedral configurations, which, however, are arranged differently in the two cases.

The configuration about the D_1 atoms is more complex and less readily interpretable.

It is illuminating to consider also the Pauling valences, calculated from the expression, D (1) $-$D (n) = 0.6 log n, the numbers for which are given in Table IV. In this scheme, the usual valence would be about 6 for Fe, Cr or Mo. In χ-phase, it appears that only the D_1 atoms are of abnormally low valence. This is in contrast to the situation for α-Mn itself, where it is indicated that the atoms in positions 2*a* and 8*c* also have low valence [4]. In other words, two sets of low-valent Mn atoms in the α-Mn structure can be replaced by the larger Mo atoms, without detectable distortion of structure and with no abnormally low valence any longer associated with atoms in these sites. This result as well as the size considerations suggest that χ-phase may not be an electron-type compound, but that its formation is governed primarily by size factors.

As a consequence of this study, it would seem that other ternary systems containing Mo and Cr could form the same structure. It is implied that the atomic fraction of Mo could be fixed at 10/58, and different proportions of Cr with another element such as Co would then have to be investigated.

Acknowledgement

The author gratefully acknowledges the contribution of Mr. R. Waterstrat to all phases of this work, especially in deducing the geometrical relationships of the structure. The advice of Dr. J. G. McMullin, as well as his provision of samples, are also happily acknowledged. Dr. B. W. Roberts kindly obtained a portion of the neutron diffraction data.

References

1. Andrews, K. W. and Brookes, P. E. Metal Treatment and Drop Forging, July 1951, p. 301.
2. McMullin, J. G., Reiter, S. F. and Ebeling, D. G. Equilibrium Structures in Fe-Cr-Mo alloys. Trans. ASM **46** (1954).
3. Kasper, J. S. and Decker, B. F. The Crystal Structure of Co-Cr Sigma Phase. To be published.
4. Pauling, L. J. Am. Chem. Soc. **69** (1947) 542.

SOME OBSERVATIONS ON HETEROGENEOUS NUCLEATION OF SODIUM CRYSTALS FROM ATOMIC BEAMS*

L. YANG,† C. E. BIRCHENALL,‡ G. M. POUND,† and M. T. SIMNAD†

A vapor effusion apparatus was developed to measure critical supersaturation ratios for nucleation of metal crystals on various substrates. Deposition from sodium vapor beams was studied as a function of temperature and lattice misfit between the body-centered cubic sodium crystal and the various crystalline substrates. These substrate surfaces probably were coated with adsorbed gas films. The critical supersaturation ratios for the deposition of sodium are very high, ranging from 10^{19} at 159°K to 10^{11} at 213°K. The data are fitted by a rate equation whose kinetic coefficient was derived on the basis of an adsorption and surface diffusion mechanism. This treatment leads to an evaluation of the standard free energy of adsorption of the metal atoms. The critical nucleus size is calculated from the data to be about the size of a unit cell (9 Na atoms). The potencies of the metal substrates (face-centered cubic, Ag, Pt, Cu and Ni) for catalysis of nucleation are about the same. The potency of CsCl (body-centered cubic) is much higher than that of the metal substrates, possibly indicating a smaller gas adsorption on the CsCl surface. However, there is a small decrease in catalytic potency with increase in disregistry at the higher temperatures in qualitative agreement with the Turnbull-Vonnegut theory.

QUELQUES OBSERVATIONS SUR LA CONDENSATION HÉTÉROGÈNE DE CRISTAUX DE SODIUM À PARTIR D'UN FLUX D'ATOMES

On a développé un appareil d'effusion de vapeur, en vue de mesurer les rapports critiques de sursaturation pour la germination de cristaux métalliques sur divers supports. Le dépôt, à partir de flux de vapeur de sodium, a été étudié en fonction de la température et de la différence du degré d'ajustement entre le cristal cubique centré de sodium et la structure cristalline des divers supports. Les surfaces de support étaient, probablement, couvertes de couches de gaz adsorbé. Les rapports critiques de sursaturation pour le dépôt de sodium sont très grands et vont de 10^{19} à 159°K jusqu'à 10^{11} à 213°K. Les données obtenues sont en accord avec une équation de vitesse, dont le coefficient cinétique a été déterminé en se basant sur un mécanisme d'adsorption et de diffusion sur la surface. Les dimensions calculées du germe critique sont celles de la maille cristalline (9 atomes de Na). Le pouvoir catalytique de germination, des métaux utilisés comme supports (Ag, Pt, Cu, Ni, tous cubiques à faces centrées), est à peu près le même. Le pouvoir de CsCl (cubique centré) est de beaucoup supérieur à celui des supports métalliques, ce qui indique, probablement, une adsorption moins importante des gaz sur la surface de CsCl. On note, cependant, une légère diminution du pouvoir catalytique quand le degré d'ajustement diminue aux températures plus élevées, en accord qualitatif avec la théorie de Turnbull-Vonnegut.

EINIGE BEOBACHTUNGEN ZUR HETEROGENEN KONDENSATION VON NATRIUMKRISTALLEN AUS ATOMSTRAHLEN

Es wurde eine Dampfausströmungsapparatur entwickelt um das Verhältnis der kritischen Übersättigungen der Keimbildung von Natriumkristallen auf verschiedenen Trägern zu messen. Die Abscheidung aus Natriumdampfstrahlen wurde als Funktion der Temperatur und der Gitterfehlordnung zwischen dem kubisch-flächenzentrierten Natriumkristall und den verschiedenen kristallinen Trägern gemessen. Diese Trägeroberflächen waren wahrscheinlich mit adsorbierten Gasfilmen bedeckt. Die kritischen Übersättigungsverhältnisse für die Abscheidung von Natrium sind sehr gross; sie liegen zwischen 10^{19} bei 159°K und 10^{11} bei 213°K. Diese Werte werden in Reaktionsgleichungen eingesetzt, deren kinetische Koeffizienten auf Grund eines Adsorptions- und Oberflächendiffusionsmechanismus abgeleitet wurden. Die aus diesen Daten berechnete kritische Keimgrösse ist etwa von der Grösse der Elementarzelle (9 Na Atome). Die Fähigkeit der verschiedenen metallischen Träger, (kubisch-flächenzentriertes Ag, Pt, Cu und Ni) die Keimbildung zu katalysieren, ist gleich gross. Die entsprechende Katalysationsfähigkeit des kubisch-raumzentrierten CsCl ist wesentlich grösser als die der Metalle, was vielleicht auf eine geringere Gasadsorption auf der CsCl Oberfläche hindeuten kann. Man findet jedoch eine geringe Abnahme in der Katalysationsfähigkeit mit der bei zunehmender Temperatur abnehmenden Ordnung im Gitter; diese Erscheinung stimmt qualitativ mit der Theorie von Turnbull und Vonnegut überein.

Introduction

It is generally recognized that in the transformation of an unstable phase to a stable one by the nucleation and growth mechanism nucleation seldom occurs homogeneously. Unless special precautions are taken, it usually takes place on the surfaces of some impurities (or nucleation catalysts) which, by decreasing the free energy of formation of the nucleus, cause the nucleation rate to become appreciable at a much lower supersaturation or supercooling. There are some kinetic data available, namely those of Turnbull [1], Pound and LaMer [2], and Vonnegut [3] on crystalline nucleus formation in supercooled liquids, by which the theory of heterogeneous nucleation can be tested and the factors controlling the process analyzed. The work described here was carried out with the purpose of

*Received December 14, 1953.

†Metals Research Laboratory, Carnegie Institute of Technology, Pittsburgh, Pennsylvania.

‡Now of the Chemistry Department, Princeton University, Princeton, New Jersey.

augmenting the data on heterogeneous nucleation of metal crystals from the vapor phase so that a better understanding of this process and its controlling factors may be obtained. In the present work, the critical supersaturation for the condensation of sodium crystals from vapor on a number of substrates (or nucleation catalysts) of increasing lattice misfit with sodium was measured in the temperature range of 159°–213°K for the purpose of finding out how the structure and the temperature of the catalyst affect its potency to promote nucleation.

Although a large amount of work has been done on the structures of metal crystals condensed on substrates in connection with the study of epitaxy, very few data are available on the critical supersaturation needed to start the condensation and how it is affected by various factors. Estermann [4] in 1925 studied the condensation of Cd on various substrates in the temperature range of −83°C to −111°C and found Cd condensed at lower supersaturations on Ag than on Cu, while glass was the least effective in starting the condensation. Cockcroft [5] in 1928 made a careful study of the critical supersaturations for the condensation of Cd on Cu at six different target temperatures between −92°C and −155°C and also the condensation of Cd on Ag, Cu and glass at −137°C. He could not find any difference in the critical supersaturations for condensation on these different substrates and suggested that this might be due to the existence of a gas film on the surface of these substrates which masked the true surface forces. In 1949, Rhodin [6] measured the critical pressures of condensation of Al on glass and on different single crystal mineral surfaces, from which he deduced the binding energies between the initial layer of Al deposit and the substrates. By assuming the binding force to be van der Waals in nature, he calculated these binding energies and found that the calculated values agreed with the experimental ones. Recently, Devienne [7] studied the condensation of radioactive Cd at 300°K and found he could detect adsorption at a much lower supersturation than that extrapolated from Cockcroft's results [5].

The theory of heterogeneous nucleation of crystals from the supercooled liquid has been successfully treated by Fisher [8], Turnbull [8; 9; 11], and Hollomon [10; 11]. Also, Volmer [12] has considered nucleation in the electro-deposition of metals. However, in the present case of heterogeneous nucleation from the vapor a different mechanism may be operating, and it is thought that adsorption and surface diffusion play important roles in the nucleation process. In a separate publication [13], an equation is derived for nucleation rate from the vapor of condensed phases on substrates. In this derivation it is assumed that the atoms from the vapor become adsorbed on the substrate and travel over the surface until they either evaporate off or join other adsorbed atoms to form a stable, cap-shaped nucleus by statistical fluctuations.

This equation is:

$$(1)\quad I = (\alpha \Gamma a_0 \sigma \sin\theta/2\, mk\nu)\ (p'^2/-\Delta F_v T) \exp\left[-(2\Delta F^\circ_{ad} + \Delta F^*_D + \Delta F^*)/kT\right]$$

where

α = the condensation coefficient, assumed = 1
= fraction of adsorbed atoms striking developing nucleus that become attached

Γ = the Zeldovich nonequilibrium factor (usually not appreciably different from unity)

a_0 = substrate lattice constant

σ = condensed phase-vapor interfacial free energy/unit area

ν = vibration frequency of substrate surface atoms

m = mass of the atom being deposited

p' = equivalent partial pressure of vapor

ΔF_v = bulk free energy change/unit volume of condensed phase $= -(RT/V) \ln p'/p$

v = molar volume of condensed phase

p = equilibrium vapor pressure of bulk condensed phase

ΔF°_{ad} = standard free energy of adsorption per atom (−)

ΔF^*_D = free energy of activation of surface diffusion (+)

ΔF^* = standard free energy of formation of a critical nucleus $= 16\pi\sigma^3\phi(\theta)/3\Delta F_v^2 kT$. (+)

and

$\phi(\theta)$ = function of the substrate-condensed phase contact angle
$= (2 + \cos\theta)(1 - \cos\theta)^2/4$.

It is probably true that σ, θ, ΔF°_{ad}, and ΔF^*_D are not known with sufficient precision to permit a calculation of the critical supersaturation. However, the equation will prove useful in analyzing the present data. The coefficient terms are relatively insensitive to temperature, but the exponential is strongly temperature-dependent. Grouping the coefficient terms into a constant and assuming

$\Delta F^*_D \ll |2\Delta F^\circ_{ad}|$ or ΔF^* in the present case of sodium deposition, one gets:

$$(2) \quad I = C \cdot \exp(-2\Delta F^\circ_{ad}/kT) \cdot \exp(-\Delta F^*/kT)$$

or

$$I = C \cdot \exp(-2\Delta F^\circ_{ad}/kT \cdot \exp((-16\pi\sigma^3\phi(\theta)/3\Delta F_v^2 kT).$$

It can be shown from an evaluation of the factor C in (2) that the surface diffusion mechanism leads to a nucleation rate at least 10^2 to 10^3 greater than that calculated on the basis of direct addition of atoms to the critical nucleus from the vapor phase [13].

Due to the strong dependence of I on $\Delta F_v = -(RT/V)\ln p'/p$, it is permissible to define the critical supersaturation S as the ratio of p'/p required to make $I = 1$ cm^{-2} sec^{-1} or $\ln I = 0$ [14]. Evaluating the kinetic coefficient in (2) and rearranging [13], one gets:

$$(3) \quad (1/\Delta F^*_v)^2 = 2kT(9 + \ln p')/B\phi(\theta) - 2\Delta F^\circ_{ad}/B\phi(\theta)$$

where

$$\Delta F^*_v = -(RT/V)\ln(p'/p)_{crit.}$$

and

$$B = 16\pi\sigma^3/3.$$

This equation should provide a satisfactory description of the temperatures dependence of ΔF^*_v, the critical free energy change per unit volume of stable phase condensing on a given substrate.

An interesting relationship between the critical free energy of transformation per unit volume ΔF^*_v and the lattice misfit δ between the substrate and the substance deposited on it has been derived by Turnbull and Vonnegut [15]. The derivation is based on Turnbull's equation for the rate of heterogeneous formation of crystalline nuclei and the dislocation model of interphase boundaries developed by Van der Merwe and by Brooks. By taking into consideration the strain energy in the nucleus, these authors conclude that in the heterogeneous transformation of liquid to solid there is a parabolic relationship between $|\Delta F^*_v|$ and δ if the nucleus forms coherently on the substrate, where

$$\delta = \frac{(a_0)\text{ substrate} - (a_0)\text{ nucleus}}{(a_0)\text{ nucleus}},$$

a_0 being the lattice parameter. When the nucleus forms incoherently, the relationship is not parabolic but linear. These conclusions have not yet been tested by systematic experiments, but the present data will be considered in the light of this theory.

Experimental

1. *Arrangement of the Apparatus*

The arrangement of the apparatus is shown in Figure 1. The sodium source is a small pyrex glass boiler A with a hole of 1 mm diameter on top. The

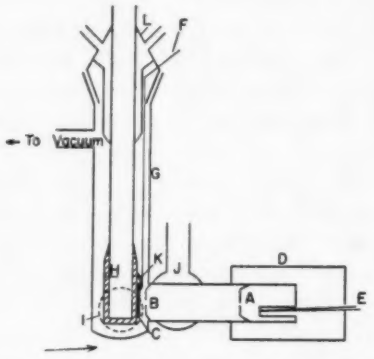

FIGURE 1. Apparatus for sodium condensation. A: orifice and boiler, orifice size—1 mm diameter. B: collimator. C: target. D: furnace. E, F: thermocouples. G: vacuum jacket. H: target support. I: flat glass window. J: cooling jacket for collimator. K: small clamp. L: condenser to protect ground joints.

boiler is heated by the furnace D which has extra windings of nichrome wire near the orifice to prevent any condensation there. The temperature of sodium in the boiler is measured with a copper-constantan thermocouple E inserted inside a thermocouple well embedded in the molten sodium. The heating current is drawn from a variac and adjusted manually. By careful observation, the temperature of the furnace in one run can be controlled to within ± 2°C. B is a collimator made of pyrex glass and sealed to the system. It has a circular hole of 2 mm diameter on the side facing the target. The collimator is cooled by dry ice-acetone mixture in the cooling jacket J so that any atom hitting the side of the collimator is condensed there. H is a copper tube sealed at one end and joined to the pyrex system at the other. The lower part of H is polished and exhibits four flat faces. The target, if it is metallic, is electroplated on H from a carefully purified bath; the thickness of the deposit is about 25 microns in each case. The plating is always done just before the target is going to be used. When a nonmetallic target like CsCl is needed, a solution of CsCl is prepared and a drop of the solution is spread on the surface of a thin microscope-slide cover glass which has been cleaned in chromic acid mixture, washed, and dried. After the water evaporates away, the glass is held against H by a small clamp K and put into the system. The temperature

of the target can be varied by putting a small heater or different cooling agents inside H. The temperature of the target surface is measured with another copper-constantan thermocouple F pressed against the target surface by the clamp K. The cooling agents used were melting diethyl ether (−114°C), melting toluene (−95°C), dry ice-acetone mixture (−78°C) and melting chloroform (−63°C). The targets used were CsCl, Ag, Pt, Cu and Ni. The distance between the orifice and the hole of the collimator is 5.5 cm and that between the latter and the target surface 0.5 cm. The glass vacuum jacket G has a flat glass window I through which the target can be examined by means of a microscope after it is brought to face the window by rotating the ground joint. The joint is protected by a water jacket L when the target is heated for outgassing.

The system is evacuated by a two-stage oil diffusion pump backed by a Cenco Hypervac mechanical pump and the pressure in the system is read from an ionization gauge.

The sodium used was of a chemically pure grade which had been further purified according to the procedures described by Strong [16]. It was distilled into the boiler in vacuum. The condensation of sodium on the target was always carried out at residual gas pressures less than 5×10^{-5} mm Hg. Even at this low residual gas pressure it is probable that considerable gas was adsorbed on the substrate surface [13].

2. *Experimental Procedures*

After the target is put in position, the system is evacuated to better than 10^{-5} mm Hg and purified sodium is distilled into the boiler through a side arm when the boiler is cooled with dry ice. After the distillation is completed, the side arm is sealed off. The temperature of the target is then brought to 350°C and pure hydrogen, freed from oxygen and water by passing through heated copper turnings and a liquid-nitrogen trap, is circulated through the system for two hours to remove any oxide layer which may be present on the target surface. The system is again evacuated and the target maintained at 350°C for another hour to outgas before it is cooled to the desired temperature. The collimator is then cooled with dry ice-acetone mixture and the temperature of the furnace brought to 150°C. It is then raised slowly, stopping at each 10°C-interval for 30 minutes. The target is rotated to face the window at the end of each interval and examined with a 40× microscope to see if there has been any deposit formed. In this way the critical temperature of condensation can be roughly fixed. The same procedures are repeated in a second experiment except that the examination of the target is made for each 5°C-increase of furnace temperature in the vicinity of the temperature found in the first run, and the waiting time is increased to one hour for higher critical condensation pressures and up to six hours for lower critical condensation pressures. The experiment is repeated until a reproducible (within ±2°C) critical temperature T_0 of the sodium source (corresponding to vapor pressure of sodium p_0) is obtained below which no condensation is observed. Since the number of sodium atoms colliding with unit target area in one second is, according to Estermann [4], $(p_0/\sqrt{2\pi mkT_0})(f_0/\pi r^2)$, which is equivalent to that produced by sodium vapor at temperature T and pressure $(p_0 f_0/\pi r^2)\sqrt{T/T_0}$, the critical supersaturation S for condensation on a target at temperature T is therefore:

$$S = \frac{p_0}{p} \cdot \frac{f_0}{\pi r^2} \sqrt{\frac{T}{T_0}} \quad (4)$$

where p is the vapor pressure of sodium at temperature T, f_0 the area of the orifice, and r the distance between the orifice and the target. For higher critical pressures of condensation p_0 of the order of 0.1 mm Hg, the amounts of sodium condensed in a given time on targets maintained at −114°C have been determined by titration with standard HCl and the results are used to calculate the supersaturation, since the effusion law may not be obeyed at these high pressures. The vapor pressure of liquid sodium is calculated from the equation: $\log_{10} p(\text{mm}) = 7.553 - (5395/T)$ [17] which is valid from 180°C to 883°C. The vapor pressure of solid sodium is calculated from the equation: $\log_{10} p_{\text{mm}} = 7.912 - 5528/T$, which was obtained from the equation for the liquid by standard methods.

Results

The results are shown in Table I. For the purpose of comparison, the data obtained by Cockcroft [5] on the condensation of cadmium on copper at six different temperatures between 118°–181°K are listed in Table II. In both tables, besides the ex-

*The momentum of the sodium atoms reaching the target surface corresponds to T_0 and not T. The calculation of supersaturation in this way involves the assumption that the sodium atoms reaching the target are all adsorbed, temporarily at least, thus attaining the temperature of the target.

TABLE I

CRITICAL SUPERSATURATION FOR THE CONDENSATION OF SODIUM ON VARIOUS SUBSTRATES

Target	Structure	D (%)	T (°K)	T_0 (°K)	p_0 (10^{-4} mm)	S	$-\Delta F^*_v$ (cals/cc)
CsCl	B.C.C.		163	493	4.01	1.66×10^{18}	563
	4.110 *A*	4.0	183	520	16.0	1.33×10^{15}	527
			199	553	62.1	1.92×10^{13}	505
			213	598	113	5.27×10^{11}	475
Ag	F.C.C.		159	513	11.3	3.22×10^{19}	593
	4.078 *A*	4.8	178	548	50.5	2.83×10^{16}	559
			195	583	196	2.28×10^{14}	534
			210	613	566	6.24×10^{12}	514
Pt	F.C.C.		159	513	11.3	3.22×10^{19}	593
	3.915 *A*	8.5	178	545	45.0	2.52×10^{16}	558
			195	587	225	2.57×10^{14}	536
			210	623	782	8.58×10^{12}	520
Cu	F.C.C.		159	513	11.3	3.22×10^{19}	593
	3.607 *A*	15.8	178	553	63.5	3.54×10^{16}	564
			195	593	284	3.24×10^{14}	541
			210	631	1010	1.01×10^{13}	522
Ni	F.C.C.		159	515	11.8	3.38×10^{19}	594
	3.517 *A*	17.9	178	548	50.5	2.83×10^{16}	560
			195	593	284	3.24×10^{14}	541
			210	633	1080	1.10×10^{13}	524

B.C.C. = body-centered cubic
F.C.C. = face-centered cubic
D = percentage difference between the lattice dimension of the target and that of sodium (B.C.C. 4.282 A)
T = target temperature
T_0 = temperature of sodium source when condensation starts
p_0 = vapor pressure of sodium at T_0
S = critical supersaturation for condensation
$-\Delta F^*_v$ = critical free energy of transformation per unit volume of condensed metal

TABLE II

CRITICAL SUPERSATURATION FOR THE CONDENSATION OF CADMIUM ON COPPER, CALCULATED FROM COCKCROFT'S DATA [5]

T (°K)	n (cm^{-2} sec^{-1})	S	$-\Delta F^*_v$ (cals/cc)
118	4×10^{12}	1.3×10^{33}	13_{73}
136	4×10^{13}	2.9×10^{27}	13_{18}
140	8×10^{13}	3.4×10^{26}	13_{05}
147	2.4×10^{14}	1.1×10^{25}	12_{94}
160	1×10^{15}	2.3×10^{22}	12_{55}
181	9×10^{15}	1.3×10^{19}	12_{18}

T = temperature of target
n = critical number of atoms per cm^2 per second arriving at the target surface for the condensation to start.
S = critical supersaturation for condensation
= $(n\sqrt{2\pi mkT})/p$, where p is the vapor pressure of Cd at T.
$-\Delta F^*_v$ = critical free energy of transformation per unit volume of condensed metal.

perimental data, the following terms calculated from these data are included:

1. The critical supersaturation for condensation S. For the condensation of sodium, this is calculated according to the method described in the preceding paragraph. For the condensation of cadmium, Cockcroft gave the critical number n of cadmium atoms reaching unit target surface /sec for the condensation to start at target temperature T, which is equivalent to that produced by cadmium vapor at temperature T and pressure $p' = n\sqrt{2\pi mkT}$. The critical supersaturation for condensation S is therefore equal to $(n\sqrt{2\pi mkT})/p$, where p is the vapor pressure of cadmium at temperature T, calculated from the equation $\log_{10} p(mm) = -5908/T - 0.232 \log T - 0.284 \times 10^{-3}T + 9.711$ [18], assuming this equation is applicable to the low target temperatures used by Cockcroft.

2. The critical free energy of transformation per unit volume of metal condensed ΔF^*_v. This is calculated from the equation:

$$\Delta F^*_v = -\frac{RT}{v} \ln S,$$

where R is the gas constant 1.98 cal/degree and $v = M/\rho$ is the molar volume of the metal crystals, M being the atomic weight and ρ the density of the solid metal.

Discussion of Results

The critical supersaturations for the condensation of sodium and cadmium in the temperature range used in these experiments are extremely high. For sodium (159°–213°K) S is from 10^{19}–10^{11} and for cadmium (118°–181°K) S is from 10^{33}–10^{19} as compared to the value of 4.2 for the heterogeneous nucleation of water vapor on gaseous ions at 275°K. This is because of the low values of T and high values of σ in these cases. The exponential term ΔF^* in equation (1) has a factor of $(\sigma/T)^3$ in the numerator and a factor $(\log S)^2$ in the denominator. A small increase of the ratio σ/T therefore needs a much higher value of S to compensate it. Also, as will be shown in the following, the substrate surfaces were not highly effective nucleation catalysts.

The correlation of the temperature dependence of the measured ΔF^*_v by equation (3) is shown in Figure 2. It is seen that the data plot to give reasonably good straight lines. This does not constitute a proof of the proposed adsorption and surface diffusion mechanism but does show that an equation based on such a mechanism can describe the data. In Figure 2, nucleation of sodium vapor on all of the metal substrates is described by the

same straight line. This probably means that the surfaces of all of the metals were masked with an adsorbed layer of residual gas. Such an hypothesis seems reasonable because at 10^{-5} mm of residual gas pressure the frequency of impacts of gaseous molecules as computed from $p/\sqrt{2\pi mkT}$ could lead to formation of an adsorbed monolayer in about 1 second, assuming that most of the impinging molecules become adsorbed. The line in Figure 2 for deposition of sodium on the CsCl substrate is considerably above that for the metal substrates, indicating that the CsCl is a more potent nucleation catalyst. Possibly this means that gas adsorption was not as complete on the CsCl surface. This hypothesis of residual gas adsorption is the subject of an extended research program in which extremely high vacua (10^{-10} mm) are being employed. At present the authors prefer to explain the above results by gas adsorption rather than in terms of structural characteristics of the substrates.

Figure 3 shows the correlation of Cockcroft's data for the nucleation of cadmium on copper by equation (3).

From the slopes of the lines in Figures 2 and 3,

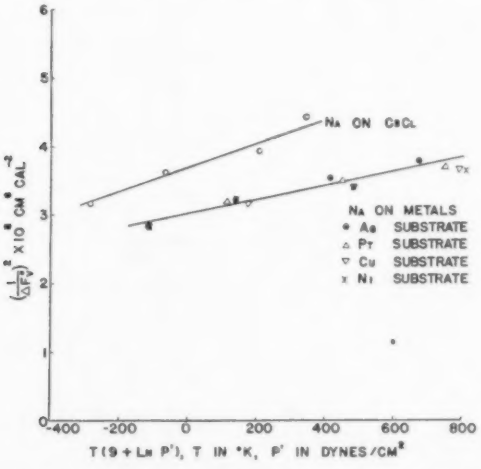

FIGURE 2. Dependence of critical free energy change on temperature. Na on various substrates.

reasonable values are obtained for $\sigma^3\phi(\theta)$. Assuming that the method of Turnbull [19] for determining the crystal-vapor interfacial free energy σ of a metal is applicable to the present case of very small critical nuclei, σ was calculated for Na and for Cd. Near the melting point, $\sigma_{Na(l)-Na(v)}$ is about 290 ergs/cm² [20] and $\sigma_{Cd(l)-Cd(v)}$ is about 630 ergs/cm² [21]. By using Turnbull's relationship [19] between the gram atomic interfacial energy and the gram atomic heat of fusion, $\sigma_{Na(c)-Na(l)}$ is about 20 ergs/cm² and $\sigma_{Cd(c)-Cd(l)}$ 70 ergs/cm². Therefore, near the melting point, $\sigma_{Na(c)-Na(v)}$ is about 310 ergs/cm² and $\sigma_{Cd(c)-Cd(v)}$ 700 ergs/cm². These values would probably be somewhat higher at the lower temperatures of the present experiments. Using appropiate values of σ and $\sigma^3\phi(\theta)$ obtained from the slopes of the lines in Figures 2 and 3, $\phi(\theta)$ for sodium on metals computes to be 0.64 corresponding to a contact angle θ of 101 degrees. The computed contact angles for sodium on CsCl and cadmium on copper are 81 degrees and 99 degrees respectively. These high contact angles indicate the

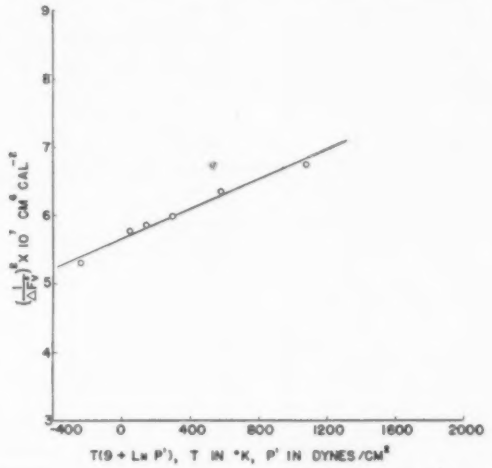

FIGURE 3. Dependence of critical free energy change on temperature. Cd on Cu (data of Cockcroft).

poor "wetting" by the sodium or cadmium of the substrates, and are consistent with the very high critical supersaturations required for deposition. This result would be expected if the metal substrates were coated with adsorbed gas films.

From the intercepts of Figures 2 and 3, the standard free energies of adsorption ΔF°_{ad} compute to be -5750 cal/gm atom for sodium on the metals, -4220 for sodium on CsCl, and $-10{,}300$ for cadmium on copper.* In a separate research program the present authors are investigating ΔF°_{ad} through equilibrium adsorption measurements involving metal vapors on various substrates.

The $-\Delta F^*_v$ for sodium condensation varies from 475 to 595 cal/cc and that for cadmium condensation from 1200–1370 cal/cc in the temperature range indicated above. Taking an average value of 530 cal/cc for the former and 1285 cal/cc for the latter and assuming the contact angle between the condensate and the substrate to be about 90

*This standard free energy of adsorption for Cd on Cu appears to be high inasmuch as it leads to an adsorption of greater than one monolayer under the conditions of Cockcroft's experiments [13].

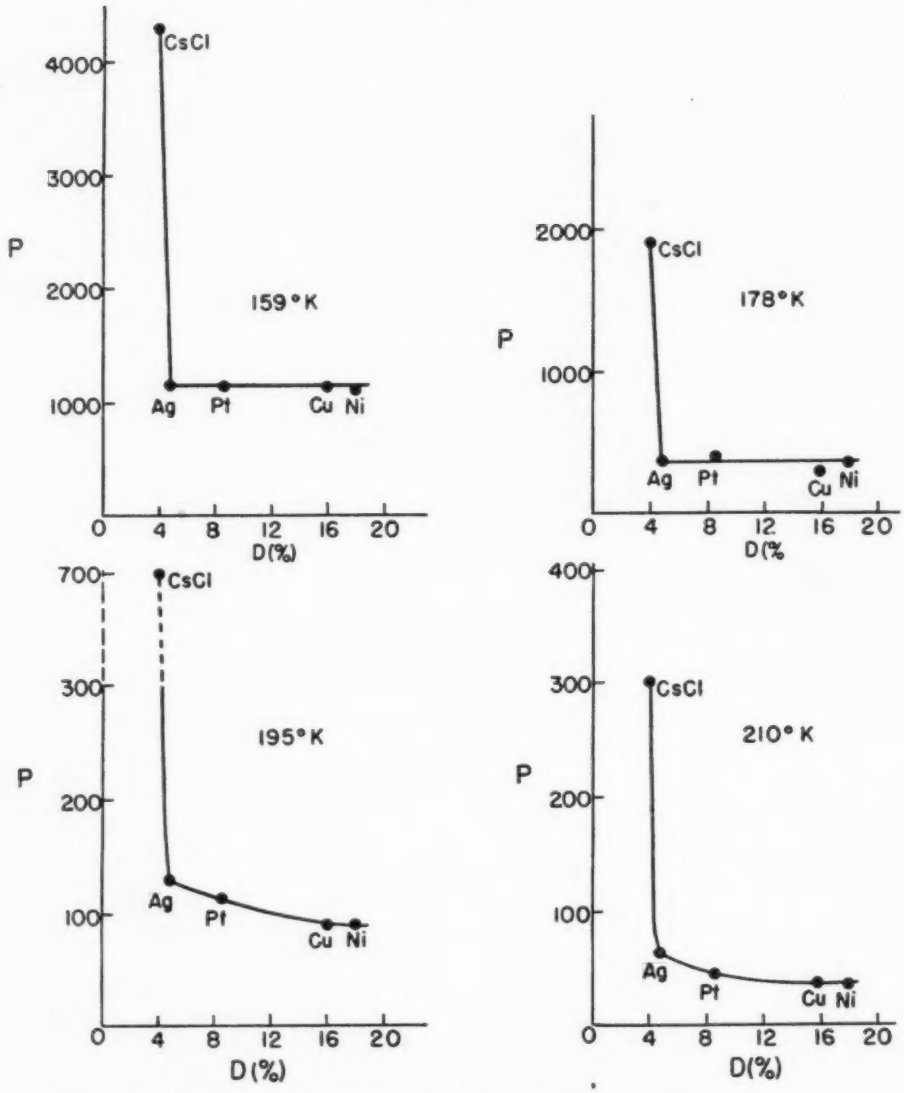

FIGURE 4. Variation of the potency with lattice misfit, P expressed in arbitrary units.

(a) = unit cell dimension

D = lattice misfit $= \dfrac{(a)_N - (a)_{target}}{(a)_{Na}} \times 100$

P = potency $= \dfrac{\text{critical supersaturation calculated for homogeneous nucleation}}{\text{critical supersaturation found experimentally}}$

[Note: CsCl data interpolated or extrapolated.]

degrees, then from the Gibbs-Thomson formula $r^* = (-2\sigma/\Delta F^*_v) \sin\theta$ we can estimate that the radius of the nucleus of critical size is about 3.0 Å for sodium ($\sigma \sim 310$ ergs/cm²) and 2.6 Å for cadmium ($\sigma \sim 700$ ergs/cm²). The diameter of the critical nucleus is therefore 6.0 Å and 5.2 Å respectively, as compared to the value of 4.3 Å for the length of the unit cell of sodium and the values of about 3.0 Å (a-axis length) or 5.6 Å (c-axis length) for cadmium. The size of the critical nucleus is therefore about the size of a unit cell of sodium (containing 9 atoms) or cadmium (containing 9 atoms). In Figure 2, two higher temperature points for the copper and nickel substrates seem to fall beyond the precision measure of the proposed correlation. In an effort to detect any systematic variation of catalytic potency for nucleation with disregistry between the sodium crystal and the substrate, a potency function P was

defined and plotted versus disregistry. P is defined as S_0/S, where S_0 and S are the critical supersaturations needed respectively for the homogeneous nucleation and the heterogeneous nucleation on a particular substrate at the same temperature. It must be pointed out that P thus defined represents the ability of the nucleation catalyst to make the process less homogeneous, i.e., to cause a bigger deviation of S from its corresponding S_0 at the same temperature. When the P-values of different substances are compared at the same temperature, a higher P means a lower S, since S_0 is a constant. S_0 was calculated by means of the Becker-Doering equation [22] for homogeneous nucleation from the vapor. The necessary crystal-vapor interfacial free energy was estimated as described above. The results are shown in Figure 4. For the metallic substrates there is almost no difference in their potencies at lower target temperatures (159° and 178°K). At higher target temperatures (195°K and 210°K), there is a small but unambiguous increase in potency with decrease of lattice misfit between the substrate and sodium. The same effect is shown in the plot of Figure 5. These results are in general

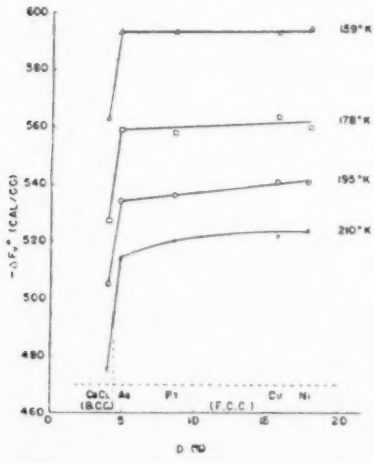

FIGURE 5. Measured critical free energy change versus substrate disregistry with sodium (B.C.C.).

qualitative agreement with the theory of Turnbull and Vonnegut [15] that relates critical free energy change and disregistry with the substrate in liquid-crystal nucleation. It may be that the hypothesized film of residual gas adsorbed on a substrate is not as thick at the higher temperatures, allowing the surface forces of the substrates to exert some effect. However, the present authors propose to defer discussion of this point until more data become available.

Acknowledgment

The authors would like to express their sincere thanks to Dr. Robert F. Mehl for many helpful discussions.

The research described in this paper was sponsored by the Geophysics Research Division, Air Force Cambridge Research Center, Cambridge, Massachusetts, under Contract No. AF 19(122)-185.

References

1. TURNBULL, D. J. Chem. Phys. **20** (1952) 411.
2. POUND, G. M. and LA MER, V. K. J. Am. Chem. Soc. **74** (1952) 2323.
3. VONNEGUT, B. J. Colloid Sci. **3** (1948) 563.
4. ESTERMANN, I. Zeit. Elektrochem. **31** (1925) 441.
5. COCKCROFT, J. D. Proc. Roy. Soc. **A119** (1928) 293.
6. RHODIN, T. N., JR. Trans. Faraday Soc. (1949), Discussion on Crystal Growth, p. 218.
7. DEVIENNE, F. M. J. Phys. Radium **13**, no. 2 (1952) 53.
8. TURNBULL, D. and FISHER, J. C. J. Chem. Phys. **17** (1949) 71.
9. TURNBULL, D. J. Appl. Phys. **21** (1950) 1022.
10. HOLLOMON, J. H. Thermodynamics in Physical Metallurgy (Cleveland, Ohio, Amer. Soc. Metals, 1950) 161–77.
11. HOLLOMON, J. and TURNBULL, D. Progress in Metals Physics, vol. 4 (New York, Interscience, 1952).
12. VOLMER, M. Zeit. Elektrochem. **35** (1929) 555.
13. POUND, G. M., SIMNAD, M. and YANG, LING. J. Chem. Phys. (in press).
14. POUND, G. M. Ind. Eng. Chem. **44** (1952) 1278.
15. TURNBULL, D. and VONNEGUT, B. Ind. Eng. Chem. **44** (1952) 1292.
16. STRONG, J. Procedures in Experimental Physics, p. 534.
17. International Critical Table, vol. III, p. 205.
18. KUBASCHEWSKI, O. and EVANS, E. LL. Metallurgical Thermochemistry. p. 298.
19. TURNBULL, D. Thermodynamics in Physical Metallurgy (Cleveland, Ohio, Amer. Soc. Metals, 1950) 282–306.
20. QUINCKE, G. Ann. Physik **135** (1886) 621.
21. HOGNESS, T. R. J. Am. Chem. Soc. **43** (1921) 1621.
22. BECKER, R. and DOERING, W. Ann. Physik **24** (1935) 719.

A RADIOACTIVE TRACER STUDY OF SILVER CONDENSATION ON SUBSTRATES*

LING YANG, M. T. SIMNAD and G. M. POUND†

A vapor effusion apparatus was devised to study the deposition of a metal by radioactive tracer techniques. This apparatus is useful because it can measure amounts of less than a complete monolayer of deposited metal. In general, experimental conditions were such that, although supersaturation was above the critical, rate of supply of atoms was very slow. The condensation coefficients of silver vapor on substrates of gold and of glass at 192°C were measured as a function of time. The observed increases in condensation coefficient with time on the glass substrates are explained in terms of nucleation and growth on the substrate surface. The condensation coefficients of silver vapor on substrates of silver, gold, platinum, nickel, and glass at 192°C were measured with the time of condensation fixed at one hour. The lattice misfits between silver and these targets are 0, 0.18, 3.96, and 13.7 per cent, respectively. The corresponding condensation coefficients are 1.0, 0.99, 0.86, and 0.64, respectively, while that on glass is 0.31. Thus there seems to be a continuous decrease of condensation coefficient with increase of lattice misfit, which illustrates the importance of lattice disregistry in the condensation process. The variation of condensation coefficient with substrate metal indicates that there probably was no appreciable film of adsorbed gas on these substrate surfaces.

UNE ÉTUDE AUX TRACEURS RADIOACTIFS DE LA CONDENSATION DE L'ARGENT SUR DES SURFACES DE SUPPORT

Un appareil d'effusion de vapeur a été conçu de façon à permettre l'étude du dépôt d'un métal par les techniques des traceurs radioactifs. L'utilité de cet appareil se manifeste par le fait qu'il permet de mesurer des quantités inférieures à une couche monoatomique, complète, de métal déposé. En général, les conditions expérimentales étaient telles, que malgré une sursaturation supérieure à la valeur critique, la vitesse d'alimentation en atomes était très faible. Les coefficients de condensation de vapeur d'argent, sur des supports en or et en verre, à 192°C, furent mesurés en fonction du temps. Les accroissements du coefficient de condensation avec le temps, observés sur les supports de verre, sont expliqués en termes de germination et de croissance sur ces supports. Les coefficients de condensation des vapeurs d'argent sur des supports d'argent, d'or, de Platine, de nickel et de verre, à 192°C, ont été mesurés pendant un temps de condensation constant, fixé à une heure. Les départs de l'ajustement parfait entre les réseaux de l'argent et de ces supports sont de 0, 0,18, 3,96, et 13,7 pour cent respectivement. Les coefficients de condensation correspondants sont de 1,0, 0,99, 0,86, et 0,64 respectivement, alors que celui pour le verre est de 0,31. Il paraît y avoir, donc, une diminution continue du coefficient de condensation avec l'augmentation du manque d'augmentation entre les réseaux, ce qui met en évidence l'importance de l'ajustement du réseau dans le processus de condensation. La variation du coefficient de condensation avec le métal de support indique qu'il n'y avait probablement pas de couche importante de gaz, adsorbée sur la surface.

EINE UNTERSUCHUNG DER KONDENSATION VON SILBER AUF TRÄGERN MIT HILFE VON RADIOAKTIVEN INDIKATOREN

Es wurde eine Dampfausströmungsapparatur entwickelt um die Kondensation eines Metalles mit Hilfe von radioaktiven Indikatoren zu untersuchen. Der Wert dieser Apparatur besteht darin, dass sich das niedergeschlagene Metall in Mengen, geringer als eine vollständige Atomschicht, messen lässt. Im allgemeinen sind die experimentellen Bedingungen so, dass, obwohl die kritische Übersättigung überschritten ist, die Geschwindigkeit der Atomzufuhr sehr gering ist. Die Kondensationskoeffizienten von Silberdampf auf Gold- und Glasträgern wurden bei 192°C als Funktion der Zeit gemessen. Die beobachteten Zunahmen der Kondensationskoeffizienten auf Glasträgern mit zunehmender Zeit werden auf Grund von Keimbildung und Wachstum auf der Trägeroberfläche erklärt. Die Kondensationskoeffizienten von Silberdampf auf Silber-, Gold-, Platin-, Nickel- und Glasträgern wurden bei 192°C und einer auf eine Stunde festgesetzten Kondensationszeit gemessen. Die Gitterfehlordnung zwischen Silber und diesen Trägern beträgt 0; 0,18; 3,96 und 13,7% in der oben erwähnten Reihenfolge. Die dazugehörigen Kondensationskoeffizienten sind 1,0; 0,99; 0,86; 0,64 und 0,31 für Glas. Somit scheint eine kontinuierliche Abnahme des Kondensationskoeffizienten mit wachsender Gitterfehlordnung vorzuliegen. Diese Beobachtung zeigt die Bedeutung der Gitterbauabweichungen für den Kondensationsprozess. Die Tatsache, dass sich der Kondensationskoeffizient ändert, wenn man das Trägermetall variiert, deutet darauf hin, dass sich auf diesen Trägeroberflächen wahrscheinlich kein nennenswerter adsorbierter Gasfilm befand.

I. Introduction

In the preceding paper [1], the critical supersaturation for deposition from the vapor of metal crystals on substrates was discussed. The data given there clearly represented a relatively simple process of heterogeneous nucleation and accordingly were readily susceptible to mathematical treatment. In the present work, the condensation coefficient for deposition of silver from atomic beams on various substrates is considered. The condensation coefficient‡ is here defined as the ratio of the number of metal atoms remaining

*Received December 22, 1953.

†Metals Research Laboratory, Carnegie Institute of Technology, Pittsburgh, Pennsylvania.

‡Notice that this condensation coefficient is different from the one mentioned in equation (1) of the preceding paper [1]. There it referred to the fraction of adsorbed atoms striking the developing nucleus that become attached to the nucleus at least temporarily.

fixed on the substrate to the total number that strike the substrate.* It is clear that this condensation coefficient will be determined by the processes of nucleation and crystal growth occurring on the substrate. Accordingly, this phenomenon is not as simple as critical supersaturation and will require a more elaborate mathematical treatment for its description. Nevertheless, the experimental results for condensation coefficients as a function of time and lattice disregistry with silver will prove instructive.

In the present work, experimental conditions were such that, although supersaturation was above the critical, rate of supply of atoms was very slow. Accordingly, these measurements required a radioactive tracer technique that could measure amounts of less than a complete monolayer of deposited metal.

In the preceding paper [1], it was hypothesized that films of adsorbed residual gas covered the cold metal substrates. It is believed that no such films existed in the present study, because the measured condensation coefficient varies markedly with substrate metal. Actually, one might expect this because of the higher substrate temperature (192°C) in the present work.

There are very few other data for condensation coefficients of metal vapors on substrates. Recently, Devienne [4] studied the condensation of radioactive cadmium at 300°K and found he could detect adsorption at much lower supersaturations than those extrapolated from Cockcroft's results [5]. He also found that the condensation coefficients of radioactive Sb on Cu, Zn, glass, and Al were in the ratio of 1:0.59: 0.53: 0.44. His metal substrates were mechanically polished.

II. Arrangement of the Apparatus

The apparatus used for the evaporation of silver is shown in Figure 1. The silver source is a small Mo crucible *A* having a hole 1 mm in diameter at its top and containing about 30 mg of silver. The crucible is sitting on top of a Pt-Pt 10 per cent Rh thermocouple *G* and is surrounded by a tungsten spiral *E* and a Mo shield *B* (1/16 in. thick). Outside *B* there is another stainless steel shield, *C*, which has a circular hole of 10 mm diameter at its center. Above the hole there is a steel shutter *D* which can be opened or closed by means of a magnet outside the glass vacuum jacket *L*. The target *J*, which is 75 mm away from the crucible orifice, is held against a Kovar metal tube *H* by a stainless steel holder *I*. It can be heated or cooled by putting a small heater or a cooling agent in the Kovar tube which is sealed to a glass tube connected to the inner ground joint. The current for heating the target and that for heating the Mo crucibles

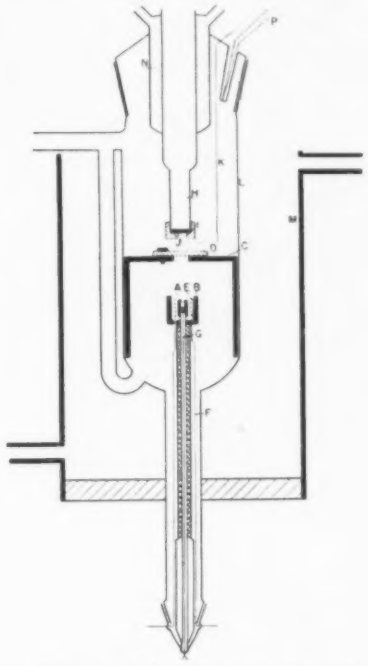

FIGURE 1. Apparatus for silver condensation. A: Mo crucible. B: Mo shield. C: stainless steel shield. D: steel shutter. E: tungsten spiral. F: lead wire for heating current. G: Pt-Pt Rh thermocouple. H: Kovar metal tube. I: stainless steel specimen holder. J: specimen. K: alumel-chromel thermocouple. L: pyrex vacuum jacket. M: water jacket. N: water jacket to protect ground joint. P: alumel-chromel thermocouple to measure the cold junction temperature of *K*.

are drawn from two Variacs connected to a constant voltage transformer. The variation of the temperature of the target (190°C to 350°C) and that of the Mo crucible (700°C to 1000°C) is within ±3°C and no special care has to be taken to watch them. The temperature of the target is measured with an Alumel-Chromel thermocouple *K* pressed against the target surface by springs. The cold junction of *K* is measured by another Alumel-Chromel thermocouple *P*. The whole vacuum jacket *L* is cooled by water in the cooling jacket *M*.

III. Preparation of the Silver Sample

In a small volume of chemically pure HNO_3, 514 mg of 99.99 per cent pure silver are dissolved

*Considering that the mean translational kinetic energy ($3kT/2$) of the atoms in the atomic beam is probably small relative to the standard free energy of adsorption under the present experimental conditions, it seems safe to assume that no atoms rebound from the surface by semielastic collision and that all atoms become temporarily adsorbed before evaporating off or joining a growing metal crystallite [1; 2; 3].

and 10 mg of radioactive silver in the form of $AgNO_3$ are added. After thorough mixing, the silver is precipitated as AgCl which is then reduced to Ag with H_2 at about 400°C. 0.8 mg of this active sample is weighed out on a gold assay balance, which is sensitive to 0.01 mg, and dissolved in a small amount of HNO_3. The solution is then diluted to 1 cc, and different small amounts of this solution are weighed out and spread on glass plates or silver discs. These specimens are counted with a Geiger counter for a total number of 12,288 counts and the required times are recorded, from which the number of counts per minute for each specimen is obtained. The values obtained, after being

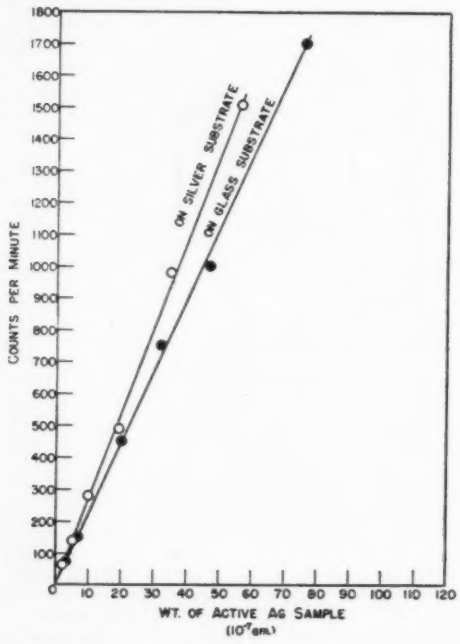

FIGURE 2. Weight vs. activity for the active silver sample used.

Substrate	*Sample wt.* (10^{-7} gm)	*Activity* (c/min)
Silver	2.0	64
	5.1	140
	10.0	280
	19.2	490
	35.0	980
	56.6	1507
Glass	3.0	70
	7.2	150
	20.0	450
	32.0	751
	47.2	1005
	76.0	1702

corrected for the activity due to background, are used to construct two calibration curves of weight of silver versus number of counts per minute, one for silver on glass and the other for silver on silver (Figure 2). For the same weight of silver, the number of counts on the silver substrate is found to be slightly higher than that on glass, probably because the back-scattering of the silver substrate is higher than that of the glass substrate. The strength of the active silver prepared in this way is such that it gives 100 counts per minute for a deposit 1 cm^2 in area and a complete monolayer thick.

IV. Experimental Procedures

After the target is put in position, the whole system is evacuated to about 10^{-5} mm Hg. The shutter *D* is closed and the Mo crucible is heated to about 1000°C and the target to 350°C. The evacuation is continued until the ionization gauge indicates a residual gas pressure of about 5×10^{-5} mm Hg. The target and the Mo crucible are then brought to the desired temperature and the shutter *D* is opened to make an exposure of a predetermined period of time. The shutter is then closed, the system cooled down, and the target counted

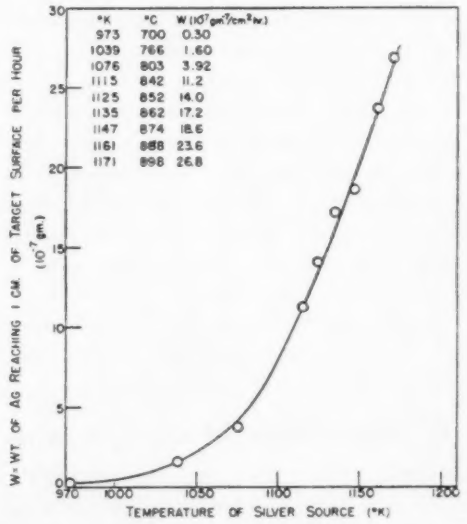

FIGURE 3. Amounts of silver reaching unit target area per hour at different temperatures of the silver source.

for its activity. From the counting results and the calibration curve, one can find out how much deposit is on the target.

For the calculation of the condensation coefficient, the number of silver atoms arriving at the target surface per unit area per second for different temperatures of silver source must be known. Although this may be calculated from the effusion law, it was decided to measure it experimentally so that the results may be more accurate. This is

done by using silver targets (99.99 per cent pure, polished, degreased, etched lightly in 5 per cent KCN, washed and dried) cooled with dry ice-acetone mixture. Each target is exposed one hour to a silver source kept at some constant temperature. The targets are then counted for their activity. It is assumed that at such a low target temperature (−78°C) each silver atom that strikes the target surface stays there. The counting results, after correction for the activity of the background, are converted to the amounts of silver reaching unit area of the target surface per hour by using the "weight activity" calibration curve of Figure 2. The plot of the amount of silver reaching unit area of the target per hour versus the corresponding crucible temperature is shown in Figure 3.

V. Experimental Results and Discussion

Condensation coefficients* have been measured for silver depositing on glass and gold with the targets kept at 192°C but with the temperature of the Mo crucible and the time of condensation varied. The glass targets are microscope-slide cover glasses, cleaned in chromic acid cleaning

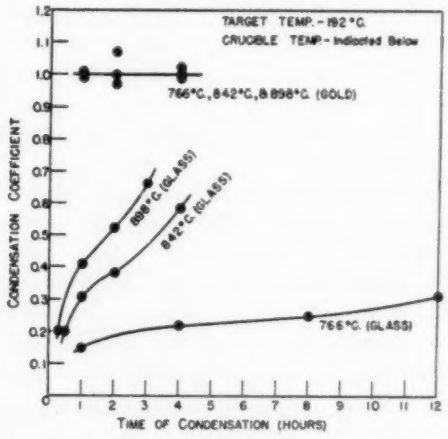

FIGURE 4. Condensation coefficients of silver deposited on glass and on gold. This condensation coefficient is an average over the whole time.

mixture and washed and dried. The gold target is a gold disc (99.99 per cent pure), polished, degreased, etched lightly in 5 per cent KCN solution, and washed and dried. The results are tabulated in Table I. In Figure 4 the variation of the condensation coefficient with time of condensation is plotted

*The condensation coefficient measured represents the average value over the total time.

TABLE I

VARIATION OF THE AMOUNT OF SILVER CONDENSED AND THE CONDENSATION COEFFICIENT WITH TIME OF CONDENSATION

Target	Temperature of silver Source (°C)	Time of condensation (hours)	Amount of condensation (10^{-7} gm/cm²)	Condensation coefficient (ave. over total time)
glass (192°C)	700	8, 10, 12 or 22	negligible	
	766	1	0.24	0.15
		4	1.4	0.22
		8	3.2	0.25
		12	6.0	0.31
	842	½	1.1	0.20
		1	3.5	0.31
		2	8.5	0.38
		4	26	0.58
	898	¼	1.8	0.20
		1	11	0.41
		2	28	0.52
		3	53	0.66
gold (192°C)	766	1	1.6	1.0
		2	3.1	0.97
		4	6.5	1.0
	842	1	11	1.0
		2	24	1.0_7
		4	46	1.0_2
	898	1	27	1.0
		2	55	1.0
		4	112	1.0

Note: For the condensation of silver on gold targets, the amount of condensation is deduced from the activity of the target by using the "weight ~ activity" calibration curve for silver deposited on silver.

for a number of silver source temperatures. Table II gives the supersaturations corresponding to a target temperature of 192°C and the various source temperatures. These supersaturations were com-

TABLE II

SUPERSATURATIONS CORRESPONDING TO A TARGET TEMPERATURE OF 192°C AND VARIOUS SILVER SOURCE TEMPERATURES

Silver source temp., °C	Supersaturation, p'/p_0
700	2.59×10^{12}*
766	1.43×10^{13}†
842	1.03×10^{14}†
898	2.25×10^{14}†

*Sub-critical for deposition of silver on glass.
†Supercritical for deposition of silver on glass and on gold.

puted [1] using the calibration curve of Figure 3 and the data of McCabe and Birchenall [6] for the vapor pressure of silver.

For the glass targets at a crucible temperature of 700°C, the activity does not increase with time although the target shows a small amount of radioactivity after being exposed to the silver vapor. For 8, 10, 12, and 22 hours of exposure, the activity is always less than 5 counts per minute. This shows that the supersaturation* is below the critical value [1] and the nucleation rate is so low that very little condensation has occurred. At a crucible temperature of 766°C, the activity of the target is found to increase with the time of exposure, indicating that the supersaturation is above the critical value so that the nucleation rate becomes appreciable. Nevertheless the amount of deposit condensed in 8 hours is still less than a complete monolayer if the deposit were evenly distributed over the whole target surface. There is therefore a certain crucible temperature between 700°C and 766°C, below which no appreciable condensation can occur. However, even for crucible temperatures above the critical value, not all the atoms hitting the target surface are captured. As shown in Figure 4, for crucible temperatures 766°C, 842°C and 898°C, the condensation coefficients are all very small at the beginning of the condensation but increase with the time of condensation. The rate of increase of the condensation coefficient is very rapid at the beginning, then becomes slower, but becomes rapid again as the condensation continues. This is shown by the change of the slopes of the curves in Figure 4 with time of condensation.

The following hypothesis is proposed to explain these phenomena. From the very small condensation coefficients observed at the beginning of the condensation, one might infer that on glass targets at 192°C the nucleation of the silver deposit starts at isolated spots on the glass surface.† The atoms arriving after the nucleation has started are captured only if they hit the surface of the target in the vicinity of these initial nuclei. Most of them evaporate away after staying on the glass surface for a short time. Only those stay that can join the nuclei already present by surface diffusion or form some other nuclei. As the condensation goes on, the condensation coefficient increases because of the increasing availability of crystallization sinks [7] for the adsorbed silver atoms. This increase in availability of sinks is due in part to the formation of new nuclei and partly to the spreading of the crystals already on the surface. The new nuclei provide additional "point" sinks to catch the adsorbed atoms diffusing over the surface before they can evaporate. The spreading crystals provide circumferential length of crystal edges as well as crystalline area which can serve as sinks for the adsorbed atoms. Initially, the sharp increase in availability of sinks (hence the condensation coefficient) with time is mainly due to the formation of new nuclei. After a while, the preferred sites‡ for nucleation on the glass surface have become occupied and nucleation rate decreases sharply. Therefore, the rate of increase of the condensation coefficient becomes lower. Due to the slow rate of supply of atoms to the surface, most of the crystals have not yet become large, i.e., the silver crystals do not yet occupy a large fraction of the surface area. Eventually, the silver crystals do begin to cover an appreciable fraction of the surface area. Their contribution to the increase in availability of sinks with time, due to lateral growth, becomes important. At this point, the increase of condensation coefficient with time becomes more rapid again. The condensation coefficient finally will approach the value of unity, but probably not until after a number of layers of silver atoms has accumulated. The authors are presently attempting a mathematical formulation of this process to describe the curves for deposition on glass shown in Figure 4.

When the same experiments are carried out on gold targets at these temperatures, the condensation coefficient is found to be always equal to unity, no matter how long the condensation has been going on. This indicates that every atom arriving at the target surface is captured. This does not mean that each captured silver atom is a critical nucleus in the classical sense [8] that its chemical potential is equal to that of the vapor. Rather it means that the rate of evaporation of adsorbed atoms is much less than the rate of arrival of atoms to the surface in this case of deposition at highly supercritical saturations. No attempt has been made to determine the critical supersaturation, which is probably very low.

Thus, on gold, the condensation coefficient at the supersaturations used here has the value of unity and should drop gradually to zero as the temperature of the silver source approaches the critical

*Table II.

†This is corroborated by autoradiographic evidence.

‡These may be cracks or small devitrified regions.

value. On glass, the condensation coefficient at the supersaturations used here is less then one and decreases gradually to zero as the critical temperature of the silver source is approached. Of course, these are two extreme cases. For targets having various amounts of lattice misfit with silver, they may behave either like gold or like glass, depending upon the structural or other factors.

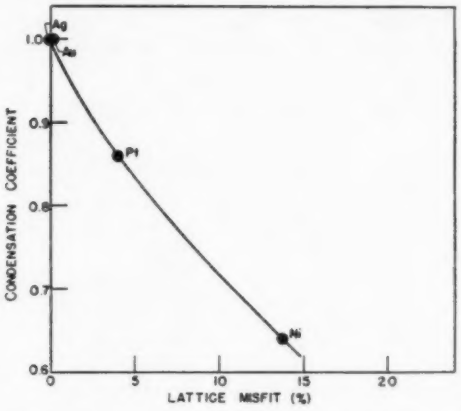

FIGURE 5. Variation of condensation coefficients of silver with the lattice misfit between silver and the target material.
Target temperature: 192°C.
Crucible temperature: 842°C
Time of condensation: 1 hour

$$\text{Lattice misfit} = D = \frac{(a)_{Ag} - (a)_{target} \times 100}{(a)_{Ag}}$$

"a" = unit cell dimension
[NOTE: On glass the condensation coefficient is 0.31.]

We have made a few measurements of the condensation coefficients of silver on silver, gold, platinum,* nickel,† and glass, with the target kept at 192°C, the crucible at 842°C, and the time of condensation fixed at one hour. The lattice misfits between silver and these metal targets are 0, 0.18, 3.96 and 13.7 per cent respectively. It is found that the condensation coefficients are 1.0, 0.99, 0.86 and 0.64 respectively, while that on glass is 0.31 (Figure 5). There seems to be a continuous decrease of condensation coefficient with increase of lattice misfit, which illustrates the importance of structural similarity in the condensation process [9; 10; 11].

*This hypothesis is consistent with a plot of condensation coefficient versus average deposit thickness.

†The platinum and nickel targets are all 99.99 per cent pure, polished, degreased, etched lightly in aqua regia and dilute HCl respectively, and washed and dried just before being used.

Acknowledgement

The authors would like to express their sincere thanks to Dr. Robert F. Mehl for many helpful discussions.

The research described in this paper was sponsored by the Geophysics Research Division, Air Force Cambridge Research Center, Cambridge, Mass., under Contract No. AF 19 (122)–185. Additional support was received from projects sponsored by the Office of Naval Research.

References

1. YANG, L., BIRCHENALL, C. E., POUND, G. M. and SIMNAD, M. T. Acta Met. **2** (1954) 462.
2. POUND, G. M., SIMNAD, M. T. and YANG, LING. To be published.
3. ESTERMANN, I. Zeit. Elektrochem. **31** (1925) 441.
4. DEVIENNE, F. M. J. Phys. Radium **13**, no. 2 (1952) 53.
5. COCKCROFT, J. D. Proc. Roy. Soc. **A119** (1928) 293.
6. MCCABE, C. L. and BIRCHENALL, C. E. J. Metals **5** (1953) 707.
7. BURTON, W. K., CABRERA, N. and FRANK, F. C. Phil. Trans. Roy. Soc. **A243** (1951) 299–358.
8. HOLLOMON, J. and TURNBULL, D. Progress in Metal Physics, vol. 4 (New York, Interscience, 1952).
9. TURNBULL, D. and VONNEGUT, B. Indusr. Engnr. Chem. **44** (1952) 1292.
10. BROOKS, H. Metal Interfaces. (Cleveland, Ohio, Am. Soc. Metals, 1952).
11. FRANK, F. C. and VAN DER MERWE, J. H. Proc. Roy. Soc. **198A** (1949) 216.

THE EFFECT OF METAL SURFACE CONDITION ON THE ANODIC OXIDATION OF TANTALUM*

D. A. VERMILYEA†

When tantalum is anodized at constant current two different types of behavior are observed, depending on whether the metal surface is rough or polished. With polished sheet, an efficiency of 98 per cent is obtained up to the spark voltage, and no change in the character of the oxide surface is observed. With rough sheet, apparent efficiencies greater than 100 per cent are observed above a critical voltage depending on the nature of the original metal surface. In addition, minute depressions are observed on the surface of the oxide film. The same behavior is observed for many different dilute aqueous solutions. It is suggested that minute bubbles, formed at points of electrical breakdown, result in a decrease in effective area and hence an apparent efficiency greater than 100 per cent. The depressions result when the oxide grows up around the bubbles. These effects appear to be the result of a rough surface rather than the presence of impurities.

L'EFFET DE L'ÉTAT DE SURFACE DU MÉTAL SUR L'OXYDATION ANODIQUE DU TANTALE

Quand on anodise le tantale à courant constant, le comportement du métal est différent suivant que la surface est rugueuse ou polie. Sur des tôles polies on obtient un rendement de 98 pour cent jusqu'à la tension d'étincelle, et on ne note pas de changement dans le caractère de la surface de l'oxyde. Sur des tôles rugueuses on constate des rendements apparents de plus de 100 pour cent, au-dessus d'une tension critique qui dépend de l'état de la surface originale. En plus, de petites cavités apparaissent sur le film d'oxyde. Le même comportement est constaté dans le cas de solutions aqueuses, diluées. Il est suggéré que des bulles minuscules, qui se forment aux points de détérioration du contact électrique, provoquent une diminution de la surface effective, ce qui donne un rendement apparent, supérieur à 100 pour cent. Les cavités apparaissent quand l'oxyde se forme autour des bulles. Ces effets paraissent être le résultat des rugosités de la surface, plutôt que des impuretés.

DER EFFEKT DES ZUSTANDES DER METALLOBERFLÄCHE AUF DIE ANODISCHE OXYDATION VON TANTAL

Wenn Tantal mit konstantem Strom anodisiert wird, werden zwei verschiedene Verhaltungsweisen beobachtet. Diese Erscheinung hängt davon ab, ob die Metalloberfläche rauh oder poliert ist. An poliertem Blech wird eine Ausbeute von 98% bis zur Funkenspannung erhalten, und es kann keine Änderung in der Oxydoberfläche beobachtet werden. An rauhem Blech werden scheinbare Ausbeuten von über 100% oberhalb einer von der Art der Ausgangsoberfläche abhängenden kritischen Spannung beobachtet. Ausserdem können kleine Vertiefungen in der Oberfläche des Oxydfilms beobachtet werden. Das gleiche Verhalten wird in vielen verschiedenen verdünnten wässrigen Lösungen gefunden. Zur Erklärung dieser Erscheinung wird angenommen, dass kleine Bläschen, die sich an den Punkten des elektrischen Durchschlags bilden, die wirksame Oberfläche verringern und dadurch zu einer mehr als 100%igen scheinbaren Ausbeute führen. Die Vertiefungen treten auf, wenn das Oxyd über die Bläschen wächst. Diese Effekte scheinen ihre Ursachen in einer rauhen Oberfläche und nicht so sehr in Verunreinigungen zu haben.

Introduction

In a previous paper [1] data for the kinetics of anodic oxidation of tantalum were presented. In that investigation all specimens were chemically polished before they were used. The necessity for using chemically polished specimens became apparent during the course of some preliminary observations of anodic oxidation, when it was noticed that the surface condition exerted a marked effect on the formation of an oxide film above a certain voltage. The present paper is concerned with this effect of surface condition. As in the previous paper, the thin, amorphous, nonporous type of anodic film is the one of interest here.

Guntherschulze and coworkers [2] found that during anodic oxidation of tantalum at constant current the voltage rose linearly with time up to the "spark voltage" (see curve 1 of reference 1). In attempting to reproduce the portion of these curves up to the spark voltage, it was observed that the voltage-time plot often deviated from linearity as shown in Figure 1. Curve 1, for sheet with a very rough surface, shows that the voltage rose linearly with time to about 40 volts, then rose more rapidly and continued to rise at a more rapid rate until the spark voltage was reached. Bubbles were observed at the anode above the point when the voltage-time curve became nonlinear. With smoother sheet the voltage at which the curve departed from linearity was higher (120 volts) and the maximum slope was less. With etched sheet the curve was linear to 200 volts and departed only slightly from linearity. With chemically polished sheet the curve was linear up to the spark voltage, and no bubbles were observed below the spark voltage.

*Received January 11, 1954.
†General Electric Research Laboratory, The Knolls, Schenectady, New York.

An electron microscope study was made to determine the cause of the deviations from linearity. Specimens of 0.0005-inch cold-rolled tantalum sheet and 0.010-inch electropolished sheet were anodized at the various voltages shown in Figure 2. Each specimen was then thoroughly cleaned by stripping six successive coatings made by applying a solution of 10 per cent nitrocellulose in amyl acetate. The final replicas were made by applying a solution of 1 per cent nitrocellulose in amyl acetate. The replicas were stripped, transferred to copper screens, shadow cast with palladium at 15 degrees, and examined.

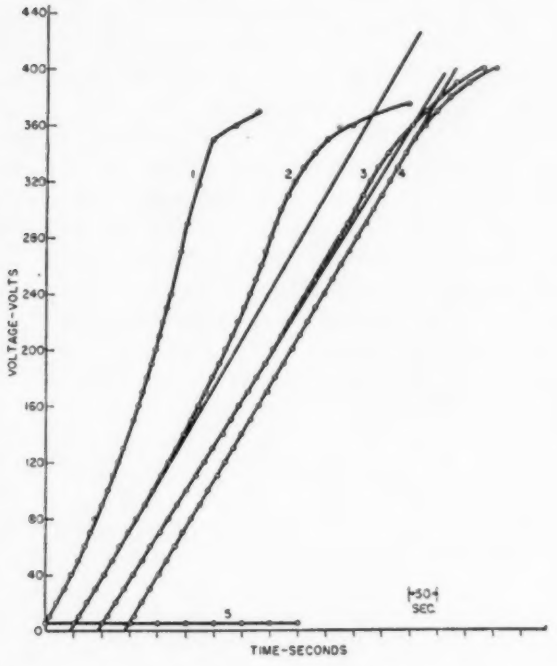

FIGURE 1. Tantalum sheet with different surface conditions anodized in 0.2% $Na_2B_4O_7 \cdot 10\ H_2O$ + 0.75% H_3BO_3 balance water. Curve 1, Run 99a: as rolled and annealed; surface very rough. Curve 2, Run 100: as cold-rolled to .0005" (95%); surface smoother. Curve 3, Run 104: as etched in 3 HF, 1 HNO_3, 1 H_2SO_4; surface matte, scratches removed. Curve 4, Run 107: as dip-polished in 1 HF, 2 HNO_3, 5 H_2SO_4; surface smooth and bright. Curve 5, Run 99h-1: abraded on 3/0 paper; surface very rough. (All specimens at 2 ma/cm.²)

Results and Discussion

The results are shown in Figures 3 to 14. Figure 3 shows the rough surface of the rolled sheet. After anodization at 50 volts, the oxide surface was much smoother than the original metal surface. At 120 volts, where the first deviation of the voltage-time curve from linearity occurred, the surface was still smoother, but many small depressions (projections on the replica) were observed. At 180 volts the surface was still smoother and contained more depressions, which appeared to be arranged in rows suggestive of the original rolling scratches. The projections increased in number and size as the voltage was raised, until finally at 370 volts a new type of surface structure appeared. This new structure, shown in Figure 8, was presumably caused by the sparks which became visible above approximately 350 volts.

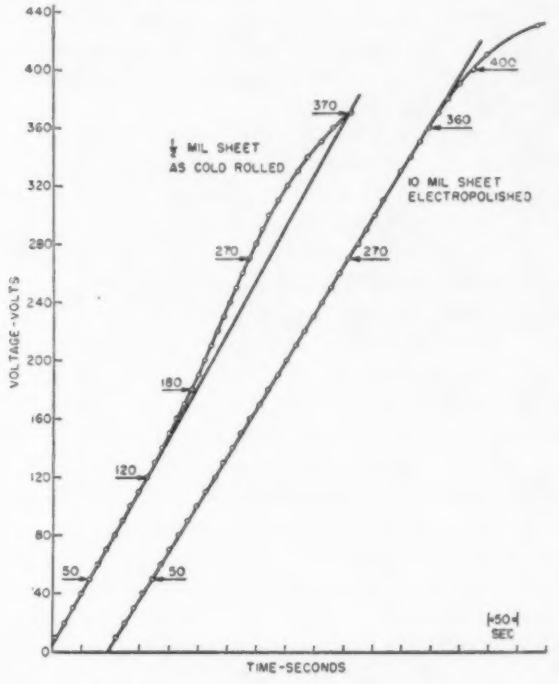

FIGURE 2. Voltages at which specimens for electron microscope studies were prepared. Specimens taken at voltages indicated by arrows.

Figure 9 shows the relatively smooth electropolished surface. Many small depressions, probably small pits produced by the electropolishing, appear at random on the surface. Little surface change occurred on anodizing this material at voltages up to 360 volts, as shown by Figures 10, 11, and 12. At 360 volts a few areas contained a new structure, again presumably caused by the sparks which appeared at 350 volts. In Figure 13, taken above the spark voltage, it appears that some disruption of the film occurred at one point and spread radially. In some experiments, sparks have been observed to start at one point on the surface and wander rapidly for a total distance as great as one centimeter. Figure 14 shows an

advanced stage of surface destruction far above the spark voltage.

The two series of micrographs for the two types of surface conditions show that for electropolished sheet, which gives a linear voltage-time curve below the spark voltage, there is essentially no disruption of the surface of the oxide film until the spark voltage is reached. For the rough, as rolled sheet, which gives a nonlinear voltage-time curve below the spark voltage, depressions appear on the oxide surface above the voltage where the voltage-time curve becomes nonlinear. The arrangement of these depressions in rows parallel to original rolling marks suggests that the roughness of the underlying metal surface played some role in their formation.

This effect was investigated using a total of 13 different electrolytes in dilute solutions. The same behavior was obtained for a given surface condition with all of the electrolytes. It was also observed that the initial linear portion of the curves had the same slope regardless of the electrolyte and for both annealed and cold-rolled material. These facts suggest that the anodic oxidation of tantalum, in general, and in particular the effects observed at constant current, are not dependent on the electrolyte as long as dilute aqueous solutions are used.

Using the interference color step gage described in the preceding paper, the thickness was measured as a function of voltage. It was found that the thickness was proportional to the voltage up to the spark voltage whether the voltage-time curve was linear or not. It is known that anodic oxidation of tantalum is 98 per cent efficient in the region where the voltage-time curve is linear [1]. When the voltage, and hence the thickness, begins to increase at a more rapid rate, the efficiency would thus appear to be greater than 100 per cent. For example, the greatest slope of the voltage-time curve in curve 2 of Figure 1 would indicate an efficiency of 130 per cent if the efficiency during the linear portion is taken as 98 per cent.

These facts suggest that the phenomena observed during anodic oxidation of rough-surfaced tantalum at constant current may be explained as follows. Formation of the oxide film proceeds normally until a voltage is reached where electrical breakdown occurs. This breakdown may occur because of the enhanced electric field near a sharp point or because in the process of growth the oxide becomes highly stressed in the region of a sharp corner and a crack appears. The appearance of visible bubbles at the surface suggests that a very minute bubble forms at each point where a breakdown occurs. From the results given in the previous paper it appears that there is very little overvoltage, if any, for the formation of Ta_2O_5 anodically, while oxygen evolution requires about a volt of overvoltage. The current will, therefore, pass through the part of the oxide not shielded by gas bubbles, and each bubble thus decreases the effective area slightly. As the oxide grows it will grow up around the bubble, thus leaving a shallow depression in the oxide surface. The depressions which were observed with the electron microscope appear to be roughly spherical. As the voltage increases still further more bubbles would form as breakdowns occur at less drastic faults while the existing bubbles remain and the oxide grows up around them. Thus, the depressions in the oxide surface will increase in size and number. The constant current, now passing through a reduced area, will cause a more rapid growth of the film as was observed.

If this hypothesis is correct the apparent increase of efficiency should be a measure of the area covered by bubbles. From a count of the number of depressions present in Figure 7 the amount of the surface covered was estimated as 14 per cent of the total area. If the area was reduced by 14 per cent the efficiency would be increased to 116 per cent, which is considerably lower than the 130 per cent measured from the slope of curve 2 of Figure 2 at 270 volts. Using another micrograph of a specimen formed at 270 volts, however, the area covered by depressions was estimated as 35 per cent, which would correspond to an efficiency of 154 per cent. Probably there is a considerable variation from area to area of a specimen depending on the exact surface condition.

It has been suggested that the effects observed at constant current were caused by impurities present on the surface rather than by electrical breakdowns at surface roughness. In order to test this suggestion, a polished specimen was scratched with a diamond point and anodized. When the specimen was heavily scratched with deep scratches, no oxide formation occurred at 2 ma/cm^2, although at a higher current density oxide formation did occur. A specimen lightly scratched over its entire area showed a behavior very similar to that obtained for the rolled sheet. Since the chemically polished sheet itself gave a linear voltage-time curve, and since it is doubtful if any diamond particles were

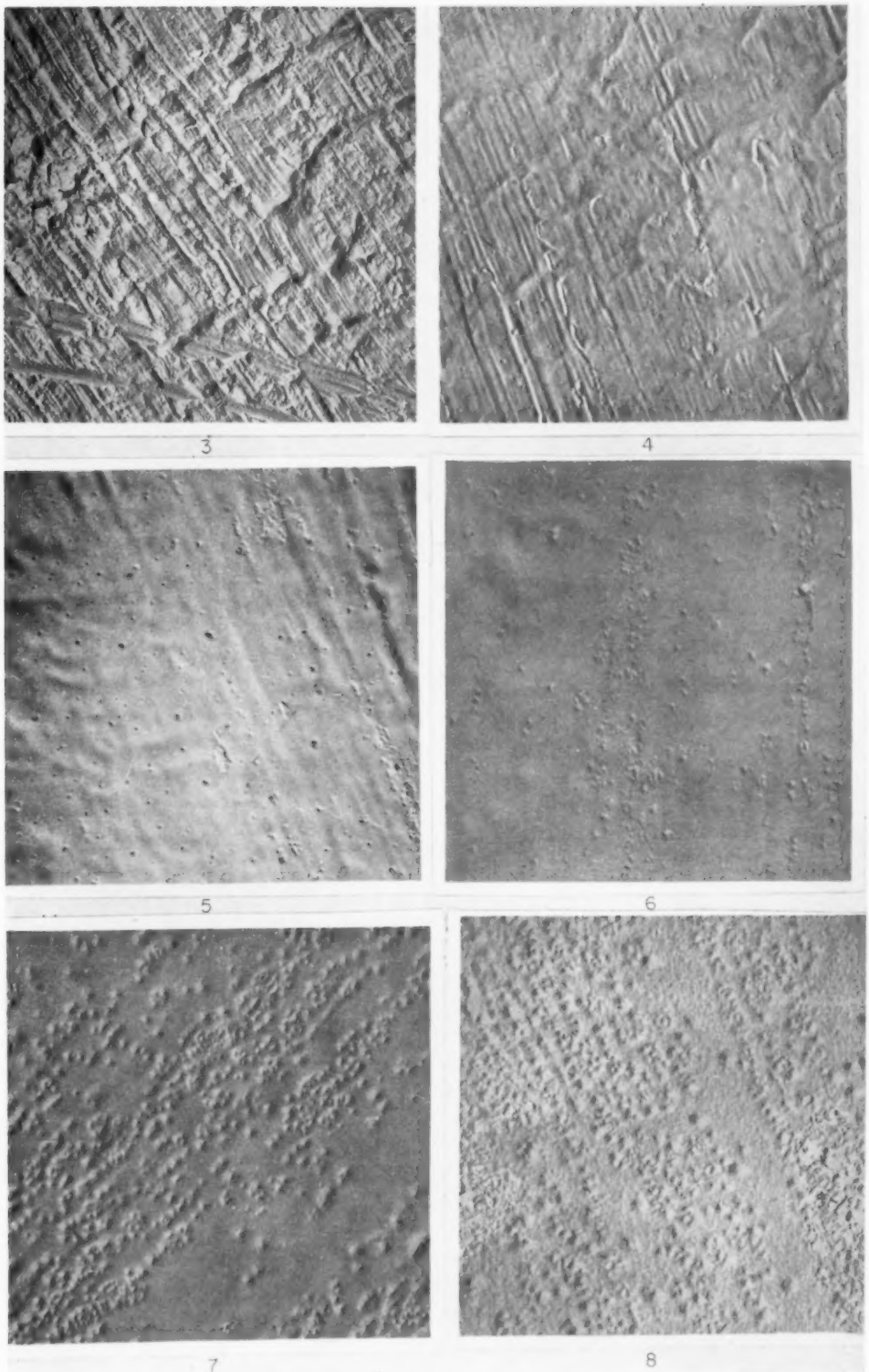

PLATE I (all figures reduced by ½ in reproduction). FIGURE 3—Rolled tantalum sheet. FIGURE 4—Rolled tantalum sheet anodized at 50 volts. 7500×. FIGURE 5—Rolled tantalum sheet anodized at 120 volts. 7500×. FIGURE 6—Rolled tantalum sheet anodized at 180 volts. 7500×. FIGURE 7—Rolled tantalum sheet anodized at 270 volts. 7500×. FIGURE 8—Rolled tantalum sheet anodized at 360 volts. 7500×.

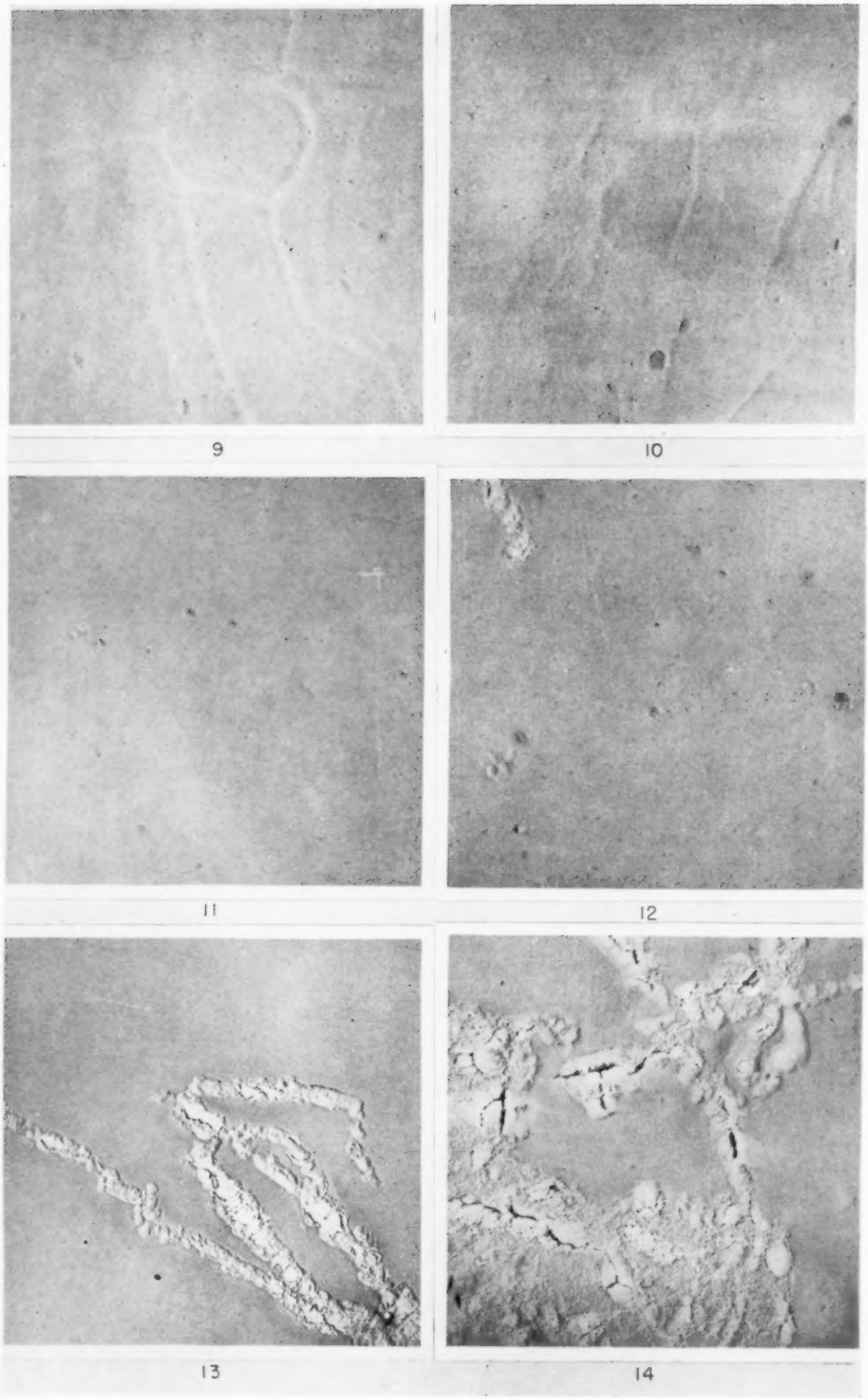

PLATE II (all figures reduced by $\frac{1}{2}$ in reproduction). FIGURE 9—Electropolished tantalum sheet. 7500×. FIGURE 10—Electropolished tantalum sheet anodized at 50 volts. 7500×. FIGURE 11—Electropolished tantalum sheet anodized at 270 volts. 7500×. FIGURE 12—Electropolished tantalum sheet anodized at 360 volts. 7500×. FIGURE 13—Electropolished tantalum sheet anodized at 400 volts. 7500×. FIGURE 14—Electropolished tantalum sheet anodized at 460 volts. 7500×.

left on the tantalum, it was concluded that impurities do not cause the deviation from linearity and surface depressions which were observed.

Acknowledgment

The author was extremely fortunate in having the benefit of the advice and assistance of E. F. Fullam in making the electron micrographs used in this paper. He is also indebted to D. Turnbull for the suggestion of using the electron microscope to study the effect of surface condition and for many helpful discussions. A great deal of background material and valuable suggestions were obtained during discussions with members of the capacitor laboratory.

References

1. VERMILYEA, D. A. Acta Met. **1** (1953) 282.
2. GUNTHERSCHULZE, A. and BETZ, H. Electrolyt-Kondensatoren (Berlin, M. Krayn, 1937).

THE FORMATION OF ANODIC OXIDE FILMS ON TANTALUM IN NON-AQUEOUS SOLUTIONS*

D. A. VERMILYEA†

The anodic films formed on tantalum in many non-aqueous solutions have been found to consist of two layers. Next to the metal there is a layer of Ta_2O_5 with the same characteristics as that of films formed in aqueous electrolytes, while between the Ta_2O_5 film and the solution there is a layer which is characteristic of the forming solution. Changes in the relative thicknesses of the two layers with formation rate, temperature, and forming solution result in a dependence of formation rate on the history of the film.

During anodic oxidation it has been found that the tantalum ions move out through the Ta_2O_5 film to react with oxygen at the oxide-electrolyte interface.

LA FORMATION DE FILMS ANODIQUES SUR LE TANTALE DANS DES SOLUTIONS NON-AQUEUSES

Il a été constaté que les films anodiques, formés sur le tantale, dans des solutions non-aqueuses, consistent en deux couches. En contact immédiat avec le métal on trouve une couche de Ta_2O_5 ayant les mêmes caractéristiques que les films formés dans des électrolytes aqueux, alors qu'entre la couche de Ta_2O_5 et la solution il y a formation d'une couche dont le caractère dépend de la solution. Les changements dans les épaisseurs relatives des deux couches, en fonction de la vitesse de formation, de la température et du genre de solution, donnent lieu à une dépendance de la vitesse de formation sur l'histoire du film. On a constaté que pendant l'oxydation anodique, les ions du tantale se déplacent à travers la couche de Ta_2O_5 pour réagir avec l'oxygène à l'interface oxyde-électrolyte.

DIE BILDUNG VON ANODISCHEN OXYDFILMEN AUF TANTAL IN NICHTWÄSSRIGEN LÖSUNGEN

Es wurde gefunden, dass die anodischen Filme, die sich auf Tantal in vielen nichtwässrigen Lösungen bilden, aus zwei Schichten bestehen. Direkt am Metall befindet sich eine Ta_2O_5-Schicht, die die gleichen Eigenschaften wie die in wässrigen Elektrolyten auftretenden Filme hat, während sich zwischen dem Ta_2O_5 Film und der Lösung eine für diese Lösung charakteristische Schicht befindet. Änderungen im Dickenverhältnis der beiden Schichten mit veränderter Bildungsgeschwindigkeit, Temperatur und Elektrolytlösung rufen eine Abhängigkeit der Bildungsgeschwindigkeit von der Vergangenheit des Filmes hervor.

Es zeigte sich, dass sich während der anodischen Oxydation Tantalionen durch den Ta_2O_5 Film hindurchbewegen um mit dem Sauerstoff an der Grenzfläche Oxyd-Elektrolyt zu reagieren.

The kinetics of growth and structure of anodic tantalum oxide films formed in aqueous solutions were discussed in a previous report [1]. It has been found that when the solution in which the anodic film is formed is largely non-aqueous the composition of the film is markedly different from that of films formed in aqueous solutions. The present report discusses the influence of the forming solution on film structure and on the formation kinetics.

Experimental

Three types of solutions were used in the work to be discussed. The first two consisted of either H_2SO_4 or H_3PO_4 plus water, while the third was a glycol base solution containing $Na_2B_4O_7$ as the electrolyte.‡ (This solution will be referred to below as "solution *A*.") The power supplies for constant current and constant voltage operation together with the switching and timing circuits and the constant temperature bath have been described previously [1]. Thickness measurements were made by comparison with the calibrated optical step gage discussed in the previous paper. All of the tantalum used was obtained from Fansteel Metallurigcal Company in the form of 0.005 in. sheet, and was chemically polished before use. Information concerning the macrostructure of the films was obtained by etching the films in hydrofluoric acid solutions and recording the thickness as a function of etching time.

Results and Discussion

The rate of formation of Ta_2O_5 on tantalum in aqueous solutions depends only on the instantaneous field and temperature, and is not at all dependent on previous history. In non-aqueous solutions, however, the rate of growth under specified conditions was found to be dependent on both the previous formation rate and the previous formation temperature. For example, Figure 1 shows plots of optical thickness versus log time for specimens held at 155 volts, 30°C in solution *A* after prior formation to 2067 Å in the same solution at 97°C and at 30°C. The lines are

*Received January 20, 1954.

†General Electric Research Laboratory, Schenectady, New York.

‡Any one of a variety of such solutions is satisfactory. One which works very well consists of 85–90% Ethylene Glycol, 5% $Na_2B_4O_7 \cdot 10\,H_2O$, 5–10% H_2O.

roughly parallel but the specimen previously formed at 97°C had a much greater thickness at a given time. The rate of growth at 2600 Å was 4.2 Å/sec for the specimen previously formed at 97°C and only 0.081 Å/sec for the specimen formed entirely at 30°C. In another test, specimens were anodized to 90 volts in solution *A* at 26°C using 2 ma/cm² and 0.2 ma/cm². For both specimens the voltage was then held constant at 90 volts and the current allowed to decrease to 0.005 ma/cm². The film which had been formed to

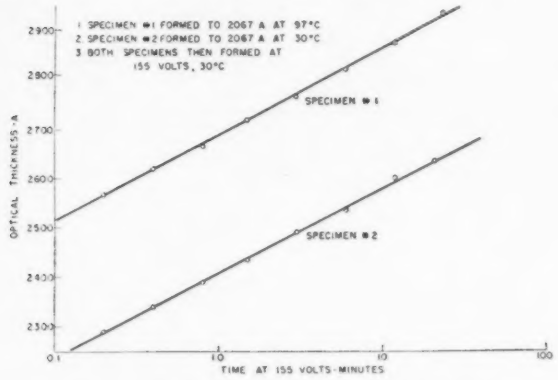

FIGURE 1. Thermal history during anodic oxidation.

90 volts at 2 ma/cm² had a final thickness of 1401 Å, while the film formed at 0.2 ma/cm² had a final thickness of 1505 Å. A change in prior formation rate by a factor of 10 has thus produced a 15 per cent change in the field required for the final formation under identical conditions.

The fact that the kinetics of formation of anodic films in non-aqueous solutions is thermal and rate history dependent while no such behavior is observed for formation in aqueous solutions suggests that the composition of a film depends on the solution in which it is formed. There is additional evidence for this assumption. For example, the thickness of films formed in non-aqueous solutions may be as much as 50 per cent less than that of films formed in aqueous solutions under the same conditions of voltage, temperature and current density. In addition, the efficiency of oxidation, assuming Ta_2O_5 formed and comparing weight changes with Faraday's law, was greater than 100 per cent in all the non-aqueous solutions studied, and as great as 210 per cent for formation in concentrated H_2SO_4.

After the above information had been obtained, it was observed that the capacity per unit area was the same for films formed under the same conditions of voltage, temperature, and current density in all solutions except concentrated H_2SO_4. The optical thickness, however, was never the same in any two different solutions, and all the evidence pointed to a difference in composition for films formed in different solutions. If the composition was different, then presumably the field required to cause a given current to flow through the film at a particular temperature would also be different. Thus, the thickness at a given voltage would be different, in agreement with the observations of optical thickness. It was not at all clear, however, why the capacity per unit area should be the same for films formed under the same conditions in different solutions.

The reasons for the observed behavior were discovered by the use of the technique of dissolving films in HF, recording thickness as a function of time. In the work to be described, it should be noted that the "thickness" quoted will refer to the optical thickness measured with an interference color step gage which is made up of specimens with Ta_2O_5 films of different thicknesses. If the thickness of a film of different composition (and hence different refractive index) is estimated by comparison with the gage, a value is obtained which is not the true thickness, so that only relative thickness measurements are possible.

When a film which has been formed in an aqueous solution is dissolved in HF, the rate of solution is constant, as shown in Figure 2. On dissolving a film formed in a non-aqueous solution, however, it is found that the film dissolves at two different rates. Figure 2 shows the results of dissolving a film formed in solution *A*. The initial rate of solution is very rapid, but when the film thickness has reached 750 Å the rate decreases. Similar behavior is exhibited by films formed in H_2SO_4 plus water and in H_3PO_4 plus water, as shown by Figures 3 and 4. In H_2SO_4 solutions (and presumably in others also) the relative thickness of the inner layer decreases as the amount of water in the solution decreases; it is either very thin or nonexistent in H_2SO_4 solutions above about 80 per cent H_2SO_4. In 85 per cent H_3PO_4 the outer part of the film dissolves more slowly than the inner part. The inner layer of these films always dissolves at the same rate as a Ta_2O_5 film formed in an aqueous electrolyte.

These results suggest that films formed in these non-aqueous solutions* consist of a layer of Ta_2O_5

*Except concentrated H_2SO_4 solutions.

next to the metal and one of different composition between the Ta_2O_5 and the solution. No attempt has been made to determine the composition of the second film; it may consist of solvated Ta_2O_5 or of another compound entirely.

An explanation may now be given for the fact that the capacity per unit area is the same for films formed under the same conditions in different solutions* although the optical thickness is different.

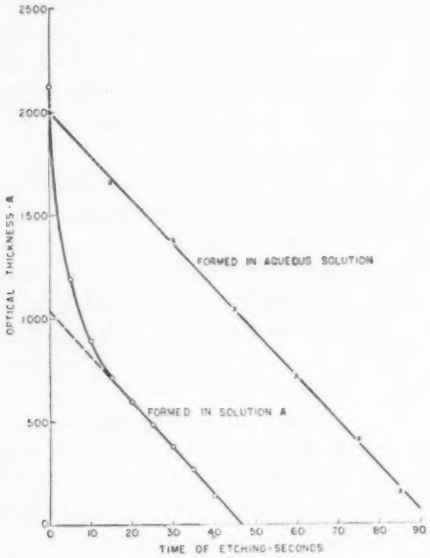

FIGURE 2. Corrosion in HF of films formed in aqueous and non-aqueous solutions.

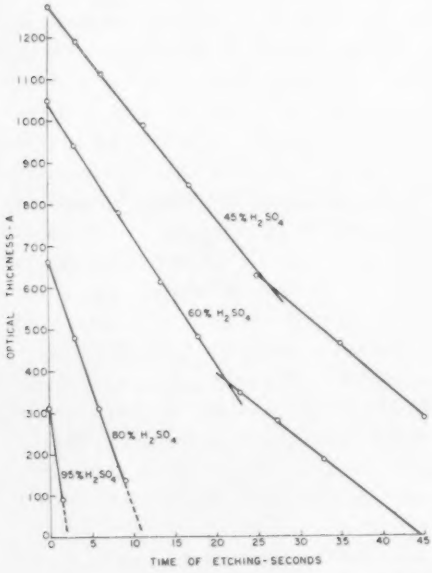

FIGURE 3. Corrosion in HF of films formed in H_2SO_4–H_2O solutions.

*Except concentrated H_2SO_4 solutions.

The fact that the capacity per unit area of films formed to the same voltage in all solutions is the same, implies that the charge density at the metal-oxide and oxide electrolyte interfaces is the same in all solutions. Consider now one of the duplex films. The film is equivalent electrically to two condensers in series, the inner one having a Ta_2O_5 dielectric and the outer one having a different dielectric material characteristic of the forming

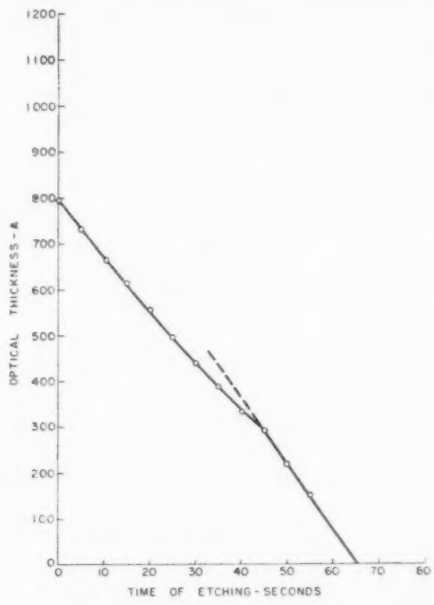

FIGURE 4. Corrosion in HF of an anodic film formed in 85 per cent H_3PO_4.

solution. For either condenser we have during formation at a given current density

$$Q = CV_f = \text{const.} \tag{1}$$

in all solutions where Q is the charge density at the interfaces of the dielectric, V_f is the voltage across the layer, and C is the capacity per unit area. Since the capacity per unit area is given by:

$$C = \frac{K}{4\pi X} \tag{2}$$

where K is the dielectric constant and X the thickness of the layer, we have

$$Q = \frac{K}{4\pi}\ \frac{V_f}{X} = KE_f = \text{const.} \tag{3}$$

in all solutions where E_f is the electric field in the dielectric during formation.

In the Ta_2O_5 layer of a film formed in any solution, therefore, the electric field during formation is the same. Thus, the fact that the capacity per

unit area is the same for films formed under the same conditions in different solutions means that the same electric field in the Ta_2O_5 layer is required to produce a given current density at a given temperature in any solution (except concentrated H_2SO_4 solutions). It is clear, therefore, that the rate-controlling step of the process of film formation occurs in the Ta_2O_5 layer of the film.

Because the rate-controlling step is in the Ta_2O_5 layer, therefore, anodic films formed on tantalum under the same conditions of voltage, temperature and current density in any solution which produces a duplex film consisting of Ta_2O_5 next to the metal will have the same capacity per unit area. The optical thickness, on the other hand, depends on the thicknesses and refractive indices of both layers, and so may easily be different for films formed in different solutions. No determination of the true total thickness of these duplex films has been made, so it is not possible to determine either the dielectric constant or refractive index of the outer layer of the film.

Since the thickness of the outer layer of the film formed in H_2SO_4 plus water was a function of the composition of the electrolyte, it was thought that it might also be a function of the rate and temperature of formation. In order to test this hypothesis, specimens were anodized in Solution *A* at 95°C using current densities of 1.5 and 15 ma/cm². At 1.5 ma/cm² for an apparent total thickness of 2230 Å, 1340 Å or 60 per cent was Ta_2O_5. In a film formed at 1.5 ma/cm² and 30°C, the Ta_2O_5 layer was only 33 per cent of the total thickness. Thus, as the temperature is increased, the percentage of Ta_2O_5 in the film increases. At 95°C and 15 ma/cm², the Ta_2O_5 layer was 53 per cent of the total, a slight decrease compared to the lower rate.

The rate and thermal history observed when tantalum is anodized in non-aqueous solutions and the thickness measured optically is now understandable. Consider two specimens of tantalum, one formed to a given voltage at room temperature, the other formed first for a short time at a high temperature, then at room temperature to the same voltage as the first specimen. The film on the first specimen will have a Ta_2O_5 layer comprising about 35 per cent of the total thickness. The other specimen, during the part of its formation at high temperature, will have a film containing 60 per cent Ta_2O_5, while the film added at the lower temperature will again be 35 per cent Ta_2O_5. As a result the final film formed on the second specimen will have a thicker Ta_2O_5 layer than the first specimen. It has been observed that the film formed in aqueous electrolytes, which consists of Ta_2O_5, is thicker optically than a film formed to the same voltage at the same temperature and current density in a non-aqueous electrolyte. For a given total thickness, therefore, the greater the percentage of Ta_2O_5 in one of these duplex films, the thicker it will appear. Finally, therefore, prior formation at a high temperature is seen to result in a film which is optically thicker after final formation under a specified set of conditions at a lower temperature than one formed only at the lower temperature. Figure 1 shows that the specimen performed at 95°C is indeed optically thicker than the one formed only at 30°C. The same type of reasoning indicates that a slower prior formation rate should result in an optically thicker film, as is actually observed.

One final experiment using the technique of dissolving the film is of interest. In concentrated H_2SO_4 solutions, as pointed out above, the Ta_2O_5 layer next to the metal may be absent. A Ta_2O_5 film was formed in 1 per cent Na_2SO_4 to about 225 Å, and this specimen was then anodized further in 80 per cent H_2SO_4. The results of dissolving this film in HF are shown in Figure 5.

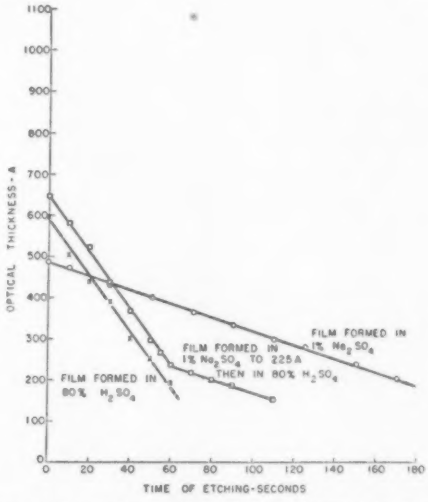

FIGURE 5. Corrosion in HF of films formed in 1 per cent Na_2SO_4 and 80 per cent H_2SO_4.

It may be seen that a rapid initial rate of solution changes abruptly at 232 Å to a slower rate. The data for the solution of films formed only in 80 per cent H_2SO_4 and only in H_2O are also shown, and it is apparent that the initial rate for the duplex film is that characteristic of the 80 per cent H_2SO_4

film, while the final rate is characteristic of Ta_2O_5. It may be concluded that the Ta_2O_5 film has remained in place next to the metal and has increased only very slightly in thickness. This would be possible if tantalum is the only mobile material in the Ta_2O_5 film. It would also be possible if oxygen were mobile and moved in through the Ta_2O_5 to react with tantalum at the inner interface while at the same time the outer portion of the Ta_2O_5 layer was converted to the sulphuric acid type of film at the same rate that new Ta_2O_5 was formed. No detectable attack or alteration of Ta_2O_5 occurs upon prolonged exposure to concentrated H_2SO_4 when no current is flowing, and it seems likely that the assumption of mobile tantalum in the Ta_2O_5 film is more reasonable.

Conclusions

1. Films formed in many non-aqueous solutions consist of a layer of Ta_2O_5 next to the tantalum and a layer of material characteristic of the solution between the Ta_2O_5 and the solution.

2. The relative thickness of each of the layers in these duplex films changes with formation rate and temperature. These changes result in rate and thermal history, that is, the rate of formation under specified conditions depends on the previous formation rate and temperature.

3. Tantalum is the mobile material during anodic formation of Ta_2O_5.

Acknowledgement

The author acknowledges the helpful criticisms by D. Turnbull during the preparation of the manuscript.

Reference

1. VERMILYEA, D. A. Acta Met. **1** (1953) 282.

A FUNDAMENTAL INVESTIGATION OF THE MECHANISM OF SINTERING*

E. B. ALLISON and P. MURRAY†

Part I is concerned with the mechanism of sintering. Data on the sintering of fluorides are obtained by a continuous, dilatometric method, and the effects of initial compacting pressure and particle size distribution of the powder are also investigated.

The results are analysed in relation to two recent theories of sintering based on a plastic flow model. One of these theories (proposed by Shuttleworth and Mackenzie) is also applied to Clark and White's data for the sintering of glass spheres. It is shown that, while the two mathematical relations may be fitted to experimental sintering data, neither mechanism accounts completely for the effect of compacting pressure and particle size distribution.

Activation energies for the flow process are derived, the values being approximately 35 and 90 kcal/mole for sodium and calcium fluoride respectively.

The Clark-White mechanism is critically reviewed, and it is shown that their empirical term is not related to particle size as they suggested. Alternative explanations regarding the inclusion of the empirical term are proposed. Additional evidence is required regarding the way in which flow occurs in an assemblage of spheres before the appropriate mathematical rate equations can be developed.

Further indication that a plastic flow mechanism is operative in sintering is obtained by applying Herring's analysis to the sintering data for different size fractions of calcium fluoride.

Part II is concerned with the measurement of the flow properties of glass and sodium fluoride at elevated temperatures, and the subsequent comparison of the flow constants with those deduced from sintering data.

Scott's theory of compression of discs is applied to subsidence-time curves obtained for glass and sodium fluoride at various temperatures. It is found that a sample of soda glass tested at 655°C behaves as a Newtonian fluid, the viscosity being approximately 5×10^8 poises. Sodium fluoride, however, in the temperature range 870° to 970°C, appears to behave as a Bingham solid. The yield stress values are of the order of 10^6 to 10^7 dynes/cm^2 and the viscosity coefficients range from 10^9 to 10^{10} poises.

Values of yield stress and viscosity deduced from sintering data using the Shuttleworth-Mackenzie equations are of the same order of magnitude as those determined experimentally.

UNE INVESTIGATION FONDAMENTALE DU MÉCANISME DE FRITTAGE

La première partie traite le mécanisme de frittage. Les données sur le frittage de fluorures sont obtenues par une méthode dilatométrique, continue; les effets des pressions de serrage initial et de la distribution granulométrique de la poudre furent aussi investiguées. Les résultats sont analysés en relation avec deux théories récentes de frittage, basées sur un modèle d'écoulement plastique. Une de ces théories (proposée par Shuttleworth et Mackenzie) est aussi appliquée aux données de Clark et White concernant le frittage de sphères de verre. On montre que malgré que les expressions mathématiques des deux théories soient en accord avec les données expérimentales sur le frittage, aucun des deux mécanismes ne justifie complètement l'effet des pressions de serrage et de la distribution granulométrique. On détermine les énergies d'activation pour le processus d'écoulement, elles sont d'environ 35 et 90 kcal/mol, respectivement pour le fluorure de sodium et le fluorure de calcium. Une critique du mécanisme de Clark et White est faite et il est montré que le terme empirique de leur expression n'est pas, contrairement à leur suggéstion, lié aux dimensions des grains. On propose d'autres explications concernant l'inclusion du terme empirique. Des preuves supplémentaires, relatives à la façon dont s'opère l'écoulement dans un assemblage de sphères, seraient nécessaires avant qu'il soit possible de développer les équations de vitesse appropriées. D'autres indications, supportant l'idée qu'un mécanisme d'écoulement agît dans le frittage, sont obtenues en appliquant l'analyse de Herring aux données sur le frittage de différentes catégories de grosseur des grains de fluorure de calcium. La deuxième partie traite, pour commencer, les mesures des propriétés d'écoulement du verre et du fluorure de sodium aux températures élevées; une comparaison entre les constantes d'écoulement ainsi obtenues et celles qu'on déduit des données sur le frittage, suit. La théorie de Scott, sur la compression de discs, est appliquée aux courbes tassement-temps, obtenues pour le verre et le fluorure de sodium à diverses températures. Il est constaté qu'un échantillon de verre à la soude, essayé à 655°C, se comporte comme un fluide Newtonien, la viscosité étant d'environ 5×10^8 poises. Toutefois, le fluorure de sodium, dans l'intervalle de températures allant de 870° à 970°C, se comporte comme un solide de Bingham. Les tensions d'écoulement sont de l'ordre de 10^6 à 10^7 dynes/cm^2 et les coefficients de viscosité vont de 10^9 à 10^{11} poises. Les valeurs des tensions d'écoulement et de viscosité, déduites des données sur le frittage, en se servant des équations de Shuttleworth et Mackenzie, sont du même ordre de grandeur que celles qu'on a déterminées expérimentalement.

EINE GRUNDSÄTZLICHE UNTERSUCHUNG DES SINTERUNGSVORGANGS

Teil I behandelt den Sinterungsvorgang. Mit Hilfe von kontinuierlichen Dilatometermessungen wurden Angaben über das Sintern von Fluoriden gewonnen. Ausserdem wurde der Einfluss des Ausgangspackungsdruckes und der Teilchengrössenverteilung des Pulvers untersucht.

Diese Resultate werden im Hinblick auf zwei kürzlich veröffentlichte Theorien des Sinterns, die sich auf Modellvorstellungen des plastischen Fliessens stützen, analysiert. Eine dieser Theorien (die von Shuttleworth und Mackenzie vorgeschlagen) wurde ausserdem auf die von Clark und White am Sintern von Glasskugeln gewonnenen Resultate angewandt. Es zeigt sich, dass obwohl die beiden mathematischen Beziehungen mit den experimentellen Sinterungsdaten in Einklang gebracht werden

*Received October 9, 1953.

†Atomic Energy Research Establishment, Harwell, England.

können, keine der vorgeschlagenen Elementarvorgänge die Wirkung des Packungsdrucks und der Teilchengrössenverteilung völlig erklären kann.

Die Aktivierungsenergien für den Fliessprozess wurden abgeleitet. Für Natrium- und Kalziumfluorid betrugen die entsprechenden Werte 35 kcal/mol und 90 kcal/mol.

Der von Clark und White vorgeschlagene Elementarvorgang wird kritisch diskutiert, und es wird gezeigt, dass ihr empirischer Faktor nicht in der von ihnen angegebenen Weise zur Teilchengrösse in Beziehung steht. Andere mögliche Erklärungen für die Einbeziehung des empirischen Faktors werden vorgeschlagen. Erst wenn mehr Material über die Art und Weise, in der Fliessen innerhalb eines Kugelaggregates beginnt, vorliegt, können die geeigneten mathematischen Geschwindigkeitsbeziehungen entwickelt werden.

Weitere Hinweise auf die Möglichkeit eines plastischen Fliessprozesses im Sintern ergeben sich, wenn man Herrings Analyse auf die Resultate der Sinterung von verschiedenen Teilchengrössenanteilen von Kalziumfluorid anwendet.

Teil II behandelt die Messungen der Fliesseigenschaften von Glass und Natriumfluorid bei höheren Temperaturen und den Vergleich der Fliesskonstanten mit den aus den Sinterresultaten abgeleiteten Daten.

Scotts Theorie der Kompression von Scheiben wurde auf die an Glass und Natriumfluorid erhaltenen Abklingung-Zeit Kurven angewandt. Es zeigte sich, dass sich eine bei 655°C untersuchte Probe von Sodaglass wie eine Newton'sche Flüssigkeit mit einer Viskosität von etwa 5×10^8 poises verhielt; Natriumfluorid verhält sich jedoch zwischen 870°C und 970°C anscheinend wie ein Bingham'scher Festkörper. Die Werte der Fliesspannung liegen zwischen 10^6 und 10^7 dynes/cm^2 und die Koeffizienten der Viskosität zwischen 10^9 und 10^{10} poises.

Die aus den Sinterresultaten mit Hilfe der Shuttleworth-Mackenzie'schen Gleichungen abgeleiteten Werte der Fliesspannung und der Viskosität liegen in der gleichen Grössenordnung wie die experimentellen Daten.

Introduction

One of the most widely used methods of producing refractory shapes is that of cold-pressing and sintering, and, in practice, the rate at which sintering occurs and the porosity of the final product are of importance. The present work, however, has been designed to yield information pertinent to the fundamental mechanism underlying sintering.

Material can be transported by several mechanisms, namely, (i) evaporation-condensation, (ii) diffusion or (iii) macroscopic flow. Evaporation-condensation can be ruled out as a general mechanism since there are many cases in which rapid shrinkage occurs at temperatures where the vapour pressures are negligible. Considering diffusion as a possible mechanism in sintering, Shuttleworth [1] has made calculations which indicate that such a mechanism is far too slow to account for the experimental results. Furthermore, one of the most important features of the isothermal bulk density-time curves is that the densities appear to attain a limiting value which is temperature-dependent. This suggests that sintering is governed by *two* parameters. Further evidence regarding this point was obtained by Cannon, Clark and White [2] who plotted the logarithm of the time required to reach a given degree of sintering at various temperatures against the reciprocal of the absolute temperature. The resulting plot was a curve, indicating that the rate of sintering could *not* be described by a single parameter. Evidence such as this suggests that plastic flow (involving two parameters) rather than diffusion is operative in sintering.

In view of the above considerations, the present work has been concerned with an attempt to prove the validity of a plastic flow theory as applied to sintering. Two such theories have been proposed recently, one by Clark and White [3] which is applicable to the early, open-pore stage of sintering and the other by Shuttleworth and Mackenzie [1] which is applicable to the closed, isolated pore stage. Isothermal shrinkage-time curves obtained by a continuous, dilatometric method provide accurate data with which the validity of these theories may be tested. Furthermore, additional evidence has been obtained by studying the effect of particle size and initial compacting pressure upon sintering characteristics. The materials used in this investigation were sodium and calcium fluorides since these possess the following advantages:

(*a*) there are no phase changes,

(*b*) sintering temperatures are relatively low (less than 1000°C),

(*c*) the general characteristics of fluorides (e.g., ionic radii) are not very different from those of the refractory oxides, thus leading the way to a general theory.

A more rigid test of these plastic flow equations can be obtained by comparing the rheological properties of the fluorides at elevated temperatures with the sintering data. This forms the subject of the second part of this paper. Compression testing offers several advantages, namely, (i) direct application of the load, obviating the use of chucks; (ii) the use of relatively simple apparatus for applying the load and measuring the deformation; and (iii) test pieces are of simple shape and do not require machining. Consequently, the flow

properties of sodium fluoride and a soda glass have been determined by measuring the rate of subsidence of thin discs of material under a constant load. Under these conditions, the viscosity coefficients and yield stresses may be evaluated by the application of Scott's [4] analysis.

I. Sintering Data and Plastic Flow Mechanisms

Experimental Procedure

The spectrographic analyses of the fluorides used throughout this investigation are given in Table I.

TABLE I

SPECTROGRAPHIC ANALYSES OF THE FLUORIDES

Fluoride	Impurities %					
	Mg	Si	Ti	Zn	Al	Sr
NaF	0.015	2.0	< 0.02	0.01	< 0.01	< 0.02
CaF_2	0.3	0.2	0.02	< 0.01	0.1	0.3

All experimental compacts were made by cold-pressing. Before pressing, the chemically pure calcium fluoride was calcined at 1100°C and ground in an agate mortar to pass a 150 B.S. sieve. Compacts of this fluoride were pressed at 48,000 psi. The sodium fluoride as received was sieved −330 B.S. sieve and pressed at 8,000 psi. Pressings were made without a binder. At a later stage, the effect of moulding pressure and variation of the particle-size distribution of the CaF_2 powder were also investigated.

Normally, the shrinkage of preformed refractory materials on sintering is followed by measurement of the volume changes after given heat treatments (i.e., by discontinuous methods), but in the case of fluorides which sinter below 1000°C, it was possible to use a more accurate dilatometer method to obtain shrinkage-time curves at different temperatures. The dilatometer consisted of a closed-end fused silica tube, 1 in. in diameter, to the top of which was cemented a dial gauge graduated in 0.0001 in. Changes in the height of the compact, which was placed in the bottom of this tube, were transmitted to the dial gauge by a central silica tube. With this arrangement, changes in the dimensions of the system itself are very small and can be neglected. The apparatus was placed in a nichrome wound furnace for a length of 6 in. of the silica tube. To prevent heating of the dial gauge by radiation from the furnace, close fitting "Syndanyo" collars were fixed round the dilatometer. The temperature of the compact was measured by a thermocouple inserted in the inner tube with its junction situated 1 mm from the surface of the compact.

Initially, the temperature range in which significant shrinkage occurred was determined by heating the compacts at a constant rate. From these preliminary runs it was possible to define the temperature range in which rapid shrinkage occurred and in the subsequent isothermal experiments, compacts were heated rapidly to given temperatures in this range, the temperature held constant, and the variation of shrinkage with time measured over periods up to four hours. In assessing the zero point for the shrinkage-time data, the point at which the linear shrinkage exactly balanced the thermal expansion that had occurred was taken, since at this point the bulk density is equal to that of the compact initially. The linear shrinkages thus obtained were converted to volume shrinkages, it being assumed that the shrinkage was isotropic. Measurement of the sintered compacts after removal from the apparatus showed that this was not strictly true, but the errors involved were small and of the order of 0.5 per cent of the bulk density.

Results

The initial heating curves obtained with CaF_2 and NaF are shown in Figure 1 together with those

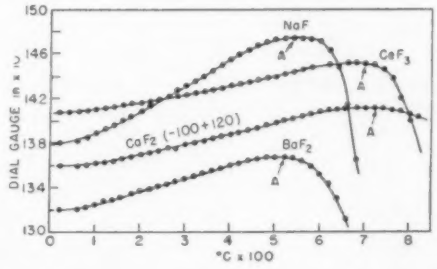

FIGURE 1. Dilatometer heating curves for various fluorides.

determined on BaF_2 and CeF_3. These latter powders were used as received and compacted at 8000 psi. These curves are the product of two opposing factors, namely, thermal expansion and shrinkage due to sintering. Hence the curves show a peak, shrinkage (and sintering) starting just prior to this peak. Values of the coefficient of thermal expansion taken from the linear parts of the curves, at temperatures well below the peak temperature are given in Table II.

It is of interest to note that the thermal expansion increases with decreasing cation valency, the difference being particularly marked in the case of

TABLE II

THERMAL EXPANSION DATA FOR THE FLUORIDES

Fluoride	Linear expansion coefficient (in./in./°C)
CeF_3 (as received)	18.8×10^{-6}
BaF_2 (as received)	20.6
CaF_2 (calcined, − 100 + 120)	21.4
CaF_2 (calcined, − 300)	25.9
NaF (as received, − 330)	38.9

the univalent and divalent fluorides. Although this is in qualitative accord with the theoretical work of Megaw [5], the quantitative relationship that the thermal expansion coefficient is proportional to the coordination number of the cation divided by the square of the cation valency is not substantiated.

Comparison of the values for the compacts made from the two grades of CaF_2 powder shows that the expansion coefficient is higher for the finer grade, indicating that some expansion is taken up in the interstices of the coarser powder compacts. The thermal expansions of the fluorides are high, suggesting that the thermal shock properties of fluoride refractories are likely to be very poor.

The temperatures at which shrinkage overbalances thermal expansion for the above materials, indicated by the peaks on the heating curves (Figure 1), are given in Table III.

TABLE III

SHRINKAGE TEMPERATURE DATA FOR THE FLUORIDES

Fluoride	Temperature at which shrinkage overbalances expansion	Melting Point °C	T/Tm (T and Tm expressed in °K)
CeF_3 (as received)	720°C	1460	0.57
BaF_2 (as received)	540	1353	0.50
CaF_2 (calcined, −100+120)	720	1418	0.58
CaF_2 (calcined, −300)	760	1418	0.61
NaF (as received, −330)	560	995	0.66

Thus shrinkage begins when the value of T/Tm is approximately 0.5–0.6. It may be noted that this provides one point of difference between the sintering of ionic solids and metals. The latter, in general, must be heated closer to the melting point, although in some cases the presence of oxide films on the metal particles may be responsible for this effect.

Linear shrinkage-time and porosity-time data for CaF_2 and NaF are shown in Figures 2 and 3. With CaF_2, compacts of 5–10 per cent porosity can be obtained by sintering in the region of 950°C, whereas with NaF, at the temperatures employed, the minimum porosity was 14 per cent. In both cases the shapes of the shrinkage-time curves indicate that there is a limiting shrinkage for each particular temperature. At the temperatures investigated, this limit will only be attained after much longer times than those of these tests.

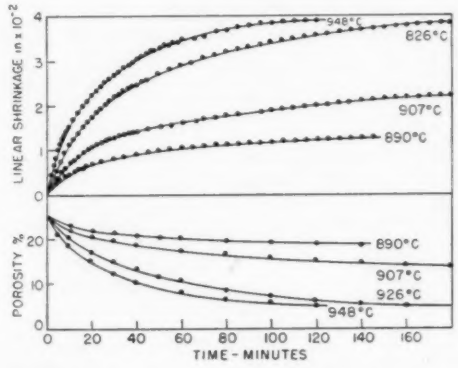

FIGURE 2. Shrinkage-time and porosity-time curves for calcium fluoride (calcined −150 B.S. sieve).

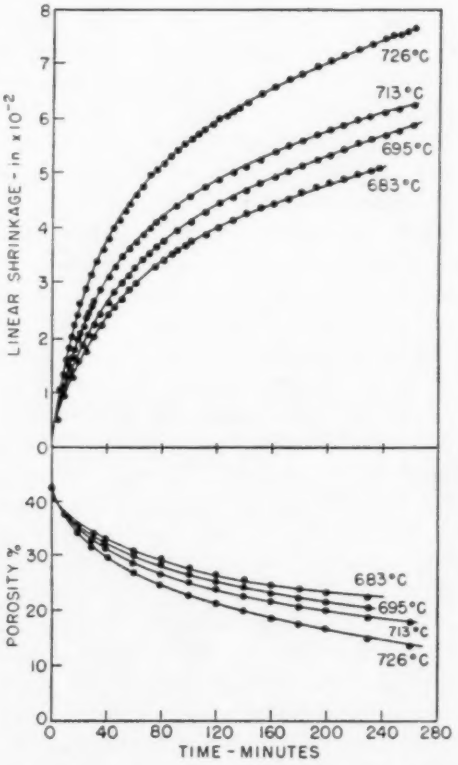

FIGURE 3. Linear shrinkage-time and porosity-time data for sodium fluoride (as received, −330 B.S. sieve).

The effect of increase of compacting pressure is shown in Figure 4 relating to the sintering of CaF_2 at 890°C. The porosity-time curves are roughly parallel, the final porosity being lower at the higher pressures. This is probably entirely due to the lower initial porosity of the more highly pressed compacts. The curves of Figure 4 indicate that no matter how long the sintering time, the compacts of higher initial porosity will never attain as low a porosity as those made at the higher compacting pressures.

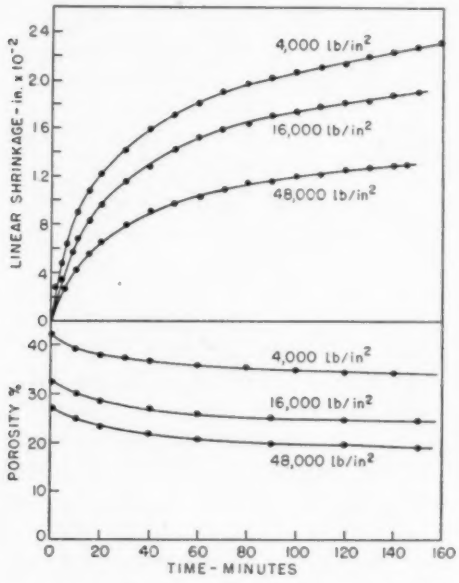

FIGURE 4. Effect of compacting pressure on the sintering of calcium fluoride (calcined −150 B.S. sieve) at 890°C.

The effect of variation of the particle-size distribution of the powder on the shrinkage behaviour of the compacts was investigated by sieving out three fractions (−100 + 120, −250 + 300, and −300 B.S. sieve) from the CaF_2 calcined at 1100°C and ground in an agate pestle and mortar. The particle-size distributions of the two finer fractions were determined turbidimetrically and are shown in Figure 5. The −250 + 300 fraction gave an irregular distribution due to "blinding" of the sieve resulting in retention of the finer particles. The sintering behaviour of compacts (pressed from these fractions at 24,000 psi) at 890°C is shown in Figure 6. Because of its irregular particle-size distribution, the initial porosity of the compacts made from the −250 + 300 fraction is lower than that of the compacts made from the −300 fraction. As regards the sintering behaviour, the effect of particle-size is partly reflected in the difference in the initial porosities of the compacts. The curves, however, indicate that a greater decrease in porosity is obtained (with decreasing particle-size) than can be accounted for by the initial difference in porosity. There are thus two effects of particle-size:

(1) With decreasing particle-size, better packing is obtained, resulting in a decreased initial porosity for the same compacting pressure and hence a lower sintered porosity.

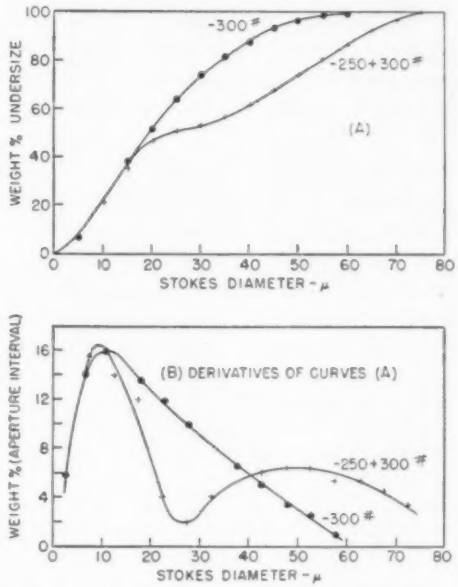

FIGURE 5. Particle-size distribution curves for calcium fluoride.

(2) With decreasing particle-size, not only is the shrinkage rate increased, but the limiting shrinkage

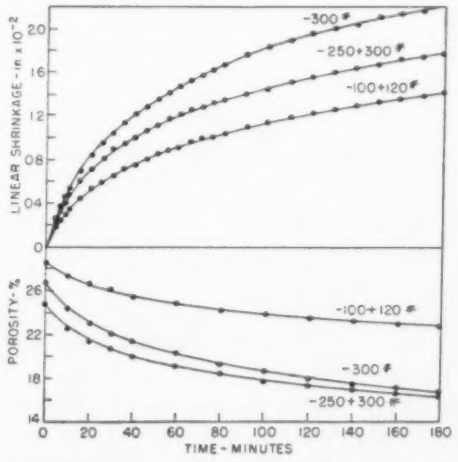

FIGURE 6. Effect of particle-size on the sintering behaviour of calcium fluoride at 890°C.

is also increased, resulting in a further decrease in sintered porosity over and above that due to better compacting.

Analysis of the Isothermal Shrinkage Data

The isothermal shrinkage curves described above provide accurate data by which to test the various mathematical expressions derived from the recent physical mechanisms designed to explain sintering phenomena by macroscopic flow. The two most important types of mechanism are those proposed by Clark and White [3] and Mackenzie and Shuttleworth [1].

(*a*) *The Clark-White Mechanism*

This mechanism is modelled on an assemblage of spherical particles, shrinkage (and sintering) being attributed to movement of the surface layers towards the points of contact by capillary forces. Lenses of the material are thus formed between the particles (Figure 7), and by considering the

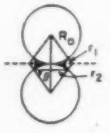

FIGURE 7. Schematic representation of lens formation.

forces acting and the rate of flow of material into these lenses, equations are derived for the rate of volume shrinkage both for viscous flow and for flow of the Bingham type (i.e., where the material possesses a finite yield point). The latter is considered to be the type of flow operative in the sintering of oxides and fluorides. The relevant rate equation is:

$$(1)\quad \frac{d\bar{V}}{dt} = K\,\frac{\frac{1}{\rho}+q_0}{\frac{1}{\rho}+V}\,\frac{n\sqrt{1-x^2}}{2}\left[2+\frac{x}{(1-x)}-\frac{1}{\sqrt{1-x^2}}-\frac{X}{1+V\rho}\right]$$

where K is a velocity constant, expressed in c.c./gm/sec and is equal to

$$\frac{\gamma h^3}{\rho\eta^{l}R_0^3},$$

γ is the surface tension, η is the viscosity, R_0 is the initial radius of the spheres, h is the thickness of the moving layer, l is the length in the direction of stress over which shearing occurs, ρ is the specific gravity of the material, q_0 is the initial pore volume per gram, n is the number of points of contact between each sphere and its neighbours (e.g., for cubic packing $n = 6$), $\bar{V}$ is the volume shrinkage per gram and is equal to

$$V\,\frac{\left(\frac{1}{\rho}+q_0\right)}{\left(\frac{1}{\rho}+V\right)},$$

V is the volume of the lenses associated with one gram of spheres at time t and is given by

$$\frac{3n}{4\rho}\left[\frac{1-x}{x}\right]^2\left[1-\sin^{-1}x\frac{\sqrt{1-x^2}}{x}\right],$$

x being $\sin\theta$ (Figure 7), X = a constant which varies only with temperature, being given by

$$\frac{3R_0lS}{2h\gamma},$$

and S is the yield stress in shear.

Since a range of particle-sizes is present in the actual compacts, the shrinkage in the early stages would be expected to be conditioned by that of the finer particles, the coarser fractions making an increasing contribution as shrinkage proceeds. This is equivalent to an increasing value of R_0, and was allowed for empirically, by Clark and White, by replacing R_0 by $R_0(1+V)^{2/3}$ in equation (1) which thus becomes:

$$(2)\quad \frac{d\bar{V}}{dt} = K\,\frac{\frac{1}{\rho}+q_0}{\frac{1}{\rho}+V}\,\frac{n\sqrt{1-x^2}}{2}\left[2+\frac{x}{1-x}-\frac{1}{\sqrt{1-x^2}}-\frac{X}{3\sqrt{1+V\rho}}\right]\frac{1}{(1+V\rho)^2}$$

These equations were applied to the sintering data for the two fluorides, the linear shrinkage-time curves first being converted to $\bar{V}$-time curves, assuming that the shrinkage was isotropic. In equation (2), ρ and q_0 are known for a given compact, n and X are constants, and V and $\bar{V}$ are functions of x which vary with time. Hence, for various values of x and X, it is possible to calculate values of $\bar{V}$ and $(1/K)\cdot(d\bar{V}/dt)$. Plotting $Kdt/d\bar{V}$ against $\bar{V}$, a series of curves is obtained for various values of X, the area under which, expressed in appropriate units, gives values of Kt. If the values of Kt thus obtained from one curve (i.e., constant X) are divided by the times corresponding to the relevant $\bar{V}$ on the experimental curves, values of K are obtained. The value of X chosen

determines whether or not the "K" is constant along the experimental curve. In this way, values of K and X can be selected to fit the data, and calculated shrinkage-time curves can be obtained for comparison with the experimental data. A typical example is worked out in detail in Appendix 1.

The calculated curves agree remarkably well with the experimental ones as shown in Figure 8

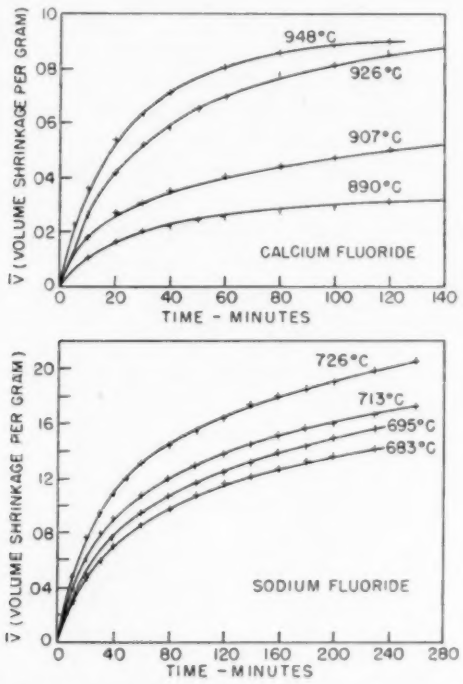

FIGURE 8. Comparison of calculated and experimental sintering curves for the fluorides. Full lines, calculated curves; +, experimental points.

for calcium and sodium fluorides. The values of K and X obtained are reported in Tables IV and V.

TABLE IV

SINTERING DATA FOR CALCIUM FLUORIDE

Compacting pressure 48,000 psi; $\rho = 3.18$; $q_0 = 0.107$ cc/gm; n assumed equal to 8

T°C	T°K	$10^3/T$°K	K	$\log_{10} K$	X
948	1221	0.819	5.90×10^{-6}	$\bar{6}.771$	2.4
926	1199	0.833	3.53×10^{-6}	$\bar{6}.548$	2.3
907	1180	0.848	2.25×10^{-6}	$\bar{6}.352$	4.0
890	1163	0.860	1.30×10^{-6}	$\bar{6}.114$	5.5

log K is plotted against $10^3/T$°K, in Figure 9; reasonably straight lines are obtained, indicating that the results obey the Arrhenius equation:

TABLE V

SINTERING DATA FOR SODIUM FLUORIDE

Compacting pressure 8,000 psi; $\rho = 2.79$; $q_0 = 0.254$ cc/gm; n assumed equal to 8.

T°C	T°K	10^3T/°K	K	$\log_{10}K$	X
726	999	1.001	5.27×10^{-6}	$\bar{6}.722$	1.8
713	986	1.014	3.94×10^{-6}	$\bar{6}.596$	2.0
695	968	1.033	3.12×10^{-6}	$\bar{6}.494$	2.1
683	956	1.046	2.81×10^{-6}	$\bar{6}.449$	2.3

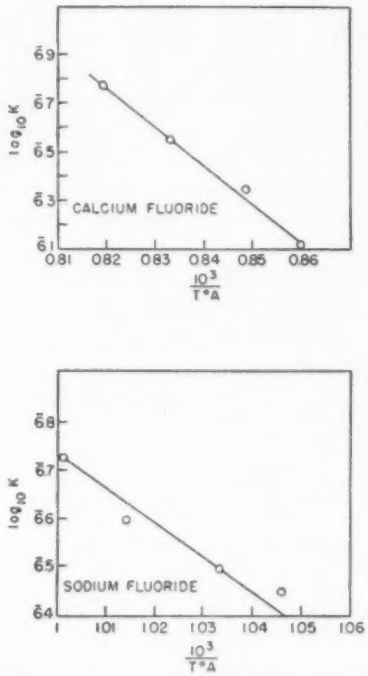

FIGURE 9. Arrhenius plots for the fluorides (Clark-White equation).

$$K = A\, e^{-E/RT}$$

The activation energies E and the values of $\log_{10}A$ are given in Table VI. The values obtained by Clark and White for magnesia and alumina are included for comparison.

Comparison of the parameters for the flow process for fluorides and oxides shows that the

TABLE VI

ARRHENIUS PARAMETERS FOR THE SINTERING OF FLUORIDES AND OXIDES

	E cal/mole	$\log_{10} A$
NaF	32,600	1.86
CaF_2	73,700	7.96
MgO	43,000	0.51
Al_2O_3	87,000	4.42

activation energies are of the same order. In both cases, the $\log_{10}A$ value is higher for the higher E-value, but there is insufficient data to draw any definite conclusions. One other point of significance is that the activation energies for the cubic lattices NaF and MgO are low (30,000 to 40,000 cal/mole), whereas the fluoride lattice CaF_2 and α-Al_2O_3 (trigonal) require much higher E-values for initiation of the flow process. This suggests that the simple cubic lattice is much easier to deform in shear than the more complex types.

The application of equation (2) is valid only when the lenses at the points of contact are separate and distinct from each other. As sintering proceeds, a point will be reached at which merging of the lenses occurs, leading to the development of separate spherical pores. Elimination of these closed pores would then proceed by some other mechanism. The point at which closed pores will form depends upon the type of packing assumed in the initial compacts; with 8 points of contact per sphere, closed pores would be formed when the value of x is approximately equal to 0.8. Thus the lower limits of porosity below which equation (2) should not hold would be

	Initial porosity %	Lower limit of porosity .% (corresponding to $x = 0.8$)
NaF	42	34
CaF_2	26	17

Figure 8 shows that the curves calculated from equation (2) fit the experimental points closely down to the lowest porosities obtained for each fluoride (5 per cent and 14 per cent for CaF_2 and NaF respectively). This is well below the range of porosity over which equation (2) should be valid theoretically.

However, an indication that the Clark-White mechanism does break down at high degrees of sintering has been obtained by calculating the values of $\bar{V}$ at which, according to equation (2), shrinkage will stop. From equation (2) $d\bar{V}/dt = 0$, i.e., shrinkage stops when

$$\left[2 + \frac{x}{1-x} - \frac{1}{\sqrt{1-x^2}} - \frac{X}{3\sqrt{1+V\rho}}\right] = 0.$$

X is known, V varies with x and hence the value of x which satisfies this condition can be obtained. Thus $\bar{V}_\infty$, the limiting shrinkage at infinite time can be deduced. The limiting values, together with the corresponding limiting porosities P_∞, are given in Table VII.

Thus, by extrapolation to infinite time using equation (2) negative porosities are obtained. It is evident, therefore, that the equation is not valid at low porosities, and that some other mechanism, which is slower, must become operative.

TABLE VII

LIMITING VOLUME SHRINKAGES AND POROSITIES FOR THE FLUORIDES

CaF_2			NaF		
T°C	$\bar{V}$ cc/gm	P_∞ %	T°C	$\bar{V}$ cc/gm	P_∞ %
948	0.13	negative	726	0.31	negative
926	0.14	negative	713	0.25	negative
907	0.06	13.1	695	0.24	3.5
890	0.03	19.2	683	0.20	11.8

The shrinkage-time curves obtained for increasing initial compacting pressure for CaF_2 at 890°C have also been examined using equation (2). The curves are shown in Figure 10; good fits are again obtained, the K- and X-values being given in Table VIII.

TABLE VIII

SINTERING DATA FOR CaF_2 AT 890°C FOR DIFFERENT COMPACTING PRESSURES

Compacting pressure psi	Initial porosity %	K	X
4,000	42.5	3.22×10^{-6}	3.5
16,000	32.5	1.77×10^{-6}	3.75
48,000	25.0	1.30×10^{-6}	5.5

Compacting pressure has a marked effect on both K, the velocity constant, and also on X which is a measure of the yield stress at any temperature. K is decreased by 250 per cent, while X is increased by 60 per cent. Equation (2) may be written shortly as

$$\frac{d\bar{V}}{dt} = K \frac{\left(\frac{1}{\rho} + q_0\right)}{\left(\frac{1}{\rho} + V\right)} n \left[f(x) - g\frac{(X)}{(x)}\right] h(x)$$

and hence compacting pressure will affect both q_0, the initial pore volume per gram and also n, the number of points of contact per sphere. Hence both $d\bar{V}/dt$ and the integrated $\bar{V}$-time curve would be affected. It is difficult to see however, how compacting pressure can affect K and X which are defined as follows:

$$K = \frac{\text{surface tension (thickness of the moving layer)}^3}{\text{specific gravity} \times \text{viscosity} \times (\text{particle radius})^3 \times \text{length of shear}},$$

$$X = \frac{3 \times \text{particle radius} \times \text{length of shear} \times \text{yield stress in shear}}{2 \times \text{surface tension} \times \text{thickness of the moving layer}}$$

Compacting pressure may possibly result in two effects

(*a*) Degradation of the particles resulting in the production of finer particles. This, however, would have the opposite effect to that observed, viz., K would increase and X decrease.

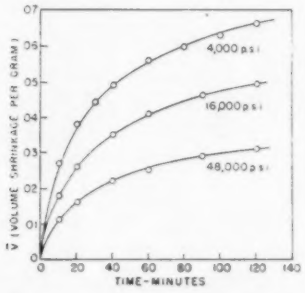

FIGURE 10. Application of the Clark-White equation to the sintering curves for CaF_2 compacted at different pressures, temperature 890°C.

(*b*) An increase in the area of the interface of contact of the particles. This would not be expected to affect any of the factors determining K and X.

It is concluded, therefore, that the mechanism in its present stage of development cannot account for this effect of compacting pressure.

The curves obtained for decreasing particle size for CaF_2 at 890°C can also be fitted closely by equation (2); the curves are shown in Figure 11, data being given in Table IX.

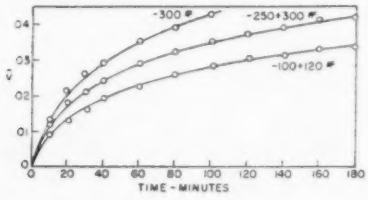

FIGURE 11. Application of the Clark-White equation to different size fractions of CaF_2. Full lines, calculated curves. ⊙, experimental points, temperature 890°C.

TABLE IX

SINTERING DATA FOR CaF_2 AT 890°C FOR DECREASING PARTICLE SIZE

Compacting Pressure 24,000 psi

Grading B.S. sieves	Average particle size microns	K	X
− 100 + 120	135 (approx.)	7.76×10^{-7}	5.0
− 250 + 300	50	1.20×10^{-6}	4.6
− 300	12	1.41×10^{-6}	3.9

Since $K = (\gamma h^3/\rho\eta l R_0^3$ and $X = (3R_0 lS)/(2\gamma h)$, then K should increase with decreasing particle-size while X should decrease. Table IX shows that the results are in agreement with the prediction. The agreement is, however, not quantitative since, considering the two closely graded fractions ($-100 + 120$ and $-250 + 300$), the decrease in particle radius of approximately 50 per cent should result in an eightfold increase in K and 50 per cent reduction in the value of X. In practice, however, the effect is much smaller, K being increased by about 50 per cent and X being decreased by about 10 per cent.

It has been shown that the Clark-White equation fits the experimental sintering data during the early stages of sintering (i.e., open, connected pores). The equation at present, however, cannot account for the effect of compacting pressure on sintering nor does it give quantitative agreement with the effect of particle-size on sintering. A further important point arising from particle-size considerations is that, even though closely graded fractions were used for the fluoride work (e.g., between 150 and 125μ), it is still necessary to include the empirical correction term for particle-size distribution to obtain calculated curves which fit the experimental data. This indicates that the correction term cannot be related to particle-size distribution. If the correction term is omitted, the true theoretical sintering curve will not fall away sufficiently with time, and to account for the deviation it would seem that the isothermal velocity constant must decrease along the volume shrinkage-time curve. The extent of the variation necessary to fit the experimental curve can be determined as follows:

The Bingham solid equation containing the empirical term may be written:

$$(3)\quad \frac{1}{K_c}\frac{d\bar{V}}{dt} = \left(\frac{\frac{1}{\rho} + q_0}{\frac{1}{\rho} + V}\right)\frac{n\sqrt{1-x^2}}{2}$$

$$\left[2 + \frac{x}{1-x} - \frac{1}{\sqrt{1-x^2}} - \frac{X}{(1+V\rho)^{1/3}}\right]\cdot\frac{1}{(1+V\rho)^2}$$

where K_c is the velocity constant and the agreement with experiment is given by the inclusion of the empirical term.

Considering the case of the sintering of NaF at 713°C (see Appendix 1) assuming $X = 1$ for the sake of simplicity, values of $1/K_c(d\bar{V}/dt)$ can be

obtained for various values of x. If we omit the correction term the equation becomes

$$(4)\quad \frac{1}{K}\frac{d\bar{V}}{dt} = \left(\frac{\frac{1}{\rho}+q_0}{\frac{1}{\rho}+V}\right)\frac{n\sqrt{1-x^2}}{2}\left[2+\frac{x}{1-x}-\frac{1}{\sqrt{1-x^2}}-\frac{X}{1+V\rho}\right].$$

Again assuming $X = 1$, values of $(1/K)(d\bar{V}/dt)$ can be calculated for various values of x. The variation in K necessary for agreement between theory and experiment can thus be found as in Table X.

TABLE X

VARIATION IN K NECESSARY TO FIT THE SINTERING CURVE FOR NaF AT 713°C.

x	$\frac{1}{K_c}\frac{d\bar{V}}{dt}$	Q	A	$\frac{1}{K}\frac{d\bar{V}}{dt}$	$\frac{K_c}{K}$
0.90	20.85	2.887	7.739	22.36	1.073
0.87	16.28	3.180	5.722	18.17	1.116
0.84	12.92	3.420	4.455	15.25	1.182
0.80	10.00	3.680	3.435	12.64	1.264
0.77	8.26	3.830	2.907	11.13	1.350
0.74	6.69	3.885	2.305	9.73	1.450
0.70	5.23	3.973	2.120	8.43	1.61
0.60	2.79	3.950	1.528	6.04	2.17

$$Q = \left(\frac{\frac{1}{\rho}+q_0}{\frac{1}{\rho}+V}\right)\frac{n\sqrt{1-x^2}}{2}$$

and

$$A = \left(2+\frac{x}{1-x}-\frac{1}{\sqrt{1-x^2}}-\frac{X}{1+V\rho}\right)$$

Hence K must decrease by a factor of 2 over the range $x = 0.90$ to $x = 0.60$ (x being the sine of the lens angle, Figure 7) for agreement between theory and experiment. Closed, isolated pores, are, however, formed at approximately $x = 0.80$, so that over the valid range of the mechanism, a decrease in K of 25 per cent, is sufficient to account for the discrepancy.

The Clark-White velocity constant K is given by $\gamma h^3/\rho\eta l R_0^3$, where h is the thickness of the moving layer, l is a length in the direction of flow and B_0 is the original particle radius. Furthermore, to account for the variation in K necessary to fit the experimental curve, Clark and White suggested that in the actual compacts a range of particle-sizes was present. However, the use of closely graded fractions in the present series of experiments tends to disprove this hypothesis. Consideration of the parameters involved in K gives several alternative explanations for a decrease in K with time at constant temperature.

(1) The Clark-White theory assumes that h, the thickness of the moving layer, remains constant as sintering proceeds. This is the case for Newtonian fluids, but it would not appear to be true for materials of the Bingham type; below a certain critical transmitted stress, the element which is at the lowest part of the stress gradient will become stationary, i.e., the stress at this point is less than the yield value. As sintering proceeds and the stress decreases still further, the thickness of the "stationary plug" in the centre of the particle will increase until, finally, when the applied stress falls to the value of the yield point, flow will cease and h is zero. The relation between h and stress (and therefore time) is, therefore, as follows:

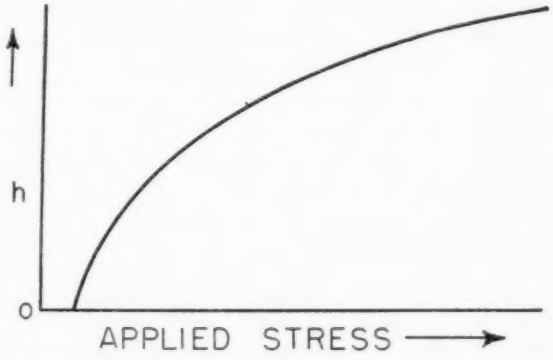

Thus the value of K will fall as sintering proceeds due to h decreasing.

(2) An obvious explanation of the deviation in the K-values is that the flow process may not be of the simple Bingham type. Much of the work done on the deformation of metals and ionic solids indicates that strain-hardening occurs, i.e., the apparent yield point rises with increasing deformation. Furthermore, several workers have found that the relation between shear rate and applied stress is more complex than the simple Bingham equation, a power law often being applicable.

(3) Clark and White postulate that the particle radius gradually decreases as sintering proceeds. Thus from their equations:

$$R^2 = \frac{R_0^3}{1 + V\rho}$$

where R is the radius at time t, R_0 the initial radius, V the volume of lenses associated with 1 gm of spheres, and ρ the specific gravity. In the author's opinion, however, during the early stages of sintering, and possibly up to the closed pore stage, the particle radius probably remains constant and the shrinkage is effected by a "merging together" of the particles. This is in direct contradiction to the Clark-White hypothesis. Kuczynski's [6] experiments on the sintering of glass particles to flat plates suggests that there is no systematic decrease in R with time. His results are reported in Table XI.

TABLE XI

VARIATION OF PARTICLE RADIUS R WITH TIME FOR GLASS PARTICLES (KUCZYNSKI)

t(min)	R (cm)
10	2.41×10^{-2}
15	2.35
20	2.61
25	2.52
30	2.20
40	2.47

(b) The Shuttleworth-Mackenzie Mechanism

The pressed compact is regarded as a solid mass containing isolated, spherical pores of equal size. It is assumed that deformation during sintering is due to surface tension, and that the effect of surface tension in closing the pores is equivalent to the application of an external pressure to the surface of the compact. Two equations of state are considered, that for a Newtonian fluid and that for a Bingham solid, and equations relating the apparent density to the sintering time are derived. For the fluorides, it was assumed that the equation of state relating to the Bingham solid was the appropriate model, and the corresponding equation is:

$$(5) \quad \frac{d\rho}{dt} = \frac{3}{2}\left(\frac{4\pi}{3}\right)^{1/3} \frac{\gamma n^{1/3}}{\eta} (1-\rho)^{2/3} \rho^{1/3} \left[1 - a\left(\frac{1}{\rho} - 1\right)^{1/3} \log_e \left(\frac{1}{1-\rho}\right)\right]$$

where ρ is the relative density at time t, γ the surface tension, n the number of pores per cc of real material, η the viscosity (at infinite rate of shear) and

$$a = \sqrt{2}\left(\frac{3}{4\pi}\right)^{1/3} \frac{T_c}{2\gamma n^{1/3}},$$

T_c being the yield stress.

In the mechanism proposed, it is implied that for pores of equal size, sintering will result in a decrease in their size but the total number n will remain constant. If, however, there is a distribution of pores of different sizes, sintering will result in the disappearance of the smaller pores so that n will decrease. In the application of equation (5) to the fluoride data it has been assumed that n remains constant.

As rate plots are sensitive and tend to magnify errors, calculated density-time curves have been obtained by graphical integration for comparison with the experimental curves. For various values of K and a, values of $dt/d\rho$ at various values of ρ are calculated from equation (5). $dt/d\rho$ is then plotted against ρ, the area under the curve giving values of t at various values of ρ. In this way, values of K and a can be selected to fit the experimental data, and calculated curves can be obtained for comparison with the experimental density-time curves. A typical example is worked out in detail in Appendix 2. Curves are shown in Figures 12 and 13 for calcium and sodium fluorides respectively,

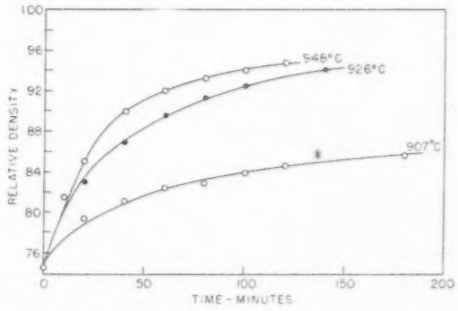

FIGURE 12. Comparison of calculated and experimental sintering curves for calcium fluoride (S–M equation). Full lines, calculated curves, ⊙ and ●, experimental points.

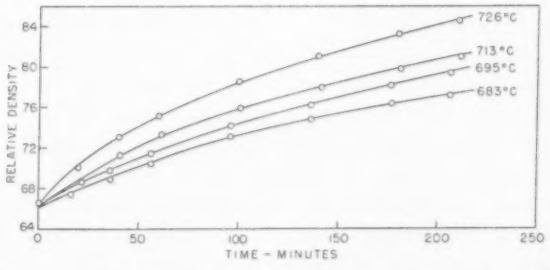

FIGURE 13. Comparison of calculated and experimental sintering curves for sodium fluoride (S–M equation). Full lines, calculated curves; ⊙, experimental points.

which show that good agreement is obtained, particularly in the case of NaF.

The equation holds from approximately 35 per cent downwards, but, theoretically, closed pores will not be formed in sintering until much lower porosities are obtained. Thus it is evident that the Shuttleworth-Mackenzie equation can be extrapolated above the upper limits of porosity (17 and 34 per cent for CaF_2 and NaF respectively), and still fit the experimental data closely. The porosity limits given above are theoretical ones; in practice, open connected pores probably persist down to and below 10 per cent porosity, depending on factors such as particle-size distribution and the proximity of the sintering temperature to the fusion point of the material.

The values of K and a for the two fluorides are given in Tables XII and XIII.

TABLE XII

SINTERING DATA FOR CALCIUM FLUORIDE

Compacting pressure 48,000 psi.; S.G. = 3.18; n assumed constant

T°C	T°K	$10^3/T$°K	K (sec^{-1})	$\log_{10}K$	a
907	1180	0.848	8.80×10^{-4}	$\bar{4}.945$	0.92
926	1199	0.833	2.08×10^{-3}	$\bar{3}.319$	0.87
948	1221	0.819	4.17×10^{-3}	$\bar{3}.620$	0.88

TABLE XIII

SINTERING DATA FOR SODIUM FLUORIDE

Compacting pressure 8,000 psi; S.G. = 2.79; n assumed constant

T°C	T°K	$10^3/T$°K	K (sec^{-1})	$\log_{10}K$	a
683	956	1.046	1.13×10^{-4}	$\bar{4}.054$	0.85
695	968	1.033	1.45×10^{-4}	$\bar{4}.161$	0.85
713	986	1.014	1.74×10^{-4}	$\bar{4}.240$	0.85
726	999	1.001	2.60×10^{-4}	$\bar{4}.416$	0.85

The velocity constant K has the dimensions of reciprocal time as compared with the units of cc/gm/sec for the Clark-White velocity constants. Values of the latter can be converted to the same basis as the Shuttleworth-Mackenzie constants by multiplying the values given in Tables IV and V by the specific gravity of the material. In both cases, a and X are pure numbers representing the effect of temperature on the ratio of the yield stress to surface tension. The Arrhenius plots of $\log_{10}K$ against $10^3/T$°K are shown in Figure 14, the activation energies and $\log_{10}A$ values being as follows:

	E	$\log_{10}A$
CaF_2	103,600	16.11
NaF	36,700	4.45

The activation energies are appreciably higher than those obtained using the Clark-White equation, that for CaF_2 being 50 per cent and for NaF 12 per cent higher.

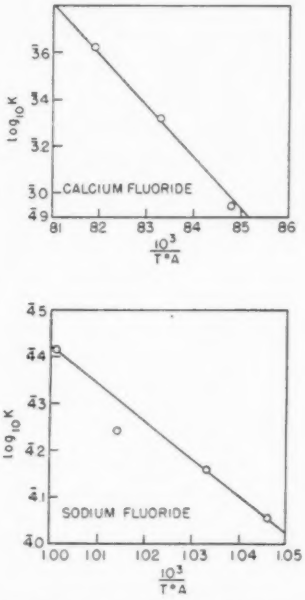

FIGURE 14. Arrhenius plots for the fluorides (Shuttleworth-Mackenzie equation).

Clark and White determined the sintering characteristics of a pressed compact of glass particles, and applied their plastic flow equation to the results. The present authors have applied the Shuttleworth-Mackenzie equation to these sintering curves. The experimental and theoretical curves are compared in Figure 15 which shows that

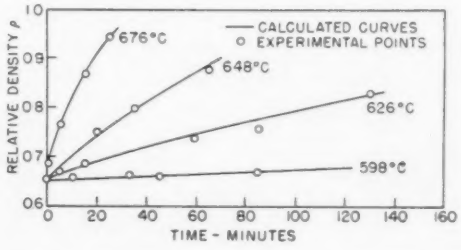

FIGURE 15. Application of the Shuttleworth-Mackenzie equation to the sintering of glass spheres.

good agreement is obtained. The values of the velocity constant K are given in Table XIV; the

value of a is zero showing that the glass behaves as a Newtonian fluid.

TABLE XIV

SINTERING DATA FOR GLASS

°C	°K	$10^3/°K$	$K(sec^{-1})$	$\log_{10}K$	a
598	871	1.148	1.04×10^{-6}	$\bar{5}.017$	0
626	899	1.112	5.80×10^{-6}	$\bar{5}.763$	0
648	921	1.086	1.73×10^{-4}	$\bar{4}.238$	0
676	949	1.055	6.41×10^{-4}	$\bar{4}.807$	0

The Arrhenius plot is shown in Figure 16; a straight line is obtained corresponding to an activation energy of 84,700 cal/mole.

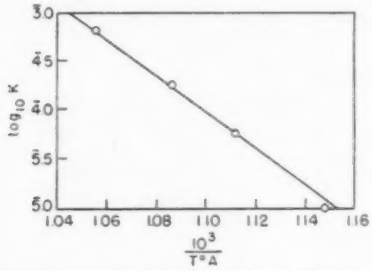

FIGURE 16. Arrhenius plot for glass (Shuttleworth-Mackenzie equation).

The sintering curves obtained with different initial compacting pressures have also been fitted using equation (5). Good agreement is obtained as is shown in Figure 17. The values of the constants are given in Table XV.

Increasing values of the compacting pressure will result in a decrease of the initial porosity of the compact. The main effect of increased compacting pressure is to reduce the pore size, the number of pores (associated with 1 cc of real material) remaining the same. From this, it follows that varying compacting pressure should have no effect on the values of K and a. Table XV shows that trebling the compacting pressure has not altered K, but has slightly reduced the value of a.

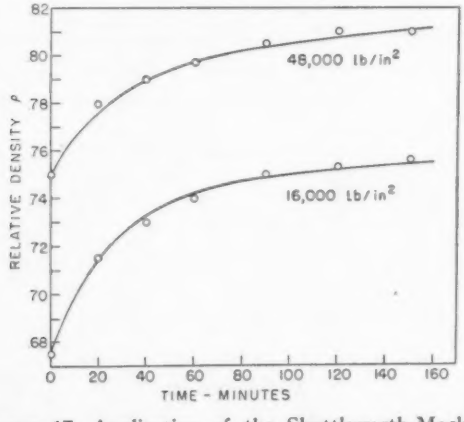

FIGURE 17. Application of the Shuttleworth-Mackenzie equation to the sintering of CaF_2 compacted at various pressures. Full lines, calculated curves; ⊙, experimental points. Sintering temperature 890°C.

TABLE XV

SINTERING DATA FOR CaF_2 AT 890°C FOR DIFFERENT COMPACTING PRESSURES

Compacting pressure (psi)	Initial porosity %	K sec^{-1}	a
16,000	32.5	7.7×10^{-2}	1.04
48,000	25.0	7.7×10^{-2}	0.97

The curves of Figure 18 show that equation (5) also gives satisfactory agreement when applied to the sintering of different size fractions of calcium fluoride; the values of the constants are given in Table XVI.

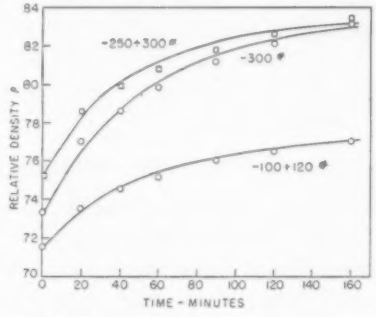

FIGURE 18. Application of the Shuttleworth-Mackenzie equation to the sintering of different-size fractions of CaF_2. Full lines, calculated curves. ⊙ and ⊡, experimental points. Sintering temperature 890°C.

TABLE XVI

SINTERING DATA FOR DIFFERENT SIZE FRACTIONS OF CaF_2 AT 890°C

Compacting pressure 24,000 psi

Grading B.S. sieves	K	a	$K\alpha$
− 100 + 120	8.34×10^{-4}	1.02	8.50×10^{-4}
− 250 + 300	1.04×10^{-3}	0.95	9.88×10^{-4}
− 300	8.34×10^{-4}	0.95	7.93×10^{-4}

The smaller the particle-size of a powder, then, the greater is the number of particles (and therefore the closed pores) associated with 1 cc of real material. Furthermore, since a is inversely proportional to $n^{1/3}$ and K is directly proportional to $n^{1/3}$, the value of a should decrease and that

of K increase with decreasing particle size. Table XVI shows that the a values do tend to decrease with decreasing particle size; the K-values, however, show no regular variation. Furthermore, the values of K and a are given by:

$$K = \frac{3}{2}\left(\frac{4\pi}{3}\right)^{1/3}\left(\frac{\gamma n}{\eta}\right)^{1/3}$$

and

$$a = \sqrt{2}\left(\frac{3}{4\pi}\right)^{1/3}\frac{T_c}{2\gamma_n^{1/3}}$$

Therefore, $Ka = (3\sqrt{2}/4)(T_c/\eta)$. Since the present experiments were carried out at one temperature (890°C), the ratio T_c/η must be a constant, and hence the values of Ka should be constant. Referring to Table XVI, the Ka-values show a 24 per cent variation; the values, however, have no definite trend.

The application of the Shuttleworth-Mackenzie mechanism to the present data may be summarized as follows. The experimental data obey equation (5) reasonably well, and the predictions of the mechanism regarding the effect of compacting pressure agree with experiment. The results of the particle size experiments, however, are not in complete accord with equation (5).

Discussion of Plastic Flow Mechanisms

The fact that the two stages of sintering, namely (*a*) the open, connected pore stage, and (*b*) the closed, isolated pore stage, may be described by two mathematical relations based on macroscopic flow cannot be taken as proof of the validity of the respective mechanisms. The determination in the present work of the effects of compacting pressure and particle-size on sintering was an attempt to obtain additional evidence. Neither mechanism accounts completely for the observed facts; it is possible, however, that the discrepancies may be rectified by slight modifications of the mechanism.

One way of indicating the basic mechanism of transport in sintering has been derived by Herring [7] in a theoretical treatment of the effect of change of scale on sintering phenomena. Two partially sintered assemblages are considered, the linear dimensions of the second being λ times that of the first. Thus if spherical particles of radius R, are sintered until the radius of the area of contact of adjacent grains is a_1, similarity will require $R_2 = \lambda R_1$ and $a_2 = \lambda a_1$. The time Δt_1 required to produce a given change in shape of the first assemblage is a function of time Δt_2 required to produce a geometrically similar change in the second assemblage. The functions for the four possible basis mechanisms of transport are given by Herring as

Basic mechanism of transport	*Scale relationship*
Plastic flow	$\Delta t_2 = \lambda \Delta t_1$
Evaporation and condensation	$\Delta t_2 = \lambda^2 \Delta t_1$
Volume diffusion	$\Delta t_2 = \lambda^3 \Delta t_1$
Surface diffusion	$\Delta t_2 = \lambda^4 \Delta t_1$

This analysis has been applied to the calcium fluoride data. The times required to obtain the same reduction in porosity for the two fractions $-100 + 120$ and $-250 + 300$ mesh are shown in Table 17. The particle sizes of these two fractions are $124\mu - 152\mu$ and 50μ respectively, and hence the value of λ should lie between 2.48 and 3.04.

TABLE XVII

RELATION BETWEEN SINTERING TIME AND PARTICLE SIZE FOR CaF_2

Reduction in porosity %	$\Delta t_{135\mu}$ (approx.) min.	$\Delta t_{50\mu}$ min.
0.5	4	2
1.0	8	4
1.5	13.5	6
2.0	20	9
2.5	29	12
3.0	39	16
3.5	52.5	21
4.0	69	27
4.5	89.5	36
5.0	117	45

$\Delta t_{50\mu}$ is plotted against $\Delta t_{135\mu}$ in Fig. 19, which shows that the results obey the equation:

$$\Delta t_{135\mu} = 2.47\ \Delta t_{50\mu}$$

thus indicating that a plastic flow mechanism is operating in sintering. The value of 2.47 for λ agrees with the predictions of Herring's theory.

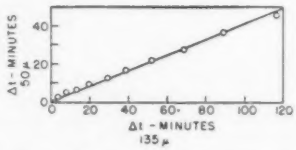

FIGURE 19. Relation between particle-size and sintering time.

Conclusions

Dimensional changes of pressed compacts of fluorides have been studied dilatometrically. The

thermal expansions of the fluorides are high, indicating that their thermal shock resistance will be very low. Furthermore, the thermal expansion increases with decreasing cation valency. Shrinkage (and sintering) begins at a temperature approximately equal to 0.5 of the melting point (in °K), and thereafter the sintering process is governed by the initial compacting pressure applied and the particle size of the powder.

Clark and White's plastic flow equation has been applied to the sintering data. Their equation may be written in the form:

$$\frac{d\bar{V}}{dt} = K \,.\, f(x)\,[g(x) - h(x)]$$

where $\bar{V}$ = volume shrinkage/gram, and $f(x)$, $g(x)$ and $h(x)$ are functions of x; x is the sine of the lens angle θ (Figure 7).

Good agreement is obtained, and the equation fits the results over a wider range than should be valid theoretically. However, the equation breaks down at high degrees of sintering, a slower mechanism becoming operative. Velocity constants have been obtained, and application of the Arrhenius relation gives activation energies of 73,700 and 32,600 cal/mole for CaF_2 and NaF respectively. These values suggest that the simple cubic lattice (NaF) is easier to deform than the more complex fluorite type (CaF_2). The Clark-White mechanism qualitatively explains the effect of particle size on sintering, but it does not account for the effect of compacting pressure.

The present work shows that, even when using closely graded fractions, the empirical term in the equation must be included. Hence, this term is not related to particle-size as Clark and White suggested; alternative explanations are proposed below.

(*a*) The Clark-White velocity constant K is given by $\gamma h^3/\rho\eta l R_0^3$ and they assume that h(the thickness of the moving layer) is constant. For materials of the Bingham type, however, a stationary "plug" of material will form when the stress falls below a critical value, i.e., h(and therefore K) will decrease.

(*b*) The present authors suggest that the particle radius remains constant during the early stages of sintering, shrinkage being effected by a 'merging' of the particles. This suggestion, which is borne out by Kuczynski's experiments on the sintering of glass spheres to flat plates, is in direct contradiction to the Clark-White hypothesis.

(*c*) An obvious explanation of the necessity of the empirical term is that the flow process operative may not be of the simple Bingham type.

The sintering data have also been analyzed by means of the Shuttleworth-Mackenzie mechanism. The results obey the equation:

$$\frac{d\rho}{dt} = K \,.\, f(\rho)\,[1 - a \,.\, f'(\rho)]$$

where $f(\rho)$ and $f'(\rho)$ are functions of the relative density (ρ), and K and a are constants. The Arrhenius plot of the velocity constants (K) gives activation energies of 103,600 and 36,700 cal/mole for calcium and sodium fluoride respectively. The predictions of the mechanism regarding the effect of compacting pressure agree with experiment, but the results of the particle size experiments are not in complete accord with theory.

The mechanism has also been applied to Clark and White's data for the sintering of glass spheres. The experimental curves obey the equation:

$$\frac{d\rho}{dt} = K \,.\, f(\rho)$$

indicating that the glass behaves as a Newtonian fluid. Application of the Arrhenius equation gives an activation energy of 84,700 cal/mole.

In addition, the sintering curves for two different-size fractions of calcium fluoride have been analysed by Herring's method. The results obey the equation:

$$\Delta t_2 = \lambda \Delta t_1$$

where Δt_1 and Δt_2 are the times required to produce geometrically similar changes in the two compacts, and λ is a constant.

This provides additional evidence that a plastic flow mechanism is operative in sintering.

APPENDIX I

Application of the Clark-White Equation to a Sintering Curve

e.g. NaF −330 mesh. Pressed at 8,000 psi. Temp. 713°C.

Variation of V with x

$$V = \frac{3n}{4\rho}\left(\frac{1-x}{x}\right)^2\left[1 - \theta\frac{\sqrt{1-x^2}}{x}\right]$$

$n = 8$ $\rho = 2.79$

x	$\left(\frac{1-x}{x}\right)^2$	θ (deg)	θ (rad)	$\left[1-\theta\frac{\sqrt{1-x^2}}{x}\right]$	V
.60	.445	36° 52′	.6440	.144	.138
.70	.184	44° 24′	.7749	.210	.0830
.74	.124	47° 42′	.8325	.245	.0653
.77	.0894	50° 24′	.8797	.268	.0515
.80	.0625	53° 6′	.9267	.305	.0409
.84	.0365	57° 6′	1.9965	.360	.0283
.87	.0222	60° 30′	1.0559	.406	.0193
.90	.0123	64° 12′	1.1205	.458	.0121

Variation of $\bar{V}$ with x

$$\bar{V} = V\left(\frac{\frac{1}{\rho}+q_0}{\frac{1}{\rho}+V}\right)$$

Initial bulk density = 1.633 gm/cc
Initial porosity = 41.5 per cent

Initial pore volume/gm $= q_0 = .415 \times \frac{1}{1.633}$
$= .2543$

$$\frac{1}{\rho} = .3584\,\frac{1}{\rho} + q_0 = .6127$$

x	V	$\left(\frac{1}{\rho}+V\right)$	$\bar{V}$
.60	.138	.496	.171
.70	.0830	.441	.115
.74	.0653	.424	.0945
.77	.0515	.410	.0770
.80	.0409	.399	.0628
.84	.0283	.387	.0448
.87	.0193	.378	.0313
.90	.0121	.371	.0200

Variation of $\frac{1}{K}\cdot\frac{d\bar{V}}{dt}$ with x

$$\frac{1}{K}\cdot\frac{d\bar{V}}{dt} = \left(\frac{\frac{1}{\rho}+q_0}{\frac{1}{\rho}+V}\right)\frac{n\sqrt{1-x^2}}{2}$$

$$\left[2+\frac{x}{1-x}-\frac{1}{\sqrt{1-x^2}}-\frac{X}{3\sqrt{1+V\rho}}\right]\frac{1}{(1+V\rho)^2}$$

x	$\left(\frac{1}{\rho}+V\right)$	$\sqrt{1-x^2}$	$x/1-x$	$\frac{1}{\sqrt{1-x^2}}$	$(1+V\rho)$	$(1+V\rho)^{\frac{1}{3}}$	$(1+V\rho)^2$	$\frac{1}{K}\cdot\frac{d\bar{V}}{dt}$
.60	.496	.800	1.500	1.250	1.385	1.114	1.918	$2.062(2.250-X/1.114)$
.70	.441	.714	2.333	1.401	1.232	1.072	1.518	$2.615(2.932-X/1.072)$
.74	.424	.671	2.841	1.490	1.182	1.057	1.397	$2.780(3.351-X/1.057)$
.77	.410	.640	3.344	1.563	1.144	1.046	1.309	$2.925(3.781-X/1.046)$
.80	.399	.600	4.000	1.667	1.114	1.036	1.241	$2.968(4.333-X/1.036)$
.84	.387	.539	5.236	1.855	1.079	1.025	1.164	$2.935(5.381-X/1.025)$
.87	.378	.490	6.711	2.041	1.054	1.017	1.111	$2.865(6.670-X/1.017)$
.90	.371	.436	9.000	2.294	1.034	1.011	1.069	$2.700(8.706-X/1.011)$

Values of $K\frac{dt}{d\bar{V}}$ are then calculated for various values of X as shown below.

	$X=1$		$X=2$		$X=3$		
x	$\frac{1}{K}\cdot\frac{d\bar{V}}{dt}$	$K\cdot\frac{dt}{dV}$	$\frac{-1}{K}\cdot\frac{d\bar{V}}{dt}$	$K\cdot\frac{dt}{dV}$	$\frac{1}{K}\cdot\frac{d\bar{V}}{dt}$	$K\cdot\frac{dt}{dV}$	$\bar{V}$
.60	2.787	.359	.936	1.068	—	—	.171
.70	5.23	.191	2.786	.359	.348	2.87	.115
.74	6.69	.150	4.055	.247	1.425	.702	.0945
.77	8.26	.121	5.46	.183	2.665	.375	.0370
.80	10.00	.100	7.14	.140	4.27	.234	.0628
.84	12.92	.0774	10.06	.0945	7.20	.139	.0448
.87	16.28	.0614	13.46	.0743	10.65	.0939	.0313
.90	20.85	.0479	18.18	.0550	15.50	.0645	.0200

These values of $K \cdot \frac{dt}{d\bar{V}}$ are plotted against $\bar{V}$ as in Figure $A(1)$.

The areas under the curves give values of Kt at various values of $\bar{V}$. The Kt values are then divided by the corresponding times read off from the experimental curve. The value of X chosen determines whether the K values thus obtained are constant. In the present example, taking $X = 2$:

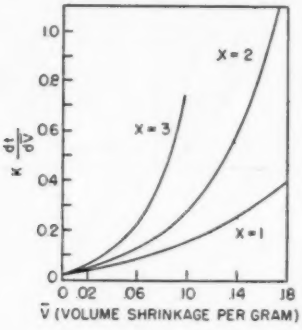

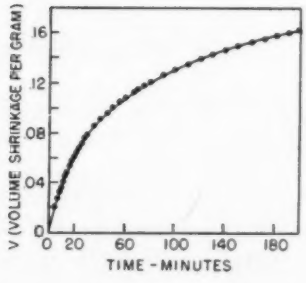

FIGURE A(1). Calculated $K(dt/dv)/\bar{V}$ curves.
FIGURE A(2). Experimental sintering curve.

$\bar{V}$	$Kt \times 10^3$	t(min)*	t(sec)*	K	t_{min}(calcd. $K = 3.94 \times 10^{-4}$)
.02	0.90	—	—	—	3.8 min
.04	2.32	10½	630	3.84×10^{-4}	9.8
.06	4.54	19	1,140	3.99	19.2
.08	7.80	31½	1,890	4.13	32.9
.10	12.40	50½	3,030	4.10	52.4
.12	19.06	79½	4,770	4.00	80.5
.14	28.8	123½	7,410	3.89	122
.16	43.0	192	11,520	3.73	182

*Values read off from experimental curve [Figure A(2)].
Av. $K = 3.94 \times 10^{-4}$

APPENDIX II

Application of the Shuttleworth-Mackenzie Equation to a Sintering Curve

$$(1)\quad \frac{1}{K} \cdot \frac{d\rho}{dt} = (1-\rho)^{2/3}\,\rho^{1/3}\left[1 - a\left(\frac{1}{\rho} - 1\right)^{1/3} \cdot \log_e\left(\frac{1}{1-\rho}\right)\right]$$

Experimental Sintering Curve (plotted in Figure B(1)).

t(min)	0	20	40	60	80	100
Relative density (ρ)	.700	.775	.825	.855	.880	.900

Using the above equation values of $\frac{1}{K}\frac{d\rho}{dt}$ are calculated for various values of a, e.g.,

ρ	$a = .80$	$a = .84$	$a = .82$
.70	.1090	.0944	.1015
.75	.0836	.0699	.0767
.80	.0602	.0476	.0539
.85	.0379	.0267	.0318
.90	.0235	.0146	.0189

$K \cdot \frac{dt}{d\rho}$ is then plotted against ρ so that a series of curves is obtained as shown in Figure B(2). The area under these curves gives the values of $K \cdot t$ at various values of ρ. Division of these values of Kt by the corresponding times on the experimental sintering curve gives the value of K. This process is carried out until a value of 'a' is chosen such that K remains constant along the curve.

		$a = .82$		$a = .84$		$a = .80$	
ρ	t*	Kt	$K \times 10^2$	Kt	$K \times 10^2$	Kt	$K \times 10^2$
.70	0.0	0	—				
.75	12.0	0.557	4.64	0.605	5.04	0.515	4.30
.80	28.8	1.332	4.63	1.470	5.11	1.210	4.20
.85	55.5	2.552	4.60	2.877	5.18	2.253	4.06
.90	100.0	4.617	4.62	5.46	5.46	3.915	3.92

*From Figure B(1). N.B. The units of K are min^{-1}.

Thus, in the present case, K decreases when 'a' = .80, increases when 'a' = .84, and remains constant when 'a' has the value .82. The sintering curve of Figure B(1), may, therefore, be represented by equation (1), the values of 'a' and 'K' being 0.82 and 4.62×10^{-2} respectively.

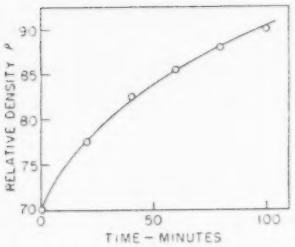

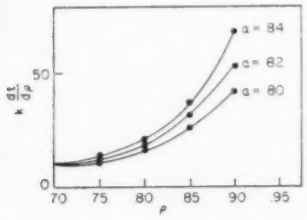

FIGURE B(1). Experimental sintering curve.
FIGURE B(2). Calculated $K(dt/d\rho))/\rho$ curves.

II. Comparison of Experimental and Calculated Flow Constants

Theory of the Deformation of Thin Discs

(*a*) *General*

A simple and common method of determining the creep properties of materials at elevated temperatures is to study the compression of cylinders which have a height/diameter ratio of 2.5 to 4. Under these conditions, the cylinder usually subsides at a decreasing rate until a point is reached when the deformation rate accelerates and finally results in failure of the specimen. If, however, the height/diameter ratio is very small (of the order of 0.3) then the deformation process is very different; the thickness of the disc decreases to a limiting value without rupture. It was this latter case which was analysed by Scott [4] who derived equations relating the rate of subsidence of the disc to the applied stress and the flow constants of the material. A summary of his analysis is given in the following sections.

(*b*) *Development of general flow equation*

When a thin disc is compressed the material flows radially outwards. This implies the presence of a horizontal pressure gradient, the pressure decreasing from the centre outwards. On grounds of symmetry, the flow, except near the edge, must be horizontal and radial; hence the pressure (and the pressure gradient) at all points on any one cylindrical surface coaxial with the disc must be the same. It is assumed that the layers of material in contact with the confining surfaces do not slip over these surfaces.

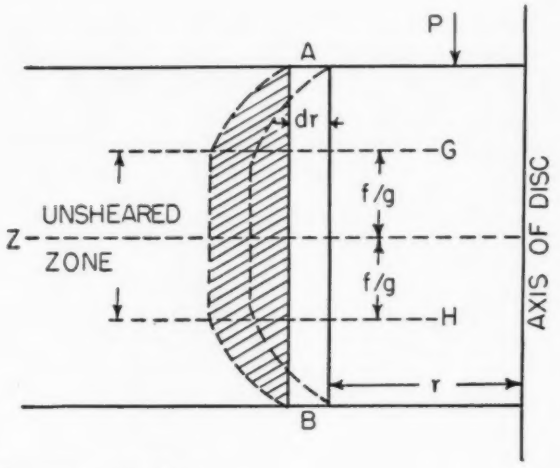

P = compressive force
V = volume of disc
R = radius of disc
θ = thickness of disc
$d\theta$ = decrease in thickness in time interval dt ($d\theta$ is negative)
p = pressure in material at distance r from the axis

Horizontal pressure gradient at distance r from axis $= -g = dp/dr$.

Therefore pressure difference across annulus AB $= g \cdot dr$.

Therefore total shearing force acting horizontally on the annulus at a distance y from the mid-plane $z = g \cdot dr \cdot 2\pi ry$.

Therefore shear stress acting horizontally on the annulus at a distance y from the mid-plane $z = gy$.

Now the general equation relating shear rate to the applied stress is:

$$\text{Shear rate} = \frac{dv}{dy} = \left(\frac{F-f}{c}\right)^n \tag{6}$$

where v = horizontal velocity of the material at a distance y from the mid-plane z, F is the applied stress, f is the yield stress, c is the viscosity, and n is a positive numerical constant. Substituting gy for F in equation (6) gives

$$\frac{-dv}{dy} = \left(\frac{gy-f}{c}\right)^n \tag{7}$$

Flow will not occur if gy is $< f$ so that there is a zone of unsheared material extending to a distance f/g on each side of the mid-plane. Thus when the annulus AB is displaced by the outward flow of material it takes up the form shown by the broken lines.

An expression relating the variation of v with the distance y is obtained by integrating equation (7) and introducing the condition that $v = 0$ when $y = \theta/2$. By further integration of $v \cdot dy$, and taking into account that in the non-sheared zone (GH) v is constant, an expression is obtained for the area (shaded in the figure) swept out by the annulus in time dt:

$$(8) \quad \frac{2 \cdot dt}{g^2 c^n}\left[\frac{(\tfrac{1}{2} g\theta - f)^{n+2}}{n+2} + \frac{f(\tfrac{1}{2} g\theta - f)^{n+1}}{n+1}\right]$$

During the time dt the thickness of the disc decreases by an amount $d\theta$ so that the volume of material flowing into the shaded area is

$$-\pi r^2 \cdot d\theta$$

Therefore shaded area $= -\frac{1}{2} r \cdot d\theta$.
Equating this to equation (8) we obtain:

$$(9) \quad (n+1)(\tfrac{1}{2} g\theta - f)^{n+2} + f(n+2)(\tfrac{1}{2} g\theta - f)^{n+1} + (n+1)(n+2)\frac{c^n g^2 r}{4} \cdot \frac{d\theta}{dt} = 0.$$

The above equation describes the deformation of a disc of material obeying the general equation:

$$\text{shear rate} = \left(\frac{F - f}{c}\right)^n$$

Equation (9) cannot be conveniently solved, and, therefore, it is necessary to consider particular cases.

(c) Consideration of particular cases

Materials may be conveniently classified, from a rheological point of view, in the following way:

(1) Yield stress $f = 0$
  (a) $n = 1$ Newtonian liquid
  (b) $n > 1$ Pseudo-plastic
(2) Yield stress f is finite
  (a) $n = 1$ Bingham body
  (b) $n > 1$

The application of equation (9) to the above cases is considered in the following sections.

(i) *Case 1 where $f = 0$*

Putting $f = 0$ in equation (9) gives:

$$g^n(\tfrac{1}{2}\theta)^{n+2} = -(n+2)\, c^n r \cdot \frac{d\theta}{dt}$$

Now $g = -\dfrac{dp}{dr}$, hence by integrating $-g \cdot dr$ with respect to r, and introducing the condition that $p = 0$ when $r = R$, the following expression is obtained for p:

$$p = \frac{2nc(n+2)^{1/n}}{(n+1)\,\theta^{\frac{n+2}{n}}} \cdot \left(\frac{d\theta}{dt}\right)^{1/n} [r^{\frac{1}{n}+1} - R^{\frac{1}{n}+1}]$$

Since the material is a fluid, this pressure acts horizontally and vertically on the confining surfaces. Hence the integral of this pressure over the surface of the disc of material must equal the compressive force P; i.e.,

$$P = \int_0^R 2\pi r \cdot dr \cdot p$$

from which we obtain the expression:

$$\frac{-d\theta}{dt} = \frac{(3n+1)^n \theta^{n+2} P^n}{(2\pi nc)^n (n+2)\, R^{3n+1}}$$

or, since $\pi R^2 \theta = V$:

$$(10) \quad \frac{-d\theta}{dt} = \frac{(3n+1)^n\, \pi^{\left(\frac{n+1}{2}\right)}\, \theta^{\left(\frac{5n+5}{2}\right)}\, P^n}{(2nc)(n+2)\, V\left(\frac{3n+1}{2}\right)}$$

Equation (10) may be written in the form:

$$(11) \quad \log D = \left(\frac{5n+5}{2}\right)\log\theta + n\log P - n\log c - \left(\frac{3n+1}{2}\right)\log V + \log\left[\frac{(3n+1)^n\, \pi^{\left(\frac{n+1}{2}\right)}}{2^n n^n (n+2)}\right]$$

where D = rate of decrease in thickness of disc.

In any one experiment the last four terms are constant, and the $\log D - \log\theta$ curve is therefore a straight line of slope $(5n+5)/2$. From this curve the value of n may be determined, and, since P and V are also known, the value of the viscosity (c) may be calculated.

(ii) *Case 2 where f is finite*

As the thickness of the disc decreases, the compressive force is spread over an increasingly large area, so that the pressure and the pressure gradient must continuously decrease. Thus the thickness of the non-sheared zone (which is equal to $2f/g$) must increase and finally become equal to θ, when flow ceases. Therefore, the limiting thickness $\theta_L = 2f/g$.

The value of this limiting thickness may be calculated as follows:

Equation (9) can be written in the form:

$$(12) \quad (\tfrac{1}{2}g\theta - f)^{n+1}[\tfrac{1}{2}(n+1)\, g\theta + f] = -(n+1)(n+2)\, c^n g^2 r \frac{d\theta}{dt}$$

When $\theta = \theta_L$, $d\theta/dt = 0$, and therefore both sides of equation (12) become equal to zero.

Therefore $\frac{1}{2} g\theta_l - f = 0$; i.e.,

$$\theta_L = \frac{2f}{g}$$

Now $g = -dp/dr$ and therefore $dp = -(2f)/(\theta_L)\, dr$

Integration of this with respect to r gives p, and by integrating $2\pi r \cdot dr \cdot p$ and then equating to P we obtain the expression:

$$\theta_L = \left(\frac{4V^3 f^2}{9\pi P^2}\right)^{1/5} \tag{13}$$

or

$$f = \frac{3\pi^{1/2} P\, \theta_L{}^{5/2}}{2V^{3/2}} \tag{14}$$

Thus the yield stress f may be determined directly by experiment, since the limiting thickness θ_L can be determined and P and V are known.

The general form of the $\log D - \log \theta$ curve for finite values of f may be deduced as follows: As $\theta \to \theta_L$, $D \to 0$ so that as $\log \theta \to \log \theta_L$, $\log D \to -\infty$. Furthermore, when θ is very large compared to f (i.e., f is negligible), then the curve becomes a straight line as represented by equation (11). Thus the $\log D - \log \theta$ curve will be as shown in Figure 20.

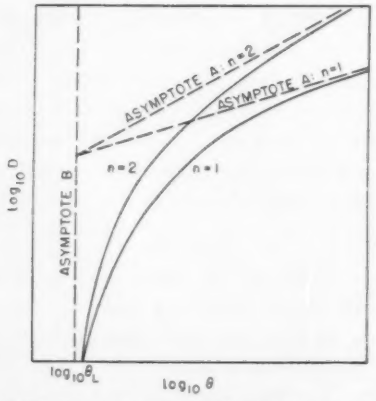

FIGURE 20. General form of the $\log D - \log \theta$ curve.

A more detailed treatment of the $\log D - \log \theta$ curve may be attempted for the case where f is finite and $n = 1$. Thus, putting $n = 1$ in equation (9) gives:

$$g^3 - g^2\left(\frac{3f}{\theta} - \frac{6cr \cdot d\theta}{\theta^3 dt}\right) + \frac{4f^3}{\theta^3} = 0$$

There is no general solution of the above equation. It can, however, be written in the form:

$$g\left(1 + \frac{4f}{g^3\theta^3}\right) = \frac{3f}{\theta} - \frac{6cr \cdot d\theta}{\theta^3 dt}. \tag{15}$$

Under appropriate experimental conditions the term $4f^3/g^3\theta^3$ can be made so small that, as an approximation, it may be considered as constant, i.e., it is assumed that g is independent of r. The approximate magnitude of $4f^3/g^3\theta^3$ can then be deduced as follows:

Since g is independent of r, integration of the equation $dp = -g \cdot dr$ gives $p = g\ (R - r)$; further integration of $2\pi r \cdot dr \cdot p$ between the limits $r = 0$ and $r = R$ gives $P = \frac{1}{3}\pi R^3 g$, or

$$g = 3\pi^{1/2} P\theta^{3/2} V^{-3/2}.$$

By inserting this value of g in the expression $4f^3/g^3\theta^3$, putting $\theta = x \cdot \theta_L$, and then substituting for θ_L from equation (13), it is found that:

$$\frac{4f^3}{g^3\theta^3} = \tfrac{1}{2} x^{-15/2}$$

Inserting this value of $4f^3/g^3\theta^3$ in equation (15) and substituting $-dp/dr$ for g:

$$-dp(1 + \tfrac{1}{2}x^{-15/2}) = \frac{3f \cdot dr}{\theta} - \frac{6cr \cdot dr}{\theta^3} \cdot \frac{d\theta}{dt}$$

Integration of the above expression gives the value of p, and on further integration of $2\pi r \cdot dr \cdot p$ it is found that:

$$-\frac{d\theta}{dt} = \frac{2\pi P\theta^5}{3cV^2} \cdot (1 + \tfrac{1}{2}x^{-15/2}) - \frac{2\pi^{1/2} f\theta^{5/2}}{3cV^{1/2}}$$

where

$$x = \frac{\theta}{\theta_L}$$

Substituting $x \cdot \theta_L$ for θ, and substituting for f from formula (14) gives the expression:

$$-\frac{d\theta}{dt} = \frac{\pi P \theta_L{}^5}{cV^2}\left(\frac{2}{3}x^5 - x^{5/2} + \frac{1}{3}x^{-5/2}\right)$$

or

$$\log D = \log\left(\frac{\pi P \theta_L{}^5}{cV^2}\right) + \log\left(\frac{2}{3}x^5 - x^{5/2} + \frac{1}{3}x^{-5/2}\right) \tag{17}$$

which is the equation of the $\log D - \log \theta$ curve for the case when f is finite and $n = 1$. When $x > 1.6$, $\frac{1}{3}x^{-5/2}$ is negligible, and at high values of x, $x^{5/2}$ is negligible compared with $\frac{2}{3}x^5$. Thus at high values of x the curve becomes a straight line obeying the equation:

$$\log D = \log\left(\frac{\pi P \theta_L^5}{cV^2}\right) + \log\left(\frac{2}{3} \cdot x^5\right)$$

or

$$\log D = \log\left(\frac{2\pi P}{3_c V^2}\right) + 5 \log \theta \quad (18)$$

This straight line is the asymptote A shown in Figure 20, and the asymptote B is given by

$$\log \theta = \log \theta_L = \frac{1}{5} \log\left(\frac{4V^3f^2}{9\pi P^2}\right)$$

The co-ordinates of the point of intersection of these asymptotes are:

$$\frac{1}{5} \log\left(\frac{4V^3f^2}{9\pi P^2}\right) : \log\left(\frac{8Vf^2}{27cP}\right)$$

The most convenient method of applying the above theory to a set of experimental results is as follows:

The general $\log D - \log \theta$ curve and its two asymptotes are plotted on tracing paper. Since P, V, c and f can be chosen arbitrarily, it is convenient to put $\log (\pi P \theta_L^5 / cV^2) = 0$ and $\theta_L = 1$; asymptote B is then identical with the $\log D$ axis and the abscissa ($\log \theta$) becomes equal to $\log x$. This general curve is placed over the experimental one; if the two curves fit, then the material is a Bingham body, and values of c and f can be calculated from the co-ordinates of the point of intersection of the asymptotes.

If $n > 1$ then the exact form of the $\log D - \log \theta$ curve cannot be determined. In this case, therefore, n may be determined by making $g\theta$ very large (i.e., use high loads) so that f is negligible. The $\log D - \log \theta$ curve is then a straight line obeying equation (11), so that n may be determined from the slope of the line, and hence c calculated from equation (11).

(d) Discussion of possible errors

Scott pointed out that there are two factors which can affect the validity of the above theory, namely:

(i) Equation (16) was derived by an approximate method and it can be shown that if $x = 1.15$, the value of $d\theta/dt$ given by (16) is in error by less than 3 per cent, the error decreasing as x increases. When $x < 1.15$, $d\theta/dt$ is usually too small to be measured accurately, and therefore, equation (16) is a sufficient approximation for practical purposes.

(ii) The theory assumes that the material under test is in the form of a very short cylinder. In practice, however, the disc has a rounded edge so that the material near the edge flows under less restricted conditions and, therefore, probably absorbs less energy. The volume of material in the edge portion decreases as the disc becomes thinner so that the equations are more nearly correct the greater the ratio of R to θ.

The above considerations indicate that the theory can be applied only over a certain range of sample thickness. To obtain as wide a range as possible, P should be high so as to make the limiting thickness θ_L as small as possible.

One further point is that Scott's theory is applicable to non-porous discs of material. If the material under test possesses considerable porosity, then, presumably, the flow process will be affected, particularly if the specimen dilates on compression.

Experimental Work

The experimental* discs were cut from a rod of soft soda glass and their faces ground to make sure that they were plane and parallel. Small discs of sodium fluoride were made by cold-pressing at 67,500 lb./sq in. 7.5 per cent of Winnothene wax being present to act as a lubricant. The discs were then slowly heated up to 600°C to remove the wax, and then fired for two hours at 950°C. The porosities of the fired discs were of the order of 5 per cent. Lower porosities could be obtained by firing at temperatures closer to the melting point (1000°C) but this was not practical since it usually resulted in some distortion of the discs. Hot-pressing in Nimonic dies was unsuccessful due to chemical reaction between the fluoride and the die; very low porosities (<1 per cent) could be attained by hot-pressing in graphite dies, but this was not attempted in the present series of experiments. The initial height/diameter ratio of the specimens varied from 0.25 to 0.40.

A diagram of the compression equipment used for the present work is shown in Figure 21. Weights (W) were applied to one end of the tubular beam (B) which was 63 cm long. The load was transmitted to the specimen through the ball-bearing (S) acting on the short, steel push rod (R) which, in turn, acted upon the alumina push rod (T). The steel push rod was held in a vertical position by a loose fitting, vertical sleeve (V) rigidly attached to the horizontal strut (H). The specimen (C), which was held between the two alumina plates

*The composition of the glass for these experiments was as follows: SiO_2 69.2%, Na_2O 16.2%, CaO 6.1%, Al_2O_3 3.4%, MgO 3.2%, B_2O_3 1.2%. Other oxides 0.7%.

(P), was located at the centre of a nichrome-wound furnace. The furnace was controlled by a Variac and a Cambridge regulator, so that the temperature was constant to within ±2°C. Temperatures were measured by a Pt-Pt/13% Rh thermocouple (F), the junction of which was located just above the upper alumina plate. The deformation of the

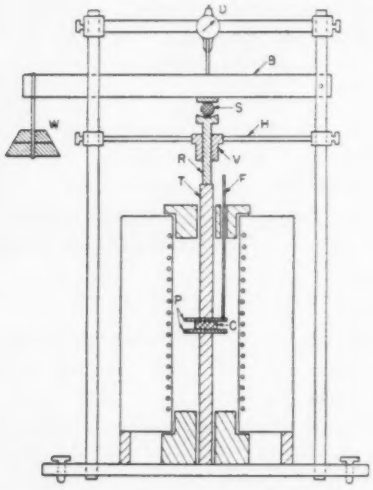

FIGURE 21. Diagram of compression equipment.

specimen was followed by a dial gauge (D) reading to 0.0001 in., which was rigidly fixed over the beam and directly above the push rods.

A specimen of known thickness and diameter was placed between the alumina plates and the reading of the dial gauge noted. The temperature was then raised at a rate of 10°C/minute until the desired temperature was attained. [NOTE: During this time the dial gauge reading increases due to thermal expansion of the specimen and the alumina push rods. The thermal expansion of the specimen may be obtained by carrying out a blank run with a specimen of known thermal expansion.] The specimen was allowed to soak for half an hour to give a uniform temperature throughout the specimen. The load was then applied and readings of the dial gauge noted at regular time intervals.

Deformation-time curves were obtained at several temperatures, the load applied ranging from 6 $\times 10^6$ to 2 $\times$ 10^7 dynes.

Results

Two subsidence-time curves for glass at a temperature of 655°C are shown in Figure 22 for loads of 1.11 $\times$ 10^7 and 6.295 $\times$ 10^6 dynes. The differentials of these curves, i.e., the log D – log θ curves, are plotted in Figure 23, where it can be seen that good straight lines are obtained, indicating that the glass has no finite yield point. There is some deviation from the straight lines at the beginning of the curves; this may be due either to (1) surface irregularities of the specimen, or (2) loading errors; i.e., the load was not applied smoothly or instantaneously. The slopes of these lines [which are equal to $(5n + 5)/2$] are equal to 5, so that $n = 1$. Thus, this particular soda glass behaves as a Newtonian liquid at a temperature of 655°C. The relevant data for these two experiments together with the viscosity coefficients calculated from it are given in Table XVIII.

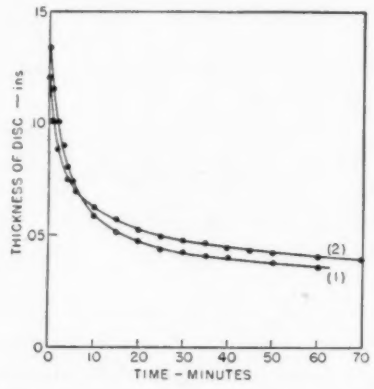

FIGURE 22. Subsidence-time curves for glass at 655°C two different loadings.

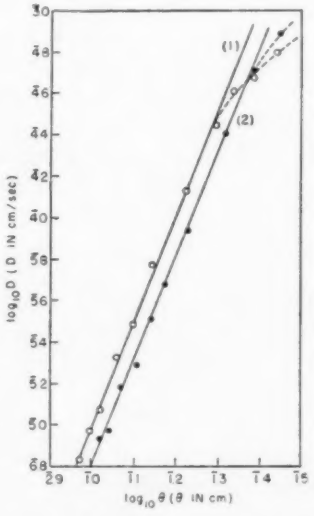

FIGURE 23. log D – log θ curves for glass at 655°C, two different loadings.

TABLE XVIII

FLOW CONSTANTS FOR GLASS AT 655°C

	Run no. 1	Run no. 2
Volume of specimen V	0.220 cc	0.198 cc
Compressive force $P^{655°}$	1.11×10^7 dynes	6.295×10^6 dynes
Yield stress	0.0 dynes/cm²	0.0 dynes/cm²
n	1.0	1.0

Inserting these values in equation (11) gives the following values for the viscosity:

4.81×10^8 poises $\quad$ 5.32×10^8 poises

The value of 5×10^8 poises for the viscosity coefficient at 655°C compares favourably with the results of Poole and Gensamer [8] who found that, for glasses lying within approximately the same composition range as the present sample, the viscosity ranged from 10^8 to $10^{9.5}$ poises at 655°C.

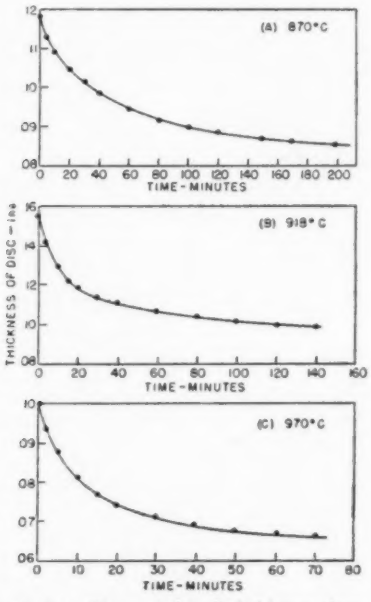

FIGURES 24 (*a*), (*b*), and (*c*). Subsidence-time curves for NaF at various temperatures.

Subsidence-time curves for sodium fluoride at three different temperatures are plotted in Figures 24 (A), (B), and (C). The flow properties of the material were derived from these curves using the method described previously, i.e., the experimental log D – log θ curves were constructed and compared with the theoretical Bingham curve plotted on tracing paper. It was found that the experimental results agreed quite well with the theoretical curve, and indicated that the fluoride behaves as a Bingham body. The points of intersection of the asymptotes were noted, and from the co-ordinates values of C and f were calculated. The relevant data is given in Table XIX.

Theoretical log D – log θ curves have been calculated from the above data and are plotted in Figures 25 (A), (B) and (C), experimental values being included for comparison. Good agreement is obtained.

The best method of determining the value of n is to arrange the experimental conditions so that the log D – log θ plot extends up to the linear portion

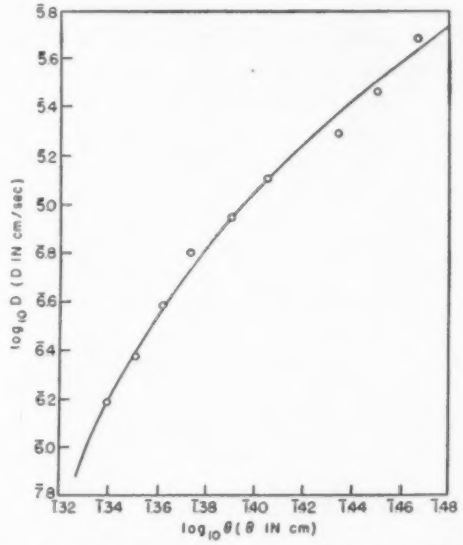

FIGURE 25(*a*). log D – log θ curve for NaF at 870°C. Full line, theoretical Bingham curve; ⊙, experimental points.

of the curve, when n may be determined from the slope of this line. Figures 25 (A), (B) and (C) show that the present series of experiments did

TABLE XIX

FLOW CONSTANTS FOR NaF

Temperature °C	870	918	970
Volume of specimen (cc)	0.197	0.256	0.164
Comprehensive force (dynes)	2.055×10^7	1.815×10^7	1.580×10^7
Co-ordinates of point of intersection of asymptotes	$(\bar{1}.296 : \bar{5}.11)$	$(\bar{1}.355 : \bar{5}.28)$	$(\bar{1}.179 : \bar{5}.40)$
f(dynes/cm²)	1.06×10^7	9.13×10^6	5.61×10^6
c(Poises)	2.77×10^{10}	1.82×10^{10}	3.84×10^9

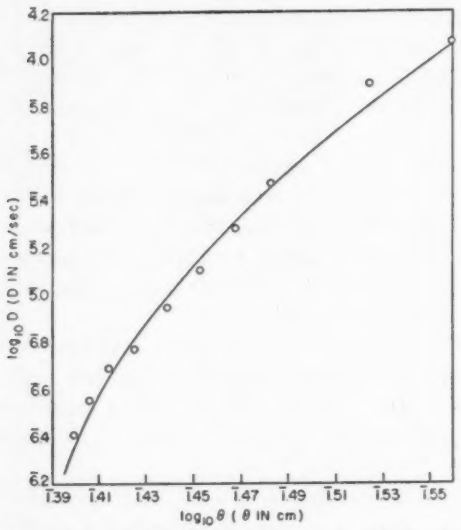

FIGURE 25(*b*). log D − log θ curve for NaF at 918°C. Full line, theoretical Bingham curve. ⊙, experimental points.

not cover such a wide range, and, therefore, n could not be directly determined by this method. To extend the range it is necessary to make $g\theta$ very large relative to f and since θ must not be too high because of the edge effect mentioned previously, the only solution is to increase the compressive force P (and therefore g). This was

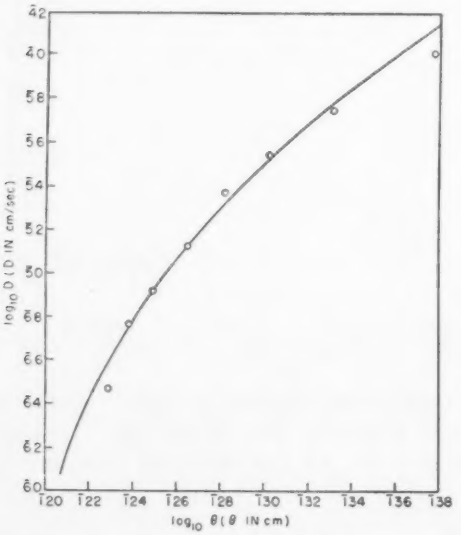

FIGURE 25(*c*). log D − log θ curve for NaF at 970°C. Full line, theoretical Bingham curve; ⊙, experimental points.

not attempted in the present work, principally because it was felt that the deformation rates would be too high to permit accurate measurement. For these higher rates of subsidence it would probably be an advantage to use some form of self recording dilatometer.

Flow Contents Deduced from Sintering Data and Comparison with Experimental Values

Several equations, based on plastic flow theory, have been proposed to describe sintering phenomena. One of these equations, developed by Clark and White, contains too many parameters to permit detailed analysis. The Shuttleworth-Mackenzie theory, however, can be more readily analysed so that constants may be derived from sintering data. The relevant equations are given below:

For Newtonian liquids:

$$\frac{d\rho}{dt} = k\,h(\rho) \tag{19}$$

For Bingham solids:

$$\frac{d\rho}{dt} = k\,h(\rho)\,[1 - a\cdot h'(\rho)] \tag{20}$$

where

$$k = \frac{3}{2}\left(\frac{4\pi}{3}\right)^{1/3}\frac{\gamma n^{1/3}}{c},\ h'(\rho) \text{ and } h(\rho) \tag{21}$$

are functions of ρ, and

$$a = \sqrt{2}\left(\frac{3}{4\pi}\right)^{1/3}\frac{f}{2\gamma n^{1/3}} \tag{22}$$

where ρ is the relative density of the compact, γ the surface tension, n the number of pores/cc of real material, f the yield stress, and c the viscosity.

Combining equations (21) and (22) gives:

$$ka = \frac{3\sqrt{2}}{4}\frac{f}{c} \tag{23}$$

Values of k and a, taken from the report previously mentioned, are presented below. Flow constants have been derived from this data and are compared with the values determined experimentally.

The following data refers to Clark and White's results for the sintering of glass spheres, the com-

TABLE XX

SINTERING DATA FOR GLASS

°C	k (min^{-1})	a
598	6.25×10^{-4}	0
626	3.48×10^{-3}	0
648	1.04×10^{-2}	0
676	3.85×10^{-2}	0

position of the glass being similar to that used in the present work.

The glass spheres used by Clark and White were about 12μ in diameter so that $n^{1/3}$ is of the order of 10^3. To calculate c it is necessary to assume some value for the surface tension, which will be of the order of several hundred dynes/cm at these temperatures. Two values for γ have been assumed, namely, 300 and 400 dynes/cm, and inserting these values into equation (21) gives the following viscosity coefficients:

TABLE XXI

CALCULATED VISCOSITY COEFFICIENTS FOR GLASS

	γ = 300 dynes/cm		γ = 400 dynes/cm	
°C	C	$\log_{10} C$	C	$\log_{10} C$
598	6.97×10^{10}	10.843	9.29×10^{10}	10.968
626	1.25×10^{10}	10.097	1.67×10^{10}	10.223
648	4.19×10^{9}	9.622	5.58×10^{9}	9.747
676	1.13×10^{9}	9.053	1.51×10^{9}	9.179

These viscosity values, together with those determined experimentally, are plotted in Figure 26. Included in this figure are the results of Poole and Gensamer [8] who measured the viscosities of a number of glasses of varying composition; the shaded area is applicable to glasses lying within the composition range:

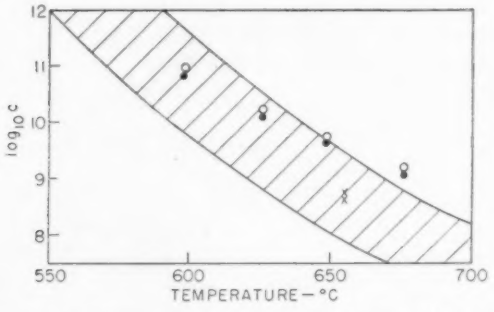

FIGURE 26. Comparison of viscosity coefficients for glass. Shaded area: Poole and Gensamer's results.

Composition range: SiO_2 69.0%; Na_2O 14.9–20.2%; CaO 9.4–4.7%; Al_2O_3 6.2%

× Experimental values using plastometer.

Composition: SiO_2 69.2%; Na_2O 16.2%; CaO 6.1%; Al_2O_3 3.4%; B_2O_3 1.2%; other oxides 0.7%

⊙ Derived from sintering data: γ = 400 dynes/cm

● " " " " γ = 300 dynes/cm

SiO_2: 69.0%; Na_2O: 14.9 → 20.2%; CaO: 9.4 → 4.7% and

Al_2O_3: 6.2%.

All the sets of values agree reasonably well with each other.

Application of the Shuttleworth-Mackenzie equation to the sintering curves for sodium fluoride gave the following values for k and a:

TABLE XXII

SINTERING DATA FOR NaF

°C	k (sec^{-1})	a	$k\,a$
683	1.13×10^{-4}	0.85	9.60×10^{-5}
695	1.45×10^{-4}	0.85	1.23×10^{-4}
713	1.74×10^{-4}	0.85	1.48×10^{-4}
726	2.60×10^{-4}	0.85	2.21×10^{-4}

It was seen previously (equation 23) that $ka = 1.06 \times (f/c)$. Thus, from Table XXII above, the values of the ratio f/c will be:

°C	683	695	713	726
f/c	9.06×10^{-5}:	1.16×10^{-4}:	1.40×10^{-4}:	2.09×10^{-4}

These values are plotted in Figure 27 (A), together with those determined experimentally by compression of sodium fluoride discs. Even though the temperature ranges of the two sets of data do not overlap, the results show that the f/c ratios derived from the sintering data are of the correct order of magnitude. This is revealed rather more

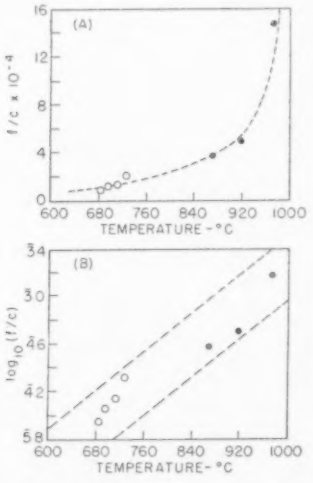

FIGURES 27(*a*) and (*b*). Comparison of flow constants for sodium fluoride. ●, experimental values; ⊙, deduced from sintering data.

clearly by plotting $\log_{10}(f/c)$ against temperature as in Figure 27 (B).

Conclusions

The deformation characteristics of a glass and sodium fluoride have been studied by means of a parallel-plate plastometer, and the data thus obtained analysed graphically as suggested by Scott. At a temperature of 655°C, the soda glass behaves as a Newtonian fluid, the viscosity coefficient being approximately 5×10^8 poises. There was some deviation from ideal Newtonian flow at the beginning of the test, but this may be due to surface irregularities of the specimen or loading errors. On the other hand, sodium fluoride appears to behave as a Bingham solid, the yield stress values and the viscosity coefficients being of the order of 10^7 dynes/cm^2 and 10^{10} poises respectively.

It is to be noted that the best method of determining the value of n in the equation

$$\text{shear rate} = \left(\frac{F-f}{c}\right)^n$$

is to apply high loads so that f is negligible compared to F, and the material behaves as a Newtonian fluid. Under these conditions the deformation rate would probably be rather high, and therefore the use of a self-recording dilatometer would be advantageous. A further point of importance is that the specimens used should possess, if possible, zero porosity. The presence of pores will probably affect the mechanism of deformation, particularly if dilation occurs on compression.

Yield stress values and viscosity coefficients have been deduced from sintering data using the equations of Shuttleworth and Mackenzie. These values are in reasonable agreement with those determined experimentally. From this, it would appear that the plastic flow mechanism proposed by Shuttleworth and Mackenzie goes some way towards explaining sintering phenomena.

Acknowledgement

The authors wish to express their gratitude to the Director, A.E.R.E., for permission to publish this paper.

References

1. Shuttleworth, R. and Mackenzie, J. K. Proc. Phys. Soc. **62** (1949) 833.
2. Cannon, J. H., Clark, P. W. and White, J. Trans. Brit. Cer. Soc. **52** (1953).
3. Clark, P. W. and White, J. Trans. Brit. Cer. Soc. **49** (1950) 305.
4. Scott. Trans. I.R.I. **7** (1931) 1.
5. Megaw, H. D. Z. Kryst. **100** (1938) 58.
6. Kuczynski, G. C. J. Appl. Phys. **20** (1949) 1160.
7. Herring, C. J. Appl. Phys. **21** (1950) 301.
8. Poole, J. P. and Gensamer, M. J. Amer. Cer. Soc. **32** (1949) 220.

EXPERIMENTAL IRON CARBONYL POWDERS*

F. E. JAUMOT, Jr. and L. MULDAWER†

The strain and crystallite size in an experimental iron powder produced by a carbonyl process have been determined by the method of Warren and Averbach. Using FeK_α and MoK_α radiation, the shapes of nine powder diffraction lines were obtained for the powder and for a well-annealed "standard." From Fourier analyses of these lines, coefficients of line profiles due only to strain and crystallite-size broadening were obtained. A curve of the logarithm of these coefficients as a function of the order of the diffraction lines gave crystallite sizes and strains. Values obtained for these quantities in the [100], [110], and [111] directions were: 53 Å, 73 Å, and 80 Å for the crystallite sizes, and 3.5×10^{-3}, 6.3×10^{-3}, and 2.2×10^{-3} for the strains, respectively.

Samples of carbonyl iron powder were annealed for two hours at various temperatures. Relative peak heights, half-widths and line positions were determined. Line profiles were analyzed and particle size and strain determined. It was found that annealing produced a diminution in the lattice parameter accompanied by a corresponding reduction in the strain. The strain recovery is approximately 85 per cent complete at about 350°C. Crystallite size increased from 70 Å in the untreated powders to over 1200 Å in the powder annealed at 450°C. Growth below 350°C was relatively small. Speculations are presented as to the cause of the initial distortion and the nature of the annealing process.

POUDRES EXPÉRIMENTALES DE CARBONYL DE FER

La déformation et les dimensions des cristaux d'une poudre expérimentale de fer, produite par un procédé "carbonyl," furent déterminées en se servant de la méthode de Warren et Averbach. Les formes de neuf raies de diffraction furent obtenues pour cette poudre et pour un échantillon standard bien recuit, en employant les radiations FeK_α et MoK_α. Une analyse de Fourier de ces raies, a permis de déterminer les coefficients de profil des raies dus exclusivement à la déformation et de l'élargissement des raies dû aux dimensions des cristaux. Une courbe du logarithme de ces coefficients, en fonction de l'ordre des raies de diffraction, a donné les dimensions des cristaux et les déformations. Les valeurs suivantes furent obtenues pour les directions [100], [110], et [111] respectivement: 53 Å, 73 Å, et 80 Å pour les dimensions des cristaux et $3{,}5 \times 10^{-3}$, $6{,}3 \times 10^{-3}$ et $2{,}2 \times 10^{-3}$ pour les déformations.

Des échantillons de poudre de fer carbonyl on été recuits pendant deux heures à diverses températures. On a déterminé les hauteurs relatives des maxima, les demi-largeures et les positions des raies. Les profils des raies furent analysés et les dimensions des particules, ainsi que les déformations en furent déterminées. Il fut constaté que le recuit produisait une diminution du paramètre du réseau accompagné d'une réduction correspondante de la déformation. A 350°C environ 85 pour cent de la déformation sont restaurés. Les dimensions des cristaux vont de 70 Å pour une poudre non traitée à plus de 1200 Å pour une poudre recuite à 450°C. En dessous de 350°C la croissance des cristaux était relativement faible. On discute des hypothèses concernant les causes de la distortion initiale et le caractère du processus de recuit.

EXPERIMENTELLE EISENKARBONYLPULVER

Die inneren Spannungen und die Korngrösse von experimentellen, in einem Karbonylprozess dargestellten Eisenpulver, wurden mit Hilfe eines von Warren und Averbach entwickelten Verfahrens gemessen. Neun Linienprofile von mit Fe K_α und Mo K_α-Strahlen aufgenommenen Pulverdiagrammen wurden für das Pulver und eine gut ausgeglühte "Standardprobe" aufgenommen. Aus der Fourieranalyse dieser Linien wurden Profilverbreiterungskoeffizienten erhalten, die entweder nur den inneren Spannungen oder nur der Teilchengrösse zuzuschreiben sind. Eine Kurve des Logarithmus dieser Koeffizienten als Funktion von n, der Ordnung der Beugungsmaxima, ergab Teilchengrössen und innere Spannungen. Die in den [100] [110] und [111] Richtungen erhaltenen Werte waren 53 Å; 73 Å; 80 Å für die Korngrössen und $3{,}5 \times 10^{-3}$; $6{,}3 \times 10^{-3}$ und $2{,}2 \times 10^{-3}$ für die inneren Spannungen.

Karbonyleisenpulverproben wurden zwei Stunden bei verschiedenen Temperaturen geglüht. Die relative Höhe der Maxima, die Halbwertbreiten und die Lage der Linien wurde vermessen. Die Linienprofile wurden analysiert, und Teilchengrösse und innere Spannungen wurden bestimmt. Es zeigte sich, dass die Glühung eine Verminderung der Gitterkonstanten hervorrief, die von einer entsprechenden Verminderung der inneren Spannungen begleitet war. Bei 350°C war etwa 85% der Spannungserholung erfolgt. Die Teilchengrösse stieg von 70 Å im unbehandelten Pulver auf mehr als 1200 Å in einem bei 450°C geglühten Pulver an. Unterhalb von 350°C wachsen die Teilchen nur wenig.

Es werden spekulative Erklärungen der Ursache der Anfangsverzerrung und des Wesens des Glühprozesses mitgeteilt.

Introduction

In the course of a general study of iron powders, we became interested in the properties of powders prepared by the carbonyl process. Specifically, we have studied the broadening of X-ray diffraction lines due to the small crystallite size and strain in an experimental carbonyl iron, prepared and donated by General Aniline and Film Corporation, and designated by them as P-818.

The powder is prepared by deposition from an iron carbonyl vapor and exhibits a macrostructure

*Received September 10, 1953; in revised form December 7, 1953.

†Franklin Institute Laboratories for Research and Development, Philadelphia, Pennsylvania.

consisting of concentric spherical shells, usually called an "onionskin" structure. Presumably this structure is due to alternate deposition of layers of relatively pure iron followed by carbon-rich iron. Electron micrographs of the P-818 powder indicate that the particles are roughly spherical, with a mean diameter of approximately 20,000 Å. It should be emphasized that this particle diameter is several orders of magnitude larger than the dimensions of the crystallites within the particles.

In addition to the determination of the crystallite size and strain in the "as prepared" powders, we have studied some aspects of the annealing kinetics of this powder. The powders are of interest in this respect because of the information to be gained concerning the nature of the strain and small crystallite size in the untreated powder.

The technique used to separate the strain, or distortion, broadening and the broadening due to crystallite size was that described by Warren and Averbach [1; 2; 3; 4]. They have shown that for either type broadening the shape of the diffraction peak can be represented by a Fourier series:

$$(1) \qquad P = K \sum_{n=-\infty}^{\infty} A_L(l_0) \cos\left(\frac{4\pi}{\lambda} L \sin\theta\right),$$

where

$l_0 = \sqrt{h^2 + k^2 + l^2}$; h, k, l are the Miller indices;

$L = na_3$, where n is the defining integer of the Fourier coefficients, and a_3 is a length in the crystal.

Further, they have shown that if both types of broadening are present, the coefficients $A_L(l_0)$ may be written as a product of coefficients, each representing one type of broadening:

$$(2) \qquad A_L(l_0) = A_L{}^P \cdot A_L{}^D(l_0)$$

where, for crystallite size,

$$(3) \qquad A_L{}^P = \frac{1}{N} \sum_{i=|n|+1}^{\infty} (i - |n|)\, n_i$$

and for distortion,

$$(4) \qquad A_L{}^D(l_0) = \left\langle \cos \frac{2\pi l_0 \Delta L}{a} \right\rangle_{av}.$$

Here, n_i is the number of columns of unit cells of length i cells, perpendicular to the reflecting planes; N is the total number of cells; a is the lattice parameter; and ΔL is the change in L for a given value of L.

The coefficient $A_L{}^P$ is independent of the order of the diffraction line, while $A_L{}^D$ can be approximated, for small n and l_0, by an exponential

$$\left(\left\langle \cos \frac{2\pi l_0 \Delta L}{a} \right\rangle \rightarrow \exp\left[-\frac{2\pi^2 l_0{}^2 < \Delta L^2 >}{a^2}\right]\right)$$

the argument of which is proportioned to the square of the order, as well as the mean square strain. Thus, if we plot the logarithm of A_L *versus* the square of the order of the lines, the intercepts on the axis of ordinates give ln $A_L{}^P$, and the initial slopes are proportional to the root mean square strains.

The above method of analysis was used in both phases of the work to be discussed, and we believe that this is the first time that this powerful technique has been used in a study of distortion produced in growth (as contrasted to cold-work distortion) and to the annealing kinetics of such distortion.

I. Strain and Crystallite Size in the Untreated Powder

The Experimental Method

The line profiles needed for the analyses were obtained from powder briquettes, $\frac{1}{8} \times \frac{1}{4} \times 1$ in., pressed (24,000 p.s.i.) using the "as prepared" powder with a binder of Duco cement. The intensities were determined by a point-by-point count using a conventional Geiger counter spectrometer. An average of 75 points were taken each time the line was "counted," and each line was "counted" three times. Line profiles of each diffraction line were taken for both the sample exhibiting line broadening and for a well-annealed sample, or "standard." The diffraction peaks were corrected for instrumental broadening including the K_α doublet by the method due to Stokes [5], using the Lipson-Beevers strips. This gave the coefficients, A_L, of a line profile due only to crystallite size and distortion.

A total of nine lines were studied using MoK_α radiation: the (110), (211), (220), (321) and (422); the (200) and (400); and the (222) and (444). The (110), (211), (220) and (200) lines were also analyzed using FeK_α radiation.* These lines gave information about three directions in the crystal, namely those perpendicular to the (110), (100) and (111) planes. The fact that the (110), (211) and

*The background correction was difficult to make in the case of molybdenum radiation. A check of our technique was provided by the duplication of several of the lines using FeK_α radiation. The Fourier coefficients are, of course, independent of the radiation.

(321) planes gave identical values for particle size and strain is an interesting result of the experiment.

Inasmuch as iron is elastically anisotropic and the coefficients A_L contain explicitly a contribution due to strain in the lattice, it is interesting that those lines which correspond to directions in the crystal having the same value of Young's modulus were those which yielded identical results. The set of lines including the (110), (211), (220), (321) and (422) all represent directions in the iron crystal which have a Young's modulus of 22,500 Kg/mm². These planes are the slip planes in iron. In the cases of the (100) and the (111) sets of lines, no other directions were found which had similar Young's moduli. These planes correspond to directions in the crystal having the minimum value of Young's modulus, or the fracture planes, and the maximum value. A similar correlation with the values of Young's modulus was observed by McKeehan and Warren [6] for the case of cold-worked, thoriated tungsten.

The coefficients, A_L, of the line profile obtained by correcting the broadened lines for instrumental broadening, were plotted against the parameter L. Figure 1 shows the resulting curves for the five lines of the (110) set.

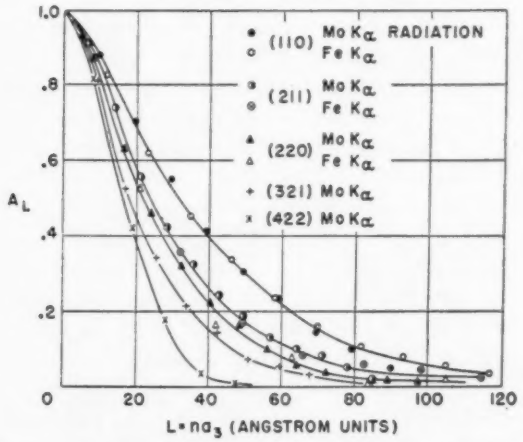

FIGURE 1. Fourier coefficients A_L (l_0) plotted against L for various directions in the crystal.

Values of A_L for constant values of L were taken from this set of curves and the logarithm of A_L plotted as a function of the square of the order of the diffraction lines as shown in Figure 2. The intercepts of these curves on the axis of ordinates gave the logarithm of the crystallite size coefficients, A_L^P, and the initial slopes gave the root-mean-square strains.

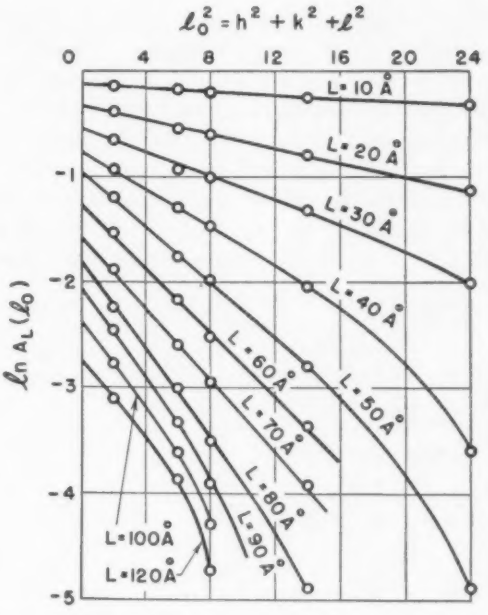

FIGURE 2. Plot of ln A_L (l_0) *versus* l_0^2 for various lengths L.

Results

Figure 3 gives the curve of the crystallite size coefficients as a function of the length of a column of cells in the crystal. The mean size of the crystallites is then given by the reciprocal of the negative initial slope of this curve. The value obtained in the [110] direction (from Figure 3) is approximately 70 Angstroms.

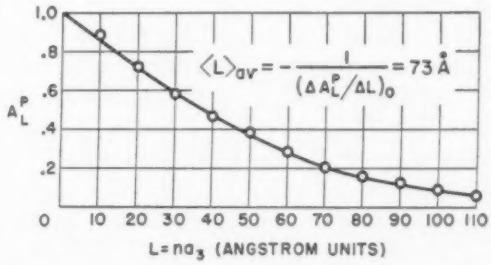

FIGURE 3. Plot of A_L^P *versus* L for the [110] direction in iron carbonyl powder.

The term *mean crystallite size* or *dimension* as used in this paper, is the measured value of the mean length of a column of cells in the crystallite, the columnar axes of which are along the given direction. Consequently the reported values are not true dimensions of a crystallite, since it is possible to show that the mean length of columns of cells, L, is always less than the largest crystallite dimension, d.

Figure 4 gives the root-mean-square strain as a function of distance in the crystal. These strains can be computed in three ways, as indicated in the figure. As we mentioned above, they can be computed from the initial slopes of the curves of ln A_L *versus* l_0^2. In addition, we can obtain values for the $A_L{}^P$ from the plot of $A_L{}^P$ *versus* L, which then can be divided into A_L to give the coefficients, $A_L{}^D$, due to distortion broadening. From these, we

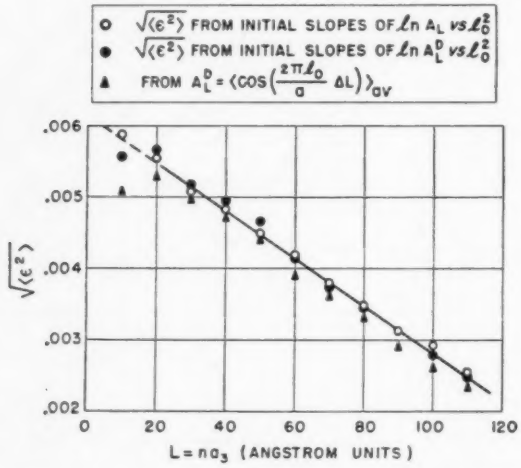

FIGURE 4. Root-mean-square strain in the [110] direction as a function of distance in the crystal.

can compute strain from the cosine representation (equation 4), or assuming the exponential approximation to be valid, we can compute the rms strains from a plot of the logarithm of $A_L{}^D$ versus l_0^2. In view of the relatively large error inherent in taking slopes of logarithmic curves, the agreement is good. The small amount of scatter in the data points leads us to believe that the strain values are accurate to better than ± 0.0005. The values of the strain at very small distances, obtained by extrapolation, is probably good to ± 0.001.

Using entirely similar analyses to the one described for the (110) set of lines, we have obtained the values of the crystallite size and strain for the [100] and [111] directions in this material. Table I gives the maximum values of the strain and the mean crystallite sizes in these directions, along with those for the [110] direction. We have included in the table the values of Young's modulus for the given directions and the values of the stresses corresponding to the strains if a Hooke's law is assumed to hold.

TABLE I

CRYSTALLITE SIZE AND STRAIN IN UNTREATED CARBONYL IRON POWDER

Crystal direction	Mean crystallite size (Å)	R.M.S. strain	Young's Modulus	Stress* (kg/mm²)
[100]	53	3.5×10^{-3}	13,500	47
[110]	73	6.3×10^{-3}	22,500	142
[111]	80	2.2×10^{-3}	29,000	64

*Computed using a Hooke's law relation

Discussion of Results

The data indicate that there is an rms strain of about 6×10^{-3} in the [110] direction over very small distances. It was observed from lattice parameter measurements (see Part II) that there was an apparent macroscopic strain of about 2.7×10^{-3} in this direction. Thus, the evidence is that there is a combination of micro- and macro-strain, where by a micro-strain we mean those strains with equal probability of being positive or negative, and whose regions of influence extend only over small distances in the crystal. It is to be noted that the rms strain apparently decreases with distance in the crystal in a linear fashion. As McKeehan and Warren have pointed out [6], the small crystallite size (i.e., the small dimensions of the regions over which the averages are taken) makes interpretation of the strain ambiguous. Thus we can say little more of this feature than it indicates that the strain is not constant throughout the crystal.

Very little significance is to be attached to the stresses given in Table I, since the validity of Hooke's law is extremely uncertain. At the same time there is a definite correlation with the elastic anisotropy of the material as is shown by the fact that all lines of the set, referred to as the (110) set, give similar values.

The values of the stresses given in Table I do, however, allow us to make a comparison with Taylor's values [7] for the stress in carbonyl iron which were computed in a similar manner. Using a different carbonyl iron powder (Mond Nickel Co.) and a different technique for determining the strain, Taylor obtained a value for the stress of about 130 tons/sq in. This compares favorably with our value of approximately 100 tons/sq. in. However, Taylor found a crystallite size of 200 Å, which is considerably larger than our values.

Berteaut [8], on the other hand, found the broadening of the lines from carbonyl iron powder to be due entirely to crystallite size of about 70 Å. In a private communication he stated that his work indicated negligible strain. However, his conclusions were based on the analysis of a single (110) line, which does not allow precise determination of the strain. Thus, the agreement of our value with his may be due to his powder having a larger crystallite size together with a strain which was neglected in the analysis.

A word as to the accuracy of the crystallite size measurements. Errors in this type of analysis can be quite large and are difficult to evaluate. However, we feel that the dimensions of the mean columnar lengths given here are reasonably accurate, particularly in the [110] direction, since two separate determinations by different experimental techniques (see Part II) showed excellent agreement. A rather arbitrary estimate of the over-all accuracy of the crystallite dimensions is approximately ±5 Å, with an accuracy of ±3 Å in the [110] direction. In any event, it is quite definite that the dimensions given in Table I differ by amounts greater than the error and consequently some size anisotropy is present.

An obvious interpretation of this size anisotropy is that deposition of the powder occurs in such a way that platelets or needles are formed, the major platelet plane or needle direction being a given one. However, the major direction of growth has not been determined although numerous possibilities have been examined.

Let us now consider the nature of the untreated powder. Chemical analyses yielded the following for P-818 powder, in weight percent: Fe, 97.89; N, 0.54; C, 0.71; others, 0.84 (by difference). Thus these considerable impurities must play a major role in producing the strain. There is reason to believe (see Part II) that the strain is caused principally by very highly dispersed precipitates, and in particular by nitrides. Carbon is also present to a considerable extent either in monolayers or highly dispersed carbides. (Ref. 7; see also Part II). The strain anisotropy could then be explained on the basis of precipitation on preferred planes.

Carbonyl iron powders are formed at temperatures in the neighborhood of 200°C [9], and hence it is probable that certain atomic migrations and precipitation occur. The temperature of formation presumably aids polygonization but the high impurity content restricts the scale of polygonization. The interior of the subcrystals so formed must be strained in order for the measured rms strain to be so large. This strain is too large to be due to dissolved carbon (10); thus the conclusion that it is due to widely dispersed impurities. The restricted polygonization probably accounts for the observed small crystallite dimensions. This interpretation of the nature of the untreated powders leads us to believe that we are measuring sub-grain (rather than normal crystallite) dimensions since the X-ray scattering from sub-grains is presumed to be incoherent.

II. Annealing Kinetics in an Experimental Carbonyl Iron Powder

Experimental Method

In order to learn something of the nature of the distortions, and of the causes of the apparent small crystallite size of this iron carbonyl, powders were heat treated for two hours at 150°C, 250°C, 300°C, 350°C, 400°C, and 450°C. The powders were then pressed into briquettes similar to those used in Part I of this paper.

The details of the experimental method were changed in some respects from those described above because of the greater number of lines that were involved in the analyses. The line profiles were obtained from these samples by automatic recording of the intensities from the Geiger tube on a strip chart recorder. The accuracy of lines obtained in this way is not so great as for "point-by-point" counting, but the agreement of results obtained on untreated powder by this method and by "point-by-point" counting was sufficiently good so that the difference in labor involved made the automatic recording virtually mandatory.

In addition to the change in the method of recording intensities, only lines of the (110) set were analyzed in detail for the anneal study. For this work, FeK_α was the only radiation used and consequently only the (110), (211), and for the higher temperature anneals where the intensity was appreciable, the (220) lines were analyzed. These, of course, represent different crystallographic planes rather than different orders of the same plane, but the data of Part I indicate that this procedure is valid.

In all other respects the method of determining the crystallite size and strain was similar to that described in Part I.

Results

In addition to the strain and crystallite size, the relative peak-heights, half-breadths, and the line positions of the (110) lines were determined as a function of temperature and are tabulated in Table II. These quantities were determined in order to obtain a qualitative picture of the annealing process.

TABLE II

(110) Diffraction Line Parameters as a Function of Annealing Temperatures for Carbonyl Iron Powders

Anneal temp. (°C)	Peak height (arbitrary units)	Half-breadths (deg. in 2θ)	Line positions (2θ in deg.)
No treatment	18.5	1.165	56.88
150	19	1.150	56.90
250	21	1.000	56.92
300	29	0.700	56.95
350	62	0.320	57.01
400	92	0.240	57.01
450	108(?)	0.225	57.03
A standard	225	0.130	57.04

A "pictorial" view of the effects of annealing temperatures may be seen in Figure 5, where we have plotted A_L as a function of distance in the

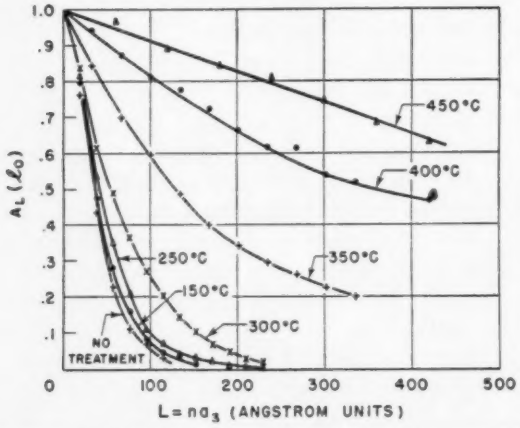

Figure 5. Plot of Fourier coefficient A_L (l_0) *versus* L for the (110) diffraction lines obtained after annealing for two hours at temperature indicated.

crystal for various temperatures, for the (110) line. In particular, the large differences in the lines at 300°C and at 350°C show graphically the fact that the strain is reduced to 15 per cent of its original value at 350°C, and also that this is the lowest annealing temperature studied for which there is an appreciable change in crystallite size.

Figure 6 is a combined plot of the strain and crystallite size in the [110] direction and the peak position of the (110) line, as functions of annealing temperatures. The values shown in Figure 6 are summarized in Table III.

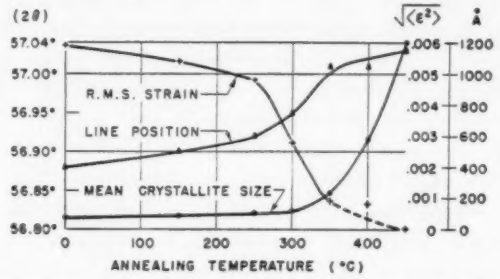

Figure 6. Root-mean-square strain and crystallite size in the [110] direction, and the position of the (110) line as functions of annealing temperature.

TABLE III

Crystallite Size and Strain as a Function of Annealing Temperature for the [110] Direction

Anneal temp. (°C)	Mean crystallite size (Å)	R.M.S. strain	Line position (110) line (2θ in degrees)
No treatment	73	5.9×10^{-3}	56.88
150	84	5.4×10^{-3}	56.90
250	101	4.8×10^{-3}	56.92
300	116	2.8×10^{-3}	56.95
350	230	0.9×10^{-3}	57.01
400	580	0.8×10^{-3}	57.01
450	1200	—	57.03

In addition to the above results obtained from detailed examination of particular lines, three important results were obtained from an examination of the complete patterns given by these powders. First, no evidence for tetragonality (due to martensite) was observed for any annealing temperature or for the untreated powder. Second, there was no evidence of lines due to precipitates in the spectra of the untreated powder. Diffraction lines corresponding to cementite and nitride precipitates were looked for in particular. Third, lines which could be identified as being due to Fe_4N appeared in the pattern of the powder annealed at 250°C. These lines became sharper and more intense in the spectra of the powders annealed at higher temperatures. However, no carbide lines were observed for any annealing temperature.* A. Taylor [7] has reported Fe_4N

**Note added in proof:* We have observed lines identified as due to Fe_3C in the X-ray pattern of powders annealed for much longer times (40 hours at 350°C.)

present in his carbonyl powders, in some cases in the untreated powders. He reports no observable carbides, although other workers [11; 12] have reported carbide formation on annealing.

Discussion of Results

Figure 6 shows that both line position and strain have almost reached their equilibrium value after two hours at 350°C. It is evident that the major effect of the anneal at this temperature has been a strain recovery since the crystallite size has only begun to increase. Then with increasing annealing temperatures, the subcrystal walls move to give the observed grain growth. Since it is more difficult to move these walls than to move isolated defects to the boundary it is to be expected that strain recovery occurs at lower temperature than sub-grain growth.

Without more specific information it is possible only to speculate on the details of the recovery and sub-grain growth. However the appearance and the behaviour of the diffraction lines corresponding to Fe_4N at the higher annealing temperatures provide clues as to the probable mechanism. Presumably, on annealing, the highly dispersed impurities in the untreated powder agglomerate with a consequent reduction in strain. It is likely that a major portion of the agglomeration (particularly of the carbon) occurs in the subcrystal boundaries, and it is these boundaries which move in the course of the subcrystal growth.

It is evident that there are still many questions to be answered as to the nature of carbonyl iron powders. However, we believe that this work justifies, at least for P-818 carbonyl iron, the following conclusions:

1. The crystallite dimensions determined are probably due to sub-grains. These sub-grains are nonspherical.

2. The interiors of the sub-grains are highly strained, presumably due to widely dispersed impurities.

3. Recovery occurs at temperatures below 350°C, probably due to impurity agglomeration.

4. Crystallite growth is observed at temperatures below the generally accepted recrystallization temperatures, presumably due to motion of sub-grain boundaries.

Acknowledgements

This work was supported in part by the Office of Naval Research and in part by the Atomic Energy Commission. The authors also wish to extend their appreciation to Dr. R. L. Smith for many helpful discussions, and to Dr. A. Taylor for supplying us with a copy of his manuscript.

References

1. Warren, B. E. and Averbach, B. L. J. Appl. Phys. **21** (1950) 595.
2. Warren, B. E. and Averbach, B. L. J. Appl. Phys. **23** (1952) 497.
3. Warren, B. E. and Averbach, B. L. J. Appl. Phys. **23** (1952) 1059.
4. Warren, B. E. and Averbach, B. L. Imperfections in Nearly Perfect Crystals (New York, Wiley, 1952), p. 152.
5. Stokes, A. R. Proc. Roy. Soc. **61** (1948) 382.
6. McKeehan, M. and Warren, B. E. J. Appl. Phys. **24** (1953) 52.
7. Taylor, A. Soft Magnetic Materials for Telecommunications (New York, Interscience Publishers Inc., 1953).
8. Berteaut, Felix. Ph.D. Thesis, University of Grenoble, 1949.
9. Altmann, G. D. F.M.T.V., June, 1949.
10. Williamson, G. K. and Smallman, R. E. Acta Cryst., **6** (1953) 361.
11. Rooksby, H. P. Cantor Lectures, Royal Society of Arts, 1942.
12. Jack, K. H. J. Iron and Steel Inst. **169** (1951) 26.

THE EFFECT OF PHASE TRANSFORMATIONS ON THE ORIENTATION OF ZIRCONIUM CRYSTALS*

J. W. GLEN and S. F. PUGH†

The orientation relations suggested by Burgers for the phase change in zirconium are used to deduce the possible orientations which can arise after one or two transformations starting from either a hexagonal or a body-centered-cubic lattice, and their relative probability is assessed assuming that at each stage all possible transformations are equally probable. The results of this analysis are compared with the known behaviour of zirconium and titanium crystals and rolled zirconium strip; it appears that a first transformation is determined only by the orientation relations, but the second is not, for the original orientation almost invariably returns. The possible reasons for this are examined; one which has so far received little attention is that simple dislocations in the parent phase can only all return to simple dislocations after a second transformation if the original orientation returns. The reasons for the observed texture of crystal bar zirconium are discussed, and experiments suggested to indicate the importance of the various factors.

L'EFFET DES TRANSFORMATIONS DE PHASES SUR L'ORIENTATION DE CRISTAUX DE ZIRCONIUM

Les relations d'orientation suggérées par Burgers sont utilisées pour déduire les orientations qui peuvent apparaître après une ou deux transformations, partant soit d'un réseau hexagonal, soit d'un réseau cubique centré. Les probabilités relatives de ces transformations sont évaluées en supposant qu'à chaque étape toutes les transformations sont également probables. Les résultats de cette analyse sont comparés au comportement connu des cristaux de zirconium et de titane, et de bandes laminées de zirconium; il apparaît qu'une première transformation est déterminée uniquement par des relations d'orientation, mais la deuxième ne l'est pas, car l'orientation primitive revient presque toujours. Les raisons possibles de ce fait sont examinées; une de ces raisons n'a reçu que peu d'attention avant, à savoir, que les dislocations simples dans la phase primitive ne peuvent toutes redevenir des dislocations simples, après une deuxième transformation, que si l'orientation primitive réapparaît. Les raisons d'apparition de textures dans des barres de zirconium sont discutées et des expériences, qui indiqueraient l'importance des divers facteurs, sont suggérées.

DIE WIRKUNG DER PHASENUMWANDLUNGEN AUF DIE ORIENTIERUNG VON ZIRKONIUMKRISTALLEN

Es werden unter Zugrundelegung der von Burgers für die Phasenumwandlung im Zirkon vorgeschlagenen Orientierungsbeziehungen alle Orientierungen abgeleitet, deren Entstehen entweder nach einer oder nach zwei Umwandlungen möglich ist, wenn man entweder vom hexagonalen oder vom kubisch-raumzentrierten Gitter ausgeht. Die relative Häufigkeit ihres Auftretens wird unter der Annahme abgeschätzt, dass in jedem Stadium alle möglichen Umwandlungen gleich wahrscheinlich sind. Die Resultate dieser Analyse werden mit dem bekannten Verhalten von Zirkon- und Titankristallen und von gewalztem Zirkonblech verglichen. Es scheint, als sei eine erste Umwandlung ausschliesslich durch die Orientierungsverhältnisse bestimmt; dies trifft jedoch nicht auf die zweite Transformation zu, denn die ursprüngliche Orientierung tritt fast unweigerlich wieder auf. Die möglichen Ursachen für diese Erscheinung werden diskutiert. Ein Gesichtspunkt, der bisher wenig beobachtet wurde, ist, dass einfache Versetzungen in der Ausgangsphase nach einer zweiten Transformation nur dann wieder völlig in einfache Versetzungen zurückgeführt werden können, wenn die ursprüngliche Orientierung zurückkehrt. Die Ursachen für die an kristallinen Zirkonstäben beobachtete Textur werden diskutiert, und es werden Versuche zur Abschätzung des Einflusses der verschiedenen Faktoren vorgeschlagen.

1. Introduction

From room temperature to 862°C ± 5° zirconium has a close-packed hexagonal structure; from this temperature to its melting point at about 1800°C it is body-centered cubic. Crystal bar is usually grown by deposition of the metal on a tungsten or zirconium wire heated by passing an electric current through the wire in a cool vessel containing zirconium iodide vapour, the temperature of deposition being above 900°C. In 1934, Burgers [1] noticed that the crystal bar had flat faces all parallel to the bar axis and with either six sides at 60 degrees or, more rarely, four sides at 90 degrees. Crystallographically, these faces were not equivalent at low temperatures, though both types were sometimes basal (0001) planes. He argued that at the high temperature they must have been {110} faces of the body-centered cubic lattice, since these alone give a zone of six faces at 60 degrees or four at 90 degrees in the holosymmetric class of the cubic system. In this way he could deduce the exact orientation of the β (body-centered-cubic) grains and, by measuring the orientation of the resulting α (hexagonal) grains, he deduced that the orientation relation for the β- to α-phase change was that one of the six {110} planes of the β-structure became the (0001) plane of the α, while one of the ⟨111⟩

*Received October 12, 1953.
†Atomic Energy Research Establishment, Harwell, England.

directions in the β-structure became one of the $\langle 11\bar{2}0 \rangle$ directions in the α-structure.

These orientation relations have since been found to be at least approximately valid for lithium [2] and titanium [3; 4], while the remaining elements having both a hexagonal and a body-centered-cubic modification, thallium [5] and hafnium [6], may reasonably be expected to follow them as well.

If these orientation relationships alone determined the orientations of grains arising after transformation, it would be possible to predict not only what orientations are to be expected after a given number of transformations starting from a given texture, but also what their relative probability would be. These predicted results can then be compared with the observed textures to obtain information on whether the assumption that the orientation relations alone determine the new orientations is correct. The predictions can also be used to explain the structure of crystal bar.

2. Analysis of Possible Orientations after Transformations of Single Grains

In this section we shall consider the orientations that can arise after one or two transformations, starting from either a body-centered-cubic or a hexagonal orientation. First, a hexagonal orientation can transform into six body-centered-cubic orientations. This arises because the three $\langle 11\bar{2}0 \rangle$ directions* in a (0001) plane are at 60 degrees while the two $\langle 111 \rangle$ directions are at 70°32′. Thus, although the (0001) plane must become a $\{110\}$ plane only one of the three $\langle 11\bar{2}0 \rangle$ directions can become a $\langle 111 \rangle$ direction, and the other $\langle 111 \rangle$ direction may lie on either side. This is shown in Figure 1, which represents the (0001) plane of the hexagonal phase AA, BB and CC are the $\langle 11\bar{2}0 \rangle$ directions which can become $\langle 111 \rangle$ directions. The other possible $\langle 111 \rangle$ directions are shown by the remaining lines. Thus, for example, if A becomes one $\langle 111 \rangle$ direction, either A_1 or A_2 will become the other $\langle 111 \rangle$ direction in this plane. If the orientation laws alone decide the probability of these, all six are equally probable.

Next, we shall consider the possible orientations arising after a transformation from a single cubic orientation, a case which has already been considered by Burgers [1]. As there are six $\{110\}$ planes, there are six possible (0001) planes after

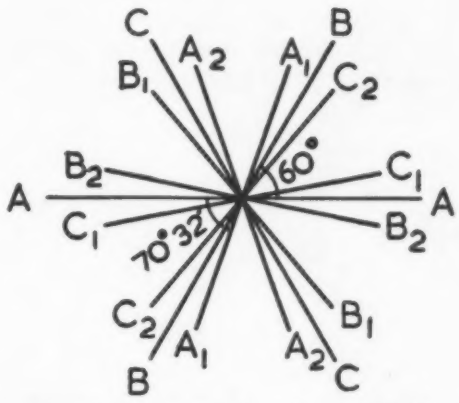

FIGURE 1. Diagram to illustrate the possible orientations after one transformation of a hexagonal structure.

transformation, and in each of these there are two possible sets of $\langle 11\bar{2}0 \rangle$ directions, one for each $\langle 111 \rangle$ direction in the original $\{110\}$ plane. These possible orientations are shown in Figure 2, which is a standard stereographic projection of the cubic orientation, the $\langle 110 \rangle$ diads and the $\langle 111 \rangle$ triads being marked. For a given $\langle 110 \rangle$ direction such as A, the plane corresponding to the great circle XCY becomes the basal plane and the two possible sets of $\langle 11\bar{2}0 \rangle$ directions are Y with the two points marked A_1, and X with the two points marked A_2. Each of the six $\langle 110 \rangle$ directions thus gives two hexagonal orientations. In this way 12 hexagonal orientations can arise, each of equal probability.

We are now in a position to discuss the orientations which can arise after two transformations

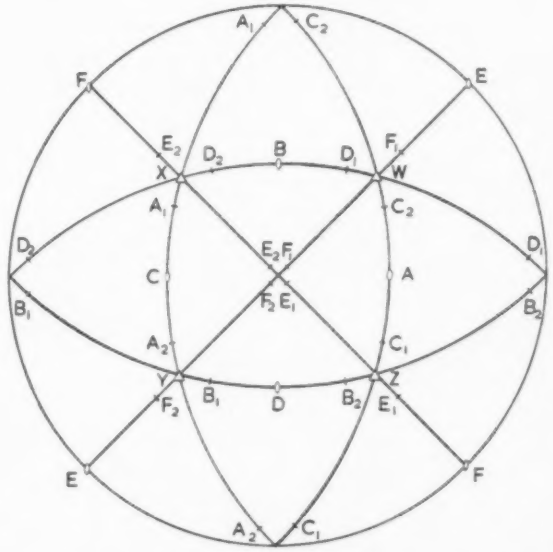

FIGURE 2. Stereogram of the possible orientations after one transformation of a body-centered-cubic structure.

*It will henceforward be assumed that Miller-Bravais indices (with four figures) refer to the hexagonal, and Miller (three figures) to the body-centered-cubic phase.

of a hexagonal lattice. Since after the first transformation six cubic orientations arise, and each of these can yield 12 hexagonal orientations, there

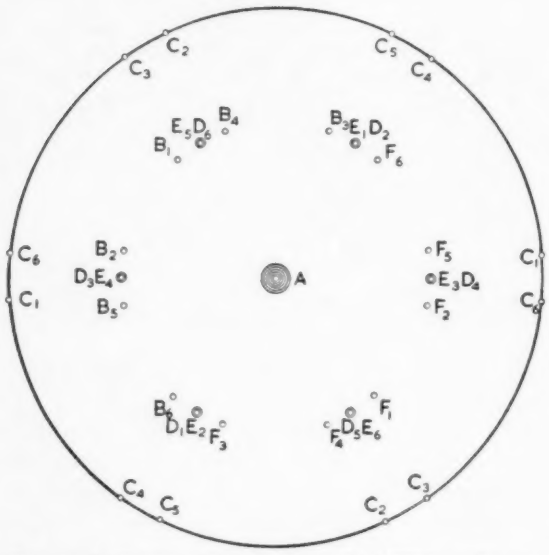

FIGURE 3. Stereogram of the possible (0001) poles after two transformations of a hexagonal structure.

are a total of 72 different orientation paths; but these do not all necessarily yield different orientations, for one hexagonal orientation may appear from more than one of the intermediate cubic orientations. Thus, for example, the original orientation can reappear from any of the six cubic orientations, and will thus be six times more probable than an orientation reached by only one path. To see how many of the paths yield the same orientations, Figure 3 was constructed; this shows on a stereographic projection, centered on the pole of the original (0001) plane, all the possible {110} poles after one transformation. All poles except the centre are marked with a letter for each time they occur; the points with a given suffix are the {110} poles of one cubic orientation. The centre should have six suffixes, one for each possible orientation. These points are all thus possible new (0001) poles and, considering also the $\langle 11\bar{2}0 \rangle$ directions, those points with two letters can be shown to yield three orientations, one with twice the probability of the other two.

The full analysis shows that 57 orientations can arise. Their relation to the original orientation and their relative probabilities are shown in Tables I and II.

A similar analysis can also be made for the orientations arising after two transformations of a body-centered-cubic structure. Again, 72 paths are possible, but some of these lead to identical final orientations. The full analysis shows that

TABLE I

PROBABILITY OF VARIOUS ORIENTATIONS AFTER TWO TRANSFORMATIONS OF A HEXAGONAL STRUCTURE

Category	No. of orientations	No. of paths leading to each	Total no. of paths	Remarks
1	1	6	6	Orientation of original hexagonal crystal
2	2	3	6	(0001) $\parallel^t$ original (0001), $\langle 11\bar{2}0 \rangle$ at 10°32
3	6	2	12	one $\langle 11\bar{2}0 \rangle$ $\parallel^t$ one original $\langle 11\bar{2}0 \rangle$, (0001) at 60° to original (0001)
4	36	1	36	(0001) at 60° to original (0001)
5	12	1	12	(0001) at 90° to original (0001)
Total	57		72	

TABLE II

ORIENTATION RELATIONS AFTER TWO TRANSFORMATIONS OF A HEXAGONAL STRUCTURE

Category in Table I	No. of orientations	Angle from original $\langle 11\bar{2}0 \rangle$ which became $\langle 111 \rangle$				Angle from original [0001]			
		New [0001]		New $\langle 11\bar{2}0 \rangle$		New [0001]		New $\langle 11\bar{2}0 \rangle$	
1	1	90°	0°	60°	60°	0°	90°	90°	90°
2	2	90°	70°32′	10°32′	49°28′	0°	90°	90°	90°
3	6	90°	0°	60°	60°	60°	90°	41°25′	41°25′
4	12	35°16′	70°32′	54°55′	76°2′	60°	35°16′	48°50′	80°54′
4	12	35°16′	70°32′	54°55′	76°2′	60°	90°	41°25′	41°25′
4	12	90°	70°32′	10°32′	49°28′	60°	35°16′	48°50′	80°54′
5	12	35°16′	70°32′	54°55′	76°2′	90°	35°16′	24°74′	84°74′

TABLE III

PROBABILITY OF VARIOUS ORIENTATIONS AFTER TWO TRANSFORMATIONS OF A BODY-CENTERED CUBIC STRUCTURE

Category	No. of orientations	No. of paths leading to each	Total no. of paths	Remarks
1	1	12	12	Orientation of original b.c.c. crystal
2	12	2	24	Original orientation rotated 60° about a $\langle 110 \rangle$ direction
3	4	3	12	Original orientation rotated 70°32′ about a $\langle 110 \rangle$ direction
4	12	1	12	Original orientation rotated 10°32′ about a $\langle 110 \rangle$ direction
5	12	1	12	Original orientation rotated 40°28′ about a $\langle 110 \rangle$ direction
Total	41		72	

41 orientations arise. The results are summarized in Table III.

Further transformations will give an even greater number of possible orientations, and exact analysis becomes lengthy; it is of interest to see, however, how some important orientations are retained. As we have already seen after two transformations of a hexagonal structure, 1/12, or 8.3 per cent, of the material returns to its original orientation. After another two, about 2.4 per cent is still in its original orientation. Similar results for other cases are shown in Table IV.

Arguments of this kind show that a specimen would, on these assumptions, rapidly lose any preferred orientation it might have.

TABLE IV

THE EFFECT OF DOUBLE TRANSFORMATION ON ORIENTATION OF HEXAGONAL STRUCTURE

Case considered	Percentage of crystals after two transformations	Percentage of crystals after four transformations
Crystals returning to original hexagonal orientation	8.3%	2.4%
Crystals having [0001] parallel original [0001]	16.7%	4.2%
Crystals having a $\langle 11\bar{2}0 \rangle$ parallel given original $\langle 11\bar{2}0 \rangle$	13.9%	3.7%

3. Prediction of the Effect of Transformation of Preferred Orientation

Using the results presented in the last section, it is possible to predict the change of preferred orientation occurring in a transformation. Here again the assumption is made that all possible transformation paths are equally likely.

(a) *Single transformation of a sample of body-centered-cubic lattice structure with a [111] fibre texture.*

This texture is the major texture of crystal bar zirconium in the β-range. The transformation of a single grain has been considered above. In Figure 2, W, X, Y and Z were the original $\langle 111 \rangle$ directions and A, B, C, D, E and F the resulting (0001) poles; W, X, Y, Z, A_1, A_2, . . . F_1, F_2 the resulting $\langle 11\bar{2}0 \rangle$ directions. To obtain the pole figure of a given hexagonal plane it is necessary to bring one of the $\langle 111 \rangle$ directions (say X) to the centre of a stereographic projection and then to draw small circles centered on X through all poles of the desired type of plane. The density of poles on each circle is proportional to the number of poles marked on the circle and inversely proportional to its radius. These operations are shown in Figure 4 for the (0001) poles and Figure 5 for the $\{11\bar{2}0\}$ poles. It is also of interest to see what directions now lie in or near the original [111] fibre direction, and these have been tabulated in Table V. This shows that if the assumptions are correct, one half of the grains would have a $\langle 11\bar{2}0 \rangle$ direction within 11 degrees of the fibre direction, and the other half would have [0001] at 35°16′.

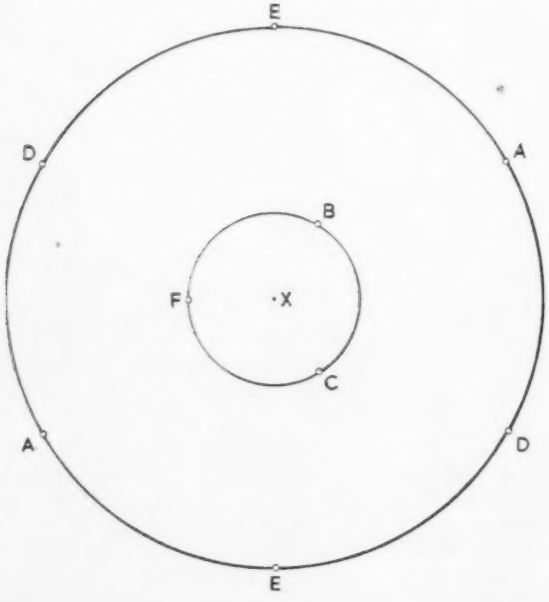

FIGURE 4. Predicted (0001) pole figure after one transformation of a specimen with a [111] fibre texture.

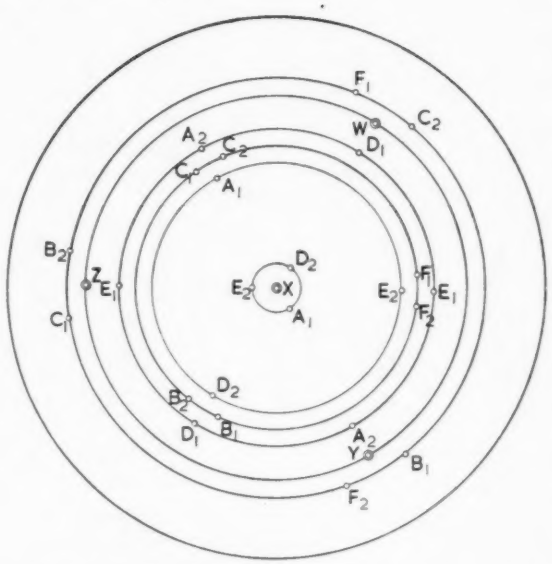

FIGURE 5. Predicted $\{11\bar{2}0\}$ pole figure after one transformation of a specimen with a [111] fibre texture.

TABLE V

TEXTURE AFTER ONE TRANSFORMATION OF A BODY-CENTERED CUBIC SPECIMEN WITH A [111] FIBRE TEXTURE

Axis nearest to original [111]	Angular deviation from original [111]	No. of orientations
$\langle 11\bar{2}0 \rangle$	0°	3
$\langle 11\bar{2}0 \rangle$	10°32′	3
[0001]	35°16′	6

(b) *Single transformation of a sample of hexagonal structure with a $[11\bar{2}0]$ fibre texture*

This texture is the one predicted for recrystallized zirconium wire (see sec. 5 below). Figure 6 shows a stereographic projection of the possible transformations centered on one of the original $\langle 11\bar{2}0 \rangle$ directions (6). The possible {111} poles arising from this hexagonal structure are shown; the horizontal line through the centre can be considered as the trace of the plane of Figure 1. The {111} pole figure is obtained by drawing circles through the {111} poles. The number of paths leading to various orientations near the original $[11\bar{2}0]$ fibre axis is shown in Table VI; this shows that two thirds of the grains would have a {111} pole within 11 degrees of the fibre axis and the other

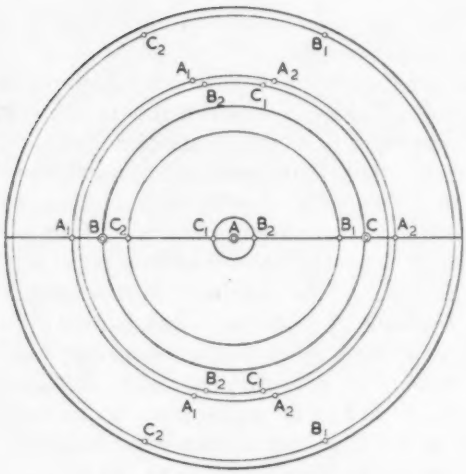

FIGURE 6. Predicted {111} pole figure after one transformation of a specimen with a [11$\bar{2}$0] fibre texture.

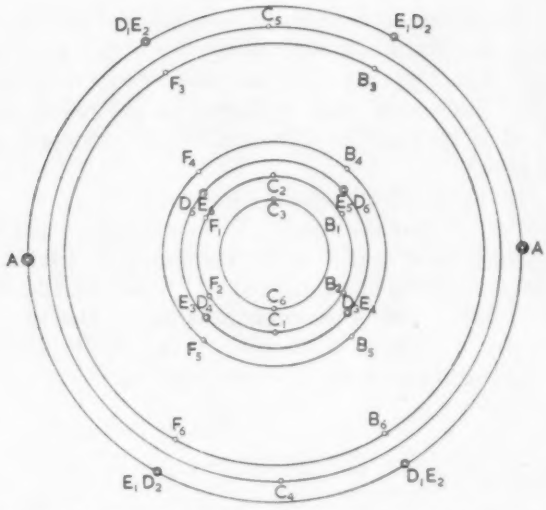

FIGURE 7. Predicted (0001) pole figure after two transformations of a specimen with a [11$\bar{2}$0] fibre texture.

third a ⟨110⟩ direction within 6 degrees of this direction.

TABLE VI

TEXTURE AFTER ONE TRANSFORMATION OF A HEXAGONAL SPECIMEN WITH A [11$\bar{2}$0] FIBRE TEXTURE

Axis nearest to original [11$\bar{2}$0]	Angular deviation	No. of orientations
⟨111⟩	0°	2
⟨111⟩	10°32′	2
⟨100⟩	5°16′	2

(c) *Double transformation of a sample of hexagonal structure with a [11$\bar{2}$0] fibre texture*

The double transformation of a single hexagonal crystal has been considered above, and the results are shown in Tables I and II, while the poles of the various possible (0001) planes have been plotted in Figure 3. To obtain the final (0001) pole figure it is necessary to rotate Figure 3 until a ⟨11$\bar{2}$0⟩ direction is at the centre. This gives the points of Figure 7, the pole *A* being six times as probable, and the poles marked with two circles twice as probable as the others. The pole figure is again given by small circles centered on *A* through all these points.

(d) *Double transformation of a sample of hexagonal structure with texture for cold-rolled and recrystallized zirconium*

This texture consists [7; 8] of two orientations, both having a ⟨11$\bar{2}$0⟩ direction in the rolling direction, and with basal planes inclined at about 30 to 40 degrees to the plane of the strip. The resulting (0001) pole figure can be found from Figure 3 by rotating the poles through the required number of degrees about an original {11$\bar{2}$0} pole, such as the one at the top of the figure. Figure 8 shows the resulting (0001) pole figure if the 30 degree angle is used. It is thus directly comparable with the pole figures found by McGeary and Lustman [7], and they have attempted to predict the pole figure by a similar calculation to the present one. They did not, however, include all the possible

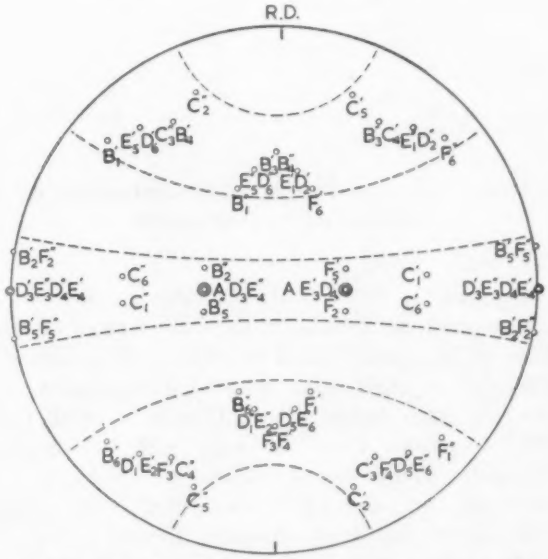

FIGURE 8. Predicted (0001) pole figure after two transformations of a specimen having the preferred orientation found for recrystallized rolled zirconium by McGeary and Lustman [7].

transformations from cubic to hexagonal and have only one third of the total number of points. The pole figure for $\{10\bar{1}0\}$ has also been predicted, using this time the 40–degree angle found by Keeler, Hibbard and Decker [8]. It is shown in Figure 9.

In Figure 8 all letters correspond to a pair of paths, so that each point has a number of paths leading to it that is twice the number of letters marked. The points marked '*A*' have the 12-fold multiplicity of *A* as well as that of the other letters. In Figure 9 all poles have a multiplicity equal to the number of circles marked.

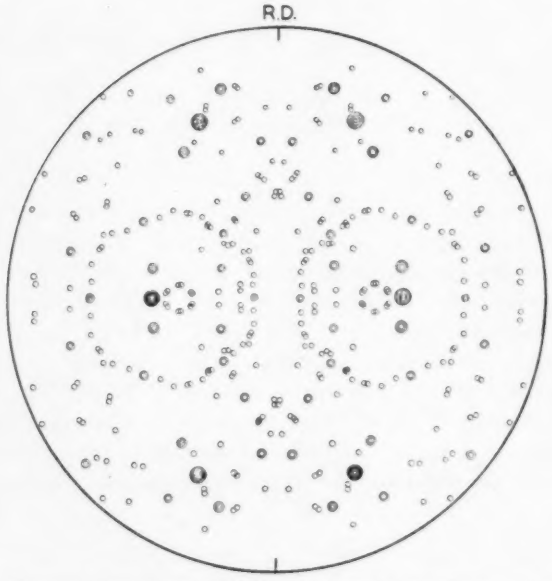

FIGURE 9. Predicted $\{10\bar{1}0\}$ pole figure after two transformations of a specimen having the preferred orientation found for recrystallized rolled zirconium by Keeler, Hibbard, and Decker [8].

4. Comparison of Predicted Orientations with Observed Orientations

(a) *Single crystals*

Burgers [1] deduced that a large single crystal of β-zirconium, grown by deposition from zirconium iodide vapour, transformed on cooling to many different crystals with various orientations, all obeying the simple orientation rule, and that crystals grown from the melt probably behave similarly. This seems extremely probable, as Newkirk and Geisler [4] have used the transformation of an ingot of titanium formed from the melt to show that titanium has the same orientation rule. In the subsequent discussion it seems reasonable to assume that the observations made on either zirconium or titanium are equally valid for the other metal.

The predictions made in Section 2 show that, if Burgers' rule alone determined the transformation, as it appears to do for the transformation of virgin β-material, then 41 different orientations would be possible for material starting from a given β-grain after two transformations; however, Burgers and Ploos van Amstel [10] observed that in polycrystalline zirconium, the original β-grain reappeared with the same orientation after a period in the α-phase, which implies that some further condition is operating, besides Burgers' rules, to determine the transformation of the α-zirconium formed from the β-phase. It is not known what happens to a single crystal of α-zirconium or titanium formed by recrystallisation in the α-range, when it is heated into the β-range and then recooled, though Burgers and Ploos van Amstel [9] observed that the martensitic α-structure formed from a β-crystal tended to reappear on subsequent heating and cooling, and Newkirk and Geisler [4] have observed the same phenomenon on an isolated α-crystal formed in the same way; it also returned to its original orientation even after many hours at 1000°C.

From this latter result it would appear improbable that any mechanism involving internal stresses can be responsible for the reappearance, and, while preferred nucleation at impurities is a possibility, it does not seem a likely explanation for the reappearance of the grains of the high temperature phase when these have been formed by grain growth. It seems more probable that the reversibility is due to the influence of lattice defects such as stacking faults or unusual dislocations arising from the transformation, which might be eliminated only by the particular reverse transformation which leads to the return of the original grain. Such faults might arise from normal dislocations present in the parent grain, which become dislocations with Burgers' vectors in directions quite different from the usual slip direction in the transformed structure. Such dislocations will only all return to normal, low energy, dislocations if the second transformation is the reverse of the forward one. To take a definite case, if the (0001) plane of an α-crystal becomes the (110) plane of the β-phase by a mechanism similar to that suggested by Burgers [1], then dislocations which had Burgers' vectors in the directions $[11\bar{2}0]$, $[1\bar{2}10]$ and $[\bar{2}110]$ will now have Burgers' vectors $[1\bar{1}1]$, $[\bar{1}11]$ and $[1\bar{1}0]$.

The first two are usual active dislocations for the body-centered-cubic structure, but the third is not, and can only return to a usual hexagonal dislocation if (110) is the {110} plane that becomes (0001). In this example, two final orientations are clearly possible, but they differ only by 10 degrees, and have the (0001) plane in common; they might easily not be recognized as distinct.

A final possible cause for the reappearance of the original orientation is that the mechanism by which the first transformation is produced could work in reverse to reinstate the original orientation (for example, if a dislocation mechanism were used, the dislocation would retrace its path) but it might not be possible to find so easily the necessary mechanism to produce other orientations.

The observation that the high temperature modification reappears could also be due to retained stress and grain-boundary energy, though it would seem desirable to have the same explanation for both phenomena.

(b) *Pole figure observations*

The effect of a double transformation on a pole figure has been observed on rolled zirconium and titanium annealed in the α-range. Using the observed pole figure for such material before transformation, the predicted pole figures for (0001) and $(10\bar{1}0)$ poles have been computed in section 3d. The resulting pole figures agree reasonably well with those found experimentally by McGeary and Lustman [7] for zirconium. This does not necessarily imply that all possible paths occur on two transformations of recrystallized α-zirconium, as the pole figures are not very different from the purely cyclic prediction plus a large background of random orientations. The same difficulty occurs even in the case of the more quantitative $(10\bar{1}0)$ pole figure of Keeler, Hibbard and Decker [8], as, although the pole figure predicted in Section 3d has only 1/12 the intensity in its major spots that the original structure had, the remainder is so scattered that it could easily be thought to be simply a large increase in background. Keeler, Hibbard and Decker state that the texture remains sharp after cycling, but this does not necessarily mean that the background had not apparently increased. The same argument applies to the textures observed on rolled titanium by McHargue and Hammond [10], which are similar to those of zirconium. It is thus impossible from this evidence alone to show whether the predictions using the transformation rule above are obeyed, though single-crystal observations on transformed unrecrystallized grains, if they are applicable to the recrystallized structure, imply that the process is purely cyclic, and that the transformation rules are obeyed together with extra conditions which determine the particular orientation developed in the second transformation.

5. Growth of Large Crystals in Crystal Bar

The growth of large β-zirconium crystals in crystal bar is not difficult to explain, since Burgers and Ploos van Amstel [9] have shown that grain growth is fairly rapid at the deposition temperature; the main difficulty is to account for the preferred orientation of the crystals. Burgers [1] deduced that the larger crystals have either a $\langle 111 \rangle$ or, more rarely, a $\langle 100 \rangle$ axis lying within 5 degrees of the rod axis. The corresponding external forms are six {110} faces at 60 degrees round the rod axis and four {110} at 90 degrees. These will be referred to as "hexagonal" and "square" crystals respectively. In many rods, over 75 per cent of the length is in the "hexagonal" crystals.

The first mechanism that we shall consider for developing such a structure is that the crystal orientation arises from the orientation of crystals in the wire on which the zirconium is deposited. This orientation has not been directly determined in zirconium, but it can be deduced from the preferred orientations found in α-zirconium using Burgers' transformation rules. Both McGeary and Lustman [7], and Keeler, Hibbard and Decker [8] found $[10\bar{1}0]$ parallel to the rolling direction in zirconium strip, in general agreement with the observation of Burgers, Fast and Jacobs [11] that the ideal fibre texture of zirconium wire is $[10\bar{1}0]$. The change of the rolling texture on annealing can be regarded as a 30-degree rotation about the [0001] axes of the grains [7; 8]. This would give a $[11\bar{2}0]$ fibre texture in a wire heated to the top of the α-range, and as this is the fibre texture found in titanium [10], which has a similar rolling structure, it is reasonable to assume it for zirconium. In section 3b the texture of such a wire after transformation has been deduced; two thirds of the crystals have $\langle 111 \rangle$ directions within 10 degrees of the rod axis, and the remainder have a $\langle 100 \rangle$ direction within 5 degrees. Thus, if these orientations were maintained during growth, the observed orientations would be obtained and their ratio would be of the right order of magnitude.

It is claimed that crystal bar grown on a tungsten wire has the same appearance as that grown on

zirconium wire. Since the wire texture for tungsten is [110], while the zirconium crystals grown onto it have a [111] fibre texture, it is necessary to assume that the rule of epitaxy is [110] $\|^l$ [111]. This should be checked experimentally; the lattice parameters of the two metals differ by 15 per cent so that parallel crystal orientations are not to be expected. It is known that regular epitaxy occurs since single crystals of zirconium have been grown on single crystals of tungsten—a fact that in itself shows that the underlying orientation affects the resulting structure.

Another possible reason for the large proportion of crystals with a ⟨111⟩ axis parallel to the rod axis is the low surface energy of these crystals. Whenever a crystal has grown to such a size that it occupies the complete cross section of the bar, it can develop faces by surface migration of atoms. {110} faces, being close-packed, have low energy and tend to develop, and, for a given volume of crystal in a rod approximately circular in cross section, the least surface area of {110} faces will be formed in a crystal with a [111] direction parallel to the axis, as this can give the "hexagonal" zone of {110} faces. Such a crystal thus has lower energy than one in any other orientation, and will thus tend to grow at the expense of less favourably oriented crystals.

A third possible explanation has been suggested by Jones [12]. This depends on the most favourable growth direction in a crystal being deposited from the vapour. If it be assumed that ⟨111⟩ axes are the directions of fastest growth (as seems likely, both because they are the most densely packed directions, and because they are perpendicular to ⟨110⟩ directions, which are normal to the planes that develop, and hence probably the directions of minimum growth), then crystals with {110} planes parallel to the rod can grow rapidly in the rod direction, particularly if they have a ⟨111⟩ axis parallel to the rod axis. Such crystals will thus tend to encroach on other crystals.

The following experiments are suggested to choose between the above three theories. If a cast wire of zirconium, or any wire free from [11$\bar{2}$0] fibre texture, is used to grow iodide zirconium, then crystal bar will not develop *if* and only if the first theory is correct. The other suggestions are harder to verify directly, but if a rod of random orientation is heated to about 1200°C under conditions similar to those occurring during the growth of crystal bar, but modified to prevent the rapid deposition of zirconium, then if the preferred orientation develops, it must do so by preferential grain growth, for which the second theory alone can account. If this experiment does not tend to develop the preferred orientation, then it must develop during the growth process and this could be due to the third mechanism.

The first theory could also be checked by verifying that crystal bar grown on tungsten wire has the same preferred orientation and by determining the law of epitaxy at 1200°C.

It is of course possible that all three mechanisms are active, the first providing crystals of the two orientations, while the second and third account for the increase in proportion of "hexagonal" to "square" crystals.

If either the first or the second mechanism occurs—that is to say, large grains arise from grain growth at the deposition temperature—it follows that to produce bar free from large grains the deposition temperature should be kept as low as possible. Burgers and Ploos van Amstel [10] have shown that occasional cooling into the α-range during deposition is more likely to increase the β-grain size than to reduce it, as such treatment stimulates β-grain growth.

6. Conclusions

An analysis of the number of possible orientations which can arise after two transformations according to Burgers rules has shown that large numbers of orientations are possible. Experimental evidence implies that, although after one transformation any orientation consistent with the transformation rules can arise, the second transformation returns the structure to its original orientation. Thus only one orientation occurs out of 41 geometrically possible for an β–α–β-transformation and, for the case of an α-grain formed from the β-phase by transformation, only one (the original) occurs out of 57 geometrically possible for an α–β–α-transformation. The various factors that could be responsible for this behaviour have been discussed. Two that have hitherto been given little attention are that irregularities in the original lattice can only be restored without an increase in energy if the original orientation returns, and that the transformation mechanism occurs in such a way that a source for the reverse transformation is easily found, whereas that for any other is not. The development of the texture and faces of crystal bar zirconium has also been discussed, and three possible mechanisms suggested; these depend on crystal growth on the substrate texture, surface

energy considerations, and the preferred growth direction, respectively.

Acknowledgements

The authors wish to thank Dr. W. M. Lomer for valuable discussion, Dr. H. M. Finniston for the original suggestion which led to this work and his subsequent advice, and the Director, A.E.R.E., for permission to publish this paper.

References

1. Burgers, W. G. Physica **1** (1934) 561.
2. Barrett, C. S. Transformations in pure metals. Symposium (1948) held at Cornell University on Phase Transformations in Solids (New York, John Wiley, 1951) p. 343.
3. McHargue, C. J. Acta Cryst. **6** (1953) 529.
4. Newkirk, J. B. and Geisler, A. H. Acta Met. **1** (1953) 372.
5. Lipson, H. and Stokes, A. R. Nature **148** (1941) 437.
6. Duwez, P. J. App. Phys. **22** (1951) 1174.
7. McGeary, R. K. and Lustman, B. Trans. A.I.M.E. **191** (1951) 994.
8. Keeler, J. H., Hibbard, W. R., Jr. and Decker, B. F. Trans. A.I.M.E. **197** (1953) 932.
9. Burgers, W. G. and Ploos van Amstel, J. J. A. Physica **5** (1938) 305.
10. McHargue, C. J. and Hammond, J. P. Trans. A.I.M.E. **197** (1953) 57.
11. Burgers, W. G., Fast, J. D. and Jacobs, F. M. Z. Metallkunde **29** (1938) 410.
12. Jones, E. R. W. Private communication.

SOME OBSERVATIONS ON THE ANELASTIC PROPERTIES OF COPPER AND TIN BRONZES*

K. J. MARSH†

Investigations have been made into the low-frequency damping of copper and certain tin bronzes, using the method suggested by Kê. Damping curves were obtained at two frequencies, and the various features of these—peak damping, peak temperature and activation energy—were compared with the results of impact-tensile tests on the same materials; but no correlation was found. A simple model is suggested to account for the damping effects in terms of the properties of the grains. The damping at amplitudes higher than those used by Kê was examined and curves showing the variation of damping with amplitude were obtained. Some measurements were made of the torsional creep of copper at low amplitudes and at various temperatures, but the results were not consistent and did not fit the equations proposed by Kê. A reduction in the torsional creep and the damping was found in materials of large grain size.

QUELQUES OBSERVATIONS SUR LES PROPRIÉTÉS ANÉLASTIQUES DU CUIVRE ET DES BRONZES D'ÉTAIN

On a investigué l'amortissement du cuivre et de certains bronzes d'étain, en employant la méthode suggérée par Kê. Des courbes d'amortissement furent obtenues pour deux fréquences; diverses caractéristiques de ces courbes, à savoir: les maxima d'amortissement, les températures correspondantes à ces maxima et les énergies d'activation, ont été comparées avec les résultats d'essais de traction par choc sur les mêmes matériaux, mais aucune corrélation n'a été trouvée. On suggère un simple modèle pour expliquer l'amortissement en termes des propriétés des grains. On a examiné l'amortissement aux amplitudes supérieures à celles qu'a utilisées Kê, ce qui a permis d'obtenir des courbes donnant la variation de l'amortissement en fonction de l'amplitude. On a mesuré, dans quelques cas, le fluage en torsion, du cuivre, à des basses amplitudes et à diverses températures, mais les résultats n'étaient pas compatibles avec les équations proposées par Kê. Dans des matériaux à gros grains on a constaté une réduction du fluage en torsion et de l'amortissement.

EINIGE BEOBACHTUNGEN DER ANELASTISCHEN EIGENSCHAFTEN VON KUPFER UND ZINNBRONZEN

Mit Hilfe der von Kê vorgeschlagenen Methode wurde die Niederfrequenzdämpfung von Kupfer und von gewissen Zinnbronzen untersucht. Mit zwei verschiedenen Frequenzen wurden Dämpfungskurven aufgenommen, und die verschiedenen Charakteristika dieser Kurven—Maximaldämpfung, Temperatur am Maximum und Aktivierungsenergie—wurden mit den Resultaten von Schlag-Zugversuchen am gleichen Material verglichen. Es konnten keine Beziehungen zwischen den beiden Versuchsreihen gefunden werden. Es wird ein einfaches Modell vorgeschlagen, das die Dämpfungseffekte auf Grund der Eigenschaften der Kristallite erklärt. Es wurde die Dämpfung bei Amplituden, die grösser als die von Kê benutzten waren, untersucht, und Kurven der Änderung der Dämpfung bei veränderter Amplitude wurden aufgenommen. Es wurden einige Torsionsmessungen des Kriechens von Kupfer mit kleinen Amplituden und bei verschiedenen Temperaturen durchgeführt; die Resultate waren jedoch widerspruchsvoll und genügten nicht den von Kê vorgeschlagenen Gleichungen. Für Materialien mit grosser Korngrösse wurde eine Verminderung des Torsionskriechens und der Dämpfung gefunden.

I. Introduction

The plastic properties of polycrystalline materials are influenced both by the intrinsic properties of the single crystals forming the grains and by the restrictions adjacent grains impose on one another. While the deformation of single crystals has been studied extensively, and a fairly complete understanding is now possible of the processes which contribute to it, no such quantitative appreciation of the mechanisms by which polycrystalline aggregates deform is yet possible. Observations of the progress of deformation under creep conditions show that adjacent grains may undergo relative movement without great change of shape or orientation; the motion takes place along the grain boundaries and occurs at low loads, suggesting that the boundaries themselves behave as a viscous liquid. This is not surprising in view of the comparatively disordered atomic arrangement which must in general be present when the regular lattices of grains of differing orientation meet. In such disordered regions, moreover, normal solubility relationships need not apply and they may therefore offer favoured locations for stranger atoms; these may well influence markedly the effective "viscosity" of the layer.

Kê [1] has recently attempted to give a quantitative significance to the effective viscosity of grain boundaries. He took as his simplified model a solid composed of elastic grains cemented by a viscous fluid. When stress is applied to such a hypothetical material, it is relaxed locally by shear along favourably oriented grain boundaries.

*Received December 10, 1953.

†Formerly at the British Non-Ferrous Metals Research Association; now at Research Station, Anglo-Iranian Oil Company, Sunbury-on-Thames, England.

Flow occurs until opposing elastic stresses are built up, for example, at grain corners which oppose the applied stress. Kê's predictions on the basis of this model were borne out to his satisfaction by experiments on the damping capacity, creep and creep recovery of several metals, notably aluminium.

Investigations of the type made by Kê in his experiments offered the possibility of confirming a hypothesis proposed by Eborall which formed the basis of a method for improving the hot working properties of certain tin bronzes [2], and of obtaining information on the general properties of grain boundaries. In a series of impact-tensile tests carried out in the Association's laboratories on copper and tin bronzes containing up to 9 per cent tin it was found that, at elevated temperatures, the addition of tin caused a reduction in the energy to fracture and in the total elongation; the fracture tended to be intercrystalline at the highest temperatures, particularly as the tin content was increased. The temperature at which embrittlement set in was found to depend on the rate of straining, and a comparison of the results of the impact-tensile tests with those of slow tensile tests gave an activation energy of roughly 50,000 cal/gm. Eborall suggested that the reduced impact-tensile strength of the bronzes was due to weakening of the grain boundaries by the preferential segregation of tin to grain boundary regions. According to his view the grain boundaries should be strengthened by elements of high melting point whose atomic diameter differed considerably from that of copper. Further tests showed that small additions of a number of such elements including zirconium, titanium and beryllium effected a considerable improvement in the mechanical properties. It was also found from creep and stress-rupture tests that the addition of zirconium caused a slight improvement in the creep resistance of a 5 per cent tin bronze; while the elongation at fracture was considerably increased.

In order to test the theory, an independent method of investigating the properties of the grain boundaries was required and the methods used by Kê offered an indirect way of doing so. At the same time it would be possible to make a critical examination of the validity of Kê's views.

The present report gives a description of the apparatus and of a series of investigations on the damping properties, at low amplitudes, of some of the materials used in the mechanical tests. It also describes observations of the effect of amplitude of swing on the damping characteristics and gives the results of a series of experiments on the torsional creep of copper under low stress.

II. Apparatus and Methods

(*i*) *Description of Apparatus*

A diagram of the apparatus used is given in Figure 1.

(*a*) *Furnace.* The furnace consisted of a steel tube 1.5 in. in bore with five separate windings of "Nichrome" wire spaced evenly along its length. These five heaters were regulated independently by rheostats and it was possible to control the temperature along the central part of the tube to be uniform within ±1.5°C. A differential expansion-

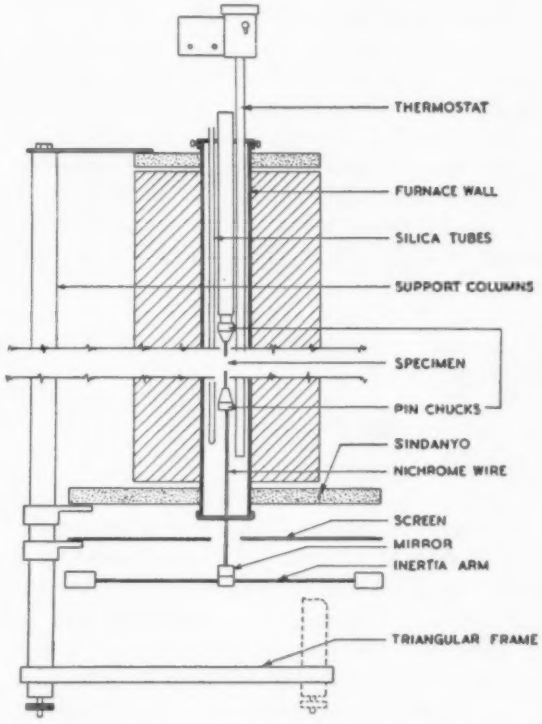

FIGURE 1. Furnace and torsion pendulum for damping capacity measurements.

type thermostat was used to provide temperature control to within ±1°C. Two silica tubes were inserted through holes in the top cap of the furnace. The first contained three thermocouples arranged at the top, middle and bottom of the specimen length; while the second was used for introducing an auxiliary specimen having the same previous history as the test specimen. This could be withdrawn as required for X-ray or metallographic examination.

(*b*) *Specimen assembly.* The material to be tested was in the form of a wire 30 cm in length and about 0.075 cm in diameter. This was suspended in the furnace with its upper end firmly gripped by a pin chuck welded to a steel tube rigidly fixed to the top cap of the furnace. The lower end was similarly attached to a "Nichrome" wire protruding from the bottom of the furnace. In the later experiments the grips were changed to flat steel plates with V-grooves.

For the damping experiments the specimen was made to oscillate torsionally by means of a horizontal swing bar attached to the "Nichrome" wire. The frequency of oscillation could be altered by changing the weights on the bar. A small mirror was attached to the assembly and the amplitude of swing observed with a lamp and scale.

To carry out torsional creep experiments, a small coil was attached to the protruding "Nichrome" wire between the poles of a permanent magnet so that it acted like a moving coil galvanometer with the test specimen as the suspension. To apply a load to the specimen, a constant current was passed through the coil and the strain was measured with a lamp and scale. The deflection with a hard-drawn specimen was found to be proportional to the current up to amplitudes considerably greater than those used in the experiments.

(*ii*) *Experimental Procedure*

For each experiment a 30 cm length of the material under test was mounted in the apparatus and, before heating, the furnace was flushed for an hour with a mixture of white-spot nitrogen and hydrogen which had been passed through alkaline pyrogallol and dried. The specimen was then annealed for the required time with a gas flow through the furnace of about 0.4 litre/min. A short length of the specimen material was placed in one of the silica tubes and was heated at the same time as the test specimen. This could be removed after the anneal for comparison with the test length at the end of the experiment. The furnace was then held at various temperatures for damping measurements to be made.

For the experiments at strains of about 10^{-5} (i.e., those used by Kê) the deflections were observed visually. The logarithmic decrement was obtained either from the deflections on one side of the zero or by noting the time for the amplitude to fall a fixed amount and measuring the frequency. In the experiments at larger amplitudes the deflections were recorded photographically with a drum-recording camera. Experiments were usually carried out at two frequencies so that the activation energy could be calculated, as described below.

Before annealing the specimen for creep tests, the current in the coil was adjusted to give a fixed deflection of the assembly with the hard-drawn wire. This was found to be a more satisfactory method of obtaining a constant load than that of using a fixed current in the coil since it was not possible to obtain a sufficiently exact setting of the coil in the magnet to give a reproducible load in different tests. The creep was usually measured for periods of up to two hours; this was observed photographically for the first three minutes and then visually. In all the experiments described, the maximum surface strain was of the order of 10^{-5}. A creep recovery curve was obtained by noting the deflections after the stress had been released.

III. Investigations of Damping at Low Amplitudes

(*i*) *Initial Tests on Reproducibility of Results*

The aim of the experiments was to measure the loss of energy in the torsional vibrations of the wire, so it was essential that energy losses in the apparatus itself should be reduced to a minimum. Such losses are most likely to occur in those parts of the apparatus connected with gripping the specimen, due to the relative movement of neighbouring parts under severe localised stresses. To assess the unwanted loss effects, a specimen of fully-softened copper was mounted in the furnace and the damping measured, at room temperature when the bolts fixing the top pin chuck to the top cap, and those fixing the top cap to the furnace wall, were successively loosened. No significant difference in damping was found. To test the efficacy of the pin chucks, measurements of damping were made at room temperature after a specimen had been removed from the furnace and replaced four times. The values were in good agreement with each other and with a fifth value when the pin chucks had been deliberately loosened. It did not appear therefore that the mounting of the specimen was critical.

(*ii*) *Comparison with Published Results*

Three curves were obtained of the variation with temperature of damping and rigidity, using copper, for comparison with a similar curve published by Kê [3]. The material used was a specially refined high-purity copper supplied by Johnson Matthey and Co. having the following

analysis: 0.0002% Fe, < .0003% Pb, 0.0001% Ni, <0.001% Ag. This was received as 5/16 in. rod and was drawn down to wire 0.05 cm or 0.075 cm diameter with intermediate bright anneals. In each experiment a new wire was mounted in the furnace and annealed for 4½ hours at 450°C. After annealing, the furnace was cooled to room temperature and observations made by heating to the required series of temperatures in the range 20°C–450°C. No significant difference in grain size was observed between test pieces withdrawn after the anneal and at the end of the experiment. For the first two experiments, wire of 0.050 cm diameter was used and in the third experiment the diameter was 0.075 cm.

The three curves were similar and a typical curve is given in Figure 2. In this it can be seen

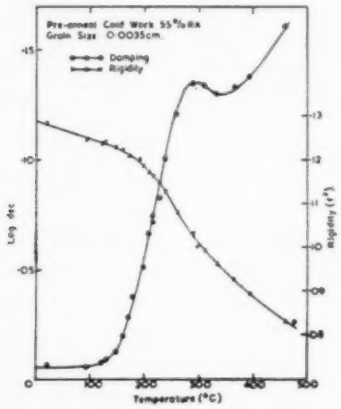

FIGURE 2. Variation of damping and rigidity with temperature: copper.

that the logarithmic decrement rises to a maximum value of 0.14 at about 290°C. After a slight decrease above this temperature the damping increases again at higher temperatures. The rigidity, which is plotted as the square of the oscillation frequency, decreases linearly with temperature with a more rapid fall near the temperature of the damping peak. These curves show the same characteristics as the curve for copper published by Kê and the peak value of damping is similar.

The temperature at which the peak occurs differs from that in the published curve, but according to Kê it can be related to it through the following parameter, which is constant for a given material:

$$f \cdot d \cdot \exp(H/RT)$$

In this f = frequency, d = grain size, H is an activation energy, R the gas constant = 1.99 cal/mol/°C, T = absolute temperature. In Kê's experiments $d = 0.03$ cm, $f = 1$ cps. and the peak occurred at 350°C. In the investigations reported $d = 0.0035$ cm and $f = 0.36$ cps. Taking $H = 35{,}000$ on the basis of Kê's work, it is calculated that under these conditions the peak should occur at 290°C. This is identical with the temperature observed.

(iii) Experiments with Material of Larger Grain Size

According to Kê's analysis, a value for the activation energy of the process causing the damping may be obtained from tests on materials of differing grain size. Some further experiments were therefore carried out with copper of larger grain size.

In the first experiment, copper wire of 0.05 cm diameter was used. This was cold-stretched to 4 per cent RA after annealing and was then annealed in the apparatus for 4 hours at 450°C, giving a grain size of 0.024 cm; eight times that of the previous specimen. The curves of damping and rigidity against temperature are shown in Figure 3. It can be seen that the damping peak was

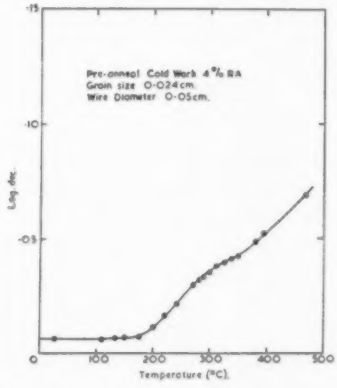

FIGURE 3. Variation of damping with temperature: copper.

considerably reduced in amplitude and was barely resolved, so that it was not possible to determine its temperature with accuracy. On subsequent examination, several grains were found to extend right across the specimen. In experiments on aluminium Kê [4] found a similar reduction in damping when the grain size was comparable with the wire diameter.

In a second experiment a specimen of larger diameter was used. This was given a reduction of 1.8 per cent after annealing and had a diameter of 0.075 cm. The grain size at the end of the experiment was 0.012 cm. Initially the specimen was

annealed for 14 hours at 450°C and the damping at this temperature was measured after 8, 10 and 14 hours. During this time its value decreased continually. The temperature was reduced to 300°C, where the peak was expected, to find out whether the damping was also falling at this temperature. After 7 hours at 300°C no change in damping had occurred. Starting from room temperature, a curve was plotted up to about 350°C, above which it became obvious that the damping was still falling. During a further 6 hours at 450°C the damping at this temperature decreased continually.

The fall in damping capacity as high temperature annealing is prolonged throws doubt on the precision with which the height of the damping peak and the temperature at which it occurs can be estimated. The whole damping curve clearly consists of two components; one, the peak associated by Kê with viscous movement at the grain boundaries, and the other, due to some cause not yet understood, the form of which did not become constant in Kê's experiments until after long annealing. This "background damping" was shown by Kê [5] to depend on the previous deformation and thermal history of the material.

(iv) Experiments at Two Frequencies: Copper

An alternative method leading to values for the activation energy, which was used by Kê, is to carry out identical damping experiments at two frequencies. This has the merit that the same specimen can be examined at each frequency so that the effects of differences in previous history between specimens of different grain size are eliminated. From Kê's views it is expected that the effect of increasing the frequency should be to shift the damping curve to higher temperatures without altering its form. The activation energy H can be calculated from the following equation

$$H = \frac{R \log_e (f_1/f_2)}{1/T_2 - 1/T_1}$$

where R = the gas constant, f_1 and f_2 the frequencies of test, and $(1/T_2 - 1/T_1)$ the shift in the damping curve, T being measured on the absolute scale.

A specimen of copper wire as used in the previous experiments was examined at two frequencies. Initially annealed material was cold drawn to 32 per cent RA and was annealed for 9½ hours at 580°C. It had been intended to continue annealing until the damping at this temperature reached a constant value but the material was so soft that there was a continuous shift of zero, and accurate measurements were not possible. The curves of damping against frequency are shown in Figure 4. The expected temperature shift with frequency occurs and the two curves are similar in shape. The grain size of the material measured subsquently was 0.0090 cm. The specimen was examined at frequencies of 0.305 cps. and 1.29

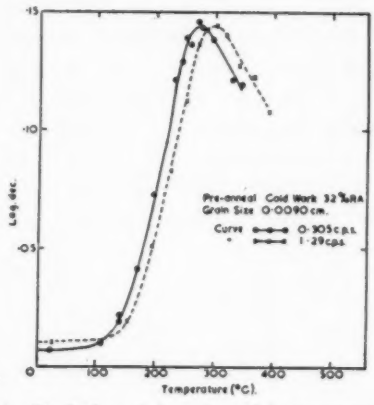

FIGURE 4. Variation of damping with temperature at two frequencies: copper.

cps. These frequencies and those quoted in subsequent sections refer to measurements at room temperature; although the frequency varied with temperature, the ratio of the frequencies at similar points on each pair of damping curves was always found to be roughly constant.

With the values obtained from these curves the activation energy was calculated to be

$$H = 37{,}000 \text{ cal/mol}$$

The result is in reasonable agreement with Kê's corresponding figure of 35,000 cal/mol.

(v) Experiments with Plain Tin Bronzes

With Kê's observations confirmed and a reproducible technique established, the experiments were extended to include some of the tin bronzes used in the impact-tensile tests referred to in the Introduction. The materials used were from the batch of high-purity vacuum-cast copper-tin alloys whose impact-tensile properties were determined in these tests and these had the nominal compositions:

91/9 Cu/Sn
94/6 Cu/Sn
97/3 Cu/Sn

Before carrying out damping capacity measure-

ments, each material was annealed until the damping at 600°C, the annealing temperature, became constant. The treatment required varied slightly with the material. The 9 per cent alloy was first annealed for 7 hours at 500°C when portions of the auxiliary specimen were examined by the X-ray back-reflection method. The material was not fully recrystallized and the annealing temperature was raised to 600°C. After a further 6 hours, well-defined spots were obtained on the X-ray photograph; the damping had then become fairly constant. Succeeding specimens were found to require an anneal of about 13 hours at 600°C for the damping to reach a stable value.

Each material was examined at frequencies of about 0.4 and 1.8 cps. and data obtained on the variation of damping and rigidity with temperature. The damping curves for these three alloys showed a marked difference from that of pure copper but no obvious differences between each other. Typical curves are those for the 6 per cent tin bronze, given in Figure 5, in which the logarithmic decre-

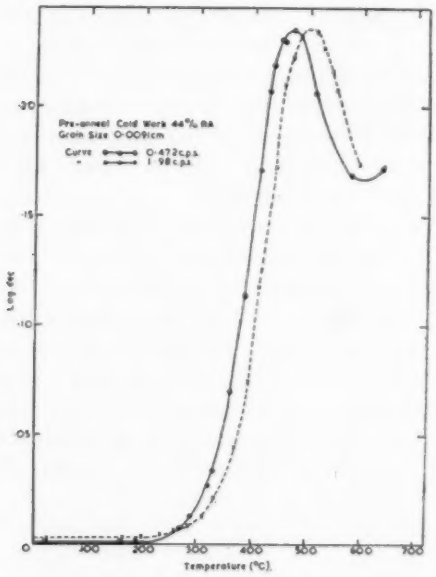

FIGURE 5. Variation of damping with temperature at two frequencies: 6 per cent tin bronze.

ment has a peak value of 0.24 at 465°C and 500°C, in contrast with the value of 0.14 at 270°C and 290°C obtained with copper. From each pair of curves an activation energy was calculated. Details of the thermal treatment of the alloys are given in Table I while the experimental results are summarised in Table II.

TABLE I

FINAL PREPARATION OF MATERIALS

Material	Copper	9% Sn bronze	6% Sn bronze	3% Sn bronze	3% Sn bronze +Be	9% Sn bronze +Ti
Final cold work (% RA)	32	47	44	44	69	53
Final anneal	9½ hr, 580°C	7 hr, 500°C 6 hr, 600°C	13 hr, 600°C	12½ hr, 600°C	16 hr, 650°C	16½ hr, 600°C 16½ hr, 600°C
Final grain size (cm)	0.0090	0.0071	0.0091	0.0052	0.016	0.0035

TABLE II

SUMMARY OF DAMPING RESULTS

Material	Copper	9% Sn bronze	6% Sn bronze	3% Sn bronze	3% Sn bronze Be	9% Sn bronze Ti
f_1 cps	1.29	1.81	1.98	1.79	2.23	1.57
f_2 cps	0.305	0.434	0.472	0.441	0.275	0.211
log. dec. 1	0.15	0.24	0.24	0.22	0.14	0.12
log. dec. 2	0.15	0.24	0.24	0.22	0.15	0.10 0.11
T_1°C	293	490	500	498	509	475 462
T_2°C	270	445	465	483	445	425
H cal/ mol	37,000	41,000	49,000	36,000	35,000	—

f = frequency. T = temperature of peak.

(vi) *The Damping of Tin Bronzes with Small Additions*

Two alloys which had shown marked reduction of hot brittleness in comparison with the plain tin bronzes were selected from the same melts as were used for the mechanical tests; the first was a 3 per cent tin bronze with 0.05 per cent beryllium and the second a 9 per cent tin bronze with 0.1 per cent titanium.

The damping curves obtained for these two materials are given in Figures 6 and 7 respectively. With the beryllium-containing alloy, the peak damping occurs at approximately the same tem-

peratures as in the plain tin bronzes as may be seen by comparing with Figure 5, but the value of the damping 0.14, is lower. The temperatures at which the low-frequency peaks occur in Figures 5 and 6 cannot be compared directly since different frequencies were used.

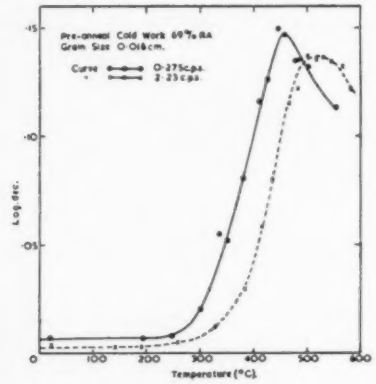

FIGURE 6. Variation of damping with temperature at two frequencies: 3 per cent tin bronze containing 0.05 per cent beryllium.

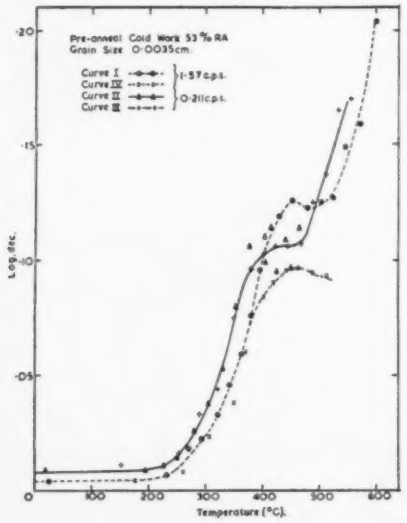

FIGURE 7. Variation of damping with temperature at two frequencies: 9 per cent tin bronze containing 0.1 per cent titanium.

Results with the titanium-bearing alloy were irregular. After annealing for 16½ hours at 600°C, the damping was measured at a frequency of 1.57 cps. as the furnace was cooled to room temperature and curve I of Figure 7 was obtained. This shows a peak with a value of 0.12 at 470°C. When the furnace was heated again and the damping measured at a frequency of 0.21 cps. the values of damping fell on a smooth curve to 400°C but above that temperature they became erratic (curve II). In order to examine the material under similar conditions to those of the high-frequency test, the specimen was further annealed for 16½ hours at 600°C. When the furnace was again cooled, a smooth curve was obtained for the damping at the lower frequency and this had a peak value of 0.10 at about 425°C (curve III). Below 400°C the points were coincident with those obtained before the second anneal. On repeating the higher-frequency experiment by heating from room temperature, the damping values were found to coincide with the first set up to 400°C but above that temperature they formed a peak with a value of 0.099 (curve IV) considerably below that of the first peak. The results of these experiments are included in Table II.

(*vii*) *Discussion*

According to Kê, the damping or energy dissipation measured in these experiments is due to stress relaxation by a relative movement of elastic grains in which the grain boundaries behave in a viscous manner. The energy lost by the sliding of adjacent grains over each other depends solely on the product of the applied force and the distance moved; at low temperatures, when the grain boundaries are highly viscous, little movement takes place and the energy loss is negligible; at elevated temperatures the viscosity is low so that the maximum allowable movement takes place when only a small stress is applied and the dissipation of energy is again low. Between these two extremes, however, where both factors of the product are significant, there is a greater dissipation of energy resulting in a damping peak at some temperature. Kê shows that the absolute temperature T at which the peak occurs depends on the grain size d and the frequency f through the parameter.

$$f \cdot d \cdot \exp(H/RT),$$

where H is an activation energy and R the gas constant.

It is of interest to examine how this expression may be derived and to see further what significance attaches to the magnitude of the damping peak and the temperature at which it occurs.

Consider, for example, a grain boundary film of viscosity η between two grains one of which can have an unlimited movement over the other in the plane of the boundary.

Let z be the thickness of the boundary film.

If a stress $s = s_0 \sin \omega t \cdot$ is applied, the velocity V of the movable grain is found from the usual equation:

$$s_0 \sin \omega t \cdot = \eta \cdot V/z$$

If y is the relative displacement of one grain from a standard position this can be written as

$$(1) \qquad s_0 \sin \omega t \cdot = \eta \cdot 1/z \cdot \frac{dy}{dt}$$

Solving this differential equation gives

$$(2) \qquad y = \frac{s_0 z}{\eta \omega} \cos \omega t.$$

The energy loss per unit area for a small movement dy is given by the product $s \cdot dy$. Substituting from (1) and (2) and integrating over a cycle we obtain the energy loss per unit area as

$$(3) \qquad \Delta E = \frac{\pi s_0^2 z}{\eta \omega}$$

In this equation the energy loss increases as the frequency is decreased or as the temperature is increased, since η is a function of temperature. It therefore represents the equation for the low-temperature portion of an ideal damping curve.

Equation (2) shows that the movement can become unlimited as η is decreased but in practice the movement of grains over each other is severely restricted by the presence of neighbouring grains. We have to limit the movement, therefore, to some maximum value $\pm Y$. Thus, above a certain temperature, movement occurs during only part of the time when the force is acting, and once the movement is restricted it can be shown that the energy decreases again.

Hence the equations give rise to a damping peak at a particular temperature. The maximum energy loss occurs when the grain is just moving within the restricted zone, i.e., when $y = Y$. By taking the maximum value of $\cos t \cdot$ in (2) we can write

$$(4) \qquad Y = \frac{s_0 z}{\eta \omega}$$

The next step is to determine a value for the maximum slip distance Y, and there are several possible ways of representing this. Kê [4] suggests that the slip distance is dependent on the grain size. If it depended only on this we could write

$$(5) \qquad Y = 1/k \cdot d$$

Substituting this in equation (4) gives the relation

$$(6) \qquad \eta \omega d = k s_0 z$$

We can put $\eta = \eta_0 \exp(H/RT)$ and $\omega = 2\pi f$ and we obtain a parameter relating frequency, grain size and peak temperature,

$$(7) \qquad f \cdot d \cdot \exp(H/RT) = s_0. \text{ (const.)}$$

This differs from Kê's parameter in that the peak temperature depends on the stress; but the experimental evidence described in the next section suggests that the peak temperature is independent of the stress level. The discrepancy probably lies in the assumption that the slip is proportional to grain size only when it is evident that slip along any boundary must involve elastic or plastic deformation of the grains, and this must depend on the applied stress.

The assumptions may be extended therefore by including the stress as a factor affecting slip distance, so that we can write,

$$(8) \qquad Y = c \cdot s_0 \cdot d$$

When this is substituted in equation (4) we obtain Kê's parameter

$$(9) \qquad f \cdot d \cdot \exp(H/RT) = \text{const.}$$

Both these assumptions, however, are based on the idealised concept of grains with smooth boundaries, but the grain boundaries met in practice are probably far from smooth on a submicroscopic scale; and the irregularities must play a far larger part in hindering the relative movement of the grains than the grain corners themselves. A single projection in two otherwise plane and unimpeded surfaces can prevent all movement until the grains are deformed elastically or otherwise by the applied stress; and any movement which occurs will depend on the amount of deformation and, hence on the stress. The number and size of such projections in a given length of grain boundary would be independent of grain size and would be related to the previous history of the specimen. A third possibility, therefore, for representing the slip distance is to make it proportional only to the stress so that

$$(10) \qquad Y = m s_0$$

where m is a constant related to the elastic modulus and grain boundary roughness.

Substituting this in equation (4) gives

$$(11) \qquad \eta \omega m = z,$$

which leads to a new parameter

(12) $m \cdot f \cdot \exp(H/RT) = \text{const.}$

This contains m instead of the grain-size factor in Kê's parameter and means that a change in peak temperature after a heat treatment would be attributed to a change in grain-boundary roughness rather than to an increase in grain size. Annealing, for example, would increase m by lowering the elastic modulus and smoothing the grain boundaries; the peak would then be shifted to a higher temperature.

Equation (3) can be written in terms of the damping capacity ψ. This is the ratio of the energy dissipated to the maximum strain energy. The total energy dissipation is proportional to the product of ΔE and the grain boundary area per unit volume which in turn is proportional to $1/d$.
Hence

$$E \propto \Delta E \cdot \frac{1}{d}$$

The stress s_0 on a typical grain boundary is also proportional to the macroscopic stress S so that

$$\psi \propto \frac{E}{S^2} \propto \frac{\pi z}{\eta \omega d} \tag{13}$$

If we now substitute the value of $\eta\omega$ appropriate to the peak from (11) we have an expression for the peak damping; i.e.,

$$\psi \propto \frac{m}{d} \tag{14}$$

It may be noted that if we apply the same argument to equation (8) we obtain the result that

$$\psi \propto c$$

This is in accord with Kê's suggestion that the peak damping is independent of grain size so that the assumption that slip distance depends on stress as well as grain size appears to be implicit in his model.

However equation (14) shows that the height of the damping peak is a function of grain size and grain-boundary roughness. Hence it would be expected that with large grains the peak would be reduced and this may account for the reduction of the damping peak observed by Kê with specimens of increased grain size. In practice, strict inverse proportionality of peak damping with grain size would not be expected since not all the grain boundaries in a unit volume are contributing to the damping; some, for example, are so inclined that there is no shear stress along the boundary, while others are on the outside surface of the specimen.

Where damping peaks of different heights are obtained from materials with similar grain sizes these may be due to changes in m; that is, to grain-boundary roughness. Annealing and mechanical working may therefore be expected to affect the peak damping. Alternatively, when the peak is reduced by small additions of foreign elements, this may be due to the blocking of certain boundaries by the preferential segregation of the addition. This would reduce the effective grain-boundary area of the basis material and so give a lower peak. The modified boundaries would have their own characteristic viscosity which would give rise to a damping peak at some other temperature.

When experiments are carried out at similar stress levels and frequencies, the ratio of the viscosities at any temperature can be obtained from the temperature difference of the peaks. The experiments reported above show that there is a marked difference between the peak temperature of copper and the copper alloys but that the alloys show no difference between themselves. The experimental conditions are sufficiently similar for broad comparisons to be made and a rough calculation based on equation (11) gives the ratio of the grain-boundary viscosities in copper to that in the alloys as 1: 12,000. This appears to be the case even with the addition of sufficient beryllium to cause a marked change in the mechanical properties.

The activation energy for a given material can be calculated by carrying out experiments at different frequencies since this does not involve any assumptions regarding the constants in equation (4). Wherever the curves are sufficiently reproducible this has been done, but the accuracy of the calculation is not very high. The activation energy therefore, is only useful as a criterion for comparison when large and consistent differences are observed and in these experiments the differences cannot be regarded as significant.

The foregoing analysis applies only to the case of viscous grain boundaries between elastic grains; but in practice the damping curves do not represent the damping due purely to viscous slip and there is evidently a contribution from a further mechanism. This "background" damping cannot be separated from the grain-boundary peak and itself varies with the previous history of the specimens. As a result of this, the uncertainties of interpretation at this stage are so great that discussion can only be speculative. However if Kê's interpretation is accepted, the results show clearly that the addition of tin to copper does not reduce the viscosity of the

boundaries in small movements but, on the contrary increases it. On this basis, the interpretation of the observations on tensile ductility must involve other quantities, perhaps relating to the fracture process rather than to the stress redistribution which precedes it. An alternative view might be that the movements preceding fracture are much larger than those postulated in the damping; the latter being only a few atomic distances; and that the mechanism of movement might alter with increasing displacement. It was thought worth while, therefore, to conduct a few experiments on damping at higher amplitudes and on torsional creep, to see if some clearer differentiation could be made between the experimental materials which might serve as an empirical basis for the rapid assessment of creep performance. These experiments failed to suggest such a basis and are simply recorded without extensive discussion, in case the results may later prove to have some value.

IV. The Effect of Amplitude on Damping

(*i*) *Increased Amplitudes*

In the experiments so far described, the maximum surface strain on the specimen was of the order of 10^{-5} (corresponding to a deflection of 6 cm on a screen 3 metres from the galvanometer suspension). With a grain size of 0.009 cm this would involve a maximum movement at the grain boundaries of about 9 Å or 3 atomic diameters. The grain boundary movement occurring during the course of conventional creep tests may well be of the order of thousands of angstroms. It is possible that damping experiments at low amplitudes involve a different mechanism of grain-boundary movement from that operative during creep so some experiments were carried out to investigate the damping at strains differing from those normally employed with a Kê apparatus.

(*a*) *Experimental details.* Two series of observations were made on the damping of high-purity copper at relatively high amplitudes; the first at one frequency, and the second at two frequencies so that an activation energy could be calculated. In order to make accurate measurements of the individual amplitudes of swing, a drum-recording camera was used. Each of the two specimens examined was given a final reduction of 44 per cent RA and was annealed for 4 hours at 600°C, giving a grain size of 0.0064 cm. As the results of each experiment were essentially similar, only the more detailed experiment at two frequencies will be described.

For each reading the assembly was swung to give an initial surface strain of about 7×10^{-5} and the logarithmic decrement was calculated for deflections corresponding to strains of 2.1×10^{-5} and 4.2×10^{-5} as the oscillations died away. Curves were then plotted of the variation of these values with temperature for frequencies of 2.12 cps and 0.35 cps at room temperature. Figure 8 shows the

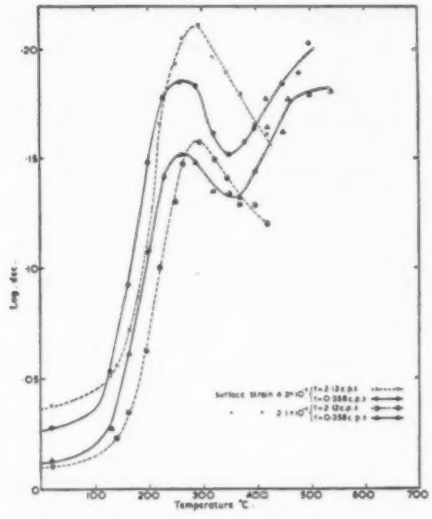

FIGURE 8. Variation of damping with temperature at two frequencies and two surface strains: copper.

damping curves at the two strains for each frequency. The low-strain curves are similar to each other and to the corresponding curve obtained in the first experiment; but the curves at the higher strain differed considerably and were not reproducible. It should be emphasised that the pair of values at each temperature were taken from different points in the same train of oscillations. Several sets of swings were recorded at each temperature and these were found to be quite consistent with each other, showing that the specimen underwent no appreciable internal change during the taking of readings at these amplitudes.

(*b*) *Activation energy.* The damping at the low strain was plotted against the reciprocal of the absolute temperature and from the shift in the curves at the two frequencies an activation energy was calculated having the following value:

$$H = 28{,}000 \text{ cal/mol.}$$

It was not possible to calculate the activation energy from the curves at the higher strain because they were too dissimilar.

(*c*) *Variation of damping with amplitude.* The

records taken at various temperatures in the high-frequency experiment were analysed in detail to find the variation of damping with amplitude. Four of the curves obtained are given in Figure 9, in which the vertical lines represent the strains at which the values for Figure 8 were taken. The temperatures selected represent, respectively, the damping at room temperature, the position of greatest slope, the peak, and the high-temperature region. Above strains of 2×10^{-5} the damping was found to vary with amplitude at all temperatures.

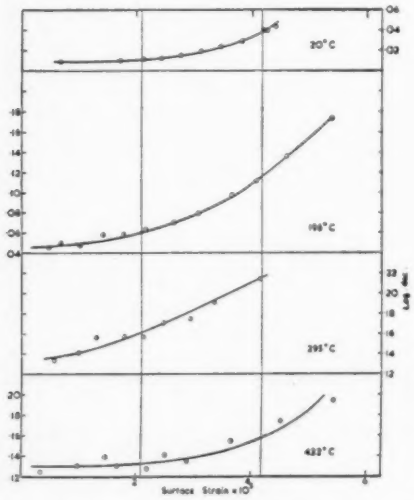

FIGURE 9. Variation of damping with strain: copper.

(*d*) *Damping at greater amplitudes.* Before the specimen was removed from the furnace a further set of observations were made at even greater amplitudes such that the initial strain was about 20×10^{-5}. It was not possible to measure the damping at strains greater than 10^{-4} since, above this value, the suspension system was too highly damped. The variation of damping with strain at several temperatures is shown in Figure 10.

(*ii*) *Damping at Various Strains with Increased Grain Size*

To investigate the effect of increased grain size on the damping, an experiment was carried out on similar lines to the one described above, using a copper specimen with a larger grain size. This specimen was given a 44 per cent reduction and annealed for 24 hours at 950°C in an atmosphere of nitrogen plus hydrogen. After being mounted in the apparatus it was annealed again for 16 hours at 600°C. This produced a grain size of about 0.1 cm and most of the grains stretched across the entire width of the specimen.

The damping was first measured for strains less than 0.22×10^{-5} at frequencies of 2.27 cps and 0.329 cps. The curves were coincident over the range examined and showed no trace of a damping peak around 300°C. Figure 15, curve I, shows the variation of damping with temperature; the damping was fairly constant up to about 300°C but, above, it increased slowly with temperature. This

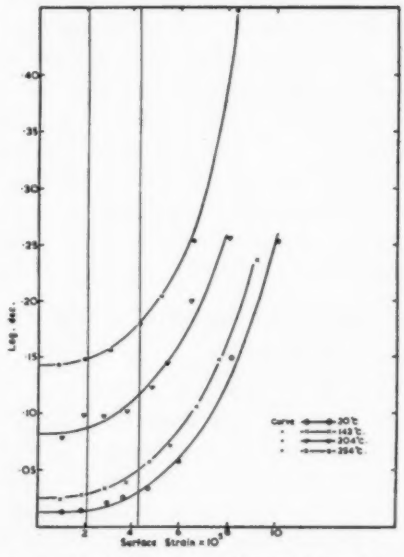

FIGURE 10. Variation of damping with strain: copper.

increase may correspond with the background damping observed in experiments with smaller grain sizes but its values are much lower, as may be seen by comparison with, for example, Figure 2.

Following this, the damping was again measured from trains of oscillations in which the initial strain was 7×10^{-5} and the logarithmic decrement was calculated for strains of 2.1×10^{-5} 4.2×10^{-5} and 6.3×10^{-5} at each temperature. The variation of damping within this range of strains was not so great as with the smaller grain specimens but the general level of damping above 250°C was considerably higher than that measured at the lowest strain. The three curves obtained at these strains are given in Figure 15.

(*iii*) *The Damping at Reduced Amplitudes*

Throughout the experiments described in the preceding sections the specimen had been gripped in the apparatus by pin chucks. The increase in damping at higher amplitudes may possibly be associated with the method of gripping the speci-

men since originally this was only intended to be used for tests at low amplitudes. A detailed test was carried out using the pin chucks to see if a variation of damping with amplitude could be detected at strains below those normally employed (i.e., 10^{-5}).

A damping curve was obtained in which the maximum surface strain on the specimen did not exceed 0.25×10^{-5}. Without touching the specimen in any way, a second set of observations was then made in which the maximum surface strain was 1.3×10^{-5}. At all temperatures the damping was found to be slightly higher in the second experiment at the higher strain. This result was contrary to that obtained in the original tests on the apparatus so it was decided to see if the effect was reproducible with new grips.

(*iv*) *The Use of New Grips*

A new set of grips was made consisting of two flat steel plates which could be bolted firmly together. The specimen was gripped between these in *V*-grooves.

Using these grips, a number of tests was carried out on a specimen of copper wire. This had been given a previous reduction of 44 per cent RA and was then annealed in the furnace for 16 hours at 500°C, giving a final grain size of 0.0068 cm. The following sequence of observations was then made:

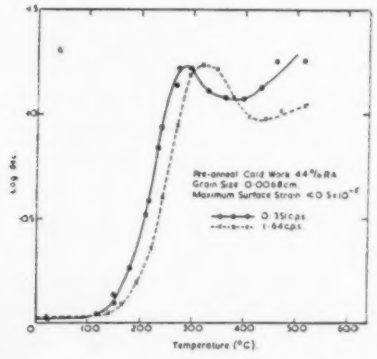

FIGURE 11. Variation of damping with temperature at reduced amplitudes: copper.

(*a*) Before annealing, the damping of the cold-drawn wire was measured at room temperature up to a strain of 7×10^{-5}. The logarithmic decrement had a value of 0.007 and did not change appreciably over this range of amplitude.

(*b*) The specimen was annealed and cooled to room temperature. Measurements of damping were then made for a frequency of 1.64 cps as the temperature was raised and the maximum strain was kept below 0.5×10^{-5}. The specimen was cooled to room temperature, and the damping again measured to ascertain whether any change had occurred during the test, but none was observed.

(*c*) The inertia arms were changed for a repeat experiment with the same maximum strain but at a frequency of 0.351 cps. Before taking any readings, the specimen was held for an hour at 500°C to relieve any stresses caused by changing the inertia arms, and then measurements were made as the furnace was cooled. Figure 11 shows the damping curves obtained from these two sets of observations and with this data the activation energy was calculated to be

$$H = 31{,}000 \text{ cal/mol}$$

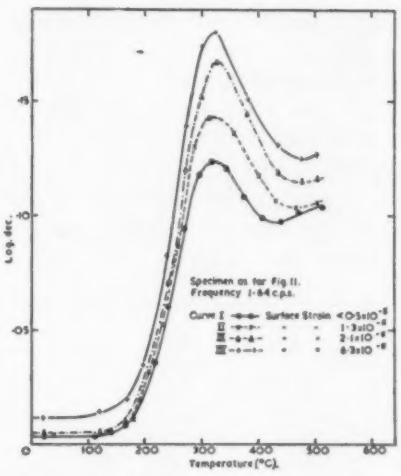

FIGURE 12. Variation of damping with temperature at various strains.

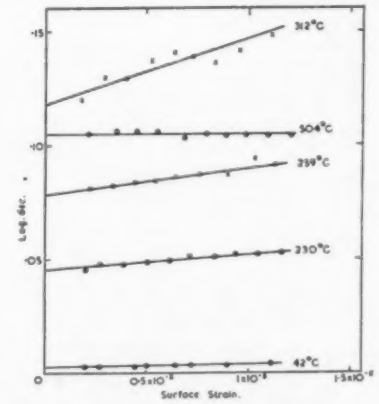

FIGURE 13. Variation of damping with amplitude: copper. Maximum surface strain $1{\cdot}3 \times 10^{-5}$.

(*d*) After replacing the high-frequency inertia arms and giving stress relief for 1 hour at 500°C, damping measurements were made at a strain of 1.1×10^{-5}. Curve II of Figure 12 shows that the damping was slightly higher than that of the experiment at lower strains (curve I). Detailed analyses were made at several temperatures of the variation of damping with amplitude and these are given Figure 13.

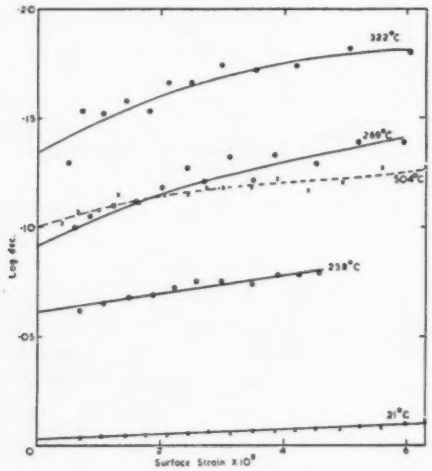

FIGURE 14. Variation of damping with amplitude: copper. Maximum surface strain 7×10^{-5}.

(*e*) A final set of observations was made in which the initial strain was increased to 7×10^{-5} and the damping was measured at several points as the oscillations died away. Curves III and IV in Figure 12 show the damping at strains of 6.3×10^{-5} and 2.1×10^{-5}. The detailed analysis of individual trains of oscillations are given in Figure 14.

(*v*) *Discussion of Results*

Although the damping has been found to vary with amplitude in all of these tests, the way in which it does so is not consistent; whereas in Figures 9 and 10 the damping increases considerably as the amplitude increases, it shows a tendency to flatten off in the curves of Figure 14. Since different grips were used in these experiments it is reasonable to suppose that much of the inconsistency can be attributed to spurious damping caused by losses associated with the grips. Fortunately the effect is not very pronounced with the pin chucks at strains of the order of 10^{-5} so the experiments described in section II can be regarded as having been carried out in conditions leading to unimportant grip losses. The difficulty arises with the interpretation of the variation of damping with amplitude at strains greater than this. Of the two variations represented by Figures 9 and 10 on the one hand and Figure 14 on the other, those of Figure 14 obtained with the new grips are regarded as more reliable since, before performing the experiment, no change of damping with amplitude could be detected in the hard-drawn wire up to strains of 7×10^{-5}. While the expansion at high temperatures might be expected to loosen the grips and to allow slipping to take place, this effect would become greater as the temperature increased; but, in fact, the greatest variation of damping with amplitude is observed around 300°C, the peak temperature, and at 504°C the slope of the curves has decreased. It therefore seems likely that the results reported in subsection (*iv*) give a fairly accurate indication of the behaviour of the specimen itself.

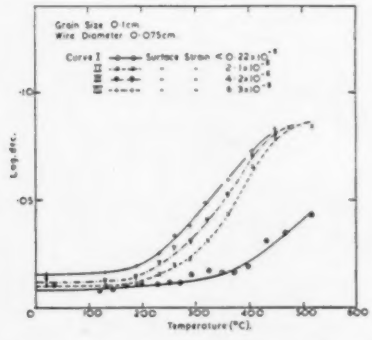

FIGURE 15. Effect of amplitude on damping with specimen of large grain size: copper.

The curves in Figure 13, which covers the range of strains normally used with the Kê apparatus, suggest that even at low stress levels there is a small linear dependence of damping on amplitude and that this is greatest in the region of the peak temperature. These results are not sufficiently extensive, however, to establish a general rule, and remain to be confirmed by further experiments. In Figure 12 the surface strain is increased by a factor of 12 but no change is apparent in the temperature of the damping peak. The same effect was observed in the experiments described in section I and is illustrated by Figure 8, although the strains do not cover such a wide range. It is evident, therefore, that stress or strain should not appear in any parameter relating temperature and other experimental factors.

The activation energy for copper has been measured in experiments carried out at three different strains and the values are collected for

comparison in Table III. These values do not show any general trend as might be expected if a different mechanism came into play at higher strains.

TABLE III

Surface strain	0.5×10^{-5}	10^{-5}	2.1×10^{-5}
Activation energy cal/mol	31,000	37,000	28,000

V. Torsion Creep Experiments

It is evident that these measurements of damping are not suitable for studying the mechanism associated with the large grain movements observed in creep; but it should be possible to link up the tests at low strains with the conventional creep tests by carrying out torsional creep tests at different levels of elastic strain, commencing with the strains used in Kê-type damping experiments. Kê [1] showed that, with aluminium, torsional creep and stress relaxation tests gave the same activation energy as the damping tests and he suggested that the same mechanism, namely, grain-boundary slip, was responsible for all three phenomena. Before carrying out the tests at different stress levels it was thought desirable to perform a series of tests at different temperatures and one stress to see how far the results corresponded with those of Kê. A low stress was chosen to reduce the complication of plastic deformation so that grain boundary slip would be the dominating mechanism.

(*i*) *Tests on Copper*

A series of tests was carried out at various temperatures and the stress was chosen to give a strain of 0.88×10^{-5} in the hard-drawn wire before annealing. The specimens were of the high-purity copper used in all the damping tests and each was given a final reduction of 44 per cent RA followed by an anneal in the apparatus of 16 hours at 500°C. This gave an average grain size of 0.007 cm. The creep tests were performed at temperatures ranging from 140°C to 402°C and at the end of each test the deflection was observed after the stress had been removed, so that a creep recovery curve could be drawn.

Three typical creep curves are given in Figure 16 in which the deflection on a screen 2½ metres from the assembly is plotted against the time in minutes. The same curves are also given in Figure 17 in which values of dt/do are plotted against time; dt is the deflection at a time t and do is the instantaneous deflection at $t = 0$. In this type of curve the creep strain is related to the elastic strain and creep curves with different elastic strains can be compared with each other.

Although the points in each experiment were usually found to be on a smooth curve, the reproducibility of the curves was not very good and in

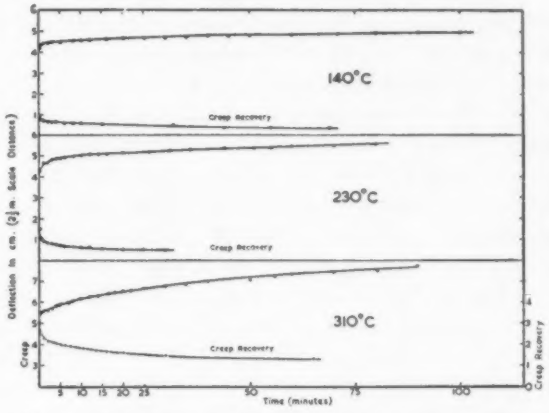

FIGURE 16. Creep and creep recovery curves: copper.

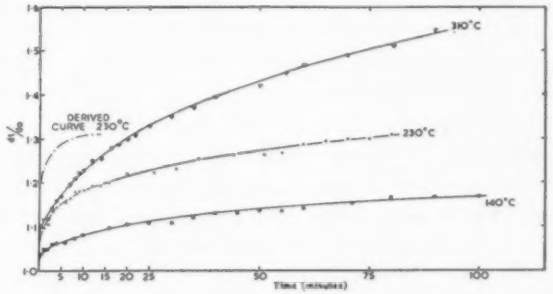

FIGURE 17. Creep in terms of instantaneous deflection (dt/do): copper.

the worst case the creep changed by a factor of two in a repeat experiment. This uncertainty makes it difficult to investigate the relationship between creep and temperature and it is only possible at present to make a few general observations on the creep behaviour.

(*a*) The amount of creep in a given time increased with the temperature of the experiment with the exception of a few experiments which are regarded as anomalous. The increase in creep was not as much as would be expected if the results conformed to an activation law. The results were analysed by the method described by Kê [1] in which the time t is observed for the curves to reach the same value of dt/do at various temperatures.

An activation energy H can then be calculated from the equation:

$$\frac{d(\log_{10} t)}{d(1/T)} = \frac{H}{2.3R}$$

where T is the absolute temperature and R the gas constant. Curves of $\log_{10} t$ against $1/T$ for different values of dt/do should therefore be parallel straight lines with the gradient $H/(2.3R)$. In these experiments, however, the points obtained in this way were so scattered that it was not possible to obtain even a rough value for the activation energy.

(*b*) The general form of the curves is similar to that published by Kê for aluminium and is not unlike conventional creep curves carried out at higher stresses. It would be expected that if the creep were solely due to slip at grain boundaries, it would tend to zero at long times when all the grain boundaries were relaxed; but in the experimental curves the creep continues at a steady rate at times considerably longer than the order of the relaxation time. A theoretical creep curve was derived from the damping curve of Figure 4, using the relaxations derived by Zener [6] and is shown in Figure 17. In the course of this derivation, use is made of a value for activation energy in order to convert damping values at various temperatures into creep values at various times. This implies that the conversion can only be made when one relaxation process is involved: it is probable that two processes are occurring in these experiments and these may have widely differing activation energies so that the equations are not strictly applicable. However, the derived curve illustrates the difference between the experimental curves and those expected from theoretical considerations; essentially it differs from the experimental curve in that the initial creep rate is greater and that it tends to zero at longer times. In Figure 4 the damping curve shows only a small contribution by the background damping and if this had been greater the derived creep curve would have continued to increase. There is good reason, therefore, to assume that the background damping and "steady-state" creep are due to the same process. That this process is related in some way to the slip of grain boundaries is indicated by the fact that with specimens of larger grain size not only is the damping peak eliminated but also the background damping is reduced (compare for example Figures 11 and 15). Under these conditions the creep is also reduced as was shown by a creep experiment at 402°C with copper of increased grain size (about 0.1 cm) in which the creep was almost negligible; there was a small amount of movement during the first 10 minutes, after which the deflection remained steady until the end of the test: at 30 minutes the value of dt/do was 1.040 compared with a value of 1.505 in a specimen with a grain size of 0.0070 cm tested under similar conditions.

(*c*) The curves have been found, within the limits of experimental error to conform to an equation of the type

$$dt/do = 1 + at^b;$$

in other words, to an equation of the Andrade type but with a negligible "viscous" (K) term. The values of a were found to lie in the range 0.14 to 0.58 and the values of b in the range 0.25 to 0.40 but no correlation could be found between either of these and the temperature.

The work carried out so far is not sufficiently advanced for any general conclusions to be reached. The relation of the curves at various temperatures to each other is at present obscured by the lack of reproducibility of the results and until this is improved it will not be possible to derive any useful information on the effect of stress and temperature on creep.

VI. General Conclusions

1. The damping capacity of copper and several tin bronzes has been measured by the method used by Kê and gives results considered to indicate the viscosity of the grain boundaries; these show that the addition of tin to copper increases their viscosity. The values for the activation energy of the grain-boundary flow process are subject to considerable experimental error and are not sufficiently accurate to differentiate between the grain-boundary characteristics of the materials examined.

2. The height of the damping peak appears to be the most significant feature of the results, but depends on a number of factors which are not yet fully understood and therefore cannot be used to indicate what properties would be obtained in creep and hot impact-tensile tests.

3. The damping effects and corresponding effects in torsional creep experiments which are also reported, are most evident in materials of small grain size and are reduced in materials of larger grain size. This is consistent with the view that they are associated with the relative movement of the grains at the boundaries.

4. The damping curves contain a contribution from a "background" damping effect, which can have a marked influence on the height and position of the damping peak. This background varies with the heat treatment of the specimen and experiments should only be carried out after annealing until it reaches a stable value. In experiments with materials of comparatively large grain, where the peak is reduced, the background is also lowered; it may thus be associated with plastic deformation in the grains caused by relative movement at the grain boundaries.

5. The damping varies with amplitude even at the smallest amplitudes used and the dependence on amplitude is greatest in the region of the peak damping. The nature of the dependence varies with the type of grip used. The peak damping temperature is unaffected by the stress level in the range examined.

6. Difficulty has been encountered in obtaining reproducible creep curves but in general the amount of creep in a given time does not increase with temperature as much as would be expected if the results conformed to an activation law, with an energy of activation similar to that found for the damping. The curves conform to an equation of the type:

$$dt/do = 1 + at^b,$$

where b is the order of 1/3.

Acknowledgments

The author wishes to thank the Director and Council of The British Non-Ferrous Metals Research Association for permission to publish this paper. He is indebted to Dr. G. L. J. Bailey, Mr. R. Eborall and Dr. S. Harper for many valuable discussions during the course of the work.

The work described in this paper was made available to members of the B.N.F.M.R.A. in a confidential research report issued in October, 1952.

References

1. Kê, T'ing Sui. Phys. Rev. **71** (8) (1947) 533.
2. Eborall, R. Unpublished work.
3. Kê, T'ing Sui. J. Appl. Phys. **20** (9) (1949) 274.
4. Kê, T'ing Sui. Phys. Rev. **72** (1) (1947) 41.
5. Kê, T'ing Sui. J. Appl. Phys. **21** (5) (1950) 414.
6. Zener, C. Elasticity and Anelasticity of Metals (Chicago, Univeristy of Chicago Press, 1948).

Wachstum und kristallographische Orientierung von Dendriten*

Durch experimentelle Untersuchungen ist bekannt, dass die Hauptwachstumsrichtungen von Dendriten in Schmelzen oder Lösungen niedrig indizierte kristallographische Richtungen sind, die als Dendritenachsen bezeichnet werden. Dieser Befund zeigt, dass für die Richtung des dendritischen Wachstums nicht Spitzenwirkungen o.ä. verantwortlich ist, sondern dass die Anisotropie der Reaktionsfähigkeit der verschiedenen kristallographischen Flächen einen wesentlichen Einfluss hat. Unter der Reaktionsfähigkeit einer Fläche verstehen wir die Wahrscheinlichkeit, dass ein in die betreffende Grenzfläche eintretender Gitterbaustein tatsächlich fest im Gitter gebunden wird.

Die Tabelle zeigt, dass die Dendritenachse nicht, wie gelegentlich vermutet wurde [1], die dichtest besetzte Gittergerade des betreffenden Kristalls ist. Eine naheliegende Vermutung wäre, dass die Dendritenachse sich senkrecht zu Flächen sehr grosser Wachstums-Aktivität (=Wahrscheinlichkeit der Bildung von Flächenkeimen) einzustellen sucht, da die Wachstumsgeschwindigkeit v_n in Normalenrichtung einer Fläche deren Wachstums-Aktivität proportional ist. Nun sind aber Flächen grosser Aktivität sehr wenig dicht mit Atomen belegt; sie werden deshalb durch die mit grosser Tangentialgeschwindigkeit v_t wachsenden dichtest belegten Flächen, die ja kleinste Wachstums-Aktivität und niedrigste Absorptionsenergie haben, aufgezehrt.

Offensichtlich kommt es für die Möglichkeit zu dendritischem Wachstum darauf an, dass sich die zur Dendritenachse senkrechte Fläche (als Dendritenfläche bezeichnet) überhaupt ausbilden kann.

Wir verstehen unter der primitiven Gleichgewichtsform eines Kristalls denjenigen Körper, der von den dichtest gepackten Flächen und—falls dies noch keinen allseitig begrenzten Körper ergibt, —den nächst dichtest gepackten Flächen begrenzt wird. v_n' bezeichnet die Wachstumsgeschwindigkeit einer der primitiven Gleichgewichtsform des Kristalls angehörigen Fläche (im allgemeinen diejenige kleinster Wachstums-Aktivität und v_n'' die Wachstumsgeschwindigkeit der Dendritenfläche. Die Ausbildung der Dendritenfläche ist nur möglich, wenn die Ungleichung

$$v_n' > v_n'' \cos \phi$$

erfüllt ist. (Siehe Abb.). ϕ ist dabei der Winkel zwischen der Dendritenachse und der Normalen zur Gleichgewichtsfläche. Diese Ungleichung wird am ehesten erfüllt sein für die langsamst wachsende (also dichtest belegte) Kristallfläche, die

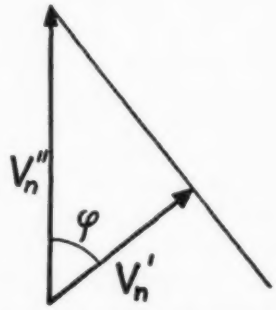

Die Bedingung für die Bildung frei wachsender Dendriten.
(*a*) $v_n' < v_n'' \cos \phi$: Keine Dendritenbildung möglich

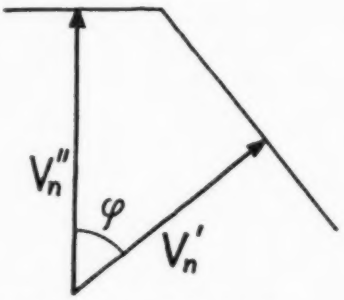

(*b*) $v_n' = v_n'' \cos \phi = v'_{krit}$: Kritischer Fall

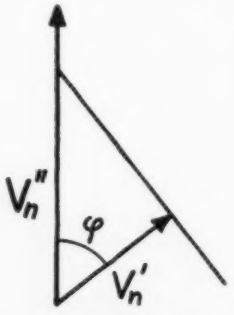

(*c*) $v_n' > v_n'' \cos \phi$: Normalfall des dendritischen Wachstums. Auf Grund der Aktivität der beiden Flächen entstehen abgerundete Kristallformen.

nicht zur primitiven Gleichgewichtsform gehört. In Übereinstimmung mit den Angaben in der Tabelle ist dies im allgemeinen die zweitdichtest

*Received January 19, 1954.

Gittertyp	Dendriten achse	dichtest besetzte Gittergerade	Flächen der primitiven Gleichgewichtsform	Nächstdichtest belegte Fläche
kubisch raumzentriert	⟨100⟩ (1)	⟨111⟩	{110}	{100}
kubisch flächenzentriert	⟨100⟩ (1) (2)	⟨110⟩	{111}	{100}
hexagonale dichteste Packung	⟨10$\bar{1}$0⟩ (1) (2)	⟨11$\bar{2}$0⟩	(0001) {10$\bar{1}$0}	{10$\bar{1}$0}
tetragonal raumzentriert	[110] (1) [1$\bar{1}$0] (2)	[001]	(100) (010)	(110) (1$\bar{1}$0)
Na-Cl-Typ	⟨110⟩ (4)	⟨100⟩	{100}	{110}

besetzte Gitterebene.* Lediglich die hexagonale dichteste Kugelpackung macht hier eine Ausnahme, da die zweitdichtest belegten Ebenen {10$\bar{1}$1} der primitiven Gleichgewichtsform angehören, sodass an ihre Stelle die drittdichtest belegten Ebenen {10$\bar{1}$0} als Dendritenflächen treten. Auch dies ist in Übereinstimmung mit den Beobachtungen.

Weinberg und Chalmers [2] haben für die Dendritenachse diejenige Richtung vorgeschlagen, in der sie sich mit der Maximalzahl dichtest gepackter Flächen umgibt, und zwar in der Weise, dass die Achse den Winkel zwischen zwei dichtest gepackten Ebenen halbiert. Diese aus der Erfahrung abgeleitete Regel trifft zu für die von Weinberg und Chalmers betrachteten Gittertypen. (Flächenzentriert-kubisch und raumzentriert tetragonal— bei der hexagonalen dichtesten Kugelpackung sind kompliziertere Überlegungen notwendig). Beim NaCl-Typ dagegen liefert die Regel kein mit der Erfahrung übereinstimmendes Ergebnis.

Dendritisches Wachstum kann also eintreten, wenn v_n' mindestens so gross geworden ist, dass

$$\frac{v_n'}{v_n''} = \cos \phi$$

gilt. Dies erfordert eine verhältnismässig grosse Keimbildungshäufigkeit auf der dichtest belegten Fläche, wie sie nur weit vom Phasengleichgewicht entfernt auftritt (grosse Übersättigung oder starke Unterkühlung). In diesem Bereich ist die Keimbildungshäufigkeit so gross, dass die Reaktionsfähigkeit von dichtest gepackten Flächen mit derjenigen von Stufenflächen [3] vergleichbar wird und somit runde Kristallformen möglich sind.

Nachdem durch das obige Kriterium über die Wachstumsrichtung des Dendriten entschieden ist, wird für die wirkliche Ausbildung eines frei wachsenden Dendriten die Spitzenwirkung wesentlich. Wie schon Weinberg und Chalmers [2] betont haben, wird die Keimbildungshäufigkeit bei frei wachsenden Dendriten zur Spitze hin grösser. Der Wachstumsmechanismus ist auch bei dem hier vorliegenden schnellen Wachstum grundsätzlich derselbe, wie beim langsamen Wachstum. Es handelt sich hier ebenfalls um ein seitliches Auswachsen der dichtest belegten Flächen Randwachstum mit der Erweiterung, dass die Wachstumsgeschwindigkeit senkrecht zu diesen Flächen vergleichbar ist mit der tangentialen Wachstumsgeschwindigkeit.

J. Schlipf und A. Seeger

Max Planck-Institut für Metallforschung, Stuttgart, und Institut für theoretische und angewandte Physik der Technischen Hochschule, Stuttgart

*Alle diese einfachen Überlegungen gelten natürlich nur, solange nicht durch Fremdstoffzusätze die Potentialverhältnisse an den Kristallflächen grundlegend geändert werden.

Literaturnachweis

1. Nix, F. C. und Schmid, E. Z. Metallkde. **21** (1929) 286.
2. Weinberg, F. und Chalmers, B. Canad. J. Phys. **30** (1952) 488.
3. Burton, W. K., Cabrera, N. und Frank, F. C. Philos. Trans. **A243** (1951) 299.
4. Graf, L. Z. Metallkde. **42** (1951) 336, 401.

Solubility of Nitrogen in α-Iron†

The small solubility of nitrogen in α-iron has recently been measured in the range of temperature from 570°C to 170°C in two different ways; by Dijkstra [1] using the mechanical relaxation phenomenon, and by Borelius, Berglund and Avsan [2] using the method of isothermal calorimetry. The results of these two investigations differed by a factor of about two, and we have been searching for the source of this discrepancy by new measurements of both kinds.

Dijkstra made his measurements on wires with a diameter of 0.6 mm, used as the suspension wire of a torsional pendulum with a period of vibration of about one second. He determined the maximum logarithmic decrement Δ for small amplitudes, which for this period occurs at about 20°C. The concentration c of nitrogen in solution was assumed

†Received January 21, 1954.

to be proportional to Δ. The ratio of c to Δ was determined by measurements of the resistivity and use of the relationship between resistivity and concentration of nitrogen obtained by Köster. The value of c/Δ was determined at concentrations below 0.015 weight % but was assumed to be constant in the whole range covered by the damping measurements or up to about 0.1%. The logarithmic decrement Δ was measured after aging at different temperatures in order to obtain the equilibria at these temperatures. At temperatures between 250°C and 300°C a metastable equilibrium, occurring before the stable one, could be clearly observed. In Figure 2, which shows the atomic ratio of N to Fe on a logarithmic scale against the reciprocal of the absolute temperature, the values obtained directly from the graphs of Dijkstra are shown by the circles on the left side of the dotted horizontal lines.

The present investigation on the relaxation phenomenon was performed in another way. Instead of observing the oscillations of a thin wire, the nitrogen content of which had to be determined indirectly, we studied the relaxation after-effect of a spiral of such dimensions (about 200 grams of weight) that the amount of nitrogen put into it could be determined simply by its increase of weight. The method had been developed in this Laboratory by Lindstrand, whose work is still unfinished and unpublished. The spirals used were of a technically pure iron with small impurities of Si, Mn, P, S, C, and N. They were purified from C and N by heat treatment in wet hydrogen and loaded with various amounts of N in a mixture of NH_3 and H_2. The measurements were made at −18°C where the time constant for the exponential relaxation of N in α-Fe is 25 seconds. The spiral was fixed at its upper end. The lower end was turned an angle ϵ_1 of about 50 degrees, kept there for a sufficient time, and quickly released. The after-effect was recorded and its starting value ϵ_2, just after the release was determined. According to the theory of simple relaxation phenomena the ratio ϵ_2/ϵ_1 is related to the maximum logarithmic decrement Δ determined by Dijkstra by the formula

$$\frac{\epsilon_2}{\epsilon_1} = \frac{2}{\pi}\Delta \qquad (1)$$

In Figure 1 the experimental values of ϵ_2/ϵ_1 are shown as a function of the content of nitrogen. The specimens were in all cases quenched from a temperature where all N was in solution and special care was taken to prevent precipitation during quenching. At low concentration the ratio of ϵ_2/ϵ_1 to c has very nearly the value found and used by Dijkstra. At the higher values of c there are large discrepancies, the nature of which will be discussed in a later publication. By means of the diagram of Figure 1 the results of Dijkstra have been recalculated. We are aware, however, of the uncertainty of this calculation owing to the fact that Dijkstra's measurements were made at +20°C, ours at −18°C. The corrected values are given in Figure 2 by the circles at the right ends of the dashed horizontals. Using the diagram of Figure 1, we have also made a few determinations

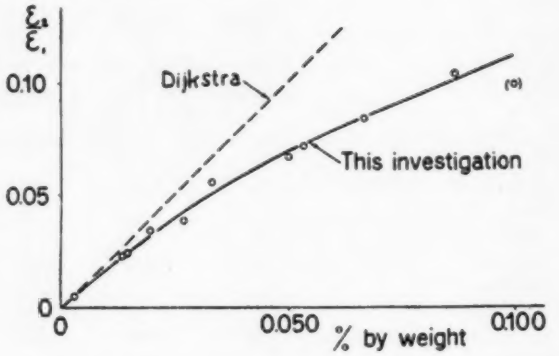

FIGURE 1. After-effect as a function of the content of nitrogen in per cent by weight.

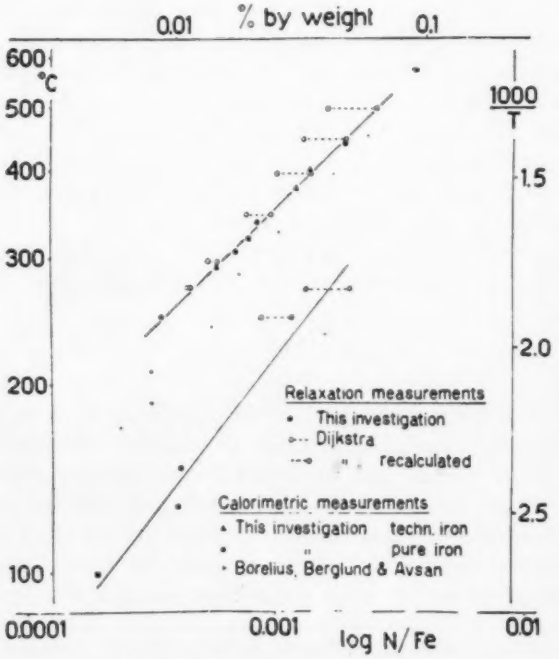

FIGURE 2. Part of the logarithmic equilibrium diagram Fe–N.

of the solubility limit, by measurements on the same samples as above quenched from temperatures where the nitride and N in solution were in equilibrium. The results are shown in Figure 2 as filled circles and fit well with the corrected values of Dijkstra.

In search of the source of the discrepancies, we have also repeated the calorimetric measurements of Borelius, Berglund and Avsan. In these measurements a sample of some 100 grams weight was first heated to a temperature T, in order to get a certain amount c of nitrogen in solution into equilibrium with an excess of nitride. The sample was then rapidly cooled to the measuring temperature where most of the dissolved nitrogen precipitates. The heat evolved, corrected in order to correspond to full precipitation, may be written $Q = L \cdot c$, where L, the heat of solubility, is determined from measurements at different temperatures by the thermodynamic relationship $\ln Q = \text{const.} - L/RT$. In order to obtain absolute Q-values, the apparatus was calibrated by means of Peltier heat evolved in the junction of a thermocouple put into a central boring in the sample. It had been observed that the way the thermocouple was arranged in the measurements of Borelius, Berglund and Avsan was not quite satisfactory, giving rise to a disturbing chimney effect. An improved arrangement gave Q-values which were about 17 per cent smaller than those obtained earlier. Three measurements in the range from 295° to 405°C on the same technically pure iron as used by Borelius, Berglund and Avsan with an initial content in weight percent of 0.01 Si, 0.07 Mn, 0.002 P, 0.007 S, 0.017 C, and less than 0.003 N, shown by the filled triangles in Figure 2, now gave full agreement with the results of our relaxation measurements. A measurement at 324°C shown by a filled square in Figure 2, on a sample of a very pure iron from the laboratories of Philips in Eindhoven, kindly put to our disposal by Mr. Fast, also gave full agreement with the results from the sample of technically pure iron.

The solubilities obtained by Borelius, Berglund and Avsan in the lower range of temperature from 170 to 250°C now seemed definitely too high, and it could be suspected that the precipitation was a mixture of that of the stable phase Fe_4N and the metastable phase observed by Dijkstra. New measurements performed in a slightly different way at temperatures between 100°C and 150°C showed that it was possible to obtain the precipitation in two steps, the first representing the metastable equilibrium and the second the stable one. Three calorimetric measurements on the iron obtained from Mr. Fast at 100°C, 130°C, and 150°C combined with the recalculated results of the damping measurements of Dijkstra at 250 and 275°C gave the metastable solubilities shown by the three filled squares in Figure 2, and the metastable phase boundary line drawn in the figure.

The results of this investigation will be given and discussed in more detail in a paper by Åström, planned for publication in the Arkiv för Fysik.

HANS U. ÅSTRÖM and G. BORELIUS

Department of Physics
Royal Institute of Technology
Stockholm

References

1. DIJKSTRA, L. J. J. Metals **1** (1949) 252.
2. BORELIUS, G., BERGLUND, S., and AVSAN, O. Arkiv f. Fysik **2** (1950–1) 551.

Radiation Ordering in Cu_3Au*

There appears to be a rather basic disagreement in both the conditions under which the phenomenon of radiation ordering results and the mechanism by which it occurs. It has been suggested [1] that this phenomenon was connected with the production of Frenkel defects during the bombardment and it was in fact cited as evidence that interstitial atoms or vacant lattice sites increase the diffusion rate. On the other hand Cook and Cushing [2; 3] interpreted their experiments to indicate that the radiation ordering was dependent on the slow neutron flux. They consequently ruled out the influence of structural defects, attributing radiation ordering to the presence of mercury and in some cases to zinc and nickel impurities created by a transmutation process resulting from the capture of slow neutrons by the nucleus. The mechanism by which these impurity atoms increase the diffusion rate is not clear but presumably the authors assumed that these atoms play the role which is customarily attributed to vacant lattice sites or interstitial atoms in the diffusion process.

It would seem that the relative influence to radiation ordering of structural defects produced by the elastic collisions of fast particles as compared to the chemical defects produced by nuclear reactions could be estimated by consideration of the effects of fast electrons as compared with reactor neutrons. In the former case, with electrons having energies

*Received January 19, 1954; in revised form February 5, 1954.

of the order of a few Mev, the number of transmutations produced will be extremely small compared to the latter case. Recently the experimenters at Harwell studied the effect of 3 Mev electrons on the ordering rate of Cu_3Au [4]. They found a pronounced increase in the rate of ordering as a result of a relatively small bombardment. If these data are representative of radiation ordering it seems that structural defects must play a role in the increased ordering rate.

Recent results obtained at Oak Ridge [5] suggest that substantial radiation ordering can occur during reactor bombardment even when the number of chemical defects formed by nuclear reactions is small. On Cu_3Au samples prepared by heat treatment to minimize the contribution of domain walls to the electrical resistivity (the samples had a domain size in excess of 10^{-3} mm with the order within a domain equal to the equilibrium order at 375°C), the resistance was observed to decrease before appreciable mercury was formed. The data are plotted in Figure 1. It should be noted that a

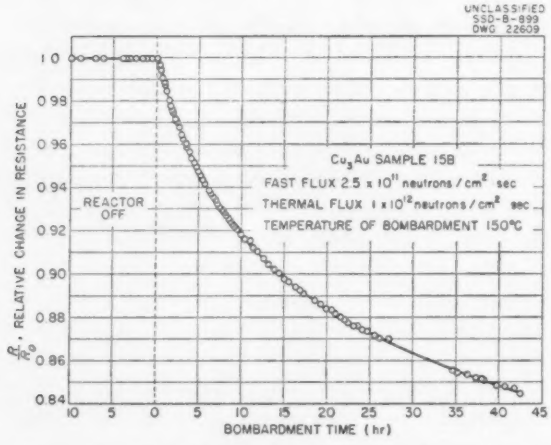

FIGURE 1. The effect of neutron irradiation on the resistance of partially ordered Cu_3Au. The original resistivity was 7.92 micro-ohm cm. The resistivity of Cu_3Au at equilibrium at 150°C is 5.50 micro-ohm cm. After 500 hours at a flux of 2.5×10^{11} fast neutrons/cm² sec and 1×10^{12} thermal neutrons/cm²/sec the resistivity dropped to 5.94 micro-ohm cm.

resistance decrease, well beyond experimental error, is detected after the first hour of reactor radiation. The fraction of gold atoms transmuted to mercury in this period computed on the basis of a capture cross section of 100 barns, a flux of 10^{12} nv, and a half life of three days, is less than 1×10^{-8}. Even after 20 hours the amount of mercury is only of the order of one part in a million. It would be surprising if such small amounts of mercury could change the diffusion rate so substantially.

The above remarks probably require some modification of the deductions made by the Chalk River group as to the effects of transmutations. The principal evidence cited to substantiate the important role attributed to transmutations is the diminution of radiation ordering when the sample is bombarded in a neutron converter (a thimble of fissionable material which converts thermal neutrons to fast neutrons). It was assumed that the predominant factor introduced by the converter was a reduction of slow neutron flux and the effects of a corresponding increase in the fast neutron flux were ignored. While it would appear at first sight that an increase in the fast neutron flux should increase the magnitude of radiation ordering if it were associated with structural defects formed by fast neutron interactions, a more careful analysis seems to show that the increased fast flux in Cook and Cushing's experiment could be responsible for the suppression of radiation ordering. This apparent anomaly can be rationalized by considering a localized region of Frenkel defects. One of the components of the Frenkel defect, say the vacancy, will have a high jump frequency in comparison to the other component, say the interstitial atom [6]. At an appropriate temperature, the vacancy will be free to move while the interstitial atom will remain relatively fixed. While many vacancies will combine with interstitials and the defect pair thus annihilated some of the vacancies will escape from the damaged region and increase the ordering rate as they wander throughout the crystal. The number of jumps the defect can make, if we assume that the number of other type defects, such as dislocations, capable of trapping vacancies are small, will depend on the probability that they will encounter a damaged region and be annihilated by the residual interstitial atoms.

If the above picture is applicable then the damaged regions will affect the diffusion rate in two competitive ways. Increasing the number of damaged regions will increase the number of defects available for diffusion but at the same time will decrease the efficiency of the defect by decreasing the number of jumps.

In the case of sample 15B and 18A of Figure 2 it is apparent that the latter factor is the more important, as increasing the fast flux reduces the magnitude of the radiation ordering. It would be

expected that the magnitude of the observed effects in the case of the sample exposed to the higher fast flux should increase to that of the sample exposed to the lower fast flux if the temperature of bombardment is raised to increase the mobility of the defects by a factor corresponding to the increase in the fast flux.

The effectiveness of the damaged regions as a sink for vacant lattice sites can be determined

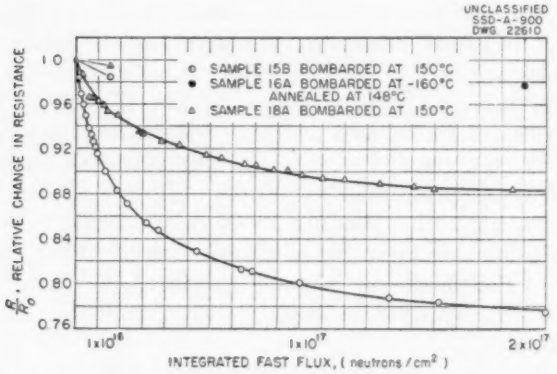

FIGURE 2. The effect of fast neutron flux on the rate of radiation ordering. Sample 15B was bombarded in a flux of 2.5×10^{11} nv fast neutron and 1×10^{12} nv thermal neutrons at +150°C. Sample 16A was bombarded in a flux of 2×10^{11} nv fast neutrons and 1×10^{12} nv thermal neutrons at −160°C. It was annealed at 148°C to cause the degree of ordering indicative of the point at 2×10^{17} nvt. Sample 18A was bombarded in a flux of 1×10^{12} nv fast neutrons and 1×10^{12} nv fast neutrons and 1×10^{13} slow neutrons at 150°C.

experimentally. By bombarding the samples at temperatures where the jump frequency of the vacancies is negligible a concentration of damaged regions can be created before the defects are allowed to move. In this way a study of the efficiency of the defect as a function of the number of damaged regions can be made. The results of one experiment of this type are shown in Figure 2. Sample 16A, which was bombarded at −160°C to an integrated fast flux of 2×10^{17} nvt and then annealed to equilibrium at 148°C, is ordered only slightly in comparison with samples bombarded for equivalent integrated fast fluxes at high temperatures where the vacancies were permitted to migrate at low concentrations of damaged regions. It is perhaps noteworthy that samples 15B and 16A were exposed to very nearly the same integrated slow neutron flux. It thus appears that these data offer experimental evidence that the diffusion-producing defects are annihilated in the localized neutron damaged region.

In conclusion it should be noted that the proposed mechanism of radiation ordering is probably somewhat oversimplified in that defect combinations probably move rather than the individual defects. There is evidence [5] which shows that there is not a single activation energy, but rather a continuous spectrum, associated with radiation ordering. It may be, however, that the concept introduced here as a simple picture will be an aid in the basic understanding of radiation effects.

T. H. BLEWITT and R. R. COLTMAN

Oak Ridge National Laboratory
Oak Ridge, Tennessee

References

1. BLEWITT, T. H. and COLTMAN, R. R. Phys. Rev. **85** (1952) 384.
2. COOK, L. G. and CUSHING, R. L. Acta Met. **1** (1953) 539.
3. ——— Acta Met. **1** (1953) 549.
4. ADAM, J., GREEN, A., and DUGDALE, R. A. Phil. Mag. **43** (1952) 1216.
5. To be published.
6. It is not clear which component of the Frenkel defect is the most mobile. It has been arbitrarily assumed that the vacancy is the more mobile defect.

Self-Diffusion in Lead*

I. Lattice and Grain-Boundary Diffusion

In the course of an investigation of the influence of impurities on self-diffusion in lead (see part II) we found some differences between the values for self-diffusion in pure lead as given by Seith and Keil [1], and the values we measured. Moreover, we observed grain-boundary diffusion at temperatures lower than about 260°C., whereas no grain-size effect was noticed by the previous authors.

Seith and Keil calculated the rate of self-diffusion in lead from the decrease in surface-activity, a method which does not seem to give always reliable results. We determined once more the lattice self-diffusion in lead following the sectioning method and using single crystals for the lower temperature region.

From the experiments with polycrystalline specimens at lower temperatures we were able to calculate the average grain-boundary self-diffusion in lead with the aid of the theory of Fisher [2], as was done by Hoffman and Turnbull [3] and more recently by Slifkin, Lazarus and Tomizuka [4] for silver.

Starting from high-grade lead metal-foil (Merck, Darmstadt) polycrystalline specimens (average grain-size 1 mm) were vacuum-cast and single

*Received March 22, 1954.

crystals were grown from the melt as described by Tiedema and Kooy [5]. After annealing, the specimens were covered with a thin layer of radioactive lead (Thorium B) and heated in an electric furnace with a controlled temperature for several days. After the diffusion anneal the specimens were sectioned on an ordinary lathe into layers of 0.01-mm thickness (on the average, 15 layers in a definite experiment). From the weight and the radioactivity of each layer the concentration-penetration curve was obtained.

The diffusion coefficient for lattice self-diffusion D_L was calculated from the equation [6]:

$$\log c = \text{const} - [\log e/(4D_L t)]x^2,$$

where c is the concentration of radioactive atoms at penetration x, and t is the diffusion time.

The average diffusion coefficient for grain-boundary self-diffusion D_G was calculated from the equation (2):

$$\log c = \text{const} - [2^{\frac{1}{2}}(D_L/D_G\delta)^{\frac{1}{2}} \log e/(\pi D_L t)^{\frac{1}{4}}]x,$$

where δ is the thickness of the grain boundary.

In Figure 1 all data so far obtained are plotted versus reciprocal absolute temperature. The lines

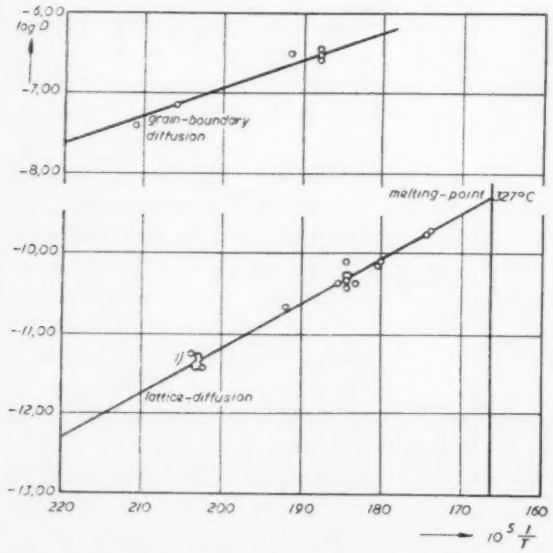

FIGURE 1. Observed diffusion coefficients for lattice- and grain-boundary self-diffusion in lead plotted versus reciprocal absolute temperature.
') In this temperature range 8 points were measured.

are drawn as the most probable lines. The equations of these lines appear to be: $D_L = 1.17$ exp $(-25700/RT)$ cm²/sec for lattice self-diffusion and $D_G = 0.81$ exp $(-15700/RT)$ cm²/sec for grain-boundary self-diffusion, if the thickness of the grain boundary is assumed to be 10 Å.

As with silver [3; 4], the activation energy for the average grain-boundary diffusion is much lower than the energy for lattice diffusion; this is to be expected on the basis of all diffusion mechanisms that have been seriously considered so far.

II. Effect of Impurities

Self-diffusion provides the simplest form of diffusion and has the smallest chance to be interfered with by disturbing influences. For this reason experiments on self-diffusion, both in pure metals and in alloys, can contribute largely to the understanding of the mechanism of metallic diffusion. Recently, Le Claire [7], extending Zener's [8] theory of D_0, showed that the experimental results strongly favour the vacancy mechanism in face-centered cubic metals.

It might be possible to increase the rate of self-diffusion by introducing an excess of vacancies into the metal. As Seitz [9] suggested, this could be done by alloying the metal with an "impurity-metal."

We measured the self-diffusion of lead in four lead-alloys, containing respectively 1 at. % silver, 1 at. % cadmium, 1 at. % and 1.5 at. % tin. All alloys were annealed for about a week at 300–310°C. As the solubilities of silver, cadmium and tin in lead are, respectively, about 0.1 at. %, 3 at. % and 3 at. %, the silver-alloy lies in the two-phase region, whereas the cadmium- and tin-alloys are homogeneous.

The metals used were high-grade lead (Merck, Darmstadt), "purest" silver (Drijfhout, Amsterdam), cadmium "for standard cells" (Merck, Darmstadt) and tin (Johnson and Mathey, London). By melting together weighed quantities of the components, polycrystalline specimens (average grain-size 1 mm) were obtained. The diffusion coefficients were measured in the same way as for pure lead (see part I).

In Figures 2 to 5 the experimental results so far obtained are plotted versus reciprocal absolute temperature. The line drawn in each figure is that for pure lead. It appears that the rate of self-diffusion of lead in these alloys is the same as in pure lead, within the experimental error. Our experiments on the lead-silver-system are in close agreement with the experiments of Seith and Keil [10], whereas Hoffman and Turnbull [11] observed a marked influence of lead on the self-diffusion of silver.

Further experiments are in progress to check the observed diffusion-coefficients. The results and details of all experiments will be published later.

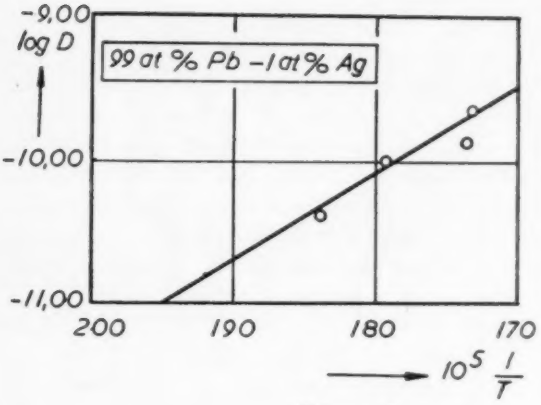

FIGURE 2

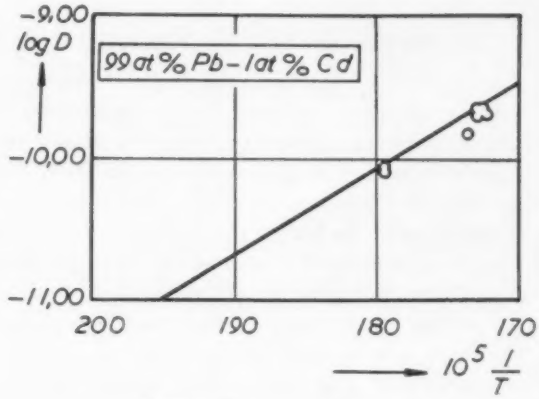

FIGURE 3

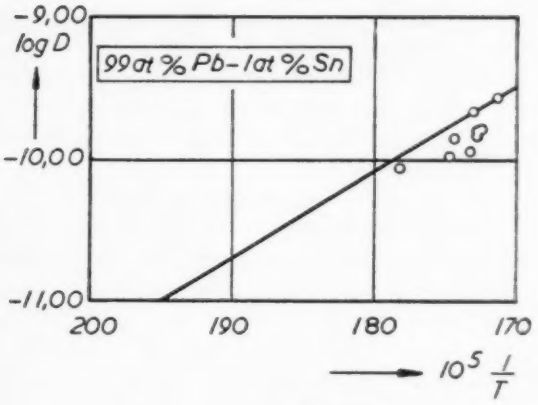

FIGURE 4

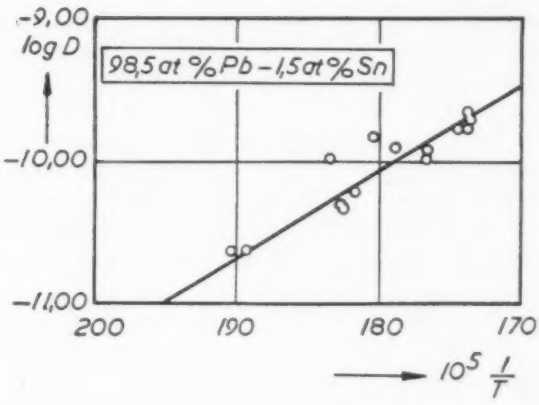

FIGURE 5

FIGURES 2–5. Observed self-diffusion coefficients of lead in lead-silver-, lead-cadmium- and lead-tin-alloys. The line drawn is that for pure lead.

The writer is extremely grateful to Professor G. J. Sizoo and his collaborators of the Physical Laboratory of the "Vrije Universiteit" at Amsterdam for their care in depositing the radioactive layer on the specimens and to Dr. T. J. Tiedema of the Laboratory for Physical Chemistry of the "Technische Hogeschool" at Delft for his help in preparing the single crystals. He is indebted to Professor W. G. Burgers for helpful discussions.

"Researchgroup Metals F.O.M.-T.N.O." sponsored by Z. W. O.

B. OKKERSE

Laboratory for Physical Chemistry
Technical University
Delft, Netherlands

References

1. SEITH, W. and KEIL, A. Z. Metallk. **25** (1933) 104.
2. FISHER, J. C. J. Appl. Phys. **22** (1951) 74.
3. HOFFMAN, R. E. and TURNBULL, D. J. Appl. Phys. **22** (1951) 634.
4. SLIFKIN, L., LAZARUS, D. and TOMIZUKA, T. J. Appl. Phys. **23** (1952) 1032.
5. TIEDEMA, T. J. and KOOY, C. L. D. Appl. Sci. Res. **A3** (1952) 391.
6. BARRER, R. M. Diffusion in and through Solids (Cambridge, 1941) p. 45.
7. LE CLAIRE, A. D. Acta Met. **1** (1953) 438.
8. ZENER, C. J. Appl. Phys. **22** (1951) 372.
9. SEITZ, F. Acta Cryst. **3** (1950) 355.
10. SEITH, W. and KEIL, A. Z. phys. Chem. **B22** (1933) 350.
11. HOFFMAN, R. E. and TURNBULL, D. J. Appl. Phys. **23** (1952) 1409.

Elastic Strains around an Interstitial Atom*

In a paper in this ussue Tucker and Sampson [1] have shown how precision X-ray measurements of lattice parameter may be used to detect interstitials in radiation damaged metals. To estimate the size of the elastic strains caused by an interstitial atom in the lattice they fit an equation for an elastic displacement at a center of pressure (equation 6) to the atomic displacements calculated by the author [2] for copper. Because these displacements were calculated roughly in a situation where emphasis was concentrated on the energy of the interstitial and because the atomic displacements of third nearest neighbors were arbitrarily set equal to zero, it was decided to reexamine the subject more carefully.

In the course of this reexamination it was discovered that there was an error in the definition of δ as given [3] for interstitial configuration. As used there in the minimization of the closed shell repulsive energy δr_0 (not δd) should be the magnitude of the displacement of second neighbors. Here d is the lattice constant and r_0 is the nearest neighbor distance. The values in Table II [3] correspond to the definition as used here but the formulas and values in Table III are in error. To correct replace δ by $\delta/2^{1/2}$. The net result is to lower slightly the energies of Configuration B relative to C so that they nearly coincide on the basis of either interaction potential U_a or U_b.

Originally only the repulsion of closed ion core shells had been considered in determining the atomic displacements. If one now assumes that the displacements of second nearest neighbors, third nearest neighbors, etc., fall off as r^{-2} according to the elastic formula, then some attractive force will be needed to give lattice stability. The simplest device to add to our model to insure stability was to introduce a constant inward radial force or hydrostatic pressure sufficient to hold the δ-neighbors at their equilibrium positions with no interstitial present and first neighbors undisplaced. With this pressure and the U_a repulsive potential the distortion energy was minimized. Material outside a radius of $1.7d$ was treated as an elastic continuum and contributed less than 5% of energy at all times. With this model the equilibrium value of δ was 0.05_2. The equilibrium value of ϵ turned out to be 0.21 as before. An alternate procedure for introducing lattice stability is to replace the repulsive potential with a Morse function [4]. With the same value for ϵ it was found that the equilibrium value of δ was 0.04_0. A smaller displacement might be reasonably expected in this case since the Morse function gives a "softer" potential.

Finally some consideration has been given to fitting the elastic formula to the atomic displacements found for the asymmetrical C-configuration [2]. These displacements vary markedly in direction and magnitude and exhibit axial rather than radial symmetry. By employing as generating functions spherical harmonics of higher order [5] (in this case second and fourth) in addition to the spherically symmetric function, it was possible to fit approximately the atomic displacement found for this configuration. At large distances only the spherically symmetric function contributes appreciably to the strains. The size of this contribution is roughly comparable to the radial strain found for the symmetric configuration B, though possibly 20 or 30 per cent larger. Since there is some likelihood that configuration C rather than B may be the stable one for the interstitial atom, it is fortunate that the strain pattern at large distances from the interstitial is roughly independent of the choice of configuration.

To sum up, an investigation of the atomic displacements in the neighborhood of an interstitial atom in a copper lattice has been fitted to a radial elastic displacement at large distances of the form bd^3/r^2. Alternate atomic force models, a repulsive ion core potential modified to give lattice stability and a Morse potential, give a value for b of 0.04 to an accuracy of about 20 per cent.

The authors wishes to express his thanks to Drs. Tucker and Sampson for pointing out the interest in this problem and for their helpful criticism of this letter.

H. B. HUNTINGTON

Physics Department,
Rensselaer Polytechnic Institute.

References

1. TUCKER, C. W. and SAMPSON, J. B. Acta Met. **2** (1954) 433.
2. HUNTINGTON, H. B. Phys. Rev. **91** (1953) 1092.
3. See ref. 2, p. 1094.
4. SLATER, J. C. Introduction to Chemical Physics (New York: McGraw-Hill Co., 1939), p. 454.
5. LOVE, A. E. H. Mathematical Theory of Elasticity (Dover, 1944), p. 249.

*Received March 18, 1954.

On the Relation of the Disordering of a Superlattice to the Melting of the Disordered Alloy*

In a recent note [1], Oriani has drawn attention to a relation between the critical temperature of disordering of an alloy, T_c, and the solidus temperature, T_s, of the disordered alloy of the same temperature. He finds that the mean T_c/T_s is 0.63 ± 0.06 for 1-to-1 alloys and 0.55 ± 0.10 for the 1-to-3 alloys. Though unexplained, the correlation appears to exist and is quite intriguing. However, some questions may be raised by a consideration of this ratio in certain ternary alloys.

Consider the substitution of gold for silver in β-AgZn. The critical temperature is a function of the gold content, T_c being higher with higher gold content [2]. This is to be expected since pure AuZn is presumably ordered up to T_s [3]. The ζ-to-β transformation, which occurs at 280°C in pure AgZn, cannot be considered as a true order-disorder transformation and only with gold substitutions can the $\beta' \rightarrow \beta$ transformation be observed. By extrapolation of T_c as a function of gold content, it was shown that pure AgZn should disorder near 270°C. Thus, T_c/T_s varies from about 0.56 for pure AgZn to 1.00 for pure AuZn.

Similar experiments can be performed with AgCd. For an alloy of 10 per cent Au, 40 per cent Ag, 50 per cent Cd the critical temperature is 375°C [4]. Again, the ζ-to-β transformation cannot be considered as an order-disorder transformation and 440°C (the temperature of the $\zeta \rightarrow \beta$ transformation) is much too high. A rough estimate of T_c for pure AgCd can be obtained by extension of the β' portion of the curve of electrical resistance as a function of temperature [5]. A reasonable estimate is 325°C. In these alloys, then, T_c/T_s varies from 0.61 for pure AgCd to 1.00 for pure AuCd. Note that this improves agreement for pure AgCd with the mean value of T_c/T_s for 1-to-1 alloys.

It should be pointed out that AuCd does not disorder at 267°C, nor is it thought to disorder at all below T_s [6; 7]. Electrical resistance measurements in the region of the supposed order-disorder transformation give no indication of any change taking place [4].

It may be that such carefully contrived ternary alloys must be placed in a separate category. The above examples may or may not invalidate the correlation observed by Oriani. However, any explanation of the correlation must also explain the effect of third element substitutions.

L. MULDAWER
Physics Dept., Temple University
Philadelphia, Pennsylvania

*Received April 29, 1954.

References

1. ORIANI, R. A. Acta Met. **2** (1954) 343.
2. MULDAWER, L. J. Appl. Phys. **22** (1951) 663.
3. OWENS, E. A. and EDMUNDS, I. G. Proc. Phys. Soc. (London) **50** (1938) 389.
4. MULDAWER, L. Unpublished research.
5. MULDAWER, L., AMSTERDAM, M., and ROTHWARF, F. Trans. A.I.M.E. **197** (1953) 1458.
6. ÖLANDER, A. J. Am. Chem. Soc. **54** (1932) 3819.
7. BYSTRÖM, A. and ALMIN, K. E. Acta Chem. Scand. **1** (1947) 76.

Metallurgical Abstracts, General and Nonferrous. Vol. 19, New Series, 1951–1952. London: The Institute, 1952. Pp. 895.

This last volume of Metallurgical Abstracts has 896 wide columns of abstracts containing references to approximately 5000 papers; this in one year! The enormous number of papers that a metallurgist could conceivably be concerned with makes abstracting services essential, whether one is concerned with either the scientific or the practical aspects of metallurgy. Although there are other metallurgical abstracts—including the ASM's Metals Review which has the merit of promptness—the English Metallurgical Abstracts meet the requirements of the physical or nonferrous metallurgist better than all the others. The Abstracts are long enough to give a clear picture of what is covered, are written by abstractors obviously conversant with the subject matter, and are well classified and indexed so that one does not need to skim over large numbers of irrelevant entries.

An important feature of Metallurgical Abstracts is the bibliography and particularly the Book Review section. The latter has the rare quality of honesty. All books are not automatically to be recommended. Far too many are written just because a publisher saw a chance to make a penny by having a title in a field where a gap was known to exist. The reviewers selected for Metallurgical Abstracts show no reluctance to criticize the author or the publisher and this should have a salutary effect. The reviews by H. W. G. Hignett and J. S. G. Thomas are consistently good reading.

In reviewing Metallurgical Abstracts adverse criticism is impossible and only minor suggestions can be made. One can deeply deplore the fact that the Institute of Metals and their older sister, the Iron and Steel Institute, have not combined their nonferrous and ferrous abstracts into a single publication. From a scientific standpoint there is little harm done since the present Abstracts includes the most important papers on structure, deformation, and transformation in steels, as well as other metals. One wonders what advantage is gained by including abstracts of the host of United States Atomic Energy Commission and other United States government progress reports. These are written hurriedly according to the calendar or contract by investigators mainly to justify the continuation of their contracts. If the authors are proud of their work these reports are followed by a paper in one of the regular technical journals, and no purpose is served by cluttering up abstracts and indices with preliminary undigested potboilers.

The recent publication of a decennial index, arriving a whole decade after the period covered, will facilitate literature searches prior to 1943. It is greatly to be hoped that the index covering the succeeding ten volumes will be given a very high priority, for a search through more than ten annual indices is a discouragement to the user.

C. S. SMITH

The Journal of the Institute of Metals. Vol. 50, 1951–1952. N. B. Vaughan, Editor. London: The Institute, 1952. Pp. 683.

Reviewing a single volume of a journal is like commenting upon one stone in a building. Each volume of "JIM" is not expected to be a complete textbook of metallurgical science and practice. One asks only that it provide a place for publishing advanced research in the physics and chemistry of metals and a medium wherein industrial metallurgists can keep in touch both with advancing science that may be useful to them and with the changing patterns of industrial operations. The emphasis should be on the new, not the established.

The present volume includes several excellent papers on constitution of alloys (which has always been an important feature of English metallurgy), a number of papers on sub-crystal formation, on the role of grain boundaries in deformation, a few papers on stress corrosion, and four papers on titanium and its alloys. The problems of the founder are represented by two papers on metal-mold reactions and one on grain refinement by inoculation. The recent broadening of scope of the Institute is reflected in the 30-page symposium on metal economics included in the present volume, while the 86-page symposium on equipment for thermal treatment is an expression of the long-standing interest in industrial aspects of metallurgy. A man who intends to call himself a metallurgist must have some familiarity with all these aspects of his subject, and a young man can find no better post-textbook than this journal. He should not skip those parts that do not concern the minutiae on his thesis.

As the reviewer placed this volume on his shelves, he noticed the coincidence that it was exactly the fiftieth from the first he received in joining the

Institute in 1923. It is interesting to compare volume 80 with volume 30. Both volumes have several papers on the constitution of alloys and both have a single paper on quaternary alloys. X-ray diffraction was hardly used metallurgically in 1923, and the difference between the two volumes is in large degree attributable to the impact of X-ray diffraction on the understanding of metal structure. The 22nd May Lecture, which appeared in volume 30, was by the late great Walter Rosenhain, and it brought to many metallurgists for the first time some understanding of what the then-new methods of X-ray diffraction meant to their subject. He mentions the amorphous grain boundary, a concept which passed completely out of fashion and now back again. The 42nd May Lecture in volume 80 is on "The Place of Plastics in the Order of Matter." It is a useful summary of the kind of plastic available and a warning to metallurgists that structural materials are no longer their exclusive prerogative (perhaps even foreshadowing as great a change in metallurgy as did Rosenhain's lecture). The writer remembers the skepticism of the oldtimers in the audience in 1923: perhaps the metallurgist of the future will be a broader man, concerned also with covalent and ionic as well as metallic bonds.

X-ray studies no longer have the field of scientific metallurgy to themselves as much as they did a decade ago, and volume 80 contains many examples of a renaissance of microscopic methods, particularly as applied to the formation and movement of sub-grain boundaries. The study of deformation mechanisms, as the microscopist but not the diffractionist has always known, can be properly understood only by consideration of structure at all scales and the interaction between them. The superb paper by Ulick Evans on corrosion in 1923 has no counterpart in 1952, though corrosion is still with us.

In 1923 the National Physical Laboratory reported investigations on the effects of oxygen in copper; in 1952 the Australian Commonwealth Research Organization reports studies of oxygen in titanium. Dilatometry is replaced by thermoelastic analysis in studying transformations. Studies of casting temperature, and volume change on solidification in the earlier volume are replaced with investigations of grain refinement and metal-mold reactions in 1952. The early concern with red stains on sheet brass seems to have no counterpart in volume 80, largely because of the great advance in heat treating equipment which is described in the symposium.

The greatest difference between volumes 80 and 30 is the presence of 76 papers in the latter volume and 17 in the former —725 quarto pages versus 407 octavo. The same kinds of metallurgical problems seem to be still with us, but they require many more words and many more people to study them. Yet with all this, there is an impressive increase in understanding, less to be learned by rote and more to be understood as an application of a principle. It is significant, too, that in 1923 the Institute was able largely to avoid economic matters, while in 1952 a most important discussion was held on metal resources, both primary and secondary.

Readers of ACTA METALLURGICA are mostly concerned with the science of metals; many of them are physicists. Those who call themselves metallurgists can scarcely afford to be without a set of the journal under review. As a mirror of progress in all aspects of metallurgy beyond smelting, it is unmatched. Though Institute headquarters are in London, membership is international, and though foreign members can rarely attend meetings, they will find that the information in the Journal knows no national boundary. "JIM" is a fine publication and continues through the years to serve the double function of reporting current methods and theories and leading the changes in both science and practice on which the future depends.

C. S. SMITH

SOME CURRENT PAPERS IN OTHER JOURNALS

Acta Crystallographica, Vol. 7

April, 1954

The Determination of Pseudosymmetric Structures. P. VOUSDEN.

The β-Uranium Structure. J. THEWLIS and H. STEEPLE.

'Mean Strains' in Worked Aluminium. P. GAY and A. KELLY.

The Diffraction of X-rays by Close-packed Crystals Containing both 'Growth Stacking Faults' and 'Deformation or Transformation Stacking Faults'. R. GEVERS.

'β-Tungsten' as a Tungsten Oxide. G. HÄGG and N. SCHÖNBERG.

The (hki0) Reflexions of Graphite. G. E. BACON.

An X-ray Examination of the Spinel-type Mixed Oxide, $MgFeAlO_4$. G. E. BACON and A. J. E. WELCH.

On the Crystal Structures of the β- and γ-Phases in the System Indium-Tin. R. M. SCREATON and R. B. FERGUSON.

On the structure of CuAu II revealed by electron diffraction. SHIRO OGAWA and DENJIRO WATANABE.

Further complexities in the lamellar structure of alkali felspars. J. V. SMITH and W. S. MACKENZIE.

Archiv für das Eisenhüttenwesen

Heft 1–2 (Januar/Februar, 1954)

Das metallurgische Verhalten der Chromerze. D. HOENES und GEORG VOLKERT.

Zur Frage der Qualitätsuntersuchung des Stahlwerksteeres. A. ROSENGREN.

Wirkungsweise und Handhabung der Flussmittel für das Feuerverzinken. JOSEPH HILLE.

Die Probenahme von Erzen und Schlacken bei der Eisenerzeugung. KURT MOHL.

Wechselbeanspruchung und Kristallzustand. III. Zur Frage nach den Beziehungen zwischen Kristallitverformung und Verfestigung oder Schädigung. HERMANN MOLLER und MAX HEMPEL.

Die Kerbschlagzähigkeit weicher Feinkornstähle im ungealterten und gealterten Zustand. HEINZ KORNFELD.

Untersuchungen über die Kristallisation von Nickel-Kohlenstoff-Legierungen und von Gusseisen. ERICH SCHEIL.

Festigkeitseigenschaften von Lichtbogenschweissungen bei wassergehärtetem Thomasstahl. JAKOB COLBUS.

Verfahren zur Erzielung von Zwischenstufengefüge in zylindrischen Teilen mittleren Durchmessers aus Chrom-Molybdan-Vergütungsstahl. WALTER EILENDER und HEINRICH AREND.

Schnellpolieren metallographischer Schliffe aus Gusseisen. ERLING JUUL NIELSEN.

Journal of the Chemical Society

April, 1954 (Partial Contents)

A Comparison of Chemical and Electrolytic Methods of Reduction. M. G. FOUAD and J. F. HERRINGSHAW.

Journal of the Institute of Metals, Vol. 82

April, 1954

The forgeability, creep strength, and ductility of molybdenum and some of its alloys. J. H. RENDALL, S. T. M. JOHNSTONE, and W. E. CARRINGTON.

The arc melting of metals and its application to the casting of molybdenum. G. L. HOPKIN, (Mrs.) J. E. JONES, A. R. MOSS, and D. O. PICKMAN.

The Pressure welding of molybdenum. A. R. MOSS.

Factors influencing brittleness in aluminium-magnesium-silicon alloys. I. R. HARRIS and P. C. VARLEY.

Techniques for the investigation of thermal conditions in continuous casting. D. M. LEWIS.

The use of autoradiography for finding the solidification boundary in continuously cast aluminium. J. L. PUTMAN.

May, 1954

The domain structure of ferromagnetic metals. L. F. BATES.

The influence of extrusion direction on the corrosion and stress-corrosion of aluminium-copper-magnesium alloys. E. A. G. LIDDIARD and WINIFRED A. BELL.

A redetermination and interpretation of the titanium-rich region of the titanium-chromium system. (Mrs.) M. K. MCQUILLAN.

Resistivity anomalies in the nickel-chromium system as evidence of ordering reactions. ROLF NORDHEIM and NICHOLAS J. GRANT.

X-ray determination of the alpha-phase boundary of the copper-indium alloy system. R. O. JONES and E. A. OWEN.

Some further observations on the fatigue process in pure aluminium. P. J. E. FORSYTH.

The system uranium-mercury. B. R. T. FROST.

The ternary compound E in the system aluminium-chromium-magnesium. (Miss) K. LITTLE.

Revue de Métallurgie 51e Année

Numéro 3, Mars 1954

Mesures statiques et dynamiques du module d'élasticité de matériaux frittés. J. BARDUCCI et R. CABARAT.

Contribution à l'étude des mises au mille de coke des hauts fourneaux. M. BRUN et J. SZCZENIOWSKI.

Calcul, construction et comportement des engrenages trempés à la flamme. H. W. GRÖNEGRESS.

Influence d'une addition de zirconium sur la texture cristalline des demiproduits en alliage d'Al filés à la presse et traités thermiquement. J. HÉRENGUEL et M. SCHEIDECKER.

Etude de la précipitation submicroscopique dans les alliages réfractaires nickel-chrome tenaces à chaud du type 80–20. B. BAILLIE et J. POULIGNIER.

Le dosage de l'hydrogène dans les soudures à l'arc des aciers doux. Mode d'expression des résultats. M. ROUX.

Etude des échantillons de laitiers prélevés au convertisseur Thomas sur charges soufflées sans addition de chaux. PAUL KOZAKEVITCH et PIERRE LEROY.

Influence des joints intergranulaires des métaux et alliages sur certaines propriétés mécaniques au voisinage du point de fusion. CHRISTIAN BOULANGER.

PREFERRED ORIENTATION IN α-URANIUM*

C. M. MITCHELL and J. F. ROWLAND†

The preferred orientation of uranium rolled in the α-range has been investigated by X-ray diffraction using a spherical specimen in the Geiger counter spectrometer. Complete figures of the principal pole distributions have been obtained without absorption correction.

At low rolling temperatures, a texture is obtained having principal pole maxima corresponding to a single unit cell orientation. The (001) and (100) pole maxima lie in the plane normal to the rolling direction at 30 and 60 degrees respectively to the compression axis; the (010) pole maximum is parallel to the rolling direction. At higher rolling temperatures near the recrystallization point a duplex texture is obtained, having a common (001) pole maximum at 20 degrees to the compression axis, and having the (010) and 110) poles parallel to the rolling direction.

The unit cell probability distribution has been derived using two principal pole distributions, and from this the inverse pole figures have been calculated, giving the distributions of the compression axis and of the rolling direction over the unit cell.

A direct comparison of the rolling figures predicted by Calnan and Clews is obtained from the inverse pole figures. Good agreement is obtained with the figures predicted for rolling at low temperatures where deformation occurs predominantly by twinning with a small amount of slip. The rolling figures obtained at high temperatures giving the duplex texture are not in agreement with Calnan and Clews.

A treatment of the deformation of α-uranium during tension, compression and rolling is described, using the glide mechanisms determined by Cahn, which is compatible with both the low- and high-temperature textures.

The reorientation of the (010) axial and the duplex (010)-(110) axial textures upon recrystallization has been investigated. The (010) texture is shown to be relatively stable under recrystallization. The duplex texture undergoes reorientation to give a single component texture having the (151) pole axial. A (100) pole maximum occurs along the rolling direction which is shown to be due to overlapping of four symmetric components.

LES ORIENTATIONS PRÉFÉRENTIELLES DANS L'URANIUM-α

On a investigué, au moyen de la diffraction des rayons X, l'orientation préférentielle de l'uranium-α laminé, en se servant d'un échantillon sphérique, monté sur un "spectromètre" à compteur Geiger. Des figures polaires, complètes, pour les distributions principales des pôles, furent obtenues sans correction pour l'absorption. Aux basses températures de laminage on obtient une texture, dont les maxima principaux des pôles correspondent à une orientation unique de la maille cristalline. Les maxima des pôles (100) et (001) se trouvent dans le plan perpendiculaire à la direction de laminage, à 30° et à 60°, respectivement, par rapport à l'axe de compression; le maximum du pôle (010) est parallèle à la direction de laminage. Aux températures plus élevées de laminage, proches du point de recristallisation, une texture double est obtenue, ayant un maximum du pôle (001) commun à 20° par rapport à l'axe de compression, et dont les pôles (010) et (110) sont parallèles à la direction de laminage. La probabilité de la distribution de la maille a été déterminée en se servant de deux distributions principales des pôles; partant de là, les figures polaires, inverses, furent calculées, ce qui a donné les distributions des axes de compression et des directions de laminage dans la maille. En se basant sur les figures polaires, inverses, on obtient une comparaison directe avec les figures de laminage prédites par Calnan et Clews. On constate un bon accord avec les figures prédites pour le laminage aux basses températures, où la déformation s'opère principalement par maclage avec très peu de glissement, Les figures obtenues aux températures plus élevées de laminage, donnant des textures doubles, ne s'accordent pas avec les prédictions de Calnan et Clews. On décrit un traitement de la déformation de l'uranium pendant la traction, la compression et le laminage, en employant le mécanisme de glissement déterminé par Cahn, qui est en accord avec les textures obtenues aux basses, ainsi qu'aux hautes températures de laminage. On a investigué la réorientation de la texture axiale (010) et de la texture axiale, double (010)-(110) lors de la recristallisation. Il est constaté que la texture (010) est relativement stable pendant la recristallisation. La texture double subit une réorientation donnant une texture simple, dont l'axe est constitué par le pôle (151). Un maximum polaire (001) qui se présente le long de la direction de laminage est dû à un enchevauchement de quatre composantes symétriques.

TEXTUREN IM α-URAN

Die bevorzugten Orientierungen von im α-Gebiet gewalztem Uran wurden an einer kugelförmigen Probe mit Hilfe eines Zählrohr-Spektrometers röntgenographisch gemessen. Vollständige Polfiguren wurden ohne Korrekturen für Absorption erhalten.

Bei tiefen Walztemperaturen trat eine Textur auf, deren Hauptpolmaxima einer einzigen Elementarzellorientierung entsprach. Die Maxima der (001) and (100) Pole liegen in der zur Walzrichtung senkrechten Ebene und 30° resp. 60° zur Kompressionsrichtung. Das (010) Polmaximum ist der Walzrichtung parallel. Bei höheren Walztemperaturen, die in der Nähe des Rekristallisationspunktes lagen, trat eine Doppeltextur auf; sie hat ein gemeinsames (001) Polmaximum 20° von der Kompressionsrichtung und die (010) und (110) Pole parallel zur Walzrichtung.

Die Elementarzellverteilungsfunktion wurde unter Zugrundelegung von zwei Hauptpolverteilungen berechnet. Daraus wurden dann inverse Polfiguren berechnet, die die Verteilung der Kompressionsrichtung und der Walzrichtung in Bezug auf die Elementarzelle angeben.

*Received October 14, 1953; in revised form December 8, 1953.

†Physical Metallurgy Division, Mines Branch, Department of Mines and Technical Surveys, Ottawa, Ont.

Diese inversen Polfiguren konnten direkt mit den von Calnan and Clews angegebenen Walzfiguren verglichen werden. Die für Walzen bei tiefer Temperatur angegebenen theoretischen Figuren stimmten gut mit den röntgenographisch erhaltenen überein. In diesem Fall erfolgt die Verformung im wesentlichen durch Zwillingsbildung mit geringer Gleitung. Die für hohe Temperaturen erhaltenen Walzfiguren, die die Doppeltextur aufweisen, stimmen nicht mit Calnan und Clews' Angaben überein.

Es wird eine allgemeine Behandlung der Verformung von α-Uran durch Zug, Druck oder Walzen beschrieben; die von Cahn gefundenen Gleitprozesse, die sowohl die Tief- als auch die Hochtemperaturtexturen erklären, werden der Beschreibung zu Grunde gelegt.

Weiterhin wird die Reorientierung der (010)- und der Doppel (010)-(110) Axialtexturen während der Rekristallisation untersucht. Die (010) Textur erweist sich während der Rekristallisation als relativ stabil. Die Doppeltextur erfährt eine Reorientierung, die zu einer Einkomponententextur mit einem (151) Pol führt.

Ein in der Walzrichtung auftretendes (001) Maximum rührt von der Überlagerung von vier symmetrischen Komponenten her.

1. Introduction

The action of single crystal glide in producing preferred orientation in polycrystalline metals undergoing deformation by extension and compression, and the combined action of these during rolling, has been the subject of a series of papers by Calnan and Clews [1] who have studied the production of textures in the face-centered cubic system, and have predicted textures for the body-centered cubic [2] and close-packed hexagonal [3] systems and for α-uranium [4] in the orthorhombic system, using the glide systems outlined by Cahn [5]. The prediction for α-uranium has received only partial verification in the textures found in round rods by Harris [6].

An investigation of the preferred orientation in uranium plate-rolled in the α-range, below the recrystallization temperature, has been carried out by a method developed in these laboratories [7] using spherical specimens with the Geiger counter spectrometer. The method has enabled complete principal pole distributions to be obtained without absorption correction, and these have been found to have a high degree of resolution. A mounting of this type has been described in a recent article by Jetter and Borie [8].

It is demonstrated that the probability distribution of the unit cell can be determined from two principal pole distributions and this relation has been used to produce inverse pole figures, the probability distributions of the compression axis and the rolling direction on the stereographic projection of the unit cell. Quantitative figures have been obtained which can be compared directly with the distributions predicted by Calnan and Clews.

The orientations can be described in terms of two components, a low-temperature form having distribution maxima corresponding to a single unit cell orientation and a duplex orientation occurring at higher rolling temperatures. The low-temperature form is in agreement with the figure predicted by Calnan and Clews when glide is considered produced by twinning alone, but the duplex orientation does not agree with the predicted distribution where slip and twinning are considered to occur simultaneously. This has made it necessary to re-examine the deformation mechanism under combined twinning and slip.

The orientation figures employed in studying the deformation modes have been produced by rolling below the recrystallization point. The investigation of the preferred orientation in the α-phase range has been extended by recrystallizing the rolled material. A description of the reorientation on recrystallization has been obtained, which together with the rolling figures accounts for all orientations presently reported in flats and round rods treated below the transformation point.

2. Derivation of the Inverse Pole Figure

The Probability Distribution of the Unit Cell

The intensity distribution of the diffracting planes can be represented by the function $\rho(h_0k_0l_0)$ per steradian where the direction of the distribution vector lies long the diffracting plane normal and therefore coincides with the sphere radius passing through the spectrometer centre. The integral of the distribution over the sphere surface

$$\int_0^{4\pi} \rho(h_0k_0l_0)\, d\Omega = n \tag{1}$$

where n is the number of cooperating crystallographic planes of indices $(h_0k_0l_0)$ in the unit cell.

The position of a unit cell in a given reference system is fixed by stating the position of two lattice plane poles; the probability of the unit cell having this orientation can then be expressed by stating the compound probability of the simultaneous orientation of the two poles. For convenience the reference poles may be chosen as principal

unit cell directions which can be orthogonal in the orthorhombic system, and systems of higher symmetry.

Let $\bar{p}_A$ and $\bar{p}_B$ be the intensity distributions of the principal poles A and B in the reference system formed by the rolling direction R, the compression axis C normal to the rolling plane and the transverse axis T normal to R and C. Where α is the angle between $\bar{p}_A$ and C and β is the angle between the projection of $\bar{p}_A$ in the rolling plane R–T and the rolling axis R, the distribuion probability of $\bar{p}_A$ for angular increments $d\alpha$ and $d\beta$ is

$$p_A \, d\Omega = p_A \sin \alpha \, d\alpha \, d\beta.$$

The associated distribution vector $\bar{p}_B$, where pole B is orthogonal to A in the unit cell, can be considered to lie in the plane normal to $\bar{p}_A$ at an angle δ to the trace of the plane containing $\bar{p}_A$ and the C-axis, as illustrated in Figure 1a, where A coincides with the (001) pole and B with the (100) pole. The associated distribution vector $\bar{p}_B$ has an equal *a priori* probability of orientation in the plane normal to $\bar{p}_A$ and the probability of the unit cell having the orientation $\{\bar{p}_A; \bar{p}_B\}$, within the incremental angles $d\alpha$, $d\beta$, $d\delta$, is

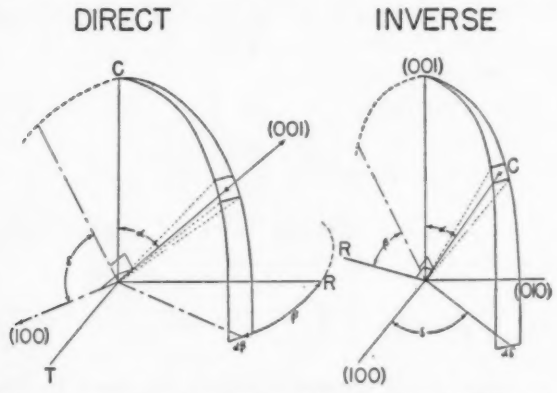

FIGURE 1. Transformation of the (001) and (100) principal pole distributions into the inverse pole figure giving the compression axis C distribution over the unit cell.

$$(2) \qquad \sigma_{AB} = \frac{p_A \, p_B \, d\Omega \, d\delta}{\int_{\Omega=0}^{4\pi} p_A \left\{ \int_0^{2\pi} p_B \, d\delta \right\} d\Omega} = \frac{1}{N} p_A \, p_B \sin \alpha \, d\alpha \, d\beta \, d\delta$$

The Inverse Pole Figure

The probability distribution of the principal rolling directions over the unit cell can be derived directly from the unit cell probability distribution. The C-axis distribution over the unit cell can be derived by translating the axes to the principal unit cell directions. The angle between (001) and C is α, the angle between the R-axis and (100) is β, and the angle between (100) and the projection of CA in the (001) plane is δ, as illustrated in Figure 5b. The probability of this orientation

$$d\sigma_{C-R} = d\sigma_{(100),(001)}.$$

The C-axis will have the same direction in the unit cell for rotations about C and the probability distribution of C is determined by permitting β to vary from 0 to 2π.

$$(3) \qquad p_{(C)} = \frac{p_{001} \left\{ \int_0^{2\pi} p_{100} \, d\beta \right\} \sin \alpha \, d\alpha \, d\delta}{\int_{\Omega=0}^{4\pi} p_{001} \left\{ \int_0^{2\pi} p_{100} \, d\beta \right\} \sin \alpha \, d\alpha \, d\delta}$$

3. Measurement of Preferred Orientation

The Spherical Specimen Mount

The motions of the spherical specimen and the construction of the holder are shown in Figures 2 and 3. An eccentric shaft is mounted on the spectrometer axis, and the sphere mount rotates on this shaft. The degree of eccentricity is equal to the radius of the spherical specimen, so that the spectrometer rotation axis lies in the tangent plane at the sphere apex. A second independent

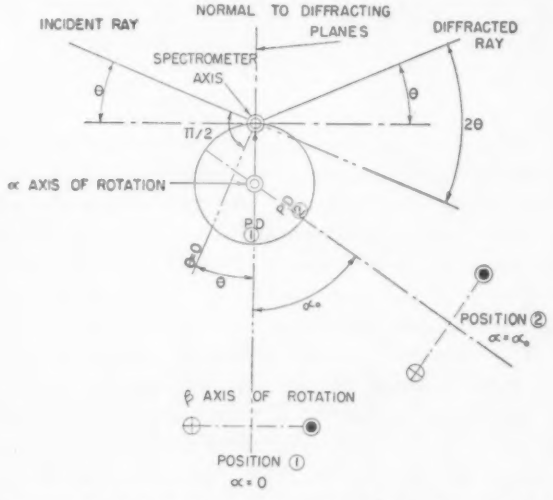

FIGURE 2. Schematic representation of the sphere motions. The tangent plane to the sphere at the intersection with the spectrometer axis is maintained in the diffracting position by rotation of the specimen mount at 1/2 the angular velocity of the scanning slit.

rotation of the sphere is obtained by an axis normal to the first axis passing through the sphere centre. In traversing, the eccentric shaft rotates with the spectrometer axis at half the angular velocity of the scanning slit, and the tangent plane at the apex of the sphere remains in the diffracting position.

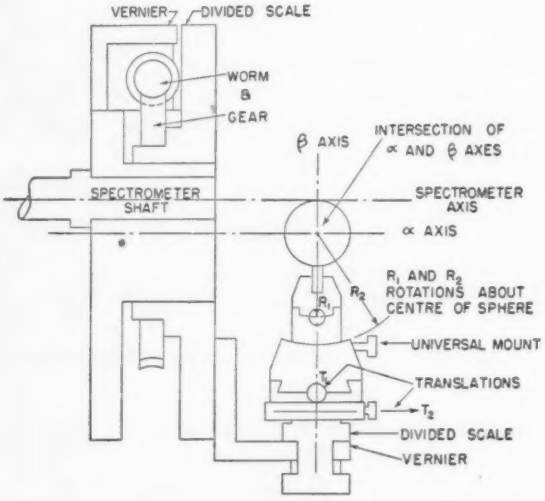

FIGURE 3. Section of the spherical specimen mount. A universal crystal mount is employed in addition to the motions shown in Figure 2 to enable the sphere to be centred, and to permit alignment of a given direction in the specimen with the β-rotation axis.

The specimen is set in a universal mount aligned with this axis, having two transverse motions at right angles for centering the specimen and two 30-degree arcs which rotate the sphere about its centre, and permit any radius within this solid angle to be aligned with the second rotation axis, as illustrated in Figure 3.

The spherical specimen mount permits a progressive analysis of the distributions of several crystallographic planes. If a distribution maximum of one set of planes of indices $(h_0k_0l_0)$ is aligned along the β-rotation axis, the maxima of an associated set of planes (hkl) will lie on a cone of semi-apex angle equal to the angle

$$\alpha\{(h_0k_0l_0) \wedge (hkl)\}$$

between the poles in the unit cell. The hkl pole distribution maxima can be located by rotating the sphere in the plane of incidence through this angle, and turning the sphere through one full rotation about the β-axis. As illustrated in Figure 4,

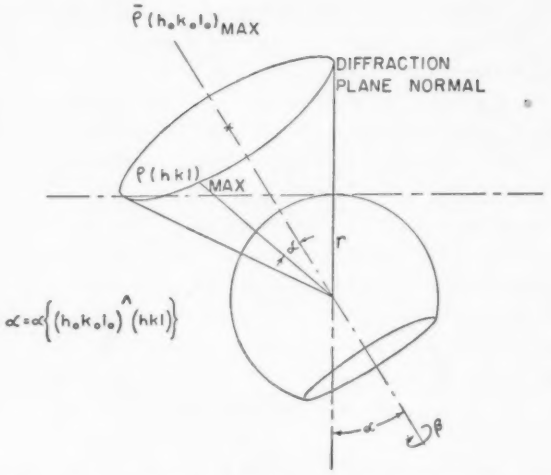

FIGURE 4. The locus of the distribution maximum of pole (hkl) passes through the diffracting position in a rotation from $\beta = 0°$ to $\beta = 360°$, when the pole $(h_0k_0l_0)$ distribution maximum is aligned with the rotation axis and $\alpha = \alpha\{(h_0k_0l_0) \wedge (hkl)\}$.

the β-rotation brings all poles on the cone surface through the diffracting position.

The Normalised Pole Figure

The normalisation factor P in the relation

$$\rho_{(hkl)} = \frac{I_D(hkl)}{P}$$

can be obtained directly from a complete pole figure by the summation

$$(4) \qquad P(hkl) = \frac{1}{n}\int_0^{4\pi} I_D(hkl)\, d\Omega$$

and can be determined without reference to the geometry of the spectrometer. When only a section of a pole figure is required or where comparison between the normalisation factors is used in checking the validity of a distribution, the θ-dependence of the normalisation factor must be known.

The distribution intensity of a pole can be calculated directly from the intensity of the diffraction line. Where the beam of intensity, I_0, per unit cross section is incident over a small region at the apex of the sphere, the diffracting area A_p can be treated as flat and parallel to the tangent plane; the integrated diffracted intensity for a specimen of linear absorption μ,

$$(5) \qquad I_D = \rho(h_0k_0l_0)\,\frac{\sin\theta}{2\mu}\cdot\frac{I_0Q\cdot A_p}{2R_0\sin\theta}$$

per unit length of scanning slit at radius R_0.

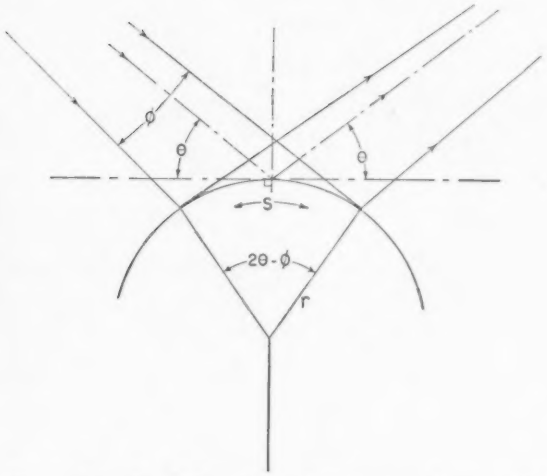

FIGURE 5. The diffracting region in a specimen of high absorption, limited by the incident and diffracted rays tangent to the specimen surface.

At low θ-values the length of arc in the plane of incidence will be defined between the limits formed by tangent incident and diffracted rays as illustrated in Figure 5. If the incident beam has a cross section $w_p \cdot l_p$ and a divergence ϕ_0,

$$A_p = (2\theta - \phi_0)\, r \,.\, l_p \qquad \text{for } \theta < \theta_s$$

$$A_p = \frac{w_p l_p}{\sin\theta} \qquad \text{for } \theta > \theta_s$$

where

$$\theta_s = \tfrac{1}{2} \sin^{-1} \frac{R_0 \phi_0}{r}$$

The ratio of the normalisation factors will be given by the relation

$$(7) \qquad \frac{P(hkl)}{P(h_0k_0l_0)} = \frac{Q(\theta)}{Q(\theta_0)} \frac{A_p(\theta)}{A_p(\theta_0)}$$

Specimen Preparation

The specimens used have been in the form of three-quarter spheres $\frac{1}{2}$ in. in diameter. The rolled plate was drilled and tapped and an arbor mounted normal to the surface. The arbor was then mounted in a lathe and the sphere formed, using a jig mounted on the compound rest, which rotated a tool point inward on a circle of variable radius, having its centre on the lathe rotation axis. An alternative method of cutting the sphere is described by Jetter and Borie [8].

The worked surface was removed by electropolishing using a solution of chromic acid in acetic acid (25 gm CrO_3 in 130 ml acetic acid and 7 ml water) at a current density of .5 to 1 ampere/cm^2. A smooth surface of high reflectivity was obtained by this procedure.

4. Orientation in Uranium Rolled Below the Recrystallization Point

The preferred orientation in uranium plate has been determined for two rolling temperature ranges, corresponding to deformation with slight (010) slip and deformation with a large degree of slip.

The polar distributions of the principal unit cell directions for plate, reduced 60 per cent in cross section by rolling after heating to a low temperature, are shown in Figure 6(i). In this temperature range Cahn [5] proposes twinning as the principal mode of deformation. The (001) pole distribution is shown in 6(i)*b* to be sharply defined about the transverse plane, and the polar distribution in this plane has a maximum at 30 degrees to the *C*-axis as shown in 6(i)*a*. The distribution of the (010) pole in the plane of (001) maximum was obtained by aligning the (001) maximum pole with the β-axis and scanning over a complete β-rotation; the distribution 6(i)*c* shows a sharply defined (010) lobe having its maximum along the rolling direction *R*. The definition of this lobe was checked by making cuts in the *C*–*T* plane, shown in 6(i)*d* where peaks of low intensity inclined at 20 degrees to the *T*-axis were obtained, and in the *C*–*R* plane shown in 6(i)*e* which showed an equal distribution to that in the (001) maximum plane. The (100) distribution in the *C*–*T* plane is shown in 6(i)*f* to have maxima at 20 degrees to the *T*-axis, corresponding to the inclination of the (010) peaks in this plane. The associated (001) and (100) pole maxima have a deviation of 10 degrees from a right angle, and are orthogonal with the (010) maximum; within this deviation the polar figures are consistent with a single orientation component in which the (001) and (100) maxima lie in the transverse plane, and the (010) maximum is directed along the rolling axis *R*. The stereographic projection of the (001) and (010) distributions are shown in Figure 7(i).

The polar distributions of the principal unit cell directions for a plate rolled at a temperature close to the recrystallization point, with a 60 per cent reduction of area are shown in Figure 6(ii). In this temperature range, Cahn predicts that (010) slip will predominate. The (001) distributions in the transverse plane shown in 6(ii)*a* and in the *C*–*R* plane shown in 6(ii)*b* are seen to be closely equiva-

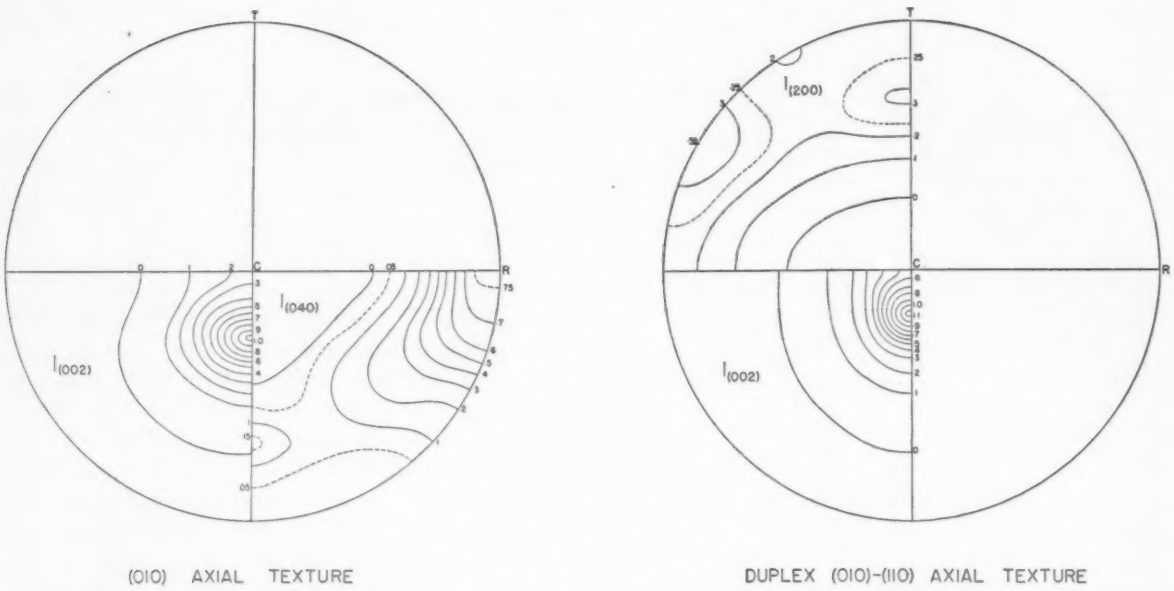

FIGURE 7. Stereographic projection of the principal pole distributions in rolled uranium plate. I, (010) Axial texture. II, Duplex (010)-(110) axial texture.

lent to the (001) distribution in the low-temperature rolling shown in 6(i)*a* and *b*; the angle of inclination of the (001) maximum to the *C*-axis is 20 degrees. The distribution of the (100) pole in the plane of (001) maximum was obtained as before by turning the β-axis into coincidence with one (001) pole maximum. The distribution of (100) in this plane shows two maxima in each quadrant, as illustrated in 6(ii)*c*, one lying in the *C*–*T* plane, equivalent to the (100) maximum in the low temperature case, shown in Figure 6(i)*f*, and one inclined at 30 degrees to the rolling axis *R*. Traverses taken in planes passing through these maxima are shown in Figure 6(ii)*c*, *d* and *e*. The

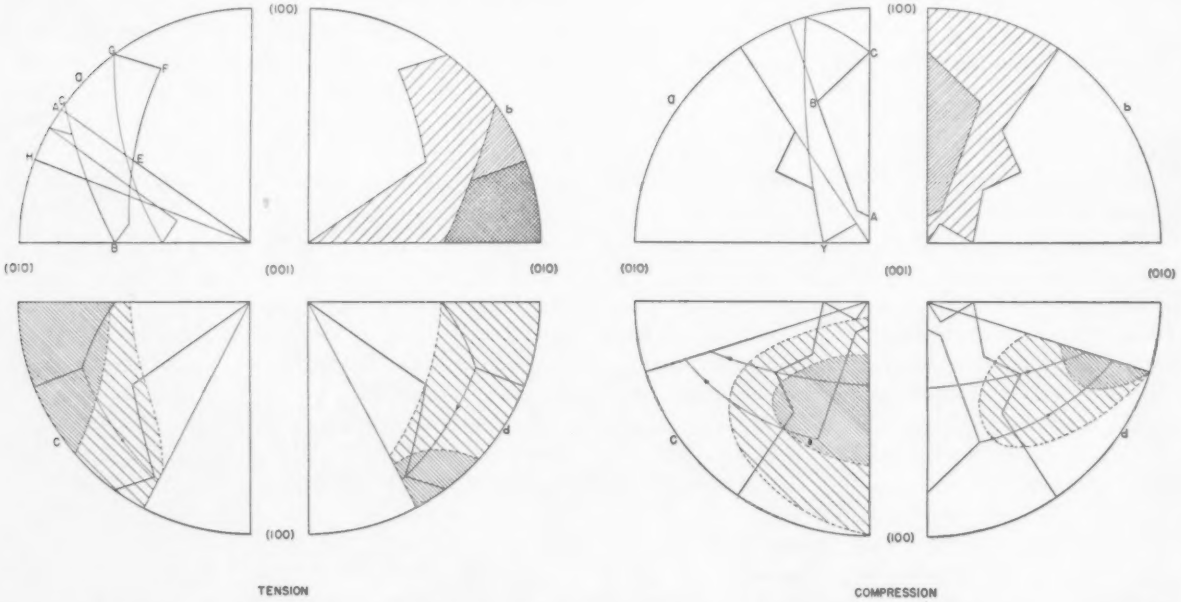

FIGURE 8. I Tension and II Compression axis distributions over the unit cell predicted by Calnan and Clews. (*a*) Twin boundaries; (*b*) Texture resulting from twinning alone; (*c*) Texture resulting from twinning and some slip; (*d*) Texture resulting from twinning with a large amount of slip.

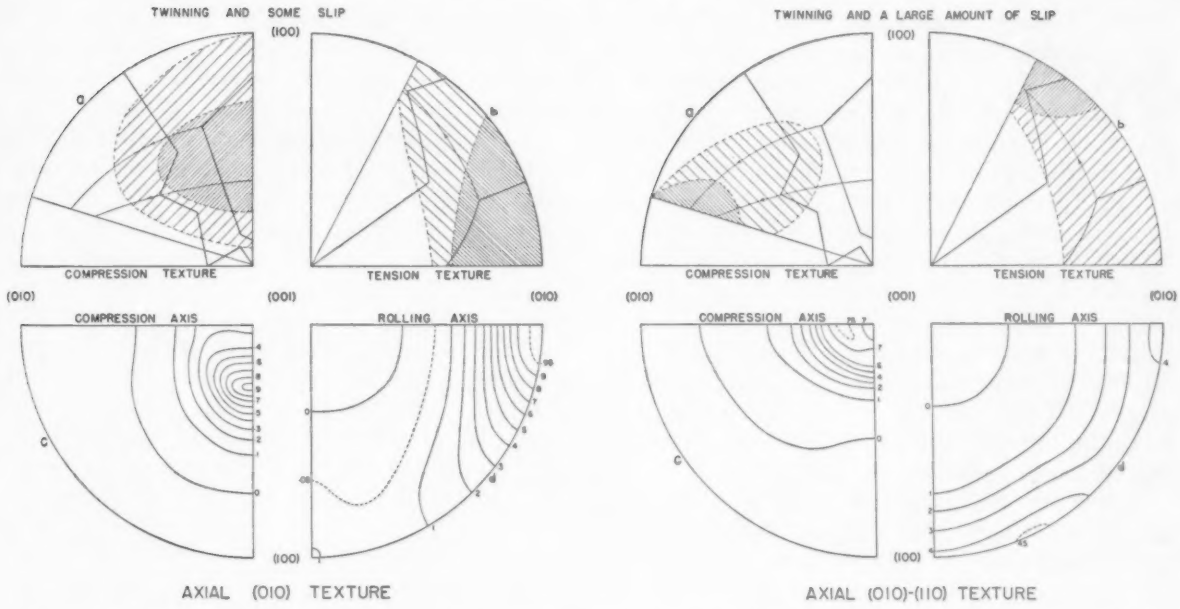

FIGURE 9. Inverse pole figures of the rolled plates derived from the principal pole figures of Fig. 7, together with the distributions predicted by Calnan and Clews for these rolling temperatures.

(100) distribution about the plane of (001) maximum is approximately equal in the two components and is equivalent to the (001) distribution about the transverse plane. The orientation is duplex; one component is equivalent to the low-temperature distribution having the (001) and (100) maxima in the transverse plane, with (001) at 20 degrees to the *C*-axis and the (010) maximum along the rolling direction; the second component has the same (001) maximum and the (100) and (010) maxima lie in the (001) maximum plane, the (100) maximum at 30 degrees to the rolling axis *R* and the (010) maximum at 60 degrees to the *R*-axis. In the second orientation the (110) pole lies within a few degrees of the rolling axis. The stereographic projection of the (001) and (100) pole distributions are shown in Figure 7(ii).

5. Deformation of α-Uranium

Comparison of Predicted and Experimental Inverse Pole Figures

Predicted stress-axis distributions over the unit cell have been derived by Calnan and Clews for α-uranium under tension and compression and these have been combined to give predicted rolling figures for plate rolled in the α-range with different degrees of twinning and slip. The inverse pole figures, giving the probability distribution of the compression axis and the rolling axis over the unit cell can be derived directly from the principal pole figures following equation (7). On the basis of the quantitative *C* and *R* distributions obtained in this experiment it has been possible to compare the results directly with the figures predicted by Calnan and Clews, and these are not in agreement.

The stress-axis distributions predicted by Calnan and Clews for tension and compression are shown as stereographic projections in Figures 8(i) and 8(ii). The distributions for twinning alone, on the twin system $K_1(130)$: η_2 [110], and the related systems $K_1(112)$: η_2 [312] and $K_2(112)$: η_1 [312] are shown in 8(i)*b* and 8(ii)*b*. The predicted modifications in these figures due to slip on the (010) plane in the direction [100] are shown in *c* and *d*, for increasing amounts of slip.

The inverse pole figures for the *R* and *C* distributions of the single component orientation texture, obtained by low-temperature rolling, are shown in Figure 9(i)*c* and *d*, the predicted distributions for twinning with a small degree of slip being shown for comparison in Figures 9(i)*a* and *b*. It will be seen that both the extension axis and compression axis figures are in close agreement with the predicted distributions. The compression axis maximum occurs on the (001)-(100) axis at 30 degrees to (001), and the rolling axis *R* maximum is coincident with the (010) axis. The orientation texture at low temperature is therefore in excellent agreement with the predicted twinning distribution.

The R and C distributions derived from the principal pole figures of the duplex (010)-(110) texture obtained in high-temperature rolling near the recrystallization point, are shown in Figure 9(ii)c and d; the predicted distributions for combined twinning and slip being shown for comparison in 9(ii)a and b. The extension axis R distribution has a maximum on the (010)-(100) zone at 30 degrees to the (100) axis, as predicted, but it shows a component whose maximum is coincident with the (010) pole as in the low-temperature texture. The compression axis C distribution has no maximum corresponding to that predicted on the (001) (130) axis, but has a zone of maxima lying on a cone with a semi-apex angle of 20 degrees, coaxial with the (001) axis.

The duplex orientation therefore has a residual texture equivalent to that observed in low-temperature rolling, corresponding to deformation by twinning with a small amount of slip, and a new component having the compression axis C maximum near the (001)-(130) zone within 20 degrees of the (001) pole and the R maximum, on the orthogonal (001)-(110) zone, lying in the (001) plane.

A Revision of the Theory of the Deformation of α-Uranium

Two possibilities can be considered in accounting for the discrepancy between the experimental textures and those predicted by Calnan and Clews. The first is that additional glide systems are operating which modify the orientation mechanism; the second is that an error has been made in applying deformation theory using the present slip systems. One additional twin $K_1(121)$: η_2 [311] has been identified by Cahn [5], having a high shear $s = .329$ compared to $s = .228$ for (112) and $s = .299$ for (130) twins. Further possible twins have been proposed by Frank [9] as $K_1(110)$: η_2 [310] and $K_1(011)$: η_2 [011] but these have not been observed experimentally at present. Cross slip on the (110) plane has been observed by Cahn in the possible directions [112] or [110], the latter being equivalent to the glide of twin K_1 (110): η_2 [310].

The agreement of the low-temperature rolling texture with the predicted texture for twinning with a small amount of slip indicates that the discrepancy is probably due to the action of slip at higher rolling temperatures. An examination of the deformation produced by the (130) and (112) twinning systems in combination with (010) slip has therefore been carried out to determine if a consistent orientation mechanism can be obtained on these systems alone. The modifications produced by further glide systems can then be examined.

The resolved shear stress on the most favourably oriented twinning system is shown for tension glide in Figure 10c and for compression glide in Figure 10d, plotted on the stereographic projection of the unit cell. In deriving the resolved shear stress, and the reorientation due to twinning the twins $K_1(112)$; η_2 [312] and $K_2(112)$: η_1 [312] can be treated as approximately equivalent. The reorientation by twinning in K_1 (112): η_2 [312] occurs by reflection in the (112) plane and in K_2 (112):η_1 [312] by reflection in the plane normal to [312] which is within a few degrees of (112). The resolved unit shear stress

$$S = \cos \chi \cos \lambda,$$

where χ is the angle of the stress vector to the pole of the glide plane; λ is the angle of the stress vector to the glide direction; the K_2 (112): η_1 [312] twin has $K_1 \approx (172)$; and the K_1 (112): η_2 [312] twin has $\eta_1 \approx (172)$; so that

$$\lambda([312]) \doteq \chi(112)$$

and

$$\chi(172) = \lambda([172])$$

and the resolved shear stresses are nearly equal.

The positions of low resolves shear stress $S \lesssim 0.1$ on the diagrams 10c and d represent the stable regions, in which twinning is least probable. In tension the stable region surrounds the (010) pole and in compression the stable region lies close to the (010) plane. The resolved shear stress on the (010) plane is shown in Figure 10a for tension and 10b for compression. The action of (010) slip in tension is to cause the stress vector to rotate along the great circle to the glide direction [100], and the action in compression is to cause the stress vector to rotate along the great circle to the (010) pole. The great circle paths from the stable regions are shown on the diagrams.

The reorientation due to (010) slip in compression can be considered to cause rotations from the stable twinning region to points $C1$ to $C4$ on the zone (001)-(130). The positions $C2$ to $C4$ correspond to the stable region proposed by Calnan and Clews. The resolved shear stress on the (130) and (112) twinning systems rises to $S \approx 0.4$ between the limits $C2$ and $C4$. Reorientation by (130) twinning will return the stress vectors to the points $C2'$, $C3'$ and $C4'$ near the original positions along

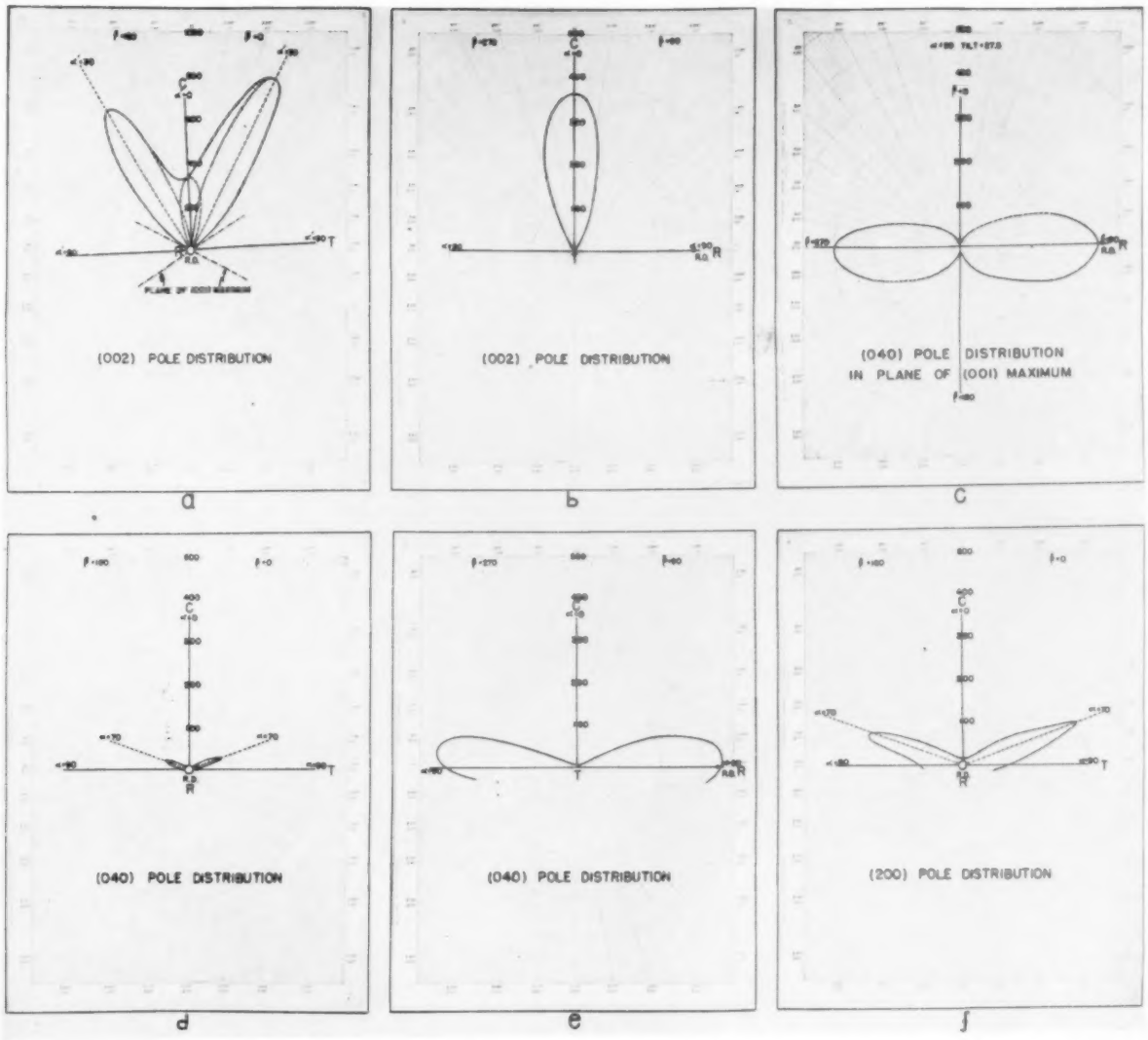

FIGURE 6.(i) Polar graphs of the principal pole distributions in uranium rolled in the α-range. Plate rolled at a low temperature. Single component texture having the (010) pole maximum parallel to the rolling direction.

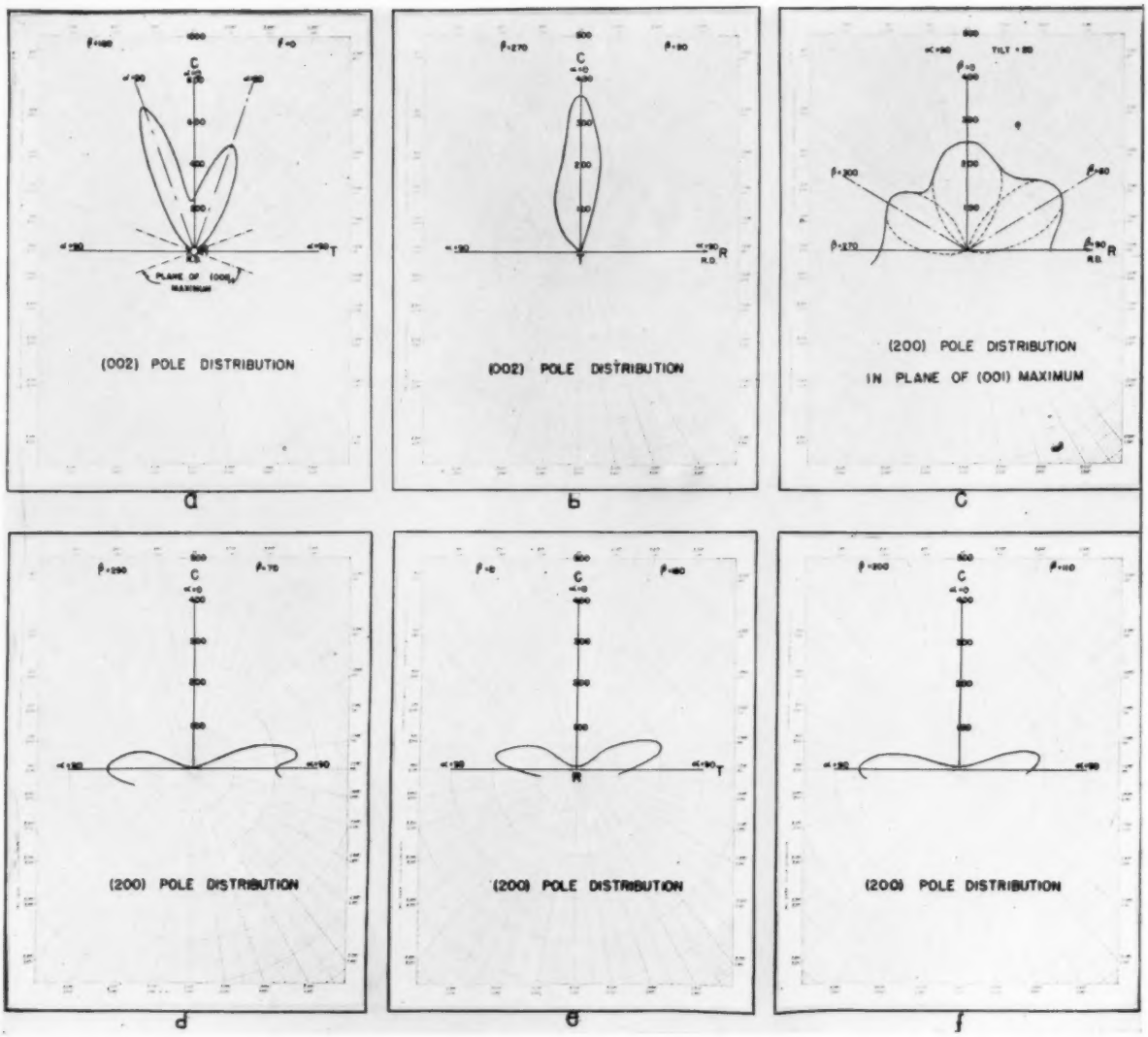

FIGURE 6(ii). Polar graphs of the principal pole distributions in uranium rolled in the α-range. Plate rolled at a temperature near the recrystallization point. Duplex texture having the (010) pole and (110) pole parallel to the rolling direction.

the (001)-(100) zone axis. The (112) twinning will orient the stress vectors at *C2″*, *C3″* and *C4″* in the stable region along the (001)-(100) zone within 45 degrees of the (001) pole. (010) slip occurring in this region will cause rotation of the compression

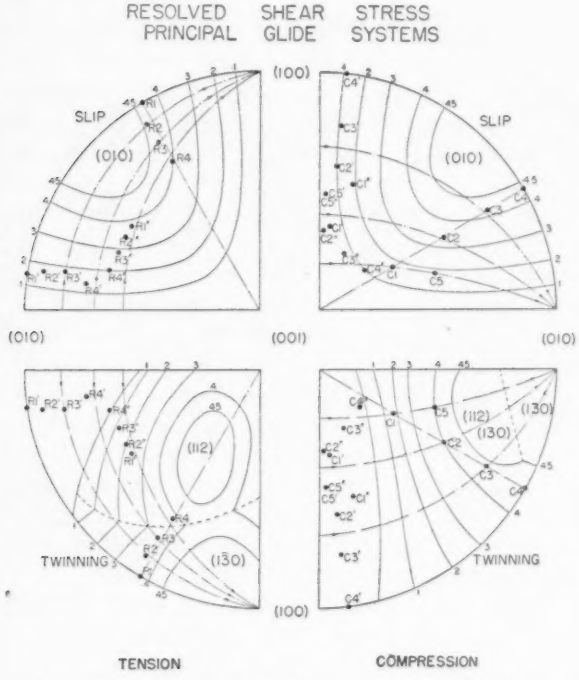

FIGURE 10. The resolved shear stress on the most favourable glide systems. (*a*) (010) slip in tension; (*b*) (010) slip in compression; (*c*) (130) and (112) twinning in tension; (*d*) (130) and (112) twinning in compression.

axis toward the (010) pole. The resolved shear stress S on the (010) plane is low over the great circle paths nearest to the (001) pole and is zero along the (001)-(010) zone. Compression axis rotation will be sluggish over this region. On the great circles to (010) at 20 and 30 degrees to (001) the shear stress on the twinning systems rises to $S \doteq 0.3$ at *C5* and *C2*. Reorientation by (130) and (112) twinning will occur to *C5′* and *C2′* and to *C5″* and *C2″* respectively, these points lying near the (001)-(100) zone at greater than 45 degrees to (001). In this region cycling will occur with higher resolved shear stress on the (010) plane over the great circle paths, (130) twinning returning the vectors to the (001)-(100) zone axis, until (112) twinning causes reorientation near the (001) pole. The compression axis maximum will therefore be formed along the (001)-(100) zone within 45 degrees of the (001) pole. As the (010) slip increases, with increasing deformation temperature, the rate of cycling will increase and the compression axis maximum will move along the (001)-(100) zone to a region of lower (010) shear stress about the (001) pole.

The tension axis distribution produced by (130) and (112) twinning acting alone has a maximum surrounding the (010) pole where the resolved shear stress $S \lesssim 0.1$. Under (010) slip the tension axis will rotate along the great circle toward the (100) pole, into a region of high (010) shear stress. The great circle paths enter an area of high resolved shear stress on the (130) twinning plane near the (001)-(110) zone. Reorientation by (130) twinning of points *R1* to *R4* in this zone will return the tension axis to *R1′*, *R2′*, *R3′* and *R4′* in the region near the (010) pole and a cycle of (010) slip and (130) twinning will be established between these regions. Twinning on the (112) system will cause reorientation of *R1*, *R2* and *R3* to *R1″*, *R2″* and *R3″* on the great circle between *R4* and the (100) pole. As these points pass *R4* under (010) slip reorientation to *R4′* by (130) twinning or to *R4″* by (112) twinning will transfer the tension axis to the region near the (010) pole. The combined action of (130) and (112) twinning under (010) slip therefore sets up a closed cycle. Two maxima are formed, one about the (010) pole coincident with the maximum for twinning alone, and one about the (110) pole. The relative concentration about the (110) pole will increase with increasing (010) slip at high deformation temperatures.

The rolling figures can be derived directly from the compression axis and tension axis distributions providing the corresponding component maxima are orthogonal. The tension axis component having its maximum about the (010) pole will be orthogonal with the compression axis maximum on the (001)-(100) zone. The tension axis component having its maximum about the (110) pole will be orthogonal with a compression axis maximum on the (001)-(130) zone, a corresponding compression axis maximum occurring on the zone (001)-($1\bar{3}0$). Where these maxima are within 20 to 30 degrees of the (001) pole they will lie within the region of minimum resolved shear stress on both the (010) slip and the (130) and (112) twinning systems. It follows, therefore, that, for orthogonality between the compression and tension axis maxima in the rolling texture, dispersion of the compression axis maximum must occur on a cone about the (001) pole. As slip increases and the tension axis component about the (110) pole builds up, resolution should be observed in the com-

pression axis maximum along the (001)-(130) and (001)-(1$\bar{3}$0) zones.

The experimental results are in substantial agreement with the textures predicted by this mechanism. The inverse pole figures are shown in Figures 9(i) and 9(ii). The rolling axis distribution in the low-temperature texture has its maximum about the 010 pole, and the corresponding compression axis maximum lies on the (001)-(100) zone at 30 degrees to the (001) pole. At higher rolling temperatures the second distribution maximum in the rolling axis distribution is found at the (110) pole. The compression axis maximum has moved to within 20 degrees of the (001) pole and lies on a cone surrounding the pole, compatible with unresolved maxima orthogonal to the tension axis components, on the zones (001)-(130), (001)-(100) and (001)-(1$\bar{3}$0).

6. Recrystallization of Rolled Uranium

The change in orientation produced by annealing for short periods above the recrystallization point has been investigated for the single-phase and duplex orientation textures. The specimens were immersed in a lead bath at a temperature near the recrystallization point for ten minutes and quenched to room temperature. The specimens were then electropolished and examined by polarized light to ensure that grain growth had been initiated in the worked material, and textures having small equiaxed grains were used in measuring the orientation.

The principal pole distribution for the single-phase (010) structure after recrystallization is shown in Figure 11(i). Comparison with the pole distribution before recrystallization, Figure 7(i) shows that some dispersion has occurred, but that the distribution maxima have not altered. The microphotograph of this texture shows definite grain growth and the annealing was repeated at a higher temperature without substantial change in the orientation texture, although large grain effect was encountered. Therefore the single phase (010) texture is effectively stable under recrystallization.

The principal pole distribution for the (010)-(110) duplex structure after recrystalliztion is shown in Figure 11(ii). Comparison with the pole distribution before recrystallization Figure 7(ii), shows that considerable change in orientation has occurred.

The (010) distribution has maxima inclined at 20 degrees to the *R*-axis, the (001) distribution is broadened about the transverse plane *C*–*T* and shows evidence of partially resolved maxima, and the (100) distribution shows maxima at 15 degrees to the transverse plane and a new maximum along the zone *R*–*C* at 75 degrees to the *C*-axis.

The symmetry of the rolling figure gives equal distributions in the eight quadrants, and the principal pole distributions have been divided into a single component for the quadrant. The figure was determined for each principal pole distribution by separating components along the principal

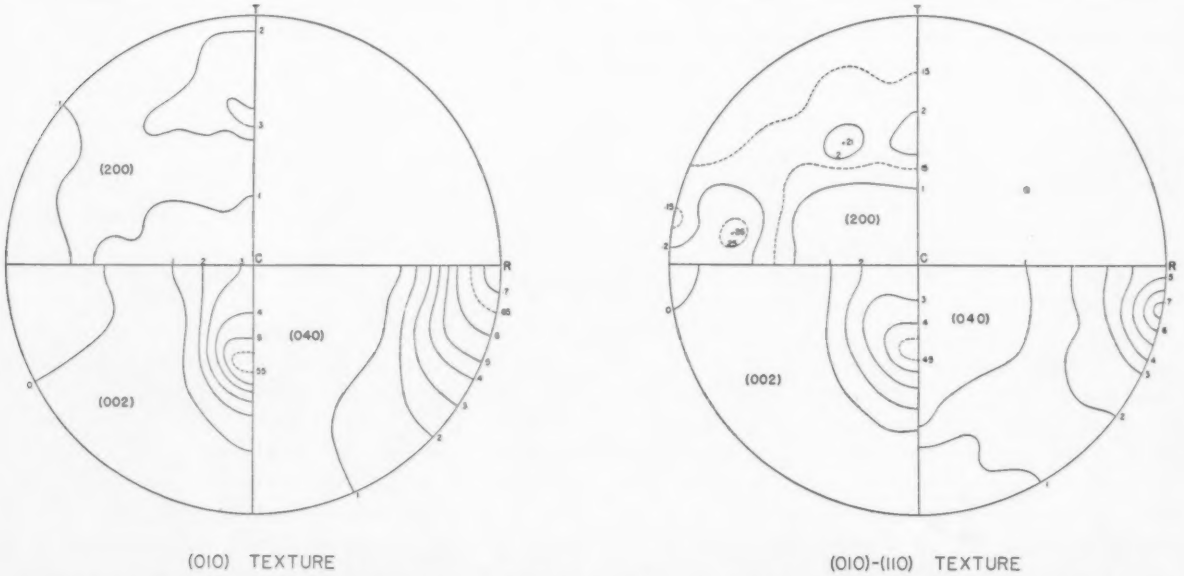

(010) TEXTURE (010)-(110) TEXTURE

FIGURE 11. Modification of the principal pole distributions in rolled α-uranium by recrystallization. I, Recrystallization of the (010) axial texture found in plate rolled at low temperature. II, Recrystallization of the duplex (010)–(110) axial texture found in plate rolled at temperatures near the stress release point.

planes *R–C*, *C–T* and *T–R* which act as mirror planes in the rolling figure. The (001) distribution proved to be isolated from contributions from the lower hemisphere, and components were readily extracted, as shown in Figure 12(i) to give components circular symmetry about the (001) maxima. The (100) and (010) components were obtained by resolving components along the rolling axes, and assuming mirror symmetry about the plane of (001) maximum. Application of this symmetry to axial points gave a distribution of intensities over the pole figure which acted as a first approximation in dividing components. The (100) and (010) components are shown in Figures 12(i) and 12(ii) and are closely equivalent, having approximately elliptical section, with the major axis lying in the plane of 001 maximum, and of the equal intensity distribution about this plane.

In the unresolved texture, if the (001) pole maximum is assumed to lie in the transverse plane, the (140) pole will lie close to the rolling axis. The resolved duplex recrystallization texture has a single-unit cell orientation, whose principal pole maxima lie as shown in Table I, having the (151)

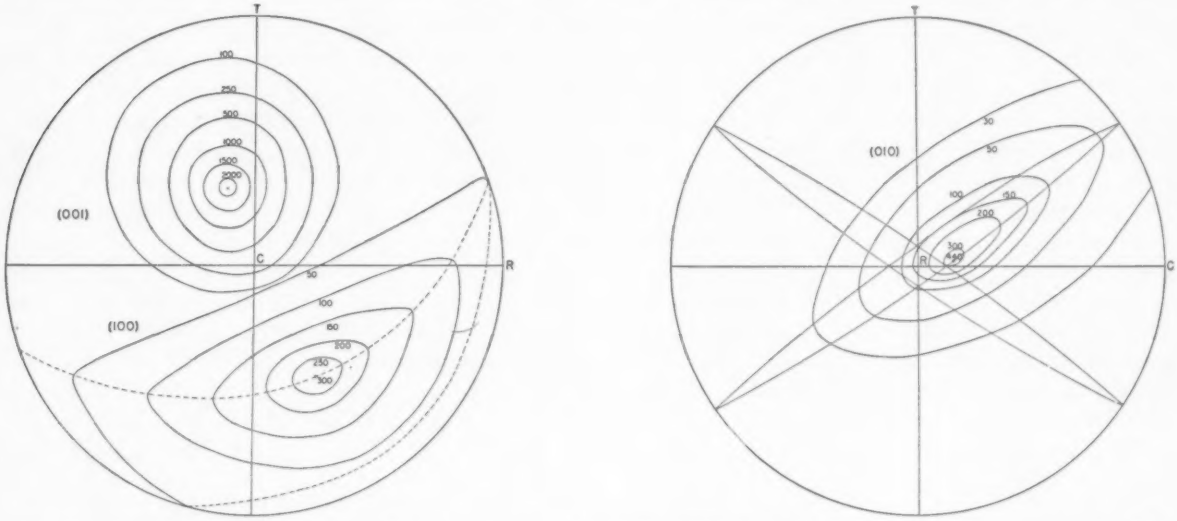

FIGURE 12. Resolution of the recrystallization texture of the duplex (010)–(110) axial orientation into components which are equal in each octant of the sphere. The (100) pole maximum appearing along the rolling direction in Fig. 11–II is due to contributions from four (100) components along the *C–R* axis.

TABLE I

PRINCIPAL POLE DISTRIBUTION MAXIMA

		Type	(100) *C*	(100) *T*	(100) *R*	(010) *C*	(010) *T*	(010) *R*	(001) *C*	(001) *T*	(001) *R*	Axial pole
1. ROLLING TEXTURES	Low-temperature texture	1	60°	30°	90°	90°	90°	0°	30°	60°	90°	010
	High-temperature duplex texture	2	70°	20°	90°				20°	70°	90°	010
		3	90°	63°	27°				20°	70°	90°	110
2. RECRYSTALLIZATION TEXTURES	Low-temperature rolling	1	60°	30°	90°	90°	90°	0°	37°	53°	90°	010
	High-temperature rolling	4	61°	42°	61°	90°	80°	10°	37°	53°	90°	140
		5	15°	82°	18°	–	–	–	–	–	–	100
	Component	4	54°	45°	66°	66°	80°	25°*	35°	56°	78°	151

*Centre of 200 contour

pole approximately parallel with the rolling direction. The (100) maximum along the rolling direction is seen to be due to the overlapping of four equal (100) lobes, along the rolling axis, and does not represent a new orientation component.

7. Conclusions

The rolling and recrystallization textures determined in this experiment are summarised in Table I. A consistent explanation of the experimental rolling textures has been put forward based on the (130) and (112) twinning systems and (010) slip. The low-temperature texture coincides with the texture predicted for twinning with some (010) slip, the inverse pole figure maxima for the *C* and *R* distributions lying within the regions of minimum resolved shear stress for the (130) and (112) twinning planes. A concentration of the *C* axis near the (001) pole in this texture is explained by the action of (112) twinning after (010) slip, which results in a *C* axis concentration in the region of low resolved shear stress on the (010) plane, along the (001)-(010) zone. For rolling at low temperatures the tension axis *R* distribution has a single maximum about the (010) pole. At higher rolling temperatures increases of (010) slip causes a second component to develop about the (110) pole, the action of (130) and (112) twinning being to return the axis to the region of the (010) pole, and establish a closed cycle. In the compression axis distribution, increase of the (010) slip at higher rolling temperatures causes movement of the maximum along the (001)-(100) zone toward the (001) pole, and dispersion to the (001)-(130) and (001)-($1\bar{3}0$) zones, orthogonal with the tension axis maximum about the (110) pole.

The recrystallization of the (010) axial texture produced at low temperatures occurred without change of principal pole maxima, some increase in dispersion being observed. The axial (010) texture occurring alone is therefore effectively stable under recrystallization. Reorientation of the duplex (010)-(110) axial texture occurred giving a single component texture having the (151) pole axial, the major reorientation occurring in the (110) axial component. A (100) pole maximum occurs along the rolling direction which is shown to be due to overlapping of four components of the (151) texture.

8. Acknowledgements

This paper was presented by permission of the Deputy Minister, Department of Mines and Technical Surveys, Ottawa, Ontario.

The authors wish to acknowledge the encouragement of Dr. John Convey, Director of the Mines Branch, and the helpful suggestions of Dr. R. L. Cunningham, Head of the Metal Physics Section in their supervision of this problem.

They would also like to thank Mr. J. A. Perry, Head of the Metal Forming Laboratory, for carrying out the rolling of the uranium plate used in these experiments.

References

1. Calnan, E. A. and Clews, C. J. B. Phil. Mag. **41** (1950) 1085.
2. ——— Phil. Mag. **42** (1951) 616.
3. ——— Phil. Mag. **42** (1951) 919.
4. ——— Phil. Mag. **43** (1952) 93.
5. Cahn, R. W. Acta Met. **1** (1953) 49.
6. Harris, G. B. Phil. Mag. **43** (1952) 113.
7. Mitchell, C. M. American Crystallographic Association, Abstracts of the Meeting at New Hampton, N.H., 1950.
8. Jetter, L. K. and Borie, B. S. J. Appl. Phys. **24** (1953) 532.
9. Frank, F. C. Acta Met. **1** (1953) 71.

THE DEBYE TEMPERATURE OF $AuCu_3$ AS A FUNCTION OF LONG-RANGE ORDER PARAMETER*

D. B. BOWEN†

Simultaneous measurements of resistance have been made on partially ordered and disordered $AuCu_3$ wires. The resistance measurements are made over the temperature range from 4.2°K to 77°K. The differing behavior of the temperature dependent portions of the resistivities of the two wires has been interpreted as an increase of Debye temperature in the ordered sample. The total change observed from disorder to complete order is 22 degrees. Some thermodynamic implications of these changes are discussed. A suggestion is made that the appearance of long-range order, as distinguished from short-range order, must be accompanied by changes in the spectrum of lattice oscillation. The basis for this suggestion is presented.

LA TEMPÉRATURE DE DEBYE DE $AuCu_3$ EN FONCTION DU PARAMÈTRE D'ORDRE À GRANDE DISTANCE

On a mesuré simultanément la résistance de fils de $AuCu_3$ désordonnés et partiellement ordonnés. Ces mesures de résistance furent effectuées dans un intervalle de température allant de 4,2°K à 77°K. Le comportement différent des parties de la résistivité des deux fils, dépendant de la température, fut interprété comme un accroissement de la température de Debye de l'échantillon ordonné. Le changement total, observé depuis le désordre jusqu'à l'ordre complet est de 22°.

Certaines implications thermodynamiques de ces changements sont discutées. On suggère que l'apparition d'ordre à grande distance, contrairement au cas de l'ordre à petite distance, doit être accompagnée de modifications du spectre des oscillations du réseau. La base de cette suggéstion est présentée.

DIE DEBYE TEMPERATUR VON $AuCu_3$ ALS FUNKTION DER FERNORDNUNGS-KOEFFIZIENTEN

An Drähten von teilweise geordnetem und von ungeordnetem $AuCu_3$ wurde der elektrische Widerstand gleichzeitig gemessen. Diese Widerstandsmessungen wurden in einem Temperaturbereich von 4, 0°K bis 77°K durchgeführt. Das unterschiedliche Verhalten des temperaturabhängigen Anteils des Widerstands der beiden Drähte wurde als eine Erhöhung der Debye-Temperatur in der geordneten Probe gedeutet. Die Gesamtänderung, die beim Übergang vom ungeordneten zum völlig geordneten Zustand beobachtet wurde, betrug 22°. Es werden einige thermodynamische Konsequenzen dieser Änderungen diskutiert. Es wird die Hypothese vorgeschlagen, dass das Vorhandensein einer Fernordnung, im Gegensatz zu einer Naheordnung, von Änderungen im Spektrum der Gitterschwingungen begleitet sein muss. Die Basis für diese Hypothese wird dargelegt.

Introduction

Siegel [1] has measured the influence of degree of long-range order on the elastic constants of $AuCu_3$. The changes that he has observed imply a change in the spectrum of lattice oscillations. There should be a smaller relative proportion of lower-frequency modes as order increases. These modal changes will have corresponding thermodynamic changes associated with them. Nix and Shockley [2] have emphasized the importance of including this source of ordering potential in any complete theory of the phenomenon, but they lacked data on which to base any quantitative conclusions. A Debye model can be used as a first approximation to estimate the thermodynamic changes to be expected. The dependence of the thermodynamic functions on Debye temperature can be found in many texts on statistical mechanics. To investigate this dependence of Debye temperature on degree of order, direct comparisons of the temperature dependence of the electrical resistivity of a disordered sample and partially ordered samples are made. From these comparisons the differences in Debye temperature between the partially ordered samples and the disordered sample are deduced in terms of the conductivity theory of Gruneisen [3].

Experimental

The alloy was prepared from Johnson Matthey pure copper and S. S. White pure gold. These metals were reported to have a purity of 99.999 per cent. The pure metals were weighed in the correct proportion (25 atomic per cent gold, 75 atomic per cent copper) to within 0.01 per cent. The alloy was formed by melting in vacuum. After melting there was a weight loss that could have altered the composition by 0.5 per cent only if the loss were all concentrated in one constituent. The slug of alloy was rolled, and then drawn into wire 0.0035 in. in diameter.

The method of measurement has been discussed for a different application [4]. Simultaneous measurements of resistance are made on a disordered

*Received November 27, 1953; in revised form February 8, 1954.

†Atomic Energy Research Department, North American Aviation, Inc., Downey, California.

sample and a partially ordered sample over the temperature range from 4.2°K to 77°K. From this direct comparison the difference in Debye temperature between the two can be directly inferred. The same disordered sample is used as a reference throughout a series of measurements in which the degree of order of the other sample is varied. The samples are heat-treated after being mounted in a lavite holder so that no direct handling of the wires is required. The disordered sample was heated in vacuum for two hours at 400°C, then quenched in water. A variety of heat treatments was used to achieve the partial orderings to be reported.

It is necessary to have a reasonably accurate value for the Debye temperature of the disordered reference sample. The resistivity of this sample as a function of temperature is shown in Figure 1.

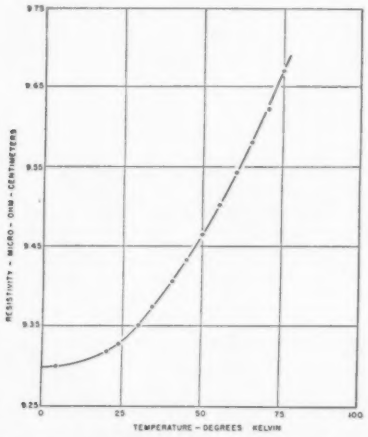

FIGURE 1. Resistivity of $AuCu_3$ as a function of temperature.

From these data a mean value of 175°K for the Debye temperature of disordered $AuCu_3$ is obtained. A spectrum of values from 170°K to 185°K is required to fit the data exactly at each point.

The change in Debye temperature and the standard deviation of the change as a function of degree of order is determined by the procedure given in Reference 4. The data are shown in Figure 2 as a function of residual resistivity. The ordered samples have a larger Debye temperature than the disordered sample.

In order to see if the method of disordering produced significant changes in the Debye temperature, a partially ordered sample was disordered by irradiation with alpha-particles in the Crocker Laboratory 60-inch cyclotron at the University of California. The energy of the particles striking the specimen was 35 Mev. The range of alpha-particles in Cu_3Au at this energy is about twice the 0.0035-inch diameter of the wires. The total integrated beam (which was uniform to better than 3 per cent) was 16 μamp-hrs/cm^2. The specimen was refrigerated during the irradiation, its temperature being kept below −150°C. The radiation increased the residual resistivity of the sample from 3.7 to 8.3

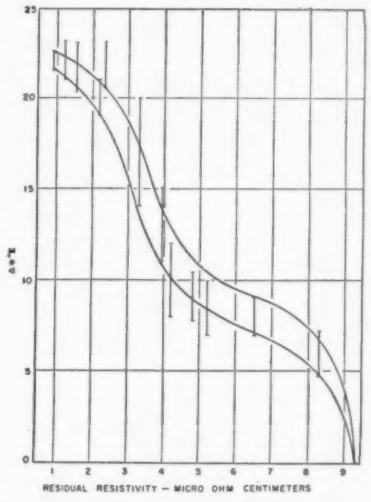

FIGURE 2. Change in Debye temperature as a function of residual resistivity.

micro-ohm-centimeters. To the accuracy of the Debye temperature determination the change observed was equal to that to be expected in a sample thermally treated to this residual resistivity (see Figure 2).

Implied Thermodynamic Relations

Let us accept, as suggested in the Introduction, that the temperature-dependent portion of the resistivity changes with degree of order because of a change in the spectrum of lattice oscillation. At temperatures in the vicinity of room temperature and below, atom movements are so slow that all of our samples can be considered as being in metastable equilibrium, and the thermodynamic variables can be estimated on the basis of the Debye model. These estimates are subject to the several reservations discussed in detail in Reference 4. The difference in internal energy, E, and work content (Helmholtz free energy), A, per unit Debye temperature difference between samples is plotted as a function of temperature in Figure 3. These values arise exclusively from the lattice oscillations. Their analytic form is obtained by differentiating the thermodynamic functions, as given in texts on

statistical mechanics, with respect to Debye temperature.

It is interesting to note that the lattice oscillations contribute less internal energy, but more work content to an ordered than to a disordered sample. The total limiting internal energy difference from lattice oscillations between an ordered and a disordered sample is estimated in this Debye approximation to be 44 cal/mole or 0.45 cal/g. This represents about 8.7 per cent of the total internal energy difference as measured by Sykes and Jones [6]. The remaining 91.3 per cent is presumably independent of temperature, and in the usual quasi-chemical theories would be made a function of order parameter only.

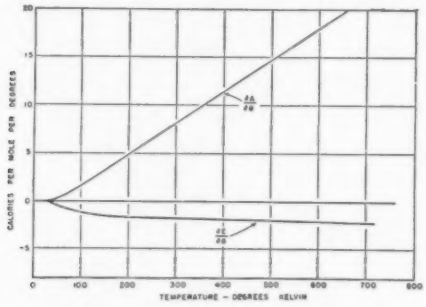

FIGURE 3. The temperature dependence of the partial derivatives of the work content and the internal energy with respect to the Debye temperature.

Although the lattice oscillations make only a small contribution to the total ordering energy the contribution may be of importance to long-range order. Qualitatively, one may say that the lattice oscillations provide a mechanism for transmitting the long-range order information. Let us consider a sample ordered within antiphase domains. When the domains are very small, or only nuclei, there are many single atomic exchanges that result in a reduction of the total antiphase surface, and hence of the internal energy from short range ordering forces. However, as the domains grow the population of single exchanges that will result in a net reduction of the antiphase surface decreases, and may vanish. For further domain growth a rearrangement of the surface is required that involves several cooperating atomic interchanges. From considerations of short range forces only, one would expect these events to be governed by the laws of random walk of boundaries, and hence their probability decreases rapidly with domain size. On the other hand, the larger domains will have a lower vibrational free energy than the small ones because of the additional entropy from the extra long wave modes they can support (considering the scattering properties of the antiphase boundary as equivalent to a semi-rigid wall). This will favor their growth at the expense of the smaller domains at all stages of their growth even though the antiphase surface is not decreased by the exchange. (The surface must not be increased either, but exchanges are possible that leave the total antiphase surface constant but alter the volumes of adjacent domains.) Thus this long-range force will bias the random walk of the antiphase surface in favor of the larger domain and accelerate the ordering process. This suggests that the vibrational free energy may be the long-range order dependent factor that determines the rate at which ordering takes place.

These ideas may be pertinent to some other alloy systems. The silver-gold system, for instance, exhibits a tendency to short range order [7], but has not been ordered in a long-range sense. For this system the atomic radii and the Debye temperature of the constituents are nearly equal. Hence, there is little tendency for the spectrum of lattice oscillations to change either from lattice strains or composition fluctuations, and consequently there should be little or no long-range vibrational ordering energy. On the other hand, the atomic radii of copper and zinc may be as much as 25 per cent different. Hence, one might expect very large changes in the spectrum of lattice oscillations of beta-brass when the degree of order changes, and indeed the elastic moduli are observed to change by large amounts [8; 9].

Acknowledgements

The author is indebted to Mr. Haruo Hori for making the many measurements, and to Mr. Bert Harwick for planning and supervising the irradiation. This paper is based on studies conducted for the Atomic Energy Commission.

References

1. SIEGEL, S. Phys. Rev. **57** (1940) 537.
2. NIX, F. C. and SHOCKLEY, W. Rev. Mod. Phys. **10** (1938) 1.
3. GRUNEISEN, E. Ann. d. Phys. **16** (1933) 530.
4. BOWEN, D. B. and RODEBACK, G. W. Acta Met. **1** (1953) 649.
5. OWEN, A. E. and SIMS, G. M. Phil. Mag. **38** (1947) 342.
6. SYKES, C. and JONES, F. M. Proc. Roy. Soc., London **157A** (1936) 213.
7. NORMAN, N. and WARREN, B. E. J. Appl. Phys. **22** (1951) 483.
8. GOOD, W. A. Phys. Rev. **60** (1941) 605.
9. RINEHART, J. S. Phys. Rev. **58** (1940) 365.

X-RAY MEASUREMENTS OF LOCAL ATOMIC ARRANGEMENTS IN ALUMINUM-ZINC AND IN ALUMINUM-SILVER SOLID SOLUTIONS*

P. S. RUDMAN and B. L. AVERBACH†

The X-ray diffuse scattering from Al-Zn solid solutions has been measured at equilibrium above the solubility temperature. Observations were made for compositions ranging from 5 to 50 atomic per cent zinc at 400°C, and at 300 and 500°C for a 10 atomic per cent zinc alloy. The diffuse scattering exhibits a strong small-angle component, and this has been interpreted in terms of Zn and Al-rich clusters. The excess of like neighbors does not appear to extend beyond the first shell of atoms, and the average nearest neighbor excess has been measured. The diffuse scattering from an Al-10 atomic per cent Ag solid solution at 540°C has also been measured, and a similar clustering has been observed.

The quasi-chemical theory is used to compare the X-ray results with the measured thermodynamic data and an apparent agreement is obtained.

DES MESURES AUX RAYONS X DES ARRANGEMENTS ATOMIQUES LOCAUX DANS LES SOLUTIONS SOLIDES Al-Zn ET Al-Ag

La dispersion diffuse des rayons X par des solutions solides fut mesurée à l'équilibre, au-dessus de la température de solubilité. Les observations ont été faites dans l'intervalle des compositions allant de 5 à 50 pour cent en atomes de zinc, à 400°C et aussi pour 10 pour cent en atomes de zinc, à 300 et à 500°C. La dispersion diffuse manifeste une petite, mais forte composante angulaire, qui a été interprétée en termes d'amas riches en Zn et en Al. L'excès de voisins semblables ne paraît pas s'étendre au delà de la première couche d'atomes; l'excès moyen de voisins semblables a été mesuré. On a aussi mesuré la dispersion diffuse par une solution solide de 10 pour cent en atomes d'Ag dans l'Al, à 540°C; on a constaté l'existence d'amas semblables à ceux des solutions Al-Zn. La théorie quasi-chimique est utilisée pour comparer les résultats obtenus par l'emploi des rayons X, aux données thermodynamiques, mesurées, et on constate qu'il paraît y avoir un accord entre les deux.

RÖNTGENOGRAPHISCHE MESSUNGEN DER ÖRTLICHEN ATOMANORDUNG IN Al-Zn UND IN Al-Ag LEGIERUNGEN

Die diffuse Streuung der Röntgenstrahlen wurde an festen Al-Zn Lösungen, die sich oberhalb ihrer Löslichkeitstemperatur im Gleichgewicht befanden, gemessen. Die Messungen wurden bei 400°C an festen Lösungen mit einem Zinkgehalt zwischen 5 und 10 Atomprozent und bei 300°C und 500°C an einer Legierung mit 10 Atomprozent Zink durchgeführt. Die diffuse Streuung wies eine starke Kleinwinkelkomponente auf, und diese Erscheinung wird auf zink- und aluminiumreiche Aggregate zurückgeführt. Der Überschuss gleicher Nachbaratome scheint nicht über die erste Atomschale hinaus vorhanden zu sein; der mittlere Überschuss gleichartiger Nachbaratome wurde gemessen. Die diffuse Streuung an einer festen Lösung von 10 Atomprozent Ag in Al wurde bei 540°C gemessen, und es wurde eine ähnliche Aggregation gefunden.

Die röntgenographischen Ergebnisse werden im Rahmen der qusai-chemischen Theorie mit den thermodynamisch gemessenen Werten verglichen, und es wird eine scheinbare Übereinstimmung erhalten.

Introduction

Local atomic arrangements in solid solutions may be studied by means of diffuse X-ray scattering, and there have been several measurements in systems which form superlattices on cooling below a critical temperature. In such alloys there is a preference for unlike nearest neighbors above the critical temperature and this type of local arrangement is usually called short range order [1].‡ Diffuse scattering measurements from two systems in which heterogeneous precipitation occurs on cooling have also been reported. In gold-nickel solid solutions [2] it was shown that there was a preference for unlike neighbors above the miscibility gap and it was concluded that on cooling, the separation into two phases, one rich in nickel and the other in gold, occurred because of the large difference in atomic sizes. A comparison of the thermodynamic and X-ray data for gold-nickel alloys also indicated that the heat of formation must contain a strain energy term when the solid solution is formed from atoms of different sizes [3]. In an aluminum-20 per cent silver (by weight) alloy diffuse scattering measurements [4] above the solubility temperature indicated that there was a preference for like nearest neighbors; that is, a clustering of like atoms in the solution.

This paper describes X-ray data obtained from aluminum-zinc solid solutions above the solubility temperature. Aluminum has an appreciable solubility for zinc (see Figure 1), and since both atoms are almost identical in size it might be expected that the local atomic arrangements could be interpreted in terms of a simple statistical theory. The free energies and entropies of mixing have recently been

*Received December 5, 1953.

†Department of Metallurgy, Massachusetts Institute of Technology, Cambridge, Massachusetts.

‡The local order measurements have been summarized in reference [1].

measured for these solutions [5] and these are correlated with the X-ray data. A better understanding of the precipitation process is also obtained in the light of the measured atomic arrangements in the equilibrium solid solution.

Similar X-ray data on an aluminum-silver alloy are also reported.

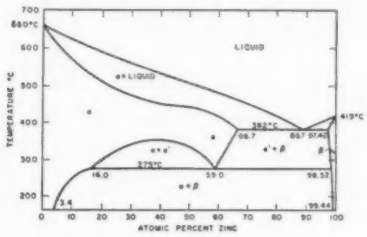

FIGURE 1. Aluminum-zinc system.

Experimental Procedure

The alloys were made by the induction melting of high purity metals, and strips were produced by alternate cold rolling and annealing. There was some grain growth during the measurements at 400°C, and some preferred orientation due to rolling, but these factors probably introduced little error in the diffuse scattering measurements.

Transmission powder patterns were taken using a bent fluorite monochromator and CoKα radiation from a half-rectified power supply run at 22 kv. Thus $\lambda/2$ and $\lambda/3$ were suppressed, and exposure times were of the order of 40 hours. The sample was a foil approximately 0.005 in. thick and was supported in a furnace in an evacuated camera. The temperature of the foil was measured by a Pt-(Pt, 10% Rh) thermocouple welded to it, and the camera arrangement is indicated in Figure 2. It

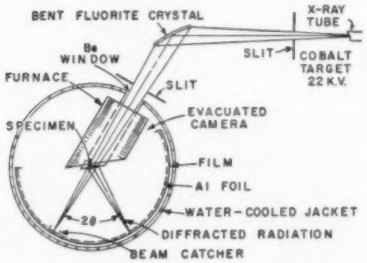

FIGURE 2. Transmission camera geometry.

was impossible to make measurements on quenched alloys since precipitation was detected immediately on cooling to room temperature.

A hand spectrometer (see Figure 3) was used to obtain the diffuse scattering in absolute units. The diffuse intensity was measured in the spectrometer at the same temperatures used for the transmission photograms, and the intensity was standardized by making identical measurements on a block of lucite [1]. It was thus possible to fit the spectrometer and the photographic data and obtain a

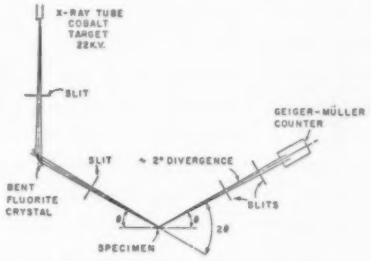

FIGURE 3. Geiger counter spectrometer geometry.

final curve in absolute units. The spectrometer sample was maintained at temperature in an atmosphere of dry hydrogen by means of the arrangement shown in Figure 4.

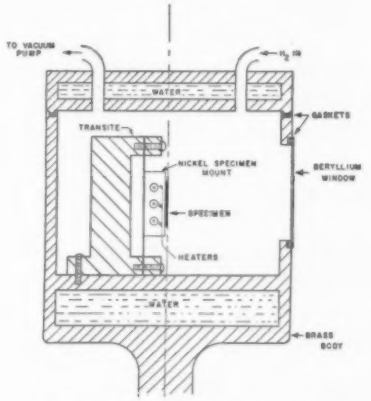

FIGURE 4. Cross section of high temperature spectrometer chamber.

X-Ray Theory

It has been shown [6] that the component of the diffuse scattering arising from local atomic arrangements in a powder pattern of a binary alloy of atoms of equal size is given by:

$$(1)\quad \frac{I(S)}{N} = m_A m_B (f_B - f_A)^2 \left\{1 + \sum_{i=1}^{\infty}{}' C_i \alpha_i \frac{\sin Sr_i}{Sr_i}\right\}$$

where

$$S = \frac{4\pi \sin\theta}{\lambda},$$

$$\alpha_i = 1 - \frac{p_i}{m_A} = \text{short range parameter},$$

m_A = atomic fraction of A-atoms,
C_i = number of atoms in i^{th} shell,
p_i = probability of finding an A-atom in the i^{th} shell about a B-atom,
r_i = distance between i^{th} neighbors.

The coefficients α_i describe the deviations of the solid solution from randomness, and it is these α_i's which must be extracted from the X-ray data. Fourier methods have been used to obtain the α_i's, but more recently Flinn [7] has developed a modified Fourier treatment which allows a weighting of the more accurate low angle data and minimizes the termination effects. We have used this modified Fourier treatment, but in these experiments there were several advantages in the use of a least squares procedure.

Rearranging equation (1):

$$K(S) = \sum_{i=1}^{\infty}{}' C_i\alpha_i \frac{\sin Sr_i}{Sr_i} \tag{2}$$

where

$$K(S) = \frac{I(S)}{Nm_Am_B(f_B - f_A)^2} - 1.$$

Since the Fourier transformation indicated that α_i was essentially zero for $i > 2$, equation (2) could be approximated by

$$K(S) = C_1\alpha_1 \frac{\sin Sr_1}{Sr_1} + C_2\alpha_2 \frac{\sin Sr_2}{Sr_2}. \tag{3}$$

The least-squares procedure requires the minimization of the quantity:

$$\sum_S \Delta^2 = \sum_S [C_1\alpha_1 x + C_2\alpha_2 y - K(S)]^2 \tag{4}$$

with respect to $C_1\alpha_1$ and $C_2\alpha_2$.

One obtains

$$\begin{cases} C_1\alpha_1 \sum_S x^2 + C_2\alpha_2 \sum_S xy = \sum_S xK(S) \\ C_1\alpha_1 \sum_S xy + C_2\alpha_2 \sum_S y^2 = \sum_S yK(S) \end{cases} \tag{5}$$

where

$$x = \frac{\sin Sr_1}{Sr_1}, \; y = \frac{\sin Sr_2}{Sr_2}.$$

These two simultaneous equations may then be solved for $C_1\alpha_1$ and $C_2\alpha_2$.

Experimentally, the low-angle data are the most accurate. At high angles there is a large temperature diffuse contribution, and the diffuse scattering must be obtained by extrapolating under Bragg reflections. The manner in which the transformation method weights the data is thus of prime importance. Considering equation (5), the weighting function of the least squares method is essentially the envelope of the sin Sr_1/Sr_1 curve. In the modified Fourier method the weighting function is $S \exp[-a^2S^2]$, and the data are weighted by S alone in the formal application of the Fourier method. These three weighting factors are plotted in Figure 5, normalized at the point $S = 2.0$. The

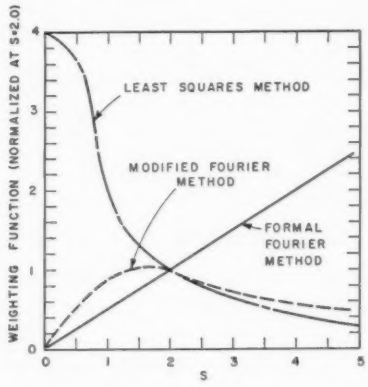

FIGURE 5. Transformation weighting functions.

advantage of the least squares procedure is not general and arises in this case only because the diffuse scattering can be described in terms of sin x/x functions. If a size effect is present [6] an additional cosine term is introduced and the advantage of the least squares method is lost.

The experimentally observed intensity is not simply $I(S)$, but rather:

$$(I(S) + I_T + I_C)\,[q]\,[A(\theta, \mu)] \tag{6}$$

where

I_T = temperature diffuse,
I_C = Compton modified,
q = polarization factor,
$A(\theta, \mu)$ = absorption factor.

All the factors except I_T are easily computed [1] and hence separable from $I(S)$. By introducing the simplifying assumptions of independence of vibrations and randomness of solution, an approximate expression for I_T was derived:

$$\frac{I_T}{N} = (m_Af_A + m_Bf_B)^2 - \left(m_Af_A \exp\left[-\frac{S^2\overline{u^2}_A}{2}\right] + m_Bf_B \exp\left[-\frac{S^2\overline{u^2}_B}{2}\right]\right)^2 \tag{7}$$

where

$\overline{u^2}_A$, $\overline{u^2}_B$ are the mean-square displacements from

the equilibrium lattice positions, and these were calculated using a mean Debye temperature and the respective masses of the atoms.

Experimental Results

Some representative microphotometer traces for the Al-Zn system are presented in Figure 6 for a

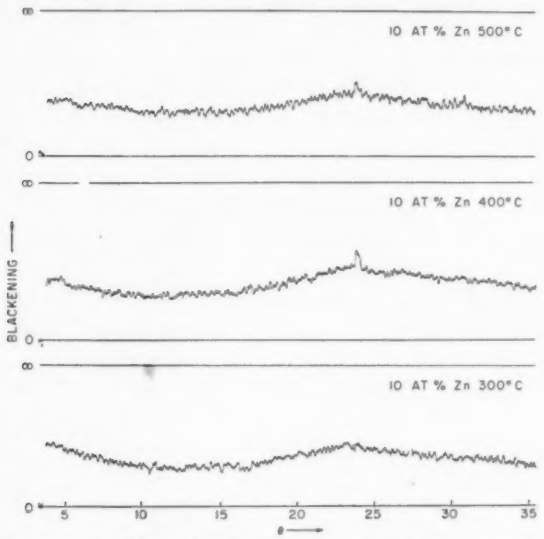

FIGURE 6. Microphotometer traces of diffuse scattering from aluminum-zinc alloys (CoKα radiation).

composition of 10 atomic per cent Zn at temperatures of 300, 400 and 500°C. There is a small-angle component that decreases as the temperature is increased corresponding to a diminution in α_1. A second diffuse maximum (coming under the (111) and (200) Bragg reflections) remains approximately constant and this component is due to temperature diffuse scattering. This temperature diffuse modulation was not taken into account by the calculated temperature scattering and the minimizing of this error is left to the inherent weighting in the transformation operation. Figure 7 shows the measured diffuse scattering on an absolute intensity scale for

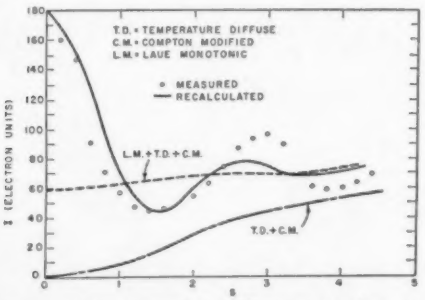

FIGURE 7. Aluminum-zinc diffuse scattering at 400°C. 50 atomic per cent zinc.

a 50 atomic per cent zinc alloy measured at 400°C. Also included are the calculated temperature diffuse and Compton modified contributions. The recalculated intensity using only the value of α_1 obtained by the least squares method is given in the same figure. Although a value for α_2 was obtained, the erratic variation with composition showed that these coefficients were not significant but merely helped to produce a better least squares fit.

The coefficient α_1 was measured at 400°C for a series of aluminum-zinc solid solutions containing 5-50 atomic per cent zinc. An attempt was also made to measure the variation of α_1 with temperature for the 10 atomic per cent alloy but the variation was small; at other compositions, the temperature could not be varied sufficiently without danger of melting. The coefficient α_1 at 400°C is shown as a function of composition in Figure 8, and

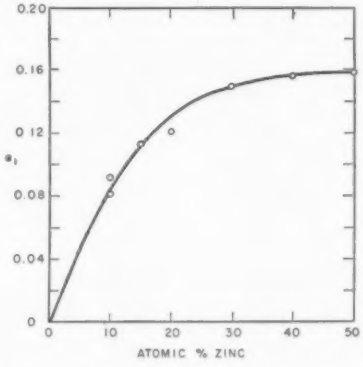

FIGURE 8. Short-range parameter for aluminum-zinc alloys at 400°C.

the results are summarized in Table I in terms of a more tangible quantity, the average number of zinc atoms in the first shell about an aluminum atom.

All of the alloys exhibited positive values of α_1 and this indicates that there was a preference for like neighbors in these solid solutions. The preference for like neighbors increases as the solution becomes more concentrated and the maximum effect probably occurs at the 50 atomic per cent composition. It is interesting to note that at 400°C in a 50 atomic per cent alloy, a given atom has about one more like nearest neighbor than it would have had in a random solution. Since the second neighbor coefficients, α_2, appear to be very nearly zero it may be inferred that the excess of like neighbors does not extend beyond the first shell of atoms.

Similar results were obtained in an alloy of aluminum-10 atomic per cent silver. The coefficient α_1 was positive and the preference for like neighbors is also listed in Table I.

TABLE I

CLUSTERING IN AL-ZN SOLID SOLUTION

		400°C		
		No. Zn atoms in first shell		
m_{Zn}	α_1	Random	Observed	Difference
.10	.08	1.2	1.1	.1
.15	.11	1.8	1.6	.2
.20	.13	2.4	2.1	.3
.30	.15	3.6	3.06	.54
.40	.156	4.8	4.05	.75
.50	.16	6.0	5.04	.96

EFFECT OF TEMPERATURE

		Al–.10 Zn		
		No. Zn atoms in first shell		
Temp. °C	α_1	Random	Observed	Difference
300	.09	1.2	1.09	.11
400	.08	1.2	1.10	.10
500	.075	1.2	1.11	.09

		Al–Ag–540°C		
		No. Ag atoms in first shell		
m_{Ag}	α_1	Random	Observed	Difference
.10	.15	1.2	1.02	0.18

Discussion of Results

In order to compare the X-ray measurements of local atomic arrangement with measured thermodynamic quantities it is necessary to connect the two concepts by a statistical theory of solid solution formation. A prevalent approach [8; 9] ascribes the entire heat of mixing to nearest neighbor chemical bonding terms, and it has been shown recently [3; 10] that this approach does not have general applicability. If lattice strain energy arising from a dissimilarity in atomic sizes or electronic contributions arising from a change in electron distribution are involved in solid solution formation, the chemical bonding approach may be completely in error [3]. The aluminum-zinc system, however, appears to be well adapted for this type of treatment. The X-ray data indicate that the atoms have almost identical sizes and there is thus no strain energy contribution. In addition, the liquid solutions in this system also show positive heats of mixing, indicating a nearest neighbor interaction energy which is independent of the presence of a lattice. There is no information available on the possible changes in the average electron configuration, but these can be neglected for the moment and considered separately if the quasi-chemical theory fails.

The relative molar integral heat of mixing is given as:

$$(8)\quad H^M = \frac{zN_0m_A}{2}(E_{AA} - E_{AA}^0) + \frac{zN_0m_B}{2}(E_{BB} - E_{BB}^0) + p_{AB}\left(E_{AB} - \frac{E_{AA} + E_{BB}}{2}\right)$$

where

z = number of nearest neighbor atoms,
E_{ij} = nearest neighbor interaction energy,
E_{jj}^0 = nearest neighbor interaction energy in the pure metals (the E's are inherently negative quantities),
p_{AB} = number of (AB) bonds per gm-atom of solution,
N_0 = Avogadro's number.

Assuming that E_{AA} and E_{BB} are independent of composition and equal to their values in the pure metals (E_{AA}^0 and E_{BB}^0), equation (8) becomes:

$$(9)\quad H^M = p_{AB}\nu$$

where

$$\nu = E_{AB} - \frac{E_{AA} + E_{BB}}{2}.$$

It should be noted that ν need not be assumed constant since E_{AB} may vary with composition. If we take A as aluminum and B as zinc, a difficulty arises with the assumptions leading to equation (9) since the term $(E_{BB} - E_{BB}^0)$ must include a term for the virtual transformation $Zn(HCP) \rightarrow Zn(FCC)$. There appears to be no way to measure this quantity directly, but since the transformation involves only a change in stacking it is probably small. The apparent agreement between the X-ray and thermodynamic results indicated later appears to substantiate this assumption.

Takagi [8] has shown that the number of (AB) pairs is given by

$$(10)\quad \frac{p_{AB}^2}{(zN_0m_A - p_{AB})(zN_0m_B - p_{AB})} = \exp\left[\frac{-2\nu}{kT}\right]$$

which may be approximated by

$$(10a)\quad \frac{p_{AB}}{zN_0} = m_Am_B\{1 - m_Am_B[\exp(2\nu/kT) - 1]\}.$$

By definition

$$(11)\quad \frac{p_{AB}}{zN_0} = m_Am_B(1 - \alpha_1).$$

Therefore, from an X-ray determination of α_1, ν may be evaluated from equation (10a) and H^M

from equation (9). The relative integral heat of mixing computed in this way is shown in Figure 9 along with the values of H^M measured by thermodynamic methods [5]. The agreement is within the experimental error of each type of determination.

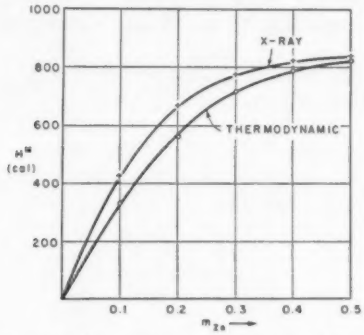

FIGURE 9. Aluminum-zinc relative integral heat of mixing at 400°C.

Takagi [8] has derived an expression for the relative integral entropy of mixing for a solution containing an arbitrary number of (AB) bonds.

$$(12)\quad \frac{S^M}{R} = (z-1)(m_A \ln m_A + m_B \ln m_B) - \frac{z}{2}\left[2\frac{p_{AB}}{zN_0}\ln\frac{p_{AB}}{zN_0} + \left(m_A - \frac{p_{AB}}{zN_0}\right)\ln\left(m_A - \frac{p_{AB}}{zN_0}\right) + \left(m_B - \frac{p_{AB}}{zN_0}\right)\ln\left(m_B - \frac{p_{AB}}{zN_0}\right)\right]$$

Figure 10 shows the excess configurational entropy calculated from the X-ray data using equation (12) and the excess entropy calculated from the emf

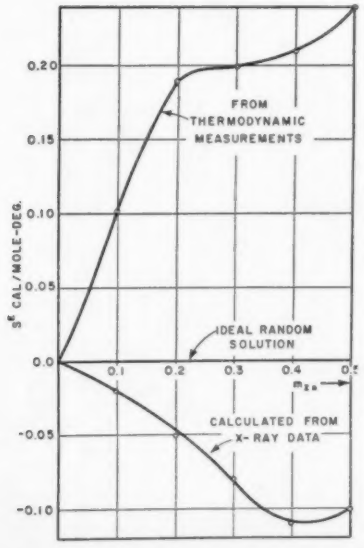

FIGURE 10. Aluminum-zinc excess molar entropy at 400°C.

measurements. The excess entropies of the random ideal solutions are zero and those calculated from the X-ray data are less than zero because of the clustering within the solution. The thermodynamic data are above the ideal curve, but this discrepancy may be within the experimental error.

If the assumption is made that the internal energy of the solution is made up of a sum of independent terms:

$$E = E(\text{chemical bonding}) + E(\text{strain}) + E(\text{change in vibrational spectrum}) + E(\text{electronic changes}) + \ldots$$

then X-ray measurements of local atomic arrangement would be influenced principally by E(chemical bonding). The relative integral entropy would then contain the analogous terms:

$$S^M = S^M(\text{atomic configurations}) + S^M(\text{changes in vibrational spectrum}) + S^M(\text{electronic changes}) + \ldots.$$

The entropy changes arising from lattice strain would appear only as the volume was changed and this effect may be neglected. The electronic entropy term is probably negligible, being of the same order of magnitude as the electronic specific heat. A positive vibrational contribution to the entropy should be reflected in a small positive contribution to H^M. In Figure 10 the configurational entropy determined from the X-ray data is below that of the measured thermodynamic value, while in Figure 8 the enthalpy calculated from the X-ray data is above the measured value. It is possible that the differences in both cases arise from experimental errors.

The energy relationships in aluminum-zinc solid solutions are thus apparently accounted for on the basis of a chemical bonding theory, with the X-ray and emf results in substantial agreement.

Acknowledgments

The authors are indebted to the U.S. Atomic Energy Commission for sponsoring this research program. We also wish to thank Dr. P. A. Flinn for his many valuable contributions, Dr. J. E. Hilliard for supplying and discussing the thermodynamic data used, and Mr. M. Commerford for his aid in obtaining the X-ray data.

This work was performed under the sponsorship of the U.S. Atomic Energy Commission under Contract AT(30–1)–1002 and represents a portion of the thesis presented by P. S. Rudman in partial fulfilment of the requirements for the degree S.M. in metallurgy at the Massachusetts Institute of Technology, Cambridge, Massachusetts.

References

1. WARREN, B. E. and AVERBACH, B. L. The Diffuse Scattering of X-Rays. Modern Research Techniques in Physical Metallurgy (A.S.M. 1953) 95.
2. FLINN, P. A., AVERBACH, B. L., and COHEN, M. Local Arrangements in Gold-Nickel Alloys. Acta Met. **1** (1953) 664.
3. AVERBACH, B. L., FLINN, P. A., and COHEN, M. Solid Solution Formation in the Gold-Nickel System. Acta Met. **2** (1954) 92.
4. WALKER, C. B., BLIN, J., and GUINIER, A. Mise en évidence des hétérogénestes d'une solution solide en équilibre. Comptes rendus **235** (1952) 254.
5. HILLIARD, J. E., AVERBACH, B. L. and COHEN, M. Thermodynamic Properties of Solid Aluminum-Zinc Alloys. Acta Met. **2** (1954) 621.
6. WARREN, B. E., AVERBACH, B. L. and ROBERTS, B. W. Atomic Size Effect in X-ray Scattering of Alloys. J. Appl. Phys. **22** (1951) 1493.
7. FLINN, P. A., RUDMAN, P. S., and AVERBACH, B. L. The Interpretation of Diffuse X-Ray Scattering from Powder Patterns of Solid Solutions. Acta Cryst **7** (1954) 153.
8. TAKAGI, Y. Statistical Theory of Binary Alloys. Proc. Phys. Math. Soc. (Japan) **23** (1941) 44.
9. FOWLER, R. H. and GUGGENHEIM, E. A. Statistical Thermodynamics (Cambridge, 1939) 350–366.
10. ORIANI, R. A. Thermodynamics of Ordering Alloys. Acta Met. **1** (1953) 144.

THE EFFECT OF A SURFACE OXIDE FILM ON TORSIONAL RELAXATION*

B. I. EDELSON† and W. D. ROBERTSON‡

The effect of a surface oxide film on the torsional relaxation of polycrystalline cadmium wires was investigated. The phenomenon of reversal when the film is removed during relaxation, known as the abnormal after-effect, is shown to be a reproducible effect directly dependent on the presence and elastic properties of a surface film. Various physical parameters, such as metallurgical history of the metal, film conditions and time functions, are varied in relaxation tests to show this dependence. An explanation of the abnormal after-effect is given in terms of a two-component mechanical model. An equivalent explanation of the abnormal after-effect may be given in terms of the dislocation barrier theory.

L'EFFET D'UNE COUCHE D'OXYDE À LA SURFACE, SUR LA RELAXATION EN TORSION

On a investigué l'effet d'une couche d'oxyde à la surface, sur la relaxation en torsion de fils polycristallins de cadmium. Il est montré que le phénomène d'inversion, quand la couche est enlevée pendant la relaxation, connu comme la répercussion anormale, est un effet reproductible qui dépend directement de la présence et des propriétés élastiques de la couche à la surface. Divers paramètres physiques, tels que l'histoire métallurgique du métal, les conditions de la couche et des fonctions du temps sont variés dans les essais de relaxation, en vue de montrer cette dépendance. Une explication de la répercussion anormale est donnée en termes d'un modèle mécanique à deux composantes. Une explication équivalente peut être donnée en termes de la théorie de barrière de dislocations.

DER EFFEKT EINES OBERFLÄCHENOXYDFILMES AUF DIE TORSIONSNACHWIRKUNG

Es wurde der Effekt eines Oberflächenoxydfilmes auf die Torsionsnachwirkung von polykristallinen Kadmiumdrähten untersucht. Es wird gezeigt, dass die als "anomale Nachwirkung" bekannte Erscheinung der Umkehrung beim Ablösen des Filmes während der Relaxion ein reproduzierbarer Effekt ist, der direkt von der Anwesenheit und von den elastischen Eigenschaften des Oberflächenfilmes abhängt. Um dieses Abhängigkeitsverhältnis zu zeigen wurden verschiedene physikalische Parameter, wie die metallurgische Vorgeschichte des Metalls, die Filmeigenschaften und die Zeitkonstanten in den Nachwirkungsversuchen variiert. Es wird eine Erklärung der anomalen Nachwirkung im Rahmen eines mechanischen Zweikomponentenmodells gegeben; eine entsprechende Erklärung der anomalen Nachwirkung kann auf Grund der Theorie der Versetzungshindernisse gegeben werden.

Introduction

If a metallic wire is twisted beyond its elastic limit and the applied stress is released, there occurs an instantaneous elastic recovery followed by a time-dependent relaxation. This relaxation, called the normal after-effect, is such that the wire recovers, approximately, an equal number of angular units in equal increments of the logarithm of time [1]. When recovery in degrees is plotted against log time a straight line is obtained, except near zero time and near infinite time.

It was suggested by Cottrell [2] that, in accordance with the current concept of plastic deformation, an elastic film on the surface of a wire constitutes a barrier to those dislocations associated with torsional deformation that ordinarily pass through the external surface and, accordingly, they should concentrate beneath the surface film. The extent to which the dislocations are blocked defines the residual elastic stress associated with the torsional deformation. After removal of the applied stress the wire untwists in accordance with the normal after-effect. If, during the untwisting, the surface film is quickly removed—by etching, for example—the dislocations still concentrated at the surface are released and they escape from the metal; this corresponds to a motion in the direction of the original deformation, opposite to the existing motion, and should manifest itself by a change in the rate of the normal after-effect. Barrett [3; 4] observed this phenomenon in single crystals of zinc and in polycrystals of iron, zinc and cadmium. In some cases the wire actually reversed (moved in direction of original twist) after removal of the surface layer. This reversal Barrett termed an "abnormal after-effect." In other cases the untwisting was merely slowed and the resultant plot showed a decrease of slope.

In the first paper [3] Barrett established the existence of the effect in zinc and iron. Subsequent work [4] indicated: (1) the abnormal effect did not originate from a thermal transient or acid attack on the metal itself; (2) the sensitivity of the method

*Received December 8, 1953.

†Lieutenant, U.S.N., Hammond Metallurgical Laboratory, Yale University, under sponsorship of the U.S. Naval Postgraduate School, Monterey, California.

‡Hammond Metallurgical Laboratory, Yale University.

was great enough to detect very thin films (those formed in air at room temperature in less than one hour); (3) that moderate plastic deformation did not disrupt the coherency of the film to the extent of eliminating the effect; and (4) that prior cold work increased the magnitude of the normal after-effect.

In addition to the preceding interpretation of the abnormal after-effect, there is an alternative, or equivalent, explanation that is generally consistent with the experimental facts reported by Barrett, namely, that a coherent elastic film on the surface of a plastically deformed wire constitutes a two-component mechanical system. Twisting the wire and film produces an elastic stress at the surface causing the wire to recover at a greater rate than it would in the absence of a film. The sudden removal of the film allows the wire to seek its own recovery rate, even reversing temporarily to the position it would have assumed in the absence of the film. The investigation described below was designed to evaluate this hypothesis in terms of new experiments and to determine how far the two interpretations can be considered equivalent.

The following determinations are necessary to obtain the data required to form a self-consistent set from which unambiguous conclusions can be formulated:

(1) The difference in relaxation behaviour of an oxidized wire and a clean wire, including the effect of etching.

(2) The effect of previous history of the metal (cold-working and annealing) on the abnormal after-effect.

(3) The effect of thickness of the oxide film.

(4) The effect of holding time prior to release of load.

(5) The effect of a delay in removing the surface film.

(6) The effect of twisting a clean wire and then applying the film after twisting.

Experimental Procedure

For preliminary work the apparatus developed by Barrett [4] was used. Several metals were tested with various cold-working and annealing treatments, types of surface films, and concentrations of acids to obtain normal and abnormal after-effects as distinct as possible. This preliminary work showed that polycrystalline cadmium with an anodic film, and dilute sulfuric acid as etchant, was the most effective of the combinations tested.

For quantitative work it was necessary to employ precision timing; to eliminate accidentally introduced bending, tensile and compressive stresses; to control the exact amount of twist and the time of holding after twist; to eliminate possible buoyancy, wetting and thermal transient effects; and finally, to provide for the application of a surface film subsequent to twisting.

The apparatus shown in Figure 1 was developed

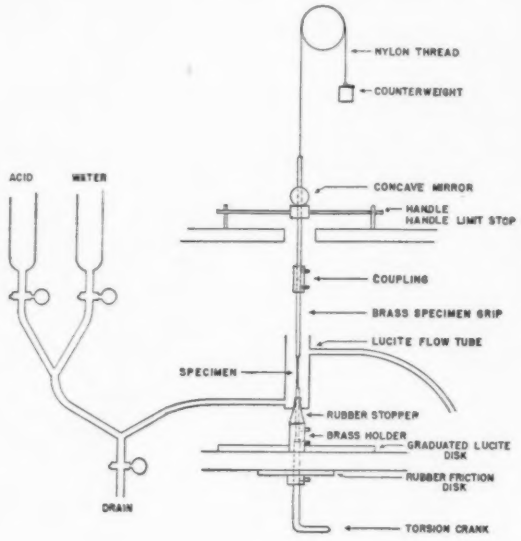

FIGURE 1. Schematic drawing of apparatus.

to meet the above requirements. The wire specimens, each 5.6 cm long and 1.11 mm in diameter, were cemented in brass grips with a DeKhotinsky-type wax having a softening point of about 140°C. Length of specimens between grips was 4.0 cm. No evidence was found of plasticity in the cement. The bottom grip was rigidly fastened to a graduated lucite disk and to the crank used for twisting the wire. Amount of twist was determined by matching the graduated disk with a line on the base of the apparatus. The top grip was rigidly coupled to a handle and concave mirror. The assembly was maintained vertical by a nylon thread and counterweight, resulting in a net tensile force of 1.3 gm. The specimen was enclosed by a lucite tube through which water or the acid etchant could be circulated. The bottom grip passed through a rubber stopper which remained stationary during the twisting operation. Two burettes were connected to the inlet of the flow tube and they permitted changing of the medium from water to acid, as desired. A drain valve and overflow tube were also provided; in this way liquid level remained constant and the

specimen was always immersed which precluded significant temperature changes or other effects due to immersion.

The apparatus and following procedure permitted the wire to be twisted, held, released and its relaxation observed with a minimum of handling. When the crank was turned, the grip holder, lucite disk, specimen and its grips, and the handle and mirror turned with it; the flow tube and rubber stopper remained stationary. If the crank were turned far enough, the handle encountered two handle limit stops fixed to the top of the apparatus which prevented its further turning. This fixed the top of the specimen, upper specimen grip and mirror in the "zero position". Further turning of the crank twisted the specimen. When the specimen was twisted the required amount and held for the prescribed time, the crank was reversed until the handle was free of the limit stops; zero time was marked; and the specimen was allowed to relax. Since a rubber friction disk held the crank, holder and bottom grip stationary, untwisting of the wire was transmitted to the mirror via the upper grip. A galvanometer lamp and scale together with an electric timer, were used to record the movement of the mirror.

Commercially pure cadmium, obtained from the New Jersey Zinc Company, was used. Specimens were prepared by casting into bars, rolling and then drawing to the same final diameter (1.11 mm). Unless otherwise indicated, specimens having a grain size about 1/100 of the wire diameter were used in the cold-worked condition, produced by approximately 60 per cent reduction in area. Experiments with wires at various times after drawing demonstrated that the effect of annealing at room temperature was negligible.

Surface films were produced in a cell consisting of the specimen as anode, a platinum cathode, and a 1N sodium hydroxide electrolyte. It was found that 2.5 volts (0.02 amp/cm^2) gave a very satisfactory anodic film in 20 minutes. The film formed was cadmium hydroxide [5], which is insoluble in water but dissolves readily in 2 per cent sulfuric acid.

The standard procedure was to prepare wires of the final diameter about 6 feet long and then wash with organic solvent, acid, water and alcohol to remove traces of lubricant and foreign matter. The wires were then cut to the standard length (5.6 cm), anodized, cemented in grips and then tested in the apparatus. During the tests the liquid media, always at room temperature, were allowed to circulate slowly through the flow tube to maintain constant conditions and dissipate heat. All runs were made at room temperature (23°C to 25°C). All wires were twisted 180 degrees in approximately 4 seconds. The etchant used in every case was 2 per cent H_2SO_4. The ends of the grips were coated with paraffin to prevent galvanic action between the acid and the brass grips. Unless specifically stated otherwise the following parameters were kept constant. The time from commencement of twist to release of load was 30 seconds. The wire was twisted, held, and allowed to relax while surrounded by distilled water. The etchant was applied at 400 seconds after release of load.

Experimental Results

Effect of Anodic Film

An investigation was made to determine the effect of an anodic film on the relaxation behaviour of cold-worked polycrystalline cadmium. The tests were conducted in quadruplicate in order to determine the degree of reproducibility. Four specimens were anodized in the standard manner, and four were etched in 2 per cent H_2SO_4 for five minutes prior to the run. The resulting data are given in Figure 2 where strain (in degrees) is plotted as a function of log time. The figures in parenthesis represent the normal after-effect strain rate, ex-

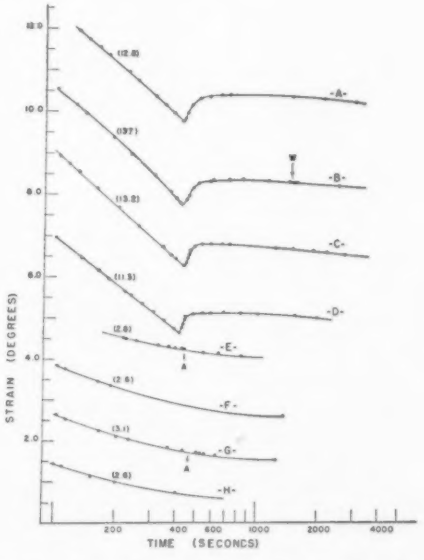

FIGURE 2. Comparison of after-effect curves of anodized and nonanodized specimens. Curves are in quadruplicate: -A- through -D- were anodized; -E- through -H- were not anodized. *W* indicates water added. *A* indicates acid added. Figures in parenthesis indicate strain rate (in tenths of a degree recovered between 200 and 400 seconds).

pressed in tenths of a degree strain recovered between 200 and 400 seconds.

The abnormal after-effect is very clearly demonstrated and associated with the removal of the film. Prior to the removal of the film, the slope of oxidized specimens is linear and the deviation of the slope is less than 10 per cent from the mean. The magnitudes of reversal in tenths of a degree are 6.4, 5.5, 5.4 and 4.9, respectively. The behaviour of the etched wires is markedly different; the strain rate is only about one quarter of that obtained with anodized wires and is not linear. Although acid replaced the control media, water, at points marked *A* on curves -E- and -G-, no effect was observed. Water replaced acid at point marked *W* on curve -B-. Again no effect was noticed. At no time, in this or succeeding experiments, was acid attack of the metal indicated, either by formation of bubbles or by change in diameter of the specimen after the run.

Effect of Cold Working

Polycrystalline cadmium wires (all 1.11 mm in diameter) were identically prepared except for the amount of cold work following a full anneal of one hour at 250°C. After standard anodizing treatment these wires were tested to determine the effect of cold-working on the normal and abnormal after-effects and the results are shown in Figure 3. The specimen representing zero per cent reduction in area was annealed for 1 hour at 250°C after the final drawing operation.

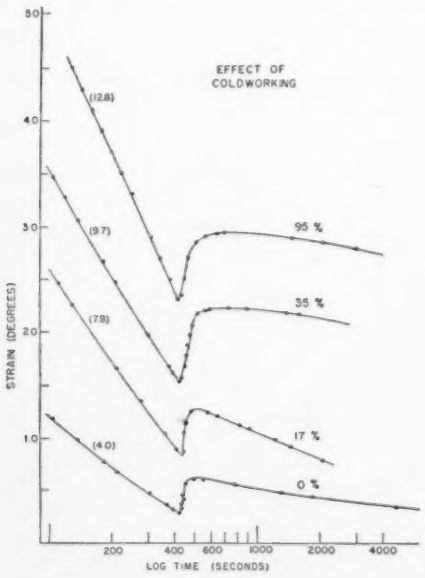

FIGURE 3. Effect of cold work on after-effect curves Percentages indicate amount of reduction in area after last anneal. 0 per cent cold work indicates 250°C anneal after drawing.

As might be anticipated, increasing amounts of cold work increase the normal strain rate when the anodic coating is the same. Likewise, increasing the amount of cold work has a tendency to increase the magnitude of reversal, in fact it is 3.3, 4.5, 6.9 and 6.4 tenths of a degree from zero to 95 per cent reduction, respectively.

Effect of Annealing Temperature

Using the specimens in the highly cold-worked condition (95 per cent reduction in area) a series of runs were made to determine the effect of subsequent annealing. Accordingly, specimens of this wire were annealed in air at various temperatures for one hour, then anodized in the standard manner. The plots of strain *versus* log time are given in Figure 4. Here the initial strain rate became less

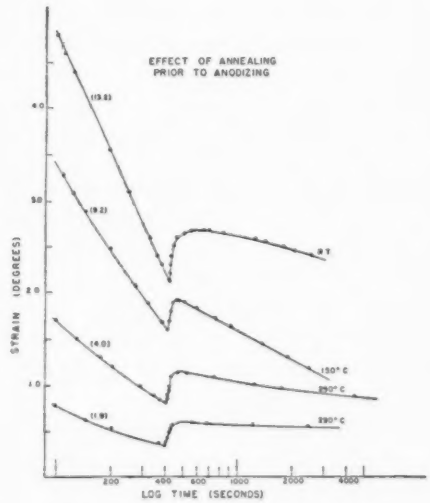

FIGURE 4. Effect of annealing for one hour at various temperatures on after-effect curves.

with increasing annealing temperature. The amount of reversal (in tenths of a degree) also decreased with increasing annealing temperature. These two quantities are plotted in Figure 5.

The effect of annealing, as well as that of cold-working, demonstrates the influence of the metallurgical history of the wire on its relaxation behavior. These results might have been predicted on the basis of mechanical properties, by noting that increasing annealing and decreasing cold work both facilitate plastic deformation, leaving a smaller portion of the original twist recoverable and therefore decreasing the amount and rate of relaxation.

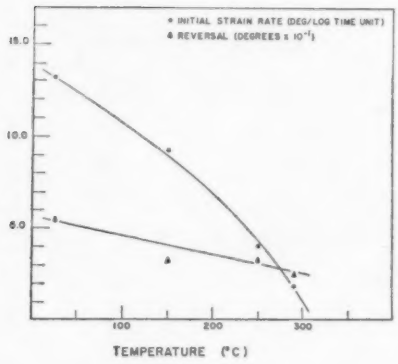

FIGURE 5. Effect of annealing at various temperatures for one hour prior to anodization on initial strain rate and amount of reversal.

Effect of Thickness of Oxide Film

A series of runs was made to determine the effect of thickness of the anodic film. Successive specimens of cold-worked wire were anodized for various lengths of time, all at 2.5 volts. The results are shown in Figure 6. Differences in anodizing time could be noted visually: the one-minute film was a blackish-brown (probably mostly oxide); films produced by longer anodizing times were successively lighter (hydroxide); and the 40-minute film was a very light gray, appearing slightly spongy. The nonanodized specimens again showed no reversal upon application of acid (applied at *A* in Figure 6). The one-minute specimen showed

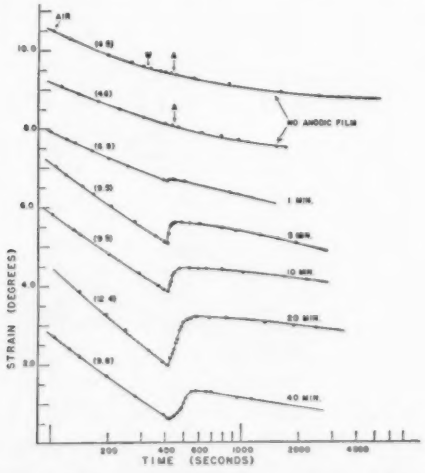

FIGURE 6. Effect of anodizing time at 2.5 volts on after-effect curves of cold worked cadmium.

only a very slight reversal. All others displayed an appreciable reversal of the same order of magnitude, although the longer the anodizing time the longer was the time during which the reversal took place.

The two nonanodized runs were identical, except that as an additional control the first run (No. 115) was twisted and released in air and distilled water first added at 300 seconds. This treatment had no evident effect on the results. The data for these runs are tabulated in Table I.

TABLE I

EFFECT OF FILM THICKNESS

Run no.	Anodizing time	S_1*	R†	t‡
115	0	4.5	—	—
115A	0	4.6	—	—
132	1 min	6.0	0.6	(very short)
128	5 min	9.5	5.4	10
129	10 min	9.5	5.8	20
116D	20 min	12.4	12.5	55
130	40 min	9.8	6.8	95

*S_1, Initial strain rate expressed in tenths of a degree recovered between 200 and 400 seconds.
†R, Magnitude of reversal in tenths of a degree.
‡t, Time, in seconds, for 2/3 of R to occur.

These results show that a thin film increases the initial strain rate considerably, but an additional increase of the film thickness does not further increase the initial slope, but does significantly increase the time for reversal to occur.

Effect of Holding Time on Normal After-Effect

Since the "clean" wire did not behave like the anodized wire, it was found necessary to establish the character of the normal after-effect occurring in a wire without the applied film. A suitable variable for examining the relaxation of a wire, independent of the surface condition, was found to be the time of holding in the twisted condition prior to release.

A group of nonanodized specimens were twisted in distilled water, held for various lengths of time and released. The holding time was computed from commencement of twist to release of load. The plot of strain *versus* logarithm of elapsed time after release of load, Figure 7, indicated that the initial strain rate varied with the time held. In all cases the resultant plot is not exactly a straight line, but rather an S-shaped curve which would extrapolate to zero slope at zero time and at infinite time. The central portion may appear linear for a relatively long period of time. However, to be strictly comparable, the slopes must be computed during the same time interval, in this case between 200 and 400 seconds. Examination of the slopes for various holding times in Figure 7 shows that, in the seg-

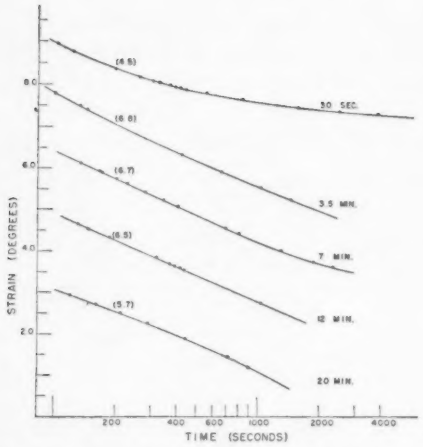

FIGURE 7. Effect of holding time on after-effect curves of non-anodized wires. Holding time was computed from commencement of twist to release of load.

ments plotted, the first three slopes are decreasing in value with increasing holding time, the 12-minute curve is almost linear, and the 20-minute curve increases in value. It appears, then, that these curves have typical anelastic characteristics: increasing the holding time has the effect of moving the inflection point to later time. The slopes during identical time intervals first increase and then decrease with increasing holding time as shown in Figure 8.

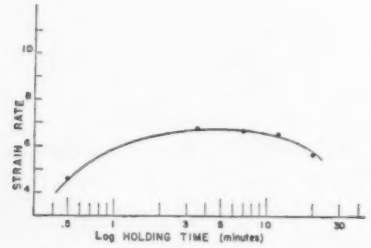

FIGURE 8. Effect of holding time on strain rate of non-anodized wires.

Effect of Delayed Etching Time

The experiments performed by Barrett [3; 4] indicate that the reversal should die out if removal of the film is delayed. Investigation along this line failed to verify this finding. Tests were made using cold-worked cadmium in the standard manner except that the time of replacing water with acid was varied from 200 to 3200 seconds. The resultant data are shown in Figure 9. The amount of reversal and the time during which reversal continued increase with increasing time at which the film is removed. It is especially noteworthy that when the acid was added at 3200 seconds the run was continued for another six hours at the end of which time the reversal still had not died out. The results of this series are tabulated in Table II. Since the initial slope (S_1) varied slightly throughout these runs it was felt that the ratio of the amount of reversal (R) to the initial slope was more significant than R alone. The amount of reversal, the ratio of reversal to initial slope and the time during which reversal occurred all increase with increasing time of adding acid.

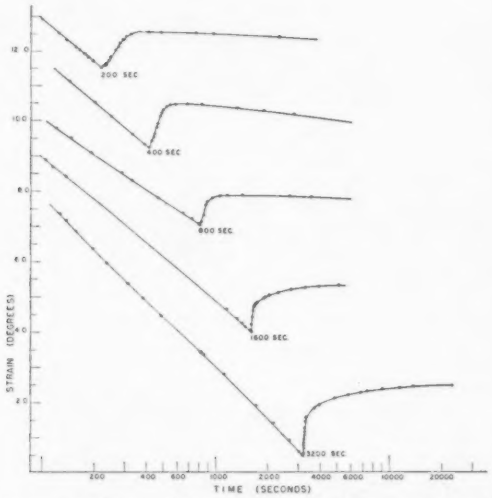

FIGURE 9. Effect of time of replacing water with acid on after-effect curves.

TABLE II

EFFECT OF DELAYED ETCHING TIME

Run no.	Time of adding acid (seconds)	S_1	R	R/S_1	t
127	200	11.8	10.0	.85	57
116A	400	12.6	9.5		
B	400	13.4	13.9	$\overline{11.7}$.$\overline{92}$	$\overline{60}$
C	400	12.4	11.8		
D	400	12.4	12.5		
124	800	10.5	9.5	.91	60
125	1600	12.0	14+	1.17	286
126	3200	14.5	20+	1.38	550

The Inverse Abnormal After-Effect

It has been amply demonstrated that the removal of a film, applied prior to twisting, caused a reversal of the normal after-effect. As a final

critical test of the effect of a film, the order of oxidizing and twisting was inverted by applying the anodic film to the twisted wire while maintaining all other variables constant.

A cylindrical platinum mesh cathode was inserted in the flow tube, and a specimen was mounted in the apparatus in the nonanodized condition. The specimen was then twisted 180 degrees in the usual manner and held for 12 minutes. During this time the flow tube was filled with sodium hydroxide and the specimen anodized at 2.5v for 10 minutes. Upon completion of anodizing the flow tube was drained, flushed, and filled with distilled water. At the end of the 12 minutes the load was released and the recovery noted. At 400 seconds the water was replaced with acid. The effect was opposite to that previously experienced upon etching. Upon attack with acid, the rate of untwisting *increased*, rapidly at first, and then settled down to a rate which was *greater* than the original rate. Two of these runs are plotted in Figure 10 as curves -A- and -B-.

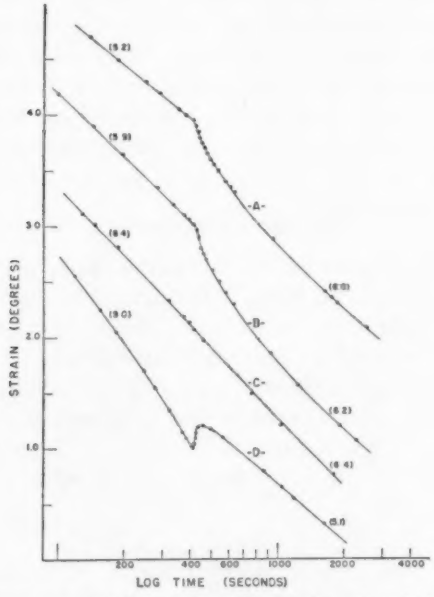

FIGURE 10. Effect of inverting order of twisting and anodizing on after-effect curves. Curves –A– and –B– represent wires which were first twisted, then anodized, then released; curve –C–, twisted and released without anodizing; curve –D–, anodized first, then twisted and released.

As control runs, tests were made on wires treated in the following manner. The specimens were mounted in the apparatus as above. They were then anodized for 10 minutes in the apparatus. Following anodization the sodium hydroxide was replaced with water. The specimens were twisted 180 degrees, held for 12 minutes and released. One of these runs is plotted as curve -D- in Figure 16. Its initial slope was greater than in the runs described above, and when the acid was admitted the "normal 'abnormal after-effect' " occurred, involving a reversal and settling down to a lesser slope. As a final control, a nonanodized wire was held in the twisted position for 12 minutes and then released. Its plot (Curve -C-) shows an intermediate slope corresponding to that finally assumed by -A-, -B- and -D-, after removal of the film. The reproducibility here was quite good and the trend of relaxation immediately after adding the acid very pronounced, as summarized below:

1. Anodizing after twist: Low initial strain rate, increasing upon acid attack.
2. No anodizing: Intermediate strain rate, no effect upon acid attack.
3. Anodizing before twist: High initial strain rate, decreasing upon acid attack.

Discussion

The preceding experiments appear to demonstrate conclusively that the abnormal after-effect is a reproducible phenomenon, directly dependent on the presence and the elastic properties of a film on the surface of a plastically deformed wire. Where the present work duplicates that of Barrett, general agreement is found except with respect to the effect of the time at which the film is removed from the surface. The data obtained show that the latter effect is contrary to that indicated by Barrett.

The phenomena may be accounted for in detail on the basis of a simple mechanical system composed of the plastically deformed wire surrounded by a coherent, elastic film. In the absence of the film, the wire untwists at its characteristic anelastic rate which is determined by the temperature and metallurgical history. If, however, the wire is coated with a coherent, elastic film, the stress resulting from the initial twist is such that the untwisting of the wire is accelerated as shown by the comparison of normal after-effect rates for unoxidized and oxidized wires (Figure 2). A graphic analogy may be drawn between the untwisting wire and the hand of a clock which proceeds at its own regulated speed. If the hand were made of rubber, an externally applied torque would displace the hand to an advanced position; when the external force is removed the hand returns to the position it would have attained without the external force.

In the present case the normal recovery of the wire is forced by the elastic stress imposed by the film to proceed at a rate greater than normal. When the film is removed the wire reverts to a strain and strain rate it would have had in the absence of the film, assuming equal initial conditions. This requires a reversal of the untwisting motion which is the observed abnormal after-effect. In order to cause an elastic reversal of .5 degree, an hydroxide film one micron thick must withstand a stress of 10^9–10^{10} dynes/cm^2. This stress is less than that computed by Orowan [6] (10^{11} dynes cm^2) as the theoretical limit, and is similar to that found by Roscoe [7], Phillips and Thompson [8], and Coffin and Weiman [9] in bending and creep experiments.

The wire does not adopt the new strain instantaneously because a finite time is required to remove the film; in fact, about 60 seconds for the films used in these experiments. Furthermore, the wire may have so far exceeded its normal recovery due to the maintenance of stress in the elastic film that it is plastically deformed and approaches the equilibrium position in a time-dependent manner from the opposite direction. This is demonstrated in the case of delayed removal of the film where reversal continues for a prolonged period after the film is removed, and the period of reversal increases with extended delay in removing the film (Figure 9).

The final test involving an inversion of the order of twisting an anodizing (Figure 10) is a clear demonstration of the effect of the properties of the film and fully conforms with the preceding mechanical description of the observed phenomena. The normal recovery is, in this case, retarded by the initially unstressed film which is stressed elastically during untwisting and so behaves as a brake on the normal rate. Removal of the film permits the wire to accelerate to its normal rate which, in this particular experiment, is that of the unoxidized wire.

Clearly, the observed facts may be accounted for by the simple mechanical concept of a two-component mechanical system comprised of the anelastically recovering metal and its elastically stressed film. The equivalency of this explanation with the dislocation model proposed by Barrett lies in the relation of a surface barrier to plastic deformation.

The torsional plastic deformation generates dislocations which are able to move through the structure of the metal, even in a cold-worked condition, but which accumulate beneath a surface film which is elastically harder than the adjacent metal. These dislocations, if released, would contribute to the permanent or plastic, torsional, deformation of the wire. The normal after-effect is not caused by the migration of these surface-accumulated dislocations, but is a function of the cold-worked condition of the wire and is an internal relaxation occurring within the multitude of interior grains in an anelastic fashion. The dislocations, then, remain adjacent to the surface barrier in a field of high strain energy. This stress concentration caused by the accumulation of dislocations may be thought of as the atomistic analogue of the elasticity of the film. When the film is dissolved, the dislocations are released, and the wire undergoes further plastic deformation in the direction of original twist. The release of dislocations, then, in the mechanical picture, appears as the abnormal after-effect. The fact that the abnormal after-effect does not diminish in magnitude as a result of delay in the removal of the film (Figure 9) is a demonstration that the dislocations remain concentrated at the surface.

Since no attempt has been made here to explain the normal after-effect itself in terms of dislocations, a dislocation analogue to account for the influence of a surface film on the initial strain rate cannot be given.

Acknowledgements

The authors wish to express their appreciation to Professor A. S. Nowick for extensive discussions and to the Office of Naval Research for financial assistance under Contract Nonr-305(00).

This paper constitutes part of a thesis by B. I. Edelson, submitted in partial fulfilment of requirements for the degree of Master of Science to the Faculty of the Department of Metallurgy, Yale University.

References

1. Zener, C. Cold Working of Metals, (Cleveland, Ohio, American Society for Metals, 1949), p. 180.
2. Cottrell, A. H. Dislocations and Plastic Flow in Metals (London, Oxford University Press, 1953), p. 54.
3. Barrett, C. S. Acta Met. **1** (1953) 2.
4. Barrett, C. S. J. Metals **5** (1953) 1652.
5. Huber, K. J. Electrochem. Soc. **100** (1953) 376.
6. Orowan, E. Rep. Phys. Soc. Progr. Phys. **12** (1949) 192.
7. Roscoe, R. Phil. Mag. **21** (1936) 399.
8. Phillips, D. J. and Thompson, N. Proc. Phys. Soc. (London), **63B** (1950) 839.
9. Coffin, F. D. and Weiman, A. L. J. Appl. Phys. **24** (1953) 282.

THE ELASTIC CONSTANTS OF COPPER ALLOYS*

J. R. NEIGHBOURS† and CHARLES S. SMITH‡

The elastic constants of single crystals of dilute solutions of Al, Si, Zn, Ga and Ge in Cu have been determined by the ultrasonic pulse method. Alloying causes a decrease in all the fundamental constants, C_{44}, $(C_{11}-C_{12})/2$ and $(C_{11}+2C_{12})/3$, the relative decrease in $(C_{11}-C_{12})/2$ being the greatest. The changes in shear constants C_{44} and $(C_{11}-C_{12})/2$ have been interpreted in terms of the known electrostatic and ionic contributions to these constants for copper. The large decrease in $(C_{11}-C_{12})/2$ is attributed to the change in ion-ion interactions, upon alloying. The electrostatic shear stiffness of an alloy is found to be nearly equal to the electrostatic term for copper times the square of the electron atom ratio.

LES CONSTANTES D'ÉLASTICITÉ DES ALLIAGES DE CUIVRE

On a déterminé les constantes d'élasticité de solutions diluées de Al, Si, Zn, Ga et Ge dans le cuivre, par la méthode de pulsation ultra-sonique. L'addition de ces éléments produit une diminution de toutes les constantes fondamentales, C_{44}, $(C_{11}-C_{12})/2$ et $(C_{11}-C_{12})/3$; la diminution relative de $(C_{11}-C_{12})/2$ étant la plus importante.

Les changements des constantes de cisailliement C_{44} et $(C_{11}-C_{12})/2$ furent interprétés en termes des contributions électrostatiques et ioniques, connues, à ces constantes pour le cuivre. La diminution importante de $(C_{11}-C_{12})/2$ est attributée à la modification des interactions entre les ions, lors de l'addition des éléments d'alliage. Il fut constaté que la rigidité électrostatique en cisaillement d'un alliage était approximativement égale au terme électrostatique pour le cuivre multiplié par le carré du rapport du nombre d'électrons au nombre d'atomes.

DIE ELASTIZITÄTSKONSTANTEN VON KUPFERLEGIERUNGEN

Die Elastizitätskonstanten von verdünnten Lösungen von Al, Si, Zn, Ga und Ge in Cu wurden mit Hilfe einer Ultraschallimpulsmethode bestimmt. Legieren rief eine Verringerung in allen fundamentalen Konstanten, C_{44}, $(C_{11}-C_{12})/2$ und $(C_{11}-2C_{12})/3$ hervor. Die relative Verringerung war in $(C_{11}-C_{12})/2$ am grössten. Die Veränderungen in den Scherungskonstanten C_{44} und $(C_{11}-C_{12})/2$ wurden auf Grund der im Kupfer bekannten Beiträge der elektrostatischen und Ionenkräften zu diesen Konstanten gedeutet. Die starke Abnahme von $(C_{11}-C_{12})/2$ wird den beim Legieren erfolgenden Änderungen in den Ion-Ion Wechselwirkungen zugeschrieben. Es wurde gefunden, dass die elektrostatische Scherungssteifheit einer Legierung nahezu gleich dem elektrostatischem Glied für Kupfer mal dem Quadrat des Elektron: Atom Verhältnisses ist.

Introduction

The elastic constants of a single crystal are of interest because of the information they give about the nature of the binding forces in solids. The elastic constants of some simple crystals have been investigated both theoretically and experimentally.

Of interest here is the calculation [1] of the elastic constants of copper from fundamental principles and the recent dynamic [2] measurement of these same constants. More recently, one of the authors [3] has investigated the elastic constants of a Cu-4 per cent Si single crystal and has interpreted the change in shear constants starting from Fuchs' theory of the elastic constants of copper. The present work is an extension of this type of analysis to other copper-alloy single crystals.

Experimental Procedure

Copper alloy single crystals were prepared in a manner similar to that previously described [4]. Briefly, the method, which is a modification of the Bridgman technique, is to slowly cool a hydrogen atmosphere furnace through the solidus point of the alloy, the alloy charge, contained in a graphite crucible, being placed in a region of high temperature gradient.

The alloys were prepared by melting the solvent in a large graphite crucible and then rapidly adding the solute. Except when adding the solute, the carbon crucible was covered, thus ensuring a reducing atmosphere. After holding the charge at an elevated temperature for some time, a portion of it was cast into one of the small crucibles used for crystal growth. The cast ingot was cleaned in nitric acid and the inside of the graphite crucible was polished smooth before the ingot in its crucible was placed in the crystal growing furnace.

After removal from the crystal growing furnace, the ingots were etched in nitric acid to develop any grain boundaries. A back reflection Laue photograph taken with the X-ray beam parallel to the cylinder axis of the ingot determined the orientation of the ingot. A small cylinder to be used for the acoustic measurement was then sawed from the ingot using a thin water-cooled abrasive wheel. The end faces of this cylinder were surface ground

*Received January 5, 1954; in revised form February 15, 1954.

†Now at Rensselaer Polytechnic Institute, Troy, N.Y.
‡Case Institute of Technology, Cleveland, Ohio.

until flat and parallel and then given a metallographic polish. Two small disks were also sawed from the ingot adjacent to each face of the cylinder. Chemical analyses of these disks by the James H. Herron Company gave an accurate determination of the composition of the cylinder.

The longitudinal and transverse acoustic wave velocities were measured by the pulsed ultrasonic method [5]. The crystal cylinders were cut from selected ingots with their axes as close as convenient to the [110] direction. Near this direction the fundamental shear constants are measured nearly directly and the numerical reduction of the data converges rapidly.

After the velocity measurements had been completed on a crystal cylinder, one of its polished faces was electropolished to remove the cold worked surface layer. A back reflection Laue photograph was then taken from this polished face and orientation of the crystal cylinder then determined using the least squares method [4].

The elastic constants of the crystal were then calculated using the approximation method [6]. The results of these calculations for various copper alloys are shown in Table I, where Zener's notation for the fundamental shear constants $C = C_{44}$ and $C' = (C_{11} - C_{12})/2$ has been used. Also included in Table I are the elastic constants for copper [2].

In order to calculate the elastic constants for a given crystal, one must also know its density. The densities used to obtain the elastic constants in Table I were computed from the composition as determined by chemical analysis and the lattice parameter-composition data in the literature [7].

Several things are evident upon examination of Table I. In general, all three fundamental elastic constants, C, C', K^{-1} decrease upon alloying. This is in qualitative agreement with the work of Smith [8], and Koster and Rauscher [9] in which Young's modulus was found to decrease when a solute was introduced into copper. The constant most affected is C', where the percentage change upon alloying is about five times as great as for the other constants. The elastic anisotropy, C/C', increases with composition upon alloying, increasing relatively faster for the higher valence solutes.

Measurement of the acoustic wave velocities is felt to be good to 0.5 per cent. The elastic constants appearing in Table I are then thought to be good to 1.0 per cent, since the square of the velocity enters into the calculation of the elastic constants.

TABLE I

ELASTIC CONSTANTS OF COPPER ALLOYS IN UNITS OF 10^{12} DYNE CM^{-2}

(The elastic constants of pure copper as measured by Lazarus (2) are included for comparison.)

Alloy	Atom composition (per cent)	$C = C_{44}$	$C' = (C_{11} - C_{12})/2$	$K^{-1} = (C_{11} + 2C_{12})/3$	Anisotropy C/C'
Cu	0	0.756	0.237	1.396	3.19
CuZn	4.59	0.742	0.221	1.339	3.36
CuAl	4.81	0.749	0.221	1.363	3.39
	9.98	0.766	0.209	1.316	3.66
CuGa	1.58	0.743	0.229	1.345	3.25
	4.15	0.741	0.221	1.357	3.36
CuSi	4.17	0.748	0.218	1.387	3.43
	*5.16	0.749	0.210	1.328	3.56
	7.69	0.741	0.197	1.395	3.67
CuGe	1.03	0.750	0.228	1.362	3.29
	1.71	0.750	0.224	1.332	3.35

*The elastic constants of this alloy crystal have been reported previously [3]. However a new chemical analysis shows that the composition is actually different than previously stated. The composition is used to calculate the density and hence the elastic constants so these quantities have been changed correspondingly in the current listing.

In the course of growing these alloy crystals some crystals resulted in which segregation was evident. These segregated crystals were all characterized by the following:

1. A wood-grain like appearance on the sides of the ingot and appearance of a fine rectangular grid on the polished faces of the crystal cylinders. This grid etched in nitric acid to a corresponding system of etch pits on such crystals.

2. Attenuation so high that accurate velocity measurement was impossible.

3. Uniformly poor back reflection Laue photographs.

These segregated crystals were useless for the elastic constant work.

Many specimens were produced, however, *without* these three obvious characteristics although there was no major change in growing technique; such good specimens were used for the present work. It may be commented in this connection that the acoustic test for segregation may be expected to be sensitive. A stiffness variation results from a composition variation and while the former is small, the visible periodicity of the composition

variation in bad crystals was around one-half millimeter which is just the acoustic wave length. High acoustic scattering leading to high attenuation, as observed in bad crystals, is just what one expects. On the other hand the good crystals exhibited attenuation which was indistinguishable from that of pure metals. It is felt, therefore, that the results of this paper are descriptive of alloy crystals of at least small segregation.

It is proper to enquire, however, what would be the effect of segregation on the measured elastic constants and therefore on the conclusions of this paper. For this purpose one may compare an ideal alloy crystal of uniform composition x with a model of a segregated crystal. The latter may be taken for simplicity as consisting half of material of composition $2x$ and half with composition zero. The velocities which would be "observed" may be calculated by assuming the conclusions made in this paper, and the two "crystals" will be found to be indeed different. The observed velocity in these experiments is a time average whereas what one would like to have is the space average, or better, the square of the velocity averaged over space. Since *averages* are involved, however, one does not expect more than a second order effect and this turns out to be the case. The detailed arithmetic for the comparison described above shows that the error arising in segregation is less than the ordinary experimental uncertainty of velocity measurement which has been stated.

The large scale homogeneity of the alloy crystals is best measured by the chemical analyses. The first crystals measured were the low and high composition Si alloys. From the three inch cropped ingots four thin disks were taken for analysis at roughly even intervals along the length. For the low Si crystal the chemical results were 1.84, 1.93, 1.88, 1.76 and for the high Si crystal, 3.44, 3.45, 3.64, .3.74, expressed in weight per cent Si. This homogeneity was felt to be good enough and subsequently the analyses were confined to disks cut adjacent to each end of the acoustic specimen, which, it should be noted was only one centimeter long. As it turned out most of the other crystals appeared to be better than the figures just given for Si. Thus the analyses quoted in pairs for the various specimens were as follows: Al, 2.09–2.10, 4.48–4.49; Ga, 1.69–1.77, 4.51–4.54; Ge, 1.16–1.18, 1.90–1.78; Si, 1.84–1.93, 3.45–3.64. For the reason named later the germanium analysis was questioned and so the whole acoustic specimen of the higher compositon was analyzed, yielding the value 1.95, which was used. The middle Cu–Si specimen was a gift to this laboratory and was in the form of a large diameter disk. Our own analysis of a single piece taken from the specimen next to the acoustic path yielded the value quoted. The Cu–Zn specimen was a gift from Horizons Incorporated of Cleveland, Ohio, and our single analysis agreed with theirs at 4.72 weight per cent. The uncertainty in composition indicated by these analyses is insignificant in its effect on the elastic constants of the specimens.

Interpretation

Fuchs' theoretical calculation [1] of the elastic shear constants starts by writing the energy per atom of the crystal as:

$$U = U_E + U_I + U \text{ (volume only)} \tag{1}$$

Here U_E represents the electrostatic potential energy of an f.c.c. structure of positive point charges imbedded in a uniform negative charge distribution. The term U_I is the repulsive exchange interaction energy between closed shell ion cores.

The shear constants $C = C_{44}$ and $C' = (C_{11} - C_{12})/2$ are calculated by imagining an appropriately strained crystal, calculating the energy in the strained state, and differentiating twice with respect to the shear strain. Only the energy terms U_E and U_I contribute to the elastic shear constants since the other terms are assumed to be functions of volume only. The resulting four terms have been called the electrostatic stiffnesses C_E, C'_E and the ionic stiffnesses C_I, C'_I. The electrostatic stiffnesses C_E, C'_E are the contributions from the electrostatic energy to the elastic shear constants C and C'. In the actual calculation of the electrostatic stiffnesses, the only contribution [10] is from the lattice of positive point charges, the uniform negative charge distribution not contributing to the shear constants. The ionic stiffnesses are the contributions to C and C' from the ion exchange energy. The numerical results of Fuchs are $C_E = 0.257$, $C'_E = 0.0286$, $C_I = 0.63$, $C'_I = 0.225$, all in units of 10^{12} dyne cm^{-2}.

The analytical results of Fuchs for the electrostatic stiffnesses are

$$C_E = 0.9478(2e^2/a^4) \qquad C'_E = 0.1058(2e^2/a^4) \tag{2}$$

where a is the lattice parameter.

The ionic stiffnesses may be written as

$$C_I = 2a^{-3}y(y-3)W \qquad C'_I = a^{-3}y(y-7)W \tag{3}$$

where W is the repulsive energy of a single pair of

ions which has been assumed by us to have the exponential form ($W = Ae^{-r/\rho}$).

Some simple assumptions [3], about the effects of alloying have been made previously in considering the elastic constants of a copper-silicon alloy. The electrostatic stiffnesses contain the charge squared, and it is reasonable to assume that these terms for the alloy will be given by equation (2), multiplied by a factor Z^2. This statement may be regarded as a definition of Z which for the moment may be regarded as an empirical parameter.

Equation (3) shows that the ionic stiffnesses are proportional to the bond energy W. Simply then, in the dilute range, the effect on these terms of adding solute atoms would be proportional to the number of solute atoms added, that is to the atomic concentration, x. The proportionality constant, denoted α, will then be an empirical parameter which measures the ionic effect. Since the exponential W will control both these terms a single parameter α has been assumed to be adequate.

According to the above then, the shear constants for the alloy will be given as

$$(4) \qquad C = C_E Z^2 + C_I(1 + \alpha x), \qquad C' = C'_E Z^2 + C'_I(1 + \alpha x).$$

The changes in elastic constants due to alloying will be, of course,

$$(5) \qquad \Delta C = C_E(Z^2 - 1) + C'_I \alpha x, \qquad \Delta C' = C'_E(Z^2 - 1) + C'_I \alpha x.$$

However, all of the solutes considered expand the copper lattice upon alloying, some more than others. From equation (2) it may be shown that the changes in the electrostatic stiffnesses due to a change in lattice constant are

$$(6) \quad \delta C_E/C_E = -4\delta a/a \qquad \delta C'_E/C'_E = -4\delta a/a$$

Similarly [3], the changes in the ionic stiffnesses are

$$(7) \quad \delta C_I/C_I = -17.8\delta a/a \quad \delta C'_I/C'_I = -17.3\delta a/a$$

The change in the shear constant due to a change in lattice constant would then be the sum of the changes in electrostatic and ionic stiffnesses. The difference between this calculated change owing to lattice parameter change and the observed change in elastic shear constant is ascribed to the effect of alloying per se, i.e., the insertion of foreign atoms into the lattice. These latter differences are the quantities ΔC and $\Delta C'$ which have been used in equation (5). Similarly, the ionic and electrostatic stiffnesses introduced into equation (5) are those for an expanded lattice, calculated according to equation (6) and equation (7).

Thus, in recapitulation, the values for ΔC, $\Delta C'$, C_E, C'_E, C_I, C'_I are all adjusted for the change in lattice parameter upon alloying. When these values are introduced into equation (5) Z and α may be determined. Then the values of Z and α which appear in Table II are expected to be characteristic of introducing solute atoms into an expanded copper lattice. Thus they describe the effect of alloying alone.

From inspection of Table II, it is clearly evident that the empirical parameter Z very nearly equals the electron atom ratio q, and one is justified in concluding on an *experimental* basis that these quantities are equal. One would expect the parameter α to be nearly independent of composition for the specimens in a given alloy system. We feel that Table II shows that α is indeed independent of composition within the experimental error. Thus the reasonable behaviour of both parameters is held to be justification for the present empirical analysis.

TABLE II

THE PARAMETERS Z AND α FOR COPPER ALLOYS

Alloy	Atom composition (per cent)	α	Z	q, electron-atom ratio
CuZn	4.59	−1.0	1.08	1.05
CuAl	4.81	−0.9	1.11	1.10
	9.98	−0.8	1.25	1.20
CuGa	1.58	−1.4	1.03	1.03
	4.15	−1.0	1.09	1.08
CuSi	4.17	−2.5	1.13	1.13
	5.16	−3.0	1.18	1.16
	7.69	−3.0	1.25	1.23
CuGe	1.03	−3.6	1.06	1.03
	1.71	−3.3	1.09	1.05

The experimental values of Z and α are a synthesis of a large number of physical quantities coming from both experimental and theoretical sources. It hardly seems profitable to discuss in detail the accuracy of the final parameters other than to say that it is felt that $(Z^2 - 1)$ and α are good to about five per cent as implied in Table II. The chemical composition is probably the most important single measurement entering

into these results appearing as it does in the density, as a coefficient of α, and in q the quantity with which Z is compared. In this connection it will be noted that in the Cu–Ge alloys Z departs most markedly from q, and that α is exceptionally high. A higher Ge composition would put *both* parameters more nearly in line with those for the other alloys. The chemical analysis of these specimens was however repeated with essential agreement with the first analysis and the results are reported as found.

This analysis has been carried out with Fuchs' theoretical stiffnesses as the starting point. The electrostatic terms are reasonably sure both physically and in respect to agreement with experiment, notably in the case of sodium. The theoretical ionic terms seem to us to be quite questionable, however, both from the point of view of the original theory, and because they do not in fact give the actual elastic constants of copper at room temperatures. (The agreement at absolute zero is probably better.) However, there seems to be little doubt that physically the two effects, electrostatic and ionic, are present and that the ionic effect enters in about the *relative* magnitudes of the Fuchs values, and that it varies rapidly with r as supposed here. These properties are all that are actually required by the present analysis. It actually makes little difference, for example, whether one makes the lattice parameter correction or not, or whether one uses the Fuchs ionic stiffnesses or empirical ones obtained by subtracting the electrostatic terms from the experimental constants of copper.

Discussion

It was first pointed out by Jones [11] and Hume-Rothery [12] that the electron-atom ratio q is the important quantity determining the limit of solid solubility in these alloys and in others. The electron-atom ratio here again appears to have an important role, this time determining the electrostatic stiffnesses of these alloys.

The electrostatic shear stiffnesses of pure copper were calculated by Fuchs on the basis of an assumed model of positive point charges imbedded in a *uniform* valence electron charge distribution. Our result, that $Z \cong q$, can be shown to be reasonable, as a first approximation, by extending the Fuchs model to the substitutional alloy. The alloy picture then is that of an array of positive point charges imbedded in again a negative charge distribution which is uniform at a density now of q electrons per atomic volume. The positive charges statistically have the value $V_A = 1$, the solvent valence, and V_B the solute valence. As previously stated the only contribution to the shear stiffnesses is from the point charges when the negative charge is uniformly distributed. The Coulomb energy of the positive charges will be a sum of terms V_iV_j/R_{ij} which must be differentiated twice to give the stiffnesses. If we consider all pairs of ions at a given spacing R_{ij} and in a given orientation, it is easy to show that $\overline{V_iV_j} = q^2$. This conclusion holds for all sets of pairs and hence the electrostatic stiffnesses of the model are given directly by $C = C_0q^2$, and therefore $Z = q$. The important restriction of this argument is that the valence charge must be uniform.

With the experimental result that $Z \cong q$ in mind it is tempting to reverse the above reasoning and conclude that the valence electron charge is indeed uniformly distributed in these copper alloys. The validity of the reverse reasoning is questionable, and the resulting conclusion is obviously false on physical grounds. It has been long recognized that in a substitutional alloy the valence charge must pile up in the vicinity of the more highly charged solute ions, effectively screening their excess charge in part [13]. With the solute ion charge partially screened one would be led to expect as a second crude approximation of the model for the alloy that Z should be less than q. However such considerations take no account of redistribution of the screening charge and the resulting possible stiffness contribution when the crystal is sheared. In any case the present results indicate that if anything Z is slightly greater than q. The problem of interpreting the observed Z's in any but a crude manner would appear to be difficult. We are inclined to avoid a definite conclusion, merely commenting that the present result suggests to us a more uniform valence charge distribution than we had supposed beforehand.

The values of α appearing in Table II are all negative. This behaviour is reasonable since it is the *ion core* interaction which must be considered in the stiffness equations, and the solute ion cores Zn^{+2}, Ga^{+3}, and Ge^{+4} must surely be smaller than Cu^{+1}. For this series of ion cores the electron configuration is identical with only the nuclear charge changing in the series. The ion cores Al^{+3} and Si^{+4} have a different electron configuration from Cu^{+1} but the net ion charge makes for a smaller core with these solutes also. Hartree cal-

culations have been carried out [14] for the ions Cu^{+1}, Ga^{+3}, Al^{+3}, Si^{+4} and confirm these statements. The charge distributions for all three solute ions are smaller than Cu^{+1}; Si^{+4} is smaller than Al^{+3}; and furthermore Al^{+3} is smaller than Ga^{+3}.

The parameter α is increasingly negative in the sequence Zn, Ga, Ge and in the sequence Al, Si as previously predicted [3] on the basis of just the reasoning quoted above. However, α also decreases in the order Al, Ga and in the order Si, Ge, contary to the previous prediction and contrary to what one would expect simply from the sizes of the Hartree charge distributions for Al^{+3} and Ga^{+3}.

One model used by Smith and Burns for estimating the empirical parameter α is to assume that the solute-solute and solute-copper interactions are all zero and that there are no local distortions. Then α simply measures the number of broken bonds and should equal -2 for this model. The value -2 is then a lower limit on α; considering the solute-solute and solute-copper ion interactions to be only weakened, rather than broken, would have the effect of raising α above this lower limit.

In fact, the values of α for the solutes Si and Ge surpass this lower limit. In itself, this is not too surprising, in view of the simple picture presented. In this picture, moreover, the low values of α can be easily understood as being due to movement of the nearest neighbors of the solute ion [3].

The ideas presented here represent a somewhat different approach to understanding alloys. In contrast to the idea of atomic diameter, one thinks instead of ion core diameter. That this is actually different can be seen when one considers substituting a solute atom such as Zn into the copper lattice. In the usual atomic picture, the Zn atom which is supposed to be larger than Cu would produce local compressions, whereas the ion core is expected to be smaller than the Cu ion and would then produce a local tension. Thus the nearest neighbor movements would be opposite in the two cases.

Summary

The elastic constants of several copper alloy single crystals have been measured by the pulsed ultrasonic method. The changes upon alloying have been interpreted with regard to two parameters, Z and α. The electron atom ratio and Z have been shown to be nearly equal experimentally. The ionic parameter α is found to be smaller (larger absolute magnitude) as the solutes progress to the right in the periodic table.

Acknowledgments

The authors wish to acknowledge the assistance of Mr. John C. Scarlett with the experimental work and the participation of Mr. Roger Bacon in some helpful discussions pertaining to this work. This work was supported by the Office of Naval Research.

References

1. Fuchs, K. Proc. Roy. Soc. **A153** (1936) 622; **157** (1936) 444.
2. Lazarus, D. Phys. Rev. **76** (1949) 545.
3. Smith, Charles S. and Burns, J. W. J. Appl. Phys. **24** (1953) 15.
4. Neighbours, J. R., Bratten, F. W. and Smith, Charles S. J. Appl. Phys **23** (1952) 389.
5. Huntington, H. B. Phys. Rev. **72** (1947) 321.
6. Neighbours, J. R. and Smith, Charles S. J. Appl. Phys. **21** (1950) 1338.
7. Abstracted in K. Polmanteer's Master's Thesis TM 65 (1950), Case Institute of Technology.
8. Smith, A. D. N. J. Inst. Metals **80** (1951) 477.
9. Koster, W. and Rauscher, W. Z. Metalkunde **39** (1948) 110.
10. Price, W. J. Phys. Rev. **72** (1947) 514.
11. Jones, H. Proc. Roy. Soc. **A144** (1934) 225.
12. Hume-Rothery, Mabott and Channel-Evans, Phil. Trans. Roy. Soc. **A233** (1934) 1.
13. Mott, N. F. and Jones, H. The Theory of the Properties of Metals and Alloys (London, Oxford University Press, 1936) p. 87.
14. Hartree, D. R. Reports on Progress in Physics, **11** (1946–47) 113.

X-RAY MEASUREMENT OF ORDER IN CuAu*

B. W. ROBERTS†

The long-range order in CuAu has been measured with a Geiger counter spectrometer using filings quenched from various annealing temperatures. The long range order is essentially perfect at low temperature, and decreases to about 0.97 at 380°C, where the material changes to CuAuII. Short-range order coefficients were determined from measurements of the diffuse intensity from a single crystal of CuAu. The coefficients indicate a preference for unlike nearest neighbors, and they are qualitatively similar to those for Cu_3Au. An outward shift of the 100 and 300 diffuse peaks suggests but does not prove the existence of a microlayering, similar to CuAuI, even above the critical temperature.

DES MESURES AUX RAYONS X DE L'ORDRE DANS CuAu

On a mesuré l'ordre à grande distance CuAu au moyen d'un spectromètre à compteur Geiger, en employant des limailles trempées à partir de différentes températures de recuit. L'ordre à grande distance est essentiellement parfait aux basses températures et diminue jusqu'environ 0,97 à 380°C, où le matériau change en CuAuII. Les coefficients d'ordre à petite distance furent déterminés par des mesures de l'intensité diffusée, donnée par un monocristal de CuAu. Ces coefficients indiquent une préférence pour des voisins directs, dissemblables, et sont qualitativement similaires aux coefficients correspondants dans Cu_3Au.

Un déplacement vers l'extérieur des maxima diffusés, donné par 100, 300, suggère, mais ne prouve pas, qu'il y existe une micro-stratification ressemblant à CuAuI, même au-dessus de la température critique.

RÖNTGENOGRAPHISCHE MESSUNGEN DES ORDNUNGSGRADES IN CuAu

Die Fernordnung von CuAu wurde mit einem Zählrohrspektrometer an Feilspänen, die von verschiedenen Glühtemperaturen abgeschreckt worden waren, gemessen. Bei tiefen Temperaturen war die Fernordnung praktisch vollkommen; sie nahm auf etwa 0,97 bei 380°C ab, bei dieser Temperatur wandelt sich das Material in CuAu II um. Die Naheordnungskoeffizienten wurden aus Messungen der diffusen Intensität an einem CuAu-Einkristall ermittelt. Sie zeigen eine Bevorzugung für ungleiche nächste Nachbarn, und ähneln qualitativ den Cu_3Au-Koeffizienten. Eine Verschiebung der diffusen 100 und 300 Maxima nach aussen deutet darauf hin, dass selbst oberhalb der kritischen Temperatur, wie im CuAu I, eine Mikroschichtung vorhanden ist. Diese Erscheinung wird jedoch durch die Verschiebung der Maxima nicht bewiesen.

I. Introduction

Near the composition CuAu the critical temperature for long-range ordering is $T_c = 408$°C. Above T_c the material is disordered face-centered cubic.‡ Below 380°C it forms an ordered tetragonal structure with the 002 planes alternately copper and gold. Between 380°C and 408°C there is a complex orthorhombic structure which Johansson and Linde [1] have called CuAuII to distinguish it from the ordered tetragonal form known as CuAuI. The CuAuII structure is derived from that of CuAu I by following the tetragonal structure for 5 unit cells along the b-axis and then interchanging the Cu and Au layers for the next 5 unit cells.

For CuAuI the long-range order parameter S is a measure of how completely the gold layers are occupied by gold atoms and the copper layers by copper atoms. Quantitative values of S are obtained from a comparison of the integrated intensities of the superstructure and the fundamental reflections. At temperatures above T_c, the short-range order parameter α measures how far the composition of the neighboring atoms about any origin atom differs from the average sample composition. Short-range order produces modulations in the diffuse scattering, and quantitative values of α are obtained from an analysis of the modulations.

II. Long-Range Order in CuAuI

For tetragonal CuAuI we will represent Cu atoms by A, and Au atoms by B. The correct Cu atom positions will be called α, and the correct Au atom positions will be called β. The long range order parameter S is then defined by $S = r_\alpha - w_\beta$, where r_α is the fraction of α-positions rightly occupied, and w_β is the fraction of β positions wrongly occupied. For perfect order S equals unity, and for complete randomness it equals zero. For partial long-range order the structure factor takes the two forms:

$h + k$ = even, hkl unmixed $F^2 = 4(f_B + f_A)^2$
Fundamental reflection,

$h + k$ = even, hkl mixed $F^2 = 4\ S^2(f_B - f_A)^2$
Superstructure reflection.

*Received February 4, 1954.

†General Electric Research Laboratory, Schenectady, N.Y.; formerly at Massachusetts Institute of Technology, Cambridge, Massachusetts.

‡Cell dimensions: FCC: $a = 3.867$ A (quenched from 600°C); Orthorhombic: $a = 3.954$, $b = 39.66$, $c = 3.652$ A; Tetragonal: $a = 3.967$ A, $a/c = 1.078$ (quenched from 300°C).

It is evident that the long-range order parameter S can be determined from the ratio of the integrated intensities of a superstructure reflection and a fundamental reflection.

For diffraction from a powder sample the integrated intensity per unit length of diffraction line is given by

$$P = km\ (LP)\ F^2\ A(\theta)\ T(\theta),$$

where k is a constant for all reflections, m is the multiplicity, (LP) is the Lorentz polarization factor, $A(\theta)$ is the absorption correction and $T(\theta)$ is the Debye temperature factor. Using the Norelco Geiger counter spectrometer and a flat faced briquet sample, P is proportional to the peak area and the absorption correction $A(\theta)$ is nearly independent of angle. Calling A_{SS} and A_F the areas under a superstructure and a fundamental peak, the long range order parameter is given by

$$(1)\quad S^2 = \frac{A_{SS}}{A_F}\ \frac{[m(LP)(f_B + f_A)^2 A(\theta)\ T(\theta)]_F}{[m(LP)(f_B - f_A)^2 A(\theta)\ T(\theta)]_{SS}}.$$

The CuAu sample was prepared by melting C.P. copper shot and 99.99 per cent gold wire in an evacuated Vycor tube and homogenizing for 15 hours at 750°C. Analysis of the final sample showed 49.7 atomic percent Au. Filings from the ingot were used for the powder samples. The samples were annealed at various temperatures below T_c by heating in evacuated Pyrex tubes and quenching in water. The annealing times were set using the half-ordering times found by Kallback, Nystrom and Borelius [2]. Temperatures were measured with a chromel-alumel thermocouple with the junction placed in contact with the evacuated tube. No attempt was made to determine accurately the transition temperatures. The loose filings were placed in a sample holder to give a flat faced sample. The patterns were run at room temperature with a Norelco spectrometer using filtered CuKα radiation.

Values of S were computed from equation (1) by comparing the area of a superstructure peak with that of a nearby fundamental peak. Since only neighboring peaks were compared it was assumed as a first approximation that $A(\theta)\ T(\theta)$ was the same for both peaks. Table I lists the values of S obtained by comparing six superstructure peaks with two sets of fundamentals for various annealing temperatures.

The values of S in Table I are too large if the superstructure peak is on the high-angle side of the fundamental and too small for the reverse case. This effect cannot be due to either extinction or the lack of a temperature factor correction. It appears to be due to a surface roughness absorption factor which gives a bigger absorption effect the smaller the angle between the beam and the sample surface. The effect is to be expected for a sample of filings whenever the linear absorption coefficient is very high. The same effect has been observed in intensity measurements from tungsten filings [3]. An approximate correction for the surface roughness effect is obtained by averaging the seven sets of values in Table I. A plot of the average S-values

TABLE I

LONG-RANGE ORDER VALUES FOR CuAu ANNEALED AT VARIOUS TEMPERATURES

T°C	207	254	283	304	320	341	352	367	380
Time (hrs.)	100	38	37	22	15	29	18	9	15
				Compared with 200–002 Fundamental					
001	0.860	0.862	0.853	0.868	0.849	0.842	0.835	0.841	0.860
110	0.921	0.945	0.912	0.922	0.908	0.897	0.900	0.901	0.871
201	1.040	1.031	1.056	1.013	1.022	1.000	1.025	1.020	1.042
112	1.030	1.042	1.033	1.029	1.039	1.020	1.022	1.055	1.004
				Compared with 220–202 Fundamental					
112	0.917	0.935	0.933	0.931	0.948	0.929	0.921	0.932	0.853
221	1.063	1.016	1.037	1.016	1.047	1.047	1.064	1.040	1.003
310	1.081	1.054	1.054	1.043	1.029	1.077	1.067	1.089	1.027
				Average S					
	0.988	0.984	0.983	0.975	0.977	0.973	0.976	0.982	0.951

normalized to unity at $T/T_c = 0.5$ is shown on Figure 1. We conclude that long-range order in CuAuI is practically perfect at low temperature and decreases by about 3 per cent on raising the temperature to 380°C.

To prove that the small change in long-range order is real, precision measurements have been made of the axial ratio a/c. Powder patterns were

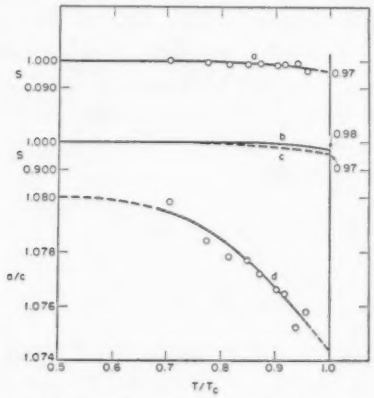

FIGURE 1. (*a*) Experimental values of long range order S for CuAu. (*b*) Values of S from the Li theory. (*c*) Values of S from the measured a/c curve. (*d*) Measured a/c ratio.

made in a 114 mm camera using filtered CuKα radiation. The samples were made up from the same annealed filings recorded in Table I. The a/c ratios were computed from the combinations 200–002, 220–202, 420–402, and 420–204. The averaged values are shown on Figure 1 plotted against T/T_c where T_c is taken as 408°C. There is a definite decrease in the a/c ratio with rising temperature as observed previously by Gorsky [4].

For a high degree of order a relation between S and c/a can be obtained by a formal averaging of characteristic distances. Let l_{AA}, l_{BB} and l_{AB} be distances characteristic of nearest neighbor pairs AA, BB and AB. If $\bar{l}_1$ is an average nearest neighbor distance for two atoms in a 002-plane and $\bar{l}_2$ is an average nearest neighbor distance between atoms in adjacent 002 planes

$$2\bar{l}_1 = (r_\alpha^2 + w_\beta^2)\, l_{AA} + (r_\beta^2 + w_\alpha^2)\, l_{BB} + 2(r_\alpha w_\alpha + r_\beta w_\beta)\, l_{AB}$$

$$\bar{l}_2 = r_\alpha(r_\beta l_{AB} + w_\beta l_{AA}) + w_\alpha(r_\beta l_{BB} + w_\beta l_{AB}).$$

For the CuAuI structure $\sqrt{2}\ \bar{l}_2/\bar{l}_1 = (1 + c^2/a^2)^{\frac{1}{2}}$ and using the relations for long range order $r_\alpha = r_\beta = (1 + S)/2$ and $w_\alpha = w_\beta = (1 - S)/2$, together with the condition that c/a is close to unity, we obtain the approximate relation

$$S^2 = (1 - c/a)\, B/4 \tag{2}$$

where

$$B = \frac{l_{AA} + l_{BB} + 2l_{AB}}{l_{AA} + l_{BB} - 2l_{AB}}.$$

The value of B in equation (2) is assumed to be independent of S and is determined from the experimental value of c/a at $S = 1.0$. A plot of S determined from the c/a values by means of equation (2) is shown on Figure 1. The agreement with the S-values determined from intensity measurements is surprisingly good in view of the assumptions involved in equation (2). Based on a different line of reasoning, Li [5] has derived a relation between S and c/a which is similar to equation (2).

In Cu_3Au [6] the long-range order drops continuously to about $S = 0.8$ at T_c and then goes discontinuously to zero. In CuAuI the long-range order drops by only about 3 per cent up to 380°C where the structure changes to that of CuAuII. In the CuAuII range (380°C – 408°C) the data at 390°C indicated a lower degree of long-range order although the structural relations are not strictly comparable to those in CuAuI. At 408°C the long-range order drops discontinuously to zero as indicated by powder patterns and Geiger counter observations on a single crystal.

III. Measurement of Short-range Order in CuAu

Above 408°C, CuAu is statistically face-centered cubic and only a short-range order exists. The experimental measurements of the short-range order and the evaluation of the data were carried out following the method used by Cowley [7] on Cu_3Au. In the face-centered cubic lattice, the position of one lattice point relative to another can be represented by

$$r_{lmn} = la'_1 + ma'_2 + na'_3$$

where lmn are certain integers and $a'_1\ a'_2\ a'_3$ are each half of the usual cubic axes $a_1\ a_2\ a_3$. In terms of the $a'_1\ a'_2\ a'_3$, the corresponding reciprocal vectors are $b'_1\ b'_2\ b'_3$ and the diffraction vector can be represented by

$$\left(\frac{s - s_0}{\lambda}\right) = h_1 b'_1 + h_2 b'_2 + h_3 b'_3$$

where $h_1 h_2 h_3$ are continuous variables. The short-range order parameter α_{lmn} is defined by

$$\alpha_{lmn} = 1 - (P_{lmn}/m_A)$$

where α_{lmn} is the order parameter for neighbors at a distance lmn, and P_{lmn} is the probability of finding an A atom as an (lmn) neighbor of a B-atom. In a sample containing N atoms, with A and B present in proportions m_A and m_B, in addition to the sharp crystalline reflections, there will be a diffuse intensity characteristic of the short range order given by

$$(3) \quad (I_{eu})_{SRO} = N m_A m_B (f_A - f_B)^2 I'_{SRO}$$

where

$$(4) \quad I'_{SRO} = \sum_l \sum_m \sum_n \alpha_{lmn} \exp [2\pi i(lh_1 + mh_2 + nh_3)].$$

As seen from (4), the corrected short-range order intensity I'_{SRO} is periodic in reciprocal space, with periods $b'_1\, b'_2\, b'_3$ which are double the reciprocal vector lengths $b_1 b_2 b_3$ corresponding to the usual cubic axes. The short-range order parameters α_{lmn} are the coefficients of the Fourier series for I'_{SRO} and can be evaluated in the usual way by

$$(5) \quad \alpha_{lmn} = \int\int\int_0^1 I'_{SRO} \exp [-2\pi i(lh_1 + mh_2 + nh_3)]\, dh_1\, dh_2\, dh_3.$$

Single crystals of CuAu (49.7 atomic per cent Au) were grown from the melt by lowering the temperature at about 13°C per hour to a temperature of 600°C where they were quenched. Flat plates about 1 cm in diameter and 0.2 cm thick were cut with surfaces parallel to the (100) planes. The spectrometer mount allowed a sufficient range of orientation of the crystal to permit measuring the diffuse intensity throughout the necessary volume in reciprocal space.

For measurements at high temperature the crystal was enclosed by a cylindrical foil cover and maintained in flowing dried nitrogen. CuKα radiation was monochromated by a bent quartz crystal which focussed on the sample. The $\lambda/2$ component from the monochromator was corrected by using a balanced Ni-Al filter, balanced at $\lambda/2$. The slit system limited the divergence of the primary and the scattered beam to less than three degrees. By tolerating this amount of divergence there was sufficient intensity for measurement with a Geiger counter.

The correction for temperature diffuse scattering was determined by measuring the total diffuse scattering at a number of positions in reciprocal space with the crystal quenched in the disordered form and held at temperatures of 150°C, 27°C and −145°C. Assuming the temperature diffuse scattering to be linearly proportional to the absolute temperature, the difference between the extrapolated values for O°K and T°K is taken as the correction for a sample held at T°K. The Compton modified scattering is independent of temperature and can be computed from tabulated values. Each intensity reading was the difference between the readings with the Ni filter and the Al filter. This difference automatically eliminates the general counter background, and also both scattering and fluorescence radiation from the $\lambda/2$ and $\lambda/3$ wavelengths. The working equation for I'_{SRO} was then

$$(6) \quad I'_{SRO} = k(I_D - I_T - I_C) \frac{1}{(1 + \cos^2 2\theta \cos^2 2\theta')} \frac{1}{(f_{Au} - f_{Cu})^2}$$

where I_D is the difference of the Ni and Al filter readings, I_T is the temperature diffuse scattering, I_C is the Compton modified intensity, and θ' is the Bragg angle for the quartz monochromator. Determining the constant k amounts to getting the intensities in electrons units per atom, and this can be done by comparing with the high-angle scattering from paraffin or by using the fact that $\alpha_{000} = 1.0$ and hence from (5)

$$\int\int\int_0^1 I'_{SRO}\, dh_1\, dh_2\, dh_3 = 1.0.$$

The latter method was used.

Preliminary measurements of intensity along the $h_1 00$-axis of reciprocal space for a crystal quenched from 500°C are shown in Figure 2a. Positions along the axis are represented by the usual (hkl) indices, thus the fundamental reflections (200) and (400) are at positions $h_1 = 1$ and $h_1 = 2$. To avoid confusion both fundamental and diffuse peaks will be designated by the usual (hkl) indices throughout this paper. There are two unexpected features in the curve of Figure 2a for the crystal quenched from 500°C. The (100) and (300) diffuse peaks are displaced appreciably toward larger angle, and there is an asymmetry about the fundamental reflections (200) and (400) with the intensity higher on the small-angle side. To investigate further these two unexpected features, the diffuse intensity was measured throughout the $(h_1 h_2 0)$ plane in reciprocal space for the crystal quenched from 500°C. The results are represented by the

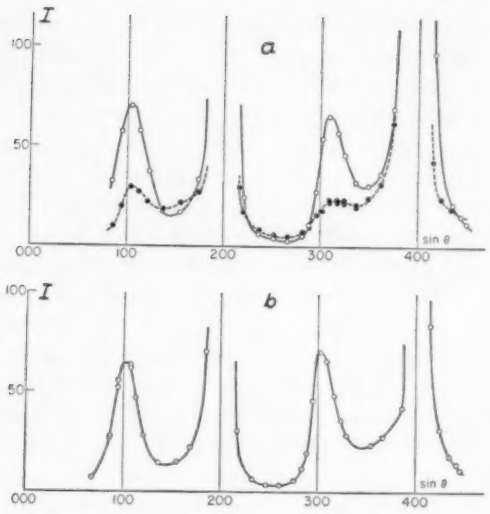

FIGURE 2. Measured intensity along the $h_1 00$ line, corrected for f^2 and polarization variation only. (*a*) CuAu,——— quenched from 500°C,– – – – – – – – measured at 480°C. (*b*) Cu_3Au, quenched from 500°C.

contours of Figure 3. The diffuse peaks at (100) and (300) are shifted outward while those at (110), (210) and (310) are not displaced. In CuAu the diffuse peaks due to short-range order are roughly spherical rather than having the pronounced disk shape which Cowley [7] found for Cu_3Au.

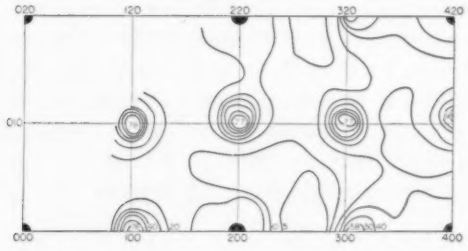

FIGURE 3. Measured intensity, corrected for f^2 and polarization dependence, in the $h_1 h_2 0$ plane for a crystal of CuAu quenched from 500°C.

Since quenching is always uncertain, the diffuse intensity was next measured with the crystal held at 480°C. The intensity distribution along the $h_1 00$-line is shown in Figure 2a. A contour plot for the $hk0$-plane of reciprocal space, with the crystal held at 450°C, is shown by Figure 4. The diffuse peaks in both plots are lower than those of the quenched sample (100) and (300) are still displaced toward large angle, and a pronounced temperature diffuse scattering appears around the fundamental reflections (200) and (400). The two curves of Figure 2a are not strictly comparable since the 480°C trace was attenuated 26 per cent by the foil surrounding the crystal. However, even after this attenuation correction is made, the 100 and 300 peaks for the sample held at 480°C are about one half those observed for the sample quenched from 500°C. This is an indication that although the quench was adequate to prevent the formation of visible superstructure lines, it was not adequate to maintain the short-range order in a state characteristic of 500°C.

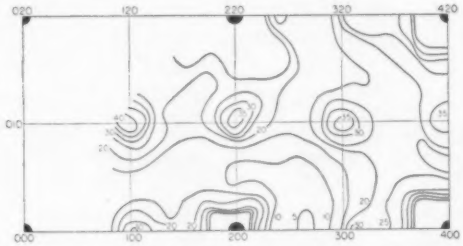

FIGURE 4. Measured intensity, corrected for f^2 and polarization dependence, in the $h_1 h_2 0$ plane for a crystal of CuAu held at 450°C.

It seems to be experimentally established that there is an outward displacement of the 100 and 300 diffuse peaks in disordered CuAu, but the significance of the effect is not certain. It has been shown that for a disordered binary alloy in which both the atomic sizes and the scattering factors are different, there is a modulation in the diffuse scattering due to the size effect [8]. For plots of intensity along the $h_1 00$-line, such as those of Figure 2, the size effect adds a term $-16\pi^2\beta_1 h_1 \sin 2\pi h_1$, and for the Cu-Au system the size effect coefficient β_1 is positive. This term raises the intensity in the regions 100–200 and 300–400, and lowers it in the region 200–300. In addition to explaining the observed difference in background level in these regions, the size effect term will automatically produce an outward shift of the 100 and 300 diffuse peaks. Figure 2b shows the intensity variation along the $h_1 00$-line for Cu_3Au quenched from 500°C. The size-effect variation in the background level is clearly seen, together with an outward shift of the 100 and 300 peaks which is smaller than the shift observed for CuAu.

Another explanation of the outward shift can be related to the ordered structure of CuAu. In the ordered structure, the 002-planes are alternately gold and copper and there is a marked contraction of the *c* axis, resulting in an outward displacement of the 001 and 003 superstructure reflections. Suppose that this same tendency for layering exists above T_c, and that there is a small contraction normal to the layers. The layered regions would be

extremely small and the layering direction would be distributed at random in the three orthogonal directions to give statistical cubic symmetry. A fundamental reflection such as 200 would receive contributions from all three orientations, 200, 020, and 002, so that its position would correspond to an average dimension. The diffuse reflections which we have called 100 and 300 would be contributed mainly by the regions whose orientations correspond to 001 and 003, and hence these diffuse peaks should exhibit an outward displacement.

From Figure 3 it is seen that there is an outward shift for the diffuse peaks at 100 and 300 but no definite shift for 100, 210 and 310. These facts are inconsistent with an explanation by either layering or size effect alone. In general the size effect will tend to displace all diffuse peaks outward, while layering displaces $00l$ outward and $hk0$ inward. A consistent explanation of the peak shifts seems possible if we assume the existence of both layering and the size effect. The diffuse peaks which have been called 100 and 300 show an outward displacement because both effects work in the same direction, and for the other diffuse peaks the two effects tend to cancel one another.

A measurement of the short-range order parameters for the various shells of neighbors is independent of whether or not a layering exists in the material, because from the measurements and method of evaluation it is an average over all neighbors of a given shell which is obtained. In terms of the hkl indices of Figure 3, measurements of the diffuse intensity were made in the prism-shaped volume bounded by 2, 0, 0; 2, 1, 0; 2, 1, 1; 2, 0, 1; 2 1/2, 1/2, 0; and 2 1/2, 1/2, 1. This choice avoided regions where the peak shift was large. Diffuse intensities were measured at about 350 points in the selected region, and the measurements were made on a crystal quenched from 500°C and on two other samples held at temperatures of 425°C and 525°C. The evaluation of the data followed the procedure used by Cowley [7] on Cu_3Au. The results are given in Table II.

Some of the shells i contain several lmn groups with different values of α_{lmn} for perfect long-range order. The values of α_i for perfect order which are given in column 5 are the appropriate averages. Complete disorder is represented by the value zero, a preference for like atoms by a positive value, and a preference for unlike atoms by a negative value of the parameter α_i.

The order parameters for the quenched sample are considerably higher than those for the samples held at temperature, indicating that the quenching of a large single crystal is inadequate to preserve the state of short-range order. For the samples held at 425°C and 525°C the order parameters are smaller but comparable to those found for Cu_3Au [7]. There is a high degree of short-range order in CuAu, as evidenced by the first neighbor parameters which are about 40 per cent of the way from complete disorder to perfect order. The second neighbor parameters seem to be too small relative to the values for higher neighbors. In view of the difficulty in correcting for temperature diffuse scattering, it could well be that these values are somewhat in error. For the two samples held at temperature, the third neighbor parameters come out approximately zero rather than negative as would be expected from the long-range order. A reversal in sign for

TABLE II

EXPERIMENTAL VALUES OF AVERAGE SHORT-RANGE ORDER PARAMETERS FOR CuAu

i	lmn	Number of sites	Perfect order α_{lmn}	Perfect order α_i aver.	α_i Measured Quenched from 500°C	α_i Measured Held at 425°C	α_i Measured Held at 525°C
1	110	4	1	−1/3	−0.158	−0.123	−0.118
	101, 001	8	−1				
2	200	6	1	1	0.210	0.048	−0.002
3	112	8	1	−1/3	−0.048	0.00	0.00
	121, 211	16	−1				
4	220	12	1	1	0.153	0.07	0.05
5	310	8	1	−1/3	−0.050	−0.03	−0.03
	301, 031	16	−1				
6	222	8	1	1	0.093	0.03	0.03
7	132, 312	16	1	−1/3	−0.035	−0.02	−0.02
	321, 213	32	−1				
8	400	6	1	1	0.070	0.02	0.00

third neighbors was found in Cu_3Au, but in this case the effect is not as certain due to the apparent uncertainty in the second neighbor values.

IV. Discussion

Long-range order in CuAu is practically perfect at low temperature, and it decreases by only about 3 per cent on raising the temperature to 380°C. This very small decrease in long-range order is quite different from the behavior observed in other binary alloys such as Cu_3Au [6], CuZn [9], and CuPt [10]. At 380°C the material changes to the orthorhombic CuAuII structure in which the long-range order is somewhat smaller, and at 408°C the long-range order goes abruptly to zero. Since the variation of order in CuAuI is terminated at 380°C by the appearance of CuAuII, it is not obvious whether the critical temperature for the variation in CuAuI is 380°C or 408°C or even a higher temperature. The measured change in the a/c ratio makes it definite that there is a small decrease in the long range order for CuAuI. Using the modified quasi-chemical theory, Li [4] has computed the long-range order curve for CuAu which is shown in Figure 1. The agreement with the measured values of S is remarkably good. Zernicke's [11] treatment of long-range order in a face centered lattice with AB composition is also in qualitative agreement.

The measured short range order coefficients for CuAu are qualitatively similar to those found for Cu_3Au and they indicate the same tendency for each atom to surround itself by unlike atoms. An observed outward shift of the 100 and 300 diffuse short-range order peaks suggests the existence of micro-regions of layered material similar to the long-range ordered structure. If this indication could be trusted it would be the most interesting result of these measurements, but unfortunately the effect is too small relative to the experimental error and the ambiguity in interpretation, to allow any really definite conclusions to be drawn.

The samples used in this study were so close to the ideal CuAu composition that no attention has been paid to the existence of possible two phase regions containing ordered and disordered material in equilibrium. Below 380°C there was no evidence for other than the highly ordered tetragonal structure and above 408°C the material was statistically face centered cubic.

Acknowledgment

The author wishes to express his gratitude for the aid and advice given by Prof. B. E. Warren during the course of this investigation. He also wishes to thank Miss R. M. Kimura for aid in the computations.

The research was sponsored by the U.S. Office of Naval Research.

References

1. Johansson, C. H. and Linde, J. O. Ann. der Physik **25** (1936) 1.
2. Kallback, O., Nystrom, J., and Borelius, G. Ingen. Vetensk. Akad. Handl. No. 157 (1941).
3. McKeehan, M. and Warren, B. E. J. Appl. Phys. **24** (1953) 52.
4. Gorsky, W. Z. Zeit. f. Phys. **50** (1928) 64.
5. Li, Y. Y. J. Chem. Phys. **17** (1949) 447.
6. Keating, D. T. and Warren, B. E. J. Appl. Phys. **22** (1951) 286.
7. Cowley, J. M. J. Appl. Phys. **21** (1950) 24.
8. Warren, B. E., Averbach, B. L., and Roberts, B. W. J. Appl. Phys. **22** (1951) 1493.
9. Chipman, D. and Warren, B. E. J. Appl. Phys. **21** (1950) 696.
10. Walker, C. B. J. Appl. Phys. **23** (1952) 118.
11. Zernicke, F. Physica **7** (1940) 565.

INTERNAL FRICTION IN OXYGEN-VANADIUM AND NITROGEN-VANADIUM SOLID SOLUTIONS*

R. W. POWERS†

Two internal friction peaks have been identified in vanadium. One occurring at 186°C for frequencies of 1 cps is associated with the stress-induced diffusion of oxygen, and the other occurring at 272°C is associated with the diffusion of nitrogen. The corresponding activation energies for these peaks were found to be 28.6 and 34.1 kcal, respectively. The skewness of the oxygen peak has been shown to be a concentration effect.

LE FROTTEMENT INTERNE DANS LES SOLUTIONS SOLIDES OXYGÈNE-VANADIUM ET AZOTE-VANADIUM

Deux maxima de frottement interne furent trouvés dans le vanadium. Un de ces maxima a lieu à 186°C pour des fréquences d'un cycle par seconde; il est dû à la diffusion de l'oxygène, induite par des tensions. L'autre a lieu à 272°C et est dû à la diffusion de l'azote. Les énergies d'activation correspondantes à ces maxima furent évaluées à 28,6 et 34,1 Kcal respectivement. On a montré que l'asymétrie du maximum associé à l'oxygène est un effet de concentration.

INNERE REIBUNG IN DEN FESTEN LÖSUNGEN VANADIUM-SAUERSTOFF UND VANADIUM-STICKSTOFF

Zwei Maxima der inneren Reibung wurden in Vanadium identifiziert. Das eine Maximum tritt bei 186°C und Frequenzen von einem Hz auf und hängt mit der spannungsinduzierten Diffusion des Sauerstoffs zusammen. Das zweite Maximum, das bei 272°C auftritt, steht mit der Diffusion des Stickstoffs in Zusammenhang. Die zu diesen Maxima gehörenden Aktivierungsenergien betrugen 28,6 Kcal und 34,1 Kcal. Es wurde gezeigt, dass die schiefe Form des Sauerstoffmaximas auf einem Konzentrationeffekt beruht.

Introduction

This investigation was undertaken to complete a gap in our understanding of interstitial diffusion in the *V* B group of the periodic table. The elements of this group, vanadium, niobium (columbium) and tantalum are all body-centered cubic metals with relatively high solubilities for oxygen and nitrogen, which occupy interstitial positions when in solution. Consequently, diffusion studies in these alloys can be conveniently undertaken by means of internal friction measurements.

Our understanding of internal friction arising from the stress-induced diffusion of interstitials in b.c.c. metals has been brought to a high level of development chiefly through the efforts of Snoek [1], Dijkstra [2] and Wert and Zener [3]. Kê [4], Ang [5], and Marx, Baker and Sivertsen [6] have carried out studies on tantalum, while niobium has been investigated by Wert [7], Ang [5], Ang and Wert [8], and Marx, Baker and Sivertsen [6]. When ductile vanadium became available in wire form, it was decided to investigate this element as well.

Materials and Apparatus

The first lot of vanadium used was obtained from A. U. Seybolt in the form of 0.040 in. wire. This metal was prepared from the calcium reduction of V_2O_5 by the method described by McKechnie and Seybolt [9]. The small pellets of vanadium so obtained had been collected into a billet by hot swaging the pellets encased in a steel can. The billet was reduced to wire by cold swaging. A second lot of wire differed from the first only in that the nitrogen content was lower. Internal friction measurements on these vanadium wires were made in a torsional pendulum similar to the one described by Kê [10].

Experimental Results

Two internal friction peaks were readily found in a specimen vibrating in torsion at 0.7 cps. One was at 181°C and the other at 265°C as shown in Figure 1 (186°C and 272°C respectively, corrected

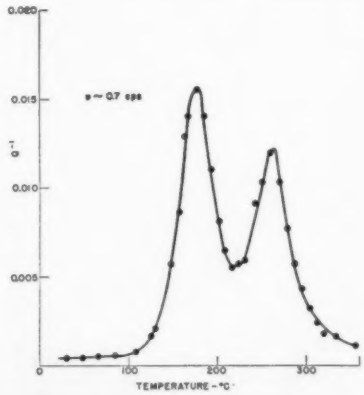

FIGURE 1. Two internal friction peaks in vanadium, Q^{-1} vs T.

*Received February 18, 1954.
†General Electric Research Laboratory, Schenectady, N.Y.

to 1 cps). The only treatment accorded this vanadium wire was an anneal in high vacuum at 850°C for eight hours. The peaks are highly reproducible. As described below, it was found that the one at 186°C is associated with oxygen and the other at 272°C with nitrogen. Moreover, the internal friction is independent of the strain amplitude as is required by the theory of stress induced diffusion. These facts indicate that damping is not associated with the motion of dislocations.

The lower temperature peak can be greatly reduced in height (from 0.0160 to about 0.0040–0.0010) by heating in a vacuum near 1550°C for four hours. Such a treatment affects the higher temperature peak to only a slight extent. Because of the high vapor pressure of vanadium, higher degassing temperatures are not practical. Degassing was carried out in an apparatus in which the vanadium wire was heated by means of its own electrical resistance.

The identification of the 186°C peak was carried out as follows. A specimen was reinserted in the degassing system. The vacuum system was flushed several times with oxygen from the laboratory main, finally filled with oxygen to 0.01 mm pressure, and isolated. The wire then was heated to 1100°C for several minutes. The pressure rapidly fell to 10^{-5} mm. Curve (*b*) of Figure 2 was subsequently

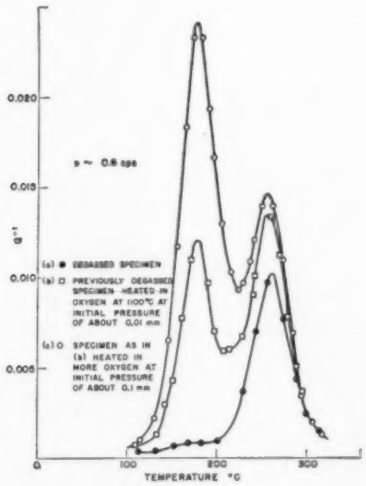

FIGURE 2. Plot illustrating identification of 186°C peak.

obtained. On repeating this procedure with this wire, but with an initial oxygen pressure of 0.1 mm, curve (*c*) was obtained. A part of the increase in the height of the high temperature peak arises from a contribution from the tail of the 186°C peak. The remainder may be due to incidental contamination as a result of the relative crudeness of the technique. However, these results as well as other cited below establish the association of the peak at 186°C with oxygen diffusion.

The identity of the 272°C peak was established with greater difficulty. The height of this peak in the first lot of vanadium wire could never be reduced below 0.0110 after the severe degassing conditions described above, and for several wires values of 0.0140 were recorded for this peak. Moreover, the highest value ever recorded after loading was only about 0.0180. This small operating range made unequivocal identification almost impossible. Consequently, a second lot of vanadium of lower initial nitrogen content was reduced to wire form. In addition, the following more elaborate technique was developed to reduce incidental contamination. Several wires were degassed as previously described. Then, small amounts of high-purity research grade gas were introduced into the degassed vacuum system from flasks isolated from this system by means of vacuum grade stopcocks. The wires were heated to 1100°C for about one-half hour. Curve (*a*) Figure 3 was obtained on a degassed specimen.

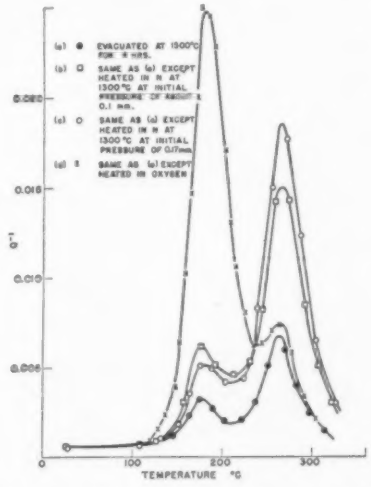

FIGURE 3. Plot illustrating identification of 272°C peak.

Curves (*b*) and (*c*) were obtained on two wires after soaking at initial pressures of nitrogen of 0.1 and 0.17 mm respectively after degassing. A fourth wire (curve *d*) was loaded with oxygen after degassing. The heights of the low-temperature peak fluctuate in a random fashion (except, of course, for curve (*d*)) presumably because it was not found possible to evacuate each time to the same oxygen level. On this basis, the high temperature peak was identified with the diffusion of nitrogen atoms.

No peak was found that could be associated with the diffusion of carbon. A vanadium wire heated at 1100°C for several hours, after a coating of Oildag was applied, displayed a bright surface. Although this indicates that the carbon had diffused into the specimen,the only effect noted in the internal friction was a slight enhancement of the oxygen peak, which likely resulted from the absorption into the specimen, during heat treatment, of oxygen adsorbed on the surface.

Activation energies for the two relaxations were determined from the shifts in the peak temperatures with changes in the frequency of vibration. The peak temperature was determined as follows: Log Q^{-1} values were plotted against $1/T$. From this plot, using linear interpolation between adjacent experimental points, values of $1/T$ corresponding to various values of Q^{-1} were determined. The arithmetic mean $(1/T)_{mean}$ of the two values of $1/T$ corresponding to a value of Q^{-1} was computed and plotted as a function of $Q^{-1}/Q^{-1}{}_{max}$ as shown in Figure 4. If the internal friction can be

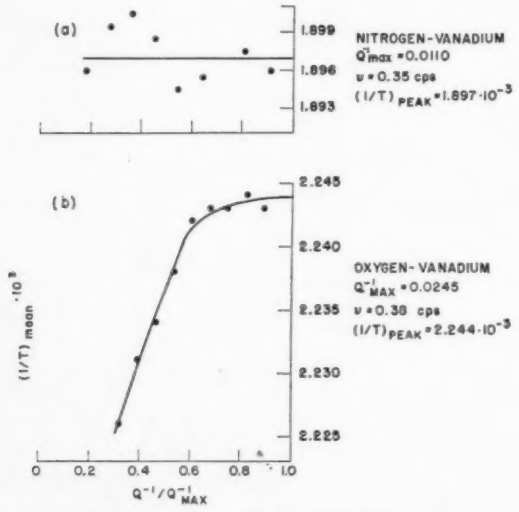

FIGURE 4. Plot illustrating peak symmetry.

described by a single relaxation time, the damping peak should be symmetric about $1/T_{peak}$ and $(1/T)_{mean}$ should remain invariant with $Q-^1$.

For the nitrogen peak, the internal friction was measured at frequencies of 0.350, 0.636, and 1.58 cps with peaks occurring at 254.2, 263.8, and 279.2°C, respectively. These results correspond to an activation energy of 34.1 kcal/mole (see Figure 5). The internal friction for this level of nitrogen in vanadium ($Q^{-1}{}_{max}$ = 0.011) can be described fairly well by a single relaxation time, as may be seen in

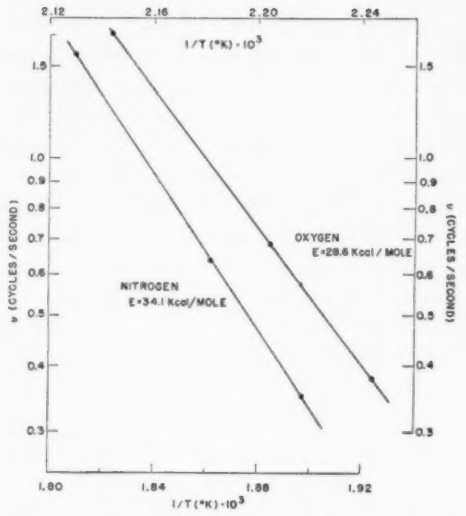

FIGURE 5. Plot of log vs $1/T$, determination of activation energy.

Figure 6. The experimental curve at one-half the peak height is only about ten per cent wider in terms of $1/T$ than the theoretical curve calculated for an activation energy of 34.1 kcal/mole. Moreover, as shown in Figure 4, the fact that values of $(1/T)_{mean}$ are constant for the entire range of Q^{-1} indicates a symmetric peak.

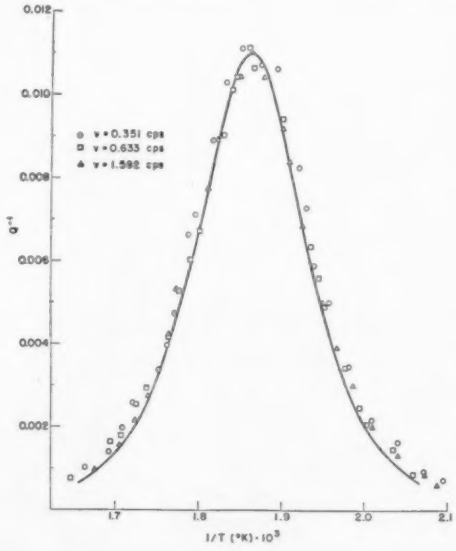

FIGURE 6. Nitrogen peak, Q^{-1} vs $1/T$, calc. + exp. data. Solid line calculated for $Q^{-1}{}_{max}$ = 0.0110, E = 34.1 kcal. Points at ν = 1.582 cps and 0.351 cps shifted along abscissae a distance corresponding to E = 34.1 kcal.

The activation energy for oxygen in vanadium was determined from measurements made at frequencies of 0.378, 0.682, and 1.72 cps. Corre-

sponding peaks were found at 172.4, 180.5, and 193.4°C. These results lead to an activation energy of 28.6 kcal/mole (see Figure 5). In order to minimize the relative effect of the slightly overlapping nitrogen peak on the measurements, these data were taken for a peak Q^{-1} value of 0.0245. (All data reported have been corrected for the contribution from the nitrogen peak as well as for background damping.) At this level of damping, the experimentally determined values of Q^{-1} are higher on the high temperature side of the peak than those calculated assuming a single relaxation time (Figure 7). The skewness of this peak is made even more

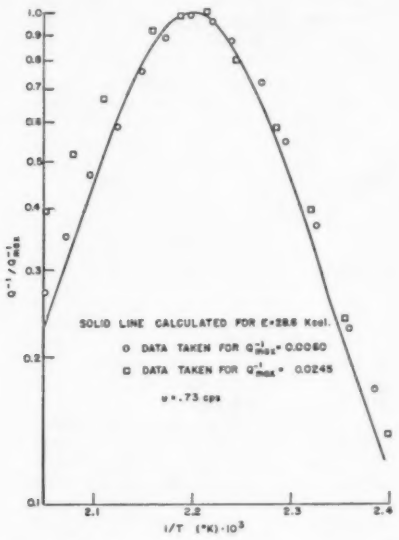

FIGURE 7. Oxygen peak, log Q^{-1} vs $1/T$, calc. + exp. data.

evident in Figure 4 wherein it may be seen that $(1/T)_{mean}$ values change markedly with Q^{-1}. However, when the internal friction was investigated in another specimen in which the maximum internal friction was only 0.0060, the experimental points were found to lie on the calculated curve in Figure 7. These results suggest that the skewness of the oxygen peak depends on the oxygen concentration.

These findings can be interpreted as follows. At small oxygen concentrations (i.e., low internal friction peak height), there is but one relaxation process and at a given temperature, only one relaxation time, $\tau = \tau_0^{(E/RT)}$. At the peak temperature, T_{peak}, the resonance condition requires that $\tau = (2\pi\nu)^{-1}$, where ν is the frequency of torsional oscillation. As the oxygen concentration is augmented, another relaxation process(es) with a relaxation time, τ_e, longer than τ, becomes increasingly important. This extra relaxation is resonant at a temperature higher than T_{peak} for a fixed frequency ν. As a result, the damping curve (log Q^{-1} vs $1/T$) is skewed with the internal friction greater on the high-temperature side of the peak than that calculated for a single relaxation time.

Similar results found with oxygen-tantalum solutions will be the subject of another report.

Acknowledgment

The author is very grateful to J. C. Fisher and A. U. Seybolt for helpful advice and criticism.

References

1. SNOEK. Physica **8** (1941) 711.
2. DIJKSTRA. Philips Research Repts. **2** (1947) 357.
3. WERT and ZENER. Phys. Rev. **76** (1949) 1169.
4. KÊ. Phys. Rev. **74** (1948) 9; **74** (1948) 914.
5. ANG. Acta Met. **1** (1953) 123.
6. MARX, BAKER, and SIVERTSEN. Acta Met. **1** (1953) 193.
7. WERT. J. Appl. Phys. **21** (1950) 1196.
8. ANG and WERT. J. Metals **5** (1953) 1032.
9. MCKECHNIE and SEYBOLT. J. Electrochem. Soc. **97** (1950) 311.
10. KÊ. Phys. Rev. **71** (1947) 533; Trans. A.I.M.M.E. **176** (1948) 448.

THERMODYNAMICS OF ORDERING ALLOYS, II. THE GOLD-COPPER SYSTEM*

R. A. ORIANI†

The solid solutions of the gold-copper system have been investigated by the galvanic e.m.f. technique. The results at temperatures higher than the critical temperatures of ordering agree with those of previous workers in showing negative deviations from Raoult's law, and a negative heat of solution. A minimum in the curve for the entropy of mixing of the disordered phase is found and is indicative of short-range order. The degrees of short-range order computed from the thermodynamic data and the quasi-chemical theory of ordering agree well with those found by X-ray diffraction. At lower temperature two-phase regions are found separating one superlattice phase from another, or from the disordered solid solution. The orthorhombic CuAuII is characterized by a relatively unsharp cusp in the curve of entropy of solution, which shows the presence of many imperfections in the superlattice.

LA THERMODYNAMIQUE DES ALLIAGES SUBISSANT LA TRANSFORMATION ORDRE-DÉSORDRE. II. LE SYSTÈME OR - CUIVRE

Les solutions solides du système or-cuivre ont été examinées par la méthode de la f.é.m. d'une pile. Les résultats obtenus à des températures supérieures à la température critique de la mise en ordre, sont en accord avec les résultats obtenus antérieurement par d'autres chercheurs, du fait qu'ils montrent une déviation négative par rapport à la loi de Raoult et des chaleurs négatives de dissolution. Un minimum est trouvé dans la courbe de l'entropie de mélange de la phase désordonnée, indiquant un ordre à petite distance. Les degrés d'ordre à petite distance calculés à partir de données thermodynamiques et en se basant sur la théorie quasi chimique, sont en accord avec les résultats obtenus au moyen de la diffraction de rayons X. Aux températures peu élevées on trouve des régions à deux phases qui, elles-mêmes, séparent deux phases différentes, ayant des surstructures, ou une phase à surstructure, de la solution solide désordonné. Le composé orthorombique CuAuII est caractérisé par une pointe peu accentuée dans la courbe de l'entropie de dissolution, ce qui indique la présence d'un grand nombre d'imperfections de la surstructure.

THERMODYNAMIK ORDNUNGSFÄHIGER LEGIERUNGEN II. DAS SYSTEM GOLD-KUPFER

Die festen Lösungen des Gold-Kupfer Systems werden mit Hilfe einer galvanischen Element Technik untersucht. Die Ergebnisse bei Temperaturen oberhalb der kritischen Ordnungstemperaturen stimmen mit den Resultaten früherer Arbeiten anderer Autoren überein, die negative Abweichungen vom Raoult' schen Gesetz und negative Lösungswärmen fanden. Es wurde ein Minimum in der Kurve der Mischungsentropie der ungeordneten Phase gefunden, und als ein Zeichen einer Naheordnung gedeutet. Das Ausmass der Naheordnung, das aus den thermodynamischen Daten und aus der quasi-chemischen Theorie des Ordnens berechnet wurde, stimmt gut mit den röntgenographisch ermittelten Werten überein. Es zeigte sich, dass sich bei tieferen Temperaturen im Zweiphasengebiete die eine Überstrukturphase von der anderen oder von der ungeordneten festen Lösung trennt. Für das orthorhombische CuAu II ist ein relativ unscharfes Maximum in der Kurve der Lösungsentropie charakteristisch, das das Vorhandensein von vielen Kristallbaufehlern in der Überstruktur zeigt.

Introduction

The gold-copper system has furnished the earliest recognized example of an ordered solid solution, and has been the subject of many investigations by many techniques. Nevertheless, the thermodynamics of the superlattices in this binary system has not been satisfactorily elucidated. The course of the activity-composition curve at 390°C obtained by Wagner and Engelhardt [1] gives no indication of the presence of superlattices. The results of Weibke and von Quadt [2] in the temperature region of the superlattices exhibit great differences between ascending and descending temperature measurements. The work of Chiche [3] is restricted to temperatures higher than those for formation of the superlattices. Heat capacity measurements through the order-disorder transformations are necessarily done as the temperature of the alloy is constantly raised, so that the alloy may not be in thorough internal equilibrium at any one instant, and of course they furnish no information on the free energy of the alloy.

Because of the great interest attaching to the gold-copper system, and because the superlattices in these alloys have served as prototypes in the theoretical analysis of the ordering phenomenon, it has been considered advisable to attempt to measure the equilibrium thermodynamic properties in the temperature region about the superlattices AuCu and $AuCu_3$. This paper describes the results of an investigation by means of the galvanic cell technique.

*Received March 4, 1954.
†General Electric Research Laboratory, Schenectady, New York.

Experimental

The galvanic cell method for the measurement of thermodynamic activities has the great advantage over the usual vapor pressure method that in principle no composition change occurs during the measurement, so that long times of waiting for equilibrium become possible. However, long holding times are feasible only if excellent electrochemical stability is achieved. The experimental arrangement in the present investigation was very similar to that described in a previous paper [4]. The electromotive force developed by the cell

$$Cu_{(s)} \mid Cu^{+} \text{ (in electrolyte)} \mid Cu(Au)_{(s)}$$

was measured as a function of temperature, alloy composition, and time. Figure 1 shows schematically the construction of the cell and of the device used for pretreatment of the electrolyte and for filling the cell. The eutectic mixture of KCl and LiCl, plus a very small amount of CuCl was melted in the auxiliary container and held at 400°C in contact with pure Cu wire, under constant evacuation, for four days. During this time, the assembled cell was also maintained at 400°C under the same vacuum. After this desiccation treatment, the seal-off was fused shut, and the molten electrolyte was forced into the cell by admitting pure argon over the liquid in the auxiliary container. When all the electrolyte had been transferred, enough pure argon was allowed to enter the cell to produce a pressure of almost 1 atm. The cell was then detached from the filling system by fusing closed the second seal-off.

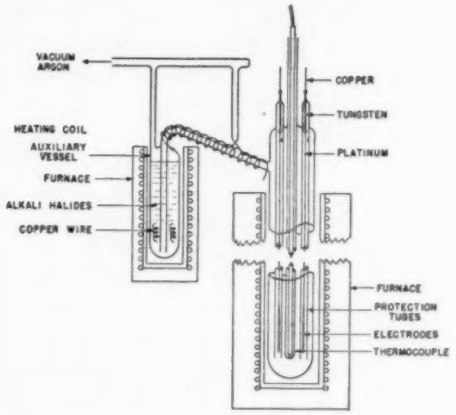

FIGURE 1. Schematic diagram of the galvanic cell and filling apparatus.

The electrodes* were cast under vacuum from A.S. and R. copper of 99.99 per cent purity and gold of 99.98 per cent purity in silica tubes. The rods were homogenized by holding for 14 days at temperatures just under the solidus points. The electrodes were fabricated by drawing and were spot-welded to the platinum suspension wires. Separate measurements for the thermal e.m.f. developed by the various connections within the cell were not made, reliance being placed on the tests carried out by Weibke and von Quadt [2] which showed the thermal e.m.f. corrections to be negligible. Temperatures were measured by means of a platinum, platinum-rhodium thermocouple calibrated by Mr. W. K. Murphy at the melting points of National Bureau of Standards samples of copper, aluminum, zinc, and tin.

Before the measurements reported here were made, some exploratory experiments in other cells were carried out in which the temperature was maintained constant for some hours and then changed to another holding temperature, the direction and magnitude of the change being chosen haphazardly. In another exploratory experiment, the entire temperature range of 100 degrees was covered in about one day. The results of those experiments were very similar to those of Weibke and von Quadt in their irreproducibility and variability of points of inflection.

The values reported here were obtained from the use of two cells, the second of which had some RbCl added to the electrolyte to permit attainment of a lower temperature without the freezing of the electrolyte. In each case, measurements were begun at a high temperature, holding the temperature fixed for a rather large length of time, then decreasing the temperature to another fixed value, and so on to the lowest attainable temperature. Then the temperature was raised intermittently in a similar fashion, save that the waiting period at each temperature continued until all the voltages became constant with time within a few hundredths of a millivolt. The values taken at positive increments of temperature are taken as more nearly equilibrium voltages because of the longer waiting times, and because of the smaller magnitude of the increments of temperature. The waiting times at constant temperature ranged from 3 to 100 hours, the average period being 24 hours.

*Thanks are due to Drs. R. W. Schmitt and J. B. Newkirk for the gifts of two alloy compositions.

Experimental Results

The experimental voltages between the pure copper electrode and the various copper-gold electrodes as a function of temperature and composition are plotted in Figure 2. In Figure 2A the results for the alloys that lie about the composition CuAu are shown; however, to avoid complicating the diagram only the values taken with positive increments of temperature are presented and data obtained at temperature above 430°C have been left out of the figure, though such data were considered in calculating the slopes of the curves in the high-temperature region. In order to include this range of compositions in Figure 2A a scale for the ordinates had to be adopted which is too small for the accuracy of the measurements. The results for compositions about Cu_3Au are shown in larger scale in Figure 2B, where values for both

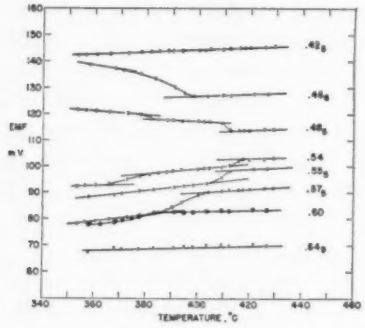

FIGURE 2A. E.m.f.-temperature curves for Au-Cu alloys near CuAu composition.

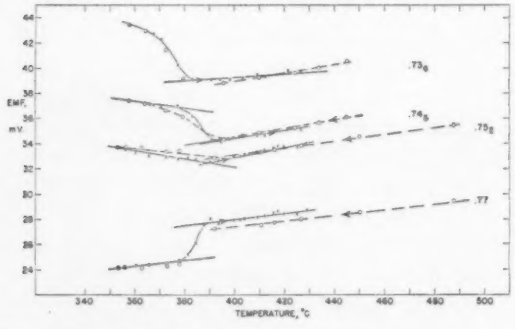

FIGURE 2B. E.m.f.-temperature curves for Au-Cu alloys near Cu_3Au composition.

negative and positive increments of temperature are given. The disparity between the two curves for $x_{Cu} = 0.77$ is about the largest observed.

Such separations between the ascending and descending branches of the curves are believed to be due to a very slow change in composition at the surface of the alloy electrodes caused by the transfer of copper and gold from one electrode to another by the agency of the reaction

$$Au_{(s)} + Cu^{+}Cl^{-}_{(liq.)} = Cu_{(s)} + Au^{+}Cl^{-}_{(liq.)}.$$

The electrolyte cannot be in equilibrium with respect to all the electrodes at any one time, since the compositions are different. The resulting transfer is considerably reduced by surrounding each electrode by a tube (see Figure 1) which dips into the electrolyte farther than does the electrode, thereby avoiding convective currents. Nevertheless, such a transfer becomes the limiting factor in an investigation with a galvanic cell when the waiting times at temperature are very long despite the fact that the concentration of Au^{+} must be extremely small. Hence, in the present work the alloy compositions contain the most uncertainty of any of the experimental quantities, probably ± 0.5 atom per cent. However, this does not sensibly vitiate the conclusions to be drawn.

In order to demonstrate the agreement of the present work at the higher temperatures with that of former investigators, present data were extrapolated to 500°C, and the activity of copper, a_{Cu}, pure copper as reference state, was calculated from $E = -(RT/F) \ln a_{Cu}$, where E is the observed potential at temperature T°K, R is the gas constant and F is the Faraday. Present values are plotted in Figure 3, together with those from

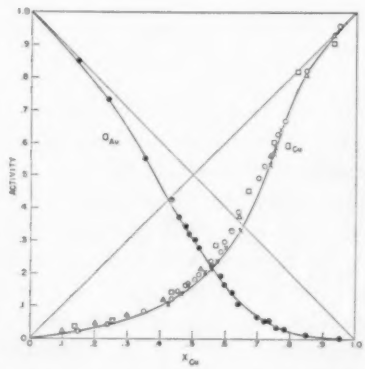

FIGURE 3. Thermodynamic activities of copper and gold in their solid alloys at 500°C. ○ Ref. 2. △ Ref. 3 (463°C.) □ Ref. 1, interpolated. × Present work, extrapolated.

the literature, and it is seen that the agreement is acceptable. The curve for a_{Au} was calculated by integrating the Gibbs-Duhem equation using excess partial molar quantities [5] based on the data of Weibke and von Quadt [2].

TABLE I

CALCULATED VALUES FROM 427°C DATA

x_{Cu}	$\Delta\bar{G}_{Cu}^{(x)}$	$\Delta\bar{G}_{Au}^{(x)}$	$\Delta\bar{G}^{(x)}$	ΔG	$\Delta\bar{S}_{Cu}^{(x)}$	$\Delta\bar{S}_{Au}^{(x)}$	$\Delta S^{(x)}$	ΔS	ΔH
.148*	−3251	214	− 299	− 879	.227	.005	.038	.867	− 272
.240*	−2506	40	− 571	−1337	−.045	.109	.072	1.168	− 520
.352*	−2440	− 30	− 878	−1783	.301	−.065	.064	1.357	− 833
.425	−2164	− 211	−1041	−1991	−.683	.483	−.013	1.346	−1050
.466	−1884	− 438	−1112	−2071	−.304	.178	−.047	1.323	−1145
.48	−1616	− 681	−1130	−2091	−.156	.043	−.052	1.323	−1167
.54	−1522	− 751	−1160	−2119	−.178	.058	−.070	1.300	−1209
.555	−1464	− 864	−1197	−2152	.027	−.190	−.070	1.294	−1246
.575	−1346	−1016	−1206	−2156	.172	−.382	−.064	1.295	−1251
.60	−1210	−1210	−1210	−2145	−.247	.230	−.056	1.281	−1249
.649	−1009	−1513	−1186	−2091	−.052	−.117	−.075	1.218	−1238
.736	− 488	−2687	−1069	−1873	.212	−.831	−.063	1.085	−1113
.745	− 400	−2940	−1048	−1834	.213	−.856	−.060	1.065	−1090
.752	− 385	−2987	−1031	−1811	.077	−.456	−.055	1.058	−1070
.77	− 295	−3278	− 981	−1732	.043	−.326	−.042	1.032	−1010
.782*	− 293	−3282	− 945	−1675	.023	−.235	−.033	1.009	− 968
.849*	− 89.0	−4145	− 701	−1292	.108	−.478	.020	0.865	− 687

*From data of Weibke and von Quadt [2].

Table I contains derived data at 427°C, a temperature slightly above the highest critical temperature for a superlattice. These excess partial and excess integral quantities were computed by equations analogous to those of (2) to (8) in reference 3; Weibke and von Quadt's data for $x_{Cu} = 0.148$, 0.240, 0.352, 0.782, and 0.849, interpolated for 427°C, have been incorporated in the calculations. The integral quantities of solution, ΔG, ΔS, and ΔH are shown in Figures 4, 5, and 6 respectively. The ΔH of solution at $x_{Cu} = 0.6$ is −1.25 kcal/g atom of alloy, and is in excellent agreement with the value of −1.24 obtained by Weibke and von Quadt at 500°C.

The nonlinear portions of the potential-temperature curves of Figure 2 that connect two linear segments are interpretable as representing the two-phase regions that must lie between any two single-phase regions. The phase diagrams of Figures 7 and 8 have been constructed from the temperatures of departure from linearity of the E-T curves; only the ascending-temperature curves have been used for this purpose because of the much greater care given

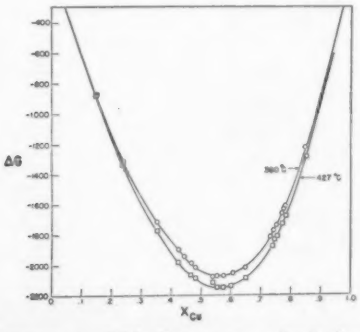

FIGURE 4. Gibbs free energy of solution.

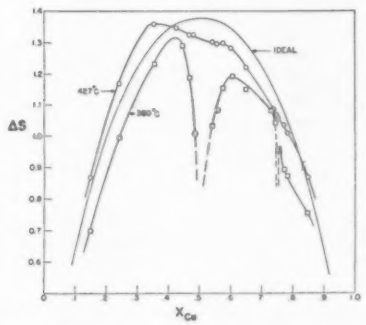

FIGURE 5. Entropy of solution; central portion of 380° curve refers to Phase II.

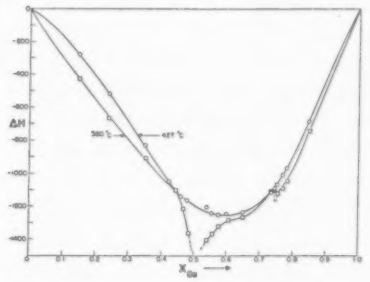

FIGURE 6. Enthalpy of solution; central portion of 380° curve refers to Phase II.

to that portion of the work. The points thus obtained from the *E-T* curves are represented in Figures 7 and 8 by solid ellipses and rectangles the size of which is a measure of the uncertainty of the position of the phase boundary. The open points in Figures 7 and 8 have been calculated from the thermodynamic requirement that an isothermal across a two-phase region is an isoactivity line; for this purpose the activity of copper was interpolated and extrapolated graphically using the measured values within the single phases. The consistency of these points with those obtained from the inflections of the *E-T* curves gives strong support for the existence of two-phase regions. However, a more direct demonstration of the presence of two-phase regions is furnished by the fact that upon going from the higher to the lower temperature phases, the *E-T* curves of Figure 2 for alloys poorer in copper than the stoichiometric composition rise in potential, whereas those richer in copper than the stoichiometric decrease in potential. This behavior is true for the transitions CuAu (disordered)→CuAu II (orthorhombic), CuAu II (orthorhombic)→CuAu I (tetragonal), as well as for Cu_3Au (disordered)→Cu_3Au (ordered), and cannot be explained except by, and is thoroughly consistent with, the composition segregation characteristics of a two-phase region.

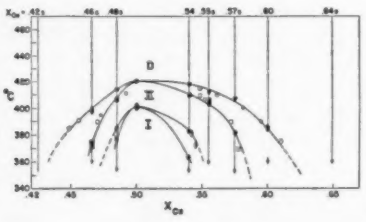

FIGURE 7. Phase relations about composition CuAu. Filled points are derived from Fig. 2A, open points from condition of isoactivity across two-phase fields.

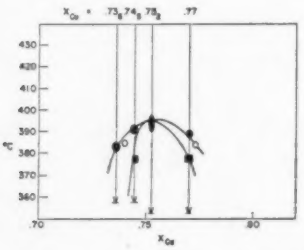

FIGURE 8. Phase relations about composition Cu_3Au. Filled points are derived from Fig. 2B, open points from condition of isoactivity across two-phase fields.

In constructing these phase diagrams, the maximum critical temperature for the CuAu D ⇌ CuAu II transformation was taken as about 421°C, in agreement with the results of Haughton and Payne [6] (about 420°), of Newkirk [7] (about 421°), of Rhines, Bond, and Rummel [8] (410°), and of Hirabayashi, Nagasaki, and Maniwa [9] (430°). The last temperature cited is apt to be high because of the dynamic nature of the heat-capacity measurement. The maximum critical temperature for the CuAu I⇌CuAu II transition was taken as about 400°C in accordance with the work of Newkirk [10] (about 395°), of Hirabayashi, Nagasaki, and Maniwa [9] (about 410°), Hirabayashi [11] (400° as estimated from c_p-curve), and Johansson and Linde [12], who found phase II in the range 410–420°.* The critical temperature at the Cu_3Au composition was set at 394°C, following the results of Haughton and Payne [6] (393°), of Nix and McNair [15] (394°), and of Keating and Warren [16] (394° ± 3°).

The activity data at the 380°C isothermal and the experimental $(\partial E/\partial T)_x$ at that temperature were used to calculate the ΔG, ΔS, and ΔH of solution. In these calculations the phase boundaries as established above were employed except that since the properties of $CuAu_{II}$ were desired, the boundaries of CuAu I were ignored and the activities and $(\partial E/\partial T)_x$ of phase II were extrapolated to the 380 degrees isothermal. The results are tabulated in Table II and presented in Figures 4, 5, and 6. The entropy and enthalpy of solution necessarily change very rapidly (see below) with composition in the region of homogeneity of a superlattice, so that many very closely spaced compositions would have to be investigated in order to establish by the present techniques the properties of a superlattice of narrow range. Such extensive information has not been obtained in the present work for CuAu I, so that Gibbs-Duhem integrations through phase I to obtain ΔS_I and ΔH_I have not been considered worthwhile. However, the large range of existence of CuAu II is notable, and permits the unambiguous demonstration of the marked decrease in ΔS of solution in the neighborhood of the stoichiometric composition that has been discussed theoretically by Olander [17]. The depth of the ΔS minimum for CuAu II cannot be established without more measurements very near and at the stoichiometric composition. The corresponding minimum

*To complete this account, it should be mentioned that Borelius, Larsson, and Selberg [13] find 408°C for II⇌D, and Nystrom [14] reports 380°C for I⇌II.

TABLE II

CALCULATED VALUES FROM 380°C DATA

x_{Cu}	$\Delta\bar{G}_{Cu}$	$\Delta\bar{G}_{Au}$	ΔG	$\Delta\bar{S}_{Cu}$	$\Delta\bar{S}_{Au}$	ΔS	ΔH
.148*	−5330	− 105	− 879	4.012	.118	.696	− 424
.240*	−4500	− 312	−1317	2.790	.430	.997	− 666
.352*	−3520	− 730	−1712	2.375	.615	1.234	− 907
.425	−3310	− 859	−1902	1.017	—	—	—
.445	−3104	−1017	−1945	1.116	1.429	1.290	−1103
.468	−3104	−1018	−1991	−3.690	5.466	1.187	−1216
.482	−2780	−1302	−2015	—	—	—	—
.485	—	—	(−2023)	− .920	2.826	1.008	−1364
.54	—	—	(−2175)	2.239	− .385	1.031	−1401
.543	−2232	−1910	−2084	—	—	—	—
.555	−2095	−2057	−2075	2.606	− .829	1.080	−1370
.575	−1879	−2338	−2075	2.836	−1.128	1.150	−1324
.576	−1879	−2337	−2070	—	—	—	—
.605	−1879	−2337	−2060	.773	1.831	1.191	−1281
.649	−1580	−2835	−2019	.807	1.774	1.148	−1269
.733	− 899	−4338	−1814	.826	1.779	1.080	−1109
.744	− 899	−4338	−1779	− .535	5.613	1.040	−1099
.745	− 851	−4477	−1775	—	—	—	—
.753	− 757	−4756	−1743	− .752	6.151	.954	−1120
.77	− 579	−5325	−1669	.424	2.455	.890	−1088
.778	− 579	−5325	−1630	—	—	—	—
.782*	− 515	−5560	−1615	.512	2.151	.870	−1047
.849*	− 252	−6720	−1230	.434	2.548	.753	− 739

*From data of Weibke and von Quadt [2].

in the ΔH curve at 380°C leads to a ΔH of transition (CuAu II→CuAu D) of at least 300 cal/g atom of alloy. The analogous minima for the Cu_3Au composition have only been indicated in Figures 5 and 6; the narrowness of the homogeneity range of this superlattice makes the compositions studied insufficient for their detailed demonstration.

Discussion

Cowley [18] has shown that above the critical temperature of ordering for Cu_3Au there is short-range order at that composition, and Roberts [19] has similarly found short-range order at the composition CuAu above the critical temperature. Quasi-chemical theory [20] of ordering based on the assumption of noninterference of pairs permits the calculation of short-range order from experimental activity coefficients, and good agreement has been found [21] at 500°C between the degree of short-range order thus computed and that found by X-ray diffraction. Table III presents a comparison of the preponderance over a random distribution of copper atoms in the first coordination shell about any one gold atom as observed by X-ray diffraction at 425°C, and as calculated by quasi-chemical theory [20] from the experimental ΔG of solution at 427°C. Included also are values of ΔH of solution calculated by quasi-chemical theory [20]

TABLE III

COMPARISON OF ATOMIC DISTRIBUTION IN FIRST COORDINATION SHELL BY X-RAY DIFFRACTION DATA AND BY CALCULATION FROM QUASI-CHEMICAL THEORY AND EXPERIMENTAL ΔG

Composition	$\alpha_1(425°)$	P[c], calcd. from α_1	$\Delta G(427°)$[d]	P, calcd. from ΔG and theory	ΔH, calcd. from ΔG and theory	ΔH[d], experimental
Cu_3Au	−0.151[a]	15.6%	−1825 cal/g atom	10.8%	−1094	−1070
CuAu	−0.123[b]	12.3%	−2120	12.9%	−1226	−1200

[a]Reference [18]. [b]Reference [19].
[c]P is the per cent excess of Au-Cu bonds in the alloy over the number that would be present for a random distribution.
[d]This work.

using the experimental figures for ΔG, and these are compared with the experimental values of ΔH at 427°C. The agreements are better than perhaps one should expect, since Li [22] has shown that the quasi-chemical theory has to be generalized to consider the tetrahedron as the local group in order to obtain a phase diagram for a f.c.c. binary system which resembles the experimental phase diagram for Au-Cu in form and in exhibiting coexistence of ordered and disordered phases about each of the superlattices.

Li's development retains all the hypotheses of the quasi-chemical theory, in particular the specification of a pairwise interaction energy that is taken as independent of composition and of the degree of order. Sato [23] and Cowley [24] have shown that an asymmetry, such as evinced by the present results for the superlattice CuAu II and by the results of Newkirk [7], can be effected by postulating a functional dependence of interaction energy on composition and on degree of order.

Hume-Rothery and Raynor [25] have pointed out that difference in the size of the components of a binary solid solution may lead to a tendency to order since a more efficient packing, and hence a lower strain energy for the system, can be achieved by surrounding any one atom by atoms of dissimilar size. It may be possible to express this strain energy factor in terms of a pairwise interaction term in the region of low solute concentration, despite the probability that the disturbance due to an atom of different size extends beyond the nearest neighbors, and thereby to bring the strain energy factor formally into the quasi-chemical theory. In any case, Zener [26] has shown that the strain energy produced by mixing atoms of disparate sizes leads to a lowering of the elastic modulus in the region about the incongruous atom, and hence to a larger vibration amplitude in that vicinity, and so to a contribution to the entropy of solution from the larger vibration randomness. Figure 5 shows that at 427°C the entropy of solution is larger than that for an ideal solution for $0 < x_{Cu} < 0.4$ and $1 > x_{Cu} > .85$ despite the short-range order that presumably exists at these compositions and temperature [27]. Thus it appears that to the configurational contribution to the entropy of solution is added another term, $\Delta S_{vib.}$, due to the excess vibration randomness caused by the 10 per cent disparity in atomic radii in the Au-Cu system. Sarolea [28] has shown that the effect of lattice vibrations is to lower the critical temperature of ordering; it is significant that the superlattice $AuCu_3$ exhibits the low critical temperature of 250°C [29] in the region of concentration which has a sizable $\Delta S_{vib.}$. In the concentration range between 0.4 and 0.85 the $\Delta S_{configuration}$ becomes small enough, i.e., the degree of short-range order becomes large enough, so that the total ΔS is less than that for an ideal solution. It is interesting to note that the ΔS curve for Mg-Cd solid solutions at a temperature somewhat higher than that for the existence of a superlattice is very similar [30] to that shown in Figure 5 for Au-Cu at 427°C.

However, whether or not the strain energy factor contributes to the tendency to order, it cannot be the sole factor, since if only the strain energy were important, the ΔH of solution would necessarily be positive, whereas the experimental value is -1.25 kcal/g atom. There must then be a specific negative "chemical" factor of larger absolute magnitude than the positive strain energy term. Hume-Rothery and Raynor [25] have suggested that the probable reason that the Au-Cu system shows complete miscibility in the solid state whereas the Ag-Cu system does not, despite the very similar size disparity between the components, is that gold is a very polarizable ion and copper ion has high polarizing ability, whereas silver ion is relatively weaker on both counts. Smith [31] has also adduced that Au is much more polarizable than Cu from the facts that although the bulk modulus of gold is larger than that of copper, the Young's modulus of gold is smaller than that of copper; that is, the resistance of gold to a unidirectional force is less than that of copper. However, it is very difficult to understand how one ion can polarize another ion when both are immersed in a highly polarizable cloud of electrons.

Ölander [17] has pointed out that the curve of entropy of solution vs. composition for a superlattice would exhibit an infinitely sharp cusp at the stoichiometric composition with $\Delta S = 0$ if the superlattice were perfectly ordered and if only configurational factors were important. The very gradual decrease in ΔS shown in Figure 5 for CuAuII as the 1 : 1 composition is approached indicates that this superlattice is characterized by many imperfections, a circumstance that probably makes possible the large extent of CuAuII in the phase diagram. According to Johansson and Linde [12] these imperfections consist of change-step boundaries at every fifth atom along the

[010] direction in this orthorhombic structure. The ordered phases CuAuI and Cu_3Au are narrower in extent and have fewer imperfections than does CuAuII; however, the degree of substitutional disorder calculated by Weibke and von Quadt [2] for CuAu, Cu_3Au, and Cu_3Au_2 from their e.m.f. data and the equations of Ölander [17] cannot be given weight because of lack of equilibrium in their measurements. In agreement with Newkirk [7], the present work finds no support for the existence of Cu_3Au_2 as a separate ordered phase.

Conclusions

1. In the disordered phase of the Au-Cu system, both components exhibit marked negative deviations from Raoult's Law, in agreement with former work. The maximum ΔH of solution is at $x_{Cu} = 0.6$ and is -1.25 kcal/g atom of alloy, in excellent agreement with the result of Weibke and von Quadt.

2. The ΔS curve of the disordered phase shows the existence of short-range order, and also gives evidence of non-configurational contributions to the entropy of mixing.

3. The degrees of short-range order calculated by quasi-chemical theory from the measured values of ΔG agree well with those measured by X-ray diffraction. It is probable that both strain energy and electrostatic interaction contribute to the ΔH of solution.

4. CuAuI, CuAuII, and ordered Cu_3Au are Gibbsian phases, separated from adjoining phases by two-phase regions.

5. The ΔH of transition for CuAuII→CuAu D is at least 300 cal/g atom of alloy. The relatively gradual cusp in the ΔS curve of CuAuII shows the relatively large amount of disorder in that phase.

Acknowledgements

It is a pleasure to thank Mrs. N. V. Doyle for assistance with the computations, and to thank Drs. D. Turnbull and E. W. Hart for helpful conversations.

This research was supported by A.E.C. Contract No. W-31-109-Eng.-52.

References

1. Wagner, C. and Engelhardt, G. Z. physik. Chem. **A159** (1932) 241.
2. Weibke, F. and von Quadt, U. Z. f. Elektrochem. **45** (1939) 715.
3. Chiche, P. Comptes rendus **234** (1952) 830.
4. Oriani, R. A. Acta Met. **1** (1953) 144.
5. Wagner, C. Thermodynamics of Alloys (Addison-Wesley Press, 1952).
6. Haughton, J. L. and Payne, R. J. M. J. Inst. Met. **46** (1931) 457.
7. Newkirk, J. B. J. Metals, Trans. A.I.M.E. (June 1953) 823.
8. Rhines, F. N., Bond, W. E., and Rummel, R. A. Interim Progress Report April 1953, Carnegie Inst.
9. Hirabayashi, M., Nagasaki, I., and Maniwa, H. J. Japan Inst. Metals **14B** (1950), No. 3, 1–5.
10. Newkirk, J. B. Unpublished data.
11. Hirabayashi, M. J. Japan Inst. Metals **15** (1951) 565.
12. Johansson, C. H. and Linde, J. O. Ann. d. Physik **25**, 1 (1936), Ser. 5.
13. Borelius, G., Larsson, L. E., and Selberg, H. Arkiv Fysik **2** (1950) 161.
14. Nystrom, J. Arkiv Fysik **2** (1950) 151.
15. Nix, F. C. and McNair, D. Phys. Rev. **60** (1941) 320.
16. Keating, D. T. and Warren, B. E. J. Appl. Phys. **22** (1951) 286.
17. Olander, A. Z. physik. Chem. **A168** (1934) 274.
18. Cowley, J. M. J. Appl. Phys. **21** (1950) 24.
19. Roberts, B. W. Paper to be submitted to Acta Metallurgica; thanks are due to the author for opportunity of seeing the manuscript.
20. Guggenheim, E. A. Mixtures (Oxford, 1952).
21. Oriani, R. A. J. Appl. Phys. **21** (1950) 1068.
22. Li, Y. Y. J. Chem. Phys. **17** (1949) 447.
23. Sato, H. Science Repts., Research Insts. Tohoku Unvi. [A] **1** (1949) 405.
24. Cowley, J. M. Phys. Rev. **77** (1950) 669.
25. Hume-Rothery, W. and Raynor, G. V. Phil. Mag **26**. (1938) 143.
26. Zener, C. Thermodynamics in Metallurgy (Am. Soc. Metals, 1950).
27. Fournet, G. Acta Met. **1** (1953) 383.
28. Sarolea, L. Physica **19** (1953) 615.
29. Hirabayashi, M. J. Phys. Soc. Japan **26** (1951) 129.
30. Trumbore, F. A., Wallace, W. E., and Craig, R. S. J. Am. Chem. Soc. **74** (1952) 132.
31. Smith, A. D. N. J. Inst. Metals **80** (1952) 477.

THE TIN-RICH INTERMEDIATE PHASES IN THE ALLOYS OF TIN WITH CADMIUM, INDIUM AND MERCURY*

G. V. RAYNOR and J. A. LEE†

New experiments on the crystal structures of the tin-rich intermediate phases γ_{Sn-In}, γ_{Sn-Hg}, β_{Sn-Hg} and β_{Sn-Cd} are briefly reported. All four phases crystallize in the simple hexagonal structure. The latter may be regarded as formed from the white tin structure by the simple displacement, along the *c*-axis, of one of the two body-centred tetragonal sub-lattices into which the structure can be divided, followed by a slight modification of the interatomic distances. The form of the first Brillouin zone for the γ_{Sn-In} type of structure is considered, and it is shown that the most probable zone is bounded by planes of the type {11.0} and {10.1}; overlapping of electrons across the {11.0} planes accounts for the dependence of the axial ratio on electron: atom ratio. The factors affecting the formation of the hexagonal phases are discussed from the point of view of a suggestion by Schubert that the appropriate Brillouin zone for white tin is bounded by {220} and {121} planes.

LA PHASE INTERMÉDIAIRE, RICHE EN ÉTAIN, DES ALLIGES D'ÉTAIN AVEC LE CADMIUM, L'INDIUM ET LE MERCURE

On rapporte brièvement de nouvelles expériences sur la structure cristalline des phases intermédiaires, riches en étain, γ_{Sn-In}, γ_{Sn-Hg}, β_{Sn-Hg}, β_{Sn-Cd}. Toutes les quatre phases ont la structure hexagonale simple. Cette dernière peut être considérée comme résultant de la structure de l'étain blanc par un simple déplacement, suivant l'axe *c*, d'un des deux réseaux tétragonaux centrés, en lesquels la structure peut être divisée, suivi d'un léger changement des distances interatomique. La première zone de Brillouin de la structure du type γ_{Sn-In} est examinée et il est montré que la zone la plus probable est limitée par des plans du type {11.0} et {10.1}; L'enchevauchement des électrons sur les plans {11.0} justifie la dépendance du rapport axial sur le rapport électrons: atomes. Les facteurs qui influencent la formation de la phase hexagonale sont discutés du point de vue de la suggéstion de Schubert, à savoir, que la zone de Brillouin appropriée de l'étain blanc est limitée par des plans {220} et {121}.

DIE ZINNREICHE ZWISCHENPHASE IN DEN LEGIERUNGEN DES ZINNS MIT KADMIUM, INDIUM UND QUECKSILBER

Es wird kurz über neue Versuche über die Kristallstrukturen der zinnreichen Zwischenphasen γ_{Sn-In}, γ_{Sn-Hg}, β_{Sn-Hg} und β_{Sn-Cd} berichtet. Alle vier Phasen kristallisieren in einfach hexagonaler Struktur. Diese kann als aus der weissen Zinnstruktur durch eine einfache Verschiebung von einem der beiden kubisch-raumzentrierten Teilgitter des Zinngitters entlang der *c*-Achse und einer anschliessenden leichten Modifizierung der Atomabstände entstanden betrachtet werden. Es wird die Form der ersten Brillouinzone für den γ_{Sn-In} Strukturtyp betrachtet, und es wird gezeigt, dass die wahrscheinlichste Zone durch Ebenen vom Typ {11.0} und {10.1} begrenzt wird. Die über die {11.0} Ebenen überlappenden Elektronen erklären die Abhängigkeit des Achsenverhältnisses vom Verhältnis Elektron: Atom. Die die Bildung der hexagonalen Phasen beeinflussenden Faktoren werden unter dem Gesichtspunkt des Vorschlages von Schubert, dass die Brillouinzone des weissen Zinns von {220} und {121} Ebenen begrenzt ist, diskutiert.

I. Introductory

Although, in the system tin-cadmium, the terminal solid solutions of tin in cadmium and of cadmium in tin enter into equilibrium below a temperature of 133°C, an intermediate phase exists above this temperature [1]. The outstanding characteristic of this phase is its high tin content (approximately 95 atomic per cent). In the tin-mercury system, a high-temperature phase of similar tin content exists above 195°C, while in the tin-indium system, a low-temperature phase with a tin-rich limit of homogeneity approaching 88 atomic per cent of tin has been observed. Crystal structure determinations have been carried out only for the tin-indium phase. Since other binary alloys of tin do not appear to contain intermediate phases of such high tin content, and since there appeared to be a possibility that the three known representatives of this class of phase were closely related, a structural investigation has been carried out, and is reported in this communication.

II. Previous Work

The relevant portions of the tin-rich equilibrium diagrams for the systems under consideration are reproduced in Figures 1, 2 and 3. The points of interest for our present purpose are as follows:

(i) Alloys consisting of the β_{Sn-Cd} phase* cannot be quenched unchanged, but decompose rapidly into the α- and γ-phases, which are the terminal solid solutions. No determination of the crystal structure of β_{Sn-Cd} has been made.

(ii) The β_{Sn-Hg} phase is also not retained on

*Received November 4, 1953.

†Department of Metallurgy, University of Birmingham, England.

*The phases under consideration are denoted by the symbol in current use in the literature, followed by the subscript chemical symbols of the components.

quenching, and its crystal structure is unknown. At approximately 215°C, β_{Sn-Hg} reacts peritectically with the liquid to form γ_{Sn-Hg}, which is stable from this temperature to room temperature, at which its homogeneity range extends from 5 to 11 atomic per cent of mercury. According to von Simson [4], who separated the phase from mercury-tin amalgams, γ_{Sn-Hg} is to be regarded as $HgSn_{12}$, with a simple hexagonal crystal structure ($a = 3.18$ Å; $c/a = 0.94$). The crystal structure and approximate lattice spacings were confirmed by Stenbeck [5] and by Løvold-Olsen [6]; the lattice spacings obtained by the latter author varied from $a = 3.2015$ kX, $c = 2.9836$ kX at 9.23 atomic per cent of mercury to $a = 3.1967$ kX, $c = 2.9770$ kX at 13.25 atomic per cent of mercury, but these values should be accepted with caution since the lattice spacing quoted for pure tin ($a = 5.8150$ kX, $c = 3.1759$ kX) agreed poorly with the generally accepted values of $a = 5.8195$ kX, $c = 3.1750$ kX.

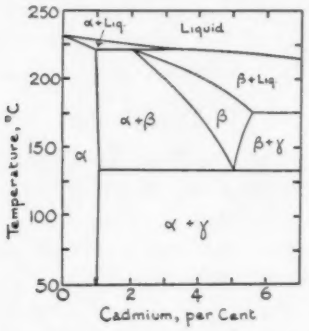

FIGURE 1. Equilibrium diagram of the tin-rich tin-cadmium alloys [1].

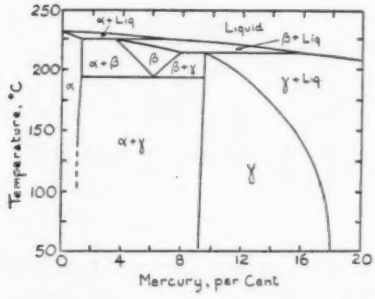

FIGURE 2. Equilibrium diagram of the tin-rich tin-mercury alloys [2].

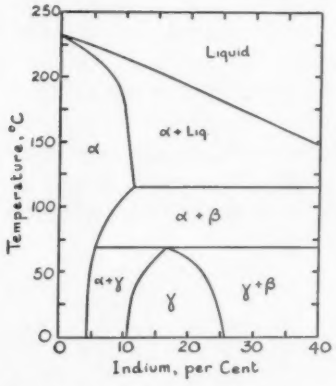

FIGURE 3. Equilibrium diagram of the tin-rich tin-indium alloys [3].

(iii) The γ_{Sn-In} intermediate phase has been denoted $InSn_{15}$ by Valentiner [7; 8], according to whom the crystal structure of the phase is basically similar to that of white tin (body-centred tetragonal, $a = 5.61$ kX, $c = 3.54$ kX). This conclusion is supported by Orlamünder [9], but in their more comprehensive examination of the system Fink, Jette, Katz and Schnettler [10] found it impossible to index the diffraction pattern of γ_{Sn-In} on the basis of the structure proposed by Valentiner, and suggested that the structure was simple hexagonal, with the following lattice spacings:

at 22.34 atomic per cent of indium $a = 3.209$ kX, $c = 2.992$ kX;

at 10.35 atomic per cent of indium $a = 3.215$ kX, $c = 2.994$ kX.

It may also be noted that there is some disagreement between the American authors [3; 10] with regard to the upper temperature of stability for γ_{Sn-In}; while Rhines, Urquhart and Hoge find that the phase is unstable above approximately 70°C, Fink and his associates suggest that γ_{Sn-In} is formed peritectically at 124°C, but they were unable to observe the expected thermal arrests on the indium-rich side of the γ_{Sn-In} composition range.

III. Present Experiments

Alloys were prepared from Chempur tin, spectroscopically pure cadmium, and pure mercury and indium supplied by Messrs. Johnson, Matthey and Co., Ltd. Carefully weighed quantities of the pure metals were melted in evacuated silica tubes, which were rotated in a furnace controlled at approximately 20°C above the liquidus temperature. The specimens were then either quenched or slowly cooled, and annealed, for the purpose of homogenization, in the same evacuated tubes. Analyses carried out on typical specimens showed that under these conditions the intended compositions were accurately attained. Filings were prepared by normal methods; those intended for exposure at room temperature received a stress-relief anneal at

an appropriate temperature, while those for exposure at a high temperature were immediately sealed in silica capillaries. Specimens were exposed to copper K_α radiation, and the high-temperature X-ray technique followed corresponded closely with that described by Berry, Henry and Raynor [11]. The following reflections occurring between 60° and 82°, were clearly resolved in to $\alpha_1\alpha_2$ doublets:

(21.2), (11.3), (20.3), (30.2), (22.1)

and all films could be indexed on the basis of a simple hexagonal unit cell containing one atom.

Experiments were made with several specimens in each system, and the spacing measurements reported below were calculated from the highest quality films; the Nelson-Riley extrapolation function was applied.

(i) The γ_{Sn-In} phase. An alloy containing 18.64 atomic per cent of indium was filed after annealing for 2 weeks at 49°C. Four closely agreeing lattice spacing measurements made at room temperature gave the following mean values:

$$a = 3.2112 \pm 0.0001\ kX,$$
$$c = 2.9928 \pm 0.0001\ kX,$$
$$c/a = 0.93196;\ 23°C.$$

(ii) The γ_{Sn-Hg} phase. An alloy with 7.193 atomic per cent of mercury was annealed for 2 weeks at 150°C. Mean values obtained from four closely agreeing measurements at room temperature were:

$$a = 3.2062 \pm 0.0001\ kX,$$
$$c = 2.9856 \pm 0.0001\ kX,$$
$$c/a = 0.9312;\ 21°C.$$

(iii) The β_{Sn-Cd} phase. An alloy containing 4.89 atomic per cent of cadmium was annealed in the homogeneous β-range and quenched. Filings were sealed in silica capillaries and exposed, after annealing to equilibrium in the high-temperature diffraction camera, at 176°C:

$$a = 3.2263 \pm 0.0001\ kX,$$
$$c = 2.9963 \pm 0.0001\ kX,$$
$$c/a = 0.92870;\ 176°C.$$

(iv) The β_{Sn-Hg} phase. The alloy selected was heat-treated as for the β_{Sn-Cd} specimen, and filings were exposed at 188°C. Results obtained were:

$$a = 3.2350 \pm 0.0001\ kX,$$
$$c = 3.0005 \pm 0.0001\ kX,$$
$$c/a = 0.92751;\ 188°C.$$

These results confirm that the crystal structures of the γ_{Sn-In} and γ_{Sn-Hg} phases, both of which are stable at room temperature, are simple hexagonal, and show clearly that the high temperature phases β_{Sn-Cd} and β_{Sn-Hg} adopt the same structure. No difference could be detected between the diffraction patterns of γ_{Sn-Hg} and β_{Sn-Hg} except for a very slight increase of the relative intensities of the (00.1) and (00.2) reflections for the β-phase.

IV. Discussion

The fact that the four tin-rich intermediate phases under discussion are isomorphous (except for axial ratio variations) is of considerable interest, since the simple hexagonal structure adopted may be closely related to that of white tin. For this purpose we express the hexagonal structure in terms of an orthorhombic unit cell, as indicated in Figure 4. If we now consider the structure formed

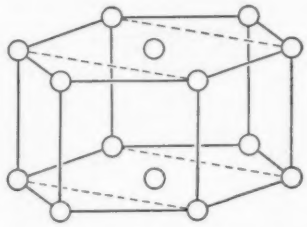

FIGURE 4. Orthorhombic unit cell derived from simple hexagonal structure.

by stacking three such unit cells as shown in Figure 5*a*, the atoms are seen to lie upon two interpenetrating body-centred orthorhombic sub-lattices, which are distinguished by full and open circles respectively. If now the sublattice of open circles is moved relatively to the other, in the direction of the a axis, by an amount equal to $a/4$, a lattice is produced in which the atomic positions are very similar to those in the white tin structure

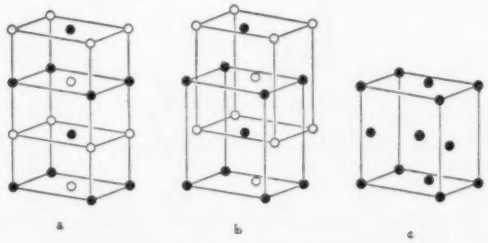

FIGURE 5. Structural relationships between the γ_{Sn-In} type of phase and white tin. a. orthorhombic structure corresponding to simple hexagonal arrangement; b. structure produced by displacement of one sub-lattice; c. white tin structure.

(Figure 5*b*). A relative contraction along the *c*-axis, allowed by the displacement of atoms denoted by open circles from positions intermediate between those denoted by full circles, completes the change to the body-centred tetragonal structure of white tin (Figure 5*c*). The γ_{Sn-In} type of structure is thus closely related to that of white tin, from which it may be derived by the reverse of the sequence of changes illustrated in Figure 5. It is probably for this reason that the simple hexagonal structure is formed only in alloys of tin with solute metals of very similar atomic diameter.

The axial ratios for the four phases examined differ, and it is of interest to plot the observed values as a function of electron : atom ratio, assuming a valency of 4 for tin (Figure 6). There is a

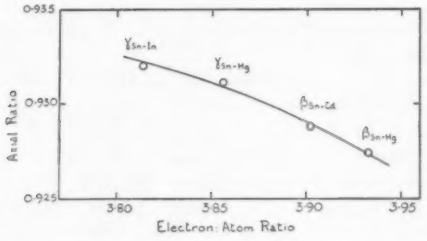

FIGURE 6. Axial ratio plotted against electron: atom ratio for phases of γ_{Sn-In} type.

definite increase in axial ratio as the electron : atom ratio decreases, which suggests strongly that the appropriate Brillouin zone is overlapped in directions at right angles to the hexagonal axis, so that a reduction in this overlap as the number of electrons per atom decreases allows the *a* spacings in the crystal to contract relative to the *c* spacings, according to the theory proposed by Jones [12]. In the diffraction pattern of γ_{Sn-In}, the two strongest low angle lines are derived from the (10.0) and (10.1) reflexions. A first Brillouin zone, containing two electrons per atom, may be formed by the planes of the type {10.0} and {00.1}, and the most probable second zone is that formed by the {10.1} and {11.0} planes, as shown in Figure 7. The volume of the polyhedron bounded by {10.1} planes only would correspond almost exactly with five electrons per atom; the volume of the Brillouin zone shown in Figure 7 corresponds with approximately 4.6 electrons per atom. The Fermi sphere which just touches the {10.1} planes has a volume corresponding with 3.31 electrons per atom, so that these planes are certain to be overlapped at 4 electrons per atom; the evidence of the axial ratio variations with decreasing electron concentration suggests that the {11.0} planes are also overlapped, giving rise to anisotropic effects when the extent of the overlap is varied. It is thus improbable that the γ_{Sn-In} structure is to be regarded as stabilized by considerations of electronic energy in the same manner as the well-known electron compounds.

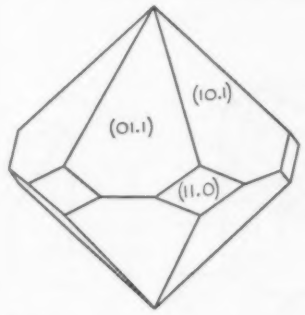

FIGURE 7. Brillouin zone formed by planes {10.1} and {11.0}.

According to Schubert [13] the appropriate Brillouin zone for the white-tin structure is not that formed by {101} planes,* as suggested by Mott and Jones [14], but by the {220} and {121} planes. This zone is illustrated in Figure 8, and the existence of

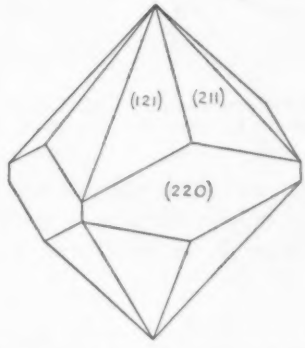

FIGURE 8. Suggested Brillouin zone for white-tin.

the γ_{Sn-In} structure gives some support for this suggestion. Since it is known that antimony decreases and indium increases the axial ratio of white tin, it is probable that the {220} planes are overlapped; a reduction in the electron:atom ratio then leads to a contraction of the *a* spacing relative to the *c* spacing. There is thus a tendency to equalize the interplanar spacings for the {220} and {121} planes. Equality, however, could be achieved

*Following the usual convention, the symbol $\{n_1 n_2 n_3\}$, used for a set of planes in a tetragonal lattice, denotes only those planes for which the third place in the symbol is either n_3 or $\bar{n}_3$).

only by an increase of the axial ratio from 0.545 to 0.575, which the cohesive forces along the c-axis may be unable to tolerate, or alternatively by a structural change. It is now important to note that, on performing the transformation from white tin to γ_{Sn-In} (Figure 5), the (220) and (121) planes of the tetragonal structure correspond with the (01.1)

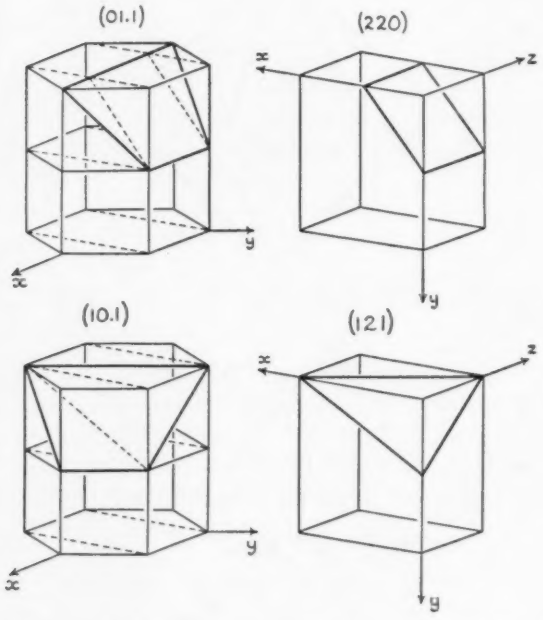

FIGURE 9. Relationship of (220) and (121) planes of white-tin to (01.1) and (10.1) planes of $\gamma_{S_n-I_n}$ structure.

and (10.1) planes of the hexagonal structure, which are equivalent in interplanar spacing. This is illustrated in Figure 9. If Schubert's suggestion is accepted, therefore, the formation of the γ_{Sn-In} structure may be regarded as due to the tendency of the {200} and {121} planes of white tin to equalize their interplanar spacings with decrease in electron : atom ratio, and the restriction of this structure to alloys of tin with solutes of lower valency may be understood.

Acknowledgements

The authors wish to acknowledge gratefully financial assistance from the Royal Society, the Department of Scientific and Industrial Research, the Tin Research Institute, and Imperial Chemical Industries, Ltd., all of which have contributed to the programme of which this work forms a part.

References

1. HANSON, D. and PELL-WALPOLE, W. T. J. Inst. Metals **59** (1936) 281.
2. GAYLER, M. L. V. J. Inst. Metals **60** (1937) 403.
3. RHINES, F. N., URQUHART, W. M., and HOGE, H. R. Trans. Amer. Soc. Metals **39** (1947) 694.
4. VON SIMSON, C. Z. Physikal. Chem. **109** (1924) 183.
5. STENBECK, S. Z. Anorg. Chem. **214** (1933) 17.
6. LØVOLD-OLSEN, L. S. Krifter Norrke Widens Kaps Akad. Oslo, 1947. (Work completed 1936.)
7. VALENTINER, S. Z. Phys. **115** (1940) 11.
8. VALENTINER, S. Z. Metallkunde **32** (1940) 31.
9. ORLAMÜNDER, E. Z. Anorg. Chem. **256** (1948) 245.
10. FINK, C. G., JETTE, E. R., KATZ, S., and SCHNETTLER, F. J. Trans. Electrochem. Soc. **88** (1945) 229.
11. BERRY, R. L. P., HENRY, W. G. and RAYNOR, G. V. J. Inst. Metals **78** (1951) 643.
12. JONES, H. Proc. Roy. Soc. **A147** (1934) 400.
13. SCHUBERT, K. Z. Metallkunde **41** (1950) 423.
14. MOTT, N. F. and JONES, H. The Theory of the Properties of Metals and Alloys (Oxford, The Clarendon Press, 1936).

THERMODYNAMIC PROPERTIES OF SOLID ALUMINUM-ZINC ALLOYS*

J. E. HILLIARD, B. L. AVERBACH, and MORRIS COHEN†

The relative thermodynamic properties of solid aluminum-zinc alloys have been determined over the complete composition range by means of a galvanic cell using a molten salt electrolyte. The results evaluated at 300°C and 380°C indicate that there is a substantial positive deviation from ideal behavior. The molar heat of mixing has a maximum value of 850 cal/gm atom (heat absorbed) at about 60 atomic per cent zinc, and the entropies of mixing are slightly greater than the ideal configurational values. For the aluminum-rich solutions, the partial quantities relative to aluminum are apparently consistent with the quasi-chemical theory, but there are large deviations from the theory in the solutions containing more than 40 atomic per cent zinc. Extrapolation of the data for solid alloys indicates that the maximum heat of mixing for the liquid alloys is 440 cal/gm atom.

LES PROPRIÉTÉS THERMODYNAMIQUES DES ALLIAGES SOLIDES ALUMINIUM-ZINC

On a déterminé les propriétés thermodynamiques, relatives, des alliages solides aluminium-zinc dans toute l'étendue des compositions, au moyen d'une pile galvanique, en employant un sel fondu comme électrolyte. Les résultats obtenus à 300° et à 380°C indiquent une déviation positive, considérable, par rapport à l'idéalité. La chaleur molaire de mélange a la valeur maximum de 850 cal par atome-gramme (chaleur absorbée) vers 60 pour cent en atomes de zinc; les entropies de mélange sont légèrement supérieures aux valeurs idéales de l'entropie de configuration. Dans le cas de solutions riches en aluminium, les quantités partielles par rapport à l'aluminium sont apparemment en accord avec la théorie quasi-chimique; il y a, toutefois, de fortes déviations par rapport aux valeurs théoriques dans le cas de solutions contenant plus de 40 pour cent en atomes de zinc. Une extrapolation des données concernant les alliages solides indique que la chaleur maximum de mélange pour les alliages liquides est de 440 cal par atome-gramme.

THERMODYNAMISCHE EIGENSCHAFTEN FESTER ALUMINIUM-ZINK LEGIERUNGEN

Die relativen thermodynamischen Eigenschaften fester Aluminium-Zink Legierungen wurden m gesamten Konzentrationsbereich mit Hilfe eines mit geschmolzenem Salzelektrolyten arbeitenden galvanischen Elements gemessen. Die bei 300° und 380°C ausgewerteten Ergebnisse deuten auf eine beträchtliche, positive Abweichung vom idealen Verhalten hin. Die molare Mischungswärme hat ihren Maximalwert von 850 cal pro Grammatom (absorbierte Wärme) bei etwa 60 Atomprozent Zink, und die Mischungsentropien sind etwas grösser als die Werte für die Idealkonfiguration. In den aluminiumreichen Lösungen sind die auf das Aluminium bezogenen Partialwerte anscheinend mit der quasi-chemischen Theorie im Einklang; es bestehen jedoch in Lösungen, die mehr als 40 Atomprozent Zink enthalten, grosse Abweichungen von der Theorie. Aus der Extrapolierung der Werte der festen Legierungen kann man das Maximum der Mischungswärme der flüssigen Legierungen zu 440 cal pro Grammatom abschätzen.

Introduction

Recent thermodynamic [1] and X-ray [2; 3] studies have demonstrated that the positive heat of mixing in solid gold-nickel alloys is attributable to the strain energy arising from the formation of solid solutions of atoms with different sizes, and that the relative bonding energies between atoms are inconsequential in determining the thermodynamic properties of the system. The aluminum-zinc system (Figure 1)‡ has a miscibility gap similar to that in the gold-nickel system, but recent diffuse X-ray studies [4] have indicated that the aluminum and zinc atoms have about the same size in solution. The strain energy is thus negligble, and barring any unforseen contribution arising from electronic changes, it was hoped that a quantitative appraisal could be made of the ability of the quasi-chemical

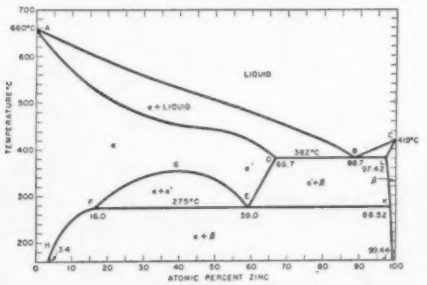

FIGURE 1. Aluminum-zinc phase diagram.

*Received January 13, 1954.

†Department of Metallurgy, Massachusetts Institute of Technology, Cambridge, Massachusetts.

‡The aluminum-zinc phase diagram, Figure 1, was drawn from the following experimental data: *Liquidus* (*ABC*). From 0 to 50 per cent zinc the curve *AB* follows the work of Gebhardt [5] and between 50 and 90 per cent interpolation is made between Gebhardt's results and those of Gayler and Sutherland [6], the latter indicating liquidus temperatures about 5°C higher. *Solidus* (*AD*). The mean was taken of three investigations [5; 6; 7] showing a maximum deviation of less than 5°C. X-ray data obtained by Ellwood [8] confirm the general shape of the curve but show a slightly greater deviation. *Solubility of Aluminum in Zinc* (*JKL*). The data of several investigators [9–13] are evaluated in the appendix. The remaining phase boundaries are drawn from the experimental data selected by Raynor [14] to be the most reliable

theory to correlate the relative thermodynamic properties with the local atomic arrangements determined by diffuse X-ray scattering experiments. This paper describes the measurement of the thermodynamic properties of solid aluminum-zinc alloys; the results of the diffuse X-ray measurements and their correlation with the thermodynamic data are given elsewhere [4].

Experimental Procedure

Aluminum and zinc are sufficiently separated in the emf series to permit the use of the galvanic cell:

Pure Al (anode)	Ionic conductor containing Al ions	Al-Zn alloy (cathode)

for the determination of the relative thermodynamic properties. A molten equimolar solution of $AlCl_3$ and NaCl (m.p. 152°C) proved suitable as an electrolyte. The successful use of a mixture containing such a high proportion of $AlCl_3$ is presumably due to the low activity of $AlCl_3$ in the solution, as indicated by its greatly reduced volatility [15].

The molten electrolyte was first purified by electrolysis at 350°C for 24–36 hours with an impressed potential of 2 volts between graphite electrodes under an atmosphere of dried argon. Since the deposition potential for hydrogen is −0.87 volts in comparison with −2.02 volts for aluminum [16], this treatment ensured virtually complete elimination of hydrogen chloride. The electrolysis also served to coagulate a finely divided black substance which always appeared when the salts were first melted. After the electrolysis, a pure aluminum spiral was kept in contact with the electrolyte for several days to assist the precipitation of the more electropositive elements, and the molten salt was then filtered through glass wool into the Vycor cups used for the emf determinations. A final treatment with pure aluminum preceded the introduction of the electrode assembly.

Sixteen alloy electrodes were prepared by melting 99.995 aluminum (supplied by the Aluminum Company of America) and 99.99+ zinc in an alundum crucible under an atmosphere of purified argon and casting $\frac{1}{4}$ inch diameter rods in a graphite mold. Wire, 0.075 in. in diameter, was obtained by swaging; the wires were etched, and material with surface defects rejected. Individual lengths were sealed in Vycor tubes under a partial pressure of purified argon and annealed in a salt bath for 5 days at 370°C. Twelve of the alloys had compositions spaced at approximately 5 atomic per cent intervals in the α solid solution range, and the remaining four were in the α'- + β-region. Chemical compositions were determined to an accuracy of 0.5 weight per cent on samples of the annealed wire. In a few cases check analyses were made on the electrodes after the runs.

The electrolytic apparatus (Figure 2) was substantially the same as that used for the gold-nickel studies [1]. Two cells were run simultaneously in individual furnaces with four or five alloy electrodes and one pure aluminum anode in each. To minimize thermal emf's the electrodes were kept as short as possible (1.4 in.) and were connected to the potentiometer by aluminum lead wires. The measured thermal emf's arising from metal-metal junctions were less than 0.01 mV. The temperature of each cell was controlled to within ±1.5°C over the zone occupied by the electrodes and was measured with a calibrated chromel-alumel thermocouple. A small flow of purified and dried argon was maintained through the cells.

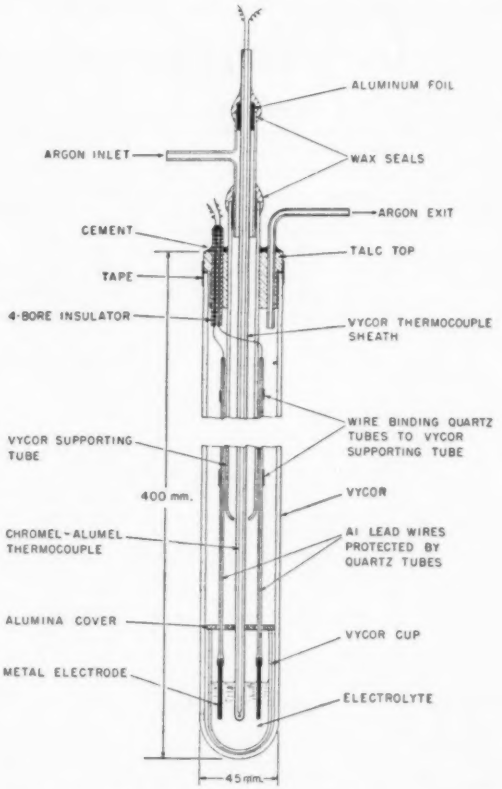

FIGURE 2. Electrolytic cell for e.m.f. measurements.

The temperature was cycled in steps of 20°C every two hours from 280°C to about 20° below the

melting point of the lowest melting alloy in a particular cell. Readings of the thermocouple and galvanic potentials were taken to a precision of 0.01 mV with a null deflection potentiometer. Each run comprised at least two complete heating and cooling cycles. The emf's of the cells were reasonably stable, though there was a slight downward drift of about 0.05 mV per 24 hours. Data obtained below 290°C tended to be erratic and were therefore discarded.

There is no single criterion which establishes the reversibility of an electrolytic cell, but its achievement in the present case is suggested by the following observations:

1. The emf values obtained on heating and cooling coincided within the limits of experimental error. (See Figure 3, for example.)

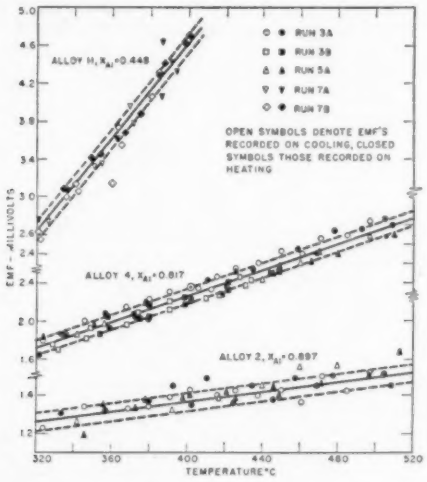

FIGURE 3. Variation of e.m.f. with temperature for three alloy electrodes against a pure aluminum anode.

2. There was no attack, apart from a slight etch, on the electrodes and there was no detectable change in their surface compositions. There was also no indication of zinc pick-up by the anode or the electrolyte, the latter analyzing less than 0.001 per cent zinc before and after each run.

3. The results derived for the solid alloys and extended to the liquid alloys were consistent with data of other investigators.

Experimental Results

Computation of Data

The various partial molar quantities relative to a standard state of pure solid aluminum can be obtained from the emf data by means of the relationships:

$$F^{M}_{Al} = -z\mathcal{F}\epsilon \tag{1}$$

$$S^{M}_{Al} = z\mathcal{F}\left(\frac{\partial \epsilon}{\partial T}\right)_{P,X_{Al}} \tag{2}$$

where the symbols are defined in Table I using notation adopted by Wagner [17]. Typical emf *vs*

TABLE I

LIST OF SYMBOLS

a_i	Activity of component i.
f_i	Activity coefficient of component i.
E_{AA}, E_{BB}, E_{AB}	Potential energies of the atom pairs (inherently negative quantities).
F^M	Relative integral molar free energy (Molar free energy of mixing).
F^E	Excess intergral molar free energy.
F^{M_i}	Relative partial molar free energy of component i ($=RT \ln a_i$).
F^{E_i}	Excess partial molar free energy of component i ($=F^{M_i} - RT \ln X_i = RT \ln f_i$).
G	Any extensive molar thermodynamic property.
H^M	Relative integral molar enthalpy (Molar heat of mixing).
H^{M_i}	Relative partial molar enthalpy of component i.
N_0	Avogadro's number.
R	Universal gas constant ($=1.99$ cal deg^{-1} mole^{-1}).
S^M	Relative integral molar entropy (Molar entropy of mixing).
S^E	Excess integral molar entropy.
S^{M_i}	Relative partial molar entropy of component i.
S^{E_i}	Excess partial molar entropy of component i ($=S^{M_i} + R \ln X_i$).
T	Absolute temperature.
X_i	Mol fraction of component i.
z	Valance of conducting ion.
Z	Coordination number, number of nearest neighbors ($=12$ for f.c.c. lattice).
ϵ	Electromotive force.
$\mathcal{F}$	Faraday's constant ($=23{,}070$ cal volt^{-1} equivalent^{-1}).
ν	Interaction Energy $= E_{AB} - \frac{1}{2}(E_{AA} + E_{BB})$.

temperature data for three alloys are shown in Figure 3. Although there is noticeable scatter, the absolute deviations are small since the emf's were low (the maximum being less than 10 mV). Since the scatter was predominantly random it was considered justifiable to analyze the data statistically. Using the least-squares method, it was found that the emf-temperature readings could be fitted adequately to equations of the form:

$$\epsilon = a + bT \tag{3}$$

where a and b are constants for a particular alloy. All the data from the two or more runs made with each alloy were included in the least-squares fitting and, in the two-phase regions, the data from all the alloys involved were considered as a whole and a single equation derived for each region. The standard deviations were also computed and

are designated by vertical lines on the plotted points in Figures 4–9.

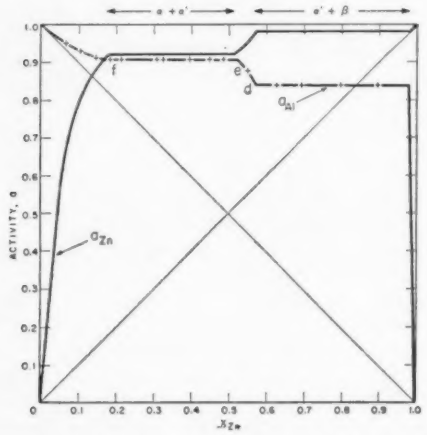

FIGURE 4. Activities of aluminum and zinc in the solid alloys at 300°C.

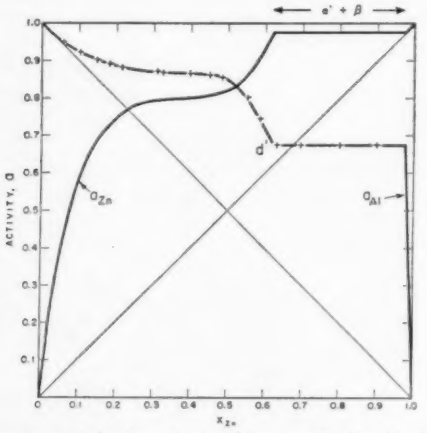

FIGURE 5. Activities of aluminum and zinc in the solid alloys at 380°C.

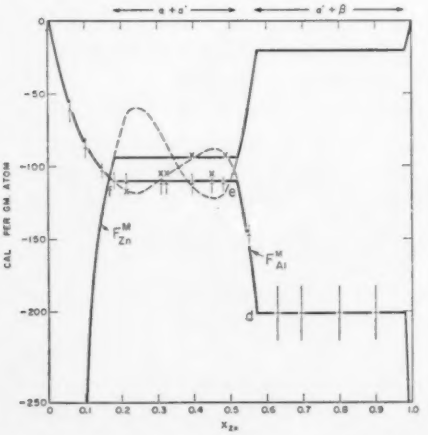

FIGURE 6. Relative partial molar free energies of aluminum and zinc in the solid alloys at 300°C.

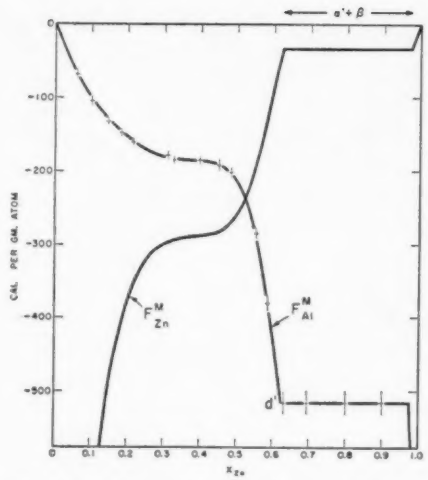

FIGURE 7. Relative partial molar free energies of aluminum and zinc in the solid alloys at 380°C.

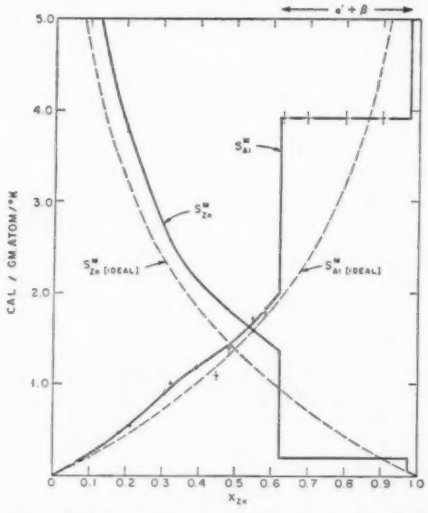

FIGURE 8. Relative partial molar entropies of the solid alloys at 380°C.

The linear relationship between the emf and temperature signifies that, within the limits of experimental error, $H^M{}_{Al}$ and $S^M{}_{Al}$ are independent of temperature over the range investigated.

Values were read from the smoothed curves for $F^E{}_{Al}$, $H^M{}_{Al}$, and $S^E{}_{Al}$ at intervals of 5 atomic per cent and the corresponding quantities for zinc were computed from the Gibbs-Duhem relation in the form [17]:

$$(4) \qquad G^M{}_A = \int_0^{X_B} \frac{G^M{}_B dX_B}{(1-X_B)^2} - \frac{X_B G^M{}_B}{(1-X_B)}.$$

The integration was performed graphically in the single-phase regions and analytically in the two-phase regions. Experimental measurements in the

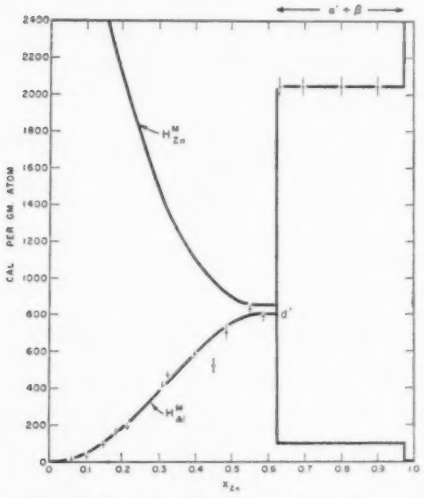

FIGURE 9. Relative partial molar enthalpies of aluminum and zinc in the solid alloys at 380°C.

narrow β-region were not feasible; hence the thermodynamic properties in this case were obtained by a method described in the appendix. The accuracy of the integration was probably about one per cent except in the range of 90–100 per cent aluminum where the error may have peen larger because of the extrapolation required. The relative integral molar properties were obtained from the relationship: $G^M = X_A G^M{}_A + X_B G^M{}_B$.

Activities and Relative Partial Molar Quantities

It is evident from the data in Figures 4–7 that aluminum-zinc solutions exhibit a large positive deviation from Raoult's law, and that this deviation increases with decreasing temperature. The pronounced flattening in the activity curves for 380°C between 25 and 50 atomic per cent zinc foreshadows the miscibility gap at lower temperatures. The phase boundaries obtained from the thermodynamic data at 300°C and 380°C are listed in atomic per cent zinc as follows (the accepted values taken from Figure 1 are given in parentheses): point f, $\alpha/\alpha' + \alpha$ at 300°C = 18.0 (20.0); point e, $\alpha'/\alpha' + \alpha$ at 300°C = 52.0 (56.2); point d, $\alpha'/\alpha' + \beta$ at 300°C = 57.5 (60.8); point d', $\alpha'/\alpha' + \beta$ at 380°C = 62.0 (66.5). The shift in positions towards the aluminum end may reflect a systematic inaccuracy in the data, although this type of measurement has poor sensitivity for locating phase boundaries.

The points marked by "X" in Figure 6 are values for the metastable solid solution calculated by extrapolating the emf-temperature equations into the two phase region. The dotted portions of the curves are the best fit that could be obtained for these values while at the same time satisfying the necessary condition:

$$(5) \quad F^M{}_{\mathrm{Zn},\alpha(\alpha')} - F^M{}_{\mathrm{Zn},\alpha'(\alpha)} = \int_{X_{\mathrm{Al}}\,\alpha'(\alpha)}^{X_{\mathrm{Al}}\,\alpha(\alpha')} \frac{X_{\mathrm{Al}}}{(1 - X_{\mathrm{Al}})} \frac{dF^M{}_{\mathrm{Al}}}{dX_{\mathrm{Al}}}\, dX_{\mathrm{Al}} = 0$$

where $X_{\mathrm{Al}}{}^{\alpha(\alpha')}$ and $X_{\mathrm{Al}}{}^{\alpha'(\alpha)}$ are the atomic fractions of aluminum at the points f and e respectively.

The experimental determinations for the relative partial molar entropies are shown in Figure 8. The values for aluminum are slightly greater than the random configurational entropy with the maximum deviation occurring at about 35 per cent zinc. The excess entropies are considered significant though, admittedly, they are only slightly greater than the experimental accuracy. The relative partial molar enthalpies are positive, as anticipated from the phase diagram, and are shown in Figure 9. (The relationships between the relative partial molar quantities at phase boundaries are considered in the appendix.)

The relative integral molar quantities F^M, H^M, and TS^M at 300°C and 380°C as functions of composition are given in Figures 10 and 11.

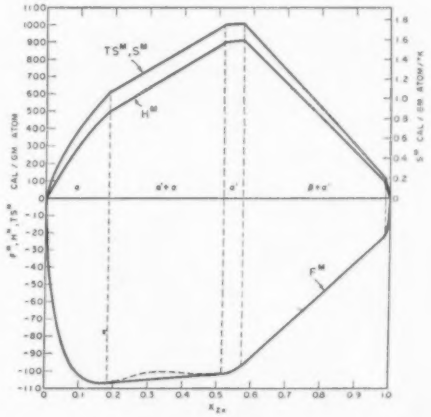

FIGURE 10. Relative integral molar properties of the solid alloys at 300°C. (Note that different scales have been employed for the negative and positive ordinates.)

It should be noted that different scales have been employed for the negative and positive ordinates and that values of S^M can be obtained from the TS^M curve by using the right hand scale. The free energy of the metastable α solution at 300°C is indicated in Figure 10 by the dotted portion of the curve. The integral molar enthalpy has a maximum positive value of about 850 cal/gm

atom (heat absorbed) at 58 atomic per cent zinc.

A check on the molar enthalpies is obtained from the work of Lyashenko [20] who used an adaptation of the method suggested by Smith [21] to measure the heat of transformation $\alpha' \rightarrow \alpha + \beta$. Lyashenko's results are plotted in Figure 12 together with those derived from an extrapolation of the H^M curve at 300°C (Figure 10) and there

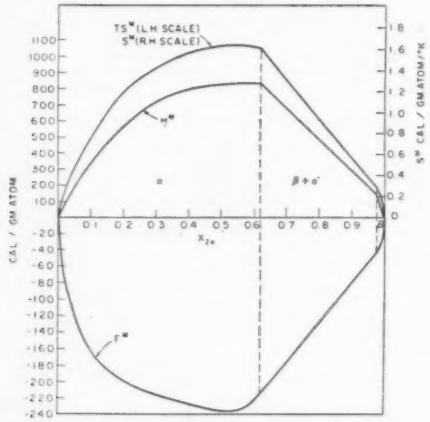

FIGURE 11. Relative integral molar properties of the solid alloys at 380°C. (Note that different scales have been employed for the negative and positive ordinates.)

appears to be reasonable agreement. The heats of decomposition of the α'-phase as measured by Schröter [22] under nonequilibrium conditions are also in approximate agreement with the curves in Figure 12.

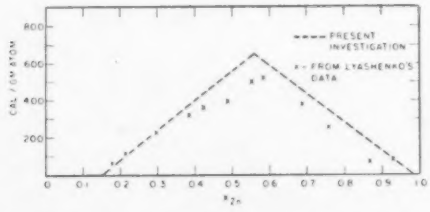

FIGURE 12. Heat of transformation: $\alpha' \rightarrow \alpha + \beta$ at 275°C. Lyashenko's results compared with data derived from H^M curve, Fig. 10.

Properties of the Liquid Alloys

From an extrapolation of the emf-temperature data to the solidus, the partial molar free energy of aluminum in the liquid alloys in equilibrium with the solid was calculated relative to a standard state of pure liquid aluminum. In converting from a solid to a liquid standard state, the following approximate relationship was used for the free energy of fusion:

$$(6) \qquad \Delta F_{Al}(\text{fusion}) = (933\text{-T})\ \Delta S_{Al}(\text{fusion})$$

where ΔS_{Al}(fusion) for pure aluminum was taken as 2.76 [23].

Figure 13 shows that the liquid solutions obey the equation:

$$(7) \quad F^E_{Al}(\text{liquid}) = RT \ln f_{Al}(\text{liquid}) = 1750 (1 - X_{Al})^2.$$

Consequently, the integral excess free energy follows the relationship:

$$(8) \qquad F^E(\text{liquid}) = 1750 X_{Al}(1 - X_{Al}).$$

If S^M(liquid) is ideal, then $H^M = F^E$, and the maximum relative integral enthalpy at $X_{Al} = 0.5$ is 440 cal/gm atom (heat absorbed), i.e., approximately half the value in the solid α solutions.

Figure 13 also includes the results obtained by Schneider and Stoll [24] from dew point measure-

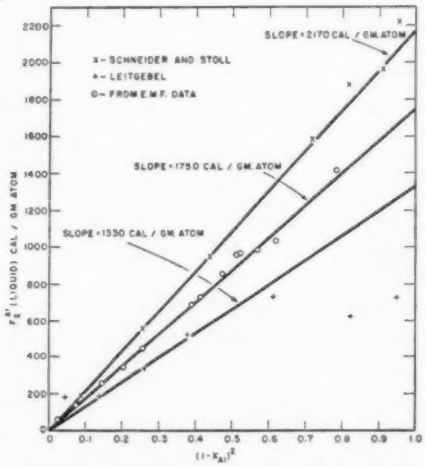

FIGURE 13. Plots of the excess partial molar free energy of aluminum in the liquid alloys versus $(1 - X_{Al})^2$.

ments of zinc vapor over the liquid alloys. Their data lead to a value of 540 cal/gm atom for H^M at $X_{Al} = 0.5$. The third set of points were calculated from the boiling point measurements of Leitgebel [25] using the following equation [26] for the vapor pressure of liquid zinc:

$$(9) \quad \log P_{Zn} = -6591/T + 5{,}657 - 0.967 \log T/1000$$

The resulting values of F^E_{Al} are very sensitive to small errors in boiling point determinations and the agreement in Figure 13 is thus as good as can be expected. These data do not agree with Kawakami's [27] value of 1200 cal/gm atom for the maximum heat of mixing, but some of Kawakami's results for other alloy systems have been questioned.

Discussion of Results

Correlation with the Quasi-Chemical Theory

The quasi-chemical theory [28–31] is a statistical treatment of the binary substitutional solutions in terms of the relative bonding energies between neighboring pairs of atoms. Lattice strains arising from mixing atoms of different sizes are neglected and the Kopp-Neumann rule is assumed to be valid. Since both of these conditions are met quite well in aluminum-zinc alloys it is instructive to test the application of this theory.

Typical expansions for the thermodynamic properties are:

$$(10)\quad F^E = ZN_0\nu X_A X_B\left\{1 - \tfrac{1}{2}\left(\frac{2N_0\nu}{RT}\right)X_A X_B - \tfrac{1}{6}\left(\frac{2N_0\nu}{RT}\right)^2 X_A X_B (X_A - X_B)^2 + \ldots\right\}$$

$$(11)\quad H^M = ZN_0\nu X_A X_B\left\{1 - \left(\frac{2N_0\nu}{RT}\right)X_A X_B - \tfrac{1}{2}\left(\frac{2N_0\nu}{RT}\right)^2 X_A X_B (X_A - X_B)^2 - \ldots\right\}$$

$$(12)\quad S^E = -\frac{ZN_0\nu X_A X_B}{T}\left\{\tfrac{1}{2}\left(\frac{2N_0\nu}{RT}\right)X_A X_B + \tfrac{1}{3}\left(\frac{2N_0\nu}{RT}\right)^2 X_A X_B (X_A - X_B)^2 + \ldots\right\}$$

and the partial properties (which are symmetrical for the two components) are given by:

$$(13)\quad F^E{}_A = ZN_0\nu X_B{}^2\left\{1 + \tfrac{1}{2}\left(\frac{2N_0\nu}{RT}\right)X_A(1 - 3X_B) + \tfrac{1}{6}\left(\frac{2N_0\nu}{RT}\right)^2 X_A(1 - 11X_B + 28X_B{}^2 - 20X_B{}^3) + \ldots\right\}$$

$$(14)\quad H^M{}_A = ZN_0\nu X_B{}^2\left\{1 + \left(\frac{2N_0\nu}{RT}\right)X_A(1 - 3X_B) + \tfrac{1}{2}\left(\frac{2N_0\nu}{RT}\right)^2 X_A(1 - 11X_B + 28X_B{}^2 - 20X_B{}^3) + \ldots\right\}$$

$$(15)\quad S^E{}_A = \frac{ZN_0\nu}{T}X_B{}^2\left\{\tfrac{1}{2}\left(\frac{2N_0\nu}{RT}\right)X_A(1 - 3X_B) + \tfrac{1}{3}\left(\frac{2N_0\nu}{RT}\right)^2 X_A(1 - 11X_B + 28X_B{}^2 - 20X_B{}^3) + \ldots\right\}.$$

If only the first power of ν is retained, the equations reduce to

$$(16)\quad F^E = H^M = ZN_0\nu\, X_A X_B$$

$$(16a)\quad S^E{}_A = S^E = 0$$

$$(16b)\quad F^E{}_A = H^M{}_A = ZN_0\nu\,(1 - X_A)^2.$$

Equations (16) are the empirical relations suggested by Hildebrand [32] and are equivalent to the assumption that the solution is random. The liquid aluminum-zinc alloys appear to follow equations (16).

In the equations (10–16) the interaction energy ν is assumed to be independent of composition. Hardy [33] has introduced the assumption that ν varies with composition according to the relationship:

$$(17)\quad ZN_0\nu = A_1X_A + A_2X_B$$

in which the parameters A_1 and A_2 are independent of composition but not necessarily of temperature. For a random solution Hardy obtains:

$$(17a)\quad F^E = A_1X_A{}^2X_B + A_2X_B{}^2X_A$$

$$(17b)\quad F^E{}_A = X_B{}^2(2A_1 - A_2) + X_B{}^3(2A_2 - 2A_1).$$

The standard states for the integral molar properties defined by the preceding equations are the pure components with the same crystal structure as the solid solution. However, the thermodynamic calculations for the integral properties are referred to a standard state of solid zinc having a hexagonal structure, whereas the α solutions and the pure aluminum are both face-centered cubic. In the absence of reliable data for the transformation Zn (HCP)→Zn(FCC), it is possible to compare directly only the partial molar quantities for aluminum, which are independent of the standard state chosen for the zinc.

Retaining only the first two terms in the equations for the excess partial free energies one obtains:

$$(18)\quad \frac{F^E{}_{Al}}{(1 - X_{Al})^2} = ZN_0\nu \quad \text{(Hildebrand)}$$

$$(19)\quad \frac{F^E{}_{Al}}{(1 - X_{Al})^2} = ZN_0\nu + \frac{Z}{RT}(N_0\nu)^2X_{Al}(1 - 3X_{Zn}) \quad \text{(Quasi-chemical)}$$

$$(20)\quad \frac{F^E{}_{Al}}{(1 - X_{Al})^2} = (2A_1 - A_2) + 2X_{Al}(A2 - A1) \quad \text{(Hardy)}$$

Experimental values of $F^E{}_{Al}/(1 - X_{Al})^2$ are plotted for the α solid solutions at 380°C vs. $X_{Al}(1 - 3X_{Zn})$ in Figure 14 and vs X_{Zn} in Figure 15. Equation (18) is invalid for these data, but equations (19) and (20) fit equally well for zinc contents up to about 40 atomic per cent. From Figure 14 a value of 280 cal/gm atom is obtained for $N_0\nu$ from the slope of the straight portion of the curve, and this is in good agreement with the value of 260 cal/gm

atom given by the intercept at $X_{Al}(1 - 3X_{Zn}) = 0$. From Figure 15, $A_1 = 2755$ and $A_2 = 1690$ and the corresponding dependence of $N_0\nu$ on composition is shown to vary from 230 to 190 cal/gm atom. Since the quasi-chemical theory accounts for the partial excess free energy of aluminum up to 40

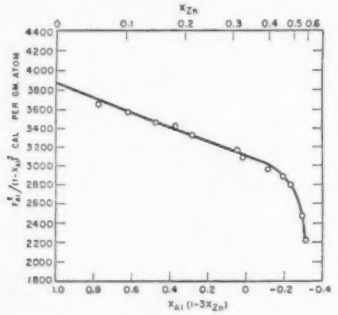

FIGURE 14. Plot of $F^E_{Al}/(1 - X_{Al})^2$ against $X_{Al}(1-3X_{Zn})$ for aluminum-zinc solutions at 380°C.

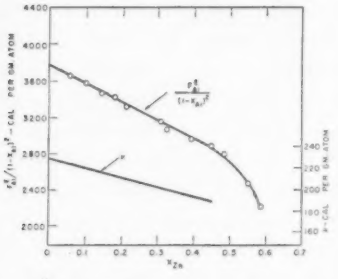

FIGURE 15. Plot of $F^E_{Al}/(1 - X_{Al})^2$ and the derived values of ν against X_{Zn} for aluminum-zinc solid solutions at 380°C.

atomic per cent zinc using only one independent parameter, the use of two independent parameters, as suggested by Hardy, appears unnecessary in this case.

Anomaly in Zinc-rich Solutions

It is apparent from Figures 14 and 15 that the thermodynamic properties do not follow the quasi-chemical equations in solutions containing more than 40 atomic per cent zinc. At least two alternative explanations should be considered. It is possible that the nature of the solution may change at the high zinc compositions. Raynor and Wakeman [34] have shown that there is a striking similarity in the aluminum-rich ends of the aluminum-silver and the aluminum-zinc systems. In each case there is a change in the direction of the solubility curve at an electron-to-atom ratio of 2.6, corresponding to 40 atomic per cent zinc in the aluminum-zinc system. The significance of the change is not understood, but it may be related to the failure of the quasi-chemical theory at approximately the same composition. It is also possible that the equations are invalid, and there may be little justification to suppose that the potential energy of a solution can be written as the sum of potentials between neighbors. Recently Friedel* has accounted for an apparent nearest neighbor interaction in terms of localized charge distributions in the vicinity of solute atoms but the resulting formulation is quite different from that of the quasi-chemical approach.

General Conclusions

A major factor governing the behavior of the aluminum-zinc solid solutions appears to be the preference of atoms to be surrounded by like neighbors. This clustering within the solid solutions has been measured by X-ray methods [4] and seems capable of accounting for the observed positive heat of mixing. Since the liquid solutions also exhibit a positive heat of mixing (about one-half as large as for the solid solutions) there may be a significant nearest neighbor interaction energy in the liquid. The quasi-chemical theories appear to fit the liquid solutions, but fail to account for the observed thermodynamic properties of the solid alloys over the entire composition range.

Although the phase diagrams of both the aluminum-zinc and the gold-nickel systems show similar miscibility gaps, their origins are quite different. The positive heat of mixing in the gold-nickel system arises mainly from the strain energy required to form the solution from atoms of different size and is not the result of a tendency toward clustering. In this respect it is significant to note that the heat of mixing in the liquid gold-nickel alloys is nil. In aluminum-zinc alloys, however, the positive heat of mixing in the solid solution is associated with clustering and it is likely that the clustering may persist even in the liquid solutions.

Appendix

Relative Partial Molar Properties in Two-Phase Regions

The thermodynamic properties of the β terminal solid solutions were derived from the measured activities in the two-phase regions and from the data on the primary solubility of aluminum in zinc. Since the maximum solubility of aluminum

*Private communication.

in zinc is only about 2.6 atomic percent, the β-phase was considered to be a dilute solution with the solvent (zinc) and the solute (aluminum) obeying Raoult's and Henry's laws respectively. Consequently, the excess partial molar quantities for aluminum are zero and those for zinc independent of temperature and composition within the β-phase region.

Let a^{β}_{Al} and a^{α}_{Al} be the activities of aluminum in the coexisting phases β and α having the compositions X^{β}_{Al} and X^{α}_{Al}, and let $a^{(\alpha+\beta)}_{Al}$ be the activity of aluminum in the $(\alpha + \beta)$ region. For equilibrium:

$$a^{\beta}_{Al} = a^{(\alpha+\beta)}_{Al} \tag{21}$$

Since

$$d \ln a = \frac{\partial \ln a}{\partial X} dX + \frac{\partial \ln a}{\partial (1/T)} d(1/T),$$

then at the phase boundary:

$$\left[\frac{\partial \ln a^{\beta}_{Al}}{\partial (1/T)}\right]_{X^{\beta}_{Al}} = \left[\frac{\partial \ln a_{Al}}{\partial (1/T)}\right]_{X^{\beta}_{Al}} + \left[\frac{\partial \ln a_{Al}}{\partial X_{Al}}\right]_{T} \left[\frac{\partial X^{\beta}_{Al}}{\partial (1/T)}\right]_{X^{\beta}_{Al}} = \left[\frac{\partial \ln a^{(\alpha+\beta)}}{\partial (1/T)}\right]_{X_{Al}}. \tag{22}$$

Since

$$\frac{R\, \partial \ln a^{\beta}_{Al}}{\partial\ (1/T)} = H^{M(\beta)}_{Al},$$

and

$$(\partial \ln a^{\beta}_{Al})/(\partial \ln X_{Al})_T = 1$$

for these solutions, this reduces to:

$$H^{M(\beta)}_{Al} = H^{M(\alpha+\beta)}_{Al} - R\left(\frac{\partial \ln X^{\beta}_{Al}}{\partial (1/T)}\right). \tag{23}$$

Similarly, for the entropy

$$S^{M(\beta)}_{Al} = S^{M(\alpha+\beta)}_{Al} - \frac{R}{T}\left(\frac{\partial \ln X^{\beta}_{Al}}{\partial (1/T)}\right). \tag{24}$$

The corresponding quantities for the zinc component, are obtained by applying the Gibbs-Duhem equation to the change in the partial molar enthalpy of zinc on passing through the $\alpha/\alpha + \beta$ boundary

$$H^{M(\alpha+\beta)}_{Zn} = H^{M(\beta)}_{Zn} - \frac{X^{\beta}_{Al}}{1 - X^{\beta}_{Al}} [H^{M(\alpha+\beta)}_{Al} - H^{M(\beta)}_{Al}] \tag{25}$$

and for the entropy

$$S^{M(\alpha+\beta)}_{Zn} = S^{M(\beta)}_{Zn} - \frac{X^{\beta}_{Al}}{1 - X^{\beta}_{Al}} [S^{M(\alpha+\beta)}_{Al} - S^{M(\beta)}_{Al}]. \tag{26}$$

Since the ratio $X^{\beta}_{Al}/1 - X^{\beta}_{Al}$ changes markedly with temperature, the values of $H^{M(\alpha+\beta)}_{Zn}$ and $S^{M(\alpha+\beta)}_{Zn}$ will be similarly affected even though the corresponding quantities for aluminum have been assumed independent of temperature.

Numerical Evaluation of Properties

Data for the primary solubility of aluminum in zinc between 270°C and 382°C are plotted in Figure 16 in the form of $\log_{10} X^{\beta}_{Al}$ versus $1/T$. The results of Löhberg [12] and the magnetic susceptibility measurements of Auer and Mann [9] both indicate an approximately linear relationship between the variables and give lines of about the same slope, but displaced from each other by an amount corresponding to a difference of about 0.3 atomic per cent aluminum. A single point due to Peirce [13] is in agreement with these two investigations, but the results of other workers

TABLE II

SMOOTHED VALUES OF SELECTED THERMODYNAMIC PROPERTIES AT 300°C

Phase field	X_{Zn}	F^{M}_{Al}	F^{M}_{Zn}	H^{M}_{Al}	H^{M}_{Zn}	F^{M}	H^{M}	S^{M}
		cal/gm atom						cal/gm atom/°K
α	0.05	− 50	−717	8	3230	− 83	169	0.436
α	0.10	− 85	−261	47	2730	−102	315	0.723
α	0.15	−103	−128	105	2320	−107	437	0.943
α	0.18	−110	− 94	150	2080	−107	497	1.056
$\alpha+\alpha'$	—	−110	− 94	285	1460	—	—	—
α'	0.52	−110	− 94	775	1010	−102	898	1.742
α'	0.55	−150	− 60	800	993	−100	906	1.755
α'	0.575	−202	− 20	800	993	− 97	910	1.758
$\alpha'+\beta$	—	−202	− 20	2045	65*	—	—	—
β	0.9828	−202	− 20*	5755*	0	− 23	99	0.213

*These values were calculated as described in the Appendix.

TABLE III

SMOOTHED VALUES OF SELECTED THERMODYNAMIC PROPERTIES AT 380°C

Phase field	X_{Zn}	F^M_{Al}	F^M_{Zn}	H^M_{Al}	H^M_{Zn}	F^M	H^M	S^M
		cal/gm atom						cal/gm atom/°K
α'	0.05	− 59	−1267	8	3380	−119	176	0.451
α'	0.10	−101	− 709	47	2870	−162	329	0.752
α'	0.15	−132	− 489	105	2460	−186	459	0.987
α'	0.20	−154	− 383	182	2100	−200	565	1.172
α'	0.25	−172	− 322	275	1780	−210	651	1.317
α'	0.30	−181	− 298	387	1480	−216	716	1.427
α'	0.35	−184	− 292	497	1250	−222	762	1.505
α'	0.40	−187	− 287	587	1100	−227	793	1.561
α'	0.45	−190	− 283	676	983	−232	814	1.600
α'	0.50	−214	− 258	759	890	−236	824	1.622
α'	0.55	−282	− 197	800	852	−235	829	1.628
α'	0.60	−430	− 87	800	852	−224	831	1.616
α'	0.62	−514	− 34	800	852	−215	832	1.603
$\alpha'+\beta$	—	−514	− 34	2045	98*	—	—	—
β	0.9744	−514	− 34*	5755*	0	− 46	147	0.296

*These values were calculated as described in the Appendix.

[10; 11] give improbably low values for the solubility of aluminum. From the slope of the line drawn through the mean of Löhberg's and Auer and Mann's data, a value of −3710 is derived for

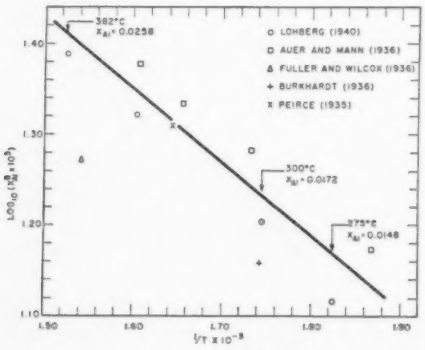

FIGURE 16. Data for the primary solubility of aluminum in zinc plotted in the form of $\log_{10}[X^{\beta}_{Al}\times10^{-3}]$ versus $1/T\times10^3$.

$R[(\partial \ln X^{\beta}_{Al})/\partial(1/T)]$. This value was used in conjunction with equations 23–26 to calculate the results marked by an asterisk in Tables II and III.

Acknowledgments

The authors are indebted to Professor Carl Wagner for many stimulating and informative discussions and to B. Howell and R. Goss for their experimental assistance.

This work was performed under the sponsorship of the U.S. Atomic Energy Commission.

References

1. SEIGLE, L. L., COHEN, M., and AVERBACH, B. L. Trans. A.I.M.M.E. **194** (1952) 1320.
2. FLINN, P. A., AVERBACH, B. L., and COHEN, MORRIS. Submitted to Acta Met.
3. AVERBACH, B. L., FLINN, P. A., and COHEN, MORRIS. Submitted to Acta Met.
4. RUDMAN, P. S. and AVERBACH, B. L. Acta Met. **2** (1954) 576.
5. GEBHARDT, E. Z. Metallkunde **40** (1949) 136.
6. GAYLER, M. L. V. and SUTHERLAND, E. G. J. Inst. Metals **63** (1938) 123.
7. BUTCHERS, E., RAYNOR, G. V., and HUME-ROTHERY, W. J. Inst. Metals **69** (1943) 209.
8. ELLWOOD, E. C. J. Inst. Metals **80** (1952) 217.
9. AUER, H. and MANN, K. E. Z. Metallkunde **28** (1936) 323.
10. BURKHARDT, A. Z. Metallkunde **28** (1936) 299.
11. FULLER, M. L. and WILCOX, R. L. Trans. A.I.M.M.E. **122** (1936) 231.
12. LÖHBERG, K. Z. Metallkunde **32** (1940) 86.
13. PEIRCE, W. M. Trans. A.I.M.M.E. **68** (1923) 767.
14. RAYNOR, G. V. Al-Zn Annotated Equilibrium Diagram (London, Inst. of Metals).
15. FINK, C. G. and SOLANKI, D. N. Trans. Electrochem. Soc. **91** (1947) 203.
16. WADE, W. H., TWELLMEYER, G. O., and YNTEMA, L. F. Trans. Electrochem. Soc. **78** (1940) 77.
17. WAGNER, C. Thermodynamics of Alloys (Cambridge, Mass., Addison-Wesley Press, 1952).
18. FINK, W. L. and WILLEY, L. A. Trans. A.I.M.M.E. **122** (1936) 244.
19. OWEN, E. A. and PICKUP, L. Phil. Mag. **20** (1935) 761.
20. LYASHENKO, V. S. Izvest. Akad. Nauk SSSR. Otdel. Khim. Nauk, (No. 3) (1951) 242.
21. SMITH, C. S. Trans. A.I.M.M.E. **137** (1940) 236.

22. SCHRÖTER, P. G. Z. Metallkunde **32** (1940) 425.
23. KELLEY, K. K. Bulletin 476, U.S. Bureau of Mines.
24. SCHNEIDER, A. and STOLL, E. K. Z. Elektrochem. **47** (1941) 527.
25. LEITGEBEL, W. Z. anorg. Chem. **202** (1931) 305.
26. LUMSDEN, J. Thermodynamics of Alloys (London, Institute of Metals, 1952) p. 141.
27. KAWAKAMI, M. Z. anorg. Chem. **167** (1927) 345.
28. KIRKWOOD, J. G. J. Chem. Phys. **8** (1940) 623.
29. BETHE, H. A. Proc. Roy. Soc. **150** (A) (1935) 552.
30. RUSHBROOKE, G. S. Proc. Roy. Soc. **166** (A) (1938) 296.
31. TAKAGI, Y. Proc. Phys. Math. Soc. (Japan) **23** (1941) 44.
32. HILDEBRAND, J. H. Proc. Nat. Acad. Sci. **13** (1927) 267.
33. HARDY, H. K. Acta Met. **1** (1953) 203.
34. RAYNOR, G. V. and WAKEMAN, D. W. Phil. Mag. **40** (7) (1949) 404.

EFFECT OF ORIENTATION DIFFERENCE ON THE PLASTIC DEFORMATION OF ALUMINUM BICRYSTALS*

K. T. AUST† and N. K. CHEN†

Single crystal and bicrystal specimens of high-purity aluminum having controlled orientations were grown from the melt using "seeding" techniques. The crystals were similarly oriented with respect to the specimen axis which was located near ⟨110⟩ in the stereographic projection. The effect of varying the orientation difference, by rotations about the specimen axis, on the tensile stress-strain curves and slip characteristics was studied up to 2 per cent deformation. An increase in orientation difference was found to have a marked effect on inhibiting the initial plastic deformation and on modifying the subsequent stages of deformation. The yield stress and the rate of strain hardening increased, and the "easy" glide region was shortened, as the orientation difference between neighboring crystals increased. The shortening of the "easy" glide region was related to the increased amount of double glide observed in the vicinity of the grain boundary. The operative slip planes in the bicrystal specimens were determined to be the same as those which occur for a single crystal stressed in a similar manner. The results were discussed in terms of a slip activation process and the obstruction of dislocations at the grain boundary.

L'EFFET DE LA DIFFÉRENCE D'ORIENTATION SUR LA DÉFORMATION PLASTIQUE DE BICRISTAUX D'ALUMINIUM

On a produit des monocristaux et des bicristaux d'aluminium de haute pureté, ayant des orientations contrôlées, par la solidification du métal liquide, en employant la technique de germination contrôlée. Les cristaux étaient orientés d'une façon similaire par rapport à l'axe de l'échantillon, qui se trouvait au voisinage de ⟨110⟩ dans la projection stéréographique. L'effet de variation de la différence d'orientation, produite par des rotations autour de l'axe de l'échantillon, sur les courbes tension-déformation en extension et sur les caractéristiques de glissement, fut étudiée jusqu'à une déformation de 2 pour cent. On a constaté qu'une augmentation de la différence d'orientation avait une influence marquée sur le freinage de la déformation plastique, initiale, et sur la modification des étapes ultérieures de la déformation. La tension d'écoulement et la vitesse de durcissement par déformation augmentent, et la région de glissement facile diminue, quand la différence d'orientation entre deux cristaux adjacents augmente. La diminution de la région de glissement facile était liée à l'accroissement du glissement double dans le voisinage du joint intercristallin. On a constaté que le glissement dans les bicristaux s'opérait sur les mêmes plans que le glissement dans des monocristaux déformés par une application similaire de tension. Les résultats ont été discutés en termes d'un processus d'activation de glissement et de l'obstruction des dislocations au joint intercristallin.

DER EFFEKT DES ORIENTIERUNGSUNTERSCHIEDES AUF DIE PLASTISCHE VERFORMUNG VON ALUMINIUMBIKRISTALLEN

Einkristall- und Bikristallproben aus Reinstaluminium mit vorgegebenen Orientierungen wurden aus der Schmelze mit Hilfe von "Keimkristallen" gezüchtet. Die Kristalle hatten in Bezug auf die Probenachse eine ähnliche Orientierung. Die Probenachse befand sich in der Nähe von 110 in der stereographischen Projektion. Bei Deformationen bis zu 2% wurde der Effekt einer Änderung der Orientierung (durch Drehungen um die Probenachse) auf die Zugspannungs-Verzerrungskurven und auf die Gleitungserscheinungen untersucht. Es zeigte sich, dass eine Vergrösserung des Orientierungsunterschiedes einen erheblichen Einfluss auf das Unterdrücken des Anfangsstadiums der plastischen Verformung und die Modifizierung der darauffolgenden Stadien hatte. Die Fliesspannung und die Geschwindigkeit der Spannungshärtung stieg an, und der Bereich der "leichten" Gleitung verringerte sich, wenn der Orientierungsunterschied zwischen den benachbarten Kristallen vergrössert wurde. Die Verringerung des Bereichs der "leichten" Gleitung wurde mit der Zunahme der Doppelgleitung, die in der Nähe der Korngrenzen beobachtet wurde, in Beziehung gesetzt. Die in den Bikristallen wirksamen Gleitebenen wurden bestimmt, und es zeigte sich, dass sie den in einem gleichartig verformten Einkristall auftretenden Gleitebenen entsprechen. Die Ergebnisse werden im Rahmen des Aktivierungsvorgangs der Gleitung und der an Korngrenzen erfolgenden Bewegungshinderung der Versetzungen diskutiert.

Introduction

In order to explain in detail the differences between the mechanical properties of single crystals and polycrystalline aggregates, several investigators [1–5] have studied the plastic deformation of specimens consisting of a few crystals of controlled orientations. In the first experiment of this type, Chalmers [1] subjected bicrystal specimens of tin to tensile stresses. The stresses required to cause an arbitrary amount of plastic deformation were measured as a function of the difference of orientation of the two crystals, both of which were so oriented that the axis of stress was always similarly oriented in relation to the crystal axes. Chalmers found that the presence of the boundary had a large influence on the stress required for plastic deformation, which increased with the orientation difference. Kawada [2] has studied the plastic deformation of zinc bicrystals. He concluded that the experimental results could be explained fairly satisfactorily by considering the

*Received January 29, 1954.
†Johns Hopkins University, Baltimore, Maryland.

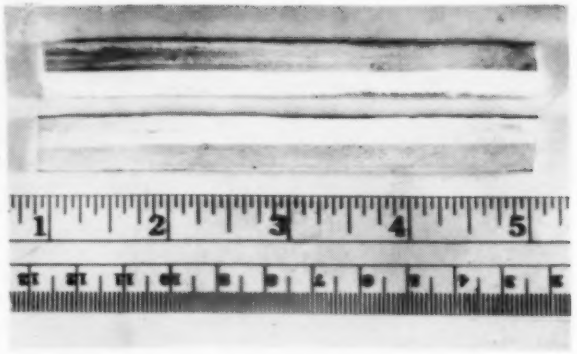

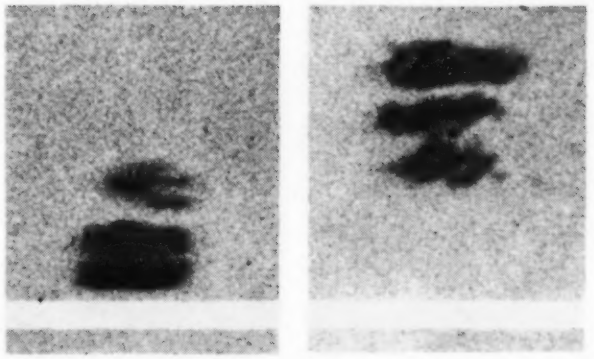

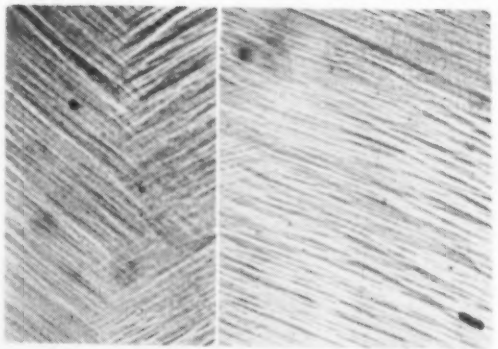

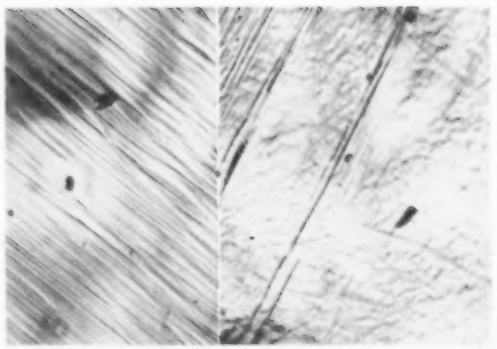

PLATE I. FIGURE 1.—Typical bicrystal specimens of aluminum showing the direction and length of the grain boundary. FIGURE 5—Enlarged Laue reflection from a crystal in specimen 6 : (*a*) before deformation, showing group of spots due to macro-mosaic structure; (*b*) after 2 per cent deformation, showing break-up of each spot. FIGURE 6—Photomicrographs showing (*a*) double glide in vicinity of grain boundary in specimen 6, $\theta = 85°$: ×100; (*b*) continuity of slip lines across grain boundary of specimen 3, $\theta = 5°$: ×1000; (*c*) clustering of slip lines in a crystal (right) of specimen 7: ×100.

mutual interaction of neighboring crystals and disregarding the mechanical properties of the grain boundary. Gilman [3] found that the stress-strain curve of a symmetric zinc bicrystal was almost identical to that of a single crystal specimen similarly oriented, in agreement with the work of Kawada [2]. Chalmers [6] believed that the proximity of a grain boundary may cause slip systems to become operative that are never detected in the single crystal. This was later confirmed in a study of the deformation of zinc tricrystal specimens [4].

Clark and Chalmers [5] examined the mechanical properties of bicrystals of aluminum having a {111} slip plane common to both crystals and inclined at 45 degrees to the specimen axis, the position of maximum resolved shear stress. The orientation difference was obtained by varying the angle θ between the ⟨110⟩ slip directions of each crystal in the common slip plane. They found that the rate of strain hardening increased, and the length of the linear stress-strain region (i.e., plastic region of "easy" glide) became shorter, as the orientation difference θ of the crystals increased from 0 to 60 degrees. However, the yield stress reached a maximum at $\theta = 30°$, the maximum slip direction orientation difference, and remained constant up to $\theta = 60$ degrees.

It was apparent that further experiments should be conducted to give additional quantitative information concerning the effects of grain boundaries before a complete understanding of the role of the grain boundary in the deformation process can be reached. In the present investigation, the stress-strain and slip characteristics were studied for a series of specimens of aluminum, each consisting of two crystals of controlled orientations separated by a longitudinal boundary. The specimens were all similarly oriented with respect to the axis of the specimen, not only for the two crystals comprising one specimen, but from specimen to specimen. The specimen axis was located within 2 degrees of the ⟨110⟩ direction, and the orientation differences were obtained by a rotation about the specimen axis.

Experimental Procedure

Aluminum of 99.997 per cent purity, obtained from the Aluminum Company of America, was used as the starting material. Graphite boats with graphite covers were machined for preparing specimens, having dimensions 1/2 in × 1/5 in. × 4–5 in. Specimen bars of suitable cross-sectional dimensions were first prepared by melting aluminum in graphite crucibles and pouring the metal into the graphite boat. A graphite boat, containing a satisfactory specimen bar and the seed crystals, was enclosed horizontally in a vycor tube closed at both ends. Single-crystal and bicrystal specimens having the desired orientations were then grown from the melt, in an argon atmosphere using "seeding" techniques previously described [7].

The specimens were etched in aqua regia in order to reveal the presence of stray crystals or striations having different orientations. The orientations of the single crystals and of each crystal in the bicrystal specimen were determined from back-reflection Laue photographs and stereographic projections. The orientation determination was accurate to only ±2 degrees as a result of the substructures or striations observed within the crystals. The specimens were wrapped in aluminum foil and annealed in air at 610 ± 5°C for 24 hours. Oxide layer which had formed on the surface during the annealing was removed by etching. Typical bicrystal specimens of aluminum are shown in Figure 1.

The specimens were electrolytically polished in a 2: 1 solution of methyl alcohol and concentrated nitric acid. Intermittent polishing periods for a total time of 30 to 40 minutes at a current density of 10 amp/sq dm resulted in a high polish and a smooth metallographic surface. The width and thickness of each specimen were measured with a traveling microscope to determine the cross-sectional area. A typical area for the various specimens was .075 sq in.

The specimens were deformed in a Tinius Olsen "Plastiversal" type of tensile testing machine. The load values could be measured to an accuracy of 1/4 lb corresponding to a stress of 3 psi. Strain over a 1–1/4 in. gauge length was obtained by using a clip gauge which was attached to the specimen in the manner described by Chen and Pond [8]. The per cent strain was measured to a value of 0.01 using the clip gauge and a SR–4 model type-K strain indicator.

After about 2 per cent deformation, micrographic examination was carried out on each specimen to determine the characteristics of the deformation markings appearing in adjoining crystals and in the immediate vicinity of the grain boundary. X-ray back-reflection Laue photograms were taken to determine the lattice rotations and the characteristics of the Laue reflections.

Experimental Observations and Results

The crystals obtained usually showed a macromosaic or striation structure which resulted in an orientation distribution of about 4 degrees. The specimen axis orientations for all of the crystals are shown in the standard cubic stereographic projection in Figure 2. A rotation about the axis

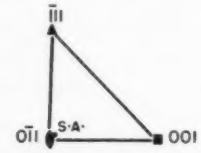

FIGURE 2. Standard cubic stereographic projection of specimen axis orientation (±2 degrees) for all crystals of specimens 1–6 inclusive.

of a bicrystal specimen would bring one crystal into coincidence with the other. This ensures that the resolved shear stresses on equivalent glide planes for every crystal are the same for a given load. Everything is therefore constant except the angular rotation θ about the specimen axis, which varies from specimen to specimen.

Typical stress-strain curves for specimens having $\theta = 5$ degrees and 85 degrees, are shown in Figure 3. Since a definite yield point was not obtained with these crystals in the present study, the linear plastic region AB shown in Figure 3 was extra-

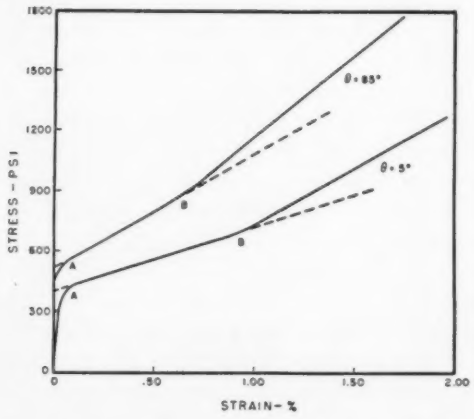

FIGURE 3. Stress-strain curves for specimens 3 and 6 having orientation differences θ of 5 and 85 degrees respectively.

polated to zero strain. The yield stress was arbitrarily defined as that value of stress obtained by extrapolating the line AB to zero strain. The slope of the "easy" glide region, AB, is a measure of the rate of strain hardening in the early stages of plastic deformation. At approximately point B, the linear region of "easy" glide ended, and the stress-strain curve rose more steeply.

The relation between the yield stress and the difference in orientation θ of the crystals in the specimen is shown in Figure 4. Table I summarizes

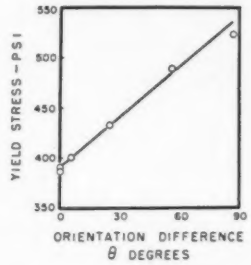

FIGURE 4. Plot of yield stress versus orientation difference θ for specimens 1–6 inclusive.

TABLE I

Specimen number	Orientation difference θ (degrees)	Yield stress (psi)	Slope of AB (psi per 0.1% strain)	% Strain at point B
1	0	392	29	0.90–0.95
2	0	390	38	0.95
3	5	402	34	0.90
4	24	435	48	0.80
5	55	490	54	0.70
6	85	525	58	0.65
7	*	515	82	0.50

*It should be noted that bicrystal specimen 7 is not in the same series as specimens 1–6 inclusive, since two angular rotations of 35° and 50° were required to bring the two crystals into coincidence. The specimen axis position of the one crystal of specimen 7 is identical with that of specimens 1 and 2, i.e., within 2 degrees of ⟨110⟩; however, the other crystal has its specimen axis within 2 degrees of ⟨111⟩.

the data for the various specimens showing the orientation difference θ versus: (i) yield stress, (ii) the slope of the "easy" glide region AB, and (iii) the approximate strain at which the "easy" glide regions ended (point B in Figure 3). It is evident that the yield stress and the rate of strain hardening (slope AB) increased, and the "easy" glide region was shortened, as the orientation difference between the crystals was increased.

X-ray back-reflection Laue patterns were obtained from each crystal in the various specimens after approximately 2 per cent deformation. The amount of lattice rotation as a result of this deformation was too small (less than 4 degrees) for accurate determination of the direction of lattice rotation. Typical Laue reflections (enlarged) before and after deformation are shown in Figure 5. A large orientation distribution due to the macro-

mosaic or striation structure is indicated in Figure 5a. It was found after 2 per cent deformation that the Laue reflections from each of the macro-mosaic crystals are broken up into high intensity regions connected by diffuse areas, e.g., Figure 5b. This observation may be interpreted in terms of crystallite fragmentation of each of the macro-mosaic crystals.

Metallographic examination after deformation revealed two sets of slip lines in each crystal of the bicrystal specimens and in the single-crystal specimens. Stereographic analysis of the slip markings indicated that these lines were traces of the $(1\bar{1}1)$ and $(\bar{1}\bar{1}1)$ planes. However, for specimens with $\theta = 0°$ and 5°, the slip markings were predominantly due to $(1\bar{1}1)$ slip, while $(\bar{1}\bar{1}1)$ slip was observed only in relatively few regions of the crystal. As the orientation difference increased, the amount of $(\bar{1}\bar{1}1)$ slip increased and was predominant in the immediate vicinity of the grain boundary. This is illustrated in Figure 6a which shows the $(\bar{1}\bar{1}1)$ slip traces on either side of the grain boundary and the $(1\bar{1}1)$ traces in the regions remote from the grain boundary for specimen 6.

Continuity of slip lines was observed across the grain boundary of specimen 3 ($\theta = 5°$), e.g., Figure 6b, and to a lesser extent across the boundary of specimen 4 ($\theta = 24°$). Striation or lineage boundaries appeared to have little effect on the continuity of slip lines across them. A distinct clustering of the slip lines was noted in the one crystal of the bicrystal specimen 7, as shown in Figure 6c, where the specimen axis orientation was located near $\langle 111 \rangle$ in the standard projection. Chen and Mathewson [9] have also observed after plastic deformation the formation of slip clusters in single crystal specimens of aluminum whose axes are oriented near $\langle 111 \rangle$.

Discussion

Chalmers [6] has pointed out that there are two factors that must be taken into account when the effects of crystal boundaries on the plastic behavior of the surrounding crystals are considered. These are the purely geometrical condition, that the material and also the strain must remain continuous; and the physical condition that the proximity of a boundary may influence the plastic deformation of the crystals. The continuity condition is not a criterion in the present experiments (omitting specimen 7) since the specimens consisted of two crystals identical with respect to the specimen axis or stress axis but rotated about this axis with respect to each other. The results, shown in Table I and in Figures 3 and 4, indicate that the proximity of a single-grain boundary has a marked effect both in inhibiting plastic deformation and in modifying the subsequent progress of deformation of the neighboring crystals. It is evident, therefore, that the continuity condition cannot by itself explain the differences between the plastic deformation of the single crystal and the polycrystalline aggregate.

The results presented in Figure 4 are in qualitative agreement with those previously obtained for tin [1]. However, the crystallography of the orientation difference is an important consideration. For instance, in the present work and for that on tin, the orientation difference was achieved by a simple angular rotation about the specimen axis. In both these cases, the yield stress progressively increased as the orientation difference increased from 0 degrees to approximately 90 degrees. Clark and Chalmers [5], however, obtained orientation differences θ between neighboring crystals of aluminum by varying the angle between the slip direction of each crystal in the common slip plane. They found that the yield stress increased slightly as θ was increased from 0 to 30 degrees and remained constant up to 60 degrees. It is evident that the crystallographic nature of the orientation difference has a significant effect on the stress at which plastic deformation begins. A rotation about the stress axis in preparing bicrystals, such as employed in the present work, has the effect of rotating slip planes in the two adjacent crystals with respect to the boundary. In fact, the greater the rotation of the seed crystal (up to 90 degrees), the greater is the primary slip plane orientation difference. Under such circumstances, it was suggested [10] that slip activation* would become increasingly difficult with increasing orientation differences; and, therefore, the yield stress would also increase with orientation difference. However, the aluminum bicrystals used by Clark and Chalmers [5] may have been all favorably oriented for slip activation by virtue of their co-planar $\{111\}$ arrangement. Thus the slip inhibition due to such a boundary may be small at the initial stages of deformation.

The data given in Table I indicate that an increase in the orientation difference resulted in an increase in the rate of strain hardening in the early

*Slip activation is designated as the process where slip bands from one crystal can initiate or activate slip bands in an adjacent crystal [10].

stages of deformation, and progressively shortened the region of "easy" glide. Similar effects were noted by Clark and Chalmers [5] for aluminum bicrystals. Double glide was metallographically observed in all specimens examined during the present study. It was also found that double glide occurred in greater amounts in the grain-boundary vicinity as the orientation difference was increased. The termination of "easy" glide has been related to the start of double glide in α-brass single crystals [11]. It is believed, therefore, that the decrease of the "easy" glide region with an increase of orientation difference may be related to the presence of double glide observed near the grain boundary. Since slip is increasingly inhibited as the orientation difference of the crystals is increased, a redistribution of resolved shear stresses may result, particularly near the grain boundary, so that new planes are stressed above their critical shear stresses.

The effect of orientation difference on the initiation of the deformation process and on the subsequent stages of deformation may be interpreted in terms of the obstruction of dislocations at the grain boundary [6; 12; 13; 14]. Two short-range forces exist which may prevent the leading mobile dislocations from penetrating the grain boundary barrier. The first is due to the stress field of the dislocations in a boundary, or simply due to the system of stresses at the regions of poor fit in the boundary if the boundary structure is not regarded as consisting of separate and distinct dislocations. The second short range force is due to a non-Hookean interaction where the law of force between atoms in the slip plane changes at the boundary as a result of the lack of continuation of the slip system across a boundary. Both these short-range forces might be expected to increase as the orientation difference of the neighboring crystals across a boundary is increased. This increase of short-range forces should result in an increase in the stress necessary, first, to drive dislocations through the grain-boundary barrier and, second, to activate dislocations on the other side of the boundary.

The results obtained from bicrystal specimen **7**, in which the specimen axis of the one crystal is near ⟨110⟩ while the axis of the other crystal is near ⟨111⟩, are noteworthy. The yield stress of the specimen approached that for specimen 6 with the largest orientation difference ($\theta = 85°$); the rate of strain hardening of specimen **7** is greater and the region of "easy" glide is still further shortened. The more complex orientation relationship existing across the grain boundary of specimen **7** might be expected to have a more marked effect on the deformation characteristics.

From the yield-stress values for the single-crystal specimens, the critical resolved shear stress required to cause plastic deformation was found to be 160 psi (112 g/mm^2). This value is in fair agreement with the critical resolved shear stress value obtained by Rosi and Mathewson [15] of 148 psi (104.5 g/mm^2) for aluminum single crystals of similar purity.

Acknowledgments

The authors wish to express their gratitude to the Office of Ordnance Research for support of their work under Contract No. DA-36-034-ORD-1153RD, and to the Aluminum Company of America for supplying the high-purity aluminum. We also wish to thank R. Maddin and R. B. Pond for their helpful advice, and B. Chalmers for making available to us some unpublished results of research.

References

1. Chalmers, B. Proc. Roy. Soc. **A162** (1937) 120.
2. Kawada, T. J. Phys. Soc. Jap. **6** (1951) 363, 485.
3. Gilman, J. J. Acta Met. **1** (1953) 426.
4. Craig, G. B. and Chalmers, B. In course of publication.
5. Clark, R. and Chalmers, B. In course of publication.
6. Chalmers, B. Metal Interfaces (A.S.M. 1952) p. 299.
7. Chalmers, B. Proc. Roy. Soc. **A196** (1949) 64.
8. Chen, N. K. and Pond, R. B. Trans. A.I.M.E. **194** (1952) 1085.
9. Chen, N. K. and Mathewson, C. H. Trans. A.I.M.E. **191** (1951) 653.
10. Chen, N. K. and France, L. L. In course of publication.
11. Maddin, R., Mathewson, C. H. and Hibbard, W. R. Trans. A.I.M.E. **175** (1948) 86; **185** (1949) 527.
12. Barrett, C. S. Structure of Metals, 2nd ed. (New York, McGraw-Hill, 1952) p. 409.
13. Cottrell, A. H. Progress in Metal Physics **4** (1953) 230.
14. Foreman, A. J. E. and Jaswon, M. A. Phil. Mag. **43** (1952) 201.
15. Rosi, F. D. and Mathewson, C. H. Trans. A.I.M.E. **188** (1950) 1159.

Transformation in Indium-Thallium Alloys*

In a communication which was entitled "Notes on Geisler's Theory of Phase Transformations with Special Reference to Indium-Thallium Alloys" [1], the authors have discussed the experimental evidence in relation to a double shear mechanism of transformation from the cubic to the tetragonal form which was proposed by Bowles and coworkers [2] and to a modified nucleation and twinning mechanism proposed by Geisler and Martin [3]. The authors state in a footnote to the communication that the terms "first" and "second" shear are used purely for convenience in describing the crystallographic change and are not meant to imply any physical resolution of the atom movements into two components. They subsequently assume the position of defending the two-shear mechanism of transformation. There is no disagreement in the general observation that the

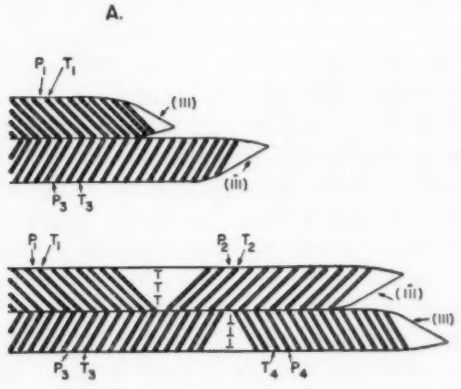

FIGURE A. Bands parallel to (101) eight crystal orientations. 4 parent orientations (P). 4 twins (T).

relation between the initial and final positions of atoms can be described by a movement which can be frequently resolved into simple crystallographic components. The disagreement arises when a mechanism based on the consecutive movements of planes of atoms along these specific components is proposed as operative during the transformation. There seems to be no justification in assuming that the *description* of these movements constitutes the *mechanism*.

The mechanism based on the consecutive movements of planes of atoms has been generally regarded as a process whereby the new structure is generated by shear, and the microstructural features, such as habit plane, macroscopic surface tilts and sub-markings, have been assigned direct roles in the generation of the new crystallographic structure. An alternative mechanism permits atom-by-atom generation of the new phase and attributes such microstructural features to shear accompanying the transformation in a broader and more general fashion [4].

In regard to the cubic to tetragonal transformation in indium-thallium alloys, I am gratified that the authors of the aforementioned communication confirm our proposal that the transformation structure can be described as 12 parent orientations with the relationship $(111)_C//(111)_T$, $[1\bar{1}0]_C//[1\bar{1}0]_T$ and 24 first-order twin orientations. Our proposal of nucleation of the tetragonal phase by the formation of coherent platelets on {111} phases also appears to be adequate. I am also grateful to the authors for pointing out the modifications needed in Figure 4 of my paper [4] to make the nucleation and twinning mechanism practically indistinguishable from the two shear mechanism. This result was the one originally desired in contrast to the obviously incompatible twinning mechanism which Bowles and coworkers chose for comparison with the experimental data. The discrepancy in Figure 4 of my paper concerned the number of orientations which may occur in a single set of main bands. Instead of twelve orientations as originally proposed, a total of eight orientations better fits the experimental data. The crystallographic details for all orientations are summarized in Table I. Orientations in a given set of main bands are apparent from the data listed under the third column of the table. For example, main bands on the (101) plane contain the parent orientations P_1, P_2, P_3 and P_4 and their twins T_1, T_2, T_3 and T_4 on the (011), $(0\bar{1}1)$, $(1\bar{1}0)$ and (110) planes, respectively, according to the experimental observations of Bowles and coworkers. The second twin of each of the parent orientations, T'_1, T'_2, T'_3 and T'_4, form on the (101) plane parallel to the set of main bands under consideration, they are at an angle of 60 degrees to the first twin, and thus can not explain the occurrence of two orientations of sub-bands at 90 degrees to each other in a single main band as I originally proposed. On the other hand, the twins T_1 and T_2 (also T_3 and T_4) are on planes at 90 degrees to each other and thus the

*Received March 31, 1954.

TABLE I

CRYSTALLOGRAPHIC FEATURES OF PRODUCT OF In-Tl TRANSFORMATION

Parent orientation	Conjugate matrix elements for (111) [1$\bar{1}$0] of tetragonal product	Planes of main band	Planes of twins* T	T'
P_1	(111) [$\bar{1}$10]	(101) (011)	(011)	(101)
P_2	(1$\bar{1}$1) [110]	(101) (0$\bar{1}$1)	(0$\bar{1}$1)	(101)
P_3	(1$\bar{1}$1) [011]	(101) (1$\bar{1}$0)	(1$\bar{1}$0)	(101)
P_4	(111) [0$\bar{1}$1]	(101) (110)	(110)	(101)
P_5	(1$\bar{1}$1) [$\bar{1}$01]	(0$\bar{1}$1) (1$\bar{1}$0)	(1$\bar{1}$0)	(0$\bar{1}$1)
P_6	($\bar{1}\bar{1}$1) [101]	(0$\bar{1}$1) (110)	(110)	(0$\bar{1}$1)
P_7	(111) [$\bar{1}$01]	(011) (110)	(110)	(011)
P_8	($\bar{1}$11) [101]	(011) (1$\bar{1}$0)	(1$\bar{1}$0)	(011)
P_9	($\bar{1}\bar{1}$1) [011]	($\bar{1}$01) (110)	(110)	($\bar{1}$01)
P_{10}	($\bar{1}$11) [0$\bar{1}$1]	($\bar{1}$01) (1$\bar{1}$0)	(1$\bar{1}$0)	($\bar{1}$01)
P_{11}	($\bar{1}\bar{1}$1) [$\bar{1}$10]	($\bar{1}$01) (0$\bar{1}$1)	(0$\bar{1}$1)	($\bar{1}$01)
P_{12}	($\bar{1}$11) [110]	($\bar{1}$01) (011)	(011)	($\bar{1}$01)

*Relative to cubic lattice to which twinning planes of tetragonal product are approximately parallel. The first column for T_1, T_2, T_3, etc. are the twins which occur in the main band on the first named plane and the second column for T_1', T_2', T_3', etc. are for the second named main band.

coexistance of the orientations P_1, P_2, T_1 and T_2 could account for the structure of a main band containing two sets of sub-bands. Such an arrangement is illustrated in Figure A which should be regarded as a more appropriate representation of the data to replace the bottom-right diagram in Figure 4 of my paper [4].

The origin of the bands with two sets of sub-bands can be explained on a more plausible basis than the chance amalgamation of the two different parent nuclei and their twins to form the single main band as proposed in the aforementioned communication. For example, during the course of growth the orientation P_1 may change to P_2 (or P_3 to P_4) as the result of growth imperfections. The two orientations in a single main band arise from coherency on two different {111} planes but they both make an angle of about 35 degrees to the plane of the main band. Thus, conditions may arise during the course of growth which energetically favor a change from coherency on one side of the tapered growing tip to coherency on the opposite side. For example, when excessive elastic distortion is encountered at the growing tip possibly due to a group of imperfections in the cubic matrix structure, a growth imperfection may arise from a change in site of coherency. Such a change produces a low angle grain boundary with the tetragonal axis rotated only 1°20′ and growth proceeds in the new parent orientation P_2 which subsequently produces its own twin T_2 behind the advancing edge. The diagrams in Figure 1A are intended to represent the before and after states of evolution of the new parent orientations during the course of growth.

The properly identified parent and twin orientations also permit an alternate interpretation of the phenomenon of "interpenetration" discussed by Bowles and coworkers. One manifestation of this phenomenon is a growing out of a new set of main bands at 60 degrees to the plane of an existing set as shown in Figure 1B. Bowles and coworkers have pointed out that of sixteen orientations present in two sets of main bands at 60 degrees to each other, only two are common. Reference to Table I shows that each parent orientation can appear in two main bands at 60 degrees to each other. For each of the two planes of main bands for a single parent orientation there is a different twin of that parent orientation. The second plane for the parent orientation P_1 alternate to that shown in Figure 1A is the (011) plane which will accommodate the seven additional orientations T_1', P_7, T_7, P_8, T_8, P_{12} and T_{12}'. An outgrowth of a new orientation of main bands could occur when through some growth irregularity the improper twin, T_1', was formed in P_1 on the (101) plane from which point proper growth for minimum strain energy would have to proceed along the (011) plane as illustrated in Figure B. The growth irregularity might originate in imperfections in the cubic matrix or a local strain condition which causes the extension of the area with parent orientation beyond the average position of the interface or which causes the formation of the twin proper for a new plane of the main band. The phenomena of the formation of areas with a second set of sub-bands and areas of interpenetration have been attributed to the inversion of sense or order of the two shears in the double-shear mechanism. Any conditions which might be used to explain these inversions probably explain the growth anomalies illustrated in Figure 1 which are dependent on energetics of growth.

One of the characteristics of martensite in general is the stimulation effect whereby the activation of a nucleus is strongly dependent upon its surroundings. The "burst" phenomenon of the martensite reaction in steels represents an example of such an effect. In order to explain the formation of large colonies of parallel main bands in In-Tl alloys, the nucleation process must be regarded as autocatalytic in such a manner that embryos

which are avilable in the disorganized grain boundary regions of the parent cubic crystals are activated by the state of stress of the existing main bands so that the new bands form parallel to the existing ones. The phenomenon of the formation of areas with a second set of sub-bands in a single main band (Figure A) might also be an embryo stimulation effect with the original parent orientation giving way to the second when the growing phase encounters an embryo of the second orientation and growth in the first orientation is impeded for some reason. According to the microstructure, the site of change from one set of sub-bands to the second appears to be haphazard except possibly in the regions where the outgrowths of the type illustrated in Figure B occur when continuity of

B.

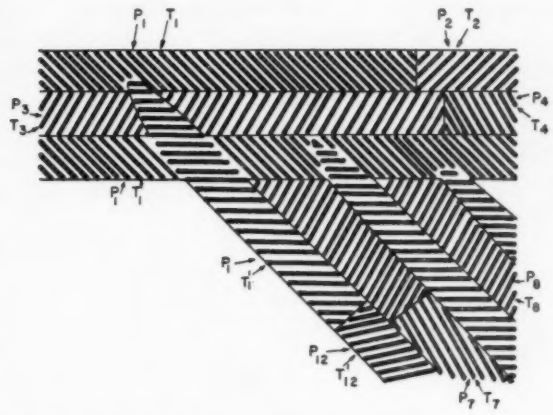

FIGURE B. "Interpenetration" of main bands on (101) and (011).

parent orientation into the two orientations of main bands must be preserved. This phenomenon of outgrowth is probably the counterpart of the cooperative phenomenon observed with iron-base alloys whereby martensite plates in one orientation stimulate nucleation and growth in certain other orientations. In that case the related orientations were such that sharing of certain of the elements for spontaneous deformation by duplex slip could account for the cooperative nature [4]. Here it is noteworthy from Figure B and Table I that common twinning planes in P_3–P_8 and P_4–P_7 are available for the main bands which interleave the main bands with the common orientation, P_1. Stimulated nucleation also plays a role in the reversibility of the martensite reaction. The ability to return to a product of the same initial orientation on heating and cooling through the transformation temperature has been observed for numerous materials and suggests that the ability to stimulate the same embryo or one of like orientation possibly through residual stresses can be retained. This type of reversibility can be reconciled with the proposal that martensite is a transformation product which is *accompanied* by shear; the objection in the aforementioned communication on the basis of the common conception that plastic deformation is generally irreversible is no longer valid. The reversibility of twinning in zinc has been demonstrated [5]. Detwinning can be produced by reversing the stress used in causing the initial twinning. Any other deformation process involving the flow of dislocations would likewise be expected to exhibit a degree of reversibility. The effect of applied stresses on propagation of the transformation demonstrates that not only do they stimulate nucleation but they also support the spontaneous deformation processes during growth. If the shear is a consequence of the generation of the new crystallographic structure, then applied stress that would promote the shear would be an aid in the growth of the new phase.

An important feature for distinguishing between the two-shear mechanism and an atom by atom mechanism accompanied by shear resides in the nature of the interface of the main bands:—whether it remains plane and of crystallographic significance as required for the plane of the first shear in the double-shear mechanism or whether it may become curved and irregular. Published micrographs for In-Tl alloys reveal that the main bands are not always smooth but reflect a slight uneveness in the termination of the twins (see [2] Fig. 1). A twinned microstructure for a partially transformed Co-Pt alloy has been published (see [4] Figure 5a) which is undeniably similar to that for In-Tl alloys. When the twins are coarse they terminate on a very irregular main band which tends to follow a {110} plane. When the twins are submicroscopic the interface between the main band and untransformed matrix is microscopically smooth but not always plane since unimpeded particles show a gradual taper to a sharp edge or point in cross section. The well-known lenticular shape of martensite in iron-base alloys is also indicative of a curved rather than plane interface. Finally transformed regions with a striated substructure have been observed with irregular outline and no resemblance to crystallographic planes. To reconcile these observations one must adopt a mechanism which does not impose discrete crystallo-

graphic significance upon the interface as does the two-strain mechanism.

There are two other possible modes of distinguishing between the two mechanisms in indium-thallium alloys. First, a precise determination of the orientation of the plane of the sub-bands should permit one to distinguish between the {111} twinning planes of the tetragonal product assumed by the growth and twinning mechanism and the {110} planes of second shear in the matrix distorted by the first shear. Such a determination has not yet been made. Second, a consideration of the stability of the twinned array should aid one in deciding whether it was necessary for the generation of the new structure or merely for accommodating the strain between the tetragonal product and the cubic parent phase. Observations on the single interface transformation in which a single crystal of one form is converted to a single crystal of the second show that the twin arrangement delineating the plane of the second shear is localized at the interface. Thus, the twins serve to accommodate the two lattices and can be annealed out without reverting back to the first strained matrix.

The ability to resolve the atom movements into two strains or shears cannot be regarded as indicative of a double shear mechanism of generation involving movement of whole planes of atoms in the discrete steps. In addition the alternate interpretations of the data for In-Tl alloys show that the microstructural features of martensite such as the habit plane, sub-band markings, and macroscopic surface tilts are not indicative of the mode of transformation to the extent that growth by shear can be distinguished from growth by atom jumps. On the other hand, to build shear mechanisms of generation on these microstructural features imposes unnecessary restrictions to the rationalizing of transformation structures. For example, macroscopic surface tilts cannot be a characteristic of the growth mechanism of martensite for they are also observed with other transformation products such as bainite, the precipitates in Cu-Be and Al-Cu alloys and ordered phases such as CoPt, FePt and CuAu, as I have pointed out in my paper. The movement of whole planes of atoms without segregation or ordering of the solute atoms as required by the diffusionless nature of martensite could not possibly describe the generation of the new structures observed in these cases. A second example of the unnecessary restrictions imposed by the double strain mechanism is the requirement of a crystallographically plane and significant interface for the operation of the first strain as described above.

With the alternative interpretations possible for the observations on indium-thallium alloys, one must be led to the conclusion that the description of the atom movements does not constitute the mechanism. Although the two mechanisms might seem practically indistinguishable in this case, there is a basic difference. The distinction is that the heterogeneous shear which causes macroscopic surface tilts is regarded as part of the process in the generation of the new crystallographic structure by the double strain mechanism whereas the shear is regarded as occurring *after* the generation of the new crystallographic structure at any particular point in or around the growing particle in the mechanism based on growth with spontaneous deformation. I support the latter viewpoint which has more far-reaching implications in rationalizing the structural aspects of transformation products. On this basis the characteristic of martensite is that it may be a sheared product and not necessarily a product of shear. The absence of long range diffusion distinguishes the martensite reaction from other transformations which may also be accompanied by shear.

A. H. Geisler

General Electric Research Laboratory
Schenectady, New York

References

1. Basinski, Z. S. and Christian, J. W. Acta Met. **1** (1953) 759–761.
2. Bowles, J. S., Barrett, C. A., and Guttman, L. Trans A.I.M.E. **188** (1950) 1478–1485.
3. Geisler, A. H. and Martin, D. L. Discussion to [2], Trans. A.I.M.E. **191** (1951) 1057–60.
4. Geisler, A. H. Acta Met. **1** (1953) 260–81.
5. Jillson, D. C. Trans. A.I.M.E. **188** (1950) 1009–18.
6. Guttman, L. Trans. A.I.M.E. **188** (1950) 1472–7.

Bending Creep of "Duplex" Zinc Single Crystals*

Zinc single crystals were grown from the melt such that two separate crystals branched from a common seed and grew side by side. The crystals of each such "duplex" pair had not only the same orientation, but also practically identical growth conditions.

Creep was measured as crystals were bent under a series of progressively higher constant uniform

*Received April 15, 1954.

bending moments reaching about 3 times the elastic limit after 4 or 5 increments. The maximum strain ($\Delta l/l$ at the surface under tension) did not exceed 10^{-3}. Over 100 runs were made on 31 crystals which included 14 duplex pairs and 3 crystals grown singly. In more than 80 per cent of the tests, run $\backsim$ 15 to 20 minutes at each load, the creep could be described within experimental error by $\eta = bt^m$, where η is the plastic shear strain (at the surface under tension, also at that under compression) and t is the time in minutes from completion of a load increment. Plotting log η against log t for the successive loads gives a series of nearly parallel straight lines (creep curves) with slope (m) ranging mostly between .20 and .32. b is a function of the previous history of the specimen and of the applied bending moment, or corresponding resolved shear stress σ (at the surface under tension). For a series of successively higher loads on a crystal, the values of log b versus σ fall roughly on a straight line; formally, $b = B(10)^{A_0\sigma}$. The log b vs. σ plots for one crystal cover a relatively small range of σ. For "soft" crystals, creep was measured with $12 < \sigma < 24$ gm/mm^2, while for the hardest crystals, $30 < \sigma < 55$ gm per mm^2. The slopes of these plots (A_0) fall mostly in the range .10–.25, usually having higher values for hard crystals. This leads to a tremendous range in the formal constant B: $10^{-64} < B < 10^{-6}$.

Though there was considerable spread in m, A_0, and stress range from one duplex pair to the next over the entire group of crystals, the two of each duplex pair were very similar in overall behaviour, often identical in some details. Even where the similarity of a duplex to its partner was not outstanding (in $\backsim$15 per cent of the runs), it resembled its partner more than almost all the other crystals of the group.

Further experiments were undertaken on duplex pairs to find the effect of the treatments listed below. One of the crystals was treated and its partner used as a "control", so that any difference in behavior found was attributable to the treatment.

(*a*) *Stress reversal.* After being bent to a strain of about $\eta = 0.6 \times 10^{-3}$, crystals were turned over and bent in the reverse direction. Substantial creep was noted at a load of about 2/3 the previous values. The m's were often a bit lower and the A_0's considerably lower. This behavior [1] was observed in $\backsim$90 per cent of the crystals subject to reverse bending.

(*b*) *Etching.* Three crystals were etched in 25 per cent HCl to remove the oxide coating and were tested immediately after rinsing and drying. The behavior at low stress was apparently unaffected. However, A_0 was somewhat higher than before and fairly rapid creep occurred before the high loads used previously were reached. This culminated in the most striking feature of "clean-surface" crystals: Under moderate stress, $\eta = 3 \times 10^{-4}$ was reached after a minute of normal creep. After another minute or so the creep rate would accelerate so that the crystal had to be unloaded to prevent excessive strain.

(*c*) *Electropolishing.* Crystals which were electropolished behaved substantially like those that had been etched. This behavior was sometimes obtained with only two sides polished, for crystals mounted with the c-axis in the plane of bending. Usually, however, four polished sides were necessary.

That crystals of a duplex pair had a common melt and very nearly the same growth conditions seemed to be the determining factor in their great similarity, rather than their growth from a common seed. Thus, several duplex pairs grown from the same seed did not show the close likeness found between members of a pair. This seems to indicate a delicate nonmonotonic dependence on impurities, and on growth conditions influencing their distribution to dislocations or other lattice defects. The crystals of a duplex pair are substantially more alike than were two crystals cut from one long crystal [2]. The latter would be expected to differ in purity due to refining action at the liquid-solid interface during growth, whereas duplex partners should have not only similar purity, but also more nearly alike impurity distributions.

The accelerating creep observed at moderate loads on clean crystals may involve reflection of dislocation loops from the surface, with a change in sign, as proposed by Frank [3].

R. EISNER

Physics Department
State Department of Iowa
Iowa City, Iowa
(Now at Westinghouse Research Laboratories,
East Pittsburgh, Pennsylvania)

References

1. SEITZ, F. Bauschinger Effect. In Physics of Metals. (New York, McGraw-Hill, 1943) p. 146.
2. WEINBERG, E. H. J. Appl. Phys. **24** (1953) 734.
3. FRANK, F. C. Report of a Conference on the Strength of Solids, Bristol, England (Physical Society of London, 1948) p. 46.

The Order-Disorder Transformation in Cu-Au Alloys Near the Composition Cu_3Au*

Jaumot and Sutcliffe [1] have recently published the results of an X-ray diffraction study which led them to propose an unusual construction in the Cu-Au phase diagram about the composition Cu_3Au. They conclude that the order-disorder transformation occurs heterogeneously with a 2-phase field on the Au-rich side of Cu_3Au and homogeneously without a 2-phase field on the Cu-rich side. The main support for this conclusion originated in the observation that during the transformation there was a resolvable separation of the 400_{ord} and 400_{disord} reflections from samples containing more than 25 per cent Au, and only a slight broadening and gradual shift of position from samples containing less. This observation confirms experimental Debye-Scherrer work reported in 1953 at which time it was pointed out [2] that through the transformation range the line shift due to the difference in a_0 of the ordered and disordered phases could be lessened or increased by the difference in composition of the conjugate phases across a 2-phase region.

An alternate interpretation of the data of Jaumot and Sutcliffe leads to a diagram which is not only normal in qualitative construction but also permits a reasonable quantitative estimate of the breadth of the 2-phase (order+disorder) regions on each side of Cu_3Au.

Continuous change of a_0 due to continuous change of the degree of long-range order

According to Figures 3b–f,† the variation of a_0 with temperature deviates from a straight line as the temperature of the sample approaches the transformation region. This deviation, also observed by Owen and Liu [3] could be ascribed to a lowering of the degree of long range order as in the case of alloys whose composition is close to 50 at.% Au [4]. Thus, in the temperature range of this curvature, the alloy is composed of a single ordered phase and the 400_{ord} reflection is sharp. At temperatures above the transformation range the reflections are also sharp since the alloy is there composed of a single disordered phase.

$\Delta a_0(D-0)$, the discontinuous change of a_0 due to the order-disorder transformation

For the present problem we wish to know the variation with composition of the lattice parameters of the disordered and of the ordered phases at temperatures which are respectively just above and just below the transformation range. The variation of a_0 (dis) with composition is given by Johansson and Linde [5]; corresponding values for the ordered phase can be approximated in the following manner.

Owen and Liu showed that the lattice parameter of Cu_3Au undergoes a discontinuous increase of 0.0044 Å as the alloy is heated through the critical temperature of ordering. This change, $\Delta a_0(D-0)$, is due only to the transformation from the ordered to the disordered phase. From the data of Jaumot and Sutcliffe (Figs. 3d–f) one can calculate corresponding values for $\Delta a_0\ (D-0)$ of 0.002_5, 0.001_3 and 0.001_8 Å for the samples containing 28, 30 and 34 at.% Au respectively. These values, plotted in Figure I, represent the differences in a_0 of the respective samples when they are in equilibrium at temperatures just above and just below the 2-phase region. Data needed to calculate values of $\Delta a_0(D-0)$ for samples containing less than 25 per cent Au are not available because the magnitudes of the discontinuities in a_0 across the 2-phase region, being small and indistinguishable from the effect of changing degree of order, cannot be read from the data (Figs. 3b and 3c). However, since long range order is not possible below about 17 percent Au [6], one can arrive at approximate values of $\Delta a_0(D-0)$ between 17 and 25 per cent Au as shown by the dashed line in Figure I.

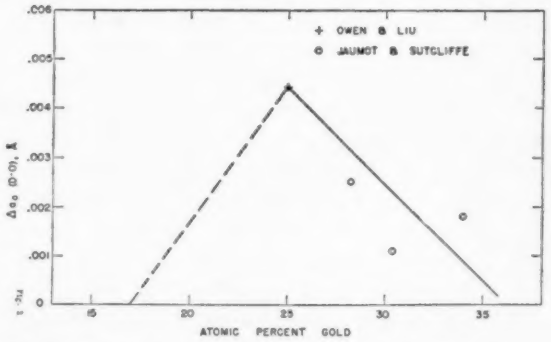

FIGURE I. Variation with composition of the discontinuous change in a_0 due to transformation only, $\Delta a_0(D-0)$.

Δa_0 (Seg), the change in a_0 due to chemical segregation

The conjugate phases of any alloy at equilibrium within a 2-phase region have different compositions, an effect commonly known as "tie-line" segregation. The compositions of the phases may be conveniently determined if the variation of crystal structure with composition is known. In the case

*Received April 20, 1954.

†Figures used in the present note are in Roman numerals; others refer to Ref. 1.

of alloys near Cu_3Au this change of crystal structure includes a change of lattice parameter, Δa_0(Seg).

Change in a_0 due to combined effects of $\Delta a_0(D-0)$ and Δa_0(Seg)

An alloy containing 28 per cent Au (see Figure 2), when in equilibrium at 378°C, will consist of two phases, one disordered having composition c_1 and the other ordered having composition c_2. Both phases are face-centered cubic but have different lattice parameters, viz., a'_0 (dis) and a'_0(ord), respectively. This much difference (0.007 Å) can easily be observed experimentally. For an alloy on the other side of Cu_3Au, however, say at 23 per cent Au and 388°C, the difference between a''_0 (dis) and a''_0 (ord) could be so slight that the coexistence of the two phases would appear only as a slight broadening and gradual shifting of the diffraction lines during the transformation as observed.

Estimation of the width of the 2-phase regions

It is assumed in the present analysis that the change in a_0 due to the order-disorder transformation, $\Delta a_0(D-0)$, is equal to Δa_0(Seg), the difference in a_0 due to the chemical segregation of the conjugate phases through the 2-phase transformation range. Justification for this assumption is found in the fact that, for alloys containing less than 25 per cent Au, the breadth of high-angle main lattice reflections increases only very slightly through the transformation range (Figures 4a and 4b) whereas for alloys containing more than 25 per cent Au the same reflections are nearly resolved into doublets (Figures 4c and 4d). The fact that there is any broadening of the 400 reflection in the case of Cu-rich alloys indicates that the assumption is not strictly valid. However, for purposes of calculation we can assume that $\Delta a_0(D-0) = \pm \Delta a_0$ (Seg). For Au-rich alloys the sign is (+); for Cu-rich alloys it is (−).

Using this assumption, $\Delta a_0(D-0)$ can be expressed as an equivalent composition change related by

$\Delta a_0(D-0) = \Delta a_0(\text{Seg}) = .005$ (Δat. per cent Au), an empirical equation derived from data of Johansson and Linde [5]. The widths of the 2-phase regions, at the compositions studied by Jaumot and Sutcliffe, were estimated by this method and are listed in Table I. The corresponding transformation temperatures were estimated from Figures 3b–f.

TABLE I

At. per cent Au	$\Delta a_0(D-0)$ observed	Δ per cent Au	Middle of transformation range Temp. °C
15.5	Disordered at all temperatures		
20.25	0.001_6	0.32	364
23.45	0.003_2	0.66	388
28.25	0.003_2	0.64	378
30.4	0.002_4	0.48	364
34.2	0.000_9	0.18	308

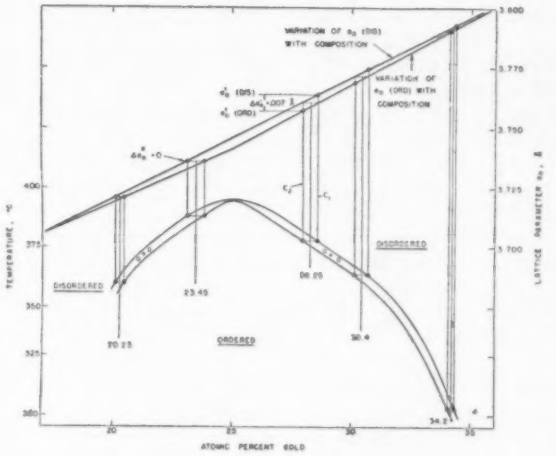

FIGURE II. *Upper figure*: Variation of a_0(dis) and a_0(ord) with composition. *Lower figure*: Portion of the Cu-Au phase diagram calculated from the data of Jaumot and Sutcliffe.

The portion of the phase diagram near Cu_3Au which results from this analysis is given in Figure II. The greatest width of the 2-phase region is about 0.75 atomic per cent and presumably occur near the stoichiometric composition.

J. B. NEWKIRK

General Electric Research Laboratory
Schenectady, New York

References

1. JAUMOT, F. E., JR., and SUTCLIFFE, C. H. Acta Met. **2** (1954) 63–74.
2. RHINES, F. N. and NEWKIRK, J. B. Trans. A.S.M. **45** (1953) 1029–55.
3. OWEN, E. A. and LIU, Y. H. Phil. Mag. **38** (1947) 354–60.
4. NEWKIRK, J. B. J. Metals June (1953) 823–6.
5. JOHANSSON, C. H. and LINDE, J. O. Ann. Physik **25** (1936) 1 *ff*.
6. KOMAR, A. and BUINOV, N. J. Exp. and Theor. Phys. U.S.S.R. **17** (1947) 555–63.

SOME CURRENT PAPERS IN OTHER JOURNALS

Acta Crystallographica, Vol. 7

Part 5, May, 1954 (Partial contents)

The nature of the specular reflexion of electrons from a crystal surface. SHIZUO MIYAKE, KAZUTAKE KOHRA and MIEKO TAKAGI.

Atomic scattering amplitudes for electron diffraction. JAMES A. IBERS and JEAN A. HOERNI.

X-ray diffraction by a layer structure containing random displacements. W. COCHRAN and E. R. HOWELLS.

A note on deformation stacking faults in hexagonal close-packed lattices. J. W. CHRISTIAN.

The intermediate Phase Zr_2Si. PAUL PIETROKOWSKY.

The crystal structure of rhodium silicide, RhSi. S. GELLER and E. A. WOOD.

The effect on metal-metal bonds of increased concentration of hydrogen in hafnium dihydride. S. S. SIDHU.

Have Hauptman and Karle solved the phase problem? W. COCHRAN and M. M. WOOLFSON.

The statistical approach of Hauptman and Karle to the phase problem. V. VAND and R. PEPINSKY.

A note on the solution of the phase problem. H. HAUPTMAN and J. KARLE.

The structure of colemanite, $CaB_3O_4(OH)_3.H_2O$, determined by the direct method of Hauptman and Karle. C. L. CHRIST, JOAN R. CLARK and H. T. EVANS.

X-ray scattering by lattice defects in neutron-irradiated single crystals of boron carbide. CHARLES W. TUCKER, JR. and PETER SENIO.

The crystal structure of TiU_2. A. G. KNAPTON.

The preparation of a $K\beta$ filter for X-ray crystallography with special reference to cromium radiation. E. KROGH ANDERSEN and C. E. SCHÄFFER.

A boundary effect on the intensity of X-rays reflected from a quartz plate. EINOSUKE FUKUSHIMA.

An analytic method for the determination of shape and location of Fourier peaks. JOSHUA LADELL and J. LAWRENCE KATZ.

Re-examination of the symmetries of iron and nickel by the powder method. F. W. VON BATCHELDER and R. F. RAEUCHLE.

Archiv für das Eisenhüttenwesen

Heft 3/4, März/April 1954

Die elektrochemischen Vorgänge bei der elektrolytischen Isolierung von Gefügebestandteilen der Stähle mit Wechselstrom. WALTER KOCH, ILSE RAMSAUER und MARK V. STACKELBERG.

Die Sauerstoffbestimmung im festen Stahl nach dem Aluminium-Diffusionsverfahren von Gotta. JEAN MASSINON, NORBERT STOLL, und MICHEL URBAIN.

Beitrag zur Prüfung von Beizzusätzen auf ihre Wirksamkeit. HUBERT HOFF und GEORG VON DER DUNK.

Beitrag zur Ermittlung der Einsatzhärtungstiefe bei Einsatzstählen. HERBERT MÜLLER.

Untersuchungen über das Umwandlungsbestreben und die Härtbarkeit von Stählen. ERICH GREULICH.

Eigenspannungen durch Oberflächenhärten mit Flammen. HANS BÜHLER.

Untersuchungen an Prüfkörpern mit bekannten Fehlern zur Kennzeichnung der Arbeitsbedingungen bei der Überschallprüfung. ERICH THEIS und KLAUS BARTELD.

Entmischungserscheinungen in einem Chrom-Nickel-Stahl mit 4,5 o/o Ni. WERNER JELLINGHAUS.

Das Durchbruchspotential passiver Eisen-Chrom-Legierungen in Sulfatlösungen. GEORG MASING, THEO HEUMANN und HEINZ JESPER.

Die Temperaturabhängigkeit der Entkohlung von Stahl durch Wasserstoff. KURT LÜCKE.

Über die Wasserstoffaufnahme austenitischer Stähle bei kathodischer Beladung. FRIEDRICH EISENKOLB und GÜNTER EHRLICH.

Journal of the Chemical Society

July, 1954 (Partial Contents)

Exchange reactions of solid oxides. Part III. Magnesium oxide. G. HOUGHTON and E. R. S. WINTER.

Exchange reactions of solid oxides. Part IV. Zinc oxide. J. A. BARNARD, E. R. S. WINTER, and H. V. A. BRISCOE.

Exchange reactions of solid oxides. Part V. Dissociation of molecular oxygen at oxide surfaces: magnesium oxide and zinc oxide. E. R. S. WINTER.

Journal of the Institute of Metals, Vol. 82

Part 10, June, 1954

Staining of clad aluminium alloy sheets during salt-bath heat-treatment. E. C. WILLIAMS and H. J. G. CHALLIS.

The constitution of gold-molybdenum alloys, with particular reference to the solubility of molybdenum in gold. G. A. GEACH and D. SUMMERS-SMITH.

Metallographic observations on cell formation and development in aluminium. J. W. KELLY and R. C. GIFKINS.

Some observations on the deformation of zinc at high temperatures. R. W. CAHN, (Miss) I. J. BEAR, and R. L. BELL.

Methods for determining the liquidus points of titanium-rich alloys. W. HUME-ROTHERY and D. M. POOLE.

Isothermal transformations of hypo-eutectoid aluminium bronzes. R. HAYNES.

Part 11, July 1954

Metals and Marine Engineering. S. F. DOREY.

Note on the constitution of the titanium-gold system in the region 0-6 atomic per cent gold. (Mrs.) M. K. MCQUILLAN.

Grain-refining additions for cast copper alloys. A. CIBULA.

Exploratory creep tests on metals of high melting point. N. P. ALLEN and W. E. CARRINGTON.

The constitution of the titanium-rich alloys of titanium, iron, and oxygen. N. P. ALLEN, T. H. SCHOFIELD, and (Mrs.) B. MELLISH.

The constitution of the copper-rich copper-zinc-gallium alloys. T. B. MASSALSKI and G. V. RAYNOR.

Revue de Métallurgie, 51e Année

Numéro 4, Avril 1954

Le soudage à l'arc des aciers auto-trempants. H. GRANJON.

Séparation des inclusions d'oxydes dans les aciers et les fontes. S. MISCHONSNIKY, CH. DUBOIS et P. BASTIEN.

L'essai de torsion à chaud appliqué à la fabrication des tubes sans soudure. J. DAUVERGNE, M. PÉLABON et J. IVERNEL.

Caractéristiques des demi-produits obtenus à partir de frittés d'aluminium oxydé. J. HÉRENGUEL et J. BOGHEN.

Etude du carbonitrure de fer hexagonal (type Fe^3N). R. BRIDELLE et A. MICHEL.

Essais de combustion à l'oxygène sur un four Martin chauffé au gaz de fours à coke carburé. G. HUSSON et J. DONNEY.

Numéro 5, Mai, 1954

Titane et alliages de titane. A. SAULNIER et R. SYRE.

Observations sur la marche des hauts fourneaux en aggloméré et minerai lorrain. J. SZCZENIOWSKI et P. THIERRY.

La métallographie du zinc pur à température élevée avec et sans contraintes. P. J. E.—FORSYTH.

Recherches industrielles sur les aciers au bore (Troisième rapport de la Commission d'Etude des Aciers au bore de l'IRSID). G. DELBART et A. KOHN.

INCLUSIONS IN IRON CRYSTALS OBTAINED BY RECRYSTALLIZATION*

T. SMITH†

A description is given of the small iron crystals included in different parts of coarse grained specimens prepared by different methods. Most of the inclusions are exact twins of the larger crystals, but some of the four twin orientations are absent. This can be explained by assuming that the twins originate by faulting on {112} planes as the crystals grow during recrystallization. The distortion in the small number of distorted inclusions which are not twins shows some systematic regularities.

INCLUSIONS DANS DES CRISTAUX DE FER OBTENUS PAR RECRISTALLISATION

On donne une description de petits cristaux de fer inclus dans diverses parties d'échantillons à gros grains, préparés par différentes méthodes. La plupart de ces cristaux sont des macles exactes des grands cristaux, mais certaines de parmi les quatre orientations de maclage sont absentes. Ceci peut être expliqué en admettant que des défauts sur les plans {112} font naître les macles durant la croissance du cristal, lors de la recristallisation. Les distorsions dans un petit nombre d'inclusions, qui ne sont pas des macles, manifestent une certaine régularité systématique.

EINSCHLÜSSE IN DURCH REKRISTALLISATION HERGESTELLTEN EISENKRISTALLEN

Es werden die kleinen Eisenkristalle beschrieben, die in verschiedenen Teilen von grosskörnigen, auf verschiedene Weise hergestellten Proben eingelagert sind. Die meisten dieser Einchlüsse waren Zwillingskristalle der grösseren Körner, jedoch fehlten einige der vier Zwillingsorientierungen. Diese Erscheinung lässt sich erklären, wenn man annimmt, dass die Zwillinge durch Stapelfehler der {112} Ebenen entstehen, wenn die Kristallite während der Rekristallisation wachsen. Die Verzerrungen in den wenigen verzerrten Einschlüssen, die keine Zwillingskristalle waren, zeigten einige systematische Gesetzmässigkeiten.

Introduction

Large crystals of many metals can be produced by annealing fine-grained material which has been appropriately deformed. It is often found that such crystals contain small regions where the lattice has a different orientation from the rest of the crystal. Thus, in face-centred metals like copper the inclusions are often twins of the parent crystal. In aluminium the inclusions are smaller and less numerous, and not always twins. They have been described, and explanations of their origin suggested in recent papers [1; 2]. Some information on the inclusions in body-centred silicon ferrite is also available [3; 4].

Inclusions in iron bear some resemblance to those in both aluminium and silicon ferrite. Four were described as early as 1928 by O'Neill [5] who found them to be twins to the parent within the limits of his experimental method. Lacombe and Berghezan [1] have also reported on them. They found that inclusions in accurate twin orientations were much more perfect than the heavily polygonized inclusions found in approximate twin orientations. It was to supplement this information and to elucidate the origin of the inclusions that this work was carried out.

Preparation of Specimens

Different types of iron and different methods of preparation have been investigated, but the specimens selected for detailed crystallographic examination were prepared as follows. Swedish iron supplied by the British Iron and Steel Research Association (AA) was machined into the form of bars 1/4 in. thick and 5 in. long. The bars were 3/4 in. wide at the ends, and tapered to 3/5 in. at the centre section. They were then annealed in moist hydrogen for 20 hours at 920°C to reduce the carbon content. As the original analysis of the iron showed 0.07 per cent carbon and all other impurities to be less than 0.02 per cent, it is probable that this treatment reduced the carbon content to less than 0.003 per cent [6]. The bars were then stretched in a tensile test machine. With a grain size of 32/mm^2 large crystals were obtained after a reduction of 2½ per cent in the central area, and a final hydrogen anneal for three days at 880°C.

A number of specimens having special characteristics were produced by giving different tapers to the bars and varying the temperature of the final anneal. In one such set each specimen contained a large number of crystals showing a size gradient along the length of the bar instead of a few large

*Received October 1, 1953; in revised form February 3, 1954.

†Department of Natural Philosophy, Marischal College, Aberdeen, Scotland.

crystals. Specimens were also prepared in which a single crystal was grown from material which showed a considerable variation in deformation.

The Distribution of Inclusions

The number of inclusions was counted with a travelling microscope (×25) after the specimen surface had been etched in dilute nitric acid (1:4). In all the crystals examined the most clearly defined difference in numbers was between the surface and the interior of the crystals; the inclusions being much less numerous in the interior. Figure 1 shows the results obtained when the number of exposed inclusions/cm² was counted after one surface of a crystal was ground away. A surface layer containing many inclusions was never found to be more than 0.3 mm thick, which is the order of magnitude of an inclusion diameter, and the figure shows that there is little change in the number of inclusions below this depth. Most of the data in this paper relate to inclusions in the surface layers. Observations on the interior inclusions indicate that they show special crystal features which will be briefly described in the final section.

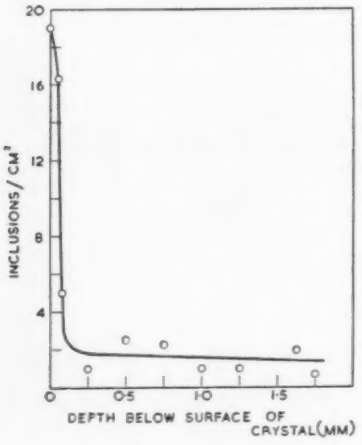

FIGURE 1. Variation of number of inclusions with depth below surface of crystal.

It seemed probable that the most important factors determining the number of inclusions in a surface would be the degree of deformation produced prior to the final anneal, and the purity of the iron. The first point was investigated by examining crystals which had been prepared from non-uniformly deformed metal. Two crystals grown from material covering the range 1–3 per cent extension, and one from material covering the range 3–5 per cent were examined. In none of these was there found to be any significant correlation between the number of inclusions/cm² in the surface layer and the deformation in the original material, and it must be concluded that the surface density of inclusions is independent of the deformation in the range from 1–5 per cent.

The influence of the purity of the iron was not so easily investigated, as different types of iron require different treatments to lead to the formation of large crystals, and it is not usually clear whether a change in the number of inclusions is due to the differing raw materials or to the different treatments. The results we obtained do not yield any general conclusion, but it is perhaps worth recording some observations on an armco iron containing 0.026 per cent carbon and 0.04 per cent nickel and sulphur. It was found that a treatment, similar to the standard method described, sometimes yielded large crystals. These were always found to be much freer from inclusions than those prepared from Swedish iron, and it is possible that this was due to the different purity of the raw material.

A final rather unexpected feature of the inclusion density was observed. It was found that the density in the surface layer of a coarse-grained specimen varied with the average crystal size in that region. The range of crystal sizes was obtained after recrystallisation as a result of the varying deformation along a strongly tapered bar. Data obtained from two bars are shown on Figure 2. It will be seen that there is an increase in the density of inclusions with the diameter of the including crystal.

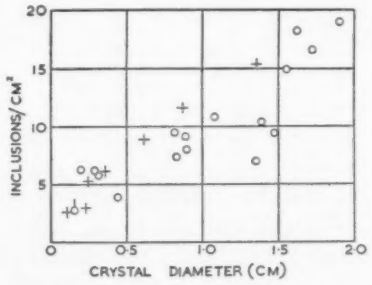

FIGURE 2. Variation of number of inclusions/cm² with crystal size for two specimens.

If the inclusions were scattered randomly over the surface area, there is a danger that the inclusion densities as measured might be underestimates, as those inclusions within a distance of $D/2$ from a crystal boundary, where D is the average diameter of an inclusion, might not have been recognized as

inclusions. The maximum error which could occur in this way can be obtained if the size distribution of the inclusions is known. Figure 3 gives this for the inclusions in a number of large crystals. When this information is used, the error obtained for a small crystal is represented by the vertical line on Figure 2. For larger crystals the maximum error becomes negligible.

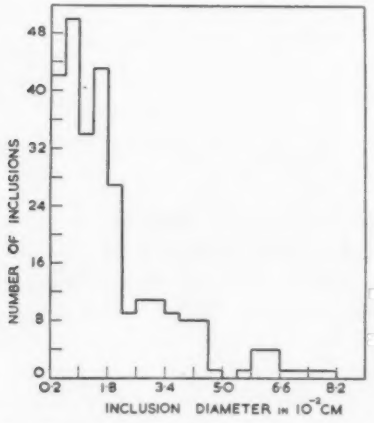

FIGURE 3. Size distribution of inclusions. The 'diameter' is the mean of the average of the greatest and least length of the inclusion in the surface layer.

The Crystallography of the Surface Inclusions

Observations with a simple goniometer showed that in each of the four crystals selected for detailed examination, most of the inclusions could be assigned to one or two groups, the inclusions within each group having the same orientation, whilst a smaller number appeared to have random orientations. Thus on one surface of crystal A, 38 inclusions fell into one group, 27 into another and 5 appeared to have a random orientation. On the other side of the crystal only one uniform group containing 37 inclusions, together with 9 random inclusions, were found. The corresponding figures for the other three crystals are shown in Table I.

TABLE I

Crystal		No. of inclusions in each uniform group		No. of random inclusions
A	Top surface	38	27	5
	Lower surface	36	0	9
B		45	0	12
C		35	30	7
D		27	26	6

Twin Inclusions

The X-ray determination of the inclusion orientation was carried out by the back-reflection Laue method. The cone angle of the X-ray beam was 5×10^{-4} radians so that with a collimator-crystal distance of 3 cm a circular patch on the crystal 0.08 cm in diameter was irradiated. When a crystal was adjusted so that one of the smaller inclusions fell within this area, two sets of diffraction spots were recorded on the film, one set due to the inclusion and the other to the parent crystal. The latter spots contained small clear areas corresponding in outline to the shape of the inclusions (Figure 4).

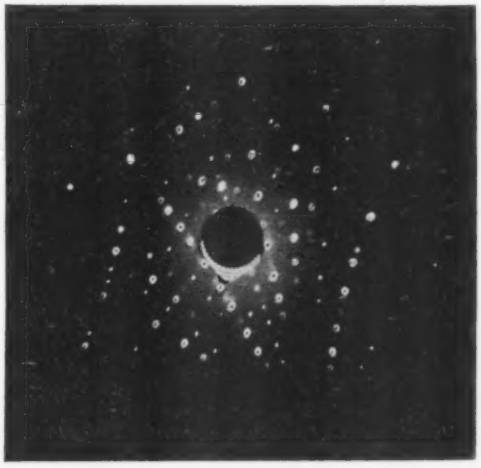

FIGURE 4. Retouched back-reflection Laue photograph showing diffraction spots from the inclusion and larger spots containing clear areas produced by parent crystal.

It was readily seen from the disposition of the diffraction spots given by inclusions originally classified in one of the uniform groups, that these inclusion lattices were related to the parent lattice in the way characteristic of twinning in a {112} plane, each group corresponding to one of the four twin possibilities. The direction of the {112} planes for crystal A are shown in Figure 5.

The observation that in each crystal no inclusions are found with more than two of the four equivalent twin orientations will be discussed in the section on the origin of the inclusions.

The exactness of the twinning relationship could most readily be obtained from an examination of certain of the diffraction spots which are produced partly by diffraction from the inclusion, and partly from the parent lattice. A feature of a twinned pair is that some planes in one crystal are parallel to planes of a similar or differing index in the other

component. Thus some {110} planes of the twin will be parallel to some {110} planes of the parent, and some {100} planes of the twin to some {122} planes in the crystal. Diffraction from {100} planes in the twin can thus fill in the clear area which would otherwise be left in the spot produced by reflection from {122} planes in the parent. Any departure from an exact twin relationship will show itself as a displacement of the two components in these composite spots.

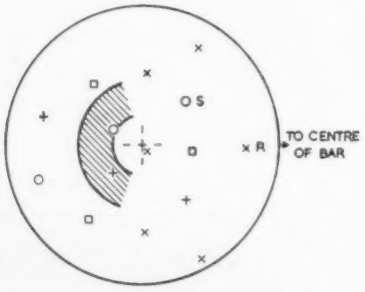

FIGURE 5. Stereogram showing orientation, relative to crystal surface, of crystal A and the twin inclusions in one of the surface layers. Shaded region corresponds to the growing crystal profile near the specimen surface. □ cube poles of crystal. ○ {112} crystal poles corresponding to twinning planes of first twin group. + {112} crystal poles corresponding to twinning planes of second twin group. × other (112) poles.

It was found in this way that the twin relationship held very exactly. In no case was there found to be a departure of more than 6′ from a strict twin relationship, and of the 42 twins examined 31 had a departure of less than 2′.

The Laue spots from neither parent nor twin showed any evidence of distortion, but considerable deformation may be present with little asterism appearing in the diffraction spots. Under favourable conditions additional information on the relative perfection of two metal crystals can be derived from observations on boundary changes taking place on prolonged annealing; so four of the twin inclusions were photographed and the crystal containing them was annealed at 880°C for three days. When the new shape of the inclusion was recorded it was found that the exposed surface of each of the inclusions had increased in area. The maximum boundary movement was 0.05 mm. As the boundary movements were regular they do not seem to be the result of adjustments to the changes produced on the specimen surface by the etching which followed the final anneal. This suggests that the driving force due to difference in perfection between the parent and inclusion is small. The deformed inclusions discussed below were rapidly absorbed under the same conditions.

Figure 6 gives a tracing of micrographs of one of the twin inclusions before and after annealing. The straight side AB is parallel to the line in which one of the {112} twin planes intersects the surface, and so along these sections the mean boundary would

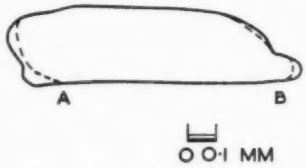

FIGURE 6. The outline of a twin inclusion: before annealing; after annealing.

appear to be nearly coherent. No change was observed in these boundaries after heating. This is similar to the immobility of coherent boundaries which has been observed in other metals, though movement of a coherent boundary is possible in iron under some conditions [7]. Along the rest of the boundary the movement was found to increase with the angle between the lines in which the boundary and the nearest {112} plane cut the surface.

Distorted Inclusions

The photographs obtained from the inclusions, which had been classified as random, were all considerably distorted. Back-reflection photographs provide a suitable method of studying such material, as in the transmission method the shape of the diffraction spots is not so completely determined by the distortion of the material. Thus a uniform distribution of the normal to a plane within a cone will lead to an approximately circular diffraction spot in the back-reflection method, but may give a radially elongated streak on a transmission photograph.

As the spots were smeared out over a considerable area, long exposures of the order of 36 hours at 20 ma and 40-kV tube voltage were required to give an adequate density. This restricted to ten the number of inclusions whose orientation was found, but shorter exposures showed that other random inclusions were similarly distorted. The positions of the cube poles of the inclusions referred to their respective parents is shown in Figure 7. It will be seen that the inclusions lie within 15 degrees of the parents, the average rotation being 8 degrees.

In view of the deformed nature of these inclusions, it is tempting to regard them simply as remnants of the original metal which have not been

absorbed by the growing grain. Even a simple Burgers boundary with a difference in tilt of the order of 8 degrees between the two crystals is far from mobile [8], and a boundary made up of more than one Burgers vector will be much less so even if it separates regions differing in perfection [9]. However, if this is the whole explanation of the history of these inclusions, certain features of the photographs are unexpected. Although the normals to a given set of planes fall within a cone of semivertical angle 2 degrees, the distribution within the cone is far from uniform. In about half the photographs the spots took the form of a small area of considerable density with a long 'tail' (Figure 8). This effect would be obtained if some of the diffracting fragments were arranged on a cylindrical surface. A stereographic plot of the normal distribution corresponding to the 'tails,' together with the poles of the parent crystals, showed that the axes of the cylinders corresponded to the axes about which the inclusions would have to be rotated to bring them into register with the parents.

FIGURE 7. Stereogram showing the mean orientation of distorted inclusions. □ Cube poles of crystals. ○ Cube poles of inclusions.

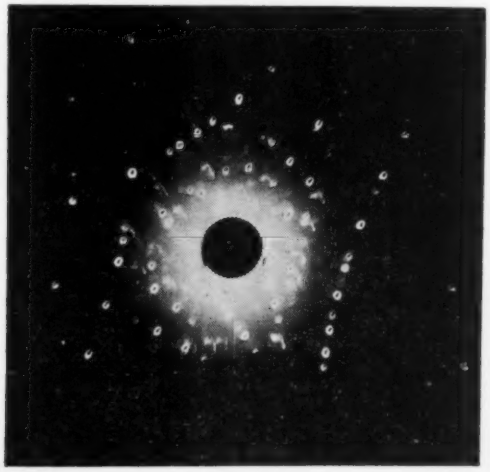

FIGURE 8. Retouched back reflection Laue photograph from distorted inclusion showing 'tailed' spots. Diffraction spots from the parent crystal are also visible.

From one of the inclusions showing a tail, a photograph was obtained when only one edge of the inclusion was irradiated. The tails were no longer recorded, although the rest of the spots appeared unchanged. So it seems that the material giving rise to the tail is concentrated in some small region within the inclusions rather than dispersed through the whole volume.

It is not possible to offer any explanation of the origin of this feature, as there seems to be no reason why this particular type of region should not be absorbed by the growing crystal.

Comparison with Inclusions in Aluminium and Silicon Ferrite

Twins giving rise to sharp spots occur in aluminium as in iron [10; 1]. It is not clear whether all four twin possibilities are observed, nor how numerous the twins are. Most of the other inclusions give rise to asterism and occur over a large range of orientations relative to the parent crystals. Examples within a few degrees of all four twin orientations are recorded [11], also many having apparently random orientations. It may be that a few of these random inclusions, having a greater than average size, do not give rise to asterism [2].

From the above results it will be seen that in iron the orientation of the inclusions can be described more simply than in aluminium. About 90 per cent of the inclusions correspond to a few of the twin possibilities, and are of comparable perfection to the parent crystal. The remainder show asterism and are grouped rather tightly at an average rotation of 8 degrees from the parent lattice. No examples of polygonized inclusions in approximate twin orientations, or of undeformed non-twins, were found. On the other hand the inclusions are more varied than those in silicon ferrite where only twin inclusions occur.

The Origin of the Twin Inclusions

The possible origin of the twins will be discussed with special reference to the absence of certain twin possibilities. As the iron showed no preferred orientation before treatment when examined by the usual X-ray transmission method, an explanation in terms of the different rates of growth of the twins is not applicable, although this may be an

important factor when strongly textured material is recrystallized [4; 12]. However, an explanation of the twin occurrence can be obtained from a consideration of the orientation of the advancing crystal boundary.

In a body-centred cubic crystal the {112} planes form a congruence of modulus 6 [13]. If, as the crystal grows into the matrix, the atoms go down in positions which do not satisfy close-packing requirements, a faulted layer results. If the normal sequence is represented by 123456123 . . . . , the most probable fault will be represented by 1234565, as this arrangement deviates least from nearest neighbour requirements. Subsequent layers will then go down in the order 12345654321, giving a new lattice mirroring the old across the {112} plane. The same relationship between the two structures can be described as a reflection across two other {112} planes, on both of which faulting would lead to the same structure. It can also be described as a reflection across one of the {111} planes, but a twin is much less likely to result from simple faulting on this plane due to the greater departure from nearest neighbour requirements.

If faulting of this type is the source of the twins obtained in the recrystallization of iron, inclusions will form when the surface of the crystal growing into the deformed matrix exposes a {112} face over some limited region, and the local disposition of atoms in the matrix or in the growing crystal is favourable to faulting.

The local arrangement of atoms may be a fragment of distorted lattice or a set of grain boundaries. In the latter case it is possible to consider the formation of the inclusions in terms of the boundary-free energies, as has been done by Fullman [14] for face-centred metals. A corner near the surface of the growing crystal A may be considered where it meets the junction of three matrix grains B, C and D (a section through A, B and C is shown in Figure 9*a*). The form of A may be taken as a pyramid. If the surface energy between A and B, A and C, and A and D is large, the crystal moving in the direction of the arrows may recrystallize as A', the twin of A, so that the boundaries will be as shown in Figure 9*b* at a later time. This type of twin formation in the corner of growing crystals has been observed in face centred metals [15; 16]. The conditions under which a twin may form is given by

$$(1)\quad S_{A'B}\,\sigma_{A'B} + S_{A'C}\,\sigma_{A'C} + S_{A'D}\,\sigma_{A'D} + S_{A'A}\sigma_{A'A} < S_{A'B}\,\sigma_{AB} + S_{A'C}\,\sigma_{AC} + S_{A'D}\,\sigma_{AD}$$

where S and σ represent the areas and energies/unit area of the boundaries. Near the outside of the specimen the growing crystal will meet at a point with two grains and the corresponding condition for the formation of twins will be

$$(2)\quad S_{A'B}\,\sigma_{A'B} + S_{A'\,C}\,\sigma_{A'C} + S_{A'A}\,\sigma_{A'A} + S'_{A'}\sigma'_{A'} < S_{A'B}\,\sigma_{AB} + S_{A'C}\,\sigma_{AC} + S'_{A'}\sigma'_{A}$$

where $S'_{A'}$ is the exterior surface area of the twin, and $\sigma'_{A'}$ and σ'_{A} the exterior surface free energies of A' and A. In both these equations the dependence of the surface energy of the boundary on the orientation of the boundary is ignored.

Once again a connection will exist between the abundance of the different twins and the growing surface of the crystal, for those twins having a twin plane with least area in the corner of the growing grain will be particularly favoured. This will usually be the {112} plane most nearly at right angles to the direction in which the mean crystal surface is moving. However, in the case of twin formation near the surface it would be possible to have a process of twin selection which was related, not to the growing surface of the crystal, but to its exterior surface. This would be the case if the surface energy terms played a predominant role in equation (2). The consideration of this special case of faulting in a grain corner is valuable in showing that under some conditions the occurrence of a large coherent twin boundary does not necessarily imply that faulting took place simultaneously over the whole of that area.

In metals having very low coherent boundary energies, the conditions for faulting in a grain corner may be often fulfilled. The requirements for the higher-energy twin boundaries in iron will be satisfied much less frequently, and faulting will only take place under particularly favourable conditions, as when one of the deformed matrix grains with which the crystal comes into contact is nearly a twin of the growing crystal. As this will be a comparatively rare occurrence, it is possible

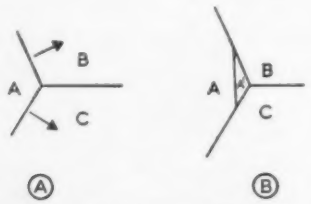

FIGURE 9. (*a*) Section through a crystal A growing into two matrix grains B, C and D. (*b*) Subsequent configuration after formation of twin A'.

that an equally important occasion of faulting will be the presence of a much smaller distorted fragment within a matrix grain. It is significant, however, that there is no increase in the number of twins with deformation.

Although the frequency with which different types of arrangement in the matrix lead to faulting is not known, it was possible to test the connection between the occurrence of the twin groups and the orientation of the exterior and interior surface of the crystal. It was easily seen that the exterior surface free energy was not the deciding factor, for in two surface layers it was found that of two twin orientations which would have had about the same surface energy, one often occurred while the other was not observed at all.

The surface of the growing crystal was more difficult to describe, for it will be subject to considerable local variation; but with the bar shape used, the mean boundary position can be roughly specified. All the crystals examined were of the same form in relation to the bar, extending from near the middle to within a few cm. from the end. By removing two of the bars from the furnace during annealing, it was clear that these crystals nucleated in the central region of greatest deformation, and after an initial period the surface advancing along the bar did not vary from the plane of cross section by more than 20 degrees.

It was noticed that those inclusions found well away from the outside of the crystal belonged to the twin groups which had a {112} plane nearest to the cross section. Thus when crystal *A* was sectioned, four of the five interior inclusions which were exposed belonged to the twin group for which *R* (Figure 5) would be a possible faulting plane. But when the stereograms of the surface inclusions were examined, it was found that some {112} planes which were approximately parallel to the cross section had no corresponding twin (c.f., pole *R* in Figure 5), and twins occurred when none of their possible {112} planes were of this type. It was observed, however, that whenever a {112} pole was found in the shaded area indicated in Figure 5—that is between 25 and 50 degrees from the centre of the stereogram, and in that half of the stereogram away from the centre of the bar—the corresponding twin always occurred in the surface layer, and not otherwise. The probability against this correspondence being due to chance is not high, but it was thought that the results might indicate that the mean lengthwise profile of the crystal surface during growth might be as shown in Figure 10. Then the {112} faces falling within this region on the stereogram would be the ones most nearly parallel to the growing crystal surface.

The profile also accounts satisfactorily for the occurrence of different groups of twins on different free surfaces. Thus on the other side of crystal *A* only one group of twins was found (Table I).

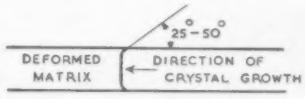

FIGURE 10. Suggested profile for growing crystal.

This is to be expected, as *S* (Figure 5) is the only pole which would occur in the shaded area corresponding to this side.

Further evidence for the close connection between the occurrence of the twins and the position of the growing surface was obtained by sectioning four of the larger inclusions found in crystal *A*. Each time it was found that there was a {112} composition plane corresponding to the pole in the shaded region, while most of the rest of the bounding surface appeared to be incoherent. A more complete investigation of the shape of the inclusion should throw light on the type of matrix accident which is usually responsible for the faulting.

Although this interpretation gives an account of some of the features of the inclusions which have been investigated in the present work, twins may sometimes originate in other ways. Grain formation by normal nucleation and subsequent failure to be absorbed, owing to a chance twin orientation, is considered to be improbable, as about the same number of inclusions would be expected to be in the exact twin orientation as in any other orientation a few degrees away, and the small increase in boundary energy between the non-coherent twin and the other inclusion would not lead to the frequent occurrence of the one, and the complete absence of the other. It also seems unlikely that the stresses which may be set up in the surface layer as a result of the recrystallization process will cause the formation of deformation twins at such a high temperature. If such twins did form, they would normally be bounded by two parallel {112} faces. In fact, the boundaries of the twin inclusions are found to be more complicated. A few do approximate to this form (Figure 6), but most of them either show one {112} plane or appear to be irregular.

A more probable special mechanism which would yield exact twins, and which differs from growth faulting, is as follows. If the growing surface of the

crystal encounters a dislocated fragment in a twin position, many of the dislocations will escape from the fragment which may then itself begin to grow into the matrix. This has been called *stimulation* [17] and has been suggested as the origin of the twins in aluminium [1; 10]. The dislocations can escape because both {112} and {110} slip planes in the fragment will lie parallel to corresponding slip planes in the growing crystal and so dislocations which were originally trapped by both the stress field of the boundary wall and by the force due to the termination of the slip planes at the fragment boundary are now acted upon only by a much reduced force due to the boundary. As the size of the stimulated fragment decreases, the mechanism becomes very similar to the mechanism which has been proposed. With a large fragment the two processes are distinct, as in stimulation there will be no necessary connection between the surface of the growing crystal and the particular twins which will occur, and the orientation of the inclusions will be determined by the orientation of the fragment rather than by the exact twin relationship. The dislocation will be able to escape most easily when the boundary is a {112} plane and may only take place under these conditions. If this is the case, faulting will be the predominating mechanism as the chances of meeting a fragment many atoms thick will be much less than finding a smaller disposition of atoms favourable to faulting.

Acknowledgement

The author wishes to express his thanks to Professor R. V. Jones, Dr. F. C. Frank, and members of this Department for useful discussions.

References

1. Lacombe, P. and Berghezan, A. Metaux et Corrosion **24** (1949) 1.
2. Tiedema, T. J., May, W. and Burgers, W. B. Acta Cryst. **2** (1949) 151.
3. Dunn, C. G. Trans. A.I.M.E. **158** (1944) 372.
4. Dunn, C. G., Daniels, F. W., and Bolton, H. J. J. Metals **188** (1950) 368.
5. O'Neill, H. J. Iron Steel Inst. **117** (1928) 689.
6. Holden, A. N. and Hollomon, J. H. Trans. A.I.M.M.E. **185** (1949) 179.
7. Garber, R. I., Gindin, M. G., Konstantinovskj and Starcev, Dokb. Akad. Nauk S.S.S.R. **74** (1950) 343.
8. Lomer, W. M. and Nye, J. F. Proc. Roy. Soc. **A212** (1952) 576.
9. Beck, P. A., Sperry, P. R. and Hu, H. J. Appl. Phys. **21** (1950) 420.
10. Lacombe, P. and Berghezan, A. Comptes Rendus **228** (1948) 93.
11. May, W., Tiedema, T. J., and Burgers, W. G. Nature **162** (1948) 741.
12. Burgers, W. G., Meijs, J. C., and Tiedema, T. J. Acta. Meta. **1** (1953) 75.
13. Cottrell, A. H. and Bilby, B. A. Phil. Mag. **42** (1951) 573.
14. Fullman, R. L. J. Appl. Phys. **21** (1950) 1069.
15. Burke, J. E. Trans. A.I.M.E. **188** (1950) 1324.
16. Fullman, R. L. and Fisher, J. C. J. Appl. Phys. **22** (1951) 1350.
17. Burgers, W. G. and May, W. Rec. des Trav. Chin. des Pays-Bas **64** (1945) 5.

THE PLASTIC DEFORMATION OF A CRYSTAL IN A POLYCRYSTALLINE AGGREGATE*

W. BOAS and G. J. OGILVIE†

Microscopic evidence is given that during plastic deformation of a polycrystalline aggregate the crystals both at the surface and in the interior are deformed inhomogeneously. In addition, it is found that slip is not always confined to {111} planes but may also occur on {100} or {110} planes. The relation between these results and the current theories of the distortion of polycrystalline aggregates is discussed.

LA DÉFORMATION PLASTIQUE D'UN CRISTAL DANS UN AGRÉGAT POLYCRISTALLIN

On présente des résultats de recherches microscopiques, montrant que lors de la déformation plastique d'un agrégat polycristallin, les cristaux sont déformés d'une façon non-homogène, aussi bien à la surface qu'à l'intérieur. On a constaté, en plus, que le glissement n'est pas toujours limité aux plans {111}, mais peut aussi avoir lieu sur les plans {100} ou {110}. La relation entre ces résultats et les théories courantes de la distorsion des agrégats polycristallins est discutée.

DIE PLASTISCHE VERFORMUNG EINES KRISTALLS IN EINEM POLYKRISTALLINEN AGGREGAT

Es wird auf Grund von mikroskopischen Beobachtungen gezeigt, dass im Laufe der plastischen Verformung eines polykristallinen Aggregates sowohl die Kristalle an der Oberfläche als auch die Kristalle im Innern inhomogen verformt werden. Ausserdem zeigte es sich, dass der Gleitvorgang nicht immer auf {111} Ebenen beschränkt ist, sondern auch auf {100} und {110} Ebenen erfolgen kann. Die Beziehung zwischen diesen Resultaten und den gegenwärtigen Theorien der Verformung polykristalliner Aggregate wird diskutiert.

I. Introduction

In a complete calculation of the plastic properties of polycrystalline aggregates from the behaviour of the crystals composing the aggregate the interaction between the crystals must be taken into account. The effect of this interaction is observed as inhomogeneous deformation of the individual crystals, even though the macroscopic deformation is homogeneous. This inhomogeneity in single-phase cubic metals and alloys is due to the anisotropic mode of deformation of the crystals and the varying constraints at their boundaries. In addition, the presence of a second phase and the type of deformation imposed on the aggregate may be equally important influences on the final behaviour.

The various sources of inhomogeneity have been studied extensively in recent years [1–6], and their importance in the behaviour of polycrystalline aggregates has been discussed [7–10]. The experimental work on pure metals has been confined exclusively to observations on crystals exposed at the surface of test specimens, and only in two-phase alloys have crystals in the interior of the specimen been investigated. The behaviour of surface crystals is not necessarily representative of the behaviour of crystals entirely surrounded by others, and the conclusions drawn from the observations on them are therefore not necessarily valid in the general case. For this reason evidence is presented in this paper to show that the deformation of crystals entirely surrounded by others is inhomogeneous in single-phase alloys. In addition, evidence is presented to show that non-octahedral slip can occur in α-brass and pure aluminium.

II. Method

The materials used were annealed high purity aluminium and α-brass strip. The average linear grain sizes were approximately 2 mm and 0.5 mm respectively. The aluminium specimens were polished electrolytically in a perchloric acid-acetic anhydride bath [11], strained 10 per cent in a tensile test and the deformed surfaces examined microscopically. The α-brass specimens were electrolytically polished in orthophosphoric acid [12] and strained 10 per cent in a tensile test. After a preliminary examination they were repolished until the new surface lay at approximately the centre of the strained test piece (approx. 4 mm thick). Traces of the slip planes were developed in the surface by the use of McLean's [13] or Jacquet's solutions [14].

III. Observations

The observations are of two types:

(*a*) structures observed at the surface of a deformed specimen,

*Received February 26, 1954.

†Division of Tribophysics, Commonwealth Scientific and Industrial Research Organization, University of Melbourne, Australia.

(*b*) structures observed after removal of the surface.

(*a*) In pure aluminium specimens extended 10 per cent, the prevailing slip system in a given crystal changes with position on its surface. This common effect (see Figure 1) is probably due to the differing constraints imposed on a crystal by its neighbours. In addition, inhomogeneous deformation in one crystal can be the direct cause of inhomogeneity in an adjacent crystal. An example of this behaviour is given in Figure 2. In one crystal, a zone of heavy shear, shown by the high concentration of slip lines, has been propagated across a grain boundary into an adjacent crystal where a different slip system to that generally prevailing has been forced to operate. This type of interaction between adjacent crystals may be observed even to the limiting case where a single slip line is propagated across a boundary initiating another slip in the adjacent crystal. An example of this effect, which has been made the subject of a separate study [15], is provided by Figure 3.

It is usual for a given crystal to have two or three different sets of slip lines on its surface. However, occasionally greater numbers may be observed. Figure 4 shows a crystal of pure aluminium in which five independent sets of slip lines appear. This effect has also been observed in α-brass specimens where a maximum of six independent sets of slip lines has been seen. Since slip on {111} planes can account for a maximum of four sets of slip lines in any one crystal, other slip planes must operate in these cases. An analysis of the slip planes on about 200 crystals has been made using measurements on the slip lines. In five crystals it was definitely established that non-octahedral slip had occurred and that {100} or {110} planes can operate as slip planes.

(*b*) Examination of the specimens which had been electropolished to half their thickness prior to etching showed similar phenomena to those described above. For example, the crystal depicted in Figure 5 has different slip systems operating in different parts of it and is directly comparable to the crystal shown in Figure 1.

A most convincing demonstration of the marked inhomogeneity of deformation that can occur is provided by the appearance of the boundaries of annealing twins in the polished surface. Examples are shown in Figures 6 and 7. The once-straight parallel boundaries are severely distorted due to the markedly different deformations that have occurred in the different parts of the crystal enclosing the twin.

IV. Discussion

Two important observations have been made in the course of this study; strong evidence has been found in support of the idea that crystals entirely surrounded by others in a metal specimen are deformed inhomogeneously, and examples have been found to demonstrate that slip in face-centred cubic metals is not necessarily confined to the {111} planes. These facts are of importance in relation to a theory developed by G. I. Taylor [16], of the plastic deformation of a face-centred cubic metal in which a deformation texture is predicted. Barrett and Levenson [17] tested Taylor's predictions experimentally and showed that at least one third of the grains do not rotate as predicted. The cause, they consider, is due to the neglect of the inhomogeneity of deformation in the calculation. The present study, in addition to confirming this idea, shows another possible cause for the unpredicted rotations. The theory assumes slip to occur only on {111} planes and therefore slip on other planes must result in deviations from the theory.

On the other hand, the stress-strain curve calculated by Taylor agrees very well with the experimental curve. This fact shows that the inhomogeneity of deformation of the crystals in an aggregate has little effect on the stress required to deform a specimen. It therefore justifies the main assumption made by Bishop and Hill [18] in their theory of the plastic distortion of a polycrystalline aggregate, i.e., "that the grains are distributed in the unit cube in such a way that there is no correlation between any component of the microscopic stress and any component of the displacement over any plane section of unit area."

References

1. Hibbard, W. R. Trans. A.I.M.E. **180** (1949) 52.
2. Collins, June and Honeycombe, R. W. K. J.C.S.I.R. **21** (1948) 59.
3. Boas, W. and Hargreaves, M. E. Proc. Roy. Soc. **A193** (1948) 89.
4. Honeycombe, R. W. K. and Boas, W. Austr. J. Sci. Res. **A1** (1948) 70.
5. Clarebrough, L. M. Austr. J. Sci. Res. **A3** (1950) 72.
6. Clarebrough, L. M. and Perger, G. R. Austr. J. Sci. Res. **A5** (1952) 114.
7. Boas, W. Proc. 7th Int. Congr. Appl. Mech. **1** (1948) 356.

1

2

3

4

PLATE I (all photographs are reduced to seven eighths). Electropolished pure aluminium extended 10 per cent. FIGURE 1—Different systems of slip lines in various places on a crystal's surface. 75×. FIGURE 2.—Deformation in one crystal passing across the boundary into an adjacent crystal. 75×. FIGURE 3—Slip lines passing from one crystal into an adjacent crystal 150×. FIGURE 4—Five sets of slip lines in the one crystal. 75×. (Note that two sets intersect at an angle of about 7 degrees.)

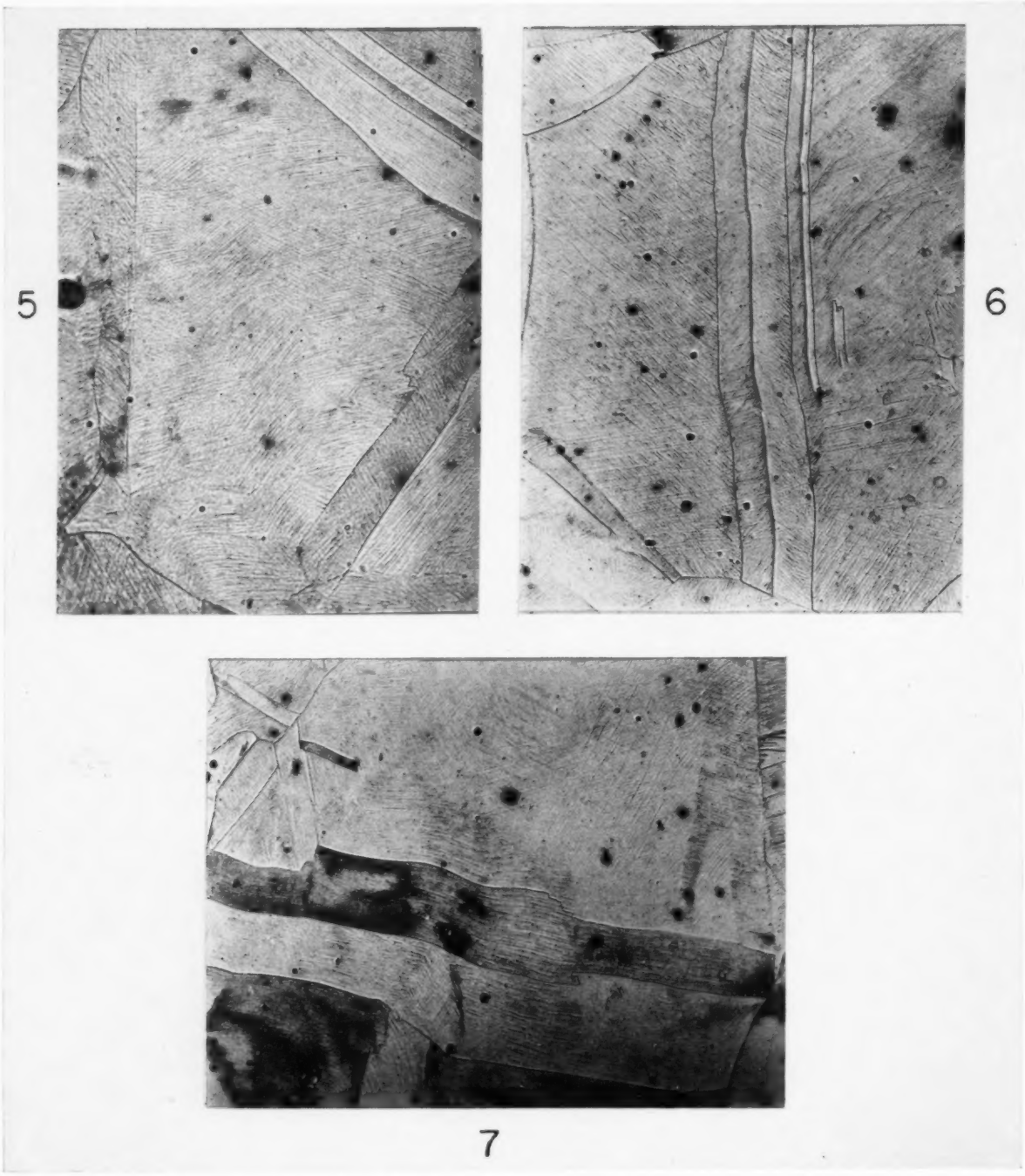

PLATE II (all photographs are reduced to seven eighths). α-brass extended 10 per cent and electropolished until the new surface lay at the centre of the original specimen and etched in McLean's reagent. FIGURE 5—Different systems of slip lines in various places on a crystal's surface. 100×. FIGURE 6—Annealing twins bent by subsequent deformation of the specimen. 100×. FIGURE 7—Annealing twin distorted in a complex fashion by the subsequent deformation. 100×.

8. BOAS, W. Helv. Phys. Acta **23** (1950) 159.
9. CHALMERS, B. Symposium on the Plastic Deformation of Crystalline Solids, Mellon Institute, Pittsburgh (1950) p. 193.
10. COTTRELL, A. H. Dislocations and Plastic Flow in Crystals (Oxford University Press, 1953) pp. 116–24.
11. LACOMBE, P. and BEAUJARD, L. J. Inst. Metals **47** (1947) 1.
12. JACQUET, P. A. Rev. Met. **42** (1945) 133.
13. MCLEAN, D. J. Inst. Metals **74** (1948) 95.
14. JACQUET, P. A. Compt. Rend. **228** (1949) 1027.
15. OGILVIE, G. J. J. Inst. Metals **81** (1953) 491.
16. TAYLOR, G. I. J. Inst. Metals **62** (1938) 307.
17. BARRETT, C. S. and LEVENSON, L. H. Trans. Amer. Inst. Min. Met. Eng. **137** (1940) 112.
18. BISHOP, J. F. W. and HILL, R. Phil. Mag. **42** (1951) 414; **42** (1951) 1298.

ON SELF-DIFFUSION IN CUBIC METALS*

F. S. BUFFINGTON† and MORRIS COHEN‡

Based on the vacancy mechanism of diffusion, a method is given for correlating the frequency factors and activation energies of self-diffusion in cubic metals. The activation energy is shown to be proportional to an appropriate elastic constant and the cube of the lattice parameter, both referred to 0°K. Reasonable agreement is found among the more recent self-diffusion determinations, with the proportionality constant being 0.0514 for face-centered cubic metals and 0.0695 for body-centered cubic metals. The theory also yields values for the fraction (λ) of the activation energy that goes into lattice straining during the elementary diffusion act. For face-centered cubic metals, λ is 0.64. For body-center cubic metals, λ cannot be calculated with any assurance because of inadequate data, but a tentative value is 0.84. These quantities, together with the above proportionality constants, permit the calculation of the self-diffusion coefficients as a function of temperature in cubic metals.

SUR L'AUTODIFFUSION DANS LES MÉTAUX CUBIQUES

On présente une méthode basée sur le mécanisme de diffusion par les lacunes réticulaires, permettant de relier les facteurs de fréquence et les énergies d'activation pour l'autodiffusion dans les métaux cubiques. On montre que l'énergie d'activation est proportionnelle à une constante élastique, appropriée, et au cube du paramètre du réseau, les deux étant rapportés à 0°K. Un accord raisonnable est trouvé parmi les déterminations récentes concernant l'autodiffusion, avec des constantes de proportionnalité suivantes: 0,0514 pour les métaux cubiques à faces centrées et 0,0695 pour les métaux cubiques centrés. Cette théorie donne aussi des valeurs de la fonction (λ) de l'énergie d'activation, qui est utilisée pour la déformation du réseau lors du processus élémentaire de diffusion. λ est égal à 0,64 pour les métaux cubiques à faces centrées, λ ne peut pas être calculé avec exactitude pour les métaux cubiques centrés à cause du manque de données précises, mais la valeur de 0,84 est proposée. Connaissant ces quantités et les constantes de proportionnalité, données ci-dessus, il est possible de calculer les coefficients d'autodiffusion dans les métaux cubiques, en fonction de la température.

DIE SELBSTDIFFUSION VON KUBISCHEN METALLEN

Es wird über ein auf dem Leerstellenmechanismus beruhendes Verfahren, mit dessen Hilfe die Frequenzfaktoren und die Aktivierungsenergien der Selbstdiffusion in kubischen Metallen in Beziehung gesetzt werden kann, berichtet. Es wird gezeigt, dass die Aktivierungsenergie einer entsprechenden Elastizitätskonstanten und der dritten Potenz der Gitterkonstanten (beides auf 0°K bezogen) proportional ist. Es wird zufriedenstellende Übereinstimmung innerhalb der neueren Bestimmungen der Selbstdiffusion gefunden, wobei der Proportionalitätsfaktor für kubisch-flächenzentrierte Metalle 0,0514 und für kubisch-raumzentrierte Metalle 0,0695 ist. Aus der Theorie lassen sich auch Werte für den Anteil (λ) der Aktivierungsenergie, der zur Verzerrung des Gitters während des elementaren Diffusionsvorgangs verwandt wird, angeben. λ beträgt für kubisch-flächenzentrierte Metalle 0,64. Wegen der unzureichenden experimentellen Daten kann λ für kubisch-raumzentrierte Metalle nicht mit Sicherheit berechnet werden; ein vorläufiger Wert beträgt 0,84. Diese Werte ermöglichen, zusammen mit den oben erwähnten Proportionalitätskonstanten, die Selbstdiffusionskoeffizienten in kubischen Metallen als Funktion der Temperatur zu berechnen.

Introduction

A somewhat different version of this paper had been submitted to Acta Metallurgica and was being reviewed when LeClaire's article on the theory of D_0 was published [1]. The two papers had several points of similarity but differed appreciably in emphasis on individual topics. Revision of the authors' paper was considered desirable so that LeClaire's contribution could be recognized and compared with the present treatment.

Both LeClaire's paper and the present one stem from Zener's [2] derivation of a relationship between the frequency factor, D_0, and the activation energy, Q_M, for self-diffusion in cubic systems. The Zener analysis was based upon general thermodynamic principles without depending upon the details of the process. In the present paper, the details of the self-diffusion process are considered. This approach has the important advantage of yielding an expression for the activation energy, Q_M, itself. Also, an equation between Q_M and D_0 is obtained, similar to that given by Zener but containing a term omitted in his derivation. The combination of the two relationships results in an equation for the self-diffusion coefficient in systems where the vacancy mechanism is operative. The relationships obtained differ in certain aspects from those given by LeClaire.

Derivation of Basic Equations

Consider an atom on a f.c.c. lattice, say at $(\frac{1}{2}\ 0\ \frac{1}{2})$, with a lattice vacancy existing at a nearest neighbor site, say (001). The elastic work necessary to move this atom to the saddle point in the direction of the vacant lattice site is required. The

*Received July 24, 1953; in revised form February 4, 1954.

†Engineering Division, California Institute of Technology, Pasadena, California.

‡Department of Metallurgy, Massachusetts Institute of Technology, Cambridge, Massachusetts.

atoms at $(\frac{1}{2}\ \frac{1}{2}\ 1)$, $(0\ \frac{1}{2}\ \frac{1}{2})$, $(0-\frac{1}{2}\ \frac{1}{2})$ and $(\frac{1}{2}-\frac{1}{2}\ 1)$ constitute the barrier to diffusion; that is, the saddle point of energy exists in the plane through the centers of these four atoms, which must "move" further apart in this plane for diffusion to occur. The resultant elastic strains are in $\langle 211 \rangle$ directions.

In b.c.c. systems, atoms at (1 0 0), (0 1 0) and (1 1 1) constitute the barrier to an atom diffusing from $(\frac{1}{2}\ \frac{1}{2}\ \frac{1}{2})$ to (1 1 0), for example. The barrier atoms are displaced in $\langle 1\ 1\ 1 \rangle$ directions.

Let F_d denote the force in direction d necessary to displace a barrier atom a distance Δx_d. With F_d, associate an area A such that the "stress" involved is $\sigma_d = F_d/A$. The resultant strain, $\epsilon_d = \Delta x_d/x_d$ is in the direction d and there are N barrier atoms involved. Accordingly, the elastic work done per diffusing atom is:

$$\begin{aligned} \Delta G_\epsilon &= N \int_0^{\epsilon_{\max}} \sigma_d A x_d \, d\epsilon_d \\ &= (\text{const.})\, \mu_d a^3 \int_0^{\epsilon_{\max}} f(\epsilon_d)\, d\epsilon_d \\ &= B_d \mu_d a^3 \end{aligned} \tag{1}$$

where a is the lattice parameter. B_d is assumed to be a constant dependent only upon the crystal structure: B_{211} for f.c.c. metals and B_{111} for b.c.c. metals. μ_d is an elastic modulus characteristic of the type and geometric arrangement of the diffusing and barrier atoms. The basic assumption made here is that $\epsilon_{\max}$ is the same in the direction d for the self-diffusion of different species of atoms in a given lattice structure. One further assumption is now introduced; namely that μ_d is directly proportional to the macroscopically measured Young's modulus in the direction d. Thus,

$$\Delta G_\epsilon = C_d E_d a^3 \tag{2}$$

where

$$C_d = B_d \mu_d / E_d.$$

The last assumption may well be questioned, since the interactions with neighboring atoms in the straining process involved in diffusion are different from those involved in measuring a modulus of elasticity. Also, atoms which are nearest neighbors to a vacancy are not quite at centers of symmetry. However, all that is required is that μ_d be directly proportional to E_d, an assumption that is verified by the constancy of K which is introduced later.

LeClaire assumes that $c_{44} + \frac{1}{2}\ (c_{11} - c_{12})$ is the appropriate modulus to use for f.c.c. metals. Values given in his Table III indicate he uses this modulus for b.c.c. metals also.

The subscript d will be omitted henceforth, but it should be remembered that C and E (and later K) refer to a particular crystallographic direction.

The change in entropy, ΔS_ϵ, corresponding to ΔG_ϵ, is

$$\begin{aligned} \Delta S_\epsilon \equiv -\frac{d(\Delta G_\epsilon)}{dT} &= -\frac{d(CEa^3)}{dT} \\ &= CE_0 a_0^3 (\phi - 3\alpha) \end{aligned} \tag{3}$$

where

$$\alpha = \frac{1}{a_0}\left(\frac{da}{dT}\right) \text{ and } \phi = -\frac{1}{E_0}\left(\frac{dE}{dT}\right),$$

the subscript 0 designating values resulting from extrapolation to $T = 0°\text{K}$. Thus,

$$\Delta G_\epsilon \equiv \Delta H_\epsilon - T\Delta S_\epsilon = \Delta H_\epsilon - CE_0 a_0 (\phi - {}_3\alpha)\ T \tag{4}$$

Assuming that the change in enthalpy due to the straining process is insensitive to temperature, then

$$\Delta H_\epsilon \cong (\Delta H_0)_\epsilon = (\Delta G_0)_\epsilon = CE_0 a_0^3 \tag{5}$$

and equation (4) becomes

$$\Delta G_\epsilon = CE_0 a_0^3 - CE_0 a_0^3 (\phi - 3\alpha)\ T. \tag{6}$$

This expression gives the change in free energy accompanying the movement of an atom to the saddle point in diffusing to a vacant nearest neighbor site.

Let $\exp(-\Delta H_v/kT)$ be the probability that there will be a vacant lattice site at a nearest neighbor position, where ΔH_v is the enthalpy change in forming a vacancy. This expression for the probability of a vacancy existing at a nearest neighbor position takes into account the change in configurational entropy due to forming vacancies in the lattice, but neglects the increase in vibrational entropy due to the greater freedom of movement acquired by the neighboring atoms. LeClaire also neglects the latter contribution to the entropy. Let Q_M be the self-diffusion activation energy per mole, and N_0 Avogadro's number. Then the fraction of Q_M that goes into elastic straining of the lattice during self-diffusion is denoted by λ, where

$$\lambda = \frac{(\Delta H_0)_\epsilon}{(\Delta H_0)_\epsilon + \Delta H_v} = \frac{N_0 (\Delta H_0)_\epsilon}{Q_M}. \tag{7}$$

(The quantity λ is the same that appears in Zener's expression for the entropy of diffusion.) Thus,

$$(8) \qquad Q_M = \frac{CN_0}{\lambda} E_0 a_0^3 = KE_0 a_0^3$$

where $K \equiv CN_0/\lambda$. Equation (8) permits the determination of the constant K for f.c.c. metals and for b.c.c. metals from existing values of Q_M for self-diffusion.

Following the treatment used by Zener and LeClaire, the entropy change per mole of diffusing atoms, ΔS, may be written as

$$(9) \qquad \frac{\Delta S}{R} = \ln\left[\frac{D_0}{\gamma \nu a^2}\right] = \frac{\lambda K E_0 a_0^3 (\phi - 3\alpha)}{R}$$

γ = an integer, whose value depends upon the lattice structure and upon the mechanism of self-diffusion. ($\gamma = 1$ for the vacancy mechanism assumed here in f.c.c. and b.c.c. metals); ν = vibrational frequency of the diffusing atom in the direction of diffusion; k = Boltzmann constant.

By combining equations (8) and (9) the following expression is obtained for the self-diffusion coefficient:

$$(10) \qquad D = \nu a^2 \exp\left[\frac{KE_0 a_0^3 \lambda(\phi - 3\alpha)}{R}\right] \exp\left[-\frac{KE_0 a_0^3}{RT}\right].$$

The vacancy mechanism is assumed in equation (10) with λ different for f.c.c. and for b.c.c. lattices. The quantity (KE_0) is taken to be in the $\langle 211 \rangle$ direction for f.c.c. metals and in the $\langle 111 \rangle$ direction for b.c.c. metals.

Determination of K and λ for F.C.C. Metals

Equation (8) was used to determine K_{211} from experimental values of Q_M for silver, lead, copper and gold. E_{211} at room temperature was calculated from the elastic constants of these metals [3], and values of ϕ were then employed to obtain E_{211} at 0°K. It was assumed that ϕ_{211} is equal to $-[dE_a/(E_a)_0 dT]$ where E_a is the Young's modulus for the polycrystalline state. Koster's [4] data for dE_a/dT were adopted, values at the lower temperatures being selected to eliminate the effect of stress relaxation by viscous slip across grain boundaries [5]. The lattice parameters at room temperature were corrected to 0°K by means of the coefficient of thermal expansion.

Table I shows that all the determinations of Q_M for silver, the single determination for lead, and the more recent data for copper and gold are in excellent agreement on K_{211}. However, the values of K_{211} calculated from the first two determinations for copper and from the first two sets of data for gold are not in line with the other K_{211} values designated by asterisks in Table I. As shown below, these earlier self-diffusion data also give λ quantities which are greater than unity.

The average of the K_{211} values indicated by asterisks is 0.0514, in agreement with the value of 0.0515 calculated from the accurate Q_M data for silver alone.

Equation (9) was used to determine the λ for f.c.c. metals. Sutton's [6] data on the elastic moduli of aluminum as a function of temperature indicate that ϕ decreases with decreasing temperature, apparently to zero at 0°K. Since similar values are not available for other f.c.c. metals, ϕ was calculated as discussed previously.

The coefficient of thermal expansion, α, decreases with decreasing temperature to zero at 0°K. Hence, the curves of α versus T of Nix and McNair [7] were employed to ascertain an average value of α for the range from 0°K to the mean diffusion temperature. The temperature dependence of ϕ and α suggests that the frequency factor D_0 is also a function of temperature. However, the temperature dependence of D_0 cannot be found experimentally since ϕ and α are sufficiently constant at the elevated temperatures where self-diffusion rates are measured. Both ϕ and α evidently approach zero at 0°K, and therefore $\Delta S \to 0$ as $T \to 0$°K in accordance with the third law of thermodynamics.

It is difficult to say what value should be adopted for the vibrational frequency, ν, of the diffusing atom in the direction of a nearest neighbor lattice vacancy. Use of the Debye frequency would imply that the potential around a lattice site is independent of whether the site is vacant or occupied. The assumption of half the Debye frequency would imply that the barrier atoms and other neighboring atoms have no influence on ν, and that the lattice vacancy effectively doubles the interatomic spacing in the direction of the vacancy. The correct value of ν is probably between the Debye frequency and half the Debye frequency, but closer to the former. In Table I values are reported as λ_D (calculated from the Debye frequency) and as $\lambda_{D/2}$ (calculated from half the Debye frequency). Fortunately, λ is not very sensitive to changes in ν; the two limiting values differ by only about 15 per cent.

Values of λ_D and $\lambda_{D/2}$ are given for silver, lead, copper and gold in Table I. The more recent self-diffusion data for copper and gold and the data

for silver and lead (designated by asterisks) indicate fair consistency. Poorer agreement in λ than in K_{211} is not surprising, however. Errors in determining D_0 are much greater than in Q_M. A 50 per cent error in D_0 (not an unusual magnitude) would result in about 15 per cent error in λ. Also, the errors in ϕ are approximately 5 per cent, resulting in a similar uncertainty in the value of λ. Because of the excellent agreement on the self-diffusion data for silver, probable values for f.c.c. metals are $\lambda_D = 0.64$ and $\lambda_{D/2} = 0.74$.

The numerical factor 0.67 appearing in LeClaire's equation (32) corresponds to λ_D and matches the value of 0.64 obtained here. However, LeClaire does not state the significance of the term. In the present treatment, this numerical factor is the fraction of the self-diffusion activation energy that goes into lattice straining, as indicated by Zener [2].

TABLE I

DIFFUSION DATA FOR FACE-CENTERED CUBIC METALS

Metal	Diffusion reference	Q_M (cal/mole)	D_0 (cm^2/sec)	K_{211}	λ_D	$\lambda_{D/2}$
Ag	Johnson	45,900	0.895	0.0519*	0.660	0.756
	Hoffman and Turnbull Slifkin, Lazarus, Tomizuka (Includes data of Johnson, Hoffman and Turnbull)	45,500	0.724	0.0515*	0.637	0.735
Pb	V. Hevesy, Seitz, Keil	27,900	5.1	0.0525*	0.658	0.721
Cu	Steigman, Shockley, Nix	57,200	11	0.0598	1.14	1.25
	Rollin	61,400	47	0.0642	1.28	1.39
	Maier and Nelson	49,000	0.6	0.0512*	0.788	0.913
	Raynor, Thomasson, Rouse	46,800	0.32	0.0490*	0.701	0.836
Au	McKay	51,000	2.1	0.0587	1.24	1.39
	V. Sagrubski	62,900	9.2	0.0724	1.27	1.40
	Kurtz and Gatos	45,600	0.625	0.0525*	0.895	1.06

*Based on most recent diffusion results.

REFERENCES

Silver: W. A. Johnson. Trans. A.I.M.E. **143** (1941) 107.
R. E. Hoffman and D. Turnbull. J. Appl. Phys. **22** (1951) 634.
L. Slifkin, D. Lazarus, and T. Tomizuka. J. Appl. Phys. **23** (1952) 1032.
Lead: G. von Hevesy. Trans. Faraday Soc. **34** (1938) 841.
Copper: B. V. Rollin. Phys. Rev. **55** (1939) 231.
J. Steigman, W. Shockley, and F. C. Nix. Phys. Rev. **56** (1939) 13.
M. S. Maier and H. R. Nelson. Trans. A.I.M.E. **147** (1942) 39.
C. L. Raynor, L. Thomassen, and L. J. Rouse. Trans. A.S.M. **30** (1942) 313.
Gold: Von. A. Sagrubski. Phys. Zeit. der Sowjetunion. **12** (1937) 118.
H. A. C. McKay. Trans. Faraday Soc. **34** (1938) 845.
A. Kurtz and H. C. Gatos. To be published in the A.I.M.E., J. Metals.

Determination of K_{111} and of λ for B.C.C. Metals

Available self-diffusion measurements on b.c.c. metals are presented in Table II. For sodium, the self-diffusion data seem to be very good. Also, accurate values of $(E_0)_{111}$, ϕ_{111}, and α are available from the work of Seigel and Quimby [8; 9]. The corresponding values of $K_{111} = 0.0695$, $\lambda_D = 0.843$, and $\lambda_{D/2} = 1.00$ for sodium are probably fairly reliable.

The differences between the Birchenall and Mehl self-diffusion data for alpha iron and those of the authors have been discussed elsewhere [10; 11]. The values of $K_{111} = 0.0585$ and 0.0716 stem from Goens and Weerts' [12] elastic constants for iron, the values of $K_{111} = 0.0625$ and 0.0765 from Kimura's [13] elastic constants. Perhaps the differences between the K_{111} values for sodium and iron arise from experimental errors in determining the elastic constants. Another possible discrepancy may lie in the fact that elastic constants are measured in ferromagnetic iron and diffusion coefficients are measured in paramagnetic iron.

TABLE II

DIFFUSION DATA FOR BODY-CENTERED CUBIC METALS

Metal	Diffusion reference	Q_M (cal/mole)	D_0 (cm^2/sec)	K_{111}	λ_D	$\lambda_{D/2}$
Na	Nachtrieb, Catalano, Weil	10,450	0.242	0.0695	0.843	1.00
Fe	Birchenall and Mehl	73,200	2300	0.0716 0.0765	1.74	1.83
	Buffington, Bakalar and Cohen	59,800	6.2	0.0585 0.0625	1.13	1.25
W	Langmuir	120,000	—	0.0658	—	—
	van Liempt	140,000	11.5	0.0767	1.28	1.39

REFERENCES

Sodium: N. H. Nachtrieb, E. Catalano and J. A. Weil. J. Chem. Phys. **20** (1952) 1185.
Iron: C. E. Birchenall and R. F. Mehl. Trans. A.I.M.E. **188** (1950) 144.
F. S. Buffington, I. D. Bakalar and M. Cohen. Chap. 6, The Physics of Powder Metallurgy, W. E. Kingston, editor (New York, McGraw-Hill, 1951).
Tungsten: I. Langmuir. J. Franklin Inst. **217** (1934) 543.
J. A. vanLiempt. Rec. trav. Chim. **64** (1945) 239.

The fact that the values of λ for iron in Table II are greater than unity may be due to errors in ϕ. Quimby and Seigel's data for sodium show that $[dE_d/(E_d)_0 dT]$ is strongly dependent upon d as might be expected in the b.c.c. system. Similar results are not available for iron, and probably

ϕ_{111} is not equal to $-[dE_a/(E_a)_0 dT]$ as assumed here.

The data for tungsten given in Table II probably do not represent actual self-diffusion values. These results are for the diffusion of thorium (Langmuir) and iron (Van Liempt) at low concentrations in tungsten. Accordingly, equation (10) was used to calculate D for self-diffusion in tungsten, assuming $K_{111} = 0.0695$ and $\lambda_D = 0.843$ as found for sodium. The D value calculated is

$$D = 0.56 \exp\left(-\frac{127{,}000}{RT}\right) \text{cm}^2/\text{sec} \qquad (11)$$

Comparison of these results for b.c.c. metals with those of LeClaire is made in the following section.

Discussion

Some available self-diffusion data have not been included in Tables I or II because the corresponding moduli of elasticity are not on hand.

According to the present findings, the fraction of Q_M which goes into the creation of lattice vacancies $(1 - \lambda)$, is somewhat smaller than previous estimates. These calculations give a maximum value for f.c.c. metals of $(1 - \lambda) = 0.36$, which is on the low side of the range 0.4 to 0.8 calculated for copper by Huntington and Seitz [14]. Possibly the assumption that ϕ_{211} is equal to $-[dE_a/(E_a)_0 dT]$ for different f.c.c. metals is open to question.* The greater ease of creating vacancies in the b.c.c. system is indicated by the maximum value of $(1 - \lambda) = 0.16$ for sodium.

The value adopted for the vibrational frequency, ν, is important in the calculation of λ. However, in using equation (10) to compute self-diffusion coefficients, the fraction of the Debye frequency assumed is immaterial. The substitution of λ_D and ν_D gives the same results as $\lambda_{D/2}$ and $\nu_{D/2}$. The same is true when equations (8) and (9) are used to evaluate Q_M and D_0. Incidentally, $Q_M = 38{,}600$ cal/mole was calculated for aluminum, and is in good agreement with the value of 37,500 obtained by Kê from internal friction measurements [5]. LeClaire's calculated value of $Q_M = 42{,}600$ cal/mole is somewhat higher principally because of his use of $c_{44} + \frac{1}{2}(c_{11} - c_{12})$ as the appropriate elastic modulus. $D_0 = 0.6$ cm^2/sec was computed for aluminum by equation (9).

*Sutton's data [6] for aluminium show that ϕ_d varies with d as follows: $\phi_{211} = 4.66$, $\phi_{100} = 5.22$ and $\phi_{111} = 4.41 \times 10^{-4}$ per °K. Thus, final evaluation of λ should be based on accurate ϕ_d values which are now available only for aluminium and sodium.

The results presented here suggest that the vacancy mechanism is probably operative in self-diffusion of f.c.c. metals. LeClaire also reaches this conclusion, although he uses the following expression for Q_M when self-diffusion occurs by the vacancy mechanism:

$$Q_M = k_1 L_s + k_2 M \frac{\mu_0}{\rho_0} \qquad (12)$$

where k_1 and k_2 are constants evaluated from existing self-diffusion data (the constants K and λ used in the present paper are also evaluated from existing self-diffusion data, but have different physical significance); L_s = latent heat of sublimation; M = atomic weight; $\mu_0 = c_{44} + \frac{1}{2}(c_{11} - c_{12})$ extrapolated to 0°K; ρ_0 = density extrapolated to 0°K. The principal difference between this expression and the one derived here is that LeClaire assumes that the change in internal energy on forming a vacancy is proportional to L_s. Self-diffusion data for f.c.c. metals show that k_1, k_2 and K_{211} all are fairly constant, so a choice between equation (8) and equation (12) is not permitted by the available experimental evidence. This situation exists because $(E_{211})_0 a_0^3 \cong$ (constant) (L_s) for f.c.c. metals, as shown in Table III. The quantity $(M\mu_0/\rho_0)$ is approximately proportional to L_s also.

TABLE III

CORRELATION BETWEEN $E_0 a_0^3$ AND L_s

Metal	$(E_{211})_0 a_0^3 N_0$*	L_s** kcal/mole	$\frac{(E_{211})_0 a_0^3 N_0}{L_s}$
Ag	885	69.46	12.8
Cu	995	81.78	12.2
Pb	531	46.77	11.4
Au	870	82.61	10.5
Al	760	75.2	10.1
Ni	1400	101.8	13.8
Metal	$(E_{111})_0 a_0^3 N_0$*	L_s** kcal/mole	$\frac{(E_{111})_0 a_0^3 N_0}{L_s}$
W	1824	201.9	9.04
Na	150.4	26.32	5.68
α–Fe	1040	96.65	10.7
K	141	22.11	6.38
Mo	1340	155.7	8.61

*E_0 is in kcal/cm^3, and a_0^3 is in cm^3. N_0 is Avogadro's number.

**Values of L_s are extrapolated to 0°K from values of ΔH and ΔC_p at 25°C, using data from U.S. Bureau of Standards Circular 500, "Selected Values of Chemical Thermodynamic Properties" (1952).

Using the data denoted by asterisks in Table I, the standard deviation of K_{211} is 2.0 per cent

compared to 4.5 per cent for k_1 and 11.5 per cent for k_2 obtained by LeClaire. However, LeClaire's values do not include the Kurtz and Gatos data for gold. In any event, both treatments favor the vacancy mechanism for self-diffusion in f.c.c. metals; on the other hand, different conclusions are reached with regard to b.c.c. metals.

The results given here for sodium lend some support to the vacancy mechamism of self-diffusion in b.c.c. metals. Sodium is the only metal for which good data are available for both self-diffusion and the variation of elastic constants with temperature. LeClaire did not include the sodium data, but found that iron and tungsten gave negative values for k_1. Consequently, he considered a ring-rotation mechanism as the most likely mode of self-diffusion in b.c.c. metals. However, as pointed out previously, the tungsten values are actually not self-diffusion data. Calculations assuming the vacancy mechanism and using equation (10) gives reasonable values of Q_M and D_0 for tungsten. The negative value of k_1 for alpha-iron found by LeClaire may result from the fact that self-diffusion data are obtained for paramagnetic iron, while elastic constants are determined for ferromagnetic iron Self-diffusion data for ferromagnetic iron at present is incomplete but will be presented in a later paper. Because of these uncertainties in both the alpha-iron and the tungsten data, it appears that calculations based on the sodium results should be considered more reliable.

The sodium data give positive values for LeClaire's constants k_1 and k_2, and do not rule out the vacancy mechanism, even on the basis of his treatment. In considering the ring-rotation mechanism, LeClaire calculates values of N_r, where N_r is one for a two-ring process and six for a four-ring process. Presumably no values of N_r between one and six exist. LeClaire found values for N_r of 2.25 for alpha-iron and 4.5 for tungsten, and claimed support for the ring-rotation mechanism,* but N_r for sodium is only 0.3 or 0.5 (depending on the modulus used). This low value for sodium would indicate an interstitial mechanism ($N_r = 0.5$) rather than a ring-rotation mechanism,† if the vacancy mechanism were not operative. However, it is believed there is insufficient evidence to exclude the vacancy mechanism for self-diffusion in b.c.c. metals.

A question naturally arises concerning the applicability of the derived equations to chemical or interdiffusion data. This point is being studied. A tentative answer is negative, since an essential assumption made in equation (1) is that ϵ_{max} is the same in direction d for the diffusion of different species of atoms in a given lattice structure. This assumption seems valid for self-diffusion, but it is probably not valid for the diffusion of A atoms in a lattice made up mostly of B atoms. Also, this assumption may not even be correct for the diffusion of B atoms in a lattice of mostly B atoms because of a non-uniform distribution of vacancies.

Dienes [15] has mentioned the possibility of negative entropies for self-diffusion. Equation (9) indicates that negative entropies may exist if $(\phi - 3\alpha)$ is negative. However, it is found experimentally that $(\phi - 3\alpha)$ is positive for cubic metals. The available data show that for cubic metals $\phi/3\alpha$ ranges from 5.5 to 10. Hence the existence of negative entropies of activation for self-diffusion in cubic systems seems unlikely, on the basis of the derivation given here. Dienes also states that negative entropies are possible for small energies of activation. Sodium has the relatively low value of $Q_M = 10{,}450$ cal/mole but $\Delta S = +3.68$ cal/mole/°K, compared to $Q_M = 59{,}800$ and $\Delta S = +6.65$ for iron, and $Q_M = 45{,}800$ and $\Delta S = +4.72$ for silver.

The discussion here is necessarily limited to cases where the vacancy mechanism is operative.

Conclusions

It is believed that equation (10) expresses the self-diffusion coefficient for f.c.c. and b.c.c. metals, based on the vacancy mechanism. The values of K and λ given in this paper should be subjected to further experimental verification. Tentative values for f.c.c. metals are:

$$K_{211} = 0.0514 \qquad \lambda_D = 0.64$$

Tentative values for b.c.c. metals are:

$$K_{111} = 0.0695 \qquad \lambda_D = 0.84$$

References

1. LeClaire, A. D. Acta Met. **1** (1953) 438.
2. Zener, C. J. Appl. Phys. **22** (1951) 372.
3. Progress in Metal Physics, B. Chalmers, Ed., vol. 2 (London, Butterworths, 1950).
4. Koster, W. Zeit. Metallkunde **39** (1948) 1.
5. Zener, C. Elasticity and Anelasticity of Metals (Chicago, University of Chicago Press, 1948).
6. Sutton, P. M. Phy. Rev. **91** (1953) 816.

*A Kirkendall effect has been found in beta brass signifying that the ring-rotation mechanism is certainly invalid for this b.c.c. phase. R. W. Baluffi and L. L. Seigle (private communication).

†See footnote, p. 656.

7. Nix, F. C. and McNair, D. Phy. Rev. **60** (1941) 597; **61** (1942) 74.
8. Quimby, S. L. and Seigel, S. Phy. Rev. **54** (1938) 293.
9. Seigel, S. and Quimby, S. L. Phy. Rev. **54** (1938) 76.
10. Buffington, F. S., Bakalar, I. D., and Cohen, M. Trans. A.I.M.E. **108** (1950) 1374.
11. Buffington, F. S., Bakalar, I. D., and Cohen, M. The Physics of Powder Metallurgy, chap. 6, W. E. Kingston, Ed. (New York, McGraw-Hill, 1951).
12. Goens, E. and Weerts, J. Physik Zeits. **37** (1936) 321.
13. Kimura, R. Physico-Math. Soc. of Japan Proc. **21** (1939) 621.
14. Huntington, H. B. and Seitz, F. Phys. Rev. **61** (1942) 315, 325.
15. Dienes, G. J. J. App. Phys. **22** (1951) 848; Phys. Rev. **89** (1953) 185.

THE INFLUENCE OF ANODIC OXIDE FILMS ON THE THERMAL OXIDATION OF ZIRCONIUM*

J. J. POLLING and A. CHARLESBY†

Changes in the thermal oxidation of zirconium due to the presence of an initial electrolytically-formed oxide layer are studied. The increase in thickness of the oxide on heating is measured optically and gravimetrically. The effect of the initial layer is the same as if it had been produced thermally, i.e., there is no difference in the oxidation behaviour of two specimens covered with initial oxide films of the same thickness, one of which has been grown electrolytically and the other thermally.

The growth of the oxide layer is approximately logarithmic up to temperatures of about 260°C, cubic at 300°C, and at higher temperatures it tends towards a quadratic function of time. For thick films there is a linear law probably due to cracking of the oxide. These rates of growth are in agreement with theoretical calculations based on the oxidation theory of Mott.

L'INFLUENCE DE FILMS D'OXYDE ANODIQUE SUR L'OXYDATION THERMIQUE DU ZIRCONIUM

On a étudié les modifications dans l'oxydation thermique du zirconium, dues à la présence d'une couche initiale d'oxyde formée électrolytiquement. L'accroissement de l'épaisseur de l'oxyde lors du chauffage est mesuré optiquement et gravimétriquement. L'effet de la couche initiale est identique à celui qui serait produit par une couche formée thermiquement, c'est-à-dire il n'y a pas de différence entre l'oxydation de deux échantillons, dont un est couvert initialement d'une couche formée thermiquement et l'autre électrolytiquement, les deux couches ayant la même épaisseur. La croissance d'une couche d'oxyde est logarithmique jusqu'à une température d'environ 260°C, elle devient cubique à 300°C, et aux températures plus élevées elle tend vers une fonction du second degré du temps. Dans le cas de couches épaisses la loi de croissance devient linéaire, probablement à cause de la fissuration de l'oxyde. Ces vitesses de croissance sont en accord avec les calculs théoriques, basés sur la théorie d'oxydation de Mott.

DER EINFLUSS ANODISCHER OXYDFILME AUF DIE THERMISCHE OXYDATION VON ZIRKON

Die durch die Anwesenheit eines ersten, elektrolytisch erzeugten Oxydfilmes hervorgerufenen Änderungen in der thermischen Oxydation von Zirkon werden untersucht. Die während der Erwärmung auftretende Dickenzunahme der Oxyde wurde optisch und gravimetrisch gemessen. Die Wirkung dieses ersten Filmes gleicht der eines thermisch erzeugten, d.h. zwei Proben, die mit Anfangsoxydfilmen gleicher Dicke überzogen sind, zeigen in ihrem Oxydationsverhalten keine Unterschiede, wenn einer der Anfangsfilme elektrolytsich und der andere thermisch erzeugt worden war.

Das Wachstum der Oxydschicht ist bei Temperaturen bis zu etwa 260°C eine logarithmische, bei 300°C eine kubische und bei höheren Temperaturen eine annähernd quadratische Funktion der Zeit. Bei dicken Filmen findet man eine lineare Abhängigkiet, was wahrscheinlich auf Aufbrechen der Oxydschicht zurückzuführen ist. Diese Wachstumsgeschwindigkeiten stimmen mit den theoretischen, auf Mott's Theorie der Oxydation beruhenden, Berechnungen überein.

Introduction

At room temperature zirconium is stable to most forms of attack by gases. The surface is rapidly oxidised to a depth of about 50 Å, but the film does not grow appreciably beyond that thickness and protects the metal from further reaction. At a few hundred degrees centigrade, however, zirconium becomes extremely reactive. Indeed, the only gases to which zirconium is stable at these temperatures are the inert gases, most of the atmospheric gases and their reaction products being soluble in the metal. Reaction with these gases greatly alters the physical properties of the metal, causing it to become brittle.

Oxide films of up to 10^4 Å thickness can be produced by anodisation of the metal in suitable electrolytes. These films are good insulators to electric current and hence to further growth by ionic flow and it was thought that they might also provide barriers to the absorption of atmospheric gases at higher temperatures.

The experiments described in this paper were made to determine the effect of anodic oxide films on the absorption of atmospheric gases by zirconium at various temperatures. At the same time the structural stability and growth of the films themselves in air at various temperatures were studied by means of changes in interference colour, and in weight.

The zirconium used by the authors was sheet metal of thickness 0.127 mm manufactured by the Kroll process (reduction of zirconium tetrachloride with magnesium) and supplied by Murex Ltd. A typical analysis of the metal is hafnium 0.5–3.0 per cent, carbon 0.15 per cent, oxygen 0.08 per cent, nitrogen 0.04 per cent.

*Received January 12, 1954.
†Atomic Energy Research Establishment, Harwell, England.

Gas Phase Reactions of Zirconium

In the next paragraphs the reactions of zirconium with some of the more common gases are briefly considered. The data given are only approximate as the results of different workers are often conflicting. This is because the physical properties of zirconium are extremely sensitive to impurities, and the concentration of these impurities varies according to the source of supply.

(*a*) *Hydrogen.* Zirconium occludes hydrogen in the same way as does palladium. The reaction commences at 300°C, becomes rapid at 400°C, but at 900°C all the hydrogen is expelled, showing that although the rate of reaction increases with temperature rise, the solubility decreases. Huddle [11] suggests that the gas dissolves in the metal in the form of positive ions to form an alloy of indefinite composition. Gulbransen and Andrew [6] showed that the reaction is dependent on pressure and deduced that no surface film is formed.

(*b*) *Oxygen.* Zirconium has a high affinity for oxygen, the product being the dioxide, ZrO_2. The reaction probably starts at about 200°C but does not become considerable till 300°C. The metal dissolves oxygen gas up to 50 at.% as a solid solution, and this remains fixed at temperatures above 1500°C. Zirconium also dissolves the oxide. Gulbransen and Andrew [6] showed that the oxidation is independent of pressure. After oxidation, specimens are blue-black in colour, but metallographic observations [8] indicated that no oxygen diffuses into the metal below 800°C. Electron diffraction studies by Hickman and Gulbransen [9] of the oxide film formed between 300 and 600°C showed the monoclinic form of ZrO_2.

(*c*) *Nitrogen.* Nitrogen gas is reported [5; 10] to dissolve in zirconium to form a solid solution up to 20 at.%. It also reacts with the metal forming the very stable nitride ZrN, which is also soluble in the metal. The nitride starts to form at about 400°C, is appreciable at 700°C and remains stable even in high vacua at 900°C. The reaction is independent of pressure, but the existence of nitride films is controversial. Gulbransen and Andrew [6] observed no coloured films up to 825°C and state that electron diffraction evidence was also negative. Hayes and Roberson [8], however, and independently Dravnieks [4], observed a faint yellow colour below 800°C which became golden at higher temperatures.

(*d*) *Air and other gases.* The above paragraphs show that zirconium reacts with the major constituents of the atmosphere at a temperature of a few hundred degrees centigrade. If the metal is allowed to absorb these gases its properties are completely altered. Hayes and Roberson [8] report that the films produced on their specimens when heated in air were bluish-black and strongly adherent up to 600°C. White spots of oxide then appeared till at 700°C the specimens became completely white. At 900°C the specimens acquired a yellow tint but this was not due to the presence of nitride. A specimen heated for one hour at 900°C increased its dimensions by about 15 per cent.

Carbon monoxide and carbon dioxide react at 400°C to form the oxide and the carbide. The oxide is distributed throughout the metal while the carbide is present only on the surface [7]. Steam attacks zirconium at 200°C, forming a loose white oxide on the surface. The halogens react at 200°C forming volatile tetrahalides.

Optical Method

The oxide films formed by anodising zirconium are transparent and show bright colours due to the interference of light reflected from the air and metal interfaces. These interference colours vary with the optical thickness of the film. A series of standard specimens can be made by anodising strips of zirconium at successively increasing voltages in steps of a few volts. Since it has been shown [1] that film thickness is proportional to voltage it is possible to estimate the thickness of any film by comparing it with the standard specimens. The colours shown by the standard specimens repeat themselves periodically so that the order of the colour must be known to judge the thickness.

If the result of heating zirconium were to increase the thickness of the oxide film without changing its structure, a change in colour of the film would be seen and the amount of the increment could be estimated by comparison with the standard specimens. If an anodised specimen were heated it would be easy to see whether the anodic film had increased in thickness or whether it resisted change. By this method the relationship between thickness and temperature could be determined.

Experimental Details

A standard specimen was made by immersing one end of a zirconium strip in dilute ammonium borate and anodising it at a high voltage, then immersing it further and anodising it again at a slightly lower voltage. The thickness of the film on the first portion is not appreciably increased by this second anodisation. The process was continued until the whole strip was anodised in portions at

successively decreasing voltages, in steps of about 4 volts. Other standard specimens were made in the same way so that a range of voltages from 0 to 200 was covered, each voltage being covered twice on different specimens.

A specimen of zirconium was anodised in portions, like the standard specimens, and heated in an oven at constant temperature while a duplicate specimen was kept at room temperature. After a given time the specimen was removed from the oven and compared with both the duplicate and the standard specimens, and the new film thicknesses on each portion estimated from its colour. This procedure was repeated at different temperatures and for different times. It was found in general that the lower-voltage portions increased in thickness while the colours of the higher-voltage portions remained the same. The minimum anodic film thickness which showed no further increase on heating in air at a given temperature for a given time is called the limiting thickness at that temperature; it is also the thickness to which all films below the limiting thickness will tend when subjected to the temperature under consideration. Often it could be only roughly estimated from the data. The process was seldom found to be completed possibly owing to inadequate time of heating. The results are given in Table I. The thicknesses are obtained from the voltages of anodisation assuming a conversion factor of 20 Å/volt [1]. A plot of limiting thickness against temperature is shown in Figure 1.

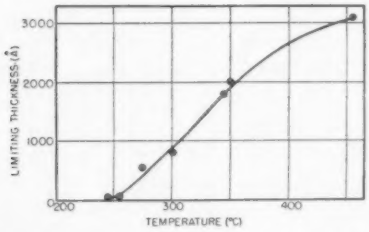

FIGURE 1. Curve showing increase in limiting thickness with temperature; specimens heated for 2 hours at temperature.

From these results it can be concluded that temperature has the effect of increasing film thickness if the initial film is sufficiently thin. If it is thick enough, however, the anodic film appears to be stable, the limiting thickness depending on the temperature and possibly to a lesser extent on the heating time. These data cannot be used to show that no gas dissolves in the metal, as a gas may permeate through the surface oxide and dissolve in the metal without altering the thickness (and hence the colour) of the film. It was therefore necessary to determine the weight changes on heating.

Gravimetric Measurements

For these tests the specimens used were squares of zirconium sheet of 5 cm edge, buffed, number-punched, degreased in trichloroethylene and acetone and washed in distilled water. They were weighed, anodised in normal ammonium borate solution to their various potentials, maintained at that potential until the leakage currents had fallen to a desired value, and weighed again. During anodisation the specimens were each suspended by one corner. These bare corners were then cut off so that the whole surface of each specimen was anodised, and the specimens were re-weighed. They were then placed in a furnace at the required temperature and removed and weighed at intervals. These measurements gave the weight increment due to thermal oxidation. It was necessary also to know the weight of the initial anodic film. This could not be determined directly by a single weighing since an anodised specimen is subjected to a number of weight changes, such as (i) a weight gain due to the anodic oxide film, (ii) a weight loss due to dissolution of the metal or its oxide in the electrolyte during anodisation, and (iii) a weight gain due to the trapping of volatile compounds, such as water, in the film during formation.

It has been reported previously [13] that the apparent weight gain due to anodic oxidation is 0.46 $\mu g/cm^2$ per volt, the weight loss due to dissolution is .02 $\mu g/cm^2$ per volt i.e., almost negligible compared with the weight of the film, and the weight gain due to the trapping of volatile compounds is .073 $\mu g/cm^2$ per volt. The true weight gain is thus 0.41$\mu g/cm^2$ per volt.

Four sets of specimens were prepared, the first set being used in a preliminary investigation and the remaining sets being subjected to temperatures of 300°, 435° and 595°C.

Preliminary Investigation

Four specimens were prepared and anodised at 0, 25, 250 and 390 volts. They were weighed, placed in an oven at 100°C and reweighed at suitable intervals. There was a detectable weight gain of the non-anodised specimen even at this low temperature, but the time required for these weight gains to become appreciable would have been excessive. The specimens were subjected to suc-

TABLE I

INCREMENTS IN FILM THICKNESS DUE TO HEATING, AND LIMITING THICKNESS AT ANY GIVEN TEMPERATURE
(Thickness estimated from interference colours)

Conditions		Initial thickness (Å)	Final thickness (Å)	Increment (Å)	Remarks and limiting thickness
Temp. of heating	Time of heating				
245°C	3 hrs	0	80	80	Process is complete. Everything below 80Å has tended to 80Å within 3 hrs.
		40	80	40	
		80	80	0	
		160	160	0	
		240	240	0	Limiting thickness 80Å.
255°C	2 hrs	0	80	80	
		80	80	0	
		120	120	0	
		160	160	0	Limiting thickness 80Å.
275°C	4 hrs	0	300	300	In 4 hours the process of oxidation is incomplete.
		120	360	240	
		240	400	160	
		400	460	60	
		600	600	0	
		800	800	0	
		1000	1000	0	Limiting thickness ∽ 550 Å.
300°C	2 hrs	0	780	780	
		200	∽600	∽400	
		380	∽460	∽ 80	
		500	600	100	
		800	800	0	
		1000	1000	0	Limiting thickness 800Å.
345°C	2 hrs	0	1360	1360	Process is incomplete even with low initial film thickness.
		80	1360	1280	
		160	1360	1200	
		340	1360	1020	
		1400	1580	180	Limiting thickness can be only guessed.
		1480	1640	160	
		1580	1740	160	
		1660	1740	80	Limiting thickness ∽ 1800Å.
350°C	2 hrs	0	800	800	Limiting thickness lies between 1600 and 2800Å, nearer the former value, say 2000Å.
		200	800	600	
		1180	1360	180	
		1260	1440	180	
		1420	1600	180	
		2800	2800	0	
		3000	3000	0	Limiting thickness ∽ 2000Å.
350°C	4 hrs	0	1240	1240	
		400	1440	1040	
		600	1440	840	
		1000	1440	440	
		1600	1800	200	
		1800	2000	200	
		2000	2060	60	
		2600	2600	0	
		2800	2800	0	
		3000	3000	0	Limiting thickness ∽ 2200Å.
455°C	2 hrs	2800	3100	300	The process is complete. This is to be expected since the maximum difference in thickness is only 300Å.
		2900	3100	200	
		3000	3100	100	
		3100	3100	0	Limiting thickness 3100Å.

cessively higher temperatures until at 300°C the thermal oxidation proceeded at a reasonable rate. The very considerable decrement in weight shown by A4 is probably due to the oxide being brushed from the surface. The results of these preliminary experiments are shown in Table II.

TABLE II

WEIGHT GAIN OF ZIRCONIUM SPECIMENS WITH TIME AT VARIOUS TEMPERATURES

Temp. (°C)	Total time of heating (hrs)	Mass increment ($\mu g/cm^2$) A1 (0V)	A2 (25V)	A3 (250V)	A4 (390V)
100	20.8	2	0	0	−18
200	5.5	2	0	−2	−24
	23.5	4	0	−4	−36
	100	6	0	−6	−45
	116	8	2	−6	−49
	163	10	2	−6	−51
	250	12	2	−6	−55
	321	14	4	−6	−57
	654	14	4	−6	−65
220	45.8	18	6	−8	−69
	87.5	20	8	−8	−71
	159	24	8	−6	−77
	255	24	12	−6	−83
	330	24	10	−8	−85
	396	26	12	−8	−89
250	16.3	28	14	−8	−89
	43.3	28	16	−6	−91
300	1.6	30	18	−6	−91
	3.7	30	18	−8	−93
	7.8	32	20	−6	−95
	27.4	40	24	−6	−91
	69.7	52	38	−4	−93
	119	70	50	−2	−93

The changes in colour of the specimens were observed. Initially A1 was metallic silver, A2 was blue, corresponding to 23 volts on standard specimens, A3 was dark grey, and A4 light grey with traces of loose white powder which could be brushed off. The colour changes were rather indeterminate. The non-anodised specimen went through a gradual succession of colours, the order of which was difficult to identify, ending with a bluish grey colour quite unlike any colour on the standard specimens. The 25-volt specimen also passed through a succession of colours which were difficult to match with the standard specimens.

Weight Changes at Constant Temperature

For the work at 300°C eight specimens were prepared, of which two were not anodised, three were anodised at 26 volts with various leakage currents, one at 130 volts, one at 200 and the last at 470 volts. The two non-anodised specimens could be checked against each other. The 26-volt specimens were used to discover the effect, if any, of temperature on specimens of different leakage currents, other than that due to the slight differences of thickness which must exist between them. When compared with the standard specimens the three 26-volt specimens, formed with leakage currents 2000, 43 and 30 $\mu a/cm^2$ at a standard formation time of 2 minutes, corresponded to potentials 23, 24 and 25 volts respectively.

After heating for 40 hours it was found that only the non-anodised and 26-volt specimens had gained in weight, while the 130-volt film afforded protection from atmospheric attack. Differences in leakage current had no great effect; the specimens behaved as though higher leakage currents were equivalent to slight decrements in voltage of formation. The weight gains are plotted in Figures 2 and 3. The two non-anodised specimens behaved similarly, as was expected, and the experimental scatter can be clearly seen in the graph.

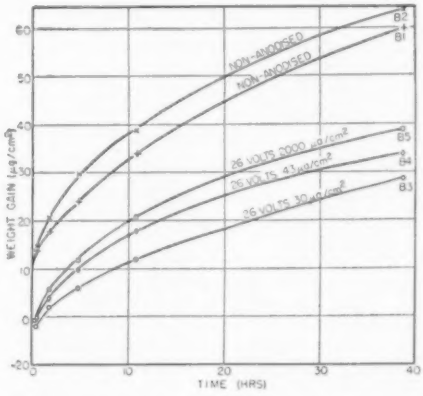

Figure 2. Weight gain of anodised and non-anodised specimens heated at 300°C in air.

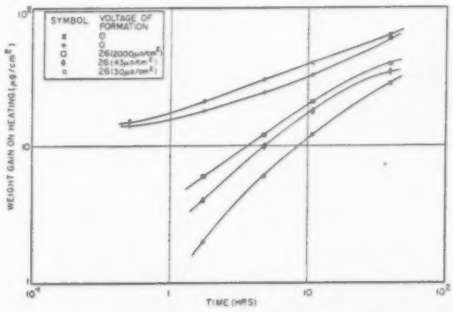

FIGURE 3. Weight increase at 300°C due to thermal oxide only.

TABLE III

COLOUR CHANGES OBSERVED AFTER HEATING AT 435°C IN AIR

Total time of heating (hrs)	Colour changes and equivalent formation voltages						
	C1 (0 V)	C2 (50 V)	C3 (100 V)	C4 (150 V)	C5 (200 V)	C6 (250 V)	C7 (470 V)
0	Silver (0)	Golden (59)	Green (108)	Pinkish Grey (170)	Greenish Grey (?)	Deep Grey (?)	Deep Grey (?)
0.25	Blue Green (31)	Orange (68)	Yellow Green (115)	Purplish Grey (180)	Dark Green (?)	Deep Grey (?)	Deep Grey (?)
0.75	Dark Mauve (80)	Royal Blue (84)	Red Gold (120)	Purplish Grey (180)	Dark Green (?)	Deep Grey (?)	Deep Grey (?)
1.5	Green (97)	Blue Green (100)	Greyish Red (130)	Purplish Grey (180)	Dark Green (?)	Deep Grey (?)	Deep Grey (?)

The anodisation voltages equivalent to these colours (obtained from standard specimens) are given in brackets.

Two more sets of specimens, C1–7 and D1–7, each anodised in steps of 50 volts up to 250 volts, and including a 470-volt specimen, were heated at 435° and 595°C respectively. The results are shown in Figures 5 and 7. One unexpected phenomenon which was observed in these two runs was a very great increase in the rate of absorption of atmospheric gases after the runs had progressed for many hours. This may have been due to cracking of the film and dissolution of atmospheric gases in the metal. At 435°C interference colours were seen up to 1½ hours of heating, as shown in Table III, after which the specimens assumed a medium grey colour which remained permanent. At 595°C no interference colours were seen as the specimens became grey within ten minutes. After 20 hours they were light brown, very crinkled and brittle.

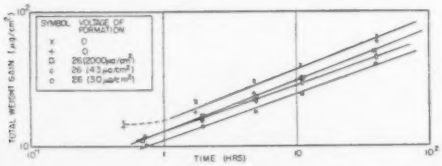

FIGURE 4. Total weight increase at 300°C (anodic plus thermal film). The mean slope is 0.35, i.e., growth is approximately cubic.

Analysis of Results

The curves in Figures 3, 5 and 7 show the weight increases due to thermal oxidation alone. At any one temperature the effect of the oxide layer deposited electrolytically is to reduce the initial uptake of gas by the metal. For long periods of heating the relative difference between the variously

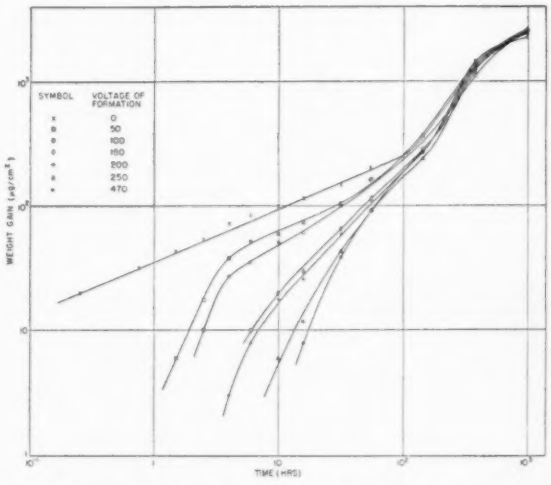

FIGURE 5. Weight increase at 435°C due to thermal oxide only.

anodised samples becomes negligible. If we assume that the oxide formed electrolytically is identical with that obtained by heating, then the only difference between the curves at a given temperature should be in the time factor; the non-anodised specimens take a certain time, t_0, to reach the same state of oxidation as has already been obtained electrolytically. If, therefore, the total weight increase (anodic plus thermal) is plotted against $t + t_0$ the curves should coincide. The time t_0 can be determined from the known weight of the anodic film (0.41 μg/cm² per volt) and the thermal oxidation curve for a non-anodised specimen. Thus for a specimen anodised at 200 volts the weight of the anodic layer is $200 \times 0.41 = 82$ μg/cm², and at

435°C the time t_0 needed for non-anodised metal to reach this film thickness is six hours. A small correction factor of .073 $\mu g/cm^2$ per volt must also be added to the total weight gain to allow for evaporation of water, etc., from the film. The initial weight gains taken in the first few minutes while the evaporation was taking place will be erroneous.

Figures 4, 6 and 8 show that the curves corrected in this manner are linear and close together. In the

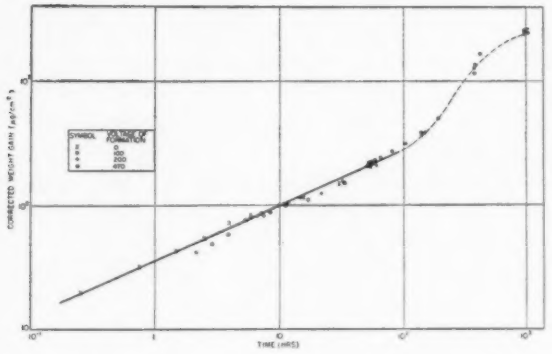

FIGURE 6. Total weight increase at 435°C (anodic plus thermal film) corrected for initial time factor and loss of volatile compounds. The slope is 0.445, i.e., growth is approximately quadratic. After about 100 hrs. the growth rate is linear.

case of oxidation at 300°C the curves do not coincide exactly. This is probably due to the assumption that the weight of volatile compounds included in the film is proportional to voltage.

It is concluded that at these temperatures there is no essential difference between the oxide layer formed electrolytically in aqueous ammonium borate, and that produced by heating.

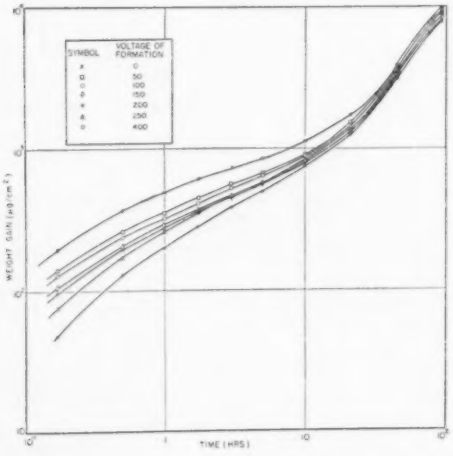

FIGURE 7. Weight increase at 595°C due to thermal oxidation only.

In the theory of oxidation given by Mott [12] a barrier exists between the metal and the oxide. Under the influence of an electric field across the oxide, metal ions are able to surmount the barrier, and flow into the oxide layer, resulting in a thicker film. The electric field may be produced either by the passage of electrons to the outer surface of the oxide, as in thermal oxidation, or by the imposition of an external voltage, as in electrolytic oxidation.

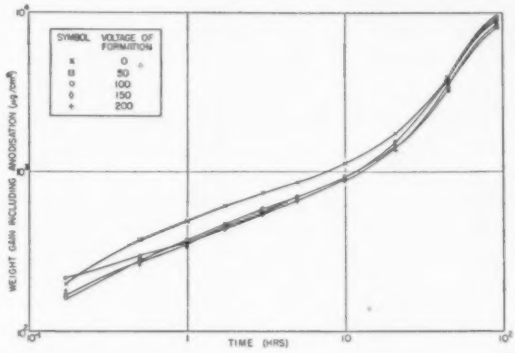

FIGURE 8. Total weight increase at 595°C (anodic plus thermal film). The slope is 0.40, i.e., the growth is approximately quadratic. After about 12 hrs. the growth rate is linear.

A calculation based on this theory, and which allows for the flow of metallic ions against the electric field, as well as with it, has been given by one of the authors [2]. This shows that the relation between oxide thickness and time depends on the value of a parameter z, equal to the product of electric field F, ion charge q and barrier width a, divided by kT. For low temperatures, when z is much greater than unity, the growth should be an approximately logarithmic function of time, and the film grows to an approximately constant thickness, which depends on the temperature. At higher temperatures, when z is about equal to one, the growth should be approximately cubic, while for lower values of z, (at still higher temperatures) the growth is parabolic. These theoretical predictions appear to apply in the oxidation of zirconium. At low temperatures, up to about 200°C, the film grows to a limiting thickness, and above 300°C it is approximately parabolic (Figure 2).

According to theoretical calculations, the logarithmic law of growth, and the concept of a limiting film thickness should fail for values of z of about 3. The value of qa/kT for zirconium is about 3.4×10^{-6} cm/volt at 20°C and 2×10^{-6} at about 250°C. The field F equals the potential across the oxide, which for thermal oxidation is about 2 volts,

divided by the film thickness δ. Thus the maximum thickness δ for logarithmic growth should equal $2 \times 10^{-6} \times 2$ divided by a factor of about 3, or about 130 Å. As seen in Table I the limiting thickness at 255°C is about 80 Å, whereas at 275°C film growth is incomplete when the thickness is 550 Å. No great accuracy can be claimed for these results, but the agreement is as satisfactory as can be expected.

Cubic growth occurs for values of z close to one. At 300°C qa/kT is about 1.7×10^{-6}, and if the potential across the film for thermal oxidation is 2 volts, and if $z = 1$, the film thickness $\delta \sim 3.4 \times 10^{-6}$ cm i.e., there is a weight increase of about 10 μg/cm^2. The weight gain of non-anodised zirconium due to heating at 300°C is 10 μg/cm^2 after 15 minutes (corresponding to $z = 1$) and 90 μg/cm^2 after 100 hours ($z \sim 0.1$). The observed slope of the weight increase/time curve at this temperature (Figure 4) is 0.35, which is close to that given in a cubic law (0.33).

At higher temperatures the observed rate of growth approximates to a parabolic law ($\delta \alpha t^{\frac{1}{2}}$) as required by the theoretical calculations. At 435° the slope of the weight increase/time curve, on a double logarithmic plot is 0.445, and at 595° it is close to 0.4. These values are lower than that predicted (0.5) possibly because the transition from the cubic to the quadratic law of growth is not complete.

After very long heating the rate of oxidation increases more rapidly than is given by a parabolic law, being approximately linear. This may be due to cracking of the very thick oxide layer, which tends to powder off the specimen. Oxidation would then depend on the rate of penetration of oxygen into the fissures. This is analogous to the electrolytic oxidation of aluminium in electrolytes such as dilute sulphuric acid, when the oxide is porous, and the law of growth is linear with time.

From the difference in weight gain after 10 hours at 435°C and 595°C the activation energy for the oxidation process can be estimated; this amounts to about 0.75 eV. or 17000 cal/mole.

Conclusions

Over the range of temperature and film thickness considered, there is no essential difference between the oxide layer formed on zirconium by thermal or electrolytic oxidation. In general the thermal oxidation of specimens with an initial anode layer proceeds as if these specimens had previously acquired the same oxide thickness by heating alone. Where the anodic film is already thicker than the oxide which would be formed by heating only, the former grows but slightly when heated; where the anodic film is thinner than the ultimate thermal growth of the oxide, the anodic film merely delays the thickening of the film on heating.

The rate of oxidation between 300° and 600°C is approximately parabolic. After prolonged heating the rate increases markedly, and becomes almost linear. This change has previously been observed by Cubicciotti, Dravnieks and Blevitzky [3] and has been ascribed by them to increased temperature of oxidation. Our experiments, which extend over a wider time range than theirs, indicate that this explanation does not hold, since the effect is observed at 435°C for a thickness of about 10^4 Å, and at 595°C at 5×10^4 Å.

Acknowledgements

The authors wish to thank Dr. H. M. Finniston for his encouragement, and Mr. A. A. Tilsley for help in the experimental work. They are grateful for permission from the Director, Atomic Energy Research Establishment, Harwell, to publish this paper.

References

1. Charlesby, A. Acta. Met. **1** (1953) 340.
2. Charlesby, A. Proc. Phys. Soc. **B66** (1953) 317.
3. Cubicciotti, D. D., Dravnieks, A., and Blevitsky, R. A.E.C. Report NP-1003, (1949).
4. Dravnieks, A. J. Amer. Chem. Soc. **72**, (1950) 3568.
5. Fast, J. D. Foote Prints **13**, 1 (1940) 22.
6. Gulbransen, E. A. and Andrew, K. F. J. Metals **185** (1949) 515.
7. Guldner, W. G. and Wooten, L. A. Trans. Electrochem. Soc. **93** (1948) 223.
8. Hayes, E. T. and Roberson, A. H. Trans. Electrochem. Soc. **96** (1949) 142.
9. Hickman, J. W. and Gulbransen, E. A. Anal. Chem. **20** (1948) 158.
10. Jafee, R. I. and Campbell, I. U.S.A.E.C. Report N.P. 266 (1948).
11. Laing, J. A.E.R.E. Report M/TN-7 (1951).
12. Mott, N. F. Trans. Faraday Soc. **43** (1947) 429.
13. Polling, J. J. and Charlesby, A. Proc. Phys. Soc. **B67** (1954) 201.

THE NITRIDES AND OXIDE-NITRIDES OF TUNGSTEN*

R. KIESSLING and L. PETERSON†

A tungsten oxide-nitride with a composition close to the formula $W_{.62}N_{.62}O_{.38}$ has been investigated by analytical and X-ray methods. It was obtained by reducing ammonium paratungstate or tungsten trioxide with ammonia, probably has metallic properties, and belongs to the interstitial compounds. It has a defective MeX-lattice with the sodium chloride structure. Only 62 per cent of the Me-positions, however, are statistically occupied by tungsten atoms, whereas probably all the X-positions are occupied, 62 per cent by nitrogen atoms and 38 per cent by oxygen.

The γ-nitride in the tungsten-nitrogen system has also been shown to be an oxide-nitride. This phase has also a defective tungsten lattice, but the vacancies are ordered. Its ideal formula is $W_{.75}(N, O)_{1.00}$, where the ratio N:O is unknown but certainly greater than for $W_{.62}N_{.62}O_{.38}$.

In conclusion there is a short discussion regarding the electronic structure of the oxide-nitrides.

LES NITRURES ET LES OXYDES-NITRURES DE TUNGSTÈNE

On a investigué par des méthodes analytiques et aux rayons X, un oxyde-nitrure de tungstène, dont la composition se rapproche de la formule $W_{0.62}N_{0.62}O_{0.38}$. Ce composé fut obtenu par la réduction d'un paratungstate d'ammoniaque ou un trioxyde de tungstène avec l'ammoniaque. Il a probablement des propriétés métalliques et appartient à la classe des composés interstitiels. Ce composé a un réseau défectueux du type—MeX avec la structure du chlorure de sodium. Toutefois, seulement 62 pour cent des positions Me sont statistiquement occupées par des atomes de tungstène, alors que les positions X sont probablement toutes occupées; les atomes d'azote en occupant 62 pour cent et les atomes d'oxygène 38 pour cent. On a montré que les nitrures γ du système tungstène-azote sont aussi des oxydes-nitrues. Cette phase a aussi un réseau défectueux du tungstène, mais les lacunes y sont ordonnées. Sa formule idéale est $W_{0.75}(N, O)_{1.00}$, où le rapport N: O est inconnu, mais certainement plus grand que dans le cas de $W_{0.62}N_{0.62}O_{0.38}$. Pour conclure, la structure électronique des oxydes-nitrures est brièvement discutée.

DIE NITRIDE UND OXYDNITRIDE DES WOLFRAMS

Ein Wolframoxydnitrid mit einer etwa der Formel $W_{0.62}N_{0.62}O_{0.38}$ entsprechenden Zusammensetzung wurde analytisch und röntgenographisch untersucht. Es wurde durch Reduktion von Ammonium-parawolframat oder Wolframtrioxyd mit Ammoniak erhalten; es hat wahrscheinlich metallische Eigenschaften und gehört zu den Einlagerungsverbindungen. Es hat ein fehlerhaftes MeX- Gitter mit einer Natriumchlorid-Struktur, in dem jedoch nur 62% der Me-Gitterplätze statistisch von Wolframatomen besetzt sind. Dagegen sind wahrscheinlich alle X-Gitterplätze besetzt, 62% mit Stickstoffatomen und 38% mit Sauerstoff.

Es wurde ausserdem gezeigt, dass das γ-Nitrid des Wolfram-Stickstoffsystems ein Oxydnitrid ist. Diese Phase ist ebenfalls ein fehlerhaftes Wolframgitter, in dem die Leerstellen jedoch geordnet sind. Die theoretische Formel dieser Verbindung ist $W_{0.75}(N,O)_{1.00}$; das Verhältnis N: O ist nicht bekannt, jedoch bestimmt grösser als für $W_{0.62}N_{0.62}O_{0.38}$.

Abschliessend wird die Elektronenstruktur der Oxydnitride kurz diskutiert.

Two nitrides of tungsten are known from earlier work. Hägg [1] reported that a nitride with a face-centred cubic metal lattice was formed if tungsten was nitrided with dry ammonia at 700–800°C. The formation of this nitride was very slow, however, and it was not possible to obtain it in a pure form; it always appeared mixed with tungsten. The phase was called the β-phase in the tungsten-nitrogen system, and assumed to have a composition of W_2N, but the formula could not be verified. Later, Kiessling and Liu [2] observed a new nitride, the γ-phase, formed at about 800–900° if tungsten was nitrided with ammonia. The γ-phase was assumed to be closely related to the β-phase. Its lattice was of the simple cubic type. The structure could not be determined but was probably closely related to that of the β-phase. The nitrogen content was assumed to be about 33 atomic per cent, as for the β-phase, but it was also impossible to obtain this phase in a pure state. It will be shown below that the γ-phase has an ordered defective lattice containing both nitrogen and oxygen.

The Existence of a Tungsten Oxide-Nitride

During experiments with the reduction of ammonium paratungstate to tungsten with ammonia, the present authors observed that a phase with a face-centred cubic metal lattice could be obtained in a pure state as the final reduction product if the reduction was carried out at a temperature of about 700°C. The phase had a grey, metallic lustre and was usually difficult to distinguish from tungsten powder. The lattice constant, about 4.138 Å was slightly greater than that of the β- and γ-phases in the tungsten-nitrogen system (4.126 and 4.122 – 4.130 Å resp.). The phase could also be obtained by reducing tungsten trioxide, a process which has been described in a patent journal [3]. However,

*Received January 15, 1954.
†Söderfors Bruk, Söderfors, Sweden.

the chemical analysis showed a tungsten content much too low and a nitrogen content too high to correspond to the formula W_2N. Large amounts of oxygen were also found to be present in the lattice. On structural grounds the formula may be written $W_xN_yO_{1-y}$, where the values of x and y both are about 0.62. Before discussing the results, which are given in Table I, the methods of analysis will be described.

The chemical analyses were carried out in the following way. Tungsten was determined by oxidizing the specimens in dry oxygen to tungsten trioxide and weighing the amount of trioxide formed. Some control analyses were carried out by dissolving the samples in a mixture of nitric and hydrofluoric acids, precipitating the tungsten as tungstic oxide, and igniting the precipitate.

Nitrogen was usually determined by heating the compound to about 1100°C and pumping the gases formed. It had been found that the phase was completely converted to a mixture of tungsten and tungsten dioxide if heated in vacuum at this temperature for 2–3 hours. During this process the nitrogen was given off, which could be checked by comparing the results with some analyses by the Kjeldahl method. The method was usually avoided, however, because of the vigorous reaction which often occurred.

The oxygen content was directly determined by reduction of the oxide-nitride with hydrogen at about 1000°C and weighing the amount of water absorbed by phosphorous pentoxide when the gas had passed the reaction zone. The residue after reduction was pure tungsten, and the completeness of the reduction could be tested by comparing the tungsten content after reduction and oxidation of the specimens. Because of the presence of oxygen in the lattice the specimens always formed a mixture of tungsten and tungsten dioxide if they were heated in vacuum at 1000–1100°C. (No trace of tungsten dioxide was observed if tungsten powder was heated in the same apparatus under the same conditions.) A probable process for this formation of tungsten dioxide is illustrated by the following reaction formula

$$W_{0.62}N_{0.62}O_{0.38} \rightarrow 0.31\ N_2 + 0.19\ WO_2 + 0.43W.$$

The tungsten dioxide is thus formed by the oxygen which is present interstitially in the oxide-nitride and which will form the dioxide when the lattice of the oxide-nitride is broken down by the evolution of nitrogen in vacuum. A mixture of 63 w.t. per cent tungsten and 37 w.t. per cent tungsten dioxide will thus be formed if the oxide-nitride is heated in vacuo. Such a mixture was prepared and the X-ray photograph compared with the residue after vacuum extraction. The photographs were very similar.

As is shown by the results in Table I, the composition of the oxide-nitride is independent of the period of nitriding, within the limits of error, if this period has been long enough. It is also

TABLE I

Formula* (according to the analyses)	W weights %	N weights %	O weights %	Density (a = 4,14Å) observed	calc. 4 metal atoms	calc. defective lattice	Method of preparation
$W_{73}N_{18}O_{45}$	89.5	5.1	4.3	12.2	19.0	14.0	paratungstate 3h, NH_3, 700° (trace of WO_2)
$W_{60}N_{21}O_{39}$	88.0	6.8	5.0	11.3	19.4	11.7	paratungstate 5h, NH_3, 700°
$W_{63}N_{21}O_{39}$	89.1	6.5	4.8	11.7	19.3	12.2	paratungstate 12h, NH_3, 700°
$W_{62}N_{43}O_{37}$	89.1	6.9	4.7	11.8	19.4	12.0	paratungstate$_6$ 48h, NH_3, 700°
$W_{53}N_{59}O_{41}$	86.8	7.3	5.8	11.4	20.3	10.5	WO_3, 3h, NH_3, 700°
$W_{63}N_{65}O_{35}$	88.6	6.9	4.3	12.0	19.4	12.2	WO_3, 7h, NH_3, 700°
$W_{64}N_{21}O_{19}$	88.4	6.4	4.7	11.5	19.4	12.4	WO_3, 11h, NH_3, 700°

*The formulas have been written with the sum of the N and O atoms in each case = 100. They thus illustrate a MeX lattice with NaCl structure where all the X-positions are occupied by the N and O atoms together and only part of the Me-positions by W atoms (73, 60, 63, 62, 53, 63 and 64 per cent resp.).

independent of whatever compound, tungsten trioxide or paratungstate, has been used for the preparation. The formula obtained if the mean value of all the analyses are used is $W_{.62}$ $N_{.62}$ $O_{.38}$ (the values after 3[h] nitriding of WO_3 or paratungstate have been excluded because of incomplete reaction time). On structural grounds, which will be discussed below, the sum of the oxygen and nitrogen atoms has been put equal to 1.00. The homogeneity range seems to be very narrow. The X-ray reflexions are those of a face-centred metal lattice with a cube-edge of 4.138 ± 0.002 Å. The intensities, but not the densities, are compatible with the assumption that 4 tungsten atoms are present in the unit cell, occupying the positions 000, $\frac{1}{2}\frac{1}{2}0$, $\frac{1}{2}0\frac{1}{2}$, $0\frac{1}{2}\frac{1}{2}$.

The densities, experimentally obtained by the pycnometric method with about 5g of the sample each time, have also been given in Table I. These densities are far too low, however, compared with the densities calculated from X-ray data with the assumption that 4 metal atoms are present in the unit cell, i.e., occupy the corners of the cube and the centres of the faces of the cubic unit cell. These calculated densities are also given, and it is evident that, even with a large experimental error in the density determination, the densities obtained are much too low to agree with the assumption of 4 metal atoms in the unit cell. The densities obtained indicate that between 2 and 3 metal atoms in the unit cell is much more probable.

Furthermore, space considerations strongly support the assumption of a face-centred tungsten lattice with tungsten atoms missing. The number of nonmetal atoms nitrogen and oxygen together is about 1, 5 to 2 times that of the number of the tungsten atoms. In a fully occupied face-centred metal lattice with a parameter of 4.14 Å there will be two types of interstices, "octahedral" and "tetrahedral" interstices. In the "octahedral" interstices a nonmetal atom will be octahedrally surrounded by six metal neighbours and the greatest radius possible for the atom will be 0.63–0.69 Å (depending on whether the radius of the tungsten atom is assumed to be 1.46 Å as obtained from this structure or 1.40 Å as obtained from other similar compounds). In the "tetrahedral" interstices a nonmetal atom will be tetrahedrally surrounded by four tungsten atoms and the greatest possible radius for an interstitial atom will be 0.33–0.39 Å. The radius of the nitrogen atom has been found for several structures to be about 0.71 Å. The radius of the oxygen atom seems to be about 0.60 Å, and if some ionisation to a negative oxygen ion occurs the value will be greater.

It is thus evident that only the octahedral interstices will have space for the nonmetal atoms, and the total number of such interstices is equal to four for the face-centred cubic cell. Thus there cannot be an oxide-nitride with a face-centred lattice with a greater number of nonmetal atoms than metal atoms unless some of the metal atoms in the face-centred lattice are missing.

There are several possibilities for the structure of such a defective lattice (see below). The most probable, in the authors' opinion, is that the nonmetal atoms oxygen and nitrogen together occupy all the "octahedral" positions of the cubic unit cell (with coordinates $00\frac{1}{2}$, $0\frac{1}{2}0$, $\frac{1}{2}00$ and $\frac{1}{2}\frac{1}{2}\frac{1}{2}$), whereas statistically about 2/3 of the metal positions in the face-centred lattice ($0\frac{1}{2}\frac{1}{2}$, $\frac{1}{2}0\frac{1}{2}$, $0\frac{1}{2}\frac{1}{2}$ and 000) are occupied by tungsten atoms and about 1/3 empty. In Table I the densities for the different specimens have been calculated on this assumption, using the formulas obtained from chemical analysis. The agreement between observed and calculated densities is very good.

It has been assumed above that the vacant sites of the metal lattice are empty. The possibility that these "holes" may be filled with nitrogen or oxygen atoms must also be considered, but may be rejected because the resulting densities would not be in accordance with the observed ones. If, for instance, all the "holes" of the lattice of $W_{.62}$ $N_{.62}$ $O_{.38}$ are assumed to be occupied by oxygen and nitrogen atoms, the formula could be written about $W_{.75}N_{.15}O_{.10}$ ($N_{.60}O_{.40}$). The density calculated for this compound would be 14,6, far too great compared with the observed density of 11.3–12.0.

There is also the possibility of vacancies both in the metal and in the nonmetal lattices. This has been suggested by Brauer for the NbO-lattice [4]. The experimental evidence makes such an assumption rather unfeasible. (A lattice with 10 per cent of the sites of the nonmetal atoms in $W_{.62}$ $N_{.62}$ $O_{.38}$ unoccupied would give a calculated density of 10.5 compared with the observed density of 11.3–12.0.)

Finally, several attempts were made to produce an ordered defective lattice of this phase. They were not successful (see below).

The Tungsten–Nitrogen System

Because of the high nitrogen content of this oxide-nitride, the presence of oxygen, and the existence of a defective lattice, a reinvestigation

of the tungsten-nitrogen system was undertaken. Starting materials were tungsten powder and ammonia, and the nitriding was carried out in a tube furnace at various temperatures and for various periods. In some experiments the ammonia was carefully dried, and all oxygen was finally removed from it by passing over zirconium hydride at about 800 degrees; in other experiments the ammonia contained small amounts of oxygen and water vapor. The following are the essential results:

The β-phase [1], assumed by Hägg to have the composition W_2N, was formed between 600°C and 850°C, and was always mixed with a much greater amount of tungsten. It had a face-centred cubic metal lattice and was formed by both pure and impure ammonia.

The γ-phase [2] was only formed if the ammonia contained small amounts of oxygen or water. It had a simple cubic metal lattice closely related to the β-phase. All the reflexions with unmixed indexes present in the β-phase were also present and strong in the γ-phase, but in addition there were weak reflexions with mixed indexes (Table II). The γ-phase too was always mixed with a much greater amount of tungsten.

It was possible to determine the crystal structure of the γ-phase, previously unknown. The reflexions are those of a simple cubic lattice (Table II),

TABLE II

γ-phase. Simple cubic, O^1_h– Pm3m. Calculated for 3 W-atoms in 3: (d) $\frac{1}{2}\,\frac{1}{2}\,0$, $\frac{1}{2}\,0\,\frac{1}{2}$, $0\,\frac{1}{2}\,\frac{1}{2}$. The observed intensities have been obtained from a film taken with monochromatic Cu radiation in a Guinier camera.

hkl	$p\|F\|^2$ (calc)	$p\|F\|^2$ (obs)
1 0 0	27	29
1 1 0	47	50
1 1 1	255	255
2 0 0	176	169
2 1 0	72	63
2 1 1	67	75
2 2 0	268	264
2 2 1	58	54
3 0 0	14	
3 1 0	53	33
3 1 1	456	370
2 2 2	147	124
3 2 0	47	39
3 2 1	91	78

except that the reflexions with unmixed indexes are much stronger than the others. The earlier investigation by Kiessling and Liu was based on the assumption that all metal positions were occupied by tungsten atoms, and it was never possible to obtain acceptable agreement between observed and calculated intensities with this assumption. A reinvestigation by the present authors showed, however, that close agreement between observed and calculated intensities was obtained if the face-centred metal lattice of the γ-phase was assumed to be an ordered defective lattice, with the metal atoms in the positions with coordinates $\frac{1}{2}\frac{1}{2}0$, $\frac{1}{2}0\frac{1}{2}$, and $0\frac{1}{2}\frac{1}{2}$, but with the atom at the corner of the cube, 000, missing (Table II).

The formula for the γ-phase should thus be $W_{.75}\,N_z\,O_{1-z}$, where z is unknown, as compared with $W_{.62}\,N_{.62}\,O_{.38}$ for the oxide-nitride described above. Attempts to determine z by nitrogen and oxygen analyses gave no reproducible results because of the small amounts present. The oxygen content of $W_{.72}\,N_z\,O_{1-z}$ is certainly much smaller than for $W_{.62}\,N_{.62}\,O_{.38}$, since the former is formed from pure tungsten and impure ammonia whereas the latter is formed from oxygen-rich tungsten compounds.

The results seem to show that at least two different oxide-nitrides exist. One, $W_{.62}\,N_{.62}\,O_{.38}$, has a defective disordered face-centred tungsten lattice, and the length of the axis of the cubic cell is 4.138 Å. The other, $W_{.75}\,N_z\,O_{1-z}$, formerly called the γ-phase in the tungsten-nitrogen system, has an ordered, defective, simple cubic tungsten lattice with the cube-edge 4.122–4.130 Å.

Because of the structural relationship between the two defective lattices of the ordered $W_{.75}\,N_z\,O_{1-z}$ and the disordered $W_{.62}\,N_{.62}\,O_{.38}$, the effect of various heat treatment was tried.

All attempts to order the defective tungsten lattice of the $W_{.62}\,N_{.62}\,O_{.38}$-phase were unsuccessful.

The ordered $W_{.75}\,N_z\,O_{1-z}$-phase (the γ-phase) changed to a face-centred cubic lattice on annealing at 890 degrees for some hours and quenching. This new face-centred lattice could again be transformed to the γ-phase if annealed for some hours in ammonia or a vacuum at temperatures below about 850°C. These reactions indicate an order-disorder transformation for the γ-phase, but no definite conclusions can be obtained, as the phases always appeared mixed with a much greater amount of tungsten.

The β-phase formed by pure, dry ammonia could not be transformed to the γ-phase, whereas the β-phase containing oxygen could be transformed.

This also indicates that the γ-phase is an oxide-nitride and not a nitride of tungsten.

Discussion

The oxide-nitrides described are of interest because they have oxygen atoms interstitially in the metal lattice. They thus belong to the same group of compounds as the carbides, borides, and nitrides of the transition metals, and are related to the oxide-nitrides of titanium [5], as well as to the oxides with the structure of the high-speed-steel carbide [6]. It is of special interest to compare the compounds

$$W_2N,\ W_{.75}\ N_z\ O_{1-z} \text{ and } W_{.62}\ N_{.62}\ O_{.38}$$

where the amount of oxygen in the lattice increases. The metal lattice is the same face-centred cubic lattice for all the phases. With increasing amount of oxygen, however, an increasing number of vacancies in the tungsten lattice appear.

This seems to support the theory advanced by one of the present authors (R. K.) for the borides of the transition metals [7], that the interstitial boron atoms (and similarly for carbon and nitrogen [8; 9]) give part of their electrons to the metal lattice. When oxygen is introduced into the tungsten nitride, some kind of N-O bonds are probably formed. Part of the electrons of the nitrogen atoms are thus engaged in bond formation with the strongly positive oxygen atoms, which tend to form negative oxygen ions. The number of electrons which can be transferred from the interstitial nitrogen atoms to the tungsten lattice thus decreases with increasing oxygen content. The electron concentration of the metal lattice thus decreases, though defects appearing in the tungsten lattice tend to maintain it.

Acknowledgements

The authors wish to thank Mr. N. Schönberg for his kind interest in this investigation and Miss B. Schöning for valuable help with various preparations and calculations.

References

1. HÄGG, G. Z. phys. Chem. **B7** (1930) 339.
2. KIESSLING, R. and LIU, Y. H. J. Metals **3** (1951) 639.
3. Brit. Pat. 635.221, August 29, 1946.
4. BRAUER, G. Z. anorg. u. allg. Chem. **248** (1941) 1.
5. EHRLICH, P. Z. anorg. Chem. **259** (1949) 1.
6. KARLSSON, N. Nature **168** (1951) 558.
7. KIESSLING, R. Acta Chem. Scand. **4** (1950) 209.
8. JACK, K. H. Proc. Roy. Soc. London **A195** (1948) 53.
9. JACK, K. H. Chem. and Ind. (1951) 1004.

FORMATION ENERGIES OF VACANCIES IN COPPER AND GOLD*

C. J. MEECHAN and R. R. EGGLESTON†

The electrical resistance of pure copper and gold has been measured as a function of temperature from room temperature to 950°C. The experimental data taken below 500°C for each metal were fitted by an expression of the form $R = A + BT + CT^2$. This equation fitted the data, within the experimental error, up to 600°C for copper and 500°C for gold. At higher temperatures the measured resistance values exceeded the extrapolated quadratic function. This additional resistance, ΔR, has been attributed to the presence of vacancies existing in thermodynamic equilibrium at the high temperatures. It was found by plotting log ΔR *vs* $1/T$ that the dependence of ΔR on temperature can be represented by the following expression:

$$\Delta R = A \exp(-E/kT).$$

Here E is presumed to be the formation energy of vacancies. The values of E determined in this manner for copper and gold are $0.90 \pm .05$ ev and $0.67 \pm .07$ ev, respectively. The activation energy for self-diffusion in face-centered cubic metals should be the sum of the formation energy and the activation energy for migration of vacancies for the particular metal. From the known energies for self-diffusion and the formation energies of vacancies given above, the activation energies of 1.17 ev and 1.54 ev are obtained for the migration of vacancies in copper and gold, respectively. Using theoretical values for the resistivity per atomic per cent vacancies, and the ΔR values determined in this paper, the vacancy density near the melting point of copper is estimated to be of the order of 1 per cent.

LES ÉNERGIES DE FORMATION DE LACUNES RÉTICULAIRES DANS LE CUIVRE ET DANS L'OR

On a mesuré la résistance électrique du cuivre et de l'or purs en fonction de la tempèrature, dans l'intervalle allant de la température ambiante jusqu'à 950°C. Les données expérimentales, obtenues pour chacun de ces métaux, en dessous de 500°C, peuvent être représentées analytiquement par $R = A + BT + CT^2$. Cette equation satisfait aux données, à l'erreur expérimentale près, jusqu'à 600°C pour le cuivre et jusqu'à 500°C pour l'or. Aux températures plus élevées, les valeurs mesurées de la résistance étaient supérieures aux valeurs extrapolées de cette fonction du second degré. Cette résistance supplémentaire ΔR fut attribuée à la présence de lacunes réticulaires qui existent en equilibre thermodynamique aux températures élevées. En portant dans un diagramme log ΔR en fonction de $1/T$ on a constaté que ΔR peut être exprimé en fonction de la température par l'equation suivante: $\Delta R = A \exp(-E/kT)$ où E représenterait l'énergie de formation des lacunes. Les valeurs de E déterminées de cette façon pour le cuivre et l'or sont de $0{,}90 \pm 0{,}05$ ev et $0{,}67 \pm 0{,}07$ ev respectivement. L'énergie d'activation pour l'autodiffusion dans les métaux cubiques à faces centrées devrait être égale à la somme de l'énergie de formation et de l'énergie d'activation pour la migration des lacunes dans le métal en question. En se basant sur les valeurs des énergies d'activation pour l'autodiffusion, connues, et les énergies de formation des lacunes indiquées plus haut, on obtient des énergies d'activation pour la migration des lacunes de 1,17 ev et 1,54 ev pour le cuivre et l'or respectivement. En employant les valeurs théoriques de la résistivité par pour cent de lacunes en atomes et les valeurs de ΔR présentées dans cet article, on a estimé la densité des lacunes au voisinage du point de fusion du cuivre à environ 1 pour cent.

BILDUNGSENERGIEN VON LEERSTELLEN IN KUPFER UND GOLD

Der elektrische Widerstand von reinem Kupfer und Gold wurde als Funktion der Temperatur zwischen Zimmertemperatur und 950°C gemessen. Die experimentellen Resultate beider Metalle unterhalb von 500°C konnten durch die folgende Gleichung beschrieben werden: $R = A + BT + CT^2$. Innerhalb der experimentellen Fehlergenzen genügte Kupfer dieser Gleichung bis zu 600°C und Gold bis zu 500°C. Bei höheren Temperaturen waren die gemessenen Widerstandswerte grösser als die aus der quadratischen Funktion extrapolierten Daten. Dieser zusätzliche Widerstand, ΔR, wird den im thermodynamischen Gleichgewicht bei höheren Temperaturen vorhandenen Leerstellen zugeschrieben. Wenn man log ΔR gegen $1/T$ aufträgt, zeigt es sich, dass man die Temperaturabhängigkeit von ΔR durch die folgende Gleichung ausdrücken kann:

$$\Delta R = A \exp(-E/kT)$$

wobei E als die Bildungsenergie der Leerstellen gedeutet wird. Die auf diese Weise ermittelten E-Werte für Kupfer und Gold sind $0{,}90 \pm 0{,}05$ eV bezw. $0{,}67 \pm 0{,}07$ eV. Die Aktivierungsenergie der Selbstdiffusion in kubisch-flächenzentrierten Metallen sollte gleich der Summe der Bildungsenergie der Leerstellen und der Aktivierungsenergie ihrer Wanderung in dem betreffenden Metall sein. Aus den bekannten Energien der Selbstdiffusion und den oben angegebenen Bildungsenergien der Leerstellen werden für die Wanderung von Leerstellen in Kupfer und Gold Aktivierungsenergien von 1,17 eV und 1,54 eV erhalten. Aus theoretischen Werten des Widerstands pro Atomprozent Leerstellen und aus den in der vorliegenden Arbeit ermittelten ΔR-Werten wurde die Leerstellendichte in der Umgebung des Schmelzpunktes von Kupfer grössenordnungsmässig zu 1% geschätzt.

Introduction

It is generally accepted that a metal damaged either by deformation [1] or high-energy particle irradiation [2] has present within it large numbers of Schottky defects. The activation energy for motion of these vacant lattice sites as well as their formation energy has received considerable attention in an effort to understand the physical behavior of metals. MacDonald [3; 4] has measured the temperature dependence of resistivity of the alkali metals. He found an "anomalous" increase in the electrical resistivity of these metals near the melting point

*Received February 6, 1954.

†Atomic Energy Research Department, North American Aviation, Inc., Downey, California.

and attributed this additional resistivity to the formation of excess vacancies generated at the higher temperatures. This extra resistivity was found to be proportional to a Boltzmann factor, $e^{-E/kT}$, where E is the energy of formation for vacancies. This work suggested to the authors that the formation energies for vacancies in copper and gold might be obtained in a similar manner.

It is the purpose of this paper to report the results of measurements of electrical resistance made on pure copper and gold as a function of temperature, and to determine the values of the formation energies of vacancies in these metals from the resistance-temperature data.

Experimental Procedure and Results

The copper and gold specimens used for these measurements were furnished by the Johnson and Matthey Company and were stated to be of 99.999 per cent purity before drawing into wire (0.009-inch diameter for copper and 0.012-inch diameter for gold). The wire was wound on a lavite frame which was in turn supported by the electrical lead wires inside a massive molybdenum cylinder which furnished thermal stability. This cylinder was placed within a vacuum furnace in which the pressure was maintained below 10^{-4} mm of mercury. The electrical connections, made of commercial purity wires of the same material as the sample, were spot welded to the sample and brought outside the vacuum furnace through Kovar seals.

The resistance measurements were made by standard potentiometric methods using Rubicon Type "B" Potentiometers. A measuring current of 0.1 ampere was used for the measurements on copper and 0.03 ampere for the gold. The usual precautions were taken so that the readings could be corrected for thermal voltages that might appear. Simultaneous measurements of temperature were made by using a chromel-alumel thermocouple, which was mounted close to the sample within the molybdenum block. The precision of measurement was within 0.5°C although the absolute accuracy may be somewhat less.

The results of the measurements are given in Tables I and II. Figure 1 shows the temperature dependence of the electrical resistance for both metals throughout the measurement range.

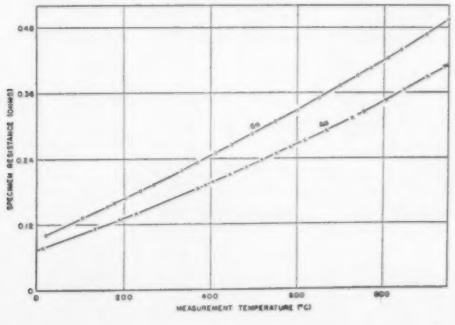

FIGURE 1. Resistance *vs* temperature curves for pure copper and gold.

TABLE I

COPPER

R_{meas} (ohms)	T_{meas} (°C)	R_{calc} (ohms)	ΔR
.15275	163.9	.15260	+.00015
.15852	179.4	.15835	+.00017
.16802	205.7	.16818	−.00016
.18064	239.2	.18084	−.00020
.19249	269.8	.19254	−.00006
.21770	334.6	.21774	−.00004
.23210	370.6	.23198	+.00012
.24933	413.5	.24920	+.00013
.26402	450.2	.26413	−.00011
.28350	497.2	.28351	−.00001
.30555	549.7	.30553	+.00002
.32716	600.3	.32711	+.00005
.34998	651.9	.34948	+.00050
.37159	699.9	.37061	+.00098
.38979	739.9	.38847	+.00132
.40420	770.6	.40232	+.00188
.42307	810.1	.42034	+.00273
.43798	840.4	.43431	+.00367
.46690	897.8	.46111	+.00579
.49350	949.3	.48555	+.00795

$\rho_{Cu}|20°C = 1.67$ micro-ohm-cm[5].

TABLE II

GOLD

R_{meas} (ohms)	T_{meas} (°C)	R_{calc} (ohms)	ΔR
.07993	17.3	.08009	−.00016
.11302	133.7	.11272	+.00030
.12992	191.6	.12970	+.00022
.14106	230.2	.14130	−.00024
.18490	369.5	.18499	−.00009
.19125	389.2	.19140	−.00015
.19677	405.8	.19684	−.00007
.20993	445.1	.20990	+.00003
.22305	483.5	.22288	+.00017
.23516	518.1	.23476	+.00040
.24706	551.6	.24644	+.00062
.25916	585.2	.25832	+.00084
.27206	620.4	.27094	+.00112
.29325	676.4	.29140	+.00185
.31459	730.4	.31157	+.00302
.32470	755.5	.32109	+.00361
.34563	805.8	.34046	+.00517
.36391	848.3	.35711	+.00680
.38655	899.1	.37737	+.00918
.40637	941.2	.39445	+.01192

$\rho_{Au}|20°C = 2.35$ micro-ohm-cm[6].

Discussion and Conclusion

The theory for electrical resistance at high temperatures, given by Mott and Jones [7], predicts a quadratic dependence of resistance on temperature for copper, silver, and gold. In addition to this temperature dependence of resistance, one might expect an "excess" resistance, ΔR, if the density of vacancies generated at the higher temperatures is sufficiently large. This extra resistance should have a Boltzmann temperature dependence. With these ideas in mind, the copper and gold data, taken below 500°C, were fitted by an expression of the form

$$R = A + BT + CT^2$$

using a least-squares criterion. In this equation R is the resistance in ohms and T is the temperature in degrees Kelvin. The coefficients A, B, and C for copper are 0.004134 ohms, 3.0955×10^{-4} ohms/°K, and 0.689×10^{-7} ohms/(°K)^2, respectively. For gold these coefficients are 0.007440 ohms, 2.2856×10^{-4} ohms/°K, and 0.742×10^{-7} ohms/(°K)^2, respectively. This expression fitted the data within the experimental error up to 600°C for copper and slightly over 500°C for gold. A calculated resistance for each point at the higher temperatures was determined by extrapolating the quadratic function to 950°C. These calculated resistance values were then subtracted from the measured values and a set of ΔR's determined. The results of this calculation are tabulated in Tables I and II. The logarithm of ΔR was then plotted as a function of $1/T$, the slope of which defines the formation energy of vacancies for the metal (see Figure 2). In this manner the formation energy of vacancies was determined to be $0.90 \pm .05$ ev in copper and $0.67 \pm .07$ ev in gold.

Dexter [8] and Jongenburger [9] have calculated the resistivity per atomic per cent vacancies for copper. Their calculations yielded 0.4 and 1.3 micro-ohm-cm per atomic per cent vacancies, respectively. Using these values and the values of ΔR from the present work, it is estimated that the density of vacancies in copper near the melting point is of the order of one atomic per cent.

The energy of formation of vacancies in gold, presented in this paper, is outside the limits of the value given by Kauffman and Koehler [10]. They concluded from quenching experiments that the formation energy should be between 1 and 2 ev. This discrepancy is unresolved at the present time.

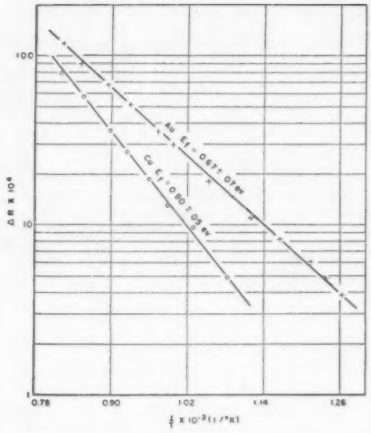

FIGURE 2. Determination of vacancy formation energies for copper and gold.

The result of this work for copper is in very good agreement with that given previously by Brinkman, Dixon, and Meechan [11]. They gave arguments for the assignment of 1.19 ev as the activation energy for migration of vacancies in copper. Subtracting this value from the activation energy for self-diffusion, they determined the formation energy for vacancies in copper to be 0.88 ev. This procedure can be used to determine the activation energy for motion of vacancies in gold. Subtracting the formation energy determined in this paper from the activation energy for self-diffusion, 2.21 ev [12], the activation energy for motion of vacancies in gold is calculated to be 1.54 ev.

LeClaire [13] has recently predicted the formation energies of vacancies in several metals including copper and gold and his results are in satisfactory agreement with those of this paper. His values for the energies of formation of vacancies in copper and gold are 0.74 ev and 0.83 ev, respectively.

Acknowledgment

The authors wish to express their deep appreciation for the enlightening suggestions offered by Mr. J. A. Brinkman and Dr. C. E. Dixon during the course of this work.

This report is based on studies conducted for the Atomic Energy Commission.

References

1. SEITZ, F. Adv. in Phys. **1** (1952) 43.
2. DIENES, G. J. Ann. Rev. of Nuc. Sci. **2** (Stanford, 1953).

3. MACDONALD, D. K. C. J. Chem. Phys. **21** (1953) 177.
4. MACDONALD, D. K. C. Erratum, J. Chem. Phys. **21** (1953) 2097.
5. SMART, J. S., SMITH, A. A., and PHILLIPS, A. J. Trans. A.I.M.M.E. **143** (1941) 272.
6. Metals Handbook (1948), p. 1116.
7. MOTT, N. F. and JONES, H. Properties of Metals and Alloys (London, 1936) p. 268.
8. DEXTER, D. L. Phys. Rev. **87** (1952) 768.
9. JONGENBURGER, P. Phys. Rev. **90** (1953) 710.
10. KAUFFMAN, J. W. and KOEHLER, J. S. Phys. Rev. **88** (1952) 149.
11. BRINKMAN, J. A., DIXON, C. E., and MEECHAN, C. J. Acta Met. **2** (1954) 38.
12. MCKAY, H. A. C. Trans. Faraday Soc. **34** (1938) 845.
13. LECLAIRE, A. D. Acta Met. **1** (1953) 438.

Note Added in Proof

F. Abeles (Comptes Rendus **237**, No. 15 (1953) 796 has recently calculated the resistivity per atomic per cent vacancies for several metals. His value for copper is 1.28 micro-ohm-cm per atomic per cent vacancies, which is in close agreement with the value given by Jongenburger. Abeles also has calculated this quantity for gold which is 1.45 micro-ohm-cm per atomic per cent vacancies. With the aid of these calculations, the density of vacancies in copper near the melting point is estimated to be 0.2 atomic per cent and in gold 0.4 atomic per cent.

ELECTRON CONFIGURATIONS IN SOME TRANSITION METAL ALLOYS*

W. H. TAYLOR†

Structural data for a number of Al-rich alloys of transition metals are reviewed, special attention being devoted to the discussion of assumptions and approximations introduced—explicitly or implicitly—in the course of the structure-analysis.

It appears that a more fundamental treatment is required for Brillouin zone measurements which, on the usual elementary interpretation, are in harmony with Raynor's suggestions of electron absorption by transition metal atoms in alloys of this kind.

Abnormally short contacts between a transition metal atom and some of the surrounding Al atoms appear to be characteristic of these structures, and—if certain assumptions made in the course of the analysis are justified—there is evidence for the absorption of about 2 electrons by Co, Mn, and Cr atoms. (No data are available for the Fe atom.)

Some of the most important lines for future development are indicated.

LES CONFIGURATIONS ÉLECTRONIQUES DANS CERTAINS ALLIAGES DES MÉTAUX DE TRANSITION

On revise les données concernant la structure de plusieurs alliages des métaux de transition, riches en aluminium. On s'arrête plus longuement à la discussion des hypothèses et approximations introduites—explicitement ou implicitement—au cours de l'analyse structurale. Il est constaté que les mesures des zones de Brillouin doivent être traitées d'une façon plus fondamentale; suivant l'interprétation élémentaire, ces mesures s'accordent avec les suggestions de Raynor, à savoir, que dans des alliages de ce genre, les atomes des métaux de transition absorbent des électrons. Des contacts anormalement courts entre un atome d'un métal de transition et certains de parmi les atomes d'Al qui l'entourent, paraissent être caractéristiques pour ces structures et, à condition que les hypothèses faites au cours de l'analyse soient justifiées, il paraît y avoir des preuves qu'environ 2 électrons sont absorbés par des atomes de Co, Mn et Cr. (Il n'y a pas de données disponibles pour le Fe.) On indique les directions les plus importantes pour les travaux futurs.

ELEKTRONENKONFIGURATIONEN IN EINIGEN LEGIERUNGEN DER ÜBERGANGSMETALLE

Die Strukturdaten einer Anzahl aluminiumreicher Legierungen der Übergangsmetalle werden kritisch zusammengestellt, und besondere Aufmerksamkeit wird den im Laufe der Strukturanalyse ausdrücklich oder stillschweigend eingeführten Voraussetzungen und Annäherungen gewidmet.

Es zeigt sich, dass für Brillouinzonenmessungen eine grundlegendere Auswertung notwendig zu sein scheint; in der üblichen elementaren Deutung sind diese Messungen im Einklang mit Raynor's Vorschlägen über die Elektronenabsorption durch die Atome der Übergangsmetalle in dieser Art Legierungen.

Für diese Strukturen scheinen die anormal kurzen Bindungen zwischen dem Übergangsatom und einigen der umgebenden Al-Atome charakteristisch zu sein. Wenn gewisse, im Lauf der Diskussion eingeführte Voraussetzungen berechtigt sind, dann zeigt das vorhandene Material, dass die Co, Mn- und Cr-Atome etwa zwei Elektronen absorbieren. (Es sind keine Werte für Fe vorhanden.)

Einige der wesentlichsten Richtungen künftiger Forschungen werden angezeigt.

I. Introduction

Anomalies in the behaviour of the transition metals Cr, Mn, Fe, Co, Ni and their alloys have long been attributed to the influence of peculiarities in the electron configurations of these metals. Fully documented discussions of some aspects of this problem have been given, for example, by Mott and Jones [1] and by Raynor [2]. The latter has shown, in particular, that many features of a number of phase diagrams can be correlated in a self-consistent scheme if it is assumed that electrons are absorbed by transition metal atoms in electron-rich alloys, so that in these circumstances the transition metals possess effectively negative valencies. In other alloys the transition metals may behave as though zero-valent, and in some cases they may have effectively positive valency. Theories of the metallic bond developed by Pauling [3] in recent years are also based, in part, on attempts to systematise the variations in physical properties, and in alloying behaviour, observed in the transition metals. They have led to suggestions about electron distribution in the transition metal atoms, and to calculations of their effective sizes in specified environments, which—though partly empirical in character—have proved of great interest.

Unfortunately the electronic systems under consideration are so complex that they have not, up to the present, been the subject of a fundamental quantum-mechanical treatment even for the atoms in the free state. Moreover, it is not easy to find experimental measurements, susceptible of direct and unequivocal interpretation, which can give information about the electron configurations in

*Received February 9, 1954.

†Crystallographic Laboratory, Cavendish Laboratory, Cambridge, England.

these complex alloys. One obvious line of attack is the accurate analysis of the crystal structures of the alloy phases, and in the last three years a number of papers have been published, on various aluminium-rich alloys of transition metals, in which Brillouin zone data, interatomic distances, and counts of electrons have been discussed in relation to the general concepts introduced by Mott and Jones, Raynor, and Pauling.

The present paper is a review of the results so far obtained for these alloys by the methods of crystal structure analysis; attention is confined to those aspects of the work which bear directly on the problem of electron configuration. The principal aim, throughout the paper, is to stress the assumptions made, and the uncertainties encountered, in the interpretation of the X-ray observations. For it is most important that the results obtained in the analysis of such complex materials shall be subjected to a cautious and critical scrutiny before they are accepted as fully established. Particularly is this the case when workers in other fields—in this case both practical and theoretical metallurgy—may use structural data as a basis for the devlopment of their own researches.

The features which appear to be characteristic of the alloy structures under discussion will be summarised in Section II, the individual structures being examined in Sections III and IV. In Section V the general conclusions reached serve to indicate possible directions for further work.

II. Features Characteristic of Aluminium-rich Transition Metal Alloys

A considerable number of aluminium-rich alloys of transition metals have now been examined, and for a few of these the atomic structures have been determined with reasonable accuracy. The following broad generalisations will serve as at least a provisional basis for the discussion of these alloys with reference to the electronic configurations of the constituent atoms; in presenting them we ignore for the time being the factors which may limit the accuracy and certainty of the conclusions reached in the individual structural investigations.

(i) Brillouin zones are prominent, indicating that electron energies are important in determining the stability of the phase structures. Moreover, the "observed" electron to atom ratios—derived from the experimentally-measured Brillouin zones—are in harmony with the assumption that electron "absorption" by the transition metal atoms takes place to about the extent proposed by Raynor.

(ii) Counts of the electron contents of the different atoms, from Fourier electron-density syntheses, indicate that the transition metals contain up to about 2 electrons additional to those in the neutral atom. Thus the amount of "absorption" in Mn and Cr is apparently considerably less than would be suggested by Raynor, and differs from the "absorption" indicated by the Brillouin zone observations on the same crystals.

(iii) The transition metal atoms make abnormally short contacts with some, but not all, of the surrounding (Al) atoms, which themselves may also show anomalous (short) interatomic distances to other Al atoms. There is some evidence, not regarded as conclusive, that the abnormally short contacts between transition metal and Al are associated with localised electron transfer between the atoms concerned.

(iv) There is a tendency for the Al atoms to form well-defined layers in the structures. Geometrically, this tendency can in some cases be associated with the occurrence of prominent Brillouin zones; its physical significance is not clear.

III. Review of the Brillouin Zone Measurements

When the existence of a prominent zone is revealed by the occurrence of a group of intense X-ray reflexions from crystal planes with similar spacings, the determination of the exact form of the zone is unambiguous when the unit cell dimensions are known. According to the theories developed for rather simple structures, the criterion of stability for a phase structure is that the zone is nearly full; in practice, it is usual to suppose that stability corresponds to the filling of the inscribed Fermi sphere when the actual zone polyhedron approximates closely to spherical form. For the much more complex structures under consideration, the assumption is made that a similar criterion can be applied in order to obtain an "observed" value of e/A corresponding to stability. In cases where the actual zone departs considerably from the spherical form, an additional assumption must be made as to the appropriate criterion to adopt, and an additional uncertainty is thus introduced in the interpretation of the measurements which are in themselves straightforward.

Published Brillouin zone measurements are summarised in Table I. For details of the alloys and of the X-ray measurements, and for drawings of the zones, the original papers should be consulted [4–14]. Values of e/A "observed", deduced on

TABLE I

BRILLOUIN ZONES

Alloy	Reference	Nature of zone	e/A for zone observed				e/A calculated			
		Range of values of $p=1/2d$ (A^{-1})	Inscribed sphere	Inscribed spheroid	Mean sphere	Filled zone	Transition metal valency assumed: 0	Mott-Jones	Raynor	Alloy composition assumed
Co_2Al_5	[4; 5; 6]	0.236 to 0.261		1.68	1.72		2.18	1.91	1.72	27.2 at.% Co
Co_2Al_9	[4; 5; 7]	0.251 to 0.258			2.12		2.45	2.27	2.14	exact Co_2Al_9
$FeAl_3$	[8]	0.238 to 0.259	1.69			2.04	2.30	1.83	1.67	23.4 Fe, 76.6 Al (at.%)
α-FeSiAl	[9]	0.229 to 0.244			1.74	1.93	2.53	2.15	2.03	32.5 Fe, 8.7 Si (wt.%)
c-FeSiAl	[9]	0.231 to 0.244			1.66	1.83	2.51	2.14	2.02	31.9 Fe, 5.6 Si (wt.%)
$MnAl_6$	[10; 11]	0.220 to 0.247			1.69		2.57	2.14	2.05	exact $MnAl_6$
β-MnSiAl	[6]	0.231 to 0.266		1.68	1.75		2.40	1.74	1.59	22.05 Mn, 6.50 Si (at.%)
$Ni_4Mn_{11}Al_{60}$	[12]	0.240 to 0.265	1.74		1.83	2.04	2.40	1.96	1.83	exact $Ni_4Mn_{11}Al_{60}$
$Cu_2Mn_3Al_{20}$	[12]	(similar)	—	(similar)	—			1.87 to 2.12	1.76 to 2.03	observed range of composition
$ZnMn_5Al_{24}$	[12]	0.231 to 0.250			1.65			1.96 to 2.00	1.85 to 1.88	observed range of composition
α-CrSiAl	[13; 14]	0.238 to 0.259	1.75				2.64	1.89	1.77	18.7 Cr, 20.3 Si (at.%)

Notes: (i) A small range of values of $p(=1/2d)$ for the planes comprising the zone indicates that it is a close approximation to a sphere.

(ii) The inscribed spheroid is prolate in both the cases quoted.

(iii) The transition metal valencies assumed in calculating the second and third values of e/A for an alloy are

Mott and Jones	Ni 0	Co −1	Fe −2	Mn −3	Cr −4
Raynor		−0.61	−1.71	−2.66	−3.66	−4.66

(iv) For information on observed ranges of composition of alloys, see references.

various assumptions about the filling of the zone, are compared with values of e/A calculated for various assumed sets of transition metal valencies together with the normal valencies Al^{+3}, Si^{+4}, Cu^{+1}, Zn^{+2}. The figures of Table I fully justify the generalisation of Section II (i) on the importance of the Brillouin zones and on the support they provide for the effective negative valencies proposed by Raynor. In view of the difficulty of deducing, without any ambiguity, a value of e/A (observed), for structures such as these, the measured zones cannot be taken to exclude effective negative valencies differing appreciably from those proposed by Raynor, though—if the zone treat-

ment is valid at all—they do appear to be quite inconsistent with the novel set of valencies suggested by Pauling in 1949 [15] (for discussion, see [12]).

The alloys $NiAl_3$ and Ni_2Al_3 also have prominent Brillouin zones, but comparison of e/A observed, with e/A calculated for valencies 0 (Mott and Jones) and −0.61 (Raynor), does not lead to such decisive information about the effective valency of Ni, in which the electron absorption is in any case not large, as in the alloys of Co, Fe, Mn and Cr for which the suggested electron absorption becomes progressively larger. It appears, in fact, [4] on the basis of a treatment similar to that applied to the data of Table I, that Ni probably has a small negative valency in $NiAl_3$ but is zero-valent in Ni_2Al_3—as might be expected in view of the smaller proportion of "free" electrons provided by Al in the latter.

To summarise, it would seem that Brillouin zone observations fully establish the importance of the electronic configurations in controlling these alloy structures, and are in general agreement with the suggestion that transition metal atoms may "absorb" electrons. It is equally clear that the interpretation of the observed zones is not yet sufficiently detailed nor certain to permit quantitative deductions about the electronic systems of the constituent atoms. The examination of these complex alloys has in fact emphasised the importance of an attempt to replace the naïve application of the simple zone treatments by a more fundamental discussion of the energy systems which they represent; in particular the meanings of the terms "free electrons" "absorption of electrons" "zone volume" need consideration.

In Section V we shall see not only that there are internal difficulties in handling the Brillouin zone data, but also that these data are apparently inconsistent with electron counts for the separate atoms.

IV. Detailed Structure Analyses

The generalisations of Section II (ii), (iii), (iv) are based on the analyses of the four structures Co_2Al_9, Mn_3SiAl_9, $MnAl_6$ and $Cr_4Si_4Al_{13}$. We now examine the results obtained in these analyses, in an attempt to see whether they are accurate and reliable or whether in the course of the analysis assumptions are made, and approximations permitted, which limit their value.

It is convenient to deal first with measurements of interatomic distances, for the special features which are encountered are subject to much less uncertainty than are the counts of electrons. For all the phase structures under discussion, the analysis was based on two-dimensional projections, supplemented by special measurements which will be described below.

(i) *Interatomic distances*

The measured interatomic distances are collected in Tables II, III, IV and V. The probable errors are estimated as not exceeding 0.03–0.04 A. for Co_2Al_9 [4; 5], 0.03 A. for Mn_3SiAl_9 [6; 13], 0.045 A. for $MnAl_6$ [10; 11], and 0.03 A. for $Cr_4Si_4Al_{13}$ [13; 14]. There seems no reason to regard these estimates as unduly optimistic, for they are based on well-established practice; special circumstances, which might modify the conclusions reached, are considered for each structure in turn.

Abnormally short contacts are observed in every case between the transition metal atom and some of the Al atoms of the surrounding polyhedron. In Co_2Al_9 there are nine Al atoms in contact with each Co atom, and the average Co-Al distance 2.47 A. is identical with that found in Co_2Al_5 and CoAl; but one of the "bonds," of length 2.37_5 A., is significantly short when compared either with this mean value or with the next longer bonds 2.43 A and 2.44 A. In Mn_3SiAl_9 the distinction between the four short contacts and the six long ones between Mn and Si, Al atoms is even more striking, and in $MnAl_6$ the contacts between Mn and Al atoms again include four short and six long ones. The polyhedron around Cr in $Cr_4Si_4Al_{13}$ includes three Si atoms making rather short contacts and three Al atoms making very short bonds, as well as three other Al atoms at a normal distance, and possibly three other Cr atoms.

Variations in contact-distances between Al atoms, though not so easily classified as those between transition metal and Al, seem in some cases to be associated fairly directly with them. Thus in Co_2Al_9 the over-all average Al–Al distance is 2.81 to 2.85A., (the precise value depending upon the maximum interatomic separation considered to constitute true "contact") which may be compared with 2.86A. in pure aluminium. There are, however, five crystallographically distinct Al atoms in the structure, which are coordinated with two Co atoms and either 7, 8 or 10 other Al atoms*; from Table II it is clear that the atom Al_0 (which makes the short "bonds" of length 2.37_5A. with two Co atoms) also makes relatively short bonds

*"Contacts" exceeding 3.0A. are excluded; if these are included, the general nature of the argument is unaffected.

TABLE II

ATOMIC ENVIRONMENTS IN Co_2Al_9

Atom	Number of adjacent Al atoms	Maximum and minimum Co-Al or Al-Al distances (A)	Average Co-Al or Al-Al distance (A)
Co	9	2.53$_5$, 2.37$_5$	2.47
Al_0	8	2.78 , 2.70$_5$	2.73$_5$
Al_1	7	2.94 , 2.72	2.84
Al_2	7	2.94 , 2.71	2.82
Al_3	10	2.94 , 2.70$_5$	2.82
Al_4	7	2.94 , 2.74$_5$	2.82

with all the surrounding Al atoms. On the other hand, in Mn_3SiAl_9 the atom Al_1 (making an exceedingly short bond 2.42A. with two Mn atoms) shows no anomalies in its contacts with ten other Al atoms at an average distance of 2.86A.; the other type atom Al_2 (normal bonds with three Mn atoms) also makes normal contacts (average 2.88A.) with nine other Al atoms, but a rather short contact with one Si atom. The Si atom, which makes these rather short contacts with six Al atoms at 2.67A.,

TABLE III

ATOMIC ENVIRONMENTS IN Mn_3SiAl_9

Atom	Number of adjacent atoms	Distances (A)		
		Maximum	Minimum	Average
Mn	2 Si			2.49
	2 Al_1			2.42
	6 Al_2	2.68	2.67	2.67$_5$
Si	6 Mn			2.49
	6 Al_2			2.67
Al_1	2 Mn			2.42
	10 Al_1, Al_2	2.97	2.77	2.86
Al_2	3 Mn	2.68	2.67	2.67$_5$
	1 Si			2.67
	9 Al_1, Al_2	2.99	2.77	2.88

Note: Where only one figure appears in the column "Distances," it is the value for all contacts of that type.

is also in contact with six Mn atoms at the short distance 2.49A. In $MnAl_6$ the atom Al_2 with an exceedingly short bond (2.43$_5$A.) to one Mn, also makes two very short contacts with other Al_2 atoms, as well as normal contacts with eight other Al atoms: all three short contacts lie in one plane. Variations in contacts between Al_1, and Al_3, and other atoms, in this structure may be less significant: they are shown in Table IV. In $Cr_4Si_4Al_{13}$ the Si atom, making a short contact with each of three Cr atoms, also makes an extremely short contact with one Al_0 atom, which, however, is itself in 4-coordination—a most unusual feature in a metallic structure. On the other hand, the atom Al_1 making very short bonds with two Cr atoms shows no other anomalously short contact distances, nor does the atom Al_2.

TABLE IV

ATOMIC ENVIRONMENTS IN $MnAl_6$

Atom	Number of adjacent atoms	Distances (A)		
		Maximum	Minimum	Average
Mn	4 Al_1			2.60
	2 Al_2			2.43$_5$
	2 Al_3			2.64
	2 Al_3			2.54
Al_1	2 Mn			2.60
	1 Al_1			2.64
	8 Al_2, Al_3	2.88	2.76	2.83
Al_2	1 Mn			2.43$_5$
	1 Al_2			2.57
	1 Al_2			2.62
	8 Al_1, Al_3	2.89	2.76	2.82
Al_3	1 Mn			2.54
	1 Mn			2.64
	9 Al_1, Al_2, Al_3	2.89	2.77	2.84

Note: Where only one figure appears in the column "Distances," it is the value for all contacts of that type.

Before accepting these anomalous transition metal to aluminium, and aluminium to aluminium contacts as physically significant, it is necessary to scrutinise the procedures followed in the structure analyses.

Except for $Cr_4Si_4Al_{13}$ the interatomic distances were determined from two-dimensional electron-density syntheses: for this alloy three-dimensional syntheses, projected on lines passing through atomic centres, led to atomic coordinates in very close agreement with those obtained from a projection. For all the alloys, however, estimates of the experimental and computational errors (see above) indicate that the anomalies in the interatomic distances are quite outside the probable range of error, and there is no reason to suppose that three-dimensional syntheses, or the use of more refined experimental measurements, would result in the disappearance of these special features.

For Co_2Al_9 no detailed discussion seems to be needed; for the space group, uniquely determined by the systematic absences in the X-ray reflexions, is centro-symmetrical, the composition of the phase is fixed, and the *b* and *c* projections used are reasonably free from overlapping of the atomic peaks.

In Mn_3SiAl_9, however, the situation is less simple. *First*, the systematic absences are compatible with any of three space groups D^4_{6h} – C6/mmc, C^4_{6v} – C6mc, and D^4_{3h} – C$\bar{6}$2c, and although there is nothing to suggest a reduction of the symmetry below that of D^4_{6h} – C6/mmc, the detailed testing of such possibilities is necessarily less rigorous than the unequivocal determination of $P2_1/a$ for Co_2Al_9. *Secondly*, the phase is observed over an appreciable range of composition, and there is slight uncertainty about the precise occupation of sites in the structure which, according to the space group symmetry, ought to contain 6 Mn, 2 Si, and 18 Al per unit cell. Thus from the analysis and density of the alloy specimen actually used for the X-ray measurements it appears that the Mn sites are not fully occupied, and that the same is true of the Si sites if the Al sites are just completely filled. Although partial occupation of the Mn sites may modify (slightly) the values observed for all contacts with Al and Si atoms—for these are averages of the actual values throughout the structure—it seems most unlikely that it can seriously affect the very considerable difference between short and long contacts to the atoms forming the surrounding polyhedron. The effect of a shortage of Si atoms is less easily predicted since Si and Al atoms may be to some extent interchangeable. *Finally*, the structure contains a "hole" of about the size which could be occupied by a Mn atom. The presence of such a well-defined unoccupied site* may have an appreciable influence on the interatomic distances, and its nature cannot be predicted; if the anomalies were observed only in this structure, they would obviously be suspect, but in fact they are similar in character in all four alloys under discussion.

TABLE V

ATOMIC ENVIRONMENTS IN $Cr_4Si_4Al_{13}$

Atom	Number of adjacent atoms	Distances (A.); Maximum	Minimum	Average
Cr	3 Si			2.41
	3 Al_1			2.46
	3 Al_2			2.77
	3 Cr			2.84
Si	1 Al_0			2.38
	3 Cr			2.41
	6 Al_1, Al_2	2.81	2.79	2.80
Al_0	4 Si			2.38
Al_1	2 Cr			2.46
	2 Si			2.81
	8 Al_1, Al_2	2.93	2.89	2.91
Al_2	2 Cr			2.77
	2 Si			2.79
	8 Al_1, Al_2	2.94	2.89	2.91

Note: Where only one figure appears in the column "Distances," it is the value for all contacts of that type.

The systematic absences in the X-ray reflexions of $MnAl_6$ are again compatible with three space groups D^{17}_{2h}–Ccmm, C^{12}_{2v}–Ccm and C^{16}_{2v}–Cc2m, but statistical tests, which clearly indicated centrosymmetry, justified the choice of the first of these. The composition of the phase corresponds closely to $MnAl_6$. A special discussion [11] shows that the highly anomalous Mn-Al_2 and Al_2-Al_2 distances are unlikely to be modified seriously in any further refinement of the structure.

For $Cr_4Si_4Al_{13}$, of the three possible (cubic) space groups, T^2_d–F$\bar{4}$3m is chosen because it alone possesses sufficient special positions to accommodate separately the Si and Cr atoms. The composition of the phase is not fixed, but for the alloy examined is fairly close to the ideal.

In all cases, therefore, there seems little reason to doubt that the interatomic distances are essentially correct and that, in particular, the anomalies are outside the probable range of error.

In discussing the possible interpretation of the observed interatomic distances it is natural to use as a basis for comparison the atomic diameters of the pure metals—Al 2.86A., Co∼2.5A., Mn∼2.6A., Cr∼2.6A., and Si∼2.65A. In such comparisons, the variation with coordination must, of course, be taken into account, and though this is a rather unreliable process, the discrepancies between observed values and "normal" values thus predicted are such as to provide strong evidence for bonding of an unusual kind. The suggested interpretation [4; 5] of the short average Co-Al distance

*The real importance of this "empty" atomic site is emphasised by the general similarity of the structure of Mn_3SiAl_9 to that of Co_2Al_5. In the comparable unit cells the atoms ($SiAl_9$) of the former occupy the same sites as (Al_{10}) of the latter, and (Mn_3 + unoccupied site) correspond to (Co_4).

in Co_2Al_9 was criticised and amended by Pauling [16]; it is probably best, for the present, to refrain from any such detailed treatments until the factors determining the forms of these structures are established with greater certainty.

(ii) *Electron counts*

Under this heading we include information about the electron-contents of the atoms in a phase, whether obtained by direct counting on a Fourier electron-density synthesis, or by other more special devices which will be described. It should not be forgotten, in considering the results obtained, that any incoherent "background" X-ray scattering is left completely out of account in the measurement of the intensities of reflexions: it is only possible to hope to demonstrate its unimportance by showing that the total energy of the coherent X-ray scattering is quantitatively in agreement with the known total number of electrons in the structure.

Electron counts are much more subject to inaccuracy and uncertainty than is the case with the interatomic distances discussed above. Among the most important adverse factors, additional to those already considered in the preceding Section (i), are the following—all of which arise for one or more of the structures treated in detail below.

(*a*) Imperfect resolution of atoms in two-dimensional projections is much more likely to result in errors in electron counts than in fixing atomic positions. For electron counts may be inaccurate on account of overlaps of the outer regions of atoms, which have no appreciable influence on the atomic peak positions.

(*b*) Absolute measurements of intensity of reflexion have not been made, and therefore at some stage in the course of the analysis the measured (or eye-estimated) relative intensities are subjected to a "scaling" operation of some kind, explicit or implicit.

(*c*) Any important modification of the scattering power of the transition metal atoms, arising from the suggested electron absorption, is probably confined to relatively small angles of diffraction. It is an inherent difficulty that there are relatively few reflexions at low angles, and moreover it is precisely in this region, where the most intense reflexions may occur, that the accuracy of measurement of intensities is liable to be affected by extinction.

In view of the complexity of the attempt to assess the significance of published data, it is convenient to take each structure in turn.

(*a*) *Co_2Al_9*. The total number of electrons in each peak, counted in arbitrary units in *b*- and *c*-projections, is probably reliable, for in both projections the peaks are fairly well resolved and the background reasonably flat.* To convert the electron counts to absolute units, the electron density between atoms was assumed to be zero. Three independent estimates of the accuracy of the counts gave a standard deviation 0.5 electron for each peak. The figures in Table VI show that the

TABLE VI

ELECTRON COUNTS IN Co_2Al_9

Atom	Co	Al_0	Al_1	Al_2	Al_3	Al_4
b-projection	29.2	12.4	12.7	12.5	11.6	11.8
c-projection	28.9	11.6	12.3	12.8	12.9	12.7
Average	29.0_5	12.0	12.5	12.6_5	12.2_5	12.2_5

Co peak count (29) differs significantly from the electron content of the neutral atom (27); it is probably not justifiable to suggest that the low count of 12.0 for Al_0 is connected with the fact that this is the Al atom making an abnormally short bond with Co. The following points need consideration in any attempt to decide whether the electron counts are reliable.

(1) In finding the correct structure, and refining it, intensities originally estimated by visual comparison with a standard scale are compared with values of F^2 calculated from the proposed structure. To bring I_{obs} into the best agreement with F^2_{calc} a conversion-factor is used which combines the effects of a number of different quantities which vary with glancing-angle θ. This procedure is necessary because, in the eye-estimation method, not only are there no *absolute* measurements of intensity, but no measurements of the actual *energy* of a reflexion are made. This "scaling" process is, in principle, in the nature of argument in a circle; for the result obtained depends upon the assumed atomic scattering powers and their variation with glancing-angle, whereas these depend upon the actual electron configurations of the atoms concerned—which is what we seek to discover; in particular, it cannot be taken for granted that the atomic f-values for (neutral) Al (13) and (neutral) Co (27) are necessarily appropriate in the alloy. Different scaling-curves result in different Fourier syntheses, and it is therefore of funda-

*Relative freedom from overlap may be taken to indicate that anisotropic thermal vibration is unlikely to vitiate the results. A flat background may be regarded as a test of the absence of serious diffraction effects due to the use of incomplete Fourier series in the synthesis.

mental importance that, so long as atomic peaks do not overlap (in projection), neither the peak positions nor the total electron contents of the various peaks are changed as a consequence of changes in the scaling curve [4].

(2) The electron-density synthesis constructed from the observed intensities will be correct—apart from the scaling effect considered above—provided that the correspondence between (scaled) I_{obs} and F^2_{calc} is sufficiently good to enable the sign ($\pm$) of each term to be chosen correctly; for the structure is centro-symmetrical. This feature of the electron-density synthesis is most important, for it follows that uncertainty about the precise value of F_{calc}, arising from uncertainty about the atomic scattering powers, has no influence on the electron-density synthesis finally obtained (except for that considered in the preceding paragraph).

(3) The electron counts would be affected by any departure from the ideal unit cell content assumed, Co_4Al_{18}. In fact, the composition of the phase is almost fixed, chemical analysis indicating only a small (relative) excess of Co, corresponding to unit cell contents $Co_{4\cdot075}Al_{18}$ or $Co_4Al_{17\cdot66}$ according as the difference from Co_4Al_{18} is supposed to be due entirely to excess Co or entirely to deficit of Al. Such small departures from the ideal would not invalidate the conclusions drawn.

We may therefore conclude that not only the *positions* of the atomic peaks, but also their total electron contents in arbitrary units reckoned above the ground level of zero electron density between atoms, are independent of any assumption about the precise form of the atomic f-curves. The conversion to absolute units as well as the fixing of the ground level, are, however, wholly dependent upon the assumption that the electron-density between the atoms is zero. Further progress in correlating interatomic distances and the apparently abnormal electron counts for Co (and possibly Al_0) in this alloy is unlikely without absolute measurements of intensities of reflexion. With these, the labour of carrying out a complete three-dimensional synthesis would be justified, for it would yield more accurate interatomic distances and direct counts of electrons in atoms without any assumption about electron density between atoms—and, of course, without the application of any "scaling" procedure.

(*b*) *Mn_3SiAl_9*. Three different treatments of the experimental measurements agree in suggesting some absorption of electrons by the Mn atom, though it is impossible to decide with any accuracy the amount of absorption.

In projection along the *c*-axis, the atomic peaks contain the numbers of electrons shown in Table VII, the background areas between peaks contain

TABLE VII

ELECTRON COUNTS IN Mn_3SiAl_9

Peak	2 Si	Mn_1	2 Al_2	Al_1
Electrons	27.0	24.2	23.7	10.9

altogether 24 electrons; the total is 404 per unit cell instead of 412 for two units Mn_3SiAl_9. Comparison of Mn with either $2Al_2$ or Al_1 suggests an excess of electrons in Mn if Al is assumed neutral, but the 2Si peak is then difficult to explain (for neutral atoms the numbers of electrons are Mn25, Si14, Al13).

In computing the electron-density synthesis the coefficients used are F_{obs}, scaled by comparison with F_{calc} for the proposed structure. The underlying basis of the method is similar to that used for Co_2Al_9 so long as electron counts are in arbitrary units—in particular there is the essential internal inconsistency in using atomic f-curves for netrual atoms (cf. ¶ (*a*) (1) above), but the structure is again centro-symmetrical (cf., ¶ (*a*) (2) above). It is in the conversion to absolute units that the treatment is fundamentally different: for Mn_3SiAl_9 it is assumed that the use of the scaling factor does yield values F_{obs} in absolute units, hence that peak counts in the resulting Fourier synthesis yield true totals of electrons. The fact that 24 electrons are then found between atoms emphasises the contrast with Co_2Al_9 where the assumption of zero electron density between atoms is the basis of the conversion to absolute units, and the total number of electrons counted in the atomic peaks then corresponds very closely with the total for the unit cell.

The alloy phase shows a fairly wide composition range: for the actual sample used, chemical analysis and density determination indicate unit cell contents 5.55–5.75 Mn, 1.65–1.70 Si, 18.0–18.5 Al atoms (according to the precise mode of calculation) instead of 6 Mn, 2 Si, 18 Al. Assuming mean values, and that the vacant Si sites are occupied by the excess Al atoms, the counts of "2 Si" (=27) and "1 Mn" (=24.2) are explained if each Mn atom on the average contains about one extra electron.

The peaks in the projection are not free from diffraction effects, nor from overlap: the accuracy of the counts for Mn and Al_2 are particularly suspect for these reasons.

For all these reasons, as well as on account of the difficulty of the 24 "background" electrons, it seems that the electron-density synthesis, in *c*-projection, is not very favourable for accurate electron counting.

An alternative treatment, the use of the (F_o-F_c) synthesis, has the advantage of removing diffraction ripples. Using only low-angle reflexions, corresponding to the range of influence anticipated for the additional electrons supposed absorbed into the *d*-shell of Mn, the synthesis obtained indicates some absorption, but owing to the very limited number of reflexions the projection is thought to be unreliable. In addition, the method is of course very dependent upon the correct choice of scaling-factor for obtaining F_o in absolute units, and upon the atomic f-curve used to calculate F_c.

The third line of attack is different, and depends upon the examination of a few selected low-angle reflexions, either measured directly by photometry of powder patterns or estimated as adjacent reflexions in single crystal patterns—with the consequence, in both cases, that the major uncertainties arising from the use of the scaling factor are removed. Two kinds of comparison are made: in one, reflexions to which Mn atoms contribute strongly are compared with a reflexion to which Mn atoms contribute nothing; in the other, reflexions for which Mn atoms contribute in phase with the resultant are compared with reflexions for which Mn atoms contribute out of phase with the resultant. Thus the comparisons are sensitive to the precise form of the atomic f-curve for Mn, at low scattering angles, and so to the electron-distribution in the Mn atoms. These measurements can be explained only if the scattering-power is enhanced above that corresponding to Mn (25) according to Viervoll and Ögrim [17]. In addition, there is some evidence—not conclusive—favouring the view that atoms Al_1 are principal contributors of electrons to the Mn atom.

In assessing the significance of this approach to the problem of electron-content, it seems that the only remaining weakness on the experimental side is the use of ratios of intensities instead of absolute integrated intensities; while in interpretation it is still necessary to assume that the shape of the atomic f-curve, its scale being adjusted to correspond with any assumed total number of electrons in Mn, is at least nearly correct for low values of $\sin\theta/\lambda$.

Thus, all methods of analysing the measurements favour the absorption of electrons by Mn; the amount is difficult to estimate, but may be put at about 2 electrons. There is some evidence that the absorbed electrons are contributed largely though not exclusively by atoms Al_1; if this is the case, the exceedingly short Mn-Al_1 contact must be associated with the localised transfer. It must be noted, in considering these findings, that for various reasons discussed above the structure is not particularly favourable for providing unique and unassailable evidence on electron configurations, so that the labour of obtaining absolute intensity measurements for a three-dimensional synthesis would probably not be justified. Moreover, the occurrence in the structure of an unoccupied cavity may confer upon it special characteristics which render it unsuited to straightforward electron-counting, though they may prove to be of vital importance for a full understanding of the structure.

(*c*) $MnAl_6$. This alloy is favourable in that it is binary with nearly fixed composition, and the statistical tests (cf., Section (i), above) support strongly the choice of the centro-symmetrical D^{17}_{2h}–Ccmm of the three space groups compatible with the systematic absences. In addition, both Mn and Al atoms appear as both single and double peaks in the two projections used (along *b*- and *c*-axes) with reasonably good resolution; in particular, in the *b*-projection a peak 1 Mn can be compared with peaks 2 Al which are nearly the same height so that the comparison becomes less dependent upon scaling operations. Three treatments of the structural data agree in suggesting absorption of electrons by Mn atoms.

Direct Fourier syntheses of electron density, with coefficients F_o scaled to absolute values by comparison with F_c, give total numbers of electrons 407 for *c*- and 413.5 for *b*-projections, compared with 412 for 4 units $MnAl_6$: these totals include "backgrounds" of 29 and 11.3 electrons, respectively. Electron counts for equal peak areas are collected in Table VIII. The procedure is entirely dependent on the accuracy of the scaling operation.

Syntheses $(F_o - F_c)$ for both projections, calculated for low-angle reflexions and using the atomic f-curves of Viervoll and Ögrim [17] for neutral Mn and Al atoms, again indicate excess electrons in Mn and deficits in Al atoms (Table VIII). Moreover, these difference-syntheses give no indication of inaccuracies in choice of atomic parameters, or of temperature factors, sufficiently serious to cast doubt on either measured inter-

TABLE VIII

ELECTRON COUNTS IN $MnAl_6$

Atom	2 Mn	Mn	$2Al_1$	$2Al_2$	Al_2	Al_3	$2Al_3$	Background
c-projection	54.3		22.2	21.4		11.8		29
b-projection		27.9	23.2		11.6		24.5	11.3
Average (single atoms)$_8$	27.5		11.4	11.1		12.0		
c-projection, assuming zero background density	56.4		25.0	24.5		11.9		(0)
Excess electrons, *c*-projection ($F_o - F_c$)	+ 2.4		− 0.9	− 1.3		− 0.2		
Excess electrons, *b*-projection ($F_o - F_c$)		+ 1.9	− 0.7		− 0.9		− 0.3	

atomic distances or electron counts. The method is, of course, entirely dependent on correct scaling, as with the F_o-syntheses.

Before the final refinement, electron counts were made [10] on one *c*-projection by assuming zero electron-density between atoms as in the case of Co_2Al_9 [5]. In this way, dependence upon a direct scaling-factor relating F_o and F_c, and upon the precise form assumed for the atomic f-curve, is avoided. Table VIII again shows an excess of electrons in the Mn peak, and the total of 406 electrons in the cell is close to the correct number 412. One weakness of these figures is that they were obtained from a projection known not to be fully refined; another is that the assumption of zero electron-density in the background is contradicted in all cases where direct scaling is used to obtain an F_o synthesis.

Summarising, it is again found that Mn appears to have about 2 excess electrons, and there is some evidence (Table VIII) that the biggest deficit is shown by atoms Al_2 which make extremely close contacts with Mn and with other atoms Al_2. No such deficit is seen for atoms Al_3 which also make rather close contacts with Mn, but these show no abnormally close contacts with other Al atoms.

(*d*) $Cr_4Si_4Al_{13}$. For this cubic crystal both two-dimensional projection and three dimensional line-synthesis were used to give the electron counts collected in Table IX. In projection, the peaks Al_1, Al_2 and $2Al_2$ are free from overlap and the counts should be reliable; but the Cr and Si peaks are too close for accurate counting. In line-synthesis, Cr, Si, and Al_0 are (necessarily) fully resolved, and if the assumption of spherically symmetrical electron-distributions is justified, the corresponding electron counts should be reliable. All these counts are placed on an absolute scale by assuming that the Si atom contains 14 electrons —a procedure which differs from any of those used in the other structures under discussion.

TABLE IX

ELECTRON COUNTS IN $Cr_4Si_4Al_{13}$

Peak	Electrons	
	From projection	From line-synthesis
Cr	27.6	25.4
Si	(14.0)	(14.0)
Al_0		13.3
Al_1	12.3	
Al_2	13.1	
2 Al_2	25.9	

Detailed consideration [14] of the actual composition of the alloy sample used leads to the conclusion that there is evidence for some absorption of electrons by Cr (probably 1 or 2 per atom), with corresponding deficit in atoms Al_1 which make a very close contact with them. Any attempt to specify the electron counts accurately is rendered more difficult by the absence of a centre of symmetry in the structure; for this results in enhancing the influence, when calculating the phases of the terms in the syntheses, of the difference between the real atomic f-curves for the Cr and Al atoms and those assumed, which correspond to neutral Cr and Al atoms.

This alloy thus falls into line with the others discussed in detail, but—partly for technical reasons connected with the symmetry of the structure—provides little new information.

V. Discussion

Any attempt at generalisation, based on the structures reviewed in the preceding sections, must

necessarily be provisional and tentative, but a number of features emerge which may be of some significance.

First, the observed prominent Brillouin zones, interpreted straightforwardly as is usual with simpler phases, consistently indicate effective negative valencies (electron absorptions) for the transition metal atoms in close agreement with the numerical values proposed by Raynor. It is, however, very difficult to accept a model of the alloy in which these atoms are supposed to have acquired negative charges as high as those proposed (e.g.) for Mn and Cr. It can also be objected that the direct counts of electrons, assuming their complete validity in each structure so far examined, do not confirm the proposed steady increase in effective negative valency along the series Co (Fe) Mn Cr, but rather suggest an absorption of the same order (about 2 electrons) for Co, Mn and Cr, or possibly a decrease for Cr to about 1 electron. It must be pointed out, in this connection, that the atoms Al and Si which are supposed to contribute 3 and 4 electrons, respectively, to the "free" electrons counted in the Brillouin zones, similarly do not give electron counts corresponding to these degrees of ionisation. Whether the electron counts are accepted as valid, or not, the Brillouin zone observations emphasise the need for making a more fundamental approach to the problem of their interpretation in these alloys than has, so far, been attempted. In a recent paper Jones [18] has examined certain aspects of the problem of "absorption" (see also, below), but a re-examination of the relation between structural stability and the filled zone, in the most general terms, is urgently needed.

A feature of these structures which appears to be firmly established and common to all is the occurrence of very short contacts between the transition metal atom and some of the surrounding Al atoms, the remaining such contacts being "normal" i.e., of lengths corresponding fairly closely with predictions from the known effective radii of the atoms in the structures of the pure elements, adjusted (semi-empirically) in accordance with the observed coordination numbers. Less firmly established, because they are revealed by interatomic distances differing from the normal by amounts which do not greatly exceed the possible error in their determination, are anomalies in the environments of those Al atoms which themselves make very short contacts with transition metal atoms. Moreover, these anomalies are found only in some of the structures, not in all.

It is rather striking that (again assuming the validity of the electron counts) there is in some cases evidence for localised transfer of electrons between Al atom and transition metal atom making a very short contact; in these cases, it is this Al atom which shows the biggest deficit in electron content (compared with Al 13) of all those in the structure.

A study of the four structures under review does not lead to an understanding of the factors which are physically important in determining their features. Some kind of localised bonding would appear to be involved, and it may be that these phase-structures should be described in relation to the coordination-groups from which they are constructed. It also seems likely that "holes" (i.e., unoccupied coordination-groups) must play a special role.

The meaning of the electron counts is very difficult to establish. At present, in spite of the general similarity of the results obtained from quite different structures, it would certainly not be justifiable to assert that electron absorption (in its most naïve sense) by the transition metal atoms has been firmly established. For all the structure-analyses suffer from the fact that no absolute measurements of intensity have been made, and from the uncertainty regarding the precise form of the atomic f-curve which should be used in the computations. In various ways, difficulties due to overlap, arising from thermal vibrations which may be anisotropic, and to diffraction ripples in the Fourier synthesis, arising from the use of incomplete series, have been overcome at least in part.

If the two major difficulties can be overcome—by making absolute measurements of intensity, and by the determination of accurate atomic f-curves—it will be of the greatest interest to see whether any electron-transfer can really be "localised" to certain Al atoms, and also to know whether there is any appreciable electron-density between atoms, either as a general background or associated with special regions. In ternaries with Si it will be particularly interesting to see whether this behaves as a normal atom or whether it should, in an alloy of this kind, be considered as truly (partially) ionised. Supposing absorption by the transition metal atom to be demonstrated conclusively, it will be necessary to know how the absorption depends upon the relative amount of Al in the alloy, whether it varies according to the nature of the coordination when this varies from one (transition metal) atom to another (of the same transition metal) in the same structure, and how the absorption varies

along the series Ni, Co, Fe, Mn, Cr. The recent work of Jones [18] to which reference has already been made, is of particular interest in connection with the last point; but a fuller discussion of its bearing on the electron counts is probably best postponed until their validity is more firmly established. In the results already obtained, though none of these aspects of the problem has been clarified, enough has been seen, in the review of Section IV, to show that the method of accurate structure-analysis can almost certainly be made to yield much information on all of them. Until the two major difficulties mentioned above have been overcome—and in particular until absolute intensity measurements are available—there is no point in a more detailed treatment of the electron counts.

VI. Conclusion

The structures discussed in this paper all belong to one class of transition-metal alloys, viz., those rich in Al. A number of simpler structures of this class are also under re-examination in the hope that they may help to build up a general picture of these alloys. In addition, the application of high-accuracy methods of measurement to the structures of both α-Mn [19] and β-Mn [20] may yield valuable information about the electron configuration of the Mn atom. The recent analyses of some sigma-phase alloys, and of β-uranium, are also of great importance for a wider discussion of the problem than is attempted here.

References

1. Mott, N. F. and Jones, H. Theory of the properties of metals and alloys (Oxford University Press, 1936).
2. Raynor, G. V. Progress in Metal Physics **1** (1949) 1–76.
3. Pauling, L. Phys. Rev. **54** (1938) 899; J. Amer. Chem. Soc. **69** (1947) 542.
4. Douglas, A. M. B. Ph.D. dissertation, Cambridge (1948).
5. Douglas, A. M. B. Acta Cryst. **3** (1950) 19.
6. Robinson, K. Acta Cryst. **5** (1952) 397.
7. Raynor, G. V. and Waldron, D. M. B. Phil. Mag. **40** (1949) 198.
8. Black, P. J. Private communication, in preparation for publication.
9. Robinson, K. and Black, P. J. Phil. Mag. **44** (1953) 1392.
10. Nicol, A. D. I. Ph.D. dissertation, Cambridge (1951).
11. Nicol, A. D. I. Acta Cryst. **6** (1953) 285.
12. Robinson, K. Phil. Mag. **43** (1952) 775.
13. Robinson, K. Ph.D. dissertation, Cambridge (1951).
14. Robinson, K. Acta Cryst. **6** (1953) 854.
15. Pauling, L. Proc. Roy. Soc. **A196** (1949) 343.
16. Pauling, L. Acta Cryst. **4** (1951) 138.
17. Viervoll, H. and Ögrim, O. Acta Cryst. **2** (1949) 277.
18. Jones, H. Phil. Mag. **44** (1953) 907.
19. Nicol, A. D. I. Private communication.
20. Bown, M. G. Private communication.

THE ANODIC OXIDATION OF URANIUM*

O. FLINT, J. J. POLLING, and A. CHARLESBY†

Over a range of 2–100 volts the anodic oxidation of uranium in ammoniacal ethylene glycol produces oxide films which are predominantly uranium dioxide in composition. The oxide formed in this manner shows considerable stability to atmospheric corrosion. During film formation at constant current the voltage rises steeply to a plateau, and subsequently increases more slowly to a second plateau. The films formed during the period of voltage rise are crystalline in character, whereas on a plateau they become amorphous.

The rate of oxidation during initial voltage rise, deduced from charge assuming maximum current efficiency, is about 16 Å/volt and 16–20 Å/volt from optical thickness measurements, assuming a refractive index of 2.0 for a film of UO_2.

Attention is drawn to similarities between thermal and anodic oxidation of uranium.

L'OXYDATION ANODIQUE DE L'URANIUM

L'oxydation anodique de l'uranium dans l'éthylène glycol ammoniacal, pour un intervalle allant de 2 à 100 volts, produit des couches d'oxyde, constituées principalement par du bioxyde d'uranium. L'oxyde formé de cette façon manifeste une résistance considérable à la corrosion atmosphérique. Pendant la formation de la couche à courant constant, le voltage s'accroît abruptement jusqu'à un plateau, et ensuite plus lentement vers un deuxième plateau. Les couches formées lors de la période d'accroissement du voltage sont cristallines, alors que le long d'un plateau il y a formation de couches amorphes. La vitesse d'oxydation pendant l'accroissement inital du voltage, déduite de la charge, en supposant un rendement maximum du courant, est d'environ 16Å/volt, et 16–20Å/volt d'après des mesures optiques d'épaisseur, en supposant un indice de réfraction de 2,0 pour un film de UO_2. On attire l'attention sur les analogies entre les oxydations thermique et anodique de l'uranium.

DIE ANODISCHE OXYDATION DES URAN

Im Bereich von 2–100 Volt erzeugt die anodische Oxydation von Uran in ammoniakalischem Äthylenglycol Oxydfilme, die vorwiegend aus Urandioxyd bestehen. Das so gebildete Oxyd ist gegen atmosphärische Korrosion recht beständig. Wird der Film bei konstanter Stromstärke gebildet, so steigt die Spannung steil bis zu einem Schwellenwert an, um dann langsamer weiter bis zu einer zweiten Schwelle aufzuwachsen. Die während des Spannungsanstieges gebildeten Filme sind kristallin, während sie auf einer Spannungsschwelle amorph werden.

Die Oxydationsgeschwindigkeit während des ersten Spannungsanstieges kann abgeschätzt werden, wenn man maximale Stromleistung annimmt; sie beträgt 16 Å/V und 16–20 Å/V aus optischen Dickenmessungen, wenn man für einen UO_2 Film den Brechungsindex 2,0 annimmt.

Es wird auf die Ähnlichkeit der Erscheinungen bei der thermischen und bei der anodischen Oxydation des Urans hingewiesen.

Introduction

The mechanism of formation of thin oxide films on metals, such as aluminium and zirconium, in air, chemically and by electrolytic methods has been studied in some detail by a number of research workers [1; 5; 10]. As a result, a theoretical framework embracing the mechanism of controlled oxidation of these metals has been evolved.

In the case of aluminium or zirconium, oxidation in air or oxygen at room temperature leads to the formation of thin stable films of some 20–30 Å thickness [2]. Further oxidation at elevated temperatures increases the film thickness parabolically.

Anodic oxidation of the two metals may produce two types of oxide film, both of an amorphous character but differing in porosity, depending on whether the oxide formed is soluble in the electrolyte. Porous films on aluminium are produced by anodic oxidation in dilute sulphuric, chromic and oxalic acid electrolytes and these films increase in thickness until equilibrium is reached between the rate of film formation and chemical solution of the oxide. During film formation the current remains fairly constant. Non-porous films on both aluminium and zirconium are formed by similar treatment in aqueous boric acid, ammonium borate and ammoniacal ethylene glycol. Here the films are practically insoluble in the electrolyte and the current density falls with time to a very low value of the order of 1 $\mu amp/cm^2$ [2]. This fact indicates that film growth has virtually ceased since prolonged current flow results in an insignificant change in film thickness. Previous work [5] has shown that the thickness of the oxide film produced is directly proportional to the formation voltage, and in the case of zirconium, reproducible interference colours can be observed at any potential up to 300 volts [3]. The colour of these films is a useful means of estimating film thickness.

The oxidation of uranium in air produces a film which is non-protective and elevation of the temperature up to about 220°C leads to the formation of UO_2; this is converted to U_3O_8 at higher

*Received February 24, 1954.

†Atomic Energy Research Establishment, Harwell, England.

temperatures. Anodic oxidation of the metal in dilute sulphuric, chromic or oxalic acids results in the dissolution of the uranium, with no visible film formation. Because of the high chemical activity of uranium and its position in the electromotive series, any surface impurity (for example an inclusion) or even slight traces of the order of 0.01 per cent of halide in the electrolyte, leads to excessive pit corrosion during anodic treatment.

It was felt that a useful comparison might be made between the oxidation of uranium under controlled electrolytic conditions and the anodic oxidation of alumium and zirconium.

Preliminary Work

Initially, uranium discs 1 in. in diameter were ground on emery paper to 4 O's grade (600 mesh) and anodised in concentrated aqueous ammonium borate at various voltages using a platinum cathode. Interference colours were formed at a potential of 1–2 volts but at higher potentials a milky pitted film developed. In N/100 ammonium borate solution this colour range was visible up to a potential of 5 volts, but electrolytic treatment for longer than 2 minutes again resulted in pitting of the base metal. Previous work has shown that uranium is readily pitted by very small concentrations of halogen ions as is the case, to a lesser degree, for aluminium. Although particular care was taken to ensure purity of the ammonium borate and triply-distilled water was employed as solvent, pitting still took place during electrolysis.

In view of the pit corrosion produced by aqueous electrolysis and the very limited range over which interference colours could be observed, anodic oxidation in a non-aqueous electrolyte was investigated. Preliminary work with ethyl alcohol gave only loose yellow oxides or hydroxides and therefore derivatives of the higher alcohols were investigated. As a first attempt uranium was anodised in water-free ethylene glycol. In this case no visible film was formed and as the conductivity of the electrolyte was of the order of 0.1×10^{-4} mhos, ammonium borate was added to increase this value. In this way thin films, showing interference colours up to 50 volts, were obtained but the reproducibility was poor.

Finally, ammoniacal ethylene glycol was used as an electrolyte. This solution is employed in the fabrication of electrolytic condensers having a long service life, and it was thought that with such an electrolyte chemical effects during oxidation would be very small. Electrolysis at room temperature produced films showing interference colours which were characteristic of formation voltage over a range of from 2–100 volts, with no pit corrosion after 2 minutes of treatment. Treatment for longer than 30 minutes, at the higher formation voltages resulted in some changes in the film, at 60 volts a yellow oxide formed loosely on top of the original film and at 80 volts, nodules of black oxide grew in pits over the surface.

A preliminary comparison of the colours produced on uranium by anodic oxidation in ammoniacal ethylene glycol and those produced on zirconium by similar electrolytic treatment in aqueous ammonium borate was made. For the purposes of this comparison a strip of uranium $10 \times 2 \times 0.4$ cm was cleaned and ground on emery paper, to 4 O's grade, and immersed in the electrolyte to within $\frac{1}{2}$ cm from the upper end, and anodised at 5 volts for 2 minutes. It was then withdrawn 1 cm and reanodised at 10 volts for 2 minutes. This process was repeated until the applied potential reached 75 volts. In this way a coloured strip was produced, each coloured band representing its respective formation voltage (Table I).

Sharp demarcation lines between each coloured band were not obtained, as with zirconium. This may have been a result of the more porous uranium oxide film which promoted creep of the electrolyte at the solution level during anodic treatment, with consequent staining.

Some preliminary runs at constant voltage and room temperature gave log i/log t curves which were

TABLE I

COMPARISON OF OPTICAL THICKNESS OF ANODIC FILMS ON URANIUM AND ZIRCONIUM

Film colour	Formation voltage on zirconium	Formation voltage on uranium
Straw	2.0	5.0
Brown	6.25	10.0
Red-brown	15.25	15.0
Purple	18.0	20.0
Deep blue	20.0	25.0
Medium blue	26.2	
Light blue	30.0	
Pale blue	35.0	30.0
Faint blue	39.0	40.0
White	45.0	50.0
Pale yellow	51.0	70.0
Pale gold	55.0	
Deep gold	59.5	
Red gold	64.0	75.0
Red	72.0	
Purple-red	76.5	

not reproducible and of variable slope. When this work was repeated at 0°C, the curves were straight lines of decreasing negative slope with increase in voltage and in all cases more uniform interference colours were obtained.

Uranium normally oxidises progressively when exposed to air; in water corrosion is much more rapid, with barnacle and pit formation taking place after a few hours. Prolonged exposure of anodic films to the laboratory atmosphere, however, produced little change in colour or texture, indicating that some degree of passivity was imparted to uranium by anodic treatment. This passivity appeared to be unchanged after 24 hours' immersion in water at room temperature, a further indication that these films were similar in character to those produced on aluminium or zirconium, by anodic treatment in aqueous ammonium borate.

Figure 1 is a typical example of a voltage/time curve of the anodic oxidation of uranium at a constant current of 0.33 ma/cm^2. By anodic treatment at constant current, any voltage change is due to film formation, since at constant temperature the voltage loss across the electrolyte is constant. In Figure 1 inset, there is a small plateau

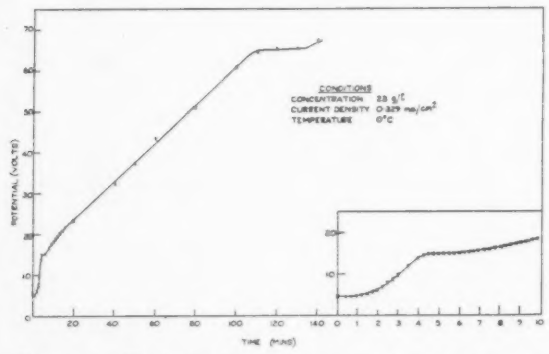

FIGURE 1. Typical voltage/time curve at constant current. Inset shows expanded version of curve for initial stage.

at 5 volts possibly due to a thin air-formed tarnish film. After two minutes the voltage rises steadily to a second plateau at 15 volts (or 11.5 volts when corrected for resistance of the electrolyte). Thereafter the voltage rises at a lower rate than the original rise until a third plateau appears at 65 volts. In the case of aluminium and zirconium, anodic oxidation in ammonium borate at constant current, gives linear voltage/time curves with no break in the continuity, (such as a plateau or sharp change in slope), until very high potentials of the order of 400 volts are reached.

Because of the preliminary results described above on the anodic oxidation of uranium in ammoniacal ethylene glycol further work in greater detail was justified.

Experimental Technique

Electrolytic cell

Throughout the work to be described, plates of uranium 5.0 × 1.9 × 0.2 cm formed by hot rolling, pickling and two final cold passes were used. The specimens were abraded on emery paper of grades down to 4 O's using petroleum ether as lubricant. They were then painted with cellulose paint to limit the anodised area to 7.6 sq cm of the side facing the cathode. A cylinder of polythene 3.75 cm in diameter, with two deep grooves 1 cm apart supported the electrodes, these being held in a parallel position by a 1 cm wide polythene spacer cut from 3 mm sheet. The assembly was lowered into the electrolyte by two leads from the ends of which were attached crocodile clips painted to prevent condensation and spray corrosion in the cell during electrolysis. During the experimental runs the solution level was maintained 0.5 cm lower than the top of the electrodes so that no galvanic couple could arise between the supporting clips and the electrodes.

To maintain steady temperature conditions the cell was supported in a Dewar flask containing melting ice for experiments at 0°C and solid CO_2 in alcohol for temperature ranges down to −40°C. At the lower temperatures the heat generated by electrolysis maintained the cell temperature about 5°C above that of the cooling bath.

To avoid absorption of water vapour from the air by the electrolyte a tube of P_2O_5 was suspended in the cell. Fully rectified smoothed d.c. current was fed to the cell through a variable series resistance of up to 50,000 ohms, to give fine control. For certain critical runs a bank of dry cells was used as a source of external current.

Specimens, after anodic treatment, were washed in running water and dried between filter papers. The effect of different formation conditions was studied in detail, as described below.

Electrolyte resistance

One important difference between uranium and the metals previously examined is that the electrical resistance of uranium oxide is low compared with aluminium and zirconium oxides, while the resistance of the ammoniacal ethylene glycol is high compared with aqueous electrolytes. It was necessary, therefore, to carry out a preliminary investiga-

tion of the properties of the organic electrolyte—its polarisation characteristics, its resistance, and the variation of these properties with temperature. This was done using two parallel platinum electrodes 7.6 sq cm in area and 1 cm apart. The polarisation effects are constant over a range of potentials and temperatures. The variation of current density with applied potential was determined. The results in Figure 2 show that the electrolyte obeys Ohm's Law, and the voltage V required to pass a current i is given by:

$$V = V_0 + iR$$

where V_0 is an initial potential of about 1.8 volts due to polarisation, and R is the resistance of the electrolyte. It is also clear from Figure 2 that the

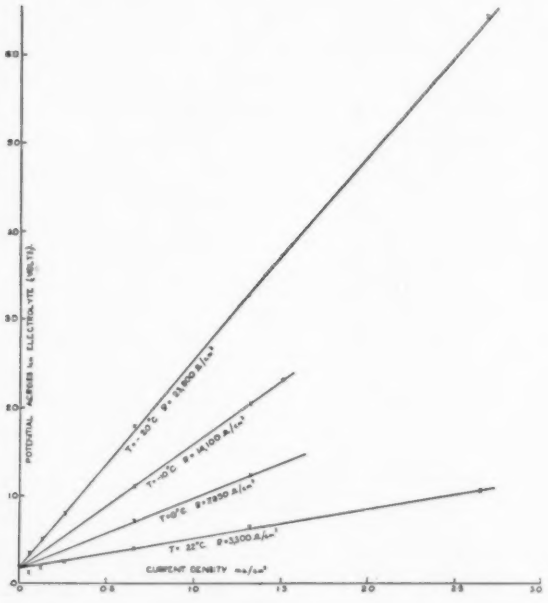

FIGURE 2. Typical voltage/current curves for ammoniacal ethylene glycol. Platinum electrodes were used spaced 1 cm apart.

resistance increases as the temperature falls. Correction factors for potential drop across the electrolyte for use in future work can be read directly from this curve. The plot of log R against $1/T$ in Figure 3 shows that the relation between resistance R and absolute temperature T may be represented by the equation:

$$R = R_0 e^{U/kT}$$

(where R_0 is the resistance to which the electrolyte tends at high temperatures, U and k being constants). Calculations based on data from the curve show that with $R_0 = 0.0269$ ohm, $U = 0.056$ electron volt.

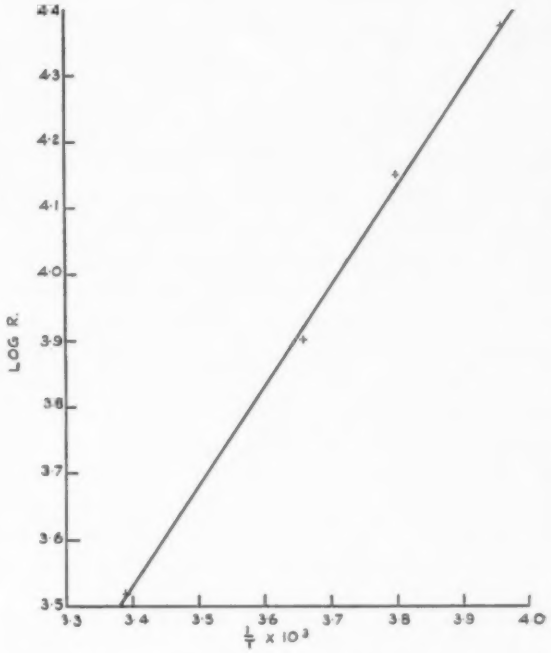

FIGURE 3. Curve showing logarithm of the resistance of the electrolyte versus the reciprocal of the absolute temperature.

The effect of variation of the concentration of ammonia in the electrolyte was studied, dilution being affected by the addition of pure B.D.H. ethylene glycol. Concentrations from saturated 70 g/l ammoniacal ethylene glycol down to 14 g/l solution were prepared and examined at 0°C. Both dilution and the combination of dry ammonia gas with glycol were exothermic. Table II shows the

TABLE II

VARIATION OF RESISTANCE WITH CONCENTRATION OF AMMONIACAL ETHYLENE GLYCOL

Ammonia content by Aliquot additions (gms/1)	Ammonia content by analysis (gms/1)	Resistance (ohms/cm²)
70	69	8,650
35	20.0	12,100
23	7.6	16,600
17.5	6.1	18,500
14.0	6.2	18,800

variation of specific resistance with dilution made by the addition of glycol to 70 g/l solution together with the corresponding chemical analysis, carried out as a straight titration of the solution against

standardized HCl using screened methyl orange, as an indicator.

From these figures it would appear that some addition compound had been formed leaving a limited quantity of "free" ammonia for titration. As was to be expected the resistance of the electrolyte increased with decrease in ammonia content.

Effect of air-formed tarnish films

As uranium tarnishes so rapidly in air and preliminary work at room temperature and 0°C had shown that any tarnish film appeared to delay the normal voltage rise during electrolysis at constant current, this effect was investigated by taking voltage/time measurements at 0°C, using specimens which had been exposed to the air from 5 minutes to 22 hours after abrading. Specimens with tarnish films were immersed for various periods in the electrolyte before anodic treatment to determine whether the delay in normal voltage rise could be removed by a simple immersion. The results are drawn as a voltage/time curve, in Figure 4. The

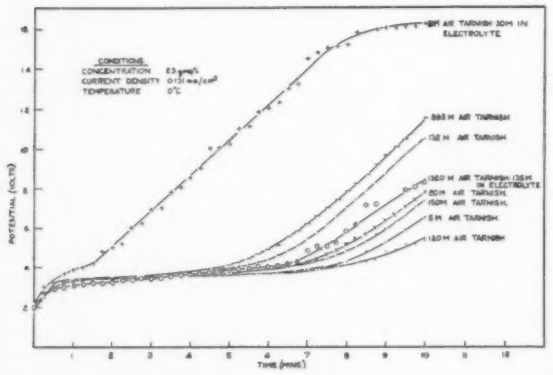

FIGURE 4. Effect of air tarnish film on voltage rise.

delay in voltage rise at the start may be due to the initial tarnish film, or to the chemical effect of immersion in the electrolyte. When the voltage finally rises the slope of each curve is nearly parallel, and may indicate that the voltage rise is similar for all specimens once the delay introduced by the tarnish film has been overcome. Variations in the curves may be due to variations in superficial surface area of the specimens and local temperature changes. Suspension of tarnished specimens in the electrolyte, prior to anodic treatment appears to eliminate the delay in voltage rise provided that the immersion time is greater than the tarnishing period. No visible change in the colour of the specimen was observed after this immersion treatment; clearly therefore, change in film thickness as a result of immersion does not appear to account for this phenomenon, nor chemical attack increase the delay.

Results

Film formation at constant current

An advantage gained from anodic oxidation at constant current is that the voltage drop across the electrolyte remains constant at constant temperature, and therefore the initial voltage V due to the electrolyte could be corrected for immediately during analysis of the results.

The cell, in this case, was connected in series with a bank of variable resistances which were decreased

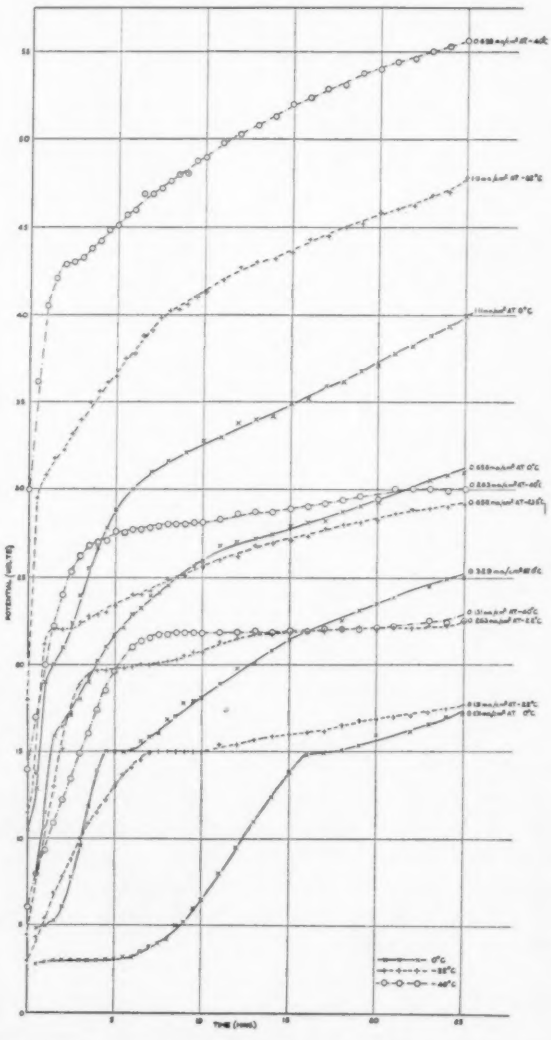

FIGURE 5. Variation of potential with time at various temperatures and current densities, in ammoniacal ethylene glycol (23 g/l).

continuously during anodic treatment in order to maintain a constant current. Current densities ranging from 0.1 to 2.5 ma/cm² were investigated, voltage/time measurements being taken at constant time intervals for various periods. This work was carried out at temperatures from 0°C to −40°C.

Figure 5 shows a series of typical voltage/time plots, using an electrolyte containing 23 g/l ammonia. This concentration was achieved through evaporation of the ammonia and not dilution with ethylene glycol, which, as has been shown, might introduce a variation in results due to the presence of complexes formed by combination of free ammonia with the diluent. All these curves show a characteristic plateau or, at the higher current densities, a sharp change of slope. In each case the voltage rises more rapidly with increase in current, as was to be expected. For each temperature studied Figures 6 to 8 show potential corrected for initial time lag due to tarnish and for resistance of electrolyte, plotted against total charge passed. At a given temperature, the increase in voltage depends mainly on the total charge passed, and only to a small extent on the current density. Moreover, the plateaux occur at very nearly the same voltage. The main features derived from these curves are summarized in Table III.

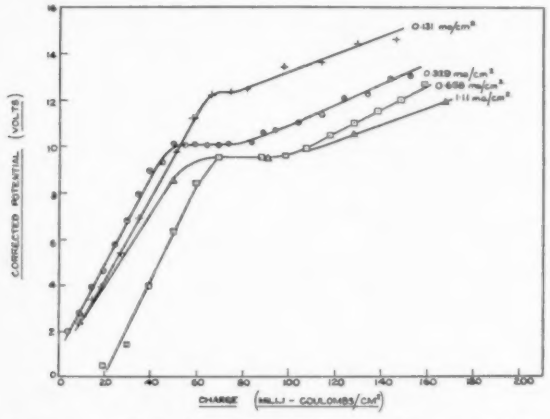

FIGURE 6. Variation of potential with charge passed at various current densities. Temperature 0°C.

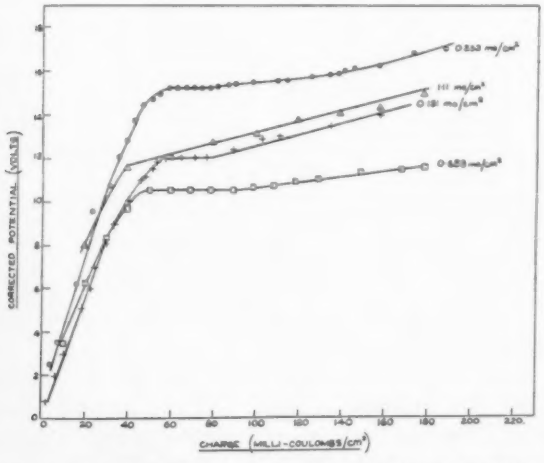

FIGURE 7. Variation of potential with charge passed at various current densities. Temperature −22°C.

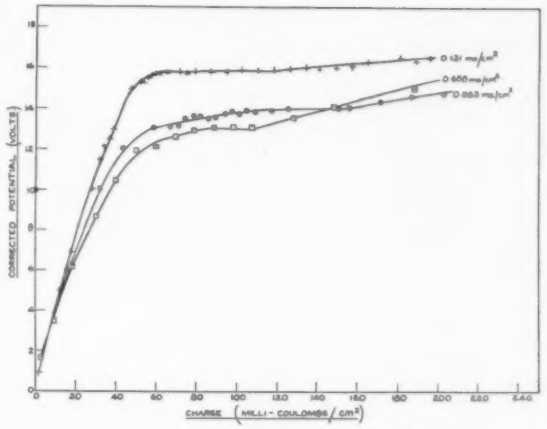

FIGURE 8. Variation of potential with charge passed at various current densities. Temperature −40°C.

TABLE III

EFFECT OF TEMPERATURE AND CURRENT DENSITY VARIATIONS DURING ANODIC OXIDATION OF URANIUM

Temperature (°C)	Current density (ma/cm²)	Potential at plateau (volts)	Charge passed to reach plateau (milli-coulombs)	Plateau length expressed as charge (milli-) coulombs)	Average plateau potential (volts)
0°	0.13	12.3	65	8	10.3
	0.33	10.0	50	25	
	0.66	9.5	65	30	
	1.11	9.5	55	25	
−22°	0.13	12.0	55	20	12.4
	0.26	15.3	55	25	
	0.66	10.5	45	30	
	1.11	12.0	45	10	
−40°	0.13	15.8	50	45	14.2
	0.26	14.0	45	25	
	0.66	13.0	50	10	

These figures show that the plateau height gradually increases with decrease in temperature, but that this change does not appear to alter markedly over the temperature range. The charge passed to reach a plateau, however, at any given current density and temperature is nearly constant, but

there is little correlation between this figure and the plateau length also expressed as charge.

Effect of dilution of the electrolyte

The primary effect of dilution on the anodic oxidation of uranium, at constant current, as seen in Figures 9*a*, *b*, *c*, and *d*, appears to be the dis-

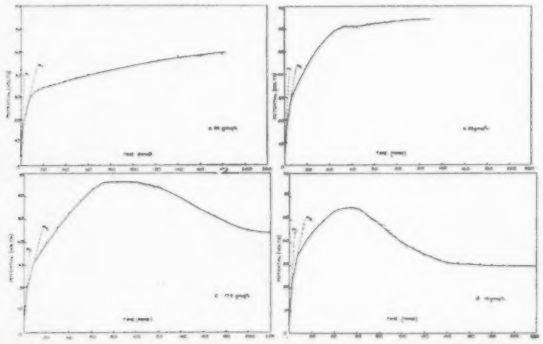

FIGURE 9. Effect of concentration of electrolyte on potential/time curve. All observations at constant current density 0.33 ma/cm², temperature 0°C.

appearance of the low voltage plateau which is replaced by two changes in slope. At 50–60 volts a plateau is also obtained after the passage of 600 milli-coulombs. At 60 volts and over, all specimens show a loose yellow powdery layer on top of the normal interference colour film. Table IV gives an analysis of these results.

TABLE IV

EFFECT OF VARIATION OF CONCENTRATION OF AMMONIA IN ELECTROLYTE ON ANODIC OXIDATION AT 0°C

Concentration (g/l NH_3)		Current density (ma/cm²)	Potential at changes in slope and plateau (P) (volts)	Charge passed to 1st and 2nd change in slope (milli-coulombs)	Plateau length expressed as charge (milli-coulombs)
Dilution	Actual				
14.0	6.2	0.33	1st 12	49	
			2nd 26	118	
			P 48		277
17.5	6.1	0.33	1st 9	25	
			2nd 26	100	
			P 60		600
23.0	7.6	0.33	1st 11.5	25	
			2nd 26	100	
			P 56.5		600
35.0	20.0	0.33	1st 17	50	
			2nd 27	100	
			P 44		600

From the table, the first change in slope occurred at an average of 12.3 volts, the second at 26 volts after the passage of 100 millicoulombs. (These figures are corrected for resistance of the electrolyte.) Similar high-voltage plateau lengths of 600 milli-coulombs were recorded in all but the most dilute solution. Thus from these results it appears that little significant change in the reaction occurs as a result of dilution, apart from an acceleration of high voltage plateau formation. The 50–60 volt plateaux formed when using solutions "diluted" only by evaporation, occurred after the passage of 3–4 coulombs rather than about 0.6 coulombs as recorded in the second case. It will be noted that the potential to reach the first change in slope is of the same order as that required to reach the plateau in solutions diluted by evaporation (of Tables III and IV).

Anodic oxidation at 1.31 ma/cm², a fairly high current density in this work, in 70 g/l concentrated electrolyte gave a film exhibiting periodic passivity, the voltage increasing by 2 volts in 14 minutes and then fluctuating with increasing amplitude (see Figure 10). Aeration of the electrolyte for short

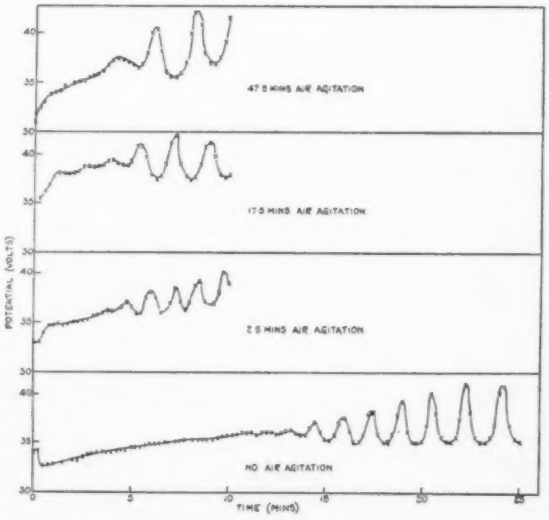

FIGURE 10. Potential periodicity during low-temperature anodisation in concentrated electrolyte, showing effect of air agitation. Concentration 70 g/l. Constant current density 1.31 ma/cm². Temperature −20°C.

periods decreases the amplitude, but does not remove the effect.

One interesting result observed at the lowest concentration examined, (14 g/l of ammonia), was the gradual fall in potential after a 48-volt plateau had been reached. This fall continued, until after

100 minutes, equilibrium was reached at 26 volts, this being nearly the original potential of the second change in slope, the curve being almost symmetrical (see Figure 9*d*). This effect could not have been due to chemical solution of uranium oxide in the electrolyte as an analysis did not reveal the presence of uranium in any detectable quantity. A similar fall in potential was also observed in the results of oxidation at 17.5 g/l dilution, though to a lesser extent.

The results described indicate either a change in chemical composition of the oxide formed or a change in physical state, at a plateau or point of sharp change in slope. A tentative suggestion at this stage was that the two plateaux formed at approximately 10–15 volts and 50–60 volts potential difference across the film corresponded to the formation of UO_2 and UO_3 (or UO_4) respectively. Similarly, the changes in slope and the plateau observed in results during oxidation in diluted solutions might also indicate these differences in oxide composition. This view is supported by the formation of loose yellow oxide above 60 volts together with black nodule formation at higher voltages. A detailed electron diffraction study of the films, taken at critical points on these curves, was undertaken to provide an answer to this aspect of the work, and is described in a separate section.

Film formation at constant voltage

A selected voltage was applied directly to the electrodes and maintained constant during electrolysis by variation of external resistances. Potentials ranging from 5 to 100 volts were employed and the variation of current with time recorded. This work was carried out at 0°C. Logarithmic current time curves drawn for the various specimens show clearly that the current falls quite rapidly with time at low formation voltages, whereas at higher voltages the fall in current is less marked (Figure 11).

In the case of aluminium, anodic oxidation at constant voltage gives extremely low values of the order of 1 μamp/cm^2 for current flow after film formation [2]. The high values recorded with uranium, about 5 ma/cm^2, may be due to greater porosity of the oxide film and the resultant increase in conductivity due to absorbed electrolyte.

Since with uranium positive the system does not obey Ohm's law during film formation, the resistance of the film is not constant, but when the applied potential is lower than the formation voltage the current passed is small, and agreement with Ohm's Law becomes closer.

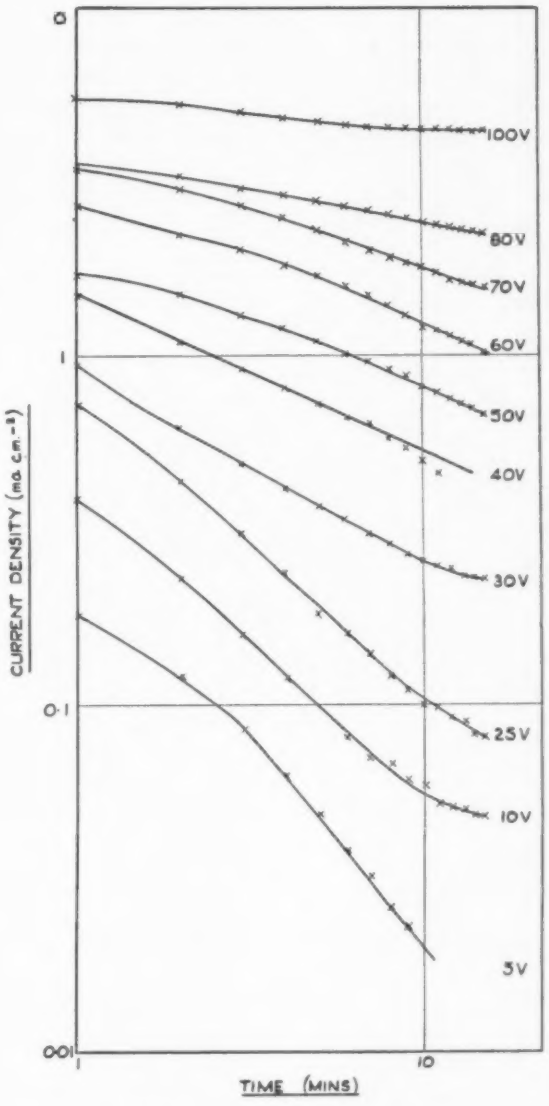

FIGURE 11. Fall of current density with time at constant voltage. Temperature in all cases 0°C.

Figure 12 is a logarithmic plot of current against potential drawn from results obtained with a specimen, formed a constant voltage having a 2-minute 25-volt film anodised at −22°C. It shows a plot AB of the same variation of current with potential corrected for the resistance of the electrolyte (23 g/l). This curve is a straight line of slope approximately 1. For a film produced under the above conditions a value for its resistance of the order of 10^5 ohms/cm^3 ($\pm$20 per cent) during a tenfold increase of current, is obtained.

It can be shown that even when film formation is

nearly complete at constant voltage, ionic current does continue to flow. A specimen was anodized at 50 volts for 15 minutes, removed, dried, and partially reimmersed in the electrolyte. Oxidation of the immersed portion was continued at the same voltage for 17 hours. The first half of the specimen was a very faint blue (equivalent to a 35–40 volt zirconium oxide film) while the second half had changed to a yellow green (103-volt zirconium film). Thus a considerable portion of the high "leakage" current is ionic, whereas in the case of aluminium and zirconium [4] the leakage current is almost entirely electronic, and little further film growth takes place after the first few minutes.

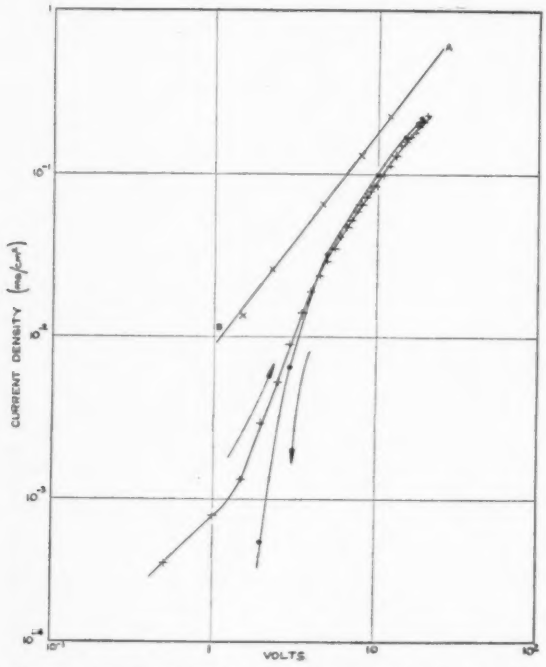

FIGURE 12. Rectification curve for 25-volt film, at −22°C.

Electron Diffraction Study of Various Films

From the results obtained by film formation at constant current, in various diluted electrolytes, positions of interest such as those of greatest gradient, change of slope and plateau were chosen on the respective voltage/time curves. These were chosen to determine whether the type of oxide film produced varied physically or chemically at each stage of film formation. Under the conditions required to reproduce these characteristic films, specimens were prepared at the Physical Laboratories of Imperial College, London. The electrolyte was removed after anodic treatment by rinsing in water, alcohol or ammonia-free ethylene glycol and drying between filter paper. To determine whether variations in the drying technique made any significant difference to the final films, the specimens were immediately transferred after drying to a 120 KV electron diffraction camera, examined and photographed. Further specimens were exposed to the laboratory atmosphere for 24 hours and re-examined to note any changes in characteristics. The loose yellow film formed on uranium at a potential of about 60 volts was removed and examined in an attempt to produce transmission patterns, and films several months old were also studied for comparison and determination of any change with age.

The results provided no support for the theory that films taken at points corresponding to sharp potential increase and plateaux, represented changes in chemical constitution of the oxide. All films clearly showed the presence of UO_2. In every case, however, films taken on samples which had been anodised at points of potential rise proved to be crystalline in nature and those taken from any point on a plateau were amorphous. The changes in slope of the potential/time curves at constant current, therefore reflect changes in the physical characteristics of the oxide film.* Films taken on samples at points of high voltage, nearer 40–60 volts, showed several extra rings in the diffraction pattern. These may be due to the presence of higher oxides of uranium but insufficient information was available for their identification. Confirmation of the presence of higher oxides was not obtained from examination of the loose yellow powder produced above 60 volts, as the detached scales employed in this study were too thick for transmission photographs. The extra rings cannot be due to the presence of water since washing the specimen in water, alcohol or ammonia-free glycol showed no significant difference. Also specimens allowed to stand overnight in air gave even clearer pictures of the UO_2 film indicating that the film had become more crystalline on ageing, but since no extra rings in the pattern developed, significant absorption of water from the air had not occurred.

The specimens prepared several months before (and examined at this stage) gave an exceptionally clear shadow edge and sharp rings with spacing

*In this study the term *amorphous structure* denotes films in which the crystallites are so small that they are below the resolution of the camera.

corresponding to UO_2. A detailed table of results together with examples of photographs taken at the various stages is given in Appendices I and II.

Film Thickness

Maximum film thickness from Faraday's laws

If a film is formed at constant current and this current is assumed to be wholly ionic, an estimate of the true thickness of the oxide film can be obtained. This assumption is justified for aluminium where the formation current is almost entirely ionic; for zirconium the efficiency is usually at least 70 per cent. At constant current the total charge passed is readily obtained and hence from Faraday's Laws the maximum weight of oxygen released at the anode is known. This can be converted into the mass of uranium oxide formed, since 8 gm of O_2 will form 67.5 gm UO_2. The density of the bulk oxide is 10.8 gms/cm^3 and if this is assumed to hold for the film, the volume of oxide produced is known [7]. Finally, if the true surface area of the specimen is taken to be equal to the apparent area, the thickness of the film can be found. During the first linear portion of the voltage/charge curve (Figure 6) the rate of growth corresponds to about 16.5 Å/volt assuming maximum current efficiency. Since the current during formation is not entirely ionic and the true surface area is greater than the apparent area, the rate of growth will actually be less than the value quoted.

Film thickness from interference colour

The colour shown by a thin oxide film is due to destructive interference of a narrow band of frequencies constituting part of the white light incident upon the film. The colours of thin films are therefore distinctive and reproducible, and if calibrated against the colours exhibited by air films of known thickness would form a reliable method of determining the optical thickness of any given film. The interference colours of thin air films have been studied by Rollett [11] and in Table V a comparison is made of the formation voltage required to produce a film of given colour on uranium, and the thickness of the air film required to show the same colour by reflection. Owing to the difficulty of identifying the colours from their descriptions, accurate matching is not easy.

If the assumption that thickness is proportional to the voltage of formation is correct and the refractive index μ is constant, the plot of voltage against equivalent air film thickness should be a straight line. Figure 13 suggests that this is the case and gives an optical growth rate of 32 Å/volt which is equivalent to an oxide growth rate of $32/\mu$ Å/volt. From Faraday's Laws a maximum value of the oxide growth rate is 16.5 Å/volt so it seems that μ is at least 2 and probably greater.

TABLE V

COMPARISON OF FORMATION VOLTAGE AND THICKNESS OF AIR FILMS

Colour	Thickness of air film required to produce colour (Å)	Formation voltage required to produce colour (volts)
Straw	1000	5
Pale brown	1045	10
Purple	1350	18
Deep blue	1400	25
Pale blue	1640	40
Faint blue	2350	50
White	2450	60
Pale yellow	3000	70

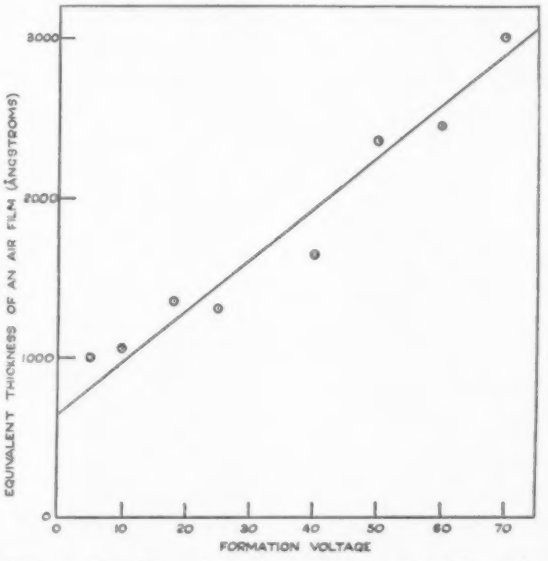

FIGURE 13. Plot of air film thickness against formation voltage required to produce the same colour.

This value is of the correct order since the indices of the oxides of zirconium (ZrO_2), aluminium (Al_2O_3), titanium (TiO_2), and plutonium (PuO_2) are 2.2, 1.77, 2.39 and 2.47 respectively. The current flowing during formation is therefore very largely ionic in character.

The curve of Figure 13 does not pass through the

origin, but indicates that even at zero voltage a film of 650 Å optical thickness, or $650/\mu$ Å = 325 Å oxide thickness, exists. This "zero thickness" can be ascribed to the average phase change on reflection which is the equivalent of a change in film thickness. In the case of tantalum, Waber and co-workers [12] found an average phase change equivalent to an oxide thickness of about 150 Å or an optical thickness of 345 Å. Since an air film thickness of only 1000 Å (i.e., total path retardation of 2000 Å) is needed for interference of frequencies at the violet end of the spectrum, and if the phase change contributes 650 Å, the oxide film need be only $325/\mu$ Å $\approx$ 162 Å thick to produce a visible colour.

Oxidation of uranium in air and water

Previous work has shown that the rate of oxidation of uranium in air at temperatures of the order of 100–250°C follows a parabolic law. In view of the characteristic thickness/time relationship observed during electrolysis the thermal oxidation of the metal in air was examined over a range of 50–200°C to determine whether plateaux also occurred under these conditions of oxide formation during the initial stages. Specimen 5 × 2.5 cm × 0.1 cm were heated in covered glass beakers in a low temperature oven, controlled to ±2°C by a Sunvic type temperature control. Films formed in air at temperatures up to 100°C were found to have reproducible interference colours and their thicknesses were estimated by comparison with air films shown in Table V. Above this temperature the heat tints traversed the whole interference colour range too rapidly for accurate comparison and thickness of film was measured by change in weight determinations. The results (Figure 14), show typical plateaux at temperatures of 74°, 90° and 100°C respectively at thicknesses equivalent to 12, 20 and 60 volts, assuming a growth rate of 16.5 Å/volt.

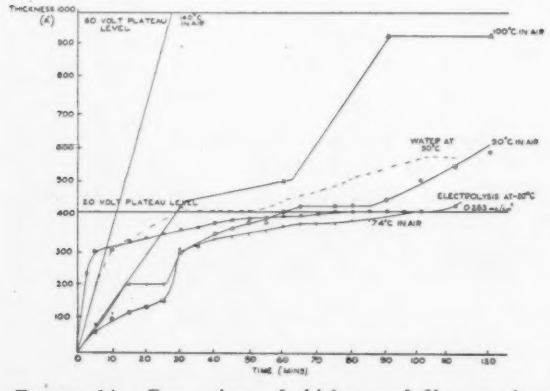

FIGURE 14. Comparison of thickness of films produced by thermal oxidation in air, anodic oxidation and immersion in water at various temperatures.

In Figure 14 is also shown the rate of oxidation at 190°C; here in agreement with previous work [8] no plateau is recorded. A thickness time curve drawn from colour comparisons for a specimen heated in distilled water, at 50°C, is reproduced in Figure 14. In this case a plateau is recorded but the rate of attack is much greater than one would expect at 50°C by thermal oxidation of the metal in air, a fact which may be due to the formation of complex hydroxides or the difference in boundary layer between metal or oxide film and medium.

One result noted after about 40 hours' oxidation in air at 190°C, was the typical partition of the uranium specimen into multiple oxide layers. This layer effect has been observed up to the maximum resolution for microscopic examination; i.e., for layers up to a thickness of 10^4 Å, in both cast and rolled material.

Discussion

In the anodic oxidation of uranium the existence of plateaux in the formation voltage/time curves, (and sharp changes in slope at the higher current densities or in dilute solutions), which occur at between 10 and 15 volts and 50 to 60 volts is somewhat surprising. Electrolysis of aluminium or zirconium in aqueous or glycol electrolytes shows no such effect in the same voltage range. The first recorded change in slope during the anodic oxidation of aluminium occurs at about 400 volts; at this potential a disruptive spark occurs in the solution at the aluminium oxide face. That this plateau formation is a fundamental characteristic of uranium is shown by the fact that variation in temperature, concentration or current density have little effect on plateau height, this being largely dependent on charge passed. Similar plateaux have been observed by other workers during the anodic oxidation of zirconium in nitric acid [9]. In this case plateaux of varying duration occurred between 8 and 10 volts in the potential/time curves.

During voltage increase to the first plateau the thickness of the films formed is directly proportional to the voltage of formation; thereafter, unless film growth virtually ceases during plateau periods, thickness estimations at higher potentials would be erroneous if based on formation voltage. Further work on the changes in film thickness over these plateaux will be carried out and reported separately. At this stage evaluation of film thickness depends largely on the correct estimation of a

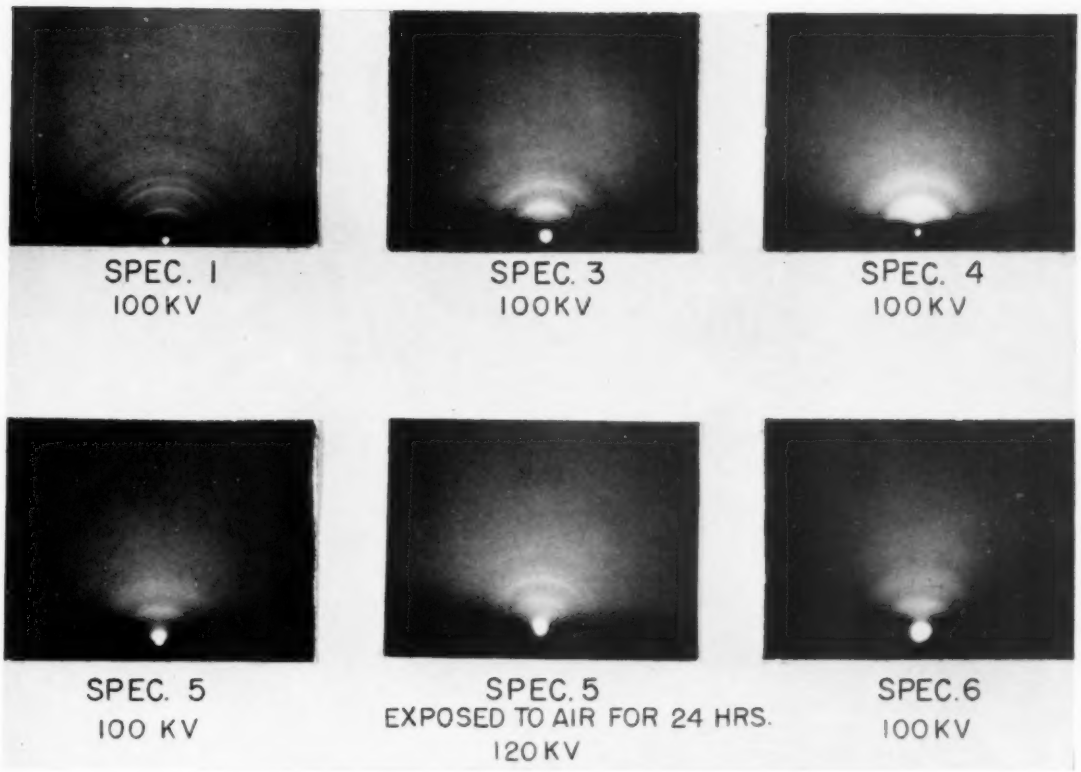

FIGURE 15. Electron diffraction pictures of oxide films on uranium.

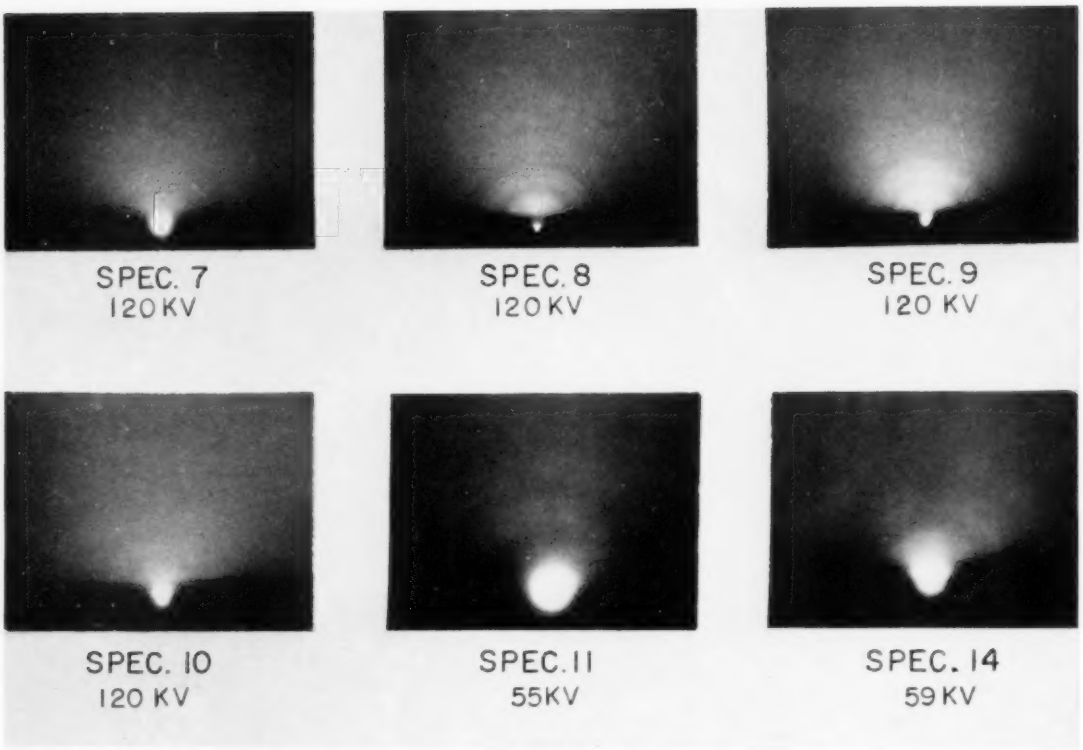

FIGURE 15 (cont.). Electron diffraction pictures of oxide films on uranium.

given series of colours in comparison with those given by Rollett in his work on the colours of thin air films. This comparison introduces a subjective error which can only be eradicated by direct physical measurements which have not, as yet, been made. The preliminary value of about 16.5 Å/volt for rate of growth of films on uranium up to the first plateau, obtained optically is of the same order as values given for other metals viz., 10 Å/volt for aluminium, 20 Å/volt for zirconium and 16 Å/volt for tantalum [13]. The rate of film growth on uranium of 16.5 Å/volt agrees favourably with a calculated maximum value of 16 Å/volt estimated from Faraday's Laws and assuming maximum current efficiency. The agreement certainly suggests that the current efficiency is high and that the methods of analysis employed in these estimations were fundamentally sound.

The electron diffraction study of films formed on uranium under various conditions has shown that in every case, at a period of potential increase, the oxide formed is crystalline in character. This is not the case for oxide films on aluminium and zirconium where the structure is amorphous, and varies only in porosity. The electron diffraction results quoted in this report indicate that changes in the physical structure of the film take place at a change from voltage rise to voltage plateau. For a plateau formed at 20 volts, at a current density of 0.7 ma/cm^2, the total energy applied to the system is equivalent to about 0.5×10^6 calories per cubic centimeter of oxide. The energy required to change the physical state of such a uranium oxide film from a crystalline to an amorphous structure is probably of the order of 10–100 calories/cm^3, by comparison with the corresponding transformation energy of the copper oxide system. Therefore, on an energy basis, such a transformation is possible, considering that the energy supplied is greater by a factor of 10^4 than that required to produce such a change. However, because of the high excess energy supplied, changes in state of the oxide layer might be due to a local heating effect, even although the thermal conductivity of the oxide is high.

The resistance of the final film which has rectification properties cannot be given in simple terms since the current in the forward direction (uranium positive) is not proportional to the applied voltage. In the reverse direction the current is approximately proportional to the applied voltage, after correction for voltage drop across the cell, and a resistance of about 10^5 ohms/cm^3 is obtained.

This preliminary survey of the anodic oxidation of uranium has also proved to be of interest since it has been shown that the controlled growth of thin films of UO_2 on the base metal imparts an appreciable degree of passivity to the surface. Uranium so treated remains protected for some hours when subsequently boiled in water, whereas untreated uranium usually undergoes general corrosion. Anodised uranium when heated in air at about 120°C shows very little change in colour (and hence in film thickness) after an eight-hour treatment, whereas freshly ground uranium surfaces become a full black in colour over a similar time, indicating that growth of a thick film has taken place. Further work on the protective nature of these films is being carried out. The similarity of air and electrolytic oxidation rate curves, moreover, suggests that the mechanism of oxidation of uranium for films up to 2000 Å in thickness, is independent of the method of oxidation, each method having fundamental features in common.

During the anodic oxidation of uranium the change in structure of the film from a crystalline to an amorphous nature is marked by the formation of a plateau on the thickness/time plot. It is postulated that at this stage a discontinuity in the film occurs. The alternate film growth and plateaux recorded may provide an explanation of the layer effect noted during thermal oxidation in air of the metal at temperatures over 150°C. Here at the plateaux or discontinuities, observed in this method of oxidation the adhesion of the oxide layers between plateaux may be less, leading to rupture of discrete layers as the rate of oxidation increases. The weakness in this explanation is the fact that no plateaux were recorded during thermal oxidation in air at 190°C although this effect may have been masked by the accelerated rate of attack.

Conclusions

The anodic oxidation of uranium in ammoniacal ethylene glycol under varying conditions of temperature, current density and concentration of ammonia, in all cases results in the formation of UO_2. Variations in the rate of voltage increase are explained by the change in physical state of the oxide, from crystalline during voltage increase to amorphous during plateau periods. The oxide film is similar in many respects to that formed on aluminium or zirconium, being passive and of the same order of thickness. Estimations of film thickness have been made by comparison with the interference colours of thin air films. Further work on the direct measurement of the refractive index of the film is in progress. A comparison between thermal oxidation in air, anodic oxidation in electrolytes

TABLE I OF APPENDIX II

PREPARATION DETAILS PRIOR TO ELECTRON DIFFRACTION

Specimen No.	Preparation	Anodic treatment					Rinse	Remarks
		Electrolyte NH_3 content	T/t time	Temp. °C	Potential volts	Current range		
1	40/s emery (600 mesh) Pet. ether rinse Acetone rinse	—	—	—	—	—		Straight into camera
2	30/s emery (400 mesh) Pet. ether rinse Acetone rinse	—	—	—	—	—		Straight into camera
3	40/s emery Pet. ether rinse Acetone rise Masking 40/s emery dry rub	23.1 g/l	17 M	−21.0	20.9	1 m/A	Water dried in filter paper	Pale yellow film
4	As (3)	23.1 g/l	18 M	−22.5	21.5	1 m/A	Water dried in filter paper	Pale yellow films with more lustre than (3).
5	As (3)	23.1 g/l	6.75M	−21.0	74.6	10 m/A	Water dried in filter paper	Partly covered with thin powder on top of yellow film
6	As (3)	23.1 g/l	20 M	−21.0	48.2	5 m/A	Ethyl Alcohol wash	Purple-blue interference colour
7	As (3)	23.1 g/l	25 M	−19.5	64.0	7 m/A	Water dried in filter paper	More loose yellow film than (4)
8	As (3)	23.1 g/l	3 M	−21	18.8	2 m/A	NH_3 glycol dried in filter paper	Specimen removed at peak of sharpest voltage rise
9	As (3)	14 g/l	5 M	− 5	23.4	3 m/A	Glycol free from NH_3 dried as (8)	Removed at change of slope
10	As (3)	14 g/l	90 M	− 5	54.0	3 m/A	As (9)	Removed at peak of slope
Specimens prepared at Harwell and examined at Imperial College								
11	As (3)	14 g/l	247 M	+ 1	27.1	2.5 m/A	Water dried in filter paper	Removed at end of slope Yellow with red streak and black barnacles
12	As (3)	23.3 g/l	130 M	+ 1.5	63.8	2.5 m/A	As (11)	Specimen covered with loose yellow film 6 days old kept in dessicator
13	As (3)	35.0 g/l	180 M	+ 1.5	49.0	2.5 m/A	As (11)	As (12)
14	Machined surface Acetone degrease	36 g/l	2 M	0	75v	—	As (11)	Purple interference colour Specimen kept on lab. bench for 3 months (Thick disc of uranium.)

TABLE II OF APPENDIX II

RESULTS OF ELECTRON DIFFRACTION EXAMINATION OF ANODIZED URANIUM
(AT A CAMERA LENGTH OF 48 CMS.)

No.	NH_3 content (gm/l)	t time (min)	Temp. (°C)	Final voltage	Current (ma)	Plate no.	Inference	Remarks
1	Original uranium surface					HV1066	UO_2 ring pattern	
3	23.1	17	−21	20.9	1	HV1067	UO_2 ring pattern	Voltage rising crystalline
4	23.1	18	−22.5	21.5	1	HV1068	UO_2 halo pattern	Plateau amorphous
5	23.1	6.75	−21	74.6	10	HV1069	UO_2 halo pattern	Plateau amorphous
ditto exposed to air 24 hours						HV1090	UO_2 ring pattern	Just coming up to plateau
6	23.1	20	−21	48.2	5	HV1072	UO_2 diffuse rings 1 extra ring	Amorphous/ crystalline
7	23.1	25	−19.5	64.0	7	HV1080	UO_2 halo pattern	Plateau amorphous
8	23.1	3	−21	18.8	2	HV1082	UO_2 ring pattern 3 extra rings	Voltage rising crystalline
9	14	5	− 5	23.4	3	HV1085	UO_2 ring pattern 4 extra rings	Voltage rising crystalline
10	14	90	− 5	54	3	HV1088	UO_2 halo pattern	Plateau amorphous
11	14	247	+ 1	27.1	2.5	h1359	UO_2 ring pattern	Min-voltage crystalline
12	23.3	130	1.5	63.8	2.5	—	no pattern	
13	35.0	180	1.5	49.0	2.5	—	no pattern	
14	36	2	—	75	—	h1355	UO_2 ring pattern	3-month specimen crystalline

and oxidation in water of uranium has shown that these processes have much in common for films up to 2000 Å in thickness.

APPENDIX I

Discussion of Electron Diffraction Results

Without exception the electron-diffraction patterns revealed a face-centred cubic structure, showing good agreement with the interplanar spacings of UO_2 (for which $a = 5.458\ kx$). The diffraction patterns ranged in clarity from haloes to sharp rings. Specimen 1 of the original surface and those of the anodized specimens 3, 8 and 9 gave patterns of sharp rings, whilst patterns from specimens 4, 5, 7 and 10 were diffuse.

Owing to the difficulty in measuring the position of the diffraction rings exactly the patterns could have corresponded to $UO_{2\cdot3}$ ($a = 5.430\ kx$) or to any composition in between UO_2 and U_3O_8. The lattice dimensions of UO, which is also face-centred-cubic but with $a = 4.92\ kx$, however, are sufficiently different from that of UO_2 ($a = 5.458\ kx$) to show that the specimens do not contain any UO.

Specimens 6, 8 and 9 gave electron-diffraction patterns showing additional rings which could not be indexed as arising from UO_2. The interplanar spacings of these patterns agree amongst themselves; those for plate HV. 1085 (Specimen 9) are given in Table III.

The rings corresponding to spacings of 4.50 and 2.185 A. could possibly be due to the presence of the U_3O_8 phase. This is not so for the 2.42 and 1.52 A rings, but it is noted that these are the same two

extra rings previously observed [6] in UO_2 patterns from mechanically polished uranium.

Recent data [7] for uranium hydroxides suggest that these four extra rings may possibly all be due to UO_3H_2O (for which $a = 6.86$, $b = 4.72$ and $c = 4.21$ kx, in the orthorhombic lattice), but until further information is obtained as to the intensities of the diffractions nothing more definite can be said. Although specimen 10 was washed in ammonia-free glycol as was specimen 9, no extra rings were recorded.

Some of the anodized uranium specimens were left in air at room temperature for 24 hours and then re-examined. The patterns showed that the uranium surface had become distinctly more crystalline, the type of oxide remaining unchanged.

Of the other uranium specimens which were anodised at A.E.R.E., Harwell, and examined at Imperial College several days later, specimens 11, 12 and 13 gave a less definite shadow edge, indicating a rough surface. Electron diffraction patterns showed the surface to be mainly amorphous but with regions of crystalline UO_2. An attempt was made to obtain transmission patterns from the powder scraped from the surface (on to a collodion film) by a razor blade, but this was not successful.

Specimen 14 of machine-surfaced uranium with a 75-volt film aged in air for three months gave an exceptionally clear shadow edge and sharp rings corresponding to the spacings of UO_2.

APPENDIX II

Notes on Specimens Prepared and Examined at Imperial College

Material

Hot-rolled uranium with two final cold passes to give smooth finish.

Electrolyte

Ammoniacal ethylene glycol of varying ammonia content.

Specimens

Samples of uranium, as above, painted with cellulose varnish (acetate) to leave area of 3.8 sq cm exposed, immediately prior to anodic treatment. All samples taken down on emery, using petroleum ether as a lubricant.

Acknowledgements

The authors wish to thank Dr. H. M. Finniston for his encouragement throughout the work and Dr. Wilman and Mr. Kerr of Imperial College, London, for their kind assistance with the electron diffraction examination of specimens. This paper is published by permission of the Director, A.E.R.E.

References

1. Cabrera, N. Comptes Rendus **220** (1945) 111.
2. Charlesby, A. Proc. Phys. Soc. **B66** (1953) 317.
3. Charlesby, A. Acta Met. **1** (1953) 340.
4. Charlesby, A. Proc. Phys. Soc. **B66** (1953) 533.
5. Günterschulze, A. Elektrolytkondensatoren (Berlin, Krayn, 1937).
6. Hart, R. K. Trans. Far. Soc. **49** (1953) 299.
7. Katz, J. J. and Rabinowitch, E. The Chemistry of Uranium. (New York, McGraw-Hill, 1951).
8. Laing, J. Private communication, A.E.R.E., 1953.
9. Misch, R. D. and Ruther, W. E. AECU Report No. 2310 (1952).
10. Mott, N. F. Trans. Far. Soc. **43** (1947) 429.
11. Rollett, A. Sitzungsb. der. Kais. Akad. der Wissenschaften, Wien, Abt. III (Physiol., Anat., Med.) **77** (1878) 177.
12. Waber, J. T., Sturdy, G. E., Wise, E. M. and Tipton, C. R. J. Electrochem. Soc. **99** (1952) 121.
13. Vermilyea, D. A. Acta Met. **1** (1953) 282.

THE DEPENDENCE OF THE THERMAL VIBRATION OF THE Cl^- ION IN NaCl, KCl, AND RbCl CRYSTALS ON THE CRYSTALLOGRAPHIC DIRECTIONS*

U. KORHONEN†

The writer has previously developed a method for the determination of the atomic scattering factor of an ion in a crystal lattice when the structure factors are known. Applying this procedure in the present paper to the NaCl, KCl, and RbCl crystals measured by Wasastjerna, he determines the atomic scattering factor values of the Cl^- ion for the reflections hOO and hhh in these crystals. When drawing, for each crystal, a curve along the points which correspond to the atomic scattering factor values obtained for the reflecticns hOO, it will be found that the values for the reflections hhh show similar deviations from this curve in all these cases. As seen from the critical error analysis, it is difficult to explain this phenomenon as resulting either from the calculation method employed or from the experimental errors. Consequently, the phenomenon can be caused only by the crystals themselves. Since the above-mentioned crystals have cubic symmetry, the phenomenon observed means, in the first place, that the anharmonic part of the amplitude of the thermal vibration is considerable and can be measured by means of X-rays.

LA DÉPENDANCE DE LA VIBRATION THERMIQUE DE L'ION Cl, DANS DES CRISTAUX DE NaCl, KCl, ET RbCl, SUR LES DIRECTIONS CRISTALLOGRAPHIQUES

L'auteur a développé antérieurement une méthode pour la détermination du facteur de dispersion atomique d'un ion dans un réseau cristallin, quand les facteurs de structure sont connus. Dans le présent article, on applique ce procédé aux cristaux de NaCl, KCl et RbCl, mesurés par Wasastjerna, pour déterminer les valeurs du facteur de dispersion atomique de l'ion Cl pour les réflexions du type hOO et hhh dans ces cristaux. Quand on trace, pour chaques cristal, une courbe le long des points qui correspondent aux valeurs du facteur de dispersion atomique, obtenues pour les réflexions hOO, on constate que les valeurs pour les réflexions hhh manifestent des déviations similaires par rapport à cette courbe, dans tous ces cas. Il apparaît de l'analyse de l'erreur critique, qu'il est difficile d'attribuer ce phénomène à la méthode de calcul qu'on a utilisée, ou à des erreurs expérimentales. Par conséquent, il ne peut être causé que par les cristaux eux-mêmes. Etant donné que les cristaux en question ont une symétrie cubique, le phénomène observé indique, en premier lieu, que la partie anharmonique de l'amplitude des vibrations thermiques est considérable et peut être mesurée au moyen de rayons X.

DIE ABHÄNGIGKEIT DER WÄRMESCHWINGUNGEN DER Cl-IONEN IN NaCl, KCl UND RbCl KRISTALLEN VON DEN KRISTALLGITTERRICHTUNGEN

Der Verfasser hat früher ein Verfahren zur Bestimmung des atomaren Streufaktors eines Ions im Kristallgitter aus den bekannten Strukturfaktoren entwickelt. In der vorliegenden Arbeit wird dieses Verfahren auf die von Wasastjerna vermessenen NaCl, KCl und RbCl Kristalle angewandt, und die Werte der atomaren Streufaktoren der Cl-Ionen in diesen Kristallen für die hOO und hhh Reflexionen ermittelt. Wenn man für jeden Kristall eine Kurve durch die den Werten der atomaren Streufaktoren für hOO entsprechenden Punkte zieht, dann zeigt es sich, dass die Streufaktoren der hhh Reflexion in allen Fällen gleichartige Abweichungen von dieser Kurve zeigen. Eine kritische Fehlerbetrachtung zeigt, dass diese Erscheinung schwerlich durch das Rechenverfahren oder durch experimentelle Fehler erklärt werden kann. Folglich kann die Erscheinung nur durch die Kristalle selbst erzeugt werden. Da die oben erwähnten Kristalle kubische Gittersymmetrie haben, bedeutet die beobachtete Erscheinung vor allem, dass der anharmonische Anteil der thermischen Wärmeschwingungen erheblich ist und röntgenographisch gemessen werden kann.

Introduction

The writer has previously developed a method [1] for the determination of the atomic scattering factor of an ion in a crystal lattice when the structure factors of this crystal are known. Supposing that the structure factors $F_{(hkl)}$ of a crystal are known and we intend to determine the atomic scattering factors $f_{1,(hkl)}$ of an ion 1, belonging to this crystal, with the position coordinates (x_1, y_1, z_1) and the ionic radius R we can proceed as follows. Let $\bar{a}, \bar{b}, \bar{c}$ be the translation group of the crystal under consideration. We imagine a crystal with the identical translation group $\bar{a}, \bar{b}, \bar{c}$ and containing only the ion 1 in the position (x_1, y_1, z_1). The structure factors of this crystal are obtained in the following way:

$$(1)\quad \begin{cases} F_{1,(hkl)} = f_{1,(hkl)}\, e^{\,i\delta(hkl)} \\ \delta_{(hkl)} = 2\pi\left(h\dfrac{x_1}{a} + k\dfrac{y_1}{b} + l\dfrac{z_1}{c}\right). \end{cases}$$

The electron distribution of this imagined crystal can now be represented by a Fourier series:

$$(2)\quad \begin{cases} \rho_1(x, y, z) = \dfrac{1}{V}\sum_{hkl} F_{1,(hkl)}\, e^{-i\Phi(hkl)}, \\ \Phi(hkl) = 2\pi\left(h\dfrac{x}{a} + k\dfrac{y}{b} + l\dfrac{z}{c}\right). \end{cases}$$

If both sides of equation (2) are multiplied with the factor $e^{i\Phi(h'k'l')}d\tau$ and integrated over the

*Received March 1, 1954.
†Institute of Physics, University of Helsinki, Finland.

period parallelepiped τ, we find, when $d\tau$ denotes the volume element,

$$(3)\quad \int_\tau \rho_1(x,y,z)\, e^{i\Phi(h'k'l')}\, d\tau = \frac{1}{V} F_{1,(h'k'l')} \int_\tau d\tau = F_{1,(h'k'l')}.$$

Because of periodicity, all the other terms on the right-hand side of equation (3) vanish. The integrand of the integral on the left-hand side of equation (3) differs from the value zero only where the electron density $\rho_1(x, y, z)$ differs from zero. We call here the sphere with the centre at (x_1, y_1, z_1) and the radius R the *ionic sphere*. Since the entire matter of the ion contributing to the scattering of radiation is situated inside that sphere (cf. Havighurst [3]), it is sufficient to extend the integral on the left-hand side of equation (3) over this ionic sphere. Thus

$$(4)\quad F_{1,(h'k'l')} = \int_{\text{ionic sphere}} \rho_1(x,y,z)\, e^{i\Phi(h'k'l')}\, d\tau.$$

Let us now revert to our original crystal. This crystal had an identical translation group and contained the same ion 1 in the identical position (x_1, y_1, z_1). Within the ionic sphere the electron distribution $\rho(x, y, z)$ representing this crystal has the same values as $\rho_1(x, y, z)$. Consequently, the value of the integral on the right-hand side of equation (4) will not be changed when the distribution $\rho_1(x, y, z)$ is substituted by the electron distribution $\rho(x, y, z)$ representing the actual crystal, and we have then

$$(5)\quad F_{1,(h'k'l')} = \int_{\text{ionic sphere}} \rho(x,y,z)\, e^{i\Phi(h'k'l')}\, d\tau.$$

Since the structure factors $F_{(hkl)}$ of the crystal are now known, it is possible to present the electron distribution $\rho(x, y, z)$ as a Fourier series:

$$(6)\qquad \rho(x,y,z) = \frac{1}{V} \sum_{hkl} F_{(hkl)}\, e^{-i\Phi(hkl)}$$

When this expression of $\rho(x, y, z)$ is substituted in equation (5),

$$(7)\quad F_{1,(h'k'l')} = \int_{\text{ionic sphere}} \frac{1}{V}\left[\sum_{hkl} F_{(hkl)}\, e^{-i\Phi(hkl)}\right] \cdot e^{i\Phi(h'k'l')}\, d\tau.$$

The integration on the right-hand side of equation (7) is feasible [1] .Thus

$$(8)\quad F_{1,(h'k'l')} = \frac{4\pi R^3}{V} \left\{\frac{1}{3} F_{(h'k'l')} + \sum_{hkl} F_{(hkl)}\, \frac{1}{\alpha^2}\left(\frac{\sin\alpha}{\alpha} - \cos\alpha\right)\right\}$$

$$\alpha = \frac{2\pi R}{d_{(h'-h,k'-k,l'-l)}}.$$

$d_{(h'-h,k'-k,l'-l)}$ in (8) denotes the distance of repetition of the lattice planes $(h' - h, k' - k, l' - l)$.

Determination of the Atomic Scattering Factors of Cl^- Ion and Discussion

In the present work the series (8) has been applied to the calculation of the atomic factors of the Cl^- ion in NaCl, KCl, and RbCl crystals on the basis of the intensity measurements carried out by Wasastjerna [2]. The continuous initial part of these intensity measurements in each crystal was carried out by using a powder plate and the photographic method developed by Wasastjerna. Finally the intensities of certain additional reflexions were determined by using the ionisation spectrometer and single crystals. In the case of NaCl, the continuous initial part ends in the reflexion 444, in the case KCl as early as 333, 511, while the even reflexions continue up to 800, and it is only in the case of RbCl that the continuous initial part extends up to the reflexion 800. Since only the continuous initial part can be used when the series (8) is applied, this involves, in the calculation of the atomic scattering factors of Cl^- ion, the breaking-off of the series after only a few terms.

The convergence of series (8) is subject to two influences. In the first place, the values of the structure factors $F_{(hkl)}$ diminish with increasing $\sin\vartheta/\lambda$, and secondly, the value of the factor $(1/\alpha^2)/(\sin\alpha/\alpha) - \cos\alpha$ becomes the smaller the more indexes hkl differ from the indexes $h'k'l'$ of the atomic scattering factor which is being determined. Consequently the convergence is considerably enhanced by the diminution of this latter factor when the values of the indexes $h'k'l'$ are considerably smaller than those of the highest indexes hkl used in the series, or, to put it more exactly, when $h'^2 + k'^2 + l'^2$ is considerably smaller than $h^2 + k^2 + l^2$. Accordingly, for the purposes of this study, the atomic scattering factor values for the reflexions h00 have been determined only up to 500 and for the hhh reflexions up to 333. There is another reason which precludes the calculation of the atomic scattering factor for reflexion 600. This is the fact that thh reflexions 600 and 442 coincide, so the

measured intensity has to be attributed chiefly to the 442 reflexion only, since the multiplicity factor of the (442) plane is 24 and that of the (600) plane only 6. When series (8) is employed to determine the atomic scattering factor for the reflexion 600, the trigonometric part connected with the structure factor $F_{(600)}$ has its maximum value (since $h' = h$, $k' = k$, $l' = l$) and is, as a rule, more than ten

TABLE I

hkl 1	F_{NaCl} Wasastj. 2	F_{KCl} Wasastj. 3	F_{RbCl} Wasastj. 4	F_{NaCl} theor. 5	F_{KCl} theor. 6	F_{RbCl} theor. 7
000	28.00	36.00	54.00	28.00	36.00	54.00
111	4.32	− 1.50	−18.21	4.04	− 1.68	−17.72
200	21.17	27.44	45.86	19.83	26.38	42.46
220	16.35	21.18	35.11	16.11	21.39	35.92
311	2.48	− 1.50	−15.21	2.38	− 1.49	−14.43
222	13.80	18.43	32.91	13.66	18.32	31.61
400	12.06	16.29	28.43	11.87	16.19	28.42
331	2.29	− 0.99	−11.79	2.31	− 0.93	−12.00
420	10.43	13.74	24.69	10.55	14.46	25.87
422	9.21	12.32	22.80	9.44	13.08	23.74
333,511	2.27	− 0.49	− 9.95	2.34	− 0.52	−10.14
440	7.39	10.10	18.31	7.71	11.02	20.29
531	2.11		− 8.28	2.30	− 0.38	− 8.67
600,442	6.74	9.41	17.77	7.04	10.20	18.88
620	6.08	8.59	16.39	6.43	9.48	17.58
533	1.87		− 7.56	2.09	− 0.34	− 7.45
622	5.58	8.09	14.51	5.88	8.83	16.48
444	5.20	7.68	14.28	5.38	8.23	15.31
551,711	*1.71*		− 6.23	1.90	− 0.32	− 6.46
640	*4.83*	7.19	12.91	4.96	7.68	14.33
642	*4.51*	6.49	11.55	4.57	7.19	13.40
553,731	*1.56*		− 5.50	1.69	− 0.31	− 5.61
800	3.92	5.98	11.00	3.89	6.30	11.74
733	*1.48*		− *4.71*	1.49	− 0.30	− 4.89
644,820	*3.68*	*5.61*	*10.20*	3.61	5.92	10.98
822,660	*3.44*	*5.30*	*9.62*	3.34	5.56	10.29
555,751	*1.30*		− *4.01*	1.31	− 0.30	− 4.27
662	*3.20*	*4.95*	*9.07*	3.09	5.21	9.65
840	*3.00*	*4.65*	*8.60*	2.87	4.87	9.05
911,753	*1.18*		− *3.57*	1.14	− 0.30	− 3.75
842	*2.78*	*4.40*	*8.20*	2.67	4.56	8.49
664	*2.68*	*4.12*	*7.75*	2.48	4.29	7.97
931	*1.08*		− *3.17*	0.99	− 0.30	− 3.30
844	*2.25*	*3.70*	*7.00*	2.15	3.78	7.04
771,755,933	*0.98*		*2.85*	0.86	− 0.30	− 2.90
1000,860	2.18	3.55	6.78	1.99	3.54	6.61
1020,862	*1.96*	*3.25*	*6.39*	1.86	3.31	6.22
773,951	*0.88*		− *2.55*	0.75	− 0.26	− 2.57
666,1022	1.77	2.98	5.79	1.74	3.12	5.86
953	*0.79*		− *2.30*	0.66	− 0.25	− 2.28
864,1040	*1.64*	*2.75*	*5.25*	1.52	2.75	5.19
1042	*1.54*	*2.58*	*4.98*	1.42	2.60	4.88
775,1111	*0.71*		− *2.07*	0.58	− 0.23	− 2.03
880	*1.36*	*2.30*	*4.44*	1.23	2.30	4.35
955,971,1131	*0.64*		− *1.82*	0.49	− 0.21	− 1.81
882,1044	*1.29*	*2.20*	*4.19*	1.15	2.16	4.09
866	*1.22*	*2.10*	*3.97*	1.08	2.04	3.86
973,1133	*0.57*		− *1.61*	0.43	− 0.20	− 1.60
1062	*1.15*	*2.03*	*3.76*	1.02	1.95	3.65
884,1200	1.06	1.92	3.63	0.94	1.81	3.43
777,1151	0.50		− 1.42	0.38	− 0.18	− 1.43

times that connected with the structure factor $F_{(442)}$. The circumstances described above introduce a certain amount of error also in the atomic scattering factor for 500.

Even with this limitation to the atomic scattering factors for the mentioned reflexions, there will be an undetermined error due to the early breaking-off of the series. Though, of course, not very great as compared with the total value of the atomic scattering factor under determination, this error still has such a considerable magnitude due to the small number of terms included that the obtained atomic scattering factor value will be somewhat dependent on chance, i.e., it will depend on which term is taken into account as the last of the series. To avoid this, the following procedure was employed in the present work.

Using the intensities measured with single crystals, the structure factor values for the reflexions up to 777 have been graphically interpolated. In the case of RbCl there remains, even after this operation, a noticeable effect from the breaking-off, which is due to the presence of the "big" Rb^+ ion. This effect was eliminated by determining, on the basis of the theoretical atomic scattering factor values, the structure factors of RbCl up to the reflexion 777. Upon this the calculation was carried out backward to give the atomic scattering factors of Cl^- ion, by means of the series (8), from which the error due to the breaking-off was obtained as the difference between the values found and the initial values. The atomic scattering factors of Cl^- ion calculated from the experimental values were then corrected by this amount.

The following considerations will show that the procedures described have no appreciable effect on the calculated atomic scattering factor values.

The atomic scattering factors of Cl^- ion, as well as those of the other ions, are functions of $\sin\vartheta/\lambda$. From the measurements we know, for certain values of $\sin\vartheta/\lambda$, the values of this function which, of course, are implicitly present in the corresponding structure factors. We are now, in a sense, carrying out an "interpolation" of the atomic scattering factor of Cl^- ion by means of the series (8) for a certain value of $\sin\vartheta/\lambda$ on the basis of the known structure factors. It is obvious that the influence on the atomic scattering factor under determination is the more insignificant the more the $\sin\vartheta/\lambda$ value of the structure factor employed differs from that $\sin\vartheta/\lambda$ value for which the atomic scattering factor of Cl^- ion is being determined with the aid of the series (8). Consequently, the structure factors "far off" in the series have no essential influence on the result, even though, in aggregate, they may cause a considerable breaking-off error. It may be mentioned, as an evidence of this, that values coinciding with those in Table II are obtained when the series are broken off even after the 800-term and the error due to breaking-off is eliminated according to the procedure used in the case of RbCl. This is the more remarkable since the series includes only 22 terms up to the 800-term, as against 50 terms up to 777, and since, moreover, interpolated values show even systematic deviations from the corresponding theoretical values, as seen from Table I.

Table I presents the structure factor values obtained from the measurements with NaCl, KCl, and RbCl crystals. The interpolated values are printed in italics. In addition, columns 5 to 7 of this table contain the theoretical structure factor values of the corresponding crystal lattices. These figures have been obtained by employing the atomic scattering factor values determined by James and Brindley [4] on the basis of Hartree's self-consistent field and using the mean-square displacements for the ions present in the crystals in question, as determined by Wasastjerna.

TABLE II

hkl	f_{Cl^-} from NaCl	f_{Cl^-} from KCl	f_{Cl^-} from RbCl	Correction due to the breaking-off	f_{Cl^-} from NaCl theor.	f_{Cl^-} from KCl theor.	f_{Cl^-} from RbCl theor.
1	2	3	4	5	6	7	8
100	15.88	16.10			15.38	15.61	
200	12.50	12.91	13.05	−0.13	11.83	12.45	12.71
300	9.47	9.70	9.39	+0.03	8.92	9.39	9.71
400	7.37	7.45	7.24	+0.18	7.11	7.45	7.61
500	5.78	5.91	6.22	−0.07	5.75	6.18	6.41
111	13.32	13.64	14.22	−0.19	12.81	13.27	13.66
222	8.04	8.22	8.79	−0.03	8.00	8.42	8.79
333	5.38	5.47	5.94	+0.27	5.53	5.72	5.83

Table II gives the values of the atomic scattering factors of Cl^- ion as calculated from series (8) according to Wasastjerna's measurements and according to the theoretical values. The atomic scattering factor of Cl^- ion for the reflexion 100, as calculated from RbCl, has not been given since the calculation of this atomic scattering factor amounts, in a sense, to an extrapolation, as the first structure factor obtained in measurement corresponds to the reflexion 111, and since, consequently, in the case of RbCl, an error in this value may easily result from the presence of the "big" Rb^+ ion.

Figure 1 gives a graphical representation of the results obtained. The h00 atomic scattering factor

values calculated from NaCl are denoted with circles and the hhh atomic scattering factors with circles topped with a cross. Similarly, solid circles and solid circles topped with a cross denote the values calculated from KCl, and squares and squares topped with a cross those calculated from RbCl.

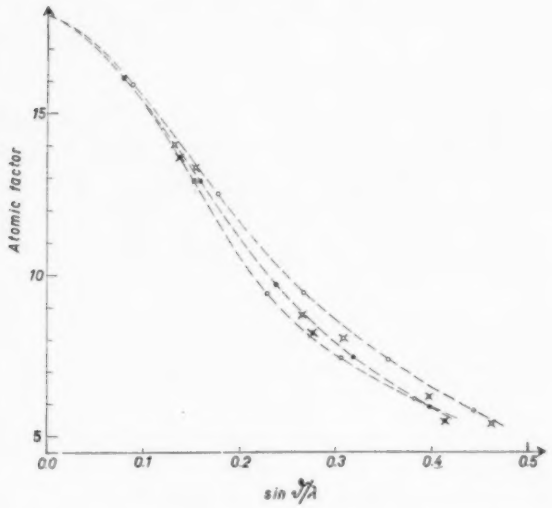

FIGURE 1. The atomic scattering factor values of Cl^- ion from NaCl, KCl, and RbCl crystals. Circles from NaCl for the hOO reflexions and circles topped with a cross for hhh reflexions. Similarly, solid circles and solid circles topped with a cross from KCl, and squares and squares topped with a cross from RbCl.

It is seen that the atomic scattering factors which are influenced only by the thermal vibration in the direction of the space diagonal, i.e., the atomic scattering factors for the hhh reflexions, depart distinctly from the curves representing the atomic scattering factors of the h00 reflexions in the case of each crystal. It seems, accordingly, that the Cl^- ion vibrates more strongly in the direction of the space diagonal in NaCl and KCl than in that of the edge, whereas conditions are inverted in the case of RbCl.

This phenomenon cannot be due to a systematic error in computing or to a possible tendency of the series (8) to favour a certain particular direction, as shown by the atomic scattering factor values of Cl^- ion calculated from the theoretical values (Table II, columns 6 to 8), which do not show any similar behaviour.

It might also be thought that these deviations could be due to some systematic error inherent in the structure factor values as measured by Wasastjerna. First of all, the question might be of a possible orientation of the crystallites in the powder plate as a consequence of which in RbCl, for example, the planes (hhh) would reach the glancing position more frequently, on an average, than the (h00) planes. A defect of this type would, however, always produce the same percentile error in all structure factors $F_{(nh,nk,nl)}$, independent of the value of n. The result of such an error in the structure factors would be that the atomic scattering factors of Cl^- ion calculated for the different reflexions would differ even at small $\sin\vartheta/\lambda$ values by the same amount as at larger $\sin\vartheta/\lambda$ values, and the absolute values even more. It is, however, evident from the values obtained (Figure 1) that, in each crystal examined, the value of the 111 atomic scattering factor differs only slightly from the curve drawn between the values of the h00 atomic scattering factors, whereas the value of the 222 atomic scattering factor shows a much more pronounced deviation. This observation also excludes the possibility that the said phenomenon might be due, for example, to secondary extinction or to a systematic error in the measurement of even against odd reflexions, i.e., "strong" reflexions against "weak" reflexions.

The only remaining possibility is, then, that this phenomenon is due to the actual crystals. With crystals examined having cubic symmetry, it should, first of all, be due to the anharmonic part of the thermal vibration. If we examine the curves obtained from the different crystals for the h00 atomic scattering factors, Figure 1, it is seen that their deviations from each other initially increase with $\sin\vartheta/\lambda$ in accordance with the exponential characteristic of the Debye factor. Later, however, this increase is no longer noticeable, and the curves even seem to approach each other. It is true that the last points on the curves are less accurate than those of the initial part, but it is not possible to explain this behaviour of the curves as resulting only from errors in the last points. The behaviour of the curves thus seems to indicate that the thermal factor is of exponential character only at small values of $\sin\vartheta/\lambda$ and differs from the exponential at larger $\sin\vartheta/\lambda$ values. This again suggests an effect of the anharmonic part on the thermal vibration (cf., e.g., H. Ott [5]).

References

1. KORHONEN, U. Ann. Acad. Scient. Fenn. **A1** (1953) 152.
2. WASASTJERNA, J. A. Soc. Scient. Fenn. Comm. Phys.-Math. XIII (1946) 5.
3. HAVIGHURST, R. J. Phys. Rev. **29** (1927) 1.
4. JAMES and BRINDLEY. Phil. Mag. **12** (1931) 104.
5. OTT, H. Ann. Phys. **23** (1938) 169.

RELAXATION EFFECTS IN SOLID SOLUTIONS ARISING FROM CHANGES IN LOCAL ORDER. I. EXPERIMENTAL*

B. G. CHILDS and A. D. LE CLAIRE†

Measurements are reported for various metallic substitutional solid solutions of the internal friction peaks which are believed to arise from changes in short-range order with stress. The solutions investigated were 5, 10, 15, 20, 25 and 30 at.% Cu Zn, 15 at.% Cu Al and 20 at.% Pt Ni. The theoretical significance of the two characteristic quantities of the peaks, the relaxation strength and the relaxation time, is discussed in terms of the degree of order, the atomic jump frequences and other relevant physical properties of the solutions.

LES EFFETS DE RELAXATION DANS DES SOLUTIONS SOLIDES, DUS AUX CHANGEMENTS LOCAUX DE L'ORDRE. I. PARTIE EXPÉRIMENTALE

On rapporte des mesures des maxima dans les courbes de frottement interne pour diverses solutions solides, métalliques, de substitution, qui seraient dus aux changements d'ordre à petite distance sous l'influence d'une tension. On a investigué les solutions suivantes: 5, 10, 15, 20, 25 et 30 pour cent en atomes Cu-Zn, 15 pour cent en atomes Cu-Au et 20 pour cent en atomes Pt-Ni. La signification théorique des deux quantités caractéristiques, relatives aux maxima du frottement interne, à savoir, la force et le temps de relaxation, est discutée en termes du degré d'ordre, des fréquences des sauts atomiques et d'autres propriétés physiques se rapportant à la solution solide.

RELAXIONSEFFEKTE IN FESTEN LÖSUNGEN, DIE AUF ÄNDERUNGEN DER NAHEORDNUNG BERUHEN. I. EXPERIMENTELLES

Es wird über Messungen der Maxima der inneren Reibung in verschiedenen metallischen Substitutionslegierungen berichtet. Es wird angenommen, dass diese Maxima auf durch Spannung hervorgerufenen Änderungen der Naheordnung beruhen. Die untersuchten festen Lösungen enthielten 5, 10, 20, 25, und 30 Atomprozent CuZn, 15 Atomprozent CuAu und 20 Atomprozent PtNi. Die theoretische Bedeutung der beiden charakteristischen Eigenschaften der Maxima, die Relaxionsstärke und die Relaxionszeit, wird in Bezug auf den Ordnungsgrad, die atomaren Platzwechselgeschwindigkeiten und andere diese Erscheinungen beeinflussenden physikalischen Eigenschaften der Lösungen diskutiert.

1. Introduction

The internal friction of metallic substitutional solid solutions measured at constant frequency as a function of temperature has, in a number of cases, been found to rise to a sharp peak. The characteristics of this particular peak, which distinguish it from other internal friction peaks, were first determined by Zener [1] and by Kê [2], for a 30 at.% solution of zinc in copper, and have been further studied by other workers [3; 4].

They are as follows:

(1) The peak occurs only for the solution and is absent for the pure components. Its height is a function of the solute concentration.

(2) The temperature at which the peak occurs and also its height are not sensitive to the mechanical condition or grain size of the particular specimens used.

(3) In the absence of other contributions to the internal friction, specimens of the solutions behave at least approximately as "standard linear solids" in the sense defined by Zener. For such solids strain is not simply proportional to the stress but the two quantities are connected also with their first time derivatives in a linear relation which, for a vibrating solid, leads to an expression for the internal friction,* Q^{-1}, in terms of the angular frequency of oscillation ω and a mean relaxation time, τ,

$$(1) \qquad Q^{-1} = \Delta_M \frac{\omega\tau}{1 + (\omega\tau)^2}.$$

The mean relaxation time τ, a characteristic of the process responsible for the internal friction, governs the exponential rate at which the strain or stress approaches its equilibrium value when the other quantity is altered by a fixed amount. Δ_M, the "relaxation strength," is a measure of the magnitude of the effect: at the top of the peak $Q^{-1}{}_{max} = \Delta_M/2$.

(4) The relaxation time closely follows an Arrhenius type equation:

$$(2) \qquad \tau = \tau_0 \exp H/RT$$

in its dependence on temperature having an activation energy, H, which is roughly the same as

*Received February 17, 1954.

†Atomic Energy Research Establishment, Harwell, England.

*Q^{-1} is the relative width of a resonance curve at half maximum amplitude. For present purposes $\log_{10}$ decrement is a more convenient measure. The two are related by

$$Q^{-1} = \frac{\log_{10} \text{dec}}{\pi \times 0.434}.$$

that for bulk diffusion. On this evidence Zener [5] interpreted the relaxation effect as being due to a preferential orientation, under the applied stress, of the axes of pairs of adjacent solute atoms into a particular crystallographic direction such that the paraxial strain set up by each pair in the lattice, as a result of the different sizes of solute and solvent atoms, would be partially relieved. The reorientation would take a finite time to reach equilibrium and so the accompanying strain would lag behind the stress and thus give rise to a dissipation of energy.

This theory has several objectionable features and is now replaced (see Section 4.1) but the essence of the theory, which lies in attributing the effect to a redistribution of atoms on lattice sites throughout the material, remains. Following the work of Zener and Kê, a systematic investigation was made by Nowick [3] with a series of AgZn solutions of Zn content from 15–30 at.%. He found that the relaxation strength for this system was five times greater than for CuZn. This difference he attributed to the relatively greater difference in the atomic sizes of Ag and Zn although this is apparent only if one takes, for the radius of the Zn atom, half the closest distance of approach of atoms in pure hexagonal Zn. It is not true for other measures of atomic size such as the Goldschmidt radius. Nowick developed a semi-empirical relation connecting the observed relaxation time with the mean rates of movement of the two species of atoms as measured, using radioactive tracers, in diffusion experiments. Although not entirely satisfactory it is a distinct improvement on the earlier relation of Le Claire [6] which, based on the simple Zener model, took the rate of movement of solute atoms alone as governing the relaxation time.

Both Nowick and Le Claire have pointed out the advantages which may be gained from using the effect to study small-scale atomic movements in cases where conventional diffusion techniques are inapplicable on account of the long times and high temperatures that these require. However, before the greatest benefit can be gained from using the effect in such studies a more detailed knowledge of the atomic movements involved will be necessary. This paper and the following one are intended as contributions to this understanding.

The following paper is concerned with the development of a new theory for the relaxation strength which is free from the objectionable features of Zener's theory. In particular it accounts satisfactorily for the differences in the relaxation strengths of the CuZn, CuAl and AgZn systems and moreover shows that the difference in the atomic size is not the only nor even the most important factor governing the relaxation strength.

In the present paper an account is given of an investigation which has provided further data for three solid solutions, CuZn, CuAl and PtNi. Of these systems the one studied in most detail was CuZn. This was chosen since diffusion and thermodynamic data for it are relatively extensive and reliable and since it was known to show the effect. The compositions used were nominally 5, 10, 15, 20, 25 and 30 at.%.

Measurements on the CuAl and PtNi systems were made at single concentrations of 15 and 20 at.% respectively. The CuAl system was selected, before the theory was developed, since both components have the same crystal structure f.c.c. but have widely different lattice spacings, and since the solubility limit of CuAl are comparable to that of CuZn. The PtNi system was chosen on account of the low mobility of vacancies in Pt at room temperature. It was hoped with this alloy to study the increase in the number of vacancies above equilibrium, brought about by neutron bombardment of the lattice, by observing the consequent decrease in the relaxation time.

Spectrographically pure materials only were used in the alloys.

2. Experimental Details

The internal friction measurements were made with the specimens in torsional oscillation at low frequencies.

Two wires of the specimen material about 15 cm long and 1 mm diameter were mounted side by side in the centre section of a tubular furnace. The upper ends of the wires were clamped in V-grooves on either side of a stainless steel wedge which in turn was bolted to a pyrophilite plug attached to the furnace. The lower ends of the wires were clamped and silver soldered in to the ends of 2.5 mm diameter nichrome rods which projected out of the bottom of the furnace.

Various inertia members were attached to the bottom of one of these rods and this rod, with the corresponding wire, formed the torsion pendulum. The second wire was used as a dummy for temperature measurement, fine chromel and alumel thermocouple wires being soldered to the midpoint and ends. Its temperature and temperature distribution were assumed, in view of the similarity in mounting, to be also those of the wire under test.

The dummy wire could be made uniform in temperature to within 1°C by separately adjusting the currents through the three sections of the furnace winding. The temperature range which could be covered with the furnace was from 20°C to 650°C.

Because of the contribution to the total internal friction which is believed to arise, above about 300°C from relative movements of the grains in the specimens and which normally obscures the effect under consideration, it was necessary before assembling the wire under test, to coarsen its grain size to about 1 mm and thus reduce the total boundary area of the grains. For the 5 and 10 per cent wires, still further coarsening was necessary and these wires were made to consist of only one or two grains.

After assembly in the apparatus the wires were annealed for several hours at 600°C to remove strains introduced by handling.

The frequency range covered extended from 0.3 to 50 c/s. Up to about 3 c/s the decrements of the oscillations were measured using a lamp and scale device. Above that, photographic recording on a moving film was employed. The maximum amplitudes of oscillation in both cases were not allowed to exceed a torsional strain of 6×10^{-5}. At this strain there was no dependence of decrement on amplitude.

The possibility of an influence on the decrement, near the peaks, of the tensile load on the wire (which differed for each frequency) was examined by increasing the load tenfold without changing the natural frequency. No such effect was found.

In the experiments on each wire of a particular composition, three runs were made over the temperature range up to 600°C for each of the frequencies used, the observations being most numerous in the region of the peak.

At the end of the tests each wire was divided into sections of about one inch in length and these were analysed separately to give the average composition of the wire and the variation in composition along its length. For the CuZn wires the composition was never exactly uniform on account of distillation of Zn from hotter to colder parts of the wire during the preliminary annealing. The variation from the mean, however, never exceeded 1 per cent Zn. No such distillation occurred for the CuAl and PtNi wires and these were uniform in composition, at least within the limits of error of the analysis (0.2 per cent).

3. Experimental Results

3.1 *CuZn measurements*

Typical curves of internal friction measured at 0.7 c/s as a function of the reciprocal of the absolute temperature are shown in Figure 1 for the various concentrations of Zn in Cu. The figure illustrates well the two principal ways in which the

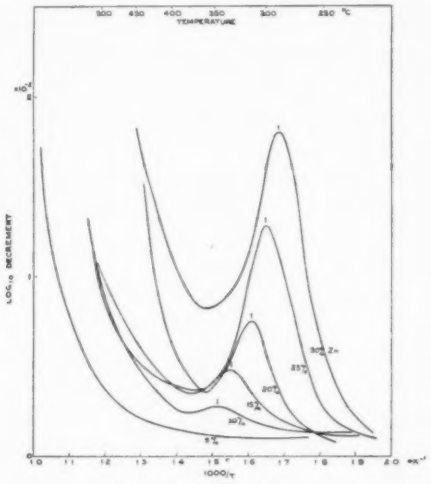

FIGURE 1. Internal friction, inverse temperature for α-brass at 0.7 cps.

effect is influenced by concentration: first through the relaxation strength—the height of the peaks above the background increases progressively—and, secondly, through the relaxation time—the peaks occur at progressively decreasing temperatures as the concentration increases.

The relaxation strength calculated from the corrected heights of the peaks (Figure 2) varies roughly as the square of the concentration the

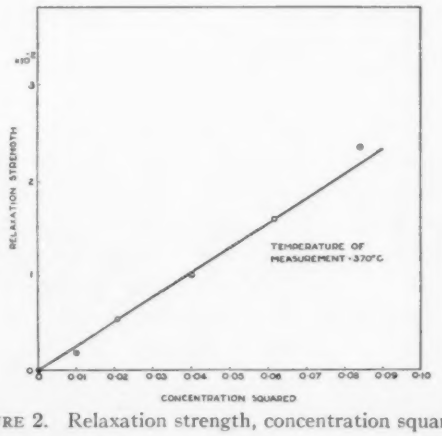

FIGURE 2. Relaxation strength, concentration squared for α-brass.

limiting Zn composition below which the effect was too small to be detected with the present apparatus being about 10 per cent. It would no doubt be possible to reduce this somewhat by evacuating the apparatus so as to reduce the *constant* background (due to air damping) and thus increase the sensitivity. However, by reason of the rise at high temperatures which occurred even for well-annealed "single crystals" (curve for 5 per cent, Figure 1) and on which the peaks are superimposed, detection of a peak in CuZn below 5 per cent is not likely.

The relaxation strength also appears to decrease slightly with increase in temperature as shown in Figure 3. The values plotted in Figure 2 have

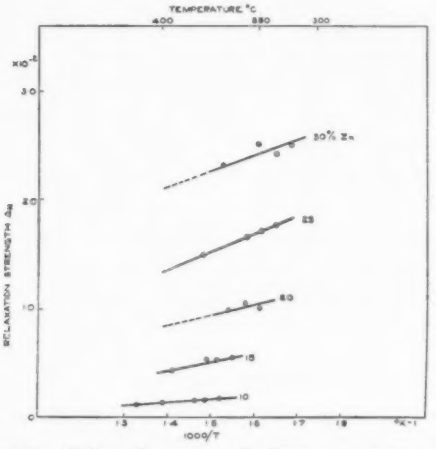

FIGURE 3. Relaxation strength, inverse temperature for α-brass.

accordingly been corrected to the same temperature.

The variation in the position of the peak with frequency and concentration may be seen from Figure 4, in which the logarithm of the relaxation time at the peak ($=-\log\omega$) is plotted against the inverse temperature. For a given concentration $\log\tau$ varies linearly with $1/T$ as expected, the curves for higher concentration being displaced towards lower temperatures.

At a fixed temperature the relaxation *rate* ($=1/\tau$) decreases monotonically with increasing concentration. This is closely paralleled by the behaviour of the atomic jump rate in diffusion and provides evidence in support of the interpretation of the effect in terms of atomic rearrangements. Further evidence is provided by comparing the activation energies for the two processes (table, Figure 4). In both cases H decreases from about 42.5 kcal/mol at 10 per cent to 37.3 kcal/mol at 30 per cent. No such dependence of H on τ, as expected theoretically and as Nowick claims for AgZn, could be detected here, possibly because of the more limited range of τ. Direct measurements of the rate of relaxation of strain on removing an applied stress, which might have extended the range, were tried but did not give results accurate to better than a factor two. This was because the effect for CuZn with its relatively smaller relaxation strength was masked by other relaxation effects of an unknown nature with the result that the apparent relaxation time was a function of the duration of stress.

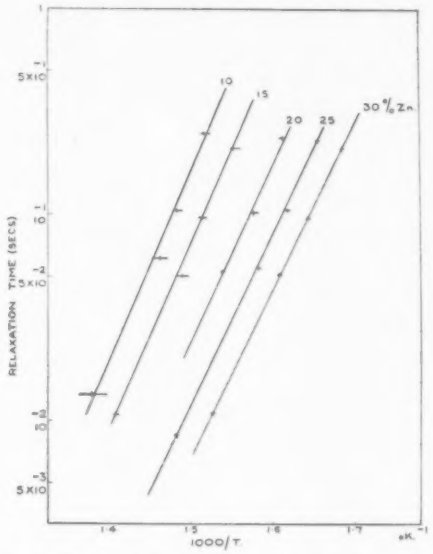

FIGURE 4. Log relaxation time, inverse temperature for α-brass.

Nominal concentration percent Zn	True concentration percent Zn	τ_0 $\times 10^{15}$ sec	H kcal/mol	H Diffusion kcal/mol	
10	10.9	1.8	42.3±3	42.5	[9]
15	14.5	2.45	41.3±1.5	41.4	[9]
20	20.0	3.2	39.5±1.0	38.2	[9]
25	24.8	5.0	37.6±0.6	—	
30	29.0	6.2	37.3±1.0	38.3	[6]

If we assume equation (1) to be valid for the shape of the peaks so that the relaxation process is characterised by a single time then H can be calculated also from the width of the peaks by means of equations (1) and (2). The values thus obtained of H for the CuZn alloys are smaller than those found from the shifts in the peaks by amounts of up to 10 kcal/mol, the peaks being broader than the theoretical curves for the corresponding relaxation strengths. This is attributed to there being a narrow

range of relaxation times on account of the variations in concentration along these wires. It was in fact observed that the more nearly uniform the wires were in composition the more nearly the peak width approached that given by equation (1) with the observed value of Δ_M.

The constant factor τ_0 also appears to vary systematically (Figure 4), increasing with increasing concentration. This contrasts with AgZn where according to Nowick τ_0 is independent of concentration. No great significance can be attached to this, both because of the extreme sensitiveness of τ_0 to errors in the experimental value of τ and also because the Arrhenius equation with constant H may only be valid over limited ranges of temperature. (See Section 4.2.)

3.2 *CuAl and PtNi measurements*

The curves for the 15 per cent CuAl alloy were similar to those for CuZn and are not reproduced. The corrected relaxation strength was 1.76×10^{-2} compared with 0.58×10^{-2} for the equivalent composition of CuZn—a factor of three greater.

The activation energy for the relaxation process, calculated from the displacement of the curves, was 42.8 ± 1.7 kcal/mol, about the same as CuZn.

For this alloy in which the composition, as mentioned, was uniform along the wire the standard linear solid equation (1) is closely obeyed; the value of H (42.0 kcal/mol) calculated from the widths of the peaks, agrees well with the above value.

For the 20 per cent NiPt alloy measurements were made at 0.25 and 1.2 c/s from 20–650°C. Within this range no peak could be detected. Above 450°C and continuing above 650°C the internal friction increased rapidly. This was not part of the peak being sought, however, since the curves for the two frequencies were not displaced. The relaxation strength of NiPt is thus either very small compared with that for the equivalent CuZn alloy (less than one-seventh) or the peak, if comparable in magnitude, must be above 650°C.

An estimate of the temperature of the peak may be made since, whether Le Claire's or Nowick's expression is used, τ is of the order $a^2/12D$, where a is the lattice parameter and D the diffusion coefficient (see Section 4.2). Then from the experimental relation of Kubaschewski and Ebert [7] for the diffusion of Ni in Pt at *15 per cent* concentration.

$$D = 7.75 \times 10^{-4} \exp \frac{-43.1 \times 10^3}{RT},$$

the peak for 0.5 c/s, if it exists, should occur at 480°C. The difference in the diffusion rates of a 15 and 20 per cent alloy is not likely, by analogy with other systems, to be more than a factor of two, but even if the values used or the equation itself are in error by a factor of 100 the peak should still be within the range of temperature studied.

It thus seems probable that the relaxation effect for PtNi is indeed much smaller than for CuZn.

3.3 *High-temperature internal friction*

The remaining feature of interest in the internal friction curves is the monotonic increase with temperature which was always observed at high temperatures (see Figure 1). This effect was not studied systematically but certain of its characteristics have appeared in the course of this work. It seems to be composite in nature: a large part is associated with the granular structure of the specimen since, on coarsening the grain size, the internal friction at a particular temperature decreased from a relatively large value for fine grained specimens down to a much smaller but still finite value for well annealed single crystal wires. The high-temperature internal friction is also very sensitive to the state of strain in the wire: a slight degree of cold work produced by bending the wire, straightening it and then reannealing it at 600°C, changes the shape of this position of the curve appreciably.

The relaxation time for the process responsible for this contribution is usually temperature dependent since (except for PtNi) the curves were displaced towards higher temperature with increasing frequency. It presumably corresponds to the "grain-boundary viscosity" effect studied, e.g., by Kê [2] and by Pearson [8] in which energy losses are thought to occur through relative movement of the grains.

No hypothesis can as yet be put forward for the single crystal contribution (curve for 5 per cent "single crystal," Figure 1). It is, however, in all probability a real internal friction effect since the only other likely source of energy losses of this type would be in the hard-soldered connection. This has been investigated and found not to occur.

4. Discussion

The experimental results appear to support the adequacy of the standard linear solid representation for the amplitudes of vibration used since the internal friction is independent of amplitude showing a linear relation between stress, strain and their various time derivatives and since the peaks fit closely the curve of equation (1).

4.1 *Theory of the relaxation strength*

As mentioned in the introduction, a new theory of the relaxation strength has been developed to replace Zener's elementary-pair reorientation concept and is dealt with in detail in the succeeding paper.

The theory assumes that the internal friction effects arise from a stress induced change in the degree of local order, σ, as usually understood. In developing the theory the assumptions of the quasi-chemical theory of solid solutions are employed, viz., that the total configurational energy of the solution can be adequately expressed as the sum of the interaction energies of pairs of nearest neighbour atoms and that each type of pair AA, BB and AB has its own characteristic energy W_{AA}, W_{BB}, W_{AB}. The degree of order will then be a function of the energy of mixing Δ where:

$$\Delta = W_{AA} + W_{BB} - 2W_{AB}.$$

Since Δ will in general vary with the lattice parameter, a, straining a crystal will lead to a change in the equilibrium value of σ. It is the further small change in strain which accompanies this change in σ that is observed as the anelastic strain.

The relaxation strength for torsional oscillations of a wire on this model is

$$\Delta_M = \frac{a^2 \kappa \nu}{V M kt} \frac{(1+\sigma)}{(1-\sigma)} \left(\frac{d\Delta}{da}\right)^2 g$$

where g is a geometrical factor of order unity dependent on the orientation of the supposedly single crystal wire, M_U is the appropriate unrelaxed shear elastic modulus, V is the atomic volume, and κ and ν the fractions of nearest neighbour pairs which are respectively AA or BB.

The present theory compares favourably in all respects with Zener's theory.

In the first place it is symmetrical in that it makes no distinction between solute and solvent atoms. Thus we no longer consider the movement of one type of atom alone as being responsible for the relaxation.

Secondly, allowance is made for *changes* in the total number of pairs of either type (that is, in σ) when the crystal is stressed.

Thirdly, no empirical parameters occur and all the terms can be calculated from experimentally measurable quantities.

Fourthly, it does not give unwarranted prominence, as does Zener's theory, to the influence of the relative difference in atomic size of the two species as a factor determining the relaxation strength. The difference in atomic size enters into the expressions derived for $(d\Delta/da)$ as the variation of lattice parameter with composition (f_A); thus,

$$\frac{d\Delta}{da} \propto \left(\frac{1}{a}\frac{da}{df_A}\right)\left(\frac{1}{K}\frac{dK}{df_A}\right). \tag{3}$$

But this expression contains also the variation of compressibility (K) with composition which is therefore equally as important in determining the relaxation strength as is the difference in atomic size. That the difference in size is not in fact the important factor is made evident by study of Table I where data are compared not only for the solutions already mentioned but also for three additional solutions, CuGa, AgIn and AgCd.

TABLE I

COMPARISON OF INTERNAL FRICTION DATA FOR SEVERAL SOLID SOLUTIONS

System	Solute concentration at.%	Temperature °C	τ sec.	Δ_M $\times 10^2$	Δ_M/Δ_M CuZn	$\frac{(r_{solvent}-r_{solute})}{r_{solute}}$ (Goldschmidt)
PtNi	20	20–650	—	<0.11	<0.14	0.094
CuZn	16	383	0.1	0.7	1.0	0.070
	32	331	0.1	3.4	1.0	
AgCd	32	250	0.1	5.0	1.5	0.055
CuAl	15	383	0.1	1.7	2.8	0.117
AgIn	16	270	0.1	2.9	4.1	0.091
CuGa	16	330	0.16	3.0	4.3	1.1
AgZn	16	300	0.1	3.0	4.6	0.049
	30	240	0.1	14.0	5.4	

These additional data were obtained by Pearson [8] in an investigation of the grain-boundary internal friction of a number of Cu and Ag base alloys. Because of the small grain size necessarily used in the experiments, the position and magnitude of the ordering peaks cannot be estimated very precisely from his published curves. However, this uncertainty is not sufficient to affect the order in which the solutions are arranged in the table which (see column 6) is that of increasing relaxation strength relative to that of a CuZn alloy of the same composition. Reference to column 7 of the table shows that this order is clearly different from that in which the relative differences in Goldschmidt atomic radii increase and neither can any correlation be made if some other measure of atomic size, e.g., ionic radii or the distance of closest approach of atoms in the pure components is used.

Unfortunately, lack of reliable thermodynamic data makes an absolute comparison of theory and experiment impossible for all the alloys. For CuZn,

however, the agreement is well within the limits of error imposed by uncertainties in the physical quantities involved. The greater relaxation strengths of the AgZn and CuAl systems are also satisfactorily accounted for.

4.2 *Comparison between relaxation times and diffusion rates*

If we are correct in considering the relaxation effect as due to local atomic rearrangements under stress then, whatever the precise relationship between the relaxation time and the diffusional mobilities of the atoms, τ should be of the order of the atomic jump rate $a^2/12D$. (D is the diffusion coefficient in the absence of a concentration gradient.) That this is so experimentally is shown in Figure 5 at least for 30 per cent CuZn, 15 per cent

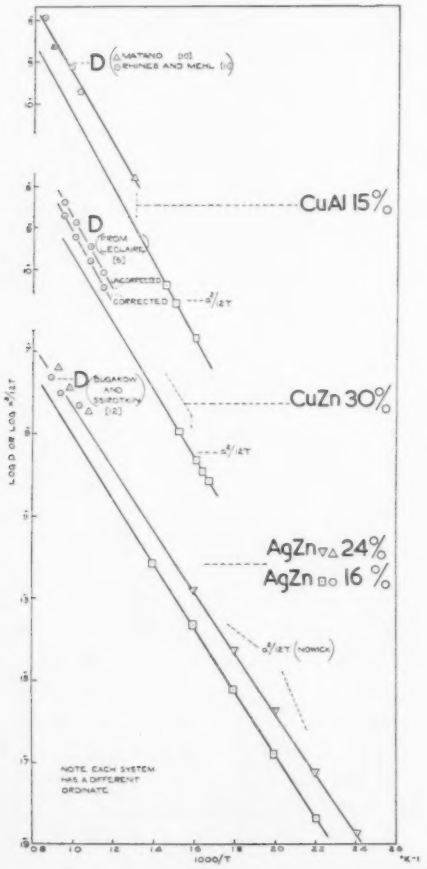

FIGURE 5. Comparison of diffusion coefficient and $a^2/12\tau$ values.

CuAl and 16 and 24 per cent AgZn, where both diffusion and relaxation data are available. It may be significant that, in this figure, the extrapolated values of $\log a^2/12\tau$ are lower than the $\log D$ values by roughly the same amount in each case with $\tau \simeq 5a/12D$.

This finding, if substantiated, would be consistent with Nowick's conclusion that τ, unlike D, is governed mainly by the diffusion rate of the more *slowly* diffusing component. No great reliance can be placed in it, however, since the D values for CuAl and AgZn are not corrected for concentration gradient and since (see below) $\log a^2/12\tau$ may not be a linear function of $1/T$.

The most satisfactory relation to date giving τ in terms of D_A and D_B the alloy self-diffusion coefficients* has been postulated by Nowick. He made the plausible assumption that since the essential atomic process involved in a change in order is the replacement, on a number of lattice sites, of one type of atom by another, then the relaxation rate $1/\tau$ should be simply proportional to Γ_r the *mean* rate at which a replacement on a given site occurs.

$$\frac{1}{\tau} = \alpha \Gamma_r . \tag{4}$$

An approximate relation for Γ_r can be calculated from D_A and D_B and is

$$\frac{1}{\Gamma_r} \simeq \frac{a^2}{24}\left(\frac{1}{f_A D_A} + \frac{1}{f_B D_B}\right). \tag{5}$$

Failing a detailed knowledge of the atomic movements involved, it is not possible to calculate α exactly. It seems unlikely, however, that equation (4) should hold at extreme limits of concentration (say below 10 or above 90 per cent) where the atoms of one type are, for the most part, distributed singly in a matrix of the other. Movements of such *isolated* atoms, if sufficiently far apart, would not affect the order or give rise to a relaxation of stress or strain and the effects observed would correspond to rearrangements involving *groups* of two or more solute atoms. One would not expect the replacement rate appropriate to this situation to be the *mean* replacement rate since the *local* atomic distribution for the particular atoms involved is different from the mean distribution. Presumably the Γ_r appropriate to the extreme concentrations will be more nearly the mean Γ_r of an intermediate concentration.

Nowick made an estimate of α by assuming for τ_0 an expression similar to that derived by Zener for the case of D_0 in *self* diffusion, namely

*$D = f_A D_B + f_B D_A$.

$$\frac{1}{\tau_0} = 12\alpha\nu \exp - \kappa \frac{H}{\mu_0} \left(\frac{d\mu}{dt}\right),$$

ν being the atomic vibrational frequency, and μ_0 the shear modulus at 0°K, and with, in effect, the same constant K (0.55) as is appropriate for self-diffusion. It is difficult to see the justification for this since it is not obvious that such an expression would apply for high concentrations, or if so, whether K would be for all compositions the same.

For CuZn the term

$$\frac{H}{\mu_0}\frac{d\mu}{dt},$$

which is negative, decreases with composition from -11.3 at 10 per cent to -18.6 at 30 per cent. Unless K decreases with composition in roughly the same proportion, the decrease in the exponential term would easily swamp any likely change in $12\alpha\tau$ to give a nett *decrease* in τ_0 instead of an increase, as observed. No great reliance can thus be put in the value of α obtained (0.3).

Lack of data on D_A and D_B for AgZn prevented Nowick from making an empirical estimate of α assuming equations (4) and (5) to be valid. For 30 per cent CuZn, however, a comparison is possible between the measured (τ) and calculated ($\alpha\tau$) values and the logarithms of these quantities are plotted against $1/T$ in Figure 6. To obtain the

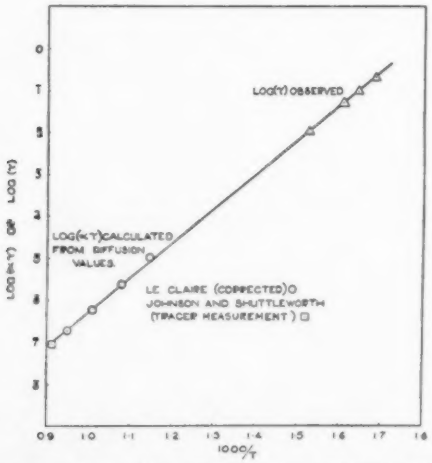

FIGURE 6. Comparison of log ($\alpha\tau$) calculated and log (τ) observed values for 30 per cent CuZn.

log ($\alpha\tau$) points in this figure, Nowick's expression was recalculated in terms of D_{Zn} and D_{Zn}/D. For D chemical diffusion values, corrected by Le Claire [6] for thermodynamic and other effects, were supplemented by a value measured in a tracer experiment by Johnson and Shuttleworth (private communication). For D_{Zn}/D the value (1.26) obtained by these observers at 825°C was used. Since ($\alpha\tau$) is relatively insensitive to D_{Zn}/D, any change in this quantity with temperature due to a possible difference in the activation energies H_{Cu} and H_{Zn} for movement of Cu and Zn atoms should not invalidate the calculation.

Reference to the figure shows that both the $\alpha\tau$ and τ values fall on the same straight line. Thus it seems likely that for 30 per cent CuZn, Nowick's relation is in fact valid with α closely equal to unity and H_{Cu} at least approximately equal to H_{Zn}.

Before the relation can be completely accepted, however, additional data for τ in the case of this composition are required at temperatures more nearly those of the diffusion measurements so as to avoid the uncertainties introduced by the extrapolation. Also, a similar comparison of $\alpha\tau$ and τ—at present impossible for lack of suitable diffusion data—is needed for the lower concentrations.

5. Conclusions

The internal friction effect under consideration is thus well established as arising from changes in short range order with stress, the relaxation time τ measuring the rate of approach of the order to equilibrium at a given temperature.

The most promising field for further development lies in a study of the kinetics of ordering at temperatures such that the relaxation time can be compared directly with the measured diffusion coefficients.

Further experimental confirmation of the theory for the relaxation strength is desirable but this is hampered at present by the scarcity of reliable thermodynamic data for other systems. The best one from this point of view is CuAu at temperatures well away from the Curie temperature where the order changes discontinuously. It is hoped to make measurements on this system in the near future.

6. Acknowledgements

It is our pleasure to record our thanks to Mrs. A. Stephenson, who ably carried out the bulk of the experimental measurements, to Mr. C. E. Austing, who performed the chemical analyses, and to Dr. H. M. Finniston for his interest and encouragement throughout the work.

7. References

1. Zener, C. Trans. A.I.M.M.E. **152** (1943) 122.
2. Kê, T. S. J. Appl. Phys. **19** (1948) 285.
3. Nowick, A. S. Phys. Rev. **88** (1952) 925.
4. Kunitomi, N. Sc. Rep. Tohoku Univ. **A5** (1953) 335.
5. Zener, C. Phys. Rev. **71** (1947) 34.
6. Le Claire, A. D. Phil. Mag. **42** (1951) 673.
7. Kubaschewski, O. and Ebert, H. Zeit. Elektrochem. **50** (1944) 138.
8. Pearson, S. Royal Aircraft Establishment, Farnborough, Report No. Met. 67.
9. Da Silva, L. C. and Mehl, R. F. Trans. A.I.M.M.E. **191** (1951) 155.
10. Matano, C. Jap. J. Phys. **9** (1934) 41.
11. Rhines, F. N. and Mehl, R. F. Trans. A.I.M.M.E. **128** (1938) 185.
12. Bugakow, W. and Ssirotkin, B. J. Tech. Phys. U.S.S.R. **7** (1937) 537.

Elastic Properties of Iron Whiskers*

It has been reported that whiskers of tin [1] and zinc sulfide [2] have elastic properties closely approaching those which have been predicted for perfect crystals [3; 4]. In this note the unusual elastic properties of iron whiskers, which have been grown in this Laboratory [5], are reported. These whiskers are believed to grow by the same mechanism which has been proposed for mercury whiskers [6]. Accordingly, they are presumed to be perfect crystals except for an axial screw dislocation. Their unusual strength, however, only demonstrates that they are perfect or near-perfect crystals.

Single whiskers were mounted on a 100–200μ quartz rod with *S*-diphenylcarbazide. A mounted whisker was attached to a micromanipulator stage so that it lay in a horizontal plane. A small quartz rod mounted on a second micromanipulator was used to strain the iron whisker while the process was observed microscopically.

The maximum strain in bending is equal to the ratio of whisker radius to bending radius. The whisker radius was determined microscopically at much higher magnifications than were used to observe the bending. The radius of bending was determined as follows. Tangents were drawn at two points on the photomicrograph of a fiber and the angle of turning, θ, was measured. The length, L, of fiber between the tangential contact points was measured. The radius of bending, R, was simply calculated by

$$R = L\theta^{-1} \tag{1}$$

The magnification of the photomicrographs was determined from a photograph of a stage micrometer under the same magnification.

Figures 1*a* and 1*b* show a 15μ iron whisker unstressed and under 0.8 per cent elastic strain. Figure 1*c* shows the same fiber after the elastic limit has been exceeded. As in the case of tin whiskers, the crystal has considerable strength at the bend. The bending angles range around 35 to 45 degrees.

The largest observed elastic strain in a smoothly bent section is 1.4 ± 0.1 per cent. It was established by X-ray diffraction [7] that an iron whisker is α-iron bounded by four (100) planes parallel to the axis. Young's modulus for α-iron normal to the (100) plane is 1.9×10^7 p.s.i. [8]. The maximum elastic stress is calculated to be 270,000 p.s.i. in a

*Received April 18, 1954.

FIGURE 1a. Iron whisker—unstressed.

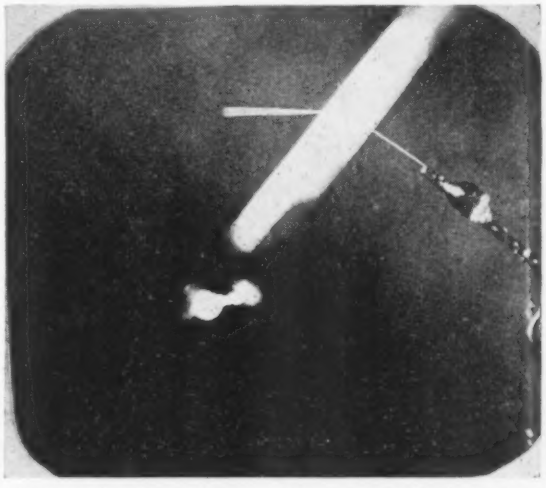

FIGURE 1b. Iron whisker—0.8 per cent elastic strain.

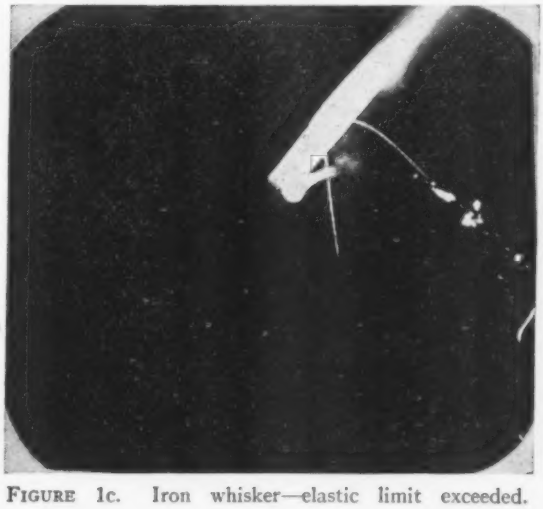

FIGURE 1c. Iron whisker—elastic limit exceeded.

smoothly bent section. The stress is to be compared to an elastic limit of 4,000 p.s.i. for a pure iron single crystal. Although no chemical analysis is available to attest the purity of the iron whiskers, impurities would not raise the elastic limit beyond 20,000 p.s.i.

Some whisker specimens show sharp bends as grown. At one such bend an "elastic" strain of 12 ± 2 per cent has been measured. This figure is well in excess of the theoretically expected elastic limit for a perfect crystal. It may be reasonably postulated that the bend is the grain boundary of two whisker segments, whose axes make a small angle with one another. The large "elastic" strain at the bend might be produced by the reversible motion of dislocations associated with the grain boundary. The effective Young's modulus for the boundary region would be much smaller than for the body of a crystal.

It has been observed that iron whiskers lose their unusual strength after exposure to air for a few days. The loss of strength occurs before visible signs of oxidation appear. This fact indicates that edge dislocations can be introduced into α-iron by oxidation.

We express our appreciation to Dr. W. L. Roth for the X-ray orientation data.

G. W. Sears
A. Gatti
R. L. Fullman

General Electric Research Laboratory
Schenectady, New York

References

1. Herring, C. and Calt, J. K. Phys. Rev. **85** (1952) 1060.
2. Piper, W. W. and Roth, W. L. Phys. Rev. **92** (1953) 503.
3. Bragg, L. and Lomer, W. M. Proc. Roy. Soc. London **A196** (1949) 171.
4. Lomer, W. M. Proc. Roy. Soc. London **A196** (1949) 182.
5. Fullman, R. L. and Gatti, A. Unpublished results.
6. Sears, G. W. Acta Met. **1** (1953) 457.
7. Roth, W. L. Private communication.
8. Metals Handbook (Cleveland, Amer. Soc. Metals, 1948) p. 430.

Chemistry of the Defect Solid State. By A. L. G. Rees. London: Methuen and Co. Ltd. New York: John Wiley, 1954. The book under review is one of the excellent *and* little Methuen Monographs on Chemical subjects. Their being little has certain advantages, particularly that the authors must stick to principles; however, that confers on them an introductory character which allows them to escape too often from difficulties. The present book successfully follows this rule and within these limits should be strongly recommended. It is mainly concerned with the fundamental role played by vacancies and interstitials in crystals on their chemical properties. As the author points out, the understanding of these properties is mainly due to C. Wagner; in fact, anybody interested in this field should be strongly advised to look into the papers published by Wagner in the thirties to avoid rediscovering something already done. As in any other sound theory, the interpretation of the chemistry of the solid state, in terms of vacancies and interstitials, had a tremendous success initially, and there is no doubt about its being fundamentally correct. However, when more detailed experimental knowledge has become available and an attempt has been made to develop the theory to a higher degree of approximation, the result has not been very satisfactory. The present book covers only the first stage of this theory, and this should have been so stated. However, this is hardly a criticism; if this book is able to encourage further work in the second stage of the theory, it should be most welcome.

In the first chapter a courageous attempt is made to classify and to propose symbols for the different types of "defects". Dislocations are not included here. That is as it should be, as very little is known concerning their influence on the chemical reactivity; and it is likely that their role will only be a minor and indirect one. The classification covers both pure and impure solids. Concerning the proposed symbols, one cannot help wondering whether they are altogether necessary. It is the experience of the present reviewer that, when one gets used to thinking in terms of vacancies and interstitials, it is not necessary to use anything but the ordinary chemical symbols. Anyhow, one cannot help but be discouraged by such a formula as:

$$\Delta + (Zn^{2+}|\square^{+}_{s})\ (O^{2-}|\square^{-}_{s}) \rightleftarrows (e_2|Zn^{2+}|\Delta) + \square^{+}_{s} + \square^{-}_{s} + \tfrac{1}{2}\, O_2 \uparrow ,$$

which apparently means the dissociation of ZnO. Chapter II gives an excellent introduction to the statistical mechanics and the wave mechanics of the solid state containing "defects."

The best known reaction in solids is the oxidation of metals. The theory is developed in Chapter V but only to the first approximation mentioned above. This is not enough to explain the experimental data actually known, for instance, among many others, the effect of crystallographic orientation well established by the work of Gwathmey and his co-workers. A second approximation is badly needed, and attention to this point might have been profitable.

Chapter VI gives a short review of the role of "defects" on the catalytic properties of solids. This is a very promising field of research, and a complete review of it should be very welcome. According to one of the references in the present book, Dr. Rees seems to have one in preparation.

The book as a whole is very pleasantly written. It is unfortunate that the author has chosen a rather queer title. The word "defect" seems entirely unnecessary; in fact, if solids did not contain "defects," there would be hardly any Chemistry of the solid state. Besides the use of the word "defect" to describe vacancies and interstitials, though widely used, seems altogether unsatisfactory to this reviewer, as they are not defects of the crystal lattice.

N. CABRERA

CURRENT PAPERS IN OTHER JOURNALS

Acta Crystallographica, Vol. 7

Part 6–7, July 1954 (Partial Contents)

Long-range-short-range order in calcic plagioclases as a continuous and reversible function of temperature. FRITZ LAVES and JULIAN R. GOLDSMITH.

A suggested explanation of the occurrence of forbidden X-ray reflections in the α-phase. J. A. BLAND.

A review of the Al-O and Si-O distances. J. V. SMITH.

Generalisation du principe de focalisation de Bragg-de Broglie. A. J. ROSE.

The Crystal structure of $Cs_2I_8(Cs_4I)$. E. E. HAVINGA, K. H. BOSWIJK and E. H. WIEBENGA.

Sign determination in crystal structure analysis. K. LONSDALE and H. J. GRENVILLE-WELLS.

X-ray diffraction by close-packed crystals with "growth stacking faults" assuming an n-layer influence. R. GEVERS.

The determination of the crystal structure of $Ni_4Mn_{11}Al_{60}$. KEITH ROBINSON.

The effect of anisotropic thermal vibration on the atomic scattering factor. W. COCHRAN.

The lattice spacings of lead-rich substitutional solid solutions. C. TYZACK and G. V. RAYNOR.

A study of clay minerals by electron-diffraction diagrams due to individual crystallites. GORO HONJO and KAZUHIRO MIHAMA.

A construction giving the projection of the point $h00$ on to the $0kl$ plane in reciprocal space, for non-orthogonal axes. E. W. RADOSLOVICH.

On precipitation of metastable centres in solid solutions NaCl-$CaCl_2$. SHIZUO MIYAKE and KAZUO SUZUKI.

A method for setting the equi-inclination angle. D. SAYRE.

The accuracy of electron-density maps in X-ray analysis: correction. D. W. J. CRUICKSHANK.

Archiv für das Eisenhüttenwesen

Heft 5/6, Mai/Juni, 1954

Die Bindung und das Verhalten des Schwefels in Hochofenschlacke und Huttenwolle. HANS ERNST SCHWIETE und LUDWIG ZAGAR.

Der verstärkte Angriff des Zinks auf Eisen im Temperaturgebiet um 500°. DIETRICH HORSTMANN.

Der Einfluss eines Antimongehalts in eisengesättigten Zinkschmelzen auf ihren Angriff auf Eisen. DIETRICH HORSTMANN.

Die Probenahme von Kohle und Koks. FRANZ TREFNY.

Die Probenahme von Ferrolegierungen und ihren Erzen. HUBERT WIRTZ.

Die Teilchengrösse des Eisennitrids bei der Ausscheidung aus einem an Kohlenstoff und Stickstoff übersättigten α-Eisen. WERNER KÖSTER und LOTHAR BANGERT.

Die Ausscheidung des Kohlenstoffs in α-Eisen während der Auslagerung. WINIFRED DAHL und KURT LÜCKE.

Der Austenitzerfall der übereutektoidischen Manganstähle. WERNER JELLINGHAUS, ADOLF ROSE und HANS HOLETZKO.

Einige grundsätzliche Betrachtungen zu den Umwandlungen des Austenits in der Perlit- und Zwischenstufe. WERNER JELLINGHAUS und EDUARD HOUDREMONT.

Die Härte des Martensits in Abhängigkeit von seinem Kohlenstoffgehalt. MUZAFFER SAGISMAN.

Ermittlung von Eigenspannungen aus röntgenographischen Gitterkonstanten-Messungen. VIKTOR HAUK.

Versuche über die Leistung des 31-MeV-Betatrons bei der Durchstrahlung von Stahl. HERMAN MÖLLER, WALTER GRIMM and HELMUT WEEBER.

Fehler bei der Messung des Ummagnetisierungsverlustes von Elektroblechen an Epstein- und Ringproben. ROBERT OCHSENFELD.

Journal of the Institute of Metals, Vol. 82

Part 12, August, 1954

A study of preferred orientation in extruded, drawn, and annealed copper. PAUL G. BASTIEN and J. POKORNY.

The cleavage fracture of pure polycrystalline zinc in tension. G. W. GREENWOOD and A. G. QUARRELL.

Preferred orientation in rolled uranium sheet. J. ADAM and J. STEPHENSON.

The constitution of the system silver-lithium. W. E. FREETH and G. V. RAYNOR.

The systems magnesium-lithium and magnesium-lithium silver. W. E. FREETH and G. V. RAYNOR.

Journal of the Institute of Metals, Vol. 83

Part 1, September, 1954

Grain-boundary movement, slip, and fragmentation during creep of aluminium-copper, aluminium-magnesium, and aluminium zinc alloys. D. MCLEAN and M. H. FARMER.

Fatigue Phenomena in high-strength aluminium alloys. R. F. HANSTOCK.

The ageing characteristics of some ternary aluminium-copper-magnesium alloys with copper: magnesium weight ratios of 7 : 1 and 2.2 : 1. H. K. HARDY.

A high-resolution evaporated-carbon replica technique for the electron microscope. D. E. BRADLEY.

The formation and removal of twins in titanium during deformation. A. T. CHURCHMAN.

La Metallurgia Italiana, Vol. XLVI

N. 2, febbraio, 1954

Esame della superficie dei metalli con il micropscopio elettronico e con la diffrazione elettronica. K. HUBER: experimental part: DR. LASKE.

Ossidazione a caldo ed ossidazione anodica del cadmio. Ricerche sulla struttura dei film. G. BIANCHI.

N. 3, marzo, 1954

La microscopia a contrasto di fase nella metallografia e nella mineralogia. R. MITSCHE.

Studio teorico e sperimentale su alcuni fenomeni di dezincificazione negli ottoni. P. LOMBARDI. IIparte: Mezzi per prevenire i fenomeni di dezincificazione.

N. 4, aprile, 1954.

Proprietà di acciai da contruzione a basso contenuto di carbonio, legati con fosforo e rame. Parte II: Comportamento alla ossidazione a temperature elevate—Fenomeni di ossidazione accelerata dell'acciaio in presenza di fosforo e rame. N. COLLARI e N. FONGI.

Studio teorico e sperimentale su alcuni fenomeni di dezincificazione negli ottoni. Parte III: Metodi di studio dei fenomeni di dezincificazione e risultati ottenuti su ottoni monofasici alfa e ottoni bifasici alfa + beta allo stato crudo e ricotto con aggiunta di inibitori. P. LOMBARDI.

Lo stagno come materiale di protezione. G. BIANCHI.

N. 5. maggio, 1954

Attualità nel campo della produzione del piombo. G. ROLARDI.

Le fasi di Hume-Rothery nei sistemi a più di due componenti –IV–La fase $NiCuAl_2$ (7 : 4). FRANCESCO MAZZOLENI.

L'analisi spettografica dello zinco e delle leghe di zinco nel laboratorio della Soc. Montevecchio a Porto Marghera. G. SCACCIATI and A. D'ESTE.

RELAXATION EFFECTS IN SOLID SOLUTIONS ARISING FROM CHANGES IN LOCAL ORDER. II. THEORY OF THE RELAXATION STRENGTH*

A. D. LeCLAIRE and W. M. LOMER†

The lattice dimensions of an alloy depend upon the degree of short-range order σ. Thus the equilibrium value of σ in a strained crystal will in general differ from that in the unstrained crystal and in addition to the elastic strain following an applied stress, there will be an anelastic strain arising from the change to the new stress induced equilibrium value of σ. An internal friction peak frequently found in substitutional solid solutions is attributed to this type of anelastic effect and on the basis of the regular solution model a calculation is made of the associated relaxation strength δ. Very satisfactory agreement is found between the theoretical values of δ and the measured values for α-CuZn, α-AgZn and CuAl alloys.

The theory is critically compared with an earlier interpretation of the experimentally observed effect by Zener, who employed a concept of stress induced reorientation of solute atom pairs.

LES EFFETS DE RELAXATION DANS DES SOLUTIONS SOLIDES, DUS AUX CHANGEMENTS LOCAUX DE L'ORDRE. II. LA THÉORIE DE LA RELAXATION

Les dimensions du réseau dépendent du degré d'ordre à petite distance σ. Ainsi, la valeur d'équilibre de σ dans un cristal déformé sera, en général, différente de cette valeur dans un cristal non-déformé. En plus de la déformation élastique, due à la tension appliquée, il y aura une déformation anélastique, provoquée par le passage à la nouvelle valeur d'équilibre de σ, induite par la tension. Un maximum de la courbe de frottement interne, souvent constaté dans le cas de solutions solides de substitution, est attribué à ce genre d'effet anélastique; en se basant sur le modèle de solution régulière, on a calculé la relaxation δ associée à cet effet. Il est constaté que les valeurs théoriques de δ et les valeurs mesurées pour les alliages Cu-Zn α, Ag-Zn α, et Cu-Al sont en bon accord. La théorie est comparée d'une façon critique à une interprétation antérieure des effets observés expérimentalement, due à Zener, et basée sur le concept de réorientation de paires d'atomes de soluté, induite par des tensions.

RELAXIONSEFFEKTE IN FESTEN LÖSUNGEN, DIE AUF ÄNDERUNGEN DER NAHEORDNUNG BERUHEN. II. THEORIE DER RELAXIONSSTÄRKE

Die Gitterabmessungen einer Legierung hängen von dem Grad der Naheordnung σ ab. Folglich wird der Gleichgewichtswert von σ in einem verzerrten Kristall im allgemeinen von dem in einem unverzerrten Kristall verschieden sein; zusätzlich zu der einer äusseren Spannung folgenden elastischen Verzerrung wird eine unelastische Verzerrung vorhanden sein, die bei der Umlagerung zu dem neuen, spannungsinduzierten Gleichgewichtswert σ entsteht. Ein häufig in Substitutionslösungen gefundenes Dämpfungsmaximum wird einem derartigen anelastischen Effekt zugeschrieben, und mit Hilfe eines Modells einer regulären Lösung wird die dazugehörige Relaxionsstärke δ berechnet. Die Übereinstimmung zwischen den theoretischen Werten von δ und den an α-CuZn, α-AgZn und CuAl-Legierungen gemessenen Werten ist sehr zufriedenstellend.

Die Theorie wird kritisch mit einer früheren Deutung des experimentell beobachteten Effektes bei Zener verglichen, der die Idee einer spannungsinduzierten Reorientierung gelöster Atompaare zu Grunde liegt.

1. Introduction

The deformation of a solid under stress may take place in two stages. There is always an "elastic" strain which is effectively instantaneous, proportional to the stress, and reversible in that it disappears on removing the stress. But in addition internal processes may occur in the solid as a result of the stress which produce an additional strain, but which require some finite time for their completion. These relatively slow processes, and the additional strain they produce provided it also is reversible and proportional to the stress, are referred to as "anelastic" [1].

The usual dynamic characteristic of an anelastic process is its "relaxation time," which is a measure of the time required for the process to be effectively completed. The modulus of elasticity measured in a time short compared with the relaxation time, e.g., by a dynamic method employing a suitably high frequency, (the unrelaxed modulus M_u) is greater than the relaxed modulus (M_r) measured under conditions such that the total strain, elastic + anelastic is observed. The usual static characteristic of a relaxation process is the *Relaxation Strength* δ_M defined as

$$\delta_M = \frac{M_u - M_r}{M_u}.$$

A previous paper [2] discusses the evidence for the occurrence in metal substitutional solid solutions of an anelastic effect arising from the diffusion-like movement of individual atoms, and in particular describes an extensive set of measurements on several solid solutions. It is the purpose of this

*Received February 17, 1954.
†Atomic Energy Research Establishment, Harwell, England.

paper to discuss the theoretical interpretation of the relaxation strength observed in such experiments. An understanding of the relaxation time is a problem in diffusion theory which still awaits a completely satisfactory solution.

2. Zener's Theory

The first attempt at a theoretical interpretation of the relaxation strength is due to Zener [3]. Zener points out that solute atoms generally have a size different from that of the solvent atoms and so produce an elastic distortion in the lattice. In cubic substitutional solid solutions, isolated solute atoms produce a field of distortion with cubic symmetry, but adjacent pairs of solute atoms produce a distortion with uniaxial symmetry. Thus when the solute atoms are larger than the solvent atoms, as in α-brass, the lattice around a pair is extended more along the axis of the pair than in any other direction. When the stress is zero pair axes are distributed at random over the several crystallographically permissible directions, but when, say, a tensile stress is applied to the crystal, the solute pairs will tend to become oriented so that their axes are along those crystallographically allowed directions which make the least angle with the tensile axis.

The preferential redistribution of pair axes will be effected by the movement of one or both of the atoms of a pair over a distance of the order of an atomic spacing (a) so that the relaxation time will be of order a^2/D as is, in fact, observed, D being the diffusion coefficient.

There are two major points in connection with Zener's model, which in the authors' opinion are in need of clarification.

The first is concerned with the mechanism itself for it is by no means immediately clear why such a rotation of pairs of solute atoms should lead to a relaxation of the strain, and hence why it should occur at all. Consider Figure 1, which shows a pair of solute atoms (X) before and after a rotation induced by a tensile stress in the direction indicated by the arrows. In the direction of the stress the numbers of X–X bonds and of O–O bonds are each increased by one and the number of X–O bonds is decreased by two. Zener attributes the relaxation effects to the difference in size of solute and solvent atoms, so it is natural for us first to assign a definite bond length to each type of atom pair. Then if the X–O bond length is the mean of the X–X and O–O bond lengths, the average lattice dimensions of the crystal will be a linear function of the composition. Under such conditions, however, the average dimensions of the crystal in the direction of the stress would not be altered as a result of the rotation shown in Figure 1. With such assumptions the model does not then account for the relaxation effects observed in cases where the lattice parameter varies linearly with composition, as, for example, in α-brass. These considerations apply whatever the degree of short-range order, so that the difficulty cannot be resolved by introducing this factor.

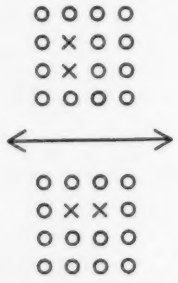

FIGURE 1. The rotation of the axis of a pair of solute atoms.

An essential defect of the argument lies in the assumption that the bond lengths are invariant, i.e., that both species of atom are incompressible. When this restriction is removed it is not difficult to see that a rotation of solute pairs could produce a change in average dimensions and hence a relaxation effect. Roughly speaking, one would expect the effect to be greater, the larger the difference in compressibilities of the two species.

The second difficulty is in connection with Zener's calculation from the model of a rough value for the strength, a value which he finds to be of the same order of magnitude as that found experimentally. Zener's expression for the relaxation strength δ_E is:

$$\delta_E = n E_U (\partial e/\partial n_p)^2/4kT \tag{1}$$

where n is the number of solute pairs per unit volume, E_U the unrelaxed Young's Modulus and k and T have their usual meaning. $(\partial e/\partial n_p)$ is the rate of change of strain e with change in the number of pairs n_p aligned along the preferred crystallographic direction. Zener equates $\partial e/\partial n_p$ to $r\ (1/b)\ (db/dp)$ where $(1/b)\ (db/dp)$ is the relative change with composition p of the lattice parameter b and r is a numerical coefficient which he supposes to be less than one but of the order of magnitude of unity. Since δ_E depends on r^2, some justification of this assumption of the order of magnitude of r would appear to be necessary. When r is put equal to one we have the relation $(\partial e/\partial n_p) = (1/b)(db/dp)$

which is tantamount to saying that a change in the number of pairs lying along one direction produces a change in the average concentration along that direction—viz., an increase of one solute atom for each pair rotated—and that the anelastic strain results from this increase in concentration. But no change at all in the average concentration throughout the sample can be produced by rotations of pairs or by any other kind of redistribution of solute atoms and least of all along one particular direction. Therefore, although it may be reasonable to suppose that $(\partial e/\partial n_p)$ is proportional to $(1/b)(db/dp)$ it is by no means immediately obvious why r should be even of the order of magnitude of unity.

Zener's model may also be criticised on other but less serious points.

At concentrations much above 5–10 per cent it is quite inadequate to refer only to pairs of solute atoms, for solute atoms will occur predominantly in much more complicated groupings. In any case, the nearer we approach the 50 at.% composition the more arbitrary becomes any distinction between solute and solvent. A satisfactory theory should treat both species of atoms in a symmetrical manner and should not need to distinguish a solute from a solvent.

The number of pairs is assumed constant in Zener's treatment, no allowance being made for the possibility of pairs breaking up or new pairs being formed when the stress is applied.

The final point is that no proper account is taken of tendencies towards short range order or segregation.

The present work aims at constructing a more complete and satisfactory theory which will remove the objections we have discussed above and in particular justify the order of magnitude of r assumed by Zener, and bring out the importance of the compressibilities in determining the relaxation strength. We shall find that the latter two points are closely connected.

3. Relaxation Effects arising from Changes in Short-Range Order

It is well known that the lattice dimensions of an alloy depend upon the degree both of long and of short range order present in the alloy. Thus the equilibrium value of order in a strained crystal will in general differ from that in the unstrained crystal and in addition to the elastic strain following an applied stress there will be an anelastic strain arising from the change to the new stress induced equilibrium value of order.

Anelastic effects arising from changes with stress of long range order have previously been observed and discussed [4]. The present paper deals with a relaxation effect which is assumed to arise from changes in short-range order, i.e., from changes in the numbers of the different types of pairs of atoms. The discussion is based on the assumptions of the theory, as developed by Bethe [4], Guggenheim [5], Takagi [6] and others, of what Guggenheim has called "strictly regular solutions."

The essential assumption is that the total configurational energy can be adequately expressed as the sum of the energies of interaction of pairs of nearest neighbour atoms. The contributions to the energy of an AA pair, BB pair and an AB pair in a solid solution of A and B we designate respectively as W_{AA}, W_{BB} and W_{AB}. When the mixing energy $W_{AA} + W_{BB} - 2W_{AB} \equiv \Delta$ is zero, the atoms are distributed at random on the lattice sites and the solution is said to be "ideal." Solutions for which Δ is finite are known as "strictly regular" and the value of Δ determines the departure of the numbers of different types of pairs from those found in "ideal" solutions, i.e., the degree of short range order σ. Since Δ will in general vary with the lattice dimensions, straining a crystal will lead to a change in the equilibrium value of σ, and it is the further small change in strain which accompanies this change in σ, that is observed as the anelastic strain.

Such a model satisfies the essential condition that it should lead to a relaxation time of the order a^2/D as observed experimentally, for a change in local order is effected by the movement of atoms over distances of the order of the atomic spacing.

It is to be noted that the model provides for a relaxation of a purely hydrostatic pressure whereas that of Zener does not. Such a relaxation has not yet been looked for experimentally.

We proceed now to a calculation of the relaxation strength based on this model.

(a) *The unstressed crystal*

We suppose the crystal to be composed of Np atoms of type A and $Nq = N(1 - p)$ atoms of type B distributed on the N sites of a lattice, each of which are surrounded by z equivalent nearest neighbour sites. We shall assume that the normal modes of the lattice are independent of the configuration of the atoms, so that since we are primarily interested only in changes of configura-

tion we need only consider the configurational contribution to the free energy.

The total number of pairs of atoms is $N \cdot z/2$. An AB pair may be oriented in any of the z-directions, but it is convenient to consider only $z/2$ positive directions in the lattice and then to distinguish between AB and BA pairs. Let κ, λ, μ and ν be the fractions of pairs which are AA, AB, BA and BB respectively. In a completely random solid solution $\lambda = \mu = pq$. The degree of short-range order in a non-random solution will be defined by the equation $\lambda = pq\,(1 + \sigma)$. It can be shown that $\kappa = p - \lambda$ and $\nu = q - \lambda$ so that κ, λ, μ and ν are not independent quantities but are related through the common parameter σ by the equations

$$\left.\begin{aligned} \kappa &= p\,(p - q\sigma) \\ \lambda &= pq\,(1 + \sigma) \\ \mu &= qp\,(1 + \sigma) \\ \nu &= q\,(q - p\sigma). \end{aligned}\right\} \tag{2}$$

We require first to obtain a relation between the W's and the corresponding equilibrium value of σ.

The free energy of the solid solutions may be written, with the above assumptions as

$$F = N z/2\,(\kappa W_{AA} + (\lambda + \mu)\,W_{AB} + \nu W_{BB}) - kT \log g\,(N, p, z, \kappa) \tag{3}$$

where $g(N, p, z, \kappa)$ is the number of ways of arranging Np atoms of A and $N(1 - p)$ atoms of B on a lattice with co-ordination number z such that the total number of AA pairs is $\kappa N \cdot z/2$.

An exact expression for g is not available. We shall make use of the approximate expression derived by Chang [8], Takagi [7] and others:

$$g = \left\{ \frac{(p^p q^q)^{z-1}}{(\kappa^\kappa \lambda^\lambda \mu^\mu \nu^\nu)^{z/2}} \right\}^N .$$

For a given lattice spacing and therefore given values of the W's, the equilibrium value of σ is given by the condition $(\partial F/\partial \sigma)_s = 0$. From equation (3), with the expression for g inserted, this condition leads, noting that $\partial\kappa/\partial\sigma = -\partial\lambda/\partial\sigma = -\partial\mu/\partial\sigma = \partial\nu/\partial\sigma$, to

$$\frac{\kappa\nu}{\lambda\mu} = \exp\,(-\Delta/kT). \tag{4}$$

This equation expresses the well-known "quasi-chemical" condition of equilibrium [6]. It may be written in terms only of σ or of κ through the relations

$$\frac{\kappa\nu}{\lambda\mu} = \frac{(p - q\sigma)(q - p\sigma)}{pq(1 + \sigma)^2} = \frac{(q - p + \kappa)}{(p - \kappa)^2} . \tag{5}$$

It will be convenient to summarise at this stage some of the other properties of the model which we shall use later.

The free-energy change on forming the solution from its components, assumed of the same structure, is given by:

$$\Delta F = F(\text{eq. } 3) - pN \cdot z/2 \cdot W_{AA} - qN \cdot z/2 \cdot W_{BB} \tag{6}$$

The Heat of Solution is therefore

$$\begin{aligned} \Delta H = \Delta F - T\frac{\partial \Delta F}{\partial T} &= -N \cdot z/2 \cdot \lambda \left(\Delta - T\frac{\partial \Delta}{\partial T}\right) \\ &= -N z/2\,(p - \kappa) \left(\Delta - T\frac{\partial \Delta}{\partial T}\right). \end{aligned} \tag{7}$$

The chemical activity coefficient γ_A of the A component, referred to pure A as standard state, is given by the equation 9,

$$kT \log \gamma_A\, p = (1/N)\ \{\Delta F + (1 - p)\,(\partial \Delta F/\partial p)_T\}$$

from which we find

$$\log \gamma_A = \tfrac{1}{2} z\,(\log)\,\kappa - 2 \log p). \tag{8}$$

Equation (6) assumes that W_{AA} and W_{BB} are the same in the alloy as in the pure components, i.e., that the interatomic distances are the same. The equations (7) and (8) derived from (6) will then in general be more approximate than (4).

(*b*) *The strained crystal*

When the crystal is strained homogeneously the average nearest neighbour interatomic spacing, which is the same in all directions in the unstrained crystal, will now in general be different for each of the $z/2$ directions in the crystal. We denote the several interatomic spacings by a_i and the corresponding values of the W's by W_{AA_i}, W_{BB_i} and W_{AB_i} $(i = 1, \ldots z/2)$. As a result of the changes in the W's there will be changes in the equilibrium degree of short range order, and we can define a degree of order σ_i for each direction i which expresses, through equations of the type (2), the fraction of those pairs lying in the direction i which are of the several types; σ_i will in general be different for each direction. We shall assume that an equilibrium condition of the type (4) holds for each of the $z/2$ directions in the crystal so that

$$\frac{\kappa_i \nu_i}{\lambda_i \mu_i} = \frac{\kappa_i(q - p + \kappa_i)}{(p - \kappa_i)^2} = \exp\,(-\Delta_i/kT) \tag{9}$$

where $\Delta_i = W_{AAi} + W_{BBi} - 2W_{ABi}$ and κ_i is the fraction of the pairs lying in the ith direction which

are of type AA, with similar definitions for $\lambda_i\mu_i$ and ν_i.

We now write for the free energy of the strained crystal

$$F = N\sum_{i=1}^{z/2}(\kappa_i W_{AA_i} + (\lambda_i + \mu_i)\, W_{AB_i} + \nu_i W_{BB_i}) - kT \log g(N, p, z, \kappa_1 \ldots \kappa_{\frac{z}{2}})$$

where g is the number of ways of arranging Np atoms of A and $N(1-p)$ atoms of B on the N sites of a crystal so that the numbers of pairs of each type counted along any one direction corresponds to the required value of σ_i in that direction. The nature of g will not concern us but consistency would demand that it be of a form to lead to the equilibrium relations (9).

Let e be some measure of the strain and s the corresponding stress producing it. If the crystal is in complete equilibrium under this stress so that $(\partial F/\partial\sigma) = 0$ for each i, then s is given by

$$s = -\frac{1}{V}\left(\frac{\partial F}{\partial e}\right)_{\bar{\sigma}}$$

where $\bar{\sigma}$ denotes the equilibrium values of σ_i and V is the total volume of the crystal; thus

$$s = -\frac{N}{V}\sum_{i=1}^{z/2}(\bar{\kappa}_i W'_{AA_i} + (\bar{\lambda}_i + \bar{\mu}_i)\, W'_{AB_i} + \bar{\nu}_i W'_{BB_i})\frac{da_i}{de}$$

where the bar denotes the equilibrium value, and where W'_{AA_i} is written for $\partial W_{AA_i}/\partial a_i$.

The relaxed modulus of elasticity M_r is then given by $(ds/de)_T$ where in forming the differential coefficient the degree of order is allowed to change with the strain so as to maintain values of σ_i corresponding to equilibrium, as signified by the complete differentials. Thus

$$M_R = -(N/V)\Big[\sum_i (\bar{\kappa}_i W''_{AA_i} + (\lambda_i + \mu_i)\, W''_{AB_i} + \bar{\nu}_i W''_{BB_i})\left(\frac{da_i}{de}\right)^2 + \sum (\bar{\kappa}_i W'_{AA_i} + (\lambda_i + \mu_i)\, W'_{AB} + \nu_i W'_{NN})\left(\frac{d^2 a_i}{de^2}\right) + \sum_i \left(\Delta'_i \frac{\partial \bar{\kappa}_i}{\partial e}\frac{da_i}{de}\right)\Big]. \quad (10)$$

The unrelaxed modulus M_U is given by $(\partial s/\partial e)_{\bar{\sigma}\,T}$ where the partial differentials signify that the degree of order $\bar{\sigma}$ is to be kept constant in forming the differential coefficient. M_U is thus given by equation (10) without the third summation term. It follows immediately that the relaxation strength δ_M is given by:

$$\delta_M = \frac{M_u - M_r}{M_u} = (N/V)(1/M_u)\sum_i \Delta'_i \frac{\partial \kappa_i}{\partial e}\cdot\frac{da_i}{de} \quad (11)$$

$\partial\kappa_i/\partial e$ may be expressed in terms of Δ' by differentiation of the equilibrium condition (9). We find that

$$\frac{\partial \kappa_i}{\partial e} = \frac{1}{kT}\cdot \Delta'_i\, pq(p - q\sigma_i)(q - p\sigma_i)\left(\frac{1+\sigma_i}{1-\sigma_i}\right)\left(\frac{da_i}{de}\right).$$

Thus

$$\delta_M = (N/V)(1/kT)(1/M_u)\sum_i (\Delta'_i)^2\, pq(p - q\sigma_i)(q - p\sigma_i)\left(\frac{1+\sigma_i}{1-\sigma_i}\right)\left(\frac{da_i}{de}\right)^2.$$

For the small strains usually employed in relaxation experiments very little error will be introduced if we replace the σ_i by the uniform value of σ for the unstrained crystal and assume that Δ_i is the same for each i. Thus

$$\delta_M = (N/V)(1/kT)(1/M_u)(\Delta')^2\, pq(p - q\sigma)(q - p\sigma)\left(\frac{1+\sigma}{1-\sigma}\right)\sum_i \left(\frac{da_i}{de}\right)^2. \quad (12)$$

δ_M is therefore determined by the atomic volume, the composition, the degree of local order and the variation of the ordering energy Δ with interatomic spacing. The summation term at the end of equation (12) is a geometrical factor determined by the nature of the strain imposed on the crystal.

It is to be noted that $pq(p - q\sigma)(q - p\sigma) = \kappa\nu$, i.e., the product of the fractions of AA and of BB pairs. Equation (12) is therefore symmetrical in its reference to the two atomic species.

4. The Evaluation of the Relaxation Strength

We now consider the evaluation of the various terms occurring in equation (12).

(a) *The geometrical factor*

(i) *Hydrostatic stress.* M becomes the bulk modulus K and de is the relative change in volume dV/V when s is the pressure; da/de is the same for each direction and $3da_i/a_i = dv/v = de$. Thus

$$\sum_i \left(\frac{da_i}{de}\right)^2 = (z/2)(a^2/9).$$

We note also for future reference that

$$\sum_i \frac{d^2 a_i}{de^2} = 0. \tag{14}$$

(ii) *Pure shear.* For the two important cases of b.c.c. and f.c.c. lattices and for shears for which c_{44} and $(c_{11} - c_{12})/2$ are the appropriate moduli, it is not difficult to show that

$$\left.\begin{aligned} \sum_i \left(\frac{da_i}{de}\right)^2 &= a^2/2 \ (M = C_{44}) \\ \sum_i \left(\frac{da_i}{de}\right)^2 &= a^2/4 \ (M = (C_{11} - C_{12})/2) \end{aligned}\right\} \text{f.c.c.} \tag{15a}$$

$$\left.\begin{aligned} \sum_i \left(\frac{da_i}{de}\right)^2 &= 4a^2/9 \ (M = C_{44}) \\ \sum_i \left(\frac{da_i}{de}\right)^2 &= 0 \qquad (M = (C_{11} - C_{12})/2) \end{aligned}\right\} \text{b.c.c.} \tag{15b}$$

Equation (15b) shows that there would be no relaxation for a (110) $[1\bar{1}0]$ shear in a b.c.c. crystal, as was pointed out by Zener [3]. Experiments on the type of relaxation effect we are considering are usually performed with the specimen in the form of a wire which is made the support of a torsional pendulum. The rigidity modulus G for a single crystal wire whose axis makes with the principal axes of the crystal angles whose direction cosines are γ_1, γ_2, γ_3 is given by

$$G^{-1} = (1/c_{44}) + 2[2/(c_{11} - c_{12}) - 1/c_{44}]\,\phi$$

where

$$\phi = \gamma_1^2 \gamma_2^2 + \gamma_1^2 \gamma_3^2 + \gamma_2^2 \gamma_3^2.$$

If δ and δ' represent respectively the relaxation strengths for a c_{44} and a $(c_{11} - c_{12})/2$ shear, then the relaxation strength observed with a torsional pendulum using a single crystal wire of orientation γ_1, γ_2 and γ_3 is found from the above equation to be [3]*

$$\delta_G = \frac{c'\delta + 2(c\delta' - c'\delta)\phi}{c + 2(c - c')\phi} \tag{16}$$

where for convenience we write $c_{44} = c$ and $(c_{11} - c_{12})/2 = c'$. All the experimental measurements have been carried out by the torsional pendulum method on wires of f.c.c. substances and so provide values of δ_G. For f.c.c. material δ and δ' are given by equation (12) with (15a) and the expression for δ_G for a wire of orientation ϕ becomes, from equation (16)

$$\delta_G = (N/V)(1/kT)(\Delta')^2 a^2 \cdot pq(p - q\sigma)(q - p\sigma) \tag{17}$$

$$\left(\frac{1+\sigma}{1-\sigma}\right)\left\{\frac{c'/2\,c + (c/2c' - c'/c)\phi}{c' + 2(c - c')\phi}\right\}.$$

(b) The degree of local order

Two methods are available for its estimation:

(i) By measurement of the intensity distribution of X-rays or neutrons scattered at low angles from the crystal. Such measurements have been made for a few alloys; the results are usually expressed in terms of κ, λ, etc., from which σ can immediately be obtained.

(ii) From thermodynamic measurements such as of the equilibrium vapour pressure over the alloy of one of the components, when this is much greater than the vapour pressure of the other component, or of the e.m.f. of a cell whose two electrodes are composed respectively of the alloy and of one of the pure components. Such measurements lead directly to the activity coefficient γ of one or other of the alloy constituents. κ, and therefore σ, may then be calculated from equation (8).

(c) The variation of Δ with interatomic distance $(d\Delta/da = \Delta')$

We shall describe three methods, two of which involve relating $d\Delta/da$ to other directly measurable properties of the alloy and a third which makes use again of the thermodynamic measurements referred to under (*b*) (ii).

(i) It is not difficult to relate $d\Delta/da$ to the variation of lattice parameter with short range order.

For a given degree of order, which may or may not be that corresponding to thermodynamic equilibrium, the interatomic spacing is derived from the condition $(\partial F/\partial a)_\kappa = 0$, i.e.,

$$N(z/2)\{\kappa W'_{AA} + (\lambda + \mu)\, W'_{AB} + \nu W'_{BB}\} = 0.$$

Taking the total differential of this expression with respect to a leads to

$$\frac{da}{d\kappa} = \frac{\Delta' N(z/2)}{N(z/2)\{\kappa W''_{AA} + (\lambda + \mu) W''_{AB} + \nu W''_{BB}\}}$$

The denominator on the R.H.S. is closely related to the Unrelaxed Bulk Modulus K_u, as can be seen from equations (10), (13) and (14). Thus

*Equation (16) is given by Zener as equation (14) in reference [3]. Zener also gives [equation (13)] an expression for Δ_E, the relaxation strength for a wire strained in tension. This is not appropriate for the present treatment because it is derived on the assumption, not valid here, that there is no relaxation of a hydrostatic stress.

(18) $K_u = -(N/V)(z/2)\{\kappa W''_{AA} + (\lambda + \mu)W''_{AB} + \nu W''_{BB}\}$

and hence

$$(19) \qquad \Delta' = \frac{9KV}{N(z/2)a}\left\{\frac{1}{a}\frac{da}{d\kappa}\right\}.$$

This provides a useful expression for estimating Δ' in the few cases for which $da/d\kappa$ has been measured. The equation will be employed also in connection with a later discussion of Zener's theory.

(ii) The variation of lattice parameter with composition is known for most metal solutions; a simple expression may be obtained for it involving Δ'.

When both a and κ assume their equilibrium values the two conditions $(\partial F/\partial a)_\kappa = 0$ and $(\partial F/\partial \kappa_a = 0$ are simultaneously satisfied, i.e.,

$$(20) \qquad \left.\begin{aligned} \kappa W'_{AA} + (\lambda + \mu)\, W'_{AB} + \nu W'_{BB} &= 0 \\ \Delta + kT \log (\kappa\nu/\lambda\mu) &= 0 \end{aligned}\right\}.$$

When the composition p changes, both κ and a change. If equilibrium values of κ and a are maintained for all compositions, the total differentials of (20) with respect to p must be zero. From this condition we find after some reduction

$$\frac{9K_uV}{Na^2(z/2)}\cdot\frac{da}{dp} + \Delta'(2p-1)(1+\sigma) + (W'_{AA} - W'_{BB}) = \Delta' pq\frac{d\sigma}{dp}$$

and,

$$\Delta'\frac{da}{dp} + kT\frac{\sigma(q-p)}{pq(q-p\sigma)(p-q\sigma)} = kT\frac{(1-\sigma)}{(p-q\sigma)(q-p\sigma)(1+\sigma)}\frac{d\sigma}{dp}.$$

Eliminating $d\sigma/dp$, and with further reduction, we obtain

$$\frac{da}{dp} = -\frac{N.(z/2)a^2}{9VK_B}\left\{\frac{\Delta'(1-2p)(1+\sigma)}{(1-\sigma)} - (W'_{AA} - W'_{BB})\right\}.$$

In order to eliminate $(W'_{AA} - W'_{BB})$, we note that at the composition $p = \frac{1}{2} = q$

$$\left(\frac{da}{dp}\right)_{p=\frac{1}{2}} = \frac{N(z/2)}{9}\left(\frac{a^2}{VK_B}\right)_{p=\frac{1}{2}}(W'_{AA} - W'_{BB}).$$

Thus

$$\Delta' = -\frac{9}{N(z/2)}\left\{\frac{VK}{a^2}\cdot\frac{da}{dp} - \left(\frac{VK}{a^2}\frac{da}{dp}\right)_{p=\frac{1}{2}}\right\}\frac{(1-\sigma)}{(1+\sigma)(1-2p)}.$$

Now in many cases, K varies much more rapidly with composition than either a or da/dp, so that we can write Δ' approximately as

$$(21) \qquad \Delta' = -\frac{9V}{N(z/2)a^2}\cdot\frac{da}{dp}\left\{K - K_{p=\frac{1}{2}}\right\}\frac{(1-\sigma)}{(1+\sigma)(1-2p)}$$

$$(22) \qquad \simeq \frac{9VK}{N(z/2)a}\left(\frac{1}{a}\frac{da}{dp}\right)\left(\frac{1}{K}\frac{dK}{dp}\right)\left(\frac{1-\sigma}{1+\sigma}\right).$$

dK/dp is known for a few alloys, so that this is quite a useful expression.

(iii) The Thermodynamic method. Δ may be determined, from activity coefficient measurements, for various temperatures at each composition and Δ then calculated from the equation

$$(23) \qquad \Delta' = d\Delta/da = (1/a\alpha)\, d\Delta/dT$$

where α is the coefficient of linear expansion.

A convenient expression for $d\Delta/dT$ which requires a knowledge of Δ at only one temperature, may be readily derived from equations (4), (5) and (8)

$$(24) \qquad \frac{d\Delta}{dT} = \frac{\Delta}{T} + \frac{p(1-2p)+\kappa}{(p-\kappa)(1-2p+\kappa)}\cdot\frac{2k}{Tz}\frac{d\log\gamma}{d(1/T)}.$$

When independent measurements of the heats of solution are also available, these may be combined with the values of Δ derived from the activity measurements to give another estimate of $d\Delta/dT$ for from equation (7),

$$(27) \qquad \frac{d\Delta}{dT} = \frac{1}{T}\left\{\frac{\Delta H}{(z/2)(p-\kappa)} + \Delta\right\}.$$

5. Comparison with Experiment

(a) CuZn alloys

Early measurements on this system were made by Kê [10] and by Zener [11] for roughly 30 at.% alloys. The previous paper [2] reports measurements on alloys of various compositions between 10 and 30 per cent. All the measurements, except those of Zener, were made by the torsional pendulum method so that the relaxation strengths derived from them are to be represented by equation (17). The values of δ_G are shown by crosses in Figure 2.

In the absence of X-ray studies of short range order in α-brass, σ must be estimated from thermodynamic measurements. The vapour pressure of

zinc over α-brass of various composition has been measured by Herbenar, Siebert and Duffendack [12] and Lumsden [13] has shown that the activity coefficients γ calculated from their measurements, and referred to pure liquid zinc as standard state, may be represented by the equation $RT \log_e \gamma = 4.2T + d$, where d is a constant depending only on the composition. Values of d were derived from Lumsden's published graphs and the equation used to determine γ at 400°C.

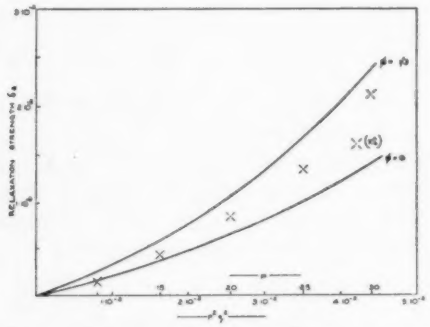

FIGURE 2. The relaxation strength δ_G of CuZn alloys strained in torsion, as a function of composition. p = atomic fraction of Zn, q = atomic fraction of Cu—Theoretical values for $\phi = \frac{1}{3}$ and 0. $\times$ Experimental values.

This temperature was chosen at which to estimate γ as being sufficiently close to the temperatures at which δ_G was measured for the value at 400°C to be obtained by extrapolation without serious error, while not requiring too extensive an extrapolation of the vapour pressure measurements.

The values of γ were corrected so as to refer to pure solid zinc as the standard state and σ and Δ derived from them through equations (8) and (5). Δ' was then obtained from equation (23) and (24).

Lumsden has derived from the same vapour pressure measurements an equation for the heat of solution of solid zinc in solid copper as a function of concentration, $\Delta H = -7770p + 3150p^2/q$ cal/mole. This represents excellently the values of ΔH measured directly by Weibke [14] and by Körber and Oelson [15], and so may be regarded as an estimate of ΔH independent of the vapour pressure measurements. It was used with the values of Δ derived from the vapour pressure measurements to give from equation (25) a second estimate of Δ'.

The compressibilities of CuZn alloys of 18 per cent zinc and 35.6 per cent zinc composition have been measured by Mehl and Maier [16]. An admittedly rough extrapolation of these results to 50 per cent zinc enabled a third estimate of Δ' to be obtained, using equation (21).

These results are summarised in Table I.

TABLE I

p (at. fraction of Zn)	σ at 400°C	Δ' (ergs/cm) eqs (24) and (23)	eq. (21)	eq. (25)	Av. Δ'
.1	.0575	$-.38.10^{-4}$	$-.14.10^{-4}$	$-.33.10^{-4}$	$-.28.10^{-4}$
.15	.0855	$-.36.10^{-4}$	$-.15.10^{-4}$	$-.34.10^{-4}$	$-.28.10^{-4}$
.20	.113	$-.34.10^{-4}$	$-.15.10^{-4}$	$-.34.10^{-4}$	$-.28.10^{-4}$
.25	.141	$-.35.10^{-4}$	$-.16.10^{-4}$	$-.29.10^{-4}$	$-.27.10^{-4}$
.30	.168	$-.37.10^{-4}$	$-.17.10^{-4}$	$-.26.10^{-4}$	$-.27.10^{-4}$

The elastic constants of α-brass were derived from the measurements at room temperature of Fenn, Hibbard and Lepper [17], and roughly corrected to give values at 400°C.

The relaxation strengths of a wire strained in torsion were then calculated from equation (17) for the range of compositions shown in Table I and for the two values of $\phi = 0$ and $\frac{1}{3}$, these being the values corresponding to the minimum and maximum values respectively of $\delta_G : \phi = 0$ for a single crystal wire whose axis is parallel to the [001] direction in the crystal and $\phi = \frac{1}{3}$ for a wire with the [111] direction parallel to the wire. Polycrystalline wires are usually employed in the experiments; their values of δ_G will be between the values corresponding to $\phi = 0$ and $\phi = \frac{1}{3}$.

The results are shown in Figure 2. There is a surprisingly good agreement between theory and experiment. However, the comparatively wide spread in the values of the independent estimates of Δ' for each composition indicates that this good agreement is in part a matter of good fortune, although the use of the extreme values of Δ' in computing δ_G would by no means alter the order of magnitude of the theoretical result: the constancy over the composition range of the average value of Δ' shown in the last column of Table I might warrant our having some confidence in it.

(*b*) *α-AgZn alloys*

Nowick [18] has carried out extensive observations on this system for compositions of 15–30 at.% zinc, using again the torsion pendulum method; when his results are extrapolated to 400°C they show relaxation strengths which are roughly four to five times larger than those observed for copper zinc alloys.

The physical data on the silver zinc system available for the computation of theoretical relaxation

strengths are much less complete than for the copper zinc system, but are adequate at least to account for the differences observed between the relaxation strengths of the two systems.

Thus the elastic constants of α-AgZn crystals are not known but estimates of them can be made by assuming that they are in the same ratio to the corresponding constants of CuZn crystals as those of silver are to copper. Thus for AgZn, C_{44} is 0.58 times and $(C_{11}-C_{12})/2$ is 0.66 times the corresponding values for CuZn. These being roughly equal we take an average value of 0.62 and so find that the last factor in equation (17) is $1/0.62 = 1.6$ times greater for AgZn than for CuZn. The average interatomic distance in AgZn alloys is about 2.85×10^{-8} cm compared to 2.5×10^{-8} cm for CuZn alloys. This, together with the change in the elastic constants, will, according to equation (17), account for an increase of δ_G for AgZn alloys over that for CuZn alloys by a factor of 1.45. Thus the larger part of the difference in δ_G for these two alloys must be attributed to differences in Δ' or in σ, or in both.

The only data available for the estimation of these quantities are the vapour pressure measurements of Zn over AgZn alloys of composition 5–30 at.% Zn, carried out by Birchenall and Cheng [19]. The logs of the activity coefficients γ at each composition studied, as computed from these measurements, vary linearly with $1/T$, the reciprocal of the temperature, over the range of temperatures at which the pressures P were measured. Such linear plots were used to obtain by extrapolation the values of γ at 400°C and from these, values of σ and Δ' were calculated. The results are shown in Table II. The values of Δ' are seen to vary very considerably with composition, and those for 17 and 23 per cent Zn would lead to values of δ_G several orders of magnitude smaller than the observed values. Believing the rapid variations with composition to be due to errors arising from the linear extrapolation of $\log \gamma \backsim 1/T$ plots down to 400°C, Δ' was re-evaluated at 600°C, with the results shown in the last column of Table II. An even more rapid variation of Δ' with composition is apparent at this temperature. We must then conclude that such a variability cannot be due to errors of extrapolation and that the vapour pressure measurements are not sufficiently accurate to produce a value of Δ' in which we can have any confidence, except perhaps at 10.5 per cent Zn where the values of Δ' for 400° and 600° agree quite closely; we should not expect Δ' to vary much with temperature. Furthermore, Δ' is positive only for the 10.5 at.% figures and such is the sign of Δ' we are to expect for AgZn. This follows from equation (22). da/dp for AgZn is opposite in sign to da/dp for CuZn, but we should expect the sign of dK/dp to be the same for both alloys, since the bulk moduli of Ag and Cu are both greater than that of Zn. Therefore, since Δ' is $-ve$ for CuZn, it should be $+ve$ for AgZn.

TABLE II

THE VALUES FOR AgZn ALLOYS OF σ AND Δ' AT 400°C AND OF Δ' AT 600°C

P (at. fraction of Zn)	σ at 400°C	Δ' (ergs/cm) at 400°C	Δ' (ergs/cm) at 600°C
.105	.0315	+.43	+ .42
.173	.0633	−.019	− .32
.235	.0919	−.029	− .36
.297	.1303	−.57	−1.20

It is interesting that when linear plots of log (vapour pressure) against $1/T$ are extrapolated down to 400°C, the resulting values of the pressure no longer monotonically increase with composition, that for 17.3 per cent Zn being less than that for 10.5 per cent. This suggests that a separation into two phases should occur at some temperature above 400°C, a behaviour for which there is no other evidence and which is inconsistent with the positive values of Δ derived at each composition from the pressures at this temperature. Errors, except for 10.5 per cent, in the experimentally determined values of $\log P$ as a function of $1/T$ would account both for this behaviour and the inconstancy of Δ', for this is very sensitive to the rate of variation of $\log P$ with $1/T$.

We shall assume then that $\Delta' = 0.42\ 10^{-4}$ ergs/cm. Comparing this with the average value of Δ' for CuZn, derived from the vapour pressure measurements, viz., $0.36\ 10^{-4}$ ergs/cm, the change in δ_G arising from the increase of Δ' is by a factor $(0.42/0.36)^2 = 1.35$.

Only the value of σ at 10.7 at.% Zn can be taken as reliable. This is 0.0315 compared with .0603 for a CuZn alloy of the same composition. The term in equation (17) containing σ is therefore 0.0069 compared with .0047 for the CuZn alloy so that a further increase in δ_G by a factor $.0069/.0047 = 1.5$ is to be expected from the decrease in σ.

Considering all the contributions to the change in δ_G, we expect δ_G for AgZn alloys to be about three times greater than that for CuZn alloys,

which is nearly the difference observed experimentally. If we were to compare our single estimate of Δ' for AgZn with the average of the three estimates of Δ' for CuZn viz., .28 10^{-4} ergs/cm, then we should find a value of δ_G for AgZn nearly five times larger than that for CuZn as is observed experimentally.

Nowick also observed that the relaxation strengths of different specimens of the same composition covered a range of values and this he was able to relate to differences between the specimens of their degree of preferred orientation. The larger relaxation strengths were found for those specimens which had the smaller torsion modulus, a behaviour which is to be expected from the present theory as can be seen by considering equation (12). Taking the above estimates of the shear constants the ratio of the maximum to the minimum values of δ_G, calculated from the last term of equation (17), is about 1.7 for a specimen of 30 at.% Zn. Nowick reports for a series of alloys of this composition values of δ_G (at 220°C) varying from 7.3 to 4. 10^{-2}, the ratio of which is 1.8. This variability between specimens can then be interpreted as an orientation effect.

Nowick attributes the higher relaxation strengths observed in AgZn alloys to the difference in size between Ag and Zn atoms being twice that between Cu and Zn atoms, presumably taking as the atomic diameter of zinc the closest distance of approach of atoms in the basal plane of the pure zinc structure. The atomic size difference enters into the determination of δ_G, through equation (22), as $(1/a)\ (da/dp)$. This is a little *smaller* for AgZn than for CuZn alloys so that the higher relaxation strengths of AgZn alloys are not due to atomic size differences, for their effect alone would be to produce a lower value of δ_G for AgZn. A comparison of the Goldschmidt radii for Cu, Zn and Ag atoms would have led to the same conclusion.

(*c*) *Copper-aluminium alloys*

The measurements reported in the previous paper show that the relaxation strength for a 15 per cent Al alloy at 400°C is about three times greater than that for a CuZn alloy of the same composition.

The interatomic distance a and the variation of a with composition do not differ appreciably from those for CuZn alloys.

No data are available on the elastic constants of CuAl alloys, but the values for pure Al do not differ so very appreciably from those for pure Zn for us to expect any appreciable difference between the elastic constants of CuZn and CuAl alloys at such fairly low concentrations as 15 at.% of Zn or Al respectively.

The increased relaxation strength of the CuAl over that of the CuZn alloy must then be due to differences for the two systems of σ or Δ' or both.

There exist no thermodynamic data for CuAl from which σ or Δ' could be calculated. However, it has recently been shown [20] by X-ray methods that in AgAl alloys the number of Ag-Ag bonds is greater than corresponds to a random solid solution of the two elements, i.e., σ is $-ve$. We may perhaps assume that the same is true for CuAl alloys although we have no means of estimating the magnitude of σ. Let us assume that $\sigma = 0$. Then the term in equation (17) containing σ becomes 0.0162 for a 15 per cent alloy compared with .0098 for a CuZn alloy of the same composition.

Consider now equation (21) for Δ': this quantity increases with decrease in σ and for a change from $\sigma = .085$ for CuZn to $\sigma = 0$ for CuAl, the increase is by a factor $1.085/.915 = 1.19$. Thus the change is δ_G arising from this change alone in Δ' is by a factor $(1.19)^2 = 1.4$.

Thus the total increase in the relaxation strength of a 15 per cent CuAl alloy over that for a 15 per cent CuZn alloy is by a factor $(.0162/.0098)1.4 = 2.3$. The experimentally observed increase is by a factor $\backsim 3$. Since σ is most probably less than zero, so that the increase in δ_G is really by a factor > 2.3, we may say that the increased value of δ_G in CuAl alloys could be wholly accounted for as due to the different degrees of local order existing in CuAl and in CuZn alloys.

Mehl and Maier [16] measured the compressibility of a 16 at.% Al alloy. This result, with the known compressibilities of pure Al and pure Cu, was used to give an admittedly very tentative estimate of $(K_{p=\frac{1}{3}} - K_{p=0.15})$ for use in equation (21). This was found not to differ appreciably from the corresponding value for CuZn. Thus the change in Δ', as expressed by (22) most probably derives principally from changes in σ, as assumed above.

(*d*) *Nickel-platinum alloys*

The absence of any peak in the experiments described in the previous paper on a 15 at.% Pt alloy shows that δ_G is certainly less than about 10^{-3} and so well below that of the other alloys investigated. The data required for an estimation of the theoretical value of δ_G are not available. This result, however, illustrates well the fact that an appreciable atomic size difference ($\backsim$10 per cent) is not a sufficient condition for the occurrence of an appreciable relaxation effect.

6. Discussion

Equation (17) represents an expression for the strength of the relaxation arising from the stress induced redistribution of atoms in substitutional alloys which appears capable of providing theoretical values of the relaxation strength in good agreement with experimental measurements and which is free from the more obvious shortcomings of Zener's earlier theory, referred to at end of section 2.

It will be clear that the change from the unstressed distribution in which σ is the same for each direction to the distribution under stress where σ varies with direction, can be imagined as taking place, at least in part, by rotation of the axes of pairs of atoms from one direction to another, so that Zener's essential concept is retained but appears only as a simplified way of describing the relaxation process, applicable only for concentrations so low that there are no groupings of solute atoms more complicated than pairs. It is interesting to note that the average degree of order $(\sum_i \sigma_i)/(z/2)$ is unchanged by application of a pure shear stress, as may readily be shown when it is realised that $\sum_i i\,(da_i/de)_{\text{shear}} = 0$. Thus for this type of deformation Zener's tacit assumption that the total number of solute pairs remains constant, is substantiated, although there may well of course be pairs which break up with an equal number of new pairs formed.

The importance, discussed in Section 2, of the compressibilities of the two constituent species in determining δ_G is best made apparent by consideration of equation (22). If both species of atom were incompressible K would not change with composition and Δ' and hence δ_G would be zero. Furthermore, the larger the difference in the bulk moduli of the two species the larger in general might we expect dK/dp to be and so the greater the relaxation strength.

Let us now compare equations (19) and (22) for Δ'. If we ignore in equation (19) the order term, which is always roughly unity, we find that $(1/a)\ (da/d\kappa) \simeq (1/K)\ (dK/dp) \cdot (1/a)\ (da/dp)$. When allowance is made for differences in notation, it is readily seen that Zener's coefficient r, discussed in Section 2, is of the same order as $(1/K)\ (dK/dp)$. Whether or not this is unity, as Zener assumed was always so, can *only* be determined by appeal to experiment in each case. For CuZn alloys, $(1/K)\ (dK/dp)$ being roughly 0.4 at 20–30 per cent Zn, r is in fact of order unity so that Zener's assumption led him to the correct order of magnitude of δ_G in this case. For alloys the constituents of which have nearly equal compressibilities, r would most probably be very much less than one.

Zener's theory leads one to expect the relaxation strength to be larger the greater the difference in size of the alloy constituents. This is true in so far as Δ', as given by (22) is proportional to $(1/a)\ (da/dp)$ but a larger size difference might well be compensated by a smaller value of $(1/K)\ (dK/dp)$, so that differences in atomic size are *not* a sufficient criterion for determining the relative relaxation strengths of a series of alloys, as has sometimes been supposed.

For the two systems which have been studied over a range of composition, viz., CuZn and AgZn, δ_G is found to be roughly proportional to the square of the concentration of Zn i.e., to p^2. This is as might be expected from equation (1) based on Zener's theory, for n_p the number of solute pairs is proportional to p^2 if we assume $\sigma = 0$. But no such simple dependence on composition is apparent from equation (17) and for $\sigma = 0$, $\delta_G \propto p^2q^2$. δ_G is plotted against p^2q^2 in Figure 1 and clearly departs noticeably from a proportionability with p^2q^2. This is in part due to variation of a and the elastic constants with composition but principally to σ not being zero, and it so happens that the departure is such as to make δ_G appear more nearly proportional to p^2 than to p^2q^2. It follows that if corrections can be made for the variation of the elastic constants and of a with composition, a departure from the law $\delta_G \propto p^2q^2$ indicates a non-random solid solution, so that measurements of the variation of relaxation strength with composition may be useful in the study of short-range order. For a $+ve$ σ the curve of $\delta_G \backsim p^2q^2$ is convex towards the abscissa as in Figure 1; for σ $-ve$ it is convex towards the ordinate.

Basic to the whole development of the theory presented in this paper has been the assumption that the total free energy of a solid solution is adequately represented by the configurational contribution alone and that this can be expressed sufficiently well as the sum of the interaction energies of nearest neighbour pairs of atoms, quantities we have represented by W_{AA}, etc. Thus the electronic and vibrational contributions are to be regarded as having been ignored or, at best, as included in the W terms so that changes in electronic and vibrational energy are always proportional to changes in configurational energy. It is, however, interesting to note that it is unnecessary to take explicit account of the electronic contribu-

tion to the total free energy when calculating δ_G for a pure shear deformation, for the electronic energy is, in the usual approximation, a function only of the total volume, which is unchanged by shear. Equation (17) does not then suffer from our having ignored the electronic energy.

We have also tacitly assumed in the development of the theory that each atom resides on a point of an ideal lattice so that the distance between any neighbouring pair of atoms is the same, whatever the species constituting the pair. This will not of course be exactly true for atoms of unequal size.

Attempts have frequently been made to refine theories of solid solutions based on these assumptions. Thus one may separate the total configurational energy into two parts, the one being the sum of the energies of interaction when the atoms reside on the points of a perfect lattice, whose dimensions are the average lattice parameters as measured by X-ray methods, and the other a strain energy arising from the displacements from those lattice points which the atoms necessarily suffer because of their unequal sizes. We have in effect assumed that the interaction energy and the strain energy may be added and the sum denoted by one of the three quantities W_{AA}, etc., according to the bond type.

It is interesting to compare from this point of view the present theory of relaxation effects with that of Zener. Whereas we attribute the relaxation effects to the fact that the total interaction energy in a strained crystal can be lowered by a redistribution of atoms, i.e., a change in directional order, Zener attributes them to a lowering only of the strain energy contribution to the total interaction energy. To what extent the relaxation effects are in fact due to changes with interatomic distance of the strain energy contribution and to what extent due to changes in the interaction energy as defined in the last paragraph could no doubt be deduced by a development of the theory treating separately the two contributions to the configurational energy.

7. Acknowledgements

The authors are much indebted to Mrs. A. Stephenson for the care with which the numerical calculations for this paper were carried out. Our thanks are also due to Mr. B. G. Childs for many valuable discussions, to Dr. H. M. Finniston for his continued interest and encouragement, and to Sir John Cockcroft, F.R.S., Director of the Atomic Energy Research Establishment, for permission to publish the paper.

8. References

1. Zener, C. Elasticity and Anelasticity of Metals (University of Chicago Press, 1948).
2. Childs, B. G. and Le Claire, A. D. Acta Met. **2**, (1954).
3. Zener, C. Phys. Rev. **71** (1947) 34–8.
4. Gorsky, W. S. Physik, Zeitschr. Sowjet. **8** (5) (1935) 562.
5. Bethe, H. A. Proc. Roy. Soc. **A150** (1935) 552.
6. Guggenheim, E. A. Mixtures (Oxford University Press, 1952).
7. Takagi, Y. Proc. Physico-Math. Soc. Japan **23** (1) (1941) 44.
8. Chang, T. S. Proc. Camb. Phil. Soc. **35** (1939) 265.
9. Guggenheim, E. A. Thermodynamics: An Advanced Treatment for Physicists and Chemists (North Holland Publ. Co., 1949), p. 174.
10. Kê, Ting Sui. J. Appl. Phys. **19** (1948) 285.
11. Zener, C. Trans. A.I.M.M.E. **152** (1943) 122.
12. Herbenar, A. W., Siebert, C. A. and Duffendack, O. S. Trans. A.I.M.E. **188** (1950) 323.
13. Lumsden, J. Thermodynamics of Alloys (London, Institute of Metals, 1952).
14. Weibke, F. Z. Anorg. Chem. **232** (1937) 289.
15. Körber, F. and Oelson, W. Mitt. Kaiser-Wilhelm Inst. Eisenf. Dusseldorf, **19** (1937) 209.
16. Mehl, R. F. and Maier, B. J. J. Amer. Chem. Soc. **50** (1928) 55.
17. Fenn, R. U., Hibberd, W. R. and Lepper, H. A. J. Metals (Trans. A.I.M.E. **188**), (1950) 175.
18. Nowick, A. S. Phys. Rev. **88** (4) (1952) 925.
19. Birchenall, C. E. and Cheng, C. H. J. Metals **1** (7) (1949) 428.
20. Walker, C. B., Blin, J. and Guinier, A. C.R. Acad. Sci. Paris, **235** (1952) 254.

DIE KINEMATISCHE AUFNAHME VON FEINSTRUKTURÄNDERUNGEN*

A. BOETTCHER, R. THUN und H. TREUPEL†

Eine neue Methode zur Untersuchung rasch ablaufender Gitterumwandlungen mittels Elektronenstrahlen sowie der Aufbau einer entsprechenden Apparatur wird beschrieben, bei der man durch eine Schlitzblende schmale Segmente des Debye-Scherrer-Diagramms ausblendet, welche auf einer bewegten Photoplatte kontinuierlich aneinandergereiht aufgenommen werden.

Bei stehendem Objekt, das während der Aufnahme getempert werden kann, erhält man ein Zeitdiagramm der Feinstrukturänderung, während eine Aufnahme des durch den Elektronenstrahl bewegten Objekts unter konstanten Versuchsbedingungen die räumliche Strukturverteilung im Präparat wiedergibt. An einigen Beispielen wird die Anwendungsmöglichkeit des Verfahrens gezeigt.

Es erscheint besonders für die Untersuchung von Phasenumwandlungen sowie Diffusions- und Korrosionsvorgängen geeignet. Die Aufstellung der Zustandsdiagramme von Zwei- und Dreistoffsystemen wird durch das angegebene Verfahren wesentlich erleichtert.

A CONTINUOUSLY RECORDING ELECTRON DIFFRACTION CAMERA FOR STUDIES OF CRYSTAL STRUCTURE TRANSITIONS

A new electron diffraction camera for investigating rapidly proceeding lattice transitions is described. The outstanding new features of the apparatus are a screen with a slit diaphragm and a photoplate which moves behind the slit. The moving photoplate is exposed by the direct electron beam and by two small portions of each diffraction ring. The resulting pattern consists of parallel lines instead of rings. The new method permits the continuous recording of both structure transformations and the distribution of different crystalline components over an extended flat sample. Various applications for which the method is particularly valuable are presented.

OBSERVATIONS CINÉMATOGRAPHIQUES DE CHANGEMENTS DE LA STRUCTURE CRISTALLINE

On décrit une nouvelle méthode d'investigation de transformations rapides du réseau au moyen d'un faisceau d'électrons, ainsi que la construction de l'équipement qui s'y rapporte. L'emploi d'un système de fentes permet d'enregistrer, d'une façon continue, de petits segments des raies de Debye-Scherrer sur une plaque photographique mobile. En opérant avec un échantillon stationnaire, qui peut être chauffé pendant l'exposition, on obtient un diagramme de la structure cristalline en fonction du temps, alors qu'avec un échantillon mobile, qui se déplace sous le faisceau d'électrons dans des conditions constantes, on obtient un diagramme donnant la structure spatiale de l'échantillon. On donne plusieurs exemples montrant les possibilités d'application de cette méthode, qui paraît convenir tout particulièrement aux investigations des changements des phases, des problèmes de diffusion et de corrosion. Cette méthode facilitera la détermination des diagrammes des phases pour des alliages binaires et ternaires.

Seit Jahren gewinnen Untersuchungen von Festkörperreaktionen, Ausscheidungsvorgängen und Phasenumwandlungen im festen Zustand zunehmend an Bedeutung, da die Aufklärung der diesen Erscheinungen zugrundeliegenden Mechanismen eine wesentliche Förderung der Werkstoffphysik verspricht. Es besteht daher Interesse an Verfahren, welche die derartige Vorgänge begleitenden Veränderungen der Kristallgitterstruktur kontinuierlich zu verfolgen gestatten.

Die klassische Methode der Feinstrukturanalyse, das Röntgeninterferenzverfahren, ist für derartige Untersuchungen der Gitterkinetik nicht ohne weiteres geeignet, da wegen des geringen Streuvermögens von Materie für γ-Quanten die für die Aufnahme eines Strukturdiagramms erforderliche Zeitdauer gross ist im Verhältnis zur Lebensdauer intermediärer Gitterzustände, so dass schnelle Strukturwechsel nicht erfasst werden können. Man kann diese Einschränkung der Röntgenmethoden zwar dadurch zum Teil ausgleichen, dass man nach Rösler und Ruff [1] die Veränderung der Intensität nur eines Bragg-Reflexes registriert, nach Boettcher und Thun [2] das Diagramm durch kontinuierliche getrennte Abtastung mehrerer Streuwinkelbereiche gewinnt oder die Strahlungsintensität nach Schall [3] durch Verwendung einer Röntgenblitzröhre steigert und dadurch die Belichtungszeit entsprechend verkürzt. Diese Röntgenverfahren bedingen jedoch entweder eine Beschränkung auf die Registrierung ausgewählter Einzelteile des Beugungsdiagramms oder im Falle der Röntgenblitzmethode einen grossen experimentellen Aufwand, sofern die für solche Zwecke notwendige Aufnahmefrequenz erzielt werden soll.

Diese Schwierigkeiten werden vermieden, wenn

*Received January 30, 1954.
†Degussa, Hanau, Germany.

die kinematische Aufzeichnung von Feinstrukturänderungen durch Elektroneninterferenzen erfolgt, da Elektronen an Materie stark gestreut werden und Strahlen hoher Intensität mit einfachen elektronenoptischen Anordnungen zu erzielen sind. Kossel und Möllenstedt [4; 5; 6], die als erste Elektroneninterferenzen zur Registrierung strukturkinetischer Vorgänge benutzten, haben vollständige Debye-Scherrer Diagramme mit einer normalen Kinokamera in schneller Einzelbildfolge aufgenommen. Dieses Aufnahmeverfahren bringt jedoch bei langsamen Diffusions- und Ausgleichsvorgängen einen grossen Verbrauch an Filmmaterial mit sich, da wegen der Möglichkeit rascher Zwischenumwandlungen nicht auf eine hohe Bildwechselzahl verzichtet werden kann. Nachteilig ist ferner, dass jedes Einzeldiagramm gesondert indiziert werden muss und die Zuordnung entsprechender Reflexe auf verschiedenen Einzelbildern nicht sicher möglich ist.

Zur Lösung dieses Problems wurde von Boettcher u. Mitarbeitern [7] [8; 9; 10] ein neuartiges Abbildungsprinzip angegeben, das neben der einfachen Registrierung strukturkinematischer Vorgänge auch die Aufzeichnung der Strukturverteilung in einem flächenhaft ausgedehnten Objekt ermöglicht (Abb. 1). Der Elektronenstrahl enger

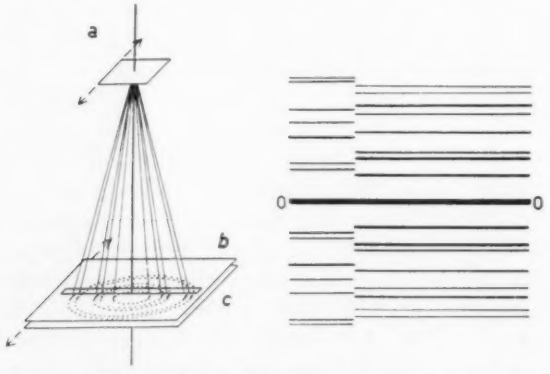

Abb. 1. Kinematische Elektronenbeugung (schematisch). Links Prinzipskizze: (*a*) Objekt, (*b*) Spaltblende, (*c*) Photoplatte. Rechts: Diagrammschema.

Apertur durchstrahlt wie üblich das Objekt und entwirft das Debye-Scherrer-Diagramm auf eine mit Leuchtsubstanz belegte Spaltblende, welche in einem linearen, über den Primärfleck verlaufenden Teilsegment des Beugungsbildes den Interferenzkegel hindurchtreten lässt. Dieses Teilsegment enthält mit dem Zentralfleck und je zwei symmetrisch zu diesem liegenden Punkten der auftretenden Debye-Scherrer-Ringe alle zur Auswertung eines solchen Diagramms erforderlichen Elemente, sofern in der Probe keine starken Texturen oder zu grossen Kristallite auftreten.

Der so ausgeblendete Strahl schwärzt die unter der Blende und senkrecht zum Blendenspalt kontinuierlich bewegte Photoplatte, auf der die Teilsegmente der Beugungskegel in steter Folge aneinandergereiht werden. Das Plattenbild enthält also statt eines Primärflecks eine Primärgerade und statt der Ringe je zwei symmetrisch zur Primärgeraden verlaufende Reflexlinien. (Diese sind dann ein Bild der Streuwinkelzeitfunktion, wenn die zeitliche Konstanz der Strahlungswellenlänge gewährleistet ist.)

Durchstrahlt man die Probe an einer gleichbleibenden Stelle und tempert sie während der Aufnahme, so erhält man ein Strukturdiagramm als Funktion der Temperatur. Bewegt man aber die Probe synchron zum Plattenvorschub durch den Strahl, so gibt das Diagramm die geometrische Verteilung der im Präparat auftretenden Strukturen wieder. Wegen der geringen Durchdringungsfähigkeit von Elektronen und der dadurch bedingten geringen Präparatdicken handelt es sich praktisch immer um eine Registrierung der flächenhaften Verteilung von Strukturen.

Aufbau der Apparatur

Abb. 2 zeigt die Kamera schematisch im Schnitt, Abb. 3 gibt ihren Aufbau wieder. Der Kathodenkopf für 40 bis 90 kV Strahlspannung kann zur Strahljustierung in allen Richtungen gegen die Objektkammer gekippt und verschoben werden.

Die mit der Rückwand dieser Kamera abnehmbare Objekthalterung (Abb. 4) wurde mit hoher Präzision gefertigt. Das Präparat kann auf ihr in zwei zueinander senkrechten Koordinaten verschoben werden, wobei der Antrieb über Spindeln von Hand oder durch einen regelbaren Gleichstrommotor über ein Wechselgetriebe erfolgt.

Das Objekt wird durch einen elektrisch geheizten Strahlofen erwärmt, in dem sich gegen Störfelder abgeschirmte Schlitze zum Durchtritt des Elektronenstrahls befinden. Die Temperaturmessung erfolgt durch Thermoelemente, die durch Beobachtung bekannter Phasenumwandlungen und des Gitterzusammenbruchs reiner Metalle bei Erreichung des Schmelzpunktes geeicht wurden. Die Genauigkeit der Temperaturmessung ist durch Störungen des Strahlungsgleichgewichts und den Einfluss der Elektronenstrahlenenergie begrenzt und beträgt ungefähr $\pm 15°C$. Der Präparatwechsel erfolgt durch das abnehmbare Einblickfenster der Objektkammer.

Mit dieser ist das Kameragehäuse durch einen Tubus über ein Vakuumventil verbunden, durch das eine Flutung der Objektkammer während des Wechselns der Photoplatte vermieden werden kann. Der Wagen für den Transport der Photoplatte vom Format 6 × 18 cm² läuft in diesem Gehäuse auf Schienen und kann durch den Antriebsmotor in

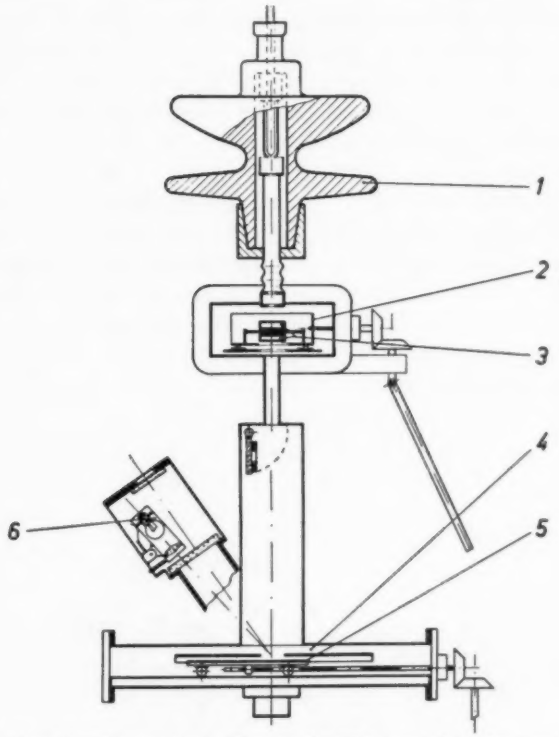

ABB. 2. Kinematische Kamera für Elektroneninterferenzen (Schnittzeichnung). (1) Strahlkopf, (2) Objektschlitten, (3) Ofen für Objektheizung, (4) Kamera, (5) Plattenwagen, (6) Einblicktubus mit Lichtmarkengeber.

verschiedenen, festen Übersetzungsverhältnissen synchron zum Objektvorschub bewegt werden.

Direkt über der Platte befindet sich der Blendenträger mit der Schlitzblende. Seine Einstellung, die durch einen besonderen Einblicktubus kontrolliert wird, erfolgt so, dass der Primärfleck des Leuchtschirmbildes genau auf den Blendenspalt fällt. Der Blendenträger besitzt ferner zur wahlweisen Benutzung eine grosse Blendenöffnung für die Aufnahme üblicher Debye-Scherrer-Diagramme. In dem Einblicktubus befindet sich ein manuell betätigter Lichtmarkengeber, durch den charakteristische Objekttemperaturen auf der Platte markiert werden.

Charakteristisch für die Leistungsfähigkeit der Anlage ist ihr zeitliches und geometrisches Auflösungsvermögen. Das zeitliche Auflösungsvermögen liegt in der Grössenordnung der für ein Bildsegment erforderlichen Belichtungszeit, die bei dieser Anlage etwa 1 sec beträgt, d.h. Strukturänderungen, die rascher ablaufen, können nicht mehr getrennt registriert werden. Eine Erhöhung der Zeitauflösung ist ohne Schwierigkeit durch Verwendung elektronenoptischer Hilfsmittel möglich.

Das für die feinstrukturelle Aufnahme ausgedehnter, zeitlich konstanter Objekte wesentliche geometrische Auflösungsvermögen wird bei der beschriebenen Anordnung durch den Durchmesser des Primärstrahls in der Objektebene begrenzt und liegt bei 50μ. Durch Verwendung einer Feinstrahlsonde kann auch dieses wesentlich erhöht werden.

Ergebnisse

1. *Zeitdiagramme*

In Fortführung älterer Untersuchungen [11] wurde der Diffusionsvorgang in dünnen AgAl-Aufdampfschichten untersucht. Diese wurden durch quantitative Verdampfung entsprechender Legierungen hergestellt. Infolge der unterschiedlichen Dampfdrucke beider Legierungskomponenten entsteht im Kondensat eine Disproportionierung, die bei dessen Erwärmung durch Diffusionsausgleich verschwindet.

In Abb. 5 ist das kinematische Diagramm einer Schicht aus der Ausgangslegierung AgAl 88/12 wiedergegeben; während der Aufnahme wurde bis zu 350°C erwärmt und dann auf 200°C abgekühlt. Bei ungefähr 300°C vollzieht sich die Umwandlung der α-in die β' (Ag_3Al)-Phase. Aus der Umwandlungsgeschwindigkeit lassen sich Rückschlüsse auf die Grösse der Diffusionskonstanten innerhalb des Systems ziehen, ausserdem scheint die ausschliessliche Ausbildung der β'-Phase die Existenz eines endlichen Homogenitätsbereiches dieser Phase wahrscheinlich zu machen. Da Ag_3Al einer Al-Konzentration von ungefähr 8 Gewichtsprozent entspricht und die Ausbildung der β'-Phase bei einer Ausgangslegierung von 88/12 erfolgte, kann auf unterschiedliche Kondensationsbedingungen der beiden Komponenten geschlossen werden.

Als weiteres Beispiel sei in Abb. 6 die Aufnahme eines CuSb 65/35-Präparates bei Temperung bis zu 670°C gezeigt. Oberhalb des Diagramms sind die Bereiche markiert, in denen die einzelnen Phasen auftreten. Die Phasenausbildung erfolgt hier langsamer als in Abb. 5. Interessant ist die unmittelbar zu erkennende Änderung der Gitterkonstanten der β'-Phase mit der Temperatur. Während der Abkühlung wird das Gefüge so

grobkristallin, dass nur noch wenige Kristallite durchstrahlt und dadurch die Debye-Scherrer-Ringe in Punkte aufgelöst werden, wie das Teilstück eines normalen Diagramms ganz rechts in Abb. 6 zeigt. Dies führt zu unsymmetrischem Verschwinden der Reflexlinien im kinematischen Diagramm, wie es in dessen nicht identifiziertem Teil zu erkennen ist. Ausgeprägte Texturen rufen ähnliche Erscheinungen hervor.

Neuerdings wurde diese Methode auch von Trillat [12] übernommen, der eine Aufnahme aus dem System CuAl wiedergibt.

In besonders übersichtlicher Weise lässt das Verfahren den Ablauf von Phasenumwandlungen in Abhängigkeit von der Temperatur erkennen. Als Beispiel sei hier die Phasenumwandlung der Verbindung Ag_2S bei Erwärmung gegeben. Die Untersuchungen wurden an synthetischem Ag_2S durchgeführt.

Nach älteren Untersuchungen von Emmons, Stockwell und Jones [13], Palacios und Salvia [14] u.a. hat Ag_2S bei Zimmertemperatur rhombisch fl.z.Struktur und wandelt sich bei 180°C in die kubisch r.z. Hochtemperaturform um. Bei Abkühlung erfolgt wieder Rückumwandlung bei180°C in die rhombische Tieftemperaturphase.

Abb. 7 zeigt die Aufnahme der Phasenumwandlung des Ag_2S bei der Erwärmung. Bei Zimmertemperatur lassen sich die Reflexe in Übereinstimmung mit den von Glocker [15] angegebenen Gitterkonstanten (a = 4,77 Å, b = 6,92 Å, c = 6,99 Å) rhombisch indizieren. Bei 180°C verschwinden die meisten Reflexe, es bleiben nur diejenigen des kubisch r.z. Gitters erhalten (a = 4,88 Å). Darüber hinaus zeigt die Aufnahme bei genauer Auswertung, dass die ursprünglich rhombische Tieftemperaturphase bei der Erwärmung bis zur Umwandlungstemperatur langsam tetragonal wird. Dies tritt unmittelbar in Erscheinung bei den Reflexen des Typs $(hkl)(hlk)$, die sich während der Erwärmung einander nähern und kurz vor der Umwandlungstemperatur von 180°C zu einem

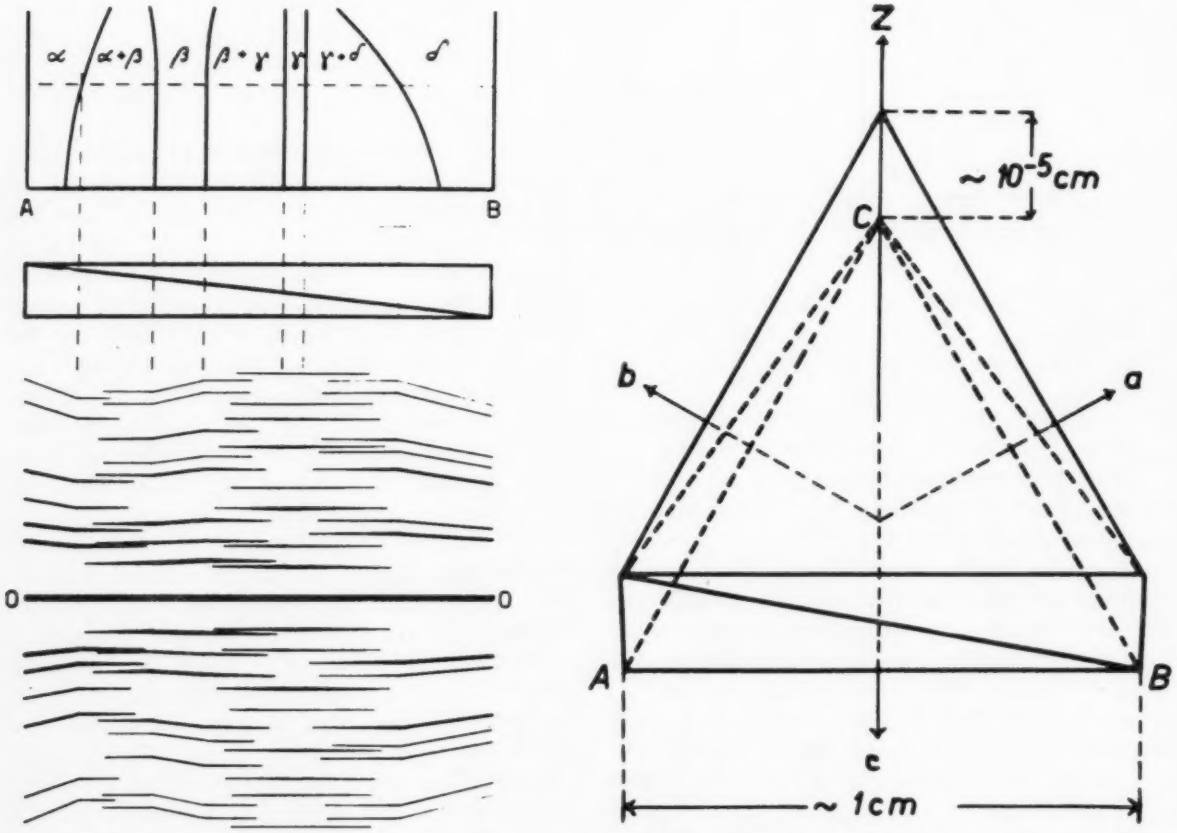

ABB. 8. Schema einer Keilaufdampfung zur Untersuchung von Zustandsdiagrammen. *Links* für Zweistoffsysteme: oben: Zustandsdiagramm, mitte: Schnitt des undiffundierten Präparates, unten: Schema einer Aufnahme. *Rechts* für Dreistoffsysteme. Lage der aufgedampften Komponenten im Präparat.

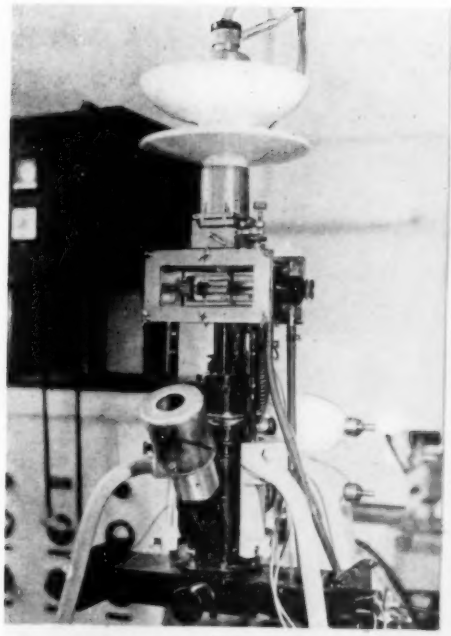

3

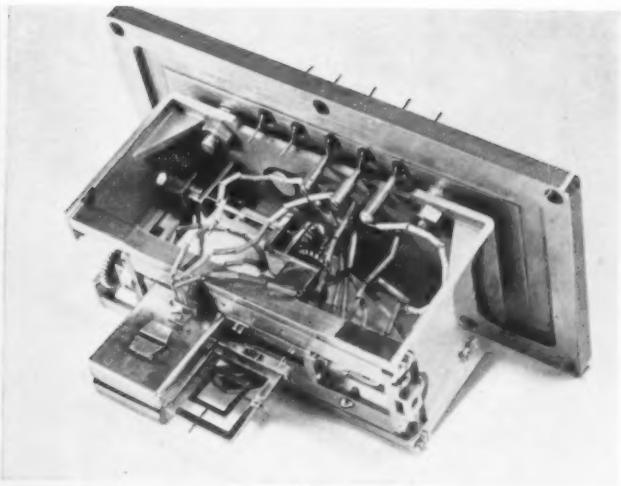

4

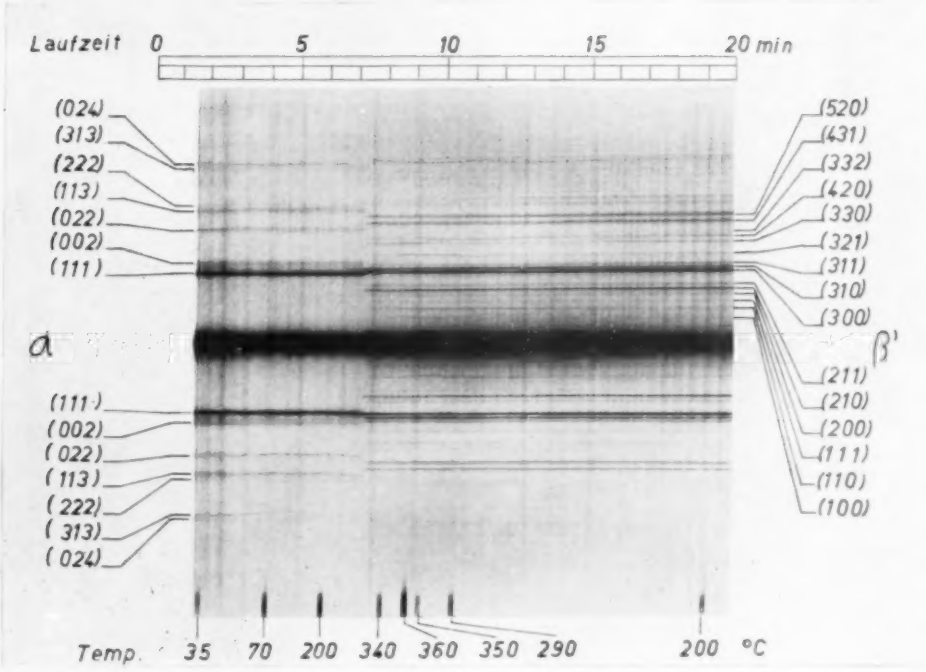

5

PLATE 1. ABB. 3—Ansicht der kin. Beugungsanlage. ABB. 4—Objektschlitten mit Ofen. ABB. 5—Kinematisches Diagramm von AgAl 88/12. Strahlspannung 76 kV. Temperatur 20–350–200°C.

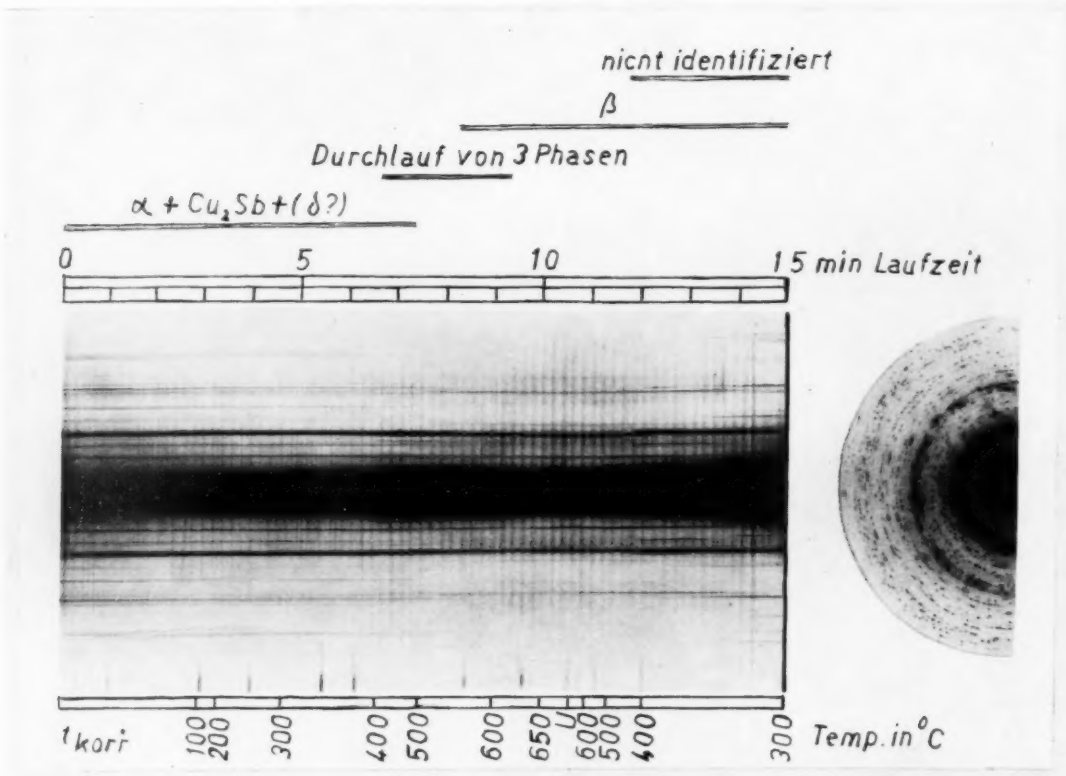

6

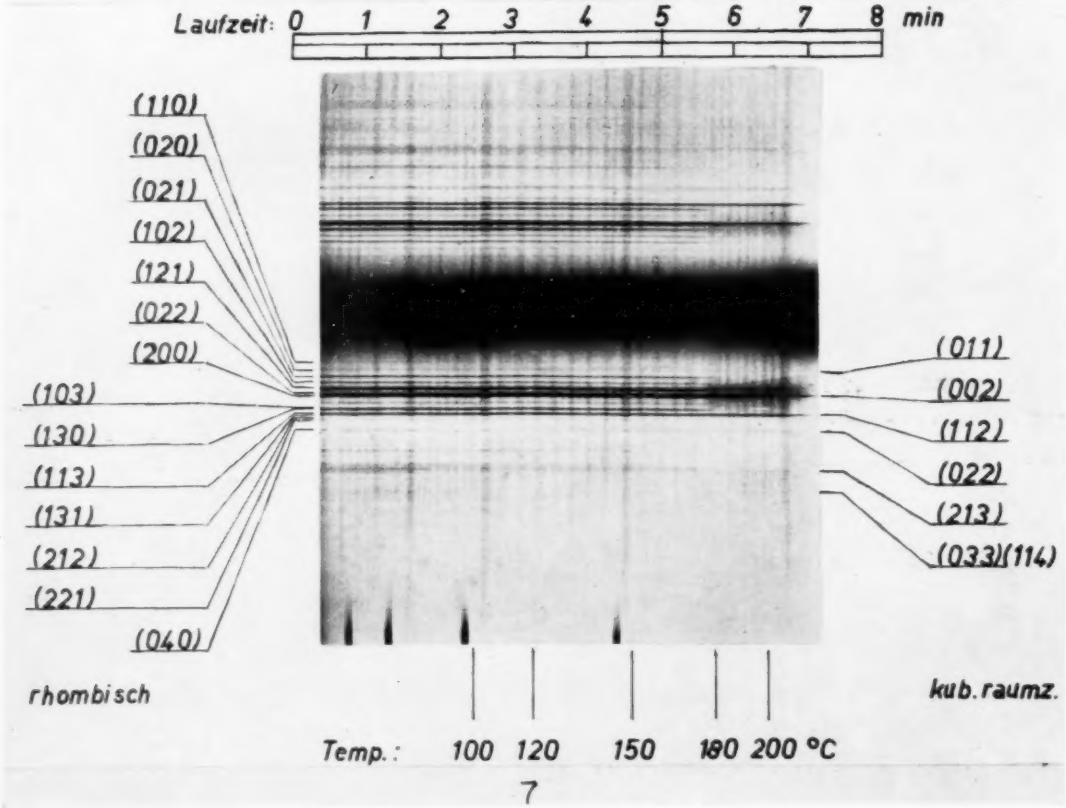

7

PLATE II. ABB. 6—Kinematisches Diagramm von CuSb 65/35. Strahlspannung 71 kV. Temperatur 20–670–300°C.
ABB. 7— Kinematisches Diagramm von Ag_2S. Strahlspannung 74 kV. Temperatur 100–220°C.

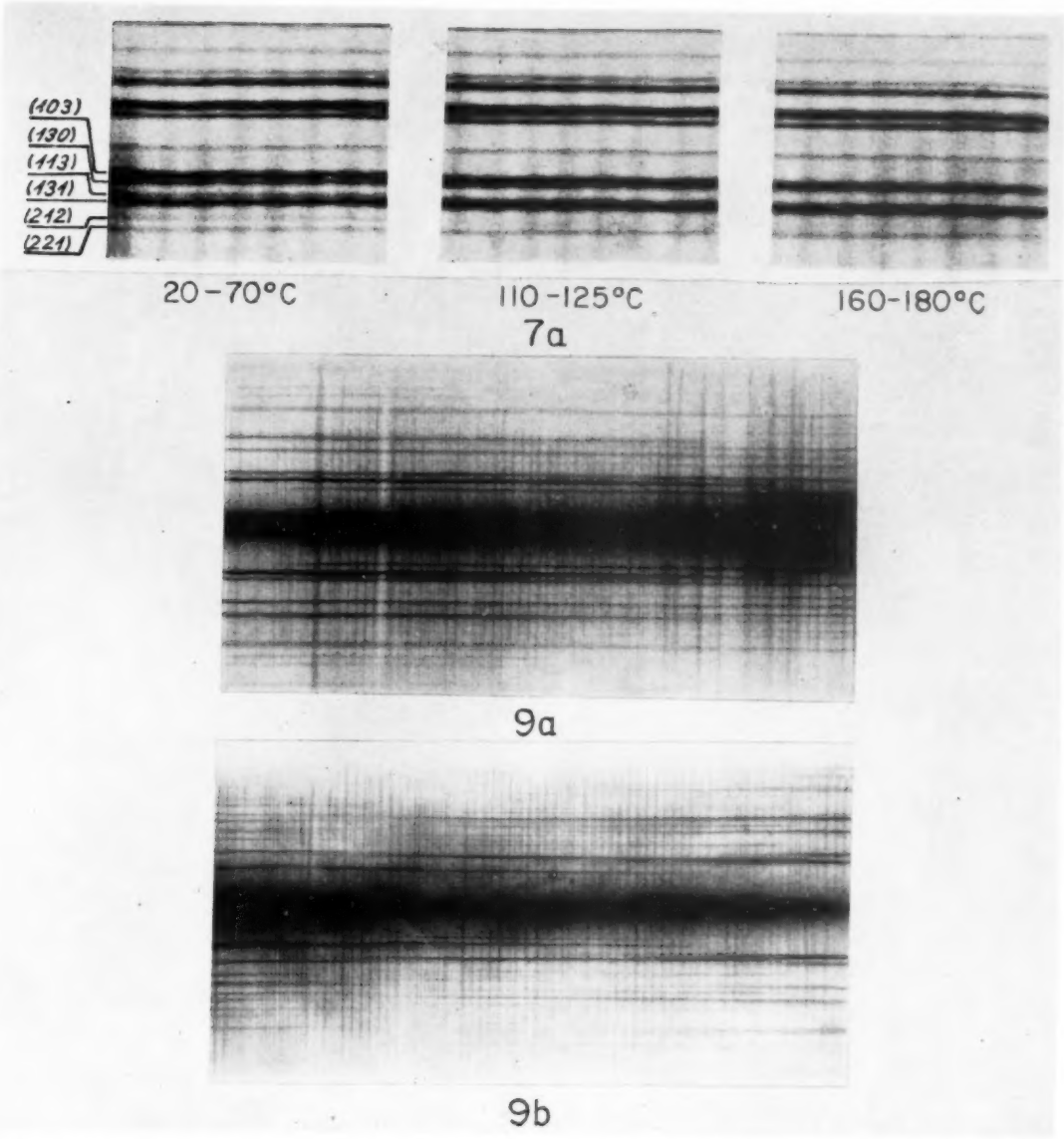

PLATE III. ABB. 7a—Ag_2S Phasenübergänge (Teilvergrösserung). ABB. 9—Kinematisches Diagramm eines Au-Sn-Keilpräparates: (*a*) undiffundiert; (*b*) diffundiert.

einzigen Reflex vereinigen. Wegen des geringen Unterschiedes der *b*- und *c*-Achsen liegen diese Reflexe dicht benachbart, so dass diese Einzelheit in Abb. 7 schwer zu erkennen ist.

Abb. 7*a* zeigt eine Ausschnittsvergrösserung dieser Aufnahme aus den Temperaturbereichen 20 bis 70°C, 110 bis 125°C und 160 bis 180°C, auf der die Annäherung der Reflexe (103)(130), (113)(131) und (212)(221) erkennbar ist. Der gleichmässige Verlauf dieser Änderung der Gitterkonstanten mit der Temperatur legt es nahe, hier nicht von einer Phasenumwandlung zu sprechen, sondern von einer Erhöhung der Gittersymmetrie durch anisotrope Wärmeausdehnung. Der bei etwa 180°C erfolgende Übergang der tetragonalen zur kubisch r.z. Hochtemperaturphase verläuft ungleich schneller.

Die vorliegenden Aufnahmen lassen jedoch eindeutig erkennen, dass auch hier die Umwandlung im einzelnen Gitterbereich keine spontane ist, sondern in schnellem Ablauf über intermediäre Gitterzustände erfolgt. Einzelheiten hierüber werden an anderer Stelle veröffentlicht werden.

2. *Flächendiagramm*

Alle bisher gezeigten Aufnahmen waren Temperaturdiagramme, die von einem Objektpunkt bei feststehendem Präparat gemacht wurden.

Interessante Möglichkeiten bietet indessen auch das bei bewegtem Objekt aufgenommene "Flächendiagramm", welches die geometrische Verteilung der Strukturen im Objekt wiedergibt. Ein Beispiel hierfür ist ein besonders einfaches Verfahren zur schnellen Aufklärung von Zwei- und Dreistoffsystemen. Zur Herstellung geeigneter Präparate werden die Komponenten des zu untersuchenden Systems entsprechend Abb. 8 als gegenläufige oder um je 120° gedrehte Keile übereinander gedampft. Tempert man ein derartiges Präparat, so wird der Diffusionsausgleich senkrecht zur Objektfläche schnell erfolgen, da hier nur Diffusionswege von höchstens einigen hundert ÅE zur Einstellung des Gleichgewichts notwendig sind. In der dafür benötigten Zeit ist der Ausgleich innerhalb der einige mm ausgedehnten Fläche zu vernachlässigen.

Man hat nun an jedem Flächenpunkt des Präparates ein Konzentrationsverhältnis der Komponenten, welches allein aus der Geometrie der aufgedampften Keile folgt. Für eine quantitative Indentifizierung ist eine Bestimmung der Keildicken erforderlich, die am einfachsten nach der Methode der Mehrfachinterferenzen von Tolansky [16; 17] erfolgt. Das vollständige Zustandsdiagramm gewinnt man durch mehrere Aufnahmen bei verschiedenen konstanten Temperaturen, nachdem jedesmal das Erreichen des Gleichgewichtszustandes abgewartet wurde. Die Aufnahme eines solchen Keilpräparates von Au und Sn vor und nach dem Diffusionsausgleich ist in Abb. 9 wiedergegeben. Da dieses Verfahren gegenüber den bisher bekannten röntgenographischen Methoden die vollständige Strukturanalyse eines Systems mit sehr viel geringerem Arbeits- und Zeitaufwand ermöglicht, wird seine Weiterentwicklung in einer zurzeit noch nicht abgeschlossenen Untersuchung besonders gefördert.

Literatur

1. RÖSLER, U. und RUFF, W. La metallurgia italiana n. 8–9 (1952) 475/87.
2. BOETTCHER, A. und THUN, R. D. Patentanmeldung **B26** 429 IX b/42 k vom 9.7.1953.
3. SCHALL, R. Z. f. angew. Phys. **2** (1950) 83/88.
4. KOSSEL, W. und MÖLLENSTEDT, G. Optik **1** (1946) 163.
5. MÖLLENSTEDT, G. Phys. Bl. **3** (1947) 201.
6. MÖLLENSTEDT, G. Optik **3** (1948) 68/74.
7. BOETTCHER, A. D.P. 845 275 vom 7.9.1949.
8. BOETTCHER, A. und THUN, R. Physikalische Verhandl. **3** (1952) 115.
9. BOETTCHER, A. und THUN, R. Optik 11 (1954) 22/31.
10. BOETTCHER, A. Vorgetragen in Bad Neuenahr, Jahreshauptversammlung der Deutschen Gesellschaft für Metallkunde 2–5.10.52.
11. BOETTCHER, A. Z. f. angew. Phys. **2** (1950) 193/203.
12. TRILLAT, J. J. und TAKAHASHI, N. Extrait des Comptes rendus des séances de l'Académie des Sciences **236**, 790–792, séance du 23 février 1953.
13. EMMONS, STOCKWELL und JONES. Am. Miniral. **11** (1926) 326.
14. PALACIOS und SALVIA. An. Soc. Esp. Fisica Quim. **29** (1931) 269.
15. GLOCKER, R. Materialprüfung mit Röntgenstrahlen (Springer Verlag 1949) 248.
16. TOLANSKY, S. Multiple Beam Interferometry (Oxford, Clarendon Press, 1948).
17. MCLAUCHLAN, A., SCOTT, G. D., und SENNET, R. S. J. Appl. Phys. **21** (1956) 843/46.

RECHERCHES EXPÉRIMENTALES SUR LA MICROSTRUCTURE DE LA SOLUTION SOLIDE CUIVRE-ZINC 65/35 POLYCRISTALLINE TRÈS FAIBLEMENT DÉFORMÉE PAR TRACTION ET SUR SON ÉVOLUTION AU RECUIT ENTRE 200 ET 600°C.*

P. A. JACQUET†

I. En vue de l'interprétation des mécanismes des processus de déformation plastique, de restauration, de polygonisation et de recristallisation, il est d'un grand intérêt de pouvoir suivre avec la micrographie, et parallèlement aux diagrammes de rayons X, l'évolution de la microstructure d'un métal en fonction de l'intensité de la déformation, puis au cours de traitements thermiques variés.

Si l'on admet, conformément à l'opinion actuelle, que les rassemblements de certaines dislocations dans le réseau d'un métal pur ou d'une solution solide homogène constituent des domaines d'attaque priviligiée, il devient possible d'envisager de localiser ces défauts, et, par suite, de suivre leur évolution sous l'effet des traitements mécaniques et thermiques.

En fait, les méthodes jusqu'ici utilisées n'ont donné que des renseignements partiels dont les plus évidents concernent les sous-joints de polygonisation typique. Pour tenter d'améliorer ces résultats il est indispensable de disposer d'une technique d'attaque extrêmement sélective, sensible et fidèle.

Le présent travail expose les détails d'une telle méthode adaptée au cas particulier de la solution solide α cuivre-zinc à 35% de zinc, et donne les premiers résultats obtenus avec des éprouvettes soumises à une très minime déformation plastique, puis chauffées entre 200 et 600°. Cette technique, d'une grande simplicité, convient pour la micrographie optique et pour les empreintes de micrographie électronique. Elle a permis déjà de mettre en évidence les glissements dans les grains à l'intérieur de l'éprouvette, et l'évolution ultérieure de la microstructure au cours du recuit, jusqu'au stade final de la polygonisation typique. On est donc en droit d'invoquer son emploi dans les études sur le fluage et la fatigue du laiton α, phénomènes jusqu'à présent peu accessibles par la micrographie, et dont les mécanismes font intervenir la dynamique des dislocations.

EXPERIMENTAL RESEARCH ON THE MICROSTRUCTURE OF THE POLYCRYSTALLINE SOLID SOLUTION COPPER-ZINC 65/35 VERY SLIGHTLY DEFORMED IN TENSION, AND ITS EVOLUTION DURING ANNEALING BETWEEN 200° AND 600°C.

In order to interpret the mechanisms of the processes of plastic deformation, recovery, polygonization and recrystallization, it is of great interest to be able to follow the evolution of the microstructure of a metal, as a function of the degree of deformation and subsequently during various heat treatments, using simultaneously micrographic and X-ray techniques.

Assuming that, as presently believed, accumulations of certain dislocations in the lattice of a pure metal or of a homogeneous solid solution constitute preferred regions of easy etching, one can consider the possibility of localizing such imperfections and subsequently of following their evolution under the effect of mechanical and heat treatments. In fact, the previously used methods gave only partial information, of which the most evident are concerned with typical polygonization sub-boundaries. In order to improve those results it is necessary to use a highly selective, sensitive and accurate etching technique. In the present work, the details of such a method are given. The method has been adapted to the particular case of the α copper-zinc solid solution containing 35 per cent Zn. The first results obtained on specimens, which were very slightly plastically deformed and then heated between 200° and 600°, are given. The technique is very simple and is suitable for both optical micrography and electron microscope replicas. It has already shown glide in the grains inside the specimen, and the subsequent evolution of the microstructure during annealing, up to the end of the typical polygonization. It is, therefore, expected that this method will enable one to study creep and fatigue in α brass, both of which involve the dynamics of dislocations and were, so far, hardly accessible to investigations by micrographic methods.

EXPERIMENTELLE UNTERSUCHUNGEN ZUR FEINSTRUKTUR EINER POLYKRISTALLINEN FESTEN KUPFER-ZINK LÖSUNG (65/35), DIE EINER SEHR GERINGEN ZUGVERFORMUNG UNTERWORFEN WAR, UND ZUR AUSBILDUNG DIESER STRUKTUR BEIM GLÜHEN ZWISCHEN 200 UND 600°C.

Wenn man die Elementarprozesse der plastischen Verformung, der Erholung, der Polygonisation und der Rekristallisation deuten will, so ist es von grossem Interesse, die Ausbildung der Feinstruktur eines Metalles als Funktion des Deformationsgrades und während verschiedenartiger nachfolgender Wärmebehandlungen gleichzeitig metallographisch und röntgenographisch verfolgen zu können.

Wenn man, wie z.Z. allgemein üblich, annimmt, dass die Aggregationen gewisser Versetzungen im Gitter reiner Metalle oder homogener fester Lösungen die beim Ätzen bevorzugt angegriffenen Stellen darstellen, dann sollte es möglich sein, solche Fehlstellen zu lokalisieren und dann ihre Entwicklung unter der Wirkung von mechanischen Einflüssen und Wärmebehandlung zu verfolgen.

In der Tat haben die bisher benutzten Verfahren nur unvollständige Informationen gegeben—die klarsten Angaben betrafen die typischen Polygonisations-subkorngrenzen. Um diese Resultate zu verbessern ist es notwendig, ein sehr selektives, empfindliches und genaues Ätzverfahren zu verwenden.

Die vorliegende Arbeit berichtet die Einzelheiten eines solchen Verfahrens, das speziell auf den Fall einer festen Lösung von Kupfer-Zink mit 35% Zink angewandt wurde. Die ersten Ergebnisse

*Received February 25, 1954.

†Ingénieur Contractuel des Constructions et Armes Navales; Marine Nationale, Paris, France.

an geringfügig verformten und zwischen 200 und 600°C geglühten Proben werden angegeben. Dieses sehr einfache Verfahren kann sowohl auf Proben für Lichtmikroskopie als auch auf Abdrücke für Elektronenmikroskopie angewandt werden. Mit Hilfe dieses Verfahrens war es bereits möglich, Gleitung in Kristalliten im Zentrum der Proben und die darauf folgende Ausbildung einer Feinstruktur beim Glühen bis zum Ende des typischen Polygonisationsstadiums zu zeigen.

Auf Grund dieser Ergebnisse kann man annehmen, dass man mit Hilfe dieses Verfahrens Kriech- und Ermüdungserscheinungen im Messing, die man bisher optisch kaum untersuchen konnte, und mit denen dynamische Versetzungsvorgänge verbunden sind, untersuchen kann.

Introduction

Le polissage électrolytique que nous avions préconisé dès 1935 pour la préparation des spécimens métallographiques [1] a contribué aux substantiels progrès de la physique des métaux durant ces dernières années [2], par exemple dans les domaines de la déformation plastique et de la recristallisation. En particulier il a permis de reconnaitre avec le microscope le phénomène de la polygonisation dans les gros cristaux métalliques que révélent d'autre part les diagrammes de rayons X [3], et d'étudier ses relations avec d'autres processus [4].

Parfois le polissage électrolytique n'intervient que comme une méthode de finition permettant d'obtenir une surface de haut degré de poli, privée de toute trace des perturbations structurales que produisent immanquablement les procédés mécaniques habituels. Dans d'autres cas le polissage seul n'est pas suffisant, et il doit être suivi d'une attaque destinée à révéler les détails de la microstructure, dont on est ainsi certain qu'elle est bien spécifique du spécimen. Les conditions d'une telle attaque sont elles-mêmes très importantes et doivent, par conséquent, être adaptées à chaque cas particulier, ce qui n'est pas sans laisser trop souvent une large part à l'empirisme.

La présente étude montrera que précisément dans le domaine de la déformation plastique et de la polygonisation une technique micrographique spéciale est susceptible de faire apparaitre des phénomènes qui échappent complètement à l'observation avec les méthodes classiques.

Notre but initial était d'essayer d'apporter une réponse précise à la question suivante encore controversée [5]. Existe-t-il dans la masse d'une éprouvette soumise à une très faible traction des modifications de la microstructure qui traduisent le déformation révélée par les lignes de glissement sur la surface préalablement polie?

Une étude antérieure sur le cuivre [6], et les travaux plus récents de McLean [7] et de Ogilvie [8] sur les laitons, ont prouvé qu'avec une méthode d'attaque assez sensible les traces des glissements se retrouvent sous forme de stries encore loin sous la surface. Certaines de ces expériences ont provoqué des critiques [9], qui, d'ailleurs, ne nous paraissent pas fondées. Cependant on peut objecter que les résultats se rapportent à des spécimens assez fortement déformés. Or il est bien évident que dès le moment où l'écrouissage devient assez considérable pour modifier les propriétés physiques et physicochimiques du métal, l'effet se traduira sur sa structure. De plus, les conditions de l'examen doivent éliminer toute possibilité de déformations parasites, ce qui exige de grandes précautions qui ne paraissent par avoir été toujours respectées.

Nous avons eu également l'occasion d'étudier le cas particulier des déformations produites par l'abrasion et le polissage mécanique des alliages cuivreux, du fer et des aciers [2; 10; 11]. Les perturbations du réseau cristallographique s'étendent alors parfois à une grande distance sous la surface, mais les nombreux facteurs qui interviennent ne permettent pas encore de déduire du seul aspect micrographique le détail des processus en cause.

Ces dernières recherches ont eu cependant l'avantage de faire apparaitre l'extrême sensibilité de la méthode d'attaque employée pour les laitons α, puisqu'elle s'est révélée capable de déceler des traces infimes de déformation plastique qui ne sont pas visibles sur les diagrammes de rayons X.

Aussi avons nous songé à utiliser cette méthode dans le cas beaucoup plus simple d'une déformation par traction sous faibles charges. La netteté des résultats obtenus nous a ensuite incité à examiner de la même façon les effets des traitements thermiques sur la microstructure des éprouvettes préalablement déformées, avec l'espoir d'apporter une contribution expérimentale à l'importante question du mécanisme de la polygonisation et de ses relations éventuelles avec la restauration et la recristallisation.

Comme on le verra, les observations effectuées et les conclusions qui en ont été tirées sont loin d'avoir épuisé les possibilités de la méthode micrographique restreinte au cas particulier d'une solution solide cuivre-zinc polycristalline homogène. Aussi en exposant nos résultats avons nous surtout le désir qu'ils suscitent d'autres expériences

plus complètes et plus systématiques, par exemple dans le domaine de la fatigue et du fluage où l'on peut logiquement s'attendre à rencontrer une évolution structurale justiciable de la technique proposée.

I. Étude de la Déformation Plastique

1. *Méthode Expérimentale*

Nature des spécimens

Quelques essais préliminaires ayant montré que la sensibilité de la méthode micrographique est d'autant meilleure que la teneur en zinc, dans les limites correspondant à la phase α, est plus élevée, on a choisi un alliage titrant 64,5% de cuivre et 35,4% de zinc, avec comme seules impuretés 0,07% de fer, moins de 0,027% de plomb et des traces indosables de silicium, nickel et aluminium.

Les microéprouvettes de traction de 30 mm de longueur entre têtes et 3 mm de largeur sont découpées dans de la planche laminée à froid de 6,9 à 0,9 mm, soit une réduction de 87%. L'examen micrographique ne révèle aucune trace de phase étrangère ni d'inclusions insolubles. Les diagrammes de rayons X confirment l'absence de phase β et donnent une valeur de la maille en accord avec la composition établie par l'analyse chimique.

Traitement avant déformation

Après que ses deux faces ont été rendues bien planes chaque éprouvette est placée entre deux plaquettes du même alliage et recuite à 600 ± 10°C dans un four à air. Le refroidissement s'effectue dans le four lui-même. La mince pellicule d'oxyde est éliminée dans l'acide phosphorique à 10%. On procède ensuite au polissage électrolytique avec la méthode habituelle [6], c'est-à-dire dans une solution aqueuse concentrée d'acide phosphorique de densité 1, 4, pendant une durée de 60 minutes. La micrographie montre que la surface est privée de toute couche d'oxydation interne, et que les grains ont une taille moyenne comprise entre 0,05 et 0,1 mm.

Bien entendu toutes les précautions sont prises pour que pendant les manipulations l'éprouvette ne puisse subir aucune déformation.

Conditions de la déformation

Pour les charges inférieures à 3 kg/mm² la traction est faite sur un appareil très simple construit au laboratoire. Une micromachine Amsler avec enregistrement de la courbe effort-allongement est utilisée pour les charges plus élevées.

Les lignes de glissement sont détectées par l'examen sous le microscope de la surface aussitôt après la traction. La méthode du contraste interférentiel en lumière polarisée de Nomarski [12] rend aisée l'exploration rapide de toute la superficie.

Méthode d'attaque [13]

L'attaque est effectuée d'abord sur l'éprouvette qui vient de subir la traction, puis après des polissages électrolytiques successifs de façon à dissoudre des épaisseurs croissantes de l'alliage.

L'éprouvette placée verticalement joue le rôle d'anode dans une solution à 18–20°C d'hyposulfite de sodium à 0,2%, sous une densité de courant de 1,5 A/dm² pendant 60 secondes. La cathode est une plaquette d'acier inoxydable 18/8 disposée à 20 mm de l'anode.

Chaque attaque s'effectue rigoureusement dans les mêmes conditions et exige un électrolyte fraichement préparé. Ici encore on prend les plus grandes précautions pour éviter la moindre déformation des spécimens. Ce mode d'attaque produit toujours une pellicule solide de composés sulfurés, de composition exacte inconnue, dont la couleur apparemment uniforme présente en réalité sous le microscope les teintes d'interférence des lames minces, en relation, ainsi que nous le verrons, avec la structure du support.

Si cette pellicule solide est dissoute par immersion de une seconde dans l'acide chlorhydrique concentré l'aspect observé au microscope dépend de l'état de l'éprouvette. En l'absence de toute déformation plastique seuls sont visibles les joints de grains et de macles, l'examen sous les plus forts grossissements optiques jusqu'à 2000 diamètres, ne révélant qu'une attaque homogène non résolue de la matrice. En revanche, des domaines de dissolution sélective apparaissent à l'intérieur des grains pour lesquels l'effort de traction a atteint la limite d'élasticité. C'est sur ces effets spécifiques que repose précisément l'intérêt de la technique d'attaque anodique.

Micrographie électronique

Grâce à l'obligeance de MM. M. Mathieu et R. Castaing* certains de nos spécimens ont pu être examinés au microscope électronique par M. Baillie. La méthode utilisée est celle de la double empreinte [14] consistant à déposer sur la surface attaquée une mince pellicule d'aluminium qui est ensuite oxydée anodiquement.

*Département des Matériaux de l'Office National d'Études et Recherches Aéronautiques (O.N.E.R.A.)

Examens aux rayons X

Nos éprouvettes ont été examinées aux rayons X par Madame A. R. Weill. Les diagrammes sont pris chaque fois sur un même point, au centre de la partie utile, d'abord avant toute déformation, puis après traction sous des charges croissantes.

La méthode utilisée est celle des diagrammes en retour avec une anticathode de cobalt, une tension de 30 kV et un débit de 3 m A. Le collimateur mesure, 0,6 mm et la distance film-échantillon est de 55 mm.

2. *Résultats*

Observations micrographiques

Après la traction sous différentes charges comprises entre 1 et 4 kg/mm² l'examen de la surface indique qu'au-dessous de 2,5–2,9 kg/mm² les lignes de glissement sont limitées à quelques uns seulement des grains dans la partie utile de l'éprouvette, et ces lignes sont d'autant moins fréquentes que la charge est plus faible. A partir de 3–3,5 kg/mm² les glissements intéressent tous les grains et comportent en général deux, et même trois, systèmes d'orientation. En continuant à augmenter la charge le début de l'allongement mesurable se situe autour de 3,6–3,8 kg/mm².

Dans l'étude de la microstructure on a choisi trois éprouvettes chargées respectivement sous 1 kg/mm² (éprouvette N° 1)–3 kg/mm² (éprouvette N° 2) et 3,8 kg/mm² (éprouvette N° 3). Leurs états de déformation globale appréciés par la densité des lignes de glissement, étaient respectivement, pratiquement nul, net et assez considérable. Il est à remarquer que pour l'éprouvette N° 3, où l'allongement était à peine mesurable la surface polie est restée très plane, sans le moindre indice de la "peau de crapaud" qui se manifeste si aisément à l'essai de traction au delà de la limite d'élasticité.

Nous décrirons d'abord les résultats relatifs à l'éprouvette N° 2 qui a donné lieu à l'étude la plus systématique. L'exploration de toute la partie utile, après la traction, puis après l'attaque anodique, et enfin après dissolution du film coloré, conduit aux observations suivantes:

1°. La pellicule solide présente sur chaque grain une coloration spécifique, c'est-à-dire que son épaisseur dépend de l'orientation cristallographique, exactement comme dans les autres cas bien connus en métallographie (sulfure et oxyde sur le cuivre, oxyde sur l'aluminium, sur le fer et sur la solution solide nickel-chrome, etc.)

D'une façon générale la couleur est très uniforme sur chaque grain, sauf quelques indices de variations locales dont un exemple est visible, sous forme de domaines triangulaires plus contrastés, dans le grain 1 vers ses voisins 2 et 6 (figure 1). Nous verrons que ce phénomène d'hétérogénéité de coloration prend une importance beaucoup plus grande dans les grains situés à l'intérieur de l'éprouvette.

2°. Les lignes de glissement qui sont très continues à travers tous les grains se couvrent de très petits points plus ou moins espacés, qui sont visibles à la fois par un effet de gravage, et par leur couleur généralement bleu foncé quelle que soit la teinte du grain correspondant.

3°. Après élimination de la pellicule solide les points de dissolution sélective deviennent plus apparents (figures 3 et 4).

4°. On note de notables variations de la densité des points d'attaque d'un grain à un autre et aussi à l'intérieur de chacun d'eux. Bien souvent, cette densité est maximum près des frontières intergranulaires.

5°. Les alignements de points d'attaque existent parfois là où n'apparaissent pas de lignes de glissement. C'est le cas dans le grain 6 où de tels alignements se forment parallèlement à la limite rectiligne de son voisin le grain 5, d'ailleurs en position de macle (cf. figures 1 et 3).

6°. Les joints de grains et de macles sont aussi le siège d'une attaque toujours très continue et relativement profonde (évaluée à 200 Å au moins par la méthode interférentielle de Nomarski).

L'examen au microscope électronique de l'empreinte prise sur la même éprouvette après dissolution du film coloré, c'est-à-dire dans l'état où sont faites les micrographies ordinaires des figures 3 et 4, confirme la nature discontinue des microdomaines de dissolution sélective (figures 5 à 8). On peut voir qu'il s'agit de microfigures de corrosion qui possèdent bien, malgré leur forme plus ou moins irrégulière, la symétrie du cube. D'autre part la matrice présente une sous-structure spécifique du grain considérée, et consistant soit de fibres parallèles très serrées, soit d'une sorte de réseau cellulaire, d'ailleurs moins apparent. Ces deux aspects traduisent très vraisemblablement l'attaque générale de la solution solide donnant naissance à la mince pellicule de composés sulfurés. Il est normal, par conséquent que cette sous-structure soit, comme les microfigures de corrosion, en relation avec l'orientation cristallographique. Par exemple lorsque les domaines d'attaque profonde se présentent en carrés assez bien

formés, deux arrêtes opposées sont parallèles à la direction générale des fibres, tandis que la diagonale correspond à la ligne de glissement, c'est-à-dire que la surface coupe le grain en question suivant un plan voisin de (100).

Le fait que l'on n'observe pas sur les micrographies électroniques les traces des lignes de glissement comprises entre les microfigures de corrosion peut être dû à cette attaque générale régulière de la matrice. Cependant, de telles traces se distinguent sur les micrographies ordinaires, de sorte la véritable explication serait plutôt que les variations de microprofil produites sur la surface par les glissements sont trop faibles pour pouvoir être décelées avec la méthode d'empreinte utilisée.*

D'ailleurs, contrairement à ce qu'on pourrait penser la visibilité des lignes de glissement sous le microscope optique n'implique pas qu'elles s'accompagnent de dénivellations considérables. On sait, par exemple, que les spirales de croissance sur les faces des cristaux sont faciles à observer, même à des grossissements peu élevés, alors que les mesures indiquent des niveaux distants de moins de 50 Å [12].

Les expériences qui viennent d'être décrites prouvent que les stries produites par l'attaque anodique correspondent bien à la dissolution préférentielle de certains domaines très petits et très localisés sur les lignes de glissement. Indépendamment de son intérêt propre qui sera discuté plus loin, ce résultat nous met en possession d'un moyen très sûr pour trancher, au moins dans le cas particulier de l'alliage examiné, la question de la propagation en profondeur des glissements, ou plutôt des perturbations cristallographiques qui y sont liées. Pour cela il suffira de retirer par polissage électrolytique des épaisseurs croissantes à partir de l'état brut de traction, et de soumettre chaque fois la nouvelle surface à une attaque anodique.

Les aspects ainsi obtenus sont tout à fait comparables à ceux qui ont été trouvés sur la surface initiale. L'exploration en profondeur a été pousée jusqu'à 0,30 mm seulement, car au delà l'éprouvette devient trop mince, l'effet de dissolution s'exerçant aussi sur l'autre face, pour pouvoir être manipulée sans risquer de nouvelles déformations.

La figure 9 a montré qu'après dissolution de 0,15 mm les différences entre les caractéristiques d'attaque sur la tête non déformée et sur la partie utile de l'éprouvette sont encore suffisament nettes pour être visibles à l'échelle macrographique.

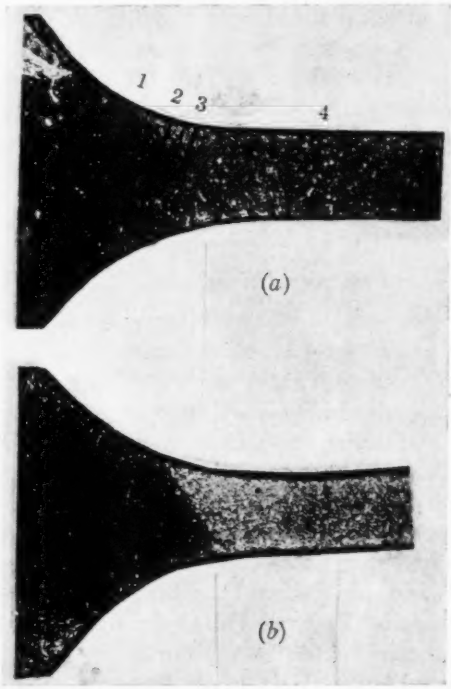

FIGURE 9. Macrographies en éclairage oblique après attaque anodique et dissolution du film coloré. (*a*) Eprouvette N° 2 (traction sous 3 kg/mm²)—Dissolution de 0,15 mm avant l'attaque (×4,5). (*b*) Eprouvette N° 3 (traction sous 3,8 kg/mm²)—Dissolution de 0,23 mm avant l'attaque (×4,5).

Les figures 10 à 13 correspondent aux quatre types de microstructure que l'on peut reconnaitre avant l'enlèvement du film coloré. Sur la tête (région 1 de la figure 9a), où l'alliage est resté à l'état recristallisé initial, les joints sont seuls attaqués, chaque grain présentant une coloration spécifique parfaitement uniforme (figure 10). Sur toute la longueur de la partie utile, à partir d'une petite distance du congé, l'abondance des systèmes de stries traduit l'importance de la déformation plastique; tous les grains présentent sensiblement la même coloration bleue avec des renforcements d'intensité qui dessinent des bandes orientées (figure 11). En se rapprochant du congé les stries deviennent de moins en moins nombreuses, les grains tendent à se différencier par la couleur du film mais les teintes sont très hétérogènes car les bandes transgranulaires sont encore bien marquées (figures 12 et 13).

Après dissolution de la pellicule solide l'explora-

*Dans cette méthode l'épaisseur de la couche d'alumine est constante et les contrastes sur la photographie correspondent à des inclinaisons variables par rapport au faisceau d'électrons, et non pas à des différences d'épaisseur comme c'est le cas avec les empreintes plastiques.

1

2

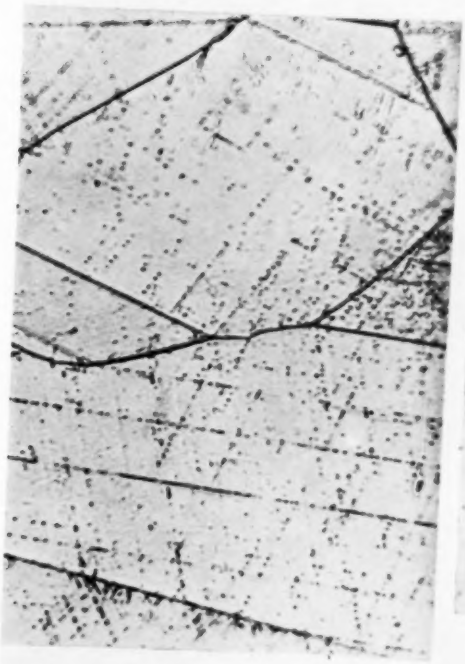

3

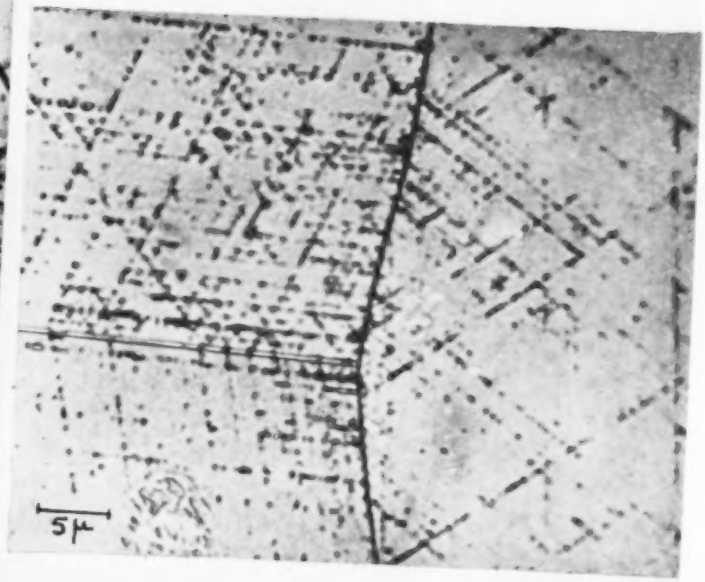

4

PLANCHE 1. Surface de l'éprouvette après traction sous 3 kg/mm². Figures 1, 2, 3—même champ avant attaque, après attaque, après dissoluton du film coloré (1000×). Figure 4—autre endroit dans la même region (2000×). Sur la figure 2 les grains 1 sont colorés en orange, le grain 2 en mauve, les grains 3 en mauve-rose, le grain 5 en jaune et le grain 6 en rose orange: les shies sont bleu-violacé.

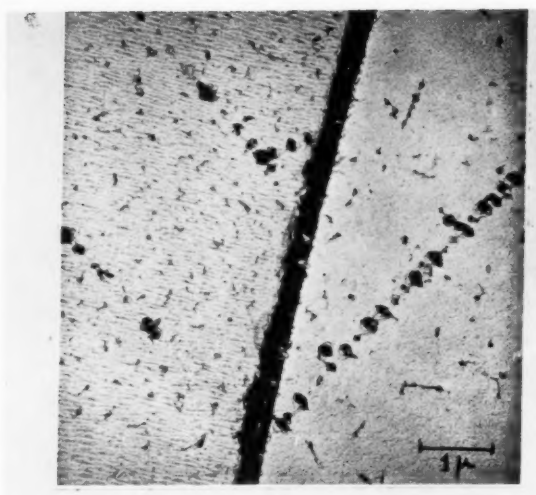

5

6

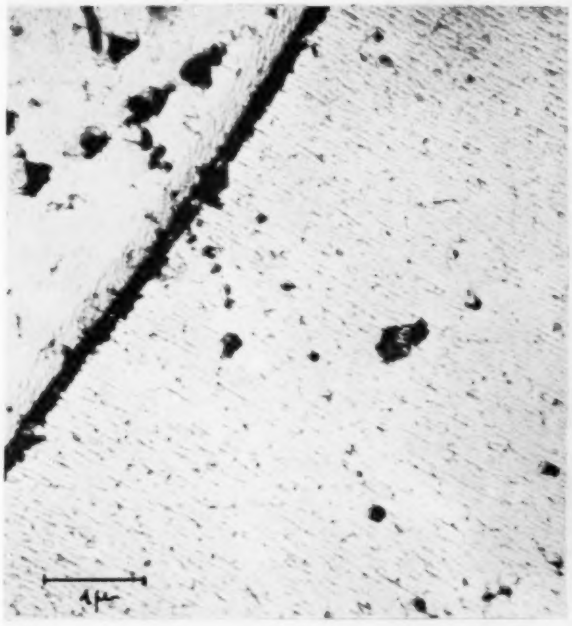

7

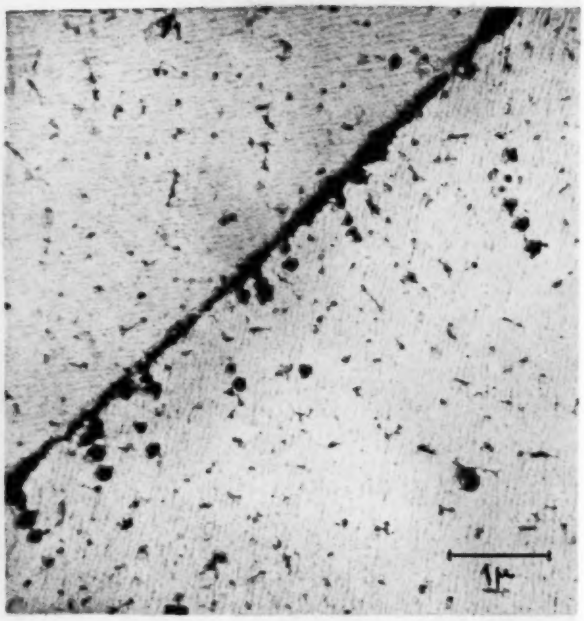

8

PLANCHE II. Quelques exemples de micrographies électroniques de la surface correspondant aux micrographies optiques figures 3 et 4. Figures 5 et 6 (11,000 ×); Figures 7 et 8 (14,800×).

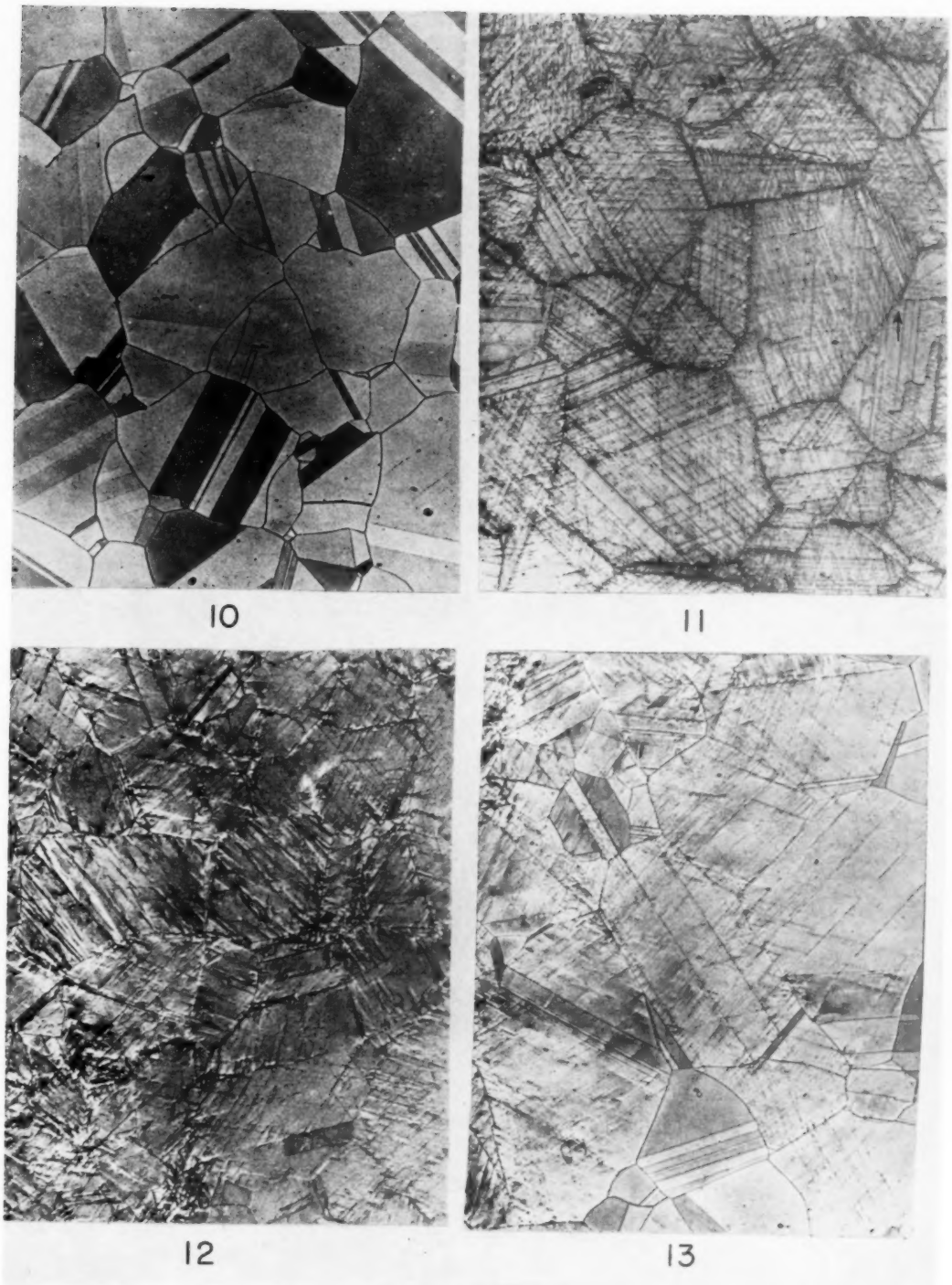

PLANCHE III. Microstructure des différentes régions repérées sur la macrographie. Figure 9*a*. Photographies prises avant dissolution du film coloré. Figure 10—region 1. Figure 11—region 4. Figure 12—region 3. Figure 13—region 2 (160×).

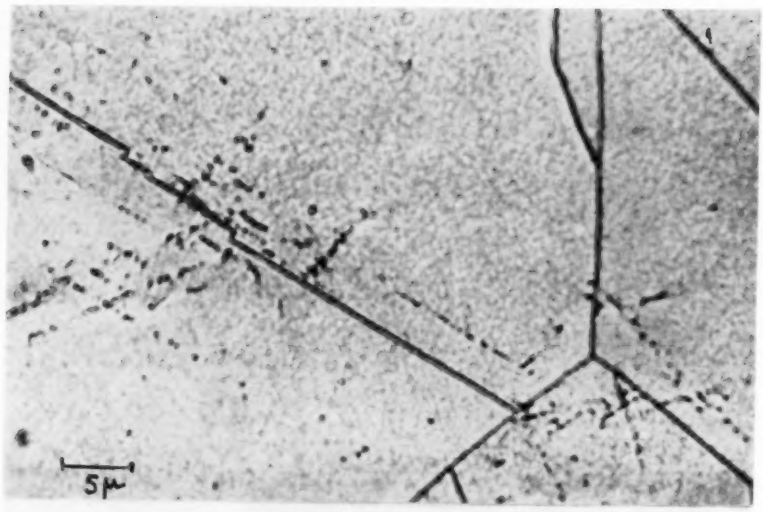

14

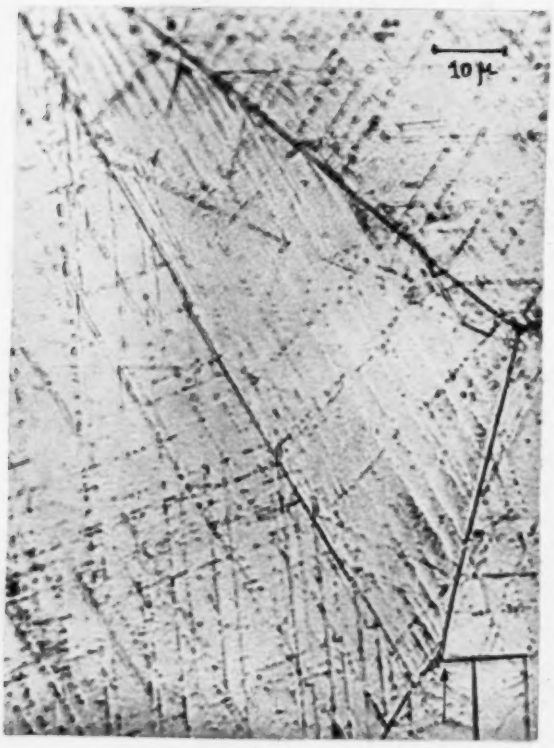

15

PLANCHE IV. Micrographies sur la surface correspondant à la macrographie figure 9*a*. Figure 14—Traces de déformation à la limite des régions 1 et 2 (2000×). Figure 15—Endroit repéré par la flèche sur la figure 11. Remarquer près des limites du grain triangulaire le gravage plus intense correspondant aux bandes de colorations différentielles (1000×).

PLANCHE V. Figure 16—Exemple d'hétérogénéité de la déformation plastique dans un grain. Après la traction de l'éprouvette N° 2, dans la direction correspondant à la hauteur de cette micrographie, la surface est polie pour dissoudre environ 80 microns puis attaquée et immergée 1 seconde dans ClH pour dissoudre le film coloré (2000×).

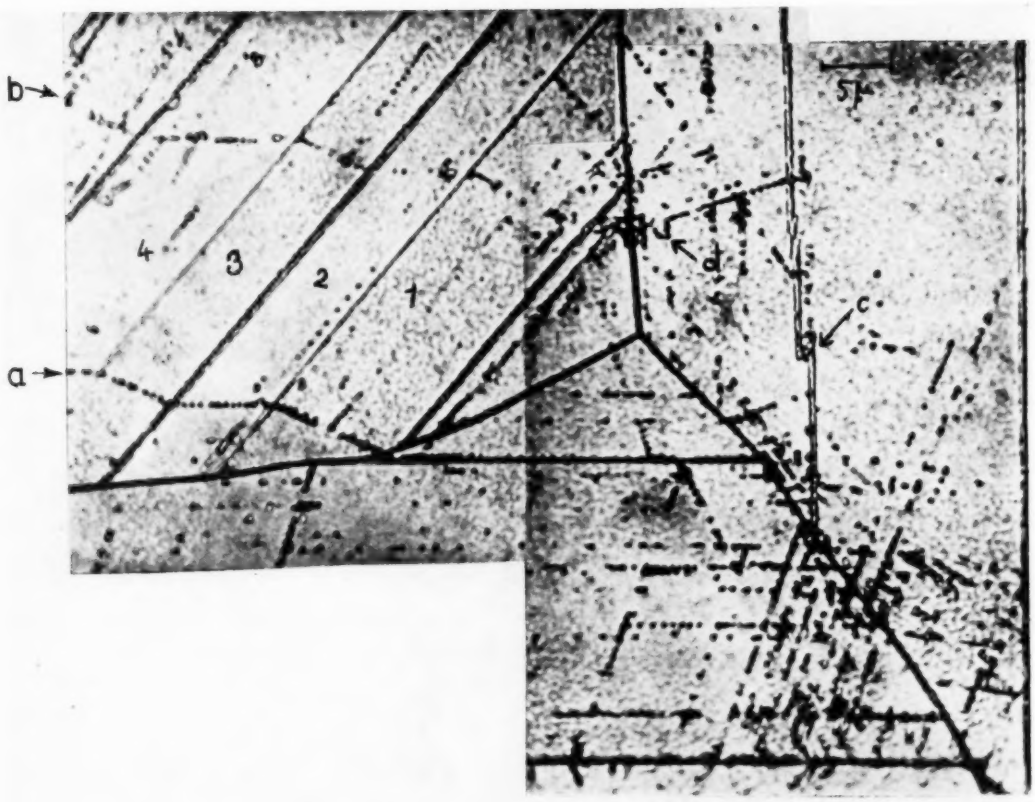

17

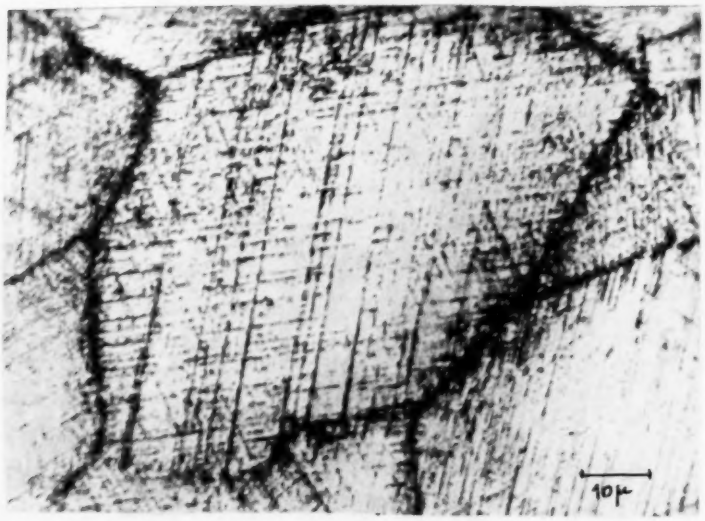

18

PLANCHE VI. Figure 17—Autre endroit du spécimen de la figure 16. *a* et *b*: deux lignes de point d'attaque qui se propagent à travers les macles 1, 2, 3, 4. *c*: décrochement d'un joint de macle donnant naissance à un alignement de points d'attaque. *d*: "cross slip" (2000×). Figure 18—Eprouvette No 3; dissolution de 15 microns après traction sous 3,8 kg/mm². Remarquer le gravage général de la matrice autour des joints intergranulaire (1000X).

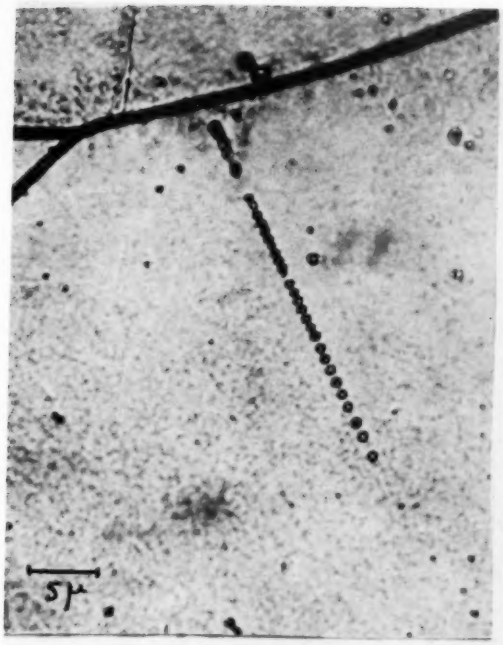

19

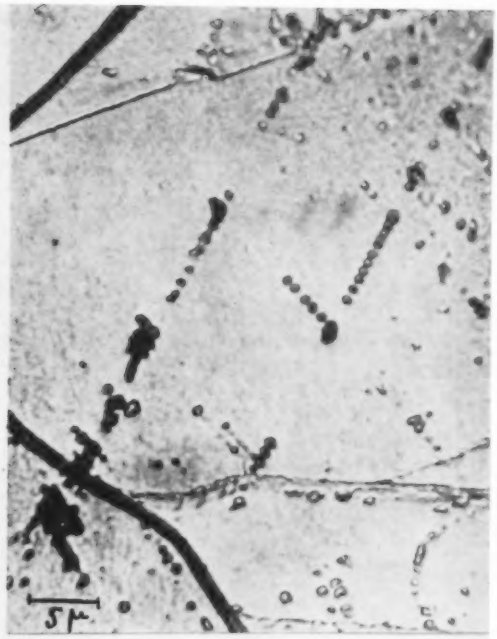

20

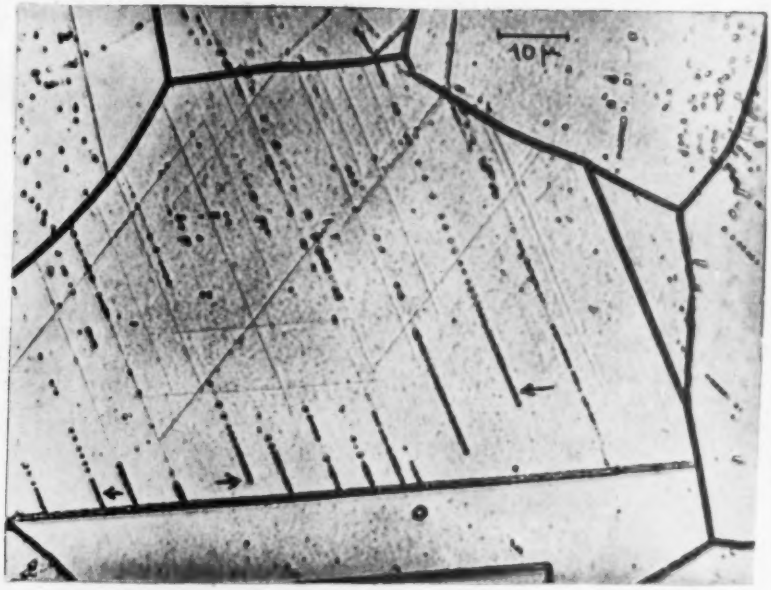

21

PLANCHE VII. Eprouvette No 1 (traction 1,0 kg/mm²). Attaque de la surface immédiatement après la traction. Figure 19—Microfigures de corrosion sur une ligne de glissement (2000X). Figure 20—"Cross-slip" dans un grain (2000X). Figure 21—Après une nouvelle traction de 2,5 kg/mm² les lignes de glissement qui apparaissent sont indépendantes des premières qui se trouvent matérialisées par les points d'attaque (1000X).

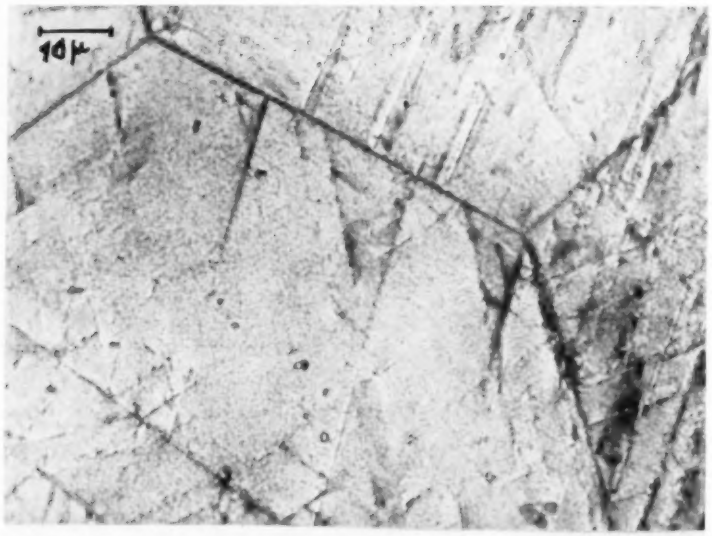

23

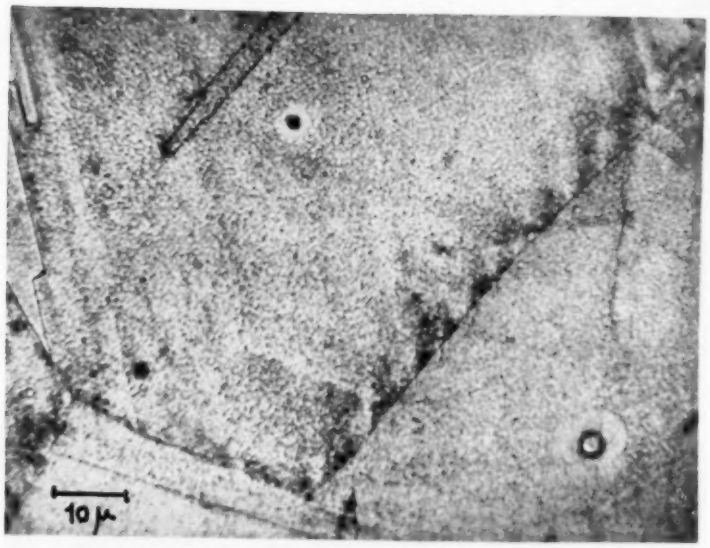

24

PLANCHE VIII. Figure 23—Variations d'intensité de la coloration bleue du film sur les grains de l'eprouvette No 2 attaquée après dissolution de 21 microns (1000X). Figure 23—Bandes de colorations différentielles à 0,7 mm sous la surface d'un bloc de laiton a 66% de cuivre soumis à l'action de la lime (1000X).

tion sous les forts grossissements montre que la région intermédiaire comprise entre celles où les déformations sont respectivement nulles et nettes, contiennent quelques grains avec des points d'attaque formant des segments de stries plus ou moins localisées près des frontières (figure 14). Dès que l'on atteint sur la même surface les zones de déformation appréciable, on observe, entre les alignements de micro-figures de corrosion, une attaque homogène un peu plus forte de la matrice sur les domaines où se trouvaient les bandes de colorations différentielles (figures 15).

La caractéristique la plus évidente de la microstructure observée à tous les niveaux sous la surface est l'extrême hétérogénéité de la répartition des microfigures de corrosion. Leur densité minimum est presque toujours localisée au centre des grains et leur densité maximum vers la périphérie. Ainsi sur le grain de la figure 16 les stries d'attaque sont abondantes et orientées selon trois systèmes, près du joint inférieur; elles sont moins nombreuses et orientées dans une seule direction près du joint supérieur; elles sont très rares dans la région intermédiaire. Les localisations d'attaque sont également visibles sur la figure 17 où l'on remarque en particulier vers la gauche les deux stries parallèles *a* et *b*, qui traversent plusieurs macles en conservant leur écartement. On note aussi d'autres particularités fréquentes, tels que des "cross-slip", et des alignements prolongeant des décrochements le long des frontières de macles (indiqués en *d* et *c* sur la figure 17).

L'éprouvette N° 3 chargée sous 3,8 kg/mm² jusqu'au début de l'allongement mesurable donne lieu aux mêmes observations et montre encore en particulier l'extrême hétérogénéité de la déformation plastique matérialisée par les stries. Dans l'ensemble, ces stries sont plus nombreuses et plus continues et on voit apparaitre ici une attaque générale de la matrice plus intense dans un domaine de 2 à 5 microns autour de beaucoup des joints de grains (figure 18 que l'on comparera à la figure 16). Ces particularités traduisent la plus grande intensité de la déformation plastique par rapport à l'éprouvette chargée sous 3 kg/mm², la différence étant assez considérable pour être visible sur une macrographie (figure 9).

Considérons maintenant l'éprouvette N° 1 soumise à la traction sous la charge de 1 kg/mm². Les lignes de glissements, très difficiles à détecter si on n'utilise pas le contraste de phase interférentiel de Nomarski, n'existent que dans un très petit nombre de grains répartis en trois ou quatre régions près des bords de la partie utile. Chacune de ces lignes donne lieu à une attaque ponctuelle très discontinue. La figure 19 montre une succession de microfigures de corrosion (un peu plus volumineuses ici parce que l'échantillon brut de traction a subi deux électrolyses dans le réactif) de plus en plus écartées à mesure qu'elles s'éloignent du joint de grains. Un autre aspect également très fréquent, assimilable au "cross slip," est visible sur la figure 21.

Cette éprouvette a été utilisée pour examiner comment s'effectue une deuxième déformation sous une charge un peu plus élevée de 2,5 kg/mm² encore inférieure à celle correspondant au début d'allongement mesurable. Ainsi qu'on pouvait s'y attendre les nouvelles lignes de glissement se forment en dehors des précédentes matérialisées par les points d'attaque. Dans le grain de la figure 21 les premières n'intéressaient qu'un seul système et les secondes apparaissent simultanément selon ce système et dans deux autres directions. Une série d'expériences de ce genre serait utile pour suivre d'une façon systématique l'influence de divers facteurs, par exemple l'orientation cristallographique, la direction et la valeur de l'effort sur les proportions et localisations relatives des lignes de glissements aux divers stades de la déformation.

Observations aux rayons X

Les diagrammes de rayons X en retour pris au centre de la partie utile de l'éprouvette N° 2, à l'état recuit initial, puis après deux tractions sous 1,5 et 3 kg/mm² sont donnés figure 22. La comparaison des trois clichés montre une différence nette seulement dans le cas de la deuxième traction; les taches sont un peu plus nombreuses et présentent un léger étalement. Toutefois, en l'absence du diagramme de l'état initial non déformé il serait difficile de tirer une conclusion définitive.

Lorsque les lignes de glissement sont peu nombreuses et limitées seulement à quelques uns des grains il est impossible de déceler aux rayons X ces traces de déformation.

Ceci permet de conclure que la technique d'attaque micrographique est beaucoup plus sensible que les rayons X puisqu'elle peut montrer la présence de glissements dans un grain isolé au milieu d'un grand nombre d'autres non déformés.

3. *Discussion des résultats*

Le phénomène classique d'apparition des lignes de glissement sur la surface polie du métal était considéré jusqu'à présent comme la seule manifes-

tation visible d'une faible déformation. Or en étudiant la dissolution préférentielle qui ne se produit qu'avec les éprouvettes ayant subi une déformation plastique—aussi minime soit-elle—nous avons pu révéler des perturbations de la microstructure non seulement sur la surface, mais dans les régions sous-jacentes. Ces perturbations cor-

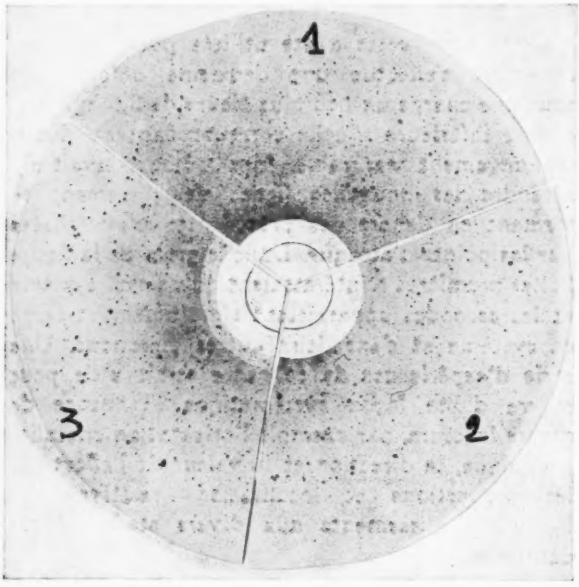

FIGURE 22. Diagrammes en retour pris au même endroit (milieu de la partie utile) de l'éprouvette N° 2. Radiation du cobalt, collimateur de 0,6 mm. 1, Avant la traction. 2, Après traction sous 1,5 kg/mm². 3, Après traction sous 3 kg/mm².

respondent à un accroissement de réactivité chimique de très petits domaines plus ou moins espacés le long des glissements.

Avant de poursuivre la discussion il est nécessaire de rappeler les faits expérimentaux suivants:

1°. La durée de l'attaque anodique n'a aucune influence sur le nombre et la position des points de dissolution sélective. Ainsi, une deuxième électrolyse a seulement pour effet d'augmenter très légérement leur taille sans en faire apparaître de nouveaux.

2°. Les points de dissolution sélective sont des figures de corrosion de symétrie cubique mesurant 0,07 à 0,5 micron, séparées par des distances très variables qui dans le cas des alignements compacts sont de l'ordre de grandeur de leur dimension propre et peuvent descendre à moins de 0,1 micron. Il existe d'ailleurs une certaine périodicité dans la distribution de ces microdomaines le long d'un glissement ainsi qu'on le voit sur les figures 16, 19 et 21: très rapprochés près des joints intergranulaires ils s'écartent progressivement en s'en éloignant.

Dans l'état actuel des connaissances sur le mécanisme de la déformation des cristaux métalliques nos résultats ne paraissent pouvoir s'interpréter qu'en admettant une relation entre les microdomaines d'attaque sélective et certaines dislocations du réseau accumulées sur les glissements.

Plusieurs auteurs ont montré que sur les faces des cristaux de carbure de silicium les points d'émergence des dislocations en hélice constituent des points d'attaque privilégiée vis à vis des réactifs chimiques [15].

Dans un remarquable travail Vogel et ses collaborateurs [16] ont réussi à observer sous le microscope optique les dislocations en arête individuelles alignées sur la limite séparant deux domaines très faiblement désorientés dans des spécimens de germanium. Avec une attaque acide spéciale chaque dislocation est matérialisée par une micropiqûre conique distante de sa voisine d'une longueur égale à celle calculée à partir de la désorientation.

Plus récemment des figures d'attaque distantes de quelques microns ont été produites suivant une technique non précisée, sur les faces (111) de cristaux de germanium déformés plastiquement [17]. Elles sont alignées sur les lignes de glissement, et l'auteur rapproche ce résultat de celui du travail mentionné ci-dessus.

D'autre part, les expériences de Castaing et Guinier [17] apporteraient une preuve indirecte de la présence des dislocations dans le réseau déformé de la solution solide aluminium-cuivre, en montrant qu'au cours de la décomposition thermique à basse température les plaquettes de la phase θ' se localisent de préférence sur les lignes de glissement.

De son côté Amelinckx [19] a examiné la répartition des figures de corrosion sur la surface d'une éprouvette d'aluminium constituée de gros cristaux, faiblement déformée de façon à faire apparaître quelques lignes de glissement. Il constate qu'après l'attaque acide certaines figures de corrosion se localisent sur ces lignes, tandis que d'autres sont placées d'une façon quelconque dans les cristaux et aussi sur leurs frontières. Cette expérience est critiquable, car dans les conditions de polissage électrolytique utilisé avant la déformation (bain acide perchlorique-alcool, forte densité de courant) il doit se former une pellicule d'alumine relative-

ment épaisse (20) susceptible de se rompre ensuite, en particulier le long des lignes de glissement, ce qui favorise bien entendu une dissolution préférentielle du métal. En outre l'auteur ne dit pas si le même effet est observé dans les couches sous-jacentes à la surface.

Notre technique expérimentale est à l'abri d'une telle critique et les raisons qui nous font estimer qu'elle apporte une preuve plus directe à la présence des dislocations, et à la plus grande réactivité chimique du réseau là où elles sont localisées,* reposent sur les caractéristiques suivantes des microfigures de corrosion:

1°. Elles possèdent une taille extrêmement faible, comprise entre 0,07 et 0,5 micron. Or, d'après la micrographie publiée par Vogel et ses collaborateurs, chaque microfigure matérialisant une dislocation a un diamètre évalué à 0,2–0,5 micron.

2°. Elles sont strictement réparties sur les lignes de glissement à la surface et sur des stries qui correspondent à ces mêmes glissements à l'intérieur de l'éprouvette.

3°. Elles sont plus abondantes dans les régions voisines des joints de grains, alors qu'on ne peut faire aucune distinction entre l'aspect des différentes portions d'une même ligne de glissement qui traverse un grain.

4°. Lorsqu'elles sont rassemblées elles dessinent des aspects typiques, tels qu'on peut en attendre d'après des considérations théoriques développées sur les dislocations. Par exemple l'alignement des points d'attaque sur la figure 19, et ceux indiqués par les flèches sur la figure 21, présentent une remarquable analogie avec le schéma d'une séquence de dislocations venant buter contre un obstacle dans une ligne de glissement (21).

La preuve la plus formelle que des dislocations sont bien responsables des effets observés est apportée par l'étude de l'évolution de la microstructure lorsque les éprouvettes très faiblement déformées sont traitées entre 200 et 600°C. Ainsi que nous le montrerons dans la seconde partie les microdomaines d'attaque sélective abandonnent progressivement leurs positions sur les stries discontinues pour former les contours d'une sous-structure de type cellulaire de plus en plus grossière jusqu'à l'aspect typique de la polygonisation. L'évolution parallèle des diagrammes de rayons X confirme que l'on assiste bien aux transformations prévues par la théorie des dislocations pour expliquer la genèse de l'état dit polygonisé à partir de l'état déformé.

Examinons maintenant les renseignements qui peuvent être tirés des effets relatifs à la pellicule solide colorée. Nous avons vu qu'après dissolution des couches superficielles de l'éprouvette, seuls les grains libres de toute trace de déformation prennent à l'attaque anodique une couleur très homogène spécifique de leur orientation. En admettant que la coloration du film soit seulement fonction de son épaisseur la couleur traduit le degré de réactivité du plan cristallographique parallèle à la surface. Cet effet spécifique de l'orientation tend à s'effacer pour les grains ne contenant qu'un petit nombre de glissements et alors apparaît le curieux phénomène des domaines de coloration différentielle; leur disposition géométrique est en relation avec les divers systèmes de stries, ce que nous discuterons plus loin. Lorsqu'on atteint les régions de forte déformation, c'est-à-dire sur la partie utile au délà des congés, tous les grains sont uniformément recouverts d'un film bleu avec des renforcements d'intensité qui dessinent des bandes parallèles à certaines stries.

Etant donné que dans la succession des teintes d'interférence de 1er et de 2ème ordre des films minces d'oxydes ou de sulfures, le bleu vient après les autres couleurs, c'est-à-dire correspond ici à un maximum de réactivité du support, tout se passe comme si les perturbations du réseau, révélées par les microfigures de corrosion, s'accompagnaient d'un phénomène rendant la masse entière de la matrice plus réactive, au point de masquer l'effet propre de l'orientation. D'autre part, la présence des bandes d'un bleu plus foncé prouve que cet accroissement de réactivité est maximum sur certaines régions cristallographiquement définies.

Pour expliquer les différences de réactivité correspondant à l'effet dit des bandes de coloration différentielle on pourrait penser à des désorientations locales suivant un processus assimilable au "Kinking" mais cette hypothèse ne paraît pas compatible avec un certain nombre de particularités observées. Tout d'abord la plupart des bandes sont elles-mêmes morcelées en domaines de teintes légérement différentes qui peuvent prendre la forme triangulaire (figure 23). D'autre part, les renforcements d'intensité de coloration, c'est-à-dire les régions de réactivité maximum, se localisent près des joints de grains (figure 15). Enfin,

*Si une éprouvette polie, puis soumise à la traction, est abandonnée à l'air sec il apparaît parfois, outre un film d'oxyde mince, des micropiqûres de taille encore inférieure aux points d'attaque anodique, et alignées, comme ceux-ci sur des lignes de glissement.

ces bandes sont le plus facilement observées lorsque la déformation n'est ni trop faible, ni trop forte, et nous avons vu qu'elles n'apparaissent pour ainsi dire pas sur la surface brute de traction, mais seulement dans les régions sous-jacentes.

Il est intéressant de mentionner que les bandes transgranulaires ont été trouvées dans le laiton α déformé par abrasion [10] (figure 24) et nous les avions alors attribuées à un phénomène en relation avec les tensions internes créées par l'hétérogénéité de la déformation plastique. A l'époque, le seul argument présenté était une remarquable analogie entre les aspects micrographiques et ceux observés par Nye [22] en examinant par la méthode photo-élastique des feuilles transparentes de chlorure d'argent polycristallines soumises à la traction.

Dans un récent travail relatif à la croissance des films de sulfures sur divers métaux Hoar et Tucker [23] observent qu'après une légère déformation par flexion d'une éprouvette de cuivre polie électrolytiquement, le film produit au contact d'une solution de poly-sulfures alcalins présente en certaines régions (au voisinage des joints de grains et sur des lignes de glissement) une forte biréfringence sous l'éclairage en lumière polarisée. Les auteurs se référant également aux résultats de Nye estiment que ce phénomène indique la présence de contraintes dans le film aux endroits où existent des tensions, ou distortions, du réseau métallique sous-jacent. Cette explication rejoint la nôtre, avec la seule particularité que la sensibilité de l'attaque anodique est telle que l'effet des contraintes se traduit par un accroissement de la vitesse de sulfuration, d'où des différences de couleur directement observables. Cependant, si le film anodique est trop épais le grain apparaît uniformément coloré, mais les domaines redeviennent visibles sous la lumière polarisée. On peut d'ailleurs parfois les distinguer encore après dissolution du film grâce au gravage un peu plus intense de la matrice (figure 15).

Une autre preuve que les tensions internes sont la cause probable des variations de coloration à l'intérieur des grains est donnée par l'étude des effets du recuit. Nous verrons dans la deuxième partie que les bandes s'estompent progressivement et finissent par disparaître au moment où la microstructure révélée par les points d'attaque est nettement modifiée. Or Nye constate que le recuit ne change pas la répartition des contraintes dans les cristaux de chlorure d'argent déformés, mais réduit leur intensité puis les élimine si la température est suffisament élevée, sans provoquer d'ailleurs la recristallisation.

Conclusions

1°. La méthode d'attaque anodique dans la solution d'hyposulfite de sodium dilué s'est révélée être d'une extrême sensibilité pour la mise en évidence des très faibles déformations par traction de la solution solide polycristalline cuivre-zinc à 35% de zinc.

2°. Cette méthode fait apparaître sur les lignes de glissement des microfigures de corrosion de taille comprise entre 0,07 et 0,5 micron, et séparées les unes des autres par des distances très variables pouvant devenir du même ordre de grandeur que leur dimension propre.

3°. Les mêmes microdomaines d'attaque sélective se produisent encore après dissolution par polissage électrolytique d'épaisseurs notables de matière. Ils forment alors des systèmes de stries plus ou moins discontinues, ce qui prouve que l'apparition des lignes de glissement sur la surface, seul signe extérieur visible de la déformation, est accompagnée de perturbations de réseau qui intéressent les régions profondes de l'éprouvette.

4°. La densité des stries et le nombre de points d'attaque qu'elles comportent sont très variables d'un grain à un autre et à l'intérieur d'un même grain, traduisant ainsi l'extrême hétérogénéité de la déformation plastique d'un agrégat polycristallin soumis à la traction sans allongement appréciable. D'une façon générale les portions centrales des grains sont les plus pauvres en microdomaines d'attaque priviligiée.

5°. Conformément à des faits expérimentaux déjà connus nous admettons que les microdomaines de dissolution préférentielle sont en relation avec la présence des dislocations dans le réseau. La deuxième partie de notre étude montrera que cette interprétation est entièrement confirmée par les nouveaux aspects micrographiques observés au cours du recuit de ces éprouvettes entre 200 et 600°.

6°. Outre les attaques localisées la méthode anodique produit un film très mince de composés sulfurés de composition exacte encore inconnue. En l'absence de toute trace de déformation plastique la couleur, donc l'épaisseur, du film ne dépend que de l'orientation du grain (phénomène d'épitaxie). Ce facteur d'orientation diminue d'importance avec le degré de déformation, et il ne se manifeste plus lorsque le réseau est suffisament

perturbé. On montre que ceci est dû à un accroissement de la réactivité globale de la solution solide, mais les variations locales d'intensité des colorations observées sur la superficie de chaque grain considéré, prouvent l'existence de degrés de réactivité. Ce phénomène proviendrait d'une hétérogénéité de la répartition des tensions internes induites par la déformation plastique, elle même très hétérogène.

Bibliographie

1. JACQUET, P. A. Nature **135** (1935) 1076; Comptes Rendus **201** (1935) 1473.
2. JACQUET, P. A. Rev. Métall. **48** (1951) 1.
3. LACOMBE, P. et BEAUJARD, L. Rev. Métall. **45** (1948) 317; J. Inst. Metals **74** (1947) 1.
   GUINIER, A. et LACOMBE, P. Métaux et Corrosion **23** (1948) 212.
4. WOOD, W. A. et RACHINGER, W. A. J. Inst. Met. **76** (1949) 237;
   CRUSSARD, C., AUBERTIN, F., JAOUL, B., et WYON, G. Progress in Metal Physics **2** (1950) 193;
   MCLEAN, D. et TATE, A. E. L. Rev. Métall. **48** (1951) 765.
5. BROWN, A. F. Phil. Mag. Suppl. **1**, N° 4 (1952) 427.
6. JACQUET, P. A. Rev. Métall. **42** (1945) 133.
7. MCLEAN, D. J. Inst. Metals **74** (1947) 95.
8. OGILVIE, G. J. J. Inst. Metals **81** (1953) 491.
9. HIBBARD, W. R. Trans. A.I.M.E. **175** (1948) 123.
10. JACQUET, P. A. Rev. Métall. **47** (1950) 355; La Metallurgia Italiana, N° **2** (1950) 43.
11. JACQUET, P. A. Journées Métallurgiques d'Automne de la Société Française de Métallurgie, Paris, 1953. A paraître dans Rev. Métall.
12. NOMARSKI, G. et WEILL, Madame A. R. Journées Métallurgiques d'Automne de la Société Française de Métallurgie, Paris, 1953. A paraître dans Rev. Métall.
13. JACQUET, P. A. Comptes Rendus **228** (1949) 1027; voir aussi réf. [10].
14. FERT et DARGENT, R. Comptes Rendus **235** (1952) 1623;
    DARGENT, R. Métaux-Corrosion-Industries **28** (1953) 285.
15. GEVERS, R., AMELINCKX, S., et DE KEYSER, W. Naturwiss **39** (1952) 448.
    HORN, F. H. Phil. Mag. **43** (1952) 1210.
    GEVERS, R. J. Chimie Physique **50** (1953) 321.
16. VOGEL, F. L., PFANN, W. G., COREY, H. E., et THOMAS, E. E. Phys. Rev. **90** (1953) 489.
17. GALLAGHER, C. J. Amer. Physical Soc., Rochester Meeting, 1953, résumé dans Phys. Rev. **91** (1953) 846.
18. CASTAING, R. et GUINIER, A. Comptes Rendus **228** (1949) 2033.
19. AMELINCKX, S. Phil. Mag. **44** (1953) 1048.
20. JACQUET, P. A. Métallographie de l'aluminium et de ses alliages, Publication O.N.E.R.A., N° 51, 1952.
21. COTTRELL, A. H. Theory of dislocations. Progress in Metal Physics **4** (1953) 205.
22. NYE, J. F. Nature **161** (1948) 367; Proc. Roy. Soc. **A198** (1949) 190.
23. HOAR, T. P. et TUCKER, J. P. J. Inst. Metals **81** (1953) 665.

RECHERCHES EXPÉRIMENTALES SUR LA MICROSTRUCTURE DE LA SOLUTION SOLIDE CUIVRE-ZINC 65/35 POLYCRYSTALLINE TRÈS FAIBLEMENT DÉFORMÉE PAR TRACTION ET SUR SON ÉVOLUTION AU RECUIT ENTRE 200 ET 600°C
II. ÉTUDE DE LA MICROSTRUCTURE DE RECUIT*

P. A. JACQUET†

L'étude de l'évolution au cours de recuits étagés de la microstructure de déformation décrite dans la première partie, a mis en évidence deux faits importants : la polygonisation des grains, stade ultime du traitement, et l'existence d'étapes intermédiaires permettant d'envisager le processus de la polygonisation.

L'observation des mêmes endroits en cours d'évolution montre l'influence prépondérante de l'hétérogénéité et de l'intensité de la déformation plastique par traction. On est conduit à admettre que les rassemblements de dislocations formant les sous-joints présentent des différences de stabilité thermique. Jusqu'à l'apparition de la polygonisation typique la croissance des domaines et leur degré de perfection sont étroitement associés.

Outre les dissolutions sélectives permettant de définir la sous-structure, la méthode d'attaque utilisée produit sur la surface une mince pellicule solide dont les caractéristiques de coloration se sont révélées d'une très grande sensibilité à l'évolution thermique de la solution solide déformée.

EXPERIMENTAL RESEARCH ON THE MICROSTRUCTURE OF THE POLYCRYSTALLINE SOLID SOLUTION COPPER-ZINC 65/35 VERY SLIGHTLY DEFORMED IN TENSION, AND ITS EVOLUTION DURING ANNEALING BETWEEN 200° AND 600°C. II. A STUDY OF THE ANNEALING MICROSTRUCTURE

The study of the evolution of the deformation microstructure during annealing in steps, described in the first part, has revealed two important facts: the polygonization of the grains, which is the ultimate stage of the treatment, and the existence of intermediate stages, which enable one to consider the process of polygonization. The observation of the same areas during the evolution shows the preponderant influence of heterogeneity and of the amount of plastic deformation in tension. One is led to admit that the arrays of dislocations forming the sub-boundaries exhibit differences in thermal stability. Up to the appearance of the typical polygonization, the growth of domains and their perfection are closely associated. Beside the selective dissolution, which enables one to define the structure, the etching method used in the present work produces on the surface a thin, solid film, having colouring features which are very sensitive to the thermal evolution of the deformed solid solution.

EXPERIMENTELLE UNTERSUCHUNGEN ZUR FEINSTRUKTUR EINER POLYKRISTALLINEN FESTEN KUPFER-ZINK LÖSUNG (65/35), DIE EINER SEHR GERINGEN ZUGVERFORMUNG UNTERWORFEN WAR, UND ZUR AUSBILDUNG DIESER STRUKTUR BEIM GLÜHEN ZWISCHEN 200 UND 600°C. II. UNTERSUCHUNG DER FEINSTRUKTUR NACH DER WÄRMEBEHANDLUNG

Die Untersuchung der Ausbildung der Deformationsfeinstruktur während schrittweiser Glühungen wurde in Teil I beschrieben. Diese Untersuchung hat zwei wichtige Tatsachen gezeigt: Die Polygonisation der Kristallite, die das Endstadium der Behandlung darstellt, und das Vorhandensein von Zwischenstadien, die eine Diskussion des Polygonisationsprozesses möglich machen.

Beobachtungen an ein und derselben Stelle der Probe während der Ausbildung der Feinstruktur zeigen den dominierenden Einfluss der Heterogenität und des Ausmasses der plastischen Zugverformung. Es scheint, als hätten die Versetzungsreihen, die die Subgrenzen bilden, unterschiedliche thermische Stabilitäten. Bis zum Auftreten der typischen Polygonisation ist das Wachstum der Bereiche und ihre Fehlerfreiheit eng miteinander verknüpft.

Wegen der selektiven Auflösung, die eine Beschreibung der Struktur gestattet, zeigt das in der vorliegenden Arbeit verwandte Ätzverfahren einen feinen festen Film auf der Metalloberfläche. Dieser Film zeigt charakteristische Verfärbungen, die der thermischen Strukturveränderung der verformten festen Lösung sehr empfindlich folgen.

I. Méthodes expérimentales

Les essais préliminaires ont porté sur une éprouvette qui avait subi une légère déformation dans des conditions assez mal définies de traction et de flexion (éprouvette N° 4). L'éprouvette N° 3, déjà décrite dans la première partie, nous a servi pour l'étude systématique. Rappelons qu'elle avait subi une traction sous 3,8 kg/mm² jusqu'au début de l'allongement mesurable.

La technique expérimentale employée consiste en une suite de traitements de durée variable aux températures de 200, 400, 500 et 600° (±5°). Après chaque recuit la surface est repolie électrolytiquement, puis attaquée en anode dans la solution d'hyposulfite de sodium. Les conditions de cette attaque sont exactement les mêmes que celles adoptées pour la mise en évidence des microstructures de déformation, c'est-à-dire : solu-

*Received February 25, 1954.

†Ingénieur contractuel des Constructions et Armes Navales, Marine Nationale, Paris, France.

tion à 0,2% dans l'eau distillée, température 20°, courant de 55 mA, durée Imn.

Le refroidissement après traitement a lieu dans le four, et on prend toujours les plus grandes précautions pour éviter les déformations accidentelles. Bien que le chauffage s'effectue à l'air, l'éprouvette étant placée entre deux plaques du même alliage, l'oxydation est faible jusqu'à 500°. Elle devient plus notable à 600°, mais reste néanmoins assez superficielle si la durée du séjour ne dépasse pas 1 heure.

La croûte d'oxyde doit être éliminée avant le polissage, ce qui est facilement obtenu en laissant séjourner l'éprouvette dans l'acide orthophosphorique à 10% pendant une quinzaine de minutes. Après ce nettoyage il ne subsiste que la couche d'oxydation interne, extrêmement mince jusuq'à 500°, et qui est dissoute au cours du polissage électrolytique. Toutefois, dans les expériences où l'on examine l'évolution de la structure à des endroits repérés sur la surface, la durée du polissage doit être limitée, afin que la dissolution reste inférieure à une dizaine de microns. Dans ces conditions, pour les températures de 500 et 600° il subsiste encore des traces d'oxydation, visibles sous forme de points de corrosion de taille notable, d'ailleurs impossibles à confondre avec les microdomaines de dissolution sélective définissant la microstructure.

Les observations micrographiques ont été limitées ici au microscope optique sous le grossissement maximum de 2000 diamètres (objectif à immersion d'huile d'ouverture numérique = 1,30). Elles sont complétées par la prise de diagrammes de rayons X dont les conditions et les résultats seront donnés dans un appendice rédigé par Madame A. R. Weill.

II. Résultats

1. *Eprouvette N° 4*

Cette éprouvette, qui avait subi une légère traction accompagnés de flexion, présentait la microstructure striée typique d'une déformation globale relativement minime, et d'ailleurs absente dans certains grains. Après un recuit de 2 heures à 690 ± 5° suivi d'un polissage électrolytique pour retirer environ 40 microns, l'attaque ne révèle plus les stries, ni les bandes de colorations différentielles de l'état déformé, mais une sorte de réseau cellulaire constitué de lignes très fines uniformément colorées en bleu, quelle que soit la teinte du film sur les grains correspondants. Ce réseau se détache particulièrement bien à l'observation en lumière polarisée (figure 1).

Lorsque le film solide est éliminé dans l'acide chlorhydrique, la sous-structure apparaît avec une grande netteté (figure 2), ce qui indique un effet de dissolution sélective exactement comme dans le cas de la microstructure de déformation. Cependant, alors que les stries étaient, en général, des alignements de points plus ou moins espacés, les lignes du réseau sont davantage continues, bien que des ponctuations existent encore (par exemple, à droite sur la figure 2).

L'exploration de toute la superficie de l'éprouvette montre que sur la partie utile certains grains ne possèdent aucune sous-structure, et il en est ainsi évidemment pour tous les grains près des têtes où n'existait aucune trace de déformation. D'autre part, les cellules de cette sous-structure n'ont pas une taille homogène, par exemple elles sont très petites en face de la macle à la partie supérieure du grain figure 2.

La figure 1 montre le cas, d'ailleurs unique, d'un très petit grain qui s'est formé en face d'une macle (à gauche) dans une région où la sous-structure est particulièrement fine.

La microstructure interne des grains ainsi mise en évidence présente une ressemblance très étroite avec celle qui correspond à l'état dit polygonisé du métal. Les diagrammes de rayons X pris sur cet échantillon (voir Appendice) comportent le morcellement des taches caractéristiques de la polygonisation, c'est-à-dire que les cellules observées au microscope sont bien les domaines, ou sous-grains, plus ou moins désorientés les uns par rapport aux autres.

Si l'éprouvette est alors soumise à une nouvelle traction de 3,5 kg/mm² jusqu'à apparition des lignes de glissement sur la surface, puis repolie et attaquée, on fait apparaître simultanément les sous-joints et les stries de déformation (figure 3). Après dissolution du film coloré les forts grossissements montrent que les discontinuités d'attaque des glissements sont souvent en relation avec la sous-structure et que, d'autre part, les sous-joints peuvent être soit des lignes continues, soit des alignements de points ; ces divers aspects sont montrés sur la figure 4 où l'on voit également que les sous-grains, nettement marqués par leurs contours, peuvent être divisés eux-mêmes en domaines plus petits, beaucoup moins bien définis.

Le fait que les glissements ne présentent que très exceptionnellement un changement de direction appréciable en traversant les frontières des

TABLEAU I

SUITE DES TRAITEMENTS SUR L'EPROUVETTE No 3

Expérience no	Traitement de l'éprouvette	Epaisseur (en microns) retirée après le traitement	Figures correspondantes
1	Traction sous 3, 8 kg/mm²	230	6 (et 9 b de la 1 ère partie)
2	Comme 1 + 1 h.à 200°	45	
3	Comme 2 + 13 h.à 200°	35	7
4	Comme 3	50	8
5	Comme 4 + 3 h. à 400°	10	9, 10
6	Comme 5	15	5a, 11, 12, 16, 17
7	Comme 5 + 1 h.à 500°	8	5b, 13, 19, 20, 23, 26
8	Comme 7 + 2 h.à 500°	6	14, 18, 21, 22, 24
9	Comme 8 + 45 mn. à 600°	6	15, 25, 27, 28

sous-grains prouve le très faible degré de désorientation des domaines de polygonisation.

2. *Eprouvette N° 3*

Le tableau I donne les conditions des traitements successifs subis par l'éprouvette à partir de l'état recristallisé normal, et l'épaisseur enlevée électrolytiquement avant l'attaque.

On voit que, dans les expériences 7, 8 et 9 la quantité de matière enlevée au polissage est très faible, d'où la possibilité de suivre l'évolution de la structure sur les mêmes endroits repérés. Il est regrettable que ce mode opératoire n'ait pas été utilisé dès le début, c'est-à-dire pour les premiers stades du recuit qui sont précisément les plus intéressants. Cette lacune devra sans aucun doute être comblée dans un travail ultérieur, plus systématique, avec l'aide du microscope électronique.

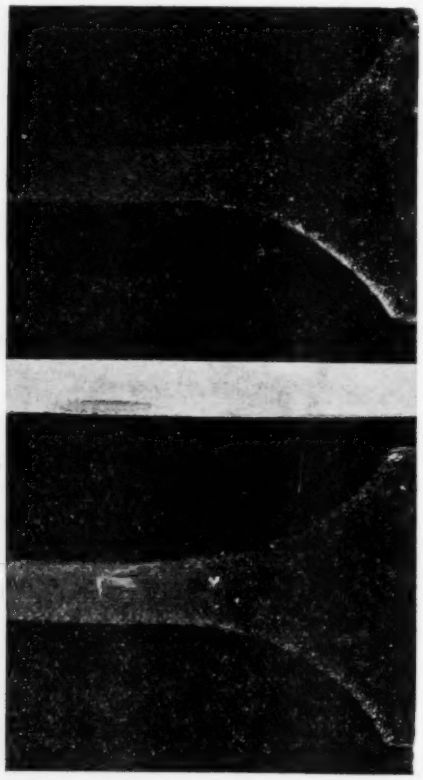

Figure 5.

Avant de décrire dans le détail les aspects observés après chaque traitement, nous remarquerons que l'évolution est déjà décelable à l'échelle macroscopique. Les nombreuses stries d'attaque sur les grains déformés (figure 6) se traduisent sous l'éclairage oblique par un fort contraste par rapport aux têtes bien polies (figure 9*b* de la Première Partie). Ce contraste n'évolue pas après le recuit de 14 heures à 200°, mais il diminue notablement à la suite du traitement supplémentaire de 3 heures à 400° (figure 5*a*) pour devenir à peine perceptible après le troisième recuit de 1 heure à 500° (figure 5*b*). D'où l'on conclue que les caractéristiques de l'attaque se modifient au cours du recuit à partir d'une température suffisante, dans le sens d'une restriction des microdomaines de dissolution préférentielle.

Recuit à 200°. Après 14 heures à 200° les bandes de colorations différentielles sont au moins aussi marquées qu'à l'état brut de déformation (figure 7). Après enlèvement du film on voit que la dissolution sélective perd son caractère très ponctué et tend à envahir des domaines initialement non réactifs, d'où la microstructure confuse visible sur la figure 8.

Recuit à 400°. Un traitement de 1 heure à 400° n'entraine pas de modifications appréciables; au bout de 3 heures à la même température, l'évolution est très nette. D'une façon générale les bandes colorées s'estompent et leurs limites deviennent très floues (figures 9 et 10). Les attaques sélectives

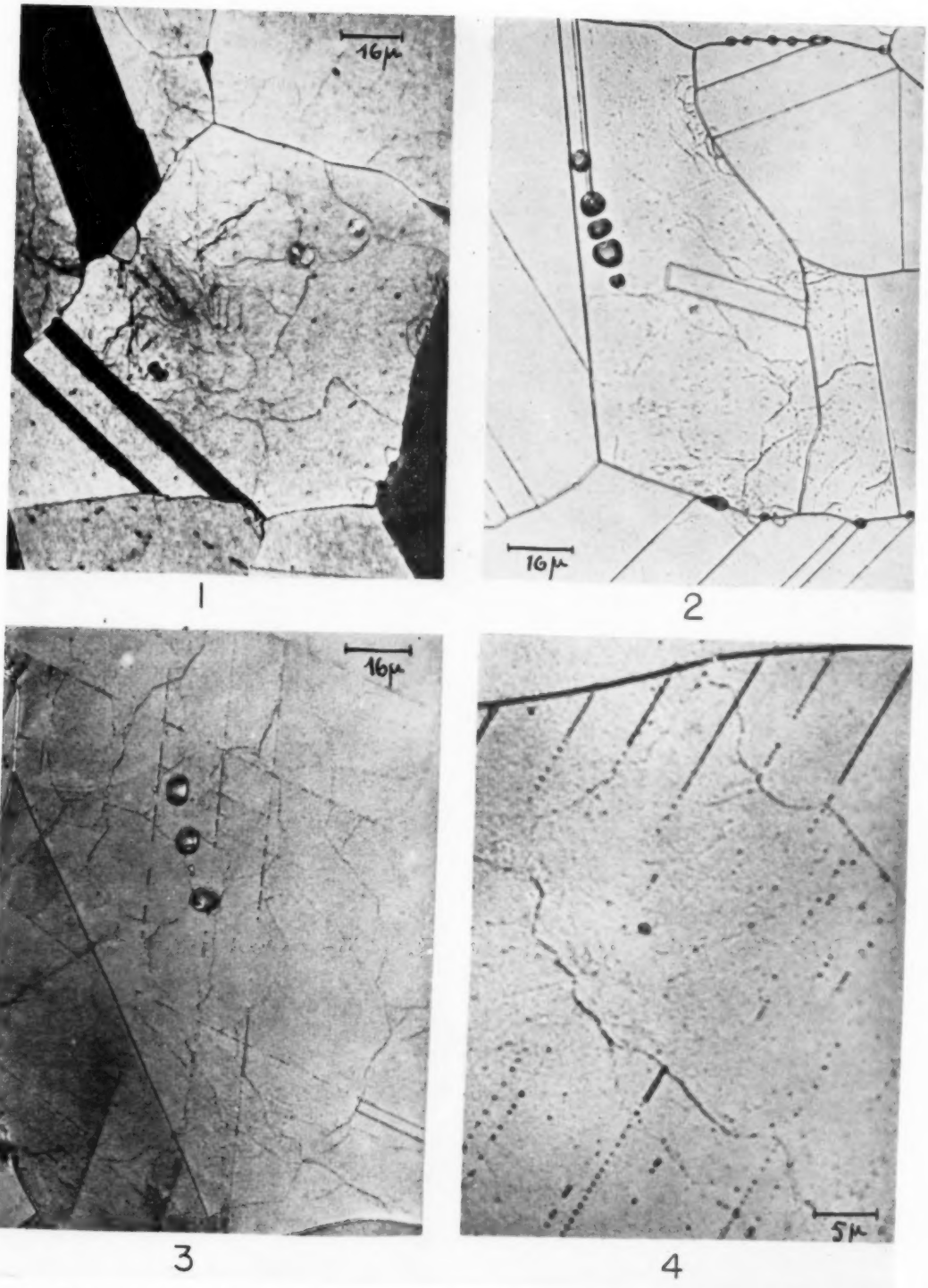

PLANCHE I. Eprouvette N° 4 déformée par traction accompagnée d'une légère flexion, recuite 2 h. à 600° puis polie pour dissolution de 40 μ et attaquée. Figure 1—Examen en lumière polarisée de la surface avec son film coloré (630×). Figure 2—Autre endroit, après dissolution du film (630×). Figure 3—Nouvelle traction sous 3,5 kg/mm², polissage pour dissolution de 60μ puis attaque anodique (630×). Figure 4—Même spécimen après dissolution du film (la ligne épaisse en bas est un joint intergranulaire (2000×). Figure 5—Eprouvette N° 3—Photographies avec éclairage oblique (4,5×). (*a*) Attaque après recuit 14 h. à 200° + 3 h. à 400°. (cf. fig. 9*b* de la 1ère Partie). (*b*) Attaque après recuit supplémentaire 1 h. à 500°.

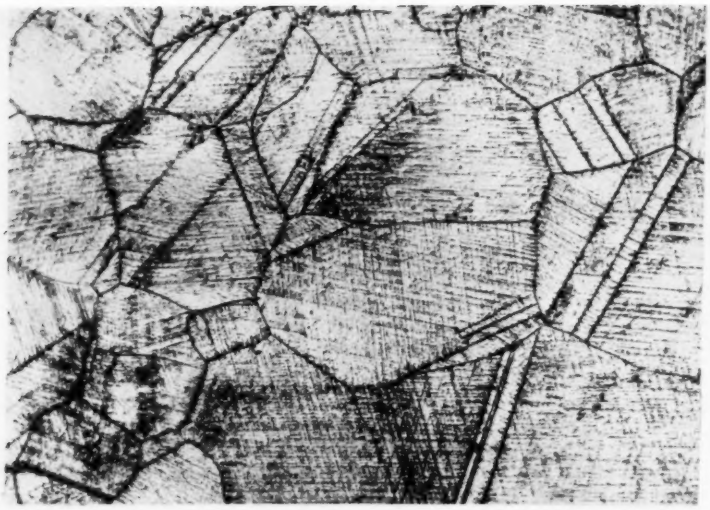

6

7

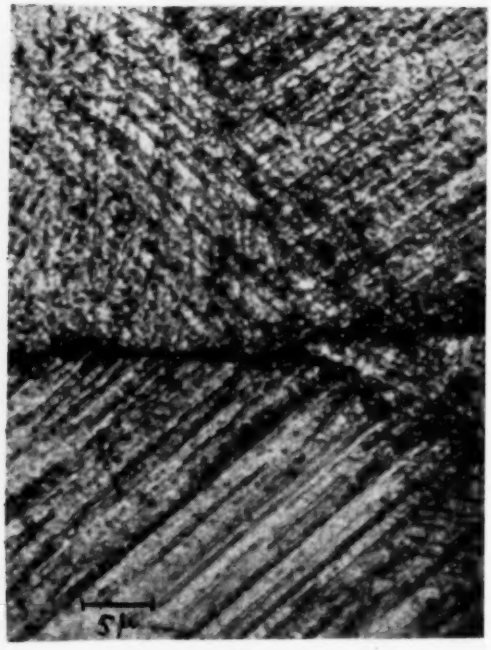

8

PLANCHE II. Figure 6—Microstructure de l'éprouvette N° 3 après la traction et avant les recuits (400×). Figure 7—Recuit 14 h. à 200°. Bandes de colorations différentielles sur le film solide (les parties claires sont colorées en jaune et les parties sombres en bleu foncé (1000×). Figure 8—Même spécimen après dissolution du film coloré (2000×).

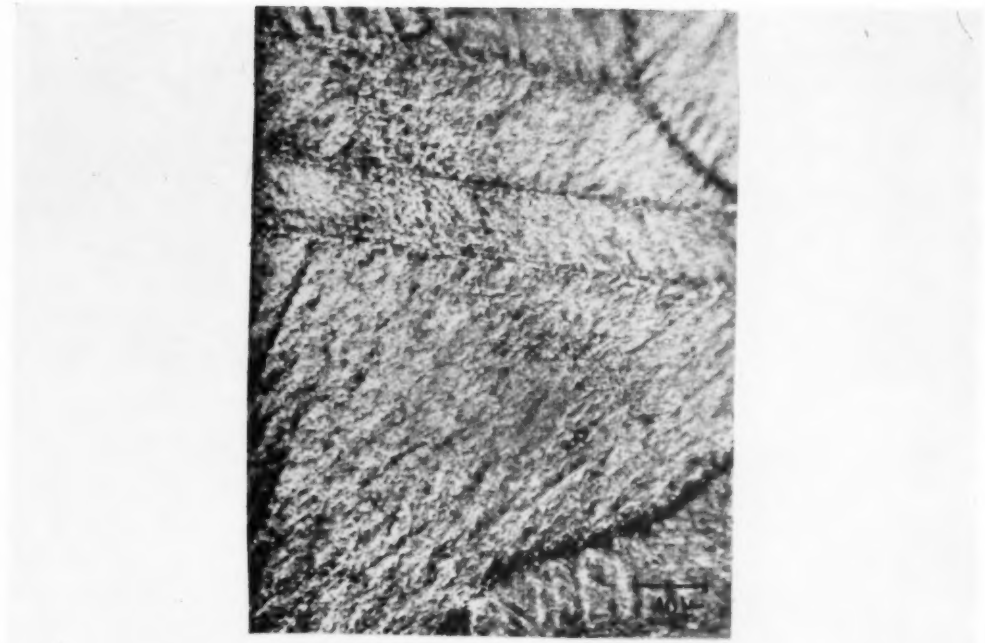

9

10

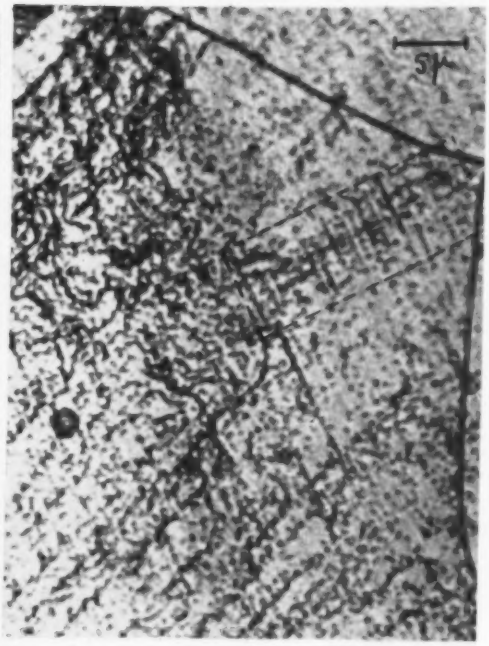

11

PLANCHE III. Nouveau recuit de 3 h. à 400°. Photographies de la surface avec son film coloré. Figure 9—Bandes bleuâtres très floues (1000×). Figure 10—Région à gauche du grain de la figure 9 (2000×). Figure 11—Autre région (2000×).

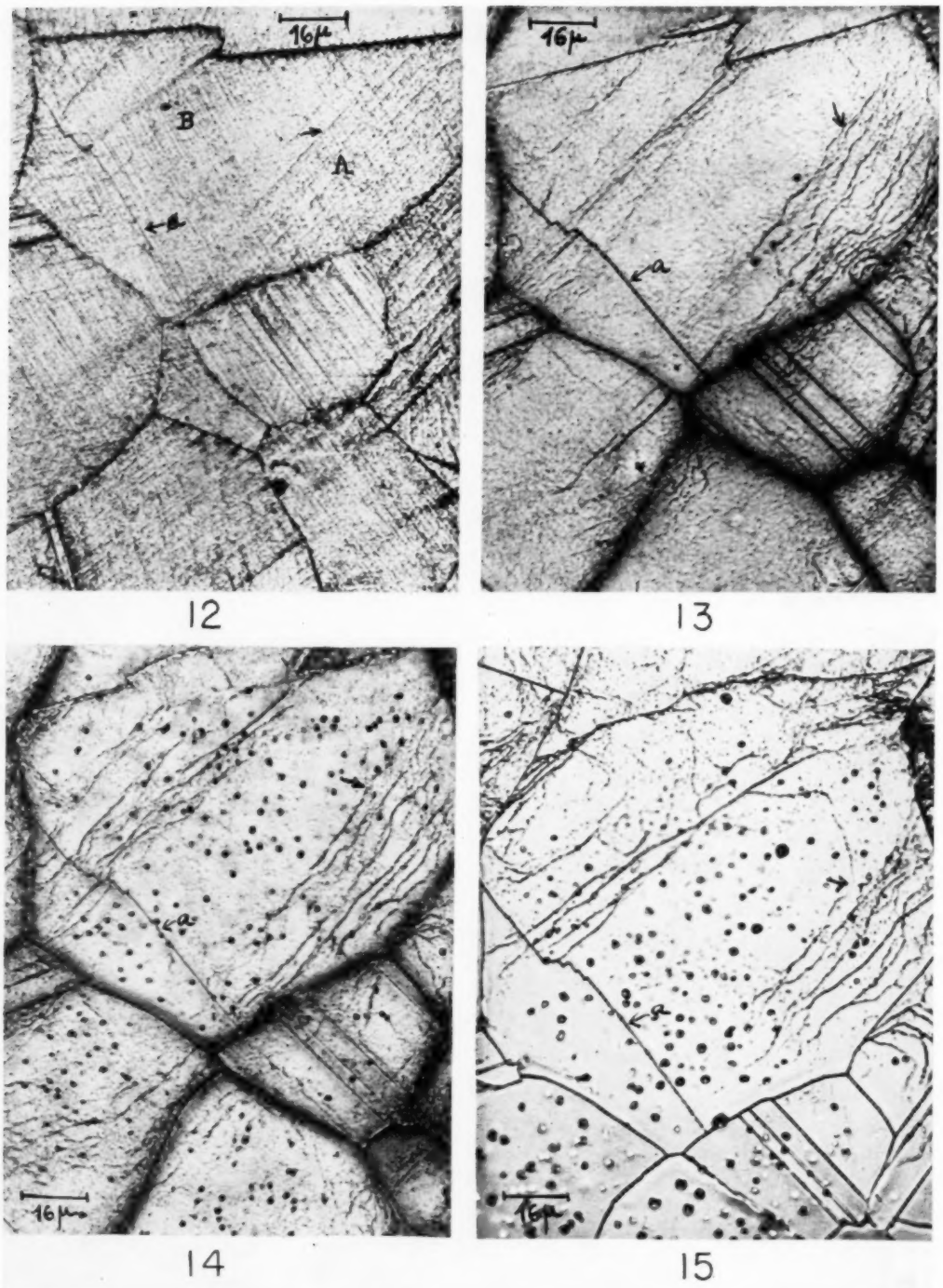

PLANCHE IV. Même endroit de l'éprouvette examiné après divers recuits (630×). Figure 12—14 h. à 200° + 3 h. à 400° (film coloré enlevé). Figure 13—Comme fig. 12 + 1 h. à 500° (avec le film coloré). Figure 14—Comme fig. 13 + 2 h. à 500° (avec le film coloré). Figure 15—Comme fig. 14 + 45 mn à 600° (film coloré enlevé).

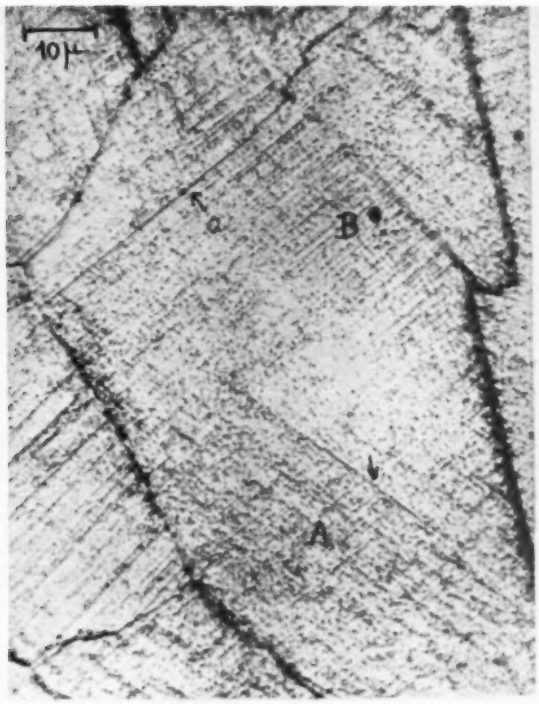

16

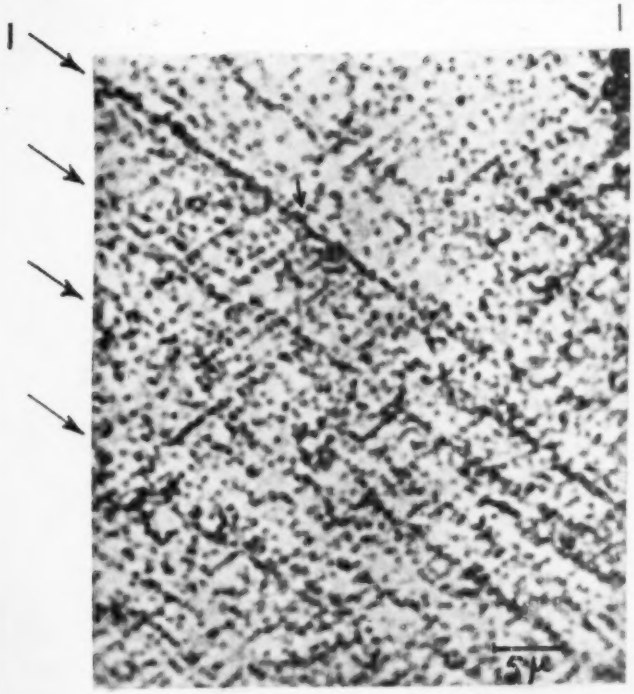

17

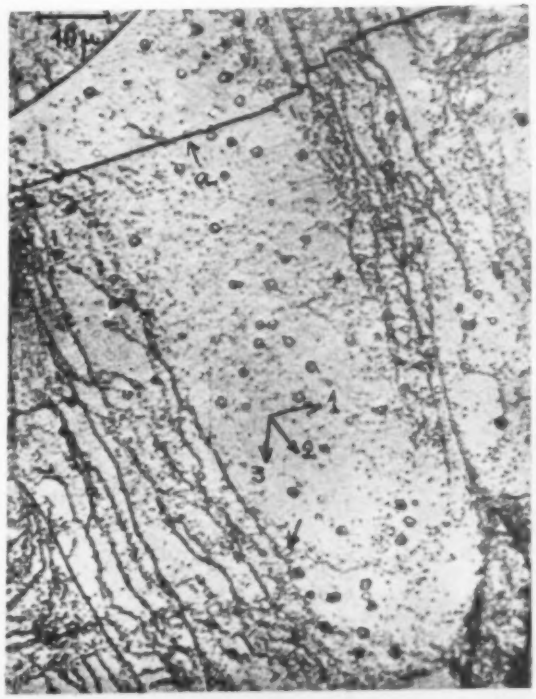

18

PLANCHE V. Grain en haut du champ de la figure 12 (tourné de $\pi/2$ environ). Figure 16—Recuit 14 h. à 200° + 3 h. à 400° (1000×). Figure 17—Partie inférieure droite du grain fig. 16; la flèche indique le même endroit; les flèches latérales montrent les zones qui préfigurent les positions approximatives des sous-joints après le recuit de 3 h. à 500° (cf. fig. 18) (2000×). Figure 18—Comme figure 16 + 3 h. à 500° (1000×).

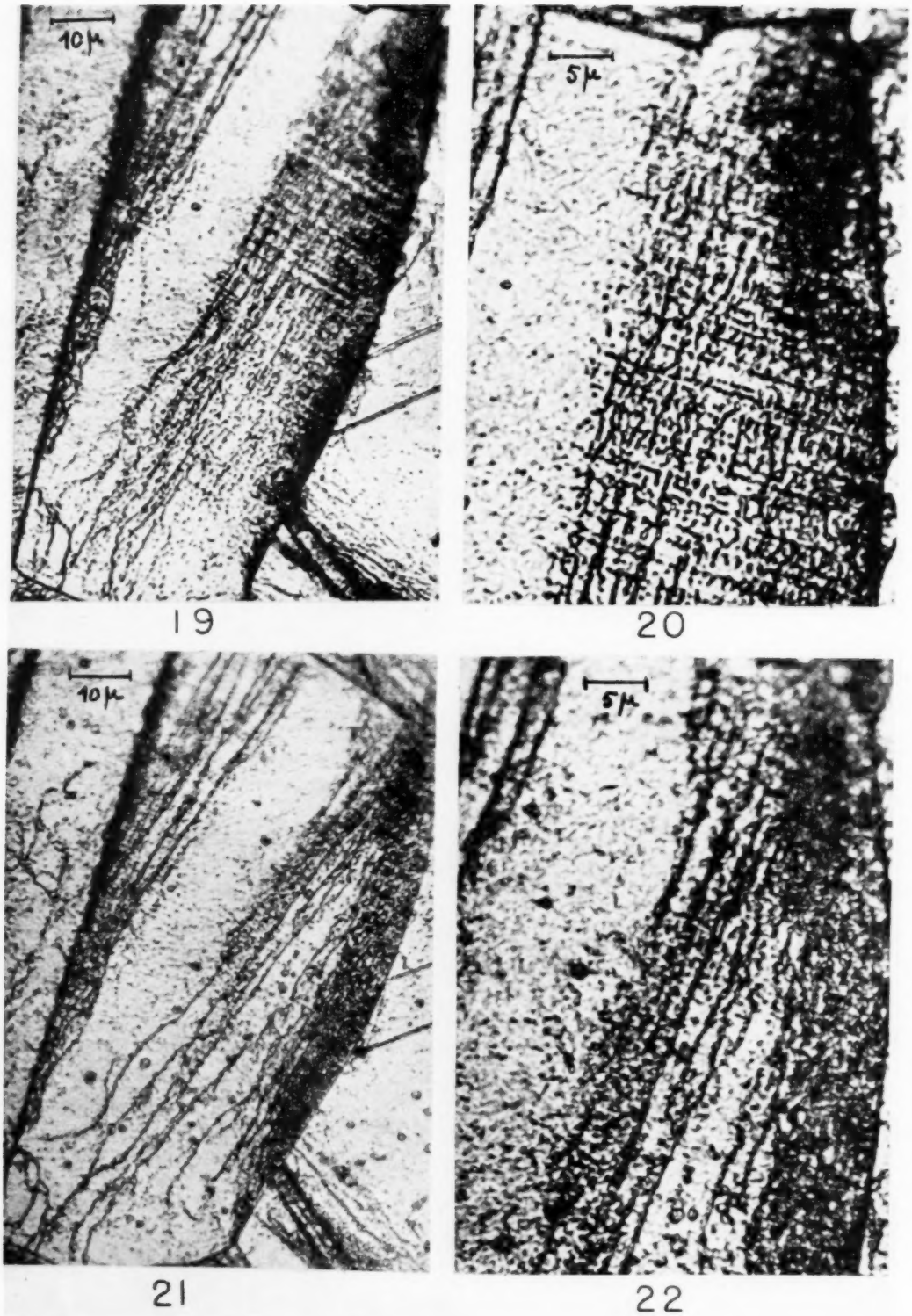

PLANCHE VI. Influence de la durée du recuit à 500° sur la sous-structure d'un même grain. Figure 19—Recuit 14 h. à 200° + 3 h. à 400° + 1 h. à 500° (1000×). Figure 20—Partie supérieure du champ fig. 19 (2000×). Figure 21—Comme figure 19 + 2 h. à 500° (1000×). Figure 22—Partie supérieure du champ fig. 21 (2000×).

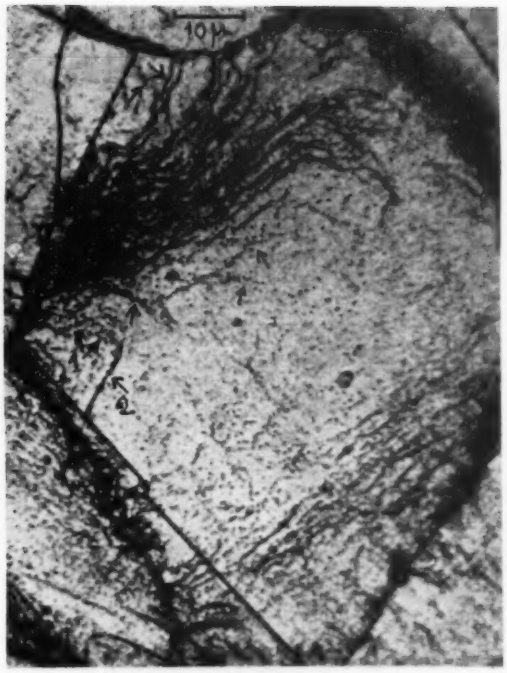

23

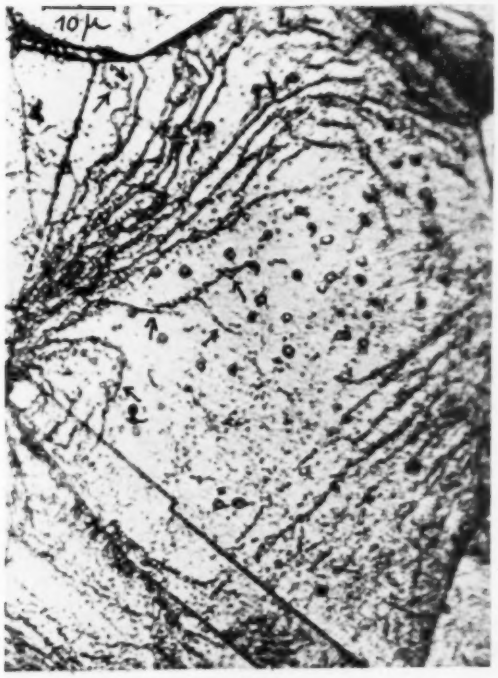

24

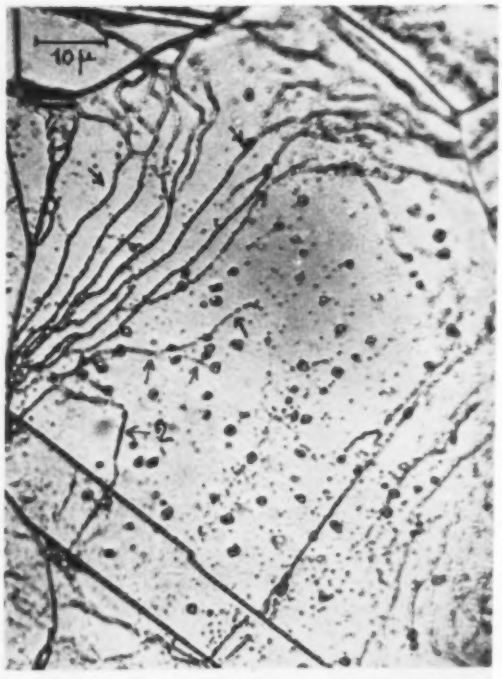

25

PLANCHE VII. Sous-structure d'un même grain après divers recuits (1000×). Figure 23—14 h. à 200° + 3 h. à 400° + 1 h. à 500°. Figure 24—Recuit supplémentaire 2 h. à 500°. Figure 25—Recuit supplémentaire 45 mn à 600°. La comparaison avec les figures 23 et 24 montre la disparition des sous-joints "secondaires" à l'intérieur du domaine limité par le sous-joint "primaire" 2.

26

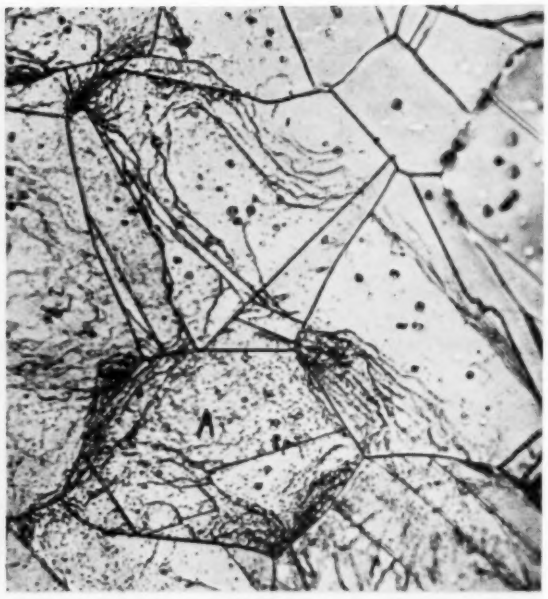

27

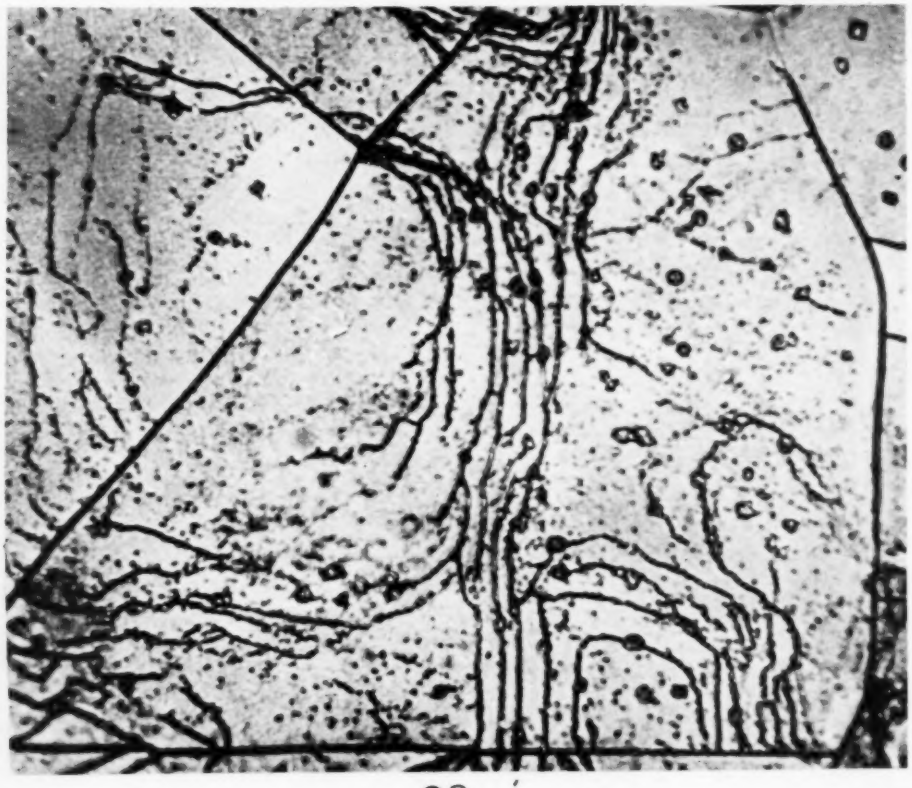

28

PLANCHE VIII. Figure 26—Recuit 14 h. à 200° + 3 h. à 400° + 1 h. à 500° (630×). Figure 27—Même champ après recuit supplémentaire 2 h. à 500° + 45 mn à 600°. Remarquer l'évolution de la sous-structure du grain A (630×). Figure 28—Autre champ du spécimen figure 27. Les gros points d'attaque localisés en majorité sur les sous-joints sont des restes de l'oxyde formé pendant le traitement à 600° et non éliminés par le polissage électrolytique (1600×).

se présentent sous trois aspects bien distincts dont les proportions respectives varient non seulement d'un grain à un autre, mais dans les différentes régions d'un même grain. La figure 11 en donne un exemple typique, car l'on y voit simultanément (*a*) des traces d'alignements rectilignes ponctuels qui sont des restes de stries ; (*b*) des rassemblements de points dessinant des contours polygonaux plus ou moins réguliers ; (*c*) des segments de lignes continues assez épaisses formant un réseau à mailles serrées. Sur le grain de la figure 10 existent seulement les contours polygonaux discontinus. Il est à remarquer que toutes les localisations d'attaques apparaîssent colorées en bleu intense sur un fond de teinte homogène, généralement bleu, quel que soit le grain considéré.

Les micrographies des figures 12, 16 et 17 prises à ce stade du recuit possèdent un intérêt particulier du fait qu'on a pu suivre leur évolution ultérieure à 500 et 600°. L'hétérogénéité de l'attaque est bien visible sur le grain à la partie supérieure de la figure 12, vu à plus forts grossissements figures 16 et 17. On remarque surtout les traces de stries parallèles au joint de macle *a* et la zone centrale peu attaquée séparant deux domaines *A* et *B* à microstructure complexe comportant de très petits segments fortement inclinés sur les alignements de points matérialisant les restes des glissements.

Recuit à 500°. Il suffit de 1 heure à 500° pour faire disparaître les derniers restes des bandes de colorations différentielles, et accentuer beaucoup les hétérogénéités de la microstructure amorcées à 400° (figure 13). Les petits segments qui étaient localisée dans les régions *A* et *B* du grain 1 font place a des lignes épaisses assez continues, sensiblement parallèles entre elles et à la direction des segments initiaux, et en première approximation perpendiculaires aux anciens glissements qui maintenant ne sont plus visibles. Quant à la zone centrale elle est morcelée en d'assez nombreux petits domaines définis par des contours où l'attaque ponctuée est extrêmement faible. Cette même sous-structure cellulaire se retrouve d'ailleurs dans la partie supérieure gauche du grain, au-delà de la petite bande des lignes en faisceaux. La comparaison de la figure 13 avec la figure 12 de l'état antérieur montre que la nouvelle sous-structure est bien en relation avec l'ancienne. (Sur ces deux figures la flèche repère le même endroit.)

D'autres régions de l'éprouvette présentent des aspects très analogues. La figure 26 montre par exemple des faisceaux serrés de lignes épaisses occupant de larges portions à la périphérie des grains, alors que les régions centrales ont une sous-structure cellulaire à peine visible qui existe seule sur toute l'étendue d'autres grains.

Les figures 19 et 20 montrent un autre cas très intéressant d'hétérogénéité. Le grain contient à sa partie supérieure droite des restes très nets de stries de glissement et de très petits segments rigoureusement normaux à ces stries, prolongeant les lignes en faisceaux développées sur la moitié inférieure. Plus à gauche on distingue le réseau cellulaire, puis au bord du joint un nouveau faisceau.

Une augmentation de la durée du recuit à 500° tend à faire disparaître les différences de sous-structure de grain à grain, tout en conservant les variations locales caractéristiques de chacun d'eux. Les rassemblements de lignes peu nombreuses, donc assez espacées, n'évoluent pratiquement pas, (figure 14 que l'on comparera à la figure 13), alors que les faisceaux de lignes serrées deviennent moins fournis. Ces deux aspects sont visibles également sur la figure 24 où l'on remarquera en particulier la stabilité des lignes repérées par les flèches (cf. figure 23). La comparaison des figures 21 et 22 avec les figures 19 et 20 montre également comment apparaîssent les sous-joints continus: par "soudure" de segments épais déjà bien orientés.

Dans les régions où les lignes continues sont absentes, c'est-à-dire presque toujours vers le centre des grains, le réseau cellulaire est maintenant un peu mieux visible, parce que l'attaque générale de la matrice étant moins intense, les contours ponctués se détachent avec davantage de netteté (figures 14, 18 et 24).

En ce qui concerne les caractéristiques du film solide coloré produit par l'attaque, on observe dès la première heure de recuit à 500° la disparition complète des bandes de colorations différentielles encore faiblement observables après le recuit à 400°. La couleur de la pellicule est uniforme sur l'ensemble des grains, quelle que soit leur orientation, toutefois plus foncée le long de leurs frontières et sur les éléments de la sous-structure (lignes continues et points séparés). Cet aspect n'évolue pas en prolongeant le traitement à 500°.

Recuit à 600°. La tendance vers un état d'équilibre structural commun à tous les grains se précise au cours du traitement de 45 minutes à 600° (figures 15, 25, 27 et 28). Chaque grain est alors morcelé en domaines fermés ayant conservé le type initial fibreux ou cellulaire. Les frontières du

type fibreux correspondent en général à une attaque plus continue que celle des cellules, dont le nombre a d'ailleurs diminué par rapport aux états antérieurs.

Il est remarquable qu'après ce recuit à 600° réapparaîssent les teintes du film solide spécifiques de chacun des grains (effet d'épitaxie) qui caractérisaient l'état non déformé. Sur ces colorations très différentes les sous-grains se distinguent par une teinte bleu-foncé.

III. Discussion des Résultats

L'essai préliminaire avec l'éprouvette N° 4 apporte deux résultats nouveaux et a une importante conséquence. Il prouve en effet : (1°) que la solution solide cuivre-zinc à 35% de zinc soumise à une très faible déformation, subit par un recuit ultérieur à 600° les transformations qui conduisent au phénomène de polygonisation classique ; (2°) que ce phénomène peut exister dans un spécimen polycristallin, alors que jusqu'à présent il avait été seulement observé et étudié avec les monocristaux ou les assemblages d'un petit nombre de très gros grains.* D'autre part, puisque la même technique d'attaque révèle d'abord les perturbations du réseau associés à la déformation plastique par glissements, puis, après le recuit, les frontières des sous-grains de polygonisation, nous sommes en droit de conclure que les microdomaines de dissolution sélective sont bien, comme nous l'avons admis dans la première partie de l'étude, en relation avec les dislocations. De ce fait on pouvait donc espérer pouvoir observer sous le microscope les stades intermédiaires prévus par la théorie de la polygonisation, mais que les techniques actuelles de la micrographie et des rayons X n'ont pas encore réussi à montrer. Dans les cas les plus favorables ces techniques ne décèleraient que les sous-grains dont la taille minimum est comprise entre 10 et 100 microns [1].

Les recuits étagés effectués sur l'éprouvette N° 3 avaient donc pour objet d'essayer de suivre l'évolution progressive de la sous-structure des grains depuis l'état déformé jusqu'à l'état typiquement polygonisé. A notre connaissance, la seule étude tentée dans ce sens est celle de Dunn et Daniels avec les gros cristaux de ferrosilicium, mais dans ces expériences les étapes de l'évolution sont peu nombreuses [2].

Remarquons tout d'abord que le résultat général le plus frappant est la grand hétérogénéité de la microstructure à l'intérieure de chaque grain à tous les stades du recuit. Nous avons vu que cette remarque vaut également pour l'état initial déformé, mais ici les différences sont beaucoup plus remarquables. Dans le premier cas il s'agissait, en effet, de simples variations de la répartition et de la densité des points d'attaque de forme et de taille très comparables. Ici s'observent des types d'aspects radicalement différents dont la localisation varie à l'intérieur des divers grains, tout en présentant une certaine constance de répartition. Il est à noter aussi que, surtout aux premiers stades, tous les grains n'atteignent pas au même moment le même état structural.

Ce sont précisément les hétérogénéités de la déformation initiale, telles qu'elles se traduisent par la densité des microdomaines de dissolution (figure 6 et plusieurs figures de la première partie) qui conditionnent toute l'évolution ultérieure au cours du chauffage (voir par exemple figure 26), résultat en parfait accord avec un mécanisme basé sur les dislocations.

L'attention doit donc se porter principalement sur les transformations de la sous-structure au début du recuit. Malheureusement notre étude n'est pas sans présenter à ce point de vue de notables lacunes. D'une part, il aurait été nécessaire d'observer les effets des traitements à 200 et 400° sur des endroits repérés du spécimen brut de déformation. Or l'examen systématique d'un même champ n'a été fait qu'à partir de l'éprouvette déjà traitée á ces températures. D'autre part, les phénomènes initiaux se déroulent à une échelle qui est à l'extrême limite du pouvoir de résolution du microscope optique, c'est-à-dire que la micrographie électronique permettrait sans aucun doute une bien meilleure définition.

Sens général de l'évolution entre 200 et 500°. Le recuit à 200° entraîne une modification assez sensible de la microstructure dans certains grains. L'attaque présente en effet les deux caractéristiques suivantes: (1°) elle donne non plus des alignements de points distincts, mais des domaines continus très étroits (0,25 à 0,5 micron) dont les bords ne sont pas parfaitement rectilignes, et qui s'allongent sur des distances parfois considérables, surtout au voisinage des frontières intergranulaires ; (2°) elle envahit des régions situées entre les stries, sous forme d'un gravage généralisé non résolu sous les plus forts grossissements optiques (figure 8).

Ces aspects nouveaux pourraient traduire les mouvements des dislocations sur les plans de

*GUINIER et TENNEVIN ont cependant montré, à l'aide des rayons X, la polygonisation dans une éprouvette d'aluminium contenant des grains de 0, 2 mm [1].

glissements actifs et les débuts de leur nouvelle répartition dans le réseau, interprétation qui demanderait à être confirmée par des expériences sous les conditions d'observation indiquées plus haut. La discussion des diagrammes de rayons X apporte d'ailleurs d'autres renseignements qui ne sont pas en désaccord avec la micrographie (voir Appendice).

Il est intéressant de noter que dans leur travail sur le ferrosilicium Dunn et Daniels ont mis aussi en évidence par la micrographie un stade précoce du recuit qui est, à l'échelle près (le grossissement étant de 200 seulement), très comparable à celui décrit ici (voir la figure 10 du mémoire réf. 2).

C'est à partir du traitement de 3 heures à 400° que l'évolution de la microstructure devient assez nette dans la quasi-totalité des grains pour pouvoir être différentiée sans aucune ambiguïté de celle de l'état initial. Les figures 10, 11, 12, 16 et 17 indiquent une réorganisation complète des microdomaines d'attaque, à l'intérieur de chaque grain. En gros, cette réorganisation conduit à deux types extrêmes faciles à distinguer. Le premier comporte des points bien séparés dessinant de petites cellules plus ou moins nettement définies (figure 11), et le second des segments continus dont la taille, la forme et le nombre sont très variables, pouvant, par exemple, s'enchevêtrer pour constituer un réseau serré (région en haut à gauche figure 11), ou rester assez localisés, tout en prenant une orientation générale commune d'aspect fibreux (région de la figure 17 limitée à sa partie supérieure par la ligne sensiblement continue repérée par la flèche 1).

A ces types de sous-structure de recuit précoce peuvent se superposer des restes de microattaques correspondant aux stries caractéristiques de la déformation. C'est le cas des segments discontinus qui sont toujours associés à des lignes de points bien parallèles. Ainsi, sur la figure 17 les segments font avec ces restes de stries très discontinues un angle de 75°. Il en est de même pour le grain figure 11 dans la petite portion encadrée où l'angle est ici de 90°. Enfin nous en verrons un exemple encore plus net après le recuit supplémentaire de 1 heure à 500° (figure 20).

Déjà à ce stade apparaît une relation évidente entre l'intensité de la déformation et le type de sous-structure, relation qui se précisera encore par la suite. Les cellules définies par les segments formés de points bien séparés naissent manifestement dans les grains ou portions de grains plus pauvres en glissements, tandis que le réseau de lignes épaisses et continues correspondent à des régions initialement très riches en stries ; une situation intermédiaire est celle des petits segments associés à des restes d'attaque sur les glissements.

Une telle relation est en accord avec la théorie basée sur les dislocations. Celle-ci prévoit, en effet, le rôle important de la courbure du réseau, car les dislocations étant concentrées dans les plans de glissements actifs, le nombre de systèmes de glissement mis en jeu au cours de la déformation conditionne les proportions respectives des dislocations de signes contraires et la distribution ultérieure de celles en excès. Il est donc normal que là où l'attaque mettait en évidence une accumulation de dislocations sous forme de plusieurs systèmes d'alignements de points, impliquant une forte courbure du réseau, apparaisse la nouvelle organisation en lignes continues enchevêtrées. Par contre, dans les régions où le petit nombre de points d'attaque traduisait la pauvreté relative en dislocations, et la plus faible courbure du réseau, on doit s'attendre à rencontrer le type de sous-structure cellulaire à contours ponctués discontinus. Le premier cas s'observe en général vers la périphérie des grains et le second dans les portions centrales (figure 16 de la première partie, et figure 23).

Il semble donc qu'à ce stade initial du recuit nous assistions surtout au processus de concentration des dislocations conduisant à la formation de murs ou parois. La théorie voudrait que cette étape de la polygonisation soit précédée d'un processus de neutralisation des dislocations de signes contraires. Les seuls aspects micrographiques ne permettent pas de mettre en évidence un tel phénomène, à moins d'en voir une preuve dans la microstructure relativement plus claire après recuit à 400°, par rapport à l'état de recuit à 200° (cf par exemple la figure 8 avec les figures 10, 11 et 17). D'ailleurs dans ce domaine de la confrontation des expériences avec la théorie il faut garder une grande prudence, car nous avons à faire ici à un réseau plus compliqué que celui traité par les théoriciens, d'autre part il existe plusieurs types de dislocations, et en ne considérant même que le type en arête nous n'avons aucun renseignement sur l'excès de dislocations d'un signe donné, sachant seulement qu'il doit être maximum dans les régions où la courbure du réseau est la plus grande.

Toujours d'après la théorie, les murs de dislocations se placent normalement à la direction des

glissements. Or dans notre éprouvette déformée la plupart des grains contiennent deux, et parfois même trois, systèmes de stries (figure 6), de sorte qu'il n'est pas facile de vérifier la localisation prévue, puisque les endroits examinés après recuit à 200 et 400° n'avaient pas été repérés à l'état initial. Selon Dunn et Daniels [2] quand il existe deux systèmes de glissement sur un monocristal de ferrosilicium déformé, les sous-joints qui se forment au recuit sont orientés normalement à celui qui serait le plus "actif." La figure 21 de la Première Partie prouve qu'à la traction du laiton polycristallin les premières lignes de glissement apparaissent selon un seul système, les autres intervenant ensuite. Donc pour résoudre la question de la position exacte des amorces de sous-joints il faudrait déterminer, par des expériences préliminaires, l'ordre d'apparition et la position des systèmes de stries dans les grains dont on étudierait ensuite la sous-structure de recuit.

Sur certaines des micrographies il est visible que les premiers indices des sous-joints dans les régions notablement déformées se localisent normalement aux traces du seul système de glissement rendues visibles par des points d'attaque (figure 20). Il existe des preuves, et nous les discuterons plus loin, que cette localisation peut se faire parallèlement à un autre système de glissement, lorsque celui-ci est lui-même encore visible et est orienté dans une direction presque normale par rapport au premier.

Aucun effet net d'orientation des sous-joints ne peut-être reconnu aux stades précoces du recuit dans les deux cas extrêmes des régions très fortement déformées, où les segments sont enchevêtrés (figure 11), et des régions contenant le minimum de déformation, où se forment les cellules à contours ponctués à peine décelables.

Nous avons vu que les résultats des traitements de 1 heure, puis de 2 heures à 500° sont caractérisées par l'apparition de sous-grains maintenant bien nets et à contours fermés, présentant le type fibreux ou le type cellulaire selon qu'ils naissent respectivement dans les régions de forte ou de faible déformation. On pourait dire que ces sous-grains résultent de la croissance des très petits domaines esquissés par les segments plus ou moins continus déjà présents après le recuit à 400°. En réalité il paraît difficule de parler de croissance en donnant à ce terme son sens habituel en métallographie, où le grossissement d'un grain se produit par simple déplacement de tout ou partie de son contour fermé préexistant.

Sous-structure "fibreuse." Pour essayer de comprendre la genèse des sous-joints du type fibreux, les figures 19 à 22, planche VI, présentent un intérêt tout particulier. Sur la figure 19 ces sous-joints se distinguent à la partie inférieure du grain et deviennent de moins en moins nets à mesure qu'ils se rapprochent de la partie supérieure où ils finissent par se perdre dans une sous-structure confuse qui se résout au grossissement 2000 en petits segments parallèles entre eux et perpendiculaires à des restes très apparents de stries de glissements (figure 20). Après le traitement complémentaire de 2 heures à la même température de 500° les figures 21 et 22 prouvent que : (1°) sur la moitié inférieure du grain les sous-joints sont devenus beaucoup plus nets, en même temps qu'ont disparu la plupart des points d'attaque dispersés ; (2°) les mêmes sous-joints se prolongent maintenant sans discontinuité sur la partie supérieure où les restes de stries de glissement ne sont plus visibles.

D'autres cas analogues sont donnés par les figures 17 et 18 d'une part, 23 et 24 d'autre part. Après 3 heures à 500° la portion du grain qui possédait la sous-structure figure 17 (correspondant à une étape d'évolution apparemment un peu moins avancée que celle de la figure 21) donne les mêmes sous-joints continus et fibreux (figure 18, cf. figure 21). Sur la figure 23 les rassemblements diffus de points d'attaque repérés par les flèches 1, au bord du large faisceau développé sur la partie gauche du grain, se concentrent en lignes bien définies après le traitement supplémentaire de 2 heures à 500° (figure 24). Les régions supérieure et inférieure du même faisceau évoluent respectivement comme les portions inférieure et supérieure du grain des figures 19 et 21.

L'ensemble de ces résultats montre que l'évolution qui conduit à la formation des sous-grains du type fibreux, à partir du moment où la sous-structure est nettement différentiée par rapport à l'état déformé, impliquerait un processus de migration et de concentration des dislocations vers et dans des plans dont les positions paraissent déjà à peu près fixées, et qui se précisent au cours du recuit. En effet, les écartements des régions indiquées par les flèches latérales sur la figure 17, et sur lesquelles l'attaque est un peu plus intense correspondent sensiblement, compte tenu du grossissement, aux distances qui séparent les sous-joints apparaissant dans la même région (figure 18). On remarquera d'ailleurs que ces zones peuvent être distinguées aussi sous un plus faible grossisse-

ment (figure 16) et que la première d'entre elles (flèche 1) correspond exactement à la limite qui sépare les deux régions A et B où se forment, d'une part, la sous-structure fibreuse, et d'autre part, la sous-structure dite "cellulaire." Nous examinerons plus loin si ces plans, où se concentrent les dislocations, sont en relation avec la microstructure de déformation.

La preuve que les sous-joints sont bien la conséquence des processus de migration et de concentration des dislocations est apportée par le fait que leur accroissement de netteté coïncide avec la disparition progressive des microdomaines d'attaque encore localisés sur les restes de glissements ou déjà dispersés. Le microscope optique paraît indiquer que les attaques dispersées ne sont pas réparties d'une façon quelconque dans la matrice, mais dessinent des contours plus ou moins discontinus de très petits domaines de l'ordre de 2 à 4 microns (figures 11 et 17). On pourrait donc dire que la disparition de ces contours correspond à un grossissement des domaines qu'ils délimitent, à condition d'ajouter que cette croissance se bloque contre des parois déjà matérialisées, et qui, de ce fait, se trouve parfois renforcées par un nouvel apport de dislocations.

Il n'est pas douteux que la cinétique des processus de migration et de concentration des dislocations pendant le recuit à 500°, déduite des aspects micrographiques, est conditionnée par leur distribution initiale telle qu'elle résulte des recuits antérieurs, et qui est elle-même fonction de l'état de déformation primitif. En effet, nous limitant toujours, pour l'instant, à la seule sous-structure fibreuse localisée dans les régions de déformation maximum, nous observons à un stade donné, et à l'intérieur d'un même grain, de grandes hétérogénéités dont il est facile de voir des exemples sur les figures 22 et 23. Ainsi, pour le grain de la figure 22 le recuit supplémentaire de 2 heures à 500° n'a aucun effet sur la sous-structure de la zone qui borde jusqu'à une distance de 5–10 microns le joint à droite, et cette sous-structure très confuse, encore mieux visible sur la figure 20 correspond, comme celle de la figure 11 à un rassemblement de petits segments très enchevêtrés et sans orientation définie. De même sur la figure 23 la base du faisceau en haut à gauche, où les fibres sont très serrées et assez bien orientées, conserve encore une structure fine après le recuit supplémentaire de 2 heures à 500° (figure 24).

Revenons maintenant à l'importante question de la position des sous-joints fibreux par rapport aux glissements. Considérons pour cela le grain de la figure 16. Il comporte deux portions A et B qui se différentient à ce stade du recuit (14 heures à 200° + 3 heures à 400°) par le nombre de systèmes de glissement encore présents sous forme de traces de stries d'attaque. Dans la partie A on voit surtout les systèmes 1 et 2 et des indices du système 3 (pour plus de clarté ces directions sont portées sur la figure 18), alors que dans la région B le système 1 est seul présent. Or, à ce même stade les premiers indices de sous-joints sont : dans la région B des petits segments (très comparables à ceux sur la figure 20, mais toutefois moins nets) se plaçant à 90° par rapport au système 1, et dans la région A des domaines d'attaque assez diffus concentrés autour de la direction du système 2, lequel fait un angle de 75° environ avec la direction du système 1.

Au cours des traitements à 500° les sous-grains deviennent bien définis et dans les deux régions A et B leur plus grande dimension a conservé l'orientation générale fixée à l'étape antérieure. Leurs frontières présentent d'ailleurs de franches sinuosités, ayant tendance dans la région A à se placer à 90° par rapport au système de glissement 3, de même que les lignes continues qui ferment le contour de ces sous-grains fibreux.

Par conséquent dans les grains, ou portions de grains, déformés contenant plusieurs systèmes de lignes de glissement, les dislocations qui, pendant le recuit se déplacent sur les plans correspondants, peuvent se concentrer sur l'un d'entre eux pour amorcer les parois des domaines de polygonisation, lorsque l'orientation de celui-ci est assez voisine de 90° par rapport à un autre système. Il est probable d'ailleurs que cette condition d'orientation ne suffise pas, et qu'il doive exister en outre certaines relations entre les proportions respectives des dislocations sur les divers systèmes, proportions qui varient beaucoup d'un endroit à un autre et peuvent expliquer le caractère sinueux des sous-joints. Dunn et Daniels [2] ont mis en évidence des aspects analogues aux nôtres dans les cristaux de ferrosilicium laminés à 12% et recuits, tandis que dans les mêmes cristaux déformés par flexion les sous-joints sont remarquablement rectilignes et parallèles.

Sous-structure "cellulaire." Dans les portions généralement localisées vers le centre des grains* l'évolution à 500° est difficile à saisir, parce que les

*Et qui s'étendent au grain entier dans les régions de l'éprouvette voisines des têtes où nous avons montré que les glissements étaient en nombre très limité.

contours des sous-grains, ici grossièrement équiaxes, sont indiqués par des alignements ou des rassemblements de points très discrets qui se détachent sur un fond présentant une attaque de grande finesse. Les effets les plus apparents de l'augmentation de la durée du recuit à 500° sont de réduire l'importance de cette attaque généralisée, d'augmenter quelque peu la netteté de certains sous-joints et de diminuer au contraire, jusqu'à la faire disparaître, l'attaque de certains autres (cf. figures 13–14 et figure 23–24). Ces effets peuvent, ici encore, s'interpréter comme traduisant la migration et la concentration des dislocations.

Les attaques beaucoup plus discrètes dans les régions de faible déformation par rapport à celles qui mettent en évidence les sous-joints fibreux continus, sont bien en accord avec le fait que les dislocations y sont relativement peu nombreuses. Cette faible proportion est non seulement une conséquence de la distribution initiale (figure 6), mais provient aussi de ce que les courbures du réseau étant limitées, l'excès de dislocations d'un signe donné doit être certainement inférieur à ce qu'il est dans les portions très riches en glissements. Il est fort possible que le processus de neutralisation se poursuive encore, au moins au début, pendant le recuit à 500°, car des traces d'attaques en stries sont encore décelables à ce stade.

Perfection des domaines de polygonisation. Après les recuits à 200, 400 et 500° les dislocations se sont rassemblées pour former dans beaucoup de grains, mais non dans tous, les contours de domaines dont le nombre, la taille et la forme varient en relation avec l'hétérogénéité de la déformation plastique initiale. Pouvons-nous dire que chaque domaine a acquis à ce stade le degré de perfection qui caractérise les sous-grains de polygonisation typique? La discussion des aspects micrographiques donnée ci-dessus justifie, sans aucun doute, une réponse négative reposant surtout sur le fait que les points d'attaque ne sont pas strictement localisés sur les sous-joints. On verra d'ailleurs plus loin (dans l'Appendice), que les diagrammes de rayons X confirment le caractère encore très imparfait de la grande majorité des domaines de polygonisation.

Le recuit complémentaire de 45 minutes à 600° accentue l'évolution amorcée à la fin du séjour à 500° et la provoque dans les grains ou portions de grains restés jusqu-là plus ou moins en retard (par exemple le grain A, figures 26 et 27). Les attaques continues ou ponctuelles se détachent avec une remarquable netteté sur un fond très bien poli (figure 15, 25 et 28), suggérant que le stade de polygonisation typique a été atteint, c'est-à-dire que chacun des domaines morcelant le grain posséderait maintenant un bien meilleur degré de perfection. Effectivement, les diagrammes de rayons X pris sur l'éprouvette comportent la division des taches caractéristiques de l'état polygonisé (voir Appendice).

Croissance des sous-grains. La grande mobilité des sous-joints de polygonisation serait une caractéristique importante qui les différentieraient des joints intergranulaires normaux. Elle expliquerait la croissance des domaines, observée à la fois avec le microscope et avec les rayons X, quand un échantillon polygonisé est soumis à un nouveau recuit. On admet cependant qu'un état d'équilibre peut être atteint à partir duquel la croissance s'arrête. On a dit également que le processus de croissance pourrait correspondre au développement des domaines les plus parfaits aux dépens de ceux qui le sont le moins [1].

Comme on a pu s'en rendre compte au cours de la discussion qui précède, nos résultats conduisent à préciser le mécanisme possible de la croissance des sous-grains, phénomène sur lequel les connaissances d'ordre expérimental sont d'ailleurs assez vagues.

La première preuve micrographique de la mobilité des contours des domains de polygonisation a été apportée par Lacombe et Beaujard [3]. Leur micrographie montre simultanément sur un spécimen d'aluminium pur à très gros cristaux polygonisés, la trace des anciens sous-joints et celle des nouveaux apparus à la suite d'un deuxième traitement à 600°. Il est clair que ce traitement a produit un réarrangement complet, mais contrairement à ce qu'on attendrait, les nouvelles positions sur le cristal principal correspondent à un nombre de sous-grains presque double de celui à l'état antérieur. En revanche, sur la petite portion visible d'un cristal adjacent il y a réduction notable du nombre des domaines sans modification de l'aspect général. Une explication possible du comportement aberrant du grain principal serait une déformation accidentelle au cours des manipulations entre les deux recuits.*

Le mémoire de Dunn et Daniels [2] contient

*Des systèmes de stries ayant l'apparence de lignes de glissement sont visibles sur la micrographie. Elles ne peuvent que matérialiser une déformation plastique postérieure au deuxième traitement thermique, donc sans influence sur les nouveaux sous-grains également visibles. Il n'en serait pas de même, évidemment, si des glissements s'étaient produits aussi après le premier recuit. Nous avons pu nous rendre compte à nos dépens de l'extrême facilité avec laquelle un spécimen relativement mince tend à se déformer, et les chances d'un tel accident augmentent, bien entendu, avec la taille des grains.

plusieurs exemples micrographiques de croissance des sous-grains pendant le recuit de gros cristaux de ferrosilicium polygonisés. Elle se traduit par l'augmentation de la distance, jusqu'à 10 fois, qui sépare leurs frontières bien rectilignes et parallèles. Les auteurs l'expliquent par une migration de ces frontières, mais admettent aussi, sans trop y insister, l'intervention partielle d'un phénomène de "disparition" de certains sous-joints. Nous verrons plus loin que sur quelques figures du mémoire de Dunn et Daniels, ce phénomène ressort d'une façon frappante. En tout cas, contrairement à l'observation de Lacombe sur l'aluminium, les stades successifs de croissance des domaines de polygonisation du ferrosilicium conduisent à des aspects micrographiques cohérents, c'est-à-dire que ces domaines deviennent moins nombreux tout en conservant leur disposition générale.

L'examen d'endroits repérés sur l'éprouvette soumise aux recuits étagés nous indique que contrairement au phénomène banal de grossissement d'un métal polycristallin, la croissance des domaines de polygonisation ne correspond pas aux déplacements de leurs limites. De plus, nous avons donné de nombreux exemples de sous-joints conservant, à partir du moment où ils sont bien formés, leurs positions exactes pendant les recuits ultérieurs.

Pour interpréter l'évolution de la sous-structure micrographique au chauffage entre 400 et 600°, nous n'emploierons donc pas l'expression "mobilité" des sous-joints qui laisse sous-entendre une analogie avec certains phénomènes de croissance des grains, observés par exemple par Beck et ses collaborateurs [4]. Nous préférons baser l'explication possible des faits sur une notion de stabilité thermique des sous-joints, ou plutôt des dislocations qu'ils contiennent.

A une étape assez précoce du recuit, des dislocations se rassemblent à certains endroits du réseau perturbé pour former des parois de grande stabilité que nous appelerons "sous-joints primaires." Ils délimitent des domaines, ou "sous-grains primaires," eux-mêmes morcelés en "sous-grains secondaires" par d'autres rassemblements de dislocations formant des "sous-joints secondaires" moins stables que les précédents. A ce moment le grain peut être considéré comme contenant déjà les larges domaines de polygonisation, relativement assez désorientés les uns par rapport aux autres, qui seront décelés au stade final. Chacun d'eux est encore très imparfait du fait de son morcellement en nombreux sous-grains secondaires avec de faibles degrés de désorientation. Les micrographies traduisent bien cet état d'imperfection qui explique que la polygonisation ne soit pas encore visible sur les diagrammes de rayons X (voir Appendice).

En augmentant la durée du chauffage, ou mieux en élevant la température, les sous-joints secondaires disparaissent, probablement par migration des dislocations individuelles qui iraient se fixer sur les sous-joints primaires, comme le suggère l'accroissement de netteté de ceux-ci. Dans le cas des régions à faibles courbures du réseau, il n'est pas exclu que la disparition des sous-joints secondaires soit dûe, en partie ou en totalité, au processus de neutralisation. La nouvelle configuration résultante se traduira par un grossissement apparent des vrais domaines de polygonisation, ou sous-grains primaires, et par un accroissement de leur degré de perfection. Finalement apparaîtra l'état structural typique de la polygonisation, c'est-à-dire la division de chaque grain en un petit nombre de domaines plus ou moins désorientés les uns par rapport aux autres, mais individuellement assez parfaits, pour qu'ils se manifestent sur les diagrammes de rayons X.

D'après ce schéma il n'y aurait donc pas de discontinuité entre les deux étapes extrêmes correspondant, la première à la visibilité au microscope du réseau serré d'alignements des dislocations (recuit 3 heures à 400°), et la seconde à la polygonisation classique (dernier recuit de 45 minutes à 600°). En d'autres termes, à chaque stade du recuit existerait une certaine hiérarchie des parois de dislocations, ou sous-joints, définie probablement par des facteurs en relation avec les dislocations, et avec le degré de perfection du réseau dans les domaines contigüs. On conçoit que cette hiérarchie soit d'autant plus facile à mettre en évidence que l'état considéré est plus éloigné de la configuration supposée stable (voir plus loin).

L'interprétation proposée explique pourquoi les deux caractères de l'état polygonisé, taille et perfection des domaines, évoluent en même temps, et soient respectivement d'autant plus grande et meilleure que le recuit est plus avancé. On doit tenir compte aussi de l'intensité de la déformation plastique initiale qui conditionne la distribution des dislocations et leur nombre. Ainsi l'évolution est plus rapide dans les régions de très faible déformation (près des têtes de l'éprouvette) où l'on observe les domaines les plus grands et les plus parfaits.

L'examen attentif des micrographies publiées par Dunn et Daniels [2] révèle des aspects très

comparables à ceux trouvés dans le laiton, tendant à prouver que le grossissement des domaines de polygonisation dans le ferrosilicium s'effectue selon le même mécanisme. Cependant ces aspects ne suffiraient pas à eux seuls pour décrire le phénomène parce que les étapes du recuit sont largement espacées, les observations successives sont faites sous faible grossissement optique (× 200) et non exactement aux mêmes endroits ; et enfin la méthode de détection des sous-grains n'est probablement pas d'une extrême sensibilité. Nous signalerons tout particulièrement la figure 4 du mémoire original concernant un gros cristal déformé par laminage. Après le premier recuit de 10 minutes à 950° la sous-structure comporte des bandes parallèles et un réseau cellulaire dont il subsiste, après le recuit ultérieur de 1 heure à 1200°, des restes très apparents, sous forme d'alignements de points à l'intérieur de très gros domaines, généralement très alongés dans la direction des bandes primitives, et limités par des lignes épaisses.

On peut se demander jusqu'à quel point l'état de polygonisation typique, celui que nous obtenons au recuit de 45 minutes à 600°, est stable. Certains auteurs ont dit avoir trouvé encore la polygonisation dans des monocristaux portés jusqu'au voisinage du point de fusion du métal, mais nous estimons que ces preuves expérimentales sont insuffisantes, car il doit être difficile d'affirmer que des traces de déformations ne se sont pas produites sous l'effet de contrainte mécanique, par exemple, au début du refroidissement, ou comme conséquence de la formation d'oxyde superficiel. La rétrogradation apparente de la polygonisation typique vers une étape antérieure, effectivement constatée avec notre éprouvette N° 3 après un nouveau recuit de 1 heure 30 à 600°, ne peut qu'être attribuée à une déformation non intentionnelle pendant les manipulations.

En tous cas, pour cette éprouvette N° 3 la sous-structure au stade du recuit 45 minutes à 600° présente des signes indiscutables de "dissolution" partielle de certains sous-joints qui ne sont plus, en effet, des lignes continues, mais des alignements de points distincts (figures 15, 25 et 28). Dans l'éprouvette N° 4 traitée 2 heures à 600° nous avons vu qu'il existe à la fois des sous-joints ponctués et continus limitant de larges domaines où peuvent être parfois devinées des traces de sous-structure secondaire (figure 4). Toutes ces observations sont des indices de l'instabilité, sinon de toutes les frontières des domaines de polygonisation, au moins de certaines d'entre elles. Le fait qu'un sous-joint initialement sous forme d'une ligne continue se transforme en une séquence de points distincts traduit : (1°) son appauvrissement en dislocations ; (2°) la tendance des domaines qu'il sépare à prendre la même orientation. Si ce processus se poursuivait, il conduirait à une diminution du nombre des sous-grains et peut-être à leur disparition complète, c'est-à-dire au rétablissement de l'homogénéité d'orientation et de perfection du réseau dans la masse entière du grain. La vérification de cette hypothèse exigerait une éprouvette épaisse, une atmosphère de recuit non oxydante et de grandes précautions pendant les manipulations. On devra aussi tenir compte de certaines remarques concernant les conclusions tirées des aspects micrographiques, et que nous allons rapidement discuter.

Les micrographies montrent la raréfaction des microdomaines d'attaque sélective à mesure que le recuit progresse, mais il ne faudrait pas tirer de cet effet des conclusions trop absolues du point de vue de phénomènes qui se déroulent à l'échelle de la maille atomique. Nous pouvons seulement affirmer qu'il existe une relation entre les points de dissolution préférentielle et la présence de certaines dislocations. Le fait qu'une attaque ne se produise plus là où elle était observée à un stade antérieur peut seulement s'interpréter comme la preuve certaine d'une diminution de la concentration des dislocations à cet endroit, et non comme celle de leur disparition complète.

D'ailleurs, les micrographies électroniques sur l'éprouvette déformée nous avaient révélé des points de dissolution de l'ordre de 0,1 micron, c'est-à-dire invisibles au microscope optique. Par conséquent il n'est pas exclu que la disparition d'une attaque constatée sous les plus forts grossissements du microscope optique corresponde à une simple diminution de son intensité. Un indice assez sérieux en faveur d'une telle hypothèse est fourni par la micrographie figure 4 : le large sous-grain bien délimité (sauf à sa partie inférieure comprise entre les deux flèches) contient des segments à peine résolus qui marqueraient des restes sous-structure antérieure. Toutefois, étant donné que ces aspects sont à l'extrême limite des possibilités du microscope employé, nous ne sommes pas en mesure d'affirmer qu'ils existent à l'intérieur de tous les sous-grains. En tout cas les rayons X prouvent que ce spécimen est dans l'état polygonisé typique, c'est-à-dire que la majorité des domaines ont acquis une taille et un degré de perfection du

réseau suffisants pour être visibles sur les diagrammes.

Caractéristiques du film solide coloré. Quelques aspects du film coloré, aux différentes étapes du recuit, méritent d'être maintenant discutés.

La disparition complète des bandes de colorations différentielles entre 400 et 500°, c'est-à-dire au moment où commence à évoluer d'une façon très sensible la microstructure d'attaque, est en faveur de l'origine que nous avons attribuée à ces bandes, à savoir l'hétérogénéité de répartition des tensions internes, elles-mêmes en relation avec la non-homogénéité de la déformation plastique dans le masse de chacun des grains. Rappelons que dans ses expériences sur les feuilles polycrystallines de chlorure d'argent déformées, Nye a observé la disparition progressive des bandes biréfringentes pendant le recuit [5].

L'identité de coloration générale de tous les grains, qui caractérisait l'alliage à l'état brut de déformation, existe encore après le recuit de 3 heures à 500°. A ce stade les variations locales de teinte d'un grain donné correspondant aux attaques (points isolés, frontières plus ou moins continues des sous-grains) sont bleu foncé, ce qui s'explique ici encore, par un maximum d'épaisseur du film, simple conséquence de la dissolution préférentielle. En outre, le film est également plus épais sur une bande étroite de part et d'autre des joints intergranulaires. Ce phénomène traduit une réactivité chimique plus grande de la solution solide dont l'origine n'est pas claire, et qui n'existe d'ailleurs pas pour les joints de macles.

Il est très remarquable que la coloration spécifique de l'orientation cristallographique du grain ne réapparaisse qu'après le recuit final, c'est-à-dire 45 minutes à 600°, au moment où le microscope et les rayons X indiquent l'état de polygonisation typique caractérisé par le petit nombre des sous-grains et par la perfection du réseau de chacun d'eux. A toutes les étapes précédentes l'effet d'orientation serait donc inhibé par le degré d'imperfection encore élevé qui se traduit sur les micrographies (sous-joints secondaires) et sur les diagrammes de rayons X.

IV. Resumé et Conclusions

1° La très grande sensibilité de la méthode d'attaque anodique a permis d'observer comment évolue, au cours de recuit successifs entre 200 et 600°, la microstructure des éprouvettes faiblement déformées par traction, étudiées dans la Première Partie du travail.

2° Ainsi ont pu être mis en évidence dans le laiton α polycristallin deux faits importants : la polygonisation des grains, stade ultime du traitement thermique, et l'existence d'étapes intermédiaires intéressantes du point de vue des processus donnant naissance à l'état polygonisé.

3° Les aspects observés confirment que les microdomaines d'attaque sélective sont bien en relation avec la distribution de certaines dislocations, car ils sont, d'une façon très générale, en accord avec le mécanisme de polygonisation fondé, selon la terminologie moderne, sur les modes de réarrangement des dislocations dans le réseau cristallographique perturbé.

4° Toutefois, la théorie classique manquait jusqu'ici d'appui expérimental pour préciser, d'une part les premiers stades de réarrangement, d'autre part le processus de croissance des domaines déjà polygonisés.

L'évolution de la microstructure à l'échelle du microscope optique apporte à ce double point de vue quelques renseignements qu'il conviendrait, d'ailleurs, de confronter, avec les idées théoriques.

5° Le premier recuit de 14 heures à 200° provoque une nette transformation de la microstructure de déformation, mais à une échelle qui est au-delà du pouvoir de résolution optique. Les aspects beaucoup plus confus suggèrent un accroissement du nombre de microdomaines de dissolution préférentielle et leur extension dans des zones initialement non réactives.

6° L'examen des mêmes endroits attaqués après les traitements à 400, 500 et 600° montre que dès le recuit de 3 heures à 400° pour quelques uns des grains, et après 1 heure à 500° pour la majorité d'entre eux, les attaques sélectives amorcent des contours qui se précisent ensuite et restent stables jusqu'au stade ultime de la polygonisation. Ces contours définissent des domaines relativement volumineux à l'intérieur desquels d'autres points d'attaque disparaissent progressivement.

7° On est ainsi conduit à penser que les parois constitués de rassemblements de dislocations présentent des degrés de stabilité thermique variables. Les plus stables constituent les sous-joints que nous avons appelés primaires. Ils délimitent des sous-grains qui persistent encore après 45 minutes à 600°. Les autres sont les sous-joints secondaires qui n'existent plus au moment où la polygonisation typique est incontestable.

8° Jusqu'au stade où les rayons X montrent l'apparition de la polygonisation (voir Appendice) les phénomènes de croissance *apparente* et de

perfectionnement du réseau des sous-grains seraient donc étroitement associés. Cependant, même à cet état tous les sous-joints ne sont pas équivalents. Les uns, attaqués en lignes continues, doivent séparer des domaines de désorientation mutuelle plus grande que celle des domaines séparés par des alignements de points plus ou moins espacés. Ces deux formes peuvent d'ailleurs coexister sur un même contour fermé.

9° Le problème de la stabilité des sous-joints de polygonisation typique n'a pas été abordé. Il est d'ailleurs difficile, car l'on devra éviter toute possibilité d'apparition de traces de déformation plastique pendant les expériences.

Certains aspects micrographiques indiquent que la stabilité thermique n'est probablement pas identique pour tous les sous-joints, ce qui laisserait prévoir une croissance des domaines par un mécanisme analogue à celui conduisant à la polygonisation typique.

10° La grande hétérogénéité de la déformation plastique se traduit sur les microstructures de recuit. A une température donnée les divers grains et les différentes régions de chacun d'eux ne sont pas au même état. La localisation des deux types de sous-joints et leurs stabilités thermiques relatives sont en relation avec l'intensité des déformations telle que la révèlent les stries d'attaque à l'état initial non recuit.

11° Les sous-joints continus rassemblés en faisceaux apparaissent dans les zones périphériques des grains riches en glissements, donc où les courbures du réseau sont les plus grandes. Ils prennent alors une orientation générale perpendiculaire au seul système de glissement encore apparent. S'il existe dans le même grain des régions où sont encore visibles des traces d'un deuxième système d'orientation assez proche de 90° par rapport à l'autre, les sous-joints se forment parallèlement à ce deuxième système.

Dans les portions de moindre déformation, c'est-à-dire à plus faibles courbures du réseau, les sous-joints sont limités par des alignements de points discrets, conséquence probable de la pauvreté relative en dislocations du signe en excès. Cette sous-structure est seule présente dans les grains voisins des têtes des éprouvettes où l'effort de traction était minimum.

12° Outre les dissolutions sélectives définissant la microstructure, la méthode d'attaque anodique produit sur la surface un mince film solide de composés sulfurés dont les caractéristiques de coloration se sont révélées aussi d'une grande sensibilité à l'évolution thermique de la solution solide déformée.

Les bandes de coloration différentielles qui existent dans les grains déformés, et que nous avons attribuées aux tensions internes, s'estompent à 400° et disparaissent complètement après 1 heure à 500°. Les colorations spécifiques de l'orientation des grains (effet d'épitaxie) qui se manifestent sur l'alliage recristallisé non déformé, ne réapparaissent qu'au stade de la polygonisation typique, c'est-à-dire quand les sous-grains relativement peu nombreux ont atteint un degré de perfection suffisant.

13° A aucun stade nous n'avons pu observer d'indice de recristallisation dans l'éprouvette utilisée pour l'étude de l'évolution de la microstructure de recuit. En revanche, un exemple unique d'apparition d'un trés petit grain a été trouvé dans l'éprouvette déformée par traction et flexion et portée à 600°. Ce résultat doit être souligné, car il prouve la possibilité d'étudier sur une même éprouvette de laiton de section variable les relations encore peu connues entre la polygonisation et la recristallisation.

Références

1. Guinier, A. and Tennevin, J. Researches on the polygonization of metals. Progress in Metal Physics **2** (1950) 177.
2. Dunn, C. G. and Daniels, F. W. J. Metals **3** (1951) 147.
3. Lacombe, P. and Beaujard, L. Sub-boundary structure in high purity aluminium. Report of a conference on Strength of Solids, (Bristol, Physical Society, 1947), p. 91.
4. Voir par exemple Beck, P. A. and Sperry, R. J. Metals, **2** (1950) 468A.
5. Nye, J. F. Proc. Roy. Soc. **A198** (1949) 190.

APPENDICE

Examens qualitatifs aux rayons X de la polygonisation d'une solution solide cuivre-zinc a 65/35.*

Mme. A. R. WEILL†

On a effectué un certain nombre de diagrammes de rayons X en retour, focalisés ou non, sur les éprouvettes étudiées au microscope par P.A. Jacqet. On a observé en particulier divers degrés de polygonisation après recuits à 600° suivant le taux de la déformation initiale. Aux déformations les plus faibles correspondent les polygonisations les plus fines qui se traduisent par des chapelets ou des essaims de taches fines, nettes et très voisines. Lorsque l'éprouvette soumise à une faible traction subit des traitements étagés, on observe après

*Received March 19, 1954.
†Ingénieur contractuel des Constructions et Armes Navales, Marine Nationale, Paris, France.

un premier recuit d'une dizaine d'heures à 200° un accroissement de la perturbation du réseau cristallographique. Ce résultat semble devoir être interprété par l'intervention d'une tendance à l'équipartition des dislocations préalablement distribuées de manière très hétérogène. Les traitements thermiques à 400°C et à 500°C provoquent des réarrangements localisés, plus aisés à observer un microscope qu'aux rayons X, du moins lorsque les examens sont effectués par les méthodes banales sur des échantillons massifs et polycristallins. On peut cependant, en s'appuyant sur les résultats obtenus par micrographie apercevoir des groupes de taches diffuses indiquant l'accolement de domaines encore très imparfaitement cristallisés et sensiblement désorientés. Cette étape précède la formation de blocs élémentaires faiblement désorientés les uns par rapport aux autres. Ces arrangements, caractéristiques de la polygonisation finale, ne sont généralisés dans la solution solide cuivre-zinc à 65% de cuivre qu'après recuit à 600°.

QUALITATIVE X-RAY EXAMINATIONS OF THE POLYGONIZATION OF A 65/35 COPPER-ZINC SOLID SOLUTION

A number of X-ray back-reflection photographs, using both focused and non-focused beams, have been taken on the samples studied by means of microscopic methods by P. A. Jacquet. In particular, various degrees of polygonization, which depend on the amount of initial deformation, have been observed after annealing at 600°. The finest polygonizations correspond to the smallest deformations; the polygonization is indicated by arrays or randomly distributed groups of fine spots, which are well defined and very closely spaced. When a sample is extended very slightly and then annealed in steps, an increase in the distortion of the lattice is observed after the first annealing step of about ten hours at 200°. This result should probably be interpreted as a tendency towards an equipartition of the dislocations, which are at first distributed in a very heterogeneous way. Heat treatments at 400° and at 500°C lead to localised rearrangements, which are more easily observed by means of a microscope than with X-rays, at least when the common methods of examination are used on massive, polycrystalline samples. It is possible, however, by correlating the results obtained from micrographic examination with those obtained by means of X-rays, to notice groups of diffuse spots which indicate the joining of still very imperfectly crystallized and perceptibly misoriented domains. This stage preceeds the formation of elementary blocks, which are slightly misoriented with respect to one another. In the copper-zinc solid solution containing 65% of copper, those arrangements which are characteristic of the final polygonization, appear only after annealing at 600°.

QUALITATIVE RÖNTGENOGRAPHISCHE UNTERSUCHUNGEN DER POLYGONISATION EINER FESTEN KUPFER-ZINK LÖSUNG (65/35)

Von den von P. A. Jaquet mikroskopisch untersuchten Proben wurden eine Reihe von Röntgenrückstrahlaufnahmen, sowohl mit fokusiertem als auch mit nichtfokusiertem Strahlengang, hergestellt. Nach Glühung bei 600° C wurden verschiedene Polygonisationsgrade beobachtet, deren Ausmass von dem Ausmass der vorhergehenden Verformung abhing. Die schwächste Polygonisation entsprach der geringsten Verformung; diese Polygonisation zeigt sich im Röntgenbild als Reihen oder ungeordnete Gruppen feiner Schwärzungsflecken, die wohldefiniert oder nahe benachbart sind. Wenn eine Probe leicht gedehnt und dann schrittweise geglüht wird, zeigt sich nach der ersten Glühung von 10 Std. bei 200° C ein Anwachsen der Gitterverzerrung; dieses Ergebnis lässt sich wohl als eine gleichmässigere Verteilung der vorher sehr heterogen verteilten Versetzungen deuten. Glühungen bei 400° und 500° C führen zu örtlichen Umgruppierungen, die sich leichter mikroskopisch als röntgenographisch nachweisen lassen, wenn man die üblichen Untersuchungsmethoden an grossen massiven Proben anwendet. Es ist jedoch möglich, die mikroskopischen und röntgenographischen Ergebnisse miteinander in Beziehung zu setzen; man findet Gruppen diffuser Schwärzungsflecken, die darauf hindeuten, dass die noch immer ziemlich fehlgeordneten und missorientierten Bereiche beginnen, sich zusammenzulagern. Dies geschieht, bevor sich eine Struktur von Elementarblöcken, die gegeneinander leicht missorientiert sind, bildet. In Kupfer-Zink Legierungen, die 65% Kupfer in fester Lösung enthalten, treten derartige Strukturen, die für das endgültige Polygonisationsgefüge charakteristisch sind, erst nach Glühungen bei 600° C auf.

Introduction

En même temps que se poursuivaient les examens au microscope, on a effectué par les méthodes courantes de diffraction de rayons X un certain nombre de diagrammes sur les mêmes éprouvettes (N° 3 et N° 4) au cours de leurs traitements.

Bien qu'il ne s'agisse aucunement d'une étude systématique, ces quelques sondages ont mené à des observations qui paraissent devoir être signalées, notamment en ce qui concerne l'influence sur le réseau cristallographique des premiers et des derniers traitements effectués sur l'éprouvette N° 3 (P. A. Jacquet, mémoire II, tableau I).

Nous nous proposons donc de décrire ces expériences et de suggérer une interprétation plausible des résultats.

Résultat des Observations

Une première éprouvette (N° 4) a été examinée aux rayons X après que les observations au microscope aient permis de reconnaître que la polygonisation des grains y était quasi-générale.

On a pris un diagramme en retour avec un foyer bien défini* formé de deux lignes d'intensités inégales. Sur le cliché focalisé la grande majorité des taches, sinon toutes, montre qu'il s'agit à la fois des réflexions caractéristiques du cobalt (anneau 400 en α, encadré par les anneaux 420 et 331 en β) et de réflexions de Laue dues au spectre continu (figure 1).

Les agrandissements de groupes de taches montrent l'accolement des domaines, et la finesse de certains d'entre eux (figure 2) prouve la qualité de la cristallisation des blocs élémentaires. On retrouve en effet l'image exacte du foyer donnée par nombre de ceux-ci.

La polygonisation est encore visible sur un diagramme en retour du type banal (figure 3a) pris avec un foyer quelconque et la radiation du cuivre. L'avantage de cette méthode est de permettre la comparaison avec les diagrammes pris antérieurement (voir P. A. Jacquet, mémoire I, figure 22) sur un échantillon faiblement étiré ou sur une pièce témoin non déformée (figure 3b).

*L'appareil a été utilisé avant achèvement du réglage du foyer. On disposait au moment de l'étude d'un foyer bilinéaire.

L'éprouvette n° 4 ayant été déformée assez irrégulièrement on a cherché si d'autres types de polygonisation, — plus fins ou plus grossiers — apparaissaient en dehors de la partie utile. En fait les clichés pris en ces différents points sont tous très comparables, quoique la finesse des taches soit légèrement variable.

Par exemple, dans la région du congé, près de la tête, on obtient un diagramme focalisé dont les taches sont très finement subdivisées en éléments bien nets (figure 4).

En se fondant sur les critères de reconnaissance de la polygonistaion obtenus sur ces échantillons massifs et polycristallins on a entrepris de scruter l'éprouvette N° 3, après les différents traitements thermiques qu'elle devait subir (voir tableau I, mémoire de P. A. Jacquet, IIème partie).

Le point milieu de la partie utile de l'éprouvette a été systématiquement examiné après chaque traitement. La région du congé, qui a subi une plus faible déformation a été analysée après les premiers et les derniers traitements.

L'influence du traitement à 200° sur l'éprouvette se déduit des diagrammes reproduits à la figure 5 dont la partie supérieure est relative au milieu de l'éprouvette, la partie inférieure à la région du congé. Les diagrammes de gauche et de droite ont été pris respectivement après la traction (3,8 kg/mm^2) et à la suite d'un traitement de 14 heures à 200°.

Au centre, l'état écroui se traduit par des taches larges, déplacées de la position théorique des anneaux,* et des taches de Laue très floues (figure 5a). Après traitement, les réflexions caractéristiques prennent une notable extension périphérique, restant peu nettes et discontinues (figure 5b).

Le diagramme pris dans la région du congé, plus faiblement écrouie que la précédente, est caractérisé par des taches moins étalées que les précédentes (figure 5c). Le traitement a pour effet de produire une multiplication des réflexions qui dépasse largement ce que l'on serait en droit d'attendre d'une simple amélioration de la qualité cristalline des domaines réflecteurs (figure 5d).

Dans ces deux régions, l'effet obtenu est surprenant et dépasse le simple rétablissement géométrique qui résulterait de la disparition des distorsions.

Examinons maintenant le centre de l'éprouvette au cours des traitements à 400°, 500° et à 600°. Les diagrammes ordinaires (figure 6*a* et *b*) évoluent vers la formation de plus en plus précise de l'anneau Debye Scherrer, les arcs sont souvent ponctués, mais ce n'est que lorsque l'on atteint la température de 600° que la polygonisation est franchement marquée par une très fine subdivision des taches (figure 6*c*). A ce même stade de recuit (traitement final de 600°), la région du congé présente une polygonisation plus nette encore que le centre (figure 6*d*) : il n'y a plus d'arcs Debye Scherrer mais des taches en essaims, d'aspect analogue à celles obtenues par l'examen de l'échantillon N° 4 (comparer avec la figure 3*a*).

Les diagrammes focalisés, pris au centre de l'éprouvette après les derniers traitements à 400°, 500° et 600° présentent à des degrés divers des signes plus ou moins nombreux de polygonisation.

Après 3 heures à 400° (figure 7*a*) on voit quelques réflexions nettes, jamais franchement isolées, se dessiner dans des taches floues. Ces mêmes signes sont plus marqués, plus fins aussi et plus nombreux, après le dernier traitement à 500° (figure 7*b*). Dans le premier cas, on ne peut parler de polygonisation qu'en s'appuyant sur les résultats obtenus au microscope, dans le second cas, les rayons X se suffisent à eux-mêmes.

Enfin après avoir porté l'échantillon à 600° (figure 7*c*) on retrouve l'aspect caractéristique de la polygonisation, bien que les domaines élémentaires soient souvent encore indiqués par des taches floues, en tout cas bien moins nettes que celles obtenues dans le cas de l'éprouvette N° 4 (comparer la figure 7*c* avec les figures 1 et 4).

En résumé, malgré la faible dispersion des clichés, qui n'autorise pas la mesure de la désorientation des domaines, on peut juger qualitativement du mécanisme des phénomènes précédant la polygonisation.

Les domaines écrouis se morcellent en éléments plus ou moins perturbés et ceci dans tout l'échantillon dès le traitement à 200°. L'affinement des blocs élémentaires se continue ensuite, tandis que leur désorientation décroît, conformément à la théorie.

Aux stades ultérieurs (recuits à 400° et 500°) on voit se dessiner sur certaines taches des signes de polygonisation qui se précisent lorsque les recuits sont prolongés.

Ce n'est qu'en portant l'échantillon à 600° que ces marques sont généralisées et de netteté beaucoup plus accusée.

Dans la région où la déformation initiale était

*En fixant la distance film échantillon à 43 mm environ, on recueille sur le film plan, à partir du centre, les anneaux (333) β, (420) α, (422) β, et (331) α, avec la radiation du cuivre.

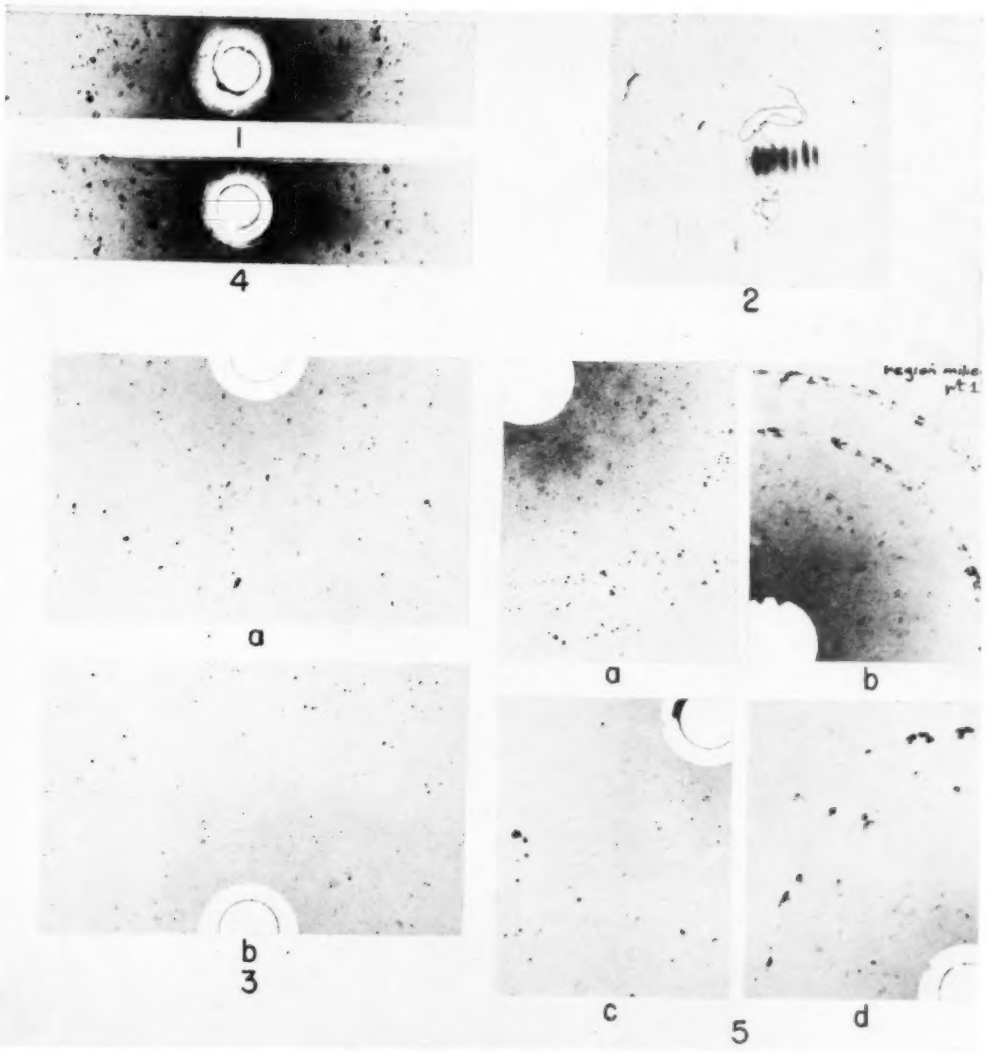

PLATE I. (All figures reduced to three-fourths.) Figure 1—Diagramme focalisé du centre de l'éprouvette N° 4 fortement polygonisée. Rayons de retour. Radiation du cobalt. Figure 2—Agrandissement d'un groupe de taches. Figure 3—Diagramme en retour de l'éprouvette N° 4: (*a*) fortement polygonisée; (*b*) état non déformé. Radiation du cuivre. Figure 4—Diagramme focalisé de l'éprouvette N° 4 fortement polygonisée (Région du congé). Rayons de retour. Radiation du cobalt. Figure 5—Influence du traitement à 200°: (*a*) milieu de l'éprouvette N° 3—après déformation; (*b*) milieu de l'éprouvette; N° 3—traitée 14 h à 200°; (*c*) région du congé de l'éprouvette N° 3—après déformation; (*d*) région du congé de l'éprouvette N° 3—traitée 14 h. à 200°.

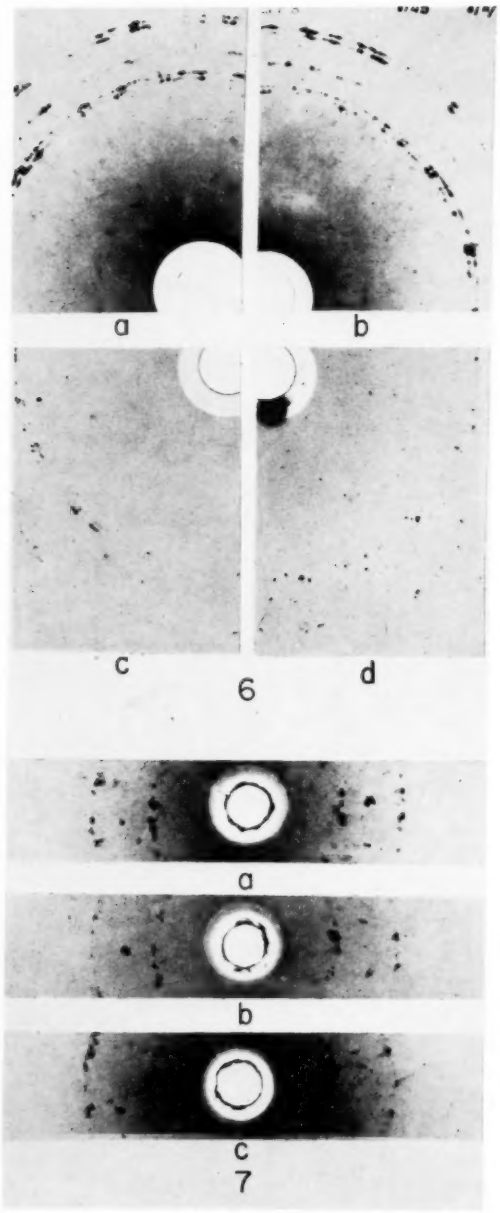

PLATE II. Figure 6—Influence des traitements successifs. Milieu de l'éprouvette N° 3: (*a*) 14 h. à 200° + 1 h. à 400°; (*b*) comme (*a*) + 2 h. à 400° + 1 h. à 500°; (*c*) comme (*b*) + 2 h. à 500° + 45 mn à 600°; (*d*) Région du congé même traitement que (*c*). (Diagrammes en retour—Radiation du cuivre.) Figure 7—Influence des traitements successifs: (*a*) dernier traitement: 3 h. à 400°; (*b*) dernier traitement: 3 h. à 500°; (*c*) dernier traitement: 45 mn à 600° (diagrammes focalisés en retour—Radiation du cobalt).

le plus faible la désorientation des domaines sera la plus faible, sans toutefois être aussi réduite que dans le cas de l'échantillon de référence (cf. figures 6*c*, 6*d* et 3*a*).

Discussion des Résultats

Cherchons à analyser le phénomène observé par le microscope et par les rayons X et que produit un traitement thermique de 14 heures à 200° sur un échantillon très faiblement déformé.

La micrographie montre la très grande hétérogénéité de la déformation plastique : à la forte densité de glissements, donc de dislocations, au voisinage du joint de grain correspond un état de fortes tensions, bien différent de celui qui règne vers le milieu du grain.* Il en résulte des variations du paramètre moyen de la solution solide ce qui se traduit par l'allongement radial des taches du diagramme (figures 5*a* et 5*c*).

Le traitement à 200° doit permettre aux dislocations de se disposer d'une manière moins hétérogène, correspondant à un état de plus faible énergie —du même coup s'opère une sorte de nivellement des tensions.

Le microscope montre que la réactivité de la surface augmente alors considérablement,** et ceci en tous points, cependant que l'allure des diagrammes de rayons X change radicalement. Au centre de l'éprouvette, si les taches perdent leur allongement radial au bénéfice de leur extension périphérique, elles se divisent en même temps en chapelets aux éléments irréguliers (figure 5*b*). Dans la région du congé on assiste à une multiplication considérable des domaines réflecteurs, sans que des relations de voisinage ne se fassent jour.

Dans le premier cas le microscope révélait de nombreux glissements, dans le second—où la déformation est sensiblement plus faible, ces marques étaient très rares. Il n'est donc pas autrement surprenant que la répartition des dislocations avant le traitement étant bien différente dans chaque cas, la sous-structure soit également différente après un même revenu.

Les observations faites aux rayons X peuvent être rapprochées de celles de Wood et de ses collaborateurs [1; 2], reprises et interprétées par G. B. Greenough et Mrs. E. Smith [3] comme indiquant différents stades de la polygonisation de l'aluminium au cours du fluage ; bien que, dans le cas du laiton, déformation et recuit soient opérés en deux temps.

Sans pouvoir préciser—dans l'attente de nouvelles expériences plus systématiques, le mécanisme du réarrangement des dislocations, on peut cependant envisager deux processus, d'ailleurs apparentés, et menant tous deux, après une série de nouveaux traitements à deux états polygonisés quelque peu différents.

Au centre, dès le premier traitement, on se trouve en présence de sous-grains très perturbés, mais dont l'accolement est esquissé. Les traitements ultérieurs auront pour effet de diminuer la densité des dislocations dans les sous-grains en facilitant les annulations de défauts de signes contraires, et en réduisant déjà à partir des traitements à 500°, mais surtout à 600°, la désorientation des domaines élémentaires adjacents.

Dans la région du congé, des domaines de cristallisation régulière, dont les réflexions sont déjà très fines après le traitement à 200°, se regroupent à 600° en essaims polygonisés. De nouvelles expériences seront nécessaires pour préciser l'évolution au cours des stades intermédiaires. Il se peut, étant donné que la composition de l'alliage est trés voisine de celle qui correspond à la limite de stabilité de la phase α—d'ailleurs difficile à déterminer avec précision [4]—que l'on se trouve en présence de modes de diffusion des atomes, ou d'interaction entre atomes de deux espèces et dislocations d'un type très particulier.

On sait par ailleurs que Harrington et Jester [5] ont étudié pour des laitons à 85/15 et à 65/35 l'influence de traitements thermiques modérés de différentes durées (entre 150° et 225°, et de 4 à 100 heures) sur la conductibilité électrique des éprouvettes. Toutefois ce qui risque de rendre la comparaison fallacieuse, c'est que ces échantillons avaient subi préalablement des laminages extrêmement importants, soit 37% ou 60% de réduction.

Il peut être intéressant cependant de noter en vue de nouvelles études systématiques sur les conséquences des faibles déformations dans les laitons α, que dans le cas de ces très forts laminages, les auteurs observent au revenu un accroissement du durcissement, maximum au bout de 4 heures de traitement à 200° pour le laiton 65/35 le moins déformé. Tandis que le laiton le plus déformé (60%) s'adoucit très sensiblement lorsque le traitement est prolongé jusqu'à 100 heures, l'autre déformé à 37% et pareillement traité conserve la dureté acquise. Dans le même temps, la conductibilité électrique augmente.

Pour expliquer leurs résultats, les auteurs émettent l'hypothèse d'un durcissement structural par formation d'un précipité.

Cette hypothèse est aujourd'hui tout à fait

*Mémoire I de P. A. Jacquet (figure 16).
**Mémoire II de P. A. Jacquet (figures 7 et 8).

exclue, non seulement parce que le précipité en question n'a jamais été observé, mais surtout parce que l'allure de la limite de séparation des phases α et β a précisément la courbure inverse de celle qui est observée lorsqu'il y a précipitation.

A l'époque déjà, Maddigan, dans la discussion du mémoire de Harrington et Jester suggérait un mécanisme de migration des dislocations expliquant l'accroissement de dureté, et simultanément la formation de germes de recristallisation.

Encore une fois, bien que les conditions des expériences soient entièrement différentes, puisque dans le cas des faibles déformations il n'est pas question de recristallisation, il est intéressant de rapprocher le phénomène que nous avons étudié d'un cas plus complexe, mais de grande importance pratique—où l'effet que nous signalons pourrait persister, tout en demeurant localisé et sans doute mêlé à celui de recristallisation.

Si nous n'avons pas fait de mesures de dureté, l'observation au microscope de la surface très réactive après le traitement à 200°,* l'allure des diagrammes de rayons X correspondants, semblent tous deux indiquer une augmentation de la dureté.

L'accroissement de conductibilité constaté par les mêmes auteurs pose une question intéressant la manière dont les dislocations entraînent les lacunes du réseau en se réorganisant, et les conséquences de leurs migrations sur l'état d'ordre ou de désordre cuivre-zinc du réseau.

Conclusion

En résumé on ne peut par les techniques que nous avons employées ici qu'entrevoir les grandes lignes du phénomène, mais le fin détail de l'évolution échappe. Il serait nécessaire de recourir du point de vue des rayons X à des méthodes comme celles de Guinier ou Tennevin [6] ou à des examens par microfaisceaux [7] pour préciser les dimensions des domaines élémentaires aux différents stades précédant la polygonisation. Ceci permettrait de préciser les hypothèses avancées au sujet des migrations de dislocations, et comme l'a indiqué P. A. Jacquet, le microscope électronique serait également d'un grand secours pour l'étude des sous-joints.

Dans l'état actuel des expériences, il paraît difficile d'invoquer une autre interprétation de celle qui découle du mécanisme le plus simple de ceux qui se présentent à l'esprit, étant donné que les dislocations doivent se répartir suivant l'état énergétique le plus bas. Une faible énergie thermique serait suffisante, vu l'état de tension de la matrice, pour amorcer des migrations et des annulations de défauts de signes contraires, sans toutefois qu'un réseau de sous-joints puisse s'établir. Le traitement de 14 heures à 200° assurerait en quelque sorte une équipartition des perturbations par rapport à l'état antérieur.

Les modifications de structure créées par ce mécanisme évolueraient lors des traitements à 400 et 500° vers des réorganisations plus radicales, la mobilité des dislocations devenant alors plus grande.

Dans le cas des déformations préalables les moins accentuées, le premier traitement semble surtout épurer les sous-grains en annihilant un certain nombre de défauts. Là où les glissements étaient apparus en grand nombre, les relations d'orientation entre domaines élémentaires se dessinent déjà pour se confirmer aux cours des traitements ultérieurs aux températures de 400° et 500°, quand les mouvements de dislocations sont plus amples.

A partir du traitement à 600°, et dans les deux cas étudiés, apparaissent des signes caractéristiques de la polygonisation, avec cette différence que dans la région préalablement la moins déformée les essaims sont plus ramassés, dans l'autre cas la désorientation des domaines élémentaires est plus grande.

Nous remercions bien vivement M. Jacques Friedel de nous avoir fait bénéficier de son expérience pour l'interprétation de nos résultats.

*Mémoire II de P. A. Jacquet (figure 8).

Références

1. Wood, W. A. et Rachinger, W. A. J. Inst. Metals **76** (1949) 237.
2. Wood, W. A. et Scrutton, R. F. J. Inst. Metals **77** (1950) 423.
3. Greenough, G. B. et Smith, Mrs. E. M. J. Inst. Metals **77** (1950) 435.
4. Beck, L. H. et Smith, C. S. Trans. A.I.M.E. **188** (1952) 1079.
5. Harrington, R. H. et Jester, T. C. Trans. Amer. Soc. Metals **30** (1942) 124.
6. Guinier, A. et Tennevin, J. Acta Cryst. **2** (1949) 133.
7. Hirsch, P. B. et Kellar, J. N. Acta Cryst. **5** (1952) 162, 168 et 172.

A RELAXED VACANCY MODEL FOR DIFFUSION IN CRYSTALLINE METALS*

N. H. NACHTRIEB and G. S. HANDLER†

A mechanism for diffusion in solid metals is proposed in which the rate-limiting atom movements occur within small regions of disorder in the crystal. The disordered regions consist, on the average, of 12 to 14 atoms which have relaxed inward around a lattice vacancy, and have an energy content about the same as the equivalent number of atoms in the liquid state.

UN MODÈLE DE LA DIFFUSION DANS DES MÉTAUX CRISTALLINS, BASÉ SUR DES LACUNES RÉTICULAIRES, RELACHÉES

On propose un mécanisme de diffusion dans des métaux solides, dans lequel les mouvements atomiques qui limitent la vitesse ont lieu au sein de petites régions désordonnées du cristal. Ces régions désordonnées consistent, en moyenne, en 12 à 14 atomes qui ont été relâchés vers l'intérieur autour d'une lacune réticulaire, et dont l'énergie est approximativement la même que celle d'un nombre équivalent d'atomes à l'état liquide.

EIN SPANNUNGSFREIES LEERSTELLENMODELL DER DIFFUSION IN KRISTALLINEN METALLEN

Es wird ein Diffusionsmechanismus in festen Metallen vorgeschlagen, bei dem die geschwindigkeitsbegrenzenden Atombewegungen innerhalb kleiner fehlgeordneter Bereiche des Kristalls erfolgen. Diese fehlgeordneten Bereiche bestehen im Durchschnitt aus 12 bis 14 Atomen, die um eine Gitterleerstelle gruppiert sind und sich in diesem Komplex spannungsfrei anordnen. Der Energieinhalt dieser Anordnung ist etwa gleich dem der gleichen Anzahl von Atomen im flüssigen Zustand.

Introduction

Atom movements in crystalline solids have been best explained in terms of lattice imperfections, notably vacant lattice sites and interstitial atoms. The latter are believed to be responsible for the diffusion of small atoms in a host lattice of atoms of large radius, while the former provide the widely accepted mechanism for self-diffusion in pure metals and in alloys in which the atom radii are not widely different (i.e., substitutional solid solutions). The vacancy model is apparently fundamentally correct for such cases, and its essential features will doubtless be retained in more elaborate theories of solid state self-diffusion. It shares with other mechanisms a rather serious defect, however; it offers no ready means of predicting the rates and activation energies for diffusion or of relating these kinetic quantities to the bulk physical properties of metals. Its real value has been qualitative . . . conceptual, rather than quantitative. Even the most thorough-going discussion of the energy of formation and movement of vacancies in copper by Huntington and Seitz [1] disagrees with experiment by about 35 per cent.

The point of view advanced in this paper is that it may be more consistent with experimental evidence to consider a model for diffusion in which the elementary acts are not the creation and movement of a simple vacancy, but rather the creation of a small region of disorder whose movement through the crystal is the origin of exchange. Two essential differences are implied in this notion: (1) that the energy of formation of the imperfection must take into account a larger region of the crystal, and (2) that the elementary atom movements are not isolated events, but cooperative motions involving a number of atoms.

The basis for regarding diffusion as a kind of small-scale cooperative phenomenon is a relation which has been found to exist between the activation energies for diffusion in cubic metals and their latent heats of fusion [2]. The simple relation

$$\Delta H = 16.5\, L_m \tag{1}$$

obtained from a study of the effect of hydrostatic pressure on the rate of self-diffusion in sodium, applies to six f.c.c. and b.c.c. metals and to α-white phosphorous within experimental error, as Table I shows. The relation does not apply to lead with the same precision, although our recent measurements on this metal give an activation energy more nearly in agreement with equation (1) than does the less precise determination of Hevesy, Seith, and Keil [3]. It is interesting to note that no similar relation exists between the activation energy for diffusion and the latent heat of vaporization. Taken at face value, equation (1) suggests that diffusion in cubic metals is in some way related to fusion. The simple vacancy model, on the other hand, would lead one to expect a connection with sublimation.

*Received February 4, 1954.
†Institute for the Study of Metals, University of Chicago.

TABLE I

OBSERVED AND CALCULATED ENTHALPIES OF ACTIVATION FOR DIFFUSION

Substance	Structure	L_m cal/g atom	ΔH (obs)	ΔH (calc)
Au	f.c.c.	3060	51,000	50,280
Ag	f.c.c.	2730	45,950	44,850
Cu	f.c.c.	3110	48,000 54,000	50,920
Co	f.c.c.	3700	61,900	60,790
Fe	f.c.c.	3630	59,700	59,640
Pb	f.c.c.	1190	27,900 24,500*	19,650
P_4 (white)	b.c.c.	601	9,360*	9,920
Na	b.c.c.	636.2	10,450	10,450

*Data of the authors, not yet published.

The Enthalpy of Activation

On any lattice imperfection model of diffusion we may regard the "experimental" activation energy as consisting of two terms: (1) an enthalpy of *formation*, ΔH_1, of the particular lattice defect which is antecedent to diffusion, and (2) an enthalpy of *activation*, ΔH_2, for the movement of atoms involved in measurable diffusion over macroscopic distances. ΔH_1 is the difference in heat content of an infinitely large crystal containing N lattice defects of the appropriate kind and the same crystal devoid of such defects. We assume that the equilibrium density of such imperfections in a pure substance is determined solely by the temperature and pressure. In the simple vacancy theory the lattice imperfections are considered to be discrete voids whose spherically inscribed volume is about equal to the atom volume. The energy of formation of such a void would be twice the latent heat of vaporization per atom if the atom were taken to the vapor.

It is here that the present model departs from the discrete vacancy theory, by the proposal that the vacancy volume is locally distributed. In effect, the vacancy dissolves in the lattice as a result of the inward relaxation of the neighboring atoms. We shall refer to such dispersed vacancies and to the complex of atoms most closely associated with the excess volume as "relaxions," and retain the term "vacancy" in its familiar sense to denote a discrete atom void. Several questions are immediately suggested. How many atoms comprise a relaxion? What is the basis for expecting an inward, rather than an outward, relaxation of atoms around a vacancy? What is the energy of formation of a relaxion? What is the configuration of atoms within a relaxion? Finally, what is the equilibrium concentration of relaxions?

In an attempt to answer the first question, let us note two inferences which may be drawn from equation (1):

1. The invariance of ΔH over a wide range of temperatures implies that the average number of atoms associated with a relaxion is constant.

2. The coefficient 16.5 is somewhat larger than the number of nearest neighbors in a f.c.c. lattice (12) and of the sum of the nearest and next nearest neighbors in a b.c.c. lattice (14).

Let us draw the naive conclusion that the number of atoms most closely associated in a relaxion is of the order of 12 to 14, realizing that it is somewhat arbitrary to set any definite boundary on the disordered region.* We may expect the energy changes associated with these displacements to be related to the latent heat of fusion and the volume change to be related to the volume change on melting (see later). The independence of relaxion size with temperature implied by (1) is at first surprising. One might have expected the size distribution as well as the number distribution to depend exponentially upon temperature, according to such heterophase fluctuation theories as Frenkel [4] has discussed. The reason for the invariance of relaxion size with temperature appears to be the short-range character of the interatomic forces. Relaxation of atoms about a vacancy is accompanied by a decrease in free energy, and most of the energy change arises from the movement of the nearest (and in the case of b.c.c. lattices, next nearest) neighbors.

That an inward, rather than an outward, displacement of the atoms surrounding a vacancy is to be expected may be argued on logical grounds if a suitable potential function can be found. No rigorous method is known, however, for computing the potential energy of an atom in a metallic crystal. Pair potential functions are incorrect in principle, although useful for rough estimates if the forces are sufficiently short range. Regardless of the exact form of the potential function, we recognize that it must have the property of repulsion for sufficiently close interatomic distances and attraction for great separations. For any crystal of minimum energy there is a balance

*We neglect in this approximation contributions to the relaxion energy which might be described as interfacial energy or strain energy. Their effect would be to decrease the number of atoms which are regarded to comprise a relaxion. Properly, of course, there is no interface and the use of an interfacial energy term is somewhat artificial.

between the forces of attraction and repulsion appropriately summed over all atoms in the crystal. The last two statements can be true only if the net forces between nearest neighboring atoms are repulsive. It then follows that removal of an atom from the interior of a metallic crystal must result in an inward movement of its nearest former neighbors.* Removal of an ion from the interior of an ionic crystal, on the other hand, would result in outward relaxation of the neighboring ions because of the repulsion of their Coulomb fields.

Energy of Formation of Relaxions

An exact calculation of the energy of a relaxion relative to the perfect crystal would require a detailed balance of all interactions and is not possible with approximate potential functions. A rough calculation with an admittedly imperfect function is nevertheless worth while, merely to indicate that large relaxation energies are involved. Slater [5] has represented the energies of the alkali metals by means of a Morse function:

$$U_0 = L(e^{-2a(r-r_0)} - 2e^{-a(r-r_0)}) \tag{2}$$

where U_0 is the energy of the crystal at 0°K, L is the latent heat of vaporization (26.2 kcal/g atom for sodium), r_0 is the nearest interatomic distance (3.72A), and a is a parameter derived from compressibility measurements (0.67 for sodium). Such a function disregards all interactions between atoms farther apart than nearest neighbors, and in so doing ignores the fact that the net force between nearest neighbors is repulsive. The energy per atom pair for a b.c.c. structure will then be given by

$$E_0 = \frac{L}{8}(e^{-2a(r-r_0)} - 2e^{-a(r-r_0)}). \tag{3}$$

Relaxation of the eight nearest atoms surrounding the vacancy and of the six next nearest atoms to a closest-packed configuration gives −13.0 kcal. Combined with the 26.2 kcal required to produce a vacancy and a surface atom gives 13.2 kcal as the energy of formation of a relaxion. The agreement with the observed activation energy (10.45 kcal) is as good as can be expected in view of the crude assumptions which underlie the calculation.

Equation (1), first obtained for b.c.c. sodium, applies equally well to f.c.c. metals, as Table I indicates. The f.c.c. lattice is close-packed, however, and no relaxation about a vacancy is possible if the atoms are regarded as hard spheres. Presumably, considerable polarization must take place if inward relaxation is to occur in such structures.

Structure of Relaxations

In the foregoing we have discussed in rough terms the energy, ΔH_1, required to form a lattice imperfection involving 12 to 14 atoms by a symmetrical relaxation about a vacancy and have proposed that it amounts to about 12 to 14 times the latent heat of fusion per gram atom. Such a region would have a density about 7 to 8 per cent lower than that of the normal crystal if the vacancy volume were entirely localized within it. We believe that the density is only 3 to 4 per cent lower, for reasons to be discussed in the last section. If this is so, such a region would have about the same heat content as the same number of atoms in the liquid state. A symmetrical relaxion would then be one of the configurations of the liquid state. Atom movements within a relaxion resulting from the absorption of phonons would cause the configuration to progress through less symmetrical atom arrangements more typical of the liquid state. Within a relaxion atoms are considered to squeeze or roll past one another, but the movement of any one atom would entail the correlated movement of the remaining atoms.† In effect, atom movements within a relaxion are considered to take place with a rate and activation energy comparable to that observed for diffusion in liquids.

Activation Enthalpy for Atom Movement

If the enthalpy of relaxion formation is taken to be $\Delta H_1 = 14\ L_m$ for sodium, there remains for the enthalpy of activation for atom movements, ΔH_2, about $2.5\ L_m$. This amounts to about 1600 cal in the case of sodium, in reasonably good agreement with the experimental value (2580 cal) for the activation energy for diffusion in liquid sodium. With such comparative freedom for atoms to pass from one configuration in a relaxion to

*It is worth calling attention to the very instructive magnet model of a two-dimensional crystal which Hilsch has described. Rod-form magnets axially suspended by threads from a central point take up a close-packed hexagonal array in a plane. The repulsive forces are due to the magnetic dipole interaction, and vary as $1/r^4$; the simulated attractive forces are the restoring gravitational component, and vary as r for small displacements. Such a model shows complete inward relaxation of the surrounding magnets when a central one is released from the array to simulate a vacancy.

†In this connection it is interesting to call attention to Zener's ring diffusion model (Acta Cryst. 3, 1950, 346), wherein a ring of 4 atoms cooperatively rotates through an angle of 90 degrees in the elementary diffusion act.

another, there would still be no macroscopic diffusion if the relaxion were anchored to the particular lattice site where it was formed. Propagation of a symmetrical relaxion would constitute a vacancy wave which would produce macroscopic diffusion in the same manner as the movement of a discrete vacancy, however. We assume that a relaxion moves through the crystal with a Brownian-like course because of scattering by phonons. The process may be likened to "melting" and "freezing" one or two atoms at a time with an activation energy of the order of Lm. Since the activation energy for diffusion in monatomic liquids is of comparable magnitude, we think it likely that the cooperative movement* of atoms within a relaxion is a process of similar probability. In effect, this is to propose that the various diffusion mechanisms . . . vacancy, interstitial, direct exchange, and ring rotation . . . are partial truths and that an eclectic approach may be nearer to the true situation.

Concentration of Relaxions

If we assume that relaxions move through a metal lattice by a process which is comparable to small-scale melting, it is possible to make a simple estimate of their average concentration. Let X represent the fraction of all atoms which are present in relaxions at a given temperature and pressure, and let the average number of atoms per relaxion be denoted by g. Then if D_s and D_l are the self-diffusion coefficients for the solid and liquid at a given temperature, the fractional number of relaxions is simply

$$n = \frac{X}{g} = \frac{1}{g} \cdot \frac{D_s}{D_l}. \tag{4}$$

D_l can be estimated from the Stokes-Einstein equation

$$D = \frac{kT}{6\pi\eta r}. \tag{5}$$

For sodium, however, unpublished experimental diffusion coefficients in the liquid state are available,† together with the activation energy for extrapolation of the data to the undercooled range. Figure 1 shows a plot of $\log D$ versus $1/T$ for liquid and solid sodium. Table II lists the relevant data, together with the fractional number of relaxions calculated for five temperatures. The values range from 5.74×10^{-6} at 0.3°C to 2.95×10^{-4} (extrapolated to the melting point), and are consistent with general estimates of the fractional numbers of vacancies present in metals correspondingly near to their melting points.

TABLE II

CONCENTRATION OF RELAXIONS IN SODIUM

T(°C)	D_s (obs)	D_l (calc)*	X	n
0.3	9.22×10^{-10}	1.15×10^{-5}	8.04×10^{-5}	5.74×10^{-6}
39.4	1.31×10^{-8}	2.08×10^{-5}	6.29×10^{-4}	4.49×10^{-5}
69.3	5.26×10^{-8}	3.00×10^{-5}	1.76×10^{-3}	1.26×10^{-4}
94.2	1.43×10^{-7}	3.88×10^{-5}	3.68×10^{-3}	2.63×10^{-4}
97.5	1.65×10^{-7}	4.00×10^{-5}	4.13×10^{-3}	2.95×10^{-4}

*Calculated from $D_l = 1.33 \times 10^{-3} \exp(-2580/RT)$ (unpublished data of Mr. R. E. Meyer for self-diffusion in liquid sodium). The results are not materially altered if D_l is calculated from viscosity data with the Stokes-Einstein equation.

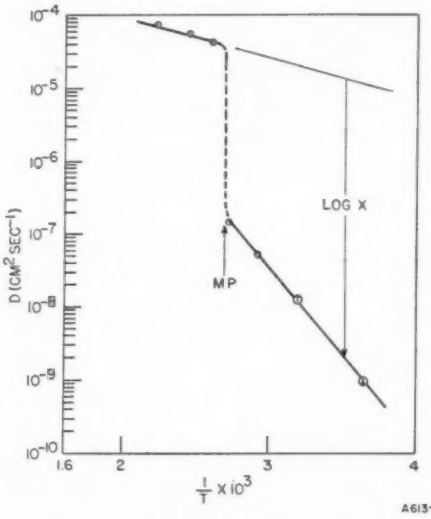

FIGURE 1. Diffusion in solid and liquid sodium.

Activation Volume for Diffusion

Further evidence that diffusion in solid metals may be regarded as a small scale cooperative phenomenon having some of the characteristics of melting may be deduced from the effect of hydrostatic pressure on the rate of self-diffusion. The activation volume for diffusion is defined in a completely general way by the relation

$$\left(\frac{\partial \Delta F}{\partial P}\right)_T = \Delta V_{act} \tag{6}$$

*Observation of the magnet model is instructive in this connection. Readjustments involving many magnets occur when a vacancy is created. The motions are so rapid and complex that it has not been possible to observe a relaxion wave.

†Mr. Robert E. Meyer has measured the rate of self-diffusion in sodium between 101.7°C and 176.5°C in this laboratory. The measured D_l is 4.15×10^{-5} cm² sec^{-1} at 101.7° and the activation energy is 2580 cal/g atom. These values may be compared with 4.17×10^{-5} cm² sec^{-1} and 2470 cal/g atom, obtained by use of Andrade's data (Proc. Roy. Soc. Lond. **A157**, 1936, 264) for the viscosity of liquid sodium at the same temperature and with the ionic radius (0.95A) for r in equation 5.

where ΔF is the activation free energy. ΔV_{act}, like the activation free energy, enthalpy, and entropy, is a composite quantity and can be regarded as consisting of a volume change for the formation of N relaxions, ΔV_1, and a volume change for their movement and the movement of atoms within them, ΔV_2. Following Zener [6] we may define ΔF by means of the expression

$$D = \gamma a^2 \nu e^{-\Delta F/RT} \tag{7}$$

where ν is the average lattice vibrational frequency, a is the lattice parameter, and γ is a constant determined by the lattice geometry and the assumed jump mechanism. Its value is unity for b.c.c. lattices for a vacancy mechanism.

The limitations of equation (7) must now be noted. It was derived for mechanisms in which the elementary jump distance is well defined and geometrically related to the lattice parameter. Moreover, it is implicit that a single characteristic lattice frequency may be used with sufficient approximation to the truth. In the relaxion model, however, many atom movements take place on a scale small compared to the lattice parameter and unrelated to it in any simple manner. Further, the dominant vibration frequency in a relaxion must be somewhat lower than in a flawless portion of a crystal. In the face of these apparent objections, we nevertheless use equation (7) for the following reasons. Measureable diffusion occurs only when interchanged atoms are left in the wake of a moving relaxion. Only those movements of atoms within a relaxion contribute to diffusion which involve displacements amounting to mass rotation by one atom distance. Lesser movements are merely anharmonic vibrations which restore the atoms to their original sites on the perfect lattice. Such relaxions with sub-marginal heat content do not contribute to diffusion until an energy fluctuation (absorbed phonon) occurs. γ is a constant, and its particular value will not affect the value of the derivative

$$\Delta V_{act} = -RT\left(\frac{d \log D/\gamma a^2 \nu}{dP}\right)_T. \tag{8}$$

Finally, it is the variation of ν with P which concerns us, not ν, itself. Grüneisen's relation shows that for sodium ν increases only 16 per cent for a 20 per cent increase in crystal density, and since a^2 and ν vary in opposite ways with pressure, their product is constant to within 4 per cent for pressures up to 12,000 atmospheres. Without serious error we could have taken ΔV_{act} to be $-RT$ $[d \log D/dP]_T$. In other words, this amounts to ignoring the change in the entropy of activation with pressure.

Figure 2 shows the fractional variation of ΔV_{act} and ΔV_{fusion} as a function of pressure up to 12,000 atmospheres at 90°C for sodium. We note that equation (8) gives the activation volume referred to one mole of relaxions, and that for comparison with the volume change on fusion per

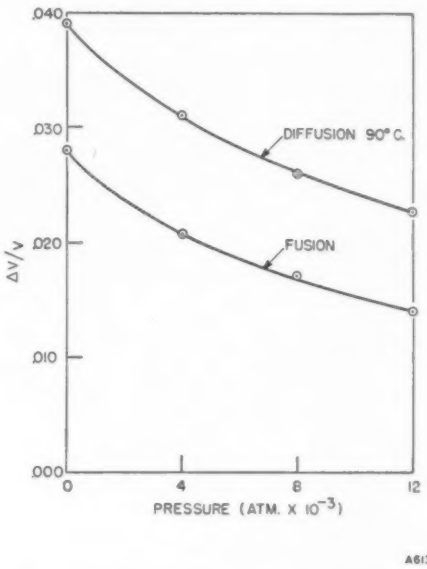

FIGURE 2. Volume changes (fusion and diffusion) for sodium as a function of pressure.

gram atom it must be divided by the number of atoms in a relaxion. The interesting point to note is that the two quantities are of similar magnitude, and their variation with pressure is also similar. We should expect ΔV_{act} to be larger than ΔV_{fusion}, since the former includes ΔV_2, the activation volume for the movement of atoms and relaxions. An experimental determination of the activation volume for liquid diffusion would now be interesting.

Acknowledgements

It is a pleasure to acknowledge the many helpful suggestions and criticisms offered by members of the Institute for the Study of Metals. The authors are particularly indebted to Professor Cyril Stanley Smith and to Professor Charles S. Barrett for their encouragement and advice.

This research was supported by the United States Air Force under Contract No. AF33(616)–2090.

References

1. HUNTINGTON, H. B. and SEITZ, F. Phys. Rev. **61** (1942) 315.
2. NACHTRIEB, N. H., WEIL, J. A., CATALANO, E., and LAWSON, A. W. J. Chem. Phys. **20** (1952) 1189.
3. HEVESY, G. V., SEITH, W., and KEIL, A. Z. Physik **79** (1932) 197.
4. FRENKEL, J. Kinetic Theory of Liquids (Oxford University Press, 1946), p. 383.
5. SLATER, J. C. Introduction to Chemical Physics (New York, McGraw-Hill, 1939), p. 452.
6. ZENER, C. J. Appl. Phys. **22** (1950) 373.

A STUDY OF THE PLASTIC DEFORMATION OF COPPER SINGLE CRYSTALS*

C. R. CUPP† and B. CHALMERS‡

Single crystals of copper having uniform rectangular cross-sections, and of known orientations, were tested in axial tension using a "soft" tensile machine in which the applied load was independent of the resulting strain. During the course of stepwise loading of each specimen, a delay was found to occur between the beginning of the addition of each small stress increment and the resumption of plastic strain. The length of the delay time, in the order of a few seconds, was found to depend to some extent on the length of the waiting period, prior to the addition of a stress increment, during which time the load on the specimen is constant. The effect may be considered as a type of yield point phenomenon. Other results of this work indicated an effect of dissolved hydrogen on the mechanical properties of the specimens, and a transition point in the stress-strain curves of the specimens during the early stages of plastic strain.

UNE ÉTUDE DE LA DÉFORMATION PLASTIQUE DE MONOCRISTAUX DE CUIVRE

Des monocristaux de cuivre de section réctangulaire, uniforme, et dont l'orientation était connue, furent soumis à une extension axiale dans un appareil de traction permettant d'appliquer une charge indépendamment de la déformation résultante. Lors de l'application étagée d'une charge à chaque échantillon, on a constaté qu'il y avait un délai entre le commencement de l'addition de chaque petit accroissement de charge et la reprise de la déformation plastique. Il fut constaté que la durée du délai (de l'ordre de quelques secondes) dépendait, dans une certaine mesure, de la durée de la période d'attente qui précédait l'addition d'un accroissement de tension et pendant laquelle la charge sur l'éprouvette restait constante. Cet effet peut être considéré comme un phénomène de limite d'écoulement. D'autres résultats de cette recherche indiquent un effet de l'hydrogène dissous dans le métal sur les propriétés mécaniques des éprouvettes et un point de transition dans les courbes tension-déformation des éprouvettes en question, pendant les premiers stades de la déformation plastique.

EINE UNTERSUCHUNG DER PLASTISCHEN VERFORMUNG VON KUPFEREINKRISTALLEN

Kupfereinkristalle mit gleichförmigem rechteckigem Querschnitt und mit vorbestimmten Orientierungen wurden unter einachsigem Zug untersucht; es wurde eine "weiche" Zugmaschine benutzt, bei der die angelegte Last von der resultierenden Dehnung unabhängig war. Wenn man die einzelnen Proben schrittweise belastete, zeigte sich eine zeitliche Verzögerung zwischen dem Anlegen der zusätzlichen äusseren Spannung und dem Wiederbeginn der plastischen Verformung. Die Länge dieser zeitlichen Verzögerung, die von der Grössenordnung einiger Sekunden war, hing zu einem gewissen Grade davon ab, wie lange man bis zum nächsten Belastungsschritt wartete, d.h. die Probe unter konstanter Belastung hielt. Man kann diesen Effekt als eine Art Fliesspunktserscheinung betrachten. Andere Ergebnisse dieser Untersuchung deuten auf einen Einfluss des gelösten Wasserstoffes auf die mechanischen Eigenschaften der Proben hin; ausserdem zeigte sich ein Umkehrpunkt in den Spannungs-Dehnungskurven in den ersten Stadien der plastischen Verformung der Proben.

Introduction

A number of investigators have observed and studied the delay time which may occur between the application (or increase) of a stress, and the observation of the resulting strain. Such observations are closely associated with the existence of yield phenomena. The present paper describes a delay effect that has been observed in single crystals of copper; it appears to be distinct from any of the effects described previously. The delay phenomena reported in the literature are the following:

Clark and Wood [1] made a series of rapid-load tests, using stresses exceeding the room-temperature static-elastic limit, on a 0.19 per cent carbon annealed steel for which the static stress-strain curve exhibits a definite yield point, and on other steels which do not exhibit definite yield points. It was concluded that a definite time delay in the initiation of plastic deformation is associated only with materials for which the static stress-strain curve exhibits a definite yield point. In later work, Wood and Clark [2] studied the influence of temperature on this time delay. In order to compare the results of rapid load tests with more conventional test results, static tests were made on 0.17 per cent carbon steel at temperatures of −60°C, 23°C, 65°C, and 121°C. Stepwise loading was used, allowing approximately two minutes to elapse between points. It was noted that the static stress-strain relationships obtained at 65°C and 121°C show clearly the phenomenon of strain ageing. At these temperatures appreciable strain ageing evidently takes place in the approximately two-minute interval between successive load increments. During the

*Received February 10, 1954.
†Research Dept., The International Nickel Co. of Canada, Ltd., Copper Cliff, Ontario, Canada.
‡Division of Applied Science, Harvard University, Cambridge, Massachusetts.

performance of these tests, it was noted that "in several instances, the secondary yield points exhibit a definite delay time for the resumption of plastic deformation." Except that these tests were on polycrystalline alloy specimens, and the plastic strain somewhat higher, the effect described in the quotation above is similar to that studied in the present work. In another study, Wood and Clark [3] investigated the effect of the presence and near-absence of carbon and nitrogen upon the delayed-yield phenomenon in steel. The delay was found to occur in steel which had been wet-hydrogen treated to remove the static upper yield point. They concluded that in order to remove completely the effects of carbon and nitrogen upon the mechanism of yielding, the concentrations of those elements would have to be reduced to considerably lower values than were present in the wet-hydrogen treated material.

Gensamer and Mehl [4] tested single crystals and polycrystals of iron by dead-weight loading in increments of between 70 g/mm^2 and 140 g/mm^2 and plotting strain-versus-time curves after each increment of stress. The load increments were added at intervals varying from six hours to five days. In all cases for stresses above the yield point, there was an initial delay time before flow began; the rate of extension then reached a maximum and finally decreased to zero. When the next increment of stress was added, the same behaviour was observed. A valid comparison of these particular observations with others cannot be made since the strain sensitivity was not indicated, and the purification of the specimens reduced the carbon content only "to the limit for detection under the microscope," which may be a relatively high interstitial impurity content which would affect the plastic properties of the material.

McReynolds [5], while studying stepped stress-strain curves of pure (99.996% Al) polycrystalline aluminium, apparently observed a phenomenon which is similar to that studied in the present work. This was not mentioned in the text but it may be seen in Figure 2 of McReynold's paper that, after holding the stress constant for 15 minutes and then increasing the stress, the strain did not increase to any marked degree until a fairly large stress increment had been made.

The presence of a yield point in body-centered cubic and close-packed hexagonal metals containing small quantities of interstitial solute elements is well known. This, and the absence of well-established yield points in face-centered cubic metals have been discussed recently by Smallman *et al.* [6] who observed yield points at liquid-air temperatures in single crystals of commercially pure aluminium and in binary alloys of superpure aluminium containing copper, zinc and hydrogen. In all cases, ageing treatments at elevated temperatures were needed to induce the yield points. Under similar conditions superpure (greater than 99.99% Al) aluminium crystals gave no yield phenomenon.

The purpose of this paper is to present evidence of a yield phenomenon in single crystals of copper, some observations on the effect of hydrogen on the mechanical properties of the crystals, and some observations on a transition in the stress-strain curve of copper crystals.

Experimental Procedure

Specimens were prepared from copper supplied by Messrs. Johnson, Matthey and Co., Ltd. who reported the major impurities to be silver (0.0003%–0.0005%), nickel (0.0003%), and lead (<0.0004%) with faintly detectable amounts of gallium and calcium.

The single crystals were grown in a machined graphite boat which was fitted with a suitable cover and heated in argon in a furnace which has been described by Gow and Chalmers [7]. The crystals were usually grown in pairs originating from the same nucleus so that two crystals of the same crystallographic orientation could be compared after different thermal treatments. The crystals were separated by electrolytic cutting in order to prevent strains introduced into the crystal by mechanical working. Each crystal was approximately 5½–6 in. long, ½ in. wide, and 3/16 in. thick. The crystallographic orientation of each specimen was determined from Laue back-reflection patterns by means of Greninger's technique [8]. The specimens were each annealed for periods of time ranging from two to six days (the majority for six days) in vacuum ($<5 \times 10^{-5}$mm Hg), purified hydrogen, or argon. In all cases, the annealing temperature was in the range 975°–1000°C.

An optical extensometer was carefully clamped in position on a specimen, and the specimen then mounted in the balanced "soft" tensile testing machine. Descriptions of the extensometer and the testing machine are to be found elsewhere [9]. A slowly increasing tensile load was applied to the specimen until the elastic limit had been reached. It was possible to record a few stress-strain

measurements prior to the onset of plastic deformation. These strain measurements, however, can be accepted only as approximations. Once the elastic limit of the specimen had been exceeded, small amounts of load were added to the specimen at recorded time intervals. The increment of stress in the specimen at each loading was in the order of 10–20 g/mm². After the addition of a load increment to the specimen, the total load and the specimen's elongation were measured and recorded. At the end of a desired time interval, hereafter called the *ageing time* (usually in the order of minutes), during which the specimen remained under a constant load, the elongation was again recorded in some cases, and in all cases another load increment was added to the specimen. The time interval, hereafter called the *delay time* (in the order of seconds), between the beginning of the addition of a load increment and an increase of plastic extension was carefully measured and recorded.

In order to eliminate the possibility that a spurious delay time was introduced by the machine or by the method of observation, it became necessary to examine the procedure critically. For this purpose, motion pictures were used to record the behaviour of the light beam reflected from the optical extensometer on the specimen. The delay time was recorded on film by photographing the reflected light beam and, in the same field, a small electric light which indicated the time required for the addition of a load increment. To show that the delay time could not be due to the equipment or procedure, similar photographs were made when the extensometer was mounted on the system shown in Figure 1. The steel ring shown was made of black oil-tempered spring steel and was designed so that a given load increment on the spring, mounted in place of a specimen, would cause the same amount of extension as that occurring (on an average) in the copper crystals due to the same load increments. Thus the distance between the gauge marks on the brass dummy bars shown increased the same amount as on a specimen under an equal load. However, the ring remained elastic, while the copper specimen had deformed plastically.

The specimen extensions were recorded to the nearest micron (strain = 2×10^{-5}cm/cm on a 5 cm gauge length); the stresses were recorded to the nearest g/mm² in the range 0–300 g/mm², the sensitivity of the measuring system decreasing somewhat above that.

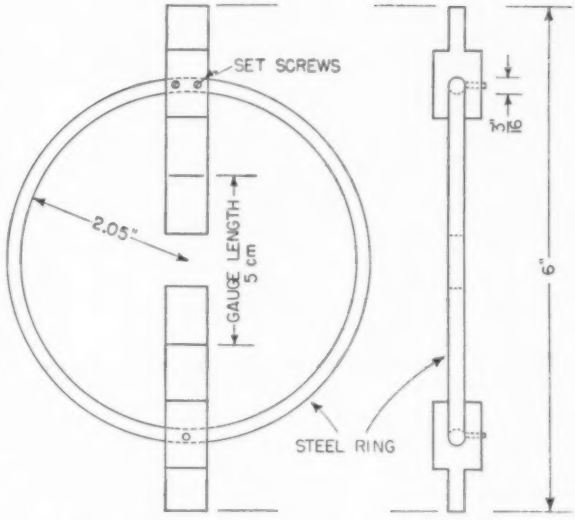

FIGURE 1. Steel test spring with brass dummy bars.

Observations

As has already been stated, a marked delay was found to occur between the beginning of the addition of a load increment and the observed onset of continued plastic strain. This delay was measured by using a stopwatch and visual observations, and was confirmed by photographing the elongation of the crystal specimens as indicated by the light beam from the optical extensometer. The rate of loading during the addition of a stress increment was also measured, and from this information, and the delay time recorded during each stress increase, some portions of the stress-strain curves of typical crystals have been developed in detail, and are shown in Figures 2–5. The figures located under each constant-stress portion of the curves indicate the ageing time in minutes during which the specimen was held at the indicated stress level. Usually a sequence of three or four measurements was recorded, with a shorter ageing time for each subsequent step of the sequence. In most cases it may be seen that the rise in stress, prior to an increase in plastic strain, is dependent on the length of the ageing time at which the specimen had been held before the load was increased. The curved portions of the stress-strain curves are quite arbitrary since no attempt was made to determine the exact strain value at the time of completion of a load addition. However, the curved sections show reasonably well the behaviour of the specimens. It may be seen that there are two distinct types of "steps" on the stress-strain curve. The most common type has a rounded

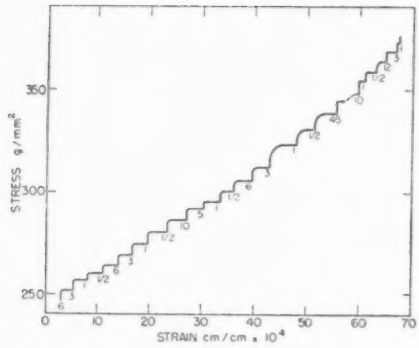

FIGURE 2. Portion of stress-strain curve for crystal 11A.

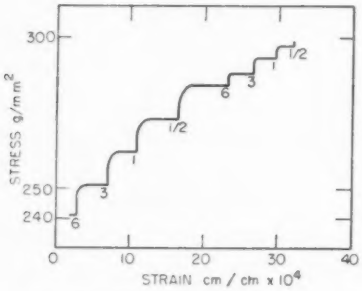

FIGURE 3. Portion of stress-strain curve for crystal 11B.

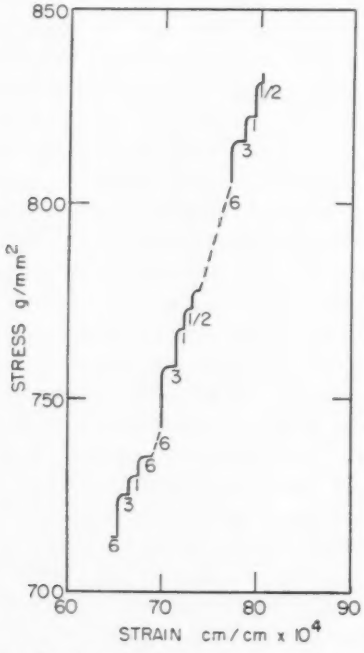

FIGURE 4. Portion of stress-strain curve for crystal 12B.

corner resulting from the fact that plastic strain was detected prior to the completion of a load increment addition. The other type of step has a sharp transition from the vertical rise in the stress

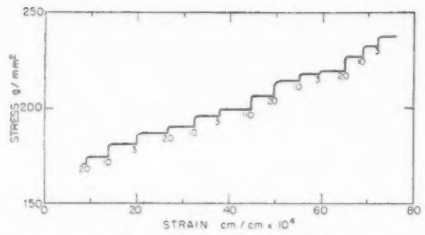

FIGURE 5. Portion of stress-strain curve for crystal 15.

to the horizontal increase in strain at a constant stress. This results from the delay time being equal to, or longer than, the time required for the addition of a load increment.

Figure 6 shows a number of curves of delay times plotted against the waiting period prior to each delay measurement. The curves are numbered as sequences, with each succeeding set of measurements being made on the crystal at higher stress level. It may be seen that the delay times increased with the ageing period. The shortest waiting period is shown as one-half minute. This minimum ageing time was chosen since both visual and photographic records indicated that an elapsed time of between 10 and 30 seconds was required for the rate of strain of the crystals to become imperceptible. When the copper crystals were *immediately* subjected to a higher load, there was no delay time and, therefore, no yield point. It was mentioned that it took from 10 to 30 seconds after the completion of a load addition before the rate of strain became too slow for detection. Therefore, an immediate reloading simply increased the already perceptible rate of strain.

In testing the steel spring system described earlier, it was found that the delays, following ageing periods of the same order as those used for

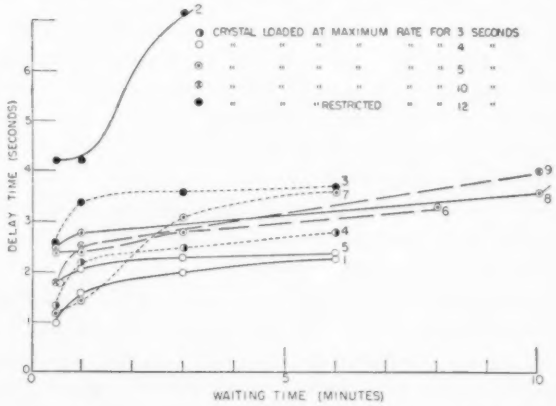

FIGURE 6. Ageing-time versus delay-time curves for crystal 11B.

the copper, were too short to be readily measured by visual observations. Photographic records indicated that the delays were less than one-half second so that, for the crystal specimens, any delay above one-half second was entirely due to the behaviour of the copper, and could not be due to inertia or friction in the testing equipment. Also, unlike the behaviour of the metal crystals, perceptible deflection of the steel spring ceased within one-quarter second after loading had stopped.

The stress-strain curves for some typical specimens of particular interest are shown below in Figures 7–11 and the specimens' orientations are shown in Figure 12. The long dashes to zero stress on some of these diagrams indicate the course of the stress-strain curve during unloading, and the shorter dashes show the curve during reloading to the same stress. The solid circles on the curve for crystal No. 15 indicate that the measurements

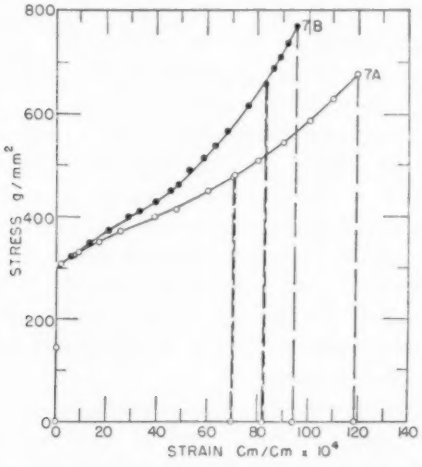

FIGURE 7. Stres-strain curves for crystals 7A and 7B.

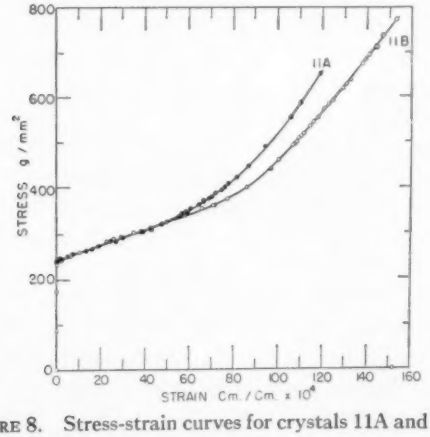

FIGURE 8. Stress-strain curves for crystals 11A and 11B.

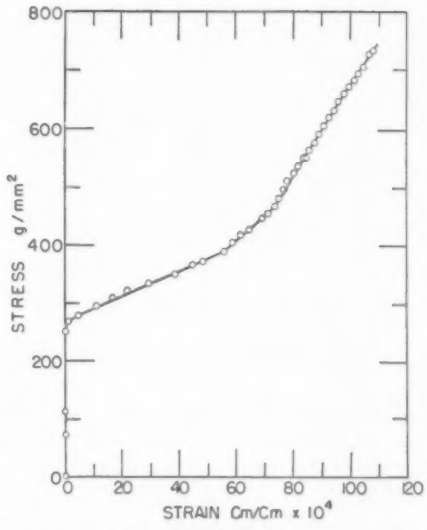

FIGURE 9. Stress-strain curve for crystal 14.

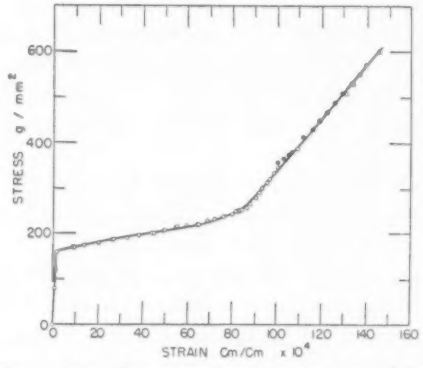

FIGURE 10. Stress-strain curve for crystal 15.

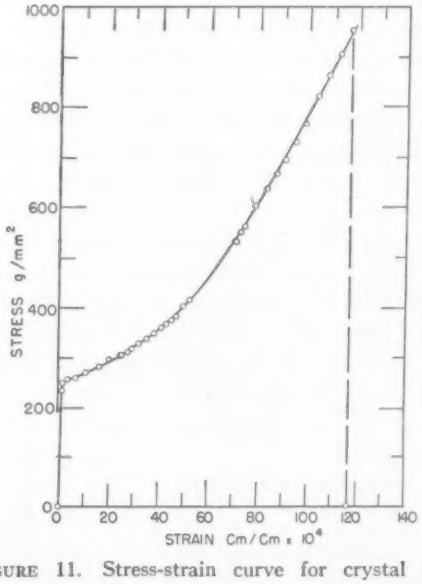

FIGURE 11. Stress-strain curve for crystal 16.

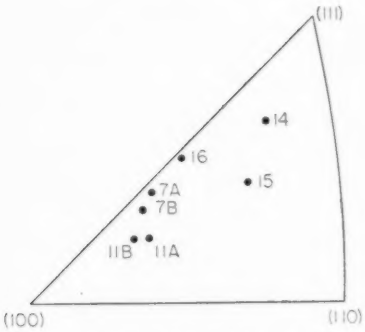

FIGURE 12. Crystallographic orientation of specimens.

were obtained while the base of the specimen was packed in solid carbon dioxide. All curves are drawn through the stress-strain conditions at the end of the ageing periods, and do not show the steps which are given, in detail, elsewhere.

The crystals 7A and 7B (Figure 7) are of the same orientation but were annealed *in vacuo* for 72 hours and 50 hours respectively. The critical resolved shear stress was approximately the same for each crystal, but the rate of work-hardening for crystal 7B was considerably higher than that for 7A.

Crystals 11A and 11B (Figure 8) are of the same orientation and were annealed, prior to testing, for 146 hours. Crystal 11A was annealed 41 hours in hydrogen, and 105 hours *in vacuo*, while 11B was *in vacuo* the entire time. In this case the critical resolved shear stress was exactly the same for each crystal, while the rate of work-hardening was the same for each in the first part of the plastic region of the stress-strain curve, and greater in the second part of the curve (which started at a lower strain) for crystal 11A. In all cases where identical crystals were annealed for equal times in different atmospheres, the specimen annealed in hydrogen had a higher rate of work-hardening and, in two instances, a slightly higher critical resolved shear stress.

Each of crystals 14, 15 and 16 (Figures 9–11) has two definite rates of work-hardening in the plastic region of the stress-strain curves. Table I shows the region of easy glide and the path (in degrees) which the pole of the specimen axis traverses during classical single slip.

TABLE I

Crystal number	15	14	16
Region of easy glide (cm/cm$\times 10^4$)	75	55	20
Single slip path (degrees)	12	7	1

Summary and Discussion

A type of yield phenomenon has been observed in single crystals of "superpure" copper tested at room temperature. A new feature of the present results is that the yielding has been found to occur in a face-centered cubic material with less than 0.002 per cent. substitutional impurities present. It has been found that ageing for a few minutes *in situ* at 26°C, and under the maximum load to which the specimen had been subjected up to the time of ageing, is effective in producing yielding. Since a "soft" tensile machine was used, it was impossible to obtain a fall in load at the beginning of plastic deformation. However, the sudden yielding and subsequent rapid deformation was indicative of the presence of a yield point which could be obtained by suitable ageing treatment, and which was absent if ageing was not allowed.

It is interesting to note that the stress-strain curves shown in Figures 2–5 resemble the stepped stress-strain curves found for various alloys [10; 11]. However, the stepped curves for the alloys were obtained by loading the specimens at a steady and quite rapid rate, while the present curves result from discontinuous and slow loading. In other work on alloys [12], discontinuous, but rapid, loading was used.

The dislocation theory mechanism proposed by Cottrell to explain strain-ageing effects and yield phenomena accounts for the behaviour which has been observed here. It has already been pointed out [6; 12] that a substitutional solute should be able to cause a yield point which would be expected to be weaker than the well-known yield point in the iron-carbon system. This is in agreement with the present observations.

The consistent effect of developing a higher rate of work-hardening and/or a higher critical resolved shear stress by annealing one of two identical crystals in hydrogen would suggest that this atom in solution affects the slip mechanism. However, the effects of minor crystalline substructures should be determined before it is definitely concluded that the hydrogen alone is responsible for the effect.

Lücke and Lange [13] have shown that crystals of aluminium stretched in tension show easy glide, provided they are pure and have orientations which avoid double slip. Figure 13 shows their results on two crystals of pure aluminium, one of which, A, deformed initially by single slip and showed a region of easy glide in which hardening was very small, while the other, B, deformed by multiple slip and began hardening immediately. Curve B is similar to some results obtained here, but curve A does not indicate the sharply defined region of

more rapid work-hardening which has been found for copper crystals. The two regions of easy glide and more difficult glide may be seen in all the stress-strain curves obtained with the single crystals of copper. A similar transition point in the stress-strain curve has been observed in polycrystalline aluminium-base alloys [16], in high-

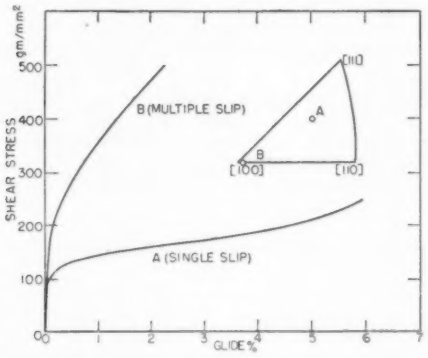

FIGURE 13. Stress-strain curves of pure aluminium crystals (after Lücke and Lange).

purity aluminium single crystals (17; 18), and in copper crystals [19]. Masing and Raffelsieper [14] have shown that the region of easy glide in aluminium became smaller the nearer the initial orientation was to one giving multiple slip, and this has been confirmed here as shown in Table I. It should however, be noted that the increase in the rate of work-hardening took place long before multiple slip would normally be expected to operate.

Acknowledgement

The authors wish to thank the National Conference of Canadian Universities and the International Nickel Company of Canada, Limited, who provided a fellowship for this research. They also thank Dr. C. Elbaum for his valuable assistance in this work, and Dr. L. M. Pidgeon who provided facilities for this work in the Department of Metallurgical Engineering at the University of Toronto.

References

1. CLARK, D. S. and WOOD, D. S. Proc. A.S.T.M. **49** (1949) 717.
2. WOOD, D. S. and CLARK, D. S. Trans. A.S.M. **43** (1951) 571.
3. WOOD, D. S. and CLARK, D. S. Trans. A.S.M. **44** (1952) 726.
4. GENSAMER, M. and MEHL, R. F. Trans. A.I.M.E. **158** (1944) 207.
5. MCREYNOLDS, A. W. Trans. A.I.M.E. **185** (1949) 32.
6. SMALLMAN, R. E., WILLIAMSON, G. K., and ARDLEY, G. Acta Met. **1** (1953) 126.
7. GOW, K. V. and CHALMERS, B. Brit. J. Appl. Physics **2** (1951) 300–303.
8. GRENINGER, A. B. Trans. A.I.M.E. **117** (1935) 61.
9. CLARK, R. and CUPP, C. R. To be published.
10. KRUPNIK, N. and FORD, H. J. Inst. Metals **81** (1953) 601.
11. EBORALL, R., LACK, M., and PHILLIPS, V. A. Bull. Inst. Metals **1** (1952) 58.
12. PHILLIPS, V. A., SWAIN, A. J., and EBORALL, R. J. Inst. Metals **81** (1953) 625.
13. LÜCKE, K. and LANGE, H. Z. Metallkunde **43** (1952) 55.
14. MASING, G. and RAFFELSIEPER, J. Z. Metallkunde **41** (1950) 65.
15. BECKER, J. J. and HOBSTETTER, J. N. Trans. A.I.M.E. **5** (1953) 1231.
16. JAOUL, B. and CRUSSARD, C. Rev. Mét. **47** (1950) 589.
17. CRUSSARD, C. Rev. Univ. Mines (Congrès A. I. Lg., Section Métallurgie physique 1947), 41.
18. JAOUL, B. and CRUSSARD, C. J. Inst. Metals **80** (1953) 690.
19. DALTON, A. L. and HONEYCOMBE, R. W. K. Unpublished work.

NOTE ON THE DISORIENTATION AND IMPURITY SUBSTRUCTURES IN ZINC SINGLE CRYSTALS*

K. F. HULME†

The systematic distribution of impurity when crystals are grown from the melt under certain conditions has been investigated for the case of zinc. The relationship of this impurity substructure to disorientations within the crystal has been studied using the Berg-Barrett technique; it was found that in some cases the disorientation boundaries and the impurity-rich regions coincided. The results are discussed briefly in the light of the theory of dislocations.

UNE NOTE SUR LES SOUS-STRUCTURES QUI PROVIENNENT DE LA DÉSORIENTATION ET DES IMPURETÉS, DANS DES MONOCRISTAUX DE ZINC

On a fait une investigation, dans le cas du zinc, de la distribution systématique des impuretés, lorsque des cristaux sont formés, sous certaines conditions, à partir du métal liquide. La méthode de Berg-Barrett fut utilisée pour la détermination de la relation entre la sous-structure due aux impuretés, et la désorientation au sein du métal. On a constaté que dans certains cas les joints des régions désorientées et les régions d'impuretés coïncident. Ces résultats sont brièvement discutés en termes de la théorie des dislocations.

BEMERKUNGEN ZUR FEHLORDNUNGS- UND VERUNREINIGUNGSFEINSTRUKTUR IN ZINKEINKRISTALLEN

Die systematische Verteilung von Verunreinigung in unter gewissen Bedingungen aus der Schmelze gezüchteten Kristallen wurde an Zinkkristallen untersucht. Das Verhältnis dieser Verunreinigungsstruktur zu Fehlordnungen innerhalb des Kristalls wurde mit Hilfe der Berg-Barrett Technik untersucht. Es zeigte sich, dass in einigen Fällen die Fehlordnunsgrenzen und die an Verunreinigung reichen Gebiete zusammenfielen. Die Resultate werden kurz im Rahmen der Theorie der Versetzungen diskutiert.

Introduction

Chalmers and his co-workers have recently published several papers on the imperfections of single crystals of metals grown from the melt. One of these papers [1] described observations of disorientations within single crystals. The crystals investigated were found to be divided into parallel rods by low-angle boundaries; the direction of the axes of the rods was intermediate between the direction of maximum temperature gradient during growth and a prominent crystallographic direction (in the case of tin the [110] direction). The dimensions of the rods and the disorientations between them depended on the growth conditions; rod diameters of 1 mm, and disorientations of 2 degrees were typical for tin grown at the rate of 10 cm/hr.

In another paper [2], a second type of imperfection was described; this was the effect of impurities in the melt on the growing crystal. Buerger [3] had recorded an example of this substructure and the association with impurity in the melt had been made by Smialowski [4]. A smooth growth front advancing into an impure melt is only possible under certain conditions; when these conditions are not satisfied the solid-liquid interface becomes corrugated and the impurity in the resulting crystal is concentrated into the walls of an impurity substructure. Rutter and Chalmers [2] made observations on the growth front by pouring the remaining melt away when growth of a single crystal was incomplete; they found that the corrugation produced a roughly hexagonal network in most cases; the onward movement of this pattern, as growth proceeded, caused the crystal to be divided into hexagonaloid pencils with impurity concentrated in the walls between the pencils. Autoradiography was used to prove that the impurity lay in the walls of the structure. The connection with the etching patterns previously observed on single crystals by Buerger [3] and Smialowski [4] was obvious. The axes of the pencils were parallel to the axes of the disoriented rods described above, although the two types of imperfection were otherwise quite distinct; the diameter of the pencils was dependent on the speed of growth but was typically 0.05 mm for 40 cm/hr growth rate. Back-reflection Laue photographs of a crystal displaying this impurity substructure showed that there could be random orientation differences of up to 15′. [2, p. 22].

The present paper is an account of some further work on these two types of imperfection in crystals of zinc.

*Received March 2, 1954.
†H. H. Wills Physical Laboratory, University of Bristol, England.

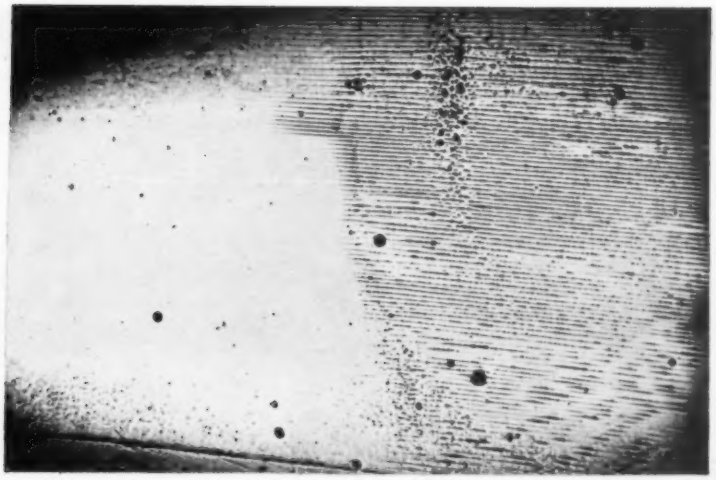

1

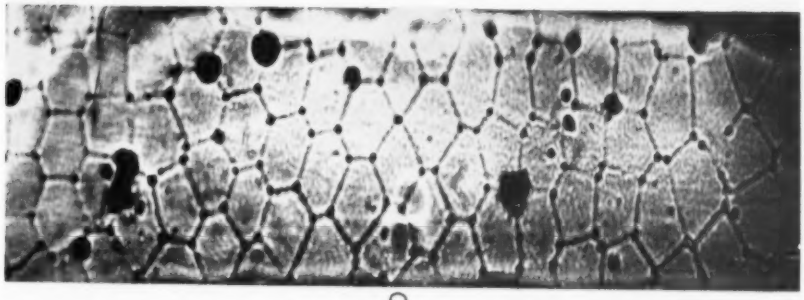

2

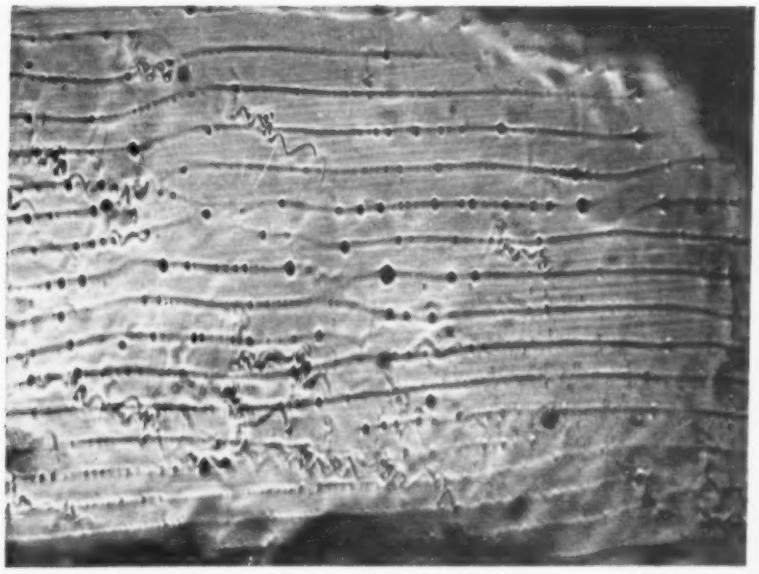

3

PLATE I. Figure 1.—Top surface of zinc single crystal after electropolishing showing start of impurity substructure. 6X. Figure 2.—Cross section of impurity structure. 47X. Figure 3.—Cross section of impurity substructure. 47X.

4

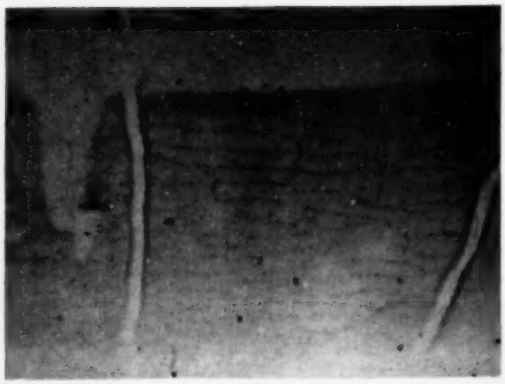

5

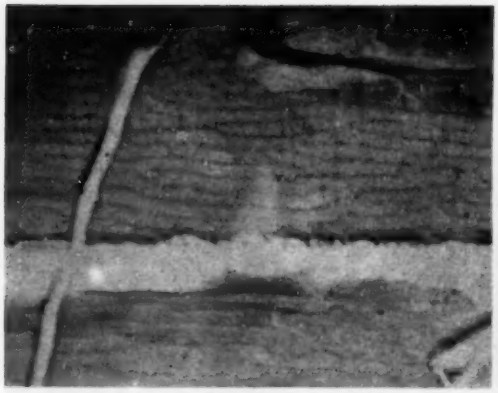

6

7

PLATE II. Figure 4.—(All figures reduced to two-thirds in reproduction.) Berg-Barrett photograph 36.X. 18 hours' exposure. Distance from specimen to plate approximately 5 mm. Figure 5.—Berg-Barrett photograph. 36.X. 48 hours' exposure. Distance from specimen to plate; approximately 3 mm. Figure 6.—Berg-Barrett photograph. Details as for Fig. 5. Figure 7.—Optical micrograph of crystal used for Figs. 4, 5, 6. 36.X.

The Preparation of the Crystals and Microscopical Examination

The crystals were grown from 99.99 per cent+ purity zinc ("Tadanac") in an atmosphere of 99 per cent purity argon by the travelling furnace method. A graphite boat was used to hold the zinc; it was 15 cm long, 2 cm wide and 7 mm deep; the orientation of the crystals grown was controlled by seeding with a small crystal of predetermined orientation. The technique followed closely that described in a paper by Chalmers [5]. The speed of travel of the furnace was 2 cm/hr for all the crystals described below.

After removal from the boat the crystals were subjected to a crystallographic etching reagent [6]. This did not make any orientation differences visible; this was in contrast to the observations of Teghtsoonian and Chalmers [1], although it must be noted that their tin crystals were grown at a somewhat higher growth-rate.

After light mechanical polishing of the surface to be examined with "Brasso" on a "Selvyt" pad the crystals were electrolytically polished in 20 per cent CrO_3 solution; a current at the lower end of the polishing range made the impurity structure conveniently visible for low-power microscopical examination. This was due to the fact that during electrolytic polishing the impurity-rich portions dissolve most rapidly. The surface profile thus produced was readily detectable under the microscope when the surface was slightly out of focus.

Measurements showed that for crystals grown by the method described above the temperature gradient at the solid-liquid interface falls during growth. The impurity content of the bulk melt also rises slowly during growth as a result of convection in the melt. The criterion for the appearance of the impurity substructure therefore becomes satisfied at a well-defined stage during growth; thereafter, the substructure prevails. For crystals of zinc grown as described above the last 2 cm to grow invariably showed this substructure; Figure 1 shows the top surface of a crystal and it is seen that the impurity substructure has started at a reasonably well-defined plane; in the photograph the growth direction was from left to right. In Figure 2 a cross section very near the end of another crystal is shown; it shows the typical roughly hexaganoloid cells described by previous workers.

In agreement with the observations of Smialowski [4] it was found that when growth took place along a direction in the basal plane the hexagonaloid cells were greatly elongated and became in fact lamellae parallel to the basal plane. This lamination occurred when the basal plane was horizontal in the boat during growth and thus did not appear to have a direct relationship to possible convective flow in the melt across the interface; the streamlines of the convective flow would be perpendicular to the lamination. Figure 3 is a cross section perpendicular to the growth direction of a crystal showing this type of impurity substructure; the crystal had been slightly deformed by hand after electropolishing to cause slip lines which delineate the basal plane; the slip lines are visible between the heavy black lines which are the impurity-rich regions.

Description and Use of the Berg-Barrett Technique

The Berg-Barrett technique has been used to study the orientation differences in a crystal showing the impurity substructure. The technique, originally used by Berg [7], improved by Barrett [8] and recently used by Honeycombe [9], in a study of deformation bands, is a form of X-ray microscopy.

The surface from which the Berg-Barrett photographs described below were obtained was a cross section a few millimetres from the termination of growth of a crystal grown and prepared by the method given above. The orientation, which was determined by a back-reflection Laue photograph, was such that the growth axis was inclined at 85 degrees to the [0001] direction and 11 degrees to the [2110] direction; the impurity substructure was therefore in the form of laminations parallel to the trace of the basal plane.

The X-rays used were those from a vertical line source 1 cm × 1 mm on a copper target; a 0.02 mm Ni filter was used and the radiation obtained consisted predominantly of the $CuK_{\alpha_1\alpha_2}$ doublet. The specimen was held in a goniometer 72 cm. from the source. When the specimen had been oriented correctly, Bragg reflection occurred from the surface and a fine-grain photographic plate placed close to the surface and approximately parallel to it was used to record an X-ray image of the surface. Kodak Maximum Resolution Plates were very suitable and graininess of the image was not observable at the magnifications used during the subsequent microscopical examination of the plate. The photographic plate was screened from the incident X-ray beam and was placed as close to the specimen as possible without interfering

with the incident beam. It was found to be most convenient to use angles of incidence on the surface of between 5 and 20 degrees and Bragg angles between 5 and 45 degrees.

Figure 4 is a mosaic obtained from three micrographs of a single Berg-Barrett photograph of the surface; it is a negative as are also Figures 5 and 6. (By this is meant that blackening indicates X-rays have been reflected strongly from that region of the crystal and vice versa.) Light scratches were scribed on the surface of the specimen to assist comparison between various photographs of the same area. Two, which appear as broad white horizontal lines on Figure 4, are parallel to the trace of the basal plane and two others which are not straight run roughly vertically across the area. The end of a fifth is seen at the right. In this photograph the projection of the incident X-ray beam on the surface was parallel to the two horizontal scratches and runs from right to left across the photograph.

Figures 5 and 6 are enlargements of another Berg-Barrett photograph of the same area; in this photograph the projection of the incident X-ray beam on the surface was perpendicular to the horizontal scratches and from top to bottom. The area covered by Figure 5 corresponds to the bottom left-hand area of Figure 4, whereas Figure 6 corresponds to the top right-hand area of Figure 4. Although the Bragg planes operative were not ascertained, detailed comparison leads to the conclusion that the reflection used for Figures 5 and 6 was different from that used for Figure 4. Dust particles stuck to the emulsion are visible in some of the photographs; these are difficult to avoid and impossible to remove if they are picked up when the emulsion of the plate is wet.

An optical micrograph of the surface was taken after the X-ray photographs had been obtained; unforeseen attack of the surface had taken place since electropolishing and has considerably reduced the visibility of the impurity substructure. The lamellae can be made out running horizontally in Figure 7, which corresponds to the left-hand lower portion of Figure 4. The appearance of the crystal before the corrosion was very similar to Figure 3, except that in this case there was no intentional deformation and therefore no slip lines.

The Interpretation of the Photographs

The details of the X-ray photographs are attributed to the following effects:

1. Parts of the crystal which are disoriented so that they fail to satisfy the Bragg condition will appear white. This is exemplified by the scratches and by the block-like regions in the top right of Figure 4. Further, the X-ray source is not of uniform intensity and the selection by neighbouring areas of the crystal of different portions of the source will result in intensity differences; these variations of intensity will be smooth if the crystal has no disorientation boundaries, provided the source itself has smooth variations of intensity, but if there are disorientations the parts of the crystal on different sides of the disorientation boundary will select X-rays from widely differing points on the source and a sharp change of intensity will be observed between the X-ray images. There are examples of this in Figure 4 also.

2. Adjacent portions of the crystal with a disorientation boundary separating them will not only select their X-rays from different parts of the source (provided this is possible) but will send off their reflected rays at different angles. In the photographs this will result in the images of the two parts of the crystal either overlapping a little or failing to meet; the disorientation boundary will be seen as a black line in the first case or a white one on the second. Figures 4, 5 and 6 show this effect. Disorientations may be measured by this means, except components of disorientations corresponding to rotations about the normal to the Bragg reflecting plane used. Typical disorientations as shown in the photographs are of the order 5′.

3. The intensity of X-rays reflected will also be affected by any variation in the extinction. It is thought that disorientation boundaries and the impurity-rich regions may be effective in reducing the extinction although the result on the photographs—black lines—is difficult to disentangle from the overlap effect mentioned above. The fact that slip lines on deformed crystals appear as regions of increased reflecting power on Berg-Barrett photographs is known [7] and lends support to the view that dislocation boundaries cause reduced extinction in their immediate neighbourhood. Many of the black lines in Figures 4, 5 and 6 are attributed to this effect, especially those running perpendicular to the basal planes.

4. The fact that the incident radiation is not strictly monochromatic but consists of the $CuK_{\alpha_1\alpha_2}$ doublet means that in fact two images of each point of the surface will be formed. The Bragg condition is:

$$\lambda = 2d \sin \theta$$

The angular difference between the two images is then given by $\delta\theta = \delta\lambda/2d \cos \theta \sim 3'$ in this case.

No spurious black or white lines will appear on the photographs from this effect but where there are details they will be blurred.

The conclusions to be drawn from a comparison of Figures 4, 5, 6, and 7 are as follows:

(i) Twins have been produced near the scratches; they are responsible for the jagged edges of the scratches and the inclination of their traces to the basal plane trace is in agreement with the computed value for the cross section. The dark vertical lines coming down from some of the more prominent twins in Figure 4 are thought to be accommodation kinks made visible because of effect (3) above.

(ii) The disorientation boundary running stepwise downwards in the top right of Figure 4, which is seen by reason of effects (1) and (2), is a strong one; it is also visible in Figure 6 as a white line. The fact that there is an overlap in Figure 4 and the opposite in Figure 6 is not necessarily inconsistent; the reflections used are different.

(iii) The crystal is split into blocks by low-angle boundaries. Figure 4 shows this very strikingly.

(iv) Where the boundaries run approximately horizontally in the X-ray photographs they coincide with the impurity-rich regions. The general trend and the spacing of the lines correspond in Figures 5 and 7 and the bottom left of Figure 4. A detailed comparison of a line of recognizable shape is possible. This is the line running from left to right starting from the extreme left vertical scratch in Figure 4, four lines below. the bottom horizontal scratch; compare it with the first line below the horizontal scratch in Figure 5 and the fourth line below the bottom scratch in Figure 7 (the scratches appear of different width in the three cases).

Discussion

The block-like structure revealed by the X-ray photographs brings to mind the mosaic structure postulated by Darwin [10] to explain the intensity of X-ray reflections; but block dimensions in the range 10^{-4}cm to 10^{-6}cm were needed by this theory whereas the dimensions of the blocks in Figure 4 are larger than 10^{-2}cm. Also it must be remembered that a systematic distribution of the impurity exists in the crystal from which the photographs were obtained.

The low-angle boundaries in the crystal can be regarded as arrays of dislocations; experimental evidence of this has been provided by Vogel *et al* [11]. A possible mechanism for the production of the dislocations responsible for the low-angle boundaries they found in tin has been given by Teghtsoonian and Chalmers [1]. Whatever the method of production of dislocations, it appears that during the rearrangement behind the solid-liquid interface the impurity-rich layers of the impurity substructure provide resting places for many of them. The interaction between solute atoms and dislocations is well known [12] and the fact that the interaction is greater for edge dislocations than screw dislocations may have some relation to the fact that the low-angle boundaries in crystals grown from the melt found by Chalmers and Teghtsoonian [1] and Vogel [11] consisted of edge dislocations.

Acknowledgements

I wish to thank Dr. F. C. Frank for his continued interest, helpful discussion and advice, and Mr. K. E. Puttick for much valuable advice on experimental techniques. I am indebted to the University of Bristol for a maintenance grant.

References

1. Teghtsoonian, E. and Chalmers, B. Can. J. Phys. **29** (1951) 370.
2. Rutter, J. W. and Chalmers, B. Can. J. Phys. **31** (1953) 15.
3. Buerger, M. J. Zeit. für Krist. **89** (1934) 195.
4. Smialowski, M. Z. für Metallkunde **29** (1937) 133.
5. Chalmers, B. Can. J. Phys. **31** (1953) 132.
6. Barrett, C. S. Structure of Metals, 2nd ed. (London, McGraw-Hill, 1953), p. 194.
7. Berg, W. Naturwiss. **19** (1931) 391.
8. Barrett, C. S. Trans. A.I.M.E. **161** (1945) 15.
9. Honeycombe, R. W. K. J. Inst. Metals **80** (1951) 39.
10. Darwin, C. G. Phil. Mag. **43** (1922) 800.
11. Vogel, F. L., Pfann, W. G., Corey, H. E., and Thomas, E. E. Phys. Rev. **90** (1953) 489.
12. Cottrell, A. H. Report of a Conference on the Strength of Solids, University of Bristol (London, Physical Society, 1948), p. 30.

THE EFFECT OF SHORT-TIME MODERATE FLUX NEUTRON IRRADIATIONS ON THE MECHANICAL PROPERTIES OF SOME METALS*

F. W. KUNZ and A. N. HOLDEN†

Single crystals of iron, lead and zinc were irradiated at room temperature to a total flux of 10^{18} nvt to determine the effect of neutron irradiation on the mechanical properties of these metals. The flow stress of the iron and zinc crystals as measured from load versus elongation curves was markedly increased after the neutron exposure. The flow stress of the lead crystals remained unchanged after irradiation. Irradiated iron crystals were annealed at temperatures ranging from 200°C to 500°C for times ranging from one to 10^4 minutes, following which they were tested in tension to determine the extent of recovery of the mechanical properties. The extent of recovery was determined by comparing the observed yield strength of the partially recovered crystals with yield strength of crystals in both the irradiated and unirradiated condition. An equation of the form $\tau = A \exp(Q/kT)$ was found relating the time for any fixed amount of recovery to the absolute recovery temperature. The determined activation energy for recovery Q is equal to the activation energy for self-diffusion in iron. Various radiation hardening mechanisms are also critically reviewed.

L'EFFET DE L'IRRADIATION DE COURTE DURÉE PAR UN FLUX MODÉRÉ DE NEUTRONS SUR LES PROPRIÉTÉS MÉCANIQUES DE CERTAINS MÉTAUX

On a irradié des monocristaux de fer, de plomb et de zinc, à la température ambiante, jusqu'à un flux total de 10^{18}nvt, en vue de déterminer l'effet de l'irradiation aux neutrons sur les propriétés mécaniques de ces métaux. La tension d'écoulement du fer et du zinc, mesurée à partir de la courbe charge-élongation, était considérablement plus élevée après l'irradiation aux neutrons. La tension d'écoulement des cristaux de plomb restait inchangée après l'irradiation. Les cristaux irradiés de fer furent recuits à des températures allant de 200°C à 500°C pendant des temps allant d'une minute à 10^4 minutes, ensuite ils furent soumis à des essais de traction en vue de déterminer le degré de la restauration des propriétés mécaniques. Le degré de la restauration fut déterminé en comparant la tension d'écoulement des cristaux partiellement restaurés à la tension d'écoulement des cristaux à l'état normal et à l'état irradié. On a trouvé une équation de la forme $\tau = A\exp(Q/kT)$ qui relie le temps nécessaire pour une restauration déterminée à la température absolue de restauration. L'énergie d'activation déterminée pour la restauration, Q, est égale à l'énergie d'activation pour l'autodiffusion dans le fer. Divers mécanismes de durcissement par irradiation sont revisés d'une manière critique.

DIE WIRKUNG EINER KURZEN NEUTRONENBESTRAHLUNG MÄSSIGER INTENSITÄT AUF DIE MECHANISCHEN EIGENSCHAFTEN EINIGER METALLE

Eisen-, Blei- und Zinneinkristalle wurden bei Zimmertemperatur mit einer Geamteinstrahlung von 10^{18} nvt bestrahlt um die Wirkung von Neutronenbestrahlung auf die mechanischenEigenschaften dieser Metalle zu ermitteln. Die aus Last-Dehnungskurven gemessene Fliesspannung der Eisen- und Zinkkristalle nahm nach der Neutronenbestrahlung merkbar zu, während sich in den Bleikristallen die Fliesspannung nicht durch Bestrahlung ändert. Die bestrahlten Eiseneinkristalle wurden in einem Temperaturbereich zwischen 200°C und 500°C geglüht. (Glühzeiten zwischen einer und 10^4 Minuten) Danach wurden sie unter Zug untersucht, um das Ausmass der Erholung der mechanischen Eigenschaften zu bestimmen. Das Ausmass der Erholung wurde durch Vergleich der Streckgrenzen von teilweise erholten, bestrahlten und unbestrahlten Proben ermittelt. Es zeigte sich, dass eine Gleichung der Form $\tau = A \exp(Q/kT)$ die für ein festgesetztes Ausmass der Erholung erforderliche Zeit mit der absoluten Glühtemperatur in Beziehung setzt. Die so ermittelte Aktivierungsenergie der Erholung Q ist gleich der Aktivierungsenergie der Selbstdiffusion in Eisen. Es werden ausserdem verschiedene Vorstellungen über den Mechanismus der Strahlungsverfestigung kritisch diskutiert.

Introduction

Until recently very little was known about the effect of neutron irradiation on the mechanical properties of metals. The extent of knowledge included only that the indentation hardness of metals was increased by such radiation and that the increase in hardness was less marked for metals hardened by some other means prior to irradiation.

The work of Blewitt *et al.* [1] with copper single crystals provided the first information of a fundamental nature about radiation damage to mechanical properties. Blewitt found that the critical shear stress for slip in copper was increased markedly by exposure to neutrons in a reactor, but that the strength of the crystals, after extensive plastic flow had occurred, was not seriously different from that of unirradiated specimens. In other words, the flow curves for irradiated and unirradiated copper crystals merge at higher strains.

Blewitt *et al.* [2] also observed that the recovery from radiation-induced damage to the mechanical properties of copper required annealing in the

*Received March 7, 1954.

†Knolls Atomic Power Laboratory, Schenectady, New York.

neighborhood of 300°C for times consistent with the activation energy for self-diffusion in copper.

Because of the useful results obtained by Blewitt with copper crystals, it seemed important that similar studies be made with single crystals of other metals, particularly those with different crystal structures. Such studies are described in this paper. In addition, both X-ray studies and elastic-constant measurements were made with polycrystals in order to reveal if possible the nature of the defects causing damage and these results are reported. Finally, an attempt has been made to assess several mechanisms for the effect of radiation on mechanical properties, in so far as is possible with certain critical experiments either to be carried out or to be confirmed.

Experimental Methods

Large iron crystals were grown in 0.037 inch-thick decarburized strip steel by a strain-anneal technique. Tensile specimens were machined from the crystals and subsequently carefully annealed. Two or more tensile specimens of the same orientation were cut from each crystal, so that an unirradiated control specimen was available for comparison with each specimen irradiated. One very large iron crystal was cut into sixteen (16) identical tensile specimens, and all but two were irradiated. The fourteen (14) irradiated crystals were given recovery treatments at various temperatures and for various times to determine the activation energy for recovery from mechanical damage. Another large iron crystal was cut into eight (8) specimens, four of which were irradiated. The effect of varying strain rate on both irradiated and unirradiated crystals was studied with the eight specimens.

Zinc crystals were grown by progressive solidification in glass tubes. These crystals were about 0.180 inch in diameter and 6 inches long. They were cut in half so that in every case two 3-inch long crystals of identical orientation were available, one for a control test and the other for irradiation.

Lead crystals 0.125 inch in diameter were grown in split graphite molds by a progressive solidification technique. They were also 6 inches long and cut in half to provide similar pieces for irradiation and control.

Tensile tests on all crystals were done at room temperature in a screw-loading tensile machine with automatic recording of crosshead motion and load. Care was taken to use identical initial crosshead separations and identical rates of crosshead travel for each set of irradiated and unirradiated crystals. However, different initial separations and rates of motion were used for different metals.

All irradiations were done at Brookhaven for periods of about one week in an air-cooled portion of the reactor. Fluxes were approximately 10^{12} thermal neutrons/cm^2/sec and temperatures were less than 50°C.

In addition to the single crystal tensile data, X-ray diffraction data were obtained from polycrystalline specimens of zinc, brass, copper and magnesium. These specimens were carefully machined and annealed and the positions of Debye rings were determined with either a Geiger counter X-ray spectrometer or a focusing back-reflection film camera. Duplicate specimens of each metal were irradiated to 2.4×10^{18} nvt and were examined in the same manner. The work was difficult because of the increased background of the irradiated specimens, and a technique of shielding all but the entrance slit of the Geiger counter was used to carry out this study. The background was maintained at the same high level during examination of the unirradiated specimens by keeping an irradiated sample in a nondiffracting position proximal to the specimen being studied.

Finally, polycrystalline specimens of copper and aluminum were machined to the form of cylinders suitable for use with the ultrasonic pulse equipment for measuring elastic constants as described by Reynolds [3]. These cylinders were carefully annealed and the elastic properties measured both before and after irradiation.

In all tensile tests and X-ray examinations both the control specimen and the irradiated specimen were tested or examined on the same day to eliminate any chance variation in equipment or technique. This was not done with elastic measurements, as the same specimen was measured before and after irradiation.

Results

Iron—The effect of 10^{18} nvt of radiation on the plastic flow behaviour of iron crystals is shown for two typical crystals in Figure 1. In these tests the yield stress was increased about 90 to 100 per cent by irradiation. The early flow stress was raised by irradiation but after some 16 per cent elongation the two curves came together and there was little or no difference thereafter. The tensile strength of irradiated and unirradiated crystals was the same within experimental error. The ductility of the irradiated crystals was not decreased. In fact,

the irradiated crystals fractured at a greater per cent elongation.

The results of the recovery tests on the sixteen identical iron crystals were as follows: The yield stress of the crystals after irradiation as determined with two crystals was about 10,500 psi. The yield stress before irradiation as determined with two annealed crystals was 7,000 psi. The yield stress of each of the remaining twelve irradiated crystals after annealing for differing times at either 300, 275, 250 or 225°C, was found to lie at some value between 7,000 and 10,500 psi. These yield stress values are indicated for each specimen on Figure 2 where yield stress is plotted against the logarithm of the annealing time. A cross-plot of the logarithm of the time at half recovery of yield stress τ against $1/T$, as shown in Figure 3 gives a line whose slope indicates an activation energy of 3.1 ev. This value is precisely the value for self-diffusion in iron [4].

The effect of strain rate on the stress strain curve of an iron crystal is shown in Figure 4 for an unirradiated crystal and in Figure 5 for an irradiated crystal of the same orientation.

Zinc—The results of tensile tests on both annealed and 2.4×10^{18} nvt irradiated zinc single crystals are shown in Figures 6, 7 and 8. The crystals used to obtain Figures 6 and 7 were of quite soft orientations and deformed several per cent by slip before twinning occurred. The crystal

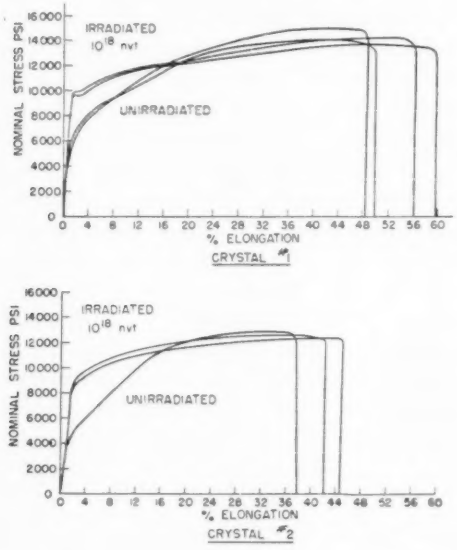

FIGURE 1. Effect of irradiation on mechanical behavior of pure iron single crystals.

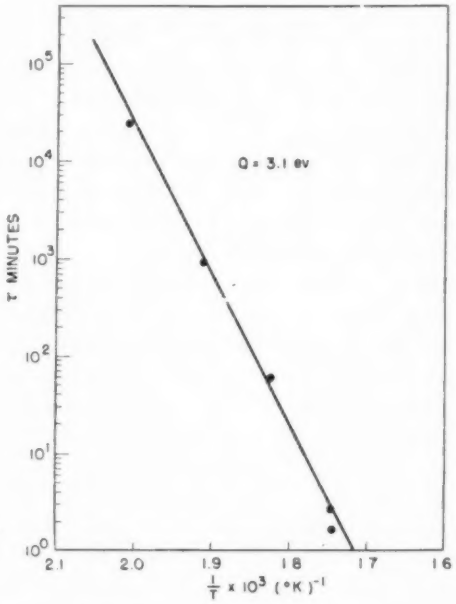

FIGURE 3. Temperature dependence of the recovery time for neutron irradiated iron single crystals.

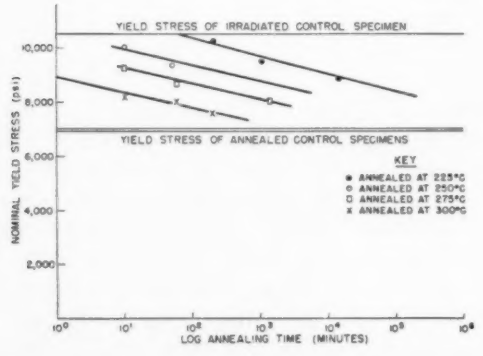

FIGURE 2. The effect of temperature on the recovery of irradiated single crystals of iron.

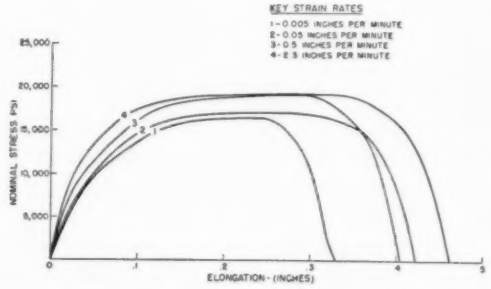

FIGURE 4. Nominal stress vs. elongation at various strain rates for non irradiated iron sheet crystal of identical orientation.

of Figure 8 was of an orientation that twinned almost immediately. It was found that crystals having soft orientations were strengthened several times by irradiation, particularly for the early stages of plastic flow. Crystals with twinning orientations were apparently little affected by irradiation since they could be deformed at about the same stress irradiated as unirradiated.

Lead—The effect of neutron irradiation on the tensile behavior of lead single crystals is shown in Figures 9 and 10. The flow stress and ultimate strength of the lead crystals were not affected seriously by 2.4×10^{18} nvt. The ductility, however, as measured by per cent elongation to fracture was increased by irradiation, in one case by a factor of 2.5 Because of the nature of necking in these single crystals of lead (i.e., thin knife-edge) it is difficult to say whether the load-elongation curve

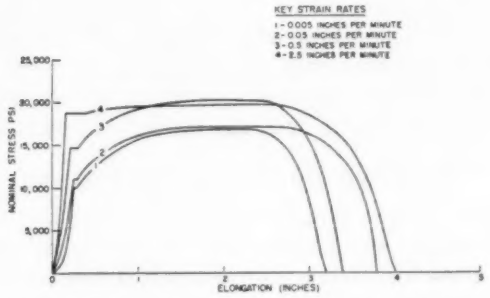

FIGURE 5. Nominal stress vs. elongation at various strain rates for irradiated iron sheet crystals of identical orientation.

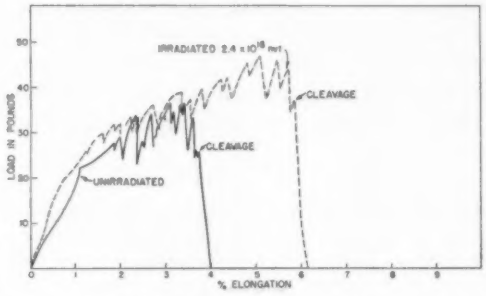

FIGURE 8. The effect of neutron irradiation on zinc single crystals of similar orientation.

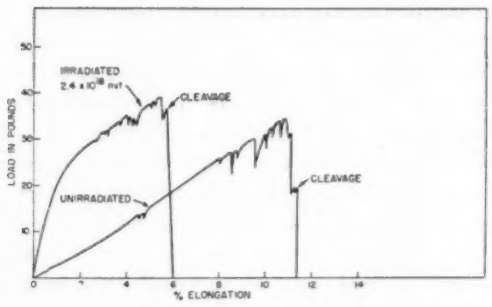

FIGURE 6. The effect of neutron irradiation on zinc single crystals of similar orientation.

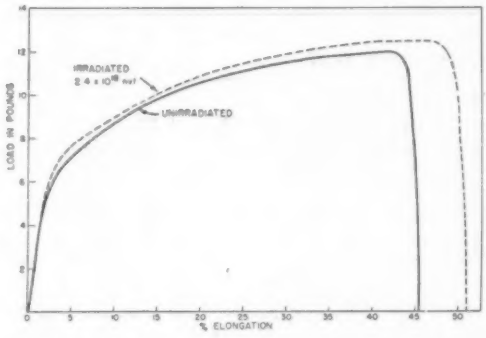

FIGURE 9. The effect of neutron irradiation on lead single crystals of similar orientation.

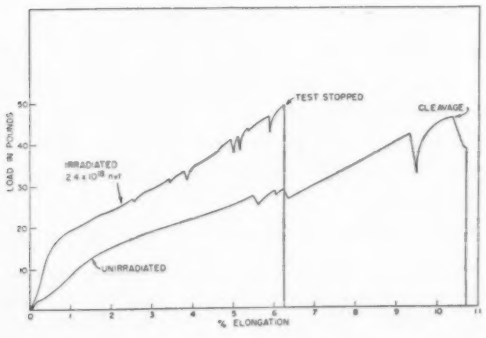

FIGURE 7. The effect of neutron irradiation on zinc single crystals of similar orientation.

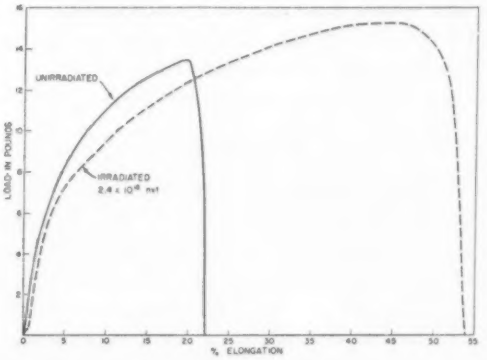

FIGURE 10. The effect of neutron irradiation on lead single crystals of similar orientation.

gives a true picture of the increase in ductility.

X-ray examination—In the case of copper and magnesium, there was some line-broadening but no detectable line shift. The zinc proved too radioactive to study with the Geiger counter even with 2 inches of lead covering all of the Geiger counter except its slit system. The brass showed both line broadening and line shift. The line shift in brass, however, was of the nature of an isotropic expansion. This expansion was more accurately confirmed with a focusing back-reflection camera.

Elastic constants—The results of elastic measurements after 2.4×10^{18} nvt of radiation compared with the elastic measurements before irradiation are shown in Table I for 2S aluminum and for two

TABLE I

RESULTS OF THE ELASTIC CONSTANT MEASUREMENTS

Specimen	$V_L\times10^5$ cm/sec	$V_S\times10^5$ cm/sec	$G\times10^{11}$ dynes/cm²	$E\times10^{11}$ dynes/cm²	Poisson ratio
Al #1 Annealed	6.46	3.12	2.63	7.09	0.348
Al #1 Irradiated	6.30	3.13	2.65	7.08	0.336
Al #2 Annealed	6.47	3.16	2.71	7.28	0.344
Al #2 Irradiated	6.27	3.19	2.76	7.34	0.330
Cu #1 Nat. Res. Corp. Annealed	4.63	2.30	4.71	12.58	0.336
Cu #1 Irradiated	4.62	2.26	4.55	12.21	0.342
Cu #2 OFHC Annealed	4.71	2.34	4.87	13.01	0.336
Cu #2 Irradiated	4.72	2.34	4.87	13.02	0.337

different grades of copper. The precision of a single value of velocity is about 0.02×10^5 cm/sec, but the reproducibility of the velocity is about 0.1×10^5 cm/sec.

In all cases, the changes observed after irradiation are small, and they are not consistent as to magnitude or direction. For all practical purposes, one can say that the exposure to neutrons reported here had no effect on elastic properties.

Discussion

It is now apparent that irradiation hardens (raises the yield and early flow stress) all common metal crystal structures—face-centered cubic, body centered cubic, and hexagonal close packed. It is also certain that recovery of mechanical properties from radiation damage requires a process with an activation energy equal to that for self-diffusion in the metal.

In the case of low melting-point metals such as lead, radiation recovery must proceed at room temperature. No ready explanation for the apparent increase in ductility of lead has occurred to the authors. Small increases in strain-to-fracture values were also observed with irradiated iron.

The X-ray results have thus far indicated only line-broadening and slight isotropic expansion. The elastic measurements have shown little or no change. Evidently much higher exposures to neutrons will be required to obtain changes that can be interpreted in the case of both the X-ray and elastic constant measurements. Plastic mechanical measurements are more sensitive to the submicroscopic defects produced by radiation than either elastic or X-ray measurements.

Radiation Hardening Mechanisms

If we assume that the damage produced in a metal by high-energy neutron radiation consists of atoms in interstitial lattice positions and lattice vacancies from which the atoms have been knocked, the mechanical behavior of metals might be affected in at least three ways. First, the random defects may interfere with the motion of dislocations. Second, the defects may anchor dislocations in the Cottrell fashion. Third, the defects may agglomerate and cause precipitation hardening of the metal.

Random defects—Let us first consider that interstitials or vacancies simply impede the motion of dislocations because they are regions of high local compression (or tension) which interfere with dislocation motion. It is obvious that a high density of defects would be required to hamper seriously a dislocation in motion. Furthermore, if the effect of single randomly positioned defects on moving dislocations is the principal cause of radiation hardening, the activation energy for recovery from radiation hardening should be consistent with the activation energy for diffusion of vacancies and interstitials.* We know, however, from the measurements made here and by Blewitt and co-workers that recovery from radiation hardening requires the same activation energy as self-diffusion, which is from two to ten times greater than the energy at which the defects should move.

Cottrell anchoring—A second possible effect of

*The activation energy values for diffusion of vacancies or interstitials are still equivocal. Huntington [5] has assigned the values of 0.25 ev for interstitially displaced atoms and 0.7 ev for vacancies in copper. Overhauser [6] agrees with 0.7 ev for vacancies but insists that interstitials require an even higher energy. It seems certain that both defects must move with an activation of 1.2 ev or less.

vacancies and interstitially displaced atoms on mechanical properties is that of segregation at dislocations and consequent anchoring of the dislocations in the Cottrell [7] fashion. Pure edge dislocations in any of the simple metal structures would not be anchored in this way, since the displaced atom or the vacancy would merely add on or subtract from the extra plane of the dislocation and cause a jog in its singular line that does not impede its motion. Marx, Cooper, and Henderson [8] have suggested that many of the interstitials and vacancies in fact might be swept out by plastic deformation. Displaced atoms or vacancies cannot cause a jog in a screw dislocation, nor can they anchor screw dislocations under all conditions. In face-centered cubic structures screw dislocations cannot be anchored by either interstitials or vacancies since the stress fields of these defects are spherical while the field of a screw dislocation is amost pure shear and there can be practically no interaction. In body-centered cubic metals screw dislocations will again not be anchored by vacancies, but the interstitial in body-centered cubic metals will prefer a $\frac{1}{2}$, $\frac{1}{4}$, 0 position where it does produce a shear distortion and therefore can anchor the screw component of any dislocation.

It was pointed out recently by Ardley and Cottrell [9] that interstitial defects can anchor the half-dislocations that are the glide units in face-centered cubic metals. Such dislocations have the added advantage that they cannot be annihilation sinks for vacancies or interstitials since half-dislocations cannot be jogged. One might also point out that the hardening produced in copper by radiation manifests itself in a yield point type of initial flow curve similar to the flow curve for brass—that is, it behaves as if hardened by a Cottrell mechanism.

It is apparent from the foregoing discussion that one probably can select the proper combination of displaced atom or vacancy and dislocation type for Cottrell anchoring in any crystal structure. The problem in a Cottrell mechanism is to explain readily the unique value of activation energy for recovery from radiation damage, i.e., the self-diffusion activation energy. It is doubtful that so large or so precise a value of activation energy would come out of a calculation of the interaction of the various appropriate dislocations with displaced atoms or vacancies, although such calculations have not been made.

To a first approximation the local strain resulting from an interstitially displaced iron atom is but little greater than that resulting from a true interstitial carbon atom. This is apparent if one calculates the size of a carbon atom as Cottrell [10] has done from Lipson and Parkers [11] experimental data on martensite dilatation. The evident large size of the carbon atom probably arises from the lack of metallic binding of that atom. The importance of the similarity in size of the carbon and the displaced atoms lies in the fact that their interactions with dislocations should also be similar, and the recovery process for any Cottrell-anchoring radiation damage mechanism should require a lower activation energy than that for self-diffusion.

Agglomeration of defects—A third possible mechanism for the effect of vacancies and interstitially displaced atoms on mechanical properties is the formation of interstitial agglomerates. The agglomerates form on close-packed planes strictly analogous to stacking faults, but compressed into an interstitial layer. Their formation is energetically feasible because any addition to the agglomerate shares among two or more interstitials the burden of distorting the local lattice. The formation is kinetically feasible because of the high mobility of the interstitially displaced atoms.

The effect of such agglomerates is to harden a metal just as precipitation from supersaturated solution hardens certain alloys. The particles impede dislocation motion, and conceivably might even anchor dislocations in the Cottrell fashion if the agglomerate is very small (three or four atoms). The agglomerate offers the further advantage that it may be stable at relatively small size and thus may require self-diffusion activation energies to bring about recovery. A weak point in a damage theory based on agglomerates is that X-ray evidence for agglomerates is lacking. If the agglomerates are large one might expect an effect similar to the stacking fault effects observed by Paterson [12] or Warren and Warekois [13], but if they are small (three to ten atoms) the effect may be one of isotropic expansion. The latter effect is all that we have observed. It is possible that agglomerates may show up similar to Guinier-Preston zones in precipitation.

Critical experiments—Of the three possibilities discussed here, and there are no doubt still others, the formation of interstitial agglomerates seems most feasible to the authors, at least until certain critical experiments have been done.

Recent work by Overhauser [6] has shown that copper irradiated with deuterons at 78°K recovers

all but 25 per cent of the damage to electrical conductivity on warming to room temperature. The remaining 25 per cent of damage requires higher temperature annealing to bring about recovery. These experiments may indicate that at low irradiation temperatures (78°K) most of the damage consists of random interstitially displaced atoms and lattice vacancies which would affect the mechanical properties but little while seriously affecting the electrical properties. Warming up could then cause diffusion of the interstitials and considerable annihilation by interstitial-vacancy collision. Nevertheless, many small agglomerates of interstitials could form during the warm-up and these would be stable up to self-diffusion temperatures and could cause the remnant of conductivity damage and most of the radiation hardening. The critical check for such behavior is to irradiate a copper crystal at 78°K without warming the crystal between the irradiation and the tensile test. The mechanical behavior of such an irradiated crystal tested at 78°K should show little hardening over a similar but unirradiated crystal tested at 78°K. Finally, a crystal that had been irradiated at 78°K, warmed to room temperature, and cooled back to 78°K should show considerable hardening in the low-temperature test. The low temperature mechanical test is a critical test for either the Cottrell or the agglomerate mechanism of radiation hardening, since either will require interstitial diffusion. The tests are, of course, difficult to make.*

Another critical test for agglomerate formation is to measure the electrical conductivity change in directions normal and parallel to the close-packed basal planes in an hexagonal crystal during irradiation. Since plate agglomerates can only form parallel to the basal planes, the $\Delta R/R$ values in the two directions should show a difference during any plate formation. Such measurements should be made on both room temperature and cold (78°K) irradiated crystals as well as on crystals cold irradiated and subsequently warmed to room temperature.

One might predict on the basis of a Cottrell mechanism that radiation damaged metals should strain-age. If, after dislocations had been released from the anchoring interstitially displaced atoms by some form of plastic deformation, and if the load were released and the specimen aged, a subsequent test should show that the dislocations had been re-anchored. Of course, many interstitially displaced atoms once freed from dislocations would be annihilated by vacancies and perhaps many would be swept out by the deformation itself, but some aging ought to occur.

*Such a test was made recently in a rather preliminary fashion by Blewitt and co-workers at Oak Ridge, and though the results have not been published and the conditions during the irradiation are not positively known, it is fair to assume that apparently either diffusion of defects is not required for radiation hardening or the defects diffuse more rapidly than has yet been suggested. The test should be repeated. Meanwhile, the authors are indebted to Blewitt for this preliminary information.

Acknowledgements

The authors wish to acknowledge assistance received through many discussions with J. E. Burke, C. W. Tucker, H. B. Huntington, J. B. Sampson, and C. A. Bruch concerning radiation damage experiments and mechanisms. The assistance of P. Senio with certain X-ray work and of M. B. Reynolds with the elastic constant work is appreciated.

The Knolls Atomic Power Laboratory is operated by the General Electric Company for the United States Atomic Energy Commission under contract No. W-31-109 Eng. 52.

References

1. Blewitt, T. H., *et al.* Study of the Effect of Radiation on Metal Crystals, TID-5015.
2. Redman, J. K., Coltman, R. R., and Blewitt, T. H. Bull. Am. Phys. Soc. **28** (April 30, 1953) 24.
3. Reynolds, M. B. Trans. A.S.M. **45** (1953) 839.
4. Birchenall, C. E. and Mehl, R. F. Trans. A.I.M.E. **188** (1950) 144.
5. Huntington, H. B. Phys. Rev. **91** (1953) 1092.
6. Overhauser, A. W. Phys. Rev. **90** (1953) 393.
7. Cottrell, A. H. The Yield Point in Single Crystal and Polycrystalline Metals. Symposium on Plastic Deformation of Crystalline Solids, Mellon Inst., Pittsburgh (1950) p. 60.
8. Marx, J. W., Cooper, H. G., and Henderson, J. W. Phys. Rev. **88** (1952) 106.
9. Ardley, G. W. and Cottrell, A. H. Proc. Royal Soc. **219** (1953) 328.
10. Cottrell, A. H. and Bilby, B. A. Proc. Phys. Soc., London **62A** (1949) 49.
11. Lipson, H. and Parker, A. M. B. J. Iron and Steel Inst. **149** (1944) 123.
12. Paterson, M. S. J. Appl. Phys. **23** (1952) 805.
13. Warren, B. E. and Warekois, E. P. J. Appl. Phys. **24** (1953) 951.

X-RAY LINE BROADENING FROM METALS DEFORMED AT LOW TEMPERATURES*

M. S. PATERSON†

Comparative measurements of the X-ray line broadening in copper, aluminium and nickel, plastically deformed by various amounts at room temperature and at liquid air temperature, have been made and the behaviour at room temperature of specimens previously deformed at the low temperature studied. Also, some measurements have been made of the effects of change of temperature or of direction of straining during the deformation.

It appears that recovery or self-annealing does not, in general, limit the line broadening, but support is given to the hypothesis that the broadening is due to internal stresses which cannot exceed the yield stress of the cold-worked metal. Stress-strain tests on specimens similar to the line-broadening specimens show that the course of the line-broadening with increasing plastic deformation is roughly parallel to the yield stress versus strain curve, and the internal stresses estimated from the observed line broadening are of the same order of magnitude as the macroscopic yield stress. The influence of the temperature of deformation is practically the same on both the line broadening and the yield stress at large plastic strains.

Finally, the origin of the internal stresses mainly responsible for X-ray line broadening is discussed briefly and it is suggested that the major contribution to the broadening arises from elastic distortion of the glide lamellae.

L'ÉLARGISSEMENT DES RAIES DES RAYONS X PROVENANT DE MÉTAUX DÉFORMÉS AUX BASSES TEMPÉRATURES

On a mesuré l'élargissement des raies de rayons X dans le cas du cuivre, de l'aluminium et du nickel, déformés plastiquement à des degrés différents, à la température ambiante et à la température de l'air liquide. Une étude a été faite du comportement à la température ambiante d'échantillons précédemment déformés aux basses températures. On a aussi mesuré l'effet de changements de température et de la direction de tension pendant la déformation. Il apparaît que la restauration, ou "l'auto-recuit," ne limite, en général, pas l'élargissement des raies, toutefois, on considère comme plausible l'hypothèse que l'élargissement est dû aux tensions internes qui ne peuvent pas dépasser la tension d'écoulement du métal écroui. Des essais tension-déformation sur des éprouvettes semblables à celles des essais d'élargissement des raies montrent que l'évolution de ce dernier, en fonction de l'augmentation de la déformation plastique est approximativement parallèle à la courbe de la tension d'écoulement en fonction de la déformation. Ces essais montrent aussi que les tensions internes estimées à partir de l'élargissement observé des raies sont du même ordre de grandeur que la tension macroscopique d'écoulement. Aux grandes déformations plastiques l'influence de la température de déformation sur l'élargissement des raies et sur la tension d'écoulement est pratiquement la même. Pour terminer, on discute brièvement l'origine des tensions internes, dont dépend avant tout l'élargissement des raies. Il est aussi suggéré que la contribution la plus importante à l'élargissement des raies provient de la distorsion élastique des lamelles de glissement.

VERBREITERUNG DER RÖNTGENLINIEN IN BEI TIEFEN TEMPERATUREN VERFORMTEN METALLEN

Vergleichende Messungen der Linienverbreiterung der Röntgenreflexionen in Kupfer, Aluminium, und Nickel, die bei Zimmertemperatur und der Temperatur der flüssigen Luft in verschiedenem Masse plastisch verformt worden waren, wurden durchgeführt; ausserdem wurde bei Zimmertemperatur das Verhalten von bei der Temperatur der flüssigen Luft verformten Proben untersucht. Weiterhin wurden einige Messungen über den Einfluss der Änderung der Temperatur oder der Richtung der Verzerrung während der Verformung angestellt.

Es scheint, als ob Erholung im allgemeinen nicht das Ausmass der Linienverbreiterung begrenzt; das vorliegende Material unterstützt die Hypothese, dass die Linienverbreiterung auf inneren Spannungen beruht, die nicht grösser als die Fliesspannung des kaltbearbeiteten Metalles sein können. Spannungs-Dehnungskurven von Proben, die den zur Messung der Linienverbreiterung aufgenommenen Kurven entsprachen, zeigten, dass der Verlauf der Linienverbreiterung bei wachsender plastischer Verformung annähernd parallel der Fliesspannung-Verzerrungskurve verläuft; die aus den beobachteten Linienverbreiterungen geschätzten inneren Spannungen sind von gleicher Grössenordnung wie die makroskopische Fliesspannung. Im Gebiet grosser plastischer Verformungen beeinflusst die Verformungstemperatur die Linienverbreiterung und die Fliesspannung in gleicher Weise.

Der Ursprung der für die Linienverbreiterung der Röntgenreflexionen im wesentlichen verantwortlichen inneren Spannungen wird kurz diskutiert, und es wird die Hypothese dargelegt, dass die elastische Verzerrung der Gleitlamellen den Hauptbeitrag zur Linienverbreiterung darstellt.

1. Introduction

Although the influence of plastic deformation at room temperature on the breadth of X-ray diffraction lines from metals has been studied extensively, very little attention has been given to the behaviour at lower temperatures. Wilson and Thomassen [1] and Hutchison [2] have shown that, in the case of aluminium, plastic deformation at a low temperature (−78°C and liquid air temperature, respectively) can give rise to a greater X-ray line

*Received March 22, 1954.

†Cavendish Laboratory, Cambridge University, England. Now at Department of Geophysics, Australian National University, Canberra, Australia.

broadening than is observed after deformation at room temperature.

In the present work, more extensive experiments have been made on several metals to study the influence of increasing amounts of plastic deformation at liquid nitrogen temperature on the X-ray line broadening. In addition, a close comparison of the strain-hardening behaviour with the line broadening has been made from stress-strain measurements. A preliminary note on some of the line-broadening measurements has already been published [3].

2. Materials and Specimens

The metals used were high-conductivity copper, commercially-pure aluminium and commercially-pure nickel. The specimens were cut from cold-drawn wires of about 0.5 mm diameter, which were annealed so that the metal was in a recrystallized and strain-free condition.

3. X-ray Line-Broadening Experiments

(a) *Mode of Deformation*

Torsion was chosen as the mode of deformation because of the ease with which it can be carried out at liquid nitrogen temperature and followed by an X-ray exposure at the same temperature. Since the depth of penetration of the X-ray beam is small compared with the specimen diameter, the observed line broadening corresponds to the plastic strain at the surface of the specimen. Only in the case of aluminium is the depth of penetration of the X-ray beam appreciable, the plastic strain varying by about 10 per cent over the portion of the specimen contributing significantly to the intensity of the reflection.

The torsion apparatus was attached to a Unicam single crystal X-ray camera. The lower specimen chuck assembly, which was screwed to the spindle in place of the usual specimen holder, was free to move longitudinally so that the specimen did not buckle when it elongated slightly during the torsion.

During the experiments at low temperature, both specimen chucks were immersed in liquid nitrogen,* a thin stream of which was also allowed to flow down the specimen to ensure that its temperature was very close to that of liquid nitrogen. The upper chuck was surrounded by a funnel-shaped reservoir; the annular gap between its lower opening and the chuck could be adjusted in order to control the rate at which the liquid nitrogen flowed down the specimen into the reservoir surrounding the lower chuck. The chucks were mounted on "Paxolin" assemblies in order to insulate them thermally from the body of the apparatus.

This arrangement permitted experiments of the following nature. A specimen of annealed metal could be cooled to the temperature of liquid nitrogen and then plastically deformed by a specified amount; while the specimen remained at the low temperature, the X-ray exposure could be made. Furthermore, the same specimen could be deformed by successive, known amounts and X-ray exposures made after each increment of strain, without raising its temperature during the whole course of the experiment.

(b) *Measurement of X-ray Line Breadth*

A back-reflection, photographic method, using flat film, was chosen for the X-ray measurements in order to obtain maximum sensitivity. The experimental conditions were rigidly standardized during the whole series of experiments, so that for any particular metal the instrumental broadening (that is, the incidental broadening due to finite size and divergence of X-ray beam, etc.) was constant, and the total line breadth for an annealed specimen was taken as its measure. By correcting for this broadening (see later), the broadening due solely to the effects of the plastic deformation could be obtained. Table I summarizes the radiations used and the reflections studied in the present experiments. The use of filters has been avoided where practicable in order to keep the duration of experiments at low temperature as short as possible.

TABLE I

RADIATIONS USED AND REFLECTIONS STUDIED

Specimen	Target	Filter	Sin θ for K_α lines at room temperature		
			(311)	(331)	(420)
Copper	Mn	None	0.964	—	—
	Cu	None	—	0.928	0.953
Nickel	Cu	Ni	—	0.953	0.978
Aluminium	Co	None	—	0.963	0.988

The pinhole collimator gave an X-ray beam wider than the specimen, so that the effective divergence of the beam was governed by the dia-

*Liquid oxygen was used in the experiments on nickel.

meter of the specimen and the first pinhole (0.5 mm). Since the specimen was a wire in a vertical position, the effective collimation of the beam was best in a horizontal plane, and the line-breadth measurements were always made on the horizontal diameter of the diffraction ring.

A manually operated, null-method microphotometer (Dobson type) was used for the measurement of the variation of density across the diffraction lines on the X-ray photographs. A sufficient length of the film was scanned on each side of a line in order to permit the interpolation of the background density across the line. The density distribution of the line itself was then found by subtracting this background from the measured density distribution. The exposure times in the experiments were adjusted so that the maximum density was kept within the linear density-exposure range of the film.

The measure taken for the line breadth is the "integral breadth," that is, the area of the intensity distribution curve of the line divided by the maximum ordinate.

(c) *Correction to Line-breadth Measurements*

Firstly, the measured line breadths have been corrected for the α-doublet of the incident radiation. Using a procedure identical with that described by Rachinger [4], a sufficient number of lines were resolved to allow a set of correction curves to be constructed for obtaining the breadths of the single α-components for all the lines.

In X-ray photographs made at low temperatures, the diffraction lines are shifted to slightly higher angles than at room temperature, so that the line breadths do not correspond exactly to the same geometrical conditions as apply at room temperatures. The angular broadening will vary approximately in proportion to $\tan\theta$ (or $\sec\theta$, which is practically the same at large θ), and the angle at which the diffracted X-ray beam strikes the film will be different. Therefore, after correcting for the α-doublet, the line breadths for low temperature conditions have been corrected to correspond as nearly as possible to the same angles of diffraction as those measured at room temperature; the breadths corresponding to the two temperatures are then directly comparable. The change is only of the order of a few per cent (the correction factors used are given in Table II), except in the case of the (420) reflection from aluminium.

Finally, correction was made for the instrumental broadening. Strictly, it should have been applied to the low-temperature breadths before the corrections mentioned in the previous paragraph, but in the present work no significant error will arise from the reversed order of these corrections. The method used for the instrumental broadening correction is described elsewhere [5]. It is based on Jones' method [6], but the basic integral equation is solved directly by numerical means, avoiding assumptions about the shapes of the lines; in fact, the true shape of the broadened line is given by the calculation. In the present experiments, the correction for instrumental broadening was carried out by this method for lines of various breadths, obtained from the different metals, for both room temperature and low temperature conditions. The α-doublet corrections need not have been made previously but some saving in labour resulted since the calculations of the instrumental broadening corrections of a single α-component take less time than for a doublet and the effect of varying doublet separation has already been eliminated. The same curve for the shape of the diffraction line from annealed specimens was used in all the calculations since it was found to be substantially the same for different metals, with a breadth of approximately 0.01 radians.

TABLE II

LOW-TEMPERATURE CORRECTION FACTORS

Reflection	Copper (311)	Aluminium (331)	Aluminium (420)	Nickel (331)	Nickel (420)
Low temperature correction factor	0.98	0.97	0.84	0.99	0.96

With the results of these calculations, the correction graph shown in Figure 1 was obtained; within the limits of experimental error it seems possible to use a common mean curve for the different metals. This curve has been used for correcting all the experimental results for instrumental broadening (in the case of nickel where the value of the instrumental broadening was slightly different from that on which Figure 1 is based, the correction curve was plotted in the form used by Jones).

(d) *Accuracy*

At least two films were exposed for each condition of the specimen. Thus, since photometer measurements were made at both ends of the horizontal diameter of the Debye-Scherrer rings, four measured values of line breadth were obtained; the average of these has been taken as the observed line breadth. From consideration of the

scatter in the individual measurements, it is estimated that the error made in comparing the corrected values of line broadening should not be more than about ±5 per cent, or at most ±10 per cent. The absolute accuracy is more difficult to estimate but the results are unlikely to be more than about ±20 per cent in error.

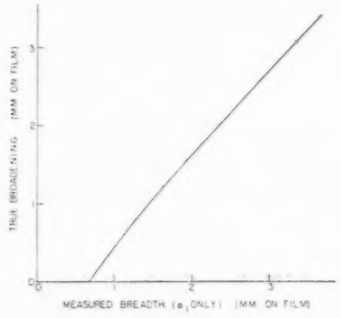

FIGURE 1. Correction curve for instrumental broadening.

4. Results of X-ray Line-broadening Measurements

The manner in which the X-ray line-broadening develops with increasing plastic deformation, both at room temperature and at liquid-nitrogen temperature,* is shown in Figures 2, 3(a) and 4 for copper, aluminium and nickel, respectively. The low temperature results refer to experiments in which the specimen was kept at the low temperature during both deformation and X-ray exposure.

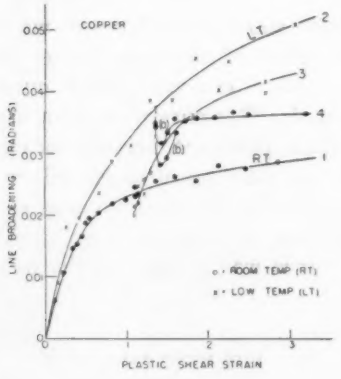

FIGURE 2. Effect of plastic deformation on broadening of (311) reflection from copper. 1: Deformation at room temperature. 2: Deformation at low temperature. 3: Deformation at low temperature after strain 1.09 at room temperature. 4: Deformation at room temperature after strain 1.36 at low temperature.

*See footnote p. 824.

In further experiments, the line breadth was measured immediately after the specimen, deformed at the low temperature, had been brought to room temperature and then at subsequent times on remaining at room temperature. For copper, the line breadth was the same, within limits of experimental error, after the specimen had been brought to room temperature as it was at the low temperature (allowing for the slightly different angles of diffraction) and no subsequent change of line breadth was observed even after the specimen had remained for nine months at room temperature. The line breadth for a specimen deformed at room temperature also showed no recovery after nine months.

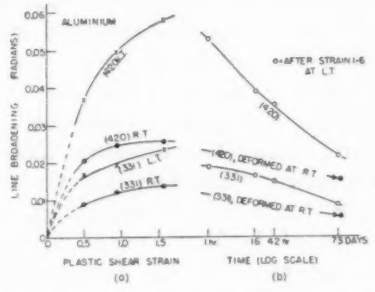

FIGURE 3. (a) Effect of plastic deformation at room temperature (R.T.) and at low temperature (L.T.) on broadening of (331) and (420) reflections from aluminium.
(b) The recovery of the line broadening from aluminium at room temperature.

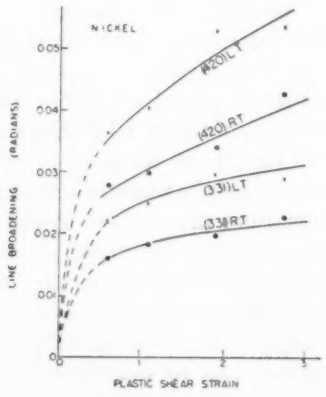

FIGURE 4. Effect of plastic deformation at room temperature (R.T.) and at low temperature (L.T.) on broadening of (331) and (420) reflections from nickel.

In the case of aluminium, appreciable slow changes in line breadth occurred at room temperature, subsequent to deformation at liquid nitrogen temperature. This is shown in Figure 3(b), which refers to specimens for which the initial conditions

corresponded to the final points in Figure 3(a). It is seen that a specimen deformed at room temperature showed similar recovery of the line breadth when measurements were made after several months.

In the case of nickel which had been deformed at the low temperature, there appeared to be a slight recovery (about 10 per cent) in line breadth during a period of one month at room temperature.

The curves 3 and 4 in Figure 2 refer to measurements on the course of the line-broadening in copper when, in one case, a specimen was deformed at liquid-nitrogen temperature to a plastic shear strain of 1.36 and the deformation then continued at room temperature, and when, conversely, the deformation was continued at liquid-nitrogen temperature after an initial plastic shear strain of 1.09 at room temperature. Additional measurements confirm the existence of the initial "dip" in the first curve.

5. Stress-Strain Tests

(a) *Experimental*

A simple apparatus for making torque and twist measurements on small wire specimens was designed in order to study the stress-strain behaviour of specimens under conditions similar to those used in the line-broadening experiments. The specimens of copper, aluminium and nickel used in the stress-strain experiments were taken from the respective batches of specimens that had been prepared for the line-broadening experiments.

The general design of the apparatus is shown in Figure 5. The torque applied to the specimen S is indicated by the elastic twist in the beryllium-copper wire D connecting the spindle C and the upper specimen chuck assembly Q, A, as shown by the movement of the pointer E over the scale F. Since there are no bearings or other sources of friction between the torque-measuring device and the specimen, the torque applied to the beryllium-copper wire is equal to the torque applied to the specimen, provided it is not set into oscillation. The torque-measuring device was calibrated by attaching to its lower end a disc of known moment of inertia in place of the chuck assembly and measuring the period of natural torsional oscillation of the system. The angular twist in the specimen is measured by the rotation of the upper chuck assembly, the lower chuck being fixed to the frame.

The stress-strain tests can readily be done at liquid-nitrogen temperature by surrounding the specimen and chucks with a Dewar flask of liquid nitrogen. The "Paxolin" pieces P, Q serve for thermal insulation.

The apparatus was of ample sensitivity to give results of greater accuracy than was required for comparing them with the X-ray line-broadening results.

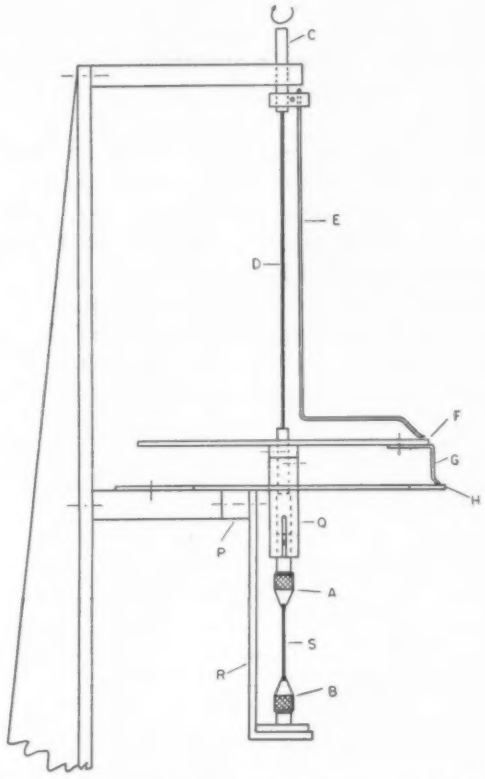

FIGURE 5. Apparatus for measuring torque-twist curves of small metal wires.

For obtaining shear stress-strain curves from the torque-twist measurements, the method described by Nadai [7] has been used. Since, owing to the assumptions underlying this method, it is only valid for simple experiments in which the conditions are constant throughout, it cannot be applied where the temperature or direction of straining has been changed during the course of the experiment. In the latter cases, only torque-twist curves can be given, but these permit some qualitative conclusions about the course of the stress-strain curves.

In deriving the shear stress-strain curves, a correction has been made for the slight increase in length and the accompanying decrease in diameter of the specimen during torsion. In the apparatus,

the upper chuck is free to move longitudinally, and rough measurements were made of the magnitude of the longitudinal strain in order to carry out the corrections (detailed measurements of this nature have been made by Swift [8]). It was interesting to note that greater longitudinal strains were observed at liquid-air temperature than at room temperature for a given strain; thus, the longitudinal strain during torsion appears to depend on the degree of strain-hardening.

(b) *Results*

The stress-strain curves in shear for copper, aluminium and nickel, both at room temperature and at liquid-nitrogen temperature, are given in Figure 6. These curves correspond to the line-broadening curves of Figures 2, 3(a) and 4.

Figure 7 gives the torque versus surface shear strain curves for copper obtained when the temperature was changed during the course of the deformation; the sequences used in the corresponding line-broadening experiments have been followed (c.f., Figure 2). The dashed lines indicate the course of the torque curves when the temperature is constant throughout the experiment.

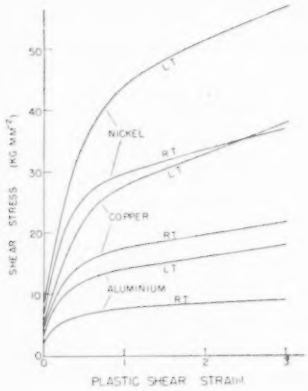

FIGURE 6. Stress-strain curves in shear for copper, aluminium and nickel at room temperature and at low temperature.

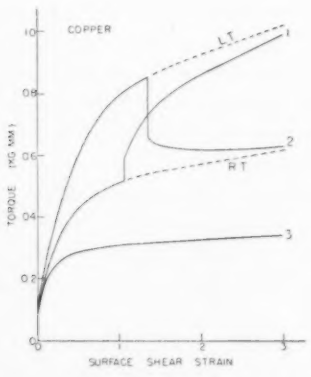

FIGURE 7. Torque-twist curves for copper. 1: At low temperature after straining to 1.09 strain at room temperature. 2: At room temperature after straining to 1.36 strain at low temperature. 3: Cyclic straining at room temperature.

6. Reversed Deformation at Room Temperature

A copper specimen was given a surface plastic shear strain of 0.8 by twisting in one direction and the broadening of the (311) line was found to be 0.021 radians. The specimen was then twisted in the opposite direction; after a strain of 0.05 the line-broadening was 0.019 radians, but when a strain if 0.8 had been reached (so that the total algebraic strain was zero), the line-broadening was 0.021 radians again. Thus, there is possibly a slight decrease in the line-broadening at first when twisting in the opposite direction, but after complete reversal of the strain, no significant change is observed. The final line-broadening is smaller, however, than would be caused by the same absolute strain applied unidirectionally.

In another experiment a copper specimen was given successive 0.05 increments of surface plastic shear strain in opposite directions (that is, the wire was twisted back and forth) until a total absolute strain of 2.2 had been reached, the total algebraic strain being zero. The line-broadening resulting from this cyclic straining was 0.009 radians, only one third of that resulting from the same absolute strain applied unidirectionally. Also, the diffraction ring was not uniform, indicating much less disorientation in the crystals than in the case of unidirectional straining.

The curve 3 in Figure 7 shows the manner in which the torque needed for plastic deformation at room temperature increases during cyclic straining with 0.05 plastic strain amplitude, as described in the previous paragraph. Here the torque is plotted against the total absolute value of the plastic shear strain. Although a stress-strain curve cannot be derived directly from this result, it suggests that the cyclic straining is accompanied by a lower strain hardening than is unidirectional straining.

7. Discussion

(a) *Influence of Temperature*

The results described in § 4 show that the X-ray line-broadening arising from plastic deformation at low temperatures is greater than that arising from an equal plastic strain at room temperature. Furthermore, if the metal that has been deformed at the low temperature is brought to room tem-

perature, its line-broadening is found not to change appreciably within the time needed for an X-ray exposure (about ½ hour); at most, there appears a slow recovery subsequently. These observations show that, in general, the apparent limiting of the line-broadening of a metal during cold-work at room temperature cannot be due to a recovery, or self-annealing, which is effective at room temperature within the time of an X-ray exposure. For recovery is unlikely to be appreciable at liquid-nitrogen temperature, and the much greater line-broadening that would be expected to result from deformation at this temperature should disappear rapidly when the specimen is brought to room temperature [3].

The observation of greater line-broadening after plastic deformation at low temperature also argues against the view that the metallic grain contains an "elementary crystalline unit" (crystallite), with a size characteristic of the metal, into which the grain has been fragmented when the limit to the line-broadening at room temperature is reached [9; 10]. The existence of a fundamental unit of smaller size would have to be assumed at lower temperatures.

A comparison of the yield-stress versus plastic-strain curves (Figure 6) with the line-broadening versus plastic-strain curves of Figures 2, 3(a) and 4 for each temperature reveals a considerable similarity. Not only are the curves of roughly parallel course, but, for the larger strains, the yield-stress and line-broadening values developed at the low temperature are greater by approximately the same factor than the values developed at room temperature for a given metal.

The experiments on copper in which the temperature was changed during the deformation also reveal a general similarity between the behaviour of the yield stress and the line-broadening, except in the neighbourhood of the strain at which the temperature was changed (the stress-strain curves are assumed to be qualitatively similar to the torque-twist curves of Figure 7).

It would appear, therefore, that the X-ray line broadening in a cold-worked metal is closely related to its yield stress. The curve of line-broadening versus plastic strain flattens out in a similar manner to the stress-strain curve, and the temperature at which the deformation is carried out has a similar influence on both curves. This supports the hypothesis that the line-broadening is due mainly to internal stresses which cannot exceed the current yield stress of the metal during the course of its deformation [11; 12; 13]. The influence of the temperature of deformation on the development of the line-broadening would, therefore, be a consequence of the influence of the temperature of deformation on the strain-hardening.

(b) *X-ray Line Broadening and Internal Stresses*

A number of workers [13; 14; 15, etc.] have estimated the magnitude of the internal stresses corresponding to the observed line-broadening and compared it with the macroscopic tensile strength of the metal, showing that the two quantities are of the same order of magnitude. The present measurements permit a more direct comparison of line broadening and stress-strain properties, so the quantities in Table III have been derived, for certain values of plastic shear strain, from the

TABLE III

INTERNAL STRESSES DEDUCED FROM LINE-BROADENING

Metal	Reflection	Line-broadening	Crystallite size ($\times 10^{-6}$ cm)	Average internal strain ϵ	Corresponding internal stress (kg mm^{-2})	Measured yield stress in shear (kg mm^{-2})
Copper, after strain 2.5 at room temp.	(311)	0.00287	2.82	0.00193	21	20.7
Copper, after strain 2.5 at low temp.	(311)	0.00470	1.67	0.00327	36	35.5
Aluminium, after strain 1.5 at room temp.	(331)	0.00135	4.88	0.00094	6.5	8.0
	(420)	0.00260	4.34	0.00104	7	
Aluminium, after strain 1.5 at low temp.	(331)	0.00232	2.84	0.00164	11.5	15.2
	(420)	0.00570	1.98	0.00228	16	
Nickel, after strain 2.5 at room temp.	(331)	0.00215	2.34	0.00172	36	35.3
	(420)	0.00385	1.88	0.00209	44	
Nickel, after strain 2.5 at low temp.	(331)	0.00300	1.68	0.00240	50	54.5
	(420)	0.00550	1.32	0.00299	63	

curves of Figures 2, 3(a), 4 and 6. The average internal strain ϵ corresponding to the line-broadening β has been obtained from $\epsilon = \frac{1}{4}\beta \cot \theta$, and the Young's modulus for polycrystalline metal* used in estimating the internal stresses. An accurate calculation of the internal stresses cannot be made since the lack of knowledge on the nature of the system of internal stresses prevents the appropriate values of the elastic moduli being chosen. However, Table III shows that, at large plastic strains, there is a complete agreement in order of magnitude between these estimated internal stresses (column 6) and the macroscopic yield stress in shear (column 7); the close numerical agreement is most probably fortuitous. Thus, if the line-broadening is due mainly to internal stresses, the current value of the yield stress seems, in general, to set a limit to the line-broadening during the course of plastic deformation.

Alternatively, the present experiments provide suitable data for use in Bragg's theory of the strength of metals [16]. The measured yield stresses fall within the range predicted by the theory.

(c) *The Nature of Internal Stresses Responsible for X-ray Line-Broadening*

The inadequacy of macroscopic residual stresses or intercrystalline (Heyn) stresses to account for the observed magnitude of the broadening, the occurrence of considerable line-broadening from single crystals [17], and the extent of the internal stresses deduced by Warren and Averbach [18] suggest that the internal stresses mainly responsible for X-ray line-broadening in cold-worked metals occur in small regions within the individual crystals. It seems likely that these stresses arise from the inhomogeneous elastic distortion of the glide lamellae (that is, the regions between the glide zones or "slip bands"). Nye's studies on silver chloride [19] indicate that the most prominent internal stresses correspond to complex elastic bending of the glide lamellae. Also, bending of the glide lamellae is evident in many photomicrographs of deformed metals. A rough estimate shows that the amount of bending needed to explain the line-broadening would not be unreasonable; if the half-thickness of the lamellae is of the order of 10^{-4} cm, then the radius of curvature corresponding to a maximum strain of 10^{-3} would be of the order of 0.1 cm. Of course, the situation will usually be more complicated than this on account of multiple glide.

*The values used were: Copper 11,000 kg mm^{-2}; Aluminium 7,000 kg mm^{-2}; Nickel 21,000 kg mm^{-2}.

Acknowledgements

The author is indebted to Professor E. Orowan, F.R.S. for suggesting the initial experiments and for stimulating discussions and suggestions throughout the progress of the work. The work was done in 1947 and 1948 during the author's tenure of the Angas Engineering Scholarship (University of Adelaide) and an Australian Council for Scientific and Industrial Research Studentship.

References

1. Wilson, J. E. and Thomassen, L. Trans. Am. Soc. Metals **22** (1934) 769.
2. Hutchison, T. S. Nature **162** (1948) 374.
3. Paterson, M. S. and Orowan, E. Nature **162** (1948) 991.
4. Rachinger, W. A. J. Sci. Instrum. **25** (1948) 254.
5. Paterson, M. S. Proc. Phys. Soc. **A63** (1950) 477.
6. Jones, F. W. Proc. Roy. Soc. **A166** (1938) 16.
7. Nadai, A. Plasticity (New York, McGraw-Hill, 1931), p. 126.
8. Swift, H. W. Engineering **163** (1947) 253.
9. Wood, W. A. Proc. Roy. Soc. **A172** (1939) 231.
10. Wood, W. A. and Rachinger, W. A. Nature **161** (1948) 93; J. Inst. Metals **75** (1949) 571.
11. van Arkel, E. A. Physica **5** (1925) 208.
12. Stokes, A. R., Pascoe, K. J., and Lipson, H. Nature **151** (1943) 137.
13. Megaw, H. D. and Stokes, A. R. J. Inst. Metals **71** (1945) 279.
14. Haworth, F. E. Phys. Rev. **52** (1937) 613.
15. Smith, C. S. and Sticlkey, E. E. Phys. Rev. **64** (1943) 191.
16. Bragg, Sir Lawrence. Strength of Solids (Physical Society, 1948), p. 26; Proc. Camb. Phil. Soc. **45** (1949) 125.
17. Caglioti, V. and Sachs, G. Z. Phys. **74** (1932) 647.
18. Warren, B. E. and Averbach, B. L. J. Appl. Phys. **21** (1950) 595.
19. Nye, J. F. Nature **161** (1948) 367; Proc. Roy. Soc. **200** (1949) 47.

THE RESISTIVITY-TEMPERATURE-CONCENTRATION RELATIONSHIPS IN THE SYSTEM NIOBIUM-TITANIUM*

S. L. AMES and A. D. McQUILLAN†

The resistivity of a series of β-phase niobium-titanium alloys has been measured over the temperature range 88°K to 1173°K. The form of the resistivity-temperature-concentration relationships is abnormal, particularly at low temperatures. Additions of titanium to niobium cause a progressive increase in resistivity and a decrease in the temperature coefficient of resistance until, in β-phase alloys containing less than 25 at.% niobium, the temperature coefficient of resistivity becomes negative. Although the β-phase in alloys containing less than 20 at.% niobium cannot be retained at low temperatures, extrapolation of the isothermal resistivity-concentration curves for the β solid-solution to zero niobium content seems to indicate that pure β-titanium would show a semi-conducting type of behaviour at temperatures approaching the absolute zero. The validity of the extrapolation is discussed.

LES RELATIONS ENTRE LA RÉSISTIVITÉ, LA TEMPÉRATURE ET LA CONCENTRATION DANS LE SYSTÈME COLOMBIUM-TITANE

On a mesuré la résistivité d'une série d'alliages colombium-titane sous la forme de la phase β, dans l'intervalle de température allant de 88°K à 1173°K. Les relations entre la résistivité, la température et la concentration sont anormales, surtout aux basses températures.

Des additions de titane au colombium causent une augmentation progressive de la résistivité et une diminution du coefficient de température de la résistance; finalement, dans les alliages de la phase β contenant moins de 25 pour cent en atomes de colombium, ce coefficient devient négatif. Quoiqu'il ne soit pas possible de retenir aux basses températures la phase β dans des alliages contenant moins de 20 pour cent en atomes de colombium, une extrapolation des courbes résistivité-concentration pour la solution solide β jusqu'à une teneur nulle en colombium, paraît indiquer que le titane pur se comporterait comme un semi-conducteur aux températures proches du zéro absolu. La validité de cette extrapolation est discutée.

DIE BEZIEHUNGEN ZWISCHEN WIDERSTAND, TEMPERATUR UND KONZENTRATION IM SYSTEM NIOB-TITAN

Der Widerstand einer Reihe von β-Niob-Titan Legierungen wurde in einem Temperaturbereich von 88°K bis 1173°K gemessen. Die Form der Beziehung zwischen Widerstand, Temperatur und Konzentration ist anormal, vor allem bei tiefen Temperaturen. Titanzusätze rufen eine stetige Zunahme des Widerstandes des Niobs und eine Abnahme des Temperaturkoeffizienten des Widerstandes hervor, bis in β-Legierungen, die weniger als 25 Atomprozent Niob enthalten, der Temperaturkoeffizient des Widerstandes negativ wird. Obwohl β-Legierungen mit weniger als 20% Niob bei tiefen Temperaturen nicht beständig sind, scheinen doch die auf Nb→0 extrapolierten isothermen Widerstand-Konzentrationskurven der β-festen Lösungen darauf hinzudeuten, dass reines β-Titan bei Temperaturen in der Nähe des absoluten Nullpunktes ein halbleiterähnliches Verhalten zeigen würde. Die Berechtigung einer solchen Extrapolierung wird diskutiert.

I. Introduction

The resistivity-temperature curve of pure metallic titanium has been determined by several investigations [1; 2] and its general form established. Figure 1 shows the curve obtained for the iodide titanium used in this investigation. The discontinuity observed at 1155.7°K (882.5°C) is due to the allotropic transformation from the low-temperature, close-packed hexagonal α-titanium to the high-temperature, body-centred cubic β-titanium. The curve for β-titanium is unusual in having an extremely low temperature coefficient. In the limited temperature region over which the resistivity of β-titanium has been determined, its increase in resistivity with temperature appears to be fairly linear, although Wyatt [2] has reported a slight discontinuity in slope in the curve at 1473°K. Since the resistivity of a normal pure metal tends to zero at the absolute zero of temperature, it would be expected that the resistivity-temperature curve of β-titanium (if this form of titanium could exist below the temperature of the transformation) would bend steeply towards zero resistivity in the

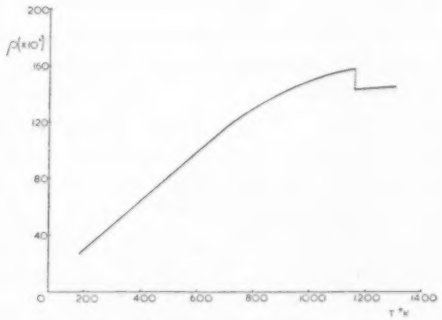

FIGURE 1. Resistivity-temperature curve of iodide titanium used in present investigation. Experimental points have been omitted, these being extremely numerous and showing little scatter. The resistivity ρ is in ohm cm. units.

*Received March 29, 1954.

†Department of Physical Metallurgy, University of Birmingham, England.

temperature range between 1155.7°K and absolute zero.

An extrapolated value of the room temperature resistivity of β-titanium can be derived from previously published results. Adenstedt, Pequignot and Raymer [3], in an investigation of the vanadium-titanium system, obtained values for the room temperature resistivity and temperature coefficient of resistance of a series of β solid-solutions. The room temperature resistivity-concentration curve obtained by these workers is remarkably linear and does not show the usual parabolic form resulting from solid-solution scattering of the conduction electrons (usually expressible as a function $c(1-c)$ where c is the atomic fraction of one component of the binary system). If this curve is extrapolated to zero vanadium content, the estimated resistivity of pure β-titanium at room temperature thus obtained is slightly greater than that of β-titanium at 1173°K. Furthermore, the temperature coefficient of resistance at room temperature, of β-vanadium-titanium alloys extrapolated to zero vanadium content, indicates that pure β-titanium has a very low or even a negative temperature coefficient of resistance at this temperature. If the figures for the resistivity and temperature coefficient of resistance of pure β-titanium at room temperature are valid, then the behaviour of this material is far from that to be expected of a normal metal. Such a conclusion warrants further investigation.

The fact that the allotropic transformation of pure titanium cannot be suppressed prevents the direct determination of the resistivity of β-titanium below the transformation temperature. Further information about the probable form of the resistivity-temperature curve can, therefore, only be obtained by extrapolation from a series of resistivity-temperature curves for various concentrations of an addition element which stabilizes the β-phase. The present investigation was carried out in order to provide the data necessary for this type of approach.

The systems of titanium with vanadium, niobium, tantalum and molybdenum all possess the characteristics essential for this investigation. Each of these elements depresses the allotropic transformation temperature of titanium, and is soluble in β-titanium at elevated temperatures over the whole range of composition. In these systems, furthermore, it is possible to retain the β-phase by water-quenching alloys which, under equilibrium conditions, would be two phase ($\alpha + \beta$) at room temperature. At concentrations below a critical amount of any of the above mentioned elements, however, a diffusionless transformation of β- to α-phase takes place during quenching. The occurrence of this type of transformation imposes a lower limit for the concentration of the addition element in retained β-phase solid-solutions. Of the four possible alloying elements, niobium was selected as being most suitable for three reasons: (1) the atomic size of niobium is almost exactly equal to that of titanium, (2) it is in the adjacent group of the periodic table and would not, therefore, be expected to differ greatly in electronic structure from that of titanium and (3) the difference between the melting point of niobium and titanium, although large, is not great enough to make the production of homogeneous titanium-niobium alloys excessively difficult.

II. Experimental Procedure

High-purity iodide titanium containing a small amount of zirconium ($\simeq$ 0.2 at.%), prepared by the Foote Mineral Company, and spectrographically pure niobium supplied by Messrs. Johnson, Matthey, Ltd., were used as the starting materials for the preparation of a series of niobium-titanium alloys. In order to obtain homogeneous specimens, ingots resulting from melting the component metals together in an argon arc-furnace were cold-rolled to thin sheets, which were then coiled and remelted. After hot-forging to break up the as-cast structure and removal of the contaminated surface layers, the alloys were cold-swaged to 2 mm diameter rod. The rods were sealed into evacuated silica tubes, homogenised for 70 hours at 1000°C and then cooled by plunging the silica tubes, unbroken, into water. Under these conditions of cooling, it would seem probable that all alloys containing less than 35 at.% niobium might possibly contain some precipitated α-phase, as may be seen from the titanium-rich portion of the constitutional diagram of the niobium-titanium system, determined by Hansen, Kamen, Kessler and McPherson [4] and shown in Figure 2. The broken line superimposed on the diagram is the M_s temperature of the diffusionless β- to α-phase transformation for this system obtained by Duwez [5]. The alloys containing 20, 25 and 34 at.% niobium were therefore reheated to 900°C for 15 minutes in a molten tin bath, water-quenched, and subsequently surface-cleaned by pickling in a hydrofluoric acid-nitric acid solution. Micro-examination revealed that the specimens consisted

entirely of retained β-phase, as is illustrated by Figure 3 which shows the microstructure of a 20 at.% niobium alloy.

In order to minimise the effects of surface contamination of the alloys, which occurs even at very low pressures, the surface area/volume ratio of the resistance specimens was kept as low as possible. Furthermore, the necessity of maintaining the whole specimen at a uniform temperature

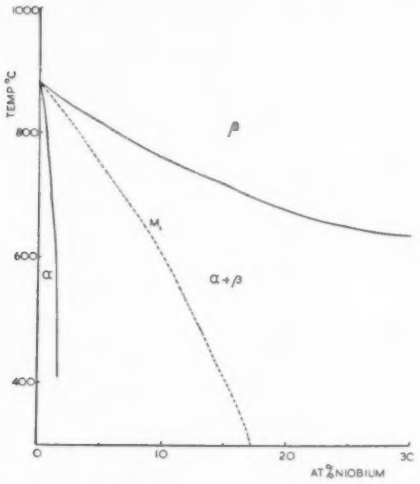

FIGURE 2. Constitutional diagram of titanium-rich portion of niobium-titanium system after Hansen *et al.* [4]. The M_s boundary is taken from Duwez [5].

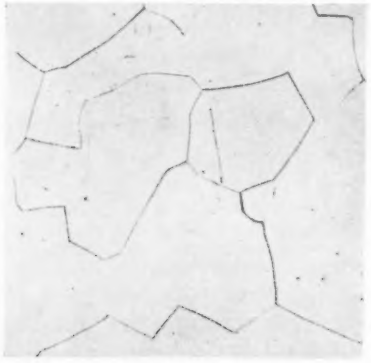

FIGURE 3. Microstructure of water-quenched 20 at.% niobium-titanium alloy. Retained β. Etched in 2 per cent H.F., 2 per cent H_2O_2 in water. 150X.

severely limited the length of specimen which could be used. Both these considerations would lead to the choice of a specimen with a very low resistance and hence to a loss in accuracy in the measurement of this quantity. The actual choice of specimen size and form used was the result of a compromise between the two requirements, a rod 4 cm in length and 2 mm diameter being eventually selected.

The arrangement of the resistance apparatus used is illustrated in Figure 4. The current and potential contacts to the specimen were made of titanium metal in order to reduce the effect of contamination of the alloys at high temperatures by diffusion, and took the form of small titanium blocks and screws. The screws were found to have no tendency to loosen or stick even after heating for some hours at temperatures in the neighbourhood of 900°C. In order to facilitate the operation of changing specimens, the thermocouple, current, and potential leads were all sealed into a cold-setting plastic plug which was mounted in the apparatus by means of a demountable O-ring seal. The vacuum obtainable within the apparatus was of the order of 10^{-6} mm of mercury at 1000°C. A double-balance bridge method [6] was used for measurements of resistance.

For the determination of the resistivity-temperature curves at temperatures above room temperature, the specimen assembly, contained in a

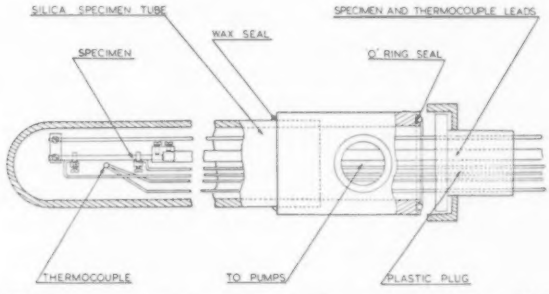

FIGURE 4. Arrangement of the apparatus for high temperature resistance determinations.

continuously evacuated silica tube as shown in Figure 4, was inserted in a tube furnace having a constant temperature region 9 in. in length. When low-temperature resistivity readings were required, the assembly was removed from its silica envelope and placed in a Dewar flask through which cold dry gas could be passed. Whether the high-temperature measurements are taken before or after the low temperature measurements is immaterial in the case of high niobium alloys. This is not true, however, for quenched alloys in which the retained β-phase is metastable at low temperatures. Such alloys are found to precipitate α-phase on heating above a certain temperature which depends on the composition of the particular alloy. It is necessary, therefore, in determining the resistance-temperature relationship for these specimens, to take measurements with increasing temperature starting from the lowest temperature. At the onset of β-phase precipitation, which was

marked by a pronounced discontinuity in the slope of the resistance-temperature curve, measurements were discontinued and the specimen was heated at 950°C to rehomogenise. Its resistance was then determined at a series of decreasing temperatures from 950°C until the precipitation of α-phase again prevented further measurement. The curves for titanium-rich alloys have, therefore, a temperature region in which no experimental values can be obtained. It is, however, possible to estimate with a reasonable degree of probability, the form of the curves within the region in which the β-phase is decomposing.

The specific resistivity of the β-phase alloys could not be determined when using the arrangement shown in Figure 4 because of the uncertainty in the effective length of the specimen between the potential contacts. In order, therefore, to permit the conversion of the experimental results from resistance to specific resistivity values, the specific resistivity of each alloy specimen was obtained at room temperature from an independent experiment using knife-edge potential contacts, the separation of which was accurately known. The specific resistivity values for titanium-rich alloys which had been quenched in order to retain the β-phase are subject to some error because of the necessity of removing surface contamination occurring during quenching by a pickling treatment which causes changes in the diameter of the specimen rods and slight surface pitting. The accuracy with which the mean diameter of the specimens can be measured is thus reduced, the estimated uncertainty in the values of the specific resistivity of the specimens concerned being about 2 per cent. The probable error in the values of the resistance of all the specimens as a function of temperature is 0.5 per cent, no allowance being made for thermal dilation.

III. Results

In order to eliminate the temperature-independent contribution of the solid-solution scattering to the resistivity of the alloys, the experimental results for each alloy have been plotted in Figure 5 in terms of the ratio of the resistivity at a given temperature to the resistivity of the same alloy at 1173°K. This particular reference temperature was chosen to allow the resistivity-temperature curve of pure β-titanium to be included in the series of curves. The results given in Figure 5 may be converted to a specific resistivity scale by combining them with the room temperature specific resistivity measurements of the same series of alloys which are plotted as a function of alloy concentration in Figure 6.

The isothermal resistivity-concentration curve of niobium-titanium alloys shows a form very similar to that obtained by Adenstedt *et al.* for the vanadium-titanium system, the curve of which is, for comparison, also presented in Figure 6. Like

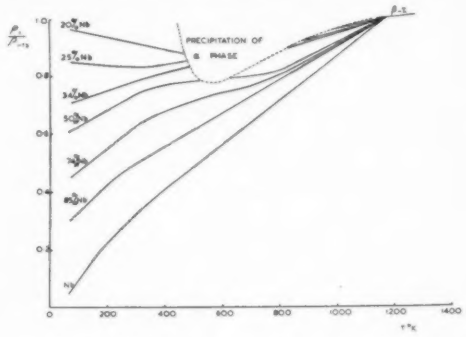

FIGURE 5. Relative resistivity $\frac{\rho_T}{\rho_{1173}}$ — temperature curves for a series of niobium-titanium alloys. Because of the large number and the small amount of scatter in the experimental points, these have been omitted.

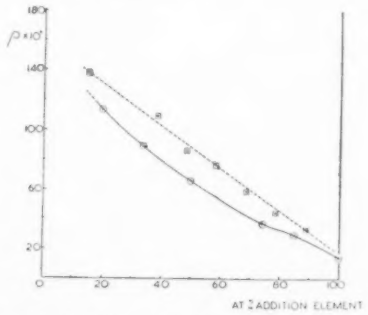

FIGURE 6. Resistivity ρ in ohm cm at room temperature of β-phase titanium alloys as a function of addition element. ——Niobium-titanium (present investigation). — — — Vanadium-titanium (after Adenstedt *et al.* [3]).

those for vanadium alloys, the results for niobium do not exhibit the expected parabolic form, although a slight distortion of the otherwise steeply sloping resistivity-concentration curve in Figure 6 at about 85 at.% niobium may indicate that a component due to solid-solution scattering is present, but is almost completely masked by another effect. Extrapolation of our results to zero niobium content is difficult, firstly because the curvature is apparently increasing continuously with increasing titanium concentration, and secondly because no estimate of the extent of the solid-solution scattering contribution for titanium-rich alloys is possible. It would be imagined,

however, that unless a very large decrease in resistivity with concentration takes place in β-phase alloys containing less than 20 at.% niobium, the estimated resistivity of pure β-titanium at room-temperature cannot lie much below 140×10^{-6} ohm cm. This is in agreement with the extrapolated result from the resistivity-temperature curve of Adenstedt *et al.* The small difference between this value and that for stable β-titanium at 1173°K (143×10^{-6} ohm cm) cannot be reconciled with the assumption that β-titanium behaves as a normal pure metal, in which an approximately fourfold increase in resistivity would be expected to occur on heating from room temperature to 1173°K.

The form of the family of relative-resistivity/temperature curves given in Figure 5 is also anomalous, especially at low temperatures. With increasing titanium content, the temperature coefficient of resistance at low temperatures decreases until, for the 25 and 20 at.% niobium alloys, it becomes negative. The results plotted in Figure 5 have been used to derive the isothermal resistivity-concentration curves at a number of temperatures, shown in Figure 7. The shape of

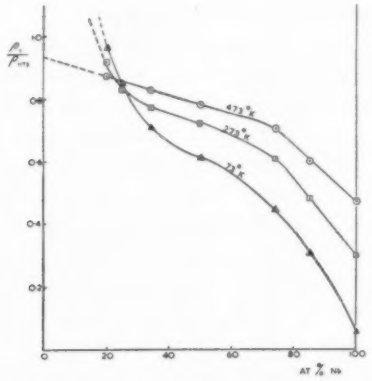

FIGURE 7. Isothermal relative-resistivity/concentration curves for β-phase niobium-titanium alloys, derived from the results shown in Figure 5.

these curves indicates that there is a tendency for the magnitude of the rate of increase in resistivity with increasing titanium content to become progressively larger at lower temperatures. If this trend were to be continued at niobium contents below those which could be investigated, it would seem that pure β-titanium should have a resistivity-temperature curve which, at temperatures below 473°K, rises steeply with decreasing temperature. Since the temperature coefficient of resistance of β-titanium is positive at 1173°K, the hypothetical resistivity-temperature curve would have a minimum lying between 473° and 1173°K. This is the type of curve to be expected of an intrinsic semi-conductor.

The evidence on which the foregoing argument is based depends largely on the resistivity values for metastable β solid-solutions. Before discussing the results further, therefore, it is necessary to consider the factors which may affect the reliability of these values. The first of these is the possibility that retained β-alloys undergo a reversible martensitic transformation at low temperatures, which could perhaps cause an increase in resistivity of the alloys with decreasing temperature, of the type observed. In order to be sure that the results obtained for β-phase titanium-rich alloys are not, at any rate, due to a microscopically visible transformation, the 20 at.% niobium-titanium alloy was subjected to a further micrographical examination after prolonged immersion in liquid air. On reheating to room temperature, no trace of martensitic α-phase was found, nor was any of the surface rumpling which would be expected to occur if a reversible martensitic change had taken place at temperatures below room temperature observed. If a transformation did take place on cooling to liquid-air temperature, it must, therefore, have occurred on a submicroscopical scale. X-ray examination of the specimen at room temperature showed no trace of lines due to the hexagonal lattice of α-titanium, although this again is not absolutely conclusive since submicroscopic α-phase formed by a martensitic transformation would be expected to give rise to diffuse X-ray reflections.

One further piece of evidence is available which would suggest that no reversible martensitic change is taking place in metastable β-phase alloys. The low-temperature, resistance-temperature curves of these materials were identical when obtained by heating or cooling experiments. Since hysteresis would be expected to occur if a martensitic change were present, it may be concluded, therefore, that all the available evidence suggests that no decomposition of metastable β-phase alloys takes place.

There is another possible cause of error in interpretation of the resistivity measurements which applies only to the 20 at.% niobium alloy. During the course of this work it was found that slight plastic deformation at room temperature of this alloy when in the retained condition causes the formation of a small amount of α-phase by a shear mechanism, as may be seen in Figure 8.

Such behaviour has previously been observed by Machlin and Weinig [7] in a metastable molybdenium-titanium alloy. It is probable, therefore, that in mounting the 20 at.% niobium specimen in the resistance apparatus, some martensitic α-phase was produced in the neighbourhood of the potential contacts. As the pressure due to the contacts was extremely localised, it is felt that the errors thus introduced into the low-temperature resistance measurements would not be great. In order to test

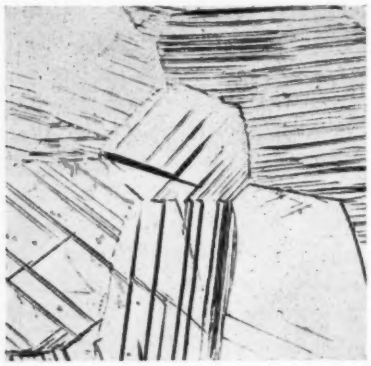

FIGURE 8. Microstructure of retained β-phase in the 20 at.% niobium-titanium alloy, shown in Figure 3, after plastic deformation. 175X.

whether the presence of some martensitically produced α-phase in the resistance specimen would enhance the possibility of further transformation on cooling to liquid air temperature, the specimen shown in Figure 8 was cooled in liquid air and reexamined. No additional α-phase or surface rumpling was observed.

IV. Discussion

Assuming, on the basis of the above discussion, that no breakdown of the metastable β-phase titanium-niobium alloys is occurring, detailed consideration of the trends shown by the whole series of niobium-titanium alloys seems to indicate that even small additions of titanium to niobium have anomalous resistivity effects. The resistivity-temperature curves of niobium-rich alloys (Figure 5) show a flattening at about 570°K which becomes more pronounced as the titanium content increases. The effect appears to be a development from the change in curvature observed in the resistivity-temperature curve of pure niobium at 120°K. Additions of titanium increase the temperature at which this change takes place and also increase its magnitude. It is unfortunately not possible to follow the effect in alloys containing less than 50 at.% niobium because the temperatures at which it would be expected to occur lie within the region in which α-precipitation prevents measurements from being made. It is possible, however, that further development of the same effect in alloys containing more than 50 per cent at.% titanium is responsible for the progressively decreasing values of the temperature coefficient of resistance of alloys containing increasing concentrations of titanium. On the other hand, in view of the S-shape of the isothermal resistivity-concentration curves at 73°K and 273°K seen in Figure 7, it is more probable that two combining effects are present, one more effective in niobium-rich alloys and the other in titanium-rich alloys.

The existence of semiconducting properties in a metal implies a full electron band with a finite gap between it and the conducting electron band. If β-titanium could exist below the transformation temperature and behaved as a semi-conductor, it is difficult to see how it could comply with this requirement and yet remain body-centred cubic. At present, therefore, no explanation can be offered for the anomalous resistivity results in the β-phase niobium-titanium alloys.

It is of some importance to obtain further information on the resistivity-temperature-concentration curves in other titanium systems with elements as different as possible from niobium. Preliminary experiments on the hydrogen-titanium system have shown that additions of hydrogen produce only small changes in resistivity in titanium. Hydrogen is known to depress the $\beta \rightarrow \alpha$ transformation in titanium [8] and it is hoped that the results of a current investigation on this system will yield information which may supplement that presented here.

V. References

1. McQUILLAN, A. D. J. Inst. Metals **78** (1950–51) 249.
2. WYATT, J. L. Trans. A.I.M.E. **197** (1953) 903.
3. ADENSTEDT, H. K., PEQUIGNOT, J. R. and RAYMER, J. M. Trans. A.S.M. **44** (1952) 990.
4. HANSEN, M., KAMEN, E. L., KESSLER, H. D. and McPHERSON, D. J. Trans. A.I.M.E. **191** (1951) 881.
5. DUWEZ, P. Trans. A.S.M. **45** (1953) 934.
6. LAWS, F. A. Electrical Measurements (New York, McGraw-Hill 1938) p. 185.
7. MACHLIN, E. S. and WEINIG, S. Acta. Met. **1** (1953) 480.
8. McQUILLAN, A. D. Proc. Roy. Soc. **A204** (1950) 309.

THE STRUCTURE OF THE $Co_3W_9C_4$ PHASE*

N. SCHÖNBERG†

The formula of the ternary so called χ-phase in the Co-W-C system has been found to be $Co_3W_9C_4$. The structure has been determined from X-ray powder photographs. The crystal axes of the hexagonal unit cell with the atoms in the space-group $D_{6h}^4 - P6_3/mmc$ are $c = a = 7.826$ Å. The cell contains two formula units $Co_3W_9C_4$. Three Co and 15 W atoms are located at the corners of slightly deformed octahedra oriented in such a way that each atom is common for two such octahedra. The remaining three Co and three W-atoms occupy the greatest lattice holes of the resulting framework. Two C-atoms are situated at the centres of trigonal prisms of six W-atoms and six C-atoms at the centres of octahedra of one Co and five W-atoms. These interstitial groupings of C-atoms are characteristic of the WC and W_2C structures respectively. The low affinity of carbon for cobalt is evident from the low Co-C coordination number. The intermetallic coordination number is high (10 to 12).

LA STRUCTURE DE LA PHASE $Co_3W_9C_4$

Il a été trouvé que la formule de la phase ternaire χ du système Co-W-C est $Co_3W_9C_4$. La structure fut déterminée au moyen de diagrammes de diffraction de rayons X, en employant la méthode des poudres. Les axes de la maille hexagonale, dont les atomes sont disposés dans le groupe spatial $D_{6h}^4 - P6_3/mmc$ sont $c = a = 7,826$Å. La maille contient deux unités de formule $Co_3W_9C_4$. Trois atomes de Co et 15 atomes de W se trouvent aux coins d'octaèdres légèrement déformés, qui sont orientés d'une manière telle que chaque atome est commun à deux des octaèdres en question. Les trois atomes de Co et les trois atomes de W restants occupent les plus grands des espaces libres du réseau résultant de l'arrangement décrit plus haut. Deux atomes de C se trouvent aux centres de prismes trigonaux de six atomes de W, alors que six atomes de C se trouvent aux centres des octaèdres formés d'un atome de Co et cinq atomes de W. Ces groupements interstitiels des atomes de C sont caractéristiques de WC et W_2C respectivement. La faible affinité du carbone pour le cobalt apparaît d'une façon évidente du petit nombre de coordination de Co-C. Le nombre de coordination intermétallique est élevé (10-12).

DIE STRUKTUR DER $Co_3W_9C_4$-PHASE

Die Formel der ternären sogenannten Phase im System Co-W-C wurde zu $Co_3W_9C_4$ bestimmt. Die Struktur wurde röntgenographisch aux Pulveraufnahmen bestimmt. Die Achsen der hexagonalen Elementarzelle mit Atomen in der Raumgruppe $D_{6h}^4 - P6_3/mmc$ sind $c = a = 7$, 826 Å. Die Elementarzelle enthält zweimal die Formeleinheit $Co_3W_9C_4$. Drei Kobalt-und 15 Wolframatome befinden sich in den Ecken leicht verformter Oktaeder, die so angeordnet sind, dass jedes Atom zwei solchen Oktaedern gemeinsam angehört. Die restlichen drei Co und drei W Atome befinden sich in den grössten Gitterlöchern des so entstandenen Skeletts. Zwei C Atome befinden sich in den Mittelpunkten der aus sechs W Atomen bestehenden trigonalen Prismen, und sechs C Atome in den Mittelpunkten der aus einem Co Atom und fünf W Atomen gebildeten Oktaeder. Diese Zwischengitteranordnungen sind für die WC resp. W_2C Struktur charakteristisch. Die geringe Affinität von Kohlenstoff und Kobalt zeigt sich deutlich in der niedrigen Co-C Koordinationszahl. Die intermetallische Koordinationszahl ist gross (10-12).

Introduction

In 1952 [1] Rautala and Norton published diagrams of stable and metastable equilibria in the Co-W-C system. In addition to the η-phase, Co_3W_3C, their study revealed the existence of two double carbides, called θ and χ, of the proposed compositions Co_3W_6C and $Co_3W_{10}C_4$ respectively. The η-phase was first studied by Adelsköld, Sundelin, and Westgren [2] although the isomorphous iron-tungsten carbide was known earlier [3]. The Co_2W_4C phase reported by Kislyakova [4] is obviously identical with the θ-phase, and the same formula is given by Kiessling [5; 6]. According to the two last-mentioned authors the only difference in the configuration between the η- and θ-phases is that 16 Co-atoms have been replaced by 16 W-atoms in a 16-fold atomic position in the latter case. In order to accentuate the close relationship between the two phases Kiessling has designated them by η_1 and η_2, respectively.

While a two-phase range evidently exists between the two η-carbides, many of the analogous η-oxides [7; 8] have the homogeneity limits closely corresponding to the compositions $Me_3' Me_3''O$ and $Me_2' Me_4''O$ without any intermediate two phase range. This has been observed for the following combinations of atoms: Me′ = Mn, Fe, Co, Ni, Cu, and Me″ = Ti [7]. On the other hand the η-oxides and nitrides of Me′ = Mn, Fe, Co, Ni and Me″ = Mo, W have fairly narrow homogeneity ranges with the phase composition corresponding to the general formula $Me_3' Me_3''$ (O or N) [8].

The present structure determination was started to see if any Co-C bonds exist in the lattice and

*Received March 30, 1954.
†Institute of Chemistry, University of Uppsala, Uppsala, Sweden.

whether the C-atoms are located at the centres of metal atom octahedra—as in the W_2C and η-phases —or at the centres of trigonal prisms, as in WC.

Experimental

Finely powdered metals—Co (Riedel–de Haën, *puriss.*) and W (Söderfors, 99.9 per cent)—and carbon (soot) were used as starting materials for the preparations. Powder mixtures with the Co/W ratios equal to 3:8, 1:3, 3:10 and the W/C ratios equal to 5:2 and 3:1 were pressed into brickettes weighing 5–10 g and sintered in graphite or zirconia crucibles in a graphite tube resistance furnace at a temperature of 1600°C for one hour. The phase analysis and structure determination was performed by means of powder photographs taken in focusing cameras of the Guinier type using monochromatized Cu-$K\alpha$ and Cr-$K\alpha$ radiation. For measurements of the high-angle reflections additional photographs were taken with Hägg-Phragmén type focusing cameras. It was evident from the phase analysis that the composition of the phase corresponds to the formula $Co_3W_9C_4$ rather than $Co_3W_{10}C_4$. The chemical analysis of a seemingly homogeneous sample gave the composition $Co_{2.94}W_{9.03}C_{4.00}$.

Discussion of the Structure

According to Rautala and Norton the χ-phase has hexagonal symmetry with the crystal axes $c = a = 7.848$ Å, which was confirmed in the present study. The c/a ratio differs from unity to such a small extent that it is hardly possible to detect it in the photographs. A slight broadening of several diffraction lines could be seen, but in spite of the good resolution powder in the Guinier cameras it was not possible to separate the coinciding *hkl* reflections. Attempts to replace a small fraction of the W-atoms with Ti or Nb and thereby to cause a deformation of the lattice were in vain. As the ratios between the $\sin^2\theta$ values are comparatively small integers it is possible to index the photographs using rather small unit cells of cubical, tetragonal or orthorhombic symmetries. An excessively great percentage of absent reflections makes the choice of any of these cells most unlikely, however.

The observed dimensions of the phase were $c = a = 7.826$ Å ($V = 415.1$ Å^3). The observed density was 14.8 which corresponds to two formula units $Co_3W_9C_4$ per unit cell, giving a calculated density value of 15.05.

The powder reflections with $h = k$ and $l = 2n+1$ are absent in the photograph. The space-group with the highest symmetry for which this condition is characteristic is D_{6h}^4–$P6_3/mmc$. The unit cell contains 6 Co-, 18 W- and 8 C-atoms, and the atoms have to be distributed over probable combinations of four 2-fold, two 4-fold, two 6-fold and three 12-fold positions. If the Co-Co, Co-W, and W-W mean distances are assumed to be at least 2.50, 2.60 and 2.70 Å respectively, it is evident that the combinations with all atoms in 2-, 4-, and 6-fold positions have to be excluded. Hence 12 W-atoms are assumed to be located in 12 (i) x,0,0, or 12 (j) x,y,1/4, or 12 (k) x,2x,z. The 12 (i) position is characterized by the absence of reflections with h-$k = 3n$ and odd l and can be excluded because the 301 reflection is very strong. A calculation of a few $p|F|^2$ values shows that the 12(j) position is also most unlikely. For the remaining 12 (k) position the following limits are valid for the parameters: $0.18 < x < 0.22$ and $0 < z < 0.08$. From considerations of space the remaining two groups of 6 W and 6 Co-atoms, then both have to be located in the position 6 (h) x,2x,$\frac{1}{4}$ with an ordered or disordered distribution, because all other combinations will give some abnormally small intermetallic distances. Before the calculation of the x_h parameters it is seen that the only possible positions for the C-atoms are 2 (c) $\frac{1}{3}$, $\frac{2}{3}$, $\frac{3}{4}$ and 6 (g) $\frac{1}{2}$,0,0, if the W-C distances are assumed to be at least 2.10 Å. The limits for the parameters in 12 (k) can then be restricted within the probable limits $0.19 < x < 0.21$ and $0.06 < z < 0.08$. The x-parameters for the Co- and W-atoms will then lie within the limits $0.88 < x < 0.92$ and $0.52 < x < 0.57$. The intensity distribution in the photograph shows that the 6 Co + 6 W-atoms are distributed at random over the two 6 (h) positions. A systematic variation of the parameters within the limits given above and a comparison between the calculated $p|F|^2$ values and the observed intensities—for the reflections 100, 101, 201, 112, 300, 301, 212, and 203—showed that good agreement is obtained for the values given below.

3 Co + 3 W	in 6 (h) x,2x,$\frac{1}{4}$	with $x = 0.890$ (I)
3 Co + 3 W	in 6 (h) x,2x,$\frac{1}{4}$	with $x = 0.555$ (II)
12 W	in 12 (k) x,2x,z	with $x = 0.205$ and $z = 0.075$
2 C	in 2 (c) $\frac{1}{3}$,$\frac{2}{3}$,$\frac{1}{4}$	
6 C	in 6 (g) $\frac{1}{2}$,0,0.	

The calculated and observed intensities are compared in Table I and the interatomic distances are listed in Table II.

The metal atoms in the 6 (h) II and 12 (k) posi-

TABLE I

CALCULATED AND OBSERVED INTENSITIES FOR THE $Co_3W_9C_4$ PHASE. Cu-$K\alpha$ RADIATION.

hkl	$\sin^2\theta_{calc.}$	$\sin^2\theta_{obs.}$	$I_{calc.}$	$I_{obs.}$	*hkl*	$\sin^2\theta_{calc.}$	$\sin^2\theta_{obs.}$	$I_{calc.}$	$I_{obs.}$
1,0,0	0.0129		0	0	4,2,0			2	
1,0,1	0226		0	0	5,0,2	3621	3621	24	25
1,1,0	0388	0388	62	75	4,0,4			6	
0,0,2			21		1,0,6			0	
2,0,0	0517	0516	51	75	4,2,1	3717	3715	9	10
1,0,2			20		3,3,2	3880	3885	8	15
2,0,1	0614	0614	57	75	1,1,6			9	
1,1,2	0776		0	0	5,1,0			0	
2,1,0	0905	0908	67	125	4,2,2	4009	4008	8	25
2,0,2			78		3,2,4			8	
2,1,1	1002	0999	0	200	2,0,6			9	
1,0,3			196		5,1,1			2	
3,0,0	1163	1161	47	40	5,0,3	4106		5	0
3,0,1	1260	1262	371	350	3,1,5			0	
2,1,2	1293	1292	180	200	4,1,4	4267		0	0
2,0,3	1390	1394	205	200	5,1,2	4397	4394	13	40
3,0,2			1		2,1,6			32	
0,0,4	1552	1553	5	25	4,2,3	4493	4499	8	10
2,2,0			21		4,0,5			6	
3,1,0	1681	1681	5	5	6,0,0	4655	4656	17	200
1,0,4			2		3,0,6			184	
3,1,1	1778	1780	0	5	6,0,1	4753	4754	63	75
2,1,3			3		4,3,0	4785	4779	39	40
2,2,2	1940	1945	13	25	5,0,4			10	
1,1,4			6		4,3,1			2	
3,0,3	2036		0	0	5,1,3	4882	4884	88	125
4,0,0			13		3,2,5			22	
3,1,2	2069	2065	27	40	1,0,7			2	
2,0,4			13		5,2,0			14	
4,0,1	2166		6	0	6,0,0	5044	5041	15	75
3,2,0			27		3,3,4			17	
4,0,2	2457	2456	5	75	2,2,6			15	
2,1,4			45		5,2,1	5140	5134	14	25
3,2,1			6		4,1,5			12	
3,1,3	2554	2552	6	15	4,3,2			4	
1,0,5			4		4,2,4	5170	5168	3	10
4,1,0	2715		0	0	3,1,6			4	
3,0,4			6		2,0,7	5270		0	0
4,1,1	2812	2812	9	5	5,2,2	5431	5434	10	10
4,0,3	2942	2947	23	40	6,0,3	5528		3	0
2,0,5			17		6,1,0			5	
4,1,2	3103		0	0	5,1,4	5560	5570	6	10
2,2,4			2		4,0,6			1	
5,0,0	3233	3229	3	15	6,1,1			1	
3,1,4			10		4,3,3	5658		3	0
5,0,1			1		5,0,5			1	
3,2,3	3330	3334	228	200	2,1,7			0	
2,1,5			0		5,2,3	5916	5918	59	75
3,3,0	3492	3494	26	25	3,0,7			40	
0,0,6			7		6,1,3	5949	5952	4	25
4,1,3	3588	3584	45	200	3,2,6			23	
3,0,5			176						

tions form a framework of slightly deformed octahedra with all their corner atoms common for two such octahedra. The octahedral centres are occupied by C-atoms in the positions 6 (*g*) $\frac{1}{2},0,0$; $0,\frac{1}{2},0$; $\frac{1}{2},\frac{1}{2},0$; $\frac{1}{2},0,\frac{1}{2}$; $0,\frac{1}{2},\frac{1}{2}$; $\frac{1}{2},\frac{1}{2},\frac{1}{2}$. The remaining metal atoms in the 6 (*h*) I position are located in the six resulting lattice holes in the unit cell and have metallic 10-coordination, while the former atoms

TABLE II

INTERATOMIC DISTANCES IN THE $Co_3W_3C_4$ PHASE.

Atom	Surrounding atoms	Interatomic distance, Å	
(Co,W) in 6 (*h*) I	2 (Co,W) in 6 (*h*) I	2.58	2.60
	2 (Co,W) in 6 (*h*) II	2.62	
	4 W in 12 (*k*)	2.72	2.76
	2 W in 12 (*k*)	2.85	
(Co,W) in 6 (*h*) II	2 (Co,W) in 6 (*h*) I	2.62	2.62
	2 (Co,W) in 6 (*h*) II	2.62	
	4 W in 12 (*k*)	2.95	2.99
	4 W in 12 (*k*)	3.03	
W in 12 (*k*)	2 (Co,W) in 6 (*h*) I	2.72	2.89
	1 (Co,W) in 6 (*h*) I	2.85	
	2 (Co,W) in 6 (*h*) II	2.95	
	2 (Co,W) in 6 (*h*) II	3.03	
	1 W in 12 (*k*)	2.74	2.96
	2 W in 12 (*k*)	3.01	
	2 W in 12 (*k*)	3.02	
C in 2 (*c*)	6 W in 12 (*k*)	2.21	
C in 6 (*g*)	2 (Co,W) in 6 (*h*) II	2.10	
	4 W in 12 (*k*)	2.13	

are surrounded by 12 metal atoms at contact distances. As a mean the observed Co-W and W-W distances are 2.61 and 2.96 Å respectively. The intermetallic W-W distances are thus 5 per cent greater than those in the pure metal corrected for 12-coordination. It is of interest to note that 2 C-atoms are located in trigonal prisms of 6 W-atoms and 6 C-atoms in octahedra of 1 Co + 5 W-atoms and that the interatomic metal-carbon distances in the two types of interstitial groupings agree well with those observed in WC and W_2C respectively.

Acknowledgement

The author wishes to thank Professor G. Hägg for his kind interest in this study. A grant from Statens Tekniska Forskningsråd is gratefully acknowledged.

References

1. RAUTALA, P. and NORTON, J. T. Trans. A.I.M.E. **4** (1952) 1045.
2. ADELSKÖLD, V., SANDELIN, A., and WESTGREN, A. Z. anorg. Chem. **212** (1933) 401.
3. WESTGREN, A. Jernkontorets Ann. **117** (1933) 1.
4. KISLYAKOVA, E. N. Zhur. Fiz. Khim. **17** (1943) 108.
5. KIESSLING, R. Discussion of the paper by P. Rautala, and J. Norton, J. Metals **5** (1953) 745.
6. KIESSLING, R. Symposium on the Reactivity of Solids, Gothenburg, Sweden, June 9-13, 1952.
7. KARLSSON, N. Nature **168** (1951) 558.
8. SCHÖNBERG, N. Acta Chem. Scand. (1954). In press.

THERMAL DIFFUSION IN SOLID ALLOYS*

L. S. DARKEN† and R. A. ORIANI‡

The phenomenon of thermal diffusion (Ludwig-Soret effect) has been observed in three solid binary alloys, αFe-N, αFe-C, and Au-Cu. The interstitial solutes migrate to the higher temperature region of the specimen, as also does Cu in Cu-Au. The quantity, heat of transfer, appearing in the thermodynamic equations is interpreted as arising from the asymmetric dissipation of activation energy after a unit step in diffusion. For the case of vacancy mechanism of diffusion an explicit relation is developed with which the experimental results are rationalized.

LA DIFFUSION THERMIQUE DANS LES ALLIAGES SOLIDES

On a observé la diffusion thermique (l'effet Ludwig-Soret) dans trois alliages binaires, solides, Fe-N α, Fe-C α, et Au-Cu. Les solutés interstitiels se déplacent vers les régions de haute température, ce qui est aussi le cas de Cu dans Cu-Au. La grandeur dite chaleur de transport, qui apparaît dans les équations thermodynamiques, est interprétée comme provenant de la dissipation asymétrique de l'énergie d'activation après un déplacement unitaire dans le processus de diffusion. On a développé une relation explicite pour le cas du mécanisme lacunaire de diffusion au moyen de laquelle les résultats expérimentaux sont rendus rationnels.

DIE THERMISCHE DIFFUSION IN FESTEN LEGIERUNGEN

Die Erscheinung der thermischen Diffusion (Ludwig-Soret Effekt) wurde an drei festen binären Legierungen, Fe-N, Fe-C und Au-Cu beobachtet. Die Lösungsatome in Zwischengitterplätzen wandern in den wärmeren Teil der Probe; das gleiche Verhalten zeigt Cu in Cu-Au. Die in den thermodynamischen Gleichungen erscheinende Grösse, die Übertragungswärme, wird folgendermassen interprätiert: Sie rührt von der asymmetrischen Abfuhr der Aktivierungsenergie nach einem elementaren Diffusionsschritt her. Für den Fall des Leerstellenmechanismus der Diffusion wurde eine explicite Beziehung abgeleitet, die die experimentellen Ergebnisse verständlich macht.

The establishment of a concentration gradient in a binary solution by means of a temperature gradient has long been known as thermal diffusion when the phenomenon occurs in the gaseous state, and as the Ludwig-Soret effect when in the liquid state. Much experimental work has been done on this effect in mixtures of organic liquids and in aqueous solution of inorganic salts [1–5]; Ballay [6] investigated the Ludwig-Soret effect in liquid metals. The amount of work done on thermal diffusion in the solid state is much less. Reinhold [7; 8] and collaborators studied the phenomenon in solid solutions of various salts; however, Jost [9] notes that deGroot [10] points out that not all the concentration change observed by Reinhold can be attributed to the Soret effect since large concentration differences were observed only if the hot and cold parts of the system belong to different phases. Ballay [6] has looked for the Soret effect in three solid alloys with negative results. As a by-product of an investigation on the electro-migration of carbon in austenite, Lebedev [11] observed the diffusion of carbon to the hotter section of a specimen heated by passage of alternating current.

The present paper reports a few measurements on thermal diffusion in gold-copper alloys, of nitrogen in α-iron and of carbon in α-iron, together with a simple atomistic interpretation of the relevant phenomenological equations which adequately rationalizes the observations.

Experimental

The apparatus employed to observe thermal diffusion in Fe-N alloys is shown in Figure 1. That

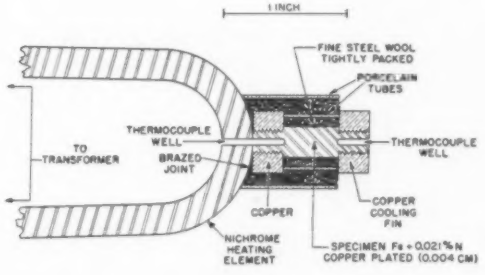

FIGURE 1. Apparatus for thermal diffusion in iron alloys.

for Fe-C alloys was similar except for replacement of the threaded end parts of the specimen by copper, in an attempt to minimize decarburization. The temperature gradient was established by providing good thermal contact between one end of the specimen and a large mass held at a high temperature, while the other end of the specimen was allowed to lose heat through a copper cooling fin to the ambient air. The magnitude of the temperature difference

*Received April 5, 1954.
†Research Laboratory, United States Steel Co., Kearny, N.J.
‡Research Laboratory, General Electric Co., Schenectady, N.Y.

was varied by varying the size of the cooling fin. A blank run with a specimen drilled completely through showed that the temperature gradient was substantially uniform. The temperature was measured by a fine platinum, platinum-rhodium thermocouple pushed in hard against the bottom of the thermocouple well.

The specimens for Fe-C thermal diffusion were made from ingot iron (Mn, 0.028%; P, 0.014%; S, 0.029%; Si, 0.003%; C, 0.016%). Those for Fe-N thermal diffusion were first decarburized, then nitrided to 0.021% N by equilibration with nitrogen gas at 1000°C. The specimens were copper-plated, diffusion-annealed, and then prepared for metallographic examination. For the Fe-N alloys, this preparation consisted of holding the specimen at 500°C for ten minutes to put nitride in solution, followed by holding at 300°C for one hour to develop nitride "needles." It should be emphasized that the nitrogen was completely in solution during the diffusion anneal. The metallographic examination showed a greater predominance of nitride needles toward the hot end of the specimen. Subsequently, four equal sections (0.25 cm) were made, with the cuts normal to the axis of the temperature gradient, and used for nitrogen analyses by the distillation of ammonia method.

Since diffusion rates in substitutional solid solutions are much smaller than those in interstitial solutions, a different type of apparatus was necessary to observe thermal diffusion in gold-copper alloys. This device is shown in Figure 2,

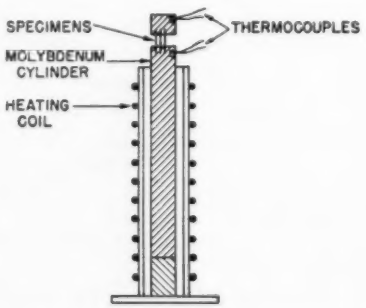

FIGURE 2. Schematic diagram for apparatus for thermal diffusion in gold-copper alloys.

and consists of a long molybdenum cylinder surrounded by a heating element. Three specimens in the form of fine wires, 0.4 mm diameter by 5 mm, are inserted into 0.4 mm diam × 1.5 mm holes in the face of the molybdenum cylinder. The top ends of the three specimens are similarly inserted into holes in the lower face of a short molybdenum cylinder which acts as a cooling fin. The length of specimen in the space between the two molybdenum cylinders is about 2 mm. The temperatures are measured by fine platinum, platinum-rhodium thermocouples. The entire assembly is within a glass envelope which permits evacuation and degassing. The diffusion anneal (described later) took place under 5 mm Hg pressure of argon to suppress vapor-phase transfer of metal.

After the diffusion anneal, the specimens were enclosed in separate Pyrex ampoules under argon, held at 500°C for 24 hours and water-quenched in order to retain the disordered solid solution. The compositions along the axis of the specimen were measured by taking a series of Debye-Scherrer diffraction patterns using a fine pencil of X-rays the diameter of which was about twice the specimen diameter. After calculation of the lattice parameter, a_0, the composition can be obtained from the composition-lattice parameter data of Johansson and Linde [12].

Experimental Results

Table I presents the results on the effect of a temperature gradient on the concentration of nitrogen in ferrite. It will be noticed that the loss of nitrogen was small, probably because the slight oxide film was an effective barrier to the diffusion of nitrogen. These results are shown in Figure 3 to show clearly the pronounced tendency of nitrogen to migrate to the hot end and to emphasise the minimum in two of these curves. Such minima (or maxima) are to be expected whenever the temperature of the cold end is so low that the diffusion in

TABLE I

THERMAL DIFFUSION OF NITROGEN IN α-IRON
(original %N = 0.021)

Run	Sample sections	Temp. °C	Time, hrs.	% Nitrogen
A	1 (hot end)	766		.028
	2		24	.020
	3			.017
	4 (cold end)	418		.019
B	1 (hot end)	803		.026
	2		24	.016
	3			.018
	4 (cold end)	510		.021
C	1 (hot end)	756		.033
	2		96	.019
	3			.013
	4 (cold end)	622		.010

that region is effectively frozen, and the demand of the hot end of the specimen for solute or for solvent must be met by the zone of the specimen at intermediate temperature. However, in run *C* where the cold-end temperature was considerably higher than in the other two runs, and where the holding time was four times longer, there is no trace of a minimum; extensive thermal diffusion occurred throughout the entire specimen. These results give no evidence that a steady state was attained.

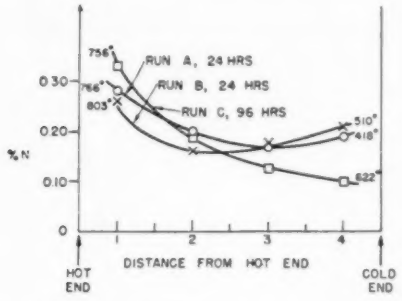

FIGURE 3. Thermal unmixing in iron-nitrogen alloys.

The data for the thermal diffusion of carbon in ferrite, shown in Table II, are rather less convincing because, due to decarburization, the carbon content nowhere rose significantly over the original value. However, keeping in mind the relative immobilization of carbon at the cold end, and hence giving greater weight to the carbon contents of sections 1 and 2 of the specimens, it seems clear that there has been a consistent relative enrichment in carbon in section 1 at the expense of section 2. The general form of the carbon distribution is somewhat similar to that for nitrogen distribution for the shorter time runs, in that the concentration change in the colder end is small and a minimum concentration is found near the center. It seems reasonable to suppose that decarburization was small at the colder end and became progressively more severe toward the hotter end. On this hypothesis only the hotter end would in each case have contained considerably more carbon if decarburization had been avoided. Thus carbon in ferrite appears to migrate in a thermal gradient in the same direction as nitrogen—toward the higher temperature region; this is also the same direction of migration as found by Lebedev for carbon in austenite.*

TABLE II

THERMAL DIFFUSION OF CARBON IN α-IRON
(original %C = 0.016)

Run	Sample sections	Temp. °C	Time, hrs.	% Carbon
A	1 (hot end)	677		.018
	2		24	.010
	3			.014
	4 (cold end)	525		.018
B	1 (hot end)	696		.015
	2		48	.009
	3			.013
	4 (cold end)	537		.015
C	1 (hot end)	690		.016
	2		96	.007
	3			.009
	4 (cold end)	554		.011

For study of thermal diffusion in gold-copper alloys, two samples which contained 26.5 at.% Au were used. Figure 4 shows the lattice parameter along the axis of one of these specimens after a diffusion run lasting 32 days, hot end at 830°C, cold end at 435°C. Since in this region the variation of lattice parameter with composition is [12] 2 at.% Au per 0.01 *Kx*, there has been an enrichment in gold towards the lower temperatures by about 0.4 at.%, and an impoverishment in gold at the hotter end by about 1.4 at.%.

Because the X-ray beam had an appreciable diameter, some two times larger than the specimen diameter, the observed diffraction pattern must correspond to an average composition in the region observed. The diffraction pattern from the hot end was clearly double and gave rise to two definite lattice parameters; this corresponds to a region of the specimen completely within the high-temperature molybdenum cylinder. It is presumed that the double diffraction pattern arises because in this isothermal zone a steep concentration gradient was established due to the depletion of gold at, and just beyond, the interface of the cylin-

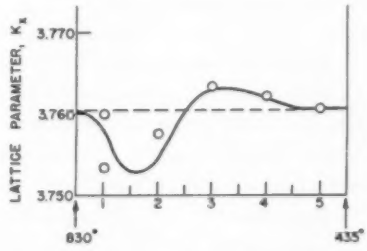

FIGURE 4. Thermal unmixing in gold-copper alloys.

* From Lebedev's [11] Figure 3 one can estimate that the original per cent carbon was 0.35 to 0.40 and that the final per cent carbon after 20 hours in a temperature gradient of unknown magnitude was about 0.6% in the hotter zone and about 0.3% in the colder zone.

der by virtue of the temperature gradient at this point. The isothermal diffusion produced two regions of nearly constant composition, one at the point of minimum gold content, and the other at the far end of the specimen. The curve of Figure 4 has been drawn in accordance with this hypothesis. The cold end of the specimen displays the same immobilization of diffusion that was evident in the case of the Fe-C alloys.

The second specimen of 26.5 at.% Au unfortunately underwent some loss of copper by oxidation during the heat treatment prior to the measurement of lattice parameters. However, the Debye-Scherrer pattern from the hot end also showed two definite lattice parameters, so that thermal diffusion must have occurred.

Discussion

In the case of the iron-nitrogen alloys, the flux J of nitrogen may be represented phenomenologically [13] for linear diffusion (at low concentration) in the presence of thermal and concentration gradients as:

$$J = - D \frac{\partial C}{\partial x} - D' C \frac{\partial T}{\partial x}$$

where D is the ordinary diffusivity; D' is the thermal diffusion coefficient, C is concentration of nitrogen, T is temperature and x is distance along the axis of the cylinder. The first term on the right is obviously the Fick's law term. This equation may be very simply applied for either of two simple cases. The first corresponds to sufficiently long time that steady state is achieved and $J = 0$. In this event $-\partial \ln C/\partial T = D'/D$, the Soret coefficient, designated s_T. Thus at steady state a plot of $\ln C$ or $\log [\%N]$ against T would be expected to be almost linear as the Soret coefficient is usually not strongly temperature dependent. Such a plot for run C, shown in Figure 5, exhibits curvature particularly at the low temperature end, and hence indicates that steady state was not fully achieved. The slope of this curve at the highest temperature, where steady state would be approached more rapidly, corresponds to $s_T = -0.021$, or to a concentration change of a factor of almost ten per 100 degrees. This value corresponds to a minimum estimate since the true steady-state value may be even higher. The extent of thermal separation is surprisingly large in comparison to that [9] observed in gases and liquids.

The second simple case pertains to times sufficiently short that the first (Fick's law) term in the equation for the flux may be ignored. Treating runs A and B in this manner as short time runs, and considering the flux across the plane of the minimum (Figure 3), where $\partial C/\partial x$ is zero at both the initial and final times, permits an approximate evaluation of D'. As this method is rather sensitive to the small errors in the nitrogen balance a detailed description does not seem warranted. It leads again to a Soret coefficient of about -0.02. This method also leads to a low value by virtue of the neglected term. In spite of the uncertainties it supports the previous estimate.

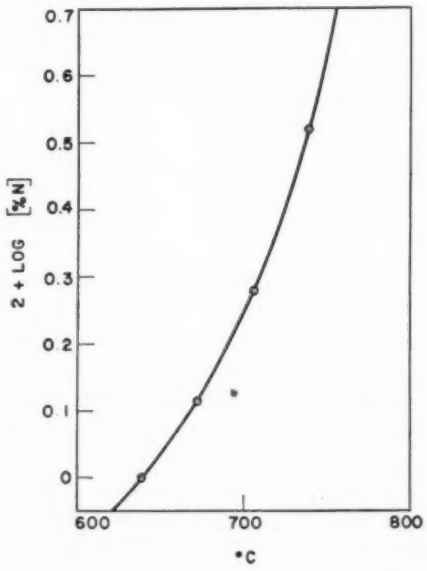

FIGURE 5. Plot for estimating Soret coefficient for nitrogen in ferrite (Run C).

An estimate of the Soret coefficient for the case of the gold-copper alloy may be made with the aid of an equation developed by deGroot [13; 14] for the progress with time of the separation under the action of a thermal gradient. Utilizing the observed enrichment in copper of 1.4 atomic per cent, $s_T \approx -0.0002$.

These observations can also be treated from the point of view of the thermodynamics of irreversible processes [13]. For the case of a binary solution in mechanical equilibrium under a temperature gradient,

$$(1) \quad J_1 = - J_2 = L_{11} \left[- \frac{1}{c_2} (\partial \mu_1 / \partial c_1) \operatorname{grad} c_1 - (Q^*_1 - h_1 + h_2) \frac{\operatorname{grad} T}{T} \right],$$

in which c_i is the mass fraction of component i;

μ_1 is the chemical potential per unit mass of component 1; h_i is the partial specific enthalpy of solution of i; T is the absolute temperature; J_i is the flux of i relative to the center of mass of the system, in g/sec/cm²; and L_{11} is a phenomenological coefficient with positive sign—it is the same coefficient that would appear in the equation for isothermal diffusion. The "heat of transfer" Q^*_1 can be shown by application of the Onsager reciprocity relations to be given by $J_q = Q^*_1 J_1 = -Q^*_1 J_2$ at zero temperature gradient, where J_q is the energy flux. Thus, Q^*_1 is the energy transported by unit mass of either component relative to the center of mass of the system.

Starting with a homogeneous binary solid solution, directly upon impressing a gradient of temperature, grad $c_1 = 0$, so that initially,

$$(2) \qquad J_1(t=0) = -L_{11}(Q^*_1 - h_1 + h_2)\frac{\text{grad } T}{T}.$$

Thus, the sense of J_1 will be the sense of grad T when the quantity $(Q^*_1 - h_1 + h_2)$ is negative. At subsequent times, the concentration gradient established by the temperature gradient will tend to be counteracted by diffusion driven by the concentration gradient, so that a steady state of zero net mass flow will eventually obtain. In these circumstances, the Soret coefficient s_T, a measure of the separation effected by the temperature gradient, may be defined as

$$(3) \qquad s_T = -\frac{d \ln c_1}{c_2\, dT} = \frac{D'_{12}}{D_{12}} = \frac{(Q^*_1 - h_1 + h_2)}{c_1 T\,(\partial\mu_1/\partial c_1)} = \frac{Q^*_1}{RT^2}.$$

The last equality is valid only for an ideal solution; the D_{12} is the diffusivity for ordinary isothermal diffusion; and D'_{12} is an analogously defined diffusivity for thermal diffusion. Thus, the larger the heat of transfer, the larger the unmixing effected by a given temperature difference.

The thermodynamic theory cannot take one further into the elucidation of the Soret effect; the all-important quantity Q^*_1 must be interpreted and evaluated in terms of some explicit kinetic model, since the amount of energy transferred by a unit step of the diffusion process depends upon the details of the mechanism of that process. Denbigh [15] has stressed that an activated process provides the opportunity for a transfer of energy from one zone to another in a medium. Hiby and Wirtz [16], independently of thermodynamic considerations, carry through a kinetic analysis in which the energy of detachment of an atom from its neighbors in a liquid solution is thought of as referring to the region at temperature T of the origin of the diffusing atom, and the energy of hole formation refers to the region, at $T + dT$, to which the atom is going. By equating, at the stationary state, the rates of jumping in either direction, they obtain

$$s_T = -\frac{(q_{1H} - q_{1L}) - (q_{2H} - q_{2L})}{RT^2},$$

in which q_{iH} is the energy of detachment of atom i from its neighbors, and q_{iL} is the energy for formation of a hole. The assumption is usually made that $q_{1L} = q_{2L}$.

Prigogine, de Brouckere, and Amand [3] adopt the kinetic scheme of Hiby and Wirtz, but proceed to express the energies of detachment in terms of pairwise binding energies, ϵ_{ij}, between nearest neighbors, and assume $\epsilon_{12} = (\epsilon_{11}\epsilon_{22})^{\frac{1}{2}}$. Denbigh [15] has endeavored to correlate the thermodynamic heat of transfer with the energies of detachment, and concludes that the thermodynamic and kinetic formulations are equivalent if

$$Q^*_1 = (q_{1H} - q_{1L}) - (q_{2H} - q_{2L})$$

for an ideal solution. He then formulates the energies of detachment in terms of nearest-neighbor interactions.

Thus, the emphasis has been laid on interpreting the energy of transfer in terms of the binding energies of the atoms in their normal rest positions. This appears inherently wrong, since such an interpretation purports to explain the details of a dynamic process by the properties of the initial and final states. It is now stressed that the heat of transfer is associated, and in principle calculable from, the manner in which, on the everage, a statistical fluctuation concentrates energy about a small region, and from the manner in which the activation energy is dissipated into the lattice after the unit step of diffusion. More specifically, the difference in spatial distribution of the activation energy before and after a unit diffusion step is the controlling factor behind the heat of transfer. Although the theory of lattice dynamics is at present inadequate to make this concept quantitative, a simple formulation is possible when the unit diffusion step is an atom-vacancy exchange.

Considering such a mechanism for diffusion in solid solutions, then J_1 can be produced by atom 1 exchanging with a vacancy from left to right, or by atom 2 exchanging with a vacancy from right to

left. Each such unit process is characterized by its own activation energy per atom, ϵ_1 and ϵ_2, respectively, assuming a sufficiently random distribution of atomic species so that all vacancies are essentially alike. In general, ϵ_1 need not equal ϵ_2. By a statistical fluctuation energy has been concentrated in a region about a vacancy, so that an exchange of an atom with the vacancy is possible. This excess thermal energy collects itself into the potential energy of an activated complex; the probability of the exchange of species i with the vacancy will be proportional to $(P_{vi})e^{-\epsilon_i/kT}$, where P_{vi} is the probability of finding a vacancy adjacent to an atom of species i. After any one such exchange, the potential energy of the activated complex will be reconverted to kinetic energy having in general a spatial distribution about the region considered different from that characterizing the activated complex. For purposes of formulation, a portion of this energy may be thought of as residing in the lattice matrix about the atom-vacancy couple, so that the "center of gravity" of this portion of ϵ_i remains essentially fixed. Another fraction, $\eta_i\epsilon_i$, may be considered to travel with the jumping atom, whereas the third fraction, $\nu_i\epsilon_i$, may be considered to travel with the vacancy. Thus, any one atom-vacancy exchange may move the "center of gravity" of the activation energy along with the jumping atom or with the vacancy. If the former is the case, then heat must be supplied to the region of origin of the atom in order to keep it at constant temperature; on the other hand, if more energy moves with the vacancy than with the atom, then heat must be removed from the region of the origin of the atom in order to maintain isothermal conditions. Since Q^*_1 is the net heat supplied, one may write

$$(4) \quad Q^*_1 = P_v \{n^0_1 e^{-\epsilon_1/kT} \cdot (\eta_1 - \nu_1)\, \epsilon_1 - n^0_2 e^{-\epsilon_2/kT} \cdot (\eta_2 - \nu_2)\, \epsilon_2\}$$

where n^0_i is the number of i-atoms per gram of solution, and P_{v1} has been set equal to $P_{v2} = P_v$ for simplicity.

Therefore, equation (2) becomes

$$(5) \quad J_1(t=0) = -L_{11}P_v [n^0_1 e^{-\epsilon_1/kT} \cdot (\eta_1 - \nu_1)\, \epsilon_1 - n^0_2 e^{-\epsilon_2/kT} \cdot (\eta_2 - \nu_2)\epsilon_2] \frac{\text{grad } T}{T}$$

where $(-h_1+h_2)$ has been neglected as being usually of too small a magnitude to be considered. If one considers the case of thermal diffusion in iron alloys, letting C or N be component 1, then $\epsilon_1 \ll \epsilon_2$ by virtue of the interstitial nature of the carbon and nitrogen, so that the exponential factors are of overriding importance in establishing the inequality

$$n^0_1 \epsilon_1 e^{-\epsilon_1/kT} \gg n^0_2 \epsilon_2 e^{-\epsilon_2/kT}$$

Hence, in order to describe the experimental finding that carbon and nitrogen migrate to the hotter side, one must conclude that $(\eta_1 - \nu_1) < 0$; that is, when carbon or nitrogen in iron exchanges with an interstitial vacancy, the vacancy takes with it a larger fraction of the activation energy than does the solute atom. This result is perhaps not too surprising when one considers that the newly formed vacancy is in a much looser medium than is the interstitial atom, so that the atoms surrounding the vacancy are able to partake of vibrations of larger amplitude, that is, of greater energy. The heat of transport is therefore negative —heat must be removed from the region of origin of the diffusing atom in order to maintain isothermality. Conversely, if a temperature gradient is forced upon the system, carbon or nitrogen must diffuse to the higher temperature, the heat of transfer being discharged into the lower temperatures behind the diffusing atom.

The case of the thermal diffusion in the gold-copper alloy cannot be analyzed so unambiguously because ϵ_1 and ϵ_2 cannot be so disparate as for interstitial alloys. Since Cu is a smaller atom than Au, ϵ_{Cu} is probably smaller than ϵ_{Au}, so that letting 1 = Cu, $e^{-\epsilon_1/kT} > e^{-\epsilon_2}/kT$. (It might be remarked that, in the case of substitutional alloys, the ϵ_i refers to the experimental activation energy per atom less the energy for forming a vacancy; in interstitial alloys, the vacancies presumably have no temperature dependence, so that here ϵ_i is in fact the experimental activation energy per atom.) However, the other factors in each of the two terms within the brackets in equation (5) retain importance. The small numerical difference between the two terms, reflected in the small magnitude of the separation effect observed in Au-Cu, cannot be ascribed to any specific factor. The magnitude, and even the sign, of the Soret effect in substitutional solutions appear to depend on the fine details of the dissipation of the activation energies of the two possible exchanges.

Other diffusion mechanisms have heats of transport due to the asymmetry in the dissipation of the activation energy. However, no simple way is apparent for their formulation. In general, it appears that the Soret effect in solid solutions is in

principle a means for the study of diffusion dynamics, but present theoretical treatments are inadequate for the treatment of the empirical results.

Acknowledgments

The authors wish to acknowledge the assistance of Mr. Warren S. Briggs and Mr. E. W. Filer (U.S. Steel Corp.) in the experimental work on the iron alloys. They are likewise grateful to Dr. J. B. Newkirk and Mr. W. G. Martin (General Electric Co.) for their cooperation in the laborious X-ray measurements on the gold-copper alloys, as well as to Drs. E. W. Hart and R. W. Schmitt (General Electric Co.) for helpful conversations.

References

1. CHIPMAN, J. J. Am. Chem. Soc. **48** (1926) 2577.
2. DEGROOT, S. R., GORTER, C. J. and HOOGENSTRAATEN, W. Physica **10** (1943) 81.
3. PRIGOGINE, I., DE BROUCKERE, L. and AMAND, R. Physica **16** (1950) 577.
4. THOMAES, G. Physica **17** (1951) 885.
5. TANNER, C. C. Trans. Faraday Soc. **23** (1927) 75; **49** (1953) 611.
6. BALLAY, M. Rev. Metallurgie (Memoires) **25** (1928) 427.
7. REINHOLD, H. Z. Elektrochem. **35** (1929) 627; Z. physik. Chemie **A141** (1929) 137.
8. REINHOLD, H. and SCHULZ, R. Z. physik. Chemie **A164** (1933) 241.
9. JOST, W. Diffusion in Solids, Liquids, Gases. (New York, Academic Press, Inc. 1952).
10. DEGROOT, S. R. L'effet Soret. Thesis, Amsterdam, 1945.
11. LEBEDEV, T. A. Metallurg (Leningrad) **15** (1940) 61.
12. JOHANSSON, C. H. and LINDE, J. O. Ann. Physik **25** (Ser. 5), 1 (1936).
13. DEGROOT, S. R. Thermodynamics of Irreversible Processes. (New York, Interscience, 1951).
14. DEGROOT, S. R. Physica **9** (1942) 699.
15. DENBIGH, K. G. Trans. Faraday Soc. **48** (1952) 1.
16. WIRTZ, K. and HIBY, J. W. Physik. Z. **44** (1943) 369.

ETCHPITS AND DISLOCATIONS ALONG GRAIN BOUNDARIES, SLIPLINES AND POLYGONIZATION WALLS*

S. AMELINCKX†

This paper describes some preliminary results of a study of the distribution of dislocations in crystals of rock salt by means of the etching process. It is shown that a one to one relation can be established between dislocations and etchpits. This applies as well to dislocations in small angle grain boundaries, as to dislocations produced by slip. Both Taylor and Burgers dislocations etch. In particular, formulae for the dislocation density in asymmetrical pure tilt boundaries are verified. The mixed character (tilt and twist) of a particular boundary could be visualized.

It was further shown that etchpits are produced along slip traces, visible as well as invisible ones.

LES FIGURES D'ATTAQUE ET LES DISLOCATIONS LE LONG DES JOINTS INTERCRISTALLINS, LES LIGNES DE GLISSEMENT ET LES PAROIS DE POLYGONISATION

On décrit dans cet article quelques résultats préliminaires d'une étude de la distribution de dislocations dans des cristaux de sel gemme au moyen du processus d'attaque. On montre qu'il est possible d'établir une relation directe, d'unité pour unité, entre les dislocations et les figures d'attaque. Ceci s'applique aussi bien aux dislocations dans des joints intercristallins à petit angle qu'aux dislocations produites par glissement. Les deux types de dislocations (de Taylor et de Burgers) apparaissent sous l'attaque. Il a été possible, en particulier, de vérifier des formules donnant la densité des dislocations dans des joints asymétriques qui résultent d'une inclinaison simple entre les deux cristaux. Le caractère mixte d'un joints résultant d'une inclinaison et d'une rotation des cristaux a pu être représenté.

ÄTZGRUBEN UND VERSETZUNGEN AN KORNGRENZEN, GLEITLINIEN UND POLYGONISATIONSGRENZEN

Die vorliegende Arbeit beschreibt einige vorläufige Ergebnisse einer Untersuchung von Versetzungen in Steinsalzkristallen mit Hilfe einer Ätztechnik. Es zeigt sich, dass eine direkte Beziehung zwischen Versetzungen und Ätzgruben nachgewiesen werden kann, und zwar sowohl für Versetzungen in Kleinwinkelkorngrenzen als auch für Versetzungen, die im Gleitprozess erzeugt wurden. Sowohl Taylor-als auch Burgersversetzungen lassen sich ätzen. Es wurden speziell die Formeln der Versetzungsdichte in asymmetrischen reinen Neigungskorngrenzen experimentell verifiziert. Die verschiedenen Komponenten (Neigungs-und Verwerfungskomponenten) einer bestimmten Korngrenze konnten auf diese Weise deutlich gemacht werden.

Weiterhin wurde gezeigt, dass sowohl auf sichtbaren als auch auf unsichtbaren Gleitspuren Ätzgruben entstehen.

Introduction

In the course of a study of the etching process—mainly of rock salt—some results were obtained which permit the conclusion that a one-to-one relationship was established between etchpits and dislocations. The dislocations were of both types (Taylor and Burgers); they were either initially present in the crystal (in sub-boundaries) or created by deformation. We give here some preliminary results. (The detailed account has to be reserved for publication as part of a thesis at Ghent University.)

Experimental Procedures

Fresh cleavage faces of "single" crystals of rock salt grown from the melt were etched with alcohol, then washed in ether, and rapidly dried on filter paper. In the described way, small well-developed polygonal etchpits could be obtained in a reproducible way. Their polygonal shape was used at the same time to orient the specimen.

Three kinds of specimens were investigated:

(*a*) Well-annealed specimens. A substructure of small angle boundaries, similar to the veining structure of annealed aluminium single crystals [1], was found. A great number of the boundaries could be resolved into separated etchpits.

(*b*) Specimens deformed by compression. Separated etchpits were developed along the slip traces.

(*c*) Bent and annealed specimens. Dislocation walls, due to polygonization, could be visualized by means of etchpits.

Observations

We will now summarize some of the results which were obtained.

(a) *Sub-boundaries*

The cleavage faces were found to consist of slightly disoriented crystal grains. This could be shown by means of the interference method introduced by Françon [2]. This method shows small orientation differences as differences in colour.

*Received April 14, 1954.

†Laboratorium voor Kristalkunde, Rozier, 6, Gent, Belgium.

5

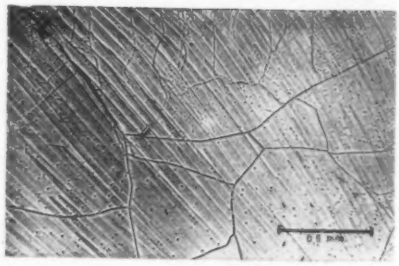

1

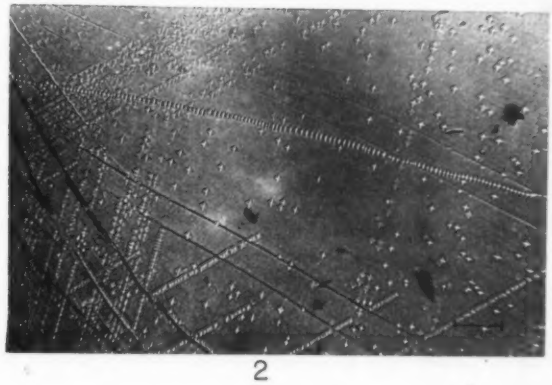

2

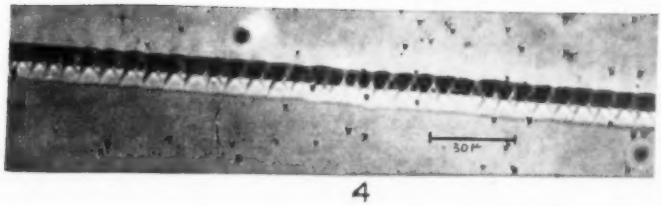

4

PLATE I. (All figures reduced to two-thirds). Figure 1—The "veining" structure in rock salt single crystals at small magnification. Figure 2—Etched slip lines and one grain boundary. Note the difference in etching between slip lines and grain boundary. Figure 4—Boundary showing two kinds of etchpits. The boundary is probably an alternation of Taylor and Burgers dislocations. Figure 5—Polygonization walls.

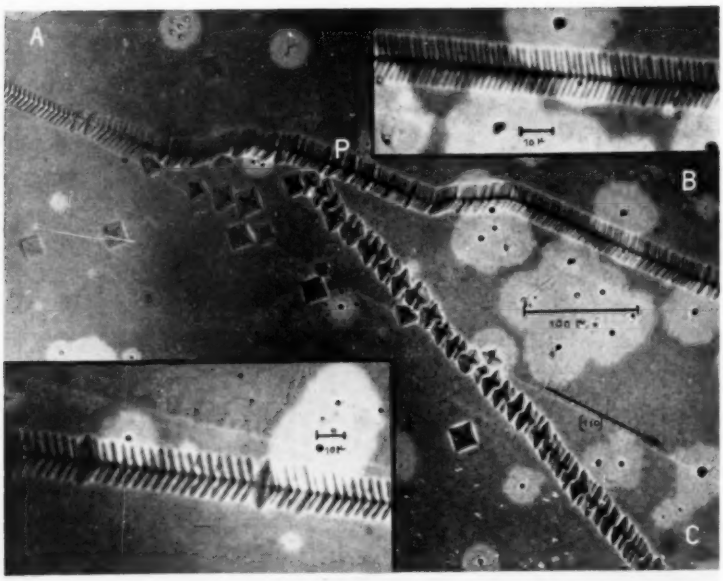

3

PLATE II. (Figure reduced to two-thirds.) Figure 3—Branching point of three pure tilt boundaries.

Etching revealed the existence of a "veining" structure similar to that found in annealed aluminium single crystals [1]. Rows of etchpits were developed along the boundaries of the crystal blocks. In many cases well separated etchpits were obtained (see Figures 1 and 2).

The relation $\vartheta = b/D$ (ϑ = angle of tilt, b = Burgers-vector, D = distance between dislocations) for a symmetrical pure tilt boundary was recently verified on germanium crystals by Vogel, Pfann, Corey and Thomas [3]. The distance D was simply derived from the distance between etchpits. The measurement of the angle ϑ is difficult when the crystals are of microscopic size. From the observation of resolved etchpits, verification of more general formulae is, however, *also* possible *without* knowledge of the angle ϑ. This can be done in a simple way in two cases.

1. When a pure tilt boundary changes orientation, the dislocation density should change, as can be derived from formulae developed by Read and Shockley [4]. When ρ is the density of the symmetrical boundary, the total density ρ' of dislocations in an asymmetrical boundary making an angle ϕ with the direction of the symmetrical one should be:

$$\rho' = \rho(\sin\phi + \cos\phi) \tag{1}$$

2. When three (in general asymmetrical) pure tilt boundaries meet, the following relation should hold

$$\sum_{i=1}^{3} \frac{\rho'_i}{\sin\phi_i + \cos\phi_i} = 0, \tag{2}$$

where ρ'_i are the total dislocation densities and ϕ_i the angles of the boundaries with the direction of the symmetrical boundary.

This relation follows from the fact that $\sum_{i=1}^{3} \vartheta_i = 0$; it holds for a simple cubic lattice. In what concerns the present case the rock salt lattice can be considered as such. There are indeed sets of mutually perpendicular slip planes, e.g., (110) and ($\bar{1}$10), with slip vectors which are also mutually perpendicular.

The relations (1) and (2) could now be verified by measuring distances between etchpits and angles ϕ.

Figure 3 represents three pure tilt boundaries which meet in P. Inset (a) is an enlargement of a part of PB, while (b) is an enlargement of part of PA.

Measurements give:

Boundary	$\rho'_{obs.}$*	ϕ**	$\rho'_{calc.}$*	$D_{obs.}$
BP	46.7	$<1°$	46.7	2.14μ
AP	29.9	3°	28.5	3.34μ
CP	23.3	22°	17.9	4.29μ

*Expressed in dislocations per 100μ.
**ϕ angles are measured in the same region where dislocations are counted.

We have now indeed very approximately: $28.5 + 17.9 \simeq 46.7$, so that (2) is satisfied within the accuracy of the measurements. Part of the boundary PA changed orientation. Measurements give:

Boundary	ϕ	$\rho'_{obs.}$	$\rho_{calc.}$
first part	3°	29.9	28.5
second part	29°	40	29.3

The agreement between 28.5 and 29.3 is good.

These observations prove in a striking way the dislocation structure of small-angle grain boundaries. They allow further the conclusion that one etchpit developed with the described method really corresponds to one dislocation.

That the substructure is a genuine structure of the crystal is proved by the observation that both halves of a cleaved specimen produce etch patterns which are rigorously mirror images, even when etched in slightly different condition.

Detailed observation of some grain boundaries in well-annealed specimens revealed a regular succession of etchpits of different development. The boundary of Figure 4 shows a regular alternation of etchpits of different depths. This structure cannot be a coincidence as the same sequence is continued all along the boundary. This particular structure simply results when a slight difference in dissolution velocity is assumed between two successive centres of attack. Such a difference could, for example, exist between the points of emergence of Taylor dislocations and Burgers dislocations. It is indeed to be expected, when the crystal is sufficiently well annealed, that impurities will concentrate along Taylor dislocations, but much less or not at all along pure Burgers dislocations [5]. This could result in a slightly different rate of dissolution. It is not impossible that the difference in geometry between the two dislocations alone is sufficient to cause a difference in dissolution rate. In every case we feel that the only explanation for the observed etch pattern of this particular grain boundary is that it consists of a regular alternation of Taylor and Burgers dislocations.

It will be seen on the photographs that a number of etchpits seem to be distributed at random within the "grains." They correspond, however, to

real features as even the patterns of these etchpits were exact mirror images on both halves of a cleavage. It was found that after a long anneal their number decreases and that they also tend to arrange themselves so as to form very small-angle boundaries. We think that these randomly distributed etchpits might find their origin in the three-dimensional network of single dislocation lines which was postulated by Mott [6].

(b) *Sliplines*

It was already shown on aluminium crystals that slip lines could be etched [7]. It proved difficult, however, to get well-resolved etchpits so that there was some doubt as to the exact relation between etchpits and dislocation density. Two other authors have since confirmed the possibility of producing etchpits along slip lines [8; 9]. In none of these cases could a clear-cut correspondence be reached. In the case of rock salt, we believe that a one-to-one correspondence could be established. This follows from the arguments under (a) and from the fact that for the sliplines the distance between etchpits could in some cases be kept larger than in grain boundaries so that even better resolution is possible.

Specimens were treated in two ways: (1) A freshly cleaved specimen was deformed while under observation, until slightly visible sliplines were developed, and then etched. (2) A specimen was deformed, cleaved and both halves etched.

The experiments under (2) gave etch patterns which were again exact mirror images of both the etch pattern of the substructure and the etch pattern of the slip traces. This proves again that the process is reproducible, and it permits the retention of a "replica" of the dislocation structure of a specimen. This opens the way to experiments concerning the evolution of a distribution of dislocations under the influence of heat treatment or strain. It is hoped to follow strain-induced movement of a single dislocation in this way. Moreover, by cleaving away thin slices, the distribution of dislocations in the interior of a crystal can be reconstructed.

The experiments on sliplines confirmed that etchpits are formed at both Taylor and Burgers dislocations. This follows from the following considerations. When, for instance, slip occurs along a (101) plane in a cleavage prism of NaCl compressed along [100], dislocation loops will in general reach (001) as well as (010). The slip vector being $\frac{1}{2}[\bar{1}01]$, the loops will cut the (001) face with a Burgers component, while the (010) plane will be cut as pure Taylors. The slip traces on (001) will be parallel to the cube edge while they will form an angle of 45 degrees with the cube edge on the (001) plane. Thus visible sliplines will only be produced on the (001) face. Etching, however, takes place not only along the visible trace on (001) but also along the trace with (010). Figure 2 gives an example of slip traces of both types.

As can be seen, dislocations in boundaries etch somewhat more easily than dislocations produced by slip. This will be evident from the argument given above about the effect of annealing (formation of Cottrell atmosphere). The experiments under (2) prove further that the etching of slip lines does not depend upon the presence of a step, as might be thought if only visible slip lines would etch.

(c) *Polygonization*

Specimens were bent under water and then annealed during various intervals of time and at different temperatures. In a typical case the specimens were found to be polygonized after 6 hours at 650°C. The polygonization of rock salt was already studied earlier by Konobejevsky and Mirer [10], by means of ordinary Laue photographs.

Our specimens were prisms bent about the [010] axis. When cleaved along the (100) or (001) face, polygonal cleavage faces were produced. On these faces the polygonization could be seen directly by means of the observation method of Françon, which is very sensitive to orientation differences. The polygon domains are seen as narrow, differently coloured, strips [11].

The side face, i.e., the (010) face, was etched. Photograph 5 gives an example of the etch patterns obtained. It is evident that the dislocation walls have two orientations. They are situated in planes (101) or $(\bar{1}01)$; some of the walls contain parts belonging to two of the planes.

Conclusions

From the observations it is now clear that not only chemical attack takes place most easily at dislocations [12], but also simple dissolution. It is further proved that both screw and edge dislocation are etched.

The observations illustrate in a striking way the theory concerning the dislocation structure of small-angle grain boundaries, as formulated by Burgers [13] and Read and Shockley [4]. It even proved possible to see directly such fine details as the succession of two different types of dislocations.

The etching at dislocations produced by slip seems now to be proved unambiguously. A detailed

analysis of the geometry of dislocations produced by slip has not yet been made, but the described method seems promising. The procedure of cleavage for producing fresh surfaces has a marked advantage over electrolytic polishing as no complication due to surface layers of foreign substances are to be feared.

Acknowledgments

This work is part of a research scheme supported by I.R.S.I.A. (C.E.S.). I wish to thank Professor Dr. W. Dekeyser for his continued interest in this work.

References

1. LACOMBE, P. Report of a conference on the Strength of Solids, University of Bristol (London, Physical Society).
2. FRANÇON, M. Revue d'optique **31** (1952) 65.
3. VOGEL, F. L., PFANN, W. G., COREY, H. E., and THOMAS, E. E. Phys. Rev. **90** (1953) 489.
4. READ, W. T. and SHOCKLEY, W. Phys. Rev. **78** (1950) 275.
5. COTTRELL, A. H. Dislocations and Plastic Flow in Crystals (Oxford University Press, 1953).
6. MOTT, N. F. Phil. Mag. **43** (1952) 1151.
   See also HEDGES, J. M. and MITCHELL, J. W. Phil. Mag. **44** (1953) 223.
7. AMELINCKX, S. Phil. Mag. **44** (1953) 1048.
8. JACQUET, D. A. Comptes Rendus **237** (1953) 1248.
9. ABDOU, A. H. Phil. Mag. **45** (1954) 105.
10. KONOBEJEVSKY, S. and MIRER, I. Z. Krist. **81** (1932) 69.
11. AMELINCKX, S. Nature. In press.
12. GEVERS, R., AMELINCKX, S., and DEKEYSER, W. Naturwiss. **19** (1952) 448.
    GEVERS, R. J. Chem. Phys. **50** (1953) 321. *See also* HORN, F. H. Phil. Mag. **43** (1952) 1210.
13. BURGERS, J. M. Proc. Kon. Ned. Akad. Wet. **42** (1939) 293.

STRAIN HARDENING IN FACE-CENTRED CUBIC METAL CRYSTALS*

J. SAWKILL† and R. W. K. HONEYCOMBE‡

Gold single crystals have been deformed in a shear apparatus of the type developed by Röhm and Kochendörfer. Metallographic examination revealed that the deformation mainly did not occur by slip on the octahedral system oriented for shear, but rather on the system which would operate during tensile deformation. Bending occurred in the vicinity of the grips.

A comparison has been made of the tensile deformation of aluminium and gold crystals. In both cases, deformation bands of two types were observed, but the size of these inhomogeneities and the disorientations resulting from them were much smaller in the gold crystals. The shapes of the stress-strain curves, and in particular, the occurrence of easy glide were very dependent on orientation in both metals. The possible effect of deformation bands on the duration of easy glide, and on strain-hardening is discussed.

LE DURCISSEMENT PAR DÉFORMATION DES CRISTAUX DE MÉTAUX CUBIQUES À FACES CENTRÉES

On a soumis de monocristaux d'or à une déformation dans un appareil de cisaillement du type concu par Röhm et Kochendörfer. Un examen métallographique a permis de constater que la déformation se produisait avant tout sur les plans qui auraient opéré pendant une déformation par traction et non pas sur le système octaèdrique qui était orienté pour le cisaillement. Il y avait de la flexion au voisinage des mordaches. On a comparé la déformation par traction des cristaux d'or à celle des cristaux d'aluminium. Dans les deux cas on a constaté la présence de bandes de déformation de deux types, mais l'étendue de ces hétérogénéités et des désorientations qui en résultaient était beaucoup plus faible dans les cristaux d'or. La forme des courbes tension-déformation et en particulier l'apparition du glissement facile dépendaient beaucoup, dans les deux cas, de l'orientation. L'effet possible des bandes de déformation sur la durée du glissement facile et sur le durcissement par déformation est discuté.

SPANNUNGSBEDINGTE VERFESTIGUNG IN KUBISCH-FLÄCHENZENTRIERTEN METALLKRISTALLEN

In einer der von Röhm und Kochendörfer ähnlichen Scherungsapparatur wurden Goldeinkristalle verformt. Die metallographische Untersuchung zeigte, dass die Verformung im wesentlichen nicht durch Gleitung auf den für Scherung günstig orientierten Oktaederebenen erfolgt, sondern auf dem Gleitsystem das bei Zugverformung wirksam sein würde. In der Nähe der Klammern treten Biegungserscheinungen auf.

Die Zugverformung von Aluminium- und Goldkristallen wird verglichen; in beiden Fällen wurden zwei Arten von Deformationsbändern beobachtet; das Ausmass dieser Inhomogenitäten und die auftretenden Fehlordnungen waren jedoch in den Goldkristallen viel geringer. Die Form der Dehnungskurve und vor allem das Auftreten der "leichten Gleitung" hing in beiden Metallen stark von der Orientierung ab. Der Einfluss, den die Deformationsbänder möglicherweise auf die Dauer der "leichten Gleitung" und auf die spannungsbedingte Verfestigung haben, wird diskutiert.

I. Introduction

In recent years metallographic investigations [1; 2; 3; 4] have shown that inhomogeneities play an important part in the deformation of pure aluminium. These inhomogeneities, which can be broadly classified as deformation bands, are regions of the crystal which differ in orientation from the mother crystal, the difference increasing with the amount of deformation. Two types of deformation band have been distinguished by Honeycombe [4]. On one hand there are kink bands, the nature of which has been studied by several workers. These are essentially narrow bands initially normal to the slip plane and to the slip direction and which involve a double curvature of the lattice within their confines. Kink bands separate blocks of the crystal differing in orientation from each other which are relatively free from macroscopic distortion, and which occupy a much larger volume than the bands. It has been shown that kink bands, when present, contribute largely to the X-ray asterism streaks whereas the undistorted blocks give rise to the intensity maxima often imposed on these streaks.

The other type of deformation band known to occur in deformed aluminium is the band of secondary slip [4; 5]. These are lamellar regions initially approximately parallel to the operative slip plane in which primary slip is very weakly developed or absent. After heavier deformations these regions are revealed as preferred sites for slip on a secondary plane, or frequently step-like slip alternately on the primary and secondary planes. These bands, too, result in disorientations which will give rise to intensity maxima in X-ray asterisms, but they do not in the early stages involve lattice bending.

*Received April 14, 1954.

†Formerly postgraduate student, Department of Metallurgy, University of Sheffield, now at P.C.S. Laboratory, Cambridge, England.

‡Senior Lecturer in Physical Metallurgy, University of Sheffield, England.

It has been suggested [4; 20] that deformation bands are one of the causes of strain-hardening in cubic metal crystals in so far as they act as barriers to the passage of the primary slip processes, but this view is now far from being widely accepted. This hypothesis would receive strong support if it were found that cubic metal crystals deformed so as to avoid the formation of deformation bands showed a much smaller degree of strain-hardening. During the last twenty years a number of attempts have been made to deform metal crystals by pure shear without the occurrence of inhomogeneities or asterisms. Some success has attended experiments on hexagonal metal crystals [6] which in any case show much lower rates of strain-hardening than cubic metal crystals. However, similar experiments with cubic metals have been without avail until recently Röhm and Kochendörfer [7] claimed to have deformed aluminium crystals by pure shear along the slip plane in a slip direction; the deformation appeared to be accompanied by much less strain-hardening than in a normal tensile test. Furthermore, asterisms were absent and the crystals recovered completely on annealing. This work has been criticised by Read [8] on the grounds that the method of testing used was incapable of giving a pure shear. It thus seemed that further experimental work was needed to settle this question.

A survey of the recent literature on the deformation of metals reveals that investigations on aluminium greatly preponderate. While the reasons for this are not far to seek, there exists a real danger that the ease of study of deformation phenomena in this metal will lead to generalisations which may later be found to be invalid. For this reason the present work on shearing of crystals was done primarily with gold single crystals. The second part of the paper is a comparison of the behaviour of gold and aluminium crystals of similar orientations when deformed in tension at room temperature.

II. Preparation of Crystals

Single crystals of gold of square cross section (approximately 3 mm × 3 mm × 80 mm) and purity 99.995 per cent, were grown from the melt in a split graphite mould. A variation of the Bridgman technique was used for growing the crystals. The mould sat vertically in an evacuated Mullite tube, which was surrounded by a furnace wound to produce a marked temperature gradient. Instead of moving the mould through the furnace all parts were stationary, and once the gold was molten the temperature was lowered by reducing the current in the furnace windings by means of a motor-controlled variac. A light aqua-regia etch determined whether the crystals were single or not. The single crystals were electropolished in the manner described by Kushner [9] and the orientations were determined by the back-reflection Laue method.

Single crystals of aluminium (99.99 per cent) were prepared by a variation of the strain-anneal method with dimensions 3 mm × 3 mm × 300 mm lengths of 7.5 cm were cut from these crystals and were electropolished.

III. The Shear Experiments

(a) *Previous Work*

Bausch [10] attempted to deform metal crystals by simple shear along the slip plane in the slip direction by gripping short, carefully oriented specimens, and by moving the grips relative to each other so as to exert a shearing stress. Bausch, and also Burgers and Lebbink [11] who repeated the experiments with aluminium, found that the deformation was accompanied by X-ray asterisms, indicating that it was not homogeneous. More recently Röhm and Kochendörfer [7] confirmed these results but found that no asterisms occurred in the X-ray patterns when the length of the specimen was markedly increased. Figure 1 shows

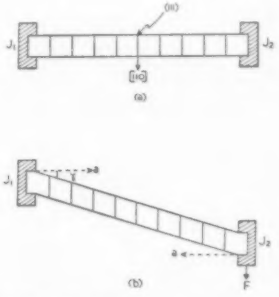

FIGURE 1. (*a*) Before deformation. (*b*) After deformation.

schematically the type of test they carried out. Figure 1*a* shows the specimen prior to deformation with an octahedral plane normal to the longitudinal axis of the specimen and a [110] direction in that plane parallel to the subsequent direction of shear. On moving the grips parallel to each other in opposite directions it was claimed that the result shown in Figure 1*b* was obtained, namely, a simple shearing of the crystal. Measurement of the force F and the angle γ enabled a shear stress-

strain curve to be calculated. Plotting their results in this way, Röhm and Kochendörfer found a linear hardening curve very similar to that obtained for hexagonal metals. Furthermore, asterism was absent below about 25 per cent slip. Below this strain no slip lines were visible to the naked eye, but this is hardly surprising as the state of the surface was unsuitable for careful observations.

Read [8] has criticised this method of deformation on the grounds that the stress distribution is highly complicated and is unlikely to lead to pure shear over the whole length of the crystal. He concluded that deformation was due to both slip on the slip plane, and to rotation of the lattice due to plastic bending at the ends, combined with an axial elongation required to prevent motion of the ends towards each other. Read also suggested that the rotation at the ends might explain the lack of slip and asterism in the middle of the crystal, for in these regions the strain may actually have been small. To overcome these difficulties Read pointed out that if the ends were allowed to move freely then the axial force would become very small. Measurement of the rotation of the central part of the crystal in these circumstances should lead to the evaluation of the contribution of the two components of the deformation referred to above. More recently Kanzaki [22] has examined experimentally the stress-strain relationships of this mode of deformation in copper crystals, and has also concluded that much of the deformation is due to bending.

(b) *Present Work*

A number of gold single crystals were grown but none had an octahedral plane normal to the longitudinal axis. Figure 2 shows the orientations of

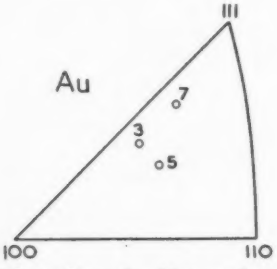

FIGURE 2. Orientations of gold crystals used in the shear experiments.

three crystals, Au 3, 5, and 7, which by a simple rotation resulted in an octahedral plane in the position shown in Figure 3a. A further rotation brought a [110] direction parallel to the intended direction of shear. The crystals were fixed in the required position by mounting the ends in steel cups using Woods metal. Finally the mounted crystal was placed in the shear apparatus, which will not be described in detail as it follows the same principle as that used by Röhm and Kochendörfer except that one grip could slide towards the other during deformation if desired. Figure 4 shows the shearing jig with a crystal in position. It was constructed so that it could be used in a Hounsfield

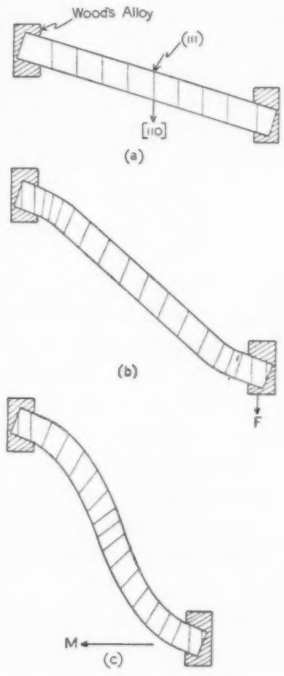

FIGURE 3. (*a*) Gold crystal before deformation. (*b*) After deformation. (*c*) After deformation allowing motion in direction M.

tensometer whereby a tensile stress imposed by the machine resulted in the displacement of one grip relative to the other such that the perpendicular distance between them remained the same. At several stages during the deformation, the electropolished crystal was examined microscopically and by X-ray diffraction. Some photographs were taken with the X-ray beam parallel to the direction of application of the load. The main observations were:

1. Slip lines were observed microscopically at very small deformations.

2. From the beginning of deformation two slip systems operated.

3. Plastic bending was observed near the ends, with consequent rotation of the lattice between (Figure 3*b*). The bending was limited to a few millimetres near the grips.

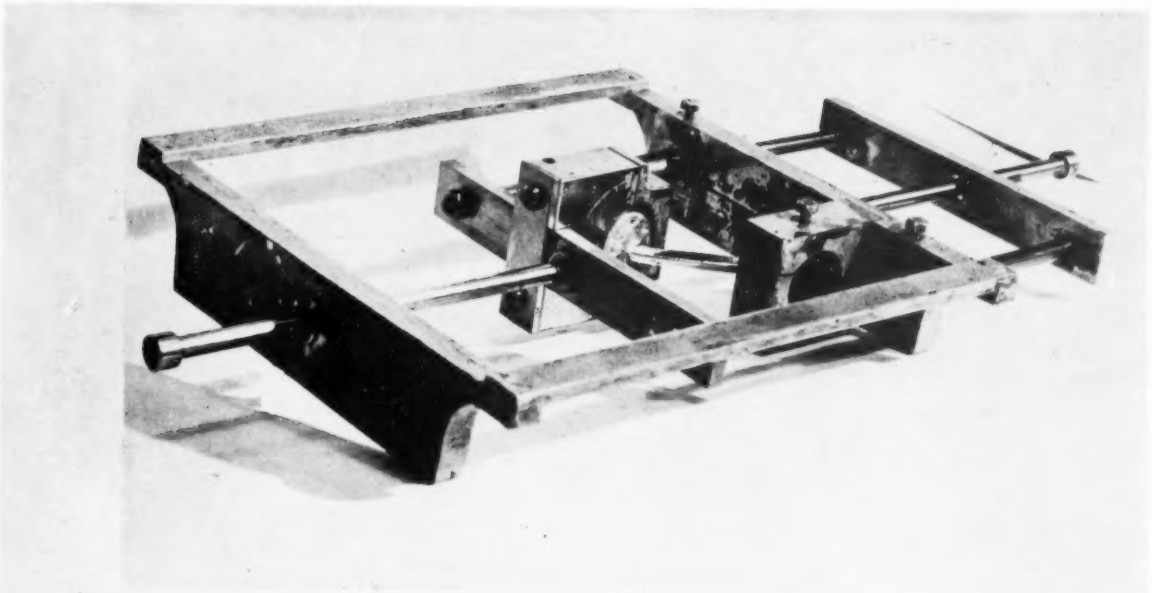

4

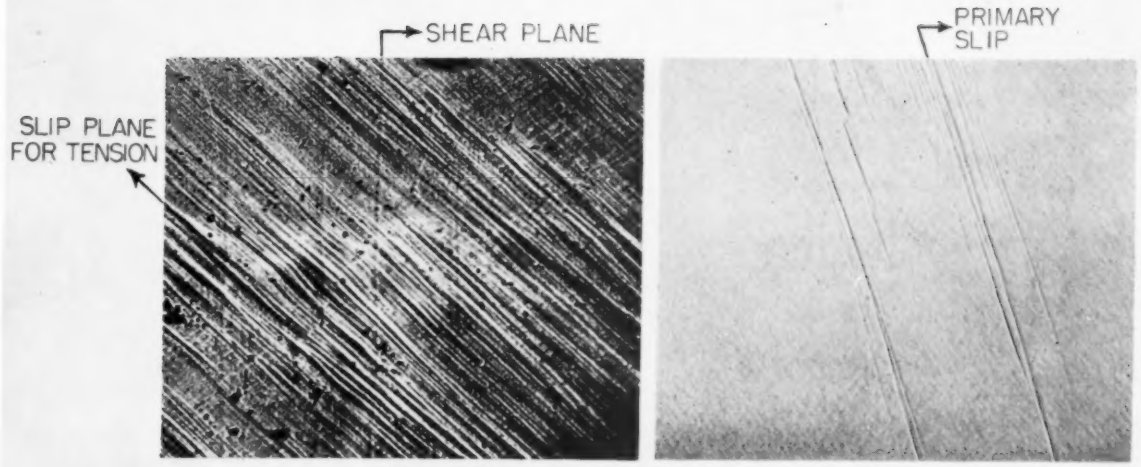

5 8

PLATE I. Figure 4—The shear apparatus. Figure 5—Crystal Au 3 after fairly large "shear." 140X. Figure 8—Micro-slip in a crystal near [100]. 100X.

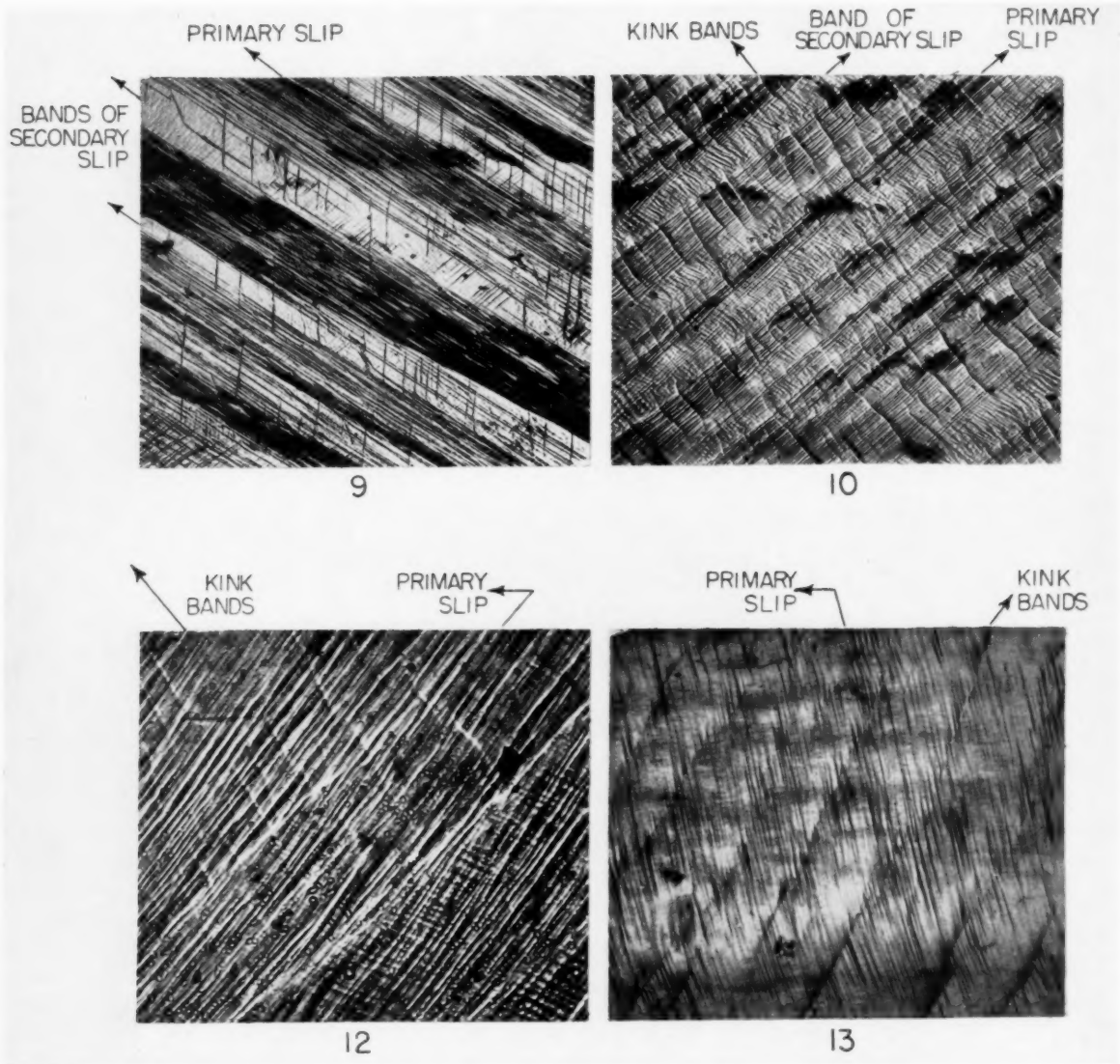

PLATE II. Figure 9—Crystal Al 1; 10 per cent tensile strain. 66X. Figure 10—Crystal Al 2; 11.3 per cent tensile strain. 66X. Figure 12—Crystal Au 13; 24 per cent tensile strain at room temperature. 330X. Figure 13—Crystal Au 12; 33 per cent tensile strain at 575°C. 130X.

4. No kink bands were observed microscopically.

5. There was no measurable asterism over the unbent part of the crystal, but some was observed near the grips.

The observed slip traces were plotted on a stereographic projection and it was found that one of these was the shear plane for which the crystal was oriented (Figure 3*a*). The other system taking part in the deformation was that which had the highest shear stress for a load along the crystal axis; that is, it was the system which would normally operate first in a tensile test. Microscopic observations indicated that the majority of the slip occurred on this system. For example, Figure 5 is a photomicrograph of the middle of crystal Au 3 after fairly heavy apparent shear. The traces of the shear plane for which the crystal was oriented are very few whereas the tension slip system is markedly developed. The rotation of the lattice relative to the original position in the middle of the crystals became substantial as the deformation proceeded and in the case of Au 7 amounted to 40 degrees at the end of the experiment, the duration of which was determined by the magnitude of the axial load, for the crystals in all cases eventually pulled out of the Wood's metal grips.

In order to make a comparison with Röhm and Kochendörfer's results, the shear stress-strain curve for crystal Au 7 was plotted assuming that deformation had occurred by pure shear. Figure 6

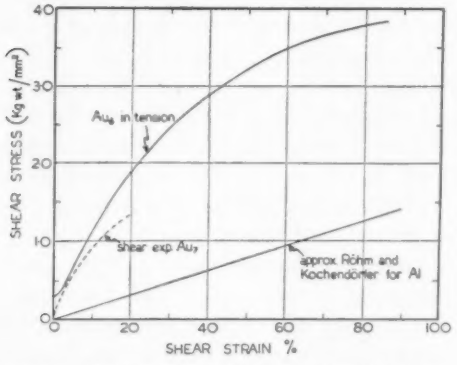

FIGURE 6. Shear stress-strain curves for Au 6 in tension, Au 7 in shear compared with the results of Röhm and Kochendörfer.

shows that the resulting curve lies much higher than that obtained by Röhm and Kochendörfer for aluminium crystals, but it does not show such strong apparent strain-hardening as crystal Au 6, which was deformed in tension. The metallographic results, however, show that the plotting of a shear stress-strain curve for this type of test is not justified, and no definite conclusions can be drawn from its shape.

Finally, following Read's suggestion, free lateral movement of the grips was allowed in the direction *M* (Figure 3*c*) with the result that the bending previously localised near the grips now extended over most of the length of the specimen. In these circumstances an analysis of the type suggested by Read was clearly impossible.

IV. The Tension Experiments

Lücke and Lange [12] have shown that the shape of the stress-strain curves of high-purity aluminium crystals is markedly dependent on the orientation of the crystals relative to the tension axis. Crystals with orientations away from the boundaries of the stereographic triangle show a region between 0 and 5 per cent extension where the rate of hardening is small; this is the so-called easy-glide range which may persist up to strains of 20 per cent in silver and gold crystals [18]. The curves subsequently showed more rapid work-hardening. In three crystals, this rapid hardening occurred from the beginning of the deformation. Two of these crystals had orientations near [100] and then rapid hardening was ascribed to the multiple slip which occurs from the beginning of the deformation for these orientations. The third crystal had an orientation on the [111]–[110] boundary such that for a tensile stress, the resolved shear stress was equal for two [110] directions in the same octahedral plane. Current dislocation theories [9; 10] of strain-hardening do not explain why this orientation should give a high strain-hardening curve.

From Lücke and Lange's detailed investigation it thus emerges there are three orientations which would bear further detailed study:

(*a*) The symmetrical orientations in which two or more separate slip planes operate from the beginning of deformation. The cube orientation is a good example as no less than four different planes can take part in the deformation.

(*b*) The symmetrical orientations in which slip can take place in two different directions on the same slip planes.

(*c*) The "typical" orientations towards the centre of the stereographic triangle. Crystals in this region show easy glide.

An understanding of the behaviour of these three different types of crystal should throw light on the problem of strain hardening. To this end, aluminium crystals (99.99 per cent purity) of these

orientations were prepared, and were examined microscopically and by X-rays in some detail during tensile deformation. At the same time, for reasons already mentioned, it was deemed advisable to do a similar set of experiments with gold crystals. A number of these were grown, amongst which were three in the categories *a*, *b* and *c* above, and thus a direct comparison could be made of the behaviour of aluminium and gold of high purity.

1. *Aluminium*

The orientations of the aluminium crystals referred to are given in Figure 7. Crystal Al 1, as

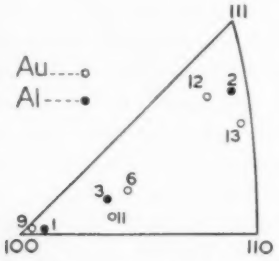

FIGURE 7. Orientations of gold and aluminium crystals pulled in tension.

might be expected from its proximity to [100], did not deform uniformly. The primary slip plane was different in two major parts of the crystal, and altogether four different slip planes were observed. A typical region is illustrated in Figure 9 after 10 per cent strain. A general characteristic of this type of crystal is that the operative slip systems are not uniformly distributed. The primary slip bands occurred in packets with large regions between them which were deficient in primary slip and were preferred regions for slip on the other almost equally favoured planes. Small amounts of slip on these alternative planes minimised the passage of primary slip in these regions, but there was no evidence that the slip on these planes occurred prior to the primary slip. Rather the primary slip occurred initially in isolated bands which subsequently spread laterally by addition of other bands. During this process, the secondary slip occurred in the empty regions, i.e., in the region where slip on the alternative planes can occur without interruption.

In the earliest stages of the deformation, these symmetrically oriented crystals show a peculiar rumpling (Figure 8) which covers the *entire* surface of the crystal and appears unrelated to the subsequent slip. It is now clear that this phenomenon is directly connected with the deformation and is in fact a manifestation of what Brown and Honeycombe [13] have called "*micro-slip*," while Kuhlmann-Wilsdorf and Wilsdorf [14] have used the term "*elementary structure*" to describe the same phenomenon. In the case of nonsymmetrically oriented crystals, micro-slip occurs as very closely spaced lines involving displacements of 150 Å or less; these are parallel to the subsequently formed coarse slip which is a familiar manifestation of plastic deformation. However, in symmetrically oriented crystals, the micro-slip does not occur exclusively on one set of planes, but wanders on a very fine scale from one to another because more than one plane is in a favoured orientation. This results in a microscopic rumpling in which crystallographic directions are very difficult to discern.

As has been previously reported, no kink bands were observed in crystals with orientations of type *a* above. The dominant microscopic feature is the marked inhomogeneity of the slip which results in almost macroscopic bands of secondary slip, which develop from the early stages of the deformation, becoming progressively disoriented from adjoining regions of the crystal as deformation proceeds. Crystal Al 2 was close to the [111]–[110] boundary; however, Figure 10 shows a photomicrograph of this crystal after about 11 per cent extension in tension. The expected primary system has operated but there are pronounced bands of secondary slip. In addition, kink bands have occured and are clearly visible in the photograph, in contrast to the behaviour of Al 1. It was difficult to associate the structures in the bands of secondary slip with any given slip system.

Crystal Al 3 behaved in what, for convenience, has been referred to as a typical way. Slip occurred primarily on a single slip system and kink bands developed in the usual way. Bands of secondary slip were far less pronounced, which is to be expected because the crystal orientation is well away from the boundaries of the stereographic triangle.

Stress-strain curves were plotted for the three crystals (Figure 11). For the purposes of comparison with Lücke and Lange's results the curves were plotted on a shear stress-shear strain basis; they coincided almost exactly with those of Lücke and Lange. Al 3 showed a small region of easy glide whereas Al 1 hardened rapidly from the beginning, however, Al 2 hardened most rapidly of the three. The only difference between Al 2 and Al 3 which could be observed in the microstructure was that in the former there were marked bands of secondary slip.

2. *Gold*

In all, five crystals were examined during tensile deformation. Crystals Au 6, 9, and 13 were deformed at room temperature and stress-strain curves obtained. Crystals Au 11 and Au 12 were deformed at 275°C and 575°C respectively but in these two cases, stress-strain curves were not obtained. All crystals were subjected to X-ray and metallographic examinations. The orientations of the crystals are plotted in Figure 7.

Crystal Au 9 had an orientation similar to that of Al 1, and multiple slip could be expected at a very early stage of the deformation. As in the case of the aluminium crystal, the primary slip plane differed in different parts of the crystal. The primary slip was again in bunches separated by pronounced bands of secondary slip, in which there was little evidence of individual slip bands. At the later stages of the deformation, three slip planes other than the primary one were detected. No kink bands were observed at any stage of the deformation, and after 30 per cent tensile strain, the asterism in X-ray back reflection Laue photographs was only about 2 degrees. The asterism did not appear to correspond to bending about the usual [211] axis of rotation.

Crystal Au 13 can be compared with Al 2 as the orientations are very similar, being close to the [111]–[110] boundary. The microstructure (Figure 12) had a general similarity to that of the corresponding aluminium crystal (Figure 10), although the slip was on a finer scale and was somewhat masked by the early appearance of microslip. Bands of secondary slip were present although they were not as pronounced as in Al 2. Striations were visible within the bands although again they could not be related to any octahedral plane. Kink bands were observed although they were very fine and closely spaced (0.02 mm apart), and the rotations associated with them small; this is supported by the X-ray Laue patterns which after 33 per cent extension only revealed asterisms with a spread of 1½degrees. So far as could be determined, the axis of rotation was the classical [211].

Crystal Au 6 corresponded closely with Al 3, both having orientations towards the centre of the stereographic triangle. The crystal deformed by slip on a single system but no kink bands could be detected optically at any stage of the deformation. X-ray Laue patterns were taken at different points along the specimen and in general no marked asterisms were observed. This suggested that either the kink bands were absent or the disorientations associated with them were very small. Bearing in mind that the spacing of these bands is dependent on the temperature of deformation, some qualitative experiments were carried out at elevated temperatures on crystals with similar orientations to Au 6. Au 11 was deformed at 275°C but again no kink bands could be observed; however, when Au 12 was deformed at 575°C, kink bands were observed microscopically (Figure 13). It was confirmed that they occurred initially on a (110) plane perpendicular to the active slip direction. At a tensile strain of 30 per cent the asterism spread was 5 degrees and the axis of rotation was [211] normal to the slip direction which adequately describes the rotation in a kink band. The band spacing at this temperature was about 0.1 mm.

The stress-strain curves for Au 6, 9, and 13 were converted to shear-stress/shear-strain curves (Figure 11). It is interesting to compare their behaviour

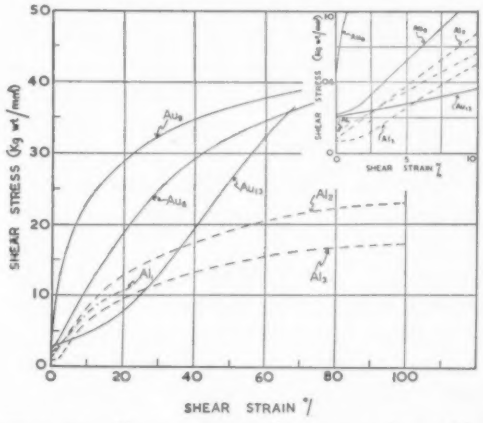

FIGURE 11. Shear stress-strain curves for gold and aluminium crystals deformed in tension.

with those of the aluminium crystals of similar orientation, bearing in mind the fact that the two metals were deformed at very different temperatures relative to their melting points. Au 9 and Al 1 had similar types of hardening curve—rapid initially, but gradually falling off—whereas Au 6 and Al 3 showed initially a region of easy glide followed by more rapid strain-hardening. However Au 13 gave a very different stress strain curve to Al 2, although the orientations were quite similar. Au 13 had a prolonged region of easy glide covering about 15 per cent glide strain, while Al 2 showed the most rapid hardening of the three chosen orientations.

V. Discussion

The shear experiments have shown that with gold crystals, pure shear was in no case obtained.

The work of Röhm and Kochendörfer is not entirely convincing because no microscopic examination of their crystals was made to determine whether slip had occurred exclusively on the one suitably oriented system. In the present experiments such observations have been made and it was clear that slip did not occur solely on the octahedral system oriented for shear; in fact, most of the deformation appeared to take place on the octahedral plane along which the resolved shear stress was greatest for a tensile stress along the crystal axis. The observations clearly support Read's interpretation of this type of deformation, namely, that it is a combination of plastic bending in the vicinity of the grips and of tensile deformation along the greater part of the specimen. In the experiments with gold the initial position of the long axis of the crystal was in no case horizontal; this may account for observed differences in the shape of the shear stress-strain curve (Figure 6).

Röhm and Kochendörfer observed little asterism in their crystals after deformation, and it had thus been assumed that the deformation was particularly homogeneous. It would be surprising if asterisms were absent in X-ray photographs taken in the vicinity of the grips; the present experiments have clearly shown bending in these regions. The small amount of asterism in the middle of the crystals could arise from two causes. Firstly, the actual deformation there might be quite small, particularly if much bending had occurred in the vicinity of the grips. Secondly, as we have shown, at least two slip systems take part in the deformation of the central part of the crystals even in the early stages; crystals where this occurs during simple tension do not develop kink bands and, as a consequence, the asterisms are usually not severe. So it is reasonable to assume that kink bands were absent in their shear experiments, but this does not imply that the deformation necessarily took place by pure shear.

In the present experiments on gold, little asterism was detected in the central portion of the "sheared" crystals even after large strains, but this was also true for the gold crystals deformed in tension. So to associate absence of asterism with homogeneity of deformation is a dangerous simplification. In tensile deformation of aluminium, it has been established that the asterism streaks arise principally from kink bands [15]. Clearly, then, the extent of the asterism depends primarily on the extent of the disorientations within the bands and to a lesser extent on the number of bands impinged on by the X-ray beam. Earlier work on aluminium [4] and the present work on gold have shown that for a given deformation several factors influence the extent of the disorientations within kink bands. These are

(*a*) *The temperature of deformation.* The higher this is, the larger the disorientations in the individual bands, and the larger the spacing between the bands,

(*b*) *The orientation of the crystal.* In extreme cases, such as crystals of symmetrical orientation, the bands are absent, but in between extremes the spacing varies with the orientation as do the individual disorientations,

(*c*) *The purity and nature of the metal.* In general, impurities tend to reduce the size of kink bands and also their spacing. Different metals do not behave identically.

The comparative tensile experiments on aluminium and gold have shown that the behaviour of aluminium is not unique and that similar phenomena occur in gold. In the tensile experiments on gold at room temperature, kink bands were detected in only one crystal, and then they were much finer than those observed in similar aluminium crystals. This observation is in keeping with the temperature dependence of the size of kink bands. Aluminium crystals deformed further from the melting point, e.g., in liquid air, develop kink bands but these are usually so fine that they are not detected microscopically until after relatively heavy deformations. The gold crystal deformed at 575°C confirmed this trend by developing bands much coarser than those produced during deformation at room temperature. Again the asterism observed was greater (5 degrees) and the spacing of the bands was 0.1 mm compared with 0.02 mm at room temperature.

The same general influence of orientation holds with gold and aluminium. Crystals of both metals, with orientations close to the boundaries of the stereographic triangle, show marked formation of bands of secondary slip. The stress-strain curves of aluminium and gold crystals with orientations near the centre of the stereographic triangle both show easy glide while the orientations near [100] strain harden rapidly from the beginning of the deformation.

An anomaly exists in the case of crystals with orientations near the [111]–[110] boundary. Both show kink bands and bands of secondary slip, but

whereas the aluminium initially hardens rapidly, the gold shows an initial pronounced region of small hardening. The stress-strain curve for Al 2 is very similar to that for a crystal used by Lücke and Lange; both crystals had an orientation on the [111]–[110] boundary. Here the two preferred slip systems involve different slip directions in the *same* plane. Microscopically, one cannot easily differentiate between these two systems for they produce the same primary slip traces. Measurement of the lattice rotation with respect to the stress axis indicates that crystal Al 2 slips primarily on one system, but it is likely that there will be interference from the other system. These results on aluminium may be of importance in view of the fact that recent work by Edwards, Washburn, and Parker [21] shows that zinc crystals harden more when the orientation is such that the resolved shear stresses are the same for two slip directions in one plane. The gold crystal Au 13 near the [111]–[110] boundary behaved entirely differently although it appeared to exhibit the same microscopical phenomena. Clearly, there is a need for further investigation of orientations near this boundary, for these results as they stand cannot be satisfactorily explained. The exact significance of shear stress-strain curves in such circumstances is also in doubt.

In the early stages of plastic deformation, the influence of orientation on hardening is already evident. At strains less than 1 per cent the familiar coarse slip is an infrequent occurrence, but the crystal surfaces are already uniformly covered with micro-slip, the spacing of which is such (less than 150 Å) that interaction between dislocations on adjacent slip planes becomes a feasible mechanism of hardening. In symmetrically oriented crystals the micro-slip is not confined to one slip system, but forms a network over the whole crystal. It is suggested that this multiple micro-slip is largely responsible for the initial marked increase in strain-hardening in these crystals. With other orientations, the initial hardening due to micro-slip on one system is followed by a region of easy glide during which the coarse slip develops.

Cottrell [17] has suggested that the easy glide range in cubic metal crystals is equivalent to the usual stress-strain curves of hexagonal crystals, and represents a region of laminar flow with low hardening. In this view the end of easy glide represents the onset of turbulent slip characterised by the development of kink bands and associated secondary slip.* Andrade and Henderson [18] have shown that the range of easy glide in silver and gold crystals increases with decreasing temperature. Furthermore, it also depends on the crystal orientation. These factors have also been referred to as significant variables in the development of kink bands. The present authors take the view that the length of the easy glide range is dependent on the extent of the disorientations developing in the individual kink bands, because they are a measure of the effectiveness of the bands as barriers to the passage of dislocations. At low temperatures the disorientations are smaller and the easy glide range is longer. The above experiments have shown that in gold the individual kink bands involve smaller disorientations for a given strain and so are less effective barriers than those in aluminium. There should thus be a correlation between the extent of easy glide and the disorientations as shown by X-ray diffraction, Andrade and Henderson's results confirm this.

The hypothesis implies that kink bands have a hardening influence; however, a recent theoretical study by Mott [16] indicates that piled up dislocations in a deformation band cannot contribute substantially to the hardening as no long-range stress field exists. Furthermore symmetrically oriented crystals harden very rapidly from the beginning of the deformation without the formation of kink bands. However, it is well known that slip bands do stop abruptly in kink bands, particularly in the later stages of deformation when they are preferred regions for slip on other systems. Cottrell has put forward the view that the presence of this secondary slip leads to hardening by kink bands as there is full opportunity for sessile dislocations to be produced. It is now suggested that the onset of secondary slip is controlled by the amount of rotation within the kink band, so the resulting hardening will depend on those variables which influence the magnitude of the kink band, viz., temperature of deformation and orientation. As the temperature of deformation is raised, the kink bands become coarser, the disorientations larger, and consequently the secondary slip occurs at an earlier stage. So the easy glide range is restricted and eventually eliminated.

Crystals of symmetrical orientations develop slip

*Unpublished experiments by Honeycombe on aluminium support the view that kink bands are pronounced only after the end of easy glide. The easy glide range increased with decreasing temperature.

on alternative systems at a much earlier stage of the deformation, as shown by the appearance of bands of secondary slip. This could account for their more rapid rate of work-hardening and the absence of easy glide.

Easy glide appears to occur only in metals of high purity and in some solid solutions free from second-phase impurities (e.g. alpha-brass). In these cases, well-defined slip bands are present, and it is possible to observe where large dislocation pile-ups occur; the mean free path of a slip band or group of dislocations is large, i.e., of microscopic dimensions and it is considered that in these circumstances the microscopic inhomogeneities such as kink bands have considerable influence. Andrade and Henderson's observations [18] that surface films on silver markedly influence the extent of easy glide is in keeping with this viewpoint. In less pure metals, and in alloys with fine precipitates, the mean free paths of dislocation groups are often so small that no slip bands are observed microscopically. In these cases the fine dispersions of a second phase limit the movement of the slip packets, and thus must play a significant role in the work hardening.

Acknowledgments

We are much indebted to Mr. R. C. Jewell of the Sheffield Smelting Company for the loan of the high-purity gold. We gratefully acknowledge helpful discussions with Professor A. G. Quarrell, Dr. B. A. Bilby and Dr. G. B. Greenough.

References

1. Laloeuf, A. and Crussard, C. Rev. Met. **48** (1951) 462.
2. Cahn, R. W. J. Inst. Metals **79** (1951) 448.
3. Chen, N. K. and Mathewson, C. H. J. Metals **3** (1951) 653.
4. Honeycombe, R. W. K. J. Inst. Metals **80** (1951) 49.
5. Calnan, E. A. Acta Cryst. **5** (1952) 557.
6. Parker, E. R. and Washburn, J. A.S.M. Seminar on Modern Research Techniques in Physical Metallugry, (1953) p. 186.
7. Röhm, F. and Kochendörfer, A. Z. Metallk. **41** (1950) 265.
8. Read, W. T. Symposium on the Plastic Deformation of Crystalline Solids, Pittsburgh, 1950, p. 111 (discussion).
9. Kushner, J. B. Products Finishing **7** (2) (1942) 42.
10. Bausch, K. Z. f. Physik **93** (1935) 479.
11. Burgers, W. G. and Lebbink, W. J. Trav. Chim. des Pays Bas **64** (1945) 321.
12. Lücke, K. and Lange, H. Metallk. **43** (1952) 55.
13. Brown, A. F. and Honeycombe, R. W. K. Phil. Mag.1 **42** (1951) 1146.
14. Kuhlmann-Wilsdorf, D. and Wilsdorf, H. Acta. Met. **1** (1953) 394.
15. Gay, P. and Honeycombe, R. W. K. Proc. Phys. Soc. **A64** (1951) 844.
16. Mott, N. F. Phil. Mag. **43** (1952) 1151.
17. Cottrell, A. H. Progress in Metal Physics, **4** (1953) 243 *et seq.*
18. Andrade, E. N. Da C. and Henderson, C. Phil. Trans. Roy. Soc. **A244** (1951) 177.
19. Von Göler and Sachs, G. Z. Physik **55** (1929) 581.
20. Mott, N. F. Proc. Phys. Soc. **B64** (1951) 729.
21. Edwards, E. R., Washburn, J. and Parker, E. R. J. Metals **5** (1953) 1525.
22. Kanzaki, Hiroshi. J. Appl. Phys. **24** (1953) 811.

DEFORMATION TEXTURES OF FACE-CENTRED CUBIC METALS*

E. A. CALNAN†

A number of investigations of the deformation of single crystals have shown that the crystals tend to rotate past the orientation where duplex slip would start before the second slip plane begins to function. The effect is very slight in aluminium but marked in α-brass. Starting from these observations the present treatment shows how such differences lead to the different deformation textures of, on the one hand, aluminium and copper, and on the other, α-brass and certain copper base solid solution alloys. The method follows that previously described in a series of papers by Calnan and Clews but gives more detailed consideration to the derivation of sheet rolling textures.

TEXTURES DE DÉFORMATION DE MÉTAUX CUBIQUES À FACES CENTRÉES

Plusieurs investigations de la déformation de monocristaux ont permis de constater que les cristaux tendent à tourner au-delà de l'orientation pour laquelle le glissement double commencerait, avant que le deuxième plan de glissement commence à fonctionner. Dans l'aluminium cet effet est très faible, mais il est plus marqué dans le laiton α. En partant de ces observations, le présent traitement montre comment de telles différences mènent aux différentes textures de déformation, d'une part de l'aluminium et du cuivre, et d'autre part du laiton α et de certains alliages du cuivre sous forme de solution solide. Cette méthode suit celle qui fut décrite antérieurement dans une série d'articles de Calnan et Clews, mais elle considère avec plus de détails la détermination des textures de laminage dans les tôles.

DEFORMATIONSTEXTUREN IN KUBISCH-FLÄCHENZENTRIERTEN METALLEN

Eine Anzahl Untersuchungen der Verformung von Einkristallen haben gezeigt, dass die Kristalle die Tendenz haben, über die Orientierung, bei der Doppelgleitung beginnen würde, hinaus zu rotieren, ehe die zweite Gleitebene aktiv wird. In Aluminium ist der Effekt nur gering, in α-Messing jedoch recht ausgeprägt. Die vorliegende Arbeit geht von diesen Ergebnissen aus und zeigt, wie derartige Unterschiede zu den verschiedenen Deformationstexturen von Aluminium und Kupfer einerseits, von α-Messing und gewissen Kupferlegierungen des festen Lösungstyps andererseits, führen können. Die angewandte Untersuchungsmethode wurde bereits in einer Serie von Arbeiten von Calan und Clews beschrieben; in der vorliegenden Studie wird jedoch mehr auf die Einzelheiten der Ableitung der Walztexturen eingegangen.

Introduction

The deformation textures of face-centred cubic metals have been the subject of many experimental investigations, see for example Barrett [1], and it has been established beyond doubt that while aluminium and copper have very similar textures, certain copper base solid solutions including 70–30 brass have a markedly different texture. The matter has not been resolved in the various treatments which have been proposed for the explanation of textures on the basis of the operative slip mechanisms, Barrett [1], since all these metals slip on the $\{111\}\langle 110\rangle$ system and should accordingly have the same texture. In the light of some recent experimental work, Murphy and Calnan, [2] on the behaviour of α-brass single crystals in tension, the present paper shows how the differences in texture may be explained and in so doing presents a more satisfactory method for the prediction of cubic rolling textures than that described previously by Calnan and Clews [3; 4].

The experimentally determined textures are listed in Table I. The only fully quantitative results are the rolling textures of Hu, Sperry, and Beck [5], who used Geiger-Muller Counter methods for their determinations. These can be described adequately only by reference to the actual pole figures since, for instance, their description of the aluminium rolling texture as a scatter around (7, 12, 22) [84$\bar{5}$] near (123) [1$\bar{2}$1] does not account entirely for all the intensity maxima in the pole figure. However, it is clear from Table I that the two types of textures are those corresponding to copper and 70–30 brass, which are: (i) drawing textures: [111] with an intermediate [100] texture for copper, and [111] alone for brass; (ii) compression and compression rolling textures: [110] with a spread to [311] and [100] for copper, [110] with a spread to [311] and [111] for brass; (iii) rolling textures: a texture near (123) [1$\bar{2}$1] for copper, and (110) [1$\bar{1}$2] for brass.

The treatment for the prediction of deformation textures which is being extended here is based on a knowledge of the deformation modes of the metal, that is to say, the particular crystallographic slip and twinning systems. In view of the generally satisfactory results obtained by this method for body-centred cubic metals, Calnan and Clews [4], Calnan [6], hexagonal metals, Calnan and Clews [7], Williams and Eppelsheimer [8], and ortho-

*Received March 5, 1954.
†National Physical Laboratory, Metallurgy Division, Teddington, England.

TABLE I

EXPERIMENTALLY DETERMINED DEFORMATION TEXTURES IN FACE-CENTRED CUBIC METALS

Deformation	Metal	Texture	Reference
Drawing*	Cu	[111] †	Hibbard [15]
	Au	" †	"
	Ag	" †	"
	Ni	" †	"
	Pb	" †	"
	Al	" †	"
	Cu solid solutions with ≯ 1% Al, 5% Zn, 30% Ni	" + [100] component after 50% reduction which vanishes after 95% reduction	Hibbard[16]
	Cu solid solutions with >2% Al, 8% Zn	[111]	Hibbard [16]
Compression	Cu solid solutions with ≯1% Al, 5% Zn, 30% Ni	[110] with a spread to [100] and [311]	Hibbard and Trout [17]
	Cu solid solutions with >2% Al, 8% Zn	[110] with a spread to [111] and [311] and some concentration at [111]	Hibbard and Trout [17]
"Compression Rolling" (rolling with many passes, each pass in a different direction)	Al	[110] with a spread to [100] and [311]	Barrett and Levenson[18] Barrett [1] p. 447
	Ni	"	
	Cu	"	"
	70–30 brass	[110] with a spread to [111] and [311] and some concentration at [111]	"
Rolling	Al	"Scatter around orientations near (123) [1$\bar{2}$1]," see pole figure.	Hu, Sperry and Beck [5]
	Cu	"	"
	70–30 brass	[110] [1$\bar{1}$2]	"

*The only pure tension experiments are those of Calnan and Williams [19] who found some evidence in aluminium of a texture near [211] rather than [111].

†Earlier workers reported an additional [100] component but these results corresponded to lesser reductions than that used by Hibbard.

rhombic metals, Calnan and Clews [9], it is reasonable to look for the origin of the different face-centred cubic textures in the behaviour of their single crystals. The relevant differences are: (*a*) in aluminium and copper the active and latent slip systems work-harden equally such that when crystal rotation has taken place to give equal resolved shear stresses on two systems these both come into operation, whereas in α-brass considerable inequality has been observed to occur in certain cases, Göler and Sachs [10], Maddin, Mathewson and Hibbard [11], (*b*) the cross-slip (slip on two planes in the common slip direction) observed in α-brass [11, *loc. cit.*] is of a much more pronounced character than that found in aluminium Cahn [12]. The essential features of the recent experimental observations of Murphy and Calnan is that the existence of the unequal hardening referred to in (*a*) above has been demonstrated for a range of orientations in the neighbourhood of the [100] [111] boundary of the unit triangle and that it can be shown how cross-slip is the logical outcome of such an effect. The fundamental cause for this effect could well be that proposed by Ardley and Cottrell [13] who have shown that in α-brass a yield point is obtained when the zinc content exceeds about one per cent and have explained this on the basis of "atmospheres" of zinc atoms locking the dislocations. However, the starting point of the present treatment is the observation of unequal hardening of the slip systems and so the treatment is independent of any atomic scale explanation of the hardening phenomena.

Tension and Compression Textures

The derivation of the tension texture is illustrated for the case of equal hardening on all the slip systems, i.e., for copper, by Figure 3 of the original Calnan and Clews paper [3], Figure 1 of the present paper. The arrows I and II indicate respectively the rotations resulting from single and duplex slip. The relative amounts of the two components are expected to depend upon the path which the effective stress, T_e, follows from the stress axis orientation to a minimum of resolved shear stress. The part of the path which lies wholly within the unit triangle produces single crystal slip and the part along a unit triangle boundary produces duplex slip. For a grain of original applied stress axis u near the [100] [111] boundary the path which T_e is most likely to follow (the line of quickest descent) is almost entirely along the boundary. Therefore duplex slip is the most likely mode and the grain will rotate in the direction II. There is a small possibility of some single-crystal slip—that is to

say, slightly more slip on one of the duplex systems, which results in the general direction of rotation deviating slightly from the pure duplex direction II towards the single-crystal direction I. From such considerations the general trends of rotation shown in Figure 2 are derived.

Consider now the case of α-brass where the

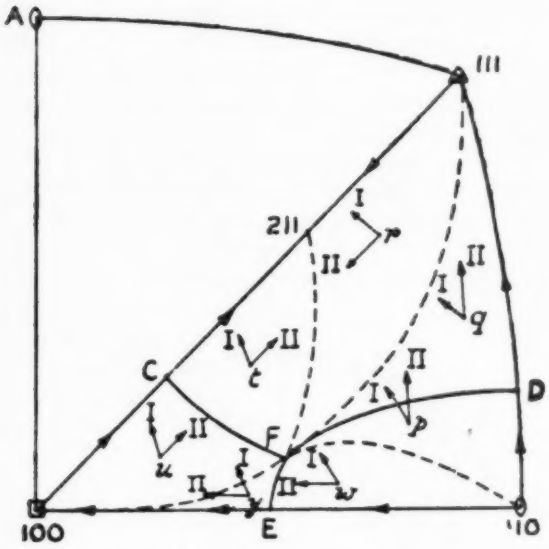

FIGURE 1. Lines of quickest descent from the shear stress peak, F, and directions of rotation due to single crystal slip (→ I) and duplex slip (→ II) in copper under tension.

boundary dividing the areas of primary and conjugate slip is no longer the [100] [111] line but is removed to the position shown in Figure 3, Murphy and Calnan [2]. This increases greatly all the single-crystal path lengths for the movement of the effective stress and correspondingly increases the likelihood of single crystal rotations. The general trends of rotation are thus as shown in Figure 3. The major difference between Figures 2 and 3 is that for the latter, α-brass, there is no longer a tendency for orientations to rotate towards [100] and thence

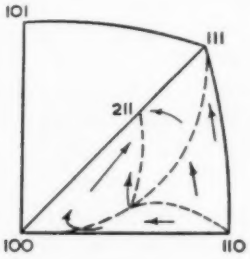

FIGURE 2. General trends of rotation in copper under tension.

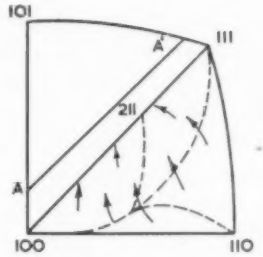

FIGURE 3. General trends of rotation in α-brass under tension. AA' is boundary between primary and conjugate slip.

proceed along the boundary towards [211]; instead they move much more directly towards [211].

There is some complication in the neighbourhood of [111]. Although no direct evidence is available for the nature of the boundary between primary and conjugate slip in this vicinity, it seems highly probable that it may be deduced by extrapolation of the known part. It has been suggested by Kuhlmann-Wilsdorf and Wilsdorf [14] that mixed slip (a common slip plane, two active slip directions) should be more prevalent in brass. It will be seen that the highest probability for this to occur is for orientations along the [110] [111] boundary, the systems being the primary one $(11\bar{1})$ [101] and the system $(1\bar{1}\bar{1})$ [011], Figure 4. The rotations

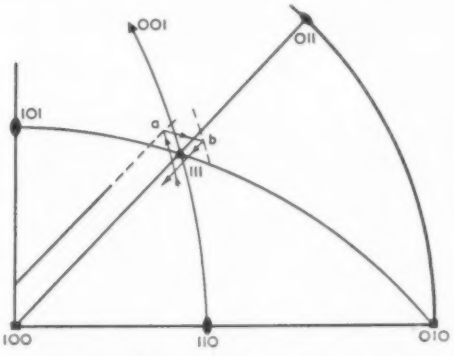

FIGURE 4. Rotations in the vicinity of [111] due to mixed slip in α-brass under tension.

corresponding to these systems are respectively towards [101] and [011], the resultant being along the great circle including [110], [111] and [001]. Figure 4 shows how the stress axis under this rotation moves across the [100] [111] boundary to a point a, thence with mixed slip on the conjugate system, approximately parallel to [101] [111] [010], to b, followed by mixed slip on the $[1\bar{1}\bar{1}]$ plane back towards the original unit triangle. The result of such a complication may well be to cause some persistence of the [111] tension texture in brass.

Thus the pure tension textures for both copper

and brass are ultimately [211] but with the former there should be intermediate [100] and [111] textures while for brass there should be a more persistent [111] intermediate texture.

The compression textures may be deduced in similar fashion. Figures 5 and 6 show the trends of rotation for copper and brass respectively and it will be seen that the former leads to an intermediate [100] texture which is absent in brass. The effect of cross-slip, which is more prevalent in brass, is to make the [111] orientations persist in compression but to a lesser extent than in tension. The experimentally determined drawing and compression rolling textures are not strictly comparable with these pure tension and compression textures and therefore comparison with experiment will be postponed until the predicted drawing and rolling textures have been derived.

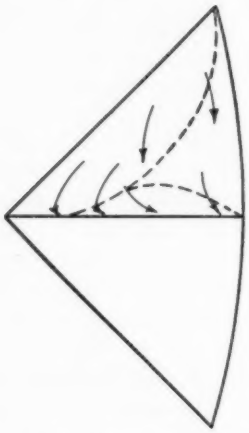

FIGURE 5. General trends of rotation in copper under compression.

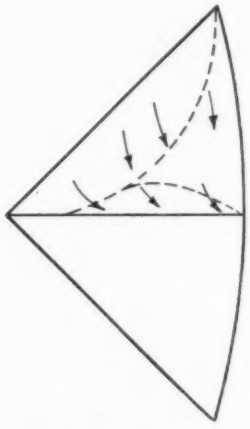

FIGURE 6. General trends of rotation in α-brass under compression.

Drawing Textures

The process of wire-drawing will be simulated in the present treatment by a tensile stress in the direction of drawing together with a circular array of compressive stresses perpendicular to this direction. The compressive stresses correspond to the complex stresses exerted by a circular die on the material being drawn through it. Thus for a grain with tension axis denoted by a certain point in the unit triangle, there are compressive stresses operative at every point on the great circle normal to the tension axis.

Consider the case of copper. The tension rotations lead to [111], [211], and [100] and thus the radial compressive stresses tend to become aligned along one of the great circles C_1, C_2 and C_3, corresponding to these points, Figure 7. The radial stresses will not be equally favourable for initiating slip and the predominating ones will be those nearest the centres of their particular unit triangles. The resulting compression rotations towards the appropriate $\langle 110 \rangle$ directions are shown by the arrows in Figure 7. It will be seen that on C_1 and C_3 the compression rotations are exactly equal and opposite in successive triangles along the great circle and that there is consequently no disturbance of the tension texture. For C_2, however, the compression rotations are not balanced and there will be a general rotation of the great circle towards C_1 so bringing the tension axis to [111].

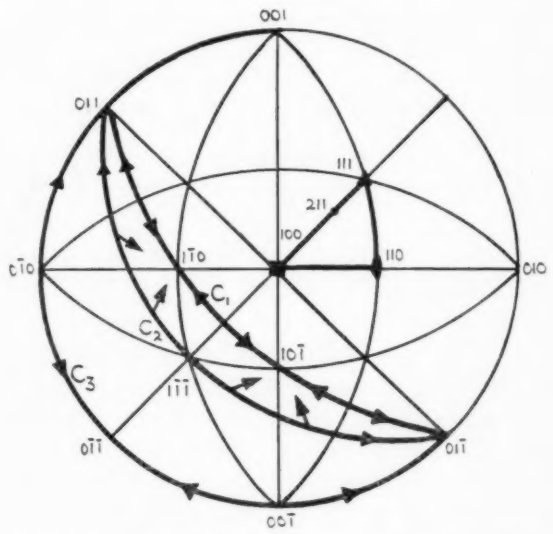

FIGURE 7. Standard stereographic projection illustrating the derivation of the drawing texture in face-centred cubic metals.

Thus a double fibre texture will result having [111] and [100] as fibre axes. After severe deformation the [111] and [100] intermediate tension textures decrease in intensity, leaving a single [211] texture. This will have the effect of finally eliminating the [100] drawing texture and causing some spread to the [111] component. The ultimate texture will thus be an axis between [111] and [211] where the tension rotation towards [211] is balanced by the compression rotations towards [111].

In α-brass the [100] intermediate component of the tension texture is absent, Figure 3, and thus there will be no tendency for the compression stresses to be aligned on the great circle C_3 and hence no intermediate [100] drawing texture. These results are in accord with the experimental observations listed in Table I bearing in mind the fact that the observed textures designated [111] do comprise some spread around this point. It would be useful nevertheless to have some further quantitative measurements on the magnitude of this spread of orientation for comparison with prediction.

Sheet Rolling Textures

As in previous attempts to derive the sheet rolling texture, the process will be simulated by compression parallel to the rolling plane normal and tension in the rolling direction, perpendicular to the rolling plane normal. Thus a grain may have its rolling plane normal (compression axis) represented by a point p in the unit triangle [100] [110] [111], Figure 8, and its rolling direction (tension axis) at a particular point on the great circle p' whose pole is p. The polycrystalline aggregate will therefore be represented by compression axes all over the triangle [100] [110] [111] and tension axes all over the area 90 degrees from this triangle, viz., the areas a, b, c . . . k. The effect of simultaneous tension and compression rotations has now to be considered, that is to say, to a particular compression axis must be applied the appropriate compression rotation compounded with the rotation of this point resulting from the appropriate tension rotation of the tension axis, and *vice versa* for the tension axis orientation.

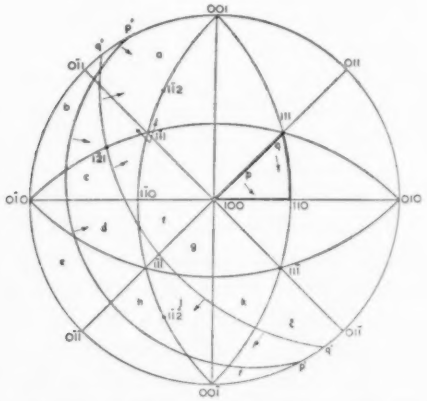

FIGURE 8. Standard stereographic projection illustrating the derivation of the sheet rolling texture of α-brass.

Since the component rotations of compression and tension for copper and brass have been shown above to be different it may be expected that the resulting sheet textures are different. The respects in which they differ must now be demonstrated in detail. Consider first the somewhat simpler case of brass. For compression axes in the unit triangle [100] [110] [111] the variation of compression rotations over the triangle may be reasonably adequately described by the two typical orientations p and q, for which the compression rotations are those shown by the arrows →. The tension axes lying on the corresponding great circles p' and q' are rotated by the compression as shown by similar arrows. The effect of these rotations in the triangles a, b, c, etc., where in each there are also the tension rotations shown in Figure 3, will now be discussed for each of the triangles in turn. In triangle a the tension rotation towards [1$\bar{1}$2] is in general accord with the compression arrows →, and the mutually satisfactory end-point (110) [1$\bar{1}$2] will be reached. In triangle b some orientations adjacent to the boundary with triangle a will move into the latter and join the (110) [1$\bar{1}$2] texture. The remainder will move towards [1$\bar{1}$1] but between this point and [1$\bar{2}$1] the tension and compression rotations are almost in opposition. However, referring to Figure 4 it will be seen that the tension rotations may continue out of triangle b to meet the great circle boundary [1$\bar{1}$0] [1$\bar{1}$1] [001], especially as the most favourable slip system for triangle b is the (11$\bar{1}$) [1$\bar{1}$0] which is a mixed slip system of the primary compression system (11$\bar{1}$) [101]. From the [1$\bar{1}$0] [1$\bar{1}$1] [001] boundary a tension rotation will take place towards [1$\bar{1}$2] without disturbing the compression end-point [110] and so the texture (110) [1$\bar{1}$2] will be reached. In triangle c also both tension and compression lead to the vicinity of [1$\bar{1}$1] and it seems likely that here also the effect will occur by which the tension rotations lead out of the triangle, parallel to [1$\bar{1}$0] [1$\bar{1}$1], and so to triangle a and the end-point (110) [1$\bar{1}$2].

Similar arguments may be applied to the rotations in d, e, f, and g, which will reach the vicinity

of [1$\bar{1}\bar{1}$] and thence move to the end-point (110) [1$\bar{1}\bar{2}$]. The latter is also the immediate end-point for triangles *h* and *j* and probably for *k*, while the orientations in *l* rotate out of the triangle to join triangle *a*. Thus a texture of (110) ⟨211⟩ is reached by all the orientations and may therefore be expected to form the complete rolling texture.

This result is in good agreement with the experimental pole figure of Hu, Sperry, and Beck [5] Figure 9. The small spread around the (110)

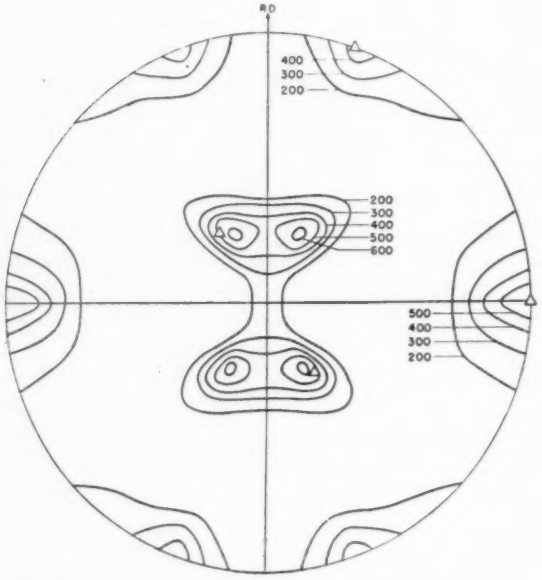

FIGURE 9. (111) pole figure of "inside texture" of 95 per cent rolled strip of commercial 70.30 brass (Hu, Sperry and Beck).

⟨211⟩ texture which they observed may be due to the fact that all the material has not quite reached the end-point after 95 per cent reduction or to experimental variations in the rolling procedure. The isthmus across the centre of the pole figure must be due to material with a (111) plane in the rolling plane and may perhaps be the retention of a small amount of this (111) component of the compression texture mentioned previously. With very severe rolling it would presumably disappear.

Turning now to the case of copper and aluminium, the tendency of both compression and tension rotations to lead first towards [100] before turning towards [110] and [211] respectively, together with the inability of an orientation to cross the boundary of a unit triangle without changing its slip system, immediately introduces considerable complications. It will be appreciated that the following explanation is by no means rigorous but in view of the complexity of the problem, in particular the rapid variation of rotation direction for small orientation differences, an analytical treatment of the polycrystalline case presents great difficulty.

Consider the orientations in detail, Figure 10. In the primary compression unit triangle I there are three quite distinct directions of rotations corresponding to the regions (i), (ii) and (iii). For compression axes in region (i) the tension axes must lie mainly in the areas bounded by the great

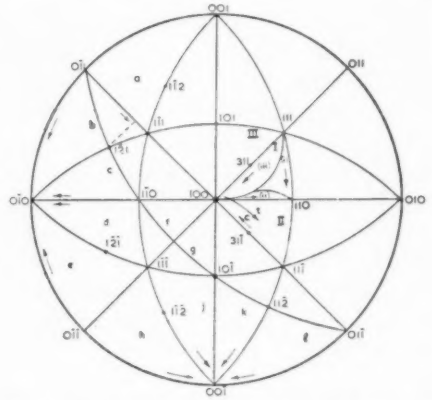

FIGURE 10. Standard stereographic projection illustrating derivation of the sheet rolling texture of copper.

circles [001] [1$\bar{1}$0] [00$\bar{1}$] and [0$\bar{1}$1] [1$\bar{1}$0] [01$\bar{1}$]. The compression rotation indicated by the arrow in region (i) corresponds to a rotation about [1$\bar{1}$0] which when applied to the tension axes tends to sweep them from the [0$\bar{1}$1] [1$\bar{1}$0] [01$\bar{1}$] great circle to the [001] [1$\bar{1}$0] [00$\bar{1}$]. Compounding this rotation with the tension rotations appropriate to each triangle in turn it will be seen that in triangle *a* the tension rotations lead to [001] and [11$\bar{1}$] and finally to [1$\bar{1}\bar{2}$], all of which are on the compression end-point great circle [001] [1$\bar{1}$0] [00$\bar{1}$] and thus the mutually satisfactory texture (110) [1$\bar{1}\bar{2}$] is reached. In the part of triangle *b* under consideration, that between [0$\bar{1}$1], [1$\bar{1}$1], and [1$\bar{2}$1], the compression rotations will pull some tension axes into triangle *a* to join the (110) [1$\bar{1}\bar{2}$] texture while some remain in the neighbourhood of (110) [1$\bar{1}$1]. The rolling direction for the latter texture is not a true end-point and there will be some spread of rolling direction towards [1$\bar{2}$1] with a consequent small spread on the rolling plane normal (compression axis) near (110). Such conclusions for the various triangles are summarized in Table II.

The region (ii) of the compression unit triangle may then be considered. To this there correspond tension axes in the area bounded by the great

TABLE II

COMPONENTS OF ROLLING TEXTURE OF COPPER

Compression axis region	Tension axis region	Area over which tension axes initially occur (measured in unit triangles)	Textures: {110} ⟨1$\bar{1}$2⟩	Textures: near {110} ⟨1$\bar{1}$1⟩	Textures: Spread {311} ⟨1$\bar{1}$2⟩
(i)	*a*	1	(110) [1$\bar{1}$2]		
	b	½		near (110) [1$\bar{1}$1]	
	c	½		"	
	d	< ½		near (110) [1$\bar{1}$1]	
	e	< ½		"	
	f	½		"	
	g	½		"	
	h	< ½	(110) [1$\bar{1}$2]		
	j	1	"		
	k	⅔	"		
	l	⅔	"		
	Totals		~3½	~1½	
(ii)	*a*	1	(110) [1$\bar{1}$2]		
	b	1			(31$\bar{1}$) [1$\bar{2}$1]
	c	1			"
	d	1			(311) [1$\bar{2}$1]
	e	1			"
	h	1	(110) [1$\bar{1}$2]		
	Totals		2		4
(iii)	*b*	⅔			(31$\bar{1}$) [1$\bar{2}$1]
	c	⅔			"
	d	1			(311) [1$\bar{2}$1]
	e	1			"
	f	⅓			"
	g	⅓			"
	h	1			(311) [1$\bar{1}$2]
	j	1			"
	k	⅔	(101) [11$\bar{2}$]		
	l	⅔	"		
	Totals		1⅓		6
Weighted grand totals (relative)*			50	10	100

*The areas (i): (ii): (iii) are 7: 3: 15. The individual region totals are multiplied in these ratios before adding into the grand total.

circles [001] [0$\bar{1}$0] [00$\bar{1}$] and [001] [1$\bar{1}$0] [00$\bar{1}$]. The compression rotation is represented by a rotation about [001], which swings tension axes across from [001] [0$\bar{1}$0] [00$\bar{1}$] to [001] [1$\bar{1}$0] [00$\bar{1}$]. In triangle *a* this clearly leads again to the (110) [1$\bar{1}$2] texture. In triangle *b* the tension rotation towards [1$\bar{2}$1], that is to say, about an axis in the general region of [10$\bar{1}$], will tend to swing the compression axis into triangle II and is likely to join with the spread of texture which develops from orientations in region (iii). Geometrically equivalent textures to this and the (110) [1$\bar{1}$2] occur for the other triangles as listed in Table II.

There now remains the more complex region (iii) of the compression triangle I. The tension axes lie approximately between [0$\bar{1}$1] [0$\bar{1}\bar{1}$] [01$\bar{1}$] and [0$\bar{1}$1] [1$\bar{1}$0] [01$\bar{1}$]. The compression rotation corresponds to a rotation about [0$\bar{1}$1], i.e., sweeping tension axes from [0$\bar{1}$1] [1$\bar{1}$0] [01$\bar{1}$] to [0$\bar{1}$1] [0$\bar{1}\bar{1}$] [01$\bar{1}$]. The tension rotations in the neighbourhood of the latter great circle, shown by arrow →, would tend to accumulate the tension axes around [0$\bar{1}$0] and [00$\bar{1}$] at the time when the compression axis in triangle I has reached [100]. These textures of (100) [0$\bar{1}$0] and (100) [00$\bar{1}$] are not final end-points, since the tension rotations now lead towards [1$\bar{2}$1], [1$\bar{2}\bar{1}$], [1$\bar{1}\bar{2}$], or [11$\bar{2}$]. Consider the first of these tension rotations which corresponds to a rotation about [10$\bar{1}$]. This will swing the compression axis out of triangle I into II as shown by the arrow → t. The compression axis reaching the neighbourhood of [31$\bar{1}$] coincides with the tension axis reaching [1$\bar{2}$1]. The compression rotation in triangle II, however, represented by the arrow → c, tends to throw the tension axis away from [1$\bar{2}$1] towards the interior of triangle *b*, and it seems possible that the tension axis moves round to the neighbourhood of the [0$\bar{1}$1] [1$\bar{1}$1] boundary. Certainly in this latter region, extending from [1$\bar{2}$1] to the adjacent point of the [0$\bar{1}$1] [1$\bar{1}$1] boundary, as shown by the broken line, the tension rotations are directly opposed to the compression rotation → c of triangle II. It thus appears that this will be a very persistent texture, that is to say, compression axes near [31$\bar{1}$] and tension axes from [1$\bar{2}$1] across to the [0$\bar{1}$1] [1$\bar{1}$1] boundary.

Similar arguments may be applied to the other triangles. For example, for triangle *e* the tension rotation from [0$\bar{1}$0] towards [1$\bar{2}\bar{1}$] throws the compression axes back from [100] to the vicinity of [311] as does also the rotation [00$\bar{1}$] [1$\bar{1}\bar{2}$] in triangle *h*. These textures as listed in Table II for the compression region (iii) are all of equivalent form,

similar to $(31\bar{1})$ $[1\bar{2}1]$ although based on different triangles, except for triangles *k* and *l* for which the tension rotations throw the compression axis towards [101]. Although the derivation of this texture has been made on the basis of movement first to the neighbourhood of (100) $[0\bar{1}0]$ and (100) $[00\bar{1}]$ it is by no means certain that such complete movement actually occurs. It is possible that the irregular movements of adjacent grains enable them to reach the final texture of opposing tension and compression rotations by rather shorter paths, and this may be especially so for orientations initially in the vicinity of the final texture.

Summing up the textures in Table II, it appears that there are three components: (a) the spread of orientation near (311) $[1\bar{1}\bar{2}]$, (b) the straightforward (110) $[1\bar{1}2]$ texture, and (c) a component near (110) $[1\bar{1}1]$. The relative amounts of these textures, obtained by totalling for the various tension axis triangles and then weighting the totals in proportion to the compression axis region areas, can only be considered as very approximate. The results can be described by saying that the major component (a) is about twice as important as component (b) while (c) is present in only a very small amount.

These components must now be combined on a pole figure for comparison with the experimental results. Considering the representation of the spread component (a) it will be seen from Figure 11 that such a texture consisting of a small spread of orientation near [311] with a somewhat larger spread from $[1\bar{1}\bar{2}]$ to the adjacent $[1\bar{1}\bar{1}]$ $[0\bar{1}\bar{1}]$ boundary can conveniently be represented by a 15-degree rotation about [111] of the texture with rolling plane normal [311] and rolling direction 90 degrees from [311] on the $[1\bar{1}\bar{1}]$ $[0\bar{1}\bar{1}]$ line. Although it should be pointed out that other rotation axes slightly removed from [111] operating on slightly different textures could also give generally similar spreads of orientation, the [111] axis may be taken as typical of these axes. On the (111) pole figure, Figure 12, the poles of the individual components

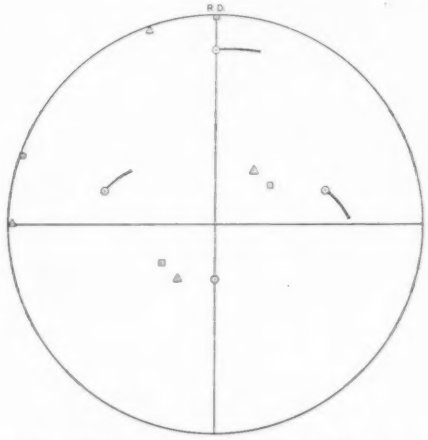

FIGURE 12. (111) pole figure. ⊙ spread of orientation near $(311)[1\bar{1}\bar{2}]$. ▲ $(110)[1\bar{1}2]$. ⊡ $(110)[1\bar{1}1]$.

are shown, and from these and the symmetrical orientations of the same form (the "mirror-image" poles) combined in the proportions derived above, the semi-quantitative pole figure of Figure 13a may be drawn. One feature here requires special attention. The maximum about 30 degrees from the centre of the pole figure which corresponds to a certain pole in the texture (a) has no spread at all since this is the actual [111] rotation axis. This

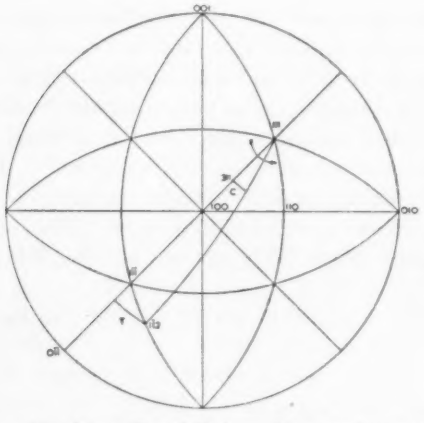

FIGURE 11. Lines *C* and *T* show the spread of orientation obtained by rotating the texture with (311) as rolling plane and rolling direction 90 degrees from [311] on the $[1\bar{1}\bar{1}][0\bar{1}\bar{1}]$ line by 15 degrees about [111].

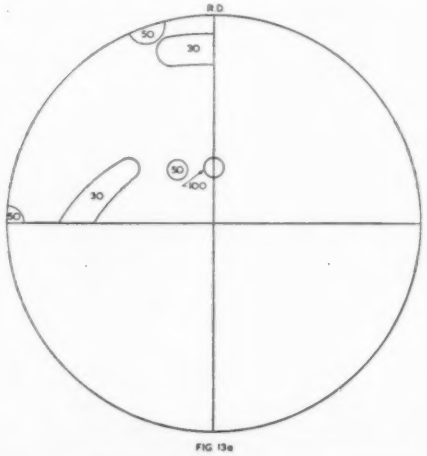

FIGURE 13a. Predicted (111) pole figure for copper. Spread of orientation of 5 degrees on each pole position of Fig. 12.

maximum, and its "mirror image," will therefore be particularly intense since the number of grains to which it corresponds is elsewhere spread over a much larger area of the pole figure.

In Figure 13b is shown the experimental pole figure of Hu, Sperry, and Beck [5] and it will be noted at once that the high-intensity maxima near the centre of the figure, which have hitherto been somewhat difficult to interpret, are explained by the rotation axis poles of the texture (a) just dis-

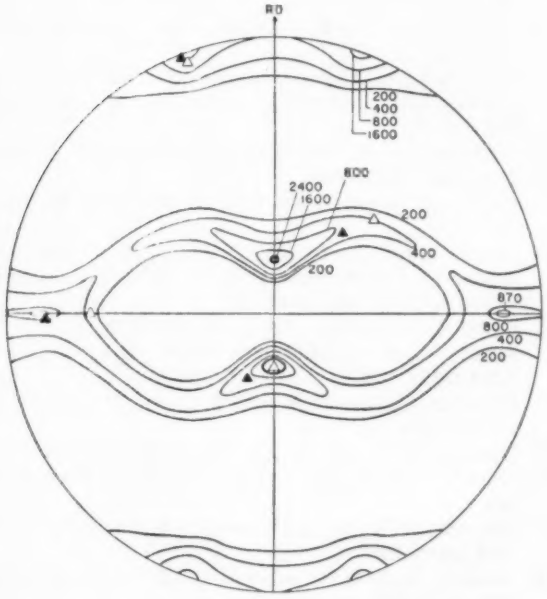

FIGURE 13b. Experimental (111) pole figure of tough pitch copper strip, 96 per cent reduction. Hu, Sperry and Beck [5].

cussed. These predicted maxima, 30 degrees from the centre, do not agree precisely with the observed positions, 22 degrees from the centre for copper and 25 degrees for aluminium. The observed maxima correspond to positions of the compression axis in triangle I, Figure 10, a few degrees from [311] towards [211] and since such positions also conform to the general argument above, the discrepancy, though interesting, is not considered serious. The synthesis of the complete texture from textures (a) and (b) in the relative proportions of 2: 1 implies that isolated maxima of the former should be twice as intense as isolated maxima of the latter. In this particular case comparison may be made between the texture (a) maximum 30 degrees from the centre of the pole figure with the texture (b) maximum in the transverse direction, i.e., 90 degrees from the rolling direction on the periphery. It will be seen that experimentally the magnitudes are: (a) 2400–1600, (b) 870–800. In view of the assumptions in the treatment, this seems satisfactory agreement. Hu, Sperry, and Beck have reported very slight differences in the textures of aluminium and copper; for example, the positions of the very strong maxima near the centre. The treatment above hardly permits a detailed differentiation between these two textures, but it is feasible that such a difference might result from a very slight difference in slip behaviour, by no means as marked as that between copper and brass, but of the same general type.

To sum up briefly: in copper some of the grains go to the spread of orientation near (311) $[1\bar{1}2]$ and some to the (110) $[1\bar{1}2]$ texture, while in α-brass the predominance of single crystal slip and the ability of the stress axis to cross the unit triangle boundary enables all the grains to attain the (110) $[1\bar{1}2]$ texture so that the (311) $[1\bar{1}2]$ texture does not form.

There remains to comment on the predicted compression textures and the observed compression and compression rolling textures. The compression rotations in Figures 5 and 6 indicate the development of (110) textures for both copper and brass but with an intermediate (100) texture for the former and some persistence of the (111) texture for brass due to cross-slip. This is in accord with Hibbard and Trout's compression textures after 90-degree reduction. The treatment here predicts that after very severe reduction only a (110) texture should occur, but there are no experimental results by which this may be verified.

Much more severe reductions have, however, been obtained by Barrett and his co-workers using compression rolling, i.e., rolling with many passes, each pass in a different direction. They concluded that the wide scatter of orientations to [100] and [311] in the case of aluminium would exist after any reduction since it was but little altered in reduction from 98 to 99.9 per cent. The predictions for compression rolling are the textures in the compression unit triangles of I, II, etc. of Figures 8 and 10. Since it was concluded in discussion of Figure 8 that for α-brass the compression end-point [110] is attained ultimately for all orientations, the final compression rolling texture should be [110], with previously some spread via [311] to [111]. Barrett's observations on α-brass which show the spread to [311] and [111] refer to 97 per cent reduction so it is not quite certain whether the

final end-point has in fact been attained. For copper or aluminium, on the other hand, Figure 10, the opposition of tension and compression rotations does indeed produce the spread of orientations via [100] to [311] from the final end-point [110] in accord with observation, and it is possible that not even 99.9 per cent reduction is sufficient to eliminate the cyclic movement of orientations in this spread.

Conclusions

Although the treatment leaves much to be desired in the procedure for deriving the crystal rotations resulting from the simulation of rolling textures by simultaneous tension and compression, it may now claim to demonstrate how metals of the same crystal structure and slip systems develop quite different deformation textures. These differences are believed to stem directly from the fundamental effect of foreign atoms in the lattice and may thus provide a useful link between macroscopic properties and atomic behaviour. The establishment of such a link may well prove valuable in that it is much more convenient to measure preferred orientations and deduce the slip behaviour, and hence the behaviour of the foreign atoms, than to attempt to measure the two last effects directly.

Acknowledgements

The work described above has been carried out as part of the general research programme of the National Physical Laboratory, and this paper is published by permission of the Director of the Laboratory.

References

1. Barrett, C. S. Structure of Metals, 2nd ed. (London, McGraw-Hill, 1953) pp. 442 et seq.
2. Murphy, Heather M. and Calnan, E. A. To be published.
3. Calnan, E. A. and Clews, C. J. B. Phil. Mag. **41** (1950) 1085.
4. Calnan, E. A. and Clews, C. J. B. Phil. Mag. **42** (1951) 616.
5. Hu, H., Sperry, P. R., and Beck, P. A. Trans. A.I.M.E. **194** (1952) 76.
6. Calnan, E. A. Thesis, University of London, 1952.
7. Calnan, E. A. and Clews, C. J. B. Phil. Mag. **42** (1951) 919.
8. Williams, D. N. and Eppelsheimer, D. S. J. Inst. Metals **81** (1953) 553.
9. Calnan, E. A. and Clews, C. J. B. Phil. Mag. **43** (1952) 93.
10. Göler, V. and Sachs, G. Z. Physik. **55** (1929) 581.
11. Maddin, R., Mathewson, C. H. and Hibbard, W. R. Jr. Trans. A.I.M.E. **185** (1949) 527.
12. Cahn, R. W. J. Inst. Metals **79** (1951) 129.
13. Ardley, G. W. and Cottrell, A. H. Proc. Roy. Soc. **A219** (1953) 328.
14. Kuhlmann-Wilsdorf, D. and Wilsdorf, H. Acta Met. **1** (1953) 394.
15. Hibbard, W. R., Jr. J. Inst. Metals **77** (1950) 581.
16. Hibbard, W. R., Jr. Trans. A.I.M.E. **185** (1949) 598.
17. Hibbard, W. R., Jr. and Trout, D. E., Trans. A.I.M.E. **185** (1949) 620.
18. Barrett, C. S. and Levenson, L. H. Trans. A.I.M.E. **127** (1940) 112.
19. Calnan, E. A. and Williams, Betty E. Trans. A.I.M.E. **194** (1952) 743.

ELECTRON-OPTICAL OBSERVATIONS OF TRANSFORMATIONS IN EUTECTOID STEEL*

G. W. RATHENAU† and G. BAAS‡

The transformation of austenite into pearlite and *vice versa* has been studied on pure eutectoid steel by direct observation, applying electron-emission microscopy.

Pearlite colonies generally cross austenite grain boundaries. Strain induced grain boundary migration occurs within the austenite. Stimulation of austenitic twins has been observed on austenitizing partially transformed austenite.

OBSERVATIONS AU MOYEN DU MICROSCOPE À ÉMISSION ÉLECTRONIQUE DES TRANSFORMATIONS DANS L'ACIER EUTECTOÏDE

On a étudié la transformation de l'austenite en perlite, et vice-versa, dans un acier eutectoïde, pur, en se servant du microscope à émission électronique. Des amas de perlite traversent, en général, les joints intercristallins de l'austenite. Dans l'austenite, on constate l'existence d'une migration des joints induite par la déformation.

Une stimulation de macles austenitiques fut observée lors de l'austenitisation d'austenite partiellement transformée.

ELEKTRONENOPTISCHE BEOBACHTUNGEN DER TRANSFORMATION IN EUTEKTOIDEM STAHL

Die Umwandlung von Austenit in Perlit und von Perlit in Austenit wurde an reinem, eutektoidem Stahl durch direkte Beobachtung des Vorgangs am Elektronenemissionsmikroskop untersucht.

Im allgemeinen überschreiten Perlitgruppen die Korngrenzen des Austenits. Innerhalb des Austenits erfolgt spannungsinduzierte Korngrenzenwanderung. Anregung zur Bildung von Austenitzwillingen wurde bei der Rückumwandlung von teilweise transformiertem Austenit beobachtet.

Grain growth in metals and alloys has been observed directly in application of electron-emission microscopy [1]. Applying a newly developed electron-emission microscope, which allows resolution of details of the order of 10^{-5} cm, the authors have in the past studied two kinds of grain growth: the recrystallization in homogeneous NiFe alloys with a pronounced rolling texture [2] and the formation of new crystals during the phase transformation $\alpha \rightleftharpoons \gamma$ in SiFe [3]. This paper deals with the formation of pearlite in eutectoid steel and the reverse process of austenitizing as studied directly with the emission microscope.

Experimental

Eutectoid carbon steel of high purity (0.81% C by weight) prepared in the high vacuum melting apparatus of J. D. Fast [4], has been used throughout. Specimens as in Figure 1 were prepared. They were heated by a tungsten filament. A magnified image of their polished surface S was formed by the electrons which were emitted after either Cs or Ba or both had been evaporated on to this surface. By this activation with electropositive atoms the work function for electron emission is reduced. Furthermore, contrast is obtained in the electron optical image of the surface since absorption of activator atoms by metals depends on the exposed lattice plane. Therefore grains of identical composition, but different orientation are represented with different brightness. In a heterogeneous alloy the different phases can also be recognized by a difference in brightness. When comparing light-optical (after suitable etching) and electron-optical images of the same spot of pearlite, excellent agreement was found.

A description of the electron-emission microscope and its handling will be given elsewhere.

Growth of Pearlite Colonies within a Matrix of Austenite

The cooling of the austenite specimen which had been heated to above 1000°C occurred by its radiation after the current through the filament in Figure 1 had been reduced.§ Generally the nodules of pearlite originated at grain boundaries or imperfections of the surface as shown in Figure 2. This figure does suggest already that a colony of pearlite can pass over an austenite grain boundary without change of orientation of the composing ferrite and cementite, the brightness of these constituents being the same for two parts of a pearlite colony at either side of the original boundary between two austenite grains. Figure 3 gives a typical example of the crossing of grain boundaries

*Received April 20, 1954.

†Physical Laboratory, University of Amsterdam, Netherlands.

‡Philips Research Laboratories, N. V. Philips' Gloeilampenfabrieken, Eindhoven, Netherlands.

§The austenite pearlite transformation was observed at a temperature of about 700°C, that is to say just below the eutectoid temperature.

by pearlite colonies. Figure 4 shows an austenitic twin boundary being crossed by a pearlite colony. The photographs make clear that in the pure alloy an individual lamella of cementite as well as of ferrite generally crosses an austenite boundary. Sometimes a change of direction of the lamella which may be sudden (Figure 5d), or continuous, is to be seen near the crossing of the boundary.

Hull and Mehl [5] formerly gave incidental examples of such crossing. However, G. V. Smith and Mehl [6] found indications of an orientation relationship between austenite and ferrite in

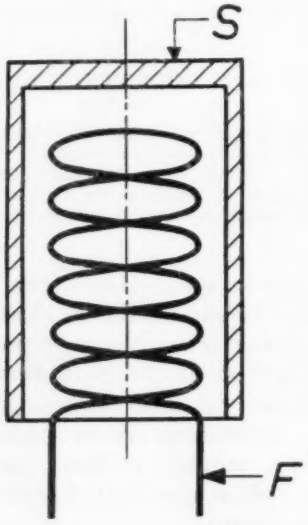

FIGURE 1. Schematic representation of specimen. S: polished surface represented in the electron optical image. F: filament.

pearlite. C. S. Smith [7], on the other hand, gives another interpretation of the experimental results obtained by G. V. Smith and Mehl and regards the orientations as being distributed at random except for the avoidance of certain orientations. This avoidance, he suggests, is caused by the well-known fact that only highly disordered boundaries can move at measurable speed, lateral diffusion along them being extremely high. Our experiments are inadequate to test this hypothesis. They do indicate, however, that one and the same pearlite colony can grow in different austenitic grains with rates varying at most by about a factor of 10 (Figures 5d and f).

We have observed that often the grain boundary between two austenitic grains migrates when a pearlite colony approaches. Generally the boundary between the austenite grains moves towards the approaching pearlite colony as is shown in Figures 5b, 5d and 6 and schematically sketched in Figure 7.

The following explanation is probably appropriate. The changes in volume accompanying the eutectoid transformation give rise to imperfections of the austenite lattice, which are the more numerous the smaller is the distance to the moving pearlite-austenite interface. A grain boundary motion towards the approaching pearlite therefore

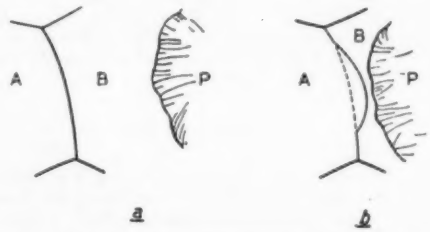

FIGURE 7. Schematic representation of grain boundary displacement between austenite grains A and B. According to our explanation, grain B is strained by changes in volume accompanying the eutectoid transformation. Therefore, movement of boundary towards approaching pearlite P may reduce strain energy.

may reduce the strain energy. Strain induced grain boundary migration in high-purity Al has been described and discussed by Beck, Sperry and Hu [8].

Austenitizing of Pearlite

On heating a material which had been completely transformed into pearlite a great number of germs of austenite are formed which coalesce into larger grains.

We reheated the eutectoid steel, after it had been partially transformed into pearlite, to a temperature just above the eutectoid temperature. It turned out that, as shown in Figure 8, the pearlite starts to be absorbed by the austenite crystal from which it originated. At first, cementite lamellae remain undissolved within the retransformed austenite (Figures 8b and 8c).

It can be seen from Figures 8 and 9 that the retransformed austenite crystal forms many twins. Generally one colony of pearlite produces during transformation only one of the possible sets of spinel twins. Often, the number of twins which are formed at the austenite-pearlite interface during the initial stages of retransformation is of the same order of magnitude as the number of ferrite lamellae in the same area. During the growth of the

2a

2b

3a

3b

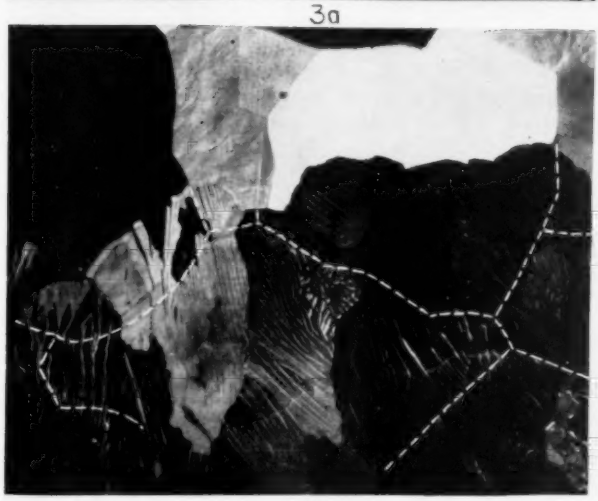

3c

4a

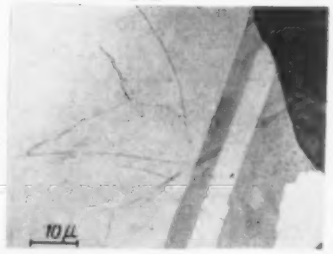

4b

PLATE I. FIGURE 2.—Origin of pearlite nodule: (a) at boundary between two austenite grains, (b) at imperfection within austenite grain. FIGURE 3.—Crossing of austenite grain boundaries by pearlite colonies: (a) Beginning of pearlite invasion at bottom of figure. (b) Same field as in Figure 3a at a later moment. (c) Same photomicrograph as in Fig. 3b. Former austenite grain boundaries indicated by dashed line. FIGURE 4.—Coherent twin boundaries crossed by pearlite colonies. In (b) the spot where former twin has been located is still visible, owing to insufficient vacuum. Part of pearlite-austenite boundary indicated by dotted line.

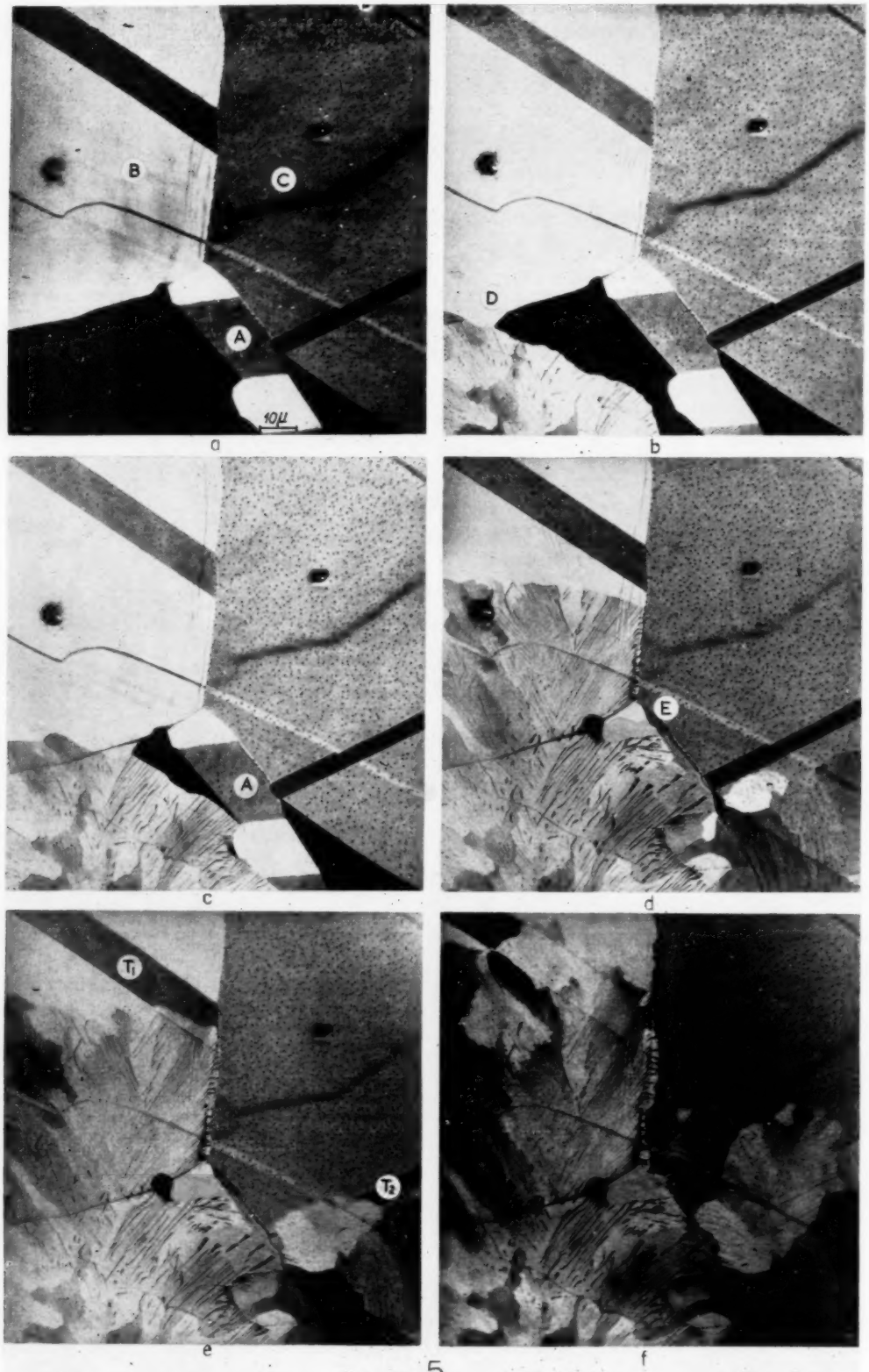

5

PLATE II. FIGURE 5.—Complete survey of austenite→pearlite transformation just below the eutectoid temperature; time between (a) and (f) 4 minutes. (a) Austenite matrix. (b) Pearlite invasion at left bottom corner; at *D* displacement of austenite grain boundary towards approaching pearlite. (c) Pearlite colony reaches grain *A*. (d) Different rates of growth of same pearlite colony in grains *A* and *B* of (a). Sudden change in direction of pearlite lamellae at boundary between grains *B* and *C* of (a). At right bottom corner unhampered crossing of austenite grain boundary by pearlite colony. At *E*, again, grain-boundary displacement towards approaching pearlite. (e) Coherent boundaries of twins T_1 and T_2 crossed by pearlite colonies. (f) Different rates of growth of same pearlite colony in grains *B* and *C* of (a) [cf. (e)]. (g) Growth of austenite by slight increase of temperature.

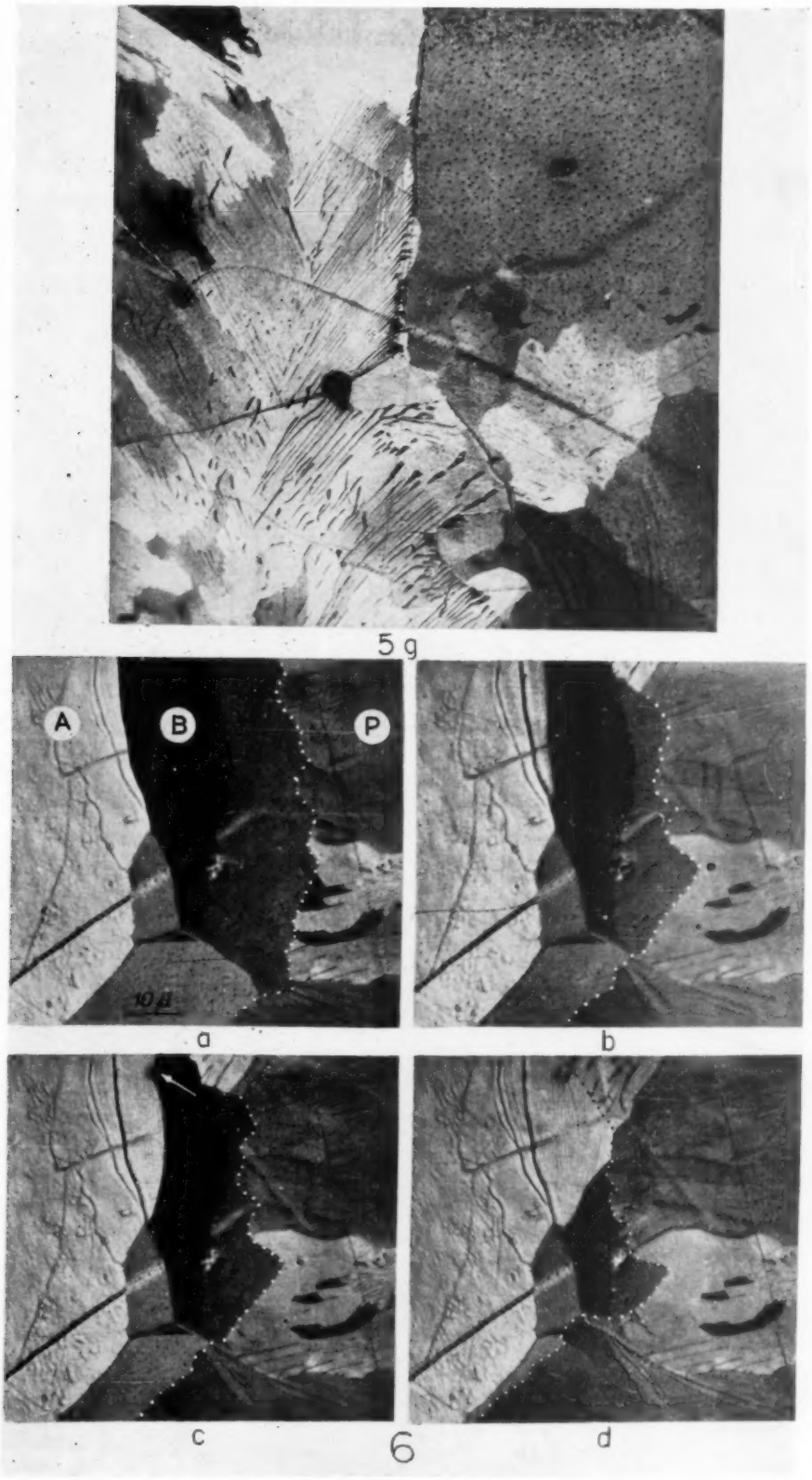

PLATE III. FIGURE 6—Displacement of boundary between two austenite grains *A* and *B* in the direction of approaching pearlite. Migrating boundary is hindered by inclusion indicated by arrow in (c). Dotted line indicates austenite pearlite boundary.

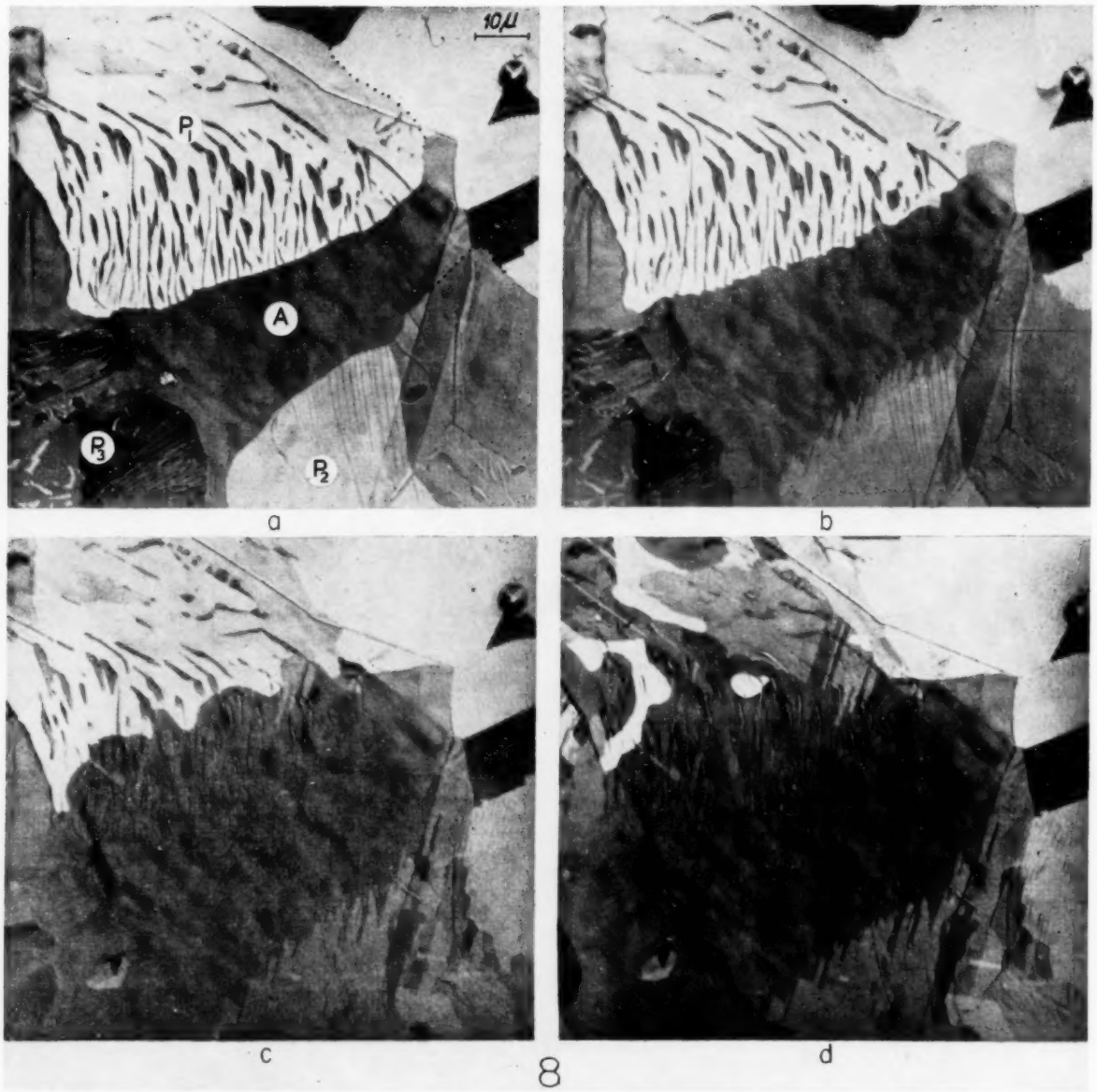

PLATE IV. FIGURE 8—Pearlite→austenite transformation just above the eutectoid temperature; time between (a) and (d) 1 minute. (a) Austenite grain A from three sides invaded by pearlite, indicated as P_1, P_2 and P_3. Part of austenite-pearlite boundary indicated by dotted line. (b) Start of retransformation of pearlite to austenite. Pearlite areas P_1, P_2 and P_3 are absorbed by austenite grain A. The still undissolved cementite lamellae of P_1 are clearly visible. In P_2 formation of nearly as many twins as the number of cementie lamellae in this area. (c) and (d) Course of austenitizing process. Twins in area P_1 are parallel to those in area P_2, indicating that these areas have been retransformed in the same austenite orientation.

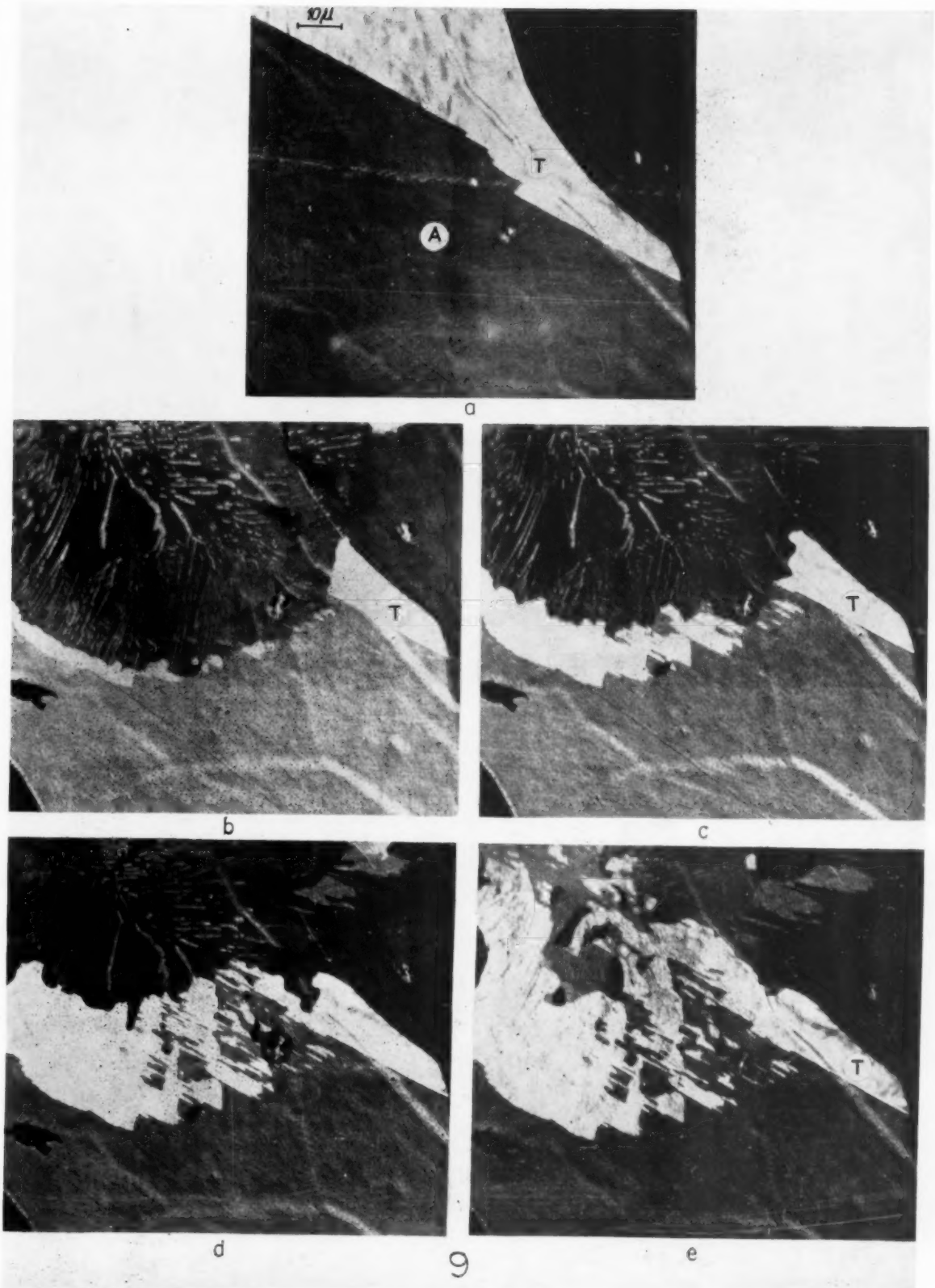

PLATE V. FIGURE 9—(a) Austenite grain *A* with its twin *T* before transformation. (b) Pearlite colony formerly grown into grain *A* of (a) is reabsorbed by this grain. Retransformed area has the same orientation as twin *T*. (c), (d) and (e) Course of austenitizing process. During growth of retransformed austenite with same orientation as twin *T*; this austenite twins again at many spots and it does so in the orientation of the original grain *A* of (a).

twins twinning back occurs and it does so in the orientation of the original austenitic crystal (Figures 8 and 9). Probably the generation of twins is to be explained by the hindrance of grain growth of the original austenitic grain by undissolved cementite. That set of twins might be chosen of which the boundary energy at the boundary of the yet undissolved cementite within the austenite region is minimum. It is not yet clear why the orientation of the secondary twins is always that of the original crystal. Burgers and co-workers [9] have described a similar phenomenon in which a twin of an aluminium crystal after its creation by "stimulated nucleation" grows at a higher rate than the stimulating crystal. It might be worth while to investigate whether the rate of growth of the original Al crystal was hampered by insoluble impurities clinging to its boundary, and whether the nucleation of a twin at its surface was a relatively cheap way out to continue rapid grain growth. It is also conceivable that slip accompanying the transformation is at the base of the observed twinning, [10].

References

1. See, for example. BRÜCHE, F. and JOHANNSON, H. Phys. Z. **33** (1932) 898.
   BURGERS, W. G. and PLOOS VAN AMSTEL, J. J. A. Physica **4** (1937) 5, 15; **5** (1938) 305, 313.
2. RATHENAU, G. W. and BAAS, G. Physica **17** (1951) 117.
   RATHENAU, G. W. Rev. Met. **48** (1951) 923.
3. RATHENAU, G. W. 9e Conseil de Physique Solvay, Brussels, 1952.
   RATHENAU, G. W. and BAAS, G. Métaux **29** (1954) 139.
4. FAST, J. D., LUTEIJN, A. I. and OVERBOSCH, E. Philips Techn. Rev. **15** (1953) 114.
5. HULL, F. C. and MEHL, R. F. Trans. Amer. Soc. Metals **30** (1942) 381.
6. SMITH, G. V. and MEHL, R. F. Trans. A.I.M.E. **150** (1942) 211.
7. SMITH, C. S. Trans. Amer. Soc. Metals **45** (1953) 533.
8. BECK, P. A. and SPERRY, P. R. J. Appl. Phys. **21** (1950) 150.
   BECK, P. A., SPERRY, P. R. and HU, H. J. Appl. Phys. **21** (1950) 420.
9. BURGERS, W. G. and SANDEE, J. Physica **9** (1942) 741; BURGERS, W. G. Physica **9** (1942) 987.
   BURGERS, W. G. and MAY, W. Rec. Trav. chim. Pays-Bas **64** (1945) 5;
10. cf. also BURGERS, W. G., MEYS, T. C. and TIEDEMA, T. J. Acta Met. **1** (1953) 75.

The Influence of Aluminum on the Occupation of Lattice Sites in the TiAl Phase*

During the course of the development of alloys based on the γ-titanium aluminum (TiAl) phase, it was found desirable to know the effect of aluminum additions on the crystal structure of the alloy. The gamma-phase is stable from the equiatomic composition (36 weight per cent aluminum) to 70 atomic per cent aluminum (60 weight per cent) at the peritectic temperature of 1340°C [1].† At the equiatomic composition, stoichiometric TiAl, the structure is isomorphous with CuAu, an ordered face centered tetragonal [2; 3]. Coordinates of the atoms in the unit cell are as follows:

Titanium atoms: (0,0,0), (1/2,1/2,0)

Aluminum atoms: (1/2,0,1/2), (0,1/2,1/2)

This gives a structure composed of alternate layers of titanium and aluminum atoms.

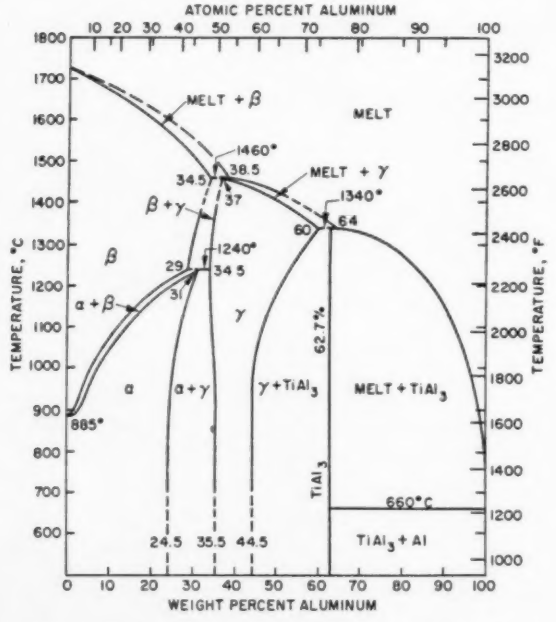

FIGURE 1. The titanium-aluminum phase diagram.

At aluminum compositions greater than the equiatomic composition, the lattice adjustment might involve: (*a*) breakdown of long range order, (*b*) preservation of long-range order but the evacuation of titanium sites, (*c*) preservation of long-range order as much as permitted by the replacement of titanium atoms by aluminum atoms, (*d*) some compromise of (*a*) with (*b*) or (*c*). A quantitative study of the intensity of the diffraction lines as a function of alloy content was selected as a method for determining by which of the alternatives the lattice adjusts itself to the increasing aluminum content. A Norelco Geiger counter spectrometer with filtered characteristic copper radiation was used for this work.

To provide a basis for comparison, the ratios of intensities of the (220) line to the (110) line were calculated for conditions (*b*) and (*c*). The calculations were based on the standard intensity equation and included Lorentz and polarization factors, an absorption factor and an approximation of the Debye-Waller temperature factor. For the Norelco spectrometer, the Lorentz and polarization factors are identical to that for the conventional powder cameras. However, because the angle of incidence is equal to the Bragg angle, the absorption term is constant [4] and equal to $1/2\mu$ where μ is the absorption coefficient. Atomic scattering factors were taken from a standard source [5]. Values for the

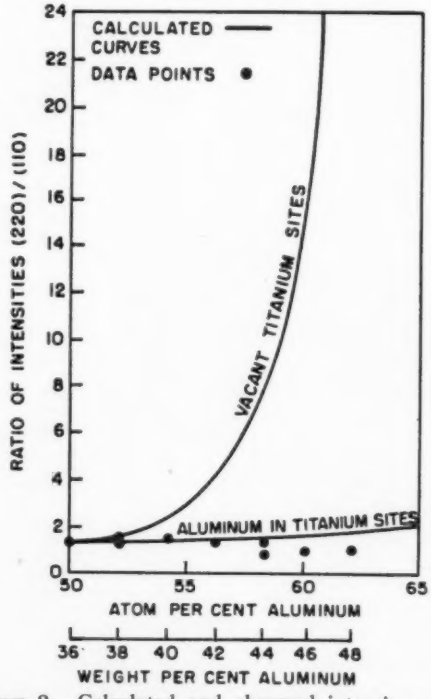

FIGURE 2. Calculated and observed intensity ratios of (220)/(110).

*Received November 13, 1953.

†Numbers in parantheses refer to the bibliography.

Lorentz and polarization factors and the mass absorption coefficients were taken from the Metals Reference Book [5]. In computation of terms, it was assumed that TiAl had lattice constants $a = 3.978$ kX and $c = 4.066$ kX. Data from reference[1]showed that it was possible to assume lattice constants to be very nearly unchanged with increases in aluminum content. A characteristic temperature of 400°K was assumed to be reasonable, since TiAl has a single crystal structure and metallic properties. The characteristic temperatures of titanium and aluminum [5] are 342° and 394°K, respectively.

Powders were filed or crushed from homogenized lump samples of alloys containing 36, 38, 40, 42, 44, 46 and 48 weight per cent aluminum. The powders were sealed in Vycor bulbs and re-solution treated for 10 minutes at 1200°C and water quenched. The powders were then screened through a 200-mesh screen before mounting in the specimen holder.

TABLE I

COMPARISON OF OBSERVED AND CALCULATED LINE INTENSITIES IN THE PHASE TiAl

Atomic per cent Al	Radio intensity (220)/(110)		
	Measured	Calculated	
		Al in Ti sites	Vacant Ti sites
50	1.25	1.221	1.221
52.1	1.26, 1.51		
54.2	1.50		
55		1.428	2.873
56.2	1.25		
58.2	0.74, 1.35		
60		1.715	15.172
60.2	0.94		
62.1	1.00		
65		2.117	113.11*
70		2.727	4.624

*Ratio becomes infinite at 63.6 atomic per cent Al.

The measured and calculated line intensity data are summarized in Table I and graphically presented in Figure 1. The measured data unambiguously demonstrate that aluminum atoms replace titanium atoms on (0,0,0) or ($\frac{1}{2}$,$\frac{1}{2}$,0) sites but otherwise preserve long range order. Were a breakdown of long-range order to occur simultaneously, the curve of measured data would be expected to lie on a curve of generally steeper slope.

The authors wish to express their appreciation to the Wright Air Development Center, U.S. Air Force, for sponsorship and permission to publish. This work was performed under Contract AF 33(616)-196. Special thanks are due to Mr. J. B. McAndrew for alloys furnished.

R. P. ELLIOTT
W. ROSTOKER

Armour Research Foundation,
Illinois Institute of Technology,
Chicago, Illinois.

References

1. BUMPS, E. S., KESSLER, H. D., and HANSEN, M. Trans. A.I.M.E. **194** (1952) 609; J. Metals, June, 1952.
2. OGDEN, H. R., MAYKUTH, D. J., FINLAY, W. L., and JAFFEE, R. I. Trans. A.I.M.E. **191** (1951) 1150; J. Metals, December, 1951.
3. DUWEZ, P. and TAYLOR, J. L. Trans. A.I.M.E. **194** (1952) 70; J. Metals, January, 1952.
4. AVERBACH, B. L. Trans. A.I.M.E. **197** (1953) 87; J. Metals, January, 1953.
5. Internationale Tabellen zur Bestimmung von Kristallstrukturen, vol. 2, Ann Arbor, Mich.: J. W. Edwards, (1944) pp. 571–2.
6. SMITHELLS, C. J. *Metals Reference Book* (New York: Interscience Publishers, Inc., 1949), pp. 150–1.

Diffraction Studies of Possible Ordering in α-brass*†

Recently there has been some evidence to point to possible ordering in the α-brasses. Matsumoto, Saito, and Sugihara have concluded from their specific heat measurements that there is a possibility of ordering in the α-brasses [1]. In particular they observed an anomally in the specific heat curves for the α-brasses for the temperature range from 200 to 260°C and explained these results upon the basis of a change in local or short range order in α-brass at these temperatures. In connection with the study of radiation damage effects in α-brass ordering has been suspected. Rosenblatt has annealed 70–30 α-brass, previously annealed at 350°C and cooled to room temperature, at 190°C for six weeks. He observed a decrease of .90±.03% in the electrical resistivity of α-brass measured at −196°C after the anneal at 190°C [2].

A series of diffraction experiments was carried out to determine whether order in α-brass could be detected by this method. A single crystal of 70–30 α-brass was cut on the (110) face and annealed at 190°C for 6 weeks [3]. This temperature was chosen from examination of the specific heat

*Received April 6, 1954.
†Work done under contract with the U.S. Atomic Energy Commission.

anomaly as the most likely temperature at which some degree of order would be produced. After this anneal the crystal was first examined with X-rays for possible superlattice reflections. Any appreciable long range order should easily be detected in a single crystal by the presence of superlattice reflections whose integrated reflections would be proportional to the square of the Bragg and Williams Long Range Order Parameter, S. Examination of the crystal with X-rays did not reveal such reflections.

On comparing the structure factor of a superlattice reflection to that of a fundamental reflection for the case of neutron diffraction one finds it to be about 10 to 100 times more favorable than for the case in X-ray diffraction. The diffraction experiments were continued using neutron diffraction techniques to detect the possibility of both long and short range order in α-brass, and maximum values were assigned to the degree of order in α-brass at 190°C.

The single crystal was mounted in transmission and the counter slits were made large enough so as to include all the radiation scattered by the crystal as it passed through the Bragg position. The crystal was rotated such that the (110) family of planes reflected. In Figure 1 the solid curve is the observed

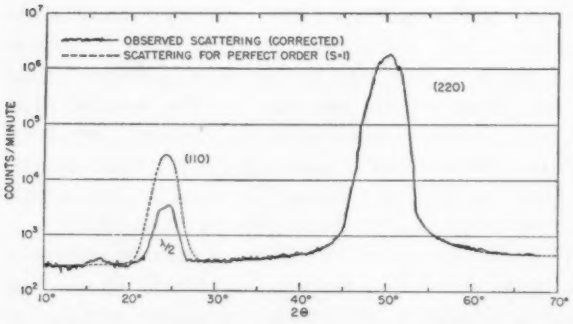

FIGURE 1. Neutron scattering from α-brass minus background corrected for absorption and change in irradiated volume and predicted scattering for perfect order, S = 1.

neutron scattering from α-brass minus the background with no sample in the beam in counts per minute, corrected for absorption and change in irradiated volume. The dashed curve indicates the expected (110) superlattice reflection for perfect long range order and the half wavelength component of the primary beam diffracted from the (220) fundamental reflection. The wavelength producing the observed peak at the (110) position was determined by observing the transmission of this reflection through a set of samarium filters.

Figure 2 shows curves for the transmission through Sm of a 1.08 Å beam of neutrons containing varying percentages of half wavelength contamination. The open circles correspond to the observed transmission of the (110) reflection. The wavelength producing the (110) reflection is almost entirely due to half wavelength and at most about 1 per cent of the reflection is due to full

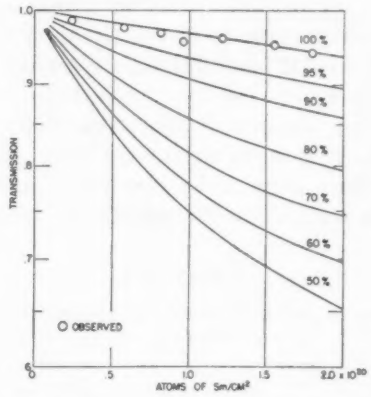

FIGURE 2. Transmission through Sm filters of 1.08 Å neutron beam containing varying percentages half wavelength contamination and observed transmission of (110) reflection.

wavelength. The integrated (110) reflection due to full wavelength was found to be at most .13 per cent of the theoretical value for perfect order corresponding to a maximum value for S of .0365. The intensity of the main beam was observed and the integrated (110) reflection was computed using the coherent cross sections σ_{coh}(Cu) = 7.3 barns and σ_{coh}(Zn) = 4.1 barns and a Debye temperature of 313°K. The observed (220) reflection was 1.3 per cent larger than calculated by this method.

In order to detect the possible short range order scattering from α-brass a careful examination was made of the diffuse scattering along the (110) direction of the crystal. This scattering was put in absolute units of barns/atom by standardizing diffuse intensities with vanadium. Figure 3 shows the observed diffuse scattering from α-brass. Assuming the ordering process in α-brass and Cu_3Au to be similar the diffuse scattering to be expected from α-brass for three temperatures above the critical temperature, T_c, was computed. Of the three computed curves the solid curve corresponds to the scattering from the short-range order expected for a temperature $T = 1.02\ T_c$, the curve with one dash to a temperature $T = 1.10\ T_c$, and the curve with two dashes to a temperature

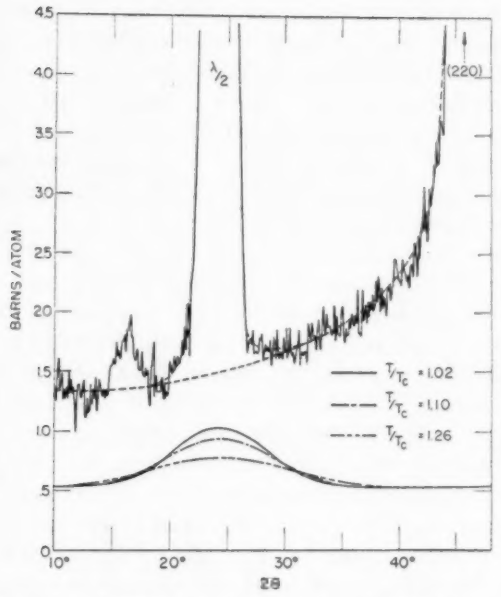

FIGURE 3. Diffuse scattering and expected short-range order scattering from α-brass using coefficients for $T/T_c = 1.02$, 1.10 and 1.26.

$T = 1.26\ T_c$. These diffuse scattering curves were computed from Cowley's short-range order coefficients in Cu_3Au for the temperature indicated [4] and the diffuse scattering equation

$$I_{Diff} = .7\ \sigma_{inc}(\mathrm{Cu}) + \{\sigma_{inc}(\mathrm{brass}) - .7\ \sigma_{inc}(\mathrm{Cu})\}$$
$$\times \sum_{l\alpha}^{a} \sum_{m\alpha}^{a} \sum_{n\alpha}^{a} \alpha_{lmn} \exp\left[-2\pi i(lh_1 + mh_2 + nh_3)\right]$$

where $\sigma_{inc}(\mathrm{Cu}) = .7$ barn, and $\sigma_{inc}(\mathrm{brass}) = .586$ barn were used.

The diffuse scattering and hence the short range order corresponding to the first two temperatures would probably be noticeable in the observed pattern. However, the scattering corresponding to the last temperature and hence the short range order is too small to be detected. The maximum amount of short range order in α-brass at 190°C is roughly that corresponding to a temperature 1.26 or more T_c. From this one would predict a critical temperature of about 95°C or lower.

Order was not detected by diffraction techniques. A maximum value for S in α-brass at 190°C is .0365. Assuming the ordering in α-brass and Cu_3Au to be similar the short range order present probably does not exceed that expected to be present at a temperature of $1.26\ T_c$. The critical temperature is probably 95°C or lower. Thus a small amount of order is permitted and probably would agree with Rosenblatt's results. A critical temperature as low as predicted would account for the difficulty of producing and detecting order in α-brass.

D. T. KEATING

Brookhaven National Laboratory
Upton, New York

References

1. MATSUMOTO, H., SAITO, H., and SUGIHARA, M. Sc. Rep. Res. Inst. Tohoku Univ., Ser. **A4** (1952) 481.
2. ROSENBLATT, D. B., SMOLUCHOWSKI, R., and DIENES, G. J. Radiation Induced Changes in the Electrical Resistivity of α-brass, Bull. Am. Phys. Soc. **29** No. 3 (1954).
3. Crystal furnished by F. Rhines, Carnegie Institute of Technology.
4. COWLEY, J. M. J. Appl. Phys. **21** No. 1 (1950) 24–30.

The Superlattice in Sendust*

The magnetic and electrical properties of iron rich Fe-Si-Al alloys have been studied in some detail, principally in Japan [1], in an attempt to discover suitable substitutes for high nickel alloys. In particular, the magnetic alloy Sendust, containing 8–11% Si, 4.5–8% Al, exhibits peak initial and maximum permeabilities and lowest resistivity, magnetostriction and crystal anisotropy at a composition close to 9.6% Si, 5.5% Al. From electrical and magnetic measurements, Yamamoto [1] concluded that a superlattice of the Fe_3Al type is formed in Sendust cooled slowly from 900°C and that the disordered state is retained by quenching from around 600°C. Later X-ray work by Ogawa and Matsuzaki [2] confirmed that a superlattice $Fe_3(Si,Al)$ exists at room temperature in slowly cooled Fe-Si-Al alloys over a range of compositions. Up to the present time, however, no X-ray work appears to have been reported on other than slowly cooled alloys.

Arising from work in these laboratories [3], a limited investigation has been undertaken to determine the transition temperature for the order-disorder transformation in Sendust. The material used was an alloy of composition by weight 9.7% Si, 5.5% Al, remainder Fe, corresponding to an atomic composition 15.4% Si, 9.4% Al, 75.2% Fe. The cast alloy was ground to powder of 300 mesh and then homogenised by heating for 3 hours at 1000°C, after which a number of samples were enclosed in evacuated silica tubes and subjected to the following different heat treatments for subse-

*Received March 9, 1954.

quent X-ray examination (using unfiltered iron radiation):

(*a*) Annealed for 2½ hours at 900°C, furnace-cooled to 650°C, held at this temperature for 24 hours and then furnace-cooled to room temperature.

(*b*) Heated for 2½ hours at 900°C and then oil-quenched.

(*c*) Heated for 10 minutes at 1350°C and then water-quenched.

In addition, diffraction patterns were obtained from a sample of the (as ground) cold-worked powder and from a specimen held at 900°C in a high-temperature camera during the course of the exposure.

In all cases, the patterns indicated a face-centred cubic structure and exhibited the 111, 200, 311, 222, 331 and 420 lines corresponding to an Fe_3Al type of superlattice as described by Bradley and Jay [4]. Since, for the X-ray wavelengths available, the scattering factors of iron and silicon are almost identical, it was not possible to determine whether the atoms of these two elements take up ordered positions with respect to each other.

The 311α and 400β reflections on some of the films were microphotometered and the relative peak intensities I, and half breadths B, are given in Table 1.

TABLE 1

MICROPHOTOMETER MEASUREMENTS

Sample	I_{311}/I_{400}	B_{311}/B_{400}
Annealed and furnace-cooled	1.25	1.0
Oil-quenched from 900°C	0.87	0.9
Water-quenched from 1350°C	0.70	1.0
Cold worked (ground in ball mill)	0.43	0.8

The lattice parameters at 24°C for the annealed and water-quenched samples were found to be 5.6846 and 5.6854 ± 0.0002 Å respectively.

The above observations lead to the following conclusions:

(1) A superlattice of the Fe_3Al type exists in Sendust after a wide variety of heat treatments, even including rapid quenching from a temperature close to the melting point (approximately 1400°C). The ordered structure is also maintained up to at least 900°C. It therefore appears either that the critical temperature for the order-disorder transformation lies very close to or above the melting point, as in Cu_3Sb, or that the transformation cannot be suppressed by quenching.

(2) Quantitative measurements of line intensities show that the superlattice lines decrease in intensity with cold work or rapid cooling from high temperatures. This is probably due to a reduction in the degree of order. Owing to uncertainties connected with extinction effects and the fact that Sendust is a ternary alloy, no attempt has been made to estimate the degree of order in the samples after the different treatments.

An alternative explanation for the reduction in intensity of the superlattice lines could be that, on quenching, some of the sample transforms to a partially ordered superlattice with the FeAl type of structure, as in the binary Fe-Al system for aluminium in excess of 25 atomic per cent [4]. It seems unlikely, however, that this is the case because (a) the I_{222}/I_{400} ratio decreases on quenching instead of increasing as in the Fe-Al system; (*b*) the I_{200}/I_{220} ratio from visual inspection does not increase markedly, if at all; (*c*) the 311-reflection is still present; and (*d*) the lattice spacing increases instead of decreasing.

(3) The small increase in lattice parameter on quenching from 1350°C is consistent with the interpretation placed upon the intensity measurements, viz., a reduction in the degree of order with rapid cooling [5].

(4) Measurement of line breadths showed no appreciable increase in breadths of the superlattice lines compared with the main lines on quenching. Although the measurements had to be made at fairly low θ values (~35°), they indicate that no significant change from long range to short range order occurs on quenching.

The authors desire to thank Mr. K. Bailey for the preparation and heat treatment of the samples of Sendust, and the Chief Scientist, Department of Supply, Australia, for permission to publish this note.

R. I. GARROD and L. M. HOGAN

Defence Standards Laboratories,
Melbourne,
Victoria,
Australia.

Reference

1. "Magnetic and Electrical Heating Element Alloys Developed in Japan." Australian Scientific Mission to Japan, Report No. J.261 (1946).
2. OGAWA, S. and MATSUZAKI, Y. Science Repts. Tôhoku Univ., First Ser. **3** (1951) 50.
3. THURLBY, E. G. Metal Progr. **60** (1951) 83.
4. BRADLEY, A. J. and JAY, A. H. Proc. Roy. Soc. (London), **A136** (1932) 210.
5. OWEN, E. A. and MACARTHUR SIM, G. Phil. Mag. **38** (1947) 342.

Grain Boundary Shear in Aluminum*

Grain-boundary shear, as well as what appears to be alternate shear and grain boundary migration, has been observed in high-purity (99.995%) aluminum deformed in creep.

Tricrystal test pieces, which had been grown from the melt, were used. They were 10 cm long, 2 cm wide and 0.4 cm thick and were of the form shown in the heavy outline of Figure 1. In the

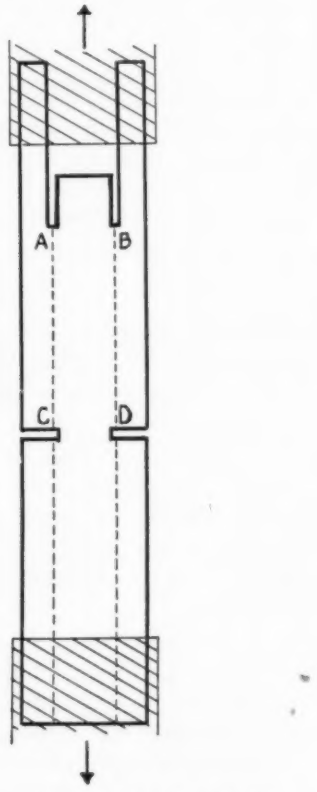

FIGURE 1. Front surface of tricrystal specimen (schematic).

drawing AC and BD are the traces of the boundaries subjected to shear when a tensile load is applied to the specimen. Points A and B are the ends of two mica inserts which were removed after the tricrystal was grown; the cuts at C and D were made with a fine saw. Before the specimens were tested, they were electropolished and scribed with a set of fine scratches to act as fiducial marks.

In the preliminary tests seven specimens of the type shown were tested. All had component crystals oriented in the same way; the two outside crystals had a ⟨100⟩ direction parallel to the specimen axis and perpendicular to the front surface: the centre crystal had a ⟨110⟩ direction parallel to the specimen axis and ⟨100⟩ perpendicular to the front surface. One complete boundary trace was observed through a window in the furnace and scratch positions were measured on either side of the boundary trace during the test. Specimen temperatures were kept at 550 ± 2°C and the loads applied per unit boundary area under shear varied from 350 to 500 grams/cm², being constant for any one test.

Observations

All of the specimens tested showed appreciable, and approximately uniform, boundary shear along the central portion of the four boundary traces. Curves relating boundary shear with time, as measured on one boundary trace during the test, were obtained for four of the seven specimens tested. The major parts of the resultant curves were straight lines, indicating a constant rate of shear near 10^{-5} mm/minute. Two of the four specimens showed a higher rate of shear in the early part of the test; the others remained essentially constant. The total average boundary shear of the four specimens ranged from 0.07 mm to 0.14 mm with deformation of the component crystals over the averaged region of the specimen being less than 0.01 mm. Tests were continued for times ranging from 80 to 210 hours.

All of the boundary traces observed appeared to show some evidence of boundary migration, either along their entire length or in isolated regions. The boundaries moved irregularly in a direction perpendicular to the specimen axis away from the centre crystal, for distances which varied appreciably along any one boundary trace. It did not appear that they moved continuously since periodic traces of their position appeared to be left on the specimen surface. At each of these boundary traces, the fiducial mark showed a sharp discontinuity. From this it would appear that shearing of one crystal with respect to its neighbour took place by an alternate shear and boundary migration process. It is not clear whether shear actually stops when the boundary migrates or whether the rate of boundary movement is too rapid to observe any effect of the shear on the fiducial scratches. With magnifications of 1000× the scratch steps at the boundary traces still appeared sharp and the scratch segments between the trace lines straight. In several cases, near the end of the boundary where a few large steps were formed, it was clearly observed during the test that the first step appeared at the boundary, increased in size, and then stopped

*Received April 12, 1954.

increasing when a new boundary trace and subsequent step appeared.

Some of the observations discussed above are illustrated in Figures 2, 3 and 4. Figure 2 is a composite photograph of a specimen surface after deformation, in which the boundary traces are vertical. The positions of the horizontal fiducial scratches are indicated by the arrows. The right boundary has sheared, as shown by the steps in the scratches crossing it, but shows little boundary migration. The entire left boundary on the other hand has migrated as well as sheared. Figure 3 is a more detailed picture of this boundary at one scratch showing the steps in the scratch. Figure 4 is a photograph of another specimen showing boundary migration similar to that of Figure 2, in which the lower part of the specimen has been etched. Initially the boundary trace was a straight line at 1, which on the etched portion is shown to be at 2, the final boundary position.

Figure 3 also shows families of fine lines of varying length inclined to the boundary traces. These lines are confined nearly entirely to the surface between the initial and final boundary. It is believed that these are traces of slip lines of {111} planes because of their regularity and direction.

The observed behaviour of the boundaries under shear suggests that a mechanism analogous to the "strain induced boundary migration" described by Beck [1], could be operative. In the present investigation the boundaries subjected to shear were not microscopically straight. As a result, when shear took place, strains would be introduced in the component crystals in the vicinity of the boundary, a preponderance of this strain probably being confined to the crystal more favourably oriented for deformation to take place. Following Beck's mechanism, when the difference in strain of the crystals at the boundary becomes sufficiently large, the boundary will move in such a manner that the less strained crystal will grow at the expense of its more highly strained neighbour, stopping when it has swept through the strained region. Further shear would then take place at this new boundary position and the process would be repeated.

This could then account for the periodicity of the boundary shear and migration process observed. It could also account for the irregular shape of the boundary traces, the orientation of the material swept through by the boundary, and that occasionally no boundary movement occurs on segments of the initial boundary when sheared. The slip lines observed above could be a manifestation of the strains in the vicinity of the boundary produced during shear.

A more extensive investigation is under way in which it is hoped to obtain more complete data on the reproducibility of boundary shear rates, as well as the dependence of shear rates on temperature, stress, and relative orientation of the crystals forming the boundary.

This paper was published by permission of the Deputy Minister, Department of Mines and Technical Surveys, Ottawa, Ontario.

F. WEINBERG

Physical Metallurgy Division, Mines Branch,
Department of Mines and Technical Surveys
Ottawa, Ontario, Canada

Reference

1. BECK, PAUL A. Metal Interfaces (A.S.M., 1952).

Equilibrium Segregation of Silicon at Grain Boundaries in Nickel-Iron-Copper-Molybdenum Alloys*

In a study of the microstructures of high-purity nickel-iron-copper-molybdenum soft magnetic alloys it has been noticed that etching effects occur which closely resemble those reported by Perryman [1] for tin bronzes.

A number of alloys containing between 0.01 and 0.03% silicon have been examined microscopically after various heat treatments. The nominal composition of the alloys was 77% Ni, 14% Fe, 5% Cu, 4% Mo. Spectrographic analysis showed that the strongest impurity was silicon. Other impurities were manganese and magnesium, about 0.005% of each being present in all alloys.

Specimens were prepared for microscopical examination by chemical polishing and electrolytic etching under standard conditions. The polishing bath contained 20 ml acetic, 10 ml nitric, and 4 ml hydrochloric acid; for electrolytic etching, a bath of 20% (by volume) sulphuric acid was used with a potential difference of 3 volts.

The first evidence of equilibrium segregation was found in specimens annealed in pure hydrogen at 1050°C for three hours and furnace-cooled. The intensity of etching increased with silicon content, and within any particular specimen varied greatly from one grain boundary to another (Figure 1).

*Received May 15, 1954.

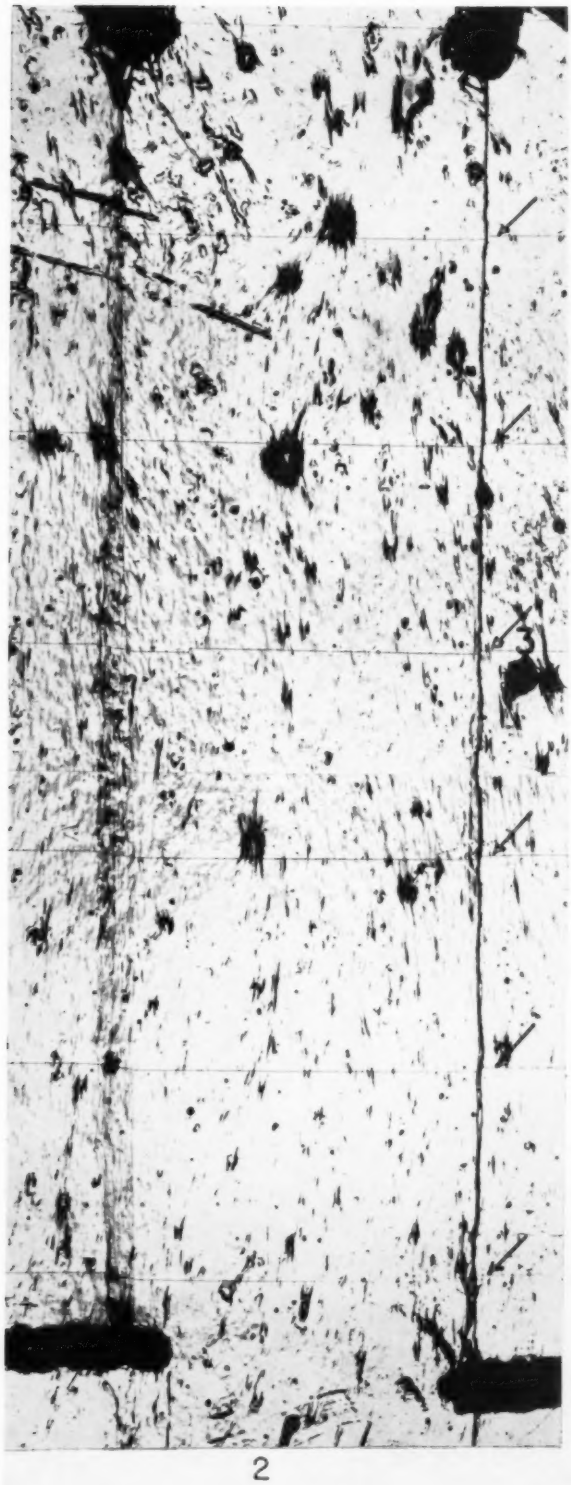

2

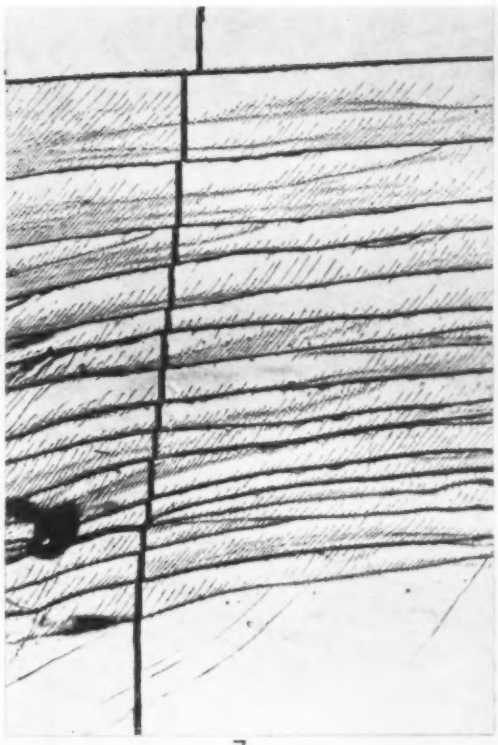

3

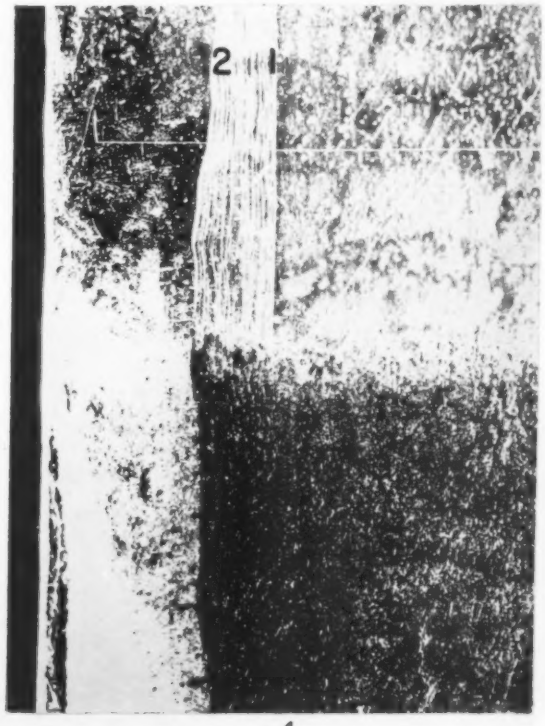

4

PLATE I. (All figures reduced by two-thirds.) Figure 2—Front surface of tricrystal specimen after deformation. Scratches, indicated by arrows, 5 mm apart. (Note: The step in the centre crystal of scratch 3 was accidently introduced in the ruling). Figure 3—Detail of scratch crossing left boundary of Fig. 2 (100×). Figure 4—Specimen similar to that of Fig. 2 in which the lower portion has been etched.

Twin boundaries were very lightly etched indeed and were frequently observed only through relief.

If specimens in this condition were heated to 800°C for ten minutes and quenched in hydrogen, these effects could be largely, but not entirely, suppressed. (Quenching from 700°C did not produce suppression.) They returned, however, after reheating to 600°C. In a specimen containing 0.02% silicon grain boundary segregation could be detected after twenty minutes and was quite pronounced after one hour.

The explanation of these effects seems to be that the equilibrium concentration of silicon is higher at the boundaries than in the crystals themselves, especially at temperatures below 800°C. The nature of the etching suggests that the concentration of silicon at a boundary depends on the disorientation between the grains meeting at the boundary.

R. E. S. WALTERS

Post Office Engineering Dept.
Research Branch,
Dollis Hill,
London, England

Reference

1. PERRYMAN, E. C. W. J. Metals **5** (1953) 906.

BOOK REVIEW

Procedures in Experimental Metallurgy by Seybolt and Burke. New York: John Wiley and Sons Inc.

When, in 1939, Strong's book—*Procedures in Experimental Physics*—was published, several directors of research laboratories remarked that this was the most valuable book to their organizations that had appeared for many years. The companion volume by Seybolt and Burke for men working with metals is in the same category. It is certain to save hours, weeks or months of labor for countless graduate students and research men in industrial and governmental laboratories concerned with studies of metals. While the authors state that it was written for physicists and physical chemists or other investigators new to the study of metals, there will be few metallurgists who cannot also get new ideas on experimental techniques from the volume.

The chapter headings indicate the scope of the book: (1) Methods of Obtaining High Temperatures; (2) Measurement of High Temperatures; (3) Control of Temperature; (4) Refractories; (5) Controlled Atmospheres; (6) Vacuum Systems; (7) Melting and Casting; (8) Heat Treating Techniques; (9) Fabrication of Metals; (10) Powder Metallurgy; (11) Preparation of Pure Metals and (12) Preparation of Metal Single Crystals.

The book aims at helping the experimentalist decide on the best experimental procedure by informing him of the pitfalls and difficulties of several approaches and methods of overcoming these troubles. In several months use of the book and discussions with other users of the book, I have found that everyone has been helped with ideas from this book. At times, additional ideas have appeared from other sources but even in these cases, the book must be credited with a stimulation effect.

Two of the most useful items in the book are a table on the properties and applications of ceramic materials and a table on commercially available pure metals, with their sources identified.

The only criticism is that the details of many operations are omitted or given in too brief a form. For example, if you wish to know how to make a high-frequency coil with flattened copper tubing, this book will not help you. The research worker or experimentalist gets a lot of help but in general he is still going to have to conquer the bugs that differentiate between a successful procedure and one that, for him, does not work.

R. M. Brick

SOME CURRENT PAPERS IN OTHER JOURNALS

Acta Crystallographica, Vol. 7

Part 8–9, September, 1954 (Partial Contents)

The crystal structure of samarium. A. H. DAANE, R. E. RUNDLE, H. G. SMITH, and F. H. SPEDDING.

An X-ray microbeam study of polycrystalline specimens of aluminium and iron deformed in tension. A. KELLY.

The use of Fourier analysis in the interpretation of X-ray line broadening from cold-worked iron and molybdenum. G. K. WILLIAMSON and R. E. SMALLMAN.

A new photographic method for studying the texture of large single crystals. A. R. LANG.

The determination of signs of structure factors from the intensities. W. COCHRAN.

Electron diffraction by electropolished surfaces and mean inner potentials of silver and copper. S. YOSHIDA.

Optical-diffraction methods for deducing the effects of hydrogen atoms on X-ray intensities. P. R. PINNOCK and H. LIPSON.

Conversion of Norelco fluorescent spectrograph to an X-ray diffractometer. R. J. WEISS, J. J. DE MARCO, and G. WEREMCHUK.

Archiv für das Eisenhüttenwesen

Heft 7–8, Juli-August, 1954

Zur Metallurgie des Hochofens. T. KOOTZ, A. MICHEL und H. RELLERMEYER.

Struktur von Zinküberzügen auf Grund elektrochemischer Ablösung. W. KATZ.

Das System Eisen—Schwefel—Sauerstoff und seine Bedeutung als Grundlage der Umsetzungen von Eisensulfiden mit Schwefeldioxyd zu Eisenoxyden und Schwefeldampf. N. G. SCHMAHL.

Elektrographische Schnellerkennung von legierten Stählen und Legierungen der Eisenmetalle. E. FITZER.

Präzisionsbestimmung von Eisen und von Eisenoxyden nebeneinander. W. KANGRO und G. WIEBKE.

Beitrag zur photometrischen Bestimmung von geringen Siliziumgehalten im Stahl. H. WOLK.

Beziehung der Mikrohärte zur Makrohärte. W. SCHULTZE und L. SCHIMMER.

Beziehungen zwischen Mikro- und Makrohärte an Ferrit- und Aluminiumkristalliten. A. SCHEPERS und W. BARTHOLOME.

Massänderung von Einsatzstählen beim Einsatzhärten. B. FINNERN.

Bedingungen für die Auslösung und das Auftreten des Sprödund Verformungsbruches auf Grund der Eigenschaften der Versetzungen. A. KOCHENDÖRFER.

Aufstickung von Rohren aus austenitischem Chrom-Nickel-Molybdän-Stahl durch Stickstoff beim Innendruckversuch bei 700°F. BRAUMANN und H. KRÄCHTER.

Erhöhung der Anfangspermeabilität von niedriglegierten Eisen-Silizium- und Eisen-Aluminium-Legierungen durch oxydierendes Glühen bei niedrigen Temperaturen. H. FAHLENBRACH und E. HOUDREMONT.

Die magnetische und elektromagnetische Sortentrennung von Stahlhalbzeug und Massenteilen. F. FÖRSTER.

Beitrag zur Theorie des elektrolytischen Polierens. E. KNUTH-WINTERFELDT.

Journal of the Chemical Society

September, 1954 (Partial contents)

Studies in the chemistry of quadrivalent germanium: Ion-exchange studies of solutions of germanates. D. A. EVEREST and J. E. SALMON.

The magnetic susceptibility of lanthanum. O. M. HILAL and F. A. SALEH.

October, 1954 (Partial contents)

Liquid metals. I. The surface tension of liquid sodium: the vertical-plate technique. C. C. ADDISON, D. H. KERRIDGE, and J. LEWIS.

Journal of the Institute of Metals, Vol. 83

Part. 2, October 1954

Influence of cold deformation on the Young's modulus of some non-ferrous metals. M. COOK, T. LL. RICHARDS, and G. F. BIDMEAD.

The solid solution of cadmium in zinc. J. R. BROWN.

Growth twins in crystals of low co-ordination number. E. BILLIG.

Twinning and untwinning in polycrystalline magnesium. R. L. WOOLEY.

The viscosity of copper and some binary copper alloys. W.R. D. JONES and W. L. BARTLETT.

The bainitic transformation of the beta phase in copper-zinc alloys. R. D. GARWOOD.

Part 3, November, 1954

The creep and fatigue properties of some wrought complex aluminium bronzes. J. MCKEOWN, D. N. MENDS, E. S. BALE, and A. D. MICHAEL.

The effect of strain rate and temperature on the resistance of aluminium, copper and steel to compression. J. F. ALDER and V. A. PHILLIPS.

The selective oxidation of nickel-chromium alloys at high temperatures. J. MOREAU and J. BÉNARD.

Diffusion of nitrogen and oxygen in titanium. R. J. WASILEWSKI and G. L. KEHL.

Isothermal transformation of eutectoid aluminium bronzes. R. HAYNES.

Strain-ageing in 70: 30 brass. B. B. HUNDY.

Journal of Metals. Vol. 6

September, 1954, Part 1 (Partial contents)

Manganese modification of the Fe-S-O system. D. C. HILTY and W. CRAFTS.

Equilibrium pressure measurements above ZnS from 680° to 825°C. C. L. MCCABE.

Creep-rupture characteristics of Al-Mg solid-solution alloys. A. W. MULLENDORE and N. J. GRANT.

Ferromagnetism of certain manganese-rich alloys. E. R. MORGAN.

Precipitation of iron oxide from alpha Fe-O solid solutions. A. U. SEYBOLT.

Removal of copper from iron-copper-carbon alloys. F. C. LANGENBERG and R. W. LINDSAY.

Influence of oxygen and nitrogen in solution in alpha titanium on the friction coefficient of copper on titanium. W. R. YANKEE and E. S. MACHLIN.

Diffusion of boron in alpha iron. P. E. BUSBY and C. WELLS.

September, 1954, Part 2

Preferred orientation of cold-rolled uranium foil. W. SEYMOUR.

Effects of temperature on the deformation of beta brass. C. S. BARRETT.

Stress-strain characteristics and slip-band formation in metal crystals: Effect of crystal orientation. F. D. ROSI.

Rate of self-diffusion in polycrystalline magnesium. P. G. SHEWMAN and F. N. RHINES.

Etch pits and dislocations in germanium and silicon. J. J. OBERLY.

Electron optical study of oxidation of high purity iron at low oxygen pressures. E. A. GULBRANSEN, W. R. MCMILLAN and K. F. ANDREW.

Self-diffusivity along edge-dislocation singular lines in silver. A. A. HENDRICKSON and E. S. MACHLIN.

High pressure oxidation of metals: Tantalum in oxygen. R. C. PETERSON, W. M. FOSSELL, JR., and M. E. WADSWORTH.

Coefficients of thermal expansion for zirconium. R. B. RUSSELL.

Mathematical methods for zone-melting processes. H. REISS.

Viscosity and density of liquid lead-tin and antimony-cadmium alloys. H. J. FISHER and A. PHILLIPS.

On the nucleation of pearlite. M. E. NICHOLSON.

Effect of tempering on the hardness of retained austenite. P. STARK and B. S. LEMENT.

Ordering reaction of the Cu_4Pd alloy. A. H. GEISLER and J. B. NEWKIRK.

Method of using a fine-focus X-ray tube for examining the surface of single crystals. L. G. SCHULZ.

Mechanism for the origin of recrystallization nuclei. J. P. NIELSEN.

Correlation between microstructure and resistivity of transforming Ti-Mn alloys. D. J. DELAZARO and D. W. LEVINSON.

Decrease of density during plastic deformation of nodular cast iron. W. R. CLOUGH and M. E. SHANK.

Revue de Métallurgie 51e Année

Numéro 7, juillet, 1954

Recherches sur un défaut se présentant au laminage de laiton à 67% de cuivre et 33% de zinc. J. MARÉCHAL.

Analyse de pièces métalliques en cuivre et en plomb, provenant de l'épave romaine, dite du Grang-Congloué. A. R. WEILL.

Evolution structurale par revenu d'un alliage Cu-Be 2%. A. SAULNIER.

Granulation de surface après déformation plastique: Relation avec les conditions d'écrouissage et de recuit. J. HÉRENGUEL et F. SANTINI.

Procédés de chromage thermique O.N.E.R.A. et traitements thermiques des aciers chromisés. PH. GALMICHE.

Association d'un traitement thermique élémentaire et d'un traitement thermochimique de cémentation par le chrome "Chromisation integrée." PH. GALMICHE.

Les possibilités de l'autoradiographie quantitative par des mesures microphotométriques. A. KOHN.

Numéro 8, août, 1954

La fin du Néolithique et l'apparition des métaux. A. A. SANFOURCHE.

Alliages de titane et de silicium. D. A. SUTCLIFFE.

Détections des discontinuités dans les tubes métalliques par courants électriques induits. G. GAUTHIER.

Sur le durcissement secondaire dans un acier au chrome-molybdène. L. HABRAKEN.

Observations sur le palier élastique des aciers. R. DE STRYCKER.

Quelques applications du sondage ultrasonoscopique des rails. L. BEAUJARD et V. HUSAREK.

Sur la viscosité des laitiers de hauts fourneaux. P. KOZAKEVITCH.

Zeitschrift für Metallkunde

Heft 13, Juni, 1954

OFHC-Kupfer. M. HEBERLEIN.

Elektrothermisches Umschmelzen von Kupferkathoden. W. SCHWARTZ.

Die Herstellung von Kupferbändern auf pulvermetallurgischem Wege. H. FRANSSEN.

Über den Aufbau des Systems Kupfer-Blei-Sauerstoff. E. GEBHARDT und W. OBROWSKI.

Beitrag sur Kenntnis des Systems Kupfer-Blei-Sauerstoff. W. HOFMAN und J. KOHLMEYER.

Eigenschaftsänderungen während der Aushärtung einer Kupfer-Chrom-Legierung. W. KÖSTER und W. KNORR.

Über die Erholung der inneren Reibung von Messing unmittelbar nach der Verformung. W. KÖSTER und E. STOLTE.

Untersuchungen im System Kupfer-Antimon. K. SCHUBERT und M. ILSCHNER.

Untersuchungen im System Kupfer-Tellur. K. ANDERKO und K. SCHUBERT.

Photometrisches Schnellverfahren zur Bestimmung von Kupfer in Weissmetall. H. WIEDMANN.

Eine neue photometrische Schnellbestimmung für Tellur in Kupfer-Tellur-Legierunen zur Überwachung des Schmelzbetriebes. W. NIELSCH und G. BÖLTZ.

Korrosionsschutz bei der Verarbeitung von Kupferlaugen. W. TEWORTE.

Über das chemische Glänzen von Messing und Neusilber. G. SCHMID und H. SPÄHN.

Der Einfluss des Sauerstoffs auf das Oberflächenverhalten von Kupfer. F. ERDMANN-JESNITZER und F. GÜNTHER.